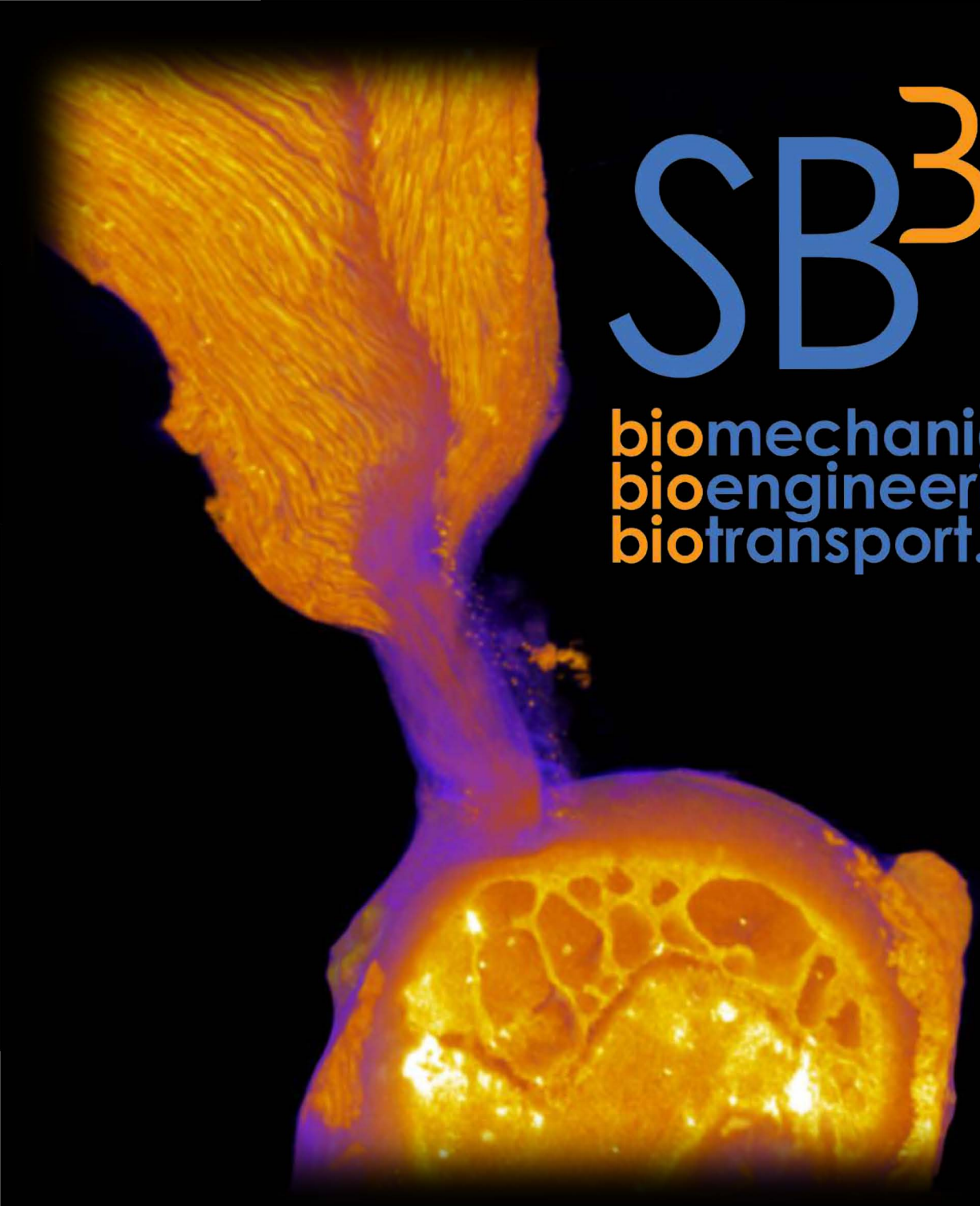

SB³C

biomechanics.
bioengineering.
biotransport.

Proceedings of the 2019 Summer Biomechanics, Bioengineering, and Biotransport Conference

June 25 - 28, Seven Springs, PA

ISBN: 978-0-578-51234-1

1 Podium Sessions

Tuesday, June 25	3:45PM - 5:15PM

Thermal Damage Processes in Tissues — Sunburst

Session Chair: Rupak Banerjee *University of Cincinnati*
Session Co-Chair: Liang Zhu *University of Maryland Baltimore County*

3:45PM **Adventures In Thermal Therapy: From Surgery To Cancer Treatment** SB^{3}C2019-001
John Pearce[1], [1]*The University of Texas at Austin, United States*

4:00PM **Microwave Thermal Therapy of Benign Adrenal Adenomas For Treatment of Primary Aldosteronism** SB^{3}C2019-002
Punit Prakash[1], Martin O'Halloran[2], Michael Dennedy[2], [1]*Kansas State University, United States,* [2]*National University of Ireland - Galway, Ireland*

4:15PM **Metabolize Or Die: John Pearce'S Fascination With Bioenergetics In Cancer, and What We Know (and do Not Know) Now** SB^{3}C2019-003
Michael Graner[1], Petr Paucket[2], Natalie Serkova[3], Anthony Fringuello[1], Steven Ojemann[1], Aviva Abosch[1], Julia Craft[1], Xiaoli Yu[1], [1]*University of Colorado Denver, Anschutz Medical Campus, Department of Neurosurgery, United States,* [2]*University of Colorado Denver, Anschutz Medical Campus, Department of Neurology, United States,* [3]*University of Colorado Denver, Anschutz Medical Campus, Department of Anesthesiology, United States*

4:30PM **Examining Arrhenius Kinetics Over A Large Temperature Range** SB^{3}C2019-004
Daipayan Sarkar[1], Peiyuan Kang[1], Zhenpeng Qin[1], [1]*University of Texas at Dallas, United States*

4:45PM **Heating Protocol Design Affected By Thermal Damage Model In Magnetic Nanoparticle Hyperthermia For Cancer Treatment** SB^{3}C2019-005
Manpreet Singh[1], Qimei Gu[1], Ronghui Ma[1], Liang Zhu[1], [1]*University of Maryland Baltimore County, United States*

Tuesday, June 25	3:45PM - 5:15PM

Heart Valve Mechanics and Cardiovascular Devices — Snowflake

Session Chair: Ankush Aggarwal *University of Glasgow*
Session Co-Chair: Ali Akyildiz *Erasmus Medical Center*

3:45PM **A Physiologically-Driven Biaxial Bioreactor System To Investigate Valve Interstitial Cell Phenotypic State After Surgical Repair** SB^{3}C2019-006
Salma Ayoub[1], Jordan Graves[1], Chung-Hao Lee[2], Michael Sacks[1], [1]*The University of Texas at Austin, United States,* [2]*The University of Oklahoma, United States*

4:00PM **Restriction of Annulus Movement Alters The Dynamic Deformation and Strain Distribution of The Tricuspid Valve Leaflets: A Simulation Study** SB^{3}C2019-007
Keyvan Amini Khoiy[1], Rouzbeh Amini[1], [1]*The University of Akron, United States*

4:15PM **Tricuspid Valve Leaflet Strains In The Beating Ovine Heart** SB^{3}C2019-008
Manuel Rausch[1], Mrudang Mathur[1], William Meador[1], Marcin Malinowski[2], Tomasz Jazwiec[2], Tomasz Timek[2], [1]*University of Texas at Austin, United States,* [2]*Spectrum Health, United States*

4:30PM **Materially Heterogeneous Annuloplasty Ring Reduces Loading On Posterior Annular Sutures** SB^{3}C2019-009
Beatrice Ncho[1], Eric Pierce[1], Ajit Yoganathan[1], [1]*Georgia Institute Of Technology, United States*

4:45PM **3d Reconstructions of Deployed Coronary Stents In The Clinical Setting: Investigation of Distortion Effects From Curvature On The Circumferential Orientation of Oct Images** SB^{3}C2019-010

Mark Elliott[1], David Molony[2], Brigham Smith[3], Sarang Joshi[1], Habib Samady[2], Lucas Timmins[1], [1]*University of Utah, United States,* [2]*Emory University School of Medicine, United States,* [3]*University of Utah School of Medicine, United States*

5:00PM **Effects of Right Ventricular Assist Device On Treating Pulmonary Arterial Hypertension: An In-Silico Study Using Image Based Biventricular Modeling Framework** SB^{3}C2019-011

Sheikh Mohammad Shavik[1], Lik Chuan Lee[1], [1]*Michigan State University, United States*

Tuesday, June 25	**3:45PM - 5:15PM**

Cardiovascular Biomechanics and Tissue Engineering — Wintergreen

Session Chair: Joao Soares *Virginia Commonwealth University*
Session Co-Chair: Zhijie Wang *Colorado State University*

3:45PM **Controlling Compliance of Polycaprolactone/gelatin Tissue Engineered Vascular Graft In A Rat Model** SB^{3}C2019-012

Kenneth Furdella[1], Shinichi Higuchi[1], Kang Kim[1], William Wagner[1], Jonathan Vande Geest[1], [1]*University of Pittsburgh, United States*

4:00PM **A Bio-Chemo-Mechanical Computational Model of Tissue Engineered Vascular Graft Development In Vivo** SB^{3}C2019-013

Ramak Khosravi[1], Abhay Ramachandra[1], Jason Szafron[1], Christopher Breuer[2], Jay Humphrey[1], [1]*Yale University, United States,* [2]*Nationwide Children's Hospital, United States*

4:15PM **Role of Hyaluronic Acid In Regulation of Contractile Forces In Heart Valve Tissue Constructs** SB^{3}C2019-014

Ying Lei[1], Luciano Bortolin[1], Frank Benesch-Lee[1], Teniola Oguntolu[1], Kristen Billiar[1], [1]*Worcester Polytechnic Institute, United States*

4:30PM **Adipose Stromal Cell Secreted Factors Induce The Elastogenesis Cascade Within Aortic Smooth Muscle Cells** SB^{3}C2019-015

Aneesh Ramaswamy[1], Rachel Sides[1], Eoghan Cunnane[2], David Vorp[1], Justin Weinbaum[1], [1]*University of Pittsburgh, United States,* [2]*University of Pittsburgh; Royal College of Surgeons in Ireland, United States*

4:45PM **Quantifying and Modeling Spatial Heterogeneity In Valve Interstitial Cells** SB^{3}C2019-016

Emma Lejeune[1], Alex Khang[1], Michael Sacks[1], [1]*University of Texas at Austin, United States*

5:00PM **Cyclic Stretch Causes Liberation of Caveolin-1 In Extracellular Vesicles From Vascular Smooth Muscle Cells** SB^{3}C2019-017

Mohammad Shaver[1], Jessica Molina[1], Joshua Daniel Hutcheson[1], [1]*Biomedical Engineering Department of Florida International University, United States*

Tuesday, June 25	**3:45PM - 5:15PM**

Mechanics of Cartilage in Health and Disease — Seasons 1-3

Session Chair: Corinne Henak *University of Wisconsin-Madison*
Session Co-Chair: Corey Neu *University of Colorado Boulder*

3:45PM **Focal Chondral Defects In The Dysplastic Hip Cause Activity- and Size-Dependent Increases In Stress and Strain** SB^{3}C2019-018

Jocelyn Todd[1], Travis Maak[1], Jeffrey Weiss[1], [1]*University of Utah, United States*

4:00PM **Mechanical Property Changes In The Tibial Plateau Cartilage Following Traumatic Injury and Repair Procedures To The Lapine Knee** SB^{3}C2019-019

Patrick Vaughan[1], Feng Wei[1], Albane Fauron[1], Loic Dejardin[1], Tammy Haut Donahue[2], Roger Haut[1], [1]*Michigan State University, United States,* [2]*University of Massachusetts - Amherst, United States*

4:15PM **Collagen-Derived Residual Stress Enhances The Biphasic Lubrication Property In Articular Cartilage** SB^{3}C2019-020

Hiromichi Fujie[1], Soh Morishita[1], Seido Yarimitsu[1], [1]*Tokyo Metropolitan University, Japan*

4:30PM **Shorter More Regular Activity Improves Cartilage Function Compared To Longer Less Regular Activity** SB^{3}C2019-021

Brian Graham[1], Axel Moore[2], David Burris[1], Christopher Price[1], [1]*University of Delaware, United States,* [2]*Imperial College London, United Kingdom*

4:45PM **Impact of Decorin On Cartilage Pericellular Matrix Micromechanics and Chondrocyte Mechanotransduction** SB^{3}C2019-022

Daphney R. Chery[1], Prashant Chandrasekaran[1], Qing Li[1], Biao Han[1], Su Chin J. Heo[2], Renato V. Iozzo[3], Motomi Enomoto-Iwamoto[4], Robert L. Mauck[2], Lin Han[1], [1]*School of Biomedical Engineering, Science and Health Systems, Drexel University, United States,* [2]*Department of Orthopaedic Surgery, University of Pennsylvania, United States,* [3]*Department of Pathology, Anatomy and Cell Biology, Thomas Jefferson University, United States,* [4]*Department of Orthopedics, University of Maryland, United States*

5:00PM **Through-Thickness Patterns of Shear Strain Change With Early-Stage Progression of Osteoarthritis** SB^{3}C2019-023

Franz Maier[1], Courtland G. Lewis[2], David M. Pierce[1], [1]*University of Connecticut, United States,* [2]*Hartford Healthcare, United States*

Tuesday, June 25 | 3:45PM - 5:15PM

Reproductive and Abdominal Biomechanics — Seasons 4-5

Session Chair: Raffaella De Vita *Virginia Tech*
Session Co-Chair: Kristin Miller *Tulane University*

3:45PM **Material Property Characterization of Human Cervical Tissue Based On Biphysical Viscoelastic Model** SB^{3}C2019-024

Lei Shi[1], Joy Vink[2], Ronald Wapner[2], Kristin Myers[1], [1]*Department of Mechanical Engineering, Columbia University, United States,* [2]*Department of Obstetrics and Gynecology, Columbia University, United States*

4:00PM **Effects of Pelvic Organ Prolapse On The Biaxial Biomechanical Behavior of Post-Menopausal Uterosacral Ligament** SB^{3}C2019-025

Elvis Danso[1], Jason Schuster[1], Isabella Johnson[1], Emily Harville[1], Laurephile Desrosiers[2], Leise Knoepp[2], Kristin Miller[1], [1]*Tulane University, United States,* [2]*Ochsner Clinical School, United States*

4:15PM **Rupture Mechanisms of The Vagina Under Inflation** SB^{3}C2019-026

Jeffrey McGuire[1], Woowon Lee[2], Kimani Toussaint[2], Caleb Stine[1], Jennifer Munson[1], Raffaella De Vita[3], [1]*Virginia Tech, United States,* [2]*University of Illinois at Urbana Champaign, United States,* [3]*Virginia tech, United States*

4:30PM **Remodeling of The Diabetic Urinary Bladder: A Comparison of An Obese and A Lean Animal Model of Type Ii Diabetes** SB^{3}C2019-027

Marissa Grobbel[1], Matthew Lewis[1], Anne Tonson[1], Robert Wiseman[1], Sara Roccabianca[1], [1]*Michigan State University, United States*

4:45PM **Lactating Human Breast Response To Infant Oral Movements** SB^{3}C2019-028
Diana Alatalo[1], Lin Jiang[1], Fatemeh Hassanipour[1], *[1]The University of Texas at Dallas, United States*

5:00PM **Contribution To The Understanding of The Genese of The Ligamental System of The Pelvic System** SB^{3}C2019-029
Olivier Mayeur[1], Mathias Brieu[2], Michel Cosson[3], *[1]Centrale Lille, France, [2]California State University, United States, [3]CHR Lille - Jeanne de Flandres, France*

Tuesday, June 25	**3:45PM - 5:15PM**

Biomedical Engineering Education — Hemlock

Session Chair: Sara Wilson *University of Kansas*
Session Co-Chair: Choon Hwai Yap *National University of Singapore*

3:45PM **Broadening Research Exposure and Research Participation In Mechanical Engineering: Findings From The Umbc Me S-Stem Scholarship Program** SB^{3}C2019-030
Liang Zhu[1], Ronghui Ma[1], Deepa Madan[1], Charles Eggleton[1], L. D. Timmie Topoleski[1], Shuyan Sun[1], *[1]University of Maryland Baltimore County, United States*

4:00PM **Lessons Learned: Five Years of The Biomedical Engineering In Simulations, Imaging, and Modeling (bme-Sim) Reu Site** SB^{3}C2019-031
Stephanie George[1], *[1]East Carolina University, United States*

4:15PM **Incorporating Clinical Rotations, Online Lectures, and Business Concepts In Bme Senior Capstone Design: Are We There Yet?** SB^{3}C2019-032
Alan Eberhardt[1], Joel Dobbs[1], *[1]University of Alabma at Birmingham, United States*

4:30PM **Outcomes of Incorporating Clinical Simulation Laboratories In Biomedical Engineering Education** SB^{3}C2019-033
Anita Singh[1], Dawn Ferry[1], *[1]Widener University, United States*

4:45PM **Industrial Ergonomics Risk Assessment Meets Research In The Biomechanics Classroom** SB^{3}C2019-034
Johannes Brombach[1], Megan DeRidder[2], Laurel Kuxhaus[2], *[1]University of Applied Sciences, Germany, [2]Clarkson University, United States*

5:00PM **On The Role of Project-Based Active Learning Techniques On Computer Programming Self-Efficacy of Undergraduate Biomedical Engineering Students and The Interactive Effects of Gender** SB^{3}C2019-035
S. Cyrus Rezvanifar[1], Rouzbeh Amini[1], *[1]The University of Akron, United States*

Tuesday, June 25	**3:45PM - 5:15PM**

Respiratory, Lymphatic, Ocular and Other Organ System Fluid Mechanics — Fox Den

Session Chair: Jessica Oakes *Northeastern University*

3:45PM **Numerical Modeling of Lamina Cribrosa Hemodynamics** SB^{3}C2019-036
Yi Hua[1], Bryn L. Brazile[1], Ian A. Sigal[1], *[1]University of Pittsburgh, United States*

4:00PM **Particle Deposition Correlates With Wall Shear Stress Divergence In Human Airways** SB^{3}C2019-037
Ali Farghadan[1], Kamran Poorbahrami[2], Sahar Jalal[3], Jessica Oakes[2], Filippo Coletti[3], Amirhossein Arzani[1], *[1]Northern Arizona University, United States, [2]Northeastern University, United States, [3]University of Minnesota, United States*

4:15PM **Computational Modeling of Pathogen Leakage Through N95 Respirators** SB^{3}C2019-038
Prasanna Hariharan[1], Neha Sharma[2], Gavin D'Souza[2], Suvajyoti Guha[1], Rupak Banerjee[2], Matthew Myers[1], *[1]US Food and Drug Administration, United States, [2]University of Cincinnati, United States*

4:30PM **Regional Targeting of Therapeutic Particles In Healthy and Asthmatic Lungs** SB^{3}C2019-039
Kamran Poorbahrami[1], Sean Fain[2], David Mummy[2], Jessica Oakes[1], *[1]Northeastern University, United States, [2]University of Wisconsin-Madison, United States*

4:45PM **Differential Effects of Bladder Outlet Obstruction Associated Pressure Cycling On Urothelial Cell Inflammation and Fibrosis In Vitro** SB^{3}C2019-040
Cody Dunton[1], Todd Purves[2], Francis Hughes[2], Jiro Nagatomi[1], *[1]Clemson University, United States, [2]Duke University Medical Center, United States*

5:00PM **Effect of Airway Cilia Properties On Its Physiological Functioning** SB^{3}C2019-041
Uduak George[1], *[1]San Diego State University, United States*

Wednesday, June 26	**9:30AM -11:00AM**

Drug Delivery in Cancer, Ocular, and Central Nervous Systems — Sunburst

Session Chair: Ying Li *University of Connecticut*
Session Co-Chair: Bryn Martin *University of Idaho*

9:30AM **In Vivo Measurement of Bevacizumab Diffusion Coefficient In The Rabbit Vitreous Humor Using Fluorescein Labeling** SB^{3}C2019-042
Anita Penkova[1], Shuqi Zhang[1], Komsan Rattanakijsuntorn[2], Mark Humayun[1], Juan Carlos Martinez[1], Alejandra Gonzalez Calle[1], Ana Galesic[1], Abegail Tadle[1], Mattew Pratt[1], Mark Thompson[1], Satwindar Sadhal[1], *[1]University of Southern California, United States, [2]Ubon Ratchathani University, Thailand*

9:45AM **Precise Targeting of Polr2a As A Therapeutic Strategy For Human Triple Negative Breast Cancer** SB^{3}C2019-043
Jiangsheng Xu[1], Xiaoming He[1], *[1]University of Maryland, United States*

10:00AM **Characterization of Injection-Induced Tissue Swelling During Subcutaneous Injection of Biologics** SB^{3}C2019-044
Yingnan Shen[1], Bumsoo Han[1], *[1]Purdue University, United States*

10:15AM **Analysis of Convective and Diffusive Transport In The Brain Interstitium** SB^{3}C2019-045
Lori Ray[1], Jeff Iliff[2], Jeff Heys[1], *[1]Montana State University, Chemical & Biological Engineering, United States, [2]Ohsu, United States*

10:30AM **Three-Dimensional Nonlinear Biphasic Finite Element Model of Backflow During Flow-Controlled Infusions Into The Brain** SB^{3}C2019-046
Gustavo Orozco[1], Joshua Smith[2], Jos Garca[3], *[1]University of Eastern Finland, Finland, [2]Lafayette College, United States, [3]Universidad del Valle, Colombia*

10:45AM **Relating Chemical and Physical Properties of Oligonucleotide Polyelectrolyte Complex Micelles** SB^{3}C2019-047
Alexander Marras[1], Jeffrey Vieregg[1], Jeffrey Ting[1], Matthew Tirrell[1], *[1]University of Chicago, United States*

Wednesday, June 26	9:30AM -11:00AM

Growth Remodeling and Repair I — Snowflake

Session Chair: Colleen Witzenburg *University of Wisconsin*
Session Co-Chair: Sara Roccabianca *Michigan State University*

9:30AM **Structural Remodeling and Volumetric Growth In The Right Ventricle Under Pulmonary Arterial Hypertension** SB^{3}C2019-048
Reza Avaz[1], Emilio Mendiola[1], Michael Sacks[2], *[1]UT Austin, United States, [2]University of Texas at Austin, United States*

9:45AM **Mathematical Modeling of Regional Hypertensive Aortic Remodeling Reveals A Critical Role For Inflammation** SB^{3}C2019-049
Marcos Latorre[1], Matthew Bersi[2], Jay Humphrey[1], *[1]Yale University, United States, [2]Vanderbilt University, United States*

10:00AM **Effect of Glucose On The Interlamellar Bonding of Arterial Elastin** SB^{3}C2019-050
Ruizhi Wang[1], Xunjie Yu[1], Yanhang Zhang[1], *[1]Boston University, United States*

10:15AM **Cortical Thickness Differences Emerge From Passive Physical Forces Generated By Growth** SB^{3}C2019-051
Maria Holland[1], Ellen Kuhl[2], Alain Goriely[3], *[1]University of Notre Dame, United States, [2]Stanford University, United States, [3]University of Oxford, United Kingdom*

10:30AM **Targeting Cadherin-11 For Renal Fibrosis** SB^{3}C2019-052
Tessa Huffstater[1], Leslie Gewin[1], W. David Merryman[1], *[1]Vanderbilt University, United States*

10:45AM **Plastic Remodeling of Collagen Upon Tumor Growth Alters Fluid Transport Properties of The Extracellular Matrix** SB^{3}C2019-053
Jacopo Ferruzzi[1], Meng Sun[1], Anastasia Gkousioudi[1], Anahita Pilvar[1], Darren Roblyer[1], Yanhang Zhang[1], Muhammad Zaman[1], *[1]Boston University, United States*

Wednesday, June 26	9:30AM -11:00AM

Celebration of YC Fung's 100th Birthday — Wintergreen

Session Chair: Grace O'Connell *UC Berkeley*

9:30AM **Yc Fung Symposium Introduction** SB^{3}C2019-054
Robert Nerem

9:45AM **Pulmonary Arterial Mechanics: Something Old, Something New, Something Borrowed, Something Blue** SB^{3}C2019-055
Naomi Chesler[1], *[1]University of Wisconsin - Madison, United States*

10:00AM **Coronary Calcifications: From Vesicles To Plaque Rupture** SB^{3}C2019-056
Natalia Maldonado[1], Luis Cardoso[2], Sheldon Weinbaum[2], *[1]New York City College of Technology, United States, [2]The City College of New York, United States*

10:15AM **The Impact of Hemodynamic Reflex Compensation Following Myocardial Infarction On Subsequent Ventricular Growth** SB^{3}C2019-057
Colleen Witzenburg[1], Jeffrey Holmes[2], *[1]University of Wisconsin, United States, [2]University of Virginia, United States*

10:30AM **Effect of Ltbp-3 On The Circumferential and Axial Mechanics of The Aorta In A Mouse Model of Marfan Syndrome** SB^{3}C2019-058

Arina Korneva[1], Arunika Makam[2], Jay Humphrey[1], Chiara Bellini[2], *[1]Yale University, United States, [2]Northeastern University, United States*

10:45AM **Contribution of Matrix Remodeling To Biaxial Mechanics of Right-Ventricular Myocardium In Pulmonary Arterial Hypertension** SB^{3}C2019-059

Daniela Velez-Rendon[1], Justin Shieh[2], Daniela Valdez-Jasso[2], *[1]University of Illinois at Chicago, United States, [2]University of California San Diego, United States*

Wednesday, June 26 | 9:30AM -11:00AM

Biomechanics of Lower and Upper Extremities — Seasons 1-3

Session Chair: Mariana Kersh *University of Illinois at Urbana-Champaign*
Session Co-Chair: Jennifer Wayne *Virginia Commonwealth University*

9:30AM **Flexion Angle Dependent Differences In Joint Kinematics and Acl Force In Response To Applied Loads Are Conserved Throughout Skeletal Growth In The Porcine Stifle Joint** SB^{3}C2019-060

Stephanie Cone[1], Danielle Howe[1], Emily Lambeth[1], Jorge Piedrahita[2], Jeffrey Spang[3], Matthew Fisher[1], *[1]North Carolina State University and the University of North Carolina – Chapel Hill, United States, [2]North Carolina State University, United States, [3]University of North Carolina – Chapel Hill, United States*

9:45AM **A Novel Geometric Ratio To Predict The Flexion Gap In Total Knee Arthroplasty** SB^{3}C2019-061

Shady Elmasry[1], Peter Sculco[1], Timothy Wright[1], Andrew Pealre[1], Michael Cross[1], David Mayman[1], Cynthia Kahlenberg[1], Geoffrey Westrich[1], Carl Imhauser[1], *[1]Hospital for Special Surgery, United States*

10:00AM **Micromotion In Tibial Components Recovered Post Mortem: A Pilot Study** SB^{3}C2019-062

Heath Baskin[1], Elie Ghanem[1], Jack Lemons[1], Alan Eberhardt[1], *[1]University of Alabama at Birmingham, United States*

10:15AM **Computational Mechanics Demonstrate How A Transcondylar Screw Enhances Healing of Subchondral Bone Cysts** SB^{3}C2019-063

Lance Frazer[1], Elizabeth Santschi[2], Kenneth Fischer[1], *[1]University of Kansas, United States, [2]Kansas State University, United States*

10:30AM **A Generalized Framework For Objective Determination of Functional Musculoskeletal Joint Coordinate Systems** SB^{3}C2019-064

Tara Nagle[1], Ahmet Erdemir[1], Robb Colbrunn[1], *[1]Cleveland Clinic, United States*

10:45AM **Cartlage Contact Stiffness Effects On Contact Pressure and Area At The Elbow Joint** SB^{3}C2019-065

Jonathan Parman[1], Cuneyd Gunay[2], Akin Cil[1], Antonis Stylianou[1], *[1]University of Missouri - Kansas City, United States, [2]Eskisehir Osmangazi University, Turkey*

Wednesday, June 26	9:30AM -11:00AM

Ocular Biomechanics — Seasons 4-5

Session Chair: Rouzbeh Amini *The University of Akron*
Session Co-Chair: Andrew Feola *Atlanta VA and Georgia Institute of Technology*

9:30AM **A Multiscale Finite Element Modeling Approach To Characterize Iris Deformation** SB^{3}C2019-066
Vineet Thomas[1], Sam Salinas[1], Anup Pant[1], Syril Dorairaj[2], Rouzbeh Amini[1], *[1]The University of Akron, United States, [2]Mayo Clinic, United States*

9:45AM **Correlation of Human Lamina Cribrosa Strain Response To Axon Counts In The Optic Nerve Across Racioethnic Donor Eyes** SB^{3}C2019-067
Hirut Kollech[1], Reza Behkam[1], Katelyn Axman[1], Jr-Jiun Liou[1], Jonathan Vande Geest[1], *[1]University of Pittsburgh, United States*

10:00AM **Tensile Behavior of Anterior and Posterior Corneal Flaps Subjected To Cxl Treatment Procedure** SB^{3}C2019-068
Hamed Hatami-Marbini[1], *[1]University of Illinois at Chicago, United States*

10:15AM **Genomic Loci Modulating Ocular Compliance In Mice** SB^{3}C2019-069
Elizabeth Boazak[1], Cassandra Chu[1], Rebecca King[2], Joseph Sherwood[3], Darryl Overby[3], Eldon Geisert[2], C. Ross Ethier[1], *[1]The Georgia Institute of Technology, United States, [2]Emory University, United States, [3]Imperial College London, United Kingdom*

10:30AM **Characterizing The Actin and Gfap Network Structure of The Astrocytic Lamina In Mouse Eyes** SB^{3}C2019-070
Yik Tung Tracy Ling[1], Mary Pease[2], Harry Quigley[2], Thao (Vicky) Nguyen[1], *[1]Department of Mechanical Engineering, Johns Hopkins University, United States, [2]Wilmer Eye Institute, Johns Hopkins University, United States*

10:45AM **Snapshot Polarized Light Microscopy To Visualize and Quantify Collagenous Soft Tissue Microstructure At 156 Frames/second** SB^{3}C2019-071
Bin Yang[1], Po-Yi Lee[1], Bryn Brazile[1], Ian Sigal[1], *[1]University of Pittsburgh, United States*

Wednesday, June 26	9:30AM -11:00AM

Human Movement and Gait — Hemlock

Session Chair: Wu Pan Zagorski *Lear Corporation*
Session Co-Chair: Antonis Stylianou *University of Missouri Kansas City*

9:30AM **A Human Cadaveric Model For Quantifying Knee Joint Mechanics During Simulated Gait: Effect of Astm and Iso Derived Input Profiles** SB^{3}C2019-072
Amanda Wach[1], Olufunmilayo Adebayo[1], Caroline Brial[1], Tony Chen[1], Russell Warren[1], Peter Torzilli[1], Suzanne Maher[1], *[1]Hospital for Special Surgery, United States*

9:45AM **Predicted Gait Alterations Due To A Unilateral Reduction In Muscle Synergies** SB^{3}C2019-073
Marleny Arones[1], Carolynn Patten[2], Benjamin J. Fregly[1], *[1]Rice University, United States, [2]University of California, United States*

10:00AM **System Identification of Pressure-Measuring Insoles For Determining Ground Reaction Force During Walking** SB^{3}C2019-074
Jessica DeBerardinis[1], Janet S. Dufek[1], Mohamed B. Trabia[1], Yann Le Gall[2], Nicolas Da Silva Sacoto[2], *[1]University of Nevada Las Vegas, United States, [2]Ecole Superieure d'Electronique de l'Ouest, France*

10:15AM **Utilizing Cross-Correlation To Determine Phase Shift In Gait Data For A Neural Prosthesis** SB^{3}C2019-075
Martin L. Tanaka[1], David Hudson[1], *[1]Western Carolina University, United States*

10:30AM **Movement Patterns In Dancers** SB^{3}C2019-076
Rita Patterson[1], Nathan Hersberger[1], Elizabeth Balyakina[1], Sajid Surve[1], *[1]University of North Texas Health Science Center, United States*

10:45AM **Can Superhydrophobic Slip Flow Improve Centrifugal Blood Pump Performance and Reduce Blood Damage?** SB^{3}C2019-077
Wei Xuan Chan[1], Vivek Vasudevan[1], Jia Jun Low Adriel[1], Janani Venkatesan[1], Choon-Hwai Yap[1], *[1]National University of Singapore, Singapore*

Wednesday, June 26 | 9:30AM -11:00AM

Data Driven Fluid Mechanics Modeling and Visualization — Fox Den

Session Chair: Alejandro Roldan-Alzate *University of Wisconsin-Madison*

9:30AM **Non-Invasive Diagnostics of Coronary Artery Disease Using Machine Learning and Computational Fluid Dynamics** SB^{3}C2019-078
Kritika Iyer[1], Christopher J. Arthurs[2], Cyrus P. Najarian[1], S.M. Reza Soroushmehr[1], Brahmajee K. Nallamothu[1], C. Alberto Figueroa[1], *[1]University of Michigan, United States, [2]King's College London, United Kingdom*

9:45AM **Statistical Modeling For Assessment of Aneurysm Rupture Status - Implications For Japanese and Finnish Populations** SB^{3}C2019-079
Felicitas Detmer[1], Sara Hadad[1], Sven Hirsch[2], Philippe Bijlenga[3], Yuya Uchiyama[4], Juhana Frsen[5], Juan Cebral[1], *[1]George Mason University, United States, [2]ZHAW University of Applied Sciences, Switzerland, [3]University of Geneva, Switzerland, [4]Tokyo University of Science, Japan, [5]Kuopio University Hospital, Finland*

10:00AM **Accelerating Cardiovascular Model Building With Convolutional Neural Networks** SB^{3}C2019-080
Gabriel Maher[1], Nathan Wilson[2], Alison Marsden[1], *[1]Stanford University, United States, [2]Open Source Medical Software Corporation, United States*

10:15AM **Cardiac Motion Tracking From Noisy Ultrasound Images - Exploiting Cyclic Constraint Fitted To Non-Ridgid Image Registration** SB^{3}C2019-081
Hadi Wiputra[1], Wei Xuan Chan[1], Yoke Yin Foo[1], Yu Zheng[1], Sheldon Ho[1], Choon Hwai Yap[1], *[1]National University Of Singapore, Singapore*

10:30AM **Deep Neural Networks For Hemodynamic Analysis of Human Thoracic Aorta** SB^{3}C2019-082
Liang Liang[1], Wenbin Mao[2], Wei Sun[2], *[1]Department of Computer Science at University of Miami, United States, [2]Georgia Institute of Technology and Emory University, United States*

10:45AM **Effect of Nonlinear Elastic Properties of Arterial Walls On Pulse Wave Propagation** SB^{3}C2019-083
Alberto Coccarelli[1], Sanjay Pant[1], Ankush Aggarwal[2], *[1]Swansea University, United Kingdom, [2]University of Glasgow, United Kingdom*

Wednesday, June 26	11:15AM -12:45PM

Biotransport in a Tumor Microenvironment — Sunburst

Session Chair: Sihong Wang *The City College of New York*
Session Co-Chair: Rana Zakerzadeh *University of Texas at Austin*

11:15AM **Fast Tumor Spheroid Growth In Microfluidic Device** SB^{3}C2019-084
Yaling Liu[1], Chris Uhl[1], Yuyuan Zhou[1], *[1]Lehigh University, United States*

11:30AM **A Microfluidic Tissue Array For Mid-Throughput Drug Screening Using Tumor Tissues For Personalized Medicine** SB^{3}C2019-085
AH Rezwanuddin Ahmed[1], Xuejun Jiang[2], Sarat Chandarlapaty[2], Sihong Wang[1], *[1]The City College of New York, United States, [2]Memorial Sloan Kettering Cancer Center, United States*

11:45AM **Circulating Tumor Cell Transport and Adhesion In Microfluidic Devices** SB^{3}C2019-086
Jifu Tan[1], Zhenya Ding[2], Wei Li[2], *[1]Northern Illinois University, United States, [2]Texas Tech University, United States*

12:00PM **An In Vitro Tumor Platform For Modeling Breast Tumor Stromal Interactions and Characterizing The Subsequent Response** SB^{3}C2019-087
Manasa Gadde[1], Marissa Rylander[1], *[1]University of Texas at Austin, United States*

12:15PM **Computational Fluid Dynamics Model of Pressurized Intraperitoneal Aerosol Chemotherapy: Gravity Matters!** SB^{3}C2019-088
Mohammad Rahimi-Gorji[1], Leen Van de Sande[1], Charlotte Debbaut[1], Patrick Segers[1], Wouter Willaert[1], Wim Ceelen[1], *[1]Ghent University, Belgium*

12:30PM **Microtissues For Biomechanical Investigations of Angiogenesis** SB^{3}C2019-089
M.K. Sewell-Loftin[1], Priscilla Hwang[1], Joshua Katz[1], Steve George[2], Gregory Longmore[1], *[1]Washington University School of Medicine in St. Louis, United States, [2]University of California, Davis, United States*

Wednesday, June 26	11:15AM -12:45PM

Cardiac Mechanics — Snowflake

Session Chair: Manuel Rausch *University of Texas at Austin*
Session Co-Chair: Colleen Witzenburg *University of Wisconsin*

11:15AM **A Robust 3d Constitutive Model For The Passive Properties of Left Ventricular Myocardium** SB^{3}C2019-090
David Li[1], Reza Avazmohammadi[1], Samer Merchant[2], Tomonori Kawamura[3], Edward Hsu[2], Joseph Gorman[3], Robert Gorman[3], Michael Sacks[1], *[1]The University of Texas at Austin, United States, [2]University of Utah, United States, [3]University of Pennsylvania, United States*

11:30AM **Fast Predictions of Cardiac Growth During Ventricular Dyssynchrony** SB^{3}C2019-091
Pim Oomen[1], Colleen Witzenburg[2], Thien-Khoi Phung[1], Kenneth Bilchick[1], Jeffrey Holmes[1], *[1]University of Virginia, United States, [2]University of Wisconson, United States*

11:45AM **Role of Talin1 In Cardiac Fibroblasts On Cardiac Hypertrophy** SB^{3}C2019-092
Natalie Noll[1], Qinkun Zhang[1], Hind Lal[1], W. David Merryman[1], *[1]Vanderbilt University, United States*

12:00PM **Modeling of Anisotropic Reverse Cardiac Growth In Response To Local Alteration of Electromechanics** SB^{3}C2019-093

Jayavel Arumugam[1], Ghassan Kassab[2], Lik Chuan Lee[1], *[1]Michigan State University, United States, [2]California Medical Innovations Institute, United States*

12:15PM **The Effect of Collagen Heterogeneity On Rat Myocardial Infarct Mechanics In A Multiscale Fiber Network Model** SB^{3}C2019-094

Christopher Korenczuk[1], William Richardson[2], Victor Barocas[1], *[1]University of Minnesota - Twin Cities, United States, [2]Clemson University, United States*

12:30PM **Analyzing The Biomechanical Response of Failing Right Ventricular Tissue To Sacubitril/valsartan Treatment** SB^{3}C2019-095

Danial Sharifikia[1], Claire Tushak[1], Evan Benza[2], Kang Kim[3], Marc Simon[3], *[1]Department of Bioengineering, University of Pittsburgh, United States, [2]Heart and Vascular Institute, University of Pittsburgh Medical Center (UPMC), United States, [3]Department of Bioengineering, University of Pittsburgh; Division of Cardiology, School of Medicine, University of Pittsburgh; Heart and Vascular Institute, University of Pittsburgh Medical Center (UPMC); McGowan Institute for Regenerative Medicine, Univer, United States*

Wednesday, June 26	**11:15AM -12:45PM**

Celebration of YC Fung's 100th Birthday — Wintergreen

Session Chair: Spencer Lake *Washington University in St. Louis*

11:15AM **Osmotic Swelling Behavior of The Pregnant Mouse Cervix and The Contribution of Hyaluronic Acid** SB^{3}C2019-096

Charles Jayyosi[1], Shanmugasundaram Nallasamy[2], Priya Madhukaran[2], Mala Mahendroo[2], Kristin Myers[1], *[1]Columbia University, United States, [2]University of Texas Southwestern Medical Center, United States*

11:30AM **From Biomechanics To T Cell Affinity To Systems Immunology My Path In Biomedical Engineering That Is Inspired By Dr. Yc Fung** SB^{3}C2019-097

Ning Jiang[1], *[1]University of Texas at Austin, United States*

11:45AM **A Mathematical Model For The Post-Implant Collagen Maturation Behavior of Engineered Tissues** SB^{3}C2019-098

Michael Sacks[1], *[1]University of Texas at Austin, United States*

12:00PM **Non-Invasive Brillouin Moduli and Membrane Fluctuation Measurements of Live Tumor Cell Nuclei** SB^{3}C2019-099

Anya Roberts[1], Vijay Singh[1], Peter So[1], Roger Kamm[1], *[1]Mit, United States*

12:15PM **A Micromechanical Model For Collagenous Tissues and Applications To Study Growth and Remodeling** SB^{3}C2019-100

Thao Vicky[1], *[1]Johns Hopkins University, United States*

12:30PM **Yc Fung Symposium Conclusion** SB^{3}C2019-101

Savio Woo

Wednesday, June 26	**11:15AM -12:45PM**

Mechanics of Cartilage and Meniscus — Seasons 1-3

Session Chair: Deva Chan *Rensselaer Polytechnic Institute*
Session Co-Chair: David M Pierce *University of Connecticut*

11:15AM **Mechanical Property Changes In The Meniscus In A Novel Closed Joint Animal Impact and Surgical Model** SB^{3}C2019-102

Gerardo Narez[1], Albane Fauron[2], Loic Dejardin[2], Feng Wei[2], Roger C. Haut[2], Tammy L. Haut Donahue[1], *[1]University of Massachusetts, Amherst, United States, [2]Michigan State University, United States*

11:30AM **Non-Invasive Mri Assessment of Meniscus and Cartilage Changes In A Large Animal Model of Meniscus Injury** SB^{3}C2019-103

Kyle Meadows[1], Sonia Bansal[2], John Peloquin[1], Liane Miller[2], Jay Patel[2], Kamiel Saleh[2], Michael Hast[2], Miltiadis Zgonis[2], Robert Mauck[2], Dawn Elliott[1], *[1]University of Delaware, United States, [2]University of Pennsylvania, United States*

11:45AM **Maintaining Cartilage Hydration During Sliding Part 2: Modes and Competitive Recovery Rates** SB^{3}C2019-104

David Burris[1], Axel Moore[2], Brian Graham[1], Jamie Benson[1], Caroline Kook[1], Steven Voinier[1], Christopher Price[1], *[1]University of Delaware, United States, [2]Imperial College London, United Kingdom*

12:00PM **Collagen Fiber Orientation and Mechanical Properties Correlate Across Human Articular Cartilage Zones** SB^{3}C2019-105

Kristine Fischenich[1], Joseph Wahlquist[1], Virginia Ferguson[1], *[1]University of Colorado at Boulder, United States*

12:15PM **Toward Quantifying Changes In The Collagen Network of Human Articular Cartilage During Early-Stage Osteoarthritis** SB^{3}C2019-106

Szarek E. Phoebe[1], Magnus B. Lilledahl[2], Courtland G. Lewis[3], David M. Pierce[1], *[1]University of Connecticut, United States, [2]Norwegian University of Science and Technology, Norway, [3]Hartford Healthcare, United States*

12:30PM **Type III Collagen Is A Key Regulator of Collagen Fibrillar Structure In Cartilage Pericellular Matrix** SB^{3}C2019-107

Chao Wang[1], Becky Brisson[2], Qing Li[1], Masahiko Terajima[3], Motomi Enomoto-Iwamoto[4], Mitsuo Yamauchi[3], Susan Volk[2], Lin Han[1], *[1]Drexel University, United States, [2]University of Pennsylvania, United States, [3]University of North Carolina, United States, [4]University of Maryland, United States*

Wednesday, June 26	**11:15AM -12:45PM**

Injury: Imaging — Seasons 4-5

Session Chair: Steve Rowson *Virginia Tech*
Session Co-Chair: Liming Voo *Johns Hopkins University Applied Physics Laboratory*

11:15AM **A Comparison of The Deformation Response of The Brain To Mild Acceleration In The Axial and Sagittal Planes In A Healthy Volunteer** SB^{3}C2019-108

Andrew Knutsen[1], Arnold Gomez[2], Jerry Prince[2], Philip Bayly[3], John Butman[4], Dzung Pham[1], *[1]The Henry M Jackson Foundation, United States, [2]Johns Hopkins University, United States, [3]Washington University in St. Louis, United States, [4]National Institutes of Health, United States*

11:30AM **Longitudinal Head Impact Exposure and White Matter Integrity Analysis Among Returning Youth Football Players** SB^{3}C2019-109

Mireille Kelley[1], Jillian Urban[2], Derek Jones[2], Elizabeth Davenport[3], Logan Miller[2], Beverly Snively[4], Alexander Powers[5], Christopher Whitlow[6], Joseph Maldjian[3], Joel Stitzel[2], *[1]Virginia Tech-Wake Forest School of Biomedical Engineering and Sciences, United States, [2]Virginia Tech-Wake Forest University School of Biomedical Engineering and Sciences, United States, [3]Department of Radiology, University of Texas Southwestern, United States, [4]Department of Biostatistical Sciences, Wake Forest School of Medicine, United States, [5]Department of Neurosurgery, Wake Forest School of Medicine, United States, [6]Department of Radiology (Neuroradiology), Wake Forest School of Medicine, United States*

11:45AM **Imaging and Mechanical Characterization of The Pia-Arachnoid Complex** SB^{3}C2019-110

Nikolaus Benko[1], Emma Luke[2], Yousef Alsanea[1], Brittany Coats[1], *[1]University of Utah Mechanical Engineering, United States, [2]University of Rochester Biomedical Engineering, United States*

12:00PM **Mechanical and Interfacial Characterization of Meningioma Through Mr Imaging** SB^{3}C2019-111
Efe Ozkaya[1], Dominic Nistal[2], Zeynep Suar[1], Alexander Chartrain[2], Cassandra Gologorsky[3], Priti Balchandani[2], Raj Shrivastava[2], Mehmet Kurt[1], *[1]Stevens Institute of Technology, United States, [2]Icahn School of Medicine at Mount Sinai, United States, [3]Cornell University, United States*

12:15PM **A Network-Based Brain Injury Metric For Concussion Prediction** SB^{3}C2019-112
Shaoju Wu[1], Wei Zhao[1], Bethany Rowson[2], Steve Rowson[2], Songbai Ji[1], *[1]Worcester Polytechnic Institute, United States, [2]Virginia Tech, United States*

12:30PM **Changes In Brain Tissue In Vivo Deformation Following Decompression Surgery In Chiari Patients** SB^{3}C2019-113
Maggie Eppelheimer[1], Blaise Simplice Talla Nwotchouang[1], Soroush Heidari Pahlavian[2], John Oshinski[3], Daniel Barrow[3], Rouzbeh Amini[1], Francis Loth[1], *[1]The University of Akron, United States, [2]USC Stevens Neuroimaging and Informatics Institute University of Southern California, United States, [3]Emory University, United States*

Wednesday, June 26	**11:15AM -12:45PM**

UG Design Competition — Hemlock

Session Chair: Michael Moreno *Texas A&M University*
Session Co-Chair: Ted Conway *Florida Institute of Technology*

11:15AM **Design and Optimization of A Finger-By-Finger Vibrational Therapy** SB^{3}C2019-114
Joshua Posen[1], George Durrant[1], Samuel Langlois[1], Chirsteen Abdalla[1], Gary Drzewiecki[1], *[1]Rutgers University, United States*

11:30AM **Jogging Stroller Attachment Device For Natural Arm Motion** SB^{3}C2019-115
Tamara Chambers[1], Amy Ramos[1], Meghan Blanks[1], *[1]Embry-Riddle Aeronautical University, United States*

11:45AM **Assistive Device For Stretching Exercise In Patients With Frozen Shoulder Syndrome** SB^{3}C2019-116
Maria Owsiak[1], Monsour Al Awami[1], Ryan Daher[1], Scott Goeltz[1], Rebecca Gomezrueda[1], Russel Maurer[1], Andrew Saylor[1], Ria Mazumder[1], *[1]Widener University, United States*

12:00PM **Wearable Robotic Wrist Orthosis For Stroke Rehabilitation** SB^{3}C2019-117
Neshat Baset[1], Dona Antony[1], Mahdi Haghshenas-Jaryani[1], Muthu Wijesundara[1], *[1]University of Texas at Arlington Research Institute, United States*

12:15PM **Design of 3d Printed Robotic Glove Augmenting Manual Manipulation of Humans** SB^{3}C2019-118
Mason Araujo[1], Immanuel Ponminissery[1], Seok Chang Ryu[1], *[1]Texas A&M University, United States*

12:30PM **Assistive Device For Muscular Degeneration In The Upper Arm** SB^{3}C2019-119
Alexandria Barber[1], Emily Eaton[1], Jillian Farmer[1], Samantha Gladd[1], Natalie Jagelski[1], Jenny Lin[1], *[1]Clarkson University, United States*

Wednesday, June 26	**11:15AM -12:45PM**

Translational Cardiovascular Diagnosis and Treatment — Fox Den

Session Chair: John LaDisa *Marquette University*

11:15AM **Analyses of Hemodialysis Arteriovenous Fistula Geometry Obtained By Serial Magnetic Resonance Imaging** SB^{3}C2019-120
Yong He[1], Daniel Pike[2], Yan-Ting Shiu[2], Prabir Roy-Chaudhury[3], Alfred Cheung[2], Scott Berceli[1], *[1]University of Florida, United States, [2]University of Utah, United States, [3]University of Arizona, United States*

11:30AM **Effect of Gravity On Hemodynamics In Cerebral Aneurysms - An In Vitro Study** SB^{3}C2019-121

Melissa Brindise[1], Sean Rothenberger[1], Susanne Schnell[2], Michael Markl[2], David Saloner[3], Vitaliy Rayz[1], Pavlos Vlachos[1], *[1]Purdue University, United States, [2]Northwestern University, United States, [3]University of California San Francisco, United States*

11:45AM **A Nonlinear Mechanics-Based Virtual Coiling Method For Intracranial Aneurysm** SB^{3}C2019-122

Seyyed Mostafa Mousavi Janbeh Sarayi[1], Robert J. Damiano[1], Palak Patel[1], Gary Dargush[1], Adnan H. Siddiqui[1], Hui Meng[1], *[1]University at Buffalo, The State University of New York, United States*

12:00PM **Computational Assessment of Left-Ventricular Outflow Tract Hemodynamic Alterations In Discrete Subaortic Stenosis** SB^{3}C2019-123

Jason Shar[1], Sundeep Keswani[2], Jane Grande-Allen[3], Philippe Sucosky[1], *[1]Wright State University, United States, [2]Texas Children's Hospital, United States, [3]Rice University, United States*

12:15PM **Blood Flow Modeling of Cerebral Aneurysm Treated With Intrasaccular Flow Diverting Devices** SB^{3}C2019-124

Fernando Mut[1], Bong Jae Chung[2], Juan Cebral[1], *[1]George Mason University, United States, [2]Montclair State University, United States*

12:30PM **Impact of Post-Tavr Patient-Specific Geometry On Neo-Sinus Flow: A Computational Fluid Dynamics Study** SB^{3}C2019-125

Shelly Singh-Gryzbon[1], Sanchita Bhat[1], Vahid Sadri[1], Joseph Choi[1], Mandy Salmon[1], Zhenglun (Alan) Wei[1], Philipp Ruile[2], Franz-Joseph Neumann[2], Philipp Blanke[3], Ajit Yoganathan[1], *[1]Georgia Institute of Technology, United States, [2]University Heart Center Freiburg-Bad Krozingen, Germany, [3]St Paul's Hospital and University of British Colombia, Canada*

Thursday, June 27 | 9:30AM -11:00AM

PhD Paper Competition: Cell & Tissue Engineering — Sunburst

Session Chair: Tamara Bush *Michigan State University*
Session Co-Chair: Zhenpeng Qin *The University Of Texas At Dallas*

9:30AM **Igf-1 Suppresses Trpv4 Osmosensation Through The Map7 Binding Domain In Chondrocytes** SB^{3}C2019-126

Nicholas Trompeter[1], Lauren Hurd[1], Joseph Gardinier[2], Victor DeBarros II[1], Mary Boggs[1], Randall Duncan[1], *[1]University of Delaware, United States, [2]Henry Ford Health System, United States*

9:45AM **High-Velocity Stretching Causes Mechanically-Induced Tau Pathology In Neurons** SB^{3}C2019-127

Nicholas Braun[1], Dezhi Liao[1], Patrick Alford[1], *[1]University of Minnesota - Twin Cities, United States*

10:00AM **Introduction of Heterogeneous Cell Properties For Modeling Emergent Stress Fields In Multicellular Systems** SB^{3}C2019-128

Zachary Goldblatt[1], Heather Cirka[1], Habibeh Ashouri Choshali[1], Nima Rahbar[1], Dannel McCollum[2], Kristen Billiar[1], *[1]Worcester Polytechnic Institute, United States, [2]UMASS Medical School, United States*

10:15AM **Concentration Dependent Tgf-Beta Internalization Rate In Engineered Musculoskeletal Tissues** SB^{3}C2019-129

Sedat Dogru[1], Danial Sharifikia[1], Samuel Sze[1], Michael Albro[1], *[1]Boston University, United States*

10:30AM **A Micropatterning Approach To Study Cellular Communication Via Mechanical Forces In Fibrous Microenvironments** SB^{3}C2019-130

Christopher Davidson[1], Brendon Baker[1], *[1]University of Michigan, United States*

10:45AM **Endothelial Nitric Oxide Synthase Glycosylation Is A Potential Target For Reducing Endothelial Dysfunction** SB^{3}C2019-131

Sarah Basehore[1], Alisa Morss Clyne[1], *[1]Drexel University, United States*

Thursday, June 27	9:30AM -11:00AM

PhD Paper Competition: Imaging, Injury, and Biomedical Engineering Education — Snowflake

Session Chair: Corinne Henak *University of Wisconsin-Madison*
Session Co-Chair: Victor Barocas *University of Minnesota*

9:30AM **Developing A Stem+m Identity In Underrepresented Minority Groups Through Sports and Biomechanics** SB^{3}C2019-132

Brittany Marshall[1], Amy Loya[2], John Drazan[3], Anthony Prato[4], Nicole Conley[5], Stavros Thomopoulos[1], Katherine Reuther[1], *[1]Columbia University, United States, [2]Rensselaer Polytechnic Institute, United States, [3]University of Pennsylvania, United States, [4]SUNY Geneseo, United States, [5]Union College, United States*

9:45AM **3d Strain Gradients Correlate With Murine Myocardial Infarct Severity** SB^{3}C2019-133

Arvin Soepriatna[1], John Boyle[2], Abigail Clifford[1], Alex Yeh[1], Semih Bezci[3], Grace O'Connell[3], Craig Goergen[1], *[1]Purdue University, United States, [2]Washington University in Saint Louis, United States, [3]University of California Berkeley, United States*

10:00AM **Development of A Dual-Venc 4d Flow Mri Framework For The Generation of Patient Specific Aortic Finite Element Models** SB^{3}C2019-134

Jamie Concannon[1], Kevin Moerman[1], Peter Dockery[1], Peter McHugh[1], Christof Karmonik[2], Patrick McGarry[1], *[1]National University of Ireland Galway, Ireland, [2]MRI Core, Debakey Heart and Vascular Center, Houston Methodist, TX, USA, United States*

10:15AM **5-Ht2b Antagonism Controls Border Zone Mechanics To Improve Outcomes Following Myocardial Infarction** SB^{3}C2019-135

J. Caleb Snider[1], Qinkun Zhang[1], Hind Lal[1], W. David Merryman[1], *[1]Vanderbilt University, United States*

10:30AM **An Integrated Machine Learning-Inverse Finite Element Approach For Identification of Patient-Specific Material Properties of The Aortic Wall From Clinical Ct Images** SB^{3}C2019-136

Minliang Liu[1], Liang Liang[2], Fatiesa Sulejmani[1], Xiaoying Lou[3], Glen Iannucci[3], Edward Chen[3], Bradley Leshnower[3], Wei Sun[1], *[1]Georgia Institute of Technology, United States, [2]University of Miami, United States, [3]Emory University, United States*

10:45AM **Comparative Analysis of Head Impact Kinematics In High School and Collegiate Football Using Mig2.0 Instrumented Mouthguard** SB^{3}C2019-137

Ileana Pirozzi[1], Michael Fanton[1], Chiara Giordano[1], Sohrab Sami[1], India Rangel[1], William Mehring[1], Pritha Roy[1], Brett Avery[1], Michael Zeineh[1], Gerald Grant[1], David Camarillo[1], *[1]Stanford University, United States*

Thursday, June 27	9:30AM -11:00AM

PhD Paper Competition: Extracellular Matrix Biomechanics — Wintergreen

Session Chair: Alejandro Roldan-Alzate *University of Wisconsin-Madison*
Session Co-Chair: Bahareh Behkam *Virginia Tech*

9:30AM **Plasticity and Elasto-Plastic Damage Mechanics Using Reactive Constrained Solid Mixtures: A Modeling Approach For Biomedical Materials** SB^{3}C2019-138

Brandon Zimmerman[1], Gerard Ateshian[1], *[1]Columbia University, United States*

9:45AM **Inflammatory and Non-Inflammatory Synovial Fluids Exhibit Distinct Tribological Phenotypes** SB^{3}C2019-139

Elizabeth Feeney[1], Devis Galesso[2], Cynthia Secchieri[2], Roberta Ramonda[3], Lawrence Bonassar[1], *[1]Cornell University, United States, [2]Fidia Farmaceutici S.p.A., Italy, [3]University of Padua, Italy*

10:00AM **Failure Mechanisms In The Tendon Enthesis Under Quasistatic, Cyclical, and Pathological Loading** SB^{3}C2019-140
Mikhail Golman[1], Adam Abraham[2], Iden Kurtaliaj[2], Brittany Marshall[2], Guy Genin[3], Victor Birman[4], Stavros Thomopoulos[2], *[1]Columbia Univeristy, United States, [2]Columbia University, United States, [3]Washington University in St. Louis, United States, [4]Missouri Science & Technology, United States*

10:15AM **Real-Time Measurement of Collagen Architecture and Deformations At Sub-Micron Resolution** SB^{3}C2019-141
Po-Yi Lee[1], Bin Yang[1], Ian A Sigal[1], *[1]University of Pittsburgh, United States*

10:30AM **Collagen Fatigue Damge Evolves With Creep Strain and Is Strain Rate Dependent** SB^{3}C2019-142
Jared Zitnay[1], Gang Seob Jung[2], Allen Lin[1], Zhao Qin[2], Yang Li[1], Markus Buehler[2], S. Michael Yu[1], Jeffrey Weiss[1], *[1]University of Utah, United States, [2]Massachusetts Institute of Technology, United States*

10:45AM **Collagen Denaturation Occurs Upon Tissue Failure In Energy Storing Tendons** SB^{3}C2019-143
Allen Lin[1], Jared Zitnay[1], Alexandra Allan[1], Jeffrey Weiss[1], *[1]University of Utah, United States*

Thursday, June 27	**9:30AM -11:00AM**

Bone Mechanics — Seasons 1-3

Session Chair: Daniel Nicolella *Southwest Research Institute*

9:30AM **Metabolic Acidosis Causes Physio-Chemically Induced Mechanical and Compositional Changes To Murine Bones** SB^{3}C2019-144
Kathryn Morozov[1], Brian Wingender[1], Anna Peterson[1], Alix Deymier[1], *[1]UConn Health, United States*

9:45AM **Effect of Hydration On Mechanical Properties of Individual Collagen Fibrils and Extrafibrillar Matrix** SB^{3}C2019-145
Heber Martinez Barron[1], Wei Gao[1], Xiaodu Wang[1], *[1]University of Texas at San Antonio, United States*

10:00AM **Effects of Exercise and Posture On Subchondral Bone Density and Thickness of Sheep** SB^{3}C2019-146
Hyunggwi Song[1], John Polk[1], Mariana Kersh[1], *[1]University of Illinois at Urbana-Champaign, United States*

10:15AM **Statistical Shape Analysis For The Assessment of Proximal Femur Shape Features Meaningful To Osteoporotic Risk of Fracture** SB^{3}C2019-147
Alessandra Aldieri[1], Mara Terzini[1], Cristina Bignardi[1], Alberto L. Audenino[1], Umberto Morbiducci[1], *[1]Politecnico di Torino, Italy*

10:30AM **Nondestructive Mapping of 3d Bone-Implant Contact and 3d Peri-Implant Strain** SB^{3}C2019-148
Yuxiao Zhou[1], Chujie Gong[1], Mehran Hossaini-Zadeh[2], Jing Du[1], *[1]The Pennsylvania State University, United States, [2]Temple University, United States*

Thursday, June 27	**9:30AM -11:00AM**

Frontiers in Experiments, Imaging, and Modeling in Tissue Solid Mechanics — Seasons 4-5

Session Chair: Adrian Buganza Tepole *Purdue University*
Session Co-Chair: Mathias Brieu *California State University - Los Angeles*

9:30AM **Choroidal Swelling Is Predicted To Cause Significant Optic Nerve Head Deformation: Potential Relevance To Sans** SB^{3}C2019-149

Andrew Feola[1], Brian Samuels[2], Brandon Macias[3], Michael Stenger[4], Nimesh Patel[5], C. Ross Ethier[6], *[1]Atlanta VA and Georgia Institute of Technology, United States, [2]University of Alabama at Birmingham, United States, [3]KBRwyle, United States, [4]Nasa-jsc, United States, [5]University of Houston, United States, [6]Georgia Tech, United States*

9:45AM **Biomechanical Characterization of Active and Passive Properties of Murine Branch Pulmonary Arteries** SB^{3}C2019-150

Abhay B. Ramachandra[1], Jay Humphrey[1], *[1]Yale University, United States*

10:00AM **Effects of Long Term Spinal Cord Injury On The Mechanical Behavior of The Urinary Bladder Extracellular Matrix** SB^{3}C2019-151

Tyler Tuttle[1], Heidi Lujan[1], Stephen DiCarlo[1], Sara Roccabianca[1], *[1]Michigan State University, United States*

10:15AM **Multi-Scale Model of Pressure-Driven Hypoxia In The Skin Resulting From Microvascular Collapse** SB^{3}C2019-152

Vivek Sree[1], Manuel Rausch[2], Adrian Buganza Tepole[1], *[1]Purdue University, United States, [2]The University of Texas at Austin, United States*

10:30AM **A Comparative Classification Analysis of Abdominal Aortic Aneurysm By Machine Learning Algorithms** SB^{3}C2019-153

Balaji Rengarajan[1], Wei Wu[1], Crystal Weidner[2], Satish Mukul[3], Mark Eskandari[4], Ender Finol[1], *[1]Department of Mechanical Engineering University of Texas at San Antonio San Antonio, TX, U.S.A., United States, [2]Department of Management Science and Statistics University of Texas at San Antonio San Antonio, TX, U.S.A., United States, [3]Department of Thoracic & Cardiovascular Surgery, Allegheny General Hospital Allegheny Health Network Pittsburgh, PA, U.S.A., United States, [4]Division of Vascular Surgery, Feinberg School of Medicine Northwestern University Chicago, IL, U.S.A., United States*

10:45AM **Design, Calibration, and Preliminary Testing of A System To Measure The Viscoelastic Properties of A Pacinian Corpuscle** SB^{3}C2019-154

Tiffany Senkow[1], Emily Chandler[1], Amy Moeller[2], Victor Barocas[1], *[1]University Of Minnesota, United States, [2]Twin Cities Orthopedics, United States*

Thursday, June 27	**9:30AM -11:00AM**

Rehabilitation and Assistive Technologies — Hemlock

Session Chair: Sara Wilson *University of Kansas*
Session Co-Chair: Carrie Peterson *Virginia Commonwealth University*

9:30AM **The Effect of Intermittent Theta Burst Stimulation On Biceps Corticomotor Excitability In Nonimpaired Individuals and Individuals With Tetraplegia** SB^{3}C2019-155

Neil Mittal[1], Blaize Majdic[1], Carrie Peterson[1], *[1]Virginia Commonwealth University, United States*

9:45AM **Inertial Measurement Units Used To Quantify Arm Elevation Angles of Manual Wheelchair Users and Able-Bodied Controls Throughout A Typical Day** SB^{3}C2019-156

Brianna Goodwin[1], Stephen Cain[2], Meegan Van Straaten[1], Emma Fortune[1], Melissa Morrow[1], *[1]Mayo Clinic, United States, [2]University of Michigan, United States*

10:00AM **Exercise Therapy Affects Glenohumeral Kinematics In Patients With Isolated Supraspinatus Tears** SB^{3}C2019-157

Luke Mattar[1], Camille Johnson[1], Tom Gale[1], Adam Popchak[1], James Irrgang[1], William Anderst[1], Volker Musahl[1], Richard Debski[1], *[1]University of Pittsburgh, United States*

10:15AM **Changes In Hand Function Due To Basal Joint Suspensionplasty** SB^{3}C2019-158

Joshua Drost[1], James Clarkson[1], Tamara Bush[1], *[1]Michigan State University, United States*

10:30AM **Macroscopic Surface Deformation of Retrieved Glenoid Components For Total Shoulder Arthroplasty** SB^{3}C2019-159

Giuliana Davis[1], Noah Bonnheim[1], Louis Malito[1], Stephan Gunther[2], Tom Norris[3], Lisa Pruitt[1], *[1]Department of Mechanical Engineering, University of California, Berkeley, United States, [2]Martha Jefferson Hospital, United States, [3]San Francisco Shoulder, Elbow & Hand Clinic, United States*

10:45AM **Development of An Annular Flow Mechanism For Maintaining Intraocular Pressure With A Glaucoma Drainage Device** SB^{3}C2019-160

Sara Wilson[1], Anna Donovan[1], Hussain Alantari[2], Paul Munden[3], Ronald Dougherty[1], *[1]University of Kansas, United States, [2]University of Missouri - Kansas City, United States, [3]Oklahoma City VA Health Care System, United States*

Thursday, June 27 | 9:30AM -11:00AM

Ventricular and Valvular Flow — Fox Den

Session Chair: Lakshmi Prasad Dasi *Ohio State University*

9:30AM **Aortic Sinus Vortex Spatio-Temporal Variations With Leaflet Calcification** SB^{3}C2019-161

Hoda Hatoum[1], Lakshmi Prasad Dasi[1], *[1]The Ohio State University, United States*

9:45AM **An Initial Fluid Mechanics Study of Bioprosthetic Heart Valves In An Accelerated Dynamic Environment** SB^{3}C2019-162

Sailahari Ponnaluri[1], Ming-Chen Hsu[2], Michael Sacks[3], Keefe Manning[1], *[1]The Pennsylvania State University, United States, [2]Iowa State University, United States, [3]University of Texas, United States*

10:00AM **Experimental Testing of Polymeric Tavr Valve Performance In Patient-Specific Models** SB^{3}C2019-163

Brandon Kovarovic[1], Oren Rotman[1], Marvin Slepian[2], Danny Bluestein[1], *[1]Department of Biomedical Engineering, Stony Brook University, Stony Brook, NY, United States, [2]Sarver Heart Center, University of Arizona,Tucson, AZ, United States*

10:15AM **Comparative Quantification of Mitral Regurgitation By Computer Modeling and Simulated Echocardiography** SB^{3}C2019-164

Wenbin Mao[1], Andrs Caballero[1], Rebecca Hahn[2], Susheel Kodali[2], Wei Sun[1], *[1]Georgia Institute of Technology, United States, [2]Columbia University Medical Center, United States*

10:30AM **The Effects of Anterior Mitral Leaflet Laceration On Left Ventricular Flow With Transcatheter Mitral Valves: An In Vitro Study** SB^{3}C2019-165

Thomas Easley[1], Vahid Sadri[1], Pranav Dorbala[1], Norihiko Kamioka[2], Vasilis Babaliaros[2], Ajit Yoganathan[1], *[1]Georgia Institute of Technology, United States, [2]Emory University, United States*

10:45AM **Patient-Specific Modeling of The Left Ventricular Hemodynamics Using The Chimera Overset Mesh Technique** SB^{3}C2019-166

Federico Can[1], Matteo Selmi[2], Gianluca De Santis[3], Alberto Redaelli[4], Patrick Segers[1], Joris Degroote[5], *[1]IBiTech bioMMeda, Department of Electronics and Information Systems, Ghent University, Belgium, [2]Division of Cardiac Surgery, Department of Surgery, Universit di Verona, Italy, [3]FEops NV, Belgium, [4]Department of Electronics, Informatics and Bioengineering, Politecnico di Milano, Italy, [5]Department of Flow, Heat and Combustion Mechanics, Ghent University, Belgium*

Thursday, June 27	11:15AM -12:45PM

PhD Paper Competition: Computational Biomechanics and Diagnostic Models

Sunburst

Session Chair: Chiara Bellini *Northeastern University*
Session Co-Chair: Craig Goergen *Purdue University*

11:15AM **Designing Tissue Engineered Vascular Grafts For Young and Aged Hosts: In Vivo, Ex Vivo and In Silico Study** SB^{3}C2019-167

Piyusha Gade[1], Keewon Lee[1], Yadong Wang[2], Anne Robertson[1], *[1]University of Pittsburgh, United States, [2]Cornell University, United States*

11:30AM **Computational Fluid Dynamics Modeling of Myocardial Bridging Using Coronary Angiography** SB^{3}C2019-168

Mohammadali Sharzehee[1], Ran Gao[2], Yuan Chang[2], Jiangping Song[2], Hai-Chao Han[3], *[1]University Of Texas At San Antonio, United States, [2]Fuwai Hospital, China, [3]Professor, United States*

11:45AM **Axial Stretch Modulates Lymphatic Contractility: An Experimental-Computational Approach In A Novel Rat Tail Model** SB^{3}C2019-169

Mohammad S. Razavi[1], Julie Leonard-Duke[1], Rebecca Hardie[1], Brandon Dixon[1], Rudolph Gleason[1], *[1]Georgia Institute of Technology, United States*

12:00PM **Simulation of Cardiac Flow: Analysis of Geometry Simplification** SB^{3}C2019-170

Fanwei Kong[1], Christoph Augustin[2], Kevin Sack[3], Shawn Shadden[1], *[1]Department of Mechanical Engineering, University of California, Berkeley, United States, [2]Institute of Biophysics, Medical University of Graz, Austria, [3]Division of Biomedical Engineering Department of Human Biology, University of Cape Town, South Africa*

12:15PM **A Combined Mri Arterial Spin Labeling and Computational Modeling Strategy To Quantify Patient-Specific Blood Flow and Perfusion In Cerebrovascular Occlusive Disease** SB^{3}C2019-171

Jonas Schollenberger[1], Luis Hernandez-Garcia[2], C. Alberto Figueroa[3], *[1]Department of Biomedical Engineering, University of Michigan, United States, [2]fMRI Laboratory and Department of Biomedical Engineering, University of Michigan, United States, [3]Departments of Surgery and Biomedical Engineering, University of Michigan, United States*

12:30PM **Evaluation of Artificial Neural Networks As A Potential Rupture Discrimination Model** SB^{3}C2019-172

Sricharan S Veeturi[1], Hamidreza Rajabzadeh-Oghaz[1], Jason M Davies[1], Hui Meng[1], *[1]University at Buffalo, United States*

Thursday, June 27	11:15AM -12:45PM

PhD Paper Competition: Morphogenesis, Development, Growth, and Remodeling

Snowflake

Session Chair: Kristin Miller *Tulane University*
Session Co-Chair: Jeffrey Weiss *University of Utah*

11:15AM **Systematic Modulation of Cell-Cell Adhesion In Vivo Modulates Epithelial Tissue Mechanics and Remodeling** SB^{3}C2019-173

Xun Wang[1], Karen Kasza[1], *[1]Columbia University, United States*

11:30AM **Relating Bone Strain To Local Changes In Radius Microstructure Following 12 Months of Axial Forearm Loading In Women** SB^{3}C2019-174

Megan Mancuso[1], Karen Troy[1], *[1]Department of Biomedical Engineering, Worcester Polytechnic Institute, United States*

11:45AM **Effects of Reproduction and Lactation History On Rat Maternal Bone Mechano-Responsiveness and Osteocyte Microenvironment** SB^{3}C2019-175

Yihan Li[1], Ashutosh Parajuli[2], Chantal de Bakker[1], Hongbo Zhao[1], Wei-Ju Tseng[1], Rebecca Chung[1], Liyun Wang[2], X. Sherry Liu[1], *[1]University of Pennsylvania, United States, [2]University of Delaware, United States*

12:00PM **Biphasic Network Model of Collagen and Elastin Remodelling Recapitulates Compositional and Organizational Changes During Aortic Growth and Development** SB^{3}C2019-176

Ryan Mahutga[1], Victor Barocas[1], *[1]University of Minnesota, United States*

12:15PM **Pregnancy and Lactation Impair Subchondral Bone Leading To Reduced Rat Supraspinatus Tendon Failure Properties** SB^{3}C2019-177

Ashley Fung[1], Snehal Shetye[1], Yihan Li[1], X. Sherry Liu[1], Louis Soslowsky[1], *[1]University of Pennsylvania, United States*

12:30PM **Modeling Adaptive Remodeling of The Bladder Wall During Aging** SB^{3}C2019-178

Fangzhou Cheng[1], Lori Birder[1], Paul Watton[2], Anne Robertson[1], *[1]University of Pittsburgh, United States, [2]University of Sheffield, United States*

Thursday, June 27	**11:15AM -12:45PM**

PhD Paper Competition: Cellular Mechanics, Drug Delivery, and Therapeutics — Wintergreen

Session Chair: Sarah Bentil *Iowa State University*
Session Co-Chair: Brendon Baker *University of Michigan*

11:15AM **Membrane Wrapping Efficiency of Elastic Nanoparticles During Endocytosis: Size and Shape Matter** SB^{3}C2019-179

Zhiqiang Shen[1], Huilin Ye[1], Xin Yi[2], Ying Li[1], *[1]University of Connecticut, United States, [2]Peking University, China*

11:30AM **Neck Skin Thermal Features As A Measure of Stenosis In The Carotid Artery: Computational and In-Vivo Study** SB^{3}C2019-180

Ashish Saxena[1], Eddie Yin Kwee Ng[1], Vignesh Raman[1], Soo Teik Lim[2], *[1]Nanyang Technological University, Singapore, [2]National Heart Center Singapore, Singapore*

11:45AM **A Cold-Responsive Nanoparticle Enables Intracellular Delivery and Rapid Release of Trehalose For Fast Freezing of Stem Cells** SB^{3}C2019-181

Samantha Stewart[1], Xiaoming He[2], *[1]Unviersity of Maryland, College Park, United States, [2]University of Maryland, College Park, United States*

12:00PM **Engineering and Characterization of Collagenase-Expressing Salmonella Typhimurium For Enhanced Interstitial Transport In Tissue** SB^{3}C2019-182

Eric Leaman[1], Bahareh Behkam[1], *[1]Virginia Tech, United States*

12:15PM **A Systematic Approach To The Thermal Mitigation of Irreversible Electroporation Therapy** SB^{3}C2019-183

Timothy O'Brien[1], Melvin Lorenzo[1], Yajun Zhao[1], Robert Neal, II[2], John Robertson[1], S. Nahum Goldberg[3], Rafael Davalos[1], *[1]Department of Biomedical Engineering and Mechanics, Virginia Tech, United States, [2]AngioDynamics, United States, [3]Department of Radiology, Hadassah Hebrew University Hospital, Israel*

12:30PM **Optical Opening of Blood-Brain Barrier For Macromolecules Penetration By Laser Excitation of Vasculature-Targeted Plasmonic Nanoparticles** SB^{3}C2019-184

Xiaoqing Li[1], Hejian Xiong[1], Vamsidhara Vemireddy[2], Xiuying Li[1], Monica Giannotta[3], Heather Hayenga[1], Edward Pan[2], Shashank Sirsi[1], Elisabetta Dejana[3], Robert Bachoo[2], Zhenpeng Qin[1], *[1]University of Texas at Dallas, United States, [2]University of Texas Southwestern Medical Center, United States, [3]FIRC Insititute of Molecular Oncology Foundation, Italy*

Thursday, June 27	11:15AM -12:45PM

Musculoskeletal Tissue Engineering — Seasons 1-3

Session Chair: Alix Deymier *UConn Health*
Session Co-Chair: Spencer Szczesny *Pennsylvania State University*

11:15AM **Recapitulating The Complex Biomechanical Properties of Intervertebral Disc Using Tunable 3d Printing** SB^{3}C2019-185
Samantha Marshall[1], Timothy Jacobsen[1], Kevin Anton[1], Archana Murali[1], Nadeen Chahine[1], *[1]Columbia University, United States*

11:30AM **Orientation and Size of The Porcine Anterior Cruciate Ligament Vary Between Yorkshire and Yucatan Breeds At Early Adolescence** SB^{3}C2019-186
Stephanie Cone[1], Danielle Howe[1], Emily Lambeth[1], Jorge Piedrahita[2], Lynn Fordham[3], Jeffrey Spang[3], Matthew Fisher[1], *[1]North Carolina State University and the University of North Carolina – Chapel Hill, United States, [2]North Carolina State University, United States, [3]University of North Carolina – Chapel Hill, United States*

11:45AM **For Ligaments, Material Stiffness Is Not What It Appears To Be: How To Build More Accurate Material Models and Implications On Acl Graft Selection** SB^{3}C2019-187
Callan Luetkemeyer[1], Ellen Arruda[1], *[1]University of Michigan, United States*

12:00PM **An Engineered Biomaterial Microenvironment To Direct The Formation of A Living Barrier To Seal Cartilage Defects** SB^{3}C2019-188
Jay Patel[1], Claudia Loebel[1], Brian Wise[1], Kamiel Saleh[1], James Carey[1], Jason Burdick[1], Robert Mauck[1], *[1]University of Pennsylvania, United States*

12:15PM **Sustained Release of Tgf-3 From Heparinized Collagen Biofabric Induces Chondrogenic Differentiation of Human Mesenchymal Stem Cell Macromass** SB^{3}C2019-189
Hyungjin Jung[1], Phillip McClellan[1], Ozan Akkus[1], *[1]Case Western Reserve University, United States*

Thursday, June 27	11:15AM -12:45PM

Nano to Micro Multiscale Mechanics — Seasons 4-5

Session Chair: Kristin Myers *Columbia University*
Session Co-Chair: Vicky Nguyen *Johns Hopkins University*

11:15AM **A Computational and Experimental Study of Short Bowel Syndrome Biomechanics** SB^{3}C2019-190
Hadi S. Hosseini[1], Jordan S. Taylor[1], James C. Y. Dunn[1], *[1]Stanford University, United States*

11:30AM **A Discrete Fiber Network Model of Arterial Elastin Considering Inter-Fiber Crosslink** SB^{3}C2019-191
Xunjie Yu[1], Yanhang Zhang[1], *[1]Boston University, United States*

11:45AM **In Vivo Lamin A/c Deficiency Maintains Bulk Nuclear Shape and Stiffness, But Leads To Abrogated Intranuclear Mechanics and Chromatin Organization** SB^{3}C2019-192
Soham Ghosh[1], Adrienne Scott[1], Jessica Kelly[1], Benjamin Seelbinder[1], Xin Xu[1], Stephanie Schneider[1], Corey Neu[1], *[1]University of Colorado Boulder, United States*

12:00PM **Tunable Dna Nanocalipers Capable of Applying Forces To Biomolecules** SB^{3}C2019-193
Jenny Le[1], Kyle Crocker[1], Michael Darcy[1], Michael Poirier[1], Ralf Bundschuh[1], Carlos Castro[1], *[1]The Ohio State University, United States*

12:15PM **Microstructure of Tendon Reveals Helically Wrapped Fibrils With The Potential To Mediate Mechanical Load Transfer By Friction** SB^{3}C2019-194

Babak N. Safa[1], John Peloquin[1], Jessica Natriello[1], Jeffrey Caplan[1], Dawn Elliott[1], *[1]University of Delaware, United States*

12:30PM **Deformation Characteristics of The Rat Pia-Arachnoid Complex Through Multimodal Imaging** SB^{3}C2019-195

Zeynep M. Suar[1], Gloria Fabris[1], Luke Langner[1], Mehmet Kurt[1], *[1]Stevens Institute of Technology, United States*

Thursday, June 27	**11:15AM -12:45PM**

Vascular Biomechanics — Hemlock

Session Chair: Patrick Alford *University of Minnesota*
Session Co-Chair: Seungik Baek *Michigan State University*

11:15AM **Uncertainty Analysis of Vascular Surrogate Models** SB^{3}C2019-196

Zhenxiang Jiang[1], Jongeun Choi[2], Seungik Baek[1], *[1]Michigan State University, United States, [2]Yonsei Unversity, South Korea*

11:30AM **Effect of Calcification & Fibrous Tissue Features On Rupture Risk In Atherosclerotic Plaques** SB^{3}C2019-197

Bas Vis[1], Hilary Barrett[1], Astrid Moerman[1], Frank Gijsen[1], Ali Akyildiz[1], *[1]Erasmus Medical Center, Netherlands*

11:45AM **Initiation of Dissection In The Aortic Arch** SB^{3}C2019-198

Brian FitzGibbon[1], Kevin Moerman[1], Peter McHugh[1], Patrick McGarry[1], *[1]National University of Ireland Galway, Ireland*

12:00PM **Comparative Biomechanical Phenotyping of The Murine Central Vasculature** SB^{3}C2019-199

Jay Humphrey[1], *[1]Yale University, United States*

12:15PM **Regional Anisotropic Mechanical Characterization of Porcine Pulmonary Arteries** SB^{3}C2019-200

Narasimha Rao Pillalamarri[1], Sourav Patnaik[1], Senol Piskin[1], Ender Finol[1], *[1]University of Texas at San Antonio, United States*

12:30PM **Investigating The Effects of Extracellular Stiffness On Vascular Smooth Muscle Cell Stress and Mechanical Properties** SB^{3}C2019-201

Elizabeth Shih[1], Patrick Alford[1], *[1]Department of Biomedical Engineering at University of Minnesota Twin Cities, United States*

Thursday, June 27	**11:15AM -12:45PM**

Patient-Specific Flow and Physiology — Fox Den

Session Chair: Amirhossein Arzani *Northern Arizona University*

11:15AM **Cardiac Flow Dynamics of Healthy Volunteers : Sex Differences** SB^{3}C2019-202

David Rutkowski[1], Gregory Barton[1], Christopher Francois[1], Alejandro Roldan-Alzate[1], *[1]University of Wisconsin-Madison, United States*

11:30AM **Wall Shear Stress Topological Skeleton Identification In Cardiovascular Flows: A Practical Approach** SB^{3}C2019-203

Valentina Mazzi[1], Diego Gallo[1], Karol Cal[1], Muhammad O. Khan[2], David A. Steinman[3], Umberto Morbiducci[1], *[1]Polito BIOMed Lab, Department of Mechanical and Aerospace Engineering, Politecnico di Torino, Turin, Italy, [2]Cardiovascular Biomechanics Computation Lab, Department of Pediatrics Stanford University, Stanford, United States, [3]Biomedical Simulation Laboratory, Department of Mechanical & Industrial Engineering University of Toronto, Toronto, Canada*

11:45AM **Patient-Specific Fluid-Structure Interaction Analysis of A Bicuspid Aortic Valve** SB^{3}C2019-204

Monica Emendi[1], Ram Ghosh[2], Matteo Bianchi[2], Francesco Sturla[3], Filippo Piatti[3], Alberto Redaelli[1], Danny Bluestein[2], *[1]Politecnico di Milano, Italy, [2]Stony Brook University, United States, [3]IRCCS Policlinico San Donato, Italy*

12:00PM **Introduction of A Simple 2d Computational Model To Predict Risk of Coronary Obstruction During Transcatheter Aortic Valve Replacement** SB^{3}C2019-205

Megan Heitkemper[1], Hoda Hatoum[1], Amirsepher Azimian[1], Breandan Yeats[1], Jennifer Dollery[1], Bryan Whitson[1], Gregory Rushing[1], Juan Crestanello[1], Scott Lilly[1], Lakshmi Prasad Dasi[1], *[1]The Ohio State University, United States*

12:15PM **Machine Learning For Discrimination of Posterior Communicating Artery Aneurysm Rupture Status** SB^{3}C2019-206

Felicitas Detmer[1], Daniel Lckehe[2], Fernando Mut[1], Martin Slawski[1], Sven Hirsch[3], Philippe Bijlenga[4], Gabriele von Voigt[2], Juan Cebral[1], *[1]George Mason University, United States, [2]Leibniz University Hannover, Germany, [3]ZHAW University of Applied Sciences, Switzerland, [4]University of Geneva, Switzerland*

12:30PM **A Reduced Order Modeling Method For Cardiovascular Flow** SB^{3}C2019-207

Mehran Mirramezani[1], Shawn Shadden[1], *[1]University of California, Berkeley, United States*

Friday, June 28	**12:00PM - 1:30PM**

Biotransport in Thermal Therapy and Cryopreservation — Sunburst

Session Chair: R. Lyle Hood *University of Texas at San Antonio*
Session Co-Chair: Nilay Chakraborty *University of Michigan Dearborn*

12:00PM **Whole Body Hyperthermia Induced Interstitial Fluid Pressure Reduction and Enhanced Nanoparticle Delivery To Pc3 Tumors** SB^{3}C2019-208

Qimei Gu[1], Shuaishuai Liu[1], Arunendra Saha Ray[1], Lance Dockery[1], Marie-Christine Daniel[1], Charles Bieberich[1], Ronghui Ma[1], Liang Zhu[1], *[1]University of Maryland Baltimore County, United States*

12:15PM **Quantification of Tissue Electrical and Thermal Response Due To High Frequency Irreversible Electroporation: A Pilot Study In Ex Vivo Perfused Livers** SB^{3}C2019-209

Melvin Lorenzo[1], Tim O'Brien[2], Kenneth Aycock[1], Navid Manuchehrabadi[3], Rafael Davalos[1], *[1]Department of Biomedical Engineering and Mechanics Virginia Polytechnic and State University, United States, [2]Virginia Department of Biomedical Engineering and Mechanics Virginia Polytechnic and State University, United States, [3]AngioDynamics, United States*

12:30PM **Magnetic Nanoparticle Hyperthermia For Pancreatic Cancer: A Computational Study** SB^{3}C2019-210

Anilchandra Attaluri[1], Sri Kamal Kandala[2], Robert Ivkov[3], *[1]The Pennsylvania State University - Harrisburg, United States, [2]University of Texas MD Anderson Cancer Center, United States, [3]Johns Hopkins University School of Medicine, United States*

12:45PM **In Situ Photo-Inactivation of Proteins By Molecular Hyperthermia** SB^{3}C2019-211

Peiyuan Kang[1], Xiaoqing Li[1], Stephanie Shiers[1], Hejian Xiong[1], Theodore Price[1], Zhenpeng Qin[1], *[1]The university of texas at dallas, United States*

1:00PM **Diffusion Limited Cryopreservation of Arterial Tissue To 1.5 Mm With Radiofre-Quency Heated Metal Forms** SB^{3}C2019-212

Zonghu Han[1], Zhe Gao[1], Anirudh Sharma[2], John Bischof[2], [1]*University Of Minnesota, United States,* [2]*University of Minnesota, United States*

1:15PM **Counterintuitive Scaling Effects In The Developing Thermomechanical Stress During Cryogenic Cooling of The Kidney With Implications To Electromagnetic Rewarming For Organ Banking** SB^{3}C2019-213

Prem Solanki[1], Yoed Rabin[1], [1]*Carnegie Mellon University, United States*

Friday, June 28	**12:00PM - 1:30PM**

Aneurysm Mechanics — Snowflake

Session Chair: Spandan Maiti *University of Pittsburgh*
Session Co-Chair: Yanhang (Katherine) Zhang *Boston University*

12:00PM **Patient-Specific Estimation of Ascending Thoracic Aortic Aneurysim Growth and Remodeling: Fem Based Constrained Mixture Model** SB^{3}C2019-214

S. Jamaleddin Mousavi Mousavi[1], Stephane Avril[1], [1]*Mines Saint-Etienne, Univ Lyon, Univ Jean Monnet, INSERM, U 1059 Sainbiose, Centre CIS, F - 42023 Saint-Etienne France, France*

12:15PM **Machine Learning Prediction of Rupture Strength of Ascending Aortic Aneurysm Tissue** SB^{3}C2019-215

Xuehuan He[1], Anna Ferrara[2], Yuanming Luo[1], Ferdinando Auricchio[2], Jia Lu[1], [1]*University Of Iowa, United States,* [2]*Universit degli Studi di Pavia, Italy*

12:30PM **Wall Stress and Geometric Measures In Electively Repaired Abdominal Aortic Aneursyms** SB^{3}C2019-216

Balaji Rengarajan[1], Wei Wu[1], Mirunalini Thirugnanasambandam[2], Shalin Parikh[2], Raymond Gomez[1], Ender Finol[1], [1]*Department of Mechanical Engineering University of Texas at San Antonio San Antonio, TX, U.S.A., United States,* [2]*UTHSA/UTHSA Joint Graduate Program in Biomedical Engineering University of Texas at San Antonio San Antonio, TX, U.S.A., United States*

12:45PM **A Particle-Based Model Reveals An Insidious Feed-Back Loop Between Aortic Lamellar Disruption and Cell Apoptosis** SB^{3}C2019-217

Hossein Ahmadzadeh[1], Jay Humphrey[1], [1]*Yale University, United States*

1:00PM **Alterations In Biomechanical Properties of Aortic Wall In A Mouse Model of Marfan Syndrome** SB^{3}C2019-218

Nazli Gharraee[1], Rahul Raghavan[1], Yujian Sun[1], Susan Lessner[1], [1]*University of South Carolina, United States*

1:15PM **Can The Elastase Induced Aneurysm Model Be Used To Study Remodeling In Saccular Aneurysms** SB^{3}C2019-219

Chao Sang[1], David Kallmes[2], Watkins Simon[1], Anne Robertson[1], [1]*University of Pittsburgh, United States,* [2]*Mayo Clinic, United States*

Friday, June 28	**12:00PM - 1:30PM**

Mechanobiology - a Symposium in Memory of Christopher R. Jacobs — Wintergreen

Session Chair: Eno Ebong *Northeastern University*
Session Co-Chair: Ed Guo *Columbia University*

12:00PM **Adhesion Models For Cell Migration Simulator On Continuous Substrate** SB^{3}C2019-220

Jay Hou[1], Liam Tyler[1], Daniel Keefe[1], David Odde[1], Victor Barocas[1], [1]*University of Minnesota, United States*

12:15PM **Red Blood Cell Biomechanics In Chronic Fatigue Syndrome** SB^{3}C2019-221

Amit Saha[1], Brendan Schmidt[2], Arun Kumar[2], Amir Saadat[1], Vineeth Suja[1], Vy Nguyen[2], Justin Do[2], Wendy Ho[2], Mohsen Nemat-Gorgani[1], Eric Shaqfeh[1], Anand Ramasubramanian[2], Ronald Davis[1], *[1]Stanford University, United States, [2]San Jose State University, United States*

12:30PM **Development of Recombinant Inner-Ear Motor Protein Prestin Equipped With Affinity Tag** SB^{3}C2019-222

Michio Murakoshi[1], Hiroshi Wada[2], *[1]Kanazawa University, Japan, [2]Tohoku Bunka Gakuen University, Japan*

12:45PM **Inhibition of Gsk-3 By Licl Does Not Affect Msc Differentiation In Vitro Or Bone Formation In Situ** SB^{3}C2019-223

Alyssa Oberman[1], Angela Patel[1], Glen Niebur[1], *[1]University of Notre Dame, United States*

1:00PM **Mechanical Feedback and Cooperativity In A Theoretical Model of Airway Smooth Muscle Cell-Matrix Adhesion** SB^{3}C2019-224

Linda Irons[1], Markus Owen[2], Reuben O'Dea[2], Bindi Brook[2], *[1]Yale University, United States, [2]University of Nottingham, United Kingdom*

1:15PM **Extracellular Matrix Stiffness Regulates Calcium Oscillations In Multicellular Ensembles, But Not In Isolated Cells** SB^{3}C2019-225

Suzanne Stasiak[1], Ryan Jamieson[1], Harikrishnan Parameswaran[1], *[1]Northeastern University, United States*

Friday, June 28	**12:00PM - 1:30PM**

Imaging and Mechanics of Ligament and Tendon — Seasons 1-3

Session Chair: Mona Eskandari *University of California Riverside*
Session Co-Chair: Mariana Kersh *University of Illinois at Urbana-Champaign*

12:00PM **Elastography Evaluation of The Elbow Ulnar Collateral Ligament In Overhead Throwing Athletes** SB^{3}C2019-226

Seyedali Sadeghi[1], Dov Bader[1], Daniel Cortes[1], *[1]Penn State University, United States*

12:15PM **Assessment of Tendon Hydraulic Permeability Using Osmotic Loading and Biphasic Finite Element Modeling** SB^{3}C2019-227

Babak N. Safa[1], Ellen Bloom[1], Andrea Lee[1], Michael Santare[1], Dawn Elliott[1], *[1]University of Delaware, United States*

12:30PM **Three Dimensional Morphological Changes In Carpal Tunnel Ligament Arch In Response To Wrist Compressive Forces** SB^{3}C2019-228

Rakshit Shah[1], Zong-Ming Li[1], *[1]Hand Research Laboratory, Department of Biomedical Engineering, United States*

12:45PM **Fibroblast-Like Synoviocytes Alter Matrix Mechanics & Neuronal Mmp-1 Expression Under Tensile Failure To Different Degrees Depending On Concentration** SB^{3}C2019-229

Meagan Ita[1], Nicholas Stiansen[1], Sarah St Pierre[2], Beth Winkelstein[1], *[1]University of Pennsylvania, United States, [2]Worcester Polytechnic Inst, United States*

1:00PM **Aging Adversely Affects Different Rat Rotator Cuff Tendons Similarly** SB^{3}C2019-230

Joseph Newton[1], George Fryhofer[1], Snehal Shetye[1], Ashley Rodriguez[1], Andrew Kuntz[1], Lou Soslowsky[1], *[1]University of Pennsylvania, United States*

1:15PM **Comparison of The Deformation Behavior of The Anterior Cruciate Ligament In Response To Various External Knee Loadings** SB^{3}C2019-231

Satoshi Yamakawa[1], Richard Debski[1], Hiromichi Fujie[2], *[1]University of Pittsburgh, United States, [2]Tokyo Metropolitan University, Japan*

Friday, June 28	12:00PM - 1:30PM

Injury: Models — Seasons 4-5

Session Chair: Brittany Coats *University of Utah*
Session Co-Chair: Mehmet Kurt *Stevens Institute of Technology*

12:00PM **Development of Finite Element Model of Subhuman Primate Brain and Investigation of Diffuse Axonal Injury Thresholds Induced By Head Rotation** SB^{3}C2019-232

Tushar Arora[1], Priya Prasad[2], Liying Zhang[1], *[1]Wayne State University, United States, [2]Prasad Engineering, LLC, United States*

12:15PM **Development of A Computational Biomechanics Mouse Model For Traumatic Axonal Injury** SB^{3}C2019-233

Connor Bradfield[1], Liming Voo[1], KT Ramesh[2], *[1]Johns Hopkins Applied Physics Lab, United States, [2]Johns Hopkins Department of Mechanical Engineering, United States*

12:30PM **A Study of The Brain-Skull Interface Conditions of The Worcester Rat Head Injury Model (wrhim)** SB^{3}C2019-234

Wei Zhao[1], Brian Stemper[2], Songbai Ji[1], *[1]Worcester Polytechnic Institute, United States, [2]Marquette University & Medical College of Wisconsin, United States*

12:45PM **Probabalistic Analysis of Injury Risk Using Human Body Finite Element Models** SB^{3}C2019-235

Travis Eliason[1], Matthew Davis[2], Derek Jones[2], Daniel Nicolella[1], *[1]Southwest Research Institute, United States, [2]Elemance, United States*

1:00PM **Characterization of Injured Brain Tissue After Controlled Cortical Impact** SB^{3}C2019-236

Suhao Qiu[1], Wenheng Jiang[2], Changxin Lai[1], Tianyao Wang[3], Wei Chen[2], Luyang Tao[2], Mingyuan Gao[2], Jun Liu[3], Jianfeng Zeng[2], Yuan Feng[1], *[1]Shanghai Jiao Tong University, China, [2]Soochow University, China, [3]Fudan University, China*

1:15PM **A Model of Tension-Induced Organization of Subcortical Axons During Cortical Folding of The Brain** SB^{3}C2019-237

Kara Garcia[1], Christopher Kroenke[2], Philip Bayly[3], *[1]Indiana University School of Medicine, United States, [2]Oregon Health and Science University, United States, [3]Washington University in St. Louis, United States*

Friday, June 28	12:00PM - 1:30PM

Cardiovascular and Musculoskeletal Device Design — Hemlock

Session Chair: Amy Throckmorton *Drexel University*
Session Co-Chair: Lucas Timmins *University of Utah*

12:00PM **Synthesis and Characterization of Porous Shape Memory Polymer Materials For Use In The Design of Implantable Medical Devices** SB^{3}C2019-238

Robert Kunkel[1], Jingyu Wang[1], Jishan Luo[1], Bradley Bohnstedt[2], Yingtao Liu[1], Chung-Hao Lee[1], *[1]University of Oklahoma, United States, [2]University of Oklahoma Health Sciences Center, United States*

12:15PM **Dual-Support Mechanical Assistive Technology For Pediatric and Young Adult Patients** SB^{3}C2019-239

Carson Fox[1], Randy Stevens[2], Joseph Rossano[3], Francisco Arabia[4], Amy Throckmorton[1], *[1]Biomedical Engineering, Drexel University, United States, [2]St. Christopher's Hospital for Children, United States, [3]Cardiology, The Children's Hospital of Philadelphia, United States, [4]Cardiothoracic Surgery, University of Arizona, United States*

12:30PM **Durable and Flexible Superhydrophobic and Blood-Repelling Surface With Shape-Customizable Features For Biomedical Applications** SB^{3}C2019-240

Zhe Li[1], Ba Loc Nguyen[2], Junmin Xue[3], Graeme MacLaren[4], Choon Hwai Yap[1], *[1]Department of Biomedical Engineering, National University of Singapore, Singapore, Singapore, [2]National University of SingaporeDepartment of Biomedical Engineering, National University of Singapore, Singapore, Singapore, [3]Department of Material Science and Engineering, National University of Singapore, Singapore, Singapore, [4]Department of Surgery, Yong Loo Lin School of Medicine, National University of Singapore, Singapore, Singapore*

12:45PM **Quantifying The Capacitance and Resistance of A Double-Walled Aortic Stent-Graft Prototype** SB^{3}C2019-241

Shannen B Kizilski[1], Omid Amili[1], Filippo Coletti[1], Rumi Faizer[1], Victor H Barocas[1], *[1]University of Minnesota, United States*

1:00PM **Developement and Evaluation of An Intratracheal Aerosol Delivery Device For Avian Wildlife Conservation Efforts** SB^{3}C2019-242

Carlos Ruvalcaba[1], Susana Ramirez-Perez[1], Stephanie Ortega[1], Lisa Tell[1], Jean-Pierre Delplanque[1], *[1]University of California Davis, United States*

Friday, June 28	**12:00PM - 1:30PM**

Thrombosis Hemolysis and Mechanical Circulatory Support — Fox Den

Session Chair: Keefe Manning *The Pennsylvania State University*

12:00PM **Superhydrophobicity and Vortex Generators Potential To Reduce Thrombogenicity After Prosthetic Valve Implantation** SB^{3}C2019-243

Hoda Hatoum[1], David Bark[2], Hamed Vahabi[2], Sanli Movafaghi[2], Brandon Moore[2], Marcio Forleo[2], Arun Kota[2], Ketul Popat[2], Lakshmi Prasad Dasi[1], *[1]The Ohio State University, United States, [2]Colorado State University, United States*

12:15PM **A Multiscale Model For Simulating Platelet Aggregation: Correlating With In Vitro Results** SB^{3}C2019-244

Peng Zhang[1], Prachi Gupta[1], Jawaad Sheriff[1], Changnian Han[1], Marvin J. Slepian[2], Yuefan Deng[1], Danny Bluestein[1], *[1]Stony Brook University, United States, [2]University of Arizona, United States*

12:30PM **3d Flexible Non-Newtonian Computational Framework To Study Thrombosis Initiation** SB^{3}C2019-245

Sabrina R. Lynch[1], Christopher J. Arthurs[2], Zelu Xu[3], Onkar Sahni[3], Jose A. Diaz[1], C. Alberto Figueroa[1], *[1]University of Michigan, United States, [2]King's College London, United Kingdom, [3]Rensselaer Polytechnic Institute, United States*

12:45PM **Refining A Numerical Model For Device-Induced Thrombosis** SB^{3}C2019-246

Ling Yang[1], Steven Deutsch[1], Keefe Manning[1], *[1]Department of Biomedical Engineering, The Pennsylvania State University, United States*

1:00PM **Investigation of The Interplay Between Blood and Thrombus Mechanical Properties: A 3d Fluid-Solid Interaction Model** SB^{3}C2019-247

Fatama T. Huda[1], Tarek Abdel-Salam[1], Nathan E. Hudson[1], Ali Vahdati[1], *[1]East Carolina University, United States*

1:15PM **Numerical Models of Valve-In-Valve Deployment To Evaluate The Risk of Leaflets Thrombosis** SB^{3}C2019-248

Halit Yaakobovich[1], Dar Weiss[1], Uri Zaretsky[1], Shmuel Einav[1], Gil Marom[1], *[1]Tel Aviv University, Israel*

Friday, June 28	1:45PM - 3:15PM

Biotransport in Disease Detection and Therapy — Sunburst

Session Chair: Zhongping Huang *West Chester University*
Session Co-Chair: Rebecca Heise *Virginia Commonwealth University*

1:45PM **Accurate Detection of Differential Interaction Strengths In Energy Landscapes Using Machine Learning** SB^{3}C2019-249

Ahmad Haider[1], Alan Liu[1], Todd Sulchek[1], *[1]Georgia Institute of Technology, Atlanta, United States*

2:00PM **Aerosolized Surfactant Replacement Therapy In An In Vivo Rodent Lung Injury Model** SB^{3}C2019-250

Franck J Kamga Gninzeko[1], Michael Valentine[1], Sahil Chindal[1], Susan Boc[2], Sneha Dhapare[1], Michael Hindle[1], Dale Farkas[1], P. Worth Longest[1], Rebecca Heise[1], *[1]Virginia Commonwealth University, United States, [2]Virginia Commonealth University, United States*

2:15PM **Numerical Analysis of Dense Suspension Rheology of Red Blood Cells In A Shear Flow** SB^{3}C2019-251

Naoki Takeishi[1], Marco Rosti[2], Yohsuke Imai[3], Shigeo Wada[1], Luca Brandt[2], *[1]Osaka University, Japan, [2]Royal Institute of Technology (KTH), Sweden, [3]Kobe University, Japan*

2:30PM **Deep Learning Assisted Label-Free On-Chip Selective Extraction of Single-Cell-Laden Droplets From Oil Into Aquous Solution With Dielectrophoresis** SB^{3}C2019-252

Alisa White[1], Yuntian Zhang[2], Gang Zhao[2], Xiaoming He[1], *[1]University of Maryland College Park, United States, [2]University of Science and Technology of China, China*

2:45PM **Biotransport In The Glymphatic System: Measuring and Modeling Flow Through Perivascular Spaces** SB^{3}C2019-253

Humberto Mestre[1], Jeffrey Tithof[2], Ting Du[1], Wei Song[1], Weiguo Peng[1], Amanda Sweeney[1], Genaro Olveda[1], John Thomas[2], Maiken Nedergaard[1], Douglas Kelley[2], *[1]University of Rochester Medical Center, United States, [2]University of Rochester, United States*

Friday, June 28	1:45PM - 3:15PM

Vascular Pathology and Disease Progression — Snowflake

Session Chair: Umberto Morbiducci *Politecnico di Torino*

1:45PM **Prediction of Carotid Restenosis Risk After Endarterectomy By Hemodynamic and Geometric Analysis: A 5-Years Follow-Up** SB^{3}C2019-254

Diego Gallo[1], Maurizio Domanin[2], Christian Vergara[3], Umberto Morbiducci[1], *[1]Politecnico di Torino, Italy, [2]Universit di Milano, Italy, [3]Politecnico di Milano, Italy*

2:00PM **Comparison of Healthy and Pulmonary Hypertension Hemodynamics** SB^{3}C2019-255

Senol Piskin[1], Ender A. Finol[1], *[1]University Of Texas At San Antonio, United States*

2:15PM **Functional Characterization of Arteriovenous Fistula On Swine Models Using Mri** SB^{3}C2019-256

Eleonora Tubaldi[1], Jose A. Rosado-Toro[1], Diego Celdran-Bonafonte[1], Prabir Roy-Chaudhury[1], *[1]University of Arizona, United States*

2:30PM **Impact of Hemodynamics and Endothelial Glycocalyx On Cancer Cell Adhesion To Vascular Wall Endothelium** SB^{3}C2019-257

Solomon Mensah[1], Alina Nersesyan[1], Ian Harding[1], Mark Niedre[1], Vladimir Torchilin[1], Eno Ebong[1], *[1]Northeastern University, United States*

2:45PM **Pulmonary Artery Hemodynamic Changes In Pediatric Patients With Ventricular Septal Defects** SB^{3}C2019-258
Melody Dong[1], Weiguang Yang[1], Marlene Rabinovitch[1], Jeffrey Feinstein[1], Alison Marsden[1], *[1]Stanford University, United States*

3:00PM **Fluid-Solid Growth Modeling of Pulmonary Vascular Tree: Establishing A Homeostatic Baseline State** SB^{3}C2019-259
Hamidreza Gharahi[1], Seungik Baek[1], Vasilina Filonova[2], C. Alberto Figueroa[2], *[1]Michigan State University, United States, [2]University of Michigan, United States*

Friday, June 28	**1:45PM - 3:15PM**

Mechanobiology - a Symposium in Memory of Christopher R. Jacobs — Wintergreen

Session Chair: Kara Garcia *Indiana University School of Medicine*
Session Co-Chair: Tammy Haut Donahue *University of Massachusetts Amherst*

1:45PM **An Active Chemo-Mechanical Model Predicts Adhesion and Microenvironmental Regulation of 3d Cell Shapes** SB^{3}C2019-260
Xingyu Chen[1], Veronika te Boekhorst[2], Peter Friedl[2], Vivek Shenoy[1], *[1]University of Pennsylvania, United States, [2]University of Texas MD Anderson Cancer Center, United States*

2:00PM **Myosin-Independent Regulation of Cell and Nuclear Structures In Wavy Patterns** SB^{3}C2019-261
Bor-Lin Huang[1], Chin-Hsun Huang[1], Richard Assoian[2], Pen-hsiu Grace Chao[1], *[1]National Taiwan University, Taiwan, [2]University of Pennsylvania, United States*

2:15PM **Mapping 3d Mechanical Strains During Tissue Formation With A Novel Fibronectin-Based Nanomechanical Biosensor** SB^{3}C2019-262
Daniel Shiwarski[1], Joshua Tashman[1], Alkis Tsamis[1], Quintin Jallerat[1], Malichi Blundon[1], John Szymanski[1], Brooke McCartney[1], Lance Davidson[2], Adam Feinberg[1], *[1]Carnegie Mellon University, United States, [2]University of Pittsburgh, United States*

2:30PM **Tendon Enthesis Cilium Assembly Is Driven By Mechanical Loading and Hedgehog Signaling** SB^{3}C2019-263
Fei Fang[1], Andrea Schwartz[2], Stavros Thomopoulos[1], *[1]Columbia University, United States, [2]Washington University in St. Louis, United States*

2:45PM **Sensing The Curvature: Protrusive Sensitivity of Invasive Breast Cancer Cells** SB^{3}C2019-264
Apratim Mukherjee[1], Bahareh Behkam[1], Amrinder Nain[1], *[1]Virginia Tech, United States*

3:00PM **Towards Fiber-Level Traction Force Microscopy In Collagen Gels** SB^{3}C2019-265
Lauren Bersie-Larson[1], Jay Hou[1], Victor Barocas[1], Paolo Provenzano[1], *[1]University Of Minnesota, United States*

Friday, June 28	**1:45PM - 3:15PM**

Spine Biomechanics — Seasons 1-3

Session Chair: Alicia Jackson *University of Miami*
Session Co-Chair: Daniel Cortes *Penn State University*

1:45PM **Inhibition of The Integrin Beta-1 Subunit Increases Strain Thresholds For Peripheral Neuron Dysfunction and Injury** SB^{3}C2019-266
Sagar Singh[1], Beth Winkelstein[1], *[1]University of Pennsylvania, United States*

2:00PM **Vertebral Endplate Remodeling Reduces Small Molecule Diffusion Into Degenerative Intervertebral Discs** SB^{3}C2019-267

Beth Ashinsky[1], Edward Bonnevie[1], Sai Mandalapu[1], Stephen Pickup[1], Chao Wang[2], Lin Han[2], Robert Mauck[1], Harvey Smith[1], Sarah Gullbrand[1], *[1]University of Pennsylvania, United States, [2]Drexel University, United States*

2:15PM **In-Plane Shear Mechanical Characterization of The Lumbar Facet Capsular Ligament** SB^{3}C2019-268

Emily Bermel[1], Arin Ellingson[1], Victor Barocas[1], *[1]University of Minnesota - Twin Cities, United States*

2:30PM **Direct Quantification of Intervertebral Disc Water Content Using Magnetic Resonance Imaging** SB^{3}C2019-269

Bo Yang[1], Michael Wendland[1], Yu Ma[1], Grace O'Connell[1], *[1]University Of California Berkeley, United States*

2:45PM **Location-Wise Fatigue Damage Prediction For The Intervertebral Disc Annulus of The Cervical Spine** SB^{3}C2019-270

Adhitya Vikraman Subramani[1], Phillip Whitley[2], Harsha Teja Garimella[2], Reuben Kraft[1], *[1]Pennsylvania State University, United States, [2]CFD Research, United States*

3:00PM **Bone Volume Fraction Vs. Bone Mass Density As A Predictor For Mechanical Properties of The Cancellous Bone of Human Lumbar Vertebral Bodies** SB^{3}C2019-271

Francesco Travascio[1], Abeer Al-Barghouthi[2], Loren Latta[1], *[1]University of Miami, United States, [2]Max Biedermann Institute for Biomechanics, Mount Sinai Medical Center, United States*

Friday, June 28	**1:45PM - 3:15PM**

Growth Remodeling and Repair II: Musculoskeletal System — Seasons 4-5

Session Chair: Reuben Kraft *Penn State University*
Session Co-Chair: Johannes Weickenmeier *Stevens Institute of Technology*

1:45PM **Murine Rorator Cuff Tendinopathy Models: The Role of Muscle Loading** SB^{3}C2019-272

Adam Abraham[1], Fei Fang[1], Mikhail Golman[1], Panagiotis Oikonomou[1], Stavros Thomopoulos[1], *[1]Columbia University, United States*

2:00PM **The Effect of Fatigue On The Impact Response of Rat Ulna** SB^{3}C2019-273

Chenxi Yan[1], Mariana Kersh[1], *[1]University of Illinois Urbana Champaign, United States*

2:15PM **Microindentation Maps Two Gradients In Mechanical Properties Across The Zones of The Growth Plate** SB^{3}C2019-274

Kevin Eckstein[1], Karin Payne[2], Virginia Ferguson[1], *[1]University of Colorado at Boulder, United States, [2]University of Colorado at Anschutz, United States*

2:30PM **Fibrous Network Topography Regulates Fibrotic Phenotypes In Annulus Fibrosus Cells** SB^{3}C2019-275

Edward Bonnevie[1], Sarah Gullbrand[1], Beth Ashinsky[2], Tonia Tsinman[1], Dawn Elliott[3], Harvey Smith[1], Robert Mauck[1], *[1]University of Pennsylvania and CMC VA Medical Center, United States, [2]University of Pennsylvania, CMC VA Medical Center, and Drexel University, United States, [3]University of Delaware, United States*

2:45PM **Mitochondria Function, Structural, and Mechanical Outcomes After Exposure To Near-Infrared Light During Tendon Maturation and Adult Healing** SB^{3}C2019-276

Ryan Locke[1], Elisabeth Lemmon[1], Ellen Dudzinski[1], Sarah Kopa[1], Harrah Newman[1], Elahe Ganji[1], Megan Killian[1], *[1]University of Delaware, United States*

3:00PM **Primary Synovial Fibroblast-Collagen Gels Exhibit Unique Tensile Failure Properties & Microstructure From 3t3-Collagen Gels** SB^{3}C2019-277

Meagan Ita[1], Harrison Troche[1], Beth Winkelstein[1], *[1]University of Pennsylvania, United States*

Friday, June 28	1:45PM - 3:15PM

Soft Tissue Mechanics — Hemlock

Session Chair: Kristin Myers *Columbia University*
Session Co-Chair: Joao Soares *Virginia Commonwealth University*

1:45PM **Contact Experiments Reveal Pressure Evolution In Soft Hydrated Interfaces** SB^{3}C2019-278
Christopher Johnson[1], Jiho Kim[1], Alison Dunn[1], *[1]University of Illinois at Urbana-Champaign, United States*

2:00PM **Harmonic Shear Wave Imaging: A New Elastography Method To Evaluate Mechanical Properties of Soft Tissues** SB^{3}C2019-279
Seyedali Sadeghi[1], Daniel Cortes[1], *[1]Penn State University, United States*

2:15PM **Strong Triaxial Coupling and Anomalous Poisson Effect In Collagen Networks** SB^{3}C2019-280
Ehsan Ban[1], Hailong Wang[2], J Matthew Franklin[3], Jan Liphardt[3], Paul Janmey[1], Vivek Shenoy[1], *[1]University of Pennsylvania, United States, [2]University of Science and Technology of China, China, [3]Stanford University, United States*

2:30PM **Fiber Orientation and Structure Characterization of Pregnant and Nonpregnant Human Uterus** SB^{3}C2019-281
Shuyang Fang[1], James McLean[2], Christine Hendon[2], Joy Vink[3], Kristin Myers[1], *[1]Department of Mechanical Engineering Columbia University, United States, [2]Department of Electrical Engineering Columbia University, United States, [3]Department of Obstetrics and Gynecology Columbia University Medical Center, United States*

2:45PM **Cadherin-11 Regulates Aortic Valve Interstitial Cell Force Generation and Mechanical Properties** SB^{3}C2019-282
Matthew Bersi[1], Meghan Bowler[1], W. David Merryman[1], *[1]Vanderbilt University, United States*

3:00PM **A Volumetric Growth Model For Healing Post-Infarction Scar** SB^{3}C2019-283
Derek Bivona[1], Ana Estrada[1], Jeffrey Holmes[1], *[1]University of Virginia, United States*

Friday, June 28	1:45PM - 3:15PM

Emerging Computational and Experimental Methods in Fluid Mechanics — Fox Den

Session Chair: C. Alberto Figueroa *University of Michigan*

1:45PM **A Multiscale Flow-Mediated Platelet Adhesion Model and Its Experimental Validation** SB^{3}C2019-284
Peng Zhang[1], Jawaad Sheriff[1], Peineng Wang[1], Marvin J. Slepian[2], Yuefan Deng[1], Danny Bluestein[1], *[1]Stony Brook University, United States, [2]University of Arizona, United States*

2:00PM **Deep-Learning Based Region-of-Interest Selection In 3d Cerebrovascular Images** SB^{3}C2019-285
Tatsat Rajendra Patel[1], Prakhar Jaiswal[1], Nikhil Paliwal[1], Adnan H Siddiqui[1], Rahul Rai[1], Hui Meng[1], *[1]University at Buffalo, United States*

2:15PM **A Forward Incremental Prestressing Approach For Nonlinear Fluid-Structure Interaction Hemodynamics** SB^{3}C2019-286
Nitesh Nama[1], Miquel Aguirre[2], Jay D. Humphrey[3], C. Alberto Figueroa[1], *[1]University of Michigan, United States, [2]Mines Saint-tienne, France, [3]Yale University, United States*

2:30PM **Fsi Modeling of Cyclic Aspiration For Acute Ischemic Stroke Patients** SB^{3}C2019-287
Bryan Good[1], Francesco Costanzo[1], Scott Simon[2], Keefe Manning[1], *[1]The Pennsylvania State University, United States, [2]Penn State Hershey Medical Center, United States*

2:45PM **A Systematic Methodology For Correcting Pc-Mri and Cfd Incompatibilities** SB^{3}C2019-288
Thomas Puiseux[1], Anou Sewonu[2], Franck Nicoud[1], Simon Mendez[1], Ramiro Moreno[2], *[1]IMAG, Univ. Montpellier, CNRS, France, [2]ALARA Expertise, France*

3:00PM **Reduced-Order Leaflet Models For Numerical Experiments On Transcatheter Aortic Valves** SB^{3}C2019-289
Shantanu Bailoor[1], Jung-Hee Seo[1], Hoda Hatoum[2], Lakshmi Prasad Dasi[2], Rajat Mittal[1], *[1]Johns Hopkins University, United States, [2]Ohio State University, United States*

Friday, June 28	**3:30PM - 5:00PM**

Multiscale Biotransport in Hemodynamics and Lymphatics — Sunburst

Session Chair: Brandon Dixon *Georgia Institute of Technology*
Session Co-Chair: Mona Eskandari *University of California Riverside*

3:30PM **Biotransport In The Glymphatic System: Pulsation, Peristalsis, and High Blood Pressure** SB^{3}C2019-290
Humberto Mestre[1], Jeffrey Tithof[1], Ting Du[1], Wei Song[1], Weiguo Peng[1], Amanda M. Sweeney[1], Genaro Olveda[1], John H. Thomas[1], Maiken Nedergaard[1], Douglas H. Kelley[1], *[1]University of Rochester, United States*

3:45PM **Micro Particle Image Velocimetry For In Vitro Assessment of Patient Specific Whole Blood Rheology** SB^{3}C2019-291
Erdem Kucukal[1], Yuncheng Man[1], Ailis Hill[1], Shichen Liu[1], Jane Little[1], Umut Gurkan[1], *[1]Case Western Reserve University, United States*

4:00PM **Patient-Specific Metrics From Quantitative Rheology of Whole Sickle Blood Using Microfluidics** SB^{3}C2019-292
Jose Valdez[1], Yvonne Datta[2], John Higgins[3], David Wood[1], *[1]University of Minnesota-Department of Biomedical Engineering, United States, [2]University of Minnesota-Department of Medicine, United States, [3]Harvard University-Department of Systems Biology, United States*

4:15PM **Instability of Phospholipid Bilayer Under Shear Flow: Molecular Dynamics Simulation** SB^{3}C2019-293
Taiki Shigematsu[1], Kenichiro Koshiyama[2], Shigeo Wada[3], *[1]Global Center for Medical Engineering and Informatics, Osaka University, Japan, [2]Graduate School of Technology, Industrial and Social Sciences, Tokushima University, Japan, [3]Graduate School of Engineering Science, Osaka University, Japan*

4:30PM **Computational Simulations of Thrombolytic Therapy In Acute Ischaemic Stroke** SB^{3}C2019-294
Boram Gu[1], Andris Piebalgs[1], Yu Huang[1], Dylan Roi[2], Kyriakos Lobotesis[2], Rongjun Chen[1], Simon A. Thom[3], Xiao Yun Xu[1], *[1]Department of Chemical Engineering, Imperial College London, United Kingdom, [2]Imaging Department, Charing Cross Hospital, Imperial College Healthcare NHS Trust, United Kingdom, [3]National Heart & Lung Institute, Imperial College London, United Kingdom*

4:45PM **Combined Microfluidic-Computational Approach To Quantify The Effect of Sickle-Cell Disease On Blood Rheology** SB^{3}C2019-295
Marisa Bazzi[1], Jose Valdez[2], David Wood[2], Victor Barocas[2], *[1]Department of Chemical Engineering and Material Science University of Minnesota, United States, [2]Department of Biomedical Engineering University of Minnesota, United States*

Friday, June 28	3:30PM - 5:00PM

Cardiovascular Mechanics: Other — Snowflake

Session Chair: Seungik Baek *Michigan State University*
Session Co-Chair: Sourav Patnaik *University of Texas at San Antonio*

3:30PM **Mechanical Characterization of Atherosclerotic Coronary Arteries By Ex-Vivo Inflation Testing and Inverse Finite Element Modeling** SB^{3}C2019-296
Su Guvenir[1], Giulia Gandini[1], Irene Berselli[2], Veronica Codazzi[2], Francesco Migliavacca[2], Claudio Chiastra[2], Frank J.H. Gijsen[1], Ali C. Akyildiz[1], *[1]Erasmus Medical Center, Netherlands, [2]Politecnico Di Milano, Italy*

3:45PM **Histomechanical Analysis of Decellularized Porcine Internal Thoracic Arteries** SB^{3}C2019-297
Colton Kostelnik[1], Wayne Carver[2], John Eberth[2], *[1]University of South Carolina - Department of Biomedical Engineering, United States, [2]University of South Carolina School of Medicine - Department of Cell Biology and Anatomy, United States*

4:00PM **Understanding The Transmural Variation In Extracellular Matrix Fiber Orientation Using Multi-Photon Microscopy** SB^{3}C2019-298
Anastasia Gkousioudi[1], Jacopo Ferruzzi[1], Yanhang Zhang[1], *[1]Boston University, United States*

4:15PM **Kinematic Analysis of Murine Cardiac Hypertrophy Using High-Frequency Four-Dimensional Ultrasound** SB^{3}C2019-299
Frederick Damen[1], Mauro Costa[2], Craig Goergen[1], *[1]Purdue University, United States, [2]The Jackson Laboratory, United States*

4:30PM **Selective Stiffening of A Myocardial Infarct Improves Predicted Systolic Function Without Impairing Filling** SB^{3}C2019-300
Kyoko Yoshida[1], Ana Estrada[1], Jeffrey Holmes[1], William Richardson[2], *[1]University of Virginia, United States, [2]Clemson University, United States*

4:45PM **Hypertension-Induced Changes In The Mechanical Behvaior of The Left Ventricular Wall** SB^{3}C2019-301
Marissa Grobbel[1], Ari Hollander[1], Analeeza Dubay[1], Emma Darios Flood[1], Kibrom Alula[1], Gregory Fink[1], Stephanie Watts[1], Lik Chuan Lee[1], Sara Roccabianca[1], *[1]Michigan State University, United States*

Friday, June 28	3:30PM - 5:00PM

Biofabrication and 3D in Vitro Systems — Wintergreen

Session Chair: Matthew Fisher *NC State University*
Session Co-Chair: Anna Grosberg *University of California, Irvine*

3:30PM **Bioprinting 3d Breast Epithelial Spheroids To Study Vascular Interactions In Human Cancer** SB^{3}C2019-302
Swathi Swaminathan[1], Alisa Morss Clyne[1], *[1]Drexel University, United States*

3:45PM **Fabricating 3d Cellular Aggregates Via Laser Direct-Write Bioprinting: Size- and Shape-Controlled Embryoid Bodies and Tumor Spheroids** SB^{3}C2019-303
David Kingsley[1], Cassandra Roberge[1], David Corr[1], *[1]Rensselaer Polytechnic Institute, United States*

4:00PM **Fluid-Structure Interaction At Drop-Drop Interface During Drop-On-Demand Printing of Hydrogel-Based Soft Materials** SB^{3}C2019-304
Cih Cheng[1], George T. C. Chiu[1], Bumsoo Han[1], *[1]Purdue University, United States*

4:15PM **Directed Self-Assembly of 3d In Vitro Tissue Models Using Droplet Microfluidics** SB^{3}C2019-305
Jasmine Shirazi[1], Michael Donzanti[1], Jason Gleghorn[1], [1]*University of Delaware, United States*

4:30PM **Engineering A 3d Model of Ductal Carcinoma In Situ Using Multimaterial Fresh 3d Bioprinting** SB^{3}C2019-306
Joshua Tashman[1], Thomas Hinton[1], Daniel Brown[2], Daniel Shiwarski[3], Andrew Lee[1], Andrew Hudson[1], Adrian Lee[2], Adam Feinberg[1], [1]*Carnegie Mellon University, United States,* [2]*University of Pittsburgh, United States,* [3]*Canegie Mellon University, United States*

4:45PM **Integrating In Vitro and In Silico Technologies: Development of A Perfusion Bioreactor and Its Digital Twin** SB^{3}C2019-307
Liesbet Geris[1], Mohammad Mehrian[1], Sebastien de Bournonville[2], Toon Lambrechts[2], Jean-Marie Aerts[2], Frank Luyten[2], Ioannis Papantoniou[2], [1]*University of Lige, Belgium,* [2]*KU Leuven, Belgium*

Friday, June 28	**3:30PM - 5:00PM**

Mechanics and Modeling of Musculoskeletal Soft Tissues — Seasons 1-3

Session Chair: Sara Roccabianca *Michigan State University*
Session Co-Chair: Adrian Buganza Tepole *Purdue University*

3:30PM **Sex-Dependent Orientation and Size of The Anterior Cruciate Ligament Throughout Skeletal Growth In The Porcine Stifle Joint** SB^{3}C2019-308
Danielle Howe[1], Stephanie Cone[1], Jorge Piedrahita[2], Lynn Fordham[3], Jeffrey Spang[3], Matthew Fisher[1], [1]*North Carolina State University and the University of North Carolina- Chapel Hill, United States,* [2]*North Carolina State University, United States,* [3]*University of North Carolina- Chapel Hill, United States*

3:45PM **Decorin, Alone and In Tandem With Biglycan, Alters Viscoelasticity In Aged Tendons** SB^{3}C2019-309
Ryan Leiphart[1], Snehal Shetye[1], Stephanie Weiss[1], Louis Soslowsky[1], [1]*University of Pennsylvania, United States*

4:00PM **Bath Osmolarity Alters Multiscale Mechanics and Damage In Tendon** SB^{3}C2019-310
Ellen Bloom[1], Andrea Lee[1], Dawn Elliott[1], [1]*University of Delaware, United States*

4:15PM **Quantifying Differences In The Mechanical Properties of The Flexor and Extensor Muscles In The Human Forearm Using Mr Elastography** SB^{3}C2019-311
Daniel Smith[1], Andrea Zonnino[1], Peyton Delgorio[1], Raymond Duda[1], Fabrizio Sergi[1], Curtis Johnson[1], [1]*University of Delaware, United States*

4:30PM **Sex-Related Differences In Carpal Arch Morphology** SB^{3}C2019-312
Kishor Lakshminarayanan[1], Rakshit Shah[1], Zong-Ming Li[1], [1]*Hand Research Laboratory, Department of Biomedical Engineering, United States*

4:45PM **Utilizing Arfi Imaging To Predict Linear Region Modulus of Tendons From Toe Region Data** SB^{3}C2019-313
Gerald A Ferrer[1], Waqas Khalid[1], Volker Musahl[1], Kang Kim[1], Richard E Debski[1], [1]*University of Pittsburgh, United States*

Friday, June 28	3:30PM - 5:00PM

Injury: Biomechanics — Seasons 4-5

Session Chair: Songbai Ji *WPI*
Session Co-Chair: Yuan Feng *Shanghai Jiao Tong University*

3:30PM **Shear Wave Propagation and Estimation of Material Parameters In A Nonlinear, Fibrous Material** SB^{3}C2019-314
Zuoxian Hou[1], Ruth Okamoto[1], Philip Bayly[1], *[1]Washington University in St.Louis, United States*

3:45PM **Shock Wave Propagation In Brain Tissue** SB^{3}C2019-315
Donghoon Keum[1], Soroush Assari[1], Kurosh Darvish[1], *[1]Temple University, United States*

4:00PM **Effect of Corpus Callosum Demyelination On Murine Brain Injury Mechanism** SB^{3}C2019-316
Javid Abderezaei[1], Gloria Fabris[1], Zachary Lopez[1], Cassandra Gologorsky[2], Johannes Weickenmeier[1], Mehmet Kurt[1], *[1]Stevens Institute of Technology, United States, [2]Cornell University, United States*

4:15PM **High-Rate Anisotropic and Region-Dependent Properties In Human Infant Cranial Bone** SB^{3}C2019-317
Robert Metcalf[1], Jessica Comstock[2], Brittany Coats[1], *[1]University of Utah, Mechanical Engineering, United States, [2]University of Utah, Pediatric Pathology, United States*

4:30PM **Bilateral Skull Fractures Due To Controlled Head Drops In Infant Porcine Specimens** SB^{3}C2019-318
Patrick Vaughan[1], Alexis Goots[1], Todd Fenton[1], Roger Haut[1], Feng Wei[1], *[1]Michigan State University, United States*

4:45PM **Estimates of High-Risk Single and Cumulative Head Impact Doses In American Football** SB^{3}C2019-319
Adam Bartsch PhD[1], *[1]Prevent Biometrics, United States*

Friday, June 28	3:30PM - 5:00PM

Government Perspectives on Multiscale Biomechanics, Bioengineering, and Biotransport — Hemlock

Session Chair: Alisa Morss Clyne, *University of Maryland*

Grace Peng, *NIH Program Director,* Division of Discovery Science & Technology and Mathematical Modeling, Simulation, and Analysis
Michele Grimm, *NSF Program Director,* Biomedical Engineering
Laurel Kuxhaus, *ASME Federal Fellow*

Friday, June 28	3:30PM - 5:00PM

Pediatric and Congenital Fluid Mechanics — Fox Den

Session Chair: Amy Throckmorton *Drexel University*

3:30PM **Stent Intervention Improves Flow Distribution and Vascular Growth In Porcine Pulmonary Artery Stenosis** SB^{3}C2019-320
Ryan Pewowaruk[1], Klarka Mendrisova[1], Carolina Larrain[1], Christopher Francois[1], Luke Lamers[1], Alejandro Roldan-Alzate[1], *[1]University of Wisconsin - Madison, United States*

3:45PM **Shear Stress Modulates Cardiomyocyte Proliferation Via Endothelial Cell-Cardiomyocyte Signaling** SB^{3}C2019-321

Matthew Watson[1], Lauren Black[2], Erica Kemmerling[3], *[1]Tufts University, Department of Mechanical Engineering and Department of Biomedical Engineering, United States, [2]Tufts University, Department of Biomedical Engineering, United States, [3]Tufts University, Department of Mechanical Engineering, United States*

4:00PM **Computational Surgical Planning For Peripheral Pulmonary Artery Stenosis In Children With Alagille and Williams Syndromes** SB^{3}C2019-322

Ingrid Lan[1], Weiguang Yang[2], Jeffrey Feinstein[3], Alison Marsden[3], *[1]Bioengineering, Stanford University, United States, [2]Pediatric Cardiology, Stanford University, United States, [3]Bioengineering and Pediatric Cardiology, Stanford University, United States*

4:15PM **Fluid-Structure Analysis of A Collapsible Axial Impeller and Protective Cage For Dysfunctional Fontan Physiology** SB^{3}C2019-323

Matthew Hirschhorn[1], Evan Bisirri[1], Randy Stevens[2], Joseph Rossano[3], Amy Throckmorton[1], *[1]Drexel University, United States, [2]St. Christopher's Hospital for Children, United States, [3]Children's Hospital of Phildelphia, United States*

4:30PM **Mechanics and Efficiency of The Zebrafish Embryonic Heart Tube** SB^{3}C2019-324

Alireza Sharifi[1], Alex Gendernalik[1], Deborah Garrity[1], David Bark Jr.[1], *[1]Colorado State University, United States*

4:45PM **Whole Embryonic Heart Ultrasound Imaging, Motion Tracking and Flow Simulations Reveal Hemodynamic Role of Embryonic Atria** SB^{3}C2019-325

Sheldon Ho[1], Wei Xuan Chan[2], Nhan Phan-Thien[2], Choon Hwai Yap[2], *[1]Biomedical Engineering, National University of Singapore, Singapore, [2]National University of Singapore, Singapore*

2 Poster Sessions

2.1 Poster Session I	Wednesday, June 26 12:45PM - 2:15PM

Posters - BS Level Competition: Cardiovascular System

Assessment of Pulmonary Arterial Structure and Its Association With Right Ventricular Function SB[3]C2019-P001

Frankangel Servin[1], Rebecca R Vanderpool[2], Rajesh Janardhanan[3], Jose Rosado[4], Franz P Rischard[5], Jason X.J Yuan[6], *[1]University of Arizona, Department of Biomedical Engineering, United States, [2]University of Arizona, Department of Biomedical Engineering, Division of Translational and Regenerative Medicine, United States, [3]University of Arizona, Department of Medical Imaging, United States, [4]University of Arizona, Department of Medical Imaging, United States, [5]University of Arizona, Division of Pulmonary, Allergy, Critical Care and Sleep Medicine, United States, [6]University of Arizona, Division of Translational and Regenerative Medicine, United States*

Quantitative Analysis of Flow Distribution Within The Fetal Heart Using In-Vitro 4d Flow Mri SB[3]C2019-P002

Lucille Anzia[1], Katrina Ruedinger[1], Shardha Srinivasan[2], Barbara Trampe[1], Timothy Heiser[1], J. Igor Iruretagoyena[2], Alejandro Roldan-Alzate[1], *[1]University of Wisconsin Madison, United States, [2]University of Wisconsin School of Medicine and Public Health, United States*

On The Use of Pentagalloyl Glucose For Mechanistic Suppression of Abdominal Aortic Aneurysm SB[3]C2019-P003

Vangelina Osteguin[1], Sourav Patnaik[1], Alycia Berman[2], Craig Goergen[2], Ender Finol[1], *[1]University of Texas at San Antonio, United States, [2]Purdue University, United States*

Novel Method of Detecting The Effect From Inhaled Anesthetics On Peripheral Venous Pressure Waveforms SB[3]C2019-P004

Kaylee Henry[1], Ali Al-Alawi[1], Md Abul Hayat[1], Patrick Bonasso[2], Hanna Jensen[1], Jingxian Wu[1], Kevin Sexton[2], Morten Jensen[1], *[1]University of Arkansas, United States, [2]University of Arkansas for Medical Sciences, United States*

Fluvastatin Decreases Endothelial Nitric Oxide Synthase O-Glcnacylation SB[3]C2019-P005

Danika Meldrum[1], Sarah Basehore[1], Alisa Morss Clyne[1], *[1]Drexel University, United States*

Investigations of The Chordae Tendineae'S Mechanical Properties of Porcine Atrioventricular Heart Valves SB[3]C2019-P006

Colton Ross[1], Devin Laurence[1], Yan Zhao[2], Ming-Chen Hsu[3], Ryan Baumwart[4], Yi Wu[1], Chung-Hao Lee[1], *[1]The University of Oklahoma, United States, [2]The University of Oklahoma Health Sciences Center, United States, [3]Iowa State University, United States, [4]Oklahoma State University, United States*

Relationship of Platelet Adhesion With Surface Topography In The Penn State Pvad SB[3]C2019-P007

Cecilia Richardsen[1], Ashlyn Mueser[1], Branka Lukic[2], Christopher Siedlecki[2], William Weiss[2], Keefe Manning[1], *[1]Pennsylvania State University, United States, [2]Penn State Hershey Medical Center, United States*

Mouse Aortic Mechanical Properties From Finite Element Model Optimized To Match Ring-Pull Experiments SB[3]C2019-P008

Carl Schoephoerster[1], Ryan Mahutga[1], Victor Barocas[1], *[1]Department of Biomedical Engineering, University of Minnesota-Twin Cities, United States*

A Computational Study of The Role of The Pericardium On Cardiac Function In Normal and Hypertensive Hearts SB[3]C2019-P009

Emilio A. Mendiola[1], Huan Nguyen[1], Reza Avaz[1], Michael S. Sacks[1], *[1]The University of Texas at Austin, United States*

Estimating The Contribution of The Endovascular Catheter On Cerebral Hypoperfusion During Mechanical Thrombectomy SB[3]C2019-P010

Christina Ngo[1], Jeffrey Pyne[2], Jaiyoung Ryu[3], Shawn Shadden[2], *[1]Department of Bioengineering, UC Berkeley, United States, [2]Department of Mechanical Engineering, UC Berkeley, United States, [3]Department of Mechanical Engineering, Chung-Ang University, South Korea*

Alteration of The Mechanical Response of Porcine Tricuspid Valve Anterior Leaflets Following Exposure To De-Ionized Water SB^{3}C2019-P011

Margaret Clark[1], Samuel Salinas[1], Rouzbeh Amini[1], *[1]The University of Akron, United States*

On The Distribution of Aortic Valve Cusp Calcification SB^{3}C2019-P012

Varshini Guhan[1], Megan Heitkemper[1], Lakshmi Prasad Dasi[1], *[1]The Ohio State University, United States*

An Investigation of Layer-Specific Tissue Biomechanics of Porcine Atrioventricular Valve Anterior Leaflets SB^{3}C2019-P013

Cortland Johns[1], Katherine Kramer[1], Anju Babu[1], Chung-Hao Lee[1], *[1]Biomechanics and Biomaterials Design Lab, School of Aerospace and Mechanical Engineering, The University of Oklahoma Norman, OK, USA, United States*

A Study of Pressure Dynamics Across A Stenotic Orifice SB^{3}C2019-P014

Tori Burton[1], Hoda Hatoum[1], Lakshmi Prasad Dasi[1], *[1]Department of Biomedical Engineering at The Ohio State University, United States*

A Study of The Effects of An Increased Beat Rate On The Penn State Pediatric Ventricular Assist Device SB^{3}C2019-P015

Brady Houtz[1], Sailahari Ponnaluri[1], Maureen Gallagher[1], Charlee Dawson[1], Bryan Good[1], Steven Deutsch[1], Keefe Manning[1], *[1]Pennsylvania State University, United States*

Hemodynamics of Coronary Artery Aneurysms In Kawasaki Disease An Idealized Aneurysm Model SB^{3}C2019-P016

Alex Lu[1], Noelia Grande Gutierrez[1], Alison Marsden[1], *[1]Stanford University, United States*

Fluid Dynamics Study of An Implantable Blood Pump For Patients With A Failed Fontan Circulation SB^{3}C2019-P017

Cody Kubicki[1], Bryan Good[1], William Weiss[2], Keefe Manning[1], *[1]The Pennsylvania State University, United States, [2]Penn State Hershey Medical Center, United States*

Posters - BS Level Competition: Musculoskeletal, Respiratory, Ocular and Other Systems

Heterogeneity and Anisotropy In The Microscale Energy Dissipating Properties of The Knee Meniscus SB^{3}C2019-P018

Kevt'her Hoxha[1], Chao Wang[1], Biao Han[1], Robert Mauck[2], Lin Han[1], *[1]Drexel University, United States, [2]University of Pennsylvania, United States*

2d Or Not 2d; Comparing 2d and 3d Measurements of Collagen Microstructure SB^{3}C2019-P019

Gosia Fryc[1], Bin Yang[1], Alexandra Gogola[1], Bryn Brazile[1], Yi Hua[1], Tian Yong Foong[1], Ian A. Sigal[1], *[1]University of Pittsburgh, United States*

The Effect of A Cannabinoid Receptor 2 Agonist On Motor Function After Blast-Induced Neurotrauma SB^{3}C2019-P020

Bayan Alturkestani[1], Soroush Assari[1], Ola M Sharaf[1], Ian Hendricks[1], Sara J. Ward[1], Ronald F. Tuma[1], Kurosh Darvish[1], *[1]Temple University, United States*

Drone Blade Induced Skin Laceration and Eye Injury Risk; An Investigation of Skin and Eye Surrogate Models SB^{3}C2019-P021

Lauren Duma[1], Mark Begonia[2], Barry Miller[1], Stefan Duma[1], *[1]Virginia Tech, United States, [2]Virgina Tech, United States*

Direct Measurement of Collagen Fiber Orientation Along The Surface of Ligaments and Tendons of The Knee In A Porcine Model SB^{3}C2019-P022

Emily Lambeth[1], Stephanie Cone[1], Matthew Fisher[1], *[1]North Carolina State University and the University of North Carolina - Chapel Hill, United States*

Elastase Treatment Increases and Accelerates Stress Relaxation In Tendon. SB^{3}C2019-P023

James Abraham[1], Jeremy Eekhoff[2], Spencer Lake[3], *[1]Department of Mechanical Engineering and Materials Science at Washington University in St. Louis, United States, [2]Department of Biomedical Engineering at Washington University in St. Louis, United States, [3]Department of Mechanical Engineering and Materials Science at Washington University in St. Louis , Department of Biomedical Engineering at Washington University in St. Louis , Department of Orthopaedic Surgery at Washington University in St. Louis, United States*

Ultrasound Shear Wave Elastography of The Anterior Cruciate Ligament SB^{3}C2019-P024

Gabi Schwartz[1], Rachel Heller[1], Seyedali Sadeghi[1], Daniel Cortes[1], *[1]Penn State, United States*

Extracellular Matrix Stiffness Alters Chondrocyte Phenotype Through Trpv4 Regulation SB^{3}C2019-P025

Ryan Skinner[1], Mallory Griffin[1], Nicholas Trompeter[1], Cindy Farino[1], Omar Banda[1], John Slater[1], Randall Duncan[1], *[1]University of Delaware, United States*

Asthmatic and Healthy Airway Morphology Measured From Ct-Based Geometries SB^{3}C2019-P026

Irina Pyataeva[1], Kamran Poorbahrami[1], Ellesse Cooper[1], Ben Piperno[1], David Mummy[2], Sean Fain[2], Jessica Oakes[1], *[1]Northeastern University, United States, [2]University of Wisconsin-Madison, United States*

Contributions of Collagen Ii, Laminin, and Fibronectin To Vitreoretinal Adhesion In Human Eyes SB^{3}C2019-P027

Joseph Phillips[1], Christopher Creveling[1], Brittany Coats[1], *[1]University of Utah, United States*

Rapid Quantitative Assessment of Postural Control Function For Mild Traumatic Brain Injury: Evaluation of A Portable Force Plate Device SB^{3}C2019-P028

Jonathan VanPaepeghem[1], Kunal Dave[1], Liying Zhang[1], *[1]Wayne State University, United States*

Mechanical Influence of Graphitic Carbon Nitride Filler On Poly(vinyl Alcohol) Thin Film Hydrogels For Wound Healing SB^{3}C2019-P029

Bradley Henderson[1], Katelyn Cudworth[1], Andrew Clifford[2], Dylan Quintana[2], John Thurston[2], Trevor Lujan[1], *[1]Boise State University, United States, [2]College of Idaho, United States*

A Novel Workflow For Generation of Patient-Specific Asthmatic Airway Models From Ct Data SB^{3}C2019-P030

Ellesse Cooper[1], Kamran Poorbahrami[1], Ben Piperno[1], David Mummy[2], Sean Fain[2], Jessica Oakes[1], *[1]Northeastern University, United States, [2]University of Wisconsin, United States*

Water Sport Head Injuries; Ability of Helmets To Reduce Head Impact Accelerations SB^{3}C2019-P031

Brock Duma[1], Mark Begonia[1], Casey Charron[1], Stefan Duma[1], *[1]Virginia Tech, United States*

The Influence of Radiographic Projection Angle On Visualization of The Subtalar Joint SB^{3}C2019-P032

Kalebb Howell[1], Nicola Krahenbuhl[2], Rich Lisonbee[1], Beat Hintermann[2], Charles Saltzman[1], Andrew Anderson[1], Alexej Barg[1], Amy Lenz[1], *[1]University of Utah, United States, [2]Kantonsspital Baselland, Switzerland*

Effects of Volumetric Boundary Conditions On The Compressive Mechanics and Modeling of Passive Skeletal Muscle SB^{3}C2019-P033

Anurag Vaidya[1], Benjamin Wheatley[1], *[1]Bucknell University, United States*

Posters - MS Level Competition: Solid Mechanics

The Effect of In Vivo Ionizing Radiation On The Micromechanics of Mouse Vertebrae SB^{3}C2019-P034

Tongge Wu[1], Megan Pendleton[1], Noah Bonnheim[1], Joshua Alwood[2], Tony Keaveny[1], *[1]University of California, Berkeley, United States, [2]NASA Ames Research Center, United States*

Investigating Sex-Specific Accuracy of Proximal Femur Coordinate Systems Derived From Statistical Shape Models SB^{3}C2019-P035

Carla Winsor[1], Xinshan Li[2], Ju Zhang[3], Corinne Henak[1], Heidi-Lynn Ploeg[4], *[1]University of Wisconsin - Madison, United States, [2]University of Sheffield, United Kingdom, [3]Auckland Bioengineering Institute, New Zealand, [4]Queen's University, Canada*

Effects of Collagenase and Elastase On The Mechanical Properties of Porcine Abdominal Aorta SB^{3}C2019-P036

Celeste Blum[1], Chris Korenczuk[2], Victor Barocas[2], *[1]University of Minnesota - Twin Cities, United States, [2]University of Minnesota- Twin Cities, United States*

Finite Element Simulation Framework For Investigating Pathological Effects On Organ-Level Tricuspid Valve Biomechanical Function SB^{3}C2019-P037

Devin Laurence[1], Emily Johnson[2], Ming-Chen Hsu[2], Arshid Mir[3], Harold Burkhart[3], Yi Wu[1], Chung-Hao Lee[1], *[1]University of Oklahoma, United States, [2]Iowa State University, United States, [3]University of Oklahoma Health Sciences Center, United States*

An Integrated Opto-Mechanical System For Quantification of Dynamic Microstructure and Mechanics of Heart Valve Tissues SB^{3}C2019-P038

Samuel Jett[1], Zachary Schuermann[1], Arshid Mir[2], Harold Burkhart[3], Chung-Hao Lee[1], *[1]Biomechanics and Biomaterials Design Laboratory, School of Aerospace and Mechanical Engineering, The University of Oklahoma Norman, OK, USA, United States, [2]Division of Pediatric Cardiology, Department of Pediatrics, University of Oklahoma Health Sciences Center, Oklahoma City, OK, USA, United States, [3]Division of Cardiothoracic Surgery, Department of Surgery, University of Oklahoma Health Sciences Center, Oklahoma City, OK, USA, United States*

Computational Analysis of Unhelmeted Bicycle Accidents Through Multi-Body and Finite Element Simulations SB^{3}C2019-P039

Lise Gheysen[1], Michel Woering[2], Markos Kapeliotis[2], Jos Vander Sloten[2], *[1]UGent, Belgium, [2]KU Leuven, Belgium*

Repeated Non-Injurious Loading Induces Changes In Local Mechanics & Collagen Fiber Organization That May Be Injurious SB^{3}C2019-P040

Travis Kotzur[1], Beth Winkelstein[1], *[1]University of Pennsylvania, United States*

Investigation of Scaling Techniques Used For Developing Brain Injury Criterion By Finite Element Models of The Primate and Human Head Simulating Head Rotation SB^{3}C2019-P041

Tushar Arora[1], Priya Prasad[2], Liying Zhang[1], *[1]Wayne State University, United States, [2]Prasad Engineering, LLC, United States*

Determination of Tissue Level Injury Threshold For Ocular Trauma By Finite Element Analysis SB^{3}C2019-P042

Kunal Dave[1], Liying Zhang[1], *[1]Wayne State University, United States*

Computational Analysis of Lisfranc Surgical Repairs SB^{3}C2019-P043

M. Tyler Perez[1], John Owen[1], Robert Adelaar[2], Jennifer Wayne[1], *[1]Virginia Commonwealth University, United States, [2]McGuire VA Medical Center, United States*

McDespot Quantitative Mri Correlates With Articular Cartilage Material Properties SB^{3}C2019-P044

Matthew Grondin[1], Fang Liu[1], Michael Vignos[1], Richard Kijowski[1], Corinne Henak[1], *[1]University of Wisconsin-Madison, United States*

Characterization of Shear Wave Speed-Stress Relationship In Collateral Ligaments SB^{3}C2019-P045

Jonathon Blank[1], Joshua Roth[1], Darryl Thelen[1], *[1]Department of Mechanical Engineering, University of Wisconsin-Madison, United States*

Tribocorrosion Behavior of Metallic Implants: A Comparative Study of Cocrmo and Ti6al4v SB^{3}C2019-P046

Mihir Patel[1], Edward Cudjoe[1], Jae Joong Ryu[1], *[1]Youngstown State University, United States*

An Age-Aware Constitutive Model For Human Sclera Incorporating Experimentally-Measured Collagen Fiber Tortuosity SB^{3}C2019-P047

Tian Yong Foong[1], Yi Hua[1], Alexandra Gogola[1], Rouzbeh Amini[2], Ian A. Sigal[1], [1]*University of Pittsburgh, United States,* [2]*University of Akron, United States*

Posters - MS Level Competition: Biotransport, Fluids, Tissue Engineering and Dynamics

Stochastic Model For Platelet Spreading Under Flow SB^{3}C2019-P048

Iain Briongos[1], Peter Hammes[1], David Bark[1], [1]*Colorado State University, United States*

Evaluating Single Muscle Contraction Using Electrical Stimulation and Shear Wave Elastography SB^{3}C2019-P049

Heer Patel[1], Seyedali Sadeghi[1], Daniel Cortes[1], [1]*The Pennsylvania State University, United States*

Implementing Real-Time Extrinsic Muscle Control In A Robotic Gait Simulator For Investigating Lower Extremity Function SB^{3}C2019-P050

Watson Spivey[1], Cody O'Cain[1], Bronislaw Gepner[1], Edward Sprately[1], Jason Kerrigan[1], [1]*University of Virginia, Center for Applied Biomechanics, United States*

Evaluation of Accuracy of Four Muscle Models Using Intramuscular Pressure A Surrogate For Muscle Force SB^{3}C2019-P051

Grant Boggess[1], Mohammad Shorijeh[1], Filiz Ates[2], William Litchy[2], Krista Coleman-Wood[2], Kenton Kaufman[2], BJ Fregly[1], [1]*Rice University, United States,* [2]*Mayo Clinic, United States*

The Effects of Ankyloglossia On The Tongue Motility of Infants During Breastfeeding SB^{3}C2019-P052

Yiela Saperstein[1], David Elad[2], Andrew Laine[1], Scott Siegel[3], Catherine Watson Genna[4], [1]*Columbia University, United States,* [2]*Tel Aviv University, Israel,* [3]*Stony Brook University, United States,* [4]*Private Practice, United States*

Development of A Computational Model of Braided Stent For Cerebral Aneurysm Treatment SB^{3}C2019-P053

Shunya Shiozaki[1], Tomohiro Otani[1], Shigeo Wada[1], [1]*Department of Mechanical Science and Bioengineering, Graduate School of Engineering Science, Osaka University, Japan*

Accelerometers Used To Measure Magnitude and Frequency of Hand Movement For Children With Cerebral Palsy During Constraint Induced Movement Therapy SB^{3}C2019-P054

Brianna Goodwin[1], Emily Sabelhaus[2], Ying-Chun Pan[1], Kristie Bjornson[1], Kelly Pham[1], William Walker[1], Katherine Steele[1], [1]*University of Washington, United States,* [2]*Seattle Children's Hospital, United States*

Reduction of Wall Shear Strain Rates In Arteriovenous Graft Venous Anastomoses SB^{3}C2019-P055

Dillon Williams[1], Guy Genin[1], Mohamed Zayed[1], [1]*Washington University, United States*

Flow Through Soft Tissue Equivalents: Measuring The Hydraulic Permeability of Collagen Gels SB^{3}C2019-P056

Christopher Vidmar[1], Brittany Fisher[1], Victor Lai[1], [1]*Department of Chemical Engineering at the University of Minnesota-Duluth, United States*

Effect of Different Inlet Velocity Profiles On Patient-Specific Cfd Simulations of Healthy Trachea SB^{3}C2019-P057

Bipin Tiwari[1], Tarun Kore[1], Sandeep Bodduluri[2], Surya Bhatt[2], Vrishank Raghav[1], [1]*Auburn University, United States,* [2]*University of Alabama at Birmingham, United States*

Quantifying Distortion Energy In Collagen Matrices Subjected To Complex Loads Using A Biaxial Bioreactor SB^{3}C2019-P058

Katherine Hollar[1], Danielle Siegel[1], John Everingham[1], Abdullah Ahmad[1], Alvaro Morfin[1], Gunes Uzer[1], Trevor Lujan[1], [1]*Boise State University, United States*

An Intercalating Crosslinkable and Biocompatible Hydrogel System For Resurfacing Damaged Cartilage SB^{3}C2019-P059

Brian Wise[1], Jay Patel[1], Claudia Loebel[1], Jason Burdick[1], Robert Mauck[1], [1]*University of Pennsylvania, United States*

Engineering Spatial Gradients of Diamagnetic Particles and Cells In Hydrogels Using Negative Magnetophoresis SB^{3}C2019-P060

Hannah Zlotnick[1], Andy Clark[2], Xuemei Cheng[2], Robert Mauck[1], *[1]University of Pennsylvania, United States, [2]Bryn Mawr, United States*

Posters - Fluids: Cardiovascular Fluid Mechanics

Computational Hemodynamics & Complex Networks Integrated Platform To Study Intravascular Flow In The Carotid Bifurcation SB^{3}C2019-P061

Karol Cal[1], Diego Gallo[1], Valentina Mazzi[1], Stefania Scarsoglio[1], Muhammad O. Khan[2], David A. Steinman[3], Luca Ridolfi[1], Umberto Morbiducci[1], *[1]Polito BIOMed Lab, Department of Mechanical and Aerospace Engineering, Politecnico di Torino, Turin, Italy, [2]Cardiovascular Biomechanics Computation Lab, Department of Pediatrics, Cardiology, Stanford University, Stanford, United States, [3]Biomedical Simulation Lab, Department of Mechanical & Industrial Engineering, University of Toronto, Toronto, Canada*

Automatic Techniques For Determining Boundary Condition Parameters In Computational Haemodynaics SB^{3}C2019-P062

Christopher J. Arthurs[1], C. Alberto Figueroa[2], *[1]King's College London, United Kingdom, [2]University of Michigan, United States*

Developing A Scalable Open-Source Solver To Simulate Hemodynamics In The Human Pulmonary Vasculature SB^{3}C2019-P063

Narasimha Rao Pillalamarri[1], Senol Piskin[1], Ender Finol[1], *[1]University of Texas at San Antonio, United States*

Solution Adaptive Refinement of Cut-Cell Cartesian Meshes Improves Mechanical Heart Valve Simulation Performance SB^{3}C2019-P064

Ryan Pewowaruk[1], Tim Ruesink[1], Yanheng Li[2], David Rowinski[2], Alejandro Roldan-Alzate[1], *[1]University of Wisconsin - Madison, United States, [2]Convergent Science, United States*

Uncertainty Quantification of Outflow Boundary Conditions On Non-Invasive Pressure Quantification In Aortorenal Artery System SB^{3}C2019-P065

Huidan (whitney) Yu[1], Monsurul Khan[1], Hao Wu[1], Xiaoping Du[1], Alan Sawchuk[1], *[1]Indiana University-Purdue University Indianapolis, United States*

Modeling Pulse Wave Propagation For Idealized and Physiological Arteries With Fluid-Structure Interactions In Febio SB^{3}C2019-P066

Jay Shim[1], Vittorio Gatti[1], Pierre Nauleau[1], Grigorios Karageorgos[1], Elisa Konofagou[1], Gerard Ateshian[1], *[1]Columbia University, United States*

In Vitro Volumetric Lagrangian Particle Tracking and 4d Pressure Field In A Left Ventricle Model SB^{3}C2019-P067

Hicham Saaid[1], Matteo Novara[2], Jason Voorneveld[3], Christiaan Schinkel[4], Jos Westenberg[5], Frank Gijsen[6], Patrick Segers[1], Pascal Verdonck[1], Johan Bosch[6], Sasa Kenjeres[4], Daniel Schanz[2], Sebastian Gesemann[2], Andreas Schrder[2], Tom Claessens[7], *[1]BioMMeda, Institute Biomedical Technology Ghent University, Belgium, [2]Institute of Aerodynamics and Flow Technology, German Aerospace Center (DLR), Germany, [3]Thoraxcenter Biomedical Engineering, Erasmus Medical Center, Netherlands, [4]Department of Chemical Engineering Delft University of Technology, Netherlands, [5]Department of Radiology Leiden University Medical Center, Netherlands, [6]Thoraxcenter Biomedical Engineering Erasmus Medical Center, Netherlands, [7]Department of Materials, Textiles And Chemical Engineering, Ghent University, Belgium*

Impact of Different Bifurcation Stenting Techniques On The Endothelial Shear Stress Within A Peripheral Bifurcation SB^{3}C2019-P068

Azadeh Lotfi[1], Tracie Barber[1], *[1]UNSW Australia, Australia*

Improvement and In Vitro Validation of A Finite Element Based Virtual Coiling Method For Intracranial Aneurysm SB^{3}C2019-P069

Robert Damiano[1], Saeb Ragani[1], Adnan Siddiqui[1], Jason Davies[1], Hui Meng[1], *[1]University at Buffalo, United States*

Automated Segmentation of Cerebral Arteries From Patient-Specific 3d Cerebrovascular Images Using Deep-Learning and Group Morphology SB^{3}C2019-P070

Tatsat Rajendra Patel[1], Nikhil Paliwal[1], Prakhar Jaiswal[1], Adnan H Siddiqui[1], Rahul Rai[1], Hui Meng[1], *[1]University at Buffalo, United States*

Fabrication of A Flexible Idealized 3d Printed Aortic Dissection For In Vitro Analysis SB^{3}C2019-P071

Sylvana Garca-Rodrguez[1], Alexander B. Holtz[1], Huairen Zhou[1], Rafael Medero[1], Alejandro Roldan-Alzate[1], *[1]University of Wisconsin-Madison, United States*

Experimental Evaluation of Two Fast Virtual Stenting Algorithms For Modeling Flow Diverters In Patient-Specific Intracranial Aneurysms SB^{3}C2019-P072

Saeb Ragani Lamooki[1], Vincent Tutino[1], Nikhil Paliwal[1], Setlur Nagesh[1], Robert Damiano[1], Adnan Siddiqui[1], Hui Meng[1], *[1]University at Buffalo, United States*

Adhesion Effect On Localization of Deformable Micro-Particles In Blood Flow SB^{3}C2019-P073

Huilin Ye[1], Zhiqiang Shen[1], Ying Li[1], *[1]University of Connecticut, United States*

4d Flow Mri Determination of Windkessel Parameters For Patient Specific Cardiovascular Simulation SB^{3}C2019-P074

Ryan Pewowaruk[1], Alejandro Roldan-Alzate[1], *[1]University of Wisconsin - Madison, United States*

Differences In Parent Artery Geometry Between Acom and McA Aneurysms SB^{3}C2019-P075

Fernando Mut[1], Megan Lawson[1], Juan Cebral[1], *[1]George Mason University, United States*

Predicting Aneurysmal Degeneration In The Dissected Thoracic Aorta: A Computational Fluid Dynamic Approach SB^{3}C2019-P076

Arianna Forneris[1], Alina Ismaguilova[1], Giampaolo Martufi[1], Jehangir Appoo[1], Elena Di Martino[1], *[1]University of Calgary, Canada*

Patient-Specific Evaluation of Post-Tevar Hemodynamic Performance In Aortic Dissection SB^{3}C2019-P077

Selene Pirola[1], Claudia Menichini[1], Baolei Guo[2], Simone Saitta[1], Weiguo Fu[2], Zhihui Dong[2], Xiao Yun Xu[1], *[1]Imperial College London, United Kingdom, [2]Fudan University, China*

Image-Based Assessment of The Hemodynamic Performance of Surgical and Transcatheter Aortic Valve Replacements SB^{3}C2019-P078

Selene Pirola[1], Omar A. Jarral[1], Mohammad Y. Salmasi[1], Declan P. ORegan[1], John R. Pepper[2], Thanos Athanasiou[1], Xiao Yun Xu[1], *[1]Imperial College London, United Kingdom, [2]Royal Brompton and Harefield NHS Fundation Trust, United Kingdom*

Hemodynamic Characteristics Associated With Cerebral Aneurysms Evolution SB^{3}C2019-P079

Seyedeh Fatemeh Salimi Ashkezari[1], Fernando Mut[1], Juan Raul Cebral[1], *[1]George Mason University, United States*

Intensity of Stenosis-Induced Flow Instabilities of The Internal Carotid Artery: A Computational Approach SB^{3}C2019-P080

Viviana Mancini[1], Aslak W. Bergersen[2], Kristian Valen-Sendstad[2], Patrick Segers[1], *[1]IBiTech bioMMeda, Ghent University, Belgium, [2]Department of Computational Physiology, Simula Research Laboratory, Norway*

Predicting Thrombosis Risk In The Left Atrial Appendage of Human Heart SB^{3}C2019-P081

Breandan Yeats[1], Hoda Hatoum[1], Thura Harfi[1], Lakshmi Prasad Dasi[1], *[1]The Ohio State University, United States*

Effects of Subject-Specific, Spatially Reduces, and Idealized Boundary Conditions On The Predicted Hemodynamic Environment In The Murine Aorta SB^{3}C2019-P082

Kelly Smith[1], Samer Merchant[1], Edward Hsu[1], Lucas Timmins[1], *[1]University of Utah, United States*

Pre-Procedural Patient-Specific In-Silico Deployment of Sapien and Evolut Transcather Aortic Valves SB^{3}C2019-P083

Sri Krishna Sivakumar[1], Hoda Hatoum[1], Jennifer Dollery[1], Scott Lilly[1], Lakshmi Prasad Dasi[1], *[1]The Ohio State University, United States*

Effects of Resolution and Dynamic Range of Dual-Venc 4d Flow Mri On Flow Measurements In Cerebral Aneurysms: In Vitro 4d Flow Study In A Scaled Model SB^{3}C2019-P084

Sean Rothenberger[1], Melissa Brindise[1], Joseph Muskat[1], Susanne Schnell[2], Pavlos Vlachos[1], Vitaliy Rayz[1], *[1]Purdue University, United States, [2]Northwestern University, United States*

In-Silico Characterization of Patient-Specific Pulmonary Hypertension Hemodynamics SB^{3}C2019-P085

Narasimha Rao Pillalamarri[1], Senol Piskin[1], Sourav Patnaik[1], Alifer Bordones[1], Vitaly Kheyfets[2], Ender Finol[1], *[1]University of Texas at San Antonio, United States, [2]University of Colorado, Denver, United States*

Development of An Experimental System Exploring The Efficacy of Cyclic Aspiration On Clot Displacement In A Cerebral Thrombectomy Model SB^{3}C2019-P086

Joshua Kugel[1], Connor Foust[1], Bryan Good[1], Keefe Manning[1], *[1]The Pennsylvania State University, United States*

Posters - Solid Mechanics: Bone Mechanics

Assessing Femural Implant Failure Risk By Applying Controllable Torque With Robot Manipulator and 6 Dof Sensor SB^{3}C2019-P087

Marius Gudauskis[1], Abel Pietros[2], Brian L. Davis[2], Brandon Jonard[3], *[1]Institute of Mechatronics, Kaunas University of Technology, Lithuania, [2]Department of Biomedical Engineering, The University of Akron, United States, [3]Department of Orthopaedics, Summa Healthcare System, United States*

Drill Plunge In Orthopedic Surgery Defined SB^{3}C2019-P088

Scott Baskerville[1], Ted Conway[1], Samantha Schultz[1], *[1]Florida Institute of Technology, United States*

A Preliminary Study On Correlations Between Microarchitectural Parameters of Human Trabecular Bone SB^{3}C2019-P089

Pengwei Xiao[1], Joel Gomez[1], Matthew Kirby[1], Ed Guo[2], Xiaodu Wang[1], *[1]The University of Texas at San Antonio, United States, [2]Columbia University, United States*

Posters - Solid Mechanics: Cardiovascular Tissue Mechanics

Three-Dimensional Anisotropic Residual Stresses In The Abdominal Aorta SB^{3}C2019-P090

Taisiya Sigaeva[1], Gerhard Sommer[2], Gerhard A. Holzapfel[3], Elena Di Martino[1], *[1]University of Calgary, Canada, [2]Graz University of Technology, Austria, [3]Graz University of Technology, Norwegian University of Science and Technology, Austria*

A Biomechanics-Based Risk Prediction Metric For Thoracic Aortic Dissection SB^{3}C2019-P091

Spandan Maiti[1], James Thunes[1], Leonid Emerel[1], Thomas Gleason[1], David Vorp[1], *[1]University of Pittsburgh, United States*

Physiologic Strength of Ascending Thoracic Aortic Tissue Depends On Stress Biaxiality SB^{3}C2019-P092

James Thunes[1], Ronald Fortunato[1], Thomas Gleason[1], David Vorp[1], Spandan Maiti[1], *[1]University of Pittsburgh, United States*

Inverse Mixed Strain Method For Aneurysm Stress Analysis SB^{3}C2019-P093

Yuanming Luo[1], Jia Lu[1], *[1]the University of Iowa, United States*

Microstructural Characterization of Intraluminal Thrombus In Abdominal Aortic Aneurysms SB^{3}C2019-P094

Pete Gueldner[1], Sourav Patnaik[1], Senol Piskin[1], Mirunalini Thirugnanasambandam[1], Satish Muluk[2], Ender Finol[1], *[1]University of Texas at San Antonio, United States, [2]Allegheny General Hospital, United States*

Material Characterization of Atherosclerotic Plaques With Virtual Fields Method SB^{3}C2019-P095

Ronald van den Berg[1], Stephane Avril[2], Frank Gijsen[1], Ali Akyildiz[1], *[1]Erasmus Medical Center, Netherlands, [2]Mines Saint-Etienne, France*

Microstructure-Based Finite Element Modeling Framework For Simulating Passive Inflation of The Left Ventricle SB^{3}C2019-P096

Ce Xi[1], Ghassan Kassab[2], Lik Chuan Lee[1], *[1]Michigan State University, United States, [2]California Medical Innovations Institute, United States*

A Thermodynamically Motivated Cross-Bridge Cycling Framework To Predict Myofibril Remodeling Under Conditions Accosiated With Lv Hypertrophy SB^{3}C2019-P097

Eoin McEvoy[1], Patrick McGarry[1], *[1]National University of Ireland Galway, Ireland*

Contractility Modelling Towards Predicting Eccentric Hypertrophy In A Patient-Specific Heart Model SB^{3}C2019-P098

Ryan Coleman[1], Eoin McEvoy[1], Patrick McGarry[1], *[1]NUI Galway, Ireland*

Cardiac Growth and Remodeling: Using Machine Learning To Correlate Cell and Organ Scales SB^{3}C2019-P099

Mathias Peirlinck[1], Francisco Sahli Costabal[2], Kevin Sack[3], Jenny Choy[4], Ghassan Kassab[4], Julius Guccione[5], Matthieu De Beule[1], Patrick Segers[1], Ellen Kuhl[2], *[1]Ghent University, Belgium, [2]Stanford University, United States, [3]University of Cape Town, South Africa, [4]California Medical Innovations Institute, Inc., United States, [5]University of California at San Francisco, United States*

Changes In The Anisotropic and Viscoelastic Properties of The Ovine Right Ventricle Under Chronic Pressure Overload SB^{3}C2019-P100

Wenqiang Liu[1], Michael Nguyen-Truong[1], Elisabeth Gray[1], Jeremiah Easley[1], Eric Monnet[1], Christian Puttlitz[1], Zhijie Wang[1], *[1]Colorado State University, United States*

Mechanical Characterization of Bovine Embolus Analogs For Investigating Acute Ischemic Stroke Recanalization SB^{3}C2019-P101

Gretchen Hiller[1], Bryan Good[1], Keefe Manning[1], *[1]Department of Biomedical Engineering The Pennsylvania State University University Park, PA, United States*

Assessment of Ascending Aortic Wall Stresses For Nondissected Patients With Bicuspid Aortic Valve and Dissected Patients With Tricuspid Aortic Valve SB^{3}C2019-P102

Sreyas Ravi[1], David Vorp[1], Spandan Maiti[1], *[1]University of Pittsburgh, United States*

Application of Digital Image Correlation To The Local Strain Analysis of Mouse Aortas: Novel Method To Create Speckle Pattern SB^{3}C2019-P103

Liya Du[1], Brooks Lane[1], John Eberth[1], Susan Lessner[1], *[1]University of South Carolina, United States*

Towards An Ultrasound Imaging Framework For Transmural Evaluation of Right Ventricular Myocardial Fiber Orientation Under Loading SB^{3}C2019-P104

Danial Sharifikia[1], Marc Simon[2], Kang Kim[2], *[1]Department of Bioengineering, University of Pittsburgh, United States, [2]Department of Bioengineering, University of Pittsburgh; Division of Cardiology, School of Medicine, University of Pittsburgh; Heart and Vascular Institute, University of Pittsburgh Medical Center (UPMC); McGowan Institute for Regenerative Medicine, Univer, United States*

Improved Strain Analysis of Left Ventricular Function Post Myocardial Infarction In Mice SB^{3}C2019-P105

Danielle Wilson[1], Zhen Zhu[1], Stephanie George[1], Jitka Virag[1], *[1]East Carolina University, United States*

Structural Changes In The Progression of Pulmonary Arterial Hypertension SB^{3}C2019-P106

Erica Pursell[1], Daniela Valdez-Jasso[1], *[1]Ucsd, United States*

Dynamic Mechanics of Cyclically Stretched Vascular Smooth Muscle Cells SB^{3}C2019-P107

Taylor Rothermel[1], Patrick Alford[1], [1]*University of Minnesota - Twin Cities, United States*

Mechanics of The Bulbus Arteriosus In Zebrafish: Why The Shape of The P-D Loop Is Crucial SB^{3}C2019-P108

Matthias Van Impe[1], Patrick Sips[2], Julie De Backer[2], Patrick Segers[1], [1]*Ghent University, Belgium,* [2]*Ghent University Hospital, Belgium*

The Effect of Leaflet Residual Strains On Aortic Valve Dynamics SB^{3}C2019-P109

Rana Zakerzadeh[1], Ming-Chen Hsu[2], Michael Sacks[1], [1]*University of Texas at Austin, United States,* [2]*Iowa State University, United States*

Effects of -80c Freezing Onthe Biomechanical Response of Tricuspid Valve Leaflets SB^{3}C2019-P110

Samuel Salinas[1], Margaret Clark[1], Rouzbeh Amini[1], [1]*The University of Akron, United States*

Role of Glycosaminoglycans In Biaxial Mechanical Behaviors of Porcine Atrioventricular Heart Valve Leaflets SB^{3}C2019-P111

Chung-Hao Lee[1], Colton Ross[1], Devin Laurence[1], Lauren Evans[1], Jacob Richardson[1], Anju Babu[1], Ean Beyer[1], Yi Wu[1], Gerhard Holzapfel[2], Arshid Mir[3], Harold Burkhart[3], [1]*The University of Oklahoma, United States,* [2]*Graz University of Technology, Austria,* [3]*The University of Oklahoma Health Sciences Center, United States*

State of The Art Simulation of The Early Stages of Bioprosthetic Heart Valve Fatigue SB^{3}C2019-P112

Will Zhang[1], Rana Zakerzadeh[2], Michael Sacks[2], [1]*University of Michigan, United States,* [2]*The University of Texas at Austin, United States*

Image-Based Simulation of The Mitral Valve Repair Surgery In Ischemic Mitral Regurgitation Patients SB^{3}C2019-P113

Amir Khalighi[1], Bruno Rego[1], Robert Gorman[2], Joseph Gorman[2], Michael Sacks[1], [1]*The University of Texas at Austin, United States,* [2]*University of Pennsylvania, United States*

A Non-Invasive Method To Quantify Aortic Valve Leaflet Deformation SB^{3}C2019-P114

Bruno Rego[1], Samuel Potter[2], Alison Pouch[3], Robert Gorman[3], Michael Sacks[2], [1]*University of Texas at Ausin, United States,* [2]*University of Texas at Austin, United States,* [3]*University of Pennsylvania, United States*

Collagen Architecture, Cellularity, and Biaxial Mechanics of Ovine Tricuspid Valve Leaflets SB^{3}C2019-P115

William Meador[1], Mrudang Mathur[1], Marcin Malinowski[2], Tomasz Jazwiec[2], Tomasz Timek[2], Manuel Rausch[1], [1]*The University of Texas at Austin, United States,* [2]*Spectrum Health, United States*

Quantification of Simultaneous Structure, Strain, and Stress Behaviors In Layered Soft Tissues SB^{3}C2019-P116

Samuel Potter[1], Will Goth[1], James Tunnell[1], Michael Sacks[1], [1]*The University of Texas at Austin, United States*

The Role of Sclerostin In Calcific Aortic Valve Disease SB^{3}C2019-P117

J. Ethan Joll[1], W. David Merryman[1], [1]*Vanderbilt University, United States*

A Spatial Mean Curvature Map of The Aortic Valve-Relevance To Calcification SB^{3}C2019-P118

Amanda Barreto[1], Asad Mirza[1], Sharan Ramaswamy[1], [1]*FIU-Biomedical Engineering Department, United States*

Posters - Solid Mechanics: Growth Remodeling and Repair

Matching Material and Cellular Timescales Maximizes Cell Spreading On Viscoelastic Substrates SB^{3}C2019-P119

Ze Gong[1], Spencer Szczesny[2], Steven Caliari[3], Elisabeth Charrier[1], Ovijit Chaudhuri[4], Xuan Cao[1], Yuan Lin[5], Robert Mauck[1], Paul Janmey[1], Jason Burdick[1], Vivek Shenoy[1], [1]*University of Pennsylvania, United States,* [2]*The Pennsylvania State University, United States,* [3]*University of Virginia, United States,* [4]*Stanford University, United States,* [5]*University of Hong Kong, Hong Kong*

Extracellular Matrix Microstructure Modulates Myofibroblast Differentiation Within 3d Fibrous Microenvironments In Vitro SB^{3}C2019-P120

Daniel Matera[1], Brendon Baker[1], [1]*University of Michigan, United States*

Architecture and Function of Chick Embryonic Heart Cells Are Mediated By Geometric Ecm Patterning Cues SB^{3}C2019-P121

Bernard Cook[1], Patrick Alford[1], [1]*University of Minnesota, United States*

Three-Dimensional Ct Morphometric Image Analysis of The Clivus and Sphenoid Sinus In Chiari Malformation Type I SB^{3}C2019-P122

Blaise Simplice Talla Nwotchouang[1], Maggie Eppelheimer[1], Paul Bishop[2], Dipankar Biswas[1], Janna Andronowski[1], Jayapalli Bapuraj[3], David Frim[4], Rick Labuda[5], Rouzbeh Amini[1], Francis Loth[1], [1]*University of Akron, United States,* [2]*Cleveland Clinic, United States,* [3]*University of Michigan Health System, United States,* [4]*University of Chicago, United States,* [5]*Conquer Chiari, United States*

Controlled Release From Mechanically-Activated Microcapsules In Developing Tissue Microenvironments SB^{3}C2019-P123

Ana Peredo[1], Yun Kee Jo[1], Daeyeon Lee[1], George Dodge[1], Robert Mauck[1], [1]*University of Pennsylvania, United States*

Finite Element Modeling To Study Musculoskeletal Growth: A Comparison of Node and Element-Based Approaches SB^{3}C2019-P124

Danielle Howe[1], Nikhil Dixit[2], Katherine Saul[2], Matthew Fisher[1], [1]*North Carolina State University and the University of North Carolina- Chapel Hill, United States,* [2]*North Carolina State University, United States*

Mitral Valve Leaflet Remodeling Following Myocardial Infarction SB^{3}C2019-P125

Bruno Rego[1], Amir Khalighi[1], Eric Lai[2], Robert Gorman[2], Joseph Gorman[2], Michael Sacks[1], [1]*The University of Texas at Austin, United States,* [2]*University of Pennsylvania, United States*

A Machine Learning Material Model For Soft Tissue Remodeling SB^{3}C2019-P126

Wenbo Zhang[1], Tan Bui-Thanh[1], Michael Sacks[1], [1]*The University of Texas at Austin, United States*

Biomechanical Restoration Potential of Pentagalloyl Glucose After Arterial Extracellular Matrix Damage SB^{3}C2019-P127

Sourav Patnaik[1], Narasimha Rao Pillalamarri[1], Senol Piskin[1], Mirunalini Thirugnanasambandam[1], Vangelina Osteguin[1], Gladys P. Escobar[2], Eugene Sprague[2], Ender A. Finol[1], [1]*University of Texas at San Antonio, United States,* [2]*University of Texas Health San Antonio, United States*

Low-Energy Mechanical Impacts To Articular Cartilage Increase At Least One Anabolic Protein In Chondrocytes SB^{3}C2019-P128

Stephany Santos[1], Kelsey Richard[1], Melanie C. Fisher[2], Caroline N. Dealy[2], David M. Pierce[1], [1]*University of Connecticut, United States,* [2]*University of Connecticut Health Center, United States*

Alpha Smooth Muscle Actin-Expressing Bone Marrow Progenitor Cells Contribute To Tunnel Integration Following Acl Reconstruction SB^{3}C2019-P129

Timur Kamalitdinov[1], Keitaro Fujino[1], Yaping Ye[1], Xi Jiang[1], Snehal Shetye[1], Ashley Rodriguez[1], Miltiadis Zgonis[1], Andrew Kuntz[1], Nathaniel Dyment[1], [1]*University of Pennsylvania, United States*

In Silico Modeling of Soft Tissue Failure From Subfailure Damage To Complete Rupture SB^{3}C2019-P130

Ronald Fortunato[1], Anne Robertson[1], Chao Sang[1], Spandan Maiti[1], [1]*University of Pittsburgh, United States*

Myofibroblast Activation In Synthetic Fibrous Matrices Composed of Dextran Vinyl Sulfone SB^{3}C2019-P131

Christopher Davidson[1], Danica Jayco[1], Daniel Matera[1], William Wang[1], Brendon Baker[1], [1]*University of Michigan, United States*

Interaction of Pentagalloyl Glucose With The Microenvironment of Macrophages SB^{3}C2019-P132

Sourav Patnaik[1], Vangelina Osteguin[1], Tina Rodgers[1], Rohini Vishwanath[1], Craig Goergen[2], Dan Simionescu[3], Gabriela Uribe[1], Ender Finol[1], *[1]University of Texas at San Antonio, United States, [2]Purdue University, United States, [3]Clemson University, United States*

Posters - Cell & Tissue Engineering: Quantitative Micro/Nanodevices

Rapid Actuation and Tunable Control of Dna Machines SB^{3}C2019-P133

Alexander Marras[1], Stephanie Lauback[2], Ze Shi[3], Gaurav Arya[4], Ratnasingham Sooryakumar[5], Carlos Castro[5], *[1]University of Chicago, United States, [2]Juniata College, United States, [3]University of California San Diego, United States, [4]Duke University, United States, [5]Ohio State University, United States*

High-Throughput Cell Mechanical Property Measurements From Creep Experiments In An Extensional Flow Microfluidic Device SB^{3}C2019-P134

Huda Irshad[1], Safwa Ali[1], Gwendolyn Cramer[1], Jonathan Celli[1], Joanna Dahl[1], *[1]University of Massachusetts Boston, United States*

Posters - Cell & Tissue Engineering: Cardiovascular

A Computational Approach For Optimal Design of Tissue Engineered Vascular Grafts SB^{3}C2019-P135

Jason Szafron[1], Abhay Ramachandra[1], Christopher Breuer[2], Alison Marsden[3], Jay Humphrey[1], *[1]Yale University, United States, [2]Nationwide Children's Hospital, United States, [3]Stanford University, United States*

Curling Angle Measurement of Lv Bi-Layered Surface Strip Reviews Residual Stress In The Epicardium SB^{3}C2019-P136

Xiaodan Shi[1], Yue Liu[2], Katherine Copeland[1], Sara McMahan[1], Song Zhang[3], Ryan Butler[3], Yi Hong[1], Michael Cho[4], Pietro Bajona[5], Huajian Gao[2], Jun Liao[1], *[1]University of Texas at Arlington, United States, [2]Brown University, United States, [3]Mississippi State University, United States, [4]University of Texas Arlington, United States, [5]University of Texas Southwestern Medical Center, United States*

Effects of Microgravity On 3d Bioprinted Constructs To Assess Cardiovascular Disorders SB^{3}C2019-P137

Likitha Somasekhar[1], Prabhuti Kharel[1], Kenia Nunes[1], Paul Gatenholm[2], Kunal Mitra[1], *[1]Florida Institute of Technology, United States, [2]Chalmers university of Technology, Sweden*

Patient Specific, In Vitro Studies of Pathologies Caused By Heart Disease Associated Lamin A/c Mutations SB^{3}C2019-P138

Mehrsa Mehrabi[1], Richard Tran[1], Halida Widyastuti[1], Cecilia Nguyen[1], Michael V. Zaragoza[1], Anna Grosberg[1], *[1]University of California, Irvine, United States*

Adipose Stromal Cell Derived Extracellular Vesicles Induce Elastin and Collagen Deposition By Aortic Smooth Muscle Cells SB^{3}C2019-P139

Eoghan Cunnane[1], Aneesh Ramaswamy[1], David Vorp[1], Justin Weinbaum[1], *[1]University of Pittsburgh, United States*

Posters - Cell & Tissue Engineering: Mechanobiology - a symposium in memory of Christopher R. Jacobs

Tissue-Engineered Intra-Arterial Barrier For Mechanobiology Studies SB^{3}C2019-P140

Sara Ben Saadon[1], David Elad[1], *[1]Tel Aviv University, Israel*

The Role of Prestress In Calcification of Human Coronary Artery Smooth Muscle Cells In Vitro SB^{3}C2019-P141

Amirala Bakhshian Nik[1], Daniela Medina[1], Manuel Garcia Russo[1], Walter Heatherly[1], Joshua Daniel Hutcheson[1], *[1]Florida International University, United States*

Regulation of Nuclear Architecture, Mechanics and Nucleo-Cytoplasmic Shuttling of Epigenetic Factors By Cell Geometric Constraints SB^{3}C2019-P142

Farid Alisafaei[1], Doorgesh Sharma Jokhun[2], GV Shivashankar[2], Vivek Shenoy[1], [1]*University of Pennsylvania, United States,* [2]*National University of Singapore, Singapore*

Computational Models of Endothelial Cell Biochemical Responses To Shear Stress SB^{3}C2019-P143

Jonathan Garcia[1], Alisa Morss Clyne[1], [1]*Drexel University, United States*

Perlecan Deficiency Impairs The Intracellular Calcium Signaling In Mechanically Loaded Bone and Osteocytes SB^{3}C2019-P144

Shaopeng Pei[1], Sucharitha Parthasarathy[1], Ashutosh Parajuli[1], Jerahme Martinez[1], Mengxi Lv[1], Sida Jiang[1], Danielle Wu[2], Shuo Wei[1], X. Lucas Lu[1], Mary C. Farach-Carson[2], Catherine B. Kirn-Safran[1], Liyun Wang[1], [1]*University of Delaware, United States,* [2]*University of Texas Health Center, United States*

A Modified Bioreactor Configuration To Study Effects of Low Intensity Pulsed Ultrasound Treatment SB^{3}C2019-P145

Abdolrasol Rahimi[1], Zach Pittz[1], Nicholas Weaver[1], Natasha Case[1], [1]*Saint Louis University, United States*

Design and Computational Modeling of An Ultrasound Bioreactor For Stimulation of Cell-Seeded Scaffolds SB^{3}C2019-P146

Jacob Crapps[1], Abdolrasol Rahimi[1], Natasha Case[1], [1]*Saint Louis University, United States*

Pulsatile Electromagnetic Fields Regulate Bone Integrity Through Activation of Voltage Sensitive Calcium Channels SB^{3}C2019-P147

Abigail Dela Paz[1], Case Gregory[1], Randall Duncan[1], Mark Mirotznik[1], [1]*University of Delaware, United States*

Posters - Cell & Tissue Engineering: Other

Creating The Storkel: A Water Occluding Device For Accidental Submersion With A Tracheostoma SB^{3}C2019-P148

Claire M. Chaisson[1], Samantha K. Denning[1], Kelli E. Grimes[1], William J. Pelowski[1], Michael A. Valleau[1], Byron D. Erath[1], [1]*Clarkson University, United States*

Dynamic Tracking of Fluorescently Labeled Type I Collagen Molecules; Direct Quantification of Molecular Association With Native Fibrils SB^{3}C2019-P149

Seyed Mohammad Siadat[1], Jeffrey Ruberti[1], [1]*Northeastern University, United States*

Mechanical Advances In Cardiopulmonary Resuscitation SB^{3}C2019-P150

Jeffrey Stransky[1], Morgan Dean[1], Thomas Merrill[1], Jennifer Kadlowec[1], [1]*Rowan University, United States*

2.2 Poster Session II	Thursday, June 27 12:45PM - 2:15PM

Posters - Biotransport

Thermal Analysis of Partial Vitrification With Application To Large-Size Cryopreservation SB^{3}C2019-P151

Purva Joshi[1], Yoed Rabin[1], [1]*Carnegie Mellon University, United States*

Point-of-Care Diagnosis of Respiratory Syncytial Virus By Digital Nanobubble Detection SB^{3}C2019-P152

Yaning Liu[1], Varsha Godakhindi[1], Ruth Levitz[2], Jeffrey Kahn[2], Zhenpeng Qin[1], [1]*University of Texas at Dallas, United States,* [2]*University of Texas Southwestern Medical Center, United States*

Safe Duration of A Person Soaking Inside A Hot Tub: Theoretical Prediction of Temperature Elevations In Human Bodies Using A Whole Body Heat Transfer Model SB^{3}C2019-P153

Myo Min Zaw[1], Manpreet Singh[1], Ronghui Ma[1], Liang Zhu[1], [1]*University of Maryland Baltimore County, United States*

Creating A Distinct Capture Zone In Microfluidic Flow Greatly Enhances The Throughput and Efficiency of Cancer Detection SB^{3}C2019-P154

Jiangsheng Xu[1], Xiaoming He[1], [1]*University of Maryland, United States*

Fundamental Aspects of Paper-Based Microchip Electrophoresis Ph Gradient SB^{3}C2019-P155

Muhammad Noman Hasan[1], Ran An[1], Asya Akkus[1], Derya Akkaynak[2], Adrienne Minerick[3], Umut Gurkan[1], [1]*Case Western Reserve University, United States,* [2]*Princeton University, United States,* [3]*Michigan Technological University, United States*

Robustness of Convolutional Neural Networks For Malaria Parasite Identification In Thin Blood Smear Images With Adversarial Image Noise SB^{3}C2019-P156

Bill Sun[1], Liang Liang[2], [1]*Walton High School, United States,* [2]*Department of Computer Science at University of Miami, United States*

Towards Patient Specific Vascular Navigation of Therapeutics SB^{3}C2019-P157

Luke Puller[1], Matthew Charles[1], Darien Perez[1], Scott Anderson[1], Anilchandra Attaluri[1], [1]*The Pennsylvania State University - Harrisburg, United States*

Theoretical Evaluation of Temperature Elevation, Thermal Damage, Tumor Porosity Enhancement, and Magnetic Nanoparticle Migration In Tumors During Local Heating SB^{3}C2019-P158

Manpreet Singh[1], Ronghui Ma[1], Liang Zhu[1], [1]*University of Maryland Baltimore County, United States*

Aloe Alginate Hydrogels For Cervical Cancer Treatment: Antioxidant and Drug Release Activity SB^{3}C2019-P159

Sierra McConnell[1], Patrick Charron[1], Rachael Oldinski[1], [1]*University of Vermont, United States*

Modelling Lymph Propulsion In A Series of Pumping Lymphangions SB^{3}C2019-P160

Ghazal Adeli Koudehi[1], Matthias Van Impe[1], Carlos Alejandro Silvera Delgado[1], Charlotte Debbaut[1], Christophe Casteleyn[1], Pieter Cornillie[1], Patrick Segers[1], [1]*Ghent University, Belgium*

A 2d Axisymmetric Computational Model For The Study of Mass Transport Into Lymphatic Capillaries and Pre-Collector Vessels SB^{3}C2019-P161

Carlos Alejandro Silvera Delgado[1], Ghazal Adeli Koudehi[1], Matthias Van Impe[1], Charlotte Debbaut[1], Patrick Segers[1], [1]*Ghent University, Belgium*

Microfluidic Assessment of Red Blood Cell Deformability and Microvascular Occlusion Risk In Malaria and Sickle Cell Disease SB^{3}C2019-P162

Yuncheng Man[1], Erdem Kucukal[1], Quentin Watson[1], Jurgen Bosch[1], Jane Little[1], Peter Zimmerman[1], Umut Gurkan[1], [1]*Case Western Reserve University, United States*

Microfluidic Assessment of Red Blood Cell Detachment In Simulated Microvascular Flow SB^{3}C2019-P163

Utku Goreke[1], Shamreen Iram[1], Gundeep Singh[1], Jane A Little[1], Michael Hinczewski[1], Umut A Gurkan[1], *[1]Case Western Reserve University, United States*

Effects of Leaky Tumor Vasculature On Tissue Stress and Porosity In A Biphasic Model of Brain Glioma SB^{3}C2019-P164

Julian Rey[1], Malisa Sarntinoranont[1], James Ewing[2], *[1]Mechanical and Aerospace Engineering, University of Florida, Gainesville, FL, United States, [2]Henry Ford Health System, Detroit, Michigan, United States*

Modelling Advection-Based Nanoparticle Drug Delivery To The Left Ventricle Using A Splitting Method For Advection-Diffusion Kinetics SB^{3}C2019-P165

Alexandra Diem[1], Kristian Valen-Sendstad[1], *[1]Simula Research Laboratory, Norway*

Posters - Design Dynamics & Rehabilitation

Comparison of Principal Component Analysis and Non-Negative Matrix Factorization In Prediction of Unmeasured Muscle Excitations SB^{3}C2019-P166

Di Ao[1], Mohammad Shourijeh[1], Carolynn Patten[2], Benjamin Fregly[1], *[1]Rice University, United States, [2]UC Davis, United States*

Variance In Swimmer Symmetry Due To Effort and Fatigue SB^{3}C2019-P167

Casey Main[1], Craig Goehler[1], *[1]Valparaiso University, United States*

Joint Stiffness Modulation of Gait Variability In A Stroke SB^{3}C2019-P168

Geng Li[1], Di Ao[1], Mohammad Shourijeh[1], Marleny Arones[1], Carolynn Patten[2], Benjamin Fregly[1], *[1]Rice University, United States, [2]UC Davis, United States*

Analytical Calculation of Musculoskeletal Joint Stiffness SB^{3}C2019-P169

Mohammad S. Shourijeh[1], Di Ao[1], Carolynn Patten[2], Benjamin J. Fregly[1], *[1]Rice University, United States, [2]UCDavis, United States*

Identifying Postural Instability Using Topological Data Analysis SB^{3}C2019-P170

Kyle Siegrist[1], James Chagdes[1], Amit Shukla[1], Ryan Kramer[2], Michael Cinelli[3], *[1]Miami University, United States, [2]Air Force Research Laboratory, United States, [3]Wilfrid Laurier University, Canada*

A Novel Strategy For Concurrent Reduction of Fluid Reduction of Fluid Drag and Protein Adsorption For Cardiovascular Medical Devices. SB^{3}C2019-P171

Cheng Yi-Chih[1], Yap Choon Hwai[1], *[1]National University of Singapore, Taiwan*

Integrated Switchable Ventricular Assist Device For Pediatric Patients SB^{3}C2019-P172

Harut Sarkisyan[1], Randy Stevens[2], Amy Throckmorton[1], *[1]Biomedical Engineering, Drexel University, United States, [2]St. Christopher's Hospital for Children, United States*

Experimental Modeling of Coronary Intervention: Towards Computational Simulation SB^{3}C2019-P173

Maxwell Bean[1], David Jiang[2], Sam Stephens[1], Megan Laughlin[1], Hanna Jensen[1], Barry Uretsky[3], Lucas Timmins[2], Morten Jensen[1], *[1]University of Arkansas, United States, [2]University of Utah, United States, [3]University of Arkansas for Medical Sciences, United States*

Agonist / Antagonist Control Combining Mixed Sensitivity Design and Iterative Learning SB^{3}C2019-P174

Patrick Schimoler[1], Jeffrey Vipperman[2], Mark Carl Miller[1],*[1]Allegheny General Hospital, United States, [2]University of Pittsburgh, United States*

Analysis of A Poly(ethylene Glycol) Diacrylate (PEGDA) Optical Sensor-Based Whispering Gallery Mode Shift Subjected To Shock Wave Impact SB^{3}C2019-P175

Ling Zhang[1], Maurizio Manzo[2], Sarah Bentil[1], *[1]Iowa State University, United States, [2]University of North Texas, United States*

Exercise Therapy Affects Glenohumeral Joint Stability In Patients With Isolated Supraspinatus Tears SB^{3}C2019-P176

Luke Mattar[1], Camille Johnson[1], Tom Gale[1], Adam Popchak[1], James Irrgang[1], William Anderst[1], Volker Musahl[1], Richard Debski[1], *[1]University of Pittsburgh, United States*

Biceps Voluntary Activation: Method To Calculate Pre-Stimulus Moment Affects Magnitude But Not Reproducibility SB^{3}C2019-P177

Thibault Roumengous[1], Paul Howell[1], Carrie Peterson[1], *[1]Virginia Commonwealth University, United States*

Posters - Education

Effectiveness of An Extensively Active and Authentic Learning Environment In An Undergraduate Biomedical Engineering Module A Case Study In A South-East Asian Cohort SB^{3}C2019-P178

Vivek Vasudevan[1], Alberto Corrias[1], Martin Buist[1], Hwa-Liang Leo[1], Choon-Hwai Yap[1], *[1]National University of Singapore, Singapore*

Injury Prevention Via Computer Modeling of Stud Traction SB^{3}C2019-P179

Justin Rittenhouse[1], Peter Gustafson[1], *[1]Western Michigan University, United States*

An Ecg Analysis Determining The Impact of Mother'S Metabolic Equivalent Value In Pregnancy On Infant Heart Rate Variability SB^{3}C2019-P180

Alexandra Williams[1], Colby Jolly[1], Christy Isler[1], Kelley Haven[1], Edward Newton[1], Linda May[1], Stephanie George[1], *[1]Ecu, United States*

For Your Information: Student Evaluations of Teaching Are Biased Against Women and Faculty of Color SB^{3}C2019-P181

Naomi Chesler[1], Dante Fratta[2], Elizabeth Harris[1], Wayne Pferdehirt[1], Heidi Ploeg[3], Barry Vanveen[1], *[1]University of Wisconsin - Madison, United States, [2]University of Wisconsin-Madison, United States, [3]Queens University, Canada*

Incorporating National Biomechanics Day Into Biomechanical Engineering Courses SB^{3}C2019-P182

Sara Wilson[1], *[1]University of Kansas, United States*

Posters - Fluids: Cardiovascular Fluid Mechanics

Developing The Components of A Multiscale Computational Platform In The Design of A Geometrically Tunable Blood Shunt For Norwood Recipients SB^{3}C2019-P183

Ellen Garven[1], Kara Spiller[1], Randy Stevens[2], Amy Throckmorton[1], *[1]Drexel University, United States, [2]St. Christopher's Hospital for Children, United States*

Quantifying Hemodynamics In Hypoplastic Left Heart Syndrome SB^{3}C2019-P184

Banafsheh Zebhi[1], Hadi Wiputra[2], Lisa Howley[3], Bettina Cuneo[3], Dawn Park[3], Hilary Hoffman[3], Lisa Gilbert[3], Choon Hwai Yap[2], David Bark Jr[1], *[1]Colorado State University, United States, [2]National University of Singapore, Singapore, [3]Children's Hospital Colorado, United States*

On The Quantification of Hemodynamics In The Ascending Aorta To Predict Pathogenesis In Bicuspid Aortic Valve Disease SB^{3}C2019-P185

Tejas Canchi[1], Sargon A Gabriel[1], Mustafa Gok[1], David F Fletcher[2], Stuart Michael Grieve[1], *[1]The Heart Research Institute, Australia, [2]The University of Sydney, Australia*

Multiple Mitraclips: The Balancing Act Between Pressure Gradient and Regurgitation SB^{3}C2019-P186

Shelley Gooden[1], Hoda Hatoum[1], Konstantinos Boudoulas[1], Lakshmi Prasad Dasi[1], *[1]The Ohio State University, United States*

Basilica-Type Leaflet Laceration To Reduce Risk of Thrombosis In Transcatheter Aortic Valve Replacement SB^{3}C2019-P187

Hoda Hatoum[1], Pablo Maureira[2], Scott Lilly[1], Lakshmi Prasad Dasi[1], *[1]The Ohio State University, United States, [2]Centre Hospitalier Universitaire de Nancy, France*

Early Diagnosis of Reduced Leaflet Mobility After Transcatheter Aortic Valve Replacement SB^{3}C2019-P188

Hoda Hatoum[1], Jung-Hee Seo[2], Shantanu Bailoor[2], Scott Lilly[1], Rajat Mittal[2], Lakshmi Prasad Dasi[1], *[1]The Ohio State University, United States, [2]Johns Hopkins University, United States*

Hemodynamics, In Addition To Morphology, Predicts Long-Term Outcome of Intracranial Aneurysms Treated With Flow Diverters SB^{3}C2019-P189

Nikhil Paliwal[1], Jason Davies[1], Adnan Siddiqui[1], Hui Meng[1], *[1]University at Buffalo, United States*

Correlation of Computational Instantaneous Wave-Free Ratio With Fractional Flow Reserve In The Case of Multiple Intermediate Coronary Artery Stenosis In A Left Main Bifurcation SB^{3}C2019-P190

Arash GhorbanniaHassankiadeh[1], David S. Marks[2], John F. LaDisa, Jr.[1], *[1]Marquette University and Medical College of Wisconsin, United States, [2]Medical College of Wisconsin, United States*

The Effects of Oscillatory Shear Regulation On Paracrine Signaling Between Vascular Endothelial Cells and Vascular Smooth Muscle Cells SB^{3}C2019-P191

Chia-Pei Hsu[1], Alexandra Tchir[1], Joshua Hutcheson[1], Sharan Ramaswamy[1], *[1]Florida International University, United States*

Non-Linear Cd31 Expression In Vascular Endothelial Cells In Response To Increasing Oscillatory Flow Conditions SB^{3}C2019-P192

Alexandra Tchir[1], Chia-Pei Hsu[1], Sharan Ramaswamy[1], *[1]Florida International University, United States*

Intra-Valvular Pressure Dynamics and Valve Specific Pressure Recovery In Transcatheter Aortic Valve Replacement: Implication On Validity of Echo Derived Gradient SB^{3}C2019-P193

Hoda Hatoum[1], Maurice Alston[1], David Orsinelli[1], Gregory Rushing[1], Susan O'Neil[1], Nancy Matre[1], Konstantinos Boudoulas[1], Scott Lilly[1], Lakshmi Prasad Dasi[1], *[1]The Ohio State University, United States*

Design of A Cost-Effective Cardiac Flow Loop For Testing Tavr Placement In Patient-Specific Anatomy SB^{3}C2019-P194

Christine Buffinton[1], Benjamin Conser[1], M. Laura Beninati[1], Shikhar Agarwal[2], *[1]Bucknell University, United States, [2]Geisinger Medical Center, United States*

Effect of Leaflet Opening Geometry On Turbulent Characteristics For Prosthetic Aortic Valve Applications SB^{3}C2019-P195

Megan Heitkemper[1], Hoda Hatoum[1], Jun Kim[1], Lakshmi Prasad Dasi[1], *[1]The Ohio State University, United States*

In Vitro Forward Flow Performance of The Konect Resilia Aortic Valved Conduit SB^{3}C2019-P196

Vahid Sadri[1], Immanuel David Madukauwa-David[1], Ajit Yoganathan[1], *[1]Georgia Institute of Technology, United States*

Posters - Fluids: Respiratory and Other Fluid Mechanics

Autonomous Pumping In A Physical Model of A Multi-Lymphangion System SB^{3}C2019-P197

John Montani[1], Luke Riexinger[1], Lance Munn[2], James Baish[1], *[1]Bucknell University, United States, [2]Harvard Medical School, United States*

Culture of Lymphatic Endothelial Cells In A Custom Bioreactor For Studies Combining Stretching and Fluid Shear Stress SB^{3}C2019-P198

Caleb Davis[1], Walter Cromer[2], David Zawieja[2], Michael Moreno[1], *[1]Texas A&M University, United States, [2]Texas A&M Health Science Center, United States*

In Vitro Anthropomorphic Model of The Cerebrospinal Fluid System: Application To Subarachnoid Hemorrhage Filtration SB^{3}C2019-P199

Lucas Sass[1], Mohammadreza Khani[1], Gabryel Conley Natividad[1], Elliott Marsden[1], Shavaine Byass[1], Omolola Bangudu[1], Aaron McCabe[2], Laura Zitella Verbick[2], Shivanand Lad[3], Bryn Martin[1], *[1]University of Idaho, United States, [2]Minnetronix Neuro, Inc., United States, [3]Duke University, United States*

Impact of Cerebrospinal Fluid Filtration On Subarachnoid Hemorrhage Clearance: A Computational Fluid Dynamics Study SB^{3}C2019-P200

Mohammadreza Khani[1], Lucas Sass[1], M. Keith Sharp[2], Aaron McCabe[3], Laura Zitella Verbick[3], Shivanand Lad[4], Bryn Martin[1], *[1]University of Idaho, United States, [2]University of Louisville, United States, [3]Minnetronix Neuro, Inc., United States, [4]Duke University School of Medicine, United States*

Towards Physiologically-Relevant Vocal Fold Models For Voiced-Speech Investigations SB^{3}C2019-P201

Mohsen Motie-Shirazi[1], Natalie Jagelski[2], Byron Erath[1], *[1]Clarkson University, United States, [2]Clarkson Univeristy, United States*

Computational Methodology To Estimate Resistance To Cerebrospinal Fluid Motion In The Spinal Canal For Chiari Patients With Specific and Nonspecific Symptoms SB^{3}C2019-P202

Alaaddin Ibrahimy[1], Rafeeque Bhadelia[2], Abraham Bezuidenhout[2], Francis Loth[1], *[1]The University of Akron, United States, [2]Beth Israel Deaconess Medical Center, United States*

Multiphase Fluid Dynamics of Shear-Thinning Droplets In A Microfluidic Flow-Focusing Device SB^{3}C2019-P203

Ali Bozorgnezhad[1], Jason Gleghorn[1], *[1]University of Delaware, United States*

Posters - Solid Mechanics: Injury

Fracture Patterns In Concentrated 4-Point Bending of The Ovine Femora: The Effects of Age and Rate of Loading SB^{3}C2019-P204

Patrick Vaughan[1], Feng Wei[1], Roger Haut[1], *[1]Michigan State University, United States*

The Importance of Skull Morphology In Remote Blunt Impact Induced Fracture Initiation SB^{3}C2019-P205

Paul Snyder[1], Steven Rundell[2], Todd Fenton[1], Roger Haut[1], Feng Wei[1], *[1]Michigan State University, United States, [2]Explico Engineering Company, United States*

Subject-Specific Madymo Analysis of A Low Speed Rear-End Collision SB^{3}C2019-P206

David Sproule[1], Stephanie Rossman[1], Paul Snyder[1], Keith Button[1], Brian Weaver[1], Steve Rundell[1], *[1]Explico Engineering, United States*

Development of A Portable Suction Device For Combat Medics SB^{3}C2019-P207

Forhad Akhter[1], Austin Schoppe[1], Omar Navarro[1], Christopher Carroll[1], Priya Jain[1], Ricardo Pescador[1], Robert De Lorenzo[2], Bruce D. Adams[2], Yusheng Feng[1], R. Lyle Hood[1], *[1]University of Texas at San Antonio, United States, [2]University of Texas Health Science Center at San Antonio, United States*

Finite Element Model of Neonatal Brachial Plexus and Spinal Cord SB^{3}C2019-P208

Anita Singh[1], Christian D'Andrea[2], Sriram Balasubramanian[2], *[1]Widener Univ, United States, [2]Drexel Univ, United States*

Development of Visual Analysis Tracking Method For Use In Conjunction With Novel Animal Model of Mtbi SB^{3}C2019-P209

Allison Gleason[1], Lisa Pruitt[1], Daniela Kaufer[1], Ellen Parker[2], *[1]University of California - Berkeley, United States, [2]Dalhousie University, Canada*

Biomechanical Response of The Mandible To Blunt Impact and Corresponding Biofidelity of The Focus Headform SB^{3}C2019-P210

Charles Weisenbach[1], Jodie Gomez[1], Andrea Dargie[1], Ray Daniel[1], Valeta Chancey[2], Frederick Brozoski[1], *[1]U.S. Army Aeromedical Research Laboratory, United States, [2]U.S. Army Aeromedical Research Laborary, United States*

Converting The Worcester Head Injury Model From Abaqus To Ls-Dyna SB^{3}C2019-P211

Kianoosh Ghazi[1], Wei Zhao[1], Songbai Ji[1], *[1]Worcester Polytechnic Institute, United States*

Quasi-Linear Viscoelastic Fitting of Thoracic Tissues and Ballistics Gel For Modeling Behind Armor Blunt Trauma SB^{3}C2019-P212

Madelyn Eaton[1], Robert Salzar[1], *[1]University of Virginia, United States*

Inhibiting Spinal Phospholipase A2 Prevents Pain and Modifies Spinal Neuron Activity & Glutamate Signaling Early After Nerve Root Compression SB^{3}C2019-P213

Julia Quindlen-Hotek[1], Sonia Kartha[1], Prabesh Ghimire[1], Beth Winkelstein[1], *[1]University of Pennsylvania, United States*

Viscoelastic Response of Shock Wave Impacted Brain Tissue SB^{3}C2019-P214

Annastacia McCarty[1], Ling Zhang[1], Sarah Hansen[1], William Jackson[1], Sarah Bentil[1], *[1]Iowa State University, United States*

Effects of Excessive Impact On Bone Conduction In Contact Sports SB^{3}C2019-P215

Shinji Hamanishi[1], Namkeun Kim[2], Seongho Mo[2], Takashi Watanabe[1], Yoshihiro Aoki[1], *[1]Sendai National College of Technology, Japan, [2]Incheon National University, South Korea*

Properties of The Six Layers of The Gray Matter SB^{3}C2019-P216

Arpad Bakonyi[1], Alan Faitelewicz[2], Siavash Hashemi[2], Ali Sadegh[2], *[1]University of Applied Sciences Technikum Vienna, Austria, [2]The City College of the City Univ. of New York, United States*

Helmeted Head-Neck Kinematics With Localized Impacts and Implications For Brain Injury Metrics SB^{3}C2019-P217

Narayan Yoganandan[1], John Humm[1], Mark Meyer[1], Frank Pintar[1], Tyler Rooks[2], Frederick Brozoski[2], Joseph McEntire[2], Valeta Chancey[2], *[1]Medical College of Wisconsin, United States, [2]Usaarl, United States*

Investigate The Variations of The Head Impact Response In A Rodent Head Impact Acceleration Model By Finite Element Modeling SB^{3}C2019-P218

Runzhou Zhou[1], Liying Zhang[1], *[1]Wayne State University, United States*

Injury Risk Curves Using A Novel (bayesian) Techinque To Describe Human Tolerance In Impact Biomechanics SB^{3}C2019-P219

Nicholas DeVogel[1], Anjishnu Banerjee[1], Narayan Yoganandan[1], *[1]Medical College of Wisconsin, United States*

Designing An Impact Pendulum To Test Different Concussion Prevention Helmet Acessories SB^{3}C2019-P220

Farryl Groder[1], Efe Ozkaya[1], Luca Conetta[2], Mehmet Kurt[1], *[1]Stevens Institute of Technology, United States, [2]The Packer Collegiate Institute, United States*

Head Impact Characterization In Men'S and Women'S Collegiate Rugby SB^{3}C2019-P221

Emily Kieffer[1], Grace Pierce[1], Chase Vaillancourt[1], Steven Rowson[1], *[1]Virginia Tech, United States*

History Dependent Damage Modelling For Axonal Fiber Tracts of The Brain SB^{3}C2019-P222

Ritika Menghani[1], Ouniol Aklilu[1], Reuben Kraft[1], *[1]The Pennsylvania State University, United States*

Chestband-Based Injury Metrics In Far-Side Impacts SB^{3}C2019-P223

Yuvaraj Purushothaman[1], John Humm[2], Hans Hauschild[2], Klaus Driesslein[2], Frank Pintar[2], Narayan Yoganandan[2], *[1]Medical College Of Wisconsin, United States, [2]Medical College of Wisconsin, United States*

Application of Six-Year-Old Child Human Body Finite Element Models With Accurate Anatomical Characteristics For Understanding The Injury Mechanisms SB^{3}C2019-P224

Haiyan Li[1], Yongqiang Huang[1], Wenle Lv[1], Shihai Cui[1], Lijuan He[1], Shijie Ruan[1], Chunxiang Wang[2], *[1]International Joint Research Centre of modern automobile safety technology, Tianjin University of Science and Technology, China, [2]Tianjin Children Hospital, China*

Effect of Microstructural Variation In The Biomechanics of Oligodendrocyte-Neuron Co-Cultures SB^{3}C2019-P225

Zeynep M. Suar[1], Mateusz Urbanski[2], Gloria Fabris[1], Carmen V. Melendez-Vasquez[2], Mehmet Kurt[1], *[1]Stevens Institute of Technology, United States, [2]Hunter College, United States*

An Atlas-Based Finite Element Model of Mouse Brain For Controlled Cortical Impact SB^{3}C2019-P226

Changxin Lai[1], Suhao Qiu[1], Yuan Feng[1], *[1]Shanghai Jiao Tong University, China*

Biomechanical Characterization of Ovine Pia Arachnoid Complex SB^{3}C2019-P227

Gabryel Conley Natividad[1], Sophia Theodossiou[1], Nathan Schiele[1], Gordon Murdoch[2], Goutham Burla[1], Gabriel Potirniche[3], Bryn Martin[1], *[1]University of Idaho, Department of Biological Engineering, United States, [2]University of Idaho, Department of Animal and Veterinary Science, United States, [3]Univerisyt of Idaho, Department of Mechanical Engineering, United States*

Posters - Solid Mechanics: Joint and Spine Mechanics

Template Models For Surface Manipulation of Musculoskeletal Extremity Regions SB^{3}C2019-P228

Sean Doherty[1], Ben Landis[1], Tammy Owings[1], Ahmet Erdemir[1], *[1]Cleveland Clinic, United States*

A Parametric Study of Transcondylar Screw Effectiveness To Enhance Healing of Subchondral Bone Cysts of Varied Sizes SB^{3}C2019-P229

Lance Frazer[1], Elizabeth Santschi[2], Kenneth Fischer[1], *[1]University of Kansas, United States, [2]Kansas State University, United States*

Reducing Kinematic Data Uncertainty During Mechanical Testing of Orthopaedic Implants: The Benefits and Pitfalls of Auxiliary Motion Capture Systems SB^{3}C2019-P230

Callan Gillespie[1], Quinn Saluan[1], Tara Nagle[1], Joe Little[2], Willy Theodore[2], Robb Colbrunn[1], *[1]Cleveland Clinic, United States, [2]360 Knee Systems, United States*

Effect of Pelvis and Limb Position On Radiographic Leg Length Discrepancy Measurement: A Sawbones Model SB^{3}C2019-P231

Isaac Livshetz[1], Awais Hussain[1], Matthew Robinson[1], Farid Amirouche[1], Mark Gonzalez[1], *[1]University of Illinois College of Medicine at Chicago, United States*

Clinical Representation of Joint Coordinate System Forces SB^{3}C2019-P232

Callan Gillespie[1], Tara Nagle[1], Robb Colbrunn[1], *[1]Cleveland Clinic, United States*

Biomechanics of Three-Level Cervical Fusion Comparing A Stand-Alone Cage Construct To Anterior Plate and Cages Construct - A Cadaveric Study SB^{3}C2019-P233

Robert McGuire[1], Abeer Al-Barghouthi[2], Loren Latta[3], Francesco Travascio[3], *[1]University of Mississippi, United States, [2]Max Biedermann Institute for Biomechanics, Mount Sinai Medical Center, United States, [3]University of Miami, United States*

A Posture Controlling Test Device To Dynamically Load Lumbar Spinal Columns SB^{3}C2019-P234

John Humm[1], Narayan Yoganandan[2], *[1]Medical College of Wisconsin and Marquette University, United States, [2]Medical College of Wisconsin, United States*

3d Surface Kinematics of The Lumbar Facet Capsular Ligament During Inflation Testing SB^{3}C2019-P235

Elizabeth Gacek[1], Emily Bermel[1], Arin Ellingson[1], Victor Barocas[1], *[1]University of Minnesota Twin-Cities, United States*

Dorsal Subluxation of The First Metacarpal At The Basilar Thumb Joint During Key Pinch: Comparison To Osteoarthritis Grading Systems SB^{3}C2019-P236

Nolan Norton[1], Brandon Barnds[2], Terence McIff[2], E. Bruce Toby[2], Kenneth Fischer[1], [1]*University of Kansas, United States,* [2]*University of Kansas Medical Center, United States*

Wheelchair Seat Position and Footprint Length Effects On Shoulder and Elbow Angles On Graded Surfaces SB^{3}C2019-P237

Amogha Vijayvargiya[1], Sarah Bass[2], Hailee Kulich[2], Alicia Koontz[2], [1]*University of Pittsburgh, United States,* [2]*Human Engineering Research Laboratories, United States*

Posters - Solid Mechanics: Musculoskeletal Soft Tissue Mechanics

An Alternative Method To Characterize Poroelastic Material Properties of Murine Articular Cartilage SB^{3}C2019-P238

Alexander Kotelsky[1], Joseph Carrier[1], Mark Buckley[1], [1]*University of Rochester, United States*

Comparison of The Effects of Boundary Lubricants On The Tribological Rehydration of Articular Cartilage SB^{3}C2019-P239

Margot Farnham[1], David Burris[1], Christopher Price[1], [1]*University of Delaware, United States*

Effect of Counterface Surface Roughness On Tribological Rehydration of Articular Cartilage SB^{3}C2019-P240

Meghan Kupratis[1], Margot Farnham[1], David Burris[1], Christopher Price[1], [1]*University of Delaware, United States*

Maintaining Cartilage Hydration During Sliding Part 1: The Effect of Migration Length SB^{3}C2019-P241

Jamie Benson[1], Caroline Kook[1], Axel Moore[2], Steven Voinier[1], Christopher Price[1], David Burris[1], [1]*University of Delaware, United States,* [2]*Imperial College London, United Kingdom*

Improved Methods For Mechanically Testing Foot and Ankle Ligaments: Preparation, Length Estimation, Environmental Maintenance, and Semi-Automation SB^{3}C2019-P242

Alexander Berardo-Cates[1], Christopher Prasanna[2], Levi Davis[1], Mathew Kindig[2], William Ledoux[3], Joseph Iaquinto[1], [1]*Center for Limb Loss and MoBility, University of Washington, United States,* [2]*Center for Limb Loss and MoBility, United States,* [3]*Center for Limb Loss and MoBility, University of Washington, Department of Orthospedics and Sports Medicine, United States*

Testing Medial Ulnar Collateral Ligament Fatigue Failure SB^{3}C2019-P243

David Jordan[1], Alexander Kharlamov[2], Patrick Schimoler[3], Patrick DeMeo[2], Mark Carl Miller[3], [1]*University of Pittsburgh, United States,* [2]*Allegheny General Hospital, United States,* [3]*Allegheny General Hospital and University of Pittsburgh, United States*

Experimental Measurement of Embryonic Tendon Multiscale Mechanics SB^{3}C2019-P244

Benjamin Peterson[1], Spencer Szczesny[1], [1]*Pennsylvania State University, United States*

Femoral Tunnel Location Affects Acl Excursion During Knee Flexion SB^{3}C2019-P245

Patrick Schimoler[1], J. Jared Guth[1], Alexander Kharlamov[1], J. Daniel Thompson[1], Sam Akhavan[1], Mark Carl Miller[1], [1]*Allegheny General Hospital, United States*

Utilization of Multi-Foci Arfi Imaging To Generate Larger Tendon Displacement SB^{3}C2019-P246

Gerald A Ferrer[1], Waqas Khalid[1], Volker Musahl[1], Kang Kim[1], Richard E Debski[1], [1]*University of Pittsburgh, United States*

Using Optical Tracking To Calculate Non-Recoverable Strain In The Glenohumeral Capsule SB^{3}C2019-P247

Jocelyn Hawk[1], Calvin Chan[1], Robert Tisherman[1], Richard Debski[1], [1]*Orthopaedic Robotics Laboratory, United States*

3d Strain Components and Their Viscoelastic Behavior For Knee Meniscus Tissue In Circumferential Tension Under Stress Relaxation and Creep SB^{3}C2019-P248

John Peloquin[1], Michael Santare[1], Dawn Elliott[1], [1]*University of Delaware, United States*

Intramuscular Pressure and Shear Modulus of Lower Leg Muscles Are Correlated SB^{3}C2019-P249

Seyedali Sadeghi[1], Dov Bader[2], Daniel Cortes[1], *[1]Penn State University, United States, [2]Penn State College of Medicine, United States*

Development of Displacement-Controlled Multiaxial Stretching Device For Characterising Viscoelastic Properties of Female Pelvic Floor Tissue SB^{3}C2019-P250

Katie Harte[1], Gary Menary[1], Alex Lennon[1], *[1]Queen's University Belfast, United Kingdom*

Body Position Effects On Thigh Soft Tissue Properties SB^{3}C2019-P251

Justin Scott[1], Sheng Chen[1], Sara Roccabianca[1], Tamara Reid Bush[1], *[1]Michigan State University, United States*

Python-Inspired Grasping Teeth For Tendon To Bone Repair SB^{3}C2019-P252

Iden Kurtaliaj[1], Ethan Hoppe[2], Dong Hwan Yoon[2], Lester Smith[3], Victor Birman[4], Guy Genin[2], Stavros Thomopoulos[1], *[1]Columbia University, United States, [2]Washington University, United States, [3]Indiana University, United States, [4]Missouri Science & Technology, United States*

Optimizing Non-Linear Mechanical Behavior of Soft Tissues In Finite Element Model of Human Thigh SB^{3}C2019-P253

Eli Broemer[1], Sheng Chen[1], Justin Scott[1], Tamara Bush[1], Sara Roccabianca[1], *[1]Michigan State University, Mechanical Engineering, United States*

Design of A Novel Biaxial Mechanical Testing System and Protocols For Analysis of Biological Tissues and Tissue-Engineered Constructs SB^{3}C2019-P254

Mingliang Jiang[1], Michael Moreno[1], *[1]Texas A&M University, United States*

Dissimilar Linear Friction Welding (lfw) Technology For Manufacturing of Functional Materials: Bi-Metallic Ti6al4v-Cocrmo Joint Implants SB^{3}C2019-P255

David Irwin[1], Christina Seydlorsky[1], Agraha Gautam[1], Aspen Glaspell[1], Kyosung Choo[1], Jae Joong Ryu[1], *[1]Youngstown State University, United States*

Posters - Solid Mechanics: Multiscale Mechanics, Reproductive, Ocular and Others

Automated Fiber Orientation Quantification In Three Dimensional Images SB^{3}C2019-P256

Jeremy Eekhoff[1], Spencer Lake[1], *[1]Washington University in St. Louis, United States*

The Effect of Composition and Hydration On The Mechanics of Carbonated Apatite SB^{3}C2019-P257

Brian Wingender[1], Masashi Azuma[1], Christina Krywka[2], Paul Zaslansky[3], John Boyle[4], Alix Deymier[1], *[1]UConn Health, United States, [2]Zentrum fr Material- und Kstenforschung GmbH, Germany, [3]Charit - Universittsmedizin Berlin, Germany, [4]Columbia University, United States*

Application of Micro-Raman Spectroscopy To Mechanical Characterization of Hydrogels SB^{3}C2019-P258

Hui Zhou[1], John M. Maloney[1], Alexander M. Knapp[1], Malisa Sarntinoranont[1], Chelsey S. Simmons[1], Ghatu Subhash[1], *[1]University of Florida, United States*

High Fidelity Modeling of 3d Euler Buckling and Stress Transmission Through Mother-Daughter Crosslink Captures Reversible Collapse In Compressing Dendritic Actin Mesh SB^{3}C2019-P259

Jyothirmai Simhadhri[1], Preethi Chandran[1], *[1]Howard University, United States*

Ultrashort Laser Fragmentation of Plasmonic Gold Nanoparticles: Coulomb Expolsoion Versus Photothermal Evaporation SB^{3}C2019-P260

Peiyuan Kang[1], Daipayan Sarkar[1], Zhenpeng Qin[1], *[1]The University of Texas at Dallas, United States*

In Vivo Estimation of Optic Nerve Sheath Stiffness Using Noninvasive Mri Measurements and Finite Element Modeling SB^{3}C2019-P261

Chanyoung Lee[1], Jesse Rohr[2], Austin Sass[2], Stuart Sater[2], Bryn Martin[2], Arslan Zahid[1], John Oshinski[1], C. Ross Ethier[1], *[1]Georgia Institute of Technology and Emory University, United States, [2]University of Idaho, United States*

Peripapillary Deformation and Its Relation To Material Properties of The Eye Globe SB^{3}C2019-P262

Jafar A. Mehr[1], Heather M. Moss[2], Hamed Hatami-Marbini[1], *[1]University of Illinois at Chicago, United States, [2]Stanford University, United States*

The Effects of Size and Location of Laser Peripheral Iridotomy On The Changes In Pressure Difference Across The Iris Following Dilation SB^{3}C2019-P263

Anup Pant[1], Rodolfo Repetto[2], Syril Dorairaj[3], Rouzbeh Amini[1], *[1]University of Akron, United States, [2]University of Genoa, Italy, [3]Mayo Clinic, United States*

In Vivo Measurements of Trabecular Meshwork Stiffness SB^{3}C2019-P264

Ross Ethier[1], Guorong Li[2], Chanyoung Lee[1], Ke Wang[1], Iris Navarro[2], Joseph Sherwood[3], Karen Crews[4], Sina Farsiu[2], Cheng-Wen Lin[4], Dan Stamer[2], *[1]Georgia Tech/Emory, United States, [2]Duke University, United States, [3]Imperial College London, United Kingdom, [4]Aerie Pharmaceutical, United States*

A Comparison of Two Continuum Modeling Approaches For Corneal Stroma Mechanical Response SB^{3}C2019-P265

Shuolun Wang[1], Hamed Hatami-Marbini[1], *[1]University of Illinois at Chicago, United States*

Microsturctural Changes At The Vitreoretinal Interface With Region and Age In Human Eyes SB^{3}C2019-P266

Christopher Creveling[1], Yousef Alsanea[1], Brittany Coats[2], *[1]The University of Utah, United States, [2]University of Utah, United States*

Development of A Finite Element Simulation To Estimate Corneal Elasticity SB^{3}C2019-P267

Usmaan Siddiqui[1], Nathan Gallant[2], *[1]University of South Florida, United States, [2]Univeristy of South Florida, United States*

Clot Contraction: Investigating The Impact On Clot Mechanical Behavior and Microstructure SB^{3}C2019-P268

Sarah Johnson[1], Juyu Chueh[2], Matthew Gounis[2], Michael Glivarry[3], Ray McCarthy[3], Patrick McGarry[1], Peter McHugh[1], *[1]National University Of Ireland Galway, Ireland, [2]University of Massachusetts Medical School, United States, [3]Cerenovus, Johnson & Johnson, Ireland*

Arterial Stiffness Compared Across Scales: From Cells To Extracellular Matrix To Vessels SB^{3}C2019-P269

Bart Spronck[1], Jay D. Humphrey[1], *[1]Department of Biomedical Engineering, Yale University, United States*

Review of Hyperelastic Modeling of Brain Tissue SB^{3}C2019-P270

Kristen Cirincione[1], Joshua Smith[1], *[1]Lafayette College, United States*

On The Viscoelasticity of Extra- and Intra-Parenchymal Bronchi SB^{3}C2019-P271

Samaneh Sattari[1], Mona Eskandari[1], *[1]University of California, Riverside, United States*

Does The Random Generation Algorithm Affect The Results of Numerical Models For Mechanical Response of Filamentous Networks? SB^{3}C2019-P272

Hamed Hatami-Marbini[1], *[1]University of Illinois at Chicago, United States*

Vascular Remodeling and Proteoglycan Accumulation In The Aorta of Progeria Mice Result In Fatal Cardiovascular Effects SB^{3}C2019-P273

Sae-Il Murtada[1], Yuki Kawamura[1], Alexander Caulk[1], Nicole Guerrera[2], Hossein Ahmadzadeh[1], Nathan Maulding[2], Kristin Zimmerman[2], Dar Weiss[1], Marcos Latorre[1], Dillon Kavanagh[2], Zhenwu Zhuang[2], Demetrios Braddock[2], Jay Humphrey[1], *[1]Yale University, United States, [2]Yale School of Medicine, United States*

Mechanical Effects of Fiber Interweaving SB^{3}C2019-P274

Bingrui Wang[1], Yi Hua[2], Fengting Ji[2], Ian A. Sigal[2], *[1]Southwest Jiaotong University, China, [2]University of Pittsburgh, United States*

A Connectome-Based Network Model To Simulate Prion-Like Protein Propagation In Neurodegenerative Diseases SB^{3}C2019-P275

Xuesong Zhang[1], Johannes Weickenmeier[1], *[1]Stevens Institute of Technology, United States*

Determination of The Linear Viscoelastic Behavior of Aponeurosis SB^{3}C2019-P276

Keith Grega[1], Benjamin Wheatley[1], *[1]Bucknell University, United States*

Mri-Based Analysis of 3d Printed Patient Specific Prostate Slicing Molds SB^{3}C2019-P277

David Rutkowski[1], Shane Wells[1], Brian Johnson[1], Wei Huang[1], David Jarrard[1], Joshua Lang[1], Steve Cho[1], Alejandro Roldan-Alzate[1], *[1]University of Wisconsin-Madison, United States*

Murine Vaginal Wall Biaxial Contractile Response Following Elastase Digestion SB^{3}C2019-P278

Gabrielle Clark[1], Laurephile Desrosiers[2], Leise Knoepp[2], Kristin Miller[1], *[1]Tulane University, United States, [2]Ochsner Clinical School, United States*

Toward Fast and Accurate Automated Female Pelvic Floor 3d Geometric Model Reconstruction Based On Deep Convolutional Neural Networks SB^{3}C2019-P279

Fei Feng[1], James A. Ashton-Miller[2], John O.L. DeLancey[3], Jiajia Luo[1], *[1]University of Michigan Shanghai Jiao Tong University Joint InstituteShanghai Jiao Tong University, China, [2]Department of Mechanical EngineeringUniversity of MichiganAnn Arbor, United States, [3]Department of Obstetrics and GynecologyUniversity of MichiganAnn Arbor, United States*

Viscoelastic Mechanical Behavior of Decorin Knockout Mouse Cervical Tissue SB^{3}C2019-P280

Nicole Lee[1], Charles Jayyosi[1], Shanmugasundaram Nallasamy[2], Mala Mahendroo[2], Kristin Myers[1], *[1]Columbia University, United States, [2]Department of Obstetrics and Gynecology and Green Center for Reproductive Biology Sciences University of Texas Southwestern Medical Center, United States*

Determination of The Active and Passive Mechanical Properties of The Non-Pregnant Murine Cervix SB^{3}C2019-P281

Cassandra Conway[1], Gabrielle Clark[1], Mala Mahendroo[2], Kristin Miller[1], *[1]Tulane University, United States, [2]University of Texas Southwestern Medical Center, United States*

Traction Force Microscopy On Human Aortic Smooth Muscle Cells SB^{3}C2019-P282

Claudie Petit[1], Alain Guignandon[2], Stephane Avril[1], *[1]Ecole des Mines de Saint-Etienne, SaInBioSE INSERM U1059, France, [2]Universite Jean Monnet, SaInBioSE INSERM U1059, France*

Posters - Cell & Tissue Engineering: Musculoskeletal

Effects of Solvent and Gelatin Concentration Near-Field, Direct-Write Electrospinning of Gelatin SB^{3}C2019-P283

Zachary Davis[1], Paul Warren[1], Matthew Fisher[1], *[1]North Carolina State University and University of North Carolina - Chapel Hill, United States*

Volumetric Intensity Histogram Analysis Method For Quantification of Fatty Infiltration Following Rotator Cuff Repair SB^{3}C2019-P284

Victoria Webster-Wood[1], Phillip McClellan[2], Lekha Kesavan[1], Greg Learn[2], Ozan Akkus[2], *[1]Carnegie Mellon University, United States, [2]Case Western Reserve University, United States*

Fiber Morphology and Tensile Modulus of Melt Electrowritten Scaffolds Are Dependent On Process Parameters SB^{3}C2019-P285

Paul Warren[1], Zachary Davis[1], Matthew Fisher[1], *[1]North Carolina State University and University of North Carolina - Chapel Hill, United States*

Translation of An Engineered Porcine Accessory Carpal Osteochondral Unit As A Model For Treatment of Thumb Oa SB^{3}C2019-P286

Brendan Stoeckl[1], Hannah Zlotnick[1], Megan Farrell[1], Liane Miller[1], Josh Baxter[1], Thomas Schaer[1], Michael Hast[1], David Steinberg[1], Robert Mauck[1], *[1]University of Pennsylvania, United States*

Muscle and Tendon Derived Extracellular Matrix Promotes Expression of Myotendinous Junction Specific Integrins In Myoblast Cell Culture SB^{3}C2019-P287

Lewis Gaffney[1], Matthew Fisher[1], Donald Freytes[1], *[1]North Carolina State University and the University of North Carolina – Chapel Hill, United States*

Posters - Cell & Tissue Engineering: Organs Morphogenesis and Development

Smooth Muscle Differentiation Actively Patterns The Airway Epithelium During Branching Morphogenesis SB^{3}C2019-P288

Katharine Goodwin[1], Andrej Kosmrlj[1], Celeste Nelson[1], *[1]Princeton University, United States*

The Effects of Oxygen and Air-Liquid-Interface Culture On Human Bronchial Epithelial Cell Differentiation SB^{3}C2019-P289

Sonya Kouthouridis[1], Julie Goepp[1], Carolina Martini[1], Elizabeth Matthes[1], John Hanrahan[1], Christopher Moraes[1], *[1]McGill University, Canada*

Ectopic Sources of Fibroblast Growth Factor 10 Drive Epithelial Buckling and Supernumerary Bud Formation In Cultured Embryonic Lungs. SB^{3}C2019-P290

Kara Peak[1], Victor Varner[1], *[1]The University of Texas at Dallas, United States*

Posters - Cell & Tissue Engineering: Other

Bioelectric Gradients Emerge Downstream of Mechanical Forces In Epithelial Tissues SB^{3}C2019-P291

Brian Silver[1], Celeste Nelson[1], *[1]Princeton University, United States*

Characterization of Collagen/keratin Hydrogels As An Extracellular Matrix For 3d In Vitro Thermal Stress Studies SB^{3}C2019-P292

Kameel Isaac[1], Neda Ghousifam[1], Sean Brocklehurst[1], Mark Van Dyke[2], Marissa Rylander[1], *[1]UT Austin, United States, [2]Virginia Polytechnic Institute and State University, United States*

Microrna Sequencing of Ascs Undergoing Endothelial-Genesis SB^{3}C2019-P293

Shahensha Shaik[1], Elizabeth Martin[1], Daniel Hayes[2], Jeffrey Gimble[3], Ram Devireddy[1], *[1]Louisiana State University, United States, [2]Pennsylvania State University, United States, [3]LaCell LLC, United States*

In Vitro Degradation of Electrospun Polycaprolactone Tissue Engineered Scaffolds Under Cyclical Dynamic Loading SB^{3}C2019-P294

Johane Bracamonte[1], Sarah Saunders[1], Sam Cole[2], Gilbert Annohene[2], Gary Tepper[2], Joao Soares[2], *[1]Virginia Commowealth University, United States, [2]Virginia Commonwealth Universi, United States*

Transcorneal Electrical Stimulation Shown To Reduce The Signs of Glaucoma SB^{3}C2019-P295

McKay Cavanaugh[1], Assraa Jassim[2], Lucy Coughlin[2], Jessica Stukel[1], Denise Inman[2], Rebecca Willits[1], *[1]The University of Akron, United States, [2]Northeast Ohio Medical University, United States*

Optimization of Topographical and Mechanical Properties of Peg-Da Based Hydrogels For Promoting Neurodegeneration SB^{3}C2019-P296

David Hall[1], Sourav Patnaik[1], Ender Finol[1], Gabriela Romero Uribe[1], *[1]University of Texas at San Antonio, United States*

Maintaining Multipotency of Neural Stem Cells Using Synthetic Fgf Peptide Microenvironments SB^{3}C2019-P297

Diana Philip[1], Elena Silantyeva[1], Matthew Becker[1], Rebecca Willits[1], [1]*The University of Akron, United States*

Huvec Tubular Formation On Bio-Inspired Vascularization Substrate SB^{3}C2019-P298

Luis Garcia[1], Patrick Charron[1], Rachael Oldinski[1], [1]*University of Vermont Engineered Biomaterials Research Laboratory, United States*

SB³C2019
Summer Biomechanics, Bioengineering and Biotransport Conference
June 25 -28, Seven Springs, PA, USA

ADVENTURES IN THERMAL THERAPY: FROM SURGERY TO CANCER TREATMENT

John A. Pearce (1),

(1) Department of Electrical and Computer Engineering
The University of Texas at Austin
Austin, TX, USA

INTRODUCTION

While thermal treatment has been used therapeutically for millennia there are still many useful and interesting avenues of investigation open to study. In my view it will remain a vital clinical treatment for the foreseeable future. My goal today is to convince new investigators of the rich and fertile ground available to the perpetually curious in thermal therapy. The opportunities are virtually unbounded.

My own adventure was originally motivated by almost 5 years of clinical experience in the Department of Surgery at the Medical University of South Carolina. We worked closely with folks in the Burn Unit developing devices and strategies. We experienced some adverse outcomes related to electrosurgery burns; consequently my PhD dissertation research at Purdue University was on the topic of electrosurgical dispersive electrodes. Over the past 43 years of research the problems we encountered ran the gamut from very basic undergraduate engineering fundamentals to the most challenging advanced science and engineering principles.

METHODS

Here's how to get involved in thermal therapeutics: 1) Find an amenable pathologist colleague with whom to collaborate. The best work I have been able to complete has been with my long-term pathologist colleague, Dr. Sharon Thomsen. This collaboration opened so much in the way of other sciences and their far-reaching influences, for which I am eternally grateful. 2) Be ever alert for interesting avenues of investigation: if you see something cool, don't hesitate to go there, even if you have to learn a lot. Sitting in on courses on Cell Biology, Tumor Biology and 2 semesters of Biochemistry launched the last 5 years of my work in so many new directions its just not funny. All of the recent work stemmed from the chance purchase of a book The Systems Biology of Cancer. I highly recommend all of those courses. Be curious, branch out. 3) Establish effective collaborative relationships with industrial colleagues and partners in the medical device industry. Our collaboration with Valleylab (now Medtronic Minimally Invasive Therapies), for example, resulted in "Ligasure", the first RF system capable of reliably sealing large arteries and veins. I believe that some of those colleagues are here today. The Ligasure system now has multiple competitors (i.e. imitators), illustrating its ubiquitous contributions in open and laparoscopic surgery. I assure you, I'm not selling these devices … I have no financial interest in any vessel sealing entity (dang it).

As your work continues, never forget the basic engineering fundamentals. Quite by luck (rather than any grand strategy on my part) I have had strong educational backgrounds in both electrical and mechanical engineering and have used all of it most of the time. Perhaps this stems from my initial quandary as a newly admitted student to Clemson University in 1964. I couldn't decide between Mechanical and Electrical Engineering, so after long deliberations I finally pulled out a quarter and it came up Mechanical. My 43 years of research is a combination of heat transfer, thermodynamics and electromagnetic field theory, so I guess I never did decide. That's the fun of it, actually.

SOME EXAMPLE THEORY

The fundamental relation describing irreversible thermal alterations has been the Arrhenius model for first order irreversible reactions, which can be configured to predict the remaining concentration of undamaged tissue constituent, $C(\tau)$, relative to the initial concentration, $C(0)$:

$$ln\left\{\frac{C(0)}{C(\tau)}\right\} = \int_0^{\tau} A\, e^{\left\{\frac{-E_a}{RT}\right\}}\, dt \qquad (1)$$

where: A = the "frequency factor" (1/s), E_a = the activation energy (J/mole), R = the gas constant (J/mole/K), and T = temperature (K). The temperature history (from the bioheat equation) can be used with such a calculation to compare numerical model results with histology and other experimental assessment variables. This simple formulation works very well when applied to structural proteins, but fails for functional protein cascades at moderate (hyperthermic) temperatures, for which the sequences of reactions are higher order. [1] It can be successfully applied when coupled to a temperature-dependent time delay. [2] Direct comparison between histology and numerical creates a powerful combination of theory and experiment, the best kind of science in my view.

RESULTS

Analysis by this thermal damage model and the careful application of basic thermodynamics led directly to development of the Ligasure system, for example. Other models based on this formulation can predict thermally-induced collagen shrinkage, a prime component of almost all cosmetic surgery by RF and laser sources.

DISCUSSION

Results like Ligasure don't come along very often in a career and must be thoroughly appreciated when they do. We had a very large number of failed vessel seals before the underlying physics were resolved to result in a practical system. However, thermal therapy is an excellent avenue by which significant advances in patient care can be realized. After all is said and done, that's what we all hope for, I would say.

Happy research and please do seriously consider this arena of investigation. It's fascinating.

ACKNOWLEDGEMENTS

This work has been partially funded by the O'Donnel Foundation, the Texas Advanced Research Program, the Whitaker Foundation, Valleylab Inc., and the National Science Foundation. The assistance of many graduate and undergraduate students (far too numerous to be individually listed) is gratefully acknowledged.

REFERENCES z

[1] Pearce, J. A., 2013, "Comparative analysis of mathematical models of cell death and thermal damage processes," International Journal of Hyperthermia, 29(4), pp. 262-280.

[2] Pearce, J. A., 2015, "Improving Accuracy in Arrhenius Models of Cell Death: Adding a Temperature-Dependent Time Delay," Journal of Biomechanical Engineering, 137(12), p. 121006.

SB³C2019
Summer Biomechanics, Bioengineering and Biotransport Conference
June 25 -28, Seven Springs, PA, USA

MICROWAVE THERMAL THERAPY OF BENIGN ADRENAL ADENOMAS FOR TREATMENT OF PRIMARY ALDOSTERONISM

Punit Prakash (1), Martin O'Halloran (2), M. Conall Dennedy (3)

(1) Dept of Electrical & Computer Engineering
Kansas State University
Manhattan, KS, USA

(2) College of Engineering and Informatics
National University of Ireland, Galway
Galway, Ireland

(3) Lambe Institute of Translational Research
National University of Ireland, Galway
Galway, Ireland

INTRODUCTION

Primary aldosteronism (PA) accounts for 5 - 12% of all hypertension and confers a higher risk for cardiovascular and cerebrovascular complications compared to age and blood pressure (BP) matched essential hypertension[1], [2]. Despite this, PA remains under-diagnosed and under-treated, largely due to the lack of definitive management options for the majority of affected individuals[1], [3]. PA is driven by unregulated aldosterone secretion from unilateral (40%) or bilateral (60%) aldosterone producing adenomas (APA) (0.5-2 cm^3) or aldosterone producing cell clusters (APCC) (<0.5 cm^3), and is characterized biochemically by raised aldosterone and suppressed renin[4], [5]. The current definitive approach to unilateral PA is surgical adrenalectomy. Bilateral disease is managed medically using mineralocorticoid receptor antagonists (MRA), and is often poorly tolerated due to off target anti-androgen effects of MRAs. Only ~30% of all individuals diagnosed with PA undergo surgery, and collateral resection of normal cortex limits the option of surgery to unilateral disease, given the inevitable risk for adrenocortical insufficiency with bilateral adrenalectomy[6], [7]. There exists a need for improved definitive options for treatment of unilateral and bilateral PA alike, not offered by currently available therapeutic modalities. An ideal approach would selectively eliminate or defunctionalize pathological aldosterone producing adenomas (APA), while simultaneously preserving normal adjacent adrenal cortex.

The standard approach for localizing APAs following diagnosis of PA is with adrenal venous sampling[8]. The recent development of ^{11}C metomidate PET/CT imaging has enabled, for the first time, localization of APAs within adrenal glands, paving the way for the development of localized treatment approaches for PA[8], [9]. Thermal ablation, which is in clinical use for minimally-invasive image-guided treatment of cancers in the liver and other sites, presents a plausible approach for partial treatment of an adrenal gland[10]. Some clinical case series have used radiofrequency ablation (RFA) to treat unilateral functioning adrenocortical adenomas, with clinical and biochemical outcomes demonstrating resolution of PA-associated endocrinopathy[10], [11]. However, these studies did not spare normally-functioning adrenal cortex adjacent to the pathological lesions, and did not provide supporting histology or molecular data to demonstrate the cellular-level effects of heat on the adrenal gland. Compared to other energy modalities for thermal treatments, microwave energy offers the advantages of rapid treatment, and is minimally impacted by tissue heterogeneities[12]. However, (1) the relationship between biological effects of heating and applied thermal history (intensity and duration of heating) on adrenal cells is unknown; (2) currently available microwave heating technology is optimized for thermal ablation of large tissue volumes (diameter > 20 mm), and is ill-suited to minimizing thermal damage to tissue adjacent to offending APAs[11]; (3) inserting ablation probes into adrenal targets is technically challenging; and (4) there are no means to assess the functional status of adrenal tissue immediately following thermal therapy.

Our team is developing a minimally invasive solution for definitive management of APAs: image-guided, cortically-sparing, microwave thermal therapy (MWT) that targets APAs and areas of high autonomous aldosterone production, and preserves areas of ipsilateral normally functioning adrenocortical tissue. Here, we report on our preliminary *in vivo* studies assessing the effects of microwave heating on adrenal cell survival and function.

METHODS

Collaborative work between our labs has investigated the effects of ablative MWT on porcine adrenal gland *in vivo.* All in vivo studies were conducted at Kansas State University under approved Institutional

Animal Care and Use Committee protocol number #4019. We aimed to achieve targeted subtotal adrenocortical ablation (adrenal volumes 0.8 – 1.2cm^3), with preservation of non-targeted tissue. We applied MWT under direct surgical visualization, using a lateralized, non-penetrative approach to normal swine adrenal cortex (n=8 animals). Ablation was performed with a 2.45 GHz directional microwave antenna, previously reported by our group [13]. We assessed tissue histologically, at 48 h post ablation for evidence of coagulative necrosis, heat-induced cellular damage, steroidogenic enzyme expression, and immune infiltration. These data were matched to biochemical measurement of serum concentrations of steroids pre- and post-ablation.

RESULTS

At 48 h post-MWT, coagulative necrosis was induced in the targeted adrenal cortex with disruption of steroidogenic enzyme expression, while the non-targeted cortex remained intact, without evidence of inflammation or upregulated heat-induced damage markers (see Fig. 1). Importantly, steroidogenic enzyme expression was preserved in non-targeted tissue and this was accompanied by normal post-procedural circulating steroid concentrations.

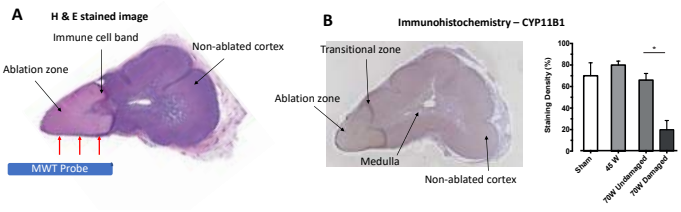

Figure 1: Hematoxylin and Eosin (H&E) staining of porcine adrenal cortex at 48 h following 70 W, 60 s ablative MWT illustrates an area of coagulative necrosis (ablation zone), with preserved normal histological appearance in non-targeted cortex.

DISCUSSION

We conclude from this work that our approach to subtotal adrenocortical ablation is technically feasible and that this merits development. However, further specific details of adrenocortical cellular response to heat are required. Specifically, further insight into the dose-dependent effects of heating on adrenocortical function may identify sub-ablative thermal doses that enable disruption of APAs, while maximally sparing adjacent normal adrenocortical and medullary tissue. Our ongoing *in vitro* studies are geared towards identifying the relationship between duration and intensity of heating on adrenocortical cell survival, cellular damage, and steroidogenesis (i.e. cell function).

ACKNOWLEDGEMENTS

We gratefully acknowledge support from the KSU Johnson Cancer Research Center and the European Research Council under the European Union's Horizon 2020 Programme/ERC Grant Agreement BioElecPro n. 637780. and REALTA no. 75308. P. Prakash acknowledges support of the Paul L. Spainhour Professorship in Electrical Engineering.

.

REFERENCES

[1] S. Monticone *et al.*, "Prevalence and Clinical Manifestations of Primary Aldosteronism Encountered in Primary Care Practice," *J. Am. Coll. Cardiol.*, vol. 69, no. 14, pp. 1811–1820, Apr. 2017.

[2] G. L. Hundemer, G. C. Curhan, N. Yozamp, M. Wang, and A. Vaidya, "Cardiometabolic outcomes and mortality in medically treated primary aldosteronism: a retrospective cohort study," *Lancet Diabetes Endocrinol*, vol. 6, no. 1, pp. 51–59, 2018.

[3] P. Mulatero, S. Monticone, J. Burrello, F. Veglio, T. A. Williams, and J. Funder, "Guidelines for primary aldosteronism: uptake by primary care physicians in Europe," *J. Hypertens.*, vol. 34, no. 11, pp. 2253–2257, 2016.

[4] S. Boulkroun *et al.*, "KCNJ5 mutations in aldosterone producing adenoma and relationship with adrenal cortex remodeling," *Mol. Cell. Endocrinol.*, vol. 371, no. 1–2, pp. 221–227, May 2013.

[5] K. Omata *et al.*, "Aldosterone-Producing Cell Clusters Frequently Harbor Somatic Mutations and Accumulate With Age in Normal Adrenals," *J Endocr Soc*, vol. 1, no. 7, pp. 787–799, Jul. 2017.

[6] T. A. Williams *et al.*, "Outcomes after adrenalectomy for unilateral primary aldosteronism: an international consensus on outcome measures and analysis of remission rates in an international cohort," *Lancet Diabetes Endocrinol*, vol. 5, no. 9, pp. 689–699, 2017.

[7] J. W. Funder *et al.*, "The Management of Primary Aldosteronism: Case Detection, Diagnosis, and Treatment: An Endocrine Society Clinical Practice Guideline," *J. Clin. Endocrinol. Metab.*, vol. 101, no. 5, pp. 1889–1916, 2016.

[8] M. J. Wolley and M. Stowasser, "New Advances in the Diagnostic Workup of Primary Aldosteronism," *J Endocr Soc*, vol. 1, no. 3, pp. 149–161, Mar. 2017.

[9] T. J. Burton *et al.*, "Evaluation of the sensitivity and specificity of (11)C-metomidate positron emission tomography (PET)-CT for lateralizing aldosterone secretion by Conn's adenomas," *J. Clin. Endocrinol. Metab.*, vol. 97, no. 1, pp. 100–109, Jan. 2012.

[10] M.-H. Yang, Y.-S. Tyan, Y.-H. Huang, S.-C. Wang, and S.-L. Chen, "Comparison of radiofrequency ablation versus laparoscopic adrenalectomy for benign aldosterone-producing adenoma," *Radiol Med*, vol. 121, no. 10, pp. 811–819, Oct. 2016.

[11] A. Sarwar *et al.*, "Clinical Outcomes following Percutaneous Radiofrequency Ablation of Unilateral Aldosterone-Producing Adenoma: Comparison with Adrenalectomy," *J Vasc Interv Radiol*, vol. 27, no. 7, pp. 961–967, Jul. 2016.

[12] C. L. Brace, "Radiofrequency and microwave ablation of the liver, lung, kidney, and bone: what are the differences?," *Curr Probl Diagn Radiol*, vol. 38, no. 3, pp. 135–143, Jun. 2009.

[13] B. T. McWilliams, E. E. Schnell, S. Curto, T. M. Fahrbach, and P. Prakash, "A Directional Interstitial Antenna for Microwave Tissue Ablation: Theoretical and Experimental Investigation," *IEEE Trans Biomed Eng*, vol. 62, no. 9, pp. 2144–2150, Sep. 2015.

SB³C2019
Summer Biomechanics, Bioengineering and Biotransport Conference
June 25 -28, Seven Springs, PA, USA

METABOLIZE OR DIE: JOHN PEARCE'S FASCINATION WITH BIOENERGETICS IN CANCER, AND WHAT WE KNOW (AND DO NOT KNOW) NOW

Michael W. Graner (1), Petr Paucek (2), Natalie J. Serkova (3), Anthony Fringuello (1), Steven Ojemann (1), Aviva Abosch (1), Julia Craft (1), Xiaoli Yu (1)

(1) Department of Neurosurgery
University of Colorado Denver, Anschutz Medical Campus
Aurora, Colorado, USA

(2) Department of Neurology
University of Colorado Denver, Anschutz Medical Campus
Aurora, Colorado, USA

(3) Departments of Anesthesiology and Radiology
University of Colorado Denver, Anschutz Medical Campus, Aurora, Colorado, USA

INTRODUCTION

Dr Pearce had a scientific "dalliance" with cellular apoptosis, the rather organized and structured means of programmed cell death, and he enjoyed modeling such processes in the context of hyperthermia [1]. He was also intrigued by the relationships amongst the members of the apoptotic process and their roles in cellular metabolism (eg, cytochrome C as a critical player in mitochondrial electron transport, but also as an intermediary in apoptosis). The connections between metabolism and apoptosis become "altered states" in cancer, where the Warburg Effect (a shift towards glycolysis and away from oxidative phosphorylation despite adequate oxygen, ie, aerobic glycolysis) and a stunning avoidance of apoptosis are standard features. However, bioenergetic flexibility is also prevalent in tumors. The consequences of the Warburg Effect may have benefits for tumors, but there are questions as to the ultimate mechanistic relevancy, and numerous controversies surrounding the Warburg Effect impacts remain [2].

Our work has done little to clarify this situation. Here we will show that tumor stress responses induce elements of glycolysis that correlate with tumor growth (and recurrence) [3]. We also show that tumors release extracellular vesicles (EVs), virus-sized membrane-enclosed particles, that can promote stress responses and push a glycolytic phenotype in both tumor cells and in the "normal" cells of the tumor microenvironment. The tumors we work with are high-grade gliomas such as glioblastomas (GBMs), the worst of the brain tumors with universally fatal outcomes. We hope to show here that tumor stress tends to eventually benefit the tumor, and may be tied to the altered metabolic states that coincide with resistance to therapies. On the other hand, using canine lung cancer cells, we do suggest that such stresses may "set up" the tumor for therapeutic interventions aimed directly at the stress response itself.

METHODS

Cell lines include U87MG (GBM, from ATCC); F3-8 and E8-5 (GBMs, UCD Neurosurgery); STAR line (K9 lung tumor, UCD Neurosurgery) [3] [4] [5]. Human tumor tissues and human normal brain samples were acquired in UCD Neurosurgery (COMIRB, protocol no. 13-3007). Exosomes/extracellular vesicles were collected by concentration, filtration, and differential centrifugation and were characterized by standard means [4].

Drug treatments with temozolomide and PU-H571 were as described [3] [5]. Metabolic studies were performed as described [3]. Two-photon microscopy was utilized to measure changes in bound/free NADH. Cells were stressed by heat shock (42degC, 2hrs) and by induction of the unfolded protein response (UPR) by treatment with 1mM DTT for 4 hrs [3] [5]. Cells were allowed to recover for 24 hrs.

Phospho-signaling and apoptosis arrays were performed as described; cell survival was measured by MTS assay and by soft agar colony formation [3] [4] [5].

RESULTS

We have shown that inducing stress such as the UPR can promote metabolic shifts in U87GBM cells (Fig 1) along with profound resistance to temozolomide, the standard-of-care chemotherapy for GBMs (Fig 2). Thus, stress induction, mirrored by metabolic changes, coincided with resistance to drug-driven apoptosis. However, in a canine lung cancer model, UPR induction followed by treatment with an HSP90/GRP94 inhibitor did result in reduced proliferation (with prolonged treatment, Fig 3). The apoptotic phenomena under stress were mostly muted, with survival characteristics enhanced (Fig 4), but overcome in targeted drugs. We also show that tumor EVs (F3-8) incubated on a human brain slice can shift the ratio of bound/free NADH, indicative of glycolysis on tumor cells themselves (Fig 6).

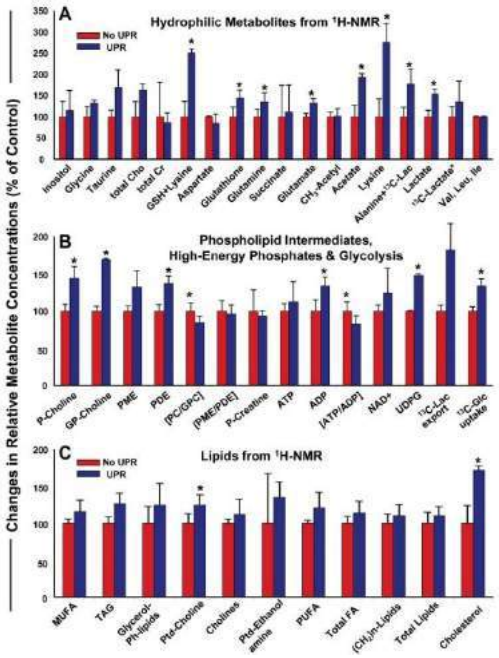

Fig 1: NMR-based quantitative metabolomics of U87MG cells in unstressed (red bars) vs UPR-stressed cells (blue bars)

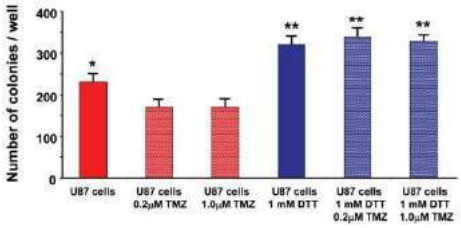

Fig 2: Soft-agar assay measuring U87 MG colony growth after drug treatment, without (red) or with (blue) UPR stress induction

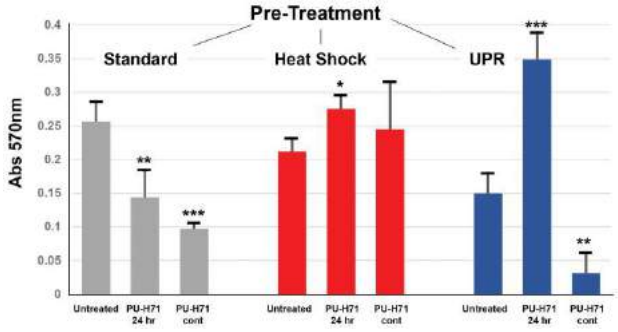

Fig 3: Soft-agar assay measuring STAR cell growth following standard conditions, heat shock, or URP induction in the presence or absence of PU-H571, an inhibitor of HSP90/GRP94

DISCUSSION

Our results show that tumor stress can alter the metabolic phenotype of brain tumor cells and can engender those cells with therapeutic resistance. However, tumor stress may also put the tumor in a vulnerable setting, where inhibiting proteins that enable stress survival (eg, heat shock/chaperone proteins such as HSP90 and GRP94) may result in tumor cell death amidst the stress. Exosomes/EVs released by

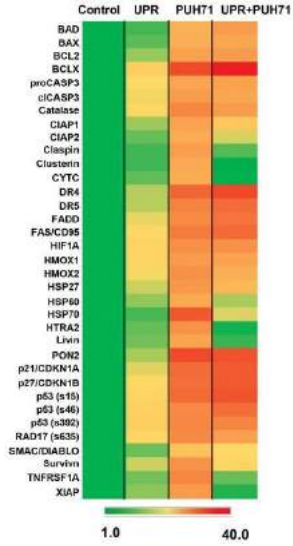

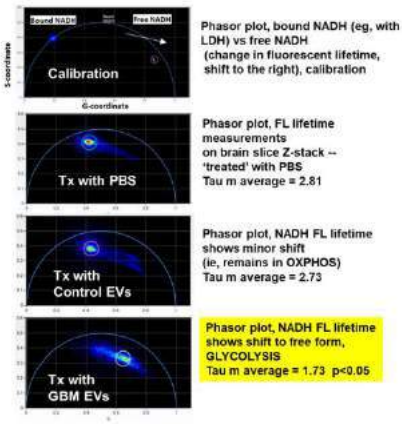

Fig 5: 2-photon microscopy of EV-tx human brain slices showing phasor plot shift towards free NADH

Fig 4: Apoptosis array with expression changes in key apoptotic and anti-apoptosis proteins following UPR and/or drug therapy

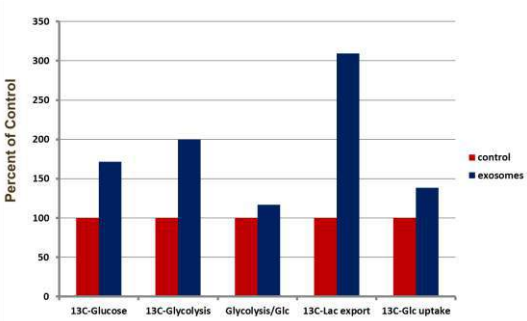

Fig 6: Incubation of GBM EVs on GBM cells induces glycolysis

tumors may also affect the metabolic phenotypes of recipient cells, including normal cells of the tumor microenvironment. This adds layers of complexity to an already disturbing outlook for targeting metabolism or its apoptotic counterparts. Certainly Dr Pearce would love to generate equations describing these events.

ACKNOWLEDGEMENTS

NIH/NIBIB 1R01 EB016378
University of Colorado Dept of Neurosurgery
University of Colorado Cancer Center
Cancer League of Colorado

REFERENCES

[1] Pearce JA Int J Hyperthermia. 2013 Jun;29(4):262-80. doi: 10.3109/02656736.2013.786140..
[2] Liberti MV, Locasale JW Trends Biochem Sci. 2016 Mar;41(3):211-218. doi: 10.1016/j.tibs.2015.12.001. Epub 2016 Jan 5.
[3] Epple L et al, PLoS One. 2013 Aug 15;8(8):e73267. doi: 10.1371/journal.pone.0073267. eCollection 2013.
[4] Oushy S et al, Philos Trans R Soc Lond B Biol Sci. 2018 Jan 5;373(1737). pii: 20160477. doi: 10.1098/rstb.2016.0477.
[5] Graner A, et al, Int J Hyperthermia. 2016 Dec 20:1-15. doi: 10.1080/02656736.2016.1256503

SB³C2019
Summer Biomechanics, Bioengineering and Biotransport Conference
June 25 -28, Seven Springs, PA, USA

EXAMINING THE LIMITS OF ARRHENIUS KINETICS OVER A LARGE TEMPERATURE RANGE

Daipayan Sarkar[1], Peiyuan Kang[1], Zhenpeng Qin[1, 2, 3]

(1) Department of Mechanical Engineering
The University of Texas at Dallas
Richardson, TX, USA

(2) Department of Bioengineering
The University of Texas at Dallas
Richardson, TX, USA

(3) Department of Surgery
University of Texas at Southwestern Medical Center
Dallas, TX, USA

Topic Areas: Biotransport, Therapeutics and Biotransport, Thermal Damage Processes in Tissues Celebrating Dr. John Pearce's 70th Birthday

ABSTRACT

Thermal denaturation of proteins has significant impact on cell injury in focal cancer thermal therapies as well as fundamental studies of protein folding and unfolding. For focal therapies, Arrhenius kinetics is a simple yet widely used model to predict cell injury[1-3] up to 70 °C or 343 K. We have previously examined the kinetics of protein denaturation and found that the kinetic parameters including activation energy E_a (kcal/mol) and frequency factor A (s^{-1}) are correlated with each other, thus providing a simple method to fit the kinetic parameters from experimental data. Furthermore, we found that the activation energy tends to decrease when extending to higher temperatures[4]. However, the validity of Arrhenius kinetics extending beyond this temperature range (>> 70 °C or 343 K) or over a wide temperature range remains a long-standing fundamental question for focal therapy and protein unfolding. Previous experimental investigations of protein unfolding have been predominately conducted by small temperature perturbations (e.g. temperature jump spectroscopy), while molecular simulations are limited to small timescales (microseconds) and high temperatures to observe unfolding. Thus, it remains unclear how fast a protein unfolds across a large temperature range.

To examine the temperature dependent protein denaturation at high temperatures, we have recently developed a technique called molecular hyperthermia[5] that uses nanosecond pulsed heating of individual plasmonic nanoparticles to create precise localized heating. Molecular hyperthermia generates very high temperatures (~85 % of critical temperature of water or 550 K) in a very localized region (nanometers), without any global temperature rise of the bulk solvent. Connecting this with protein unfolding measurements at low temperatures using temperature-jump experiments (T-jump)[6], we observe that the kinetics of protein unfolding is less sensitive to temperature change at the higher temperatures, which significantly departs from the Arrhenius behavior extrapolated from low temperatures. To account for this effect, we propose the use of a reaction-diffusion model[7] that modifies the temperature-dependence of protein unfolding by introducing a diffusion limit. Analysis of the reaction-diffusion model provides general guidelines in the behavior of protein unfolding (reaction-limited, transition, diffusion-limited) across a large temperature range from physiological temperature to extremely high temperatures. The experimentally validated reaction-diffusion kinetics of protein unfolding is an important step towards understanding protein-unfolding kinetics over a large temperature range. It also calls for future studies to examine this model for other protein molecules.

REFERENCES

1. Pearce, J. A. *Journal of Biomechanical Engineering* 2015, 137, (12), 121006.
2. Pearce, J. A. *International Journal of Hyperthermia* 2011, 27, (8), 741-750.
3. He, X.; Bischof, J. C. *Crit Rev Biomed Eng.* 2003, 31, (5&6), 67.
4. Qin, Z.; Balasubramanian, S. K.; Wolkers, W. F.; Pearce, J. A.; Bischof, J. C. *Annals of Biomedical Engineering* 2014, 42, (12), 2392-2404.
5. Kang, P.; Chen, Z.; Nielsen, S. O.; Hoyt, K.; D'Arcy, S.; Gassensmith, J. J.; Qin, Z. *Small* 2017, 13, (36).
6. Huttmann, G.; Birngruber, R. *IEEE Journal of Selected Topics in Quantum Electronics* 1999, 5, (4), 954 - 962.
7. Sarkar, D.; Kang, P.; Nielsen, S.; Qin, Z., Non-Arrhenius Reaction-Diffusion Kinetics for Protein Unfolding over a Large Temperature Range -submitted, 2019.

SB³C2019
Summer Biomechanics, Bioengineering and Biotransport Conference
June 25 -28, Seven Springs, PA, USA

HEATING PROTOCOL DESIGN AFFECTED BY THERMAL DAMAGE MODEL IN MAGNETIC NANOPARTICLE HYPERTHERMIA FOR CANCER TREATMENT

Manpreet Singh, Qimei Gu, Ronghui Ma, Liang Zhu

Department of Mechanical Engineering
University of Maryland Baltimore County
Baltimore, Maryland, USA

INTRODUCTION

Advancement in computational resources in recent years has allowed accurate theoretical simulation based on scanned images of tumors and nanoparticle concentration distribution in magnetic nanoparticle hyperthermia. This leads to determination of heating protocols for individualized designs specific for targeted tumors and their nanoparticle distributions.

Although many cell survival models have been developed and tested, the original Arrhenius integral developed by Henriques, often coupled with simulated temperature elevations in tumors during transient heat transfer process, has been used extensively in hyperthermia treatment to quantify extent of thermal damage in tumor regions. Recently, Pearce[1] observed that the Arrhenius model does not capture the initial shoulder region representing no cell death initially after heating starts. The Arrhenius model was then modified by Pearce to include a time-delay accounting for the initial cellular activities before cell apoptosis can occur.[1]

In this study, we implement both the traditional Arrhenius model and the Pearce model in designing heating protocols for magnetic nanoparticle hyperthermia. MicroCT scans of tumors implanted on mice by prostatic cancer (PC3) cells are used to generate a realistic tumor physical model and a 3-D distribution of volumetric heat generation rate when the tumor is subject to an alternating magnetic field. Coupled with the temperature elevations in tumors, both thermal damage models are implemented to determine the heating time needed to induce thermal damage to the entire tumor.

METHODS

MicroCT scans of five resected PC3 tumors are used for this study, obtained from a previous study.[2] The microCT scan of the tumor was then used to generate a tumor physical model of a uniform material.[3] The tumor was then attached to a previously generated mouse body to mimic the situation in the original animal experiments.[3] The volumetric heat generation rate distribution Q'''_{MNH} in each tumor was obtained from that in Gu et al.[2] The Pennes bioheat equation[4] is the governing equation for simulating the transient temperature field during magnetic nanoparticle hyperthermia:

$$\rho_t c_t \frac{\partial T_t}{\partial t} = k_t \nabla^2 T_t + \omega_t \rho_b c_b (T_b - T_t) + Q'''_{met,t} \qquad (1)$$

$$\rho_c c_c \frac{\partial T_c}{\partial t} = k_c \nabla^2 T_c + \omega_c \rho_b c_b (T_b - T_c) + Q'''_{met,c} + Q'''_{MNH} \qquad (2)$$

where subscripts t and c denote tissue and cancer, respectively. Magnetic nanoparticles are only deposited in the cancer region. All the thermal properties such as density ρ, specific heat c, thermal conductivity k, blood perfusion rate ω, boundary conditions, and initial condition are the same as that in Lebrun et al.[3]

The thermal damage at any tumor location is assessed by the following equation:

$$\Omega(x,y,z,\tau) = A\int_0^{\tau} \exp\left[-\frac{E_a}{R_u T_c(x,y,z,t)}\right]dt - A\int_0^{\tau_d} \exp\left[-\frac{E_a}{R_u T_c(x,y,z,t)}\right]dt \qquad (3)$$

where the time delay τ_d either is zero for the traditional Arrhenius model, or or is temperature-dependent in the Pearce model[1] as:

$$\tau_d = 2703 - 49.6 * T(x,y,z,t) \qquad (4)$$

where the coefficients in Eq. 4 are specific to the PC3 cells. Note that the temperature in Eq. 4 is in Celsius. The designed heating time for causing permanent damage to the entire tumor is determined when Ω is larger than or equal to 4 in the tumor.

Implementing Eq.3 and Eq.4 in simulation is difficult since the time delay depends on local tumor temperature that keeps changing

with time. Examining Eq. 3, one finds that the heating time is determined by the tumor location with the lowest temperature. In this study, we first simulated the steady temperature to determine the tumor location with the lowest value. Then, we performed the simulation of the transient heat transfer process to determine the temperature rising curve verse time at this tumor location. The temperature rising was finally plotted with the curve of Eq. 4. It yields an intersection between those two curves, which gave the time delay τ_d. All the simulations were performed by COMSOL software.

RESULTS

Figure 1 gives the color contours of the generated volumetric heat generation rates on a cross-sectional plane, induced by the magnetic nanoparticles deposited inside the five tumors. The physical model of the mouse with an attached tumor is shown in Figure 2.

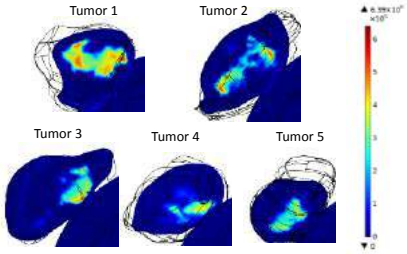

Figure 1: Generated volumetric heat generation rate (W/m^3) on a cross-sectional plane in the five tumor models in COMSOL.

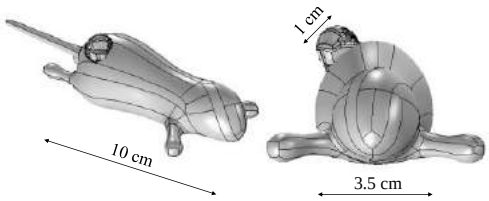

Figure 2: A simplified mouse model with an attached tumor.

Color contours of the simulated steady state temperature fields are illustrated in Figure 3. Most of the elevations occur in the tumor region, however, there is some heat conduction from the tumor to the mouse body. The maximal temperature inside the five tumors varies from 68.77°C to 77.91°C. The location of the lowest temperature inside each tumor is also identified at the interface between the tumor and mouse body. Figure 4 shows how the time delay for this location is determined in one tumor. The time delay calculated as 494 seconds, from the intersection of the two curves in Figure 4. The time delay varies from 346 to 534 seconds in the tumor group.

The heating time required to damage the entire tumor is listed in Table 1 using both the traditional Arrhenius integral and Pearce modified model with a time delay. It is interesting to see that both thermal damage models give very similar results. The Pearce thermal damage model leads to a longer time than that predicted by the traditional Arrhenius model, with less than 6% increase in the designed heating time. This may be due to the relatively large temperature elevations in the tumor, and typically heating time required is dramatically reduced when the temperature is much higher than 43°C. Showing in Figure 4, during the initial heating period before the apoptosis occurs ($t < \tau_d$), tumor temperature is low, around 44.5°C (45.6±1.7°C in the tumor group). When one uses the traditional Arrhenius model, the accumulative thermal damage within the initial time delay duration, shown by the second term on the right of Eq. 3, is small, around 0.36±0.08. Later the tumor temperature increases significantly to 50.36±2.87°C. To compensate the unaccounted initial thermal damage (2nd term on the right of Eq. 3) in the Pearce model, a longer heating time is needed than that in the traditional Arrhenius model. For tumor 1, the steady state temperature at the lowest temperature location is around 47.3°C, the required heating duration is 104 s (1.73 min) longer than that predicted by the traditional Arrhenius model.

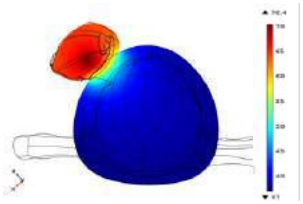

Figure 3: Steady state temperature field on a cross-sectional plane in both the tumor and its surrounding mouse body.

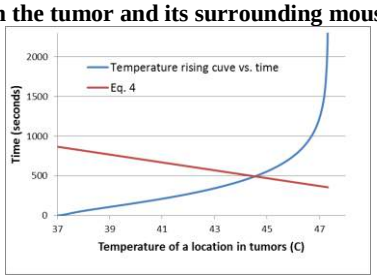

Figure 4: A typical temperature rising curve verse time at a tumor location, and the time delay relationship in Eq.4.

Table 1: Determined heating time (minutes) to damage the entire tumor using both thermal damage models.

	Tumor 1	Tumor 2	Tumor 3	Tumor 4	Tumor 5
Traditional	33.13	22.35	36.00	15.05	14.72
Pearce	34.87	23.24	37.44	15.82	15.34
	5.25%	3.98%	4%	5.12%	4.21%

SUMMARY

In this study, both the traditional Arrhenius model and Pearce model are implemented to quantify tumor thermal damage in magnetic nanoparticle hyperthermia. Theoretical simulations are performed to predict transient temperature elevations in five PC3 tumors implanted on the flank of a mouse model. Previously obtained volumetric heat generation rate distribution due to injected nanoparticles in the tumors is implemented to induce temperature rise. To damage the entire tumor, the traditional Arrhenius model predicts that the average heating time needed is 24.24 minutes, similar to that in our previous study. The modified damage model by Pearce excluding the thermal damage in an initial time delay leads to a minor increase in the required heating time as 25.34 minutes. The mild effect may be due to the relatively high tumor temperature achieved in the tumors. The effect of the modified damage model may be significant when the temperature elevation is modest from 37°C.

ACKNOWLEDGEMENTS

This research was supported by an NSF research grant (CBET-1705538). The research was performed in partial fulfilment of the requirements for the PhD degree by Manpreet Singh from University of Maryland Baltimore County, Baltimore, Maryland, USA.

REFERENCES

[1] Pearce, ASME *J Biomech. Eng*. 137(12):121006, 2015.
[2] Gu et al., ASME *J Heat Transfer*, 141(3):032402, 2019.
[3] Lebrun et al., *Journal of Thermal Biology*, 62:129-137, 2016.
[4] Pennes, *Journal of Applied Physiology*, 1:93–122, 1948.

A PHYSIOLOGICALLY-DRIVEN BIAXIAL BIOREACTOR SYSTEM TO INVESTIGATE VALVE INTERSTITIAL CELL PHENOTYPIC STATE AFTER SURGICAL REPAIR

Salma Ayoub (1), Jordan Graves (1), Chung-Hao Lee (2), Michael S. Sacks (1)

(1) Institute for Computational Engineering and Sciences
The University of Texas at Austin
Austin, TX, USA

(2) School of Aerospace and Mechanical Engineering
The University of Oklahoma
Norman, OK, USA

INTRODUCTION

Despite the phenomenal level of reliability of heart valves, more than five million people are diagnosed with valvular disease in the United States each year, with approximately 95,000 annular valve replacement surgeries and 20,000 mortalities per year [1]. Though ring annuloplasty for mitral regurgitation is beneficial in the short-term, it has been shown to be less promising in the long term, with repair failure as high as 60% [2-3]. Mechanical stress is a strong etiological factor: alterations in mechanical loading caused by surgical repair lead to stress-induced changes in mitral valve interstitial cell (MVIC) function that affect both tissue structure and composition, ultimately leading to repair failure. In this work, we develop a robust experimental-computational approach that allows us to answer specific questions on mitral valve (MV) mechanobiology and provides insight into the micromechanics of surgically repaired valves. This work is thus three-fold: the first part focuses on the design and development of a planar biaxial bioreactor system. The second part involves the use of an established finite element model of the mitral valve [4] to estimate *in vitro* pre-stresses and functional stresses before and after different surgical repair scenarios. We then use the biaxial bioreactor system to apply the estimated stresses to stimulate MV samples and follow-up with downstream biological assessments of the valves.

METHODS

Biaxial bioreactor design and development: In brief, a biaxial stretch device was developed to replicate the complex physiological biaxial strains of the MV. The design consists of four linear actuators and two load cells, one on each axis. A four-pillared stacking system in the middle of the system holds the specimen chamber, which is made of wear-resistant and temperature-stable polysulfone **(Fig. 2A-C)**.

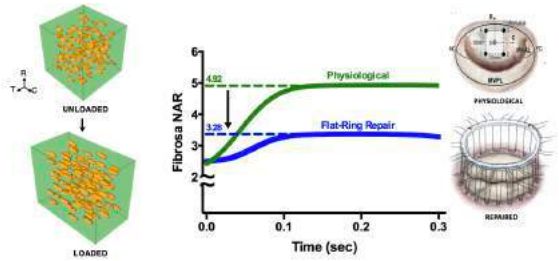

Figure 1. A model-driven experimental design: simulations of MVIC nuclear aspect ratio (NAR) using a macro-micro finite element model from [5] to drive experiments in the BBR.

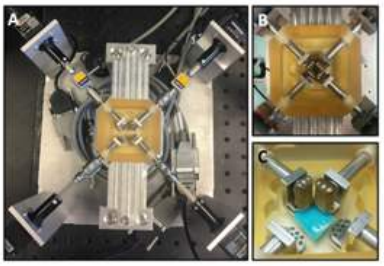

Figure 2. (A) Biaxial bioreactor system. (B) Top view of specimen chamber, (C) Tissue attachment system (tissue phantom in blue).

Estimating in-vivo stresses: The estimated stresses from the finite element inverse modeling framework **(Fig. 2)** are reported in **Table 1**. To emulate the physiological environment, pre-stresses are applied to the samples. Samples are then cyclic stretched from pre-stress to normal

physiological stress. Two groups were used in the bioreactor studies: (1) Normal/Physiological and (2) Post-Ring Repair.

Tissue preparation and bioreactor treatment: Fresh ovine hearts were collected from lamb (6-10 months, 150-175 lbs.) from a local USDA approved abattoir (Mercantile Meat Processing Company, Utopia, Texas) within 30 minutes of slaughter. MV anterior leaflets (MVAL) were isolated on-site and submerged in ice-cold Hypothermosol FRS (Sigma-Aldrich, St. Louis, MO) for transport to the laboratory. Once in the laboratory, cruciform shaped samples (5-7 mm × 3-4 mm, circumferential × radial) were dissected from the clear zone of the anterior leaflet and mounted onto the specimen chambers. Control samples were acquired using the same approach. Samples were cut from the clear zone of the anterior leaflets, snap frozen with liquid nitrogen, and stored at -80°C. For each bioreactor treatment group, 3 (n = 3) MVs were used. Each specimen chamber was filled with 12 mL of media. The specimen chamber was then attached to the system base of each bioreactor housed within the incubator (37°C, 5% CO_2). Samples were then stretched for a total of 48 hours.

ECM Biosynthesis and Cell activation: Samples were fixed with formalin, embedded in paraffin, sectioned (5μm), and stained with Movat pentachrome to analyze layer-specific morphological changes. Staining for α -SMA was performed to quantify VIC activation. Collagen, elastin, and glycosaminoglycan content were quantified using the Sircol, Fastin, and Blyscan assays, respectively.

RESULTS

Mitral valve interstitial cell deformation under normal/physiological stress: In some of our more recent work, we identified MV interstitial cell deformation as a key player in leaflet tissue homeostatic regulation and as such, used it as the metric that makes the critical link between *in vitro* responses to simulated equivalent *in vivo* behavior [5]. Similarly, in this work, we use MVIC deformation to make the same link. We first quantified the nuclear aspect ratio (NAR) in the control ovine samples (juvenile) as well as the NAR in the pre-stress state and the normal/physiological state.

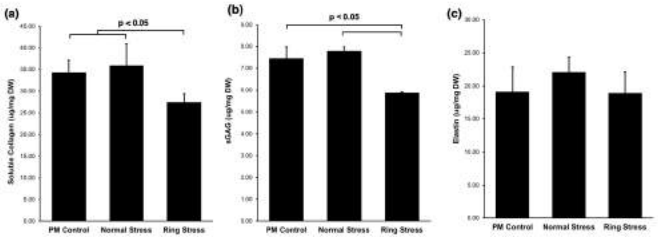

Figure 3. Extracellular matrix composition for the three groups: (1) Control, (2) Normal Stress, and (3) Post-Flat Ring Annuloplasty Stress. All bar graphs, mean ± SEM, *n* = 3. ECM content (s-GAG, collagen, and elastin) quantified with colorimetric assays is presented in μg/mg dry weight. (a) collagen, (2) sGAG, (3) elastin.

Biosynthetic response: homeostasis and ring repair: The Sircol assay demonstrates that although there appears to be a decrease in acid-pepsin soluble collagen after biaxial bioreactor treatment under post-annuloplasty ring stresses, from 34.31 ± 4.97 μg/mg DW (dry weight) for the control group to 27.47 ± 1.90 μg/mg DW, such a difference is not statistically significant ($p > 0.05$). The Sircol assay also demonstrates that the normal stress group has a relatively similar ($p > 0.05$) amount of collagen to the control group, 35.93 ± 4.96 μg/mg DW and 34.31 ± 4.97 μg/mg DW, respectively **(Fig. 3a)**. Blyscan results indicate that the amount of sulfated glycosaminoglycans remains relatively the same after a 48-hr bioreactor treatment under normal physiological stress, whereby the sGAG content is 7.46 ± 0.51 μg/mg DW and 7.80 ± 0.18 μg/mg DW for the control and normal stress groups, respectively. This said, there is a statistically significant drop in sGAG content after a bioreactor treatment under post-flat ring repair stresses ($p < 0.05$), whereby the sGAG content is 5.88 ± 0.04 μg/mg DW **(Fig. 3b)**. The Fastin colorimetric assay indicates that the elastin content, though it changes, is not statistically different across the three groups: 19.10 ± 3.73 μg/mg DW, 22.10 ± 2.23 μg/mg DW, 18.91 ± 3.23 μg/mg DW for the control, normal stress, and ring stress groups, respectively **(Fig. 3c)**.

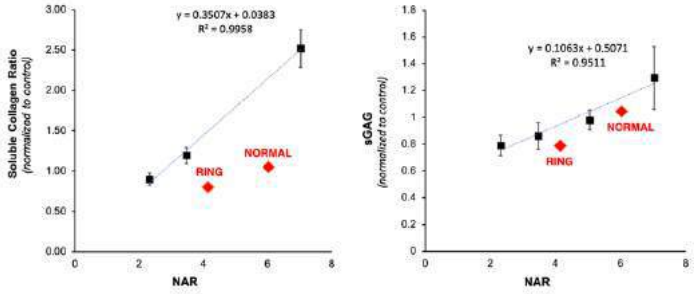

Figure 4. Soluble collagen and sGAG synthesis related to MVIC nuclear aspect ratio. Results from our recent work on MVIC biosynthesis under stretch [5] compared to results from this study.

Mitral valve interstitial cell phenotypic activation after ring stress treatment: Phenotypic activation of VICs is characterized by an upregulation of α-SMA, whereby MVICs become myofibroblast-like and begin to actively remodel the ECM, highlighting the fact that VIC phenotypic state is linked to the remodeling demands of the tissue. The SMA stains shows that the level of phenotypic activation of valve interstitial cells in the control group is similar to the one in the normal stress group. The ring stress group stains, however, show a clear decrease in SMA, highlighting a decreased phenotypic activation after a lower stress level stimulation for 48 hours in the bioreactor.

DISCUSSION

The integrated experimental-computational approach presented in this work allowed us to truly emulate *in vivo* loading conditions and reproduce *in vivo* cellular deformations, quantified by the NAR, in our *in vitro* biaxial bioreactor system. We were able to bridge the crucial gap between the *in vivo* functional and *in vitro* experimental configurations by applying pre-stresses estimated from the inverse modeling framework [4], and also subsequently applied normal/physiological stresses. Most importantly, we were able to validate our hypothesis that cell deformation, more specifically, nuclear deformation is the main driver for VIC mechanobiological response. Our approach can, in the future, serve as a platform for identifying biomechanical treatments that optimize surgical repair and elucidate mechanisms of disease progression.

ACKNOWLEDGEMENTS

NIH grant R01HL119297 to MSS and AHA Pre-Doctoral Fellowship 17PRE33420135 to SA and SDG 16SDG27760143 to CHL. The authors acknowledge Brenda Rodriguez-Nino and Michelle Lu.

REFERENCES

[1] Go et al. *Circulation*, 129:228-92, 2014. [2] Flameng et al., *Circulation*, 107: 1609-13, 2003. [3] Gillinov et al., *J Thorac Cardiovas Surg*, 135:885-93, 2008. [4] Lee et al. *Biomech Model Mechanobiol,* 1-20, 2017. [5] Ayoub et al. *Journal of Royal Society Interface*, 14, 2017.

SB³C2019
Summer Biomechanics, Bioengineering and Biotransport Conference
June 25 -28, Seven Springs, PA, USA

RESTRICTION OF ANNULUS MOVEMENT ALTERS THE DYNAMIC DEFORMATION AND STRAIN DISTRIBUTION OF THE TRICUSPID VALVE LEAFLETS: A SIMULATION STUDY

Keyvan Amini Khoiy, Rouzbeh Amini

Biomedical Engineering Department
The University of Akron
Akron, Ohio, USA

INTRODUCTION

In order to develop new surgical techniques for tricuspid valve (TV) repair and improve the available strategies, it is necessary to have an accurate FE model for the TV. Such a model can be used to simulate surgical procedures and predict the outcomes before the surgery is performed, helping the surgeon to preplan the procedure so as to maximize the quality of the result. This model could also be used in the development of new prosthetic heart valves that can more accurately mimic the behavior of a native valve. Such a development will facilitate in-silico examination of valve repair techniques and will aid in predicting alterations in the biomechanical behavior of TV following such surgeries. While a couple of finite element (FE) models of TV are presented in the literature [1, 2], no study has simulated the effects of TV environmental changes (due to surgeries or diseases) on its mechanical behavior.

In our previous studies [3, 4], a material model was developed to represent the mechanical behavior of the TV in response to estimated environmental strains due to the transvalvular pressures. Moreover, using sonomicrometry, we were able to measure TV annulus and septal leaflet deformations [5]. In the current study, we have utilized our previous studies to establish an FE model of TV to simulate the valve mechanical behavior. We then used this FE model to evaluate the effects of restricting the annulus movement (which normally happens during rigid ring annuloplasty) on TV deformations and strain distributions.

METHODS

The average sonocrystal positional data of the annulus obtained using sonomicrometry [5] were used to reconstruct the three-dimensional geometry of the annulus, and the valve apparatus were reconstructed on top of the annulus geometry using the measurements taken from excised porcine TVs (Figure 1).The number of chordae connected to the free edge and on the ventricular surface of each leaflet were also counted and included in the model (Figure 2 a).

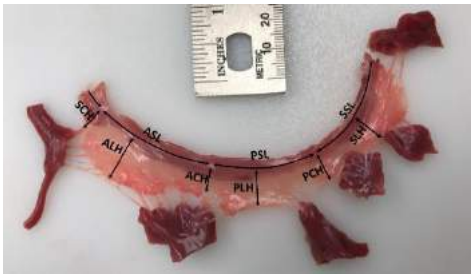

Figure 1: Dimensions used in TV geometry development, anterior segment length (ASL), posterior segment length (PSL), septal segment length (SSL), anterior leaflet height (ALH), posterior leaflet height (PLH), septal leaflet height (SLH), anteroposterior commissure height (ACH), posteroseptal commissure height (PCH), and anteroseptal commissure height (SCH).

The TV was assumed to have three papillary muscles, each considered as a single point in which all the chordae of that area merge. The positions of these points were chosen based on the observations made for porcine heart TVs. First-order chordae (chordae on the edges) were assumed to be distributed uniformly along the edge for each leaflet. Second-order chordae (chordae on the leaflets) were assumed to be uniformly distributed on the surface of each leaflet and positioned at a distance about one-third of the total leaflet length from the leaflet distal (free) edges.

The developed TV geometry (Figure 2a) was imported into Abaqus (Dassault Systèmes, Vélizy-Villacoublay, France) for FE modeling. A

structured technique was implemented to mesh the leaflets using standard linear quadratic-shape shell elements with an approximate global size of 0.5 mm while the thicknesses of the anterior, posterior, and septal leaflets were considered to be 0.313 mm, 0.346 mm, and 0.491 mm, respectively [3]. The chordae were meshed using standard linear truss elements with an approximate global size of 7 mm and a cross-sectional area of 0.171 mm^2 [1, 6] (Figure 2b).

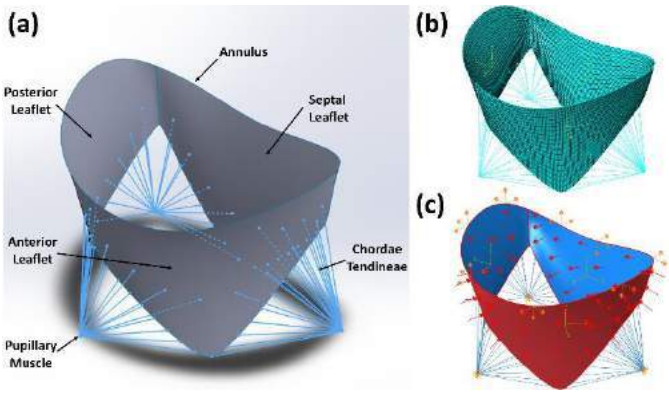

Figure 2: (a) Developed TV geometry, (b) finite element mesh, (c) computerized model, including loading and boundary conditions.

A linear elastic model with parameters (modulus of elasticity = 0.4 MPa, Poisson's ration = 0.45) obtained from the literature [7] was used to represent the mechanical responses of the leaflets. Chordae tendineae mechanical response was modeled using an isotropic hyperelastic Ogden material model [2]. The papillary muscles were considered to be fixed and the time dependent relative transvalvular pressures was applied on the surface of the leaflets (Figure 2 c).

In the first simulation, previously quantified dynamic deformation of the annulus was imposed as the boundary condition and the closure of the valve was simulated. Then, the annulus was kept fixed to mimic the ring annuloplasty and the simulation was repeated.

RESULTS

The developed model was used to simulate the closure of TV. In Figure 3 the deformation of the valve during the simulation is illustrated at different time points.

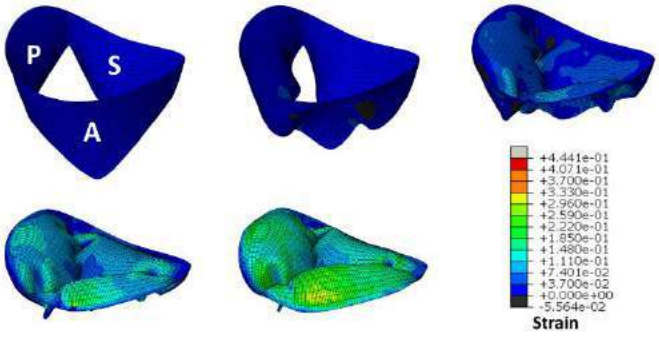

Figure 3: Maximum in-plane principal strain distribution illustrated over the anterior (A), posterior (P), and septal (S) valve leaflets during the valve closure simulation.

The color map in this figure shows the maximum in-plane principal strain distribution. The maximum principal strain was under 25% for most locations, and the strains appeared to be uniform at the belly areas over the surface of the leaflets. The strains in the belly area of the septal leaflet ranged from approximately 8 to 15%.

The simulation resulted in maximum in-plane principal stresses as high as 120 kPa. The distribution of the stresses shows that the anterior leaflet experiences the highest stress, while the septal leaflet experiences the lowest stress.

Figure 4 shows the comparison between the strain distribution of the septal leaflet for the simulation with a fixed annulus and the simulation with moving annulus boundary conditions.

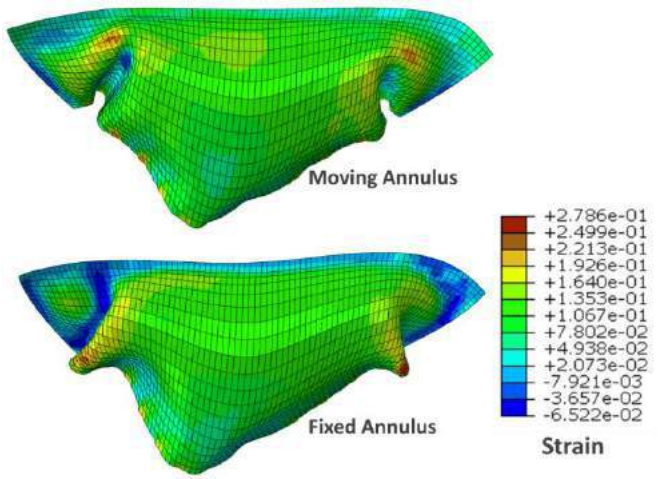

Figure 4: Comparison of effects of changes in the annulus boundary conditions on the strain distribution and deformations of the septal leaflet.

DISCUSSION

We used a finite element model to examine the effect of annular restrictions on TV leaflet deformation. The septal leaflet maximum in-plane principal strain distribution from the simulation ($\sim 8-15\%$) was comparable to the values we measured experimentally ($\sim 11\%$) [5]. Moreover, the levels of the stresses in the FE model (120 kPa) were analogous to the estimated values for normal physiological stress levels on the leaflet surfaces [3] from the biaxial experiments (the values ranged roughly from 80 kPa for the septal leaflet to 130 kPa for the anterior leaflet).

As shown in Figure 4, there was a slight increase in the range of the strains in the belly area following annular restriction. However, for the areas in the proximity of the commissures, the strain distributions and the leaflet deformations were notably altered. This alteration in the strain distribution and leaflet deformation indicated that changes in the normal biomechanical environment of TV (due to valvular treatments or diseases) can affect the valve mechanical responses, leading to potential tissue degeneration and long-term valvular failure.

ACKNOWLEDGEMENTS

Funding was provided in part by the American Heart Association (Grant No. 16SDG27770088).

REFERENCES

[1] Stevanella, M., et al., *Med Eng Phys*, 32:1213-1223, 2010.
[2] Kong, F., et al., *Ann Biomed Eng*, 1-16, 2018.
[3] Amini Khoiy, K., et al., *J Biomech Eng*, 138:104504, 2016.
[4] Amini Khoiy, K., et al., *J Biomechanical Eng*, 140:094503-094503-094511, 2018.
[5] Amini Khoiy, K., et al., *J Biomech Eng*, 138:111006, 2016.
[6] Lim, K. O., *Jpn J Physiol*, 30:455-464, 1980.
[7] Lim, K. H., et al., *J Heart Valve Dis*, 14:386-392, 2005.

SB³C2019
Summer Biomechanics, Bioengineering and Biotransport Conference
June 25 -28, Seven Springs, PA, USA

TRICUSPID VALVE LEAFLET STRAINS IN THE BEATING OVINE HEART

**Manuel K. Rausch (1,2), Mrudang Mathur (3), William D. Meador (2), Marcin Malinowski (4)
Tomasz Jazwiec (4) Tomasz A. Timek (4)**

(1) Aerospace Engineering
University of Texas at Austin
Austin, TX, USA

(2) Biomedical Engineering
University of Texas at Austin
Austin, TX, USA

(3) Mechanical Engineering
University of Texas at Austin
Austin, TX, USA

(4) Cardiothoracic Surgery
Spectrum Health
Grand Rapids, MI, USA

INTRODUCTION

The tricuspid leaflets are an integral part of the tricuspid valve apparatus that directs blood from the right atrium into the right ventricle and prevents regurgitant blood flow from the right ventricle to the right atrium. Between the open and closed states of the valve, the leaflets undergo very large deformations and experience large strains. However, exactly how large these strains are is currently unknown because they have never been directly measured *in vivo*. Knowledge of these strains is not only important to our basic understanding of tricuspid valve function, it could also be important for diagnostic purposes. Specifically, the leaflet strains are a result of the transvalvular pressure, contraction of the peri-valvular tissue and, indirectly via the chordae tendineae, of ventricular contractions. Thus, deviations from normal strains may be indicative of disease of any of these structures or could be predictive of future disease. The purpose of this current study is to establish a baseline measurement of the tricuspid valve leaflet strains.

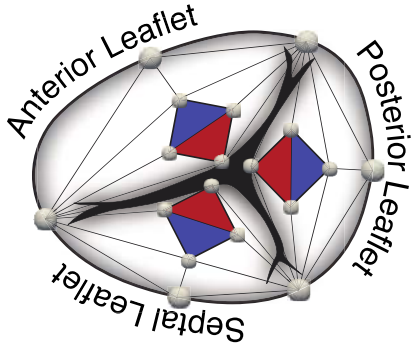

Figure 1: Schematic of tricuspid valve leaflets with sonomicrometry crystals on annulus and leaflets. Blue delineates the leaflet belly region, while red delineates the leaflet free edge. The black lines illustrate the full leaflet triangulation that will later be used in combination with a subdivision scheme to create smooth leaflet surfaces.

METHODS

To determine *in vivo* strains in the tricuspid valve leaflets, we implanted sonomicrometry crystals around the tricuspid valve annulus (6) and on each tricuspid valve leaflet (12, 4 per leaflet) of five sheep in an open heart surgery, see Figure 1. After weaning the animals off cardiopulmonary bypass, we recorded the crystal locations throughout the cardiac cycle alongside hemodynamic data in the beating hearts under open pericardium, open chest conditions.

We computed *in vivo* strains by first interpolating crystal locations in the reference configuration and the deformed configuration via linear shape functions, viz.,

$$\boldsymbol{X}(\theta^1,\theta^2)=\sum_{I=1}^{n} N_I(\theta^1,\theta^2)\boldsymbol{X}_I,\ \boldsymbol{x}(\theta^1,\theta^2)=\sum_{I=1}^{n} N_I(\theta^1,\theta^2)\boldsymbol{x}_I. \quad (1)$$

Here, $N_I(\theta^1,\theta^2)$ are aforementioned linear shape functions, and $\boldsymbol{X}_I$ and $\boldsymbol{x}_I$ are the crystal coordinates in the reference configuration (at end-diastole) and spatial configuration, respectively. Based on the partial derivatives of the shape functions, we next computed the covariant base vectors in both configurations,

$$\boldsymbol{G}_\alpha(\theta^1,\theta^2)=\sum_{I=1}^{n} \partial N_I/\partial\theta^\alpha \boldsymbol{X}_I,\ \boldsymbol{g}_\alpha(\theta^1,\theta^2)=\sum_{I=1}^{n} \partial N_I/\partial\theta^\alpha \boldsymbol{x}_I, \quad (2)$$

while we determined the contravariant counterparts to the above bases via the covariant surface metric in the reference configuration $G_{\alpha\beta}=\boldsymbol{G}_\alpha\cdot\boldsymbol{G}_\beta$, i.e.,

$$\boldsymbol{G}^\alpha = G^{\alpha\beta}\boldsymbol{G}_\beta, \text{ where } G^{\alpha\beta}={G_{\alpha\beta}}^{-1}, \text{ with } \alpha,\beta=1,2 \quad (3)$$

and via the covariant surface metric in the current configuration $g_{\alpha\beta}=\boldsymbol{g}_\alpha\cdot\boldsymbol{g}_\beta$, i.e.,

$$\boldsymbol{g}^\alpha = g^{\alpha\beta}\boldsymbol{g}_\beta, \text{ where } g^{\alpha\beta}={g_{\alpha\beta}}^{-1}. \quad (4)$$

Moreover, we computed the Green-Lagrange strain tensor as,

$$\boldsymbol{E}=E_{\alpha\beta}\boldsymbol{G}^\alpha\otimes\boldsymbol{G}^\beta, \text{ where } E_{\alpha\beta}=\frac{1}{2}\left[g_{\alpha\beta}-G_{\alpha\beta}\right]. \quad (5)$$

RESULTS

We included five animals in our study which all recovered well after coming off bypass, i.e., their hemodynamic data normalized before we record crystal coordinates. Based on our finite kinematic approach, we calculated area strain, radial strain, and circumferential strain in the bellies and the free edges of each leaflet and illustrated them throughout the normalized cardiac cycle. Because of space limitations, we are showing the results for the anterior leaflet only, see Figure 2A. These data demonstrate that strains varied throughout the cardiac cycle. They were largest during systole when the transvalvular pressure is highest, and were minimal during diastole. Also, the strain data demonstrates heterogeneity in radial and circumferential strains, between the belly region and the leaflet region, as well as anisotropy between the two strains. Specifically, strains were overall larger in the radial direction than in the circumferential direction.

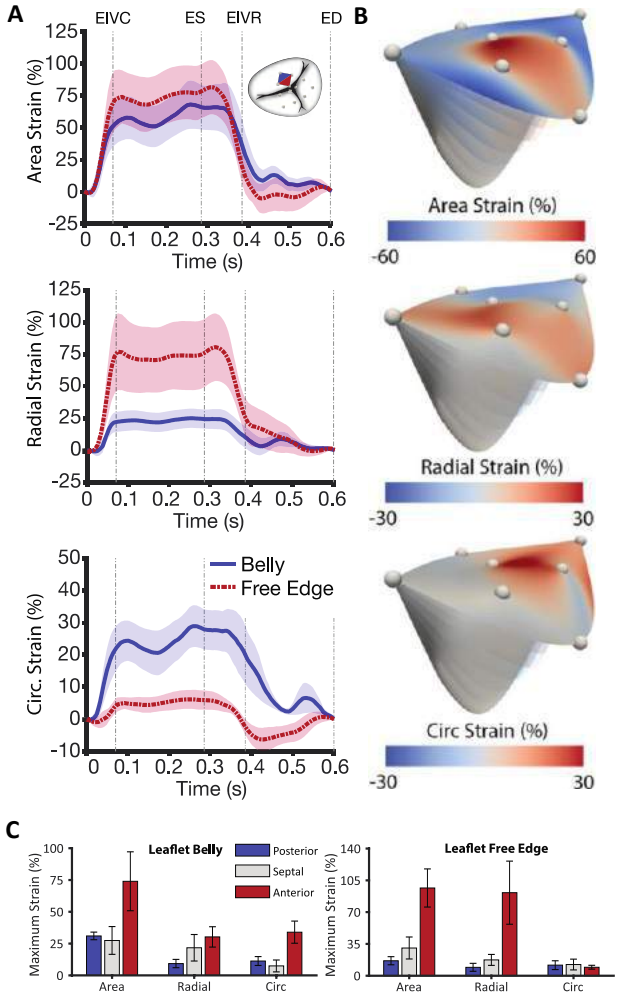

Figure 2: A) Area strain, radial strain, and circumferential strain in the belly and free edge of the anterior leaflet throughout the cardiac cycle. B) Area strain, radial strain, and circumferential strain across the entire anterior leaflet surface between end-diastole and end-isovolumetric contraction. The surface reconstruction is based on the Loop triangular subdivision surface algorithm and an iterative optimization method to ensure that the surfaces interpolate the original crystal coordinates. C) Comparison of peak strains between leaflets, strain types, and leaflet regions.

Additionally, we illustrate all strain types across the entire anterior leaflet surface. The grey configuration in Figure 2B is end-diastole, while we show the strain contours on the leaflet state at end-isovolumetric contraction. All strains show significant heterogeneity with the largest strains either in the leaflet belly or at the free edge, see Figure 2B. Note, strains toward the annulus are likely negative due to annular contraction during systole.

Finally, in Figure 2C, we show a comparison between leaflets, types of strain, and leaflet regions in terms of peak strain, i.e., the largest strain throughout the cardiac cycle. Using a three-way ANOVA (which included "subject" as a random effect), we found that strains are significantly larger in the anterior leaflet ($p=0.003$) and that strains are larger in the radial direction than in the circumferential direction ($p=0.044$).

DISCUSSION

This is the first time direct measurements of *in vivo* tricuspid leaflet strains have been reported. All previous strain measurements have been performed in an *in vitro* right heart simulator [1], an *in vitro* beating heart model [2], or through computational simulations [3]. Interestingly, our measurements are not well-aligned with previous data. Specifically, our strains are larger than those reported in the *in vitro* beating heart model by Khoiy et al. (who only reported strains in the septal leaflet) [1]. Additionally, our findings contradict those made in the *in vitro* right heart simulator by Spinner et al [2]. In detail, our strains in the anterior leaflet exceed Spinner et al.'s, while our measurements in the posterior leaflets are smaller. Although comparison to *in silico* findings by Kong et al. is challenging as they did not report quantitative data, analysis of their strain maps shows relatively good agreement with our data in that their strains are largest in the anterior leaflet (agreeing with us) and that peak strains are as large as ~50% [3]. However, in contrast to us, they found circumferential strains to be larger than radial strains. Note, a comparison between the three studies is difficult, among other reasons, as they used different methodologies. Additionally, all measurements have been made in different species. Hence, to gain more confidence in our findings and shed additional light on the strains in the tricuspid valve leaflets, more work is needed. Specifically, we are planning to include more animals in our study to improve confidence. Also, our methodology should be applied to other species to allow for better comparison to previous data.

In conclusion, for the first time, we report *in vivo* strains in the tricuspid valve leaflets. Combining sonomicrometry with a finite strain kinematic framework, we computed area, radial, and circumferential strains across the entire leaflet surfaces and throughout the full cardiac cycle. We found that strains were significantly larger in the anterior leaflet than in the posterior or septal leaflets and that radial strains were larger than circumferential strains. We believe our work is another important step toward a deepened understanding of the tricuspid valve leaflets, which will aid our basic scientific understanding of the valve itself and better inform future surgical and technological strategies toward tricuspid valve repair.

ACKNOWLEDGEMENTS

We acknowledge funding through an internal grant by the Meijer Heart and Vascular Institute at Spectrum Health.

REFERENCES

[1] Khoiy et al., *J Biomech Eng*, 138:111006, 2016.
[2] Spinner et al., *Ann Biomed Eng*, 40:996-1005, 2012.
[3] Kong et al., *Ann Biomed Eng*, 46:1112-1127, 2018.

SB³C2019
Summer Biomechanics, Bioengineering and Biotransport Conference
June 25 -28, Seven Springs, PA, USA

MATERIALLY HETEROGENEOUS ANNULOPLASTY RING REDUCES LOADING ON POSTERIOR ANNULAR SUTURES

Beatrice E. Ncho (1), Eric L. Pierce (1), Charles H. Bloodworth(1), Akito Imai (2), Keitaro Okamato (2), Yoshiaki Saito (2), Robert C. Gorman (2), Joseph H. Gorman (2), Ajit P. Yoganathan (1)

(1) The Wallace H. Coulter Department of Biomedical Engineering
Georgia Institute of Technology
Atlanta, GA, USA

(2) Gorman Cardiovascular Research Group, Perelman School of Medicine, University of Pennsylvania, Philadelphia, PA, USA

INTRODUCTION

Surgical repair by undersized ring annuloplasty remains one of the most common methods of treatment for ischemic mitral regurgitation (IMR) [1]. Although usually successful, reports indicate recurrence of moderate to severe MR in approximately one third of treated patients within 12 months of surgery [2]. A recognized cause of recurrent MR after annuloplasty is ring dehiscence, and is estimated to underlie 13-42% of reoperations for failed annuloplasty repairs [3]. This phenomenon challenges repair durability, and occurs when mechanical loading on sutures attaching the annuloplasty ring to the mitral annulus pull out from the tissue. Its consequences are often severe, and can include device migration, embolization, endocarditis and increased patient morbidity. Clinical reports have indicated dehiscence to be more common along the posterior annulus [4].

Previous studies establish that the forces experienced by the annuloplasty sutures are influenced by ring design (shape, stiffness), ring-annulus sizing, suture position and region. These studies suggest that suture retention could be improved by incorporating flexibility in novel ring designs. Despite these advantages of flexibility, rigidity is required to restore normal annular geometry in IMR patients who have undergone significant annular distortions. As such, in pursuit of an optimized ring design, we present a novel materially heterogeneous ring that could incorporate benefits of flexibility and rigidity. We hypothesize that the segmental flexibility of this ring will reduce loading on the posterior annulus like the flexible ring, while maintaining minimal loss to the repair efficacy of a rigid saddle-shaped ring.

METHODS

Creation of novel heterogeneous annuloplasty ring. Materially heterogeneous rings were created with rigid anterior and posterior, and flexible commissural segments. These rings were created to match the geometry of the Profile 3D ring (Medtronic, Dublin, Ireland).
Profile 3D rings of three ring sizes (24, 26 and 28) were subjected to micro-computed tomography (μCT) imaging in a Siemens Inveon scanner (Siemens Medical Solutions USA, Inc., Malvern, PA). These images were segmented, smoothed and reconstructed to obtain the ring geometry. For each ring size, molds were designed in SolidWorks (Dassault Systemes, Waltham, MA) and 3D printed from Clear Resin material (Formlabs, Boston, MA) at 0.001" resolution (3D Printing Tech, Atlanta, GA). Rigid cores were designed in SolidWorks and 3D printed from titanium (Ti-6Al-4V) via direct metal laser sintering (resolution < 0.001"). Heterogeneous rings of each size were overmolded atop the titanium inserts with a fast-setting silicone (shore hardness: A40).

Suture force transducers and annuloplasty ring attachment. Each ring was instrumented with 10 custom suture force transducers. These transducers are strain gage-based, designed to report tension on each individual suture as a positive force. The transducer positions around the ring circumference represented mitral annular positions with one transducer on each of the left and right trigones, one each on the antero-lateral (3 o'clock) and postero-medial (9 o'clock) commissures, two on the inter-trigonal positions (11 and 1 o'clock) of the anterior annulus, and four on the inter-commissural positions of the posterior annulus (4, 5, 7 and 8 o'clock).

***In-vivo* testing and surgical protocol.** The instrumented rings were tested in 6 healthy Dorsett hybrid sheep.

Prior to cardiopulmonary bypass, epicardial 2-D, 3-D echocardiography and Doppler were collected to assess ventricular function, transmitral gradients and MR grade. After establishment of bypass, each animal's mitral annulus size was measured, and the ring was selected to undersize the animal's mitral valve by two sizes. Ten mattress sutures (2-0 Ticron with Y-31 needles, Covidien, Mansfield, MA) were placed around the mitral annulus, and through the mounting holes of the transducer. After left atrial closure, the animal was weaned from bypass, and Doppler, 2-D, and 3-D echocardiography were collected to assess ventricular function, transmitral gradients and mitral regurgitation (MR) grade. Cyclic suture forces (F_C) were then recorded during cardiac cycles with a maximum LVP (LVP_{max}) of 100, 125, and 150 mmHg. F_C was compared to previously reported values with the fully-rigid Profile 3D [5] and fully-flexible prototype [6] rings.

All animals received care according to protocols approved by the Institutional Animal Care and Use Committee at the University of Pennsylvania, and in compliance with the guidelines for humane care.

RESULTS

F_C was observed to increase with increasing levels of $LVP_{max.}$ In healthy subjects mean F_C increased with LVP, from 1.38 ± 0.97 N (100 mmHg), to 1.61 ± 1.12 N (125 mmHg), and 1.80 ± 1.24 N (150 mmHg). Averaged over 6 subjects, the maximum and minimum F_C's were 3.09 ± 1.38 and 0.90 ± 0.60 N and again located at 1 and 9 o'clock, respectively.

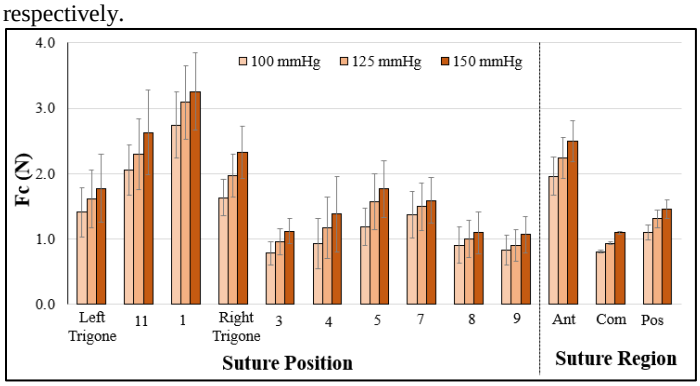

Figure 1: Suture force (F_C) in healthy subjects for each LVP_{max} at all suture positions. Shown: Fc mean ± standard deviation (N). Grouped F_C are presented at the right, Left trigone – right trigone, ant (anterior); 3 and 9 o'clock, com (commissural); and 4-8 o'clock, pos (posterior).

In comparison to homogeneous fully-rigid Profile 3D and fully-flexible prototype rings in healthy subjects, use of the heterogeneous ring overall decreased mean F_C by 0.50N from the fully- rigid Profile 3D case (2.10 ± 1.08 N vs 1.60 ± 1.12 N), and F_C was overall similar to fully-flexible prototype ring (1.58 ± 1.25 N vs 1.60 ± 1.12 N). ANOVA indicated pair wise differences between the fully- rigid Profile 3D and heterogeneous ring ($p<0.001$), but non-significance between the heterogeneous and fully-flexible prototype.

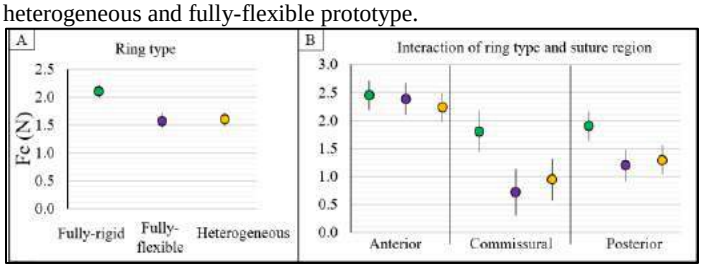

Figure 2: Comparison of heterogeneous ring suture force (FC) data with that of previously measured rings fully- rigid Profile 3D, and fully-flexible prototype ANOVA results (A) Main effects of ring type, (B) Interaction effects of ring type and suture region. Plots indicate F_C means and 95% confidence intervals (N); pairs whose 95% confidence intervals do not overlap differ significantly ($p<0.05$).

DISCUSSION

This ring design featured rigid anterior and posterior segments interposed by flexible commissural segments. As a whole, its construction was more similar to the fully-rigid alternative than to the fully-flexible (with its rigid titanium cores occupying approximately 60% of its circumference). Yet, in terms of the observed F_C dynamics, its performance more closely matched that of the fully-flexible ring. Across all suture positions, mean F_C when using the heterogeneous ring was 24% ($p<0.001$) lower than when using the fully-rigid ring, but only 1.27% ($p= 0.851$) higher when using the fully-flexible ring. Examining these same comparisons by region, we observe all three rings agreed within 8% in the anterior region. These suggests that suture loading in this region is primarily driven by the cardiac motion itself rather than by the ring construct. In the commissural region, the heterogeneous ring reduced F_C by 0.86 N ($p<0.001$) vs. the fully-rigid but increased by 0.22 N ($p= 0.420$). vs. the fully-flexible. This significant reduction was likely a direct result of the heterogeneous ring's flexible commissural segments. Finally, in the posterior region, the heterogeneous ring reduced F_C by 32% ($p<0.001$) vs. the fully-rigid but increased by 4.7 % ($p= 0.420$) vs. the fully flexible. This further reduction was likely an *indirect* result of the flexible commissural segments.

Ongoing experiments with the heterogeneous ring in diseased IMR subjects indicate F_C dynamics follow similar trends. Overall F_C is significantly less than those observed in healthy subjects (1.29 ± 0.63 N vs 1.60 ± 1.12 N, $p<0.01$). These initial findings show that repair effectiveness of mitral regurgitation was 100% in all IMR subjects as their MR grade moved from 2+ or 3+ before ring implantation to none after surgical repair.

Successively, while the flexible commissural segments of the heterogeneous ring confer a benefit by reducing posterior suture loads relative to the fully-rigid case, the rigid posterior will simultaneously confer a benefit relative to the fully-flexible case, by enabling more effective downsizing of dilated mitral annuli. This is demonstrated by the elimination of MR in preliminary IMR subjects. Additionally, the rigid, saddle-shaped anterior segment is likely to benefit leaflet curvature and coaptation and decrease leaflet stress.

A few limitations specific to this novel ring and its comparisons with other rings should be noted. The rigid sensors likely caused stiffening across all positions for all rings. Particularly the case for flexible ring material, thus the benefits to F_C of ring flexibility may be even greater than we were able to detect. Nonetheless, manual manipulation of the instrumented rings revealed this effect to be relatively small. Furthermore, the fully - flexible prototype ring had a flat geometry based on the Physio ring (Edwards LifeSciences, Irvine, CA) and this could potentially confound the intended force comparisons between ring types. However, previous investigation comparing the saddle-shaped Profile 3D and flat Physio rings observed no differences in mean F_C between these geometries [5]. Additionally, given all subjects were terminal, long term repair efficacy with this ring type was not evaluated.

Overall this study demonstrates that a materially heterogeneous annuloplasty ring can reduce loading on the structurally weaker posterior annulus, without compromising repair efficacy suggesting a positive approach to reduce the potential of harm associated with suture dehiscence.

ACKNOWLEDGEMENTS

This study was partially supported by the National Heart, Lung and Blood Institute (R01HL113216), and a grant from the National Science Foundation (DGE-1148903; ELP). The author B.E.N holds an International Fellowship from American Association of University Women (AAUW).

REFERENCES

[1] Acker, M et al., *N Engl J Med*, 370:23-32, 2014.
[2] McGee, E et al., *J Thorac Cardiovasc Surg*, 128:916-924, 2004.
[3] Gillinov, A et al., *J Thorac Cardiovasc Surg* , 113:467-473, 1997.
[4] Levack, M et al., Ann Thorac Surg, 94:2132, 2012.
[5] Pierce, E et al., *J Thorac Cardiovasc Surg*, 155:131-139, 2018.
[6] Pierce, E et al., *J Biomech*, 75:58-66, 2018.

SB³C2019
Summer Biomechanics, Bioengineering and Biotransport Conference
June 25 -28, Seven Springs, PA, USA

3D RECONSTRUCTIONS OF DEPLOYED CORONARY STENTS IN THE CLINICAL SETTING: INVESTIGATION OF DISTORTION EFFECTS FROM CURVATURE ON THE CIRCUMFERENTIAL ORIENTATION OF OCT IMAGES

Mark R. Elliott (1), David S. Molony (2), Brigham R. Smith (3), Sarang Joshi (1,4), Habib Samady (2), Lucas H. Timmins (1,4)

(1) Department of Biomedical Engineering
University of Utah
Salt Lake City, Utah, USA

(2) Division of Cardiology
Emory University School of Medicine
Atlanta, Georgia, USA

(3) Division of Cardiovascular Medicine
University of Utah School of Medicine
Salt Lake City, Utah, USA

(4) Scientific Computing and Imaging Institute
University of Utah
Salt Lake City, Utah, USA

INTRODUCTION

The non-physiologic mechanical loads that vascular stents place on arterial tissue have been identified as contributing factors for the failure of these devices due to neointimal hyperplasia and stent thrombosis [1, 2]. Indeed, computational models evaluating the post-stent mechanical environments in generalized vascular geometries have provided insight on the role of mechanics in stent failure. However, current understanding of the impact of mechanics in device failure at the lesion-specific level, and the development of pre-interventional planning strategies, is limited in the clinical setting. This shortcoming is a direct result of the lack of understanding of the post-deployment stent and vessel geometry at the required resolution for modeling efforts. Towards the development of lesion-specific stenting strategies, we recently development and validated a framework to reconstruct the 3D post-deployed stent geometry through the fusion of optical coherence tomography (OCT) and micro-computed tomography (μCT) image data in a well-controlled experimental setup [3].

To advance this research into the clinical setting, the aim of this investigation was to extend the established framework and reconstruct the *in vivo* 3D post-deployed stent geometry through the fusion of angiographic and OCT imaging data.

METHODS

Clinical Data Biplane coronary angiography and OCT image data from patients (n = 2) undergoing percutaneous coronary intervention for treatment of a flow limiting lesion were retrospectively analyzed. An Integrity® BMS (ID: 3.0 mm, length: 18 mm; Medtronic, Minneapolis, MN) was implanted in the mid-left anterior descending (LAD) coronary artery in one patient, and the other patient had a Xience Alpine™ (ID: 3.0 mm, length: 42 mm; Abbott Vascular, Santa Clara, CA) also implanted in the mid-LAD.

OCT Stent Strut Detection and Angular Drift Correction Stent struts were automatically identified in the OCT image data utilizing a modified version of a previously described algorithm [3]. Briefly, raw 16-bit OCT image data were windowed to remove the catheter and perivascular image data and axial-lines (A-lines) were classified as containing a stent strut or the lumen boundary based on unique signal characteristics (e.g., peak prominence, intensity decay, width of signal). Strut centroids were determined by adjoining contiguous strut define A-lines and accounting for strut thickness. Application of the A-line classification scheme to all images in the OCT pullback resulted in a 3D point cloud of the deployed stent (OCT_{PC}).

Upon examination of the OCT_{PC} , an angular (circumferential) drift in the orientation of the OCT images was observed. As the stent reconstruction algorithm is dependent on an accurate orientation of OCT-derived stent struts, the relationship between curvature and angular drift, which has been noted previously in intravascular ultrasound image data [4], was investigated to establish a *correction factor* for fusion with angiography data. A torsion-free (i.e., planar) experimental test bed, consisting of four 2 mm-wide, 'U'-shaped channels of constant curvature (κ = 0, 1/60, 1/30, 1/20 mm^{-1}) at least 54 mm long, was manufactured out of Delrin® using a CNC-machine (Fig. 1A). An OCT catheter (Dragonfly™ OPTIS™, Abbott Vascular) was guided into each channel, and OCT images were acquired in both "high-resolution" and "survey" mode (54 mm and 74 mm length scans, respectively, with images separated by 0.1 mm and 0.2 mm, respectively) via automatic pullback.

The circumferential orientation of each acquired image was determined by identifying the opening at the top of the channel, defining a line across the channel opening, and calculating the angle between the defined line and the first A-line of the image. The analysis resulted in angle versus image position (axial location) data. A *correction factor*

due to the drift was calculated by averaging the angular drift per mm for each curved channel evaluated and performing a linear regression to identify a relationship between curvature and angular drift per mm. Furthermore, image orientation angles versus position data were calculated across multiple pullbacks of the same channel to evaluate reproducibility.

Deformed Stent Geometry Reconstruction The angular drift *correction factor* was applied to the OCT_{PC} prior to fusion with angiography data. Segmented OCT images were fused with a catheter centerline derived from biplane angiography [4]. A wireframe model derived from μCT image data (14.8 μm isotropic voxels) of a stent identical to the one deployed *in vivo*, but rather deployed in a stress-free environment (i.e., open-air) was created. The wireframe was spatially co-registered to the OCT_{PC} through an initial bending along the catheter centerline. Subsequently, the wireframe was deformed to the geometry of the OCT_{PC} through an constrained iterative deformation process directed by diffeomorphic metric mapping [3]. Following convergence, a volume derived from the stent strut cross-sectional area was lofted about the deformed wireframe, resulting in a continuous, high-resolution 3D reconstruction of the *in vivo* stent geometry.

RESULTS

A positive correlation was observed between curvature and the magnitude of angular drift, such that the angular drift was greater with increasing channel curvature values (Fig. 1). For curvature values of 0, 1/60, 1/30, and 1/20 mm^{-1}, the average angular drift per mm of pullback was 0.10º ± 0.06º, -0.05º ± 0.02º, -0.24º ± 0.05º, -1.0º ± 0.05º, respectively ($p < 0.05$ for all, Fig. 1B). Linear regression demonstrated the relationship between curvature (κ) and angular drift per mm (Δdeg) as $\Delta deg = -21\kappa + 0.23$. Finally, strong reproducibility in the calculated image orientation angle and position data was observed across the scanned data at either acquisition rate (i.e., "high-resolution" or "survey"). The cross correlation of the angle versus image position data from each pullback mode showed highest correlation near zero lag with correlation values of 0.84, 0.97, 0.85, and 0.87 for $\kappa = 0$, 1/60, 1/30, and 1/20 mm^{-1}, respectively.

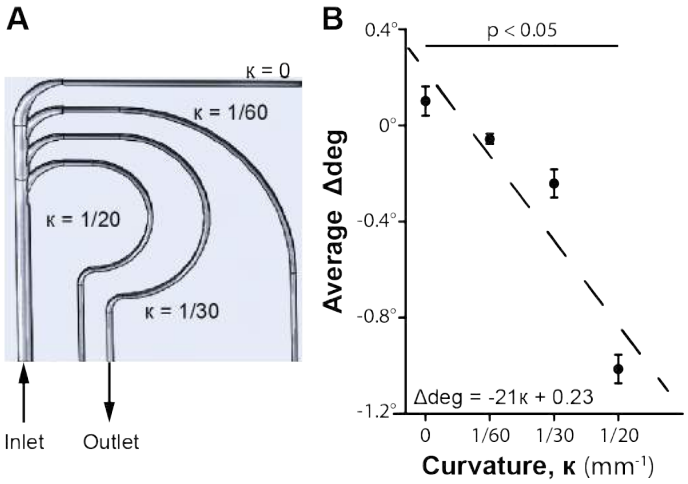

Figure 1: Angular drift experimental test bed and results. (A) A schematic of the experimental setup with constant curvature channels. (B) Average angular drift versus channel curvature with fitted linear regression (dashed line).

Implementation of the angular drift *correction factor* into the stent reconstruction algorithm had an observable effect on the OCT_{PC}. The catheter path for the OCT scan of the Xience Alpine™ stent had an average curvature of 0.04 ± 0.02 mm^{-1}, resulting in an average angular drift of -0.75º ± 0.41º per mm, which accumulated to an angular drift of -29.6º at the proximal end of the stent. Catheter curvature, angular drift, and accumulated angular drift values were 0.05º ± 0.03º, -0.95º ± 0.57º per mm, and -18.2º, respectively, for the Integrity® BMS. A representative example of the automatic 3D stent reconstruction algorithm, which includes angular drift correction, for the *in vivo* deployed Xience Alpine™ is shown in Figure 2. Note the agreement in stent strut location and orientation between the OCT_{PC} and deformed wireframe around the catheter centerline. Most importantly, the deformed, high-resolution wireframe, derived from μCT, provides a continuous stent geometry, which is not observed in sparse OCT-derived stent point-cloud.

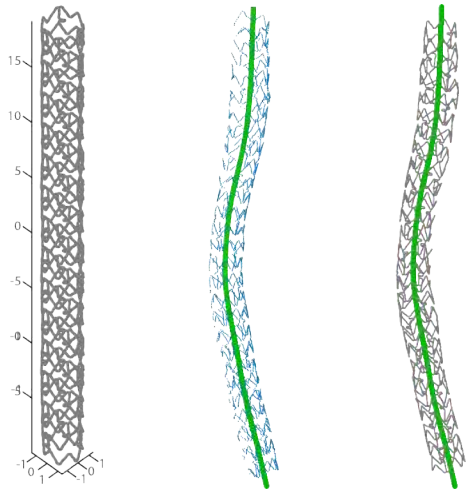

Figure 2: Wireframe coregistration and deformation to catheter centerline and OCT_{PC}. From left to right, the wireframe model before coregistration, the OCT_{PC} fused with the angiographic defined catheter centerline (green), and the completed reconstructed stent that is bent along the catheter centerline and deformed to the OCT_{PC}.

DISCUSSION

Our investigation highlights the influence that vessel curvature has on OCT image angular (circumferential) drift, and the requirement for drift correction when reconstructing a deployed vascular stent from OCT image data. We identified a relationship between angular drift and vessel curvature and proposed a *correction factor* to account for this image distortion. Finally, we integrated the image correction into our established stent reconstruction framework [3], demonstrating the feasibility to reconstruct a high-resolution 3D geometry of a deployed coronary stent through the fusion of clinically relevant imaging modalities. Future studies to validate the *in vivo* stent reconstruction algorithm are warranted, as we have previously performed experimentally [3], to ensure accurate geometries prior to post-stent mechanical environment model predictions.

REFERENCES

[1] Duraiswamy, N., *J. Biomech. Eng.*, vol. 131, p. 061006, 2009.
[2] Timmins, L. H., *Lab. Invest.*, vol. 91, pp. 955–67, 2011.
[3] Elliott, M. R., *IEEE Trans. Med. Imaging*, (in press).
[4] Wähle, A., *IEEE Trans. Med. Imaging*, vol. 18, pp. 686–699, 1999.

EFFECTS OF RIGHT VENTRICULAR ASSIST DEVICE ON TREATING PULMONARY ARTERIAL HYPERTENSION: AN IN-SILICO STUDY USING IMAGE BASED BIVENTRICULAR MODELING FRAMEWORK

Sheikh Mohammad Shavik, Lik Chuan Lee

Department of Mechanical Engineering
Michigan State University
East Lansing, Michigan, USA

INTRODUCTION

Pulmonary arterial hypertension (PAH) is a debilitating disease that is characterized by an abnormally elevated pulmonary artery (PA) pressure (> 25 mmHg). Without treatment PAH progresses rapidly and adversely affects the right ventricle (RV) function, eventually leading to heart failure and death [1]. The elevated PA and RV pressure due to a high afterload in PAH can cause unusual ventricular deformation, such as a left ventricular septal bow (LVSB) in which the septum wall bulges towards the left ventricle (LV). Moreover, long-term functional, structural, and geometrical changes such as enlargement of the RV also occur as the disease progresses. Left ventricular assist devices (LVAD) have been successfully used in the past to treat patients who have left heart failure. Recently, right ventricular assist device (RVAD) has been proposed as a treatment for PAH patients to unload the RV. Because the RV is different from the LV in terms of its structure, geometry and operation, the effects of RVAD on RV may be different from that of LVAD on the LV. Few studies, however, have investigated the effects of RVAD and all computational studies have neglected the effect of RVAD on the ventricular mechanics. To address this limitation, we developed an image based biventricular computational modeling framework to investigate the effects of RVAD in PAH patients.

METHODS

Patient specific biventricular geometry was constructed from the cine magnetic resonance (MR) images of one normal human subject and two PAH patients who had different degree of remodeling. For the PAH patients, one of them had severe RV remodeling (PAHR) with a large RV end-diastolic volume (EDV) and the other had little remodeling (PAHN) and normal RV chamber size and volume (**Fig. 1**). Finite element (FE) meshes were generated using these geometries acquired at early diastole when the LV and RV pressures were at their lowest values in the cardiac cycle. Myofiber helix angle was varied linearly in the transmural direction across the ventricular wall from $60°$ at the endocardium to $-60°$ at the epicardium [2] using a Laplace-Dirichlet Rule-Based algorithm. We assumed a homogeneous helix angle distribution due to the lack of experimental measurements in humans.

The biventricular FE models were coupled to a closed loop circulatory model (**Fig. 1A**) that describes both systemic and pulmonary circulations. The modeling framework consists of eight compartments with four components each (ventricle, atrium, artery and vein) in the systemic and pulmonary circulation. The systemic and pulmonary vessels (arteries and veins) were modeled using their electrical analogs and the contraction of left and right atriums (LA and RA) were modeled using a time varying elastance function. The RVAD flow was simulated using the pressure gradient – flow characteristics of the Synergy™ continuous flow miniature pump (CircuLite Inc, Saddle Brook, NJ) with operating speeds between 20 to 28krpm. Flow through the RVAD was sourced from the RV and ejected to PA.

An active stress formulation was used to describe the mechanical behavior of the myocardial tissue in the cardiac cycle. In this formulation, the first Piola stress tensor $\boldsymbol{P}$ was decomposed additively into a passive ($\boldsymbol{P_p}$) and an active ($\boldsymbol{P_a}$) stress tensor. The active stress tensor has the form $\boldsymbol{P_a} = P_a\, \mathbf{e_f} \otimes \mathbf{e_{f_0}}$, where $\mathbf{e_f}$ and $\mathbf{e_{f_0}}$ denote the local myofiber direction in the current and reference configurations, respectively. The active stress P_a behavior was described by a previously developed active contraction model [3] in which the contractile force is dependent on the sarcomere length. The passive stress tensor was defined by $\boldsymbol{P_p} = dW/d\boldsymbol{F}$, where W is a strain energy function of a Fung-type transversely-isotropic hyperelastic material [4] and $\boldsymbol{F}$ is the deformation gradient tensor.

The biventricular FE models were divided into 3 material regions, namely the LV free wall (LVFW), the septum and the RV free wall (RVFW) for the normal subject and the PAH patients. Contractility parameters associated with these 3 regions as well as circulatory model parameters (resistances and compliances) were adjusted to match the LV and RV pressure and volume waveforms. The simulations were run for several cardiac cycles until the steady-state pressure-volume loop was found. The cardiac cycle time for each case was also matched with the acquired heart rate of the normal subject and PAH patients.

RESULTS

The PV loops as well as both volume and pressure waveforms (not shown here) of the LV and RV predicted by the model were closely matched with the measured data for the normal subject as well as the PAH patients (**Fig. 2A**). In both PAH patients, RV peak pressure was higher compared to the normal subject while their LV peak pressure was only slightly higher than the normal subject. The LV end-diastolic volume (EDV), end- systolic volume (ESV) and ejection fraction (EF) (69% in normal vs. 64% in PAHR vs. 64% in PAHN) were similar in all 3 cases. On the other hand, RV EDV and RV ESV were both significantly larger in PAHR compared to normal, producing a substantially lower RV EF compared to the normal (37% vs. 59%).

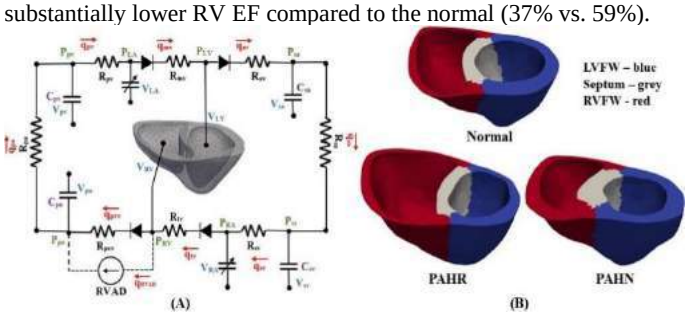

Figure 1: (A) Schematic of the biventricular FE modeling framework, (B) Unloaded geometry of normal and PAH patients with three material regions.

By contrast, PAHN had slightly lower RV EDV, RV ESV compared to the normal. RV EF in PAHN was also lower compared to the normal (51% vs. 59%) but higher than PAHR.

Implantation of RVAD produced a triangular shaped RV PV loop without any isovolumic (contraction and relaxation) periods. In addition, PA diastolic and mean pressures increased significantly together with a slight increase in the PA systolic, LA and aortic pressures (**Fig. 2B**). With increasing RVAD speed, both the PA diastolic and mean pressures increased progressively together with an increase in LV EDV and aortic pressure for both PAH cases. The increase in LV EDV and aortic pressure were, however, more pronounced in PAHR than PAHN.

Average LVFW, septum and RVFW stress were higher in both PAH patients (cf. normal) (**Fig. 2C**). RVAD reduced the average LVFW, septum and RVFW stress in PAHR whereas the stress in PAHN was almost similar to the baseline (without RVAD). Compared to the normal subject, the septum curvature (**Fig. 2D**) in the PAH patients were substantially lower than that found in the LVFW (not shown here) and PAHR had the lowest septum curvature. RVAD increased the septum's curvature in both PAH patients as it shifted towards the RV.

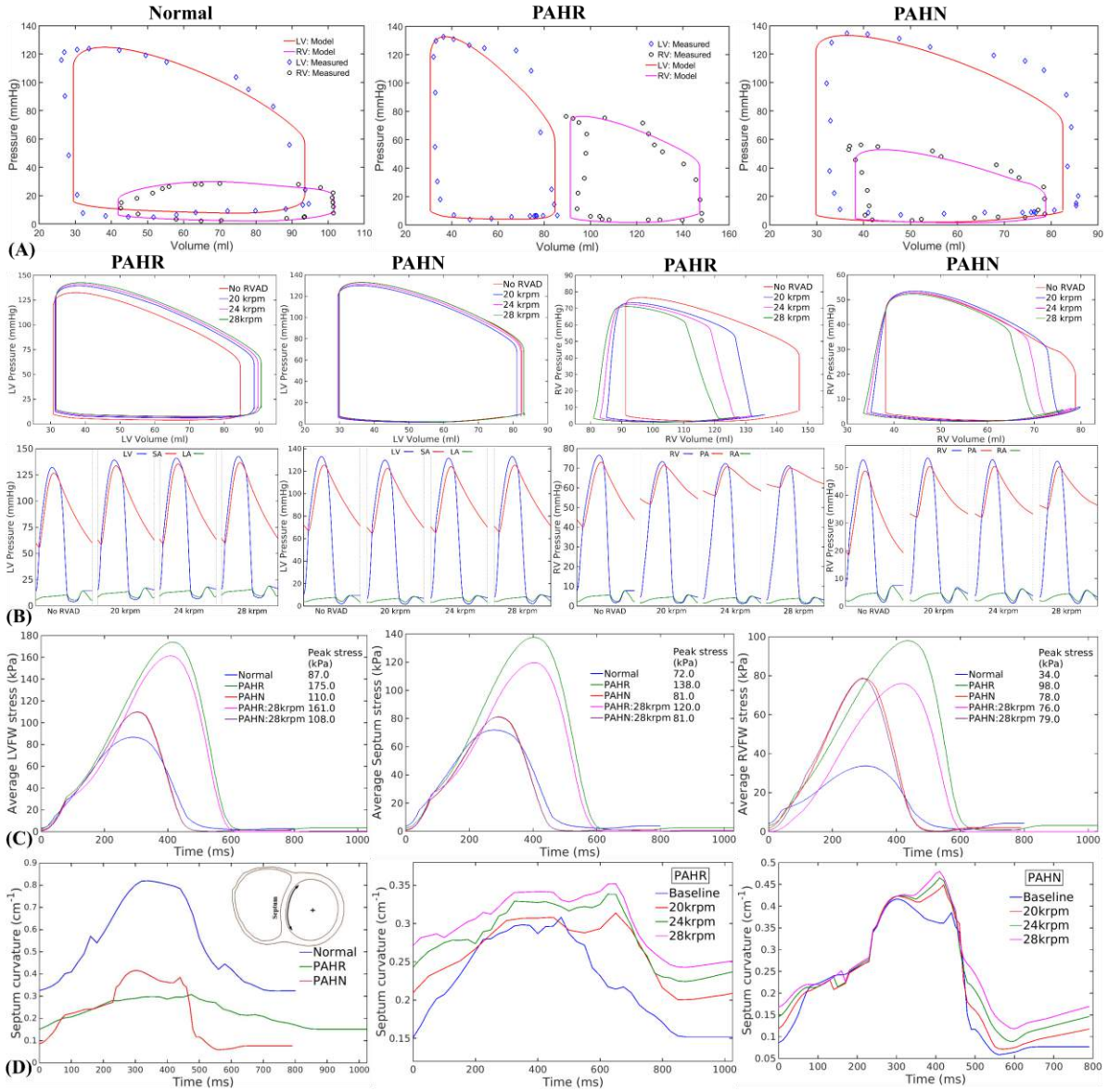

Figure 2: (A) Comparison between measurements and model predictions of LV and RV PV loops, (B) LV and RV PV loops and pressure waveforms of PAH patients at different RVAD speeds, (C) Average LVFW, Septum and RVFW stress, and (D) Septum curvature for different cases.

DISCUSSION

Based on an image-based biventricular FE modeling framework that was calibrated and matched well with **1)** PV loops, **2)** LV and RV volume waveforms and **3)** LV and RV pressure waveforms acquired from patients and normal subjects, we have shown that the implantation of RVAD is able to reduce average stress and improve the septum curvature. These positive effects are, however, compromised by an increase in the (mean and diastolic) PA pressure as well as LV EDV in PAH patients with severe RV remodeling. Thus, while RVAD can help reduce RV load, it may worsen LV function by increasing its preload. These findings are consistent with the previous reports of an increase in PA pressure with RVAD that depends on the severity of the disease. Similarly, we found that the effects of RVAD on hemodynamics as well as mechanics were not same in two PAH patients with different degree of remodeling. These results suggest that the RVAD flow rate should be optimized individually for each patient to minimize the adverse effects.

ACKNOWLEDGEMENTS

This work was supported by American Heart Association (AHA) 17SDG33370110, NIH R01HL134841, and NIH U01HL135842 grants.

REFERENCES

[1] Humbert, M et al., *Eur Respir J*, 36:549-555, 2010.
[2] Streeter, D et al., *Circ Res* 24:339-347, 1969.
[3] Kerckhoffs, R et al., *Ann Biomed Eng* 31:536-547, 2003.
[4] Guccione, J et al., *J Biomech Eng* 113:42-55, 1991.

SB³C2019
Summer Biomechanics, Bioengineering and Biotransport Conference
June 25 -28, Seven Springs, PA, USA

CONTROLLING COMPLIANCE OF POLYCAPROLACTONE/GELATIN TISSUE ENGINEERED VASCULAR GRAFTS IN A RAT MODEL

Kenneth J. Furdella (1), Shinichi Higuchi (2), Kang Kim (1,3,4,5), William R. Wagner (1,2,3,5), Jonathan P. Vande Geest (1,2,5)

(1) Department of Bioengineering
University of Pittsburgh
Pittsburgh, PA, USA

(2) McGowan Institute for Regenerative Medicine
University of Pittsburgh
Pittsburgh, PA, USA

(3) Department of Medicine
University of Pittsburgh
Pittsburgh, PA, USA

(4) Department of Cardiology
University of Pittsburgh
Pittsburgh, PA, USA

(5) Vascular Medicine Institute
University of Pittsburgh
Pittsburgh, PA, USA

INTRODUCTION

In the U.S., coronary artery bypass surgery occurs in over 400,000 patients with a one year patency rate ranging from 60%-95% [1, 2]. This lack of patency is attributed to graft thrombosis and/or intimal hyperplasia [3, 4]. While there are many factors that contribute to procedural failure, compliance mismatch between the implant and the native vessel is thought to be a prominent contributor and will be tested in this study [3, 5].

The current "goal standard" for a bypass procedure is an autologous vessel, but this graft is generally less compliant and usually limited due to widespread vascular disease. Hence, there is a need for a synthetic off the shelf vascular graft. The Soft Tissue and Biomechanics Laboratory has demonstrated that the compliance of a tissue engineered vascular graft (TEVG) can be modulated by using a computational and experimental approach [6]. Specifically, the user defines the material, thickness of the construct, and number of layers which will be computationally simulated to determine the formulation of a compliance specific construct.

For this study, Polycaprolactone (PCL) and gelatin were selected due to their mechanical strength and biocompatibility, respectively. The mechanical strength of PCL increases the burst strength and suturablity of the construct while gelatin provides increased biocompatibility and a fast degrading scaffold.

In this study, the composition of a vascular graft will be modulated to illustrate the role compliance facilitates in vascular graft design using a rat model. The composition of a TEVG will be modulated to create a stiff and compliance matched to rat aorta implant. This graft will then be implanted into a rat model, in vivo flow measurements will be taken, explanted, and evaluated for cell content.

METHODS

The TEVG was manufactured by electrospinning varying ratios of gelatin and PCL to create a rat aorta compliance matched (CM) and hypocompliant (Hypo) graft with 6 alternating layers of higher and lower gelatin percentage (n=3). The Hypo group was defined as having a similar compliance to commercially available DACRON or ePTFE grafts and contained about 30% gelatin or half the amount of gelatin in the CM. For electrospinning, gelatin and PCL were each dissolved into 1,1,1,3,3,3-hexafluoro-2-propanol (HFP) to create a 10% (w/v) solution and electrospun using the IME electrospinning machine. The electrospinning parameters were as follows: 50µl/min flow rate, 15kV voltage, working distance of 10cm, and 22-gauge needle tip. These acellular grafts were then cross-linked in a genipin solution for 24 hours, implanted interpositionally into the aorta of a Sprague Dawley rat for 1 month. During implantation, Doppler ultrasound was used to measure in vivo relative area change before surgery, 1, 2, and 4 weeks post implantation. The relative area change was measured at 4 locations using a cross sectional b-mode image and was calculated as follows:

$$\frac{(\text{Maximum Aorta Area} - \text{Minimum Aorta Area})}{\text{Minimum Aorta Area}}$$

After one month, the rat was sacrificed and evaluated for cellular infiltration using fluorescent microscopy. A two-way ANOVA was used to determine differences between the groups. Scaffold degradation and cell count were calculated using ImageJ. Cell count was defined as any cell within the construct, lumen of the implant, or within a cell length away from the outside of the implant. For scaffold degradation, autofluorescence of the scaffold was used to define the construct area post implantation. The explanted construct area was divided by the original area of the construct to determine the percent degradation.

RESULTS

The compliance of rat aorta, CM, and Hypo graft were $5.6\pm3.1x10^{-4}$, $4.8\pm0.09x10^{-4}$, and $1.46\pm0.15x10^{-4}$ $mmHg^{-1}$, respectively. The CM and Hypo inner diameter were 542±3µm and 548±25µm, respectively. The Hypo group had a 100% survival rate, while the CM had 2 deaths, a graft tear and an unknown cause. The average implant length was between 5-7mm. In vivo relative area measurements showed that the CM group was similar to native aorta throughout the study. The Hypo graft had a significant increase in relative area change from 7 to 14 days, **figure 1.**

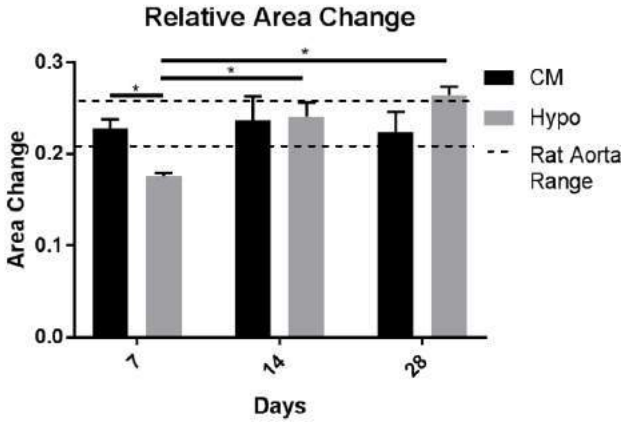

Figure 1. **Relative area change of CM and Hypo at day 7, 14, and 28 (n=3). * p<0.01.**

In vivo diameter measurements showed a slight increase in maximum diameter of the CM (590±17µm) while Hypo showed a slight decrease (520±70µm) from 14 to 28 days. The explanted diameters of the Hypo were larger than CM, 486±6µm to 370±12 µm, respectively. The 28-day cell count showed significantly more cellular infiltration in CM compared to Hypo 1908±790 to 580±181, respectively. CM also showed significantly faster degradation with 56±4% of the construct remaining compared to 77±15%. Representation images showing cellular infiltration and construct degradation are presented in **figure 2**.

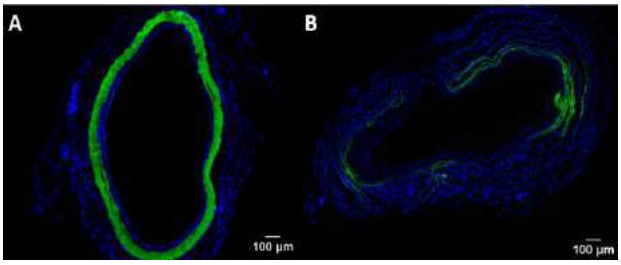

Figure 2. Representative 10 µm cross sectional images of hypo (A) and CM (B) samples. Green is autofluorescence of the implant and blue is cell nuclei.

DISCUSSION

In this study, we were successfully able to create a Hypo and CM graft to rat aorta. Our data showed that our Hypo graft became more compliance throughout the study while the CM graft remained similar to native aorta. Cellular infiltration and graft degradation were significantly higher in the CM compared to the Hypo graft.

For Hypo, this group showed an in vivo relative area shift from a Hypo/stiff to compliance matched graft from 7 to 14 days. Although there is only explant data at 28, we believe this shift in area change/compliance is from the degradation of gelatin. PCL degradation in vivo can last over two years while gelatin degrades at a much quicker rate [7]. Thus, the Hypo grafts contain around 30% gelatin with the explant showing on average a 23% loss of scaffold, thus suggesting the gain in area change/compliance is related to gelatin degradation. Even though these results are encouraging, the limited cellular infiltration, **figure 2A**, may limit the usefulness of this graft. The lack of cells could prevent vasoactivity and the incorporation of a protective endothelium that could lead to thrombosis or graft failure. Longer time points will be needed to determine if cellular infiltration is delayed.

For CM, our results show there is some difficulty implanting the CM grafts but the in vivo and explant results show great promise. Specifically, our data demonstrates that our CM graft will maintain the area change/compliance throughout implantation while promoting a high cellular infiltration. The shrinking of the in vivo to explant diameter may also demonstrate that the cells are functioning properly and depositing an extracellular matrix (ECM). With a higher cellular content and ECM deposition, this suggests that the relative area/compliance is a more beneficial scaffold than a stiff/Hypo graft.

While the results from this study are encouraging, there are some limitations. As described above, we chose to adjust the compliance of the graft by modulating gelatin content. Even though we were successful, gelatin and PCL degrade at different rates. The Hypo had about half as much gelatin as the CM and this may be a source for the differences in the groups. In the future, we would recommend evaluating similar gelatin content grafts, but with different crosslinking time to achieve a compliance match.

As we continue to evaluate this work, we will further examine the types of cells in our grafts. Specifically, we will determine the percent of endothelium, smooth muscles cells, and macrophages M1 and M2. Finally, we will evaluate collagen and elastin content using multiphoton microscopy.

ACKNOWLEDGEMENTS

This research was funded by the NIH R56 (1R56HL136517-01) and Biomechanics in Regenerative Medicine Fellowship (T32EB003392).

REFERENCES

1. Serruys, P.W., et al., *Five-year outcomes after coronary stenting versus bypass surgery for the treatment of multivessel disease: the final analysis of the Arterial Revascularization Therapies Study (ARTS) randomized trial.* J Am Coll Cardiol, 2005. **46**(4): p. 575-81.
2. Go, A.S., et al., *Heart disease and stroke statistics--2014 update: a report from the American Heart Association.* Circulation, 2014. **129**(3): p. e28-e292.
3. Pashneh-Tala, S., S. MacNeil, and F. Claeyssens, *The Tissue-Engineered Vascular Graft-Past, Present, and Future.* Tissue Eng Part B Rev, 2015.
4. Timmins, L.H., et al., *Increased artery wall stress post-stenting leads to greater intimal thickening.* Lab Invest, 2011. **91**(6): p. 955-67.
5. Hasan, A., et al., *Electrospun scaffolds for tissue engineering of vascular grafts.* Acta Biomater, 2014. **10**(1): p. 11-25.
6. Harrison, S., et al., *Computationally Optimizing the Compliance of a Biopolymer Based Tissue Engineered Vascular Graft.* J Biomech Eng, 2016. **138**(1).
7. Hwang, P.T.J., et al., *Poly(ε-caprolactone)/gelatin composite electrospun scaffolds with porous crater-like structures for tissue engineering.* Journal of biomedical materials research. Part A, 2016. **104**(4): p. 1017-1029.

SB³C2019
Summer Biomechanics, Bioengineering and Biotransport Conference
June 25 -28, Seven Springs, PA, USA

A BIO-CHEMO-MECHANICAL COMPUTATIONAL MODEL OF TISSUE ENGINEERED VASCULAR DEVELOPMENT IN VIVO

Ramak Khosravi (1), Abhay B. Ramachandra (1), Jason M. Szafron (1), Christopher K. Breuer (2), Jay D. Humphrey (1,3)

(1) Department of Biomedical Engineering
Yale University
New Haven, CT, USA

(2) Center for Regenerative Medicine
The Research Institute at Nationwide Children's Hospital
Columbus, OH, USA

(3) Vascular Biology and Therapeutics Program
Yale School of Medicine
New Haven, CT, USA

INTRODUCTION

Treatment strategies for many cardiovascular diseases often rely on replacement conduits, but the lack of suitable autologous vessels and high failure rates of synthetic materials significantly limit surgical intervention [1]. Tissue-engineered vascular grafts (TEVGs) are a promising alternative that have recently been used in clinical trials as extracardiac cavopulmonary conduits in congenital heart patients with single ventricle physiology [2, 3]. These biodegradable scaffolds are composed of a woven fabric poly(glycolic acid), or PGA, felt sealed with a 50:50 copolymer solution composed of poly(caprolactone and L-lactide), or P(CL/LA). Although safe, the primary graft-related complication is stenosis: at 5.8 years, 16% of recipients had developed critical graft stenosis (>75% decrease in luminal diameter), and the prevalence increased to 28% at the most recent follow up (11.1 years). Clearly, before routine clinical use of TEVGs can be recommended, an understanding of cellular, molecular, and biomechanical mechanisms underlying neovessel formation and their effective manipulation is required to optimize long-term conduit patency.

To investigate such mechanisms in an animal model, we implanted similar scaffolds as venous interposition grafts in the abdominal inferior vena cava (IVC) of mice for up to two years [4]. We showed that the transformation of our scaffolds into functional neovessels involves polymer degradation and immune cell infiltration, which occurs concurrently with vascular cell recruitment and extracellular matrix deposition and remodeling; moreover, the degree of macrophage infiltration is directly proportional to the incidence of TEVG stenosis. Given the myriad possible design modifications and potential pharmacological therapies that can be explored to increase graft patency, an empirical trail-and-error search for an optimal scaffold design and specific clinical interventions quickly becomes impractical.

Hence, we present a mechanistic bio-chemo-mechanical model that explicitly models interactions between the polymeric scaffold, multiple cell types, key cytokines and growth factors, matrix constituents, and mechanical stimuli, and captures graft properties that emerge from this complex interplay [5]. By combining identifiability analysis with Bayesian estimation techniques and simplex optimization, we determine non-identifiable parameter combinations, and estimate optimal model parameters that match experimental measurements in the presence of uncertainty. We then illustrate the model's clinical utility by hypothesis-driven simulations that examine the effect of altering scaffold design and administering targeted pharmacological interventions with the potential to improve graft performance.

METHODS

A dynamic system of coupled, nonlinear, constant rate ordinary differential equations governs the number of inflammatory and vascular cells, molecular concentration of cytokines and proteases, and mass density of matrix constituents in the system. The normalized mass density and evolving pore size of the degrading polymeric scaffold, along with computationally predicted intramural and wall shear stresses throughout neovessel development, serve as model inputs [6]. The model consists of 43 parameters tuned against 18 measurements from *in vivo* and *in vitro* experimental studies. Parameter bounds were chosen to be consistent with the literature or simply to be biologically reasonable when data were lacking. The administration of clodronate liposomes [7] or the TGF-β R1 kinase inhibitor SB431542 [8, 9], two pharmacological interventions employed in our murine model for the first two weeks following graft implantation to reduce the incidence of stenosis, was modeled using modified gamma distribution functions.

We use a previously published Bayesian-based estimation framework [10] to address the issue of parameter estimation in a data-

poor system in the presence of uncertainty. This framework employs adaptive Markov Chain Monte Carlo (MCMC) methods to sample from the joint posterior distribution of the unknown parameters, which are treated as random variables [11]. The estimation process is complemented with an identifiability analysis to determine unidentifiable parameters. The maximum *a posteriori* estimate is then determined on the identifiable parameters using simplex optimization [12], with the best posteriori estimate from MCMC as the initial guess to the optimization. Using a combination of Fisher information matrix (FIM) analysis and learnability metrics from MCMC simulations, we reduce the set of 43 parameters to a set of 22 identifiable parameters that can completely recover the synthetic targets. These 22 parameters were further estimated to match the desired targets. Following parameter estimation, local parameter sensitivity is determined by calculating the local sensitivity index (LSI), defined as the percentage change in the targets for a percentage change in each parameter [13]. The LSI is averaged over multiple perturbations (<10%) local to the maximum *a posteriori* estimate.

RESULTS

We began with an implanted scaffold having an initial pore radius of 20 μm (similar to those implanted in our murine model) and calibrated model parameters that yielded outputs consistent with experimental observations. Experimental targets were reproduced well, with the percent deviation between experimental targets and simulation outputs ranging from 0.16% to 6.5%. LSI analysis revealed that our model has a dominant downwind behavior, suggesting that the process of neovessel development from an implanted biodegradable scaffold may be an open-loop formulation governed less by positive and negative bio-chemo-mechanical feedback and more by the inherent immunogenicity of the scaffold. For these baseline simulations, the model predicts marked monocyte infiltration, a large number of classically activated macrophages known to contribute to graft stenosis, and a substantial number of inflammatory smooth muscle cells (SMCs) responsible for an early burst in production of stiff inflammatory collagen that adversely affects neovessel distensibility [4, 9].

Reducing the pore radius to 2 μm in our bio-chemo-mechanical model to emulate our clinically used scaffolds decreases the number of infiltrating monocytes and macrophages that enter the scaffold, and therefore reduces the number of recruited vascular cells that eventually populate the graft. Although this reduction in pore size could improve distensibility by reducing the early peak in inflammatory collagen, the inability of immune cells to enter the scaffold directly after implantation drastically compromises graft patency and reduces long-term cellularity, suggesting the need to explore alternative solutions.

When simulating clodronate administration, we observed a significant decrease in monocytes and macrophages secondary to apoptosis, markedly reduced vascular cell recruitment, and a reduction in extracellular matrix production, all consistent with empirical observations [7]. Thus, although clodronate treatment may ameliorate compliance mismatch by diminishing the peak in inflammatory collagen deposition and decrease the incidence of stenosis by inhibiting immune cell infiltration, it compromises graft cellularity and matrix production, which can have catastrophic consequences once the polymer loses load-bearing integrity.

Finally, the model revealed that administration of the TGF-β R1 inhibitor not only improves initial graft patency by inhibiting endothelial-to-mesenchymal transition and preventing the TGF-β-induced classic activation of infiltrating monocytes [9], it may also improve distensibility by significantly reducing inflammatory collagen production during early scaffold remodeling. Treatment with this inhibitor was the only simulated intervention that minimizes compliance mismatch between the implanted polymeric scaffold and the adjacent native vessel while still maintaining graft cellularity.

DISCUSSION

Our model's dominant downwind behavior suggests that variations in graft physical properties and immunogenicity may have far-reaching effects on the elicited inflammatory response, which then strongly influences the eventual patency and functionality of the remodeling graft. This may explain why early intervention with immunomodulatory therapies has proven to be so effective in reducing the incidence of stenosis (7, 8, 9). Our study also has a few limitations: first, the uncertainty in input parameters is not accounted for in the simulations or parameter estimation; second, the targets against which the parameters are estimated are from different sources that encompass varying methods, scales, and systems; third, the proposed system is mostly at a cellular scale and lacks spatial fidelity.

We emphasize the need for focused data collection and carefully designed experiments in our murine model that are explicitly intended to increase the number and diversity of experimental targets. System-specific data remain sorely lacking on the temporal and spatial profiles of immunomodulatory cytokines and the relationship between scaffold physical parameters and the elicited immune response. Increasing the number of experimental targets considered may in turn expand the number of identifiable parameters.

This mechanistic model will be integrated into a pre-existing constrained mixture theory of growth and remodeling to create a fully coupled multiscale bio-chemo-mechanical model of neotissue formation informed and validated by experimental observations. Such a model can aid in rational design by enabling us to perform an extensive series of time- and cost-efficient parametric studies that determine ideal clinical interventions and optimal scaffold parameters for achieving favorable long-term graft outcomes, which can then be evaluated experimentally in animal models and eventually be validated in clinical trials.

ACKNOWLEDGMENTS

We thank Pedro Aparicio for guidance and valuable feedback during early model formulation. This work was supported by grants from NIH (R01 HL139796, R01 HL128847, R01 HL128602, R01 HL098228, and MSTP TG T32GM07205), a Pre-doctoral Fellowship from the AHA and The Children's Heart Foundation (R. Khosravi), and a Graduate Student Research Fellowship from NSF (J. Szafron).

REFERENCES

[1] Bergmann, G et al., *J Biomech*, 34:859-871, 2001.
[1] Patterson, J et al., *Regen Med*, 7:409-419, 2012.
[2] Shinoka, T et al., *J Thorac Cardiovasc Surg*, 129:1330-1338, 2005.
[3] Hibino, N et al., *J Thorac Cardiovasc Surg*, 139:431-436, 2010.
[4] Khosravi, K et al., *Tissue Eng Part A*, 21:1529-1538, 2015.
[5] Aparicio, P et al., *J Biomech*, 49:2321-2330, 2016.
[6] Szafron, J et al., *Ann Biomed Eng*, 46:1938-1950, 2018.
[7] Hibino, N et al., *FASEB J*, 25:4253-4263, 2011.
[8] Duncan, D et al., *J Am Coll Cardiol*, 65:512-514, 2015.
[9] Lee, Y et al., *FASEB J*, 30:2627-2636, 2016.
[10] Schiavazzi, D et al., *Int J Num Meth Biomed Eng*, 33(3), 2017.
[11] Vrugt, J et al., *Int J Nonlin Sci Numer Sim*, 10:273-290, 2009.
[12] Dennis, J and Woods, D, *New computing environments: microcomputers in large-scale computing*, 11:116-122, 1987.
[13] Hamby, D et al., *Environ Monit Assess*, 32:135-154, 1994.

SB³C2019
Summer Biomechanics, Bioengineering and Biotransport Conference
June 25 -28, Seven Springs, PA, USA

ROLE OF HYALURONIC ACID IN REGULATION OF CONTRACTILE FORCES IN HEART VALVE TISSUE CONSTRUCTS

Ying Lei, Luciano Bortolin, Frank Benesch-Lee, Teniola Oguntolu, Kristen Billiar

Biomedical Engineering Department
Worcester Polytechnic Institute
Worcester, Massachusetts, USA

INTRODUCTION

The main treatment option for heart valve disease is replacement. However, mechanical prosthetic valves require lifelong anticoagulants therapy, while bioprosthetic valves tend to undergo degeneration and calcification, and both types often require follow-up surgeries. Tissue engineered heart valves (TEHVs) are a promising alternative since they have the potential to self-repair and grow. While numerous TEHVs have been developed, retraction of the leaflets often occurs involving excessive contraction of the resident cells and buildup of residual stress rather than regeneration of normal tissue. Retraction is especially detrimental since it has been shown that even a slight shortening of the leaflets can lead to regurgitation.

Hyaluronic acid (HA) has been investigated for TEHV design in the hopes that it could contribute to maintaining a healthy quiescent valvular interstitial cell (VIC) phenotype. While studies suggest addition of exogenous HA is a promising strategy to reduce retraction in TEHVs,[1,2] the effects of HA on the active contractile forces of the cells and the passive residual stress build up in the matrix remain unclear. To optimize the design of TEHVs, a better understanding of how HA interacts with the resident cells is necessary.

The goal of this work is to investigate the role of HA in regulating valvular tissue retraction. We developed a 3D tissue construct culturing and monitoring system, and created VIC-populated fibrin-based tissue models with/without HA. The active contractile and residual forces, compressive stiffness, cell alignment, and extracellular matrix (ECM) components and structures were analyzed for each group.

METHODS

Engineered tissue constructs were cultured between polydimethylsiloxane (PDMS) posts. Plugs with posts were cast using stainless steel molds. The stiffness of each post was tested using a custom bending device. Given the bending stiffness of the posts, the contractile forces of the engineered tissues could be calculated based on the deflections of the posts tracked by a monitoring system with a CMOS camera. The deflection was calculated as the difference between the original distance without tissue and the distance with tissue, divided by a factor of 2, assuming that both posts bend equally.

VICs were isolated from pig hearts obtained from a local slaughter house. They were pre-treated with 1 ng/ml TGF-β1 for 3 days before tissue casting, in which two solutions were mixed in wells and incubated for 1 h allowing gelation. In one solution, 6.6 mg/ml soluble fibrinogen was diluted in sterile Dulbecco's phosphate buffered saline with 6 mg/ml HA when applicable, while in the other one cells were suspended with 2 U/ml thrombin in media.

To separate the active cell and passive matrix contributions to tissue contractile forces, two groups of microtissues with or without HA respectively were first cultured for four days, and then incubated with 10 μM cytochalasin D (cyto-D) for 2 h to disrupt the actin network of the cells. Forces before and after cyto-D treatment were quantified. The compressive stiffness of tissues were calculated based on loading curves generated by an Instron EP1000 tensile tester with a loading rate of 0.05 mm/s and a maximum elongation of 150%. To investigate the influences of HA on the mechanical properties provided to cells at the initial stage of tissue formation, an Anton-Parr rheometer was used to perform strain sweep tests on acellular gels. The storage modulus and lost modulus were tested with strain ranging from 0.001% to 10% at 1 Hz with a cone plate of 40 mm in diameter.

The collected tissues were fixed with 4% paraformaldehyde, and H & E staining was performed to observe the general structure of the tissues using hematoxylin and eosin. Cell numbers on the sections were counted using the cell counter in ImageJ. To visualize αSMA, tissue sections were stained with primary monoclonal anti-actin αSMA, and

images were obtained through a Leica SP5 scanning confocal/DMI6000 inverted microscope. Alignment of αSMA was analyzed by OrientationJ plugin in ImageJ.

Data represents mean and standard error. Statistical significance was determined using two-way analysis of variance (ANOVA), where $p<0.05$ was considered significant.

RESULTS

We first tested the influence of varying initial cell density on tissue-generated forces and compressive stiffness in samples with/without HA. Results of groups with 1 M cells/ml and 2 M cells/ml initial cell densities suggest that incorporating HA in the scaffold could significantly reduce the contractile forces, and result in tissues with significantly higher compressive stiffness regardless of the different cell densities, as shown in Figure 1. In addition, tissues with HA have significantly reduced total and residual forces, and trend to have lower active cell contractile forces, as shown in Figure 2.

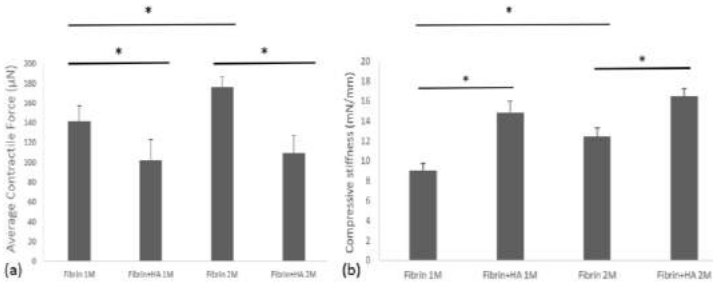

Figure 1: Effect of cell density and presence of HA on a) contractile force and (b) compressive stiffness.

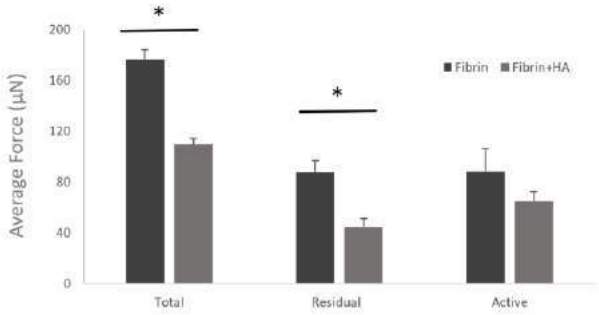

Figure 2: Total, active cell generated and passive residual forces in tissues with/without HA. (Initial cell density: 2 M cells/ml)

Histology results show that while having the same initial cell density of 2 M cells/ml, tissues with HA have denser ECM structures, more evenly distributed cells, significantly larger amount of cells and more collagen fibers secreted by the cells, as shown in Figure 3 and 4.

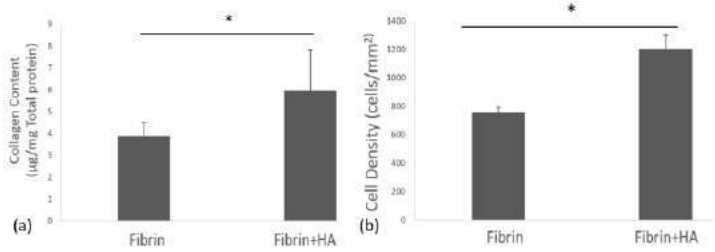

Figure 3: Collagen concentration normalized to total protein contents (a) and cell density of tissues (b) with/without HA.

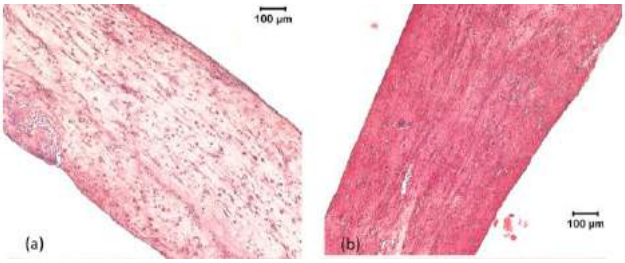

Figure 4: H&E staining of 6 micron tissue sections without (a) and with (b) HA.

For tissues with or without HA, the amounts of αSMA shown in staining images are not significantly different. (Figure 5) However, vector field map analysis suggests that αSMA fibers are well aligned along one direction in tissues with HA, while fibers have two major directions in tissues without HA (analysis not shown).

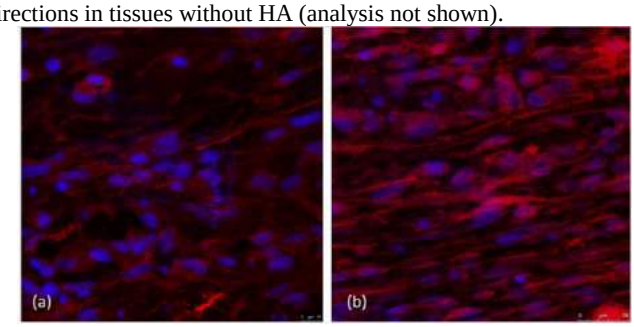

Figure 5: αSMA expression in tissues without (a) and with (b) HA.

DISCUSSION

Our results suggest that incorporating HA in the scaffold significantly reduces the passive residual forces within the ECM, and also trend to reduce active cell-generated forces, thus lessen the contraction overall. The reduction of residual forces could result from the higher initial stiffness of the scaffolds with HA. As shown in Figure 6, acellular fibrin gels with HA have 89% higher storage and loss moduli than gels without HA. In line with previous studies[3,4], the positive influence of HA on cell proliferation, migration, alignment, and secretion of collagen could also contribute to decreasing in both active and passive contractile forces. Since our current results indicate the potential of further decreasing tissue contraction by reducing the active forces, in the future we will explore the effects of growth factors on cell in these fibrin and HA based tissue models.

ACKNOWLEDGEMENTS

This work was supported by the NIH (2R15HL087257-02A1

REFERENCES

[1] Burdick, J et al., *Adv Mate*r, 23: 41-56, 2011
[2] Huang-Lee, L et al., *J Biomed Mater Res*, 28: 123-132.1994
[3] Kural, M et al., *Biomaterials*, 35: 1128-1137. 2014
[4] Quinlan, A et al., *J Biomed mater Res A*, 100: 2474-2482.2012

ADIPOSE STROMAL CELL SECRETED FACTORS INDUCE THE ELASTOGENESIS CASCADE WITHIN AORTIC SMOOTH MUSCLE CELLS

Aneesh K. Ramaswamy (1), Rachel E. Sides (1), Eoghan M. Cunnane (1,2,3), David A. Vorp (1,2,4,5,6), Justin S. Weinbaum (1,2,7)

(1) Dept of Bioengineering
University of Pittsburgh
Pittsburgh, PA 15261

(2) McGowan Institute for Regenerative Medicine
University of Pittsburgh
Pittsburgh, PA 15219

(3) Tissue Engineering Research Group
Dept of Anatomy
Royal College of Surgeons in Ireland
123 St Stephen's Green, Dublin 2, Ireland

(4) Dept of Surgery
University of Pittsburgh
Pittsburgh, PA 15213

(5) Dept of Cardiothoracic Surgery
University of Pittsburgh
Pittsburgh, PA 15213

(6) Dept of Chemical and Petroleum Engineering
University of Pittsburgh
Pittsburgh, PA 15261

(7) Dept of Pathology
University of Pittsburgh
Pittsburgh, PA 15261

INTRODUCTION

Aortic aneurysms (AA) are balloon-like enlargements of the aorta that possess a life-threatening risk of rupture, representing the 15th leading cause of death in the United States [1]. AA are most prominent in both aging populations (primarily smokers), and pediatric or young adult patients with genetic connective tissue disorders [2]. Approximately 5 million Americans over the age of 50 are living with abdominal/thoracic AA [3, 4], with over 200,000 new AAs diagnosed annually [5]. If left untreated, AA can weaken and ultimately rupture or dissect, with over 15,000 high-mortality events annually [6].

Currently, surgical intervention is governed by aortic diameter measurements. Adults are diagnosed with AA once aortic diameter exceeds 1.5-times normal value, with surgical intervention recommended after crossing a "critical diameter" of 5.5cm. Pediatric patients with 'rapid aortic expansion' exceeding 0.5cm/year undergo surgical intervention, often with several repeated surgeries with broad-targeted therapies prescribed (beta blockers, ACE inhibitors). Recent work from our group has shown that periadventitial adipose-derived stromal stem cell (ASC) delivery to a growing elastase-induced mouse aneurysm slows dilation and preserves elastic lamellae [7]. A targeted treatment to regenerate functional elastic fibers could offer a non-surgical therapeutic for adults with sub-critical AA, or an aortic maintenance therapy for children with connective tissue disorders.

While multiple mechanisms can potentially explain this ASC effect, this study tested if paracrine signaling through ASC secreted factors (ASC-SF) induced deposition of elastin by aortic smooth muscle cells (SMCs) within three-dimensional *in vitro* fibrin gel constructs. We evaluated ASC-SF effects on elastin regeneration using three different cohorts of SMCs: (1) purchased healthy adult SMCs (hSMCs); (2) adult patient-isolated SMCs from bicuspid aortic valve (BAV) non-aneurysmal aortas (BAV-NA) and thoracic AA (BAV-TAA); and (3) pediatric SMCs following aortic dilation (pSMC). Elastin analysis included several points in the elastogenesis cascade: elastin organizational protein transcription, elastic fiber organization, elastin cross-linking, and mechanical functionality.

METHODS

hSMCs were purchased from ATCC. Adult BAV SMCs were generously provided by Dr. Thomas Gleason at UPMC Presbyterian Hospital, and pediatric SMCs were isolated from ascending thoracic aorta and aortic root tissue of a two-year old patient following a Ross procedure by Dr. Victor Morell at the Children's Hospital at UPMC (genetic screening ongoing). The tissue was enzymatically digested using a solution ratio of 10mg type IV collagenase to 5mg elastase in serum-free SMC growth medium.

Fibrin gel constructs were fabricated as described [8] using a volume of 200µL and a SMC seeding density of $5x10^5$ cells/mL (**Figure 1**). A fibrinolysis inhibitor (12mM aminocaproic acid) was used to halt construct breakdown. Culture media was changed every 48-72 hours, for either 20 or 30 days in culture.

Treatment groups included: (1) No Treatment (NT), consisting of SMC growth-supplemented media; (2) ASC-SF, a 1:1 combination of SMC growth-supplemented media and ASC conditioned media, collected after 24-48 hour ASC incubations within preadipocyte growth supplemented media; and (3) Non-Conditioned Media (NCM), a 1:1 combination of SMC growth-supplemented media and fresh ASC culture media.

qPCR was used to analyze protein transcription. Human aortic elastin immunofluorescence staining was performed using an Olympus FluoView FV1000 confocal microscope (20x oil, NA=0.85 objective). Ninhydrin (insoluble elastin) and hydroxyproline (collagen) protein assays were used to quantify deposition as a percentage of total protein within the construct [9]. Uniaxial tensile testing was performed using an Instron #5543A mechanical system.

Figure 1: 3D SMC-seeded fibrin gel constructs.

RESULTS

qPCR analysis on hSMCs (**Figure 2**) revealed that both ASC-SF (4.94±0.71-fold increase vs NT control) and NCM (3.09±0.29-fold increase) induced a significant increase in SMC tropoelastin. Microfibril protein fibrillin-1 (4.22±1.10-fold increase), elastin organizational protein fibulin-5 (5.42±0.53-fold increase), and cross-linking proteins LOX (2.31±0.44-fold increase) and LOXL-1 (2.22±0.53-fold increase) were also increased with ASC-SF stimulation. LTBP-4 was significantly downregulated with both ASC-SF stimulation and NCM. NCM did not induce significant differences in fibrillin-1, fibulin-4, fibulin-5, LOX, or LOXL-1.

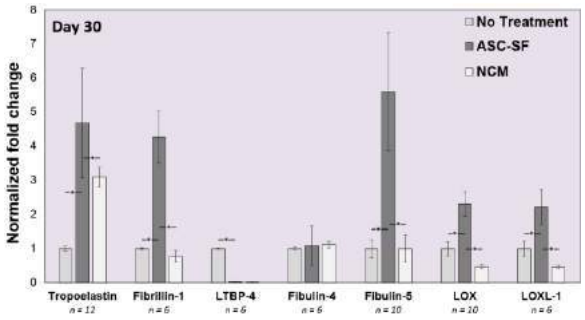

Figure 2: qPCR of hSMC elastin chaperone protein transcription.

ASC-SF stimulation of hSMC induced a 136% increase versus NT control in insoluble elastin percentage of total protein after 20 days (0.15±0.023% NT control and 0.15±0.03% NCM control, vs 0.37±0.1337% ASC-SF), and a 94% increase after 30 days (0.12±0.04% NT control & 0.098±0.038% NCM control, vs 0.25±0.07% ASC-SF) (**Figure 3**). Elastic matrix imaging revealed ASC-SF-induced continuous, thick elastic fibers. Image quantification revealed increased intersection density with ASC-SF (data not shown).

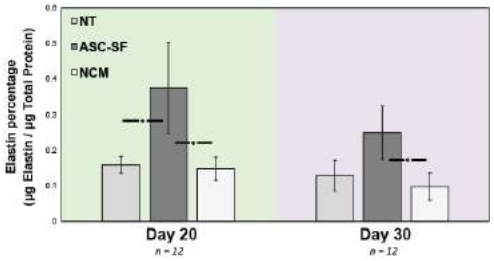

Figure 3: Insoluble elastin within stimulated hSMC constructs.

Tensile testing of hSMC constructs following 30 days of stimulation revealed an ASC-SF induced 151% increase in high elastic modulus (12.48±2.211kPA NT control vs 31.30±13.56kPA ASC-SF), while low elastic modulus remained statistically unchanged.

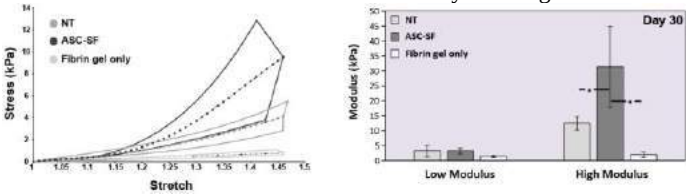

Figure 4: Tensile testing of hSMC constructs.

When cells within the construct were changed to pSMCs (**Figure 5A**), ASC-SF-stimulation resulted in a 226% increase in insoluble elastin deposition when compared to no treatment control (0.05±0.005% control, 0.19±0.05% ASC-SF).

Constructs loaded with BAV-NA cells (**Figure 5B**) saw a 102% increase with ASC-SF stimulation (0.078±0.013% NT, vs 0.16±0.06% ASC-SF). Interestingly, NCM stimulation saw a similar increase (0.22±0.028%). This trend held with BAV-TAA cells, as ASC-SF induced a 183% increase in insoluble elastin (0.058±0.010% NT, 0.16±0.042% ASC-SF), while NCM induced a 195% increase (0.17±0.069% control).

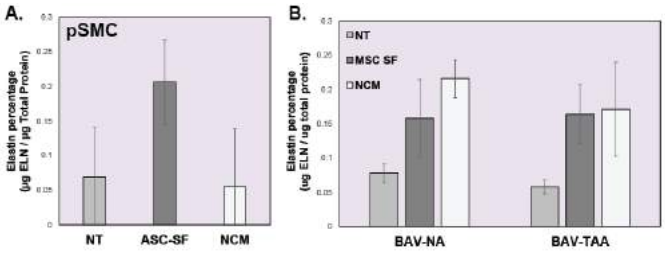

Figure 5: Insoluble elastin from patient-derived SMC constructs.

DISCUSSION

Our multi-level hSMC elastogenesis analysis shows that while NCM induces tropoelastin deposition, the accompanying milieu of elastin chaperone proteins induced by ASC-SF stimulation results in greater insoluble elastin, and increased fibril interconnectivity and mechanical functionality. We also found collagen fraction after 30 days of ASC-SF stimulation saw a 233% increase (0.045%±0.028% NT vs 0.15±0.063% ASC-SF), showing the potentially wide-ranging vascular extracellular matrix regenerative capabilities of ASC-SF.

pSMCs displayed a similar pattern of insoluble elastin stimulation to hSMCs, showing ASC-SF therapy as a potential post-surgical therapeutic mechanism to help local cells fortify vasculature after initial surgery. BAV-NA and BAV-TAA SMCs showed an increase in elastin deposition with both ASC-SF and NCM, necessitating further study as to the elastogenic components both have in common.

We conclude that ASC-SF can stimulate elastic fiber assembly by healthy adult SMCs, and both explanted pediatric and adults SMCs, possibly mediated through the increased activity of SMC-secreted elastin accessory proteins. This could potentially lead to an effective non-surgical regenerative therapy for treatment of AA.

ACKNOWLEDGEMENTS

This work was supported by the Leonard H. Berenfield Graduate Fellowship in Cardiovascular Bioengineering and National Institutes of Health T32 HL094295 (A.K.R.), the University of Pittsburgh's International Studies Fund (R.E.S.), the European Union's Horizon 2020 Research and Innovation Program under the Marie Sklodowska-Curie grant agreement 708867 (E.M.C.), the National Institutes of Health grants HL129066 and HL130784 and McCune Foundation Pediatric Device Initiative (D.A.V.), and University of Pittsburgh Competitive Medical Research Fund (J.S.W.).

REFERENCES

[1] N. Kontopodis, et al., *Front Surg*, vol. 3, p. 1, Jan 2016.

[2] D. M. Milewicz et al., *Annu Rev Genomics Hum Genet*, vol. 9, pp. 283-302, 2008.

[3] C. Fleming, et al., *Annals of Internal Medicine*, vol. 142, no. 3, pp. 203-211, Feb 2005.

[4] E. Gillis, et al., *Circ Res*, vol. 113, no. 3, pp. 327-40, Jul 19 2013.

[5] K. C. Kent et al., *J Vasc Surg*, vol. 52, no. 3, pp. 539-48, Sep 2010.

[6] K. C. Kent, *N Engl J Med*, vol. 371, no. 22, pp. 2101-8, Nov 27 2014.

[7] K. J. Blose, et al., *Regenerative Medicine*, vol. 9, no. 6, pp. 733-741, 2014 2014.

[8] J. S. Weinbaum, et al., *Tissue Engineering Part C-Methods*, Article vol. 16, no. 3, pp. 459-467, Jun 2010.

[9] B. Starcher, *Analytical Biochemistry*, vol. 292, no. 1, pp. 125-129, May 1 2001.

QUANTIFYING AND MODELING SPATIAL HETEROGENEITY IN VALVE INTERSTITIAL CELLS

Emma Lejeune (1), Alex Khang (1), Michael S. Sacks (1)

(1) Willerson Center for Cardiovascular
Modeling and Simulation
University of Texas at Austin
Austin, TX, USA

INTRODUCTION

Valve interstitial cells (VICs) play a critical role in maintaining normal valve function. Therefore, changes to the valve mechanical environment induced by both disease and surgical intervention can lead to adverse changes in VIC behavior and negative clinical outcomes. While much has been learned from tissue scale modeling of heart valves, many critical aspects of VIC regulated tissue response are only recently being investigated [1]. And, while much has been learned about VICs in isolation, the direct impact of these observations on tissue scale behavior is far from fully understood [2]. To address this gap, new strategies for bridging the cellular and tissue scales are vital. Here we present a combined experimental/computational framework to quantify and model the contractile behavior of VICs in a tunable experimental environment. We introduce statistical methods to quantify spatial heterogeneity in individual VICs, and introduce a computational framework to understand the implications of this heterogeneity across scales. The knowledge gained from this work is a step towards a better understanding and ability to potentially control how VICs remodel tissue in the native valve environment.

METHODS

Measuring spatial heterogeneity. For measurements taken within the bounds of a single cell, there is often substantial spatial variation. To understand the nature of this spatial variation, we first introduce a strategy for measuring spatial autocorrelation (similarity of spatially near points) of given properties in each cell. To do this we use the Global Moran's I statistic and compare the results to the null hypothesis that there is no spatial autocorrelation [3]. When spatial autocorrelation is high, values of I approach 1. In addition, we plot experimental semivariograms that show variance in a given property with respect to the distance between measurement points (lag) for bins of data. Here we demonstrate this method by analyzing data from a set of experiments that use atomic force microscopy (AFM) to measure the Young's Modulus of VICs derived from the Aortic Valve (AV) and Pulmonary Valve (PV). In these experiments, the cells are adhered to a two-dimensional substrate with indentation measurements taken at 40-60 discrete points per cell [3].

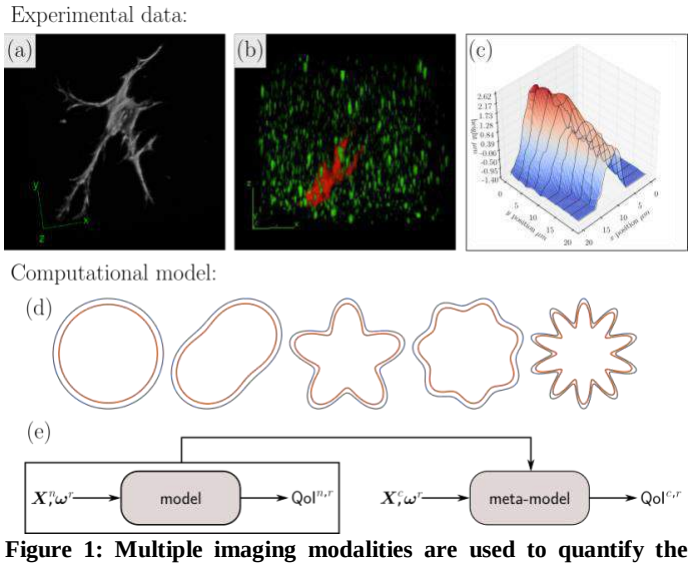

Figure 1: Multiple imaging modalities are used to quantify the spatially heterogeneous properties and irregular geometries of VICs (a-c). A suite of computational models is used to understand the implications of this heterogeneity across scales (d-e).

Gaussian process regression for interpolating experimental data. For each experimental modality, data is only available at discrete points in space. As an improvement on traditional interpolation methods, we utilize gaussian process regression (GPR), to predict properties between measurement points. Gaussian process regression is a non-parametric approach that finds a distribution over all possible functions f that are consistent with the observed data [5]. Through using GPR tuned to optimize fit on unseen data, we are better able to infer and ultimately model properties at each point in space. For example, Fig. 1c shows a GPR based interpolation of cell height acquired through AFM. This approach becomes particularly meaningful in regions where experimental data is present but sparse.

Computational analysis framework. Given experimental data describing VICs, we are able to construct a suite of computational cell models with realistic cell geometry and spatially heterogeneous cell properties. As a toy example to demonstrate the flow of the computational framework, consider a two dimensional finite element model of a cell embedded in a substrate and loaded uniaxially. We can describe the boundaries of the toy cell with a rose function:

$$\boldsymbol{x} = [\boldsymbol{R} + \boldsymbol{a}\,\boldsymbol{sin}(\boldsymbol{n}(\theta + \boldsymbol{\Phi}))]\boldsymbol{cos}\theta + \boldsymbol{x_c} \quad (1)$$

$$\boldsymbol{y} = [\boldsymbol{R} + \boldsymbol{a}\,\boldsymbol{sin}(\boldsymbol{n}(\theta + \boldsymbol{\Phi}))]\boldsymbol{sin}\theta + \boldsymbol{y_c} \quad (2)$$

where $\boldsymbol{x}$ and $\boldsymbol{y}$ are the coordinates of cell boundary, ($\boldsymbol{x_c}$,$\boldsymbol{y_c}$) is the cell center, $\boldsymbol{R}$ is the inner radius, $\boldsymbol{a}$ is the petal amplitude, $\boldsymbol{n}$ is the number of petals, and $\boldsymbol{\Phi}$ is the initial rotation. This shape is illustrated in Fig. 1d**.** In addition to geometry, we vary cell shrinkage α and average modulus E. We then choose some Quantity of Interest (QoI), such as the predicted maximum stress under a given loading condition, where the goal is to determine which simulation input parameters are most critical to that QoI. Even with this simple example, many simulations are required. To make this a tractable problem, we use a global sensitivity analysis procedure for random models [6]. This pipeline is illustrated in Fig. 1e. With this framework, we can analyze a suite of computational models that represent the variations observed in the experimental data.

Table 1. Moran's I and Z-score for each cell. Cells marked with (★) show statistically significant spatial autocorrelation.

Cell No.	I	z_I	Cell No.	I	z_I
AV-1	0.095	1.15	PV-1★	0.42	6.33
AV-2 ★	0.27	2.39	PV-2★	0.30	3.63
AV-3	-0.012	0.092	PV-3★	0.57	9.25
AV-4	-0.082	-0.31	PV-4★	0.70	10.29
AV-5	-0.023	-0.11	PV-5★	0.39	6.24
			PV-6★	0.50	7.68

RESULTS

The first result shown here is a comparison of spatial autocorrelation of stiffness in AV and PV VICs. This comparison is shown in Table 1. Critically, only one out of five AV cells shows statistically significant spatial autocorrelation in stiffness while six out of six PV cells show statistically significant spatial autocorrelation. This is also reflected in the shape of the experimental semivariogram shown in Fig. 3. For the PV cells, the spatial autocorrelation indicates that GPR is suitable for modeling spatial variation in cell modulus. For the AV cells, an alternative approach is required to generate synthetic representative models of spatial variation.

The plots in Fig. 4 show the results of running the toy problem through the computational analysis framework. First, we run a global sensitivity analysis to determine which of the varied model input parameters are the most critical. Then, we conduct a parameter sweep. Within the assumptions of this simplified model, we see that the maximum stress experienced by the cell under identical external loading conditions varies widely. In particular, we highlight the importance of cell shrinkage α and relative petal amplitude a/R.

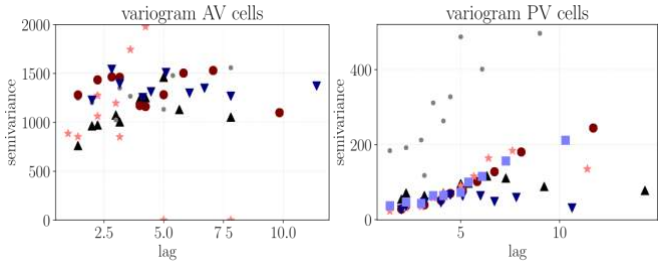

Figure 3: Experimental semivariograms for AV and PV cells.

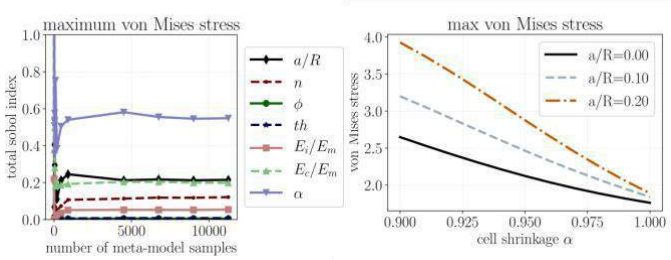

Figure 4: Left: a global sensitivity analysis on the rose model shows that cell shrinkage (α) and petal amplitude variation (a/R) are the most crucial parameters for predicting the max von Mises stress within the cell. Right: a corresponding parameter sweep.

DISCUSSION

This work on quantifying and modeling spatial heterogeneity in VICs primarily serves as a platform for future investigation into how the effects of altered cell behavior traverse scales from a bottom-up perspective. For the first time, we quantitatively show that AV and PV VICs have fundamentally different levels of spatial autocorrelation in stiffness. We also outline and demonstrate the functionality of a computational modeling framework to identify and explore mechanical mechanisms that increase our understanding of VICs and their interactions with their surroundings. Rather than simulating a single average cell with fixed parameters, our framework is set up to simulate hundreds to thousands of different cells with variable geometries and properties and interpret the results. Next, we will use our statistical techniques to generate a library of representative heterogeneous cells from experimental data and use computational modeling to test the mechanistic connection between altered cell properties and changes to experimentally observed bulk mechanical properties. Moving forward, this combined experimental/computational approach will help pave the way for understanding the impact of modified cell behavior on the tissue scale manifestation of valve disease.

ACKNOWLEDGEMENTS

This work was supported by the Peter O'Donnell, Jr. Postdoctoral Fellowship in Computational Engineering and Sciences.

REFERENCES

[1] Butcher, JT et al., *Journal of Heart Valve Disease*, 17:62, 2008.
[2] Ayoub, S et al., *Cellular and Molecular Bioengineering*, 1-16, 2018.
[3] Goodchild, MF, *Geo Books*, 37, 1986.
[4] Merryman, DW et al., *Tissue engineering*, 13:2281, 2007.
[5] Rasmussen, CE and Williams CK, *MIT press*, 2006.
[6] Hart, JL et al., *SIAM Journal on Scientific Computing*, 39:A1514, 2017.

CYCLIC STRETCH CAUSES LIBERATION OF CAVEOLIN-1 IN EXTRACELLULAR VESICLES FROM VASCULAR SMOOTH MUSCLE CELLS

Mohammad Shaver (1), Jessica Molina (1), Joshua D.Hutcheson (1)

(1) Biomedical Engineering Department,
Florida International University, Miami,
Florida, USA

INTRODUCTION

Caveolin-1 (Cav-1), an integral structural component of caveolae plasma membrane invaginations, has been reported to play important functions in atherogenesis and vascular calcification. Caveolae buffer the membrane to sudden changes in tension and mediate intracellular trafficking [2,3]. When plasma membrane tension increases caveolae flattening prevents membrane rupture. In vascular calcification, endocytosis of caveolae domains on the plasma membrane of vascular smooth muscle cells (SMCs) initiates the formation of calcifying extracellular vesicles (EVs). However, the role of plasma membrane tension in Cav-1 trafficking and EV formation in SMCs remains unknown. As pressures change over the cardiac cycle, SMCs experience cyclic mechanical stretch, causing elevated plasma membrane tension [4]. The aim of this study is to investigate the changes in Cav-1 trafficking and EV formation through application of mechanical stretch to SMCs *in vitro*.

METHODS

Porcine left coronary artery SMCs were harvested from hearts obtained from a local abattoir. The cells were expanded for no more than 7 passages and cultured on Bioflex culture plates. Cyclic stretch (5, 10 and 15%, 0.5 Hz) was applied to the SMCs for 72h using a Flexcell FX-5000T. Non-stretched SMCs were used as controls. Following mechanical stimulation, Cav-1 in SMCs and EVs collected from the culture media was assessed via western blotting. Equal protein loading was confirmed using Ponceau S staining. Immunofluorescence imaging was performed to assess changes in Cav-1 distribution within SMCs. Tunable resistive pulse sensing (TRPS) was used to quantify the number and size of EVs.

RESULTS

Western blotting showed elevated Cav-1 in non-stretched control SMCs compared to SMCs exposed to 5,10 and 15% cyclic stretches (**Figure 1A**); where 10% is considered as a physiological cyclic stretch while 5% is sub-physiological and 15% is pathological cyclic stretch [5]. However, western blotting of EVs isolated from conditioned media from these samples revealed increased of Cav-1 in EVs collected from the stretched SMCs compared to the non-stretched controls **(Figure 1B**).

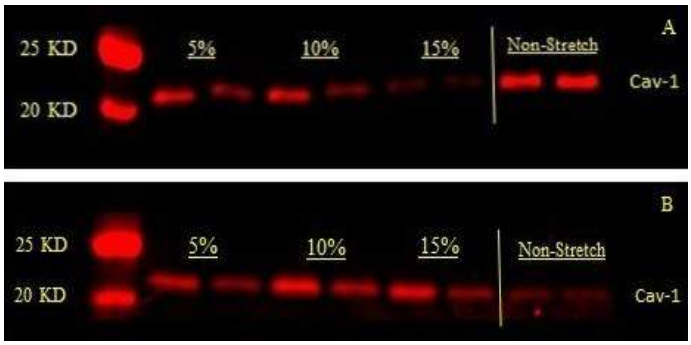

Figure1. Western blotting of intracellular (A) and EV (B) caveolin-1.

Densitometry-based quantification of n=3 independent replicates indicated a dose-dependent inverse relationship between stretch and intracellular Cav-1 (**Figure 2**). EV Cav-1 was higher in all stretched samples compared to control and exhibited a maximum in the SMCs exposed to 10% stretch.

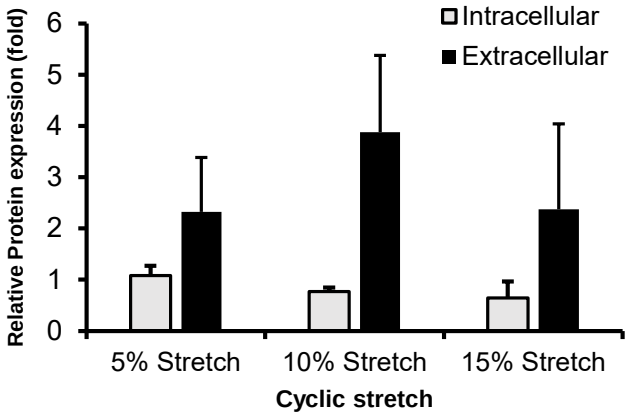

Figure 2. Values of caveolin-1 within the SMCs in comparison with the extracellular.

Immunofluorescence showed Cav-1 clustering (red fluorescence) within the cytoplasm of stretched SMCs (**Figure 3A**) compared to the non-stretch samples (**Figure 3B**), indicative of caveolae flattening and Cav-1 liberation from the plasma membrane. Actin fibers within the SMCs were identified using a green fluorescent phalloidin stain (**Figure 3A-B**).

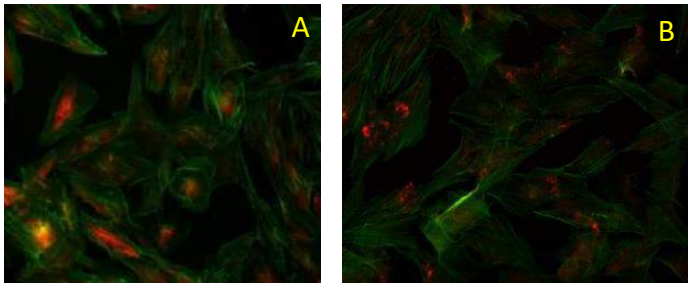

Figure 3. (A) Immunofluorescent images of SMC exposed to cyclic stretch (B) and non-stretched control SMCs.

TRPS can determine absolute concentration and size of EVs in media samples. The application of cyclic stretch led to increased EV release (**Figure 4A**). The concentration of EVs in the conditioned media from non-stretched VSMCs was $1.1x10^{12}$ EVs/mL. Exposing SMCs to 15% strain increased EV concentration to $2.x10^{12}$ EV/mL. Mechanical stretch also led to a more uniform EV size and charge distribution (**Figure 4B & 4C**).

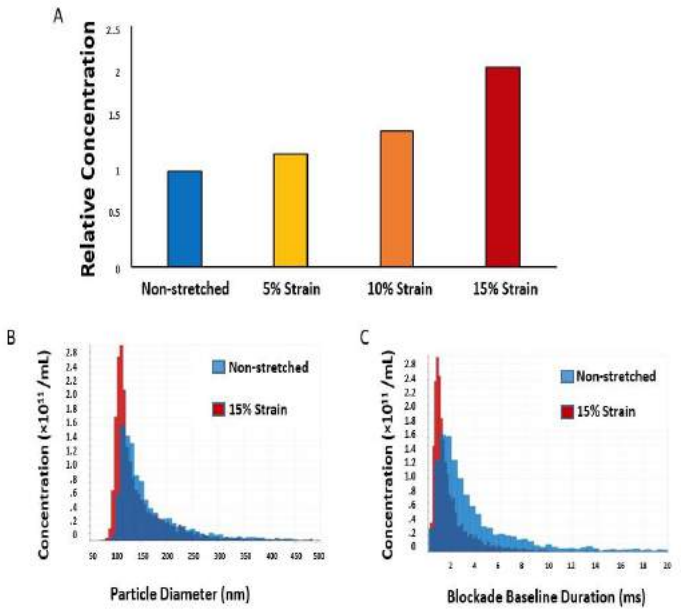

Figure 4. (A) Relative concentration of samples based on final particle count (B) EV size distribution for non-stretched control and 15% strain samples (C) EV charge distribution for non-stretched control and 15% strain samples.

DISCUSSION

The results indicate that cyclic mechanical stretch induces intracellular trafficking and subsequent release of Cav-1 in EVs of SMCs. Cav-1 has been noted to play an important role in cardiovascular diseases such as hypertension, atherosclerosis, and vascular calcification. EVs help mediate paracrine signalling and extracellular remodelling responses. Therefore, changes in Cav-1 trafficking and EV release in response to mechanical stimulation might play an important role in intercellular communication and matrix remodeling. Future studies may lead to the identification of therapeutic strategies for a number of cardiovascular diseases by modulating Cav-1 trafficking.

REFERENCES

1. Lu D et al, J R Soc Interface, 8(63):1379-85,2011.
2. Stephanie L et al, J Front physiol, 3: 280,2012.
3. Fridolfsson HN et al, J Geriatr Cardiol, 10(1): 66–74, 2013.
4. Sinha B et al, J Cell, 144(3):402-13,2011.
5. Labrosse M, ISBN 9781138197237,2018.

SB³C2019
Summer Biomechanics, Bioengineering and Biotransport Conference
June 25 -28, Seven Springs, PA, USA

FOCAL CHONDRAL DEFECTS IN THE DYSPLASTIC HIP CAUSE ACTIVITY- AND SIZE-DEPENDENT INCREASES IN STRESS AND STRAIN

Jocelyn N. Todd (1,2), Travis G. Maak (3), Jeffrey A. Weiss (1,2,3)

(1) Department of Biomedical Engineering
University of Utah
Salt Lake City, UT, USA

(2) Scientific Computing and Imaging Institute
University of Utah
Salt Lake City, UT, USA

(3) Department of Orthopaedics
University of Utah
Salt Lake City, UT, USA

INTRODUCTION

Osteoarthritis (OA) is a highly prevalent joint disease characterized by the degradation of articular cartilage and the underlying bone. The hip is one of the most common joints in the body that is affected by OA. In the hip, bony pathomorphology such as dysplasia produces abnormal loading of the cartilage. This abnormal loading on the articular cartilage can overload the tissue, resulting in focal chondral defects and subsequently the development of OA[1]. Focal chondral defects present as partial- or full-thickness voids in the articular cartilage, on the articular surface or at the osteochondral interface.

Although mechanical factors are understood to influence the initiation and progression of OA[2], the alterations in mechanics due to bony pathomorphology, the development of chondral defects, and the progression to OA are not well-understood. Due to the paucity of research on these mechanical effects, surgical treatment of chondral defects in the hip is rarely attempted. A clear understanding of the mechanical effects of these conditions would help to separate stable defects that will not expand and can potentially be treated conservatively (non-surgically) from defects that are likely to expand and thus should be treated more aggressively (i.e,. with arthroscopic or even open surgical intervention). Finite element (FE) analysis can be used to understand the mechanics of cartilage in the hip and the various effects of different sizes and locations of focal chondral defects[3]. The method allows incorporation of highly nonlinear factors, such as geometry, material properties, and loading conditions, for analysis of mechanical environments which would otherwise be nearly impossible to test *in vivo*. The objective of this study was to assess the effects of the presence and size of focal chondral defects on the time-dependent response of articular cartilage in a patient-specific, dysplastic hip during activities of daily living.

METHODS

A validated patient-specific FE model of a dysplastic hip was selected from a cohort of ten models[4] (Fig. 1A). Acetabular and femoral cartilage were represented as anisotropic biphasic materials. The solid phase consisted of a continuous ellipsoidal distribution of tension-only collagen fibrils embedded in an isotropic matrix to capture tension-compression nonlinearity, initial anisotropy, and strain-induced anisotropy[5, 6]. A physiologically realistic distribution of fibril orientation was applied through the thickness of the cartilage layers, where fibrils were aligned tangent to articular surface in the superficial zone, spherical in the middle zone, and perpendicular to the osteochondral interface in the deep zone. A continuous variation of fibril reinforcement through the thickness was achieved with a custom FEBio plugin that allows scaling of the contribution from a local element axis as a function of surface depth (https://febio.org/plugins/). Permeability was represented as strain-dependent and anisotropic to align fluid flow with the direction of the fibrils. The labrum was modeled with a biphasic transversely-isotropic material with an isotropic ground matrix and fibers aligned circumferentially. Material coefficients and parameters were determined experimentally and guided by previously published sensitivity studies[6, 7].

An intact case was compared to cases with chondral defects of 3, 7 and 15 mm in diameter at a clinically relevant location on the chondrolabral boundary[8] (Fig. 1A). Single-leg stance (SLS), gait, and squatting were simulated using three-dimensional loading and kinematics from Bergmann et al [9]. SLS was simulated by ramping to the maximum load and analyzing the response under creep for 600 s, as pilot simulations indicated that the variation of dependent variables was minimal after this time. A full cycle of gait and squatting were simulated to assess the effect of the presence and size of chondral defects on the same variables during dynamic scenarios. All models

were analyzed with FEBio (www.febio.org). The osteochondral interfaces were represented as impermeable and they were tied to rigid bodies representing the femur and pelvis. All other surfaces of the articular cartilage layers were free-draining.

For each kinematic scenario, the region around the defect (Fig 1B) was analyzed throughout the motion. The peak value over time in this region was selected for comparison between the different defect cases and activities. Maximum tensile strain on the articular surface (E_1) and maximum shear stress at the osteochondral interface (τ_{max}) were examined within the acetabular cartilage as the major dependent variables, due to the potential for collagen fibril fissuring and delamination of the cartilage from the bone, respectively. Fluid flux around the defect region was analyzed qualitatively.

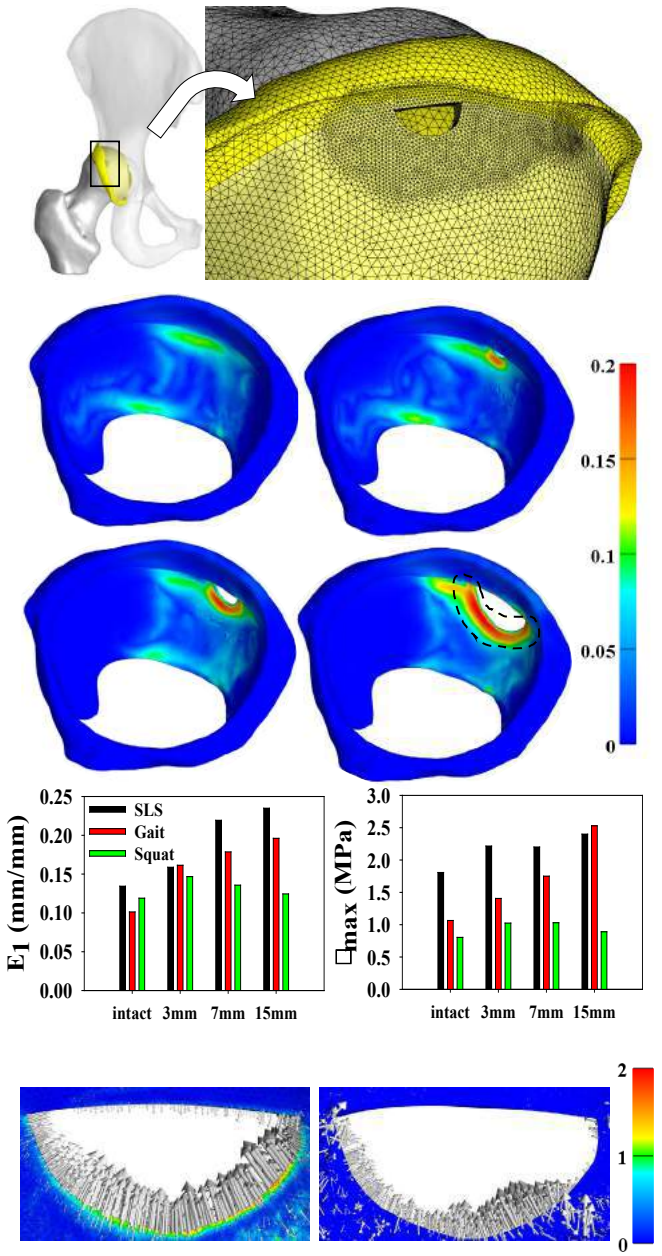

Figure 1: A) Patient-specific hip and close-up of 7 mm defect case. B) Comparison of E_1 during gait, showing the concentration in the defect region. The defect region analyzed is indicated by the black dashed line in the 15 mm case. C) Peak values of E_1 and τ_{max} during SLS, gait, and squatting. D) Comparison of magnitude and direction of fluid flux for 15 mm defect between gait and squatting cases.

RESULTS

Regardless of the activity performed, the presence of a chondral defect increased solid phase stress and strain (E_1 and τ_{max}) in the defect region compared to the intact case (Fig. 1B-C). The 15 mm defect model experienced the highest magnitude for E_1 and τ_{max}: 23.5% during SLS and 2.53 MPa during gait, respectively. For SLS and gait, E_1 and τ_{max} increased with increasing defect size. During squatting, E_1 and τ_{max} were highest for the 3 mm case and decreased slightly for the 7 mm and 15 mm defect cases. Fluid flux around the defect was much higher and concentrated in the defect region during gait and SLS compared to squatting (Fig. 1D).

DISCUSSION

Elevated solid phase stress and strain were in the defect region may put the cartilage at risk of further damage progression. However, the magnitude and trends of these variables differed based on the applied motion.

During SLS and gait, the 15 mm case experienced tensile strain within the reported range of collagen fibril failure in articular cartilage [10]. Therefore, depending on the applied loading, larger defects may have greater potential for damage progression. This may indicate a threshold defect size, beyond which more aggressive treatment strategies should be recommended; however, more cases must be tested to verify this trend, as well as to determine the threshold size.

Increasing the defect size increased the stress and strain near the defect region during gait and SLS. In these scenarios, the loading vector is more directly applied toward the defect region. Loading applied more directly to the defect will induce a higher rate of fluid loss from the defect and could elevate stresses and strains due to edge loading. This was demonstrated by increased fluid flux around the defect and indicates that loss of fluid pressurization due to different loading patterns is closely linked to increased damage in the regions. During squatting, the load was not directed towards the defect region. Interestingly, while all defect cases exhibited a localized region of elevated E_1 and τ_{max} during squatting, increasing the size of the defect from 3 mm to 7 mm and further to 15 mm decreased the stress and strain around the defect. This discrepancy in stress and strain magnitudes for increasing defect sizes indicates that the type of loading greatly affects the potential for damage progression.

ACKNOWLEDGMENTS

Supported by an LS Peery Investigator Research Grant through the Department of Orthopaedics at the University of Utah.

REFERENCES

[1] Ganz, R., *Clin Orthop Relat Res*. 466: 264-72, 2008.
[2] Guilak, F., *Best Pract Res Clin Rheumatol*. 25: 815-23, 2011.
[3] Klennert, B.J., *J Biomech*. 52: 31-37, 2017.
[4] Anderson, A.E., *J Biomech Eng*. 130: 051008, 2008.
[5] Ateshian, G.A., *J Biomech Eng*. 131: 061003, 2009.
[6] Henak, C.R., *J Biomech Eng*. 136: 021021, 2014.
[7] Todd, J.N., *J Biomech*. 69: 113-120, 2018.
[8] Kapron, A.L., *Knee Surg Sports Traumatol Arthrosc*, 2018.
[9] Bergmann, G., *J Biomech*. 34: 859-71, 2001.
[10] Sasazaki, Y., *J Anat*. 208: 681-94, 2006.

MECHANICAL PROPERTY CHANGES IN THE TIBIAL PLATEAU CARTILAGE FOLLOWING TRAUMATIC INJURY AND REPAIR PROCEDURES TO THE LAPINE KNEE

Patrick E. Vaughan (1,2), Feng Wei (1,2,3), Albane Fauron (4), Loic Dejardin (4), Tammy Haut Donahue (5), Roger C. Haut (1,3)

(1) Orthopaedic Biomechanics Laboratories
Michigan State University
East Lansing, MI, USA

(2) Department of Biomedical Engineering
Michigan State University
East Lansing, MI, USA

(3) Department of Mechanical Engineering
Michigan State University
East Lansing, MI, USA

(4) Department of Small Animal Clinical Sciences
Michigan State University
East Lansing, MI, USA

(5) Department of Biomedical Engineering
University of Massachusetts
Amherst, MA, USA

INTRODUCTION

Acute, traumatic injuries to the anterior cruciate ligament (ACL) and meniscus significantly increase the risk of a long-term, chronic disease known as post-traumatic osteoarthritis (PTOA) [1], whether or not the patient has an early surgical reconstruction of the traumatized knee [2]. Using a previously developed closed-joint knee injury lapine model, our group demonstrated that 12 weeks after traumatic ACL and meniscal injury, untreated lesions result in intraarticular soft tissue changes consistent with clinical mid to late stage PTOA [3]. While post-traumatic ACL reconstruction and meniscal debridement represent the standard of care in clinical cases, surgical treatment of the traumatized knee was not performed in our previous studies.

Osteoarthritis (OA) is a degenerative joint disease, with which the articular cartilage begins to break down and wear away over time. In order to determine the changes that occur in the mechanical properties of articular cartilage in a traumatized knee, in situ indentation relaxation tests have been the experiment of choice to extract the material characteristics of cartilage, as the method preserves the structural integrity of the tissue on the joint surface [4].

The purpose of the current study is to develop a new lapine model that combines traumatic injury and subsequent surgical repair of the knee, and perform indentation relaxation tests on the tibial plateau cartilage to document changes in mechanical properties of the cartilage over time. It was hypothesized that acute damage to the articular cartilage resulting from a controlled, traumatic impact to the lapine knee would develop chronic changes in material properties of the cartilage, consistent with the previous description of mid to late stage PTOA in the lapine model, despite the subsequent application of repair procedures to the traumatized joint.

METHODS

Traumatic ACL and meniscal tears were induced on 12 skeletally mature, anesthetized Flemish Giant rabbits. With the animal in sternal recumbency, the right knee and paw were secured into a custom fixture that allowed unrestricted anterior tibial subluxation while constraining lateromedial motion. Controlled impact was delivered by a servo-hydraulic actuator (Instron, Norwood, MA) which thrusted the tibia proximally at a rate of 0.5 Hz until ACL failure. Following debridement of the torn ACL and medial meniscus, reconstructive surgery was performed 2-3 weeks post-impact. The semitendinosus (ST) tendon's musculotendinous junction was transected while its tibial insertion was preserved. The tendon's free end was rerouted through tibial and femoral tunnels, of which intraarticular locations overlapped the ACL footprints. The ST tendon was tensioned and then secured into the femoral tunnel using an interference fit screw and periosteal sutures. A drawer test was performed to assess postoperative joint stability prior to routine closure. An IACUC approval was obtained for the study.

Animals were euthanized 1 (n=4), 3 (n=4), and 6 (n=4) months post-impact. Tissue was harvested immediately after euthanasia and refrigerated until mechanical tests were performed (within 12 h). Indentation relaxation testing was performed in a room temperature saline bath on the tibial plateau cartilage at four sites to account for both meniscus-covered and -uncovered cartilage surface (Figure 1). The cartilage thickness of each indentation site was measured by inserting a needle at a location adjacent to each site and observing when the reaction force increased due to contact with subchondral bone. A 1.59 mm diameter, spherical nonporous steel indenter was then pressed into the cartilage 30% of its thickness for 180 s, while the relaxation force-time data were collected. The mechanical tests were simulated with a previously described fibril-reinforced biphasic model

and implemented in a finite element package (Abaqus, Pawtucket, RI) [5]. The fiber modulus (E_f), matrix modulus (E_m), and tissue permeability (k) of cartilage were determined from this model. These property data were then compared with those from a previous study that uses a similar knee injury lapine model but without the surgical repair of the traumatized knee [3].

Unpaired t tests were used to compare differences in cartilage mechanical properties between impacted and contralateral control limb, and between results in the 3-month group of the current study and those from 12-week post-impact in Fischenich et al. [3], with $p<0.05$ considered as significant.

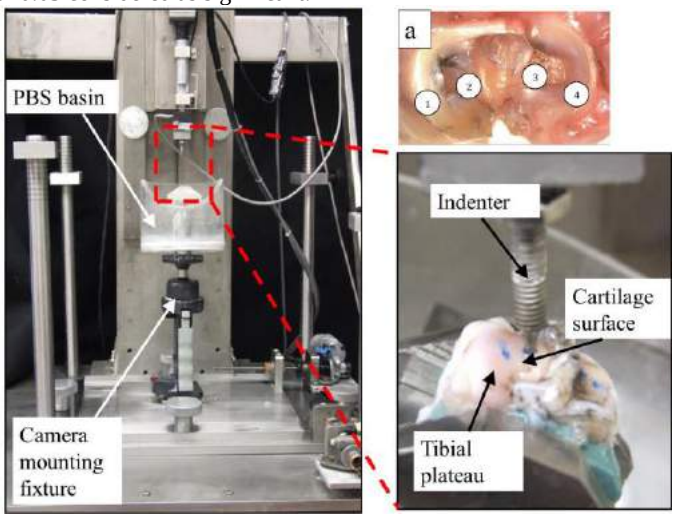

Figure 1: Experimental setup for the indentation relaxation tests with the four indentation sites on the tibial plateau (a).

RESULTS

Mid-substance ACL tears were documented in 10/12 animals, while damage to the caudal horn of the medial meniscus occurred in 8/12 animals. Mean (±SD) failure force was 859.5 ± 117.6 N, correlating with approximately 12-13 times body weight of the animal.

Cartilage thickness was significantly greater in the impacted limbs than that in the control limbs at 3 and 6 months post-impact (Table 1). Mechanical properties of the tibial plateau cartilage showed remarkable degradations of the tissue, with a significant decrease in fiber modulus at 3 and 6 months post-impact, a significant decrease in matrix modulus at all three time-points post-impact, and a significant increase in tissue permeability at all three time-points.

Table 1: Average tibial plateau cartilage thickness and mechanical properties at three different time-points. * Denotes significant difference with p<0.05 between control and tested limb.

Group	Cartilage Thickness t (mm±SD)	Fiber Modulus E_f (MPa±SD)	Matrix Modulus E_m (MPa±SD)	Tissue Permeability k (10^{-14} m^4/Ns)
Left Tibial Plateau (control, average of covered and uncovered sites)				
1-month	0.29 ± 0.08	48.9 ± 15.0	1.52 ± 0.52	6.39 ± 4.11
3-month	0.42 ± 0.09	51.2 ± 13.4	1.49 ± 0.21	6.58 ± 3.01
6-month	0.26 ± 0.05	45.2 ± 10.8	0.99 ± 0.24	7.73 ± 5.99
Right Tibial Plateau (tested, average of covered and uncovered sites)				
1-month	0.38 ± 0.06	35.5 ± 19.1	0.85 ± 0.14*	20.6 ± 5.22*
3-month	0.64 ± 0.12*	15.7 ± 11.2*	0.50 ± 0.11*	21.9 ± 7.45*
6-month	0.47 ± 0.09*	4.78 ± 6.67*	0.41 ± 0.13*	47.7 ± 11.5*

In addition, a comparison of the current results with those from a previous study [3] under the same time-point (12 weeks post-impact) showed that no statistically significant difference was observed in the mechanical properties of the impacted tibial plateau cartilage between studies (Figure 2).

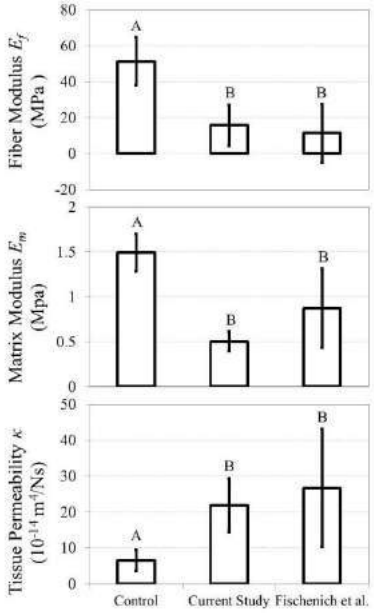

Figure 2: Comparisons of mechanical properties in tibial plateau cartilage between the current study and Fischenich et al. [3]. Means that do not share a letter are significantly different.

DISCUSSION

This closed-joint knee injury model successfully and reliably generated traumatic mid-substance ACL tears and in most cases, meniscal damage. Repair procedures were then successfully performed for surgical treatment of the traumatized knee. ACL reconstruction and meniscal debridement replicated current surgical management of these injuries. Thus, this study provides a combined *injury* and *repair* model that can be used to study clinically relevant damages to the menisci, articular cartilage and subchondral bone associated with traumatic ACL rupture. Additionally, the fibril-reinforced biphasic model used in the current study accurately fitted the experimental curve, extracting both the instantaneous (fiber modulus) and equilibrium (matrix modulus) responses and tissue permeability.

The mechanical property results suggested significant degenerative changes of articular cartilage due to a traumatic knee impact, despite surgical repair of the traumatized joint. In addition to mechanical properties, as the ongoing project also uses morphological, functional, histological and imaging analyses, soft tissue lesions due to traumatic knee injury could be correlated to clinical progress of PTOA using this new animal model. This new model will therefore allow evaluations of the efficacy of an early intraarticular pharmacological intervention (P188) post-trauma.

ACKNOWLEDGEMENTS

The study is funded by DOD grants W81XWH-16-1-0735 and W81XWH-16-1-0734. The authors thank Mr. Clifford Beckett for technical assistance in the project.

REFERENCES

[1] Felson, DT, *Radiol Clin North Am*, 42(1):1-9, 2004.
[2] Myklebust, G, and Bahr, R, *Br J Sports Med*, 39(3):127-131, 2005.
[3] Fischenich, KM et al., *J Biomech*, 48(2):246-253, 2015.
[4] Mow, VC et al., *J Biomech Eng*, 102(1):73-84, 1980.
[5] Golenberg, N et al., *Int J Exp Comput Biomech*, 1(1):58-75, 2009.

COLLAGEN-DERIVED RESIDUAL STRESS ENHANCES THE BIPHASIC LUBRICATION PROPERTY IN ARTICULAR CARTILAGE

Hiromichi Fujie (1), Soh Morishita (1), Seido Yarimitsu (1)

(1) Biomechanics Laboratory
Faculty of System Design, Tokyo Metropolitan University
Tokyo Japan
fujie@tmu.ac.jp

INTRODUCTION

Articular cartilage is heterogeneous and consists of three zones: superficial, middle, and deep zones. Previous studies indicated that articular cartilage surface could be split along collagen fiber direction in response to insertion of a dissecting needle [1]. This phenomenon is known as "split-line" that would suggest a collagen-derived residual stress is contained in articular cartilage. In fact, sliced cartilage specimens from mature animals tend to curve due to residual stress (Figure 1). In the present study, the effect of residual stress on the biphasic lubrication property in articular cartilage was analyzed [2].

Figure 1 Natural curvature of articular cartilage after sliced from a porcine femur (surface faces up)

METHODS

A fiber-reinforced 2-dimensional poroelastic cartilage model was developed on Abaqus 6.14 (Dassault Systemes, US), while referring to our previous study [3]. Cartilage of 3 x 1.5 mm was assumed to consist of fiber-reinforced poroelastic elements. Each element consisted of a pore pressure, plane strain element (CPE4RP) as a model of proteoglycan, and laterally oriented spring elements (SPRING A) as a model of collagen fibers. While the permeability, Poisson' ratio, and coefficient of friction for solid-to-solid contact of proteoglycan were obtained from previous studies [4-6], the elastic moduli of proteoglycan and collagen fibers were determined through a curve fitting procedure to a confined compression test (Table 1). Note that the modulus of the collagen fibers was set to be dependent on compressive strain. This model was termed as standard model (SD model). Then, residual stress was contained in the collagen fibers in the surface layer of 0.3 mm in thickness by applying 1%-5% of tensile strain to collagen fibers. These models were termed as residual stress models (RS1-RS5 models). A rigid cylinder of 1 mm in diameter was translated on the cartilage model with a contact force of 0.1 N at a friction speed of 0.05-10.0 mm/s. The coefficients of start-up and dynamic friction were calculated from the integral of shear stress divided by the integral of contact pressure.

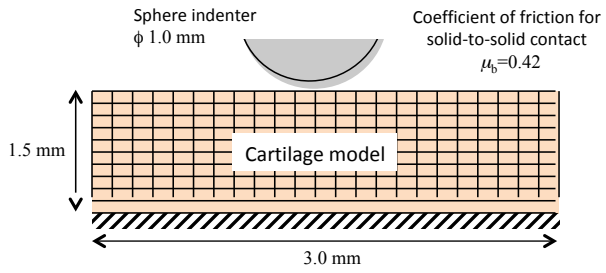

Figure 2 Fiber-reinforced 2-dimensional poroelastic articular cartilage model in a friction test against a cylindrical indenter

Table 1 Mechanical properties of the proteoglycan and collagen fiber of articular cartilage model

Proteoglycan				Collagen fiber	
Modulus (MPa)	Poisson's ratio	Permeability (10^{-15} m^4/Ns) $k = k_0 \exp(M\varepsilon_m)$*		Modulus (MPa)** $E_f = E_{f0} + E_{f1}\varepsilon_f$	
E_m	ν_m	k_0	M	E_{f0}	E_{f1}
0.15	0.42**	6.44****	2.64 ***	0.01	6.4

*Lai, W. M.,et al., 1980. Biorheology. **Li L. P., et al., 1999. Clin Biomech. ***Susa T., et al., 2010. 6thWCB. ****Nakamura, R., et al., 2014. 7thWCB.

RESULTS

At 1 mm/s of friction speed, the coefficient of start-up friction at the first cycle was approximately 0.21 in SD model while it was slightly higher in RS models (Figure 3). However, at the second cycle of friction, the coefficient was approximately 0.16 in SD model while it was much lower in RS models; approximately 0.11 in RS1 model and 0.13 in other RS models. The coefficient of dynamic friction in the 1st and 2nd friction cycles was also lower in RS models than in SD model. This trend of decreasing coefficients of start-up and dynamic friction in RS models was also observed at other friction speeds.

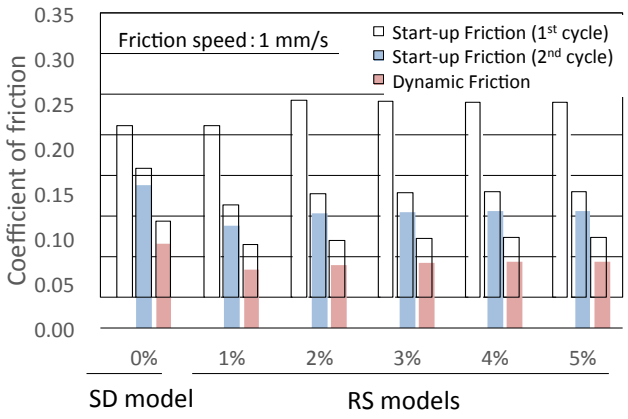

Figure 3 Coefficients of start-up friction at the 1st and 2nd cycles of friction and averaged coefficient of dynamic friction at a speed of 1 mm/s in SD and RS models of articular cartilage

DISCUSSION

It was found that the residual stress in arterial wall played a role in decreasing its pressure gradient in a previous study [7]. To our knowledge, the present study is the first one that clarified the effect of residual stress on the lubrication property of articular cartilage. The coefficients of start-up and dynamic friction were decreased in RS models as compared with SD model, with the largest decrease observed at 1% of strain remained in collagen fibers (RS1 model) at friction speed of 1 mm/s. The modulus of collagen fibers in RS models was higher than that in SD model due to the contained residual stress. Thus, negative pressure behind the contact area was higher in RS model, shown in black in Figure 4, than in SD model, which caused a rapid rehydration in the region and higher fluid load support at the second and further friction cycles (Figures 4 & 5). Note that the coefficient of start-up friction was lower at a friction speed of 1 mm/s (cycle of 2s) as compared with 10 mm/s (cycle of 0.2s). Therefore, it is suggested that collagen-derived residual stress enhances the biphasic lubrication property in articular cartilage, with the most significant effect appeared around walking speeds.

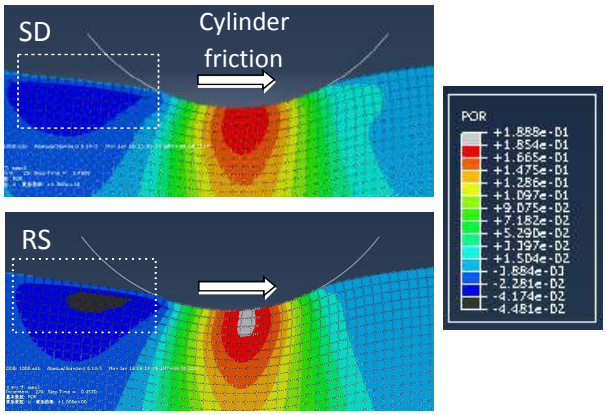

Figure 4 Interstitial fluid pressure in articular cartilage at the 2nd cycle of friction at a speed of 1 mm/s in SD (top) and RS (bottom) models of articular cartilage

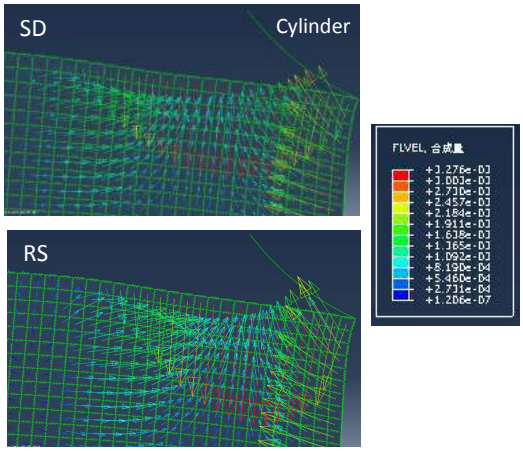

Figure 5 Flow rate in articular cartilage just behind contact area (focusing on the dotted line squares in Figure 4) at the 1st cycle of friction at a speed of 1 mm/s in SD (top) and RS (bottom) models of articular cartilage

ACKNOWLEDGEMENTS

The present study was supported by JSPS KAKENHI Grant Number JP16H03172.

REFERENCES

[1] Below S, et al, Arthroscopy, 2002.
[2] Fujie H, et al, Biosurf Biotribol, 2018.
[3] Fujie H, et al, Biosurf Biotribol, 2015.
[4] Susa T, et al, Trans of the SBC (ASME), 2011.
[5] Nakamura R, et al, Proc of the WCB, 2014.
[6] Li LP, et al, Clin Biomech, 1999.
[7] Vaishnav RN, Vossoughi, Biomed Eng II, Pargamon Press, 1983.

SB³C2019
Summer Biomechanics, Bioengineering and Biotransport Conference
June 25 -28, Seven Springs, PA, USA

SHORTER MORE REGULAR ACTIVITY IMPROVES CARTILAGE FUNCTION COMPARED TO LONGER LESS REGULAR ACTIVITY

Brian T. Graham (1), Axel C. Moore (2), David L. Burris (1,3) Chirstopher Price (1,3)

(1) Mechanical Engineering
University of Delaware
Newark, Delaware, USA

(2) Materials and Bioengineering
Imperial College London
London, UK

(3) Biomedical Engineering
University of Delaware
Newark, Delaware, USA

INTRODUCTION

Our sedentary lifestyle has been associated with increased risk of cardiovascular disease, metabolic disorders, cancers, and all-cause mortality.[1,2] On this basis, the CDC has recommended a minimum of 30 minutes of daily exercise in order to maintain health.[1] Nonetheless, a pervasive impression exists among the lay public, and among many practitioners, that osteoarthroses result from 'wear and tear'; leading to concerns that even moderate activity can promote cartilage wear. However, innumerous studies refute this relationship, instead, epidemiological studies indicate that moderate physical activity can decrease risk of joint disease.[3,4]

The link between exercise and cartilage health is at least partially understood. Static loading (during sitting and standing) pressures the interstitial fluid of cartilage, which preferentially supports loads, minimizes tissue strains and shear, and reduces frictions.[5,6] However, because cartilage is porous, load-driven exudation drives fluid losses and defeats this interstitial lubrication.[6] Consequently, loss of interstitial fluid due to compressive loading represents a serious impediment to cartilage's mechanical, tribological, and biological function. However, during articulation, cartilage recovers interstitial fluid and pressure, as evidenced by *in vivo* observations of activity-induced joint-space (cartilage) thickening.[7,8]

Links between joint movement and cartilage hydration, hydration and mechanical function, and mechanical function and chondrocyte function suggest that activity promotes cartilage health by preventing the detrimental mechanical, tribological, and biological effects of cartilage dehydration. However, direct insight into practical matters such as how activity should be prescribed to support and optimize joint health outcomes (how much and how often) has been sorely lacking. This is in part due to the fact that the gold standard platform for conducting 'controlled' studies of cartilage tribology and mechanobiology, the stationary contact area, induces rapid fluid exudation without providing any mechanism for competitive recovery, leading to functional compromise of the tissue and an inability to realistically study the link between cartilage tribology and health.

Recently, we have shown that by enlarging cartilage explant samples to allow for the creation of a convergent wedge at the leading edge of the stationary contact area (cSCA), one can drive sliding-induced fluid and deformation recoveries (which we term 'tribological rehydration') similar to that observed *in vivo*.[9] Follow-up studies have suggested that sliding-induced hydrodynamic pressures restore cartilage hydration by competing directly against the load-induced exudation process, and this restoration of hydration and interstitial pressurization facilitates both surface lubrication and solute transport.[10,11] Here, we leverage the cSCA testing configuration to determine if and how one distributes of a fixed volume of activity (i..e 30 min. of sliding) affects cartilage strain, which we use as a real-time predictor of cartilage health, within a simulated day of joint activity.

METHODS

19 mm diameter osteochondral cylinders (n = 5) were harvested from the femoral condyles of mature bovine stifles and tested on a uni-directional pin-on-disc materials tester (a.k.a. tribometer). When compressed against the glass disc, the curvature of the cartilage explants creates a convergence zone at the contact periphery that permits hydrodynamic effects during siding that are necessary for tribological rehydration.[9] Since the contact area is kept stationary relative to the cartilage, this geometry is referred to as a convergent stationary contact area (cSCA).[9] Explants were subject to a 150-min 'equivalent day' (based on area-exudation scaling of time); which consisted of 90-min 'awake' period in which a constant 5N load (~0.25MPa) was applied, and a 60-min 'sleep' periods in which the load was reduced to 0.1N load

and held (**Figure 1A**). The awake period was further divided into a 30 min 'active' (100mm/s sliding) and 60 min inactive 'sedentary' period. Each specimen (n = 5 explants) was subjected to five different equivalent daily activity regimens in a random order, consisting of 1 (1x30-min), 3 (3x10), 6 (6x5), 15 (15x2), or 30 (30x1) equally spaced bouts (see **Figure 1B**). Direct measurements of normal force, friction force, compression, and thickness were used to quantify a number of biomechanical outcomes including compressive strain, friction coefficient, contact radius, contact pressure, shear stress, effective modulus, interstitial pressure, and fluid load fraction (**Figure 1C**).

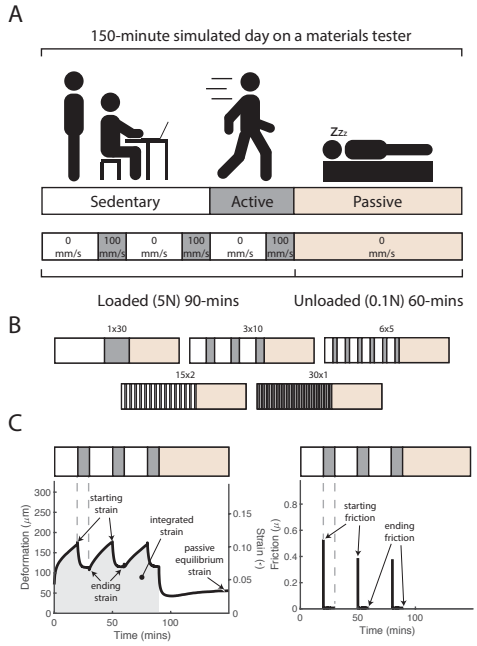

Figure 1: Figure caption centered below the graphic.

RESULTS

The data in **Figure 1C** illustrates the effects of loading, sliding, and resting on the deformation and strain recovery responses, and friction response of cSCA articular cartilage (data for 3x10-min activity paradigm shown). When loaded statically, the deformation jumps more or less immediately to 100 um, which represents the elastic response of cartilage. Over time under static load, deformations increase due to load-induced fluid exudation. Subsequent high-speed sliding restores thickness via tribological rehydration to nearly the original 'elastic' limit of 100 um; this rehydration process also restores interstitial pressure (not shown) and lubrication (friction coefficient).

Increasing the regularity of activity bouts (decreasing sedentary interval length) within our fixed 30-min of 'daily' activity substantially reduced the total loss of interstitial fluid as illustrated by **Figure 2A**. Increasing the number of bouts from 1 ('daily') to 30 ('half-hourly') decreased max strain accumulation and the loss of interstitial fluid by 80%, while also decreasing the extent of sliding friction at the start-of-sliding (**Figure 2B**). However, for a fixed volume of 'daily' sliding activity (30-min), strain at the end of each sliding bout, at the end of the loaded portion of the day, and at the end of the overnight unloading period were insensitive to the regularity of activity (or the length of contiguous time spent sedentary).

DISCUSSION

Our results demonstrate that the tribomechanical functions of cartilage are significantly affected by the length of sedentary bouts they are exposed to when controlling for total sedentary (60-min) and active (30-min) time in the cSCA. The results provide new insights into both cartilage biomechanics and cartilage function. The application of static load causes cartilage to lose interstitial fluid and pressure, and lubricity when sliding/activity is initiated.[6,9] Without any change in load, sliding-induced tribological rehydration reverses this exudation, restoring numerous biomechanical functions.[9] Because exudation increased over time, the detrimental biomechanical effects of inactivity increased with sedentary bout length. From a cartilage biomechanics standpoint, the results demonstrate that shorter and more regular bouts of intermittent activity are preferred to longer and less regular bouts.

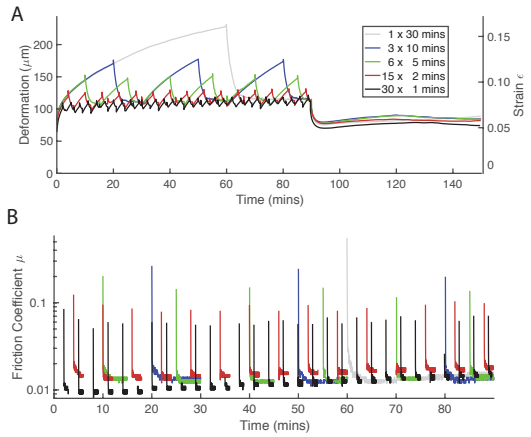

Figure 2: A) Deformation/strain and B) Friction traces for a representative sample subjected to the 5 different activity regimens tested in the present study.

The cSCA, and the discovery of tribological rehydration, offers us an opportunity to speculate about mechanistic connections between exercise, inactivity, joint health, and cartilage degradation. While it is intuitive that exercise might promote physical 'wear and tear' of joints, which are bearings after all, our results suggest the counterintuitive possibility that activity-induced mechanical damage is actually least likely to occur under conditions of sliding and joint activity that co-opt tribological rehydration to prevent the excessive loss of interstitial hydration and lubrication.

In conclusion, the result of this work demonstrates that the regularity of the ex vivo activity regimen, specifically the duration of each sedentary bout, has a significant effect on the biomechanical functions of cartilage. In more practical terms, the results suggest that brief but regular movement patterns (*e.g.* every hour) may be biomechanically preferred to long and infrequent movement patterns (*e.g.* a long walk after a sedentary work day) when controlling for daily activity volume (*e.g.* 30 minutes).

ACKNOWLEDGEMENTS

This work was supported by the NSF BMMB [1635536]. All opinions, findings, and conclusions are those of the authors and do not reflect views of the NSF.

REFERENCES

1. U.S. HHS (1996), 2. Diaz, *Annals Int Med* (2017), 3. Williams, *Med. Sci. Sport. Exerc.* (2013), 4. Hannan *J Rheumatol* (1993), 5. Mow, *J. Biomech.* (1984), 6. Ateshian, *J. Biomech.* (2009), 7. Ingelmark, *Upsala Lakareforen. Forh.* (1948) 8. Eckstein, *J. Anat.* (2006), 9. Moore, *Osteoarthr. Cartil.* (2017), 10. Graham, *Osteoarthr. Cartil.* (2017), 11. Graham, *J. Biomech* (2018),

SB^{3}C2019
Summer Biomechanics, Bioengineering and Biotransport Conference
June 25 -28, Seven Springs, PA, USA

IMPACT OF DECORIN ON CARTILAGE PERICELLULAR MATRIX MICROMECHANICS AND CHONDROCYTE MECHANOTRANSDUCTION

D. R. Chery (1), P. Chandrasekaran (1), Q. Li (1), B. Han (1), S. J. Heo (2), R. V. Iozzo (3), M. Enomoto-Iwamoto (4), R. L. Mauck (2), L. Han (1)

(1) School of Biomedical Engineering, Science and Health Systems, Drexel University, Philadelphia, PA, United States.

(2) Department of Orthopaedic Surgery, University of Pennsylvania, Philadelphia, PA, United States.

(3) Department of Pathology, Anatomy and Cell Biology, Thomas Jefferson University, Philadelphia, PA, United States.

(4) Department of Orthopedics, University of Maryland, Baltimore, MD, United States.

INTRODUCTION

In articular cartilage, the pericellular matrix (PCM) is a structurally distinct, 3-5 μm thick region surrounding chondrocytes that occupies the space between the further-removed territorial/ interterritorial matrix (T/IT-ECM) and the cell [1]. Cartilage PCM is defined by the exclusive presence of type VI collagen [2]. In comparison to the further-removed T/IT-ECM, the PCM has a higher concentration of aggrecan, perlecan, type IX collagen and fibronectin, and has mechanical and structural properties that are distinct from the T/IT-ECM [3]. Serving as the immediate microenvironment of each cell, it has been hypothesized that the PCM serves as a transducer for biomechanical, biophysical and biochemical signals between the cell and the ECM [3]. For example, studies have found that the PCM is critical to many mechanosensitive cell activities such as cell adhesion, migration, solute transport and mechanotransduction [4-6]. However, the contribution of each molecular constituent to the PCM properties is not fully understood [1]. This study investigated the role of decorin, a small leucine rich proteoglycan, in the mechanical properties of cartilage PCM. In normal cartilage, decorin can bind to many different molecules [7] including: collagens II [8] and VI [9], aggrecan [10] and transforming growth factor-β (TGF-β) [11]. In chondrocyte culture, decorin is one of the first molecules that accumulates in the newly formed PCM [12]. In addition, we recently showed that decorin-null murine cartilage develops with a much reduced proteoglycan content and impaired mechanical properties [13]. Based on these findings, this study tests the hypothesis that decorin is crucial for establishing PCM micromechanical properties and chondrocyte mechanotransduction.

METHODS

Sample preparation. Tibial condyles were harvested from 3-day (newborn), 2-week (juvenile) and 3-month old (adult) wild-type (WT) and decorin-null (*Dcn*$^{-/-}$) mice [14]. Following our established procedure, the Kawamoto's film-assisted method [15] was used to obtain unfixed 5 μm-thick cryo-sections for AFM testing.

Immunofluorescence-guided AFM-nanomechanical mapping. Cryo-sections were labeled by immunofluorescent antibodies specific for collagen VI, the biomarker of cartilage PCM [2]. Guided by the IF-images, AFM-nanomechanical mapping was performed using a Total Internal Reflection Fluorescence (TIRF) 3D-Moleuclar Force Probe (MFP-3D) in PBS (R = 2.25 μm, k = 1 N/m, 10 μm/s indentation rate), following established procedures [16]. Using a custom Matlab code and IF-images, the moduli of PCM and T/IT-ECM moduli were analyzed separately.

Collagen fibril structural analysis. For both genotypes, additional 20-μm thick cryo-sections were prepared at all ages. Samples were treated with Karnovsky's fixative, dehydrated in hexmethyldisilazane and imaged under a scanning electron microscope (Zeiss Supra 50VP SEM) to visualize collagen fibrils [17]. Diameter of the fibrils were quantified in ImageJ.

Intracellular $[Ca^{2+}]_i$ signaling under osmotic stimuli. Intact tibial articular cartilage of both genotypes at all three ages was labeled with Ca-520^{TM} AM in DMEM at 37° C for 1-hour. Time-series confocal images were taken to track the intracellular calcium signal of cells, $[Ca^{2+}]_i$ every 2 seconds for up to 15 min [18]. Osmotic stimuli were applied by varying ionic strength (IS) of DMEM in hypotonic (165 mOsm, IS = 0.075 M), isotonic (330 mOsm, IS = 0.15M) and hypertonic (550 mOsm, IS = 0.23M) conditions for all three ages [19]. To test the role of sGAGs in chondrocyte $[Ca^{2+}]_i$ signaling, additional juvenile cartilage was treated with chondroitinase-ABC (ChABC) in DMEM for 12 hours to remove CS-GAG [20]. Time series images were taken in the same conditions as above. The responsive rate, $\%R_{cell}$, for each sample was calculated as the fraction of responsive cells over total cell counts within a region of interest.

RESULTS

Guided by collagen VI IF-imaging, we separately analyzed the moduli of the T/IT-ECM and the PCM (Fig 1a). For juveniles and adults, *Dcn*$^{-/-}$ cartilage PCM showed significantly lower modulus than that of WT. However, this difference was absent in newborns. Under SEM, we also found a mild, but significant increase in collagen fibril diameter in the PCM in adults, but not in newborns or juveniles (Fig. 2). Spontaneous intracellular $[Ca^{2+}]_i$ oscillations were observed for

both genotypes under all three osmotic conditions. In isotonic DMEM, adult *Dcn*$^{-/-}$ chondrocytes had significantly lower $\%R_{cell}$ than WT, while juvenile and newborn chondrocytes were not different than WT. This trend was consistent in hypotonic and hypertonic conditions as well, with $\%R_{cell}$ decreasing with increases IS for both genotypes (Fig. 3a). Upon depletion of sGAGs, there was a significant decrease in $\%R_{cell}$, reaching levels similar to that of a loss of decorin (Fig. 3b).

DISCUSSION

This study showed that decorin is a crucial component of the cartilage PCM, impacting micromechanics and chondrocyte mechanotransduction. Previously, we showed that decorin plays an indispensable role in mediating the assembly and stability of the aggrecan network in cartilage [13]. As a result, decorin null cartilage develops much lower aggrecan content and shows impaired biomechanical properties during post-natal growth. In cartilage, aggrecan is more concentrated [2], and undergoes faster turnover in the PCM [21]. Here, using our newly established method integrating Kawamoto's film-assisted cryo-sectioning [15] with IF-guided AFM [16], we further show that decorin directly mediates the structural integrity and micromechanics of the PCM (Figs. 1,2). On one hand, given that the PCM is where newly synthesized aggrecan is localized [22], decorin possibly mediates the integration of newly synthesized aggrecan. On the other hand, as chondrocytes are highly sensitive to their PCM micromechanical environment, decorin may also affect chondrocyte activities via mediating the integrity of PCM.

Indeed, we noted that the loss of decorin significantly reduces chondrocyte intracellular $[Ca^{2+}]_i$ signaling in adults. $[Ca^{2+}]_i$ signaling is one of the earliest cell mechanoresponses to its micromechanical environment [23]. We found a reduction in $\%R_{cell}$ that correlates well with the changes in PCM modulus, where the effect is absent in newborn and juvenile tissue, but becomes significant in adult tissues (Fig. 3a). In the PCM, the localization of proteoglycans, primarily aggrecan, provides a specialized, highly negatively charged microenvironment for residing chondrocytes. When hypotonic stimuli were applied to enhance the electrical double layer repulsion in the matrix, $\%R_{cell}$ increased accordingly. In *Dcn*$^{-/-}$ cartilage, we attribute the reduction of $\%R_{cell}$ to the decreased aggrecan content in the PCM. Indeed, when CS-GAGs were removed in WT cartilage, a similar trend of decreased $\%R_{cell}$ was observed (Fig. 3b). Therefore, we hypothesize that, during post-natal cartilage growth, decorin regulates chondrocyte mechanosensitive activities by mediating aggrecan content and assembly and the micromechanical properties of the PCM.

ACKNOWLEDGEMENTS

This work was supported by NIH AR066824, NSF CMMI-1662544, and the Penn Center for Musculoskeletal Diseases (PCMD) (NIH P30AR050950). We thank the Singh Center at the University of Pennsylvania for the use of the TIRF-MFP-3D.

REFERENCES

[1] Guilak, F et al., *Matrix Biol* 71-72:40-50, 2018. [2] Poole, CA et al., *J Histochem Cytochem* 39:1175-1187, 1991. [3] Wilusz, RE et al., *Matrix Biol* 39:25-32, 2014. [4] Evanko, SP et al., *Arterioscler Thromb Vasc Biol* 19:1004-1013, 1999. [5] Han, Y et al., *Proc Natl Acad Sci U S A* 101:16689-16694, 2004. [6] Itano, N et al., *Proc Natl Acad Sci U S A* 99:3609-3614, 2002. [7] Gubbiotti, MA et al., *Matrix Biol* 55:7-21, 2016. [8] Douglas, T et al., *Biomacromolecules* 7:2388-2393, 2006. [9] Wiberg, C et al., *J Biol Chem* 276:18947-18952, 2001. [10] Wiberg, C et al., *J Biol Chem* 278:37698-37704, 2003. [11] Hildebrand, A et al., *Biochem J* 302 (Pt 2):527-534, 1994. [12] Chang, J et al., *Histochem J* 29:515-528, 1997. [13] Han, B et al., *Trans ORS* 38:248, 2017. [14] Danielson, KG et al., *J Cell Biol* 136:729-743, 1997. [15] Kawamoto, T et al., *Methods Mol Biol* 1130:149-164, 2014. [16] Wilusz, RE et al., *J R Soc Interface* 9:2997-3007, 2012. [17] Li, Q et al., *J Biomech* 48:1364-1370, 2015. [18] Heo, SJ et al., *Sci Rep* 5:16895, 2015. [19] Zhou, Y et al., *Ann Biomed Eng* 44:1138-1147, 2016. [20] Wilusz, RE et al., *J Mech Behav Biomed Mater* 38:183-197, 2014. [21] Quinn, TM et al., *Ann N Y Acad Sci* 878:420-441, 1999. [22] Bayliss, MT et al., *J Biol Chem* 275:6321-6327, 2000. [23] Guilak, F et al., *J Biomech* 47:1933-1940, 2014.

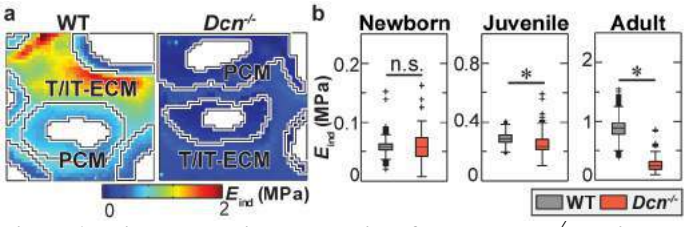

Figure 1: Micromechanical properties of WT and *Dcn*$^{-/-}$ cartilage PCM. a) Representative modulus maps (20 × 20 μm^2) of 3-month old WT and *Dcn*$^{-/-}$ cartilage. T/IT-ECM and PCM regions were distinguished and partitioned from collagen VI IF-images. b) Box-and-whisker plots of PCM indentation modulus (n = 4 for each genotype and age, *: $p < 0.001$ between WT and *Dcn*$^{-/-}$).

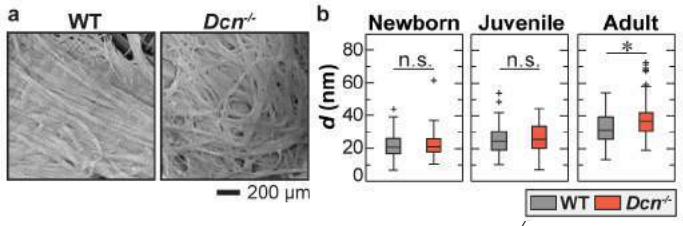

Figure 2: Collagen fibril structure of WT and *Dcn*$^{-/-}$ cartilage PCM. a) Representative SEM images of adult WT and *Dcn*$^{-/-}$ cartilage PCM collagen fibrils. b) Box-and-whisker plots of PCM fibril diameters, d_{nm}, at all three ages (n = 3 for each genotype and age, *: $p < 0.01$).

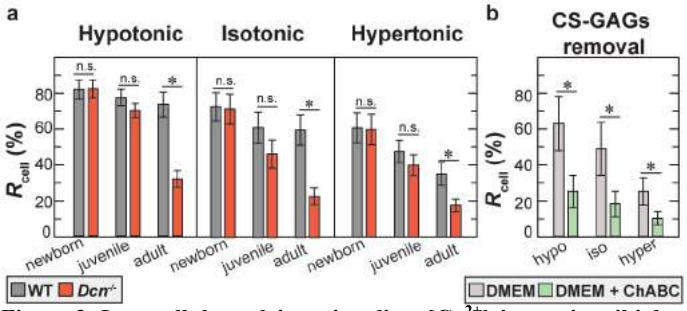

Figure 3: Intracellular calcium signaling, $[Ca^{2+}]_i$ in murine tibial chondrocytes. a) Comparison of percentage of $[Ca^{2+}]_i$ responding cells ($\%R_{cell}$) between WT and *Dcn*$^{-/-}$ for three ages under different osmotic conditions (mean ± 95 % CI from ≥ 50 responding cells pooled from n = 3 animals, *: $p < 0.05$). b) Effect of 12 hr chondroitinase ABC (ChABC) treatment on $\%R_{cell}$ for juvenile cartilage in DMEM (mean ± 95 % CI from ≥ 30 responding cells pooled from n = 2 animals, *: $p < 0.05$).

SB³C2019
Summer Biomechanics, Bioengineering and Biotransport Conference
June 25 -28, Seven Springs, PA, USA

THROUGH-THICKNESS PATTERNS OF SHEAR STRAIN CHANGE WITH EARLY-STAGE PROGRESSION OF OSTEOARTHRITIS

Franz Maier (1), Courtland G. Lewis (2), David M. Pierce (1,3)

(1) Department of Mechanical Engineering
University of Connecticut
Storrs, CT, USA

(2) Bone & Joint Institute
Hartford Healthcare
Hartford, CT, USA

(3) Department of Biomedical Engineering
University of Connecticut
Storrs, CT, USA

INTRODUCTION

In osteoarthritis (OA), degenerated cartilage eventually becomes unable to withstand normal (daily) intra-tissue mechanical loads, and begins a sustained degradation of the extracellular matrix (ECM) [1]. Currently no treatment exists to fully restore damaged or degenerated cartilage [2]. Tools to detect/monitor preclinical degeneration of cartilage may facilitate the development and validation of earlier treatments, allowing intervention before cartilage degenerates beyond repair [3]. Methods to track OA progression based on histological images, e.g. OARSI scoring [4] or adapted Mankin grading [5], are sensitive to early-stage OA but require tissue explants generally unavailable in a clinical setting. Methods used in clinical practice to quantify degeneration of cartilage rely on arthroscopic evaluation, e.g. Outerbridge [6], or magnetic resonance imaging (MRI), e.g. protocol by International Cartilage Repair Society (ICRS) [7], but are currently not sensitive enough to detect the onset of degeneration (i.e. early stage). Improved imaging techniques based on MRI have the potential for accurate, non-invasive assessment of cartilage health, particularly beyond the articular surface. However, a challenge remains to identify sensitive and reliable MRI markers associated with early OA.

OA-induced degeneration also affects collagen fiber orientation across the cartilage surface, as well as through the thickness. Desrochers et al. [8] found that minute changes in the collagen structure precede other changes (e.g. PG loss in particular) and cause alterations in the mechanical responses of cartilage at the onset of OA. Intra-tissue mechanics may thus provide more sensitive image-based biomarkers for quantifying the degeneration of cartilage. For example, Griebel et al. [9] found that changes in shear strain magnitude, measured by dualMRI, showed a stronger correlation with OA severity than T1ρ relaxometry. Such imaging methods highlight the potential of detecting the onset of OA by leveraging changes in local mechanics caused by OA.

Given the structural changes associated with the progression of OA, we hypothesized that patterns of through-thickness, large-strain shear evolve with early-stage OA. We therefore aimed to characterize changes in patterns of shear strain during early-stage OA to gauge the potential of patterns in shear strain to serve as image-based biomarkers of early-stage, preclinical OA, and to provide high-fidelity, through-thickness data for proposing, fitting, and validating constitutive models.

METHODS

Preparation of Specimens: We harvested nine lateral femoral condyles (n = 9, 67.0 ± 11.9 years old) undergoing total knee arthroplasty (TKA) at Hartford Healthcare Bone & Joint Institute. After determining the local split-line directions (SLDs), we extracted pairs of adjacent test specimens from load-bearing regions within the joint cartilages. From each pair, we used one specimen for mechanical testing (cuboid, 3×3 mm^2 footprint, full thickness), with one through-thickness plane parallel to the local SLD, and the other specimen for histological evaluation. We immediately fixed the specimens for histology in 10% neutral buffered formalin while we stored the specimens undergoing mechanical testing in PBS at -80°C prior to testing. On the day of a mechanical test, we thawed and glued the articular surface and the subchondral bone (i.e. top and bottom) of a specimen to a loading platen, ensuring a flat surface perpendicular to the stereo camera setup (front surface). We then air brushed (CM-C Plus, IWATA) a speckle pattern on the front surface using a tissue marking dye (Cancer Diagnostics, Durham, USA) diluted with deionized water (~1:1).

Histological Assessments: After decalcification in 0.5M EDTA, we embedded specimens for histology in paraffin and sectioned them at 6 µm. To determine overall cartilage health, we stained sections with Safranin-O fast green (NovaUltra Safranin O stain kit, IHC World,) and examined the slides using a light microscope. Two trained observers (FM, DMP) quantified the progression of OA using the OARSI grading

method [5]. We considered only tissues up to grade 3.5 (moderate disease, presence of vertical fissures). We binned specimens into three groups based on their OARSI grades: normal cartilage (grade < 2, group OA-1), mild OA (2 ≥ grade < 3, group OA-2), and moderate OA (grade ≥ 3, group OA-3). To assess the integrity of the through-thickness zonal architecture, we stained sections with Picosirius red (NovaUltra Sirius red stain kit, IHC World) and examined the slides under polarized light. Two trained observers (FM, LM) quantified the integrity of the zonal architecture using the PLM-CO score [10]. We binned specimens into three groups based on PLM-CO scores: normal collagen structure (score ≥ 4), mild disruption (score 3), and moderate disruption (score ≤ 2).

Digital Image Correlation During Applied Shear Strains: Using a triaxial shear-testing device (Messphysik) we performed quasi-static (75 µm/min) cyclic simple shear tests and recorded images of the deformation in the SLD. We applied 1% precompression and applied displacements corresponding to ±5, ±10, and ±15% simple shear strain. Our cyclic tests included three preconditioning cycles, and we recorded images of the fourth loading cycle to calculate patterns of displacement and strain. We completed all tests in a bath of PBS at 37°C (±1°C) including antibiotics (100U/ml penicillin and 100mg/ml streptomycin) and protease inhibitors (P2714, Sigma Aldrich) to avoid degeneration. To record images for subsequent DIC, we used a stereo camera system with two five-megapixel cameras (Manta G-505, Allied Vision).

Data Analyses: We used the commercial software Istra4D (V4.4.3.414, Dantec Dynamics) for image processing and strain calculations. We approximated the displacement field by an analytic function (bi-cubic splines) to obtain 2-D deformation gradients for subsequent strain calculations. We exported the full field of 2-D Green-Lagrange tangential shear strain and we performed further processing and analyses using MATLAB (R2017b, The MathWorks). First, we averaged (M ± SD) the shear strain values along horizontal lines at each height through the specimen's thickness to generate a through-thickness strain curve. We then grouped those curves by either OARSI grade or PLM-CO score and averaged them to obtain master curves representing normal, mildly degenerated, and moderately degenerated cartilage.

RESULTS

We successfully imaged the distribution of deformation at three applied strain levels (5, 10, and 15%) on most of the 44 specimens. Seven of our specimens showed signs of mechanical failure during testing and we excluded these data from subsequent analyses.

Histological Assessments: Our OARSI grading resulted in $n_{OA\text{-}1}$ = 17, $n_{OA\text{-}2}$ = 16, and $n_{OA\text{-}3}$ = 11 specimens per binned group. Inter-observer agreement for the unbinned OARSI grades was 0.925 and for the binned OARSI-graded groups was 1.0. Our PLM-CO scoring resulted in $n_{PLM\text{-}2}$ = 18, $n_{PLM\text{-}3}$ = 12, $n_{PLM\text{-}4\text{-}5}$ = 14 specimens per binned group. Inter-observer agreement for the unbinned PLM score was 0.735 and for the binned PLM score was 0.766.

Through-Thickness Patterns of Shear Strain: We observed three general shapes for the curves of averaged through-thickness Green-Lagrange shear strains consistent over all applied strain magnitudes (Fig. 1). We found the largest shear strains (by magnitude) at or near the articular surface. Normal tissue (OA-1) also showed a distinct relative peak in shear strain near the transition from the MZ to the DZ, near or at the advancing cartilage-bone interface. With advancing OA (mild degeneration, OA-2) the through-thickness shear strain became more homogeneous. Finally, with further advancing OA (moderate degeneration, OA-3) the shear strain became more heterogeneous with the deformation focused near the articular surface.

DISCUSSION

Histological Assessments: Semi-quantitative, histology-based methods for assessing cartilage degeneration have inherent drawbacks: e.g. these discrete categories likely cannot fully capture the dynamic,

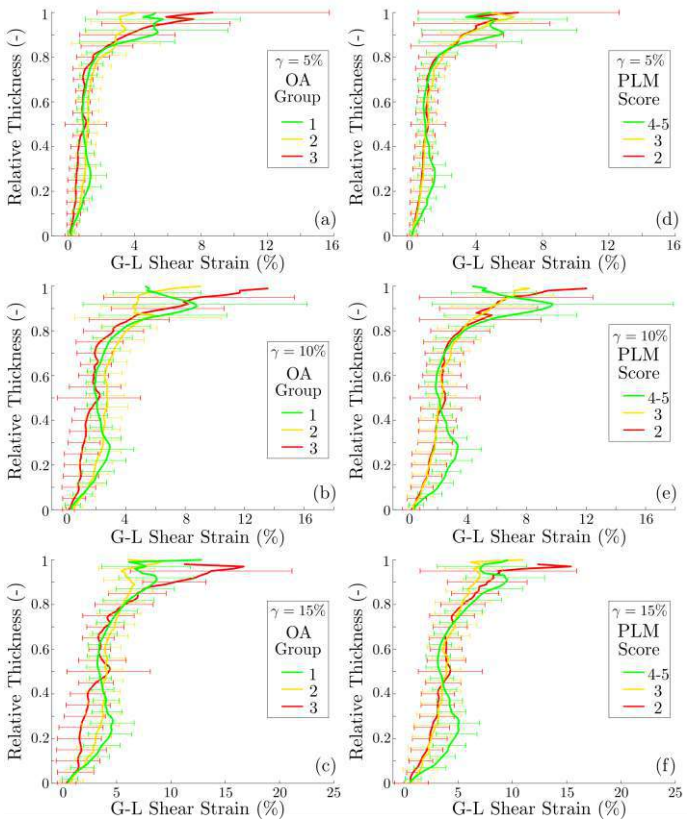

Figure 1: Green-Lagrange shear strains by OARSI grades (a-c) and PLM scores (d-f) at bulk shear strains = 5%, 10%, and 15%.

years-long progression of disease in its full complexity. Despite the good-to-excellent inter-observer agreement reported here, application of OARSI grading and PLM scoring is still subjective and automated tools may reduce potential bias.

Through-Thickness Patterns of Shear Strain: We found three general qualitative through-thickness patterns of shear strain depending on the stage of degeneration of the specimens (Fig. 1). We are the first to report a region of increased shear strains in normal cartilage in the transition from MZ to DZ, i.e. near the cartilage-bone interface.

Limitations and Conclusion: Despite predominately-external compression to cartilage *in vivo*, shear strains within cartilage tend to exceed compressive strains [11]. We found that early-stage OA presents characteristic through-thickness patterns of shear strain for normal cartilage, and mild and moderately degenerated cartilage. We propose that changes in through-thickness patterns of shear strain could provide sensitive biomarkers for early clinical detection of OA, changes that can be quantified *in*-vivo using advanced MRI protocols [9,11]. Reliable early detection will aid the development and validation of treatments.

ACKNOWLEDGEMENTS

NSF 1662429; Hartford Healthcare; L. Marshall; V. Blair.

REFERENCES

[1] Loeser +, *Arthritis Rheum*, 64:1697-1707, 2012. [2] Correa +, *Sem Cell Dev Bio*, 62:67-77, 2017. [3] Casula +, *Knee Surg Sport Traumatol Arthrosc*, 24:2046-54, 2016. [4] Pritzker +, *Osteoarthritis Cartilage*, 14:13-29, 2006. [5] Mankin +, *J Bone Joint Surg Am*, 53:523-37, 1971. [6] Outerbridge, *Bone Joint J*, 43-B:752-7, 1961. [7] Brittberg; Winalski, *J Bone Joint Surg Am*, 85:58-69, 2003. [8] Desrochers +, *Osteoarthritis Cartilage*, 20:413-21, 2012. [9] Griebel +, *Magn Reson Med*, 71:807-14, 2014. [10] Changoor +, *Osteoarthritis Cartilage*, 19:1458-68, 2011. [11] Chan +, *Scientific Reports*, 6:19220, 2016.

SB³C2019
Summer Biomechanics, Bioengineering and Biotransport Conference
June 25 -28, Seven Springs, PA, USA

MATERIAL PROPERTY CHARACTERIZATION OF HUMAN CERVICAL TISSUE BASED ON BIPHYSICAL VISCOELASTICITY MODEL

L. Shi (1), J. Vink (2), R. Wapner (2), K. Myers (1)

(1) Department of Mechanical Engineering
Columbia University
New York, NY, USA

(2) Department of Obstetrics and Gynecology
Columbia University Medical Center
New York, NY, USA

INTRODUCTION

The human cervix is essential to pregnancy for protecting the fetus before delivery, acting as a mechanical barrier. It is believed preterm birth (PTB) - defined as birth before 37 weeks of gestation - is related to a mechanically weak cervix. Therefore, the mechanical property characterization of the cervical tissue may contribute to our understanding of the causes of preterm birth.

The cervix is a soft tissue that behaves as a strong nonlinear poroviscoelastic material. It is composed of cross-linked collagen fibers embedded in a groundsubstance formed by the negatively charged proteoglycans and glycosaminoglycans [1, 2]. These components provide the anisotropic and time-dependent material response to mechanical loading. In our earlier studies, the time-dependent force response under indentation was modeled using a simple viscoelastic model [3], ignoring possible contributions of preferred collagen fibers and poroelastic mechanisms [4].

In this study, load-relaxation indentation experiments on human cervical tissue samples were conducted. This indentation test was coupled with a video extensometer to capture tissue deformation in addition to load-time data. Inverse finite element analysis (IFEA) of the indentation experiment is utilized to fit a poroviscoelastic material model to the indentation response and tissue strain. The model is informed by previous measurements of collagen fiber directionality and dispersion of each sample [5] and permeability measured from a separate set of human samples [4]. At last, statistical analysis was performed to investigate the differences in material properties between samples of different obstetric backgrounds and between different anatomical locations within each sample.

METHODS

Sample Preparation 13 non-pregnant cervical tissue slices were sectioned from 7 different consented hysterectomy patients. The thickness of the cervical slices ranged from 1.8 to 7.1 mm, with the majority being between 2.5 and 6 mm. The radii of the samples were 10 – 15 mm. The slices were stored flat in a -80°C freezer immediately after sectioning until testing.

Indentation Experiments Before scheduled indentation tests, each sample was microtomed and equilibrated in phosphate-buffered saline (PBS) at 4°C for 12 hours. The bottom surface of the cervical slices was speckled using india ink and then the edges of the bottom surface were glued to a petri dish. The cervical slice was immersed in PBS solution. Samples were put onto a glass, as shown in Fig. 1 (A). A camera was placed in front of the setup and captured the deformation of the bottom surface using a right-angle prism. Four locations (anterior, posterior, left, right) of each sample were indented (Fig. 1 (C)). A displacement-controlled, ramp-hold indentation test was conducted at each location using a 6 mm stainless steel indenter, with a ramp rate = 0.2% thickness/s and a holding time = 495 s. (Fig. 1 (B))

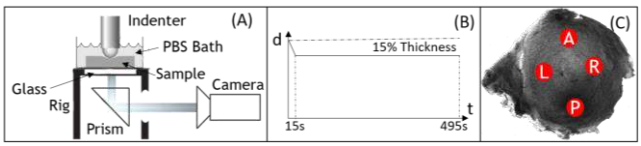

Figure 1: (A) The indentation experiment setup. (B) Testing profile of the load – relaxation experiment. (C) Four indentation locations.

FEA Model The FEA model was created in FeBio (V2.6.2, url: febio.org) to simulate the indentation experiments. As shown in Fig. 2

(B), the cervical sample was modeled as a flat half-cylinder hollow in the center, and the indenter was modeled as a hollow quarter-sphere with rigid body material. The critical points of the FEA model corresponded with those in the DIC (digital image correlation) strain map of the bottom surface generated using Vic-2D (V6, Correlated Solutions Inc.) system (Fig. 2 (A)). Points A and B were the two ends of the diameter of the canal, and C was the center of the canal. D was the indenter spot. E and F were the glued boundary and the edges of the sample, respectively. R_f^c, R_f^r, and R_f^l were the refined domain in the radial, circumferential, and axial direction to guarantee the accuracy. The z – displacement between B and E was fixed to represent the bottom surface. The symmetric boundary condition was set on the middle plane. All displacements between E and F were fixed to represent the glued boundary.

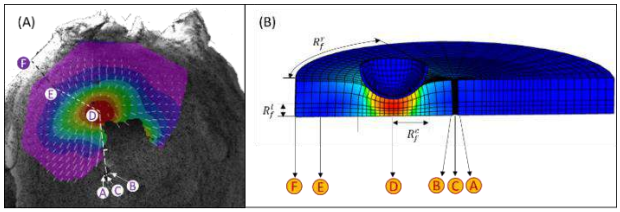

Figure 2: FEA model of the sample under indentation experiments. (A) DIC strain map of the bottom surface of the cervical tissue sample under the experiments. (B)the corresponding FEA model of the indenter and the cervical sample. The points A-F in the FEA model (B) are determined based on the points in DIC strain map (A).

Constitutive Equations The cervix was modeled as a poroviscoelastic material, where the solid component of the material is a continuously distributed fiber composite with a von Mises fiber network. The details of this kind of material are found in the FeBio user manual [5]. The material parameters of the elastic part are E, υ, ξ, b, β, and α, which were the Young's modulus, the Poisson's ratio, the fiber stiffness, the distribution coefficient, the fiber polynomial index, and the fiber exponential coefficient, respectively. The parameters of the time-dependent part are g_1, g_2, τ_1, and τ_2, where g_i's are the stiffness coefficients for each level and τ_i's are the time-decay coefficient for each level. k is the hydraulic permeability.

IFEA Process The goal of IFEA was to fit the FEA model predictions to the force-relaxation response to find the material parameters listed in Table 2 (previous IFEA was conducted using the strain maps to find anisotropic material parameters – see Table 1). The known material parameters are listed in Table 1, where ξ, b, υ, and α were obtained from previous studies and varied from slice to slice. Therefore, the range of each parameter was listed. β was fixed as 2 for exponential form of free energy density. k was chosen as 2.1×10^{-14} $m^4/N\bullet s$ according to our previous measurement. [4] The objective function of the IFEA optimization process was defined in Eq. (1).

$$\chi = \frac{1}{n}\sum_i^n \frac{\left|F_i^{EXP} - F_i^{FEA}\right|}{F_i^{EXP}} \quad (1)$$

where F_i^{EXP} is the experimental force response data at time series i, F_i^{FEA} is the corresponding FEA force response data. n is the total time series used to fit. The range of the parameters to be fitted and the optimized values are listed in Table 2.

Table 1: The material parameters obtained from previous study.

ξ	b	υ	α	β	k
$[10^{-2}, 10^3]$kPa	[0, 5]	[0, 0.499]	[0, 10]	2	$2.1\times10^{-14}m^4/N\bullet s$

RESULTS

The representative fitting results of the force – relaxation responses are shown in Fig. 3 (A). The final value of the objective function is 0.045 for this case, which is very small and proves to be a good fitting.

Table 2: The range and the optimized results of parameters.

Parameter	Range	Optimized Results (n=41)
E	$[10^{-2}$kPa, 10^2kPa]	1.65±1.48kPa
g_1	[0, 2]	0.93±0.32
g_2	[0, 2]	0.45±0.30
τ_1	[1, 100]s	25.73±23.79s
τ_2	[1, 500]s	69.76±120.09s

The one-way ANOVA statistical analysis of the parameters were conducted by dividing the samples into different groups, such as different parities (parity < 2 & > 2), different locations (anterior, posterior & left, right), and different parts of the cervix (external os & internal os). Only τ_2 was found significantly different ($p < 0.05$) at anterior and posterior compared to left and right. (Fig. 3 (B))

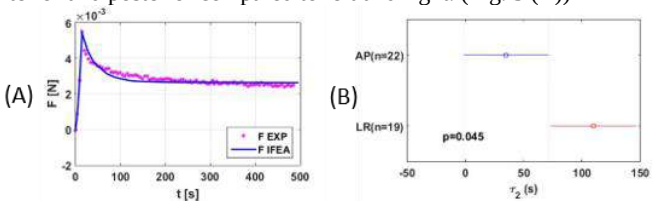

Figure 3: (A) Representative force – relaxation response to indentation and the corresponding IFEA fit for the experimental data. The final value of the objective function is 0.045. (B) Statistic analysis of the IFEA results using one-way ANOVA. Only τ_2 among different groups of quadrants (anterior and posterior vs. left and right) were found significantly different ($p < 0.05$).

DISCUSSION

The FEA model represents a good approximation of the real force – relaxation experiment appropriately. g_1 and g_2 are not far away from our previous study. τ_1 and τ_2 are very different from our previous study. [3] This is due to the additional consideration of permeability in this study compared to the previous one. It also contributes to the time – dependent response.

The main limitations of this study are that the constitutive model of the groundsubstance is a kind of general viscoelastic model with internal variables, whose physical meanings are not clear. We are studying the viscoelastic model based on reactive mixture theory, in which all variables are observable and have physical meaning. The strain maps of the bottom surface have not been fitted. The strains should also be considered in the fitting process in the future.

ACKNOWLEDGEMENTS

Research reported in this publication was supported by the NIH R01HD091153 to KM. The content is solely the responsibility of the authors and does not necessarily represent the official views of the NIH.

REFERENCES

[1] House, M et al., 2009, S. Perinatol, 33, 300-307.
[2] Myers, K et al., 2010, J. Biom. Eng., 132, 021003.
[3] Yao, W et al., 2014, J. Mech. B. Biom. Mat., 18-26.
[4] Fernandez, M et al., 2013, J. Biom. Eng., 135, 021024.
[5] Yao, W et al., 2016, PLoS ONE. 2016;11(11)
[6] Mass, S et al, 2018, FEBio User Manual V2.8, Ch. 4.

SB³C2019
Summer Biomechanics, Bioengineering and Biotransport Conference
June 25-28, Seven Springs,PA, USA

EFFECTS OF PELVIC ORGAN PROLAPSE ON THE BIAXIAL BIOMECHANICAL BEHAVIOR OF POST-MENOPAUSAL UTEROSACRAL LIGAMENT

E. Danso (1), J. Schuster (1), I. Johnson (1,2), E. Harville (2), L. Desrosiers (3), L. Knoepp (3), K. Miller (1)

(1) Biomedical Engineering
Tulane University
New Orleans, LA, USA

(2) Epidemiology
Tulane University
New Orleans, LA, USA

(3) Female Pelvic Medicine and Reconstruction Surgery
Ochsner Clinical School
New Orleans, LA, USA

INTRODUCTION

Pelvic organ prolapse (POP) is a prevalent condition characterized by the abnormal descent of female pelvic organs due to the loss of structural support. Ten percent of women in the United States undergo surgical intervention related to POP [1], and 4 out of 10 women experience reoccurrence of prolapse symptoms 2 years after surgery [3]. In the United States alone, direct cost of over a billion dollars is incurred annually for POP associated interventions [2]. Despite the epidemiologic importance of this disorder, our knowledge of its pathophysiology is limited. Although the etiology of POP has not been fully elucidated, some risk factors include mechanical injury, vaginal delivery, obesity, age, race, family history, higher parity and constipation [3, 4].

The uterosacral ligament (USL) provides structural support (Level 1) to the female pelvic floor [5]. The loss of the structural integrity of USL may induce POP. The USL is primarily composed of smooth muscle and collagen fibers, with a limited quantity of elastin [3, 5]. To assess the physiologically-relevant biomechanical properties of USL and tissue anisotropy, biaxial testing permits acquisition of biomechanical data from two axes simultaneously, thus providing a more physiologic assessment compared to standard uniaxial testing [3]. Despite this importance, biaxial USL properties have only been reported for swine [7, 8] and women without POP to date [3]. To the best of our knowledge, biaxial USL properties have not been determined for women with POP. Therefore, the objective of this study was to quantify and compare the biaxial biomechanical properties of USL from post-menopausal women with and without POP.

METHODS

USL samples were obtained (Ochsner Clinical School IRB approved: 2017.016A) from post-menopausal women with either POP (n=15, 64±7years old, 31±8 kg/m^2 BMI) or non-POP (n=11, 62±5 years old, 33±5 kg/m^2 BMI) condition following transvaginal hysterectomy surgeries (Figure 1A). Samples were snap-frozen following surgery and stored at -80°C until the day of biomechanical assessment. All the samples were from Europeans/White women, except 4 that were from African-Americans/Black women (non-POP controls). **Biaxial testing**. Samples were thawed at room temperature, cut into squares and then speckle coated with alcohol ink for strain tracking. Using a non-contacting laser micrometer, tissue thickness was measured across multiple locations and averaged. Four fish hooks were used to mount each sample side into a custom planar biaxial test device equipped with load cells (22 N) in both axes (Figure 1B). The samples were fully submerged in Hank's balance saline solution throughout the experiment. A tare load of 0.1N was applied in the X- and Y-directions, followed by 10 equibiaxial preconditioning cycles to 0.1MPa, after which the samples were allowed to equilibrate for 10 minutes. Next, samples were loaded in the X- and Y-directions to different X:Y loading ratios of 1:0.5, 1:0.75, 1:1, 0.75:1 and 0.5:1 at 0.2%/sec. For each of the loading ratios, 5 preconditioning cycles were applied. Using a custom Matlab code and a built-in minimization algorithm (*lsqnonlin*), Fung type constitutive model was fitted to the averaged experimental data for the POP and non-POP groups by minimizing the mean square error between the experimental data and model curves. The strain energy is given by

$$W = \frac{1}{2}K(e^Q - 1) \quad (1)$$

where $Q = c_1E_{xx}^2 + c_2E_{yy}^2 + 2c_3E_{xx}E_{yy}$.

The parameter K has a unit of MPa. Parameters c_1, c_2, c_3 are dimensionless, and E_{xx}, E_{yy} are Green strains. **Statistical Analysis.** All

data are presented as Mean±SD. Independent samples t-tests were used to assess differences in age, body mass index (BMI), parity, gravidity, nulliparous, nulligravid, average stress and stretch between POP and non-POP patients. Statistical significance was set to $p<0.05$. All statistical analyses were performed using SPSS software.

RESULTS

The measured thickness were 3.27±1.15 mm and 3.51±0.96 mm for the non-POP and POP specimens respectively. No statistically significant differences ($p<0.42$ (age), $p<0.439$ (BMI), $p<0.264$ (parity), $p<0.073$ (gravidity)) were identified with respect to age, BMI, parity and gravidity, between the POP and non-POP patients. USL from POP patients exhibited statistically significantly ($p<0.00001$) larger stretches when subjected to either 1:1 or 0.75:1 loading ratios in both the X- and Y-directions (Figure 2B&D), as compared to the non-POP USL (Figure 2A&C). This indicates that the tissue from POP patients is more extensible compared to tissue from non-POP controls. Additionally, tissues demonstrated anisotropic behavior. In particular, the Y-direction in the non-POP group demonstrated higher extensibility compared to the X-direction for the 0.75:1 and 0.5:1 loading ratios ($p<0.00005$). The constitutive model described the data reasonably well ($R^2 = 0.99$, for both non-POP and POP). Table 1 shows the parameters from the averaged data obtained from the Fung constitutive model for each group. Noting that the c_1 and c_2 parameters were larger in the POP group, while c_3 was smaller in comparison to the non-POP group (Table 1).

Table 1: Parameters obtained from Fung-type constitutive model.

Group	K[MPa]	$c_1[-]$	$c_2[-]$	$c_3[-]$
Non-Prolapsed	1.27E-3	41.27	42.59	147.36
Prolapsed	8.48E-4	93.48	119.49	96.16

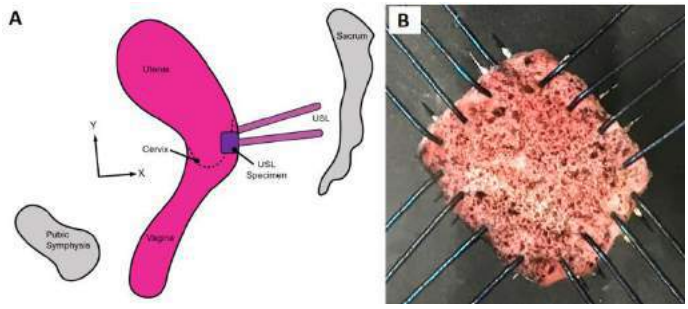

Figure 1: (A) USL specimens were obtained at the distal right and left insertions. (B) Samples were speckle-coated and mounted in a planar biaxial testing device via fishhooks.

DISCUSSION

POP tissues demonstrated increased extensibility, in particular, in the 1:1 loading ratio compared to the non-POP control USL. USLs from women with POP demonstrate significantly higher collagen type III expression than their non-POP counterparts [6]. No significant differences in collagen I expression and smooth muscle cell content, however, were identified between these two groups [6]. The significantly higher collagen III expression for the POP USL may be a contributing factor for its higher extensibility. Future work, however, is needed to identify potential statistical correlations between type III collagen content and tissue extensibility. Further, elastin may significantly contribute to tissue extensibility. Loss of elastin has been highly implicated in POP development and progression in other tissues

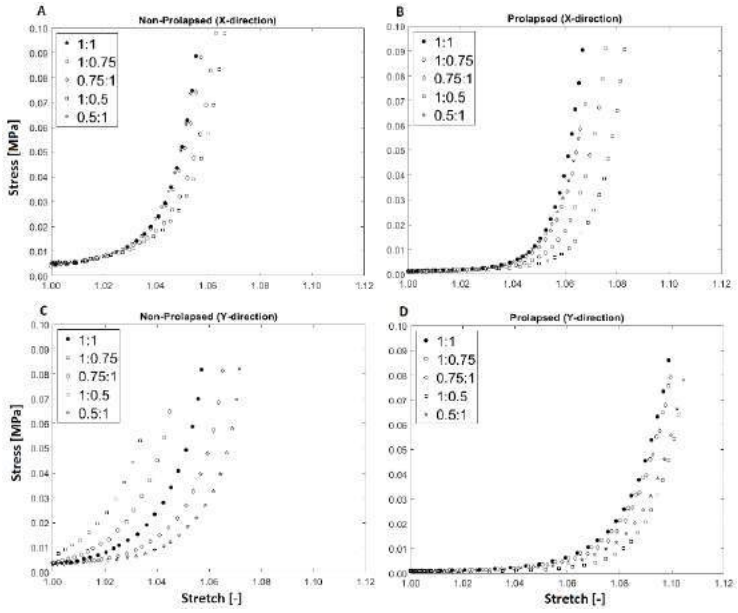

Figure 2: Representative stress-stretch plots in the X direction for non-POP (A) and POP (B) USL. Representative stress-stretch plots in the Y direction for non-POP (C) and POP (D) USL. Figure shows that POP USL exhibits more extensibility than non-POP.

within the pelvic floor [9]. The elastin composition of the USL with and without POP, however, has not been identified to date. This study also identified that the non-POP and POP USL demonstrate an anisotropic mechanical response. Generally, the USL was more extensible in the Y-direction compared to the X-direction (Figure 2). The Fung-type model was able to reasonably describe the biomechanical behavior of the non-POP and POP USL ($R^2 = 0.99$). The Fung parameters indicated that there was minimal biomechanical contribution from the ground substance (Table 1). Further, the model suggests potential remodeling of the fiber component during POP, as an increase was observed in the c_1 and c_2 compared to the controls. This may be explained by altered collagen fiber alignment, undulation, or possible alterations in the type I:III ratio. Further work is needed to identify correlations between model parameters and tissue composition, as well as to examine possible microstructural models to improve clinical relevance.

This study was not without limitations. One such limitation is the lack of racial diversity in the patient population. Current patient recruitment seeks to improve diversity. Noting, however, that the rate of POP in the African Americans/Blacks population is much lower than other racioethnic [10]

ACKNOWLEDGEMENTS

This work was supported, in part, byNIHP20-GM103629 (Miller) and the Ochsner Translational Medicine Research Initiative (Miller, Knoepp).

REFERENCES

[1] Olsen, A et al., *Obstet Gynecol*, 89:501-506, 1997.[2] Subak, A et al., *Obstet Gynecol*, 98:646-651, 2001.[3] Baah-Dwomoh, A et al., *Ann Biomed Eng*,46:2036-2047, 2018.[4]Doshani, A et al., *BMJ*,2007:335-819, 2007. [5] Ramanah, R et al., *Int Urogynecol J*, 23:1483-1494, 2012. [6] Gabriel, B et al., *Int Urogynecol J*, 16:475-479. [7] Tan et al., *Ann Biomed Eng*, 44:3225-3237. [8] Becker and De Vita, *Biom Mod mechano*, 14:549-560. [9] Goepel, R, *Acta Histochem*, 110:204-209, 2008. [10] Whitcomb E et al., *Obstet Gynecol*, 114:1271-1277, 2009.

SB³C2019
Summer Biomechanics, Bioengineering and Biotransport Conference
June 25 -28, Seven Springs, PA, USA

RUPTURE MECHANISMS OF THE VAGINA UNDER INFLATION

Jeffrey McGuire (1), Woowon Lee (2), Kimani C. Toussaint, Jr. (2), Caleb Stine (1), Jennifer Munson (1), Raffaella De Vita (1)

(1) Department of Biomedical Engineering and Mechanics
Blacksburg, Virginia, USA

(2) Department of Mechanical Science and Engineering
University of Illinois at Urbana Champaign
Urbana and Champaign, Illinois, USA

INTRODUCTION

During childbirth the female pelvic floor endures substantial stretching, frequently resulting in tearing of the vaginal wall and major surrounding tissues and organs. Childbirth-related maternal trauma is the primary etiological factor of pelvic floor disorders (PFDs) such as urinary incontinence, fecal incontinence, and prolapse. These disorders affect one out of three adult women, representing a major healthcare concern in the U.S. Although the prevalence of PFDs increases with childbirth, there are currently no quantitative methods that can predict maternal trauma and the development of PFDs. In this study, we conduct inflation tests together with the digital image correlation (DIC) method to determine the tear behavior of the vaginal wall using the rat as an animal model. Inflation tests are preferred over planar biaxial tests since they are physiologically more relevant and prevent tearing at the hooks that are used in planar biaxial testing [1]. We also analyze the collagen fiber organization in the regions where the tears form using second harmonic generation (SHG) imaging. This micro-mechanical analysis reveals the possible mechanisms of vaginal tears.

METHODS

This study was approved by the Institutional Animal Care and Use Committee (IACUC) at Virginia Tech. Eight (n = 8) vaginal tracts were isolated from eight virgin Sprague-Dawley rats (~3 months old). Initial axial, radial, and thickness measurements were taken using a CMOS camera (Thorlabs Inc.) on a dissecting microscope. Each specimen was then mounted onto two dispensing needles which allowed one end of the vaginal tube to freely move while being inflated. After mounting, specimens were dyed blue with an aqueous methylene blue solution (1% w/v) and speckled with an aerosol fast dry gloss white paint. This created a high contrast speckle pattern on the surface of the specimen for non-contact strain measurements. Throughout the preparation process, the specimens were hydrated with phosphate buffered saline (PBS). Specimens were housed in an acrylic water bath filled with PBS and inflated with PBS via a computer-controlled syringe pump (New Era Pump Systems Inc.) to a pre-load of 0.2 psi as measured by a 50 psi pressure transducer (Omega Engineering Inc.). This point was established as the reference configuration. Specimens were pre-conditioned for 20 cycles at 4.7 mL/min up to a 100% increase in volume and back to the reference configuration. Following a 10 minute long period of rest, specimens were inflated at 4.7 mL/min until rupture. High-resolution images of the specimens were taken during inflation via two CMOS cameras (Basler Inc.) equipped with c-mount lenses (Schneider Optics Inc.). Non-contact strain measurements were performed with a DIC system (Correlated Solutions Inc.). Once testing was completed, specimens were removed from the setup, kept hydrated, and the rupture site was imaged using the SHG imaging. Specimens were placed on a motorized stage of a Zeiss LSM 880 upright confocal microscope (Zeiss). Backward-SHG imaging was performed with a 140 fs Ti:Sapphire laser (Coherent Inc.) centered at 780 nm at 80 MHz repetition rate. The beam was

deflected into the back port of the microscope and scanned across the vaginal specimens by a galvanometric x-y scanner. The beam was passed through a 690 nm dichroic mirror and focused onto the specimen. A 20X non-immersion microscope objective and a 40X oil-immersion microscope objective were used for imaging. The average excitation power illuminating the specimen was approximately 30 mW as measured by a power meter (Newport Corp.). The backscattered SHG signal from the specimen traveled through the objective and was collected by reflected to a detector after going through a 690 nm long-pass dichroic beam splitter. The SHG signal was isolated by a secondary beam splitter followed by a 390 nm bandpass filter (Semrock). Two-dimensional images were acquired from various depths into the specimen.

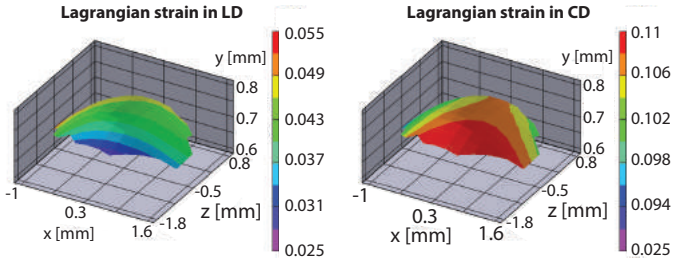

Figure 1: Lagrangian strains in the longitudinal direction (LD) and circumferential direction (CD) for a representative vaginal specimen at a 118 kPa pressure. For this specimen failure occurred at 119 kPa pressure. Note that the z-axis is oriented along the longitudinal axis of the vagina.

RESULTS

Rupture of the vaginal wall consistently occurred in the central region away from the clamps. The main axis of the tear was oriented along the longitudinal direction (LD) of the vagina. The tissue was observed to strain far more in the circumferential direction (CD) than in the LD (Figure 1(a)-(b)). Larger strains in the CD were expected, but in the LD the strain was surprisingly near zero. The average axial Lagrangian strain at failure was 0.41 ± 0.38 in the CD compared to 0.05 ± 0.03 in the LD. The average pressure at rupture was 106.8 ± 26.2 kPa, which corresponded to an average maximum stress of 1035 ± 254 kPa and 487 ± 123 kPa in the CD and LD, respectively. Paired t-tests confirmed a statistically significant difference between the average failure stresses ($p < 0.001$) and strains ($p = 0.032$) in the two directions.

Images collected using the SHG imaging after mechanical testing showed that the collagen fiber orientation changes through the thickness of the specimens (Figure 2 (a)-(b)). However, fibers seemed to be preferentially aligned along the LD of the vagina. In regions that were close to the tear, the fibers appeared to be oriented along the edges of the tears (Figure 2 (c)-(d)). Moreover, post-failure analysis of the vaginal specimens via SHG imaging revealed three primary failure mechanisms: delamination, collagen fiber failure, and collagen fiber re-orientation.

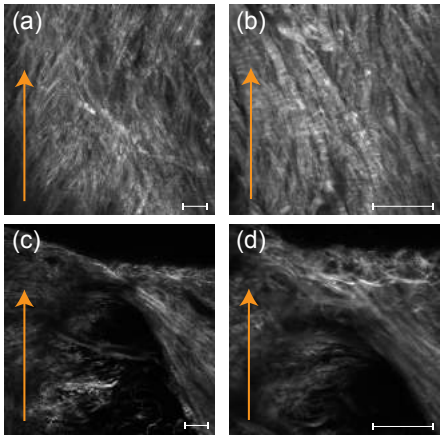

Figure 2: (a)-(b): Collagen fibers in the dorsal region of the rat vagina, near the rectum, at 20X and 40X magnifications. (c)-(d): Collagen fibers in the ventral region of the rat vagina, near the urethra, where tearing occurred. The orange arrow indicates the LD of the vagina. Scale bar=50 μm.

DISCUSSION

This study presents the first mechanical characterization of the rat vagina up to under inflation. Our results demonstrated that the vagina is highly anisotropic and undergoes large deformations (Figure 1). The strain in the LD was significantly lower than in the CD due to the preferred orientation of the collagen fibers in the LD (Figure 2(a)-(b)). Our results indicated a nearly zero and sometimes negative strain in the LD. It is possible that the complex strain behavior may be determined by the magnitude of the applied strain relative to the in-vivo strain as shown in a previous study performing inflation of murine vaginas [3].

Under inflation, we observed that the vaginal specimens successfully failed in regions away from the clamped ends. Our SHG analysis of these regions showed that the primary mechanisms of tear formation are delamination, collagen fiber failure, and collagen fiber re-orientation. Future studies will be conducted to determine the tear propagation mechanisms under inflation. Knowledge about the tear behavior of the vagina can guide the development of new prevention and treatment strategies for maternal birth trauma.

ACKNOWLEDGEMENTS

This work was supported by NSF Grant No. 1511603.

REFERENCES

[1] Robison, K.M. et al., *J. Biomech. Eng.*, 139(10):104504, 2017.
[2] McGuire, J. et al., *J. Biomech. Eng.*, 2019, doi: 10.1115/1.404243.

SB³C2019
Summer Biomechanics, Bioengineering and Biotransport Conference
June 25 – 28, Seven Springs, PA, USA

REMODELING OF THE DIABETIC URINARY BLADDER: A COMPARISON OF AN OBESE AND A LEAN ANIMAL MODEL OF TYPE II DIABETES

Marissa R. Grobbel (1), Matthew T. Lewis (2), Anne Tonson (2) Robert W. Wiseman (2), and Sara Roccabianca (1)

(1) Department of Mechanical Engineering
Michigan State University
East Lansing, MI, United States

(2) Department of Physiology
Michigan State University
East Lansing, MI, United States

INTRODUCTION

Diabetic cystopathy is a form of neurogenic bladder dysfunction that occurs in diabetic patients experiencing peripheral neuropathy. Loss of connection between the urinary bladder and the nervous system dulls the sensation of fullness in the bladder. This causes delays in voiding, leading to chronic over-filling of the bladder. This type of volume overload has been shown to cause changes in extracellular matrix (ECM) content, wall thickness, tissue compliance, and inflammation in the bladder [1, 2, 3]. Furthermore, obesity — often associated with type II diabetes, specifically — also has been shown to increase systemic inflammation, which could induce even further remodeling to the bladder wall (e.g., high level of inflammation are often associated with fibrosis in the remodeling of the lungs, liver, and heart). Finally, stiffening of the bladder wall associated with fibrosis can diminish the bladder distensibility, which in turn could increase the urine storage pressure, posing a threat to kidney function of these patients. For these reasons, it is crucial to understand what specific changes are taking place in the ECM within the bladder. In this study, we have measured experimentally the mechanical behavior of the ECM of urinary bladders from a lean and an obese rat model of type II diabetes. We then employed a Fung-type exponential isotropic strain energy function to model the experimental data, and quantify material parameters for each model of type II diabetes.

METHODS

Uniaxial ring tests were conducted using transversely sliced, decellularized rings of urinary bladder tissue from: **Goto-Kakizaki** rats (**lean diabetic, GK-D**, *n = 5*), **Zucker diabetic fatty** rats (**obese diabetic, ZDF-D**, *n = 4*), Wistar as a control for GK-D animals (GK-C, *n = 6*), and lean ZDF littermate as a control for ZDF-D animals (ZDF-C, *n = 4*) [4]. Before the ring tests were conducted, each ring was decellularized through a 48 hour soak in a 1% sodium-dodecyl sulfate solution to isolate the ECM. Following this procedure, the rings were mounted on a uniaxial testing machine using suture and submerged in a modified, calcium-free Krebs buffer. Each ring was subjected to a pre-load of 2-3g. Finally, the ring test consisted of: 10 cycles at 5% stretch (preconditioning), 5 cycles at 10% stretch, 5 cycles at 20% stretch, and 5 cycles at 30% stretch.

Assuming incompressibility and isotropic behavior of the tissue, the final loading curves of the stress-strain data from these tests were then fitted to a Fung-type material model, Eq. 1.

$$W = c\left(e^{k(I_1(C)-3)} - 1\right) \tag{1}$$

Two parameters, c and k, have been reported for each test group, see **Table 1**. Additionally, the product $2ck$ was also used in the comparison of different groups, as this term serves as an important parameter in the equation for theoretical stress, Eq. 2.

$$t_{11} = 2ck\left(\lambda^2 - {}^1/_{\lambda}\right)e^{k\left({}^{\lambda^2-2}/_{\lambda^{-3}}\right)} \tag{2}$$

While k has an effect on the entire curve, 2ck is specific to the toe-region, which will provide crucial information about compliance at low stresses.

Additionally, histological analyses were performed to assess changes in the extracellular matrix due to remodeling—namely elastin and collagen fibers—and mast cell activation, which is indicative of inflammation. To measure elastin fiber, collagen fiber, and mast cell content, the slices were stained with Verhoeff-Van Gieson (VVG), Picrosirius Red (PSR), and a modified toluidine blue (t-blue),

respectively. Because mast cells are present regardless of inflammation, simply counting the number of mast cells present in the tissue samples or estimating an area fraction would not provide sufficient information about inflammation in the urinary bladder. Instead, mast cell activation was estimated through a ranking system: 1-completely inactive (no granulation), 2-beginning activation, and 3-completely inactive (high granulation). Mast cells were counted and ranked to provide an overall score of activation for each sample.

RESULTS

Our experimental results showed that the ECM of bladders collected from both GK-D and ZDF-D diabetic animals presented an increase in compliance when compared to their respective controls, namely Wistar (GK-C) and ZDF lean littermates (ZDF-C), **Figure 1**. Furthermore, we observed that the ECM of bladders from ZDF animals, both the ZDF-C and ZDF-D, show a higher compliance when compared to GK animals, GK-C and GK-D, respectively. The only two groups that showed no difference were GK-D and ZDF-C.

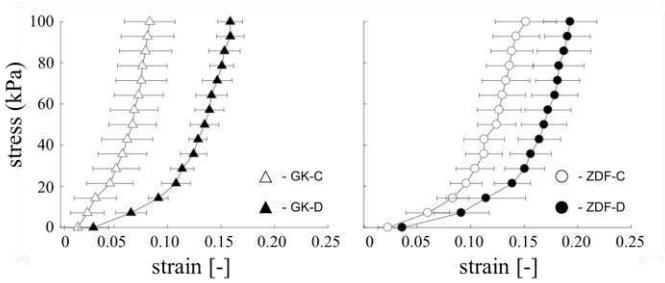

Figure 1. Stress-strain data from uniaxial ring test. Each point represents average (error bars showing standard deviation) strain from all samples in each group. Data shown is from final loading curve.

The model proved useful in identifying where differences between the groups are present in regards to the mechanical parameters. Specifically, a decrease in c and k when comparing controls to diabetic, using a student t-test, is present in both the GK and ZDF models ($p < 0.05$), **Table 1**. The differences in 2ck were significant across all test groups except for ZDF-C v. GK-D and ZDF-C v. GK-C (the comparison ZDF-C v. GK-C was close to significance, $p = 0.061$).

Table 1. Optimized material parameters for each test group.

Group	c (***avg*** ± *stdev*)	k (***avg*** ± *stdev*)	2ck (***avg*** ± *stdev*)
ZDF-C	**0.466** ± *0.113*	**36.067** ± *13.428*	**32.039** ± *7.374*
ZDF-D	**0.271** ± *0.090*	**25.983** ± *4.370*	**14.055** ± *5.496*
GK-C	**0.725** ± *0.342*	**79.625** ± *26.131*	**121.931** ± *79.230*
GK-D	**0.433** ± *0.193*	**31.839** ± *6.986*	**25.72** ± *8.417*

Histological analyses are ongoing but have shown thus far a potential increase in elastin fiber content and mast cell activation in ZDF-D compared to ZDF-C, **Figure 2**. Additionally, ZDF-D appears to have thinner collagen fibers than ZDF-C.

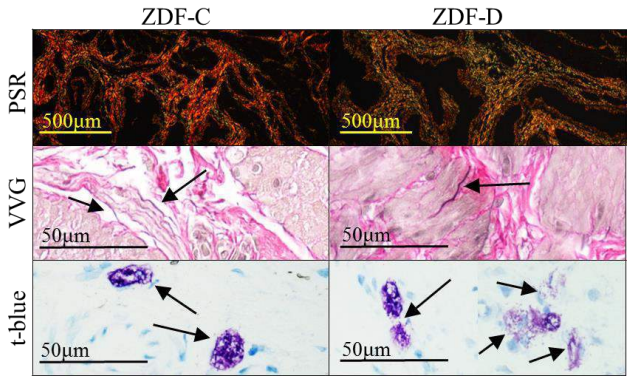

Figure 2. Histological stains from ZDF-C and ZDF-D groups. Arrows show elastin fibers and mast cells.

DISCUSSION

While GK and ZDF rat models are both useful models of type II diabetes, they result in significantly different remodeling of the urinary bladder ECM. Though in both models the ECM was more compliant in diabetic bladders than controls, ZDF diabetic bladders are significantly more compliant than GK diabetic. Differences in compliance were especially significant in the toe-region of the stress-strain curves, suggesting that the diabetic bladders are especially compliant at low physiological stresses. Because the bladder fills at low-pressure, this decrease in compliance at low stress could have a large impact on urinary bladder function in vivo.

Changes in the mechanical behavior of the bladder ECM are the result of remodeling of the bladder tissue, which we have observed through histology. It is also known that tissue remodeling could be exacerbated by systemic or localized inflammation, which is evident in soft tissues such as lungs, liver, and the heart. Hence, the increase in mast cells recruitment and activation in the wall of ZDF-D bladders could suggest that inflammation is triggering a more dramatic remodeling in this model when compared to the GK. An increase in elastin fibers, as well as thinning of collagen fibers could also contribute to the increase in compliance of the tissue.

These results strongly suggest that there is remodeling of the ECM within the bladder wall in both of the models studied. The response however seems to be more prominent in the bladder of obese animals. We suggest that inflammation could play a key role in this difference, since a higher level of systemic inflammation is generally associated with obesity. However, in order to draw a conclusion such as this, further histological analyses will need to be performed on the GK groups. Results of this study help us to understand the differences in mechanical behavior of the urinary bladder affected by obese and non-obese diabetic cystopathy.

ACKNOWLEDGEMENTS

We kindly thank the MSU investigative histopathology lab for help with staining our samples.

REFERENCES

[1] G. Liu & F. Daneshgari. *Am J Physiol Regul Integr Comp Physiol* 2006.
[2] C.C. Wang et. al. *Urology* 2009.
[3] M.Y. Donath & S.E. Shoelson SE. *Nat. Rev. Immunol.* 2011.
[4] M. Shiota & R.L. Printz. *Animal Models in diabetes research* 2012.

SB^{3}C2019
Summer Biomechanics, Bioengineering and Biotransport Conference
June 25 -28, Seven Springs, PA, USA

LACTATING HUMAN BREAST RESPONSE TO INFANT ORAL MOVEMENTS

D. Alatalo* (1), L. Jiang* (1), F. Hassanipour (1)

(1) Department of Mechanical Engineering
The University of Texas at Dallas
Richardson, Texas, USA

INTRODUCTION

Breastfeeding provides nourishment and other responses in both infants and mothers that promote survival. The biomechanics of breastfeeding have been studied for over half a century, primarily by clinicians. Four primary stages of latch-on have been identified (see Fig. 1). Latch-on and suckling involves positive pressures applied by the lips, mandible, maxilla, tongue, and palate. The movement of the tongue creates a negative intra-oral vacuum. The vacuum pressure created during breastfeeding has been investigated for decades. Studies show that infants who are unable to maintain a negative vacuum frequently have difficulty extracting sufficient milk and mothers suffer from sore and damaged nipples. Additionally, a healthy suckling pattern creates a sinusoidal intra-oral vacuum [1]. Previous works have modeled the effect of vacuum pressure on milk flow within the breast. However, the effects of positive pressure on milk flow have been largely ignored, either because they are deemed negligible or simply because clinical recordings of these pressures do not exist. Recent experimental work captured the positive peripheral oral pressure exerted on the areola during breastfeeding in conjunction with intra-oral cavity ultrasound imaging and vacuum. The objective of this study is to understand the relationship between positive compression and negative vacuum pressures on the geometry of the nipple during suckling with milk expression.

METHODS

Collection of pressure data, ultrasound images, and 3D scans of the breast before and after feed was obtained as outlined by Alatalo et al. [2] for six breastfeeding infants ranging in age from 6 days to 4.5 months. Arbitrary white noise and unpredictable outliners in raw sensor data for both vacuum and compression were filtered in MATLAB using a polynomial de-noising algorithm known as BUTTERWORTH.

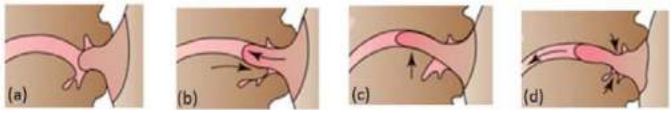

Figure 1: Latch-on is when the infant attaches to the nipple and begins to suckle. The four stages of successful latch-on are (a) infant's lips clamp, (b) tongue pulls the nipple into oral cavity, (c) tongue pushes the nipple to the hard palate, and (d) infant's gums compress the nipple [1].

Periods of milk transfer were visually identified in ultrasound videos. For each mother-infant dyad, 1-2 suck cycles with milk transfer were chosen for measurements of nipple dimension changes based on clarity of imaging. Calibration used a self-decided base-line in images. A self-programmed measurement system was achieved in MATLAB to measure average dimension changes of the nipple width and length with tongue moving up and tongue moving down (see Fig. 2).

Prefeed and postfeed 3D scans of the breast were captured using Polhemus FASTSCAN and the .dxf files were imported into SolidWorks for measurements of nipple. The nipple was assumed to be cylindrical in shape and two orthogonal cross-sectional areas were used to calculate an average value for nipple width (NW) and nipple length (NL). Since no clinical signs of tissue damage were noted after feeding, the nipple was assumed to experience total elastic compression/torsion. The prefeed measurements and ultrasound measurements were used to calculate the apparent strain ratio using Equation (1), where L_i and W_i are the initial length and width and L_f

*Shared first authorship

and W_f are the length and width at different times during milk transfer or nutritive suck cycle.

$$\nu = \frac{\frac{L_f}{L_i} - 1}{1 - \frac{W_f}{W_i}} \quad (1)$$

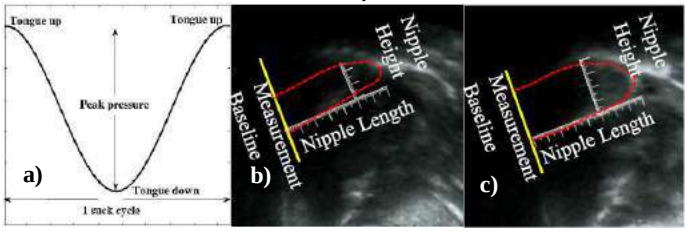

Figure 2: Nipple dimension measurement in ultrasound images. (a) Vacuum peaks when tongue moves down. (b) Tongue moving up (lowest vacuum). (c) Tongue moving down (strongest vacuum)

RESULTS

All infants applied sinusoidal compression patterns on the areola during suckling for both maxilla and mandible, which has not been previously reported particularly for the maxilla (see Fig. 3). The change in compression (3.63 kPa) is considerably smaller than the change in vacuum (-13.77 kPa) during nutritive suckling. Correlation between compression and vacuum pressures was moderate for only the 2 youngest infants with correlations coefficients of 0.57 and 0.72.

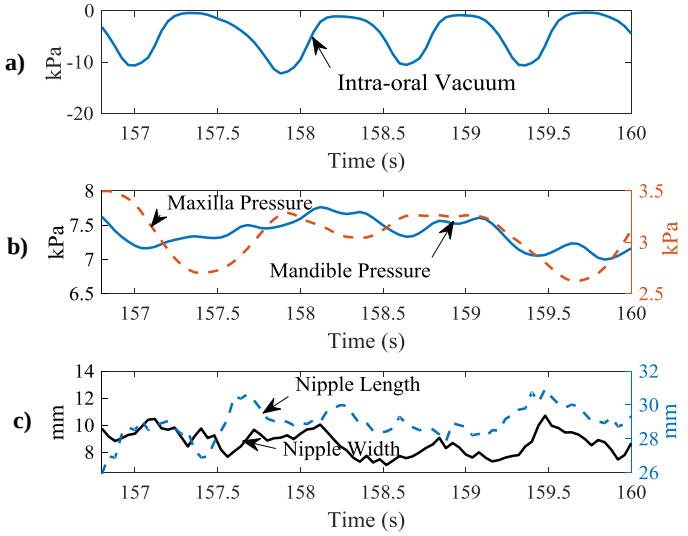

Figure 3: Sinusoidal patterns are evident in (a) vacuum pressure, (b) compression pressures, and (c) nipple dimensions.

The nipple dimensional changes in response to compression and vacuum pressures showed that compression dominates nipple deformation. Ultrasound images show that when the tongue is down, milk is expressed from the nipple and milk continues to be expressed as the tongue rises up toward the palate. When the tongue is down, the vacuum pressure is at its lowest but the nipple is at its shortest length. Whereas when the tongue is up, the vacuum is higher but the nipple is longer. Thus, the dominate pressure that impacts the deformation of the nipple appears to be the positive pressure applied by the tongue and palate, not the vacuum.

Strain ratio calculations showed large variation between dyads over time (see Fig. 4.) with mean values ranging from 0.13 to 0.65. Postfeed nipple measurements showed volume changes when compared to prefeed dimensions ranging from -315 mm^3 to 1166 mm^3.

Correlations between strain ratio and vacuum pressure were strong for 3 dyads (>0.7) but weak for the other 3 dyads (<0.3). A summary of findings is presented in Table 1.

Table 1: Mean values plus standard deviations for all dyads.

Nipple Height Changes	1.56±0.24 mm
Nipple Length Changes	3.00±0.37 mm
Intra-oral Vacuum Changes (min-max)	-13.77±4.86 kPa
Peripheral Oral Pressure Changes (min-max)	3.63±3.53 kPa
Strain Ratio	0.39±0.19

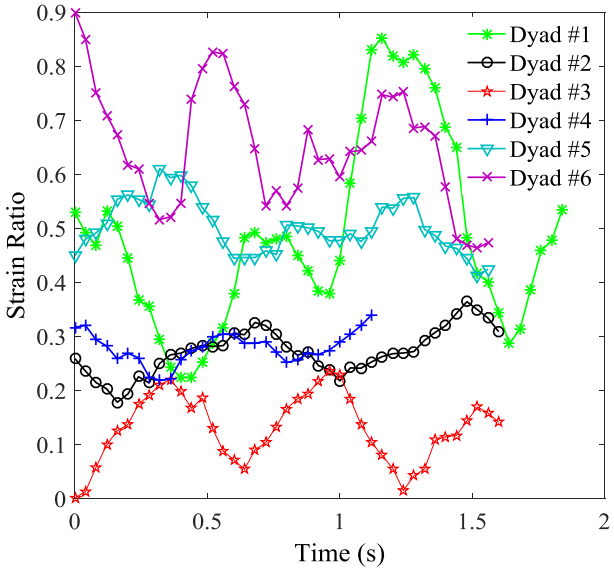

Figure 4: Strain ratio of the nipple during nutritive suckling varies greatly between dyads but in a sinusoidal.

DISCUSSION

The dynamics of breastfeeding are extremely complex and require novel methods to capture data. The oscillatory compression of the areola by the maxilla has not been previously reported and would not be obvious to external observers since the maxilla does not appear to move after forming a teat. Rather movement of the mandible is generally evaluated for correct suckling patterns. The small variations in compression pressure under maxilla and mandible are sufficient to occlude milk ducts under the areola. The lack of correlation in older infants between compression and vacuum suggests that as infants mature they develop two methods of controlling milk flow.

Compression dominates the nipple deformation, however the dominate pressure over milk flow remains unsolved [1]. The variations in strain ratio during nutritive suckling are likely related to volume changes within the nipple. These results challenge the current practice of assuming a Poisson's ratio near or at 0.5 for breast tissue during lactation. Further study is planned.

ACKNOWLEDGEMENTS

The authors wish to thank all the mothers who volunteered for this study. This material is based upon work supported by the National Science Foundation under Grant Numbers 1454334 and 1614350, National Science Foundation Graduate Research Fellowship Program under Grant 1746053, and Eugene McDermott Graduate Fellowship.

REFERENCES

[1] Geddes, DT et al., Early Human Dev, 84 (7):471-477, 2008.
[2] Alatalo, et. al., J.of Biomech Eng. Accepted, 2019.

SB³C2019
Summer Biomechanics, Bioengineering and Biotransport Conference
June 25 -28, Seven Springs, PA, USA

CONTRIBUTION TO THE UNDERSTANDING OF THE GENESE OF THE LIGAMENTAL SYSTEM OF THE PELVIC SYSTEM

O. Mayeur (1), M. Brieu (2), M. Cosson (1,3)

(1) olivier.mayeur@centralelille.fr, LaMcube, ULille-CNRS-Centrale Lille, Cité scientifique CS 20048, F-59000 Lille, France

(2) mbrieu@calstatela.edu, Dept. Mechanical Engg, California State University, CA, USA

(3) michel.cosson@chr-lille.fr, LaMcube, ULille-CNRS-Centrale Lille, Hôpital Jeanne de Flandres - CHRU de Lille, F-5900 Lille, France

INTRODUCTION

The physiology and pathology of the pelvic organs remains a key question in terms of mechanical modelling to reach a better understanding of pelvic trauma. The pelvic system, and its suspension elements, presents a complex equilibrium related to the mechanical properties of tissues involved and their geometries [1]. Disturbance of such an equilibrium may induce pathophysiology mobility such as genital prolapse, which is a major health problem concerning 30% of the women population [2]. Different anatomical structures seem to play a key role in that balance and the authors have remained on the role of the pelvic muscles. Recently it has been demonstrated that the uterosacral ligaments also play an important role in supporting organs [3, 4]. This complex equilibrium might be impacted by the life events such as aging, pregnancy or delivery.

During pregnancy, a modification of the pelvic floor appears [5]. During life time and aging evolution of the anatomy is also reported [6, 7]. The evolution of the pelvic floor and the ligaments that sustain the pelvic organs seems to be one of the key factors of pathology such as prolapse [8]. However, while study are reporting some observance of the evolution of the pelvic suspension with age and/or physio-pathology no understanding of the mechanism of evolution is proposed.

The objective of this work is to propose a mechanical approach to explain the evolution of the pelvic suspension. In a fisrt par, a generic model of the pelvic anatomy will be introduced to model the pelvic suspensions. In a second part, an optimization process will be proposed to minimize and homogenized the stress-strain equilibrium within the suspension device modeled. The analysis of the obtained result will propose an explanation of the pelvic suspension element whose appearance will be interpreted as a remodeling process aiming at uniformly distributing the strain within the suspension elements.

METHODS

The approach used in this study is purely numerical. It is based on one side on a refined model of the pelvic cavity, fully reconstructed with medical imaging technics [9] and on the other side on Finite Element method under large strain [10]. The images data provided from a healthy patient with no medical history and in agreement with ethical approval. MRI was performed thanks to classical parameters used for clinical gynecologic examination. Segmentation and contouring of all the organs allowed us to obtain the bone structures and main organs of the pelvis such as the vagina, the rectum, the uterus and the bladder. This geometrical information makes it possible to know precisely the position of the organs on the pelvic cavity. CAD tools are used to generate a representative surface of the level I support. This anatomical area is characteristic for our study because the constitutive structures (uterosacral and cardinal ligaments) provide a support of the vagina cervix [11]. The limits of this surface correspond to precise anatomical zones (fig.1a), following an anteroposterior trajectory, posterior face of the pubis (z1), arcus tendinous (z2), sacrospinous ligaments (z3) and the sacrum (z4). This surface is also in interaction with the positions of reconstructed organs such as the bladder, the cervix and the rectum (fig.1b).

Parameterization of this surface was performed to apply pressure levels on different areas (fig1a). The pressures may be oriented normal to the surface or oriented at a specific inclination. A study was conducted to select the most appropriate configuration, in accordance with the dynamic MRI analysis performed in previous team work [11].

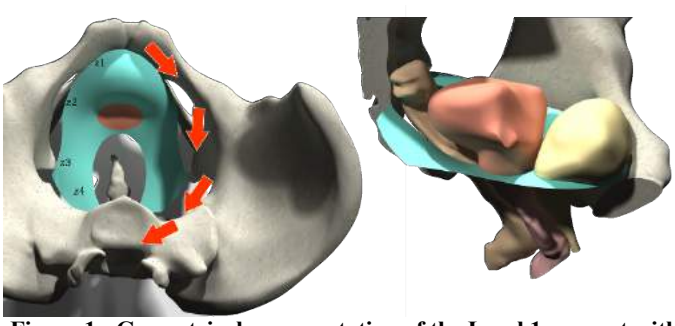

Figure 1: Geometrical representation of the Level 1 support with location. a) Anatomical areas near the bone structures and b) integration of the 3D organs.

The study aims to analyze the deformations that undergoes on this anatomical area. We chose a "generic" material with mechanical properties (E_0 = 0.3MPa, Poisson ratio = 0.45) closed to the analyze carried out on the ligamentous tissues [13, 14]. We assume that the material is linear elastic, undergo small strain and stress, homogeneous and thickness of the surface is constant. Numerical simulations is performed on Abaqus CAE. The convergence of the calculation, as well as a mesh sensitivity study, was carried out in order to guarantee the validity of the results. Considering that the remodeling process aims at reaching a stress-strain equilibrium for cells, and since where considering only applied stress problems, we have introduced an optimization procedure aiming at reaching a strain equilibrium by minimizing the difference between the maximum and the minimum of strain. The variable optimized is the effective local stiffness, assumed as homogeneous at the initial stage.

RESULTS

A first simulation (fig 2a) allows us to provide an analysis of the principal strain levels, by considering a surface with a homogeneous stiffness E_0 value. The strain is observed to be highly heterogeneous. Based on those results, we have implemented an optimization process on the FE method to minimize the gap between the maximum and minimum deformations making varying the local stiffness. With this optimization process, we are able to homogenize the deformations by modifying, for each element of the mesh, the mechanical properties by a ratio of E_0. Taking into account the strain level in our analysis is in accordance with literature review which reveals that the damage of the pelvic tissues is dependent to the deformation [15].

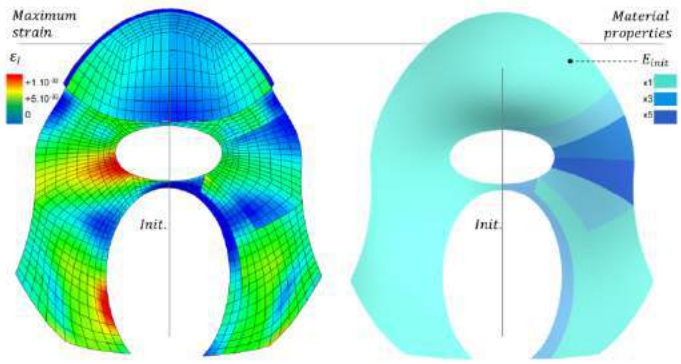

Figure 2: Comparison between initial simulation (with homogenous material) and optimization process results (with un-homogenous material) - a) Strain level and b) material properties map.

At the end of the optimization loop, a map of the floor can be plotted (fig2b). On fig. 2 representation, we can observe on the left hand side the homogeneity of the strain, and on the right hand side the areas where the material properties must be rigidified to normalize the strain level. Homogeneous mechanical property on the considered surface leads highly heterogeneous strain fields. However, the introduction of the optimization process proposed, leads to homogenize the strain field by densify locally the material and increasing its stiffness. It leads to make uterosacral ligaments appearing with module stiffenes 3 times higher than E_0 to reduce the strain level. In the same way, the areas corresponding to the cardinal ligaments are also more densify with a ratio of 4xE0.

DISCUSSION

The literature reveals that quadruped animals have no utero-sacral ligaments. It also reveals that in the childhood and even at the foetal stage, women have neither utero sacral ligaments nor cardinal ligaments [6, 7] while old women have very stiff and thick uterosacral and Cardinale ligaments [8].

The optimization process we have developed is initially considering a suspension surface with homogeneous mechanical properties. It is a model of a connective tissues which function aims at providing a suspension to pelvic organs. Since the stiffness is homogeneous in this initial surface of suspension, no specific sub-domain can be highlighted. The optimization process introduce aims at homogenizing the strains answering to a stress-strain equilibrium expectation. The results of this optimization process highlights to zone with densified mechanical properties which are corresponding to the location of uterosacral and cardinal ligaments.

CONCLUSION

The genese of pelvic ligaments is not well understood. The approach we are proposing tends to show that pelvic ligaments, and more specifically, are appearing with age to reach stress-strain homogenized equilibrium within the pelvic system.

Further study, using this approach, may lead to propose some remodeling models of the pelvic system with respect to the loadgin history of patients.

REFERENCES

[1] Mayeur, O et al., *Annals of Biomed Eng*, 44(1):202-212, 2016.
[2] Samuelsson, E et al., *Am J Obstet Gynecol,* 180:299-305, 1999.
[3] Wei, JT et al., *Clin Obstet Gynecol*, 47(1):3-17, 2004.
[4] Cosson, M et al., *Int Urogynecol J*, 24(1):105-12, 2013.
[5] O'Boyle, AL et al., *Int Urogynecol J*, 14(1):46-9, 2003.
[6] Ramanah, R et al., *Int Urogynecol J,* 23:1483-1494, 2012
[7] Ramanah, R et al., *Int Urogynecol J Pelvic Floor Dysfunct 19:1565-1570*, 2008.
[8] DeLancey JOL. *American Journal of Obstetrics & Gynecology*, 166t, 1992.
[9] Jiang Z. et al., Strain, 51(3): 235-247, 2015.
[10] Lamblin G. et al., *Archives of gynecology and obstetrics,* 294, 2017.
[11] Mayeur O. et al., Biomed.Simulation, Book series, 8789, p. 220-227, 2014
[12] Rubod C. et al., Int. Urogynecology J., 24(12): 2093-2098, 2013.
[13] Rubod C. et al., Int. Uro-gynecology J, 19(6): 811-816, 2008
[14] Chantereau P. et al., Int. Urogynecology J 25(11): 1547-1553, 2014.
[15] Clay JC., Int. Uro-gynaecology, 21(12): 1535-1538, 2011.

SB^{3}C2019
Summer Biomechanics, Bioengineering and Biotransport Conference
June 25 -28, Seven Springs, PA, USA

BROADENING RESEARCH EXPOSURE AND RESEARCH PARTICIPATION IN MECHANICAL ENGINEERING: FINDINGS FROM THE UMBC ME S-STEM SCHOLARSHIP PROGRAM

Liang Zhu (1), Ronghui Ma (1), Deepa Madan (1), Charles Eggleton (1), L. D. Timmie Topoleski (1), Shuyan Sun (2)

(1) Department of Mechanical Engineering
University of Maryland Baltimore County
Baltimore, Maryland, USA

(2) Department of Psychology
University of Maryland Baltimore County
Baltimore, Maryland, USA

INTRODUCTION

Since 2008, many public universities have undergone continuous and substantial budget cuts, while the number of students enrolling in Mechanical Engineering (ME) programs continues to grow. Financial difficulty has forced some community college students to forego pursuing a 4-year BS degree. Many of our students pursuing a BS degree in the ME program have to seek employment outside of engineering to pay for their education. This limits their time available to focus on their course work. For the 2010 cohort of our ME freshmen, the 4 year retention rate was around 50% and the 4 year graduation rate was 23%. The retention and graduation rates were even worse in underrepresented minority (URM) students and transfer students.

Studies[1-3] have demonstrated that integrating a research experience into a student's education program improves retention rates, and plays a role in increasing the percentage of students pursuing graduate degrees. Despite efforts at the university level, very few undergraduate students on our campus attend regular research seminars in the STEM departments and less than 10% of the undergraduate students actively participate in research. This may be due to lack of information, conflict of schedules, as well as the depth of the research topics. We believe that providing students with research opportunities and actively exposing them to STEM advancements would lead not only to more students applying and/or transferring to our ME undergraduate program, but also retaining them through graduation. Extra effort is needed to inspire students' interest in research, especially interdisciplinary research.

Starting in 2010, the ME department at UMBC has been awarded three NSF S-STEM grants to increase student diversity, improve retention, and provide successful paths toward job placement and graduate study in our department. In addition to scholarships and faculty mentoring, we implemented approaches to integrate research into various aspects of our curriculum, including visiting community colleges, giving research seminars to community college students and UMBC students, organizing lab visits for undergraduate students, and providing undergraduate research opportunities. In this study, we asked students to complete a survey after specific research related educational activities. Data analyses were conducted to evaluate whether the perceived experiences from exposure to research differed by ethnic group, family educational background, whether they are community college transfers, and whether the students are part of a scholarship program. The survey results were also used to measure the satisfaction of the participants from the research related activities, and to collect feedback for future improvements.

METHODS

Two short surveys were designed, one for community college visits, and the other for ME lab tours. An ME faculty member visited a community college and gave a seminar typically consisting of three parts: a description of the ME S-STEM Scholarship Program at UMBC, the transfer process to the ME program, and ongoing research projects in the faculty's lab at UMBC. The lab tour at UMBC was scheduled during a University "free-hour" so that all ME undergraduate students could attend. During the lab visit, the faculty gave a Powerpoint presentation, and then a show and tell session, followed by a Q&A session to answer their questions. The surveys were given to all participants after the events and were collected on the site. Both surveys were similar, with only 15 questions covering information about their demographic background, their previous exposure to research and research experience, and their satisfaction to the event. All survey results were entered into EXCEL for data analyses. Not all participants answered every question in the survey. Percentages of participations were calculated based on the sample size of individual groups stated by the participants.

RESULTS

We received 27 surveys after the community college visit and 58 surveys after the ME lab tour. Figure 1 gives the demographic data of the participants. The percentages of any specific group were higher than 19%, and thus provided good sample sizes for analyses. In both surveys, more than 30% of the participants were female or URMs defined as African Americans, Hispanics, and Native Americans.

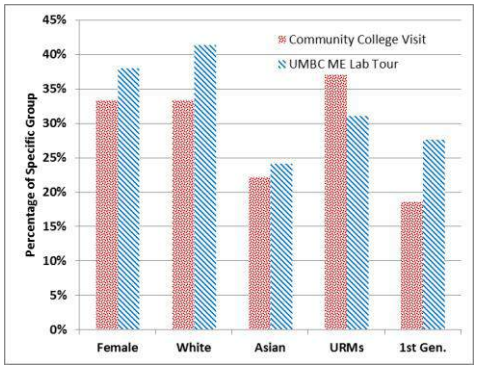

Figure 1: Percentages of participants' demographic data.

We wanted to know whether the students had any exposure to research by attending any research seminar before the event. Overall, 37% (community college students) and 21% (UMBC participants) of the participants attended at least one research seminar. The percentages of participants in specific groups are shown in Figure 2. Exposure to research in the URM group and the group of the 1st generation of college students is better in the community college students; however, in the UMBC ME participants, those two groups' exposure to research is much lower than the White group. Contrary to stereotype, exposure to research for Asian students in community colleges and in the ME department also trailed that for the White group.

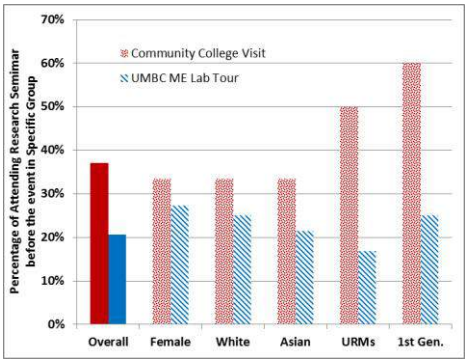

Figure 2: Percentages of attending at least one research seminar before the event in individual groups

The ME undergraduate students can apply for scholarships at UMBC. Three scholarship programs identified by the participants are the ME S-STEM Scholarship Program that our team is managing, the Meyerhoff Scholarship Program at UMBC, and the CWIT Program by the College of Engineering and Information System at UMBC. All three scholarship programs not only provide financial assistance, but also engage their scholars in research. Our program also promotes community college transfer students to pursue research.

Overall, among the 58 participants in the UMBC survey, 21% attended a seminar, and 19% did research in a lab. The positive impacts of those scholarship programs on the research participations of students in the ME department at UMBC are illustrated in Figure 3. Note that the solid bars represent participation percentage of their previous attendance of a research seminar, while the pattern bars represent participation percentage of the students who actually did research in a research lab before the event. As shown in the bars on the left, for all the 34 participants in at least one scholarship program, 29% of the 34 participants attended a seminar and had at least one research experience in a lab, both exceed the overall averages of 21% and 19%, respectively. However, among the 23 participants who were not in any scholarship program, only 9% attended a research seminar and 0% worked in a research lab. The data from the 15 participants who originally transferred from a local community college illustrate similar trends. Among the 11 community college transfer students who are in at least one scholarship program, 9 of them (or 82%) attended a research seminar and 3 of them (27%) had an opportunity working in a lab. However, for the 4 community college transfer students not in any scholarship program, only 1 of them (25%) attended research seminars, and none of them worked in a research lab.

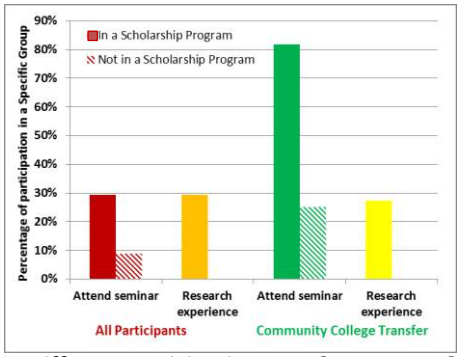

Figure 3: Different participation rates between students in a scholarship program or students not in any scholarship program in the ME department at UMBC.

More than 88% of the participants after the community college visit and 100% of the participants after the lab tour stated that they understood more of the technical content of ongoing research projects. More than 70% (community college) and 88% (UMBC lab tour) were satisfied with the overall event. 71% of the community college students would like to attend future seminars offered by ME faculty. For the UMBC ME students, 86% stated that the experience made them more interested in pursuing undergraduate research, and 97% of them are interested in attending another lab tour in the future.

SUMMARY

Survey data were collected after several research related events sponsored by the ME S-STEM Scholarship Program at UMBC. Exposure to research measured by attending a research seminar was low for the participants, around 37% in community college students and 21% in ME students at UMBC. There is little correlation between students' demographic background and their research exposure and their opportunity of working in a research lab. The results show the positive impact of the scholarship programs at UMBC on the research exposure and research experience, while the impact is more evident in students originally transferred from a community college. The overall satisfaction rates to the events were high, suggesting rationale to continue to offer those research related events to students.

ACKNOWLEDGEMENTS

This research was supported by an NSF S-STEM grant (DUE-1742170).

REFERENCES

[1] Hensel, N.H. and Cejda, B.D. Council on Undergraduate Research. Washington, D.C., 2014.

[2] Lopatto, D. *CBE - Life Sciences Education* Vol. 6, No. 4, pp. 297-306, 2007.

[3] Lopatto, D. *Peer Review*, 12(2), 2010.

SB^{3}C2019
Summer Biomechanics, Bioengineering and Biotransport Conference
June 25 -28, Seven Springs, PA, USA

LESSONS LEARNED: FIVE YEARS OF THE BIOMEDICAL ENGINEERING IN SIMULATIONS, IMAGING, AND MODELING (BME-SIM) REU SITE

Stephanie M. George (1)

(1) Department of Engineering
College of Engineering and Technology
East Carolina University
Greenville, NC, USA

INTRODUCTION

Quality undergraduate research opportunities (URO) increase understanding of how to conduct a research project, confidence in skills, and awareness of graduate school [1]. In addition, such programs can clarify, refine, and reinforce STEM career path goals [2] and increase the likelihood of pursuing a graduate degree in a STEM field [3]. Research shows UROs have the same affect or greater on under-represented minorities (URM) [2]. Thus, engaging URM in URO may increase the retention rate and matriculation into STEM graduate programs. This is critical because while African-Americans and Hispanics make up 7% and 8.8% of the STEM BS degrees awarded, they only make up 1.8% and 2.3% of PhDs awarded (white students make up 77% of PhDs awarded) [4,5].

Research Experiences for Undergraduates (REU) Sites funded by the National Science Foundation have provided numerous students with UROs. The REU Site in Biomedical Engineering in Simulations, Imaging, and Modeling (BME-SIM) was initially funded in 2014 (EEC-1359183) and renewed in 2017 (EEC-1659796). The goals of the BME-SIM REU program are to provide quality research experiences increasing awareness of and application to graduate school. The purpose of this study is to provide an example program framework, report outcomes for the past five years, and share lessons learned.

METHODS

The BME-SIM program provides research experiences for 10 students (initially 8 students) for 10 weeks each summer. Each student has an individual research project and faculty mentor. The projects are bound by a methodological theme, simulations, imaging, and modeling, instead of an application or disease pathology [6]. Because of this, students learn techniques that are relevant to a wide variety of applications, and not traditionally taught in an undergraduate curriculum. The faculty mentors span six departments (Engineering, Kinesiology, Health Education and Promotion, Physical Therapy, Communication Sciences and Disorders, and Physics) and four colleges providing a culture of multidisciplinary research. Running an REU site consists of four tasks; recruitment, assessment, follow-up, and summer program.

Recruitment. The BME-SIM recruitment campaign includes a national component (program website, social media, email, professional organizations, webinars, and NSF website) and a targeted regional component (partner institutions and site visits). During the planning process partner institutions and faculty liaisons were identified within a 3-hour radius of campus. The institutions (8) include minority serving institutions, community colleges, and predominantly undergraduate/MS serving institutions.

Program Assessment. Program assessment is conducted by an external evaluator and includes a pre/post survey (in-house), and pre/post writing sample assessment. Feedback on program components, mentoring, and environment is solicited.

Follow-Up. Follow-up involves an online survey 3 and 9 months following the program and annually thereafter. The first survey focuses on national conference attendance. All students are funded by the grant to attend the Biomedical Engineering Society (BMES) annual meeting which provides an opportunity to share research with a larger audience and reconnect after the summer. The latter surveys track career (graduate school, job), academic (major, GPA, honors), and research (abstracts, publications, experiences) outcomes.

Summer Program. Delivery of the summer program is the largest task and can be subdivided into structured program elements, professional development, mentoring, and research projects. Here the focus will be on the first three. The program schedule can be found in

Table 1. The BME-SIM program includes several **structured program elements** designed to build camaraderie and facilitate research dissemination. The summer begins with a campus tour, team building program, and informal cookout with the mentors. Formal training begins with a 2-day research bootcamp to help prepare the students for their research project and get them acclimated to ECU. Key deliverables for the students include research plan (Week 3), oral presentation (Week 9), poster presentation (Week 10), personal statement (Week 10) and BMES abstract submission (Week 10).

Our **professional development series** is designed to provide information on graduate school (application, funding, fellowships), career paths (program panel, graduate school student panel), and soft skills (communication, social media, networking). Based on feedback, special communication workshops have been developed and implemented in years 4 and 5. These workshops are offered by the University Writing Center and Speech Communication Center. Quality **mentoring** is a top priority for the BME-SIM program. To extend the reach of our program, we have developed a home institution mentor model [7]. Each student is matched to a faculty member from their home institution who they meet with before and after the program. The hope is to not only provide quality mentoring while on campus, but also when they return to their home institution. Summer faculty mentors are chosen based on their mentoring experience; with informal training provided prior to the program.

Table 1: REU Summer Program Schedule (S: Social, PE: Program Element, CW: Communications Workshop, PD: Professional Development)

Week	Activities
1	S: Campus tour, team building challenge, cookout, team trivia, ice cream social; PE: 2-day Research Bootcamp
2	CW: Literature Reviews: Making Synthesis Happen; PD: Graduate School Application; S: Bowling
3	CW: Professional Communication Skills; PD: Graduate Program Presentation; S: Board Game Night
4	CW: Personal Statements: Packing a Punch in 1-2 pages; PD: NSF Graduate Research Fellowship
5	S: Baseball game; PD: Building a Professional Social Media Presence
6	CW: Mock Interview and Elevator Speech; PD: How to Compose a Scientific Poster
7	PD: Graduate Student Panel; CW: Scientific Writing
8	CW: Practice Presentation; PD: Speed-Networking Event
9	PE: Oral Presentations; S: Women in STEM
10	PD: Research Conferences: What to Expect; PE: Poster Presentations; S: Celebration Lunch

RESULTS

To-date 45 students have participated in the BME-SIM program. Twenty-five (55.5%) participants were women and 20 (44.4%) were underrepresented minority students of which 12 were women. The majority of students were from R2 institutions or lower (86.7%) with 42.2% of students from masters level institutions or lower. All learning outcomes significantly increased (p *value* < 0.05) following the summer program. Outcomes include understanding the research process, confidence in research skills, understanding how scientists work on problems, understanding how to design and implement a research project, development of identify as a scientist/engineer, understanding the role of modeling in biomedical engineering, increase knowledge of graduate school and career opportunities, and developing a meaningful mentoring relationship. Of the students who have graduated, 75% (21) have gone on to graduate programs with 16 pursuing STEM degrees.

DISCUSSION

Based on our five years of experience, we report on some of our lessons learned and current challenges.

Recruitment. A concerted effort is required to recruit our target students (female, URM, low socioeconomic status, and veteran students along with students with disabilities and those from institutions with limited research opportunities). Reliance on the NSF directory and website presence is generally not enough. We have found targeted recruiting through partner institutions, and programs that recruit or target similar students (NIH MARC, McNair Scholars, and NSF LSAMP) to be successful. In-person recruiting through site visits and conferences have also been extremely successful. We have experimented with live webinars, hosting our second one this year.

Mentoring. It is important to have clear expectations for the faculty mentors. Our faculty mentors are actively participating in the research process and often meet daily with students. Because our graduate program is relatively new, graduate students are part of the mentoring program, but primary mentoring (both research and career) is accomplished by our faculty mentors. To complement our current mentoring plan, we are investigating cultural competence training programs to help create a more inclusive environment. It is important that all students feel like they belong.

Administrative Burden. Organizing program logistics (housing, dining, stipend, hiring, travel, programming) can be time consuming, especially if there is not a central office to coordinate. As PI, I am primarily responsible for the above duties. As the second REU site on campus, many protocols were not in place so we had to write them. While this is a summer program, work is required all year long.

Follow-up. In order to evaluate the long term success of the program, all participants must be tracked through their undergraduate careers and post-graduation. In order for tracking to be successful, a strong sense of community must be established during the program. Further, alternate contact information should be collected including permanent address, non-school email, and phone numbers. Follow-up surveys are sent by email, LinkedIn, then text, and finally a phone call. Based on feedback from students, we recommend sharing research updates and achievements so that students can see how their work has contributed to the bigger picture. Another option for sustaining long term follow-up is to offer incentives for survey completion, such as a drawing for a gift card.

Appropriately Scoped Projects. Finally it is important to provide students with appropriately scoped projects to be completed in 10 weeks. This has involved some trial and error and reflecting on what has worked in the past. Faculty mentors must also be willing to adapt projects to fit the skills and interests of their students.

In conclusion, an REU program takes careful planning and a dedication to training the next generation of students.

ACKNOWLEDGEMENTS

National Science Foundation EEC-1359183 and EEC-1659796. Co-PI Zachary Domire and Evaluator Nathaniel von der Embse.

REFERENCES

[1] Russell, S et al., *Science*, 316.5824: 548-549, 2007.
[2] Lopatto, David, *CBE-Life Sciences Education*, 6.4: 297-306, 2007.
[3] Eagan, M et al., *Am. Educ. Research Journal*, 50: 683-713, 2013.
[4] NSF, *Division of Science Resources Statistics*. NSF 09-317, 2009.
[5] NSF, *National Center for Science and Engineering Statistics*. NSF 12-328, 2012
[6] George, S et al., *J of Biomechanical Eng.* 139 (7), p.071002, 2017.
[7] George, S et al., *Proceedings of the 123rd ASEE Annual Conference and Exposition*, June 26-29, New Orleans, LA, 2016.

SB³C2019
Summer Biomechanics, Bioengineering and Biotransport Conference
June 25 -28, Seven Springs, PA, USA

INCORPORATING CLINICAL ROTATIONS, ONLINE LECTURES AND BUSINESS CONCEPTS IN BME CAPSTONE DESIGN: ARE WE THERE YET?

Alan W. Eberhardt (1), Joel H. Dobbs (2)

(1) Dept. of Biomedical Engineering
University of Alabama at Birmingham
Birmingham, Alabama, USA

(2) Collat School of Business
University of Alabama at Birmingham
Birmingham, Alabama, USA

INTRODUCTION

Since 2001, with the support from the National Science Foundation (RAPD and GARDE programs), the lead author has run the senior capstone experience in which biomedical engineering (BME) student teams design and prototype assistive technologies for people with disabilities. In 2013, with the receipt of an NIH R25 award, a working partnership was formed with the UAB Collat School of Business to bring engineering and business students together to develop functional prototypes and commercialization strategies around new medical device designs. The co-author joined as a team instructor, and the Biodesign text [1] was adopted as a resource for students to gain an appreciation for clinical needs finding and screening, establishing the market for their product, and in developing an operating plan for development of a commercial product. In the past two years, UAB Solution Studios™ was piloted as a source for clinical matchmaking between engineering/business students and clinical mentors.

By bringing engineering and business students together, the capstone design course has focused on team-based learning with students of truly multidisciplinary backgrounds. In the past 5 years, we have incorporated a number of experiences in order to promote commercialization of devices developed during the two-semester sequence. The following article provides our current approach and the steps that led to this point.

METHODS

BME 498 Product Development and BME 499 Capstone Design represent the two-semester capstone course sequence required by all BME seniors at our institution. We have coordinated class times to allow BME students to be joined by business students enrolled in a senior entrepreneurship elective series (ENT 424 New Product Development/ENT 426 Practicum in Commercialization). The fall semester begins with clinical shadowing to determine device needs and ideate potential solutions. Using an approach modeled after Stanford Biodesign [1], students work to "identify, invent and implement" medical and assistive devices for local clients. Teams form around clinical needs of their choosing. Market analyses are performed as a preliminary vetting of the needs. Need specifications are turned into engineering design constraints and the students are coached through the process of brainstorming and evaluation using the Pugh Method [2]. Concurrently, the students begin their investigation into business development for their medical devices, including IP and patent landscapes, and business models using the "Business Model Canvas" [3]. On-line modules were created where Biodesign readings and quizzes were assigned as homework, prior to in-class instruction. Regulatory topics include medical device classes and FDA approval processes. As part of the original R25, we expanded our instructional efforts around how to work effectively in teams. Lectures include project management, the classic "five dysfunctions" of a team [4], and how to have "crucial conversations" [5] to help students resolve team issues that arise during the year. In BME 498, a series of writing assignments culminate in a formal Design Proposal that includes concepts for a functional prototype as well as a marketable design. The teams are required to have signature approvals from their client, as well as that of a lab manager, who has mentored the team throughout the ideation and design process. The fall semester ends with an oral presentation to a "Shark Tank" that includes faculty from the Harbert Institute for Innovation and Entrepreneurship (HIIE).

Spring semester emphasizes building of functional prototypes and formulation of a commercialization strategy. BME students take part in manufacturing rotations where they gain hands-on experiences with state-of-the-art methods for machining metals and forming plastics and composites. In this manner, we ensure that students have adequate

access to equipment and expertise to help fabricate their prototype devices. Business topics are continued, including project management and the use of Gantt charts. Students are required to present Gantt charts for the 14-week development of their working device as well as a one-year Operating Plan that includes research and development and financial planning of their "marketable device," including plans for verification and validation, and a complete Risk Analysis.

Over the past five years, we have experimented with different approaches where the business students "split off" from the BME students at various times during the second semester. In the current iteration, the business students left the BME teams at the start of the second semester in order to pursue development of commercialization strategies for three projects. These projects were selected by the Shark Team in the first semester based on their commercial potential.

Additional engineering lectures are provided on an as-needed basis, including finite element analysis, motor/bearing selection, and/or structural frame design. As projects take final shape, teams with patentable ideas submit IP disclosures to our tech transfer office in the HIIE. The students perform verification testing (as is feasible) and demonstrate some form of customer validation of the final working product. The Final Design Presentation includes a 3-minute video investor pitch, a scientific poster, and demonstration of their working device, held during the final BME seminar for the term. This seminar is attended by BME faculty, students, clients and members of the HIIE.

In recent years we have begun offering extra credit for submission and/or participation in student design competitions, such as the Design of Medical Device Conference in Minneapolis, MN, as well as the annual RESNA Conference and the SB3C, among others.

Various surveys were used to assess the effects of changes made to the course. In BME 498, students were asked to provide their input regarding the length of time and quantity of clinical rotations, which served as the source for their year-long project activities. In addition, the students who participated in the UAB Solution Studios™ web platform were asked specifically if it enhanced their experience. Later on, students in BME 499 were asked if they preferred the on-line learning module approach piloted in BME 498, as compared to the traditional PowerPoint style lectures given in class during BME 499. IDEA surveys were examined for student comments regarding the inclusion of business students, problems with team dynamics, etc.

RESULTS

IDEA survey results have consistently indicated student satisfaction levels exceeding 4.5/5 with respect to "Progress on Relevant Objectives,", as well as "Excellent Course" and "Excellent Instructor." The results of the student surveys (Fig. 1) indicated that 92% (36/39) preferred the online approach, with a consensus that "doing the lectures on-line freed up valuable class time for working on our design projects." 69% (27/39) responded favorably, indicating that "more time for rotations would allow us the opportunity to better vet the project opportunities." In this case 80% (16/20) students who participated in UAB Solution Studios™ indicated that their overall experience was enhanced.

Other results indicated that the majority of teams functioned well together – for example, in fall 2018, only two teams experienced problems with teammates, which seemed to center around two scenarios: i. a BME student who was overly committed to honors research and/or medical school preparation that prevented them from spending adequate time on their capstone project or ii. a business student who took the course less seriously than their BME counterparts, resulting in a "takeover" by BME students where they simply did all the business work themselves. In the past three years, we have had multiple student teams take part in student design competitions, and three teams that took 2nd or 3rd place (e.g., Fig. 2). Feedback from these experiences has been extremely positive.

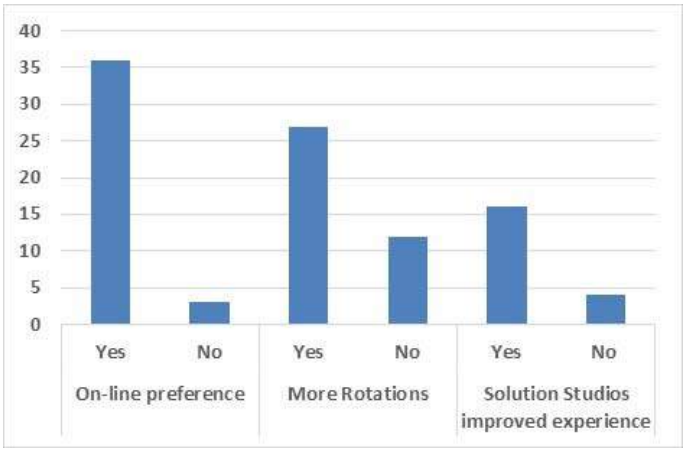

Figure 1: Survey results from BME capstone experience.

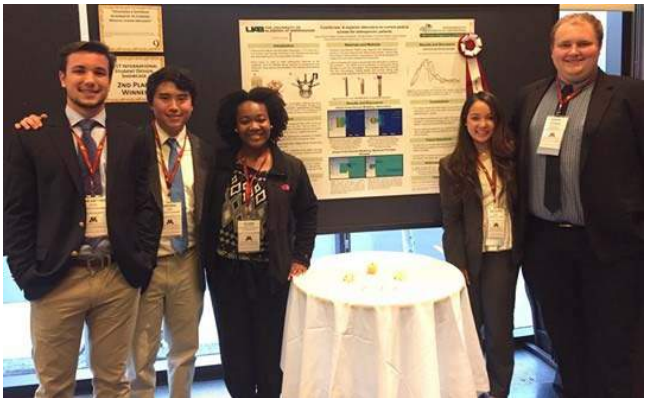

Figure 2: A BME team taking second place at the 2017 Design of Medical Device Conference

DISCUSSION

Senior capstone design continues to be a success story for the Department of Biomedical Engineering at UAB. The involvement of business and engineering is viewed extremely favorable by the upper administration and is often cited as a shining example of interdisciplinary education at our institution. The establishment of the online modules, the use of UAB Solution Studios™ for clinical matchmaking, the use of sharks to evaluate commercial potential, and the encouragement of teams to apply to student design competitions, all have worked to enhance the success of our program.

ACKNOWLEDGEMENTS

The authors gratefully acknowledge financial support from National Science Foundation CBET-1263941 and National Institutes of Health 1R25HD078327-01A1.

REFERENCES

[1] Zenios, et al., 2010, Biodesign: The Proc of Innov Med Tech
[2] Pugh, 1981, Proc. Inter. Conf. Eng. Design
[3] Osterwalder & Pigneur, 2010, Business Model Generation, Wiley.
[4] Lencioni, 2002, The five dysfunctions of a team. Jossey-Bass.
[5] Patterson, et al., 2013, Crucial Accountability, 2nd ed, McGraw Hill.

OUTCOMES OF INCORPORATING CLINICAL SIMULATION LABORATORIES IN BIOMEDICAL ENGINEERING EDUCATION

Anita Singh (1), Dawn Ferry (2)

(1) Department of Biomedical Engineering
Widener University
Chester, PA, USA

(2) School of Nursing
Widener University
Chester, PA, USA

INTRODUCTION

Simulation laboratories are primarily used in nursing education to simulate real world scenarios through the inclusion of role-play, standardized patients, virtual simulation, and computerized mannequins. While the primary goal of biomedical engineering education is to train the next generation of engineers who can tackle the problems at forefront of healthcare and related fields, their preparedness requires a different approach than other basic engineering disciplines. Biomedical engineers should be trained to work in real-world health care settings where most medical device industry emerges. Inability to perform and translate their knowledge in these setting can prove to be the biggest setback in today's biomedical engineering education. To overcome this problem, we investigated utilizing teaching approaches currently employed in the training of health care providers and assess their use in better preparedness of biomedical engineers who perform in similar environments.

METHODS

A total of 20 BME seniors were matched with 20 Nursing Juniors in a semester long (BME448: Medical Device and NURS338: Evidence-based practice) course. The BME and Nursing faculty worked collaboratively to create an interdisciplinary environment by bringing the engineering and nursing students together in one classroom setting. To further their collaborations and enhance their communication skills, the teams were exposed to two different simulation labs.

Simulation Labs

The two simulation classes (75 minutes long and accounting for 7% of the total course contact hours), included three scenarios that prompted collaboration and communication among students from these two disciplines. Student learning was further fostered by orienting them to the environment, debriefing them about the scenarios, and making them aware of their roles in troubleshooting the problem they were to observe in these settings. During the first simulation class, in teams of two comprising of one engineering and one nursing student, students attended two scenarios (10 minutes each). Both scenarios were device/equipment based. In the first scenario, an actor was positioned in the observation room while waiting to be diagnosed with a beeping intravenous (IV) device. In the second scenario, a mannequin was showing signs of distress while being hooked up to the gas (Figure 1).

Figure 1: Engineering Students embedded in simulation based clinical scenarios to trouble shoot gas-line related problem

These scenarios were specifically created so that the team could successfully fix the problem through effective communication and coordinated actions. A 15-minute debriefing was conducted immediately following each simulation where students assessed their

performance and were provided with feedback from instructors, who were observing them throughout the process from the outside through a camera placed in the room. During the second simulation class, students were again teamed up in pairs consisting of one engineering and one nursing student and introduced to a scenario that was more clinically oriented. Also, another such student team observed their performance from outside the room through the camera placed in the room to offer student-oriented feedback during debriefing (Figure 2).

Figure 2: Student observing from outside the room

The scenario consisted of a mannequin who was admitted to the emergency room with blurred vision. The goals for the team were to make a diagnosis of his condition, administer the required medication, and offer the correct treatment option. The overall goal of this simulation was to better prepare engineering students for real-world clinical scenarios. Knowing clinical settings, understanding roles played by all individuals in providing care to the patients and family, knowing procedures involved during the care process, and feeling comfortable in these environments to ask relevant questions are all critical to the training of biomedical engineers.

Survey

With Institutional Review Board approval, voluntary anonymous student surveys were obtained to evaluate the impact of the clinical immersions through simulation labs (Table 1). These items were measured on a yes/no and Likert-type scale ranging from 1 (strongly disagree) to 5 (strongly agree).

RESULTS

As shown in Figure 1, the three simulation scenarios promoted better learning than slides explaining these scenarios. These simulation scenarios allowed them to demonstrate their ability to communicate with the other providers of the healthcare team, to use critical thinking skills learned through the engineering program, and an active hands-on learning environment. Students agreed that having a nursing partner in the room during these individual simulation scenarios made the experience more realistic. Students felt confident in providing specific rationales for their actions during the simulation scenarios. Overall, the simulation scenarios helped students better understand their role in the healthcare industry as an engineer. Students agreed that the experience was novel to engineering education and should be part of future offerings.

Table 1: Survey Questions

Q1: The knowledge gained through the simulation experience can be transferred to the clinical setting
Q2: The offered simulation scenarios promote better learning than slides explaining these scenarios
Q3: The individual simulation scenario allowed you to demonstrate your ability to communicate with the other providers of the health care team
Q4: The individual scenario allowed you to use the critical thinking skills learned through the engineering program during the simulation
Q5: The faculty provided constructive feedback and discussion after the simulation scenarios
Q6: You can provide specific rationales for your actions during the simulation scenarios
Q7: The nursing partner in the room during the individual simulation scenario made the experience more realistic
Q8: Simulation lab provided an active hands-on learning environment
Q9: The simulation lab experience is novel to engineering education and should be offered in future offerings
Q10: Simulation lab helps you better understand your role in health-care industry as an engineer

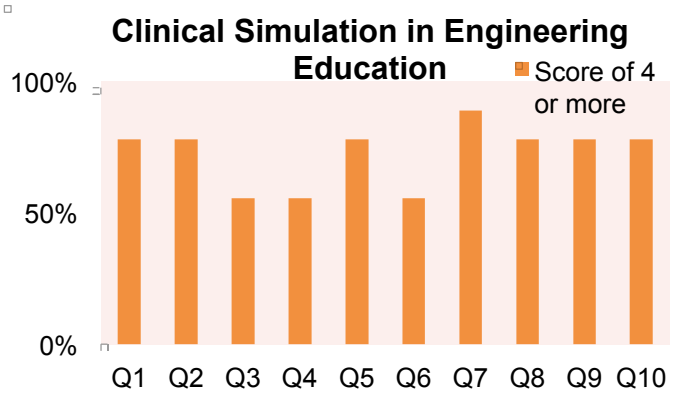

Figure 3: Survey Results

CONCLUSION

Simulation labs can successfully be used in biomedical engineering education due to its proven efficacy in offering a safe, controlled environment in which problem-based learning can be fostered to achieve better preparedness of future biomedical professionals.

ACKNOWLEDGEMENTS

Research reported in this publication was supported by the National Institute of Biomedical Imaging and Bioengineering of the National Institutes of Health under Award Number R25EB023857.

SB³C2019
Summer Biomechanics, Bioengineering and Biotransport Conference
June 25 -28, Seven Springs, PA, USA

INDUSTRIAL ERGONOMICS RISK ASSESSMENT MEETS RESEARCH IN THE BIOMECHANICS CLASSROOM PROJECT

Johannes Brombach (1,2), Megan E. DeRidder (2), Laurel Kuxhaus (2)

(1) Department of Engineering & Management
University of Applied Sciences
Munich, Germany

(2) Mechanical & Aeronautical Engineering
Clarkson University
Potsdam, NY USA

INTRODUCTION

Students crave real-world applications of their studies and such examples increase student engagement, improve learning, and better prepare students for their careers. Context-rich projects, especially those for which the 'answer' remains unknown, foster an entrepreneurial mindset [1]. Opportunities for students to engage in the inquiry-based process of being a researcher and translating the results to the real world are limited in the traditional curriculum. For example, students often engage with the research process in a prescribed manner (traditional laboratory exercises with a detailed instruction manual), or by reading published work. To engage students in an open-ended way, it is helpful to direct students to a well-defined topic such as the risk of spinal injury.

Musculoskeletal disorders (MSD), especially injuries of the spine, are a burden for the individual and an economic problem for society. In Germany 22.1 % of the sick leave days as well as production losses of 13 Billion Euro are connected to MSD [2]. According to the Bureau of Labor Statistics (BLS) in the US, 33% of all worker injury and illness cases are attributed to MSD. In the United States the annual prevalence of lower back pain ranges from 15 to 20% of the working population [3]. Workplace design requires a constant improvement of knowledge about the interaction of the human being in the work system [4, 5], and is therefore well-suited for open-ended industry-focused class projects.

Here, we present an example of a context-rich research-based class project that requires students to use their classroom knowledge to link a research experiment to a real-world ergonomics application.

METHODS

This undergraduate class project merged practical risk assessment tools used in industry with ongoing fundamental biomechanics research topics in a highly interactive undergraduate course. Briefly, students worked together to critically analyze experimental results from ongoing laboratory research at Clarkson University, with the goals of explaining the experimental results using basic biomechanics principles and translating the results to workplace ergonomic recommendations.

Prior to beginning the project, students learned basic ergonomics and biomechanics concepts in the classroom, with a typical week shown in Table 1. In a term paper, completed individually near the start of the project, each student examined a specific topic in relation to risk assessment (e.g. in sport or industry). Journal articles were analyzed weekly [6] and specific homework assignments fostered technical skills (Table 1). For the project, the class of 32 undergraduate students was then divided into 8 teams. The overall task was to critically analyze a research study performed at Clarkson University [7,8] and translate the results to an ergonomic risk assessment. The project was coached on a weekly basis for 10 weeks. Students were encouraged to explore both German and US content for their term paper topic of choice. Methods used to establish connections include literature searches, experiments and ergonomic risk assessments. Assessment included a short presentation near the beginning of the project, and a longer presentation by each team at the end of the semester. Instructor evaluation of the logic of the student presentations was based on classic scientific quality criteria (e.g. objectivity, reliability, validity).

Table 1: Typical class schedule and content

Monday *50 min*	Wednesday *50 min*	Friday *50 min morning + 90 min afternoon*
Ergonomics and biomechanics lecture: anthropotechnics, occupational physiology, risk identification.		Project related Journal Club (morning); Coaching activity for term paper and project work (afternoon)

The published work was introduced to the students by one of the study's authors. In brief, ex-vivo cervine lumbar spinal motion segments were subject to low-angle low-load cyclic loading, up to 40,000 cycles. Some specimens showed evidence of ring apophysis fractures, and the load displacement data and hysteresis loops (in the force displacement plots) during cyclic loading indicate that the damage occurred gradually, i.e. without trauma [7]. Students were tasked with explaining the results using basic biomechanics principles and translate the results to the workplace using current risk assessment tools.

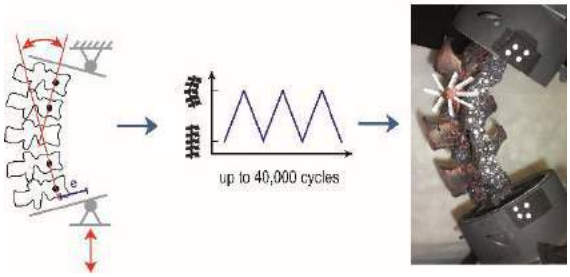

Figure 1: Schematic of experiments in [7].

Students had learned through classroom instruction and individual problem solving that workplace risk assessment is based on models of degradative effects of repeated motion on the musculoskeletal system over long-term data plots. Spinal injury risk assessment is based on the analysis of the human spine and the physical pressure that occurs due to the working situation. Generally, the consensus is that higher loads and a higher frequency will lead to a higher risk of injury.

The resulting damage from low-load high-repetition loads is contrary to the current consensus. Students were tasked to explore how traditional ergonomics risk assessment tools could be used in situations where these low-load high-repetition loads exist. Each team was given a unique question to focus on, as presented below.

- How certain are the results of the new study?
- Which situation in industry could yield to a stress level "low-load high-repetition loads"? Are there other studies that support these results? (2 Teams: different approaches and statistical analysis)
- How would that be assessed (with usual or advanced ergonomics methodologies)?
- How does the age-and-gender-related limits based on the load-bearing capacity of spinal elements compare?
- How does the flexibility of the spine influence the risk (in general)?
- Which different "dose-response models" exist and how would a revised "dose-response model" look like? (2 teams: research and new ideas)

Instructor feedback steered students towards appropriate aspects of the risk assessment and suggestions for further investigations were made. Students compared different "Dose Models" from ergonomics literature [9] and biomechanics literature. At the conclusion of the project, each group presented a 15-minute presentation, with one of the authors of the original study in attendance.

RESULTS

The presentations exceeded the instructor's expectations. In general, the students were highly involved in the research and found many interesting published studies, and explored related research areas. For example, they questioned if an increase in flexibility might not be a positive indicator like it has been discussed in sports biomechanics. That widened the scope of the project and lead to engaging discussions.

Students appeared engaged with the topic throughout and asked detailed questions. The instructor observed that student questions tended to be critical towards characteristics of the experimental design such as: limited sample selection, the difference between the cervine model and a human cadaver, the freezing of disc and potentially altered kinematic properties, temperature and moisture considerations, and the realism of the number of cycles and frequency. Students also found other published studies to support their ideas. For example, after finding a study that showed recovery after 10000 cycles and a rest period of 18h, [10] students suggested studying this with future laboratory experiments.

While students readily found fault with the published work and could eagerly suggest improvements, they remained challenged to provide suggestions that could be feasibly implemented given the realities of research funding and available resources. Thus, this project provided opportunity for students to confront some of the harsh realities of performing research in the real world.

Students also struggled to come up with an explanation the unexpected findings of the research study using basic biomechanics principles. They were challenged to question the widely-accepted paradigm that only high-load high-repetition loads cause injury. Despite encouragement, they did not consider that the mechanical characteristics of soft tissues change with the speed of the motion and become increasingly hard and less flexible, even though they recognized that the specimens lost liquid during loading. As described in [7] the spinal flexion-extension movement was controlled and the forces measured. With reduced forces over the course of the experiment, tensile forces were necessary to fully extend the spine. Students did not recognize this as a different mechanical loading scenario, or consider that the micro fractures may have occurred due to this. Future scientific work might investigate how intermittent rest and recovery periods would alter the results, and future iterations of this project might include additional emphasis in lessons on the importance of recognizing when a loading scenario changes.

DISCUSSION

This project offered students opportunities to link their classroom knowledge by translating contemporary experimental results into real-world implementation, e.g. by recommending study of the effect of rest breaks during low-load high-frequency tasks. The instructor benefited from this discussion process, and the researchers benefited from hearing the students' ideas to further the work. Students also considered a global perspective, merging recommendations from Germany with those from the US. Students discovered differences between available public datasets between the two countries. As a result of this style of project, the students develop an entrepreneurial mindset, and the instructor benefits widely. In this specific case, the utility of this research comes from the translation of the laboratory results into actionable recommendations for workers. Other educators may consider using a similar approach to engage students with both the research process and an industrial application in the classroom.

REFERENCES

[1] Rae+, *TJEE*, 2017
[2] Liebers+, *BAuA*, 2016
[3] van der Beek & Frings-Dresen, *Occ Env Med*, 1998
[4] Robson+, NIOSH 2001
[5] Brombach and Kurz, GfA Press, 2015
[6] Corbiere and Kuxhaus, *JBME*, 2016
[7] Corbiere+, *J Biomech*, 2016
[8] Gale+, JOR Spine, 2018
[9] Jäger+, Industrial Ergonomics 25, 2000
[10] Johannesse+, *Ann Biomed Eng*, 2004

SB³C2019
Summer Biomechanics, Bioengineering and Biotransport Conference
June 25 -28, Seven Springs, PA, USA

ON THE ROLE OF PROJECT-BASED ACTIVE LEARNING TECHNIQUES ON COMPUTER PROGRAMMING SELF-EFFICACY OF UNDERGRADUATE BIOMEDICAL ENGINEERING STUDENTS AND THE INTERACTIVE EFFECTS OF GENDER

S. Cyrus Rezvanifar, Rouzbeh Amini

Department of Biomedical Engineering
The University of Akron
Akron, Ohio, USA

INTRODUCTION

Active learning significantly improves students' educational achievements as compared to passive learning [1, 2]. In Biomedical Engineering (BME), active learning can be incorporated through various techniques such as problem- and project-based learning [3]. Such approaches lead to students' deeper and more efficient retention of new concepts. During the past two decades, perceived self-efficacy has been increasingly considered as a highly effective predictor of students' motivation and learning, as well as an important contributor to their academic development [4, 5].

Over the past two years, we investigated how project-based active learning techniques used in a biomedical computing class affected the self-efficacy of undergraduate BME students, while also examining the main and interactive effects of gender. We hypothesized that project-based active learning techniques enhance computer programming self-efficacy and expectation of success in undergraduate biomedical engineering students.

METHODS

This study was carried out under an official exemption by the Institutional Research Board at the University of Akron. In our project-based learning approach, three-member student groups were instructed to build a heart rate monitor/activity tracker using Arduino UNO microprocessors interfacing with MATLAB and MATLAB Mobile (Fig.1), as described in our previous publication [6].

Seven-point Likert-scale anonymous surveys with 14 questions were collected prior to and following the project within all three sections. Due to the anonymous nature of the surveys, two-way ANOVA with significance level set at α=0.05, along with post-hoc Tukey's tests were used to statistically compare the pre- and post-activity self-efficacy scores across genders.

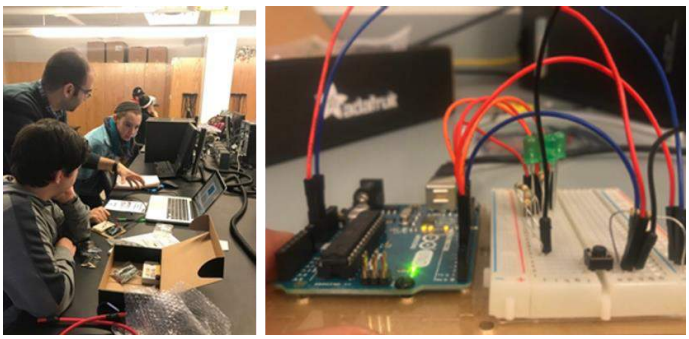

Figure 1. Hands-on experience through project-based learning. All of the groups were required to build a heart rate monitor/activity tracker using Arduino UNO microprocessors interfacing with MATLAB and MATLAB Mobile.

RESULTS

For the entire cohort of participants, the overall average score for *clearer vision of programming application in engineering* (Question 1) *and BME careers* (Question 3) significantly improved upon the completion of the hands-on project. Similarly, for the entire cohort, *the expectation of success in a future BME career that involves developing medical devices* (Question 14) significantly increased after they completed their project (Fig.2).

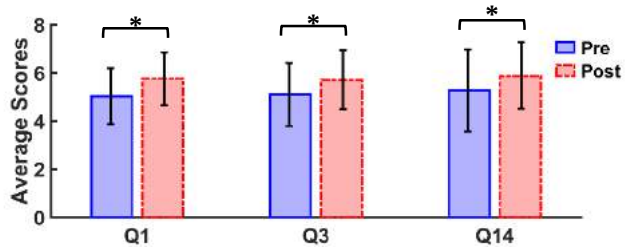

Figure 1. Average scores (± SD) of Questions 1, 3, and 14 which indicated significant differences between pre- and post-activity. "*" indicates statistically significant difference.

Given the combined pre- and post-activity scores, a significant difference was observed between female and male students' *self-confidence about understanding the most complex course material* (Question 6): the combined average score of the female group was 4.81±1.37 (N = 58), as opposed to a combined average score of 5.33±1.23 for the male group (N = 63). In addition, female students were significantly less willing to *have a future career in BME that involves intensive computer programing* (Question 11) (females combined average score = 3.23±1.90 and males combined average score = 3.99±1.60).

Comparing pre- and post-activity scores, only among the male students, we observed a statistically significant improvement in one's *clear vision of the application of programming concepts in engineering and BME careers* (Questions 1 and 3). In pre-activity results, the average scores for these measures were rather higher in female students compared to male students; however, they only slightly increased to post-activity average scores below those of male students (Fig.3).

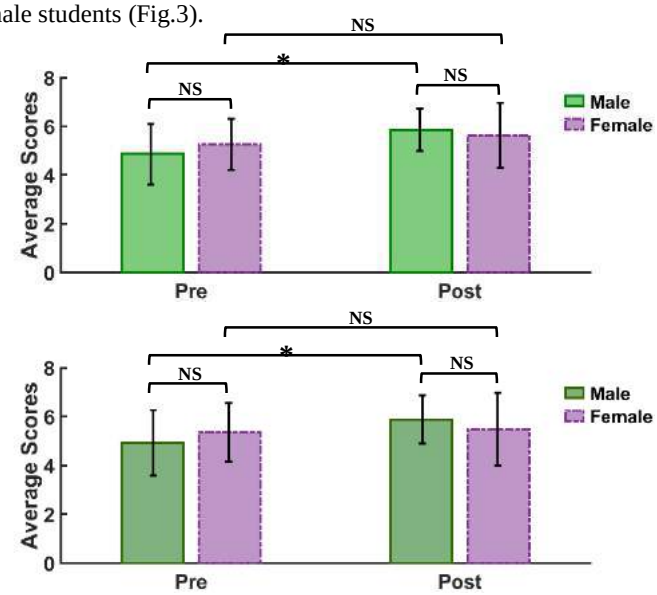

Figure 3. Average scores (± SD) of female and male students in pre- and post-activity results of Questions 1 (top) and 3 (bottom). "*" indicates statistically significant difference.

DISCUSSION

The results of this study agree well with the existing literature on the positive impacts of active learning techniques on students' learning experience [1, 7, 8]. Hands-on projects provide students with an opportunity to apply their theoretical knowledge into solving a real-life problem, which enhances their perspective on the practical applications of course material and boosts their self-efficacy in relatively complicated topics such as computer programming.

The significantly lower *self-confidence about understanding the most complex course material* and *expectation of success in BME careers with intensive programming* observed in our female students can be attributed to multiple factors, including but not limited to lesser previous experience in computer programming and sociocultural barriers for women entering STEM fields [9]. On the other hand, the higher pre-activity average score of female students' in *clear vision of the application of programming in engineering and BME careers* can be interpreted as the relatively more informed decision of female students upon entering engineering fields, supposedly due to the foregoing sociocultural factors.

We observed a significant improvement in students' *expectation of success in a career that involves developing medical devices*, without a significant increase in their "willingness" for such career—according to another question within the survey. This finding implies that students were already aware of the nature of such careers, and that the enhancement in their expectation of success is a sheer indicator of improved self-efficacy, and not due to obtaining "new information".

In summary, the results of this study confirm our hypothesis that project-based active learning techniques enhance computer programming self-efficacy and expectation of success in BME careers in undergraduate biomedical engineering students. The lower average scores of the female students, measured in a number of self-efficacy and expectation of success questions, further justifies the need for the continual efforts of "Women in Engineering" societies and K-12 outreach programs in order to raise public awareness toward aforementioned sociocultural factors. These earnest efforts will help eliminate barriers for women entering STEM fields and will enhance their corresponding self-efficacy and expectation of success. For both female and male students, we strongly believe that the foregoing improvements achieved through the completion of hands-on projects have direct influence on students' motivation and performance, and would maximize the accomplishment of learning objectives.

ACKNOWLEDGEMENTS

The authors acknowledge the Doctoral Teaching Program in College of Engineering at The University of Akron for providing teaching fellowships for S. Cyrus Rezvanifar.

REFERENCES

[1] Freeman, S. et al., (2014). *Proceedings of the National Academy of Sciences*, 111(23), pp. 8410–8415.
[2] Handelsman, J. et al., (2004). *Science*, 304(5670), pp. 521–522.
[3] Clyne, A. M., and Billiar, K. L. (2016). *Journal of Biomechanical Engineering*, 138(7), p. 070804.
[4] Bandura, A., (1977). *Psychological Review*, 84(2), p.191.
[5] Zimmerman, B.J., (2000). *Contemporary Educational Psychology*, 25(1), pp.82-91.
[6] Ham, T., et al. (2018). *Journal of Biomechanical Engineering*, 140(8), 081007
[7] Prince, M. (2004). *Journal of Engineering Education*, 93(3), p.223
[8] McCarthy, J.P. & Anderson, L. (2000). *Innovative Higher Education* 24: 279.
[9] Ceci, S. J., et al. (2009). *Psychological bulletin*, 135(2), 218.

SB³C2019
Summer Biomechanics, Bioengineering and Biotransport Conference
June 25 -28, Seven Springs, PA, USA

NUMERICAL MODELING OF LAMINA CRIBROSA HEMODYNAMICS

Yi Hua (1), Bryn L. Brazile (1), Ian A. Sigal (1,2)

(1) Department of Ophthalmology
University of Pittsburgh
Pittsburgh, PA, USA

(2) Department of Bioengineering
University of Pittsburgh
Pittsburgh, PA, USA

INTRODUCTION

Glaucoma is a potentially blinding disease characterized by irreversible damage to the retinal ganglion cell axons within the optic nerve head, where the axons pass through the lamina cribrosa (LC) and exit the eye. [1] The mechanisms underlying the development and progression of glaucoma remain unclear. It is hypothesized that deformations of the optic nerve head, for example due to increased intraocular pressure, may in turn compress capillaries and compromise perfusion to LC astrocytes and axons, contributing to neural tissue distress and eventually retinal ganglion cell axon death. [2] To understand the potential contribution of perfusion on glaucomatous neuropathy, we must therefore understand how LC hemodynamics are altered by capillary occlusion. The LC capillaries form a complex interconnected network, in which blood can take a number of routes. Hence, the effects of occlusion are much more difficult to predict and understand than in a relatively simple arterial tree.

Our goal in this project was to understand the changes in LC hemodynamics caused by capillary occlusion. Specifically, we used a specimen-specific map of LC vasculature to develop a numerical model of LC hemodynamics. We then evaluated the effects of occluding some capillaries or arterial inlets. To understand potential differences in regional sensitivity to occlusion we repeat the virtual experiments with occlusions in different LC quadrants.

METHODS

Serial histological sections (thickness: 16 µm) were obtained from a monkey optic nerve head, in which the blood vessels had been labeled with a fluorescent dye. [3] The sections were imaged with fluorescence microscopy at a resolution of 0.73 µm per pixel and registered to one another. A 3D stack was created of the registered images to obtain a Z-projection of maximum intensity of three sections through the LC. The result was then skeletonized, and any isolated branches were removed to ensure that all vessels were connected except at the periphery for blood inflow and the center for outflow (Figure 1). [4, 5] The skeleton was converted into a mesh of the LC vasculature suitable for solving flow numerically.

We assumed blood as an incompressible Newtonian fluid. [6] The hemodynamics boundary conditions are illustrated in Figure 1. A fluid mechanics approach was used to predict the blood pressure and blood flow velocity within the vessels. As a first approximation, we assumed the flow is one-dimensional, such that only the average flow velocity was solved for each cross-section of a vessel.

The LC vasculature was divided into four quadrants: nasal (N), temporal (T), superior (S) and inferior (I). The blood flow in the model as reconstructed was considered the baseline. To evaluate the impact on LC hemodynamics of capillary occlusion we considered two tests: First, to test minor occlusions, we gradually removed from the model 1, 2 and then 3 vessels in each quadrant. Second, to test the effect of a major occlusion in one of the feeder vessels of the circle of Zinn-Haller, we eliminated blood inflow in all but one of the inlets in a quadrant.

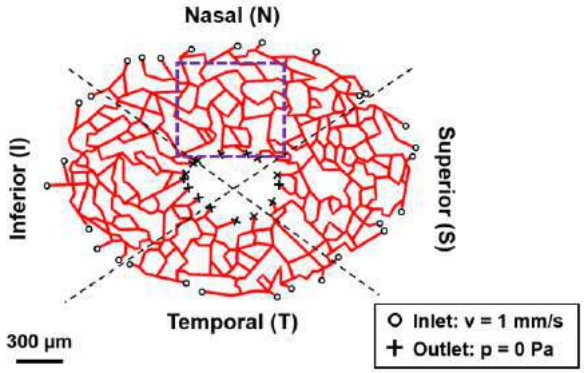

Figure 1. A specimen-specific model of LC vasculature generated from monkey optic nerve head. An inlet velocity (v) of 1 mm/s was applied at the periphery to simulate the blood flow originated from the Circle of Zinn-Haller, a variably complete anastomotic ring of arteries around the LC. An outlet pressure (p) of zero was applied at the center to simulate the blood drainage via the central retinal vein. The dashed square indicates the region where we removed the vessels in the nasal quadrant.

RESULTS

Due to space limitations, we only present the results related to the changes made to the nasal quadrant. The results observed for other quadrants were similar. The effects of removing a few capillaries on

LC blood pressure and velocity are shown in Figure 2. The effects of reducing blood inlets from 9 to 1 are shown in Figure 3.

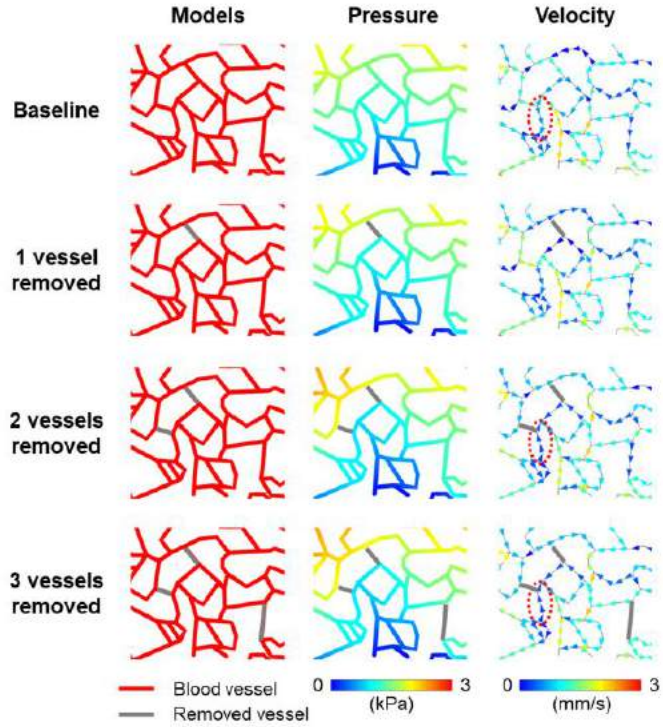

Figure 2. Color map of the blood pressure (second column) and blood flow velocity (third column; arrows indicate the direction of the velocity) predicted by the models with and without removing the blood vessels (first column). The flow was highly resilient to removing the vessels. Interestingly, flow reversal was observed in a vessel adjacent to the ones removed (an example is highlighted by the dotted red ellipse in the third column).

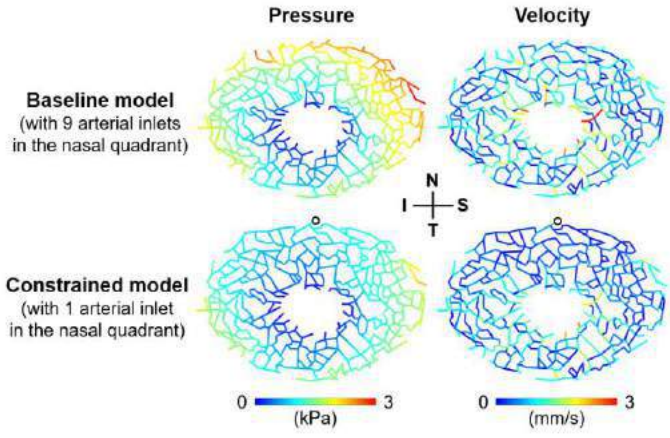

Figure 3. Color map of the blood pressure (left column) and blood flow velocity (right column) predicted by the models with 9 (baseline, top row) and 1 (constrained, bottom row) arterial inlets in the nasal quadrant, respectively. The small black circle in the bottom row indicates the single arterial inlet left. Reducing the number of arterial inlets decreased the blood pressure and blood flow velocity inside the vessels.

DISCUSSION

We studied LC hemodynamics using a numerical model based on specimen-specific LC vasculature of a monkey. To test the robustness of LC hemodynamics to artery occlusions, we reduced virtually the number of arterial inlets and removed a couple of vessels in each LC quadrant. Our models predicted that: (1) removing a few vessels within the LC had a very small effect on the overall blood flow behavior in the LC, though the effects were larger locally; (2) an occlusion of a feeder artery resulting in no blood inflow in most of the inlets substantially decreased the blood pressure and blood flow velocity, with effects throughout the LC.

The minor effects of removing a few vessels suggest that LC defects, for instance such as could occur from a hemorrhage, may also have a limited impact on the LC. [7, 8] Even though the magnitude of blood flow velocity did not change substantially with the removal of the vessels, we observed flow reversal in a few adjacent vessels. This is consistent with the observation by Fu et al. that modeling the retinal blood flow with the loss of several retinal capillaries. [9] It is unclear if this reversal behavior is physiologically realistic. Improvements in imaging and in vivo measurement of LC blood flow are needed to confirm model predictions.

We found that LC hemodynamics was highly influenced by the number of arterial inlets to the LC. LCs with fewer arterial inlets exhibited lower blood pressure and blood flow velocity inside the vessels. A decreased blood velocity inside can reduce oxygen transport to the surrounding neural tissues. [10] Our findings suggest that occlusion of the circle of Zinn Haller could have a substantial impact on LC hemodynamics. In vivo evaluation of the sensitivity of the feeder arteries to compression when under elevated IOP is necessary to confirm our predictions.

In summary, we developed a model of LC hemodynamics based on specimen-specific data. Our findings suggest that the interconnected network of capillaries in the LC increases its robustness by decreasing sensitivity to occlusion of some capillaries. The interconnectivity is, however, insufficient to completely compensate for the compromised blood flow resulting from an occluded feeder vessel. All four sectors had similar sensitivities. Ongoing efforts are directed toward developing more advanced 3D models of LC vasculature and to quantify oxygen and nutrient diffusion.

ACKNOWLEDGEMENTS

Supported by National Institutes of Health Grants R01-EY023966, T32-EY017271, and P30-EY008098; Research to Prevent Blindness; and the Eye and Ear Foundation (Pittsburgh, PA, USA).

REFERENCES

[1] Quigley, HA, *Prog Retin Eye Res*, 18:39-57, 1999.
[2] Moore, D et al., *Clin Ophthalmol*, 2:849-861, 2008.
[3] Brazile, B et al., *IOVS*, 59:1220, 2018.
[4] Chuangsuwanich, T et al., *IOVS*, 57:6167-6179, 2016.
[5] Carichino, L et al., *IOVS*, 53:2836-2836, 2012.
[6] Guidoboni, G et al., *J Coupled Syst Multiscale Dyn*, 1:1-21, 2013.
[7] Suh, MH et al., *Ophthalmology*, 123:2309-2317, 2016.
[8] Kiumehr, S et al., *Arch Ophthalmol*, 130:552-559, 2012.
[9] Fu, X et al., *PLOS Comput Biol*, 12:e1004932, 2016.
[10] Beard, DA et al., *Ann Biomed Eng*, 29:298-310, 2001.

SB³C2019
Summer Biomechanics, Bioengineering and Biotransport Conference
June 25 - 28, Seven Springs, PA, USA

PARTICLE DEPOSITION CORRELATES WITH WALL SHEAR STRESS DIVERGENCE IN HUMAN AIRWAYS

Ali Farghadan (1), Kamran Poorbahrami (2), Sahar Jalal (3), Jessica M. Oakes (2), Filippo Coletti (3), Amirhossein Arzani (1)

(1) Department of Mechanical Engineering
Northern Arizona University
Flagstaff, AZ, USA

(2) Department of Mechanical Engineering and Bioengineering
Northeastern University
Boston, MA, USA

(3) Department of Aerospace Engineering and Mechanics
University of Minnesota
Minneapolis, MN, USA

INTRODUCTION

Lungs are directly exposed to harmful aerosols, which increases the vulnerability of the respiratory and cardiovascular systems. On the other hand, recent developments in inhalation treatment for various lung diseases highlight the need to understand deposition processes. Wall shear stress (WSS) is a substantial parameter in biological flows. We have recently used WSS vectors to study near-wall transport in cardiovascular flows [1, 2]. WSS divergence (WSSdiv) represents near-wall normal velocity and could be used to study transport towards or away from the wall [1]. In this study, we test our hypothesis that particle deposition in lung airways correlates with WSSdiv. Specifically, we hypothesize that particle deposition mainly occurs in regions of positive WSSdiv (near-wall velocity towards the wall) and that there is a correlation between deposition concentrations and positive WSSdiv magnitudes. Computational fluid dynamics (CFD) simulations were performed to quantify the airflow in the upper tracheobronchial tree. A comprehensive comparison between the numerical simulation and magnetic resonance velocimetry (MRV) measurements were made to validate the CFD simulation. We performed global and regional statistical analyses on a case-control and six patient-specific models (2 healthy and 4 asthmatic)

METHODS

Velocity and WSS data were obtained from CFD simulations. In the case-control, a mesh with a total of 5.3M linear tetrahedral elements with five layers of boundary layer meshing was created via the open source SimVascular software (simvascular.org). The open-source finite element solver Oasis (github.com/mikaem/Oasis), which is a CFD solver with minimal numerical dissipation, was used to solve the fluid flow. The same lung model was 3D printed and MRV measurements were performed to quantify time-resolved 3D velocity. The outlet resistances in CFD simulations were tuned such that each lobe outflow had less than 1% relative error with respect to the corresponding experimental outflow measurements. The case-control simulations and experiment were done assuming steady flow with Reynolds number of 1500 at the trachea. WSS and velocity field along with particle deposition locations for six patient-specific models with unsteady inhalation were obtained from a recent study [3].

WSSdiv scalar field is derived from time-averaged WSS vector field at the surface. The near-wall normal velocity can be written as a scale of WSSdiv ($\nabla \cdot \boldsymbol{\tau}$) [1]:

$$u_n = -\frac{1}{2\mu} \nabla \cdot \boldsymbol{\tau} \; \delta n^2 + O(\delta n^3) \; , \tag{1}$$

where δn is the distance normal to the wall and μ is dynamic viscosity. Hence, positive and negative WSSdiv could exemplify flow impingement and separation, respectively.

Lagrangian particle tracking throughout inhalation is performed for all models (by solving the Maxey-Riley equation). We released particles at the inlet of case-control (steady flow) with two conditions. First, it was made sure that the entire surface is covered with 250K particles and the interactions between the particles were ignored. Second, particles were released in a staggered fashion in accordance to parabolic inlet profile such that in total around 1M particles were integrated. Also, on average 3.5M particles were released for the other six patient-specific models (unsteady flow) and tracked throughout inhalation.

To quantify the density of particles, we defined the normalized deposition concentration as:

$$\mathrm{DC} = \frac{N_e}{A_e} \times \frac{A}{N_d} \tag{2}$$

Where N_e is the number of particles at the surface element, A_e is the area of that element, A is the entire lung surface area, and N_d is the total number of deposited particles during inhalation. The second fraction in Eq. 2 is the normalization coefficient. Deposition percentage (DP) is defined as the ratio of particles deposited in the upper tracheobronchial tree (N_d) to the total number of released particles at the inlet (N_t). Also, negative DC is the ratio of cumulative DC in negative WSSdiv region to the sum of all DCs.

RESULTS

Representative results are presented in this section. Figure 1 shows the experimental and numerical models. We performed a comparison between MRV [4] and CFD secondary flow patterns and velocity magnitude on the locations shown in Fig. 1. A very good agreement between CFD and MRV methods can be seen in Fig. 2.

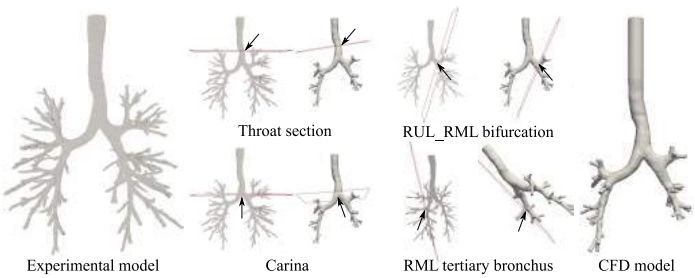

FIGURE 1: The experimental and CFD models. The slices on the models show the locations where the comparison is made.

The scattered DC vs. WSSdiv results are shown in Fig. 3. The majority of particle deposition occurs in positive WSSdiv regions.

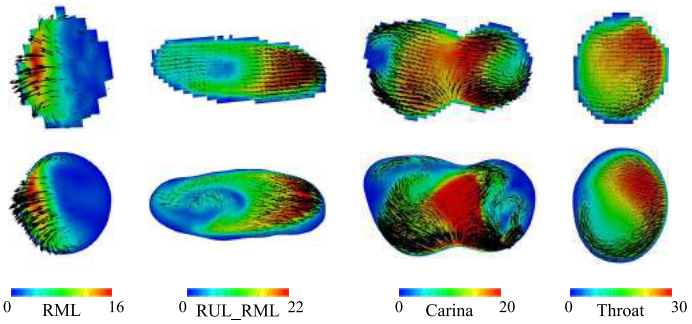

FIGURE 2: MRV (voxel-based) velocity field (top row) and CFD velocity field at the same location (bottom row). The secondary flow motion is shown with black vectors on the top of velocity magnitude (cm/s).

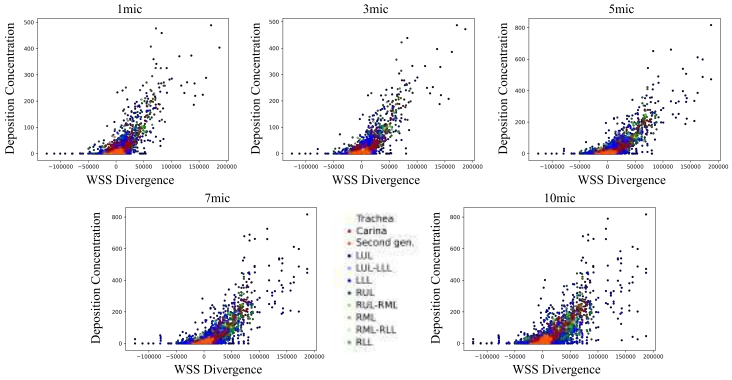

FIGURE 3: Deposition concentration vs. WSS divergence plots for 1, 3, 5, 7, and 10 microns diameter particles (case-control model). Colors represent various regions in the lungs as shown in Fig. 4.

Pearson's correlation coefficients (for the data in positive WSSdiv region) are shown in Table 1. A strong correlation is seen between positive WSSdiv and DC. Correlation values drop as larger particles are considered. This is expected as larger particles tend to deviate more from the fluid pathlines. The same investigation on

Table 1: The DP and negative DC are shown for each particle diameter. Pearson's correlation coefficients are calculated for positive WSSdiv data with respect to DC.

Diameter	Stokes number	DP	negative DC	Pearson's values
1 μm	2.8×10^{-4}	3.5%	11%	0.83
3 μm	2.5×10^{-3}	4.6%	10%	0.84
5 μm	7.0×10^{-3}	7.5%	9.7%	0.83
7 μm	1.4×10^{-2}	15%	10%	0.79
10 μm	2.8×10^{-2}	41%	15%	0.67

six patient models (unsteady flow) shows that our conclusions are extensible (results not shown). One notable observation is negative DC, which shows that the majority of deposition occurs at positive WSSdiv as expected. We also performed a regional analysis in each specific division shown in Fig. 4 (results not shown), and the spatial integral of positive WSSdiv (over each region) was strongly correlated to the spatial integral of DC.

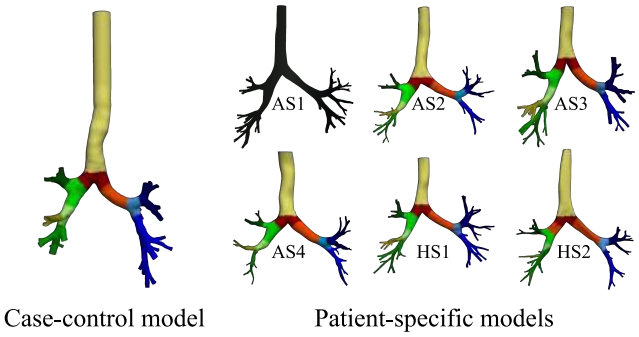

FIGURE 4: Case-control and patient-specific models are divided into localized regions for a regional analysis. Healthy subjects (HS) and asthmatic subjects (AS) were studied.

DISCUSSION

Numerical simulation of particle transport in the lung airways has been widely studied in recent years and has provided insight into detrimental airborne aerosol deposition and optimal particle transport for therapeutic developments. However, no previous studies have shown a strong relationship between particle deposition quantifications and fluid flow characteristics. In this study, we compared and validated our highly resolved CFD simulations with MRV measurements of the same upper tracheobronchial tree model. Lagrangian particle tracking was performed over a range of Stokes numbers. Deposition concentration (DC) was defined to quantify the deposition patterns and enable statistical analysis. As only a small fraction of DC occurs in the negative WSSdiv regions (Table 1 and Fig. 3), we directed our analysis to the positive WSSdiv side. Positive WSSdiv has a strong linear correlation with DC indicating higher deposition concentrations in regions with greater positive WSSdiv. Additionally, our conclusions were verified in six diseased and healthy patient-specific models with physiologic unsteady flows.

Our study introduces WSSdiv as a parameter that is quantified on the airway wall and provides a strong correlation with particle deposition. Our group has previously demonstrated the important role that topological features in WSS play in determining near-wall biochemical localization patterns in cardiovascular flows [1, 2]. Such transport processes are often considered passive where biochemicals follow fluid flow. However, aerosols in lung airways may have their own inertia, causing them to deviate from fluid pathlines. Nevertheless, our results showed that WSS could still be used to predict particle deposition patterns in the range of particle diameters that are of interest in the conducting airways.

ACKNOWLEDGEMENTS

Support from Northern Arizona University is acknowledged.

REFERENCES

[1] Arzani, A. and Gambaruto, A. M. and Chen, G. and Shadden, S. C. Lagrangian wall shear stress structures and near-wall transport in high-Schmidt-number aneurysmal flows. *Journal of Fluid Mechanics*, **790**, 158–172, 2016.

[2] Farghadan A, Arzani A. The combined effect of wall shear stress topology and magnitude on cardiovascular mass transport. *International Journal of Heat and Mass Transfer*, **131**, 252–260, 2019.

[3] Oakes J. M. et al. Patient-specific computational simulations of hyperpolarized 3He MRI ventilation defects in healthy and asthmatic subjects. *IEEE Transactions on Biomedical Engineering*, in press, 2018.

[4] Jalal S., Moortele T. V., Nemes A., Amili O., Coletti F. Three-dimensional steady and oscillatory flow in a double bifurcation airway model *Physical Review Fluids*, **3**, 103101(23), 2018.

COMPUTATIONAL MODELING OF PATHOGEN LEAKAGE THROUGH N95 RESPIRATORS

Prasanna Hariharan (1), Neha Sharma (2), Gavin D'Souza (2), Suvajyoti Guha (1), Rupak K. Banerjee (2), Matthew R Myers (1)

(1) Division of Applied Mechanics
Center for Devices and Radiological Health
Silver Spring, MD, USA

(2) Department of Mechanical and Materials Engineering
University of Cincinnati
Cincinnati, Ohio, USA

INTRODUCTION

During an airborne pandemic or bio-terror attack, N95 respirators could form the first line of defense against hazardous bio-aerosols. The effectiveness of PPEs is strongly dependent on preventing aerosol leakage through gaps between the human face and PPE in addition to the intrinsic penetration through the respirator's porous layers [1, 2]. The leakage through gaps can be significantly reduced by performing fit testing and selecting the appropriately sized respirator. However, during a public health emergency, fit-testing of respirators may not be possible and leakage of aerosol through the gaps could compromise the effectiveness of the PPE. Hence, it is important to locate the leakage sites (gaps) and quantify the gap surface area and aerosol leakage for different face and masks combinations.

This paper presents a computational fluid dynamics (CFD) approach for quantifying the aerosol leakage through respirators for multiple human face-respirator combinations under realistic flow conditions. The gap surface area for different face-respirator combinations has been recently quantified by our group [3]. This study takes the CFD model further and establishes a relationship between the amount of aerosol leakage and the gap surface area for each of the face-respirator combinations. The leakage results from this study will be combined with our recently published comprehensive risk assessment models [4] to quantify the infection risk to pediatric and adult populations when exposed to various types of bio-pathogens such as Bacillus anthracis or Influenza virus.

METHODS

Four adult headforms and two brands of respirators, shown in Fig. 1, were selected for evaluating the gaps between the face and respirator. The geometric data of the headforms were obtained from an anthropomorphic survey of 3,997 US workers, conducted at the National Personal Protective Technology Laboratory at the Center for Disease Control [5], and categorized based on shape and size as: small, medium, large, and short/wide. Subsequently, mannequins resembling realistic solid models of each of the headforms were obtained using 3D printing (Materialise, Inc.). The two respirator brands, labeled as Model A and Model B, belonged to the class of N95 surgical respirators, which are certified by the National Institute for Occupational Safety and Health (NIOSH) and regulated by the US Food and Drug Administration (FDA). Therefore, eight unique headform-respirator combinations were obtained by donning each of the two respirators on all four headforms.

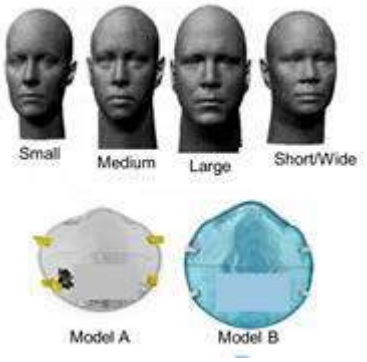

Figure 1: An image of headforms and N95 respirators

Computed Tomography (CT) was used to capture the gap between the face and the mask for different mask-face combinations. Before the CT scans, the inside layer of the mask was coated with a thin layer of

gold to enhance the pixel intensity of the mask layer relative to the face. The CT slices were reconstructed using Mimics and 3-matics software and converted to 3D CAD geometry. A computational domain of size 150x150x200 mm^3 which includes the face, respirator and the surrounding enclosure are shown in Fig 2. An inlet tube of diameter, 6 mm, was attached to the front side of the enclosure (opposite the face and respirator), while the outlet was modeled as a circular region (diameter = 6 mm) on the mouth (Fig. 2). The domain was then meshed into finite volumes consisting of tetrahedral elements using commercial meshing software (3-matic, Materialise Inc.). The mesh around the face and respirator region was refined to accurately solve the leakage flow through the gaps. Subsequently, the meshed computational domain was exported to a commercial CFD solver, CFX (Ansys, Inc.).

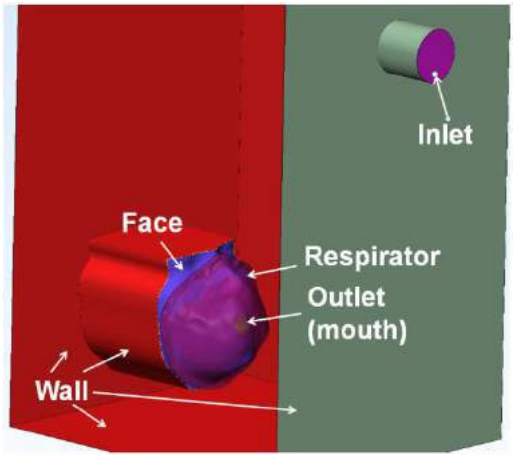

Figure 2: A computational domain of the face-resiprator model surrounded by a bounding box

A 3-step numerical methodology was adopted for simulating the airflow and aerosol transport around and through the face-respirator geometry.

In the first step, the porous media properties (porosity and linear resistance coefficient) of the masks were obtained by performing a no-leakage CFD simulation of the masks attached to the flat plate. For this simulation, all the aerosol penetration was assumed to happen through the porous layers of the mask. The pressure drop required across the mask to attain the necessary flow was measured experimentally for all two masks. Subsequently, the mask porosity and the linear resistance coefficient were adjusted in the CFD simulations until the pressure drop matched with the experimental data. After completion of first stage, for mask Model A, the simulation with 10LPM intake flow rate resulted in porosity value of 0.5 and linear resistance coefficient value of 93700 kg $m^{-3}s^{-1}$, while the simulation with 70LPM intake flow rate resulted in porosity value of 0.5 and linear resistance coefficient value of 89800 kg $m^{-3}s^{-1}$.

In the second step, fluid flow simulation through the face-respirator geometry was performed using the mask properties obtained from the first stage. An inlet boundary condition of zero static pressure was specified at the inlet and mass flow rate was specified at the mouth outlet. This combination of boundary conditions simulates a suction flow through the inlet. Subsequently, the amount of fluid flow through the leakage sites and through the porous layers of the mask was determined.

In the third step, a particle tracking algorithm was used to track the leakage of aerosols through the leakage sites between face and the respirators. The flow split between the leakage sites and the mask (obtained from the second step) was provided as the input for this stage. The input parameters for aerosol transport including the density (2250 kg/m^3) and aerosol size (100 nm) were obtained from the experimental studies. Finally, the amount of aerosol leakage was obtained as a function of flow rate to understand the relationship between the gap surface area and the leakage percentage for different face-respirator combinations.

RESULTS

The variation of flow leakage as a function of gap surface area for two different intake flow rates of 10 LPM and 70 LPM is shown in Fig. 3. The gap surface area for the eight human face-respirator combinations were obtained from image based modeling and ranged from 29.45mm^2 to 409.43mm^2 [3], while the flow leakage varied from 20% to 95%. The rate of increase of flow leakage is observed to be high up to a gap surface area of 200 mm^2 beyond which it stabilizes to a value of ~90%. As expected, flow leakage is observed to increase with gap surface area.

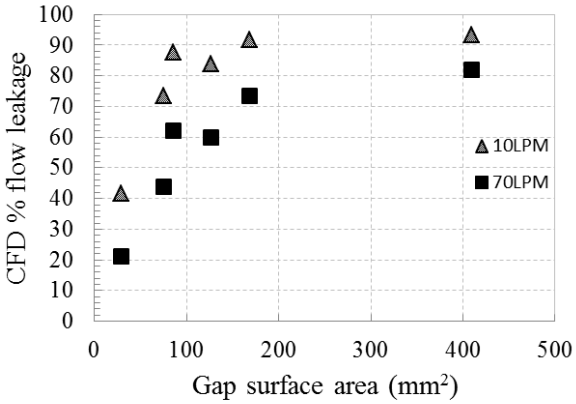

Figure 4. Variation of CFD simulations based flow leakage with gap surface area for intake flow rates of 10LPM and 70LPM

DISCUSSION

Future studies will provide the relation between gap surface area and aerosol leakage (instead of the flow leakage reported here). The aerosol leakage % obtained from the CFD will also be validated with the experimental results. Subsequently, the leakage results will be input to our comprehensive risk assessment model [4] to quantify the infection risk to pediatric and adult populations when exposed to various types of bio-pathogens.

REFERENCES

[1] Grinshpun SA,et al. J Occup Environ Hyg; 6:593–603.
[2] Shaffer RE et al. J Nanopart Res; 11:1661–1672.
[3] D'Souza et al. DMD conference, 2017.
[4] Myers et al. Mathematical Medicine and Biology; Oct 25, 2016;
[5] Zhuang Z et al.J Occup Environ Hyg; 2: 567–76

SB³C2019
Summer Biomechanics, Bioengineering and Biotransport Conference
June 25 -28, Seven Springs, PA, USA

REGIONAL TARGETING OF THERAPEUTIC PARTICLES IN HEALTHY AND ASTHMATIC LUNGS

Kamran Poorbahrami (1), Sean Fain (2,3,4), David G. Mummy (2), Jessica M. Oakes (5)

(1) Department of Mechanical and Industrial Engineering, Northeastern University, Boston, MA, USA.

(2) Departments of Biomedical Engineering, (3) Medical Physics, and (4) Radiology, University of Wisconsin-Madison, WI, USA.

(5) Department of Bioengineering, Northeastern University, Boston MA, USA.

INTRODUCTION

Targeting drug particles to specific regions in the lungs in asthmatic subjects may improve therapeutic response while reducing side effects, benefiting the 10-15 percent of patients with uncontrolled asthma [1]. Contributing factors of ventilation heterogeneity, airway remodeling, and mucus plugging make it challenging to deliver therapeutics to obstructed airways, resulting in inadequate dose concentrations. Identifying the variables that most influence regional deposition is the first step towards targeting inhaled medications. Previously, we developed a framework that combines imaging data (e.g. MRI and CT) with computational fluid dynamic simulations to study the structural-functional abnormalities in healthy and asthmatic lungs [2]. Here, we extend this framework to include particles and apply it to predict airway dose concentrations and test delivery conditions on particle fate in the lungs.

METHODS

We perform unsteady computational fluid dynamics and particle transport (CFD-PT) simulations in six human airways: 2 healthy subjects (HS1 and HS2) and 4 asthmatic subjects (AS1-2 mild/moderate, and AS3-4 severe), all of whom underwent CT and MRI. Airway models were created based on each subject's CT images at FRC [2]. We registered and integrated hyperpolarized (HP) ^{3}He MRI and CT data to model the regional ventilation defects [2] as resistance boundary conditions.

An open-source finite element solver (SimVascular [4]) is used to solve the unsteady three-dimensional Navier-Stokes equations for an incompressible Newtonian fluid (density = 1.2E-6 g/mm^3 and viscosity = 1.81E-5 $g/mm-s$). We prescribe a parabolic velocity profile on the trachea entrance based on the waveform presented by Longest et. al., which models generic use of a dry powder inhaler:

$$\begin{cases} Q(t) = \frac{Q_{max}}{T_{Q_{max}}} t & 0 \le t \le T_{Q_{max}} \quad (1a) \\ Q(t) = Q_{max}\, cos\left(\frac{\pi(t-T_{Q_{max}})}{2(1-T_{Q_{max}}/T_f)} t\right) & T_{Q_{max}} < t \le T_f \quad (1b) \end{cases}$$

where Q_{max} is the peak flowrate set to 61.4 L/min, $T_{Q_{max}}$ is the time when the flowrate reaches its peak, and T_f is the inhalation time (set to 1.22 s and 4.86 s, respectively).

The airway resistances within the conducting airways (R_{3D}) are calculated by dividing the time averaged pressure gradients by the trachea flowrates. In addition, we calculate wall shear stress (WSS):

$$WSS = \int_S \mu \frac{d\mathbf{u}}{d\mathbf{n}} dS \quad (2)$$

where μ is viscosity, **u** is the velocity vector, and **n** is the normal vector to the wall.

Following the airflow simulations, 3 μm diameter particles are released and tracked throughout inhalation by solving a force balance equation that incorporates gravity and drag. Particles are marked as deposited once they intersect with airway wall, and the remaining particles are assumed to be delivered to the lung periphery. We compute total and regional deposition for each subject, and to visualize deposition hotspots, we calculate the area-normalized number of deposited particles in each surface element with respect to the total deposited particles:

$$NP = \frac{N_e \sum T}{N_T \sum e} \quad (3)$$

where N_e is the number of deposited particles within a surface element, $\sum e$ and $\sum T$ is the element and total surface area, respectively, and N_T is the total number of deposited particles.

We hypothesize that the time and injection locations that particles are released are important variables linked to the particle's fate within the lung. To test this hypothesis, time frames corresponding with enhanced deposition efficiency are identified by recording particle deposition over inhalation time and are correlated with the particle injection time. We then alter particle release time frames to enhance the fraction of particles delivered to the central or peripheral airways.

In addition, we study the correlation between particle initial locations (at the start of the inhalation) and the lobe that they are delivered to. We choose a severe asthmatic subject (AS3) for this analysis. Our aim here is to improve delivery to the Right Middle lobe, which has the highest segmental ventilation defect percentages (SVDP indicates inability to deliver inhaled gas).

RESULTS

Time averaged wall shear stress (TAWSS) is calculated by averaging the WSS over inhalation time (Figure 1A). In Table 1 we present the TAWSS normalized by $\sum T$. AS3 has the lowest R_{3D} in comparison to the other subjects due to its larger distal airways [2]; airway resistances are reversely correlated to the fourth power of airway diameter. High regions of TAWSS are located at the distal airways of AS4 (Fig. 1A), likely because this subject's airways are smaller and less circular than the other subjects [2], leading to higher velocity magnitudes and near-wall gradients. The velocity streamlines show helical-type patterns, likely because this subject has asymmetric airways, including curved and irregularly shaped airways (Fig. 1B).

While total deposition within the conducting airways are similar among the healthy subjects (which agrees with our previous study [4]), we see larger variations among the asthmatic subjects (Table 1). Despite similar asthma severity, the percentages of

deposited particles is almost 10 times less in AS3 than in AS4, suggesting that far more particles are delivered to the lung periphery in AS3.

Table 1. *Simulated total deposition for the three particle sizes, resistances within the 3D airways (R_{3D}), and area normalized time averaged wall shear stress for the six subjects*

Subjects	Deposition (Percent)			R_{3D}	$\overline{TAWSS}$
	1μm	3 μm	5 μm	cmH_2O-s/ml	g/mm-s2
HS1	4.4	26.6	68.7	6.9E-3	1106
HS2	4.4	26.6	73.5	7.9 E-3	1800
AS1	5.6	33.4	79.1	4.8 E-3	2034
AS2	7.8	40.3	81.7	13.8 E-3	1023
AS3	2.6	5.9	21.6	0.1 E-3	602
AS4	8.7	56.3	90.6	31.9 E-3	1542

We choose to either enhance or reduce central airways deposition based on an arbitrary threshold of 30% central airway deposition (Fig. 1C). To enhance conducting airway deposition in HS1, HS2, and AS3, we release particles only during the times of peak flowrates (between 1.2 to 2.5s). To enhance peripheral delivery in subjects AS1, AS2, and AS4, which have relatively higher central deposition fractions, we release particles only during the slower flowrate times (3.2 to 4.5s). Fig. 1C shows the results of these alterations, total dosimetry in subject AS4 is reduced from 56% to 32% (Fig. 1D and 1E).

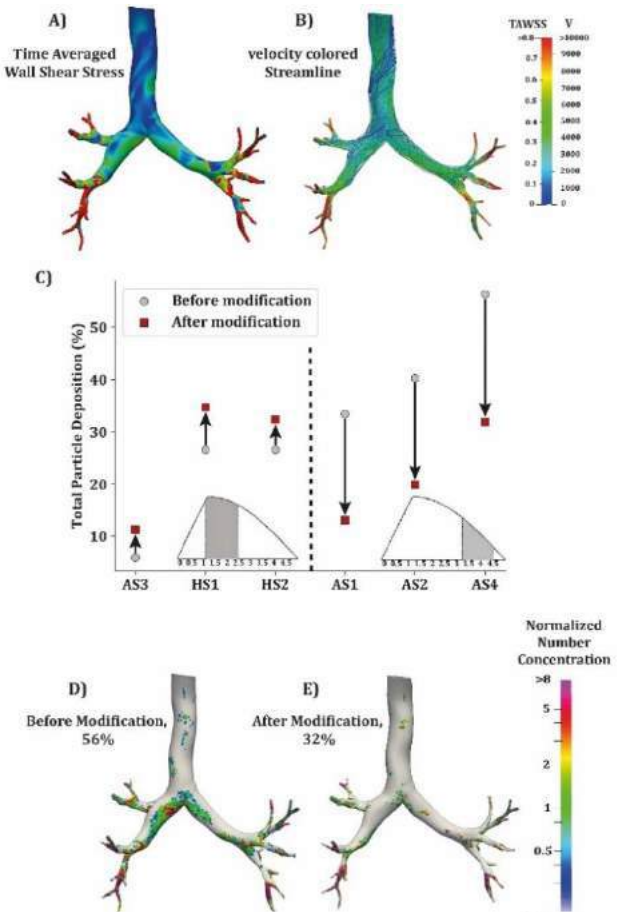

Figure 1*. Time averaged wall shear stress (A), velocity colored streamlines (B), variations of central/peripheral deposition due to altering the particle release time (C, left/right), and AS4 number concentration before and after modification (D-E)*

We correlate lobar deposition with the release locations of particles on the trachea face for subject AS3, in order to investigate the influence of the particles' initial locations on regional deposition. Subpanel of Fig. 2A shows the trachea inlet, where the colors represent the concentration of deposited particles in the Right Middle lobe (highest SVDP). Leveraging these results, we change the initial location of the 3 μm particles in order to deliver them to the lobe with the highest ventilation defects. Fig. 2A shows the percentage of particles that deposited on the walls of the airways that leads to a specific lobe and Fig. 2B shows the particles delivered to that lobe's periphery. By altering the seeding location of particles, we are successful in increasing regional deposition within the Right Middle lobe (RM) from 6 to 11 % and the delivery percentage from 10 to 43%.

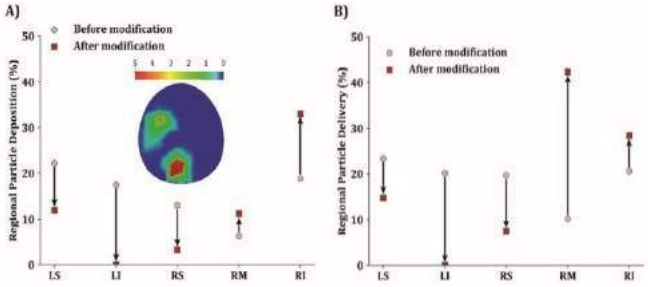

Figure 2. *Lobar deposition percentages and the initial location of the Right Middle Lobe (RM) deposited concentrations (panel A) and lobar delivery percentages (panel B) for subject AS3, before and after seeding modifications. LS=Left Superior, LI=Left Inferior, RI=Right Inferior, and RS=Right Superior.*

DISCUSSION

Asthma is typically controlled by direct delivery of therapeutics to the lung. Optimization of drug delivery may lead to a reduction in the total dosage, potentially reducing adverse side effects while preventing future exacerbations. We performed a patient-specific airflow and aerosol simulation in healthy and asthmatic airways and found that (1) total and regional tissue dosimetry varies between asthmatic subjects, (2) central vs. peripheral deposition can be adjusted by altering the aerosol bolus injection time, and (3) lobar targeting can be achieved by altering the seeding locations of particles. This knowledge brings us one step closer to our ultimate goal of optimizing drug delivery based on each patient's needs. Here, we focus on the link between the initial location of the particles on the trachea inlet and their destination lobe, however therapeutics are inhaled through the mouth and the particles will likely re-distributed by the time they pass the trachea. Therefore, we plan to add the extra-thoracic airways in our future studies.

ACKNOWLEDGEMENTS

This work is supported by NIH/NHLBI R21 HL140436-01. Human data collected was facilitated by: NIH/NHLBI R01 HL069116; R01 HL080412; U10 HL109168; NIH/NCATS UL1TR000427.

REFERENCES

[1] Global Asthma Network, Auckland, New Zealand, Tech. Rep., 2014.

[2] Oakes J. M. et al. IEEE Transactions on Biomedical Engineering, in press, 2018.

[3] Updegrove, Adam, et al. Annals of biomedical engineering 45.3 (2017): 525-541.

[4] Poorbahrami, K., and J. M. Oakes. Clinical biomechanics (Bristol, Avon) (2018).

SB³C2019
Summer Biomechanics, Bioengineering and Biotransport Conference
June 25 -28, Seven Springs, PA, USA

DIFFERENTIAL EFFECTS OF BLADDER OUTLET OBSTRUCTION ASSOCIATED PRESSURE CYCLING ON UROTHELIAL CELL INFLAMMATION AND FIBROSIS IN VITRO

Cody L. Dunton (1), J. Todd Purves (2, 3), Francis M. Hughes (2), Jiro Nagatomi (1)

(1) Department of Bioengineering
Clemson University
Clemson, SC, USA

(2) Department of Surgery, Division of Urology
Duke University Medical Center
Durham, NC, USA

(3) Department of Pediatrics
Duke University Medical Center
Durham, NC, USA

INTRODUCTION

Partial bladder outlet obstruction (pBOO) is a condition that affects one-sixth of the worldwide population[1] and is typically diagnosed by the presence of lower urinary tract symptoms (LUTS) such as hesitancy, weak stream, and incomplete bladder emptying. In addition, pBOO is frequently accompanied by inflammation leading to fibrosis of the bladder wall tissue and reduced tissue compliance[2]. Early evidence of pBOO is generally determined by a voiding pressure increase as the bladder contracts against the obstruction. As pBOO progresses, the storage pressure within the bladder also increases due to changes in bladder tissue compliance. Thus, it was hypothesized that changes in voiding and/or storage pressure associated with pBOO disease progression may induce activation of pro-inflammatory and pro-fibrotic mechanosensitive pathways in the urothelium.

Our previous in vitro study demonstrated that exposure of bladder urothelial cells to simulated elevated voiding pressures (40 cm H_2O for 1 minute) as well simulated elevated storage pressures (15 cm H_2O for 60 mintues) both induced an increase in extracellular ATP release[3]. Moreover, exposure of these cells to elevated hydrostatic pressure led to an increase in activation of intracellular caspase-1, part of inflammasome cascade. We concluded that the pressure-induced ATP release led to additional ATP-induced ATP release via activation of P2X7 receptor, which then resulted in caspase-1 activation via activation of P2X4 receptor[3]. These results provided a potential mechanism at the cellular-level for a previous *in vivo* study that demonstrated elevated levels of caspase-1 preset in the urothelium of pBOO rats[4]. In the present study, we exposed urothelial cells to simulated pressure cycling profiles in order to elucidate the mechanisms for increased collagen content found in the bladders of pBOO rats[5]. Specifically, we compared the effects of early stage pBOO (elevated voiding pressure), and late stage pBOO (elevated voiding and storage pressures) on caspase-1 activation and pro-fibrotic gene expression *in vitro*.

METHODS

For experiments investigating the role of hydrostatic pressure magnitude during storage/voiding cycles on inflammation and fibrosis, a custom apparatus[6] was used to expose rat urothelial cell line MYP3 cells to sustained pressure over designated time intervals. Briefly, the system consisted of a computer that ran a custom LabView program (National Instruments) with a pump and pressure transducer to monitor and regulate the pressurized environment within a closed chamber. Cells were plated at $1.2x10^6$ cells/well in sterile 6 well cell culture plates and incubated for 48 hours until the cells reached 90% confluence. The complete F-12K media was then replaced with complete media containing 25 mM MOPES buffer immediately prior to exposure to hydrostatic pressure in order to minimize the effects of basal extracellular ATP levels on the results after exposure to pressure. Cells were subjected to pressure cycles for 24 or 72 hours of either 0 cmH_2O for 175 minutes followed by 30 cmH_2O for 5 minutes to simulate unobstructed bladder cycling, 0 cmH_2O for 175 minutes followed by 75 cmH_2O for 5 minutes to simulate early stage (ES) pBOO, or 15 cmH_2O for 175 minutes followed by 75 cmH_2O for 5 minutes to simulate late stage (LS) pBOO. Following exposure, RNA was isolated using a commercially available RNA isolation kit (Qiagen) and purified with DNase (Thermo Scientific). RT-PCR was conducted on the purified RNA following the established protocol of a commercially available qRT-PCR kit (Invitrogen) with primers designed to amplify a region of mRNA corresponding to regions of target genes that lack homology with other subtypes. Separate cells exposed to the same cyclic pressure regime for 24 hours were lysed

and intracellular caspase-1 activity was measured using an established method[4,7].

Each experiment was performed in triplicate, with a minimum of three repetitions (n=3). The mean values of the data from the repetitions were calculated using SAS software (SAS Institute) and compared using single-factor analysis of variance (ANOVA). When a statistically significant difference was displayed, a *post hoc* pairwise analysis was conducted using the Tukey-test. P-values less than 0.05 were considered statistically significant.

RESULTS

MYP3 cells exposed to simulated early stage (ES pBOO) and late stage (LS pBOO) pressure cycling for 24 hours exhibited similar gene expression for collagen type I (Col I), collagen type III (Col III), lysyl oxidase (LOX), or prolyl 4-hydroxylase (P4H) (Figure 1A). However, cells exposed to these pressure cycling conditions resulted in increased level of intracellular caspase-1 activity in both ES pBOO (1.15-fold) and LS pBOO (1.21-fold) when compared to the non-pressure treated control. Unlike the 24 hour experiments, MYP3 cells exposed to ES pBOO pressure cycling for 72 hours demonstrated decreased levels of collagen type III expression and increased levels of prolyl 4-hydroxylase expression compared to cells exposed to unobstructed pressure conditions. In addition, MYP3 cells exposed to LS pBOO pressure cycling for 72 hours demonstrated decreased levels of collagen type III expression, but also demonstrated increased levels of both prolyl 4-hydroxylase and collagen type I expression compared to cells exposed to unobstructed cycling conditions (Figure 1B). The data also indicates a trend of increasing expression of collagen type I and prolyl 4-hydroxylase and decreases expression of collagen type III and lysyl oxidase as pBOO progresses.

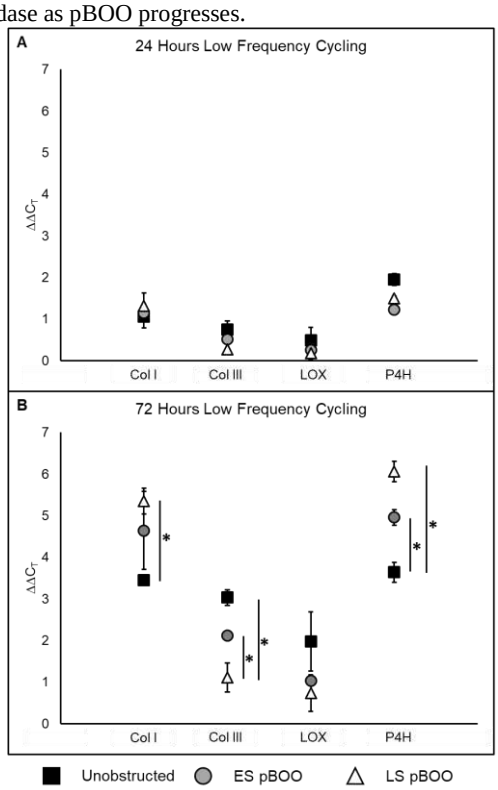

Figure 1: Gene expression of cells exposed to simulated early and late stage pBOO pressure cycles of unobstructed, early stage (ES), and late stage (LS) pBOO for 24 (A) and 72 (B) hours *in vitro*. Results are mean ± SEM; *P<0.05, n=3.

DISCUSSION

Although changes in the mechanical environment have long been correlated with the progression of pBOO associated disorders, the role of specific mechanical cues in disease progression has yet to be elucidated. In the present study, we hypothesized that changes in pressure cycling associated with different stages of pBOO resulted in progression of associated disorders. Using a custom set-up, we exposed urothelial cells to simulated early stage and late stage pressure cycling and determined the effect of pressure variation on precursors of inflammation and genes associated with fibrosis. Results indicate that increased voiding pressure and storage pressure associated with early stage and late stage pBOO resulted in increased activation of intracellular caspase-1, indicating activation of the NLRP3 inflammasome within 24 hours of pressure exposure. Simulated early stage pBOO and late stage pBOO pressure cycling also resulted in increased collagen type I and prolyl 4-hyroxylase as well as decreased collagen type III after 72 hours. Increased collagen type I and prolyl 4-hyroxylase content indicates fibrosis of the tissue and is consistent with previous findings that demonstrated BOO rats exhibited increased levels of collagen in urothelial cells[5]. The collagen type I/III ratio also increases with progression of the simulated pressure cycles. It has been reported that the ratio of collagen type I/III is an important indicator of fibrosis as increased collage type I/III ratio is correlated with changes in tissue compliance[8] and that there is an increase in collagen type I/III ratio in rabbit ventricles in response to pressure overlaod[9]. Further research, however, is needed to elucidate the underlying mechanisms by which elevated pressure and distention trigger ATP release and intracellular caspase-1 activation in order to improve understanding of mechanically induced bladder pathologies such as pBOO.

ACKNOWLEDGEMENTS

Funding Sources: NIH (R01DK103534, P20GM103444), NSF (1264579)

REFERENCES

[1] Irwin, D.E. et al., *BJU Int*, 108:1132-1138, 2011.
[2] Metcalfe, P.D. et al., *BJU Int*, 106:1686-1694, 2010.
[3] Dunton, C.L. et al., *Int Urol Nephrol*, 50:1607-1617, 2018.
[4] Hughes, F.M., J Urol, 195:1598-1605, 2016.
[5] Hughes, F.M., *Am J Physiol*, 313:F603-610, 2017.
[6] Stover, J. et al., *Ann Biomed Eng*, 35:1585-1594, 2007.
[7] Hughes, F.M., *Am J Physiol*, 306:F299-F308, 2013.
[8] Wei, S. et al., *J Cardiac Failure*, 5:117-126, 1999.
[9] Low, R.B. et al., *Biochem J*, 263:709-713, 1989.

SB³C2019
Summer Biomechanics, Bioengineering and Biotransport Conference
June 25 -28, Seven Springs, PA, USA

EFFECT OF AIRWAY CILIA PROPERTIES ON ITS PHYSIOLOGICAL FUNCTIONING

Uduak Z. George

Department of Mathematics and Statistics
San Diego State University
San Diego, CA, United States

INTRODUCTION

Mucus clearance in the airway is regulated by carpets of cilia on the epithelial layer of the lungs. Each cell of the epithelium contains about 200-500 cilia that beat synchronously with each performing about 20-30 beating cycle per second [1]. Bordering the epithelial layer and surrounding the cilia is the periciliary liquid (PCL) that lubricates the epithelial layer. The mucus layer is sandwiched between the PCL and the air in the core airways. The PCL and mucus layer are also referred to as the airway surface liquid (ASL) [2]. PCL is known to facilitate mucus clearance by providing a favorable environment for the beating cilia [3]. The impairment of mucus clearance is often devastating and may result in inflammation [4] and infection [5] in the airways. It has also been observed that people born with certain abnormal ciliary structure may have reduced mucociliary transport efficiency. Permanent changes in ciliary structure and function results in mucus retention [6]. We seek to understand the mechanism by which changes in ciliary structure affect its functional role and causing mucus clearance to fail. We speculate that changes in ciliary structure would affect its biomechanical properties and structural integrity and impede the proper functioning of mucociliary transport.

METHODS

A computational model describes the lung airways. The cilia are represented as an elastic solid. The PCL and mucus layer are modeled as fluids with different density and viscosity. We consider three different cases:

I. PCL occupy the whole region of ASL (i.e. no mucus is present).
II. Physiologically healthy mucus occupies the whole region of ASL (i.e. PCL is absent).
III. Highly viscous mucus occupies the whole region of ASL (i.e. no PCL is present).

We choose the geometry of the model to correspond to a cross-section of a bronchi (Figure 1A). Model geometry and parameter values are chosen to correspond to experimental observations [7]. The radius of a cilium is approximately 0.1μm and its height is 8μm long [8]. The lung is continuously undergoing cyclic changes in pressure gradient, a necessity for gaseous exchange. The model investigates the resilience of cilia to deformation during exposure to normal cyclic pressure gradient in the airways.

Navier-Stokes equation for airway surface liquid

Let $\Omega = \Omega_A \cup \Omega_c$ denote the lung airways in $\boldsymbol{\mathcal{R}}^2$ with Ω_A the region resided by the airway surface liquid and Ω_c the cilia. Let $\boldsymbol{v} = \boldsymbol{v}(\boldsymbol{x}, t)$ denote the velocity of the airway surface liquid (ASL), $p = p(\boldsymbol{x}, t)$ the pressure at the ASL, ρ_F and μ_F the density and dynamic viscosity of the ASL respectively. The airway mucus and PCL are assumed to be incompressible viscous fluids. The motion of the mucus and PCL is governed by the incompressible Naiver-Stokes equation defined in a bounded domain $\Omega_A \subset \boldsymbol{\mathcal{R}}^2$. The equation of motion is:

$$\rho_F(\partial_t \boldsymbol{v} + (\boldsymbol{v} \cdot \nabla)\boldsymbol{v}) = \nabla \cdot \boldsymbol{\sigma}, \quad \text{in } \Omega_A, \ t \in (0, T) \tag{1}$$

$$\nabla \cdot \boldsymbol{v} = 0, \quad \text{in } \Omega_A, \ t \in (0, T) \tag{2}$$

where $\boldsymbol{\sigma} = -p\boldsymbol{I} + 2\mu_F \boldsymbol{D}(\boldsymbol{v})$ is the fluid Cauchy stress tensor and $\boldsymbol{D}(\boldsymbol{v}) = \frac{1}{2}\left((\nabla \boldsymbol{v} + (\nabla \boldsymbol{v})^T)\right)$ is the symmetrized gradient of **v**. $\boldsymbol{I}$ is the identity tensor in $\boldsymbol{\mathcal{R}}^2$. Values of ρ_F and μ_F for ASL are 1×10^3kg/m^3 and 0.001Pa·s respectively (for case I, no mucus is present).

Elastic model for cilia

We denote by $\boldsymbol{u} = \boldsymbol{u}(\boldsymbol{x},t)$, $\boldsymbol{x} \in \Omega_c$, $t \in (0,T)$, the displacement of the cilia. We assume that cilia is a homogeneous isotropic material and the displacement gradient for cilia is small (i.e. $\nabla \boldsymbol{u} \ll 1$) and the equilibrium equation is [9]:

$$\rho_s \, \partial_{tt}\boldsymbol{u} = \nabla \cdot \boldsymbol{S}, \quad \text{in } \Omega_c, \; t \in (0,T) \tag{3}$$

where $\boldsymbol{S}$ is the linearized Saint Venant-Kirchhoff model that describes the mechanical property of cilia.

$$\boldsymbol{S} = \mu(\nabla \boldsymbol{u} + (\nabla \boldsymbol{u})^T) + \lambda (\nabla \cdot \boldsymbol{u}) \boldsymbol{I}, \quad \text{in } \Omega_c, \; t \in (0,T)$$

Here, μ and λ are the Lamé constants, describing the compression and distortion of the cilia. The constants μ and λ can be expressed as [10]: $\mu = \frac{E}{1+\upsilon}$, $\lambda = \frac{E\upsilon}{(1+\upsilon)(1-2\upsilon)}$, where E is the modulus of elasticity (Young modulus) of a cilium, υ the contraction ratio (Poisson ratio) of cilium and ρ_s is the density of cilium. Value of ρ_s and υ used in the model is 1.11×10^3kg/m^3 and 0.49 respectively.

*Young modulus for motile cilia*Let a denote the radius of a cilium, E its Young modulus and I its area moment of inertia then $EI = 6 \times 10^{-22}$Nm^2 [11]:

where $I = \frac{\pi a^4}{4} = \frac{\pi(0.1\times 10^{-6})^4}{4} = 0.78546 \times 10^{-28}$m^4.

Given that $EI = 6 \times 10^{-22}$Nm^2, we can write that

$E = \frac{6\times 10^{-22}\text{Nm}^2}{0.7859\times 10^{-28}\text{m}^4} = 7.639 \times 10^6$N/m^2

Coupling condition for the elastic model and Navier-Stokes equation

We apply a linear coupling at the ASL-cilia interface by imposing continuity of stresses at the interface. That is at the interface the normal stress experienced by the cilia is equal to the normal fluid stress.

Let **n** denote the outward pointing unit normal at the ASL-cilia interface, the coupling condition at the ASL-cilia interface is expressed as follows: $\boldsymbol{\sigma} \cdot \boldsymbol{n} = -\mathbf{S} \cdot \mathbf{n}$ on the ASL-cilia interface.

Pressure gradient in the airways

The maximum local pressure drop in the airways is higher before forced inhalation (about 120 Pa) compared to before quiet inhalation (about 8 Pa) [12]. We note that local pressure gradient is higher compared to the linear pressure gradient because of local bifurcations of the airways at different generations.

RESULTS

The pressure boundary condition at the inlet and outlet of the domain mimics the pressure gradient in the airways and the model is simulated for $T = 1$ sec. Simulation results (for case I) is presented in Figure 1B. The von Mises stress is higher at the stalk than at the tip of the cilia. Increase in pressure drop leads to an increase in the deformation of cilia. The deformation of cilia decreases for increasing Young's modulus. The values of the Young's modulus are chosen to correspond to typical values for normal and abnormal cilia.

DISCUSSION

The pressure gradient in the airways during inhalation and exhalation causes a displacement of the peri-cilia liquid and this in turn deforms the cilia. Deformation of the cilia would decrease the effective stroke of cilia. The model shows that changes in ciliary structure may influence cilia dynamics and in turn the transport of mucus. Most models seek to understand the active transport of mucus in the airway, a contribution of this work is in showing that changes in ciliary structure would affect its biomechanical properties and structural integrity and impede the proper functioning of mucociliary transport.

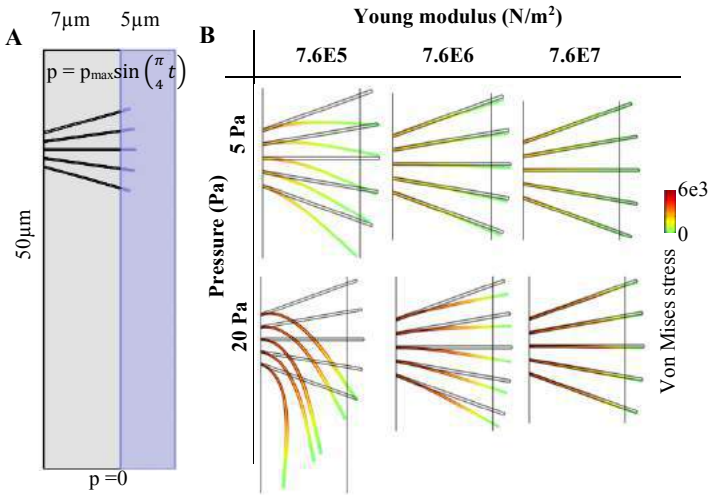

Figure 1: A. Model domain in $\mathcal{R}^2$ representing a cross-section of a bronchi. B. Stress distribution in cilia for different values of Young modulus and pressure P_{max} at t=1sec. Top row, P_{max} = 5 Pa. Bottom row, P_{max} = 20 Pa. Top row from left to right: Young modulus increases by an order of 10. Same for bottom row. Color scale shows the distribution of von Mises stress. Red is high and green is low. Deformed geometry at t = 1sec is superimposed on the undeformed initial geometry (t=0).

ACKNOWLEDGEMENTS

The author would like to acknowledge the funding support from San Diego State University.

REFERENCES

1. Kurbatova, P., et al., *Model of mucociliary clearance in cystic fibrosis lungs.* J Theor Biol, 2015. **372**: p. 81-8.
2. Matsui, H., et al., *Coordinated clearance of periciliary liquid and mucus from airway surfaces.* J Clin Invest, 1998. **102**(6): p. 1125-31.
3. Button, B., et al., *A periciliary brush promotes the lung health by separating the mucus layer from airway epithelia.* Science, 2012. **337**(6097): p. 937-41.
4. Mall, M., et al., *Increased airway epithelial Na+ absorption produces cystic fibrosis-like lung disease in mice.* Nat Med, 2004. **10**(5): p. 487-93.
5. Matsui, H., et al., *A physical linkage between cystic fibrosis airway surface dehydration and Pseudomonas aeruginosa biofilms.* Proc Natl Acad Sci U S A, 2006. **103**(48): p. 18131-6.
6. Del Donno, M., et al., *The effect of inflammation on mucociliary clearance in asthma: an overview.* Chest, 2000. **118**(4): p. 1142-9.
7. Fahy, J.V. and B.F. Dickey, *Airway mucus function and dysfunction.* N Engl J Med, 2010. **363**(23): p. 2233-47.
8. Rydholm, S., et al., *Mechanical properties of primary cilia regulate the response to fluid flow.* Am J Physiol Renal Physiol, 2010. **298**(5): p. F1096-102.
9. Bodnár, T., G.P. Galdi, and S. Necasová, *Fluid-Structure Interaction and Biomedical Applications*. 2014, Springer.
10. Johnson, C., *Numerical solution of partial differential equations by the finite element method.* 1987, Cambridge: Cambridge University Press.
11. Hill, D.B., et al., *Force generation and dynamics of individual cilia under external loading.* Biophys J, 2010. **98**(1): p. 57-66.
12. Chovancova, M. and J. Elcner, *The pressure gradient in the human respiratory tract. EPJ Web of Conferences*, 2014. **67**.

SB^{3}C2019
Summer Biomechanics, Bioengineering and Biotransport Conference
June 25 -28, Seven Springs, PA, USA

IN VIVO MEASUREMENT OF BEVACIZUMAB DIFFUSION COEFFICIENT IN THE RABBIT VITREOUS HUMOR USING FLUORESCEIN LABELING

Anita N. Penkova (1), Shuqi Zhang (1), Komsan Rattanakijsuntorn (6), Mark S. Humayun (3,5) Juan C. Martinez (5), Alejandra Gonzalez Calle (5), Ana Galesic (4), Abegail Tadle (4), Matthew R. Pratt (4), Mark E. Thompson (4), Satwindar S. Sadhal (1,2)

(1) Department of Aerospace & Mechanical Engineering (2) Department of Ophthalmology
(3) Department of Biomedical Engineering (4) Department of Chemistry
(5) Department of Ophthalmology, Roski Eye Institute

University of Southern California
Los Angeles, California, USA

(6) Department of Mechanical Engineering, Faculty of Engineering,
Ubon Ratchathani University, Ubonratchathani, Thailand

INTRODUCTION

In making progress towards ocular drug delivery, predictive modeling along with corresponding experimentation has taken an important role. While sophisticated computational models for drug transport are being developed, it is fundamentally important to obtain the relevant biophysical parameters for the ocular tissues. One of the important parameters in this regard is the mass diffusion coefficient of the vitreous humor. A large body of literature exists on the measurement techniques in the vitreous humor, and a concise review of these works has been provided by Penkova et al. [1]. They discuss the advantages of the visualization techniques such as MRI and fluorescence that provide a snapshot of drug distribution profile provided, of course, the drug can be labeled with a contrast agent. Penkova and coworkers [2, 3] have developed the 'contour method' for measuring the diffusion coefficient for various drugs and contrast agents.

METHODS

The procedure consists of injecting a drug labeled with a contrast agent into the vitreous humor and tracking its spread therein by MRI. The image intensity distribution upon calibration provides the concentration snapshot at the various time points when the image is taken. At the same time the concentration distribution can be theoretically predicted on the basis of the diffusion equation solution for a given initial deposition of a bolus of a drug/contrast agent. A comparison of the theoretical and the experimental distributions and minimizing the difference (least-squares best fit) while floating the unknown diffusion coefficient D returns the value of D. For real drugs, this technique relies on successful labeling of the drug with a contrast agent. Our goal for the current work has been to establish the diffusion coefficient for bevacizumab. With this drug, labeling it with gadolinium for MR imaging has not been very successful. Therefore, we have resorted to applying the contour method with fluorescence imaging. We have in fact been able to label bevacizumab with fluorescein.

Labeling Bevacizumab

We labeled bevacizumab with Alexa Flour 488 dye. A 20µl bolus of the labeled drug with concentration of 6.74µM was injected into the vitreous of a with a 30G hypodermic needle via pars plana (1.5mm away from the limbus) of an anesthetized dutch-belted rabbit at a slow rate of 2µl/min over a period of 10 minutes using a syringe pump. The slow rate gave a nearly spherically symmetric bolus. In order to not disturb the imaging process, the needle was not removed after the completion of the injection.

Imaging

Using the HRA+OCT Spectralis (Heidelberg Engineering, Inc; Heidelberg, Germany) and its fluorescein angiography software (Figure 1), a series of images of the diffusion labeled bevacizumab had been acquired every 30 second during the injection period (10 minutes) and every 15 minutes thereafter for a total period of three hours. Images were acquired using a wide field 55° lens focused on the needle inserted into the mid-vitreous (Figure 1). To analyze the intensity of the images and their labeled-bevacizumab distribution, MatLabR 2016a software (MathWorks, Inc; MA, USA), was used. The images show that the drug initially distributes around the needle but with time a more spherical bolus shape emerges.

Figure. 1: In vivo set up acquisition.

Analysis

From the raw intensity data, color maps of the drug distribution were constructed. These contours were compared with the theoretical intensity distribution. We approximated the initial bolus to be spherical in shape and used the distribution (see [1, 4]) for an infinite medium around the bolus,

$$c(r,t) = c_0\left\{\frac{1}{2}\left[\operatorname{erf}\left(\frac{a-r}{\sqrt{4Dt}}\right) - \operatorname{erf}\left(\frac{a+r}{\sqrt{4Dt}}\right)\right] - \frac{1}{r}\sqrt{\frac{Dt}{\pi}}\left[e^{-\frac{(a-r)^2}{4Dt}} - e^{-\frac{(a+r)^2}{4Dt}}\right]\right\}, \qquad (1)$$

where $c(r,t)$ is the labeled bevacizumab intensity distribution, c_0 is the initial signal intensity of the bolus, a is the bolus radius, r is the spherical distance from the bolus center, t is the time. For the timescale involved, the infinite-medium approximation is quite good [2]. It should be noted that since the relationship between signal intensity and bevacizumab concentration is linear, we do not need a calibration curve. Additionally, since the diffusion equation is linear, inverse problem for obtaining the diffusion coefficient from the data is invariant with the intensity to concentration conversion (and hence no need for a calibration curve). A comparison of the theoretical distribution in Equation (1) with the signal intensity data returns the value of D.

RESULTS AND DISCUSSION

A large set of signal intensity data has been acquired, and a colormap example is given in Figure 2. A theoretical model based on a spherical bolus of the drug and its quantitative comparison with experimental data provided the value of the unknown diffusion coefficient, giving approximately $D = 4\times10^{-7}\text{cm}^2/\text{s}$ for bevacizumab (149 kDa). This value is somewhat higher than that for Gd-Immunoglobulin (160 kDa) for the ex vivo bovine vitreous but about the same order of magnitude ($2.1\times10^{-7}\text{cm}^2/\text{s}$). As discussed by Penkova et al. [1], the contour method using MRI has provided very accurate measurements of the diffusion coefficients for various Gd-labeled molecules. However, when such labeling presents challenges, fluorescein labeling provides an alternative. With bevacizumab, the fluorescein labeling alternative worked out very successfully, and led to in vivo through-the-lens imaging with a dutch-belted rabbit. The analysis of the imaging data gave for

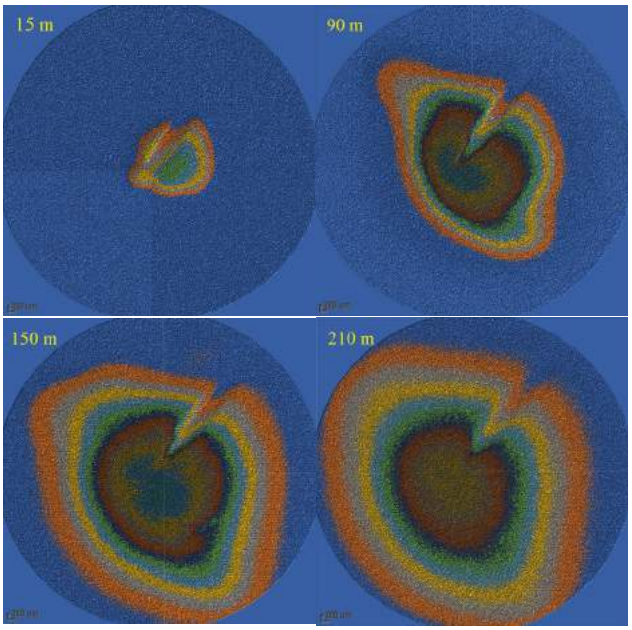

Figure 2: Colormapped images of the fluorescein-labeled bevacizumab signal intensity distribution at 15, 90, 150 and 210 minutes. The indentation is the needle mark.
Colormap key for intensity data:

the rabbit vitreous the fluorescence intensity distribution which is proportional to the labeled bevacizumab concentration. The current results provide information towards developing a comprehensive model for fluid flow and transport in the eye. However, experimental and analytical refinements in the approach are being explored to provide a higher degree of experimental accuracy.

ACKNOWLEDGEMENTS

This work has been supported by the National Eye Institute under the NIH Grant No. 5R01EY026599

REFERENCES

[1] A. Penkova, R. Moats, M. S. Humayun, S. Fraser and S. S. Sadhal, "Diffusive Transport in the Vitreous Humor: Experimental and Analytical Studies," invited review article, *ASME J. Heat Transfer,* 2019. DOI: 10.1115/1.4042297

[2] A. Penkova, K. Rattanakijsuntorn, S. Sadhal, Y. Tang, R. Moats, P. M. Hughes, M. R. Robinson and S. S. Lee, "A technique for drug surrogate diffusion coefficient measurement by intravitreal injection, " *Int. J. Heat Mass Transfer,* **70**: 504–514, 2014. http://dx.doi.org/10.1016/j.ijheatmasstransfer.2013.11.002,

[3] K. Rattanakijsuntorn, A. Penkova and S. S. Sadhal, "Mass diffusion coefficient measurement for vitreous humor using FEM and MRI," *IOP Conf. Series: Mat. Sci. Engin.,* **297**: 012024: 1-9, 2018.

[4] S. Li, A. Jeong and M. Hastings, "Magnetic Resonance Imaging Study of Current and Ion Delivery into the Eye during Transscleral and Transcorneal Iontophoresis," *Invest. Ophthalmol. Vis. Sci.,* **45**(4): 1224-1231, 2004.

SB³C2019
Summer Biomechanics, Bioengineering and Biotransport Conference
June 25 -28, Seven Springs, PA, USA

PRECISE TARGETING OF POLR2A AS A THERPEUTIC STRATEGY FOR HUMAN TRIPLE NEGATIVE BREAST CANCER

Jiangsheng Xu[1,2], Xiaoming He[1,2*]

(1) Fischell Department of Bioengineering,
University of Maryland
College Park, MD, USA

(2) Comprehensive Cancer Center,
The Ohio State University
Columbus, OH, UAS

INTRODUCTION

Triple negative breast cancer (TNBC) is negative for the expression of oestrogen and progesterone receptors, and absent of human epidermal growth factor receptor 2 (HER2) overexpression[1]. These receptors are molecular targets for treating breast cancer. As a result, other than olaparib, a poly(ADP-ribose) polymerase inhibitor that can benefit a small subset of TNBC patients with *BRCA* mutation, no approved targeted therapies are available for most TNBC patients. Standard chemotherapy is the only approved option, but it is ineffective with undesired side effects[2,3]. Therefore, new targeted therapies are critically needed for TNBC.

TP53 is the most frequently mutated or deleted gene in triple negative breast cancer (TNBC). Both the loss of *TP53* and the lack of targeted therapy are significantly correlated with poor clinical outcomes, making TNBC the only type of breast cancer that has no approved targeted therapies. Through in silico analysis, we identified *POLR2A* in the *TP53*-neighboring region as a collateral vulnerability target in TNBC tumours, suggesting that its inhibition via small interfering RNA (siRNA) may be an amenable approach for TNBC targeted treatment. To enhance bioavailability and improve endo/lysosomal escape of siRNA, we designed pH-activated nanoparticles for augmented cytosolic delivery of *POLR2A* siRNA (siPol2). Suppression of POLR2A expression with the siPol2-laden nanoparticles (siPol2@NPs) leads to enhanced growth reduction of tumours characterised by hemizygous *POLR2A* loss. These results demonstrate the potential of the pH-responsive nanoparticle and the precise *POLR2A* targeted therapy in TNBC harbouring the common *TP53* genomic alteration.

METHODS

The Cancer Genome Atlas analysis. The Cancer Genome Atlas primary (origin: METABRIC Nature 2012 & Nat Commun 2016, and Cell 2015) and metastatic (origin: France 2016) breast cancer data were downloaded from cBioPortal, which included copy number variation at segment levels in log-ratio, copy number variation at gene levels estimated by using the GISTIC2 algorithm, RNA-seq for gene expression in base-2 log scale, and patient information on oestrogen receptor, progesterone receptor, and HER-2/neu status. We analysed the correlation between gene copy number and the corresponding gene expression as previously described[4]. The triple-negative breast cancer (TNBC) subtypes, defined by PAM50 profiling test, included all the basal-like and claudin-low groups.

Synthesis of nanoparticles. The nanoparticles were synthesized using the double-emulsion method[45], with slight modification. First, chitosan was modified with a guanidine group according to the literature to form chitosan-guanidinate (CG). The guanidine group is a common functional group in many natural products including the naturally occurring amino acid *L*-arginine.

RESULTS

TP53 is frequently inactivated by mutation or deletion in a majority of human tumours. The Cancer Genome Atlas analysis shows that 53% (202 out 380) of TNBC cases bear the hemizygous loss of *TP53* (**Fig. 1a**). More severe stages of TNBC are associated with higher frequencies of patients with hemizygous *TP53* loss **(Fig. 1b)**. This indicates one copy of *POLR2A* is enough to maintain cell survival. This positive correlation is also validated in a panel of TNBC cell lines (**Fig. 1c**). In immunohistochemical analysis using a tumour tissue microarray containing 100 TNBC samples, the expression of *POLR2A* was scored according to the staining intensity and proportion of signals in each sample (**Fig. 1d**).The *TP53* deletion is included in a large fragment deletion of Chr17p that spans over ~19.8 megabases of DNA in TNBC and other human breast cancers (**Fig. 1e**). The *POLR2A* gene is almost always co-deleted with *TP53* in the Chr17p deletion region (**Fig. 1f**). Although one allele deletion of the Chr17p fragment significantly

decreases mRNA expression of *POLR2A*, Accordingly, the copy numbers of *POLR2A* in the tumour tissue samples were determined and shown that a tight correlation was validated between *POLR2A* copy numbers and protein expression levels (**Fig 1g**). Collectively, these data suggest inhibition of POLR2A is an amenable approach for targeted treatment of TNBC.

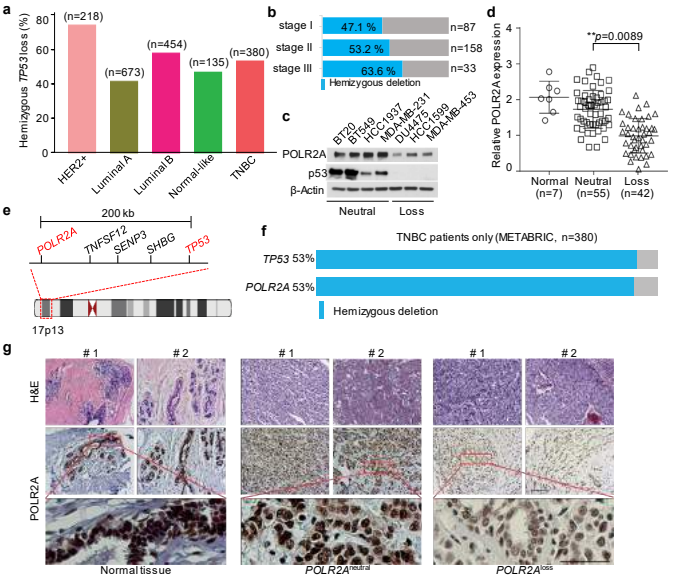

Figure 1: *POLR2A* is almost always deleted together with *TP53* in triple negative breast cancers

We developed a core-shell nanoplatform for delivering siPol2 to target *POLR2A*. The core contains siRNA and chitosan modified with guanidine. The guanidine group can react reversibly with CO_2 to form chitosan-guanidinate-CO_2 (CG-CO_2) in a pH dependent manner, which is utilized to capture/store CO_2 at neutral pH for release at reduced pH such as that (~5) inside endo/lysosomes. Typical transmission electron microscopy images of the siPol2-laden nanoparticles (siPol2@NPs) are shown in **Fig. 2a**. The siPol2@NPs have a spherical morphology and core-shell structure. The size of the nanoparticles synthesized using CG without CO_2 is not significantly affected by either pH 6.0 or pH 5.0 These results indicate that the CO_2 generation from CG-CO_2 encapsulated in the nanoparticles under low pH (particularly pH 5.0) conditions could expand and/or break open the nanoparticles, to give the "nano-bomb" effect. The migration of siPol2 into electrophoretic agarose gel is almost completely inhibited by nanoparticle encapsulation with negligible release at pH 7.4 (**Fig. 2b**). Moreover, the strong signal observed under pH 5.0 closely resembles the free siPol2 band. Under pH 6.0, smaller bands indicating slower release of the siRNA could be seen. These data demonstrate the low pH activated "nano-bomb" effect of the nanoparticles could trigger the release of the encapsulated siPol2. Furthermore, the siPol2@NPs were observable for at least 24 h in serum while most of the free siPol2 degraded shortly and no siPol2 was discernible after 3 h (**Fig. 2c**). These data indicate the nanoparticles could enhance the stability of the siPol2 in blood and allow for pH triggered release of the siRNA.

To exclude potential genetic differences across cell lines, we generated two isogenic HCC1937 cell lines with hemizygous loss of *POLR2A* using CRISPR (clustered regularly interspaced short palindromic repeat)/Cas9. The wild type HCC1937 is $TP53^{+/mut}$, $POLR2A^{+/+}$ ($POLR2A^{neutral}$). The parent and two isogenic $POLR2A^{loss}$ HCC1937 cells exhibited similar cell growth rates, confirming hemizygous deletion of *POLR2A* does not affect cell survival. siPol2@NPs decreases POLR2A expression in all the cells. (**Fig. 2d**). However, hemizygous loss of *POLR2A* (HCC1937$^{loss\text{-}1}$and HCC1937$^{loss\text{-}2}$) markedly sensitizes the HCC1937 cells to siPol2@NPs (**Fig. 2e**). As expected, siNT@NPs or free siPol2 had no substantial effect on the cell proliferation. POLR2A expression is reduced in isogenic HCC1937 cell lines (**Fig. 2d, e**, control groups). Collectively, these data show the materials in the nanoparticles (other than siPol2) do not have an effect on POLR2A expression in cells or their proliferation, and siPol2@NPs effectively kill $POLR2A^{loss}$ isogenic TNBC cells.

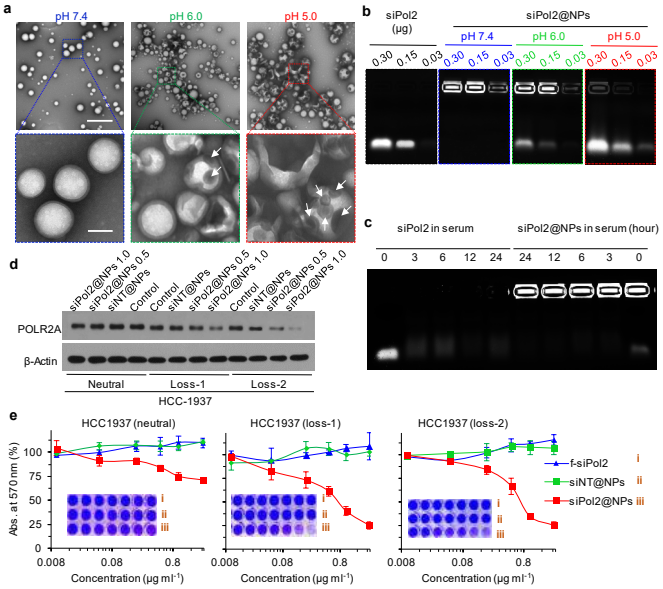

Figure 2: Synthesis and characterization of nanoparticles for stabilizing and delivery *POLR2A* targeting siRNA.

DISCUSSION

In this study, by analysing TNBC databases, we reveal that *POLR2A* gene is almost always co-deleted with *TP53* in the Chr17p deletion region, and 53% of TNBC harbours this heterozygous deletion. Moreover, the POLR2A expression levels are highly correlated with the copy number of *POLR2A*, rendering cancer cells with heterozygous loss of *TP53* vulnerable to POLR2A inhibition. This collateral loss of *POLR2A* with *TP53* prompted us to use RNAi to precisely target *POLR2A* for TNBC treatment. To overcome the hurdles to cytosolic delivery of siRNA for RNAi, we developed a unique nanoplatform with a low pH-activated "bomb-like" effect for endo/lysosomal escape. This improves cytosolic delivery of siPol2 to inhibit POLR2A in $TP53^{loss}$ cells.

ACKNOWLEDGEMENTS

This work was partially supported by grants from American Cancer Society (ACS #120936-RSG-11-109-01-CDD) and NIH (R01CA206366) to X.H., and Pelotonia post-doctoral Fellowship to J.X.

REFERENCES

[1] Dent, R., et al., *Clin. Cancer Res.* **13:**429-4434, 2007.
[2] Denkert, C., ey al., *Lancet* **389:**2430-2442, 2017.
[3] Mayer, E. L., et al., *J. Clin. Oncol.* **34:**3369-3371, 2016.
[4] Liu, Y., et al., *Nature* **520:**697-701, 2015.
[5] Wang, H., et al., *Chem. Commun. (Camb)* **51:**7733-7736, 2015.

CHARACTERIZATION OF INJECTION-INDUCED TISSUE SWELLING DURING SUBCUTANEOUS INJECTION OF BIOLOGICS

Yingnan Shen, and Bumsoo Han

School of Mechanical Engineering
Purdue University
West Lafayette, IN, USA

INTRODUCTION

Recent emergence in biologics provides effective solutions to treat a variety of diseases that presently have no other treatment options available. These biopharmaceuticals include vaccines, blood and blood components, somatic cells, and recombinant therapeutic proteins. Major limitations of the biologic drugs are attributed to difficulties in effective delivery, which significantly increases the treatment cost and the burden on the health care sector [1]. Subcutaneous (SQ) injection of biologics has been thought as a promising delivery route to address this problem. However, due to large molecular weights of biologic drugs, pain and discomfort are induced during SQ injection. This poses significant challenges for broader use of biologic drugs, design and development of injection and infusion devices, and quality of patient's life [2, 3]. Thus, it is critically important to be able to assess and quantify the extent of the injection-induced pain and discomfort (IPD). However, current available methods are mostly very subjective and inadequate to quantify the extent of IPD.

In this study, we developed a biomimetic platform to quantify spatiotemporal tissue swelling during SQ injection of biologics, and to predict associated increase in mechanical stress and interstitial fluid pressure (IFP) of tissues. Our overarching hypothesis is that the IPD is caused by tissue swelling and subsequent increase in mechanical stress and IFP of tissues near injection sites. This mechanical stress and fluid pressure stimulate nociceptors, which are primarily present at the dermis of the skin. Accurate measurement of tissue swelling, thus, can be a quantitative and predictive indicator of the IPD. We constructed and tested an experimental setup capable of measuring injection-induced swelling of engineered tissue constructs, dermal equivalents.

METHODS

A schematic of the testing platform is shown in Figure 1. The platform consists of injection system, imaging system and engineered tissue constructs (ETCs). The injection system infuses or injects biologic drugs and macromolecules into the ETCs at various injection rates to simulate a wide range of injection conditions. The ETCs are prepared by seeding quantum dot (QD)-labeled fibroblasts in collagen matrices whose mechanical and chemical properties are designed to mimic the dermal layer of skin. The imaging system includes a fluorescence macro/microscope (MVX10, Olympus, PA, USA) and a CCD camera (Aqua, QImaging, Canada), and images QD-labeled fibroblasts during injection of biologics drugs, and determine the spatiotemporal deformation of ETCs.

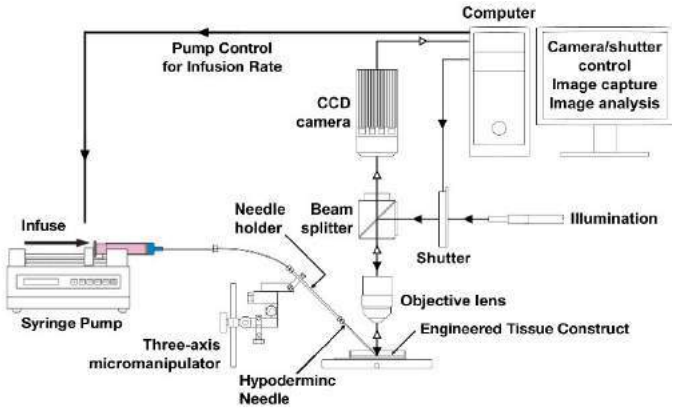

Figure 1. Schematic of experimental setup.

The detailed description of the construction of engineered tissues can be found in our prior publications [4, 5]. Briefly, the early human foreskin fibroblasts were cultured up to 17th passage and consistently harvested at 80 ~ 90 % confluency. The collected cells were labeled with quantum dots (Qtracker 655, Invitrogen, OR, USA) by being mixed with the labeling solution and incubated for 45 min. After incubation, the cells were washed twice to remove the excess quantum dots. To construct the engineered tissue mimicking the dermal layer of skin, the labeled fibroblasts were suspended in 1.5 mL of type I collagen solution (Corning, MA, USA) containing 3 mg/mL collagen, and the cell concentration was 2×10^5 cells/mL.

The collagen solution containing labeled fibroblasts was placed in a cylindrical hole punched through a PDMS layer filling a petri dish. The dimension of the hole is 11 $cm^2 \times 1$ cm. The engineered tissue was generated when the fibroblasts-contained collagen solution polymerized at 37 ℃ for 1.5 hours. After being incubated with complete culture

medium for 24 hours, as shown in Figure 2, the fibroblasts embedded in collagen matrix developed a dendritic morphology and were still labeled with QDs. Figure 2(b) shows that the QDs accumulate in the cytoplasm.

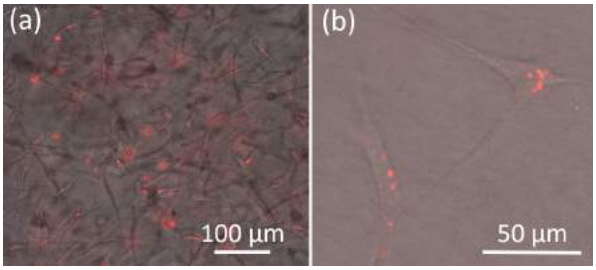

Figure 2. (a) Labeled fibroblasts, embedded in collagen matrix. (b) Quantum dots accumulate in the cytoplasm of dendritic fibroblasts.

As shown in Figure 3(a), a conventional 27-gauge needle was manipulated to penetrate into the engineered tissue. The injection rate ranged within 0.3 ~ 3 mL/min, and distilled water was injected as a preliminary experiment which aims to validate the platform and estimate the range of the injection-induced tissue swelling. During the injection, the tissue was continuously imaged with a 0.2 s interval. As shown in Figure 3(b), the QD-labeled cells were visualized with a TRITC filter, and the fluorescence image showed the entire tissue was labeled by fluorescence particles.

The acquired sequential images were cross-correlated to estimate the local deformation rates throughout the tissue during the injection. Briefly, a pair of consecutive images was put into the DaVis software (LaVision, MI, USA), and each of the images was divided into a grid of 32 × 32 pixels (1 pixel equals 4 µm) interrogation windows. The density of the fluorescence particle pairs was large enough to guarantee that there were typically no less than 4 fluorescence particles in each window. The interrogation windows in the consecutive images were cross-correlated to generate correlation peaks, the location of which provided the deformation rate vector in the corresponding window. For example, the vector marked in Figure 4 was generated in a 32 × 32 pixels interrogation window containing 7 fluorescence particles which were used to perform cross-correlation. Multi-pass processing was used with decreasing interrogation window size (2 iterations of 64 × 64 pixels followed by 3 iterations of 32 × 32 pixels) and 50% overlap, and finally the deformation vector field throughout the tissue was generated.

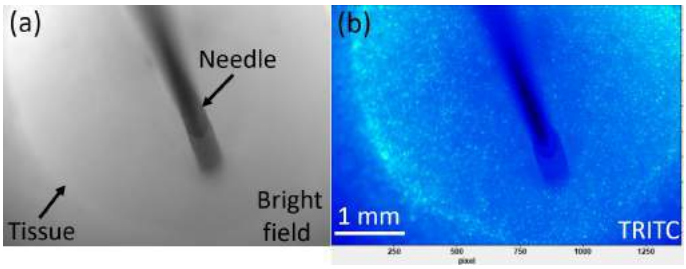

Figure 3. Brightfield and fluorescence (TRITC filter) images of the engineered tissue during the injection.

RESULTS AND DISCUSSION

A representative spatiotemporal deformation rate of the dermal equivalent at the initiation of the injection (2 mL/min) is shown in Figure 4. The deformation rate vector field of the tissue was determined in terms of µm/s. The tissue swelling during the injection is clearly shown by the vector field, and the vectors indicating the largest local deformation rates locate close to the needle injection site. The largest deformation rate is up to 28 µm/s, and the deformation rate gradually decreases below 6 µm/s when it reaches the outskirt of the tissue. The region without vectors is due to that the needle blocks the view of the tissue, as well as that the deformation of the tissue due to the penetration of the needle causes the area near the injection site to be out of focus.

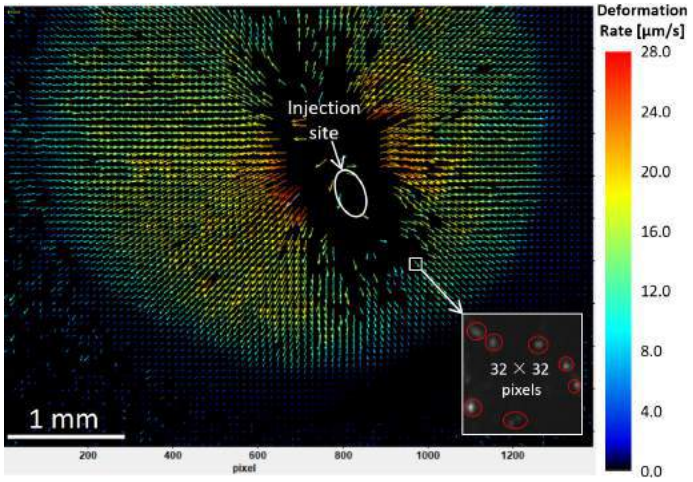

Figure 4. Deformation rate vector field indicating the tissue swelling at the initiation of the injection (2 mL/min).

In the present study, we demonstrated the feasibility of measuring injection-induced deformation, which is expected to cause IPD using dermal equivalents and digital image correlation. The underlying rationale is that most nociceptors are present at the dermal layer, even though injection occurs at the SQ layer. However, we plan to further develop the ETCs by adding adipocytes, hyaluronic acids and fibronectins to create more realistic dermal and subcutaneous tissue models. The platform can also measure transport of biologic drugs at various injection conditions. Ultimately the platform will provide a reliable test bed to systematically design and optimize biologic drugs, their injection devices and schemes.

ACKNOWLEDGEMENTS

This study was partially supported by a Program Project Grant from the Purdue Institute of Drug Discovery, and by the Purdue Center for Cancer Research through NCI P30 CA023168.

REFERENCES

[1] Jones, G. B., et al. (2017) "Subcutaneous drug delivery: An evolving enterprise." *Sci. Transl. Med.* **9** (405), eaaf9166.

[2] Sato, M., et al. (2013) "FRI0174 Pain assessment for subcutaneous injection of biologics in the treatment of rheumatoid arthritis." *Ann. Rheum. Dis.* **72** (Suppl 3), A430.

[3] Curtis, J. R., et al. (2011) "Injection-site burning and stinging in patients with rheumatoid arthritis using injectable biologics." *Curr. Med. Res. Opin.* **27** (1), 71.

[4] Teo, K. Y., et al. (2010). "Spatiotemporal measurement of freezing-induced deformation of engineered tissues." *J. Biomech. Eng.* **132**(3), 031003.

[5] Teo, K. Y., et al. (2011). "Effects of freezing-induced cell–fluid–matrix interactions on the cells and extracellular matrix of engineered tissues." *Biomaterials* **32**(23), 5380.

SB^{3}C2019
Summer Biomechanics, Bioengineering and Biotransport Conference
June 25 -28, Seven Springs, PA, USA

ANALYSIS OF CONVECTIVE AND DIFFUSIVE TRANSPORT IN THE BRAIN INTERSTITIUM

Lori A. Ray (1), Jeffrey J. Iliff (2,3), Jeffrey J. Heys (1)

(1) Chemical & Biological Engineering
Montana State University
Bozeman, MT, USA

(2) Anesthesiology and Perioperative Medicine &
(3) Knight Cardiovascular Institute
Oregon Health Sciences University
Portland, OR, USA

INTRODUCTION

Transport of interstitial molecules is an essential link in many physiological processes of the brain: communication, nutrient delivery, waste clearance. For example, transport governs the dynamics of pathological molecules that transit the extracellular space (ECS); impairment of the clearance of mis-aggregating proteins is believed to underlie the vulnerability of the aging and injured brain neurodegeneration. Despite advances in imaging and experimental techniques, the nature of transport mechanisms at the smallest scales remain elusive. Mathematical modelling validated using available experimental data offers a powerful tool for investigating hypotheses regarding extracellular transport of molecules in brain tissue. Here we use a finite-element model to investigate interstitial transport mechanisms, especially the potential for convection and its relevance to interstitial solute transport, for which there is conflicting evidence.

Brain tissue is comprised of cells along with the extracellular space (ECS) between cells. The ECS is a continuously-connected network filled with interstitial fluid (ISF), where interstitial transport occurs. Researchers have established the presence of a perivascular space (PVS) surrounding penetrating vasculature that is connected to cerebrospinal fluid (CSF), providing a potential source of interstitial fluid and efflux route for interstitial solutes and fluid (Figure 1). The PVS is surrounded by a sheath of astrocytic endfoot processes. To enter or exit the ECS via the PVS, molecules must pass through small gaps between endfeet.

There is strong evidence that transport in the PVS is more rapid than can be explained by diffusion, possibly transport by convective flow or dispersion [1-3]. Mestre et. al. used particle tracking of fluorescent microspheres to measure velocity in the PVS *in vivo,* reporting a mean speed around 19 $\mu m\ s^{-1}$ in the same direction as blood flow [4]. There is conflicting evidence whether interstitial transport is dominated by diffusion, or convection plays a role [1,2,5].

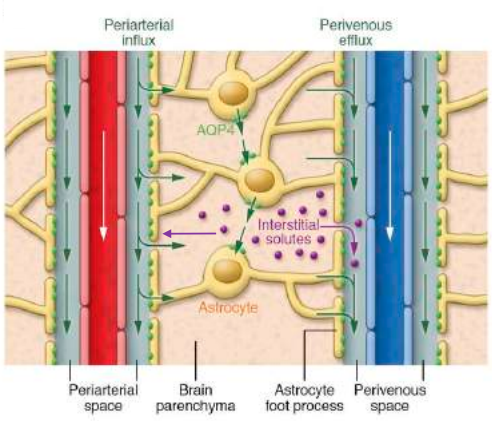

Figure 1. Illustration of proposed interstitial transport in brain tissue where fluid (green arrows) moves from the CSF along the periarterial space following penetrating vasculature deep into the brain. The fluid enters the interstitium, where interstitial solutes (purple) and fluid are transported to and out the perivenous space [6].

Real-time Iontophoresis (RTI) experiments offer a well-established data set for brain transport, where analysis assumes diffusion-only transport in a homogenous material. RTI experimental data displays a consistent level of variability among data sets [7-9], which leads one to question whether some physical phenomena has

been overlooked that may be uncovered by applying different transport models. We hypothesize the inclusion of convection and heterogeneous perivascular efflux may account for the observed experimental range.

METHODS

Despite the incredible complexity of brain tissue, transport of molecules has been successfully described using relatively simple porous media models [6]. A 3D finite-element model of transport in a small volume of brain tissue (< 0.5 mm^3) was developed using Darcy's Law and the mass-transport equation adjusted for porous media[6]:

$$v = -k'(\nabla P) \quad (1)$$

$$\nabla \cdot v = 0 \quad (2)$$

$$\frac{\partial c}{\partial t} = D^*\nabla^2 c + \frac{s}{\alpha} - v \cdot \nabla c \quad (3)$$

where: c = concentration in the ISF, D^* = apparent diffusivity = D/λ^2, λ = tortuosity, s = source term, and α = void volume = V_{ECS}/V_{total}. The mass-transfer resistance at the endfeet is modelled using a small percentage of the interstitial diffusivity for a narrow region surrounding vessels. Communication between the PVS and the interstitium is applied through boundary conditions at the vessel walls. The resulting system of partial differential equations is solved using FEniCS [10].

RESULTS

Figure 2 shows agreement between the range in Cserr's RTI data (grey) [9] and the range of concentration curves for simulations performed with an average superficial bulk velocity of v=50 μm min^{-1} (blue) combined with diffusion and perivascular efflux. Similar results are observed for other data sets [7,8]. Contributions from tissue variability were found to account for less than a third of the data range.

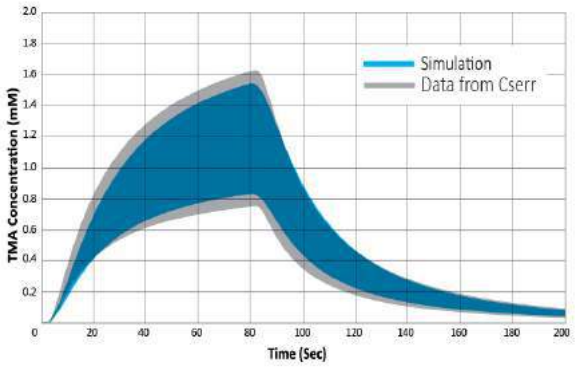

Figure 2. Range in TMA concentration curves for experimental data in rats (Cserr et al., n=33 [9]) compared with simulations of diffusion and convection (v=50 μm min^{-1}) with perivascular efflux (blue, n=112). RTI uses tetramethylammonium (TMA) as its molecular probe.

TMA is a small molecule (114Da) with a relatively fast diffusivity. Molecules of interest in brain transport, such as beta amyloid (4.5kDa) and tau (45kDa), thought to play a significant role in neurodegenerative pathologies, are larger and have slower diffusivities. The Péclet number (Pe) is a ratio of convective to diffusive transport rates, allowing comparison of the relative importance of the two mechanisms.

$$Pe = \frac{rate\ of\ convection}{rate\ of\ diffusion} = \frac{Lv}{D} \quad (4)$$

Dextran-3kDa (Dex3), of similar in size to beta amyloid, has a Péclet number of 4 (Figure 3), meaning convection will have an effect similar in magnitude to, or potentially greater than, diffusion within the brain. Many molecules of interest to brain pathologies are larger than Dex3, therefore, the magnitude of convective transport due to bulk flow is likely to be of similar or greater magnitude than diffusive transport.

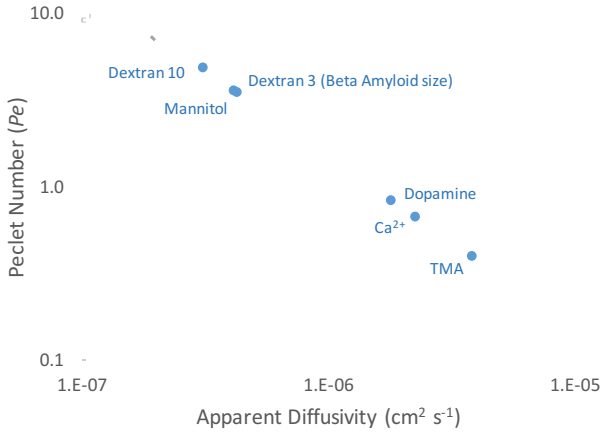

Figure 3. Péclet number versus apparent diffusivity for molecules of interest in brain transport. L=250 μm, v=15 μm min^{-1}, and D^* specific to each molecule. For $Pe \approx 1$, diffusive and convective rates are balanced; for $Pe > 1$, convection exceeds diffusion.

DISCUSSION

This work compares the range in simulated RTI concentration curves inherent to different transport mechanisms to experimental range. There are other possible contributions to experimental range not included in the present analysis: tissue damage, physiologic variations, and experimental variations. Therefore, the range attributable to perivascular efflux and convection may be less, suggesting less vascular heterogeneity and/or lower convective velocities.

Even at lower convective velocities, the analysis supports that molecular transport in the ISF may occur by both diffusion and convection, with both mechanisms potentially relevant and the apparent diffusivity, related to molecular size, determining which is dominant. There is limited experimental data on transport specifically in the brain interstitium. Iliff et. al. interpret tracer-study results as being caused by convective flow [2]. Smith et. al. interpret results of similar experiments in favor of diffusion only [1]. Mestre et. al. demonstrate the methods used by Smith result in hindered tracer transport [5].

In conclusion, simulations show that published RTI experimental ranges allow for bulk flow superficial velocities up to v=50 μm min^{-1}; corresponding to intrinsic ISF velocities on the order of 100 μm min^{-1} ($v_i = v/0.2$). A quantitative finding useful to scientists developing approaches for evaluating slow interstitial bulk flow over long distances. Results also support the hypothesis of perivascular routes of influx and efflux allowing exchange between the brain interstitium, the CSF, and perivenous drainage out of the brain.

ACKNOWLEDGEMENTS

J.H. and L.R. were partially supported by the NSF (DMS-1361240).

REFERENCES

[1] Smith, AJ et. al., *Elife*, 6:e27679, Aug 21 2017.
[2] Iliff, JJ et.al., *Science of Translational Medicine*, 4:147, Aug 2012.
[3] Asgari, M et. al., *Scientific Reports*, 6:38635, Dec 2016.
[4] Mestre, H et. al., *Nature Communications*, 9:4878, Nov 2018.
[5] Mestre, H et. al., *Elife*, 7, Dec 2018.
[6] Nicholson, C, Reports on Progress in Physics, 64:815-884, 2001.
[7] Kress, BT et. al., *Annals of Neurology*, 76:845-861, Dec 2014.
[8] Xie, L et. al., *Science*, 342:373-377, Oct 2013.
[9] Cserr, HF et. al., *Journal of Physiology-London*, 442:277-295, 1991.
[10] Logg, AM et. al., *The FEniCS Book*, Berlin: Springer, 2012.

SB³C2019
Summer Biomechanics, Bioengineering and Biotransport Conference
June 25 -28, Seven Springs, PA, USA

THREE-DIMENSIONAL NONLINEAR BIPHASIC FINITE ELEMENT MODEL OF BACKFLOW DURING FLOW-CONTROLLED INFUSIONS INTO THE BRAIN

Gustavo A. Orozco (1), Joshua H. Smith (2), José J. García (3)

(1) Department of Applied Physics
University of Eastern Finland
Kuopio, Finland

(2) Department of Mechanical Engineering
Lafayette College
Easton, PA, USA

(3) Escuela de Ingeniería Civil y Geomática
Universidad del Valle
Cali, Colombia

INTRODUCTION

Convection-enhanced delivery (CED) is a technique to deliver controlled therapeutic agents for the treatment of tumors and brain diseases such as Parkinson's [1]. Despite CED studies in animals having shown encouraging results [2,3], clinical trials [4,5] have reported low effectiveness of CED, primarily due to the poor drug distribution. This lack of efficacy has been, in some cases, related to backflow, a phenomenon in which the infused medication flows toward the surface of the brain through the annular gap created outside of the cannula surface during the insertion.

Some clinical investigations have reported the influence of anatomical structures, such as the ventricles, the convolutions of the tissue, and the longitudinal fissure, on the loss of volume infused and on backflow [6,7]. Based on these effects, researchers have suggested recommendations for improving CED protocols, e.g., locate the cannula at a depth of no less than 2 mm in the cerebral cortex, place the cannula at a distance of no less than 10 mm from the ventricles and interhemispheric fissure, and perform the infusion in the peritumoral zone [8,9].

Analytical and numerical models have complemented the clinical and experimental CED studies to establish the variables that reduce backflow [10,11]. We developed a finite element model of infusion that incorporates backflow and includes material and geometrical nonlinearities to predict fluid distributions and mass transport under flow-controlled infusions [12,13]. Nevertheless, this computational model does not include the effect of anatomical structures of the brain. While a recent 3D transport model within a tumor has been developed to elucidate drugs delivery during CED [14], that study did not consider backflow or infusion-induced deformation of the brain tissue.

Hence, the aim of this study was to develop a 3D human brain nonlinear biphasic finite element model of backflow to investigate the influence of anatomical structures during flow-controlled infusions. Backflow length predictions were compared under the influence of ventricular pressure and the position of the cannula relative to the ventricles.

METHODS

A healthy subject was imaged using an MRI scanner (3.0T scanner, General Electric). This MR imaging was conducted according to the ethical guidelines of Universidad del Valle, Colombia, and written informed consent was obtained from the volunteer. The acquired 3D MRI data was used to segment the brain, including the ventricles, corpus callosum, and longitudinal fissure, in 3DSlicer (Harvard University, USA) and then the geometry was imported into Abaqus (v6.14, Dassault Systèmes) where a finite element (FE) model was developed (Fig. 1).

The 3D FE infusion model was defined by two parts: (1) a cylindrical domain that includes two special layers of elements to represent backflow, based on our previous studies [11-13], and (2) the 3D brain geometry with a hole into which the cylindrical backflow domain assembles. This strategy allows for easily modifying the location of the cannula (Fig. 1).

The brain tissue was represented as a poro-hyperelastic medium composed of solid and fluid phases. The solid phase was represented with the Ogden-type compressible energy function W, described as

$$W(\bar{\lambda}_1,\bar{\lambda}_2,\bar{\lambda}_3)=\sum_{i=1}^{N}\frac{2\mu_i}{{\alpha_i}^2}\left({\bar{\lambda}_1}^{\alpha_i}+{\bar{\lambda}_2}^{\alpha_i}+{\bar{\lambda}_3}^{\alpha_i}-3\right)+\sum_{i=1}^{N}\frac{1}{D_1}(J-1)^{2i}, \quad (1)$$

where $\bar{\lambda}_1,\bar{\lambda}_2,\bar{\lambda}_3$ are the principal deviatoric stretch ratios, α_i, μ_i, and D_1 are material parameters, and J is the determinant of the deformation gradient tensor. The hydraulic conductivity κ, which relates the flow

rate to the gradient of fluid pressure via Darcy's law, was allowed to vary with strain as

$$\kappa = \kappa_o exp(M\, e), \qquad (2)$$

where κ_o is the initial hydraulic conductivity, e is the volumetric dilatation, and M is a dimensionless coefficient. The material parameters were taken from values reported in the literature and used in previous infusion simulations [11-13] (Table 1).

The external surface of the brain was fixed to simulate the restraint caused by the skull. Likewise, a null fluid pressure was implemented on the external surface and adjacent faces of the longitudinal fissure.

To understand the impact of brain structures and the distance CD between the cannula and the ventricles, simulations were performed with three CDs (4, 20, and 36 mm), two ventricle pressures (VP, 0 and 100 Pa), and two infusion flow rates (1 and 4 µL/min), for a total of 12 simulations.

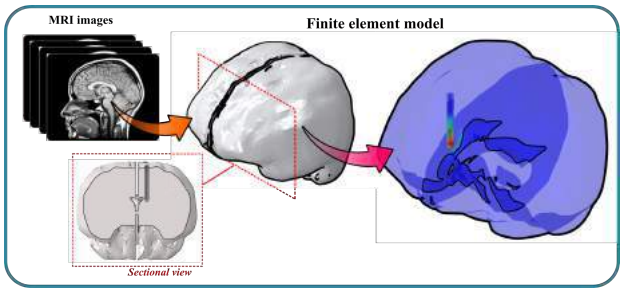

Figure 1: MRI images used to construct a brain geometry. The FE model includes the ventricles and longitudinal fissure. The model can evaluate different catheter positions (sectional view).

Table 1: Material parameters used in the FE simulations.

Parameter	Value
Energy function exponent, α_1	-4.7
Shear modulus, μ_1	2000 Pa
Poisson's ratio, v	0.35
Initial hydraulic conductivity k_0	2 mm^4 N^{-1} s^{-1}
Nonlinear conductivity, M	1
Radius catheter, r_c	0.98 mm
Flow rate, Q	1 and 4 μL min^{-1}

RESULTS

Numerical infusions with zero ventricle pressure displayed similar predictions of backflow length for the CDs of 20 and 36 mm and each flow rate (Fig. 2a). Compared to these results, the backflow lengths for a CD of 4 mm was smaller for both flow rates, and the fluid was observed to escape to the ventricle (Fig. 2b).

Models with a VP equal to 100 Pa showed an increase of fluid flow through the tissue and away from the ventricles, and a backflow length rather independent of the CD. For a CD of 4 mm the backflow length increased 167% and 80%, for the flow rates of 1 µL/min and 4 µL/min, respectively, when compared to the results obtained with a VP of 0 Pa (Fig. 2a). For the two larger CDs, similar values of backflow length were obtained for both VPs studied, particularly, fluid flow reached the external brain surface (~ 45 mm) for the higher flow rate.

DISCUSSION

This study presents a novel 3D biphasic finite element model of backflow during flow-controlled infusions into a realistic human brain geometry that considers material and geometrical nonlinearities. Anatomical details such as the ventricles, the corpus callosum, and the longitudinal fissure were included in the model.

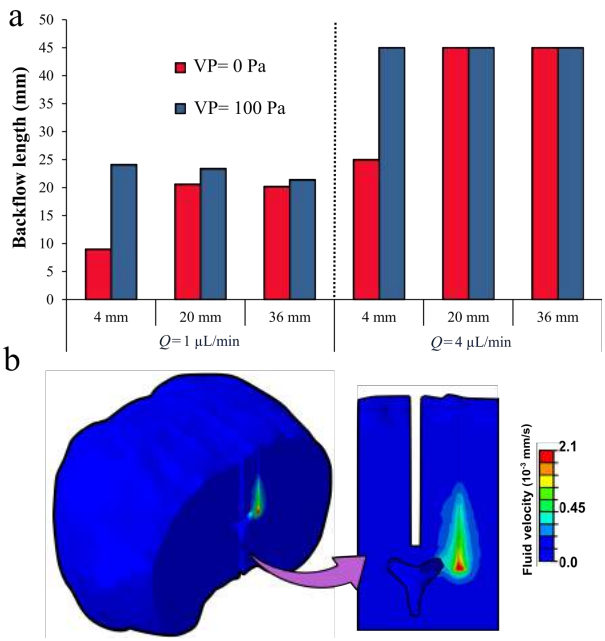

Figure 2: (a) Backflow length predictions for each flow rate (1 and 4 µL/min) with three catheter distances (4, 20, and 36 mm) and two ventricular pressures (0 and 100 Pa). (b) Fluid velocity distribution for a catheter distance of 4mm and zero ventricle pressure. The model predicts the leakage of fluid to the ventricles.

Increase in backflow length with CD might be associated with the increment of hydraulic resistance through the tissue relative to that through the annular gap that forms around the catheter. When VP is nonzero, this hydraulic resistance causes the infused fluid to flow away from the ventricles and either toward the longitudinal fissure or to the external brain surface. In contrast, the smaller backflow length when the VP was zero and the CD was 4 mm can be attributed to the smaller hydraulic resistance that allows leakage into the ventricles.

This model enables researchers to more accurately predict backflow lengths when accounting for both anatomical structures and deformation of the brain tissue.

ACKNOWLEDGEMENTS

The authors appreciate the support of the University of Eastern Finland, Lafayette College and Universidad del Valle to undertake this study. Thanks for Marie Skłodowska-Curie grant agreement No 713645 and Colciencias grant agreement No. 110656933826.

REFERENCES

[1] Bobo, R. H. et al., *PNAS*, 91:2076–2080, 1994.
[2] Brady, M. L. et al., *J Neurosci. Methods*, 229:76–83, 2014.
[3] Rosenbluth, K. et al., *J Magn Reson Imaging*, 36:1339–1346, 2012.
[4] Sampson, J. H. et al., *J Neurosurg*, 113:301–309, 2010.
[5] Heiss, J. D. et al., *Neurosurgery,* 2018. doi:10.1093/neuros/nyy480.
[6] Valles, F. et al., *Neurosurgery*, 65:579–585, 2009.
[7] Sampson, J. H. et al., *AJR Am J Roentgenol*, 188:703–709, 2007.
[8] Tanner, P. et al., *Neurosurgery*, 61:E880-882, 2007.
[9] Sampson, J. H. et al., *Neurosurgery*, 60:ONS89-98, 2007.
[10] Raghavan, R. et al., *Phys Med Biol*, 55:281–304, 2010.
[11] García, J. J. et al., *J Comput Nonlinear Dynam*, 8:011017–8, 2012.
[12] Orozco, G. A. et al., *Med Biol Eng Comput*, 52:841–849, 2014.
[13] Orozco, G. A. et al., *Rev Ingeniería Biomédica*, 8:56-64, 2014.
[14] Zhan, W. et al., *J Control Release*, 271:74–87, 2018.

SB³C2019
Summer Biomechanics, Bioengineering and Biotransport Conference
June 25 -28, Seven Springs, PA, USA

RELATING CHEMICAL AND PHYSICAL PROPERTIES OF OLIGONUCLEOTIDE POLYELECTROLYTE COMPLEX MICELLES

Alexander E. Marras (1,2), Jeffrey R. Vieregg (1,2), Jeffrey M. Ting (1,2), Matthew V. Tirrell (1,2)

(1) Institute for Molecular Engineering
University of Chicago
Chicago, IL, USA

(2) Institute for Molecular Engineering
Argonne National Laboratory
Lemont, IL, USA

INTRODUCTION

Developing effective non-viral methods for delivery of nucleic acids and other macromolecular therapeutics is one of the most pressing challenges for nanomedicine and polymer science [1,2]. The potential power of engineered nucleic acids as therapeutic agents is severely limited by the difficulty of overcoming the physical and biological barriers to using them as practical drugs. Polyelectrolyte complex micelles (PCMs, core-shell nanoparticles formed by complexation of a polyelectrolyte with a hydrophilic charged-neutral block copolymer) offer a solution to this critical problem. Still, few systematic studies have been conducted on how parameters such as polymer charge density, hydrophobicity, and choice of charged group influence PCM properties, despite evidence that these strongly influence the complexation behavior of polyelectrolyte homopolymers. Using small angle X-ray scattering (SAXS) and electron microscopy we investigate the relationship between the physical properties of oligonucleotide PCMs and chemical properties of the nucleic acids and block copolymers that form them. For instance, differences in charge density and hydrophobicity have been individually suggested to provide increased complex stability, but we find that other factors may disrupt this trend. These observations narrow the design space for optimizing therapeutic PCMs and provide new insights into the rich polymer physics of polyelectrolyte self-assembly.

METHODS

Poly((vinylbenzyl) trimethylammonium) (pVBTMA) homopolymers and pVBTMA-PEG block copolymers were synthesized by aqueous reversible addition-fragmentation chain transfer (RAFT) polymerization as described by Ting et al. [3]. Poly(lysine) (pLys), pLys-PEG, and oligonucleotides were purchased. PCMs were prepared using a salt-annealing method [4]. Briefly, the polyelectrolytes were mixed in PBS buffer, then concentrated NaCl solution was added to obtain 1M final concentration to dissolve the complexes. The salt concentration was then slowly reduced over 36 h by step dialysis to a final working concentration of 1x PBS. SAXS measurements were made at the Advanced Photon Source at Argonne National Laboratory. Background subtraction and fitting were performed using multi-level modeling macros in the Irena software package for Igor Pro. PCMs were also imaged using cryo transmission electron microscopy (TEM) and traditional negative-stained TEM. Phase and morphology of homopolymer complexes were observed by bright field optical microscopy. To assess the stability of micelles vs. salt, micelle samples were titrated with 5M NaCl and light scattering intensity was measured.

RESULTS

In order to evaluate pVBTMA as a cationic polymer for nucleic acid delivery, we first prepared PCMs using pVBTMA-PEG block copolymers and single-stranded DNA oligonucleotides and compared them to PCMs assembled from pLys-PEG block copolymers of similar lengths. Both cationic polymers readily formed spheroidal PCMs when mixed with DNA, with low polydispersity in radius, and we observe a marked increase in PCM radius with charged block length.

For double-stranded DNA, we observe long, wormlike micelles with the pLys-PEG block copolymers, consistent with our previous report [4], but in this case we see a qualitative difference for PCMs prepared with pVBTMA-PEG. These micelles exhibit low polydispersity in radius, with fitted values very similar to those found for pLys-PEG PCMs, but the lengths are shorter and highly variable between and within samples [5]. Figure 1 depicts the distinct shapes and phases we obtain by adjusting parameters of our starting materials. These include spherical micelles, flexible cylindrical micelles, liquid coacervate droplets, and solid-like precipitates.

The critical ionic strength required for dissolution provides a measure of the stability of a given complex. To compare the stability of our PCMs, we titrated concentrated NaCl and observed changes in light scattering intensity. We found that pVBTMA-PEG PCMs are considerably less stable than those containing pLys-PEG, and observe a similar trend for homopolymer complexes. Likewise, we see phase transitions occurring at lower salt concentrations in pVBTMA-DNA complexes compared to pLys-DNA complexes.

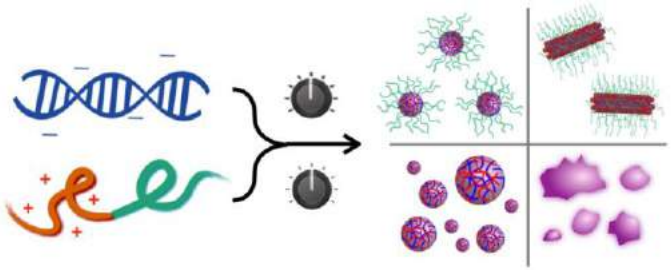

Figure 1: Complexation between nucleic acids (polyanion) and hydrophilic cation-neutral block copolymers forms phase separated structures. This study explores the effect of chemical parameters determining the physical properties of polyelectrolyte complexes.

DISCUSSION

Investigations of polycations for nucleic acid delivery have focused on hydrophilic polymers such as pLys, poly(ethyleneimine), poly(amidoamine), and cationic polysaccharides, many of which are analogs of natural products. This may represent a missed opportunity, as synthetic polymers provide access to diverse bio-orthogonal structural motifs and allow tuning of intermolecular interactions (hydrophobicity, hydrogen bonding, cation-pi, etc.) over a wider range than is possible with naturally-inspired polycations. This study was designed to provide a test of these tunable characteristics. Namely, pVBTMA has a larger linear charge density than pLys, has an aliphatic backbone and aromatic side chains, is largely unable to form hydrogen bonds, and contains a permanent positive charge rather than the ionizable primary amine.

We show many similarities and some marked differences when comparing PCMs formed by the two polycations. Oligonucleotide PCMs formed with pLys-PEG and pVBTMA-PEG show that micelle radius is controlled by the length of the charged block but largely insensitive to oligonucleotide length, suggesting this may be a universal property for PCMs. We find the hybridization state of the nucleic acid is a key parameter in determining the shape of the micelles, where, for both polycations, single-stranded oligonucleotides produce spheroidal PCMs, while double-stranded oligonucleotides generate elongated PCMs. We observe major discrepancies for PCMs with double-stranded oligonucleotides, where pLys-PEG forms micron-scale worm-like micelles, but pVBTMA-PEG forms much shorter cylindrical micelles that are highly polydisperse, implying some mechanical instability in this system. pVBTMA-PEG PCMs also proved to be less stable in high NaCl conditions, suggesting the interactions between nucleic acids and pVBTMA are weaker than those with pLys, despite higher charge density, increased hydrophobicity, and non-susceptibility to neutralization. The large structural differences between pLys and pVBTMA suggest that the similarities in PCM properties we observe may be universal, while the differences provide useful leads for further investigation into the physics of polyelectrolyte self-assembly as well as possible solutions to the pressing problem of nucleic acid delivery.

ACKNOWLEDGEMENTS

This work used resources of the Advanced Photon Source, a U.S. Department of Energy (DOE) Office of Science User Facility operated for the DOE Office of Science by Argonne National Laboratory under Contract No. DE-AC02-06CH11357. Parts of this work were carried out at the Soft Matter Characterization Facility and the Advanced Electron Microscopy Facility of the University of Chicago. The authors thank Xiaobing Zuo for his assistance with the SAXS data acquisition and Tera Lavoie for assistance with electron microscopy.

REFERENCES

[1] Pelaz, B., et al., *ACS Nano*, 11:2313-2381, 2017.
[2] Dowdy, S.F., *Nat Biotechnol*, 44:6518-6548, 2017.
[3] Ting, J.M., et al., *ACS Macro Lett*, 7:726-733, 2018.
[4] Lueckheide, M., et al., *Nano Lett*, 18:7111-7117, 2018.
[5] Marras, A.E., et al., *Polymers*, 11:83, 2019.

SB^{3}C2019
Summer Biomechanics, Bioengineering and Biotransport Conference
June 25 -28, Seven Springs, PA, USA

STRUCTURAL REMODELING AND VOLUMETRIC GROWTH IN THE RIGHT VENTRICLE UNDER PULMONARY ARTERIAL HYPERTENSION

Reza Avaz (1,2), Emilio A. Mendiola (1), Michael S. Sacks (1,2)

(1) Willerson Center for Cardiovascular Modeling and Simulation, Institute for Computational Engineering and Sciences, The University of Texas at Austin, Austin, USA

(2) Department of Biomedical Engineering, The University of Texas at Austin, Austin, USA

INTRODUCTION

Pulmonary arterial hypertension (PAH) imposes pressure overload on the right ventricle (RV), leading to a substantial RV enlargement via simultaneous growth of cardiac myocytes and remodeling of the collagen fiber architecture [1, 2]. The effects of these alterations on the functional behavior of the RV free wall (RVFW) and global cardiac function remain largely unexplored. Computational rodent heart models (RHM) of the normal and hypertensive states [3-4] can be quite valuable in gaining insights into the pathophysiology of myocardium remodeling.

Recently, we developed high-fidelity biventricular finite-element RHMs using extensive data collected from rat hearts at normal and post-PAH time points [3]. In the current study, we extended our model to predict the *time-course* adaptations of RV under PAH from normal state to post-PAH state. Our model accounted for growth processes driven by sarcomerogenesis and collagen fibrosis, coupled with myo- and collagen fiber reorientation events. We used our model to investigate the correlations between the alterations in the wall stress, the remodeling of the RVFW microstructure, and the shape changes in the RV during the development of PAH. To the best of our knowledge, this is the first work to investigate the interaction between fiber remodeling and volumetric growth in the heart. Ultimately, the detailed description of organ-level remodeling patterns predicted by in-silico models such as ours could replace the traditional measures of RV dimensions and volume that often lead to gross and limited information on cardiac performance.

METHODS

Time-course measurements. The time-course variation of RV pressure was measured in PAH animal models during 30 days after monocrotaline (MCT) injection (Fig. 1). The pressure remained in an approximately plateaued constant for a large part of the post-injection period. A key assumption in our model was that the volumetric growth and fiber remodeling were limited to this phase (Fig. 1).

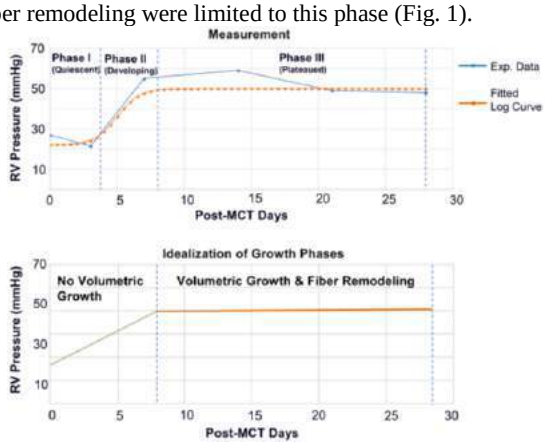

Figure 1: (Top) Time-course pressure data during the development of MCT-induced PAH. (Bottom) Limitation of G&R processes to the plateau phase of pressure development.

Growth model. Our volumetric growth model to induce RV dilation is based on multiplicative decomposition of deformation gradient expressed as

$$\mathbf{F} = \mathbf{F}^{e}\,\mathbf{F}^{g} \qquad (1),$$

where $\mathbf{F}^{e}$ and $\mathbf{F}^{g}$ denote the elastic and growth parts of the deformation, respectively. To generate an eccentric hypertrophy in the RV, we adopted the following form for $\mathbf{F}^{g}$

$$\mathbf{F}^{g} = \mathbf{I} + (\vartheta^{g} - 1)\,\mathbf{N} \otimes \mathbf{N} \quad (2),$$

where $\mathbf{N}$ is the fiber direction. A specific strain-driven evolution law for the growth multiplier ϑ^{g} is given by [4]

$$\dot{\vartheta}^{g} = k^{g}(\vartheta^{g})(\lambda^{e} - \lambda^{h}) \quad (3),$$

where $k^{g}(\vartheta^{g})$ is a limiting function [4], and λ^{e} and λ^{h} denote elastic and homeostatic stretches, respectively.

Fiber remodeling model. In this work, the fiber remodeling is driven by the adaptation of fibers orientation towards the axis with the largest stretch. Through this mechanism, the fibers adapt their orientation following a change in the direction of the largest stretch (denoted by $\mathbf{E}^{max}$) and/or in the value of the largest stretch. Accordingly, the angular velocity stimulus is expressed as

$$\boldsymbol{\omega} = \vartheta^{r}\,\mathbf{N} \times \mathbf{E}^{max} \quad (4),$$

where ϑ^{r} is the remodeling multiplier governing the speed at which the fiber direction reorientation takes place. Its evolution is given by

$$\dot{\vartheta}^{r} = k^{r}(\vartheta^{r})(1 - \mathbf{E}^{max} \cdot \mathbf{E}_{h}^{max}) \quad (5),$$

where the subscript 'h' denotes to the homeostatic state. The evolution of the fiber direction is then calculated by [5]

$$\dot{\mathbf{N}} = \boldsymbol{\omega} \times \mathbf{N} \quad (6),$$

RESULTS

Significant dilation of the RV was observed while the left ventricle underwent little notable change. The RV end-diastolic volume increased by approximately 200%, from 40.1 to 78.3 uL (Fig 2). The stroke volume of the RV was nearly preserved. A small amount of hypertrophy of the RVFW was also noted (Fig 2). Evolution of the growth multiplier throughout the cycles identified locations of the RVFW that experienced the greatest amount of growth. Although the growth multiplier increased rather uniformly throughout the RVFW, the posterior corner was an area of growth concentration.

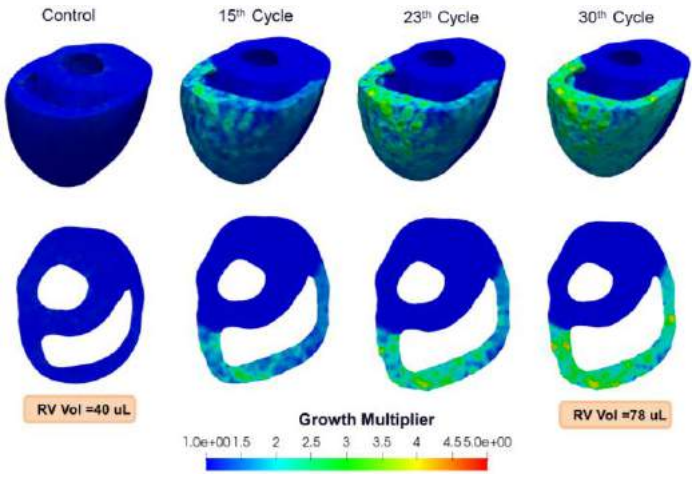

Figure 2: Short-axis views of the evolution of the FE RHM from the control to post-PAH state simulated by 30 growth cycles.

A large part of the dilation occurred at later cardiac growth cycles (Figs. 2 and 3) that significantly reduced the ejection fraction. This indicates that the dilation advances once the heart has exhausted other adaptations available to maintain the cardiac output. A nearly uniform fiber reorientation across the RVFW thickness (~ 22° from the circumferential direction) was consistent with previous histological studies [1]. In contrast to RV dilation and fiber reorientation that took place rapidly at later stages, myocardial contractility and stiffness seemed to increase early on during the maturation of the PAH (Fig. 3).

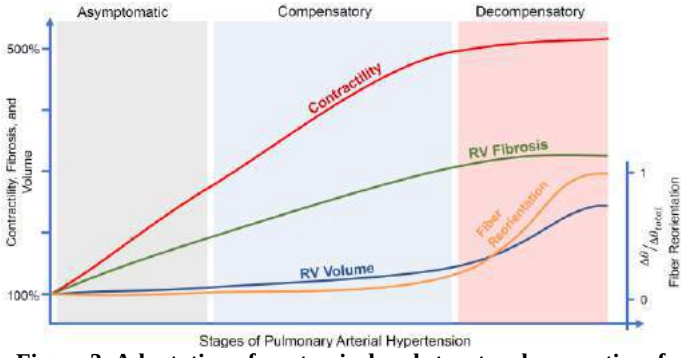

Figure 3. Adaptation of anatomical and structural properties of the RV from the asymptomatic to decompensatory states.

DISCUSSION

In this work, we took an essential step towards the modeling and predicting the multiscale growth and remodeling events in the RV during PAH with a focus on integrating remodeling events at the fiber level (such as fiber reorientation) with the volumetric growth of the RVFW and RV at the tissue and organ levels.

Our model results suggest that augmentation of the intrinsic contractility of myofibers is among the first remodeling events through which the RV strives to maintain the cardiac output against the pressure overload. In fact, the RV first exhausts its capacity to increase the contractility of RVFW myofilaments, which could go up to five fold (Fig. 3), before it succumbs to a rapid dilation to maintain the output. The changes in the contractility is accompanied by an increase in passive stiffness of RVFW which, based on our previous studies [1,2], we suspect to stem from the deposition of new collagen fibers and changes in the existing collagen structure. On the other hand, our model suggests that the reorientation of the fibers towards the longitudinal (apex-to-base) direction is rather a *maladaptive* mechanism that does not improve the overall contractility and ejection fraction of the RV and advances together with RV dilation at the later stages of PAH development. In this connection, we inferred from our simulations that although the fibers remodeling is assisting with the restoration of the wall stress in the circumferential direction, it undermines the contractility of the RV by shifting the circumferential contractility mode (seen in a normal heart) toward a more isotropic contraction. To fully understand the multiscale nature of these events, our next step is to separate the remodeling effects of myofibers and its contractile machinery from alterations in collagen content and structure.

ACKNOWLEDGEMENTS

RA was supported by the NIH, under grants 5F32HL132543-03 and K99HL138288-01A1, and by AHA grant 18CDA34110383.

REFERENCES

[1] Hill, MR et al, *Ann Biomed Eng*, 42:2451-65, 2014.
[2] Avaz, R et al, *APL Bioeng*, 1:016105, 2017.
[3] Avaz, R et al, *Ann Biomed Eng*, 47:138-53, 2019.
[4] Goktepe, S et al, *J Theor Biol*, 265:433-42, 2010.
[5] Kuhl, E et al, *J Mech Phys Solids*, 53:1552-73, 2005.

SB³C2019
Summer Biomechanics, Bioengineering and Biotransport Conference
June 25 -28, Seven Springs, PA, USA

MATHEMATICAL MODELING OF REGIONAL HYPERTENSIVE AORTIC REMODELING REVEALS A CRITICAL ROLE FOR INFLAMMATION

M. Latorre (1), M. Bersi (2), J. Humphrey (1,3)

(1) Department of Biomedical Engineering
Yale University
New Haven, CT, USA

(2) Department of Biomedical Engineering
Vanderbilt University
Nashville, TN, USA

(3) Vascular Biology and Therapeutics Program
Yale School of Medicine
New Haven, CT, USA

INTRODUCTION

Uncontrolled hypertension is a major risk factor for myriad cardiovascular diseases. Among its many effects on the body, hypertension increases central artery stiffness, which in turn is now known to be both an initiator and indicator of disease and disease propensity. Despite extensive clinical, animal, and basic science studies, the biomechanical mechanisms by which hypertension drives aortic stiffening remain unknown. In this work, we show that a new computational model of aortic remodeling can capture salient effects of induced hypertension on the thoracic and abdominal aorta in a common mouse model of disease characterized primarily by regional adventitial fibrosis in the presence of marked inflammation. Because the model treats the aortic wall as a constrained mixture of different constituents having different material properties and rates of turnover, one can gain increased insight into underlying biomechanical mechanisms of aortic remodeling.

METHODS

We model the infrarenal abdominal aorta (IAA) and descending thoracic aorta (DTA), of 19-week old male *Apoe*$^{-/-}$ mice rendered hypertensive via a continuous infusion of AngII at 1000 ng/kg/min for up to 28 days [1], using a constrained mixture framework for growth (changes in mass) and remodeling (changes in microstructure) that includes mechanical stress and inflammatory cell density as drivers of matrix turnover [2]. Comparisons with other recent constrained mixture formulations suggest that the artery is immuno-mechano-biologically equilibrated after two-to-four weeks of hypertensive development. This finding allowed us to obtain best-fit values of constituent-specific material parameters from available biaxial data collected from pressure-diameter and axial force-length tests after predetermined durations of AngII infusion (0, 4, 7, 14, 21, and 28 days) for both regions [1]; in particular, we used a single model that allows many quantities to evolve over time, with gain-type parameters for constituent production and rate parameters for constituent removal, including an additional dependence on inflammatory cell density, estimated based on equilibrium relations [2].

RESULTS

Model results suggest that the aorta can mechano-adapt to blood pressure elevation in the absence of inflammation, but marked increases in inflammation drive a maladaptive response. Numerical simulations predict well the observed results, including differences in medial versus adventitial growth and remodeling and bulk biaxial mechanical measurements in both normotensive and hypertensive states, with the IAA and DTA mechano-adapted by 14 days, but the DTA markedly maladaptated after 14 days of AngII infusion, when significant inflammation and adventitial fibrosis manifested most dramatically (Figure 1).

Model results also suggest that this fibrosis occurs via a marked increase in the rate of deposition of collagen having different material properties in the absence of a compensatory increase in the rate of matrix degradation, and moreover that

effects of inflammation appear to persist for long periods after removing the exogenous stimulus.

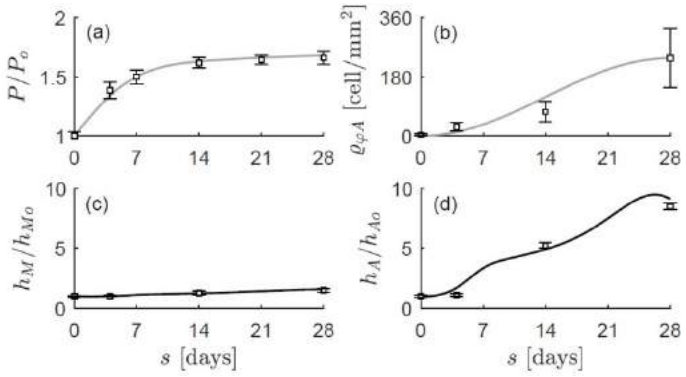

Figure 1: Model predictions (black lines) of medial (c) and adventitial (d) thickening for the DTA following a rapid 1.68-fold increase in systolic pressure (grey lines, model inputs) that persists up to 28 days (a) and an associated, retarded increase in inflammatory cell density (b). The model predicts well the experimentally measured (open squares with error bars [1]) adventitial versus medial thickening consistent with an exuberant production of inflammatory collagen in the adventitia.

DISCUSSION

Computational models of vascular adaptation and maladaptation can provide increased insight in progressive changes in geometry, structure, and properties in hypertension, including those due to mechano-adaptation and those due to immuno-maladaptation. Indeed, our simulations support the concept that controlling inflammation appears to be key to reducing fibrosis. Such therapeutic strategies, however, should not compromise the proteolytic activity of the wall that is essential for mechanical homeostasis. Whereas such homeostasis is promoted by negative feedback loops, as captured by the stress-difference term in our stimulus function, fibrosis appears to be driven either by positive feedback or no feedback, as modeled presently.

ACKNOWLEDGMENTS

This work was supported, in part, by grants from the US NIH (R01 HL105297, U01 HL116323, U01 HL142518, and P01 HL134605).

REFERENCES

[1] Bersi, MR et al., Differential cell-matrix mechanoadaptations and inflammation drive regional propensities to aortic fibrosis, aneurysm or dissection in hypertension, *J Royal Soc Interface*, 14(136): 20170327, 2017.

[2] Latorre M, Humphrey JD, Modeling mechano-driven and immuno-mediated aortic maladaptation in hypertension, *Biomech Model Mechanobiol*, 17:1497-1511, 2018.

EFFECT OF GLUCOSE ON THE INTERLAMELLAR BONDING OF ARTERIAL ELASTIN

Ruizhi Wang (1), Xunjie Yu (1), Yanhang Zhang (1,2)

(1) Department of Mechanical Engineering
Boston University
Boston, MA, USA

(2) Department of Biomedical Engineering
Boston University
Boston, MA, USA

INTRODUCTION

Aortic dissection is a clinically challenging disease with a high rate of mortality [1]. It starts with a tear in the intima and propagates in the media [2]. Failure of various microstructural constituents can occur simultaneously during this process. As one of the major load-bearing proteins in the artery, elastin forms a 3D cross-linked fiber network of which ~29% are oriented in the transmural direction [3]. Thus, arterial elastin not only provides the tissue with in-plane stiffness and strength, but also plays an important role in maintaining the integrity and resisting damage propagation in the aorta.

Diabetes has been found to be closely associated with cardiovascular disease progression and vascular remodeling. Earlier stiffening of the arterial wall among diabetic patients has been attributed to glycation crosslinks of elastin and collagen [4]. Our previous studies have shown that arterial elastin exhibits larger stiffness and hysteresis in both the circumferential and longitudinal directions with glucose exposure [5]. Interestingly, in a nationwide case-control study, reduced risk of thoracic aortic dissection was found in patients with diabetes [6]. This study aims to investigate the change of interlamellar bonding properties of arterial elastin with glucose treatment. Peeling tests were carried out on glucose treated porcine elastin. Peeling force as well as dissection energy were quantified and compared for samples with different duration of glucose treatment.

METHODS

Porcine thoracic aortas were cut into circumferential and longitudinal rectangular strips of about 40 mm × 10 mm. Purified elastin network was obtained using a cyanogen bromide treatment method [7]. Samples were then incubated in 2 M glucose solution and were allowed to equilibrate at 37°C for 7, 14, 21 or 28 days. Elastin samples without any further treatment were also tested and served as a control. Apart from the glucose-treated and control samples, one group of elastin samples were incubated in 1× phosphate buffered saline (PBS) solution at 37°C for 21 days for comparison.

A 10 mm incision was introduced at one end of each sample to initiate dissection. Steady-state mode-I peeling tests were conducted using a uniaxial tensile tester (Instron, Norwood, MA). A schematic of the experimental setup is shown in Figure 1a. Briefly, one side of the sample was fixed while the other side was pulled away at an extension rate of 0.2 mm/s. Peeling force and displacement were recorded until complete separation. To keep chemical balance, samples were submerged in glucose (glucose-treated groups) or PBS (PBS-treated and control groups) solution during experiments.

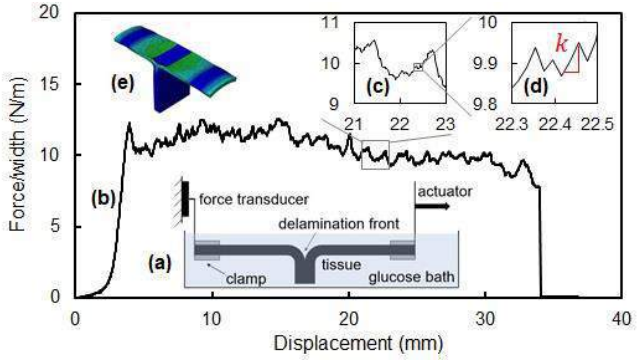

Figure 1: (a) Schematic of the experimental setup; (b) a representative force/width-displacement curve obtained from peeling tests; (c) and (d) zoom-in graphs of the force/width-displacement curve showing high-frequency oscillation of the peeling force; (e) finite element model.

The energy release rate, G_c, i.e., the energy required to split a unit area of interface, can be calculated as [8]

$$G_c = (W_{ext} - W_{elastic})/L \quad (1)$$

where $W_{ext} = 2Fl$ is the external work done by the peeling force, and $W_{elastic} = F(l - L)$ is the elastic energy stored in the tissue. F is the mean peeling force per unit width of the sample strip. L and l are length of the sample strip in the original and stretched states, respectively. Experimental data are summarized and plotted with mean ± standard deviation. Two-tailed unpaired t-tests were used for analysis with $p < 0.05$ considered as statistically significant.

RESULTS

A representative curve of peeling force per unit tissue width versus displacement is shown in Figure 1b. Averaged peeling force/width (F/W) and energy release rate (G_c) of elastin before and after glucose treatment are plotted in Figure 2. Compared with untreated samples, glucose treatment increased both F/W and G_c significantly in the circumferential direction (Figure 2a). However, compared with the untreated group, significant increase in F/W and G_c in the longitudinal direction did not occur until 21 and 28 days of treatment time, respectively (Figure 2b). No drastic change can be observed for F/W and G_c with longer glucose treatment beyond day 7.

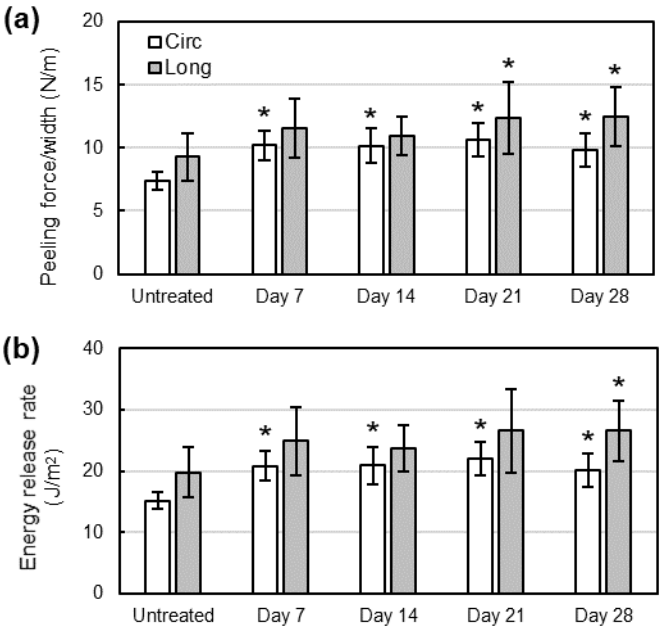

Figure 2: Change of (a) peeling force/width and (b) energy release rate before and after glucose treatment for 7, 14, 21, and 28 days in the circumferential (Circ) and longitudinal (Long) directions. (n=6~9, *p<0.05).

Averaged G_c of samples treated with PBS was plotted in Figure 3. Compared with the untreated group, G_c of samples treated with PBS exhibited a slight decrease in both circumferential and longitudinal directions, though no significant statistical difference was found. G_c of samples treated with glucose increased significantly compared to samples treated with PBS for the same amount of time. Also, glucose or PBS treatment has little influence on the direction-dependent phenomena of steady-state peeling of arterial elastin, as peeling tests along the longitudinal direction require larger values of F/W and G_c than the circumferential direction in all sample groups.

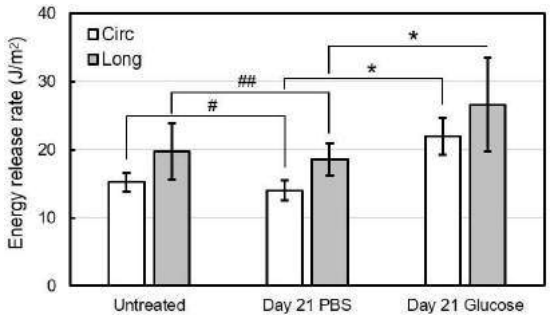

Figure 3: Comparison of energy release rate of elastin in the circumferential and longitudinal directions for untreated, and after treated with PBS or glucose for 21 days. (n=6~9, #p=0.11, ##p=0.47, *p<0.05).

DISCUSSION

Our study shows that glucose has a prominent effect on the interlamellar bonding of arterial elastin. Results of peeling tests demonstrate that larger force and energy are needed to delaminate glucose treated elastin. The most notable change seems to happen within the first week of glucose treatment, however there is a rising tendency of the mean peeling force/width and energy release rate over the incubation time (Figure 2). This suggests that the contribution of arterial elastin to interlamellar bonding is enhanced by longer glucose exposure. This effect can be further confirmed by comparative studies made in Figure 3. Submerging elastin samples in PBS alone for the same amount of time did not lead to a stronger interlamellar adhesion.

Results from the current study are consistent with the inverse relationship reported by Prakash et al. [6], that diabetic patients are better protected from aortic dissection. Higher glucose concentration can accelerate non-enzymatic glycation which may induce intermolecular and interfibrillar crosslinks. This provides a possible mechanism for the higher G_c obtained here. However, influences of glucose on the dissection properties of other interlamellar components, and on the stiffening and failure behavior of the intimal layer of arteries are not clear. Therefore, more studies are needed before we can form a thorough understanding on the relationship between diabetes and the occurrence of aortic dissection. It is worth noting that the peeling force oscillates at a high frequency (Figures 1c and 1d) which is a result of microstructural failure events. The slope of a ramp up of peeling force can be related to local interlamellar stiffness. Finite element models employing the cohesive theory of fracture (Figure 1e) will be developed based on tissue-level mechanical properties and microstructural failure evidence to better understand glycation and interlamellar bonding in aortas.

ACKNOWLEDGEMENTS

The authors would like to thank Dr. Xin Brown for assistance with the testing facility as well as Dr. Yunjie Wang for providing helpful research suggestions. This study was supported by a grant from National Institute of Health (2R01HL098028).

REFERENCES

[1] Khan, IA and Nair, CK., *Chest*, 122: 311-328, 2002.
[2] Thubrikar, MJ et al., *J Med Eng Technol*, 23: 127-134, 1999.
[3] O'Connell, MK et al., *Matrix Biol*, 27: 171-181,2008.
[4] Sims, TJ et al., *Diabetologia*, 39: 946-951, 1996.
[5] Wang, Y et al., *J Mech Behav Biomed Mater*, 49: 244-254, 2015.
[6] Prakash, SK et al., *J Am Heart Assoc*, 1: e000323, 2012.
[7] Lu, Q et al., *Biomaterials*, 25: 5227-5237,2004.
[8] Sommer, G et al., *J Biomech Eng*, 130: 021007, 2008.

SB^{3}C2019
Summer Biomechanics, Bioengineering and Biotransport Conference
June 25 -28, Seven Springs, PA, USA

CORTICAL THICKNESS DIFFERENCES EMERGE FROM PASSIVE PHYSICAL FORCES GENERATED BY GROWTH

Maria A. Holland (1), Ellen Kuhl (2), Alain Goriely (3)

(1) Aerospace & Mechanical Engineering
University of Notre Dame
South Bend, IN, USA

(2) Mechanical Engineering
Stanford University
Stanford, CA, USA

(3) Mathematical Institute
University of Oxford
Oxford, UK

INTRODUCTION

Genetic, biochemical, geometric, and physical factors interact during morphogenesis, the biological development of shape. The roles and relationships of these factors in the developing human brain is of great interest. Recently, in addition to findings of genetic influence on folding, the biomechanics research community has found increasing evidence that the folding pattern in mammalian brains is correlated with physical forces and instabilities.

Cortical thickness, a characteristic biomarker for a wide variety of neurological disorders, is known to vary widely within individual healthy adult human brains, between 1.5 and 4.5mm in different regions. This variation is observed consistently between individuals, with gyri, or outer folds, consistently thicker than sulci, or inner folds (Fig. 1). Previous studies have suggested a genetic influence [1,2], but it remains unclear whether these thickness variations are a cause or consequence of cortical development.

Here we model cortical development in a computational simulation, a non-biological physical experiment, and an analytical solution, and show that this bifurcation occurs naturally as a result of the passive physical forces generated by growth [3]. Additionally, we investigate thickness patterns in a large dataset of typically-developing adult humans.

METHODS

Nonlinear umerical simulations were performed in a custom MATLAB code, modeling finite growth to represent isotropic, morphogenetic growth in the "cortex" (i.e., a thin stiffer layer adhered to a thicker, softer substrate). The stiffness ratio between the two materials was chosen to be ~3.

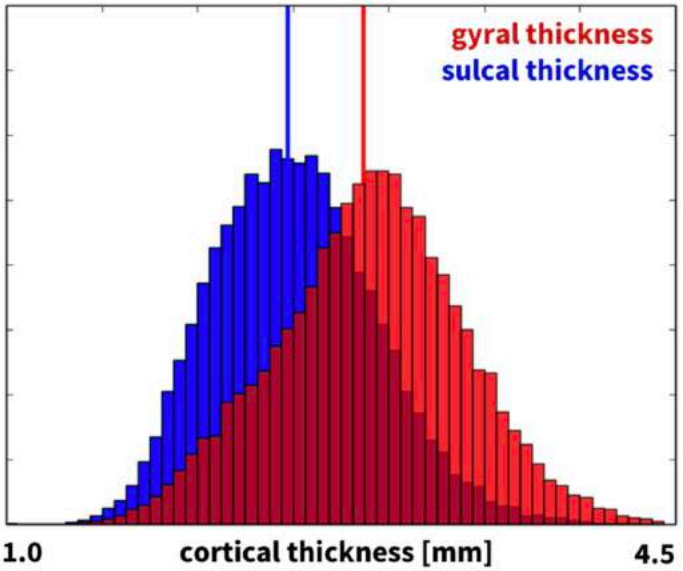

Fig. 1: Histograms of regional cortical thickness in N=564 adults from age 7-64 (from [3])

Polymer experiments were performed using a prestretched silicon substrate and adhering a thinner, stiffer silicon film before slowly releasing the prestretch. The stiffness ratio between the two polymers was about 4.6.

The analytical solution was based on a model of morphoelastic instability caused by the homogeneous growth of an elastic film on an

elastic half space. Using a variational method, the folding mode with the lowest elastic energy was selected. Close to the instability point, the solution also details the shape of the folds, which were used to compare gyral and sulcal thicknesses.

To assess gyral and sulcal thicknesses in healthy adults, N=564 MRI scans were obtained from the public Autism Brain Imaging Data Exchange database [4], which contains anatomical, functional, behavioral, and phenotypic data. Preprocessing had previously been performed using Freesurfer [5], and the Destrieux atlas [6] was used to distinguish gyral and sulcal regions.

RESULTS

Our numerical simulations show that, after instability, gyri are consistently thicker than sulci, even when subject only to the passive forces generated by growth-induced instability (Fig. 2). Eventually, gyri can attain up to 1.8 times the thickness of sulci.

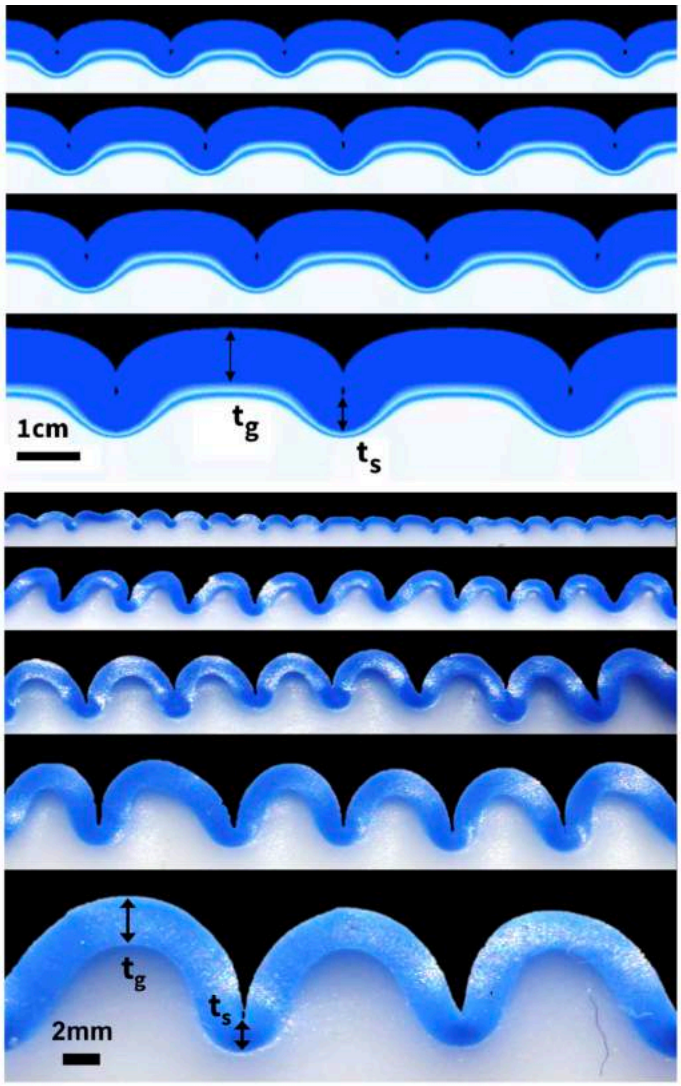

Fig. 2: Cortical development in numerical simulations (top) and polymer experiments (bottom) (both from [3])

When considering the results of the polymer experiments, as well as the lobe-specific thickness in adult humans, we find that they follow similar patterns (Fig. 3). After bifurcation, gyri continue to thicken nonlinearly, while sulci begin to thin. In each of these systems, even those without genetic or biochemical influence, gyri consistently become significantly thicker than sulci, and at similar rates.

DISCUSSION

Cortical thickness is a characteristic biomarker for a wide variety of neurological disorders. While recent studies suggest that thickness variations are primarily the result of genetic events, our work demonstrates that geometric and physical events alone could be sufficient to induce cortical patterning. Together, this suggests that genetic, geometric, and physical factors interact in human brain development.

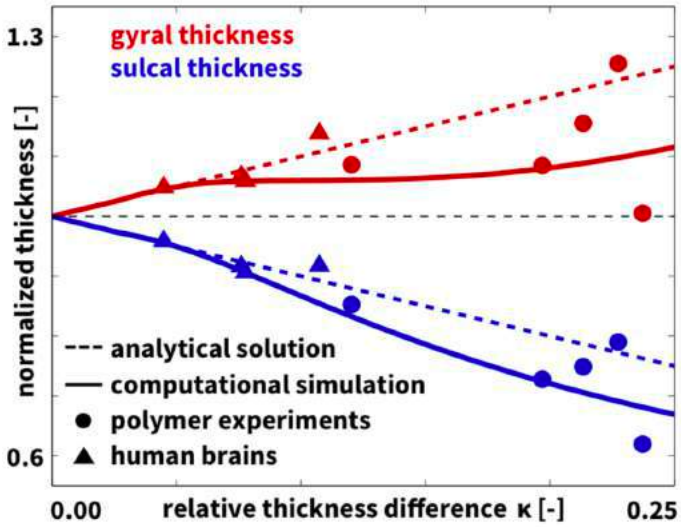

Fig. 3: Evolution of cortical thickness difference as thickness increases (from [3]).

Importantly, understanding the causes and consequences of cortical thickness variations can provide insight into the development, diagnostics, and treatment of neurological disorders.

ACKNOWLEDGEMENTS

This work was supported by Notre Dame's Advanced Diagnostics & Theraputics Discovery Fund Award (MAH), the Stanford Bio-X IIP and NSF Grant No. CMMI 1727268 (EK), and the EPSRC Grant No. EP/R020205/1 (AG).

REFERENCES

[1] Fernández V, Llinares-Benadero C, Borrell V, *EMBO J.* 35 (2016) 1021–1044.
[2] Zhang T, Razavi MJ, Li X, Chen H, Liu T, Wang X, *Sci. Rep.* 6 (2016) 37272.
[3] Holland MA, Budday S, Goriely A, Kuhl E, *Phys. Rev. Lett.* 121 (2018) 228002.
[4] Di Martino A et al., *Mol. Psychiatry* 19 (2014) 659–667.
[5] Dale AM, Fischl B, Sereno MI, *NeuroImage* 9 (1999) 179–194.
[6] Destrieux C, Fischl B, Dale A, Halgren E, *NeuroImage* 53 (2010) 1–15.

SB³C2019
Summer Biomechanics, Bioengineering and Biotransport Conference
June 25 -28, Seven Springs, PA, USA

TARGETING CADHERIN-11 FOR RENAL FIBROSIS

Tessa M. Huffstater (1), Leslie S. Gewin (2), W. David Merryman (1)

(1) Biomedical Engineering
Vanderbilt University
Nashville, Tennessee, USA

(2) Nephrology & Hypertension
Vanderbilt University Medical Center
Nashville, Tennessee, USA

INTRODUCTION

Chronic kidney disease (CKD) is a fibrosis-mediated disease caused by severe or prolonged injury to the kidneys. Currently, there are very few pharmacological treatment options for CKD, while dialysis and kidney transplants are still considered the primary treatment options. Cadherin-11 (CDH11) is a transmembrane protein involved in cell-cell adhesion that has been implicated in rheumatoid arthritis, and calcific aortic valve, and whose inhibition has been shown to significantly improve outcomes in these diseases.[1–4] CDH11 has also been recently identified as a biomarker for renal fibrosis.[5] The current study investigates the effects of CDH11 knockdown and inhibition in CKD to test CDH11 as a novel drug target for renal fibrosis.

METHODS

CKD was induced using two models of renal fibrosis: aristolochic acid nephropathy and unilateral ureteric obstruction (UUO). The first is a toxin-induced injury, whereby 10-week-old mice were injected with 2-4 mg/kg of aristolochic acid (AA) daily for one week. Mice were sacrificed at 6 weeks, at which point blood and kidneys were collected for analysis. The second model is a classic surgically-induced model of tubulointerstitial fibrosis, UUO, wherein one kidney is externalized and the ureter is ligated with a suture. Mice were sacrificed a week following the surgery, at which point kidneys were collected for analysis.

In both injury models, transgenic mice of wild-type (*Cdh11*$^{+/+}$), heterozygous (*Cdh11*$^{+/-}$), and null (*Cdh11*$^{-/-}$) genotypes were used to evaluate the effects of genetically inhibiting CDH11. To study CDH11 functional inhibition, C57BL/6J mice were injured and simultaneously injected with a CDH11 blocking antibody (SYN0012) or isotype control (IgG2a). To evaluate changes in function, morphology, and gene expression, several interrogative techniques were employed, including histological analysis, qPCR, and atomic force microscopy (AFM).

RESULTS

In preliminary studies, CDH11 expression was found to be elevated as much as 20-fold in injured kidneys relative to healthy controls (data not shown). In both injury models used, genetic inhibition of CDH11 results in improved outcomes and amelioration of disease (**Figure 1**). CDH11-heterozygous and null mice had significantly higher survival rates and diminished expression of renal injury markers compared to wild type littermates. Genetic inhibition of CDH11 also improved morphology (by Masson's trichrome stain) evident in the reduced incidence of tubule dilation, nephron damage, and immune infiltrate seen with CDH11 knockdown when compared to wild type. Tissue stiffness – measured using AFM in areas of fibrosis (αSMA-positive) – was reduced in mice with CDH11 knockout compared to wild type. Flow cytometry identified a reduction in lymphocyte invasion among CDH11 knockdown and knockout mice compared to wild type.

Similar results were obtained with pharmacological inhibition of CDH11 using SYN0012 (**Figure 2**). In these

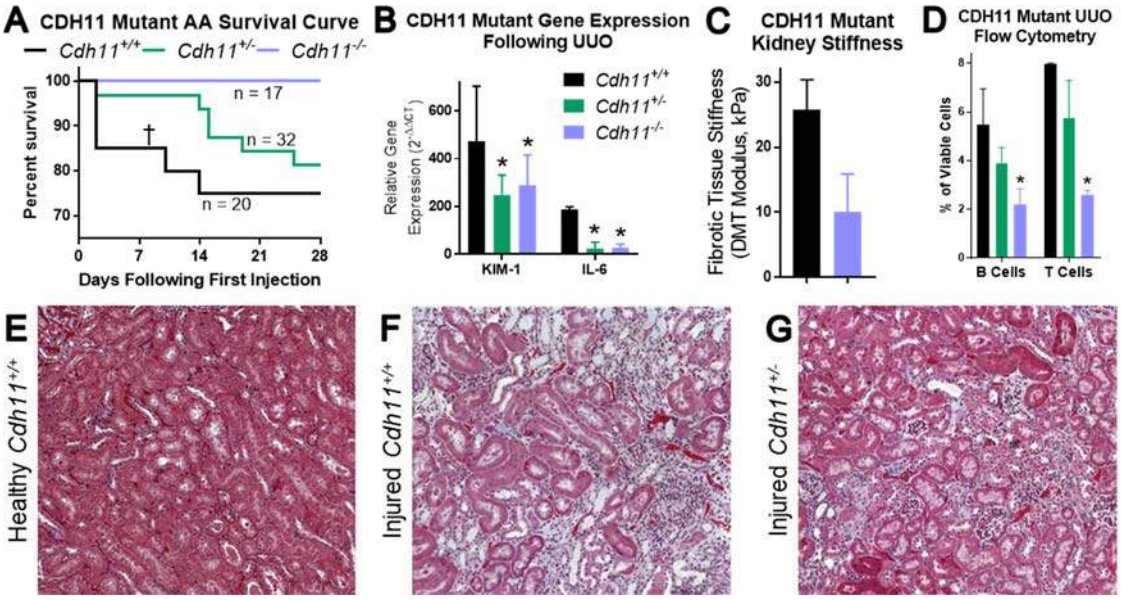

Figure 1. *Cdh11*$^{+/-}$ and *Cdh11*$^{-/-}$ mice have lower mortality rates (A), diminished expression of tubular injury and inflammatory markers (B), reduced tissue stiffness (C), decreased infiltration of inflammatory cells (D), and preserved morphology (E-G) following kidney injury compared to *Cdh11*$^{+/+}$ littermates. Images taken at 10X. † indicates trend of $p < 0.05$; * indicates $p < 0.05$ compared to Cdh11$^{+/+}$.

studies, injured mice that received the CDH11-blocking antibody had significantly improved morphology and significant reduction of renal injury, fibrotic, and inflammatory markers compared to mice that received the isotype control.

DISCUSSION

The results of this study clearly identify targeting CDH11 as an effective means of improving outcomes in murine renal fibrosis models. These studies demonstrated drastic differences in renal morphology, with both overall tissue health and immune infiltrate significantly improved with CDH11 inhibition, which was supported by reduction in the expression of renal injury and fibrotic markers. The reduction in fibrotic tissue stiffness is a particularly novel and impactful find, as previous studies have shown that stiffer tissues can alter extracellular matrix production and induce fibrosis.[6,7] Based upon these data, CDH11 is a compelling target for therapeutic intervention in patients with CKD and its mechanism should be more fully investigated.

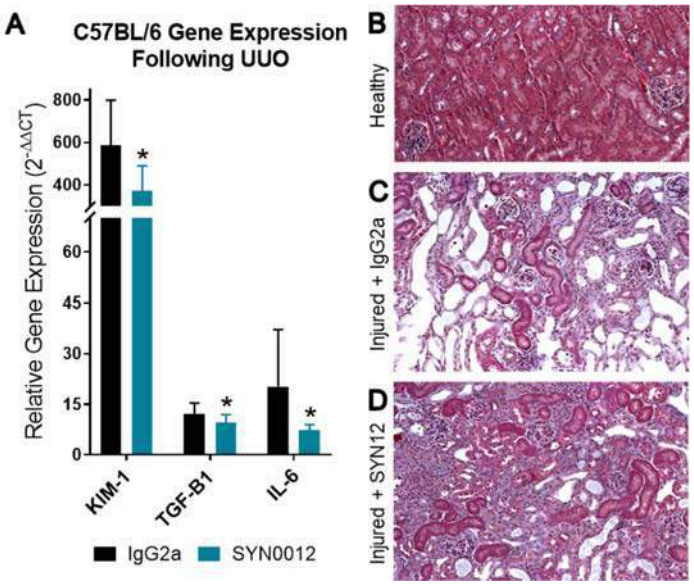

Figure 2. Administration of CDH11 blocking antibody SYN0012 results in reduced expression of tubular injury, fibrotic, and inflammatory markers (A) as well as preserved morphology (B-D) following kidney injury compared to injection with isotype control (IgG2a). Images taken at 10X. * indicates $p < 0.05$ compared to IgG2a.

ACKNOWLEDGEMENTS

This work was funded by the NIH (R35 HL135790).

REFERENCES

1. Clark CR, et al. *Circulation*. 2017;135(24):2448-2450.
2. Hutcheson JD, et al. *ATVB*. 2013;33(1):114-120.
3. Schneider DJ, et al. *FASEB J*. 2012;26(2):503-512.
4. Kiener HP, et al. *Arthritis Rheum*. 2009;60(5):1305-1310.
5. Craciun FL, et al. *J Am Soc Nephrol*. 2016;27(6):1702-1713.
6. Szeto SG, et al. *J Am Soc Nephrol*. 2016;27(10):3117-3128.
7. Yasuda T, et al. *J Clin Invest*. 1996;98(9):1991-2000.

SB³C2019
Summer Biomechanics, Bioengineering and Biotransport Conference
June 25 – 28, Seven Springs, PA, USA

PLASTIC REMODELING OF COLLAGEN UPON TUMOR GROWTH ALTERS FLUID TRANSPORT PROPERTIES OF THE EXTRACELLULAR MATRIX

Jacopo Ferruzzi (1), Meng Sun (1), Anastasia Gkousioudi (2), Anahita Pilvar (3), Darren Roblyer (1), Yanhang Zhang (1,2), Muhammad H. Zaman (1,4)

(1) Department of Biomedical Engineering
Boston University
Boston, MA, USA

(2) Department of Mechanical Engineering
Boston University
Boston, MA, USA

(3) Department of Electrical Engineering
Boston University
Boston, MA, USA

(4) Howard Hughes Medical Institute
Boston University
Boston, MA, USA

INTRODUCTION

The tumor microenvironment represents a complex and highly dynamic biological system which includes a remodeled extracellular matrix (ECM). A malignant phenotype is established not only due to genetic mutations, but also because of altered biochemical and biomechanical interactions between a tumor and its microenvironment. In particular, tumors generate both compressive and tensile forces [1], and typical biomechanical alterations observed in tumors include ECM stiffening and interstitial fluid pressurization. The established view is that ECM stiffening is caused by collagen deposition, reorganization and cross-linking, while fluid pressurization is due to leaky and disorganized blood vessels [2]. However, ECM remodeling by tumors typically involves collagen densification, which can also affect fluid transport properties and lead to interstitial fluid pressurization. Thus, there is a need for improved characterization of ECM mechanics, remodeling and how evolving ECM properties affect tumor progression.

Type I collagen is the predominant fibrous constituent of the ECM and reconstituted collagen gels are commonly used as substrates for 3D cell cultures. The mechanical properties of collagen gels are commonly assessed using rheometry and uniaxial tension, while their compressive properties are still poorly understood [3]. Here, we used a reductionist system – the tumor spheroid embedded in 3D collagen I – to quantify the extent of compressive matrix remodeling upon spheroid growth. We characterize the structural and mechanical properties of collagen networks at various concentrations (1-4 mg/mL), before (control) and after chemical cross-linking. Confined compression testing, continuum biphasic modeling, and discrete network dynamics were employed to provide a detailed understanding of the mechanisms underlying compressive matrix remodeling upon tumor growth. Overall, we show that tumor growth induces localized compression of the ECM via plastic remodeling, which in turn impacts convective fluid transport.

METHODS

Multicellular spheroids were generated using ~10^3 MCF-10A cells (ATCC) and were fully embedded in collagen gels of various densities, which were prepared as described below. Spheroid growth and matrix remodeling were examined by means of time-lapse imaging (Leica DMI 6000B) and multiphoton microscopy (Bruker Ultima Investigator). Collagen gels for biomechanical testing were prepared using rat tail type I collagen (BD Biosciences) at concentrations of 1, 2, 3, 4 mg/mL using established protocols [4]. For each concentration, half of the gels (controls) were exposed to regular deionized water (dH_2O), while the other half was cross-linked chemically by adding glutaraldehyde (GA) diluted in dH_2O on top of the self-assembled gels. Microstructural characterization of collagen networks was allowed via second harmonic generation (SHG) imaging both before and after biomechanical testing. Confined compression tests were carried out by preparing collagen gels within cylindrical PDMS wells and by using a DHR-2 rheometer (TA Instruments) equipped with a porous indenter to compress the samples. Stress relaxation tests with steps of 3-5% were applied at a constant rate of 1%/s and followed by a holding period of 180 s, during which the deformation remained constant while the force decreased to a plateau.

In virtue of the elevated content of water, collagen gels were modeled as biphasic mixtures consisting of a solid phase (collagen fiber network) and a fluid phase (interstitial liquid). From a constitutive standpoint, the hydraulic permeability was assumed to be isotropic and strain-independent, while the solid phase was modeled using a Yeoh strain energy function [5]. The material parameters and the hydraulic permeability were determined via nonlinear least squares by means of a two-step fitting procedure [6]. A mechanistic network model was also developed to gain further insights into the mechanisms of compressive remodeling. A 3D random network was generated and cross-linked within a volume of 50 μm^3. Stretching and bending potentials govern

collagen fiber mechanics [7], while cross-linked nodes exchange forces until they exceed a breaking force. The mechanical behavior of the simulated network depends on the Young's modulus of individual fibers and by the cross-link breaking force. Therefore, these two quantities were varied parametrically to reproduce qualitatively the different behaviors observed experimentally

RESULTS

MCF-10A spheroid growth over 48 hours was found to be nearly independent from collagen concentration. Cell proliferation induced collagen deformations that were radially compressive and tangentially tensile (Figure 1a). Furthermore, SHG imaging of collagen revealed that collagen densified around the spheroid boundary instead of propagating its deformation in the bulk of the collagen matrix (Figure 1b). Motivated by these findings, we investigated collagen gel mechanics under confined compression and found that control gels develop modest reaction forces at each step of compression. After chemical cross-linking with GA, collagen gels displayed a distinct stiffening, lower energy dissipation, and frank rupture at large deformations. Microstructural features of the networks were found to be controlled by collagen concentration, not by cross-linking. However, cross-linked networks exhibited significantly higher autofluorescence with respect to controls, which indicates that the intrinsic fiber properties were altered by treatment with GA. Biphasic modeling showed that control gels display lower shear moduli but also lower hydraulic permeabilities, with respect to their cross-linked counterparts. The lower permeabilities, which cause higher peaks and slower decays in interstitial fluid pressure upon compression, were associated with the presence of plastic deformations in correspondence of the gel surface (Figure 2). The densification of collagen on the surface of the gel after compression was reminiscent of the densification observed around the spheroid boundary after 48 hours of proliferation. Additional insights into the mechanisms of compressive remodeling were gained from the network model. In fact, baseline simulations reproduced behaviors that were qualitatively similar to those observed in control networks. We found that both fiber stiffening (i.e., increase in Young's modulus) and cross-link strengthening (i.e., increase in breaking force) were required to reproduce behaviors similar to those observed after GA treatment. Conversely, these results suggest that cross-link rupture and fiber buckling under compressive loads underlie collagen densification and compressive matrix remodeling.

DISCUSSION

Altered cell-matrix interactions are implicated in the initiation and progression of multiple pathologies. In particular, malignant tumors are characterized by increased collagen deposition and stiffness, and such fibrotic features have been shown to play a causative role in cancer invasion [8]. A better understanding of tumor-driven ECM remodeling using realistic *in vitro* models, such as the multicellular spheroid embedded in a 3D collagen gel, will lead to a better understanding of the metastatic feedback loop existing between ECM densification and tumor invasion / metastasis. Our approach combined 3D cell culture models, microstructural characterization, biomechanical testing, and modeling at multiple length scales. We investigated the structure-function relationship in control and cross-linked gels, and found that the latter behave elastically, while the former display plastic behaviors even at small strains. Localized densification upon compression reduces the hydraulic permeability of control gels, which suggests that the fluid transport properties of the tumor ECM are altered by tumor growth. This finding implies that interstitial fluid pressurization can arise also from ECM remodeling, and not only from a leaky tumor vasculature. Furthermore, a remodeled ECM can act as a transport barrier that is responsible for the development of hypoxia and poor drug delivery.

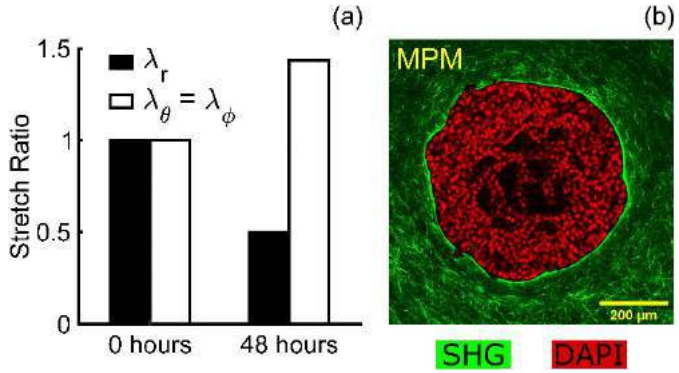

Figure 1: (a) Radial (λ_r) and tangential ($\lambda_\theta = \lambda_\phi$) deformations imposed at the matrix boundary by MCF-10A spheroid growth in collagen for 48 hours. (b) Localized deformation of collagen around the spheroid boundary shown as a dense collagen layer from SHG.

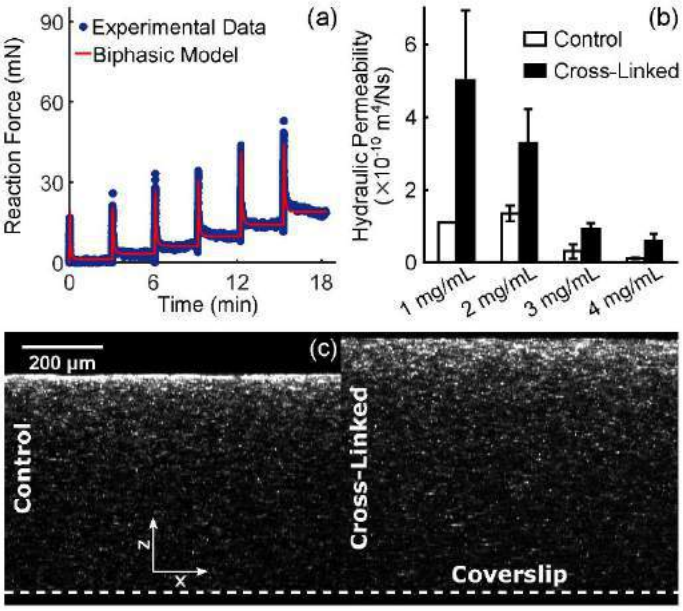

Figure 2: (a) The biphasic model captures well the stress relaxation response of collagen gels. (b) The resulting hydraulic permeabilities decrease with increasing collagen concentration and are consistently lower in control gels. (c) After compression, plastic deformations and localized densification of collagen at the gel surface are present in control, but not in cross-linked, gels.

ACKNOWLEDGEMENTS

This work was funded by NIH grant U01 CA202123. We acknowledge Haig Aboyan, Robert Sabatelle, and Avanelle Onaifo for collecting preliminary data.

REFERENCES

[1] Provenzano, P.P. et al., *BMC Med*, 4: 38, 2006.
[2] Mitchell, M.J. et al., *Nat Rev Cancer*, 17: 659-675, 2017.
[3] van Oosten, A.S., *Sci Rep*, 6: 19270, 2016.
[4] Harjanto, D. et al., *PLoS One*, 6: e24891, 2011.
[5] Yeoh, O.H., *Rub Chem Tech*, 63: 792-805, 1990.
[6] Ateshian, G.A. et al., *J Biomech*, 30: 1157-1164, 1997.
[7] Kim, T. et al., *Exp Mech*, 49: 91-104, 2009.
[8] Pickup, M.W. et al., *Cancer Res*, 73: 5336-46, 2013.

SB³C2019
Summer Biomechanics, Bioengineering and Biotransport Conference
June 25 -28, Seven Springs, PA, USA

PULMONARY ARTERIAL MECHANICS: SOMETHING OLD, SOMETHING NEW, SOMETHING BORROWED, SOMETHING BLUE

Naomi C. Chesler

Department of Biomedical Engineering
University of Wisconsin-Madison
Madison, WI USA

INTRODUCTION

As early as 1966, YC Fung was advancing understanding of blood flow in the lungs [1]. According to an oral history [2], he first studied the lung in order to solve a problem posed by Dr. Benjamin Zweifach, a famous microcirculatory physiologist, which led to an even more exciting, long-lasting, and productive collaboration with Sidney Sobin, a pulmonary physiologist. According to the oral history, because so little was known about tissue mechanics when he entered the field, he had to measure it all: "From geometry, anatomy, histology, mechanical properties, to physiology and pathology."

So the study of arterial mechanics, even pulmonary arterial mechanics, is quite old. That said, since the 1960s there have been many advances that have facilitated the study of pulmonary arterial mechanics, including imaging technologies (i.e., echocardiography, MRI, optical coherence tomography, second harmonic imaging, and others), instrumentation (e.g., 1.2F pressure catheters, ultrasound-based flow sensors), biological innovations (e.g., microRNA, CRISPR/Cas9), and computational modeling approaches. As a result, there is much knowledge of pulmonary arterial mechanics to be gained that is new.

While YC Fung initially focused his attention on the pulmonary vasculature and developed techniques to study the "lesser" circulation specifically, the field of vascular mechanics is dominated by attention to the systemic circulation. As a consequence, many approaches to investigating pulmonary arterial mechanics are borrowed ones designed for measuring systemic arterial mechanics. Significant differences in mean and pulse pressure, relative wall thickness, branching pattern and even luminal oxygen concentration call the appropriateness of these into question. The common illustrations in which pulmonary arteries are blue and systemic arteries are red belie a host of other differences in structure and function that have physiological and pathological consequences.

REPRESENTATIVE METHODS & RESULTS

Direct measurements of large pulmonary artery mechanics can be obtained ex vivo in static [3] or dynamic conditions [4] by controlling transmural pressure in cannulated arteries while diameter is measured by standard, dynamic light microscopy since the pulmonary artery wall is so thin relative. As shown in Figure 1, chronic pulmonary hypertension alters both static and dynamic properties of pulmonary arteries as a nonlinear function of frequency [4].

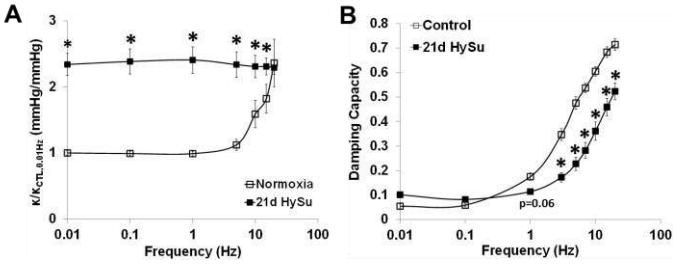

Figure 1: Frequency-dependent (A) structural stiffness κ normalized to κ of control at 0.01 Hz and (B) and damping capacity of pulmonary arteries from control animals and those exposed to 21 days of pulmonary hypertension (21d HySu). N = 5 per group. * p<0.05 vs. control. See [4] for methodological details.

If arteries cannot be cannulated, which is often the case for the short segments in the highly branching pulmonary vascular network, mechanics can be measured in contrast-perfused lungs [5] or in vivo [6] by quantifying diameters at known pressures using computed tomography, as shown in Figure 2, ultrasound, or magnetic resonance imaging.

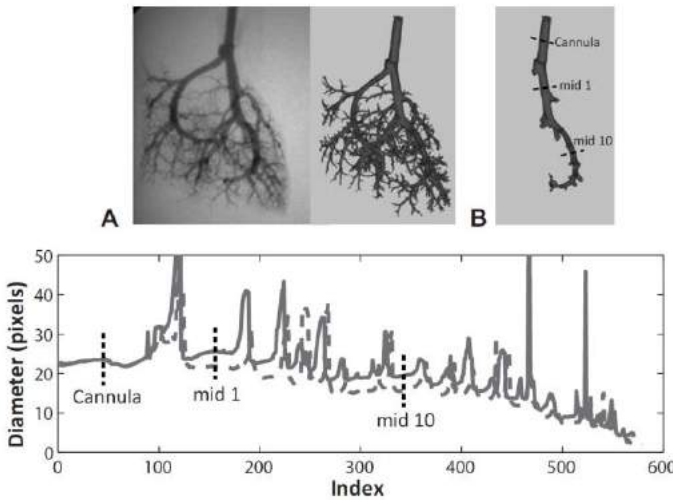

Figure 2: (A) Planar computed tomography images of lung arteries reconstructed into 3D volumes. A 3D surface mask used to isolate (B) the right principal pathway. Then, the centerline coordinates and best fit diameters can be found for the principal pathway. (Bottom panel) Representative measurements of the mid-branch diameter for the first segment (mid 1) and the 10th segment (mid 10) as well as the pulmonary artery cannula (Cannula) at two different pressures. From [5].

Alternatively, large pulmonary arterial mechanics can be estimated from area-flow relationships non-invasively [7] (Figure 3) or pulmonary vascular impedance invasively [8, 9] (Figure 4). Distal pulmonary arterial mechanics can be estimated from pressure-flow relationships assuming all small arteries have the same stiffness [10].

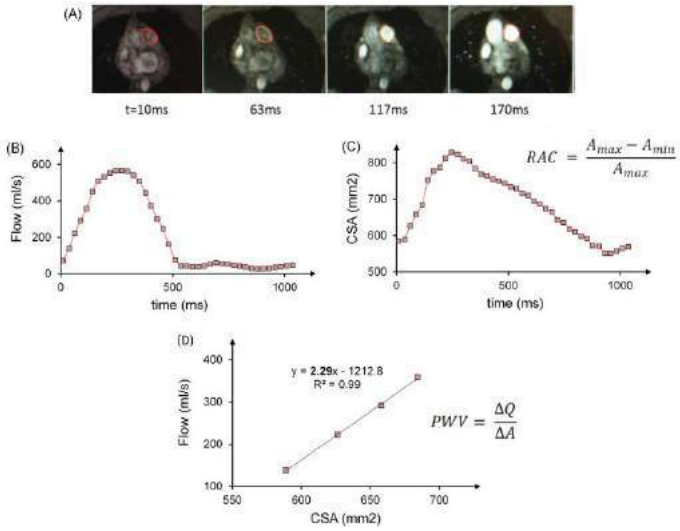

Figure 3. (A) Time-lapse of magnetic resonance images of main pulmonary artery (PA) cross-section during early systole. (B) and (C) Flow rates and cross-sectional area (CSA) of the main PA were assessed based on the contours shown in the images (red). (D) Flow and CSA are measured from the MRI phase contrast-derived velocity maps integrated over the MRI magnitude-derived area. PWV velocity is calculated as the slope of QA plot at early systole. From [7].

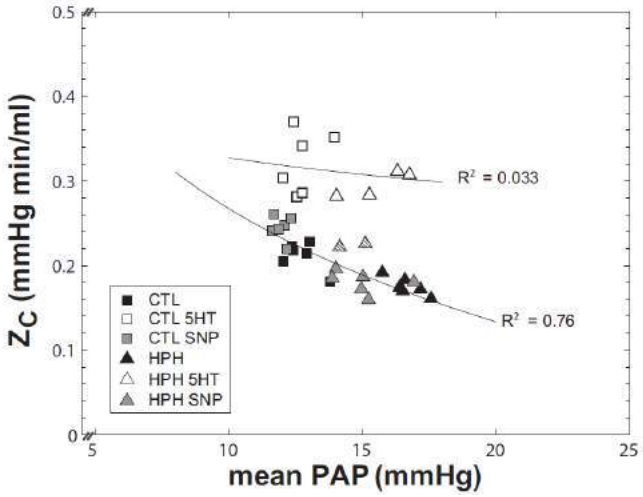

Figure 4. Characteristic impedance (Z_C) as a function of mean pulmonary artery pressure (mean PAP) for control (CTL) and chronically hypoxic (HPH) lungs untreated, treated with serotonin (5HT, white) or sodium nitroprusside (SNP, gray). From [8].

DISCUSSION

Pulmonary arterial mechanics are critical to the ability to exercise, the progression of disease, and right ventricular function. Building on the foundational insights of Professor YC Fung, our knowledge of pulmonary arterial mechanics has grown exponentially since his first forays in this field over 50 years ago. But some things haven't changed; we still begin with geometry and anatomy to assess mechanical properties and use mechanics to understand physiology and pathology.

ACKNOWLEDGEMENTS

The creativity and hard work of past and current members of the Vascular Tissue Biomechanics lab are gratefully acknowledged.

REFERENCES

1. Fung, Zweifach, and Intaglietta, Circ Res, 1966. **19**(2): p. 441-61.
2. Nebeker, *Yuan-Cheng "Bert" Fung: An oral history conducted in 2000*. 2000, Hoboken, NJ USA: IEEE History Center.
3. Chesler, Thompson-Figueroa, and Millburne, J Biomech Eng, 2004. **126**(2): p. 309-14.
4. Wang, Lakes, Golob, Eickhoff, and Chesler, PLoS One, 2013. **8**(11): p. e78569.
5. Vanderpool, Kim, Molthen, and Chesler, J Appl Physiol (1985), 2011. **110**(1): p. 188-98.
6. Bellofiore, Henningsen, Lepak, Tian, Roldan-Alzate, Kellihan, Consigny, Francois, and Chesler, J Biomech Eng, 2015. **137**(4): p. 044501.
7. Forouzan, Warczytowa, Wieben, Francois, and Chesler, J Cardiovasc Magn Reson, 2015. **17**: p. 109.
8. Vanderpool, El-Bizri, Rabinovitch, and Chesler, Biomech Model Mechanobiol, 2013. **12**(1): p. 33-42.
9. Vanderpool, Naeije, and Chesler, Ann Biomed Eng, 2010. **38**(5): p. 1854-61.
10. Chesler, Argiento, Vanderpool, D'Alto, and Naeije, Conf Proc IEEE Eng Med Biol Soc, 2009. **2009**: p. 173-6.

SB³C2019
Summer Biomechanics, Bioengineering and Biotransport Conference
June 25 -28, Seven Springs, PA, USA

CORONARY CALCIFICATIONS: FROM VESICLES TO PLAQUE RUPTURE

Natalia Maldonado (1), Luis Cardoso (2), Sheldon Weinbaum (2)

(1) Electrical Engineering,
New York City College of Technology
Brooklyn, NY, USA

(2) Biomedical Engineering
The City College of New York
New York, NY, USA

INTRODUCTION

Approximately half of all cardiovascular deaths associated with acute coronary syndrome occur with the rupture of a vulnerable plaque, when a thin fibrous cap overlying a lipid rich core is ripped or fissured under the action of high blood pressure [1]

Clinical studies show that calcium score is an excellent predictor of cardiovascular morbidity and mortality, and coronary calcification is the most widely used marker of the advancement of atherosclerosis [2]; However, the identification of atheromas prone to rupture and the cause of subsequent acute cardiovascular events, such as myocardial infarction and stroke, is still challenging. Criteria based on morphology and tissue composition such as fibrous cap thickness, vasa-vasorum, necrotic core size, and macrophage infiltration [3] have been found to be relevant, but insufficient, to identify vulnerable plaques and assess the risk of rupture. Moreover, the link between calcification and plaque rupture is still controversial.

Formerly, the prevailing view was that the presence of calcification within atherosclerotic plaques acted as a biomechanical stabilizer. Indeed, large calcifications easily detected with coronary computed tomography (CT) do not seem to increase plaque vulnerability [4]. However, recent studies indicate an inverse relationship between cardiovascular risk and calcification density [5], and spotty or speckled areas of calcification, observed from intravascular ultrasound (IVUS) or optical coherence tomography (OCT) are a good indicator of susceptibility of rupture [6]. These observations provide insights into the role calcification may play in the stability of the atherosclerotic plaque and suggest that it is not only the amount of vascular calcification, but the morphology, size and location that affect plaque vulnerability.

A biomechanical explanation for the contribution of low density, spotty calcifications to plaque rupture is centered on subcellular microcalcifications that exist within the thin fibrous cap of atherosclerotic plaques [7]. Finite-element modelling of the stress distribution within plaques indicates that these microcalcifications promote material failure of the fibrous cap [8,9]. Their presence within it greatly increases the stress in the intimal tissue, leading to rupture and the subsequent thrombus formation and vessel occlusion. Microcalcifications (μCalcs) > 5μm within the cap have been shown to produce a 200–700% increase in peak circumferential stress, which transforms a stable plaque into a vulnerable one [10].

The origin of these dangerous microcalcifications remains largely unknown; In-vitro studies suggest that vascular calcifications form as part of an active, cell-mediated process involving the differentiation of multipotent cells and VSMCs into osteoblast-like cells. The osteochondrogenic transformation of SMCs in the vasculature initiate the formation and release of specialized phospholipidic membrane-bound bilayer structures with sub-micron diameter size named matrix vesicles (MVs) [11]. Calcium phosphate accumulates inside these matrix vesicles, forming hydroxyapatite crystals similar to bone formation. Once the mineral inside the MVs grows and penetrates the membrane, it can mineralize in the interstitial space [12] and grow, possibly following a passive crystal growth mechanism.

In this study, we examine individual human atheroma considering gross morphological features and the presence of calcified particles of sizes ranging from the subcellular level, to large calcifications a few mm in diameter. The quantitative analysis of the detailed axial progression of calcification within the necrotic core and fibrous cap of the atheroma, provides novel insights into the coronary calcification process.

METHODS

Specimens: Ninety-six human coronary arteries were harvested from 32 atherosclerotic whole human hearts obtained from the National

Disease Research Interchange. All procedures were approved by Institutional Animal Care and Use Committees of the City College of New York, NY.

High Resolution Micro Computed Tomography Scanning: Coronary specimens were scanned using a high resolution micro computed tomography (HR-μCT) system (1172, SkyScan, Belgium) at 2.1-μm resolution. Histology: Atheromas were processed for high-fidelity histological analysis of non-decalcified coronary arteries [12]. using Alizarin Red S, von Kossa and Trichrome staining.

μCalcs quantification: HR-μCT images of the atheromas were binarized to segment the calcified particles from the soft tissues in the atheroma using a global thresholding method [12] The volume, position and equivalent spherical diameter was calculated for each calcified particle. The size of the necrotic core was measured as the maximum area in the intima beneath the fibrous cap. Then, the region of the plaque of minimum cap thickness was identified and measured as the shortest distance between the necrotic core and the lumen

RESULTS

The quantitative analysis of calcifications within the atheroma reveals distinct patterns: microcalcifications at the core boundary, microcalcifications within the core, large calcifications within the core and advanced calcifications. The first pattern, microcalcifications at the core boundary, describes what seems to be the initial stage of calcification development, submicron and micron-size calcified particles that are aligned at the interface between the soft tissue and the necrotic core, possibly constrained by the internal elastic lamina in Figure 1A. The atheroma looks like a soft plaque, characterized by a mixed lipid/necrotic core, containing a few isolated μCalcs within the core, and 0.5 - 5μm size μCalcs appearing as a fuzzy/dotted border at the core boundary. The second pattern includes microcalcifications within the core, in which small calcified particles < 100μm diameter are dispersed within the necrotic core. As shown in Figure 1B, μCalcs > 5μm visible at 2.1-μm resolution cluster to form more abundant and larger μCalcs within the core. The third pattern is characterized by large calcifications within the core, where calcifications > 100μm diameter either fuse together or grow through a crystallization process forming a calcification front and large calcifications in the core (Figure 1C). Large calcifications within the core may form large shells, which may fracture radially. The last pattern comprises advanced calcifications, which can grow until they completely fill the entire core area forming an advanced calcified plaque (Figure 1D), in some cases growing beyond the core and extending into the tunica media. Advance calcifications may also undergo fracture and form calcified nodules with fibrin deposition. These calcified nodules are sometimes seen protruding into the lumen, where they have been associated with a thrombogenic response and cardiovascular events.

Most atheroma (75.4%) exhibit a combination of 2 or more of the patterns described above. As shown in Figure 1, all four calcification patterns are found at contiguous locations in this single atheroma along its axial length.

DISCUSSION

One of the key contributions of this study using HR-μCT is to gain a better understanding of the calcification process that fibroatheromas undergo. Large calcifications > 50μm in diameter, that were often thought to be external to lipid/necrotic core are actually a part of a process in which microcalcifications agglomerate and form a crystallization front that advances from one boundary of the core and then spreads inward. We observed four distinct calcification patterns in the lipid /necrotic core that suggest different stages of calcification progression.

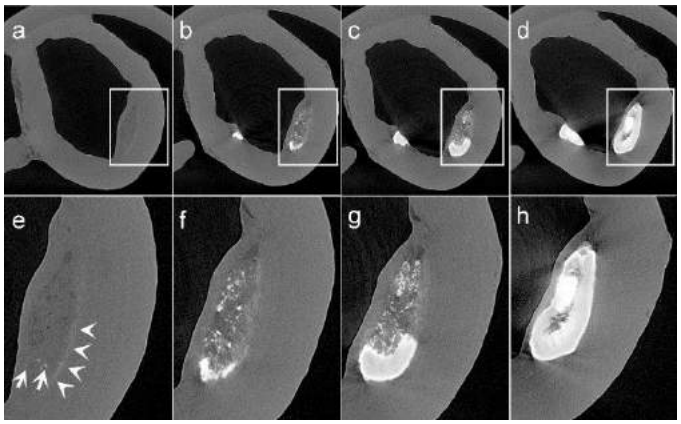

Figure 1. Sequence of images from a human atheroma taken approximately 250μm apart from each other displaying the spatial progression of calcification process in atheroma. (**A**, **E**) a soft plaque, characterized by a mixed lipid/necrotic core, containing few isolated μCalcs within the core, (**B**, **F**) submicron μCalcs cluster to form more abundant and larger μCalcs within the core of the lesion, (**C**, **G**) microcalcifications further agglomerate to create a larger macrocalcification within the core, (**D**, **H**) the calcification fills the entire core area.

The frequency of each of these four patterns is quantified and it is shown that ¾ of all atheromas exhibit two or more of the patterns. Small μCalcs accumulating at the borders of the core are the most commonly found pattern in this sample of 72 atheromas. Consistent with our findings, previous studies had described the presence of submicron size calcifications in the early stages of plaque progression; However, the use of high-resolution 3D images of the entire plaque, allows a unique description of the calcification process, that links the findings of calcified matrix vesicles with the large calcifications routinely seen in the clinic.

Elucidating the active process wherein cellular-derived vesicles serve as nucleating foci for the formation microcalcifications within the plaque provides hope that therapeutic strategies may be developed to target dangerous microcalcifications. As future studies progress our understanding of the nucleating events of mineralization, the development of preventive strategies for calcification or therapeutic interventions that may reduce calcification or shift it to a more favorable phenotype may be within reach

ACKNOWLEDGEMENTS

This research has been supported by NIH HL136431, DK103362, National Science Foundation 0723027, 1229449, 1333560 and 1662970.

REFERENCES

[1] Virmani, R et al., J Interv Cardiol.,16(3):267–272. 2003
[2] Otsuka, F et al., Arterioscler Thromb Vasc Biol; 34:724–736. 2014
[3] Virmani R, et al., The Vulnerable Atherosclerotic Plaque. Blackwell; 2007
[4] Lin TC, et al., Ann Biomed Eng. Oct; 34(10):1535-41. 2006
[5] Criqui MH, et al., JAMA; 311(3):271-8. 2014
[6] Ehara S, et al., Circulation. Nov 30; 110(22):3424-9. 2004
[7] Kelly A, Maldonado N, et al. PNAS; 110:10741–10746. 2013
[7] Maldonado N, et al., Am J Physiol Heart; 303:H619–628. 2012
[8] Hutcheson J, et al. Curr Opin Lipidol; 25(5): 327–332. 2014
[9] Maldonado N, et al. J Biomech; 46:396–401. 2013
[10] Hutcheson J, et al. Nature Materials 15, 335–343. 2016
[11] Bertazzo, S. et al. Nature Mater. 12, 576–583. 2013
[12] Maldonado N, et al., Int J Cardiov Imag; 31(5): 1079–1087. 2015

SB³C2019
Summer Biomechanics, Bioengineering and Biotransport Conference
June 25 -28, Seven Springs, PA, USA

THE IMPACT OF HEMODYNAMIC REFLEX COMPENSATION FOLLOWING MYOCARDIAL INFARCTION ON SUBSEQUENT VENTRICULAR GROWTH

Colleen M. Witzenburg (1), Jeffrey W. Holmes (2,3)

(1) Department of Biomedical Engineering
University of Wisconsin
Madison, WI, USA

(2) Department of Biomedical Engineering
University of Virginia
Charlottesville, VA, USA

(3) Department of Medicine
University of Virginia
Charlottesville, VA, USA

INTRODUCTION

Post-infarction heart failure is an important problem because it is common, with an incidence of 16 to 30% [1], and it is difficult to treat, with a 1-year mortality of 31 to 45% [1,2]. The development of heart failure following myocardial infarction (MI) is driven by a number of processes, however changes in regional mechanics play a central role by triggering myocyte elongation and left ventricular (LV) dilation.

Although the extent of post-infarction hypertrophy and dilation correlates with infarct size, there is striking variability in individual patients, particularly among those with moderately sized infarcts (15-25%) [3]. We hypothesized that compensatory reflexes that act to preserve mean arterial pressure following MI might be an important source of this variability. These reflexes trigger a suite of responses through the sympathetic nervous system, including an increase in heart rate, an increase in contractility of the surviving myocardium, arterial vasoconstriction, and venous vasoconstriction. Sympathetic activation not only directly promotes myocyte hypertrophy through intracellular signaling pathways, but also indirectly modulates hypertrophy by affecting the load placed on the myocardium. Thus, variability in post-infarction sympathetic activation could represent both a source of individual variability in the extent of LV remodeling and a target for therapies aimed at reducing that remodeling.

Studying post-infarction reflex compensation is complicated by the fact that some of the responses listed above cannot be directly determined from routinely available hemodynamic data. Thus, we used a computational model to reinterpret published hemodynamic measurements to better understand the contributions and variability of the individual compensatory mechanisms following MI. We then employed a published growth model to predict how variability in compensation might translate to variability in global LV remodeling.

METHODS

Modeling the Compensatory Response Post-Infarction

Compensatory responses post-infarction were modeled using our recently published compartmental model of the LV coupled to a circuit model of the circulation to simulate hemodynamics throughout the cardiac cycle [4]. Four model parameters reflect the primary hemodynamic compensations that occur in response to myocardial infarction: heart rate (HR), systemic vascular resistance (SVR, changes with arterial vasoconstriction), end-systolic elastance of the non-infarcted compartment (E_n, changes with myocardial inotropic state), and stressed blood volume (SBV, changes with venous vasoconstriction). Heart rate was prescribed directly in the model. We estimated SVR using the measured ratio of mean arterial pressure to cardiac output. The contractility of an intact ventricle is typically quantified by the slope of its end-systolic pressure-volume behavior [5,6]. In an infarcted heart, however, this slope depends not only on the behavior of the surviving contractile myocardium but also on the behavior of the non-contractile infarct region. Thus E_n could not be measured directly. Furthermore, SBV is rarely reported because measuring it typically involves circulatory arrest [7,8]. Therefore, we used the model to fit E_n and SBV simultaneously by minimizing the sum squared error in other experimentally reported hemodynamic values: LV end-diastolic pressure, the maximum derivative of LV pressure, and mean arterial pressure.

Simulating Left Ventricular Growth

To capture how differences in hemodynamic compensation can lead to differences in subsequent ventricular hypertrophy, we used our previously published model of post-infarction growth [4]. Briefly, an increase in the maximum circumferential strain drives dilation and an increase in the maximum radial strain drives thickening. No changes to

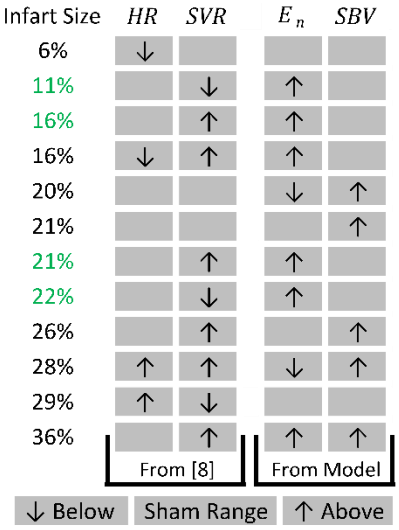

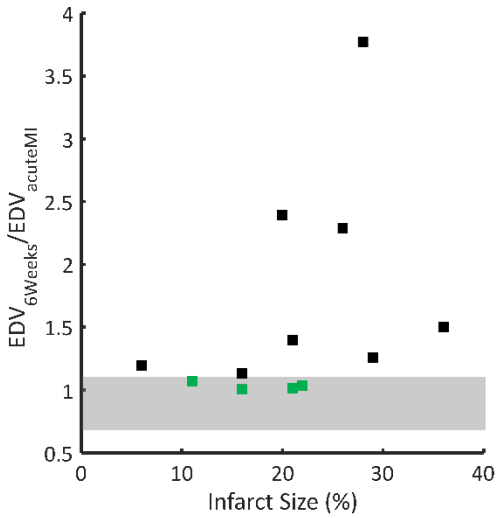

Fig. 1 A) Computed compensatory reflex profiles and B) predicted change in LV end-diastolic volume 6 weeks post-infarction for each infarct dog from [8].

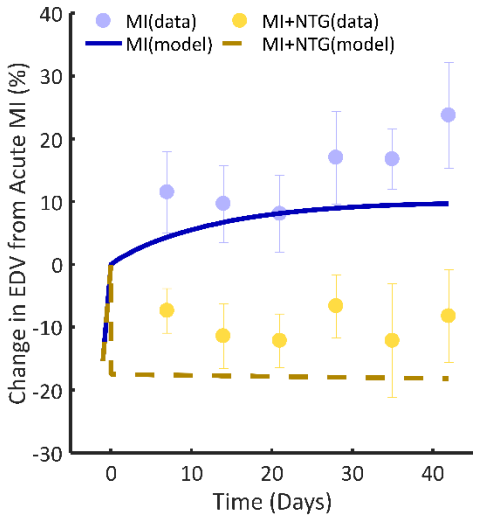

Fig. 2 The change in end-diastolic volume over 6 weeks with and without nitroglycerin.

the previously published growth parameters were made for this study.

RESULTS

Variability in Post-Infarction Compensation and LV Dilation

We fitted individual data from 4 sham and 12 acutely infarcted dogs originally published by [9] to assess the variability in compensatory responses post-infarction. Our optimization procedure matched the reported hemodynamics well (sum squared error < 9% in all cases), and optimized values were insensitive to initial guesses. There was a high degree of individual variability in the reported (HR and SVR) and fitted (E_n and SBV) responses to MI (Fig 1A). Overall, there was no clear relationship between infarct size and the compensatory mechanisms employed.

We tested whether the variability in hemodynamic compensation observed for [9] would lead to variability in predicted ventricular hypertrophy by simulating 6 weeks of ventricular growth for each infarct animal. We assumed hemodynamic parameters remained stable at their acute post-infarction values. Although the predicted change in end-diastolic volume (EDV) generally increased with infarct size (Fig. 1B), there was considerable variability, due in part to the mix of compensatory mechanisms employed. Animals with little dilation are labeled in green in Fig. 1. Interestingly, those with the least predicted dilation all exhibited increases in the contractility of the surviving myocardium with little change in heart rate or venoconstriction.

Effects of Therapeutic Intervention on Compensation and LV Dilation

We also simulated data from [10] in which nitroglycerin was administered following coronary occlusion to test the model's ability to assess changes in post-infarction hemodynamic compensation due to drug treatment. On average, dogs in that study compensated primarily by increasing heart rate. Simulated treatment with the vasodilator nitroglycerin reduced systemic vascular resistance and to a lesser degree stressed blood volume. Heart rate and myocardial contractility both increased, suggesting that animals relied more on these mechanisms.

Next, we tested whether the hemodynamic change induced by nitroglycerin would lead to different growth predictions by simulating 6 weeks of ventricular growth utilizing the acute hemodynamic parameters fitted above. We compared the predictions to data on the effect of nitroglycerin on post-infarction remodeling reported by [11]. In the absence of nitroglycerin treatment, the model correctly predicted the observed post-infarction increases in LV volume (Fig. 2). With infarction plus nitroglycerin treatment, the model predicted an acute drop in LV volume (Fig. 2) but no subsequent dilation, consistent with the results reported by [11]. Data show mean ± SE.

DISCUSSION

The model simulations presented here suggest that post-infarction reflex compensation could be both a source of individual variability in the extent of LV remodeling and a target for therapies aimed at reducing that remodeling. We found a strikingly wide range of compensatory reflex profiles in response to MI. Most animals employed one or two mechanisms, but in some cases heart rate, systemic vascular resistance, or myocardial elastance actually reduced in individual dogs even as they compensated with other mechanisms. This variability in compensation translated to variability in the degree of predicted LV dilation consistent with variability reported in the literature. Treatment with a vasodilator had the expected result of shifting the compensatory response away from arterial and venous vasoconstriction and towards increased heart rate and myocardial contractility. Importantly, this shift reduced predicted LV dilation, a prediction that matched prior experimental studies well.

Heart failure is one of the most difficult to treat and deadly complications of MI. We propose that there may be opportunities to intervene early after infarction to prevent or reduce LV dilation that leads to failure, and that computational models can play an important role in customizing therapies to account for variability among individuals.

ACKNOWLEDGMENTS

This work was supported by funding from the National Institutes of Health (U01 HL 127654, JWH) and the American Heart Association (17 POST 33660943, CMW).

REFERENCES

[1] Benjamin, E. et al., *Circulation*, 137:e67-492, 2018. [1] Chen, J. et al., *Circulation*, 128:2577-84, 2013. [3] Wu, E. et al., *Br Heart J*, 94:6:730-6, 2008. [4] Witzenburg, CM. et al., *J Cardiovasc Trans Res*, 11:2:109-22, 2018. [5] Suga, H. et al., *Circ Res*, 32:3:314–22, 1973. [6] Grossman, W., et al., *Circulation*, 56:5:845–52, 1977. [7] Magder, S. & De Varennes., B. *Crit Care Med*, 26:6:1061–4, 1998. [8] Gelman, S.. *Anesthesiology*, 108:4:735–48, 2008. [9] Hood, WB. et al., *Circ Res*, 21:2:191-9, 1967. [109] Theroux, P. et al., *Circulation*, 53:2:302–14, 1976. [10] Jugdutt, BI. & Khan MI. *Circulation*, 89:5:2297–307, 1994.

SB³C2019
Summer Biomechanics, Bioengineering and Biotransport Conference
June 25 -28, Seven Springs, PA, USA

EFFECT OF LTBP-3 ON THE CIRCUMFERENTIAL AND AXIAL MECHANICS OF THE AORTA IN A MOUSE MODEL OF MARFAN SYNDROME

Arina Korneva (1), Arunika Makam (2), Jay D. Humphrey (1,3), Chiara Bellini (2)

(1) Department of Biomedical Engineering
Yale University
New Haven, CT, USA

(2) Department of Bioengineering
Northeastern University
Boston, MA, USA

(3) Vascular Biology and Therapeutics Program
Yale School of Medicine
New Haven, CT, USA

INTRODUCTION

Marfan syndrome (MFS) is an autosomal dominant disorder of connective tissues that results from mutations to the gene coding for the extracellular matrix glycoprotein fibrillin 1. Alongside other glycoproteins, fibrillin 1 associates with elastin to form the elastic fibers that endow the aortic wall with sufficient compliance to accommodate changes in blood flow throughout the cardiac cycle. Although MFS patients also manifest skeletal and ocular disorders, it is their predisposition to develop aneurysms of the ascending aorta (TAA) that often threatens their life.

Reduced fibrillin 1 content accelerates elastic fiber degradation due to mechanical fatigue [1] and increased MMP activity mediated by TGFβ [2]. TGFβ is secreted by the cell as a large latent complex, where the small latent complex consisting of TGFβ and a TGFβ propeptide is covalently linked to a latent TGFβ binding protein (LTBP). It has been shown that the interaction between fibrillin 1 and LTBP-3 mediates the sequestration of TGFβ in the matrix in vitro [3]. Furthermore, absence of LTBP-3 renormalizes signaling downstream of TGFβ and improves the survival rate in the *Fbn1*$^{mgR/mgR}$ mouse model of MFS [3]. Here we report a mechanical characterization of the ascending (ATA) and proximal descending (DTA) thoracic aorta from *Fbn1*$^{mgR/mgR}$:*Ltbp3*$^{-/-}$ mice compared to MFS and control vessels.

METHODS

Mechanical testing. Aortic specimens between the aortic root and the diaphragm were excised from 8-9 week-old mice. Following removal of perivascular tissue and ligation of lateral branches, specimens were secured to glass cannulae and coupled to a computer-controlled biaxial device in preparation for mechanical testing. Arteries were acclimated and preconditioned with cyclic pressurization to in vivo pressures, while maintained at their preferred in vivo axial stretch (λ_z^{iv}). Biaxial protocols consisted of cyclic pressurization between 10 and 140mmHg, with the specimens held at constant axial length (λ_z^{iv} and $\lambda_z^{iv} \pm 5\%$), and cyclic axial extension up to an axial force of 40-60mN, with constant luminal pressure (10, 60, 100, and 140 mmHg). Outer diameter, luminal pressure, axial force, and axial stretch were measured online during testing. Tested specimens were fixed in formalin overnight and sent for histological analysis.

Constitutive modeling. Aortic tissue was modeled as a (pseudo)hyperelastic material, i.e. we postulated the existence of a strain energy potential W, from which stress and stiffness were obtained by first and second order differentiation with respect to an appropriate measure of deformation. We assumed a four-fiber-family form of W to capture the isotropic contribution of the amorphous matrix and transversely isotropic behavior of ECM fibrillar proteins,

$$W(\mathbf{C}, \mathbf{M}^j) = \frac{c}{2}(I_\mathbf{C} - 3) + \sum_{i=1}^{4} \frac{c_1^i}{4c_2^i}\left\{\exp\left[c_2^i\left(IV_\mathbf{C}^i - 1\right)^2\right] - 1\right\},$$

where c, c_1^i, and c_2^i are material parameters, $\mathbf{C} = \mathbf{F}^\mathrm{T}\mathbf{F}$ is the right Cauchy-Green deformation tensor, $\mathbf{F}$ is the deformation gradient tensor, $I_\mathbf{C}$ and $IV_\mathbf{C}^i$ ae the first and fourth invariants of $\mathbf{C}$, $\mathbf{M}^j$ is a vector in the fiber direction, and $det\mathbf{F} = 1$ for assumed incompressibility. Experimental values of stress were inferred as radial averages. Material parameters were estimated with a nonlinear least-square regression and used to simulate the mechanical response of the aorta under loading conditions of interest.

Assessment of the skeletal manifestations of MFS. An Inveon™ micro-PET/CT scanner with an 80-W, 35- to 80-kVp tungsten-anode X-ray source (Siemens) was used to acquire whole-body CT scans of mice placed in a prone position following euthanasia. Cross sectional images

were segmented in Mimics (Materialize) to create a 3D model of the skeleton. The kyphotic curve of the thoracic spine was characterized using dorsal-ventral asymmetries in the length of the vertebrae between T4 and L6 [4].

RESULTS

Gross anatomy. Although *Fbn1*$^{mgR/mgR}$:*Ltbp3*$^{-/-}$ mice have lower body mass (21.9 ± 1.5g) compared to controls (29.2 ± 0.4g), the ratio between the systolic diameter of the ATA and their body mass falls within the confidence intervals for normal allometric scaling (Figure 1). This suggests that absence of LTBP-3 prevents or retards aneurysm formation in MFS mice, at least to 9 weeks of age.

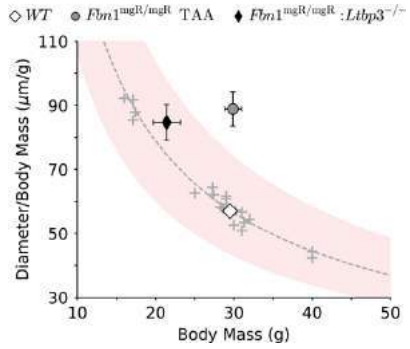

Figure 1: Normal allometric scaling for the ATA diameter

Circumferential mechanics. Figure 2 displays the mechanical behavior of the ATA in the circumferential direction as estimated from biaxial tests. While the Pressure *vs*. Outer diameter (A) and the Cauchy stress *vs*. stretch (B) response of aneurysmal MFS mice clearly reflects the effects of fragmentation of elastic fibers within the media [2], the curve for *Fbn1*$^{mgR/mgR}$:*Ltbp3*$^{-/-}$ mice overlaps that for controls. Consistently, absence of LTBP-3 restores normal values of circumferential stiffness (C), a parameter that was shown to strongly correlate with the propensity for and the development of thoracic aortic aneurysms [5]. Results for the DTA (not shown) mirror those for the ATA.

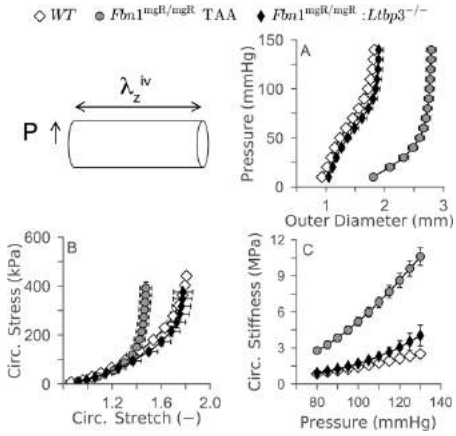

Figure 2: Circumferential mechanics of the ATA

Axial mechanics. Despite the reduced elastic fiber fragmentation in the *Fbn1*$^{mgR/mgR}$:*Ltbp3*$^{-/-}$ aorta, both the DTA and the ATA of double mutant mice have limited axial extensibility. The in vivo axial stretch (λ_z^{iv}) in the ATA of *Fbn1*$^{mgR/mgR}$:*Ltbp3*$^{-/-}$ mice (1.41 ± 0.02) is comparable to that of MFS mice (1.42 ± 0.06) and significantly reduced from WT mice (1.70 ± 0.04). Similarly, the in vivo axial stretch of the DTA is 1.44 ± 0.03 and 1.45 ± 0.03 in *Fbn1*$^{mgR/mgR}$:*Ltbp3*$^{-/-}$ and MFS mice, respectively, compared to 1.60 ± 0.05 in controls (Figure 3, A). Furthermore, the DTA from both *Fbn1*$^{mgR/mgR}$:*Ltbp3*$^{-/-}$ and MFS mice maintained a significant curvature upon excision, while the control DTA remained fairly straight (B). Given that the basis of this behavior was not microstructurally-related, we shifted our focus on surrounding organs and tissues that impose structural constraints to the aorta. Amongst those, the spine provides support to the DTA, which is tethered to the vertebrae by the intercostal arteries.

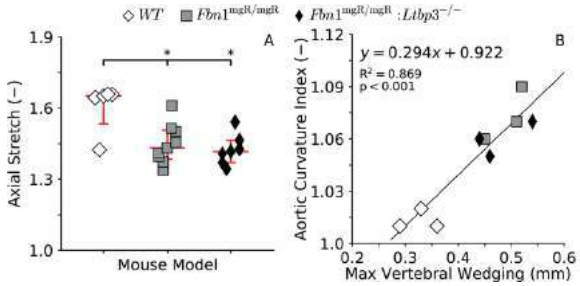

Figure 3: Axial stretch and curvature of the DTA

Thoracic kyphosis. The kyphotic curve of the thoracic spine was exacerbated in MFS mice, as indicated by the pronounced wedging of the vertebrae in the dorsal-ventral plane (Figure 3, B). Furthermore, a strong correlation existed between the curvature of the unloaded aorta and the degree of spinal kyphosis, suggesting that the spine may play a role in the axial development of the aorta throughout somatic growth.

DISCUSSION

Increased TGFβ activity often characterizes syndromic or familiar connective tissue disorders that predispose affected individuals to the development of thoracic aortic aneurysms, including MFS. Consistent with this observation, the mechanical analysis of the *Fbn1*$^{mgR/mgR}$:*Ltbp3*$^{-/-}$ aorta is consistent with the thought that renormalization of TGFβ signaling through removal of LTBP-3 [3] protects MFS mice from thoracic aneurysms up to 9 weeks. First, double mutant aortas exhibited normal diameter compared to weight-matched controls. Second, absence of LTBP-3 reduced the predisposition towards aortic dilatation by contributing to the decrease in circumferential stiffness [5].

Despite normalizing circumferential properties, absence of LTBP-3 did not restore the axial mechanics of the thoracic aorta in MFS mice. While the progressive fragmentation of the elastic fibers is responsible for the decreased in vivo stretch of the MFS aorta, other mechanisms may influence the axial mechanics of the *Fbn1*$^{mgR/mgR}$: *Ltbp3*$^{-/-}$ aorta, where elastic fibers are intact. The correlation between the curvatures of the aorta and the spine that emerged from our analysis hints to a possible coupling between the development of the vascular and skeletal systems that could influence the axial behavior of the aorta. Although the connection between the spine and the thoracic curvature necessitates further investigation, our results suggest that the skeletal phenotype might influence the vascular phenotypes in MFS.

ACKNOWLEDGEMENTS

We thank the Rifkin lab at NYU for providing the mice.

REFERENCES

[1] Ferruzzi, J et al., *Cardiovasc Res*, 92:287-295, 2011.
[2] Neptune, ER et al., *Nat Genet*, 33:407-411, 2003.
[3] Zilberberg, L et al., *Proc Natl Acad Sci*, 112:14012-14017, 2015.
[4] Li, B et al., *Bone Res*, 5:16053, 2017.
[5] Bellini, C et al., *J R Soc Interface*, 14: 20161036, 2014.

SB³C2019
Summer Biomechanics, Bioengineering and Biotransport Conference
June 25 -28, Seven Springs, PA, USA

CONTRIBUTION OF MATRIX REMODELING TO BIAXIAL MECHANICS OF RIGHT-VENTRICULAR MYOCARDIUM IN PULMONARY ARTERIAL HYPERTENSION

D. Vélez-Rendón (1), Justin Shieh (2), D. Valdez-Jasso (2)

(1) Department of Bioengineering
University of Illinois
Chicago, IL, United States

(2) Department of Bioengineering
University of California San Diego
La Jolla, CA, United States

INTRODUCTION

Right-ventricular (RV) function is a good prognostic indicator in pulmonary arterial hypertension (PAH), a progressive vasculopathy that commonly results in intractable RV failure and premature death. It has been shown in humans and animal models of PAH that the RV hypertrophies in response to increased RV systolic pressure, which can be associated with tissue fibrosis and altered end-diastolic stiffness. However, the extent to which altered RV chamber stiffness is due to increased RV wall stiffness, altered extracellular matrix (ECM) content or altered intrinsic ECM material properties remains unclear. Our recent (unpublished) measurement and model analysis of changes in RV geometry and hemodynamics suggest that by 6 weeks of PAH in a sugen-hypoxia animal model, RV end-diastolic chamber stiffness is significantly greater than baseline and that increase cannot be explained by the increased RV wall thickness alone. Hence, we sought to determine the extent to which increased resting myocardial material stiffness in this model could be attributed to changes in myocardial ECM content or changes in biaxial stress-strain properties of decellularized RV myocardium. We also found that the biaxial stress-strain tests in ionic and decellularized RV myocardium are well approximated by exponential strain energy functions first proposed by Y-C Fung, and we propose a new mixture based constitutive theory that allows these experimental measurements to be used in a novel strain energy formulation that accounts for matrix pre-stress in the myocardium and allows the contributions of ECM, myocytes and their interactions to the total strain energy to be separately identified.

METHODS

Male Sprague-Dawley rats were injected with a single dose of 20mg/kg of Sugen (SU5416, Sigma-Aldrich), a VEGF receptor inhibitor, and were placed in a hypoxia (10% oxygen) chamber for 3 weeks to induce PAH. Three weeks post returning to normoxia, *in-vivo* hemodynamic measurements were taken to assess ventricular function. The control group was untreated and maintained in normoxia.

Immediately after the hemodynamic measurements, the heart was harvested and the RV isolated and dissected. A square sample of the free wall was excised and oriented with one primary axis from the apex to the RV outflow-tract. Thickness, weight and surface dimension measurements were made. Four custom-made hooks were placed on each side of the sample and attached to the pulley-system of the Bose Electro Force planar biaxial testing device. While kept in an oxygenated and temperature-controlled bath of PBS, 4 material markers placed on the surface of the specimen were brought into the visual field of the optical tracking system to compute the deformation gradient tensor. The mechanical testing consisted of stretch-controlled biaxial tests with biaxial ratios of 1:0.5, 1:0.25 ,1:1, 0.5:1, and 0.25:1, all recorded after 15 cycles of preconditioning. After obtaining the mechanical properties of the RV myocardium, the sample underwent a decellularization protocol to isolate the RV ECM. The decellularization protocol consisted of sequential exposure of specimens to Tris-buffered solution with 0.1% phenylmethylsulfonyl fluoride (PMSF), 1% Triton X-100, and 0.1% SDS for 48 h each. To prevent loss of the graphite markers, the specimens were placed securely in cell strainers, while on a stirring plate at room temperature as done previously [1]. At the conclusion of the decellularization protocol, the ECM-only specimens were kept in a -4 C refrigerator for 24 hours. In room-temperature PBS, the RV ECM specimens underwent the same biaxial testing protocol as the RV myocardium after the matrix sample dimensions were measured.

From the marker positions, the deformation gradient tensor $\boldsymbol{F}$ was calculated for each loading cycle. From $\boldsymbol{F}$, the components of the in-plane Green strain tensor E were calculated using $\boldsymbol{E} = \frac{1}{2}(\boldsymbol{F}^{\mathrm{T}}\boldsymbol{F} - \boldsymbol{I})$. The shear components of $\boldsymbol{E}$ were negligible in all test specimens, so only the

normal apex-outflow tract and circumferential component E_{11} and E_{22} were analyzed. The 1st Piola–Kirchhoff (PK) stress tensor $\boldsymbol{P}$ was calculated from the measured loads in grams and the specimen dimensions. The 2nd PK stress tensor $\boldsymbol{S}$ was determined using $S = PF^{-T}$ [1]. Assuming a pseudoelastic, hyperelastic material response, the tissue-level 2nd PK stress $\boldsymbol{S}$ is derived from the strain energy as [2]

$$\mathbf{S}(\mathbf{E}) = \frac{\partial \Psi(\mathbf{E})}{\partial \mathbf{E}} - p\mathbf{C}^{-1} \qquad (1)$$

where the Lagrange multiplier p accounts for the incompressible nature associated with non-fibrillar tissue components [3]. In our case, p was eliminated as a result of the configuration of planar biaxial testing. Using the experimentally obtained **S-E** data, we fitted a Fung-type model (Equation 2) to first obtain the Ψ for each specimen. A set of model parameter that described the strain-energy of the RV myocardium and ECM in normo- and hypertension was achieved through gradient-based nonlinear optimization *fminsearch* function in Matlab (2018b).

$$\psi(E_{11}, E_{22}) = c(e^{a_1E_{11}^2 + a_2E_{22}^2 + a_3E_{11}E_{22}} - 1) \qquad (2)$$

RESULTS

RV ECM samples significantly thinned (0.13 mm in control to 0.38 mm in PAH) and shorten in the normal directions (by 3 mm in control and 1mm in PAH) from their intact state. The decellularized to intact volume-ratio or hydrated volume-fraction went from 0.144 in control to 0.119 in PAH. The shortening or change in dimensions can be visualized in the pixel position of the markers (Figure 1A). Nevertheless, the intact and decellularized samples' Green strain space closely overlaps (Figure 1B).

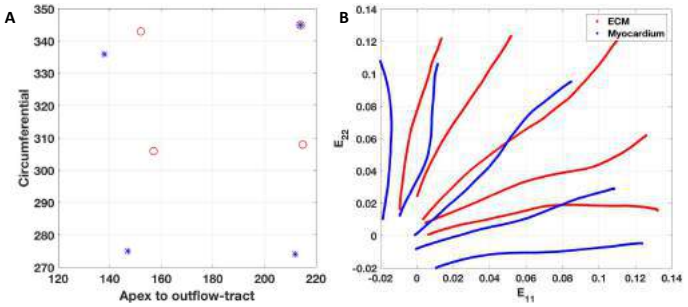

Figure 1: A. Camera field of view of the material markers at the center of the intact (blue) and decellularized (red) RV samples. B. Green strain space of an intact and decellularized RV sample.

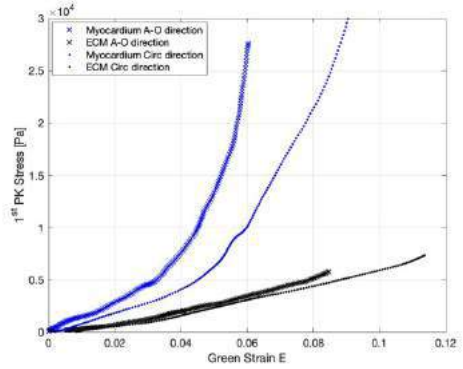

Figure 2: Equi-biaxial stress-strain relations of RV myocardium and ECM of a normotensive animal. As previously shown [1], the RV display an anisotropic tissue response, with the apex to outflow tract being the stiffer direction in intact and decellularized states.

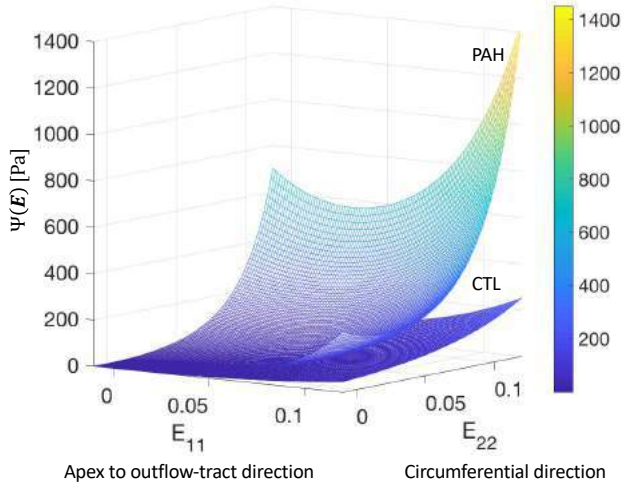

Figure 3: Strain-energy surfaces of the ECM of normo (CTL)- and hypertensive (PAH) rat.

Equi-biaxial stress-strain relationships of the control and PAH samples show both the myocardium and ECM being anisotropic materials, with the apex to outflow-tract direction being the stiffer direction (Figure 2). When comparing the strain-energy surfaces of the ECM of a normo- and hypertensive animal, the PAH sample is significantly stiffer even after accounting for the smaller hydration volume fraction.

DISCUSSION

Results show that while the amount of matrix increased, the volume fraction did not due to the significant hypertrophy. However, the PAH matrix was significantly stiffer and this contributed a greater amount to myocardium stiffness. This suggests that alterations to the fiber and/or molecular structure of the ECM such as increased diameter or decreased tortuosity of coiled perimysial fibers and/or increased collagen crosslinking may have played an important role in increased RV end-diastolic stiffness in PAH before any systolic decompensation. Classical Fung-type exponential strain energy functions do an excellent job of fitting the biaxial responses of both the intact and decellularized tissue. However, the fact that the matrix significantly shrinks from the reference state suggests the existence of prestresses in the matrix and collagen that are in equilibrium in the unloaded state. A mixture theory that properly represents the contributions of matrix and cells to the intact tissue properties in this experiment may account for these pre-stresses and may require the inclusion of additional terms in the constitutive equations to reflect interactions between myocytes, matrix and water.

ACKNOWLEDGEMENTS

Funded by the American Heart Association Scientist Development Grant 16SDG29670010, and UIC College of Engineering Seed Fund.

REFERENCES

[1] Valdez-Jasso *et al.* J Physiology, 2012 Sep 15;590(18):4571-84

[2] Fung. Biomechanics, Mechanical Properties of Living Tissues; Spring Verlag, NY,1993.

[3] Sacks and Chuong. J Biomech Eng; 115(2); 202-205, 1993.

SB³C2019
Summer Biomechanics, Bioengineering and Biotransport Conference
June 25 -28, Seven Springs, PA, USA

FLEXION ANGLE DEPENDENT DIFFERENCES IN JOINT KINEMATICS AND ACL FORCE IN RESPONSE TO APPLIED LOADS ARE CONSERVED THROUGHOUT SKELETAL GROWTH IN THE PORCINE STIFLE JOINT

Stephanie G. Cone (1), Danielle Howe (1), Emily P. Lambeth (1), Jorge A. Piedrahita (2), Jeffrey T. Spang (3), Matthew B. Fisher (1,3)

(1) Department of Biomedical Engineering
North Carolina State University and
University of North Carolina – Chapel Hill
Raleigh, NC, USA

(2) College of Veterinary Medicine
North Carolina State University
Raleigh, NC, USA

(3) Department of Orthopaedics
University of North Carolina – Chapel Hill
Chapel Hill, NC, USA

INTRODUCTION

The incidence of anterior cruciate ligament (ACL) injuries has been increasing significantly in skeletally immature populations over the past decade [1]. ACL injuries are most commonly treated through surgical reconstruction procedures which are designed to restore function and stability to the knee joint under both translational and rotational loading conditions. Interestingly, in the mature knee joint, less translation (~3-5 mm) and axial plane rotation (~5-7°) occurs under applied tibial loads when the joint is extended compared to when the joint is flexed [2,3]. Joint flexion has implications in surgery. For example, the flexion angle of the knee can influence the force carried in the native ACL [3]. Likewise, flexion angle at the time of ACL graft fixation can have a substantial effect on the force carried by the reconstruction graft [3]. Additionally, joint laxity, which varies by knee flexion, can be used as an intraoperative measure of ACL graft function [2]. These flexion-dependent behaviors of different tissues under anterior tibial translation at full extension versus flexed positions depend on tissue engagement. Previous work in our lab has shown that the resulting kinematics from applied tibial loads is age-dependent with greater normalized translation in younger joints [4,5]. It is important to determine if the impact of flexion angle on joint laxity and ACL function is conserved throughout skeletal growth, potentially helping to inform optimal joint flexion during ACL reconstruction of pediatric patients. Here, we hypothesized that joint laxity under applied anterior-posterior and varus-valgus loads would be decreased and the percentage of applied anterior tibial force carried by the ACL would be decreased at full extension (40° in the pig) versus 60° of flexion across juvenile and adolescent stages in the porcine knee model.

METHODS

Hind limbs were collected from female Yorkshire cross-breed pigs representing four age groups ranging from juvenile to late adolescent stages (3-18 months, n=22 total). All soft tissue was dissected away from the femur and tibia in order to expose the surface of the bones, and a fiberglass epoxy was fixed to the bones inside of molds that were designed to fit custom-built clamps. Joints were mechanically tested using a 6 degree-of-freedom universal force sensing robotic system (KUKA/SimVitro) which is capable of operating under both kinematic and kinetic control.

The following biomechanical tests were performed using the robotic system. A passive path was established for each limb by moving the tibia from full extension (40° in the pig) to 90° of flexion and finding the kinematic positions with minimized loads in the remaining 5 degrees of freedom. The kinematics for passive path positions at 40° and 60° of flexion were recorded. Scaled anterior-posterior tibial loads and varus-valgus moments were applied to the joints at both 40° and 60° of flexion while loads in the remaining degrees of freedom were minimized. The kinematic paths were recorded and repeated in intact, AM bundle deficient, and ACL deficient (AM and PL) bundle deficient) states and the resulting loads were recorded. The kinematic paths were exported for further processing. Parameters of interest included anterior-posterior tibial translation (APTT) and varus-valgus rotation (VVR) under applied loads. The principle of superposition was applied to determine the *in situ* forces carried by the ACL and its bundles at maximum anterior translation and varus and valgus rotation [5]. Normality of data sets was confirmed. Statistical analysis consisted of repeated measures ANOVA testing with Tukey's post hoc analysis where age and flexion angle were the main effects, and flexion angle as a repeated measure ($p<0.05$).

RESULTS

Under the application of anterior-posterior tibial loads, APTT of the joint varied significantly as an effect of flexion angle ($p<0.05$) with no significant effect due to age ($p>0.05$) or the interaction of age and angle ($p>0.05$). Specifically, increasing knee flexion resulted in mean APTT increases from extension (40° of flexion) to 60° of flexion of 1.6 mm at 4.5 months (19%), 1.4 mm at 6 months (21%), and 1.3 mm at 18 months (18%) (Fig. 1). These increases were statistically significant in all but the 3 month age group.

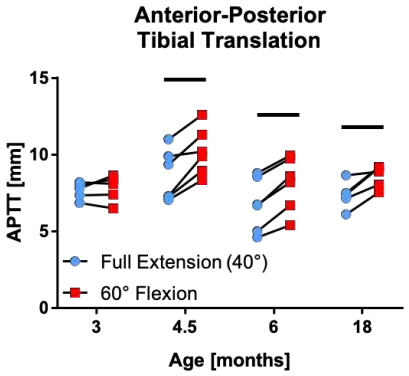

Figure 1: Anterior-posterior tibial translation (APTT) is greater at 60° of flexion relative to full extension during growth. Connected points show data from individual specimens, bar shows $p<0.05$ between angles.

Joint rotation under applied varus-valgus moments were also measured. We found a significant effect due to age, flexion angle, and the interaction term ($p<0.05$). Unlike APTT, we found that increasing flexion angle resulted in greater VVR in the 3, 4.5, and 6 month age groups ($p<0.05$), but not in the 18 month age group ($p>0.05$). The increase in flexion angle resulted in mean increases of 1.8° (3 months), 2.8° (4.5 months), and 2.2° (6 months) in the separate age groups. These effects due to flexion angle were coupled with an overall decrease with age of ~11° from 16.9° (full extension) and 18.7° (60° of flexion) in the 3 month group to 6.2° (full extension) and 7.4° (60° of flexion) at 18 months. Significant decreases occurred between 3 months and all older groups, and from 4.5 months to the remaining older groups ($p<0.05$) (Fig. 2).

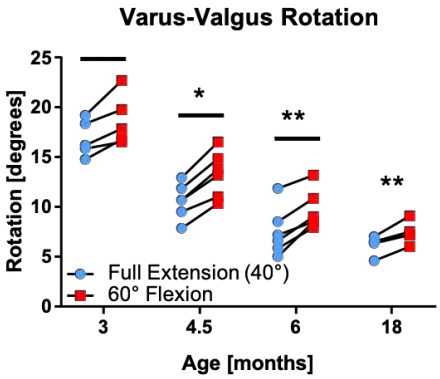

Figure 2: Varus-valgus rotation (VVR) decreased with increasing age in growth, and increased with joint flexion. Connected points show individual specimens, bar indicates $p<0.05$ between angles, *$p<0.05$ vs. 3 months, **$p<0.05$ vs. 3 and 4.5 months.

In addition to changes in joint kinematics, knee flexion had a significant effect on the forces carried in the soft tissues ($p<0.05$) while there was no significant effect due to age or the interaction term ($p>0.05$). Specifically, the ACL carried an average of 72% of the total applied anterior force in the joint at full extension which was significantly less than the mean 87% carried at 60° of flexion ($p<0.05$, Fig. 3). Furthermore, flexion angle had a significant effect ($p<0.05$) on the relative contributions of the AM and PL bundles of the ACL to resisting anterior force. The AM bundle of the ACL carried significantly more force at 60° of flexion compared to 40° of flexion ($p<0.05$, data not shown).

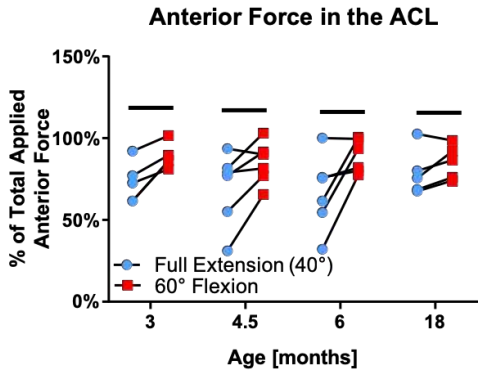

Figure 3: The ACL carried significantly less of the applied anterior tibial load ($p<0.05$) at full extension compared to 60° of flexion. Connected points show data from individual specimens, bar shows $p<0.05$ between angles.

DISCUSSION

In this study, we report significant increases in both translational and rotational joint laxity as a result of increasing knee flexion in skeletally immature pigs. Interestingly, these results were statistically significant in early through late adolescent groups for APTT while they were statistically significant in juvenile through mid-adolescent groups for VVR. Both translational and rotational laxity decreased as an effect of increasing age. Additionally, we found that the ACL carried a greater portion of applied anterior forces in flexed positions across juvenile and early adolescent porcine groups. These results are similar to previous studies focusing on the kinematic [2,3] and kinetic [6] properties of mature joints, while expanding our knowledge of the biomechanics of skeletally immature knees. While this study focused on a female model, future work will focus on expanding the data set to include male specimens and a greater range of ages. Additionally, the information gathered here may be used to motivate a non-invasive human study in pediatric and adolescent populations to investigate knee laxity at different flexion angles. Given that flexion angle is an important consideration for ACL graft function in adults, these findings may be important in developing age-specific clinical practices for a rapidly growing population of young patients with ACL injuries.

ACKNOWLEDGEMENTS

We would like to thank the Swine Education Unit (NC State) for their contributions to this work. Funding provided by NSF (DGE-1252376) and NIH (R03-AR068112, R01-AR071985).

REFERENCES

[1] Collins SL et al., *Ped Therapeut,* 4:196, 2014; [2] Harner CD et al., *Am J Sports Med,* 28(4):460-465, 2000; [3] Hoher J et al., *Am J Sports Med,* 29(6):771-776, 2001; [4] Cone SG et al., *J Orthop Res,* 35(12):2725-2732, 2017; [5] Cone SG et al., *World Congress of Biomechanics*, 2018; [6] Livesay GA et al., *J Orthop Res,* 15(2):278-284, 1997.

SB³C2019
Summer Biomechanics, Bioengineering and Biotransport Conference
June 25 -28, Seven Springs, PA, USA

A Novel Geometric Ratio To Predict The Flexion Gap In Total Knee Arthroplasty

S. Elmasry (1), P. Sculco (2), T. Wright (1), A. Pearle (2), M. Cross (2), D. Mayman (2), C. Kahlenberg (2), G. Westrich (2), C. Imhauser (1)

(1) Department of Biomechanics
Hospital for Special Surgery
NYC, NY, USA

(2) Adult Reconstruction and Joint Replacement Service
Hospital for Special Surgery
NYC, NY, USA

INTRODUCTION

Total knee arthroplasty (TKA), despite high rates of long-term implant survival, still suffers from elevated incidence of patient dissatisfaction of up to 15% [1]. These high rates of dissatisfaction are, in part, attributed to improper ligament tensioning during TKA implantation, which may lead to joint instability [2]. Ligament tensioning is clinically evaluated by assessing the gaps between the femur and the tibia in response to varus and valgus moments applied with the knee flexed and extended. Achieving equal (i.e. balanced) medial and lateral gaps is a common surgical target for successful TKA. Measured resection (MR) and gap balancing (GB) are commonly used techniques for gap balancing. In MR, femoral component placement relies solely on bony landmarks. This technique ignores the role of the restraining collateral ligaments in driving knee mechanics, which may lead to inconsistent knee function following TKA implantation [3]. In contrast, in GB, collateral ligament geometries and tensions dictate the rotation of the femoral component. This technique, however, may cause excessive internal or external rotations if the medial or lateral collateral ligaments (MCL &LCL) are deficient [3]. Therefore, we developed a new geometric measurement, "the MCL ratio", which accounts for the geometry of both the femur and the insertions of the medial collateral ligament (MCL) when placing the femoral component. Our objective was to determine whether the MCL ratio can predict the flexion gaps produced from MR and GB techniques to help define the rotation of the femoral component to achieve balanced gaps.

METHODS

Six computational knee models were virtually implanted with both MR and GB techniques based on our previously-developed framework (all males; age 33 ±15 years) [4]. A posteriorly stabilized implant system was utilized. In both MR and GB models, the distal femoral cut and the proximal tibial cut were perpendicular to the femoral and tibial mechanical axis, respectively. The only difference between MR and GB was the amount of external rotation of the femoral component. Specifically, in the MR models, the femoral component was aligned parallel to the transepicondylar axis (TEA). In contrast, in the GB models, the femoral component was externally rotated at 90^0 of flexion until equal gaps are achieved (within 2 mm), which reflects equal tension in MCL & LCL (Figure 1).

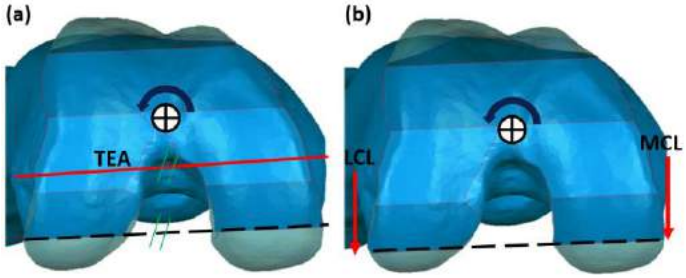

Figure 1: Posterior bony cuts for the placement of the femoral component for (a) measured resection where the component is externally rotated until it is parallel to the TEA, and (b) gap balancing, where the component is externally rotated until achieving equal tensions in the MCL and LCL

The collateral and capsular ligaments in each model were represented with twenty ligament fibers. Standardized ligament properties, including slack length and linear stiffness, were

controlled for the structural properties of the ligaments across all models [5]. Knee flexion from full extension to 90° under 500 N of compression was applied to simulate a common intraoperative examination. Then, to assess the lateral and medial gaps, varus and valgus moments of ±20 Nm were applied at full extension and 90^0 of flexion, which reflect common intraoperative assessments [6]. The difference in the medial and lateral gaps at full extension and at 90° of flexion was measured for both MR and GB. Next, the MCL ratio, which is a ratio between the distances of the femoral insertions of the anterior fiber of the MCL to the posterior and distal cuts, was calculated (Figure 2). Finally, this ratio and the difference between the medial and lateral gaps at 90° of flexion for both the MR and GB knee models were compared for each knee model.

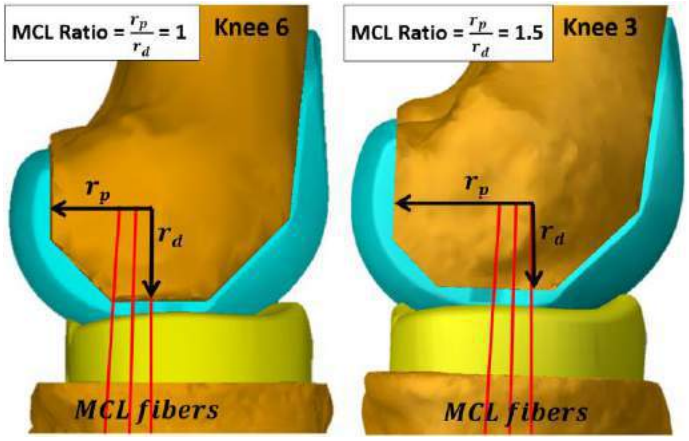

Figure 2: The MCL ratio is a ratio between the distances of the femoral insertions of the anterior fiber of the MCL to the posterior and distal cuts

RESULTS

The medial and lateral gaps at full extension were balanced (difference < 1.0 mm) for both MR and GB models. The external rotation that is required to achieve balanced gaps at 90° of flexion was the same for both MR and GB models of knees one, two, and six (Table 1). These three knee models yielded difference in flexion gaps of <1.0 mm and an MCL ratio <1.1 for both MR and GB (Figure 3). In contrast, knee models three, four, and five produced different external rotation between MR and GB (Table 1). Specifically, in MR, knee models three, four, and five were unbalanced and produced a gap difference and MCL ratio ranging from 3.6 to 10 mm and from 1.2 to 1.5, respectively (Figure 3). In contrast, in GB, knee models three, four, and five required more external rotation than in MR (Table 1). Moreover, the MCL ratio was lower in GB than in MR for knee models three, four, and five decreasing from 1.5 to 1.3, from 1.2 to 1.1, and from 1.4 to 1.2, respectively (Figure 3).

Table 1: External rotation of the femoral component for the six knee models using measured resection (MR) and gap balancing (GB) models in degrees

	Knee 1	Knee 2	Knee 3	Knee 4	Knee 5	Knee 6
MR	2.5°	0.6°	1.3°	1.6°	4°	2.5°
GB	2.5°	0.6°	6.3°	2.6°	7°	2.5°

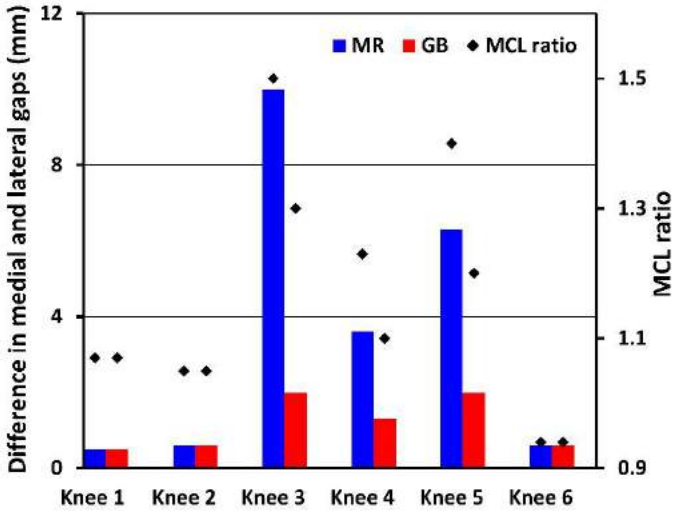

Figure 3: The MCL ratio closely followed variations in the difference of the medial and lateral gaps at 90° of flexion for both MR and GB

DISCUSSION

Despite aligning the femoral component parallel to the TEA and having balanced gaps at full extension, three out of six knees were unbalanced in the MR models and produced a difference between the medial and lateral gaps >2 mm in flexion. Our findings challenge current clinical thinking that alignment of the femoral component with the TEA yields consistent gaps from knee to knee [7]; rather, our findings indicate that this variability in gaps is likely due to high interpersonal geometric variation in the femoral condyles as well as the MCL insertion. Interestingly, even though ligament properties and component placement were standardized across each knee model, the external rotation required to achieve balanced flexion gaps (i.e. < 2 mm) ranged from 0.6° to 7° (Table 1). The MCL ratio, however, may provide a useful reference for femoral component rotation in TKA; specifically, the less was the MCL ratio, the less was the difference between the medial and lateral gaps (Figure 3). The relationship between the MCL ratio and the gap difference at 90° of flexion can be explained by the ability of this ratio to capture the isometry of the MCL between extension and flexion. In conclusion, the MCL ratio could be a useful measure to guide femoral component placement to achieve more predictable knee function following TKA.

ACKNOWLEDGEMENTS

Clark Foundation, Kirby Foundation

REFERENCES

[1] Song S., JoA, 29(2): 360-4, 2014; [2] Athwal K., Clinincal Biomech, 29(2): 119-28, 2014; [3] Dennis A., CORR, 468: 102-7, 2010; [4] Kia M., JBiomechEng, 138(5):051010, 2016; [5] Kia M., CORR, 476(1): 113-23, 2018; [6] Meere P., AAOS, 2014; [7] Mantas J., JoA, 7(4):531-5, 1992.

SB³C2019
Summer Biomechanics, Bioengineering and Biotransport Conference
June 25 -28, Seven Springs, PA, USA

MICROMOTION IN TIBIAL COMPONENTS RECOVERED POST-MORTEM: A PILOT STUDY

Heath M. Baskin (1), Elie S. Ghanem (2), Jack E. Lemons (1,2), Alan W. Eberhardt (1)

(1) Department of Biomedical Engineering
University of Alabama at Birmingham
Birmingham, Alabama, USA

(2) Department of Orthopedic Surgery
University of Alabama at Birmingham
Birmingham, Alabama, USA

INTRODUCTION

Total knee arthroplasty (TKA) is among the most successful medical procedures, providing patients long term function, reduced pain and improved quality of life. By 2030, the demand for primary TKA is projected to exceed 3 million [1]. Despite the success, some device revision rates remain as high as 12.9% after ten years [2], translating into significant numbers of revision surgeries annually. A leading cause for revision TKA is aseptic loosening following stable fixation at the time of implantation, with mechanical loss of fixation over time and/or particle induced osteolysis. In the present study, we quantified radiolucency and micromotion in tibial components in TKA devices retrieved post mortem, which were still attached to host bone. We hypothesized that radiographic lucency would be indicative of high rates of micromotion and associated with visual evidence of wear and corrosion.

METHODS

Six (6) specimens recovered post mortem ("en bloc") were obtained from RTI Biologics (Alchua, FL) that we presume were still functioning at the time of patient death. Device manufacturer and patient information including height, weight, age, and time in service were noted for analysis (Table 1). The tibial components were radiographed and scored for lucency according to the Knee Society TKA Radiographic Evaluation and Scoring System [3] using ImageJ software (Research Service Branch). In doing so, scores were given by the thickness (mm) of radiolucent lines in seven different zones in the anterior/posterior views of the tibial components. If lucency occurred in more than one zone the scores were added giving a single total score for each device. Clinically, a score of less than 4 is considered insignificant, 5 - 9 signifies follow-up needed, and greater than 10 predicts the device is approaching failure.

Micromotion was measured using an approach modified from Peters et al., [4]. Each en bloc tibial specimen was thawed at room temperature for 24 hours and equipped with four rods extending from the anterior, medial, posterior, and lateral tibial tray, affixed to the device by cyanoacrylate (Fig. 1). The tibial component was potted using Custom Tray Material (GC America Inc.) and fastened to the baseplate of an 858 Mini Bionix (MTS Systems Corporation) uniaxial testing station. A custom fixture was fabricated and attached to the actuator of the MTS to allow in vitro loading of the polyethylene of the tibial component using a femoral ball. Four linear variable differential transducers (LVDT, Stellar Technology Inc. Amherst, NY) were affixed to the tibia using a custom halo. The LVDTs were positioned so that each rod was fastened to the peg of the tibial construct, measuring liftoff and compression of the medial, lateral, anterior, and posterior tray, accounting for the distance of each LVDT from the edge of the tibial construct. Loads equal to 1.8 times the body weight were applied to the medial and lateral articulating surfaces of each component [4]. A cumulative micromotion value was determined by adding the absolute values of compression and lift-off for each specimen.

Four MyDAQ drivers (National Instruments, Austin, TX) were coupled with LabVIEW (National Instruments, Austin, TX) and a program was developed in which voltages were captured from the LVDTs, plotted against time into a user interface while simultaneously output into an Excel spreadsheet. Each LVDT was carefully calibrated by measuring the physical distance correlating to the full range of voltage (2.792 mm). This program allowed the correlation between micromotion and load supplied by the 858 Mini Bionix.

RESULTS

All tibial radiographic scores were below 4, which indicates that the lucencies present were not clinically significant [3]. All lucencies

found occurred around the tibial tray; none were found around tibial keels. The radiographs were further analyzed by an orthopedic surgeon (Ghanem) who concluded that all implants were cemented with no signs of scalloping due to osteolysis.

As expected, loading of the medial/lateral bearing surfaces of tibial components resulted in the largest compressive displacements of the medial/lateral tibial tray, respectively. Three components (170R, 170L and 395L) displayed liftoff of the opposing side and compressive displacements larger than 150 µm – a value associated with fibrous tissue formation at porous implant surfaces [5]. The cumulative magnitude of micromotion from each implant significantly correlated to time in service ($p = 0.0378$, Fig. 2). Furthermore, radiographic scores showed a strong correlation to levels of micromotion ($p = 0.0206$). Devices exhibiting radiolucency (170R, 170L and 395L) had the highest rates of micromotion among those tested.

DISCUSSION

The aim of this study was to establish the testing methodologies necessary to quantify radiolucency and micromotion for retrieved tibial components that were still affixed to the host bone. The methods were then applied to six devices for which we had patient data including time in service. The results suggested that micromotion was positively correlated with time in service. To our disappointment, radiographic images revealed little evidence of osteolysis or scalloping that might be correlated with the measured micromotion. The largest values of medial compression (-515.24 µm, -444.06 µm) occurred for two specimens with a small lucency under each medial plateau; however, a small lucency was also observed under the medial plateau of one other device that yielded only 8.8 µm of displacement under medial compression. In general, specimens exhibiting any amount of tibial lucency, even clinically insignificant levels (score < 4), experienced more micromotion on average when compared to specimen that did not (p-value = 0.0206). It should be noted that during testing, deformation of the cancellous bone may have affected the measurements [6]. No bone mineral density measurements or structural assessments were performed.

The secondary aim of this study was to investigate whether micromotion of en bloc specimens correlated to wear and corrosion. The results showed that micromotion of these en bloc devices did not correlate with the area of inflammatory cell induced corrosion (ICIC, $p = 0.7872$) or polyethylene wear scores ($p = 0.1481$, data not shown).

The study was limited by the small number of en bloc specimens obtained from our collection for which we had patient data. All tibial components were cemented and were designs marketed in the late 1990's to early 2000's. In the future, we hope to continue these efforts and include more contemporary design features, including highly crosslinked polyethylene.

ACKNOWLEDGEMENTS

The authors gratefully acknowledge financial support from the UAB Department of Orthopedic Surgery and NIBIB-BRP Grant 5 RO1 EB001715-02.

REFERENCES

[1] Kurtz et al., JBJS, 89-A, 4, 2007.
[2] Labek et al., JBJS, 93-B, 3, 2011.
[3] Ewald, CORR, 248, 1989.
[4] Peters et al., CORR, 409, 2001.
[5] Jasty et al., JBJS, 79-A, 5, 1997.
[6] Kraemer et al., JOA, 10, 2, 1995.

Table 1. En bloc specimen data

Device	Company	Age	Height (in.)	Weight (lbs.)	Service (Years)	Date of Death
209 R	Zimmer	49	64	200	3	6/28/2005
209 L	Stryker	49	64	200	3	6/29/2005
395 L	Depuy	88	68	178	4	2/6/2008
099 L	Sulzer	93	63	110	4	5/13/2007
170 R	NA	74	70	219	9	2/18/2007
170 L	NA	74	70	219	9	2/19/2007

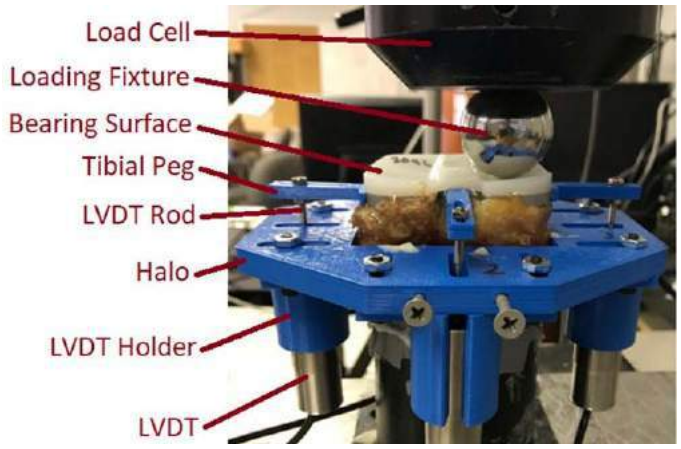

Figure 1. Micromotion test set-up.

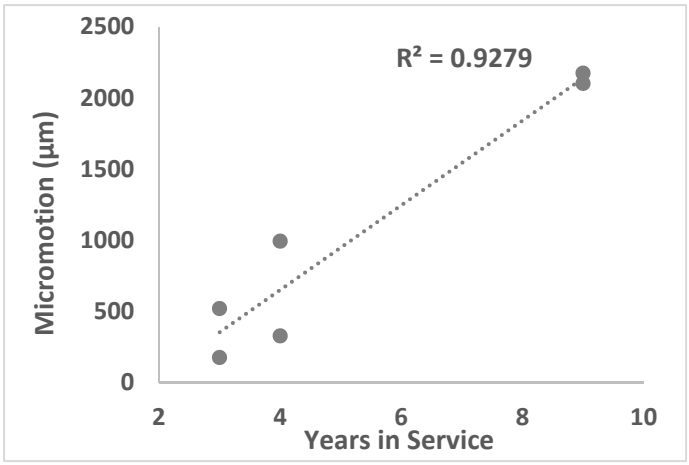

Figure 2. Micromotion measurements versus time in service, which showed a strong positive correlation.

SB³C2019
Summer Biomechanics, Bioengineering and Biotransport Conference
June 25 -28, Seven Springs, PA, USA

COMPUTATIONAL MECHANICS DEMONSTRATE HOW A TRANSCONDYLAR SCREW ENHANCES HEALING OF SUBCHONDRAL BONE CYSTS

Lance L. Frazer (1), Elizabeth M. Santschi (2), Kenneth J. Fischer (1, 3)

(1) Bioengineering Program
University of Kansas
Lawrence, KS, USA

(2) Equine Surgery
Kansas State University,
Manhattan, KS, USA

(3) Mechanical Engineering
University of Kansas
Lawrence, KS, USA

INTRODUCTION

Subchondral bone cysts (SBCs) occur in young horses bred for racing, most often in the medial femoral condyle (MFC). These SBCs result in lameness and secondary pathologies such as meniscal tears and cartilage damage. Traditional treatments attempt to reduce local inflammation and promote bone healing by anti-inflammatory agents and debridement, but rates of radiographic healing are less than 20% [1].

While a horse may become "sound" after traditional treatments, the risk for re-injury and lameness exists if the void remains in the MFC. In a study by Frazer et al., high shear stresses (above yield) were found in the boundary of a SBC at high load, and increased stresses were reported in the medial meniscus with a femoral SBC [2]. In order to reduce the risk of re-injury and secondary meniscal injury, treatment strategies should focus on bone growth in the void.

A recently developed treatment which places a transcondylar lag screw across the void has shown high success rates in both lameness resolution and radiographic healing [3], but the mechanism of healing remains unclear. Understanding how a screw promotes bone formation would provide information to both improve the surgery and possibly develop more treatments in the future. As such, a previously developed finite element model of an equine stifle joint was used to test and predict the transcondylar screw's primary mechanism of promoting healing [2].

Bone apposition will occur on free surfaces of bone with appropriate mechanical stimulus [4]. Lag screws create compression along their long axis and this mechanical change may promote bone formation in the void. We hypothesize that the lag screw treatment strategy stimulates bone growth on the inner lining of the SBC by increasing the mechanical stimulus the bone experiences. Furthermore, we hypothesize that the lag screw alters the direction of the principal stresses surrounding the MFC to be transverse to the normal trabecular orientation.

In this study, finite element analysis was utilized to quantify the bone remodeling stimulus with and without a transcondylar lag screw through an equine MFC with a 2 cm^3 void. Screw placement method, compression across the screw, steps allowed per day, and joint load were all varied to determine characteristics of the surgery and rehabilitation strategy most conducive to bone apposition.

METHODS

Previous work by our lab developed a finite element model of an equine stifle joint in extension with a 2 cm^3 void in the MFC under gallop ground reaction force loading [2]. The present study used this model with an added sclerotic region of bone of thickness 5 mm (as seen clinically) outside of the SBC. The sclerotic density was assumed to be 1.0 g/cm^3 and given a corresponding modulus of 3770 MPa using

$$E = 3770\,\rho^3 \quad (1)$$

for the density-modulus relationship [5]. The remaining bone tissue was assigned properties using the same relationship. Cartilage material properties were lowered from our previous study to better represent the tissue response at lower loads and strain rates experienced in a post-operative environment (E = 8 MPa, $\nu = 0.45$).

Criteria for Effectiveness: To evaluate the efficacy of various surgical treatment strategies, Beaupre, Carter, and Orr's theory of bone remodeling was adopted [4, 6]. The standard tissue stimulus (Ψ) was calculated to predict bone resorption, apposition, or no net change,

$$\Psi = \left(\sum_{day} n_i \sigma_{b_i}^m\right)^{\frac{1}{m}} \quad (2)$$

where n_i is the number of cycles per day (for a given load), σ_{b_i} is a bone tissue-level effective stress based on strain energy density, and m is an

empirical constant assumed to be 6 for the horse [7]. We assumed the standard attractor state (ideal reference stimulus) of 50 MPa and a "dead zone" of ± 20% (i.e. 40-60 MPa). Thus, values of $\Psi > 60$ MPa predict bone apposition, and values of $\Psi < 40$ MPa predict bone resorption.

We also calculated third principal stress (compression), σ_{III}, directions, to indicate the preferred direction of trabecular alignment.

General Boundary Conditions and Analysis Procedures: Depending on the analysis, a varying magnitude of uniform pressure was applied to the proximal femur. The quadriceps tensile force on the superior aspect of the patella to prevent unrealistic femoral anterior translation was scaled down from our previous study to 100 N [2]. The proximal aspect of the femur was constrained in varus-valgus (0°) and flexion/extension rotations (155°). The tibia was fully constrained, and all femoral translations and internal rotation were allowed. Frictionless contact was defined between all articulating surfaces using general contact in ABAQUS. Stimulus, Ψ, was calculated on the interior surface elements of the SCL, and a percentage of the available surface area exceeding 60 MPa (predicting bone formation) was calculated. Peak strain values were also calculated.

Effect of Screw Compression: For all models with a transcondylar lag screw, a simplified screw (40 mm length and 4.5 mm diameter cylinder, E = 200 GPa) was constructed with a 6 mm head and tapered at the axial end. The head was constrained by contact with the outside of the bone and the tip was tied to the bone. Screw compression of 0 N, 75 N, 150 N, and 300 N was applied axially to simulate tightening.

Effect of Daily Cycles (steps during rehabilitation): This study also investigated the effects of increasing the number of steps, cycles per day (cpd), by adjusting n_i in Equation 2. Three n_i values were chosen as 750, 3000, and 6000 cycles per day.

Effect of Joint Load: Three different magnitudes of load were placed on the proximal femur to simulate joint load during different activities. Pure stall confinement was estimated to be 900 N, 1800 N corresponded to hand-walking loads, and 3000 N was used for light exercise. These three joint loads capture post-surgery activity for the first few weeks to months.

Effect of Screw Placement: Screws were placed from abaxial to axial in the MFC (i.e. from medial surface toward central femur). Three screw placements were tested: a proximodistal oblique transcondylar (PDO) screw that passed through the central void, a proximal horizontal screw that intersected the proximal aspect of the void (PH), and a distal horizontal screw through the central cavity of the void (DH).

RESULTS

As expected, increasing joint load, screw compression or steps per day all increased the predicted bone formation area (BFA, Table 1). Under no conditions did strains approach yield. More interesting were the results for screw placement, which indicate that the proximal horizontal screw is less effective in developing BFA and does not substantially change the principal stress directions (Figure 1).

Table 1: Predicted bone formation area (BFA) as a percent of void surface area at 3000 N joint load with increasing levels of screw compression and daily cycles (steps).

3000 N load			
Model	BFA% 750 cycles	BFA% 3000 cycles	BFA% 6000 cycles
Void only	5	19	31
Void/PDO hole	20	53	66
Void/ SSS 0 N	24	59	72
Void/SSS 75 N	30	63	75
Void/SSS 150 N	37	68	78
Void/SSS 300 N	50	76	84

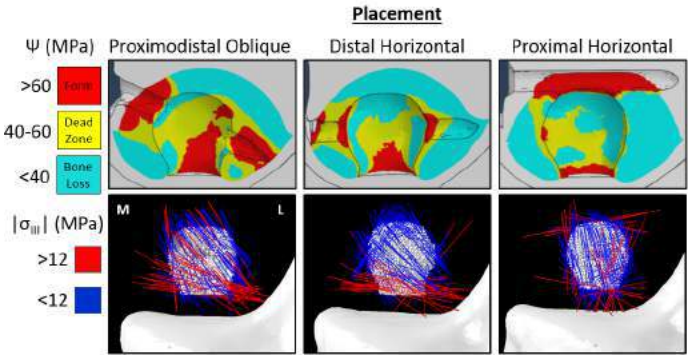

Figure 1. Top: Surface stimulus with an 1800 N joint load, 300 N stainless lag screw compression, and 3000 cpd for three screw placements. Bottom: Corresponding third principal stress vectors for bone immediately around the void. L=lateral, M=medial.

DISCUSSION

The transcondylar screw treatment of MFC SBC focuses on altering the biomechanical environment of the SBC to promote bone healing. The changes in bone stress stimulus and the reorientation of principle stresses caused by the transcondylar screw in this model suggests that the screw alters the mechanical environment to promote healing. As expected, increasing the lag screw compression, the loading cycles per day, and the joint loading all increase the stress stimulus, but only the lag screw compression reorients the principal stresses. The results of the screw placement comparison are consistent with clinical observations of poor bone healing after placement of a proximal horizontal lag screw.

There are a number of limitations to this study. All configurations tested were variations of a single finite element model based on a single healthy stifle joint. The SBC shape and the sclerotic region were idealized to match what is commonly seen clinically. The joint loading was estimated, as there are no kinetic data for the equine stifle. Also, the bone remodeling theory framework is based on limited samples that do not include equine data. While absolute values may be questioned, the relative values of stress stimulus and the reorientation of compressive principal stress clearly indicate the relative effectiveness of the lag screw treatment versus conservative treatment.

The results from this computational study support the use of a proximodistal oblique transcondylar lag screw to treat SBCs in the equine MFC and indicate the mechanisms that promote bone formation.

ACKNOWLEDGEMENTS

Supported by the Madison and Lila Self Graduate Fellowship.

REFERENCES

[1] Ortved KF, et al., *Equine Vet J.* 2012;44:606-13.
[2] Frazer LL, et al., *Vet Surg* 2018; DOI: 10.1111/vsu.13139
[3] Santschi EM, et al., *Veterinary Surgery* 2015;44:281-8.
[4] Beaupre GS, et al.. *J Orthopaedic Research* 1990;8:651-61.
[5] Carter DR, Hayes WC. *J Bone Joint Surg* [Am] 1977;59:954-62.
[6] Beaupre GS, et al.. *J Orthopaedic Research* 1990;8:662-70.
[7] Whalen RT, et al., *Journal of Biomechanics* 1988;21:825-37.

SB³C2019
Summer Biomechanics, Bioengineering and Biotransport Conference
June 25 -28, Seven Springs, PA, USA

A GENERALIZED FRAMEWORK FOR OBJECTIVE DETERMINATION OF FUNCTIONAL MUSCULOSKELETAL JOINT COORDINATE SYSTEMS

Tara F. Nagle (1), Ahmet Erdemir (2), Robb W. Colbrunn (1)

(1) BioRobotics Lab
Lerner Research Institute
Cleveland Clinic
Cleveland, Ohio, USA

(2) Department of Biomedical Engineering
Lerner Research Institute
Cleveland Clinic
Cleveland, Ohio, USA

INTRODUCTION

In biomechanics research, local coordinate systems (CS) of bones are typically defined based on anatomical landmarks. While using anatomical landmarks is a convenient approach for defining local CSs, it is sensitive to the variability in properly locating the landmarks. This variability is caused by excess soft tissue, the existence of osteophytes and other abnormalities, and the characterization of landmarks as contoured surfaces; not discrete points. Variability in collecting anatomical landmarks can result in vastly different CS definitions, and different kinematic representations of joint motion [1]. Even if landmarks are properly identified, it is not guaranteed that the CSs would be optimally aligned with the mechanical axes of the joint.

The aim of this study was to establish a generalized linear least squares (LLS) optimization approach to calculate the functional CSs of bones belonging to any joint utilizing a three-cylindrical joint kinematic chain decomposition method, from motion data.

METHODS

Optimization Method

a. Data Collection

The generalized framework for calculating functional CSs requires the collection of two low-resistance motion profiles; 1A) rotation about the axis fixed on the Base Reference Frame (BRF) and 2A) rotation about the axis fixed on the Relative Reference Frame (RRF).

b. Optimizing Coordinate System Origins

Kinematic data collected from motion profiles 1A and 2A can be used to redefine origins using the LLS optimization approach for calculating the hip origin established by Piazza et.al [2]. Collected kinematics should be recalculated using the redefined CS origins resulting in motion profiles 1B and 2B, respectively.

c. *Optimizing Base Reference Frame Orientation*

Transformed kinematic data from the first motion profile (1B) can be used in a LLS optimization for calculating respective axes on the two bones that are best aligned throughout the motion.

The change in orientation for the BRF and RRF can be reduced to orientation changes to the fixed Base axis (θ_1, θ_2) and its respective axis on the RRF (φ_1, φ_2), which are the metrics to be calculated.

The orientation of the axis of interest in the BRF $(B_{r_{xa}}, B_{r_{ya}}, B_{r_{za}})$ and RRF $(R_{r_{xa}}, R_{r_{ya}}, R_{r_{za}})$ can be determined using a LLS optimization, where a is the axis of interest $(x, y,$ or $z)$. The square of the difference between the a axes belonging to the BRF and RRF for each samples shall be calculated and the total error differentiated with respect to components of x, ($B_{r_{xa}}$, $B_{r_{ya}}$, $B_{r_{za}}$, $R_{r_{xa}}$, $R_{r_{ya}}$ and $R_{r_{za}}$), yielding Equation 1 when set to zero, where A is a symmetric 6 x 6 matrix.

$$Ax = 0 \tag{1}$$

Because Equation 1 is not solvable for $x \neq 0$, the following can be used where x is an eigenvector of A corresponding with the smallest eigenvalue, λ.

$$Ax = \lambda x \Longrightarrow 0 \tag{2}$$

Once x is solved, it must be scaled so that the vectors $[B_{r_{xa}} \;\; B_{r_{ya}} \;\; B_{r_{za}}]$ and $[R_{r_{xa}} \;\; R_{r_{ya}} \;\; R_{r_{za}}]$ are unit vectors. The change in orientation for the BRF and RRF can be described using rotation matrices, R_B and R_R, as a function of $(\theta_x, \theta_y, \theta_z)$ and $(\varphi_x, \varphi_y, \varphi_z)$, respectively. Depending on the axis of interest, (θ_1, θ_2) and (φ_1, φ_2) can be calculated as Euler angles from the R_B and R_R definitions.

Collected kinematics should be recalculated using the redefined CS orientations resulting in motion profiles 1C and 2C, respectively.

d. Optimizing Relative Reference Frame Orientation

The LLS optimization method used for optimizing the BRF orientation can also be used for redefining the orientation of the RRF. Transformed kinematic data from the second motion profile (2c) should be used and the methods should be followed in the same manner, but with the axis of interest being that of the fixed RRF. Collected kinematics should be recalculated using the redefined Relative CS orientation resulting in motion profiles 1D and 2D, respectively.

Experimental Methods

Twelve fresh-frozen, cadaveric leg specimens, femoral head to foot were procured (6 female, 6 male, age: 40-79, BMI: 20-30). Optotrak motion Tracking sensors (Northern Digital Inc., Waterloo, Canada) were secured to the tibia and femur. Five trained observers digitized anatomical landmarks on the leg. For testing purposes, two sets of anatomical CSs were established using the Grood & Suntay definition [3] for the tibia and femur from the collection of digitized points; average anatomical (AA) and median variance anatomical (MVA) CSs. The specimens were prepared for biomechanical testing on a simVITRO® Universal Musculoskeletal Simulator (Cleveland Clinic, Cleveland, OH).

Testing was performed using AA-CSs and MVA-CSs. The knee underwent a flexion/extension (FE) profile and internal/external rotation (IR/ER) profiles at 0°, 30°, 60° and 90° flexion.

The optimization method for redefining functional CSs was performed. Kinematic data collected from the FE and IR/ER profiles were used in the optimization as motion profiles 1A and 2A, respectively. Because the IR/ER profile was performed four times, at four different flexion angles, the unit vector redefining the tibia IR axis ($[R_{r_{xa}} \quad R_{r_{ya}} \quad R_{r_{za}}]$) was calculated at each flexion angle, averaged, and scaled back to a unit vector.

Analysis Methods

The convergence of the two functional (AF and MVF) CS sets to a common solution was measured in the form of reproducibility, where the resultant differences between the tibia origins and femur origins, and the angles between the femur FE axes and the tibia IR/ER axes were measured between the two sets. Reproducibility of the anatomical (AA and MVA) CSs were calculated as well for comparison. Paired, equal variance, 2-tailed *t* tests were performed to evaluate the reproducibility of anatomical CSs compared to functional CSs.

RESULTS

The CS reproducibility was significantly improved between the functional CS definitions compared to the anatomical (Figure 1).

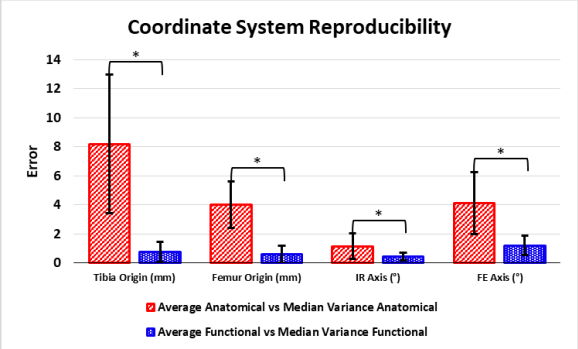

Figure 1: Average CS reproducibility error between anatomical CSs (AA and MVA) and between functional CSs (AF and MVF). * represents significant difference ($p<0.05$)

The off-axis range of motion during discrete flexion decreased significantly for all degrees of freedom except superior when comparing kinematics calculated from the AF-CS and AA-CS sets (Figure 2).

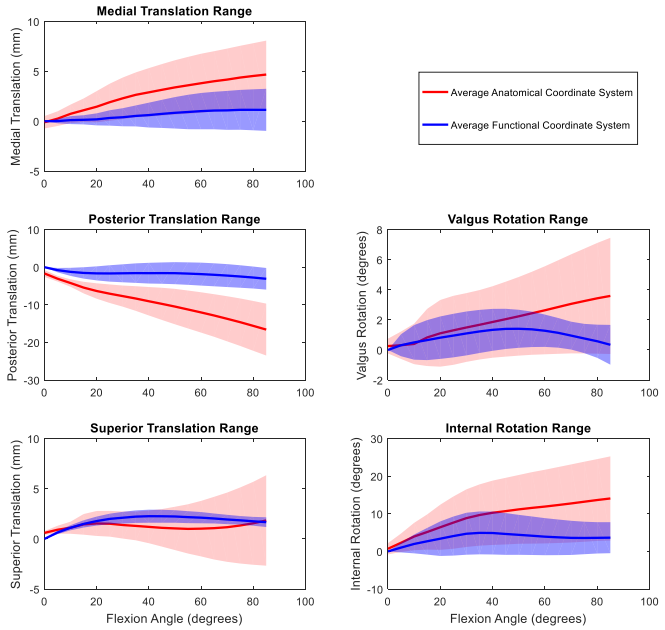

Figure 2: Average off-axis range of motion for FE profiles measured using the AA and recalculated using the AF CS sets. Shaded region represents one standard deviation amongst the twelve specimens.

DISCUSSION

In this study, a generalized framework was presented for objectively calculating functional CS definitions and the methodology was shown to be robust over 12 knee joints. Since the reproducibility in functional CSs is greater than in anatomical CSs, the use of functional CSs provides a more objective way for representing kinematic data so that it can be better compared amongst a population. Additionally, functional CSs could likely change as the joint is surgically altered, and these deviations might provide an important metric for evaluating surgical conditions.

This method was developed to be used on any joint utilizing the three-cylindrical joint kinematic chain decomposition method, and utilizes kinematic data of the joint moving through low resistance motion paths. This method is limited with joints like the hip or spine, where there are many possible low resistance motion paths, preventing this method from finding a singular solution.

ACKNOWLEDGEMENTS

The authors would like to acknowledge Quinn Saluan's testing support. This material is based upon work supported by the JSPS under Grant No. 17H02151, the NIH under Grant No. R01GM104139 and Grant No. R01EB024573.

REFERENCES

1. Morton, N.A., et al., *J Orthop Res*, 25:1221-1230, 2007.
2. Piazza, S.J., et al., *J Biomech*, 37:349-356, 2004.
3. Grood, E.S. and W.J. Suntay, *J Biomech Eng*,. 105:136-44, 1983.

SB³C2019
Summer Biomechanics, Bioengineering and Biotransport Conference
June 25 -28, Seven Springs, PA, USA

CARTILAGE CONTACT STIFFNESS EFFECTS ON CONTACT PRESSURE AND AREA AT THE ELBOW JOINT

Jonathan Parman (1), Cuneyd Gunay (2), Akin Cil (1,3), Antonis Stylianou (1)

(1) Department of Civil and Mechanical Engineering
University of Missouri – Kansas City
Kansas City, MO, USA

(2) Department of Orthopaedics and Traumatology
Eskisehir Osmangazi University
Eskisehir, Turkey

(3) Department of Orthopaedics
Truman Medical Centers
Kansas City, MO, USA

INTRODUCTION

Upper extremity use depends largely on the elbow joint. The elbow serves as a link in the lever arm system that positions the hand, as a fulcrum of the forearm lever, and as a load-carrying joint. Because of the centrality of the elbow joint to the upper extremity, loss or diminished function of the elbow results in significant deficits in upper extremity function and loss of independence. Articular cartilage defects of the capitellum are typically seen in overhead athletes. These cartilage defects eventually cause pain, inability to compete at the desired level, functional impairment, and lead to osteoarthritis [1,2]. Treatment of osteochondritis dissecans (OCD) of the capitellum is often guided by the size, stability, and containment of the defect. The effects of altered cartilage stiffness at a typical OCD location has not been investigated. The objective of this study is to identify the influence of altered cartilage stiffness at a defect location on the magnitude and distribution of contact pressure in the elbow.

METHODS

A previously developed computational multibody model created from a cadaver specimen (61 years, male, right arm) was used in this study [3,4]. The model was created in ADAMS (MSC Software Corporation, Santa Ana, CA) using three-dimensional bone and cartilage geometries segmented from CT and MRI images using 3D Slicer (www.slicer.org). The model included three bundles for the lateral ulnar collateral ligament (LUCL), three bundles for the radial collateral ligament (RCL), three bundles for the anterior band of the medial collateral ligament (MCL), three bundles for the posterior band of the MCL, and two bundles for the annular ligament. All ligaments were modeled as non-linear force elements that included the "toe" region [3,4,5]. The humeral cartilage was divided into discrete hexahedral rigid bodies with a 3 x 3 mm cross-sectional area. Each discrete cartilage body was rigidly fixed to the humerus and a contact constraint was defined between each humerus cartilage body and the radius and ulna cartilage geometries (equation 1).

$$F_c = k_c\delta^n + B_c(\delta)\dot{\delta} \quad (1)$$

Where F_c is the contact force, k_c is the contact stiffness, δ is the interpenetration of the geometries, n is a power exponent, $\dot{\delta}$ is the velocity of the interpenetration, and B_c is a damping coefficient. The model is shown in figure 1.

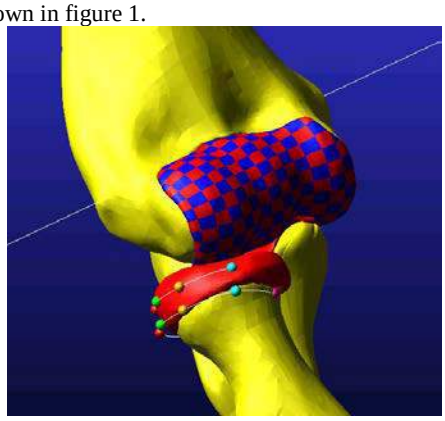

Figure 1: Elbow model with discrete cartilage.

Contact parameters were determined by optimization to a validated finite element model [6]. The initial contact stiffness was set at 40 N/mm. A humerus cartilage defect of 10mm diameter was created at the center of the capitellum at a 45 deg angle from the humeral axis. Three cartilage conditions were studied, no defect (ND), defect contact

stiffness 10 times higher than normal (HD) simulating a treated OCD lesion with microfracture resulting in fibrocartilage formation, and contact stiffness 10 times lower than normal (SD) simulating an untreated OCD lesion. For each cartilage scenario two conditions were simulated; a static simulation with the elbow in full pronation and fixed at 20 deg flexion with a compressive load of 377N on the humerus and a dynamic simulation of full flexion-extension of the elbow joint.

RESULTS

Under static loading, the SD condition resulted in an increase in contact area from 675 mm^2 to 702 mm^2 with no change in the maximum contact pressure. The HD condition increased the maximum contact pressure from 3.7MPa to 11.4MPa but did not result in any change of the contact area (figure 2). Both the SD and HD conditions increased the contact area on the medial humerus cartilage (trochlea) side with the HD condition causing a decrease in the maximum contact pressure on the trochlea from 3.7MPa to 2.1MPa (figure 3).

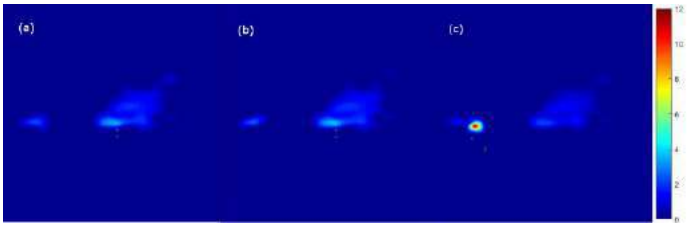

Figure 2: Contact pressure under static load. ND condition (a), SD condition (b), HD condition (c).

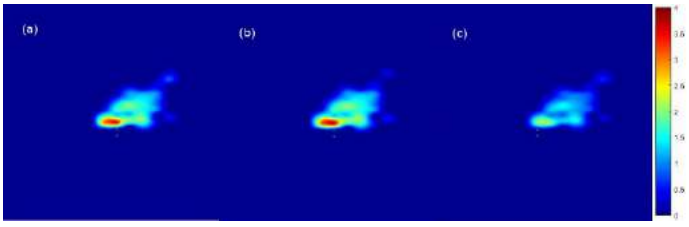

Figure 3: Ulno-humeral contact pressure under static load. ND condition (a), SD condition (b), HD condition (c).

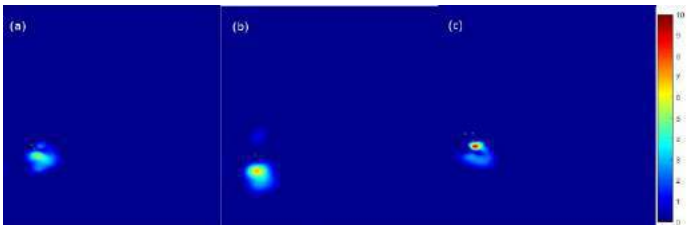

Figure 4: Contact pressure during dynamic simulation (90 deg flexion shown). ND condition (a), SD condition (b), HD condition (c). For all the figures, the top of the figure corresponds to the posterior side of the humeral cartilage, bottom of the figure corresponds to the anterior side. Left is lateral (radius contact) and right is medial (ulna contact).

During flexion/extension the lower cartilage stiffness condition at the defect side, (SD) resulted in an increase in the contact area on the capitellum whereas the higher cartilage condition, (HD) caused a decrease. In terms of contact pressure on the capitellum, both altered stiffness conditions resulted in an increase of contact pressure (figure 4). Table 1 shows these results at a flexion angle of 90 deg.

Table 1: Contact pressure and contact area on the radial side at 90 flexion.

Contact Area (mm^2)			Contact Pressure (MPa)		
ND	SD	HD	ND	SD	HD
117	189	108	5.3	7.0	8.9

DISCUSSION

The purpose of this study was to investigate the influence of changes in the contact stiffness of humeral cartilage at the capitellum on the humero-ulna and humero-radial joint under static and dynamic conditions.

A decrease in the contact stiffness resulted in an increase of the contact area under all conditions without an increase in contact pressure. A higher contact stiffness at the defect side did not alter the contact area over the whole elbow joint but caused an increase on the trochlea. This in turn caused a decrease in contact pressure in the medial humerus cartilage with an accompanied large increase of contact pressure on the capitellum. Under dynamic conditions both softening and hardening of the cartilage at the defect side caused an increase in the contact pressure at the capitellum.

These results suggest that changes in the contact stiffness affect the pressure distribution both on the ulno-humerus and radio-humerus articulations. These changes may alter the mechanical response of the joint and predispose the elbow to degenerative changes ultimately leading to osteoarthritis.

The results of the current study are very limited because all simulations were done on one cadaver-derived model and only under full pronation conditions. Further studies on the effects of cartilage mechanical properties and defect locations throughout the whole envelope of elbow motion are needed.

ACKNOWLEDGEMENTS

The research was partially funded by the Franklin D. Dickson Endowment, School of Medicine, University of Missouri – Kansas City.

REFERENCES

[1] Bauer M, Jonsson K, Josefsson PO, et al. 1992. Osteochondritis dissecans of the elbow. A long-term follow-up study. Clin Orthop Relat Res: 156-160.

[2] Bae DS, Ingall EM, Miller PE, et al. 2018. Early results of single-plug autologous osteochondral grafting for osteochondritis dissecans of the capitellum in adolescents. J Pediatr Orthop.

[3] Rahman M, Cil A, Stylianou AP, 2016. Prediction of elbow joint contact mechanics in the multibody framework. Med Eng Phys 38:257-266.

[4] Rahman M, Cil A, Bogener JW, et al. 2016. Lateral collateral ligament deficiency of the elbow joint: A modeling approach. J Orthop Res 34:1645-1655.

[5] Blankevoort L, Kuiper JH, Huiskes R, et al. 1991. Articular contact in a three-dimensional model of the knee. J Biomech 24:1019-1031.

[6] Renani MS, Rahman M, Cil A, et al. 2018. Calibrating multibody ulno-humeral joint cartilage using a validated finite element model. Multibody System Dynamics 44:81-91.

A MULTISCALE FINITE ELEMENT MODELING APPROACH TO CHARACTERIZE IRIS DEFORMATION

Vineet S. Thomas (1), Sam D. Salinas (1), Anup D. Pant (1), Syril K. Dorairaj (2), Rouzbeh Amini (1)

(1) Department of Biomedical Engineering
The University of Akron
Akron, OH, US

(2) Department of Ophthalmology
Mayo Clinic
Jacksonville, FL, US

INTRODUCTION

Insight into iris biomechanics plays an important role in understanding the pathophysiology of primary angle-closure glaucoma (PACG). Since abnormality in the iris and its interference with aqueous humor flow are established contributing factors in the closure or narrowing of the anterior chamber angle (e.g. via pupillary block), the iris has been studied extensively in the context of PACG [1].

Major component of the iris stroma are the striated collagen fibrils which provides support while undergoing continuous large mechanical deformation [2]. It is, however, unclear how regulation of these collagen fiber synthesis in an iris stroma relate to the iris stiffness. In general, cells sense and respond to changes in their surroundings by relaying signals to the nucleus. When stromal cells are subjected to mechanical stimuli in the micro-environment, the cytoskeleton of the cell exerts mechanical stresses on the nucleus. As a result, the shape of the nucleus is altered. This nuclear alteration results in the functional and morphological alteration of the cells [3].

We are able to predict changes in the microenvironment under different macro-scale loading for other soft tissues using our multiscale computational framework [4]. This approach links the volume-averaged stress in micrometer-scale representative volume elements (RVEs) to a macro-scale (millimeter-scale) FE continuum. In this study, for the first time, we characterize porcine iris tissue using our multiscale model and further investigate the stromal cell deformation in association with the collagen fiber reorientation, which is currently unknown.

METHODS

Whitcomb et al. (2009) [5] published uniaxial test data for both intact iris and excised iris sections in radial and azimuthal directions. We employed the uniaxial tension test data from the excised iris in the radial direction as a reference in order to fit the multiscale model response and obtain its parameters. A three-dimensional finite element model of the sample was generated and meshed with 330 elements using Abaqus (Dassault Systèmes, Vèlizy-Villacoublay, France). For the current study, we assumed isotropic fiber networks with anisotropy index α =10% and preferred fiber direction μ = 0°, throughout the sample. The mathematical definitions of the anisotropy index and preferred fiber direction are provided in our previous publications [6]. Strain of ~15% was applied to the model by simulating displacement boundary conditions uniaxially on the boundary nodes of the sample.

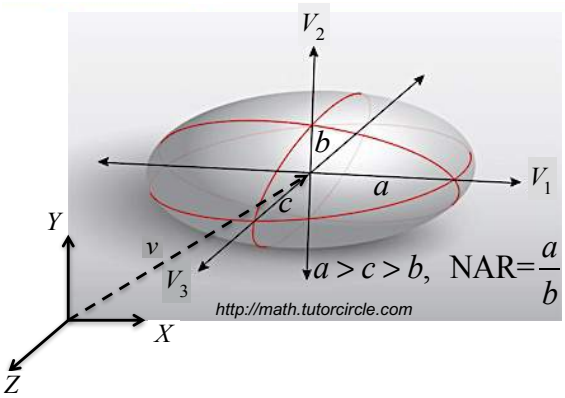

Figure 1: An ellipsoidal geometry was assumed for the cell nucleus [7]. The nuclear aspect ratio (NAR) was defined as the ratio of the largest to the smallest length of semi axes.

For our study, we considered the nuclear aspect ratio (NAR) as a measure to quantify cellular deformation (Fig. 1). To obtain NAR, DAPI-stained image stacks were used to reconstruct surfaces of the nuclei using a voxel-based 3-D image processor. Images were then segmented using ImageJ and the average NAR of the 3D reconstructed nuclei was measured. Based on the obtained images, an average initial NAR of 2.0 was considered for this study. An ellipsoidal geometry was assumed for the cell nucleus based on other studies in the literature [7]. The equation $\mathbf{(x-x_0)^T A(x-x_0)}$, where $\mathbf{x_0}$ is the coordinate of the center, **A** can be written as $\mathbf{QDQ^T}$,where **Q** is a symmetric matrix whose columns represent the principal axes of the ellipsoid and **D** is the diagonal matrix with squared inverses of the length of the semi-axes along the diagonal elements, was used to construct the nucleus geometry. The NAR was defined as the ratio of the largest to the smallest eigenvalue of A.

RESULTS

Figure 2a shows the deformed profile of the FE model in the final step of the uniaxial stretch simulation. The multiscale model fitted the uniaxial test data with R^2 value of 82 %. The model fitting parameters for the iris are as follows: shear modulus -G = 3.5 kPa, threshold fiber stretch ratio - λ_c = 1.01, fiber modulus - E_f = 4.5 kPa and parameter that governs the nonlinearity of the response -β = 1.0 (Fig. 2b).

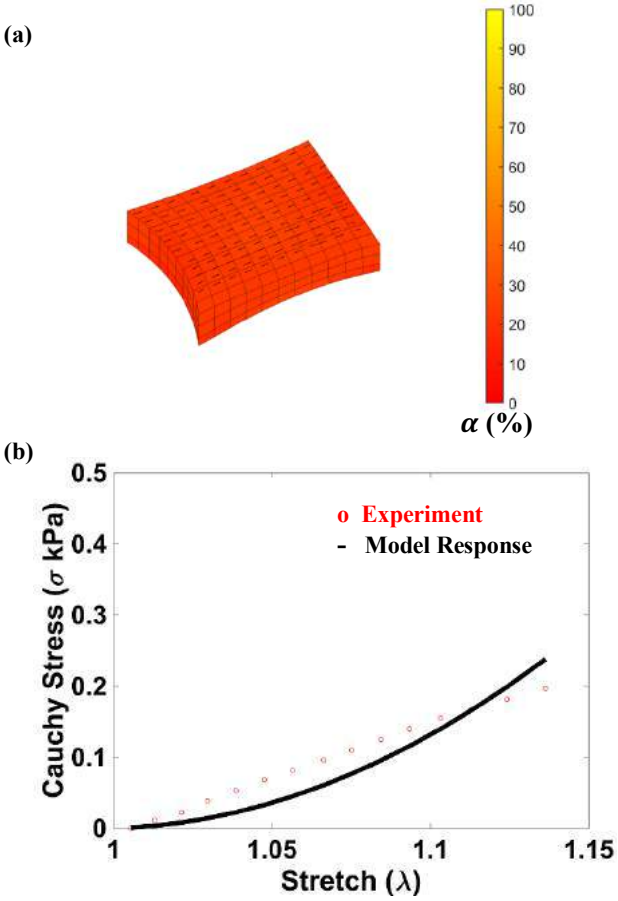

Figure 2: (a) Deformed Configuration of the FE model under uniaxial stretch. (b) Multiscale model response after fitting the model parameters to the experimental data for the uniaxial extension of a porcine iris specimen (R^2 = 82%).

The nucleus was initially assumed to be along the main fiber direction. Figure 3 shows the deformed configuration of the fiber network chosen from the boundary element plotted with the deformed configuration of the nucleus. The NAR of the deformed nucleus was 1.9.

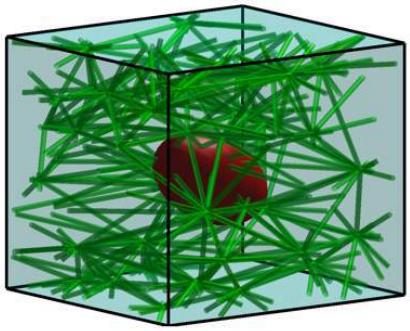

Figure 3: RVE with a 3D ellipsoidal geometry of the nucleus (in red) in the deformed state with the surrounding ECM collagen fiber network (in green)

DISCUSSION

Cellular configuration linked with ECM fiber architecture vary nonlinearly in response to tissue level stresses. From Fig. 3, it can be observed that nucleus deforms and realigns in association with the surrounding ECM fiber network in response to the mechanical loading. Cell level deformations are influenced through complex micro-mechanical interactions that occur within physiological conditions, imparting altered stress levels on the nucleus due to changes in the cell cytoskeleton, which affects an array of cell functions. Gene expression and protein synthesis has been associated directly to certain optimal change in nuclear shape [8].

We investigate nuclear deformation in stromal cells, which is an important factor in mechanical regulation of genome and gene expression. While recent studies show that ECM collagen I content increases in PACG irides, it is unclear how regulation of collagen synthesis in iris stroma relates to the iris stiffness. Although there is considerable understanding of relationship between mechanical stimulation on cellular processes, identifying specific mechanisms responsible for vital physiological phenomenon remains poorly understood. Our multi-scale modelling approach can provide insight into complex cell-matrix interactions which can aid in identifying such specific mechanisms.

ACKNOWLEDGEMENTS

Computations were facilitated by a supercomputing resource grant from the Ohio Supercomputer Center (Columbus, OH). Funding for this study was provided in part by a grant from BrightFocus Foundation (G2018177). The assistance from Murtada, Alzayer, Neda Rashidi, and Mickey Shah in quantification of the undeformed cell nuclei is also acknowledged.

REFERENCES

[1] Amini, R et al., *Invest Ophthalmol Vis Sci*, 53(3):1188-94, 2012.
[2] Marshall, G. E. et al., *Br J Ophthalmol,* 77:515-524, 1993.
[3] Cho, S. et al., *J Cell Biol,* 216(3): 305, 2017.
[4] Stylianopoulos, T. et al., *Comput Methods Appl Mech Eng*, 196(31-32):2981-90, 2007.
[5] Whitcomb, J. E. et al., *Exp Eye Res*, 89: 456-461, 2009.
[6] Pant, A.D. et al., *Acta Biomater,* 67:248-258, 2018.
[7] Huang, H. S. et al., *J Biomech Eng*, 129(6):880-889, 2007.
[8] Thomas, C.H. et al., *Proc Natl Acad Sci*, 99(4):1972-77, 2002.

SB³C2019
Summer Biomechanics, Bioengineering and Biotransport Conference
June 25 -28, Seven Springs, PA, USA

CORRELATION OF HUMAN LAMINA CRIBROSA STRAIN RESPONSE TO AXON COUNTS IN THE OPTIC NERVE ACROSS RACIOETHNIC DONOR EYES

Hirut G. Kollech (1), Reza Behkam (2), Katelyn Axman (2), Jr- Jiun Liou (2), Jonathan P. Vande Geest (2,3,4)

(1) Computational Modeling and Simulation
University of Pittsburgh
Pittsburgh, PA, USA

(2) Department of Bioengineering
University of Pittsburgh
Pittsburgh, PA, USA

(3) McGowan Institute for Regenerative Medicine
University of Pittsburgh
Pittsburgh, PA, USA

(4) Louis J. Fox Center for Vision Restoration
University of Pittsburgh
Pittsburgh, PA, USA

INTRODUCTION

Glaucoma refers to a group of neuronal degenerative disease that damage the retinal ganglion cells (RGCs) at the optic nerve and leads to irreversible vision loss. The most common type, primary open angle glaucoma (POAG), is the second leading cause of blindness, and it is expected to affect 110 million people worldwide by 2040 [1-3]. In the US, the disease is more prevalent in African descent (AD) and Hispanic ethnicity (HE) when compared to European descent (ED) [4-6]. While the risk factors include ocular hypertension, age, elevated intraocular pressure (IOP) and ethnicity, there is sufficient evidence to suggest that differences in the biomechanical properties of the optic nerve head between these racial and ethnic groups contribute to this increased risk [7-8].

The optic nerve head (ONH) contains the lamina cribrosa (LC) which is a porous collagenous disc that undergoes significant remodeling in the presence of POAG [9-10]. The LC and the posterior sclera play a critical mechanical role in protecting RGC axons as they exit the eye through the ONH. Although there are several studies showing that eyes of AD and HE donors exhibit LC microstructure and biomechanical response that are significantly different than ED [11- 13], the correlation between the LC biomechanical response and RGC axonal health across racioethnic groups has not been studied. Therefore, the purpose of this study is to investigate correlation between the axon count and the LC strain response in non-glaucomatous samples across the racioethnic groups.

METHODS

Nine non-glaucomatous human donor samples (n=3 from the racioethnic groups: AD, ED and HE) were used for this study. Pressure inflation experiments were conducted on each donor LC at 5, 15, 30 and 45 mmHg while simultaneously collecting 3D images using a multiphoton microscope. A maximum intensity projection from second harmonic generation (SHG) is shown in Figure 1. Digital volume correlation (DVC) algorithm was used to generate 3D displacement fields [14]. These DVC results were used to calculate the Green strain components.

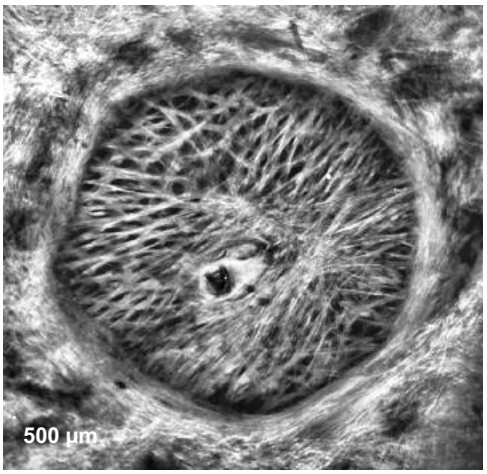

Figure 1: Representative mean intensity projection of the collagen (SHG) in a human LC

In addition, embedded optic nerve cross sections of the same nine samples were visualized on a Nikon Eclipse 90i microscope using a montaging method with Nikon NIS-Elements software. The method used individually imaged 60X magnifications with autofocus capabilities and a 15% overlap. A montage of an axon cross section of one of the samples is shown in Figure 2. Axon counts were quantified using an established and validated semi-automated axon counting software [15]. Statistical analysis was done using Pearson correlation to study the relationship between LC strain and axon counts.

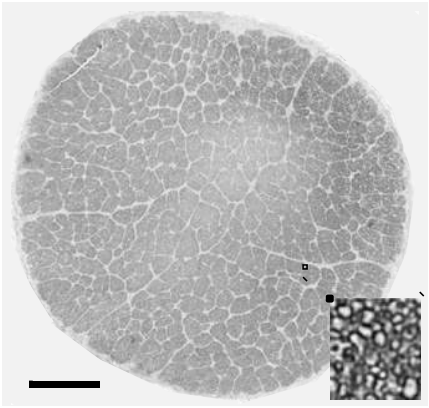

Figure 2: Microscope image of full optic nerve cross section. Dark sections indicate bundles of axons separated by lighter connective tissue. Scale bar denotes 500 microns.

RESULTS

Figure 3 shows the axons counts in the racioethnic groups. There were no significant differences in axon counts across race (p=0.54). The mean axon counts were 2.71 x 105 + 8.9 x 104 for AD (n=3), 4.73 x 105 + 3.2 x 105 for ED (n=3) and 2.96 x 105 + 2.2 x 105 for HE (n=3).

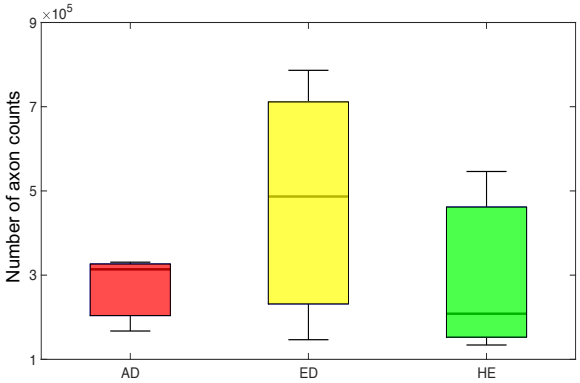

Figure 3: Axon counts across the racioethnic groups.

In addition, in the first and second pressure levels, the LC strain showed correlation to the axon count. Pearson's correlation coefficient between Peak of XY strain and axon counts were rho=0.72 (p=0.03) and rho=0.67 (p=0.051) at 15mmHg and 30 mmHg, respectively. The p-value tested the hypothesis of no correlation against the alternative hypothesis of a nonzero correlation. Figure 4 shows this correlation at 15mmHg.

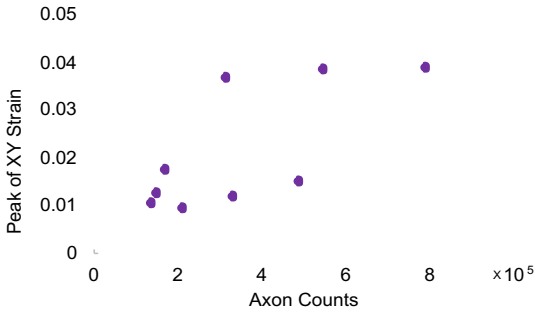

Figure 4: Correlation of axon counts to peak of XY strain at 15 mmHg (rho = 0.72, p=0.03)

DISCUSSION

The ED group showed the biggest number of axons as compared to the other two groups. Although, axon counts across races were not significantly different in our study, the AD and HE groups showed lower count of axons. As the death of RGCs is associated with progression of glaucoma, with AD and HE groups (which are at a higher risk for POAG) showing lower axon counts may be related to the development and progression of the disease.

In addition, the correlation between the shear strain XY peak and axons may contribute to mechanisms of glaucoma. Previous work done in our laboratory showed that AD had a higher strain in XY peak than ED. Higher number of axons may assist the LC from straining significantly.

On the other hand, it should be noted that only 9 samples were studied in this work. Since the number of samples is small, future study will include additional samples (both glaucomatous and non-glaucomatous) in each racioethnic group to get a better understanding of the subject. In conclusion, the results of this study showed significant correlation between the shear strain in the LC with the axons present in the optic nerve.

ACKNOWLEDGEMENTS

Research reported in this abstract was supported by the National Eye Institute under award number R01EY020890 to JPVG. The computational resources of this research were supported by University of Pittsburgh Center for Research Computing (CRC) and Pittsburgh Supercomputing Center through NSF-XSEDE award number TG-ENG160035.

REFERENCES

[1] Kapetanakis, V et al., *J Ophthalmol*, 100(1):86-93, 2016.
[2] Quigley, H et al., *J Ophthalmol*, 90(3):262–267, 2006.
[3] Tham, Y et al., *J Ophthalmol*, 121(11):2081–2090, 2014.
[4] Ferris, F et al., *A Ophthalmol*, 122(4):451–452, 2004
[5] Quigley, H et al., *A Ophthalmol*, 119(12): 1819-1826, 2001.
[6] Racette L et al., *S Ophthalmol,* 48(3):295–313, 2003.
[7] Seider, M et al., *J Glaucoma*, 18(8):595, 2009.
[8] Urban, Z et al., *IOVS*, 48(7):3209–3215, 2007.
[9] Hernanadez, M et al., *J Ophthalmol*, 109(2):180–188, 1990.
[10] Yang H et al., *IOVS*, 52(2):821–829,2011.
[11] Fazio M et al., *IOVS*, 55(11):7189-7198, 2014.
[12] Tamimi E et al., *IOVS*, 58(10):4235-4246, 2017.
[13] Yan D et al., *IOVS*, 52(2):821–829, 2011.
[14] Thirion I et al., *Medical Image Analysis* 2(3):243–260, 1998.
[15] Reynaud J et al., *IOVS*, 53(6):2951–2959, 2012.

SB³C2019
Summer Biomechanics, Bioengineering and Biotransport Conference
June 25 -28, Seven Springs, PA, USA

TENSILE BEHAVIOR OF ANTERIOR AND POSTERIOR CORNEAL FLAPS SUBJECTED TO CXL TREATMENT PROCEDURE

Hamed Hatami-Marbini

Department of Mechanical and Industrial Engineering
University of Illinois at Chicago
Chicago, Illinois, USA
Email: hatami@uic.edu

INTRODUCTION

Keratoconus is an eye disease that causes the cornea to become conical in shape. One of the treatment option to prevent the progression of this disease is corneal collagen cross-linking (CXL). In CXL, the photosensitizer riboflavin solution and ultraviolet A light (UVA) are used to create additional crosslinks in the corneal stroma [1]. These crosslinks have been shown to result in significant improvement of corneal mechanical properties.

The mechanical properties of the cornea are mainly from its extracellular matrix. The corneal extracellular matrix is composed of collagen fibers embedded in a proteoglycan matrix. The collagen fibers form sheet like structures, which are called lamellae. The composition of the collagen lamellae through the thickness of the cornea shows significant variation. In particular, anterior layers are composed of interwoven collagen lamellae while the posterior part of the cornea is composed of parallel collagen lamellae [2].

The CXL treatment has an effective crosslinking depth of a little more than about half of the thickness of the cornea. This depth has been recommended to avoid the toxic effects of UV light on the endothelium layer and other internal components of the ocular globe. There has been previous efforts in the literature in order to increase the depth of crosslinking with the hope of enhancing the stiffening effect of CXL procedure in patients. The primary objective of the present study is to determine the effects of the inhomogeneous microstructure of the cornea on the outcome of the crosslinking procedure. In other words, the present work assesses whether crosslinking the posterior part of the cornea has the same efficacy as crosslinking its anterior portion.

METHODS

Porcine eyes were obtained from a local abattoir. The corneal disks of about 800 um were divided into anterior and posterior flaps of almost equal thickness using a DSEAK system, Figure 1. From the flaps, corneal strips were prepared and soaked in the riboflavin solution for 30 minutes. The samples were then crosslinked following the Dresden protocol, i.e. they were subjected to a UVA irradiance of 3 mW/cm^2 for 30 minutes with continuous application of riboflavin solution to the strips during the crosslinking time [1]. Crosslinked specimens were tested in tension using a DMA machine (TA instruments, Maryland) at displacement rate of 2 mm/min. The same experiments were done on similar samples (control group), which were not crosslinked. The specimens in control group were subjected to similar treatment procedure with the difference that the UV light was turned off during the CXL treatment. The stress-strain curves for the samples in the control and treatment groups were compared together in order to determine the relation of CXL and microstructure of collagen fibers on improving the corneal biomechanical behavior.

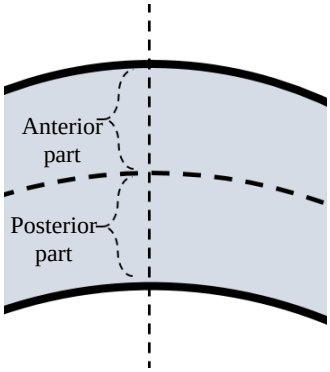

Figure 1: From corneal samples, an anterior and posterior flaps were dissected using a DSEAK system.

RESULTS

Figures 2-4 show the tensile stress-strain behavior of anterior and posterior samples from the control and treated groups. It is observed that the flaps from the anterior part of the cornea had a much stronger tensile properties compared to those of the samples from the posterior part, Figure 2. Furthermore, it is seen that the CXL treatment significantly improved the mechanical response of anterior flaps, Figure 3. However, it had an insignificant effect on the tensile response of the posterior samples, Figure 4.

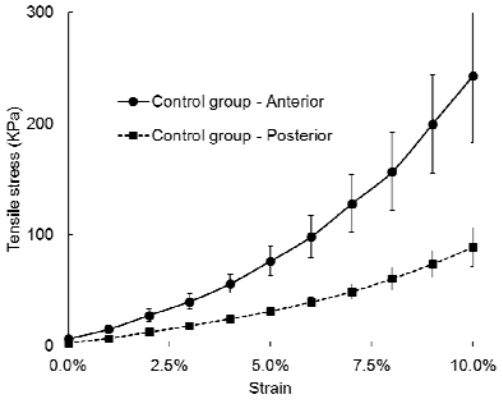

Figure 2: The tensile stress-strain response of the posterior and anterior flaps excised from the porcine cornea.

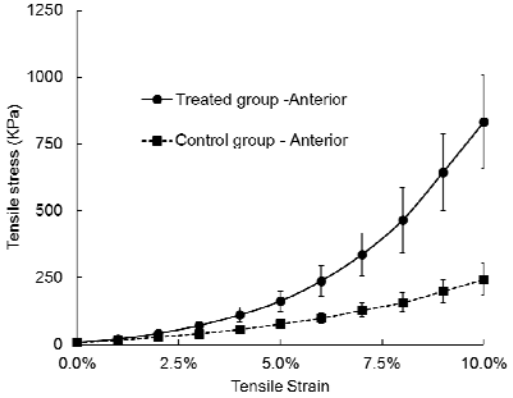

Figure 3: The effect of corneal crosslinking procedure on the tensile stress-strain response of the anterior flaps excised from the porcine cornea.

DISCUSSION

The present study compared the effects of CXL treatment on improving the tensile behavior of corneal flaps obtained from the posterior and anterior part of the cornea. The anterior flaps from the control group showed a stronger tensile properties compared to the posterior flaps, Figure 2. This finding is in agreement with previous studies [3] and is because the collagen lamellae in anterior part of the cornea are interweaved while they lie in parallel arrays in the posterior part. The interweaving of the collagen lamellae in anterior flaps induces stronger resistance to tensile force. The CXL procedure enhanced significantly the tensile behavior of anterior flaps, Figure 3. This result is also in line with general consensus in the field, i.e. the CXL treatment causes enhancement of the mechanical properties of the cornea [1,4-6]. The unexpected result is that the CXL procedure did not significantly affect the mechanical response of the posterior flaps, Figure 4. This confirms that the architecture of collagen lamellae plays an important role in the efficacy of the corneal crosslinking treatment [6]. It is noted that the depth of crosslinking in normal corneas is often limited to the top portion of the corneal thickness in order to limit the toxic effects of UV radiations on the endothelial cells. Nevertheless, the normal architecture of the corneal lamellae are expected to be disturbed because of the keratoconus disease. Thus, it is important that clinicians pay extra attention to the important role of the collagen architecture whenever they decide to use the CXL procedure for arresting the progression of this disease.

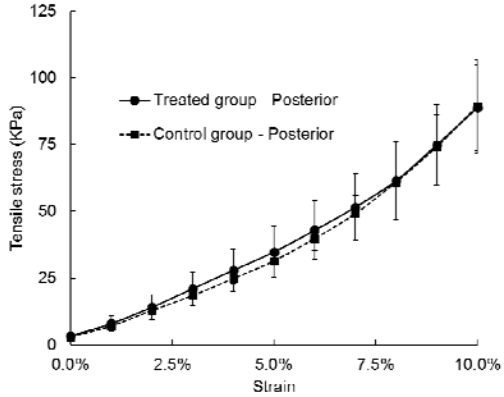

Figure 4: The effect of corneal crosslinking procedure on the tensile stress-strain response of the posterior flaps excised from the porcine cornea.

ACKNOWLEDGEMENTS

The support in part by NSF CMMI-1635290 is acknowledged.

REFERENCES

[1] Spoerl E, Huhle M, and Seiler T. Induction of cross-links in corneal tissue. *Experimental eye research* 1998; **66**: p. 97-103.

[2] Maurice DM. The structure and transparency of the cornea. *The Journal of Physiology* 1957; **136**(2): p. 263-286.

[3] Kohlhaas M, Spoerl E, Schilde T, Unger G, Wittig C, Pillunat LE. Biomechanical evidence of the distribution of cross-links in corneastreated with riboflavin and ultraviolet A light. *Journal of Cataract & Refractive Surgery* 2006; **32**(2): p. 279-283..

[4] Hatami-Marbini, H, and Rahimi A, "Interrelation of hydration, collagen cross-linking treatment, and biomechanical properties of the cornea." *Current eye research* 2016: **41** p. 616-622.

[5] Hatami-Marbini H, Jayaram SM. Effect of UVA/Riboflavin Collagen Crosslinking on Biomechanics of Artificially Swollen Corneas. *Investigative ophthalmology & visual science* 2018; **59**(2)**:** p. 764-770.

[6] Hatami-Marbini, Hamed. "Influence of Microstructure on Stiffening Effects of Corneal Cross-linking Treatment." *Journal of Refractive Surgery* 2018; **34**: p. 622-627.

SB³C2019
Summer Biomechanics, Bioengineering and Biotransport Conference
June 25 -28, Seven Springs, PA, USA

Genomic Loci Modulating Ocular Compliance in Mice

Elizabeth M. Boazak (1), Cassandra M. Chu (1), Rebecca King (2), Joseph M. Sherwood (3), Darryl R. Overby (3), Eldon E. Geisert (2), C. Ross Ethier (1,4)

(1) Biomedical Engineering
Georgia Tech/Emory University
Atlanta, GA, USA

(2) Department of Ophthalmology
Emory University
Atlanta, GA, USA

(3) Bioengineering
Imperial College London
London, United Kingdom

(4) Mechanical Engineering
The Georgia Institute of Technology
Atlanta, GA, USA

INTRODUCTION

Glaucoma is the leading cause of irreversible blindness worldwide, and is characterized by progressive damage and loss of retinal ganglion cells (RGCs), resulting in visual field loss. While glaucoma can occur at any level of intraocular pressure (IOP), elevated IOP is a known risk factor[1]. All current glaucoma treatments seek to reduce IOP, which reduces the progression of vision loss. However, a significant fraction of glaucoma patients present with normal IOPs[2,3], and it is thus widely recognized that additional risk factors remain.

The mechanisms by which elevated IOP result in RGC death are not well understood. Under elevated IOP, the optic nerve head (ONH) tissues experience abnormally high deformations, which are thought to play a major role in RGC damage. Modeling has shown that scleral stiffness plays a major role in modulating ONH deformation [4]. Recent animal and clinical data have also indicated that scleral stiffening may reduce susceptibility to glaucomatous damage[5,6]. *Therefore, we hypothesize that low scleral stiffness is a risk factor for glaucoma.* We aim to identify the genes that control scleral stiffness.

Ocular compliance (OC), ϕ, is defined as $\phi = dV/dP$, where V is ocular volume and P is IOP, and reflects corneoscleral mechanical properties. Thus, OC can be used as an indicator of scleral stiffness. We expect the genomic loci associated with OC and scleral stiffness to significantly overlap. The BXD mouse set, comprising over 100 fully mapped, inbred substrains and fully sequenced parent strains, is a powerful tool for quantitative trait locus (QTL) analysis, and specifically for the identification of candidate genes modulating OC.

Here we identify a genomic locus modulating OC using the BXD mouse set. Our initial data indicates that differences in OC can be detected between BXD mouse strains and a significant QTL was identified on chromosome 11 (chr11). Within this locus we have identified 5 candidate genes: 3 genes with nonsynonymous single nucleotide polymorphisms (SNPs) expected to disrupt protein function (Gm11939, Keratin 40, and Keratin 33b) and 2 genes that are cis-eQTLs (Smarce1 and Tensin 4).

METHODS

We measured OC using iPerfusion[7]. Following cannulation of enucleated mouse eyes, an adjustable pressure reservoir was used to apply a series of pressure steps (6.5 to 23 mmHg, range of reported IOP in BXD mice) to the eye, and the resulting flow rate into the eye was recorded. Pressure and flow data were analyzed by a Discrete Volume method, in which integration of flow traces, with adjustment for outflow, gives the change in volume of the eye following each pressure step, from which compliance was calculated. Pressure vs. compliance data were fit with the semi-empirical relationship:

$$\phi(P) = \phi_r \left(\frac{P_{r,\phi}+\gamma}{P+\gamma}\right) \qquad (1)$$

where ϕ_r is the reference compliance at reference pressure $P_{r,\phi}$, and γ is a nonlinearity parameter. ϕ_r was calculated at a reference pressure of 13 mmHg, the normal IOP of C57BL/6J mice.

Currently, we have evaluated OC in C57BL/6J (B6), DBA/2J (D2), and 14 BXD strains (n = 147, 4-16 mice per strain, male & female, ages 77-100 days). Mean OC values, normalized by eye volume, and standard errors for each strain were entered into GeneNetwork, a group of open access databases and software available for the study of gene and molecular networks, along with phenotypes. Detailed statistical and analytical methods employed by these tools are available at genenetwork.org. Candidate genes were identified within the significant QTL by assessing for SNPs, high whole-eye mRNA expression, and potential linkage to matrix or cytoskeletal mechanics as supported by the literature.

RESULTS

Compliance was successfully measured for 147 pairs of eyes using iPerfusion. From each pair, the eye with the lower uncertainty on ϕ_r was included in the strain data set. As OC is dependent on the initial volume of the eye, ϕ_r was normalized by the eye volume (**Fig. 1**). Eyes were weighed prior to cannulation and eye density[8] was used to estimate volume. Error bars indicate the 95% confidence interval on the mean. After normalization, we observed significant differences in OC between some strains (ANOVA, $p < 0.0001$). However, we note that significant differences between all strains are not required to effectively identify a QTL.

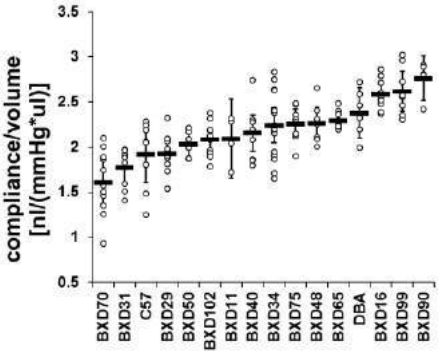

Figure 1: Mean, normalized compliance for BXD strains

The genome-wide map (**Fig. 2**) generated from the data shown in **Fig. 1** shows a significant peak on chromosome 11. The blue line indicates the total likelihood ratio statistic, a measure of the linkage between differences in traits and genotype markers. The pink and grey horizontal lines mark the threshold for significant and "suggestive" peaks, respectively. The red and green lines reflect the contributions of the B6 and D2 alleles, respectively.

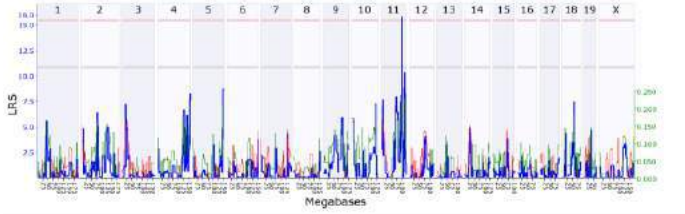

Figure 2: Interval map of volume-normalized compliance across all chromosomes

The significant peak on chr11 (**Fig. 3**) was bounded by the genomic markers rs29445436 (98.9 Mb) and rs27058443 (99.8 Mb). The positive additive coefficient for the D2 alleles (green line in LRS plot) indicates that D2 alleles increase normalized OC values. In the haplotype map shown in the upper portion of **Fig. 3**, it can also be seen that D2 (green) and B6 (red) alleles segregate around this genetic locus and that B6 alleles correspond to lower normalized OC.

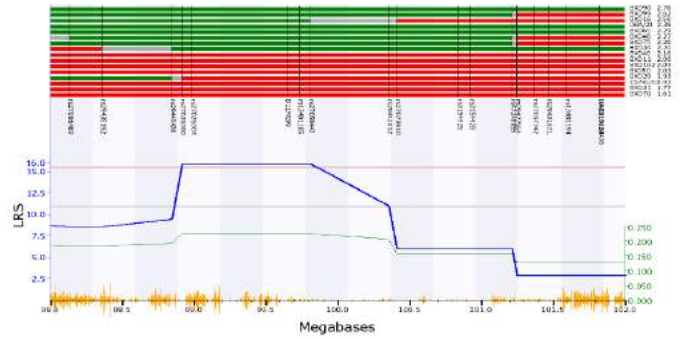

Figure 3: Haplotype map for the 16 evaluated BXD strains and map of gene locations across a subsection of chr 11.

Considering that the BXD genotyping density allows for mapping with a precision of approximately ± 1 Mb, we searched the 97.9 to 100.8 Mb region of chr11 for candidate genes involved in the regulation of OC. Tns4 and Smarce1 were identified as cis-eQTLs (i.e. their expression segregates with the parental alleles, and the genes driving the mRNA expression are located within the same region as the compliance QTL). Within this region there were also three genes with disruptive nonsynonymous SNPs (Gm11939, Krt40, and Krt33b).

DISCUSSION

We have developed methods to measure OC in mice with sufficient resolution to record significant differences between many genetic strains of mice. Our present data set has enabled the identification of five genes: Gm11939, Krt40, Krt33b, Tns4 and Smarce1, which may be involved in the modulation of corneoscleral mechanical properties. Keratins (Krt) are cytoskeletal and/or extracellular matrix proteins expressed in the eye. Tensins (Tns) are known to interact with actin filaments and β integrins in focal adhesions. In turn, how cells interact with and sense their matrix can influence gene expression and subsequently the regulation of the extracellular matrix composition. Meanwhile, Smarce1 (SWI/SNF Related, Matrix Associated, Actin Dependent Regulator of Chromatin) produces a subunit of SWI/SNF complexes, which are involved in chromatin remodeling. Future work will look for correlations between Smarce1 and extracellular matrix gene expression. The role of candidate genes in regulating corneoscleral mechanical properties remains to be evaluated.

A limitation of the current preliminary analysis is the small number of BXD strains used. Typically, robust QTL analysis is carried out with trait values from a minimum of 20 strains. Additional measurements may add and/or change the location of current significant peaks. We are continuing to evaluate additional BXD strains. Furthermore, we have been investigating alternate data analysis techniques and anticipate that better fitting of our current data will improve the precision of our OC measurements, and hence the power in the QTL analysis.

A challenge in the interpretation of our measurements is that OC reflects the mechanical behavior of the corneoscleral shell as a whole, and not the sclera alone. Direct tensile testing of mouse sclera mechanical properties is limited by tissue sample size. Additional studies relating corneal and scleral deformations using digital image correlation, as well as follow-up work to identify localization and tissue-specific changes in expression of candidate genes, are expected to yield complementary findings which will aid in data interpretation.

Thorough interrogation of the role of candidate genes in ocular mechanics, and/or successful identification of additional modulatory genes, will aid in the understanding of glaucoma pathogenesis, the identification of novel therapeutic targets, the identification of at-risk patients, and the possible development of a new mouse model for glaucoma research.

ACKNOWLEDGEMENTS

We are grateful for funding from the National Eye Institute (1R21EY026685) and the Georgia Research Alliance

REFERENCES

[1] Leske, MC et al., *Arch Ophthalmol*, 121(1):48-56, 2003. [2] Quicley, HA et al., *Arch Ophthalmol*, 119(12):1819-26, 2001. [3] Iwase, A et al., *Ophthalmology*, 111(9):1641-8, 2004. [4] Sigal, IA et al., *Invest Opthalmol Vis Sci*, 46(11):4189-99, 2005. [5] Eilaghi, A et al., *Ann Biomed Eng*, 38(4):1586-92, 2010. [6] Coudrillier, B et al., *IEEE Trans Med Imaging*, 35(4):988-99, 2016. [7] Sherwood, JM et al., *PLoS One*, 11(3):e0150694, 2016. [8] Wisard, J et al., *J Neurosci Methods* 187(2):156-66, 2010.

SB^{3}C2019
Summer Biomechanics, Bioengineering and Biotransport Conference
June 25 -28, Seven Springs, PA, USA

CHARACTERIZING THE ACTIN AND GFAP NETWORK STRUCTURE OF THE ASTROCYTIC LAMINA IN MOUSE EYES

Yik Tung Tracy Ling (1), Mary E. Pease (2), Harry A. Quigley (2), Thao D. Nguyen (1)

(1) Department of Mechanical Engineering
Johns Hopkins University
Baltimore, Maryland, USA

(2) Wilmer Eye Institute
Johns Hopkins University
Baltimore, Maryland, USA

INTRODUCTION

Glaucoma is a blinding disease characterized by the progressive degeneration of retinal ganglion cell (RGC) axons at the optic nerve head (ONH), where axons exit the intraocular space, and remodeling of the ONH tissues [1]. In human, a connective tissue lamina cribrosa (LC) serves to structurally support the axons. The LC consists of a stack of cribriform plates that when viewed en face appears as a network of connective tissue beams and pores. The pores are spanned by astrocytes that guide the RGC axons as they pass through the ONH [2]. In rodent models, the lamina consists entirely of astrocytes with long processes that wrap around the axonal bundles [3] (Fig 1a). Wang et al. [4] showed that ONH astrocytes become reactive with increased intraocular pressure (IOP); and Nguyen et al. reported that ex vivo inflation response of the mouse astrocytic lamina was stiffer in eyes subjected to 3 days of IOP elevation *in vivo* [5]. Increase IOP is also associated with axonal degeneration and blockage of axonal transport in both human and in animal models [6]. Characterizing changes in astrocytic network that precedes the degeneration of axons is important for investigation of the mechanosensitive linkages.

Morphological changes in the astrocytes caused by changes in the mechanical environment have been investigated primarily through immunostaining of their intermediate filament, GFAP [7]. However, Tehrani et al. [8] showed in longitudinal mouse optic nerve sections that actin labeling revealed fine astrocytic processes that were not visible by GFAP immunotaining. The objective of this study is to quantitatively measure and compare the spatial distribution of GFAP and actin fiber networks in the astrocytic lamina of normal mouse eyes and those subjected to 3-day IOP elevation *in vivo*. Characterization of the actin cytoskeletal network will enhance understanding of the mechanobiological response of ONH astrocytes to sustained IOP elevation.

METHODS

Specimen Preparation: Four ONH segments were obtained from two 6-month old green fluorescent protein (GFP)-glutamate transporter-GLT1 transgenic mice, which express both GFP and glutamate transporter protein, GLT1 [9]. Elevated IOP were induced in the left eyes by injecting microspheres consisting of 2 μL of 6-μm diameter beads, 2 μL of 1-μm diameter beads and 1 μL of viscoelastic compound (10 mg/mL sodium hyaluronate, Healon; Advanced Medical Optics, Inc.). The respective right eyes served as contralateral controls. The IOP was measured with a TonoLab rebound tonometer (TioLat Inc) before bead injection and before sacrificing. All mice were anesthetized after 72 hours of IOP elevation with 75/10/2 mg/kg of ketamine, xylazine and acepromazine respectively. The mice were perfused with 4% paraformaldehyde in Sorenson's phosphate buffer before enucleation. The globes were then immersed in the same fixative for an hour and were transferred into 0.1M PO_4 buffer, where the extraocular tissues were removed. ONH of 1mm length were separated from the posterior eye wall using a sharp razor blade. The optic nerve segments were cryopreserved and embedded in a mixture of 20% sucrose-buffer and OCT using a modified protocol from Barthel and Raymond [10]. The 1mm ONH segments were cryo-sectioned serially into 10μm slices using Cryostat CM3050S (Leica Biosystems) at -25 ^oC.

Immunostaining: Primary antibodies from rabbit against GFAP (1:1000, Abcam AB7260) and secondary antibodies from goat against rabbit (1:500, Invitrogen A11008) were used for GFAP labeling. ONH sections were also incubated with phalloidin (1:60, Invitrogen A1280) and DAPI (1:1000, Roche 10-236-276-001) for staining of actin filaments and nuclei respectively. All sections were mounted with Dako mounting media and covered with glass slide.

Image Acquisition: Confocal fluorescent images were obtained with a Zeiss LSM 710 confocal microscope using a Plan-Apochromat 40x objective. Three channels of images at excitation wavelength of 458nm for GFAP (Fig 1c), 561nm for actin (Fig 1e), and 405nm for nuclei were captured for each ONH section. Each channel consisted of 3 by 3 tiled images that were stitched with a 12% overlap (Fig 1a). The resulting images were exported as TIFF files for spatial characterization.

Characterizing GFAP and actin networks: Images were pre-processed with 2-D median filter and contrast-limited adaptive histogram equalization (CLAHE) to reduce noise and enhance contrast (Fig 1b). All three channels were individually binarized using Otsu thresholding method [11] followed by morphological dilation and erosion to segment the actin, GFAP and nucleus fluorescent regions. A lamina boundary was detected by tracing the outer boundary of the largest connected region in the binarized GFAP image. The boundary pixels were recorded and overlaid onto the contrast enhanced GFAP image to visually verify the accuracy of the segmentation (Fig 1b). The boundary segmentation was used to measure for each slice the (1) area of the astrocytic lamina, (2) the aspect ratio of the lamina, the (3) GFAP and (4) actin area fraction, and (5) the number of nuclei in the lamina. The aspect ratio was determined by fitting an ellipse to the boundary of lamina and calculating the ratio of the major to minor axes. The GFAP and actin area fraction were calculated as the total area of the GFAP (Fig 1d) and actin (Fig 1f) regions over the lamina area. The number of nuclei was determined by counting the number of regions with DAPI signal within the lamina. All image analyses were conducted in *Matlab* R2017a.

RESULTS AND DISCUSSION

The average area of the lamina of eyes subjected to 3-day IOP elevation in vivo was 0.057±0.007 mm^2, and the area of the lamina in the contralateral control eyes 0.053±0.001 mm^2. The lamina area for both groups increased with distance up to 400um from the retina. Previous measurements of the area of the astrocytic lamina ranged from 0.028-0.072 mm^2 in black Swiss mice [12].

The average GFAP area fraction across 4 eyes was 0.59±0.01 $\mu m^2/\mu m^2$, whereas the average actin area fraction was 0.67±0.004 $\mu m^2/\mu m^2$. The combined GFAP and actin area resulted in an average areal fraction of 0.82 $\mu m^2/\mu m^2$. The area fraction of actin was on average 13.6% larger than the GFAP area fraction in all normal and contralateral hypertension eyes. The nucleus density was on average 2.86±0.12 per 1000μm^2, which also falls in the range 0.9-12 per 1000 μm^2 reported by Mabuchi et al. [12].

As a glial cell that expresses mechanosensitive channels, its actin coverage in transverse sections may provide insights to the astrocytic reactivity that have not been previously reported. The robust image processing program allowed for further analysis of actin rearrangements and investigation of non-actin labelled regions where axonal bundles reside. Further, the spatial arrangement of cytoskeletal network within the astrocytes and overall morphology of lamina may aid the development of computational model for the investigation of mechanical properties at the ONH. It is however important to note that while GFAP labeling is specific for optic nerve astrocytes, actin and DAPI labeling can include contributions from other cell types in the lamina, such as endothelial cells.

ACKNOWLEDGEMENTS

This study is funded by NSF Award 1727104; Brightfocus Foundation G2015132 and EY001865, Wilmer Core Grant for Vision Research, Microscopy and Imaging Core Module.

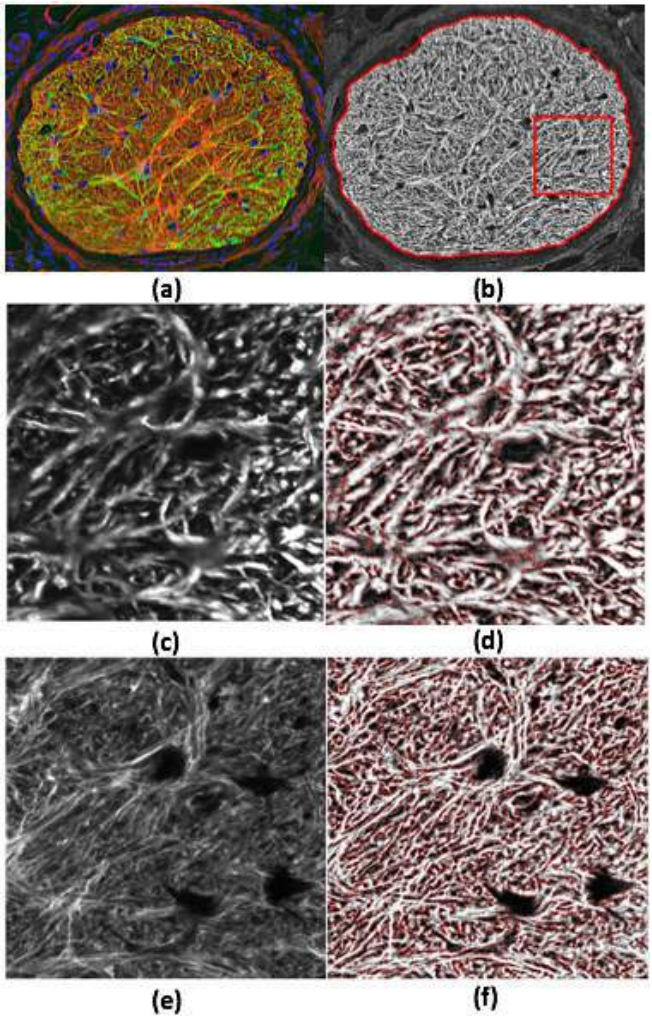

Figure 1: Fluorescent images of GFP-GLT1 transgenic mouse ONH sections acquired by LSM 710 confocal microscope, showing (a) a normal ONH section 240 μm away from the retina that was stained for GFAP (green), actin (red) and nucleus (blue), (b) GFAP channel after median filter and CLAHE, detected lamina boundary is highlighted with thick red outline. Highlighted red box represents an area of 76x76μm of lamina that were zoomed in for viewing of (c) the original GFAP and (e) actin channel. The channels were thresholded and its binarized boundary is imposed on preprocessed (d) GFAP and (f) actin images for visualization.

REFERENCES

[1] Quigley, H. and Green, W. *Ophthalmol*, 86(10):1803–1827, 1979. [2] Trivino, A et al. *Vision research* 36.14: 2015-2028, 1996. [3] Morrison, J et al. *Exp Eye Res*. Feb; 60(2):127-35, 1995 [4] Wang, R. *Invest. Ophthalmol. Vis. Sci*. 58.2:924-932, 2017. [5] Nguyen, Cathy, et al. *Invest. Ophthalmol. Vis. Sci*. 58.2: 721-733, 2017. [6] Quigley, H et al. *Invest. Ophthalmol. Vis. Sci*. 16:640–646, 1977. [7] Sun, D et al. *Journal of Comparative Neurology* 516.1:1-19, 2009. [8] Tehrani, Shandiz, et al. *Invest. Ophthalmol. Vis. Sci*. 55.10: 6945-6952, 2014 [9] Regan, R et al. J Neurosci. 27: 6607–6619, 2007. [10] Barthel LK, Raymond PA. *J Histochem Cytochem.* Sep;38(9):1383-8, 1990 [11] Otsu N. IEEE Trans Syst Man, 20(1):62–66, 1979. [12] Mabuchi, Fumihiko, et al. *Invest. Ophthalmol. Vis. Sci*. 44.10: 4321-4330, 2003

SB³C2019
Summer Biomechanics, Bioengineering and Biotransport Conference
June 25 -28, Seven Springs, PA, USA

SNAPSHOT POLARIZED LIGHT MICROSCOPY TO VISUALIZE AND QUANTIFY COLLAGENOUS SOFT TISSUE MICROSTRUCTURE AT 156 FRAMES/SECOND

Bin Yang (1), Po-Yi Lee (1,2), Bryn Brazile (1), Ian A. Sigal (1,2)

(1) Department of Ophthalmology
University of Pittsburgh
Pittsburgh, PA, USA

(2) Department of Bioengineering
University of Pittsburgh
Pittsburgh, PA, USA

INTRODUCTION

Collagen fiber microstructure and orientation are important in soft tissue dynamics and are therefore of great interest to biomechanics [1]. Hence, several techniques have been developed to measure these collagen properties, such as polarized light microscopy (PLM) [2] and second harmonic generation (SHG) [3]. These techniques, while helpful for static and quasi-static conditions, lack the temporal and/or spatial resolution necessary to study soft tissue dynamics.

To facilitate the study of the role of collagen on the dynamic properties of soft tissues and their biomechanics, we developed a technique termed snapshot PLM. Snapshot PLM captures high resolution collagen fiber microstructure and orientation in a single full-field color-image. Requiring only a single image means that snapshot PLM imaging speed is limited only by the camera frame rate. Similarly, a single image also preserves optical resolution and ability to detect small details of the microstructure, not affected by the multi-frame post-processing. Our goal in this study was to introduce snapshot PLM, and to demonstrate its high spatial and temporal resolution when applied to both static and dynamic collagenous tissues.

METHODS

Snapshot PLM imaging system – The snapshot PLM imaging system was developed by retrofitting 2 sets of polarization components into a commercial upright microscope (Olympus IX-83) [4]. A broadband white LED light source was used for illumination and a 4X strain-free air objectives were used for imaging. The image/video acquisition was automated with cellSens, a commercial software from Olympus.

Color-based collagen analysis – We conducted numerical simulations to evaluate the imaging characteristics of snapshot PLM, and to establish the algorithm to extract collagen fiber orientation from the acquired image. The color was simulated over a range of fiber orientations (0-90 degrees) and tissue retardances (0.1-1.2 radians). The RGB color was converted to HSV color (Hue, Saturation, and Value) for analysis. We established the relationship of the hue and the fiber orientation. This relationship was verified experimentally using sections of chicken tendon imaged at various known orientation angles.

Ex-vivo tissue preparation, imaging and quantification – We stretched and imaged a chicken tendon section and a whole pig chordae tendineae to demonstrate the high spatial resolution (~1μm/pixel) and high temporal resolution (~10ms/frame), respectively, of snapshot PLM. Tendons are important force transmitting materials. Fresh chicken tendon was sectioned along the longitudial fiber direction at a thickness of 30μm, and then stretched with a custom uniaxial stretcher. Chordae tendinae were chosen because they are highly dynamic during cardiac cycle, and therefore it is important to understand their dynamics and microstructure. Fresh porcine chordae tendineae (~400μm thick) was stretched by pulling manually with a tweezer during the imaging. Collagen fiber orientation during stretching was analyzed using circular statistics.

RESULTS

Color-based collagen analysis – The simulations showed a direct relationship between simulated color and collagen fiber orientation (Fig. 1a). At a given retardance, the hue and fiber orientation exhibited a unique and monotonic correlation (Fig. 1b). At a given fiber orientation, the hue is independent on the retardance. The experimental

chicken tendon verification also showed a monotonic relationship between the hue and fiber orientation, similar to that shown in Fig. 1b. Based on this curve, we developed an empirical color/angle conversion algorithm to retrieve the collagen fiber orientation.

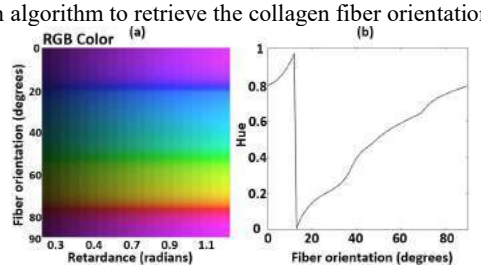

Figure 1 (a) Simulated RGB colors over a wide range of collagen fiber orientation and retardance; (b) a monotonic relationship between the hue and the fiber orientation means that there is a unique orientation at each retardance value.

Ex-vivo tissue imaging and quantification –The chicken tendon section was directly imaged with a 4X objective and the only post-processing applied to the images shown in Fig. 2 was cropping. The high resolution of snapshot PLM revealed sub-bundle details of the tendon section (Fig. 2c). Fig. 2b shows highly complex fiber deformation traces computed using DIC. Fig. 2c shows the time sequence of the uncrimping process of a crimped region (white box in Fig. 2a). After applying 16.7% stretching along the longitudinal fiber direction, collagen fibers became highly aligned with preferred fiber orientation around 5 degrees, and the standard deviation decreased from 21.3 degrees to 4.1 degrees.

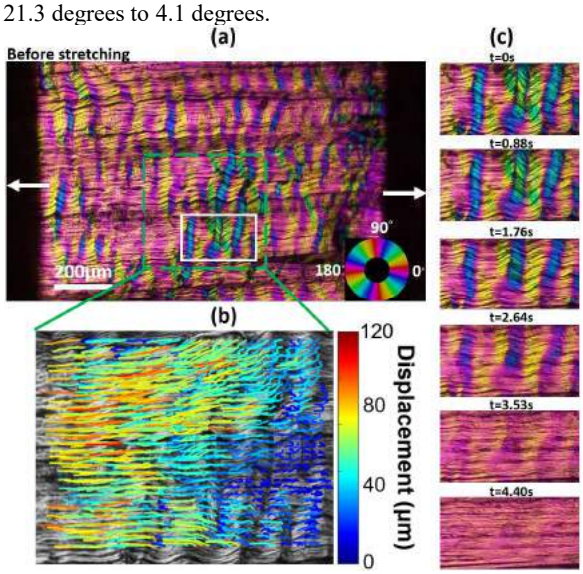

Figure 2 A 30µm-thick chicken tendon section stretched and imaged at 60 frames/second under 16.7% stretch. (a) Collagen fibers show clear crimp before stretching; (b) fiber deformation traces from DIC; (c) time-resolved uncrimping process.

The pig heart chordae tendineae uniaxial stretching was imaged at a frame rate of 156 frames/second with a 4X objective, resulting in an imaging speed of 6.5ms/frame. Snapshot PLM image revealed complex structure of the chordae tendineae, which appeared to have highly crimped collagenous structure in the core surrounded by less crimped structures as the cladding. This observation is consistent with previously reported structure of the chordae tendineae of pig mitral valves [5]. Upon applying 8.7% stretching, the fast imaging revealed the uncrimping process (Fig. 3a-d). The uniform color in the close-up images shown in Fig.3e indicates that the central collagen core lost crimp quickly and became straight. Plotting the orientation along the chordae core (dashed-line in Fig. 3e) further demonstrated the uncrimping process (Fig. 3f). The quantitative angle analysis showed that the standard deviation of collagen fiber orientation decreased from 29.2 degrees to 5.1 degrees during the stretching, primarily from fiber uncrimping, and perhaps some reorientation. The outer layer did not show significant color change, which suggests that stretching imposed minimal structural changes in this region's collagen.

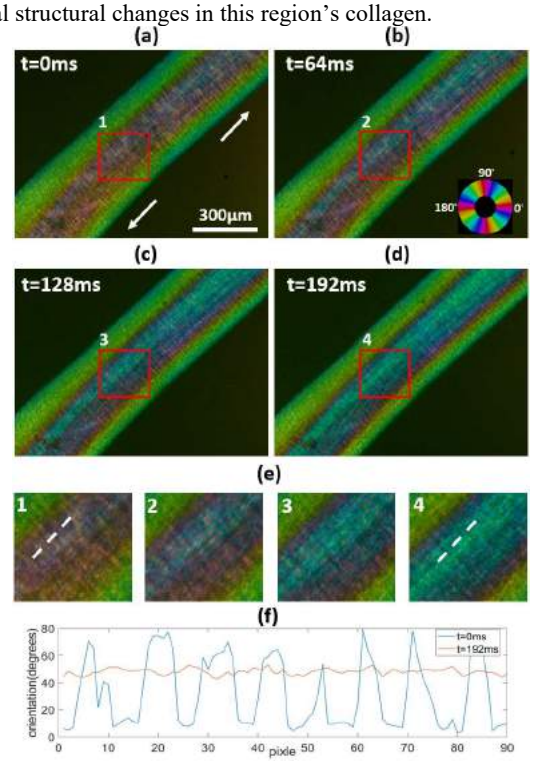

Figure 3 The pig heart chordae stretching imaged at 156 frames/second under 8.7% stretch. (a-d) Four stretching stages of the collagen core uncrimping indicated by color changes. White arrows in (a) indicate the stretching directions; (e) close-up images of the collagen core showing uncrimping; (f) plot of local orientation before and after stretching along the dashed line in (e).

DISCUSSION

We demonstrated that snapshot PLM is a fast and high-resolution imaging method, which is well-suited for real-time imaging collagenous tissues in both static and dynamic conditions. The high temporal resolution provides the opportunity to study the transient tissue deformations as well as deformations with complex trajectories that would have been missed with traditional slower imaging methods.

ACKNOWLEDGEMENTS

NIH R01-EY023966, R01-EY025011, R01-EY028662, T32-EY017271 and P30-EY008098,

REFERENCES

[1] Sacks, M et al., *J Biomech*, 42:1804-1824, 2009
[2] Jan, N. J., et al., *Biomed Opt Express*, 6(12), 4705-4718, 2015
[3] Ram, S, et al., *IEEE Trans Biomed Eng,* 65: 1617-1629, 2018
[4] Shribak, M, et al., *Sci Rep,* 5:17340, 2015
[5] Ritchie, J, et al., *Ann Thorac Surg,* 80: 189-197, 2005

A HUMAN CADAVERIC MODEL FOR QUANTIFYING KNEE JOINT MECHANICS DURING SIMULATED GAIT: EFFECT OF ASTM AND ISO DERIVED INPUT PROFILES

Amanda Wach (1), Olufunmilayo O. Adebayo (1), Caroline Brial (1), Tony Chen (1), Russel F. Warren (2), Peter A. Torzilli (3), Suzanne A. Maher (1)

(1) Department of Biomechanics
(2) Sports Medicine
(3) Research Division
Hospital for Special Surgery
New York, NY, USA

INTRODUCTION

While cadaveric models have been used to quantify the effect of injury and repair on knee mechanics, few models have captured the dynamics and contact mechanics of daily living activities. Previous cadaveric models could not dynamically control sufficient degrees of freedom [2-3] or simultaneously characterize knee kinematics and contact mechanics [4] and were most often run on complex customized machines. Confusion over the inputs required to best mimic human gait also exists and further complicated by the acceptance of two standardized sets of inputs – the ISO [5] and ASTM standards [6]. The ISO standard is an implant wear testing standard calculated from inverse dynamics gait studies of human subjects [7]. The newer ASTM standard, also intended for implant wear testing, is developed from direct load measurements from instrumented knee implants [8].

Our objectives were to: (i) develop a testing protocol to mimic walking using a commercially available six degree of freedom simulator and (ii) compare the contact mechanics and kinematics of human cadaveric knees subjected to ISO and ASTM inputs. We hypothesized that the inputs would have a significant effect on the distribution of contact forces across the knee joint.

METHODS

Following IRB approval, five intact, freshly frozen human cadaveric knees were stripped of bulk soft tissue and patella, leaving only the joint capsule. A Kirshner wire was drilled through the epicondylar axis of the femur under fluoroscopic guidance to assist with positioning during potting. Each knee was potted in full extension, such that the superior and epicondylar axes were aligned with the compression and flexion axes, respectively, of a six degree of freedom VIVO joint simulator (AMTI) and the tibial anterior axis was aligned with the anteroposterior axis of the simulator (Fig. 1). The knee was compressed with a 1kN axial load within the simulator to imitate a static standing position. Each knee was subjected with both ASTM and ISO standard gait input waveforms for 60 cycles at 0.5Hz (Fig. 2).

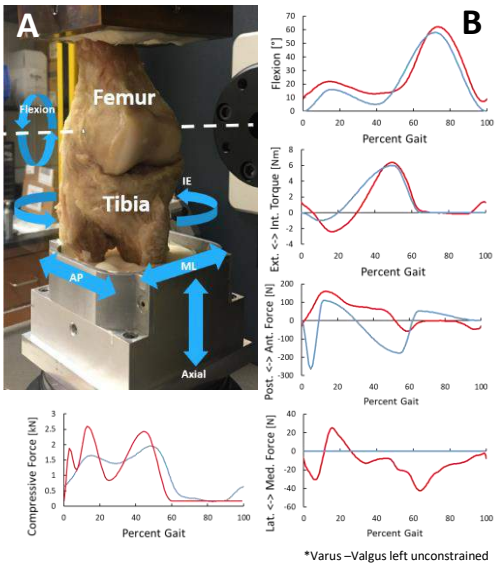

Figure 1: A) A cadaveric knee fixed in a VIVO knee simulator (AMTI) with six degrees of freedom. B) ASTM (red) and ISO (blue) inputs for simulated gait. ASTM inputs were calculated assuming a 76kg bodyweight.

Femur and tibia motions were tracked using a motion capture analysis system (Motion Analysis Corporation, CA) with retroreflective markers attached to the fixtures. Knee joint kinematics were computed using bone-fixed coordinate systems, as defined by Grood and Suntay [9]. The femoral epicondyles and most medial and lateral points of the tibial plateau were manually digitized to define the femoral flexion axis and tibial mediolateral axis; the origins of both coordinate systems were defined as the midpoints of these axes. The femoral anteroposterior axis and tibial superior axis were defined as aligned with the simulator axes. *Tibia relative to femur rotations and translations were calculated*, using the 1kN standing position as the reference position.

Contact mechanics were directly measured using a Tekscan 4011 pressure sensor placed beneath the meniscus on the medial and lateral tibial plateau and sutured to the ACL and posterior joint capsule.

Data were averaged from cycles 55-59, then averaged across specimens. Results are shown for the stance phase of gait from heel strike to toe off (0-60% of the gait cycle). Differences between the resulting kinematics and contact mechanics from ASTM and ISO standard inputs were evaluated using a paired t-test at 0%, 4%, 8%, 14%, 20%, 45% and 60% of the gait cycle ($p<0.05$).

RESULTS

Kinematics: Five knees were successfully tested with both ASTM and ISO gait input waveforms. Resulting joint kinematics were significantly different in early stance: ISO inputs resulted in higher tibial external rotation from 0-20% and a peak in tibial posterior translation at 8% of gait (Fig. 2). Knee joint kinematics were similar between the two standards from 20-60% of gait; while at 45% of gait ISO inputs resulted in higher external rotation. No differences were found between the resultant valgus rotations or medial and superior tibial translations of the ASTM and ISO standards. However, a higher variability in kinematics between specimens were measured with ISO inputs, particularly in anterior tibial translation.

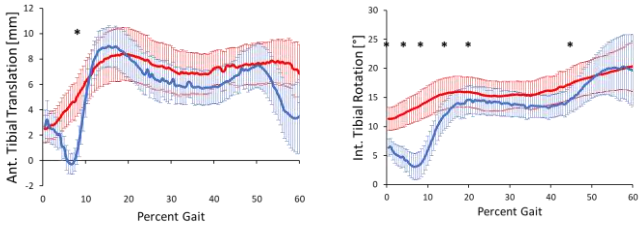

Figure 2: ASTM (red) and ISO (blue) resulting kinematics (tibia relative to femur). *p<0.05 between standard inputs

Contact Mechanics: Peak contact stresses were significantly higher at 4%, 14%, and 45% of gait with ISO standards compared to ASTM (Fig. 3A), corresponding to the compressive force inputs (Fig. 2B). No differences were found between the resultant total contact areas throughout stance. Qualitative changes in the location of contact across the tibial plateau reflect the differences in kinematics from the two standards. Specifically, the posterior tibial translation observed at 8% of gait shows a simultaneous anterior shift of weighted center of contact on the tibial plateau with ISO inputs compared to ASTM (Fig. 3B).

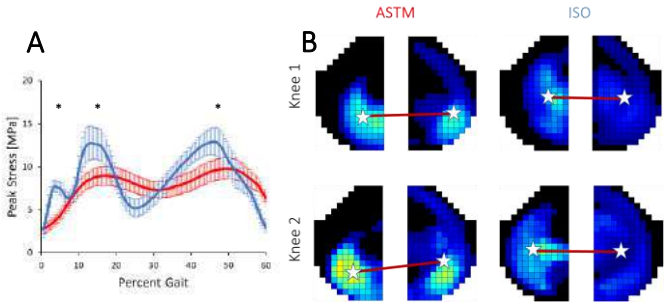

Figure 3: A) ASTM (red) and ISO (blue) resulting peak stress. *p<0.05 between standard inputs B) Example contact maps at 8% gait cycle. Weighted centers of contact are marked with stars.

DISCUSSION

We successfully developed a protocol for the application of both ISO and ASTM gait standards to cadaveric knees, using a commercially available six degree of freedom test machine. Subtle differences in kinematics and contact mechanics were evident between ISO and ASTM inputs, predominantly in translation and rotation in the early phase of stance. The ASTM standard resulted in less knee-to-knee variability in joint motion and contact mechanics. Furthermore, the peak contact stresses were higher for ISO inputs, reflecting the higher input axial forces with the ISO standard. These changes in kinematics were reflected in differences in force distribution across the tibial plateau.

Our study suggests that while it is feasible to apply both input profiles to cadaveric knees, ISO inputs, as derived from human knees, may more accurately capture the nuances of knee motion in early stance. We suggest that this model is suitable for quantification of the effects of soft tissue injury and repair on contact mechanics and kinematics.

ACKNOWLEDGEMENTS

We acknowledge the National Institutes of Health (ROI AR066635), the Clark Foundation, the Kirby Foundation, the Russell Warren Chair in Tissue Engineering, and the Stryker/ORS Women's Research Fellowship.

REFERENCES

[1] Li et al. (2004) JBJS [2]Bedi et al. (2010) JBJS; [3] Gilbert et al. (2013) J Biomech; [4] Morimoto et al. (2009) Arthroscopy [5] ISO (2009) 14243-1 [6] ASTM (2014) F3141-15 [7] Morrison (1970) J Biomech; [8] Bergmann et al. (2014) PLoS ONE; [9] Grood & Suntay (1983) ASME.

SB³C2019
Summer Biomechanics, Bioengineering and Biotransport Conference
June 25 -28, Seven Springs, PA, USA

PREDICTED GAIT ALTERATIONS DUE TO PARETIC LEG REDUCTION IN NUMBER OF MUSCLE SYNERGIES POST-STROKE

Marleny Arones (1), Carolynn Patten (2), Benjamin J. Fregly (1)

(1) Department of Mechanical Engineering
Rice University
Houston, Texas, USA

(2) Department of Physical Medicine and Rehabilitation
University of California
Davis, California, USA

INTRODUCTION

Muscle synergies may provide a helpful avenue for predicting patient function following clinical interventions, such as those arising from neurorehabilitation or orthopedic surgery. Theoretically, muscle synergies reduce the achievable control space making predicted muscle forces and consequently predicted motions more unique. In individual's post stroke, a reduced number of muscle synergies has been associated with a deterioration in walking function [1]. However, whether the degeneration in walking function is a direct result of reduced muscle synergies remains unknown.

Computational walking models coupled with optimal control provide an opportunity to test hypotheses that would otherwise be difficult or impossible to evaluate experimentally. This study aims to study the effect of reducing the complexity of locomotor control of one leg on a subject's walking function. Therefore, we predicted that differences in the number of muscle synergies assigned to one leg would be associated with differences in neuromusculoskeletal quantities.

METHODS

This study analyzed data from previously collected walking trials from one male subject suffering from chronic stroke walking dysfunctions (right-sided hemiparesis). All experimental procedures were approved by the University of Florida Health Science Center Institutional Review Board (IRB-01), and the subject provided written informed consent prior to participation. Motion capture (Vicon Corp), ground reaction (Bertec Corp), and electromyography (EMG) data (Motion Lab Systems) were collected simultaneously from the subject as he walked on a split-belt instrumented treadmill (Bertec Corp) at his self-selected speed.

The subject's neurophysiological and musculoskeletal components were taken into account using OpenSim (v3.3; [2]) and Matlab to develop four different modeling elements: a kinematic model, an EMG-driven calibration model, a foot-ground contact model, and a motion prediction model using the concept of muscle synergies. More specifically, the synergy-driven control model was calibrated using the subject's self-selected speed of 0.5 m/s using five-synergy activations per leg to track the following quantities: ground reaction forces, joint moments, joint angles, and muscle activations; see [3] for details.

The subject-specific neuromusculoskeletal model was used to develop two predictions for how the subject would walk following a reduction in the number of synergies controlling the paretic leg from the calibrated case (with five synergies) to two. Both predictions were generated using direct collocation optimal control [4], with the main difference between the two predictions being whether or not constraints were imposed in the formation of the two paretic leg synergies. In the first optimization, the two paretic leg synergy activations and synergy vectors were allowed to vary freely during the optimal control solution process. In the second optimization, the two paretic leg synergy vectors were constrained to be a linear combination of the original five paretic leg synergy vectors. Additionally, deviation of changes in the two paretic leg synergy activations from a linear combination of the original five paretic leg synergy activations were minimized in the cost function. During both predictions, the five-synergy vectors for the healthy leg were fixed to the values found during the calibration. The five-synergy activations controlling the healthy leg were allowed to change but the cost function was set to minimize the difference between the predicted and original synergy activation curves.

Technical Presentation #073

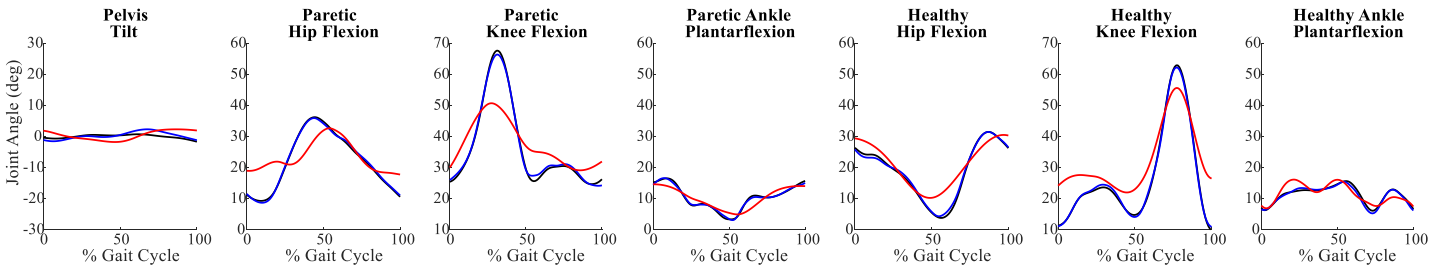

Figure 1| Comparison of joint angles produced between the different control strategies: five synergies (black line), two synergies (blue line), and two constrained synergies (red line)

The following parameters were analyzed after each prediction optimization: joint angles, joint moments, ground reaction forces and muscle activations. The NRMSE (Normalized Root Mean Square Error) values between the calibration and prediction results were calculated by normalizing each quantity by its range to identify what differences, if any, were observed and where.

RESULTS

When predicting a walking motion using two non-constrained synergies to control the paretic leg, it can be seen that there are minimal differences when compared to a walking motion produced using a five-synergy control (Figure 1). On closer inspection, there was no significant difference between the five- and two-synergy solutions when looking at the joint moments and ground reaction forces for both legs. Similarly, the muscle activations produced between the two optimizations did not significantly vary for the healthy leg, but it did vary significantly for the paretic leg (Table 1). Additionally, the stride length did not significantly vary between the five- and two-synergy walking motions (6.93% error) (Table 2).

Table 1| The average NRMSE of the muscle activations, joint moments, and ground reaction forces predicted by the model in comparison to the calibration quantities

	Muscle Activations	Joint Moments	Ground Reaction Forces
Two-synergy prediction unconstrained			
Paretic Leg	0.330	0.135	0.154
Healthy Leg	0.118	0.109	0.118
Two-synergy prediction constrained			
Paretic Leg	3.256	0.394	0.235
Healthy Leg	0.292	0.161	0.197

When predicting a walking motion using two constrained synergies to control the paretic leg, a significant difference was observed when comparing the joint angles to those generated using five synergies (Figure 1). Furthermore, a significant difference was discovered for the muscle activations, joint moments, and ground reaction forces produced by the paretic leg when comparing the five-synergy and two constrained synergy results (Table 1). Lastly, the stride length varied significantly between the five and two constrained synergy walking motions (35.3% error) (Table 2).

Table 2| Comparison of stride length between the calibration and predicted walking motions

	Stride Length (m)
Five-synergy calibration	0.701
Two-synergy prediction unconstrained	0.653
Two-synergy prediction constrained	0.453

DISCUSSION

This study evaluated the effect of reducing the number of synergies controlling the paretic leg of a stroke subject. We investigated whether reducing the control space directly resulted in the degeneration of walking function. We found that walking predictions generated using a two-synergy control over the paretic leg did not result in deterioration in walking function. Nevertheless, when the synergy activations and vectors were constrained to be a linear combination of the original five-synergy solution, deterioration in walking function was observed. The optimization predicted minor hip hiking of the paretic leg (pelvis tilt, Figure 1), which may be a direct effect of the decreased range of motion observed both at the hip and knee joints. Additionally, the joint angles of the healthy leg are forced to vary to compensate for the decrease of range of motion experienced by the paretic leg. Furthermore, the significant decrease in stride length can be directly associated with a degradation of walking performance (Table 2).

Our results support the findings from Clark et al. (2010) [1] who hypothesized that the impairment of locomotor coordination may correspond to the reduction in complexity of locomotor control. Our findings clarify that the reduction in synergies alone does not result in significant deterioration of walking performance. However, a reduction in synergies when constrained to be a linear combination of the original synergies does result in poorer walking performance.

Although our synergy-driven model predicts realistic walking motions, an important limitation of our simulation framework is that there is no enforcement of smoothness when generating muscle activations, which may be the reason why the two-synergy prediction is able to closely reproduce the walking gait generated by that of the five-synergy solution. Since the two constrained synergy model must be created from a linear combination, it doesn't have the same level of freedom to instantaneously vary the muscle activations resulting in the smaller NRMSE of the muscle activations for the two-synergy paretic leg compared to the two constrained synergy error (Table 1).

In conclusion, our findings support the idea that less complex neural control building blocks may not be the reason for degeneration of walking function; in fact, it may be that the less complex building blocks are constrained in a certain manner. Therefore, correctly identifying these building blocks may provide a channel for which neurorehabilitation interventions can be designed and locomotor impairments can be monitored.

ACKNOWLEDGEMENTS

Funding provided by the Cancer Prevention Research Institute of Texas Grant RR170026, and NSF Graduate Research Fellowship (1842494)

REFERENCES

[1]Clark, D et al., *J of Neurophysiology*, *103*(2): 844–857, 2010.
[2]Delp, S et al., *IEEE Transactions on Biomed Eng*, *54*:1940–1950, 2007.
[3]Meyer, A et al., *Frontiers in Bioeng and Biotech*, *4*: 77, 2016.
[4]Patterson, M et al., *ACM Trans. Math. Softw.*, *1*(41): 1–37, 2014.

SB³C2019
Summer Biomechanics, Bioengineering and Biotransport Conference
June 25 -28, Seven Springs, PA, USA

SYSTEM IDENTIFICATION OF PRESSURE-MEASURING INSOLES FOR DETERMINING GROUND REACTION FORCE DURING WALKING

Jessica L. DeBerardinis (1), Janet S. Dufek (2), Mohamed B. Trabia (1), Yann Le Gall (3), Nicolas Da Silva Sacoto (3)

(1) Department of Mechanical Engineering
University of Nevada, Las Vegas
Las Vegas, Nevada, United States

(2) Department of Kinesiology and Nutritional Sciences
University of Nevada, Las Vegas
Las Vegas, Nevada, United States

(3) École Supérieure d'Électronique de l'Ouest (ESEO)
Angers, Pays de Loire, France

INTRODUCTION

Pressure measuring insoles have relatively large number of pressure sensors. These insoles present an alternative for traditional instruments for measuring ground reaction force (GRF) as they can measure multiple, consecutive steps in addition to their portability. However, research validating the GRF measurements from pressure-measuring insoles has shown that they have some inaccuracies [1-2], which may be attributed to mechanical characteristics such as hysteresis of the sensors [3–5], or sensor drift [3-4]. Several researchers have attempted to address these issues through incorporating linear regression [6], load-unload calibration curves [7], polynomial adjustment of sensor drift [8], and artificial neural networks [9-10]. However, these studies were limited by their relatively small sample size. None included insole size-based analysis. The purpose of this project was to use system identification techniques to develop transfer function models that best described each of six different sizes of Medilogic® pressure-measuring insoles.

METHODS

GRF data from 29 participants was collected using pressure-measuring insoles (60 Hz) and force platforms (Kistler®, 1000 Hz). Previously published, standard biomechanical methods (IRB #724468) were used [1]. The participant demographics with respect to insole size are displayed in Table 1. The total number of data sets was 174 (29 participants x 3 trials x 2 limbs). Participants were asked to walk over two consecutive force platforms while wearing the insoles inside a pair of thin socks to allow a direct comparison between the two instruments. The GRF data from this experiment was zeroed and isolated to the steps that occurred on the force platforms.

The GRF data from each instrument were preprocessed. First, the two GRF curves of the two instruments were aligned to start at the same time instant. Equally-sized data sets were required to perform system identification, which allowed a point-by-point comparison between the results of the two instruments. Therefore, the insole data were interpolated to match the sampling frequency of the force platform. Additionally, the signal duration of the insole was adjusted to match that of force platform if the insole had a shorter stance time. If the insole had a longer stance time, the GRF from the force platform was reflected across the x-axis until the time the two signals matched. The GRF from both instruments were normalized to the participant's body weight.

Table 1: Participant demographics separated by insole size.

Insole Size (EUR)	Total #	Male /Female	Age (yr)	Body Mass (kg)	Height (cm)
35-36	5	0/5	24.4(0.8)	48.9(6.0)	156(7.3)
37-38	9	0/9	22.0(2.5)	55.1(5.3)	158(5.4)
39-40	5	0/5	24.2(2.5)	75.3(18.6)	164(2.8)
41-42	3	0/3	21.7(1.7)	84.8(7.1)	181(8.7)
43-44	4	1/4	32.3(13.9)	91.6(26.4)	173(6.3)
45-46	3	3/0	28.3(2.1)	101.2(23.5)	182(2.9)

After preprocessing, the data were separated by insole sizes. System identification was performed through the following steps:

1. One-third of the total number of data sets for each insole size were randomly selected as training data. To avoid bias, this set had an equal number of left and right trials.
2. System identification (Matlab 2018b) was used for each experimental data set to create six transfer functions of the following forms: 3 poles, 3 zeros; 4 poles, 3 zeros; 5 poles, 3 zeros; 4 poles, 4 zeros; 5 poles, 4 zeros; 5 poles, 5 zeros).

3. These estimated models were each validated on all data of an insole size. The root mean square error (RMSE) between the results of the estimated model and the force platform results was calculated and compared to the RSME between the original insole and force platform results to determine if the system identifications led to an improvement (Fig. 1).
4. The number of data sets where an estimated model improved was recorded for each model and insole size and labeled a summed improvement score, SIS. Similarly, RMSE of all cases were summed and were labeled SRMSE
5. For each estimated model, one trial that led to the most improvement were identified.

These steps were repeated for *one-sixth* the total number of trials for an insole size. The poles and zeroes of the repetitions were compared to assess the robustness of the model selection process.

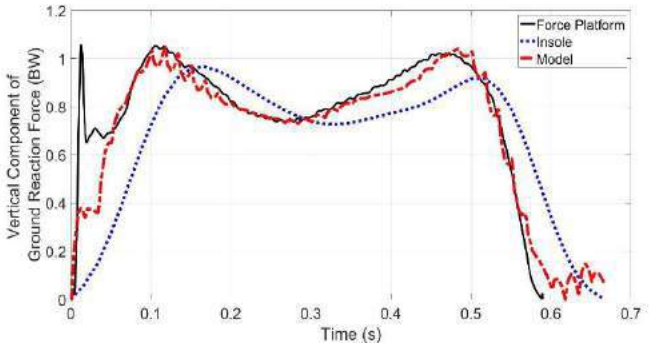

Figure 1: Exemplar set of data curves showing the improvement of the 4p 3z model (red) over the original 37-38 insole data (blue) as it better fitted the force platform data (black).

The best estimated models from the six transfer functions for each insole size were compared across all data sets of an insole size using SIS and the SRSME, respectively.

RESULTS

As shown, in Fig. 1, using system identification resulted in GRF values that were closer to those of the force platform than the original insole data. Overall, the estimated model duplicated the two peaks of the force platform curve while missing the heel strike with some noise at the end of the curve. Table 2 presented the results for all insole sizes in terms of the SRSME and SIS with best model in bold for each insole size. To help assess the robustness of the proposed approach, the locations of the poles and zeros for all repetitions of the 3p 3z model of Size 35-36 are presented in Table 3.

DISCUSSION

Despite the variability associate with different participants wearing the same insole size, it was found that the proposed approach was somewhat robust. Different repetitions during the training phase of an insole size led to the same transfer functions, as shown in Table 3. It was also found that each insole size had a distinctive transfer function that best described it, which could be due to the difference of the number and placements of sensors in each insole size. These results were similar to what was reported in [1], [5] who identified unique results of each insole size.

The results of this research show that system identification can improve the accuracy of the insoles in measuring the vertical component of the GRF. Since assessment of specific events during the gait cycle is important, future work will focus on improving specific gait variables (e.g., peak amplitudes and time to peak amplitudes) in comparison to the force platform results.

Table 2: The summed RSME and SIS for all insole sizes, combining all repetitions and the original insole RSME. The best performing model is shown in bold.

Transfer Function		Insole Size					
		35-36	**37-38**	**39-40**	**41-42**	**43-44**	**45-46**
3p 3z	**SRMSE**	**3.94**	9.00	4.47	2.26	2.88	1.58
	SIS	**29**	54	29	15	24	18
4p 3z	**SRMSE**	**3.94**	**8.27**	4.47	**2.25**	2.99	1.60
	SIS	**29**	**54**	29	**16**	24	18
5p 3z	**SRMSE**	4.17	8.29	4.74	2.45	2.87	1.91
	SIS	28	54	23	14	24	18
4p 4z	**SRMSE**	4.23	8.25	**4.46**	2.29	3.11	1.61
	SIS	29	53	**30**	15	24	18
5p 4z	**SRMSE**	4.44	8.29	4.64	2.30	**2.86**	**1.56**
	SIS	26	54	30	14	**24**	**18**
5p 5z	**SRMSE**	3.92	8.58	5.08	2.30	**2.86**	1.66
	SIS	29	53	26	16	**24**	18
Original Insole Totals	**SRMSE**	5.88	12.1	6.18	2.94	4.20	3.61

Table 3: The poles and zeros for the repetitions of the 3p 3z model for insole size 35-36. Results of trials that were similar are color coded. The best performing model is in bold.

	Poles			Zeros			SRSME/ SIS
1	-21.0 + 4.2i	-21.0 - 14.2i	-11.9 + 0i	-237.7 + 0i	-16.3 + 7.5i	-16.3 – 7.5i	4.15/29
2	-21.0 +14.2i	-21.0 - 14.2i	-11.9 + 0i	-237.7 + 0i	-16.3 + 7.5i	-16.3 – 7.5i	4.15/29
3	-36.0+ 892.3i	-36.0 – 892.3i	-5.7 + 0i	-39.2 + 0i	-20.2 + 0i	-7.8 + 0i	4.26/28
4	-36.0+ 892.3i	-36.0 – 892.3i	-5.7 + 0i	-39.2 + 0i	-20.2 + 0i	-7.8 + 0i	4.26/28
5	**-70.7+ 150.8i**	**-70.7– 150.8i**	**-10.3 + 0i**	**-2372 + 0i**	**-8.9 + 9.2i**	**-8.9 – 9.2i**	**3.94/29**

ACKNOWLEDGEMENTS

The authors would like to acknowledge the funding provided by the Barrick Graduate Research Fellowship. The authors would also like to acknowledge and thank Michael Schwob and Gaurav Arora for their contributions to this project.

REFERENCES

[1] J. DeBerardinis, *J. Rehabil. Assist. Technol. Eng.*, vol. 5, pp. 1–12, 2018.
[2] S. Barnett, *Clin. Biomech.*, vol. 16, no. 4, pp. 353–357, 2001.
[3] C. Giacomozzi, *Gait Posture*, vol. 32, no. 1, pp. 141–144, 2010.
[4] J. Woodburn, *Clin. Biomech.*, vol. 11, no. 5, pp. 301–304, 1996.
[5] A. Ghanem, *2017 Summer Biomechanics, Bioengineering, and Biotransport Conference*, 2017.
[6] A. Forner-Cordero, *Gait Posture*, vol. 23, no. 2, pp. 189–199, 2006.
[7] M. Koch, *Appl. Ergon.*, vol. 53, pp. 44–51, 2016.
[8] A. Arndt, *J. Biomech.*, vol. 36, no. 12, pp. 1813–1817, 2003.
[9] H. Rouhani, *Gait Posture*, vol. 32, no. 3, pp. 311–316, 2010.
[10] H. H. C. M. Savelberg, *Clin. Biomech.*, vol. 14, pp. 585–592, 1999.

SB³C2019
Summer Biomechanics, Bioengineering and Biotransport Conference
June 25 -28, Seven Springs, PA, USA

UTILIZING CROSS-CORRELATION TO DETERMINE PHASE SHIFT IN GAIT DATA FOR A NEURAL PROSTHESIS

Martin L. Tanaka (1) and David Hudson (2)

(1) School of Engineering and Technology
Western Carolina University
Cullowhee, NC, USA

(2) Department of Physical Therapy
Western Carolina University
Cullowhee, NC, USA

INTRODUCTION

According to the PEW Research Center, nearly 40 million people in the US live with a disability. This number represents approximately 1/8 of the population. There are many reasons that people have disabilities and some people may be helped by innovative medical devices.

To address this need, our research group is developing a neural prosthesis to assist people with muscle weakness caused by injury or disease. The device is designed to monitor movement during gait and artificially stimulate the gastrocnemius muscle at the appropriate time in the gait cycle to enhance plantar flexion to improve gait. Because people change their gait during normal movement activities, the task of determining the current position in the gait cycle in not trivial. Our third-generation neural prosthesis utilizes inertial measurement units (IMUs) attached to the foot, shank, thigh, and pelvis. Each IMU has a triaxial accelerometer and a triaxial gyroscope to monitor the direction of the gravitational force vector and the angular velocity, respectively. These sensors are used to determine the segment angles with respect to the global reference frame and through calculation, the joint angles can be determined. The neural prosthesis also utilizes foot pressure sensors to provide additional information about the gait of the user. These sensors are accessed by an integrated computer within the neural prosthesis for real-time analysis of gait. However, it is not known how accurately the IMUs and foot pressure sensors can detect actual gait characteristics.

The gold standard for measuring human movement are multi-camera systems that utilize body markers to detect movement. These camera systems have proven to be accurate and will be used as a reference for measuring the accuracy of the IMUs in the neural prosthesis. The low cost IMUs (about $5.00 US) are expected to be less accurate than the camera system (about $500k US). However, the accuracy may still be sufficient to accurately determine the phase of the gait cycle. This study was designed to determine the sensitivity of the system to measurement error. Mathematical analysis of human movement patterns were performed to determine the sensitivity of using the cross-correlation function to accurately detect phase shift in the presence of different levels of noise.

METHODS

An able-bodied individual was recruited to participate in the gait study. After being explained the nature of the study and signing the informed consent form approved by the IRB, reflective markers were placed on the lower body. The participant walked in a straight line over level ground while a camera system captured her movement.

These data were processed to determine joint angles and ground force reactions. These data sets were imported into a custom MATLAB code for data analysis. Gaussian random noise was added to the signal to simulate errors in the IMU's ability to accurately detect the exact joint angles. The probability density function is given by,

$$y(x) = \frac{1}{\sigma\sqrt{2\pi}}\, e^{\frac{-(x-\mu)^2}{2\sigma^2}} \quad (1)$$

where, μ is the mean, and σ is the standard deviation. In our case μ was zero, and σ was one, so the equation simplified to,

$$y(x) = \frac{1}{\sqrt{2\pi}}\, e^{-\frac{1}{2}x^2} \quad (2)$$

A random number generator within MATLAB was used to generate Gaussian random values with a root mean squared (rms) magnitude of one. These random values were multiplied by a noise level between 0.01 and 10 to scale the noise added to the original signal so that the effect of different levels of noise could be evaluated.

In order to comparing the data collected by the IMUs with camera system data, the data collected by the two separate systems would need

to be synchronized. Asynchronous data was simulated by randomly phase shifting two noisy gait cycle data sets between a range of 0 to 300. These data sets were analyzed using a cross correlation function to determine the phase shift between the two data sets,

$$(f \star g)(\tau) \stackrel{\text{def}}{=} \int_{-\infty}^{\infty} f^*(t) g(t+\tau) dt \qquad (3)$$

where, f and g are the two randomly shifted signals, τ is the time shift and t is time. The cross-correlation function is maximized when the two signals are best aligned and the values of τ can be determined.

Finally, the effect of noise levels ranging from 0.01 to 10 degrees rms at 0.01 degree intervals was evaluated. Each of the 1000 different noise levels was evaluated 200 times and the ability of the cross-correlation function to accurately determine the actual phase shift was determined as a function of noise level.

RESULTS

Joint angles collected using the camera system from a single gait cycle of a typical able-bodied individual are shown below (Figure 1). The results also show that a low noise level generally follows the original gait shape.

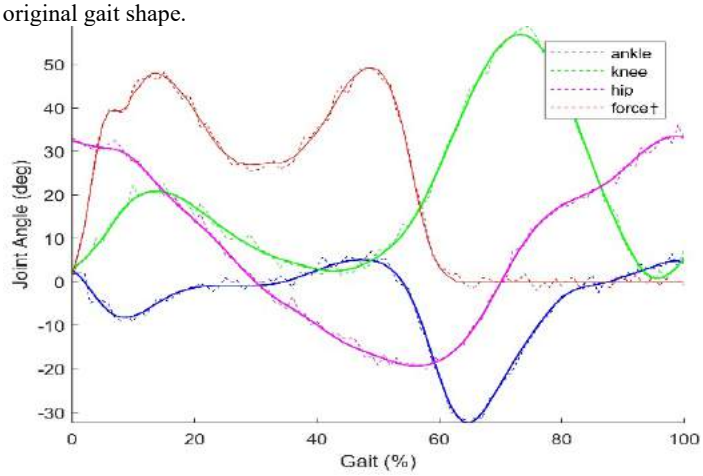

Figure 1: Natural joint angles during gait (solid lines) and gait perturbed by Gaussian random noise at one degree rms (dashed lines). †The normalized force has units of Newtons/20.

Evaluation of two randomly shifted knee joint angles, with one degree rms of noise are shown before and after synchronization (Figure 2a). The method is also able to synchronize the signals the high noise levels, ten degree rms (Figure 2b).

a)

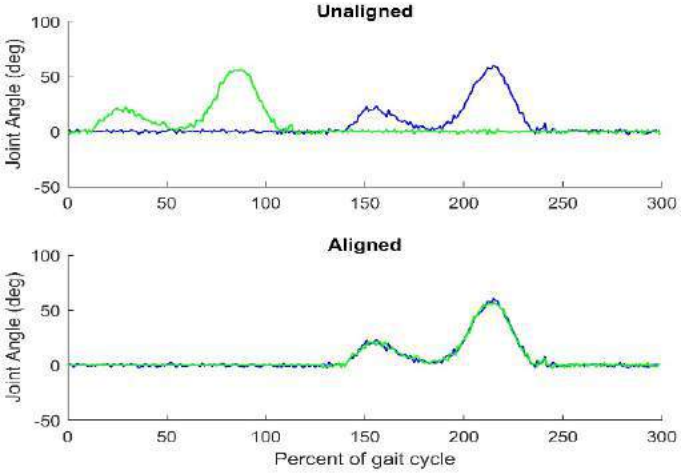

b)

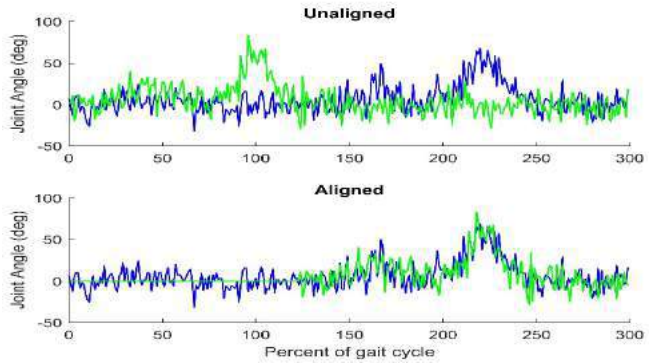

Figure 2: Synchronization of signals using the cross-correlation function at two noise levels, (a) one and (b) ten degrees rms.

The sensitivity to noise is shown in Figure 3. The results show that at a noise levels below a rms of one degree the cross-correlation function is able to determine the exact phase shift 100% of the time. By a noise level of two, the accuracy of determining exact phase shift reduces to approximately 75%. By a noise level of ten, the accuracy reduces to about 20%.

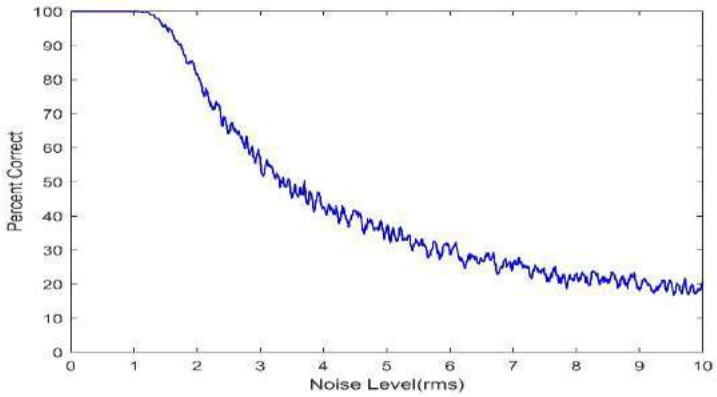

Figure 3: Percent of time shifts accurately determined using the cross-correlation function at different levels of Gaussian random noise. Data was smoothed using in a moving average of 5 points.

DISCUSSION

The results show that if the noise levels can be kept below one degree rms, they have no impact on the ability of the cross-correlation function to synchronize the data sets. However, at higher levels of noise or measurement error, the ability to exactly determine the phase shift reduces. One notable point is that even though the cross-correlation function was able to only determine accurately the phase shift only 20% of the time at the maximum noise level, the magnitude of the error was typically only 1-2% of the gait cycle (see Figure 2). This implies that even if the neural prosthesis is not able to exactly time the stimulation, it may still be close.

ACKNOWLEDGEMENTS

The authors would like to acknowledge funding from Western Carolina University's Provosts Internal Support Grant and the assistance in data collection from Kimberly Hudson and Premkumar Subbukutti.

REFERENCES

[1] Winter, DA. Biomechanics and motor control of human movement. New York: Wiley, 2009

SB³C2019
Summer Biomechanics, Bioengineering and Biotransport Conference
June 25 -28, Seven Springs, PA, USA

MOVEMENT PATTERNS IN DANCERS

Rita M. Patterson (1), Nathan Hersberger (2), Elizabeth Balyakina (2) Sajid Surve (1)

(1) Family and Osteopathic Manipulative Medicine
University of North Texas Health Science Center
Fort Worth, TX USA

(2) Medical City Fort Worth
University
Fort Worth, TX USA

INTRODUCTION

Ballet dancers have short-lived careers due to the demands placed upon their bodies throughout years of training, study, and performance. The average age a dancer retires is 34, according to the multi-country aDvANCE Project [1]. Their bodies are placed under significant stress during their professional years and injuries are common. Lower limb joint injuries have been found to be the most frequent, and length of time dancing was correlated with greatest risk for injury [2]. Faulty technique, or improper movement, has also been correlated with injury risk [3]. Early recognition of pathologic movement patterns could help prevent injuries, which could reduce injury and lengthen dancer's careers.

Of all the dance specialties, ballet is the most specific in terms of body position and movement. Ballet dancers are taught to keep the hips level and not to pronate the foot whenever the leg is lifted off the ground. It is not uncommon for amateurs to lift the left side of the hip up or pronate the foot to help lift the leg. These movements require significant flexibility and quickly adjusting the center of gravity over the standing leg, Additionally the standing leg must be constantly adjusted and ankle strength and stability are required as the entire body is balanced over one foot.

Previous research has determined that training and fatigue are important risk factors for injury during these difficult movements. Not only do dancers self-identify fatigue as a leading risk for injury [4], one study specifically showed "neuromuscular activation of the knee extensors and flexors in dancers changed in response to the dance-specific fatiguing protocol" [5]. Quadriceps and Hamstring fatigue has been shown to alter knee mechanics [6], altered mechanics of the knee have been tied to altered mechanics in the ankle [7] and alterations in the ankle have been shown to affect the knee [8]. Essentially, in the lower extremity, the motion of one joint affects motion in all the others.

This fatigue, training level, and alterations in practice versus performance tempo puts dancers at risk for injury. Specifically, abnormal kinematics at the hip or ankle can cause musculoskeletal pain or significant joint injury. For example, inversion sprains of the ankle are common in ballet dancers and lead to alterations of the intrinsic motions of that joint. An inversion sprain happens when an ankle is taken to the furthest supinated position and the ankle is rolled over the outside, injuring the ligaments within the joint. A leading risk for ankle inversion sprain is having a previous inversion sprain (Milgrom, 1991). Identifying factors that lead to changes in biomechanics of the lower extremity is important in the search for modifiable risk factors that lead to pain and injury.

The goal of this study was to evaluate proper kinematics during dance movements in an attempt to identify motions and conditions that put them at risk for injury. Additional goals are to help dancers maintain musculoskeletal health and to provide valuable information to dance teachers to prevent injuries in all levels of dancers.

METHODS

Ten professional ballerinas currently employed by the Texas Ballet Theater (https://www.texasballettheater.org/about) were studied throughout their performance season. Five men and 5 female dancers ages 20-28 (average 24 years) with an average of 16 years of training (range 7-22 years) were studied.

Reflective markers were placed on bony landmarks of the body so that Infrared cameras in the Motion analysis system (Motion Analysis Corp, Rohnert Park, CA) could register a stick-based Skelton that was used to calculate kinematics of the body parts and joint range of motion during movements (Figure 1).

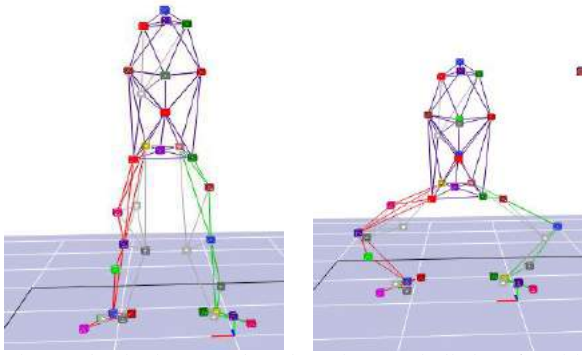

Figure 1 beginning & end motion of a Grand Plié in 2nd position.

Dancers were asked to perform 3 warm up exercises to music which included:

- Pliè in 1st and 2nd position, Demi and Grand motions (Fig 1)
- Battement avant, seconde, derrière (front, side and back)
- Dèveloppè avant, seconde, derrière (front, side and back)

Data was collected over the performance season:

- August - Beginning of the season
- November - Height of the season (busiest, most tired)
- April - End of the season

Clinical data regarding prior injuries and past and current therapies/strategies to maintain health were recorded.

Ankle Pronation/supination (sprain risk) was calculated using vector mathematics using markers between the Heel – Toe (vector u) and navicular – base of the 2nd metatarsal (vector v) using the following equation (1).

$$\cos\,\theta = \frac{u \cdot v}{||u|| \cdot ||v||} \qquad (1)$$

RESULTS

Clinical Data

Most common previous injuries

- Lower limb injury (7/10 dancers)
- Ankle sprain (4/10 dancers)
- Metatarsal fracture (2/10 dancers)
- Hamstring strain (2/10 dancers)

Most common therapy/strategy to keep healthy

- Massage (6/10 dancers).
- Physical Therapy (4/8 dancers)

Ankle Pronation/Supination variance is shown in figure 2

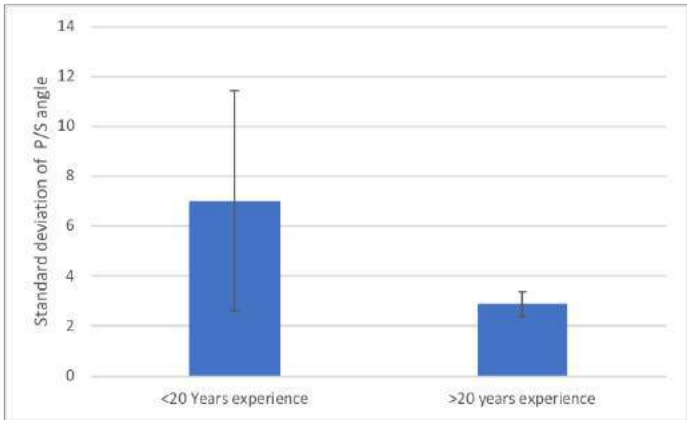

Figure 2

DISCUSSION

Professional ballet dancers are at risk for lower extremity injury. Specifically, ankle injury due to the repetitive and intense nature of the performance season. any dancers utilize alternative therapies to maintain their musculoskeletal health the most common being massage and Physical therapy.

3D kinematic data of dancer's movements during the performance season were evaluated for changes in ankle Pronation/supination motion and revealed that dancers with less experience exhibit more variation in ankle motion during basic warm up exercises. While there was very little variation in this population of professional (elite) dancers more variation would be expected in younger less experienced dancers and a potential indication of increased risk for ankle injury.

Knowledge of body kinematics could facilitate better understanding of the mechanism of injury, help identify fatigue, help dance instructors teach proper technique, and help focus clinical treatments to help prevent and identify injuries.

ACKNOWLEDGEMENTS

Special thanks to the Texas Ballet Theater for their cooperation in collecting the data. Thank you to the UNTHSC students and Human Performance Staff that helped with the data collection.

REFERENCES

[1] Jeffri, J et al. ICPSR35598-v1. 2015-05-31.
[2] Schweich, L et al. Fisioter Pesq. 2014;21(4):353-358
[3] Toledo SD, et al. Arch Phys Med Rehabil, Mar;85:S75-8 (2004).
[4] Liederbach, M eta al. J Dance Med & Sci, 5(4): 116-120, 2001.
[5] McEldowney, K.et al. J Dance Med & Sci, 17(3):109-114, 2013.
[6] Thomas, A et al. J Applied Biomechanics, 2, 159-170 (2010)
[7] Mündermann, A, et al. Arthritis & Rheumatology, 52 (9) 2005.
[8] Macrum, E. et al. J Sport Rehabilitation, 21:144-150, 2012.

SB³C2019
Summer Biomechanics, Bioengineering and Biotransport Conference
June 25-28, Seven Springs, PA, USA

CAN SUPERHYDROPHOBIC SLIP FLOW IMPROVE CENTRIFUGAL BLOOD PUMP PERFORMANCE AND REDUCE BLOOD DAMAGE?

Chan Wei Xuan, Vivek Vasudevan, Adriel Jia Jun Low, Janani Venkatesan, Choon-Hwai Yap

Department of Biomedical Engineering,
National University of Singapore
Singapore

INTRODUCTION

Centrifugal blood pumps save countless lives daily, being used in Extracorporeal Membrane Oxygenation (ECMO) circuit in the ICU, during heart surgeries, and being implanted as Left Ventricular Assist Devices (LVAD). High stresses imposed on blood by the rapidly rotating impeller [1] cause significant number of patients to suffer from severe hemolysis (in 7% of ECMO [2] and in 18% of LVAD cases [3]), which drastically reduces survival (by 6 times for ECMO [2]).

We recently proposed using superhydrophobic (SHP) coatings to enable slip-flow, so as to reduce blood stresses and blood damage, and demonstrated preliminary feasibility in a simple in-vitro pipe flow setup [4]. SHP material is a hydrophobic surface with micro-/nano-scale surface-structures which gives it enhanced fluid repellency and partial slip-flow characteristics. In the current study, we perform flow simulations to understand the potential advantages if SHP surfaces are coated on an ECMO centrifugal blood pump.

METHODS

A commercial blood pump (Maquet Rotaflow, Fig. 1a) was scanned by computed tomography, the pump features as well as measurements were extracted from the scanned DICOM images (Fig. 1b), and 3D reconstruction was done using SolidWorks® (Fig. 1c).

The model was discretized with more than 5 million tetrahedral cells and CFD simulations were performed at three flow rates: 2 LPM, 3 LPM and 5 LPM with RNG k-ε formulation to model turbulent flow in the centrifugal pump. A sliding mesh was used to rotate the impeller for at least 3.5 rotations at more than 1200 time steps per rotation. Blood was modelled as an incompressible fluid (1060 kg/m^3) with a Newtonian viscosity of 3.5 cP. Boundary conditions imposed were velocity inlet, zero pressure outlet, no slip at impeller, and partial slip / no slip at pump housing wall.

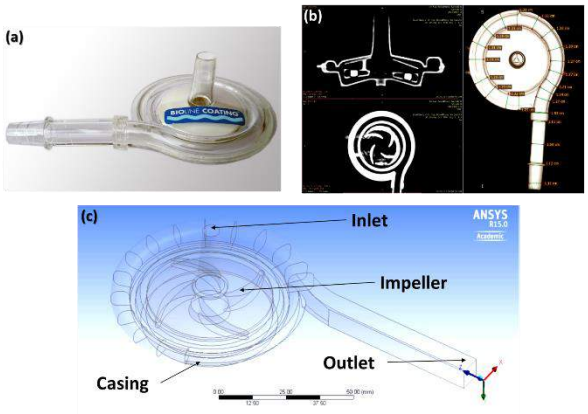

Figure 1: (a) The Maquet Rotaflow centrifugal blood pump (b) CT scan of pump head (c) Digitally reconstructed CAD model

The SHP coatings were *applied* only on the inner surface of the pump housing, and two levels of slip lengths were investigated: 0 μm (No slip) and 100 μm. The partial slip boundary conditions were imposed as,

$$\boldsymbol{u} = \beta \frac{\delta \boldsymbol{u}}{\delta \boldsymbol{n}} \quad (1)$$

where $\boldsymbol{u}$ is the velocity at the wall, β is the slip length and $\boldsymbol{n}$ is the normal vector to the wall. A stress-based measure to estimate free-plasma hemoglobin (H_E), as indicator of blood damage severity [5] was used.

$$H_E = \frac{\int_{outlet} H\boldsymbol{u}.ndS}{\int_{outlet} \boldsymbol{u}.ndS} \quad (2)$$

$$\frac{\delta H^{\frac{1}{\beta}}}{\delta t} = -u\nabla H^{\frac{1}{\beta}} + Cs^{\frac{\alpha}{\beta}}(1 - H^{\frac{1}{\beta}}) \quad (3)$$

$$s = 10^{\frac{1}{T}\int_t^{t+T} log_{10}\left(\sqrt{\frac{1}{2}\tau:\tau}\right)\mathrm{dt}} \quad (4)$$

where C (3.62x10-7), α (3.416), and β (0.785) were taken from literature [5]. s is the log average fluid scalar stress, τ is the viscous stress tensor and T is the period of rotation.

RESULTS

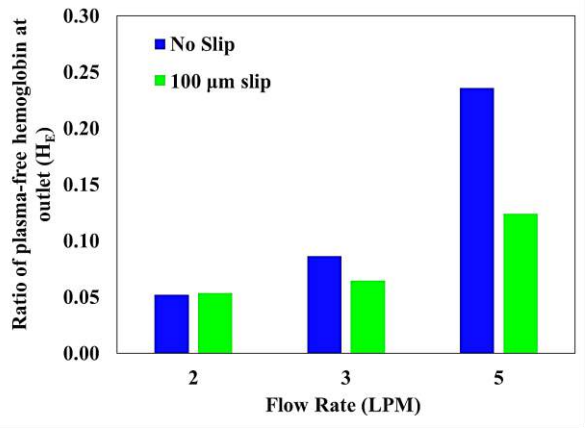

Figure 2: Ratio of free-plasma hemoglobin (H_E) at outlet for flow rates of 2 LPM, 3 LPM and 5 LPM, at slip lengths of 0 µm (No slip) and 100 µm

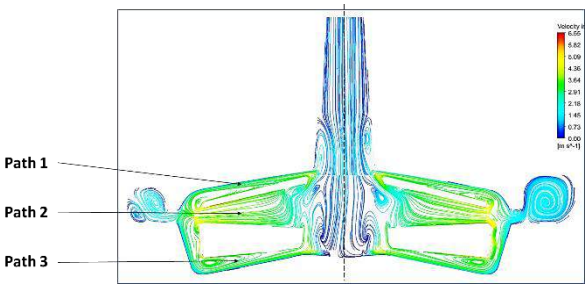

Figure 3: Streamlines of blood flow in x-y plane: Path 1 – upper gap between rotating impeller and stationary casing. Path 2 – gap between rotating impeller blades. Path 3 - lower gap between rotating impeller and stationary casing.

Simulation results (Fig. 2) showed that at lower flow rates, SHP coating did not significantly alter the blood damage. However, at a higher flow rate of 5 LPM, a significant reduction in blood damage could be achieved on the 100 µm slip surface.

The pump design allowed flow to occur in 3 paths from the inlet through the pump body (Fig. 3). Investigation of the flow fields revealed that there were reversed flows in Paths 1 and 3 (Fig. 4), which were most likely induced by high flow volumes through Path 2 that generated adverse pressure conditions for the other 2 paths. There was significant reverse flow in the No slip case, but this reduced significantly for the 100 µm slip case. Reversed flow also increased proportionately with increasing flow rate.

A higher reverse flow recirculates blood within pump, resulting in higher chances of blood damage, indicating that reduction in reverse flow is one of the factors responsible for lower blood damage with the application of SHP coatings on the inner surface of the pump housing.

Fig. 5 shows that having SHP surfaces with slip flow decreases wall shear stress (WSS) on the pump housing. Fewer surfaces have a high WSS (> 10 Pa and > 50 Pa) with increasing slip length, indicating lower chances of blood damage. Regions with high WSS are mainly distributed along Paths 1 and 3. The combined effects of reduced WSS and decreased reversed flow contributed to a lower blood damage for cases with higher slip length.

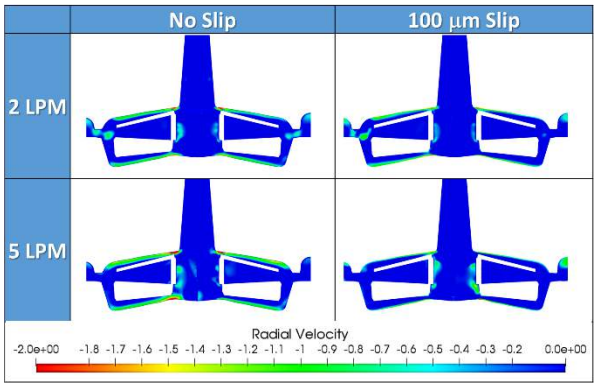

Figure 4: Reversed radial velocity contour in x-y plane in centrifugal pump (flow towards inlet) along Paths 1 and 3

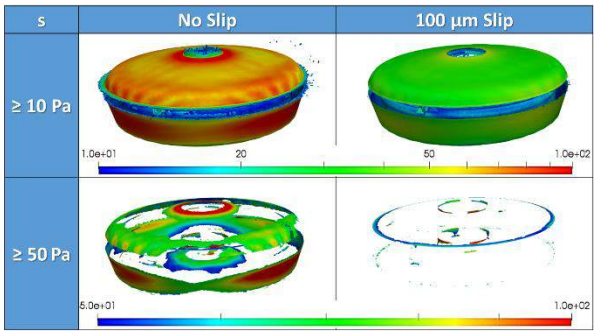

Figure 5: Contours of time- & surface-averaged WSS at 5 LPM on stationary casing for different slip lengths. WSS contours were thresholded at 10 Pa and 50 Pa, displaying regions with high WSS

DISCUSSION

Based on the results of our CFD simulations, superhydrophobic (SHP) surfaces applied on a centrifugal ECMO blood pump offered reduced WSS and, at certain flow rates (5 LPM), also reduced blood damage. However, this was observed only at slip lengths of 100 µm. With the introduction of SHP surfaces, characteristics of the flow field such as intensity of reversed flow between the impeller and housing (Paths 1 and 3) could change, which will have implications on extent of blood damage, and hence, a redesign of the pump should be conducted so as to minimize adverse flow patterns. Reversed flow in the gap between the impeller and housing have been previously acknowledged to be problematic in studies of other pump designs [6].

ACKNOWLEDGEMENTS

The Singapore Ministry of Health, National Medical Research Council Grant #NMRC/OFIRG/0060/2017 (PI: Yap).

REFERENCES

[1] Mizunuma, H., *Artif Organs*, 31:550-559, 2007.
[2] Lou, S., *Crit Care Med*, 42:1213-1220, 2014.
[3] Ravichandran, A.K., *J Heart Lung Transpl*, 33:44-50, 2014.
[4] Lai, C.Q., *Rsc Adv*, 6:62451-62459, 2016.
[5] Giersiepen, M., *Int J Artif Organs*, 13:300-306, 1990.
[6] Chua, L.P., *Artif Organs*, 30:467-477, 2006.

NON-INVASIVE DIAGNOSTICS OF CORONARY ARTERY DISEASE USING MACHINE LEARNING AND COMPUTATIONAL FLUID DYNAMICS

Kritika Iyer (1), Christopher J. Arthurs (2), Cyrus P. Najarian (1), S.M. Reza Soroushmehr (3), Brahmajee K. Nallamothu (4), C. Alberto Figueroa (1,5)

(1) Biomedical Engineering
University of Michigan
Ann Arbor, MI, USA

(2) Biomedical Engineering
King's College London
London, United Kingdom

(3) Computational Medicine and Bioinformatics
University of Michigan
Ann Arbor, MI, USA

(4) Cardiology, Internal Medicine
University of Michigan
Ann Arbor, MI, USA

(5) Vascular Surgery
University of Michigan
Ann Arbor, MI, USA

INTRODUCTION

Coronary Artery Disease (CAD) is one of the leading causes of adult mortality in the US[1,2]. CAD is characterized by plaque buildup, or stenosis, in the arteries that feed the heart, which can lead to further complications such as myocardial infarction[1,3]. The severity of the disease is typically quantified via an invasive, catheter-based diagnostic procedure that measures Fractional Flow Reserve (FFR): the ratio of pressures on either side of the stenosis under conditions of maximum flow[4,5]. Due to its invasive nature, risks, and cost, clinicians often choose not to perform FFR and rely on visual inspection of angiograms to determine whether the severity of the stenosis is high enough to warrant coronary revascularization. However, this visual inspection of the angiograms often leads to an over-estimation of the disease severity[6]. Therefore, a noninvasive, computational method to calculate FFR would greatly improve CAD diagnostics while eliminating the risks associated with the catheter-based FFR procedure. To this end, this study aims to develop a method that uses machine learning and computational fluid dynamics to compute FFR from biplane angiography image data.

METHODS

A convolutional neural network (CNN) was used for automatic vessel segmentation of synthetic and clinical biplane angiograms. The synthetic dataset was created by imaging 3D printed phantom models of a coronary tree, while clinical data was obtained from the University of Michigan hospital. Both datasets were normalized to have uniform pixel intensity and augmented to include vertical and horizontal flips. Clinical data was further pre-processed using unsharp mask filters to improve local contrast and boundary sharpness. The CNN had a Deeplab v3+ architecture[7] and was trained for 580 epochs using a batch size of 4, momentum gradient descent, cross-entropy loss, and L2 regularization (Figure 1). The network was trained separately on clinical and synthetic datasets.

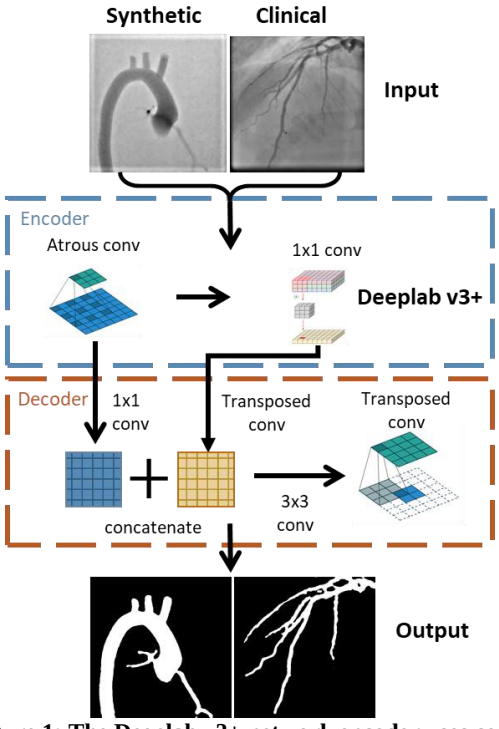

Figure 1: The Deeplab v3+ network encoder uses convolutions to identify features corresponding to blood vessels. The decoder spatially maps features to classify pixels in the input image.

Once vessels were segmented, a skeletonization algorithm based on the work of Telea *et al*. was employed to find the centerline of the vessels in the coronary tree[8]. The branchpoints of the vessel centerline were used as reference points for a back-projection algorithm. The back-projection algorithm maps the reference points from each 2D plane into 3D space using information about the position of the sources when those images were taken. Once the 3D centerline is constructed, the vessel geometry can be filled in using the local radius at each point of the centerline. Local radii are computed and stored by the skeletonization algorithm referenced above. A diagram of the back-projection algorithm is given in Figure 2.

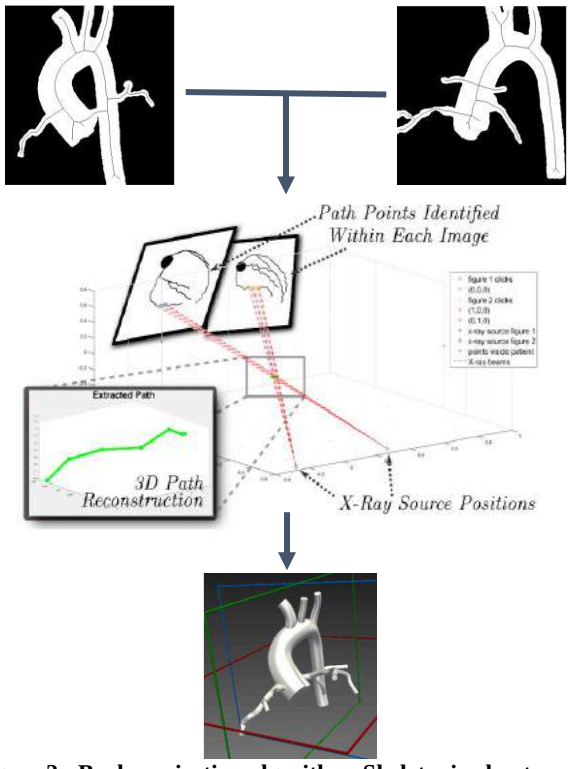

Figure 2: Back-projection algorithm. Skeletonized auto-segmented images are used to create the 3D geometry using spatial information from DICOM metadata.

Validation of the above segmentation and back-projection algorithm will be performed using the synthetic dataset. The computational hemodynamic open-source modeling software, CRIMSON, will be used to perform steady-flow simulations in the original 3D-printed geometry of the coronary tree. The simulation will yield a pressure field for the entire coronary tree, which can be used to compute FFR along the centerline of the vessels of interest. The pressure field in the original geometry will be used as a benchmark for the pressure field computed from simulations in the geometry reconstructed using the CNN and back-projection algorithms. FFR will again be calculated along the centerline of the vessels of interest, and the error between the two sets of FFR values will be calculated.

RESULTS

The accuracy of the automatic segmentation algorithm on the synthetic and clinical validation datasets is given in Table 1. The accuracy was quantified using MIOU (mean intersection over union of pixels) and the Dice score in the prediction and ground truth images. Sensitivity and specificity are also reported. Sample segmented images from the synthetic and clinical datasets are shown in Figure 3.

Table 1: Segmentation Accuracy. Accuracy in clinical data is lower as the images contain more noise and artifacts

	Synthetic Data	***Clinical Data***
Training set size	1230	927
Validation set size	152	103
MIOU	0.975	0.917
Dice	0.980	0.916
Sensitivity	0.980	0.952
Specificity	0.994	0.995

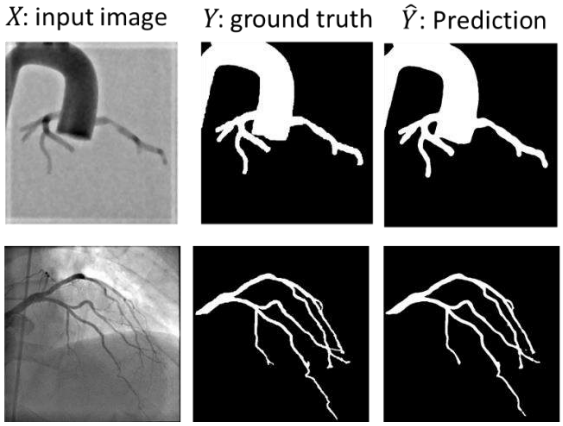

Figure 3: Segmentation Results. The top row corresponds to synthetic data, while the bottom row is clinical data. The ground truth was manually labeled by hand, and the prediction was automatically generated by the neural network.

DISCUSSION

Visual inspection of the segmentation results shows a close alignment between the true vessel in the image and the neural network's prediction of the vessel. Further improvements can be obtained by increasing the size of the clinical dataset, allowing the network to learn from a wider pool of coronary tree geometries. Image post-processing techniques can also be utilized to refine the neural network segmentation and enhance accuracy. Once the network has achieved sufficient accuracy (MIOU score of 0.95), the output images will be used to create the 3D vessel geometry using the back-projection algorithm; CRIMSON simulations will then be performed to validate the accuracy of reconstruction and compute FFR.

ACKNOWLEDGEMENTS

This work is funded by the University of Michigan Rackham Merit Fellowship, National Science Foundation Graduate Research Fellowship Program, Edward B. Diethrich M.D. Professorship, and the Michigan Institute of Computational Discovery and Engineering Fellowship.

REFERENCES

[1] Qi, X., et al. *Arch. Med. Sci.* 11:483–93, 2015.
[2] Kim, H. J. et al. *Ann. Biomed. Eng.* 38:3195–3209, 2010.
[3] CDC. Underlying Cause of Death, 1999-2017. Available at: https://wonder.cdc.gov/ucd-icd10.html.
[4] Pijls, N. H., et al. *Circulation* 87:1354–67, 1993.
[5] Pijls, N. H. J. et al. *J. Am. Coll. Cardiol.* 56:177–184, 2010.
[6] Ambrose, J. A. et al. *J. Am. Coll. Cardiol.* 12:56–62, 1988.
[7] Chen, L.-C., et al. *ECCV* 2018.
[8] Telea, A., Van Wijk, J. J. *Eurographics-IEEE TCVG VisSym* 2002.

SB³C2019
Summer Biomechanics, Bioengineering and Biotransport Conference
June 25 -28, Seven Springs, PA, USA

STATISTICAL MODELING FOR ASSESSMENT OF ANEURYSM RUPTURE STATUS – IMPLICATIONS FOR JAPANESE AND FINNISH POPULATIONS

F. J. Detmer (1), S. Hadad (1), S. Hirsch (2), P. Bijlenga (3), Y. Uchiyama (4), J. Frösen (5), J. R. Cebral (1)

(1) Bioengineering Department
George Mason University
Fairfax, VA, US

(2) Institute of Applied Simulation
□HAW University of Applied Sciences
W□denswil, Switzerland

(3) Clinical Neurosciences Department
University of Geneva
Geneva, Switzerland

(4) Graduate School of Mechanical Engineering
Tokyo University of Science
Tokyo, Japan

(5) Hemorrhagic Brain Pathology Research Group
Kuopio University Hospital
Kuopio, Finland

INTRODUCTION

Cerebral aneurysms affect up to 5% of the total population [1]. Aneurysm rupture resulting in subarachnoid hemorrhage (SAH) is associated with high mortality and morbidity [2]. At the same time, the natural aneurysm rupture risk of less than 1% per year is low compared to the risk associated with aneurysm treatment to prevent a future rupture making the decision of whether to treat an aneurysm challenging [3]. A statistical prediction model could be helpful to compare a patient's natural rupture risk against the risk of treatment.

We recently developed an aneurysm rupture probability model based on hemodynamic and geometric parameters, aneurysm location, patient gender and age using patient data obtained mainly from hospitals in the US [4]. When externally validating the model in two European cohorts, it showed a good predictive performance [5]. Different studies have shown that Finnish and Japanese populations have a higher rate of SAH compared to other populations [6, 7].

Our purpose was the evaluation of the model in Finnish and Japanese data as well as the comparison of its performance with a new model trained on data including aneurysms from Finnish and Japanese patients.

METHODS

Patient and Image Data

For model evaluation, 255 aneurysms were studied, 147 Japanese aneurysms in 138 patients and 108 Finnish aneurysms in 73 patients. In the Japanese cohort, there were 81 (58.7%) female and 57 (41.3%) male patients, 17 (11.6%) of the aneurysms were ruptured and 130 (88.4%) unruptured. Of the Finnish patients, 40 (54.8%) were female and 33 (45.2%) male, 41 (38%) of the aneurysms were ruptured, 61 (56.5%) were unruptured and 6 (5.5%) had an unknown rupture status and were excluded from the dataset resulting in a total number of 102 Finnish aneurysms.

For model development, an additional 1,631 aneurysms from US cohorts and 249 aneurysms obtained from two European (other than Finnish) hospitals were used (see [4] and [5] for a detailed description of the data).

Hemodynamic Modeling

To characterize each aneurysm's hemodynamic environment, computational fluid dynamics (CFD) simulations were performed based on the segmented angiographic images and following the same protocol as described in [4]. Briefly, unstructured grids with a maximum element size 0.2 mm were used to model the aneurysm and its surrounding arteries. Based on the aneurysm location, inflow boundary conditions were applied at the internal carotid artery (ICA) for aneurysms in the anterior circulation, at the vertebral artery (VA) for aneurysms at the posterior circulation, or the parent vessel of the aneurysm if the segmented images did not include more parts of the vascular tree. Depending on the location where the inflow boundary condition was imposed, the inflow was adjusted taking the area of the vessel into account [8]. Pressure and flow outlets were imposed as outlet boundary conditions. Numerical solutions of the unsteady Navier-Stokes equations were obtained from an in-house finite element solver [9]. To characterize the aneurysm and its hemodynamic environment, 22 hemodynamic and 25 morphological parameters were calculated based on the computed flow field as well as the 3D model. A detailed description of all parameters can be found in [4] and the references therein.

Statistical model development and evaluation

First, the previously developed model (Model-US [4]) was evaluated using all Finnish, Japanese, and combination of Japanese and Finnish datasets in terms of area under the receiver operating characteristic (ROC) curve (AUC).

Next, data from all four cohorts was divided into two parts, training and testing. To do so, from each of the four datasets (US, Europe, Japan, Finland), 10% of them were randomly excluded for testing the model while the remaining 90% were used for model training. The model was trained as described in [4] using logistic group lasso regression [10]. In a second step, interaction terms between patient population and the other continuous variables were included in the regression model. Such a model interpolates between separate models for each patient population and a global model.

The process of splitting the data into training and test sets and subsequent training of the respective models was repeated 100 times and for evaluation, the mean AUCs and their standard deviations were reported.

RESULTS

Figure 1 shows boxplots of the AUCs when evaluating the trained models in the left-out Japanese, Finnish, Finnish + Japanese combined, and all left-out data. When evaluating the US-Model in all Japanese (not only left-out data), all Finnish, and Finnish and Japanese data combined, the AUCs were 0.70, 0.72, and 0.74, respectively (shown by the black squares in Figure 1). For the models trained on the data from all four cohorts without interactions (Model_ALL_no_ints, white bars), the mean ± standard deviation AUCs were 0.65 ± 0.33 for the left-out Japanese data, 0.75 ± 0.16 for the Finnish, 0.75 ± 0.14 for Finnish and Japanese combined, and 0.83 ± 0.03 for all left-out data. The same metrics for the models including interaction terms (Model_ALL_ints, gray bars), were 0.68 ± 0.30 (Japanese), 0.79 ± 0.13 (Finnish), 0.83 ± 0.10 (Finnish + Japanese), and 0.83 ± 0.03 (all left-out data).

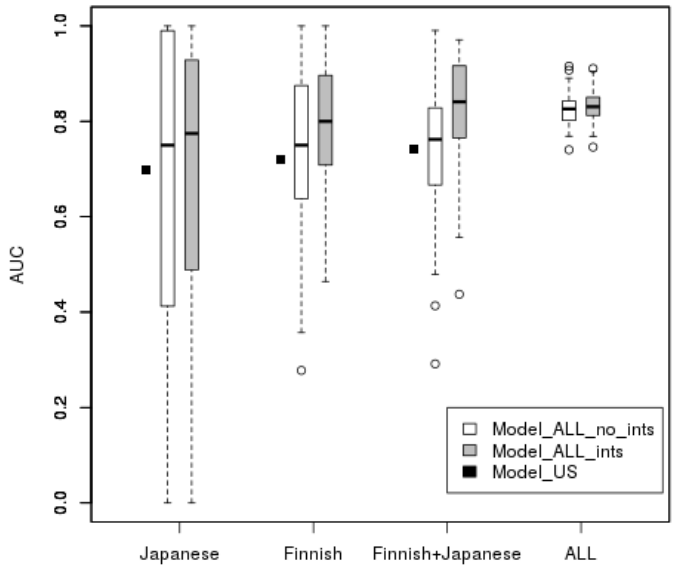

Figure 1: Boxplots of AUCs when evaluating the models in the left-out test data

DISCUSSION

When evaluating the US-model in the Japanese and Finnish data, its predictive performance in terms of AUC was largely reduced compared to the AUC when evaluated in the European data. It has previously been suggested that Japanese and Finnish populations have a higher aneurysm rupture risk [11]. The underlying mechanisms that lead to a higher rupture rate in those two populations are not clear. Our observation of the relatively poor performance of the US-model indicates that different aneurysm characteristics might be associated with rupture for these populations. This hypothesis is further supported by the fact that the model performance in the left-out Japanese and Finnish data improved significantly ($p<0.0001$) when including interaction terms in the model.

The comparatively poor performance of all the models in only the Japanese left-out data could be explained by several aspects. First, in contrast to all other cohorts, the aneurysms from the Japanese population were obtained as longitudinal data resulting in a low number of ruptured aneurysms especially in the left-out data for model evaluation. Consequently, the AUC strongly depended on the specific left-out data set (large standard deviation) and a larger dataset might be needed to get a more robust estimation of the models' performance. Second, unlike for the other data, the computational 3D models used for the CFD simulations of the Japanese aneurysms were cut at the parent vessel of the artery which might have led to differences in the computed hemodynamics and needs to be investigated further.

The developed models were trained mainly on cross-sectional data (all but the Japanese data). They provide the predicted probability that an aneurysm is ruptured rather than assessing its risk for a future rupture. The idea that these models could still be used for aneurysm risk assessment is based on the assumption that high-risk aneurysms resemble those that have already ruptured. To assess this assumption, an evaluation of the model with more longitudinal data is planned for future work.

In conclusion, our results indicate that for development of an aneurysm rupture prediction model that accurately assesses Japanese and Finnish aneurysms, the inclusion of data from these two cohorts for model training as well as interaction terms in the statistical model is necessary. When including this information, the predicative performance of such a model in Japanese and Finnish data is close to the performance in US or European data.

ACKNOWLEDGEMENTS

The European (other than Finnish) data included the publicly available AneuRisk dataset and the AneuX dataset collected and processed in the context of the @neurIST project funded by the EU commission (IST-2004-027703) and AneuX project evaluated by the Swiss National Science Foundation and funded by the SystemsX.ch initiative (MRD 2014/261).

REFERENCES

[1] Rinkel, G. J., et al., *Stroke*, 29:251-256, 1998
[2] Rivero-Arias O et al., *Cost Eff Resour Alloc*, 8:6, 2010
[3] Wiebers, D. O., *Lancet*, 362: 103-110, 2003
[4] Detmer, F. J., et al., *Int J Comput Assist Radiol Surg*, 13:1767-1779, 2018
[5] Detmer FJ et al., *Acta Neurochir*, 160:1643–1652, 2018
[6] Vlak, M. H., et al., *The Lancet*,10:*626-636*, 2011
[7] Wermer, M. J., et al., *Stroke*, 38:1404-1410, 2007
[8] Cebral, J. R., et al.,*Physiological measurement*, 29:585, 2008
[9] Cebral, J. R., et al., *IEEE Trans Med Imaging*, 24:457-67, 2005
[10] Meier L et al., *J. Royal Stat. Soc*.: Series B, 70:53–71, 2008
[11] Greving, JP et al., *Lancet Neurol*, 13:59–66, 2014

SB³C2019
Summer Biomechanics, Bioengineering and Biotransport Conference
June 25 -28, Seven Springs, PA, USA

ACCELERATING CARDIOVASCULAR MODEL BUILDING WITH CONVOLUTIONAL NEURAL NETWORKS

Gabriel D. Maher (1), Nathan W. Wilson (2), Alison L. Marsden (3)

(1) Institute for Computational and Mathematical Engineering
Stanford University
Stanford, CA, USA

(2) Open Source Medical Software Corporation
Los Angeles, CA, USA

(3) Pediatric Cardiology, Bioengineering
Stanford University
Stanford, CA, USA

INTRODUCTION

Cardiovascular disease (CVD) is the leading cause of death worldwide [1]. With recent advances in cardiac and vascular imaging, patient-specific simulations of cardiovascular hemodynamics are gaining increased clinical utility in relation to CVD [2]. Applications include development of novel surgical approaches for congenital heart disease [3], and coronary artery disease assessment [4].

In the clinic, the available time to produce simulation results is typically limited. For cardiovascular simulation in particular, high quality three-dimensional patient-specific models must be constructed for each patient, a process that delays simulation turnaround time. A common approach to build the models vessel by vessel. Specialized cardiovascular simulation software tools such as SimVascular [5], Cardiovascular Integrated Modeling and Simulation (CRIMSON) [6] and the Vascular Modeling Toolkit (VMTK) [7] can be used. The model building workflow typically begins by loading 3D medical image volume data, identifying vessels of interest, and annotating pathlines along vessel centerlines. Vessel lumen are then segmented, using 2D cross-sectional slices and interpolated to form vessel surfaces. Multiple vessels are merged, through Boolean and smoothing operations [8], producing a final 3D model.

A large and diverse body of existing work has been dedicated to the acceleration of cardiovascular segmentation [9]. However, the visual appearance of blood vessels in medical image data is subject to substantial variation making it challenging to develop general purpose algorithms that work well for the majority of cases. Recently, for image segmentation tasks, so-called Fully Convolutional Networks (FCNN) [10], have shown particular promise. However, to our knowledge, no studies have shown the utility of neural networks for modality-independent cardiovascular model building on general vascular anatomy. The closest works are the I2I network [11], which did not consider downstream applications and DeepLumen [12] which is closed-source and restricted to CT coronary artery segmentation.

We aim to use FCNNs trained for cardiovascular segmentation to accelerate the existing cardiovascular model building workflow in SimVascular by building an automated segmentation pipeline, based on Fully Convolutional Neural Networks.

METHODS

With our proposed FCNN segmentation pipeline, the first few steps of model building remain the same as is currently implemented in SimVascular [5]: users first load medical image volume data and indicate points along the pathline of the vessel of interest (Fig. 1) and 2D images are extracted along pathline at discrete intervals. However, then the extracted 2D images are automatically preprocessed and input to a FCNN that has been trained to output vessel segmentation images. Vessel lumen points are then automatically computed by applying the Marching-Squares algorithm to each FCNN output image. Using the pathline, the produced contours are reoriented in 3D space and interpolated to form the final vessel surface.

Optimal values for the neural network's parameters are found by minimizing a loss-function using example input and output images. However, in our dataset, not all blood vessels in every image volume have been segmented. To resolve this issue we introduce a new loss function that ignores regions of images that were not labeled during the labeling process. Let y be a partially labeled image, where a pixel value of 1 indicates that the labeler designated that pixel as the structure of interest and a pixel value of 0 indicates a pixel that was

not labeled. Let $\tilde{y}$ be a binary dilation of y by K pixels. Given a predicted image $\hat{y}$, our new loss function is then

$$L(\hat{y}, y) = \frac{-1}{\Sigma \tilde{y}} \Sigma \tilde{y} \left(y \log(\hat{y}) + (1 - y) \log(1 - \hat{y}) \right)$$

Conceptually, $\tilde{y}$ indicates the area of the image that the labeler focused on and only this region is considered in our loss function.

RESULTS

We compare a distance regularized level set (DRLS), threshold and each FCNN architecture via the average DICE scores on the test set (Tab. 1). FCNN indicates our neural network trained with standard loss functions and FCNN-M indicates training with our proposed masked loss function. We also measure results on small and large vessels separately by splitting the test dataset on vessel radius.

I2I-M produced better scores than I2I for all metrics when measured on small vessels ($r<0.55$cm, $p < 0.001$). Compared to reference methods, I2I-M produced better average DICE scores than DRLS and Threshold ($p<0.001$).

As a final test, users were allowed to edit segmentations and add segmentations to construct final cardiovascular models in SimVascular. The ground-truth models and those built using the proposed FCNN-M method are visually similar (Fig. 2). Inspecting the kawasaki disease case, we see that essential features of the model such as aneurysms in the coronary arteries are preserved. Using the FCNN method resulted in reductions of manual segmentations required of 73%, 57% and 71% for each case respectively.

DISCUSSION

Comparisons of the FCNN segmentation methods and the reference Threshold and DRLS algorithms shows demonstrated that neural networks improved overall performances. Both FCNN methods significantly improved average DICE scores over the reference methods, illustrating that standard algorithms such as thresholding and level sets need to be recalibrated for each image, whereas neural networks provide more automated approaches. Our results further showed that the proposed masked loss function did indeed improve the performance of both neural networks, in particular the improvement was larger for small vessels than for large vessels, achieving more precise vessel delineation in regions that are difficult to segment.

ACKNOWLEDGEMENTS

The authors acknowledge funding from NSF SI2-SSI grants 1562450 and 1339824 and the American Heart Association. The authors would like to thank Jameson Merkow and David Kriegman for their assistance in implementation of I2I, as members of the Stanford Cardiovascular Biomechanics Computation lab for user testing.

REFERENCES

[1] P. A. Heidenreich, et al., Circulation, vol. 123, 2011.
[2] A. L. Marsden, Physics of Fluids, vol. 25, 2013.
[3] A. L. Marsden, A. J. Bernstein, V. M. Reddy, S. C. Shadden, R. L. Spilker, F. P. Chan, C. A. Taylor, and J. A. Feinstein, The Journal of Thoracic and Cardiovascular Surgery, vol. 137, 2009.
[4] C. A. Taylor, T. A. Fonte, and J. K. Min, Journal of the American College of Cardiology, vol. 61, 2013.
[5] A. Updegrove, N. Wilson, J. Merkow, H. Lan, A. L. Marsden, and S. C. Shadden, Annals of Biomedical Engineering, vol. 61, 2013.
[6] R. Khlebnikov and C. A. Figueroa, Clinical Image-Based Procedures. Translational Research in Medical Imaging, 2016.
[7] L. Antiga, M. Piccinelli, L. Botti, B. Ene-Iordache, A. Remuzzi, and D. A. Steinman, Medical & Biological Engineering & Computing, vol. 46, 2008.
[8] A. Updegrove, N. M. Wilson, and S. C. Shadden, Advances in Engineering Software, vol. 95, 2016.
[9] D. Lesage, E. D. Angelini, I. Bloch, and G. Funka-Lea, Medical Image Analysis, vol. 13, 2009.
[10] S. Xie and Z. Tu, ICCV, 2015.
[11] J. Merkow, A. Marsden, D. Kriegman, and Z. Tu, Medical Image Computing and Computer-Assisted Intervention. 2016.
[12] K. Petersen, M. Schaap, D. Lesage, M. Lee, and L. Grady, GPU Technology Conference, 2017.

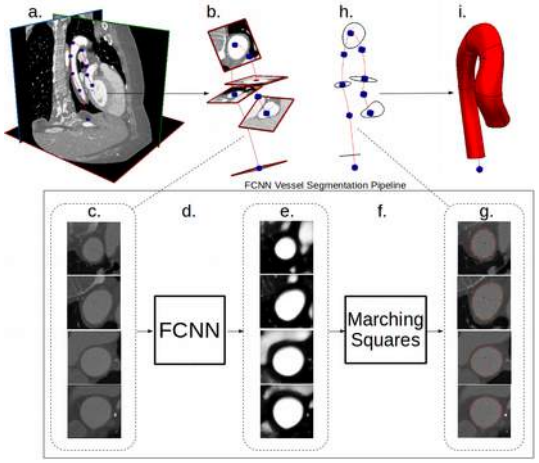

Figure 1: FCNN-based cardiovascular model building pipeline. 2D images extracted along vessel pathlines are input to the FCNN. The Marching-Squares algorithm is applied to each FCNN output segmentation image to extract the central vessel surface. Then the 2D vessel surface points are transformed back to 3D space and interpolated along the pathline to form the final vessel model.

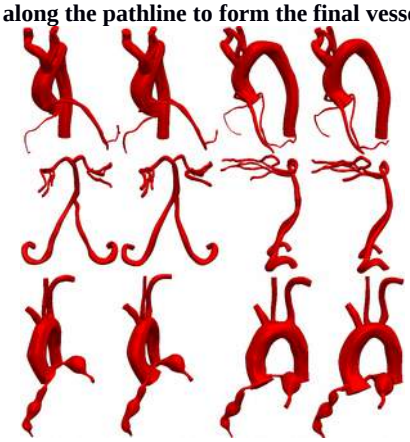

Figure 2: Comparison of cardiovascular models built using I2I-M to manually built models. First two columns are frontal views, third and fourth columns are side views. First and third columns: models built with I2I-M. Second and fourth columns: manually built models. Top to bottom: coronary artery bypass graft case (CT), carotid arteries and branch vessels (MR), Aorta and coronary arteries for a patient with Kawasaki disease (CT).

Table 1: Mean test-set DICE values, r denotes vessel radius (cm).

	all	**r > 0.55**	**r < 0.55**
FCNN-M	0.58	0.91	0.56
FCNN	0.53	0.91	0.50
Threshold	0.46	0.86	0.43
DRLS	0.43	0.85	0.40

SB³C2019
Summer Biomechanics, Bioengineering and Biotransport Conference
June 25 -28, Seven Springs, PA, USA

CARDIAC MOTION TRACKING FROM NOISY ULTRASOUND IMAGES - EXPLOTING CYCLIC CONSTRAINT FITTED TO NON-RIGID IMAGE REGISTRATION

Hadi Wiputra(1), Wei Xuan Chan(2), Yoke Yin Foo(2), Yu Zheng(2), Sheldon Ho(1), Choon Hwai Yap (2)

(1) NUS Graduate School
National University of Singapore
Singapore, Singapore

(2) Department of Biomedical Engineering
National University of Singapore
Singapore, Singapore

INTRODUCTION

Accurate tracking of cardiac tissues from clinical scans is an important task to aid the evaluation of organ function, detect disease, and aid downstream biomechanics analysis of the heart. A good method for cardiac motion tracking is non-rigid image registration, where two imaged are matched by deforming one to fit the other. This has worked very well for clean MRI images, but in noisy images such as ultrasound (US), its accuracy is limited [1]. US has lower cost than MRI, is more readily available, and in clinical fetal heart scans, US is most feasible.

Tracking difficulties are, firstly, since pairwise image registration is typically performed on consecutive time points, accumulation of tracking errors over time points will lead to tracked objects drifting away. Secondly, due to constraints in the algorithm designed to obtain smoother registration displacement calculations, tracked cardiac boundaries often underestimates the stroke volume.

In this study, we proposed a novel method for cardiac motion tracking on US images, using a mathematical model for cyclic motion of myocardial points to avoid drift, which was curve-fitted to results of a series of non-rigid image registrations. Our algorithm had the added robustness of allowing image registration of non-consecutive time points. By placing emphasis on time points when the heart was largest and smallest, we could preserve stroke volume much better. Compared to techniques reported in a recent Cardiac Motion Analysis Challenge (CMAC) [1], our technique achieved better accuracy. We successfully applied the method to cardiac scans from multiple modalities, but will focus on human fetal right ventricle (RV) US and CMAC here.

METHODS

3D Non-rigid pairwise image registration was performed with an open source module, Elastix [2]. We described a cyclic mathematical model for image coordinates motion as spatially distributed B-splines of temporal Fouriers expressions (BSF). The Fourier coefficients could be calculated at location $\vec{X}^0$ by the formula:

$$\vec{F}_f(\vec{X}^0) = \sum_{l=0}^{3}\sum_{m=0}^{3}\sum_{n=0}^{3} B_l(X_1)B_m(X_2)B_n(X_3)\vec{C}_{i+l,j+m,k+n,f} \quad (1)$$

The vector $\overrightarrow{F_o}$ denoted the Fourier coefficients in the 3 Cartesian axes at frequency *f*. B was the cubic B-spline basis function, and $\vec{C}$ was the 4D matrix of the coefficients of BSF. i, j, k were the 3D spatial index of the B-spline control points grid, and X_1, X_2 and X_3 were the Cartesian distance from the nearest B-spline control point. Next, $\vec{C}$ was optimized using Levenberg-Marquardt algorithm with objective function:

$$\overrightarrow{C^*} = argmin_{\vec{C}}\left(\frac{\sum_t \sum_{d\vec{X}\epsilon R}\left|\left|(\vec{X}^{t+1} - \vec{X}^t) - d\vec{X}\right|\right|_2}{2}\right) \quad (2)$$

Where $\overrightarrow{C^*}$ is the optimum $\vec{C}$, t is time point, T is the period of cardiac cycle, N is the maximum Fourier frequency, $d\vec{X}$ are the displacement vectors from one set of image registration results (R). $\vec{X}^t$ is described as summation of $\vec{F}_f$ in Fourier series. The initial descent value of $\vec{C}$, were calculated by Fourier decomposition and multi-level B-spline fit [3] to the displacement fields from pairwise-registration. In essence, the algorithm search for the BSF coefficients that best match the pairwise image registration results.

RESULTS

CMAC provides 15 volunteers cardiac US data with 12 tagged landmarks ground truth provided from tagged MRI. The Euclidean (*Eu*) distance error between tracked landmarks and the truth location of the landmarks, averaged across time, are shown in Figure 1, for the image tracking based on initialization (Init) BSF coefficients, and optimized

(Optim) BSF coefficients. Compared to the other three research groups participating in the challenge (Fraunhofer MEVIS, the INRIA-Asclepios Project, and Universitat Pompeu Fabra or UPF), our algorithm had lower errors. Without the iterative optimization step, our initialization BSF was found to be already comparable to the results of other groups with average *Eu* of 3.57mm. Iterative optimization reduced it further to 3.31mm, which was approximately 10% lower than the other groups (INRIA=3.76mm, MAVIS=3.72mm, UPF=3.63mm).

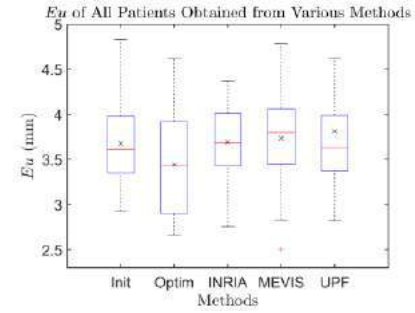

Figure 1. Box plot of Euclidean (Eu) distance error from ultrasound cardiac motion tracking. Whiskers: 1.5x of interquartile range, outliers are labeled '+', and averages as 'x'.

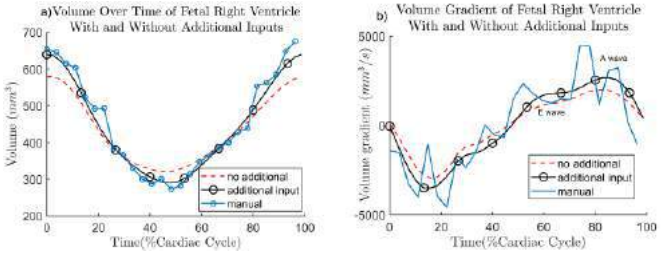

Figure 2. Comparison between the fetal RV obtained from manual segmentation and the proposed method for: a) ventricular volume and b) its gradient. Additional end diastole to end systole registration improves the stroke volume fit.

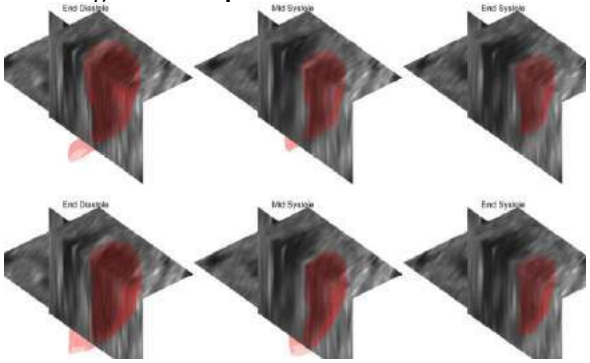

Figure 3. Tracked surface of the fetal RV, overlaid on the ultrasound images at various time points for (top) proposed algorithm and (bottom) manual segmentation.

The method was further applied to 4D human fetal cardiac US data. The volume of right ventricle (RV) across time obtained from tracking was compared against volume data from manual segmentations at all time points (Figure 2a), and a good fit was observed. The Euclidean distance error were was found to be similar to that from CMAC data, with *Eu*=0.45mm averaged over all landmarks, which was approximately 3% of the width of the RV. Our tracking method was also able to track E- and A-wave volume gradients (Figure 2b).

Since our image tracking technique utilized BSF, it naturally imposed a smoothness constraint on the curve-fitting, resulting in retardation of tracked motion. In figure 2, we could observe that the optimized BSF tracking resulted in a slight reduction of the tracked stroke volume compared to the manual segmentation truth. However, we could robustly include more pair-wise image registration displacement fields into the set of image registration results R (equation 2). By including displacement fields from end diastolic to end systolic time points, we could improve the tracked volume waveform fit, as shown the Figure 2.

To demonstrate utility in biomechanics simulation, the obtained cardiac wall displacements were used as boundary condition for computational fluid dynamics (CFD) of the fetal RV (data from a previous study [4]). Consistent E and A-wave vortex rings (Figure 4) were observed as expected [4] and CFD velocities and stroke volumes matched clinically obtained data (Table 1).

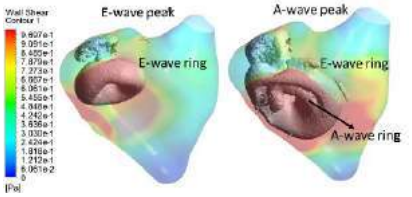

Figure 4. wall shear stress contour overlaid on top of vortex core during peak A and E waves.

Parameters	Clinic	CFD
EDV (mm^3)	675	629
ESV (mm^3)	272	285
E-wave velocity (m/s)	0.4	0.44
A-wave velocity(m/s)	0.7	0.62
Maximum pulmonary velocity(m/s)	0.6	0.68

Table 1. Cardiac physiological Parameters from clinic measurements matched CFD results.

DISCUSSION

We have implemented a novel cardiac motion tracking algorithm that could work well in noisy 4D US images, by incorporating a cyclic motion model for cardiac nodes, and curve-fitting the model to a series of non-rigid pair-wise image registration displacement fields.

BSF modelled a global motion with curve fitting across images of all time points. Other than preventing tracked nodes from drifting due to tracking error accumulation, it also enabled tracked nodes to cross over locations and time points where there were loss of signals, US shadowing by bone structure, or high noise.

The use of the B-spline spatial function also provided support to counter these localized loss of signals and high noise, as motion data from spatially-neighboring nodes can be used to bridge over areas with high noise and signal losses.

The choice of Fourier and B-spline functions are advantageous as they are continuous and easily differentiable. Further, these functions imposed a smoothness constraint naturally, which is akin to an inbuilt regularization term to the motion tracking. This simplified the form of the equation for optimisation. Further, by allowing any manner of image-pairing during image-registration, our motion tracking was robust to achieve the required stroke volume.

The performance of our proposed technique was highly encouraging, as it performed better than contemporary techniques included in the CMAC. Qualitative tracked images and quantitative tracking error computations demonstrated good performance. The algorithm should be useful for analyzing cardiac function and assist in image-based biomechanics simulations.

ACKNOWLEDGEMENTS

We acknowledge funding from Grant number MOE2018-T2-1-003

REFERENCES

[1] Tobon-Gomez C. *Medical image analysis*, 17(6), 632-648, 2013.

[2] Marstal K. *In Proc IEEE Comput Soc Conf Comput Vis Pattern Recognit Workshops* (pp. 134-142), 2016.

[3] Lee S. *IEEE Trans Vis Comput Graph*, 3(3), 228-244, 1997.

[4] Wiputra H., *Am J Physiol Heart Circ Physiol,* 311(6),1498-1508, 2016.

DEEP NEURAL NETWORKS FOR HEMODYNAMIC ANALYSIS OF HUMAN THORACIC AORTA

Liang Liang(1), Wenbin Mao(2), Wei Sun(2)

(1) Department of Computer Science
University of Miami
Coral Gables, FL, US

(2) Department of Biomedical Engineering
Georgia Institute of Technology and Emory University
Atlanta, GA, US

INTRODUCTION

Numerical analysis methods, including finite element analysis (FEA), computational fluid dynamics (CFD), and fluid-structure interaction (FSI) analysis, have been used to study the biomechanics of human tissues and organs, as well as tissue-medical device interactions, and treatment strategies. However, for patient-specific computational analysis, complex procedures are usually required to set-up the models, and long computing time is needed to perform the simulation, preventing fast feedback to clinicians in time-sensitive clinical applications.

In this study (Fig.1), by using deep machine learning (ML) techniques, we developed deep neural networks (DNNs) to directly estimate the steady-state distributions of pressure and flow velocity inside the thoracic aorta. After training on hemodynamic data from CFD simulations, the DNNs take as input a shape of the aorta and directly output the hemodynamic distributions in one second.

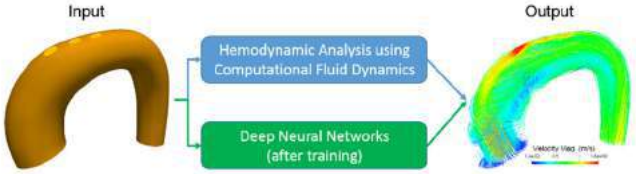

Figure 1. The proposed machine learning approach

The trained DNNs are capable of predicting the velocity magnitude field with an average error of 1.9608% and the pressure field with an average error of 1.4269%. This study demonstrates the feasibility and great potential of using DNNs as a fast and accurate surrogate model for hemodynamic analysis of large blood vessels.

METHODS

Dataset of Aorta Geometries and CFD Simulations. The DNNs were trained and tested using a dataset of 729 thoracic aorta shapes of virtual patients from our previous study[1] and corresponding CFD simulation results. As shown in Figure 2, the the aorta shape of a virtual patient (Fig.2-a1&a2, a shell mesh) is converted to a volume mesh suitable for CFD simulation (Fig.2-b1&b2). The CFD mesh is then converted to a mesh for machine learning (Fig.2-c1&c2), which has mesh correspondence[1] between patients (the same number of nodes/elements and the same nodal connectivity). The CFD simulations were performed using STAR-CCM+ (CD-adapco, Melville, NY) CFD software,

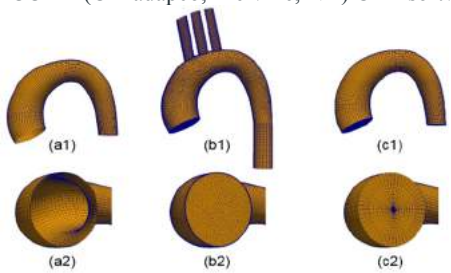

Figure 2. Three types of meshes for a virtual patient

Deep Neural Networks. In total, three DNNs with similar structures were designed to output pressure field, velocity magnitude field, and velocity vector field given an input aorta shape. The overall structure and data flow of the DNNs is shown in Figure 3. Given an input shape, a DNN will output a scalar/vector field in three steps: 1) encode the input shape as a set of scalar values, i.e. shape code; 2) conduct a nonlinear mapping of the shape code to the field code represented by a set of scalar values; and 3) decode the field code into the field values at

every node of the mesh. Autoencoders [2] to are used to obtain the shape encoding modules and field decoding modules, which are three-layer fully connected neural networks using Softplus units.

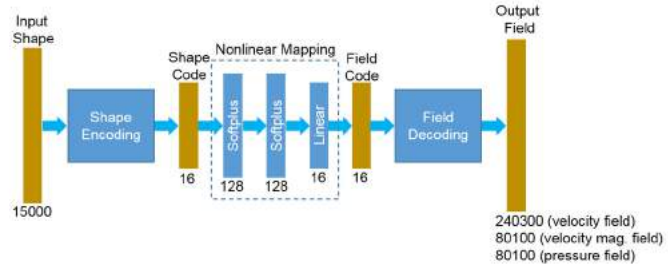

Figure 3. The structure of the DNNs

RESULTS

The performance of the DNNs was evaluated using Monte Carlo cross validation. In each round of the cross validation, 90% of the shapes and corresponding pressure/velocity field data from CFD were randomly selected as the training data to determine the parameters of the DNNs; and the remaining 10% of the CFD data were used as the testing data to obtain performance measures. The process was repeated 100 times to obtain the mean and standard deviation of each performance measure. Four performance measures were used: mean absolute error (MAE), normalized mean absolute error (NMAE), root mean square error (RMSE), normalized root mean square error (NRMSE), absolute error of the peak value (AE_peak), and normalized absolute error of the peak value (NAE_peak). The results are shown in Table 1&2&3 and Fig 4.

Table 1: Accuracy of the velocity field from the 1st DNN

RMSE (m/s)	NRMSE (%)	MAE (m/s)	NMAE (%)
0.0804 ± 0.0435	4.3699 ± 2.3456%	0.1110 ± 0.0690	6.2140 ± 4.1691 %

Table 2: Accuracy of the velocity magnitude field from the 2nd DNN

MAE (m/s)	NMAE (%)	AE_peak (m/s)	NAE_peak (%)
0.0363 ± 0.0162	1.9608 ± 0. 8367 %	0. 0260 ± 0.0417	1.2913 ± 1. 5258 %

Table3: Accuracy of the pressure field from the 3rd DNN

MAE (KPa)	NMAE (%)	AE_peak (KPa)	NAE_peak (%)
0. 0406 ± 0.1291	1.4269 ± 1.2557 %	0.0546 ± 0.1534	2.0316 ± 2.0699 %

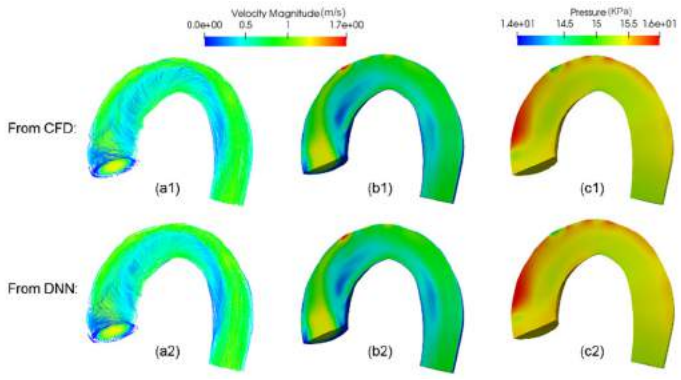

Figure 4. A representative example

DISCUSSION

Recently, ML-techniques have gained much attention in the field of biomechanics [3-6]. As an extension to our previous work on stress analysis[6], in this study, we proposed to use DNNs as an ML-surrogate to directly estimate the steady-state distributions of pressure and velocity given the aorta geometry. The trained DNNs output pressure and velocity fields within one second, and the flow characteristics predicted by the DNNs are highly consistent with those from CFD. The success of this study holds promise for the use of Machine Learning techniques to expedite the patient-specific hemodynamic analysis of human blood vessels by bypassing the time-consuming model construction and simulation processes.

In our approach, CFD is treated as a black-box and the nonlinear relationship between CFD input and output is learned by the DNNs, which decouples ML-models from hemodynamic analysis methods. On average, it took about 15 min to run a CFD simulation for each shape, which seems to be fast enough for clinical applications. However, such CFD analysis is not accurate enough compared to FSI analysis which considers the interaction between tissue and blood flow and thus takes significantly longer computation time (hours ~ days) [7]. No matter what hemodynamic analysis method is used to generate the training data, the DNNs can still have the same structures and the same processing speed for steady state hemodynamic analysis.

Since the goal of this study was to evaluate the feasibility of using ML techniques to estimate the steady-state hemodynamics of the thoracic aorta, the following simplifications in the CFD models were made to facilitate the study: (1) the aortic wall was assumed to be rigid; (2) the field data in the branching vessels were not consider as a part of the DNN output, to ease the process of establishing mesh correspondence; and (3) the same boundary conditions and properties were used because we don't have patient-specific data. These limitations will be improved in our future work.

ACKNOWLEDGEMENTS

Research for this project is funded in part by AHA Award #18TPA34230083.

REFERENCES

[1] Liang L, Liu M, Martin C, Elefteriades JA, Sun W: A machine learning approach to investigate the relationship between shape features and numerically predicted risk of ascending aortic aneurysm. Biomechanics and modeling in mechanobiology 2017:1-15.

[2] Goodfellow I, Bengio Y, Courville A: Deep Learning: The MIT Press, 2016.

[3] Brigham K, Gupta S, Brigham JC: Predicting responses to mechanical ventilation for preterm infants with acute respiratory illness using artificial neural networks. International Journal for Numerical Methods in Biomedical Engineering 2018, 34:e3094.

[4] Luo Y, Fan Z, Baek S, Lu J: Machine learning–aided exploration of relationship between strength and elastic properties in ascending thoracic aneurysm. International Journal for Numerical Methods in Biomedical Engineering 2018, 34:e2977.

[5] Cilla M, Pérez-Rey I, Martínez MA, Peña E, Martínez J: On the use of machine learning techniques for the mechanical characterization of soft biological tissues. International Journal for Numerical Methods in Biomedical Engineering 2018, 0:e3121.

[6] Liang L, Liu M, Martin C, Sun W: A deep learning approach to estimate stress distribution: a fast and accurate surrogate of finite-element analysis. Journal of The Royal Society Interface 2018, 15.

[7] Mao W, Caballero A, McKay R, Primiano C, Sun W: Fully-coupled fluid-structure interaction simulation of the aortic and mitral valves in a realistic 3D left ventricle model. PloS one 2017, 12:e0184729.

SB³C2019
Summer Biomechanics, Bioengineering and Biotransport Conference
June 25 -28, Seven Springs, PA, USA

EFFECT OF NONLINEAR ELASTIC PROPERTIES OF ARTERIAL WALLS ON PULSE WAVE PROPAGATION

A Coccarelli (1), S Pant (1), A Aggarwal (2)

(1) Zienkiewicz Centre for Computational Engineering, College of Engineering
Swansea University
Swansea, Wales, UK

(2) Glasgow Centre for Computational Engineering, School of Engineering
University of Glasgow
Glasgow, Scotland, UK

INTRODUCTION

The beating heart creates pulsating blood flow that travels through our vasculature as waves. The propagation of these pulse waves carries an immense amount of information about our cardiovascular health and has been a topic of research for many decades [1]. Our arterial network is extremely long and geometrically highly complex. Thus, the blood flow simulations for arterial networks approximate it as one-dimensional [2]. The governing equations incorporate the elasticity of the arterial wall via a constitutive relationship between pressure and cross-sectional area of the lumen. This constitutive relationship is commonly referred to as the "tube law", which is usually approximated to be linear and sometimes as other functional forms [3].

In the last decade biomechanical researchers have assembled a large dataset on the elastic properties of various arteries, which characteristically show a high nonlinearity. Several three-dimensional constitutive models have been proposed to describe the arterial elastic properties, with the so-called "GOH model" [4] being one of them most widely used. In this study, we aimed to incorporate the detailed three-dimensional constitutive relationships of arteries into the one-dimensional blood flow simulations and thereby study the effect of material nonlinearity on pulse wave propagation.

METHODS

We assume that the arteries remain perfectly cylindrical at all stages of deformation and use axisymmetric cylindrical coordinates to describe three configurations: stress-free with a known opening angle, closed at a reference pressure, and loaded at a given pressure. The arterial wall is modeled to be fully incompressible and longitudinal stretch is assumed to be fixed throughout deformation. These assumptions allow us to describe the kinematics in a single variable: the radial deformation.

After integrating the radial equilibrium condition, we get the pressure difference between inside and outside of the artery is

$$\Delta \mathrm{p} = \int_{r_i}^{r_o} (\sigma_{\theta\theta} - \sigma_{rr}) \frac{dr}{r}, \tag{1}$$

where $\sigma_{\theta\theta}$ and σ_{rr} are circumferential and radial Cauchy stresses. These are derived from a hyperelastic strain energy function ψ which is taken to be a combination of the fibrous and matrix components:

$$\psi(\mathbf{F}) = \frac{c}{2}(I_1 - 3) + \frac{k_1}{2k_2}(e^Q - 1), \tag{2}$$

where $Q = k_2[(1-\alpha)(I_1-3)^2 + \alpha(I_4-1)^2]$. For the blood flow, the one-dimensional equations of mass and momentum balance, under Newtonian flow assumption, can be written as

$$\frac{\partial A}{\partial t} + \frac{\partial (Au)}{\partial x} = 0 \tag{3}$$

and

$$\frac{\partial u}{\partial t} + u\frac{\partial u}{\partial x} + \frac{1}{\rho}\frac{\partial p}{\partial x} + \frac{8\pi\mu}{\rho}\frac{u}{A} = 0, \tag{4}$$

where A is the cross-sectional area of the lumen, u is the blood velocity, and p is the blood pressure. In order to close these equations, a tube law is required that defines the relationship between pressure and lumen area. Several different laws have been used in the literature, with the following most widely used

$$\Delta p = p_0 + \beta\left(\sqrt{A} - \sqrt{A_0}\right). \tag{4}$$

We apply our formulation to five specific artery properties reported in the literature, and also perform a parametric study by varying the various elastic parameters. We also look at the limit cases when the arterial wall is infinitely thick and infinitely thin. To match the results from linear tube law and our nonlinear one, we fit β such that the pulse wave velocity matches between the two cases.

ARTERY	Internal radius (cm)	Thickness of media (cm)	Thickness of adventitia (cm)
Rabbit carotid [5]	0.37	0.13	0.067
Human iliac adventitia [4]	0.4745	-	0.043
Human aortic arch [6]	0.9996	-	0.12
Human carotid [7]	0.37	0.13	0.067
Common iliac [8]	0.465	0.035	0.035

Table 1: Geometric details of five different arteries reported in literature (elastic properties are skipped in interest of space).

Under the approximation of no residual stresses and zero dispersion, we determined an analytical expression for the tube law (in interest of space, the final expression is skipped here). For other cases, we use numerical integration to evaluate Eq. (1).

RESULTS

The first question we explore is whether the detailed constitutive model which is nonlinear in three-dimensions can lead to a linear pressure-area relationship in one-dimension.

Using the properties for a rabbit carotid artery, we find that the stiffness of the matrix part decreases with pressure whereas that of the fibrous part increases (Fig. 1). Interestingly, the net result comes out to be approximately linear. However, for all other arteries this was not found to be the case (results not shown).

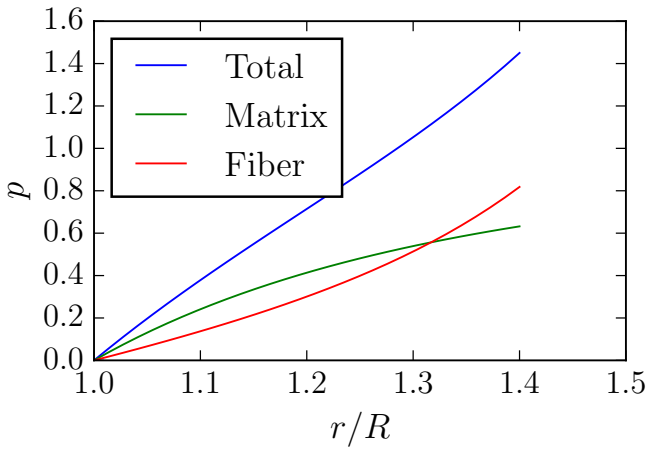

Figure 1: The pressure-area relationship for a rabbit carotid artery derived from its three-dimensional constitutive model

Next, we find the combination of elastic parameters that give a net linear response. Using the analytical expression, we noticed that the effective pressure-area relationship depends only on reduced parameters $\log(k_1 \cos^4(\beta)/c)$ and $\sqrt{k_2}\cos^2(\beta)$. Thus, we look at the range of inflation $\lambda = r/R$ up to which a linear approximation is more than 95% accurate (Fig. 2). We find that only for a small range of elastic parameters this is expected to be the case.

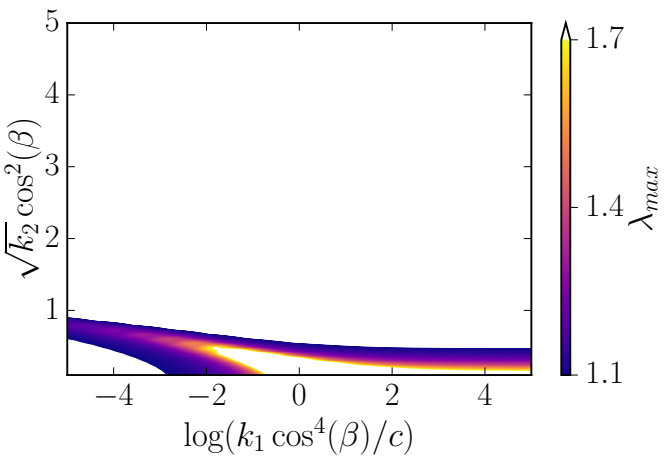

Figure 2: A contour plot of the combination of elastic parameters that lead to a net linear response

DISCUSSION

Models of pulse propagation through our arterial network have a potential of providing new ways to diagnose cardiovascular diseases. In spite of a wealth of information related to the elastic properties of different arteries, only generic tube laws are used for the pulse propagation. In this study, we present a first attempt in incorporating detailed three-dimensional information about arterial elasticity, including different layers and their specific properties. Results suggest that although for some specific arteries, a linear approximation might be appropriate, such cases are rare. Thus, we are currently investigating how this nonlinearity affects the pulse wave propagation.

ACKNOWLEDGEMENTS

This work was supported by Welsh Government and Higher Education Funding Council for Wales through the Sêr Cymru National Research Network in Advanced Engineering and Materials (Grant No. F28), and the Engineering and Physical Sciences Research Council of the UK (Grant No. EP/P018912/1).

REFERENCES

[1] Bergmann, G et al., *J Biomech*, 34:859-871, 2001.
[1] Van de Vosse, F. N., & Stergiopulos, N.. *Annual Review of Fluid Mechanics*, 43, 467-499, 2011.
[2] Alastruey, J et al. *J Biomechanics*, 44(12), 2250-2258, 2011.
[3] Olufsen, M. S., *American journal of physiology-Heart and circulatory physiology*, 276(1), H257-H268, 1999.
[4] Gasser, T. C., Ogden, R. W., & Holzapfel, G. A.. *Journal of the royal society interface*, 3(6), 15-35, 2005.
[5] Holzapfel, G. A., Gasser, T. C., & Ogden, R. W., *Journal of elasticity and the physical science of solids*, 61(1-3), 1-48, 2000.
[6] Balzani, D. (2006). Polyconvex anisotropic energies and modeling of damage applied to arterial walls. Essen: VGE, Verlag Glückauf.
[7] Holzapfel, G. A., Stadler, M., & Gasser, T. C., *Journal of biomechanical engineering*, 127(1), 166-180, 2005.
[8] Qi, N., Gao, H., Ogden, R. W., Hill, N. A., Holzapfel, G. A., Han, H. C., & Luo, X., *Journal of the mechanical behavior of biomedical materials*, 52, 108-119, 2015.

FAST TUMOR SPHEROID GROWTH IN MICROFLUIDIC DEVICE

Yaling Liu[1,2*], Chris Uhl[2], Yuyuan Zhou[2]

[1]Department of Mechanical Engineering and Mechanics
[2]Department of Bioengineering
Lehigh University, Bethlehem, PA

INTRODUCTION

Patient derived organoids have emerged as robust preclinical models for screening anti-cancer therapeutics. Current 2D culturing methods do not provide physiological responses to therapeutics, therefore 3D models are being developed to better reproduce physiological responses. 3D culturing however often requires large initial cell populations and one week to one month to grow tumors ready for therapeutic testing. As a solution a 3D culturing system has been developed capable of producing physiologically relevant tumors in an expedited fashion while only requiring a small number of initial cancer cells. .

METHODS

Device Fabrication

Bi-layer microfluidic platforms were produced following similar techniques outlined in previous microfluidic works from the Liu group45–49. The devices produced for expedited tumor spheroid growth contained a semi-permeable polycarbonate membrane which functioned to separate the apical and basal halves of the microfluidics. The circular chamber where the cancer cells were grown measured 3mm in diameter and 1.5mm in height. The straight sections of channel in the microfluidic devices measured 600µm in height and width. The use of the semi-permeable membrane within the system functioned to prevent the cancer cells introduced into the system from being washed downstream and out of the channel, which had an average pore diameter of 800nm. A depiction of the microfluidic setup can be viewed in Fig. 1.

HCT116 Spheroid Growth

Tumors were grown using HCT116 human colorectal cancer cells. The HCT116 cells used for testing were purchased from ATCC and all tests were carried out with cells within 5 passages from the initial frozen stock provided by ATCC. All spheroids utilized in this work were grown from an initial suspensions of 30 cells which were pre-formed into loose tumor spheroids via an 8 hour incubation in a low adhesion round bottom well plate under static conditions. The Ultra-Low Attachment Multiple Well Plates were manufactured by Corning that feature a covalently bound hydrogel layer that effectively inhibits cellular attachment. No additional coatings were required to facilitate spheroid formation in the round bottom wells. A hemocytometer was used to verify the concentration of cells in a stock suspension from which appropriate volumes of the suspension were separated to ensure that exactly 30 cells were introduced into each well. Due to the small number of cells used in each test, visual confirmation was performed for each well to ensure that 30 cells were present. Well containing greater or fewer than 30 cells were discarded and not used for growth testing. The pre-formed spheroids were then collected and flown into their respective microfluidic devices. Once inside the microfluidic devices, the semi-permeable membrane functioned to capture the pre-spheroids and hold them in place over the duration of the experimentation. The same process of an 8 hour incubation in a low adhesion well plate to pre-form spheroids was utilized for the static based tests. After pre-forming the initial static test case spheroids, Matrigel was added to the well plate in order to further facilitate spheroid growth over the course of 120 hours. Tumor spheroids grown under flow conditions were established as noted in the leukemia growth section at specific flow rates of $3.4X10^3$µL/hr and $3.4X10^4$µL/hr. Nutrient consumption for the HCT116 cells was also visualized and estimated as described for the leukemia cancer cells. Likewise, the HCT116 cells were maintained and grown under the same standard culturing conditions of 37ºC and 5% CO2 in an incubator as the leukemia cells.

Cancer Growth Measurements

Cancer growth was monitored daily over the course of five days with brightfield and fluorescence imaging. Data collection for spheroid growth was accomplished utilizing CellTracker™ Stain (10µM red, Thermo Fisher Scientific) and confocal microscopy (Nikon C2+, Apo 4X). Images of each cancer growth set-up were captured every 12 hours over the course of 5 days. All images were processed with FIGI (ImageJ) in order to measure HCT116 tumor sizes and cell counts for leukemia tests.

Statistical Analysis

Statistical analysis of all obtained results were run utilizing IBM's SPSS statistical software package (IBM Corp.). All of the figures have significant differences indicated above elements within the plots. One way ANOVA tests were run for each data set with confidence levels of 95% held throughout all plots. All analyses were carried out under conditions of Tukey equal variances assumed, along with tests of homogeneity of variance further verified by both Brown-Forsythe and Welch analyses.

RESULTS

On-chip cell culture and Imaging

Adherent cancer cells (HCT116) grown within the devices were first aggregated together under static culturing conditions within low adhesion well-plates. The cells were added to the wells and given 8 hours to adhere into loose spheroids before being introduced into the microfluidic devices. HCT116 cancer cells were successfully cultured within the microfluidic devices. Fig. 3b depicts representative images of HCT116 cells grown when subjected to a flow rate of $3.4X10^4$ µL/hr over the course of 120 hours. Both representative figures show overall increases in cell counts as time progresses as is indicated by the presented growth data in Fig.2a.

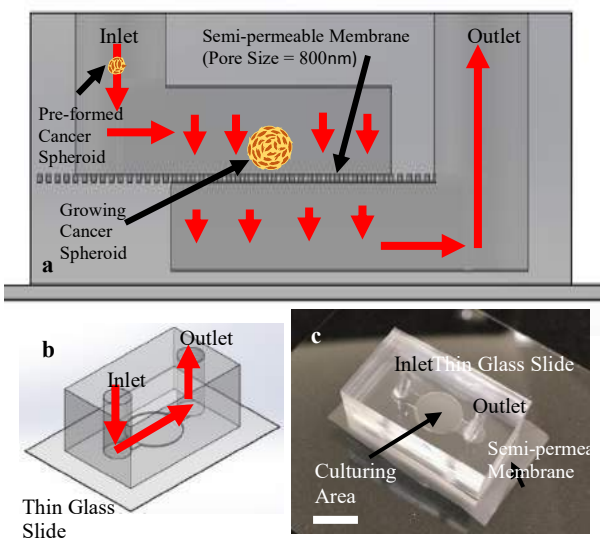

Figure. 1 Microfluidic device schema depicting device structure and cancer cell capture function utilizing semi-permeable membrane. Flow direction indicated by red arrows. (a), Device schema cross-section. (b), Device schema overview. (c), Image of sample microfluidic device utilized in experimental testing (white scale bar is 3mm long).

Cancer Growth Measurements and Nutrient Availability

Successful culturing of cancer cell lines was accomplished, as demonstrated by the growth of human colorectal (HCT116) in Fig. 2a. Growth of the cancer populations within the devices was measured directly through confocal imaging with CellTracker™ red stain. Through the application of various flow rates within the microfluidic devices, the rate of growth for the cancer cell populations was controlled. The use of convective flow allowed for a maximum of 4.76 times faster cancer cell growth when compared to the static growth cases. When compared to the static test cases, introducing $3.4X10^3$µL/hr nutrient flow into the systems containing HCT116 results in an overall increase in the cell population by a factor of 2.47 at the end of 120 hours. Even more impressive was the observed increase in HCT116 growth when supplied with a nutrient flow of $3.4X10^4$µL/hr, which resulted in a 4.76 factor increase in the cell population.

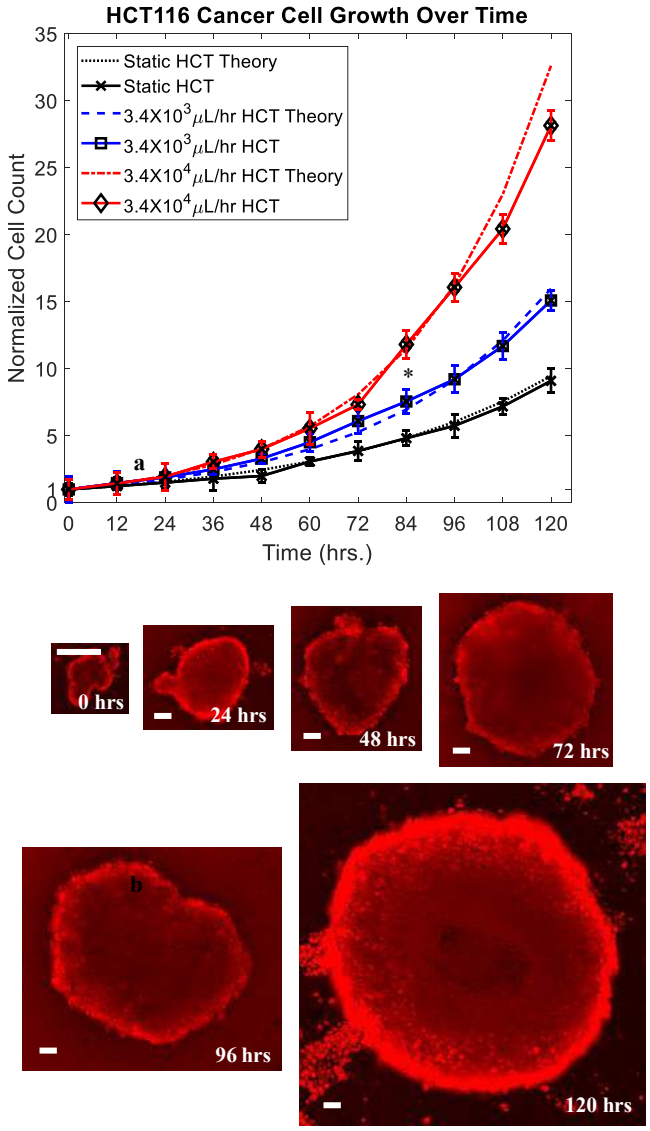

Figure 2. HCT116 cell growth over time based on flow conditions (30 cell initial count). a, Normalized HCT116 cell count over time for various flow conditions and theoretical model predictions. b, Normalized nutrient availability within microfluidic system over time for various flow conditions. Equilibrium point indicates when nutrient availability within the system can no longer satisfy the requirements of the entire cancer cell population. c, Representative fluorescence images of HCT116 tumor spheroid growth over the course of 120 hours under a flow rate of 3.4X104 µL/hr (scale bars are 60µm). Statistical significance indicated by "*" between flow based tests and static conditions and "**" between flow based tests at $p \leq 0.05$.

ACKNOWLEDGEMENTS

This work was supported by National Institutes of Health (NIH) grants R01HL131750, National Science Foundation (NSF) grants PFI:AIR-TT 1701136, DMS 1516236, and the Pennsylvania Infrastructure Technology Alliance (PITA) program.

REFERENCES

1. A. Thomas, D. Ou-Yang, L. Lorentz, V. Muzkantov, Y. Liu, "Biomimetic Channel Modeling Local Vascular Dynamics of Pro-inflammatory Endothelial Changes", *Biomicrofluidics*, 10, 014101, 2016
2. C. Uhl, V. R. Muzykantov, Y. Liu, "Biomimetic Microfluidic Platform for the Study of Transient Endothelial Monolayer Confluency and Therapeutic Transport under Mimicked Disease Conditions", Biomicrofluidics, 12, 014101, 2018
3. W. Shi, J. Kwon, Y. Huang, J. Tan, C. Uhl, R. He, C. Zhou, Y. Liu, "Facile Tumor Spheroids Formation in Large Quantity with Controllable Size and High Uniformity", Scientific Report, 68372, 2018

SB^{3}C2019
Summer Biomechanics, Bioengineering and Biotransport Conference
June 25 -28, Seven Springs, PA, USA

A MICROFLUIDIC TISSUE ARRAY FOR MID-THROUGHPUT DRUG SCREENING USING TUMOR TISSUES FOR PERSONALIZED MEDICINE

AH R. Ahmed (1), Xuejun Jiang(2), Sarat Chandarlapaty(3), Sihong Wang (1)

(1) Biomedical Engineering Department
City University of New York-City College
New York, NY, USA

(2) Cell Biology Program
Memorial Sloan-Kettering Cancer Center
New York, NY, USA

(3) Human Oncology and Pathogenesis Program
Memorial Sloan-Kettering Cancer Center
New York, NY, USA

INTRODUCTION

Cancer is recognized as a complex disease driven by genetic and epigenetic factors in individual patients. The last few decades have seen an emergence of various treatments against the disease, including chemotherapy, radiotherapy, and immunotherapy. Previous clinical studies have shown that similar genetic makeup of patients and cancer expression does not guarantee the efficacy of same treatment within these patients. A more personalized drug selection that serves the patient individually would account for the epigenetic variations presented in each patient [1]. The high expenses of the drug development process of selecting a few drugs from thousands of potential agents may inadvertently reject potentially effective drugs, which could not obtain the approval by FDA due to their adverse or undesirable effects on the majority of the population but may be effective for a small subset of the population [2]. On the other hand, there is a clinical need and merit to screen drugs for personalized treatment that minimizes adverse effects on patients and expedites selection of accurate treatment. Current methods of personalized screening involve disaggregating the cells from the original biopsy sample, and culturing them in 2D or reconstructed 3D matrices. However, under current health insurance policies, these methods are not accepted as being substantially more informative than available traditional clinical approaches [3]. Isolated cells in 2D culture lack full microenvironment, and an artificial 3D structure provides an altered non-native physical and biochemical microenvironment. Towards this end, we have developed a microfluidic tissue array (µFTA) as a platform for live culturing of tumor tissue samples directly under pathologically/physiologically relevant flow conditions. The tumor microarchitecture and microenvironment are preserved in our µFTA by virtue of never being disaggregated. Currently it has been developed as 2x4, 4x4, 6x4, or 8x4 platform for performing drug screening with mid-throughput and expected scalability up to 16x4 (16 conditions with 4 replicates per chip). The µFTA is expected to be a clinically more relevant tool for precision medicine selection over current techniques using isolated cells or reconstituted matrices.

METHODS

The µFTA is manufactured through standard soft lithography using a 3-layered construct of PDMS (polydimethylsiloxane). The 3 layers comprise of: (1) a bottom layer arrayed with traps to capture tissue pieces within a size of 0.5mmx1mmx1mm, (2) a top layer for media or drug perfusion located above the trap regions, and (3) a thin middle layer with a network of pores that provide a fluidic pathway between the top perfusion layer and the trap regions. The layers are bonded together as one complete device using oxygen plasma treatment. The tissue trap regions are situated within desired culture chambers which are hemispherical structures of 3-6mm diameter. The top perfusion layer spans to completely cover the trap region so to provide nutrients and optical clarity with a depth of at least 400µm. The pore-laden middle layer is about 40-60µm thick with each pore having a 150-250µm diameter. The design of the µFTA is continuously being optimized through CFD simulation (ANSYS and COMSOL) to provide flow velocities that are physiologically prevalent. The CFD results are verified through particle tracing velocimetry using fluorescent 2µm latex beads.

Xenograft tumors were generated by subcutaneously injecting MB-MDA 231 and BT 474 breast cancer cells with GFP in NOD-SCID mice. Patient-derived xenografts of HER2+ breast tumor (M-37) and triple negative BRCA1 mutant breast cancer (M156) were kindly provided by the Chandarlapaty lab at MSKCC. Harvested tumors were manually cut into small pieces less than 1mm^3, and then seeded into the µFTA by flow. Tumor tissues in the µFTA were cultured using

continuous flow at 1ml/day via a syringe pump in a 5% CO_2/37°C incubator. Following a 1-2 week culture, the xenografts were profiled with live-dead staining as well as EdU staining for proliferation. Doxorubicin was administered to the MB-MDA 231 samples after 2 weeks of culture, and to the M-156 samples after 1 week of culture, at a concentration of 2µg/ml, for 1 week, following which live-dead and proliferation assays were done. Histology stains for selected surface markers (HER2, EpCAM, CD44, and CD24) were performed on the M37 samples at day 0 and after day 10 of culture in the µFTA. Tissue images were captured with epi-fluorescent microscopy (AxioObserver Z1) or confocal microscopy (Zeiss LSM 700).

RESULTS

The CFD model results indicate that a 1ml/day supply of media is sufficient to maintain a flow on the order of 0.1µm/sec (Fig. 1) in accordance with its relevance to physiological flow, and has been verified using bead velocimetry. Under these culture conditions, the µFTA maintains the xenograft samples within culture for 1-3 weeks, allowing slight morphological changes or outgrowth (Fig. 2A-B), while maintaining the biopsy vitality and proliferation as noted from live-dead and EdU assays. There is no appreciable fluctuation in the expression of surface markers in the histology samples, with the exception of increased EpCAM expression. Treatment of the tissue samples to doxorubicin show a distinct clearance of the tissue as observed under phase-contrast imaging (Fig. 2 C-D).

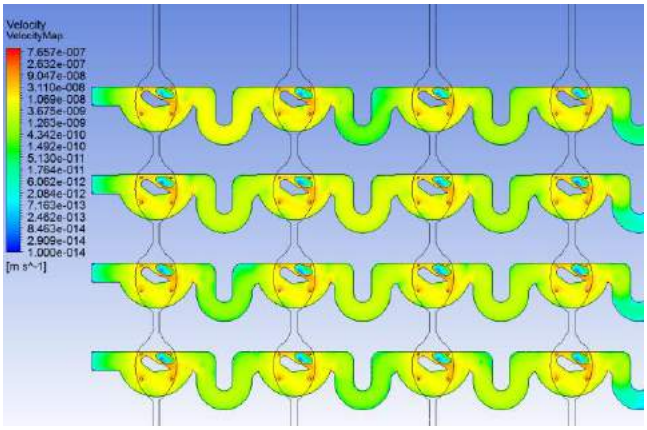

Figure 1: ANSYS CFD simulation of flow in the µFTA. The elliptical regions in the traps are modeled as porous regions to simulate tissue. Note that the velocity around this simulated tissue area reaches the order of 0.1 µm/sec.

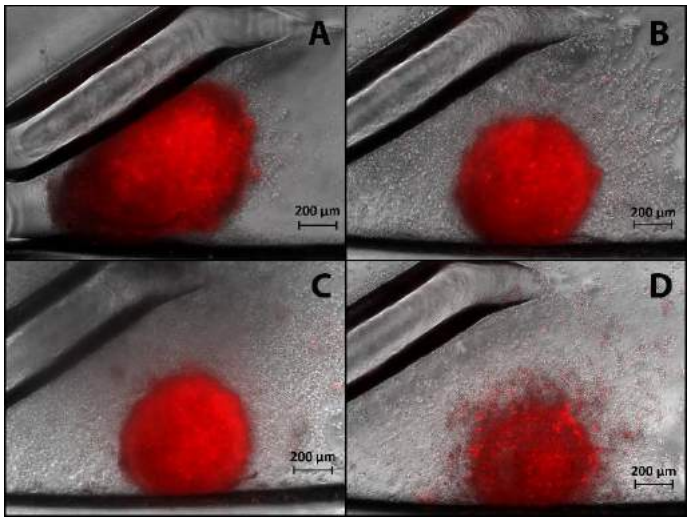

Figure 2: Culture of RFP-tagged MB-MDA 231 xenograft in the µFTA and following drug treatment. The tissue piece shown here corresponds to the tissue piece maintained in the µFTA on (A) day 1 after seeding, (B) day 5, (C) day 8, which is when doxorubicin was administered continuously at 2 µg/ml, and (D) day 6 of dox treatment, (day 14 of culture). Notable from (A) to (B) is the morphological reshaping and expansion of the tissue piece, from (C) to (D) is the visible reduction in tissue density (optical clearance of tissue) and significant removal of surface-adhered cells after the course of drug treatment. Scale bars: 200 µm.

DISCUSSION

The µFTA developed here has the potential to be a clinically relevant tool in the process of personalized medicine. In its current format, it provides a platform for conveniently seeding and culturing whole tissue samples under physiologically relevant flow conditions, with or without drugs. Depending on the format of the µFTA, different reagents can be administered onto a single chip such that varying drug treatments of assays can be performed on-chip on the whole tissue with biological replicates. The µFTA can be cascaded with different tissue types to study interorgan interaction. The versatility in the use of the µFTA is a promising technology to permit direct screening of effective drugs on patient biopsy samples to assist in a selection that would be beneficial to patients tailored to their individual cancerous tissue.

ACKNOWLEDGEMENTS

This work has been supported by the Young Investigator Award to SW from Pershing Square Sohn Cancer Alliance.

REFERENCES

Sample Reference:

[1] Goldhirsh, Aron et al., *The Lancet*, 382(9897):1021-1028, 2006.
[2] Abrahams, E et al., *J Diabetes Sci Technol*, 3(4): 680-684, 2009.
[3] Burstein, HJ et al., *J Clin Oncol*, 29(24):3328-3330, 2011.

SB³C2019
Summer Biomechanics, Bioengineering and Biotransport Conference
June 25 -28, Seven Springs, PA, USA

CIRCULATING TUMOR CELL TRANSPORT AND ADHESION IN MICROFLUIDIC DEVICES

Jifu Tan (1), Zhenya Ding (2), Wei Li (2)

(1) Department of Mechanical Engineering
Northern Illinois University
DeKalb, IL 60115, USA

(2) Department of Chemical Engineering
Texas Tech University
Lubbock, TX, 79409, USA

INTRODUCTION

Circulating tumor cells (CTCs) can lead to metastasis that accounts for 90% of the death for cancer patients[1], [2]. Thus, detecting CTCs at an earlier stage is important for diagnostics. However, detecting CTCs is very challenging, as CTCs are rare, e.g., there are only a few CTCs in 1 mL blood sample that contains billions of blood cells. Recently, microfluidic devices with micropost features have been shown in detecting CTCs successfully[3]. Different micropost sizes, separation distance, and layout has been proposed to separate CTCs from blood sample. Meanwhile, theoretical analysis and numerical simulations were performed to improve the design of the devices, e.g., a unified theoretical framework was proposed to infer the trajectories of particles in the whole device on the basis of trajectories in the unit cell[4]. The effect of post shift distance and deformability of blood cells on cell trajectories were also studied in[5], showing that it is possible to separate cells through label free method. Numerical simulations suggest better designs though combining a diffuser and a semi-cylindrical obstacles[6]. Despite these efforts, a general design principle for CTC detection considering the hydrodynamics, fluid cell interaction, cell transport and adhesion is currently not available. In the current work several numerical CTC detection simulations were performed to evaluate the binding behavior of CTCs and its diffusivity under the influence of blood cells. The numerical results on cell adhesion pattern and cellular trajectory agreed well with microfluidic experiments using human prostate cancer cells (PC-3).

METHODS

The fluid flow was solved by the lattice Boltzmann method because of its efficiency in modeling complex geometries and parallel computing. The cell membrane was modeled using a coarse grained molecular dynamics method where membrane stretching and bending were considered. The adhesion between cells and microposts was modeled as pair wise interactive Morse potential. The immersed boundary method (IBM) was used to couple the fluid motion with the solid deformation. Briefly, the solid velocity at each particle position is obtained through velocity interpolation from local fluid nodes, while the fluid feels the existence of the solid though body force terms. Details of the immersed boundary method formulation can be found in Refs[7]. The blood cell model and numerical implementation was verified in our previous publications[8], [9].

Two different microfluidic designs were considered in the study: regular layout and shifted layout. The microposts in the regular one were separated by 50 μm. The shifted one was based on the regular design but the center position of the microposts were shifted 50 um every other three row in vertical direction. A characteristic unit of the two designs device was created and periodic boundary conditions were applied to model the fluid flow. Experimentally diluted blood with PC-3 mixture (about 5000 cells/mL) was injected into the PDMS micro-fluidic device at the constant flow rate 0.12 mL/hr for 1hr to study the PC-3 cell adhesion and trajectory in the microfluidic devices.

RESULTS

The fluid flow was driven by body force with periodic boundary conditions in x and z directions. Cancer cells showed preferred adhesion locations on the surface of posts. The simulation results showed that the cells tend to settle down on the micropost surface where the shear stress is low, as indicated in the blue region in Fig. 1a. Microfluidic based experiments also confirmed that the cells do prefer adhered to those low shear stress regions, see Fig. 1b.

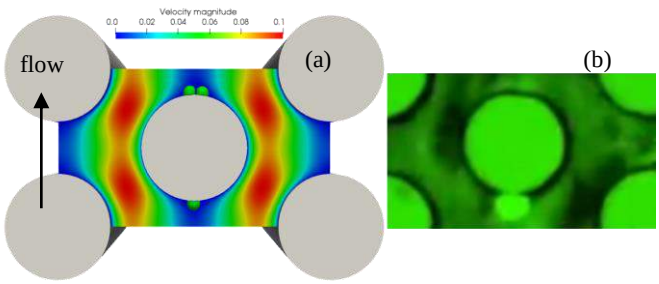

Figure 1. Cells showed preferred adhesion region on the microposts in the microfluidic device with regular design. (a) Simulation: three cells were adhered to the microposts, the background color shows the fluid velocity distribution. (b) Microfluidic experiments showing one cancer cell adhered on the front stagnant point.

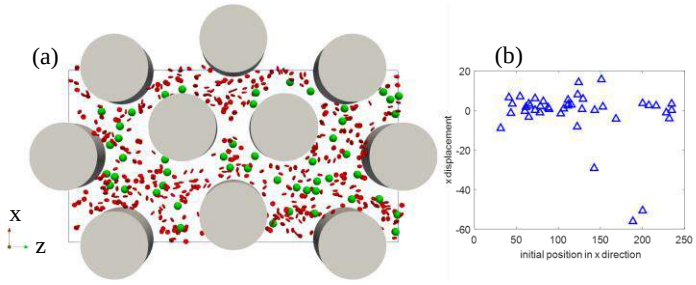

Figure 2. (a) A snapshot of the blood cells (red) and cancer cells (green) mixture in a microfluidic device with shifted design (b) the shift distance for cells after one cycle.

Blood cell mixture with cancer cells transport in microfluidic device with shifted design was also performed, as shown in Fig.2a. The cell drifting Δx in the direction perpendicular to the fluid flow was selected to quantify the cell motion in microfluidic device. Since periodic boundary conditions were applied in the simulation, the cell drifting in one cycle for micropost with a radius R=50 μm was plotted in Fig.2b. It showed that drift for most of the cells is small, with a gauss like distribution with a mean of zeros and variance of 5.6 μm. However, there are some cells showed significant drift in x direction, e.g. $\Delta x > 20$ μm, in particular in the negative x direction. The reason is due to the layout of the micropost where the resistance is smaller in the negative x direction. Simulation with micropost of different sizes showed similar pattern for the shifted distance in x direction (results not shown here).

DISCUSSION

The cell preferred adhesion location is consistent with the low shear stress region. It is expected as the ligand receptor bond is not stable at high shear stress. Thus, low shear is favorable for cell adhesion. The current model did not consider the stochastic nature of the bond formation and breaking. Another limitation is that the bond formation is instantaneous without considering the adhesion rate. Adhesion model following bell's model will be considered in the future study.

Cancer cell showed stochastic dispersion in the blood flow, as characterized by the shift distance in x direction. Cells are subjected to collisions from nearby cells, which results in a random walker like behavior. The deformability induced cell diffusion under shear flow also contribute to the cell diffusivity. If the cell trajectories can be approximated as a superposition of stream line trajectory and dispersion, then the cell micropost collision frequency can be estimated based on the device size in the flow direction and gap size perpendicular to flow direction, as cells cover device size through convection, while converting gap size by dispersion. Then, the design problem for microfluidic device optimization can be formulated as an inverse problem such that the capture efficiency is given, based on the design layout, what size of the microfluidic device should be? The hypothesis will be studied in details in the future work.

ACKNOWLEDGEMENTS

The author acknowledge the funding and computational support from Northern Illinois University.

REFERENCES

[1] D. Wirtz, K. Konstantopoulos, and P. C. Searson, "The physics of cancer: the role of physical interactions and mechanical forces in metastasis," *Nat. Rev. Cancer*, vol. 11, no. 7, pp. 512–522, 2011.
[2] K. Pantel and C. Alix-Panabières, "Circulating tumour cells in cancer patients: challenges and perspectives," *Trends Mol. Med.*, vol. 16, no. 9, pp. 398–406, 2010.
[3] S. Nagrath *et al.*, "Isolation of rare circulating tumour cells in cancer patients by microchip technology," *Nature*, vol. 450, no. 7173, pp. 1235–1239, Dec. 2007.
[4] S.-C. Kim, B. H. Wunsch, H. Hu, J. T. Smith, R. H. Austin, and G. Stolovitzky, "Broken flow symmetry explains the dynamics of small particles in deterministic lateral displacement arrays," *Proc. Natl. Acad. Sci.*, p. 201706645, 2017.
[5] T. Krüger, D. Holmes, and P. V Coveney, "Deformability-based red blood cell separation in deterministic lateral displacement devices—a simulation study," *Biomicrofluidics*, vol. 8, no. 5, p. 54114, 2014.
[6] L. Zhu, C. Rorai, D. Mitra, and L. Brandt, "A microfluidic device to sort capsules by deformability: a numerical study," *Soft Matter*, vol. 10, no. 39, pp. 7705–7711, 2014.
[7] C. S. Peskin, "The immersed boundary method," *Acta Numer.*, vol. 11, pp. 479–517, Jan. 2002.
[8] J. Tan, T. R. Sinno, and S. L. Diamond, "A parallel fluid–solid coupling model using LAMMPS and Palabos based on the immersed boundary method," *J. Comput. Sci.*, vol. 25, pp. 89–100, 2018.
[9] J. Tan, S. Sohrabi, R. He, and Y. Liu, "Numerical simulation of cell squeezing through a micropore by the immersed boundary method," *Proc. Inst. Mech. Eng. Part C J. Mech. Eng. Sci.*, vol. 232, no. 3, pp. 502–514, 2018.

SB³C2019
Summer Biomechanics, Bioengineering and Biotransport Conference
June 25 -28, Seven Springs, PA, USA

An *In Vitro* Tumor Platform for Modeling Breast Tumor Stromal Interactions and Characterizing the Subsequent Response

Manasa Gadde (1), Marissa N Rylander(1,2)

(1) Department of Biomedical Engineering
The University of Texas at Austin
Austin, TX, USA

(2) Department of Mechanical Engineering
The University of Texas at Austin
Austin, TX, USA

INTRODUCTION

Inflammatory breast cancer (IBC) is an aggressive disease with poor prognosis, accounting for 10% of breast cancer mortality [1]. It is characterized by redness and swelling of the breast and spreads rapidly and diffusely within the primary site and surrounding tissue instead of developing a lump. Contrary to its inflammatory namesake, symptoms are manifested by blockage of lymph channels and skin invasion rather than inflammation [1,2,3]. A primary factor contributing to the bleak prognosis is the difficulty of early IBC diagnosis. Approximately 50% of IBC cases lack a tumor mass and present no radiographic IBC evidence. Also, at diagnosis, the tumor has advanced to stage III or IV, most patients have lymph node metastases, and 30% of IBC patients exhibit distant metastases compared to 5% for non IBC [2,3,4]. Despite advancements in diagnostic and therapeutic approaches have improved the bleak prognosis associated with IBC but the 5 year survival rate of IBC compared to locally advanced breast cancer is still inferior.

There are currently no IBC specific therapies due to rarity of the disease combined with the lack of IBC specific diagnostic and targeting markers. Most efforts have focused on identifying driver mutations and tumor targets. While numerous comparative genomic studies of IBC and non-IBC have been undertaken, none have implicated a compelling tumor cell autonomous driver to be targeted to improve outcomes. Interestingly, most of the genes in the IBC-like signature are predicted to represent stromal cells rather than tumor cells [5]. Studies have emphasized the significance stromal cells in mediating IBC-like symptoms in animal models. This highlights the significance of understanding the interactions of tumor cells with the microenvironment in greater detail and the knowledge would enable determination of targetable biology from these interactions which would facilitate identification of patients who would benefit from such approaches. What is critically needed is a validated model to capture this complexity, identify critical spatial hetero-cellular interactions, and target them successfully in a more nuanced/physiologically relevant and high-throughput manner

To better study IBC, we have developed a novel *in vitro* breast tumor platform that possesses a matrix supportive of IBC cell representative growth incorporated with fully functional lymphatic and blood vessels for modeling critical invasion into these structures in a dynamic and spatial manner. The platform will be used to study 2 key critical features of IBC: (i) vascular sprouting and (ii) formation of IBC emboli surrounded by vascular sprouts. We will investigate the influence of macrophages, a key stromal cell in influencing IBC aggressiveness, and test the effect of various therapies such as trastuzumab on the aforementioned critical features of IBC.

METHODS

In vitro* breast tumor platform*: 14 mg/ml collagen stock solution was mixed with 10x DMEM, 1N NaOH to and supplemented with DMEM containing HER2+ breast cancer cells and THP-1 macrophages. Cancer cells used were breast HER2+ IBC cancer cell line MDA-IBC3, and non IBC HER2+ cancer cell line BT474. The collagen mixture was then injected into a PDMS mold with a needle inserted through the center and allowed to polymerize around the needle. After polymerization and removal of the needle, a cylindrical hollow void was created in the collagen which was then seeded with either telomerase immortalized microvascular (TIME) cells labeled with red fluorescence or human derived lymphatic endothelial cells (hdLECs). Lymphatic vessels were confirmed through immunofluorescent staining for lymphatic markers LYVE and Prox-1. Vessel permeability was quantified by flowing the channel with 10μg/ml fluorescently labeled 70 kDa to investigate the barrier function of the endothelium. Vessel sprouting and emboli formation were analyzed using Leica TCS SP8

confocal microscope to observe vessel sprout formation and growth followed by analysis for number of tumor emboli and sprouts, size of emboli, sprout length, thickness, and branching. Lumen formation was analyzed by perfusing the vessels with one micron green fluorescent microspheres which aggregate at the vessel walls outlining the endothelial barrier.

Trastuzumab effect: Trastuzumab treatment has shown to improve survival rates of HER2+ breast cancers. To test the influence of trastuzumab on both IBC and non IBC HER2+ tumors, Herceptin was perfused through the platforms for 24 hours followed by perfusion of fresh media for 48 hours. Next, platforms were broken down using collagenase, cells collected and lysed. Luminex bead-based multiplex assay for total and phosphorylated HER2, ERK, AKT, p38MAPK was performed.

RESULTS

We created a HER2+ i*n vitro* breast tumor platform as shown in Figure 1 capable of chemotherapeutic and cytokine perfusion. This unique platform, which will serve as the baseline platform, provides long-term, spatiotemporal characterization of multi-cellular interactions and tumor response to tissue microenvironmental conditions (matrix mechanics, cell composition, and biotransport) with high-resolution quantitative velocimetry, transport and imaging for target discovery.

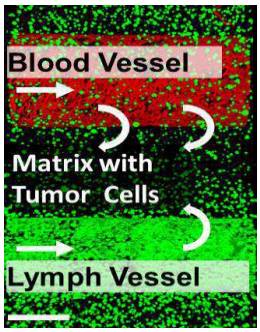

Figure 1. *In Vitro* Breast Tumor Platform: Perfusable blood (red) and lymphatic (green) vessels surrounded by collagen matrix seeded with HER2+ tumor (green) and stromal cells; scale 500 µm.

The platforms were followed for a 3 week period and imaged using confocal microscopy to analyze vessel sprouting as illustrated in Figure 2 in MDA-IBC3 platform. The sprout lengths were measured over time and we observed a significant increase in sprout lengths at later time points (Figure 2A). Additionally, at later time points we see the formation of tumor emboli surrounded by vascular nests replicating *in vivo* IBC characteristics seen in MARYX xenograft models. To test for lumen formation, vessels were perfused with 1 micron green fluorescent microsphere and as demonstrated in Figure 3, we saw the green fluorescent microspheres travel to the tips of the sprouts revealing the newly formed sprouts are patent and capable of handling flow. Additionally, we perfused trastuzumab, a HER2+ specific therapy and saw a greater sensitivity of the endothelium in the IBC *in vitro* breast tumor platform compared to non IBC breast tumor but saw a greater resistance in the IBC MDA-IBC3 tumor cells compares to non IBC BT474 cells.

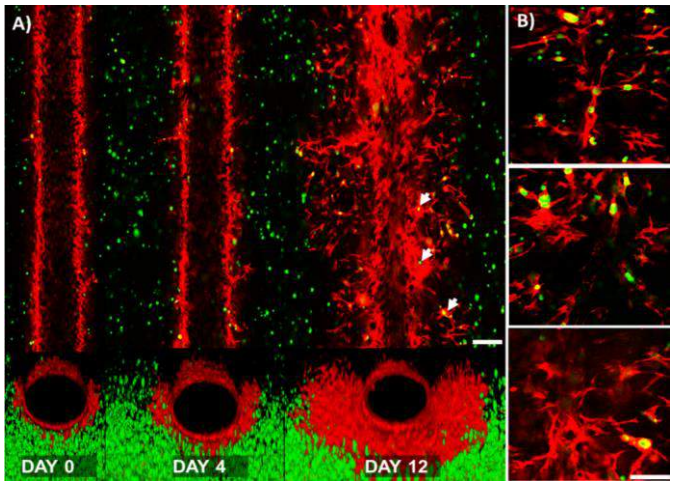

Figure 2. Established Measurable Tumor – Stromal Cell Interactions. A) Vascular sprouting dynamically observed over a three week period in the MDA-IBC3/TIME *in vitro* platform. Longitudinal cross section images of the vessel showing vessel sprouting, branching, as well formation of tumor emboli (white arrows) scale bar: 200µm; B) Close up images of emboli (green) surrounded by vascular vessel sprouts (red); scale bar 300µm

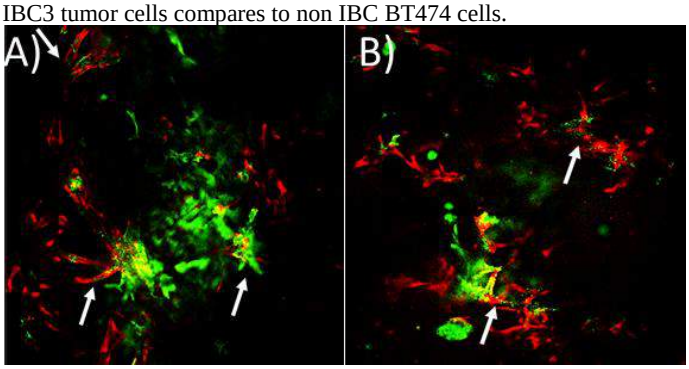

Figure 3. Patent and Functioning Sprouts. Green microspheres travel to the periphery of the newly formed sprouts as indicated by the white arrows.

DISCUSSION

IBC is an aggressive and invasive breast cancer with a poor prognosis linked to tumor-stroma interactions. Current preclinical to study IBC consist primarily of xenograft animal models which are cost prohibitive due to large number of animal required. Additionally, determining the influence of specific signaling pathways and microenvironmental stimuli on tumor progression is challenging. Here we present a novel *in vitro* breast tumor platform to model two HER2+ breast tumors and saw a difference in their behavior. The MDA-IBC3 breast tumor platform demonstrated both vascular sprouting and emboli formation, 2 key features of IBC tumors seen in *in vivo* mice models. This behavior was observed specifically in the IBC platform and was absent in the non-IBC BT474 tumor platform. Furthermore, there was a difference in the response of the tumor platforms to trastuzumab therapy. BT474 cells were more sensitive to trastuzumab but the endothelium in the MDA-IBC3 platform which presented vascular sprouting was more affected by the trastuzumab therapy. The differences in the behavior in the two platforms highlight possible molecular targets that can differentiate between IBC and non IBC tumors and lead to development of effective IBC specific therapies.

REFERENCES

[1] Fernandez, S.V., et al., *Breast cancer research and treatment*, 140(1): p. 23-33, 2013
[2] Fouad, T.M., et al., *Inflammation and Cancer*, p. 53-73, 2014.
[3] Mohamed, M.M., et al., *Journal of Advanced Research*, 5(5): p. 525-536, 2014.
[4] Giordano, S.H. and G.N. Hortobagyi, *Breast Cancer Research*, 5(6): p. 284-288, 2003.
[5] Van Laere, S.J., et al., *Clin Cancer Res*, 19:4685-96, 2013.

COMPUTATIONAL FLUID DYNAMICS MODEL OF PRESSURIZED INTRAPERITONEAL AEROSOL CHEMOTHERAPY: GRAVITY MATTERS!

Mohammad Rahimi-Gorji (1,2), Leen Van de Sande (1), Charlotte Debbaut (2), Patrick Segers (2), Wouter Willaert (1), Wim Ceelen (1)

(1) Laboratory for Experimental Surgery, Department of GI Surgery, Ghent University, Ghent, East Flanders, Belgium

(2) IBiTech – bioMMeda, Ghent University, Ghent, East Flanders, Belgium

INTRODUCTION

Pressurized IntraPeritoneal Aerosol Chemotherapy (PIPAC) is a recent and innovative drug delivery strategy developed to treat peritoneal cancer using laparoscopy [1,2]. During PIPAC, a CO_2 pneumoperitoneum is established (12-15 mmHg) and chemotherapy is nebulized to obtain a homogeneous aerosol distribution within the peritoneal cavity (Figure 1). The aerosol is generated by injecting chemotherapy-containing liquid under high pressure through a single fluid nozzle (micro-injection pump) [3]. The increased intraperitoneal pressure may overcome the elevated interstitial fluid pressure (IFP) in tumor tissue and lead to enhanced tissue penetration of chemotherapy [1].

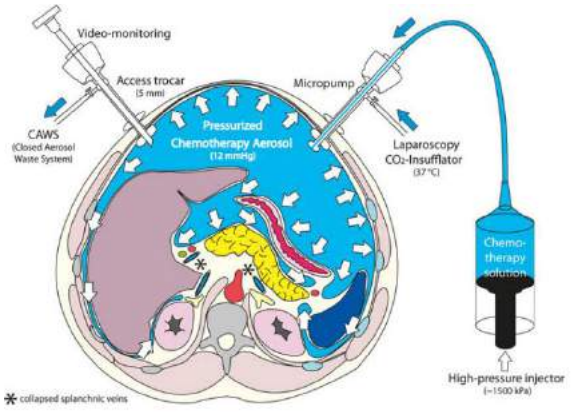

Figure 1: schematic overview of a PIPAC procedure [4].

Since tumor nodules tend to occur anywhere on the peritoneal surfaces, a *homogeneous distribution* of the aerosolized chemotherapy is of paramount importance. Preclinical experiments suggest that aerosol distribution is not uniform, probably due to the effects of gravity [5]. The use of a Computational Fluid Dynamics (CFD) model may generate important insights in how treatment parameters affect aerosol distribution during PIPAC. Here, we developed a numerical PIPAC model to investigate the effect of gravity on the distribution and deposition of aerosol particles in the peritoneal cavity in a rat model.

METHODS

A micro-computed tomography (µCT) multislice scan of the peritoneal cavity of a healthy rat (Infinity Lab, UGent) was used as input to generate the 3D simulation geometry. As we need the abdominal geometry of the rat during PIPAC, the abdomen of the rat was insufflated with CO_2 up to 8 mmHg (1066 Pa) and kept constant throughout the scan. The µCT images (DICOM files) were imported into Mimics Research software (Materialise, Belgium) (Figure 2a-b) and segmented.

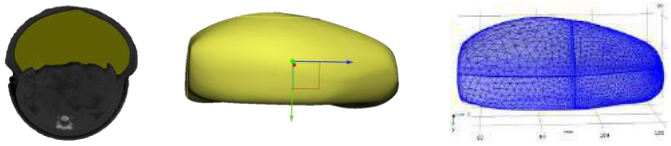

(a) (b) (c)

Figure 2: 3D reconstruction of the pressurized rat abdominal cavity: (a) 2D single slice of the CT dataset, (b) 3D reconstruction of the rat abdominal cavity and (c) the generated mesh with division of the volume in 8 subvolumes.

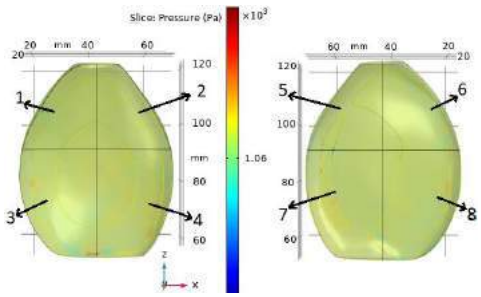

Figure 3. Geometry subdomains and illustration of the achieved homogeneous inflow (CO_2) pressure distribution.

The resulting STL-file was imported in COMSOL Multiphysics (Inc., Burlington, VT) to set up the CFD simulation. Next, a good quality mesh grid was generated resulting in 135000 tetrahedral elements. The geometry was divided into 8 subvolumes to compare different zones (Figure 2c and 3).

The first part of the CFD simulation focused on filling the abdominal cavity with CO_2 gas until its pressure equals 8 mmHg. The governing continuity and momentum equations of the CO_2 flow phase were considered under time-dependent, weakly compressible and Newtonian fluid (density of 1.98 kg/m^3 and dynamic viscosity of 1.4*10^{-5} Pa·s) assumptions. The inflow boundary condition was set to a pressure of 8 mmHg. No-slip conditions were used for the walls.

Subsequently, particle flow was simulated using Comsol's Particle Tracing Module. Similar to experimental conditions, a volume of 20 mL of the chemotherapy solution (in this study Abraxane^{TM}) was used with a volumetric flow rate of 0.8 mL/s at a fixed injector position [6]. By using the values of flow, flow rate, inlet surface area and injection time, particle inlet velocity could be calculated. The initial position (random), velocity (15.92 m/s), diameter (30 µm), density (1004.6 kg/m^3) and viscosity (1.0182 mPa·s) of individual particles were determined [6]. The time of injection was 25 s which resulted in 125000 particles being injected for each simulation. It was assumed that impacted particles do not bounce from the cavity wall, but adhere to it once the distance between particle center and the wall is less than the particle diameter. The trajectory and mass transfer calculations are based on the force balance on the particle, using the local continuous phase conditions as the particles move through the flow. Simulations were done with and without adding the gravity force in the force balance equations.

RESULTS AND DISCUSSION

The first results demonstrate that the first part of the simulation leads to a uniform pressure distribution of 8 mmHg in the peritoneal cavity filled with CO_2 (Figure 3). Figure 4 (a-b) illustrates that the aerosol distribution is not homogeneous, as is also confirmed by Khosrawipour et al. [5]. Furthermore, aerosol distribution and concentration vary considerably when taking into account gravity force. In some regions, the particle concentration was high, while it was very low for other regions. When neglecting the gravity force, the particle distribution in abdominal cavity is more homogeneous. Figure 5 displays the number of deposited particles on the abdominal wall divided in the different subvolumes (as defined in Figure 3). When considering the gravity force, most particles directly deposit in domain 6 (80% of particles). By removing the gravity force, the particle deposition in domain 6 decreases (36% of particles) and increases in other regions. Hence, these preliminary results indicate that the influence of the gravity force on aerosol distribution is significant in PIPAC and should be confirmed in validation experiments and other animal/patient- specific geometries. By considering additional forces, such as the electrostatic force [7], it may be possible to overcome the gravity force effect and improve the distribution in the abdominal cavity.

In conclusion, aerosol distribution during PIPAC therapy is significantly affected by gravity. Use of a CFD model may allow to understand particle behavior during PIPAC therapy and inform improved treatment methods.

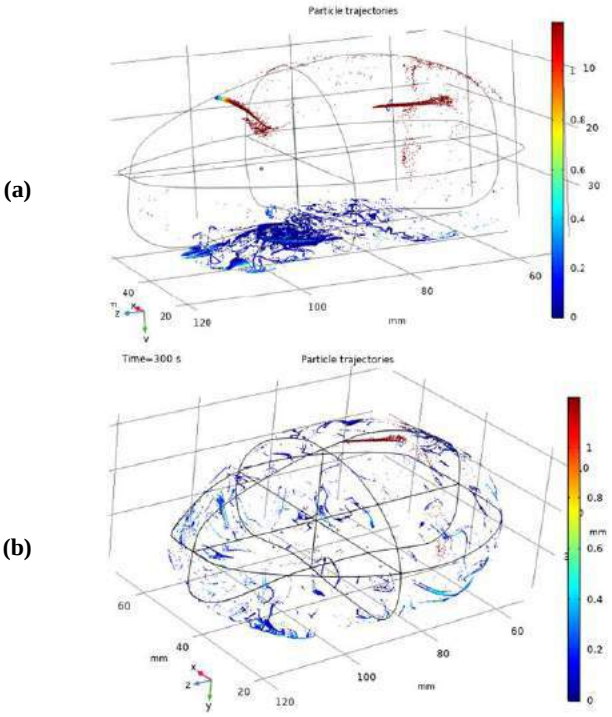

Figure 4. Particles position, (a) with gravity force and (b) without gravity force.

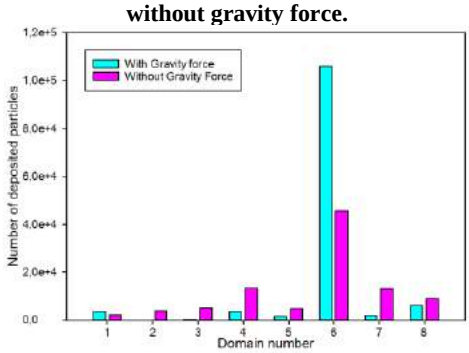

Figure 5. Comparison of number of deposited particles in different regions with and without gravity force.

ACKNOWLEDGEMENTS

This project was funded by the BOF- Ghent University, Belgium, and the Research Foundation Flanders through a post-doctoral grant (C. Debbaut; 1202418N).

REFERENCES

[1] Tempfer, C et al., Gynecologic Onc, 137:223–228, 2015.
[2] Willaert, W et al., Pleura Perit, 2: 121–128, 2017.
[3] Guhler, D et al., Surg. Endosc, 3: 1778-1784, 2016.
[4] Reymond, M et al., De Gruyter- 1st edition, 2014.
[5] Khosrawipour, V et al., Ann. Surg. Oncol, 23: 1220-1224,2016.
[6] Van De Sande, et al., Pleura and Peritoneum, 2018.
[7] Kakchekeeva, T et al., Ann Surg Oncol, 23: 592–598, 2016.

SB^{3}C2019
Summer Biomechanics, Bioengineering and Biotransport Conference
June 25 -28, Seven Springs, PA, USA

MICROTISSUES FOR BIOMECHANICAL INVESTIGATIONS OF ANGIOGENESIS

M.K. Sewell-Loftin (1), Priscilla Y. Hwang (1), Joshua B. Katz (1), Steve C. George (2), Gregory D. Longmore (1)

(1) Department Internal Medicine
Washington University School of Medicine in St. Louis
St. Louis, MO, USA

(2) Department of Biomedical Engineering
University of California, Davis
Davis, CA, USA

INTRODUCTION

Improving our understanding of the biomechanical factors that regulate tumor progression, including angiogenesis and metastasis, will permit the development of novel treatment strategies. Currently, the gold standard for cancer studies are murine models, which provide 3D physiological complexity but lack precise control over biomechanical parameters. On the other hand, many *in vitro* models permit high levels of control over mechanical inputs, however fail to exhibit the same level of complexity as *in vivo* systems. Microfluidic devices allow for a complex, 3D microenvironment that mimics *in vivo* systems while permitting improved control over multiple biomechanical parameters. The objective of this project was the development and optimization of microtissue system with independent inputs for multiple mechanical factors including spatiotemporal loading of cells and ECM-based gels, interstitial flow, and the transfer of mechanical strains between microtissues.

Cancer-associated fibroblasts (CAFs) have been shown to be key regulators of the tumor microenviroment, both in terms of secreted paracrine factors and reorganization of the ECM. Recent work in our group suggests that the mechanical behavior of CAFs is also an important factor in the growth of blood vessels, and that mechanically-inhibited CAFs cannot support vascularization in an *in vitro* model. As angiogenesis is necessary for tumor progression, an *in vitro* model allowing investigation of mechanobiological regulation of cancer-associated angiogenesis would elucidate how biomechanical factors promote tumor progression.

METHODS

Microfluidic devices were designed in AUTOCAD and generated using previously established techniques in our lab. To determine parameters for experiments, COMSOL modeling was employed to predict fluid flow patterns; experimental parameters were established to control interstitial flow between chambers. For validation, 70kDa dextran, tagged with either FITC or RhodamineB, was loaded into devices containing fibrin gels.

Angiogenesis studies were carried out by loading fibrin gels containing cells into the separate tissue chambers. On Day 0 – Normal Human Lung Fibroblasts (NHLFs) and umbilical cord blood-derived endothelial cells (ECs) were loaded into the central chamber only. On Day 4 – CAFs or normal breast fibroblasts (NBFs) were loaded separately into the side chambers in fibrin gels. The fibrin gel concentrations were maintained across the device at 10mg/mL. Several devices were loaded with NBFs or CAFs in one side chamber, with a blank fibrin gel (no cells) loaded in the opposing chamber as a control. On Day 8, the devices were fixed with 10% formalin and stained for CD31.

RESULTS

A multi-tissue chamber microfluidic device was designed to allow for control over multiple biomechanical inputs including interstitial flow, ECM and cell loading (Figure 1A). The devices I comprised of three tissue chambers connected via communication ports (4 per interface, ~20μm each), with each chamber having its own set of fluidic lines. Using COMSOL, two flow regimes were generated including a Top-to-Bottom Flow (Figure 1B) that prevented interstitial flow between chambers and an Outward Flow (Figure 1C) that permitted flow only from the center chamber two the two side chambers, with the goal of limiting diffusion of soluble factors from the side chamber to the center. Line tracings of fluid velocities in the models indicate that for the Outward Flow regime, interstitial flow levels peak ~ 0.1μm/s, which is considered a normal physiological rate.

To validate our flow models, fluorescently-tagged dextran was loaded into the chambers in the Top-to-Bottom regime and allowed to equilibrate for 24h (Figure 1D). Results indicate significantly higher FITC-dextran in the side chambers compared to the center chamber (Figure 1E, * $p < 0.01$) and significantly higher rhodamine B-dextran in the center compared to the outer chambers (Figure 1F, ^ $p< 0.01$). Following this quantification, the dextran solutions were removed and replaced with DPBS in the Outward Flow regime, demonstrating a "washout" effect of dextran. Importantly, there was almost no detectable FITC signal in the center chamber, indicating that FITC-dextran from the side chambers did not diffuse into the central chamber during the "washout" studies.

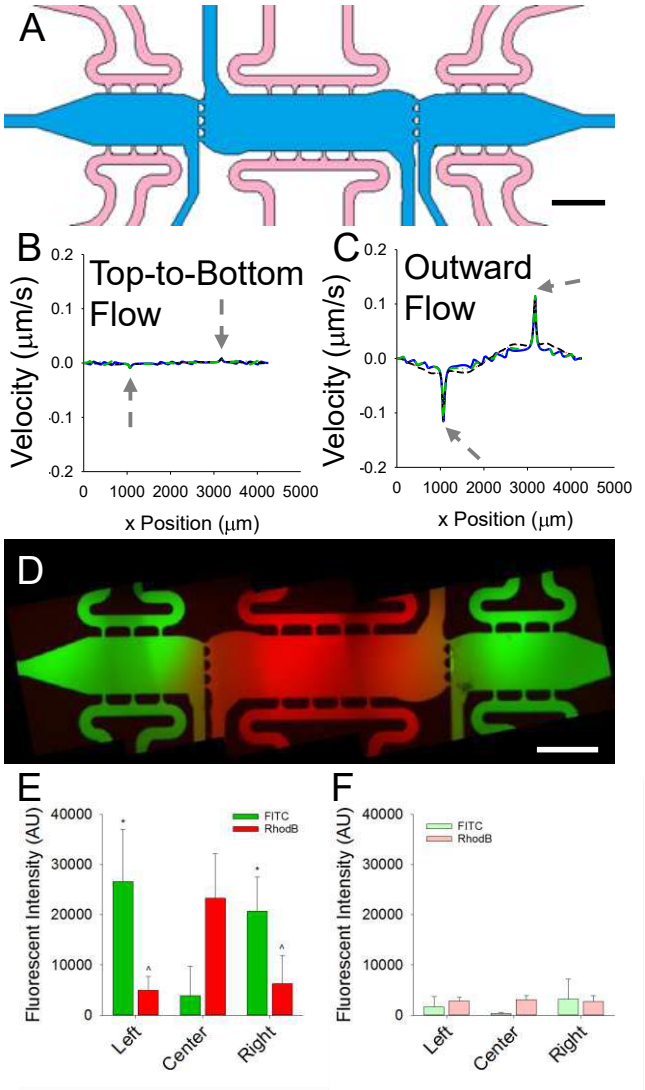

Figure 1: (A) Schematic of mutli-chambered device, with tissue chambers shown in blue; fluidic lines shown in pink. (B,C) Predicted interstitial flow velocities through communication ports. Grey arrows point to interfaces between tissue chambers for Top-to-Bottom Flow (B) or Outward Flow (C). (D) Fluorescent image of FITC- or RhodamineB-tagged dextran in multi-chamber device after 24h with Top-to-Bottom Flow. (E) Quantification of average fluorescent intensities in individual chambers of (D). * $p < 0.01$ and ^ $p < 0.01$ vs. center chamber. (F) Fluorescent intensities in individual chambers after 24h of Outward Flow with DPBS.

For angiogenesis studies, the NHLF and ECs in the central chamber supported self-assembled growth of a blood vessel network by Day4, when the side chambers were loaded. After 8 days, significant blood vessel occurred towards side chambers loaded with CAFs compared to NBFs (Figure 2A,B).

DISCUSSION

The microtissue design described in this project will allow for improved investigations of biomechanics in the tumor microenvironment. Our modeling and experimental flow studies demonstrate the ability to control flow across each tissue chamber and communication between chambers. With the Outward Flow regime, we suppressed diffusion from the side chambers toward the center chamber, thus limiting diffusion of paracrine factors secreted by CAF or NBFs into the center chamber for the angiogenesis studies. Even in the absence of these factors, the CAFs demonstrated higher levels of angiogenic potential compared to NBFs or blank control gels. The enhanced angiogenesis that occurred into the side chamber containing CAFs could be due to increased mechanical activity of CAFs compared to NBFs, supported by previous work in our group that demonstrates mechanical forces generated in the ECM can promote vascularization of a fibrin gel in the absence of secreted factors. Future studies will utilize fiducial markers in a bead tracking algorithm to determine the levels of cell-induced mechanical activity transmitted between tissue chambers. To eliminate soluble factors altogether, a series of studies utilizing magnetic beads to generate mechanical perturbations between chambers will also be completed.

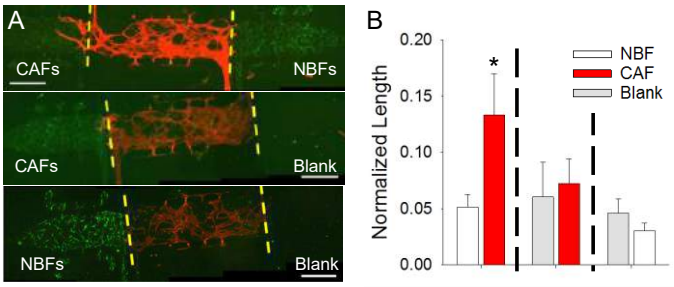

Figure 2: (A) Representative images of CD31 staining (red) in microtissues. CAFs and NBFs are shown in green. Yellow dashed lines represent interfaces between chambers. Scale bar = 500mm. (B) Quantification of vessel length in side chambers, normalized to vessel length in central chamber. * $p < 0.05$, $n > 5$ devices per condition.

ACKNOWLEDGEMENTS

The authors wish to acknowledge the following funding sources: K99-CA230202 (M.K.S.L.); R01-CM080673 (G.D.L); U54-CA143868 (G.D.L); UH3-T00048 (S.C.G); R01-CA170879 (S.C.G).

REFERENCES

[1] Hanahan, D et al, *Cell*, 144:646-674,2011. [2] Alspach, E et al, *Cancer Discovery*, 4:716-729;2014. [3] Calvo F, et al, *Nat Cell Bio*, 16: 148-168, 2011. [4] Moya, M et al, *Tissue Eng Part C*, 19: 730-737, 2013. [5] Sewell-Loftin, MK et al, *Sci Reports*, 7: 12574, 2017.

SB³C2019
Summer Biomechanics, Bioengineering and Biotransport Conference
June 25-28, Seven Springs, PA, USA

A ROBUST 3D CONSTITUTIVE MODEL FOR THE PASSIVE PROPERTIES OF LEFT VENTRICULAR MYOCARDIUM

David S. Li (1), Reza Avazmohammadi (1), Samer S. Merchant (2), Tomonori Kawamura (3)
Edward W. Hsu (2), Joseph H. Gorman III (3), Robert C. Gorman (3), Michael S. Sacks (1)

(1) Institute for Computational Engineering & Sciences
Department of Biomedical Engineering
The University of Texas at Austin
Austin, TX, USA

(2) Department of Biomedical Engineering
University of Utah
Salt Lake City, UT, USA

(3) Perelman School of Medicine
University of Pennsylvania
Philadelphia, Pennsylvania, USA

INTRODUCTION

The myocardium is a complex biocomposite of myocytes, extracellular matrix, and blood vessels, possessing an intricate structural hierarchy and exhibiting complex behavior at multiple length scales. It has been the focus of mathematical modeling for several decades. Myocardium's highly anisotropic nature demands a comprehensive 3D constitutive formulation in order for its mechanical properties to be fully captured in a model, and the tissue is commonly thought of as a locally orthotropic material at the tissue-level scale. Current modeling efforts have shown success in developing forms to fit mechanical testing datasets acquired from samples of left ventricular myocardium. However, the datasets used for fitting these models have been limited to narrowly defined deformation types that may not fully reflect the 3D variation present in the tissue or may not be appropriate for obtaining the most robust estimates of material parameters. Moreover, assessment of fitted models' ability to accurately predict behavior in non-physical states associated with disease has not been substantially explored.

To this end, we have previously implemented a theoretically-driven numerical-experimental methodology, based on optimal design of experiments, to obtain structural-mechanical measurements from ovine myocardium in full 3D. Using this optimal dataset and a well-established constitutive model for myocardium, we demonstrate the effects of incorporating multiaxial deformation modes and 3D material structure into our inverse modeling framework for parameter estimation, and we uncover possible kinematic mechanisms for the observed behavior of myocardial tissue.

METHODS

Experimental Approach

Specimens of healthy myocardium were harvested from a cohort of adult Dorset sheep (n=5), with euthanasia performed via rapid injection of potassium chloride. 1x1x1-cm cuboidal sections (Figure 1a) were cut out from the left ventricles and immediately placed in cardioplegic solution to relax into an unloaded state.

Each of the specimens was subjected to a comprehensive set of tensile, compressive, and shear deformations within our triaxial mechanical testing device (Figure 1b), specifically one-axis Simple Shear (SS) and two-axis Pure Shear (PS) deformation modes (Figure 1c), which were selected through optimal experimental design [1]. All tests were conducted immersed in cardioplegic solution maintained at 37°C, with multiple cycles in order to precondition the specimens.

Following testing, each specimen underwent diffusion tensor imaging (DTI) to determine their internal fiber structures, as measuring the diffusion of water molecules in tissue in response to magnetic fields

Figure 1: (a) Tissue specimen harvest. (b) Triaxial mechanical testing device. (c) 3D deformations. (d) Fiber structure of specimens (S1-S5). Abbreviations: left ventricle (LV), longitudinal (L), circumferential (C), radial (R), fiber (f), sheet (s), normal (n).

indicates the general orientation of myofibers within the sample. Each cuboid was scanned with magnetic field gradients of 600 mT/m. Encoding was performed along 48 directions with 500/19 TR/TE and a B-value of 800 s/mm, yielding a 40x33x38 matrix with a voxel resolution of 400 μm [2]. The fiber architecture of the specimens (Figure 1d) was determined through computing the eigenvectors in each voxel of the image using a custom MATLAB analysis routine.

Constitutive Modeling

The initial 3D constitutive model we used was introduced by Holzapfel and Ogden [3], in which the tissue features three mutually orthogonal material directions: **f**, (myo)fiber; **s**, sheet or cross-fiber; and **n**, normal to the fiber-sheet plane (Figure 1a). Formulated as a function of invariants of the right Cauchy-Green deformation tensor **C**, the strain energy ψ of the myocardium is described as

$$\psi = \frac{a}{2b}\exp\{[b(I_1-3)]-1\} + \sum_{i=\mathrm{f,s}}\frac{a_i}{2b_i}\{\exp[b_i(I_{4i}-1)^2]-1\} + \frac{a_{\mathrm{fs}}}{2b_{\mathrm{fs}}}\left[\exp\left(b_{\mathrm{fs}}I_{8\mathrm{fs}}^2\right)-1\right], \quad (1)$$

where $I_1 = \mathrm{tr}(\mathbf{C})$, $I_{4\mathrm{f}} = \mathbf{f}\cdot\mathbf{Cf}$, $I_{4\mathrm{s}} = \mathbf{s}\cdot\mathbf{Cs}$, and $I_{8\mathrm{fs}} = \mathbf{f}\cdot\mathbf{Cs}$ are invariants of **C**, and $\{a, b, \dots, a_{\mathrm{fs}}, b_{\mathrm{fs}}\}$ are fitted coefficients.

Parameter Estimation via Inverse Modeling

Our inverse modeling pipeline determines the optimal parameters needed to reproduce the experimental deformations with finite element simulations. Briefly, the optimal loading paths were prescribed onto a tetrahedral mesh whose elements were assigned material directions mapped from the DTI. The parameters for ψ were computed with nonlinear least-squares regression in order to match the model-computed stresses to experimentally measured stresses, with one set of parameters used to fit all protocols simultaneously. We first fit the model to a set of six SS protocols akin to the experiments performed by Dokos et al. [4]. The model was then fit to the optimal paths: three SS and three PS modes [1].

RESULTS

The maximum stress measured in triaxial testing bracketed a large range among specimens, especially in the PS modes. The fiber angle decreased from the endocardial to epicardial sides of the specimens. Interestingly, the fiber directions all showed a persistent "out of plane" component when projected onto the CL plane.

While the Holzafpel-Odgen model (Eq. 1) fit the six SS protocols, it was unable to capture the anisotropy in the optimal paths (Figure 2). Hypothesizing that the myocardium exhibits further modes of coupling, we incorporated additional 3D kinematics discussed in [3], extending the model to include all coupling invariant terms (I_{8ij}), given by

$$I_{8\mathrm{fn}} = \mathbf{f}\cdot\mathbf{Cn} \quad I_{8\mathrm{sn}} = \mathbf{s}\cdot\mathbf{Cn}, \quad (2)$$

to give the final form

$$\psi_{\mathrm{ext}} = \frac{a}{2b}\exp\{[b(I_1-3)]-1\} + \sum_{i=\mathrm{f,s}}\frac{a_i}{2b_i}\{\exp[b_i(I_{4i}-1)^2]-1\} + \sum_{i,j=\mathrm{f,s,n}}\frac{a_{ij}}{2b_{ij}}\left[\exp\left(b_{ij}I_{8ij}^2\right)-1\right], \quad (3)$$

which successfully fit all optimal paths (r^2=0.99) (Figure 2).

Using the identity $I_{8ij} = \lambda_i\lambda_j\cos\theta_{ij}$, we determined that the optimal loading paths cause both relative stretching (quantified by $\lambda_i\lambda_j$) and shearing (quantified by $\cos\theta_{ij}$) of fiber families in the **f**, **s**, and **n** directions, contributing to the stresses in the tissue. When examining the transmural distribution, we observed a considerable change in angle θ_{ij} throughout the specimen at maximum deformation (Figure 3).

Figure 2: Fit of the Holzapfel-Ogden model (Eq. 1) and extended model (Eq. 3) to the optimal triaxial data (black dots) of S4.

Figure 3: Distribution over transmural depth of relative stretches ($\lambda_i\lambda_j$), shearing ($\cos\theta_{ij}$), and change in angle ($\Delta\theta_{ij}$), at maximum deformation for fitted ψ_{ext} in PSCR. Subscripts: $i, j = \mathbf{f}, \mathbf{s}, \mathbf{n}$.

DISCUSSION

We applied an integrated method to determine material parameters for left ventricular myocardium using a full 3D kinematic approach incorporating transmurally varying 3D structure, leading to the first determination of material parameters for myocardium for a cohort of multiple ovine specimens. Investigation of the extended model (Eq. 3) suggested that the coupling between **f**, **s**, and **n** contained in the I_{8ij} invariants — namely, the shearing as quantified by $\cos\theta_{ij}$ — drives the need for these additional terms in order to capture the behavior of myocardium in multiaxial deformation modes. Interactions between myofibers and the surrounding collagen matrix could be a possible mechanism for these observations. Additionally, the behavior of myocardium in compression could become relevant for treatment interventions in which the heart wall is placed under non-physiological conditions, such as injection of biomaterials into the heart wall following heart attack. Ultimately, developing of more robust models in this manner will make them better suited for clinical evaluation.

ACKNOWLEDGEMENTS

NIH T32 EB007507 and F31 HL139113 to D.S.L., NIH K99 HL138288-01A1 and AHA 18CDA34110383 to R.A., and NIH R01 (HL068816, HL089750, HL070969, HL108330, HL063954) to M.S.S.

REFERENCES

[1] Avazmohammadi R et al., *Biomech Model Mechanobiol*, 17:31-53, 2018. **[2]** Abdullah O et al., *NMR Biomed*, 29:1338-1349, 2016. **[3]** Holzapfel G et al., *Philos Trans Royal Soc A*, 367:3445-3475, 2009. **[4]** Dokos et al., *Am J Physiol Heart Circ Physiol*, 283:H2650-9, 2002.

SB³C2019
Summer Biomechanics, Bioengineering and Biotransport Conference
June 25 -28, Seven Springs, PA, USA

FAST PREDICTIONS OF CARDIAC GROWTH DURING VENTRICULAR DYSSYNCHRONY

Pim J.A. Oomen (1), Colleen M. Witzenburg (1,2), Thien-Khoi N. Phung (1), Kenneth C. Bilchick (3), Jeffrey W. Holmes (1,3)

(1) Department of Biomedical Engineering
University of Virginia
Charlottesville, VA, USA

(2) Department of Biomedical Engineering
University of Wisconsin
Madison, WI, USA

(3) Department of Medicine
University of Virginia
Charlottesville, VA, USA

INTRODUCTION

In the US alone, over 5 million patients suffer from heart failure, a number that is projected to exceed 8 million by 2030 [1]. Heart failure increases the likelihood of conduction abnormalities such as left bundle branch block (LBBB), which causes uncoordinated contraction and dilation of the left ventricle, leading to reduced pump efficiency [2,3].

In the last two decades, cardiac resynchronization therapy (CRT) has emerged as a revolutionary therapy for patients with heart failure and LBBB. A CRT pacing device can restore coordinated contraction of the heart by electrically stimulating multiple locations at appropriate times. When it works, CRT can stop and even reverse the progression of heart failure, reducing the ventricle size and improving pump function. However, over 35% of patients still fail to respond to CRT [4]. One of the greatest strengths of CRT is that it can be customized to individual patients, offering the potential to improve patient response rates [3]. Yet this also presents a dilemma: there are far too many possible lead locations and pacing settings to test directly during the implantation surgery.

Computational models can address this challenge by rapidly screening many pacing options before the CRT device implantation takes place. These models could in theory be used to pre-identify pacing locations which lead not only to the best electrical and mechanical synchrony but also to the greatest long-term reduction in ventricular volume. Several finite element models have been published that are capable of predicting cardiac growth, even in response to LBBB [5]. However, these models are computationally expensive, making them impractical for routine clinical use.

In this study, we propose a computational framework that can provide fast, patient-specific predictions of cardiac growth after the onset of LBBB. Furthermore, we demonstrate that our model's initial growth predictions agree with previously published experimental data.

METHODS

Model of the heart and circulation

Mechanics of the left ventricle (LV) were modeled using a recently published compartmental model that was coupled to a circuit model of the circulation to simulate hemodynamics throughout the cardiac cycle [6]. A previously published active contraction model [7] was adapted for use in the compartmental model, while the passive material behavior was governed by an exponential relationship between LV pressure and volumetric strain. The parameters of the active and passive LV mechanical behavior were fitted to the average pressure-volume relationship of canine hearts studied previously by our laboratory [8].

Simulation of LBBB

The healthy LV wall contracts almost simultaneously, however LBBB is characterized by dyssynchronous mechanical activation of the LV wall [3,9]. Therefore, the LV was functionally split into 10 compartments [10]. All compartments shared the same pressure at any time throughout the cardiac cycle, while the compartment volumes summed to the total LV volume. This approach allowed us to set the time of onset of mechanical activation in each compartment, thus simulating LBBB. To determine the activation times for the simulations reported here, we used DENSE MRI [9] to measure the local time of onset for circumferential shortening throughout the LV wall in a dog one week after inducing LBBB using radiofrequency ablation. Baseline activation times were obtained from [9].

Strain-driven cardiac growth law

Cardiac growth was modeled by a published strain-based kinematic growth relation that allows for independent growth in the circumferential and radial direction [11]. This growth law was previously adapted for use in the compartmental model and calibrated

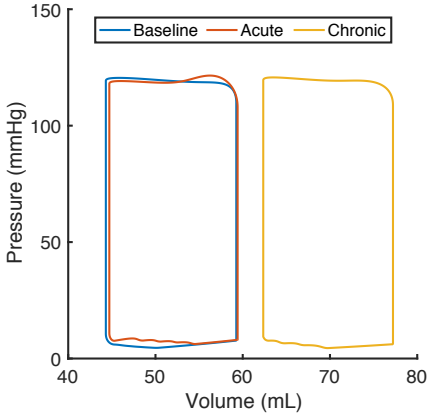

Figure 1: The pressure-volume relationship of the LV remained similar to baseline acutely after the onset of LBBB, but shifted to the right following growth.

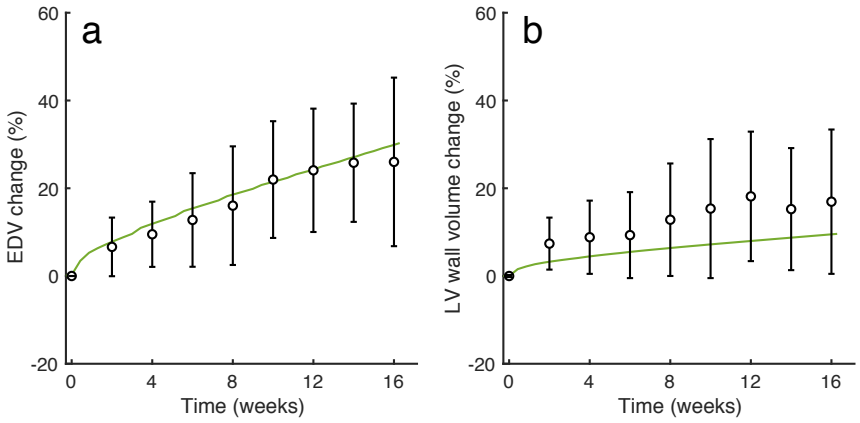

Figure 2: Predicted increases (green lines) in LV EDV (a) and wall volume (b)

based on experimental canine pressure and volume overload studies [6]. In brief, in each LV compartment, circumferential and radial strains were estimated from volumes for each compartment by assuming a thin-walled spherical geometry, and used to drive growth of the respective compartments. Dilation was driven by a change relative to baseline of the maximum circumferential strain during the cardiac cycle, whereas thickening was driven by a change of the maximum radial strain. No changes to the published growth parameters were made for this study.

Experimental data comparison

To validate our model, we compared our results to experimental data published by Vernooy et al. [2], who used radio frequency ablation to induce LBBB in dogs, and performed echocardiography measurements at baseline and every two weeks for 16 weeks after LBBB onset. These measurements were used to obtain changes in LV end-diastolic volumes (EDV) and wall volume at end-diastole. For comparison, we simulated 16 weeks of cardiac growth after the onset of LBBB in our fast computational model and predicted changes in LV EDV and wall volume, as well as pressure-volume loops.

RESULTS

16 weeks of strain-driven cardiac growth after the onset of LBBB were simulated in just under two minutes on a laptop computer. Our model results showed that, immediately after simulating LBBB, the pressure-volume loop of the total LV was similar to baseline (Figure 1). However, the changes in strain caused by LBBB led to increases in peak circumferential strain in many of the compartments and consequently caused cardiac growth (not shown). After 16 weeks of cardiac growth the pressure-volume loop shifted to the right.

Dilation was most pronounced in the latest activated compartments and was not accompanied by thickening. Without calibrating any of the growth parameters, the model-predicted evolution of EDV closely matched the experimental results (Figure 2a). The change in LV wall volume at end diastole fell well within the standard deviation of the experimental results (Figure 2b).

DISCUSSION

The goal of this study was to develop and test a fast computational framework to predict cardiac growth during ventricular dyssynchrony. The initial results of this model matched previously reported experimental results. Strikingly, this was achieved without calibrating any of the growth parameters, instead using parameters that were previously fitted to pressure and volume overload data [6]. In contrast, a previously published anatomically realistic finite-element model was only able to correctly capture growth during LBBB after changing hemodynamic parameters [5]. Moreover, the finite-element model was required to run for 3 weeks on a cluster with 12 6-core processors to simulate 4 weeks of growth [5,6], whereas our model simulated 16 weeks of cardiac growth in just under two minutes on a laptop computer, making it suitable for routine clinical use.

The current model still includes several limitations. First, wall thickening was not observed in our model, but is known to occur in late-activated regions of the LV wall during LBBB. This probably caused the underestimation of the wall volume increase shown in Figure 2b. Second, parameter sensitivity studies suggest that the choice of activation pattern and passive material properties of the myocardium strongly affect strain and therefore growth, which in our model is driven by strain. Third, for the present study the activation pattern of a single dog was obtained and simulated and compared to mean results from a separate study. Additional subject-specific, matched activation patterns and growth outcomes should be used to further test the model.

In conclusion, in the present study we demonstrated that cardiac growth, in particular LV dilation, during dyssynchrony can be predicted using a fast computational model. While this work represents just the first step towards predicting patient-specific CRT responses, we believe both the results and the time frame required to customize and run this model suggest promise for this approach in a clinical setting.

ACKNOWLEDGEMENTS

This work was supported by funding from the National Institutes of Health (HL127654) and the Seraph Foundation.

REFERENCES

[1] Mozaffarian et al., *Circulation*, 113:e38-e360, 2016
[2] Vernooy et al., *Eur Heart J*, 26(1):91-98, 2005.
[3] Bilchick et al., *J Am Coll Cardiol*, 63(16):1657-1666, 2014.
[4] Chung et al., *Circulation*, 117:2608-2616, 2008.
[5] Kerckhoffs et al., *Europace*, 14:v65-v72, 2012.
[6] Witzenburg et al., *J Cardiovasc Trans Res*, 11(2):109-122, 2018.
[7] Kerckhoffs et al., *J Eng Math*, 47:201–216, 2003.
[8] Fomovsky et al., *Circ Heart Fail*, 5(4):515-522, 2012.
[9] Auger et al., *J Magn Reson Imaging*, 46(3):887-896, 2017.
[10] Sunagawa et al., *Circ Res*, 52(2):170-178, 1983.
[11] Kerckhoffs et al., *Mech Res Commun*, 42:40-50, 2012.

SB³C2019
Summer Biomechanics, Bioengineering and Biotransport Conference
June 25 -28, Seven Springs, PA, USA

ROLE OF TALIN1 IN CARDIAC FIBROBLASTS ON CARDIAC HYPERTROPHY

Natalie, A. Noll (1), Qinkun Zhang (2), Hind Lal (2), W. David Merryman (1)

(1) Department Of Biomedical Engineering
Vanderbilt University
Nashville, TN, USA

(2) Department of Cardiovascular Medicine
Vanderbilt University
Nashville, TN, USA

INTRODUCTION

Cardiovascular disease is the underlying cause of 30.8% of all deaths in the United States annually, and continues to be the leading cause of mortality worldwide [1], [2]. Over 5.6 million adults in the United States live with congestive heart failure (HF), and nearly half will die within five years of diagnosis [3], [4]. HF patients often experience chronic left ventricular (LV) pressure overload leading to concentric hypertrophy of the LV. This persistent wall thickening leads to a reduction in LV volume, increased ventricle stiffening, and reduced elasticity resulting in diastolic dysfunction. Following injury, tissue-resident cardiac fibroblast (CF) activation occurs through a combination of mechanical strain, ventricle wall stress, and various pro-fibrotic signals such as transforming growth factor, fibroblast growth factor , and Wnt resulting in CF proliferation and switching toward a myofibroblast (MyoFB) phenotype [5], [6]. MyoFBs maintain a contractile, hyper-secretory phenotype characterized by increased α-smooth muscle actin (αSMA) and SM22α expression with excessive deposition of extracellular matrix proteins, such collagens and fibronectin. Altogether, MyoFB activity can result in increased ECM deposition resulting in increased interstitial fibrosis in the context of HF.

Talin is a focal adhesion protein that activates integrins by binding to the cytoplasmic β1 domain, resulting in increased integrin affinity for ECM ligands. CFs express two forms of Talin, with Talin1 (Tln1) being the most highly expressed. Tln1 undergoes force-induced mechanical unfolding, wherein conformational changes expose binding sites for additional focal adhesion proteins, such as vinculin, paxillin, and α-actinin [7]. This is critical for the mechanotransduction of force from the ECM to the cell's cytoskeleton and vice versa. Tln1 has been implicated in disease through modulation of integrin activation and mechanotransduction resulting in altered fundamental processes such as focal adhesion assembly, cell spreading, migration, and survival [8]. Vinculin, a binding partner of Tln1, has been shown to promote ECM fiber formation and alignment in collagen matrices. We hypothesize that MyoFB-specific deletion of Tln1 will reduce ECM matrix deposition, resulting in a decrease in interstitial fibrosis, LV hypertrophy, and preserved cardiac function in the context of HF.

METHODS

CFs were isolated from WT mice for *in vitro* experiments. XtremeGene was used to knock down Tln1 in CFs ($Tln1^{-/-}$), resulting in a 40% KD of Tln1 transcription after 48h. Control cells were treated with scramble siRNA. Cells were plated on Fibronectin treated BioFlex® culture plates after 24 hours of XtremeGene treatment and incubated for 24 hours to allow a monolayer of cells to form. Cells were placed in the FX-4000™ Tension System at 10% equibiaxial strain for 24 hours.

A tamoxifen-inducible periostin Cre mouse was bred with a $Tln1^{fl/fl}$ mouse for MyoFB specific deletion of Tln1 following injury (denoted CKO for condition knockout). Transverse aortic constriction (TAC), a model of pressure overload induced HF, was induced in WT and Tln1 CKO mice by permanent transverse aortic constriction with a 25-guage needle. Hearts were extracted 42 days post-TAC and mRNA was extracted from the flash frozen LV using TRIzol. qPCR was performed to detect transcriptional differences in tissue amongst the sham and different genotypes.

RESULTS

$Tln1^{-/-}$ and WT CFs were exposed to 10% equibiaxial strain for 24 hours. qPCR analysis after 24 hours indicated a statistically significant decrease in the relative expression of *Tln1*(schematic shown in **Fig. 1A**). This decrease coincides with a decrease in *Fn1*, with no change in *αSMA* relative expression (**Fig. 1B**). Due to a decrease in *Fn1* mRNA

expressional in Tln1$^{-/-}$ CFs, Tln1 deletion was investigated in mice in the context of the HF model TAC.

42-days following TAC, pictures taken after sacrifice showed WT mice have a significant increase in heart size as compared to Tln1 CKO mice and sham animals (**Fig. 2**). This data demonstrates that Tln1 deletion alters CF morphology in response to pressure overload induced injury.

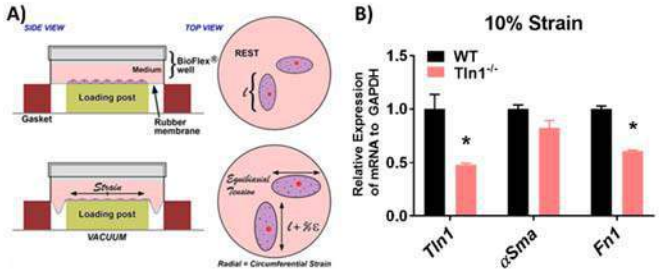

Fig. 1: A) Biaxial Strain Device B) Transcription of proteins by WT and Tln1$^{-/-}$ CFs under 10% biaxial strain. *p < 0.05.

qPCR analysis of the LV revealed an approximant 7-fold increase in transcription of the HF marker atrial natriuretic peptide (*Anp*) in the LV of WT mice as compared to sham controls (**Fig. 3A**). Furthermore, a significant reduction of *Anp* transcription back to the level of sham animals was observed in Tln1 CKO mice (**Fib. 3A**). Preliminary data show collagen1a2 (*Col1a2*), collagen3a1 (*Col3a1*), insulin-like growth factor (*Igf1*) and *αSMA* transcription levels in WT mice correlated with *Anp* transcription 42-days post TAC (**Fig. 3B**) suggesting that during HF in WT animals, these is an increase in transcription of ECM related proteins.

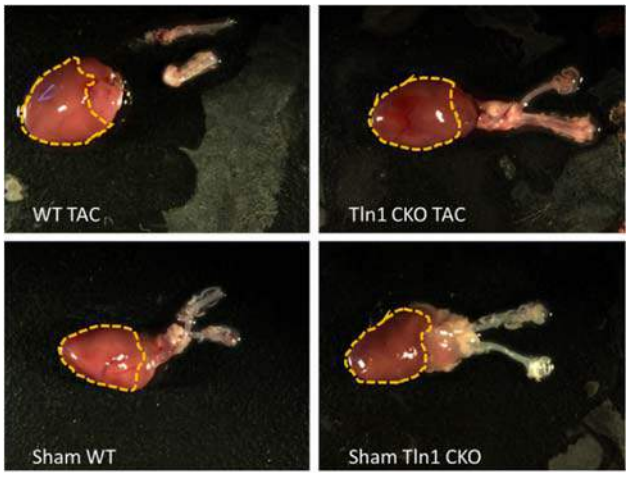

Fig. 2: Hearts and carotid arteries imaged at 1.36 times real size 42-days post TAC or Sham procedures. Ventricles are outlined in yellow.

DISCUSSION

Our initial *in vitro* findings implicate that reduction of Tln1 expression in CFs can change MyoFB phenotype under strained conditions. The reduction of *Fn1* mRNA expression in Tln1$^{-/-}$ points to Tln1 as a potential target to reduce fibrosis in the heart. As interstitial fibrosis during heart failure causes increased ventricular wall stiffening resulting in diastolic dysfunction, we believe modulating fibrosis through Tln1 is a viable approach to limit damage during pressure induced HF.

We have found that 42-days following TAC WT mice have increased ventricular size as compared to sham animals indicating hypertrophy of the ventricles occurred. Furthermore, WT TAC mice have a significant increase in the HF marker *Anp*. Both ventricular hypertrophy, and expression of *Anp* were reduced in Tln1 CKO TAC mice demonstrating that Tln1 deletion in CFs alters the heart at a tissue and cellular level in response to injury. We expect upon further analysis to see a decrease in cardiomyocyte (CM) size in the Tln1 CKO TAC mice as compared to WT TAC mice, as an increase in CM size is the main cause of ventricular hypertrophy during disease.

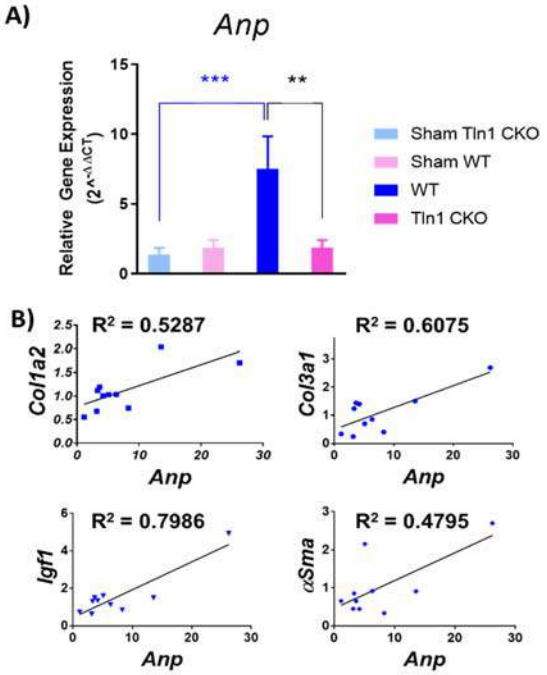

Fig. 3: mRNA transcription in the LV of mice 42-days post-TAC A) *Anp* transcription in the LV B) WT mice correlation of *ANP* with *Col1a1, Col3a1, Igf1,* and *αSMa.* ** p ≤ 0.01, *** p ≤ 0.001.

Finally, we have identified that mRNA expression of *Col1a2, Col3a1, Igf1,* and *αSMA* correlate with the mRNA expression of *Anp*. The correlation of ECM related proteins to *Anp* in WT TAC mice proposes that there is also an increase in deposition of these ECM proteins during HF. This data suggests that with a decrease in mRNA expression of *Anp*, as seen in the Tln1 CKO TAC mice, a decrease in the mRNA expression and deposition of ECM proteins may occur, resulting in a decrease in the interstitial fibrosis seen in HF.

Further exploration into the mechanical effects of Tln1 genetic deletion in CFs following TAC will provide insight into the utility of targeting Tln1 as a therapeutic approach for improve the outcomes of HF.

ACKNOWLEDGEMENTS

This work was funded by the NIH (R35-HL135790).

REFERENCES

[1] E. J. Benjamin et al, *J. Am. Heart Assoc., Circulation*, 135, 2017.
[2] National Center for Health Statistics, 2014.
[3] V. L. Roger *et al.*, *JAMA*, 292:344, 2004.
[4] N. Center for Health Statistics, 2011.
[5] J. Davis et al., *J. Mol. Cell. Cardiol.*, 70:9–18, 2014.
[6] O. Kanisicak *et al.*, *Nat. Commun.*, 7:12260, 2016.
[7] A. Haage *et al.*, *Cell Rep.*, 25: 2401–2416, 2018.
[8] R. Lugano *et al.*, *J. Clin. Invest.*, 128:3280–3297, 2018.

MODELING OF ANISOTROPIC REVERSE CARDIAC GROWTH IN RESPONSE TO LOCAL ALTERATION OF ELECTROMECHANICS

Jayavel Arumugam (1), Ghassan Kassab (2), Lik Chuan Lee (1)

(1) Department of Mechanical Engineering
Michigan State University
East Lansing, MI, USA

(2) California Medical Innovations Institute
San Diego, CA, USA

INTRODUCTION

We recently developed a cardiac growth and remodeling (G&R) constitutive model capable of describing both cellular hypertrophy and atrophy[1] that are driven by deviation from a homeostatic fiber stretch value. This model is able to predict reverse remodeling in the left ventricle (LV) when the mechanical loading is decreased. Often viewed as a favorable clinical course after heart failure (HF) treatments[2], reverse remodeling, in the form of a reduction in LV volume after CRT implantation, has been shown to be a strong predictor of lower long-term mortality and HF events[3]. While the G&R constitutive model takes into account all the mechanical states during the entire cardiac cycle, it does not describe anisotropic G&R that is necessary to reproduce asymmetric changes associated with local remodeling and reverse remodeling in the myocardium under various pacing conditions[4]. Here, we overcome this limitation by extending the reverse constitutive model to account for anisotropic growth. Specifically, we apply the model to investigate asymmetric G&R in a biventricular geometry due to alterations in electromechanics. We show that the long-term predictions of the coupled electromechanics-growth model are consistent with previous experimental studies and clinical observations[5,6] suggesting that it is possible to capture G&R features using only myofiber stretch as a stimulant.

METHODS

We let $\chi_{\kappa_0}(\boldsymbol{X}, t)$ describe the mapping from an unloaded (stress-free) reference configuration κ_0 with material point position $\boldsymbol{X}$ to a current configuration κ with the corresponding material point position $\boldsymbol{x} = \chi_{\kappa_0}(\boldsymbol{X}, t)$. The deformation gradient tensor, corresponding to a displacement field $\boldsymbol{u}(\boldsymbol{X})$, can be defined as $\boldsymbol{F} = \frac{\partial \chi_{\kappa_0}}{\partial \boldsymbol{X}}$. Under the

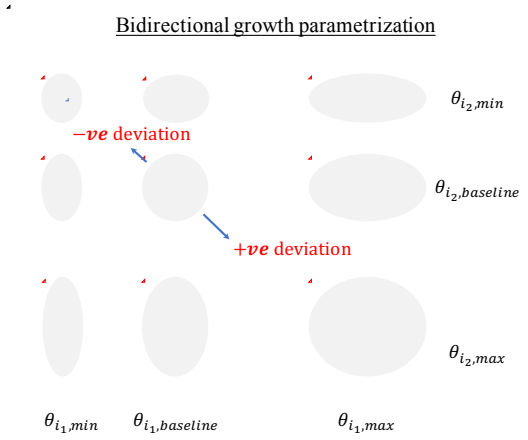

Figure 1: Schematic of anisotropic growth evolution.

volumetric growth framework[7], we considered a multiplicative decomposition of the deformation gradient tensor into an elastic component $\boldsymbol{F}_e$ and an incompatible growth component $\boldsymbol{F}_g$ i.e.,

$$\boldsymbol{F} = \boldsymbol{F}_e \boldsymbol{F}_g. \tag{1}$$

The growth deformation gradient $\boldsymbol{F}_g$ was parametrized by the growth multipliers θ_f, θ_s, and θ_n, i.e.,

$$\boldsymbol{F}_g = \theta_f \, \boldsymbol{f}_0 \otimes \boldsymbol{f}_0 + \theta_s \, \boldsymbol{s}_0 \otimes \boldsymbol{s}_0 + \theta_n \, \boldsymbol{n}_0 \otimes \boldsymbol{n}_0, \tag{2}$$

where $\boldsymbol{f}_0$, $\boldsymbol{s}_0$, and $\boldsymbol{n}_0$ are local myofiber, sheet, and normal directions in the reference configuration.

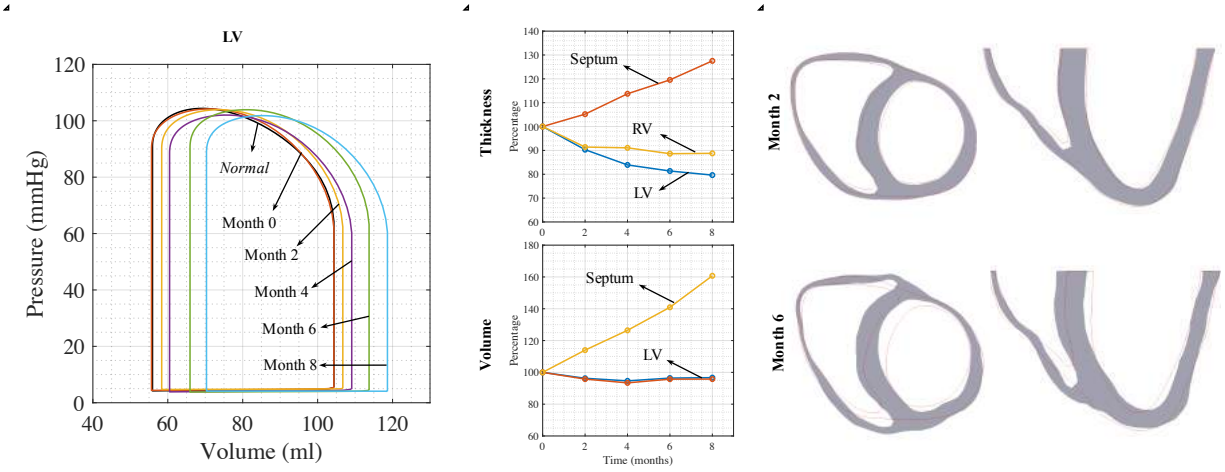

Figure 2. (Left) Evolution of left ventricular hemodynamics. (Middle) Evolution of regional volume and thickness. (Right) Geometry changes in mid short-axis and long-axis views.

Growth evolution was prescribed based on deviations of the fiber stretch λ_f from its homeostatic value $\lambda_{f,h}$, both taken with respect to the end-diastolic configuration. Specifically, the evolution of growth multipliers was of the form[1]

$$\dot{\theta}_i = k_i(\theta_i, \lambda_f) \text{ for } i = f, s, n, \tag{3}$$

where $\dot{(\ )}$ is the derivative with respect to time t, $k_i(\theta_i, \lambda_f)$ is a growth limiting function. The rate limiting function was defined as follows

$$k_i(\theta_i, \lambda_f) = \begin{cases} \frac{1}{\tau_{g,i}}\left(\frac{\theta_{max,i}-\theta_i}{\theta_{max,i}-\theta_{min,i}}\right)^{\gamma_{g,i}}(\lambda_f - \lambda_{f,h}) & \text{if } \lambda_f - \lambda_{f,h} \geq 0 \\ \frac{1}{\tau_{rg,i}}\left(\frac{\theta_i-\theta_{min,i}}{\theta_{max,i}-\theta_{min,i}}\right)^{\gamma_{rg,i}}(\lambda_f - \lambda_{f,h}) & \text{if } \lambda_f - \lambda_{f,h} < 0 \end{cases} \tag{4}$$

where subscript $i = f, s, n$ denote the association with the fiber, sheet, and normal directions. Parameters $\tau_{g,i}$, $\tau_{rg,i}$, $\gamma_{g,i}$, and $\gamma_{rg,i}$ control the rates of growth and reverse growth, respectively. The main purpose of the rate-limiting function is to restrict the evolution of the growth multipliers θ_i to lie within some prescribed limits[8] (**Figure 1**). We adopted a similar approach to separate the time scale as described in Lee et al.,[4] to integrate G&R with the electromechanics model.

Two cases differing in terms of the prescribed activation initiation location were simulated:

1. *Normal* : activation was initiated at the septum near the base,
2. *LVFW*: activation was initiated at the left ventricular free wall (LVFW) near the base.

RESULTS

There was no immediate substantial reduction in the pump function in the *LVFW* case (0 month). Changes were, however noticeable starting at 2 months in the form of a progressive LV dilation (**Figure 2**). Specifically, in the span of six months, LV end-diastolic volume (EDV) increased from 104.3ml to 113.7ml whereas end-systolic volume (ESV) increased from 55.65ml to 70.3ml. This led to a rightward shift in the LV pressure-volume (PV) loop that was accompanied by a slight change in ejection fraction (EF) from 48.7 % to 47.8 % in 6 months.

With appropriate calibration of the rate constants, the anisotropic G&R constitutive model predictions are quantitatively comparable to local and global measurements in a canine experiment with similar chronic LVFW pacing protocol[6]. In that experiment, both LV end diastolic volume and wall volume increased by 27±15 % and 15±17 %, respectively, after 6 months of pacing. Locally, the early-activated LVFW became significantly thinner by 17±17 % and the late-activated septum thickened by 23±12 % in that duration. These changes were associated with a significant increase in the cardiomyocyte diameter (18±7 %) at septum than that in LVFW. Our G&R constitutive model predicted comparable changes in global geometrical features in the form of an increase in LV end diastolic volume (9 %), wall volume (9.5 %). Comparable changes in local geometrical features were also captured by our model, which predicted an increase in septum thickness (18.5 %) and a decrease in LVFW thickness (19.7 %) (**Figure 2**).

DISCUSSION

Some of the chronic effects of LVFW pacing predicted by our model are also found in LBBB[9], which produces mechanical dyssynchrony via an opposite activation pattern (i.e., septum is activated first follows by the LVFW). Similar to LVFW pacing, LBBB is typically associated with a significant increase in LV end diastolic volume (126.6±19.3 %) in four months that is accompanied by the thickening of the late activated region and a thinning of early activated region. In contrast, LV ejection fraction decreases in LBBB (from 43±4 % to 33±6 %), which suggests that the associated asymmetrical hypertrophy may be different.

Future simulation studies on ischemic left and right bundle branch blocks cases using various pacing locations such as biventricular, right ventricular apex, His bundle, LV apex, etc., may help identify and optimize pacing locations. Such multiscale G&R simulation studies could be significant given that short-term clinical effects of pacing are not correlated with long-term outcomes[3].

ACKNOWLEDGEMENTS

This work was supported by NIH (R01 HL134841, U01 HL133359-01A1), NSF 1702987, AHA 17SDG33370110.

REFERENCES

1. Lee et al., *Biomech Model Mechanobiol*, 14(2):217-229, 2015.
2. Koitabashi N, Kass DA, *Nat Rev Cardiol*, 9:147, 2011.
3. Auricchio A, Prinzen FW, *Circ J*, 75(3):521-527, 2011.
4. Lee et al., *Biomech Model Mechanobiol*,15(4):791-803, 2016.
5. Prinzen et al., *Am Heart J*, 130:1045-1053, 1995.
6. van Oosterhout et al., *Circulation*, 98(6):588-595, 1998.
7. Rodriguez et al., *J Biomech*, 27(4):455-467, 1994.
8. Lubarda VA, Hoger A, *Int J Solids Struct*, 39(18):4627-4664, 2002.
9. Vernooy et al, *Eur Heart J*, 26:91-98, 2005.

SB³C2019
Summer Biomechanics, Bioengineering and Biotransport Conference
June 25-28, Seven Springs, PA, USA

THE EFFECT OF COLLAGEN HETEROGENEITY ON RAT MYOCARDIAL INFARCT MECHANICS IN A MULTISCALE FIBER NETWORK MODEL

C. Korenczuk (1), W. Richardson (2), V. Barocas (1)

(1) Department of Biomedical Engineering
University of Minnesota – Twin Cities
Minneapolis, MN, USA

(2) Department of Bioengineering
Clemson University
Clemson, SC, USA

INTRODUCTION

Myocardial infarction is a prevalent cardiovascular event that occurs when there is insufficient blood flow to cardiac muscle, causing myocardial damage. The healing process replaces necrotic myocytes with collagenous scar, resulting in remodeling that affects the mechanical behavior of the infarct and surrounding myocardial tissue. The changes in cardiac mechanics are often complex, and they are highly dependent on the orientation and composition of the microenvironment. Previous work has demonstrated that infarct structure can by quite heterogeneous with stark spatial variations in collagen orientations [1,2].

It is known that the microscale plays an important role in myocardial mechanics, but there remains a significant need to understand how microscale fiber alignment and architecture affect overall tissue behavior in infarcted myocardial tissue. In this study, we use collagen fiber orientation maps from infarcted rat tissue sections to study the effect of network orientation by simulating biaxial extension with 3 different networks in a multiscale finite-element model.

METHODS

Post-infarction rat myocardial tissue was sectioned into 7 μm-thick square pieces (6mm x 6mm) and stained with picrosirius red in a previous study to obtain collagen fiber orientation maps (Fig. 1A) [1]. Due to the small section thickness, tissue was not present in some areas, and fiber orientation was not measured in those regions. A linear interpolation was performed on the fiber orientation scatter data to produce a full fiber orientation map for the entire sample (Fig. 1B).

A 26x26x1 finite-element mesh was created for each tissue piece by extruding the square to a thickness of 0.25 mm, resembling a 3-dimensional tissue slab. 3 different types of network (Fig. 2) were

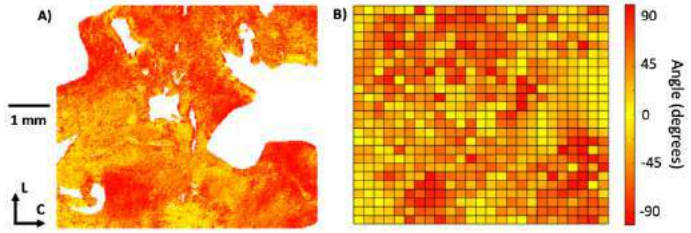

Figure 1: A) Fiber alignment map of myocardial infarcted tissue. Arrows indicate the circumferential (C) and longitudinal (L) directions. Angle in degrees is measured relative to the circumferential direction. Scale bar applies to both images. **B)** Interpolated grid of fiber alignment to fill in missing fiber information.

created to compare the effects of network orientation: 1) the same isotropic network used for every element (*isotropic* case), 2) the same aligned network used for every element, where the network was aligned in the average fiber direction for the whole sample (*homogeneous* case), and 3) differently aligned networks for each finite element based on the local fiber orientation in the area of the finite element (*heterogeneous* case). Networks were comprised of collagen fibers and a neo-Hookean component, to resemble nonfibrous material.

The network for the homogeneous case was aligned according to the overall sample orientation tensor [3],

$$T^{(sample)} = \frac{1}{1+\sum_1^N \alpha^{(el)}}\left(\frac{1}{2}I + \sum_1^N \alpha^{(el)} T^{(el)}\right) \qquad (1)$$

where $T^{(sample)}$ is the sample orientation tensor, N is the number of finite elements, $\alpha^{(el)}$ is the degree of alignment for each element

(ranging from 0-1, 0 = no alignment, 1 = fully aligned), I is the identity matrix, and $T^{(el)}$ is the orientation tensor for each element. The average fiber orientation was 43° relative to circumferential, and the degree of alignment was 0.36. The heterogeneous networks were created according to the orientation tensor for each element ($T^{(el)}$), where $T^{(el)}$ was of the same form as (1), created by averaging over the space of each individual finite element instead of the entire sample.

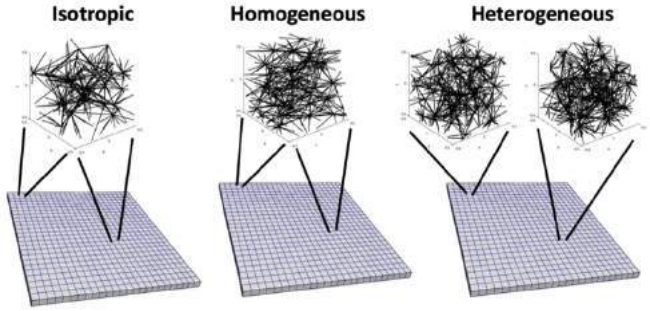

Figure 2: Isotropic (left), homogeneous (middle), and heterogeneous (right) network cases shown for the biaxial multiscale simulations.

A custom multiscale model (discussed extensively in [4]) was used to simulate equibiaxial extension of the square tissue piece for each network case. The edges of the tissue square were pulled to a final strain of 25%, with no shear stress on the boundaries.

RESULTS

Equibiaxial extension exhibited significantly different results for each of the 3 network cases (Fig. 3). The isotropic and homogeneous network case displayed a homogeneous stress and displacement field through the tissue square at 25% strain, while the heterogeneous network case exhibited significant stress and strain heterogeneity through the sample. The average von Mises stress in the isotropic case (79.19 kPa) was lower than the homogeneous (163.20 kPa) and heterogeneous cases (152.28 kPa), and the heterogeneous case exhibited the highest maximum stress (324.13 kPa) compare to the two other cases (163.39 kPa for homogeneous, 79.20 kPa for isotropic).

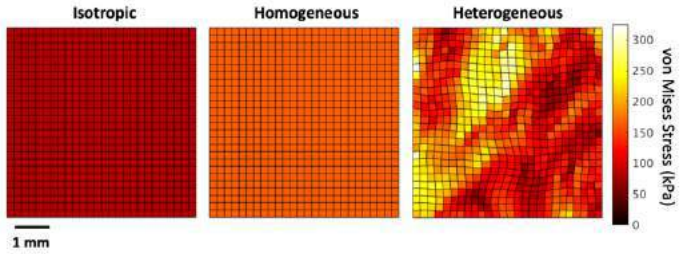

Figure 3: von Mises stresses shown at 25% equibiaxial strain for isotropic (left), homogeneous (middle), and heterogeneous (right) cases.

First Piola-Kirchhoff (PK1) stresses in the circumferential (S_{CC}) and longitudinal (S_{LL}) directions also showed differences between the 3 networks cases (Fig. 4). PK1 stresses in the isotropic case were similar in both directions, while the homogeneous and heterogeneous cases displayed anisotropy, having higher stresses in the circumferential direction compared to longitudinal. The homogeneous case reached the highest PK1 stress in the circumferential direction (943.84 kPa), compared to the lower PK1 stresses in heterogeneous (807.05 kPa) and isotropic (431.33 kPa) cases at 25% strain.

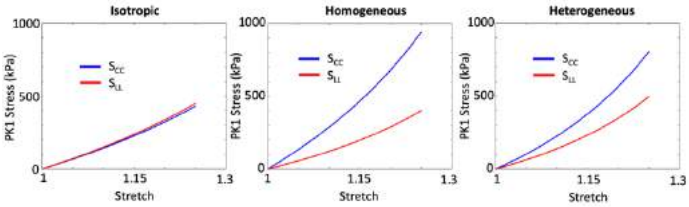

Figure 4: PK1 stresses averaged over the whole sample for the circumferential (blue) and longitudinal (red) directions for isotropic (left), homogeneous (middle), and heterogeneous (right) cases.

DISCUSSION

These results highlight the importance of the underlying tissue microenvironment, and its contribution to the overall macroscale mechanical behavior. By studying these 3 different network cases, our work shows that fiber orientation can significantly change the behavior of myocardial infarct tissue.

The von Mises stress field for the isotropic and homogeneous network cases was, as expected, homogeneous throughout, with minor differences in the maximum and minimum stresses exhibited. The homogeneous network case exhibited anisotropy, however, when comparing the directional circumferential and longitudinal stresses. Tissue anisotropy was expected, as the homogeneous network case had an alignment slightly closer to the circumferential direction.

The heterogeneous network case exhibited heterogeneity in the von Mises stress field, as well as the displacement field. Interestingly, areas of higher von Mises stress were seen in locations close to networks which were more closely aligned to the longitudinal direction. The heterogeneous network case exhibited similar anisotropy to the homogeneous network case when comparing circumferential and longitudinal PK1 stresses. The anisotropy was less pronounced in the heterogeneous case, however, which is most likely due to the heterogeneity allowing stiff and compliant sections to distribute displacements so as to reduce the overall anisotropy, similar to effects seen by Picu [5,6]. Thus, the heterogeneity leads to an increase in local stresses but a decrease in the global averaged anisotropy (and, to a lesser extent, stiffness).

Overall, this study shows how local network orientation plays an important role in the mechanics of scar tissue. Though fiber orientation is not necessarily always readily available, this work shows the need to consider network orientation when studying the mechanics of myocardial infarct tissue.

ACKNOWLEDGEMENTS

This material is based upon work supported by the National Science Foundation Graduate Research Fellowship Program under Grant No. 00039202 (CEK) and NIH grant U01 HL139471. CEK is a recipient of the Richard Pyle Scholar Award from the ARCS Foundation. The authors acknowledge Jeff Holmes and the Cardiac Biomechanics Group at the University of Virginia for the images, and the Minnesota Supercomputing Institute for computational resources.

REFERENCES

[1] Fomovsky & Holmes. (2010): AJP Heart Circ Physiol 298 (2010): H221-H228. [2] Richardson & Holmes. Biophysical J 110.10 (2016): 2266-2277. [3] Zarei, Vahhab, et al. Biomech & Modeling in Mechanobiology 16.4 (2017): 1425-1438. [4] Witzenburg, Colleen M., et al. J of Biomech Eng 139.3 (2017): 031005. [5] Picu, R. C. Soft Matter 7.15 (2011): 6768-6785. [6] Hatami-Marbini & Picu. Physical Review E 80.4 (2009): 046703.

SB³C2019
Summer Biomechanics, Bioengineering and Biotransport Conference
June 25 -28, Seven Springs, PA, USA

ANALYZING THE BIOMECHANICAL RESPONSE OF FAILING RIGHT VENTRICULAR TISSUE TO SACUBITRIL/VALSARTAN TREATMENT

Danial Sharifi Kia (1), Claire Tushak (1), Evan Benza (4), Kang Kim (1,2,3,4,5), Marc A. Simon (1,3,4,5)

(1) Department of Bioengineering, University of Pittsburgh, Pittsburgh, PA, USA

(2) Center for Ultrasound Molecular Imaging and Therapeutics, University of Pittsburgh, Pittsburgh, PA, USA

(3) Division of Cardiology, School of Medicine, University of Pittsburgh, Pittsburgh, PA, USA

(4) Heart and Vascular Institute, University of Pittsburgh Medical Center (UPMC), Pittsburgh, PA, USA

(5) McGowan Institute for Regenerative Medicine, University of Pittsburgh, Pittsburgh, PA, USA

INTRODUCTION

Pulmonary hypertension (PH) is a disease resulting in increased right ventricular (RV) afterload, ventricular remodeling and myocardial hypertrophy [1]. Pressure overload due to PH results in increased RV contractility as well as increased end-systolic and end-diastolic volumes, which if left unchecked leads to decreased RV contractility and RV failure [1]. From a biomechanical standpoint, RV myocardium experiences increased stiffness and fiber remodeling in PH which results in increased anisotropy in certain anatomic directions. This is also partly due to decreased transmural variation of myocardial fiber architecture in PH [1]. RV failure remains the main cause of mortality for PH patients, with 34-66% survival rates at 5 years post-diagnosis [2]; however, few studies have aimed to characterize the effects of PH on RV structure and function [1,3]. To date, lung transplantation remains the only curative treatment for PH.

Sacubitril/Valsartan (Sac/Val; also known as LCZ696) is a dual acting drug composed of a 1:1 mixture of neprilysin inhibitor Sacubitril and angiotensin receptor blocker Valsartan [4]. While previous hypertension therapeutics include angiotensin receptor blockers and target the renin-angiotensin-aldosterone system (RAAS), Sacubitril/Valsartan has a mode of action that targets the RAAS and Natriuretic Peptides System together. Valsartan inhibits the effects of AT1 receptor stimulation which prohibits vasoconstriction and increase of vascular tone. Sacubitril, on the other hand, increases the natriuretic peptide levels via neprilysin inhibition which results in decreased blood pressure, hypertrophy and fibrosis. As a result of this unique mechanism of action, Sacubitril/Valsartan has shown promising outcomes in reducing the risk of death for heart failure in a large placebo-controlled trial [5]. In this study, we aim to characterize the effects of preventive treatment of PH with Sac/Val on failing RV tissue using an experimental model of PH [3].

METHODS

A total of 12 male Sprague Dawley rats (8-weeks old at the start of experiments) were studied in three groups: Controls (n=4), PH with placebo treatment (n=4) and Sacubitril/Valsartan treatment (n=4). PH was induced via pulmonary artery banding (PAB). Daily doses of Sacubitril/Valsartan and placebo (same volume of water) were administered via oral gavage. At three weeks post-surgery, terminal invasive hemodynamic measurements were performed on the rats to obtain pressure-volume loops. Following hemodynamic measurements, the heart was removed and the right ventricular free wall (RVFW) was dissected and attached to a biaxial testing device (Biotester, Cell-Scale Biomaterials, Waterloo, CA). Visual tracking markers were placed on the tissue and marker deformations were recorded using a CCD camera for strain estimations. Multi-protocol biaxial testing was performed on each RVFW specimen to investigate the tissue response in a wide range of possible loading scenarios, Fig.1. Equibiaxial stress-strain response of tissues was interpolated from the multi-protocol experimental data using previously established techniques [6]. The experimental stress-strain data under multi-protocol testing was used to model the response specimens using a nonlinear anisotropic constitutive model [7]:

$$W = B_0(e^{\frac{1}{2}b_1E_{11}^2} + e^{\frac{1}{2}b_2E_{22}^2} + e^{b_3E_{11}E_{22}} - 3) \qquad (1)$$

here, B0 is the scaling factor, b1 is the stiffness in the longitudinal direction (apex to outflow tract direction), b2 is the circumferential stiffness and b3 is the coupled stiffness of the tissue. Parameter estimation was performed using a least-squares optimization algorithm (trust-region-reflective) in MATLAB (Mathworks, Natick, MA). All data were reported as sample mean ± sample standard error of the mean (SEM). Statistical comparisons were made using an unpaired Student's t-test (two-tailed) with $\alpha = 0.05$.

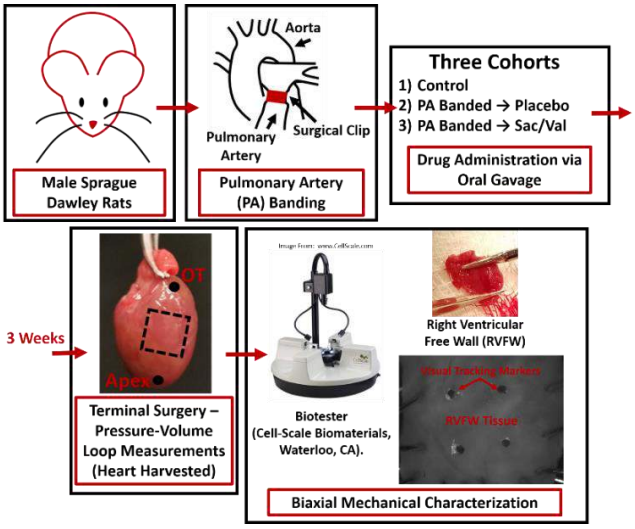

Figure 1: Graphical abstract of the framework used to evaluate RV biomechanics.

RESULTS

PA banding results in significantly increased RV systolic pressures (72.5 ± 10.5 mmHg for PAB vs. 24.5 ± 1.7 mmHg for Control) while Sac/Val leads to decreased systolic pressures (44 ± 2.3 mmHg), Fig 2a. Increased thickness due to PA banding and tissue hypertrophy (0.68 ± 0.07 mm for control vs. 1.09 ± 0.03 mm for PAB) is not recovered with Sac/Val treatment (1.01 ± 0.05 mm), Fig. 2b.

Interpolated equibiaxial stress-strain response of RVFW specimens demonstrate increased stiffness and tissue anisotropy of the RV as a result of PA banding. Sac/Val results in decreased tissue stiffness, specifically in the longitudinal direction (Fig. 3a). Constitutive modelling reveals significantly increased tissue stiffness in the longitudinal direction due to PA banding (100.3 ± 18.0 vs. 211.3 ± 29.6 KPa) while showing no significant differences in the circumferential and coupled stiffnesses (Fig. 3b). Sac/Val treatment results in significantly lower longitudinal stiffness (94.5 ± 19.3 KPa) compared to the PH group, while no statistically significant differences were found between the control and Sac/Val treatment groups.

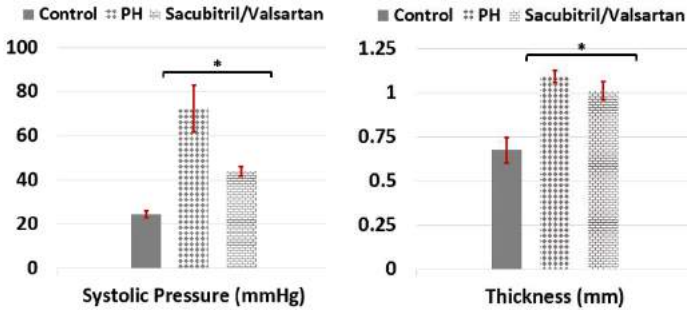

Figure 2: (a) In-vivo RV systolic pressures from terminal invasive hemodynamic measurements, (b) RVFW thickness for each cohort, *p<0.05 represents statistical variation from the control group.

DISCUSSION

RV pressure overload through PA banding resulted in increased RV systolic pressures, tissue hypertrophy, increased tissue stiffness and thickness as well as increased anisotropy. RV systolic pressures and tissue thickness and stiffness of control and PA-banded rats match

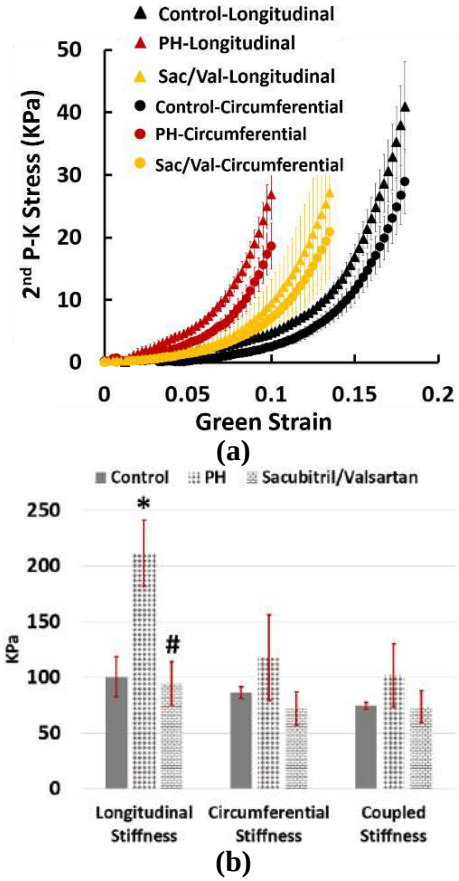

Figure 3: (a) Interpolated equibiaxial stress-strain response of each cohort, (b) Constitutive model parameters, *p<0.05 represents statistical variation from the control group, #p<0.05 represents statistical variation from the PAB group.

previously reported values [1,3]. Sac/Val treatment resulted in decreased systolic pressures and lead to near-healthy tissue biomechanical properties, suggesting the potential of Sac/Val for PH treatment.

In this study, a preventive treatment approach was employed to analyze the effects of Sac/Val on PH in a 3-week period. For future investigations, different treatment windows as well as treatment scenarios after fully developing PH needs to be studied. Also, effects of Valsartan-only treatment vs. Sac/Val needs to be evaluated for comparison purposes. Nevertheless, preliminary results suggest the promising potential of Sac/Val in lowering RV end-systolic pressure, preventing increased tissue stiffness in the longitudinal direction and RV remodeling.

ACKNOWLEDGEMENTS

This study was supported by Novartis Pharmaceutical Corporation under award number LCZ696BUSNC20T.

REFERENCES

[1] Hill, M et al., Ann Biomed Eng, 42(12):2451-2465, 2014.
[2] Pauwaa, S et al., Pulmonary Circulation, 1(3):430-431, 2011.
[3] Valdez-Jasso, D et al., J Physiol, 590(18):4571-4584, 2012.
[4] Menendez, J, J Card Fail, 2(1):40, 2016.
[5] McMurray, J et al., N Engl J Med, 371(11):993-1004, 2014.
[6] Fata, B et al., J Biomech Eng, 136(2): 021009, 2014.
[7] Choi and Vito, J Biomech Eng, 112(2): 153-159, 1990.

SB³C2019
Summer Biomechanics, Bioengineering and Biotransport Conference
June 25 -28, Seven Springs, PA, USA

OSMOTIC SWELLING BEHAVIOR OF THE PREGNANT MOUSE CERVIX AND THE CONTRIBUTION OF HYALURONIC ACID

C. Jayyosi (1), N. Lee (1), S. Nallasamy (2), P. Madhukaran (2), M. Mahendroo (2), K. Myers (1)

(1) Department of Mechanical Engineering
Columbia University
New York, NY, USA

(2) Department Obstetrics and Gynecology and Green Center for Reproductive Biological Sciences
University of Texas Southwestern Medical Center
Dallas, TX, USA

INTRODUCTION

All along pregnancy, the cervix undergoes important structural changes in order to fulfill its functional change, i.e. transforming from a closed rigid barrier to a highly deformable structure to allow safe passing of the baby at the time of delivery [1]. These structural changes known as cervical remodeling leads to a profound modification of the composition and organization of the cervix microstructure, which directly impacts the mechanical properties and function of the tissue. Abnormal and premature cervical remodeling represent a critical clinical challenge as it has been identified as a significant risk factor for preterm birth (PTB) [2], which still impacts approximately 12% of all birth [3], with often disastrous health consequences for premature babies. Hence, understanding and characterizing the biomechanical changes associated to the cervical remodeling process represent a necessary step toward a better identification of PTB etiology.

As for most soft biological tissues, the mechanical behavior of the cervix is mostly derived from the composition and organization of its extracellular matrix (ECM) [4]. Besides collagen and elastic fibers, the cervical ECM includes glycosaminoglycans (GAGs) which are macromolecules that greatly influence the mechanical behavior of the cervix as they are negatively charged. These electrical charges are embedded in the collagenous matrix and experience like-charge repulsion creating an imbalance in electrical charges between the tissue and the external environment [5]. As a result, this imbalance in charge density causes the tissue to imbibe water and swell in solutions, creating a net osmotic pressure altering the tissue mechanical properties enhancing its compressive strength [6] for instance, or increasing its rigidity [7].
With advancing pregnancy, the content of cervical GAGs evolves through the cervical remodeling process. In the mouse, while the amount of sulfated GAGs remains rather constant along pregnancy, the amount of hyaluronan (HA, a non-sulfated GAG), increases significantly toward the end at day 18 of pregnancy [8]. While HA are believed to play an important role in cervical remodeling, through the ECM disorganization toward the end of pregnancy [9], their clear impact and contribution to the mechanical/swelling behavior of the cervix is yet to be identified.

Hence, the aims of this study are to investigate the swelling tendencies of the cervix in relation to the environment osmolarity, and identify the specific contribution of HA in those tendencies, using an animal model presenting a HA depletion in the cervix.

METHODS

Non pregnant (NP, n=12) and pregnant mouse cervices at day 6 (d6, n=17), day 15 (d15, n=12) and day 18 (d18, n=17) of a 19 days pregnancy were collected and isolated from the reproductive tract. To examine the specific contribution of hyluronan to the swelling behavior, two strains of mice were used in this experiment: a wild type control strain (WT) and an HA depleted strain (HAKO).

After dissection, the samples were weighed and immediately placed in a custom built swelling bath, suspended by the inner canal. The baths were filled with NaCl solutions of 0.15M (physiologic) or 2M (hyperosmotic) concentrations, with 2mM ethylenediamineteraacetic acid (EDTA) protease inhibitor. The cervical volume change was assessed for 3h with two CCD cameras arranged perpendicularly, to image the cervix geometry during osmotic loading. Images were analyzed using a custom Matlab segmentation routine to extract measurements of the side area and the average length of the sample to estimate the cervical volume V and calculate the swelling ratio J as:

$$J = \frac{V}{V_{1st\ image}} \qquad (1)$$

To quantitatively compare the swelling kinetic between the different specimen groups, we also calculated swelling rates defined as the slope of the *J* vs. time curve.

RESULTS

Swelling kinetic in normal pregnancy

The kinetic of swelling is significantly different between physiologic and hyperosmotic solutions. The analysis of the relative volume change rate (Fig.1A-B-C) shows almost all specimen groups present a statistically different kinetic of swelling in 2M compared to 0.15M. An equilibrium is reached in the physiologic 0.15M solution after approximately 2h, while cervix keeps on swelling after 3h in 2M, as evidenced by the mid and final slope values close to 0 for the 0.15M and >0 values for the 2M (Fig.1B-C). An initial shrinkage of the volume is observed in 2M, except for d6, followed by a continuous increase in volume (Fig.1A). In physiologic solution (0.15M) the swelling ratio at equilibrium (3h) increases with advancing gestation up to day 15 and stabilizes between day15 and day18 (Fig.1D).

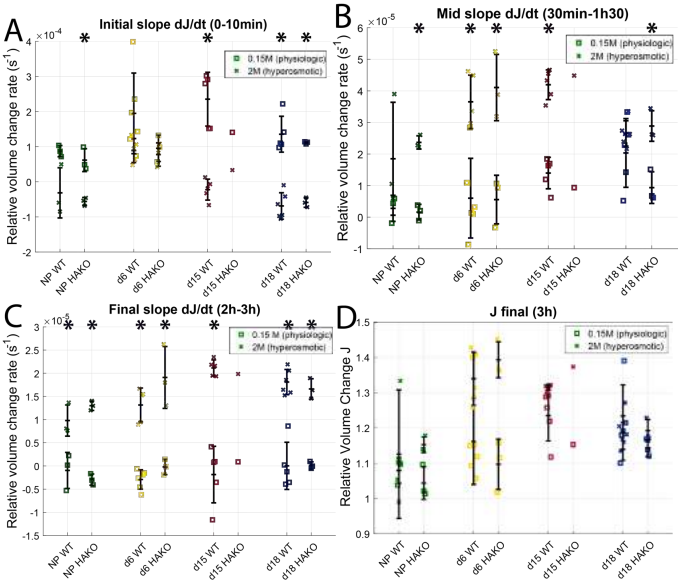

Figure 1: A-B-C) Relative volume change rate at the beginning, middle and end of the swelling experiment with advancing gestation (NP, d6, d15, d18) in both the wild type and HA depleted strains. *indicates statistical difference between the different osmolarity solutions (one-way ANOVA, p<0.05). D) Swelling ratio J after 3h of osmotic swelling.

Swelling behavior in the absence of HA

The swelling behavior of the HAKO animals is in no way different than the behavior of the wild type group. No significant difference is observed in the swelling kinetic or equilibrium properties between HAKO and WT at all gestation time point in both osmolarities (Fig.1A-B-C-D).

DISCUSSION

The different kinetic of swelling between the 0.15M and 2M conditions indicates that a different physical swelling phenomenon takes place in presence of excess NaCl ions. The Donnan equilibrium theory, usually taken to describe the swelling behavior of soft tissues does not account for the volume expansion seen in 2M when the media is saturated with NaCl ions. Some configurational entropic effects [5] could be considered in modeling approaches to describe this phenomenon, when the excessive presence of ions shields the negative charges of the GAGs., diminishing the electrostatic effects but increasing the entropic pressure creating swelling tendencies.

The increase of the equilibrium swelling ratio seen in physiologic solution (Fig.1D) is in accordance with consideration about the ECM microstructural remodeling events with pregnancy. Indeed, the cervical remodeling process is associated with a progressive disorganization of the collagenous matrix with pregnancy inducing a softening between the early stage (NP, d6) and the late pregnancy (d15, d18) [10]. This disorganization comes with a large modification of the interfibrillar spaces, which therefore enables the tissue to imbibe more water through osmotic swelling.

The contribution of HA to the mechanical/swelling behavior of the cervix remains unclear. Akgul *et al.* [11] reported that HAKO animals presented a similar matrix disorganization and increase hydration with advancing pregnancy than WT. They also found that the apparent stiffness of the tissue during load-to-break tensile testing was not altered with the absence of HA. However, they reported that HAKO cervices presented a reduced interfibrillar space compare to control animals, suggesting a possible modification of the swelling behavior. Interestingly, this reduced interfibrillar space does not influence the swelling behavior of the cervix in physiological or hyperosmotic solutions, as the swelling response of the HAKO group was not different than the WT, questioning the implication of HA in the swelling tendencies of the cervix. The swelling properties of HA have been studied through experiments conducted on HA gels or collagen-HA gels [12] showing that when they are not constrained and embedded in a collagenous matrix, HA gels swell significantly more. Those swelling characteristics also showed an important dependence on the osmolarity of the media. The absence of a distinct swelling signature of HAKO cervices could hence be explained by the contribution of other components of the ECM (other GAGs like Versican) limiting the HA impact on swelling, or compensating their contribution in HA depleted cervices.

Ultimately, the work presented here highlights that swelling tendencies of the cervix are significant and need to be accounted for in mechanical testing. Further investigation about the HA role and other GAGs contribution to swelling mechanism will help fully elucidate and further our understanding of the cervical remodeling process.

ACKNOWLEDGEMENTS

This work was supported by the Collaborative Research Travel Grant 2017 of the Burroughs Wellcome Fund and NIH R01 HD088481.

REFERENCES

[1] Timmons, B. et al., *Trends in Endo and Meta*, 21:353–361, 2010
[2] Vink, J. et al., *Seminars in Perinatology*, 41:427-437, 2017.
[3] Hamilton, B.E. et al., *National Vital Statistics System*, 62:1–20, 2013
[4] Fung, Y.C., *Biomechanics*, volume 12, Springer, New York, 1993
[5] Chahine, N.O. et al., *Biophy j*, 89:1543-1550, 2005.
[6] Yoshida, K. et al., *J Biomech Eng*, 136:021017, 2014.
[7] Lanir, Y., *Biorheology*, 24:173-187, 1987
[8] Akgul, Y. et al., *Endocrinology*, 153:3493-3503, 2012.
[9] Ruscheinsky, M. et al, *Matrix Biology*, 27:487-497, 2008
[10] Jayyosi, C. et al, *Acta Biomaterialia*, 78:308-319, 2018
[11] Akgul, Y. et al, *J of Clinical Investigation*, 124:5481-5489, 2014
[12] Lai, V. et al, *Annals of Biomedical Eng*, 44:2984-2993, 2016

SB³C2019
Summer Biomechanics, Bioengineering and Biotransport Conference
June 25 -28, Seven Springs, PA, USA

NORMALIZED SYNERGY PREDICTS CO-RECEPTOR CD8'S CONTRIBUTION TO TCR MECHANOSENSING IN HUMAN VIRAL-SPECIFIC T CELLS

Chad M. Williams (1), Alexandra A. Schonnesen (1), Ning Jiang (1,2)

(1) Department of Biomedical Engineering
University of Texas at Austin
Austin, Texas, U.S.A.

(2) Institute for Cell and Molecular Biology
University of Texas at Austin
Austin, Texas, U.S.A.

INTRODUCTION

The CD8 co-receptor contributes to TCR binding to pMHC by reducing the rate of dissociation between TCR/pMHC interaction [1]. On the MHC class one molecule, CD8 binds to the alpha 3 domain, distinctly separate from the TCR binding of the peptide, alpha 1 and alpha 2 domains [2]. Several studies have shown that the binding affinity of CD8 to MHC is independent of TCR specificity or affinity [3,4]. Using a micropipette adhesion assay, we have previously found a positive correlation between CD8 cooperation (described as synergy) and TCR affinity, with CD8 cooperation increasing with TCR affinity [5]. However, this study has been limited to a model system of transgenic mouse TCR against an array of altered peptide ligands. CD8 contribution in a native human antigen-specific T cell response remains elusive.

Here, using Hepatitis C Virus specific precursor CTLs spanning a large range of TCR affinities, we discovered that the functional responsiveness of any given TCR correlated with the contribution of CD8 to TCR/pMHC binding. Furthermore, we found that CD8 contribution to TCR/pMHC binding in the two-dimensional (2D) system was more accurately reflected by normalized synergy (CD8 cooperation normalized by total TCR/pMHC bonds) rather than synergy (total CD8 cooperation) alone. While synergy showed an increasing trend with TCR affinity, normalized synergy was demonstrated to decrease with increase of TCR affinity. Critically, normalized synergy was shown to correlate with CTL functionality and peptide sensitivity. Our results resolve the current discrepancy on CD8 contribution to TCR/pMHC binding, and demonstrate that naturally occurring high affinity TCRs are more capable of CD8 independent interactions that yield greater functional responsiveness even with CD8 blocking.

METHODS

Using a tetramer enrichment strategy described previously [6], we isolated a set of precursor CTLs that recognize human a single HCV epitope in complex with pMHC (here denoted as pMHC-CD8wt-HCV) from healthy HCV seronegative blood donors [6]. These precursor CTL clones allowed us to comprehensively examine the 2-dimensional (2D) affinity for viral antigen-specific polyclonal human TCRs. Using pMHC-CD8wt that enables CD8 binding and pMHC-CD8mut (with D227K/T228A mutations) that abrogates CD8 binding, we studied the contribution of CD8 binding to TCR mechanosensing induced T cell activation in human viral-specific T cells. The relationships between affinity and synergy and normalized synergy are defined as below. P_a, adhesion frequency; m_{TCR} or m_{CD8}, and m_{pMHC} denote site densities of TCR, CD8, and pMHC respectively; K_a, k_{off}, and t_c representing 2D affinity, 2D off-rate, and contact time; A_c is the contact area with the constant radius of 1μm; The 2D affinity measured in this way uses a product of A_cK_a, which has a unit of μm^4; $< n >/m_{pMHC}$, number of bonds formed per pMHC.

$$P_a = 1 - exp[-m_{TCR\ or\ CD8} m_{pMHC} A_c K_a (-k_{off} t_c)] \quad (1)$$

$$A_c K_a = -\ln[1 - P_a(eq)] / (m_{TCR\ or\ CD8}\ x\ m_{pMHC}) \quad (2)$$

$$< n >/m_{pMHC} = -ln[1 - P_a(eq)]/m_{pMHC} \quad (3)$$

$$synergy = \frac{<n_{TCR+CD8}>}{m_{pMHC-CD8wt-HCV}} - \frac{<n_{TCR}>}{m_{pMHC-CD8mut-HCV}} - \frac{<n_{CD8}>}{m_{pMHC-CD8wt-PPI}} \quad (4)$$

$$normalized\ synergy = \frac{Synergy}{[\frac{<n_{TCR}>}{m_{pMHC-CD8mut-HCV}}]} \quad (5)$$

RESULTS

The large affinity differences between high- and low- affinity TCRs and between TCRs and CD8 make it difficult to compare their ligand binding propensity. To simplify this comparison, we converted 2D affinity to number of bonds formed per MHC molecule [5].

For TCR, this parameter also spanned a 500-fold range similar to 2D affinity (Figure 1B). In contrast, the number of bonds formed per MHC molecule for CD8 were generally in the same range as low affinity TCRs and had little variation between TCRs where both TCR affinity and number of bonds formed per MHC molecule differed by orders of magnitude (Figure 1B). The previously described 2D method of evaluating CD8 cooperation for 2D affinity analysis subtracted the number of bonds formed by TCR/pMHC and CD8/pMHC interactions from (TCR+CD8)/pMHC interactions, and was named synergy or the change in number of bonds [5]. We demonstrated a similar trend between synergy and 2D TCR affinity as seen previously in the 2D TCR kinetic data, which showed that high affinity TCRs received more CD8 cooperation compared to low affinity TCRs (Figure 1C).

We hypothesized that the cooperation obtained as calculated by synergy was a total synergy that TCRs could receive, which was dependent on the total number of bonds that TCR/pMHC could form. Therefore, normalizing synergy by the number of TCR/pMHC bonds formed for each MHC molecule evaluates the synergy per TCR bond, which could be a more accurate parameter in the 2D setting to evaluate the cooperation between TCR and CD8. Indeed, converting synergy to normalized synergy showed that low-affinity TCRs received more cooperation, or help, from CD8 per TCR bond compared to medium- and high-affinity TCRs (Figure 1D). This corroborates the finding in previous 3 dimensional studies using protein engineered TCRs or APLs, that higher affinity TCRs are more likely to be CD8 independent in binding than low affinity TCRs. Among the three high-affinity TCRs, two were essentially independent of CD8 in terms of pMHC binding. We also have functional data to support that these CD8 minimally dependent TCR expressing CLTs are more resistant to CD8 blocking and are able to retain most of the functionality in cognate peptide stimulation compared to TCRs that are more dependent on CD8 when most of CD8 molecules are blocked. Thus, our analysis using the new parameter, normalized synergy, was able to reconcile the discrepancy between previous 3D and 2D affinity analysis on CD8 cooperation to TCR/pMHC binding.

DISCUSSION

We have shown that the T cells recognizing a naturally occurring viral peptide span an affinity range of three orders of magnitude. In our interrogation of the CD8 contribution, we established a new parameter to evaluate cooperation that can be attributed to CD8 and demonstrated that this normalized synergy correlates well with maximal functionality and peptide sensitivity. Finally, we demonstrated that CD8 independent T cells have increased functionality and sensitivity compared to those more dependent upon CD8 for binding. In the future, CD8 independent TCRs might prove beneficial for the field of adoptive cell transfer for cancer immunotherapy because these TCRs are highly sensitive and functional in response to antigen stimulation in comparison to TCRs that more heavily relied on CD8 contribution for TCR/pMHC binding.

ACKNOWLEDGEMENTS

The authors would like to thank WE ARE BLOOD, blood center, for providing the blood samples for CTL stimulations. This study was supported by NIH grant R00AG040149 (N.J.) and Damon Runyon-Rachleff Innovator Award DRR-32-15 (N.J.).

REFERENCES

[1] Garcia, C., Nature, 1996. 384.

[2] George F. Gao*†, J.T.k., Ulrich C. Gerth†,, et al., Nature, 1997. 387.

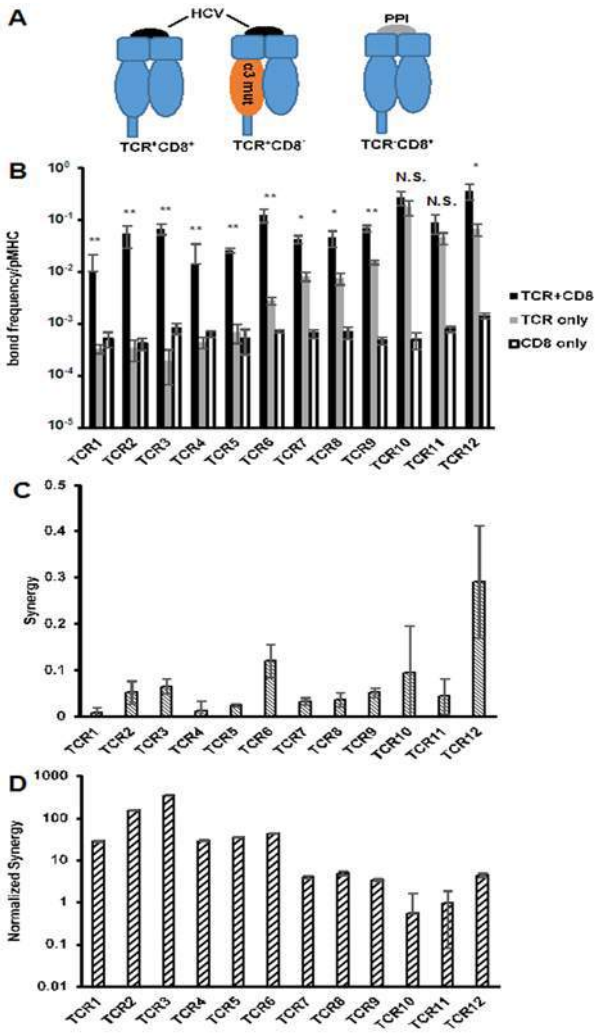

Figure 1. CD8 contribution decreases with increasing TCR affinity

(A) Schematics depicting pMHC variants used to isolate bimolecular TCR/pMHC and CD8/pMHC interaction and TCR/CD8/pMHC tri-molecular interaction. **(B)** Bond frequency per pMHC for TCR+CD8, TCR only, and CD8 only interactions with respective pMHCs for each of the functional CTLs in order of increasing 2D TCR affinity. Bond frequency per pMHC was calculated following equation 4, in materials and methods. One-way ANOVA was performed between TCR+CD8 and TCR only bond frequency to assess statistical significance between values with p-values more than 0.05 considered not significant (N.S.), p-values less than 0.01 (*) and 0.001 (**) denoted by asterisk. **(C)** Synergy was calculated for each CTL in the traditional manner following equation 5 in materials and methods, and shown in order of increasing 2D TCR affinity. **(D)** Normalized synergy was calculated following equation 6 in materials and methods, and shown in order of increasing 2D TCR affinity. Data are shown as the mean ± S.D. of at least 3 cell pairs. Error propagation was performed to obtain S.D. for normalized synergy in (**D**).

[3] Wyer, J.R., et al., Immunity, 1999. 10(2): p. 219-25.

[4] Cole, D.K., et al., Mol Immunol, 2008. 45(9): p. 2700-9.

[5] Jiang, N., et al., Immunity, 2011. 34: p. 13-23.

[6] Zhang, S.Q., et al., Sci Transl Med, 2016. 8(341): p. 341ra77.

SB³C2019
Summer Biomechanics, Bioengineering and Biotransport Conference
June 25 -28, Seven Springs, PA, USA

A MATHEMATICAL MODEL FOR THE POST-IMPLANT COLLAGEN MATURATION BEHAVIOR OF ENGINEERED TISSUES

Michael S. Sacks (1)

(1) James T. Willerson Center for Cardiovascular Modeling and Simulation
Institute for Computational Engineering and Sciences
Department of Biomedical Engineering
The University of Texas at Austin

INTRODUCTION

The optimal vascular replacement should be able to accommodate somatic growth and closely mimic the structure, function and physiology of native vessels. The field of tissue engineering attempts to create such permanent viable conduit tissue replacements, and, critically, accommodate somatic growth. Since arterial geometry greatly influences hemodynamics, replacement conduits should closely resemble the native three-dimensional arterial shape.

The most relevant studies for developing a PA conduit were conducted by Gottlieb and Hoerstrup both utilized similar methods, choice of animal model, and most importantly were focused on long-term responses [1,2]. Interestingly, while some minor (not statistically significant) changes in conduit dimensions occurred in both studies, overall the conduits were surprisingly dimensionally stable. Yet, in all studies a continued increase effective tissue modulus was consistently observed, which then leveled out by about one-year post-implant. This suggests that a tissue maturing process akin to related collagen maturation phenomena observed. Moreover, this does not appear to be a conventional growth and remodeling (G&R) phenomena in the sense that some type of restoration in homeostasis is obtained. For example, in the now classic work on residual stress in arteries and subsequent remodeling due to altered vascular pressures, restoration in transmural wall stress distributions was considered the major driver. This has been followed up by seminal work by Humphrey, Taber, and others.

Yet, to the author's knowledge, a detailed theoretical approach for the maturation behaviors of engineered tissues has yet to performed. Related work has been done on growth of the native PA, which have shown pronounced, anisotropic, and regionally heterogeneous growth. Such patterns have yet to be achieved with replacement conduits. Thus, an improved means of understanding tissue formation and remodeling in engineered tissues is necessary to further the field and ultimately develop functionally-equivalent tissues.

The principle driver of this work is to elucidate the long term in vivo remodeling processes in engineered cardiovascular tissues using models developed from first principles and based on quantifiable microstructural details. Manifestations of the maturation of collagen fiber network were explicitly modeled. Moreover, it will be shown that the growth and remodeling phenomena observed in the present study are driven by an increase in collagen modulus due the underlying process. To the best of the author's knowledge, this is the first time collagen maturation model of a large artery implant has been developed.

METHODS

Experimental database. Experimental data for this study was derived from studies by by Gottlieb and Hoerstrup [1,2]. Briefly, needle non-woven (NNW) PGA:PLLA scaffolds were cut and fabricated into conduits using manual and machine needle punching. Assemblies were mounted into a custom culturing device that immobilized the conduit and provided even seeding. BMSCs were isolated from 28 day female Dorset sheep and seeded on the conduits at 0.5-1.7 x 107 cells/cm3 in rotary culture (1 rpm).

Subsequent mechanical and structural analyses demonstrated, collectively, that the key experimental findings demonstrated that while the conduit was dimensionally stable, it underwent substantial tissue level remodeling. The specific key remodeling events are summarized in the following:

1. The conduit maintains its gross dimensions, including length, diameter, and thickness, over the entire remodeling period. Due to the stable conduit geometry and external loading conditions over the entire implant period of 100 weeks, the conduit is subjected to the same stress state throughout the maturation process. Using the Law of Laplace this is estimated to be T_{cc} =25 kPa and T_{LL} =12.5 kPa.

2. A rapid, near linear increase in γ c that ceases at about one year. No further changes in collagen modulus occur.

3. A shift towards increased collagen fiber organization, manifested as a parallel increase in average value and reduction in variance of λs .

4. 0-50 weeks: Maturation of the collagen structure, manifested as increasing modulus and a shift in mean λs and a reduction in σs.

15 5. 50-100 weeks: Maturation process appears to be complete, with no further remodeling apparent.

Model: A summary of the key equations of the modeling approach are given in Figures 1 and 2. Novel to this study is the incorporation of the time evolving collagen fiber modulus γ_c.

Total stress:

$$\mathbf{T} = -p\mathbf{I} + 2\frac{\partial \psi_m}{\partial I_1}\mathbf{B} + 2\mathbf{F}\mathbf{S}_c\mathbf{F}^T$$

Where:

$$\mathbf{S}_c(\mathbf{C},t) = \mathbf{S}_c^0(\mathbf{C},t) + \mathbf{S}_c^t(\mathbf{C},t)$$

Original fiber dissolution

Initial mass | Decay rate | Strain

$$\mathbf{S}_c^0(\mathbf{C},t) = \phi_c\gamma_c(t)\int_{\mathbf{n}}\int_1^{\lambda_{ub}} \frac{m_c^0(\mathbf{n},\lambda_s)}{M_c(t)}\, exp\left[-\int_0^t \eta_c(\mathbf{n},\lambda_s,s)ds\right]\left[\frac{1}{\lambda_s}\left(\frac{\lambda_n(\mathbf{n})}{\lambda_s}-1\right)\right](\mathbf{n}\otimes\mathbf{n})\,d\lambda_s d\mathbf{n}$$

New fiber deposition

New mass+ Stiffness increase | Decay rate | Strain

$$\mathbf{S}_c^t(\mathbf{C},t) = \phi_c\int_0^t\left\{\gamma_c(\tau)\int_{\mathbf{n}}\int_1^{\lambda_{ub}} \frac{\Delta_c(\mathbf{T})}{M_c(\tau)}\, exp\left[-\int_\tau^t \eta_c(\mathbf{n},\lambda_s,s)ds\right]\left[\frac{1}{\lambda_s}\left(\frac{\lambda_n(\mathbf{n})}{\lambda_s}-1\right)\right](\mathbf{n}\otimes\mathbf{n})d\lambda_s d\mathbf{n}\right\}d\tau$$

Figure 1 – Key equations for the time evolving stress as a function of mass changes.

Initial mass dissolution

$$\bar{\gamma}_c(t) = \gamma_c(t)\int_{\mathbf{n}}\int_1^{\lambda_{ub}} \frac{m_c^0(\mathbf{n},\lambda_s)}{M_c(t)}\cdot exp\left[-\int_0^t \eta_c(\mathbf{n},\lambda_s,s)ds\right]d\lambda_s d\mathbf{n} + \int_0^t\left\{\gamma_c(\tau)\int_{\mathbf{n}}\int_1^{\lambda_{ub}} \frac{\Delta_c(\mathbf{T})}{M_c(\tau)}\cdot exp\left[-\int_\tau^t \eta_c(\mathbf{n},\lambda_s,s)ds\right]d\lambda_s d\mathbf{n}\right\}d\tau$$

New mass deposition

Figure 2–Key equation for the time evolving collagen fiber modulus γ_c.

RESULTS

The model was able to capture the mechanical behaviors at each time point (Figure 3). Most interestingly, the model was able to faithfully simulate gradual increase in effective collagen fiber mechanical behavior and fiber recruitment (Figure 4). It is interesting to note that this evolution is direct result of the increase in in collagen modulus, which is part of the maturing process.

DISCUSSION

In the present study, a structural model-based formulation for the time evolution of a maturing collagen tissue was formulated and evaluated. The key findings included.

1. Modeling approach was able to account for time evolution of collagen crimp
2. Maintained angular fiber dispersion with an explicit constraint
3. *First model known G&R structural model that is based on evolution of material properties (fiber modulus) and not changes in boundary conditions.*

Current work includes extending the model initial implant phase and studies changes in boundary conditions (e.g. resulting from a change pressure).

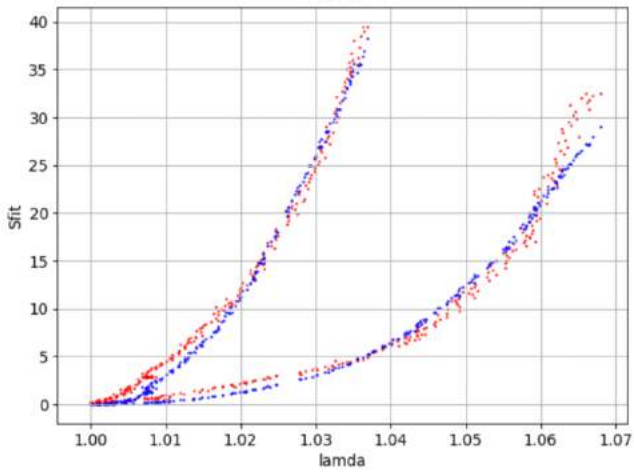

Figure 3 – Key equation for the time evolving collage

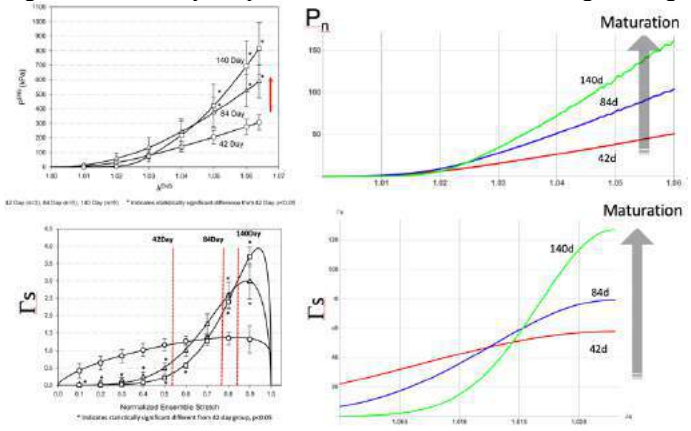

Figure 3 – Key equation for the time evolving collage

ACKNOWLEDGEMENTS

Funding by NIH R01 HL068816 is acknowledged.

REFERENCES

[1] D. Gottlieb, T. Kunal, S. Emani, E. Aikawa, D. W. Brown, A. J. Powell, A. Nedder, G. C. Engelmayr, Jr., J. M. Melero-Martin, M. S. Sacks, J. E. Mayer, Jr., In vivo monitoring of function of autologous engineered pulmonary valve, J Thorac Cardiovasc Surg 139 (3) (2010) 723–31.

[2] S. P. Hoerstrup, I. Cummings Mrcs, M. Lachat, F. J. Schoen, R. Jenni, S. Leschka, S. Neuenschwander, D. Schmidt, A. Mol, C. Gunter, M. Gossi, M. Genoni, G. Zund, Functional growth in tissue-engineered living, vascular grafts: follow-up at 100 weeks in a large animal model, Circulation 114 (1 Suppl) (2006) I159–66.

SB³C2019
Summer Biomechanics, Bioengineering and Biotransport Conference
June 25 -28, Seven Springs, PA, USA

Non-invasive Brillouin moduli and membrane fluctuation measurements of live tumor cell nuclei

A. Roberts (1), V. Singh (1), P.T. So (1), R.D. Kamm (1)

(1) Biological Engineering Department
Massachusetts Institute of Technology
Cambridge, MA, USA

INTRODUCTION

The mechanical properties of the microenvironment, cells, and their nuclei play a pivotal, interconnected role in fundamental cell processes, including cancer metastasis. But many experimental techniques used to assess mechanical properties of cells and nuclei are contact-based and/or intrusive (e.g. micropipette aspiration,[i] atomic force microscopy,[ii] micro-rheology, microfluidic constrictions, optical tweezers,[iii] and magnetic twisting cytometry) and therefore have the potential to alter the property they are intended to measure.

Here we present the first integrated system of confocal reflectance quantitative phase microscopy (QPM) and Brillouin confocal microscopy (BCM) to assess the mechanical properties of cells. Unlike other methods, QPM and BCM non-invasively measure mechanical aspects of cells and their microenvironment. Confocal reflectance QPM measures nanometer-scale thermally-driven nucleic and plasma membrane fluctuations with high sensitivity. BCM employs Brillouin light scattering to quantify intracellular longitudinal modulus. Both of these non-invasive methods employed together offer the potential to shed new light on cell and nuclear mechanics.

The ultimate goal of this study is to provide a validated method for measuring the mechanical stiffness of the nucleus in a living cell in real time during processes such as cell migration or transendothelial migration. Once established, these measurements offer the promise of providing new insights, for example, into the role of the cell nucleus in limiting the rate of migration or transmigration of a cancer cell during metastasis.

Here we take an initial step, gathering information from QPM and BCM on the same cell populations before and after a treatment that causes the cell moduli to change.

METHODS

The interaction of spontaneous acoustic phonons in the cell with light results in Brillouin scattering. The spectrometer records the small resulting frequency shift, a measure that has been shown to correlate with the shear modulus and water content of the material.[iv] BCM measures this modulus with μm level resolution in the x, y and z dimensions.

Confocal reflectance QPM can provide the μm level depth resolved optical phase information of the back scattered signal from nucleic and plasma membranes at ms temporal resolution. This phase information quantifies the height fluctuations of nucleic membranes, which are subject to thermal fluctuations around the stable equilibrium in a viscoelastic medium.

Combining the information from QPM and BCM provides the nuclear membrane and material mechanical properties.

A549 lung carcinoma cells (purchased from ATCC) were grown in cell culture in DMEM with 10% FBS and 1% Penicillin-Streptomycin. Samples for BCM were sparsely seeded on top of a 100μm tall 2.5mg/ml collagen type I gel in a 14mm diameter MatTek and samples for QPM were seeded on an uncoated 14mm diameter MatTek glass bottom surface. One population of tumor cells was treated with the chemotherapeutic 0.5μM Doxorubicin in DMEM for 24 hours and the wild-type population was grown in DMEM for 24 hours. Both samples were rinsed in complete media before imaging.

QPM measurements were carried out first. Fluctuations at the nuclear membrane over 14ms of 5 cells in the control population and 4 Doxorubicin-treated cells were measured 8 times per cell. After QPM,

we carried out BCM measurements on cells prepared the same week in the same manner for 4 cells of the control population and 4 cells of the Doxorubicin population, with 5 repeat measurements per cell in slightly different parts of the nucleus, Future experiments allow for measurement of the same 3D samples using QPM and BCM.

RESULTS

To compare QPM rheological measurements with those from BCM, we observed that 0.5uM-doxorubicin-treated A549 cells have higher nuclear fluctuations (softer nucleus) and lower Brillouin frequency (softer nuclei) (Figure 1).

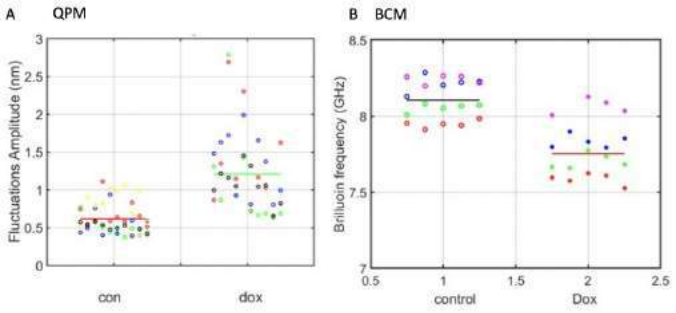

Figure 1: Confocal reflectance QPM results (A) correlate with BCM findings (B): In both instances, A549 doxorubicin treatment softens the nucleus.

DISCUSSION

Several methods can be employed to measure the rheological properties of the nucleus; however, few can do so without perturbing the cell and/or its microenvironment. Here we use light to quantify nuclear fluctuations and to quantify the Brillouin high-frequency longitudinal modulus. It has been argued that Brillouin measures water content rather than stiffness;[v] however, we show here that these Brillouin measurements of the nucleus do correlate with nuclear fluctuation measurements from QPM, a measure of the nuclear membrane stiffness. At present, there is no comprehensive theory nor computational model for either method, linking the observable quantities directly to the low frequency shear modulus of the cytoskeleton and/or nucleoplasm. Future studies will continue to improve understanding of nuclear mechanics in unperturbed cells and seek to develop a fundamental understanding of how changes in membrane, cytoskeletal or nuclear moduli affect these measurements.

ACKNOWLEDGEMENTS

We would like to acknowledge funding from the Department of Defense (DoD) through the National Defense Science & Engineering Graduate Fellowship (NDSEG) Program and from the National Institutes of Health (NIH) via the Physical Sciences of Oncology Network (U01CA202177).

REFERENCES

[i] Vaziri et al. Mechanics and deformation of the nucleus in micropipette aspiration experiment. J Biomech. 2007;40(9):2053-62.

[ii] Suresh et al. Cell and molecular mechanics of biological Nat Mater. 2003 Nov; 2(11):715-25.

[iii] Dao et al. Mechanics of the human red blood cell deformed by optical tweezers.

[iv] Scarcelli et al. Noncontact three-dimensional mapping of intracellular hydro-mechanical properties by Brillouin microscopy. Nature Methods. 2015 Dec; 12(12): 1132–1134.

[v] Overby et al. Water content, not stiffness, dominates Brillouin spectroscopy measurements in hydrated materials. Nat Methods. 2018 Aug;15(8):561-562

[i] Vaziri et al. Mechanics and deformation of the nucleus in micropipette aspiration experiment. J Biomech. 2007;40(9):2053-62.

[ii] Suresh et al. Cell and molecular mechanics of biological Nat Mater. 2003 Nov; 2(11):715-25.

[iii] Dao et al. Mechanics of the human red blood cell deformed by optical tweezers.

[iv] Scarcelli et al. Noncontact three-dimensional mapping of intracellular hydro-mechanical properties by Brillouin microscopy. Nature Methods. 2015 Dec; 12(12): 1132–1134.

[v] Scarcelli et al. Reply to 'Water content, not stiffness, dominates Brillouin spectroscopy measurements in hydrated materials'. Nature Methods. 2018 Jul; 15: 562–563

SB^{3}C2019
Summer Biomechanics, Bioengineering and Biotransport Conference
June 25 -28, Seven Springs, PA, USA

A MICROMECHANICAL MODEL FOR COLLAGENOUS TISSUES AND APPLICATIONS TO STUDY GROWTH AND REMODELING

Thao D. Nguyen

Department of Mechanical Engineering
Johns Hopkins University
Baltimore, MD, 21218

INTRODUCTION

Soft collagenous tissues, such as the sclera, tendon, and arteries, exhibit a highly organized structure composed of elastin and collagen fibers arranged in a hydrated matrix of cells, proteoglycans and other non-fibril forming proteins. The collagen fibers in the tissues often exhibit a wavy morphology in an unloaded configuration. The initial compliant toe region of the stress response of soft collagenous tissues is attributed to the straightening of the collagen fibers, and the stiff linear region is attributed to the stretching of the fibers. The degree of waviness and alignment of the collagen fibers vary greatly between tissues and are tailored to the physiological loading state and structural function of the tissues. The collagen structure of soft tissues are actively maintained and altered through the processes of growth and remodeling. For example, in the sclera, the degree of fiber alignment decreases with age[1] and the toe region of the stress-strain curve shortens significantly[2], suggesting a decrease in the fiber crimp (waviness). The collagen morphology can also influence the processes of growth and remodeling. Huang and Yannas[3] showed that deformation inhibits the enzymatic degradation of reconstituted rat-tail collagen. Furthermore, the degradation rate was lowest at the transition strain of the J-shape stress-strain curve separating the compliant region associated with fiber straightening and stiff region associated with fiber stretching.

To understand how the collagen structure influences the mechanisms of growth and remodeling and how they are in turn altered by growth and remodeling, we developed a micromechanical model for collagenous tissues that explicitly describe the anisotropic arrangement and crimp morphology of collagen fibers to describe the strain stiffening, anisotropic behavior of collagenous tissues[4]. We applied the model to investigate how these features are altered in engineered collagen constructs by cyclic loading[5] and in the mouse sclera by chronic pressure elevation. We added to the model micromechanisms of collagen enzymatic degradation and deposition to investigate how mechanical loading and the collagen structure affects the growth and remodeling processes.

METHODS

In the micromechanical model, the tissue is conceptualized as an anisotropic distribution of wavy collagen fibers, represented as sinusoidal beams, embedded in a incompressible, isotropic matrix. The planar wavy morphology has been observed in skin and the cornea, but for many other tissues, such as arteries, and engineered collagen constructs, it is an idealized representation of the non-straightness of collagen fibers that require them to bend, rotate, or be recruited before being stretched axially. The wavy fibers are assumed to be long and thin and the crimp angle is assumed to be small. This allows the analytical Euler elastica solution developed by Comninou and Yannas[6] to be applied for the deformed rotation angle $\theta(\bar{X}_1)$ and axial stretch $\lambda_f\ (\bar{X}_1)$ of the fiber midline,

$$\theta(\bar{X}_1) = \frac{\beta}{\alpha(1+\alpha)+\beta}\Theta(\bar{X}_1), \quad \lambda_f\ (\bar{X}_1) = 1 + \alpha\, cos(\theta(\bar{X}_1)). \quad (1)$$

The $\bar{X}_1$ is the normalized coordinate X_1/L along the horizontal axis about which the fiber undulate, L is the fiber length projected onto X_1, $\alpha = F/EA$, is the horizontal force applied to the wavy fiber normalized by the fiber modulus E and the fiber area $A = \pi r^2$, and $\beta = \pi r^2/L^2$ is the fiber slenderness ratio. The macroscopic fiber stretch along X_1 is defined deformed length over the original length,

$$\bar{\lambda} = \int_0^1 \lambda_f\ (\bar{X}_1)\, \frac{cos(\theta(\bar{X}_1))}{cos(\Theta(\bar{X}_1))}\, d\bar{X}_1. \quad (2)$$

The fiber model is incorporated into a distributed fiber hyperelastic constitutive model for tissues[4] by first applying the affine deformation assumption to connect the macroscopic stretch of a fiber

lying along an orientation $\boldsymbol{a_0}(\vartheta,\varphi)$ to the deformation gradient, $\bar{\lambda} = (\boldsymbol{a_0}\boldsymbol{F}^T\boldsymbol{F}\boldsymbol{a_0})^{1/2}$. We next define the fiber strain energy density as,

$$W_f = \int_0^L \frac{1}{2} E\beta[\theta(\bar{X}_1) - \Theta(\bar{X}_1)]^2 d\bar{X}_1 + \int_0^L \frac{1}{2} E\left[\lambda_f(\bar{X}_1) - 1\right]^2 d\bar{X}_1. \quad (3)$$

Then, the strain energy of the tissue can be defined within a distribute fiber hyperelastic framework as,

$$W = W_m(\boldsymbol{F}^T\boldsymbol{F}) + \langle W_f(\boldsymbol{F}^T\boldsymbol{F}, \boldsymbol{a_0})\rangle, \quad (4)$$

where $W_m(\boldsymbol{F}^T\boldsymbol{F})$ describes the incompressible isotropic matrix response and $\langle\cdot\rangle = \int_0^{2\pi}\int_{-\pi/2}^{\pi/2}(\cdot)\rho_0(\vartheta,\phi)\,sin\,\phi\,d\phi\,d\vartheta$ is the statistical average over the probability density distribution of the fiber orientation, $\rho_0(\vartheta,\phi)$. The distribution function has been estimated experimentally for many tissues using a variety of techniques, including TEM and X-ray scattering.

To model collagen deposition and degradation, we assume that collagen degradation works to reduce the fiber radius and collagen deposition works to increase the radius[4] and length of collagen fibers growing under load. We derive an evolution equation for the axial growth stretch of the fiber by assuming that collagen is deposited onto a loaded fibril in an unstressed state then solving for the updated reference length of the fiber after unloading[7]. We further assume that the rate of collagen degradation and deposition can be inhibited and stimulated, respectively, by the fiber axial strain energy density[4]. The concurrent action of these mechano-regulated deposition and degradation mechanisms allow for anisotropic volumetric growth of the tissue and remodeling of the fiber orientation distribution and tissue properties. Moreover, by making the collagen deposition and degradation dependent on the axial strain energy density of the fiber, we allow the fiber crimp morphology to affect the growth and remodeling process.

RESULTS

We applied the model as described by eq. (1)-(4) to investigate the remodeling of the mouse sclera caused by 6 week chronic elevation in the intraocular pressure (IOP) to induce glaucomatous axon damage. The increased IOP causes the sclera to expand and thin or thicken depending on the location and mouse strain[8], the pressure-strain response to stiffen significantly in the peripapillary region near the optic nerve head[8], and the collagen fiber alignment, measured by wide angle x-ray scattering (WAXS), to decrease significantly[9]. The model was applied to fit the pressure-displacement response in inflation tests of the mouse eye to determine alterations to the collagen fiber morphology and to compare the contributions of the remodeling to the shape of the sclera, collagen anisotropy, and wavy morphology to the stiffened inflation response of the tissue. Initial results suggested that the alterations to the collagen anisotropic arrangement, while statistically significant, did not significantly alter the inflation response of the peripapillary sclera beyond the experimental variation.

The model was also applied to study alterations in the stress-strain response of an acellular engineered collagen tissue caused by cyclic loading. TEM measurements showed a slight increase in the collagen fibril alignment along the loading direction and uniaxial tension tests showed an increase in the stiffness and strength of the tissue[10]. We applied the model, extended to include a fiber-level damage criteria, to investigate the effect of the cyclic loading on the mechanical properties and morphology of the collagen fiber[5]. The results showed that the increase in the fiber alignment measured by TEM was not sufficient to explain the increase in the stiffness and strength of the tissue. Cyclic loading of acellular collagen constructs significantly decreased the collagen crimp and increased the collagen stiffness beyond the experimental variation.

The micromechanical model was extended to include the effect of enzymatic degradation of collagen as described in the above section and applied the effects of mechanical loading observed in tissue-level degradation experiments for bovine corneal strips and pericardium strips[4]. The parameters of the energy-inhibited degradation law were fit to fibril-level degradation experiments[11], while parameters for the collagen fibers were fit to the tissue-level stress-strain curves[12,13]. The model successfully predicted that crimped collagen fibers are degraded until straightened, such that tissue degradation was halted when the collagen tissue stretch reached the transition stretch of the stress-strain curve as observed in experiments. The mechanical inhibition mechanism also caused the preferred orientation of the anisotropic fiber arrangement to align with the directions of the maximum principal stretch and the degree of fiber alignment to vary with the biaxial stress ratio. These findings show that mechanical inhibition of collagen degradation may play an important role in tailoring the collagen crimp morphology and anisotropic fiber arrangement to the physiological loading state of the tissue.

Finally, the model was extended to include the concurrent effects of enzymatic degradation and deposition of collagen as described in the above section[7]. We applied the model to study the growth of a spherical tissue membrane, an idealized representation of the sclera, in response to a perturbation in the internal pressure. The model was able to predict the development of stress homeostasis in the tissue, where the membrane stress recovered, after the pressure perturbation, the equilibrium value attained before the perturbation. The homeostatic stress state was determined by the properties of the collagen fibers and kinetic parameters and energy inhibition/activation energy parameters of collagen deposition and degradation. For collagen tissues with a compliant bending response (e.g., slender fibers) strain homeostasis was also developed.

In conclusion, we have developed a versatile micromechanical for the anisotropic nonlinear stress response of soft collagenous tissues. The model has been extended to incorporate fiber-level mechanisms of damage, collagen degradation and collagen deposition. We have applied the model to study how remodeling affects collagen structure and properties, particularly in mouse models of glaucoma, and how the collagen structure affects both the active and passive processes of growth and remodeling. This relatively simple model, which only includes 2 fiber-level mechanisms, can describe many important phenomena of growth and remodeling, such as the development of stress homeostasis and remodeling of collagen structures along the direction of principal stress. Future work will continue to enrich the model to predict growth and remodeling of ocular tissues in glaucoma.

ACKNOWLEDGEMENTS

TDN acknowledges support from the National Science Foundation CAREER Award No. 1253453 and the Johns Hopkins University 2016 Catalyst Award.

REFERENCES

1. Coudrillier, B. *et al. J. Biomech. Eng.* **137,** 041006 (2015).
2. Coudrillier, B. *et al. Invest. Opthalmol. Vis. Sci.* **53,** 1714 (2012).
3. Huang, C., Yannas, I.V. *J. Biomed. Mater. Res.* **11,** 137 (1977).
4. Tonge, T.K. *et al. Biophys. J.* **109,** 2689 (2015).
5. Chen, M.L. *et al. J. Mech. Behav. Biomed. Mater.* **82,** 345 (2018).
6. Comninou, M., Yannas, I.V. *J. Biomech.* **9,** 427 (1976).
7. Jia, Z., Nguyen, T.D. (2019), in preparation.
8. Nguyen, C. *et al. Invest. Ophthalmol. Vis. Sci.* **54,** 1767 (2013).
9. Pijanka, J. K. *et al. Invest. Ophthalmol. Vis. Sci.* **55,** 6554 (2014).
10. Susilo, M.E. *et al. Interface Focus* **6,** 20150088 (2016).
11. Flynn, B.P. *et al. Biomech. Model. Mechanobiol.* **12,** 291 (2013).
12. Zareian, R. *et al. Langmuir* **26,** 9917 (2010).
13. Ellsmere, J. C. *et al. Biomaterials* **20,** 1143 (1999).

SB³C2019
Summer Biomechanics, Bioengineering and Biotransport Conference
June 25 -28, Seven Springs, PA, USA

MECHANICAL PROPERTY CHANGES IN THE MENISCUS IN A NOVEL CLOSED JOINT ANIMAL IMPACT AND SURGICAL MODEL

G.E. Narez (1), A. Fauron (2), L. Dejardin (2), F. Wei (3, 4, 5), R.C. Haut (3, 4), T.L. Haut Donahue (1)

(1) Department of Biomedical Engineering
University of Massachusetts
Amherst, MA, USA

(2) Department of Small Animal Clinical Sciences
Michigan State University
East Lansing, MI, USA

(3) Orthopaedic Biomechanics Laboratories
Michigan State University
East Lansing, MI, USA

(4) Department of Mechanical Engineering
Michigan State University
East Lansing, MI, USA

(5) Department of Biomedical Engineering
Michigan State University
East Lansing, MI, USA

INTRODUCTION

The menisci are fibro-cartilaginous structures found in the knee joint that aid in joint stability, load distribution and act to protect the underlying articular cartilage from large pressures in the knee joint [1]. It has been long established that injuries to the soft tissues of the knee, primarily to the anterior cruciate ligament (ACL) and menisci, can induce post-traumatic osteoarthritis (PTOA) [2]. In order to return normal kinematics to the joint, current clinical treatment for damage to these soft tissues focuses on repairing macroscopic acute tissue damage by reconstructing the damaged ACL and removing the damaged portions of the meniscus. However, patients show signs of PTOA whether or not they receive surgical intervention [3].

A previous study by our group using a closed-joint impact lapine model demonstrated that 12 weeks following traumatic ACL and meniscal injury, there were significant morphological and mechanical changes to the menisci, which were consistent with clinical mid to late stage PTOA [4]. This study did not include surgical intervention in the traumatized joint.

The goal of the current study is to develop a new lapine model that combines a closed-joint traumatic injury with subsequent surgical repair and to determine mechanical changes in the meniscus through indentation-relaxation testing over time. It was hypothesized that damage to the menisci resulting from a controlled, traumatic impact would result in chronic changes in the mechanical properties of the tissue, even if the knee joint received surgical intervention following the traumatic injury. These results are expected to be consistent with the previous description of mid to late PTOA in the closed-joint lapine model.

METHODS

Seven skeletally mature Flemish Giant rabbits (6.81 ± 0.34 kg) were used for this study with an IACUC approval. With the animal under general anesthesia in sternal recumbency, the right knee and paw were secured into a custom fixture that allowed unrestricted anterior tibial subluxation, while constraining lateromedial motion. A controlled impact was delivered by a servo-hydraulic actuator (Instron, Norwood, MA), which thrusted the tibia proximally at 0.5 Hz until ACL failure. Peak load and time to peak were recorded. Surgical reconstruction of the ACL was performed by an orthopaedic surgeon 2-3 weeks post-impact following debridement of the torn ACL and medial meniscus. The semitendinosus (ST) tendon was transected at the musculotendinous junction while its tibial insertion was left intact. The tendon's free end was rerouted through tibial and tunnel femurs (3.2mm in diameter), which overlapped the ACL footprint. The ST tendon was tensioned and then secured into the femoral tunnel using an interference fit screw and periosteal sutures. An anterior drawer test was performed to assess postoperative joint stability prior to routine closure.

Animals were euthanized 1 (n=4) and 3 (n=3) months post-impact. Menisci were harvested immediately after euthanasia and refrigerated until mechanical tests were performed (within 18 h). Indentation relaxation testing was performed in a room temperature saline bath on the menisci as previously described [4]. Following a 20mN preload, a cylindrical steel 1.59mm diameter indenter tip was used to indent the tissue to a depth of 0.25mm and held for 900 s to reach equilibrium. Hertzian contact was assumed between an elastic half-space (the meniscus), and a rigid sphere (indenter). A Poisson's ratio of 0.01 was assigned to the meniscus. The elastic modulus and Poisson's ratio of the indenter were 210GPa and 0.3 respectively.

A custom MATLAB code was used to obtain the instantaneous and equilibrium modulus from recorded data. These were then compared to

those from a previous study that utilized a similar knee injury lapine model, but without surgical repair of the traumatized joint [4]. Minitab software (Minitab 18, Park College, PA) was used for statistical analyses. Unpaired t-tests were used to compare differences in meniscal mechanical properties between impacted and reconstructed limbs and the contralateral control limbs. Similarly, these tests were performed between results in the 3-month group of the current study and those from a 3-month post-impact group in Fischenich et al. [4]. A p-value less than 0.05 was considered significant.

RESULTS

Mid-substance ACL tears were documented in 6/7 animals, while damage to the posterior attachment of the medial meniscus occurred in 4/7 animals. Mean ± SD failure force was 900.3 ± 77.4 N.

Morphological analyses of the menisci showed increased damage in the medial meniscus compared to the lateral meniscus in the reconstructed limbs, with further degradation across time points. Tears were documented in both menisci across all time points, with increase in tear size and length at a 3-month time point. Increased maceration and synovium growth were documented on the outer 1/3 region of both menisci at a 3-month time point. Due to extreme thinning and tearing in the medial meniscus, not all three regions were able to be tested for mechanical properties.

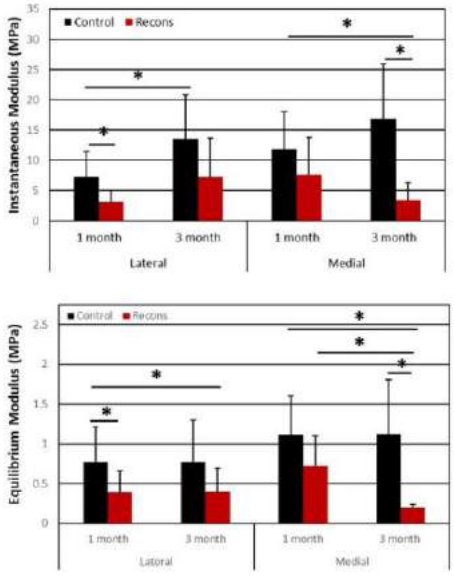

Figure 1: Comparisons of the instantaneous and equilibrium modulus in each meniscus across both time points. * denotes significant differences

In order to perform statistical analysis, the regional data were averaged for a given meniscus and specimen. A significant decrease in instantaneous modulus was found in the medial meniscus in the reconstructed limb at a 3-month time point, compared to the contralateral controls at both time points. Similarly, a significant decrease in the equilibrium modulus of the medial meniscus was observed when compared to the other groups. A significant decrease in the equilibrium modulus in the lateral meniscus was observed between the 1-month contralateral control and reconstructed limbs at both time points (Figure 1).

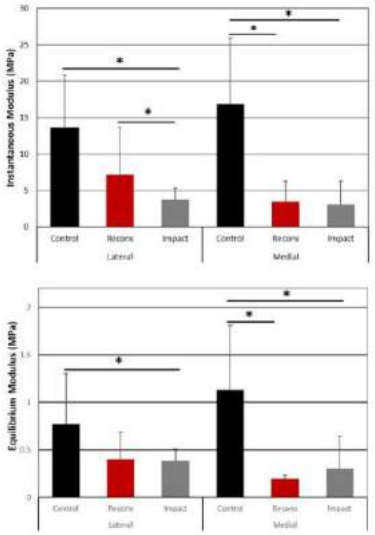

Figure 2: Comparisons of instantaneous and equilibrium modulus between the current study and that of Fischenich et al. * denotes significant differences

A comparison of the current results with those from a previous study performed by our group [4] at the same time point (3-months post impact) showed no significant differences in the instantaneous modulus of the medial meniscus between the impacted and reconstructed limb and the impacted-alone limb when compared to the contralateral control group. Similar results were observed in the equilibrium modulus. However, there were no significant differences in the lateral meniscus between the contralateral control and reconstructed limbs (Figure 2).

DISCUSSION

The closed-joint impact model was able to successfully and reliably generate ACL tears and meniscal damage, comparable to what is observed in the clinical setting. Surgical intervention to repair the damaged ACL and meniscal debridement was successfully performed as well, which replicates the current clinical gold standard. Thus, a novel closed-joint impact and surgical intervention animal model was created. This model can provide a deeper insight into the progression of PTOA that previous animal models could not achieve.

The mechanical property results suggest that surgical intervention does not prevent degenerative changes in the meniscus, specifically in the equilibrium modulus. Although the goal of surgical intervention is to return stability to the joint, the observed degradation of the tissue could be attributed to occult damage caused by the impact at the cellular level.

Future work will include histological interrogation of the tissue and the addition of a 6-month time point, as well as the validation of poloxamer 188 (P188) in aiding to prevent the onset of PTOA by inhibiting cell death in the *in-vivo* setting.

ACKNOWLEDGEMENTS

The study is funded by DOD grants W81XWH-16-1-0735 and W81XWH-16-1-0734.

REFERENCES

[1] Majewski, M et al., *The Knee*, 13(3):184-188, 2006.
[2] Felson, DT, *Radiol Clin North Am*, 42(1):1-9, 2004.
[3] Myklebust, G, and Bahr, R, *Br J Sports Med*, 39(3):127-131, 2005.
[4] Fischenich, KM et al., *J Biomech*, 48(2):246-253, 2015.

SB³C2019
Summer Biomechanics, Bioengineering and Biotransport Conference
June 25 -28, Seven Springs, PA, USA

NON-INVASIVE MRI ASSESSMENT OF MENISCUS AND CARTILAGE CHANGES IN A LARGE ANIMAL MODEL OF MENSICUS INJURY

Kyle D. Meadows (1), Sonia Bansal (2,3), John M. Peloquin (1), Liane M. Miller (2,3), Jay M. Patel (2,3), Kamiel S. Saleh (2), Michael W. Hast (4), Miltiadis H. Zgonis (2,3), Robert L. Mauck (2,3), Dawn M. Elliott (1)

(1) Biomedical Engineering
University of Delaware
Newark, DE, USA

(2) McKay Orthopedic Research Laboratory
University of Pennsylvania
Philadelphia, PA, USA

(3) Translational Musculoskeletal Research Center
CMC VA Medical Center
Philadelphia, PA, USA

(4) Biedermann Laboratory for Orthopedic Research
University of Pennsylvania
Philadelphia, PA, USA

INTRODUCTION

The meniscus serves a key function in knee load-bearing and in protecting the underlying articular cartilage against osteoarthritis (OA). The menisci are commonly injured, and injury impairs the meniscus' ability to distribute loads and often results in cartilage OA. This link between meniscus injury and OA risk is well-known in humans and has been established in small animal models [1,2,3], but the incremental progression of meniscus changes over time and the inter-relationship between cartilage and meniscus degeneration over time remain unknown. Observing this progression requires longitudinal studies with multiple time points, which in turn requires development of appropriate large-animal models and/or noninvasive human imaging.

Our group recently established a large-animal model (porcine) of meniscus injury that at one month showed loss of meniscus proteoglycan, higher contact pressure during joint loading, and cartilage degeneration that varied based on type of injury [4]. These findings demonstrated the usefulness of our model to study progressive knee joint changes after meniscus injury, but the measurement methods used were destructive and so cannot be directly translated to longitudinal studies in humans. To bridge this translational gap, non-invasive measurements with similar utility are needed.

Magnetic resonance imaging (MRI) permits noninvasive longitudinal assessment of structural and compositional changes in the knee, but MRI findings still need to be linked to tissue-level assessments to confirm their validity and interpretation. The purpose of this study was to establish this link between MRI measurements and tissue properties using our established large animal model. Specifically, we sought to identify MRI-observable pathologic remodeling in the meniscus itself and in the adjacent cartilage following meniscus injury, and to correlate these MRI findings to the joint changes previously observed in this model [4].

METHODS

Juvenile (6 month old) Yucatan minipigs underwent bilateral arthroscopic surgery in which each of the two medial menisci received one of the following interventions: sham (arthroscopy with no meniscus incision), DMM (destabilized medial meniscus, where the anterior attachment of the meniscus is transected), vertical longitudinal tear (1/3 arc length, red-white zone), or radial tear (50% of meniscus width) (n=3/treatment). Tears were created with a scalpel in the anterior part of the meniscus. Animals were sacrificed at one month and their joints were harvested for MRI followed by a series of destructive macro- and micro-scale measurements.

Two MRI sequences were acquired of the intact joints on a 3T Siemens Prisma: a multi echo T_2-weighted mapping sequence and a gagCEST sequence (both 0.58 x 0.58 x 3.00mm) and quantitatively analyzed. T_2 relaxation time is linked to water content and to deterioration of the tissue's fiber network (as fiber network degrades, water content increases and T_2 increases). GagCEST is a chemical exchange sequence that is correlated with a tissue's glycosaminoglycan (GAG) concentration [5,6]. T_2 time and gagCEST values were analyzed at and around the tear region of the anterior meniscus (or the same anatomical location in the sham and DMM cases) and in tibial cartilage in the regions covered and uncovered by the meniscus.

The destructive macro- micro-scale measurements were joint contact pressure, cartilage indentation modulus in regions covered and uncovered by the meniscus, and histology. Joint contact pressure was measured by a TekScan #6900-110 pressure sensor inserted into the medial compartment of the joint [7] under 1X body weight (400 N) at 15º of flexion. Cartilage indentation was done using a 2 mm spherical indenter on osteochondral plugs from the medial tibial plateau [8]. Histology was done using radial sections (16 microns thick) taken from the anterior horn stained with Safranin O/Fast green to measure

proteoglycan (PG) content [9]. MRI outcome measures were compared between treatments with one-way ANOVA followed by student's t-test. MRI measures were correlated with the destructive measures using a Pearson's correlations.

RESULTS

In the meniscus tear region, T_2 time was higher with a radial tear (Radial $p<0.06$); gagCEST was higher after DMM ($p<.05$) and lower after radial tear ($p<0.06$) (Fig 1). In the cartilage, T_2 time was higher in the covered region after DMM ($p<0.05$) and in the uncovered region after radial tear ($p<0.05$) (Fig 2). Cartilage gagCEST was higher in the covered region after DMM ($p<0.09$) (Fig 3).

There was a significant correlation of covered cartilage T_2 time with both contact pressure from TekScan and covered cartilage indentation modulus ($p<0.05$) (Fig 4). In the meniscus, histology slices where red stains proteoglycan were compared to gagCEST maps in paired samples and in the same region, showing similar patterns for all groups except DMM which was different than paired histology (Fig 5).

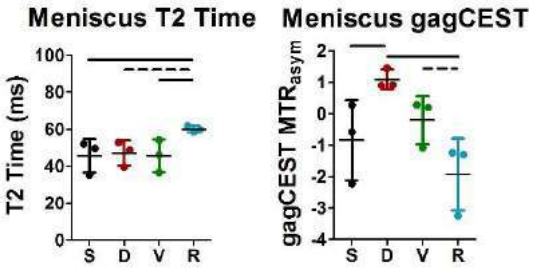

Figure 1: T_2 time and gagCEST values for meniscus in the tear region. Solid bar $p<0.05$, Dashed $p<0.1$ (S=Sham, D=DMM, V=Vertical, R=Radial)

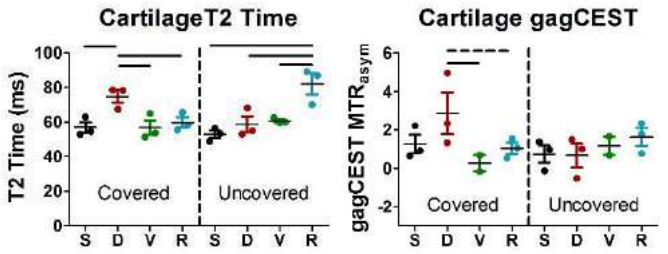

Figure 2: T_2 time and gagCEST values for cartilage. Solid $p<0.05$, Dashed $p<0.1$ (S=Sham, D=DMM, V=Vertical, R=Radial)

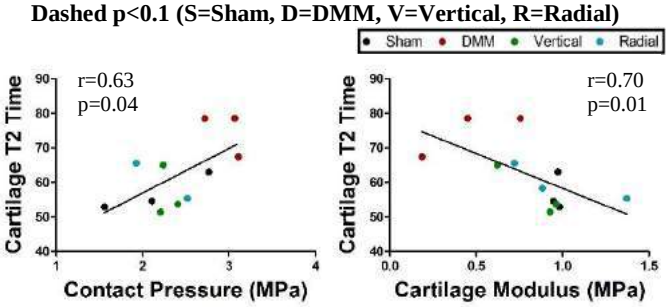

Figure 3: Correlations of Covered Cartilage Indentation Modulus and Contact Pressure to Covered Cartilage T_2 Time

DISCUSSION

This study demonstrated that non-invasive MR assessment of knee joint health can reveal degenerative changes in meniscus and cartilage resulting from injury in a large animal model. For example, imaging successfully detected meniscus changes following injury in T2 and gagCEST values that were confirmed by histology (Fig 1 and 4). These meniscus changes likely led to altered joint loading (confirmed by TekScan, Fig 3) suggesting that increased joint loading occurred in the covered region after DMM and in the uncovered region after radial tear. This altered joint loading likely caused the cartilage degeneration that was also detectable using MRI (Fig 2, 3). Further supporting functional changes following meniscus injury and altered joint loading, cartilage indentation revealed a lower modulus in injured knees which also correlated with cartilage T_2. Since TekScan requires dissection, future work will address in situ loading changes using MRI.

The DMM injury resulted in a distinct meniscus phenotype that appears more degenerative than the vertical and radial tears, as is evident by the meniscus structure/shape, the pattern of GAG staining (histology) and the higher gagCEST values (Fig 4). Additionally, the DMM injury resulted in an unusual change in the gagCEST (suggested a higher GAG content) that was contrary to histology (had less GAG). This may be due to the DMM meniscus being at a later stage of degeneration. This potential explanation is based on human cartilage studies which show that gagCEST MRI is most useful in early stage degeneration that is dominated only by loss of GAG and that T2 and morphological changes appear to bias the gagCEST in late degeneration [10]. Thus meniscus tissue remodeling and reduced fiber organization at the site of transection may cause an increased ability of water molecules to diffuse in and out of voxels during MR scanning and explain our unexpected observation of increased meniscus gagCEST in the DMM injury group. Nonetheless, the gagCEST measurement serves as an indicator that the meniscus is compositionally altered and no longer healthy (as confirmed by gross dissection and histology).

The non-invasive assessments confirmed invasive measurements, providing an important advance to allow longitudinal study of joint changes following different meniscus injuries and, ultimately, new ability to study functional changes. The correlations between invasive measures and non-invasive MRI observed here are particularly useful for guiding interpretation of MRI observations in human studies, for which longitudinal destructive measurements are impermissible, to help inform specifics about the change in function of the tissues of the knee joint. Future work will increase sample size and extend to longer time points. Our long-term goal is to determine mechanisms of post-meniscus injury joint damage and inform when and if surgical intervention should occur after meniscus injury.

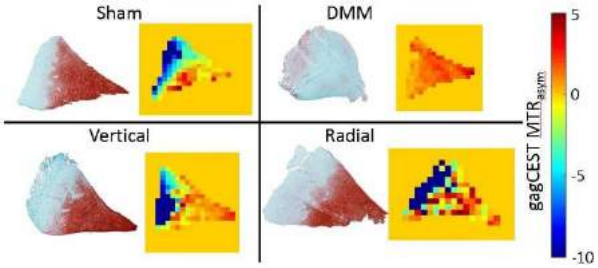

Figure 4: Representative Histology and gagCEST slices

ACKNOWLEDGEMENTS

Supported by NIH R01EB002425, U54GM104941 and Department of Veteran Affairs.

REFERENCES

[1] Glasson, S et al., *Osteoarthr. Cartil.*, 15(9):1061-9, 2007. [2] Roos, H et al., *Osteoarthr. Cartil.*, 3(4):261-7, 1995. [3] Lohmander, L et al., *Am J Sports Med.*, 35(10):1756-69, 2007. [4] Bansal, S et al., *Trans. ORS.*, 2019. [5] Mosher, T et al., *Radiology.*, 214(1):259-66, 2000. [6] Ling, W et al., *Proc Natl Acad Sci USA.*, 105(7):2266-2270, 2008. [7] Bedi, A et al., *J Bone Joint Surg Am.*, 92(6):1390-408, 2010. [8] Meloni, G et al., *Tissue Eng Part A.*, 23(13-14):663-74, 2017. [9] Pauli, C et al., *Osteoarthritis Cartilage.*, 19(9):1132-41, 2011. [10] Schmitt, B et al., *Curr Radiol Rep.*, 2(3):38, 2014.

MAINTAINING CARTILAGE HYDRATION DURING SLIDING PART II: MODES AND COMPETITIVE RECOVERY RATES

D.L. Burris[1,2], A.C. Moore[1,3], B.T. Graham[2], J.M. Benson[1], C. Kook[2], S. Voinier[2], C. Price[1,2]

(1) Biomedical Engineering
University of Delaware
Newark, DE, USA

(2) Mechanical Engineering
University of Delaware
Newark, DE, USA

(3) Bioengineering
Imperial College
London, UK

Introduction

The mechanical, tribological, and biological functions of articular cartilage depend critically on its interstitial hydration, which comprises about 75% of the free-swollen tissue. During contact, however, water content decreases until the osmotic pressure from fixed charges within the collapsing matrix fully support the applied stress; this corresponds to vanishing levels of hydration at physiological stresses (~5 MPa).

Fortunately, there is strong experimental evidence that interstitial hydration, pressure, and lubrication remain high in-vivo. One hypothesis is that cartilage slowly compacts over the day and recovers passively when unloaded at night. Coleman et al. [1] showed that strains in the human knee increase by ~3% over the day and recover by the next morning. The surprising result is not that strains increased throughout the day, but how little they increased; the back of the envelope calculation suggests more than an order of magnitude more. Their observation that evening strain correlated inversely with number of steps taken suggests that movement played a significant role.

Several observations help explain how movement disrupts load-induced exudation. Caligaris and Ateshian [2] showed that a cartilage explant retained interstitial fluid, pressure, and lubrication as long as the contact moved across the cartilage before the fluid could respond. Linn's studies on dog ankles [3] add another dimension: holding load constant, articulation quickly reversed the static exudation process. He attributed recovery to free swelling during periodic exposure of the talus to the bath and concluded that the dynamic equilibrium involved balance between loss and recovery rather than the absence of flow. Both explanations are based on migration of the contact area (MCA). Our recent studies on tribological rehydration add a third dimension [4]: using the convergent stationary contact area (cSCA), we observed consistent loss, maintenance, and recovery dynamics without changing load, without migration, and without exposing the cartilage to the bath.

Thus, static unloading and loaded articulation appear to be equally rational actions for restoring cartilage hydration following static loading. In this paper, we quantify rehydration rates of cartilage under controlled conditions to clarify if one action dominates the other and to determine the relative contributions of free swelling (outside the contact area) and tribological rehydration (inside the contact area) to articulation-induced recovery.

Methods

Materials: This study used bovine stifles from two different local sources (Herman's Quality Meats and Bowman's Butcher). Following joint dissection, a coring saw was used to extract n = 25 φ19 mm osteochondral samples. Samples were stored in and lubricated by a solution of protease inhibitor (P2714, Sigma Aldrich) dissolved in phosphate buffered saline (PBS). to a dilution of 1X based on the manufacture's recommendations. Samples were stored at 4 ºC and tested within 4 days of harvest.

Measurement device: Interstitial fluid loss and recovery rates were quantified using compression measurements from one of two custom instruments. Tribological rehydration and passive swelling rates were quantified using a unidirectional pin-on-disk tribometer comprising a stepper motor to control sliding speed, a 6-channel load cell to measure forces (± 10 mN), and a vertical nanopositioning stage to control load and measure compression (± 100 nm). Free-swelling rates were quantified using an indenter with a two axis load cell (± 10 μN) and a vertical nanopositioning stage to control load and measure compression (± 100 nm).

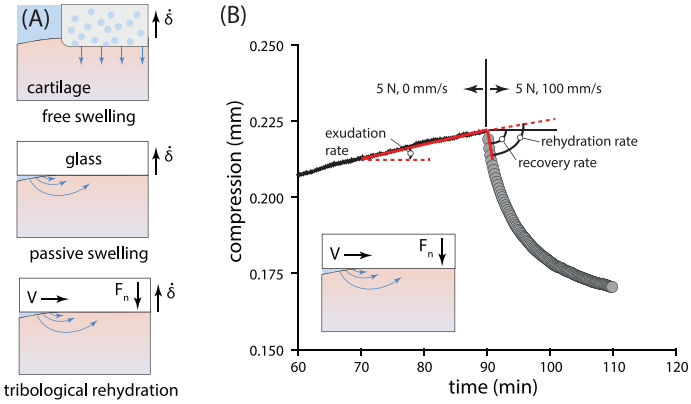

Figure 1. (A) Definitions of the three distinct fluid recovery modes measured here. (B) Illustration of a typical rehydration rate measurement. Cartilage exudes fluid during 90 min of static loading and recovers fluid during loaded sliding due to tribological rehydration; the tribological rehydration rate is the sum of the measured recovery and exudation rates (volume conservation).

Tribological rehydration: The tribometer was used to load N = 7 samples statically against a flat glass disk at a constant 5N of load. To begin, samples were loaded statically for times between 0 and 180 minutes (to vary exudation-induced strain). Following static loading, the disk began sliding at 100 mm/s (Figure 1A) to induce tribological rehydration. The recovery rate was defined as the linear regression of the first 10 seconds of this recovery process. The exudation rate was the slope of the static curve for the same strain range (Figure 1B). The tribological rehydration rate is the sum of these measured quantities (based on volume conservation).

Passive swelling: The tribometer was used to load N = 2 representative samples statically against the flat glass disk at 5N of load for 12.5 and 90 minutes, respectively. Following the static loading period, the load was reduced to 0.25 N, which allowed the instrument to track nominally unloaded passive swelling (Figure 1A). We defined the passive swelling rate as the linear regression of the first 10 seconds of this recovery process.

Free swelling: The indenter was used to load N = 9 samples statically with a ϕ6 mm porous plane-ended indenter to 75 mN for 10 min. and then unloaded to a tare load of 0.1mN, which allowed the instrument to track recovery for nominally unloaded free swelling (Figure 1A). We defined the free swelling rate as the linear regression of the first 10 seconds of this recovery process.

Results

The compression response of a representative cartilage sample to sliding following static loading is shown as a function of time for various static loading times in Figure 2A. After only 0.5 minutes of static loading, the sample continued compressing during sliding. The sample recovered thickness rapidly during sliding after 90 minutes of static loading. In all cases, sliding at 5N of load and 100 mm/s caused the sample to lose or recover fluid until reaching a dynamic equilibrium compression of 0.18 mm. Similar loaded dynamic equilibria were observed during articulation of dog ankles and human knees. It is also worth noting that every sample exhibited a specific and repeatable non-zero 'resting equilibrium deformation' between 0.05 and 0.15 mm during contact after the load was removed such that the change in strain from increased load was typically 3-10%.

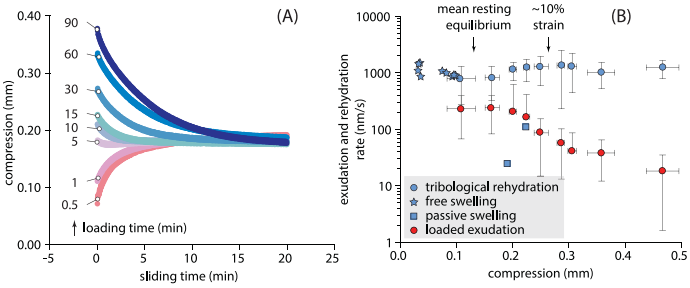

Figure 2. (A) Compression response of a single representative sample during sliding following various static loading times. (B) Summary of results: exudation, free swelling, passive swelling, and tribological rehydration rates are all plotted together as functions of compression. The 'resting equilibrium' denotes the mean compression for contact at equilibrium following load removal.

All of the rehydration and exudation rates collected for this study are plotted as functions of compression in Figure 2B. Loaded exudation rates from cartilage against glass at 5 N decreased as expected with compression from ~200 nm/s near 0.1 mm of compression to 10 nm/s near 0.5 mm of compression. The free swelling rate was 1070 ± 230 nm/s based on N=9 samples. The tribological rehydration rate was 1150 ± 690 nm/s based on 93 measurements of N=7 samples. Passive swelling rates were 20 and 100 nm/s for 90 minutes and 12.5 minutes of loading, respectively. These passive swelling rates highlight the general fact that rates correlated better with time than compression, which depended on both time and widely varying sample moduli.

Discussion

While there have been suggestions that free swelling is the fastest possible mode of fluid recovery, these are, to our knowledge, the first direct measurements of its absolute and relative rates. Free swelling rates were on the order of 1,000 nm/s and did not appear to vary significantly with strain or between samples. More importantly, free swelling rates exceeded exudation rates by 10-100 times depending on the strain, which helps explain why very little activity appears sufficient to counteract the effects of long static loading periods. This is not surprising given that free swelling occurs at a free surface and exudation requires flow through a contact area. The surprising result is that tribological rehydration rates within ***a loaded contact*** were indistinguishable. This is consistent with a fluid film enabling free swelling at the contact interface. However, it is inconsistent with the observation that the highest rehydration rates were accompanied by the highest friction coefficients (>0.4). Furthermore, our previous studies showed evidence that solutes were pushed across the contact area from the leading edge [5]. Our results appear consistent with hydrodynamic pressurization at the leading edge, but the mechanism is unclear. Passive recovery rates were far slower (10-100 nm/s) and comparable in magnitude to in-vivo measurements by the Eckstein group (27 nm/s) based on patellar recovery for human subjects resting in a scanner after deep knee bends (5% recovered in 90 minutes) [6].

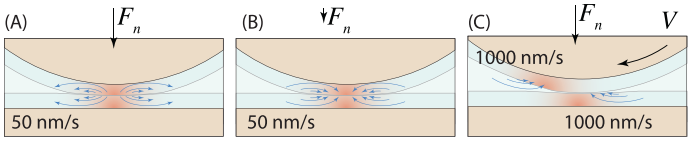

Figure 3. Interpreted flow profiles and estimated rates for a cartilage on cartilage contact under: (A) static loading; (B) static unloading; (C) loaded movement.

To move or to rest – that is the question. Following a period of static loading (standing, sitting at a desk, or sitting in an airplane), there appears to be no question that joint movement rehydrates the contact area far quicker than static unloading. During motion, free swelling rehydrates the dehydrated zone on the migrating component about as quickly as tribological rehydration rehydrates the contact zone on the stationary component; this study demonstrates that these are comparable and complementary modes. Intermittent movement, we propose, is the primary reason joints avoid reaching dangerously low levels of hydration throughout the day. While static loading has been shown to thin human patellar cartilage by 50% in an hour [6], Coleman et al. showed that strains in the knee only increased by ~3% throughout the day [1]. Given that we are active less than 10% of the day, it appears likely that strain accumulation is mitigated by a competition between long periods of slow exudation and sparse but fast periods of recovery.

Prior to 2017, migration was the only known source of articulation-induced interstitial fluid retention and recovery. On this basis, it has been concluded that hip hemiarthroplasties, which create a cSCA, defeat interstitial hydration [7]. In 2017, we demonstrated that tribological rehydration restores interstitial hydration in the cSCA; this study demonstrates that tribological rehydration rates are competitive with those associated with migration. While it is unclear if these rates persist at physiological stresses, previous conclusions should be tempered in the light of this new evidence.

Finally, these results suggest that the cSCA is just as relevant for studies of cartilage mechanics and tribology as the MCA (sphere on cartilage) while offering far more convenience to the experimenter. It removes the challenges of sample curvature, it eliminates plowing, it subjects individual cells to constant yet controllable conditions, and it lends itself well to in-situ bio-imaging [5].

ACKNOWLEDGEMENTS

The authors acknowledge support from the NSF BMMB 1635536.

REFERENCES

[1] Coleman, J. L. et. al., *J. Biomech, 46*(3), 541-1547, 2013
[2] Caligaris, M. et. al., *Osteoarthr. Cartil.*, 16(10), 1220-1227, 2008
[3] Linn, F.C., et. al., *JBJS*, 49(6), 1079-1098, 1967
[4] Moore, A.C., et. al., *Osteoarthr. Cartil., 25(1)*, 99-107, 2017
[5] Graham, B. T., et. al., *Osteoarthr. Cartil, 25(12)*, 2100-2107, 2017
[6] Eckstein, F. et. al., *J. Anat., 208(4)*, 491-512, 2006
[7] Rajan, V., et. al., *Ann Meet ORS, (2120)*, 2010

SB³C2019
Summer Biomechanics, Bioengineering and Biotransport Conference
June 25 -28, Seven Springs, PA, USA

COLLAGEN FIBER ORIENTATION AND MECHANICAL PROPERTIES CORRELATE ACROSS HUMAN ARTICULAR CARTILAGE ZONES

Kristine M. Fischenich (1), Joseph A. Wahlquist (1), Virginia L. Ferguson (1,2,3)

(1) Department of Mechanical Engineering
University of Colorado at Boulder
Boulder, CO, USA

(2) Material Science and Engineering Program
University of Colorado at Boulder
Boulder, CO, USA

(3) BioFrontiers Institute
University of Colorado at Boulder
Boulder, CO, USA

INTRODUCTION

Due to the avascular nature of the tissue, once articular cartilage is injured it has a limited healing capacity and significant damage can result in reduced quality of life and early onset osteoarthritis[1]. As we develop new treatment modalities and tissue engineered replacements, it is critical to understand the structure-function relationship of the tissue throughout the full cartilage thickness. Previous work has described variation in collagen arrangement throughout articular cartilage thickness[2] as well as mechanical anisotropy within each cartilage zone[3]. This zonal-specific anisotropy serves to distribute joint loads. However, while properties of individual articular cartilage zones have been evaluated using small, excised samples from within each zone[4,5], these assessments are complicated by testing *ex-situ* in a non-native stress environment, with imperfect sample geometry and small sample dimensions that fail to enable one to evaluate anisotropy.

In contrast, microindentation testing enables mechanical property assessment within biological tissues (i.e., *in-situ*), thus allowing observation of spatial variation in behavior with nearly intact zonal structure. Beyond just quantifying the mechanical behavior of the osteochondral tissues, it is important to observe the underlying arrangement of the tissue to evaluate relationships between structure and function. Moreover, the ability to test individual micrometer-sized regions within a tissue enables regional assessment. Thus, microindentation provides insight to tissue engineers seeking to reproduce native properties and aids in assessment of disease progression. In the current work, we sought to elucidate the structural organization and material properties in all three orthogonal directions throughout human skeletally mature, zonal articular cartilage. This was accomplished by measuring the collagen fiber orientation via second harmonic generation (SHG) and two photon fluorescence (TPF) imaging and the tensile modulus (*Et*) and compressive modulus (*Ec*) using microindentation.

METHODS

Cartilage was obtained from the femoral condyles of two male and two female human donors (55-61 years old) without a clinical history of osteoarthritis. Specimen were fresh frozen, and experienced two additional freeze thaw cycles throughout the testing process. Three 5 mm cubed samples were obtained from each donor; samples were hydrated in phosphate buffered saline (PBS) during all preparation and all mechanical testing was performed with samples submerged in 1X PBS containing 1% (v/v) Protease Inhibitors (Halt, Thermo Fisher 78438) which was replaced with fresh fluid every three days.

Microindentation was performed on a Hysitron TI-950 nanoindenter. Arrays, five indents wide and spanning the full depth of the distance from the articular surface to the zone of calcified cartilage in all three orthogonal directions (Figure 1), were placed ~10x the contact radius from the tissue corner to avoid edge effects. Direction 3 testing was conducted on the articular cartilage gliding surface, middle zone, and the deep zone. Indents were performed using a cono-spherical probe ($R = 250$ μm), spaced at 250 x 250 μm, to a max indentation depth of 12.5 μm under displacement control. The displacement rates were 1, 4, and 8 μm/s, hold time was 60 seconds, and unload rate was 1 μm/s. The articular cartilage was modeled as a nonlinear biphasic material with a Poisson's ratio near zero as proposed by Soltz and Ateshian[6] and data was applied to the indentation equation by Burris *et al.*[7]. Using the "Hertz Burris Theory" (HBT) the tensile modulus (*Et*) and equilibrium contact modulus (*Ec*) were evaluated.

The prevalence of collagen was investigated using SHG and TPF imaging (BioRad Radiance 2100 confocal and Coherent Chameleon Ultra II laser tuned to 800 nm wavelength). Imaging was performed

without staining or contrast agents on face 1 and face 2 spanning the surface, middle, and deep zones (Figure 2). Collagen I and II direction was observed from the SHG signal and measured using Image J and applying the Orientation J plugin and the finite difference gradient method[8]. The interface between articular cartilage and subchondral bone was taken as the zero axis and all collagen fiber angle measurements were calculated as the smallest absolute value from that zero axis with 90° being the highest obtainable angle.

For all statistical analysis, a linear mixed model was used with donor (and sample for mechanical analysis) as repeated variables and the direction and zone as fixed effects. A post-hoc Tukey's test was used for individual comparisons between groups with $p<0.05$ considered significant. Lastly, a linear fit between collagen fiber orientation and average *Ec* and *Et* across all zones was used to assess the correlation between the two measures.

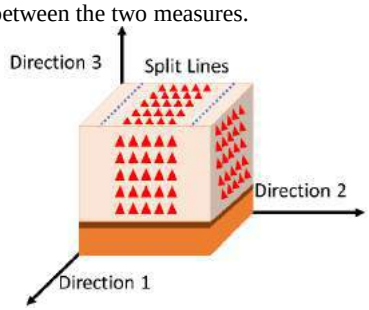

Figure 1: Sample orientation and indent location. SHG was performed on two sides, the planes normal to direction 1 and 2.

RESULTS

No outliers were found for any of the measured collagen orientation data and no significant differences ($p>0.05$) were identified between the directions 1 and 2 so data was grouped. The collagen fiber orientation was found to increase with depth relative to the articulating surface for all donors (Figure 2) and when assessed collectively the three zones were all significantly different from each other ($p<0.05$). Average orientation angles were 45.4°, 20.6°, and 8.1° for the deep, middle, and surface zones respectively.

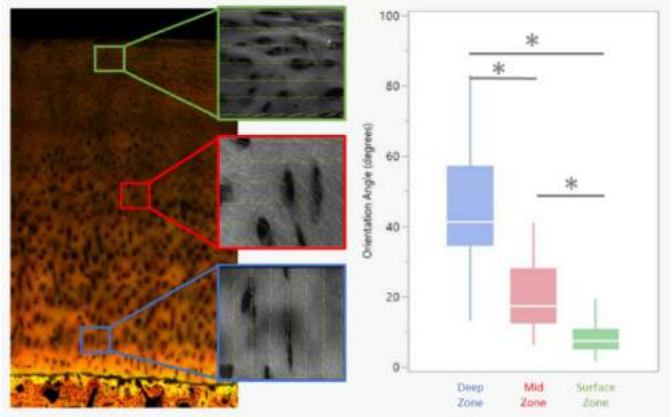

Figure 2: Left) SHG image and Orientation J vector analysis images Right) boxplot of collagen fiber orientation (face 1 and face 2 combined) vs zone*denotes significant difference.

Outliers, as determined using the Huber method[9], were removed from the mechanical analysis results. The tensile modulus regardless of direction or orientation exceeded the compressive modulus (*Et/Ec* mean = 2.04). Differences across directions were observed with direction 3 (normal to the articulating surface) being frequently significantly different ($p<0.05$) from the other two directions (Figure 3). There were also significant zonal differences identified in both the *Ec* and *Et*. In all cases, modulus values were higher in the deep zone compared to the surface zone, and this trend was most obvious when comparing *Ec* values. When correlating collagen fiber orientation to modulus, the compressive modulus had a stronger correlation compared to the tensile modulus ($R^2 = 0.45$ and 0.8, respectively) (Figure 3).

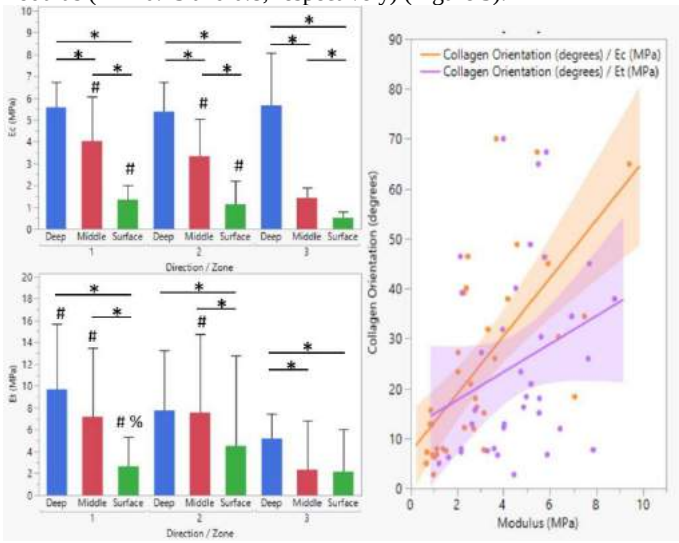

Figure 3: Left) modulus results for *Ec* and *Et* as a function of direction and zone *denotes significant differences in zones within directions, #denotes significant difference with direction 3 within zone %denotes significant difference with direction 2 within zone Right) correlation of collagen fiber orientation and modulus

DISCUSSION

These results demonstrate that microscale mechanical properties of human articular cartilage are both directionally and zonally dependent. By combining SHG and TPF, the collagen fiber orientation was mapped and compared to micromechanical assessments. Findings suggest collagen fiber orientation may be more linearly related to equilibrium contact modulus rather than tensile modulus when modeled as a nonlinear biphasic material and tested in indentation at the micron level.

These results are in agreement with previous work on bulk samples highlighting the change in collagen fiber orientation with increasing distance from the articulating surface as well as mechanical anisotropy[2–5]. Work is ongoing to analyses site-matched Raman spectroscopy data to relate mechanical and structural properties to the chemical composition of the tissue. Collectively this work will represent one of the first studies to investigate structure, mechanics, and composition in all three orientations of human articular cartilage and will help to guide future disease studies and tissue engineering strategies.

ACKNOWLEDGEMENTS

This work was supported by the National Institutes of Health [1R01AR069060].

REFERENCES

[1] Heir, S. et al., *Am J Sports Med.*, 38(2):231-237, 2010 [2] Hunziker, E. et al., *OA&C*, 10(6):432-463, 2002 [3] Jurvelin, J. et al., *Trans Orthop Res Soc.*, 217:215-219, 2003 [4] Akizuki, S. et al., *J Orthop Res.*, 4(4):379-392, 1986 [5] Robinson, D. et al., *JMBBM*, 61:96-109, 2016 [6] Soltz, M. et al., *J Biomech*, 122(6):576, 2000 [7] Bonnevie, E. et al., *Tribol Lett.*, 41(1):83-95, 2011 [8] Schneider, C. et al., *Nat Methods.*, 9(7):671-675, 2012 [9] Huber, P.J. et al., *Ann Math Stat.*, 35(1):73-101., 1964

SB³C2019
Summer Biomechanics, Bioengineering and Biotransport Conference
June 25 -28, Seven Springs, PA, USA

TOWARD QUANTIFYING CHANGES IN THE COLLAGEN NETWORK OF HUMAN ARTICULAR CARTILAGE DURING EARLY-STAGE OSTEOARTHRITIS

Phoebe E. Szarek (1), Magnus B. Lilledahl (2), Courtland G. Lewis (3), David M. Pierce (1,4)

(1) Department of Biomedical Engineering
University of Connecticut
Storrs, CT, USA

(2) Department of Physics
Norwegian University of Science and Technology
Trondheim, NOR

(3) Bone & Joint Institute
Hartford Healthcare
Hartford, CT, USA

(4) Department of Mechanical Engineering
University of Connecticut
Storrs, CT, USA

INTRODUCTION

Collagen fibers act as structural, load-bearing components in most soft biological tissues. Often, these fibers account for a majority of the tissue's mechanical strength and stiffness. In articular cartilage specifically, collagen fibers make up 15-20% of the wet weight [1] and exhibit depth-dependent orientations and fiber diameters [2]. In addition to the depth dependency, degeneration of cartilage during the development of osteoarthritis (OA) affects the collagen and its arrangement and diameter [3]. Understanding how the collagen network evolves during early-stage OA can aid in understanding the impact of evolving intra-tissue mechanics on the progression of OA. We aimed to characterize changes in the density, diameter, and orientation of collagen during early-stage OA, and to provide high fidelity, through-thickness data for proposing, fitting, and validating constitutive models.

The diameter of a single collagen fiber falls between 10 – 300 nm making it impossible to resolve single fibers using standard light microscopy [4]. Instead of using photons as in light microscopy, electron microscopy (EM) uses high-speed electrons as the energy source allowing for higher resolution. Transmission electron microscopy (TEM) specifically offers a valuable method to observe the collagen network, because specimen preparation is well suited for applications where the specimen size is on the range of millimeters, and because one aims to observe the internal morphology. TEM methods also stabilize and preserve the microstructure of tissues during imaging; thus the results still reflect the character of tissues *in vivo*.

The aim of this study is to utilize TEM and custom image analyses to visualize and quantify distributions of diameter, principal orientation, and dispersion (about this principal orientation) of collagen fibers in the early stages of OA (OARSI grades of 0, 1, 2, 3 [5]) in the superficial (SZ), middle (MZ), and deep (DZ) zones through the thickness.

METHODS

Selecting Specimens: To study cartilage spanning the course of OA progression, we obtained tissues removed during total knee arthroplasties (TKAs) at Hartford Hospital. We stored tissue at -80°C in phosphate-buffered saline (PBS) to minimize structural changes prior to fixation [6]. First, we determined the local split-line direction (SLD) by pricking the surface of the cartilage with a dissecting needle dipped in India ink [7]. We then extracted ~1-3 mm cuboid, full-thickness cartilage specimens using razor and surgical scalpel blades while identifying and marking the edge of the cuboid parallel to SLD.

We also extracted a specimen adjacent to each primary specimen for histology and OARSI grading [5]. Trained individuals independently graded randomized histological images that contained two images from each specimen. We evaluated interobserver variability and averaged grades to obtain a single OARSI grade for each specimen. Based on these grades, we chose 17 specimens (spanning the progression of OA and from multiple patients) to process for TEM imaging. These specimens allowed us to assess the inter-grade and inter-patient variability in the measured network quantities.

Preparing Specimens and Imaging via EM: We fixed the primary specimens in 3.0% glutaraldehyde, 3.0% paraformaldehyde, 0.05% w/v tannic acid in 0.1 M PIPES buffer for 2 hours [8]. Next, we trimmed off all subchondral bone and sliced the cuboids into ~0.5 mm thick pieces parallel to the imaging plane (parallel to the SLD) using a surgical scalpel before placing in the fixative overnight. We performed post-fixation with 1% osmium tetroxide for 1 hour and *en bloc* staining with 2% uranyl acetate in 50% ethanol for 15 min, followed by 2.5% Reynold's lead citrate for 3 min. We dehydrated the specimens in graded ethanol before clearing with propylene oxide. We infiltrated and embedded the specimens with Spurr's resin and polymerized the resin in a flat-bottom embedding capsule for 24 hours at 70°C.

We then cut ultrathin (50 nm) sections using an Diatome Ultra 45° diamond knife on a Leica Ultracut UCT ultramicrotome and collected the ~1-2 mm sections on copper 50 mesh grids before staining with 2% saturated uranyl acetate for 8 min and 2.5% Sato's lead citrate for 3 min. We imaged sections using a FEI Technai 12 G2 Spirit BioTWIN.

Analyzing the Images: First, we implemented a custom code using Matlab [9] that divides the images into subimages and transforms them into the Fourier domain (which rotates any linearity by 90°) to determine the angle of the principal direction based on analytical minimization of a least-squares function. We found the dispersions of fiber orientations around this direction by comparing the weight of the alignment in these principal directions to the relative weight of the directions perpendicular. We determined the distributions in fiber diameters within each image by selecting $n = 100$ fibers, one from each region in a 10×10 grid overlay, and measured their diameter using ImageJ [10]. We assigned images to specific through-thickness zones by using the relative distances from the articular surface and the following zonal definitions based on total thickness: SZ (0-15%), MZ (15-70%), DZ (70-100%) [11]. We will determine the number of images from each specimen and zone using power analysis based on a preliminary comparison of inter-grade and inter-patient variability.

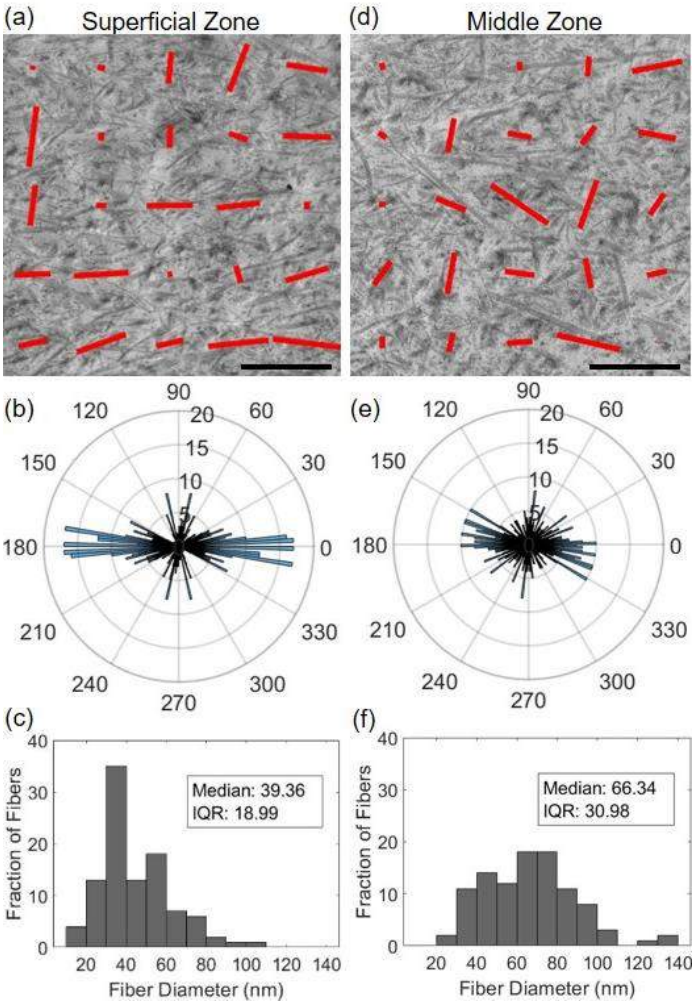

Figure 1: Representative (a,d) TEM images with local fiber orientations (red lines); polar histograms of principal directions (based on 16×16 subimages (b,e); and distribution in fiber diameters (c,f) for SZ (a-c) and MZ (d-f). Scale bar = 2 μm.

RESULTS

Figure 1 shows preliminary results from a single patient with one specimen taken from the SZ and one from the MZ. Lines overlaid on the TEM images represent the local principal orientations of collagen fibers and the degree of anisotropy ($\rho \in \{0,1\}$) by the angles and relative length of the lines, respectively [9]. The polar histograms of local principal orientations of collagen fibers where $\rho > 0.25$ (meaningful local alignment) quantify local fiber alignment by zone and visible differences between the SZ and MZ [9]. The difference in the distributions in fiber diameters between the SZ and MZ is significant ($p < 0.05$).

DISCUSSION

These preliminary results show a greater alignment in the SZ visually evident in the smaller angular distribution of local principal orientations of the fibers. This conclusion aligns with previous studies qualitatively assessing changes in fiber alignment through the thickness [2,12]. The fibers in the SZ are also on average thinner than those in the MZ, also a finding in previous studies [2,3]. However, our preliminary results show greater variation in fiber diameters in the MZ, which was not the case in [2]; additional images in our zonal comparisons will show a clearer picture. To resolve single fibers, we also needed to capture the images at a magnification that results in a single image of ~5×5 μm; to holistically characterize each zone, we will need multiple images from each zone.

Since the orientation of fibers is a key element in defining through-thickness zones within cartilage, we capture images from the through-thickness 'middle' of each zone to ensure that our images represent the respective zones. Our methods for quantifying both the local orientation and dispersion of the fibers requires dividing the initial image into sub-images. We determine and justify the optimal number of regions of interest following our previous studies [13]. Importantly, the network of collagen within human cartilage is truly three-dimensional, so our two-dimensional images do not capture any out-of-plane variations. However, based on the orientation of our imaging planes relative to the SLD, we assume that these variations are negligible.

We expect to see the local orientation and dispersion of the collagen network, and diameter of the fibers, change during to the remodeling that occurs with progression of OA (quantified via OARSI grades). The findings of this study will provide quantitative data to aid: (1) our understanding of the evolving intra-tissue mechanics on the progression of OA; (2) the development, refinement, and validation of biomechanical models of cartilage; and (3) the development of tissue-engineered biomaterials to serve as cartilage replacements.

ACKNOWLEDGEMENTS

GAANN P200A160323; NSF 1662429; Biosciences Electron Microscopy Facilities at the University of Connecticut.

REFERENCES

[1] Sophia Fox, A et al., *Sports Health*, 1:461-468, 2009. [2] Changoor, A et al., *Osteoarthritis Cartilage*, 19:1458-1468, 2011. [3] Gottardi, R, Hansen, U et al., *PlosONE*, 11:e0163552, 2016. [4] Bancelin, S et al., *Nat Commun.*, 5:4920, 2014. [5] Pritzker K et al., *Osteoarthrtis Cartilage*, 14:13-29, 2006. [6] Szarko M et al., *BMC Musculoskelet. Disord.*, 11:231, 2010. [7] Below S et al., *Arthroscopy*, 18:613-617, 2002. [8] Keene, D, Tufa, S, *Methods Cell Biol.*, 96:443-473, 2010. [9] Lilledahl, M, et al., *IEEE Trans Med. Imaging*, 30:1635-1648, 2011. [10] Schneider, C, et al., *Nat. Methods*, 9:671-675. [11] Mow, V, et al., *Basic orthopaedic biomechanics & mechanobiology*, 180-258, 2005. [12] Xia, Y, Elder, K, *J. Microsc.*, 204:3-16, 2001. [13] Schriefl, A et al, *J. R. Soc. Interface*, 9:3081-3093, 2012.

SB³C2019
Summer Biomechanics, Bioengineering and Biotransport Conference
June 25 -28, Seven Springs, PA, USA

TYPE III COLLAGEN IS A KEY REGULATOR OF COLLAGEN FIBRILLAR STRUCTURE IN CARTILAGE PERICELLULAR MATRIX

C. Wang (1), B. K. Brisson (2), Q. Li (1), M. Terajima (3), M. Enomoto-Iwamoto (4), M. Yamauchi (3), S. W. Volk (2), L. Han (1)

(1) School of Biomedical Engineering, Science and Health Systems
Drexel University
Philadelphia, PA, United States.

(2) School of Veterinary Medicine
University of Pennsylvania
Philadelphia, PA, United States.

(3) NC Oral Health Institute
University of North Carolina,
Chapel Hill, NC, United States.

(4) Department of Orthopedics
University of Maryland
Baltimore, MD, United States.

INTRODUCTION

The collagen network in the extracellular matrix (ECM) of cartilage mainly consists of heterotypic collagen fibrils of types II, IX and XI, with minute amount of collagen I. Type III collagen (collagen III), another fibril-forming collagen type, is often considered to co-assemble with collagen I, rather than collagen II [1]. Interestingly, recent literature suggested that collagen III is also present in the collagen II-rich cartilage ECM, and can contribute up to ~10% of total cartilage collagens [2]. In addition, our recent study showed that heterozygous deficiency of collagen III (in *Col3a1*$^{+/-}$ mice) results in abnormally thickened collagen II fibrils and reduced modulus of cartilage [3]. Further, literature has suggested that collagen III is more concentrated in the PCM [4], the microdomain where initial fibril assembly takes place [5]. Here, we studied the spatial distribution of collagen III in cartilage ECM and its role in mediating the structural integrity and micromechanics of cartilage. Specifically, we delineated the role of collagen III in the PCM and the further-removed, territorial/interterritorial matrix (T/IT-ECM). We focus on the role of collagen III in the structure and function of cartilage PCM.

METHODS

Sample preparation. Mice were harvested from 2-month old wild-type (WT) and *Col3a1*$^{+/-}$ BALB/c male mice. Knockout mice were unavailable due to their perinatal lethality [6]. The human articular cartilage samples were obtained at the total knee arthroplasty and de-identified for non-human subject research.

Immunohistochemistry (IHC). For mice, whole knee joint were harvested, fixed in 4% paraformaldehyde, decalcified in 10% EDTA, 6-µm-thick sagittal sections were obtained from paraffin embedded blocks, and used to stain for type III collagen (ab7778, Abcam) along with human cartilage specimen.

AFM nanoindentation modulus mapping. With the guidance of immune-labelled collagen VI (70R-CR009X, Fitzgerald) [7] on 8-µm unfixed tibia sagittal cryo-sections assisted by Kawamoto's film method [8], then AFM-nanomechanical mapping was performed using microspherical tips ($R \approx 2.25$µm, k ≈ 1 N/m, µMasch) and an MFP-3D AFM in PBS with protease inhibitors at room temperature. For each map, a 40 × 40 indentation grid was acquired over a 20 × 20 µm^2 region of interest containing well-defined, ring-like PCM terrains [9]. The effective indentation modulus, E_{ind}, was calculated using finite thickness-corrected Hertz model [10].

Collagen Structural analysis. To assess collagen fibril structure, TEM was applied to tibia sagittal sections of middle/deep zone cartilage [11]. Tibia was fixed in Karnovsky's fixative, decalcified, dehydrated with series ethanol, infiltrated and embedded following established procedures [12]. Sections were examined and imaged at 80 kV using a TEM (JEOL Ltd., Tokyo, Japan) equipped with a Gatan Orius CC Digital camera (Gatan Inc., Pleasanton, CA).

Biochemical analysis. To quantify collagen cross-link density, femoral head cartilage was collected, reduced with NaB^3H_4, hydrolyzed with 6N HCl and subjected to amino acid and cross-link analyses, as described previously [13].

Statistical test. All dataset was conformed to normal distribution after applying Kolmogorov-Smirnov test. For nanoindentation modulus and cross-link density analysis, two-sample *t*-test was applied. For collagen structural analysis, two-sample *z*-test was applied to compare the average fibril diameter, and *F*-test was applied to compare the variance. Significance level was set at $\alpha = 0.05$.

RESULTS

Collagen III immunoreactivity is found high in the PCM in healthy human cartilage, as well as in WT and *Col3a1*$^{+/-}$ murine

cartilage (Fig. 1a,b). In contrast, in OA human cartilage, collagen III was present throughout the ECM (Fig. 1a). In accordance with the known role for collagen III in regulating collagen fibril structure [14] and its more localized distribution in the PCM, TEM images showed significantly increased collagen fibril diameters with a broader distribution, i.e., higher variance (Fig. 2a-c). Meanwhile, AFM-nanoindentation showed significant reduction in the modulus of *Col3a1*$^{+/-}$ cartilage PCM, highlighting the important role of collagen III in mediating the collagen fibril assembly in the PCM (Fig. 2e). In the further removed ECM, we also observed fibril thickening and modulus reduction upon collagen III reduction, albeit to a lesser degree (Fig. 3b,c). At the tissue level, while the total collagen content was similar between the two genotypes (not shown), significant increases in the amount of both reducible (dihydroxylysinonorleucine, DHLNL) and non-reducible (deoxypyridinoline, d-Pyr) cross-links were observed in *Col3a1*$^{+/-}$ cartilage (Fig. 3d).

DISCUSSION

Given that the initial steps of collagen fibrillogenesis takes place in the PCM [5], our data showing localization of collagen III to the cartilage PCM (Fig. 1) provoke the hypothesis that collagen III could play critical roles in regulating the initial collagen fibril assembly of cartilage [5]. Indeed, the reduction of collagen III leads to pronounced structural defects of collagen fibrils networks (Fig. 2). These observations corroborate with literature showing collagen III can co-assemble with collagen II on fibril surfaces to regulate collagen II fibril assembly [15]. Taken together, our results point to a direct role of collagen III in regulating cartilage structural integrity by limiting the lateral growth of collagen II fibrils, as has been previously described for collagen I fibrils. Since the initial fibril assembly in the PCM serves the basis for the growth of T/IT-ECM [5], we also observed significant fibril thickening and modulus reduction in the T/IT ECM, despite the low concentration of collagen III. Notably, since the PCM plays key roles in mediating chondrocyte mechanotransduction [16], collagen III could also potentially regulate chondrocyte activities by influencing the PCM. We therefore propose a more comprehensive description of cartilage collagen fibrils to be a heterotypic fibrillar network of collagen II/III/IX/XI.

For articular cartilage, for the first time, we report that tissue modulus is negatively correlated with collagen cross-link density, as a result of genetic mutation. This finding may seem counter-intuitive, but it emphasizes the fact that mechanical properties are an integrated manifestation of both molecular composition and hierarchical structure [17]. While collagen cross-linking is crucial for the assembly and stability of collagen fibrils, tissue mechanical properties also largely depend on other factors such as fibril organization, packing and collagen-proteoglycan interactions. Here, loss of collagen III leads to increased cross-linking, but at the same time, disrupted collagen fibril nanostructure. With regards to the net impact of collagen III deficiency on tissue modulus, our results thus suggest that these structural defects overweigh the effect of increased cross-links. Interestingly, such observation is consistent with previous observations in fibromodulin-null tendon [18]. Therefore, for cartilage, perhaps other connective tissues such as tendon, while collagen cross-link density is an important determinant of tissue integrity, it cannot serve as a direct predictor for tissue biomechanical properties.

ACKNOWLEDGEMENTS

This work was supported by the Drexel Area of Research Excellence (DARE) Grant, the Penn Center for Musculoskeletal Diseases (PCMD) (NIH P30AR050950) and the PCMD Pilot Grant. We thank Dr. D. E. Birk and S. Adams for the help of TEM imaging.

REFERENCES

[1] Fleischmajer, R et al., *Ann N Y Acad Sci* 580:161-175, 1990. [2] Eyre, DR et al., *Eur Cell Mater* 12:57-63, 2006. [3] Price, JR et al., *Lancet Infect Dis* 17:207-214, 2017. [4] Hosseininia, S et al., *Osteoarthritis Cartilage* 24:1029-1035, 2016. [5] Wenstrup, RJ et al., *J. Biol. Chem.* 279:53331-53337, 2004. [6] Brisson, BK et al., *Am. J. Pathol.* 185:1471-1486, 2015. [7] Zelenski, NA et al., *Arthritis Rheumatol* 67:1286-1294, 2015. [8] Kawamoto, T et al., *Methods Mol. Biol.* 1130:149-164, 2014. [9] Chery, DR et al., *Trans. Orthop. Res. Soc.* 63:2017. [10] Dimitriadis, EK et al., *Biophys J* 82:2798-2810, 2002. [11] Dunkman, AA et al., *Matrix Biol* 32:3-13, 2013. [12] Dunkman, AA et al., *Matrix Biol* 35:232-238, 2014. [13] Yamauchi, M et al., *Methods Cell Biol* 143:115-132, 2018. [14] Eyre, D, *Arthritis Res* 4:30-35, 2002. [15] Wu, JJ et al., *J. Biol. Chem.* 285:18537-18544, 2010. [16] Alexopoulos, LG et al., *Acta Biomater* 1:317-325, 2005. [17] Hung, CT et al., *J. Orthop. Res.* 34:8-9, 2016. [18] Kalamajski, S et al., *J. Biol. Chem.* 289:18873-18879, 2014.

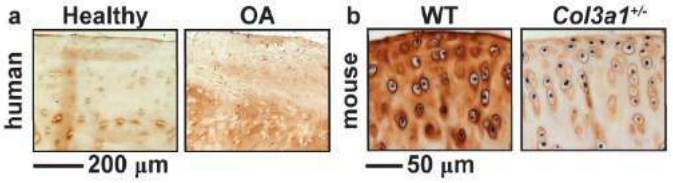

Figure 1: IHC of collagen III shows a) the localization in healthy human cartilage, and up-regulation in OA tissue, b) the localization in WT and *Col3a1*$^{+/-}$ murine tibia cartilage, and the reduction in *Col3a1*$^{+/-}$ cartilage.

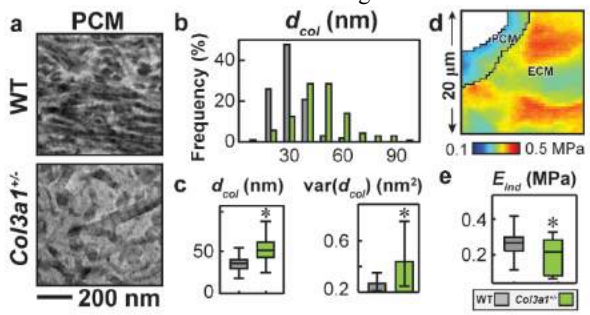

Figure 2: Structural and mechanical phenotype of *Col3a1*$^{+/-}$ cartilage **PCM**. a) TEM images show altered fibril structure. b,c) Distribution of PCM fibril diameters, d_{col}, and mean and variances. d,e) Representative modulus map of WT cartilage, and reduced E_{ind} detected in *Col3a1*$^{+/-}$ cartilage PCM. (measured from $n \geq 4$ animals, mean ± 95% CI, *: $p < 0.001$)

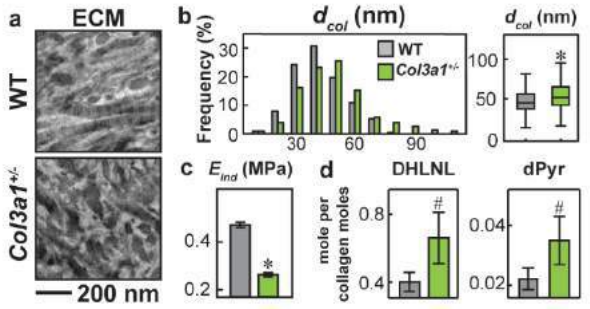

Figure 3: At tissue-level, Structural and mechanical phenotype of *Col3a1*$^{+/-}$ cartilage **ECM**. a) Typical TEM images.b) Distribution of ECM fibril diameters, increased in fibril diameter, c) decrease in modulus, and d) increase in the cross-link densities. (mean ± 95% CI, $n = 4$. *: $p < 0.001$, #: $p < 0.05$)

SB³C2019
Summer Biomechanics, Bioengineering and Biotransport Conference
June 25 -28, Seven Springs, PA, USA

A COMPARISON OF THE DEFORMATION RESPONSE OF THE BRAIN TO MILD ACCELERATION IN THE AXIAL AND SAGITTAL PLANES IN A HEALTHY VOLUNTEER

A. K. Knutsen (1), A. D. Gomez (2), J. L. Prince (2), P. V. Bayly (3), J. A. Butman (1,4), D. L. Pham (1)

(1) Center for Neuroscience and Regenerative Medicine
The Henry M Jackson Foundation
Bethesda, MD, USA

(2) Department of Electrical and Computing Engineering
Johns Hopkins University
Baltimore, MD, USA

(3) Department of Mechanical Engineering and Materials Science
Washington University in St. Louis
St. Louis, MO, USA

(4) Clinical Center
National Institutes of Health
Bethesda, MD, USA

INTRODUCTION

Traumatic brain injury (TBI) is a common health problem across the world; approximately 1.7 million emergency department visits, hospitalizations, and deaths occurred per year due to TBI from 2002 to 2006 [1]. Forms of TBI can occur as a direct result of rapid mechanical deformation of brain tissue, potentially leading to diffuse axonal injury. The purpose of this study is to use tagged magnetic resonance imaging (MRI) to quantify how the brain deformation response differs in response to mild axial and sagittal loading of the skull. Such data is important for determining brain regions that are most vulnerable to injury, as well as for validating computational models of TBI.

METHODS

One healthy volunteer (male, 31 years of age at the time of the first scan) was evaluated under a protocol approved by the Institutional Review Board at the National Institutes of Health to measure brain deformation during a mild acceleration in the axial and sagittal planes. Two devices were constructed to create reproducible loading in each of the planes [2,3]. Acceleration in the axial plane was generated when the device shaft impacted a rigid stop after the subject rotated his head approximately 32 degrees towards the left shoulder; acceleration in the sagittal plane was generated when the head cradle impacted a rigid stop after a neck extension of ~5 degrees. Angular velocity and acceleration of the device shaft were measured using an angular position sensor (MICRONOR, USA).

MRI scans were performed using a 3 T Biograph mMR (Siemens, Erlangen, Germany). For acceleration in the axial plane, a series of 12 axial slices (tag lines along the left-right and anterior-posterior axes) and 6 orthogonal slices (30 degree rotation between slices with tag lines along the inferior-superior axis) were acquired. For acceleration in the sagittal plane, a series of 13 sagittal slices (tag lines along the anterior-posterior and inferior-superior axes) and 13 axial slices (tag lines along the left-right axis) were acquired. Acquisition parameters were: temporal resolution = 18.06 ms, tag spacing = 8 mm, voxel resolution = 1.5 x 1.5 x 8 mm, slice thickness = 8 mm with a 2 mm gap between parallel slices, four repetitions per slice. The subject repeated the motion 120 times for the axial loading and 156 times for the sagittal loading. Displacement relative to the skull ($\boldsymbol{u}$) and Lagrangian strain ($\boldsymbol{E}$) were computed using the harmonic phase finite element (HARP-FE) method [4]. Eigenvalues and eigenvectors were estimated from $\boldsymbol{E}$. The first principal strain (E_1) was used in this analysis. Volume fraction, which is the number of voxels above a threshold value divided by the total number of voxels, was computed for a strain threshold of 3 percent.

Additional scans were acquired to relate measurements of brain deformation to brain anatomy and axonal structure. MPRAGE (1x1x1 mm), T2 (0.98x0.98x1 mm), and 39 diffusion weighted images (2x2x2 mm, b = 1000 s/mm^2) were acquired. The MPRAGE was segmented into different brain regions [5]. Diffusion tensors were estimated from the diffusion weighted images using TORTOISE software package [6]. Eigenvalues and eigenvectors were computed from the diffusion tensors, and fractional anisotropy was calculated. In regions labeled as white matter via segmentation and with fractional anisotropy values greater than 0.2, the first principal eigenvector ($\boldsymbol{n}$) was used to infer white matter fiber orientation. Strain along white matter fibers (E_f) was computed; only positive E_f values (stretch) were analyzed.

$$E_f = \boldsymbol{n} \cdot \boldsymbol{E} \cdot \boldsymbol{n} \quad (1)$$

RESULTS

Average peak angular velocity and acceleration were 3.7 rad/s and -230.6 rad/s^2 for axial loading and 2.0 rad/s and -346.6 rad/s^2 for sagittal loading. Figure 1 shows the distribution of E_1 and relative displacement as a function of time and in various brain regions. The zero-point on the

time axis was set to be the time of peak angular velocity. Both relative displacement and E_1 values increased to their largest values at 24-28 ms after peak angular velocity and then decayed. The regions of high relative displacement and strain differed between the two loading conditions, though the median values of both measurements were similar – 0.41 mm and 2.4 percent for axial loading versus 0.50 mm and 1.8 percent for sagittal loading. Maximum values (99th percentile of the distribution) were larger under acceleration in the axial plane(1.84 mm and 7.5 percent) than the sagittal plane (1.19 mm and 5.1 percent).

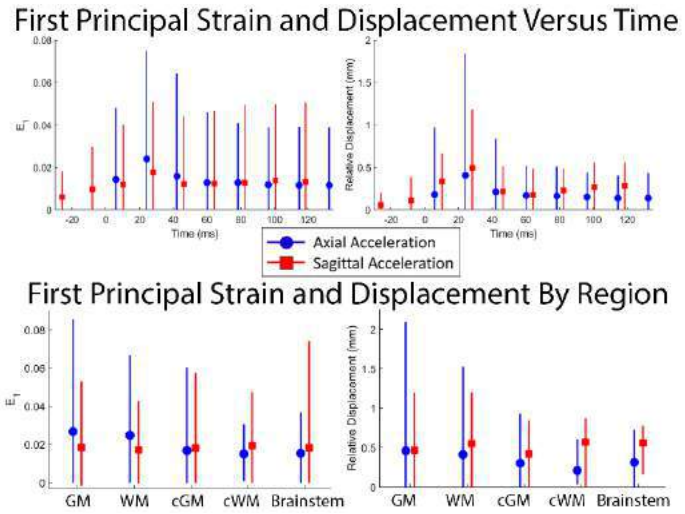

Figure 1: The top row shows the distribution of E_1 and relative displacement versus time during acceleration in the axial (blue) and sagittal (red) plane. The bottom row shows the distribution at peak deformation in cerebral gray matter (GM), cerebral white matter (WM), cerebellar gray matter (cGM), cerebellar white matter (cWM), and the brainstem. Vertical lines show the distribution from the 1st to 99th percentile; the circle and square indicate the median of the distribution. For the axial acceleration, the image used as the reference was acquired just prior to the time of peak angular velocity.

Figure 2 shows the distribution E_f as a function of time and images at the time of peak deformation. The median and maximum (99th percentile) E_f values were similar during acceleration in the axial and sagittal planes – 0.2 and 4.4 versus 0.2 and 3.9 percent. For acceleration in the sagittal plane, E_f values were largest in the brainstem and cerebellar white matter, whereas they were largest in the corpus callosum for axial loading.

At peak deformation, the volume of brain with E_1 exceeding 3 percent was almost 3 times larger in axial loading versus sagittal loading – 32.8 versus 11.3 percent. However, when only the brainstem and cerebellum are considered, the volume fraction is almost twice as large for sagittal loading compared to axial loading – 18.2 versus 9.8 percent.

DISCUSSION

This study provides high resolution 3D displacement and deformation measurements over time in a healthy volunteer in response to mild acceleration in the axial and sagittal planes. This work extends to 3D previously published work [e.g., 2-3]. Additionally, these results provide the first in vivo measurements of fiber stretch in the live human brain. The results show that regions of high strain (both E_1 and E_f) and relative displacements vary under different loading conditions, with acceleration in the axial plane leading to increased cortical strains, and acceleration in the sagittal plane yielding increased strains in the brainstem and cerebellum. These results can be compared to subject-specific computational models of TBI.

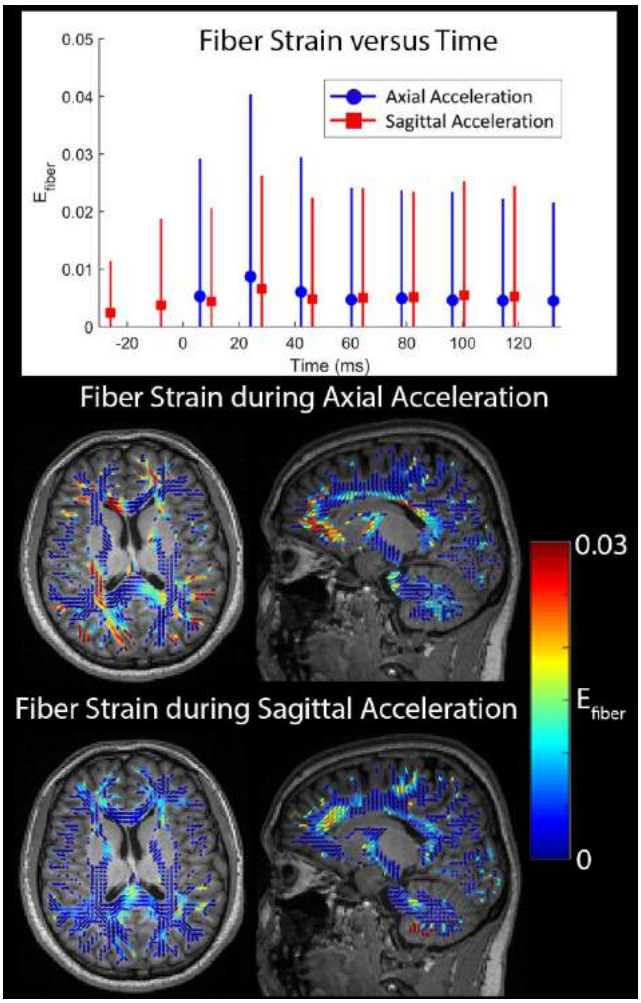

Figure 2: The top row shows the distribution of positive fiber strain (E_f) as a function of time. The vertical lines show the span of the distribution from the 1st to 99th percentile. The circle and square indicates the location of the median value for accelerative loading in the axial and sagittal planes, respectively. The bottom two rows contain images of E_f mapped to 3D ellipsoids that show the direction and orientation of the diffusion tensor.

ACKNOWLEDGEMENTS

We acknowledge funding from the National Institute of Neurological Disorders and Stroke (R56 NS055951), the Department of Defense in the Center for Neuroscience and Regenerative Medicine, and the National Institutes of Health Intramural Research Program.

REFERENCES

[1] M. Faul et al., *Handbook of Clinical Neurology*, 127: 3-13, 2015
[2] D. Chan et al., *J Biomech Engr*, 140: 101005-1-13, 2018
[3] Y. Feng et al., *J. R. Soc. Interface*, 7:1677–1688, 2010
[4] S. Roy et al., *IEEE J. Biomed Health Inform*, 19(5): 1598-1609,
[5] https://science.nichd.nih.gov/confluence/display/nihpd/TORTOISE
[6] A.D. Gomez et al., *IEEE Trans Biomed Eng*, 2018 (ePublished)

SB^{3}C2019
Summer Biomechanics, Bioengineering and Biotransport Conference
June 25 -28, Seven Springs, PA, USA

LONGITUDINAL HEAD IMPACT EXPOSURE AND WHITE MATTER INTEGRITY ANALYSIS AMONG RETURNING YOUTH FOOTBALL PLAYERS

Mireille E. Kelley (1, 2), Jillian E. Urban (1, 2), Derek A. Jones (1, 2), Elizabeth M. Davenport (3), Logan E. Miller (1, 2), Beverly M. Snively (4), Alexander K. Powers (5), Christopher T. Whitlow (6, 7), Joseph A. Maldjian (3), Joel D. Stitzel (1, 2)

(1) Virginia Tech-Wake Forest School of Biomedical Engineering and Sciences, Winston-Salem, NC, USA

(2) Department of Biomedical Engineering, Wake Forest School of Medicine, Winston-Salem, NC, USA

(3) Department of Radiology, University of Texas Southwestern, Dallas, TX, USA

(4) Department of Biostatistical Sciences, Wake Forest School of Medicine, Winston-Salem, NC, USA

(5) Department of Neurosurgery, Wake Forest School of Medicine, Winston-Salem, NC, USA

(6) Department of Radiology (Neuroradiology), Wake Forest School of Medicine, Winston-Salem, NC, USA

(7) Clinical and Translational Sciences Institute, Wake Forest School of Medicine, Winston-Salem, NC, USA

INTRODUCTION

Single-season changes in brain imaging and cognitive function have been associated with head impact exposure (HIE) metrics in contact sport athletes, but the effect of HIE on white matter alterations over multiple seasons is not well understood [1-3]. Additionally, continued research is still needed in athletes ≤18 years old because athletes at this age are undergoing structural brain growth and development of memory, problem solving, and other cognitive skills [4]. Therefore, the objective of this study was to characterize changes in HIE across multiple seasons and determine whether changes in HIE correlate with changes in imaging metrics over two consecutive seasons among youth football players.

METHODS

On-field head impact data were collected among youth football athletes between 2012 and 2017 using the Head Impact Telemetry (HIT) System for all practices and games. Study participants also completed a pre- and post-season MRI protocol, including diffusion tensor imaging (DTI). Athletes that only participated in the study for a single season were excluded from the present analysis and only returning athletes with at least two consecutive seasons of data were included. HIE was quantified in terms of number of impacts, peak linear and rotational head acceleration, and risk-weighted cumulative exposure (RWE) [5, 6]. The change in HIE metrics between consecutive seasons was also computed for each athlete. HIE was evaluated overall and stratified by session type (i.e. practices and games). ANCOVA was used to evaluate HIE variation by season (i.e. season number 1, 2, and 3) while controlling for repeated measures across seasons. Team was used as a covariate.

DTI scalar metrics, including Fractional Anisotropy (FA), Mean Diffusivity (MD), and shape anisotropy coefficients (linear anisotropy, C_L; planar anisotropy, C_P; and spherical anisotropy, C_S) were evaluated. A control group of 16 non-contact sport athletes were used to determine the total number of abnormal white matter voxels, defined as 2 standard deviations above or below the control group mean. The difference in the number of abnormal voxels between Season 1 and Season 2 was computed for each scalar metric and subject for regression analyses (ΔDTI scalar metrics: ΔFA_{voxels}, ΔMD_{voxels}, $\Delta C_{L\text{-}voxels}$, $\Delta C_{P\text{-}voxels}$, and $\Delta C_{S\text{-}voxels}$). The differences in DTI scalar metrics from Season 2 to Season 3 were not computed due to the small sample size (N=6). Linear regression analyses were performed to evaluate the relationships between changes in HIE metrics and changes in DTI scalar metrics between Season 1 and Season 2. The linear models were also adjusted for the covariates of average age between Season 1 and Season 2 preseason scans and the difference in pre- to post-season scan times between the two seasons.

RESULTS

Among the returning athletes, 33 athletes had 2 years of data, 13 athletes had 3 years of data, and 1 athlete had 4 years of data. This resulted in 109 athlete-seasons of head impact exposure data among the 47 individual returning athletes. Athletes included in the present study ranged in age from 9-13 years old. 19 of the 47 athletes had usable imaging data and HIE for two consecutive seasons.

A total of 41,148 head impacts were collected. The change in HIE measures varied among returning athletes, with some athletes experiencing increases in HIE and other athletes experiencing decreases in HIE from one season to the next. Among all returning athletes, there were no significant differences (all $p>0.05$) in HIE metrics among season number.

There were athletes with increases in the number of abnormal voxels, while others had decreases from Season 1 to Season 2. The change in total number of practice impacts demonstrated a significant positive association with all ΔDTI scalar metrics (Table 1). The change in 50th percentile impacts per practice and change in 50th percentile impacts per session were also significantly positively correlated with ΔFA_{voxels}, $\Delta C_{L\text{-}voxels}$, $\Delta C_{P\text{-}voxels}$, and $\Delta C_{S\text{-}voxels}$. Examples of the positive linear relationship between change in the number and frequency of practice impacts and ΔDTI scalar metrics are shown in Figure 1.

Table 1. Summary of linear regression analyses results between ΔHIE metrics (predictor) and ΔDTI scalar metrics (outcome) controlling for average age and the difference in time between scans between Season 1 and Season 2.

		ΔFA_{voxels}		ΔMD_{voxels}		$\Delta C_{L\text{-}voxels}$		$\Delta C_{S\text{-}voxels}$		$\Delta C_{P\text{-}voxels}$	
		Type III p	Partial R^2	Type III p	Partial R^2	Type III p	Partial R^2	Type III p	Partial R^2	Type III p	Partial R^2
Season	Δ Number of Impacts	0.06	0.21	0.08	0.19	0.05	0.23	0.07	0.21	0.07	0.20
	Δ 50th %ile Impacts/Session	***0.0004***	***0.58***	0.3	0.07	***0.0002***	***0.61***	***0.0002***	***0.62***	***0.002***	***0.49***
	Δ 95th %ile LA (g)	0.6	0.02	0.7	0.01	0.4	0.04	0.6	0.02	0.7	0.01
	Δ 95th %ile RA (rad/s^2)	0.7	0.01	0.9	0.00	0.7	0.01	0.7	0.01	0.8	0.00
	Δ RWE_{cp}	0.6	0.02	0.6	0.01	0.5	0.03	0.6	0.02	0.7	0.01
Games	Δ Number of Impacts	0.6	0.02	0.9	0.00	0.6	0.02	0.6	0.02	0.5	0.03
	Δ 50th %ile Impacts/Session	0.4	0.05	1.0	0.00	0.3	0.08	0.3	0.08	0.3	0.08
	Δ 95th %ile LA (g)	0.7	0.01	0.9	0.00	0.6	0.02	0.6	0.02	0.6	0.02
	Δ 95th %ile RA (rad/s^2)	1.0	0.00	1.0	0.00	0.8	0.01	0.8	0.00	0.9	0.00
	Δ RWE_{cp}	0.8	0.00	0.9	0.00	1.0	0.00	1.0	0.00	1.0	0.00
Practices	Δ Number of Impacts	***0.02***	***0.32***	***0.01***	***0.34***	***0.01***	***0.34***	***0.02***	***0.30***	***0.03***	***0.28***
	Δ 50th %ile Impacts/Session	***<0.0001***	***0.66***	0.1	0.14	***<0.0001***	***0.67***	***<0.0001***	***0.70***	***0.0008***	***0.54***
	Δ 95th %ile LA (g)	0.2	0.13	0.4	0.04	0.08	0.19	0.2	0.12	0.2	0.11
	Δ 95th %ile RA (rad/s^2)	0.9	0.00	0.8	0.00	0.8	0.01	0.8	0.00	1.0	0.00
	Δ RWE_{cp}	0.6	0.02	0.6	0.02	0.4	0.04	0.5	0.04	0.6	0.02

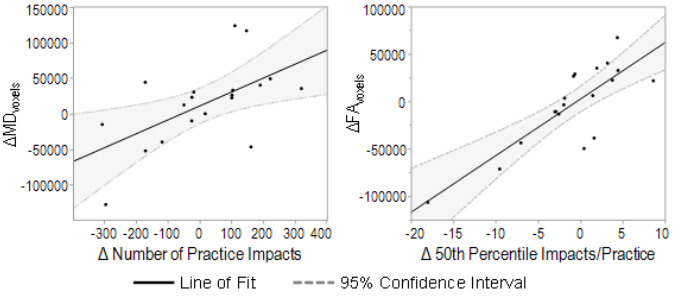

Figure 1. Δ Number of Practice Impacts vs. ΔMD_{voxels} (Left) and Δ 50th Percentile Impacts per Practice vs. ΔFA_{voxels} (Right) adjusted for average age and difference in time between scans.

DISCUSSION

This longitudinal study evaluated changes in HIE metrics and the relationship between changes in HIE and changes in neuroimaging measures among a cohort of youth football athletes. The results demonstrate that HIE can increase or decrease between seasons among individual youth football athletes and that there were no significant changes in HIE from one season to the next in this cohort. There were both increases and decreases in the number of abnormal DTI voxels from Season 1 to Season 2 and those changes were significantly positively correlated with changes in the number of practice impacts, 50th percentile number of impacts per practice, and 50th percentile number of impacts per session. While prior studies have shown single-season associations between HIE metrics and neuroimaging measures, this study suggests reduction in the number and frequency of head impacts, especially in practice, may reduce the number of abnormal imaging findings from one season to the next in youth football. The results from this study support continued efforts to reduce HIE in practice. Additionally, the study findings warrant future investigations into the long-term relationship between HIE and neuroimaging findings to better understand how reduction in subconcussive HIE may affect the brain over many years of participation in football.

ACKNOWLEDGEMENTS

Research reported in this publication was supported by the NINDS of the NIH under Award Numbers R01NS094410 and R01NS082453. The NCATS, NIH, through Grant KL2TR001421 supported Dr. Jillian E. Urban. The content is solely the responsibility of the authors and does not necessarily represent the official views of the NIH. The authors give special thanks to the Childress Institute for Pediatric Trauma at Wake Forest Baptist Medical Center for providing support for this study.

REFERENCES

[1] Davenport, EM et al., *J Neurotrauma*, 31(19):1617-24, 2014.
[2] Bazarian, JJ et al., *PLoS One*, 33(23):2133-46, 2016.
[3] Mayinger, MC et al., *Brain Imaging Behav*, 12(1):44-53, 2018,
[4] Guskiewicz, KM & Valovich McLeod, TC. *PM R*, 3(4):353-64, 2011.
[5] Rowson, S et al., *Ann Biomed Eng*, 41(5):873-82, 2013.
[6] Urban et al., *Ann Biomed Eng*, 41(12):2474-87, 2013.

IMAGING AND MECHANICAL CHARACTERIZATION OF THE PIA-ARACHNOID COMPLEX

Nikolaus A. Benko (1), Emma Luke (2), Yousef Alsanea (1), Brittany Coats (1)

(1) Mechanical Engineering
University of Utah
Salt Lake City, Utah, USA

(2) Biomedical Engineering
University of Rochester
Rochester, NY, USA

INTRODUCTION

Computational modeling has become an important tool for studying the biomechanics of traumatic brain injury. Model accuracy depends on the adequate characterization of brain materials as well as surrounding bone and soft tissue [1]. Numerous studies have characterized the material properties of cortical grey and white matter, but few efforts have focused on the pia-arachnoid complex (PAC), which connects the brain to the skull and plays a role in constraining brain deformation during injury. In this study, we image the human pia-arachnoid complex via optical coherence tomography (OCT) and conduct *in situ* mechanical testing of the PAC through fluid pressurization of the subarachnoid space.

METHODS

Studies were reviewed by the University of Utah Institutional Review Board and determined to be exempt from human study regulation. Fresh-frozen human cadaver heads (male, ages 50-86 years old, n=7) were defrosted and allowed to reach room temperature. A large craniotomy was performed on each hemisphere of the skull using an autopsy saw. Dura between the sagittal sinus and temple region was removed, exposing the PAC. Heads were placed in a stereotactic frame for OCT imaging with a Bioptigen R2200 spectral OCT scanner (Leica USA) and a 12mm telecentric lens. Scan volume was 5mm x 5mm x 1.64mm with 800A-scans per B-scan, 400 B-scans, and a single C-scan. The axial resolution of the system was 1.6µm, the lateral resolution was 6.25µm, and depth resolution was 12.5µm.

In each imaging location, a 27-gauge needle was inserted through the arachnoid membrane to inflate the subarachnoid space to physiological intracranial pressure (10±1.5mmHg). This was achieved using a custom system consisting of a Pendotech pressure monitor (model 1-06-64-04-2) and syringe pump (NE-300 New Era Pump Systems). Feedback control was provided by an Arduino Uno (Arduino AD) and MATLAB (Mathworks) program. Once the pressure had reached steady state, a volumetric scan was taken. The pressure was then increased to 20mmHg. During this inflation, a video recording of two planar B-scans was recorded using screen capture software. A second volumetric scan was obtained once subarachnoid pressure

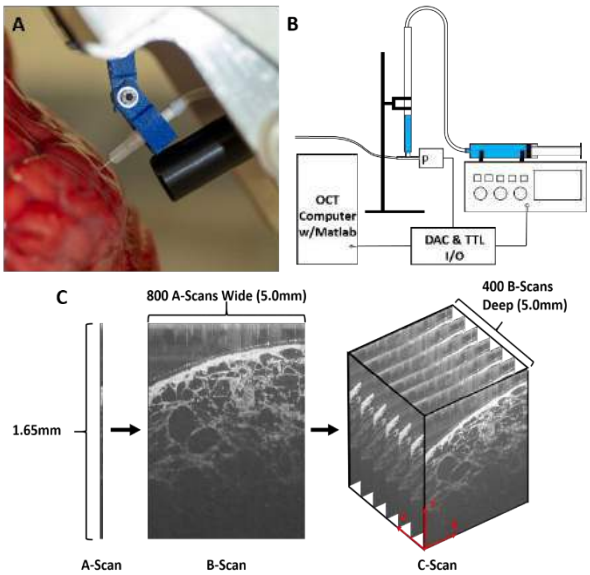

Figure 1: A: Positioning of OCT lens and pressurization system in brain. B: Schematic of the pressurization system. C: Example of a 3D volumetric scan via OCT.

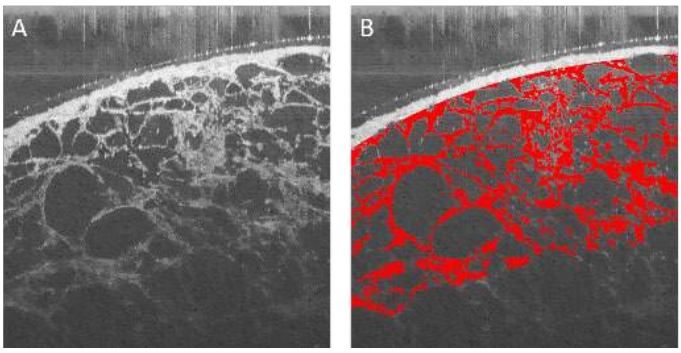

Figure 2: A: OCT image of arachnoid membrane and trabeculae. B: Segmented arachnoid trabeculae.

reached steady state. This process was repeated as the subarachnoid pressure was raised to 30mmHg. Between 8 and 12 locations were imaged for each hemisphere of each brain. Each hemisphere was subdivided into a 2x3 grid to classify regions as frontal, parietal, or occipital and as inferior or superior for a total of 12 regions per brain.

To quantify the density of trabecular fibers, three 2D slices were selected from each 3D volumetric stack. Images were masked and trabecular fibers segmented using a custom semi-automatic technique. Trabecular volume fraction (VF) was calculated by taking the ratio of segmented pixels to total pixels below the arachnoid membrane (Fig. 2). Traction stiffness of the PAC was measured in three of the seven brains. For these measurements, OCT B-scan videos captured the distance between the arachnoid membrane and cortical surface. A custom video analysis script tracked the displacement of the membrane throughout the inflation process. Displacement data were synchronized with pressure data and converted to stress and strain. Stress was defined as the measured pressure. Strain was defined as the displacement of the arachnoid membrane relative to the original segmented height. The average number of subarachnoid vessels at each location was also extracted. One-way ANOVAs with matched pairs were used to quantify regional dependencies of VF and elastic modulus. A two-way ANOVA was used to evaluate age and regional effects of modulus. A multiple regression evaluated the effect of VF and average vessel number on predictions of PAC stiffness.

RESULTS

Trabecular volume fraction, vessel count, stress, and strain were measured at 55 locations throughout the three subjects. The stress-strain response was linear in both 10-20mmHg and 20-30mmHg inflations (Fig. 3). Linear regression was used to quantify elastic moduli E_1 for 10-20mmHg tests and E_2 for 20-30mmHg tests. E_2 was significantly greater than E_1 ($p<0.0001$).

VF significantly decreased from anterior to posterior regions of the brain ($p=0.029$), while elastic modulus E_2 significantly increased from anterior to posterior regions of the brain ($p=0.03$, Fig. 4). E_2 was significantly reduced in donors $\geq$ 60 years of age ($p=0.02$). No significant trends were observed for E_1. Multiple regression analysis indicated a significant interaction effect between the number of subarachnoid vessels and volume fraction when predicting elastic modulus ($p=0.018$).

DISCUSSION

Mechanical testing of human cadaver PAC via fluid pressurization revealed a linear elastic material response. This finding matches results from an *ex vivo* test of bovine PAC in traction, and computational estimates of porcine PAC stiffness [2,3]. The overall average measured modulus of 11.7 kPa is comparable to the 61-148 kPa reported for

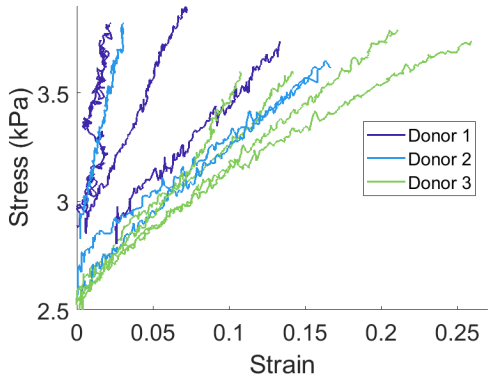

Figure 3: **Stress-strain plots from 20-30 mmHg tests in superior frontal regions.**

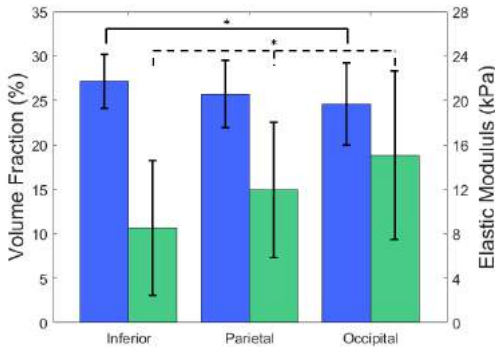

Figure 4: Regional analysis of VF (blue) and E_2 (green) in anterior-posterior groups.

bovine PAC by Jin et al. [2]. Variances between the values likely stem from species, age, and postmortem differences.

VF alone and vessel count alone did not correlate to PAC stiffness. Instead the interaction of both effects was significantly predictive of E_2, which suggests that both arachnoid trabeculae and subarachnoid vasculature dictate the local stiffness of the PAC, and that understanding the interplay between the two may be critical for improved predictions of brain/skull displacement. Further quantification of vessel size in addition to the number of vessels may shed light on these connections.

One interesting finding was a significant decrease in PAC stiffness with age in brains from donors >60 years without a corresponding change in VF or vessel number. This suggests a natural degradation of the structures and warrants further investigation into the age-dependent properties of the PAC. One limitation of the study is the unknown effect of freezing and thawing on PAC material properties This will be investigated in a future study. This study demonstrates the first known method of *in situ* imaging and material characterization of the human PAC. Results highlight the mechanical complexity of the subarachnoid space and suggest that the development of heterogeneous material models may aid in the improvement of computational models of TBI.

ACKNOWLEDGEMENTS

NSF Smart and Connected Health Award No. 1622741.

REFERENCES

[1] Zhao et al. *J Mech Behav Biomed Mater,*80:222–234, 2018
[2] Jin et al. 2007 *Stapp Car Crash ,*51:115–126, 2007
[3] Scott and Coats. *Biomech Model Mechanobiol*,15:1101–1119, 2016.

SB³C2019
Summer Biomechanics, Bioengineering and Biotransport Conference
June 25 -28, Seven Springs, PA, USA

MECHANICAL AND INTERFACIAL CHARACTERIZATION OF MENINGIOMA THROUGH MR IMAGING

E. Ozkaya (1), D. Nistal (2), Zeynep M. Suar (1), A. Chartrain (2), C. Gologorsky (3), P. Balchandani (4), R. Shrivastava (4), M. Kurt (1,4)

(1) Department of Mechanical Engineering
Stevens Institute of Technology
Hoboken, NJ, USA

(2) Department of Neurosurgery
Icahn School of Medicine at Mount Sinai
New York, NY, USA

(3) Department of Biomedical Engineering
Cornell University
Ithaca, NY, USA

(4) Translational and Molecular Imaging Institute (TMII)
Mount Sinai Hospital
New York, NY, USA

INTRODUCTION

In brain tissue it is understood that change in shear modulus can be related to pathology or intrinsic abnormalities (1). In the case of meningiomas, which account for up to 30% of all primary intracranial tumors, mechanical characterization ahead of surgery is crucial for surgical planning (2). Meningiomas are primarily treated by surgical resection. Two important determinants for complete resection include degree of firmness and adhesiveness to the surrounding healthy brain tissue (3). Recently, with magnetic resonance elastography (MRE), a novel non-invasive imaging technique, these two tumor characteristics can be addressed preoperatively (4, 5, 6). Especially, with the slip interface imaging technique, meningioma-brain interface adhesiveness can be quantified (7,8). In this study, we performed a broadband mechanical characterization protocol for meningioma through multi-frequency MRE. Multi-frequency MRE data has been transformed into frequency-independet domain through standard linear solid (SLS) model fitting by using the global mean storage and loss modulus values under three different actuation frequencies of meningioma and normal brain regions. The purpose of this is to create a consensus among neurosurgeons. Furthermore, we applied a phased-based video amplification technique on meningioma patients' data collected by cardiac gated balanced steady-state free precision (bSSFP) sequence which utilizes the heart as an intrinsic actuator (9). Through the acquired phase offset time frames, tracking the relative motion of meningioma with respect to the surrounding healthy brain tissue boundary is targeted.

METHODS

Imaging Protocol

Institutional review board approval was obtained from the Mount Sinai Hospital IRB. Nine meningioma patients aged between 35-68 (3 Female & 6 Male) underwent MRI scans in which a 3T whole-body GE MR750 Discovery MRI system (GE Healthcare, Milwaukee, WI) is used. MRE data is acquired for 48 slices via multi-slice spin echo EPI pulse sequence in the axial plane (acquisition matrix: 128×128, TE/TR=60/2000, FOV=24, 8 phases). As an MRE actuator, a head pillow (Mayo Clinic) is used under actuation frequencies of 40, 60, and 80 Hz. 3D Direct Inversion is used to obtain elastograms. Through the bSSFP sequence a short cine MRI movie capturing the meningioma regions' movement with respect to surrounding healthy brain tissue over different phases of cardiac cycle is created. Each captured frame of the cine MRI scan contains a 2D acquisition matrix of 512×512 for 24 sagittal slices of the brain except one patient having 14 sagittal slices. For each sagittal slice, 84 different phase offset is captured during a cardiac cycle. Amplification of the cine MRI dataset is done by using a bandwidth having a lower cutoff frequency of 0.01 Hz and a higher cutoff frequency of 3.0 Hz with an amplification factor of 20 (9).

Neurosurgeon grading

The neurosurgeons were asked to fill out a survey to provide information about the meningioma consistency (Extremely soft:0 - Extremely firm:10), tumor vascularity (Avascular stage:0 - Metastatic Stage:10), brain-tumor interface, (Smooth, Lobular, Fingerlike expansion, Invasive), and the extent of normal tissue preservation after meningioma resection (Poor:0 - Excellent: 10).

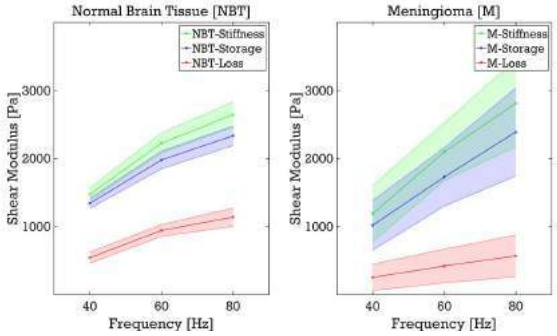

Figure 1: MRE acquisition under three actuation frequency for normal brain tissue vs. meningioma.

Pathology grading

Tumor specimens were excised and evaluated by an experienced neuropathologist at the Icahn School of Medicine at Mount Sinai, New York, NY. A trichrome stain was used to evaluate extent of collagen within the tumor (1=focal - 3=diffuse) and the level of cellularity was classified as low, moderate, or high (Figure 2).

Figure 2: Pathology grading through trichrome staining. A) Score +1, B) Score +2.5, C) Score +3.

Relative Motion Tracking

On a single sagittal slice, with the *imfreehand* command in MATLAB, meningioma boundary and the nearby brain-meningioma interface boundary were manually drawn to create binary masks. This was followed by the use of minimum eigenvalue detection algorithm from MATLAB computer vision toolbox to tag traceable corner points inside these binary mask regions (Figure 3).

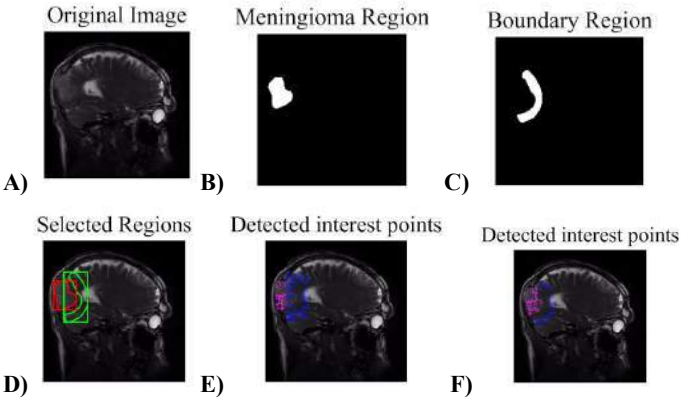

Figure 3: Relative motion tracking between meningioma and the surrounding healthy brain interface boundary region. A) Original image. B) Meningioma region. C) Interface boundary region. D) Manually selected boundaries. E) Traceable tagged points inside the rectangular regions generated by the minimum eigenvalue detection algorithm. F) Traceable tagged points inside the masked rectangular regions.

RESULTS

Stiffness maps were acquired for each actuation frequency and meningioma volumes were separated from normal brain tissue. This was followed by obtaining the average stiffness (|G|), storage (G') and loss (G'') values for meningioma and normal brain tissue (Figure 1). Steady state stiffness ($\mu 1$) and the viscosity (η) were obtained for each patient (Figure 4).

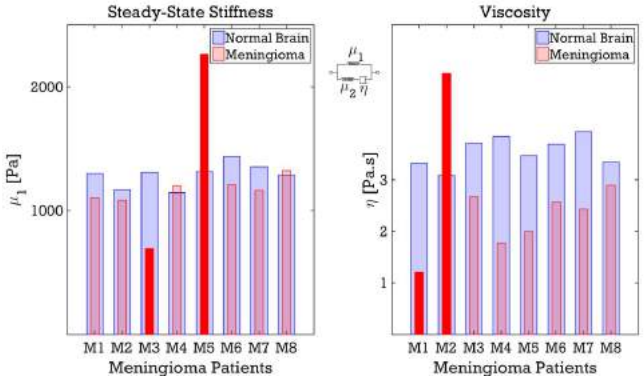

Figure 4: Strandard linear solid (SLS) material model fitting for meningioma and normal brain tissue.

A thorough examination of the link between aMRI relative displacement and neurosurgeon's resection assessment is pending. However, if we consider Patient 7 (Figure 3), the neurosurgeon assessment revealed a well-preserved arachnoid region after resection (Score=7), implying a loose connection. Our aMRI tracking results with an amplification factor of 20 demonstrate that for this patient, the maximum relative motion between the tumor and the brain is on the order of several pixels.

DISCUSSION

Our study provides the first insight into the applicability of aMRI on the characterization of brain-meningioma interface. Further phantom validation studies are needed to quantify the limits of amplification for which no other sources of noise is introduced.

REFERENCES

[1] Wuerfel, Jens et al., *Neuroimage,* 49(3):2520-2525, 2010

[2]Shiroishi, Mark S. et al., *Neurosurgery Clinics,* 27(2):145-154, 2016

[3] Oertel, Joachim et al., *Neurosurgical review*, 26(26-4):168-174, 2003

[4] Murphy, Matthew C. et al., *Journal of neurosurgery*, 118(3): 643-648, 2013

[5] Hughes, Joshua D. et al., *Neurosurgery*, 77(4):653-659, 2015

[6] Reiss-Zimmermann, M. et al., *Clinical neuroradiology*, 25(4):371-378, 2015

[7] Yin, Ziying et al., *Radiology*, 277(2):507-517, 2015

[8] Yin, Ziying, et al., *Journal of Magnetic Resonance Imaging*, 46(4):1007-1016, 2017

[9] Terem, Itamar et al., *Magnetic resonance in medicine*, 2018

SB³C2019
Summer Biomechanics, Bioengineering and Biotransport Conference
June 25 -28, Seven Springs, PA, USA

A NETWORK-BASED BRAIN INJURY METRIC FOR CONCUSSION PREDICTION

Shaoju Wu (1), Wei Zhao (1), Bethany Rowson (2), Steve Rowson (2), Songbai Ji (1,3)

(1) Department of Biomedical Engineering
Worcester Polytechnic Institute
Worcester, MA, USA

(2) Department of Biomedical Engineering and Mechanics
Virginia Tech
Blacksburg, VA, USA

(3) Department of Mechanical Engineering
Worcester Polytechnic Institute
Worcester, MA, USA

INTRODUCTION

Traumatic brain injury (TBI), including sports-related concussion, is a major public health problem in the United States (US) [1]. To date, much of the biomechanical work has centered on developing a scalar injury metric to describe head impact severity, based on which to further predict injury. Response-based injury metrics produced from impact simulations using finite element (FE) model of the human head are increasingly becoming important, as they can be related to tissue-level injury tolerances established from *in vivo*/*in vitro* experiments and clinical outcomes of TBI [2]. Studies have shown that model-estimated tissue response metrics are more effective in injury prediction than using kinematics-based brain injury metrics alone [3], [4].

An FE model of the human head provides unparalleled rich information about the state of brain mechanical responses such as strain. However, the most widely used responses from head impact simulation are either the peak maximum principal strain of the entire brain regardless of the incidence location, or the percentage of brain volume experiencing strains above a certain predefined threshold (i.e., cumulative strain damage measure; CSDM) [5]. These scalar measures treat the entire brain as a single unit. They do not and cannot inform the location or distribution of brain strains, even though such information is likely critical for studying mTBI, given the widespread neuroimaging alterations and a diverse spectrum of clinical signs and symptoms.

To account for this inherent limitation with scalar injury metrics, here we established a structural network-based "response feature matrix" to characterize brain response magnitude and distribution in both gray matter (GM) regions of interest (ROIs) and their white matter (WM) interconnections. The resulting features enabled a machine learning approach to perform a feature-based concussion classification. Three real-world injury datasets were employed to test and compare the injury prediction performance against other commonly used injury metrics using univariate logistic regression.

METHODS

We used the recently upgraded anisotropic version of the Worcester Head Injury Model (WHIM [6]) to simulate head impacts in this study. Head impacts were drawn from three injury datasets. Two reconstructed impacts were the reanalyzed NFL head impacts (N=53, 20 concussions and 33 non-injuries [7]) and reconstructed head impacts from Virginia Polytechnic Institute (VT; N=55, 11 concussions and 44 non-injuries [8]). In addition, measured head impacts using mouthguards from Stanford University were also employed (SF; N=110, 2 concussions and 108 non-injuries [9].

A brain structural network describes the anatomical connections linking a set of neural processing units, generally, cortical and subcortical ROIs [10]. Here, we employed the LONI Probabilistic Brain Atlas (LPBA40 [11]) to identify 54 cortical GM ROIs. They were used as seeding nodes to construct a brain structural network. Interregional connections between each pair of GM ROIs were identified by testing each WM fiber (obtained from the whole-brain tractography) whether it traversed the two GM ROIs under scrutiny. A global density-based thresholding was applied to the resulting connectivity matrix [12] to retain the top strongest links while removing weaker and spurious interconnections. The resulting binarized connectivity matrix was used to encode strain responses. For network nodes or GM ROIs, we choose to use the 95th percentile peak maximum principal strain to encode their responses. For network edges, injury susceptibility at a threshold level of 0.09 [13] based on WM fiber strains was used for encoding.

The utility of the network-based metric for injury prediction was illustrated using the two reconstructed injury datasets to measure "in-sample" injury prediction performance *via* leave-one-out cross-validation (LOOV). Support Vector Machine (SVM) was used as a

feature-based injury prediction method to maximize accuracy using a sequential forward feature selection (SFFS) method. The accuracy was compared with that from a single feature (i.e., a non-zero element in the matrix) and kinematics-based metrics *via* univariate logistic regression.

It was important to evaluate the performance of an injury predictor using impacts that have not been used in training for an objective comparison. Therefore, we re-trained each injury predictor using all of the samples in each of the two reconstructed impact datasets. They were then used to predict injury using impacts from the other reconstructed dataset as well as the Stanford dataset.

RESULTS

Fig. 1a shows the resulting binarized symmetric/unidirectional connectivity or adjacency matrix (1046 non-zero edges with an average of 79±184 ROI-wise fiber connections; **Fig. 1a**). A global density-based threshold (of 0.18) led to the smallest adjacency matrix without leading to an isolated node (258 unique non-zero edges with an average of 153±241 fiber connections; **Fig. 1bc**).

Fig. 2 illustrates the response feature matrices for two representative impacts drawn from each of the three injury datasets. The response feature matrices captured much richer information about the brain response state than, e.g., peak maximum principal strain.

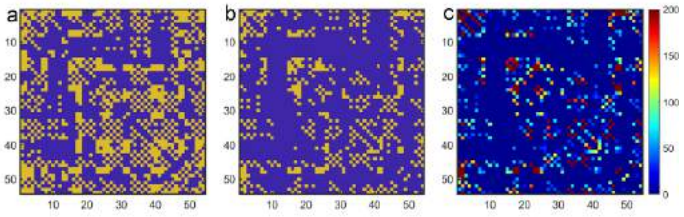

Figure 1: Binarized adjacency matrix (a) before and (b) after a global density-based thresholding to generate the smallest network and fewest edges without leading to an isolated node. (c) Nonzero edges are encoded by the corresponding number of WM connecting fibers between each WM ROI pairs (capped to 200 to improve visualization).

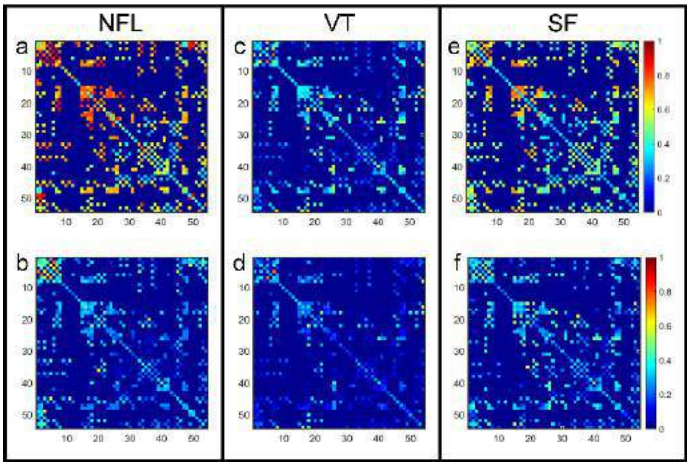

Figure 2: Representative response feature matrices that encode peak maximum principal strains (node) and injury susceptibilities of the interconnecting WM fibers (edges) for a pair of head impacts for the NFL (a: concussed b; no injury), VT (c: concussed; d: no injury), and Stanford dataset (e : loss of consciousness; f: self-reported concussion), respectively.

Cross-validation performances for the two reconstructed NFL and VT datasets are shown in **Table 1**. SVM always achieved the best accuracy as that was how it was trained. The SFFS method identified two network nodes/GM ROIs (inferior temporal gyrus left and inferior temporal gyrus right) as the most injury discriminative features for the NFL dataset. For the VT dataset, two edges/WM interconnections were identified (interconnections of inferior frontal gyrus left and middle frontal gyrus left, superior frontal gyrus left and precuneus left).

Table 1 further reports the out-of-sample injury prediction accuracy when using the same predictors re-trained on the entire NFL (VT) dataset while predicting injury occurrences for impacts in the VT (NFL) and SF datasets. Best performers were mostly the kinematic variables. However, none of the classifiers universally achieved the best out-of-sample accuracies across all of the three injury datasets.

Table 1: Summary of in-sample cross-validation accuracy (LOOV) using the reconstructed NFL and VT datasets. Out-of-sample prediction accuracies are also reported using NFL-trained predictors (NFL-trained) applied to the VT and SF datasets, and those using VT-trained predictors (VT-trained) applied to the NFL and SF datasets.

	dataset	SVM	Best single feature	a_{lin}	a_{rot}	v_{rot}
LOOV	NFL	**0.887**	0.849	0.755	0.849	0.793
	VT	**0.891**	**0.891**	0.873	0.836	0.782
NFL-trained	VT	0.818	0.836	0.800	**0.873**	0.818
	SF	0.873	0.746	0.918	0.818	**0.936**
VT-trained	NFL	0.642	0.736	0.755	**0.830**	0.774
	SF	0.846	0.646	**0.927**	0.736	0.855

DISCUSSION

The network-based brain injury metric is a compact matrix form to represent brain strain responses of important GM ROIs and their WM interconnections. A scalar metric, such as maximum principal strain of the whole brain or CSDM, is conceptually analogous to a degenerated network with only one node but no edges. Therefore, the network-based injury metric or response feature matrix extends previous scalar metrics by providing more complete information about the brain strain response state. Our performance comparisons suggested that a feature-based injury predictor *via* machine learning always outperformed others when assessed within the training samples. However, the accuracy of out-of-sample predictions depended not only on the injury predictor itself, but also on both the training and testing datasets as well. A universal "best-performer" across different datasets for out-of-sample predictions did not seem to exist based on the datasets evaluated here.

ACKNOWLEDGEMENTS

Funding is provided by the NIH grant R01 NS092853. The authors are thankful to the NFL, Biokinetics and Associates Ltd., and Dr. David Camarillo at Stanford University for data sharing.

REFERENCES

[1] CDC, 2015. [2] Yang et al., *Stapp Car Crash J.*, 50: 429–490, 2006. [3] Zhang et al., *J. Biomech. Eng.*, 126: 226–236, 2004. [4] Giordano et al., *Stapp Car Crash J.*, 58: 29–61, 2014. [5] Takhounts et al., *Stapp Car Crash J.*, 52: 1–31, 2008. [6] Zhao and Ji, *J. Neurotrauma*, 2018. [7] Sanchez et al., *Clin. Biomech.*, 2018. [8] Rowson et al., *J. Biomech. Eng.*, Under review. [9] Hernandez et al., *Ann. Biomed. Eng.*, 43: 1918–1934, 2015. [10] Sporns, *Dialogues Clin. Neurosci.*, 15(3): 247–262, 2013. [11] Shattuck et al., *Neuroimage*, 39: 1064–80, 2008. [12] Fornito et al., Boston: Elsevier/Academic Press Amsterdam, 2016. [13] Zhao et al., *Biomech. Model. Mechanobiol.*, 16: 1709–1727, 2017.

SB³C2019
Summer Biomechanics, Bioengineering and Biotransport Conference
June 25 -28, Seven Springs, PA, USA

CHANGES IN BRAIN TISSUE IN VIVO DEFORMATION FOLLOWING DECOMPRESSION SURGERY IN CHIARI PATIENTS

Maggie Eppelheimer (1), Blaise S. T. Nwotchouang (1), Soroush Heidari Pahlavian (2), John Oshinski (3), Daniel Barrow (4), Rouzbeh Amini (1), Francis Loth (1)

(1) Conquer Chiari Research Center,
Department of Biomedical Engineering
The University of Akron
Akron, OH, U.S.

(2) Laboratory of FMRI Technology (LOFT), USC
Stevens Neuroimaging and Informatics Institute
University of Southern California
Los Angeles, CA, U.S.

(3) Department of Neurosurgery,
Emory University
Atlanta, GA, U.S.

(4) Department of Radiology & Imaging Sciences
and Biomedical Engineering
Emory University
Atlanta, GA, U.S.

INTRODUCTION

Chiari malformation type I (CMI) is a neurological syndrome classified as the elongation of the cerebellar tonsils five millimeters below the foramen magnum. Patients with CMI experience symptoms including occipital headaches, neck pain, and cognitive/neurological deficits [1-3]. In addition to altered brain morphology, CMI patients demonstrate increased tissue motion [4-6], which may be the underlying cause of CMI symptoms due to repeated compression of the cerebellum, brainstem, and upper cervical cord.

Patients may be treated with posterior fossa decompression (PFD) surgery. The primary goal of this procedure is to relieve brainstem compression by altering craniocervical morphology. Eighty-four percent of patients have reported improvement in quality of life after being treated with PFD surgery [7]; however, improvement is not consistent across all symptoms or all subjects [8]. Additionally, selection of PFD candidates is primarily determined based on subjective symptomology [8]. A quantitative assessment of brain tissue motion following PFD surgery may improve candidate selection for PFD surgery.

Brain tissue motion and strain has been previously quantified before and after PFD surgery using a select number of anatomical landmarks within the cerebellum and brainstem [6]. However, tissue motion over the entirety of brain structures has yet to be quantified before and after surgery. We have previously utilized displacement encoding with stimulated echoes (DENSE) MR images to quantify brain tissue displacement in healthy individuals [9]. Within the current study, we quantified changes in brain tissue displacement and strain that occur due to surgery. We hypothesize that CMI patients will demonstrate a significant reduction in brain tissue motion and strain within the craniocervical region following PFD surgery.

METHODS

DENSE MR images before and after PFD surgery were acquired for 12 CMI patients (10 females, age 38 ± 9) in a study approved by the institutional review board. CMI patients were identified from a previous clinical imaging study based on common CMI diagnostic criteria: greater than 5 mm tonsillar descent below the foramen magnum, and the presence of CMI symptoms. All patients were referred by a single neurosurgeon (DB). Cardiac-gated, spiral cine DENSE sequences were evaluated at the mid-sagittal plane on a 3T MRI scanner (Siemens Prisma, Erlangen Germany). Acquisition parameters included: two directions of in-plane motion encoding, an encoding frequency of 0.6 cycles/mm, two spiral interleaves per heartbeat, pixel size of 1.2 x 1.2 mm^2, slice thickness of 7 mm, four signal averages, and 16-27 frames over the cardiac cycle, depending on the heart rate.

A program developed in MATLAB (Mathworks, Natick, MA) was used to quantify tissue motion using DENSE phase images in two soft tissue structures: the cerebellum and brainstem (see Fig.1). These regions of interest (ROIs) were manually identified by a single observer (ME) using midsagittal DENSE magnitude images before and after PFD surgery. The peak tissue displacement and principle strain were identified on a pixel-by-pixel basis over the cardiac cycle using 2D displacement maps obtained from DENSE phase images. These maps were used to quantify principle Lagrangian Green strains for the cerebellum and brainstem as described previously [9]. Displacement maps acquired during the first two-thirds of the cardiac cycle were used for displacement and strain calculations due to a reduction signal-to-noise ratio at the end of the MRI sequence [10]. Spatially averaged values for each ROI were calculated to quantify significant changes in mean peak displacement (MPD) and mean peak principle strain in the cerebellum and brainstem.

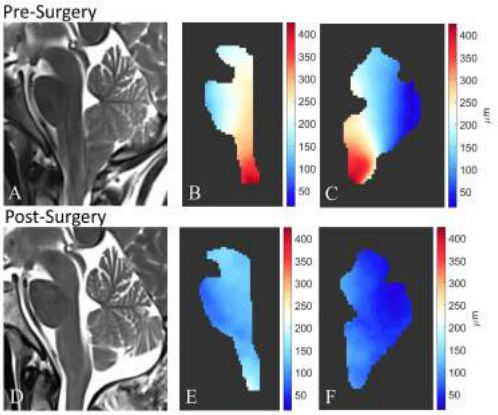

Figure 1: High-resolution T2-weighted images (A) before and (D) after surgery, and peak magnitude displacement maps of one participant before and after surgery. (B & E) Brainstem displacement maps and (C & F) cerebellar displacement maps.

To isolate regions of brain tissue demonstrating large amounts of displacement, pixels with displacement values larger than a patient's MPD were spatially averaged and compared before and after surgery. Paired t-tests were used to evaluate changes in mean peak displacement and strain post-surgery. Statistical significance was evaluated as $p < 0.05$. The Chicago Chiari Outcome Scale (CCOS) was used to assess the surgical outcome of ten out of the twelve investigated patients [11]. The CCOS evaluates post-surgical changes in four different categories: pain, non-pain symptoms, functionality, and complications. Each category is scored between 1 and 4 with 16 as the largest possible score. Pearson correlation coefficients were calculated to determine the relationship between mean peak tissue displacement and strain before and after surgery with CCOS scores.

RESULTS

Figure 1 shows changes in peak displacement maps in the cerebellum and brainstem following PFD surgery. Figure 2 shows displacement in smaller regions of tissue within the brainstem (left) and cerebellum (right) before and after surgery.

Cerebellar MPD in the superior-inferior (SI) and anterior-posterior (AP) direction significantly decreased by 34% and 46% following surgery (-51.9 ± 44.2 μm, $p = 0.002$ and -28.0 ± 22.5 μm, $p = 0.001$, respectively). Brainstem MPD in the SI direction significantly reduced by 24% following surgery (-52.0 ± 64.9 μm, $p = 0.02$). However, AP brainstem MPD did not significantly change after surgery (-10.5 ± 21.0 μm, $p = 0.13$). After quantifying displacement in smaller regions of tissue with large motion, SI and AP cerebellar displacement demonstrated a significant reduction of 45% and 56% following surgery (-103 ± 62.7 μm, $p < 0.001$ and 59.4 ± 39.0 μm, $p < 0.001$, respectively). Like brainstem MPD, smaller regions within the brainstem showed a 29% reduction in the SI direction after surgery (-75.8 ± 75.8 μm, $p = 0.008$) and 14% in the AP direction (-17.0 ± 35.2 μm, $p = 0.11$).

Additionally, the mean peak cerebellar compression and extension principle strains significantly decreased by 21% and 28% following surgery (-0.16 ± 0.18%, $p = 0.005$ and -0.18 ± 0.25%, $p = 0.03$, respectively). However, the mean peak compression and extension principle strains within the brainstem did not significantly change after surgery (-0.005 ± 0.13%, $p = 0.89$ and -0.06 ± 0.14%, $p = 0.19$, respectively). When comparing brain tissue *in vivo* deformation with surgical outcome, a significant positive correlation was found between cerebellar MPD in the SI direction before surgery with CCOS scores ($r = 0.69$, $p = 0.03$). Brainstem MPD in the SI direction before surgery was also significantly correlated with CCOS scores ($r = 0.66$, $p = 0.04$).

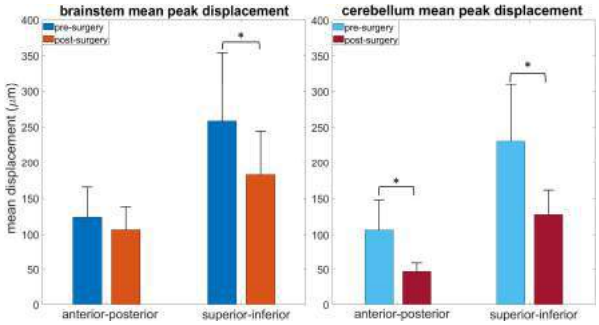

Figure 2: Changes in displacement in small regions of the brainstem (left) and cerebellum (right) before and after surgery (N = 12). Error bars represent standard deviations. *$p < 0.05$.

No significant correlations were found between mean peak soft tissue compression or extension strain with CCOS scores.

DISCUSSION

In this study, we evaluated how PFD surgery changes cerebellar and brain tissue displacement and strains using spiral DENSE MR images in 12 CMI patients before and after surgery. From this evaluation, we found a significant reduction in cardiac induced displacement (45-56%) and principle strain (21-28%) primarily within the most inferior portions of the cerebellum following PFD surgery. We also found a significant reduction in brainstem tissue displacement (29%) in the SI direction. Previously reported cerebellar tonsillar motion demonstrated a greater decrease in tonsillar displacement in the SI direction (-480 μm, -45%, $p < 0.001$) and in the AP direction (-340 μm, -48%, $p < 0.001$) [6]. Results of this same study showed a large reduction of tissue motion at the inferior portion of the spinal cord (cervicomedullary junction) in the SI (-100 μm, 17%) and AP direction (-60 μm, 14%) [6]. Additionally, Leung et al showed larger reductions in cerebellar strain (33%) following surgery. These discrepancies may be a result of using different MRI modalities and the use of single anatomical locations to quantify displacement and strain within brain tissue [6]. To address such limitations, we evaluated quantities for regions of the brain as compared to single anatomical locations.

In summary, we proved that cerebellar and brainstem tissue motion and strains within the craniocervical region reduced following surgery. Additionally, we were able to find a relationship between brain tissue mechanics and PFD surgical outcome. Our results suggest that patients with larger SI cerebellar and brainstem displacement prior to surgery may benefit from PFD surgical treatment. Such a correlation demonstrates the utility of brain tissue deformation measurements obtained from DENSE MR images to help identify which patients would benefit from surgery, and thus improve PFD selection criteria.

ACKNOWLEDGEMENTS

This work was funded by a grant from Conquer Chiari.

REFERENCES

[1] Allen, P et al., *PloS one*, 9: e94844, 2014.
[2] Fernandez, A et al., *BMC Musculoskelet Disord*, 10 Suppl 1: S1, 2009.
[3] Rogers, J et al., *Neuropsychology review*, 1-12, 2018.
[4] Hofmann, E et al., *Am J Neuroradiol*, 21: 151-158, 2000.
[5] Houston, J et al., *Journal of Neuroradiology*, 2018.
[6] Leung, V et al., *Journal of Neurosurgery: Spine*, 24: 546-555, 2016.
[7] Mueller, D et al., *Neurosurgical focus*, 18: 1-6, 2005.
[8] Giammattei, L et al., *Journal of neurosurgical sciences*, 2017.
[9] Pahlavian, S et al., *J Biomech Eng*, 140: 2018.
[10] Spottiswoode, B et al., *IEEE Trans Med Imaging*, 26: 15-30, 2007.
[11] Aliaga, L et al., *Neurosurgery*, 70: 656-665, 2011.

2019 Summer Biomechanics, Bioengineering, and Biotransport Conferecne (SB^{3}C)
SB^{3}C and the National Science Foundation (NSF)
June 25 – June 28, Seven Springs, Pennsylvania

DESIGN & OPTIMIZATION OF A FINGER-BY-FINGER VIBRATIONAL THERAPY

Joshua Posen
Rutgers University
New Brunswick, NJ, USA

George Durrant
Rutgers University
New Brunswick, NJ, USA

Samuel Langlois
Rutgers University
New Brunswick, NJ, USA

Chirsteen Abdalla
Rutgers University
New Brunswick, NJ, USA

Faculty Advisor(s)

Dr. Gary Drzewiecki
Rutgers University
New Brunswick, NJ, USA

INTRODUCTION

There are an estimated 800,000 stroke patients in the United States every year, and a "loss of protective, proprioceptive, and touch sensation" occurs in up to 65% of patients [1]. The large number of stroke patients and relative lack of individualized therapy devices or specialists begs the question of how to effectively and consistently engage patients in therapy. Proprioceptive training sessions of one hour, spread over the course of fifteen sessions, showed that each patient "improved muscle contraction in one or more muscles" and "in 4 out of 6 patients the full range of voluntary active movement emerged after therapy" [2]. Vibrational therapy is a highly promising treatment for re-establishing neuronal connections to afflicted limbs, which is needed prior to beginning movement based physical therapy.

Of the very few available vibrational therapy devices, accessibility is inhibited through either cost or ease of use. Stroke patients who wish to rehabilitate their proprioception in an affected hand will only have one functioning hand to operate any device. Thus, an at-home device which is easy to operate with one hand, is inexpensive, and can track progress over long treatment periods is of great need.

Product Design

The device is currently in its first prototype phase, with vibration motors in temporary housing and wired to DC power sources to undergo testing as seen in Figure 3. The final design is to include five vibration motors, each in a pulse oximeter finger clip, and wired to an Arduino microcontroller housing. All aspects of the circuitry such as the resistors will be stored in the housing, and the Arduino has an SD card reader attachment. The 9V output of the Arduino will power the vibration motors using an algorithm to randomly power individual motors. The Arduino will also be connected to an LCD display, which the patient will interact with. There are five buttons, one for each finger, for patient input during testing, as well as the general menu buttons. This design has been created based on the faculty advisor Dr. Drzewiecki's

During a rehabilitation treatment, the patient will turn on the device and begin the program. The vibration motors will be randomly and individually turned on, and the patient will then enter their best estimation as to what finger was stimulated. The microcontroller will track all inputs and store the data in the SD card for analysis of total patient accuracy and individual finger accuracy. This data can then be viewed by the patient to reinforce the neuronal connections established through stimulation, or provided to a physical therapist to adjust the rehabilitation program.

Budget & Market Analysis

The budget for the prototype is estimated at $100. $40 is budgeted towards an Arduino microcontroller along with an SD card attachment and SD cards. $5 is for the vibration motors and $25 is for pulse oximeter finger splints. The remaining $30 is allocated towards wiring of the vibration motors, including resistors and breadboard, as well as the housing of the Arduino and the LCD display. Lab time and preliminary testing will not have a cost in prototype development due to Rutgers University resources being available and one stroke patient subject involved in development.

The potential market size is in the hundreds of thousands.There are an estimated 400,000 patients who have suffered a stroke for the first-time and have lost proprioceptive sensation in a limb every year. A further estimate yields 250,000 patients who would benefit from the prototype glove. At a projected $180 sale price the revenue generated would be $45MM. Investments into bulk production of vibration motors, molds or 3D printing finger splints, and mass production of the housing units would easily be able to easily bring the manufacturing cost down to less than $60. A profit margin of $120 would generate profit of $30MM, so an investment of $2MM would have an ROI of $28MM.

METHODS

To validate and verify the procedures listed below, the team required specific equipment: five 12 mm diameter coin vibrator [3], five 9V power source, five 95 ohm resistors, strips of velcro, alligator clips, 25 ft of electric cable, and voltmeter/ammeter. Once collected, a temporary holding device was created to allow the team to start acquiring appreciable data. This holding consisted of a rectangular and a circular velcro strip and the 12 mm coin vibrator. (Figure 3)

Preliminary tests were used to determine at which voltage, resistance, and power the transducer would be run at for all future testing. The motor was rated for 2.7-3.3 V on the manufacturer's data sheets, after collecting data over these ranges a value of 3V was decided on. Primary tests were then conducted on Patient A's hand to determine how an injured patient would perceive the vibrational stimulation given off by the motor. The motor was attached to two of his fingers, and each was activated individually to determine if a localized region could be isolated. Three different tests were run: either one of the two transducers were activated, both the transducers were activated, or neither. Data was collected from these tests and compared from data acquired by previous iterations of designs which used a computer speaker in place of the more acute coin vibrators.

RESULTS

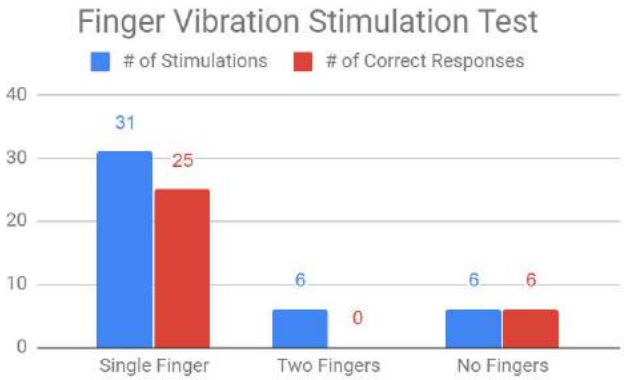

Figure 1: Data collected from Patient A's injured hand, with two 12 mm vibrators attached, they were randomly activated to determine if the individual finger can be localized from the vibration.

To acquire the data in figures 1 and 2 the same test was run with different vibration inducting devices. The data in figure 2 was from previous work done in the lab using a computer speaker. Patient A had the computer speakers attached via velcro to his fingertips and then a current was induced. He was then asked which of the five fingers he felt a sensation within. This test was then reproduced as a part of our study to determine the potential applicability of a coin vibrator instead. The data from figure one is from a shorter time period and smaller amount of tests but better results have already been found with these new devices. On single finger applied tests, there was a success rate of 80.65% while this number was never reached over the course of previous trials.

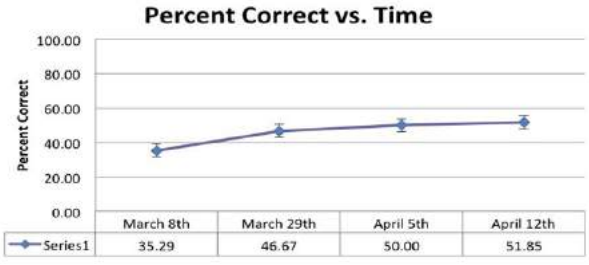

Figure 2: Data collected from a previous study on Patient A's hand, a computer speaker was used instead of the vibrating coin motor used above.

The two finger tests resulted, in zero success rates as there was an expectation that the patient would be able to realize two motors were on simultaneously. This proved to be difficult through testing, this will not prove to be a problem as later rehabilitation will be with only one activated motor at a given time.

DISCUSSION

These results have given us confidence in the approach we are taking and have allowed us to move on towards our new goal: applying this stimulation and then checking the patient for an improved sense of touch. Having a device that is capable of being discerned on each individual finger was the first step, now the group will move towards equipping the transducers with a clip to allow for single handed operation of the device.

The device will then be integrated into a system with a arduino component that will allow for randomized activation of the five transducers to allow for at-home individualized care. Altogether this system will potentially serve as a portable, user-specific system that can lead to patients strengthening the nerves required for touch in their fingers.

Separately, we wanted to acknowledge that tests were performed with two motors operating at the same time (figure 1) where the patient was unable to determine correctly that two motors were running. This was an issue as one of the 12 mm motors caused an overpowering vibrational feeling, but the fully functional device will only run one motor at a time where we have seen success.

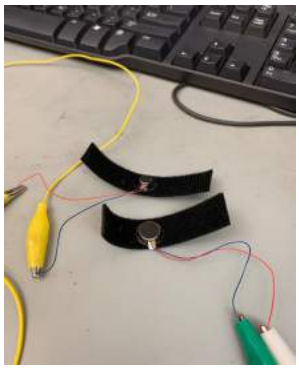

Figure 3: Image of a 12mm coin vibrator in a temporary housing for acquiring preliminary data, also pictured is a 8 mm coin vibrator used in the early stages of the project to determine the appropriate motor choice.

ACKNOWLEDGEMENTS

We would like to acknowledge the Rutgers Biomedical Engineering Department for contributing to our budget as a part of our Senior Design Course and Dr. Jay Sy for guiding us through the design and innovation process.

REFERENCES

[1] Carey, L. M., et al., *Archives of Physical Medicine and Rehabilitation*, 1993.

[2] Kiper, P., et al., *Archives of Physiotherapy*, 5:6, 2015.

[3] "12MM COIN VIBRATION MOTOR 3.4MM TYPE MODEL NFP-C1234 COIN VIBRATOR." *NFP SHOP*. N.p., n.d. Web. 14 Feb. 2019.

2019 Summer Biomechanics, Bioengineering, and Biotransport Conferecne (SB^{3}C)
SB^{3}C and the National Science Foundation (NSF)
June 25 – June 28, Seven Springs, Pennsylvania

JOGGING STROLLER ATTACHMENT DEVICE FOR NATURAL ARM MOTION

Tamara T Chambers
Embry-Riddle Aeronautical University
Daytona Beach, FL, USA

Amy Ramos
Embry-Riddle Aeronautical University
Daytona Beach, FL, USA

Meghan E Blanks
Embry-Riddle Aeronautical University
Daytona Beach, FL, USA

Author Name
Affiliation
City, State, Country

Author Name
Affiliation
City, State, Country

Author name
Affiliation
City, State, Country

Faculty Advisor(s)

Dr. Victor Huayamave
Embry-Riddle Aeronautical University
Daytona Beach, FL, USA

Author Name
Affiliation
City, State, Country

INTRODUCTION

There are numerous types of jogging strollers that include different features at significantly different prices. However, there is not one jogging stroller attachment device currently on the market that allows the user to engage the arms in the natural, fluid arm swing motion that is exhibited while running. The user is limited to one's wrists being locked in one position for the duration of the run. Restricting the arms and hands to only holding the handle bars while running may cause the end user unwanted side effects in the wrists, discomfort, or an unsatisfactory workout. Arm swing during the human gait has been shown to be an important contribution to walking, and restricting the arms while running causes the body to make unwanted adjustments [1]. At walking speeds higher than 0.8 m/s, arm swing increases, the arms move out-of-phase, while the frequency of movement is synchronized with stride frequency, coinciding with a 1:1 frequency locking between arm and leg movements [1] [2] [3]. A study by Ford et al. [1] concluded that constraining one arm swing while walking caused the opposite are swing to increase in order to maintain coordination between upper and lower body movement.

The objective was to produce a jogging stroller attachment device that encourages this "natural" arm motion instead of restricting it. The device followed strict design requirements: safe, portable, inexpensive ($100 or less), easy to use, and adjustable to runners of varying heights and running styles. Prototype testing and literature reviews have proven the need for a device that prohibits the arms from being restricted while running.

PRODUCT DESIGN

The current design for the attachment involves two lever arms that attach to the bottom side bars of the stroller, which the team deemed to be the safest attachment location by use of a Decision Matrix and a Pairwise Analysis. A telescoping clamp system allows the lever arms to retract from 3 feet to 4 feet max. Once attached to the stroller via a clamp, a cardan joint allows the lever arms to rotate along two different axes allowing any user to find the most comfortable grip for a forward-backward movement pattern.

Figure 1: Jogging Stroller Attachment Device

The design shown in Figure 1 is influenced by the movement seen from the lever arms on an elliptical machine. The user would be able to move the arms back and forward like one would if running freely. The user would be able to achieve the most natural arm swing while jogging with one's child. This sort of adaption would decrease the stresses seen at the wrist, influence proper running techniques, and minimize back problems that can occur from pushing a jogging stroller in a hunched over position.

The concept of the design was validated by building and testing a rudimentary prototype. The prototype was built using of ¾" PVC pipes, a universal joint, a clamp, and duct tape. The prototype tests were to determine if a medical cart could be moved when using the attached prototype and was a success. To quantify and better visualize the movements associated with running with the attachment device, electromyography (EMG) data was collected. The current data is limited to:

1. Natural running (no attachment device or stroller)
2. Constrained running (only with stroller)

Further testing will include the use of the attachment device on the stroller. This will then be compared to the natural running to determine if the attachment devices actually influence natural running. Relevant literature has proved that the biceps brachialis and the deltoids are activated during free running and are found to give reliable EMG data [4]. Therefore, these were the muscle activations measured.

BUDGET & MARKET ANALYSIS

The jogging stroller attachments fall in the category of assistive devices because they assist the user in engaging the arms while running. They also provide leisure to parents who want to run with their infants; therefore, this device crosses both markets.

The evolving birth rate in the United States was used as a basis to determine the number of sales of strollers in the past years. Once analyzed, the growth in the number of people who go out to run during these last years was analyzed in order to estimate the total number of final users. This data was used to determine the market outlook of the proposed device. Figure 2 shows the evolution in the number of runners in the last couple of years.

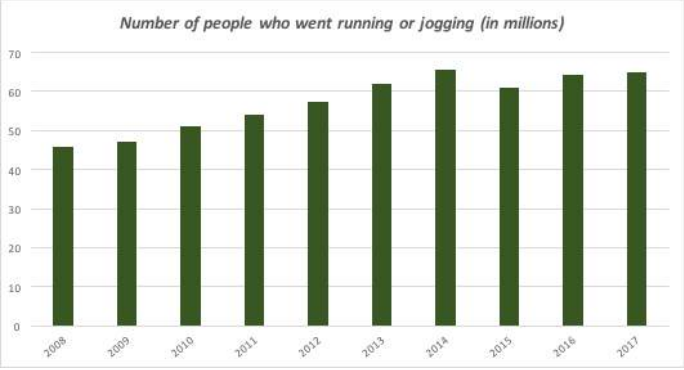

Figure 2: Number of people who went jogging or running (in millions)

As you can see in Figure 2, since 2008 the number of people who decide to go out for a run has increased considerably. As of 2016, the number of runners who were able to finish the race were around 17 million [5][8]. This number has multiplied by three in the last 20 years. Around the world there exist races, especially marathons, that are home to nearly 50,000 people willing to run for 42 km. It should be noted that in many of these competitions, the strollers are not allowed due to the possible dangers they could cause. However, in the same way, the number of marathon events has increased considerably in recent years and so has the running competitions with strollers. Based on this analysis, it can be concluded that the runners market is an emerging market.

There is a diverse array of jogging strollers currently on the market that can range anywhere between $70 to $2,000. The more frequently purchased jogging strollers range from $70 to $450. The Babytrend Expedition Jogging Stroller is a popular selling jogging stroller at Walmart for the price ranging from $73 to $126, while the BOB Revolution Flex Jogging Stroller costs $450 on Amazon. After $450, the jogging strollers come equip with an array of luxury features since there are no limitations on cost. The Thule Chariot Chinook 1 Multi-Sport Child Carrier & Stroller sells for $1,199.95 at Kohl's. Even the most popular jogging strollers do not incorporate natural arm movement.

The JogAlong stroller integrates the motion similar to that found on an elliptical machine. The designers define it as the only jogging stroller that can be considered ergonomic, since it stimulates the natural motion of the arms while the user is running. The problem with the mechanism is that it is included with the stroller. Therefore, the price increases greatly. In addition, this system is not adjustable for different heights, so as can be seen in their promotional video, it is not very ergonomic for those of a certain height. In the same way, this mechanism will not be able to adapt to any type of stroller. Therefore, it does not meet the design requirement for adaptability [5][6].

The second product currently on the market would be the elliptical stroller. The designers define this product as a mechanism composed of two fundamental elements: the stroller and the transmission mechanism of the elliptical movement. This mechanism is formed by two pedals that move up and down, moving together the stroller. The user can decide whether to engage the elliptical handle bar feature or just use the stroller as if it were a standard jogging stroller. This elliptical feature is similar to the mechanism of the teams design. However, the price is around $1,250 [5][7]. There are many other start-up companies trying to incorporate natural arm movement in their designs, but none have successfully produced this feature in an affordable attachment design.

Based on the cost of buying the materials for all three prototypes, the estimated cost per unit is $200. One of the requirements of this device is that it costs the average user $100 at the most. Producing this product on a greater scale will significantly bring down the price for the end user. Given the amount of new runners since 2008 and the price individuals are willing to spend on jogging strollers, it can be hypothesized that this attachment device will sale very well.

Using retailers such as Walmart, Inc or Target Corporation to sale the device next to the popular jogging strollers will increase the likelihood of their purchase rate.

ACKNOWLEDGEMENTS

Embry-Riddle Aeronautical University

REFERENCES

[1] M. P. Ford, R. C. Wagenaar and K. M. Newell, "Arm constraint and walking in healthy adults," *Gait and Posture* , pp. 135-141, 2007.

[2] R. C. Wagenaar and R. V. Emmerik, "Resonant frequencies of arms and legs identify different walking patterns," *Journal of Biomechanics,* vol. 33, no. 7, pp. 853-861, July 2000.

[3] S. Donker, P. Beek, R. Wagenaar and T. Mulder, "Coordination Between Arm and Leg Movements," *Journal of Motor Behavior,* 2001.

[4] J. M. Smoliga, J. B. Myers, M. S. Redfern and S. M. Lephart, "Reliability and precision of EMG in leg, torso, and arm muscles during running," *Journal of Electromyography and Kinesiology,* pp. e1-e9, 2010.

[5] A. D. Navarro, "Ergonomic Adaptable Stroller Add-On Mechanism for Running," 2018.

[6] JogAlong, "JogAlong Stroller," [Online]. Available: https://jogalong.com/. [Accessed 2019].

[7] Elliptical Stroller, "Elliptical Stroller," Legion of Creatives, [Online]. Available: https://www.ellipticalstroller.com/about.

[8] RunningUSA.org, "2017 US Road Race Trends Report is Here," March 2017. [Online]. Available: https://www.endurancesportswire.com/2017-u-s-road-race-trends-report-is-here/. [Accessed 2019].

2019 Summer Biomechanics, Bioengineering, and Biotransport Conferecne (SB^{3}C)
SB^{3}C and the National Science Foundation (NSF)
June 25 – June 28, Seven Springs, Pennsylvania

ASSISTIVE DEVICE FOR STRETCHING EXERCISE IN PATIENTS WITH FROZEN SHOULDER SYNDROME

Maria C Owsiak
Widener University
Chester, PA, USA

Mansour A Al Awami
Widener University
Chester, PA, USA

Ryan J Daher
Widener University
Chester, PA, USA

Scott J Goeltz
Widener University
Chester, PA, USA

Rebecca I Gomezrueda
Widener University
Chester, PA, USA

Russell E Maurer
Widener University
Chester, PA, USA

Andrew N Saylor
Widener University
Chester, PA, USA

Faculty Advisor

Dr. Ria Mazumder
Widener University
Chester, PA, USA

INTRODUCTION

Frozen shoulder syndrome, also known as adhesive capsulitis, is a condition where the shoulder joint has a compromised range of motion that results in extreme pain and discomfort to patients. The condition is caused by inflammatory changes in the connective tissues around the shoulder capsule area. Over time, the tissue thickens and becomes tight, allowing stiff bands called adhesions to develop. These adhesions make the movement of the joint very painful and can limit the shoulder joint's range of motion. Frozen shoulder syndrome affects various populations of people, especially, those with diabetes, hormonal imbalances, and thyroid disorders. Typically, patients of between the ages of 40 to 60 years old are most likely to develop this syndrome. Additionally, it has been seen that women are at an increased risk for frozen shoulder. [1]. The primary treatment for frozen shoulder syndrome includes a variety of strengthening and stretching exercises which are usually performed multiple times a day to improve shoulder flexibility. Some of these exercises, such as the upward arm stretch, requires assistance from another person, thereby causing dependency [2].

Therefore, the objective of this design is to make a portable assistive medical device that will allow patients to practice the upward arm stretch on their own, thereby eliminating the dependency on another person to perform this exercise.

PRODUCT DESIGN

The design as shown in Figure 1 consists of a frame (made of aluminum) on which a remote controlled electric winch (the Hiltex 11302 12V winch) is mounted. A custom made fabric strap attached to the hook at the end of the winch cable will be used to fasten the patient's elbow to the device. The included remote control on the winch will be used to raise the strapped elbow, allowing the patient to lift their arm and perform the upward arm stretch. The frame has an outer dimension of 15.5 inches x 21.3 inches. The height of the frame will accommodate a maximum patient height of 6'8'', which covers up to the 99.99th percentile of US adult male heights. Since there is no constraint on lowering down the cable the device can not only accommodate shorter patient heights but can also support patients with disabilities confined to wheelchairs. The rectangular geometry of the frame will prevent the device from toppling in any direction during use when a load is applied perpendicular to the top face of the structure. Additionally, lockable wheels included inferior to the bottom face of the frame will allow for the device's portability.

A patent search was conducted prior to the development of the design and there were no similar medical devices for treating frozen shoulder syndrome available on the market or awaiting a patent approval.

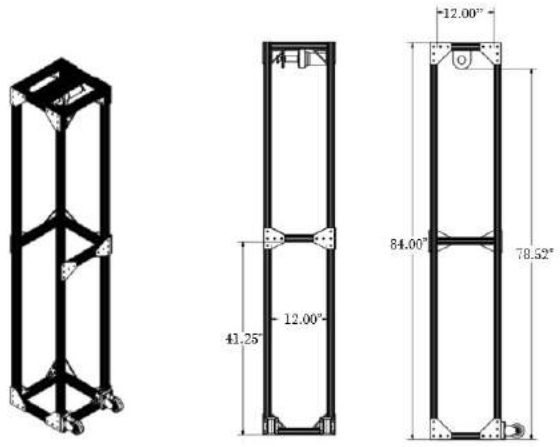

Figure 1: 2D CAD Design

Budget & Market Analysis

The current budget for designing, building, and testing of the prototype is $1000. The parts for the design cost $835 with a contingency of $165. The building and testing of this prototype don't have any costs because the team is going to carry out these tasks themselves.

In 1995, the estimated cumulative incidence of frozen shoulder syndrome was found to be 2.4 cases per 1000 people a year [3]. With the United States having a population of 328.15 million people [4], this is equivalent to 787,560 cases of frozen shoulder syndrome a year. This means that up to 787,560 units could be sold a year. At this volume, the expected cost per unit is $855. The projected sales price for the device is $1,500 per unit. The profit made on one unit at this price would be $645. If 787,560 units were sold a year, the total return on investment would be 508 million dollars in profit. Alternatively, a rental system could also be considered instead of a one-time purchase, where the device would be returned after the patient has recovered from the condition. If the patient were to be renting the device, the price would be $50 a month. Typically the condition can last anywhere from 1 month to 5 years and hence a rental system would be beneficial for short term users while the one-time purchase would be favorable to long term patients.

ACKNOWLEDGEMENTS

Funding for this project was supplied in part by the School of Engineering at Widener University, as part of the senior design program and the rest was provided by RPA Engineering.

References

1 Frozen Shoulder (Adhesive Capsulitis) Information. (2018, May 14). Retrieved from https://www.myvmc.com/diseases/frozen-shoulder-adhesive-capsulitis/

2. Frozen Shoulder. (2018, July 20). Retrieved from https://www.mayoclinic.org/diseases-conditions/frozen-shoulder/symptoms-causes/syc-20372684.

3. Rangan, A et al. "Frozen Shoulder" *Shoulder & Elbow,* Vol. 7,4: 299-307, 2015.

4. U.S. Population (Live). (2019, February 4). Retrieved from http://www.worldometers.info/world-population/us-population/

2019 Summer Biomechanics, Bioengineering, and Biotransport Conference (SB³C)
SB³C and the National Science Foundation (NSF)
June 25 – June 28, Seven Springs, Pennsylvania

WEARABLE ROBOTIC WRIST ORTHOSIS FOR STROKE REHABILITATION

Neshat Baset
Undergraduate Research Assistant
Biomedical Engineering Department
UTA Research Institute
Fort Worth, TX, USA

Dona Antony
Undergraduate Research Assistant
Biomedical Engineering Department
UTA Research Institute
Fort Worth, TX, USA

Faculty Advisors

Mahdi Haghshenas-Jaryani
Research Scientist
UTA Research Institute
Fort Worth, TX, USA

Muthu B.J. Wijesundara
Principal Research Scientist
UTA Research Institute
Fort Worth, TX, USA

INTRODUCTION

In the United States, more than 800,000 people suffer stroke every year where stroke is a leading cause of disabilities [1]. Nearly half of all stroke survivors experience loss of upper extremities function as the wrist is flexed due to increased tissue stiffness, which also means that there is an increase in required reflexive torque. Some studies have found that in a healthy wrist the static stiffness is around 20 N.mm/deg [2]. As a result of stroke, the wrist can have contractures of nearly 5° per week in the first 8 months, leading to increased stiffness of the wrist [3]. Wrist position a crucial factor in the range of motion (ROM) of the fingers. It was found that at the extreme wrist flexion and extension points, there is a lower ROM in the finger joints and hand grip force compared to when the wrist is in the neutral position. For instance, the ROM of the index metacarpophalangeal joint varies from 25.9° (±10.2°) to 84.7° (±8.6°) depending on the wrist joint angular position [4].

In order to address wrist contracture in post-stroke population, some products currently available in the market make use of splints to keep the wrist in a neutral position. According to a study done by the University of Sydney that tested the effectiveness of splints, it was concluded that wrist splinting was not effective in reducing wrist contracture after stroke [5]. Another study from the Netherlands found that static wrist-hand orthosis was not effective in preventing contractures and only caused discomfort to the stroke patients with long-term use [6]. However, studies have shown the effectiveness of dynamic wrist-hand orthosis where it was found that incorporating hand training into therapy to maintain the functionality of the wrist for the stroke survivors can help improve hand use [7]. Therefore, robot-assisted systems can be used to overcome the stiffness and dynamically put the wrist in desired positions. Soft robotic devices show promise as a therapy extender needed for motor learning while reducing the complexity, cost, and safety issues involved in conventional robotic systems. The soft robotic wrist actuator could also be used as a form of post-stroke rehabilitation in order to delay or reduce the effect of contractures in the wrist in order to help retain the ROM in the fingers.

A wrist rehabilitation has been developed for stroke patients that consists of a glove and elbow sleeve that is connected by soft robotic actuators and cable-driven mechanisms. Although this device is capable of providing wrist movement in all degrees of freedom, its effectiveness in overcoming stiffness at the wrist has not been reported [8].

PRODUCT DESIGN

Our current design is based on a soft robotic approach where it utilizes the inherent compliance of silicone rubber materials and air pressurization to generate simple bending motion of the wrist by overcoming the stiffness of the joint. This helps prevent contractures and restore mobility of the wrist and fingers.

Before determining the design parameters that could be changed in the wrist actuator, a fixed length, width, and height of the overall wrist actuator was set. After this was decided, different dimensions for the various features were set based off the shape of the bellow. The following design parameters that were set: height of the bellows, thickness of the base, thickness of the walls along the sides of the bellows, width throughout the bellows, and the heights of the inner and outer corrugations (Figure 1). Overall, there were two types of bellows used in the design process, rectangular and rounded bellows. Initially, the design began with one row of bellows spanning the entire width of the actuator. However, modifications were made to this design by creating two rows of bellows to decrease over inflation in the center. The optimized design consists of a rectangular and rounded bellowed actuator with two cavities, and inner and outer corrugations, shown in Figures 1A and 1B, which allows for lengthening and increased bending of the actuator.

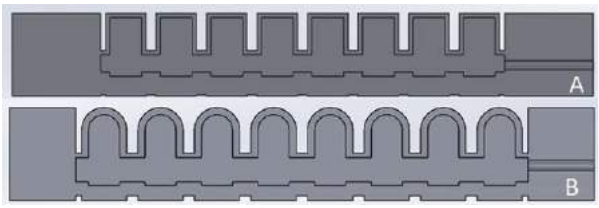

Figure 1: Inner cavity view of (A) rectangular and (B) round bellowed actuator

The commercial software SolidWorks was used to design the CAD models of the actuator (Figure 2) along with the molds used for fabrication process. For the design optimization, a finite element model of both soft robotic actuator structures that interacts with a simplified

rigid multibody model of the wrist were developed in the commercial software ANSYS. As the actuator is symmetric, half the model was used for the simulations, which were run in order to see the effects of different design parameters on wrist rotation while adding pressure to the inner cavities (Figure 3). A torsional spring with stiffness of 10.475 N.mm/deg, half the stiffness found in a healthy wrist, was considered at the joint of the wrist model to replicate the natural stiffness of the wrist. The optimized design for both geometries was obtained in order to reach the desired wrist extension of 70˚ by pressurizing the actuator with a maximum pressure of 0.2MPa over a period of 20 seconds (Figure 4). The final designs for both wrist actuators were obtained by changing the values for each design parameter until the optimum angle of rotation was achieved.

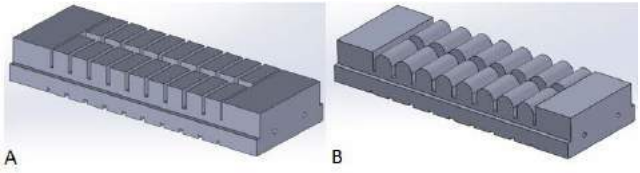

Figure 2: CAD Model of (A) rectangular wrist actuator and (B) round wrist actuator

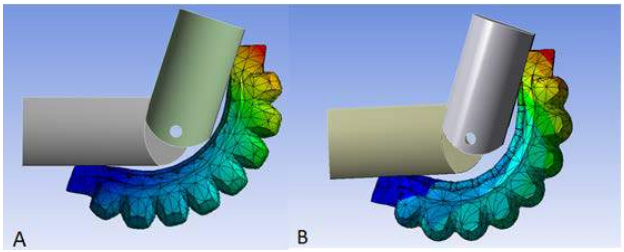

Figure 3: (A) Rectangular and (B) rounded wrist actuator simulation in ANSYS

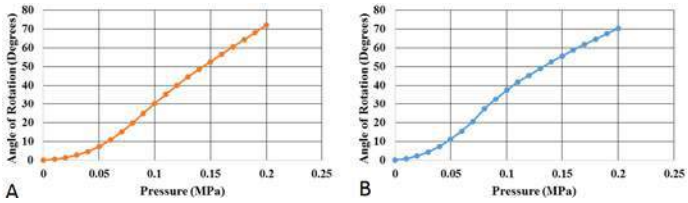

Figure 4: Angle of rotation vs pressure input (A) rectangular ridge and (B) rounded ridge

The actuator was developed through liquid polymer fabrication processes such as injection and over molding along with a wax casting process. Molds were manufactured using a stereolithography type 3D printer (ProJet SLA 6000, 3D Systems). The fabrication process consists of four steps. First, the wax pieces are made to make the inner corrugations. Second, the half-bellowed part of the actuator and end pieces are made using silicone rubber in closed molds with injection molding process. Next, the cured bellowed silicone piece and wax piece are used to over-mold on the base mold. Finally, the wax is melted out and the two end pieces are attached.

The wrist actuator is used by being attached to the underside of the hand with the help of a brace (Figure 4). To keep the actuator in place, a piece of fabric is sewn onto the brace, creating a pocket for the actuator. The actuator is then pressurized gradually by a control box (Figure 5). With the use of the embedded inertial measurement unit (IMU), the angle of extension can be measured and controlled for people with varying degrees of stiffness as shown in Figure 6. The pressurization causes the bending of the wrist upwards, providing the user with increased range of motion in the fingers, assuming the wrist begins in a contracted position.

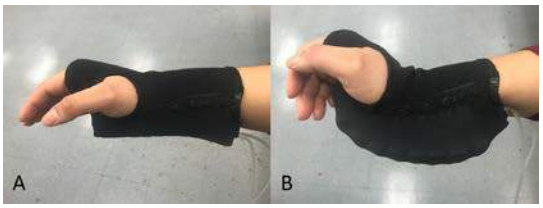

Figure 5: (A) Side view of actuator worn on hand (B) pressurized actuator

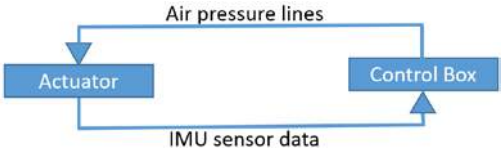

Figure 6: Schematic of sensorized soft robotic wrist and control unit

Currently, the wrist actuator is designed to be placed on the inner side of the hand and wrist, which can be difficult for some to wear if their hand is in the contracted position. However, modifications to the design can be made to overcome this issue.

BUDGET & MARKET ANALYSIS

The total cost of all the required parts to fabricate an actuator is approximately $70 where the highest cost is associated with the use of 3D printed molds. However, multiple actuators can be fabricated with the same set of molds and therefore, the cost of molds can be distributed between them. The physical rehabilitation market in the US is estimated to be a $30 billion industry growing at a rate of 7% CAGR. This is mostly due to the aging population in the US and people leading sedentary lifestyles. The robot-assisted rehabilitation market is expected to grow dramatically, reaching $2 billion by 2020. With more than 800,000 people having strokes every year in the United States and depending on the effectiveness of the wrist actuator, the commercialization plan can be expanded to meet the demand by mass producing the wrist actuator at a lower cost thus increasing the market size.

ACKNOWLEDGEMENTS

This project is partially supported by the National Science Foundation under Grant No. 1605635 and the associated Research Experience for Undergraduate (REU) supplemental funding. We would like to thank Mr. David Manivanh assisting us with 3D printing, Ms. Alexandra Lindsay for her guidance in CAD modeling of the wrist joint and Ms. Allison Palomino for her contribution. Authors also would like to thank UTA Research Institute for providing facilities and equipment.

REFERENCES

[1] Benjamin, J et al., *Circulation* vol. 135, 2017.
[2] Grey, M.J., "Viscoelastic properties of the human wrist during the stabilization phase of a targeted movement", 1997.
[3] de Gooijer-van de Groep, K et al., *Clinical Biomechanics*,35: 93-101, 2016.
[4] Latz, D et al., *Hand*, 2017.
[5] Lannin, NA et al., *Archives of Physical Medicine and Rehabilitation*, 84:297-302, 2007.
[6] Andringa, A et al., "Long-Term Use of a Static Hand-Wrist Orthosis in Chronic Stroke Patients: A Pilot Study" *Stroke Res Treat*, 2013.
[7] Barry, JG et al., *JNPT*, 36:17-24, 2012.
[8] Bartlett, NW et al., *Journal of Medical Devices*, 9, 2015.

DESIGN OF 3D PRINTED ROBOTIC GLOVE AUGMENTING MANUAL MANIPULATION OF HUMANS

Mason Araujo	**Immanuel Ponminissery**
Texas A&M University	Texas A&M University
College Station, Texas, USA	College Station, Texas, USA

Faculty Advisor(s)

Dr Seok Chang Ryu
Texas A&M University
College Station, Texas, USA

INTRODUCTION

Recently, it has come to the attention of medical professionals that surgery students are 'losing dexterity to stitch patients,' an essential skill of traditional open surgery that is sometimes the only viable option in many emergency cases including the operations in a battleground [1]. Moreover, research has shown that the physical and cognitive performance of surgeons deteriorates over time [2]. Since the chances of mistakes by fatigued, overloaded, or old surgeons increase, a system design augmenting their capabilities is necessary.

Regarding human augmentation, there has been a lot of developments in the field of virtual reality (VR) and medical training. Extensive research over the past two decades has signaled the importance of VR training in the medical field and has identified the unique benefits that such programs bring with them. As a result, Osso VR (Palo Alto, USA) has recently made successful partnerships with leading medical schools in the country. Hence, such an augmenting system needs to be developed in a way ensuring successful integration with a VR system to allow surgeons and medical students to improve their micromanipulation skills with relative ease [3].

The idea of a robotic glove (see Figure 1) was initiated by thinking about the issue above and the impact of augmenting the ability of humans in the domain of medicine. We believe that providing the surgeons with a custom-built robotic glove that can offer both a controlled motion and sufficient information allows them to achieve greater dexterity and safety mainly when they handle sensitive objects such as human organs. The system will support human motors by integrated actuators, constrain the hand motions in the desired, limited space, and provides various sensing capabilities such as precise haptics and proximity. Since the glove is manufactured using 3D printing techniques, based on the laser-scanned hand model of specific users, the fit will be natural and ergonomic, another significant attribute affecting the performance.

This paper introduces the design and mechanics of such a robotic glove augmenting human capability, focusing on the pinch motion with two fingers, thumb and index, generally used for micromanipulation, followed by our budget and market analysis.

PRODUCT DESIGN

The glove is primarily a 3D printed structure as opposed to silicone or fabric-based soft robotic gloves that have been widely studied. Although rigid materials aren't as adaptable and comfortable as their competitor, i.e. soft materials, they were used for the glove since it allows for more precise control and better repeatability of movements. Also, since the glove is 3D printed, customizable for specific users, it will improve the fit and ergonomics, leading to better task outcomes.

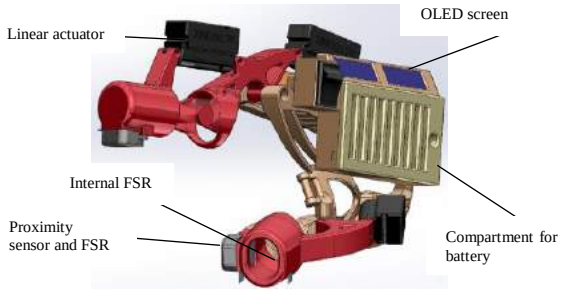

Figure 1. Schematics of a 3D printed robotic glove with actuators and sensors

Since we focus on two-digit or pinch motions, the glove is designed to help control the motions of a user's index finger and thumb. The mechanism for the index finger consists of two individual 3D printed pieces that are driven by two linear actuators. On the other hand, the structure for the thumb is a single 3D printed piece that is driven by a single linear actuator. The linear actuators are PQ12-R Micro Linear Servos manufactured by Actuonix (Victoria, Canada). A mechanics model was built (see Figure 2), and a set of experiments was conducted to validate the system performance such that the motors could resist the forces applied by the user's finger following a planned trajectory with precision. The study on resisting forces is important to verify the safe use of the designed system. If a user can break constraints pre-programmed by applying an excessive force on the linear actuators, the system loses controllability, resulting in undesired behavior. Using the model and a set of mechanics equations (see Figure 3), the results of this study for one of the motors has been shown in Figure 4. It basically shows the varying force applied on the linear actuator based on the actuation force provided by the tip of the index finger. As can be seen by the figure, it is evident that the forces are below 45N, which is the maximum force that can be sustained by the actuator. We performed experiments on the human subject whose hand was used to model the glove and determined the maximum forces

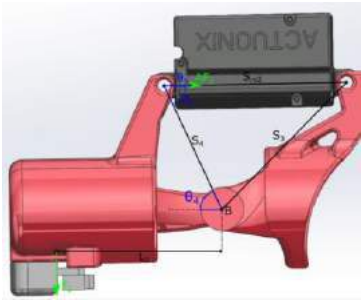

Figure 2. Mechanics model of a member of the glove

$$\alpha_2 = cos^{-1}\left(\frac{{S_4}^2 + {S_{m2}}^2 - {S_3}^2}{2 * (S_4) * (S_{m2})}\right)$$

$$\theta_5 = \theta_4 - \alpha_2$$

$$\sum M_B = F_2 * L_2 - AF_2[S_4 \sin(\theta_4) * \cos(\theta_5) - S_4 \cos(\theta_4) * \sin(\theta_5)] = 0$$

$$AF_2 = \frac{F_2 * L_2}{[S_4 \sin(\theta_4) * \cos(\theta_5) - S_4 \cos(\theta_4) * \sin(\theta_5)]}$$

Figure 3. Equations for actuation force calculation

(29.82N) applied at the tips of each segment and found that the forces were below the maximum force that could be sustained by the motor. Similar studies were conducted for all motors to validate the motor choice.

Regarding the sensing capabilities of the glove, each of finger tip parts is equipped with a proximity sensor and force sensitive resistors. The proximity sensors that we used, providing a prior-information of touch between the tip and objects for the enhanced safety, are the VCNL4040 sensors packaged within SparkFun's (Niwot, USA) Robotic Finger Sensor V2. The force sensitive resistors are Interlink's (WestLake Village, USA) FSR 402 short tail. Four of the FSRs are placed internally within the 3D printed members of the glove, sending measured interaction force values back to the microcontroller installed on the back of the hand. Based on the force information received from the FSRs, the microcontroller can actuate the members as desired. For instance, if the user wants to move the thumb upwards, he/she has to apply a force on the FSR placed on the inner top surface of the 3D printed structure for the thumb. Also, an FSR will be placed on the outside structure for the thumb as well as for the index finger. These can provide readings of the force applied by the glove on an external object. If the force exceeds a set limit, the linear actuators can prevent the user from moving it further. Similarly, the proximity sensors can

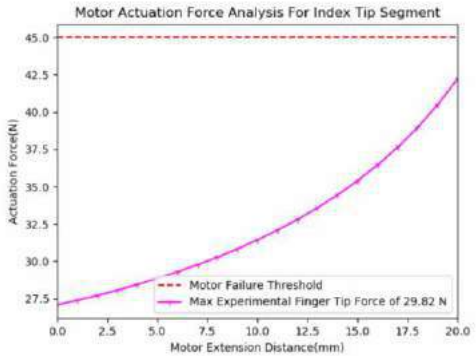

Figure 4. Results of the mechanics study

be programmed to detect a certain distance past which the actuators prevent the user from moving his/her finger.

The whole glove is powered by a 2000 mAh battery with the help of a PowerBoost from Adafruit (New York City, USA). Moreover, OLED screens made by MakerFocus are used to provide the user with visual feedback with respect to the force and proximity values. The microcontroller that is used is an Arduino Micro.

To summarize, the glove will:

- Provide user with force and proximity feedback.
- Enhance users' controllability and dexterous manipulation ability with the help of accurate actuators.
- Allow future development of VR applications with the addition of VR goggles like the Oculus.

BUDGET & MARKET ANALYSIS

The total cost of building the glove in its current state is just under US$830, summarized in Table 1. The bulk of this cost comes from the VR goggles which cost $349 and the other components make up the rest. This cost reflects a single batch run of the glove and we believe that by producing this glove in bulk would allow us to bring this cost down substantially. The only cost that might not come down would be the 3D printing manufacturing of the glove because we would not be able to make that in bulk like the other components due to the customizable nature of the system.

Table 1: Cost breakdown of a glove

Part	Quantity	Price(US$)	Total(US$)
PQ12R Motor	3	70	210
Arduino Micro	1	20	20
LiPo Battery (2000 mAh)	1	13.54	13.54
PowerBooster	1	19.68	19.68
OLED Display	2	10.99	21.98
Rocker Switch	1	0.5	0.5
FSR Sensor	6	5	30
SparkFun V2 Sensor	2	40	80
Glove Print	1	80	80
Screws	5	0.5	2.5
Oculus Rift	1	349	349
Total			827.2

ACKNOWLEDGEMENTS

The authors would like to thank Prof. Hangue Park in the Department of Electrical and Computer Engineering at Texas A&M University for his technical advice for the concept generation.

REFERENCES

[1] S. Coughlan, "Surgery students 'losing dexterity to stitch patients'", 2019.

[2] R. Blasier, "The Problem of the Aging Surgeon: When Surgeon Age Becomes a Surgical Risk Factor", *Clinical Orthopaedics and Related Research*, vol. 467, no. 2, pp. 402-411, 2008. Available: 10.1007/s11999-008-0587-7.

[3] C. Fink, "Osso VR Surgical Training Makes Push Into Med Schools", *Forbes.com*, 2019. [Online]. Available: https://www.forbes.com/sites/charliefink/2018/06/26/osso-vr-surgical-training-makes-push-into-med-schools/#576b04764f6e. [Accessed: 08-Mar- 2019].

2019 Summer Biomechanics, Bioengineering, and Biotransport Conferecne (SB^{3}C)
SB^{3}C and the National Science Foundation (NSF)
June 25 – June 28, Seven Springs, Pennsylvania

ASSISTIVE DEVICE FOR MUSCULAR DEGENERATION IN THE UPPER ARM

Alexandria J. Barber
Clarkson University
Potsdam, NY, USA

Emily F. Eaton
Clarkson University
Potsdam, NY, USA

Jillian R. Farmer
Clarkson University
Potsdam, NY, USA

Samantha M. Gladd
Clarkson University
Potsdam, NY, USA

Natalie I. Jagelski
Clarkson University
Potsdam, NY, USA

Jenny Lin
Clarkson University
Potsdam, NY, USA

Faculty Advisor

Dr. Kevin B. Fite
Clarkson University
Potsdam, NY, USA

INTRODUCTION

A reduction in bicep and shoulder muscle function can greatly alter a person's daily life. The design team's client suffers from monomelic amyotrophy [1], resulting in a major loss of muscle function in the right shoulder and bicep, and greatly limiting his ability to vertically raise the right arm. As such, his ability to perform everyday tasks has diminished, as well as the client's ability to participate in outdoor activities such as nordic skiing and hiking with poles. The proposed design is an assistive arm device, which will help an individual with decreased shoulder and bicep muscle function to regain some range of motion in the upper arm.

Many existing assistive arm devices require stationary supports, such as a table or chair, to raise an individual's arm. This greatly limits the ability to perform mobile activities for a person with reduced shoulder and bicep muscle function. In addition, current exoskeleton assistive arm devices are heavy, bulky, and require external energy devices, such as batteries or electric power. While these exoskeleton devices help to restore upper arm muscle function, the bulky and heavy design can be limiting and is not practical for everyday usage. A lightweight, mobile, self-sufficient design, such as the one proposed by the design team, would greatly improve the quality of life of individuals suffering from conditions which reduce upper arm muscle function.

This device would be useful for individuals suffering from monomelic amyotrophy, arthrogryposis multiplex congenita [2] affecting upper limb joints, muscular dystrophy [3] affecting bicep and shoulder muscle function, the early stages of Lou Gehrig's disease [4] affecting the upper arm, as well as elderly persons with weakened upper body muscles. The proposed product will provide assistance to shoulder and bicep muscles, as well as restore the quality of life of an individual with decreased shoulder and bicep muscle function.

PRODUCT DESIGN

This assistive device will reduce the workload of the bicep and shoulder muscles during activities requiring an individual to vertically raise his arm. The design consists of three main components: an upper body brace, which utilizes the back for support; a spring-loaded system, which attaches to the shoulder; and a cable with a wrist attachment, which connects the spring system to the individual's forearm. As the individual lowers his arm from a raised position, the spring stretches and gains potential energy, which is used to pull the arm back into a raised position. This device can be used for everyday activities requiring an individual to raise his arm, as well as recreational outdoor activities, such as nordic skiing and hiking.

Many assistive arm devices require attachment to stationary supports, like tables and chairs, to raise a person's arm, which limits the person's mobility and activity level. This product relies on the back and upper body for support, allowing an individual to raise his arm during mobile activities. In addition, unlike current exoskeleton products, this design does not require any external energy sources, such as batteries, to function. This design relies on simple, lightweight, and self-sufficient components to function as an assistive arm device.

In order to verify the design of the device, the prototype will be tested against functional requirements on test

subjects as well as the client that inspired this design. Tests will include load cell actuation to monitor the forces generated by the device, which may be used to ensure a properly modulated response. Throughout the design process, feasibility will be ensured in a top-down manner. This is to say that as the product develops and gains maturity the failure modes and discrepancies will be recognised and accounted for. An important aspect of assistive devices is that they conform directly to the users' needs and lifestyle. This design will be tested with very specific needs in mind. The client has expressed a love of outdoor activities and a true desire to return to full confidence in completing rigorous hikes and nordic ski trips. The design team strives to restore the client's upper body biomechanics to the range required for efficient nordic skiing motion [5]. In response to this need, the design will be tested in harsher conditions than may normally be expected; the goal is to ensure resistive feedback, even in cold weather and under rigorous activity. This will lead to many feasibility tests to ensure that the device is robust enough to not only allow the user to complete daily tasks in the comfort of his home, but to complete various outdoor activities as well.

Budget & Market Analysis

Over the course of designing, building and testing the prototype the design team should be able to stay within our $5000 budget. For our initial prototype we will be exploring the use of different elastic bands as a source of flexion. This will cost around twenty-five dollars per band. Along with this, the team will need a system to connect the bands to the user's shoulder that will cost approximately forty to fifty dollars. This will include a brace and a clip system to connect the band to the brace. After producing and testing an initial prototype, we plan on designing at least two more prototypes in order to determine the best solution possible.

Table 1: Projected Prototype Costs

Item	Price
Theraband	$25
Brace/Clip System	$50
Total Cost	$75

Our client suffers from monomelic amyotrophy [1], which typically occurs in Asia, with very few cases in the United States. The modular design enables the device to be used by a greater general population. Arthrogryposis multiplex congenita is a muscular degenerative disease that causes joints to be set in a permanently fixed or straightened position prior to birth. In some cases, a soft tissue release is necessary to improve range of motion [2]. However, muscles are weak due to the lack of motion and need assistance to initially move. Arthrogryposis multiplex congenita affects 1 in 3,000 individuals in the United States. Muscular Dystrophy causes progressive weakness and loss of muscle mass affecting 1 in 8,000 individuals worldwide [3]. The device could be used to aid those during the early stages of the disease when muscle loss has not fully progressed. Lou Gehrig's Disease affects just over 5,000 individuals in the United States per year. Lou Gehrig's Disease is a progressive neurodegenerative disease that affects voluntary muscle action, thus people progressively lose muscle function [4]. With these diseases in mind, we estimate the market size would be approximately 800 per year.

The design team does not expect to meet the full market potential until several years after releasing the product. The return on investment for the design is estimated to increase every year due to a low initial resource investment compared to the estimated net profit acquired from the final design. The cost of production would be approximately fifty dollars with a selling price of one hundred dollars per unit.

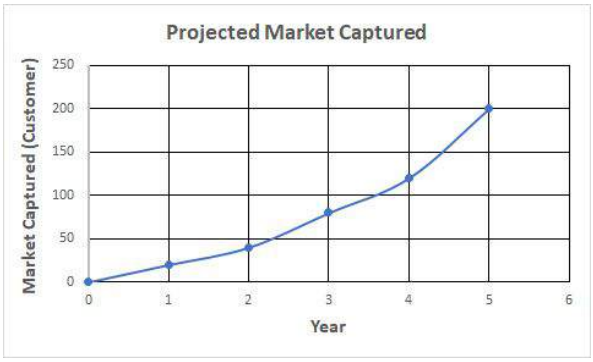

Figure 1: Market analysis graph for the first five years of projected sales.

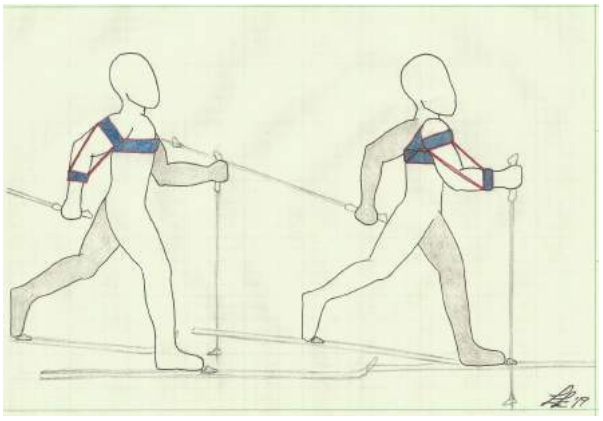

Figure 2: Design implementation sketch.

ACKNOWLEDGEMENTS

This work was supported by the National Service Foundation under Grant No. (NSF-CBET 1510367).

References

[1] Al-Ghawi, E., Al-Harbi, T., Al-Sarawi, A. et al. J Med Case Reports (2016) 10: 54.

[2] Fassier, Alice. "Arthrogryposis multiplex congenita. Long-term follow-up from birth until skeletal maturity.", *J Child Orthop,* Oct 2009, 383-390.

[3] Myotonic Dystrophy Foundation. *Types of DM, July 17, 2012.*

[4] The ALS Association. *Who Gets ALS?, June 2016.*

[5] Homberg, H.C. "Biomechanical Analysis of Double Poling in Elite Cross-Country Skiers." *American College of Sports Medicine,* Dec 2004, 807-818.

ANALYSES OF HEMODIALYSIS ARTERIOVENOUS FISTULA GEOMETRY OBTAINED BY SERIAL MAGNETIC RESONANCE IMAGING

Yong He (1, 2), Daniel B. Pike (3), Yan-Ting Shiu (4, 5), Prabir Roy-Chaudhury (6, 7), Alfred K. Cheung (4, 5), Scott A. Berceli (1, 2)

(1) Department of Surgery
University of Florida
Gainesville, FL, USA

(2) Malcom Randall
VAMC
Gainesville, FL, USA

(3) Department of Biomedical Engineering, University of Utah,
Salt Lake City, UT, USA

(4) Division of Nephrology & Hypertension, University of Utah, Salt Lake City, UT, USA

(5) George Wahlen VAMC,
Salt Lake City, UT, USA

(6) Division of Nephrology,
University of Arizona, Tucson, A□, USA

(7) Southern Arizona VA Health Care System,
Tucson, A□, USA

INTRODUCTION

An arteriovenous fistula (AVF), which is created by surgically connecting an artery to a vein directly, is the preferred vascular access for chronic hemodialysis due to its fewer complications and longer durability compared to AV grafts and central venous catheters. However, a newly created AVF needs to mature before it is cannulated for routine hemodialysis. AVF maturation requires a sufficient increase in both the lumen diameter and flow rate of the AVF vein. Yet currently the rate of AVF maturation failure remains unacceptably high. Improving AVF maturation is crucial for realizing the benefits of the Fistula First strategy, and currently there are no effective clinical treatments to enhance AVF maturation.[1]

Many factors contribute to AVF maturation failure and the exact mechanisms are not yet well understood. Disturbed and complex blood flow induced by the abrupt change in flow direction at the artery-vein anastomosis under a high flow condition may impede AVF maturation.[2] Anastomosis angles have been associated with the lumen diameter and flow rate in experimental porcine[3] and the rates of reintervention[4] and maturation[5] in patients. Nonplanarity has also been associated with maturation.[5] However, these previous clinical studies are limited in patient numbers, time points, and image resolution. Here we report the AVF geometric parameters and their associations with AVF flow rates in a multi-center study, using high-resolution MRI to follow patients longitudinally.

METHODS

From 2011 to 2016, patients with end-stage renal disease (ESRD) undergoing a new vein end-to-artery side upper-extremity AVF creation surgery were recruited at the University of Florida, University of Utah, and University of Cincinnati. Two types of MRI techniques were performed at 1 day, 6 weeks, and 6 months postoperatively using 3.0T General Electric or Siemens scanner.[6] Phase-contrast MRI was used to obtain the flow rate in the AVF. Flow rates were exacted using Segment (medviso.com/segment).[7] A contrast-free double-inversion recovery MRI sequence was used to obtain the AVF lumen images in dark blood. The AVF lumen geometry was reconstructed from the dark-blood images in Amira, and the bifurcation origin at the anastomosis and the centerlines were extracted using VMTK (www.vmtk.org).

Three geometric parameters were extracted (Fig 1). The anastomosis angle was calculated as the angle between

the lines connecting the anastomosis origin with the proximal artery (PA) and AVF vein centerline points that are 10 mm away from the origin (Fig 1A). The three points on the centerlines of PA, AVF vein, distal artery, each being 10 mm from the anastomosis origin, form the anastomosis plane. The nonplanarity angle was calculated as the angle between the anastomosis plane and the line connecting the anastomosis origin and the AVF vein centerline point that is 40 mm away from the origin (Fig 1B). Tortuosity was calculated as $(\frac{L}{D} - 1)$, where L and D are the centerline curve length and straight line length, respectively, from the anastomosis origin to the AVF vein centerline point. D was set to be 40 mm (Fig 1B).

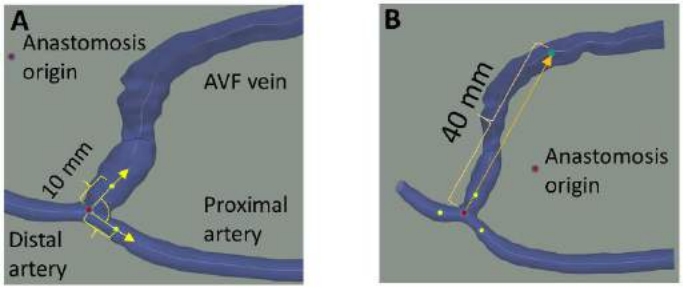

Fig 1. AVF geometric parameter definitions. (A) The anastomosis angle. (B) The nonplanarity angle and tortuosity.

Analysis of variance (ANOVA) and correlation analyses were performed to examine whether the geometric parameters changed over time and were associated with the AVF location (forearm vs. upper arm) and flow rates.

RESULTS

There were 114 patients with at least one MRI scan. There were more upper arm (63%) than forearm AVFs.

Table 1. The AVF geometric parameters and flow rates (Mean± SD) at three postoperative time points in different locations.

Anastomosis angle (degree)			
Locations	**1 Day**	**6 Weeks**	**6 Months**
Forearm	58.1±18.5	57.1±16.9	62.9±17.5
Upper arm	75.3±19.0	77.5±17.7	80.9±20.2
Nonplanarity angle (degree)			
Forearm	16.4±10.5	18.2±13.6	16.4±13.7
Upper arm	28.4±15.2	32.3±16.1	37.5±16.9
Tortuosity			
Forearm	0.10±0.07	0.11±0.08	0.11±0.09
Upper arm	0.13±0.09	0.16±0.11	0.17±0.11
Flow rate (mL/min)			
Forearm	408±249	543±326	674±422
Upper arm	633±367	821±492	887±503

Eleven AVFs were created using a two-stage method with the second surgery performed after the 6-week scan and before the 6-month scan. Due to the large geometric change of the second surgery, the 6-month scan data were not included in the analysis. The three geometric parameters and flow rates at three postoperative scans stratified by AVF locations are shown in Table 1.

Two-way ANOVA demonstrated that upper arm AVFs had significantly larger ($P < .001$) anastomosis angles, nonplanarity angles, and tortuosity than forearm AVFs, respectively; none of these geometric parameters changed significantly over time for either AVF. Similarly, upper arm AVFs also had significantly larger ($P < .001$) flow rates than forearm AVFs at all three scans. For both AVFs, flow rates increased significantly during 1 day and 6 weeks but did not increase significantly during 6 weeks and 6 months.

For both forearm and upper arm AVFs, flow rates were not significantly associated with any of the three geometric parameters at any of the three scans.

DISCUSSION

It has been well-recognized that hemodynamics affects vascular structure and function in health and diseases. Because hemodynamics is largely affected by geometric configurations, vascular geometric features have been investigated in atherosclerosis and aneurysm studies. We demonstrated that upper arm AVFs have larger anastomosis angles, nonplanarity angles, and tortuosity than forearm AVFs; however, flow rates do not correlate with these geometric parameters. The AVF flow rate is determined by the whole vasculature from the subclavian artery to superior vena cava. Geometric features in a wider range may be needed in order to explain the different AVF flow rate values. Further studies will examine the associations of these geometric parameters with the AVF lumen diameter and the rates of surgical and endovascular intervention and maturation.

ACKNOWLEDGEMENTS

This work was funded by the National Institute of Diabetes and Digestive and Kidney Diseases (U01DK082222, U01DK082189, U01DK082218, and R01DK88777).

REFERENCES

[1] Woodside, KJ et al., *Am J Kidney Dis* 71:793-801, 2018.
[2] Cunnane, CV et al., *Cardiovasc Eng Technol* 8:280-294, 2017.
[3] Krishnamoorthy, MK et al., *Kidney Int* 81:745-750, 2012.
[4] Sadaghianloo, N et al., *J Vasc Surg* 62:1583-1589, 2015.
[5] Corbett, RW et al., *J Vasc Surg* 68:152S-163S, 2018.
[6] He, Y et al., *J Biomech* 46: 165-169, 2013.
[7] He, Y et al., *J Vasc Surg* 68:1848–1857.e2, 2018.

SB³C2019
Summer Biomechanics, Bioengineering and Biotransport Conference
June 25 -28, Seven Springs, PA, USA

EFFECT OF GRAVITY ON HEMODYNAMICS IN CEREBRAL ANEURYSMS – AN IN VITRO STUDY

Melissa C. Brindise (1), Sean Rothenberger (2), Susanne Schnell (3), Michael Markl (3), David Saloner (4), Vitaliy L. Rayz (2), Pavlos P. Vlachos (1)

(1) School of Mechanical Engineering
Purdue University
West Lafayette, IN, USA

(2) Weldon School of Biomedical Engineering
Purdue University
West Lafayette, IN, USA

(3) Feinberg School of Medicine
Northwestern University
Chicago, IL, USA

(4) Department of Radiology and Biomedical Imaging
University of California San Francisco
San Francisco, CA, USA

INTRODUCTION

Hemodynamics is known to play a critical role in the progression and rupture of intracranial aneurysms (IA). Previous studies have linked hemodynamic parameters such as wall shear stress (WSS) and oscillatory shear index (OSI) to increased IA risk of rupture. However, contradictory conclusions among such studies, such as both high and low WSS linked to risk of rupture, have prevented establishing concrete mechanisms of the flow-induced aneurysm growth and the critical values of these hemodynamic risk factors.

When investigating these inconsistencies, the methodology and subsequent assumptions used must be considered. Most often, hemodynamic IA studies use patient-specific computation fluid dynamics (CFD) to solve for the velocity field within the IA. CFD studies typically assume laminar flow, rigid boundaries, Newtonian flow and neglect gravity. Some studies have measured velocities *in vivo* with three-directional phase-contrast MRI (4D Flow MRI), but the low spatiotemporal resolution of this modality inhibits accurate estimation of hemodynamic metrics in cerebral vessels. Further, because typically MRI imaging is acquired for only one patient orientation, the 4D Flow also neglects the effects of gravity. Limited experimental particle image velocimetry (PIV) studies have been completed in this domain, majority of which have been 2D - 2 velocity component studies, despite the known three-dimensionality of the flow, and have been imaged at a single orientation.

Neglecting gravitational forces is an assumption common to all hemodynamic IA studies, regardless of modality. However, the effect of gravity on the hemodynamics within a cerebral aneurysm may be significant. In this work, we experimentally investigate the effect of gravity on hemodynamic parameters in two patient-specific cerebral aneurysm models by imaging the flow at two orthogonal orientations. A "horizontal" orientation was imaged to represent a patient in a supine position in an MRI scanner and a "vertical" orientation was imaged to represent a patient standing up. Both STB orientations are compared to CFD and *in vivo* 4D Flow data.

METHODS

In vivo 4D Flow MRI velocity fields were acquired for a basilar tip aneurysm at University of California San Francisco and an internal carotid artery (ICA) aneurysm at Northwestern Memorial Hospital. *In vivo* contrast-enhanced MR angiography (basilar tip aneurysm) and non-contrast time-of-flight MR angiography (ICA aneurysm) data were segmented, and 1:1 *in vitro* silicone block models were fabricated with 3D printing. A mock circulatory flow loop mimicked *in vivo* conditions, matching inflow waveforms as well as Reynolds and Womersley numbers, and used a water-glycerol-urea blood analog [1]. Volumetric particle velocimetry images (3D – 3 velocity component) were captured for both aneurysms at both orientations. The flow in the horizontal orientation was first imaged then the aneurysm model was rotated without removing it from the flow loop. The cameras and laser volume were rotated, and the flow in the vertical orientation was imaged. Particle images were processed using Shake the Box (STB), a particle tracking based algorithm [2]. All experimental results will be referred to as 'STB' herein.

Velocity gradients and WSS were computed using radial basis functions (RBF) [3]. Three component time averaged WSS (TAWSS) was computed according to the following equation:

$$\mathrm{TAWSS} = \frac{1}{T}\int_0^T |\tau_w| dt \qquad (1)$$

where τ_w is wall shear stress (dynes/cm^2) and T is the period of the pulsatile cycle (s).

CFD velocity fields were also available for both geometries at only the same horizontal orientation as the *in vivo* 4D Flow data [4]. Horizontal STB data was acquired but post-processing of this test case is ongoing, thus comparisons herein are limited to the vertically-oriented STB and CFD.

RESULTS

Figure 1 shows the velocity pathlines for the vertically-oriented STB and horizontally-oriented CFD for both geometries. The pathlines demonstrate agreement of the general flow patterns across the two modalities for both cases.

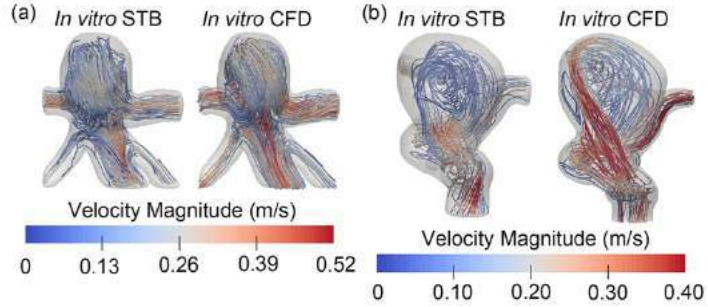

Figure 1: Velocity pathlines for vertically-oriented STB and horizontally-oriented CFD data in the (a) basilar tip and (b) ICA aneurysms. Note: length scale is different between the two geometries. (Image adapted from [4]**)**

Figure 2 compares the normalized WSS of both geometries computed using vertically-oriented STB and horizontally-oriented CFD. Despite the agreement of velocity pathlines (Fig. 1), significant differences in the low WSS regions of the STB and CFD data is observed. Specifically, for the basilar tip aneurysm a large low WSS region at the anterior proximal portion of the aneurysmal sac was present in the CFD but not the STB. For the ICA aneurysm, the vertically-oriented STB maintained a larger low WSS region than the CFD. In the horizontal orientation for both geometries, gravitational forces act in the anterior-posterior direction, pushing flow away from the anterior, towards the posterior region of the aneurysm. Conversely, in the vertical orientation, gravitational forces act in the proximal-distal direction, pushing flow in the proximal direction.

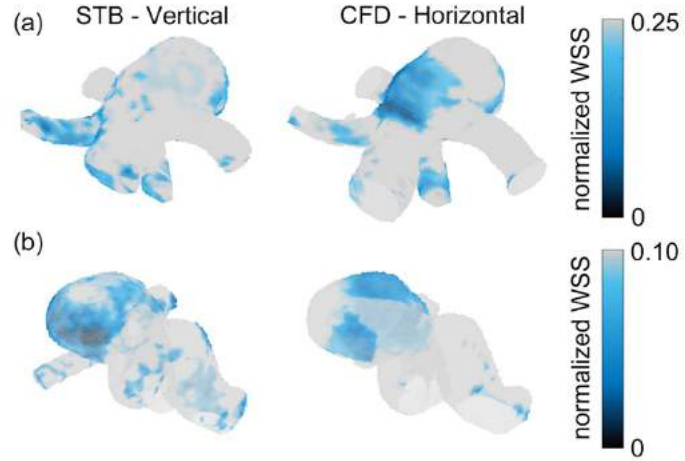

Figure 2: Normalized WSS contours for vertically-oriented STB and horizontally-oriented CFD data in the (a) basilar tip and (b) ICA aneurysms. Note: models are not shown in their acquired orientations. (Image adapted from [4]**)**

DISCUSSION

From the preliminary results presented here, it is evident that even given the same geometry, the different assumptions and limitations of each modality have a major impact on hemodynamic parameters such as WSS. The different low WSS regions based on the STB and CFD could have subsequent impact on the assessed aneurysmal stability. Thus, given the importance of this difference in WSS contours, the source of this difference must be considered.

Although variations in the inlet flow rates are possible due to the different modalities among the preliminary results, previous studies have reported that different inlet waveforms can alter WSS magnitude, but do not affect the spatial variation of WSS [5]. Therefore, it is unlikely the observed spatial WSS differences are contributed by inflow variations. Further, the same rigid wall model was used for both modalities. In the CFD, laminar flow was assumed, while STB inherently does not. However, given the similarities of flow pathlines (Fig. 1) across the modalities, it is unlikely turbulent flow behavior caused this WSS difference.

The final major difference among this comparison was the orientation: the STB was vertically oriented while the CFD was horizontally oriented. Thus, the orientation of aneurysm with respect to gravity was rotated. In the basilar tip aneurysm, the low WSS region of the CFD is located in the anterior portion of aneurysmal sac, aligning with the direction gravity would push flow away from, thereby reducing the flow velocity and WSS in that area. In the ICA case, the tortuous ICA vessel is wrapping around the aneurysm, moving horizontally at the base of the aneurysmal sac. Thus, flow entering the sac in the vertical orientation would be moving against gravitational forces, while in the horizontal orientation flow entering the aneurysmal sac would be moving orthogonal to gravitational forces. The lower flow velocity and WSS in the aneurysmal sac for the vertically oriented STB as opposed to the CFD matches the expected differences if gravitational forces in the flow are significant. Therefore, preliminary WSS analysis of both aneurysms support the notion that gravitational forces affect hemodynamic metrics such as WSS in an aneurysmal sac.

With this notion, the effect of gravitational forces, which have previously been neglected in hemodynamic IA studies, could, in part, explain some of the contradictory results that have been reported. Given that cerebral aneurysms can occur at various locations in the cerebral vasculature, the effect of gravity in each case would vary, confounding the gravitational effect across studies. However, a cross-modality comparison, as shown herein, cannot unambiguously confirm this conclusion, as too many extraneous variables could influence the results, necessitating a more direct comparison. Thus, the forthcoming results of this work, comparisons among a single modality, STB, will mitigate many of the other dependent variables and assumptions that could affect the IA hemodynamics. Ultimately these results could also be used for generating and validating orientation-dependent models, thereby enhancing hemodynamic analysis of cerebral aneurysms.

ACKNOWLEDGEMENTS

American Heart Association pre-doctoral fellowship (17PRE33670268) to Melissa Brindise is gratefully acknowledged.

REFERENCES

[1] M. C. Brindise, M. M. Busse, and P. P. Vlachos, *Exp. Fluids*, 59:173, 2018.
[2] D. Schanz et al., *Exp. Fluids*, 57(5):1–27, 2016.
[3] S. Karri et al., "*Meas. Sci. Technol.*, 20(4):045401, 2009.
[4] (Under review) M. C. Brindise et al. *Ann. Biomed. Eng.*, 2019.
[5] J. R. Cebral, F. Mut, J. Weir, and C. Putman, *Am. J. Neuroradiol.*, 32(1):145–151, 2011.

SB³C2019
Summer Biomechanics, Bioengineering and Biotransport Conference
June 25 -28, Seven Springs, PA, USA

A NONLINEAR MECHANICS-BASED VIRTUAL COILING METHOD FOR INTRACRANIAL ANEURYSM

Seyyed Mostafa Mousavi Janbeh Sarayi (1,2), Robert J. Damiano (1,2), Palak Patel (1,2), Gary Dargush (1), Adnan H. Siddiqui (2,3), Hui Meng (1,2,3,4)

(1) Department of Mechanical and Aerospace Engineering
University at Buffalo
Buffalo, NY, USA

(2) Canon Stroke and Vascular Research Center
University at Buffalo
Buffalo, NY, USA

(3) Department of Neurosurgery
University at Buffalo
Buffalo, NY, USA

(4) Department of Biomedical Engineering
University at Buffalo
Buffalo, NY, USA

INTRODUCTION

Enodvascular coils treat intracranial aneurysms (IAs) by causing them to occlude by thrombosis. Ideally, coiled IAs eventually occlude in the long-term. However, 20.8% are found incompletely occluded at treatment follow-up [1]. Computer simulations of coiling and its effect on aneurysmal flow could help clinicians predict treatment outcomes *a priori*, but it requires accurate modeling of coils and their deployment procedure. In addition to being accurate, coiling simulations must be efficient to be used as a bedside tool. To date, several virtual coiling techniques have been developed, but they lack either accuracy or efficiency. For example, finite-element-based virtual coiling methods model the mechanics of coiling and are highly accurate, at the expense of high computational cost (and thus low efficiency) [2]. Geometric-rule-based coiling techniques ignore the mechanics and therefore are computationally efficient [3], but may produce unrealistic coil deployments. In order to develop a virtual coiling method that combines accuracy and efficiency, we propose a novel virtual coiling algorithm that models coil deployment with nonlinear mechanics and nonlinear contact. Our approach is potentially more accurate than existing "simple" techniques because we model coil mechanics. It is also potentially faster than finite-element techniques because it models the most time-consuming part of these algorithms – namely contact resolution – with a novel formulation that resolves contact faster with exponential functions. Moreover, we model the coil's pre-shape as well as coil packaging into the catheter, both of which are important to model but are lacking from most existing techniques.

METHODS

In developing our algorithm, we considered three primary features of actual coiling procedures: coil geometry, coil packaging into the catheter, and coil deployment into the aneurysm. In Figure 1, we show these features in actual coil (left column) and in our model (right).

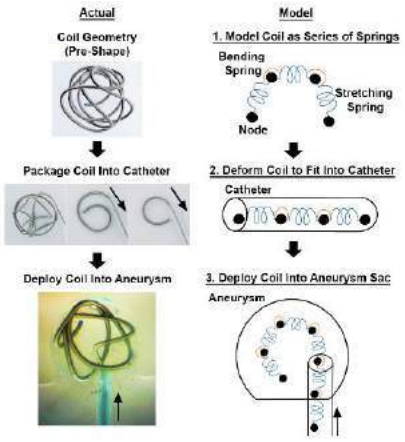

Figure 1: The three primary features of actual coil deployments were modeled in the virtual coiling algorithm.

Step 1. Modeling Coil Geometry Actual coils have a complex structure consisting of a primary wire, which is wound into a secondary spring-like structure. Moreover, in order to maximize coil distribution and clot formation in the aneurysm sac, the coils are made into a tertiary pre-shape (Figure 1, top left). To have a simplified representation of the coil structure and deployment, we modeled the coil's secondary structure as a series of equal-length linear stretching springs (with spring constants k_s) connected at nodes (Figure 1, right column). The length of each spring (l_0) was set to the diameter (d) of the coil wire. To account for bending, neighboring spring elements were connected to each other by linear bending springs (with spring constant k_b) (Figure 1, right column). Modeling a coil's geometry and mechanics as springs is more

efficient than finite-element approaches, which typically model them with higher-order beam element formulations [2].

Step 2. Deforming the Coil into the Catheter To accurately capture the mechanics of coil deployment it is important to take into account pre-packaging of the coil into the catheter, since the straightening of the coil from its pre-shape would store strain energy, which will eventually affect the deployment and final configuration of the coil. The actual physical process of packaging the coil into the catheter is depicted in Figure 1 (left middle). To deform the virtual coil into the catheter, we first determined the change in angels and orientations of neighboring spring elements required to move the coil from its pre-shape to the catheter shape. For that purpose, local coordinates were defined on each node between spring elements using Gram-Schmidt orthogonalization [4]. Then, the coil was deformed by applying the appropriate forces to the nodes. During this step, we assumed that only bending energy changes and neglect stretching energy of the coil. The total bending energy for the coil was defined by

$$W_b = \frac{1}{2} k_b \sum_j^m (\theta_j - \theta_0)\,, \qquad (1)$$

where m is the number of connections, θ_j is the angle between neighboring spring elements at the current state in the simulation and θ_0 is the angle between neighboring springs in the coil's reference pre-shape.

Step 3. Coil Deployment into the Aneurysm The final step in the coiling algorithm is deploying the coil into the IA sac (Figure 1). In the simulation, the IA sac was represented by a closed surface of tetrahedral elements. To deploy the coil, the coil was "pushed", one spring element at a time, into the IA sac, from its deformed catheter shape. The nonlinear dynamic equation of motion for the coil during deployment is given by the following nonlinear equation:

$$m\ddot{x} + c\ sign(\dot{x})\left(1 - e^{-|\dot{x}|/k}\right) = F_i + F_{c,w} + F_{c,c} + F_p. \qquad (2)$$

In this equation, the second term on the left is a nonlinear damping term in which c is the damping constant and k is a constant. This nonlinear damping term stabilizes the coil during deployment to avoid large deformations and sharp angles between neighboring springs which would be unrealistic in real life coil deployments. The right hand side of (2) contains all of the relevant forces that act on each of the coil nodes during deployment. F_0 is the force used to "push" the coil into the aneurysm and F_i is the coil's internal force defined by

$$F_i = \frac{\partial W}{\partial x_i}, \qquad (3)$$

where x_i is the position of ith coil node and W is the total internal energy. Although negligible during coil packaging, the total stretching energy for the coil W_s becomes important during deployment:

$$W = W_b + W_s\,, \qquad (4)$$

where $W_b$is the bending energy defined in (1) and W_s is the stretching energy of the coil:

$$W_s = \frac{1}{2} k_s \sum_i^n (l_i - l_0). \qquad (5)$$

Here n is the number of springs and l_i is the current length of spring elements in the simulation. In (2), F_i also contains the energy from $F_{c,w}$ and $F_{c,c}$, which are nonlinear coil-IA wall and coil-coil contact forces. These forces are defined as

$$F_{c,w} = |F_{c,w}|N, \qquad (6a)$$

$$F_{c,c} = |F_{c,c}|\frac{(\overrightarrow{x_i} - \overrightarrow{x_j})}{norm(\overrightarrow{x_i} - \overrightarrow{x_j})}, \qquad (6b)$$

where N is the normal vector of one of the tetrahedral segments of the aneurysm wall in contact with a coil segment, and x_i and x_j are the position vectors of two coil nodes involved in the contact. The magnitude of these contact forces were defined by [5]

$$|F| = \begin{cases} 0 \ \ for\ \delta_g \geq c_0 \\ \frac{P_0}{1-e}\left[\left(1 - \delta_g/c_0\right)\left(e^{1-\delta_g/c_0}\right)\right] for \quad -6c_0 < \delta_g < c_0 \\ \frac{P_0}{1-e}\left[7(e^7 - 1) - \left(6 + \delta_g/c_0\right)(8e^8 - 1)\right]\ for\ -6c_0 \geq \delta_g \end{cases}, \qquad (7)$$

where $|F|$ represents $|F_{c,w}|$ and $|F_{c,c}|$. In (7), $\delta_g = |x_i - x_j|$ is the distance between the two coil nodes in contact, and c_0 and P_0 are two model parameters that can be assumed to be approximately equal to the mean local pressure and two times the root-mean-square surface roughness of the aneurysm wall. Because the nonlinear contact forces increase exponentially as the contact distance decreases in (7), the computational time to resolve contact is fast. To solve (4) iteratively, we used a semi-implicit Euler scheme. The simulation ends once the coil is completely deployed into the IA.

Preliminary Test of the Algorithm We implemented the algorithm in Matlab and tested the code by simulating the deployment of a $3mm \times 6cm$ Stryker coil (radius $0.014605cm$) into a patient-specific internal carotid artery IA with a diameter of $3.5mm$. The pre-shape geometry of the coil was adopted from a previous study [2].

RESULTS

Figure 2 shows the intermediate and final results of the test coil deployment. It can be seen that the coil configuration changes over time during deployment, which echoes the real coil behavior when it is pushed into an aneurysm. This demonstrates that our nonlinear mechanics-based algorithm is able to capture the dynamics of coiling.

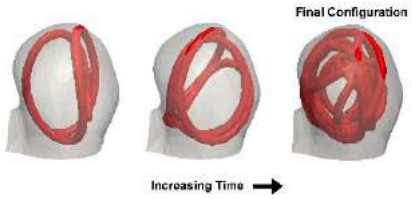

Figure 2: Coil configuration at two intermediate time points in the test deployment simulation and the final configuration.

DISCUSSION

We have demonstrated a new virtual coiling algorithm that is more realistic than existing "simple" algorithms. In one preliminary example we have shown that the simulation captures the dynamic behavior of real coil deployment. This novel method is potentially faster than the most accurate finite-element algorithms. We expect greatly increased computational efficiency from: (1) modeling a coil as a series of linear and bending spring while still maintaining coil mechanics, and (2) combining nonlinear dynamics of the coil with a novel nonlinear contact mechanics formulation. In the future, we will test the robustness of our algorithm in more patient-specific IA case, compare its efficiency against existing virtual coiling methods, and experimentally validate it.

REFERENCES

[1] Ferns, S. P. *et al.*, *Stroke*, 40:523-529, 2009.
[2] Damiano, R. J. *et al.*, *Journal of Biomechanics*. Elsevier, 48:3332–3340, 2015.
[3] Hernan .G., M. *et al.*, *IEEE transactions on medical imaging*, 32: 119–129, 2013
[4] Press, W. H. *et al.*, *Cambridge University Press*. Third: 2007
[5] Dargush, G. F. and Soom, A., *Tribiology International*. Elsevier, 100:360–370, 2016.

SB³C2019
Summer Biomechanics, Bioengineering and Biotransport Conference
June 25 -28, Seven Springs, PA, USA

COMPUTATIONAL ASSESSMENT OF LEFT-VENTRICULAR OUTFLOW TRACT HEMODYNAMIC ALTERATIONS IN DISCRETE SUBAORTIC STENOSIS

Jason A. Shar (1), Sundeep G. Keswani (2,3), K. Jane Grande-Allen (4), Philippe Sucosky (1)

(1) Mechanical and Materials Engineering
Wright State University
Dayton, Ohio, United States

(2) Division of Pediatric Surgery
Texas Children's Hospital
Houston, Texas, United States

(3) Department of Surgery
Baylor College of Medicine
Houston, Texas, United States

(4) Department of Bioengineering,
Rice University,
Houston, Texas, United States

INTRODUCTION

Discrete subaortic stenosis (DSS) is a congenital cardiac disease that is responsible for 8-30% of total left ventricular (LV) outflow tract (LVOT) obstructions in children, and up to 20% of obstructions that require surgical intervention [1]. It is characterized by a thin fibromuscular ring of tissue that forms on the interventricular septum immediately below, or sometimes fused with, the aortic valve (AV) [1]. A common morphological abnormality found among DSS patients is a steepened aortoseptal angle (AoSA), which describes the angle between the septal wall and the long-axis of the ascending aorta, and is presumed to cause turbulent blood flow conditions in the LVOT.

Present in 30-80% of DSS patients, aortic regurgitation (AR) is the most common complication of DSS [2]. AR is characterized by a reflux of diastolic blood from the aorta to the LV due to the malcoaptation of the leaflets [2]. In the context of DSS, AR has been hypothesized to result from the stenotic blood flow conditions imposed by the fibrotic lesion obstructing the LVOT [2]. Supported by observations that have shown AR progression post-obstruction relief is common with steep AoSAs, the hypothesis of this study is that LVOT abnormalities generate altered blood flow velocity, skewness, and displacement, which may contribute to abnormal leaflet dynamics and insufficiency.

Therefore, the objective of this study was to utilize 2D computational fluid dynamics (CFD) modeling incorporating patient-derived myocardial wall motion and boundary conditions to quantify the hemodynamic environment in normal (normal AoSA) and abnormal (steepened AoSA with/without DSS) LV geometries.

METHODS

LV images were obtained from a healthy 25-year-old adult male volunteer using a 3T MRI scanner (GE Healthcare Discovery MR 750w). A total of 29 temporal phases per cardiac cycle were acquired. Segmentation and reconstruction of the mid-plane of the 4-chamber view were manually performed (Fig. 1A) using Segment v2.2 R6435 (http://segment.heiberg.se) [3]. To acquire smooth displacement motion over the entire cardiac cycle with the desired temporal resolution (0.5 ms), intermediate time points were generated using cubic spline interpolation between two consecutive time frames.

LV motion was generated via implementation of a one-way fluid-structure interaction (FSI) technique in ANSYS 19. Briefly, the wall displacement prescribed in ANSYS Mechanical was transmitted to the fluid domain in ANSYS Fluent. The resulting mesh displacement and fluid flow were calculated via the arbitrary Lagrangian-Eulerian (ALE) method. Three cases were considered to isolate the impact of AoSA abnormalities and DSS on LVOT hemodynamics: LV with normal AoSA (130°), LV with steepened AoSA (110°), and LV with steepened AoSA and DSS membrane attached to the septum (Fig. 1B).

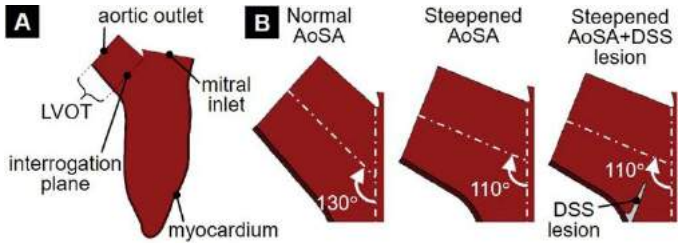

Figure 1. LV geometrical model; A) complete LV geometry, and B) different LVOT geometries considered in the study.

The DSS lesion was modeled as an isotropic linear elastic material (elastic modulus: 2 MPa, density: 1060 kg/m^3, Poisson's ratio: 0.49), and its motion was computed via two-way FSI [4]. Blood was approximated as an incompressible Newtonian fluid (density: 1050

kg/m^3, viscosity: 0.0035 Pa·s) [1]. Following a mesh sensitivity analysis, the fluid domain of the normal, steepened, and DSS geometries was meshed with 153,852, 151,248, and 152,348 cells, respectively. The turbulent flow was computed by incorporating the transitional shear stress transport $k-\omega$ model in the Reynolds-averaged Navier-Stokes equations. This model is able to handle adverse pressure gradients and flow separation that are expected in DSS.

The analysis consisted of the characterization of the flow velocity field, and the velocity profile captured at the inlet of the LVOT (Fig. 2A). In-plane jet skewness and eccentricity were quantified in terms of flow angle, θ (angle between the mean flow vector and the unit vector normal to the interrogation plane, Fig. 2A) and displacement, d (distance between the center of the LVOT and the centroid of the top 15% of velocities in the interrogation plane, Fig. 2B).

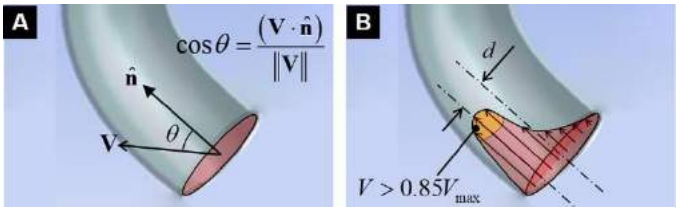

Figure 2. Interrogation plane hemodynamic endpoints: A) flow skewness, and B) flow displacement.

RESULTS

Velocity Field

While the steepened AoSA did not drastically alter LVOT flow structures, the presence of a DSS lesion substantially affected the intraventricular vortex (Fig. 3), which is known to be crucial for proper LV function. Typically clockwise within a normal LV during diastole, this vortex exhibits counter-clockwise rotation in the presence of DSS. During systole, the model predicted slight variations in flow velocity between the normal and steepened AoSA cases. The normal AoSA appeared to have a recirculation bubble forming downstream of the mitral inlet, while the steepened AoSA exhibited higher velocity magnitude closer to the septal ridge. The presence of the DSS lesion resulted in the generation of a stenotic conditions marked by a systolic jet with increased velocity magnitude due to the narrowed LVOT inlet cross section. Recirculation and vortical structures are evident on the aortic side of the DSS membrane.

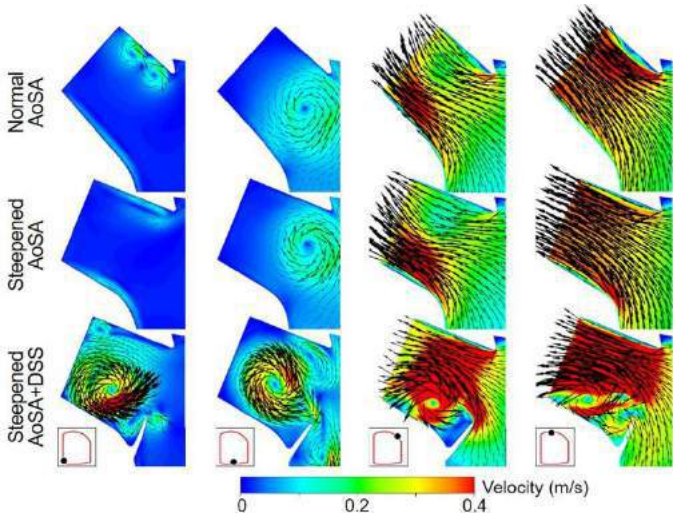

Figure 3. LVOT velocity predictions during early diastole, mid-diastole, early systole, and at peak-systole (inset: LV pressure-volume curve).

LVOT Inlet Flow Characteristics

At peak systole, the velocity profile captured at the LVOT inlet reveals a 12% increase in velocity magnitude near the septal wall ($-0.903 < r/R < -0.733$) in the steepened AoSA relative to the normal AoSA (Fig. 4A). While both the normal and steepened AoSA cases generated relatively flat velocity profiles in the interrogation plane, the presence of a DSS lesion resulted in a high-magnitude (2-fold increase vs. normal AoSA) asymmetric profile with peak velocity occurring near the middle of the LVOT. Flow skewness was increased by the steepened AoSA relative to the normal AoSA (16.8° vs. 7.2°, respectively; Fig. 4B). In addition, while the normal AoSA generated a jet displaced toward the top of the LVOT ($d/R = 0.86$), the steepened AoSA resulted in a reversed eccentricity toward the septal ridge ($d/R = -0.70$; Fig. 4C). While the DSS lesion generated an asymmetric jet with increased velocity magnitude in the unobstructed LVOT region opposite to the lesion, it resulted in decreased flow displacement relative to the normal and steepened AoSA cases ($d/R < 0.001$).

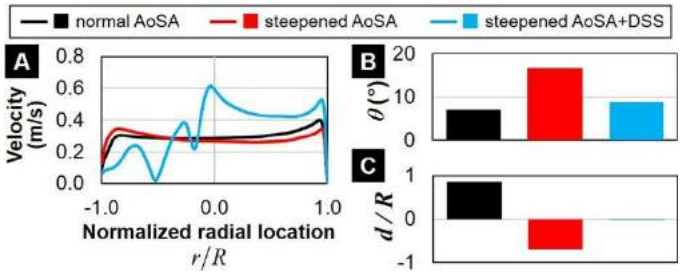

Figure 4. Peak-systolic LVOT flow characteristics: A) velocity profiles at LVOT inlet, B) flow skewness, and C) normalized flow displacement (R: local interrogation section radius).

DISCUSSION

2D LV simulations with realistic wall motion were performed to assess the effects of AoSA abnormalities and DSS on LVOT hemodynamics. In the absence of DSS, the steepened AoSA contributed to greater flow skewness and increased velocity closer to the septal wall. The presence of a DSS lesion inverted the rotation of the intraventricular vortex, a critical flow structure that aids in maintaining proper leaflet dynamics. Combined with the predicted stenotic flow conditions within the LVOT, these hemodynamic abnormalities could prove detrimental to proper leaflet function and may contribute to overall insufficiency.

Although limited by the simplified 2D geometry, this study demonstrates the existence of significant flow abnormalities in steep AoSA and DSS LVs, which may hamper leaflet dynamics and valvular function. Simulations integrating functional valve leaflets in the LV model are ongoing to elucidate valvular function and potential regurgitation in DSS.

ACKNOWLEDGEMENTS

This work was supported in part by the National Institutes of Health (NIH) grant R01HL140305. The authors would like to acknowledge Dr. Mathew Sherwood and Aaron Madaris for their assistance in the acquisition of the cardiac MRI data.

REFERENCES

[1] Massé, D et al., *Frontiers in Cardiovascular Medicine*, 5:1-9, 2018.
[2] Pickard, S et al., *Heart*, 101:1547–1553, 2015.
[3] Heiberg, E et al., *BMC Medical Imaging*, 10:1-13, 2010.
[4] Hasan, A et al., *Journal of Biomechanics*, 47:1949–1963, 2014.

SB³C2019
Summer Biomechanics, Bioengineering and Biotransport Conference
June 25 -28, Seven Springs, PA, USA

BLOOD FLOW MODELING OF CEREBRAL ANEURYSM TREATED WITH INTRASACCULAR FLOW DIVERTING DEVICES

F. Mut (1), B. J. Chung (2), J. R. Cebral (1)

(1) Bioengineering Department
Volgenau School of Engineering
George Mason University
Fairfax, VA, USA

(2) Department of Mathematical Sciences
Montclair State University
Montclair, NJ, USA

INTRODUCTION

Treatment of intracranial aneurysm using flow diverting devices have become an attractive treatment option for large and complex aneurysms where coiling alone may not be very effective due to a high chance of movement or compaction of the coils [1]. Endo-luminal flow diverting devices are placed along the parent artery and across the aneurysm orifice in order to deviate the flow away from the aneurysm thus promoting aneurysm occlusion and subsequent endothelialization and artery reconstruction. However, the main drawbacks of this approach are that 1) it requires antiplatelet therapy to prevent thrombus formation, 2) they are difficult to use in bifurcation aneurysms as one branch will be jailed. In recent years, new intra-saccular flow diverting devices have been developed [2]. These devices are built as closed braided meshes and released inside the aneurysm cavity in order to disrupt the inflow jet into the aneurysm thus promoting aneurysm thrombosis and occlusion.

As with endo-luminal devices, not all aneurysms treated with intra-saccular devices are immediately occluded after the device is implanted and some need to be retreated in follow up procedures. The purpose of this work is to study the relationship between the hemodynamic conditions created inside the aneurysm immediately after treatment with intra-saccular flow diverters and the long term outcome (complete or incomplete aneurysm occlusion) of the procedure.

METHODS

A collection of 36 aneurysms treated with intra-saccular devices was studied. 3D rotational angiography (3DRA) images were obtained before treatment. 2D digital subtraction images angiography (DSA) images were obtained immediately before and after treatment. The aneurysms were treated with the Woven EndoBridge (WEB) device [2]. The device size was chosen to be 1mm larger in diameter than the aneurysm width and 1mm smaller in length than the aneurysm depth, thus to allow the device to conform and attach to the aneurysm wall while having enough space to expand towards the fundus.

Computational models of the aneurysm and attached vessels were created from the 3DRA reconstructions [3]. A new tool called cheDeploy was created for deploying models of the intra-saccular devices within the anatomical models. The deployment procedure starts by computing the centerline of the parent vessel. From this centerline, a second straight line is created and positioned inside the aneurysm. A discrete cylinder composed of triangles is generated along this second line and expanded via a combination of radial and contact forces and also restricted to the dimensions of the target device. A braided mesh, represented as a collection of wires, is then generated based on the device characteristics (number of wires, braided angle) and mapped onto the triangular surface. If available, 2D angiography images showing the implanted device are loaded and rendered together with the vascular model and the device model using transparency. The vascular model is then interactively aligned and oriented with the aneurysm and vessels visible in the angiography images. The device model is then rotated and translated to match the implanted device. This procedure is repeated with all the available 2D angiography images until the device model matches the implanted device from all available viewpoints. Figure 1 shows the different steps of the virtual deployment procedure.

Tetrahedral meshes were generated from the anatomical models using an advancing front technique. Spheres matching the wire diameter were generated along the device model wires. Tetrahedral elements in the vascular model that were intersected by the spheres were refined several times in order to capture the effect of the wires on the blood flow (about 5 elements in the wire diameter) [4]. Meshes without the device typically contained between 2 and 5 million elements, while meshes with the deployed device ranged from 100 to 200 million elements.

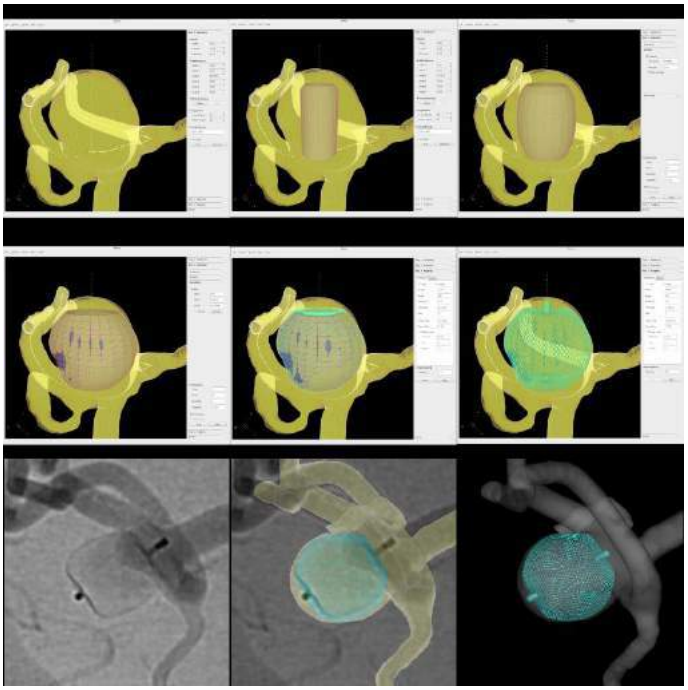

Figure 1: Virtual Deployment Procedure: From top to bottom: 1) Generation and expansion of the support cylinder, 2) Mapping of an intra-saccular device design, 3) Transparency rendering of the vascular model, device model and available 2D angiography images used for precise device placement.

Unsteady Newtonian incompressible Navier-Stokes simulations were carried out for two cardiac cycles and results from the second cycle were saved [3]. An immersed boundary strategy was utilized to solve the blood flow in presence of the deployed devices [4]. Characterization of the intra-aneurysmal hemodynamic environment before and after treatment was done by the computation of the following quantities: a) mean inflow concentration index (ICI), b) mean inflow rate into the aneurysm (Q), c) mean aneurysm velocity (VE), and d) mean aneurysm vorticity (VO). The percentage change (reduction) of these variables between the pre- and post-treatment models were also computed.

RESULTS

The aneurysms were classified into two groups: A) complete occlusion group (no filling of the aneurysm or device or filling of the device proximal recession), and B) incomplete occlusion group (filling of the device proximal compartment or filling of the device distal compartment). Of the 36 aneurysms included in this study, 18 were classified as complete occlusion and 18 were classified as incomplete occlusion.

Changes in the intra-saccular hemodynamic variables between pre- and post-treatment (i.e. device performance) were compared between the complete and incomplete occlusion groups using the non-parametric Mann-Whitney test. P-values were adjusted for multiple comparison using the Bonferroni method. For each variable with statistically significant difference, univariate logistic regressions were carried out, receiving operating characteristic (ROC) curves were created, and the area under the curve (AUC) was calculated to assess the discriminatory power of each variables.

Figure 1 compares the reduction of flow variables in the complete and incomplete occlusion groups. Small reductions of inflow (ΔQ, $p=0.01$) and inflow concentration (ΔICI, $p=0.03$) from pre- to post-treatment is associated with incomplete occlusion. Additionally, the reduction of the mean aneurysm flow velocity tends to be larger for aneurysm in the completely occluded group.

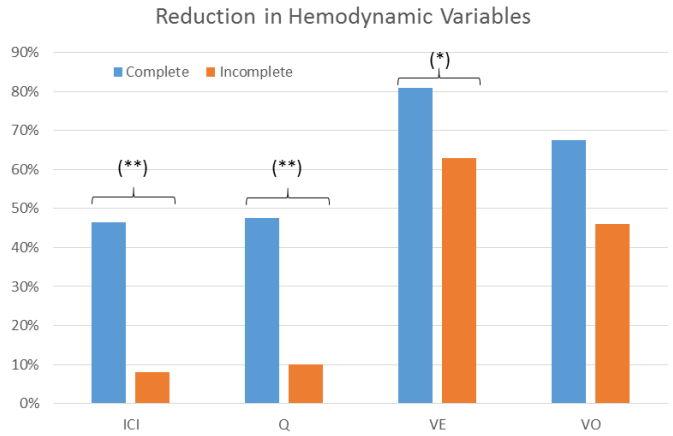

Figure 2: Reduction in intra-aneurysmal hemodynamic variables between pre- and post-treatment. Statistically significant differences ($p<0.05$) are indicated with a "*" in the univariate logistic regressions and with a "" after adjusted for multiple comparisons.**

DISCUSSION

The results of this study indicate that incomplete aneurysm occlusion after treatment with intra-saccular devices is associated with small reduction in the inflow rate and inflow jet concentration from pre- to post-treatment conditions. These results are consistent with previous studies of endo-luminal flow diverting devices [5]. Our results suggest that the change in the aneurysm inflow rate could discriminate between incomplete and complete occlusions at follow up with a predictive power of approximately 82-83%. Interestingly, the univariate logistic regression analysis also indicates that the reduction in the mean aneurysm flow velocity, which could be measured with angiography as a MAFA ratio [6], could discriminate between these groups with approximately 72% accuracy.

This study has some limitations. Patient-specific flow conditions were unavailable and therefore they were adapted from measurements in normal subjects. Vessel walls were approximated as rigid, and blood as a continuous Newtonian fluid. Placement of the virtual devices inside the vascular models were approximated by visually matching the virtual and actual device visible in the DSA images

ACKNOWLEDGEMENTS

This work was supported by the National Institutes of Health, grant number R01 NS076491.

REFERENCES

[1] Pierot, L et al., *J Neuroradiol*, 43:167-75, 2016
[2] Ding, YH et al., *AJNR*, 32:607-11, 2011
[3] Cebral, JR et al., *IEEE Trans Med Imag*, 24:457-67, 2005
[4] Appanaboyina, S et al., *Int J Num Meth Fluids*, 57:457-93, 2008
[5] Cebral, JR et al., *AJNR*, 35:1567-73, 2014
[6] Pereira, VM et al., *AJNR*, 34:805-15, 2013

SB³C2019
Summer Biomechanics, Bioengineering and Biotransport Conference
June 25 -28, Seven Springs, PA, USA

IMPACT OF POST-TAVR PATIENT-SPECIFIC GEOMETRY ON NEO-SINUS FLOW: A COMPUTATIONAL FLUID DYNAMICS STUDY

Shelly Singh-Gryzbon (1), Sanchita S. Bhat (1), Vahid Sadri (1), Joseph K.H. Choi (1), Mandy Salmon (1), Beatrice Ncho (1), Zhengun A. Wei (1), Philipp Ruile (2), Franz-Joseph Neumann (2), Philipp Blanke (3), Ajit P. Yoganathan (1)

(1) The Wallace H. Coulter School of Biomedical Engineering
Georgia Institute of Technology
Atlanta, GA, USA

(2) Department of Cardiology and Angiology II
University Heart Center Freiburg-Bad Krozingen
Bad Kroziingen, Germany

(3) Department of Radiology
St Paul's Hospital and University of British Colombia
Vancouver, BC, Canada

INTRODUCTION

Transcatheter aortic valve replacement (TAVR) has emerged as a minimally invasive option for treating intermediate and high-risk surgical patients with symptomatic aortic stenosis. Despite its success, multiple clinical reports have emerged revealing adverse events such as leaflet thrombosis [1]. Upon implantation, the transcatheter aortic valve (TAV) stent presses against the native leaflets and acts as a divider between the TAV leaflets and the aortic wall. The space between the native leaflets and the aortic wall is defined as the anatomic (native) sinus while the space between the native and TAV leaflets is defined as the neo-sinus. Early *in vitro* mechanistic studies sought to understand whether flow in the neo-sinus contributed to thrombosis on TAVR leaflets, and it was found that stasis was a predominant flow characteristic in this region [2]. However, Kapadia et al. hypothesized that the anatomical sinus may be of equal importance, affecting flow characteristics of the neo-sinus [3]. Indeed, additional studies have shown that aortic root morphology affects blood flow patterns in the sinus, potentially explaining why thrombus was observed in some patients but not all [4, 5]. Therefore, the aim of this study was to investigate the effects of patient-specific anatomical characteristics (including sinus diameter and sino-tubular junction (STJ) height) on neo-sinus flows using computational fluid mechanics (CFD).

METHODS

3D Reconstruction of Post-TAVR Anatomies. Post-procedural computed tomographic angiography (CTA) of 10 patients who underwent an Edwards SAPIEN 3 (Edwards Lifesciences, CA, USA) valve implantation at University Heart Center Freiburg-Bad Krozingen were segmented using 3D Slicer to obtain 3D reconstructions of the post-TAVR anatomies. Due to imaging artifacts, the segmented valve obtained from the patient images was not well-defined, hence the stent of the SAPIEN 3 valve was obtained via μCT scanning (Siemens Medical Solutions USA, Inc., Malvern, PA) while a parametric leaflet model (PLM) was used to create the TAV leaflets. It was matched for each patients' valve characteristics, as obtained from CTA.

Creation and *in vitro* validation of the PLM. The PLM was developed in Rhinoceros® (Robert McNeel & Associates, Seattle, WA, USA). Variables that were parameterized included valve radius, belly curvature, leaflet height, commissure height, and valve opening. The flow results obtained from CFD simulations using the PLM-derived leaflets were validated using *in vitro* flow data. A GT-TAV was deployed into an idealized aortic chamber, where GT-TAV is an in-house valve replicating the dimensions of the TAV being tested and allows optical access into the neo-sinus by using a clear acrylic cylinder to replace the native leaflets. The validated Georgia Tech Left Heart Simulator was used to replicate physiological conditions at peak systole (cardiac output 25 L/min and downstream pressure 120 mmHg) while a 2D particle image velocimetry (PIV) system was used to image the neo-sinus at its center plane. Once validated, the PLM was then used to replicate the dimensions of the SAPIEN 3 valve and coupled with the patient-specific aortic root.

Computational Model for Patient Anatomies. The fluid domain was meshed in ANSYS ICEM CFD (ANSYS, Canonsburg, PA, USA). After performing mesh independence analyses, each patient geometry was mesh with 10-14 million tetrahedral elements. A peak systolic flow rate of 25 L/min was imposed at the inlets assuming a flat velocity profile, while a pressure of 120 mmHg was used at the outlet. All structures were assumed to be rigid and non-permeable, and a no-slip boundary condition was applied at the walls. Blood was assumed to be Newtonian with a kinematic viscosity and density of 0.0036 Pa·s and 1060 kg/m^3, respectively. The governing Continuity and Navier-Stokes equations were solved using ANSYS CFX 17.1. The convergence was controlled by defining a root-mean-square residual of 10^{-6}, which was satisfied after 10 iterations per timestep.

RESULTS

Flow at peak systole was characterized by a high velocity main jet with regions of recirculation in the anatomic sinus (Figure 1). Across patients with the same valve size, there were differences in the flow fields and peak velocities due to variations in ascending aorta diameters and curvature.

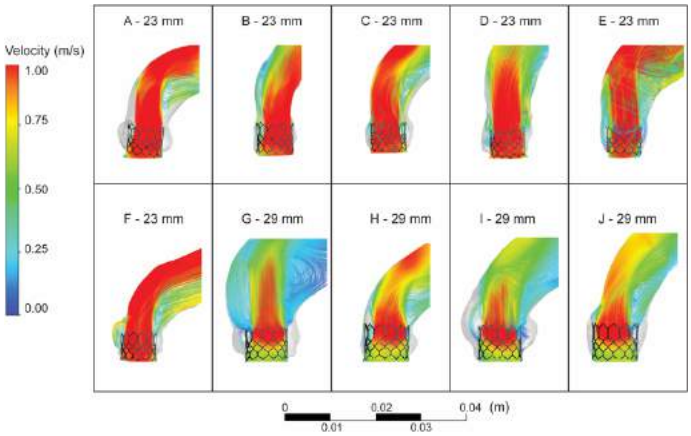

Figure 1: Streamlines of main jet velocities for n=10 patients

To better evaluate neo-sinus flow, the percentage of neo-sinus volume with low velocities ($\%Vol_{vel<v}$) was obtained for all patients. Velocity thresholds of v = 0.02, 0.05, 0.07, 0.09 and 0.1 m/s were evaluated, with the trend for v = 0.05 m/s shown in Figure 2. The results indicated that as the sinus diameter and STJ heights increased, the regions of low flow in the neo-sinus also increased.

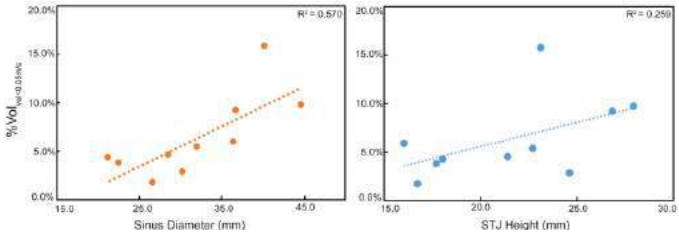

Figure 2: Percentage volume of neo-sinus with velocities below 0.05 m/s ($\%Vol_{vel<0.05m/s}$) vs sinus diameter (left) and sinotubular junction (STJ) height (right)

Analysis of wall shear stress (WSS) also showed a positive correlation between sinus diameter and STJ heights with the fraction of TAV leaflet surface area with WSS lower than 0.4 Pa ($A_{WSS<\tau}$, τ = 0.4 Pa) (Figure 3). As expected, these findings of low WSS are consistent with the regions of low velocities.

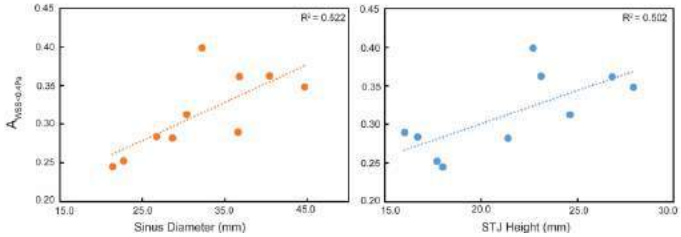

Figure 3: Fraction of TAV leaflet surface area with wall shear stress (WSS) less than 0.4 Pa ($A_{WSS<0.4Pa}$) vs sinus diameter (left) and sinotubular junction (STJ) height (right)

DISCUSSION

The proposed mechanism for thrombus formation on TAV leaflets is increased blood residence time on the leaflets as a result of reduced washout and regions of stasis of the neo-sinus [2]. It is anticipated that a combination of anatomical characteristics including sinus diameters and STJ heights, as well as TAV deployment characteristic including deployment height, tilt angle and rotation, governs the post-TAVR geometry and hence, the flow features observed. *In vitro* assessments of patient-specific hemodynamics in the neo-sinus are challenged by limited optical access of this region. Therefore, this study utilized CFD to evaluate the effects of patient-specific aortic root morphologies on neo-sinus flow under peak systolic conditions.

At peak systole, a positive correlation was observed between the anatomic sinus diameter and STJ heights and the volume of fluid in the neo-sinus with velocities below 0.05 m/s. A potential mechanism for this observed flow behavior is that as the blood entered a large anatomic sinus, its momentum was reduced and as such, had lower velocities. This in turn resulted in a slower moving fluid that entered the neo-sinus, contributing to the low flow in this region. Thrombosis is also most likely to occur in low flow or stasis regions with WSS less than 0.4 Pa, compared with an average value of 1.2 Pa in healthy vessels. Following the same trend as with the low velocity regions, WSS analyses revealed that as anatomic sinus diameter and STJ height increased, the fraction of leaflet area with WSS less than 0.4 Pa also increased.

Some simplifications and assumptions of the physiology and geometry were made in this study. First, the cardiac output was held constant across all patients in order to isolate the effects of patient-specific post-TAVR geometry on hemodynamics. Therefore, all changes in flow fields and related flow metrics were a function of geometry. Second, simulations at additional time points are necessary to quantify the transient progression of flow fields and calculate the blood residence or washout times in the neo-sinus. Third, coronary flow was excluded from the computational model in order to compare and validate with existing *in vitro* methods [2]. Fourth, the aortic wall along with the individual parts of the valve assembly (stent and leaflets) were assumed to be rigid, and the effects of the moving wall and leaflet motion would best be described via fluid-structure interaction (FSI) simulations. However, since this assumption was made for all patient anatomies, relative changes in flow fields are still valid.

Future studies of this work will involve performing FSI simulations of the TAV to simulate temporal variations in flowrate and leaflet kinematics over the cardiac cycle, enabling the quantification of washout in the neo-sinus regions.

ACKNOWLEDGEMENTS

This study was supported with funds from the Wallace H Coulter Chair Endowment and the Marvin H. & Rita Floyd Endowment; BN holds an International Fellowship from American Association of University Women; The authors acknowledge the use of ANSYS software, provided through an Academic Partnership with ANSYS, Inc.; and Ming-Chen Hsu and Fei Xu from the Department of Mechanical Engineering at Iowa State University for their assistance with the PLM.

REFERENCES

[1] Chakravarty, T et al., *Lancet*, 389:2383-2392, 2017.
[2] Midha, P et al., *Circulation*, 136:1598-1609, 2017.
[3] Kapadia, S et al., *Circulation*, 136: 1610-1612, 2017.
[4] Jahren, S et al., *Interact Cardiovasc Thorac Surg*, 27:108-115, 2018.
[5] Madakauwa-David, I. et al., *Catheter Cardiovasc Interv*, 93:134-140, 2019

SB³C2019
Summer Biomechanics, Bioengineering and Biotransport Conference
June 25 -28, Seven Springs, PA, USA

IGF-1 SUPPRESSES TRPV4 OSMOSENSATION THROUGH THE MAP7 BINDING DOMAIN IN CHONDROCYTES

Nicholas S. Trompeter (1), Lauren M. Hurd (2), Joseph D. Gardinier (3), Victor DeBarros II (2), Mary E Boggs (2), Randall L Duncan (1, 2, 3)

(1) Department of Biomedical Engineering
University of Delaware
Newark, Delaware, USA

(2) Department of Biological Sciences
University of Delaware
Newark, Delaware, USA

(3) Biomechanics and Movement Science Program
University of Delaware
Newark, Delaware, USA

INTRODUCTION

Transient Receptor Potential Vanilloid 4 (TRPV4) is a mechanosensitive ion channel that regulates chondrocyte differentiation, endochondral ossification and articular cartilage homeostasis by regulating intracellular calcium in chondrocytes. Mutations of this channel cause a gain of function of TRPV4 and leads to skeletal dysplasia, while excessive mechanical loading activation of TRPV4 has been associated with onset/progression of osteoarthritis (OA). Defining how TRPV4 regulates chondrocyte function and identifying molecular mechanisms that influence TRPV4-mediated calcium signaling may provide therapeutic targets for chondrocyte pathologies.

OA, the degeneration of the articular cartilage of diarthrodial joints, afflicts millions of Americans. While there are a number of risk factors associated with OA, aging is a dominant factor, impacting 50% of adults over the age of 65. During aging, many chondroprotective growth factors, such as Insulin-like Growth Factor-1 (IGF-1), decrease with age. IGF-1 has been shown to be chondroprotective, anti-inflammatory, and beneficial for chondrocyte function in both OA and fracture healing in the elderly (1,2) While Fraenkel, et al. (3) suggest that reduced IGF-1 levels during aging have no effect on the incidence of OA, increasing IGF-1 production in allogenic chondrocyte transplants significantly improved cartilage integrity and biomechanics of cartilage repair in the equine PTOA chip model. Here, we show that IGF-1 tonically suppresses TRPV4 activity through the actin cytoskeleton, leading us to postulate that age-related decline in IGF-1 may lead to a gain of function of TRPV4, suggesting a potential mechanism for the induction and progression of age-dependent OA.

METHODS

Human chondrocytes, murine ATDC5 chondrogenic cells (Sigma Aldrich) and HEK293 (ATCC) cells were used in these studies. Human chondrocytes with TRPV4 mutations (aa. P799L or aa. G800D) were obtained from the tissue bank at AI duPont Hospital for Children. HEK293 cells were either untransfected (HEK-UT) or transfected with TRPV4 wild type (HEK-WT) or with mutations at aa. P799L (HEK-799) or at aa. G800D (HEK-800). Chondrocytes were grown in DMEM and HEK cells were grown in MEM media (Corning) supplemented with 10% Fetal Bovine Serum (Atlas Biologicals) and 1% Penicillin/Streptomycin (Hyclone).

Calcium Imaging: Experiments were conducted as previously described (4,5). All experiments were conducted at room temperature to avoid temperature-sensitive spontaneous TRPV4-mediated calcium oscillations. Unless noted, cells were pre-treated with IGF-1 for 3 hrs prior to loading with either Fluo-4 AM or Fura-2 AM (Life Technologies). Cells were treated with cytochalasin D following loading with the fluorescent calcium chelator. Cells were challenged with 50% Hypotonic Swelling (HTS) after a 1 minute baseline was recorded.

Atomic Force Microscopy: Atomic Force Microscopy with ATDC5 cells was done as previously described (6). Cells were either untreated or treated for 3 hrs with 300 ng/ml of IGF-1, and then either treated with 1 µM of cytochalasin D. Apparent elasticity was measured on an BioScope II (Vecco, Inc.) mounted on an inverted optical microscope.

Cytoskeletal Immunostaining: ATDC5 cells were treated for 0, 1, 2, or 3 hrs with 300 ng/mL IGF-1. Actin staining with Alexa Fluor 488 phalloidin was completed as described previously (6).

Statistical Analysis: One-way or two-way ANOVAS were used to determine statistical significance, with Tukey-Kramer or Dunnett's post-hoc tests used to compare between all treatment groups or to control, respectively. p-values < 0.05 were considered significant.

RESULTS

IGF-1 is a potent chondrogenic growth factor that is essential for chondrocyte survival, proliferation, and differentiation. IGF-1 can also stimulate actin stress fiber formation (7). To confirm that IGF-1 induces actin cytoskeletal reorganization in chondrocytes, we treated ATDC5 cells with 300 ng/ml of IGF-1. As was previously presented at this conference, IGF-1 increased actin stress fiber formation in a time-dependent manner that corresponded with an increase in cell stiffness (Figure 1A). IGF-1 treatment for 3 hrs significantly increased the apparent stiffness of ATDC5 cells from ~4 kPA to ~13.5 kPA. Disruption of the actin cytoskeleton with 1 μM of cytochalasin D blocked the increase in cell stiffness induced by IGF-1. This increase in cell stiffness correlated with a significant attenuation of intracellular calcium influx in ATDC5 cells that were pre-treated for 1-3 hrs with 300 ng/ml IGF-1 (Figure 1B).

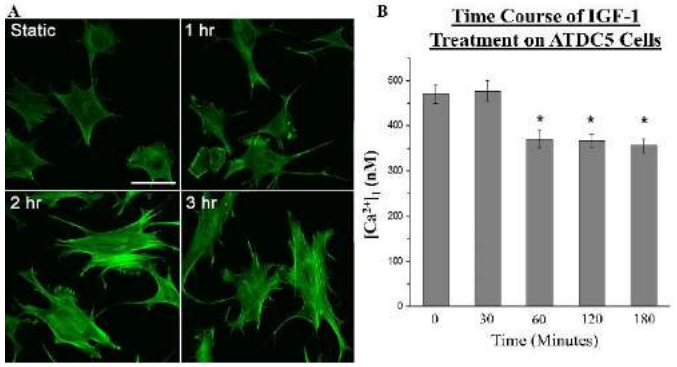

Figure 1: Time Course of IGF-1 on ATDC5 cells. A) a 3hr time course of actin staining indicates that 300 ng/ml IGF-1 increase actin stress fiber formation during 3 hrs of treatment, B) This increase in actin polymerization corresponds with a significant attenuation of Intracellular Calcium Concentration ($[Ca^{2+}]_I$) when treating cells with IGF-1 over 180 minutes prior to challenging the cells with HTS. n= 3.

Suzuki, et al. suggested that actin can bind to the microtubule associated protein 7 (MAP7) domain of TRPV4 (aa. 798-809) to regulate activity of the channel (8). To confirm these results, we utilized TRPV4 mutations in the MAP7 domain, P799L and G800D, to determine if IGF-1 regulates TRPV4 at this domain. IGF-1 suppressed the Ca^{2+} response to HTS in HEK-WT cells, similar to the repsonse observed in ATDC5 cells. The HEK-799 cells were not significantly suppressed and HEK-800 cells show a significant increase in $[Ca^{2+}]_I$ when treated with IGF-1 (Figure 2A). HEK-UT cells failed to respond to HTS, suggesting that osmosensation of HEK cells was TRPV4 dependent. These results indicate that IGF-1 exerts regulatory functions on TRPV4 through the MAP7 domain.

To further confirm that IGF-1 regulates TRPV4 through the MAP7 site, primary human chondrocytes were studied. Human Chondrocytes (HC) appear to be similarly suppressed as HEK-WT when treated with IGF-1 (Figure 2B). Human chondrocytes with a TRPV4 mutation at aa. P799L also show an attenuated response when treated with IGF-1. However, hypotonic challenge of chondrocytes with a TRPV4 mutation at aa. G800D stimulates $[Ca^{2+}]_I$, as similarly seen in the HEK-800 cells.

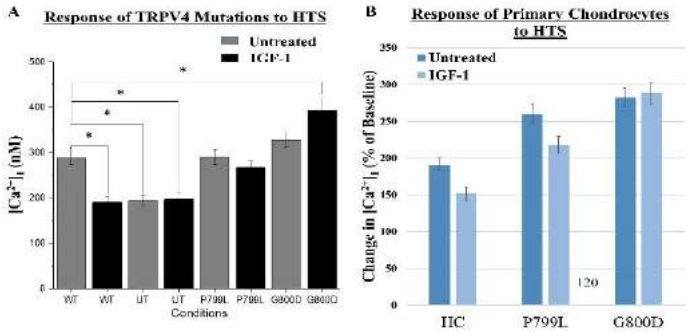

Figure 2: Effect of IGF-1 on TRPV4 Mutations. A) HEK-WT cells show significant attenuation when pre-treated with IGF-1. No suppression in HEK-799 and HEK-800 cells is noted when they are pre-treated with IGF-1. n=3. A similar trend is seen when primary human chondrocytes (HC) and human chondrocytes with TRPV4 mutations (aa. P799L and G800D) are pre-treated with IGF-1 prior to challenge with HTS. n=1.

DISCUSSION

Our findings highlight how IGF-1 tonically suppresses TRPV4 activity via reorganization of the actin cytoskeleton. During treatment with IGF-1, chondrocytes increase actin stress fiber formation to also increase chondrocytes stiffness. This stiffness was abrogated when the cells were treated with cytochalasin D. This confirms previous studies that indicate that IGF-1 rapidly stimulates actin stress fiber formation (7). Our data indicate that IGF-1 mediates this suppression through the interaction of the actin cytoskeleton at the MAP7 binding domain. When HEK293 cells were transfected with two mutations at the MAP7 domain of TRPV4, IGF-1 failed to attenuate the response of these cells to HTS. Furthermore, our data indicates that human chondrocytes respond similarly to the TRPV4 transfected HEK cells during IGF-1 pretreatment, with the caveat that these experiments need to be repeated. Interestingly, a previous study indicates that supraphysiologic IGF-1 pretreatment of TRPV4 transfected HEK cells can induce a sensitivity of TRPV4 to HTS but studies were not conducted with physiologic treatments of IGF-1 (9).

Sen, et al. have shown that the stimulation of actin stress fiber formation during IGF-1 treatment occurs through the mTORC2 pathway in mesenchymal stem cells (10). Thus, future studies will investigate if this pathway also controls chondrocyte actin fiber formation/cell stiffness during IGF-1 treatment. Physiologically, these data suggest that IGF-1 tonic regulation of the TRPV4 channel is necessary for an anabolic phenotype, while hyperactivity of this channel may cause a catabolic effect. This information could prove useful to improve therapies for OA patients and patients with other chondrocyte pathologies.

REFERENCES

[1] Griffin, D et al., *J Orthop Res*, 34:149-153, 2016.
[2] Schmidmaier, G et al., *Bone*, 31:165-172, 2002.
[3] Fraenkel, L et al., *Osteoarthr. Cartil*, 6:362-367, 1998.
[4] Hurd, L et al., *Am J Med Gen, Part A*, 165:2286-2293, 2015.
[5] Balasubramaniam, S et al., *J Biol Chem*, 290:12463-12465, 2015.
[6] Gardinier, J et al., *Cell Mol Bioeng*, 2:4-6, 2009.
[7] Kadowakis, T et al., *J Biol Chem*, 261:16141-16147, 1986.
[8] Suzuki, M et al., *J Biol Chem*, 278:51488-51453, 2003.
[9] Lee, EL et al., *Anim Cells and Sys*, 14:99-114, 2010.
[10] Sen, B et al., *J Bone Miner Res*, 29:1-23, 2015.

SB³C2019
Summer Biomechanics, Bioengineering and Biotransport Conference
June 25 -28, Seven Springs, PA, USA

HIGH-VELOCITY STRETCHING CAUSES MECHANICALLY-INDUCED TAU PATHOLOGY IN NEURONS

Nicholas J. Braun (1), Dezhi Liao (2), Patrick W. Alford (1)

(1) Biomedical Engineering
University of Minnesota – Twin Cities
Minneapolis, MN, USA

(2) Neuroscience
University of Minnesota – Twin Cities
Minneapolis, MN, USA

INTRODUCTION

Traumatic brain injury (TBI) has become a critical health concern recently due to increased awareness of its potential to cause long-term neurological deficits. Annual estimates for the number of TBIs in the US range between 1.6 and 3.8 million, and approximately 5.3 million Americans live with a disability stemming from a TBI [1]. Severe TBI and repeated mild TBI increase the risk of Alzheimer's disease (AD) and chronic traumatic encephalopathy (CTE), neurodegenerative diseases marked by hyperphosphorylation and aggregation of the tau protein into neurofibrillary tangles (NFTs) in the brain [2,3]. In healthy neurons, tau stabilizes microtubules in central nervous system axons. In tauopathic neurodegenerative diseases, tau is hyperphosphorylated by CDK5 and GSK3β, causing its aggregation into NFTs. The elevated presence of NFTs in the brains of former boxers and football players suffering from cognitive decline suggests that tau dysfunction mediates the neural deficits seen in CTE. However, it is unknown how these tau pathologies are elicited by mechanical insult of neurons during TBI.

In neurons with an AD mutation, tau is observed to mislocalize to dendritic spines, where it mediates synaptic dysfunction [3]. Here, we hypothesize that a similar mechanism is important in CTE. **We present an *in vitro* system for simulating TBI-like strains on hippocampal neurons that demonstrates a link between mechanical injury, neurodegenerative tau pathology, and functional synaptic deficits.**

METHODS

Construct Fabrication: Elastic membranes were spin coated with a 10 μm thick layer of Sylgard 527 PDMS at a 1:1 ratio of base to cross-linker. Spin-coated membranes were suspended between two custom-designed metal brackets and a Sylgard 184 PDMS ring was adhered to them to contain cell culture materials during incubation. Membranes were then coated with 100 μg/mL poly-L-lysine and 4 μg/mL laminin to permit cellular adhesion before stretching (Figure 1A).

Cell Harvest, Culture, and Transfection: Primary hippocampal neurons were harvested from newborn rat pups as previously described [3]. Hippocampi were isolated in ice-cold Earl's Balanced Medium with 1mM D-glucose before tissues were digested and cells seeded onto the stretching constructs. The day of plating was denoted as day-in-vitro 1 or DIV1. Weekly media changes were performed thereafter. A standard calcium phosphate precipitation method was used to transfect neurons with desired plasmids at DIV8. Neurons were co-transfected with DsRed and WT-Tau-GFP at a 2:1 ratio. DsRed was used to visualize the morphology of neurons, including the location of dendritic spines.

TBI Simulation, Imaging, and Electrophysiology: A high-speed linear motor was used to simulate TBI-like strains on the seeded neurons on DIV22. Strains ranged from 1-20% and strain rates from 1-1000% strain per second. Tau mislocalization to dendritic spines was quantified 24 hours after injury. Functional synaptic deficits were observed 24 hours after injury by recording miniature excitatory post-synaptic currents (mEPSCs) from neurons bathed in artificial cerebrospinal fluid with APV, tetrodotoxin, and picrotoxin to prevent action potentials [3].

RESULTS

Tau mislocalization to dendritic spines was measured after high velocity stretching (Figure 1B-C). In unstretched neurons the fraction of spines with tau was low, typical of healthy neurons. However, in neurons exposed to a single stretch of 20% strain (ε), at a strain rate ($\dot{\varepsilon}$) of 1000%/s, we found significant tau mislocalization to dendritic spines

24 hours after stretch, demonstrating that stretch-injury can drive tau pathology *in vitro* (Figure 1D). This tau mislocalization was identical to that seen in previously studied models of AD [3]. mEPSCs are the currents associated with the stochastic release of a single vesicle of neurotransmitter, and their amplitudes and frequencies can be quantified as a proxy for synaptic health or functionality [5]. We found that after a single stretch of ε = 20%, $\dot{\varepsilon}$ = 1000%/s, both the amplitude and frequency of mEPSCs decreased significantly compared to control neurons (Figure 1E-G). These results indicated that tau mislocalization and synaptic deficits can both be caused by mechanical injury alone.

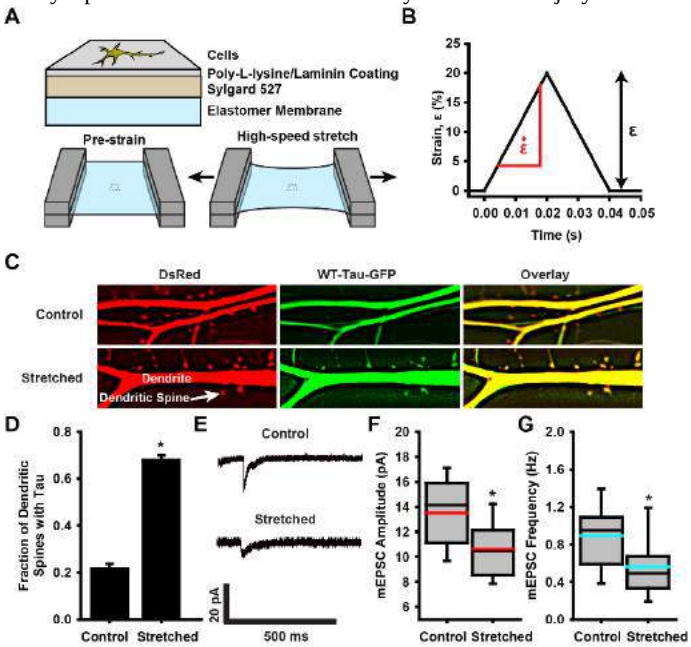

Figure 1: Mechanical injury elicits tau pathology and synaptic deficits in neurons. (A) Schematic of stretching construct with seeded neuron. (B) Example stretching protocol for ε = 20%, $\dot{\varepsilon}$ = 1000%/s. (C) Representative images of control and stretched neurons transfected with DsRed (*red, left)* to identify dendritic spines, and WT-Tau-GFP (*green, center)*. Image overlay to quantify tau mislocalization (*yellow, right)*. (D) Quantification of tau mislocalization. (E) Example mEPSC traces. (F) Amplitude of mEPSCs in control vs. stretched neurons. (G) Frequency of mEPSCs in control vs. stretched neurons. Error bars = standard deviation, * indicates statistical significance, NS indicates no statistical difference (α = 0.05) in all Figures.

Tau mislocalization was shown to be dependent on the severity or type of simulated TBI in our *in vitro* model. Stretching neurons to a high strain (ε = 20%) over a range of strain rates ($\dot{\varepsilon}$ = 1, 10, 100, 1000%/s) revealed that only the most rapid strain rate was able to cause significant tau mislocalization (Figure 2A). Similarly, tau mislocalization was dependent on the magnitude of strain. When stretched at a high strain rate ($\dot{\varepsilon}$ = 1000%/s), over a range of strain magnitudes (ε = 1, 2, 5, 10, 20%), only neurons stretched past ε = 5% displayed any significant tau mislocalization, with tau pathology worsening as strain increased (Figure 2B). To investigate whether repetitive, mild TBI simulations (like those associated with CTE) could lead to tau pathology, we stretched neurons with a previously inconsequential injury (ε = 2%, $\dot{\varepsilon}$ = 1000%/s) up to 20 times. Results revealed a cumulative effect with respect to tau mislocalization, as 10 and 20 mild-TBI simulations elicited significant tau mislocalization (Figure 2C).

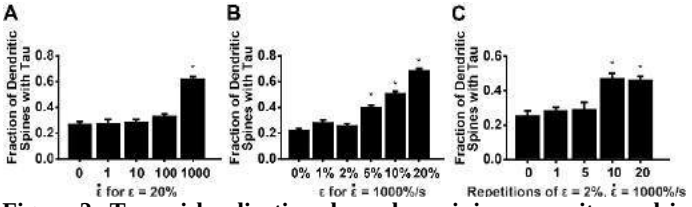

Figure 2: Tau mislocalization depends on injury severity, and is phosphorylation dependent. (A) Tau mislocalization vs. strain rate. (B) Tau mislocalization vs. strain magnitude. (C) Tau mislocalization vs. strain repetition.

In tauopathic diseases, tau is hyperphosphorylated by CDK5 and GSK3β, leading to its mislocalization. To investigate if this mechanism was preserved in our model, we used Roscovitine and CHIR-09921 to inhibit CDK5 and GSK3β, respectively. After drug treatment, severely stretched neurons did not exhibit tau mislocalization different than unstretched control neurons (Figure 3A). Additionally, these drugs prevented the decreases in mEPSC amplitude and frequency that were observed following a mechanical insult (Figure 3B-C)

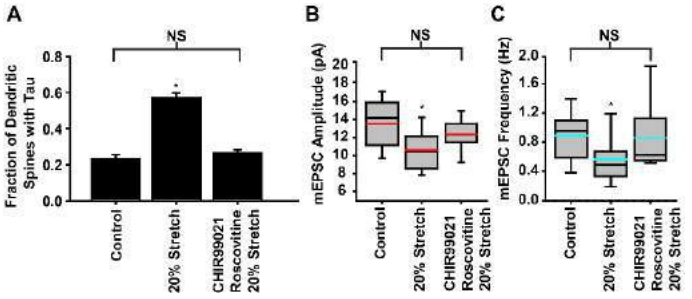

Figure 3: Kinase inhibitors block tau mislocalization and prevent synaptic deficits following mechanical injury. (A) Tau mislocalization with kinase inhibitors. (B) mEPSC amplitude with kinase inhibitors. (C) mEPSC frequency with kinase inhibitors.

DISCUSSION

Prior work has shown tau hyperphosphorylation, mislocalization, and eventual aggregation into NFTs in the brain to be hallmarks in the degenerative cascade of AD. We present a novel method of *in vitro* TBI simulation that links mechanical neuronal injury to tauopathic cellular features of AD. We have shown mechanically-induced tau mislocalization to be phosphorylation-dependent and have characterized the degree of tau mislocalization with respect to various TBI simulations, providing a cell-scale link between AD and CTE. Additionally, our model provides a connection between the tauopathic consequences of TBI and actual functional deficits in synapses of affected neurons.

ACKNOWLEDGEMENTS

We would like to thank our funding from the University of Minnesota Institute for Engineering in Medicine Seed Grant (DL, PWA), NIH-NINDS R21 (DL), NSF CMMI-1553255 (PWA) MN Office of Higher Education SCI-TBI Grant-143723 (DL, PWA), and the 3M Science and Technology Graduate Fellowship (NB).

REFERENCES

[1] Taylor CA, et al, *Surveill. Summ*, 66, 1-16, 2007.
[2] Mez J, et al., *JAMA*, 318(4), 360-370, 2011.
[3] Hoover B, et al., *Neuron*, 68(6):1067-1081, 2010.
[4] Jayapalan S, et al, *Bioinformation*, 9, 2023-30, 2013.
[5] Lin H, et al, *Biochem. Biophys. Res. Commun*, 316, 501-11, 2004.

SB^{3}C2019
Summer Biomechanics, Bioengineering and Biotransport Conference
June 25 -28, Seven Springs, PA, USA

INTRODUCTION OF HETEROGENEOUS CELL PROPERTIES FOR MODELING EMERGENT STRESS FIELDS IN MULTICELLULAR SYSTEMS

Zachary E. Goldblatt (1), Heather A. Cirka (1), Habibeh Ashouri Choshali (2), Nima Rahbar (2), Dannel McCollum (3), Kristen L. Billiar (1)

(1) Biomedical Engineering
Worcester Polytechnic Institute
Worcester, MA, USA

(2) Civil Engineering
Worcester Polytechnic Institute
Worcester, MA, USA

(3) Biochemistry and Molecular Pharmacology
UMASS Medical School
Worcester, MA, USA

INTRODUCTION

In multicellular systems, cells interact with both their extracellular environment as well as neighboring cells. Collective cell behavior has been shown to affect cell behaviors including proliferation (1), morphology (2), and apoptosis (3). Cell-cell contact causes a transfer of forces between cells, which can influence cell behavior due to the stress field that they generate and in turn sense.

There is considerable interest in accurately modeling and calculating the stresses within cell monolayers to understand the underlying mechanical factors affecting cell behavior. Predicting the emergent stress fields is commonly performed with finite element models that simulate cell contractility as prestress or thermal cooling. Additionally, monolayer stress microscopy (MSM) is used for calculating cell-layer stresses from measured traction forces. Both predictions and calculations from TFM indicate high traction stresses in the substrate at the edges of the monolayers and high cell stresses in the central region of the cell layer.

In contrast, specific mechanosensitive biomarkers indicate high cell stresses on the periphery. For example, at the aggregate edge, alpha smooth muscle actin (αSMA), a contractile protein, is highest, apoptosis is lowest, and yes-associated protein (YAP) localizes to the nucleus (1,3,4).

We hypothesize that the discrepancy between predicted cell-layer stresses and measured stress-related biomarkers is the assumption of homogeneous contractile and mechanical properties throughout the cell layer utilized in current models and calculations. In this study, we model geometrically constrained cell monolayers with heterogeneous mechanical properties and compare the simulated and computed cell-layer stresses to stress-related biomarkers.

METHODS

Porcine valvular interstitial cells (VIC) were confined to micro-contact printed circular collagen islands 200μm in diameter on 38.4kPa polyacrylamide (PA) gels prepared on glass coverslips. F-actin, G-actin, and αSMA were stained via phalloidin, fluorescent DNase 1, and anti-αSMA, respectively. Apoptosis and YAP presence were quantified via caspase-3/7 expression and anti-YAP, respectively.

For modeling of cell-layer stress, a thermal cooling finite element model of contraction was performed. Three distributions of contraction were modeled: 1) homogeneous coefficient of thermal expansion, 2) a step change heterogeneous model at half the radius of the aggregate, where the thermal expansion coefficient was reduced by 50%, and 3) an exponential distribution of thermal coefficient based on the measured distribution of cell spread area which is correlated with cell contraction in single-cell experiments (Fig. 2A). For calculation of cell-layer stress from measured traction forces, MSM was performed with three distributions of cell stiffness (modulus): 1) homogeneous, 2) step change in stiffness at half the radius, and 3) exponential distribution of stiffness (high at edge, low in center). Coefficients of thermal expansion (alpha) were normalized to have the same average value, where for each case, the integral of each curve would equal one another.

RESULTS

Protein markers associated with cell stress and contractility were first measured. It was found that the G-/F-actin ratio decreased radially from the center of aggregates to the edge (Fig. 1A). We measured a doubling of αSMA integration into stress fibers from the center to the edge of aggregates (Fig. 1B). Additionally, we observed a steady decrease of apoptotic activity from 50% present in the aggregate center to nearly 0% present in the periphery (Fig. 1C). Finally, we observed qualitatively YAP nuclear localization in peripheral cells and nuclear exclusion in central cells (Fig. 1D).

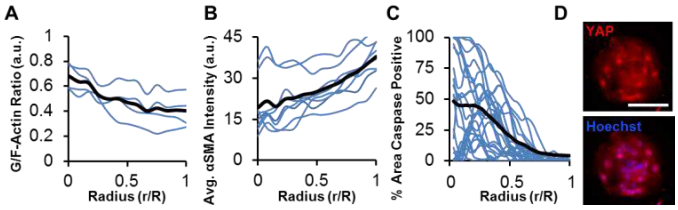

Figure 1: A) G/F-actin ratio decreases over aggregate radius. B) αSMA intensity increases with respect to aggregate radius. C) Cleaved caspase-3/7 presence decreases over aggregate radius. D) YAP nuclear localization is limited to edge cells. Scale bar=100µm.

The localization of our experimental biomarkers – higher G-actin in central region, higher αSMA incorporation into stress fibers along the edge, apoptosis occurrence in the center, and YAP localization along the periphery – suggest higher cell stress presence along the aggregate edges compared to the center.

For our homogeneous model, cell-layer stress is highest in the center and decreases towards the edge (Fig. 2B, 2D). In the heterogeneous step change model, the 50% reduction in contractility resulted in an opposite trend, where stress increases towards the edge. Finally, the continuous heterogeneous exponential model revealed an even more pronounced trend where circumferential stress is lowest in the center and increases towards the edge. The predicted substrate-level traction stresses were similar between all three conditions (Fig. 2C, 2D).

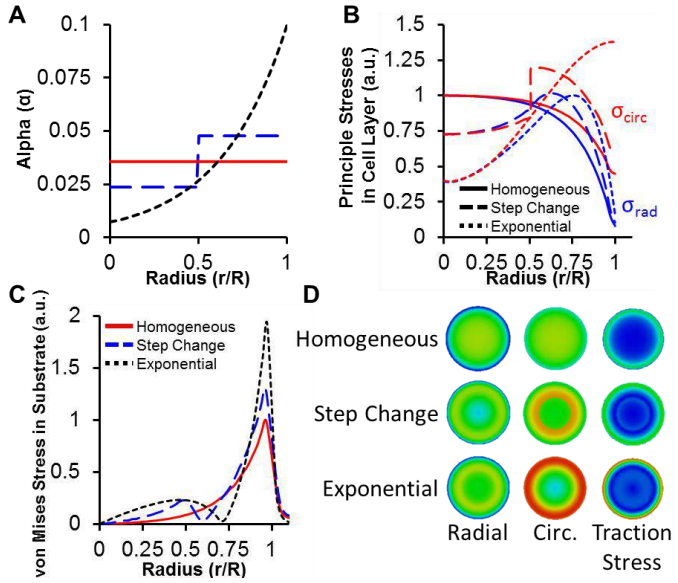

Figure 1: A) Coefficient of thermal expansion vs. radius. Corresponds to cell area vs. radius, since cell area is linearly correlated with cell contraction in single-cell studies. B) Cell-layer radial (blue) and circumferential (red) stresses for three modeling conditions for contractility. C) Predicted von Mises stresses for three modeling conditions of cell contractility as a function of radius. D) Heat maps of predicted radial, circumferential, and traction stresses for all three conditions.

To calculate the cell-layer stress using MSM, measured substrate stresses from five different aggregates were averaged together to obtain an average radial traction stress versus radius (Fig. 3A). This was input into the finite element model to obtain radial and circumferential cell-layer stresses for an average aggregate (Fig. 3B). Once again, the homogeneous case showed highest cell-layer stress in the center and lowest on the edges, while both heterogeneous cases exhibited the opposite trend.

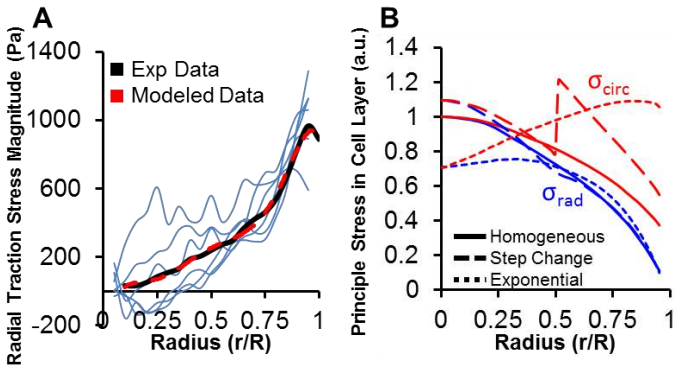

Figure 3: A) Average radial traction stresses measured from five aggregates were averaged (black line) and fit with a best fit curve (red dashed). B) Cell-layer radial (blue) and circumferential (red) stresses for three modeling conditions cell stiffness.

DISCUSSION

Here, we have found that cell-layer stresses calculated with models incorporating *heterogeneous* contractile and mechanical properties better correlate with spatial distributions of measured stress-related biomarkers than models assuming homogeneous cell-layer properties. Homogeneous assumptions of mechanical properties led to predicted stresses that are opposite to those expected by the distribution of biomarkers.

These models show that even moderate changes in cellular contractility and stiffness can have drastic effects on the cell-layer stress distribution in confined multicellular systems. Additionally, the projected traction stresses have similar patterns for all conditions, which demonstrate the need for incorporating additional biophysical data (e.g., cell spread area, aspect ratio, etc.) to accurately estimate the stress fields within the cell layers.

We present the first experimental evidence suggesting that low stresses experienced by central cells drive the biological response of aggregates. The current model is the first to incorporate heterogeneous material properties, and data show that this added complexity is required for the accurate estimation of stress distribution in our aggregates. We plan to further tune and validate this model using higher-resolution biophysical data to adjust cell contractility distributions.

ACKNOWLEDGEMENTS

This work was funded in part by a National Science Foundation CMMI 1761432 and by a WPI-University of Massachusetts Medical School Seed Grant.

REFERENCES

[1] Li, Bin et al., *J. of Biomechanics*, 42:1622–1627, 2009
[2] He, Shijie et al., *Biophysical Journal*, 109:489-500, 2015
[3] Cirka, Heather et al., *Lab Chip*, 17:814-829, 2017
[4] Dupont, Sirio et al., *Nature*, 474:179-183, 2011
[5] Chen, CS et al., *Science*, 276:1425-1428, 1997.
[6] Zhang, YH et al., *Matrix Biol.*, 30:135-144, 2011

CONCENTRATION DEPENDENT TGF-β INTERNALIZATION RATE IN ENGINEERED MUSCULOSKELETAL TISSUES

Sedat Dogru (1), Daniel Sharifikia (1), Samuel Sze (1), Michael B. Albro (1,2)

(1) Mechanical Engineering
(2) Materials Science & Engineering
Boston University
Boston, MA, USA

INTRODUCTION

Musculoskeletal tissue engineering (TE) is a promising strategy to treat degenerative disorders whereby progenitor cells are embedded in polymeric scaffolds to generate replacement tissues. Transforming growth factor beta (TGF-β) has emerged as one of the most extensively utilized mediators for promoting engineered tissue growth due to its efficacy in yielding rapid extracellular matrix (ECM) biosynthesis via cell receptor mediated signaling. Generally, TGF-β is delivered in culture medium during an *in vitro* growth phase or directly loaded into scaffolds to act on cells after *in vivo* implantation [1]. There is a growing emphasis on the importance of optimizing TGF-β delivery to cells, as growth factor excesses can lead to pathology in engineered tissues [2] or off-target pathology *in vivo* after implantation [3]. However, this optimization remains a considerable challenge, as limited work has been performed on mechanistic models that describe the transport and distribution of growth factors in engineered tissues.

We recently demonstrated that the uptake of TGF-β into engineered cartilage can be accurately described by reaction-diffusion models that account for critical interactions between TGF-β and molecular tissue constituents (scaffold, ECM, and cell receptors) [4]. In particular, TGF-β uptake is highly dependent on the rate of cell-mediated TGF-β degradation, a process that results from degradation following internalization of receptor-bound TGF-β. Accordingly, such transport models can potentially yield faithful descriptions of the distribution of TGF-β in tissues, when provided with accurate measures of this TGF-β internalization rate. Therefore, to expand our modeling capabilities, the aim of this investigation is to characterize the rate of TGF-β internalization over a range of doses that are conventionally administered in TE applications (0.3-300 ng/mL) [1] and to examine the influence of internalization on the distribution of TGF-β3 in constructs. An additional characterization is performed to verify that TGF-β degradation results from receptor mediated cell internalization.

METHODS

Tissue source: Immature bovine chondrocytes were seeded in 2% agarose (30×10^6 cells/mL) to form ∅5×1mm tissue constructs [4]. Freshly-cast constructs were maintained live in chondrogenic media or subjected to an initial freeze-thaw cycle to induce rapid devitalization.

Internalization Rate Measurements: Constructs were exposed to a chondrogenic media bath (500 μL) supplemented with TGF-β3 at an initial level of 0.3, 3, 30, or 300 ng/mL. The subsequent uptake of TGF-β3 into the construct was monitored by measuring the concentration decrease in the bath over time (TGF-β3 Duoset, R&D Systems). This transient bath decrease was modeled via our reaction-diffusion equation, which accounts for TGF-β diffusion into constructs, reversible binding to the construct scaffold/ECM, and receptor-mediated internalization by construct cells:

$$\frac{\partial C_F}{\partial t} = \underbrace{D\nabla^2 C_F}_{\text{Diffusion}} + \underbrace{\left(C_B k_r - C_F N_t k_f\right)}_{\text{Reversible binding}} - \underbrace{R_i C_F}_{\text{Internalization}} \quad (1)$$

C_F: concentration of free TGF-β, C_B: concentration of TGF-β bound to scaffold/ECM, N_t: total number of binding sites, D: TGF-β diffusivity, k_r: reverse binding constant, k_f: forward binding constant, R_i: internalization rate constant. In the presence of devitalized constructs, the TGF-β3 bath concentration decreases as a result of reversible binding to the construct scaffold/ECM. This transient decrease (n=3 constructs per concentration) was compared to a model with our binding-only reaction-diffusion equation (where R_i=0) and finite element solver (FEBio) using previously acquired diffusivity and

binding constants (D=23 μm^2/s, N_t=200 ng/mL, k_r=*2.5e-05 s^{-1}*, k_f=2.7e-06 ng.mL^{-1}.s^{-1}) [4]. In the presence of live constructs, the TGF-β3 bath concentration decreases further, as a result of a combination of reversible binding and receptor-mediated TGF-β internalization by living cells. This transient decrease (n=3 per concentration) was curve-fit with our full reaction-diffusion equation to extract the internalization rate constant R_i, using the aforementioned parameters from the binding-only model. Subsequently, the TGF-β3 internalization rate, V_i, (ng/mL internalized TGF-β per second) was calculated as the product $R_i \times C_F$.

Concentration-Dependent TGF-β Uptake Model: To assess the effect of internalization rate of TGF-β transport in constructs, we implemented an FEBio simulation (using aforementioned parameters) to model the uptake distribution of TGF-β in constructs (∅6×2.5mm) supplemented with 0.3, 3, 30, or 300 ng/mL TGF-β in a media bath.

Receptor Media Internalization Verification: To verify that the TGF-β3 bath decreases observed with live constructs result from receptor-mediated cell internalization, decreases were monitored in the presence of an alternative isoform TGF-β1, which also binds to the TGF-β type-II receptor, and thus competes for internalization with the TGF-β3 isoform. Here, transient TGF-β3 decreases were monitored in the presence of 0, 10, 100, or 1000 ng/mL TGF-β1 and compared to the response with devitalized constructs.

RESULTS

Internalization Rate Measurements: For all initial bath concentrations, in the presence of devitalized constructs, TGF-β3 bath levels decreased over time (Fig 1). These transient decreases were faithfully described by our binding-only (R_i=0) reaction-diffusion equation (R^2=0.93±0.04). In the presence of live constructs, the TGF-β3 bath concentration decreased further, but this difference was less pronounced for higher initial bath concentrations. These transient decreases were faithfully described by our full reaction-diffusion equation (R^2=0.99±0.01), allowing for successful extraction of the internalization rate constant R_i. Accordingly, R_i values decreased with TGF-β3 bath concentration (Fig 2A), ranging from 0.0123±0.0076 s^{-1} at 0.3ng/mL to 0.0002±0.0001 s^{-1} at 300 ng/mL. The internalization rate, V_i, increased with TGF-β3 bath concentration (Fig 2B), following a Michaelis-Menten reaction trend (R^2=0.99), whereby V_{max}=0.0704 ng.mL^{-1}.s^{-1}and K_M=57.34 ng/mL.

Concentration-Dependent TGF-β Uptake Model: Theoretical simulations show severe steady state concentrations gradients in constructs during the uptake of all initial bath concentrations (Fig 3). Although mitigated, gradients still persist for high 300ng/mL dose.

Receptor Media Internalization Verification: The transient decrease of TGF-β3 was mitigated in the presence of the competing TGF-β1 isoform (Fig 4). At a 100-fold TGF-β1 excess, this decrease relative to devitalized samples was no longer observed, suggesting that bath decreases are indeed attributable to TGF-β-specific receptor-mediated internalization.

DISCUSSION

Results demonstrate that our reaction-diffusion model can accurately describe the uptake of TGF-β in engineered tissues (Fig 1), allowing for the novel assessment of the TGF-β internalization rate and its variation with concentration. A striking aspect of this characterization is the remarkably high rate at which chondrocytes internalize this growth factor, as evidenced by pronounced transient concentration decreases even in the presence of the high 300 ng/mL dose. This internalization rate can be described by Michaelis-Menten reaction kinetics, consistent with an anticipated saturation of the cell receptor internalization rate at high ligand concentrations. Given the exceptionally low doses of TGF-β required to induce ECM synthesis (pM-nM range), internalization rates can greatly influence the transport and distribution of TGF-β in engineered tissues, as evidenced by highly pronounced gradients in tissue constructs (even for 300 ng/mL dose) when administered in culture media (Fig 3). The internalization rate relations advanced in this study can serve as a foundation for the development of sophisticated transport models that can predict the distribution and activity of growth factors in musculoskeletal TE applications (media supplemented or direct scaffold loaded [1]). These models can yield critical optimizations of growth factor delivery protocols, allowing for substantial improvements in tissue homogeneity [4], tissue quality [2], and reductions in off-target pathology [3].

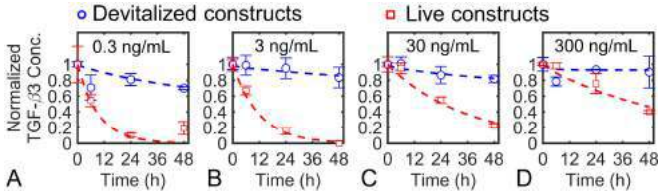

Fig 1: Transient decrease of TGF-β3 bath concentration from binding-only (devitalized) or binding + internalization (live) in constructs for initial TGF-β3 bath concentrations: (A) 0.3 ng/mL, (B) 3 ng/mL, (C) 30 ng/mL, or (D) 300 ng/mL. Dashed curves represent theoretical fit of Eq (1) to the experimental data.

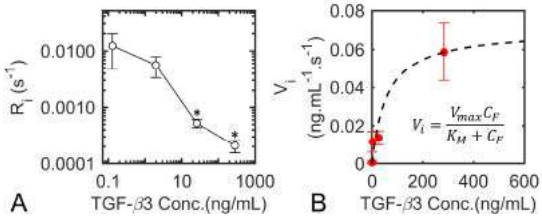

Fig 2: (A) Concentration dependent internalization rate constant of TGF-β3. *p<0.05: significant decrease from 0.3 ng/mL level. (B) Concentration dependent internalization rate, V_i. Dashed curve represents theoretical fit of Michaelis-Menten equation.

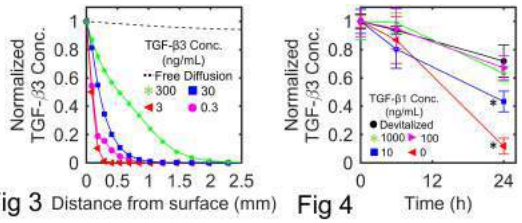

Fig 3: Predicted steady-state 1-dimensional distribution of TGF-β3 in constructs (reached at 48 hours) for varying bath concentrations using measured R_i values. Dashed curve represents 48-hour uptake in the absence of binding/internalization interactions (N_t=0, R_t=0).

Fig 4: The competing TGF-β1 isoform reduces transient decrease of TGF-β3 bath concentration. *p<0.05: significant decrease below corresponding devitalized bath concentration.

ACKNOWLEDGEMENTS: Supported by the Boston University 2018 Dean's Catalyst Award and Materials Science Innovation Grant.

REFERENCES [1] Madry+ 2014 Tis Eng B 20(2):106-25; [2] Wang+ 2018 World Congress of Biomechanics: Abstract No.3226; [3] Cahill+ 2009 JAMA 302(1): 58-66; [4] Albro+ 2016 Biomaterials 77: 173-185.

SB³C2019
Summer Biomechanics, Bioengineering and Biotransport Conference
June 25 -28, Seven Springs, PA, USA

A MICROPATTERNING APPROACH TO STUDY CELLULAR COMMUNICATION VIA MECHANICAL FORCES IN FIBROUS MICROENVIRONMENTS

Christopher D. Davidson, Brendon M. Baker

Department of Biomedical Engineering
University of Michigan
Ann Arbor, MI, USA

INTRODUCTION

The ability of cells to communicate with each other to coordinate their activity is crucial to the specification, development, and homeostatic function of all tissues. Intercellular communication via secretion of biochemical signals or through cell-surface receptors has been extensively studied [1], but more recent studies suggest an additional means via cell-generated forces propagated through the extracellular matrix (ECM). Mechanical signals are potentially faster, longer range, and more directionally focused than diffusive factors, and such communication has been observed in a variety of settings spanning different cell types, distinct ECM settings, and at scales ranging from multicellular clusters to single cells [2,3]. Despite this breadth of evidence, however, we have yet to parse the specific means and code by which cells communicate mechanically.

The generation and transmission of mechanical signals (i.e. cellular traction forces) largely depends on the mechanical properties of the underlying ECM, and fibrous microenvironments have been theorized to be an optimal structure by which tensile forces can be transmitted [4]. However, commonly used fibrous materials to study cell behavior *in vitro*, such as collagen and fibrin, lack mechanical and architectural tunability for mechanistic studies. Thus, here we developed a microfabrication-based patterning approach to study single cell behavior on tunable synthetic fibrous matrices towards further understanding the relationship between ECM physical properties and the mechanical signals sent and received by cells.

METHODS

Cell culture: Human umbilical vein endothelial cells (ECs) were cultured in endothelial growth medium supplemented with 1% penicillin-streptomycin-fungizone. Lentiviral transduction of lifeAct-GFP was utilized for live cell time-lapse imaging. Fiber network fabrication: Dextran methacrylate (DexMA) was dissolved at 0.5 g ml^{-1} in a 1:1 mixture of milli-Q water and dimethylformamide with 0.1% Irgacure 2959 photoinitiator and 0.0025% methacrylated rhodamine. This solution was electrospun, stabilized by primary crosslinking under UV light (100 mW cm^{-2}) for 60s, hydrated in varying concentrations of LAP photoinitiator solution, and then exposed again to UV light for 20s. Matrices were then functionalized with the peptide CCRGDS (RGD) to facilitate cell adhesion. Single Cell Patterning: DexMA fiber matrices were suspended over an array of microfabricated poly(dimethylsiloxane) (PDMS) wells fabricated by soft lithography. To position one cell in the center of each matrix, we fabricated a cell-patterning mold containing an array of microwells (comparable in size to a single EC) with alignment grooves corresponding to the arrayed fiber substrates (**Fig. 2a**). ECs were allowed to settle into the microwells for five minutes, and cells outside of the wells were gently flushed away with PBS. The fiber substrate was then carefully placed on top of the patterning mold via the alignment grooves and the assembly was inverted and incubated for 30 minutes to allow single cells to settle and adhere to the matrix. Staining and Microscopy: Three-channel time-lapse microscopy was performed over an 8h period during which cells spread, with imaging of F-actin, DexMA fibers, and 1 μm fluorescent microspheres (Fl-μS) embedded in fibers every ten minutes. Cells were fixed, permeabilized, and stained simultaneously with phalloidin and DAPI. For vinculin immunostaining, samples were fixed, permeabilized, blocked for 1 h in 1% fetal bovine serum, and incubated with anti-vinculin antibody (1:1000, Sigma #V9264) for 1h before counterstaining with phalloidin and DAPI. Statistics: Significance was determined by ANOVA or Student's t-test where appropriate, with significance indicated by $p<0.05$. All data presented as mean ± std.

Technical Presentation #130

RESULTS

To examine intercellular interactions in fibrous matrices, we first seeded ECs at a range of cell densities on compliant matrices. At high seeding density, ECs spread, physically reorganized matrix fibrils, and formed intercellular connections, as previously observed [5,6] (**Fig. 1a**). In contrast, at low seeding densities, isolated cells remained unspread. Although not controlling for paracrine signal effects, this experiment suggests spacing between cells and sensing of cell generated traction forces may impact cell spreading. Supporting this, cells seeded on stiff matrices showed a distinct response with a linear increase in spread area as a function of seeding density (**Fig. 1b**). Quantifying the formation of multicellular structures, we noted ECs on deformable matrices formed larger clusters than stiff matrices at the same seeding density (**Fig. 1c**).

Towards a deeper investigation of the generation and transmission of forces between cells in fibrous ECM, we sought to quantify matrix displacements from individual ECs. We developed a microfabrication-based method to precisely pattern single ECs onto fiber substrates of varying diameter (**Fig. 2a**). ECs patterned on 500 μm diameter suspended matrices of varying stiffness were stained for actin and vinculin to visualize the cytoskeleton and focal adhesions, respectively (**Fig. 2b**). Soft matrices revealed higher levels of fiber recruitment as compared to intermediate and stiff conditions. Furthermore, ECs on soft matrices exhibited increased focal adhesion size as compared to stiffer matrices (**Fig. 2b,d**). Combining this patterning technique with time-lapse confocal microscopy, we visualized matrix displacements as ECs spread and exerted traction forces. To quantify matrix displacements, Fl-μS embedded within fibers were tracked during cell spreading (**Fig. 1c**). On soft matrices, Fl-μS displacements were noted across the entire suspended matrix (up to 250 μm away from the cell centroid). With increasing matrix stiffness, however, the magnitude and range of displacements decreased, where stiff matrices displayed negligible displacements across the entire matrix (**Fig. 2c,e**).

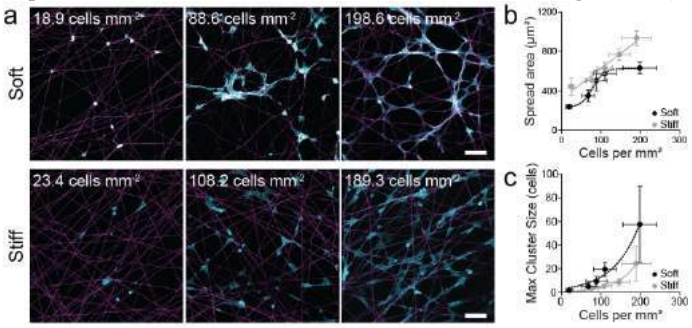

Figure 1. a) Confocal fluorescent images of phalloidin-stained ECs (cyan) and rhodamine-labeled fibers (magenta). Cell spreading (b) and maximum cell cluster size (c) as a function of seeding density and matrix stiffness. Scale bar: 100 μm.

DISCUSSION

Mechanical interactions between cells and the ECM have been shown to be crucial in many biological processes. In this work, we integrated previously developed synthetic fibrous matrices [5] with a cell patterning approach to enable investigations into how physical properties of fibrous ECM regulate intercellular mechanical communication. In initial studies, we found that compliant matrices that deform under the action of cell forces also enable cell spreading and the formation of multicellular clusters, supporting the possibility of intercellular communication via mechanical forces. To further investigate how cells send mechanical signals in the form of cell force-mediated matrix deformations, we developed a multilayered microfabrication-based method to pattern single cells onto these matrices. We found that soft matrices that promote cell spreading and clustering above threshold seeding densities reveal longer-range matrix displacements as compared to stiffer matrices. Furthermore, ECs within soft matrices also possessed larger focal adhesions than those on stiff fibers. As focal adhesion size has been previously been linked to force generation [7], this data suggests that compliant matrices could lead to increased force generation in ECs. Future work using this approach will investigate the role of other physical properties on cell adhesion, spreading, and tractions (matrix displacements) including fiber density and proximity to a rigid boundary condition (via variable fiber well diameters) with the goal of identifying the magnitudes and dynamics of force transmission that facilitate directed cell extension and migration.

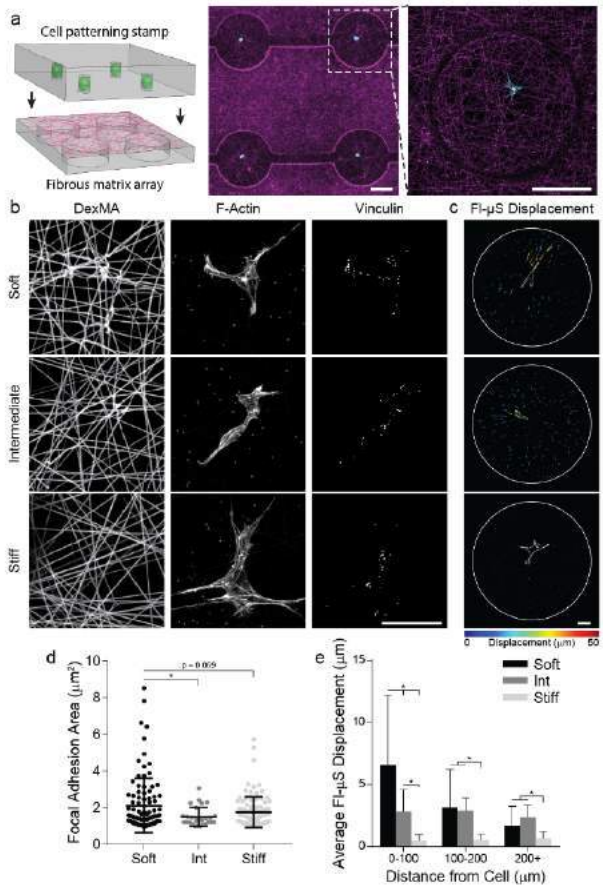

Figure 2. a) Schematic of PDMS patterning mold, fiber matrix substrates, and fluorescent image of single ECs (cyan) adhered to fibrous matrix substrates (magenta). Scale bar: 200 μm. b) Confocal fluorescent images of rhodamine-labeled DexMA fibers, phalloidin-stained ECs, and immunostained vinculin. c) Cell force-generated matrix displacement fields. Scale bars: 50 μm. Focal adhesion area (d) and Fl-μS displacement as a function of matrix stiffness.

ACKNOWLEDGEMENTS

This work was supported in part by the National Institutes of Health (HL124322). C.D.D. acknowledges financial support from the National Science Foundation Graduate Research Fellowship Program (DGE1256260).

REFERENCES

[1] Gumbiner, BM et al., *Cell*, 84:345-357, 1996. [2] Shi, Q et al. *Proc Natl Acad Sci*, 111:658-663, 2014. [3] Reinhart-King, CA et al. *Biophys J*, 95:6044-6051, 2008. [4] Wang, H et al. *Biophys J*, 107:2592-2603, 2015. [5] Baker, BM et al. *Nat Mater*, 14:1262-1268, 2015. [6] Davidson, CD et al. *Sci Rep*, 9:12, 2019. [7] Balaban, NQ et al. *Nat Cell Biol*, 3:466-472, 2001.

SB³C2019
Summer Biomechanics, Bioengineering and Biotransport Conference
June 25 -28, Seven Springs, PA, USA

ENDOTHELIAL NITRIC OXIDE SYNTHASE GLYCOSYLATION IS A POTENTIAL TARGET FOR REDUCING ENDOTHELIAL DYSFUNCTION

Sarah E. Basehore (1), Alisa Morss Clyne (2)

(1) School of Biomedical Engineering, Science, and Health Systems
Drexel University
Philadelphia, PA, USA

(2) Mechanical Engineering and Mechanics
College of Engineering
Drexel University
Philadelphia, PA, USA

INTRODUCTION

Endothelial cell (EC) dysfunction, defined as decreased nitric oxide (NO) production via endothelial nitric oxide synthase (eNOS), is a unifying precipitating factor in cardiovascular disease. NO regulates vascular tone, thrombosis, inflammation, dilation, and remodeling [1]. Steady laminar flow promotes a healthy, quiescent EC phenotype in which EC phosphorylate eNOS to produce NO [2]. However, EC in areas of oscillating disturbed flow have impaired NO production. These areas of disturbed flow are linked to EC dysfunction and diseases such as atherosclerosis [2,3].

In addition to phosphorylation, eNOS can also be glycosylated through the hexosamine biosynthetic pathway (HBP) at the same site where it is phosphorylated. In the HBP, UDP-N-acetylglucosamine (UDP-GlcNAc) is added to protein serine and threonine residues via O-GlcNAc transferase (OGT) and removed via O-GlcNAcase (OGA). EC cultured in high glucose have elevated HBP flux, which increased eNOS O-GlcNAcylation and thereby decreased eNOS phosphorylation and NO bioavailability [4-6]. eNOS O-GlcNAcylation also increased in diabetic animals, which inhibited eNOS phosphorylation and NO production [6].

While eNOS O-GlcNAcylation and its effect on eNOS phosphorylation has been studied in altered glucose conditions, eNOS O-GlcNAcylation has not yet been studied in flow. We hypothesized that steady laminar flow, but not oscillating disturbed flow, decreases eNOS O-GlcNAcylation, contributing to a healthy, quiescent phenotype. In support of this hypothesis, we measured eNOS O-GlcNAcylation in EC exposed to steady laminar and oscillating disturbed flow. We further determined how eNOS O-GlcNAcylation impacted eNOS phosphorylation, NO production, and EC dysfunction.

METHODS

Human umbilical vein endothelial cells (HUVEC) were maintained in Endothelial Growth Medium-2 supplemented with 10% fetal bovine serum, 1% penicillin-streptomycin, and 1% L-glutamine. For flow studies, 17,000 cells/cm^2 HUVEC were seeded on collagen Type 1 coated 60 x 15 mm culture dishes. A custom-built cone-and-plate device, with three independent, yet parallel samples, was used to apply shear stress to HUVEC. For laminar flow, the cone-and-plate device was programmed to administer unidirectional flow with 20 dynes/cm^2 shear stress. For disturbed flow, the device was programmed to administer oscillatory flow with 4±6 dynes/cm^2 shear stress. In some experiments, HUVEC were treated with 1 mM 2-deoxy-2-glucose (2-DG). Following 24 hours of flow, protein O-GlcNAcylation, OGT, OGA, p-eNOS, eNOS, GAPDH, and β-actin were analyzed via Western blot. Comparisons between two groups were analyzed by Student's t-test (# $p<0.05$, * $p<0.01$, ** $p<0.001$).

Glycolytic intermediates were quantified for isotopologue enrichment in stable isotope tracing experiments by mass spectrometry. 5 mM $^{13}C_6$-glucose was added to HUVECs for 5 minutes immediately after flow. 80:20 methanol:water was used to quench metabolic activity in cells. Following extraction, sample supernatants were dried under nitrogen gas and analyzed via liquid chromatography mass spectrometry.

For *in vivo* vessel analysis, the descending aorta and aortic arch from 5-month-old C57BL/6J wild type mice were dissected and sectioned. Sections were quenched in 30% hydrogen peroxide, blocked with Avidin D and Biotin blocking reagents, and analyzed for O-GlcNAcylation using a primary GlcNAc antibody (1:100), goat anti-mouse secondary antibody (1:100), and an HRP-conjugated ABC reagent. Samples were imaged using an Olympus DS60 microscope at 40x magnification.

Technical Presentation #131

RESULTS

We first measured how protein O-GlcNAcylation changed in EC exposed to 24 hours of static culture, steady laminar flow, or oscillating disturbed flow. While total protein O-GlcNAcylation was unchanged, O-GlcNAcylation of a ~140 kDa protein was decreased by approximately 75% in EC exposed to steady laminar flow. No change in protein O-GlcNAcylation was observed in cells exposed to oscillating disturbed flow (Figure 1). We confirmed that the 140 kDa protein was eNOS by immunoprecipitation and siRNA knockdown. Counterintuitively, OGT remained constant and OGA decreased in steady laminar flow by approximately 40%. These data suggest that the decrease in eNOS O-GlcNAcylation in steady laminar flow was not related to changes in OGT and OGA.

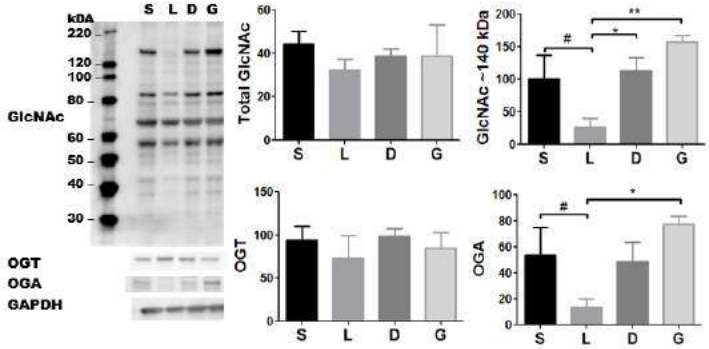

Figure 1: HUVEC adapted to steady laminar flow for 24 hours showed a specific decrease in eNOS O-GlcNAcylation without a change in total protein O-GlcNAcylation. Static ('S'), steady laminar ('L', 20 dynes/cm^2), oscillating disturbed flow ('D', 4±6 dynes/cm^2), or 5 mM glucosamine ('G', positive control) for 3 hrs. Data normalized to GAPDH.

To confirm that eNOS O-GlcNAcylation changes with flow conditions *in vivo,* we labeled mouse aortae for O-GlcNAcylated proteins in areas of laminar flow (descending aorta) and areas of disturbed flow (aortic arch) (Figure 2). We observed increased O-GlcNAc labeling in the aortic arch endothelium, suggesting that protein O-GlcNAcylation is increased in disturbed flow areas of arteries.

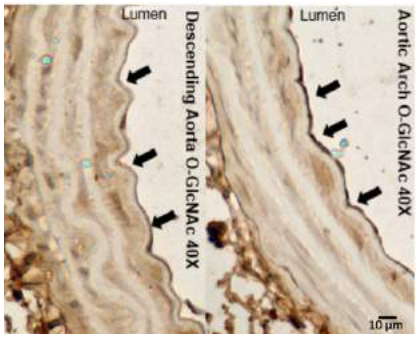

Figure 2: Protein O-GlcNAcylation was higher in the aortic arch (disturbed flow) of C57BL/6J WT female mice (5 months old) as compared to the descending aorta (laminar flow). Arrows highlight the endothelium.

We next investigated several mechanisms which might decrease eNOS O-GlcNAcylation in steady laminar flow, including decreased glucose transport, UDP-GlcNAc, as well as OGT and OGA activity. The glucose transporter GLUT1 and OGT/OGA activity remained unchanged in steady laminar flow. However, we did observe decreased UDP-GlcNAc and overall glycolytic flux, as measured via $^{13}C_6$-glucose mass spectrometry, in HUVEC exposed to steady laminar but not oscillating disturbed flow (Figure 3A). When we inhibited glycolysis in HUVEC exposed to disturbed flow via 2-DG, a glucose analog that is taken up by the cell but cannot undergo glycolysis, we effectively decreased eNOS O-GlcNAcylation (Figure 3B). These data suggest that the shear stress-induced decrease in glycolysis and hence HBP flux and UDP-GlcNAc substrate availability may lead to decreased eNOS O-GlcNAcylation.

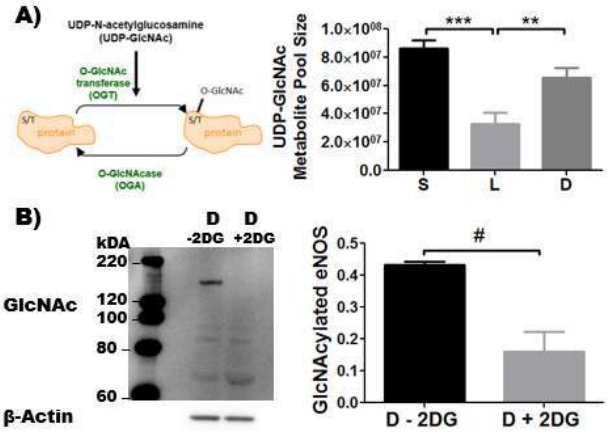

Figure 3: (A) HUVEC adapted to steady laminar for 24 hours showed decreased UDP-GlcNAc by mass spectrometry. (B) HUVEC adapted to oscillating disturbed flow ('D') + 1 mM 2-DG for 24 hours showed decreased O-GlcNAcylated eNOS compared to disturbed flow without 2DG (normalized to β-actin).

We further demonstrated that modulating OGT and OGA activity affects overall and eNOS O-GlcNAcylation. When OGA was inhibited in HUVEC exposed to steady laminar flow, eNOS O-GlcNAcylation increased and phosphorylation decreased. In contrast, when OGT was inhibited in HUVEC exposed to oscillating disturbed flow, eNOS O-GlcNAcylation decreased and phosphorylation increased. These data suggest eNOS phosphorylation and NO production can be increased in disturbed flow by decreasing eNOS O-GlcNAcylation. Thus O-GlcNAcylation may be a valid therapeutic target in EC dysfunction.

DISCUSSION

We now show for the first time that steady laminar flow, but not oscillating disturbed flow, decreases eNOS O-GlcNAcylation, which may contribute to enhanced eNOS phosphorylation and increased NO production. Additionally, modulation of eNOS O-GlcNAcylation in disturbed flow can restore eNOS phosphorylation. This research advances our understanding of EC dysfunction and may lead to novel therapies to prevent EC dysfunction. Targeting areas of disturbed flow for therapeutic interventions, such as decreasing O-GlcNAcyation, may increase NO and reduce EC dysfunction and the progression of cardiovascular disease.

ACKNOWLEDGEMENTS

This research was supported by NIH 1R01HL140239-01 and an American Heart Association GIA to AMC, as well as a GAANN fellowship to SB. We thank Dr. Vineet Bhandari and Dr. Pragnya Das for *in vivo* analysis, and Dr. Cholsoon Jang for mass spectrometry.

REFERENCES

[1] Michiels, C., *J Cell Physiol,* 2003. **196**(3): p. 430-43.
[2] Marina Noris, *Circ Res,* 1995. **76**: p. 536-543.
[3] Yetik-Anacak, G. et al., *Vascul Pharmacol,* 2006. **45**(5): p. 268-76.
[4] Federici, M., et al., *CIRCULATION,* 2002. **106**(4): p. 466-472.
[5] Du, X.L., et al., *J OF CLIN INVEST*, 2001. **108**(9): p. 1341-1348.
[6] Beleznai, T. et al., *Vascular Pharma.*, 2012. **56**(3-4): p. 115-121.

SB³C2019
Summer Biomechanics, Bioengineering and Biotransport Conference
June 25 -28, Seven Springs, PA, USA

DEVELOPING A STEM+M IDENTITY IN UNDERREPRESENTED MINORITY GROUPS THROUGH SPORTS AND BIOMECHANICS

Brittany P. Marshall (1), Amy K. Loya (2), John F. Drazan (3), Anthony T. Prato (4), Nicole C. Conley (5), Stavros Thomopoulos (1, 6), Katherine E. Reuther (1)

(1) Department of Biomedical Engineering
Columbia University
New York, New York, USA

(2) Department of Biomedical Engineering
Rensselaer Polytechnic Institute
Troy, New York, USA

(3) Department of Orthopedic Surgery
University of Pennsylvania
Philadelphia, Pennsylvania, USA

(4) Department of Psychology
SUNY Geneseo
Geneseo, New York, USA

(5) Department of Electrical, Computer, and Biomedical Engineering
Union College
Schenectady, New York, USA

(6) Department of Orthopedic Surgery
Columbia University
New York, New York, USA

INTRODUCTION

Identity has long been established as an integral facet of learning [1]. Social identity in particular, meaning the extent to which an individual perceives themselves as belonging to a social group, has been implicated as a key factor in determining an individual's sense of belonging and interest in a career or field [2]. More specifically, a STEM+M identity, a form of social identity that is the extent to which an individual feels accepted in STEM+M (Science, Technology, Engineering, Math, and Medicine), has strong implications in either affording or impeding an individual's engagement in STEM+M. This idea of STEM+M identity is of particular relevance to minority groups that have historically been underrepresented across STEM+M fields [3]. Factors limiting the STEM+M identity of minority groups include perceived lack of self-efficacy, limited mentorship opportunities, and established stereotypes in STEM+M [4,2]. If underrepresented groups felt a stronger identification as a member of the ingroup of STEM+M, there could be improved engagement and retention of these groups within STEM+M. Not only is this beneficial for the economic and social capital that these careers afford, but also for increased diversity of perspectives in STEM+M, potentially leading to innovation and better delivery of healthcare.

A necessary step in an individual developing this STEM+M identity is discovering self-efficacy in STEM+M. STEM+M self-efficacy is established when an individual constructs a belief that STEM+M has value and on that foundation finds that they are capable of success in STEM+M [4,5]. However, in order to effectively develop this self-efficacy as a means to fostering a long-term STEM+M identity, students must first be taught STEM+M though ideas that they will individually value. With emphasis on middle school age students (as research shows that career trajectories can be determined as early as middle school [5]) from underrepresented minority backgrounds, sports are a natural choice of topic on which to focus STEM+M education. Previous work has shown a positive perception of STEM through sports [6].

In this study, a basketball camp was used as a platform for demonstrating to students that a proficiency in STEM+M can improve performance not only in the classroom, but also on the court. By doing so, the value these students associate with basketball was connected to STEM+M. We hypothesized that involvement in this program would result in improved perception of STEM+M and a higher value assigned to STEM+M fields.

METHODS

In order to engage middle school students from the community in STEM+M, the research team hosted the Youth Sports Lab (YSL), a week-long summer camp at Columbia University in collaboration with 4th Family, an Albany-based nonprofit organization. YSL was a basketball training camp that used athletic performance and biomechanics as a platform for STEM+M education. The students were recruited for their interest in basketball from a Harlem-based after school program and community partner, After-School All Stars. A week of curricula was executed, with a heavy emphasis on biomechanics, including basketball drills, engineering design, and engagement with STEM+M professionals (Figure 1). The research team served as the program coordinators and coaches, and consisted of faculty and students (graduate and undergraduate) in STEM, several of whom had collegiate athletic experience. We tested the hypothesis that sports based STEM+M education would increase participants' interest in STEM+M with a 15-question survey before and after the camp. Responses were on a 5-point Likert scale. Significance was determined with a Wilcoxon signed rank test for paired nonparametric data. This survey-based

protocol was approved by the Columbia University Institutional Review Board.

	Engineering	Data Visualization/Analytics	Physiology of Sports Performance and Rehab	Presentations
Morning (9-12 PM)	Intro to week + biomechanics	Intro to statistics	Intro to physiology and injury	Poster making session
	Dynamic warmup	Dynamic warmup	Dynamic warmup	
	Basketball drills	Heat map shooting	3D motion capture session	
	Low cost combine stations	3 vs. 3 (continuous)		Basketball competitions
(12-1 PM)	Lunch	Lunch	Lunch	Lunch
Afternoon (1-5 PM)	Basketball competitions	Speaker	Speaker	Basketball competitions
	Jump plate build session	Heat map shooting	Basketball drills	Poster practice
		Jump plate session	Design experiment and collect data	Poster session

Figure 1. Sample schedule of the YSL programming.

The students were all male, about to enter grades 6-9 (age 11-14; *n* = 14). The ethnic backgrounds included African American (*n* = 5), Hispanic/Latino (*n* = 1), Caucasian (*n* = 2), and multiracial including 2 or more of the previous ethnicities (and Asian; *n* = 6) (6).

STEM Connections. Students participated in basketball drills and scrimmaging each day (as in traditional basketball camps). During the basketball drills, the students collected data on their teammates as an exercise on how data collection on metrics such as sprint speed and shooting percentage can help players work towards improved performance on the court. Students were led in a lesson on how to construct and use their own vertical jump measurement platform based on methods previously described [7].

Guest Speakers. Guest speakers were invited from STEM+M fields as examples of career paths that are available in close proximity to sports. Speakers included a Columbia Orthopedics Sports Medicine physician, a physical therapist, a motion capture technician, the Columbia women's basketball team, a Columbia Strength and Conditioning coach, and an NBA player.

Final Deliverable. The week culminated with a poster session wherein students presented the results of a research question that they answered using techniques learned during the week. Their poster session was attended by faculty members and graduate students from the Departments of Biomedical Engineering and Orthopedic Surgery. Figure 2 shows the students and coaches after finishing the poster session.

Figure 2. YSL coordinators and participants at the poster session.

RESULTS

The results from the pre- and post- survey are represented in Figure 3. A positive value indicates a greater value assigned to STEM+M. Results demonstrate significant increases in assigned value to STEM+M for 9 questions. These questions were (1) how confident are you in your ability to evaluate your strengths and weaknesses, (3) do you know what you need to practice to improve as a player, (4) do you think that math and science topics can make you a better athlete, (5) how familiar are you with sports analytics (the use of math and statistics to measure player performance in sports), (6) how familiar are you with sports science (the use of science to measure performance in sports), (8) how interested are you in pursuing a career in medicine, physical therapy, or athletic training, (9) do you think that you know how to use sports analytics and science to improve your own athletic performance, (12) do you think that you know enough about your sport to reach your goals as a player, and (15) do you think that what you learn in math and science class can be used in sports analytics?.

DISCUSSION

The significant increases in survey responses, and therefore in perception of STEM+M, demonstrates that the students' self-efficacy in STEM+M was influenced by the program, with potential impact on their long-term STEM+M identity. Even after meeting collegiate and NBA players, interest in STEM+M increased without a change in interest in sports ((2) asked how important do you think athletics are for your future career?), suggesting the impact of the STEM+M content on the students. Exposure to STEM+M leaders provided an opportunity for students to see successful professionals who look like them and demonstrated the many ways that sports and career can overlap.

The long-term goal for this project is to build student self-efficacy in STEM+M and improve their STEM+M identity to increase their opportunities for success in STEM+M. Efforts at Columbia University have been made to forge a pipeline towards STEM+M collegiate programs and careers for students in under-resourced K-12 schools [8]. This project extends this pipeline for students with personal investment in sports. The hope is that this will imbue students who are underrepresented in STEM+M with the confidence and STEM+M identity to pursue higher education and careers in STEM+M. The long-term effectiveness of this program will be assessed by following the cohorts of students in coming years as they make college and career decisions.

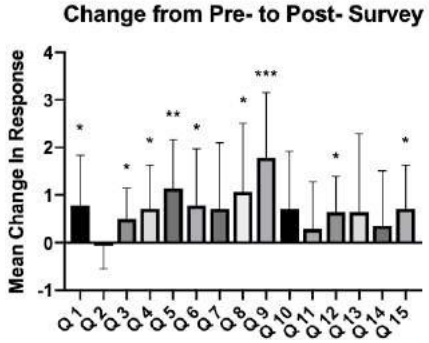

Figure 3. Change in response from pre- to post- survey on interest in STEM+M. P values denoted by: * 0.01 to 0.05, ** 0.001 to 0.01, * 0.0001 to 0.001. Standard deviation denoted with bars.**

ACKNOWLEDGEMENTS

The authors would like to thank the Carroll Laboratories of Orthopedic Surgery for its financial support of this project. We would also like to thank the Department for Biomedical Engineering for hosting the program.

REFERENCES

[1] Davidson, A, "Making and Molding Identity in Schools", 1996.
[2] Kim, A et al., *Review of Educational Research*, 88:589-625, 2018.
[3] NSF. *Women, Minorities, and Persons with Disabilities in Science and Engineering: 2017*, Special Report.
[4] Flowers, A et al., *Journal for Multicultural Education*, 10:405-417. 2016.
[5] Tai, R et al., *Science*, 312:1143-1144, 2006.
[6] Drazan, J et al., *MIT Sloan Sports Analytics Conference*, 2017.
[7] Drazan, J et al., *38th Annual International Conference of IEEE EMBC*, 2016.
[8] Kyle, A et al., *Journal of STEM Outreach*, 2018.

SB³C2019
Summer Biomechanics, Bioengineering and Biotransport Conference
June 25 -28, Seven Springs, PA, USA

3D STRAIN GRADIENTS CORRELATE WITH MURINE MYOCARDIAL INFARCT SEVERITY

Arvin H. Soepriatna (1), John J. Boyle (2), Abigail D. Clifford (3), Alex K. Yeh (1), Semih E. Bezci (4), Grace D. O'Connell (4), Craig J. Goergen (1)

(1) Weldon School of Biomedical Engineering
Purdue University
West Lafayette, Indiana, USA

(2) Department of Biomedical Engineering
Washington University in Saint Louis
Saint Louis, Missouri, USA

(3) Department of Animal Sciences
Purdue University
West Lafayette, Indiana, USA

(4) Department of Mechanical Engineering
University of California Berkeley
Berkeley, California, USA

INTRODUCTION

Coronary artery disease is the leading cause of death in the United States in 2017.[1] Despite a decrease in myocardial infarction (MI) mortality rates in the last decade, the incidence of heart failure continues to grow and remains a major public health issue.[2] While fibrotic scarring is a vital repair process post-MI, long-term outcomes of cardiac remodeling can include left ventricular (LV) dilation, hypertrophy, and ultimately heart failure.

Myocardial strain is a powerful metric for characterizing infarcted tissues. Its ability to quantitatively characterize wall kinematics at the interface between healthy and infarcted myocardium is of particular interest in the study of infarct expansion. However, most ultrasound studies focus on evaluating global metrics of LV function, such as ejection fraction and global longitudinal strain,[3] and rely on 2D analysis, which are sensitive to out of plane motion.[4] To date, a longitudinal study investigating the spatial distribution of myocardial strain following an MI has yet to be conducted. Here, we extended ultrasound strain studies to 3D to characterize the mechanical behavior of the LV near infarct border zones to understand how strain contributes to tissue remodeling.

METHODS

Animal Surgery: Fifteen male, C57BL/6 mice (age = 14±1 weeks; weight = 27±3 grams; JAX Laboratories, Bar Harbor, ME) were separated into three surgery groups: 1) sham (n=5), 2) ischemia reperfusion (n=5), and 3) permanent ligation (n=5). Mice were anesthetized with isoflurane and endotracheally intubated prior to left-thoracotomy. To induce an infarct in the LV, we either temporarily ligated the left coronary artery for 30 minutes before reperfusion or permanently ligated the vessel. In the sham group, we looped the suture around the left coronary artery without ligating the vessel. Mice were then closely monitored during recovery.

Ultrasound Imaging: All cardiac ultrasound images were collected using the Vevo2100 ultrasound system (FUJIFILM VisualSonics Inc, Toronto, Canada) with a 40 MHz transducer (MS550D). We acquired 4D ultrasound data as described previously.[5] Briefly, successive cardiac and respiratory gated 2D ultrasound videos were acquired in short-axis at 1000 Hz from the apex to the base of the LV by utilizing a linearly translating 3D motor prior to spatial registration performed in MATLAB (MathWorks Inc., Natick, MA). Ultrasound images of the LV were acquired at baseline and on days 1, 2, 3, 5, 7, 14, 21, and 28 post-surgery.

Strain Estimation: We defined a rectangular coordinate grid on the 4D data and used non-rigid registration to estimate deformation gradients directly from warping functions as described previously.[6] The estimated deformation gradient tensor **F** was then used to calculate the maximum principal component of the 3D Green-Lagrange (GL) strain tensor **E** **(Equation 1)**, where **I** is the identity matrix.

$$\mathbf{E} = \frac{1}{2}(\mathbf{F}^{\mathrm{T}}\mathbf{F} - \mathbf{I}) \qquad (1)$$

Endocardial, epicardial, and sternal artifact boundaries of the LV were segmented in SimVascular[7] at end-diastole and peak-systole and used to measure ejection fraction. We created binary masks from segmentations to isolate strain values within the myocardium. LV boundaries were then unwrapped from cartesian to polar coordinates relative to the LV apex to present maximum principal 3D GL myocardial strain in accordance to AHA's 17 segment-model.[8] We then evaluated strain profiles to estimate infarct boundaries and size. Principal strains within the infarct zone and neighboring regions were plotted as normalized radial distance from the center of the infarct, with infarct boundaries located at 0.5 normalized units. Statistical analysis was conducted using a one-way ANOVA with Tukey post-hoc analysis.

RESULTS

Mice that underwent sham surgeries did not exhibit remarkable changes in either geometry or strain profiles, while those in the permanent

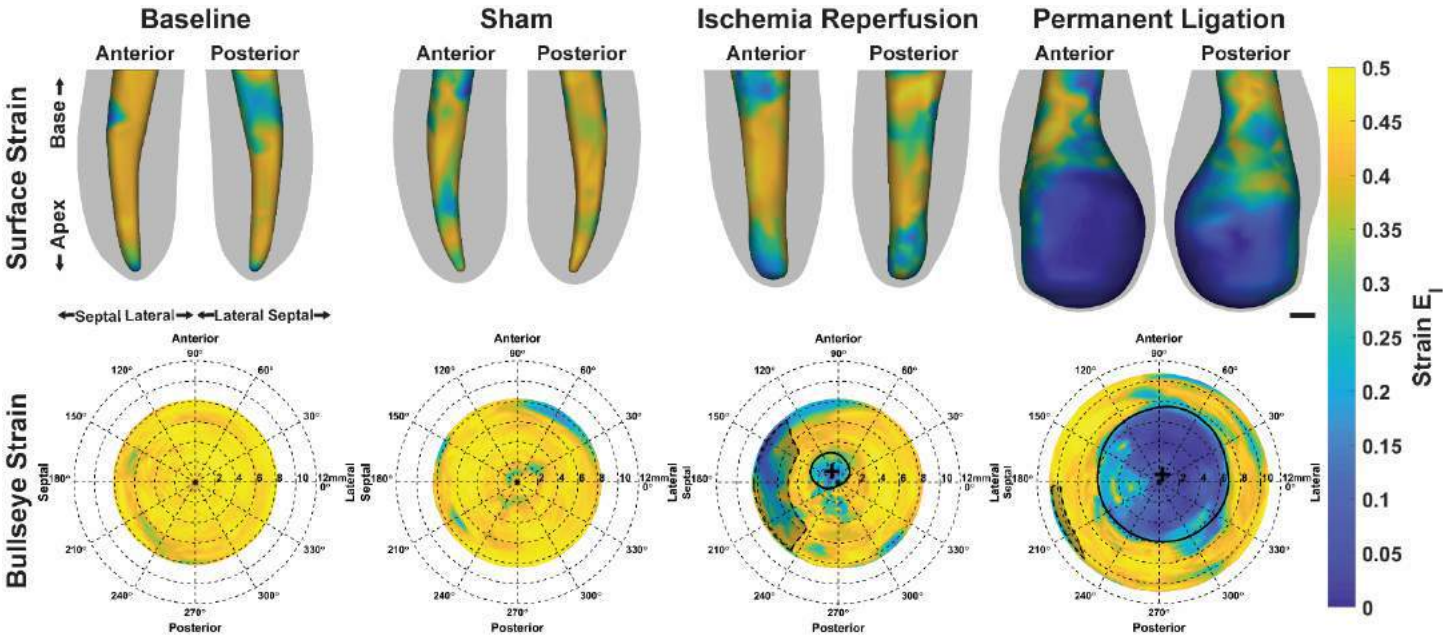

Fig. 1: Maximum principal 3D GL strain (E_l) maps of mouse LVs taken at baseline and 4 weeks post-surgery. **Top:** 3D representations of peak-systolic LV boundaries with surface strains overlaid to endocardial boundaries. Epicardial boundaries are shown in gray. Scalebar = 1mm. **Bottom:** Bullseye maps of maximum principal strain measured within the myocardium throughout a representative cardiac cycle. Strain-estimated infarct zones are outlined with solid black lines with infarct centers marked as black crosshairs. Sternal artifacts are outlined with black dashed lines.

ligation (PL) group experienced significant remodeling marked by wall thinning, LV dilation, and low strains within the infarcted myocardium (dark blue regions in **Fig. 1**). Mice in the ischemia reperfusion (I/R) group had smaller degrees of cardiac remodeling with smaller infarct sizes (IS) when compared to the PL group ($IS_{I/R}$=11±4% vs. IS_{PL}=46±15%; p<0.01). Regional analysis revealed significant reductions in maximum principal strain within the infarct zone when compared to baseline and sham groups ($E_{I,Baseline}$=0.41±0.04, $E_{I,Sham}$=0.39±0.05 vs. $E_{I,I/R}$=0.18±0.10, $E_{I,PL}$=0.06±0.03; p<0.05). The remote, healthy myocardium maintained normal contractile function with strain values of 0.40±0.03 (**Figs. 1, 2**). No statistical difference

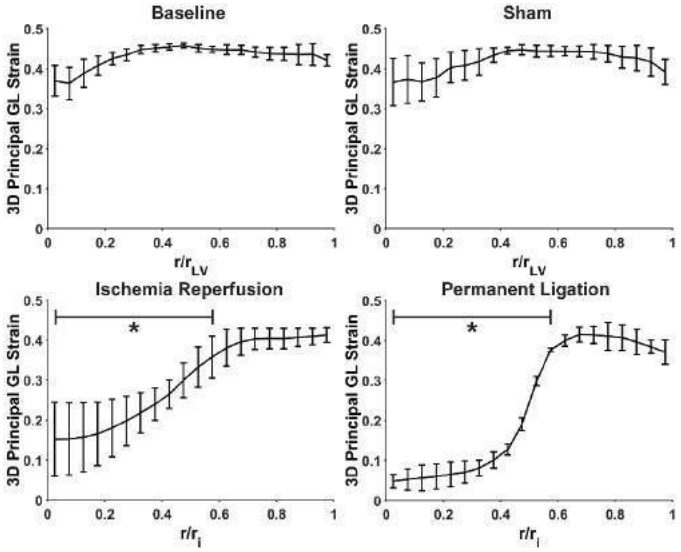

Fig. 2: Averaged strain profiles of mouse LVs at baseline and 4 weeks post-surgery. Radial distances from the apex or infarct center (r) were normalized to either the LV base (r_{LV}) or infarct boundary (r_i). Significant reductions in strain was observed within the infarct zone (r/r_i<0.5) when compared to baseline and sham group (*p<0.05).

in strain was observed in the sham group when compared to baseline. Regions of akinetic myocardium contributed to significant reductions in ejection fraction (EF) in infarcted LVs ($EF_{Baseline}$=68±3% and EF_{Sham}=66±3% vs. EF_{PL}=23±12% and $EF_{I/R}$=50±7; p<0.05).

DISCUSSION

The objective of this study was to investigate the role of myocardial strain on infarct expansion. Both permanent ligation and ischemia reperfusion models of MI have been reported in literature to have different degrees of remodeling in terms of infarct size.[9] This distinction can be clearly visualized in **Fig. 1**, by comparing areas of low-strain (dark blue) regions. Interestingly, the two models exhibited distinct strain profiles in regions adjacent to infarct boundaries (**Fig. 2**). The sigmoidal distribution of strain, along with the steep spatial strain gradient observed in the permanent ligation group are key characteristics of this MI model that undergoes severe remodeling compared to the ischemia reperfusion model, which has lower spatial strain gradient at infarct boundaries. Future work will focus on quantifying how regional myocardial strain gradients influence early stage remodeling and the directionality of expansion in asymmetrical infarcts.

ACKNOWLEDGEMENTS

This work was funded by the Hugh and Edna Donnan Fellowship and the AHA (14SDG18220010). We thank Dr. Guy Genin and Dr. Stavros Thomopoulos for their advice in the strain code development.

REFERENCES

[1] Benjamin, E.J. et al., *Circulation*, 135:e146-e603, 2017.
[2] Bui, A.L. et al. *Nat Rev Cardiol*, 8:30-41, 2011.
[3] Bhan, A. et al., *Am J Physiol Heart Circ Physiol*, 306:1371-1383, 2014.
[4] Bauer, M. et al., *Circ Res*, 108:908-916, 2011,
[5] Soepriatna, A.H. et al., *Int J Cardiovasc Imaging*, 34:713-724, 2018.
[6] Boyle, J.J. et al., *J Biomech Eng*, 2018.
[7] Updegrove, A. et al., *Ann Biomed Eng*, 45:525-541, 2017.
[8] Lang, R.M. et al., *J Am Soc Echocardiogr*, 28:1-39, 2015.
[9] Lindsey, M.L. et al., *Am J Physiol Heart Circ Physiol*, 314:812-838, 2018.

SB³C2019
Summer Biomechanics, Bioengineering and Biotransport Conference
June 25 -28, Seven Springs, PA, USA

DEVELOPMENT OF A DUAL-VENC 4D FLOW MRI FRAMEWORK FOR THE GENERATION OF PATIENT SPECIFIC AORTIC FINITE ELEMENT MODELS

J. Concannon (1), K. Moermon (1), P. Dockery (2), P. McHugh (1), C. Karmonik (3), JP. McGarry (1)

(1) Biomedical Engineering, College of Engineering & Informatics, National University of Ireland Galway

(2) Department of Anatomy, College of Medicine, National University of Ireland Galway

(3) MRI Core, Debakey Heart and Vascular Center, Houston Methodist, TX, USA

INTRODUCTION

A number of recent studies have shown higher rates of cardiac deaths following proximal compared to distal aortic stenting [1,2]. An improved understanding of the *in-vivo* mechanics of the aorta is required to uncover the biomechanisms underlying such adverse outcomes. In this study a novel 4D Flow MRI protocol is developed and implemented to allow visualisation of the dynamic deformation of and flow within the entire aorta for all stages of the cardiac cycle. For the first time, this *in-vivo* investigation uncovers a non-linear aortic compliance and heterogeneous pulse wave velocity (PVW) throughout the entire human aorta. Advanced dynamic image analysis software is developed to construct patient specific aortic finite element (FE) models. Simulations provide the first quantitative description of the *in-vivo* non-linear heterogeneous aortic material behaviour. Furthermore, a suite of histological analyses of human cadaveric aortic tissue are performed to uncover a micro-structural explanation for the aortic material behaviour uncovered by the MRI and *in-silico* investigations. Finally, the framework is used to simulate proximal and distal stenting procedures and for the first time the influence of stent position on aortic PWV is uncovered in a patient-specific model. Proximal stenting is shown to result in a higher increase in PWV than distal stenting, providing a mechanistic explanation for high mortality rates observed clinically.

METHODS

In the field of phase contrast MRI maximal sensitivity is obtained for protons moving at a velocity equal to the specified VENC value. This presents a particular challenge for determination of blood flow patterns in the aorta where flow is highly unsteady and non-uniform. The novel dual-VENC protocol proposed in this study generates a composite dataset, with a high-VENC of 200 cm/s targeted to systole and a low-VENC of 50 cm/s targeted to diastole (Figure 1(a)) following a series of VENC scouts. Analyses are performed at 10 planes along the human aorta. The boundary of the fluid domain is isolated for each plane and phase of interest to determine the lumen area as a function of space and time based on a custom-built segmentation algorithm (Figure 1(b)). For each of the planes analysed, the cross-sectional-area change ($\Delta\hat{A}$), volumetric flow rate (Q) and PWV (Figure 1(c)) are determined. Additionally, temporal compliance is investigated by plotting instantaneous area versus pressure at each location along the aorta (Figure 1(d)).

The regional aortic bioarchitecture responsible for vessel compliance is also assessed using histological and stereological techniques. Previous studies have been limited to animal tissue [3], or to a single location of the human aorta [4]. Aortic samples are harvested from 5 adult human cadavers (age range 67 – 92 years, mean 77.6 years) with no reported history of aortic disease. By excising samples at various sites along the aorta (Figure 2(a)), localized tissue fractions of both elastin and collagen are determined (Figure 2(b)). Additionally, regional wall layer thicknesses and layer specific collagen fiber orientations are also investigated for each of the sample sites. A sample collagen fiber density histogram is shown in Figure 2(c).

Finally, a patient-specific FE model of the aorta is generated directly from the MRI data (Figure 3(a)), through custom built advanced dynamic image analysis software. The aorta is modelled as a compressible anisotropic material using the modified anisotropic (MA) formulation through an Abaqus UMAT (Figure 2(c)). Regional parameter sets are found through a Levenberg-Marquardt based optimization algorithm, which minimizes the error between experimental (MRI) and simulated pressure versus area curves. Collagen fiber orientations (θ) from cadaveric specimens are used in the anisotropic formulation. Finally, two commercially available nitinol

stent-grafts are deployed into the aorta to investigate the regional effects of stenting on the vessel. The pre- and post-stenting loss in cross-sectional-area change ($\delta\Delta\hat{A}$) and gain in PWV are shown in Figure 3(d).

RESULTS

The importance of the dual-VENC composite approach to characterising aortic flow in both systole and diastole is shown in Figure 1(a), where the aortic fluid domain in diastole is not captured using the High-VENC alone ($HV_{Diastole}$). Area and flow versus time profiles for a series of aortic locations are illustrated in Figure 1(b). Percentage change in area between diastole and systole ($\Delta\hat{A}$), (which decreases distally) in addition to local PWV (which increases distally) are presented in Figure 1(c). Figure 1(d) illustrates the patient-specific pressure boundary condition used in the calculation of temporal compliance and a sample pressure versus area plot, highlighting significant strain stiffening behaviour within each cardiac cycle.

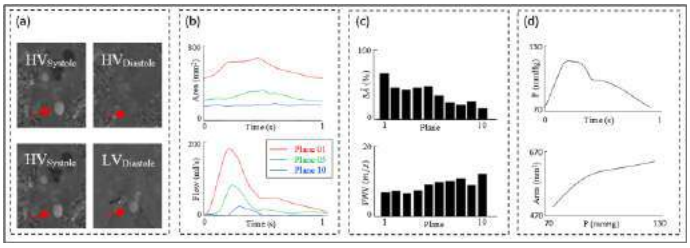

Figure 1: *In-vivo* aortic biomechanics derived from 4D Flow MRI.

Excision sites from the aorta of each cadaver in the study series are shown in Figure 2(a), which also outlines the orientation of tissue sectioning performed for both area quantification (AF) and fiber orientation (FO) analyses. A sample of each staining procedure is shown in Figure 2(b) in addition to the elastin and collagen percentage breakdown of the aortic wall for each excision location. Elastin is shown to decrease (27% vs. 17%) while collagen increases (22% vs. 53%) with increasing distance from the heart. Figure 2(c) shows post-staining, the orientation of collagen fibers within the wall, in addition to the corresponding probability density histogram. The collagen fiber orientation and dispersion data (θ and κ) are implemented into the modified anisotropic (MA) constitutive law outlined in [5].

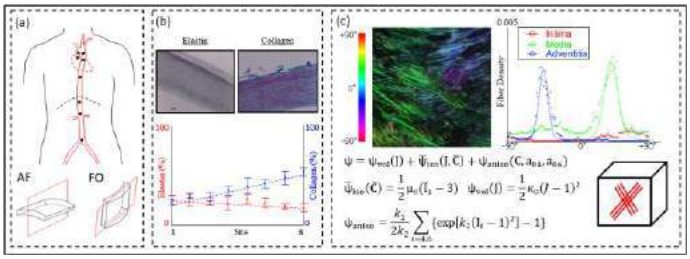

Figure 2: Characterization of regional aortic bioarchitecture.

The vessel construction algorithm used to generate a FE mesh directly from MRI data is shown Figure 3(a). Figure 3(b) (top) shows that the anisotropic non-linear MA model provides an accurate prediction of the *in-vivo* MRI behaviour, in contrast to the linear isotropic Neo-Hookean material model., Figure 3(b) (bottom) shows that a homogeneous set of material properties provides a highly inaccurate prediction of the *in-vivo* behaviour. Figure 3(c) shows the local tissue stiffness (K) plotted at each element highlighting the regional variation in compliance along the aorta in both the low- and high-pressure regimes of each cardiac cycle. Finally, the impact of stent deployment on regional compliance is shown in Figure 3(d), where a significantly larger drop in area change ($\delta\Delta\hat{A}$) in each cardiac cycle exists in the proximal (64%) compared to the distal (14%) aorta. Proximal stent deployment is also shown to have a greater increase on PWV compared to distal (129% vs 50%).

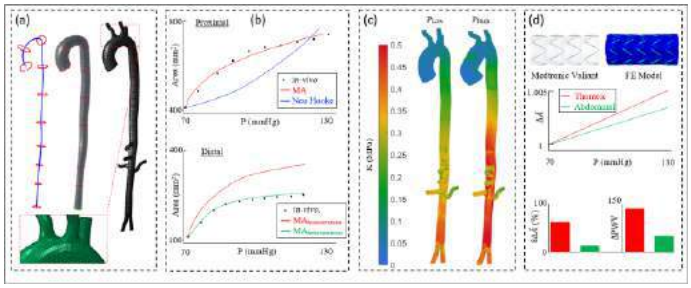

Figure 3: FE model and characterization of *in-vivo* biomechanics.

DISCUSSION

A novel dual-VENC 4D Flow MRI protocol is developed and implemented in a commercial scanner to achieve a complete characterization of the entire human aorta. Results confirm, for the first time, that the *in-vivo* aortic compliance is highly non-linear and cannot be characterized by a single value coefficient, as commonly assumed in clinical practice. In contrast, compliance is shown to alter significantly during the cardiac cycle, with significantly higher compliance being observed during periods of low blood pressure. Additionally, our *in-vivo* characterization reveals that aortic compliance is highest proximally, where a 65% change in lumen area is observed over a cardiac cycle, compared to a 15% change in lumen area in distal regions. Furthermore, the baseline PWV is lower in the thoracic than the abdominal aorta. Our comprehensive *in-vivo* characterization provides a significant advance on previous *in-vitro* mechanical testing of excised specimens of aortic tissue [6]. Our histological and stereological analyses show that elastin decreases in the distal aorta whereas collagen increases, providing a microstructural explanation for the heterogeneity in compliance observed in our *in-vivo* MRI measurements. The development of a FE model built directly from our *in-vivo* MRI data and using input from our histological studies represents a significant advance in the state of the art. Simulations provide the first computational characterization of the heterogeneity, non-linearity and anisotropy of the aorta *in-vivo*. We demonstrate that the assumption of homogeneous material behaviour, results in highly inaccurate predictions. Finally, our simulations reveal that insertion of a stent results in highly stiffened and linear vessel behaviour, in contrast to the highly compliant and non-linear behaviour of the native vessel. Proximal stenting is shown to result in a higher increase in PWV than distal stenting, providing a mechanistic explanation for the high mortality rates following proximal stent insertion clinically.

ACKNOWLEDGEMENTS

This work was funded by the Irish Research Council Enterprise Partnership Scheme and Western Vascular Institute (EPSPG/2016/194).

REFERENCES

[1] Beach et al., (2017), *J. Vasc. Surg.*, vol. 65, no. 5, pp. 1287–1296.
[2] Chaikof et al., (2009), *J. Vasc. Surg*, 50:(4):880-896.
[3] V. Saey et al., (2015), *BMC Veterinary Research*, 11(285).
[4] Y. Hosoda et al., (1984), Angiology., 35(10), pp. 615–621.
[5] Nolan et al., (2014), *J. Mech. Behav. Biomed. Mater*. (39):48-60.
[6] Krüger et al., (2016), *ICTS.*, vol. 23, no. 1, pp. 104–111.

SB³C2019
Summer Biomechanics, Bioengineering and Biotransport Conference
June 25 -28, Seven Springs, PA, USA

5-HT$_{2B}$ ANTAGONISM CONTROLS BORDER ZONE MECHANICS TO IMPROVE OUTCOMES FOLLOWING MYOCARDIAL INFARCTION

J. Caleb Snider (1), Qinkun Zhang (2), Hind Lal (2), and W. David Merryman (1)

(1) Biomedical Engineering
Vanderbilt University
Nashville, TN, USA

(2) Department of Medicine
Vanderbilt University Medical Center
Nashville, TN, USA

INTRODUCTION

Over 1.5 million Americans present with myocardial infarction (MI) annually. While mortality from acute MI has dropped dramatically in recent years, heart failure cases are on the rise and there are no effective therapies that substantially mitigate fibrosis, the underlying cause of heart failure [1]. The pervasiveness of this pathology results in substantial societal and economic costs.

MI causes permanent cardiomyocyte death, which are replaced with a stiff, collagenous scar. Heightened stress on border zone cardiomyocytes leads to scar expansion into distal myocardium and ultimately, heart failure. Where replacement fibrosis is required to prevent cardiac rupture, reactive fibrosis results in tissue stiffening and exacerbates myocardial damage [2]. The intersection of dense, collagenous scar and compliant myocardium creates a highly active environment and is the focal point of tissue remodeling and scar expansion.

Serotonin signaling is highly upregulated during cardiac injury and plays a role in fibrotic activity. Signaling through the 5-HT$_{2B}$ receptor cross-talks with TGFβ1 signaling to alter the pro-fibrotic activity of myofibroblasts [3]. The objective of this work is to understand the role 5-HT$_{2B}$ plays in scar formation. Therefore, we hypothesize antagonizing the 5-HT$_{2B}$ receptor can limit remodeling of the infarct border zone after MI to preserve cardiac function and prevent heart failure following MI.

METHODS

MI was induced in WT mice by permanent ligation of the left coronary artery. Echocardiography was performed prior to and following MI using the Vevo2100 system. Starting day of surgery and for the following 21 days, mice were treated with 1 mg/kg/day of the 5-HT$_{2B}$ antagonist RS-127445 (RS) or DMSO control. Short axis M-mode images were analyzed for cardiac structure and function, and the VevoStrain package (VisualSonics) was used to analyze long axis B-mode images for global longitudinal strain (GLS). Mice were sacrificed after 42 days. Hearts were frozen in OCT, cryosectioned at 7 μm thickness and subjected to atomic force microscopy (AFM) or histological analysis. BioScope Catalyst AFM (Bruker AXS, Santa Barbara CA) was operated in Peak Force–Quantitative Nanomechanical Mapping mode in fluid. Collagen fiber thickness was assessed using picrosirius red (PSR) staining imaged under polarized light and quantified using a color segmentation algorithm in MATLAB. Cardiomyocyte area was assessed using a wheat-germ agglutinin (WGA) stain and analyzed using a custom pipeline in the CellProfiler software. Quantitative polymerase chain reaction (qPCR) was performed on RNA isolated from flash frozen tissue. Data were analyzed using Student's t tests (for 2-group comparisons) or 2-way ANOVA (for multiple group comparisons) with mean ± SEM indicated. $P < 0.05$ was considered significant.

RESULTS

Ejection fraction in RS treated animals was preserved out to 42 days post-MI compare to control DMSO treatment (**Fig. 1A**). However, there was no change in cardiac structure indicated by similar left ventricular inner diameters during both diastole and systole (**Fig. 1B**). Since preserved structure was not the driver of improved function, we employed the VevoStrain software package to measure deformation caused by myocardial contraction to calculate GLS, a measurement of cardiac function independent of factors such as heart rate and loading conditions. GLS decreased similarly 7 days post-MI in both treatment groups, however, RS preserved contractility 21- and 42-days post-MI. Furthermore, GLS decreased from day 7 to day 21 and from day 21 to day 42 in the DMSO cohort, indicating a continued deterioration of contractility (**Fig. 1C**).

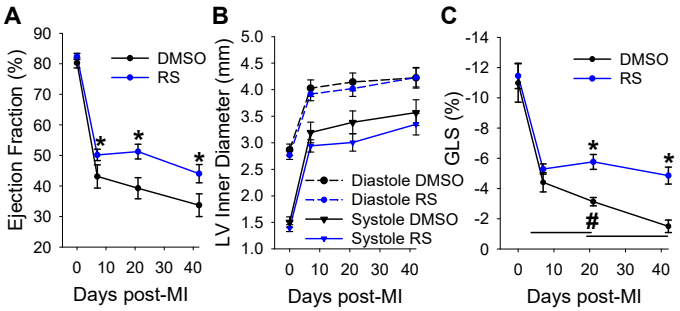

Fig. 1: Functional effect of 5-HT$_{2B}$ antagonism in response to MI. Combined echocardiographic data in WT mice treated with RS or DMSO (N=10-25). A) Ejection fraction, B) Left ventricular inner diameter, C) Global longitudinal strain. * indicates difference between treatments. # indicates difference compared to previous time point.

We then proceeded to investigate the tissue properties that lead to increased myocardial contractility 42 days post-MI. AFM was used to quantify tissue stiffness in both the scar and border zone (BZ). While scar stiffness was not reduced, BZ stiffness was noticeably reduced with 5-HT$_{2B}$ antagonism (**Fig. 2A**). PSR stain was subsequently used to assess fibrosis. There was no difference in the collagen volume fraction (data not shown). Imaging under polarized light revealed the birefringent properties of collagen fibers whose colors correspond to fiber thickness. As seen in **Fig. 2B**, there was no difference in collagen fiber thickness distribution in the scar. However, in the BZ, there was a decrease in the proportion of thicker collagen fibers with RS treatment. Control animals had more thick collagen fibers and fewer thin collagen fibers in the border zone compared to the scar.

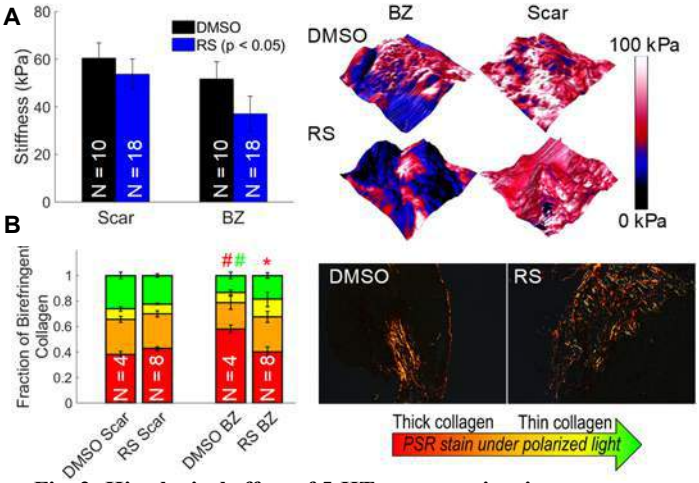

Fig. 2: Histological effect of 5-HT$_{2B}$ antagonism in response to MI. A) AFM quantification of tissue stiffness with topographical map overlaid with stiffness. B) Picrosirius red stain imaged under polarized light to assess collagen fiber thickness. * indicates difference between treatments. # indicates difference between scar and BZ.

Finally, WGA stain was used to identify the cell walls of cardiomyocytes. Quantification of the cross-sectional area determined that DMSO treated animals had larger cardiomyocytes, indicating cardiac hypertrophy (**Fig. 3A-B**). Non-scar tissue was digested and RNA isolated for qPCR analysis of *Nppa*, the gene encoding the heart failure marker ANP. We observed a decrease in *Nppa* transcription in RS treated animals (**Fig. 3C**).

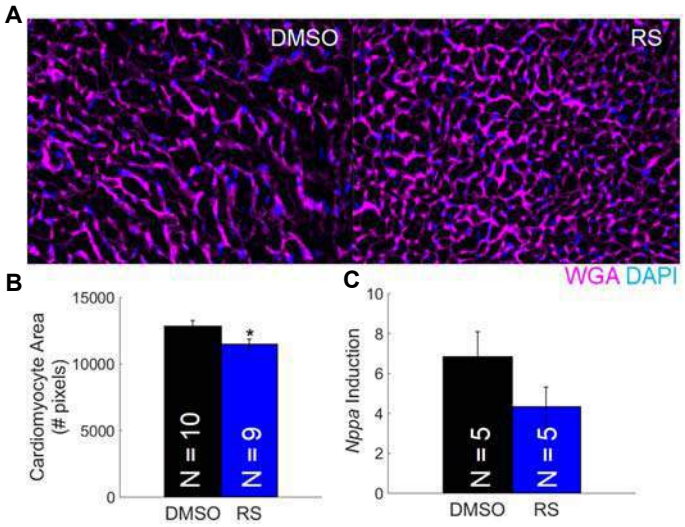

Fig. 3: 5-HT$_{2B}$ antagonism reduces heart failure markers 42 days post-MI. A) WGA stain shows decreased cardiomyocyte size and B) qPCR shows decreased expression of *Nppa*. * indicates significant difference between treatments.

DISCUSSION

Our findings indicate 5-HT$_{2B}$ is a viable target for manipulating border zone remodeling that occurs post-MI. We see that cardiac function is preserved independent of cardiac structure out to 42 days post-MI with 5-HT$_{2B}$ antagonism. This functional increase is due to preserved compliance of the left ventricle, as seen in the GLS measurement derived from wall deformation.

To understand the mechanism behind the preserved contractility, we probed the mechanical properties of the cardiac tissue. AFM analysis indicated no change in scar stiffness, however there was an effect of RS treatment in the border zone, resulting in softer, more compliant tissue. A contributing factor to this border zone stiffness is the distribution of collagen fiber thickness. RS treatment resulted in a higher proportion of thin collagen fibers, decreasing resistance to deformation.

Finally, we looked at markers of heart failure to understand the potential for 5-HT$_{2B}$ antagonism to preserve cardiac function and prevent the progression to heart failure, which is pervasive among those who have suffered MI. We first noticed a decrease in cardiomyocyte cross-sectional area with RS administration, indicating less hypertrophy. Also, *Nppa* expression, the gene encoding the heart failure marker ANP, was reduced with RS.

Our data reveal a novel approach for therapeutically controlling the mechanical environment post-MI to optimize healing and prevent the progression to heart failure. Further studies to elucidate the cell population responsible for these effects as well as further characterization of the border zone tissue are needed to solidify 5-HT$_{2B}$ antagonism as a viable therapy following MI.

ACKNOWLEDGEMENTS

This work was funded by the NIH (R35-HL135790) and AHA (18PRE34060078). Thank you to Matthew Bersi, PhD for providing the MATLAB script for histological analysis.

REFERENCES

[1] Aisagbonhi, O et al., *Dis. Models Mech.*, 4(4):469-483, 2011.
[2] Li, L et al., *Matrix Biology*, 68-69:490-506, 2018.
[3] Hutcheson, J. Et al., *J. Mol Cell Cardiol.* 53(5):707-714,2012.

SB³C2019
Summer Biomechanics, Bioengineering and Biotransport Conference
June 25 -28, Seven Springs, PA, USA

AN INTEGRATED MACHINE LEARNING-INVERSE FINITE ELEMENT APPROACH FOR IDENTIFICATION OF PATIENT-SPECIFIC MATERIAL PROPERTIES OF THE AORTIC WALL FROM CLINICAL CT IMAGES

Minliang Liu (1), Liang Liang (1, 2), Fatiesa Sulejmani (1), Xiaoying Lou (3), Glen Iannucci (3), Edward Chen (3), Bradley Leshnower (3), Wei Sun (1)

(1) Department of Biomedical Engineering
Georgia Institute of Technology and
Emory University
Atlanta, Georgia, United States

(2) Department of Computer Science
University of Miami
Coral Gables, Florida, United States

(3) School of Medicine
Emory University
Atlanta, Georgia, United States

INTRODUCTION

Accurate estimation of *in vivo* nonlinear, anisotropic mechanical properties of the aortic wall of individual patients remains to be one of the critical challenges in the field of cardiovascular biomechanics. Using multi-phase (e.g. diastole and systole) clinical images, traditional inverse methods are based on finite element (FE) updating schemes using stochastic-deterministic optimization algorithms, however, these methods are highly computationally-expensive, which can lead to thousands of nonlinear FE iterations, inhibiting rapid feedback for clinical use. Moreover, these approaches have only been validated by numerically-generated data.

In this study, we developed an integrated machine learning (ML)-inverse FE approach to identify the patient-specific material properties of the aortic wall from gated 3D CT scans. A ML model is utilized to expedite the identification process: once trained, the prediction can be made within one second. An inverse finite element method is developed using the multi-resolution direct search (MRDS) strategy, which can be applied to new aorta shapes beyond the ML training dataset. The number of iterations was significantly reduced comparing to the traditional approaches. The ML and inverse approaches have been integrated to achieve a balance between speed and accuracy (Figure 1): if the *in vivo* shapes are similar to those in the training dataset, the ML model will be invoked, otherwise the inverse method will be applied.

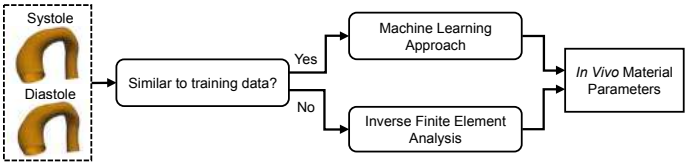

Figure 1: Framework of the integrated approach.

METHODS

Constitutive Model: A fiber reinforced hyperelastic material model [1] is used to characterize he aortic wall, given by

$$\Psi = C_{10}(\bar{I}_1 - 3) + \frac{k_1}{2k_2}\sum_{i=1}^{2}\left[e^{\{k_2[\kappa\bar{I}_1+(1-3\kappa)\bar{I}_{4i}-1]^2\}} - 1\right] \quad (1)$$

where C_{10}, k_1, k_2, κ are material parameters. θ is another parameter that defines the mean fiber direction (not shown in Eqn. (1)). The five parameters $\{C_{10}, k_1, k_2, \kappa, \theta\}$ will be identified from CT image data.

Image Registration: After image segmentation, nonlinear image registration algorithms are applied to obtain the full displacement field (i.e. mesh correspondence). Rigid iterative closest point algorithm is used to remove the rigid motion of the aorta due to heart movement during cardiac phases.

Inverse Method: The optimal set of material parameters can be found by minimizing a geometry-matching based objective function. The pre-stresses of the aorta are incorporated using the generalized pre-stressing algorithm (GPA) [2], which avoids finding the unpressurised state by iteratively performing FE simulations. Many constitutive models have highly coupled material parameters, which causes identification difficulties known as local optima. In the MRDS, multiple level representations of material parameters are established using a data science approach, and searching is performed from coarse to fine in a new space derived from 10,529 sets of stress-stretch curves.

ML Model: the ML model consists of an unsupervised shape encoding module and a nonlinear mapping module. The systolic and diastolic shapes are encoded by shape codes using principal component analysis (PCA). The nonlinear mapping between the shape codes and the material parameters is established by a neural network. For new aorta shape, a threshold value of PCA reconstruction error is used to determine whether the ML model is appropriate.

RESULTS

Experimental Validation: The inverse method was validated using pre-operative gated CT scans and corresponding surgically-resected tissue samples of two ascending thoracic aortic aneurysm (ATAA) patients (Patient 1: a 67 years old male; Patient 2: a 68 years old female). Using the MRDS, the node-to-surface errors between the image-derived and the FE-deformed systolic geometries were minimized to 0.41 mm and 0.77 mm for Patient 1 and 2, respectively.

Tissue samples were trimmed into 2~3 square-shaped specimens (2 specimens for Patient 1, and 3 specimens for Patient 2) with a side length of 20~25 mm. The specimens underwent planar biaxial tests to extract their experimentally-derived material properties. The inversely-estimated material properties were compared with the experimentally-derived material properties. Using the inversely-estimated and the experimentally-derived material parameters, stress-stretch response were computed analytically under equi-biaxial condition, and the stress-stretch curves were plotted in Figure 2. The two specimens of Patient 1 demonstrate almost identical stretch-stress response, whereas the three tissue specimens of Patient 2 show different stress-stretch responses, which indicate that the material properties are heterogeneously distributed. For both patients, the average experimental responses show relatively good agreements with the inversely-estimated responses.

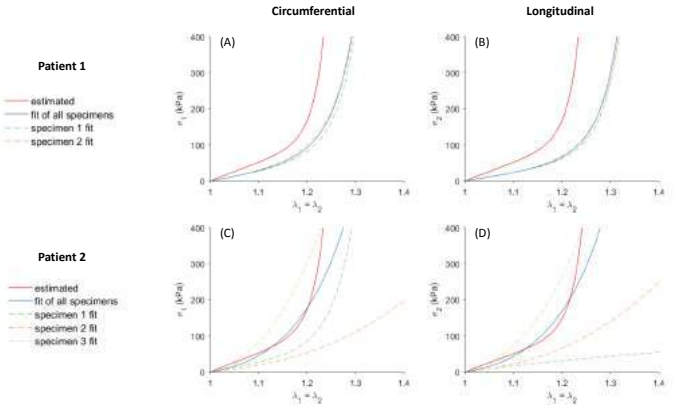

Figure 2: Equi-biaxial stress-stretch curves determined from the inversely-estimated and experimentally-derived material parameters.

Training and Testing of the ML Model: Training/ validation and testing datasets were gathered from FE simulations. Using statistical modeling methods, a large number of material parameter sets are generated from 65 sets of experimentally-derived material parameters, and virtual aorta geometries at one physiological phase (i.e., systole) are generated from 3D CT images of 25 real patients. The diastolic aorta geometries are determined from FE simulations using the virtual systolic geometries and the generated material parameters. Finally, the training/validation dataset and the testing dataset consist of 15,366 and 225 input-output pairs, respectively. Using the training/validation dataset, the performance of the neural network was assessed through leave-one-out and ten-fold cross-validations, and the neural network structure was fine-tuned.

The trained ML-model was able to predict the material parameter within one second. To evaluate the prediction of the ML-model, i.e., to examine how accurate the prediction is compared to FE simulation data, the ML-model was trained on the training/validation set and then the trained ML-model was used to predict the material parameters using shapes in the testing set as the input. The actual versus predicted material parameters in the testing set are shown in Figure 3, which indicate that the ML-predicted material parameters are in good agreement with the actual material parameters in the testing dataset.

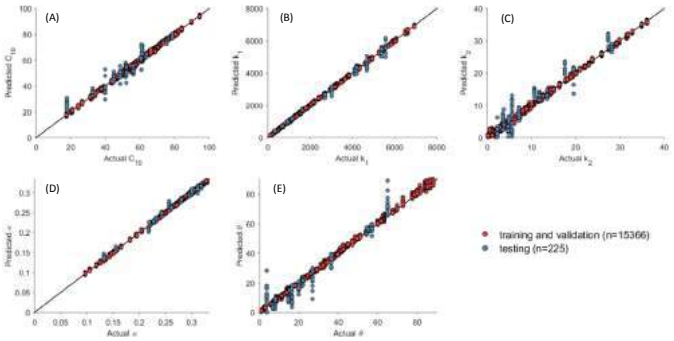

Figure 3: The actual and predicted material parameters.

DISCUSSION

The inverse method and experiments achieved relatively good agreement in the biaxial stress-stretch curves. The node-to-surface errors between the FE-deformed and the image-derived geometries were 0.41mm and 0.77mm for Patients 1 and 2, respectively, which are less than or equal to the size of a voxel (0.75×0.75×1 mm). This marks, to our knowledge, the first study that directly estimate *in vivo* nonlinear, anisotropic material properties of the ATAA from gated CT scans with validations on experimental data of planar biaxial tests.

The close match between the actual and predicted material parameters demonstrates that the ML model can predict constitutive responses with high accuracy. The computational efficiency is significantly improved using the integrated ML-inverse FE approach. If the aorta shapes are suitable for the ML approach, the material parameters can be predicted instantaneously and repeatedly, such that *in vivo* material parameter identification in real-time can be possible. If the aorta shapes are not similar with the training data, the inverse FE method can also identify the material properties in a fast and accurate manner using the MRDS strategy, which takes about 1~2 hours in a desktop PC with a quad-core CPU and a 32GB RAM.

It is known that the aortic tissue properties are heterogeneously distributed. The stress-stretch curves (Figure 2 (C) and (D)) also suggests material heterogeneity. In the current method, we only considered a simplified scenario, where the averaged *in vivo* wall thickness was used, and the averaged constitutive behavior of the aorta segment was investigated. The discrepancy in Figure 2 may be attributed to location-dependent material property distribution. In a previous study, we developed a stress-matching based strategy [3] for *in vivo* material identification, which leveraged the fact that the aortic wall is approximately statically determinate under physiological loading conditions. This strategy can be easily extended for element-wise identification of heterogeneous material parameters of the aortic wall. We are currently working to incorporate heterogeneous martial parameters identification into the integrated approach.

ACKNOWLEDGEMENTS

This study is supported in part by American Heart Association 18TPA34230083 and Georgia CTSA's Pilot Translational & Clinical Studies (PTCS) program. Minliang Liu is supported by an American Heart Association Predoctoral Fellowship 19PRE34430060.

REFERENCES

[1] Gasser, C et al., *J. R. Soc. Interface*, 3:15-35, 2006.

[2] Weisbecker, H et al., *Int. J. Numer. Meth. Biomed. Engng*, 30:857-872, 2014.

[3] Liu, M et al., *J. Mech. Behav. Biomed*, 72:148-158, 2017

COMPARATIVE ANALYSIS OF HEAD IMPACT KINEMATICS IN HIGH SCHOOL AND COLLEGIATE FOOTBALL USING MIG2.0 INSTRUMENTED MOUTHGUARD

Pirozzi I. (1), Fanton M. (1), Giordano C. (1), Rami S. (2), Rangel I. (2), Mehring W. (2), Roy P. (2), Avery B. (2), Zeineh, M. (3), Grant. G (1, 4), Camarillo D.B (1,4)

(1) Department of Bioengineering
Stanford University
Stanford, CA, USA

(2) Department of Medicine,
Stanford University School of Medicine
Stanford, CA, USA

(3) Department of Rad/Neuroimaging and Neurointervention,
Stanford University School of Medicine
Stanford, CA, USA

(4) Department of Neurosurgery,
Stanford University School of Medicine
Stanford, CA, USA

INTRODUCTION

Despite the tremendous effort in the research and clinical communities to understand the symptoms and clinical sequelae of concussions, as well as clinical management of concussion [9, 14], there has been less information regarding the mechanisms of concussions [16–17], particularly differences in impact exposure at different levels of play (e.g., age, experience, size, etc.) [18, 19]. While head impact exposure for high school and collegiate levels has been widely studied, there are few comparative investigations across levels of play. Additionally, there is surprising divergence in the current literature on the comparative differences between youth and college head kinematics, with some studies showing high school athletes experience lower severity impacts, and others suggesting the opposite [2-4].In many of these studies, however, the authors tested only one of the two age groups, and subsequently compared their kinematics parameters with those gathered by other groups, thus not accounting for the variability in experimental design and data processing.

Elucidating differences in the impact exposures experienced at different ages could guide the design of diagnostic systems and age appropriate protective gear. The purpose of this study is to compare biomechanical measures of head impact exposure, obtained through the use of our improved, instrumented mouthguard (MiG2.0), during a football season between a National Collegiate Athletic Association (NCAA) Division I football team and a small, mid-level high school football team.

METHODS

We developed an instrumented mouthguard, the Stanford MiG2.0 (***Figure 1a***), in collaboration with Intel Corporation, which measures six-DOF head impact kinematics. On the MiG2.0, linear acceleration is measured using a triaxial accelerometer (H3LIS331DL, ST Microelectronics, Geneva, Switzerland) with a range of ±400 g, sampled at 1000 Hz. Angular kinematics are measured using a triaxial gyroscope (ITG-3701, InvenSense Inc., San Jose, CA, US) with a range of ±4000 degrees/sec, sampled at 8000 Hz (***Figure 1b***). When a threshold of 10g is detected by the linear accelerometer in any of its components, the device is triggered to acquire and store 50ms of data prior to the trigger and 150ms of data post-trigger. Data is stored in an on-board flash memory chip and can be wirelessly downloaded at a future time. This device has been validated extensively in previous studies in its accuracy in measuring angular and linear kinematics [6-9]. Raw angular velocity and linear acceleration data downloaded from the device was filtered at 300 Hz using a 4th order Butterworth low-pass filter with cutoff frequency of 300 Hz. After processing, an impact detection algorithm was used to distinguish between real impacts and false positives resulting from spitting, chewing, dropping, or other spurious signals [10].

The MiG2.0 was deployed to 24 collegiate football players during the 2017 Fall NCAA season and 2018 Spring season over all practices and games through human subject protocol IRB-34943. A total of n=460 video-confirmed impacts were collected during this time period. As part of on-going efforts to instrument over 1000 high school football players at 10 high schools with the MiG 2.0, we also deployed our device to 88 participants from three high schools over the 2018 Fall season in a pilot deployment through human subject protocol IRB-46537. Thus far, we have processed and analyzed n=128 impacts that have been identified using our impact detection algorithm [10]. All data were collected in accordance with the Stanford Administrative Panels for the Protection of Human Subjects guidelines and regulations.

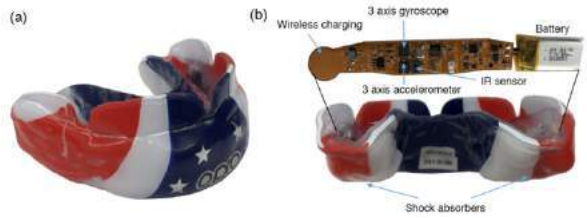

Figure 1: MiG2.0 custom-made mouthguard instrumented with a triaxial accelerometer and triaxial gyroscope (a) EVA mold (b) sensory board with wireless charging and infrared sensor for proximity detection [5].

We analyzed peak linear acceleration ($\mathbf{a_{l,p}}$), peak angular acceleration ($\mathbf{a_{a,p}}$), and peak change in angular velocity ($\Delta\mathbf{v}_{a,p}$) as biomechanical measures of interest. Probability distributions were fit to the aggregated data.

RESULTS

Head kinematics measures are summarized in **Table 1,** with the full distributions displayed in **Figure 2**. Concerning peak linear acceleration magnitudes, we found mean values of the two groups to be significantly different ($p < 0.01$), though the distributions have identical magnitudes for the 50th percentile values. Angular accelerations peak magnitude distributions, though not significantly different at the 0.01 significance level, report a higher mean impact acceleration for high school athletes than for college athletes.

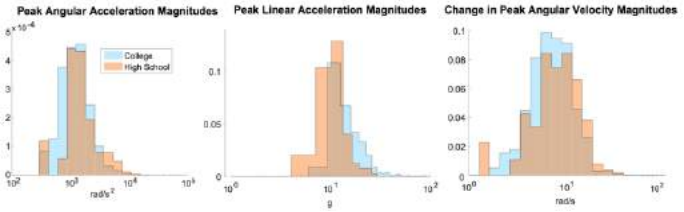

Figure 2: Head kinematics distributions for peak linear acceleration, peak angular acceleration and change in peak angular velocity magnitudes. Normalized probability density functions are graphed on log scale. The third distribution follows a log normal distribution.

	Mean	50th	95th	99th
	Peak Linear Acceleration (g), $a_{p,l}$			
High School	11.71	10.69	19.85	26.08
College	16.37	10.63	29.96	47.42
	Peak Angular Acceleration (rad/s^2), $a_{p,a}$			
High School	3084	2107	7912	12395
College	2314	1643	6216	13111

Table 1: Head impact kinematics metrics at 50th, 95th, 99th percentiles and means.

DISCUSSION

Though the distributions of head impact kinematics seem rather similar between high school and collegiate football, we summarized two interesting findings. First, we found that the collegiate linear acceleration distribution had a significantly higher mean ($p = 0.01$) , than that of high school Additionally we found the mean peak angular acceleration to be higher in high school impacts than in college impacts (though not significant at $\alpha = 0.01$).

While the first finding is intuitive given the higher level of skill, weight and age amongst other factors, at a higher level of play such as collegiate NCAA, it is surprising that peak angular accelerations are of similar magnitude in high school athletes and collegiate athletes. Given that head rotation has been hypothesized as the primary contributor to brain tissue injury [13], high school athletes may be subjected to similar levels of brain injury despite the different level of play, expertise, and muscular build. An understanding of injury biomechanics, beginning at the level of impact magnitude, could elucidate the need for prevention methods to promote health of youth athletes.

Similar studies have also found peak impact magnitudes to be higher for high school athletes than for collegiate athletes [3]. The explanation suggested by the authors is that collegiate athletes may have a more developed musculature system, that is better able to control head motion after impact [3]. However, previous research has provided evidence suggesting that the neck musculature plays a very minor role in impact biomechanics [20].

We hypothesize that the lack of high statistical significance for the difference in mean of angular acceleration magnitudes could be due to the relatively small sample size (n= 128) for high school impacts collected. As an ongoing goal to instrument over 1000 athletes at 10 high schools, we are currently processing and analyzing thousands more impacts. Moreover, we plan to assess the brain tissue strain-related response to angular and linear acceleration traces with a validated final element model of the human brain, the Global Human Body Model (GHBM), in order to quantify measures of brain injury such as maximal principal strain.

Finally, we note that, while our angular acceleration magnitudes are within range for the values previously reported in the literature (and mostly collected through the HITS system), our linear peak magnitudes are 50–79% lower than previously reported values, which range between 40g and 96g for the 95th percentile of youth football [12-15]. While early studies with instrumented helmet systems were extremely valuable in providing the first human studies in this field, our findings demonstrate increased accuracy of our measuring system, where the difference in measurements can likely be attributed to the relative motion of the helmet and the skull.

ACKNOWLEDGEMENTS

The authors would like to thank Stanford Athletics and the football teams involved in the study for their support in this research. We would also like to thank Camarillo Lab interns who aided in data collection. Research reported in this publication was supported by the National Institute of Neurological Disorders and Stroke of the National Institutes of Health under Award Number R24NS098518.

REFERENCES

[1] Centers for Disease Control and Prevention (CDC) Report: National Center for injury Prevention and Control; 2003. pp. 1–45.
[2] Cobb, B.R., Urban, J.E., Davenport, E.M. et al. Ann Biomed Eng (2013) 41: 2463.
[3] Broglio, Steven P et al. *Journal of athletic training* vol. 44,4 (2009): 342-9.
[4] *Mihalik JP, Bell DR, Marshall SW, Guskiewicz KM Neurosurgery. 2007 Dec; 61(6):1229-35; discussion 1235.*
[5] C. Giordano, L.C. Wu, C. Kuo, T. Fetters, D. Camarillo. Manuscript in preparation.
[6] L. C. Wu et al.,, J. Biomech., vol. 0, no. 0, pp. 39–47, 2016
[7] C. Kuo et al., J. Biomech., vol. 49, no. 9, pp. 1845–1853, 2016.
[8] D. B. Camarillo et al., Ann. Biomed. Eng., Apr. 2013.
[9] L. C. Wu et al., , Ann. Biomed. Eng., Aug. 2015.
[10] L. C. Wu et al., IEEE Trans. Biomed. Eng., vol. 61, no. 11, pp. 2659–68, 2014.
[12] Stitzel et al, 2019
[13] Ji, Songbai, et al. *Biomechanics and modeling in mechanobiology*13.5 (2014): 1121-1136.
[14] Daniel, Ray W. et al., *Annals of biomedical engineering* 40.4 (2012): 976-981.
[15] Kelley, Mireille E et al. *Journal of neurotrauma* vol. 34,11 (2017): 1939-1947.
[16]Guskiewicz KM et al., *JAMA* 290:2549–2555, 2003.
[17]Guskiewicz KM et al., *Am J Sport Med* 28:643–650, 2000.
[18] Field M. et al., *J Pediatr* 142:546–553, 2003
[19] McCrea M. et al., *Clin J Sport Med* 14:13–17, 2004.
[20] Fanton M. et al., IEEE Transactions on Biomedical Engineering, 2018

SB³C2019
Summer Biomechanics, Bioengineering and Biotransport Conference
June 25-28, Seven Springs, PA, USA

PLASTICITY AND ELASTO-PLASTIC DAMAGE MECHANICS USING REACTIVE CONSTRAINED SOLID MIXTURES: A MODELING APPROACH FOR BIOMEDICAL MATERIALS

Brandon K. Zimmerman (1), Gerard A. Ateshian (1)

(1) Department of Mechanical Engineering
Columbia University
New York, NY, USA

INTRODUCTION

The design of biomedical devices frequently incorporates plastic deformation as a desirable behavior. For orthopedic implants, e.g. those in the hip and knee, the material must have a Young's modulus low enough to ensure that sufficient stress will be transferred to the surrounding bones to maintain their healthy function. The search for biocompatible materials with a low elastic modulus has led researchers to various titanium alloys [1], which tend to exhibit significant plasticity. Plastic deformation may also arise during device function, e.g. the large plastic strains required to expand a coronary stent. During material selection and device design, computational modeling is required to predict *in situ* function; consequently, plasticity must be incorporated into the constitutive models of the material.

FEBio is a free finite element software package designed to meet the computational needs of the biomechanics and biophysics communities (febio.org) [2]. This study describes the formulation of a novel theoretical framework for plasticity and elasto-plastic damage based on reactive constrained solid mixtures, and its implementation into FEBio. Although plasticity has been extensively studied within the field of continuum mechanics, its dependence on internal state variable theory requires specification of evolution equations for internal variables and adds significant complexity.

We propose to model plasticity in the context of reactive constrained solid mixtures [3,4], where mechanics are governed by breaking and reforming of bonds (e.g., chemical bonds) within the material; the mechanical response is thus controlled by the material composition. Breaking and reforming of bonds is governed by chemical kinetics, subject to the axiom of mass balance. In this framework, bond concentrations represent observable state variables, obviating the need for postulating evolution equations for internal (hidden) variables. The implementation of this model into FEBio extends the available material behaviors of the software and allows simulation of the response of medical device materials to physiologic loading.

In this framework, loaded bonds break and reform in a stressed state. The deformation gradient of the stressed state is given by a constitutive assumption that describes the plastic strain field. This model naturally develops plasticity with kinematic hardening, which recovers the classical Bauschinger effect [5]. The framework is additionally enriched by allowing plastic deformation to produce damage, culminating in an elasto-plastic damage model.

METHODS

In this reactive framework, bonds which break and reform at a given time $t = u$ are referred to as u −generation bonds, where the earliest generation corresponds to $u = -\infty$. Kinematics are referred back to this earliest generation, which has a reference configuration $\mathbf{X}^s$ and is called the master reference configuration.

Consider a loaded bond which breaks and reforms into a new bond at $t = u$ with a different reference configuration $\mathbf{X}^u$. The deformation gradient of this u −generation bond is the relative deformation gradient $\mathbf{F}^u$, related to the master deformation gradient $\mathbf{F}^s = \partial\mathbf{x}/\partial\mathbf{X}^s$ via

$$\mathbf{F}^s = \mathbf{F}^u \cdot \mathbf{F}^{us} \tag{1}$$

where the mapping $\mathbf{F}^{us} = \partial\mathbf{X}^u/\partial\mathbf{X}^s$ relates the reference configuration of the u −generation to the master reference configuration, and defines the plastic deformation. Unlike the Kroner-Lee decomposition in classical plasticity, $\mathbf{F}^u$ is time-invariant and prescribed by constitutive relation; it does not represent a state variable in this formulation.

Plastic deformation is determined by a yield criterion

$$\varphi(\mathbf{F}^u) = \Phi(\mathbf{F}^u) - \Phi_m \leq 0 \tag{2}$$

where $\Phi(\mathbf{F}^u)$ is a yield measure (e.g. the von Mises stress) and Φ_m is the threshold at which yielding occurs. When $\varphi(\mathbf{F}^u) = 0$ and $\dot{\varphi}(\mathbf{F}^u) > 0$ at time $t = v$, u −generation bonds are breaking and reforming into

v −generation bonds, where $\varphi(\mathbf{F}^v) \leq 0$. To satisfy the requirement that the reforming generation be below the yield threshold, we require that the increment in the deformation between $t = v - dt$ and $t = v$ be due to plastic deformation only, where dt is an infinitesimal time increment such that the u −generation is extant at $v - dt$. We further constitutively require that this plastic deformation be isochoric, in accordance with experimental results. These constraints imply

$$\mathbf{F}^{vs} = \left(\frac{\det \mathbf{F}^s(v)}{\det \mathbf{F}^s(v-dt)}\right)^{-1/3} (\mathbf{F}^u)^{-1}(v - dt) \cdot \mathbf{F}^s(v) \qquad (3)$$

i.e. Eq. (3) constitutively defines the plastic deformation such that $\mathbf{F}^v(v)$, given by Eq. (1), satisfies $\varphi(\mathbf{F}^v) \leq 0$.

The free energy density of each bond is only a function of the relative (elastic) deformation gradient $\mathbf{F}^u$, such that the referential mixture free energy density (free energy per unit referential volume) is $\Psi_r = \sum_\alpha w^\alpha \Psi_0^\alpha(\mathbf{F}^\alpha)$, where the summation runs over all generations and w^α and Ψ_0^α are the mass fraction and referential free energy density of the α −generation. As only one generation is extant at any given time, $w^\alpha = 1$ for the extant generation and $w^\alpha = 0$ for the others.

Kinematic hardening behavior emerges naturally from the above framework by allowing multiple bond types $\alpha = 1, \ldots, n$, to exist in the mixture, each with its own yield threshold Φ_m^α, producing a Masing-like model [5]. In this simple extension, each bond type yields when its threshold is reached, and different bond types do not interact.

Damage of bonds is introduced by reducing their mass fraction such that $w^\alpha = (1 - D)w_0^\alpha$ [6]. In this expression, $0 \leq D \leq 1$ is a scalar damage variable which is a function of the plastic strain and w_0^α is the mass fraction when there is no damage. If multiple bond types are used, each has its own damage variable which is a function of the plastic strain in that bond type.

RESULTS

Several characteristic plastic behaviors have been reproduced to validate the present models of reactive plasticity and reactive elasto-plastic damage and to demonstrate agreement with experimental results.

In stress-strain curves produced from uniaxial tension testing, both perfectly plastic and kinematic hardening behavior can be observed (Fig. 1a). Perfect plasticity occurs by having only one bond type that yields at a single threshold, whereas kinematic hardening occurs when multiple bond types yield at progressively greater thresholds. Real stress-strain behavior can be recovered by incorporating plastic strain-based damage into the model; e.g. see the fit for Al-2024 in Figure 1b.

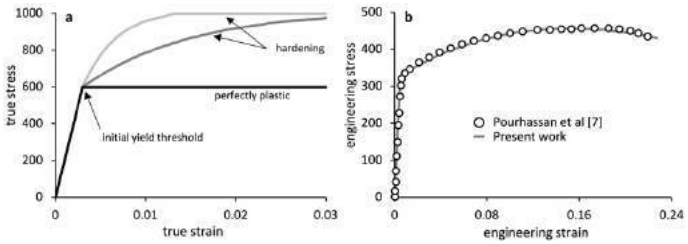

Figure 1. (a) Stress-strain behavior for different plastic parameters, recovering both perfectly plastic and kinematic hardening behavior. (b) Stress-strain curve for Al-2024, fit by adding damage to the plasticity model.

Under cyclic loading, kinematic hardening naturally emerges from this framework and recovers the well-known Bauschinger effect, where loading in one direction affects the yield threshold upon reversal. Figure 2a clearly shows compressive yielding begins much earlier than tensile yielding, as the yield surface has shifted due to previous plastic flow.

Isochoric plastic deformation is a constitutive assumption supported by experimental evidence, although careful experiments measure nonzero volume changes during plastic flow. Due to our formulation's use of multiple bond types, restricting the isochoric deformation to the plastic parts via Eq. (3) allows us to exactly predict the volumetric deformation experimentally observed during load-unload cycles (Fig. 2b) by curve-fitting the stress-strain data [8].

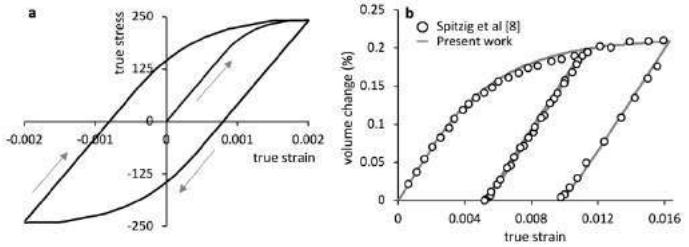

Figure 2. (a) The classical Bauschinger effect emerges from the model during cyclic loading. Grey arrows indicate loading path. (b) Predicted volume change during load-unload cycles, compared to results from maraging steel. Prediction was generated by first fitting the stress-strain curve, then simulating load-unload experiment.

Finally, strain-controlled tensile testing of a dogbone specimen produces familiar necking (Fig. 3) due to isochoric plastic flow.

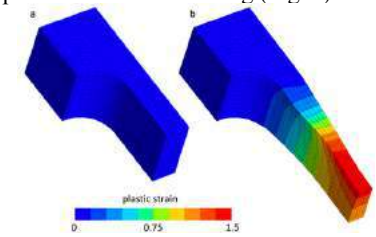

Figure 3. Necking behavior observed during FEBio simulation of strain-controlled uniaxial tension. (a) Initial geometry and (b) final fractured geometry, simulated with octant symmetry.

DISCUSSION

This study presents the formulation and finite element implementation of a reactive constrained mixture theory for plasticity incorporating damage mechanics, based on observable state variables. The behavior of the model was validated through reproduction of well-known plastic behaviors, and demonstrated both the ability to curve-fit experimental results and predict separate experiments. In contrast to classical theories of plasticity, the presented model has no need to postulate evolution equations for internal variables governing the material response; rather, the observable evolving composition (microstructure) uniquely defines the mechanical behavior.

As medical device materials often involve significant plastic effects, incorporation of the present model for plasticity into a finite element code designed for the biomechanics and biophysics community allows the use of a single software platform for finite element analyses. Further, due to the tissue-specific constitutive models available in FEBio, device plasticity may be simulated simultaneously with accurate tissue behavior. The use of reactive plasticity may also provide a level of simplicity to computational analyses, as relatively few parameters are needed to define the model.

A reactive model for plasticity also enables incorporation of tissue plasticity into biological mixtures in a consistent theoretical framework; future work is directed along this avenue of research.

ACKNOWLEDGEMENTS

NIGMS (Grant No. GM083925) and NSF GRFP (DGE-1644869).

REFERENCES

[1] Nie, L et al., *J Mech Behav Biomed Mater*, 29:1-6, 2014. [2] Maas, SA et al., *J Biomech Eng*, 134(1):011005, 2012. [3] Nims, RJ, & Ateshian, GA, *J Elast*, 129:69-105, 2017. [4] Safa, BN et al., *J Biomech Eng*, 141(2):021005, 2019. [5] Skelton, RP et al., *Mater Sci Eng A*, 238:377-390, 1997. [6] Nims, RJ et al., *Interface Focus*, 6:20150063, 2015. [7] Pourhassan, S et al., *Proc Struct Int*, 5:1355-1362, 2017. [8] Spitzig, WA et al., *Metall Trans A*, 7:1703-1710, 1976.

SB³C2019
Summer Biomechanics, Bioengineering and Biotransport Conference
June 25 -28, Seven Springs, PA, USA

INFLAMMATORY AND NON-INFLAMMATORY SYNOVIAL FLUIDS EXHIBIT DISTINCT TRIBOLOGICAL PHENOTYPES

Elizabeth Feeney (1), Devis Galesso (2), Cynthia Secchieri (2), Roberta Ramonda (3), Lawrence J Bonassar (1)

(1) Meinig School of Biomedical Engineering
Cornell University
Ithaca, NY, USA

(2) Fidia Farmaceutici S.p.A.
Abano Terme, Padua, Italy

(3) Rheumatology Unit
University of Padua
Padua, Italy

INTRODUCTION

Inferior synovial lubrication is a hallmark of osteoarthritis (OA)[1–3]. Recent studies suggest that changes in synovial lubrication and composition are highly dependent on the type of OA[4,5], though a loss of high molecular weight hyaluronic acid (HA) and reduction in synovial fluid viscosity are common[5]. HA viscosupplementation is a widely used therapy for managing the symptoms of OA. However, it is unclear how the effectiveness of HA viscosupplements varies with OA phenotype. The objective of this study was to investigate the effects of the HA viscosupplement, Hymovis®, on the lubricating properties of diseased synovial fluid (SF) from patients with non-inflammatory and inflammatory OA.

METHODS

SF was collected from the knee joints of human donors with non-inflammatory OA (n=10, age 62±10 years) and inflammatory OA (n=10, age 44±26 years) where inflammatory patients were defined as having white blood cell counts above 2000/μL and a polymorphonuclear neutrophil percentage >25%. SF samples' biophysical properties were assessed alone or in a 1:1 mixture with Hymovis, a modified HA viscosupplement. Cartilage explants were harvested from neonatal bovine stifles and loaded onto a custom tribometer in a SF or SF:HA bath. Explants were compressed to 40% strain against glass and slid at speeds of 10-0.1mm/s as friction coefficients were recorded[6]. Viscosity was quantified by shearing the fluids from 1000-1x10^{-4} 1/s on a rheometer with a 25mm cone-and-plate geometry[7]. Stribeck analysis was used to examine the frictional properties of the fluids across different modes of lubrication including high friction boundary mode, mixed, and low-friction elastoviscous mode. Stribeck curves were made by plotting friction coefficients vs. Sommerfeld number, a dimensionless parameter calculated as[7]:

$$\eta v a / L_N \quad (1)$$

that accounts for the lubricant viscosity (η), sliding speed (v), contact width (a), and contact load (L_N). Lubricin was quantified using a peanut agglutinin sandwich ELISA with mAb 9G3 as the detection antibody and purified bovine lubricin as the standard[8]. A 3-factor ANOVA and a Tukey's HSD test were performed to compare viscosities. Lubricin concentrations were compared using a t-test, and friction coefficients (0.1mm/s sliding speed) were fit to a dose-response curve with lubricin concentration.

RESULTS

Inflammatory and non-inflammatory OA samples exhibited similar shear-thinning viscous behavior. HA significantly increased the viscosity ($p<0.001$) of the fluids by a factor of over 100 at low shear rates (Fig. 1). Non-inflammatory OA samples exhibited typical Stribeck behavior in which friction coefficients decreased with increasing Sommerfeld number (Fig 2. A, B). The addition of HA reduced friction coefficients, shifted the Stribeck curve toward higher Sommerfeld numbers, and revealed a high-friction boundary mode plateau not evident for pure non-inflammatory SF. However, for inflammatory OA samples, HA did not always reduce friction coefficients (Fig. 2C,D). Inflammatory OA samples showed inconsistent Stribeck behavior (Fig. 2C, D); while several exhibited a similar magnitude of friction coefficients and Stribeck behavior like the non-inflammatory OA SF, a subset showed a vastly different behavior in which friction coefficients were higher, more variable, and increased with Sommerfeld number. This non-Stribeck-like behavior was preserved when HA was added. Lubricin concentrations were highly variable and did not differ between inflammatory and non-inflammatory SF (Fig. 3, inset). Boundary mode

friction coefficients decreased with increasing lubricin concentrations (Fig. 3). Non-Stribeck-like behavior was associated with low lubricin concentrations.

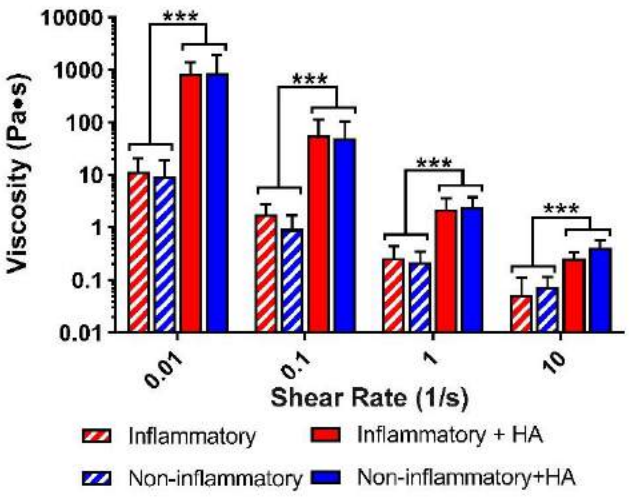

Figure 1: Inflammatory and non-inflammatory synovial fluids exhibit similar shear-thinning viscous properties which are significantly enhanced by the addition of HA (p<0.001, n=9).

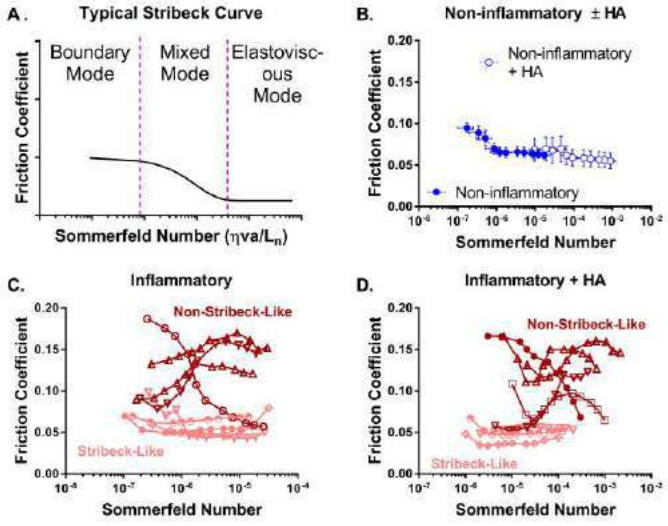

Figure 2: (A) Example of a Stribeck curve for lubricated cartilage showing high-friction boundary mode and the transition to low-friction elastoviscous mode. (B) Non-inflammatory OA samples exhibit a Stribeck-like behavior in which the addition of HA shifts the transition to elastoviscous mode to higher Sommerfeld numbers. Individual inflammatory OA samples (C,D) show unique lubrication phenotypes; some patients (pink) exhibit typical Stribeck behavior similar to non-inflammatory OA samples in (B), while others (maroon) show increasing friction coefficients with increasing Sommerfeld numbers and a larger variability in friction coefficients. Note that each symbol shape represents a single patient (C,D). (n=5-8).

DISCUSSION

HA significantly enhanced the viscosity of inflammatory and non-inflammatory OA SF. Interestingly, HA viscosupplementation was effective in reducing friction coefficients for non-inflammatory OA samples, but not necessarily for inflammatory OA samples. For some patients, friction coefficients were increased by the addition of HA. Furthermore, Stribeck analysis revealed a subset of inflammatory OA samples exhibiting higher friction and atypical Stribeck behavior where friction coefficients increased with Sommerfeld number. These atypical behaviors appear to be associated with SF composition, including lubricin and possibly HA concentrations. We have identified tribological phenotypes within inflammatory and non-inflammatory human OA SF. This suggests that distinct lubrication therapies may be advised for specific OA phenotypes.

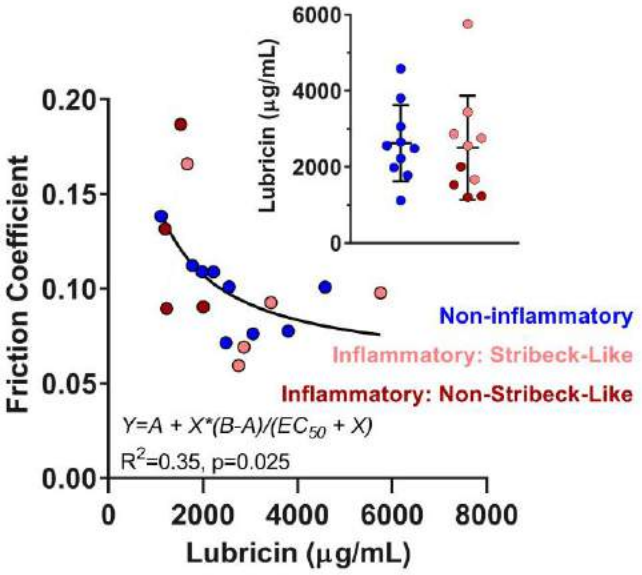

Figure 3: Lubricin concentrations were similar between inflammatory and non-inflammatory OA (inset, p=0.82). Boundary friction coefficients followed a dose-response relationship whereby increasing amounts of lubricin resulted in lower friction (n=18) Non-Stribeck-like samples (maroon) exhibited low lubricin concentrations and increased friction.

ACKNOWLEDGEMENTS

This research is supported by Fidia Farmaceutici S.p.A. and NSF GRFP DGE-1650441 (EF). We thank Heidi Reesink PhD VMD DACVS-LA, Yuyan Wang, and Jin Su PhD for assistance with ELISAs.

REFERENCES

[1] Elsaid, KA, *Arthritis Rheum*, 52:1746–55, 2005.
[2] Neu, CP, *Arthritis Rheum*, 62:2680–2687, 2010.
[3] Lee, S-S, *Proc Inst Mech Eng Part H J Eng Med*, 227:129–137, 2013.
[4] Elsaid, KA, *Arthritis Rheum*, 58:1707–15, 2008.
[5] Ballard, BL, *J Bone Jt Surgery-American Vol*, 94:e64-1–9, 2012.
[6] Gleghorn, JP, *J Biomech*, 41:1910–1918, 2008.
[7] Bonnevie, ED, *PLoS One*, 10:e0143415, 2015.
[8] Reesink, HL, *Osteoarthr Cartil*, 25:128–137, 2017.

SB³C2019
Summer Biomechanics, Bioengineering and Biotransport Conference
June 25 -28, Seven Springs, PA, USA

FAILURE MECHANISMS IN THE TENDON ENTHESIS UNDER QUASISTATIC, CYCLICAL, AND PATHOLOGICAL LOADING

Mikhail Golman (1), Adam C. Abraham (2), Iden Kurtilaliaj (1), Brittany P. Marshall (1), Guy M. Genin (3), Victor Birman (4), Stavros Thomopoulos (1,2)

(1) Biomedical Engineering
(2) Orthopedic Surgery
Columbia University
New York, NY, USA

(3) Mechanical Engineering and Material Science
Washington University in St. Louis
St. Louis, Missouri, USA

(4) Global – St. Louis and Department of
Mechanical and Aerospace Engineering
Missouri Science & Technology
St. Louis, Missouri, USA

INTRODUCTION

The enthesis is a robust fibrocartilaginous tissue that effectively transfers load across two highly dissimilar materials: tendon (soft) and bone (hard). The connection is critical to joint function, and must be both strong and tough. Although a large body of work has established the sources of strength (*i.e.*, the onset of injury) [1], the sources of toughness (*i.e.*, the energy absorption that protects against failure following the onset of injury) are largely unknown. Clinically, bone avulsion fractures or tendon mid-substance ruptures are commonly seen in high-impact injuries and in pediatric patients [2], while insertion failures are prominent for the degenerative rotator cuff tears in adult patients [3]. Because many surgical repairs fail [4], there is a pressing need to identify and eventually reconstitute the natural toughening mechanisms in the enthesis. Therefore, our aim was to perform the first characterization of these toughening mechanisms in a well-defined laboratory model of enthesis failure. We hypothesized that failure mechanisms of mouse entheses would reveal distinct molecular level injury localization and propagation in quasistatic (acute) and cyclical (degenerative) loading, and that tissue pathologies would alter these mechanisms.

METHODS

All animal procedures were approved by the Columbia University Institutional Animal Care and Use Committee. Supraspinatus tendon-to-bone units were harvested from healthy adult (>12 weeks) male C57BL6/J mice (n=72). All samples were mechanically tested in a saline bath at 25 ºC to prevent thermal collagen denaturation.

Quasi-static loading: Samples were subjected to a 0.05 N preload before being strained in tension at 0.2 %/s to 1 N, 2 N, 3 N (n=3 samples per force group), or failure (n=15). To examine the role of strain rate on tendon enthesis failure, healthy samples were also tested under three different strain rates (2 %/sec, n=10; 20 %/sec, n=10; 200 %/sec, n=10).

Fatigue loading: After pre-loading to 0.05 N, samples were either subjected to 1 Hz sinusoidal loading from 0.1-1 N (1-20 % of failure force, n=4) or 1-3 N (20-70% of failure force, n=4). To investigate molecular level damage localization in the entheses, additional samples were loaded to 10,000 cycles (n=2), 40,000 cycles (n=2), and to failure (> 50,000 cycles, n=4) using the second protocol (20-70% max failure force). The control group consisted of samples that were prepared and mounted in the mechanical tester, but not loaded (n=5).

In vivo degeneration models: To examine the effect of pathology on enthesis failures, 10-week old C57BL6/J mice (Jackson Laboratories) were subjected to two degeneration models. Underuse degeneration was induced via muscle paralysis by injecting 0.2 U of botulinum toxin (Btx) into the supraspinatus muscle (4 wk, n=10). Overuse degeneration was achieved though downhill treadmill running for 4 weeks (-15°, 22 cm/sec for 40 min/day, 5x/week; n=10). All tendon-to-bone units harvested from degeneration models were quasi-statically loaded to failure at a strain rate of 0.2 %/s.

Imaging: After mechanical testing, samples were secured at terminal displacements and either submerged in a 5% mercury chloride ($HgCl_2$, Sigma-Aldrich) for 24 hours or fixed with 4% paraformaldehyde (PFA, Fisher Sci) overnight. $HgCl_2$ solution was used as a contrast agent to enhance enthesis visualization using high resolution x-ray computed tomography (microCT, Bruker Skyscan 1272). PFA fixed samples were stained with a 15 M fluorescein-labelled collagen hybridizing peptide (F-CHP, 3Helix) to detect molecular level mechanical denaturation of collagen [5] and visualized using fluorescence microscopy. Statistical analyses was performed using one-way ANOVA with Dunnet's post-hoc test.

RESULTS

Contrast-enhanced microCT imaging of an unloaded control specimen revealed that, hidden within the well-known larger apparent attachment footprint area (Fig. 1B, blue dotted line), is a smaller, much denser primary insertion site where tendon fibers insert directly into the bone surface (Fig. 1B, green dotted line). Depending on the loading regime, there were three distinct failure modes: bone avulsion, tendon mid-substance, and tendon-bone interface (Fig. 1B-E). Under quasi-static loading conditions, healthy tendon-to-bone attachments failed either at the interface between mineralized fibrocartilage (MF) and bone (B) or extending into the trabecular bone of the humeral head (B-T), both with a mineralized "bone plug" avulsed from the insertion site (Fig. 1C, Fig 2). Imaging revealed that only 47.4 +/- 5.1 % of the apparent attachment site was avulsed, revealing a previously unknown primary attachment. This failure behavior was largely unaffected by increasing the loading rate. While stiffness was not affected by strain rate, failure load and work to failure increased at higher strain rates ($p<0.01$). All samples cyclically loaded at 20-70% failure force failed in the unmineralized fibrocartilage portion of the attachment (Fig. 1E). In contrast, samples cyclically loaded at 1-20% failure force did not fail, even after 100,000 (Fig. 1A).

Pathological tendon-to-bone attachments also exhibited exclusively avulsion-type failures. Healthy and overuse-degenerated attachments failed catastrophically, showing little post-yield behavior, while underuse-degenerated attachments failed at lower forces and showed distinct post-yield behavior (Fig. 2A). Stiffness was increased in the overuse-degenerated attachments ($p<0.01$). Maximum force was decreased in the underuse-degenerated attachments ($p<0.01$). There was an increase in fractured (avulsed) area in the underuse-degenerated attachments ($p<0.001$) (Fig.2B). Pathology caused changes in the fracture pattern: overuse-degeneration led to more failures at the interface between the MF-B, while underuse-degeneration led to more failures at the B-T interface (Fig. 2C). Bone morphometric analysis revealed that underuse-degeneration led to bone loss underlying the attachment (BMD, $p<0.0001$), while that overuse increased bone volume of the humeral head (BV/TV, $p<0.01$).

F-CHP fluorescence intensity, indicative of damage accumulation, increased with applied load or number of cycles (Fig. 3). For quasi-statically loaded samples, there was little to no fluorescent signal in the low force group (1-2N), followed by increased staining near the attachment site at higher loads (3N and failure). For cyclically loaded samples, F-CHP staining was initially concentrated in a few fibers near the tendon mid-substance (10K and 40K cycles) and ultimately propagated down the entire tendon in concentrated bands.

DISCUSSION

Mouse supraspinatus entheses exhibited three distinct failure modes: bone avulsion, tendon mid-substance failure, and tendon-bone interface failure. Results supported the hypothesis that failure mode is dependent on the loading regime. Under quasi-static loading, samples failed at the interface between mineralized fibrocartilage and bone. Consistent with previous studies of responses to monotonic loading [6,7], mechanical responses were largely strain-rate insensitive. However, avulsion area and/or the number of avulsed fragments increased with loading rate, consistent with previous observations on rate-sensitivity of bone failure [8]. For cyclical loading, samples failed at the unmineralized side of the fibrocartilage. Results suggested that the mechanisms protecting fibrocartilaginous tissue might be gradually attenuated over cyclical loading. This hypothesis was borne out by imaging of collagen damage: for quasistatic loading, damage was localized to the attachment site at loads above 3N, but for cyclical loading denaturation was attenuated at the attachment site, instead propagating through the tendon and to the distal end of the enthesis for ultimate failure.

Both overuse and underuse reduced toughness. Overuse did so by reducing failure displacement without affecting failure force, while underuse did so by reducing failure force without affecting failure displacement. Continued efforts to identify sources of strength and ductility in the enthesis hold potential to design improved tissue engineered solutions. These results demonstrate the importance of the enthesis for effectively transferring load from muscle to bone.

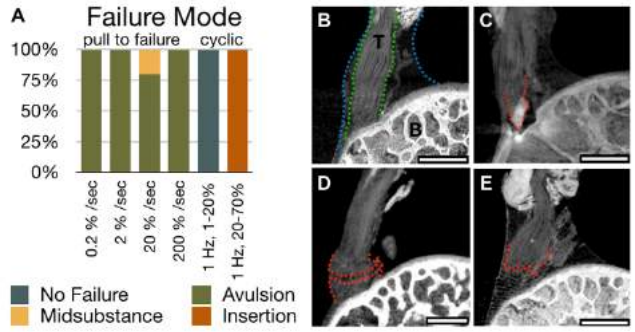

Figure 1: Failure modes distirbutions (A) and contrast enhanced uCT images of intact (B), avulsed (C), failed at mid-substance (D), and insertion (E). Red dotted line represents failure surface. Scale is 500 µm.

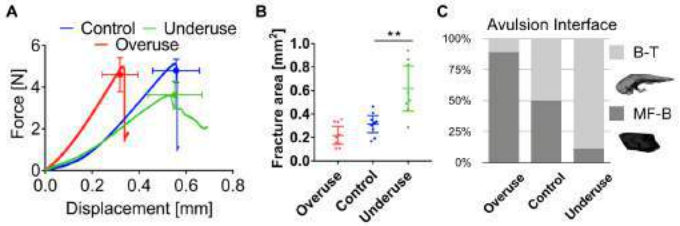

Figure 2: Failure modes in pathological murine enthesis. (A) Load-dispalcement curve (B) fracture area, and (C) failure interface distributions.

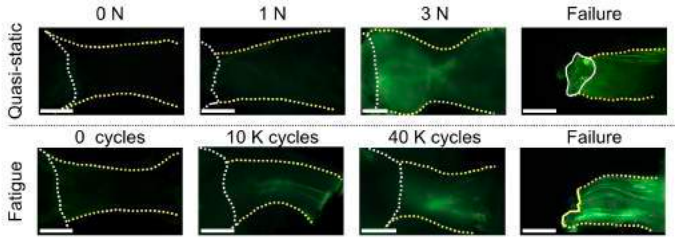

Figure 3: Representative whole-sample images of mice enthesis that were subjected to quasi-static (top) or cyclic loading (bottom). Dotted line represent outline of bone (white) and tendon (yellow). Solid line represents failure surface. Scale is 500 µm

ACKNOWLEDGEMENTS

This work was supported by NIH U01-EB016422 and R01-AR055580.

REFERENCES

[1] Genin *et al*., Biophys J. 2009 Aug 19;97(4):976-85, [2] Pedowitz *et al*., Curr Rev Musculo. Med. 2013 Dec;6(4):285-93, [3] Kim *et al*., J Bone Joint Surg Am. 2010 Apr;92(4):829-39, [4] Galatz, L et al., *J Bone Jt Surg Am*, 86-A:219-224, 2004, [5] Zitney *et al*., Nat Comm. 2017 Mar 22;8:14913, [6] Woo *et al*., J Orthorop Res. 1990 Sep; 8(5)712-2, [7] Noyes *et al*., *J Bone Joint Surg Am* **56**, 236-253, [8] Wright *et al*., Med Biol Eng. 1976 Nov; 14(6):671-80.

REAL-TIME MEASUREMENT OF COLLAGEN ARCHITECTURE AND DEFORMATIONS AT SUB-MICRON RESOLUTION

Po-Yi Lee (1,2), Bin Yang (2), Ian A. Sigal (1,2)

(1) Department of Bioengineering
University of Pittsburgh
Pittsburgh, PA, USA

(2) Department of Ophthalmology
University of Pittsburgh
Pittsburgh, PA, USA

INTRODUCTION

The optic nerve head (ONH) comprises a complex network of collagen fibers that undergoes remodeling and deformation with age and disease, such as in glaucoma [1]. The orientation and organization of collagen fibers, particularly those of the peripapillary sclera (PPS) and lamina cribrosa (LC), play an important role in the mechanical properties and deformations of the ONH [2]. Although standard polarized light microscopy allows visualizing the architecture of collagen fibers in ocular tissues, the technique requires acquiring and post-processing multiple images with different polarization states [3]. Reconstructing architecture from multiple images not only precludes time-sensitive applications, such as the study of collagen fibers dynamic response to external force, but also reduces the level of detail discernible, which prevents resolving sub-micron details.

In this study, we applied snapshot polarized light microscopy (snapshot-PLM) to ocular tissues to study their microstructure and dynamic deformations under controlled loading conditions. Compared to conventional imaging methods, snapshot-PLM captures both fiber orientation and alignment information in a single true-color image, and is therefore suitable for high-speed imaging and quantification. Our goal was to visualize load-induced changes in fiber bundle characteristics, such as shape, organization, and orientation, and to quantify tissue deformation in the LC and PPS regions. The dynamic visualization and quantification in ONH regions will provide valuable information towards better understanding of ocular biomechanics.

METHODS

Imaging setup – The snapshot-PLM imaging system was based on standard polarized microscope equipped with a pair of polarization components [4]. Objectives with 4x and 10x magnification were used for full-field or full frame rate imaging, respectively.

Sample preparation – Tendons from chicken legs were used as reference materials due to their relatively uniform architecture. The tendons were obtained fresh and fixed chemically (10% formalin) under longitudinal load to straighten and align the collagen fibers. The loaded tissues were then cryo-sectioned longitudinally at a thickness of 30 µm [5]. Sheep ONH tissues were used to investigate the structure visibility and load-induced deformations. Fresh ocular tissues from a trephined sheep ONH were cryo-sectioned into 16-µm thick sections. Note that no labels or stains or fixatives were applied to any ONH tissues or sections.

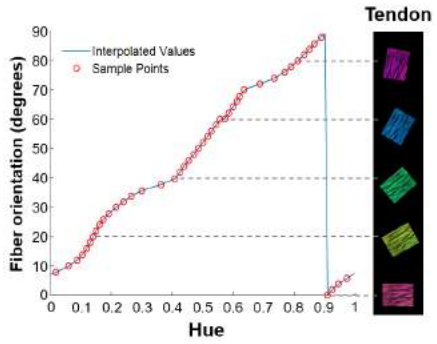

Figure 1. Circular interpolation of fiber orientation as a function of hue. The function was calibrated by imaging the chicken tendon at several known orientations. Five example orientations are shown in true color on the right-hand side.

Color-angle conversion – The color-angle conversion was calibrated by imaging at several known orientations a section of chicken tendon (Fig. 1). The tendon section rotated by a sequential increment from 0 to 90 degrees was imaged by snapshot-PLM. The

angle of rotation of the 46 images was measured by image registration, and hue was extracted. The function of hues was built by circular interpolation of the corresponding angles of rotation. The function was then used to convert snapshot-PLM images into angle maps.

Tensile testing and quantification – The ocular tissues were mounted on a custom biaxial-stretching device for dynamic testing with image acquisition at 30 frames per second. To visualize the collagen uncrimping process in the region of interest, we quantified angle distribution and generated crimp maps, which were weighted by the amplitude of crimps. We used digital image correlation (DIC) to track the fiber displacement, and then calculated the Eulerian strain from the displacement vector fields.

RESULTS

Fig. 2a shows collagen fiber organization of a sheep ONH section by snapshot-PLM before applying load. The external load altered structural features of the ONH. In the LC region, the realignment of collagen fiber bundles deformed the pores and beams. We highlighted examples where the pore width increased from 80.2 μm to 87.2 μm (white arrows), and the beam thinned remarkably from 19.0 μm to 11.7 μm (red arrows, Fig. 2b). The changes in pores or fiber bundles in LC may indicate substantial mechanical insult on the neural tissues and vasculature. The crimped collagen fibers in the LC beams were straightened under load. This is more readily visible in the PPS (Fig. 2c). This can be discerned in the reduced spread of the orientation distribution, which changed from bimodal, indicative of crimped fibers, into unimodal. (Fig. 2d).

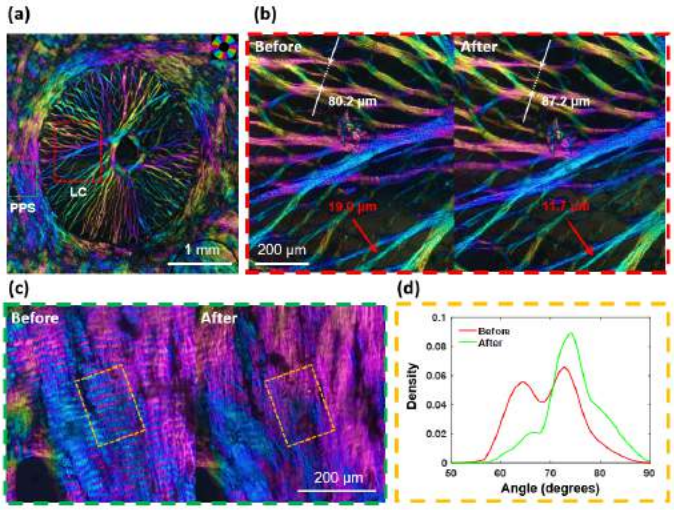

Figure 2. Visualization of a sheep ONH section by snapshot-PLM in tensile testing (4x objective). (a) True-color image of collagen fiber organization of ONH before applying load. (b) Change in LC pore (white arrows) and beam width (red arrows) under load. (c) Uncrimping process of the PPS collagen while under load. (d) Change in fiber orientation distribution in a region of (c).

Fig. 3 shows uncrimping process in the LC region. A pair of purple/yellow bands in the crimp map represents one period of crimp, and the brightness of the bands represents the crimp amplitude. Upon loading, the purple/yellow bands became less visible with a grayish appearance due to the reduced crimp amplitude. After stretching, the crimp amplitudes varied.

To study the fiber deformations in the PPS, we imaged and analyzed 104 images at various steps of loading (Fig. 4a). Stretching made the crimp less visible and caused fiber displacement. Tracking the fibers with DIC during deformation revealed that the motion trails were tortuous and anisotropic (Fig. 4b). The complex displacements indicate tissue shear, stretch, and compression. The first principal strain reached 40-80% (Fig. 4c).

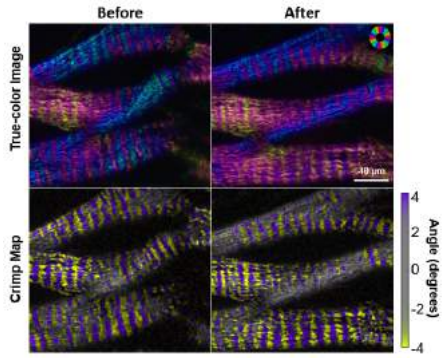

Figure 3. Uncrimping process in LC beam collagen fibers under load (10x objective). Yellow/purple crimp maps (bottom) provide better visibility of the crimp changes than true-color (top).

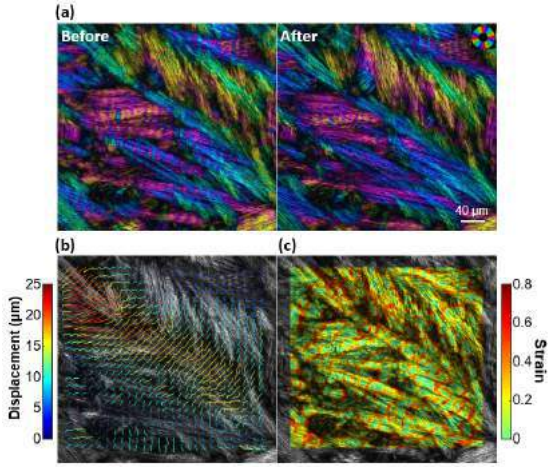

Figure 4. (a) Recording the deformation of PPS under load (10x objective). (b) Motion trails of PPS under load; the color indicates displacement in microns. (c) The first principal strain map of PPS under load.

DISCUSSION

We demonstrated that the load-induced changes in the shape and orientation of collagen fibers in ONH regions can be visualized and quantified using snapshot polarized light microscopy. The high temporal and spatial resolution of snapshot-PLM revealed sub-bundle details and highly dynamic tissue deformations in both LC and PPS regions. To the best of our knowledge this is the first direct visualization of sub-bundle deformations and crimp loss in LC and PPS. The imaging and analysis techniques can be applied to other collagenous tissues.

ACKNOWLEDGEMENTS

NIH R01-EY023966 and P30-EY008098.

REFERENCES

[1] Sigal, I. A., et al., *Exp Eye Res.*, 88(4), 799-807, 2009.
[2] Voorhees, A. P., et al., *Acta Biomater.*, 58, 278-290, 2017.
[3] Jan, N. J., et al., *Biomed. Opt. Express*, 6(12), 4705-4718, 2015.
[4] Shribak, M., *Sci. Rep.*, 5, 17340, 2015.
[5] Yang, B., et al., *J Biophotonics*, 11(8):e201700356, 2018.

SB³C2019
Summer Biomechanics, Bioengineering and Biotransport Conference
June 25 -28, Seven Springs, PA, USA

COLLAGEN FATIGUE DAMAGE EVOLVES WITH CREEP STRAIN AND IS STRAIN RATE DEPENDENT

Jared L. Zitnay (1,2), Gang Seob Jung (3), Allen H. Lin (1,2), Zhao Qin (3), Yang Li (1), Markus J. Buehler (3), S. Michael Yu (1), Jeffrey A. Weiss (1,2)

(1) Department of Biomedical Engineering
University of Utah
Salt Lake City, UT, USA

(2) Scientific Computing and Imaging Institute
University of Utah
Salt Lake City, UT, USA

(3) Department of Civil and Environmental Engineering
Massachusetts Institute of Technology
Cambridge, Massachusetts, USA

INTRODUCTION

Injuries to dense connective tissues such as tendon and ligament are often the result of overuse or age-related degeneration. The predominant hypothesis is that repeated loading cycles cause "micro-damage" in the tissue, and in the case of injury, micro-damage exceeds the rate of repair and accumulates [1]. Although the mechanisms and structures involved in load-induced micro-damage are still under investigation, it is clear that damage to collagen, the primary structural component of tendon, is involved in the micro-damage process. Indeed, previous studies using cyclic fatigue to represent repetitive use loading of tendon have demonstrated material and mechanical changes in the form of matrix disruption at the level of the collagen fibril and fiber, and decreased tissue stiffness [2]. However, the effects of cyclic fatigue loading on collagen structure at the molecular level are unknown.

We demonstrated that collagen hybridizing peptide (CHP), which hybridizes with denatured or unfolded collagen α-chains [3], can detect and quantify mechanical damage to the collagen molecule, due to monotonic tensile overload [4]. CHP binding at subfailure levels of loading, and accumulation of damage with increasing strain, demonstrated that molecular level collagen damage is a critical component of tendon mechanical damage during tensile loading. The objectives of this study were to investigate the role of molecular-level collagen damage during tendon fatigue, and to identify possible molecular level mechanisms of triple-helical fatigue damage using steered molecular dynamics (SMD) simulation. The overlying hypothesis is that molecular-level collagen damage is fundamental to the initiation and progression of fatigue damage in tendon.

METHODS

Rat tail tendon (RTT) fascicles were dissected from fresh-frozen, 6-month old, male Sprague-Dawley rats and equilibrated in 1× PBS prior to testing. Initial cross-sectional area was measured using an optical micrometer. Samples were preconditioned between 0.2 N (~2.3 MPa) and 4.6 MPa for 11 cycles, using a 6% s^{-1} constant strain rate triangle wave, then allowed to recover while unloaded for 5 min. Samples were fatigue loaded between 0.2 N and 18.5 MPa (40% of tensile strength at 1% s^{-1}) using a triangle waveform at strain rates of 0.4, 4.0, or 40% s^{-1}. Cyclic loading was applied until peak cyclic strain reached one of three predefined levels, representing increasing levels of fatigue, or failure occurred ($n \geq 5$ in all 4 groups, at each strain rate). Unloaded samples served as controls (n=12).

Following fatigue testing, samples were removed from the test system and the amount of denatured collagen was measured using a CHP based microplate assay [5]. Sample wet weight was recorded and then samples were incubated overnight at 4 °C, in a 15 μM solution of 5-FAM conjugate CHP (F-CHP; 3Helix, Inc.) to label denatured collagen. Samples were washed three times in PBS for 30 min to remove unbound F-CHP. Labeled samples were digested using proteinase K and F-CHP fluorescence was measured at 485 and 525 nm excitation and emission, respectively. Fluorescence was normalized to wet weight and the amount of denatured collagen was calculated using a standard curve for RTT fascicles. Data for peak cyclic strain and percent denatured collagen were plotted as a function of normalized number of cycles (cycle number divided by cycles to failure).

SMD simulations were performed using a representative homotrimeric collagen peptide comprised of twenty [Gly-Pro-Hyp] triplets in explicit water solution [4]. Periodic boundary conditions were applied to all directions. Each simulation was performed in the isothermal-isobaric ensemble (pressure = 1 atm and temperature = 310 K) with 1 fs simulation time step. Energy minimization and equilibrium simulations were performed before the simulated mechanical test. During equilibrium simulation, the ends of the collagen peptide were

anchored with a small force to prevent peptide bending. The SMD method was used to deform the molecule between 350 pN and 2085 pN with a constant loading speed of 3, 5, or 10 m/s. Simulations were performed with either tension dominant loading that stretches the whole triple-helical collagen molecule or shear dominant loading that corresponds to pulling a single strand out of the triple helix. Solvent accessible surface area (SASA), a measure of molecular unfolding, was computed throughout the loading simulation.

Experimental data were analyzed using mixed effects linear regressions to determine the effect of predictor variables and their interaction. Significance was determined at the α=.05 level.

RESULTS

RTT fascicles demonstrated a significant increase in the amount of denatured collagen detected by CHP binding with increased fatigue loading ($p<.001$, Fig. 1b). However, there was not a significant effect of strain rate ($p=.451$) nor interaction between fatigue level and strain rate ($p=.220$). The number of loading cycles to failure displayed a significant effect of strain rate ($p<.001$), with 250 ± 195, 920 ± 624, and 3954 ± 1115 cycles (mean ± SD) at 0.4, 4, and 40% s^{-1}, respectively. Using normalized number of cycles, however, the main effect of strain rate on peak cyclic strain was not significant ($p=.166$), while the effect of fatigue level ($p<.001$; Fig. 1a) and interaction between fatigue level and loading rate ($p=.006$) were significant.

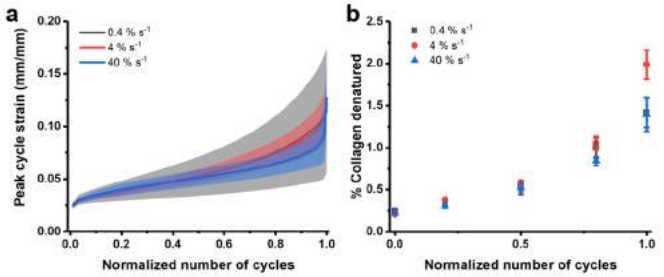

Figure 1. Normalized tissue creep (a; mean ± SD, n=10 each) and molecular damage (b; mean ± SEM, n≥5 each) due to fatigue loading. Neither the mean peak strain nor the amount of denatured collagen, as a function of normalized number of cycles, was significantly affected by strain rate.

Collagen model peptides subjected to simulated cyclic creep loading revealed that molecular strain and triple-helical unfolding, as indicated by increasing SASA, demonstrated similar strain-rate behaviors to experiments, where more loading cycles were required at faster loading rates to produce similar levels of peak cyclic strain and collagen denaturation (Fig. 2). Increased molecular strain and SASA with increasing loading cycles were observed for shear dominant, but not tension dominant loading.

DISCUSSION

A mechanism for the development of overuse tendon injury and a source for effective clinical treatment of these injuries remain elusive. We have demonstrated that tendon fatigue results in the accumulation of denatured collagen even at early levels of loading, suggesting that mechanical unfolding of the collagen triple-helix is a critical feature of fatigue damage. Both tissue level fatigue, indicated by creep strain, and fatigue damage to the collagen molecule evolve with increasing loading cycles. When normalized to cycles at failure, this evolution was independent of strain-rate, suggesting that creep strain accumulation determines fatigue damage and that collagen molecule unfolding may be a mechanism for the generation of creep strain.

The SMD results mirror the experimentally observed strain-rate dependent increase of creep strain and triple-helical unfolding with increased loading cycles. This demonstrates a possible molecular mechanism for tissue-level rate dependence of fatigue damage accumulation, and strongly indicates triple-helical unfolding as a foundational mechanism of tissue creep. Additional simulations of extended duration will enable us to assess molecular creep and SASA normalized to failure, to understand if simulated damage accumulation in isolated peptides further predicts tissue level observations. The stability of the collagen model peptide during simulated tension dominant loading, but unfolding due to shear dominant loading is in agreement with previous results demonstrating that shear load transfer via intermolecular crosslinks is the most likely mechanism for mechanical unfolding of the collagen molecule [4]. This suggests that the shear dominant loading mechanism is consistent for both monotonic and cyclic tension loading.

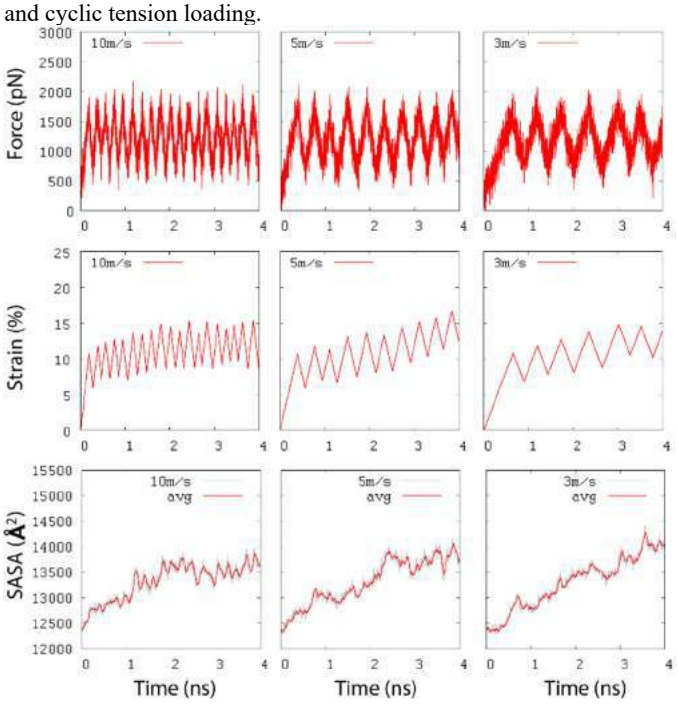

Figure 2. Applied force (top), measured strain (middle), and solvent accessible surface area (bottom) for the collagen model peptide subjected to simulated creep fatigue loading at 3, 5 and 10 m/s displacement rates. Consistent with tissue level experiments, individual molecules require more cycles to reach a similar level of creep strain or triple-helix unfolding at faster loading rates.

Our results support the hypothesis that molecular level collagen damage is fundamental to the initiation and progression of fatigue damage in tendon. Furthermore, progressive accumulation of collagen damage throughout fatigue supports the hypothesis that overuse injuries involve loading-induced damage to collagen that outpaces the remodeling capacity of the tissue, providing both a mechanistic explanation for micro-damage accumulation and a potential clinical target for the treatment and prevention of overuse injuries.

ACKNOWLEDGEMENTS

NIH F31EB023086 (JLZ). NIH R01AR071358 (JAW and SMY). ONR N00014-16-1-233 and NIH U01 EB014976 (MJB).

REFERENCES

[1] Leadbetter, W. B. *Clin Sports Med,* 11: 533-578, 1992. [2] Fung, D. T. et al. *J Biomech,* 43: 274-279, 2010. [3] Li, Y. et al. *Bioconjug Chem,* 24: 9-16, 2013. [4] Zitnay, Jared L. et al. *Nat Commun,* 8: 14913, 2017. [5] Lin, A. H. et al. *J Orthop Res*, 2018.

SB³C2019
Summer Biomechanics, Bioengineering and Biotransport Conference
June 25 -28, Seven Springs, PA, USA

COLLAGEN DENATURATION OCCURS UPON TISSUE FAILURE IN ENERGY STORING TENDONS

Allen H. Lin (1,2), Jared L. Zitnay (1,2), Alexandra N. Allan (1,2), Jeffrey A. Weiss (1,2,3)

(1) Department of Biomedical Engineering
University of Utah
Salt Lake City, UT, USA

(2) Scientific Computing and Imaging Institute
University of Utah
Salt Lake City, UT, USA

(3) Department of Orthopaedics
University of Utah
Salt Lake City, UT, USA

INTRODUCTION

Denatured collagen arises in many debilitating injuries and diseases involving connective tissues. Recently, our group has shown that permanent collagen denaturation can occur and accumulate in rat tail tendon fascicles at sub-failure levels of mechanical loading. This was the first study to definitively show that mechanical overload of musculoskeletal tissues causes permanent collagen denaturation at the molecular level [1]. However, there are differences in the structure, composition and function of different tendon types, which can be broadly categorized into either positional or energy storing tendons. The former includes tail and extensor tendons, while the latter includes the Achilles, patellar, and flexor tendons. These two tendon types differ mainly in their fibril type and the degree and type of crosslinking. Energy storing tendons have fibrils that exhibit high strain stiffening and resistance to molecular disruption, while positional tendons are more susceptible to molecular disorder upon rupture [2]. Furthermore, energy-storing tendons have trivalent crosslinks and exhibit a significantly greater crosslink density than positional tendons, whose crosslinks are divalent in nature [2,3].

A tool that has recently come to our disposal to study denatured collagen is collagen hybridizing peptides (CHPs). CHPs are short polypeptide chains that mimic the Gly-Pro-Hyp sequence of native collagen. Consequently, CHPs bind selectively with unfolded, denatured collagen strands, but not intact collagen. By using carboxyfluorescein bound CHPs (F-CHP), one is able to visualize the spatial distribution of denatured collagen. Additionally, the amount of fluorescence from F-CHPs is directly indicative of the amount of denatured collagen [4]. This study sought to characterize the evolution of denatured collagen in an energy storing tendon relative to applied strain at the tissue level. We hypothesized that denatured collagen in energy storing tendons will exhibit lower levels of denatured collagen but with the same trend as positional tendons, due to increased levels of crosslinking resisting inter-molecular sliding of the collagen α-helices.

METHODS

Rat tail tendon (RTT) fascicles were dissected from 8-week old male Sprague-Dawley rats. The samples were mechanically damaged by applying a preload of 0.03 N and stretching them in uniaxial tension to strains of 0, 5, 7.5, 9, 12, and 13.5% (n=3 for each strain group) at a rate of 0.5%/s. Rat flexor digitorum longus (FDL) tendons were dissected from the hind legs of 12-16 week old male Sprague-Dawley rats and clamped using sandpaper covered grips and cyanoacrylate. The average initial cross-sectional area was measured using an optical micrometer. After applying a preload of 0.03 N, the rat FDL tendon samples were stretched in uniaxial tension to 0, 5, 10, 12.5, 15, 17.5, 20, 22.5, 25, 27.5, and 30% strain (n=3 for 25 and 27.5% strain groups, n=5 for all other strain groups) at a rate of 0.5%/s. All mechanical tests were performed at room temperature in 1xPBS.

All samples were unloaded from the clamps and stained in 15 μM F-CHP (3Helix, Inc.) overnight at 4°C with gentle agitation. The samples were rinsed three times for 30 minutes with 1xPBS to remove unbound F-CHP. The unloaded regions of all samples were trimmed off, leaving the region subjected to tensile loading. These samples underwent proteinase K digestion as per our published protocol [4], and the fluorescence of the digest was measured in a 96-well plate using a microplate reader. The amount of fluorescence from F-CHP is directly indicative of the amount of denatured collagen in the sample.

Mean stress-strain curves for 13.5% strain and 30% strain were calculated for RTT fascicles and FDL tendons, respectively. The strain in the stress-strain curves for both tendon types was normalized to the strain at which the ultimate tensile strength (UTS) occurred. The strain values corresponding with each fluorescence measurement were also

normalized to the UTS strain. The F-CHP fluorescence at each strain level for both tendon types was calculated as a percent increase from the fluorescence of the unloaded controls (baseline).

Statistical analysis was performed by comparing the mean fluorescence of each strain group with the 0% unloaded controls within both tendon types using a two-tailed t-test. Significance was set at α=0.05.

RESULTS

The mean fluorescence of mechanically damaged rat FDL tendons was significantly greater than the unloaded control group for each strain group. This indicates that there was some amount of collagen denaturation at all strain levels. However, the amount of F-CHP fluorescence and by extension denatured collagen did not increase and accumulate until reaching the UTS, where the percent increase rises from 200% to 1300% relative to baseline. In contrast, for RTT fascicles, mean fluorescence for strain groups greater than 5% were significantly greater than the unloaded control group (Figure 1). Unlike the FDL tendons, the percent increase of F-CHP fluorescence increases until the UTS strain, where there is no further increase. The percent increase peaked at 1000% greater than baseline (Figure 1). The mean maximum stress for FDL tendons was 34.5 MPa and occurred at a strain of 19.90%. The mean maximum stress for RTT fascicles was 17.7 MPa and occurred at a strain of 10.62% (Figure 2).

DISCUSSION

F-CHP staining of energy-storing rat FDL tendons stretched to incremental strains revealed that while small amounts of denatured collagen accumulated at moderate strains, there was not any large increase in denatured collagen until initial failure of the tissue. This differs from RTT fascicles, a positional tendon, where the amount of denatured collagen accumulated until reaching the UTS and remains constant. Despite these differences in the accumulation of denatured collagen relative to the strain at UTS, the results demonstrate that mechanical overload of both tendons eventually gives rise to denatured collagen. These results are consistent with Chambers et al. [3], who reported increased molecular disruption as measured by differential scanning calorimetry in energy storing tendons. Notably, they observed this at low strain rates (1%/s), whereas at high strain rates (10%/s), there was minimal molecular disruption. Our study used a strain rate of 0.5%/s, so the results correspond with the former case.

The differences in the accumulation of collagen molecular damage between positional and energy storing tendons may be a result of the increased levels of crosslinking in energy-storing tendons [3]. Specifically, the divalent crosslinks found in positional tendons are more susceptible to intermolecular sliding of the collagen molecule during tension, while the trivalent crosslinks in energy storing tendons allow the collagen molecules within the fibrils to resist molecular sliding. The stabilization due to trivalent crosslinking prevents denaturation of the collagen molecule and unravelling of the α-chains, which is necessary for CHPs binding. Therefore, extension of the tissue occurring due to stretching of the crosslinks and their attached α-chains [5].

Interestingly, the percent increase in F-CHP fluorescence and by extension denatured collagen relative to baseline was on the same order of magnitude between RTT fascicles and rat FDL tendons (1000% vs 1300% increase). This suggests that the while the onset and mechanisms differ between the two tendon types, the incremental change in the amount of denatured collagen that eventually accumulates during tensile overload is similar.

ACKNOWLEDGEMENTS

Financial support from NIH #R01AR071358 is gratefully acknowledged. Imaging was performed at the Fluorescence Microscopy Core Facility at the University of Utah. Microscopy equipment was obtained using a NCRR Shared Equipment Grant # 1S10RR024761-01.

REFERENCES

[1] Zitnay, J et al., *Nat. Commun.* 8:14913, 2017. [2] Quigley, A et al., *Sci. Rep.,* 8:4409, 2018. [3] Chambers, N et al., *J. Orthop. Res.* 36(11):2842-2850, 2018. [4] Lin, A et al., *J. Orthop. Res.* In Print, 2018. [5] Herod, T et al., *Acta Biomater.* 42:296-307, 2016.

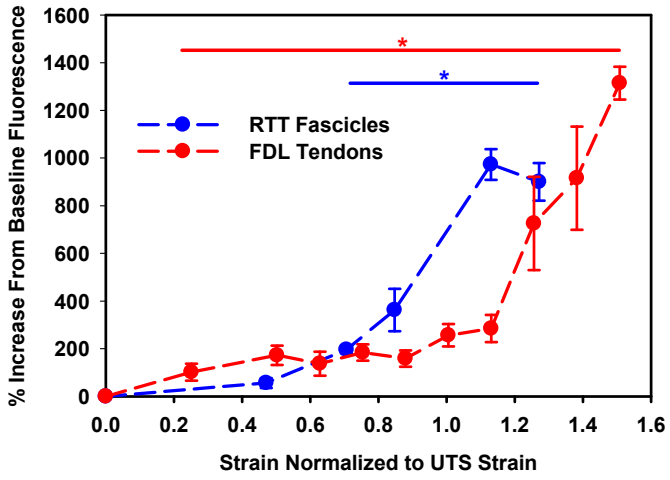

Figure 1: Percent increase in CHP fluorescence relative to baseline fluorescence as a function of strain normalized to the strain at UTS. Blue – RTT fascicles (n=3 for each group, Mean±SEM). Red – FDL tendons (n=3 for 25 and 27.5% groups, n=5 for all other group, Mean±SEM). *Significantly greater fluorescence than unloaded controls (α=0.05).

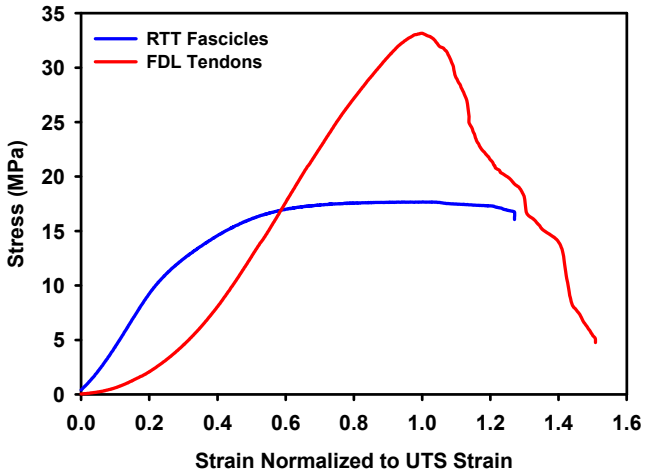

Figure 2: Mean stress-strain curves for RTT fascicles stretched to 13.5% strain (blue) and FDL tendons stretched to 30% strain (red). Strain is normalized to the strain at UTS for both tendons.

SB³C2019
Summer Biomechanics, Bioengineering and Biotransport Conference
June 25 -28, Seven Springs, PA, USA

METABOLIC ACIDOSIS CAUSES PHYSIO-CHEMICALLY INDUCED MECHANICAL AND COMPOSITIONAL CHANGES TO MURINE BONES

K. Morozov (1), B. Wingender (1), A. Peterson (1), A. Deymier (1)

(1) Dept. of Biomedical Engineering
UConn Health
Farmington, CT, United States

INTRODUCTION

Over 30 million US adults are diagnosed with chronic kidney disease (CKD) each year. CKD is characterized by a slow degradation of the kidneys leading to insufficient acid secretion and dysregulation of bicarbonate (HCO_3^-) levels in the blood [1]. Without the ability to regulate the body's acid/base balance nearly half a million CKD sufferers will develop metabolic acidosis, a drop in blood pH below 7.35, annually [2].

Without the kidneys to regulate body pH during CKD induced acidosis, the primary method of physiological buffering becomes bone resorption and dissolution. Half of bone mass is composed of a carbonate substituted apatite containing PO_4, Ca, CO_3, and Na. Upon onset of acidosis, bone dissolution begins via physio-chemical dissolution as well as activation of bone resorbing osteoclast bone cells. In both cases, the dissolution process results in the release of alkaline carbonate and phosphate containing moieties that buffer the excess acid [3]. Although bone dissolution is advantageous to the regulation of CKD induced acidosis, it can also lead to significant bone loss, osteopenia and osteoporosis, and increased fracture risk.

Establishing what occurs during the early stages of metabolic acidosis and how the mechanical properties of bones change on a shortened time scale in the pursuit of acid/base equilibrium will be substantial to developing our knowledge of musculoskeletal pH regulation. This information will serve as a platform on which to develop therapeutics to combat the earliest signs of irreparable musculoskeletal damage due to acid buffering.

METHODS

80 5-6 month-old male CD-1 mice were separated into 4 groups. The first three groups were given modified drinking water containing 0.2 M ammonium chloride (NH_4Cl) for 1, 7, and 14 days. The control group was provided with normal drinking water. After the appropriate time of acid exposure, submandibular blood draws were performed to determine blood gas concentrations after which the mice were sacrificed. Each mouse was dissected to collect he left and right femurs and supraspinatus-humerus (SH) tendon-bone complexes. Femur and SH complex samples were then analyzed via mechanical testing, micro-computed tomography (μCT), histology, and Raman spectroscopy.

For histological analysis, unfixed SH complexes were cut down to the tendon-to-bone attachment site and mounted in OCT. The samples were sectioned into ~10 μm sections using a cryostat and stained using Toluidine blue and Von Kossa. Light micrographs were taken using a Nikon Eclipse TE300 microscope. Thickness of the mineralized and unmineralized fibrocartilage layers was measured using Image J.

Both SH complexes and femurs were imaged via μCT and tested mechanically. For μCT imaging, the femurs were scanned after mechanical testing at a resolution of 12 μm in a SCANCO 40 system. The SH complexes were positioned such that humeral head pointed down which allowed the tendon to hang freely to obtain tendon cross-sectional area prior to mechanical testing. The X-ray reconstructions were analyzed to obtain bone volume/total volume (BV/TV), the cross-sectional area of the tendon, and the moment of inertia of the femurs.

Mechanical testing was done on femurs, by 3-point-bending, and SH complexes, by tensile testing, using a Mach-1 (Biomomentum, Inc.) uniaxial tensile tester with a 25-kg load cell. In both cases, samples were tested while submerged in PBS at 37ºC to simulate in-vivo bone mechanics. Femurs were tested in a standard three-point bending mount such that the medial side underwent tensile loading. The SH complex was loaded in tension using custom made 3D printed grips. The grips consisted of a bottom mount containing a bone shaped inclusion that restricted vertical movement of the humeral head to minimize the risk of growth plate failure, and a top mount consisting of a toothed clamp to secure the supraspinatus tendon. In both case, loads were applied at

constant rate until failure. The Mach-1 system provided force vs. displacement for all samples from which we calculated maximum load/stress, yield load/stress, stiffness, post-yield displacement, and the energy to failure using the µCT data.

For Raman analysis, intact femurs were cleaned of soft tissue and analyzed via a Witec alpha300 system. Carbonate levels were determined from the ratio of the 1070/960 Δcm^{-1} peak areas. Mineral:matrix ratios were determined from the 960/1030 Δcm^{-1} ratios. All measurements were made at the medial midshaft. Statistical analysis was done using one-way ANOVA tests, Tukey tests, as well as two-tailed t-tests.

RESULTS

Blood gas results indicate that ammonium chloride treatment resulted in a significant drop in pH for mice after 1 day, accompanied by a decrease in bicarbonate. This is recovered after 7 days despite continued acid loading, Fig 1. Mechanical testing showed no change in the mechanics of the SH complexes after acidosis induction. The femurs showed no change in elastic properties. However, they did exhibit a significant increase in work-to-fracture and post-yield-displacement at 7 days compared to control, Fig. 2.

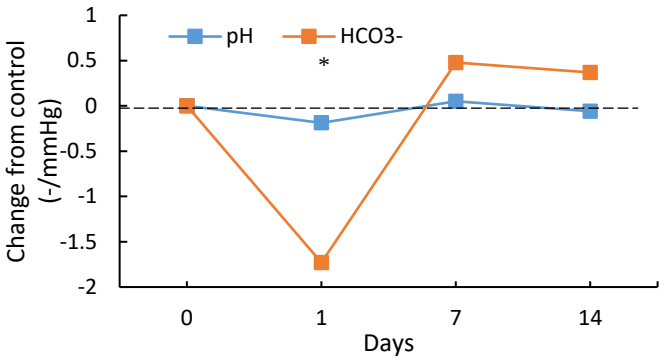

Figure 1: Standardized Changes of pH and Bicarbonate

Structurally, the tissues showed very little changes. µCT analysis showed no change in BV/TV for either the humeral head or the femoral midshaft. Similarly, measurements of mineralized and unmineralized fibrocartilage thickness at the SH attachment site from histology showed no change with acidic diet. Compositionally, both mineral:matrix and bone mineral carbonate levels were shown to decrease in the midshaft of femurs exposed to 7 days of NH_4Cl doped water.

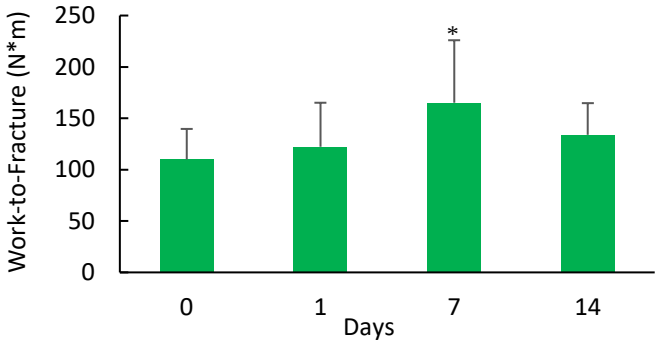

Figure 2: Mechanical Measurements of Mouse Femurs

DISCUSSION

The blood gas data confirmed that the addition of NH_4Cl to the water had induced metabolic acidosis in the mice as demonstrated by the pH and bicarbonate drop at 24 hours, Fig 1. However, despite continuous NH_4Cl administration in the mice, the pH was returned to baseline by day7 indicating that kidney function and bone dissolution were able to overcome the excess acid loading.

Previous studies have shown that induction of acidosis leads to both physio-chemical and cell-mediated bone dissolution[3]. We therefore expected that the addition of an acidic diet would lead to measurable bone loss. However, µCT analysis showed no change in BV/TV of the trabeculae in the humeral head nor the midshaft of the femur. This lack of change in the bone mass, indicated that dissolution or cellular resorption had no measurable effect on the quantity of bone present after short-term acidosis. Although this lack of change may be due to the low resolution of the µCT data, it is further supported by the histological data that indicates that there is no change in the thickness of the mineralized fibrocartilage at the SH attachment site.

Regardless of the lack of change in bone mass, the femur did exhibit a change in plastic mechanical behavior after 7 days of acidic diet. Both the post-yield displacement and the work-to-fracture increased in the 7 day mice indicating that these femurs had become tougher with acidic diet. An increase in bone toughness is usually indicative of a change in collagen quality or a decrease in bone mineral content. The later hypothesis is supported by the fact that Raman measurements indicate a decrease in the mineral:matrix ratio of the femoral midshaft. Together, these results suggest that acidosis may initially lead to a decrease in bone mineral content but not a loss in bone mass. Since osteoclasts are known to remove both mineral and collagen during the resorption process, this may indicate that physio-chemical dissolution of the bone serves as the primary mode of dissolution in short-term acidosis. In addition, the drop in mineral carbonate content supports the theory that carbonated bone mineral is preferentially dissolved to increase the bone's buffering abilities.

It is also interesting to note that the change in mechanical properties is delayed compared to the time of acidosis. The blood gas results indicate that even with an early induction of acidosis, the animals are able to recover between days 1 and 7. Despite this, bones at 7 days display modified mechanics and composition. This suggests that there may be a delay in bone dissolution relative to the start of acidosis or that continuous dissolution is necessary to recover a healthy pH.

The SH complex had been selected as a tissue of interest because the mineralized tendon attachment site does not contain bone resorbing cells; therefore, it could probe for physio-chemical dissolution without cellular participation. However, unlike the femur there were no changes in the SH mechanical properties. The lack of statistical significance may be due to the SH requiring involvement of the bone, tendon, and cartilage in the tension tests. Participation of the compliant soft-tissues may have made it difficult to measure small changes in the bone; therefore, acidosis may have affected the SH in a manner too sensitive to be recorded in our data collection.

Generally, we conclude that buffering of acidosis via physio-chemical bone dissolution had a significant effect on the bone mechanics by modifying the bone mineral content.

ACKNOWLEDGEMENTS

Funding was provided by Dr. Deymier's Startup at UConn Health. This research used the resources provided by UConn Health's Histology Core and Micro CT lab as well as Dr. David Rowe's cryostat machines. We would like to acknowledge Iden Kurtaliaj and Steve Thomopoulos at Columbia University for their assistance in sample prep.

REFERENCES

1. Prevention, C.F.D.C.a.P., *National Chronic Disease Fact Sheet*, U.S.D.o.H.a.H. Services, Editor. 2017
2. Kraut, J.A., et al. American journal of kidney diseases : the official journal of the National Kidney Foundation. **45**: p. 978-93
3. Krieger, N.S., et al. Current Opinion in Nephrology and Hypertension. **13**: p. 423-436

SB³C2019
Summer Biomechanics, Bioengineering and Biotransport Conference
June 25 -28, Seven Springs, PA, USA

EFFECT OF HYDRATION ON MECHANICAL PROPERTIES OF INDIVIDUAL COLLAGEN FIBRILS AND EXTRAFIBRILLAR MATRIX

Heber Martinez Barron, Wei Gao, and Xiaodu Wang

Mechanical Engineering,
University of Texas at San Antonio,
San Antonio, Texas, USA

INTRODUCTION

Bone is a natural composite material with a hierarchical structure consisting of three major components: mineral, organic matrix, and water. The mineral phase is considered to provide the strength and stiffness; whereas the organic matrix (collagen fibrils and non-collagenous protein matrix) is deemed to influence the toughness of bone. In addition, previous studies have shown removal of water (dehydration) from bone may lead to a significant decrease in the toughness and increase in the stiffness of bone, suggesting water plays a pivotal role in the mechanical behavior of bone [1,2].

Water is present in three different compartments in bone matrix: freely mobile water in pores, such as Haversian canals, canaliculi, and lacunae spaces; bound water at the surface of the collagen fibrils and between the collagen and mineral phase; and structural water as part of collagen and mineral molecules [3]. Water in every compartment contributes to different mechanical properties of the bone. From Granke et al [2], it has been found that amount of freely mobile water in pores correlates with the stiffness of bone, whereas bound water contributes to bone's ductility. Moreover, structural water, although its functional significance is not clear, may play a role to stabilize collagen conformation and assembly. It is known that bound water is present in both mineralized collagen fibrils (MCF) and extrafibrillar matrix (EFM). However, it is not clear on how bound water would affect the *in situ* mechanical behavior at the ultrastructural compartments. Therefore, continuing studies on nanomechanics of bone at ultrastructure levels will clearly define the role of water at these different ultrastructural compartments.

In this study, we investigated the effect of bound water on the mechanical properties (modulus and energy dissipation) of individual MCF and EFM under both dry and wet conditions using a high-resolution atomic force microscopy (AFM) system and associated techniques.

METHODS

Bone slices were prepared from a cadaveric femur of a mid-aged female donor. The slices were dissected transversely to the longitudinal direction of the diaphyseal femur. Cortical bone cores (8 mm in diameter) were first extracted from the posterior aspect of the cross section within the mid-diaphysis of the femur. Then, the cores were cut into 1.0 mm thick slices using a low-speed diamond saw with continuous irrigation of deionized water. Thereafter, both bone slices were lapped with successive grit of sand papers to the thickness of 0.1-0.2 mm, and polished using submicron alumina powder paste. The orientation of collagen fibrils in osteons was identified using cross polarized optical microscope such that AFM scans could be focused on the lamellae that contained collagen fibrils oriented parallel only to the direction of the osteon axis.

To ensure wet conditions, a 3D-printed chamber was devised to partially submerge samples in water during AFM testing. Deionized water was used to hydrate the samples for at least 60 minutes before testing. For testing under both dry and wet conditions, Peak force tapping (PeakForce QNM) AFM method was used to capture the surface topography as well as other mechanical properties, such as adhesion, deformation, elastic modulus, and energy dissipation. Samples were imaged using RTESPA-150 (Bruker, Santa Barbara, CA) cantilevers with a nominal spring constant of 5N/m, and a tip radius of 10 nm. For imaging purposes, height, peak force error, modulus, and adhesion channels were used to identify the regions of MCF and EFM. For quantitative measurements, peak force curves at each location were captured with RTESPA-525 cantilever with a nominal spring constant of 200 N/m, and a tip radius of 18 nm.

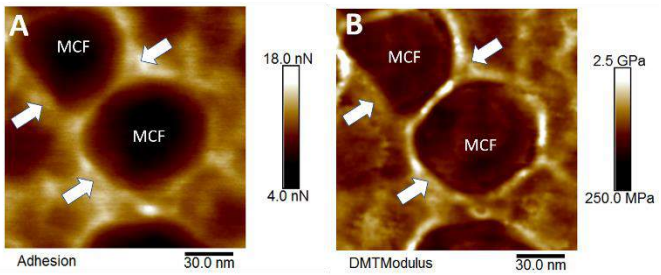

Figure 1. Adhesion(A) and DMT modulus (B) of AFM scans in the cross-section of bone indicate that the softer mineralized collagen fibrils (MCF) are surrounded by the harder EFM (white arrows).

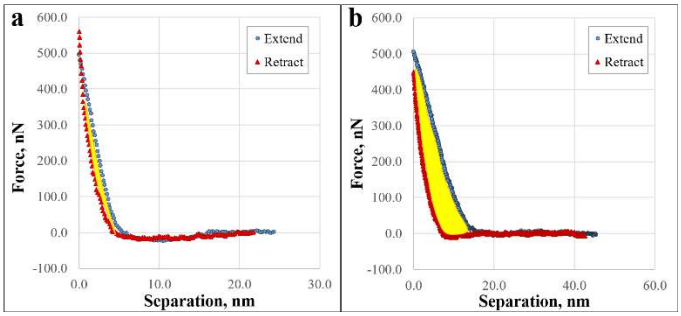

Figure 2. AFM force curves for mineralized collagen fibrils (MCF) and EFM under (a) dry and (b) wet conditions.

Approaching and retraction force curves of the MCF and EFM were recorded (**Fig 2**) using Nanoscope Analysis 1.9 software (Bruker). Young's modulus values were obtained from these curves and energy dissipation (yellow area between force curves) following the recommended models using a custom-written MATLAB script.

RESULTS

AFM scans on cross-sectional bone slices conducted in height, phase, modulus, and adhesion modes clearly demonstrated the ultrastructural features of MCF and EFM. The adhesion and modulus mapping results indicated that collagen fibrils, as a soft phase, were surrounded by a much harder EFM (**Fig.1** A-B), showing that the modulus of the EFM was about two times greater than that of MCF. The average nanoindentation modulus of MCF in the longitudinal axis was estimated to be in the range of 11.5 ± 0.29GPa. Comparing dry and wet conditions, there was about a 60% decrease in elastic modulus from dry to wet for both MCF and EFM ranging from 17.5-29.6GPa to 7.4-9.7GPa. EFM showed a higher energy dissipation (4.29±0.99mN-nm), approximately 30% more than that of MCF (3.32±1.28mN-nm) under wet conditions (**Table 1**).

DISCUSSION

The results showed that no significant differences in the elastic modulus (E) were observed between EFM and MCF under both dry and wet conditions, whereas E changed significantly from wet (7.4-9.7GPa) to dehydrated (17.5-29.6GPa) condition for both EFM and MCF. Such hydration dependent changes in elastic modulus are similar to the previous results obtained from bulk bone samples [4]. These results suggest that water plays a pivotal role in the elastic modulus and toughness of bone for both MCF and EFM. Under wet condition, EFM appears to be tougher (about 30% more) than that by MCF (3.32±1.28mN-nm) ($p < 0.05$). This implies that EFM contributes more to toughening of bone tissues *via* hydration. Both MCF and EFM under the dehydrated condition lost their capability for permanent energy dissipation (0.3-0.4mN-nm). This study provided important information regarding *in situ* mechanical properties of MCF and EFM, as well as their role in toughening of bone at ultrastructural levels.

Table 1. Experimental results under dry and wet conditions

		Sample No.	Elastic modulus (GPa)	Energy Dissipation (mN-nm)
MCF				
	Dry	01	17.5 ± 2.7	0.52 ± 0.42
		02	29.6 ± 8.5	
	Wet	01	7.4 ± 1.4	3.32 ± 1.28
		02	8.4 ± 1.7	
EFM				
	Dry	01	18.7 ± 2.4	0.77 ± 0.37
		02	21.5 ± 7.0	
	Wet	01	8.5 ± 1.9	4.29 ± 0.99
		02	9.7 ± 1.9	

ACKNOWLEDGEMENTS

The authors thankful to Mr. Juan Garduno and Joel Gomez for their assistance in sample preparations and 3D-printed chamber design, as well as Dr. Alexis Godet, who aided in the use of the cross-polarization microscope. In addition, this material is based upon work partially supported by the National Science Foundation under Grant No. 1538448. Any opinions, findings, and conclusions or recommendations expressed in this material are those of the author(s) and do not necessarily reflect the views of the National Science Foundation.

REFERENCES

[1] Jameson MW, Hood JA, Tidmarsh BG. *J Biomech*, 26(9):1055–65, 1993.

[2] Nyman JS, Anuradha R, Shen X, Acuna RL, Tyler JH, Wang X, et al. *J Biomech*, 39(5):931–8, 2006.

[3] Granke, M, Does MD, Nyman JS. *Calcif Tissue Int*, 97:292-307, 2015.

[4] Guidoni G, Swain M, Jager I. *Philos Mag* 90:553–565, 2010.

SB³C2019
Summer Biomechanics, Bioengineering and Biotransport Conference
June 25 -28, Seven Springs, PA, USA

EFFECTS OF EXERCISE AND POSTURE ON SUBCHONDRAL BONE DENSITY AND THICKNESS OF SHEEP

Hyunggwi Song (1), John D. Polk (2), Mariana E. Kersh (1,3)

(1) Department of Mechanical Science and Engineering
University of Illinois at Urbana-Champaign,
Urbana, IL, USA

(2) Department of Anthropology
University of Illinois at Urbana-Champaign,
Urbana, IL, USA

(3) Beckman Institute for Advanced Science and Technology
University of Illinois at Urbana-Champaign,
Urbana, IL, USA

INTRODUCTION

Subchondral bone is the thin layer of cortical bone that provides an interface transmitting loads between the articular cartilage and trabecular bone. The changes in subchondral properties enable to investigate differences in joint loading conditions in comparative biology, and in biomedical studies of the etiology of joint diseases such as osteoarthritis (OA) and osteoporosis. Previous studies have focused on describing patterns of the subchondral bone apparent density and relating it to inferred differences in joint load orientation and magnitude in humans [1,2] and primates [3]. However, many considerable questions remain to determine how and where the osteological changes occur due to habitual loading, and what properties of the subchondral bone respond best to 1) exercise in general, or 2) altered load orientations.

The primary goal of this study is to test whether subchondral bone density and thickness respond to experimentally induced differences in knee postures, and exercise.

METHODS

Thirty healthy juvenile sheep were used for this study beginning at the age of 60 days. Sheep were divided into three group: (i) flat treadmill exercise (0° grade; n=11), (ii) incline treadmill exercise (10° grade; n=11), and (iii) control (n=8). All the procedures were approved by the UIUC IACUC. Sheep from groups (i) and (ii) were first trained to walk on a motorized treadmill (Star Trac 4000HR, Star Trac, Irvine, CA) at moderate walking speeds and were exercised twice daily at 1.12m/s for 20 min/bout for 60 days. The duration of exercise has been shown a significant osteogenic response in sheep and other mammals [3, 4]. The control sheep were not exercised. All sheep were housed in a large indoor pen at the University of Illinois Sheep and Beef Cattle facility and were able to move freely. Access to food and water was not limited.

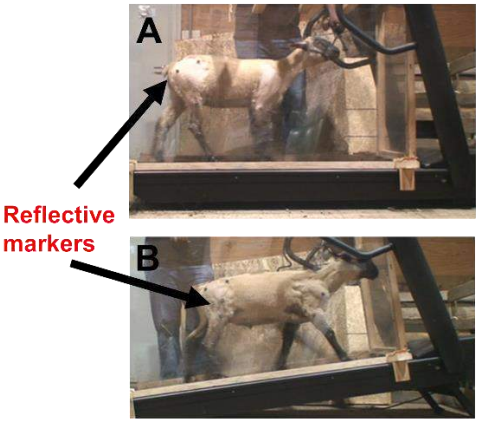

Figure 1: Sheep walking on treadmill: (A) Flat, and (B) Incline (10° grade).

Three-dimensional (3D) limb kinematic data were measured with a 6-camera Qualisys (qualisys.com) motion capture system at 160Hz. Kinematic data were collected for group (i) and (ii) only, since control group was not trained to walk on treadmill. Reflective markers were placed on standard hindlimb landmarks (Fig. 1). Joint angles were measured at mid-stance (the hoof is beneath the hip) when peak loads are experienced. All subjects were euthanized humanely, limbs were dissected, muscles and ligaments were removed, and their limb bones segments were frozen.

Subchondral bone thickness measurement was evaluated on the medial femoral condyle (MFC). Femora were scanned with microCT at 50µm voxel size using a Siemens Inveon microCT scanner

(siemens.com/inveon). Noise was removed using MATLAB (MathWorks Natick, MA, USA), and 3D representations created using AMIRA (v 6.4, Thermo Fisher Scientific, MA, USA). Each specimen was resliced through the long axis of the MFC to obtain images along the axis of the joint. Thickness data were obtained using the BoneJ plugin from imageJ. The thickness values were then extracted by fitting a contour line to the joint surface. The coordinate values were plotted in 3D surface plot in MATLAB by putting the thickness as a color matrix. Three hydroxyapatite (HA) phantoms were included in all scans (Model 092, CIRS) to convert Hounsfield Units to apparent HA density. All statistics were calculated in MATLAB with a type one error rate of α=0.05.

RESULTS

Exercised sheep experienced around 3600 more loading cycles per day than non-exercised sheep. On the incline walking, sheep used significantly more flexed knees ($p < 0.0001$) postures at mid-stance than on flat treadmills. The difference of mean knee joint angle was 8° between these two groups. A similar pattern of difference was observed when comparing the position of subchondral bone thickness between the groups of sheep. The position of the maximum subchondral thickness moved more posteriorly for the inclined group compared to flat group (Fig. 2). The maximum thickness region was distributed on the lateral-posterior subchondral bone, whereas the highest density was on the medial-anterior region. The thickness of exercise groups on the anterior region was significantly higher than that of the control group ($p<0.05$). Between flat and incline exercise groups, the flat group had a significantly higher thickness in some regions distributed over the surface than the incline group ($p<0.05$).

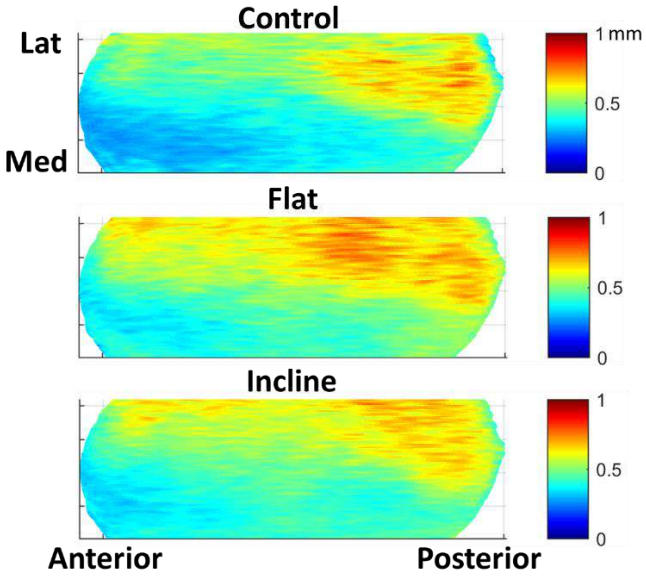

Figure 2: Averaged subchondral thickness maps of control, flat exercise, and incline exercise groups.

Also, in density maps, the medial-anterior regions in exercise groups had significantly higher density than in the control group, but it was relatively small area compared to the region that had a significant change in thickness (Fig. 3). There was no significant difference between density distribution of exercise and control groups ($p<0.05$).

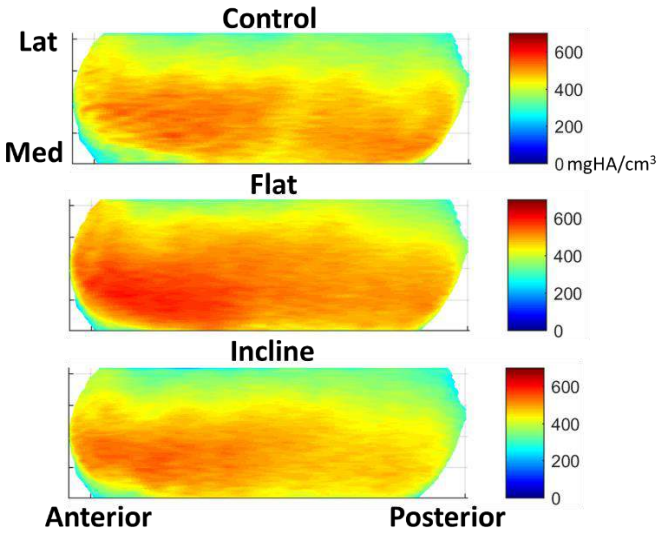

Figure 3: Averaged subchondral density maps of control, flat exercise, and incline exercise groups.

DISCUSSION

The objective of this study was to investigate whether the patterns of subchondral bone density and thickness could be affected by exercise and joint posture. Overall, there was an exercise effect on subchondral bone thickness and good correspondence between thickness-based measurement and kinematic results. As expected, higher subchondral thickness in exercised group was observed compared to control group. Also, flat group had larger area of significant thickness changes than incline group, suggesting that incline group might be loaded with smaller area on subchondral surface. On the other hand, subchondral density did not significantly respond to the loading from exercise in both flat and incline groups. Anterior subchondral thickness was significantly affected by the exercise, which had the maximum density, and this will be confirmed by analysis of range of motion of knee joint during each exercise in the future.

This is the first study that performed three-dimensional analyses of thickness and density on subchondral bone and in the future, investigating the effect of posture changes during exercise on thickness and orientation of trabecular bone, which is in deeper bone than the subchondral bone, will be done to conclude all the effects of exercise on bone. Understanding bone organization and composition, and their relationship to joint loading, will allow for the inferences relates to gait based on changes in bone as well as improvements in exercise regimens aimed to restore function after disease or injury.

ACKNOWLEDGEMENTS

This research was completed with the support of the National Science Foundation grant.

REFERENCES

[1] Schulz, et al., *Clin Orthop Relat Res*, 423:259-263, 2004.
[2] Schulz, et al., *J Shoulder Elbow Surg*, 11:174-181, 2002.
[3] Polk, et al., *Anat Rec*, 291:293–302, 2008.
[4] Robling, et al., *J Bone Miner Res*, 17:1545–1554, 2002.

SB³C2019
Summer Biomechanics, Bioengineering and Biotransport Conference
June 25 -28, Seven Springs, PA, USA

STATISTICAL SHAPE ANALYSIS FOR THE ASSESSMENT OF PROXIMAL FEMUR SHAPE FEATURES MEANINGFUL TO OSTEOPOROTIC RISK OF FRACTURE

Alessandra Aldieri (1), Mara Terzini (1), Cristina Bignardi (1), Alberto L. Audenino (1), Umberto Morbiducci (1)

(1) Polito^{BIO}Med Lab, Department of Mechanical and Aerospace Engineering, Politecnico di Torino
Torino, Italy

INTRODUCTION

Osteoporosis, a metabolic disorder which entails the reduction of bone density in terms of reabsorption and thinning of bone trabeculae, results in an altered bone strength which increases the risk of fracture. Among osteoporotic fractures, hip fracture represents a major economic and social burden in western countries [1], dramatically affecting quality of life and increasing mortality. A clinical prediction strategy accounting for specific elements of the osteoporotic patient's clinical presentation, able to assist clinicians in forming a judgment regarding treatment outcome, is therefore mandatory. At present, osteoporosis is diagnosed using Bone Mineral Density (BMD), measured through dual energy X-ray absorptiometry (DXA). Unfortunately, its predictive ability remains limited. Aiming to improve the standard diagnostic process, hip geometric features have been recently proposed as fracture predictors, although a consensus has not been achieved yet [1,2]. This study explores the risk of fracture predictive potency of specific femur shape features identified by applying a statistical shape modelling approach. The proposed approach promises to contribute to gain further insights in the role played by geometry in osteoporotic risk fracture.

METHODS

Statistical shape modelling framework Two-dimensional profiles of proximal femur were reconstructed from DXA images of twenty eight post-menopausal women. On reconstructed geometries, realigned along their shaft axes, shape analysis was carried out within the non-parametric statistical shape modelling framework proposed by Durrleman et al. [3] and implemented in *Deformetrica* (www.deformetrica.org). The first step of the analysis involves the generation of a template $\overline{\mathrm{T}}$, which represents the mean anatomical shape, from the input subject-specific shapes. Subsequently, following a forward approach [3], $\overline{\mathrm{T}}$ is mapped to each single shape T_i in the dataset, so that each T_i can be described in terms of a subject-specific transformation function ϕ_i deforming the template $\overline{\mathrm{T}}$, and by some residuals ε_i, representing features not accounted for by the deformed template:

$$\mathrm{T}_i = \phi_i \cdot \overline{\mathrm{T}} + \varepsilon_i \quad (1)$$

The individual deformation functions ϕ_i are numerically parametrized by so-called moment vectors.

Shape analysis The existence of possible associations among shape features and the risk of an hip fracture was here explored applying the Partial Least Square (PLS) regression method. PLS could indeed estimate the optimal subspace best explaining both the observed shape variance and its covariance with an external variable [4]. Here, the moment vectors parameterizing the subject-specific template deformations were gathered in an $N \times 2r$ matrix X of PLS predictors, N being the number of subjects, r the number of moments, defined as x-y pairs; PLS was thus carried out to identify deformation modes most relevant to Risk Factors (RF) derived in a previous study [2], where FE analyses on three dimensional models of the same patients were performed reproducing a sideways fall condition and the RF assessed using a principal strains based criterion. A subset of q PLS modes accounting for the 95% of the shape and RF sample variance was then considered among those previously identified. Afterwards, in order to obtain a numerical representation of each patient's collection of shape features, shape vectors $\boldsymbol{t}^i = \{t^{i,m}\}_{m=1,\dots,q}$ were derived projecting the r moment vectors onto the PLS subspace defined by the q selected modes. Shape vectors quantify how much the shape features contained within the mth mode are included in the ith patient [4]. The q shape vectors were then correlated with the response variable RF, as well as with standard

geometric descriptors [2]. Pearson correlation coefficient and Kendall's τ were calculated on normally and non-normally distributed variables, respectively. Eventually, Canonical Correlation Analysis (CCA) was applied on the shape vectors. It allowed to evaluate how much each mode correlates with the RF and consequently to estimate the deformations to be applied to the template for predicting the shape corresponding to a given RF [4]. Indeed, new moment vectors β_{RF} were calculated using CCA outputs as follows:

$$\beta_{RF} = \bar{\beta} + \frac{RF - \overline{RF}}{\sigma_{RF}} R \sum_k \rho[k] \boldsymbol{p}^k \quad (2)$$

where $\bar{\beta}$ is the average sample moment vector, $\overline{RF}$ the average RF value, σ_{RF} the RF standard deviation, and $\boldsymbol{p}^k$ the k^{th} deformation mode. R and $\boldsymbol{\rho}$, the CCA outputs, are the overall correlation coefficient and the array containing the individual correlations between each k^{th} deformation mode and the RF, respectively.

RESULTS

It was found that 11 PLS modes were necessary to describe 95% of the RF variability and 97% of the shape variability, the first 4 modes accounting for 90% of the shape variability observed in the sample. The first mode turned out, as expected [4], to be the most correlated with RF (Fig. 1), but it represents, at the same time, the most relevant mode with respect to the hip axis length (r = -0.68, $p < 0.001$), narrow neck width (τ = -0.45, $p < 0.001$) and intertrochanter width (r = -0.29, $p < 0.01$). Moreover, it accounts for 24.8% of the shape and 27.5% of the RF variability. As for the neck shaft angle, it was found to be almost equally correlated with the second and third PLS modes (II mode: r = 0.52, $p < 0.01$; III mode: r = 0.52, $p < 0.01$). CCA returned an highly correlated model (r = 0.97, $p < 0.001$), used to predict the shapes associated to an increased or decreased RF ($\pm 2\sigma$) with respect to its average value (Fig. 2). As can be observed by visual inspection, although slight variations in the hip axis length can be appreciated, the most relevant changes pertain to the neck shaft angle and the narrow neck width.

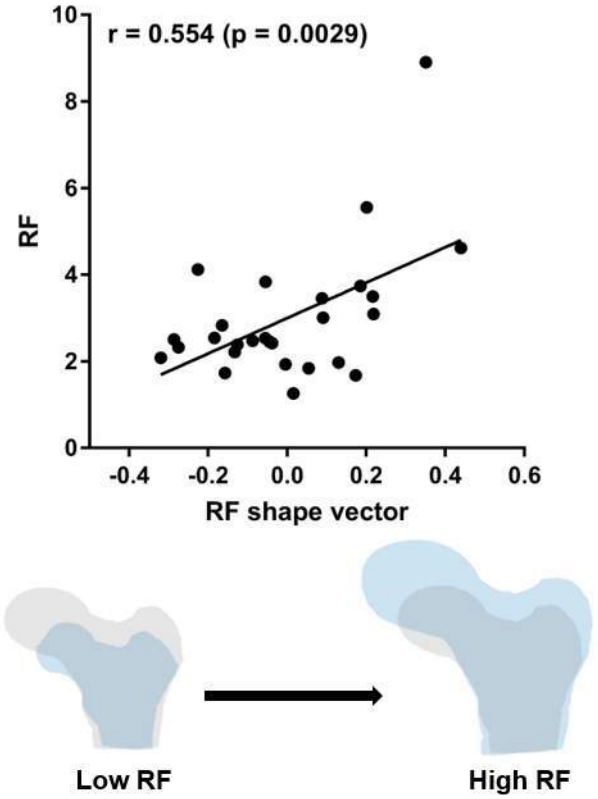

Figure 1: Correlation between the RF shape vector (associated to the first PLS mode) and RF. Below, visual assessment of the template (in grey) and of its deformations along the first PLS mode (in blue).

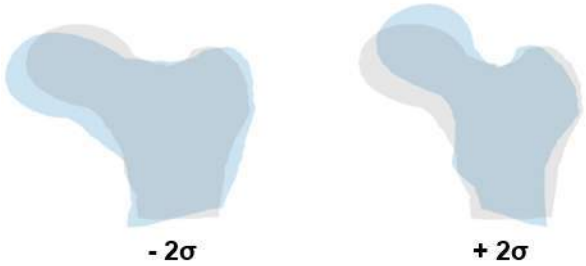

Figure 2: Template shape (in grey) superimposed on shapes predicted using CCA moment vectors and corresponding to a 2σ increased (right) and decreased (left) RF (in blue).

DISCUSSION

A statistical shape modelling approach has been here adopted to investigate the role played by geometry in the context of osteoporotic hip fracture risk. The approach was able to identify PLS modes properly capturing the dataset shape variability relevant to femur rupture risk, enforcing the predictive potency of standard DXA geometric variables. Among the limitations that could weaken the findings of this study, the limited number of patients involved, the two-dimensional proximal femur geometries investigated, and the biased input data, derived only from post-menopausal women. Nevertheless, in spite of the cited intrinsic limitations, the method appears promising to become a diagnostic tool for increased fracture risk prediction from femur shapes, providing clinicians with an empowered instrument supporting their decision. From this perspective, larger datasets will undoubtedly enhance the reliability of the models predictive power. Due to the encouraging results obtained from 2D shapes, easily achievable from available clinical images, the same approach could also be successfully applied on the 3D geometries derived from CT scans [2], not only aiming to assess the relation between 2D and 3D PLS shape patterns relevant to rupture risk, but also due to the possibility to predict 3D patient-specific shapes, not otherwise commonly accessible for osteoporotic patients using DXA derived data.

To the authors' knowledge, this represents the first study to adopt this approach in the field and it strongly corroborates the particular relevance of narrow neck width, hip axis length and neck shaft angle for fracture risk prediction, on which a consensus has not been accomplished yet [1,4].

ACKNOWLEDGEMENTS

The authors would like to thank Giangiacomo Osella, M.D., AOU San Luigi Gonzaga Hospital, Department of Internal Medicine, for the clinical data collection and Luca Rinaudo, Technologic S.r.l., Torino, Italy for his helpful collaboration.

REFERENCES

[1] Marks, R. et al., *Ageing Res Rev*, 2.1:57-93, 2003.
[2] Aldieri, A. et al., *J Biomech Eng*, 140.11, 2018.
[3] Durrleman, S. et al., *NeuroImage*, 101:35-49, 2014.
[4] Mansi, T. et al., *IEEE transactions on medical imaging*, 30.9:1605-1616, 2011.

NONDESTRUCTIVE MAPPING OF 3D BONE-IMPLANT CONTACT AND 3D PERI-IMPLAT STRAIN

Yuxiao Zhou (1), Chujie Gong (2), Mehran Hossaini-Zadeh (3), Jing Du (1)

(1) Department of Mechanical and Nuclear Engineering, The Pennsylvania State University, University Park, PA, USA

(2) Department of Biomedical Engineering, The Pennsylvania State University, University Park, PA, USA

(3) Department of Oral Maxillofacial Pathology, Medicine and Surgery, Temple University, Philadelphia, PA, USA

INTRODUCTION

Bone-implant biomechanics influenced implant stability and peri-implant healing [1]–[3]. The biomechanics of the bone-implant construct, including mechanical strain, is affected by many factors, including bone morphology [4]–[6] and mineral density [7]. Mechanical testing coupled with micro-CT was performed on dental implants that were placed in cadaveric mandible specimens to reveal relations of the bone-implant biomechanics and bone-implant contact areas. The contact area and mechanical strain in multiple bone-implant constructs were measured based on the micro-CT images. Strain distribution patterns in different specimens with different bone-implant contact areas were compared. The implications of the results on dental implant stability were discussed.

METHODS

In situ mechanical testing coupled with micro-CT were performed to nondestructively characterize 3D full-field bone-implant contact and peri-implant strain concurrently [8], [9]. Cadaveric specimens of human mandibles were obtained (IRB exempted), sectioned and imbedded. Selected teeth were extracted from each specimen and dental implants were placed immediately. A quasi-static compressive load of 100 *N* was applied to the implant through a mechanical tester (CT5000, Deben UK Limited, Suffolk, United Kingdom) to simulate the normal chewing and biting force. Micro-CT scans (Phoenix v|tome|x L300 multi-scale nano/microCT system, GE, Boston, MA) were carried out before and after loading, respectively. Micro-CT images were obtained and processed (Avizo, FEI Visualization Sciences Group, Burlington, MA) to calculate the 3D bone-implant contact areas. The displacement and strain field in the mandible bone were also calculated by digital volume correlation (DVC) of micro-CT images with and without loads (DaVis software, LaVision, Goettingen, Germany). Strain distributions in the peri-implant bone with different bone-implant contact areas were compared.

RESULTS

The dental anatomy and implant-bone morphology can be observed from the micro-CT images (Fig.1). In a transverse slice of micro-CT images for one specimen, the mismatch of the cross-sections for the alveolar socket and the dental implant can be observed. The implant were only making contact with the alveolar socket on the distal and mesial sides, but not the buccal and lingual sides (Figs. 1 and 2).
The bone-implant contact areas only partly covered the surface area of the implant, as shown in Figure.2. In a specimen with bone-implant contact area was 21.7 % of the total implant area, the maximum principal strain in the peri-implant bone strain was observed to be higher than that in another specimen with 53.6% bone-implant contact (Fig.3).

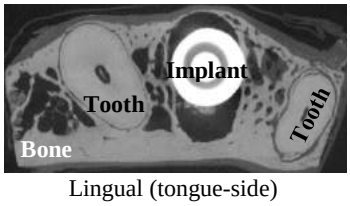

Figure 1: A virtual transverse slice of micro-CT images for a dental implant in a human cadaveric mandible

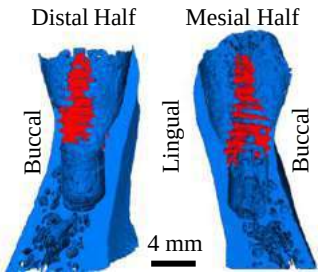

Figure 2: 3D rendered images showing bone-implant contact areas (highlighted in red)

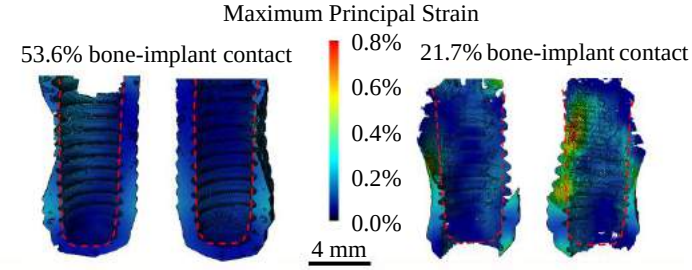

Figure 3: 3D rendered images showing the maximum principal strain in peri-implant bone for two specimens with different bone-implant contact areas.

DISCUSSION

Conventional method for measuring bone-implant contact through histology [10]–[12] can only reveal the bone-implant contact at the cut-surfaces. In this study, 3D full-field bone-implant contact areas were mapped out from the micro-CT images nondestructively. Results show that the smaller bone-implant contact area results in higher peri-implant strain in two specimens. Directions of future work includes more systematic study with larger sample size and *in vivo* study on correlation of bone-implant contact and the bone remodeling after implant placement.

ACKNOWLEDGEMENTS

The project described was supported by the National Center for Advancing Translational Sciences, National Institutes of Health, through Grant UL1TR002014. The content is solely the responsibility of the authors and does not necessarily represent the official views of the NIH. The support was made available through Penn State Clinical and Translational Science Institute (CTSI). The authors are grateful to Dr. Timothy Ryan and Mr. Timothy Stecko at the Center for Quantitative Imaging (CQI) at Penn State University for technical support on micro-CT scans.

REFERENCES

[1] R. M. Wazen, J. A. Currey, H. Guo, J. B. Brunski, J. A. Helms, and A. Nanci, "Micromotion-induced strain fields influence early stages of repair at bone–implant interfaces," *Acta Biomater.*, vol. 9, no. 5, pp. 6663–6674, May 2013.

[2] J. B. Brunski, "In vivo bone response to biomechanical loading at the bone/dental-implant interface," *Adv. Dent. Res.*, vol. 13, no. 1, pp. 99–119, Jun. 1999.

[3] G. Greenstein, J. Cavallaro, and D. Tarnow, "Assessing bone's adaptive capacity around dental implants: a literature review.," *J. Am. Dent. Assoc.*, vol. 144, no. 4, pp. 362–8, Apr. 2013.

[4] K. Akça, T. Chang, I. Tekdemir, and M. I. Fanuscu, "Biomechanical aspects of initial intraosseous stability and implant design: a quantitative micro-morphometric analysis.," *Clin. Oral Implants Res.*, vol. 17, no. 4, pp. 465–72, Aug. 2006.

[5] G. Alsaadi, M. Quirynen, K. Michiels, R. Jacobs, and D. van Steenberghe, "A biomechanical assessment of the relation between the oral implant stability at insertion and subjective bone quality assessment.," *J. Clin. Periodontol.*, vol. 34, no. 4, pp. 359–66, Apr. 2007.

[6] I. Miyamoto, Y. Tsuboi, E. Wada, H. Suwa, and T. Iizuka, "Influence of cortical bone thickness and implant length on implant stability at the time of surgery--clinical, prospective, biomechanical, and imaging study.," *Bone*, vol. 37, no. 6, pp. 776–80, Dec. 2005.

[7] I. Turkyilmaz, L. Sennerby, E. A. McGlumphy, and T. F. Tözüm, "Biomechanical aspects of primary implant stability: a human cadaver study.," *Clin. Implant Dent. Relat. Res.*, vol. 11, no. 2, pp. 113–9, Jun. 2009.

[8] J. Du, J. Lee, A. T. Jang, A. Gu, M. Hossaini-Zadeh, R. Prevost, D. A. Curtis, and S. P. Ho, "Biomechanics and strain mapping in bone as related to immediately-loaded dental implants.," *J. Biomech.*, 2015.

[9] Y. Zhou, M. A. Hernandez Lamberty, G. S. Lewis, A. D. Armstrong, and J. Du, "3D Full-Field Mechanical Measurement of a Shoulder Bone Under Implant Loading," in *TMS 2018 147th Annual Meeting & Exhibition Supplemental Proceedings. The Minerals, Metals & Materials Series.*, TMS, Ed. Cham: Springer, 2018, pp. 287–293.

[10] D. Buser, R. K. Schenk, S. Steinemann, J. P. Fiorellini, C. H. Fox, and H. Stich, "Influence of surface characteristics on bone integration of titanium implants. A histomorphometric study in miniature pigs.," *J. Biomed. Mater. Res.*, vol. 25, no. 7, pp. 889–902, Jul. 1991.

[11] S. Jun, B. M. W. Chang, H. Weber, and J.-J. Kwon, "Comparison of initial stability parameters and histomorphometric analysis of implants inserted into extraction sockets: human fresh cadaver study.," *Int. J. Oral Maxillofac. Implants*, vol. 25, no. 5, pp. 985–90, 2010.

[12] A. Wennerberg, T. Albrektsson, B. Andersson, and J. J. Krol, "A histomorphometric and removal torque study of screw-shaped titanium implants with three different surface topographies.," *Clin. Oral Implants Res.*, vol. 6, no. 1, pp. 24–30, Mar. 1995.

CHOROIDAL SWELLING IS PREDICTED TO CAUSE SIGNIFICANT OPTIC NERVE HEAD DEFORMATION: POTENTIAL RELEVANCE TO SANS

Andrew J. Feola (1,2), Brian C. Samuels (3), Brandon R. Macias (4), Michael Stenger (5), Nimesh Patel (6), C. Ross Ethier (2)

(1) Center for Visual and Neurocognitive Rehabilitation
Atlanta VA Medical Center
Atlanta, GA, USA

(2) Department of Biomedical Engineering
Georgia Institute of Technology/Emory University, Atlanta, GA, USA

(3) Department of Ophthalmology, University of Alabama at Birmingham, Birmingham, AL

(4) KBRwyle, Houston, TX, USA

(5) NASA-JSC Texas, USA

(6) College of Optometry, University of Houston, Houston, TX, USA

INTRODUCTION

Biomechanics is thought to play an important role in several ocular pathologies, including glaucoma, idiopathic intracranial hypertension, and Spaceflight-Associated Neuro-ocular Syndrome (SANS). The biomechanical environment of the posterior eye is particularly complex, since these tissues experience loading from blood pressure, intraocular pressure (IOP), cerebrospinal fluid pressure (CSFp), and choroidal deformation [1]. We focus on the optic nerve head (ONH), a region in the posterior eye which is the primary site of retinal ganglion cell injury in glaucoma and likely in other conditions. Retinal ganglion cells transmit visual information to the brain, and loss of these cells causes visual impairment; thus, understanding ONH biomechanics is an important research topic.

Here, we more specifically consider SANS, a syndrome associated with long-duration space flight and which may be related to the cephalad fluid shift and jugular venous congestion that occur in sustained microgravity [2]. A notable finding in SANS is choroidal thickening/folds, yet the functional effects of such choroidal thickening are poorly understood. Recent in-flight imaging studies indicate that the choroid swells significantly in space [3], thickening far beyond the swelling predicted to occur normally, e.g. 2.1–14.2 μL over a cardiac cycle [4]. Our goal was to develop finite element models to study how choroidal thickening and choroidal anatomy affect ONH biomechanics, with application to understanding the pathophysiology of SANS.

METHODS

We have previously described our ocular model and finite element approach [4]. In brief, we extended an existing model of the posterior eye [5], including the annular scleral ring, pia mater, dura mater, and optic nerve (Fig 1). The pia mater, dura mater and optic nerve were extended posteriorly 10 mm from the ONH. We also included a single central retinal vessel to approximate the effects of mean arterial blood pressure. We incorporated an anatomically realistic choroid based on OCT scans and average choroidal thickness measurements from the literature at specific distances away from the ONH [2]. Further, we considered two anatomical representations of the choroid: one with a ‘‘blunt’’ choroidal insertion at the ONH, and a second with a “tapered” insertion (Fig 1).

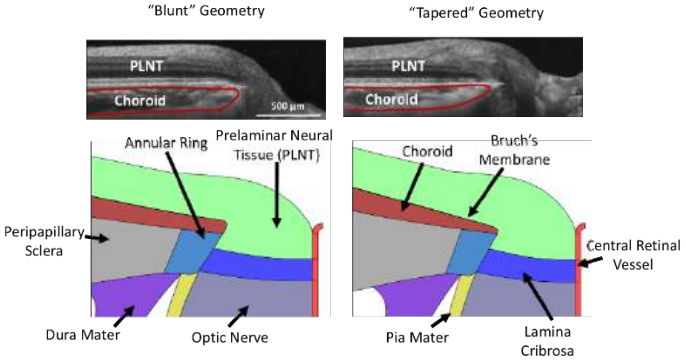

Figure 1: Top: representative OCT images at the optic nerve head (ONH) adapted from Lee et al. [8], showing choroidal geometries. Note the different choroidal terminations at the ONH. Bottom: Geometric model of the ONH/posterior eye, showing “blunt” and “tapered” choroid insertions.

The open-source program Gmsh was used to create the geometric models and for mesh generation [6], and FEBio was used as the finite element solver [7]. The model was axisymmetric, and was represented as a 3° wedge about an axis of symmetry passing though the central retinal vessel due to constraints of the FEBio solver.

The prelaminar neural tissue (PLNT), lamina cribrosa, optic nerve, central retinal vessel, and Bruch's membrane were modeled as isotropic, linear-elastic and homogenous. All other tissues were modeled as Mooney-Rivlin solids with embedded collagen fibers, distributed according to a von Mises distribution. The Young's modulus, Poisson ratio, and stiffness of the collagen fibers for each tissue component were based on previously reported values [2]. The choroid was modeled as a mixture material consisting of a linear-elastic solid matrix capable of swelling based on Donnan equilibrium. This approach allowed us to control the degree of swelling within the choroid without requiring us to model the complex geometry and behavior of the vascular bed.

Based on in-flight peripapillary OCT scans of astronauts [3], we assessed the impact of up to 50 µL of choroidal swelling, as well as the normal systolic-diastolic choroidal volume (2.1–14.2 µL, depending on ocular rigidity and other factors [4]). In addition, we examined the impact of elevating IOP to 30 mmHg without choroidal swelling, since this level of IOP puts subjects at high risk for developing glaucoma and the resulting loss of vision. Our outcome measures were the peak 1st and 3rd principal strains (95th percentile and 5th percentile) in the PLNT. All deformations and strain values were taken relative to a baseline configuration with no choroidal swelling, IOP of 15 mmHg (normal value), and mean arterial blood pressure of 57 mmHg (suitable for upright posture on earth at the level of the eye).

RESULTS

Consistent with previously reports, elevating IOP caused significant compression in the PLNT, a tissue region consisting primarily of retinal ganglion cell axons. Choroidal swelling caused significant deformation at the ONH (Fig 2), with the degree and extent of deformation being larger in the blunt vs. the tapered geometry. These differences increased as choroidal swelling became more extreme.

Figure 2: Contour plots of the computed first (red) and third (blue) principal strains in ONH tissues under an elevated IOP (30 mmHg), the upper limit of normal (physiologic) choroidal swelling (14.2 µL), and the choroidal swelling estimated to occur in astronauts (50 µL), for blunt (left) and tapered (right) choroidal geometries. All deformations are relative to a baseline condition of IOP = 15 mmHg and no choroidal swelling.

Choroidal swelling within the expected physiological range, i.e. that occurring over a cardiac cycle, led to significant cyclic strain in the PLNT. For the largest predicted extent of choroidal swelling over the cardiac cycle, strain magnitudes were either comparable to or greater than those predicted to occur as IOP was increased from 15 to 30 mmHg. However, for a choroidal swelling of 50 µL, estimated to occur in microgravity, predicted strains in the PLNT were far beyond the physiological ranges for both "blunt" and "tapered" geometries (Fig 3).

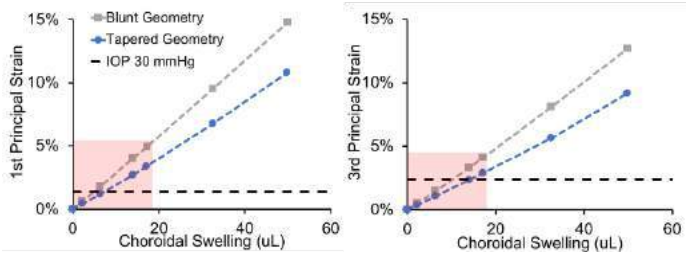

Figure 3: First (left) and third (right) principal strain versus degree of choroidal swelling. The shaded box represents the expected changes in choroidal volume and strains occurring over a cardiac cycle (normal physiology). The dashed horizontal line is the strain expected to occur due to IOP of 30 mmHg.

DISCUSSION

The chronic and significant choroidal thickening observed in some astronauts by OCT imaging is predicted to lead to significant biomechanical insult in prelaminar retinal ganglion cell axons. Specifically, we expect that such supra-physiologic choroidal thickening will lead to chronic local strain elevations many-fold greater than normal physiologic levels. This level of strain may induce remodeling at the ONH and be related to the alterations in visual function that some astronauts experience. For context, these strains are 5-7 fold greater than those expected to occur due to an elevated IOP of 30 mmHg, which is a major risk factor for developing glaucoma.

Interestingly, we found that the predicted strains in the PLNT due to normal choroidal swelling over a cardiac cycle may also exceed the deformations predicted due to an elevated IOP of 30 mmHg. Under normal conditions, individuals do not develop visual impairments due to cardiac cycle-induced changes in choroidal volume, which suggests that both the magnitude and temporal duration of choroidal swelling are important: choroidal swelling over the cardiac cycle is transient, while elevated IOP is chronic. This may be important in understanding the pathophysiology of SANS, since significant choroidal swelling can occur within 10 days of exposure to microgravity and be maintained throughout the mission. As additional astronaut and ground-based analog experimental data are gathered, we will be well positioned to use our existing models to predict the utility of various countermeasures on ONH biomechanics.

We also found that subject-specific differences in choroidal geometry at the ONH modulate the magnitude of strains due to choroidal swelling. Such anatomic features could be important risk factors for SANS and other diseases, e.g. non-arteritic anterior ischemic optic neuropathy. These results indicate that modeling of subject-specific geometries coupled with quantified choroidal changes in SANS is warranted.

ACKNOWLEDGEMENTS

Georgia Research Alliance, NASA (NNX16AT06G), Veterans Affairs (RX002342-02), and NASA Human Research Program Funding Support.

REFERENCES

[1] Burgoyne, C *Exp. Eye Res,* 93:120-132. 2011.
[2] Stenger, MB et al. Evidence Report: Risk of Spaceflight Associated Neuro-ocular Syndrome (SANS) 2017, NASA.
[3] Laurie, S et al. ARVO Annual Meeting, 2018
[4] Feola, AJ et al. *IOVS*, 59:4172-81, 2018.
[5] Sigal, I et al. *IOVS*, 45(12):4378-87, 2004.
[6] Geuzaine, C et al., Int J Num Meth Eng, 79(11):1309-31, 2009.
[7] Maas, SA et al. J Biomech Eng. 134(1):011005, 2012.
[8] Lee, K.M. et al., Acta Ophthalmologica 94: 697-708, 2016.

SB³C2019
Summer Biomechanics, Bioengineering and Biotransport Conference
June 25 -28, Seven Springs, PA, USA

BIOMECHANICAL CHARACTERIZATION OF ACTIVE AND PASSIVE PROPERTIES OF MURINE BRANCH PULMONARY ARTERIES

Abhay B. Ramachandra (1), Jay D. Humphrey (1,2)

(1) Department of Biomedical Engineering
Yale University
New Haven, CT, USA

(2) Vascular Biology and Therapeutics
Yale University
New Haven, CT, USA

INTRODUCTION

Pulmonary arteries carry deoxygenated blood from the right ventricle to the lungs in a normal circulation. In disease, pulmonaries experience an altered mechanical environment, as, for example, an increase in pressure in hypertension or volume in a single ventricle pathology. Characterizing their active and passive mechanical properties in health is a critical first step towards modeling their biomechanical behavior and understanding their remodeling in disease. Much work has been done in biaxial characterization of arteries in the systemic circulation [1-3] but there has been much less attention directed to pulmonary arteries, especially in murine species (notwithstanding a few notable exceptions [4]). While the ultimate goal is to study the human circulation and pathology, availability of diverse murine genotypes and phenotypes promises to facilitate an increased understanding of genetic and molecular aspects of diseases. Insight derived from comparisons of diverse murine systemic datasets provides strong motivation to characterize pulmonary arteries using protocols and methods that are consistent with those used to study the systemic circulation. Such consistent biomechanical phenotyping can aid inter-circulation comparisons and provide guidance for surgeries such as Fontan or Ross procedures.

METHODS

All animal protocols were approved by the Institutional Animal Care and Use Committee of Yale University. Male C57BL6/J mice (14-20 weeks of age, n = 5 per group) were euthanized with an intraperitoneal injection of Beuthanasia-D (150 mg/kg) followed by exsanguination. The pulmonary arteries were harvested from the root of the main branch to the first branching site on the right and left branches. Perivascular tissues were gently cleaned, branches were ligated, and vessels were prepared for biomechanical testing as described previously [1]. The vessel was ligated on custom-made glass cannula past the main pulmonary bifurcation at one end and at the first branching site at the distal end. The specimens were biaxially tested using a custom computer-controlled device [5]. Biomechanical testing consisted of two parts: an active characterization and a passive characterization. In the active characterization, the vessel was contracted from its in vivo state (15 mmHg and vessel-specific in vivo stretch) at isobaric conditions until the diameter reached a steady state value (after approximately 15 minutes). Here we report active results for contraction with 100 mM KCl (a membrane depolarizer) and 1μM phenylephrine (an adrenergic receptor stimulus). In the passive characterization, the vessel was subjected to two cycles of pressure-diameter tests (5-40 mmHg) at each of three different stretches (in vivo stretch, 0.95x in vivo stretch,1.05x in vivo stretch) and two cycles of force-length tests at each of the four pressures (5, 15, 25 and 40 mmHg). Note that both active and passive tests were preceded by an appropriate preconditioning step, details of which can be found elsewhere [6]. The active characterization was performed in a Krebs ringer solution at 37ºC, at a pH of ~ 7.4, and bubbled with 95% O_2 and 5% CO_2; the passive characterization was performed in buffered Hanks solution at room temperature to reduce contributions from smooth muscle tone to passive mechanics.

Keeping the analysis consistent with that used for systemic arteries, the mean mechanical behavior was modeled using a 2-D formulation, neglecting residual and radial stress [1-3]. The nonlinear passive behavior was modeled using a scalar stored energy function, under a pseudoelastic assumption. The stress and stiffness were computed from first and second derivatives of the stored energy function. The passive behavior of the vessel was modeled with a neo-Hookean model, capturing amorphous material behavior (mainly

elastin), and a four-fiber family model (along axial, circumferential and diagonal directions), capturing contributions from the structurally significant oriented constituents - smooth muscle and collagen.

Vessels not used for mechanical characterization (n=3 per group) were fixed in 10% neutral buffered formalin and stored in 70% ethanol at 4ºC for histology. The samples were stained with Verhoeff's Van Giesen (VVG) and Masson's Trichrome (MTCs). We checked for statistical differences in active, mechanical and morphometric properties between the left and right pulmonary groups using one-way ANOVA with Tukeys post-hoc analysis.

RESULTS

Results of biaxial testing are summarized in Table 1. Although right (RPA) and left (LPA) pulmonary arteries exhibit different structural behaviors, they have very similar material behaviors. That is, despite differences in size, the biaxial material properties, including passive stiffness, elastic energy storage and biaxial wall stress at in vivo pressures, are similar between RPA and LPA. Even the contractile capacity at in vivo conditions was similar between the vessels. Area fractions of the wall constituents, for example, elastin, smooth muscle and collagen, from histological quantifications were not significantly different between the left and right pulmonaries [6].

Table 1: Summary of morphological, mechanical, and histological differences between right (RPA) and left (LPA) pulmonary arteries (mean ± sem). * indicates statistically significant differences at $p < 0.05$

	RPA			LPA		
Unloaded dimensions						
Wall Thickness (μm) *	82	±	2.3	66	±	1.5
Outer Diameter (μm) *	836	±	20	669	±	6
Axial Length (mm)	3.11	±	0.25	3.51	±	0.09
Outer diameter contraction at in vivo conditions (%)						
Potassium Chloride (100mM)	31.2	±	5.7	26.0	±	2.3
Phenylephrine (1μm)	33.8	±	4.1	28.8	±	4.2
Linearized Stiffness (kPa) at Mean Pressure						
Circumferential	91.0	±	8.72	98.4	±	12.4
Axial	288	±	31.4	243	±	38.4
Stored Energy (kPa) at Mean Pressure	11.0	±	1.01	10.9	±	1.32
Area Fractions						
Elastin	0.25	±	0.07	0.26	±	0.08
Cytoplasm	0.22	±	0.05	0.18	±	0.05
Collagen	0.54	±	0.11	0.57	±	0.12

DISCUSSION

Our results show that the material properties and functional behaviors of the left and right pulmonary arteries are remarkably similar in healthy murine species. At in vivo conditions, the pulmonaries are more contractile, smaller in size, are less stiff, and they experience lower stresses than the descending thoracic aorta [7,8]. Results from these consistent methods, protocols, and analyses should serve as baselines for future biaxial experiments on murine models of pulmonary pathologies and thereby enable meaningful comparative biomechanical phenotyping across circulations.

ACKNOWLEDGEMENTS

This work was funded, in part, by grants from the NIH: R01 HL128602 and R01 HL139796.

REFERENCES

[1] Ferruzzi, J et al., *J. Biomech. Eng.*, 137: 031007, 2013
[2] Bersi, M et al., *Ann. Biomed. Eng*., 42: 1207– 1223, 2013
[3] Bellini, C et al., *J. R. Soc. Interface*, 14, 20161036, 2016
[4] Kobs, R et al., *Am. J. Physiol.* 288:H1209–H1217, 2005
[5] Gleason, R et al., *J. Biomech. Eng.*, 126: 787–795, 2004
[6] Ramachandra, A et al., *J. Biomech.* , 2019
[7] Caulk, A. et al., *J. Biomech. Eng.*, 2019
[8] Bersi, M et al., *Hypertension*, 67 (5): 890–896, 2016

SB³C2019
Summer Biomechanics, Bioengineering and Biotransport Conference
June 25 -28, Seven Springs, PA, USA

EFFECTS OF LONG TERM SPINAL CORD INJURY ON THE MECHANICAL BEHAVIOR OF THE URINARY BLADDER EXTRACELLULAR MATRIX

Tyler G. Tuttle (1), Heidi Lujan (2), Stephen DiCarlo (2), Sara Roccabianca (1)

(1) Department of Mechanical Engineering
Michigan State University
East Lansing, Michigan, USA

(2) Department of Physiology
Michigan State University
East Lansing, Michigan, USA

INTRODUCTION

The main function of the **urinary bladder (UB)** is to store and void urine through mechanical relaxation and contraction [1]. The micturition cycle is coordinated through neurological connection to the brain: when the bladder is "full" a signal is sent to the brain, which voluntarily initiates contraction of the detrusor muscle and relaxation of the external sphincter in order to empty. Loss of neurological connection inhibits perception of bladder fullness, leading to increased stored urine volume, which triggers wall remodeling. In extreme cases this leads to inability to control detrusor contraction and sphincter relaxation, preventing individuals from voluntarily emptying.

Neurogenic bladder is the term used to characterize loss of control of the UB due to brain, spinal cord, or nerve problems (e.g., parkinsonism, spina bifida, **spinal cord injury (SCI)**, and diabetes mellitus). The remodeling of the neurogenic bladder wall results in hypertrophy of the smooth muscle cells and deposition / removal of **extracellular matrix (ECM)**, i.e., fibrosis [2, 3]. Wall remodeling, particularly changes in the ECM composition, can alter the compliance, thickness, and capacity of the UB, thus changing the underlying mechanical properties. This, in turn, can significantly affect the capability of the organ to perform its physiological function. Therefore, it is important to understand how the mechanical properties of the UB wall change in the neurogenic bladder.

A previous study by Gloeckner et al. compared the passive biaxial mechanical properties of UBs from normal rats, as well as rats 10 and 14 days after SCI, and found an increase in compliance after SCI [4]. In this study, we will look at long-term changes in the UB wall mechanics by quantifying mechanical properties of the ECM of rat urinary bladders 14 weeks after SCI.

METHODS

SCI surgery was conducted on Sprague-Dawley rats (n=5) to induce paraplegia. Two ligatures (6.0 silk) were tightened around the underlying spinal cord between the second and third thoracic segments (T_2-T_3) and the spinal cord was completely transected by cutting between the ligatures with scissors.

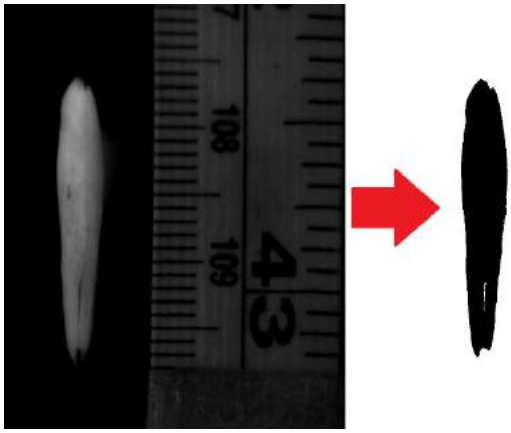

Figure 1: Front view image taken with CCD camera (left) converted to binary image (right).

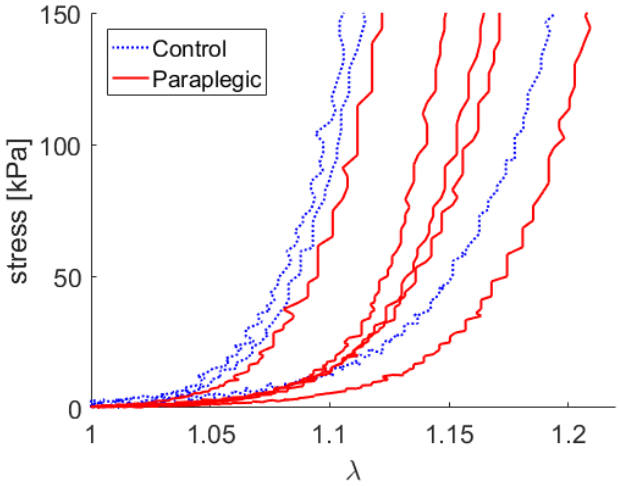

Figure 2: Stress-stretch curves from ring tests of control (blue dotted) and paraplegic (red solid) rat UBs.

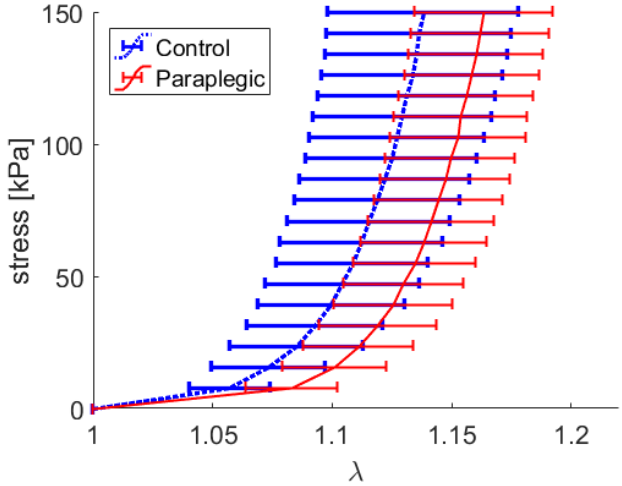

Figure 3: Stress-stretch curves of control (blue dotted) and paraplegic (red solid) rat UBs averaged by stretch at equally spaced increments of stress.

The UBs were voided by manual compression four times daily until the end of the acute recovery period (8 days), at which point the rats recover partial ability to empty independently and were manually emptied once daily. Control animals underwent the same surgical procedure, but the spinal cord was not transected (n=3). Rats were sacrificed after 14 weeks. Whole rats were frozen and stored at -20°C before dissection. The rats were thawed for 3 days at 2°C and the UBs where excised, cut into rings, placed into embedding medium for frozen tissue specimens, and frozen at -80°C.

Prior to mechanical testing, rings were thawed and decellularized to isolate the ECM. Preliminary work showed that freezing did not alter the mechanical response of decellularized rat UB rings. Based on a previous protocol for whole-heart decellularization [5], samples were soaked in heparinized saline solution for 15 minutes, 10% sodium-dodecyl sulfate solution for 48 hours, deionized water for 15 minutes, and finally 10% Triton X-100 solution for 30 minutes.

Uniaxial ring tests were performed on the decellularized UB rings. A preload of 2 gr. was applied to the samples prior to preconditioning and each set of cyclical tests. Preconditioning consisted of 10 cycles of .1 strain at a strain rate of .01 s^{-1}. The subsequent cyclical testing consisted of 5 cycles each for strains of .2, .3, and .4 at a strain rate of .01 s^{-1}. Tests were stopped if the sample ruptured or the load cell reached a maximum capacity (250 gr.). Top and side view images of the samples were captured before each set of cyclical tests. Images were converted to binary (see **Figure 1**). Median width and thickness were used to calculate cross-sectional area (A_0). The force applied to the rings was recorded during the tests with a 250 gr. capacity load cell. The length of the sample in pixels was continuously recorded with a charge-coupled device (CCD) camera.

RESULTS

Figure 2 shows the stress-stretch curves from the ring tests for both the control (blue dotted lines, n=3) and paraplegic (red solid lines, n=5) rat UBs. For each sample, the 5th loading curve of the final complete set of cycles was used. For example, if a sample ruptured or reached maximum load cell capacity during the 40% loading cycles, the 5th loading curve of the 30% loading cycles was used. **Figure 3** shows the curves for control and paraplegic averaged by stretch at incrementally spaced values of stress. Stretch (λ) is defined as the length of the sample divided by the initial length, after preload. Stress is defined as the force divided by the current cross-sectional area. Assuming incompressibility, the cross-sectional area changes by A_0/λ, where A_0 is width multiplied by the thickness, determined from top and side view images of the samples (see **Figure 1**).

DISCUSSION

The ECM of the urinary bladders of animals 14 weeks after SCI seems to be more compliant when compared to urinary bladders of control animals. This result agrees with what was previously shown for animals 10 and 14 days after SCI [4]. More SCI and control rat UBs will be tested to help validate this observation. Furthermore, UBs from rats with SCI seemed to be markedly larger than UBs from control rats. Analysis of images of rings before stretching will be used to quantify UB ring diameter and confirm this observation. Finally, histological analysis will be done on control and paraplegic rat UB samples to quantify changes in tissue morphology and ECM composition.

REFERENCES

[1] Roccabianca S, et al., *Technology*, 4(01), 30-41, 2016.
[2] Golbidi S, et al., *Frontiers in pharmacology*, 1, 136, 2010.
[3] Hackler RH, et al., *The Journal of urology*, *141(*6), 1390-1393, 1989.
[4] Gloeckner DC, et al., *The Journal of urology*, *167*(5), 2247-2252, 2002.
[5] Ott HC, et al., *Nature Medicine*, 14(2), 213, 2008.

SB³C2019
Summer Biomechanics, Bioengineering and Biotransport Conference
June 25 -28, Seven Springs, PA, USA

MULTI-SCALE MODEL OF PRESSURE-DRIVEN HYPOXIA IN THE SKIN RESULTING FROM MICROVASCULATURE COLLAPSE

Vivek D. Sree (1), Manuel K. Rausch (2), Adrian Buganza-Tepole (1,3)

(1) Mechanical Engineering
Purdue University
West Lafayette, IN, USA

(2) Aerospace and Engineering Mechanics
The University of Texas at Austin
Austin, TX, USA

(3) Biomedical Engineering
Purdue University
West Lafayette, IN, USA

INTRODUCTION

Pressure ulcers are a painful, costly, and even deadly type of injury that disproportionally affects the older adult population [1]. In fact, 7 to 23% of older adults in nursing homes and hospitals in the US suffer from pressure ulcers at one point in their stay [1]. Pressure ulcers have been described as excruciating, and their treatment costs accrue to more than 16 billion dollars every year in the US [2]. There are a multitude of factors implicated in pressure ulcer initiation and progression, including behavioral and biological factors [3]. However, one element that remains poorly understood is the effect of tissue mechanics, particularly changes in skin mechanics with aging, on pressure ulcer formation. It is now clear that compression of the tissue under applied pressure leads to ischemia, subsequently to hypoxia, and is the major driver of pressure ulcer initiation [3]. At the same time, changes in skin anatomy and mechanical behavior with aging have been documented [4]. Yet, the connection between applied pressure, ischemia, and skin anatomy and mechanical properties remains unsolved. Our work aims at bridging this gap through a novel multi-scale mathematical model.

Previous work has shown that perfusion decreases under applied loads leading to ischemia [5]. Microvasculature deformation has been suspected as a principal mechanism linking the applied loads to ischemia, but current imaging technologies are not capable of resolving the detailed deformation of the vasculature in realistic scenarios [6]. To address this challenge, we rely on a high-fidelity finite element model of a representative volume element (RVE) of the skin with a detailed microvasculature geometry. We define a homogenized metric from the RVE, the change in vessel volume fraction, and couple this variable to a tissue level model of skin mechanics and oxygen diffusion. Our model allows us to then investigate *in silico* how changes in loading, mechanical properties, and skin structure can affect susceptibility to pressure-driven ischemia and, subsequently, hypoxia.

METHODS

We create microvasculature geometries that match the geometric features of the vascular tree in the skin [7]. We adapt previous work on two-dimensional fractal generation algorithms [8] and extend these algorithms to three dimensions. The vessel tree in the skin starts at the interface between the dermis, the middle layer of the skin, and the underlying fat and muscle. At this location, the branches of the vasculature tree are 200μm in length and we assume a constant vessel diameter of 20μm [7]. The tree undergoes 8 to 10 bifurcations as it progresses through the dermis towards the interface with the epidermis, the top layer of the skin. The epidermis is avascular. Each bifurcation results in branches with a 40% reduction in length. A realistic geometry generated with our fractal algorithm is shown in Fig. 1A. The tree is imported into a CAD software and, after several postprocessing steps, results in a 1mm^3 solid RVE with a microvasculature inclusion as shown in Fig. 1B.

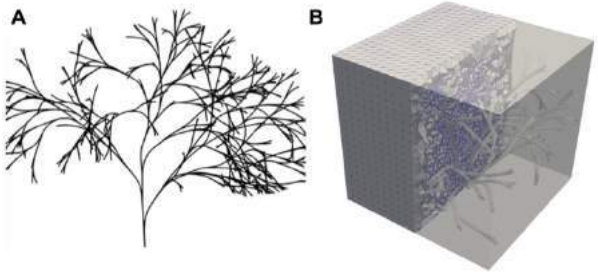

Figure 1: A) Vascular tree from our fractal generation algorithm matching features of the skin microvasculature. B) RVE finite element mesh of a 1mm^3 tissue with the vasculature inclusion.

We perform compression of the RVE in order to get the change in vessel volume fraction upon RVE deformation, see Fig. 2A. We assume the skin to behave as a compressible Neo Hookean material and we use values of the parameters reported before: $\mu_0 = 75$ kPa, $K = 350$ KPa [9]. The initial volume fraction of the vasculature is ϕ_0. The volume fraction of the deformed tree is ϕ. We generate multiple RVEs, each with a slightly different initial volume fraction. Hence, we normalize the volume change for each RVE, $\hat{\phi} = \phi/\phi_0$. We drive the simulation of the RVE by specifying the deformation between the top and bottom surfaces of the RVE while prescribing periodic boundary conditions on the lateral surfaces. In other words, we impose an average normal compression λ_z to the RVE. By tracking the change in $\hat{\phi}$ we can then construct the function $\hat{\phi}(\lambda_z)$, which is the link to our tissue scale model.

At the tissue level we have two coupled problems, one is the solution of mechanical equilibrium, for which we continue to use the Neo-Hookean model and parameters as before. We also solve for the partial oxygen pressure P_0 profile through the differential equation

$$\alpha \frac{dP_0}{dt} + \nabla \cdot \boldsymbol{q} = s_{P_0} \qquad (1)$$

Here, $\alpha = 3 \times 10^{-5}$ mlO_2/mm^3mmHg is the solubility, the flux obeys Fickian diffusion with diffusivity $D = 1.5 \times 10^{-3} mm^2/s$ [10]. The coupling of the tissue level to the RVE model is through the source term s_{P_0}. We assume that the volume fraction of the vessel geometry is correlated to the oxygen supply, we then propose $s_{P_0} = \hat{\phi} s_0$, with $s_0 = 1 \times 10^{-5}$ s^{-1} [10]. Fig. 3A shows the setup of the tissue scale model.

RESULTS

Fig. 2A shows the contours of the normal component of the Green Lagrange strain, E_{33}, when the RVE is compressed by $\lambda_z = 0.8$. The strain on the outer surfaces of the RVE is fairly homogeneous. However, inspecting cross sections inside the RVE it is evident that there are strain concentrations around the vessels. The magnification of the geometry in Fig. 2B shows vessel collapse. In fact, vessel volume fraction reduces more than 40% with less than 20% compressive strain.

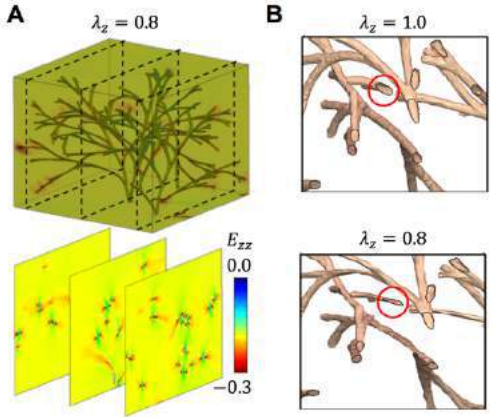

Figure 2: A) Compression of the RVE by an average stretch $\lambda_z = 0.8$ leads to homogeneous Green Lagrange strain over the RVE with higher strains near vessels. B) Magnification of vessel geometry shows collapse upon RVE compression.

We fit the function $\hat{\phi}(\lambda_z)$ based on the RVE simulations and couple to the oxygen and tissue mechanics problem of the tissue scale. Fig. 3A shows the setup of the simulation. At zero applied pressure we recover a physiological profile of partial oxygen pressure seen at the top of Fig. 3B. As the pressure is increased, the tissue deforms, leading to compression and collapse of the vasculature, reduction in the oxygen source term, and subsequent hypoxia.

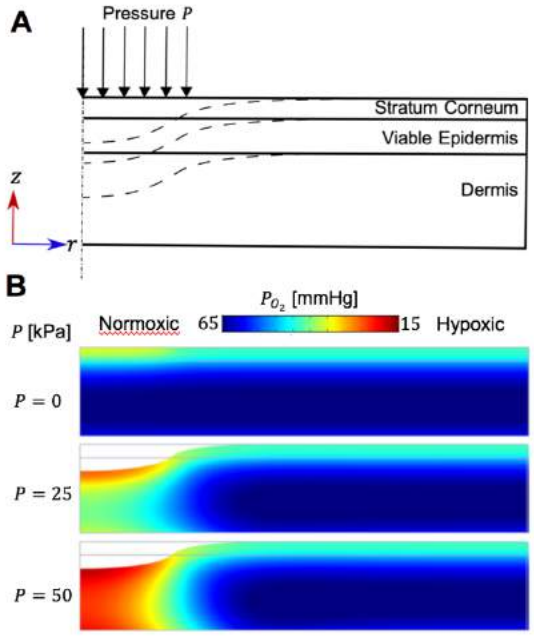

Figure 3: A) Axisymmetric tissue scale simulation accounting for the three skin layers. Pressure is applied at the top surface leading to tissue deformation. B) As the pressure increases, the coupling of normal strain and our RVE model predicts patterns of hypoxia.

DISCUSSION

Here we have shown that a multi-scale model can capture pressure-driven hypoxia in the skin. Previous work has investigated the skin microvasculature, but has disregarded full 3D vessel geometries and how these deform under applied loads [6]. We address this gap through a high-fidelity model of a RVE of the skin including realistic vessel trees. Furthermore, we then couple this model to the tissue scale oxygen diffusion tissue model, thus enabling prediction of patterns of hypoxia under applied pressure for realistic domains not available before.

One limitation of our model is the lack of a fluid problem coupling for solving the blood flow inside the vascular tree. We impose a pressure boundary condition at the inner vessel walls, but a fluid-structure interaction problem would be more realistic. Additionally, modeling blood flow would allow us to better link the RVE to the tissue scale model. Our current assumption is that vessel volume fraction is correlated with the oxygen source term. While this is a reasonable simplification it should be investigated further. Experimental calibration of the model is another key next step. Despite the limitations, this work increases our fundamental knowledge of pressure-driven hypoxia, crucial to improve treatment and prevention of pressure ulcers.

REFERENCES

[1] Demarre, et al., *I J Nurs Stud* , 52:1754-74, 2015.
[2] Lyder et al., *Patient Safety and Quality: Handbook for Nurses*, 2005.
[3] Coleman, et al., *J Adv Nurs*, 70:2222-34, 2014.
[4] Luebberding, et al., *Skin Res Tech*, 20:127-35, 2024.
[5] Loerakker, et al., *J Appl Phys*, 111:1169-77, 2011.
[6] Linder Ganz, et al., *Ann Biomed Eng*, 35:2095-2107, 2007.
[7] Cevc, et al., *J Control Release*, 118:18-26, 2007.
[8] Costabal, et al., *J Biomech*, 49:2455-2465, 2016.
[9] Pailler-Matei, et al., *Med eng Phys*, 30:599-606, 2008.
[10] Wang, et al., *Microcirculation*, 12:195-207, 2005.

SB³C2019
Summer Biomechanics, Bioengineering and Biotransport Conference
June 25-28, Seven Springs, PA, USA

A COMPARATIVE CLASSIFICATION ANALYSIS OF ABDOMINAL AORTIC ANEURYSMS BY MACHINE LEARNING ALGORITHMS

Balaji Rengarajan (1), Wei Wu (1), Crystal Wiedner (2), Satish C. Muluk (3), Mark K. Eskandari (4), Ender A. Finol (1)

(1) Department of Mechanical Engineering
University of Texas at San Antonio
San Antonio, TX, U.S.A.

(2) Department of Management Science and Statistics
University of Texas at San Antonio
San Antonio, TX, U.S.A.

(3) Department of Thoracic & Cardiovascular Surgery, Allegheny General Hospital
Allegheny Health Network
Pittsburgh, PA, U.S.A.

(4) Division of Vascular Surgery, Feinberg School of Medicine
Northwestern University
Chicago, IL, U.S.A.

INTRODUCTION

Abdominal aortic aneurysm (AAA) is an asymptomatic aortic disease characterized by the enlargement of the infrarenal segment of the aorta. Untreated AAA can rupture, which has an associated mortality of up to 90%. The current clinical management of AAA is based on assessing the size and growth of the AAA sac and clinical intervention is recommended for AAA with maximum diameter (D_{max}) > 5.5 cm in men, D_{max} > 5.0 to 5.4 cm in women. We hypothesized that using geometric indices (that best describe the shape, size, wall thickness, and curvature of the AAA), demographic information (gender and age), and biomechanical wall stress, will yield a higher accuracy when classifying electively and emergently repaired AAA than by using only D_{max}. Furthermore, by comparing the prediction accuracy of eight machine learning algorithms, we aim to select the machine learning tool that best discriminates between electively and emergently repaired AAA.

METHODS

Two groups of patients were studied: Group I, with n = 98 asymptomatic electively repaired AAA and Group II, with n = 50 symptomatic emergently repaired AAA. The abdominal computed tomography angiography (CTA) scans of the 148 AAA patients, their age and gender were obtained from an existing database in the Department of Radiology at Allegheny General Hospital (Pittsburgh, PA). The 98 asymptomatic AAA image sets were taken during routine checkup and 50 symptomatic AAA image sets were acquired no later than 1 month prior to the intervention. All segmentations were performed using custom in house segmentation scripts written in MATLAB (Mathworks, Inc., Natick, MA), collectively known as AAAVasc [1] (v1.03, The University of Texas at San Antonio, San Antonio, TX). The segmentation process exploits the difference in contrast between the AAA and its surroundings to segment lumen, inner wall and outer wall. Patient-specific geometric indices were calculated, using in house developed MATLAB scripts based on the biquintic Hermite finite element (BQFE) method. Using the point cloud generated from the segmentation process, 1D and 2D indices were calculated. Volume and surface meshes, generated with the in-house MATLAB script AAAMesh, were used to calculate the 3D indices while the BQFE method was used to compute the curvature based indices. Wall material properties were derived from the Mooney-Rivlin constitutive equation reported by Raghavan and Vorp [2]. The volume mesh file was imported to ADINA (Adina R&D, Inc., Watertown, MA) were the stress tensor components were calculated at peak systolic pressure. The protocol for generating the geometric and biomechanical metrics is illustrated in Fig. 1. Eight machine learning algorithms (Generalized Additive Model - GAM, Decision Tree - TREE, Support Vector Machine - SVM, Multivariate Adaptive Regression Splines - MARS, Random Forest - RF, Least Absolute Shrinkage and Selection Operator - LASSO, K-Nearest Neighbor - KNN, and Negative Binomial Regression - NB) were carried out to classify the 148 AAA based on 52 geometric indices, four wall stress metrics (50^{th} percentile wall stress – 50^{th}WS, 99^{th} percentile wall stress – 99^{th}WS, peak wall stress - PWS, spatially averaged wall stress - SAWS), and one demographic variable (gender). The leave-one-out-cross-validation (LOOCV) method was applied to report the accuracy of prediction for all eight algorithms. Other common performance metrics such as specificity, sensitivity and Receiver Operating Characteristic (ROC) Area under Curve (AUC) were also calculated by LOOCV.

RESULTS

The dataset consisted of 76% male patients and 23% females. It was observed that Group II AAA had a larger maximum diameter, vessel volume and surface area, and greater overall length and AAA sac

length, than Group I AAA. The intraluminal thrombus volume of Group II AAA was nearly half of that of Group I AAA, while symptomatic emergently repaired AAA have thicker walls than asymptomatic electively repaired AAA. Mean PWS for Group II was significantly higher than for Group I (139.92 ± 57.71 N/cm^2 vs. 97.45 ± 43.63 N/cm^2). The mean of the 99thWS for Group II was 66.94 ± 20.94 N/cm^2 while for Group I was 50.14 ± 16.79 N/cm^2. Similarly, SAWS had a mean of 29.72 ± 10.84 N/cm^2 and 22.03 ± 7.53 N/cm^2 for Groups II and I, respectively.

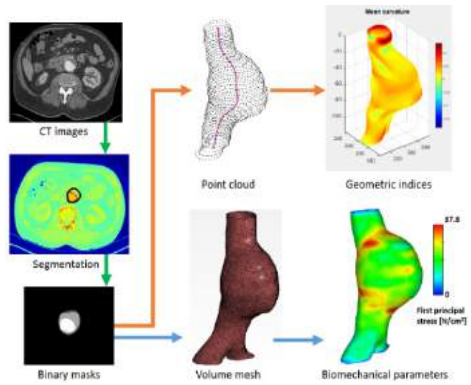

Figure 1: Schematic of the protocol for segmentation, meshing, and evaluation of the geometric indices and biomechanical parameters.

Of the eight machine learning algorithms, GAM had the highest accuracy (87%), AUC (89%) and sensitivity (78%), and was the best performing algorithm for AAA classification (see Table 1). TREE had the second best accuracy (79%) and a high sensitivity of 74%, although exhibited the lowest specificity of 82%. KNN and SVM are inefficient in predicting symptomatic emergently repaired AAA as the sensitivities for both were low (KNN = 46%, SVM = 30%). SVM also had the lowest accuracy of prediction amongst all algorithms. KNN has the highest specificity, which indicated it is effective in recognizing Group I AAA. Figure 2 shows the ROC curves for all 8 algorithms. With the variables used by GAM, the models with geometric indices alone (GAM-GEOM) and with biomechanical parameters alone (GAM-BIOM) were compared to GAM (see Table 2). GAM-GEOM had an 84% accuracy while GAM-BIOM had a 78% accuracy. Since GAM with both index types exhibited 87% accuracy, both geometric indices and wall stress metrics are needed to obtain a high classification accuracy.

Table 1: Performance metrics of the machine learning algorithms.

Model	Accuracy	AUC	Sensitivity	Specificity
SVM	0.69	0.73	0.30	0.89
NB	0.75	0.80	0.52	0.87
MARS	0.78	0.81	0.64	0.85
RF	0.78	0.83	0.56	0.90
LASSO	0.79	0.79	0.50	0.94
TREE	0.79	0.60	0.74	0.82
KNN	0.79	0.79	0.46	0.96
GAM	0.87	0.89	0.78	0.92

DISCUSSION

In the present work, wall stress metrics, geometric indices and demographic information were used to classify AAA using eight different machine learning algorithms. The techniques were applied to a data set of 98 asymptomatic and 50 symptomatic AAA, while the quality of the prediction was assessed based on the accuracy of the algorithms, sensitivity, specificity, and area under the ROC curve. While the overall accuracy of the algorithms was high, ranging from 69% to 87%, the sensitivity (i.e. the correct prediction rate for Group II AAA) was disappointingly low, ranging from 30% to 78%. In addition, to being the overall best classifier, GAM also had a high false positive detection rate or specificity (92%) which ensures that the Group I AAA are detected accurately. GAM, which is an extension of generalized linear models, assumes that the dependent variables are represented as nonlinear additive functions of the independent variables [3]. Four variables (TH_{median} - median of wall thickness; TH_{Dmax} – wall thickness at the maximum diameter; P_{above} - percentage of wall thickness below the mean thickness, in %; and SAWS) were found to have a nonlinear response to the predictor. The fast classification of GAM results largely from its use of an adaptive back-fitting procedure similar to that used in MARS to guide both the selection of variables and to identify their optimal degree of smoothing. The main contribution of this work is in finding a nonlinear predictive classifier (GAM) that makes use of patient-specific wall thickness, which significantly improves the classification of asymptomatic and symptomatic AAA based on quantitative geometric and biomechanical analyses.

Table 2: Characteristics of the three GAM models.

Model	Accuracy	AUC	Sensitivity	Specificity
GAM	0.87	0.89	0.78	0.92
GAM-GEOM	0.84	0.87	0.70	0.91
GAM-BIOM	0.78	0.80	0.58	0.89

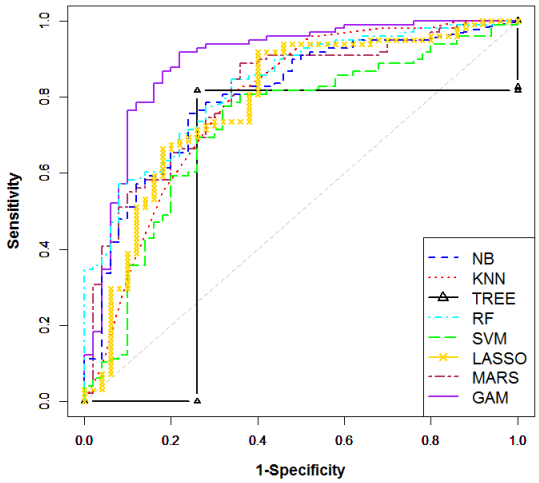

Figure 2: Receiver operating characteristic (ROC) curves of the eight machine learning algorithms applied for AAA classification analysis.

ACKNOWLEDGEMENTS

This work was supported in part by National Institutes of Health award R01HL121293.

REFERENCES

1. Shum, J et al., *Medical Physics*, 37:638-648, 2010.
2. Raghavan, ML and DA Vorp, *J Biomech*, 33:475-482, 2000.
3. Jeong, C et al., *Expert Syst Appl*, 39:3650-3658, 2012.

SB³C2019
Summer Biomechanics, Bioengineering and Biotransport Conference
June 25 -28, Seven Springs, PA, USA

DESIGN, CALIBRATION, AND PRELIMINARY TESTING OF A SYSTEM TO MEASURE THE VISCOELASTIC PROPERTIES OF A PACINIAN CORPUSCLE

Tiffany L. Senkow (1), Emily A. Chandler (1), Amy T. Moeller (2), Victor H. Barocas (1)

(1) Biomedical Engineering
University of Minnesota
Minneapolis, MN, USA

(2) Twin Cities Orthopedics
Minneapolis, MN USA

INTRODUCTION

The Pacinian corpuscle (PC) is a dermal mechanoreceptor responsible for transducing high-frequency (80-1000 Hz) vibrations [1], making it potentially important for many haptics applications, such as tactile aids for the hearing impaired and for button-click sensations. The structure of a human PC is ellipsoidal with dimensions on the millimeter scale [1]. Each PC contains a single nerve ending, surrounded by an outer core of approximately 30 collagenous lamellae separated by fluid [2]. Interaction between the lamella and fluid is responsible for filtering and transducing vibrations from the PC's outer surface to its central nerve [3]. There are several *in silico* biomechanical models of the PC, but more detailed parameters of the physical mechanoreceptor are still needed for more accurate simulations of PC dynamics.

The linear viscoelastic behavior of the corpuscle is of particular interest because it functions at high frequencies and low amplitudes, where linear viscoelasticity generally applies [4-5]. Studies often estimate the PC's viscosity to be approximately the same as that of water, which is a likely under-approximation. A previous study by our group determined an apparent Young's modulus of PCs isolated from cadaveric human hands as 1.4 ± 0.86 kPa using micropipette aspiration under steady-state conditions [6]. Also relevant, a purely kinematic study of PC under vibrational load was performed as part of a modeling effort [7], but no force measurement was made. Because the PC responds to frequencies in the 80-1000 Hz range, dynamic measurements of its biomechanical properties is crucial to understanding how the mechanoreceptor responds to *in vivo* stimuli.

In the current study, we designed, constructed, and calibrated a device to measure viscoelastic properties of the Pacinian corpuscle under physiologically relevant, i.e. millisecond, timescales as they respond to frequencies in the 50-1000 Hz range.

METHODS

We designed a system (Fig. 1) to stimulate an isolated mechanoreceptor mechanically from beneath and to measure the displacement of the PC on the opposite (i.e. top) surface. The apparatus consisted of a flat piezoelectric buzzer that provided the vibrational stimuli. The sample was placed directly on the buzzer. A polystyrene cantilever was mounted to an adjustable holder and lowered until it contacted the sample. When the sample was stimulated, the response motion of the cantilever was recorded via a laser vibrometer controller with interferometer. The input waveform to the buzzer and the vibration recordings from the interferometer were recorded simultaneously. Approximately 20 periods were recorded at each frequency with a minimum sampling frequency of 10,000 Hz.

The waveforms were characterized with Fourier analysis and fit to sinusoids. The phase difference between the displacement of the buzzer and that of the cantilever was determined to calculate the overall complex Young's modulus, of the sample.

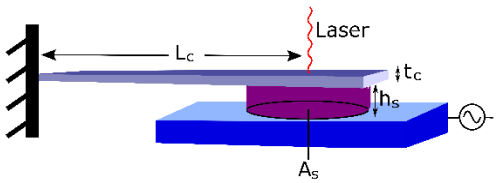

Figure 1: Schematic of the system. The sample lies between the vibrating buzzer and the cantilever. The cantilever length, L_c, cantilever thickness, t_c, sample height, h_s, and cross sectional area of the sample, A_s, are shown. Cantilever deflection at the center of the sample is measured with a laser interferometer.

Two initial calibrations were performed. First, the deflection of the cantilever under its own weight was used to estimate the modulus E of the polystyrene to be 2.3 GPa. Second, we used the system with silicone-oil viscosity standards (Brookfield Engineering Laboratories; Middleboro, MA) and analyzed only the lowest frequencies, for which it is reasonable to neglect cantilever inertia. In that limit, for a purely viscous sample, the phase, δ, is given by

$$\tan(\delta) = -E\frac{Ih_s}{\eta\omega A_s L^3} \qquad (1)$$

where I is the moment of inertia of the cantilever, h_s is the height of the sample, η is the viscosity of the sample, ω is the driving frequency, A_s is the cross sectional area of the sample, and L is cantilever length.

The University Anatomy Bequest program provided a hand specimen for PC collection. PCs were identified and isolated from the palm and finger as described previously [6]. Individual PCs were tested at room temperature. A small volume of PBS was added with a needle syringe as needed approximately every 5 minutes to maintain sample hydration. Each experiment took 20-30 minutes.

RESULTS

The phase shift between the displacement of the buzzer and the system response with 500 cP silicone oil is shown (Fig. 2a) for a range of frequencies and two cantilever lengths, 2 and 4 cm. The linear regime was used in subsequent analysis to calculate the viscosity.

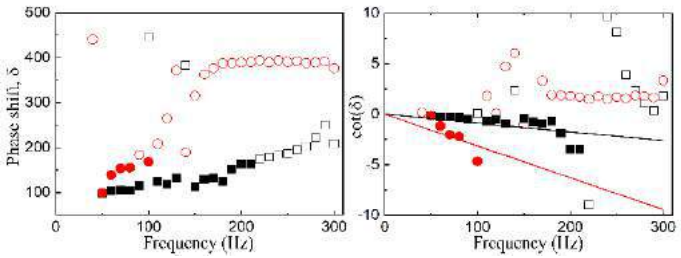

Figure 2: a) The phase difference between the buzzer displacement and the cantilever displacement at each frequency with 500 cP silicone oil. **b)** The cotangent of the phase difference. The black line is the linear regression from the 2 cm cantilever (*$-8.7x10^{-3}f$, $p=3x10^{-5}$*), and the red line is from the 4 cm cantilever *(-0.03f, p=0.009)* forcing the line through the origin. Black squares show data from the 2 cm cantilever, red circles the 4 cm cantilever. Filled shapes indicate low-ω data used in subsequent analysis.

From eqn. 1, one would expect cot(δ) to be linear in ω and cubic in L at low frequencies. As can be seen in Fig. 2b, the shorter cantilever gave excellent results, but the longer cantilever did not give a line passing through the origin, and the slope of the best fit line was only four times, not eight times that of the data for the longer cantilever. Based on eqn. 1, the viscosity of the 500 cP silicone oil was over-estimated to be 1100-1600 cP (fig. 3).

Fig. 4 shows preliminary experiments on a PC. As expected, as the cantilever length or thickness was increased, the phase shift between the displacement of the vibrating buzzer and the responding cantilever decreased. The PC samples were not analyzed with eqn. 1 because there were not enough data in the low-frequency, linear regime and because the tissue was expected to have a significant elastic component.

DISCUSSION

The creation of a new testing system was necessary to obtain reliable measurements of PC properties at high frequencies and small displacements and can be extended for measurements on other samples. Standard systems are challenged in terms of both acquisition rate and amplitude sensitivity. By coupling a laser vibrometer to the driving piezoelectric vibrator, we have overcome these barriers.

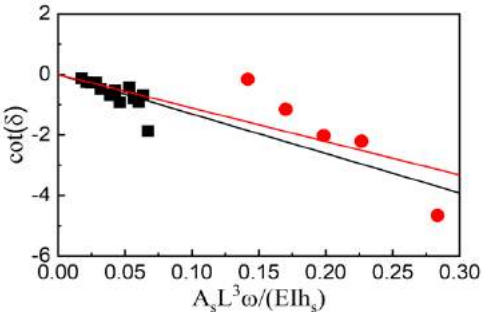

Figure 3: The cotangent of the phase difference vs. the constants from eqn. 1. Black squares show the low-ω data from the 2 cm cantilever, red circles from the 4 cm cantilever. The solid lines show the linear regression for the 2 cm (*$y=-15.7x$, $p=1.8x10^{-6}$*) and 4 cm (*$y=-11.1x$, $p=0.009$*) lengths forcing the line through the origin.

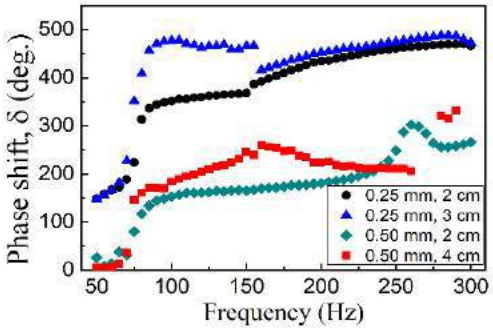

Figure 4: Preliminary experiment on a PC. A PC was tested with cantilevers of different heights (0.25 and 0.50 mm) and lengths (2 and 4 cm).

For a quasistatic (inertia-free) beam, the solution to the force balance is relatively simple, and eqn. 1 is readily derived. For calibration and testing purposes, it was fairly easy to use lower frequencies, yet the estimated viscosity of the test oils was found to be to larger than their standardized values, indicating possible confounding effects of inertia and finite sample size. To obtain more accurate estimates of the Young's modulus of the PC, especially at higher frequencies, a finite-element model of the PC and the cantilever will be needed for complete analysis.

ACKNOWLEDGEMENTS

The authors acknowledge the Minnesota Supercomputing Institute at the University of Minnesota for providing resources that contributed to the research results reported within this paper. Samples were obtained from cadaveric tissue provided, with approval, by the University of Minnesota Anatomy Bequest Program.

REFERENCES

[1] Quilliam, T. A. and Sato, M., *J. Physiol*, 167-76, 1955.
[2] Pease, D. C. and Quilliam,T. A. *J Cell Biol*, 3:3331-42, 1957.
[3] Caune, N. and Mannan, G. *J Anat*, 92(1):1, 1958.
[4] Loewenstein, G and Skalak, R., *J Physiol*, 182:346-78, 1966.
[5] Biswas, A. et al., *IEEE Trans Haptics*, 8(1):31- 42, 2015.
[6] Quindlen, J. C. et al., J *Biomech*, 63:104-9, 2017.
[7] Summers, I. R. et al., 11(1):146-50, 2018.

SB^{3}C2019
Summer Biomechanics, Bioengineering and Biotransport Conference
June 25 -28, Seven Springs, PA, USA

THE EFFECT OF INTERMITTENT THETA BURST STIMULATION ON BICEPS CORTICOMOTOR EXCITABILITY IN NONIMPAIRED INDIVIDUALS AND INDIVIDUALS WITH TETRAPLEGIA

Neil Mittal (1), Blaize C. Majdic (1), Carrie L. Peterson (1)

(1) Department of Biomedical Engineering
Virginia Commonwealth University
Richmond, Virginia

INTRODUCTION

Neuromodulation of the primary motor cortex (M1) in pair with physical therapy is a promising method for improving motor outcomes. Rationale for neuromodulation to target excitability of the corticospinal motor pathways (i.e., corticomotor excitability) is that increases in corticomotor excitability of upper limb muscles have shown to be associated with motor learning and skill acquisition [1-3]. Intermittent theta burst stimulation (iTBS) is a form of non-invasive brain stimulation which can increase corticomotor excitability and is advantageous over other forms of neuromodulation due to its short duration and low stimulation intensity [4].

The long-term goal of our study is to determine if iTBS paired with physical therapy can improve motor re-education of upper limb muscles after tendon or nerve transfer in individuals with tetraplegia. More proximal upper limb muscles, such as the biceps, can be surgically transferred to restore elbow extension. However, the ability for iTBS to increase the corticomotor excitability of proximal muscles such as the biceps brachii is currently unclear. The majority of studies involving iTBS have targeted the first dorsal interosseous (FDI) in non-impaired individuals. This is likely because the FDI is an easier target due to a high density of corticospinal neurons projecting to the muscle. These studies have found that iTBS can increase the amplitude of motor evoked potentials (MEPs) in non-impaired individuals for up to 30 minutes, however the effects often vary across participants resulting in negative findings group-wide. These results may differ in more proximal muscles, such as the biceps, due to differences in corticospinal control across flexors and extensors. One study which targeted the flexor carpi radialis (FCR), a muscle more proximal than the FDI, found that differences in the resting motor thresholds (RMT) between the FCR and its antagonist muscle (extensor carpi radialis) appeared to determine the efficacy of iTBS [5].

The purpose of this on-going study is to determine the effect of iTBS on the corticomotor excitability of the biceps, as measured by MEP amplitudes, in non-impaired individuals and individuals with tetraplegia. We hypothesize that iTBS will increase biceps MEP magnitude in non-impaired (NI) participants as well as persons with spinal cord injury (SCI). Furthermore, we hypothesize that the difference in RMT of the target and antagonist muscles (biceps and triceps respectively, RMT_T and RMT_A) will correlate with changes in MEP amplitude pre- and post-iTBS.

METHODS

Eight non-impaired individuals and four individuals with a low cervical (i.e., C5-C8) SCI have participated in this on-going study. Each participant completed three sessions of the protocol involving both active and sham iTBS, with each session separated by a minimum of three days in order to minimize the potential for carry over effects.

In each session, participants were instrumented with surface electromyography electrodes on the biceps and triceps of their dominant arm. The maximal compound muscle action potential (Mmax) was recorded from the biceps and triceps by delivering single pulse electrical stimuli to Erb's point via a bipolar stimulating electrode connected to a constant current stimulator (DS7AH, Digitimer Ltd.). Resting motor threshold (RMT) and active motor threshold (AMT) were then determined for the target muscle (biceps) by delivering single pulse transcranial magnetic stimulation (TMS) to the cortical area projecting to the biceps. RMT was also determined for the antagonist muscle (triceps). Single pulse TMS was delivered using a Super Rapid Plus stimulator (Magstim) via a 70 mm figure-of-eight coil. RMT was determined as the lowest stimulus intensity that induced MEPs of ≥ 50 μV in at least 5 of 10 consecutive stimuli with the target muscle fully relaxed. AMT was determined through the use

of an adaptive PEST software, developed by Borckardt et al., during sustained contractions of 10 ± 5% of the participant's maximum effort [6].

Fifteen biceps MEPs were recorded via single pulse TMS delivered at an intensity of 120% of RMT, at intervals 10, 20, and 30 min after sham and active iTBS. The iTBS parameters consisted of three pulses presented at 50 Hz, repeated every 200 ms for 2 s at an intensity of 80% of the participant's AMT. Two second bursts were repeated every 8 s for a total of 600 pulses [4]. iTBS was also delivered with the Super Rapid Plus stimulator. For the sham condition, a sham coil, looking identical to the active coil and making similar noise without delivering any active stimulation, was applied to the cortical area projecting to the biceps. Throughout each session, participants were kept unaware of the type of stimulation they were receiving.

Normalized MEPs (nMEP) were calculated as the MEP amplitude divided by the participant's average Mmax and averaged within each session separately for both active and sham coil in pre or post iTBS groups. A t-test was used to compare the change in nMEPs after iTBS between the active and sham coil data for both NI and SCI participant groups. Pearson's correlation was calculated for the difference between RMT_T and RMT_A, and nMEP post iTBS.

RESULTS

Magnitudes of nMEPs were increased after iTBS for the NI sham group, SCI sham group, and SCI active group ($p < 0.01$), but not NI active ($p = 0.40$). There was no difference between the post iTBS nMEP magnitudes between the active and sham coils in either group (NI $p = 0.52$, SCI $p = 0.15$). There were no correlations between post iTBS nMEP magnitude and RMT difference (1. sham coil NI; 2. active coil, NI; 3. sham coil, SCI; 4. active coil, SCI, respectively are: r^2 = 0.014, 0.014, 0.116, 0.176; all with $p > 0.05$). Mmax, RMT values, and MEP amplitudes are provided in Table 1.

Table 1: Average Mmax, resting motor thresholds (RMT) and MEP amplitudes for the NI group and SCI participants.

					pre-iTBS	post-iTBS
Subj	Session #	Mmax (mV)	RMT (Biceps)	RMT (Triceps)	MEP Amplitude (μV)	∆ MEP Amplitude (μV)
Avg NI	1	3.96	89	100	17.7 ± 15	-2.45 ± 12
	2	3.37	91	100	11.1 ± 8.6	1.45 ± 8.7
	3	3.67	86	99	12.7 ± 10	2.18 ± 12
SCI 01	1	0.950	95	100	7.74 ± 5.1	1.21 ± 2.1
	2	0.151	92	100	8.73 ± 10	14.5 ± 19
	3	1.33	97	100	18.5 ± 5.6	-7.85 ± 3.4
SCI 02	1	7.70	82	100	7.90 ± 7.8	7.12 ± 5.9
	2	9.35	80	100	13.7 ± 6.2	26.9 ± 26
	3	9.68	88	100	11. 8 ± 11	7.05 ± 1.2
SCI 03	1	0.194	77	100	49.7 ± 15	-15.0 ± 5.2
	2	0.176	80	100	49.4 ± 19	-1.69 ± 11
	3	2.75	91	98	15.0 ± 16	18.3 ± 29
SCI 04	1	0.155	95	100	7.42 ± 3.9	-0.758 ± 2.2
	2	0.297	94	100	4.17 ± 1.9	0.456 ± 0.48
	3	1.03	97	100	12.1 ± 8.3	0.354 ± 2.21

DISCUSSION

We expected that iTBS would increase the corticomotor excitability of the biceps, represented by an increase in MEP amplitudes, in both NI and SCI participants. While there did tend to be an increase in MEP amplitudes post iTBS in both groups, our t-test showed that there was no significant difference in the change of nMEPs between sham and active protocols. Additionally, while we expected there to be a correlation between the RMT difference of the target and antagonist muscles and the changes in MEP amplitudes post iTBS for both groups, our Pearson's correlation tests showed that there were no correlations.

A key outcome of this study was that both groups had not only a high degree of inter-subject variability, but also a high degree of intra-subject variability in the measured change of biceps MEP amplitudes. This was evident as a result of evaluating MEPs across multiple sessions and utilizing a sham coil as a control. Similar research done with continuous TBS has also shown varying responses across multiple sessions for each individual [7]. In addition to the variable responses seen in studies targeting the FDI, there may be some benefit in investigating the effects of iTBS on each participant in each session, rather than a group-wide analysis approach. This is further supported by other work that found the effects of iTBS on the FDI were independent across multiple sessions [8].

RMT focused inferences are of limited value with this data, as RMT intensities were frequently near or above the maximum intensity available with our stimulation unit and coil. While the use of a single coil prevents us from stimulating at an intensity that could fully capture the magnitude of MEPs in participants with higher motor thresholds, it is more realistic for a clinical approach. To circumvent this shortcoming, other studies have used a separate simulation unit and coil to record RMT and MEPs [5].

The lack of a MEP facilitatory effect of iTBS could be driven by variables that this pilot study did not account for, such as genetic factors or baseline excitability. Furthermore, the effects of iTBS may be better observed using other modalities than MEP magnitude, such as EEG measurements or MEP latency, which have been used as alternative metrics [9,10]. Finally, as this is a presentation of preliminary findings, limited sample size is a current limitation of our work.

Our preliminary data suggests that on average there are no group-wide effects of iTBS on biceps corticomotor excitability in either the NI or SCI subject groups. This provides rationale for investigating effects of iTBS on an individual basis, and suggests further work is warranted to understand factors that contribute to inter-subject and intra-subject variability.

ACKNOWLEDGEMENTS

Research reported in this publication was supported by pilot funding from the National Institutes of Health National Center of Neuromodulation for Rehabilitation, NIH/NICHD Grant Number P2CHD0886844, which was awarded to the Medical University of South Carolina.

REFERENCES

[1] Pascual-Leone A, et al., Annals of Neurology. 1993; 34(1): 33-37.
[2] Pascual-Leone A, et al., Journal of Neurophysiology. 1995; 74(3): 1037-1045.
[3] Tyc F,et al., The European Journal of Neuroscience. 2005; 21(1): 259-266.
[4] Huang, Ying-Zu, et al Neuron. 2005; 45.2: 201-206.
[5] Mirdamadi, J. L. et al., Neuroscience. 2016; 333: 132-139.
[6] Borckardt, J.J., et al. The journal of ECT. 2006; 22(3), 169-175
[7] Martin P. G. et al., Clinical Neurophysiology. 2006; 117: 2684-2690
[8] Hinder M. R. et al., Brain Stimul. 2014; 7(3): 365–371
[9] Rogasch N. C. et al., Human Brain Mapping. 2013; 34(7): 1652-1669
[10] Chang W. C. et al., Clin Neurophyiol. 2016; 127(8): 2892-2897

INERTIAL MEASUREMENT UNITS USED TO QUANTIFY ARM ELEVATION ANGLES OF MANUAL WHEELCHAIR USERS AND ABLE-BODIED CONTROLS THROUGHOUT A TYPICAL DAY

Brianna M. Goodwin, MS (1), Stephen M. Cain, PhD (2), Meegan G. Van Straaten, PT, MSPH (3), Emma Fortune, PhD (1), Melissa M. B. Morrow, PhD (1)

(1) Department of Health Sciences Research
Mayo Clinic
Rochester, MN, USA

(2) Department of Mechanical Engineering
University of Michigan
Ann Arbor, MI, USA

(3) Physical Medicine & Rehabilitation
Mayo Clinic
Rochester, MN, USA

INTRODUCTION

Of the 1.7 million wheelchair users in the United States (US), 90 percent, or 1.5 million persons use manual wheelchairs (MWCs) [1]. People with traumatic and non-traumatic spinal cord injuries (SCI) make up approximately 20% of the MWC users, and 12,000 new traumatic SCIs occur every year [2]. While MWCs are immediately available and enable independence, 63% of MWC users will have one or multiple tears of the stabilizing muscles of the humeral head in the shoulder (rotator cuff) after decades of MWC use as compared to 15% of age-matched able-bodied adults [3]. Additionally, up to 70% of MWC users will experience shoulder pain [4]. A crucial gap in knowledge exists in understanding how shoulder function of MWC users during daily living compares with the able-bodied population since MWC users function from an almost permanently seated position and use their arms as an agent for mobility and weight bearing. Further research is also needed to understand how this altered function translates to longitudinal declines in shoulder health.

Inertial measurement units (IMUs) provide an inexpensive and simple way to measure the angular velocity and acceleration of body segments in environments of daily living. IMUs have also previously been used to quantify shoulder elevation angles [5]. Shoulder angles have been associated with rotator cuff compression and impingement, which are thought to be contributing causes of shoulder pathology [6]. IMUs can be used in daily life to understand how the shoulder functions and measure the exposure of the shoulder joint to motion that increases the risk of tendon damage, which may aid in understanding the etiology of shoulder pathology.

This study aims to quantify shoulder joint motion in new (<3 yrs MWC use), mid (3-10 yrs MWC use), and chronic (>10 years MWC use) MWC users and an age and sex matched (to the new MWC users) able-bodied cohort. We hypothesize that new MWC users would have a different functional arm elevation workspace compared to their matched controls, and that this workspace would be similar between new, mid and chronic MWC users.

METHODS

The Mayo Clinic Institutional Review Board approved the study and written consent was obtained from all research participants. As part of a larger on-going investigation, a sub-set of 15 participants with SCI (five new users, five mid users, and five chronic users) and five able-bodied individuals who were age and sex matched to the new users are reported (Table 1). Participants reported the presence or absence of shoulder pain on their dominant side.

Table 1: Participant Demographics.

	Age (yrs) Mean ± SD	Sex	Level of Injury	Participants with dominant shoulder pain
Controls (New)	43 ± 12	2 M/3 F	-	0
New MWC Users	43 ± 13	2 M/3F	T4-T12	4
Mid MWC Users	33 ± 12	4 M/1 F	C6-L1	1
Chronic MWC users	49 ± 7	5 M	C6-L1	2

Participants wore three wireless IMUs (Emerald and Opal, APDM, Inc.); one on each lateral upper arm and one on the anterior of the torso. Data were sampled at 128 Hz. Participants were instructed to

wear the sensors during the entire length of a typical day, excluding bathing time. Participants performed a calibration which utilized the following movements: static upright neutral posture with upper arms resting against the thorax, right/left arm t-pose (shoulder abduction = 90º), and right/left flexion pose (shoulder flexion = 90º). Similar to El-Gohary and McNames (2012) a Kalman filter was used to estimate the orientation of each IMU relative to an inertial frame [5]. Custom Matlab (Mathworks, Natick, MA) code was written to calculate the orientations of the anatomical axes relative to the IMU-fixed reference frames from each participant's calibration movements. Arm elevation angles relative to gravity were calculated throughout the day, as well as periods of wear time [7]. Data were excluded from analysis if they did not meet the specified criteria of movement every 30 minutes. The percentage of daily wear time each participant spent in five humeral elevation bins were calculated (0-30º, 30-60º, 60-90º, 90-120º, and 120-180º).

RESULTS

For the dominant shoulder, all groups averaged over 45% of their day in 30-60º of arm elevation (Figure 1, Table 2). The new MWC users spent over 75% of their day between 0-60º while the control group spent over 70% of the day between 30-90º (Table 2). Both the mid and chronic MWC users spent over 75% of their day in the 30-90º range. Overall, all groups spent less than 5% of the day above 120º. No statistically significant differences were detected in this data set.

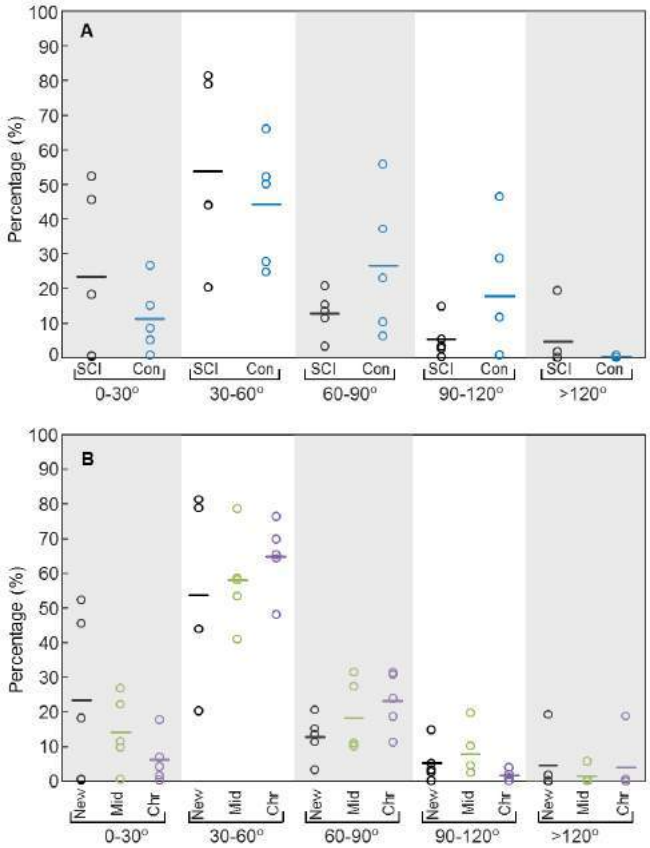

Figure 1: Percentage of time the dominant arm of each individual spent in each arm elevation range for (A) new MWC users (SCI) and age and sex matched controls (Con) & (B) new, mid, and chronic MWC users (Chr) for a day long data collection. The solid lines represent the mean of the data.

Table 2: The mean ± SD percentage of time participants spent in each arm elevation level.

	Control (%)	New (%)	Mid (%)	Chronic (%)
0-30º	13.1 ± 9.0	23.5 ± 22.0	14.2 ± 9.4	6.2 ± 6.2
30-60º	46.7 ± 15.7	53.7 ± 23.2	58.1 ± 12.2	64.9 ± 9.4
60-90º	24.6 ± 18.2	12.8 ± 5.7	18.2 ± 9.3	23.3 ± 7.6
90-120º	15.2 ± 17.7	5.3 ± 5.1	8.0 ± 6.5	1.7 ± 1.3
>120º	0.4 ± 0.2	4.7 ± 7.4	1.5 ± 2.2	3.9 ± 7.5

DISCUSSION

The purpose of this study was to report preliminary data for a subset of participants from a larger sample to demonstrate the shoulder motion of MWC users and matched controls during daily life. All groups demonstrated a primary functional workspace of the shoulder between 30-60º of arm elevation. Recent literature has suggested that the supraspinatus tendon of the rotator cuff has a higher incidence of tears than other rotator cuff tendons and impingement of this tendon likely occurs between 0-60º [8]. All MWC users spent over 70% of their day in this range, which could be indicative of a higher risk for tendon damage from impingement. A decrease in time spent in higher elevation angles (90-120º) for the MWC population is consistent with previous literature which suggests MWC users have a decreased range of motion (ROM) compared with able-bodied individuals [9]. Additionally, decreased time spent by new MWC users in the 60-90º range compared to the mid and chronic MWC users may highlight a decreased use of available ROM in the immediate years after injury due potentially to decreased trunk stability. Limitations of this study include the small sample size and the exclusion of arm plane of elevation data in our analysis (which will be enabled by an improved shoulder angle algorithm). Current understanding of shoulder impingement and pain are related to specific planes of motion. Additionally, shoulder loading was not measured.

This preliminary data demonstrated the ability to measure arm elevation throughout the day for MWC users and a matched control group. Additionally, the study reported real-world shoulder elevation trends which will be further investigated with a larger cohort and analyzed in combination with tendon pathology data. The long-term goal of this work is to understand the longitudinal connection between arm elevation angles and rotator cuff tendon pathology.

ACKNOWLEDGEMENTS

This research was supported by the Eunice Kennedy Shriver National Institute of Child Health and Human Development of the National Institutes of Health (R01 HD84423).

REFERENCES

[1] Kaye, H., et al., U.S. Department of Education, National Institute on Disability and Rehabilitation Research: Washington, DC, 2002.
[2] National Spinal Cord Injury Statistical Center, N, The University of Alabama at Birmingham, 2013.
[3] Wessels, K.., et al., JRRD, 50:351, 2013.
[4] Akbar, M., et al., J Bone Joint Surg Am, 92:23-30, 2010.
[5] El-Gohary, M., et al., IEEE Trans Biomed Eng, 59:2635-2641, 2012.
[6] Dal Maso, F., et al., Man Ther, 25:94-99, 2016.
[7] Karantonis, D. M., et al., IEEE Trans Inf Technol Biomed, 10:156-167, 2006.
[8] Lawrence, R., et al., J Orthop Res, 35 :2329-2337, 2017.
[9] Hussain, A., et al. Int J Ind Ergonom, 53:67-79, 2016.

SB³C2019
Summer Biomechanics, Bioengineering and Biotransport Conference
June 25 -28, Seven Springs, PA, USA

EXERCISE THERAPY AFFECTS GLENOHUMERAL KINEMATICS IN PATIENTS WITH ISOLATED SUPRASPINATUS TEARS

Luke T. Mattar (1), Camille C. Johnson (2), Tom H. Gale (2), Adam Popchak (3), James J. Irrgang (3,2), William J. Anderst (2), Volker Musahl (2,1), Richard E. Debski (1,2)

(1) Department of Bioengineering, University of Pittsburgh, Pittsburgh, PA, USA

(2) Department of Orthopaedic Surgery, University of Pittsburgh, Pittsburgh, PA, USA

(3) Department of Physical Therapy, University of Pittsburgh, Pittsburgh, PA, USA

INTRODUCTION

Rotator cuff tears commonly occur in the supraspinatus tendon[1], which is a primary initiator of abduction and compressor of the humeral head into the glenoid[2]. It has been theorized that maintaining the "force couple" within the rotator cuff can conserve glenohumeral joint stability in the anterior and posterior directions in the presence of a supraspinatus tear. Non-operative treatment is often the initial recommendation, but it remains unclear what factors are most important in determining whether one should undergo non-operative versus operative treatment. Structured exercise therapy programs can improve strength of the rotator cuff and scapular muscles, however it is unclear how these improvements in strength affect in-vivo translations of the glenohumeral joint. If stability is not maintained, it can lead to pain and disability limiting one's ability to perform activities of daily living. This emphasizes the importance of understanding the effect that exercise therapy has on glenohumeral joint stability during scapular plane abduction. The objectives of this study were to determine the effects of a 12-week exercise therapy program on glenohumeral kinematics and the relationship between glenohumeral abduction strength and maximum glenohumeral anterior translation in subjects with isolated supraspinatus tears during abduction in the scapular plane.

METHODS

Ten subjects (mean age 58.7 ± 5.6 years, mean BMI 27.5 ± 3.8) with a symptomatic degenerative rotator cuff tear isolated to the supraspinatus tendon were recruited for the study after providing IRB-approved written informed consent. Exclusion criteria included asymptomatic tears, previous shoulder injury, or presence of severe capsule tightness. Each subject underwent computed tomography (CT) of the affected shoulder and the images were segmented to create a 3-dimensional (3D) subject specific surface model of the humerus and scapula using Mimics 20 software package. The glenohumeral joint was imaged using biplane radiography[3]. Three trials of the motion were captured over 2 seconds per trial, starting in an adducted position and ending after maximum abduction was reached. The subjects were seated with their back straight during all trials. Digitally reconstructed radiographs from each subject and the captured biplane radiograph images were matched frame by frame using a custom model-based tracking technique (accuracy ±0.4mm and ±0.5°)[3]. Local coordinates systems for the humerus and scapula were based on a glenoid modified variation of the International Society of Biomechanics (ISB) standards[4]. Outcome measures included anterior/posterior (AP) and superior/inferior (SI) translation of the humerus with respect to the glenoid and the contact center of the humerus on the glenoid. AP and SI contact positions were normalized to glenoid width and height respectively. The normalization of the glenohumeral contact data results in the total contact path length normalized to glenoid size. Due to the variation in the amount of elevation between subjects, comparisons between pre- and post-therapy were made on an individual basis using the largest shared range of motion between data collection sessions. For all kinematic data, the trial containing the maximum elevation rotation angle was used for all analyses. Strength of the glenohumeral abductors was measured pre- and post- exercise therapy using a handheld dynamometer (Lafayette Manual Muscle Testing System). Paired sample t-tests were used to determine the difference in maximum AP translations, contact path length, and glenohumeral abduction strength pre- and post-therapy with significance set as $p<0.05$. Pearson's correlation was used to relate the changes in strength with differences in maximum anterior translations between pre- and post-exercise therapy with significance set as $p<0.05$.

RESULTS

All subjects successfully completed 12 weeks of exercise therapy. A significant reduction in maximum anterior translation of 1.7% ± 1.9% of glenoid width occurred post-exercise therapy (p=0.03). Six subjects showed a decrease in maximum anterior translation with the largest decrease being 4.8%. No increase in maximum posterior translation of 0.7% ± 2.7% glenoid width occurred post-exercise therapy (p=0.40). A significant reduction in contact path length of 16.3% ± 18.7% of glenoid size occurred post-exercise therapy (p=0.03). Eight subjects showed a decrease in contact path length with the largest decrease in contact path length being 40.6%. A significant increase in glenohumeral abduction strength was observed post-exercise therapy with an average increase of 11.3N ± 9.5N (p=0.01). Eight subjects showed an increase in glenohumeral abduction strength with the largest increase in strength being 24.5N. Although no significance was recorded, a moderate negative correlation was found (Figure 1, p=0.17, R^2=0.29, r=-0.54). As glenohumeral abduction strength improved there was a decreased maximum anterior translation. Post hoc power analysis was conducted and it was determined a significant correlation would be expected with statistical power of 80% if a subject size of 24 was tested.

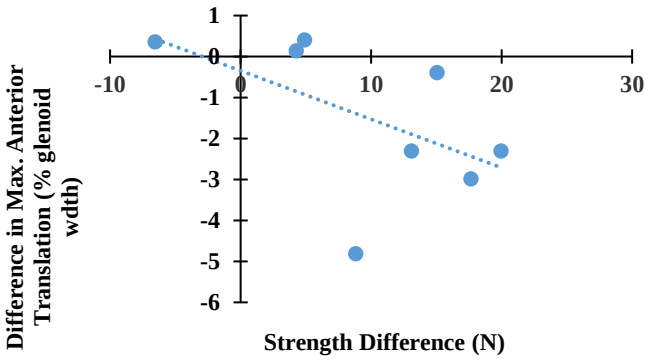

Figure 1: Correlation between the difference in glenohumeral abduction strength and difference in maximum anterior translation post-exercise therapy. Values presented are the measurements recorded post-exercise therapy minus measurements recorded pre-exercise therapy.

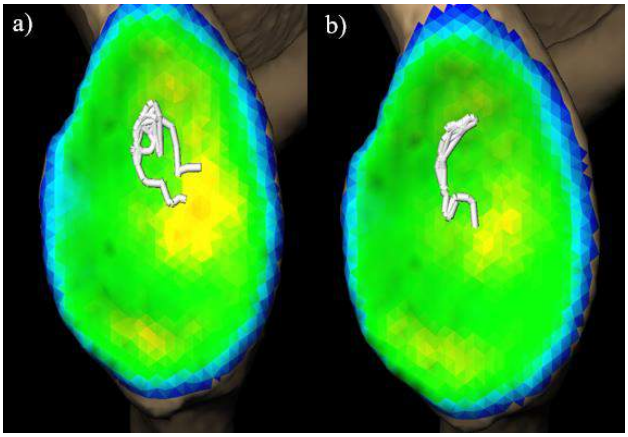

Figure 2: Representative contact path kinematics for a single subject during the scapular plane abduction task. a) Pre-exercise therapy and b) post-exercise therapy. The contact path is represented by the white line.

DISCUSSION

Our data shows that a structured exercise therapy program that focuses on restoring range of motion and strength overall successfully reduced the contact path length and maximum anterior translation and increased glenohumeral abduction strength. A significant decrease in contact path length post-therapy is indicative of greater joint stability during scapular plane abduction. The observed improvement in stability may be due to improvements in compensatory rotator cuff and scapular stabilizing muscles post-therapy as shown by the improved measures of glenohumeral abduction strength and decrease in anterior translation during the scapular plane abduction task. This may demonstrate improvements in the "force couple" of the glenohumeral joint, and could potentially be used as a clinical diagnosis for joint stability in physical therapy settings. Other studies have shown similar results regarding significant improvements in strength and contact path length in coronal plane abduction[5]. However, with a highly controlled exercise therapy program we were able to show that there may be a weak relationship between glenohumeral abduction strength and maximum translations in the anterior direction during scapular plane abduction. These findings are important clinically, as a study has shown an increase in the contact path length after rotator cuff surgery at 12 and 24 month follow-ups[6].

Limitations of the study include a small sample size and lack of cartilage on the glenoid and humerus in the model tracking technique. This may lead to overestimation of contact path length. However, because the primary objective was to determine the effects of a 12-week exercise therapy program on glenohumeral kinematics within the same subject, lack of cartilage in the model should not have affected the quantitative comparisons.

In the future, more subjects will be analyzed to determine if a significant relationship exists between the differences in clinically measured glenohumeral abduction strength and the change in maximum anterior translations during scapular abduction from before to after exercise therapy. Additionally, relationships between patient reported outcomes and glenohumeral kinematics should be investigated. Further studies should be done that analyze the effects of exercise therapy on glenohumeral kinematics longitudinally in subjects with isolated supraspinatus tears to determine if joint motion and stability is maintained over time.

ACKNOWLEDGEMENTS

Support from the National Institutes of Health grant 5R01AR069503 is gratefully acknowledged.

REFERENCES

[1] Minagawa, H et al., *J Orthop*, 10:8-12, 2013.
[2] Thompson, WO et al., *Am J Sports Med*, 24:286-292, 1996.
[3] Bey, M et al., *J Biomech Eng*, 128:604-609, 2006.
[4] Wu, G et al., *J Biomech*, 38:981-992, 2005.
[5] Miller, RM et al., *JSES*, 25:641-649, 2016.
[6] Bey, MJ et al., *Am J Sports Med*, 39:2117-2129, 2011.

SB³C2019
Summer Biomechanics, Bioengineering and Biotransport Conference
June 25 -28, Seven Springs, PA, USA

CHANGES IN HAND FUNCTION DUE TO BASAL JOINT SUSPENSIONPLASTY

Joshua P. Drost (1), James H.W. Clarkson (2), Tamara Reid Bush (1)

(1) Mechanical Engineering
Michigan State University
East Lansing, Michigan, USA

(2) Department of Surgery
Michigan State University
East Lansing, Michigan, USA

INTRODUCTION

In cases of severe thumb arthritis, surgery is often the best solution to reduce pain and improve function [1]. The most common surgery is a trapeziectomy; this is where the wrist bone at the base of the thumb (trapezium) is removed. To improve the mechanical stability of the thumb, basal joint arthroplasty replaces the bone with an alternative support for the thumb metacarpal [2]. One specific form of this replacement is a mini tightrope suspensionplasty. After the trapezium is removed, holes are drilled from the base of the first metacarpal to the proximal third of the second metacarpal. A strong braided non-absorbable suture is threaded through the bones to suspend the first metacarpal from the second, secured by two button anchors [3]. Case studies on hand surgeries have shown that this procedure is effective at reducing pain; however, research that documents the amount of the complete three-dimensional range of motion and force production recovered is lacking [3].

Therefore, the goals of this work were to 1) determine changes in motion abilities and force generation for the thumb pre- and post-surgery and 2) develop a visual representation so that the magnitude and locations of changes in hand function can be easily identified. This work will help surgeons to better understand the outcomes of surgery and could be used in the future to differentiate between surgical techniques.

METHODS

Patients undergoing a trapeziectomy with a mini tightrope suspensionplasty were enrolled in the study. Participants were tested prior to surgery, then after 6 weeks of rehabilitation and again 12 weeks post-surgery. At each time point, function was quantified through standard clinical measurements, range of motion tests, and force application. For the clinical assessment the participant filled out three questionnaires: a lifestyle/medical history, DASH (Disabilities of the Arm, Shoulder, and Hand questionnaire), and a visual analog pain scale. For reference: DASH is 0 (perfect function) to 100 (no function); the VAS pain scale is 0 (no pain) to 100 (worst pain). Also, Jamar dynamometers were used to measure power and pinch grip (Figure 1e).

Three-dimensional motion abilities were determined through four movements: 1) flexion and extension of the metacarpophalangeal joint (MCPJ) and interphalangeal joint (IPJ) (Figure 1a). 2) Radial abduction of the first carpometacarpal joint (CMCJ) and opposition to fifth MCPJ (Figure 1b). 3) Radial adduction of the first CMCJ and opposition to fifth MCPJ. 4) Palmar abduction and adduction of the thumb. Each movement was tested three times.

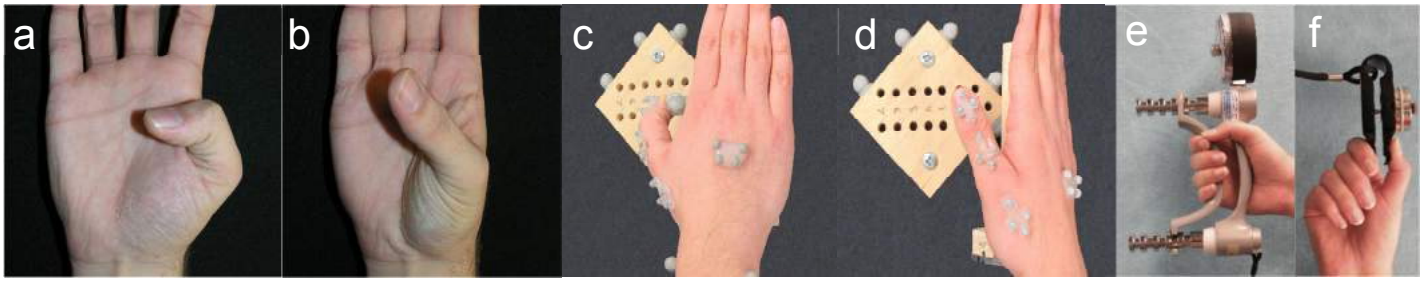

Figure 1: Testing procedure. Range of motion was measured through a) full flexion of the MCP and IP thumb joints and b) full ranges of opposition and abduction. Force capabilities were measured at multiple positions and directions; shown are c) the palm at 0° (horizontal) and force directed medially d) and palm at 60° with respect to horizontal with force directed towards the ground. Hand grip was measured using Jamar dynamometers: power grip (e) and pinch grip (f).

Maximum forces were determined in two directions in each of eight positions (Figure 1c-1d). The positions were based on varying rotation of the palm and abduction of the thumb. The palm was tested at four angles relative to the ground: 0°, 30°, 60° and 90°. At each rotation, the thumb was tested in two positions: full adduction (touching the palm) and maximal abduction of the thumb. At each position the participant was asked to apply maximal force towards the ground and then towards the hand.

RESULTS

Thus far, one patient has completed the full twelve-week study. We hypothesized that six weeks post-surgery the patient would experience reduced pain, but still demonstrate reduced function as healing of the hand was not complete. After twelve weeks we hypothesized reduced pain, improved force generation, and improved range of motion.

Clinical measures confirm our hypothesis (Table 1). After six weeks pain is deceased, both grips had similar strengths, but the dash score worsened. After twelve weeks, all clinical measures had improved as hypothesized. The DASH represents how the participant feels her hand is able to function during the tasks of daily living.

Table 1: Clinical measures before and after surgery. Power pinch grips are the average of three dynamometer trials. VAS pain and DASH are questionnaires representing how the participant feels about her pain and function.

Measure	*Pre*	*Post 6*	*Post 12*
Power Grip (N)	56.5	60.9	90.3
Pinch Grip (N)	18.7	12.9	24.5
Pain (VAS)	83	8	2
DASH	35	47	17

Range of motion tests results also confirmed our hypothesis (Figure 2). The figure on the left depicts the 3D motion of the hand as viewed from the front, showing opposition to the fifth MCP joint. A semi-transparent hand has been added to indicate the orientation of the figure. All three ranges of motion are shown together overlapping. Shown on the right are the average forces (average of four trials) at each rotation of the hand.

Six weeks post-surgery the motion space was decreased: the participant stated that while there was little pain in her hand, the CMC joint was stiff. At twelve weeks the motion space had returned to a similar size as before; however, the shape of the space had changed. Post-surgery the participant had increased palmar abduction and opposition but had reduced adduction (touch thumb to second MCPJ).

Strength abilities did not change six weeks after the surgery. However, at the twelve-week test the magnitudes were 66% larger on average. This mirrors the dynamometry data, showing that force stayed similar between pre-surgery and 6 weeks post-surgery and increased at the final test point.

DISCUSSION

The goals of this work were to determine changes in motion abilities and force generation for the thumb due to surgery and to develop a visual representation to identify the magnitude and locations of these changes.

Force abilities increased for all test conditions. This was also shown in the dynamometry measures; however, current clinical measures cannot identify the specific contribution of the thumb as they are taken together with other fingers. From our data the force generation abilities increased 10-15 Newtons. Future work will correlate thumb strength abilities to thumb posture and include force direction.

Differences in the motion shape are apparent (Fig. 2) and this is likely due to changes in the mechanics of the region. Prior to surgery, joint support came from the trapezium, a solid bone that supported load. Following surgery, the bone was removed and replaced by a suture suspension system (cable). This system is not rigid and can lead to different resultant forces on the base of the metacarpal. The suture will help stabilize the thumb motions, but differently that the solid bone structure. How the suture affects force transferal will also depend on where it is anchored in the second metacarpal. Future work will investigate suture tightrope and attachment locations and how they affect the range of motion and force production through modeling simulations.

The second goal of this project was to represent change in motion abilities visually. Figure 2 shows the range of motion of the participants thumb at each of the timepoints. Although this is a 2D representation of a 3D space, differences can be easily identified. Pre-surgery has a section to the right side showing higher extension of the thumb MCPJ. Many osteoarthritic patients exhibit hyper extension at the thumb MCPJ due to the development of a "Z" deformity, as the CMCJ subluxes progressively causing adduction of the first metacarpal generating extension forces at the MCPJ. Post-surgery tests both include a spike to the top representing the improved palmar abduction and increased opposition. These data can be viewed from any orientation, which permits easy comparisons with regard to the hand and the movement. In the future we will continue to improve the tools to display functional changes, both in making them easier to understand the orientation and adding strength abilities. We also plan to use these visualizations to compare between surgeries and treatments to understand differences in the functional outcomes.

REFERENCES

[1] Li, Y. K. et al. (2011) Plastic and Reconstructive Surgery.
[2] Huang, K. et al. (2015) Journal of Hand Surgery European Volume.
[3] Parry, J. A. and Kakar, S. (2015) Journal of Hand Surgery

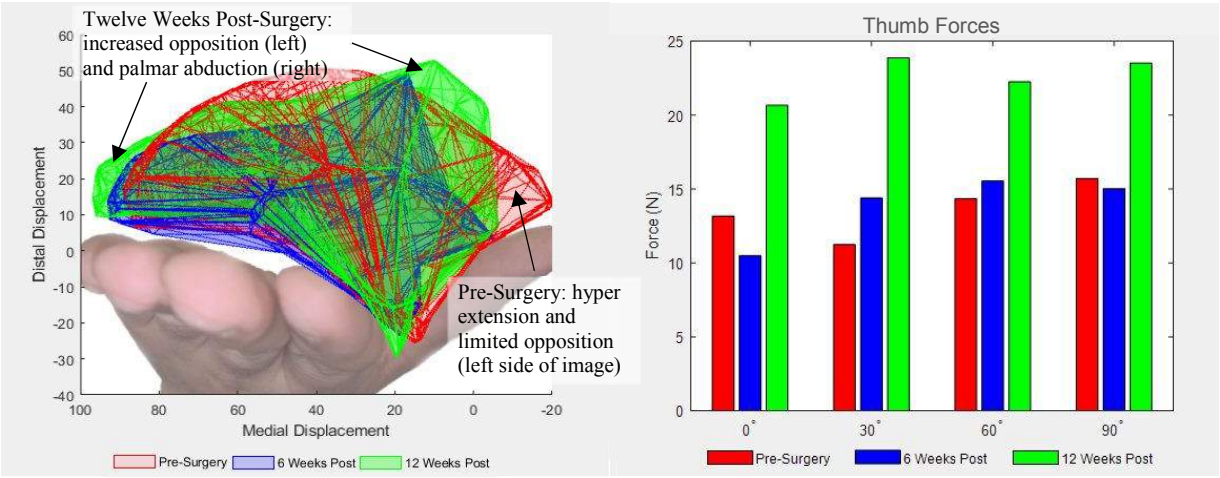

Figure 2: Changes to motion and force abilities following surgery. Left: Full range of thumb motion. The three spaces represent everywhere the thumb can reach at each time point, shown from the front. A transparent hand has been added to indicate orientation. Right: Average forces from each rotation of the hand.

SB^{3}C2019
Summer Biomechanics, Bioengineering and Biotransport Conference
June 25 -28, Seven Springs, PA, USA

MACROSCOPIC SURFACE DEFORMATION OF RETRIEVED GLENOID COMPONENTS FOR TOTAL SHOULDER ARTHROPLASTY

Giuliana M. Davis* (1), Noah B. Bonnheim* (1), Louis G. Malito, PhD (1), Stephan B. Gunther, MD (2), Tom R. Norris, MD (3), Lisa A. Pruitt, PhD (1)

(1) Department of Mechanical Engineering
University of California, Berkeley
Berkeley, CA, USA

(2) Martha Jefferson Hospital
Charlottesville, VA, USA

(3) San Francisco Shoulder, Elbow & Hand Clinic
San Francisco, CA, USA

INTRODUCTION

There are over 50,000 total shoulder arthroplasties (TSA) in the United States each year [1], making it the third most prevalent total joint arthroplasty behind total knee (TKA) and total hip (THA) arthroplasties. However, complication rates of between 10-15% in TSA [2] are higher than typically reported for TKA and THA. While the etiology of clinical failures is multi-factorial, complications related to the glenoid component have been cited as a primary cause of clinical failure in TSA [3]. Several researchers have characterized the morphology of glenoid component damage in order to elucidate the mechanisms and etiology of glenoid failure [4,5,6]. For example, repetitive translation of the humeral head along the superior/inferior (S/I) axis of the glenoid component has been associated with glenoid loosening, described as a "rocking horse" motion [7]. However, these insights have yet to result in new implant designs which demonstrate long-term clinical efficacy commensurate with other large-joint arthroplasties, suggesting that additional inquiry is required to fully understand *in vivo* biomechanical behavior and the progression of glenoid damage.

To address this issue, we analyzed the macroscopic surface deformation of twenty-five retrieved glenoid components spanning multiple component designs, surgeons and material formulations using a coordinate-measuring machine (CMM). Elucidating the macroscopic morphology of *in vivo* surface damage and comparing retrieved component geometries to their theoretical pristine conditions and patient information can provide unique insight into mechanisms of glenoid component damage and be a basis for design improvements.

METHODS

The articular surfaces of twenty-five retrieved ultra-high molecular weight polyethylene (UHMWPE) glenoid components (Table 1) were scanned using a CMM at planar isotropic resolution of 254 μm (resulting in ~10,000 point-cloud coordinates per implant). Operative data on the implant manufacturer and model were used to identify the original radius of curvature of each glenoid (i.e. pristine pre-operative geometry). Then, a custom algorithm was used to generate point-cloud coordinates of a pristine implant (i.e. "control"), which enabled comparison of the retrieval surface to its original shape.

For each retrieval, deformation was computed by subtracting, point-by-point, the retrieval point-cloud from the control point-cloud. Thus, positive deformation values denote an opening-mode, whereby the glenoid was expanded from its original shape. Two primary outcomes were considered: 1) the magnitude of deformation and 2) the spatial distribution of deformation. The magnitude of deformation was determined by separately calculating the 90th percentile of positive and negative deformations for each implant and plotting these values as a function of *in vivo* duration. The spatial distribution of deformation was determined by first calculating the 90th percentile of the absolute value of deformation of the entire point cloud, then plotting any deformations above this value on the implant surface as red (positive deformation, opening-mode) and blue (negative deformation, closing-mode). These plots were then visually compared. Both outcomes were compared against available clinical data to identify correlations between implant deformation and patient-related factors.

Table 1: Patient demographic information. Values are mean ± SD.

Time *in vivo* (months)	64.1 ± 61.5
Age at implantation (years)	57.1 ± 9.0 (n = 24)
Shoulder side	n = 14 right n = 11 left

RESULTS

Longer *in vivo* durations tended to result in larger amounts of deformation (Figure 1). The magnitude of the top 10% (90th percentile) of negative deformation was highly correlated with *in vivo* duration (R^2 = 0.61, Figure 1, blue) whereas the magnitude of positive deformation was not (R^2 = 0.00, Figure 1, red). Interestingly, summing the absolute values of the 90th percentile of positive and negative deformations slightly improved the correlation with *in vivo* duration (R^2 = 0.63, Figure 1, black), meaning that variation in damage accumulation is better explained by accounting for the interaction between deformation modes. Overall, *in vivo* duration was the best predictor of surface damage based on the available clinical factors.

In terms of the spatial distribution of deformation, the largest deformations occurred primarily at the implant edges (Figure 2). The top 10% of deformation for 76% of retrievals (19/25) was localized to the S/I edges, and of these retrievals, the mode of deformation was exclusively negative (closing) for 74% (14/19, Figure 2A) and exclusively positive (opening) for 26% (5/19, Figure 2B). Interestingly, for the 24% (6/25) of retrievals for which deformation was not localized to the S/I edges, the top 10% of deformation included a combination of both positive and negative deformations, and always involved the anterior/posterior (A/P) implant edges (Figure 2C).

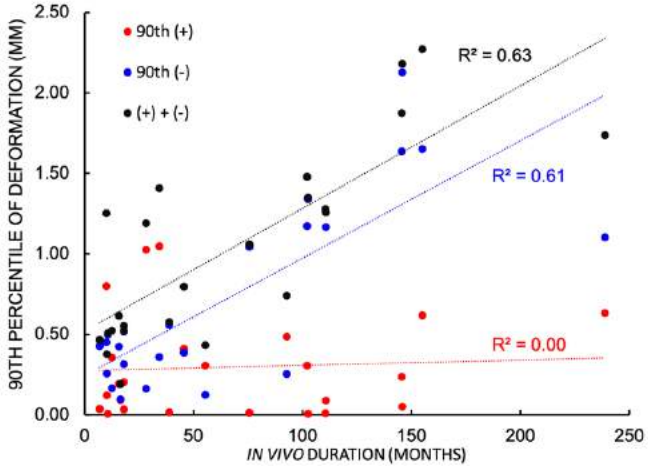

Figure 1: Magnitude of top 10% of deformation vs. *in vivo* duration.

DISCUSSION

The glenoid component in TSA is subject to a complex biomechanical environment involving both rotation and translation through a large range-of-motion [6]. This complexity, coupled with confounding variables such as fixation scheme, scapular bone quality, patient age, and physical activities, makes understanding *in vivo* loading conditions difficult. Yet, our results show consistent patterns in the magnitude and spatial distribution of deformation. For most implants, the largest deformations congregated at the S/I implant edges and are dominated by a closing mode; for a second group, the largest deformations also occur at the S/I implant edges but are dominated by an opening mode; and for a third group, both the S/I and A/P edges are recruited and a combination of opening and closing modes are evident. There were no apparent trends with respect to damage pattern as a function of reason for retrieval (n=19/25 available), patient age, or shoulder side. However, the magnitude of closing-mode damage was correlated with time *in vivo* and this correlation slightly improved when both opening and closing-mode magnitudes were combined.

Based on our current understanding of shoulder biomechanics, there is likely not a force which directly "closes" the glenoid

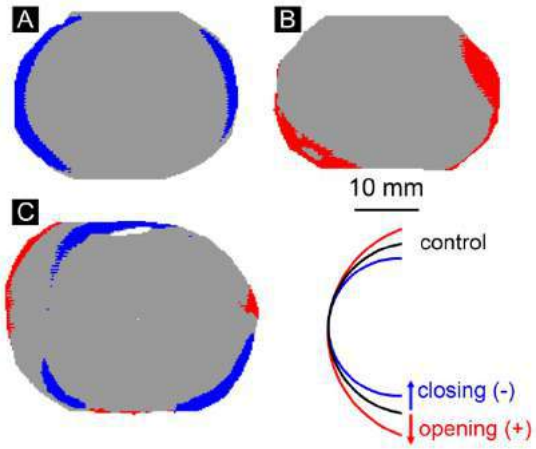

Figure 2: Spatial distribution of deformation. A) 14/25 exhibited a closing mode at S/I edges, B) 5/25 exhibited an opening mode at S/I edges, C) 6/25 exhibited mix modes with recruitment of both A/P and S/I edges

component, making it more conforming to the humeral head. However, a previous study which also reported glenoid closing using laser surface scanning suggested that a combination of wear and UHMWPE cold flow could presumably result in this type of glenoid deformation [4] following axially compressive loads exerted by the humeral head. The correlation between *in vivo* duration and closing-mode deformation reported here lends supporting evidence to this hypothesis, as both wear and cold-flow are time-dependent phenomena.

The translation of the glenoid along the S/I axis, which is thought to be a factor in edge-loading and subsequent loosening [6], could plausibly explain the opening-mode of surface deformation. The fact that this deformation mode occurs at the S/I extremes of the implant is mechanically intuitive, as it is at these locations for which the compressive loading moment-arm is largest. Interestingly, the three implants which exhibited the largest amounts of opening-mode deformation were explanted after relatively short *in vivo* durations (Figure 2B), and opening-mode damage generally did not increase with time *in vivo* (Figure 1). It is therefore possible that at shorter *in vivo* durations, perhaps when cement fixation is strongest, S/I translation serves to deform the glenoid in an opening-mode, whereas if fixation breaks down due to repeated edge loading, the "rocking-horse" motion enables translation without material deformation. This speculative hypothesis warrants further investigation.

Overall, our study provides unique insight into macroscopic glenoid deformation sustained *in vivo*. The discrete deformation patterns identified can elucidate how existing designs behave under physiologic loading, and can therefore aid in the design of components which improve TSA efficacy.

ACKNOWLEDGMENTS

REFERENCES

[1] OrthoInfo-AAOS, orthoinfo.aaos.org/en/treatment/shoulder-joint-replacement/, 2019., **[2]** Kamal, I et al., *JBJS*, 88:2279-2292, 2006., **[3]** Armstrong, A et al., *JBJS Reviews*, 1(2):e2, 2013., **[4]** Braman, JP et al., *J Orthop Res.,* 24(6):1249-60, 2006., **[5]** Gunther, SB et al., *J Arthroplasty,* 17:95-100, 2002., **[6]** Massimini, DF et al., *J bone Joint Surg Am.,* 92(4):916-26, 2010., **[7]** Strauss, EJ et al., *J Shoulder Elbow Surg.,* 18(5):819-33 2009.

* Both authors contributed equally to this work.

SB³C2019
Summer Biomechanics, Bioengineering and Biotransport Conference
June 25 -28, Seven Springs, PA, USA

DEVELOPMENT OF AN ANNULAR FLOW MECHANISM FOR MAINTAINING INTRAOCULAR PRESSURE WITH A GLAUCOMA DRAINAGE DEVICE

Sara E. Wilson (1,2), Anna M. Donovan (1), Hussain J.B. Alantari (1), Paul M. Munden (3), Ronald L. Dougherty (1,2)

(1) Mechanical Engineering
University of Kansas
Lawrence, Kansas 66045

(2) Bioengineering
University of Kansas
Lawrence, Kansas 66045

(3) Oklahoma City VA Health Care System
Oklahoma, OK 73104

INTRODUCTION

Glaucoma is an ocular disorder typically characterized by an increase intraocular pressure (IOP) that can lead to blindness.[1,2] Controlling IOP is essential to prevent vision loss. When medications are ineffective, surgery is sometimes required to treat glaucoma. A common surgical procedure is the implantation of a glaucoma drainage device (GDD) which allows drainage of aqueous humor (AH) from the anterior chamber of the eye through a small silastic tube. With such devices, a fibrous capsule forms around the GDD in the 2 to 6 weeks following implant surgery, becoming the source of resistance to AH outflow. Prior to this, IOP can be too low if not controlled. Various modifications have been created to control post-surgical IOP with limited success.[3] We have proposed a new method to modify GDDs in order to reduce the risk of early post-operative hypotony. [4,5] We propose inserting a degradable suture of appropriate diameter and length into the tubing of the GDD to provide sufficient resistance to AH outflow to maintain an acceptable IOP in the early post-operative period.[4,5] The insert would degrade over 2 to 6 weeks until fibrous capsule formation is sufficient to provide flow resistance.

METHODS

Theory

The resistance of a concentric annular insert can be modeled using Hagen-Poiseuille (H-P) theory for annular flow:[6]

$$\Delta P = \frac{8\mu L_t Q}{\pi}\left(r_2^4 - r_1^4 - \frac{\left(r_2^2 - r_1^2\right)^2}{\ln\left(\frac{r_2}{r_1}\right)}\right)^{-1} \quad (1)$$

where r_2 is the inner diameter of the tube and r_1 is the outer diameter of the insert. This model assumes fully developed, laminar flow of a Newtonian fluid. For a typical GDD tube, with an inner diameter of 300 µm and a flow rate of 2.5 µl/min, the Reynolds number is 0.20, supporting the assumption of laminar, fully developed flow. The model assumes the annular insert is concentric with the tube.

To examine this assumption, we can look to Manring's equation of eccentric annular flow: [7]

$$\Delta P = \frac{12\mu L_t Q}{\pi}\left((r_2 - r_1)^3 (r_2 + r_1)\left[1 + 3\left(\frac{e}{(r_2 - r_1)}\right)^2 \frac{r_2}{(r_2 + r_1)} + \frac{3}{8}\left(\frac{e}{(r_2 - r_1)}\right)^4 \frac{(r_2 - r_1)}{(r_2 + r_1)}\right]\right)^{-1} \quad (2)$$

where e is the distance between the centerlines of the tube and the annular insert. This model assumes that e is small. Nominally, it can be no larger than r_2-r_1.

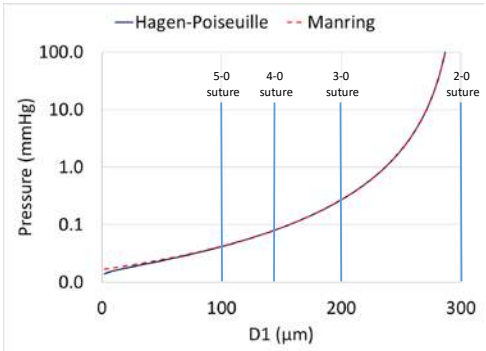

Figure 1. Hagen-Poiseuille theory and Manring equation show good agreement over the range of applicable suture diameters for a tube inner diameter of 300 µm. 3-0, 4-0 and 5-0 sutures of 8 mm in length would be appropriate for providing some resistance to flow during the early post-operative phase.

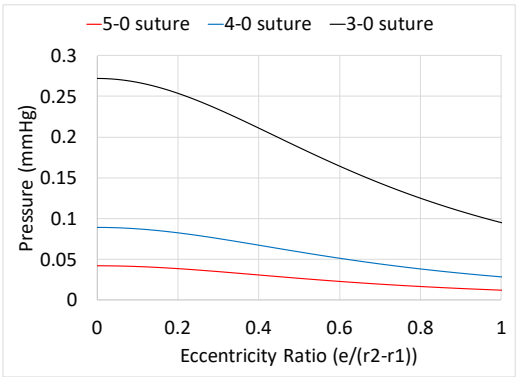

Figure 2. Flow resistance with 3-0, 4-0 and 5-0 sutures would be decreased with increasing eccentricity of the annular insert.

While the Manring equation is able to represent eccentricity in the annular insert, it has poor agreement with Hagen-Poiseuille when the annular insert has a very small diameter and pressure drops are low. In the case where the insert radius (r_1) is zero, Manring's equation should simplify to Poiseuille's law, but does not. However, the Hagen-Poiseulle equation for annular flow and the Manring equation do have good agreement over the relevant suture diameters (Fig. 1).

The Manring equation can be used to examine the effects of asymmetry of the centerline of the insert (Fig. 2). A concentric insert has the highest flow resistance. Flow resistance can be reduced by as much as 80% when the insert is against the tube wall.

These predictions of pressure assume the insert and tube diameters are exactly at the manufacturer specifications. Small variations in diameter would affect these results. Additionally, insert swelling and bends in the tubing or inserts could affect these predictions.

Experimental

The experimental setup consisted of a precision pneumatic pump, a bottle containing deionized (DI) water, microfluidic tubing and connections, a pressure transducer, a data logger, and a test section (Fig. 3)[5]. The test sample is connected in a temperature-controlled incubator (± 2 °F). A trial typically consisted of pumping DI water at the nominal human eye AH outflow rate of 2.5 µl/min, and measuring the accompanying pressure drop across the length of tubing (test sample) of interest.

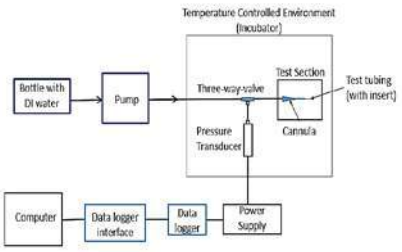

Figure 3: Schematic of microflow pressure-measuring test setup[5]

Three 4-0 and one 5-0 non-absorbable prolene sutures and one 4-0 absorbable monocryl suture were used to examine the alignment of these predictions with experimental data. Each suture was cut to a length of 8 mm and placed in a silastic tube with a nominal inner diameter of 300 µm. The system was primed for approximately 10 minutes before the trials in order to ensure that undetected air bubbles were removed from the setup. A baseline pressure reading was taken prior to insertion of the sutures. This baseline pressure drop was subtracted for pressure data during the trial.

RESULTS

The initial pressures (one day into collection) were 0.235±0.233 mmHg for the 4-0 prolene annular insert, 0.360 mmHg for the 5-0 prolene annular insert, and 0.448 mmHg for the 4-0 moncryl annular insert. Over days, the pressure increased on most of the samples (Fig. 4). Two 4-0 prolene samples had a dramatic pressure increase one after day 12 and one after day 27.

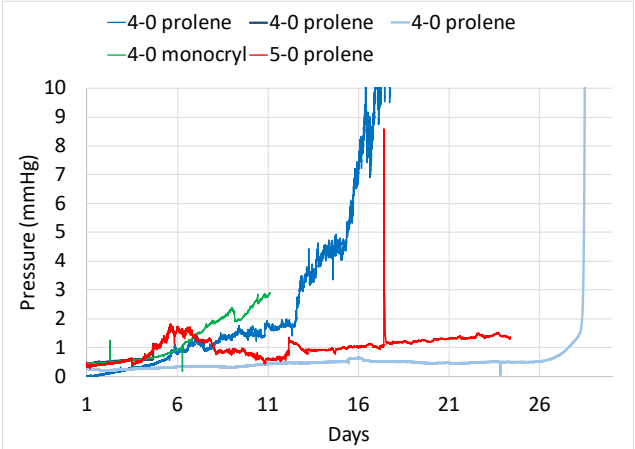

Figure 4. Flow resistance was examined for 5 suture samples. One sample had a dramatic pressure increase after day 12, possibly due to microbial contamination. Short pressure spikes are due to momentary oscillations in the flow control system.

DISCUSSION

The experimental results demonstrate general agreement with the predicted pressure, with a wide variability, likely due to variability in the actual suture diameter and possible eccentricity of the insert. Future work will look at using micro-CT to examine the exact dimensions of the inserts. Increases in pressure over the course of several days may be due to swelling of the suture. The monocryl appears to swell more than the prolene, but additional samples are needed to confirm this. The sudden dramatic increase in pressure of two prolene samples may be due to microbial contamination of the sample or displacement and bending of the sample. The monocryl sample continues to run and we expect that we should eventually see degradation of the sample and decreasing pressure. Future work will examine this degradation in order to make recommendations for the use of degradable sutures in glaucoma drainage devices.

REFERENCES

[1] Tham, Y. C, et al., *Ophthalmology*, 121 (11), 2081-90, 2014.
[2] Christakis, P.G, et al., *Ophthalmology*, 120 (11), 2232-40, 2013.
[3] Budenz, D. L., et al, *Ophthalmology*, 122 (2), 308-16, 2015.
[4] Munden, P., et al, Assoc for Research in Vision and Ophthalmology (ARVO) Annual Meeting, May 3-7; Denver, Colorado, 2015.
[5] Teo, T.H.T. et al, ASME Journal of Engineering and Science in Medical Diagnostics & Therapy 1(4), 041001-041001-8, 2018.
[6] Munson, B. R., et al., *Fundamentals of Fluid Mechanics*. 6th ed.; J. Wiley & Sons: Hoboken, NJ, 2009.
[7] Manring, N.D. *Hydraulic Control Systems*. J. Wiley & Sons: Hoboken, NJ, 2005.

SB³C2019
Summer Biomechanics, Bioengineering and Biotransport Conference
June 25 -28, Seven Springs, PA, USA

AORTIC SINUS VORTEX SPATIO-TEMPORAL VARIATIONS WITH LEAFLET CALCIFICATION

Hoda Hatoum (1), and Lakshmi P. Dasi (1)

(1) Department of Biomedical Engineering
The Ohio State University
Columbus, Ohio, USA

INTRODUCTION

The aortic sinus vortex is one of the most important and prevalent fluid dynamic features in the aortic sinuses. It is now acknowledged that the aortic sinus vortex plays a role not only in the opening and closing mechanisms of the leaflets[1], but also in the context of sinus washout and overall energy efficiency of the aortic valve system[2-4]. In addition, it was demonstrated that aortic sinus vortices initiation, entrapment and evolution play an important role in sinus stasis and washout[3,4]. Nonetheless, the factors impacting the spatio-temporal structure of the aortic valve sinus and how perturbation of this vortex can impact function, washout, and energy losses have not been completely addressed. Moore et al[3] provided an experimental study highlighting the importance of heart rate and fluid viscosity on the spatio-temporal structure in the aortic sinus vortex. Experimental studies by Hatoum et al[4] and numerical studies by Fukui et al[5] highlighted the dependence of aortic sinus vortex spatio-temporal topology on the morphology and geometry of the aortic sinuses. However, the stiffness of the leaflets and how that could impact the vortex formation, propagation and topology have not been investigated. Leaflet stiffening and its impact on the sinus vortex is critical from the standpoint of progression of calcific aortic valve disease (CAVD). This is because, in addition to genetic characteristics along with predisposition for particular inflammatory pathways fluid shear stresses and hemodynamic factors have emerged as one of the major regulators for initiation and progression of CAVD[6]. The objective of this study is to visualize and characterize the variations of the aortic sinus coherent structures as they form and evolve throughout the cardiac cycle as a function of leaflet calcification degrees (stiffer leaflets with calcification).

METHODS

A degenerated 23mm Carpentier-Edwards Perimount Magna surgical aortic valve (SAV) extracted from a patient who underwent a redo surgery (Fig.1a,b) was implanted in an aortic root model. The valve is degenerated and characterized by three leaflets with three significantly different degrees of calcific nodules: mild calcification (volume of 0.001 cm^3), moderate calcification (volume of 0.0592 cm^3) and severe calcification (volume of 0.275 cm^3). The chamber was set up into the aortic position of a pulse duplicator flow loop. Sinus hemodynamics were assessed for each of the three leaflets. Hemodynamic parameters for all conditions were maintained with a systolic to diastolic pressure of 120/80mmHg, a 1 beat per second heart rate and a cardiac output of 5Ll/min. 60 consecutive cardiac cycles of aortic pressure, pressure difference across the aortic valve (or pressure gradient as clinically recognized and as will be adopted in the sections below), and aortic flow rate data were recorded at a sampling rate of 100Hz. Time-resolved raw particle image velocimetry (PIV) images were acquired with a resulting spatial and temporal resolutions of 0.159mm/pixel and 4000Hz respectively. Circulation and viscous shear stress were calculated and leaflet tracking was performed.

RESULTS

Fig.1c and 1d show the valve configuration when it is closed and when it is open respectively. The mildly calcified leaflet almost completely opens while the severely and moderately calcified leaflets do not. Leaflet tip tracking shown in Fig.1e displays the differences among the three leaflets measured from a common point near the

centerline. As expected, the mildly calcified leaflet opens the most (4.38±0.037mm) followed by the moderately calcified (2.23±0.07mm)

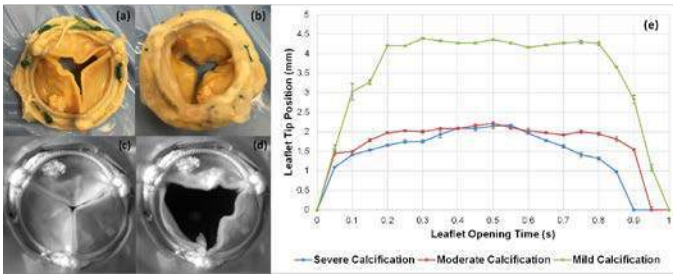

Figure 1: (a) Calcification distribution on the (a) aortic and the (b) ventricular side of the valve; (c) Closed configuration and (d) open configuration of the valve; (e) Leaflet tip position from a common point above the centerline as a function of normalized time (0 = opening; and 1 = closing).

and the severely calcified (2.16±0.02mm).

Figure 2 shows exemplary velocity and vorticity fields obtained in the sinus for the three cases. For the moderate and the severe case, the distinct absence of counter clock-wise vorticity is notable and instead presence of clockwise vorticity emanating from the separated flow boundary layer at the sinotubular junction (STJ) is entrained into the sinus.

Evaluating the circulation in the sinus area; Fig.3a shows the alternating positive and negative circulation values in the severely calcified sinus with an average circulation of -1.30x10-4 m^2/s. Fig.3b shows a prevalent negative circulation with the moderately calcified leaflet with only positive variations at the beginning and the end of the cycle. The

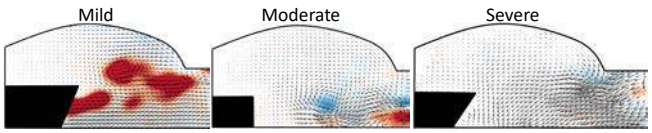

Figure 2: Velocity and Vorticity during Acceleration phase for the three cases illustrating the drastic variation in the mechanism that drives sinus flow. Flow from left to right.

circulation found was -9.47x10-4 m^2/s. Fig.3c shows a prevalent positive circulation of total magnitude of 1.85x10-3 m^2/s. In Fig.3d and 3e during systole, the mildly calcified leaflet sinus case shows the most spread-out and higher ranges of shear stress probabilities and highest magnitudes ranging from -1.5 to +1.8 Pa. Significantly higher probabilities to develop higher shear stress magnitudes were found with the moderately calcified case compared to the severely calcified one. The severely calcified case has the highest shear stress probabilities around 0.0 Pa shear stress, followed by moderate then mild. During diastole, the severely calcified leaflet case was characterized by the smallest span of shear stress. The moderately and mildly calcified cases show almost similar probability distribution range going from -0.8 Pa to 1.0Pa with similar likelihoods on the positive shear stress distribution side and higher likelihoods for higher shear stress for the mild on the negative range side.

DISCUSSION

The changes in the aortic sinus vortex evolvement can be captured and explained in Figure 4 as deduced from circulation values and from particle image velocimetry images. The degree of calcification impairs valve opening and closing mechanisms and thus it directly affects the coherent vortex structure development in the sinus. The higher the calcification degree the lower the shear stress range and likelihoods of having higher shear stress. Cell expression profiles studied by Butcher

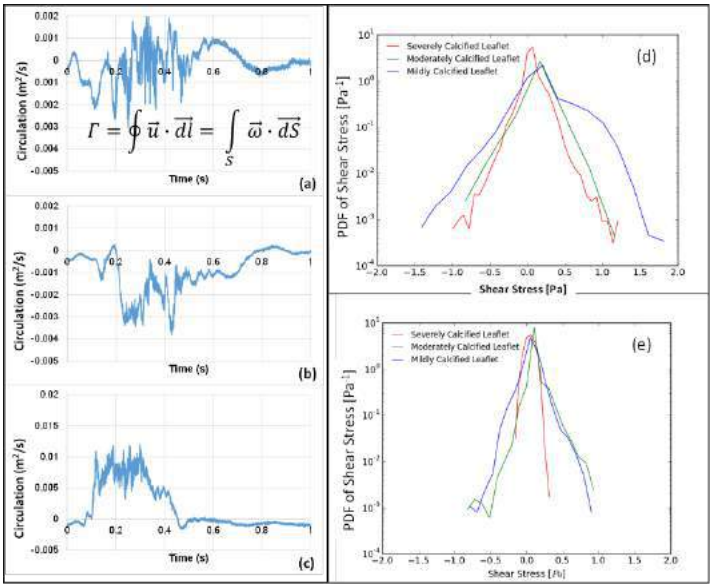

Figure 3: Variations in circulation versus time for the 3 different sinus cases with (a) severe, (b) moderate and (c) mild leaflet calcification along with Probability density function of varying shear stress distribution near the different leaflets in the sinus during (a) systole and (b) diastole.

et al[7], suggest that valvular endothelial cells are protected from oxidative, inflammatory stress and calcification beginning and propagation by shear stress. Calcification disease process is thought to be initiated by several factors, low shear stress is one of the most important ones[8]. In this study, when the shear stress is quantified in each of the three cases, during systole and probably intuitively, the larger shear stresses and the larger probabilities to obtain high stress with the smaller probabilities for near-zero shear stresses were obtained when the leaflet has mild calcification (almost fully opens). The higher the calcification density on the leaflet, the significantly smaller the shear stress distribution becomes.

Figure 4: Cartoon of sinus flow pattern differences at peak systole for the (a) severely, (b) moderately and (c) mildly calcified valve. Flow from left to right.

ACKNOWLEDGEMENTS

The research done was partly supported by National Institutes of Health (NIH) under Award Number R01HL119824.

REFERENCES

[1] Keele, K.D., *Postgraduate medical journal*, 1952. 28(324): p. 521.
[2] Van Steenhoven, A. et al., *J. of biomechanics*, 1982. 15(12): p. 941-950.
[3] Moore, BL et al., *Experiments in fluids*, 2014. 55(7): p. 1770.
[4] Hatoum, H. et al., *JTCVS*, 2018.
[5] Fukui, T. et al., *International Journal of Life Science and Medical Research*, 2013. 3(3): p. 94.
[6] Sun, L. et al., *PLoS one*, 2012. 7(10): p. e48843.
[7] Butcher, J.T. et al., *Arteriosclerosis, thrombosis, and vascular biology*, 2006. 26(1): p. 69-77.
[8] Stewart, B.F. et al., *Journal of the American College of Cardiology*, 1997. 29(3): p. 630-634

AN INITIAL FLUID MECHANICS STUDY OF BIOPROSTHETIC HEART VALVES IN AN ACCELERATED DYNAMIC ENVIRONMENT

Sailahari V. Ponnaluri (1), Ming-Chen Hsu (2), Michael S. Sacks (3), Keefe B. Manning (1,4)

(1) Department of Biomedical Engineering
The Pennsylvania State University
University Park, PA, USA

(2) Department of Mechanical Engineering
Iowa State University
Ames, IA, USA

(3) Willerson Center, Institute for Computational and Engineering Sciences, Department of Biomedical Engineering
University of Texas
Austin, TX, USA

(4) Department of Surgery
Penn State Hershey Medical Center
Hershey, PA, USA

INTRODUCTION

Approximately 280,000 people worldwide receive a heart valve transplantation per year [1]. For patients with severe regurgitation, prolapse or calcification, this is one of the best treatment options. Mechanical heart valves are more commonly implanted in patients due to their durability [2]. However, the need for life-long anticoagulant therapy motivates physicians to consider an alternative valve, specifically, bioprosthetic heart valves (BHVs). BHVs are commonly made of bovine or porcine tissue and implanted only in elderly patients due to an average valve lifespan of 10-15 years.

To test the fatigue experienced by BHVs and determine the life span, the U.S. Food and Drug Administration mandates that BHVs be tested with an accelerated wear tester (AWT). This test must adhere to the ISO:5840 guideline which indicates the valve cycling rate, the pressures they should experience, the number of cycles, and any other testing conditions [3]. In a study performed by Iwasaki *et al*., a polymer valve was cycled in three different AWTs [4]. They noticed that by increasing the cyclic rate, the lifespan of the valves were considerably shortened. Additionally the location of tears and fatigue experienced in the AWTs did not match animal experiments. Due to the high frequency testing and the non-physiological conditions observed in AWTs, the mechanism of *in vitro* fatigue may not accurately predict the fatigue mechanisms experienced *in vivo*. Therefore, this study aims to quantify the fluid dynamics of BHVs within an AWT, using high-speed particle image velocimetry (HSPIV). By developing an understanding of the fluid mechanics in an AWT environment, better fatigue tests for bioprosthetic surgical and transcatheter valves could be performed.

METHODS

To study the fluid mechanics of BHVs mounted in AWTs, an Electroforce® Durapulse™ AWT (TA Instruments, New Castle, DE) was modified for optical access. This system consists of a proximal chamber upstream of the valve, a distal chamber downstream of the valve, pressure transducers (Utah Medical Products Inc., Midvale, UT) at the base of each chamber, and a valve housing between the chambers (Figure 1A). This system was mounted on a Bose linear motor to develop pressure gradients consistent with ISO:5840. A 31 mm Hancock valve (Medtronic, Minneapolis, MN) was mounted in the Durapulse™. The Durapulse™ cycled the Hancock valve at 900 bpm in a blood analog comprised of glycerin and water, producing a density of 1.13 g/ml and an asymptotic dynamic viscosity of 3.99 cP to match the viscosity of 40% hematocrit blood. To maintain consistency with ISO:5840, a transvalvular pressure of 100 mmHg was maintained across the closed valve for approximately 20% of the cycle. The Durapulse™ recorded pressure waveforms at the distal chamber and proximal chamber and then, calculated a delta pressure (Figure 2).

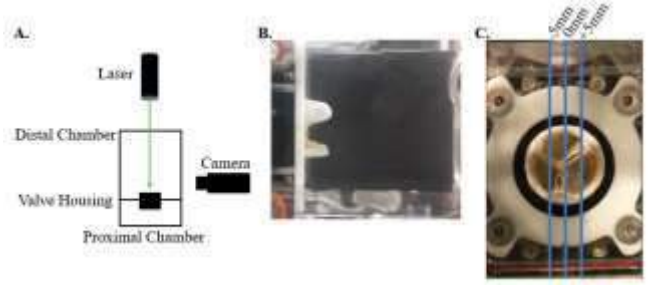

Figure 1: A. HSPIV experimental set-up with the Durapulse™, high speed camera, and laser. B. Zoomed-in view of near valve region in distal chamber. C. Front view of Durapulse™ valve region denoting the HSPIV planes of interest.

Next, the Phantom Miro-Lab 110 high-speed camera (Vision Research, Wayne, NJ) was mounted to visualize the side of the Durapulse™ chamber (Figure 1A). The camera was focused on the region directly downstream, above, and below the valve (Figure 1B) using extension tubes. A high-speed Terra PIV laser (Continuum, San Jose, CA) produced three vertical planes for collection: the centerline (0 mm) and ± 5 mm (Figure 1C). Two sets of HSPIV data were collected, an averaged set and an interpolated set, at a resolution of 26 pixels/μm. For the averaged set, 1000 image pairs were collected at 11 time points. For the interpolated set, 53 images were rapidly collected consecutively, 1.2 ms apart, to visualize any random flow phenomena that may develop. Insight 4G (TSI, Inc., Shoreview, MN) triggered image pair capture at the peak of the distal waveform and the images were processed with Tecplot Focus (Tecplot, Bellevue, WA).

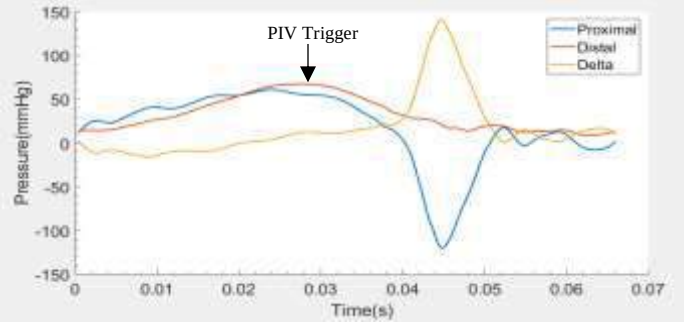

Figure 2: Durapulse™ waveform for each chamber and delta pressure. The trigger used for HSPIV is indicated.

Finally, the effective orifice area (EOA) of the heart valve was quantified. The Phantom high-speed camera was mounted to visualize the heart valve opening and closing over 11 time points through the cycle. Images were acquired in TSI's Insight 4G and processed with MATLAB (MathWorks, Natick, MA). To improve the image contrast between the valve and the open orifice area, an external light source was positioned. Valve EOA images were processed in MATLAB using the workflow shown in Figure 3.

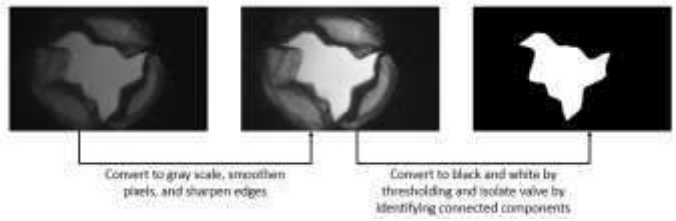

Figure 3: Workflow of processing raw valve images in MATLAB to determine the EOA

RESULTS

Starting with the effective orifice data, the valve opened for approximately 44% of the 66 ms cycle, allowing for fluid to flow into the distal chamber. As demonstrated in Figure 4, the opening was asymmetric, and the jet profile of the systolic flow could be dependent on the valve orientation. Due to valve age, the valve also did not open completely, demonstrating some stiffness associated with the leaflets. Finally, while the leaflets coapted, a twisting or pinwheel effect was observed.

Data obtained using HSPIV showed a jet formed during systole. As shown in Figure 1C, the valve orientation was such that, the larger opening would be at the top of the valve and would narrow moving downward. The jet reflected the valve opening by having the jet exit from near the top of the valve at the start of ejection (Figure 5). Looking further into the cycle, eddies randomly formed in the distal chamber. During valve closure, a large recirculation region formed consistently downstream of the valve base. This recirculation formed while the valve closed and continued until the start of the next cycle. The random eddies that formed around the valve and downstream of the valve demonstrated a level of three dimensionality.

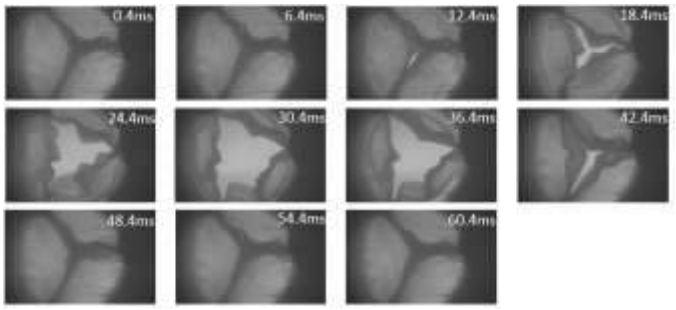

Figure 4: Raw EOA images of 31 mm Hancock valve.

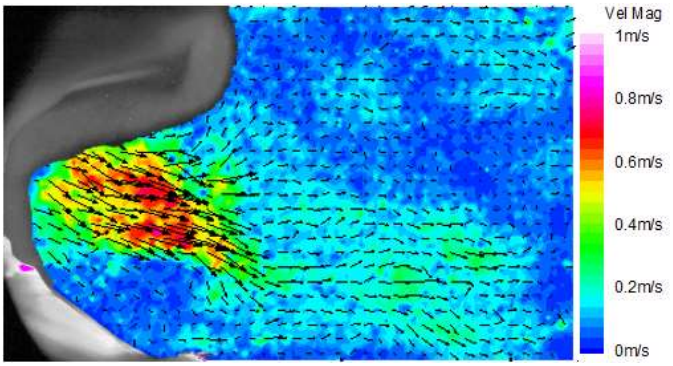

Figure 5: Centerline interpolated HSPIV flow field at the start of systole demonstrating an asymmetric jet caused by valve orientation.

DISCUSSION

These results are an initial step in understanding the flow associated with BHVs in an AWT environment, which has never been explored previously. The results demonstrated that the valve flow transitioned from a jet to a series of eddies downstream of the valve. This study was limited by the age of the valve (10 years old) which displayed a stiff behavior by not opening entirely. Gaining knowledge on the fluid mechanics, specifically, the influence of the jet, the random eddies and the non-physiological testing frequency could contribute to understanding fatigue mechanisms imparted by AWTs. The next step is to correlate the new understanding of AWT fluid mechanics to valve fatigue after cyclic testing and create new waveforms for increased physiological relevance.

ACKNOWLEDGEMENTS

Research supported by NIH HL129077.

REFERENCES

[1] Pibarot, P., Dumesnil, J.G., *Circulation*, 119:1034-1048, 2009
[2] Dasi, L.P., *et al.*, Clin Exp Pharmacol Physiol, 36(2): 225-237, 2005
[3] International Standards Organiation, ISO: 5830, Cardiovascular Implants-Cardiac Valve Prosthesis, 2005
[4] Iwasaki, K., *et al.*, *Artif. Organs*, 26(5): 420-429, 2002

SB³C2019
Summer Biomechanics, Bioengineering and Biotransport Conference
June 25 -28, Seven Springs, PA, USA

EXPERIMENTAL TESTING OF POLYMERIC TAVR VALVE PERFORMANCE IN PATIENT-SPECIFIC MODELS

Brandon J Kovarovic (1), Oren M Rotman (1), Marvin J Slepian (2), Danny Bluestein (1)

(1) Department of Biomedical Engineering,
Stony Brook University
Stony Brook, NY, USA

(2) Sarver Heart Center,
University of Arizona,
Tucson, AZ, USA

INTRODUCTION

Transcatheter aortic valve replacement (TAVR) has been a life-saving procedure for inoperable high-risk patients with severe aortic valve stenosis, as an alternative to surgical aortic valve replacement (SAVR). In recent years TAVR devices are being implanted in younger lower risk patients as an alternative to SAVR. Although valve designs and procedure approach have been refined over the past 17 years[1], those are still subject to persistent clinical complications, including poor deployed valve performance, device migration, increased risk for stroke, flow stagnation leading to device thrombosis, and leak or regurgitation flows around the valve stent (PVL or paravalvular leaks)[2]. With TAVR deployed in younger patients the device durability becomes a critical design issue. Tissue-based TAVR valves suffer faster deterioration than SAVR valves, combined with new calcific mass formation in the xenograft tissues. Several studies suggest that the method of crimping (compressing the device stent and tissue to sizes below 16F) and deployment damages the xenograft tissues and negatively impacts the durability[1].

Polymeric TAVR valves have been conceptualized to address some of the clinical complications as well as the durability associated deterioration[3]. Recent advances in hemocompatible polymeric technology are harnessed to design optimized valves that achieve similar or less thrombogenic potential achieved by tissue valves, as well as the ability to cast higher precision valve morphologies with superior valve hemodynamic performance- additionally extending the durability of the valve by preventing calcific infiltration into the valve leaflets.

Development of TAVR devices conventionally relies on idealized bench testing methods and/or *in vivo* animal testing in healthy anatomies. The discovery of clinical failures/complications, along with refinement of the device design to address them, relies on clinical experience on patients. Experimental and computational models of diseased patient-specific geometries would allow the development process of the TAVR device to study with greater detail these clinical complications and iterate device design before ever risking a patient's safety.

METHODS

Utilizing a novel self-expandable polymeric valve, PolyV-1 (PolyNova Cardiovascular Inc., Stony Brook, NY), it was compared

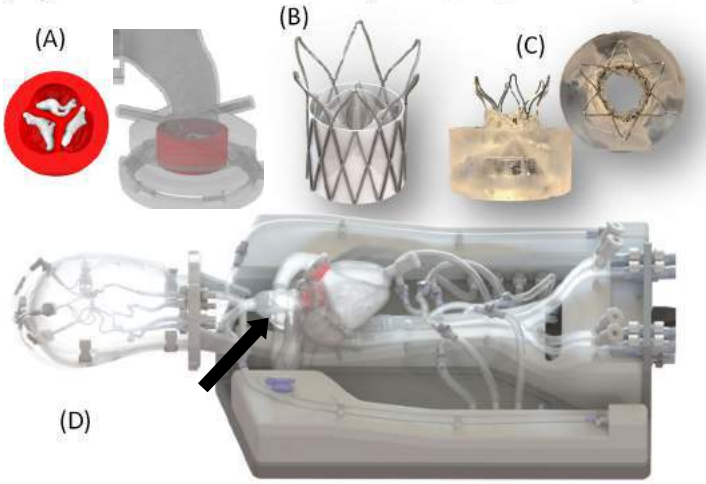

Figure 1. (A) Rendering of calcific pattern of one patient valve with matching aorta (B) Rendering of PolyV-1 design (C) Deployed PolyV-1 in the stenotic valve (D) Vascular Simulations Replicator simulator, black arrow highlighting location of patient specific anatomy placement.

against two tissue-based valves: the Carpentier-Edwards Perimount Magna Ease (PME) surgical valve (Edwards Lifesciences, CA) and the Innovare TAVR valve (Braile-Biomedica, Brazil), all of size 20mm or equivalent. Initial testing was completed in an ISO-compliant left heart simulator (Vivitro Labs, Victoria, BC) having an idealized anatomy.

Patient-specific experiments: Five patient models were reconstructed from CT scans of TAVR patients with procedural complications, obtained by Stony Brook Hospital: 3 with moderate to severe PVL, 1 with device migration, and 1 with poor post-deployment valve performance. The anatomies were scaled to fit the available TAVR valves and have equivalent oversizing in all the patients. Silicone models of the patient-specific aortic root and stenotic valve models were made by Vascular Simulations Inc (Stony Brook, NY) to interface with their Replicator simulator (Fig 1), which contains a complete silicone arterial tree of the major vessels with a functional beating left heart and a closed loop feedback system to maintain physiological flows and pressure waveforms. The anatomies were segmented with Materialise Mimics (Materialse NV, Belgium). The valves were cast with polyurethane (30A) with a uniform leaflet thickness of 400µm and semi-rigid calcifications. The aortic root was molded in a proprietary process with physiologically relevant silicone with a uniform thickness taken from the aortic lumen geometry. The Replicator simulator allows collection of hydrodynamic performance of the valves in accordance to the ISO-5840[4].

Clinical imaging: The simulator design allows the collection of imaging data comparable techniques available in the clinic. In each of the 5 geometries ultrasound continuous-wave (valve performance) and color doppler (# of regurgitant jets) are collected. Angiography images with contrast injections into the aortic root to assess leak patterns and severity as well as ventricular injections to study washout times for flow stagnations. Finally, cardiac MRA studies are collected both with phase contrast studies retrograde to the valve for accurate measures of the leak jet velocities and 4D flow analysis of the systolic jet and stagnations.

MicroCT and Computational Models: The deployed valves inside the stenotic native valves will be scanned in a µCT scanner and segmented to obtain the leak channel geometries (Fig 2). This also allows the study of the eccentricity of the stent corresponding to the calcification distribution in the native valve. The segmented geometries will then be incorporated into patient-specific computational fluid dynamics (CFD) models to determine the shear stresses and thrombogenic potential of the leak paths.

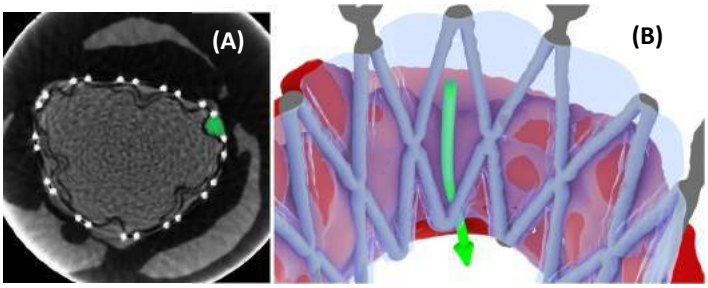

Figure 2. (A) Example µCT slice of the deployed PolyV-1 in patient-specific stenotic valve. Green highlight indicating the PVL channel (B) Rendering of segmented µCT data: gray-stent frame, red-native valve, blue- polymeric TAVR sleeve, and green arrows showing the larger PVL channel

RESULTS

Comparisons of the idealized models tested in ISO regulated traditional pulse duplicator systems to that of a patient specific replica tested in the Vascular Simulations Replicator indicates significant differences in various valve performance metrics[5]. In the idealized models (Fig 3) all three valves performed well when comparing their effective orifice area (EOA). The PolyV-1 (EOA 1.7 cm^2 at 5LPM) had equivalent or better performance as compared to a gold-standard SAVR (EOA 1.6cm^2 at 5LPM). However, in the patient-specific anatomy, all the valves suffered a performance loss and the PolyV-1 (EOA 1.3 cm^2 at 5LPM) fell below the SAVR (EOA 1.4 cm^2 at 5LPM). This is most likely due to the fact the SAVR valve was deployed without the calcified native leaflets to mimic the dissection during the surgical procedure.

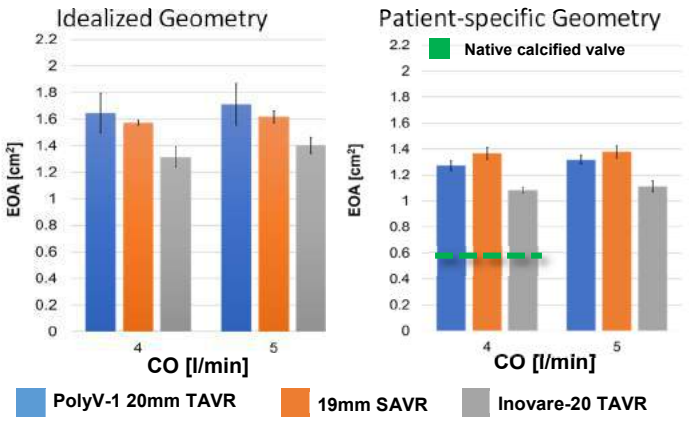

Figure 3. Hydrodynamic results of all three valves comparing the idealized geometry simulator to the patient-specific simulator.

DISCUSSION

As computational models progress with increasing complexity, so should experimental models, not only to provide validation for the computational models but also to bridge the gap with clinical measurements and techniques. The PolyV-1 performance was initially studied with a fluid-structure interaction (FSI) computational model in the idealized geometry[6] and with the advancement of these experimental techniques, the FSI can be expanded to the patient-specific model as well. The immediate goal is to establish a testing platform for testing clinical failure modes of TAVR devices and to consider these results in the device design iteration phase, the platform can also extend beyond this endeavor. The proposed methods serve to complement each other and provide deeper insight into TAVR valve performance. The simulator allows the direct comparison of many clinical imaging modalities, as well as assessment of the accuracy of the measurements. The ultimate impact and benefit to accurate and complete patient-specific models will be to reduce the risk to future patients with better devices and better-informed clinicians.

ACKNOWLEDGEMENTS

This project is supported by NIH-NIBIB Quantum Award Phase II-U01EB012487 (DB), NHLBI-STTR Phase I R41-HL134418 (DB), and NIBIB-BRP U01EB026414 (DB).

REFERENCES

[1]Rotman, O. M. et al., Expert Review of Medical Devices, 15:11. 771-791, 2018.
[2]Dasi, L. P. et al., Ann Biomed Eng, 45:2. 310-331, 2017.
[3]Claiborne, T. E. et al., Expert Rev Med Devices, 9:6. 577-94, 2012.
[4]Rotman, O. M. et al., Cardiovasc Eng Technol, 2018.
[5]Rotman, O. M. et al., Annals of Biomedical Engineering, 47:1. 113-125, 2019.
[6]Ghosh, R. et al., J Biomech Eng, 2018.

SB³C2019
Summer Biomechanics, Bioengineering and Biotransport Conference
June 25 -28, Seven Springs, PA, USA

COMPARATIVE QUANTIFICATION OF MITRAL REGURGITATION BY COMPUTER MODELING AND SIMULATED ECHOCARDIOGRAPHY

Wenbin Mao (1), Andrés Caballero (1), Rebecca T. Hahn (2), Susheel Kodali (2), Wei Sun (1)

(1) The Wallace H. Coulter Department of Biomedical Engineering
Georgia Institute of Technology
Atlanta, GA, USA

(2) Division of Cardiology
Columbia University Medical Center
New York, NY, USA

INTRODUCTION

Mitral regurgitation (MR) is the most common valvular heart disease, with a prevalence of 9.3% in the US population aged 75 and above [1]. Although Doppler echocardiography (echo) is the primary clinical tool to assess the severity of MR, quantitative assessment of MR remains challenging and a true gold standard technique is still lacking [2]. American Society of Echocardiography guidelines recommend quantifying MR primarily using two techniques [3]: the proximal isovelocity surface area (PISA) method, and the volumetric technique (VT) or the quantitative pulsed Doppler method. Clinical and *in vitro* studies have demonstrated that the 2D PISA method may significantly underestimate or overestimate the regurgitant volume (RVol) [2]. The VT method is simple in principle, however, it has not achieved a widespread usage in the clinical community.

The objectives of this study were to evaluate the fundamental assumptions in the clinical echo quantification of MR using computer modeling, identify the pitfalls in the assessment of MR severity, and propose methodologies that could correct its assessment in the clinical setting.

METHODS

Four left heart acute MR computer models with posterior mitral leaflet (PML) prolapse following chordae rupture were used in this study [4]. These models were developed from a previously validated subject-specific left heart fluid-structure interaction (FSI) computer model (72-year-old female patient), which serves as the control model [5]. PML prolapse was modeled by removing chordae elements from different chordae groups, starting from marginal and intermediate chordae, and then progressing towards partial and total chordal origins, representing a pathological process in which minimal chordae rupture precedes more extensive chordae rupture. Chordal rupture models were named based on the ruptured chordae insertions on the PML: marginal & intermediate P1 (M&I P1), marginal & intermediate P2 (M&I P2), P2 & P1, and P2 & P3, where the lateral PML scallop is P1, the central scallop is P2, and the medial scallop is P3.

For simulated echo MR quantification, the flow data from the FSI models was extracted at four discrete time instances in systole (including the instance of peak MR). To emulate the measurement of PISA in clinical practice, velocity magnitudes (i.e., the aliasing velocity) were chosen to obtain a closed and nearly hemispherical shell proximal to the orifice. The continuous wave Doppler (CWD) velocity waveform was obtained by extracting the flow velocity along a beam aligned with the regurgitant jet. By doing so, we assumed that the ultrasound beam was optimally aligned with the jet, indicating no underestimation of the velocity due to misalignment in the simulated echo measurements.

In the computer models, to account for the effect of Doppler angulation, the ultrasound probe was located 13 cm away from the mitral valve (MV) in the apical direction, representing a scan depth of 12 to 16 cm in transthoracic echocardiogram (TTE) examination in clinical practice. By projecting the velocity vectors in the direction of the ultrasound beam, the altered velocity field was used to extract the proximal flow convergence (PFC) in the simulated echo measurements (i.e., the 3D-echo PISA). In general, the 3D-echo PISA should be smaller than the true PISA (without Doppler angulation effect), as shown in Figure 1a. The surface areas of true PFC and 3D-echo PFC can be readily extracted by triangulation in the models. The hemi-elliptic (3D-HE) PISA was calculated by the measurement of three orthogonal radii and integration to obtain the surface area. Furthermore, the 2D-echo PFC was obtained by slicing the 3D isovelocity contours in an apical 4-chamber (A4ch) view (Figure 1b), or an apical 2-chamber (A2ch) view (Figure 1c). The shell radius could be easily estimated by

delineating the border of the isovelocity contour (Figure 1b, 1c), and the averaged radius was used to calculate the surface area of hemispheres.

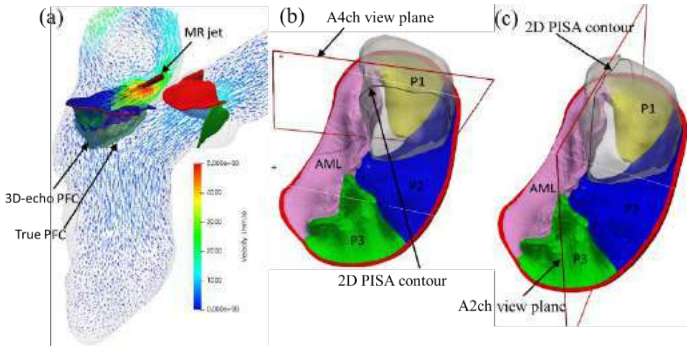

Figure 1: **(a) A representative severe MR model due to P2 & P1 leaflet prolapse at peak MR from the FSI simulation. The velocity field is shown in a cross-sectional plane with a maximum MR jet velocity around 5 m/s. The red cylinder denotes the ultrasound beam direction of the CWD in the measurement of MR jet velocity. Representative 2D-echo PFC contours were measured (b) in an A4ch view, and (c) in an A2ch view from TTE.**

RESULTS

The flow fields from the FSI simulations are treated as the ground truth values in this study. Figure 2 shows the flow rates across the aortic valve (AV) and MV during the entire cardiac cycle. The negative flow at the end of systolic in Figure 2a indicates the retrograde flow into the left ventricle (LV) during AV closing, while the negative systolic mitral flow in Figure 2b indicates the backflow into the left atrium due to the MV closing and MR. During systole, the control model had the largest forward stroke volume (SV). In the MR models, the forward SV decreased as the severity of MR increased, which is consistent with the increasing negative flow volume across the MV. Since the left ventricular size and wall motion were assumed to remain unchanged in all models, mimicking acute MR, it can be seen that the diastolic inflow rates across the MV were approximately the same for all models.

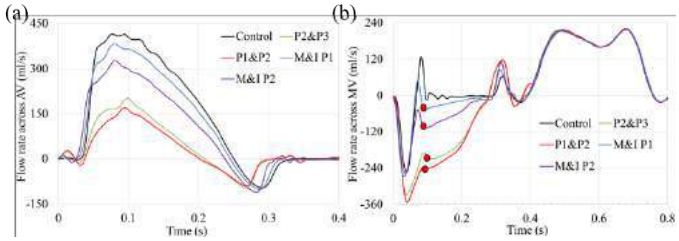

Figure 2: Flow rates across the (a) AV and (b) MV throughout the cardiac cycle from FSI simulations.

The ground truth $RVol_{MV}$ was obtained from the FSI models by integrating the negative MV flow rate curve over time. Similarly, the $RVol_{AV}$, SV_{AV}, and SV_{MV} were calculated and listed in the top section of Table 1. The combination of the SV_{AV} and $RVol_{MV}$ is known as the total SV of the LV ($LVSV$), which was used to calculate the regurgitant fraction, $RF_{MV} = RVol_{MV}/LVSV$. By using RF_{MV} as a quantitative parameter in the grading of MR severity, Table 1 shows that two MR models (P2&P3 and P2&P1) can be classified as severe MR, one moderate MR (M&I P2), and one mild MR (M&I P1). Note that the values in parenthesis denote the relative percentage error with respect to the ground truth values (i.e., FSI-$RVol_{MV}$).

Table 1: **Summary of hemodynamic parameters obtained from the FSI simulations (ground truth) and calculated from the simulated echo measurements using the PISA method at peak MR.**

	Control	M&I P1	M&I P2	P2&P3	P2&P1
FSI-$RVol_{AV}$ (ml)	4.27*	4.63	4.61	4.62	4.72
FSI-SV_{AV} (ml)	58.22	51.55	41.94	20.46	16.16
FSI-SV_{MV} (ml)	63.22	61.67	61.65	63.03	62.97
FSI-$RVol_{MV}$ (ml)	9.27*	14.75	24.32	47.19	51.53
FSI-RF_{MV} (%)	13.7	22.2	36.7	69.8	76.1
MR severity	Normal	Mild	Moderate	Severe	Severe
True PISA $RVol_{MV}$ (ml)	-	14.1 (-5%)	36.4 (50%)	82.9 (76%)	88.5 (72%)
3D-echo PISA $RVol_{MV}$ (ml)	-	12.3 (-17%)	29.8 (23%)	72.7 (54%)	76.3 (48%)
3D-HE PISA $RVol_{MV}$ (ml)	-	9.2 (-38%)	21.8 (-10%)	53.1 (13%)	58.2 (13%)
2D-A2ch PISA $RVol_{MV}$ (ml)	-	11.1 (-25%)	50.7 (108%)	92.9 (97%)	114.3 (122%)
2D-A4ch PISA $RVol_{MV}$ (ml)	-	8.1 (-45%)	28.5 (17%)	71.0 (50%)	49.1 (-5%)

DISCUSSION

We evaluated the accuracy of current echo techniques for the quantification of MR. First, we found that for the PISA method, the assumption that the isovelocity surface is perpendicular to the velocity vectors is incorrect for mitral prolapse patients, which causes inherent errors of MR measurement (overestimation). Second, the angle dependence of color Doppler imaging on the PISA may cause a systematic underestimation of MR, although is relatively small from our results (approximately 15%). Third, the 3D-HE PISA method gave the best estimation for the moderate and severe MR models. Fourth, the VT method, based on the mass conservation, is theoretically more robust. However, when calculating the SV, one should not treat the velocity measured from the pulsed wave Doppler as the mean velocity of the cross section. Our study suggested that a coefficient around 0.7 should be used to compensate for this overestimation. The accuracy of the VT method can be further improved by considering the closing volume of AV, especially in mild MR cases.

The findings of this study add in-depth insights into the identification of several pitfalls in current clinical MR quantification using 2D and 3D echo. The 3D-HE PISA method gave the best estimation for moderate and severe MR cases. Other PISA methods significantly overestimated the EROA for severe and moderate MR. The VT method is theoretically more robust compared to the PISA method. By considering correction factors due to non-flat velocity profiles and the closing volume of AV, the accuracy of the VT method can be greatly improved, even for mild MR

ACKNOWLEDGEMENTS

This work was supported in part by the NIH HL127570 grant.

REFERENCES

[1] Benjamin EJ et al., *Circulation*, 135:e146-e603, 2017.
[2] Little SH. *J Am Soc Echocardiogr*, 25:824-826, 2012.
[3] Zoghbi WA et al., *J Am Soc Echocardiogr*, 30:303-371, 2017.
[4] Caballero A et al., *Scientific reports*, 8:17306, 2018.
[5] Mao W et al., *PloS one*, 12:e0184729, 2017.

THE EFFECTS OF ANTERIOR MITRAL LEAFLET LACERATION ON LEFT VENTRICULAR FLOW WITH TRANSCATHETER MITRAL VALVES: AN *IN VITRO* STUDY

Thomas F. Easley (1,2), Vahid Sadri (3), Pranav Dorbala (3), Norihiko Kamioka (4), Vasilis Babaliaros (4), Ajit P. Yoganathan (1,3)

(1) Parker H. Petit Institute for Bioengineering and Bioscience
Georgia Institute of Technology
Atlanta, GA, USA

(2) George W. Woodruff School of Mechanical Engineering
Georgia Institute of Technology
Atlanta, GA, USA

(3) Wallace H. Coulter Department of Biomedical Engineering
Georgia Institute of Technology & Emory University
Atlanta, GA, USA

(4) Division of Cardiology, School of Medicine
Emory University
Atlanta, GA, USA

INTRODUCTION

In mitral valve (MV) disease, poor valvular geometry (e.g. annular or ventricular dilation) or valve degeneration, results in mitral regurgitation (MR) or mitral stenosis (MS). These ailments are commonly treated with surgical annuloplasty repair or bioprosthetic replacement for those not at high-risk for surgery [1]. However, these procedures can result in recurrent MR or MS that need further treatment with patients that are likely now at high-risk for surgery. These patient groups created a pertinent demand for percutaneous MV interventions. With no dedicated devices currently on the market for transcatheter mitral valves, clinicians have resorted to placing transcatheter aortic valves (TAV) into mitral annular calcification (valve-in-MAC), mitral bioprosthetic valves (valve-in-valve), and mitral annuloplasty rings (valve-in-ring) [2].

Left ventricular outflow tract (LVOT) obstruction is a potential risk from transcatheter valve replacement in the MV [2]. This is due to the anterior mitral leaflet (AML) being permanently displaced into the LVOT by the stent of the transcatheter valve. One way to proactively relieve this is through prior surgical resection of the A2 scallop during placement of a surgical prosthetic MV [3]. Another is through a new percutaneous laceration of the A2 scallop known as LAMPOON [4]. Both the use of transcatheter prosthetic valves in the mitral position and the idea to relieve LVOT obstruction to at risk patients are developing areas. Assessment of how laceration of the AML affects the flow in the LV and LVOT with a transcatheter mitral valve could help in further understanding their effects and long-term outcomes.

Motivated by this need, we studied the effects of different length AML lacerations on the LV flow field with high-speed particle image velocimetry (HSPIV). This was done through modification of a previously developed *in vitro* left heart simulator that provided a dynamically contracting LV phantom [5]. The simulator was modified to include MV leaflets and a more anatomic LVOT geometry.

METHODS

Experimental Setup

A previously developed *in vitro* left heart simulator that provided a transparent, dynamically contracting LV phantom [5] was modified to include transparent MV leaflets and a more anatomic LVOT geometry (Figure 1).

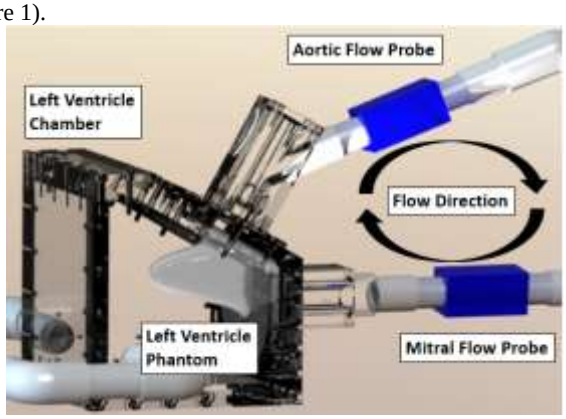

Figure 1. Schematic of left ventricle phantom and chamber.

The transparent MV leaflets were 3-D printed from µCT images of an excised porcine valve that was sized for a 29mm SAPIEN 3. During µCT, the native valvular anatomy remained intact and was mounted onto a plate where a cylinder with the dimensions of a 29mm SAPIEN 3 was inserted into the valve. This provided the correct leaflet geometry for when we place a TAV inside the rigid, printed leaflets of the

simulator. After µCT, simulated AML flail into the LVOT was done in SolidWorks (2017, Dassault Systèmes, Vélizy-Villacoublay, France) at the hinge point where the TAV stent frame ends and the leaflet would no long be taut. Lastly, different size sections of the A2 scallop of the AML were cut away in SolidWorks to mimic the resultant geometry from different lengths of LAMPOON (Figure 2).

Figure 2. Models of three LAMPOON geometries (0%, 50%, and 100%) and image of 100% LAMPOON with porcine MV and SAPIEN 3. The A2 scallop is lacerated allowing the AML to be pulled open by the TAV stent frame and the AML chordae.

The 29mm TAV used for this study was the previously validated Georgia Tech Transcatheter Aortic Valve (GT-TAV) [6]. This provided us with a transparent stent frame for better optical access during HSPIV.

Experimental Testing

Three AML lacerations of the A2 scallop were studied: 0% (no laceration), 50%, and 100% (best clinical outcome). The GT-TAV was deployed at an 80/20 ventricle/atrial ratio. A control condition with no MV leaflets and the GT-TAV placed upstream of the MV annular plane was also done to help better characterize native systole.

2-D HSPIV was performed along the central long-axis plane of the LV at 700 Hz. The resulting data was bin-averaged over 5 time points and phase-averaged over 20 cycles.

The left heart simulator was tuned to normal hemodynamics for all testing conditions (70 bpm, 35/65 systole/diastole ratio, 120/80 mmHg systolic aortic pressure) with varying cardiac output of 2.5, 5.0, and 6.5 Lpm. In order to control the pulsatile pump (Vivitro Labs, Victoria, BC, CA), record hemodynamics, and trigger HSPIV, a custom code was written in LabVIEW (2015, National Instruments, Austin, TX).

RESULTS

At 2.5, 5.0 (Figure 3A and 3B), and 6.5 Lpm, it was shown that each progression of laceration created a larger diastolic vortical structure and systolic LVOT.

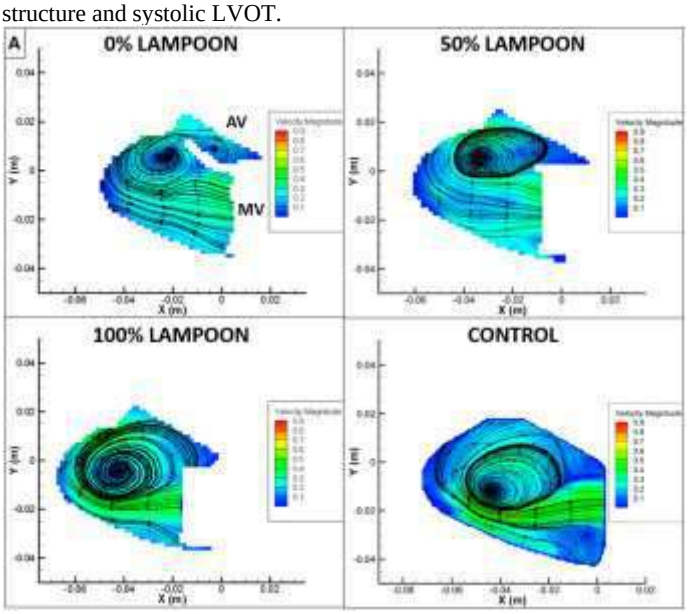

For 0%, 50%, and 100% LAMPOON at 5 Lpm, the maximum length of the vortex measured during diastole was 2.51, 3.83, and 5.30 cm, respectively. Additionally, the average velocity measured in the LVOT during peak systole was 0.711, 0.646, and 0.553 m/s, respectively.

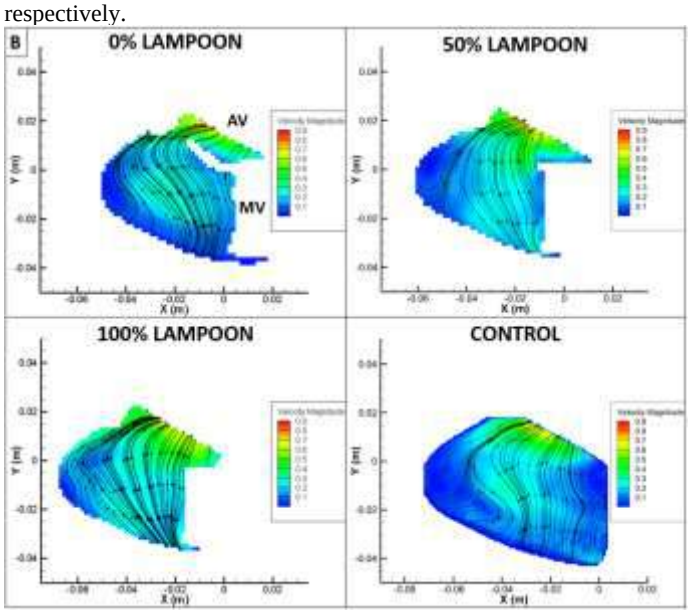

Figure 3. Left ventricular flow fields with progressing anterior mitral leaflet (AML) laceration in A) mid-diastole and B) mid-systole.

DISCUSSION

It was shown *in vitro* that the displaced anterior mitral leaflet altered the LV flow compared to the control. It was subsequently shown that with increasing AML laceration, the size of the LV diastolic vortices and systolic LVOT increased. The latter resulted in a lower velocity gradient through the LVOT with progressing laceration. Our work shows that proactively resecting or lacerating the leaflet before transcatheter mitral valve replacement can result in better flow conditions in the LV. Specifically, it can reduce obstruction of the LVOT and lead to better diastolic mixing of blood. This can translate to better function of the AV and lower blood cell residency time in the LV, respectively. The lower blood cell residency time could be important in minimizing risk of thrombosis associated with bioprosthetic devices.

Future *in vitro* work in the area will focus on the effects of different deployment heights and further understanding of the flow between the native leaflet and the prosthetic leaflet.

ACKNOWLEDGEMENTS

This work was supported by the American Heart Association under Predoctoral Fellowship 17PRE33661066 and National Heart Lung and Blood Institute under Grant R01HL119297.

REFERENCES

[1] Acker, M et al., *N Engl J Med*, 370(1):23-32, 2014.
[2] Blanke, P et al., *JACC Cardiovasc Imaging*, 10(4):482-485, 2017.
[3] David, T, *Oper Tech Thorac Cardiovasc Surg*, 17(3):194-203, 2012.
[4] Babaliaros, V et al., *JACC Cardiovasc Interv*, 10(8):798-809, 2017.
[5] Okafor, I et al., *Ann Biomed Eng*, 45(5):1305-1314, 2017.
[6] Midha, P et al., *Circulation*, 136(17):1598-1609, 2017.

SB³C2019
Summer Biomechanics, Bioengineering and Biotransport Conference
June 25 -28, Seven Springs, PA, USA

PATIENT-SPECIFIC MODELING OF THE LEFT VENTRICULAR HEMODYNAMICS USING THE CHIMERA OVERSET MESH TECHNIQUE

Federico Canè (1), Matteo Selmi (2,3), Gianluca De Santis (4), Alberto Redaelli (3), Patrick Segers (1), Joris Degroote (5)

(1) IBiTech – bioMMeda, Department of Electronics and Information Systems, Ghent University, Ghent, Belgium

(2) Division of Cardiac Surgery, Department of Surgery, Universit□ di Verona, Verona, Italy

(3) Department of Electronics, Informatics and Bioengineering, Politecnico di Milano, Milan, Italy

(4) FEops NV, Ghent, Belgium

(5) Department of Flow, Heat and Combustion Mechanics, Ghent University, Ghent, Belgium

INTRODUCTION

Accurate assessment of the physiology and function of the cardiovascular system is of paramount importance in a world with a progressively ageing population. Newer and more refined tools are needed to distinguish normal from abnormal ageing and identify subjects at risk of developing cardiovascular disease in an early stage. Thanks to the massive improvement of medical imaging, image processing and computational resources, patient-specific modeling could assist the clinicians in their diagnosis. In particular, the evaluation of fluid dynamics inside cardiac chambers by means of Computational Fluid Dynamics (CFD) may provide a fundamental fluid-mechanical insight into cardiovascular pathologies – such as ischemic heart disease, heart failure or stroke – and guide the medical team in choosing the best available treatment to restore physiological flow dynamics. Most studies addressing cardiac fluid dynamics focused on the left ventricular (LV) chamber. The LV fluid dynamics is physiologically characterized by vortex formation, which is believed to enhance among others the wash-out of the endocardial wall and favorably affects ventricular energetics, interplaying with the kinetics of both the LV endocardium and the Mitral Valve (MV) leaflets. The development of CFD models of the LV, however, has been continuously limited by the presence of complex and irregular structures (MV valve, papillary muscles, trabeculae) and by the large impulsive motion of its structures (LV endocardium and MV leaflets), which increase considerably the complexity of the model. The starting point of this study was the CFD model developed by Bavo [1] based on an Arbitrary Lagrangian Eulerian (ALE) approach, which resulted to be cumbersome in terms of stability and convergence of the solution, due to negative volume errors which limited the simulation time to 1 cardiac cycle. The Chimera technique, still relatively unemployed within the biofluids community, may overcome the aforementioned barriers as the technique describes the fluid domain with a moving 4D Boundary Layer (BL) mesh embedded in a 3D Cartesian background mesh, allowing to handle the large and impulsive motion of the LV. It is therefore our aim to develop a workflow, based on the Chimera technique, to build a patient-specific CFD model for quantitative assessment of LV flow starting from medical images. The robustness of the workflow, and especially of the Chimera technique, was tested by means of an application which aims to answer whether the torsional motion of the left ventricle has an impact on the fluid dynamics inside the chamber.

METHODS

The workflow used to build patient-specific models consists of the following steps:

1. Segmentation of the LV endocardial surfaces throughout a cardiac cycle from cine-SA MRI acquisitions;
2. Generation of the meshes: 4D BL hexahedral meshes of the LV (as component grid, cg) and an overlapping 3D Cartesian grid (as background grid, bg) [2];
3. Implementation of the torsional motion;
4. Temporal interpolation of the 4D BL LV meshes;
5. Quality check of the 4D BL meshes;
6. CFD set-up with overset meshes approach and moving boundaries.

The numerical stability of the solution was assessed by means of a mesh sensitivity study which tested the accuracy of 4 mesh combinations (2 mesh resolutions for both cg and bg). With the chosen mesh combination (edge length_{bg} = 0.5 mm, elements_{cg} = 300 k) 6 cardiac cycles were simulated in Fluent 18.2 with the assumption of Newtonian blood ($\nu = 2.9 \cdot 10^{-6}\ m^2/s$) and a time step of 3 ms. Three different

CFD cases were compared to assess the impact of torsion on the LV flow field: (i) without torsion (no Torsion), (ii) with physiological torsional motion (Torsion X1) and (iii) with torsion multiplied by a factor 2 (Torsion X2) to enhance the differences. The comparison of the CFD cases with different torsion degree was established by evaluating velocity, vorticity, Wall Shear Stress (WSS) and Residence Time (RT).

RESULTS AND DISCUSSION

Our results provide two important insights. Firstly, regardless of the torsion degree, we observed an important cycle-to-cycle variation in every simulated case. This behavior is particularly evident in the first two cardiac cycles and is reported for the CFD case with physiological torsion (Figure 1), but it occurs in all the simulated cases.

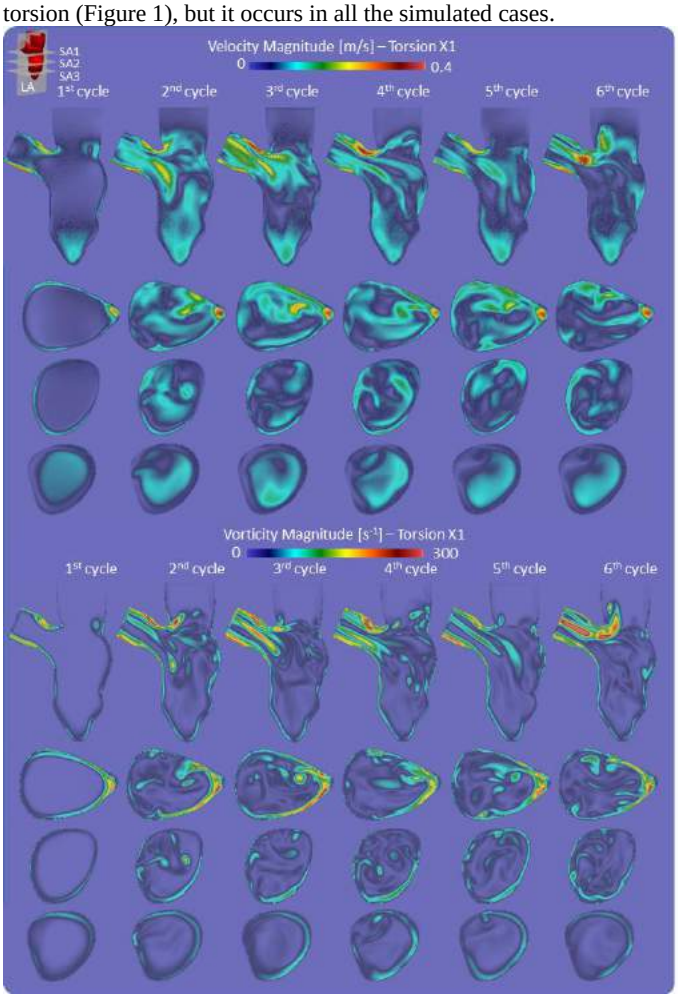

Figure 1: Cycle-to-cycle variation of velocity and vorticity during end systole in the CFD case with physiological torsion.

Secondly, accounting for torsion only leads to minor differences in the shape of velocity and vorticity contours and maximum values (Figure 2A, 2B). The main differences are located in the medial plane (SA2), which has a wider high velocity values close to the endocardial wall and an increased vorticity in the CFD cases with physiological and exaggerated torsion. The WSS distribution does not show a clear global upward or downward trend with respect to the torsion degree (Figure 2C). Torsion has, however, an (unexpected) impact on particle residence time: exaggerated torsion leads to pronounced decrease of the particles staying for less than 1 cardiac cycle (-8.8 %) at the expense of particles staying longer within the LV (+6.8 % in the case of 1T < RT < 2T, +2% in the case of RT >2T). On the other hand, the case without torsion yields less particles with RT> 2T (-1.1%). The difference between the no torsion and physiological torsion was less than one percent.

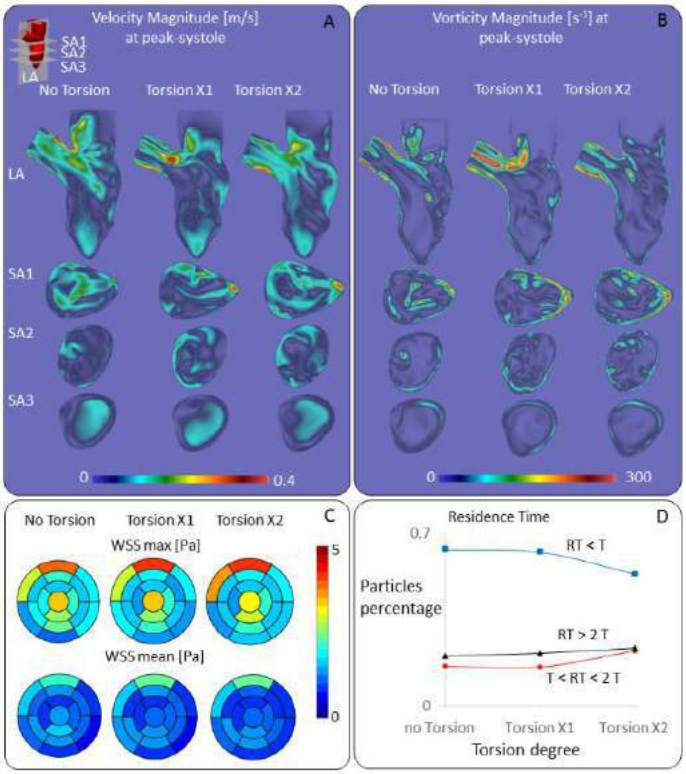

Figure 2: Investigated variables in the three simulated cases to assess whether the torsion has an impact on the LV fluid dynamics.

CONCLUSIONS

The proposed Chimera-based workflow was found to be robust for all the three CFD cases in terms of convergence and stability. Thanks to the new approach multiple cardiac cycles could be simulated, allowing us to appreciate a cycle-to-cycle variation of the flow field and how the stability of the numerical solution is reached after two cardiac cycles. This finding also raises caution with respect to our previous results, in which only one cardiac cycle was simulated. Our data further suggest only a limited impact of torsion on the studied parameters. The major differences due to the torsional motion occurred in the medial plane, where the areas associated with higher values of velocity and vorticity are more extended, but there are no pronounced differences in terms of RT and WSS. Therefore, we conclude that torsional motion by itself does not seem to largely influence the LV fluid dynamics, keeping in mind however that the model did not include the papillary muscles, the MV and assumed a smooth LV wall. The effects of the MV kinematics will be evaluated within a FSI simulation framework as further development of the current model.

ACKNOWLEDGEMENTS

This work was supported by the European Commission within the Horizon 2020 Framework through the MSCA-ITN-ETN European Training Networks (project number 642458).

REFERENCES

[1] Bavo, A et al., *J Biomech*, 50:144-150, 2017.
[2] Canè, F et al., *BioMed Research International*, 2018.

SB³C2019
Summer Biomechanics, Bioengineering and Biotransport Conference
June 25 -28, Seven Springs, PA, USA

DESIGNING TISSUE ENGINEERED VASCULAR GRAFTS FOR YOUNG AND AGED HOSTS: IN VIVO, EX VIVO AND IN SILICO STUDY

Piyusha S. Gade (1), Keewon Lee (1), Yadong Wang (2), Anne M. Robertson (1,3)

(1) Department of Bioengineering
University of Pittsburgh
Pittsburgh, PA, USA

(2) Department of Biomedical Engineering
Cornell University
Ithaca, NY, USA

(3) Department of Mechanical Engineering and Materials Science
University of Pittsburgh
Pittsburgh, PA, USA

INTRODUCTION

Pioneering works by Langille (e.g. [1]) have shown that arteries have an inherent capacity for altering their morphology in response to mechanical stimuli enabling them to maintain mechanical homeostasis; a constant, preferred mechanical state, despite altered mechanical loading. This capacity has been leveraged to develop cell-free, porous, biodegradable tissue engineered vascular grafts (TEVGs) which promote host growth and remodeling (G&R) to develop new arteries (neoarteries) in the tissue's functional site (*in situ)*. These grafts offer a much-needed alternative to using Dacron, or often unavailable autologous grafts, for treating atherosclerosis due to their ease of fabrication, reduced regulatory burden and the ability to form an adaptive tissue that is capable of G&R. One such poly (glycerol sebacate) (PGS) graft developed by Wang et al. has demonstrated mature elastin and collagen formation in the rat aorta [2] and mice carotid artery [3]. However, the fundamental mechanisms guiding neoarterial G&R are yet unknown, impeding efforts to translate this success across age and species.

Constrained mixture theory-based G&R tools [4] have been employed to understand salient features of neotissue formation in the venous circulation [5]. They are based on the knowledge that vascular tissues adapt their structure and function to achieve a certain homeostatic stress state. However, there is a need to understand the final homeostatic condition for *in situ* engineered TEVGs to translate this tool for arterial circulation. Furthermore, there is a need for biological and mechanical data to understand mass kinetics to effectively use this tool for understanding mechanisms guiding G&R. In this study, we used a combined *in vivo, ex vivo* and *in silico* approach to develop a G&R model tailored with biological and mechanical data to model arterial TEVG G&R with age. Using these tools, we aimed to answer two main questions: What is the neoarterial remodeling process in young and old animals? What is the role of graft degradation, extracellular matrix deposition and mechanics in long-term neoartery remodeling with age?

METHODS

Neoarterial G&R is modeled using the constrained mixture theory with the homogenized strain energy function (SEF) shown in equation 1. Q^{α} models graft degradation, $m^{\alpha}(\tau)$ models extracellular matrix deposition, $\widehat{W}^{\alpha}\boldsymbol{C}^{\alpha}_{n(\tau)}(s))$ is the strain energy for the "α" constituent (e.g. graft, elastin, collagen, cells),

$$W(s) = \Sigma W^{\alpha}(s) = \frac{\rho^{\alpha}}{\rho(s)} Q^{\alpha}(s)\widehat{W}^{\alpha}(\boldsymbol{C}^{\alpha}_{n(0)}(s)) + \int_0^s \frac{m^{\alpha}(\tau)}{\rho(s)} q^{\alpha}(s-\tau)\widehat{W}^{\alpha}(\boldsymbol{C}^{\alpha}_{n(\tau)}(s))d\tau \quad (1)$$

We tailored the G&R equations to young and old neoarterial remodeling by using histological and mechanical data from neoarteries in young (n = 39) and aged (n = 15) animals. Briefly, 800 μm inner diameter grafts comprised of an inner PGS core (thickness = 300 μm) and outer polycaprolactone (PCL) sheath (20 μm) were implanted in a rat carotid artery interposition model. Neoarteries were explanted at days 3, 7, 14, 30, 90 and 180 from young, and 90, 180 from old animals. Histological assessment was performed for inflammatory and synthetic cell markers. Microstructure-function relationship was assessed using a custom-designed biaxial pressure inflation system [3] which simultaneously images collagen microstructure using multiphoton microscopy (MPM) during loading. Collagen fiber orientation was assessed from MPM images obtained across the wall thickness using CT-FIRE [6].

RESULTS

Neoarterial remodeling is a highly nonlinear process. We identified two phases of remodeling for young neoarteries (YN), Phase I (Day 0 - 14) and Phase II (Day 14 – 180) (Figure 1). Phase I is dominated by a

heightened inflammatory cell response that occurs during graft degradation with an associated dramatic reduction in stiffness (day 1-7). This is followed by a sharp stiffening due to heightened collagen deposition (day 7-14) (Figure 2). Following this, Phase II

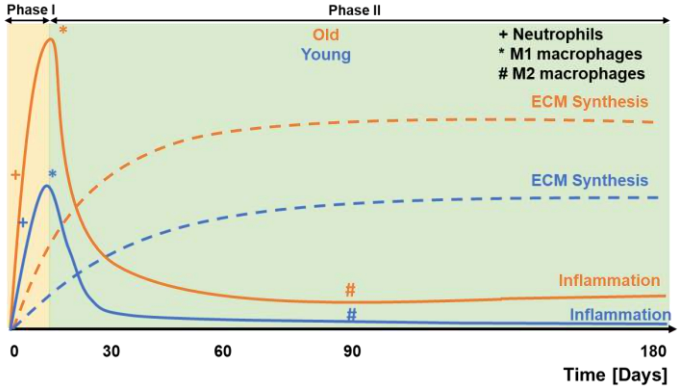

Figure 1 Schematic of qualitative features of time-course of inflammation and ECM deposition in young and old neoarteries based on histological and biochemical data at 6 time points.

response leads to a non-monotonic change in the circumferential stress-strain mechanical response in which there is an initial softening (day 14 – 90) followed by stiffening at day 180 (Figure 2). Six-month structure-function assessment of differences in homeostatic states of YNs and old neoarteries (ONs) shows that ONs have higher circumferential stiffness as compared to YNs, potentially due to the denser collagen network (Figures 2,3). YNs also exhibited bi-directional (circumferential and

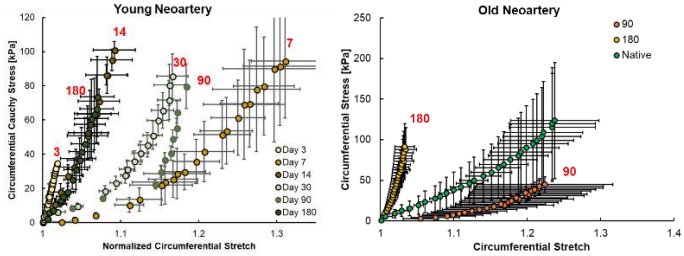

Figure 2: Temporal evolution of stress-stretch curves for neoartery in young vs old animals. Homeostatic state is altered with age showing increased circumferential stiffness at 180 days.

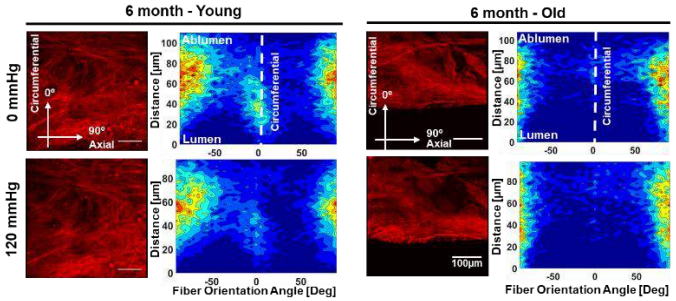

Figure 3: Stacked projections of MPM images for collagen fibers in young vs old neoarteries at 6 months with corresponding plots of collagen fiber orientation as a function of distance from ablumen. Collagen fiber orientation in ONs is less distributed.

axial) collagen fiber orientation whereas ONs had mostly axial fibers. YNs were also capable of fiber reorientation upon pressurization as opposed to ONs. Using this data for altered homeostatic states and histological data on synthetic smooth cell proliferation rates, we tailored and validated our G&R model for YN and ON remodeling. We then used this tool to leverage the interplay of graft degradation and ECM deposition for improved TEVGs. In this regards, Figure 4 shows that ONs can fail through stenosis (inward remodeling) with a low graft degradation half-life ($S_{0.5}$) of 7 days and high deposition rate. This stenosis can be mitigated by reducing the ECM deposition rate. However, simulations using this tool demonstrate a clinically useful method to avoid stenosis is to increase the degradation half-life, leading to stable remodeling.

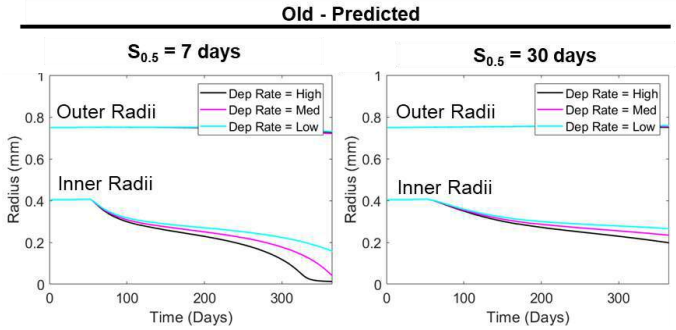

Figure 4: Predicted inner and outer neoartery radii for different graft degradation half-lives ($S_{0.5}$) and ECM deposition rates using tailored G&R tool.

DISCUSSION

To our knowledge, this is the first study that translates neoartery formation to old animals, determines factors responsible for recapitulation of ECM structure and function, and investigates their homeostatic condition. We observe that G&R in YN is a nonlinear process with an initial graft degradation and inflammation dominated phase followed by a phase of microenvironment driven mechanical remodeling toward a homeostatic state. Mechanically, collagen fiber reorientation in YNs leads to more native artery-like behavior with a toe region at lower strains and fiber recruitment at higher strain levels. In contrast, a dense collagen network combined with lack of fiber reorientation is associated with increased stiffness in ONs. Our G&R tool demonstrated the interplay of graft degradation and ECM deposition are crucial factors that need to be controlled to achieve stable long-term G&R. Biochemical evaluation show that ONs exhibit higher ECM deposition which, as our simulations suggest, coupled with slower polymer degradation half-life (faster graft degradation rate) can lead to stenosis. Thus, our results indicate that a balance of medium degradation half-life combined with lower ECM deposition rate is required for stable long-term remodeling. In summary, we assessed the longitudinal remodeling process of TEVGs in young and aged hosts. We used this knowledge to tailor our G&R computational tool and used the tool to assess salient mechanisms guiding neoarterial remodeling. In the future, this tool can be used for rational design of tissue engineered vascular devices.

ACKNOWLEDGEMENTS

This work was supported by a National Institutes of Health grant NIH/1R21HL124479-01.

REFERENCES

[1] Langille et al., *Science*, 231:405-407, 1986.
[2] Wu et al., *Nat Med*, 18:1148-1153, 2012.
[3] Lee et al., *Biomat*, 181:67-80, 2018.
[4] Humphrey et al., *Math Models Methods Appl Sci*, 12:407-430, 2002.
[5] Miller et al., *J Biomech*, 47:2080-2087, 2014.
[6] Bredfeldt J. S. et al., *J. Biomed. Opt.* 19, 016007, 2014.

SB³C2019
Summer Biomechanics, Bioengineering and Biotransport Conference
June 25 -28, Seven Springs, PA, USA

COMPUTATIONAL FLUID DYNAMICS MODELING OF MYOCARDIAL BRIDGING USING CORONARY ANGIOGRAPHY

Mohammadali Sharzehee (1), Ran Gao (2), Yuan Chang (2), Jiang-ping Song (2), Hai-Chao Han (1)

(1) Department of Mechanical Engineering
The University of Texas at San Antonio
San Antonio, TX, USA

(2) Department of Cardiac Surgery, State Key Laboratory of Cardiovascular Disease, Fuwai Hospital, National Center for Cardiovascular Diseases, Beijing, China

INTRODUCTION

A myocardial bridge (MB) is a congenital abnormality in which a segment of the epicardial coronary artery, often the middle part of the left anterior descending (LAD) artery, tunnels into cardiac muscle (myocardium). Autopsy and angiographic findings showed that the incidence rate of MB is about 20-60% and up to 16%, respectively [1]. The electrocardiogram (ECG) and angiographic measurements demonstrated that MB leads to a transient vessel compression during systole and early diastole, leading to atherosclerosis in the proximal to MB and increasing the risk of myocardial infarction [2]. The hemodynamics disturbances induced by MB are also associated with angina, arrhythmia, myocardial ischemia, and even sudden cardiac death [3].

Despite the clinical prevalence of MB, there have been relatively few hemodynamic studies of MB due to 3D transient nature of MB. The limitations of previous computational fluid dynamics (CFD) studies such as 2D modeling may underestimate the actual effect of MB on coronary hemodynamics. Therefore, the aim of this study was to assess the presence of MB on coronary hemodynamics using patient-specific 3D computational modeling.

METHODS

A patient-specific LAD model was developed based on the biplane angiograms of a LAD of a 53-year-old male patient with coronary artery disease and myocardial bridge (bridge length of 43.43 mm and compression ratio of 80%). The angiographic images were acquired at 16 frames per second using Artis zee III floor (Siemens Ltd. China) with a pixel spacing of 154μm at Fuwai Hospital. To reconstruct a realistic LAD model, 2D vessel centerlines from right anterior oblique projection (RAO) with cranial (CRA) and caudal (CAU) angulation (CRA30/RAO1 and CAU25/RAO25) were extracted from angiographic data at both end-diastole (ED) and end-systole (ES) (Fig. 1A). The coordinates and lumen diameter of 12 control points (from A to K) along each 2D centerline were imported into SolidWorks®. For each 2D view, Bezier spline was used to create the longitudinal centerline. The 2D centerlines were projected onto two orthogonal Cartesian planes and then combined to form a 3D centerline [4]. A lumen volume was generated by connecting the 12 circular cross-sections of each control point along the length of the artery using lofting (skinning) algorithm. The reduction in lumen volume was calculated as the ratio of the lumen volume change (with respect to the ED volume) to the ED volume, from ED to ES (Fig. 1B). Based on the angiographic frames, 40% of a cardiac cycle duration was related to vessel compression (VC) and the rest was for vessel relaxation (VR).

To simulate the vessel deformation, an arbitrary Lagrangian-Eulerian (ALE) formulation of mass and momentum conservation equations was implemented.

$$\frac{\partial}{\partial t}\int_V \rho dV + \int_S \rho(\boldsymbol{v}-\boldsymbol{v}_b).\boldsymbol{n}dS = 0 \quad (1)$$

$$\frac{\partial}{\partial t}\int_V \rho \boldsymbol{v} dV + \int_S (\rho \boldsymbol{v}(\boldsymbol{v}-\boldsymbol{v}_b) + p\mathbf{I} - \tau).\boldsymbol{n}dS = 0 \quad (2)$$

Where V is the control volume, ρ the blood density, S the boundary surface, $\boldsymbol{v}$ the velocity vector, $\boldsymbol{v}_b$ the moving boundary velocity vector, $\boldsymbol{n}$ the normal vector, p the pressure, $\mathbf{I}$ the unit tensor, and τ the stress tensor. Blood was modeled as a homogenous Newtonian fluid (density 1050 kgm^{-3} and dynamic viscosity 3.16mPa.s). The shear stress transport (SST) transition model was applied to capture the turbulent transition, if any occur. A user-defined function (UDF) was developed to update the new positions of the surface nodes during the simulation.

The mesh and time independency were investigated by comparing the time-averaged wall shear stress (TAWSS) over proximal, bridge, and distal segments. The results were considered reliable when the TAWSS difference became less than 3%.

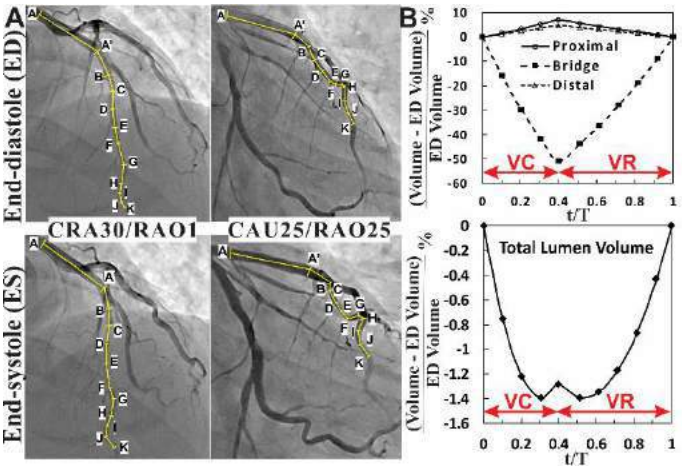

Figure 1: (A) 2D angiographic images, (B) Temporal variation of lumen volume reduction (T=cardiac cycle duration). Proximal (A-B), bridge (B-F), distal (F-K).

A structured hexahedral mesh (258795 elements) was utilized to mesh the lumen using ANSYS Meshing (v17.1). A very fine mesh near the wall with the first layer thickness of 50μm was employed to meet the requirements of the turbulence model. The inlet and outlet sections were extended by 10 and 15 times the lumen diameter along the lumen centerline to minimize the effect of inlet and outlet boundaries (Fig. 2A) [5]. Due to the lack of patient flow data, the proximal and distal pressure waveforms for a 38-year-old male patient with myocardial bridge were used (Fig. 2B) [2]. The SIMPLE algorithm along with a second-order upwind scheme was employed to solve the governing equations. The convergence criterion was set at 10^{-6} for all the residuals. A second-order temporal discretization scheme was utilized to perform transient flow simulations over three cardiac cycles with a time step of 1ms. CFD simulations were performed using ANSYS FLUENT (v17.1).

RESULTS

Our simulations showed that the reduction in mean volume flow rate during VR (7%) was higher than the VC (1%) in the MB model as compared to model without MB, due to the generated recirculation zone (Fig. 2C). In addition, the presence of MB had insignificant effect on extrema of volume flow rate (<5%) while it reduced the mean volume flow rate by 6.3% (Table 1). The effects of MB on the wall shear stress (WSS) are different at proximal, bridge, and distal segments (Fig. 3). MB resulted in a 95.5% increment in TAWSS at bridge, 8.3% and 9.6% reduction in TAWSS at proximal and distal, respectively and increased the volume-averaged flow velocity by 6.4%.

DISCUSSION

Patient-specific CFD simulations of MB were conducted to better understand its effects on coronary hemodynamics. For the given patient, although the presence of MB altered the WSS distribution significantly, it had less effect (<10%) on blood flow rate.

There are a few limitations in this study. First, the coronary arterial motion was neglected due to its minor effect [6]. Second, the diameter of control points was estimated using linear interpolation between ED and ES diameters. Despite these limitations, the current results illustrated the effects of MB on coronary blood flow and its potential role in atherosclerosis development. Further study will examine more patients with various level of MB to better understand its effects and provide inputs for clinical treatments.

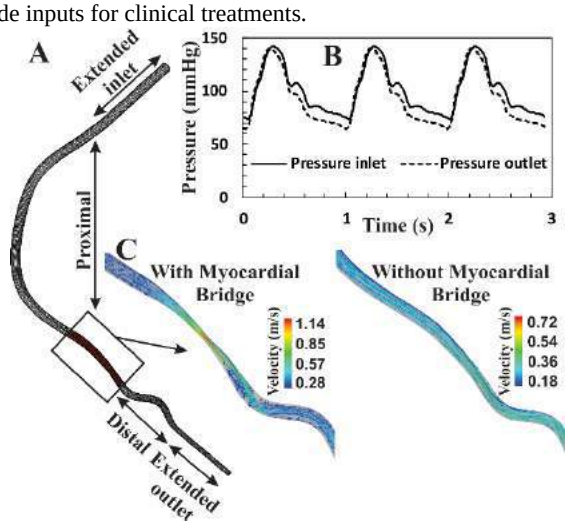

Figure 2: (A) 3D reconstructed LAD model, (B) Inlet and outlet pressure waveforms, (C) Velocity streamlines for the LAD models.

Table 1: Effect of MB on LAD volume flow rate (mL/s)

Flow rate	With MB	Without MB	Flow rate change (%)
Mean	1.73	1.85	-6.29
Maximum	3.37	3.46	-2.48
Minimum	1.31	1.29	+1.62

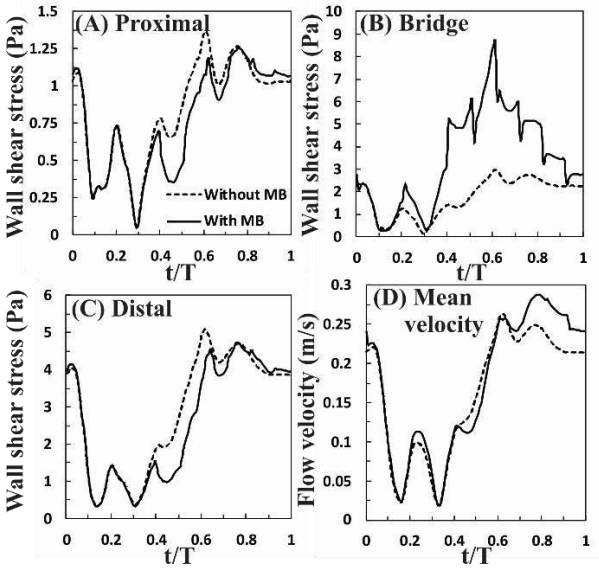

Figure 3: Temporal variation of wall shear stress and volume-averaged flow velocity over the last cardiac cycle.

REFERENCES

[1] Möhlenkamp, S et al., *Circulation*, 106:2616-2622, 2002.
[2] Javadzadegan, A et al., *J Biomech Eng*, 140:091010, 2018.
[3] Corban, MT et al., *J Am Coll Cardiol*, 63:2346-2355, 2014.
[4] Galassi, F et al., *PLOS ONE*, 13:0190650, 2018.
[5] Sharzehee, M et al., *Comput Methods Biomech Biomed Engin*, 21:219-231, 2018.
[6] Theodorakakos, A et al., *Phys Med Biol*, 53:4875–4892, 2008.

AXIAL STRETCH MODULTES LYMPHATIC CONTRACTILITY: AN EXPERIMENTAL-COMPUTATIONAL APPROACH IN A NOVEL RAT TAIL MODEL

Mohammad S. Razavi (1), Julie Leonard-Duke (2),Rebecca Hardie (2), J. Brandon Dixon (1,2), Rudolph L. Gleason, Jr. (1,2)*

(1) The George W. Woodruff School of Mechanical Engineering
Georgia Institute of Technology
Atlanta, GA, USA

(2) The Wallace H.Coulter Department of Biomedical Engineering
Georgia Tech and Emory University
Atlanta, GA, USA

INTRODUCTION

Lymphatic vessels serve as the major route to transport lymph from the interstitial space to the great veins. The dysfunction of the lymphatic system is associated with a wide range of pathologies, including lymphedema. Collecting lymphatic vessels play a key role in lymphatic transport as they serve as a pump to propel lymph against an adverse pressure gradient. These vessels are remarkably different from veins and arteries in that they have specialized smooth muscle cells that enable them to contract spontaneously. The vessels' rhythmic and synchronized contractions are orchestrated to propel lymph in an efficient way along a chain of vessels. Similar to veins and arteries, lymphatic vessels exhibit tonic constrictions (maintained contractions) to control vessel caliber as well. Mechanical stimuli (e.g., pressure/stretch), as well as biochemical stimuli (e.g., vasoactive agents such as nitric oxide), are believed to be key regulators of lymphatic contractility.

It has been shown that lymphatic muscle cells adapt their contractile force to maintain lymphatic flow under different working conditions. Mechanical regulators such as lymphatic flow and pressures modulate the vessel's contractile function via the change in calcium dynamics in lymphatic SMCs. In this regard, the mechanical stretch is believed to be a key player in the regulation of contractile force produced by lymphatic SMCs. Although mechanical regulation of lymphatic vessels in response to flow and pressure are well documented; however, less is known about the role of axial stretch in the modulation of lymphatic function. To date, there is no information available on the role of axial stretch on lymphatic contractility. Our study is the first to demonstrate the significance of axial stretch in the modulation of lymphatic contractility. We showed that collecting lymphatics from the rat tail are under axial pre-stretch and characterized the response to change in the axial stretch. This study sheds light on the effect of axial stretch and its contributions to the pumping function of lymphatic vessels.

METHODS

Animal Model. Male Sprague Dawley (SD) rats (300-350 gr) were used to limit variability. An incision (~1 cm) was made on the left or right side, near the base of the tail to gain access to the lateral tail vein. Segments of lymphatic vessels (length~1.5-2 mm, diameter~250-300 μm) were excised and were prepared for the experiments.

Ex-vivo Experiments. We improved a previously developed biaxial device to precisely measure and control transmural pressure, diameter, and axial stretch for lymphatic vessels (<300μm) (4). Using this system, the contractions under different transmural pressures/axial stretches in the mounted vessel were measured. After replacing the bath with Ca-free solution, the passive mechanical properties of lymphatic vessels were determined at different intermittent pressure and axial stretch.

Statistical analysis. A one-way ANOVA test in conjunction with Bonferroni's post hoc correction was used to determine statistical significance, ($P< 0.05$) of experimental data. Results were reported as means (±SEM).

Constitutive Model and Bootstrapping. To capture salient features of lymphatic vessel wall mechanics and to reveal its contribution to lymphatic contractility, we employ a two-dimensional constitutive framework to fit experimental data. A three-fiber family model (one-axial and two symmetric fiber families) was utilized to obtain the stored energy function as (2):

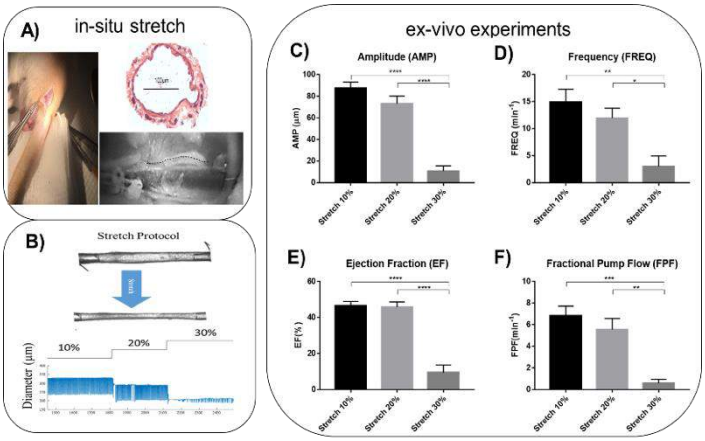

Figure 1 The results from the axial stretch experiments. A) A typical rat tail lymphatic vessel is under axial pre-stretch B) the raw data from the stretch protocol C-F) changes in contractility metrics in response to the axial stretch.

$$W = b(I_C - 3) + \sum_{i=1,2,3} \frac{b_1^i}{4b_2^i}\left\{exp\left[b_2^i((\lambda^k)^2 - 1)^2\right] - 1\right\} \quad (\mathbf{1})$$

where b, b_1^i and b_2^i are material parameters, I_C is the first invariant of the right Cauchy-Green strain tensor ($I_C = tr(\boldsymbol{C})$, $\boldsymbol{C} = diag(\lambda_r^2, \lambda_\theta^2, \lambda_z^2)$), $\left(\lambda^i\right)^2$ is the stretch of the i*th* fiber family ($\lambda^i = C_{\theta\theta}sin^2\left(\alpha^i\right) + C_{zz}cos^2\left(\alpha^i\right)$), where α^i is the fiber angle (please see Ref. ((1)). In addition, a bootstrap method with 2,000 bootstrap samples was used to check the uniqueness and respective confidence interval of fitted parameters in the constitutive model.

Confocal Imaging. An LSM 710 META inverted confocal microscope (Zeiss) was used to characterize the collagen distribution within the vessel wall. Since second-harmonic generates spectrally-isolated signals for collagen, The Non-Descanned Detector (NDD) along with the two-photon laser (800 nm) was used to excite and collect endogenous signals from the collagen fibers.

RESULTS

A typical rat tail lymphatic vessel, an isolated vessel where the vessel has been cleaned, mounted on glass micropipettes as well as H&E staining of the isolated vessel, along with the raw data from the stretch experiments are shown in (Fig. 1 A, B). The vessel is under axial pre-stretch ~20% in-situ. To determine the effect of axial stretch on lymphatic contractility, the isolated vessels were exposed to three axial stretches, 10%, 20% and 30% (Fig. 1 A-D). The amplitude of contractions decreased as the stretch increased from 10% to 20%, however, the significant reduction (50μm equal to ~90% reduction) occurred for the higher stretch of 30%. Similar trends were observed for the frequency as it decreased from 15 min^{-1} to less than 5 min^{-1} (~80% reduction), the ejection fraction decreased from 46% to 9% (~80% reduction), and fractional pump flow from 6.8 min^{-1} to 0.58 min^{-1} (~92% reduction).

The material properties of rat tail lymphatic vessels were characterized using biaxial tests (Fig. 2A). The two photon-imaging revealed that most collagen fibers are aligned in the axial direction in both low and high loading scenarios (Fig. 2B). The estimation of material and structural parameters of rat tail lymphatic vessel and their confidence interval (Eq. (1)) were obtained via regression analysis and the bootstrap technique respectively (Fig. 2C). The results suggest that rat tail lymphatic vessels show nonlinearity and experience axial stiffening with the increase in the axial stretch.

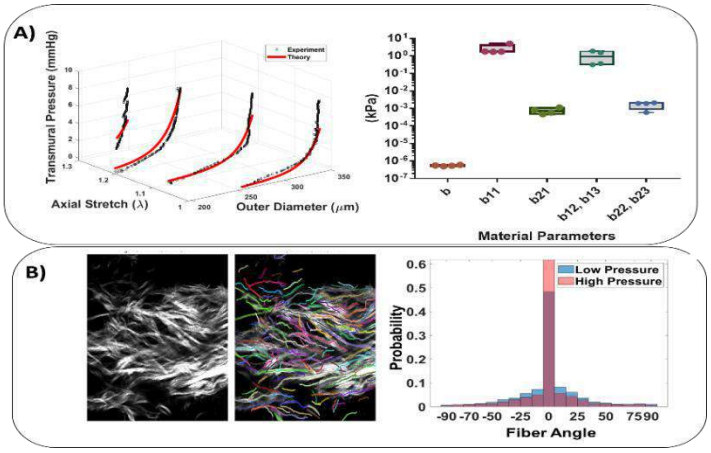

Figure 2 Passive biaxial data and modeling results. A) Representative of biaxial data from rat tail lymphatics and material properties associated with the model obtained from the nonlinear regression and bootstrapped method for four samples. B) Distribution of collagen fibers within the vessel wall obtained from the second harmonic generation (SHG) images.

DISCUSSION

Lymphatic vessels adapt their contractile function to various loading conditions (pressure, flow and external forces from skeletal muscles) which is key to serve their function as both a pump and conduit. Although there is heterogeneity in lymphatic muscle cells from different regions, previous studies suggest that muscle cells generate maximum force in a wide range of pre-load (stretch) to maintain lymphatic flow (3). Particularly, the lymphatic pressure is known to be a key regulator of lymphatic function. It is known that the increase in pressure changes the frequency and amplitude of contractions. It is believed that the change in the stretch due to the applied pressure and subsequently the change in extracellular calcium level plays a major role in the contractility changes. Here, we tested the hypothesis that the axial stretch is also a key modulator of lymphatic contractility. Our results show that the lymphatic vessels from rat tail lymphatics are under pre-axial stretch and change in the axial stretch can significantly alter the lymphatic contractions. In addition, the two-photon imaging and constitutive modeling of passive wall mechanics suggest that these vessels undergo axial loading and the most collagen fibers are aligned in the axial direction to bear the axial load.

Acknowledgments This work was supported by the AHA Predoctoral Fellowship award (17PRE33670828) and National Heart, Lung, and Blood Institute Grant R01-HL-113061.

REFERENCES

1. **Baek S**, **Gleason RL**, **Rajagopal KR**, **Humphrey JD**. Theory of small on large: Potential utility in computations of fluid-solid interactions in arteries. *Comput Methods Appl Mech Eng* 196: 3070–3078, 2007.
2. **Caulk AW**, **Nepiyushchikh Z V**, **Shaw R**, **Dixon JB**, **Gleason Jr. RL**. Quantification of the passive and active biaxial mechanical behaviour and microstructural organization of rat thoracic ducts. *J R Soc Interface* 12, 2015.
3. **Gashev AA**, **Zhang R-Z**, **Muthuchamy M**, **Zawieja DC**, **Davis MJ**. Regional Heterogeneity of Length-Tension Relationships in Rat Lymph Vessels. *Lymphat Res Biol* 10: 14–19, 2012.
4. **Gleason RL**, **Gray SP**, **Wilson E**, **Humphrey JD**. A multiaxial computer-controlled organ culture and biomechanical device for mouse carotid arteries. *J Biomech Eng* 126: 787–795, 2004.

SB³C2019
Summer Biomechanics, Bioengineering and Biotransport Conference
June 25 -28, Seven Springs, PA, USA

SIMULATION OF CARDIAC FLOW: ANALYSIS OF GEOMETRY SIMPLIFICATION

Fanwei Kong (1), Christoph Augustin (2), Kevin Sack (3,4) Shawn Shadden (1)

(1) Department of Mechanical Engineering
University of California, Berkeley
Berkeley, CA, USA

(2) Institute of Biophysics
Medical University of Graz
Graz, Austria

(3) Division of Biomedical Engineering
Department of Human Biology,
University of Cape Town,
Cape Town, South Africa

(4) Department of Surgery,
University of California, San Francisco,
San Francisco, CA, United States

INTRODUCTION

Cardiovascular diseases (CVDs) are the leading causes of mortality worldwide. The contraction and relaxation of left ventricle (LV) is the main driving force of blood circulation. Altered LV hemodynamics is believed to be associated with the initiation and progression of many CVDs. Thus, understanding and evaluating the flow pattern inside a patient LV is thought to be essential to capture, and subsequently treat, cardiovascular dysfunction at early stages to reduce the mortality and morbidity rates [1]. Computational fluid dynamics (CFD) models, often derived from patient-specific medical imaging, have been used to provide a more fundamental understanding of individual LV flow patterns and pressure fields. Such image-based modeling may advance diagnostic capabilities, treatment protocols and help guide clinicians to choose the most effective therapy of CVDs [1].

Most prior ventricular flow studies obtained LV wall geometries from *in vivo* ultrasound-based or cardiac magnetic resonance imaging (MRI) images with limited resolution [2-3]. The model geometries were often highly simplified and usually lacked the papillary muscles (PM) and the corrugated trabecular structures of the LV. Since the LV flow pattern is sensitive to geometry, it is important to understand the effect of this simplification on modeling intraventricular flow and pressure. Here we apply CFD modeling to a subject-specific porcine LV model with detailed ventricular structures and motion obtained from previous solid mechanics finite-element (FE) simulations based on high-resolution image data [4]. We simplified the detailed LV endocardial surfaces to remove PM and trabecular structures and built a smoothed model that resembles the resolution of *in vivo* MRI images. We then compare the simulated LV flow pattern and pressure of the simplified models to those of the complex model.

METHODS

Detailed model geometries were extracted from the endocardial surfaces of a subject-specific FE model constructed in a previous study [4]. Briefly, a healthy porcine heart was fixed and imaged by diffusion-tensor MRI with a high spatial resolution of 0.3 × 0.3 × 0.8 mm. The constructed model preserved detailed representations of trabecular and PM structures. The biventricular model simulated realistic dynamic beating of the heart and was validated by subject-specific and independent *in vivo* strain data obtained from echocardiography. We obtained the simulated endocardial surfaces of a total of 41 time-steps for 1 cardiac cycle. We followed conventional approaches [5-6] to avoid boundary effects on the intraventricular flow: mitral opening (MO) and aortic opening (AO) were extended from the positions of valves along the axis of the aortic outflow tract.

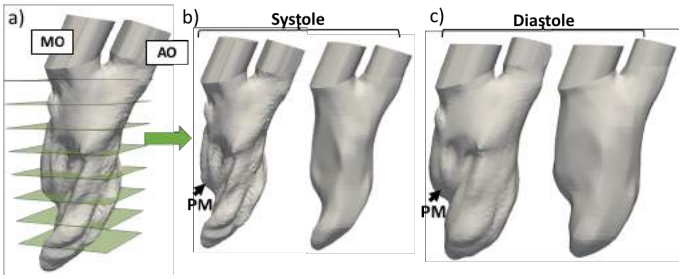

Figure 1: a) LV geometry at systole with cut planes, complex and smoothed geometries b) at systole and c) at diastole

To smooth out the PM and trabeculae structures, on the most contracted mesh surface, we sampled mesh points on cut planes that are 8 mm apart from each other and normal to the LV long axis (**fig. 1a**). From those sampled points, we selected those that form the vertices of the convex hull of the point set. We then down-sampled or linearly

interpolated the selected points to maintain a uniform distribution of mesh vertices and applied a smoothing operation to remove sharp edges caused by mesh simplification. The same mesh vertices were chosen for other phases to maintain the mesh connectivity. **Fig. 1** display a comparison between the complex and the smoothed mesh.

We applied the Arbitrary Lagrangian-Eulerian formulation of the incompressible Navier-Stokes equations with a stabilized FE Galerkin method [7] in the open-source FEniCS project to simulate the intraventricular flow and account for the moving boundary. We created a volume mesh from one surface at the start of diastole and used cubic spline interpolation to obtain 3200 interpolated surface meshes to impose the movement on the volume mesh. **Fig. 2a** shows the LV volume curve obtained from the given boundary meshes. Diastole and systole phases were determined based on rapid increase and decrease of LV volume, while the phases when the LV volume holds steadily were determined as isovolumetric contraction (IVC), and isovolumetric relaxation (IVR) phases. Pressure boundary conditions were applied at the inlet during diastole and during IVC, and at the outlet during systole and during IVR. **Fig. 2b** displays the prescribed pressure curve on mitral inlet or aortic outlet.

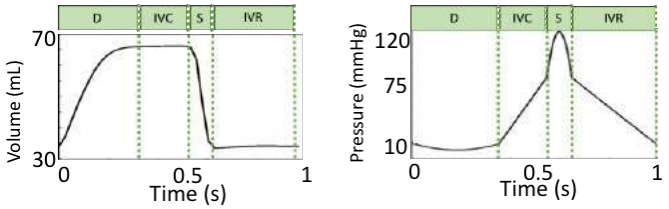

Figure 2: a) LV volume curve and b) prescribed pressure boundary condition curve of 1 cardiac cycle.

RESULTS

Based on the simulations, flow rates, maximum velocity at mitral or aortic openings, intraventricular flow velocity and pressure drop were extracted during the cardiac cycle (Fig. 3). The pressure drop was defined as the difference in pressure between apex and mitral opening at diastole or aortic opening at systole. The maximum velocity, flow rate and pressure drop curves displayed similar trends for both smoothed and complex models, while some differences in magnitudes were observed. During diastole and IVC, the largest discrepancy of flow rate happened after middle diastole when the flow rate for the smoothed model was 15.7% smaller. The maximum velocities at mitral opening and pressure drop were similar between the two models. At middle systole, the maximum velocity and flow rate at aortic opening and pressure drop were smaller by 5.4%, 14.3% and 26.9% respectively for the smoothed model than for the complex model. During IVR, small fluctuations of maximum velocity and pressure drop were observed in the complex model and not in the smoothed model.

The intraventricular flow patterns during diastole were different between the complex and the smoothed models (fig. 4 left). At middle diastole, for the complex model, the PM blocked the mitral jet and created disturbed low-velocity flow near the PMs. The mitral jet then formed two major vortices. One vortex located near the center of LV, sweeping the flow from the lateral wall to the septal wall. The other vortex centered at the bottom of LV, creating a circulation near the apex region. Without the PMs, intraventricular flow of the smoothed model was dominated by only one dominant vortex during diastole. However, the circulation did not seem to cover the apex region for the smoothed model. From middle to late diastole, the LV flow patterns were similar while the velocity magnitude decreased for both models. During systole (fig. 4 right), the intraventricular flow patterns were similar between the two models.

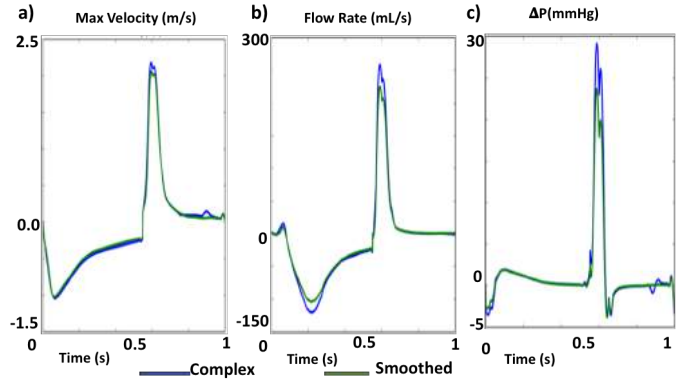

Figure 3: a) Maximum velocity and b) flow rate at mitral or aortic opening and c) pressure drop for complex and smoothed mesh

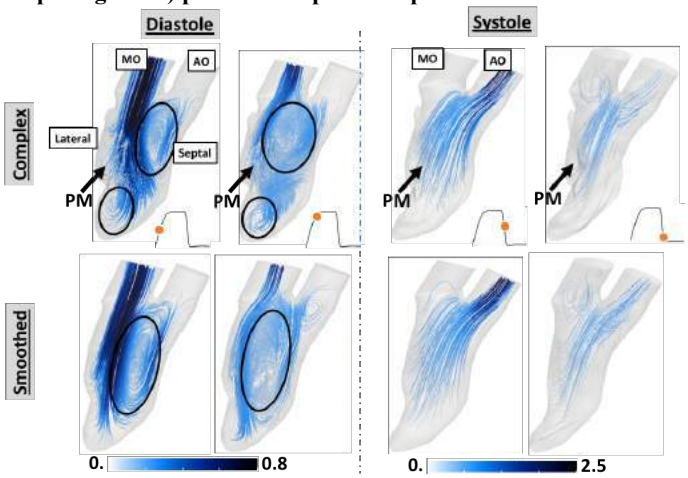

Figure 4. Comparison of velocity streamlines between complex model and smoothed model at middle diastole and middle systole. Color map represents velocity magnitude (m/s)

DISCUSSION

Simplified LV geometries have been commonly used in image-based CFD modeling of intraventricular blood flow. Our study provides useful insights on the effect of geometry simplification on LV CFD simulation by applying realistic LV wall motions obtained from both complex and smoothed model geometries. Major differences resulted from using the smoothed model were a) reduced pressure drop between apex and aortic opening at systole and b) the lack of complex flow pattern near PMs and the absent of circulatory flow near the apex region at diastole. These results also provide potential understanding of the functions of PM and trabeculae structures and were consistent with earlier findings that used simplified LV wall motions [5]. Future improvements would include adding left atrium, mitral valve and aorta structures for a more realistic inflow and outflow boundary condition, and prescribing physiological and subject-specific inlet or outlet pressure boundary conditions.

ACKNOWLEDGEMENTS

This work was supported by the National Science Foundation SI2-SSI #1663671.

REFERENCES

[1] Mittal, R et al., *J Comput Physics* 305:1065-1082, 2016
[2] Khalafvand et al., *Comput Meth Biomech Biomed Eng,*14(1):113-132, 2011
[3] Doost et al., *Biomed Eng Online*, 15(1): 101, 2016
[4] Sack, K et al *Front. Physiol*. 9:539, 2018.
[5] V. Vedula et al., *Theor. Comput. Fluid Dyn,* 30:3-21, 2016
[6] Khalafvand et al., *Int. J. Numer. Meth. Biomed. Engng*. 2014; 30:1044–1056
[7] Hoffman, J et al., *Comput Turbulent Incompressible Flow,* 2007

A COMBINED MRI ARTERIAL SPIN LABELING AND COMPUTATIONAL MODELING STRATEGY TO QUANTIFY PATIENT-SPECIFIC BLOOD FLOW AND PERFUSION IN CEREBROVASCULAR OCCLUSIVE DISEASE

Jonas Schollenberger (1), Luis Hernandez-Garcia (1,2), C. Alberto Figueroa (1,3)

(1) Department of Biomedical Engineering
University of Michigan
Ann Arbor, Michigan, USA

(2) Functional MRI Laboratory
University of Michigan
Ann Arbor, Michigan, USA

(3) Department of Surgery
University of Michigan
Ann Arbor, Michigan, USA

INTRODUCTION

Cerebrovascular occlusive disease, characterized by the buildup of plaque inside the vessel (stenosis), is a major cause of stroke. Diagnosis relies on velocity measurements in the cervical arteries via duplex ultrasonography, excluding quantification of cerebral blood flow (CBF) and tissue perfusion. However, estimation of the cerebral vasculature's capacity to compensate flow reductions via collateral pathways and autoregulation depends on this information. Considering the high anatomical variability in the Circle of Willis (CoW), there is a need to develop new clinical tools to precisely quantify CBF and perfusion.

Despite increasing use of CFD for clinical applications, patient-specific modeling of CBF has been limited by the lack of precise estimates of boundary condition parameters. Recently, a strategy to calibrate a 1D/0D model of CBF using SPECT perfusion data was proposed [1], but it required the injection of a radioactive tracer for imaging and modeled CBF was restricted to 1D.

In this work, we seek to overcome these limitations by combining a 3D multi-scale computational model of CBF with vessel-selective MRI arterial spin labeling (ASL) measurements of tissue perfusion.

METHODS

ASL measures tissue perfusion non-invasively by magnetically labeling a bolus of blood in the neck and imaging a volume of brain tissue after a short transit delay (Fig. 1). A standard (e.g. non-vessel-selective) ASL sequence was extended to acquire territorial perfusion maps by implementing cardiac-triggered super-selective pseudo-continuous ASL (SS-PCASL) [2]. In SS-PCASL, additional in-plane magnetic gradients are rotated to create a circular labeling spot which can be placed on the vessel of interest. Territorial perfusion maps provide measurements of the fractional contributions of each cervical artery to total tissue perfusion in each imaging voxel.

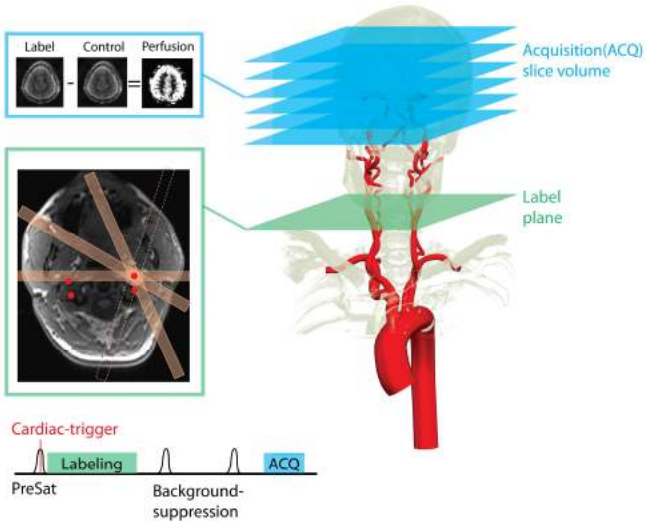

Figure 1: Cardiac-triggered SS-PCASL sequence. The sequence starts with a cardiac-triggered pre-saturation pulse, followed by vessel-selective labeling, background suppression pulses during the transit delay, and the image acquisition.

The 3D/0D framework CRIMSON [3] is used to model CBF. For physiologically meaningful results, the model needs to be informed on anatomy, flow, and pressure. Here, each outflow is coupled to a 3-element Windkessel model with parameters initially set to literature values. The goal of this work is to match the simulation to the vessel-selective ASL acquisition. Integration of ASL perfusion data into the

CFD model framework is performed in three steps (see Fig.2). 1) Segmentation of cerebral vascular territories to calculate flow splits in the CoW. 2) Estimation of cardiac-averaged CBF in each cerebral artery based on total CoW inflow through the cervical arteries (phase-contrast MRI). 3) Iterative adjustment of Windkessel parameters to match CBF estimates. In a post-processing step, Lagrangian particles are used as a metric to directly validate vessel-selective ASL images and to quantify collateral flow by counting particles at each outlet.

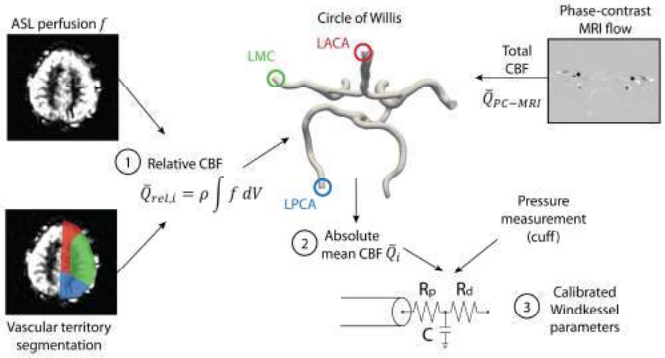

Figure 2: Workflow for estimating Windkessel parameters in the CoW using both ASL and phase-contrast MRI. LACA, LMC, and LPCA are the left anterior, middle, and posterior cerebral artery.

RESULTS

Figure 3 shows ASL territorial perfusion maps acquired in two healthy volunteers. Subject (a) presents a posterior circulation dominated by the left vertebral artery (VA). Subject (b) has an absent basilar artery and thus perfusion to the posterior circulation was solely provided by the right internal carotid artery (ICA) through the right posterior communicating artery. These perfusion results are confirmed by Time-of-Flight (TOF) MRI images.

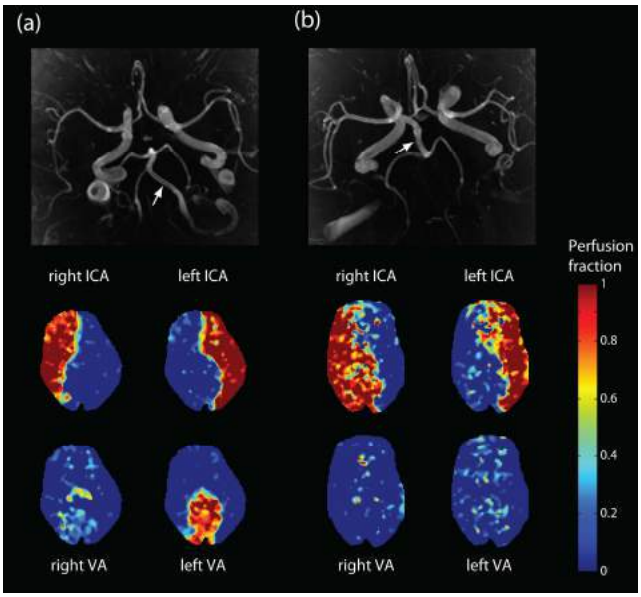

Figure 3: Axial TOF and corresponding territorial perfusion map of two subjects. The posterior circulations were perfused by the left VA (a) and the right ICA via the right posterior communicating artery (b). The increased caliber of the supplying artery is indicated by the white arrow.

Preliminary simulation results on a different patient with a left ICA stenosis are summarized in Fig. 4. Fig.4a illustrates the segmented 3D solid model based on MRI anatomical image data. Fig.4b shows the pulsatile velocity field at systole with high velocities in the stenosed vessel as well as in the contralateral ICA. Seeding of Lagrangian particles revealed an increase in contralateral flow to compensate for flow reduction in the stenosed ICA (Fig. 4c).

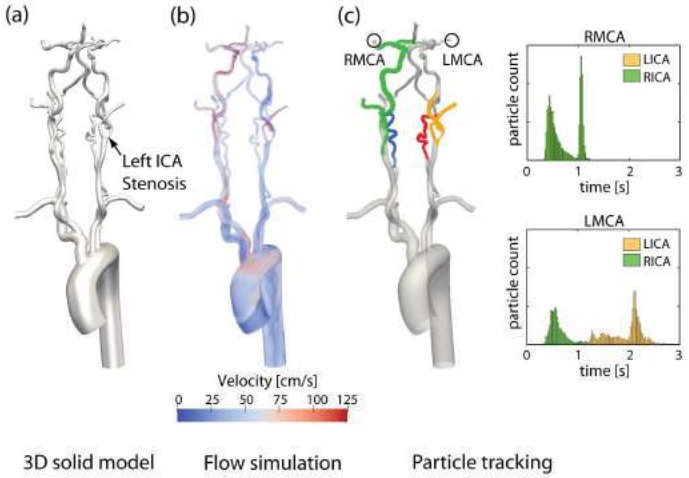

Figure 4: Computational modeling of CBF in a patient with left ICA stenosis. (a) 3D image-based reconstruction of the large arteries from the heart to the brain. (b) Simulated velocity field at systole. (c) Lagrangian particle tracking to quantify collateral flow.

DISCUSSION

Our ASL sequence offers brain perfusion measurements including territory mapping of individual cervical arteries. Our work focused on optimizing image quality and accuracy by compensating for magnetic field inhomogeneity, cardiac pulsatility, and subject movement [4]. Territorial perfusion maps have previously been successfully acquired in patients with cerebrovascular disease [5].

Simulation results reflected the contralateral flow compensation expected in a patient with carotid stenosis. However, since Windkessel model parameters were based on literature values, changes in distal vascular resistance, induced by cerebral autoregulation to compensate for the flow reduction, were not accounted for. Our proposed strategy accounts for these changes by measuring tissue perfusion. In the next step, ASL perfusion data will be processed according to the workflow outlined in Fig. 2 to calibrate the Windkessel model parameters. Our calibrated model of CBF will therefore match the patient's hemodynamics better than previously reported modeling approaches. This is a necessary step to accurately estimate collateral flow in the CoW and improve patient diagnosis and stratification in the future.

ACKNOWLEDGEMENTS

This work was supported by the Edward B. Diethrich Professorship and the German Academic Exchange Services (DAAD). Computing resources were provided by the National Science Foundation [grant 1531752] Acquisition of Conflux, A Novel Platform for Data-Driven Computational Physics (Tech. Monitor: Ed Walker).

REFERENCES

[1] Zhang, H. et al., *Ann Biomed Eng*, 44:2351-2363, 2016
[2] Helle, M. et al., *Magn Reson Med*, 64:777-786, 2010
[3] CRIMSON. The Software for Cardiovascular Modelling and Simulation. www.crimson.software
[4] Schollenberger, J. et al., *Magn Reson Med,* submitted
[5] Richter, V. et al., *AJNR Am J Neuroradiol*, 38:703-711, 2017

EVALUATION OF ARTIFICIAL NEURAL NETWORKS AS A POTENTIAL RUPTURE DISCRIMINATION MODEL

Sricharan S Veeturi (1,2), Hamidreza Rajabzadeh-Oghaz (1,2), Jason M Davies(2,3,5), Hui Meng (1,2,3,4)

(1) Department of Mechanical and Aerospace Engineering
University at Buffalo
Buffalo, New York, USA

(2) Canon Stroke and Vascular Research Center
Buffalo, New York, USA

(3) Department of Neurosurgery
University at Buffalo
Buffalo, New York, USA

(4) Department of Biomedical Engineering
University at Buffalo
Buffalo, New York, USA

(5) Department of Radiology
University at Buffalo
Buffalo, New York, USA

INTRODUCTION

In clinical practice, the decision whether to treat a newly discovered unruptured intracranial aneurysm (UIA) has been mainly based on IA size (>7mm) among other factors, as embodied in clinical scores such as ISUIA[1] and PHASES[2]: [1, 3]. However, most subarachnoid hemorrhage cases are small ruptured aneurysms(RIA) (<7mm) [4], which demonstrates that size alone is not a reliable indication of rupture risk. Identifying more reliable metrics for risk stratification is highly valuable.

Building true rupture prediction model needs longitudinal data. However, this data is scarce since the dangerous aneurysms are usually treated by clinic, which leaves us with mainly small and clinical indented as "less dangerous" UIAs. In practice, when managing UIAs, clinicians have an implicit assumption that the UIAs resembling ruptured aneurysms may be at greater danger of rupture. For instance, many studies have reported that most of the ruptured aneurysms are irregular shape; thus, clinicians are in favor of treating irregular shape UIAs [5]. Following this mindset, several studies have identified distinct morphological and hemodynamic features of ruptured IAs.

In our lab, Xiang et al. developed a composite rupture discriminator model using multi variate logistic regression based on aneurysmal morphology and hemodynamics [6]. This model could be applied on any aneurysm and identify its corresponding rupture class. The output of the predictive model can also be viewed as a continuous variable rather than just a classifier. This rupture probability for a UIA – known as ruptured resemblance score (RRS) – quantifies the similarity of the UIA to the past ruptured cohorts. In fact, those UIAs which resemble ruptured cohorts, having high RRS, may have higher likelihood of rupturing in the future, thus reasonable to get treated. The RRS model was also found to remain stable when a larger cross-sectional data was used. Recently, Varble et. al further imrpoved the model by incorporating 415 IAs and taking clinical factors into account along with morphological and hemodynamic fators[4].

All our previous classification models were built using multivariate logistic regression. Artificial Neural Networks (ANN) have been known to capture hidden nonlinear relationships of different input parameters [7, 8]. In this study, we aim to evaluate whether an ANN can better perform rupture discrimination. We also provide an example of potential application of RRS model in clinical settings.

METHODS

Data Collection, Morphologic and Hemodynamic Analyses

We took the training database used by Varble et. al [3]. The dataset consisted of 415 IAs (102 ruptured and 313 unruptured). Using the workflow shown in Figure 1, we calculated morphological and hemodynamic parameters (Table 1) for each IA. These analyses (including CFD) was already performed in Varble et al. [3].

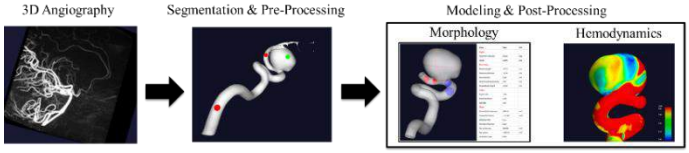

Figure 1: Work flow of image-based morphology and hemodynamics

Table 1: Input features* for the Artificial Neural Network

Clinial	Morphological	Hemodynamic
Gender	Aneurysm Size	Normalized WSS
Age	Size Ratio	OSI
Location	Aspect Ratio	RRT
Hypertension	Undulation Index	Low shear area
Family history	Ellipticity Index	Max WSS
Earlier SAH	Nonsphericity index	-

*Defined in Varble et al [3]

Development and Testing of the Neural Network

The aneurysms were randomly divided into training and testing datasets at an 85% to 15% ratio. The ratio of unruptured (U) and ruptured (R) aneurysms in both cohorts was the same. The training set had 355 aneurysms (268 U vs. 87 R), while the testing had 60 aneurysm (45 U vs. 15 R). All the parameters listed in Table 1 were used in model training.

Using the training set we built a 3-layer ANN using hold-out cross-validation to tune the hyper parameters of the neural network. We then applied the trained ANN to the testing cohort. For comparison, we also tested combined RRS model by Xiang et al. [6]

$$Odds_{combined} = \exp(0.73(SR) - 0.45(WSS) + 2.19(OSI) - 2.09)$$

and aggregate Rupture Discrimination Model by Varble et al. [3]:

$$Odds_{combined} = \exp(0.37(UI) + 1.47(OSI) - 0.12(WSS) + 2.26(Prior\ SAH) + 1.4\ (ACA) + 1.44(PCOM) - 0.79(Multiple\ IAs) - 2.91)$$

The logistic regression models give the odds that an IA is ruptured, while *RRS= Odds / (1+Odds)*[9]. ANN outputs a continuous value as well however, the value is purely mathematical. In all the classification models, a cutoff value 0.5 was used to classify the testing cohort into ruptured and unruptured aneurysms.

We compared all the models by looking at the confusion matrix as well as the Receiver Operating Characteristic (ROC) curve. To quantify the goodness of fit, we also compared the Area Under the Curve (AUC).

Application of models to clinical cases

The potential utility of RRS has gained recognition with clinicians at our center. For ambiguous UIA cases where decision-making was not straightforward, our clinicians often request us to compute RRS to confirm their treatment decision *a posteriori*. We show one of these cases to demonstrate potential application of the RRS models.

RESULTS

Performance of Rupture Discriminator Models

Table 2 reports the performance of the models on the testing cohort of 60 aneurysms (45 unruptured vs. 15 ruptured) in classifying the aneurysm rupture status.

	Model by Xiang et. al [5]	Model by Varble et. al [3]	ANN
True Positives	7 (47%)	4 (27%)	11 (73%)
True Negatives	36 (80%)	43 (96%)	33 (73%)
False Positives	9 (20%)	2 (4%)	12 (27%)
False Negatives	8 (53%)	11 (73%)	4 (27%)

Table2: Confusion matrix of testing cohort

Neural network model had the highest true positive rate (the RIA correctly classified as ruptured) and lowest false negative rate (the ruptured aneurysms misclassfied as unruptured). The ROC plots for the 3 models are shown in Figure 2. AUC for the ANN is comparable to the model developed by Varble et al [3].

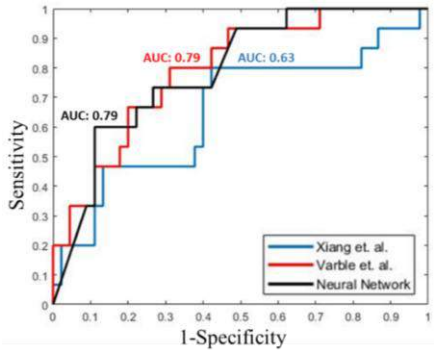

Figure 2: ROC curves of all the models

Example of Clinical Application

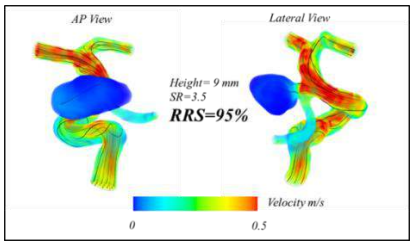

Figure 3: Velocity contours on an ambiguous UIA

Patient: A 55-year-old female on work-up for a headache. Angiography images revealed a 9 x 6 mm, narrow-necked UIA located at PComm. Decision was made to treat the IA by coils. Considering that the clinically developed rupture assessment models provided inconsistent 5-year rupture risk scores (ISUIA[1]: 14.5% and PHASES[2]: 2.4%, respectively), clinicians approached us to evaluate the rupture resemblance in terms of morphology and hemodynamics for this UIA.

Potential application of RRS: Our flow simulation revealed a stasis aneurysmal blood flow, thus low WSS on aneurysm dome. A combination of high size ratio and low WSS led to a RRS score of 95% (Xiang *et al.* model) for this UIA. While the treatment decision was made without the input of RRS, the neurosurgeons sought the RRS results to confirm their decision.

DISCUSSION & CONCLUSIONS

In this study, we have applied a well-established machine learning model (ANN) and evaluated it as a potential rupture discrimination model. Compared to the logistic regression model by Varble et. al., ANN had higher true positive rate, and lower false negative rate; however, the AUC was found to be the same between the two. Both these models showed better performance than Xiang et al., benefitting from a larger database and including clinical information in training the model. However, ANN did not improve AUC beyond Varble et al. However, for a fair evaluation, these tools need to be tested on larger and equal datasets.

Statistical models built and validated on cross-sectional data are versatile and robust and are believed to be potentially useful in the treatment of IAs [9, 10]. Xiang et al. [11] argued that UIAs that were classified as ruptured by their classification model, i.e. false positive cases, in fact highly resembled ruptured aneurysms, although they were not yet ripe for rupture. In clinical practice, such UIAs are considered as high risk, thus favoring treatment. The single UIA case presented here also highly resembled RIAs. It had a high size ratio and low WSS, an environment promoting inflammatory-cell-mediated destructive wall remodeling [12]. Although the true rupture risk of the UIA was unknown, such adverse hemodynamic environment should be eliminated for the safety of the patient. This illustrates the potential clinical utility of RRS.

ACKNOWLEDGEMENTS

This work was supported by National Institute of Health grant R01NS091075) and the Canon Medical System Corp.

REFERENCES

1. Wiebers, D.O., et al., The Lancet, 2003. **362**(9378): p. 103-110.
2. Greving, J.P., et al., Lancet Neurol, 2014. **13**(1): p. 59-66.
3. Etminan, N., et al., Neurology, 2015. **85**(10): p. 881-9.
4. Varble, N., et al., Stroke, 2018. **49**(4): p. 856-864.
5. Lindgren, A.E., et al., Stroke, 2016. **47**(5): p. 1219-26.
6. Xiang, J., et al., Stroke, 2011. **42**(1): p. 144-52.
7. Liu, J., et al., Eur Radiol, 2018. **28**(8): p. 3268-3275.
8. Paliwal, N., et al., Neurosurg Focus, 2018. **45**(5): p. E7.
9. Detmer, J., et al., Int J Com Ass Rad Surg, 2018. **13**(11): p. 67-79.
10. Detmer, J., et al.,Acta Neuroch (Wien), 2018. **160**(12): p. 25-34.
11. Xiang, J., et al. J Neurointerv Surg, 2014.
12. Meng, H., et al., AJNR Am J Neuroradiol, 2014. **35**(7): p. 54-62.

SB³C2019
Summer Biomechanics, Bioengineering and Biotransport Conference
June 25 -28, Seven Springs, PA, USA

SYSTEMATIC MODULATION OF CELL-CELL ADHESION *IN VIVO* MODULATES EPITHELIAL TISSUE MECHANICS AND REMODELING

Xun Wang (1), Karen E. Kasza (1)

(1) Department of Mechanical Engineering
Columbia University
New York, NY, USA

INTRODUCTION

Tissue remodeling is a fundamental biological process that produces the diverse shapes and structures of tissues. Mechanical factors, including forces and tissue mechanical properties, play vital roles in tissue remodeling, during embryonic morphogenesis, wound healing, and cancer metastasis [1-2]. During *Drosophila* embryonic development, tissue remodeling can be rapid. Oriented cell rearrangements and cell shape changes in the embryonic epithelium rapidly double the length of the body axis in just 30 minutes (Fig 1a) [3-5]. Cell-cell adhesion mediated by junctional proteins and contractile tension generated by actomyosin networks are thought to be key parameters in controlling epithelial tissue mechanics and remodeling [5,6]. However, it is unknown how the balance between adhesion and tension determines the mechanics and remodeling of epithelial tissues. A recent vertex model predicts that epithelial tissue mechanical behaviors can transition from solid-like to fluid-like, which could promote tissue remodeling, and that this transition depends on the balance between adhesion and tension [7]. However, *in vivo* studies of the mechanical properties of remodeling tissues have not been extensively conducted due to limitations in experimental techniques. It remains largely unexplored how mechanical properties of tissues are modulated during remodeling and development.

Here, we systematically modulate the balance between adhesion and contractile tension in epithelial tissues *in vivo* by increasing or decreasing expression of E-cadherin (E-cad), a primary cell-cell adhesion protein. We combine *in vivo* confocal imaging and quantitative image analysis to study the effects of modulating adhesion on epithelial tissue mechanics and remodeling during *Drosophila* body axis elongation. We find that increased E-cad promotes more fluid-like behaviors in static tissues that are not actively remodeling. In contrast, increased E-cad promotes more solid-like behavior in actively remodeling tissues. These quantitative *in vivo* studies of the mechanics of epithelial tissue remodeling are essential for building and testing models of epithelial mechanics. This work sheds light on the mechanical factors involved in controlling tissue remodeling during development and on the improper regulation of tissue remodeling associated with birth defects and cancer metastasis.

METHODS

Biological Materials. To visualize cell membranes, a red fluorescent marker sqh>gap43:mCherry [8] was integrated into *Drosophila* embryos. E-cad levels were modulated by the Gal4/UAS system. To decrease E-cad, expression was partially inhibited by RNAi (TRiP, Transgenic RNAi Program). To increase E-cad, overexpression was achieved using the UAS>shg:GFP transgene [9].

Time-Lapse Imaging. Embryos were dechorionated in 50% bleach and mounted in a 1:1 mixture of halocarbon oil 27 and 700, between a coverslip and an oxygen-permeable membrane (YSI). The ventrolateral region of the embryo was imaged on a Zeiss LSM880 laser scanning confocal microscope with a 40X/1.2 NA water-immersion objective. Two-color Z stacks were acquired at 1-μm steps and 15-s time intervals. Maximum intensity z-projections of 3 μm in the apical junctional plane were analyzed.

Cell segmentation, tracking, and quantification. Time-lapse movies were z-projected in ImageJ. Cells were segmented and tracked using the MATLAB-based software SEGGA [10]. Tissue elongation starts at $t = 0$. Cell shapes were quantified by the cell shape index:

$$p = P/\sqrt{A} \quad (1)$$

where P is cell perimeter and A is cell area [7]. Error bars represent standard deviations. Vertex lifetime was measured as the time between when a cell edge contracted to a vertex to when the two cells initially in contact were no longer in contact. Error bars represent standard errors. Mean values from normal distributions were compared by t-tests.

RESULTS

Cell shapes change dramatically during tissue remodeling. During *Drosophila* body axis elongation in wild-type embryos, the cell shape index *p* increases with time (Fig 1). At 10 min before the tissue begins to remodel, when the tissue is still relatively static, cells take on nearly hexagonal shapes, and *p* is close to the value predicted at the solid-fluid transition in the vertex model [7]. During body axis elongation when the tissue is dynamically remodeling, cell shapes become deformed and *p* begins to increase (Fig 1).

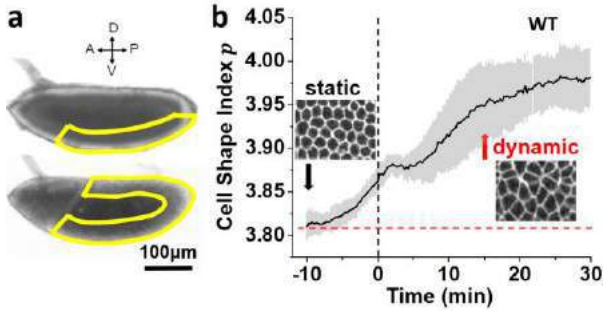

Figure 1: Cell shapes during tissue remodeling. a, The *Drosophila* body axis (yellow) elongates 2-folds in 30 min. Anterior (A), left. Dorsal (D), top. **b**, The cell shape index *p* increases with time. Predicted solid-fluid transition, red dashed line. Onset of tissue remodeling, black dashed line. Insets: Confocal images of cells. n = 5 embryos.

Cell shapes are tuned by cell-cell adhesion levels. To test the effects of adhesion on cell shapes and tissue mechanics, we systematically increased or decreased E-cad expression in the tissue. First, we examined the tissue when it is static, before remodeling begins. In embryos with normal E-cad levels, cell shapes at t = -10 min are close to that predicted at the solid-fluid transition point in the vertex model (Fig 2a). The vertex model predicts that increased adhesion should produce more fluid-like tissues [7]. We find that tissues with increased levels of E-cad display increased *p*, consistent with this prediction of more fluid-like behavior (Fig 1, 2a). Very strong decreases of E-cad produce severely disrupted cell shapes compared with normal embryos (data not shown). In contrast, when the tissue becomes dynamic and starts remodeling, the differences in *p* among embryos with different E-cad levels disappear (Fig 2b). Thus, cell shapes are tuned by E-cad expression in static tissues prior to remodeling and independent of E-cad expression levels in dynamic, remodeling tissues.

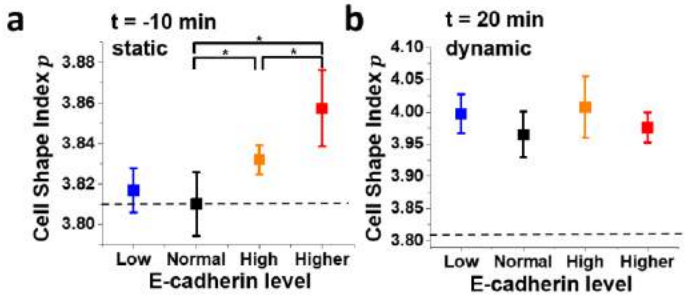

Figure 2: Cell shapes are tuned by cell-cell adhesion levels. The cell shape index *p* for embryos with different E-cad levels. Solid-fluid transition predicted by vertex model, dashed lines. **a,** At t = -10 min when the tissue is static, embryos with increased E-cad display significantly higher *p* compared to normal (P<0.05). **b,** *p* is independent of E-cad levels at t = 20 min when the tissue is dynamic.

Cell rearrangement speed shows a biphasic response to cell-cell adhesion levels. A rearrangement has two steps. First, rearrangement is initiated by contraction of a cell-cell-contact, bringing cells together at a high-order vertex. Second, vertices are resolved by the formation of new contacts between cells (Fig 3a). To test the effects of adhesion on cell rearrangement and tissue remodeling, we measured the lifetime of vertices formed during rearrangement as a measure of rearrangement speed. We find that vertex lifetime shows a biphasic relationship with E-cad levels. Reducing E-cad from normal levels produces faster rearrangement, while increasing E-cad produces slower rearrangement. Surprisingly, this trend shows that increased E-cad adhesion produces slower rearrangement, a signature of more solid-like behavior. For very high E-cad, rearrangement speed begins to increase again.

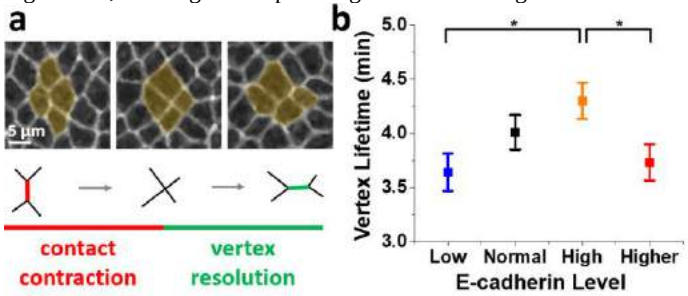

Figure 3: Cell rearrangement speed is modulated by cell-cell adhesion levels. a, Confocal images (top) and schematic (bottom) of cell rearrangement. **b,** Vertex lifetime shows a biphasic relationship with E-cad levels (P<0.05). n = 393-484 cell rearrangements.

DISCUSSION

This work, for the first time, quantitatively measures how systematic modulation of cell-cell adhesion levels influences epithelial tissue mechanics and remodeling *in vivo*, providing necessary input for models of epithelia. We find that modulation of E-cad levels influences both cell shape and rearrangement during *Drosophila* axis elongation. When the tissue is static prior to remodeling, cell shapes indicate that the tissue is at the solid-fluid transition predicted by the vertex model [7]. Increased E-cad modulates cell shapes in a manner consistent with more fluid-like behavior, at least within a working range around normal E-cad levels. When the tissue is dynamic and actively remodeling during elongation, cell shapes are independent of E-cad levels. Instead, we find that the timescale for cell rearrangement is modulated by E-cad levels in a biphasic manner, with increased E-cad producing slower rearrangement, consistent with more solid-like behavior. However, increasing or decreasing E-cad too far from normal levels produces severely disrupted tissues that abolish these trends. Together, these findings demonstrate an important role for cell-cell adhesion in tissue mechanics and remodeling during development, and indicate complex effects of modulating adhesion on the fluid-like and solid-like behavior of epithelia. Future studies of how adhesion couples to contractile tension will provide insight into how cells control tissue mechanics and remodeling, which will be essential for understanding development as well as birth defects, cancer, and wound healing in humans.

ACKNOWLEDGEMENTS

This work was supported by the NSF (CMMI 1751841). KEK holds a Career Award at the Scientific Interface from the BWF, Clare Boothe Luce Professorship, and Packard Fellowship.

REFERENCES

[1] Mongera, A et al., *Nature*, 561:401–405, 2018. [2] Friedl, P et al., *Nat Rev. Mol. Cell Biol*, 10:445-457, 2009. [3] Irvine, KD et al., *Development*, 120:827–841, 1994. [4] Butler, L C et al., *Nat Cell Biol*, 11(7):859–864, 2009. [5] Herrera-Perez, RM et al., *Curr Opin Genet Dev*, 51:88–95, 2018. [6] Heisenberg, CP et al., *Cell*, 153(5):948-962, 2013. [7] Bi, D et al., *Nature Phys*, 11(12):1074–1079, 2015. [8] Fabrowski et al., *Nat Commun*, 4:2244, 2013. [9] Lee JY et al., *PLoS Genet*, 12(5): e1006043, 2016. [10] Farrell DL et al., *Development*, 144:1725, 2017.

SB³C2019
Summer Biomechanics, Bioengineering and Biotransport Conference
June 25 -28, Seven Springs, PA, USA

RELATING BONE STRAIN TO LOCAL CHANGES IN RADIUS MICROSTRUCTURE FOLLOWING 12 MONTHS OF AXIAL FOREARM LOADING IN WOMEN

Megan E. Mancuso (1), Karen L. Troy (1)

(1) Department of Biomedical Engineering
Worcester Polytechnic Institute
Worcester, Massachusetts, USA

INTRODUCTION

Bone is a mechanosensitive tissue, with microstructure adapting to novel loading. It is hypothesized that local mechanical signals related to bone strain (magnitude, rate) are sensed by osteocytes, which signal nearby osteoblast and osteoclast cells to add bone in high strain regions and remove bone in low strain regions. This concept of localized, strain-driven adaptation is supported by studies in mice showing caudal vertebra loading yielded bone formation in areas of high strain and resorption in areas of low strain [1]. In humans, Christen et al. (2014) showed that retrospectively estimated bone strain was related to local changes in radius microstructure in postmenopausal women [2]. However, the relationship between strain magnitude and adaptation of bone microstructure has not been prospectively quantified in humans.

Previously we established a voluntary forearm loading model, in which human subjects lean their palm onto a padded load cell that provides feedback to guide load magnitude [3]. We also validated subject-specific finite element (FE) models of the forearm to simulate this loading task, enabling us to characterize the strain environment within the radius [4]. Together, these methods can be used to prospectively assign and measure radius bone strain during the loading task. In a pilot study of 23 women, we found that 14-week percent changes in bone density in the distal radius, divided into local regions by quadrant, were positively correlated with continuum FE-estimated energy equivalent strain [5]. While these results provide preliminary support of strain-driven adaptation, the continuum FE models do not explicitly consider the effect of trabecular microstructure. Recently, we have validated a multiscale modeling technique, which incorporates a micro-FE section based on High-Resolution Peripheral Quantitative Computed Tomography (HRpQCT) into the continuum forearm FE models [6]. Here, our purpose was to relate microstructure-level bone strain estimated from multiscale FE models to local, 12-month changes in trabecular microstructure measured in a prospective loading trial.

METHODS

The data reported here were obtained as part of a prospective clinical experiment, in which healthy women aged 21-40 were asked to perform four sessions of forearm loading each week over 12 months. Each session consisted of 100 loading cycles (target force 200-400 N) of the non-dominant arm. Data from all subjects (n=102) are reported elsewhere [7], and the current analysis involves a subgroup (n=7) of compliant loading subjects in the tertile experiencing the greatest increases in ultradistal bone mineral content, measured using clinical quantitative computed tomography. All subjects gave written informed consent to participate in this institutionally approved study.

HRpQCT scans were acquired for the standard distal radius site (9.02 mm axial region) with an 82 µm voxel size (XtremeCT, Scanco Medical, Switzerland) at baseline and 12 months (Fig. 1). Clinical CT scans (Brightspeed, GE Healthcare, Chicago, IL) including the scaphoid and lunate carpals and the distal-most 10 cm of the radius were acquired with a slice thickness of 0.625 mm and an in-plane resolution of 0.234 mm. A calibration phantom was included in each clinical CT scan.

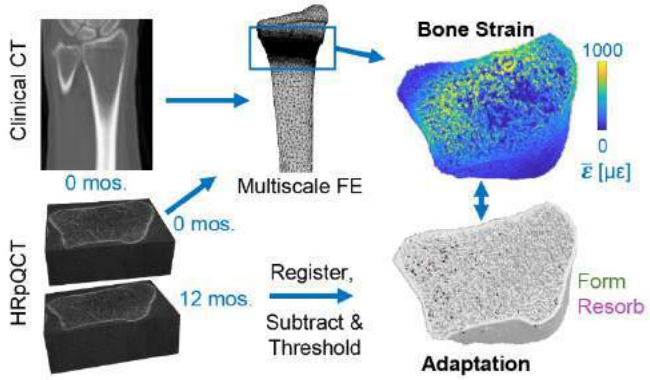

Figure 1: Overview of methods used to calculate energy equivalent bone strain, $\bar{\varepsilon}$, using CT-based multiscale FE models and identify bone adaptation sites from HRpQCT scans.

Bone strain was estimated using a previously described (6) multiscale FE modeling technique. Models consisted of proximal and distal continuum regions flanking a micro-FE region at the HRpQCT

scan site. Continuum regions were generated from segmented clinical CT scans, with 3-mm (nominal element size) quadratic tetrahedrons assigned inhomogeneous elastic moduli based on density [8]. The micro-FE sections were voxel-based meshes generated from segmented baseline HRpQCT scans. The micro-FE meshes explicitly modeled bone microstructure, with a homogenous tissue modulus (E=15 GPa) assigned to the hexahedral elements, allowing for void spaces between trabeculae. Boundary conditions were applied to the multiscale models to simulate the forearm loading task, with 300 N applied axially from the carpals towards the proximal radius. Models were solved using Abaqus 6.16 (Simulia, Providence, RI) on a parallel computing cluster. Nodal stresses and strains in the micro-FE section were exported for post-processing.

Adaptation of bone microstructure was quantified from baseline and follow-up HRpQCT scans using the algorithm presented in Christen (2018) [9] within Image Processing Language software (Scanco Medical, Switzerland). The greyscale baseline and follow-up images for each subject were aligned using 3D rigid registration [10]. The baseline and transformed follow-up greyscale images were cropped to the overlapping region, and subtracted to obtain voxel-by-voxel changes in density. Increases in density are indicative of bone formation, while decreases indicate bone resorption. To avoid the effect of noise, only clusters of at least five voxels with differences ≥225mgHA/cm^3 were identified as adaptation sites. Trabecular bone adaptation sites were identified by taking the Boolean intersection of the adaptation masks and the trabecular contour generated during the standard Scanco analysis program. A final mask overlaying the segmented baseline scan and trabecular adaptation sites was exported for post-processing.

Custom code (Matlab, Mathworks, Natick, MA) was used to calculate bone strain within formation and resorption sites. Energy equivalent strain at each FE node was calculated as

$$\bar{\varepsilon} = \sqrt{\frac{2U}{E}} \quad (1)$$

where E is elastic modulus and U is strain energy density calculated as

$$U = \frac{1}{2}[\sigma_1\varepsilon_1 + \sigma_2\varepsilon_2 + \sigma_3\varepsilon_3] \quad (2)$$

with σ_n and ε_n being the principal stress and strain components, respectively. The adaptation mask was aligned with the FE coordinates using 3D rigid registration [6]. For each voxel labeled as a formation or resorption site, an average $\bar{\varepsilon}$ was calculated for all nodes within 200 µm of the voxel coordinates (36.6 ± 5.6 nodes for formation and 56.3 ± 2.3 nodes for resorption).

Our overall hypothesis was that bone formation occurs in high strain regions, while bone resorption occurs in low strain regions. A paired t-test was used to compare mean strain in formed versus resorbed voxels within subjects (α=0.05). Formed and resorbed voxels were then pooled across subjects and binned into 25 με increments. Histograms of formation and resorption frequency, normalized to the total number of adapted voxels, were plotted as a function of strain.

RESULTS

The number of formed (33-8717) and resorbed (9-5331) voxels varied widely between subjects. On average, 0.27% of trabecular voxels were labeled as adaptation sites (formed or resorbed), while analysis of the total region showed a mean 2.01% increase in trabecular density. Mean $\bar{\varepsilon}$ was higher in formed versus resorbed voxels in six out of seven subjects (Fig. 2A, paired t-test p=0.104). Across subjects, mean $\bar{\varepsilon}$ in formed versus resorbed voxels was 314 ± 84 με versus 276 ± 35 με. The area under the normalized histograms (Fig. 2B) indicates that 61.9% of adapted voxels were formed and 38.1% were resorbed. The formation and resorption curves had peaks at 300 με and 150 με, respectively, indicating resorption is most probable at a lower strain than formation.

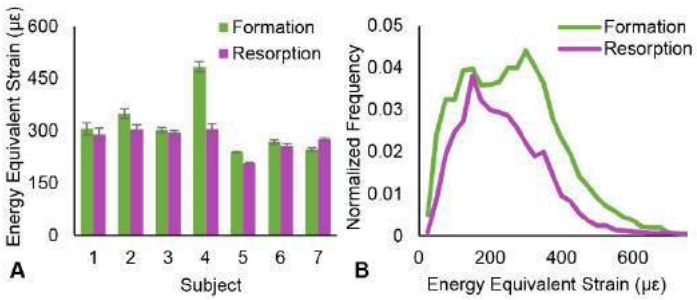

Figure 2: A) Mean $\bar{\varepsilon}$ in formed versus resorbed voxels by subject. Error bars indicate standard error. B) Formation and resorption frequency, normalized to the total number of adapted voxels.

DISCUSSION

Our purpose was to characterize the local relationship between FE-estimated bone strain and adaptation following 12 months of forearm mechanical loading. In this small sample, we found a positive, but non-significant association between higher strain and formation, and between lower strain and resorption. While the histogram distribution for resorption was clustered at lower strains (100-250 με), formation was more uniformly distributed between 150 and 400 με, potentially indicating that the likelihood of bone formation is more stochastic than that of resorption.

The major strength of this study is that bone strain was calculated for a known, prospectively assigned loading task using physiological boundary conditions. This study is limited by small sample size. Additionally, while formation and resorption were identified in all subjects, the fraction of trabecular voxels identified as adaptation sites underestimated the changes in trabecular density observed when analyzing greyscale data from the entire region. One possible explanation for this observation is that changes in density were diffusely distributed through the trabecular region, such that they were excluded as localized formation sites. Also, the method used to identify adaptation was developed for and validated using data measuring age-related bone loss in post-menopausal women [2], and may not be sensitive enough to detect more subtle, load-driven changes. Further work is needed to validate appropriate thresholds for change in density and size of adaptation site for this application. Sensitivity to detect local bone changes is also limited by the scan resolution (voxel size 82µm).

ACKNOWLEDGEMENTS

This research was fully supported by NIAMS of the National Institutes of Health under award number R01AR063691.The content is solely the responsibility of the authors and does not necessarily represent the official views of the National Institutes of Health. Support was provided by NSF IGERT (DGE 1144804) and NSF GRFP (DGE1106756). Results were obtained in part using a high-performance computing system acquired through NSF MRI grant DMS-1337943 to WPI.

REFERENCES

[1] Schulte, F et al., *PLoS ONE,* 8:e62172, 2013.
[2] Christen, P et al., *Nature Comm,* 5:4855, 2014.
[3] Troy, K et al., *J Orthop Res,* 31:1406-1413, 2013.
[4] Bhatia, V et al., *J Biomech,* 47:2759-2765, 2014.
[5] Bhatia, V et al., *J Biomech Eng,* 137:011001-1-011001-5, 2015.
[6] Johnson, J et al., *Med Eng Phys,* 44:16-24, 2017.
[7] Troy, K et al., *bioarxiv (Preprint),* 2018.
[8] Morgan et al., *J Biomech,* 36:897-904, 2003.
[9] Christen et al., *PLoS ONE,* 13:e0191369, 2018.
[10] Ellouz et al., *Bone,* 63:147-157, 2014.

EFFECTS OF REPRODUCTION AND LACTATION HISTORY ON RAT MATERNAL BONE MECHANO-RESPONSIVENESS AND OSTEOCYTE MICROENVIRONMENT

Yihan Li[1], Ashutosh Parajuli[2], Chantal MJ. de Bakker[1], Hongbo Zhao[1], Wei-Ju Tseng[1], Rebecca H. Chung[1], Liyun Wang[2], X. Sherry Liu[1]

[1] McKay Orthopaedic Research Laboratory, University of Pennsylvania, Philadelphia, PA, USA

[2] Department of Mechanical Engineering, University of Delaware, Newark, DE, USA

INTRODUCTION

The female skeleton undergoes dramatic bone loss during pregnancy and lactation [1]. Despite substantially increased bone formation after weaning, bone mass is recovered incompletely [2]. However, multiple clinical studies have shown that the history of pregnancy and lactation induces no adverse, or even a protective effect on postmenopausal fracture risk, forming a paradox. Our previous studies suggested that rats with three repeated cycles of pregnancy and lactation had attenuated estrogen-deficiency-induced bone loss later in life compared to age-matched virgins [3]. Recent studies reported that the osteocyte can actively remodel its peri-lacunar/canalicular (PLC) matrix during lactation [4, 5]. Therefore, we hypothesized that PLC remodeling induced by reproduction and lactation may prime the osteocyte microenvironment, leading to enhanced mechano-sensitivity to exert protective effects against estrogen deficiency post-menopause.

METHODS

All animal experiments were IACUC approved. 29 female, Sprague Dawley rats were assigned to 4 groups: Virgin-Intact (n=7), Reproductive-Intact (n=7), Virgin-OVX (n=8), and Reproductive-OVX (n=7). Reproductive rats underwent two reproductive cycles consisting of pregnancy, 3-week lactation and 6-week post-weaning recovery. Rats in OVX groups underwent bilateral ovariectomy surgery (OVX) at age of 10 months to simulate estrogen deficiency post-menopause. *In vivo dynamic loading:* All 6-week post-OVX and age-matched intact rats (without OVX surgery) were subjected to a 2-week dynamic, compressive loading protocol [6]. A peak load of 45N, corresponding to ~1500 με at the tibial shaft determined by strain gauges, was applied to the left tibia at 2 Hz (*i.e.*, 0.15s ramp up, 0.15s ramp down, and 0.2s dwell time), for 5 min/day over 2 weeks (5 days/week), while the right tibia remained as non-loaded control. *In vivo μCT imaging:* μCT scans of proximal tibia (Fig 1A) and tibial midshaft were performed on both tibiae right before (week 0) and two weeks after loading (week 2) using VivaCT 40 (Scanco Medical AG, voxel size 10.5μm). Percent changes between week 0 and week 2 for non-loaded and loaded tibiae were calculated. *Dynamic histomorphometry:* All rats were injected with calcein green and alizarin red on day 4 and day 12 of loading. Dynamic histomorphometry analyses were performed to evaluate double-labeled bone formation. *bSEM imaging:* The non-loaded tibial cortex (n=4/group) was subjected to scanning electron microscope in backscatter mode (bSEM, Zeiss Supra 50VP) to assess lacunar and canalicular structure. *Immunohistochemistry:* Paraffin-embedded non-loaded tibial cortex was immunostained for MMP13 to evaluate PLC remodeling enzyme expression. Ploton silver staining was performed on tibial cortex to further investigate lacunar-canalicular interconnection [7, 8]. *Statistics:* A two-way ANOVA with baseline parameters as covariate and Bonferroni corrections were used to compare loading responses between virgin and reproductive rats. Student's t-test was applied to compare lacunar/canalicular structure.

RESULTS

OVX Rats: *In vivo* μCT indicated that virgin and reproductive rats in the OVX group underwent 25% and 13% reduction in bone volume fraction (BV/TV), respectively, in the non-loaded tibia (Fig 1B). Dynamic loading attenuated the estrogen-deficiency-induced trabecular bone loss in virgin rats and abolished the bone loss in reproductive rats (Fig 1B). Loading also led to 7% increase in trabecular thickness (Tb.Th) in virgins and abolished the estrogen-deficiency-induced reduction in Tb.Th in reproductive rats (Fig 1C). However, the extent of loading responses (loaded *vs.* non-loaded) was not different in trabecular bone between post-OVX virgin and

reproductive rats. At the tibial midshaft, loading increased the polar moment of inertia (pMOI) by 7% in virgins and 13% in reproductive rats (Fig 2E). Similar results were found in cortical area (Ct.Area, Fig 2F). Moreover, ANOVA test indicated greater responses in pMOI and Ct.Area to loading (loaded *vs.* non-loaded) in post-OVX reproductive rats than in virgins. Dynamic histomorphometry suggested that loading led to 5, 16, and 96-fold increase in mineralizing surface (MS/BS), mineral apposition rate (MAR), and bone formation rate (BFR/BS) in reproductive-OVX rats (Fig 2G-I), while the loading responses in virgin-OVX rats were less pronounced. As a result, ANOVA test indicated greater response in MS/BS to loading in post-OVX reproductive rats than virgins.

Backscattered SEM images of tibial cortex showed a trend toward 11% greater lacunar area (*p=0.07*) and 33% greater canalicular area in post-OVX reproductive rats than in virgins (Fig 3). Additionally, post-OVX reproductive rats had 51% greater percent of MMP13+ osteocytes (Fig 4AB) and a trend toward 10% higher canalicular number per lacunar surface than virgins (*p=0.09*, Fig 4CD).

Intact Rats: There was minimal loading response in the tibial trabecular bone in both intact virgin or reproductive rats. Significant loading responses in pMOI and Ct.Area were detected at tibial midshaft; however, they did not differ between virgin and reproductive rats. Similarly, no difference in PLC structure, MMP13+ osteocytes, or canalicular number was found between intact virgin and reproductive rats (data not shown).

DISCUSSION

Our previous studies suggested that history of multiple cycles of pregnancy and lactation led to dramatic alterations in cortical and trabecular bone microstructure. Despite these changes, our current study found no influence of reproductive history on bone's mechano-responsiveness and osteocytes PLC structure in estrogen-replete rats. Intriguingly, when subjected to estrogen-deficiency, the history of reproduction and lactation significantly enhanced bone's mechano-responsiveness. Moreover, we found significantly increased canalicular area and osteocytic MMP13 enzyme activities, and a trend of increased lacunar area and number of canaliculi in post-OVX reproductive rats than virgins. These results suggested that the osteocytes that have experienced multiple reproductive cycles may actively regulate their lacunar-canalicular network system (LCS) and directly modulate the PLC matrix, leading to enlarged lacunae and canaliculi when subjected to estrogen deficiency. These altered osteocyte LCS microenvironment and cellular activities in response to OVX in reproductive rats may result from the osteocyte "memory" engendered by exposure to sharp estrogen withdrawal during lactation. The fluctuations in estrogen levels induced by reproductive history may condition the osteocytes to striking hormonal changes, leading to functional adaptation in osteocyte LCS microenvironment against estrogen deficiency later in life. According to the LCS fluid flow model established by Weinbaum *et al.* [9], the enlarged canaliculi and altered canalicular wall permeability due to the active PLC remodeling may change the peri-cellular fluid flow and dragging forces on peri-cellular matrix when subjected to loading, and thus affecting bone's mechano-responsiveness. Therefore, further tests with direct measurements of load-induced fluid flow in LCS [6] are necessary to establish the effects of osteocyte PLC remodeling on modulating bone's mechano-responsiveness in rats with different reproductive histories.

In summary, a history of reproduction and lactation may prime the microenvironment of osteocytes, leading to elevated mechano-sensitivity to protect maternal skeleton from estrogen deficiency. This investigation provided new insight into osteoporosis prevention and treatment for postmenopausal women based on their reproduction histories.

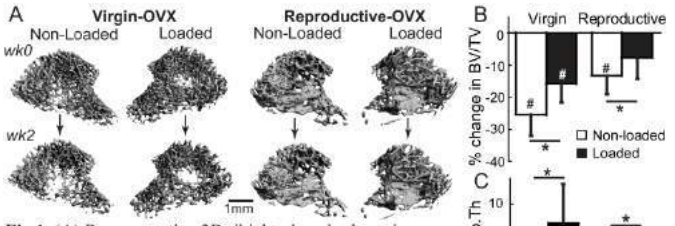

Fig 1. (A) Representative 3D tibial trabecular bone images. (B-C) Comparisons of % changes in trabecular bone between the non-loaded and loaded tibia in post-OVX virgin and reproductive rats. p<0.05: # difference between wk0 and wk2 and * between responses in the non-loaded and loaded tibia.

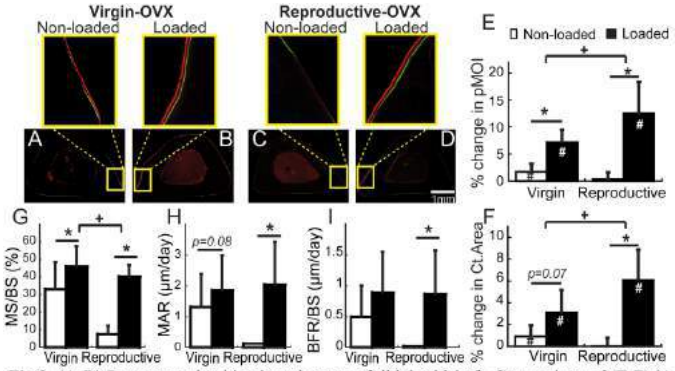

Fig 2. (A-D) Representative histology images of tibial midshaft. Comparison of (E-F) % changes in midshaft cortex, and (G-I) periosteal bone formation activities between the non-loaded and loaded tibia in post-OVX virgin and reproductive rats. p<0.05: # difference between wk0 and wk2; * between responses in the non-loaded and loaded tibia; + between loading response of virgin and reproductive rats.

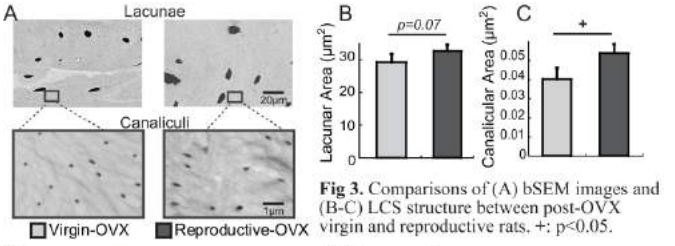

Fig 3. Comparisons of (A) bSEM images and (B-C) LCS structure between post-OVX virgin and reproductive rats. +: p<0.05.

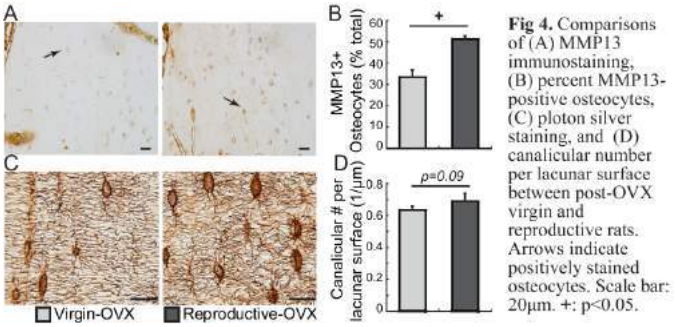

Fig 4. Comparisons of (A) MMP13 immunostaining, (B) percent MMP13-positive osteocytes, (C) ploton silver staining, and (D) canalicular number per lacunar surface between post-OVX virgin and reproductive rats. Arrows indicate positively stained osteocytes. Scale bar: 20μm. +: p<0.05.

ACKNOWLEDGEMENTS

NIH/NIAMS P30-AR069619, R03-AR065145, and R01-AR071718.

REFERENCES

[1] Kovacs CS, *Physiol Rev.*, 2015; [2] de Bakker CM *et al.*, *J Bone Miner Res.*, 2017; [3] de Bakker CM *et al.*, *J Bone Miner Res.*, 2018; [4] Qing H *et al.*, *J Bone Miner Res.*, 2012; [5] Kaya S *et al.*, *J Bone Miner Res.*, 2017; [6] Wang B *et al.*, *J Bone Miner Res.*, 2014; [7] Ploton D *et al.*, *Histochem*, 1986; [8] Dole NS *et al.*, *Cell Rep*, 2017; [9] Weinbaum S *et al.*, *J Biomech.*, 1994.

SB³C2019
Summer Biomechanics, Bioengineering and Biotransport Conference
June 25 -28, Seven Springs, PA, USA

BIPHASIC NETWORK MODEL OF COLLAGEN AND ELASTIN REMODELLING RECAPITULATES COMPOSITIONAL AND ORGANIZATIONAL CHANGES DURING AORTIC GROWTH AND DEVELOPMENT

Ryan R. Mahutga (1), Victor H. Barocas (1)

(1) Biomedical Engineering
University of Minnesota
Minneapolis, MN, USA

INTRODUCTION

Growth and remodeling (G&R) of biological tissue plays a key role in numerous diseases and is of vital importance for positive clinical outcomes. Any procedure that alters the tissue – from wound closure, to tissue grafting, to device implantation – relies on G&R. G&R processes are immensely complex involving many biological, chemical, electrical, and mechanical inputs, as well as numerous constituents making any one variable difficult to isolate. In particular, arterial G&R, including both normal and aberrant development (congenital defects, aneurysms), is fundamentally difficult to model both experimentally and computationally. Therefore, it is necessary to construct models of G&R processes that are understood to probe the effects one observes experimentally and clinically, and to isolate the interplay between stimuli. Toward this end, we have created a novel biphasic, fiber network model from primary experimental and clinical observations.

While there have been many studies on aortic development, there has been a lack of unifying theories on normal growth and maturation that can be similarly applied to aberrant development (i.e., most theories require the adjustment of many parameters to give different growth modes). Herein, we explore the idea that one can expect different growth modes from one feedback mechanism. To develop this idea, we propose two hypotheses. First, we hypothesize that tensional homeostasis drives fiber growth, maturation, and alignment, as well as dictating the time course of these actions. Second, we hypothesize that Donnan osmotic pressure due to the binding of proteoglycan-glycosaminoglycan (PG-GAG) complexes to the fiber network maintains tissue volume during loading and drives tissue growth.

METHODS

To explore our hypotheses, we have created a discrete fiber network model consisting of embedded Delaunay networks representing collagen and elastin. These networks are periodic in a unit cube domain (the representative volume element, or RVE) where the scale is determined by the network fiber properties as shown in (Eq. 1).

$$\chi = \sqrt{\frac{\pi \sum r_f^2 l_f}{\phi V}} \quad (1)$$

where χ is the RVE scale in meters per computational unit length, r_f is the fiber radius, l_f is the fiber length, ϕ is the fiber volume fraction in the RVE, and V is the computational volume of the RVE.

The constituents in this model are collagen, modeled as in [1], elastin, modeled as linear elastic [2], and PG-GAG complexes modeled through osmotic pressure based on fixed charge density (FCD). The FCD was taken to be proportional to the total fiber length in the RVE. The stress on the RVE boundary was calculated using volume averaging theory applied to these constituents.

The RVE was loaded based on the boundary loads one may expect from a developing mouse, where the blood pressure starts low prior to birth and then ramps up in the immediate post-natal period [3]. The RVE was approximated as a very small representative piece of a cylinder, and the thick-walled cylindrical approximation was used to determine the boundary conditions.

As the RVE is loaded, the fibers are remodeled according to the relation below (Eq. 2).

$$\frac{dr_f}{dt} = \frac{1}{\tau}\left(\frac{\sigma}{\sigma_\infty} - 1\right) r_f \quad (2)$$

where r_f is the fiber radius, t is time, τ is the growth time constant in days, σ is the fiber stress, and σ_∞ is the target fiber stress. The fibers are also allowed to lengthen treating the added radius as a parallel spring.

RESULTS

Simulations were performed assuming a wild-type mouse model system with typical blood pressure fit to [3] and aortic dimensions from [4]. The simulation encompassed the period from embryonic day 7.5 (E7.5) to 240 days after birth. Elastin production was ceased at day 18

(coinciding with the theory that elastin production stops shortly after birth), but collagen continued to remodel throughout the simulation.

Our simulation model system showed less growth than the experiments of Huang et al. (not shown) and Fournieri et al. (Fig 1A) [3,5]. This is likely due to the use of Delaunay networks, which are dissimilar to biological fiber networks in that they have a much higher connectivity which means there are many more redundant fibers (i.e., if a fiber is lengthened the load is shifted to another fiber that was previously unloaded rather than lengthening the whole network.). There is, however, a good agreement between the fiber volume evolution in our model system and in the experiments of Fournieri et al. (performed on rats) [5].

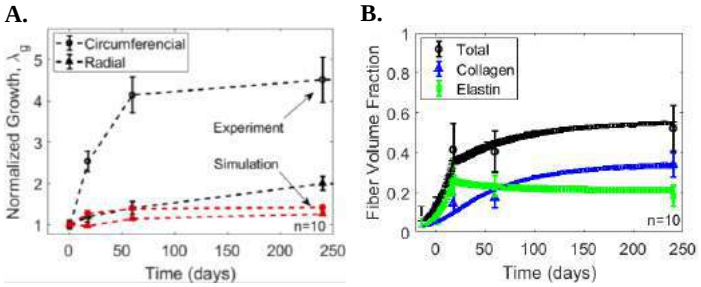

Figure 1. A. Normalized tissue growth. B. Fiber volume fraction evolution. Comparisons are made to experiments in [5] with 95% confidence intervals shown.

This model system also allowed us to track explicitly the fiber radii and rest lengths. As shown in Figure 2, collagen fibers tend to lengthen and thicken more that elastin fibers. We also note that our simulation collagen radii are comparable to those quantified by Liu et al. for mouse adventitia [6].

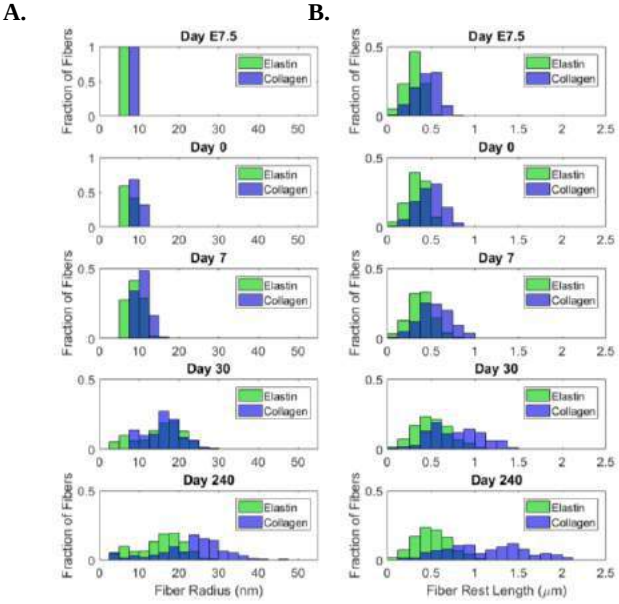

Figure 2. A. Fiber radii evolution; B. Fiber length evolution

Inspection of the networks themselves showed that in an unloaded state (i.e., with external loads removed, but still including osmotic pressure) fiber stress is held almost exclusively by elastin fibers. This is important because it implicates elastin having a major role in tissue residual stress. Additionally, as shown in Figure 4, we also see marked increases in oriented fiber area moving from the initial isotropic orientation toward the circumferential-axial plane. This is comparable to the orientations given by O'Connell et al [7].

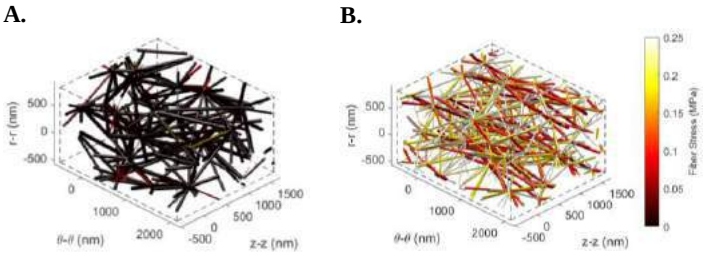

Figure 3. Unloaded networks at 240 days for A. Collagen and B. Elastin. Fiber sizes are appropriately scaled to RVE size. The colorbar shows the fiber stress overlaid onto individual fibers.

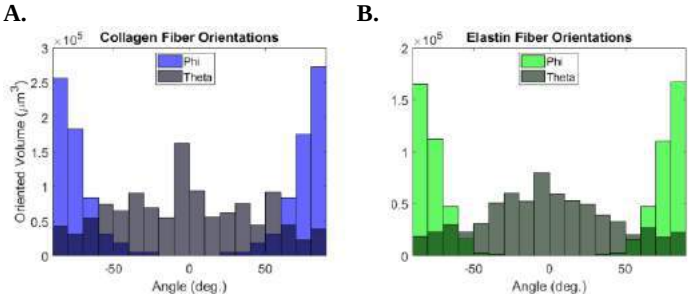

Figure 4. Unloaded network orientation distribution for A. Collagen and B. Elastin at 240 days. Theta is the angle from circumferential toward axial, and phi is the angle from radial toward the circumferential-axial plane.

DISCUSSION

This simulation framework marks a divergence from the typical continuum mechanics approach to growth and remodeling of biological tissues. Our approach represents a new method for understanding the growth of tissues as a whole, as well as providing insight into fiber-specific properties such as orientation, diameter, and length.

We have demonstrated that this model can match many features of fibers in normal development including volume fraction, radius distribution, and orientation. To this point, our simulations have shown less growth than experimental observations suggest. It is clear that our simulation framework is likely missing some detail. We suspect that this is due to the networks used. Computationally generated Delaunay networks, unlike biological networks, tend to be highly connected. Thus, these networks are insensitive to modulation of individual fibers due to the high degree of fiber redundancy in mechanical loading.

As we move towards generating more realistic and complex networks based on imaging modalities such as second harmonic generation, we will be able to garner new insights into the stress response of fibrillar networks which will be particularly important in understanding disease states such as hypertension leading to spontaneous aneurysm, and genetic disorders affecting the extracellular matrix leading to aneurysm.

ACKNOWLEDGEMENTS

The authors acknowledge funding from the National Science Foundation Graduate Research Fellowship Program (NSF GRFP) under Grant No. 00039202. The authors also acknowledge funding from the National Institutes of Health under Grant No. U01-HL139471.

REFERENCES

[1] Freed, A.D. & Doehring, T.C., *J Biomech*, 127(4), 2005.
[2] Bailey, A. J. et al., *Phil Trans R Soc Lond Series B: Biol Sci*, 2002.
[3] Huang, Y. et al., *Am J Physiol Heart Circ Physiol*, 290, 2006.
[4] Bellini, C. et al., *J. R. Soc. Interface*, 14, 2016.
[5] Fornieri, C. et al., *Art Thromb*, 12, 1992.
[6] Liu, X. et al., *PNAS*, 94(5), 1997.
[7] O'Connell et al., *Matrix Biology*, 27, 2008.

SB³C2019
Summer Biomechanics, Bioengineering and Biotransport Conference
June 25 -28, Seven Springs, PA, USA

PREGNANCY AND LACTATION IMPAIR SUBCHONDRAL BONE LEADING TO REDUCED RAT SUPRASPINATUS TENDON FAILURE PROPERTIES

Ashley K. Fung (1), Snehal S. Shetye (1), Yihan Li (1), X. Sherry Liu (1), Louis J. Soslowsky (1)

(1) McKay Orthopaedic Research Laboratory
University of Pennsylvania
Philadelphia, PA, USA

INTRODUCTION

During pregnancy and lactation, women experience hormonal and physiological changes that increase the risk of musculoskeletal joint disorders such as shoulder, lower back, wrist, and knee pain [1]. Estrogen levels rise dramatically during pregnancy followed by a rapid decline during lactation before returning to normal levels after weaning. Increased joint laxity from hormonal fluctuations [2] and substantial maternal bone loss due to increased calcium demands for fetal and infant growth [3] contribute to impaired joint function. We previously showed that rats with a history of reproduction exhibited inferior supraspinatus tendon and humeral trabecular bone properties despite a lengthy post-weaning recovery period [4]. However, the transient effects of pregnancy and lactation on the supraspinatus tendon and proximal humerus remain unknown. Therefore, the objective of this study was to evaluate changes in supraspinatus tendon mechanical properties and in the microstructure of the bony insertion site during pregnancy, lactation, and post-weaning recovery in female rats. We hypothesized that substantial bone loss during lactation would compromise the subchondral bone microstructure leading to reduced supraspinatus tendon mechanical properties.

METHODS

30 Sprague-Dawley female rats (IACUC approved) were used: virgin (n=7), end of pregnancy (n=9), 2-week lactation (n=7), and 2-weeks post-weaning (n=7). Rats in the pregnancy group were sacrificed at parturition, while the lactation group underwent pregnancy and 2 weeks of lactation. Rats in the weaning group underwent pregnancy, 2-weeks lactation, and 2-weeks post-weaning recovery. All rats were sacrificed at 7 months of age, and shoulders were harvested for supraspinatus tendon mechanical testing and subchondral and trabecular bone analysis. Mechanics: Supraspinatus tendons were marked with stain lines, cross-sectional area was measured using a custom laser device, and humeri were secured in PMMA. Right supraspinatus tendons underwent viscoelastic tensile testing, consisting of pre-conditioning, stress relaxation at a 5% strain hold for 600s, a dynamic frequency sweep at 5% strain (0.1-10Hz), and a quasi-static ramp to failure at 0.3%/s. Left supraspinatus tendons underwent fatigue cyclic loading until failure at 2Hz between loads corresponding to 7% and 40% maximum stress, determined from quasi-static results. Peak cyclic strain, secant modulus, tangent modulus, hysteresis, and laxity, were recorded at two breakpoints (ends of the primary (BP1) and secondary (BP2) phases of a triphasic fatigue life curve). Subchondral and trabecular bone analysis: Prior to mechanical testing, left proximal humeri were μCT scanned (6μm, μCT35, Scanco). Trabecular bone proximal to the humeral growth plate was analyzed. Additionally, average thickness and the mineralization gradient was calculated (Amira 6.7) across the subchondral plate, defined as the mineralized fibrocartilage of the supraspinatus tendon enthesis and subchondral bone. Briefly, a 100x120x230 voxel volume was identified in the greater tuberosity at the supraspinatus tendon insertion site. After global thresholding, the innermost layer of the subchondral bone was defined to exclude trabecular bone. Individual layers were subsequently defined outwards towards the mineralized fibrocartilage boundary. Layer intensity values were averaged to construct a mineralization gradient, normalized to the total subchondral plate thickness. Bone mineral density (BMD) was compared at 0, 0.5, and 1.0, marking the boundaries between trabecular bone, subchondral bone, mineralized fibrocartilage, and tendon. Statistics: Comparisons across groups were made using one-way ANOVAs with Bonferroni post-hoc corrections. Significance was set at $p \leq 0.05$ and trends at $p \leq 0.1$. All data is presented as mean±SD.

RESULTS

Supraspinatus Tendon Properties. Cross-sectional area was significantly increased (Fig 1A) and midsubstance modulus trended higher (Fig 1B) during pregnancy compared to virgin. After weaning, however, modulus was significantly lower than both pregnancy and lactation groups and trended lower compared to virgin (Fig 1B). Percent relaxation was also significantly greater post-weaning compared to pregnancy and lactation (Fig 1C). For fatigue, tangent stiffness at BP1 for both lactation and weaning trended lower compared to virgin and was significantly lower compared to pregnancy (Fig 1D). However, there were no differences in cycles to failure, peak cyclic strain, hysteresis, or laxity (data not shown).

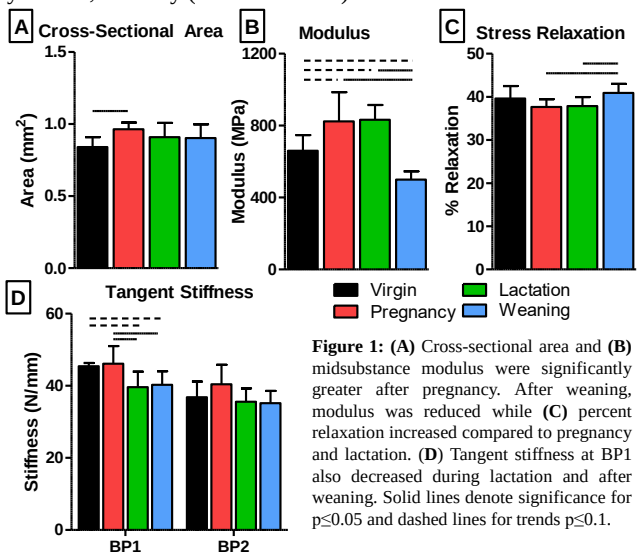

Figure 1: (A) Cross-sectional area and **(B)** midsubstance modulus were significantly greater after pregnancy. After weaning, modulus was reduced while **(C)** percent relaxation increased compared to pregnancy and lactation. (**D**) Tangent stiffness at BP1 also decreased during lactation and after weaning. Solid lines denote significance for p≤0.05 and dashed lines for trends p≤0.1.

Trabecular and Subchondral Bone Properties. Bone volume fraction (BV/TV) (Fig 2A) and trabecular number (Tb.N) (Fig 2B) was significantly lower while trabecular separation (Tb.Sp) (Fig 2C) was significantly greater during lactation compared to virgin and pregnancy groups. After weaning, BV/TV recovered with no significant difference from virgin. However, Tb.N and Tb.Sp trended lower and higher, respectively, post-weaning compared to virgin.

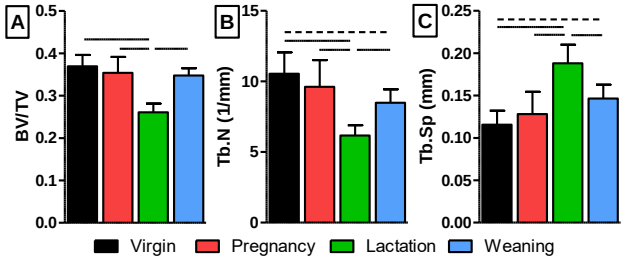

Figure 2: Lactation resulted in **(A)** decreased bone volume fraction, **(B)** decreased trabecular number, and **(C)** increased trabecular separation compared to all other groups. Solid lines denote significance for p≤0.05 and dashed lines for trends p≤0.1.

Since the predominant failure mode during quasi-static tendon testing was bony avulsion, failure properties reflect that of the insertion site and underlying subchondral bone (Fig 3A). Maximum stress (Fig 3B) and maximum strain (not shown) significantly decreased during lactation compared to virgin and pregnancy groups, but significantly recovered after weaning. At the trabecular bone-subchondral bone boundary, bone mineral density (BMD) was also significantly lower during lactation compared to virgin and pregnancy groups. After weaning, BMD remained significantly lower compared to virgin and trended lower compared to the pregnancy group. However, there were no differences in BMD between groups at 0.5, the subchondral bone-mineralized fibrocartilage interface, or at 1.0, the mineralized fibrocartilage-tendon boundary (Fig 3C). Furthermore, subchondral plate thickness trended lower in the lactation group compared to both virgin and pregnancy groups (Fig 3D).

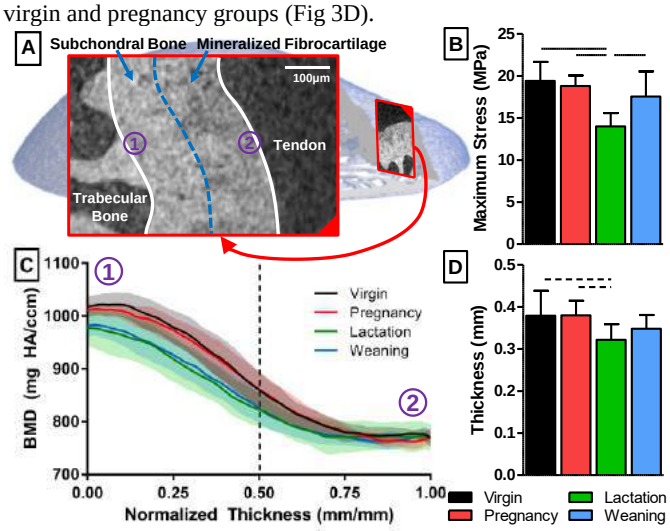

Figure 3: (A) The tendon insertion site transitions from regions of mineralized fibrocartilage to subchondral bone, forming the subchondral plate. **(B)** Maximum stress**, (C)** bone mineral density within the subchondral bone, and **(D)** overall subchondral plate thickness decreased during lactation. Solid lines denote significance for p≤0.05 and dashed lines for trends p≤0.1.

DISCUSSION

Pregnancy and lactation induced substantial changes in supraspinatus tendon and proximal humerus bone properties. Lactation impaired subchondral and trabecular bone, but properties recovered post-weaning. In contrast, supraspinatus tendon mechanical properties improved during pregnancy and these changes persisted during lactation before returning to pre-pregnancy levels post-weaning. Estrogen has been linked to increased collagen synthesis and tissue elasticity [5], providing a mechanism by which tendon properties increase by the end of pregnancy, the time at which estrogen levels peak. In contrast to bone tissue, the rapid decline of estrogen levels during lactation had no adverse effects on tendon properties, suggesting additional protective mechanisms associated with lactation.

Furthermore, bony avulsion failures and decreased maximum stress during lactation support further study into the subchondral plate microstructure. Reduced overall thickness and bone mineral density during lactation suggest that independent mechanisms modulated by osteoblast-osteoclast coupling regulation and osteocyte perilacuna-canalicular remodeling, respectively, may be at play.

Supraspinatus tendon tears most commonly occur at the insertion site, and reduced bone mineral density of the humeral head is a known risk factor [6]. Our results provide insight into the mechanisms that may govern this increased risk due to compromised bone, which may arise with menopause, aging, and other metabolic diseases. To further elucidate the onset of rotator cuff disease and hormonal regulations on tendon health, future studies will investigate the biological mechanisms underlying transient changes in tendon and bone properties during reproduction and lactation.

ACKNOWLEDGEMENTS

Study funded by NIH R03AR065145, R01AR071718, T32AR007132, and the Penn Center for Musculoskeletal Disorders (P30 AR069619).

REFERENCES

1] Kesikburun et al, *Ther Adv Musculoskeletal Dis* 10:229-334, 2018. 2] Steinetz et al, *Am J Vet Res* 69:59-67, 2008. 3] Kovacs, *Physiol Rev* 96:449-547, 2016. 4] Fung et al, *ORS* 0570, 2019. 5] Torricelli et al, *Age* 35:2125-36. 6] Meyer et al, *JSES* 13:333-337, 2004.

SB³C2019
Summer Biomechanics, Bioengineering and Biotransport Conference
June 25 -28, Seven Springs, PA, USA

MODELING ADAPTIVE REMODELING OF THE BLADDER WALL DURING AGING

Fangzhou Cheng (1), Lori A. Birder (2), Paul N. Watton (1,3), Anne M. Robertson (1,4)

(1) Department of Mechanical Engineering & Materials Science, University of Pittsburgh, Pittsburgh, PA, USA

(2) Department of Pharmacology & Cell Biology, University of Pittsburgh, Pittsburgh, PA, USA

(3) Department of Computer Science, University of Sheffield, Sheffield, UK

(4) Department of Bioengineering, University of Pittsburgh, Pittsburgh, PA, USA

INTRODUCTION

The human bladder is a highly compliant organ that can expand to store 450 ± 64.4 ml of urine at relatively low pressures of 43.5 ± 7.3 cm of H_2O in young adults (18 yrs) [1]. However, bladder compliance decreases with age [2] and the corresponding increase in wall stiffness is believed to cause lower urinary tract symptoms (LUTS) such as increased frequency of urination, urgency, incontinence, and residual volume [3,4]. In extreme cases, the associated increase in kidney pressure can lead to renal insufficiency [5].

To understand the change in bladder compliance, the bladder material properties were explored using uniaxial testing beginning in the early 70s [6] and, more recently using biaxial testing [7-10]. These studies reported the mechanical properties of bladder and suggested that bladder remodeled through alterations to material structure. However, no models of adaptive remodeling for the bladder have been introduced yet.

In this work, we integrate in situ mechanical testing and multiphoton microscopy to assess bladder mechanical properties while observing the transformation in collagen architecture under stretch. To explore the key physical mechanisms during bladder filling, a structurally motivated constitutive model is developed, driven by our database for the bladder wall [10]. A growth and remodeling framework with demonstrated success in arteries [11] is applied to bladder wall to investigate the aging process, informed by our experimental data.

METHODS

Mechanical Testing: Nine male Fischer rats (Species F344, adult and aged rats from National Institute on Aging of the NIH) were used in this study, separated by age with 4 adult rats (12 months) and 5 aged rats (21–24 months). Mechanical data (stretch vs. stress) was obtained using a customized biaxial testing system as described in [10]

Evaluation of Fiber Recruitment: Multiphoton image stacks were used to generate 3D reconstructions of collagen fiber architecture at chosen loading levels. Collagen fibers were traced in 2D slices through the depth of the 3D reconstructed model (Filament function in Imaris, Bitplane, Switzerland) [10].

Constitutive Model: The bladder was modeled as a constrained mixture [12,13] with contributions to the total strain energy per unit volume (Ψ) coming from three load bearing components within two wall layers – collagen in the detrusor smooth muscle layer (DSM) and both collagen and elastin fibers in the lamina propria layer (LP),

$$\Psi = \widetilde{\Psi}_E + \Psi_c^{LP} + \Psi_c^{DSM} \tag{1}$$

The strain energies for collagen and elastin fibers are, respectively,

$$\widetilde{\Psi}_E(\lambda_E) = \frac{k_E}{2}(\lambda_E - 1)^2 \tag{2}$$

$$\widetilde{\Psi}_C(\lambda_C) = \frac{k_C}{2}(\lambda_C - 1)^2 \tag{3}$$

where k_E and k_C are stiffness parameters; λ_E and λ_C are the fiber stretches for the elastin and collagen, respectively. Collagen fiber recruitment distributions were modeled using a triangular distribution function as described in [11] based on fiber distribution analysis of the MPM data. Briefly, the probability density function for fiber recruitment is defined in terms of distribution parameters λ_R^{min}, λ_R^{mode}, and λ_R^{max}, which are estimated by fitting data for stretch versus fraction of recruited collagen fibers to the cumulative triangular probability function. The total collagen strain energy function for each layer is then

defined as the integral of the strain energy for all collagen fibers across all recruitment stretches

$$\Psi_C(\lambda) = \int_1^{\lambda} \widetilde{\Psi}_C(\lambda_C)\rho(\lambda_R)d\lambda_R. \quad (4)$$

The probability density function for fiber recruitment, $\rho(\lambda_R)$ was defined to ensure unrecruited fibers do not contribute to strain energy.

Growth and Remodeling Framework: Motivated by [11], collagen fiber remodeling was assumed to maintain a homeostatic stretch distribution (λ_{C-AT}^{min}, λ_{C-AT}^{mod}, and λ_{C-AT}^{max}) at the maximum physiological pressure with a linear relationship for remodeling,

$$\frac{\partial \lambda_{C-R}^{min}}{\partial t} = \alpha_c \frac{\lambda_C^{max}|_{\Omega_T} - \lambda_{C-AT}^{max}}{\lambda_{C-AT}^{max}} \quad (5)$$

$$\frac{\partial \lambda_{C-R}^{max}}{\partial t} = \alpha_c \frac{\lambda_C^{min}|_{\Omega_T} - \lambda_{C-AT}^{min}}{\lambda_{C-AT}^{min}} \quad (6)$$

$$\frac{\partial \lambda_{C-R}^{mod}}{\partial t} = \alpha_c \frac{\lambda_C^{mod}|_{\Omega_T} - \lambda_{C-AT}^{mod}}{\lambda_{C-AT}^{mod}} \quad (7)$$

where $\lambda_C^{min}|_{\Omega_T}$, $\lambda_C^{mod}|_{\Omega_T}$ and $\lambda_C^{max}|_{\Omega_T}$ are the collagen stretch distributions at the threshold state; α_c is the remodeling rate. The remodeling rate of collagen in the DSM was assumed to be 3 times faster than that of the LP, motivated by experimental data where the remodeling process was found almost entirely in the DSM [10].

RESULTS

Collagen Fiber Recruitment Distribution: As shown in Figure 1, the aged bladder has a lower minimum recruitment stretch for both LP and DSM fibers compared with adult bladders. More importantly, in aged bladders, a much wider recruitment distribution was found in the DSM compared with the LP layer. The LP and DSM fibers had similar recruitment distribution length in adult healthy bladders.

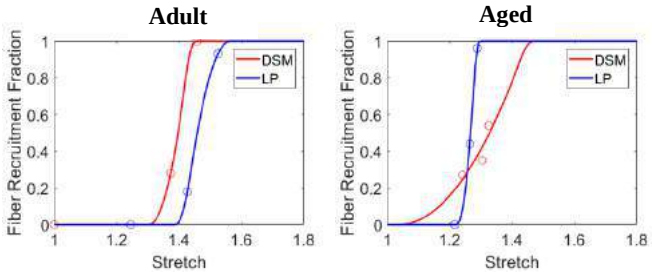

Figure 1: Tissue stretch vs. fiber recruitment fraction and associated fitted curves for both LP and DSM layers for representative adult (left) and aged (right) bladders

Collagen Fiber Remodeling: The physiological maximum pressure of rat bladder has been shown to be relatively insensitive to age, with consistent values from 12 months to 18 months and only slightly increasing by 9% at 24 months [14]. Therefore, we conjecture the aging process is not driven by changes in mechanical load on the bladder. As a much wider recruitment distribution in DSM was found in aged bladder (Fig.1), we conjecture one trigger for age related remodeling in bladder is the evolution of homeostatic stretch. Based on this conjecture and supporting data, the DSM homeostatic stretch distribution was prescribed to evolve to a wider distribution; increasing λ_{C-AT}^{max} by 0.2 and decreasing λ_{C-AT}^{min} by 0.2. The resulting evolving changes in mechanical properties (Stretch vs. Cauchy Stress) were simulated from 12 month old (adult) bladder to 24 month old (aged) bladder, Figure 2. As the DSM slowly developed a wider collagen recruitment distribution, the loading curves progressively shifted to the left, indicating a gradual loss of compliance. The predicted mechanical properties after the 48 weeks of adult bladder remodeling matched the mechanical data for aged bladder.

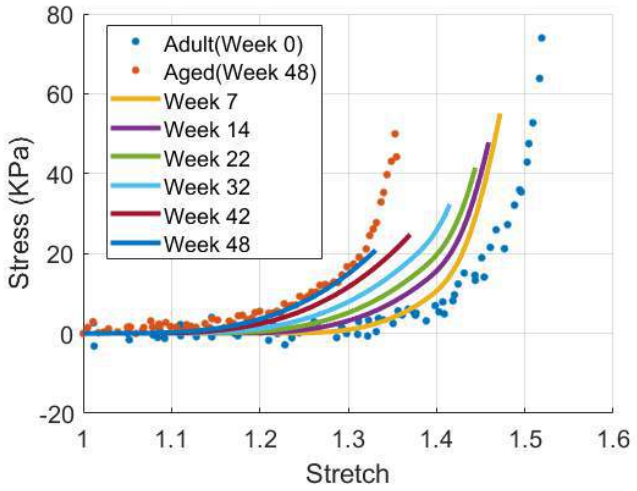

Figure 2: Experimentally measured loading curves for Adult (week 0) and Aged (week 48) bladder and simulated loading curves at multiple time points during age related remodeling

DISCUSSION

In this study, the collagen recruitment distribution was quantified and modeled using bladder data from Adult and Aged rats. A consistent feature in the aged bladder wall was an increased range in stretch for collagen recruitment in the DSM. Using our G&R approach, informed by experimental data, we examined the conjecture that age related changes in bladder wall result from aged related changes in homeostatic deposition stretch distribution. Collagen remodeling and associated changes to passive mechanical function were simulated and found to be consistent with physical data from aged rats.

ACKNOWLEDGEMENTS

This work was supported by NIH grant R01AG056944-01A1.

REFERENCES

[1] Kershen, RT et al., *J Urol*, 168:121-5, 2002.
[2] Ameda, K et al., *J Uroly*, 162:142-6, 1999.
[3] Nording, J et al., *Exp Gerontol*, 37(8-9):991-9, 2002.
[4] Hald, T et al., *Br J Uroly*, 82:59-64, 1998.
[5] Andersson, KE et al., *Neurourol Urodyn*, 33(1):9-16, 2014.
[6] Mastrigt, V et al., *Med Biol Eng and Comp*, 16(5):471-82, 1987.
[7] Chantereau, P et al., *Int Urogynecol J*, 25(11):1547-53, 2014.
[8] Natali, AN et al., *J Biomech*, 48(12):3088-96, 2015.
[9] Gloeckner, D et al., *J Uroly*, 167(5):2247-52, 2002.
[10] Cheng, F et al., *Biomech Model Mechanobiol*, 17(2):403-17, 2018.
[11] Aparicio, P et al., *J Biomech*, 49(12):2321-30, 2016.
[12] Watton, P et al., *Biomech Model Mechanobiol*, 3(2):98-113, 2004.
[13] Humphrey, J et al., *Math Mod Meth Appl Sci*, 12(3):407-30, 2002
[14] Kohan, AD et al., *Urol Res*, 28(1):33-3, 2000.

SB³C2019
Summer Biomechanics, Bioengineering and Biotransport Conference
June 25 -28, Seven Springs, PA, USA

MEMBRANE WRAPPING EFFICIENCY OF ELASTIC NANOPARTICLES DURING ENDOCYTOSIS: SIZE AND SHAPE MATTER

Zhiqiang. Shen (1), Huilin. Ye (2), Xin. Yi (3), Ying. Li (1,2,3,4)

(1) Department of Mechanical Engineering, University of Connecticut, Storrs, Connecticut, United States

(2) Department of Mechanical Engineering, University of Connecticut, Storrs, Connecticut, United States

(3) Department of Mechanics and Engineering Science, Peking University, Beijing, Beijing, China

(4) Department of Mechanical Engineering, University of Connecticut, Storrs, Connecticut, United States

INTRODUCTION

In comparison with the proliferation of viruses in nature, one of the important reasons leading to the gap between the huge number of NPs in laboratories and their poor performance in clinical applications is the lack of mechanistic understanding of the relation between NP properties and their biological activities. Despite the amount of effort that has been devoted to understanding the effects of NPs' geometry on the cellular uptake process, no solid conclusions have been drawn yet, (1) and results are inconsistent between experiments. Furthermore, the elasticity of NPs has recently attracted increasing attention for its significant role during blood circulation, penetration in solid tumors, and tumor cellular uptake. (2) Nevertheless, conflicting experimental results have been reported in terms of the relation between cellular uptake efficiency and NPs' elasticity. With these gaps between experimental results and the current understanding of the influence of NPs' geometry and elasticity in mind, we developed a coarse-grained molecular dynamics (CGMD) model for elastic NPs to systematically investigate the receptor-mediated membrane wrapping of elastic NPs with different sizes and shapes.

METHODS

Using coarse-grained molecular dynamics simulations, we systematically investigate the receptor-mediated endocytosis of elastic nanoparticles (NPs) with different sizes, ranging from 25 to 100 nm, and shapes, including sphere-like, oblate-like, and prolate-like. In our simulations, ligand and receptor densities are set as comparable to experimental values. The elastic NP is modeled by a thin elastic shell. Its elasticity can be systematically changed by tuning its bending constant. The settings in our simulations allow us to capture both the receptor diffusion kinetics and free energy changes during the membrane wrapping process.

RESULTS

As shown in Fig.1. B, the soft NP is much slower to be fully wrapped than the rigid NP. To further explore the interplay between the size and elasticity of spherical NPs, we systematically investigate soft NPs (k_{bend}= 0.1ϵ) of different radii and compare them with rigid NPs in Fig.1. C. There are two key phenomena we can observe from this comparison. First, the minimum size of spherical NPs that can be fully wrapped by the cell membrane is increased to R = 30 nm for soft NPs compared to R = 27.5 nm for rigid spherical NPs. Second, all soft NPs are less efficiently wrapped than rigid ones, and the difference between them increases as the NP radius increases. It is noteworthy that this trend in our simulations seems to conflict with the theory, (3) where the soft NPs are predicted to be more efficient.

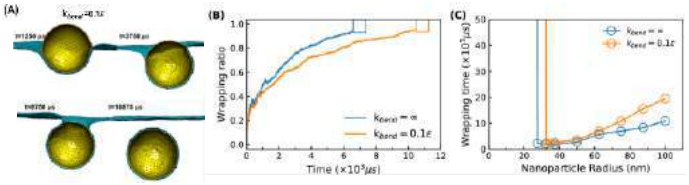

Figure 1. Membrane wrapping of soft spherical NPs. (A) Membrane wrapping of soft spherical NPs with the bending constant k_{bend} = 0.1ϵ and radius R =75 nm. (B) Wrapping ratio evolution for rigid (k_{bend}= ∞) and soft (k_{bend}= 0.1ϵ) spherical NPs with identical radii R=75 nm. (C) Wrapping time for rigid and soft spherical NPs of different radii.

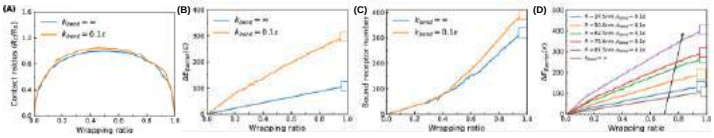

Figure 2. Free energy analysis of membrane wrapping process for spherical NPs. Comparison of (A) contact radius, (B) energy barrier change, and (C) bound receptor numbers between rigid and soft (k_{bend} = 0.1ϵ) spherical NPs at R = 75 nm. (D) Comparison of the energy barrier change between soft NPs with different radii.

The soft and rigid NPs share the same contact radius at each wrapping ratio, *f* (Fig.2. A). The total energy barriers $\Delta E_{Barrier}$ of rigid and soft NPs are given in Fig.2. B., with $\Delta E_{Barrier}$ of a soft NP much larger than that of a rigid NP at each f. Therefore, the soft NP needs to recruit more receptors to overcome a larger energy barrier at each stage after *f* = 0.4 (Fig.2. C). Due to the similar contact radius, the soft NP needs to wait longer than the rigid NP to encounter and bind extra receptors. That is also the reason that the soft NP is slower to be fully wrapped. We further calculate energy barriers of soft NPs with different sizes in Fig.2. D. It is found that the energy barrier of a soft NP is increasing with the increment of the NP size. In comparison, the energy barriers of rigid NPs with different sizes are the same. This can explain how the wrapping time difference between rigid and soft NPs is increasing with their radii, as shown in Fig.1. C.

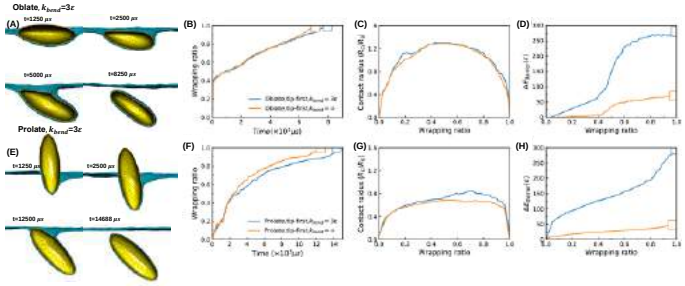

Figure 3. Membrane wrapping of oblate and prolate soft NPs with the bending constant k_{bend}=3ϵ. (A, E) Membrane wrapping process of an oblate and a prolate soft NP. (B–D) Comparisons of the wrapping ratio, contact radius, and energy barrier for rigid and soft oblate NPs. (F–H) Comparisons of the wrapping ratio, contact radius, and energy barrier for rigid and soft prolate NPs.

As shown in Fig. 3. A–D for the comparison between soft and rigid oblate NPs, it is interesting to find that their wrapping ratio evolutions are almost the same before *f* = 0.9. After that, the soft oblate NP undergoes a slower wrapping. However, as shown in Fig. 3. E–H, the wrapping of the soft prolate NP is slower than that of the rigid NP almost during the entire wrapping process. The contact radii of soft and rigid NPs are similar at all wrapping ratios for both oblate and prolate NPs. Additionally, the soft prolate NPs need to overcome a larger energy barrier during wrapping than the rigid one. Moreover, the energy barrier values in the wrapping process of soft prolate and oblate NPs are on the same order (around 300ϵ). In short, the different in contact radius between oblate and porlate NP contributes to the different wrapping efficiency difference in NPs. The large contact radius of oblate NP make it have enough receptor recruiting speed to overcome the energy barrier. While, the small contact radius causes the less efficient of soft prolate NP compared to the rigid one.

We systematically investigate the wrapping efficiency of elastic NPs with different geometries, as given in Fig. 4. The energy barrier of NPs with the same geometry decreases as the bending constant increases, leading to the scaling law between the bending constant and membrane wrapping time. Moreover, because of the significantly large contact edge length, soft oblate NPs have a high receptor recruiting speed to bind extra receptors for overcoming the increased energy barrier. Therefore, the oblate NPs are less sensitive to the variation of the bending constant.

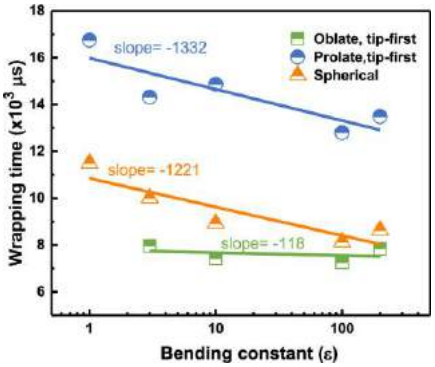

Figure 4. Wrapping time as a function of bending constant for oblate, prolate, and spherical NPs.

DISCUSSION

As we mentioned, the membrane wrapping efficiency is determined by both contact edge length and energy barrier (or thermodynamic driving force). The softer NPs are proven to need to overcome a larger energy barrier because of their deformation in both theories and simulations. But the contact edge length difference between soft and rigid NPs is determined by their mechanical properties. Specifically, in theory, by removing the volume constraint and fixing the total area, the contact edge length of soft spherical NPs in Yi and Gao's work is 20% larger than that of the rigid counterpart. (3) However, in our simulations, both the total volume and area of elastic NPs are controlled by the potential functions. Thus, the soft spherical NP has a similar contact edge to their rigid counterpart. Because of this difference, the soft NPs in Yi and Gao's work are faster than the rigid NPs to be fully wrapped, (3) while, in our simulations, soft NPs are less efficient. In experiments, the LBL capsules are hollow particles after removing the template. These particles can easily change their volumes during cellular uptake, leading to large contact lengths and high efficiencies of internalization. (4, 5) On the other hand, for the lipid-based NPs, due to the hydrophobicity of the lipid bilayer, the interior water molecules are difficult to penetrate through the bilayer. Therefore, lipid-based NPs can be considered as incompressible with constant volume, similar to the elastic NPs in the present study, which have lower cellular uptake efficiency for softer NPs. (6, 7) Therefore, our works provide an insightful explanation for these conflicting experimental results.

ACKNOWLEDGEMENTS

Z.S., H.Y., and Y.L. are grateful for the support from the Department of Mechanical Engineering at University of Connecticut. Part of this work used the Extreme Science and Engineering Discovery Environment (XSEDE), which is supported by the National Science Foundation grant number ACI-1053575. X.Y. acknowledges support from the National Natural Science Foundation of China under grant 11872005.

REFERENCES

[1] Kinnear, et al., *Chem. Rev*, 117:11476–11521, 2017.
[2] Anselmo, C et al., *Adv. Drug Delivery Rev.* 108:51– 67,2017.
[3] Yi, X et al., *Nanoscale*, *9*:454– 463,2017.
[4] Sun, H et al., *Chem. Sci.* 6:3505– 3514, 2015.
[5] Dubreuil, F et al., . *Eur. Phys. J. E: Soft Matter Biol. Phys.* 12:215–221, 2003.
[6] Takechi-Haraya, Y.et al., *Mol. Pharmaceutics* 14:2158– 2165, 2017.
[7] Takechi-Haraya, Y.et al., *Langmuir* 32:6074– 6082, 2016.

SB³C2019
Summer Biomechanics, Bioengineering and Biotransport Conference
June 25 -28, Seven Springs, PA, USA

NECK SKIN THERMAL FEATURES AS A MEASURE OF STENOSIS IN THE CAROTID ARTERY: COMPUTATIONAL AND IN-VIVO STUDY

Ashish Mr. Saxena (1), EYK Dr. Ng (2), Vignesh Mr. Raman (1), Soo Teik Dr. Lim (2)

(1) School of Mechanical and Aerospace Engineering
Nanyang Technological University
Singapore

(2) Department of Cardiology
National Heart Center
Singapore

INTRODUCTION

It has been shown in the past that the temperature variation at the neck skin surface, due to pulsatile blood flow in the carotid artery, can be used to estimate health vitals such as pulse rate [1]. Therefore, it can be established that the blood flow in the artery can be related to the heat transfer to the external neck skin surface. It is evident that the presence of the stenosis leads to a decrease in the blood flow in the carotid artery, and hence, a low blood flow to the facial and temporal arteries. In the past, using contact and non-contact thermographic methods, carotid stenosis is correlated to facial [2] or ocular [3] thermal maps. However, none of these studies investigated the effect of arterial stenosis on the heat transfer characteristics between the carotid artery flow and its surrounding tissue. The presence of stenosis will bring about changes in the heat transfer to the skin tissue, which is expected to be captured in the resulting temperature map over the external neck skin surface; possibly correlates to the degree of stenosis. Therefore, using computational and experimental methods, the present study investigates the external neck skin temperature alteration with the occurrence of stenosis in the carotid artery.

METHODS

In the present study, both computational and experimental methods are used to verify the diagnosis potential of stenosis through temperature features on the neck skin surface. In the computational work, using the geometrical data available in the literature [4], an idealized 3D carotid artery geometry is reconstructed (Fig. 1). Based on the blocked cross-sectional diameter, 75% stenosis tissue is introduced in the ICA. Further, the carotid geometry is encapsulated in a homogenous tissue, of which the thermal properties are taken from the literature [5]; resulting into a geometry resembling a trapezoid-shaped section of the human neck tissue (Fig. 1).

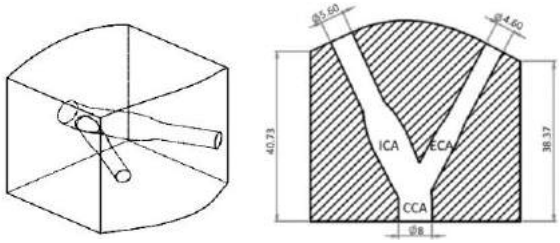

Figure 1: 3D geometry and mid-plane sectional view of the model (all dimensions are in mm)

The blood flow is assumed to be incompressible and Newtonian, with constant thermal properties. On an overall mesh size of 5 x 10^6, using finite volume method available in the FLUENT software (version 19.1) by ANSYS Inc, Navier-Stokes (blood flow) and energy (conjugate heat transfer) equations [6] are solved. Steady laminar solver, with Semi Implicit Pressure Linked Equations (SIMPLE) algorithm, is used. A convergence criterion of 10^{-10}, for velocity and temperature approximation residual, is applied. A fully developed velocity profile (at peak systolic, $U = 0.5332\ m/s$) is used at the CCA inlet, while pressure boundary condition is used at the outlet of ICA and ECA, respectively. Blood temperature is taken to be 37 °C. The top external neck skin surface is applied with ambient ($T_{amb} = 21$ °C) convective heat transfer boundary condition (heat transfer coefficient, $h = 5\ \mathrm{W}m^{-2}K^{-1}$). The side walls of the encapsulated tissue are given adiabatic condition, while the bottom surface is given isothermal core body temperature (37 °C) condition. Pennes bio-heat equation with a tissue perfusion rate of 0.4333 Kg/ms is used, along with a volumetric heat generation of 33 W/m^3.

In the experimental part of the study, Infrared (IR) thermography (using VarioCAM IR thermal camera by Infratec) is performed on 8

patients (both male and female) in the age group of 45 to 71 years old, at National Heart Center Singapore, under an ethically approved study (CIRB Ref No.: 2017/2119). Of the 8 patients, 4 belongs to the control group (0% stenosis), while the other 4 belongs to the diseased group (≥ 50% stenosis). Given the two sides of the neck are screened separately, in all, there are 16 samples (N) available for the analysis. To extract the usable thermal features, the acquired thermal images are processed as shown in Fig. 2. Taking the minimum (T_l) and maximum (T_u) temperature from the non-zero pixels of the thermal image, the cold region extraction, using temperature threshold (T_{th}) value calculated in Equation 1, is performed.

$$T_{th} = T_l + 0.3 * (T_u - T_l) \quad (1)$$

Further, to quantitatively differentiate the two groups of patients, a ratio denoted by 'R_{cn}', defined by the number of non-zero nodes with value ≤ T_{th} normalized with the total number of non-zero nodes in the image, is used. In case of the computational study, the value of T_{th} is selected based on the minimum temperature occurring in the two simulated cases (0% and 75% stenosis).

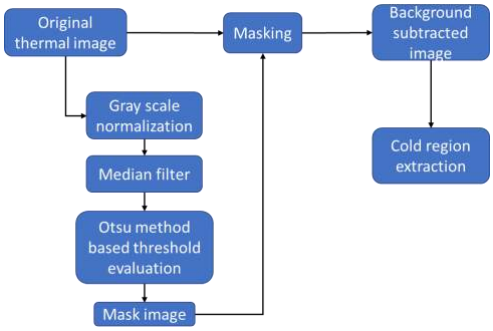

Figure 2: Thermal image processing flow chart

RESULTS

Fig. 3 shows the temperature contours, resulting from the computational study, at the mid-plane of the artery and the top skin surface. It can be observed that the presence of stenosis leads to the formation of low temperature regions in the carotid artery flow, which shall affect the heat transfer to the external neck skin surface. Fig. 4 shows the difference in the temperature features between normal and diseased case, which is found to be enhanced with the proposed cold region extraction method in the present study.

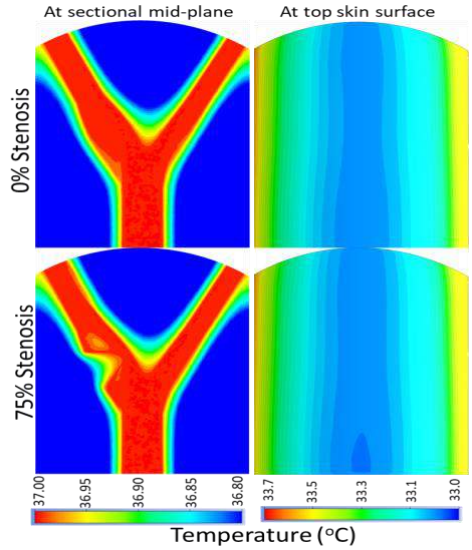

Figure 3: Temperature contours from the computational study

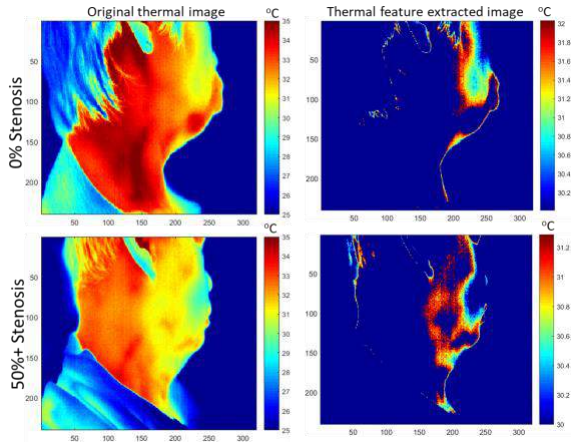

Figure 4: Original and extracted thermal images from thermography experiment

DISCUSSION

From the results, it is imperative that the occurrence of stenosis brings about changes in the thermal map on the external neck skin surface. This is marked by the presence of a vertical cold feature at the center of the top skin surface thermal map in 75% stenosis case (Fig. 3) and a higher colder region in the thermal image for 50%+ stenosis case (Fig. 4). This is further quantified by evaluating the value of R_{cn} in Table 1. For both computational and experimental studies, the value of R_{cn}, in the respective groups, is found to be alike. Furthermore, using student *t*-test, it is shown that the difference in R_{cn} value, in the two groups of patients, is significantly different (*p-value*<0.05). Hence, the present study proves the potential of IR thermography as a measure of carotid artery stenosis.

Table 1: R_{cn} value for computational and experimental study

Group	R_{cn}	
	Computational	Experimental
Control	0.10	0.09 ± 0.05
Diseased	0.17	0.21 ± 0.08
Student *t*-test	NA	*P*=0.002

ACKNOWLEDGEMENTS

The authors would like to acknowledge the SingHealth-NTU collaborative research grant (Grant number: SHS-NTU/014/2016) for the funding support to carry out this project.

REFERENCES

[1] P. Hung, K. Lee, and L. Tsai, "Contact-free Heart Rate Measurement Using Multiple Video Data," in *AIP Conference Proceedings*, 2013, vol. 57, pp. 57–66.

[2] T. D. Capistrant and R. J. Gumnit, "Detecting carotid occlusive disease by thermography.," *Stroke.*, vol. 4, no. 1, pp. 57–64, 1973.

[3] P. B. Morgan, J. V. Smyth, A. B. Tullo, and N. Efron, "Ocular Temperature in Carotid Artery Stenosis," *Optom. Vis. Sci.*, vol. 76, no. 12, pp. 850–854, 1999.

[4] B. K. Bharadvaj, R. F. Mabon, and D. P. Giddens, "Steady flow in a model of the human carotid bifurcation. Part I – flow visualization," *J. Biomech.*, vol. 15, no. 5, pp. 349–362, 1982.

[5] J. Breeze, A. West, and J. Clasper, "Anthropometric assessment of cervical neurovascular structures using CTA to determine zone-speci fi c vulnerability to penetrating fragmentation injuries," *Clin. Radiol.*, vol. 68, no. 1, pp. 34–38, 2013.

[6] A. Saxena and E. Y. K. Ng, "Steady and Pulsating Flow Past a Heated Rectangular Cylinder (s) in a Channel," *J Thermophys Heat Tr*, vol. 8722, pp. 1–13, 2017.

SB³C2019
Summer Biomechanics, Bioengineering and Biotransport Conference
June 25 -28, Seven Springs, PA, USA

A COLD-RESPONSIVE NANOPARTICLE ENABLES INTRACELLULAR DELIVERY AND RAPID RELEASE OF TREHALOSE FOR FAST FREEZING OF STEM CELLS

S. Stewart (1), X. He (1,2,3)

(1) Fischell Department of Bioengineering
University of Maryland, College Park
College Park, Maryland, United States

(2) Robert E. Fischell Institute for Biomedical Devices
University of Maryland, College Park
College Park, Maryland, United States

(3) Marlene and Stewart Greenbaum Comprehensive Cancer Center
University of Maryland, Baltimore
Baltimore, Maryland, United States

INTRODUCTION

The limited availability of living cells poses a major challenge to modern cell-based medicine like cell transplantation and cell therapy[1]. The most widely used cell banking method is cryopreservation, which involves a slow freezing procedure and storage in liquid nitrogen (LN2) to keep the cells in a state of suspended animation. This process requires the use of cell-penetrating cryoprotectants (CPAs) to protect the cells from freezing damage. However, the organic solvents used as common CPAs like dimethyl sulfoxide (DMSO) can prove highly toxic at body temperature, both *in vitro* and *in vivo*, if not sufficiently removed from the cells after thawing[2-3]. Removing CPAs is time consuming and can result in significant loss of these precious cells[1].

Trehalose is a non-reducing disaccharide commonly found in many organisms that can survive extreme freezing and/or dehydration in nature[4]. This unique sugar has been investigated as a non-toxic alternative to traditional CPAs[5]. Unfortunately, mammalian cells lack the mechanism to synthesize trehalose and their membranes are impermeable to it. Trehalose has been successfully introduced into mammalian cells through nanoparticles, however, an incubation time of 24 hours was necessary for sufficient intracellular trehalose release for cryoprotection[6]. This makes the cryopreservation lengthy and tiresome.

To address these challenges, we synthesized a cold-responsive polymer nanoparticle (PNP) to provide for efficient intracellular delivery and release of trehalose in this study. We created a polymer nanoparticle to achieve the fastest disassembly and most efficient payload release upon experiencing cold temperature (14-16°C). We confirmed nanoparticle uptake and cold-triggered intracellular release through fluorescent microscopy. We reduced the incubation time necessary for sufficient intracellular trehalose for cryoprotection to only 4 hours for human adipose-derived stem cells (hADSCs). Preliminary data showed when the cold-responsive nanoparticles were used to cryoposerve hADSCs through slow-freezing, the post-thaw viability, attachment, and proliferation proved comparable to results achieved by traditional DMSO cryopreservation. hADSC post-thaw quality was further confirmed through expression of stemness markers and multilineage differentiation capability. This success using PNPs in the slow freezing protocol led us to study their effectiveness for use in a fast freezing protocol using predehydration and ice seeding before plunging into liquid nitrogen.

METHODS

Preparation of Nanoparticles. Poly (lactic-co-glcolic acid) or PLGA (lactide:glycolid = 50:50, M_w = 5-30K) and poly (N-isopropylacrylamide-co-butylacrylate) or pNIPAM-B (NIPAM:B 8:1, M_w = 30K) were used in a double-emulsion (water-in oil-in water) method to make the nanoparticles. Trehalose (0.3mL 1.3M trehalose) was encapsulated in the aqueous core of the nanoparticles. A 2% solution of polyvinyl alcohol (PVA, M_w = 30-70K) was used as a stabilizer.

Characterization of Nanoparticles. The size and zeta potential of PNPs was examined using a dynamic light scattering system (DLS, Malvern). The morphology of PNPs was examined using a JEM 2100 LaB6 transmission electron microscope (TEM).

Cold-triggered Release. The release profile of trehalose from PNPs was quantified to confirm cold-triggered rapid release of trehalose from the nanoparticles. A tube of trehalose-laden PNPs was centrifuged ever 2 hours at 37°C/22°C for 6 hours. The tube was cooled on ice for 10 min at 4h. The amount of trehalose in the supernatant at each time point was quantified using a trehalose assay kit (Megazyme). The disassembly of the nanoparticles was also visualized by the change in turbidity of suspended nanoparticle solution.

Cell Uptake. Cellular uptake of PNPs was visualized by encapsulating doxorubicin (DOX) into the nanoparticle core instead of trehalose due to its fluorescence. hADSCs were cultured on type I collagen coated coverslips, and then incubated with medium containing DOX-loaded PNPs for 4h. Cells with or without ice cooling were studied in parallel. Cells were fixed and with LysoTracker Green and DAPI to visualize lysosome and nuclei, respectively.

Cell Cryopreservation. hADSCs were pretreated by incubation in either free trehalose in medium or trehalose-PNP medium for 4h. Cells cryopreserved without pretreatment were also studied in parallel. Cells were detached and re-suspended in culture medium containing 0.3M free trehalose. Fresh cells and cells cryopreserved using DMSO were also studied in parallel. For slow freezing, cells were transferred into a cryovial, the vial was hermetically sealed and placed into a Thermo Nalgene freezing container in the -80°C freezer overnight. Cells were then transferred to LN2 tank for storage. After 1 day of storage, cells were thawed in a 37°C water bath for further studies. For fast freezing, cells were first incubated with either free trehalose inmedium or trehalose-PNP medium for 4h. Cells were washed with 1XPBS, collected, and then resuspended in 200*u*L medium containing 0.33M trehalose in a 600*u*L plastic microcentrifuge tube. This tube was submerged into a 10% (w/v) sodium chloride bath at -4°C for 5 min to equilibrate. The tube was touched with a precooled (in LN2) copper wire to seed ice in the cell suspension, and then was transferred back into the bath for 1 min of equilibration. The tube was then plunged into LN2 to cool to -196° and stored for 24h.

Cell Quality Post-Cryopreservation. Cell viability was assessed using calcein AM and ethidium homodimer dyes immediately post-thaw. The same quantity of fresh cells and thawed cells were cultured overnight and washed with 1XPBS the next morning. Attachment was quantified as the ratio of counted thawed cells still attached to fresh cells still attached. Proliferation was calculated as the ratio of the cell numbers on days 2 and 3 to the initial cell number on day 1. Stem cell marker CD44 and differentiation marker CD31 were studied on trehalose-PNPs cryopreserved cells compared to fresh. Multilineage differentiation of cells was evaluated by adipogenic and osteogenic differentiation.

RESULTS

PNPs show a size of ~150nm at room temperature with a size peak in the distribution of 122.4nm (Figure 1A). PNPs carry a slightly negative charge, showing a zeta potential of -13mV (Figure 1B).

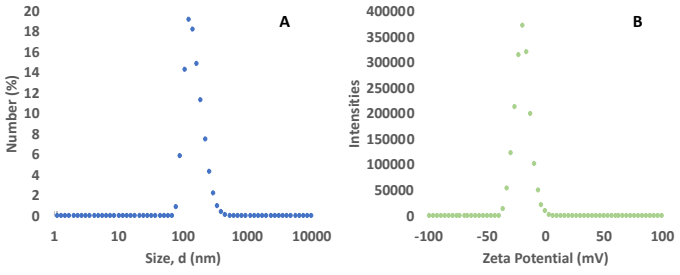

Figure 1: Dynamic light scattering data showing size and zeta potential distribution of PNPs.

PNPs showed a distinct core-shell morphology, with the trehalose encapsulated in the core of the nanoparticle (Figure 2). Encapsulating trehalose inside the core of the thermally repsponsive nanoparticle allowed it to pass through the plasma membrane of the cell and reach the cells intracellular compartment.

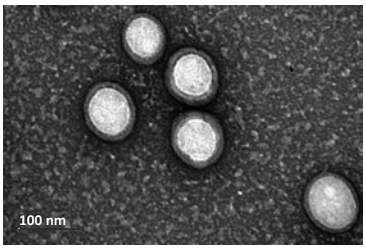

Figure 2: PNP morphology at room temperature

The PNPs showed cold-responsiveness due to the high composition of pNIPAM-B, with a lower critical solution (LCST) temperature of 14-16°C, in the nanoparticle formulation. Above the LCST, pNIPAM-B acts as a hydrophobic polymer, and is able to form nanoparticles. Below the LCST, pNIPAM-B becomes hydrophilic, and the nanoparticles irreversibly dissemble in aqueous solution. This can be seen in Figure 3, where nanoparticles in solution at room temperature (3a) are in a stable colloidal solution, appearing milky and turbid. However, once they dissemble the solution becomes more transparent as the pNIPAM-B becomes hydrophilic (3b).

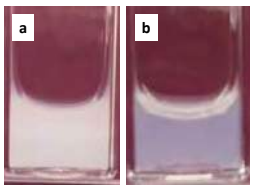

Figure 3: Cold-responsiveness of PNP in solution. (a) Room temperature (b) After ice treatment

DISCUSSION

The cold-responsive nanoparticles encapsulating trehalose synthesized in this study allowed for delivery of trehalose across the plasma membrane and controlled and rapid release of the nontoxic cryoprotectant inside of the cell. Intracellular trehalose has been shown to improve cryosurvial for mammalian cells, but previous attempts to deliver the impermeable sugar across the membrane either compromised membrane integrity (electroporation)[7], modified the cell's machinery (trehalose transporter)[8], or simply did not allow for enough intracellular accumulation in a timely manner (fluid-phase endocytosis)[9]. This method uses the cell's natural process of endocytosis to uptake the nanoparticle, and release is caused by cold temperature, which cells experience during the freezing process.

This is very different from a previous study[6], as the nanoparticle incubation time is shortened to only 4h due to the capability for rapid release. Longer incubation times may increase the chance for nanoparticle removal from cells by exocytosis, so shorter incubation times are more favorable for efficient and successful delivery. This method requires no removal step, saving time and avoiding cell loss.

This rapid release should facilitate the use of this nanoparticle to achieve intracellular trehalose for protection in fast freezing of hADSCs using predehydration and ice seeding. Predehydration by extracellular trehalose can reduce cells to their minimal volume with minimized active water inside the cell to protect from osmotic shock and intracellular ice formation (IIF) which can prove lethal. Ice seeding can release the free energy that could cause ice recrystallization during rewarming, leading to cell damage.

ACKNOWLEDGEMENTS

This work was supported by the U.S. National Institute of Health (grants R01EB012108 and R01EB023632 to X.E.)

REFERENCES

[1] Mulligan, RC, *Science*, 260:926-932, 1993. [2] Ock, SA, et al., *Cell transplantation*, 20:1231-9, 2011. [3] Davis, JM et al., *Blood*, 75:781-786, 1990. [4] Crowe, JH et al., *Ann Rev of Physiol*, 54:579, 1992. [5] Crowe, JH et al., *Nat Biotechnol*, 18:145, 2000. [6] Rao, W et al., *ACS App Mat and Interfaces*, 7:5017-5028, 2015. [7] Shirakashi, R et al., *J of Mem Bio*, 189:45-54, 2002. [8] Uchida, T et al., *Cryobiology*, 77:50-57, 2017. [9] Oliver, A et al., *Cell Pres Tech*, 2:35-49, 2004.

SB³C2019
Summer Biomechanics, Bioengineering and Biotransport Conference
June 25 -28, Seven Springs, PA, USA

ENGINEERING AND CHARACTERIZATION OF COLLAGENASE-EXPRESSING *SALMONELLA* TYPHIMURIUM FOR ENHANCED INTERSTITIAL TRANSPORT IN TISSUE

Eric J. Leaman (1), Bahareh Behkam (1,2)

(1) Department of Mechanical Engineering
Virginia Tech
Blacksburg, VA, USA

(2) School of Biomedical Engineering and Sciences
Virginia Tech
Blacksburg, VA, USA

INTRODUCTION

One of the principal impediments to the broad success of conventional chemotherapy is poor delivery to and transport within the tumor microenvironment (TME), caused by irregular and leaky vasculature, the lack of functional lymphatics, and underscored by the overproduction of extracellular matrix (ECM) proteins such as collagen. Coupled with limited specificity, the high chemotherapeutic doses needed to effectively treat tumors often lead to unacceptable levels of damage to healthy tissues. Bacteria-based cancer therapy (BBCT) is an innovative alternative. Engineered strains of species such as *Salmonella* Typhimurium have been shown to preferentially replicate in the TME, competing for cellular resources and imparting intrinsic and immune-mediated cytotoxic effects on cancer cells. Nevertheless, the myriad of successes observed *in vitro* and in murine models have not translated to the clinic, attributable to the lack of sufficient tumor colonization. High tumor collagen content has been shown to significantly hinder the intratumoral transport of macromolecules and nanoparticles [1]. Likewise, *S*. Typhimurium has been shown to poorly penetrate tumors of high collagen content relative to those with lower collagen content [2]. We hypothesize that engineering *S.* Typhimurium to express and secrete a recombinant collagenase to locally degrade tumor ECM will increase bacterial penetration, leading to enhanced retention and colonization within tumors.

Toward improving tumor colonization potential, we engineered the attenuated tumor-targeting strain *S.* Typhimurium VNP20009 [3] to secrete a heterologous collagenase and developed a microfluidic assay to systematically characterize its transport in the ECM. Results indicate significant collagen degradation and matrix remodeling by the collagenase-secreting bacteria. Our microfluidic assay allows us to visualize bacterial colonization in real time and estimate transport and growth parameters in a quasi-steady nutrient environment. This research addresses the largely unexplored question of bacterial transport in the ECM toward developing translational BBCT.

METHODS

Cloning of a Heterologous Collagenase – The matrix metalloproteinase gene *prtV* [4] was cloned from *Vibrio parahaemolyticus* EB101 (ATCC 17802) into the multiple cloning site of the pBAD LIC (8A) plasmid vector (RRID:Addgene_37501). The *araBAD* promoter was replaced with the constitutive synthetic promoter BBa_J23100, and BBa_J04450 (excluding the BBa_B0015 terminator) encoding mRFP1 was cloned downstream of *prtV* to enable fluorescent imaging during experiments. Expression and enzymatic activity was confirmed by measuring the fluorescence of collagen type I supplemented with 1% dye-quenched (DQ) collagen type I during incubation with bacteria.

Microfluidic Device Design and Fabrication – The microfluidic device was designed with 7 parallel channels separated by series of hexagonal pillars (Fig. 1) and fabricated via standard soft lithography. SU-8 photoresist was patterned onto silicon wafers at a thickness of 300 μm and used to mold polydimethylsiloxane (PDMS)-based devices. The molded PDMS device was bonded to a coverslip. Polyethylene glycol diacrylate (PED-DA; 700 Da) was then polymerized between the outermost channels in order to create permeable barriers separating media flow from adjacent channels, and 5 mg/mL collagen type I was polymerized in the center channel.

Microfluidic Experiments and Data Collection – *S*. Typhimurium VNP20009 expressing *prtV* (hereafter referred to as VNP20009*prtV*) were suspended in a buffer solution at a concentration of 5×10^7 bacteria/mL and pipetted into one of the channels adjacent to the collagen matrix, while buffer solution alone was inserted into the opposite channel. Nutrient medium and buffer solution were flowed

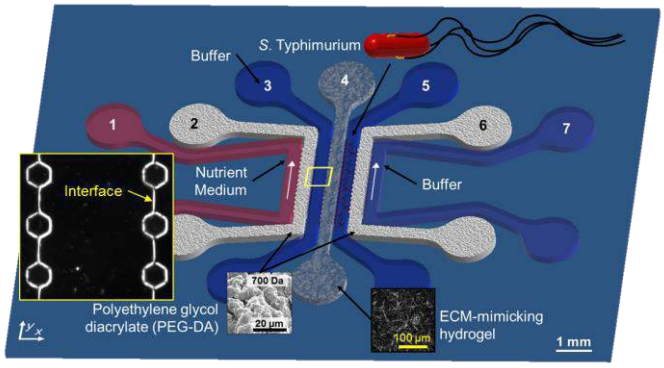

Figure 1: Microfluidic Platform for Systematic Evaluation of Bacterial Transport in ECM.

constantly through the outermost channels in order to generate a quasi-static nutrient concentration gradient across the collagen barrier (Fig. 1). The device was maintained at 37 °C and imaged every 30 min for the duration of the experiment. Confocal reflectance microscopy (CRM) was performed following time-lapse experiments.

Mathematical Model for Parameter Estimation – The bacterial transport in and colonization of the collagen hydrogel can be described by

$$\frac{\partial B}{\partial t} = \nabla \cdot D_{\text{eff}} \nabla B + k_g B \left(g - \frac{B}{k_B} \right) \quad (1)$$

where B is bacterial concentration, D_{eff} is an effective bacterial diffusivity accounting for both swimming and diffusion, k_g and g are the maximum and local growth rates, respectively, and k_B is the maximum bacterial concentration [5]. Time-lapse data were used to fit D_{eff} of strains, providing quantitative transport information.

RESULTS

We confirmed PrtV secretion and enzymatic activity against collagen type I using DQ collagen type I, which releases fluorescein upon breakdown. Fluorescence intensity increased significantly in samples containing VNP20009*prtV* but was negligible in controls (Fig. 2a). We next performed time-lapse experiments using our microfluidic assay, demonstrating bacterial transport and growth through the central collagen barrier (Fig. 2b and c). Time-lapse fluorescent images allow for a determination of relative changes in spatiotemporal bacterial concentration.

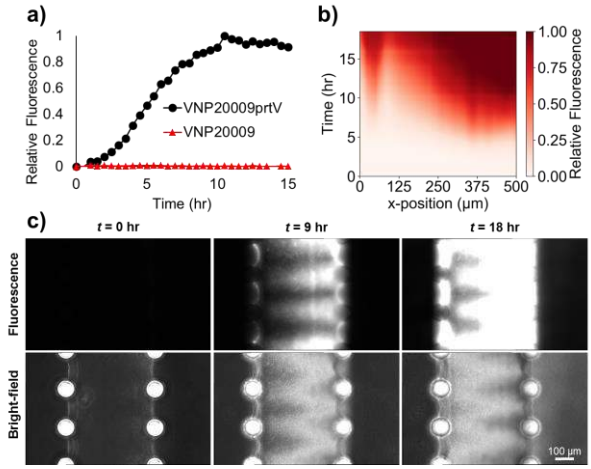

Figure 2: (a) Relative Fluorescence of DQ Collagen Type I, (b) Spatiotemporal Heatmap of Relative Bacterial Fluorescence, and (c) Representative Time-lapse Microscopy Images of VNP20009*prtV* Collagen Colonization.

CRM images recorded following experiments revealed structural differences between the collagen fiber networks of experiments with VNP20009*prtV* and controls (Fig. 3). Notably, treatment with VNP20009*prtV* led to fiber re-organization and bundling at shorter timescales (~20 hr) and a large increase in free open space within the hydrogel at long timescales (~40 hr).

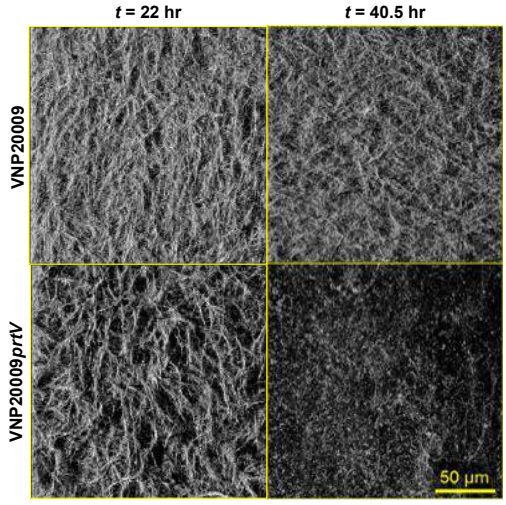

Figure 3: Shadow Projections of CRM *z*-stacked Images Reveal Structural Modifications to Collagen Networks.

DISCUSSION

We have engineered a collagenase-secreting strain of tumor-targeting bacteria toward enhancing intratumoral transport and colonization. Our preliminary results demonstrate collagen hydrogel modification by this strain, which is expected to lead to significant differences in bacterial transport between *prtV* and control strains. Our novel microfluidic platform creates a quasi-static environment through which we can systematically characterize the transport of bacteria in ECM for the first time, which we will use to optimize *prtV* expression.

Today, the rational engineering of tumor-targeting bacteria enabled by recent breakthrough achievements in medicine and biology have put BBCT on the brink of being realized as a powerful new weapon against cancer [6]. BBCT has and continues to be proven in a plethora of *in vitro* and *in vivo* animal studies. The development of strains that have (1) been shown safe for human administration and (2) demonstrated a sufficient level of tumor colonization with minimal side effects in immunocompetent hosts are the primary hurdles for translation to the clinic. The first of these challenges has been repeatedly met; addressing bacterial transport limitations in desmoplastic tumors is a largely unexplored avenue and has the potential to surmount the second.

ACKNOWLEDGEMENTS

We gratefully acknowledge support from the National Science Foundation (CAREER award, CBET-1454226).

REFERENCES

[1] Dolor, A and Szoka, F C, *Mol Pharm*, 15:2069-2083, 2018.
[2] Suh, S et al., *Adv Sci*, 1801309, 2018.
[3] Low, K B et al., *Nat Biotech*, 17:37-41, 1999.
[4] Lee, C Y et al., *Microbiology*, 141:2569-2576, 1995.
[5] Suh, S et al., In *40th Ann Int Conf IEEE EMBC*, 6162-6165, 2018.
[6] Zhou, S et al., *Nat Rev Can*, 18:727-743, 2018.

A SYSTEMATIC APPROACH TO THE THERMAL MITIGATION OF IRREVERSIBLE ELECTROPORATION THERAPY

Timothy J. O'Brien*[1], Melvin F. Lorenzo[1], Yajun Zhao[1], Robert E. Neal II[2], John L. Robertson[1], S. Nahum Goldberg[3], Rafael V. Davalos[1]

(1) Department of Biomedical Engineering and Mechanics
Virginia Tech
Blacksburg, VA, USA

(2) AngioDynamics
Latham, NY, USA

(3) Department of Radiology
Hadassah Hebrew University Medical Center
Ein Karem, Jerusalem, Israel

INTRODUCTION

Irreversible Electroporation (IRE) is an energy directed therapeutic used to treat patients with unresectable tumors. This non-thermal, minimally invasive technique can be used to target malignancies enveloping critical structures (blood vessels, major nerves, etc.) and is less influenced by the convective effects of local blood perfusion in comparison to thermal ablation technologies (radio frequency ablation, microwave ablation, etc.) [1-3]. However, in some instances, generating a sufficiently high pulsed electric field that concurrently maps the entire region of interest, while also avoiding undesirable thermal effects can be challenging. To overcome these difficult scenarios, thermal mitigation strategies have been explored [4, 5]. In many instances, surgeons performing IRE treatments use three or more monopolar IRE electrodes to encompass a large or irregularly shaped tumor. While the addition of electrodes may be useful in covering a larger ablation region, the existing method of pulse delivery has not been engineered to moderate thermal tissue damage for multi-electrode treatments. The NanoKnife™ generator is currently designed to deliver the entirety of the set number of pulses for a given electrode pair before proceeding to the next electrode pair until all of the desired electrode pair combinations have been exhausted. However, by partitioning the pulse-train into subsets of pulses and cycling between electrode pairs until the desired number of pulses is reached, thermal damage could be managed. Figure 1 illustrates these different pulsing sequences.

This study investigates the effects of various cycled pulsing paradigms in comparison to traditional pulsing schemes via a multi-electrode IRE therapy (4-electrode configuration) on the IRE lesion size, deployed electrical current, temperature changes, and treatment time. This systematic approach has the potential to improve clinical outcomes.

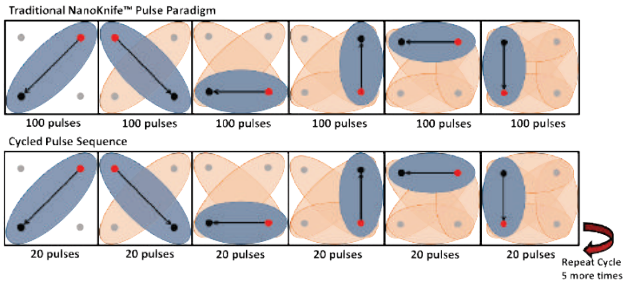

Figure 1. Schematic illustrating the differences in traditional pulsing schemes compared to a cycled pulsing paradigm for a 4-monopolar array configuration.

METHODS

All IRE treatments were performed using a 4-monopolar electrode array and the previously validated perfused organ model (porcine liver tissue) [6]. A total of five cycled pulsing variations were performed and evaluated in comparison to the NanoKnife™ (Angiodynamics, Latham, NY) pulsing scheme. After treatment, organs were dissected and treatment zones were stained using 2,3,5-triphenyl-tetrazolium chloride (TTC) to demonstrate viability. STB general purpose fiber optic temperature sensors (Luxtron m3300, LumaSense, Santa Clara, CA, USA) were positioned and adhered at the midpoint of each exposed electrode to measure temperature throughout treatments. Further, the electrical voltage and current were measured and employed to calculate the treatment energy deposition.

A finite element model was developed using a commercial finite element package (COMSOL Multiphysics, v.5.4; Stockholm, Sweden) to explore the effects of various cycled pulsing paradigms for multi electrode IRE procedures. The domain consisted of liver tissue modeled as a $12 \times 12 \times 8$ cm diameter ellipsoid and 4-monopolar NanoKnife™

electrodes modeled as cylinders of height, diameter, and spacing 1.5 cm, 1 mm, and 2 cm, respectively. The final mesh consisted of 187,418 tetrahedral elements with a maximum of 2,264,706 degrees of freedom. The electric potential distribution was captured using the Laplace equation (equation 1) and taking the gradient of the electric potential (equation 2),

$$0 = -\nabla \cdot (\sigma \nabla \Phi) \quad (1)$$

$$\vec{E} = -\nabla \Phi \quad (2)$$

This effect is captured in the model by using a sigmoidal curve previously characterized in O'Brien et al. for porcine liver tissue on the POM,

$$\sigma\left(\left|\vec{E}\right|, T\right) = \sigma_0 + \frac{\sigma_f - \sigma_0}{1 + D \cdot e^{\frac{-(|\vec{E}| - A)}{B}}} \cdot [1 + \alpha \cdot (T - T_0)] \quad (3)$$

, where σ_0 is the initial non-electroporated conductivity, σ_f is the peak electroporated conductivity, $\left|\vec{E}\right|$ is the magnitude of the electric field at any given position, and D, B, and A are fitting terms. Further, α represents the temperature coefficient, T_0 the initial temperature, and T is the temperature at any given time.

Temperature profiles were simulated using a modified Pennes' bioheat equation and implements cycled pulsing schemes using time dependent "thermal envelopes" that capture both changes in the number of cycles and cycle delays. Analytical functions enable the implementation of complex cycled pulsing schemes, where an arbitrary coefficient χ is used to simulate the on ($\chi = 1$) and off ($\chi = 0$) period of the thermal envelope. This resulted in the following equation,

$$\rho c_p \frac{\partial T}{\partial t} = \nabla \cdot (k \nabla T) - \omega_b \rho_b c_b (T - T_b) + \frac{\sigma \cdot \left|\vec{E}\right|^2 \cdot p}{\tau} \cdot \chi \quad (4)$$

, where p is the pulse width, and τ is the pulse period over which the energy was averaged.

RESULTS

The "1 pulse cycle, 0s delay" group produced the largest amount of energy, reaching an average of 2.33 ± 0.35 kJ, while the NanoKnife™ generated 2.09 ± 0.37 kJ on average. The "5 pulse cycle, 0s delay", "10 pulse cycle, 0s delay", and the "10 pulse cycle, 10s delay" produced the lowest amounts of energy during treatment, yielding an average of 1.98 ± 0.32 kJ, 1.88 ± 0.34 kJ and 1.89 ± 0.23 kJ, respectively. The "10 pulse cycle, 5s delay" pulse scheme generated an average of 2.14 ± 0.38 kJ. No statistical significance was found between experimental groups. All of the cycled pulsing schemes presented a larger ablation area on average in comparison to the 1-pulse cycle groups. The "5 pulse cycle, 0s delay" pulse paradigm produced the largest cross-sectional area, with an average area of 11.81 ± 1.97 cm^2. This pulsing paradigm was significantly different from the "1 pulse cycle, 0s delay" (8.41 ± 1.97 cm^2, $p \leq 0.0395$). The NanoKnife™ generated a cross-sectional ablation zone of 8.90 ± 0.91 cm^2 on average. Figure 2 displays experimentally measured results.

Figure 3 illustrates numerically derived time-lapse images of the thermal distribution at the first cycle of each electrode pair. The rightmost panels illustrate the thermal distribution and electric field at 50s post-treatment. Further, the boundary at which the onset of thermal damage occurs (Ω=0.53) is overlaid and outlined in green. The temperature distribution and thermal damage is much greater for the NanoKnife™ pulse paradigm than the cyclically-pulsed schemes. These results indicate that the "10 pulse cycle, 10s delay" pulse paradigm can reduce 1st degree thermal tissue injury by up to 73.95% in comparison to the traditional NanoKnife™ pulsing scheme. Further, the thermal distribution for the cycled pulsing schemes are far more uniform.

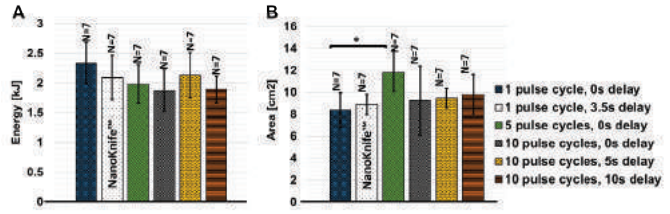

Figure 2. Experimental results illustrating the **(A)** total energy deposition throughout treatment and **(B)** cross-sectional ablation areas.

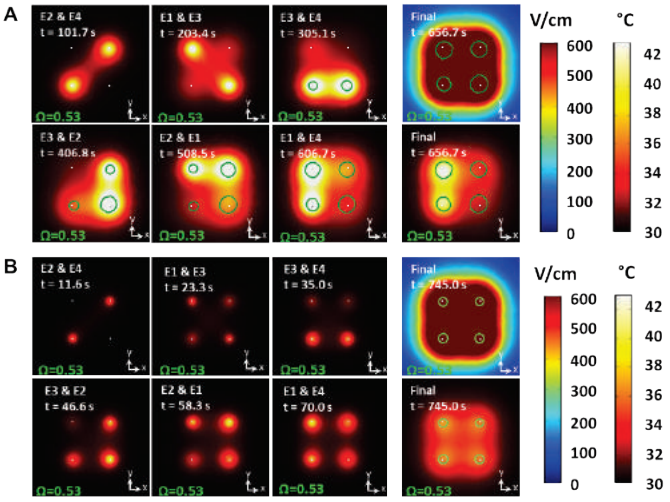

Figure 3. Numerically derived thermal distribution at the completion of each initial electrode pair activation, as well as the final electric field and thermal distribution 50 seconds post therapy is presented for a **(A)** traditional NanoKnife™ pulsing scheme and **(B)** a cycled pulsing paradigm (10 pulse cycles, 0s delay). The time at each electrode pair activation is displayed in the top left corner. The area in which the onset of thermal damage occurs (**Ω** = 0.53) is overlaid with the thermal distribution and outlined in green.

DISCUSSION

This study demonstrates the use of cycled pulse paradigms to reduce the effects of Joule heating while effectively maintaining and, in some cases, improving the IRE treatment lesion dimensions in comparison to treatments administered with a traditional pulse scheme. We have verified the effects of using pulse cycle patterns on electrical current, tissue temperature, tissue treatment lesion size, and total treatment time for several pulsing schemes experimentally using a perfused organ model. Additionally, finite element analysis verified that cycled pulsing patterns can mitigate the overall temperature distributions and thermal damage in comparison to single-cycle pulsing schemes.

ACKNOWLEDGEMENTS

This study was supported in part by AngioDynamics Inc. and the Pancreatic Cancer Action Network Translational Research Grant (PanCAN 16-65-IANN).

REFERENCES

[1] Davalos, RV et al., Ann. Biomed. Eng., 33:223-231, 2005.
[2] Al-Sakere, B et al., PloS One, 2:1-8, 2007.
[3] Weaver, JC et al., J. Cell Biochem., 51:426-435, 1993.
[4] Arena, CB et al., ASME. J Biomed. Eng., 135(11), 2013.
[5] OBrien, TJ et al., Int. J. Hyperth., 35:1, 44-55, 2018.
[6] Bhonsle, S et al., J. Vasc Interv. Radial., 27:1913-1922, 2016.

OPTICAL OPENING OF BLOOD-BRAIN BARRIER FOR MACROMOLECULES PENETRATION BY LASER EXCITATION OF VASCULATURE-TARGETED PLASMONIC NANOPARTICLES

XQ. Li (1), H. Xiong (2), V. Vemireddy (3), X. Li (2), M. Giannotta (4), H. Hayenga (1), E. Pan (3), S. Sirsi (1), E. Dejana (4), R. Bachoo (3), Z. Qin (1,2,5)

(1) Department of Bioengineering, University of Texas at Dallas, Richardson, TX 75080, USA

(2) Department of Mechanical Engineering, University of Texas at Dallas, Richardson, TX 75080 USA.

(3) Department of Neurology, University of Texas Southwestern Medical Center,

(4) FIRC Institute of Molecular Oncology Foundation (IFOM), 20139 Milan, Italy

(5) Department of Surgery University of Texas Southwestern Medical Center, Dallas, TX75390, USA.

INTRODUCTION

The blood-brain barrier (BBB) keeps an optimal environment for normal brain function[1], but also excludes most molecules from entering the brain. Temporarily overcoming the BBB to deliver molecules to the brain is critically important to studying and treating brain diseases. Current methods for BBB opening, including osmotic shock[2], focus ultrasound disruption[3] and vasoactive agents[4], lack sufficient spatial resolution for delicate brain structures.

Here, we report a new method to temporarily open the BBB by optical excitation of vasculature-targeted plasmonic gold nanoparticles (AuNPs). Ultrashort picosecond (ps) laser pulse excitation of plasmonic AuNPs leads to *in vitro* transient BBB opening possible due to a calcium-based mechanism. We further demonstrate that *in vivo* BBB opening by visualizing extravasation of Evans blue (EB) dye. Moreover, we demonstrate that the temporary optical BBB opening allows passage of anticancer drugs and antibodies (human IgG) to the brain. Compared with other approaches to open the BBB, the optical opening offers unprecedented spatial resolution to locally allow molecule penetration into the brain.

METHODS

Nanoparticle synthesis and functionalization: AuNPs were synthesized by previous reported method[5]. Then, the AuNP were functionalized with antibodies (BV16: anti-human JAM-A, BV11: anti-mouse JAM-A) for targeting JAM-A[6], one of the tight junction (TJ) proteins (**Figure 1A**).

In vitro experiments: Human cerebral microvascular endothelial cell D3 (hCMEC/D3) was used as an *in vitro* BBB model. The barrier was characterized by trans-endothelial electrical resistance (TEER), permeability and immunocytochemistry (ICC) staining. We then treated the monolayers by TJ-targeting AuNPs (AuNP-BV16), and ps laser pulses (532 nm, Full width half maximum = 28 ps), measured the BBB opening by changes in TEER and permeability (**Figure 1B**).

In vivo experiments: C57BL/6 mice were injected 36.9 μg/g AuNPs functionalized with BV11, followed by EB dye injection. We then applied ps laser through mouse skulls to excite the AuNPs on blood vessels. After 0.5 hr, mice were transcardially perfused with 25 ml PBS, followed by 4% PFA. The brain and other organs were extracted for EB extravasation imaging and histology staining (**Figure 1C**).

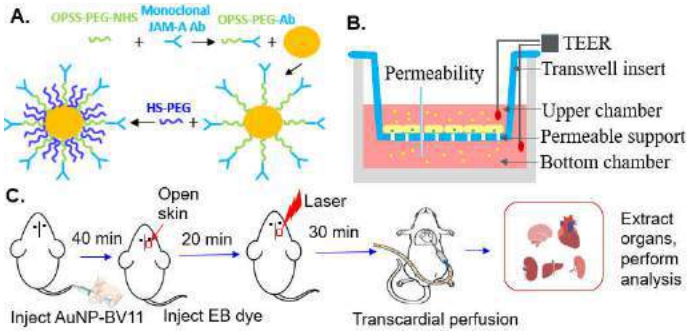

Figure 1. Methods of BBB opening *in vitro* and *in vivo*. (A) Synthesis of TJ-targeting AuNPs[7]. (B) Schematic of BBB *in vitro* model and TEER and permeability measurement. (C) Procedure of *in vivo* study.

RESULTS and DISCUSSION

Temporary BBB Opening *in vitro*

We performed ICC staining for JAM-A on hCMEC/D3 cells to determine the location of AuNP-BV16. The result shows good co-localization of AuNP-BV16 and tight junctions (**Figure 2A**). We, then, applied ps laser to monolayer treated with AuNP-BV16 and measured

the BBB temporary opening by changes in TEER and permeability. With the same pulse number, high laser energy leads to greater drop in TEER (**Figure 2B**). While with the same pulse energy, increasing pulse number leads to a larger drop in TEER values and larger permeability for 40 kDa FITC-dextran (**Figure 2C**). Cell viability testing by WST-1 assay indicates that the laser excitation of TJ-targeted AuNPs does not cause significant cell damage in our experimental conditions (Data is not shown). Moreover, we tested the Ca^{2+} response and found that Ca^{2+} transiently increased after laser illumination (**Figure 2D**).

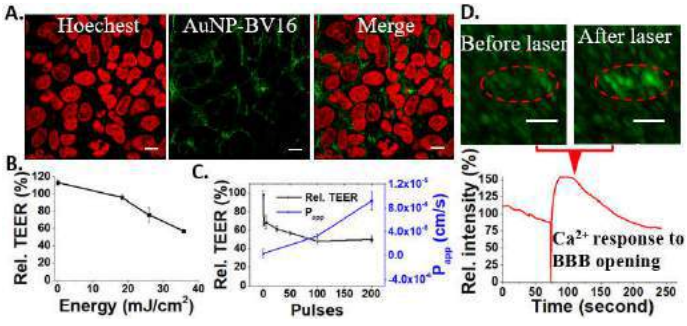

Figure 2. ***In vitro*** **BBB opening.** (A) Co-localization of TJ-targeting AuNP and TJ. Green: JAM-A, red: nuclei. Scale bar, 10 μm. (B) Normalized TEER of hCMEC/D3 monolayer treated with different laser pulse energy (25 pulses and 5Hz). (C) Normalized TEER and apparent permeability (P_{app}) of 40 kDa FITC-dextran of hCMEC/D3 monolayer treated with various laser pulse numbers (35 mJ/cm^2 and 5Hz). (D) Ca^{2+} signal response to optical BBB opening (35 mJ/cm^2, 1 pulse). The normalized intensity of fluo-4 indicates Ca^{2+} concentration. The intensity shows transient increase after laser excitation. Scale bar: 100 μm.

Temporary BBB Opening *in Vivo*

We demonstrate *in vivo* BBB opening by visualizing extravasation of EB dye, which binds to albumin in the blood and thus otherwise doesn't accumulate in a brain with an intact BBB. The result shows clear EB extravasation in the mouse treated with AuNP-BV11, while no EB extravasation in the mouse treated by AuNP-PEG (**Figure 3A**). Our optical BBB opening can reach high spatial resolution by manipulating the laser beam size. Here, we show different BBB opening area with laser beam size at 0.8 and 2.5 mm (**Figure 3B**).

To test the recovery of BBB, we administrated EB dye at 0 hour, 1 hour, 6 hours after laser excitation of TJ-targeting AuNPs. The BBB opening recovers in 6 hours with laser energy 5 mJ/cm^2 (**Figure 3C**). Next, we tested the effects of laser pulse parameters. When varying laser pulse number (1, 2, 5 pulses) with same laser pulse energy (25 mJ/cm^2), EB extravasation increased with laser pulse number (**Figure 3D**). By increasing laser pulse energy (0, 2.5, 5, 10, and 25 mJ/cm^2) and keeping the same laser pulse number (1 pulse), we observed EB extravasation starts at 2.5 mJ/cm^2 (**Figure 3E**). Analysis of the brain sections shows that the EB extravasation is deeper with increasing laser pulse energy (**Figure 3F**). Moreover, the immunohistochemistry staining shows that laser irradiation doesn't damage blood vessels (**Figure 3G**).

Lastly, we demonstrate that the temporary BBB opening allows delivery of functional molecules, such as anti-cancer drug (doxorubicin (Dox)) (**Figure 4A**) and human IgG to the brain (**Figure 4B**).

CONCLUSION

Here we report a novel method for BBB opening. Specifically, TJ-targeting plasmonic AuNPs open the BBB after excitation by a ps pulse laser *in vitro* and *in vivo*. This might be due to the nanoscale mechanical stress on the TJ molecules and Ca^{2+}-based mechanism. The biggest advantage of this optical BBB opening approach is the high optical resolution to investigate drug accumulation. This will find broad application in delivery molecules to precise brain region.

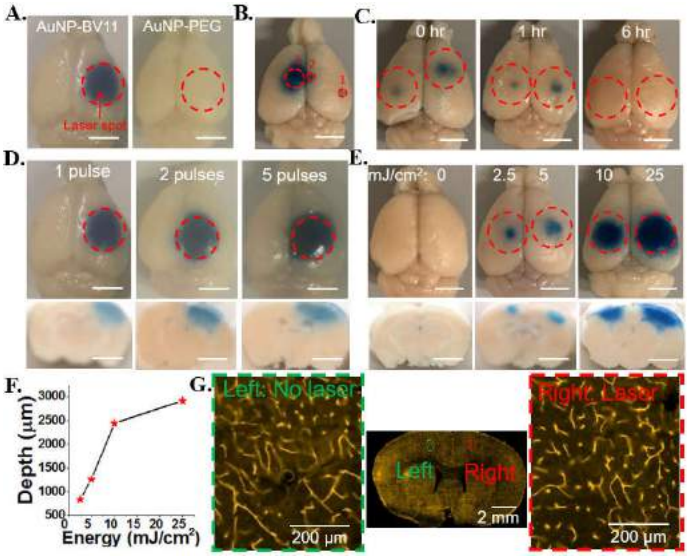

Figure 3. Temporary BBB opening i*n vivo*. (A) Effect of AuNP-BV11 targeting to TJ on BBB opening versus non-targeting AuNP-PEG (1 pulse, 25 mJ/cm^2). (B) High spatial resolution of optical BBB opening (1 pulse, 25 mJ/cm^2). Laser beam size of 1, 2, 3 is 0.8 mm, 0.8 mm, 2.5 mm, respectively. (C) Reversibility of BBB opening (1 pulse). Left hemisphere: 2.5 mJ/cm^2, right hemisphere: 5 mJ/cm^2. EB injection at 0 hr, 1 hr, 6 hr post laser irradiation. (D) Effect of laser pulse number (25 mJ/cm^2). (E) Effect of laser pulse energy (1 pulse). Scale bar of A-E: 4 mm. (F) Analysis of EB extravasation as a function of laser pulse energy. (G) Brain vascular response to optical BBB opening. 1 pulse, 5 mJ/cm^2 on right hemisphere.

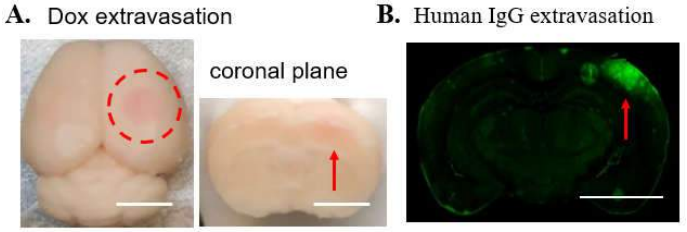

Figure 4. (A) Dox and human IgG (B) extravasation after laser irradiation. 1 pulse, 25 mJ/cm^2 on right hemisphere. Scale bar: 4 mm. Red signal in (A) indicates Dox extravasation after laser application. Green signal on the top right in (B) suggests human IgG extravasation after laser excitation.

ACKNOWLEDGEMENTS

We acknowledge funding support from Cancer Prevention & Research Institution of Texas (RP160770, RP180846).

REFERENCES

1. Tajes, M., *et al*. *Mol Membr Biol* **31**, 152-167 (2014).
2. Doolittle, N.D., *et al. Cancer* **88**, 637-647 (2000).
3. Kinoshita, M., *et al*. *Proc Natl Acad Sci* **103**, 11719-11723 (2006).
4. Gao, X., *et al. ACS Nano* **8**, 3678-3689 (2014).
5. Frens, G. *Nature-Phys Sci* **241**, 20-22 (1973).
6. Giannotta, M., *et al. EMBO Mol Med* **6**, 239-258 (2014).
7. Dai, Q., *et al*. *Angew Chem Int Ed Engl* **53**, 5093-5096 (2014).

SB^{3}C2019
Summer Biomechanics, Bioengineering and Biotransport Conference
June 25 -28, Seven Springs, PA, USA

RECAPITULATING THE COMPLEX BIOMECHANICAL PROPERTIES OF INTERVERTEBRAL DISC USING TUNABLE 3D PRINTING

Samantha L. Marshall (1), Timothy D. Jacobsen (2), Kevin Anton (2), Archana Murali (2), Nadeen O. Chahine (1, 2)

(1) Department of Orthopedic Surgery
Columbia University
New York, NY, USA

(2) Department of Biomedical Engineering
Columbia University
New York, NY, USA

INTRODUCTION

Severe back pain, one of the most common reasons for doctor visits, has been associated with degeneration of the intervertebral discs [1]. The intervertebral disc is a connective tissue between vertebral bodies that transmit load, and consists of two distinct anatomical regions with differing mechanical properties [2]. The center of the disc, called the nucleus pulposus (NP), is a highly hydrated tissue whose water content and negatively charged proteoglycans sustain the osmotic pressure that allows it to withstand large compressive forces. The annulus fibrosis (AF), which surrounds the NP, is comprised of highly oriented collagen fibers that have a high tensile strength to resist bulging [3]. The compressive modulus of native human NP ranges from 5 to 10 MPa, while the tensile modulus of native human AF ranges from 10 to 45 MPa [4,5].

Biomimetic tissue engineering approaches have been investigated to mimic the functional mechanical properties of the AF using electrospinning of PCL or PLGA fibers [6,7]. Many current research strategies for total disc engineering use two different materials for the AF and the NP and then combine these materials to create a disc composite, leaving the interface between the NP and AF vulnerable to failure under loading. Unfortunately, the biomechanical properties of the individual NP or AF scaffolds also remain orders of magnitude lower than the native disc tissue biomechanical properties.

To overcome these limitations of whole disc tissue engineering, we have developed a 3D printing approach with a flexible polymer (FPLA) to achieve a scaffold with regional elastic and viscoelastic mechanical properties that represent native AF and NP tissues. By using FPLA we can 3D print one construct that can mimic both the mechanical properties of the AF and the NP, without the need to interface two separate materials together, which can drive interfacial complications. These scaffolds may be filled with a hydrogel cell carrier to drive the creation of biological matrices. In this study, we describe the elastic and viscoelastic properties, and initial biological validation for cellular biocompatibility, and degradation behavior of this novel 3D printed scaffold.

METHODS

Scaffolds were printed from FlexiFil, a thermoplastic co-polyester elastomer/polymer blend (FPLA) (FormFutura) using a Makerbot Replicator+ 3D printer (Makerbot) with 0.4mm print nozzle. Scaffolds were printed with 0.4mm fibers with varying fiber spacing's of 1, 1.5, 2, 2.5, 3mm (Fig. 1).

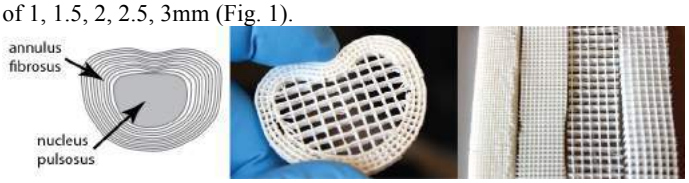

Figure 1: (Left) Schematic of IVD, (Center) 3D printed IVD scaffold consisting of an AF and NP regions, and (Right) Representative images of printed FPLA scaffolds sheets.

For evaluation of equilibrium mechanical properties, constructs were tested on an Instron UTM setup. For compressive testing, samples were compressed at a strain rate of 1 mm/min up to a maximum stain of 25% initial thickness. Young's modulus within the elastic deformation range was calculated. For tensile testing, constructs were placed under uni-axial tension and stretched until a load of 20N was reached; Young's modulus within the tensile elastic deformation range was calculated. Dynamic compressive and tensile DMA testing was done using a TA Electroforce DMA Mechanical Tester. A 5N preload was applied to samples prior to testing. For

compressive testing, samples were ramped to a 10% compressive strain after which a cyclic loading (5% to 15% strain) frequency sweep from 0.1 to 10 Hz was performed. For tensile testing, samples were ramped to 15% tensile strain followed by a cyclic loading (10% to 20% strain) applied at frequencies ranging from 0.1 to 10 Hz. Storage and Loss moduli were calculated using the DMA software. Data was analyzed with 1-way ANOVA with fiber spacing as the independent variable and Fisher LSD post-hoc test, with $p<0.05$ significant.

For evaluating biocompatibility, cells were isolated from healthy bovine lumbar spine NP tissue and were expanded in DMEM+10%FBS+1%AA in standard culture conditions up to 2 passages after which they were seeded into 24 well plates for cytotoxicity testing. Scaffold samples were cultured in 24 well plates seeded with bovine NP cells for three weeks and compared to cells culture without scaffolds. Cells were stained with 4µM Calcein AM and 2µM Ethidium Homodimer-1 and imaged using confocal microscopy to determine cytotoxicity, with green indicative of live cells and red representing the nuclei of dead cells.

Degradation tests were also performed. Samples were incubated in PBS at 37°C up to 20 weeks. Every two weeks the samples were removed from the PBS bath, dried, weighed to record any mass loss, subjected to compressive DMA testing, and scanned in a µCT to observe any mechanical degradation or morphological changes.

RESULTS

Both compressive (Fig 2a) and tensile elastic moduli (Fig 2b) of FPLA constructs decreased with increasing fiber spacing. Compared to constructs made of conventional PLA, FPLA had a significantly lower compressive elastic modulus (Fig 2a).

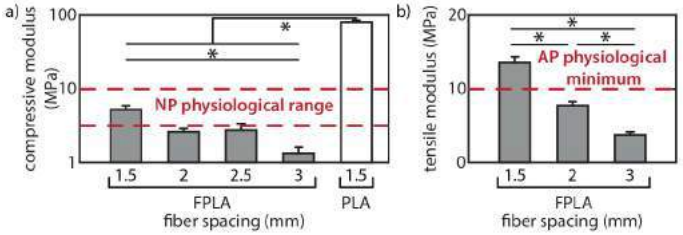

Figure 2: a) Compressive elastic modulus of FPLA constructs decreases with increasing fiber spacing. b) Tensile elastic modulus decreases with increasing fiber spacing. (* $p<0.05$).

DMA compression showed that storage and loss moduli decreased with increasing fiber spacing at all frequencies, with fiber spacing having a significant ($p<0.05$) effect on storage (Fig 3a) and loss (Fig 3b) moduli. Compressive storage modulus ranged from 1.8 MPa to 11.1 MPa, representing a range that mimics native NP tissue.

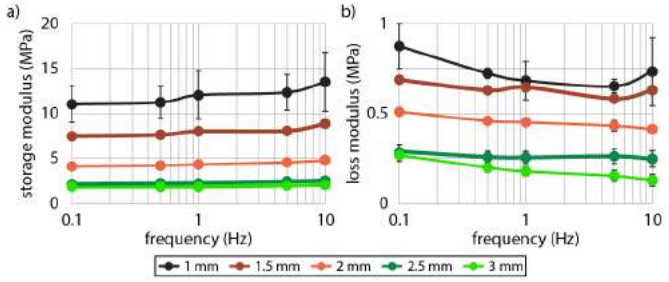

Figure 3: a) Storage modulus of FPLA constructs decreases significantly with increasing fiber spacing b) Loss modulus decreases significantly with increasing fiber spacing.

Cytotoxicity studies showed no significant changes in cell viability in either control or FPLA groups up to 3 weeks in culture, indicating FPLA scaffolds do not result in cytotoxic effects (Fig 3). From degradation studies, FPLA constructs were shown to be stable, with no signs of decrease in weight or mechanical properties to 20 weeks. µCT scans (Fig. 3) do not show major change in morphology.

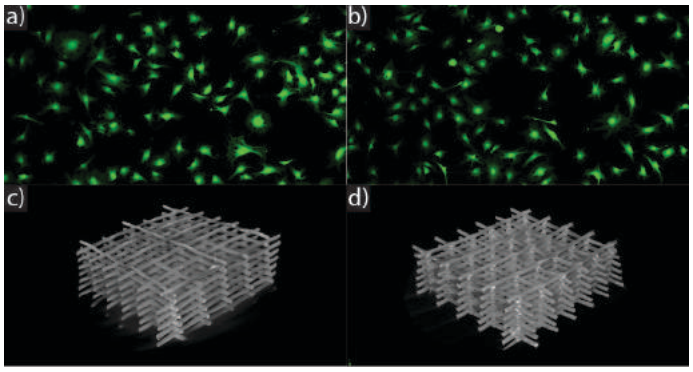

Figure 3: Representative images of live/dead Calcein AM (green) and Ethidium Homodimer-1 (red) staining of cells cultured without (a) and with (b) FPLA constructs. Representative µCT scans of a printed scaffold before (c) and after 12 weeks of degradation testing (d).

DISCUSSION

These results demonstrate that the mechanical properties of FPLA scaffolds can be tuned using 3D printing to vary the fiber spacing, and recapitulate both the compressive properties of the native NP (Fig 2a) as well as the tensile properties of native AF (Fig 2b) using a single uniform polymer material. The ability to 3D print the FPLA scaffolds allows greater control of fiber spacing, direction, and placement than other fabrication methods (e.g. electrospinning). Furthermore, we demonstrate that we are able to modulate the viscoelastic properties (storage and loss moduli) of the scaffold by varying fiber spacing, in a manner that mimics the native NP and AF viscoelasticity [8,9]. This will permit tuning of a wide range and modality of mechanical properties, leading to a mechanically biomimetic scaffold for IVD replacement. Compared to PLA (non-flexible) scaffolds with the same fiber spacing, FPLA scaffolds exhibited compressive moduli orders of magnitude lower and more physiologically relevant than conventional PLA. Additionally, we have shown that FPLA scaffolds are stables for up to 20 weeks, and they do not exert cytotoxic effects on NP cells through 3 weeks in culture, supporting the biocompatibility of the polymer. Future studies will evaluate embedding cell loaded hydrogels in the FPLA scaffold to promote extracellular matrix deposition and integration with native tissue.

ACKNOWLEDGEMENTS

Funded in part by NIH R01AR069668.

REFERENCES

[1] Serra, T. et al., *Biofabrication*. 8:35001, 2016.
[2] Urban, J.P.G. et al., *Arthritis Res. Ther.* 5:120–30, 2003.
[3] Bowles, R.D. et al., *Biomaterials.* 129:54–67, 2017.
[4] Nerurkar, N.L. et al. *Spine*. 35(8):867-73, 2010.
[5] Martin, J.T. et al., *Publically Accessible Penn Dissertations.* 2015.
[6] Lazebnik, M. et al., *Journal of Tissue Engineering and Regenerative Medicine*. 5(8):e179-87, 2011.
[7] Martin, J. T. et al., *Tissue Eng. Part A*. 23(17-18):923-34, 2017.
[8] Freeman, A.L. et al. *J Biomech.* 46(10):1714-21, 2013.
[9] Sen S. et al., *Mech Mater.* 44:93-98, 2012.

SB³C2019
Summer Biomechanics, Bioengineering and Biotransport Conference
June 25 -28, Seven Springs, PA, USA

ORIENTATION AND SIZE OF THE PORCINE ANTERIOR CRUCIATE LIGAMENT VARY BETWEEN YORKSHIRE AND YUCATAN BREEDS AT EARLY ADOLESCENCE

Stephanie G. Cone (1), Danielle Howe (1), Emily P. Lambeth (1), Jorge A. Piedrahita (2), Lynn A. Fordham (3), Jeffrey T. Spang (4), Matthew B. Fisher (1,4)

(1) Department of Biomedical Engineering
North Carolina State University and
University of North Carolina – Chapel Hill
Raleigh, NC, USA

(2) College of Veterinary Medicine
North Carolina State University
Raleigh, NC, USA

(3) Department of Radiology
University of North Carolina – Chapel Hill
Chapel Hill, NC, USA

(4) Department of Orthopaedics
University of North Carolina – Chapel Hill
Chapel Hill, NC, USA

INTRODUCTION

Porcine models are a common large animal model to study musculoskeletal tissues [1]. In particular, pigs are frequently used for research involving the anterior cruciate ligament (ACL) [1]. Within research utilizing the porcine model, several breeds have been used including Yorkshire-cross breeds and Yucatan minipig breeds [2,3]. However, variability in breeds used across studies may result in issues regarding experimental repeatability due to major differences in anatomy, growth, and mechanical loading with a large range in animal size between breeds. Further complicating the issue, previous work in our group has shown that there are major changes in the anatomy of musculoskeletal soft tissues such as the ACL during growth in the Yorkshire pig, including increases in the angle of ACL orientation and variation in the relative sizes of the anteromedial (AM) and posterolateral (PL) bundles of the ACL [2,4]. These changes in tissues during growth are of interest in order to study pediatric and adolescent clinical treatments in relevant large animal models [3]. As such, the objective of this study was to compare the orientation and size of the ACL bundles as well as femoral and tibial bone size between Yucatan minipigs and Yorkshire cross-breed pigs at two ages in early adolescence.

METHODS

Hind limbs were collected from early adolescent female pigs representing Yorkshire cross-breed and Yucatan minipig breeds at 4.5 and 6 months of age (n=6 per age and breed, n=24 total). Stifle joints were imaged at full extension in a 7.0-Tesla magnetic resonance imaging (MRI) scanner (Siemens Healthineers, Erlangen) using a double-echo steady state (DESS, voxel size=0.42x0.42x0.4 mm) sequence. Image sequences were exported to commercial software (Simpleware) for analysis and 3D models of the anteromedial (AM) and posterolateral (PL) bundles of the ACL were generated along with models of the tibial plateau and the femoral cortical bone. The cross-sectional area (CSA) of each tissue or bone was calculated, along with the length between insertion sites of each ligament using custom MATLAB code. The sagittal and coronal angles of the ACL were measured relative to the tibial plateau as described previously [2]. Statistical analysis consisted of a two-way ANOVA with age and breed as main effects and Tukey's post-hoc analysis (JMP, $p<0.05$).

RESULTS

Overall significant differences between breeds were evident with much larger joints in the Yorkshire group. All limbs were skeletally immature, with no fusion in the tibial or femoral growth plates (Fig. 1).

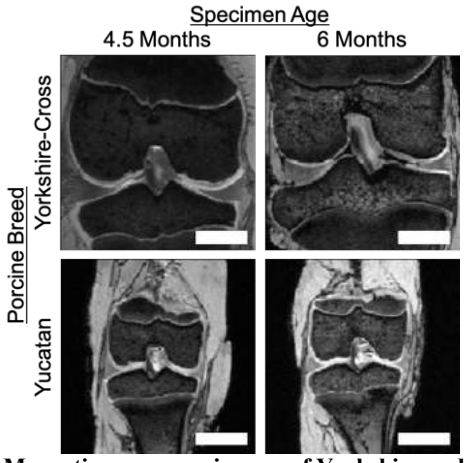

Figure 1: Magnetic resonance images of Yorkshire and Yucatan stifle joints at early adolescence (4.5 and 6 months). Scale bars represent 20mm.

ACL sagittal angle increased with increasing age ($p<0.05$), with no significant difference due to breed or interaction term ($p>0.05$). Mean values ranged by 7° in the Yucatan breed, and by 2° in the Yorkshire breed (Fig. 2). In the coronal angle, there were differences due to age, breed, and the interaction term ($p<0.05$). In Yucatan pigs, coronal angle increased by 11° from 4.5 to 6 months ($p<0.05$), while Yorkshire pigs had similar values at both ages. The Yorkshire pigs had significantly greater angles, 14°-22° higher than Yucatan pigs (Fig. 2, $p<0.05$).

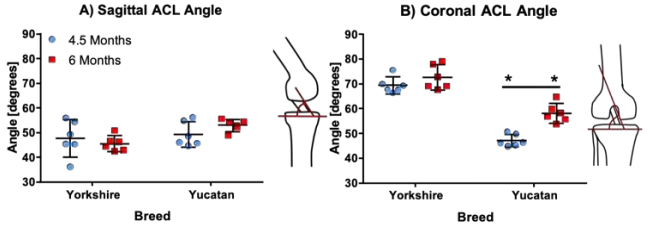

Figure 2: Coronal (A) and sagittal (B) angles varied by age and breed. Summary data show mean ± 95% C.I. * p<0.05 between breeds, bar indicates p<0.05 between ages.

The geometry of the AM and PL bundles of the ACL varied due to both age and breed between 4.5 and 6 months (Fig. 3, $p<0.05$). Specifically, the AM and PL bundle lengths varied as an effect of age and breed with a significant interaction term in the PL bundle ($p<0.05$). Mean AM bundle length values were significantly greater ($p<0.05$) in the Yorkshire breed (36.5 mm) compared to the Yucatan breed (22.1 mm) while increasing age resulted in a significant 2.0 mm increase in mean AM bundle length ($p<0.05$). In the PL bundle, the mean Yorkshire length increased by 31% with age ($p<0.05$), while the Yucatan length did not experience significant growth (Fig. 3A, $p>0.05$). An additional metric of ACL bundle size, bundle CSA, revealed significant differences in the AM bundle as an effect of age and breed ($p<0.05$) and in the PL bundle only as an effect of breed ($p<0.05$). The AM and PL bundle CSAs were 222-240% and 72-96% greater in the Yorkshire breed, respectively ($p<0.05$). The mean AM bundle CSA increased in the Yorkshire breed by 28% from 4.5 to 6 months ($p<0.05$), while the AM bundle CSA had similar values across ages in the Yucatan breed (Fig. 3B, $p>0.05$).

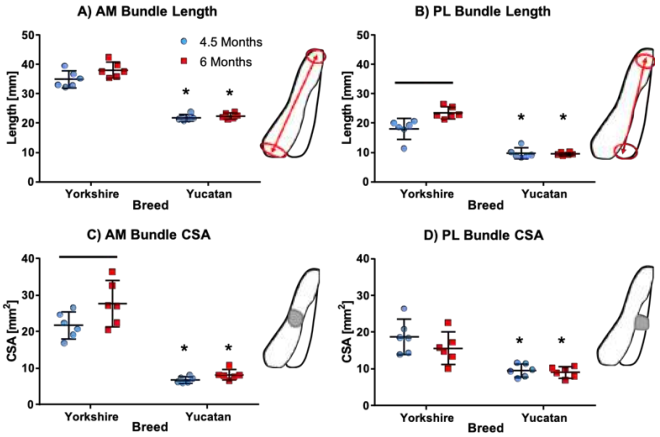

Figure 3: AM and PL length (A,B) and CSA (C,D) varied by age in some cases in Yorkshire pigs. Summary data show mean ± 95% C.I. *p<0.05 between breeds, bar indicates p<0.05 between ages.

Values of bone CSA (tibial plateau and femoral cortical bone) varied between breeds ($p<0.05$) although there was no effect due to age or interaction term ($p>0.05$) in either metric. Tibial plateau CSA was much larger in the Yorkshire pig (2164 mm^2) than in the Yucatan pig (603 mm^2) (Fig. 4A). Femoral cortical bone CSA was larger ($p<0.05$) in Yorkshire (232 mm^2) compared to the Yucatan joints (101 mm^2) (Fig. 4D). Normalization of ACL and bone sizes revealed small effects of breed and age on tissue size, although there were significant differences between breeds in the CSA of both bundles relative to the femoral cortical CSA (Fig. 4E-F, $p<0.05$), and in the PL bundle CSA relative to the tibial plateau CSA (Fig. 4C, $p<0.05$). Age had a significant effect within both breeds in the of PL CSA normalized to femoral CSA (Fig. 4F), and in the PL CSA normalized to tibial plateau CSA in the Yucatan breed (Fig 4C, $p<0.05$).

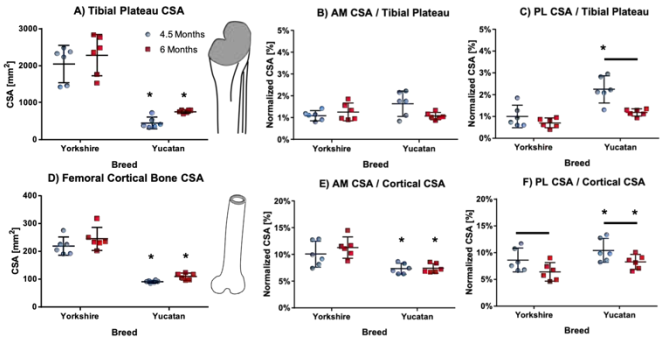

Figure 4: Tibial plateau CSA (A) and femoral cortical bone CSA (D) were significantly larger in the Yorkshire breed compared to the Yucatan breed. Normalization of bundle CSA to bony parameters (B,C,E,F) showed similar results between breeds and ages. Summary data show mean ± 95% C.I. * p<0.05 between breeds, bar indicates p<0.05 between ages.

DISCUSSION

Differences existed in overall ACL size, bone size, and some metrics of ACL orientation between Yorkshire and Yucatan pigs in early adolescence. Coronal plane ACL orientation angle experienced larger change with growth in Yucatan pigs compared to Yorkshire pigs. On the other hand, the size of the AM and PL bundles of the ACL experienced greater changes with age in Yorkshire pigs compared to Yucatan pigs. Interestingly, these soft tissue changes occurred despite no age-related changes in bone sizes in either breed. Furthermore, mean differences in ACL bundle sizes were much smaller between breeds when normalized to bone size. These results can be partially explained as the slope of the growth curves varies widely between domestic pigs and minipigs during early adolescence with increased rates and longer periods of weight gain in domestic pigs [6]. This study highlights the importance of animal breed in musculoskeletal tissue engineering studies, as age-related changes were breed-specific in both size and orientation and certain breeds may better approximate human changes [5,7]. In the future, this we will expand this study to include juvenile and late adolescent groups, and specimens will undergo functional testing to assess differences in tissue and joint mechanics. Overall, we have presented both breed-specific and age-specific changes in the orientation and size of the porcine ACL.

ACKNOWLEDGEMENTS

We would like to thank the Swine Education Unit (NCSU), Powered Research, and the Biomedical Research Imaging Center (UNC-CH) for their support. Funding provided by NSF (DGE-1252376) and NIH (R03-AR068112, R01-AR071985).

REFERENCES

[1] Cone, SG et al., *Tissue Eng Part C*, 23(11):763-780, 2017; [2] Cone, SG et al., *J Orthop Res*, 35(12):2725-2732, 2017; [3] Murray, MM et al., *Am J Sports Med,* 41(8): 1762-1770, 2013; [4] Cone, SG et al., *World Congress of Biomechanics*, 2018; [5] Kim HK et al., *Radiol,* 247(3):826-835, 2008; [6] Schuleri KH et al., *Comp Med,* 58(6): 568-579, 2008; [7] Tuca M et al., *Knee Surg Sports Traumatol Arthrosc,* 24(3):780-787, 2016.

SB³C2019
Summer Biomechanics, Bioengineering and Biotransport Conference
June 25 -28, Seven Springs, PA, USA

FOR LIGAMENTS, MATERIAL STIFFNESS IS NOT WHAT IT APPEARS TO BE: HOW TO BUILD MORE ACCURATE MATERIAL MODELS AND IMPLICATIONS ON ACL GRAFT SELECTION

Callan M. Luetkemeyer (1), Ellen M. Arruda (1,2,3)

(1) Department of Mechanical Engineering
University of Michigan
Ann Arbor, MI, USA

(2) Department of Biomedical Engineering
University of Michigan
Ann Arbor, MI, USA

(3) Program in Macromolecular Science and Engineering
University of Michigan
Ann Arbor, MI, USA

INTRODUCTION

The anterior cruciate ligament (ACL) is the most commonly injured knee ligament, and it plays a critical role in the mechanical stability of a healthy knee. Computational models can help us better understand these injuries by examining the effects of injury risk factors on ACL strain, but material models capable of predicting 3D deformations and injury continue to elude us. Our recent work has focused on how geometry can obscure mechanical measurements. We specifically address the implications of this work on the current understanding of ACL graft selection and how full-field methods may overcome this issue.

Currently, the middle third of the patient's own patellar tendon (PT) is the most commonly used graft for ACL reconstruction, but it is debated whether its material properties are sufficiently similar to that of a native ACL, as several studies have reported a larger tangent modulus for the PT than the ACL [1,2]. While it is possible that true material differences exist between the ACL and PT, we suggest that it is also possible that this difference in apparent stiffness is largely the result of differences in specimen length-to-width ratio.

Tensile tests of anisotropic materials must use samples with much larger length-to-width ratios than the isotropic standard (4:1) to achieve homogeneous uniaxial tension in the gauge section. Boundary effects create strain inhomogeneity near the gripped ends of a specimen, and mathematical analysis indicates that the length over which these effects decay is about one specimen width for isotropic materials, but much larger for anisotropic materials [3]. This finding was experimentally confirmed by Arridge and Folkes, who found that the apparent tensile modulus of a transversely isotropic polyethylene significantly increased with increasing length-to-width ratio, requiring an aspect ratio of 100:1 or more to achieve uniaxial tension [4].

While a standard PT graft has a width similar to that of the ACL, the PT graft is significantly longer than the ACL. Thus, the PT has a larger length-to-width aspect ratio than the ACL; this geometric difference alone would make the PT appear stiffer even if there were no material differences. Little of the published work comparing the mechanical responses of the PT and ACL has controlled for specimen aspect ratio. Therefore, it remains uncertain whether the PT is, in fact, a stiffer material than the ACL. Thus, the first objective of this study was to address this question by determining the effect of aspect ratio on the apparent moduli of the ACL and PT.

If homogeneous deformation states are unachievable in the ACL and PT, as we suggest, how can we build models of their material behavior? While strain inhomogeneity is a non-starter for standard material modeling methods, inhomogeneous strain fields are an asset, rather than a limitation, for full-field methods. Therefore, the second objective of this study was to use full-field methods to build material models of the ACL bundles and PT, with no assumption of strain homogeneity.

METHODS

Ovine knees were acquired from a local abattoir. The PT and anteromedial (AM) bundle of the ACL were removed, leaving small bone blocks attached at each end. The posterolateral (PL) bundle was not used due to its more complex fiber arrangement. The bone blocks were encased in moldable thermoplastic (McMaster-Carr, Aurora, OH) within a custom-made wax mold, to yield a regular shape that would be easily integrated into a horizontal materials testing system (ADMET). Samples were stretched in the mean fiber direction at 0.1 mm/s. Each specimen was tested at 4-6 length-to-width aspect ratios by removing a few fascicles from the edge of the specimen to reduce the width for subsequent tests. Statistical analysis was performed using analysis of

covariance to compare the apparent modulus vs. aspect ratio relationships.

Additionally, we recently collected full-volume displacement maps of six AM and PL bundles under tension using dual-MRI [5]. Strain fields computed from this data proved to be largely inhomogeneous. Thus, the Virtual Fields Method (VFM) was used to fit constitutive models to each full-volume displacement field. VFM is a full-field inverse method which uses the principal of virtual work to fit constitutive models to inhomogeneous deformation fields [6]. First, polynomial descriptions of the bone-ligament boundaries (entheses) were constructed using a custom MATLAB script. These polynomials were used to build virtual fields – kinematically admissible displacement fields with constant displacement along these boundaries. Collagen fiber directionality in the undeformed configuration was described with spatially continuous functions to model the splayed fiber alignment near the entheses. Custom MATLAB code was used to find the set of constitutive parameters that minimized the difference between the external and internal virtual work, according to the method described by Promma, et al [6]. Three constitutive models were considered: the Holzapfel-Gasser-Ogden (HGO) model [7], an HGO-inspired model recently published by our group [8], and a Fung-type model [9].

RESULTS

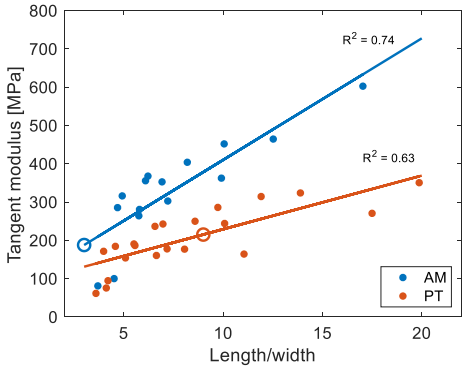

Figure 1: The peak apparent tangent modulus increased with aspect ratio for both the AM and PT (data points shown with filled dots). Medically relevant aspect ratios for each tissue (open circles) suggests that a PT graft could appear stiffer than a whole AM.

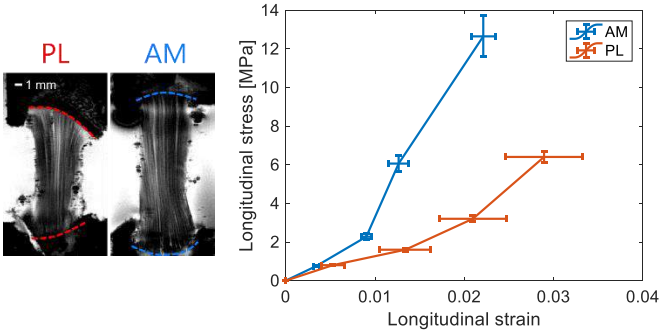

Figure 2: (a) High-resolution MRI images of ACL bundles just prior to testing show that the AM bundle has a larger length-to-width ratio than the PL bundle. (a) Volume-averaged stress-strain curves for the AM and PL bundles obtained with dual-MRI show that the AM appears stiffer than the PL.

Increased sample length-to-width aspect ratio was found to significantly increase the apparent tangent tensile modulus for the AM bundle and PT ligaments ($p < 0.001$). Additionally, AM bundle specimens exhibited a larger apparent modulus than PT specimens for a given aspect ratio ($p < 0.001$).

Volume-averaged stress-strain dual-MRI data showed that the intact AM bundle appeared stiffer than the PL bundle (see Fig. 2b), which is consistent with previous studies [9]. However, this difference could be explained by their differences in aspect ratio (see Fig. 2a). In fact, material models fit to the full-field data with VFM found no significant difference in constitutive parameters between the AM and PL bundle, with the exception of an HGO parameter which describes the degree of collagen fiber alignment ($p = 0.0017$). This is a known microstructural difference between the AM and PL bundle [10], although it has not been detected by previous modeling efforts.

DISCUSSION

The first part of this study indicates that the mechanical response of the AM bundle of the ACL and PT are significantly affected by specimen length-to-width ratio. Controlling for geometry, the AM bundle appears to be a stiffer material than the PT, contrary to the most published work on the subject [1,2]. These studies used the middle third of the PT and the whole ACL, which yielded PT and ACL samples with aspect ratios of about 9 and 3, respectively. Our results suggest that at these aspect ratios, the PT appears to be slightly stiffer than the AM bundle (see open circles in Fig. 1), even though the AM bundle is likely a stiffer material. This interpretation is supported by the recent study of Ristaniemi et al. who found that, for samples with a constant length-to-width ratio of 5, the bovine ACL was stiffer than the PT [11]. This work has two important implications beyond ACL graft selection: 1) global mechanical data cannot discern whether material differences exist between ligament groups unless all samples have the same length-to-width ratio, and 2) if accurate material models are desired for ligaments, strain inhomogeneity caused by end effects cannot be ignored.

The second part of this study demonstrates how full-field methods can take advantage of the unavoidable strain inhomogeneity when building constitutive models of ligaments and other highly anisotropic materials. Using full-field displacement measurement techniques and inverse methods, a known microstructural difference between the ACL bundles (previously identified by microstructural investigations [10]) was independently detected by a constitutive parameter found with full-field mechanics methods. This underscores the advantage of using full-field methods over standard characterization techniques to study the mechanics of biological tissues.

ACKNOWLEDGEMENTS

The authors would like to thank Andy Poli for his assistance with equipment, and Luyao Cai and Corey Neu for their help with dual-MRI data collection. This material is based upon work supported by the National Science Foundation Graduate Research Fellowship under Grant No. DGE 1256260.

REFERENCES

[1] Danto, M et al., *J Orthop Res*, 11:58-67,1993.
[2] Butler, D et al., *J Orthop Res*, 7:68-79,1989.
[3] Horgan, C, *J Elasticity*, 2:169-180, 1972.
[4] Arridge, R et al., *Polymer*, 17:495-500,1976.
[5] Luetkemeyer, C et al., *EML*, 19:7-14, 2018.
[6] Promma, N et al., *IJSS*, 46:698-715, 2009.
[7] Gasser, T et al., *JR Soc Interface*, 3:15-35, 2006.
[8] Marchi, B et al., *IJSS*, 138:245-263, 2018.
[9] Humphrey, J et al., *Crit Reviews in Biomed Eng*, 23:1-162, 1995.
[10] Skelley, N et al., *Am J Sports Med*, 43:928-936, 2015.
[11] Ristaniemi, A et al., *J Biomech*, 79:31-38, 2018.

SB³C2019
Summer Biomechanics, Bioengineering and Biotransport Conference
June 25 -28, Seven Springs, PA, USA

AN ENGINEERED BIOMATERIAL MICROENVIRONMENT TO DIRECT THE FORMATION OF A LIVING BARRIER TO SEAL CARTILAGE DEFECTS

Jay M Patel (1,2), Claudia Loebel (2,3), Brian C Wise (1,3), Kamiel S Saleh (1,2), James L Carey (1), Jason A Burdick (3), Robert L Mauck (1,2,3)

(1) McKay Orthopaedic Research Laboratory
University of Pennsylvania
Philadelphia, PA, USA

(2) Corporal Michael J. Crescenz VA Medical Center
Philadelphia, PA, USA

(3) Department of Bioengineering
University of Pennsylvania
Philadelphia, PA, USA

INTRODUCTION

Articular cartilage consists of a dense extracellular matrix that allows the tissue to undergo fluid pressurization during compressive loading. Cartilage defects compromise this function, introducing free boundaries that result in the flow of proteoglycans and other matrix elements out of the tissue [1]. Decreases in matrix density at defect boundaries make them vulnerable to progressive erosion, instigating a vicious cycle that gradually increases defect size and concludes with joint-wide osteoarthritis (OA). A barrier at this interface may functionally restore the mechanical properties of the defect boundary [2], however synthetic materials may wear or delaminate with time. In this study, we aimed to direct the formation a living fibrous barrier at the damaged cartilage interface (via targeted progenitor cell recruitment and differentiation – Fig 1A), to restore normal cartilage biomechanical function. Specifically, we sought to establish a biomaterial microenvironment (modified hyaluronic acid) that 1) enhances the attachment and mechano-biological response of MSCs at the damaged cartilage interface, 2) induces the cells to undergo fibrogenesis via mechanical cues, and 3) promotes the deposition of fibrous matrix.

METHODS

Biomaterial Microenvironment: Methacrylated hyaluronic acid (MeHA; 75kDa, 35-42% modification) was conjugated with fluorescent peptides (FITC) for visualization and fibronectin-mimicking peptides (RGD) for cellular adhesion (Fig 1B). The material was oxidized to introduce aldehydes (~30% substitution), which form covalent linkages with exposed amines in damaged tissue [3].

Cellular Response: Bovine cartilage plugs were retrieved and sectioned (6mm diameter x 100μm thick). These discs were maintained as naïve samples (ND; mimicking a focal defect) or were digested in collagenase (0.01% for 30 minutes) to mimic degenerated cartilage (D). Biomaterial was applied with 0, 5 or 15 minutes of UV cross-linking, followed by PBS washes to remove non-adhered biomaterial. Cartilage discs (both ND and D) without biomaterial served as controls. Disc-biomaterial composites were seeded with juvenile bovine MSCs (P1-P3, 500 cells per disc) for 24 hours. Samples were fixed in 10% buffered formalin, followed by staining for F-actin with phalloidin to quantify cellular spread area and for the nuclear co-factors YAP/TAZ to quantify cell mechano-response (Fig 1C) [4]. YAP/TAZ signal intensity in the nucleus and cytoplasm were quantified to obtain a measure of nuclear localization (>100 cells per group).

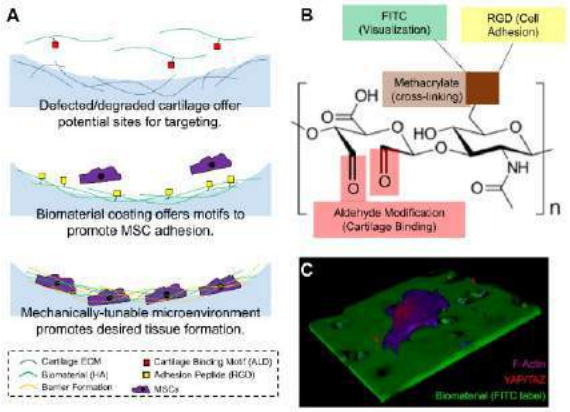

Figure 1. Approach Schematic. [A] Schematic of biomaterial binding to damaged cartilage, promoting MSC adhesion, and ultimately guiding cells towards formation of a barrier. [B] Biomaterial design with modifications to hyaluronic acid (HA). [C] Example of material applied to cartilage disc, with an adhered MSC.

Fibrogenesis and Matrix Deposition: Additional cartilage discs (both ND and D) were subjected to biomaterial application/cross-linking. Discs were seeded with 500 cells and cultured for seven days in basal media. Cells on the discs were fixed and stained for α-smooth muscle actin (α-SMA), a marker of fibrogenesis [5]. The percentage of cells positive for α-SMA fibers was calculated for six replicates. Lastly, additional samples were fixed, dehydrated, and visualized for matrix deposition via scanning electron microscopy (SEM).

Statistical Analysis: Cell area and YAP/TAZ nuclear ratio were analyzed with a one-way analysis of variance (ANOVA) with post-hoc Tukey's test. α-SMA data was compared using a replicate-matched Kruskall-Wallis test. ND and D samples were analyzed separately.

RESULTS

Confocal microscopy showed that the MeHA biomaterial infiltrated throughout the 100μm section prior to cross-linking, forming an integrated biomaterial microenvironment, around and in between chondrocytes in the cartilage matrix (Fig 1C). The biomaterial also promoted MSC adhesion (Fig 1C, Fig 2A) to the tissue-biomaterial interface, increasing cell spread area (Fig 2B). Biomaterial application and cross-linking increased YAP/TAZ nuclear localization (Fig 2C) of MSCs on both non-degraded and degraded cartilage, consistent with the increased MSC spread area (Fig 2B) and higher substrate mechanical properties (Fig 2A – insets) with biomaterial augmentation.

MSCs cultured for 7d on both nondigested and digested cartilage discs (without biomaterial; Fig 3A top) yielded a low percentage of cells positive for α-SMA fibers (13.96 and 6.95%, respectively). Biomaterial application/cross-linking (Fig 3A, bottom) significantly increased (Fig 3B) the percent of α-SMA positive MSCs on both nondigested and digested discs, indicating enhanced fibrogenesis.

Finally, samples without biomaterial (ND, D) showed little to no matrix deposition, as visualized by SEM (Fig 4, top). Conversely, application of biomaterial prior to cell seeding promoted new matrix formation (Fig 4, bottom). In fact, in the non-digested + 15min UV sample, dense collagen-like matrix was observed, to the degree that the underlying cartilage surface and MSCs were not visible.

DISCUSSION

The results of this study detail the use of a modified biomaterial to 1) promote attachment and mechano-sensation of MSCs; 2) guide attached cells towards a fibrogenic phenotype; and 3) promote matrix deposition to cover cartilage defects. These findings support the promise of creating tunable microenvironments to home and retain stem cells at the defect interface, and ultimately control their biologic response. The behavior of cells in this study is consistent with prior cell-hydrogel studies, in that cell attachment and fibrogenesis increase with substrate stiffness. The biomaterial microenvironment in this study does just that, as it utilizes both cell-adhesive and mechanical cues at the damaged interface to induce a fibrotic response. Future studies will investigate the ability of the tissue barrier to functionally seal defects and preserve cartilage integrity in an *in vivo* setting.

ACKNOWLEDGEMENTS

This work was supported by the NIH, VA, AOSSM, and CEMB. The authors thank the Mauck and Burdick Labs at Penn for their help.

REFERENCES

[1] Basalo et al., *J Biomech Eng*, 126(6):779-786, 2004.
[2] Greiner et al., *J Biomech*, 48(1):122-129, 2015.
[3] Wang et al., *Nat Mater*, 6(5):385-392, 2007.
[4] Dupont et al., *Nature*, 8(474):7350, 2011.
[5] Talele et al., *Stem Cell Rep*, 4(6):1016-1030, 2015.

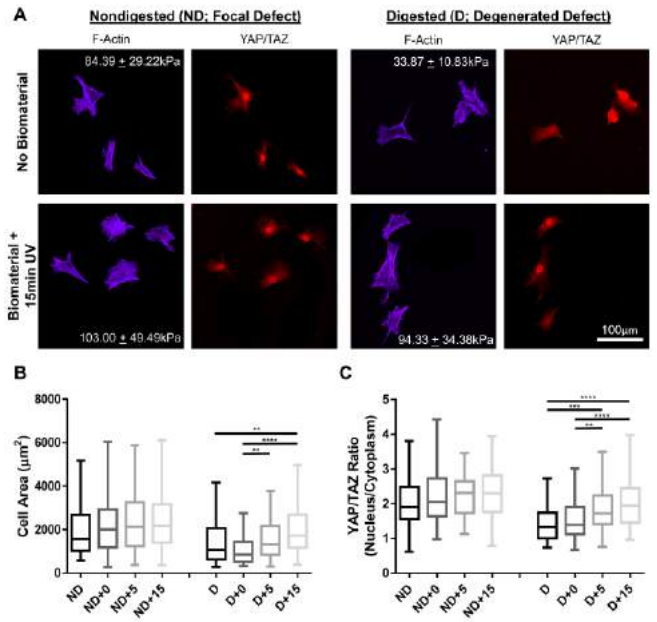

Figure 2. Cell Spreading and YAP/TAZ. [A] Representative images of F-actin and YAP/TAZ in cells on nondegraded and degraded samples, both without biomaterial (top row) and with biomaterial and cross-linking (bottom row). Quantification of [B] cell spread area and [C] YAP/TAZ ratio (nuclear:cytoplasmic) of cells on ND and D samples without biomaterial, with biomaterial (+0), and with biomaterial and crosslinking (+5, +15). n>100 cells per group. *, **, ***, **** indicate $p < 0.05$, 0.01, 0.001, 0.0001, respectively.

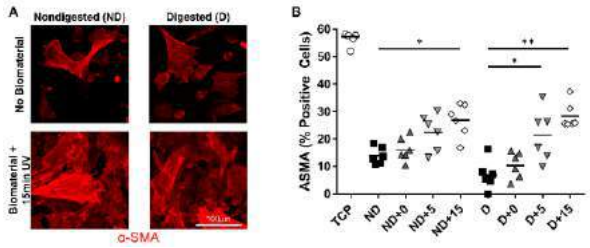

Figure 3. α-Smooth Muscle Actin. [A] Representative images of cells stained for α-SMA. [B] Percentage of cells positive for α-SMA stress fibers. n>50 cells per data point (n=6 replicates). *, ** indicate $p < 0.05$, 0.01, respectively.

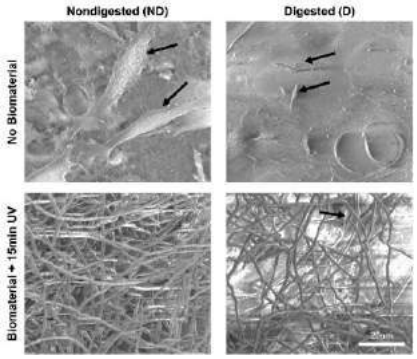

Figure 4. Barrier Formation. SEM micrographs of nondigested (ND) and digested (D) cartilage, with and without biomaterial application, following 7 days of culture with MSCs. Arrows highlight MSCs.

SUSTAINED RELEASE OF TGF-B3 FROM HEPARINIZED COLLAGEN BIOFABRIC INDUCES CHONDROGENIC DIFFERENTIATION OF HUMAN MESENCHYMAL STEM CELL MACROMASS

HJ. JUNG (1), P. McClellan (1), O. Akkus (1,2,3)

(1) Mechanical and Aerospace Engineering
Case Western Reserve University
Cleveland, Ohio, USA

(2) Biomedical Engineering
Case Western Reserve University
Cleveland, Ohio, USA

(3) Orthopaedics
Case Western Reserve University
Cleveland, Ohio, USA

INTRODUCTION

Articular cartilage plays a key role in movement of joints by providing low-friction during articulation while providing resistance to compressive loading. Cyclic loading and overloading during physiological activities may induce articular cartilage defects, and lack of blood supply limits self-healing capacity of the tissue. Current treatment strategies for cartilage defects include microfracture, drilling and abrasion arthroplasty, however, they exhibit noticeable drawbacks [1-3]. Mesenchymal stem cell (MSC) based strategies have been at the center of cartilage repair; however, induction of chondrogenic differentiation of MSCs and obtainment of engineered cartilage tissue with robust mechanical properties is an ongoing challenge

The current study proposes a novel cartilage regeneration by using a heparin-conjugated collagen fabric that is capable of releasing TGF-β3 sustainably to induce resident MSCs toward chondrogenic lineage

METHODS

Collagen biofabric: Collagen thread was prepared by an electrochemical compaction process (Fig. 1(a)) [4]. Uncrosslinked collagen threads were woven in a zig-zag pattern around a set of equidistant pins with 1 mm diameter to make a woven collagen scaffold (Fig. 1(b). The scaffold was crosslinked in genipin solution for 72 hrs.

Heparin conjugation: Genipin crosslinked scaffolds were then treated with peracetic acid / ethanol solution treatment to increase swelling ratio of collagen fabric for 4 hrs [5]. 1-Ethyl-3-(3-dimethylaminopropyl)-carbodiimide (EDC) and N-hydroxysuccinimide (NHS) (life technologies) were used to crosslink heparin molecules to the scaffold, to enhance retention and to sustain the release of TGF-β3 via affinity binding [6]. Followed incubation in 70% ethanol overnight for disinfection, 12 µl of 10 µg/ml TGF-β3 solution was applied to the scaffold and incubated overnight prior to pellet seeding.

Cell Pellets: Bone marrow derived human mesenchymal stem cells (hMSCs, passage 3) were pelletized by spinning at 500g for 12 mins (1,000,000 cells per pellet), and transferred into the scaffolds (Fig. 1(c)). The scaffolds were cultured in chondrogenic medium.

Experimental groups: 1) Negative Control: Negative control group cells in heparinized collagen biofabric without TGF-β3, 2) Treatment group: TGF-β3 was not added to the medium, however, it was loaded in heparinized collagen biofabric to demonstrate whether biofabric mediated delivery is comparable to the positive control group, 3) Positive control: the growth factor was added to chondrogenic media at 10 ng/ml.

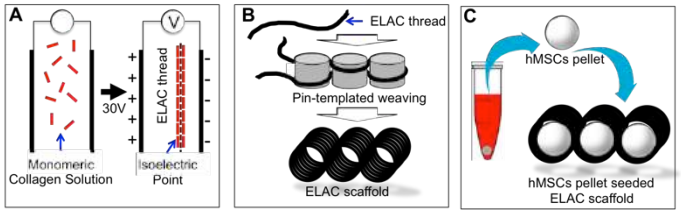

Figure. 1 Scaffold preparation. (A) Electrochemically compacted collagen thread preparation, (B) Scaffold preparation by weaving around a set of pin, (C) hMSCS pellets transfer into the scaffold.

Mechanical properties: At the end of a culture period of 28 days, the samples were loaded in unconfined compression at a constant strain-rate (0.5%/s, Rheometrics Solid Analyzer RSAII, Rheometrics Inc.,) up to 10% strain. Stress values reached at 10% strain are reported as the maximum compressive stress. Apparent Young's modulus was determined by calculating the slope of stress-strain curve

in the range of 3% to 6% strain by linear regression. 1,9-dimethylmethylene blue (DMMB) assay was performed to evaluate glycosaminoglycan (GAG) production at day 28.. The amount of DNA in the cell pellet was measured by Quant-iT™ PicoGreen™ dsDNA Assay (Thermofisher). Briefly, 100 µl of papain digested samples were mixed with 100 ul Picogreen assay solution, and fluorescence was measured by the microplate reader. Colorimetric Sircol assay (Biocolor Life Science Assays) was used to measure the amount of collagen in pellets following digestion in pepsin/acid solution at a concentration of 0.1 mg/mL of 0.5 M acetic acid at 4°C overnight. Amounts of GAG and collagen produced were normalized to amount of DNA per pellet.

Data obtained in this study were reported as mean ± standard deviation. The data were analyzed statistically using one-way ANOVA test with Tukey's pairwise comparison (Minitab 16 software, Minitab Inc.). Statistical significance is set at 95% confidence level for all tests ($p < 0.05$). Error bars in figures represent the standard deviations of the means. Six samples (N=6) were analyzed.

RESULTS

Tissue mass and mechanical properties: Weight of the treatment group (3.05 ± 0.41 mg) was significantly greater than the negative control group (0.87 ± 0.27 mg), while there was no significant difference between the treatment group and the positive control group (3.83 ± 0.31 mg) (Fig. 2(b)). Compressive modulus of the treatment group (664.95 ± 102.31 kPa) was significantly higher than the negative control group (219.47 ± 84.25 kPa), and it was not significantly different from that of the positive control group (636.51 ± 52.73 kPa) (Fig. 2(c). Strength at 10% compressive strain in the treatment group (78.17 ± 13.24 kPa) was significantly higher than the negative control group (23.99 ± 10.46 kPa), and the positive control group (61.17 ± 4.66 kPa) (Fig. 2(d)).

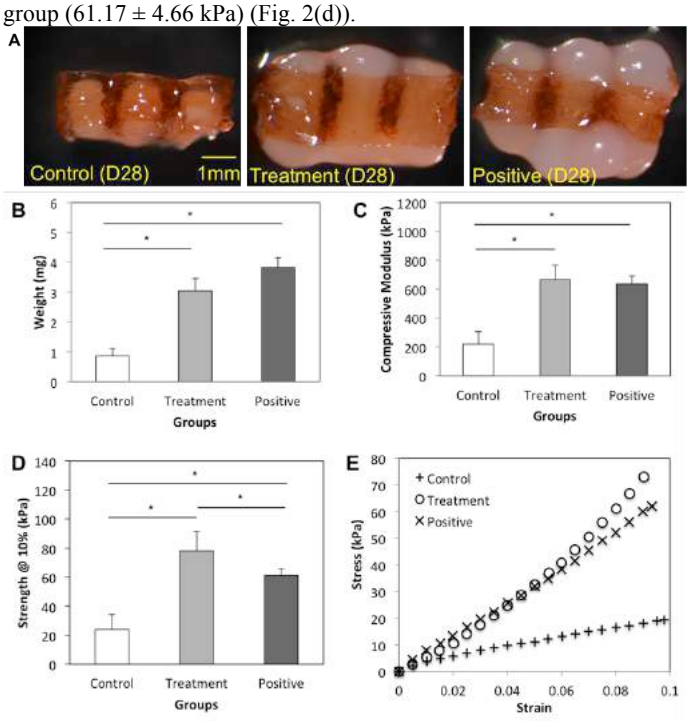

Figure. 2 Mechanical properties of scaffold / hMSCS pellet at Day 28. (A) Image of pellets after 28 days of culture, (B) Weight (mg), (C) Compressive modulus (kPa), (D) Strength at 10% compressive strain (kPa), (E) Typical stress-strain curves. *, *p < 0.05*.

There was no significant differences in the amount of DNA per hMSC pellet among the three groups at day 28 (Fig. 3(a)). The amount of glycosaminoglycan (GAG) and collagen productions per hMSC pellet in the treatment group was significantly higher than the negative control, and there was no significant difference between treatment group and positive control group (Fig. 3(b), Fig. 3(c)). Values of the assays were shown in Fig. 3(d).

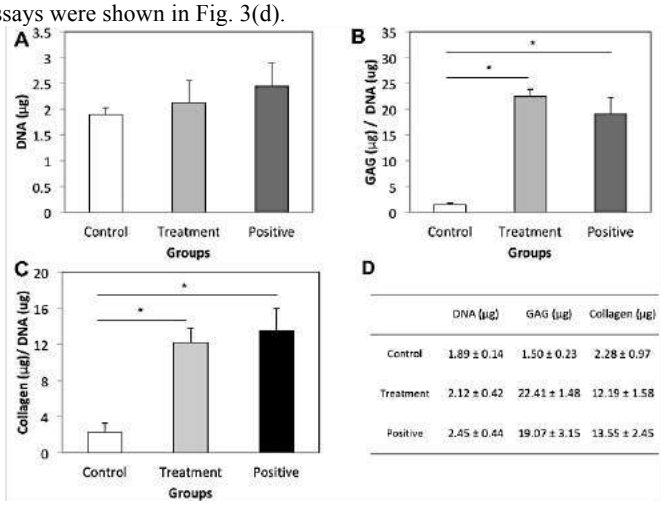

Figure. 3 Extracellular matrix synthesis of hMSCS pellets at Day 28. (A) Amount of DNA per pellet (µg), (B) Amount of glycosaminoglycan (GAG) produced per pellet (µg), (C) Amount of collagen produced per pellet (µg), (D) Values of the assay *, *p < 0.05*.

DISCUSSION

The most significant finding of this study was that sustained release of TGF-β3 from heparinized collagen scaffold had chondro-inductive effect on pelleted hMSCs. The effect was comparable to positive control groups, in which hMSC pellets were cultured in chondrogenic media supplemented with 10 ng/ml of TGF-β3. While no significant difference was found in amount of DNA per pellet among three groups, significantly higher quantities of GAG (15 fold) and collagen (5 fold) were produced by hMSC pellets in Heparin-TGF-β3 groups, compared with pellets in control group. These data indicate that TGF-β3 released from TGF-β3 bound to heparin conjugated scaffolds has potential to enhance extracellular matrix production by hMSCs. Heparinized TGF- β3 conjugated collagen scaffold may deliver growth factors locally to specific site and cells. The delivery also can guide chondrogenic differentiation of hMSCs while suppressing osteogenic differentiation of the cells. Future research will focus on utilization of TGF-β3 bound heparin conjugated scaffolds for functional cartilage tissue regeneration for cartilage defect healing in vivo.

ACKNOWLEDGEMENTS

The study was funded by National Institutes of Health (Grant Number R21-AR068616).

REFERENCES

[1] O' Driscoll SW, *J Bone Joint Surg Am.* 12: 1795-812, 1998.
[2] Magnussen RA, et al., *Clin Orthop Relat Res*. 466(4): 952-62, 2008.
[3] Kon E, et al., *Am J Sports Med.*;37(Suppl 1): 156S-66S, 2009.
[4] Cheng X, et al., *Biomaterials*. 29(22): 3278-88, 2008.
[5] Scheffler SU, et al., *Cell Tissue Bank*. 6(2): 109-15, 2005.
[6] Younesi M, et al., *Acta Biomater*. 63: 200-209, 2017

A COMPUTATIONAL AND EXPERIMENTAL STUDY OF SHORT BOWEL SYNDROME BIOMECHNAICS

Hadi S. Hosseini (1), Jordan S. Taylor (1), James C. Y. Dunn (1)

(1) Department of Surgery (Division of Pediatric Surgery), Stanford University
Stanford, CA, USA

INTRODUCTION

Intestinal failure (IF) is a rare multifactorial clinical condition that results in patient inability to sustain normal growth, nutritional and hydration status. Short bowel syndrome (SBS) is the most common cause of IF which is a devastating condition owing to loss of significant intestinal length thereby affecting the organ ability to absorb nutrients. The incidence rate of the syndrome was 22.1 per 1,000 neonatal intensive care unit admissions and 24.5 per 100,000 live births while even a higher rate was reported in premature infants [1].

Recent treatment focuses on distraction-enterogenesis where it exploits mechanical forces to increase length of small intestine. Although different techniques have been suggested to provide the mechanical force, however self-expanding springs (Figure 1A) as the source of mechanical force have shown great success in lengthening the small intestinal tract [2].

Despite great focus of recent studies on establishing a practical platform to study distraction-enterogenesis as a treatment for SBS, biomechanical factors that drive this process remained poorly studied. From previous studies and experimental observations, we hypothesized that mechanical perturbation in axial direction of intestinal tract triggers some molecular signaling pathways. This causes the tissue thickening in radial direction as well as further communication within intestinal tract even outside of distracted segment through theses signaling pathways. Here, using a combination of experiment and computational modeling, we study the biomechanics involved in distraction-enterogenesis to examine plausibility of our hypothesis.

METHODS

All animal procedures were performed in accordance with the Institutional Care and Use Committee (APLAC Protocol# 32216).

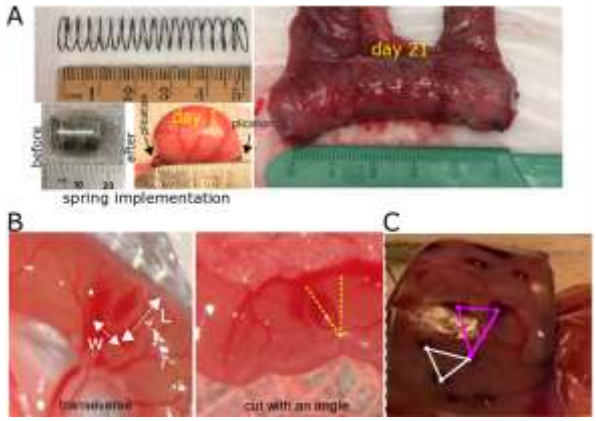

Figure 1. Experimental set up for (A) distraction-enterogenesis with lengthened distracted tissue. (B-C) Representative experiments for calculating tension and strain respectively.

Placement of in-continuity small bowel spring for distraction-enterogenesis was performed on female Yucatan pigs (S&S Farms). In brief, juvenile pigs, ages four to six weeks, were placed. Spring was confined within the bowel by plication sutures. Pigs were euthanized on day 7, 21 and 60 after the original operation. Normal segments and segments of intestine containing the springs were removed and evaluated for lengthening as well as for histologic evaluation. To characterize stress in the intestinal tract, a series of longitudinal (antimesenteric), transverse and angled cuts (Figure 1B) were made in the bowel wall with scissors. Photos were obtained of the bowel to measure the cuts characteristics for tension estimation. For strain estimation, a marking pen was used to mark points on the bowel wall to

aid in tracking the immediate expansion (Figure 1C). Coordinates of the marked dots were traced over time to be used us inputs for customized MATLAB code to analyze the elastic strains of the bowel.

Computational models for distracted-enterogenesis and cutting experiments were developed using the commercial finite-element software ABAQUS (version 2017, SIMULIA, Providence, RI). Constitutive relations (material properties) and tissue proliferation were defined via the ABAQUS user subroutine UMAT [3-5]. Here, distraction-enterogenesis processes were simulated using a continuum mechanics theory for large deformation and growth of soft tissue based on theory of Rodriguez

$$F = F^{*} \cdot G \tag{1}$$

Where G and F^* are the growth tensor and elastic deformation gradient tensor, respectively. A Neo-Hookean strain-energy density function was chosen

$$W = \frac{\mu}{2}(\bar{I}_1 - 3) + \frac{1}{D}\left[\frac{1}{2}\left(J^{*2} - 1\right) - \ln J^{*}\right] \tag{2}$$

Where μ and D are the shear modulus and volumetric compliance respectively. Values for D and μ are calculated from mechanical testing of fresh intestinal tissue along with incompressibility assumption for soft tissue.

RESULTS

Successful lengthening was observed over short (7 days) and longer (21 and 60 days) time periods after spring placement surgery. Normal segment showed an average thickness of 200±30 μm and 700±80 μm for muscularis and mucosa layers respectively, while distracted segment of jejunum showed an increase in thickness of both muscularis and mucosa layers at different time points (Figure 2).

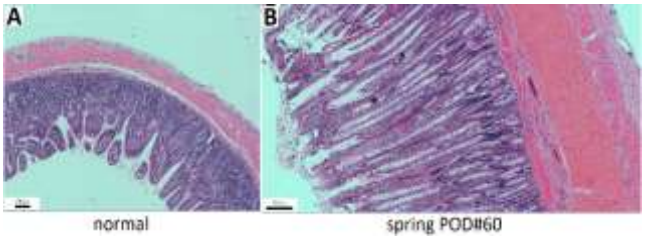

Figure 2. Representative H&E stained of segments of jejunum under different conditions (A) normal jejunum with no spring. (B) Jejunum with a compressed spring at post operation day 60.

Similar to experiment, the simulation distraction-enterogenesis begins with compressing of spring, after full compression diameter of intestinal tract was reduced by 50% at the antimesenteric side of plication segment. Lastly spring was released to be enable to move back with to simulate the distraction step. As spring is expanding, it stretches the distracted tissue to increase its length. Different view of model for different time points are represented in Figure 3C. Similar to experimental observations, different radial growth rates are defined for mucosa and muscularis layers with muscularis layer is growing faster. We examined the ability of our model to capture results given by pharmacological perturbations, as well as measures of deformation and stress. For cutting experiment, computational models were developed to mimic the condition for cutting experiment where the models include a cut in the initial geometry with length and angle of cut like experiment, then opening angle was measured at the end of the simulation. Overall results from the model agree reasonably well with the experimental measurements (Figure 3E). Strain predicted by model is consistent with

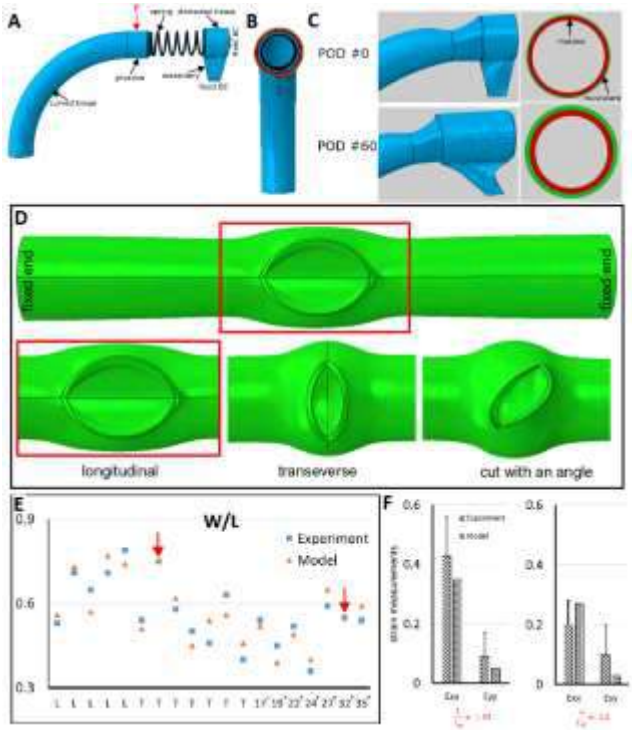

Figure 3. (A-B) Initial geometry of finite element model for distraction-enterogenesis using real geometry of self-expanding spring. (C) Different views of model at different post operation days. (D) Finite element models for different types of cut.

experimental measurements (Figure 3F). Taken together, these additional tests of the model support the plausibility of the model as well as our hypothesis.

DISCUSSION

Our experimental and modeling results show that not only there is a biomechanical feedback between axial mechanical force and lengthening but there is also a strong correlation between this mechanical force and changes in thickness of the intentional wall layers. However, our observations show muscularis layer is being more effected from the mechanical force compare to mucosa layer. First, we validated our computational models with our experimental measurements and then tested our model with further tests. Importance of modeling becomes critical for the clinical purposes where this platform can be used for predicting elastic deformation and tissue proliferation for any patient size as well as any spring characterization. This could reduce surgery risks before spring placement operation where approximate required force (spring characterizations) can be predicted by developing patient-specific finite element models

ACKNOWLEDGEMENTS

This work was supported by Coulter Foundation.

REFERENCES

[1] Wales, PW et al., *J Pediatr Surg*, 39(5):690-5, 2004.
[2] Huynh, N et al., *J Pediatr Surg*, 51(12):1983-87, 2016.
[3] Hoseini, HS et al., *Development*, p. dev.145193, 2017.
[4] Hoseini, HS et al., *Progress in Biophysics and Molecular Biology*, 137:25-37, 2018.
[5] Hoseini, HS et al., *Journal of Biomechanics*, 47(16): 3837-3846, 2014.

SB^{3}C2019
Summer Biomechanics, Bioengineering and Biotransport Conference
June 25 -28, Seven Springs, PA, USA

A DISCRETE FIBER NETWORK MODEL OF ARTERIAL ELASTIN CONSIDERING INTER-FIBER CROSSLINKING

Xunjie Yu (1), Yanhang Zhang (1,2)

(1) Department of Mechanical Engineering
Boston University
Boston, Massachusetts, USA

(2) Department of Biomedical Engineering
Boston University
Boston, Massachusetts, USA

INTRODUCTION

As one of the major extracellular matrix (ECM) components, elastin imparts the elastic property to the arterial wall in order to accommodate the physiological cyclic deformation. In aortic media, elastin forms concentric layers of elastic lamellae, within which the elastin fibers interweave into an interconnected network.

Motived by tissue structure, constitutive models of arterial wall incorporating experimentally measured structural information have been broadly studied. However, continuum mechanics based constitutive models lack fiber level geometric realism and often rely on affine deformation assumption [1]. Discrete fiber network (DFN) models have been developed to overcome the aforementioned limitations as well as to capture the local microstructural kinematics of fibrous tissue [2]. In DFN models, inter-fiber crosslinking is modeled by the intersections of two segments. Usually, these intersections were treated as pin joints [3].

In this study, a DFN model of elastin network in the arterial wall was developed based on multiphoton microscopy measured geometric features to study the contribution of inter-fiber crosslinking to ECM mechanics and fiber kinematics. Multiphoton microscopy was performed to capture the in-plane distributed cross-linked elastic fiber network within the elastic lamellae. The inter-fiber crosslinks were assumed to have a rotational stiffness that varies from zero (pinned joint) to infinity (welded joint). Finite element simulations of DFN under equi- and nonequi- biaxial stretch were performed in ABAQUS. Tissue-level stress-stretch behavior and fiber-level deformation was studied in order to understand the role of inter-fiber crosslinking properties in the response of elastin network at multiple scales.

METHODS

Sample preparation

Porcine thoracic aortas (12-24 month old) were harvested from a local abattoir and transported to laboratory on ice. Samples of approximately 20×20 mm square were cut with one edge parallel to the longitudinal direction and the other edge parallel to the circumferential direction of the artery. Purified elastin was obtained using a cyanogen bromide (CNBr) treatment to remove cells, collagen and other ECM components. Elastin samples were placed in 1× phosphate buffered saline (PBS) for further mechanical testing and imaging studies.

Mechanical testing

Equi- and nonequi-biaxial tensile tests were performed on a biaxial tensile testing device to characterize the mechanical properties of elastin network (n=3). After preconditioning, samples were subjected to eight cycles of biaxial stretch up to 1.12 with λ_l: λ_c = 1.12:1.12, 1.06:1.12, and 1.12:1.06, where λ_l and λ_c refers to stretch in the longitudinal and circumferential directions, respectively.

Multiphoton microscopy

A multiphoton microscope system (Carl Zeiss LSM 710 NLO Microscope system) with a tunable femtosecond IR pulse laser (810 nm) was used to generate two-photon excited fluorescence (2PEF) from elastin (525/45 nm). The laser scanning system was coupled with an upright microscope with a 20× water immersion objective lens for imaging acquisition (Fig. 1A). Image processing was performed in FIJI (http:/Fiji.sc/Fiji, Ashburn,VA) to obtain areal density (Fig. 1B). The fiber diameter was measured in ImageJ [4]. Fiber orientation distribution was obtained using two dimensional fast Fourier transform (2-D FFT) analysis (with the Directionality plug-in). Fiber orientation

distribution function was averaged through the thickness and used to guide the DFN generation.

Network generation

A DFN model was generated by randomly placing line segments into the given domain following the obtained orientation distribution until the desired fiber areal fraction was reached. Intersections of two segments were treated as crosslinks. Dangling ends of line segments projecting beyond the crosslinks were removed. Periodic boundary conditions were prescribed so that the DFN is continuous when tiled up in both horizontal and vertical directions (Fig. 1C).

Finite element modeling

Finite element simulations were performed in ABAQUS 6.14 (Dassault Systemes, Waltham, MA). A single layer of elastic lamella with inter-lamellar spacing was chosen to be the representative volume element (RVE). The thickness of elastic lamella is set to be the diameter of elastin fiber, while the inter-lamellar spacing was measured from cross-sectional images of elastin network to be $10\mu m$. Since the structure has two planes of symmetry, only one quarter (1mm × 1mm) of the sample was modeled [5]. The displacement of each boundary point was prescribed according to experimental settings to impose displacement boundary condition. The applied load is computed as the sum of the reaction forces at the corresponding boundary. Cauchy stresses were calculated by assuming plane stress and incompressibility. Timoshenko (shear flexible) beams elements B21H was selected considering the length to diameter ratio of the elastin fibers [5]. Fiber intersections were modeled by connecter elements with rotational stiffness changing from freely rotating to welding. The fiber diameter was set to be 3.5 μm for all the fibers. The response of elastin fibers are modeled using an entropy-based freely-jointed chain model [6]. Material parameters in the finite element model were varied to fit the tissue-level stress vs. stretch results from the DFN mode to experimental data.

RESULTS

The DFN model well recapitulated the anisotropic behavior of elastin network under equi-biaxial loading (Fig. 2A) ($r^2 = 0.99$). The model with the same material parameters was then used to predict the stress-stretch behavior of elastin network under nonequi-biaxial stretch with a good agreement with experimental data ($r^2 = 0.98$) (Fig. 2B).

To study the effect of inter-fiber crosslinking properties on tissue level behavior, we plotted the stress-stretch curves of the DFN with free rotating (pin) and welded (weld) crosslinks under equi- and nonequi-biaxial stretch in Figure 2. Changing the fiber intersection properties has little effect on the equi-biaxial stress-stretch behavior (Figure 2. A), while the model with pin joints performs slightly better in predicting nonequi-biaxial stretch. Overall, the influence of inter-fiber properties on the tissue-level response is rather small.

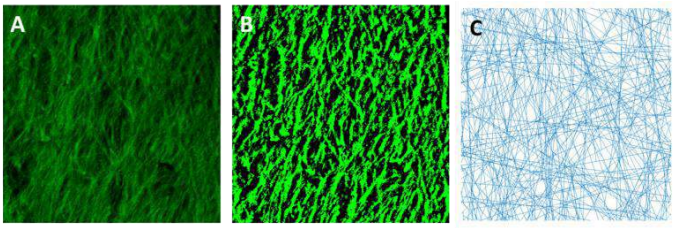

Figure 1: (A) Elastin network from multiphoton microscopy. (B) Binary image using the Otsu's method [4]. (C) DFN used for finite element simulation.

To further examine the effect of inter-fiber intersection properties on fiber-level deformation, we computed the stretch of each fiber segment with pinned and welded joints under tissue-level biaxial loading. Our findings revealed that under nonequi-biaxial stretch, the intersection properties have the most obvious effect on fiber stretch distribution. Histogram plot of fiber stretch distribution with pin joint shows two peaks that are aligned with the tissue-level stretch (1.06 and 1.12) applied at the boundary (Fig. 3A). The fiber stretch distribution of the DFN with welded joint, however, shows a single peak at a stretch value that is between 1.06 and 1.12 (Fig. 3B).

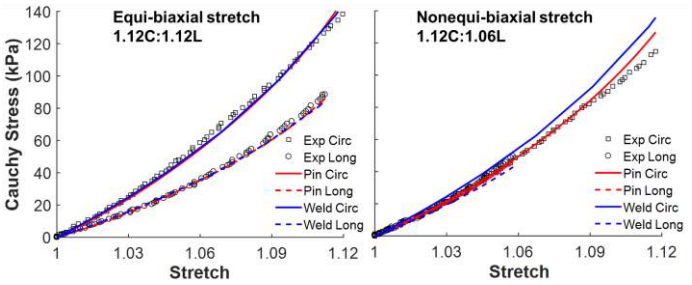

Figure 2: Comparison of the elastin stress-stretch response from simulation using the DFN model and experimental data under equi-biaxial (left) and nonequi-biaxial (right) loading.

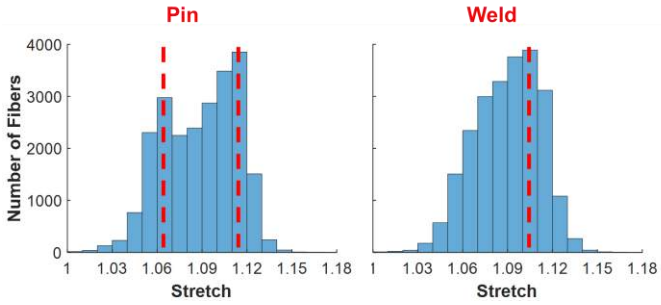

Figure 3: Fiber-level stretch distribution while pinned and welded intersection properties were assumed in the DFN model. The elastin network was subjected to nonequi-biaxial stretching.

DISCUSSION

Here we created a DFN model of arterial elastin that resembles the ECM structural properties (fiber orientation, fiber diameter, and areal density) as well as inter-fiber crosslinking. The model captures well the anisotropic and hyperelastic stress-stretch response of elastin network, and shows good fitting and predicting capabilities of elastin network under equi- and nonequi-biaxial loading conditions.

One of the main advantages of the DFN model is that it allows us to study the microstructural kinematics of fibrous tissue at large deformation. The effect of inter-fiber crosslinking properties on ECM network mechanics was studied by assuming pinned and welded intersections. Our results show that the inter-fiber crosslinking properties have an effect on fiber-level deformation. However, the tissue-level stress-stretch response remains similar despite the difference in fiber-level responses. This suggests that rotational stiffness of the crosslinks plays an important role in local fiber-level responses in the ECM network. Future work is underway to examine fiber reorientation with different inter-fiber crosslinking properties under nonequi-biaixal loading.

REFERENCES

[1] Holzapfel, G. A et al., *J Biomech Eng*, 126(2), 264-275, 2004
[2] Thunes, J. R et al., *J Biomechs*, 49(9), 1562-1569, 2016
[3] Mauri, A et al., *J Mech Behav of Biomed Mater*, 58, 45–56, 2016
[4] D'Amore, A et al., *Biomaterials*, 31(20), 5345-5354, 2010
[5] Amore AD et al., *J Mech Behav Biomed Mater* 39:146–161, 2014
[6] Kuhn W. & Grün F., *Colloid Polym Sci* 101(3):248–271, 1946

SB³C2019
Summer Biomechanics, Bioengineering and Biotransport Conference
June 25 -28, Seven Springs, PA, USA

IN VIVO LAMIN A/C DEFINICENCY MAINTAINS BULK NUCLEAR SHAPE AND STIFFNESS, BUT LEADS TO ABROGATED INTRANUCLEAR MECHANICS AND CHROMATIN ORGANIZATION

Soham Ghosh (1), Adrienne K. Scott (1), Jessica Kelly (1), Benjamin Seelbinder (1), Xin Xu (1), Stephanie E. Schneider (1), Corey P. Neu (1)

(1) Department of Mechanical Engineering
University of Colorado Boulder
Boulder, Colorado, USA

INTRODUCTION

The protein Lamin A/C in nuclear lamina forms a mesh-like structure that is thought to provide mechanical integrity and support the geometric shape of the cell nucleus. Abnormal expression or lack of Lamin A/C leads to a large class of diseases termed laminopathies, which affect mechanically stiff tissues [1]. The mechanical role of Lamin A/C is mostly elucidated through *in vitro* single cell experiments that indicate a compromised Lamin A/C leads to abnormal nuclear shape and increased strain transfer to the nucleus. However, the role of Lamin A/C *in vivo* is largely unknown. We investigated the nuclear shape and chromatin organization in normal and Lamin A/C knockout mice using intact (load- and non-load-bearing) tissues. Further, we performed *in vivo* multiscale strain measurements of skeletal muscle at tissue and intranuclear scales to understand the functional relevance of strain patterns and transfer.

METHODS

Animals: All animal experiments were performed under IACUC approved protocols. B6129S1(Cg)-*Lmna*^{tm1Stw}/BkknJ mice were purchased from Jackson Laboratory (Bar Harbor, Maine).

Visualization of nuclear shape and chromatin organization: Fibroblasts were maintained on tissue culture dish using a protrusion culture from mouse skin tissue. Skin, skeletal muscle (SM), heart, lung, and brain were collected from the euthanized animals, and were then fixed, sliced, stained (DAPI) and imaged by confocal microscopy (Nikon Eclipse Ti A1R). Skewness of the chromatin intensity distribution was calculated using a custom MATLAB code to quantify the chromatin segregation (n=3 animals, 20 nuclei/sample).

Multiscale spatial mechanics: For *in vivo* tissue and nuclear deformation measurement, we applied a neuromuscular stimulation on live mice to image and subsequently quantified the strain in skeletal muscle tissue and nucleus [2] (n=6 animals, 18 nuclei/sample).

Elastic property of tissue: Skeletal muscle was harvested from freshly euthanized mice (n=4). Elasticity of tissue was measured using atomic force microscopy (Keysight 5500 AFM System, Santa Rosa, CA, USA) using a 5 µm spherical glass tip. Further, a Hertz contact model was used to quantify the Young's modulus.

Statistics: Multifactorial ANOVA was used to test differences in sample populations. *p-value of <0.01 represents statistically significant difference in all cases.

RESULTS

Skin fibroblast nuclei showed characteristic abnormal (rough, blebbed) nuclear periphery in Lamin A/C knockout mice when plated on tissue culture plastic (TCP), but maintained the normal nuclear shape in intact tissue (Figure 1). Moreover, chromatin segregation

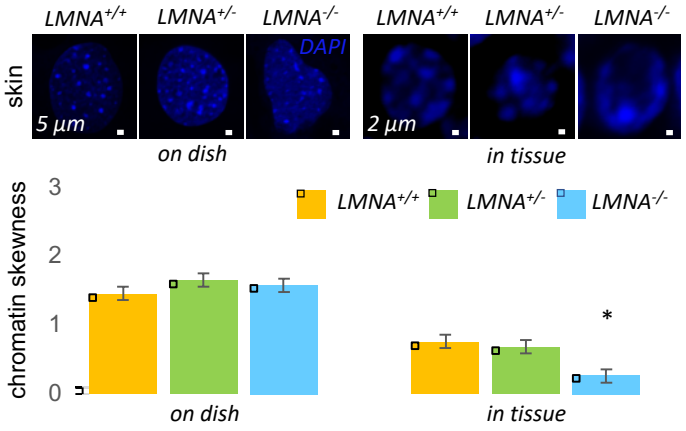

Figure 1: Lamin A/C deficiency compromises the nuclear shape in cells cultured on tissue culture plastic (TCP), but not inside intact tissue. Intranuclear chromatin architecture is not affected by Lamin A/C deficiency on TCP, but is compromised inside intact tissue.

was similar in all cases of culture on TCP, whereas in intact tissue Lamin A/C knockout cells displayed a diffuse chromatin architecture characterized by lower chromatin segregation. Besides skin, diffuse chromatin architecture in Lamin A/C knockout nuclei was observed in other relatively stiff tissues such as SM and heart (Figure 2), but not in relatively soft tissues such as brain and lung.

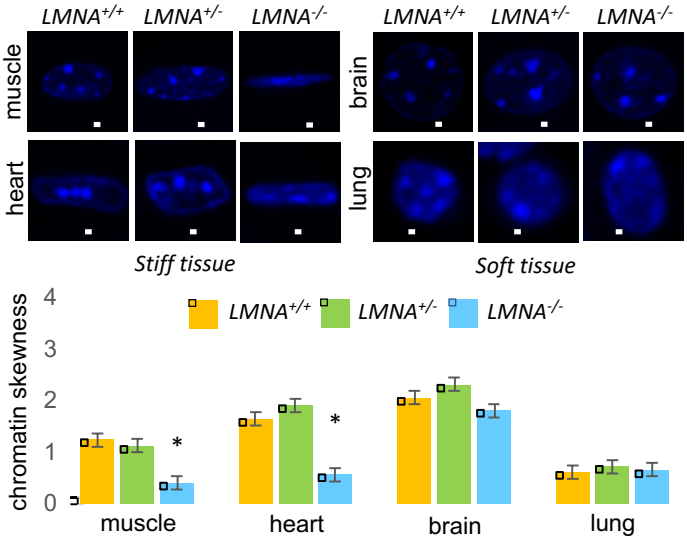

Figure 2: In stiff tissue, such as skeletal muscle and heart, intranuclear chromatin architecture is altered by Lamin A/C deficiency. Chromatin architecture is not affected by Lamin A/C deficiency in soft tissue such as brain and lung. Scale bar: 5 μm in all images.

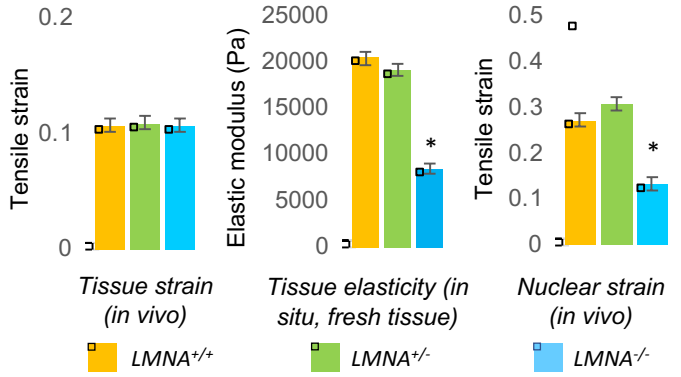

Figure 3: Multiscale strain measurement *in vivo* in murine skeletal muscle tissue and nucleus reveals that for the same tissue strain, the nuclear strain is almost half in Lamin A/C deficient mice. Elastic modulus of skeletal muscle is also nearly half in Lamin A/C deficient mice.

Intranuclear strain maps (Figure 4) showed that in wild type and Lamin A/C hemizygote mice the heterochromatin (dense chromatin region) mostly carries the tensile strain burden while the euchromatin (less dense region) carries the compressive strain burden of nuclei. In Lamin A/C knockout mice, the euchromatin carries a significantly higher tensile strain burden in nuclei.

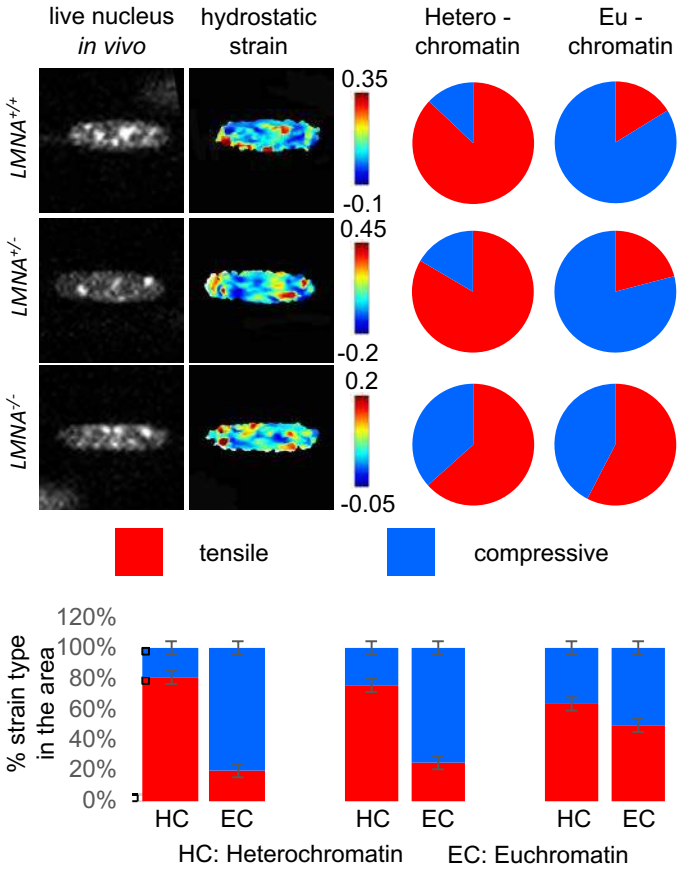

Figure 4: Intranuclear strain pattern reveal a compromised intranuclear strain distribution caused by Lamin A/C deficiency.

DISCUSSION

Nuclear shape on dish is compromised by Lamin A/C deficiency as per the findings of other groups [3], but in intact tissue it is maintained irrespective of the tissue stiffness. Our findings show that bulk nuclear mechanics is not affected by the Lamin A/C deficiency, whereas the intranuclear mechanics in SM and chromatin architecture are compromised in stiff tissues; which are affected in laminopathies. A simple scaling analysis using the strain in the nucleus and tissue (Figure 3), and estimated stresses (not shown) reveals that *in vivo* bulk elastic modulus of the nucleus is similar in all mice types, i.e. $E_{LMNA^{+/+}} \sim E_{LMNA^{+/-}} \sim E_{LMNA^{-/-}}$ (with E as the elastic modulus of the nucleus). This study indicates that *in vivo* the nuclear shape is mostly maintained by three-dimensional tissue architecture and Lamin A/C has deeper roles of maintaining chromatin architecture in a mechanically-dependent way, possibly through epigenetic mechanisms [4].

ACKNOWLEDGEMENTS

NIH R01 AR063712, NIH R21 AR066230, NSF CAREER 1349735

REFERENCES

[1] Isermann, P et al., Curr Biol, 23(24): R1113-R1121, 2013.
[2] Ghosh, S et al., ACS Biomater Sci Eng, 3(11): 2798-2805, 2017
[3] Kim, JK et al., Nat Comm, 8(2123): 1-13, 2017
[4] Stephens, AD et al., bioRxiv, 2018

SB^{3}C2019
Summer Biomechanics, Bioengineering and Biotransport Conference
June 25 -28, Seven Springs, PA, USA

TUNABLE DNA ORIGAMI NANOCALIPERS CAPABLE OF APPLYING FORCES TO BIOMOLECULES

Jenny Le (1), Kyle A. Crocker (2), Michael A. Darcy (2), Michael G. Poirier (1,2), Ralf Bundschuh (1,2), Carlos E. Castro (1,3)

(1) Biophysics Graduate Program
The Ohio State University
Columbus, OH, USA

(2) Department of Physics
The Ohio State University
Columbus, OH, USA

(3) Department of Mechanical and Aerospace Engineering
The Ohio State University
Columbus, OH, USA

INTRODUCTION

DNA origami nanostructures have strong potential for biophysical experiments because they have precisely controlled shape, tunable motion, and mechanical properties, and can be functionalized with a number of biomolecules[1-2]. Potential biophysical applications include probing molecular structure and forces, particularly on the nanoscale. Current biophysical methods have limitations for nanoscale measurements such as challenges with determining site-specific deformations, in addition to being challenging and expensive. Dynamic DNA origami can address such challenges by providing versatile devices to accommodate shape, conformational changes, and force response of biomolecules on the 10-100nm length scale. The major goal of this work is to leverage DNA origami to develop tools to study biophysical properties of the biomolecular complexes. We previously demonstrated the use of DNA nanocalipers to probe the structure and stability of nucleosomes[3], which are the fundamental packing unit of genomic DNA in cells. Here we focus on enhancing the function of DNA nanocalipers to apply tensile and compressive forces to incorporated samples. In particular, we demonstrate our ability to apply compressive forces by forcing a DNA sample into highly bent states.

METHODS

Nanocaliper Design and fabrication. The nanocaliper was designed in using the software cadnano[4] based on an 8064 nt single-stranded DNA (ssDNA) scaffold derived from the M13MP18 bacteriophage virus prepared in our laboratory[5]. The nanocalipers were folded as previously described[3]. Briefly, folding reactions contained 20 nM of scaffold and 200 nM of each staple in a solution containing ddH_2O, 5 mM Tris, 5 mM NaCl, 1 mM EDTA, and 18 mM $MgCl_2$, pH 8.0. This folding reaction was subjected to a thermal annealing similar to a previously published method[3]. Specifically, the thermal ramp consisted of rapidly heating the solution to 70 ^oC for 15 minutes, cooling down to a ramp from 63-57 ^oC for 3 hours per degree, and cooling it for 30 minutes at 4 ^oC. Folding results were characterized via agarose gel electrophoresis as previously described, and bands of well-folded structures were also characterized by transmission electron microscopy (TEM)[3, 5].

Nanocaliper Force Application. Internal strut connections can be engaged or disengaged through strand displacement[6] reactions to open or close the calipers. For displacement reactions, displacement strands for the opening actuation were added to gel-purified nanocalipers such that the staples were in 200x excess per strut and incubated for 18hrs at 37°C followed TEM imaging to verify opening. Then, displacement staples for the closing actuation were introduced to open samples in 400x excess per strut, incubated for 6hrs at 37^oC, and subjected to TEM imaging. To verify force application, a 249 bp dsDNA sample (~80 nm long) was incorporated between the ends of the arms via a biotin-streptavidin interaction. Open nanocalipers were incubated with a 2-fold excess of the dsDNA sample for 30 min at 37 °C at 250 rpm. The dsDNA-nanocaliper assemblies were then subjected to the closing actuation and prepared for TEM imaging.

RESULTS

Nanocaliper Design and Characterization. The nanocaliper design (**Fig. 1A**) is comprised of 2 arms made up of 20-helix bundles organized in an 8x3 square lattice cross section with 4 internal helices removed from the middle layer. The arms measure ~70 nm in length, ~20 nm in width, and ~7.5 nm in height. The nanocaliper arms are connected along one edge by 8 ssDNA scaffold loops, alternating between short 2nt connections to define the hinge axis of rotation and long 70 nt connections that mediate caliper mechanical properties.

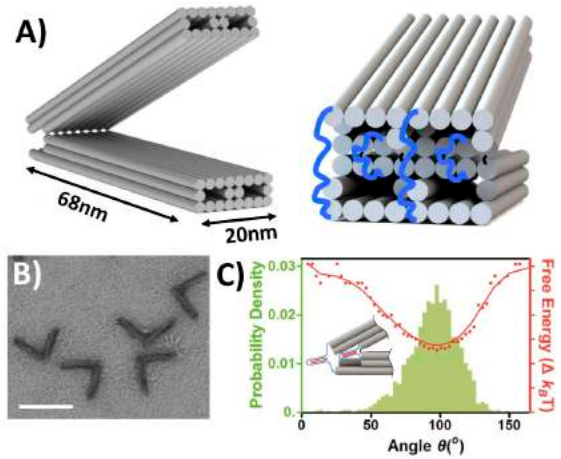

Figure 1: A) Nanocaliper design showing ssDNA linkers on the back of the hinge (blue lines) that mediate mechanical properties. B) Representative TEM images of nanocalipers. Scale bar = 100nm. C) Probability distribution and free energy landscape of nanocalipers with the linker design shown in the inset.

Gel-purified nanocalipers were imaged via TEM to confirm well-folded structures and to analyze the angular conformations (**Fig. 1B-C**). We tested a variety of nanocaliper designs where the 70 nt connections were varied from completely single-stranded to partially base-paired in a number of ways (data not shown). For the specific nanocaliper design used in this work, the 70 nt connections were pinched into a compact state (**Fig. 1C**, inset) to bias the calipers towards open angles. We analyzed at ~1500 nanocalipers over triplicate experiments. The nanocaliper exhibited a mean angle of 95° ± 2°. The uncertainty was determined by subdividing the distribution into three random subgroups, and the calculating the standard deviation of the means of those three groups. **Figure 1C** shows the probability distribution and corresponding free energy landscape, calculated assuming a Boltzmann Distribution[3].

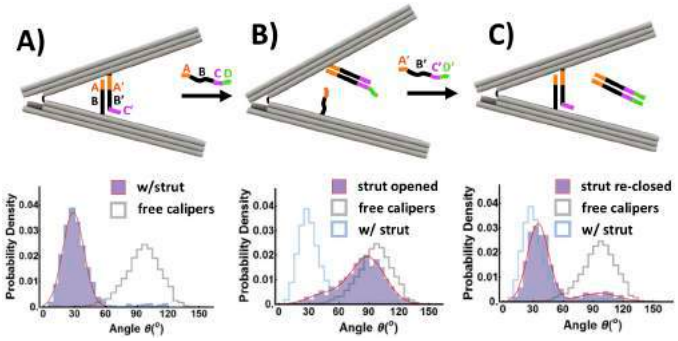

Figure 2: Nanocaliper (A) initially closed via struts, (B) actuated to open, and (C) actuated to re-close.

Nanocaliper Actuation and Force Application. We modified the nanocalipers to include 4 pairs of complementary overhangs protruding from the internal faces of the arms to form a strut that latches the arms at a specific angle. We incorporated a 19bp strut located 12nm from the vertex. The resulting probability distribution of (**Fig. 2B,** left) exhibited a mean angle of 32.7° and standard deviation of 17.0°. The internal struts were designed with a 5nt toehold to facilitate dissociation of the strut via strand displacement. Introducing the displacement strands for the open actuation resulted in a shift back to the open state (**Fig. 2B**). The slight deviation may be due to not all struts being fully displaced; nevertheless the vast majority of calipers clearly open. We further demonstrated the ability to re-close the caliper through a second strand displacement reaction illustrated in **Fig. 2C**. These results illustrate our ability to toggle from closed to open and from opened to closed, which would translate to tensile and compressive forces, respectively, when a sample is incorporated between the arms.

Finally, to verify our ability to apply compressive forces that influence the conformation of a biomolecule, we incorporated a 249 bp dsDNA sample across the ends of the arms of open calipers followed by actuating the closing nanocalipers (i.e. compression of the dsDNA sample). **Fig. 3** illustrates the closed nanocalipers with the incorporated dsDNA sample in highly bent states, which we do not observe for open nanocalipers or free the free dsDNA sample, which confirms our ability to influence the biomolecule conformation through a compressive force.

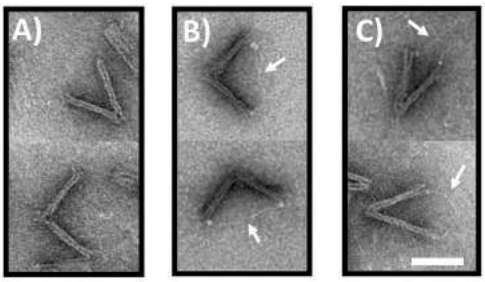

Figure 3: TEM images of (A) free nanocaliper with no sample, (B) open nanocalipers with 249bp dsDNA sample, and (C) closed nanocalipers that induce bending in 249bp dsDNA sample. The white arrows highlight the position of dsDNA. Scale bar = 50nm.

DISCUSSION

DNA self-assembly allows for the development of nanodevices with controlled shape and mechanical properties that can be actuated to reconfigure. Here we leverage these features to engineer a nanocaliper that can be toggled between an open and fixed angle state and can incorporate a biomolecule sample between the arms. We demonstrate the ability to apply compressive forces to a dsDNA sample, which forces the sample into low probability highly bent conformations. This ability to apply compressive forces opens new possibilities in force spectroscopy, since applying compression to individual biomolecules is highly challenging with other force spectroscopy methods such as optical tweezer, magnetic tweezers, or atomic force microscopy[7]. Our next steps will pursue improved quantification of applied forces and implementation of this calipers to study nucleosomes and chromatin under applied forces.

ACKNOWLEDGEMENTS

We thank the Castro, Poirier, and Bundschuh Labs for useful feedback. This work was supported by the National Science Foudantion through award #1715321 to MGP and CEC and award #1719316 to RB.

REFERENCES

1. Kearney, C. J., et al., *Advanced materials* **2016,** *28* (27), 5509-5524.
2. Rothemund, P. W., *Nature* **2006,** *440* (7082), 297-302.
3. Le, J. V., et al., *ACS nano* **2016,** *10* (7), 7073-7084.
4. Douglas, S. M., et al., *Nucleic acids research* **2009,** *37* (15), 5001-5006.
5. Castro, C. E., et al., *Nature methods* **2011,** *8* (3), 221-229.
6. Yurke, B., et al., *Nature* **2000,** *406* (6796), 605-608.
7. Neuman, K. C.; Nagy, A., *Nature methods* **2008,** *5* (6), 491-505.

3D MICROSTRUCTURE OF TENDON REVEALS HELICALLY WRAPPED FIBRILS WITH THE POTENTIAL TO MEDIATE MECHANICAL LOAD TRANSFER BY FRICTION

Babak N. Safa (1,2), John M. Peloquin (1), Jessica R. Natriello (1), Jeffrey L. Caplan (3), and Dawn M. Elliott (1)

(1) Department of Biomedical Engineering
University of Delaware
Newark, DE, USA

(2) Department of Mechanical Engineering
University of Delaware
Newark, DE, USA

(3) Delaware Biotechnology Institute,
University of Delaware
Newark, DE, USA

INTRODUCTION

The well-known hierarchical structure of tendon governs its mechanical function. However, despite decades of imaging and mechanical testing, the 3D microstructure and tendon load transfer mechanisms are still not fully known. Recent serial block-face scanning electron microscopy (SBF-SEM) has visualized three-dimensional microstructure in tail tendons [1-2] but not yet quantified the structure. Further, several load transfer mechanisms between fibrils have been suggested, including interfibrillar matrix and shear lag [3-4]. Based on the observed helical wrapping of tendon fibrils in this study, we hypothesized that these helical structures can induce frictional contact between fibrils, allowing for mechanical load transfer without a mediating matrix. The objective of this study was to quantify the 3D microstructure of rat tail tendon using SBF-SEM imaging and to study the mechanics of these helical structures via finite element (FE) analysis. The microstructure and load transfer at this scale are particularly important because the cells and the surrounding collagen fibrils interact, and these mechanical interactions may have important physiological contributions.

METHODS

A fascicle from a 3 month old male Sprague-Dawley rat was dissected and processed for SEM imaging [5]. The transverse cross-section was scanned using Apreo VolumeScope (Thermofisher Scientific) and at the end of each scan, a 200 nm layer of the block's face was removed by means of a mechanical slicer and the scanning was repeated. We scanned 432 slices that covered a total volume of (20.27 µm × 16.74 µm × 86.20 µm), where the 86.20 µm is along the fascicle's axial direction and the in-plane resolution was 10 nm/pixel.

The SBF-SEM technique is hindered by large datasets and difficult segmentation compared to 2D. Thus, for this study, a single fascicle was manually segmented in 3D (Seg3D, seg3d.org), (n=42 fibrils that spanned the entire scan length) (Fig. 1A). We confirmed that the manually segmented fibrils represented the overall population by comparing the cumulative distribution function of the fibril diameter from the 3D manually segmented fibrils to 2D automatically segmented full population for several distributed scans (not shown). Approximately half of the segmented fibrils (n=21) were in helical groups; for these fibrils we calculated the pitch (λ) by diving the scan length (86.20 µm) with the number of turns in the helices.

To study load transfer in helically wrapping fibrils, we developed a three-dimensional FE model of a pair of helical fibrils in contact (diameter = 200 nm, helix pitch = 40 µm) in FEBio (v2.8 febio.org). The model included three full fibril turns. The boundary condition was set so that each fibril had one free-end and the other end was either anchored or displaced in the axial direction for 8% of the length.

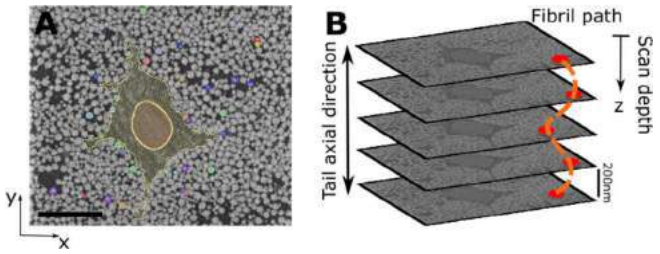

Figure 1: (A) Representative SEM image and in-plane segmentation (scale bar = 5 um), (B) SBF-SEM imaging process showing sequential stacks of images along the tendon length.

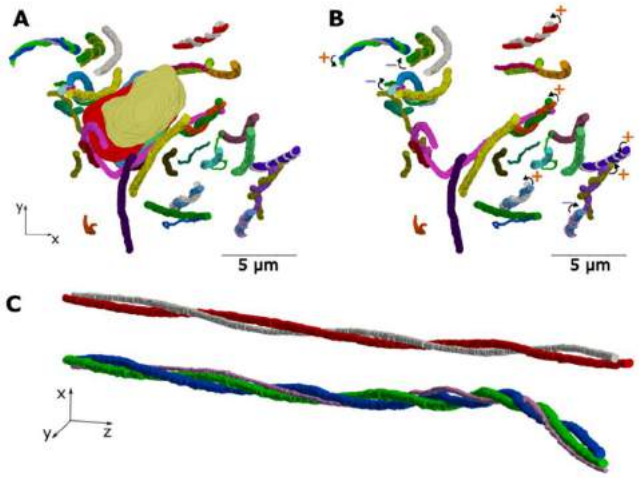

Figure 2: Many helical groups were observed in the axial view of the fibrils that are evident in the figures (A) with and (B) without the cell nuclei that were both left (-) and right (+) handed. (C) Examples of the groups of helically wrapping fibrils.

A compressible neo-Hookean constitutive relation was used with fibril properties of Young's modulus ($E = 1\text{GPa}$) and Poisson's ratio ($\nu = 0.2$). We used a frictional contact based on penalty methods in FEBio [6]. We studied three friction coefficient cases for $\mu = 0,\ 0.5,$ and 2. For analysis, we calculated the axial stress (σ) and axial normalized displacement ($\overline{u}$) along the fibrils' length, defined as

$$\overline{u}(z) = \frac{1}{\lambda}\left(u(z) - u\left(\frac{L}{2}\right)\right). \qquad (1)$$

Where, $u(z)$ is the axial displacement for distance along the fibril z-axis.

RESULTS

We observed a complex fibrillar structure, where several fibrils locally wrapped around each other (Fig. 2). These groups contained two, three, or more fibrils with both left and right-handed helical configurations (Fig. 2). Half of the fibrils (21 out of 42) of the segmented fibrils were in helical groups, although the sampling was not purely random. Of these helical fibrils, 13 fibrils had a right-handed twist and 7 were left-handed (Fig. 2B). These fibrils made an average of 2.2 ± 1.4 turns around each other along the scan-length (Fig. 2C), that also results in an overall ~39 ± 18 μm helical pitch.

The FE simulations indicated that the frictional contact can mediate load transfer and it was sensitive to frictional coefficient (Fig. 3). The fibril stress was zero with no friction ($\mu = 0$, Fig. 3B) and it increased with higher μ (Fig. 3C and D). Similarly, for the fibril deformation in the zero-friction case, there was no axial deformation, hence the fibrils slide freely (Fig. 3E). When friction is increased, the induced stress and deformation also increased, with zero-derivative plateaus at the free ends indicating no strain (which confirms the imposed stress-free boundary condition) (Fig. 3F and G).

DISCUSSION

This study used a novel serial block-face scanning electron microscopy (SBF-SEM) to demonstrate that approximately half of the segmented tendon fibrils wrapped around each other in helical groups (although additional analyses and samples are needed to confirm the ratio). Moreover, we showed that the helical mechanical contact can contribute to interfibrillar load transfer, as an additional load transfer mechanism advancing our knowledge about the structure-mechanics relationships at this length scale.

The existence of helical fibrils was previously reported, which were suggested to be left-handed [7]; however, our findings showed a

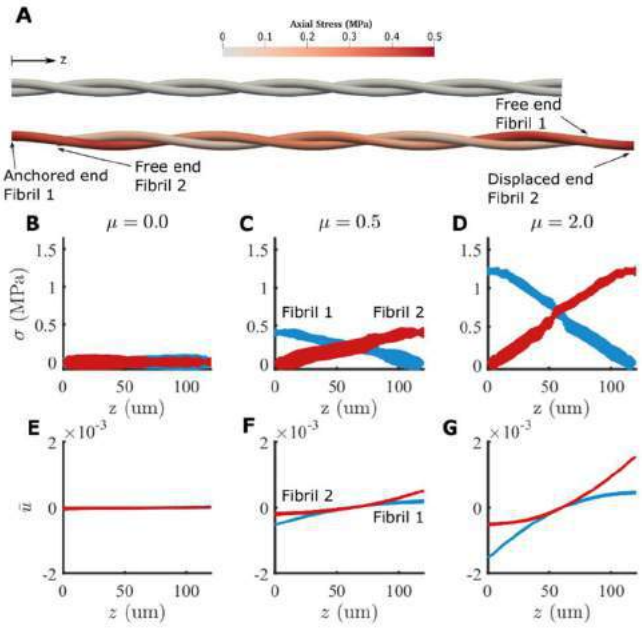

Figure 3: FE simulation of the fibrils with helical wrapping showing axial stress in (A) the undeformed (top), and deformed (bottom) ($\mu = 0.5$). With no friction ($\mu = 0$) there was no (B) stress or (E) normalized deformation ($\overline{u}$). As the frictional coefficient increases, the stress and the deformation increases for $\mu = 0.5$ (C,F) and $\mu = 2$ (D,G).

similar number of the left-handed and right-handed helical fibrils (Fig. 2B). The helical structures have been used as an explanation for the macro-scale mechanical behavior of tendon, in particular for the low stiffness of tissue at small deformations and the large Poisson's ratio in tension [8-9]. According to this study, it is possible that the grouping of these fibrils can mediate load transfer by inducing frictional contact between fibrils during axial loading.

The FE simulations indicated that frictional load transfer can be induced between fibrils, without requiring connecting matrix. This was according to the assumption that the helical fibrils have an effective free boundary condition. This is in accord with the interfibrillar sliding phenomenon that is a well-documented experimental observation in tendons, which suggests that there is some form of free boundary along the fibrils that are mechanically coupled [8]. Yet, it is unclear if these effects are caused by weak areas in the fibril or tapered ends.

In conclusion, we used SBF-SEM to visualize the three-dimensional microscale tendon structure of the fibrillar network, including helically wrapped fibrils, and performed FE analysis to demonstrate the implications of helical structures as a frictional mechanisms for interfibrillar load transfer. This mechanism should be considered as another potential mechanism for interfibrillar load transfer, in addition to interfibrillar matrix and shear lag mechanisms.

ACKNOWLEDGEMENTS NIH-NIBIB R01-EB002425.

REFERENCES

[1] Kalson *et al.*, *Elife*, 4: 2015. [2] Szczesny *et al.*, *J. Orthop. Res.*, 35: 2127–2134, 2017. [3] Ahmadzadeh *et al.*, *J. Biomech.*, 46: 2497–503, 2013. [4] Szczesny *et al.*, *J. Mech. Behav. Biomed. Mater.*, 40: 325–338, 2014. [5] Starborg *et al.*, *Nat. Protoc.*, 8: 1433–1448, 2013.[6] Zimmerman *et al.*, *J. Biomech. Eng.*, 140: 081013, 2018. [7] Franchi *et al.*, *J. Anat.*, 216: 301–309, 2010. [8] Thorpe *et al.*, *Acta Biomater.*, 9: 7948–7956, 2013. [9] Reese *et al.*, *J. Biomech.*, 43: 1394–400, 2010.

SB³C2019
Summer Biomechanics, Bioengineering and Biotransport Conference
June 25 -28, Seven Springs, PA, USA

DEFORMATION CHARACTERISTICS OF THE RAT PIA-ARACHNOID COMPLEX THROUGH MULTIMODAL IMAGING

Zeynep M. Suar (1), Gloria Fabris (1), Luke Langner (1), Mehmet Kurt (1,2)

(1) Dept. of Mechanical Engineering,
Stevens Institute of Technology,
Hoboken, NJ, USA.

(2) Translational and Molecular Imaging Institute (TMII),
Mount Sinai Hospital,
New York, NY, USA.

INTRODUCTION

To better understand the onset of damage occurring in the brain upon traumatic events, it is essential to analyze how external mechanical loads propagate through the skull and meninges and down to the brain cortex. However, despite their putative role as structural dampers protecting the brain, the mechanical properties and dynamic behavior of the meningeal layers are still poorly understood [1]. Here, we characterized the deformation characteristics following a multimodal imaging technique, where we observed the local mechanical heterogeneity of rat pia-arachnoid complex (PAC) at the microscale via atomic force microscopy (AFM) indentation experiments and the deformation response of intact PAC via OCT imaging.

METHODS

Fresh tissue staining protocol: Rat brains were dissected from adult rats immediately after death. Fragments of dura mater that had not remained on the skull were removed, and the thin PAC tissue was carefully peeled under a dissecting microscope with the help of ultrafine tweezers while the brain was still immersed in PBS. All animal and tissue work was in compliance with the Institutional Animal Care And Use Committee (IACUC) regulations.

After isolation, the meningeal tissue samples were incubated with blocking solution (0.5% milk powder in PBS) for 90 min at RT. Three PBS washing steps followed (5 min, RT). The tissue was then directly incubated overnight in a 1:300 solution of primary antibody in 0.1% milk powder in PBS, including anti-collagen I and anti-vimentin. After three more washing steps, incubation with appropriate secondary ABs for 90 min at RT. The PAC was then counterstained with Hoechst nuclear stain (20 min, RT) and washed three more times in PBS (5 min, RT). The tissue samples were immediately imaged or used for microindentation thereafter while immersed in a PBS bath.

AFM protocol: Portions of rat PAC were adhered to tissue-treated glass slides following the staining protocol. AFM indentation curves were performed on different positions of PAC immersed in PBS using tipless cantilevers (k=0.25 N/m) modified by the attachment of spherical beads (R=2.5 μm). 9x9 or 16x16 force maps at different indentation velocity (i.e. loading rate) were acquired. Contact points of indentation curves were found by combining Ratio of Variances [2] and Double Alarm [3] methods reported in literature. Force relaxation curves were obtained setting the AFM in height-clamp mode where the indentation to sample is kept constant while observing the variation of the reaction force on the cantilever. All measurements were performed within 48 hours of the animal's death. A hyperelastic material model (Ogden) was used to fit the indentation portion of the curves [4]. To avoid the large indentation regime, only the first 5 mm of the indentation curves were analyzed. The dwell curves were fit by a two term viscoelastic time relaxation model (Maxwell) [5]. Immunofluorescence stainings for confocal imaging were performed following a standard tissue staining protocol optimized for collagen-I and vimentin recognition.

OCT protocol: To determine the best scanning protocol, preliminary test scans were performed on fixed rat brains. We used the following scanning settings for imaging: 800 A-scans per B-Scan, 200 B-scans, and 3 volume repetitions over a field of view of 3 mm by 3 mm by 1.2 mm. Isolated rat brains with intact PAC were first immersed in PBS, then placed in a petri-dish and hydrated with PBS regularly. After imaging intact PAC with OCT, different levels of weight were placed on the brain and fixation were performed with 10% formalin. Same scanning settings were used to image the PAC after deformation with different loading settings.

RESULTS

Tissue stiffness probed at the microscale revealed large local heterogeneities, with a distribution mean of 4.7 ± 2.8 kPa. In particular, the Young's modulus (E) of

vascularized tissue resulted significantly higher than that of non-vascularized PAC (see Fig.1B and C and Fig.2A). We therefore hypothesize that the microanatomy of tissue must cause differential load propagation properties in different regions of the pia-arachnoid complex.

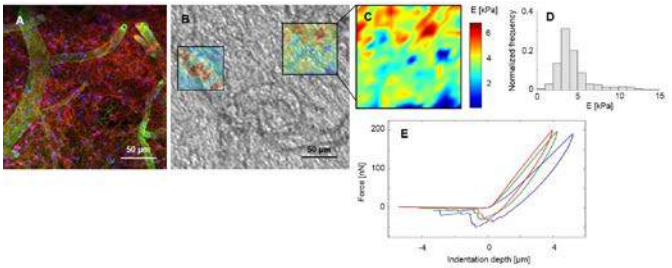

Fig1: A. Confocal imaging of peeled-off PAC. (Green: collagen-I; red: vimentin; blue: nuclei) B. Phase contrast imaging of a peeled-off PAC used during AFM indentation experiments. C. Force map showing local stiffness values and D. Young's modulus distribution as calculated from fitting all force-indentation (F-d) curves. E. Three examples of F-d curves.

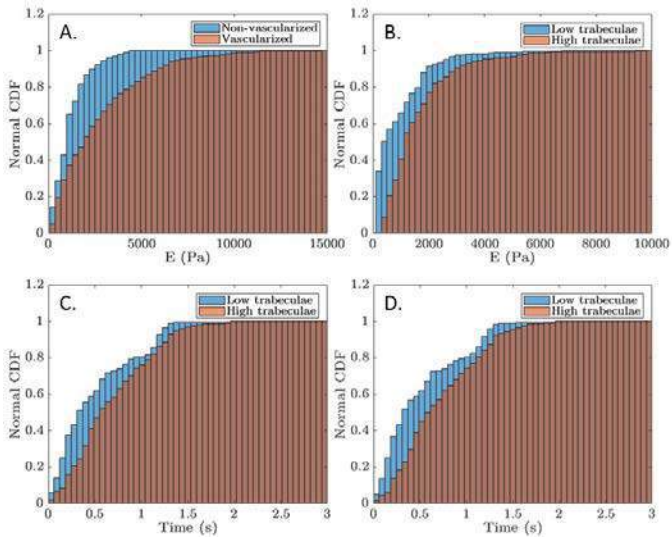

Fig2: A. Non-vascularized vs. vascularized PAC stiffness values. B. Low density vs. high density trabecular PAC stiffness values. C. Low density vs. high density trabecular PAC first relaxation term. D. Low density vs. high density trabecular PAC second relaxation term.

Higher trabecular density area showed higher stiffness values and longer relaxation times (see Fig.2), supporting the hypothesis that the trabecular structure of the PAC is an enclosing structure around the brain with higher stiffness and damping values, possibly contributing to protect the brain against impacts.

The OCT images were obtained for intact PAC on the brain and peeled-off PAC (Fig.3). The observation of trabecular structure suggests that the PAC preserve its form after removing the dura and peeling-off the PAC.

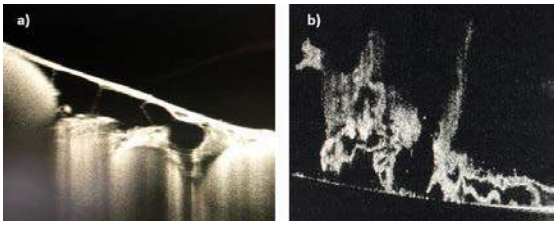

Fig3: A. Intact rat PAC anatomy observed via OCT. B. Peeled off PAC observed via OCT.

DISCUSSION

It is known that mammalian PAC displays a high regional variability both in arachnoid trabeculae density and subarachnoid vasculature distribution [6,7]. Our data highlight strong local variations in the mechanical response of this tissue, possibly relating to the differences in local vulnerability to TBI reported by [8]. Future work will attempt to better quantify the most relevant microanatomical parameters (e.g., cellular density, local trabecular orientations) and correlate them with the deformation and recovery response of tissue via coupled AFM-confocal microscopy experiments and OCT imaging.

Exploring the mechanics of this peculiar bridging structure would also be highly relevant for a number of computational applications. From a biomechanical perspective, a popular hypothesis considers the random three-dimensional structure of the collagen sheets and pillars that make up the trabeculae as a mechanically redundant structure, capable of contributing to damping and constraining brain deformation following head rotation and movement despite the small volumetric contribution of the PAC to the intracranial space [9]. The multi-phasic (liquid, solid, ions, etc.) nature of bio-interfaces make their characterization a rather challenging task. Lack of accurate experimentally-derived material parameters characterizing the brain-skull interface is a key part in TBI research. Obtaining a comprehensive quantification of the mechanical response of the meningeal interfaces would therefore bring us one step closer to accurately modeling and understanding the nature of such a complex biomaterial.

ACKNOWLEDGEMENTS

We thank Dr. Kevin Costa (Icahn School of Medicine, Mount Sinai, NY) for AFM access. This research was supported by NSF Grant No. CMMI-1826270 and CMMI-1728186.

References:

[1] X. Jin, K.H. Yang, A.I. King, J. Biomech. 44 (2011) 467–474.
[2] N. Gavara, Sci. Rep. 6 (2016) 21267.
[3] R. BenÍtez, S. Moreno-flores, V.J. BolÓs, J.L. Toca- Herrera, Microsc. Res. Tech. 76 (n.d.) 870–876.
[4] V. Borrell, O. Marín, Nat. Neurosci. 9 (2006) 1284–1293.
[5] D.C. Lin, D.I. Shreiber, E.K. Dimitriadis, F. Horkay, Biomech. Model. Mechanobiol. 8 (2009) 345.
[6] J.A. Siegenthaler, S.J. Pleasure, Curr. Opin. Genet. Dev. 21 (2011) 249–255.
[7] G.G. Scott, B. Coats, IEEE Trans. Med. Imaging 34 (2015) 1452–1459.
[8] G.G. Scott, S.S. Margulies, B. Coats, Biomech. Model. Mechanobiol. 15 (2016) 1101–1119.
[9] M.M. Mortazavi, S.A. Quadri, M.A. Khan, A. Gustin, S.S. Suriya, T. Hassanzadeh, K.M. Fahimdanesh, F.H. Adl, S.A. Fard, M.A. Taqi, I. Armstrong, B.A. Martin, R.S. Tubbs, World Neurosurg. 111 (2018) 279–290.

SB³C2019
Summer Biomechanics, Bioengineering and Biotransport Conference
June 25 -28, Seven Springs, PA, USA

UNCERTAINTY ANALYSIS OF VASCULAR SURROGATE MODELS

Z. Jiang (1), J. Choi (2), and S. Baek (1)

(1) Mechanical Engineering,
Michigan State University,
East Lansing, MI, USA

(2) School of Mechanical Engineering,
Yonsei University,
Seoul, South Korea

INTRODUCTION

Patient-specific computational modeling of vascular mechanics is an emerging area which has developed various computational tools on individual treatment. It aids in the clinical treatment by optimizing the diagnosis and prognosis prediction, and classifying staging. In vascular modeling, however, multiscale models have become more complicated and they require long computation time, which is often not acceptable in clinical practice. Therefore, there remains a pressing need for a powerful tool to reduce the computational cost while maintaining adequate accuracy. Surrogate models (SM) are methods where computational expensive physical models are approximated by faster metamodels. Although SM is promising, it reduces the complexity of the physical system, which increases modeling uncertainty. Motivated by this challenge, we present a novel framework to minimize the uncertainty caused by SM, using multi-fidelity surrogate model (MFSM) and Gaussian process upper confidence bound (GP-UCB) regression. Furthermore, a comprehensive uncertainty analysis algorithm is designed to quantify the uncertainties associated with SM and physical model respectively. For purpose of demonstration, this framework is applied to estimate patient-specific evolution prediction of abdominal aortic aneurysms (AAA) using follow-up CT images from 26 patients.

METHODS

Given two physical models that simulate for the same vascular system, a multi-fidelity vascular surrogate model (MFVSM) using the co-Kriging approach is developed to reduce the computational cost. Among two physical models, the more expensive one which provides more accurate results is taken as the high-fidelity model (HFM) while the other is defined as low-fidelity model (LFM). In this study, both are computational growth and remodeling (G&R) models which share the same constitutive relations. The HFM treats the geometry of aorta as a three-dimensional membrane model while the LFM uses a two-dimensional axisymmetric model. Moreover, in order to simulate for patient-specific aneurysm growth, two key parameters are chosen for the calibration, whereas the other parameters are fixed as given from references [1] and [2]. The first calibrated parameter is a scalar parameter that controls the stress mediated-growth of collagen fiber, K_g, which plays an important role in determining $m^k(t)$, the mass production rate of constituent *k* at time *t* per reference area. The control equation is assumed by

$$m^k(t) = \frac{M^c(t)}{M^c(0)}\left(K_g(\boldsymbol{\sigma}^k(t) - \boldsymbol{\sigma}_h^c) + m_{basal}^k\right), \quad (1)$$

where $\boldsymbol{\sigma}^k(t)$ is the stress on fiber family k at time t, $\boldsymbol{\sigma}_h^c$ is the homeostatic stress of collagen fiber, $M^c(t)$ is mass density with respect to the reference configuration at time *t*, $M^c(0)$ is the mass density of a healthy vessel at time *0*, and m_{basal}^k is a basal rate of mass production for constituent k. The second calibrated parameter is a scalar parameter that determines the elastin damage shape called θ_2. The elastin damage function, $f(s)$, is given by,

$$f(s) = \theta_1 \exp\left(-\frac{|s-\alpha|^2}{2\theta_2^2}\right), \quad (2)$$

where *s* is the coordinate defined on the centerline, θ_1 determines the magnitude of elastin degradation, and α controls the position of aneurysm, which can be identified via patient-specific CT images.

In this study, we focus on the prediction of maximum diameter of the aorta along its center line at different time, d, which is able to provide useful information in clinical practice. Then, the simulated d at different s and t from both HFM and LFM, given as functions of multiple parameter sets of K_g and θ_2, are generated for training data in MFVSM. A hierarchical random sampling is used for choosing the

initial parameter values. Due to the expensive computation, the number of samples from HFM is limited, while a larger number of samples from cheap LFM improve the prediction. Then, given the set of inputs $\mathbf{x} = \{K_g,\ \theta_2,\ s,\ t\}^T$ and the corresponding maximum diameter d, the co-kriging method is able to model $d(\mathbf{x})$ by representing the local features of physical models by the Gaussian process [3]. Specifically, Gaussian process $Z_l(.)$ and $Z_h(.)$ represents the local features of LFM and HFM respectively. $Z_h(.)$ can be approximates by $Z_l(.)$ multiplied by a scaling factor ρ plus their difference, which is the Gaussian process $Z_d(.)$:

$$Z_h(\mathbf{x}) = \rho Z_l(\mathbf{x}) + Z_d(\mathbf{x}). \quad (3)$$

The covariance among different Gaussian process can be calculated through an optimization algorithm and the best linear unbiased prediction of the intermediate values can be interpolated.

Using the follow-up CT image dataset and the trained MFVSM, a data-fitting algorithm using the least-square method is presented to estimate the physical parameters ($K_g,\ \theta_2$) as well as their uncertainty. To reduce the estimation uncertainty (EU) of parameters due to the SM, GP-UCB, an optimal algorithm to find the global maximum, is employed to explore new samplings [4]. The GP-UCB chooses a new sample location $\mathbf{x}_t$ by providing tradeoff between exploration and exploitation:

$$\mathbf{x}_t = arg\min_{x \in D} \mu_{t-1}(\mathbf{x}) + \sqrt{\beta_t}\sigma_{t-1}(\mathbf{x}), \quad (4)$$

where μ_{t-1} is average prediction of the data-fitting error, σ_{t-1} is uncertainty of the data-fitting error. It greedily selects points $\mathbf{x}_t$ such that the data-fitting error on $\mathbf{x}_t$ should be a reasonable upper bound, so that the optimized fitting results can be iteratively obtained. Based on the optimal fitting results, predictions of different physical quantities can be obtained using either HFM or MFVSM. Moreover, to provide better aid in clinical practice, we design a systematic algorithm to analyze the prediction uncertainty. First, bootstrapping, a random resampling method, is employed to provide EU of parameters caused by HFM. Second, the prediction uncertainty (PU) caused by SM and HFM modeling are estimated, respectively.

RESULTS

A test is made to exam the method. In this test, we choose $\mathbf{x} = \{K_g,\ t\}^T$ and d is the maximum diameter of the aorta. The samplings, HFM prediction, LFM prediction and MFVSM prediction are shown in **Fig. 1**. Based on the MFVSM, an optimal fitting to a follow-up CT images from a patient and associated uncertainty are obtained and shown in **Fig.2**.

DISCUSSION

The presented method provides a validated patient-specific prediction with a low computational cost. It also enables a systematic uncertainty analysis towards the computation prediction for the first time, which is essential in aiding clinical treatment. The test shows that a limited number of physical simulations is able to provide a promising MFVSM for the prediction and uncertainty analysis (**Fig. 1**). The result of uncertainty analysis gives a reasonable range of prediction, thus improving the confidence of using patient-specific computational modeling (**Fig. 2**). Furthermore, this study utilizes all 26 patient follow-up CT images to estimate computational parameters K_g and θ_2, which cannot be obtained from experiments. The population-based parameter distribution from 26 patients can be applied to improve patient-specific simulation. For example, a more practical prior distribution of K_g and θ_2 can be utilized in Bayesian Calibration studies of aorta [5].

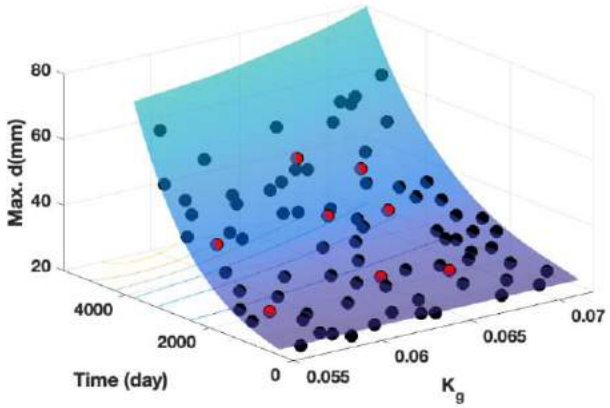

Figure 1: A plot of sampling of time and K_g and associated maximum diameter *d*. Black points show the LFM data, Red points show the HFM data and the surface shows the MFVSM predictions.

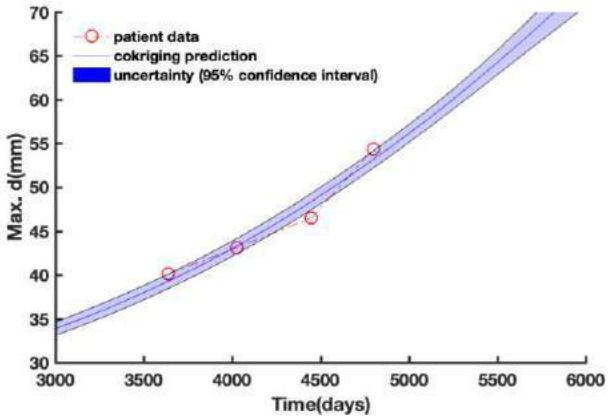

Figure 2: patient-specific optimal fitting using MFVSM and its uncertainty.

ACKNOWLEDGEMENTS

This study was supported by NIH U01 1HL135842 and R01 HL115185

REFERENCES

[1] S. Zeinali-Davarani, A. Sheidaei, and S. Baek, A finite element model of stress-mediated vascular adaptation: application to abdominal aortic aneurysms, Comput. Method in Biomech. and Biomed. Eng. 14 (2011), no. 9, 803–817.

[2] S. Seyedsalehi, L. Zhang, J. Choi, and S. Baek, Prior Distributions of Material Parameters for Bayesian Calibration of Growth and Remodeling Computational Model of Abdominal Aortic Wall, J. Biomech. Eng. 137 (2015), no.10, 101001.

[3] A.I.J. Forrester, A. Sobester, and A.J. Keane, Multi-fidelity optimization via surrogate modelling, Proceed. of the Royal Society A: Mathematical, Physical and Engineering Sciences 463 (2007), no. 2088, 3251–3269.

[4] N. Srinivas, A. Krause, S.M. Kakade, and M.W. Seeger, Information-Theoretic Regret Bounds for Gaussian Process Optimization in the Bandit Setting, IEEE Trans. on Inform. Theory 58 (2012), no. 5, 3250–3265.

[5] L. Zhang, Z. Jiang, J. Choi, C. Lim, T. Maiti, and S. Baek, Patient-specific prediction of abdominal aortic aneurysm expansion using Bayesian calibration, IEEE J. Biomed. Health Inform, accepted, 2019

EFFECT OF CALCIFICATION & FIBROUS TISSUE FEATURES ON RUPTURE RISK IN ATHEROSCLEROTIC PLAQUES

Bas Vis (1,2), Hilary Barrett (1), Astrid Moerman (1), Frank J.H. Gijsen (1), Ali C. Akyildiz (1)

(1) Dept. of Biomedical Engineering
Erasmus Medical Center
Rotterdam, the Netherlands

(2) Dept. of Biomechanical Engineering
Delft University of Technology
Delft, the Netherlands

INTRODUCTION

A major cause of myocardial infarctions and stroke events is atherosclerotic plaque rupture (1). Plaque rupture is a mechanical failure of the plaque tissue and is demonstrated to correlate with high mechanical stresses in plaques (2). Biomechanical studies have identified large lipid pool and thin fibrous cap as risk factors for plaque rupture as they lead to increased cap stresses (3). Another highly prevalent structural component in atherosclerotic plaques is the calcification. Biomechanical studies on the impact of calcifications are limited to cap and lumen stresses; however, calcification-fibrous tissue interface is a potential stress concentration location due to the large stiffness mismatch of the two tissue types (4). Recent histopathological examinations demonstrated plaque ruptures spanning from this interface to lumen (5).

The current study investigates stresses at the calcification-fibrous tissue interface in atherosclerotic plaques, their dependency on local anisotropy of the fibrous tissue and the calcification geometric features. First, morphometric analyses was conducted to identify the fiber alignment around the calcifications and the calcification geometric features regarding its shape, size and location. Secondly, computational stress analyses were performed with the local fibrous tissue anisotropy and measured calcification morphometry incorporated.

METHODS

Morphometric analyses

Carotid atherosclerotic plaques (n=16) were collected from endarterectomy operations performed in Erasmus Medical Center. The plaque samples were processed for histology. Hematoxylin&eosin-stained histology cross-sections at every 3 mm (n=380) from the decalcified plaque samples were analyzed and calcifications were identified on the high resolution histology images. The following morphometric features were measured on the histology images using NDP.view2 [Hamamatsu Photonics KK] software (Figure 1): 1) normalized radial location, D_{norm} (distance to lumen/plaque thickness), 2) normalized width, W_{norm} (calcification radial width/plaque thickness) and 3) aspect ratio, AR (calcification circumferential length/radial width). Additionally, the fiber alignment in the fibrous plaque tissue surrounding the calcification was identified.

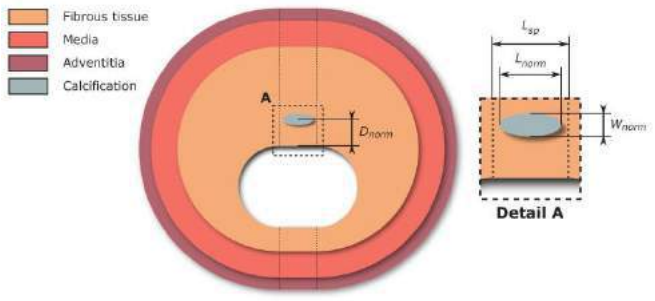

Figure 1: Illustration of the morphometric features measured and the idealized geometry used in the computational models

Computational stress analyses

Based on the morphometric analyses, 2D finite element (FE) models of the calcifications in plaques were generated (Figure 1). The idealized geometries used in the models were generated from the three morphometric measures (D_{norm}, W_{norm}, and AR) and calcification-specific models were produced. Anisotropic, hyperelastic (Holzapfel-Gasser-Ogden) material models were used for the fibrous plaque, arterial wall (adventitia & media) and calcification components in the

plaque models (6). With the FE models an intraluminal pressure of 140 mmHg was simulated under plane strain assumption and plaque stresses were computed. Maximum plaque tissue stresses along the fiber direction (S_{11}) and across the fiber direction (S_{22}) at the calcification-fibrous tissue interface were further analyzed using multivariate regression analyses and non-parametric Kruskal-Wallis *H* test for correlations to the three morphometric features and fiber orientation.

RESULTS

Of the 380 histology cross-section analyzed 65 contained calcification and was not damaged during the histology processing, allowing morphometric analyses. In these cross-sections 145 calcifications were identified and analyzed.

Of the 145 calcifications, four distinct fiber patterns in the surrounding fibrous plaque tissue were clearly identified (Figure 2). "A*ttached*" type fiber pattern, defined as fiber alignment in the circumferential direction along the radial sides of the calcification and seems to attach to the calcification at the circumferential sides, was present for 40% of the calcifications. Twenty-five per cent of the calcifications had an "encircling" fiber pattern, where fibers encapsulated the calcification. "*Pushed aside*" fiber pattern was present for 15% of the calcifications and in 10% the fibers were "*random*"ly oriented.

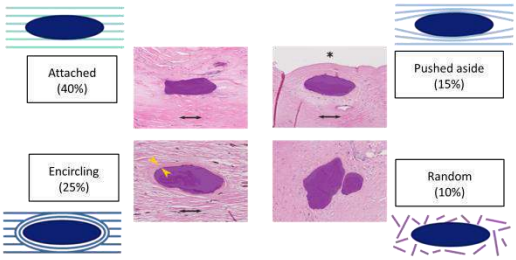

Figure 2: Four distinct fiber patterns identified in the plaque tissue surrounding the calcifications

The radial location of the calcifications in the plaque tissue, quantified by the normalized radial distance, D_{norm} (range 0-1, 0= lumen, 1=media), showed great variation for all fiber patterns but the "*random*" pattern, which was located statistically significantly abluminally (Figure 3). Regarding the shape and size of the calcifications, "*attached*" pattern clearly showed presence around larger (high W_{norm}) and more slender (high *AR*) calcifications than the other patterns (Figure 3).

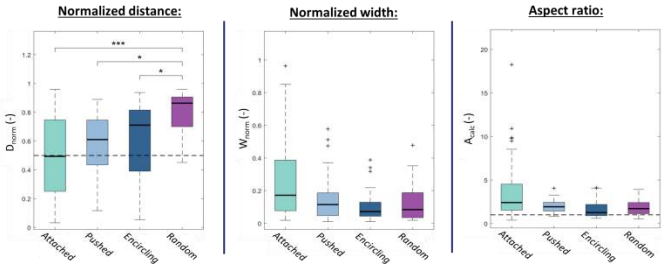

Figure 3: Measurements of the three morphometric features

The computational stress analyses demonstrated that the maximum stresses were always located at the circumferential side of the calcifications, possibly due to the high interface curvature there. The "*attached"* pattern showed statistically significantly greater maximum tissue stresses along the fibers (S_{11}) (median [Q1:Q3] = 274 [155:535] kPa) than the other patterns. The median S_{11} value was 85 kPa for "*pushed aside*" pattern, and <5 kPa for the "*encircling*" and "*random*" patterns (Figure 4). For maximum tissue stresses across the fibers (S_{22}), the stress levels were lower than S_{11} in general. "*Attached*" and "*pushed aside*" patterns had statistically significantly higher values (median= 8 & 21 kPa, respectively) than "*encircling*" and "*random*" patterns (Figure 4).

Multivariate regression analyses revealed that W_{norm} and *AR* correlated significantly and positively with S_{11} and S_{22}, implying that larger and/or slender calcifications have higher interface stresses along and across the fibers. D_{norm} was only correlated with S_{11} and correlated negatively, meaning that calcifications close to lumen have greater interface stresses along the fibers.

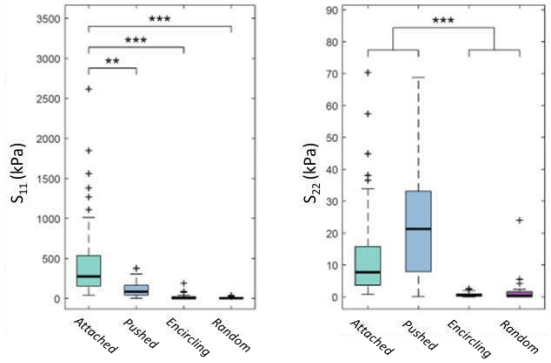

Figure 4: Computational interface stress analysis results

DISCUSSION

This study, to the authors' knowledge, is the first one performing high detail, comprehensive morphometric analyses of calcifications in atherosclerotic plaques and calcification-tissue interface stress analyses with anisotropic tissue properties implemented. The study clearly identified four distinct fiber patterns, not reported before, in the plaque tissue surrounding calcifications in atherosclerotic plaques. "*Attached*" pattern is the most prevalent one and calcifications with this pattern show the largest variance in radial location, size and shape.

Study results demonstrated that the interface stresses can reach the stress levels considered as high risk for rupture (2). This provides mechanistic explanation for the rupture observations at the calcification interfaces in histopathological examinations (5). The stresses were shown to be strongly affected by calcification location, shape and size, and the fiber pattern. "*Attached*" pattern showed the highest S_{11} stresses as the fibers in this pattern are in the circumferential direction, which is the main loading direction in atherosclerotic plaques. S_{22} stresses are much lower in general; however, they might play a critical role in plaque rupture, especially for "attached" and "pushed aside" patterns with higher S_{22} values, as possibly tissue strength across fibers is possibly lower,.

ACKNOWLEDGEMENTS

This project has received funding from the European Commission's Horizon 2020 research and innovation programme under the Marie Skłodowska-Curie grant agreement No. 749283.

REFERENCES

[1] Falk E et al., *Circulation*, 92:657, 1995
[2] Cheng, G et al, *Circulation*, 87:4, 1993
[3] Akyildiz, A et al., *Biomed Eng Online*, 10:25, 2011.
[4] Buffinton C et al, *CVET*, 5:244, 2014.
[5] Daemen, M et al., *Atherosclerosis*, 254:102, 2016.
[6] Douglas, G et al., *Annals of Biomed Eng*, 45:1462, 2017.

INITIATION OF DELAMINATION IN THE AORTIC ARCH

B. FitzGibbon (1), N. Hynes (2), S. Sultan (2), K. Moerman (1), PE. McHugh (1), JP. McGarry (1)

(1) Discipline of Biomedical Engineering
College of Engineering & Informatics
National University of Ireland Galway

(2) Dept. of Vascular & Endovascular Surgery
Galway University Hospitals
Galway, Ireland

INTRODUCTION

Aortic dissection (AD) involves the pathological separation of the layers of the aortic wall [1]. It is widely believed that this separation begins with some intimo-medial injury (entry tear). This entry tear is the antecedent for further crack propagation which is thought to occur between the elastic lamellar sheets of the media [2]. AD typically initiates in the ascending aorta near the aortic root (type A) accounting for 65-70% of cases, whilst the rest of occurrences occur distal to the left subclavian artery (type B) [3,4]. 48.6% of patients who have type A AD events do not survive long enough to reach the hospital, and the 30-day mortality rate for those who do is 47.4% [4]. These high mortality rates are due to the propagation of this crack and the creation of the pathological conduit known as the "false lumen" which frequently extends to the pericardium (3 in 4 cases of type A AD) leading to cardiac tamponade and subsequent death [5]. The false lumen may also propagate distally (particularly in type B AD) resulting in a range of malperfusion syndromes, these most commonly include stroke, acute kidney injury (AKI), paralysis, intestinal ischemia, and lower-limb ischemia [3], [6], [7].

To date no *in silico* models have been developed to examine the intramural tractions in the aortic arch and the role it plays in initiation and propagation of AD. In the present study a cohesive zone modelling approach is developed to simulate the initiation of AD in the aortic arch. An examination of the role of various geometric and material parameters in the initiation of AD under a variety of anatomical loading modes is presented.

METHODS

An idealized aortic arch geometry is created with an arch radius (R), a wall thickness (t), internal lumen radius (r), and thoracic aortic length (l). The aortic arch consists of two anatomical layers; an adventitial-medial layer (with stiffness parameter E_i); and an intimo-medial layer (with stiffness parameter E_o). The aortic arch is subject to time-dependent physiological intraluminal pressure $(P_L = 120mmHg)$.

A cohesive zone model [8] is implemented at the interface between the two layers of the aortic wall. In this fully coupled formulation both the normal and shear interface tractions are a function of the normal and tangential separations, Δ_n and Δ_t, respectively:

$$T_n(\Delta_n, \Delta_t) = \sigma_{max} \exp(1) \left(\frac{\Delta_n}{\delta_n}\right) exp\left(-\sqrt{\frac{\Delta_n^2}{\delta_n^2} + \frac{\Delta_t^2}{\delta_t^2}}\right) \quad (1)$$

$$T_t(\Delta_n, \Delta_t) = \tau_{max} \exp(1) \left(\frac{\Delta_t}{\delta_t}\right) exp\left(-\sqrt{\frac{\Delta_n^2}{\delta_n^2} + \frac{\Delta_t^2}{\delta_t^2}}\right) \quad (2)$$

σ_{max} is the maximum traction during a pure mode I separation while τ_{max} is the maximum traction during a pure mode II separation. δ_n and δ_t are the normal and tangential characteristic lengths, respectively.

Displacement boundary conditions are applied at the aortic root based on cine-MRI scans using imageJ [9]. Arch geometries containing supra-aortic vessels (brachiocephalic, left common carotid, and the left subclavian arteries) are generated using the GIBBON toolbox for MATLAB [10].

RESULTS

As shown in **Figure 1**, simulation of an applied cranial displacement at the root of the arch predict that a higher value of t/r results in

higher traction. Peak tractions are computed at the center of the arch on the inner curve. Shear tractions along the outer curve are not highly sensitive to the value of t/r. Additional traction localizations are computed at $L_{Aorta} = 0.6$, where the arch connects with the descending thoracic aorta. T_T/τ_{Max} is near-zero at $L_{Aorta} > 0.7$.

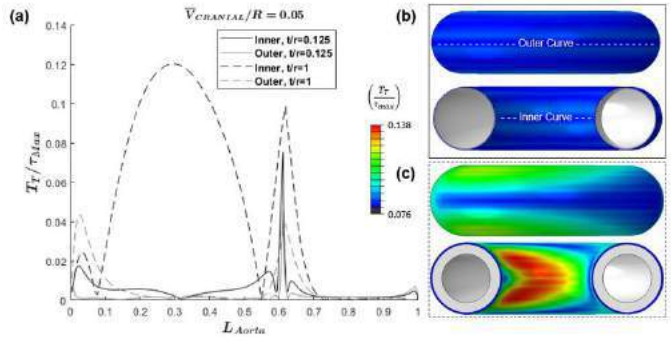

Figure 1: (a) Tangential traction (T_T) over cohesive strength (τ_{max}) vs. normalised aortic length (L_{Aorta}) for the highest and lowest permutations of t/r. The contour plots (b) and (c) show the (T_T/τ_{Max}) for $t/r = 0.125$ and $t/r = 1$ respectively.

Figure2*a* shows the variation of shear traction at the interface for three configurations of R/r_o. Maximum traction occurs in the arch when $R/r_o = 1.25$. Significant localizations are predicted in the center of the arch and also at the beginning of the descending thoracic aorta. **Figure2b** shows the magnitude of the tangential traction along the path of the inner curve of the aorta for an anterior displacement $\overline{V} = 0.15r_o$ for all values of R/r_o. Peak tractions occur in the centre of the arch along the inner curve at $L_{Aorta} = 0.4$. Two secondary peaks occur either side of $L_{Aorta} = 0.4$ with one occurring at the location of the descending thoracic aorta at $L_{Aorta} = 0.6$. Note the peak in traction at $L_{Aorta} = 0.6$ increase as the curvature of the arch increases.

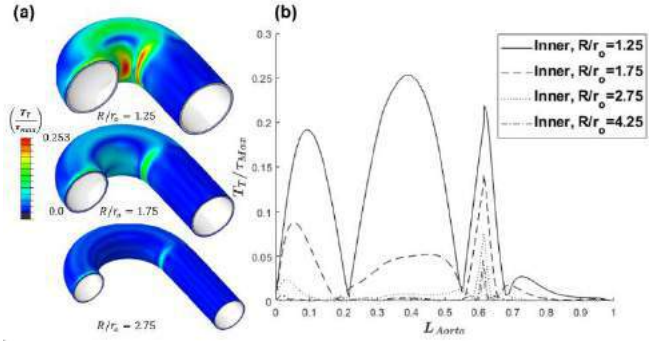

Figure 2(a) Contour plot of T_T/τ_{Max} for various values of R/r_o. (b) T_T/τ_{Max} vs. L_{Aorta} for each configuration of R/r_o.

Figure 3 shows the effect of branching vessels on shear traction in the aortic arch. Significant localizations are predicted at the ostia of the brachiocephalic, the left common carotid, and the left subclavian arteries. The peak tractions occur on the outer curve of the aortic arch between $L_{Aorta} = 0$ and $L_{Aorta} = 0.6$. The presence of supra-aortic vessels significantly increases the tractions in the arch, more so than any other geometric or material parameter identified in this study.

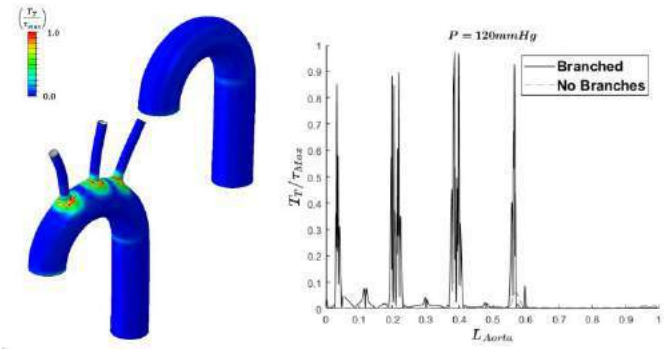

Figure 3: Contour plot showing T_T/τ_{Max} of two simulations of lumen pressurization to 120mmHg. The image on the left shows the aortic arch with supra-aortic branches, the image on the right show the aortic arch without branches.

DISCUSSION

This study explores the underlying mechanics of AD through a parametric study of the geometry of the aortic arch. Increased wall thickness is a known result of chronic hypertension, which is the primary risk factor of AD [11]. The findings of this study suggest that increased wall thickness causes significantly higher tractions in the aortic arch, resulting in an increased risk of AD. The results of this study may also suggest that for an arch with increased curvature, type A dissection is more likely to occur than type B. This principle is demonstrated in Figure 2, where for a low R/r_o (high curvature) peak tractions suggest that dissection is most likely to occur in the ascending aorta at $L_{Aorta} = 0.1$ and $L_{Aorta} = 0.4$. Whereas, for a higher R/r_o (lower curvature) peak tractions occur in the descending aorta at $L_{Aorta} = 0.6$ suggesting a type B dissection.

The current study represents the first analysis of the intramural traction state in the aortic arch under anatomical loading conditions. Results provide mechanistic insight into the relationship between arch geometry and AD risk.

ACKNOWLEDGEMENTS

B.F acknowledges funding from the Irish Research Council Enterprise Partnership Scheme (EPSPG/2016/193) and the enterprise partner, The Western Vascular Institute. B.F acknowledges the Irish Center for High-End Computing

REFERENCES

[1] Criado, FJ, *Tex. Heart Inst.* 38:694–700, 2011
[2] Gasser TC, et al., *Eur. J. Mech. - A/Solids*, 25:617–633,2006.
[3] Hagan PG, et al.,*J.Am.Med.Assoc*, 283:897–903, 2000
[4] Howard DPJ, et al.,*Circulation*,127:20, 2013
[5] Leonard JC, et al., *QJM*, 48:1, 1979
[6] Golledge J, et al., *Lancet*, 372:55–66, 2008
[7] Crawford TC, et al., *Vasc. Med.*, 21:264–73, 2016
[8] McGarry, J. P. et al. J. Mech. Phys. Solids 63, 336–362, 2014
[9] Schindelin J, et al., *Mol. Reprod. Dev.*, 82:518–529, 2015
[10] Moerman KM, *J. Open Source Softw.* 22,506, 2018
[11] Olivetti G, et al., *Circulation*, 1:19-26, 1982

SB^{3}C2019
Summer Biomechanics, Bioengineering and Biotransport Conference
June 25 -28, Seven Springs, PA, USA

COMPARATIVE BIOMECHANICAL PHENOTYPING OF THE MURINE CENTRAL VASCULATURE

Jay D. Humphrey (1,2)

(1) Department of Biomedical Engineering
Yale University
New Haven, CT, USA

(2) Vascular Biology and Therapeutics
Yale School of Medicine
New Haven, CT, USA

INTRODUCTION

Cardiovascular disease continues to be a leading cause of morbidity and mortality, and the central vasculature plays key roles in many disease manifestations. Although much has been learned from clinical studies, the inability to collect full, longitudinal data sets in patients necessitates the use of complementary animal and data-driven computational models. Of the many animal models available, the mouse has emerged as most commonly used in cardiovascular research for many reasons, including the wide availability of antibodies for biological assays and the ability to edit the genome quickly and reliably. Yet, the small size of the murine vasculature presents technical challenges in studying both the wall mechanics and the hemodynamics. Among others, our laboratory has developed unique experimental systems and approaches to enable rigorous quantification of the biomechanics of central arteries in mice. Given that one of the key advantages of mouse models is the ability to explore diverse genetic, pharmacological, and surgical manipulations, there was also a pressing need for consistent methods of both data collection and analysis. Hence, we first focused on developing custom computer-aided methods designed specifically to promote reproducibility across diverse mouse models.

In many papers, one reads of the vascular phenotype in mouse models in terms of the development or not of an aneurysm, athero-sclerosis, dissection, tortuosity, and so forth. We suggest, however, that there is also a pressing need to examine the "biomechanical phenotype," not just the clinical phenotype. That is, there is a need to quantify and compare characteristic biomechanical metrics, including multiaxial wall stress and stiffness, elastic energy storage, and contractile function in response to multiple vasoactive agonists. In this presentation, we will briefly review methods and results that enable comparative biomechanical phenotyping of murine arteries.

METHODS

Details of our methods of data collection and analysis can be found elsewhere [1-5], but briefly note the following. Central arteries experience multiaxial stresses and finite strains upon every beat of the heart. Hence, we first sought to develop a computer-controlled system capable of imposing and measuring biaxial loads and mechanical responses by cylindrical specimens. This system consists of a pump and opposing micro-stepper motors to impose multiaxial loads, and both a video-microscope and optical coherence tomography system to monitor finite deformations. Symmetrically placed upstream and downstream pressure transducers allow one to avoid complexities of geometric and viscous losses along the fluid path and thereby to infer the pressure experienced by the central region of the sample that is monitored optically. Finally, a precision load cell allows one to infer the imposed axial force. Temperature and pH control allows short-term culture and/or maintenance of endothelial and smooth muscle cell viability, and thus both active and passive testing.

Because of the existence of residual stresses and their tendency to homogenize the transmural distribution of wall stress, we often use a 2-D formulation to analyze the data [3], which is sufficient for informing fluid-solid-interaction simulations [6]. Nevertheless, we also use 3-D, layer-specific analyses to interpret results that are important for understanding mechanobiological function [4]. Regarding the former, we also use the theory of small deformations superimposed on large to compute values of the stiffness matrix that are appropriate over a cardiac cycle [2].

Whereas biaxial testing of cylindrical samples provides considerable insight into arterial health and many diseases, more complex geometries demand more complex approaches. Hence, we also developed a panoramic digital image correlation method that yields full-field geometry and surface deformations and thus, when

combined with appropriate inverse methods, information on local multiaxial wall stress and stiffness as well as local elastic energy storage [5,7]. Briefly, specimens are mounted on a custom cannula that is placed within and co-axial to the long axis of a conical mirror. A single digital camera is then moved to multiple positions to collect data on the surface of the sample sufficient for digital reconstruction of the entire surface. Following fiducial characteristics resulting from a speckle pattern placed on the surface of the sample allows one to infer local displacements at multiple levels of axial loading and pressurization, which can then be analyzed using inverse methods to determine best-fit values of material parameters in an appropriate nonlinear constitutive relation.

RESULTS

Understanding the biomechanics of vascular disease first demands an understanding of vascular health. Just as healthy humans have diverse genetic backgrounds, so too healthy mice. We have thus compared biaxial mechanical properties of so-called wild-type mice across multiple genetic backgrounds (including C57BL/6, sv129, C57BL/6 x sv129) and found that, in most cases, these mice exhibit very similar biomechanical behaviors unless generated as non-induced conditional knock-outs [8-10]. Importantly, however, there are slight differences in axial properties across different genotypes, which emphasizes the need to quantify properties biaxially [8]. Consistent comparisons of carotid artery behavior across multiple genetic, pharmacological, and surgical models reveals further that both circumferential wall stress and material stiffness tend to be maintained near normal values, even in hypertension, thus supporting the notion of a mechanical homeostasis [9].

Interestingly, an inability to control circumferential material stiffness near normal appears to be characteristic of ascending aortas that are either predisposed to aneurysmal dilatation or that have already become aneurysmal. This observation was discovered using standard biaxial testing [11], but was then confirmed using an independent panoramic digital imaging based method [5]. This finding appears to be consistent with an emerging hypothesis that thoracic aneurysms result, in part, from failed mechano-sensing or mechano-regulation of matrix [12].

It is well known that aneurysms tend to manifest within the central vasculature in either the abdominal or the thoracic aorta, the latter often in the ascending segment. There is thus a pressing need for consistent comparisons across regions to determine reasons for such predilections. Using a single model – chronic infusion of angiotensin II in *Apoe-/-* mice – we discovered marked regional differences in mechanical responses to the same insult [13]. In particular, the ascending aorta tended to exhibit aneurysmal dilatation, the descending thoracic aorta a marked fibrosis, and the suprarenal aorta dissection. Interestingly, the infrarenal abdominal aorta alone mechano-adapted to the induced hypertension. Again, the aneurysmal dilatation correlated with an increased circumferential material stiffness. In contrast, the fibrotic response correlated with an exuberant inflammatory cell infiltration while circumferential stiffness was restored whereas the dissection appeared to involve an early loss of collagen that was not sufficiently replaced during the pressure elevation, probably most importantly near branch sites. Quantifying both mechano- and immuno-biological factors is thus important in assessing regional differences in disease progression.

Finally, along with hypertension, aging is a key risk factor for cardiovascular disease. We used consistent methods to compare biomechanical changes of the aorta due to both natural aging of mice, to 100 weeks of age, and accelerated aging, due to genetic knock-out of the elastin associated glycoprotein fibulin-5. The latter proved to result in a more severe phenotype, due in part to an increased accumulation of fibrillar collagen and glycosaminoglycans.

DISCUSSION

Biomechanical phenotyping of central arteries from diverse mouse models represents a tremendous opportunity to understand better both vascular health and disease. Toward this end, however, there is a pressing need for both rigorous and reproducible methods of data collection and analysis, as called for by the NIH. Given the many different methods used by different laboratories, it is becoming increasingly more difficult to compare results across studies. In an attempt to render results easier to compare across models and regions, we developed and continued to use consistent methods of testing and data analysis. These methods have now been used to test multiple regions of the central vasculature in dozens of different mouse models. Whereas comparison of one particular manipulation – genetic, pharmacological, or surgical – against an appropriate control provides considerable insight, comparisons across multiple models provide significantly more insight [cf. 8-11,13-15]. Such biomechanical information enables a deeper understanding of both the mechanics and the mechanobiology, which of course are inextricably linked. Indeed, it is now clear that understanding the mechanobiological processes that govern extracellular matrix turnover and phenotypic modulation of the associated cells is critically important to understanding the mechanics [16]. Hence, in the words of Y.C. Fung – in his foreword to the inaugural issue of the journal *Biomechanics and Modeling in Mechanobiology* – let us continue to "enjoy the work."

ACKNOWLEDGEMENTS

This presentation is dedicated to Professor Y.C. Fung in celebration of his 100th year and his countless contributions to our field; it is an honor to be one of his many academic grandsons. This work was made possible by the many talented students and post-docs over the years with whom I have been fortunate to work, including those who established the early methods upon which our murine work rests: R. Gleason, S. Baek, J. Eberth, J. Ferruzzi, M. Bersi, and C. Bellini. Our mouse work has been supported over the past 15 years by grants from the NSF (BES-0084644) and NIH (R01 HL105297, R21 HL107768, U01 HL116323, R03 EB016810, R21 EB020968, R01 HL134712, P01 HL134605, U01 HL142518). I regret that the limited space here does not allow reference to the many, many works by colleagues that have contributed to our field in general and to my learning in particular – see, therefore, citations within the following.

REFERENCES

[1] Gleason, R.L. et al. *ASME J Biomech Engr*, 126:787-795, 2004.
[2] Baek, S. et al. *Comp Meth Appl Mech Engr*, 196:3070-3078, 2007.
[3] Ferruzzi, J. et al. *Annl Biomed Engr*, 41:1311-1130, 2013.
[4] Bellini, C. et al. *Annl Biomed Engr*, 42:488-502, 2014.
[5] Bersi, M.R. et al. *Biomech Model Mechanobiol*, 2019, in press.
[6] Cumo, F. et al. *Proceed R Soc Lond A*, 2019, in press.
[7] Genovese, K. et al. *J Mech Beh Biomed Matl*, 27:132-142, 2013.
[8] Humphrey, J.D. et al. *J Biomech*, 42:1-8, 2009.
[9] Bersi, M.R. et al. *Annl Biomed Engr*, 42:1207-1223, 2014.
[10] Bellini, C. et al. *ASME J Biomech Engr*, 139:044501, 2017.
[11] Bellini, C. et al., *J R Soc Interface*, 14:20160995, 2017.
[12] Humphrey, J.D. et al. *Science*, 344:477-479, 2014.
[13] Bersi, M.R. *J R Soc Interface*, 14:20170327, 2017.
[14] Ferruzzi, J. et al. *Biomech Model Mechanobiol*, 2019, in press.
[15] Humphrey, J.D., Tellides, G. *Am J Physiol*, 2019, in press.
[16] Humphrey, J.D. et al. *Nat Rev Mol Cell Biol*, 15:802-812, 2014.

REGIONAL ANISOTROPIC MECHANICAL CHARACTERIZATION OF PORCINE PULMONARY ARTERIES

Narasimha R. Pillalamarri (1), Sourav S. Patnaik (1), Senol Piskin (1), Ender A. Finol (1)

(1) Department of Mechanical Engineering
University of Texas at San Antonio
San Antonio, TX, USA

INTRODUCTION

Arterial compliance passively regulates pulsatile blood flow during ventricular systole [1]. In the pulmonary vasculature, the main pulmonary artery (MPA) is primarily responsible for this action. It absorbs much of the stroke volume and recoil during diastole to deliver a steady flow downstream. The remainder of the pulmonary arterial tree experiences contained multi-axial stresses on account of the local hemodynamics. Moreover, the wall thickness decreases downstream with each branching generation [2]. Consequently, pulmonary arterial wall mechanics are significantly location dependent. Therefore, modeling a precise constitutive behavior demands localized material characterization of the tissue. The long-term objective of this work is to model the mechanical behavior of pulmonary arteries and study the changes brought about by the onset of pulmonary hypertension (PH). As part of this investigation, we report on region-wise characterization of material properties in porcine pulmonary artery specimens.

METHODS

Main, left, and right pulmonary arteries from six swine of mixed Yorkshire breed were procured from Animal Technologies Inc., Tyler, TX. At the time of harvest, the animals were 6-9 months old and weighed 125-250 lb. Each of the arterial branches were divided into (i) BR – Branch, (ii) MD – Middle, and (iii) ED – End segments, as shown in Fig. 1(a). The MPA bifurcation (BF) was tested separately. Square-shaped specimens (side length $5 \pm 1\ mm$) were mounted on a CellScale Biotester (Waterloo Instruments Inc., Ontario, Canada) with orientation as shown in Fig. 1(b). Four to six specimens were tested for each region of each porcine artery. Four markers, forming a $2.5 \times 2.5\ mm$ square, were placed in the center of each specimen and a CCD camera was utilized to track the local tissue deformation.

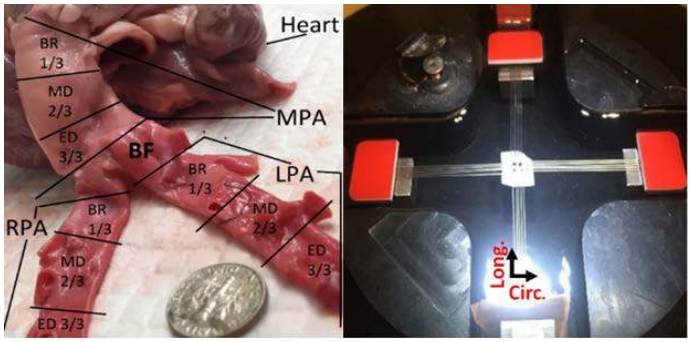

(a) **(b)**

Figure 1: (a) Arterial tree excised from porcine heart-lung section, and (b) specimen attached to the biaxial test bench.

All tests were performed in 1% PBS solution at 37℃ following the protocol described by Rogers et al [3]. An initial 5 mN tare load, followed by ten cycles of preconditioning up to 5% strain, and final tensile stretch cycle up to 45% strain was applied to each specimen. Force and stretch responses in the longitudinal and circumferential directions were recorded. Cauchy stress versus Green-Lagrange strain were used to describe the material behavior in the circumferential (x_1) and longitudinal (x_2) directions, defined by Eqs. (1) and (2),

$$\sigma_1 = \frac{F_1\lambda_1}{hL_{02}}, \qquad \sigma_2 = \frac{F_2\lambda_2}{hL_{01}} \tag{1}$$

$$\epsilon_1 = \frac{1}{2}(\lambda_1^2 - 1), \quad \epsilon_2 = \frac{1}{2}(\lambda_2^2 - 1) \tag{2}$$

where σ_i $(i = 1, 2)$ are the Cauchy stresses, ϵ_i $(i = 1, 2)$ are the Green-Lagrange strains, F_i and λ_i $(i = 1, 2)$ are the load and stretch in the x_i $(i = 1, 2)$ directions; h and L_{0i} $(i = 1, 2)$ represent the thickness and

length of each sample, respectively, before it is stretched. From the stress-strain curves, six indices were evaluated, namely: Anisotropy index, stiffness, and strain energy, each in the circumferential and longitudinal directions. Tissue thickness was measured with Vernier calipers. Anisotropy index was calculated per the definition proposed in Langdon et al [4]. Stiffness was evaluated by means of tensile modulus and strain energy calculated as the area under the stress-strain curve. For statistical analysis, one-way ANOVA tests followed by Tukey's multiple comparison tests were used to compare the region- wise indices at the 33rd, 66th and 95th percentile stresses. A probability value less than 0.05 was considered statistically significant. A Holzapfel-Gasser-Ogden (HGO) multilayer material model [5] was fitted to the experimental stress-strain curves. An optimization strategy that utilizes both genetic and Levenberg-Marquardt algorithms was used to identify the best set of HGO constants that minimizes the sum of squares of the differences between experimental and model-predicted Cauchy stresses.

RESULTS

For brevity, only the left pulmonary artery (LPA) characterization is presented in this abstract. Table 1 lists the mean constants obtained for the BR, MD and ED regions of the LPA. In the BR and MD regions, the tissue showed a near isotropic response (Figs. 2a, b). However, the ED region (Fig. 2c) presented significant anisotropy with the circumferential direction exhibiting visibly lower stresses, relative to the longitudinal direction, for identical strain values. The anisotropy index in the ED region was higher by approximately 40% and 35% relative to the BR and MD regions (Fig. 3a). The strain energy was 15% higher in the longitudinal direction (Fig. 3b). No statistically significant differences were obtained when comparing the tensile modulus in the longitudinal ($0.105 \leq p \leq 0.98$) and circumferential ($0.131 \leq p \leq 0.98$) directions at the 66th and 95th percentiles. However, remarkable differences were encountered when specimen thickness was compared amongst the BR, MD and ED regions (Fig. 4a, $p < 0.001$). Furthermore, major differences were found between the BR and ED regions, for the longitudinal tensile modulus at the 33rd percentile stress (Fig. 4b, $p < 0.05$).

Table 1: HGO constants for BE, MD and ED regions of the LPA. The definitions of c, k_1, k_2, β_m, and β_A are described in [5].

Region	c (MPa)	k_1 (MPa)	k_2	β_m (Deg.)	β_A (Deg.)
BR	0.0079	0.1097	0.466	14.89	17.2
MD	0.0025	0.0012	1.097	45.84	60.89
ED	0.0038	0.0076	1.136	73.34	72.22

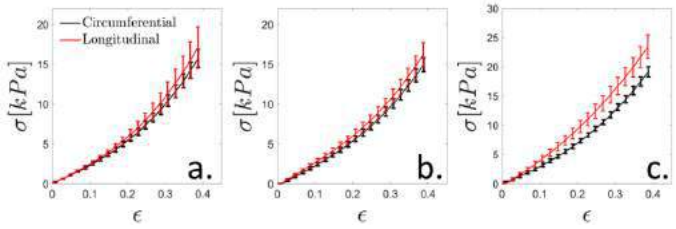

Figure 2: Stress (σ) – strain (ϵ) plots of porcine pulmonary arteries at 40% biaxial stretching; (a) Branch (BR), (b) Middle (MD), and (c) End (ED) regions.

DISCUSSION

In the present work we presented region-wise biaxial tensile testing results conducted on porcine LPA specimens. We found that the LPA is stiffer in the circumferentially compared to the longitudinal direction. Significant increase in longitudinal compliance was observed in the proximal to distal direction. As it relates to the anisotropic characteristics of large animal pulmonary arteries, our results are in close agreement with those of Cabrera and colleagues [6]. A major limitation of this work is the limited range of strain values exercised on a small sample data set, due to the available load cell capacity. Future work involves excising arterial trees up to two generations (assuming the MPA to be generation 0) and region-wise tensile testing at augmented values of strain. The subsequent implementation of the HGO model for finite element analysis simulations is expected to identify regional distributions of wall stress and displacement, which may be important, within the context of our long-term objective, to differentiate normal and PH pulmonary wall mechanics.

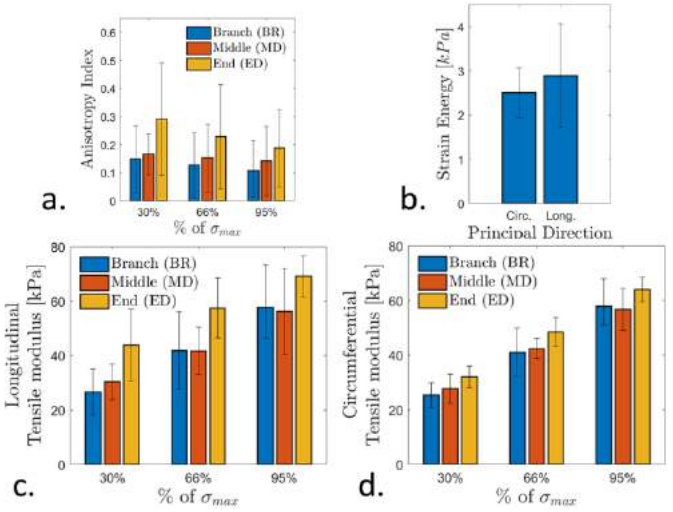

Figure 3: (a) Anisotropy index and its variability in BR, MD and ED at 33rd, 66th and 95th percentile stress, (b) Strain energy and its variability in the circumferential and longitudinal directions, (c) Longitudinal tensile modulus and its variability in BR, MD and ED at 33rd, 66th and 95th percentile stress, and (d) Circumferential tensile modulus and its variability in BR, MD and ED at 33rd, 66th and 95th percentile stress.

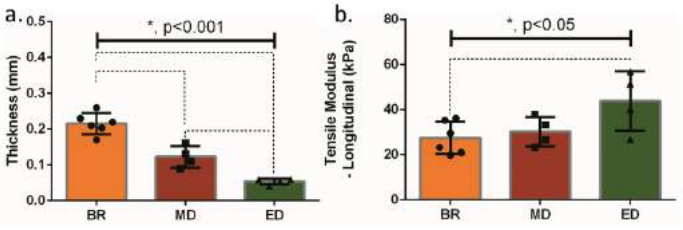

Figure 4: (a) Specimen thickness (mm) and (b) 33rd percentile longitudinal tensile modulus (kPa).

ACKNOWLEDGEMENTS

This work was supported in part by National Institutes of Health award 1R01HL121293.

REFERENCES

1. Thenappan, T et al., *Ann Am Th Soc*, 13:276-284, 2016.
2. Li, N et al., *Heart, Lung & Circ*, 21:778-781, 2012.
3. Rogers, NM et al., *Pulm Circ*, 3:936-951, 2013.
4. Langdon, SE et al., *Biomaterials*, 20:137-153, 1999.
5. Holzapfel, GA et al., *J Elasticity*, 61:1-48, 2000.
6. Cabrera, M et al., *J Biomech Eng*, 46:2075-2081, 2013.

SB³C2019
Summer Biomechanics, Bioengineering and Biotransport Conference
June 25 -28, Seven Springs, PA, USA

INVESTIGATING THE EFFECTS OF EXTRACELLULAR STIFFNESS ON VASCULAR SMOOTH MUSCLE CELL STRESS AND MECHANICAL PROPERTIES

Elizabeth D. Shih (1), Patrick W. Alford (1)

(1) Department of Biomedical Engineering
University of Minnesota – Twin Cities
Minneapolis, MN, USA

INTRODUCTION

Under pathological conditions, artery material properties are altered, influencing functions such as vessel contractility and blood flow. In some cases, like cerebral aneurysms, spatial heterogeneity in vessel properties could relate to cell mechanoadaptation, affecting tissue remodeling and determining tissue stability or failure. In vascular tissues, vascular smooth muscle cells (VSMCs) are key components in regulating the tissue's structural integrity by contracting or relaxing to adjust the vessel radius and influence blood flow, maintaining cardiovascular homeostasis. VSMC contractility and gene expression are highly sensitive to changes in extracellular mechanical properties and work in conjunction during mechanotransduction to adapt to the cell microenvironment[1]. Here, we characterize how external material properties affect cell contractility and anisotropy using traction force microscopy (TFM) and cellular micro-biaxial stretching (CμBS).

METHODS

Substrate Fabrication. Polyacrylamide (PA) gels doped with fluorescent microspheres were synthesized onto glass coverslips or PDMS membranes using previously described methods[2]. PA gel stiffness was varied by altering ratios of 40% acrylamide and 2% bis-acrylamide[3]. A layer of patterned 32 x 128 μm^2 fibronectin islands was stamped onto the top of the PA gel to facilitate cell adhesion onto the substrates. Human umbilical artery VSMCs from Lonza in between passages 5-7 were seeded onto the gel constructs, in which they adhered to the patterned fibronectin. The VSMCs were cultured overnight in supplemented Medium 199 from Gibco, incubated at 37 ºC and 5% CO_2. 24 hours before imaging, a contractile state was induced in the cells by exchanging the media with supplemented serum-free Medium 199.

Imaging and Biaxial Stretching. The constructs were imaged at 40X using a confocal microscope to obtain traction images. Brightfield images were taken of VSMCs and fluorescent images were taken of the respective underlying bead layer in the PA gel. For biaxial stretching, the constructs were mounted in a custom-designed CμBS apparatus and the elastomer membranes were stretched in increments of 5% from 0% to 20%, with brightfield and fluorescent images taken at each stretch increment. The cells were then lysed with SDS and the bead layer of the gel was imaged again at the same location and at each stretch increment. The fluorescent images of the gel layers with the adhered cells were paired with respective images of the gels without the cells to perform traction calculations.

Traction Calculation. Displacement of the beads due to cellular contraction was tracked and measured using a particle image velocimetry (PIV) ImageJ plugin between the paired images with and without the adhered VSMCs[4]. Using the displacement data with the material properties of the substrate, an unconstrained Fourier transform traction cytometry (FTTC) ImageJ plugin with a filtering regularization factor of 1E-9 calculated traction stress vectors throughout the area occupied by the cell[5]. Each vector in a specified region of the image was represented by

$$\boldsymbol{T^n} = {T_x}^n \boldsymbol{e_x} + {T_y}^n \boldsymbol{e_y} \quad (1)$$

in which $\boldsymbol{e_x}$ and $\boldsymbol{e_y}$ are the unit vectors along the x and y directions, respectively. From the traction vector field, total force vectors $\boldsymbol{f^n}$ were calculated by

$$\boldsymbol{f^n} = -{T_x}^n a^n \boldsymbol{e_x} - {T_y}^n a^n \boldsymbol{e_y} \quad (2)$$

in which n is the discrete surface and a is the area of the surface. Total force across the cell was calculated by

$$2f_i = \sum_n \frac{\boldsymbol{f_i^n} {r_i}^n}{|{r_i}^n|} \quad (3)$$

where r_i is the x or y component of the position vector r^n that maps the surface to the center of the cell such that

$$r^n = {r_x}^n \boldsymbol{e_x} + {r_y}^n \boldsymbol{e_y} \quad (4)$$

From the total force components f_i, x and y components of the First Piola-Kirchoff (PK1) stress P_i of the cell was calculated by

$$P_i = \frac{f_i}{A_i} \quad (5)$$

in which A_i is the axial or transverse undeformed cross-sectional area of the patterned VSMC (**Fig. 1A**). For biaxial stretching, P_i was calculated for each stretch increment from 0% to 20% to determine stress-strain data for further strain energy density function curve fitting.

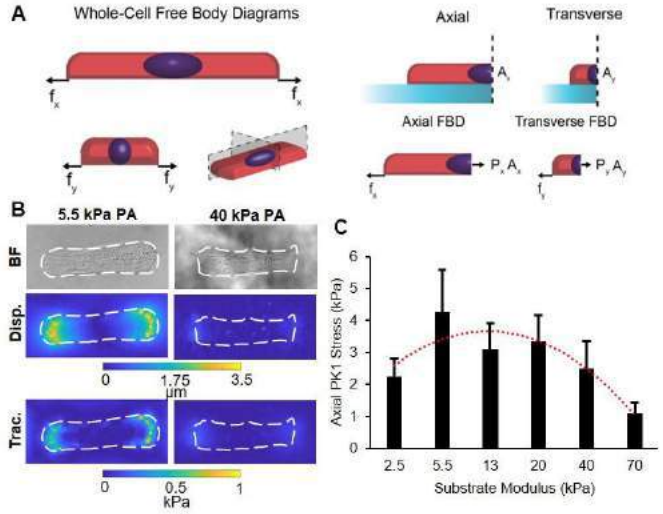

Figure 1. A. Calculation of axial and transverse PK1 stresses in a single cell[6]. **B**. Brightfield images with corresponding displacement and traction maps on two different PA substrate stiffnesses, 5.5 kPa and 40 kPa. **C**. Axial PK1 stresses of VSMCs on all substrate stiffnesses (n≈20 per group).

RESULTS

TFM studies were conducted to investigate the effect of extracellular material properties on cell stress of micropatterned VSMCs. We measured displacements of embedded microspheres in a PA gel and subsequent tractions by the contraction of VSMCs onto their substrates (**Fig. 1B**). In the lower range of substrate stiffnesses (2.5 – 5.5 kPa), the internal cell stress increased along with its external stiffness. However, as substrate stiffnesses increased (13.5 – 70 kPa), the internal cell stress followed a decreasing trend. Overall, the cell stress appeared to follow a biphasic curve as a function of substrate stiffness with stress increasing with increasing substrate modulus at low moduli and decreasing with increasing substrate modulus at higher moduli, exhibiting the highest level of contractility on a ~5.5 kPa substrate (**Fig. 1C**).

Biaxial stretching experiments were performed to study how single-cell stress-strain behavior is influenced by extracellular properties (**Fig. 2A**). Tractions were calculated for single cells at each strain to determine cell stress as a function of strain (**Fig. 2B**). For cells on the 2.5 and 5.5 kPa PA gels, the stress-strain curves appeared similar; however, the curve dropped considerably for cells on a 40 kPa substrate, complementing results from static TFM studies (**Fig. 2C**). To evaluate cell stiffness, the stress-strain curves were preliminarily fitted with a linear model to estimate an axial Young's moduli from the slope (**Fig. 2D**). Similar to results in the TFM studies, a biphasic curve was also observed in cell stiffnesses as a function of substrate stiffness. More

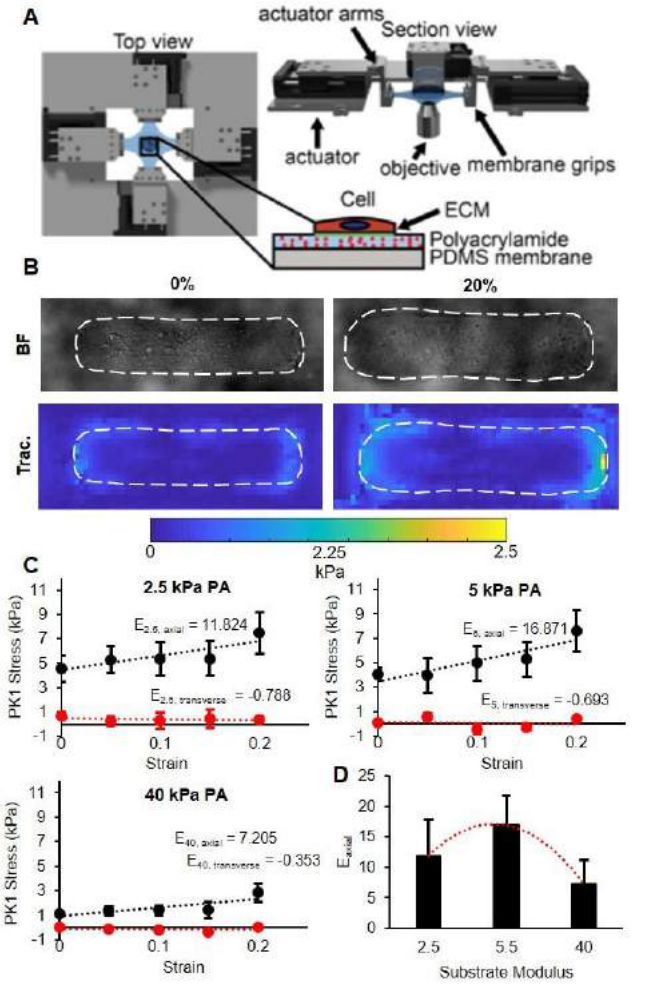

Figure 2. A. Schematic of CμBS apparatus.[2] **B**. Brightfield images of undeformed and stretched cell with corresponding traction maps. **C**. Stress-strain curves of VSMCs on different substrate stiffnesses. (n≈5 per group). **D**. Average slopes of axial stress-strain curves across different substrate stiffnesses.

data is required to significantly draw conclusions from the biaxial stretching studies and relate results to the static studies.

DISCUSSION

Our results indicate that VSMC mechanical function is mediated by extracellular mechanical properties. We found a biphasic trend in internal stress in the static studies, different stress-strain behaviors, and a corresponding biphasic curve in cell stiffness in the biaxial studies. In upcoming experiments, we will explore and model the effect of extracellular mechanics on single-cell strain energy density.

ACKNOWLEDGEMENTS

We acknowledge financial support by the US National Science Foundation (CMMI 1553255).

REFERENCES

[1] Sazonova, OV et al., *Matrix Biol*, 41:36-43, 2015.
[2] Win, Z et al., *J Biomech Eng*, 139(7), 2017.
[3] Simmons, CS et al., *Lab Chip*, 13(4):646-649, 2013.
[4] Tseng, Q et al, *PNAS*, 109:1506-1511, 2011.
[5] Butler, JP et al, *Am J Phys*, 232:C595-605, 2002.
[6] Win Z et al., *Biophys J*, 115(10):2044-2054, 2018.

SB^{3}C2019
Summer Biomechanics, Bioengineering and Biotransport Conference
June 25 -28, Seven Springs, PA, USA

CARDIAC FLOW DYNAMICS OF HEALTHY VOLUNTEERS: SEX DIFFERENCES

David R. Rutkowski (12), Gregory P. Barton (2,3), Christopher J. François (2,3,4), Alejandro Roldán-Alzate (1,2,4)

(1) Mechanical Engineering
University of Wisconsin
Madison, WI, United States

(2) Radiology
University of Wisconsin
Madison, WI, United States

(3) Medical Physics
University of Wisconsin
Madison, WI, United States

(4) Biomedical Engineering
University of Wisconsin
Madison, WI, United States

INTRODUCTION

Traditionally, cardiovascular disease has been perceived as a greater threat to male health, and literature suggests that men are at greater risk for development of cardiovascular disease than age-matched pre-menopausal women.(2) However, the prevalence of ischemic heart disease (IHD) in women is high, as it causes approximately one third of all female deaths.(3,4) Furthermore, IHD is known to be more fatal in women and the incidence of general cardiovascular disease increases distinctly in women after menopause.(2,5) Nevertheless, the true causes and detailed mechanisms driving these differences are not fully understood.

A method that has recently gained traction in the evaluation of cardiac function is flow analysis with Four-dimensional (4D) flow magnetic resonance imaging (MRI). Of particular interest in recent studies is the amount of kinetic energy (KE) dissipation and flow vortex formation in healthy and diseased ventricles.(6-14) However, the differences between sexes in kinetic energy and vorticity metrics have not yet been thoroughly examined and related to cardiac function. Therefore, the purpose of this study was to analyze the ventricular flow dynamics and cardiac function of healthy volunteers and make comparisons based on sex.

METHODS

In this IRB-approved and HIPAA–compliant study, forty healthy volunteers (twenty-one men, nineteen women) were recruited. The subjects were scanned on a 3.0T clinical system (MR750, GE Healthcare) using a 4D Flow MRI sequence known as PC-VIPR.(15) Time-resolved flow data were reconstructed into 14 time frames per cardiac cycle. Data were imported to Ensight (CEI, Apex, NC), where flow metric measurements were made at the great vessels and ventricles for each time frame of the cardiac cycle. The KE within each ventricle was then quantified through analysis of the MR image data files and ventricular volumes using Matlab (Mathworks, Natick, MA). Efficiency indices, Reynolds number, and ventricular vorticities were also processed and computed in Ensight. Two-dimensional cardiac cine images were also obtained from each patient during the 4D flow MRI session. These images were used to calculate cardiac function and cardiac strain metrics using Segment (Medviso, Lund, Sweden) (http://segment.heiberg.se). Data were compared using a Student's t-test and linear regression was used to determine the strength of correlations between measured parameters.

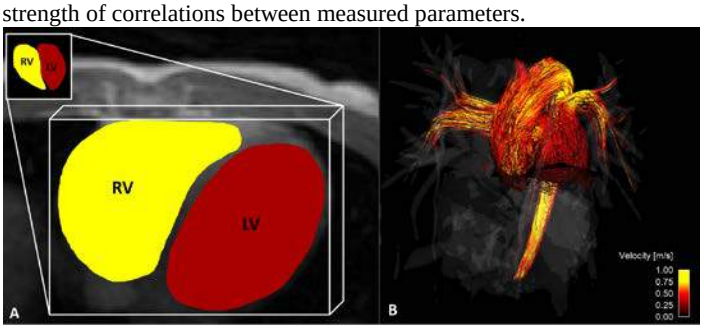

Figure 1. 4D Flow MRI was used to calculate (A) kinetic energy in the right (RV) and left (LV) ventricles. Time-averaged 4D Flow MRI magnitude data were used to segment the RV and LV (inset) and (B) flow through the main pulmonary artery (MPA) and ascending aorta (Aao)

RESULTS

Peak systolic kinetic energy was significantly higher in the left ventricle of men than it was in women (Figure 1). Additionally, peak

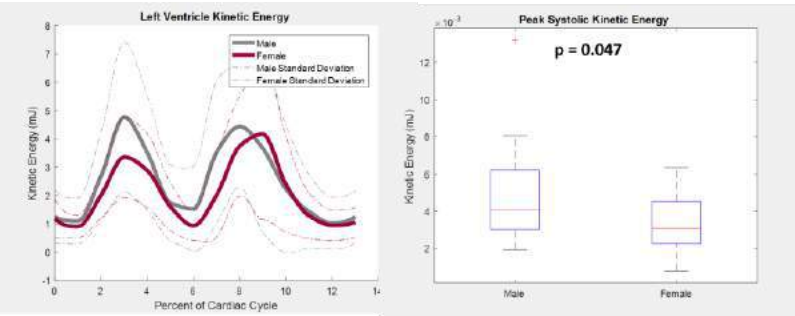

Figure 1: Left ventricle kinetic energy (KE) plotted over the cardiac cycle for male and female volunteers, along with a statistical summary on differences in peak systolic KE

LV efficiency index was higher in women than it was in men, although this result was not significant. Peak systolic and diastolic left ventricular vorticity Index was higher in women than in men (Figure 2). On average, ventricular vorticity was higher in women than in men ($p<0.001$). Preliminary Reynolds number results were significantly correlated to vorticity in both men and women (Men: $r=0.75$, $p=0.002$; Women: $r=0.59$, $p=0.026$). Global circumferential LV strain ($p<0.001$)), LV long-axis strain ($p<0.001$), and both base-($p<0.001$) and mid-($p<0.001$) and apical ($p=0.001$) left ventricle circumferential strain were significantly higher in women than in men. Furthermore, circumferential systolic ($p=0.001$) and diastolic ($p<0.001$) strain rates and long axis systolic ($p=0.02$) and diastolic ($p=0.008$) strain rates were significantly higher in women than in men. Differences in circumferential strain measurements are shown in figure 3.

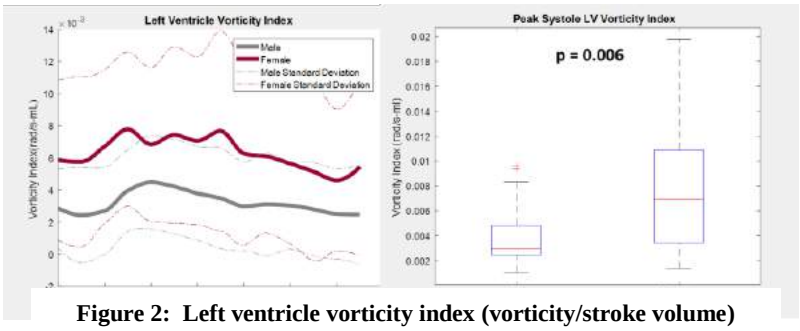

Figure 2: Left ventricle vorticity index (vorticity/stroke volume) plotted over the cardiac cycle for male and female volunteers, along with a statistical summary on differences in peak systolic vorticity index

DISCUSSION

The causes and effects of heart disease can be sex-dependent. It has been hypothesized that hormonal differences between sexes are the main drivers for the sex differences in cardiac function and disease progression. Literature suggests that estrogen can have a protective effect on the pre-menopausal female heart and leads to higher ischemia and reperfusion injury tolerance.(2) It has also been proposed that sex steroids have a significant influence on the contraction of cardiac myocytes and the regulation of autophagy during myocardial infarction.(2,5) However, the implications of these differences on the hemodynamic output of the heart are not yet understood. Through this study, it was observed that the male ventricle may be less efficient at producing flow than the female ventricle, due to higher kinetic energy dissipation, decreased myocardial strain, and less vorticity per amount

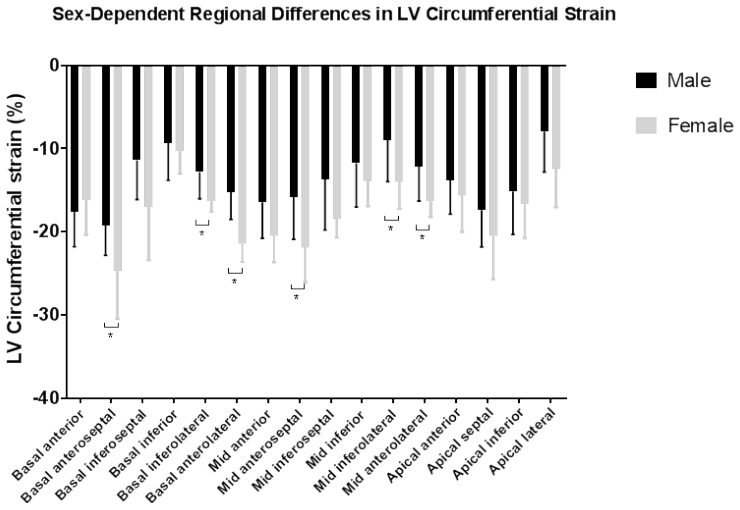

Figure 3: Summary of regional sex-dependent differences in left ventricle circumferential strain.

of generated flow. Taken together, these augmentations in cardiac function in the female sex may in part explain the beneficial effects of estrogen. However, further studies will need to confirm the relationship between sex hormones and cardiac function.

ACKNOWLEDGEMENTS

The research presented was supported by the NIH (UL1TR000427, TL1TR000429). The authors also wish to acknowledge support from GE Healthcare who provides research support to the University of Wisconsin.

REFERENCES

Sample Reference:

[1] Bergmann, G et al., *J Biomech*, 34:859-871, 2001.
[1] WorldHealthOrganization. 2017.
[2] Kolar F, et al. Acta Physiol (Oxf) 2013;207(4):584-587.
[3] Aggarwal NR, et al. Circ Cardiovasc Qual Outcomes 2018
[4] Humphries KH, et al. Front Neuroendocrinol 2017;46:46-70.
[5] Le TY, et al. Endocrinology 2014;155(2):568-575.
[6] Al-Wakeel N, et al. J Magn Reson Imaging 2015;42(6)
[7] Bermejo J, et al. Am J Physiol Heart Circ Physiol 2014
[8] Gürel E, et al. J Am Soc Echocardiogr 2016;29(5):431-440.
[9] Han QJ, et al. PLoS One 2015;10(9):e0138365.
[10] Jeong D, et al. J Thorac Cardiovasc Surg 2015;149(5):1339-1347.
[11] Kanski M, et al. J Cardiovasc Magn Reson 2015;17:111.
[12] Pierrakos O, et al. J Biomech Eng 2006;128(4):527-539.
[13] Sjöberg P, et al. Pediatr Cardiol 2017;38(4):669-680.
[14] Wong J, et al. JACC. 2015;65(10).
[15] Johnson KM, et al. Magn Reson Med 2008;60(6):1329-1336.

SB³C2019
Summer Biomechanics, Bioengineering and Biotransport Conference
June 25 -28, Seven Springs, PA, USA

WALL SHEAR STRESS TOPOLOGICAL SKELETON IDENTIFICATION IN CARDIOVASCULAR FLOWS: A PRACTICAL APPROACH

Valentina Mazzi (1), Diego Gallo (1), Karol Calò (1), Muhammad O. Khan (2), David A. Steinman (3), Umberto Morbiducci (1)

(1) PolitoBIOMed Lab, Department of Mechanical and Aerospace Engineering
Politecnico di Torino
Turin, Italy

(2) Cardiovascular Biomechanics Computation Lab, Department of Pediatrics
Stanford University
Stanford, CA, USA

(3) Biomedical Simulation Laboratory, Department of Mechanical & Industrial Engineering
University of Toronto
Toronto, ON, Canada

INTRODUCTION

The observed co-localization of "disturbed" hemodynamics and atherosclerotic lesion prevalence has led to the identification of low and oscillatory Wall Shear Stress (WSS) as a biomechanical localizing factor for vascular dysfunction [1]. However, recent evidences have underlined how consideration of only "low and oscillatory" WSS may oversimplify the complex hemodynamic milieu to which the endothelium is exposed.

In this context, recent studies have highlighted the relevance of WSS fixed points, and the stable and unstable manifolds that connect them [2][3]. These WSS topological features have a strong link with flow features like flow stagnation, separation, and recirculation, which are usually classified as "disturbed" flow. Technically, a fixed point of a vector field is a point where the vector field vanishes, while unstable/stable vector field manifolds identify contraction/expansion regions linking the fixed points. The set of fixed points and their connections form the topological skeleton of a vector field. The presence of WSS fixed points and of WSS contraction/expansion regions, highlighted by WSS manifolds, might induce focal vascular responses relevant for, e.g., early atherosclerosis, or, aneurysm rupture [3]. For these reasons, the topological skeleton analysis of the WSS vector field is of great interest and motivates the study present herein.

Lagrangian techniques have been recently proposed to identify WSS manifolds but have certain practical limitations [2]. An Eulerian approach has also been suggested, but only for 2D analytical fields [4]. Here we propose and demonstrate the use of a simple Eulerian approach for identifying WSS topological skeleton on 3D surfaces.

METHODS

Ten carotid bifurcation computational hemodynamics models from the Vascular Aging-The Link That Bridges Age to Atherosclerosis (VALIDATE) study were considered. Details on geometry reconstruction, personalized conditions at boundaries and CFD simulations are reported elsewhere [5].

Based on Volume Contraction theory, it can be demonstrated that the computation of the divergence of a vector field gives practical information about the associated dynamical system, avoiding numerical integration for manifolds identification, as required for Lagrangian technique, thus significantly reducing the computational effort. In particular, the divergence is able to (1) encase the connections between attractors and (2) identify the basins of attractions of each attractor. For this reason, here we used a divergence-based approach for WSS manifolds identification at the luminal surface of carotid bifurcations.

As WSS divergence depends by construction upon the algebraic summation of the *magnitude* of the single gradients of WSS vector components, in some cases it might fail in properly identify WSS expansion/contraction regions. In fact, these regions describe specific directional arrangements of the vectors, but both variations in magnitude and in directions are taken into account in the divergence. Consequently, here the divergence of the normalized WSS vector field was proposed:

$$\mathrm{DIV}(\boldsymbol{\tau_u}) = \nabla \cdot \left(\frac{\boldsymbol{\tau}}{\|\boldsymbol{\tau}\|_2}\right), \quad (1)$$

where $\boldsymbol{\tau_u}$ is the WSS unit vector. Eq. (1), neglecting the vector field magnitude variation but taking into account variation of directions of the vector field, correctly identifies WSS manifolds and is suitable for practical WSS topological analysis at the luminal surface of an arterial segment.

To complete the analysis, we propose a robust method to WSS fixed points identification at the luminal surface. The Poincarè index is considered here for WSS fixed points identification because of its mesh-independent and topologically invariant proprieties. Once identified, a

Jacobian analysis of WSS fixed points allows then to classify the fixed point attractive or repelling nature. The proposed practical approach for the WSS topological skeleton identification is applied to both cycle-average and instantaneous WSS vector fields.

The cycle-average WSS vector field at the luminal surface $\bar{\boldsymbol{\tau}}(\boldsymbol{x})$ is

$$\bar{\boldsymbol{\tau}}(\boldsymbol{x}) = \frac{1}{T}\int_0^T \boldsymbol{\tau}(t,\boldsymbol{x})dt \quad (2)$$

where T is the cardiac cycle duration. It was previously suggested that cycle-average WSS vector field $\bar{\boldsymbol{\tau}}$ fixed points and their associated manifolds influence the near-wall intravascular transport [2]. However, the paradoxical observation that a $\bar{\boldsymbol{\tau}}$ fixed point would have never been a real instantaneous fixed point (i.e., a null vector) along the cardiac cycle, calls into question the real physical meaning of fixed points of the cycle-average WSS vector field. In fact, from the definition of the Time-Average Wall Shear Stress (TAWSS) and from the Integral Inequality Absolute Value it follows that:

$$|\bar{\boldsymbol{\tau}}(\boldsymbol{x})| = |\frac{1}{T}\int_0^T \boldsymbol{\tau}(t,\boldsymbol{x})dt| \;\leqslant\; \frac{1}{T}\int_0^T |\boldsymbol{\tau}(t,\boldsymbol{x})|dt = \mathrm{TAWSS}(\boldsymbol{x}) \quad (3)$$

suggesting that a null value for $|\bar{\boldsymbol{\tau}}|$ does not necessarily imply the same for TAWSS. Moreover, it can be easily demonstrated that a null value for TAWSS at a specific location implies the existence there of a fixed point along all cardiac cycle. Eq. (3) highlights the need for a practical method for an in-depth analysis of the kinematics of instantaneous WSS fixed points along the cardiac cycle. Hence, WSS fixed points analysis is applied here to instantaneous WSS vector field and a measure to quantify the fraction of cardiac cycle spent by instantaneous WSS fixed points at a specific location at the luminal surface is proposed:

$$RT_{\mathrm{x_{fp}}}(\mathrm{e}) = \frac{\bar{A}}{A_e}\frac{1}{\mathrm{T}}\int_0^{\mathrm{T}} \mathbb{I}_e\big(\boldsymbol{x}_{\mathrm{fp}},\mathrm{t}\big)\ \mathrm{dt} \quad (4)$$

where $\boldsymbol{x_{fp}}(t)$ is the WSS fixed point position at time $\mathrm{t} \in [0,\mathrm{T}]$, e is the generic triangular element of the superficial mesh of area A_e, $\bar{A}$ the average surface area of all triangular elements of the superficial mesh and $\mathbb{I}$ is the indicator function.

RESULTS

An analytical vector field was used for benchmarking purposes. The proposed method was compared to the classical vector field integration approach [6] and to the recent trajectory-free method [4], providing excellent results. Then, the cycle-average WSS vector field at the luminal surface of the 10 carotid bifurcation models was analyzed. The topological skeleton of the cycle-average WSS vector field of one explanatory carotid bifurcation model, including fixed points and stable/unstable manifolds is presented in Figure 1.

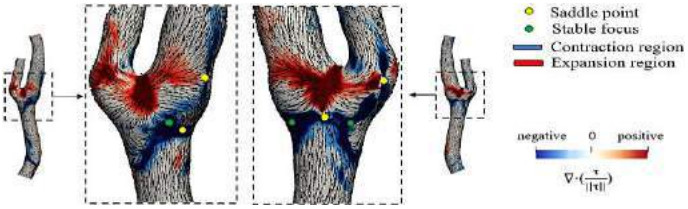

Figure 1: Topological skeleton of cycle-average WSS vector field.

The contraction and expansion patterns, identifying unstable and stable manifolds, represent the basins of attraction for the stable fixed points associated with the manifolds. Notably, all cycle-average WSS fixed points identified using the Poincarè index at the luminal surface of the 10 carotid bifurcation models were located within contraction regions, thus confirming the appropriateness of the proposed method. For an in-depth characterization of the WSS fixed points, the quantity $RT_{\mathrm{x_{fp}}}(e)$, as defined in Eq. (4), was computed on the surface of all the carotid bifurcation models and an explanatory example is presented in Figure 2. For visualization purposes, regions of interest R_{fp} were identified at the luminal surface around high $RT_{\mathrm{x_{fp}}}(e)$ areas and including the identified cycle-average WSS fixed points locations (labeled from A_C to G_C). For the explanatory model presented in Figure 2, the results of the WSS fixed points residence times analysis are summarized in Table 1 and clearly show that: (1) in regions R_{E_C} and R_{G_C} fixed points residence times were up to 30% of the cardiac cycle; (2) instantaneous WSS fixed points resided for small fractions of the cardiac cycle (range 0.0-14.5%) in cycle-average WSS fixed points identified locations; (3) interestingly, in the cycle-average WSS stable focus B_C location, the instantaneous WSS vector presented both saddle point (2%) and stable focus (2.9%) configurations along the cardiac cycle; (4) in regions $R_{D_C}, R_{E_C}, R_{F_C}$ instantaneous WSS fixed points were always of the same type as cycle-average WSS fixed points; (5) paradoxically, it emerged that at position C_C where a cycle-average WSS saddle point was identified, the instantaneous WSS vector never presented a fixed point along the cardiac cycle (we remind here that a WSS fixed point represents a focal point at the luminal surface subject to an atheroprone hemodynamic environment).

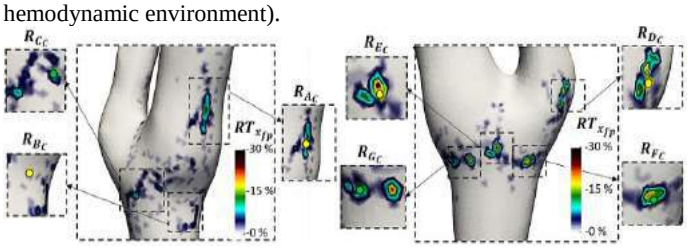

Figure 2: Map of fixed points residence time $RT_{x_{fp}}(e)$.

R_{fp}	Instantaneous WSS fixed points nature in R_{fp}	Cycle-Average WSS fixed point nature in R_{fp}	Instantaneous WSS fixed points residence time at cycle-average WSS fixed point location in R_{fp}
R_{A_C}	SPs and SFs	SP (A_C)	3.4% SPs, 0% SFs
R_{B_C}	SPs and SFs	SF (B_C)	2% SPs, 2.9% SFs
R_{C_C}	SPs and SFs	SP (C_C)	0% SPs, 0% SFs
R_{D_C}	SPs	SP (D_C)	1.5% SPs, 0% SFs
R_{E_C}	SPs	SP (E_C)	14.5% SPs, 0% SFs
R_{F_C}	SFs	SF (F_C)	0% SPs, 12.5% SFs
R_{G_C}	SPs and SFs	SF (G_C)	0% SPs, 8.2% SFs

Table 1: Summary of WSS fixed points kinematics. SPs and SFs denote Saddle Points and Stable Foci, respectively.

DISCUSSION

A practical approach to fixed points and manifolds identification was presented and applied to cardiovascular flows. The proposed approach requires the vector field and its divergence only and it can be easily implemented for 3D vector field defined on complex geometries. This practical way to analyze instantaneous WSS fixed points along the cardiac cycle allows to evaluate their residence time and how strong is local contraction/expansion using WSS divergence (data not shown). Our findings on carotid bifurcation models question the physical significance of WSS fixed points on cycle-average WSS fields, and suggest instead a focus on their dynamics. In conclusion, the practical approach proposed here could contribute to speed up studies on the physiological significance of fixed points in cardiovascular flows, in the context of the increasing interest as expressed by recent literature on this still-poorly-explored argument.

REFERENCES

[1] Morbiducci, U. et al., *Thromb Haemost*, 15: 484- 492,20016.
[2] Arzani, A. et al., *Biomech. M. Mechanobiol*., 16:787-803, 2016.
[3] Arzani, A. et al., *J Biomech*, 73: 145-152, 2018.
[4] Gary, K. et al, *Nonlinear Dynamics*, 2018.
[5] Gallo, D. et al, *Ann Biomed Eng*, 43(1): 68-81, 2015.
[6] Gambaruto, A.M et al, *Computer& Fluids*, 65:56-65, 2012.

SB³C2019
Summer Biomechanics, Bioengineering and Biotransport Conference
June 25 -28, Seven Springs, PA, USA

PATIENT-SPECIFIC FLUID-STRUCTURE INTERACTION ANALYSIS OF A BICUSPID AORTIC VALVE

Monica Emendi (1), Ram P. Ghosh (2), Matteo Bianchi (2), Francesco Sturla (3), Filippo Piatti (3), Alberto C. L. Redaelli (1), Danny Bluestein (2)

(1) Department of Electronics, Information and Bioengineering, Politecnico di Milano, Milano, Italy

(2) Department of Biomedical Engineering, Stony Brook University, Stony Brook, NY, USA

(3) 3D and Computer Simulation Laboratory, IRCCS Policlinico San Donato, San Donato Milanese, Italy

INTRODUCTION

Bicuspid aortic valve (BAV) is the most common congenital cardiac disease with an estimated incidence from 0.9% up to 2% among the world population [1]. At least one third of BAV patients develops secondary pathologies, e.g., aortic dilation or dissection as well as calcific aortic valve disease (CAVD), including aortic valve stenosis or regurgitation [2]. Altered aortic hemodynamics, characterized by abnormal flow and wall shear stresses (τ_{wall}) overloads both on aortic wall and cusps, has emerged to play a role in the pathogenesis of BAV related complications along with genetic factors [3]. According to the theory of CAVD hemodynamic etiology, an accurate quantification of stress distribution on leaflets is required to predict calcific patterns [4].

To this purpose a patient-specific fluid-structure interaction (FSI) model is herein implemented in order to accurately capture the valve dynamics and reliably compute mechanical stimuli transferred by momentum between deforming leaflets and blood flow. The most common FSI methods that were previously used to study BAV disease can be categorized as Arbitrary Lagrangian-Eulerian [4], Cut-Cell [5], and Immersed Boundary [6] method. In this study, we employed a variation of the Cut-Cell method called sub-grid geometry resolution (SGGR) which automatically adapts the Cartesian grid to the moving boundaries by implementing a curvilinear mesh. This meshing method allows to accurately capture the τ_{wall} distribution on the leaflets. Our main goal is the characterization of BAV-related flow patterns and τ_{wall} in a single patient-specific anatomy, thus overcoming previous FSI works [4, 5] adopting a parametric or paradigmatic anatomical modeling. In addition, we aim at comparing and validating the results of our FSI model against in vivo 4D flow ground-truth data. This analysis extended in time for the same patient can be helpful to guide clinical treatments and can be applied to a cohort of patients to compare relevant hemodynamics parameters and better understand the hemodynamic etiology of BAV-related complications.

METHODS

A 26-year-old female BAV patient (right-left cusps fusion) with no calcifications was enrolled for the study. MRI images were acquired at the Multimodality Imaging Section of IRCCS Policlinico San Donato on a 1.5 T scanner (Magnetom Aera, Siemens Healthcare, Erlangen, Germany). Informed consent was obtained for the patient. The geometry of the patient's aortic root (AR) was reconstructed starting from long axis cine cardiac MRI sequences acquired on 18 planes evenly rotated around the axis passing through the center of the annulus and the STJ. First, the principal AR substructures were manually traced on each plane; second, the selected points were processed, filtered and their coordinates were used to define vertexes in Gambit (Ansys, Fluent Inc., Canonsburg, Pennsylvania). These vertexes were interpolated with non-uniform rational cubic splines (NURBS) in axial and circumferential direction, that were interpolated by bicubic surfaces to obtain the 3 sinuses. The reconstruction method implemented in MATLAB (Mathworks, Inc, Natick, MA) is described in detail in [7]. To comprehensively capture the aortic helical flow patterns, LVOT and ascending aorta were included in the model using Mimics Research (Materialise NV, Leuven, Belgium).

A laminar blood flow was assumed. The blood was modeled as a Newtonian fluid with a viscosity of 0.0035 Pa·s and a density of 1060 kg/m^3. The aortic wall was preliminary modeled as a rigid body and the leaflets were modeled as hyperelastic isotropic material, using the 3rd degree Ogden model fitted on experimental data available in literature [8]. For the fused cusp, properties were averaged between the right and left coronary leaflets of a tricuspid AV, while the mechanical properties

of the non-coronary cusp were employed for the non-fused cusp. Pressure boundary conditions adjusted to the patient's heart rate were imposed at the inlet and outlet boundaries of the fluid domain. A body-fitted SGGR based FSI model was utilized because of its accurate data transfer between fluid and structural domain and incorporation of valves' leaflet thickness, hence ensuring accurate calculation of flowrates, orifice areas, mechanical stress (σ_{Mises}), and τ_{wall}. The structural part was solved by Abaqus 6.14 (SIMULIA, Dassault Systèmes, Providence, RI) and FlowVision 3.10 (Capvidia NV, Leuven, Belgium) was employed as the flow solver. FlowVision Multi-Physics Manager (Capvidia NV, Leuven, Belgium) was used to couple the two solvers during the 2-way FSI simulation.

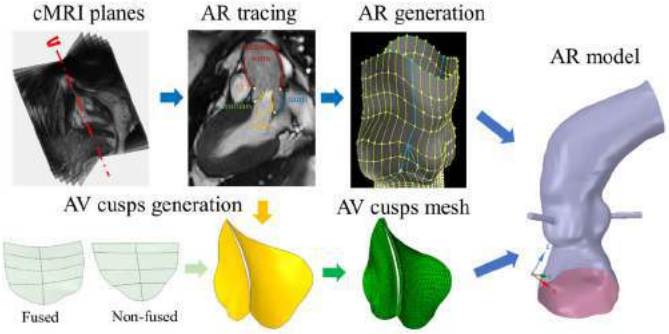

Figure 1: Patient-specific anatomy reconstruction steps. The AR anatomy is traced from cMRI images and processed in MATLAB, Gambit and ANSYS SpaceClaim to obtain the FSI model.

RESULTS

The BAV patient hemodynamics during the cardiac cycle is illustrated in Figure 2, specifically Figure 2B and 2C present the blood flow during systolic phase and Figure 2F and 2G present the diastolic flow. The systolic open configuration and the diastolic closure are shown in Figure 2A and 2E, respectively. The typical BAV asymmetric elliptical opening generated the eccentric systolic flow jet that impinged on the ascending aorta wall, potentially explaining the common BAV-induced dilation. Recirculation zones were observed in the sinuses throughout systole and a helical flow pattern was formed in the aortic arch region during peak systolic phase. The valve calculated effective orifice area (EOA) was 1.34 cm^2 and geometric orifice area (GOA) at peak systole was 1.4 cm^2.

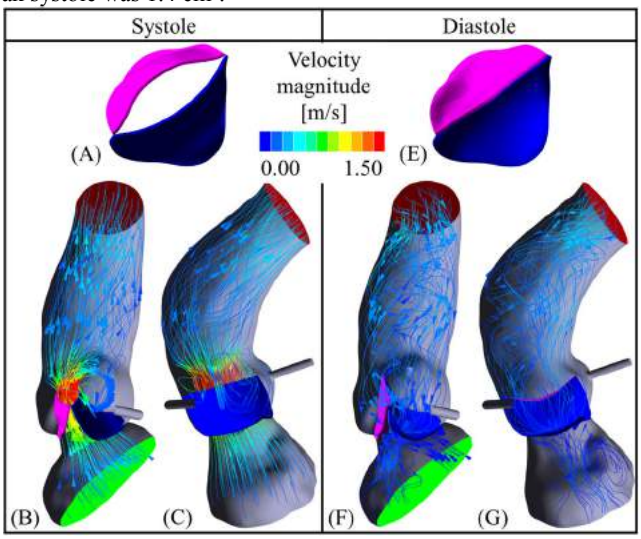

Figure 2: The BAV patient leaflets opening (A) and closing (E) and flow velocity streamlines during systole (B, C) and diastole (F, G).

The leaflets mechanical and fluid stress levels were evaluated on the ventricular side of the leaflets throughout the cardiac cycle (Figure 3). During systole, the non-fused leaflet attachment region exhibited higher level of stress if compared to the fused one (Figure 3A, B). On the contrary, the fused leaflets experienced higher stress (Figure 3E, F) during diastole. In addition, the overall σ_{Mises} magnitudes were higher in diastolic phase. The τ_{wall} magnitudes were higher on the free edge for both leaflets during systole (Figure 3C, D). During diastole, the highest τ_{wall} magnitudes were observed in the belly region, right below the coaptation region (Figure 3G, H).

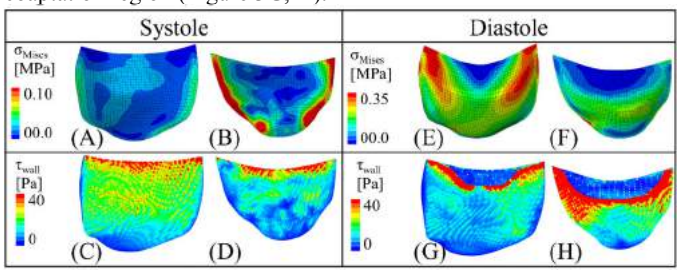

Figure 3: Mechanical and fluid stress magnitudes comparison between the fused (A, C, E, G) and non-fused (B, D, F, H) leaflets.

DISCUSSION

The distribution of leaflets WSS is similar to the one reported in previous FSI studies [4, 5] as well as the asymmetric vortices dynamics that is characterized by a larger vortex in proximity of the fused leaflet with respect to the non-fused one. This fully-coupled FSI model is able to capture regional fluid and mechanical stresses that can help localizing regions more vulnerable to damage and calcification development.

A validation of this FSI model with 4D flow data extracted from patient's phase contrast MRI, in terms of flow patterns description and estimation of main hemodynamic parameters, is in progress. Good agreement has been found between the GOA calculated from MRI and FSI analysis (GOA_{MRI}=1.5±0.2 cm^2 vs GOA_{FSI}=1.4 cm^2) at peak systole. A future development involves the full exploitation of patient-specific boundary conditions directly extracted from 4D flow data to improve the comparison between the two methods (FSI and 4D flow analysis) and to verify their reliability and accuracy. The accuracy of the FSI model will be further improved by conducting a grid independence study and modelling a compliant aortic wall.

Given the emerging off-label use of TAVR valves in BAV patients who develop CAVD at an earlier age, the feasibility of TAVR deployment will be also investigated by simulating the expansion of a commercially available self-expandable prosthesis in a calcified patient-specific BAV anatomy. This would help to inform the clinical staff whether TAVR can be considered as a safe and effective solution for BAV symptomatic patients.

ACKNOWLEDGEMENTS

Simulia and Capvidia are in an academic partnership with Dr. Bluestein. This project was supported by NIH-NIBIB-BRP U01EB026414 (DB). All the simulations were computed on Stony Brook University SeaWulf cluster. IRCCS Policlinico San Donato is a clinical research hospital partially funded by the Italian Ministry of Health.

REFERENCES

[1]Sievers, H.-H. et al., *J Thorac Cardiovasc Surg*, 133:5. 1226-1233, 2007.
[2]Ward, C., *Heart*, 83:1. 81-85, 2000.
[3]Guzzardi, D. G. et al., *J Am Coll Cardiol*, 66:8. 892-900, 2015.
[4]Cao, K. et al., *Int J Numer Meth Biomed Engng*, 33:3. e02798, 2017.
[5]Marom, G. et al., *Med Biol Eng Computing*, 51:8. 839-848, 2013.
[6]Gilmanov, A. et al., *Theor Comput Fluid Dyn*, 1-19, 2015.
[7]Votta, E. et al., *Int J Numer Meth Biomed Engng*, 33:9. e2849, 2017.
[8]Auricchio, F. et al., *Ann Solid Struct Mech*, 4:1. 1-14, 2012.

INTRODUCTION OF A SIMPLE 2D COMPUTATIONAL MODEL TO PREDICT RISK OF CORONARY OBSTURCTION DURING TRANSCATHETER AORTIC VALVE REPLACEMENT

Megan Heitkemper (1), Hoda Hatoum (1), Amirsepeher Azimian (1), Breandan yeats (1), Jennifer Dollery (3), Bryan Whitson (3), Greg Rushing (3), Juan Crestanello (1,3), Scott M Lilly, Lakshmi P Dasi (1,3)

(2) Department of Biomedical Engineering
The Ohio State University
Columbus, Ohio, USA

(3) Division of Cardiology
The Ohio State University
Columbus, Ohio, USA

(1) Department of Surgery
The Ohio State University
Columbus, Ohio, USA

INTRODUCTION

Despite the overall effectiveness of transcatheter aortic valve replacement (TAVR), complications can limit the realization of mortality and quality of life benefits for patients with severe aortic stenosis, whom conventional open-heart surgery has been deemed high risk [1-2]. Coronary obstruction is one such complication which can occur upon transcatheter valve deployment, and while a serious and potentially preventable complication, there is no consensus to which features reliably predispose risk of coronary obstruction during TAVR. Most of the guidelines developed so far have originated from clinical trials designed to exclude as many adverse outcomes as possible, which can potentially exclude a large number of potential TAVR patients, often those who have no other treatment options available. In contrast, complex computational simulations have shown potential for greater accuracy, though computational time and complexity have limited practical use. A simple, yet accurate model that is based on mechanistic insight to the precise mechanisms of coronary obstruction is essential to be able to reliably predict which patients could safely be treated with TAVR. Herein, we introduce a simple mechanistic index that can predict which high risk patients (i.e. patients with coronoary artery height (h) < 14 mm and/or Sinus of Valsalva diameter (SOVd) < 30mm) are not actually at risk and are indeed candidates for TAVR pre-operatively, allowing for the most patients possible to safely undergo TAVR without coronary obstruction. An overarching objective of this study is to better understand the physical mechanism of coronary obstruction beyond the conventional parameters of *h* and *SOVd* alone.

METHODS

A patient specific 2D model was developed to assess risk of coronary obstruction during TAVR for 28 patients out of 600 aortic stenosis patients flagged as high risk for coronary obstruction (defined as meeting h < 14 mm and/or $SOVd$ < 30 mm) during TAVR at The Ohio State University Wexner Medical Center between January 2014 and September 2018. Informed consent was obtained from all patients and the study complied with the Institutional Review Board of The Ohio State University. With respect to the outcomes for these 28 patients, 23 received TAVR successfully while 5 patients did not receive a successful TAVR. These five include 1 male who suffered coronary obstruction, 2 females who underwent surgical aortic valve replacement with visual confirmation of coronary obstruction by the operating surgeon, and 1 male and 1 female who each had extremely low lying coronaries and were deemed surgically inoperable due to age and received medical management. The 2D model that was developed accounts for patient specific parameters beyond h and $SOVd$, including cusp length (L) (Figure 1A), coronary ostium size (d) (Figure 1B), the distances between the coronary ostium and the respective annulus to STJ line (W) (Figure 1B) and calcification size (t) (Figure 1C), measured from pre-TAVR CT images. From these measurements, the closest distance between native aortic valve cusp and the corresponding coronary artery ostium, DLC_{2D}, was calculated using the Pythagorean theorem Equation (1):

$$DLC_{2D} = \sqrt{(\Delta x)^2 + (\Delta y)^2} \quad (1)$$

Where Δx and Δy are the horizontal (x-direction) and vertical distances (y-direction) between a point on the cusp (P_c) and a point on the upper coronary ostium (P_o) respectively. Δx and Δy are each related to the measured parameters using Equation (2) and (3), respectively:

$$\Delta x = w - t \quad (2)$$

$$\Delta y = h + d - L \quad (3)$$

An idealized aortic root, measured parameters, and the calculated index are shown in Figure 1D,E. DLC_{2d} was then indexed with the coronary artery diameter, d, to yield a representative measure of the fractional

obstruction of the native cusp "eclipsing" the ostium (DLC_{2D}/d). A fractional value greater than unity indicates that the gap available for blood flow is greater than the coronary artery diameter. The 2D model was validated using a more complex 3D computational model that was previously developed and validated in-vitro performed using 3D printed flexible patient-specific aortic root geometries. Briefly, the pre-procedural patient specific aortic root, calcium nodules and cusps were segmented from pre-TAVR CT images using Mimics Research 18.0 (Materialise, Belgium). The segmented aortic wall, cusps and calcium nodules were then discretized in 3-Matic Research 13.0 (Materialise, Belgium). An example of the segmented aortic root (red) and cusp with calcification (yellow) anatomy before TAV implantation is depicted in Figure 1F. Finite element analysis (FEA) was performed on each patient-specific 3D anatomical model using Abaqus/Explicit 6.9 software (Simulia, Providence, RI, USA) to simulate the opening of a TAV device stent that pushes the native cusps open towards the coronary ostium. The distance from cusp to coronary ostium (DLC_{3d}) was measured post simulation, and indexed with the coronary artery diameter, *d,* to yield DLC_{3D}/d (Figure 1 G-H). A Mann Whitney comparison of means test was performed for the patient groups under the indices *h* and *SOVd* as well as the DLC_{2D}/d and DLC_{3D}/d. Sensitivity and specificity analyses were also performed for these four indices.

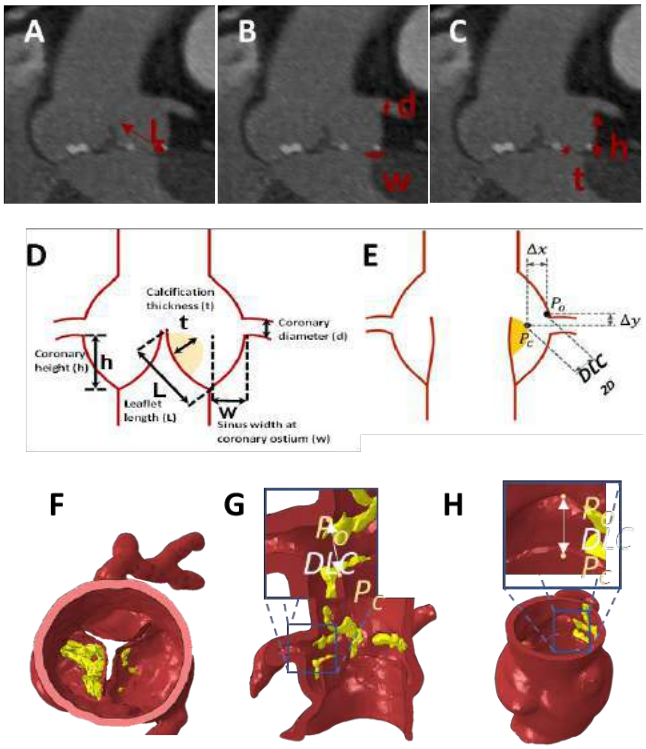

Figure 1: (A-D) Aortic root measurements; (E) Idealized schematic representing the calculated minimum distance following a TAVR (DLC_{2D}); (F) Example of patient specific aortic root with left and right coronary artery; The measured distance from the closest point on the leaflet to the upper ostium of the coronary artery (*DLC*) from (G) example finite element simulated post-TAVR aortic root with *DLC* from top view (H) and side view

RESULTS

Sensitivity and specificity analyses revealed that a cut off of DLC_{2D}/d < 0.65 was predictive with 100% sensitivity and 78.3% specificity, while a cut off of DLC_{3D}/d < 0.7 was predictive with 100% sensitivity and 95.7% specificity (Figure 2). The optimal sensitivity and specificity of *h* and *SOVd* in this high-risk group was only 60% and 40% respectively for a cut off *h* =10 mm and *SOVd* of 30.5 mm. DLC_{2D}/d and DLC_{3D}/d between the two groups of patients were significantly different ($p < 0.00078$ and $p < 0.0018$ respectively) while neither *h* nor *SOVd* were significantly different ($p > 0.32$) (Figure 3).

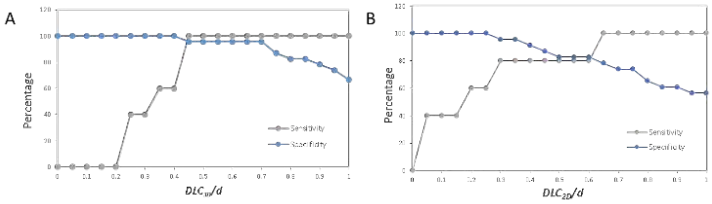

Figure 2: Sensitivity and Specificity of LCAh, SOVd, DLC_{3D}/d, and DLC_{2D}/d to predict coronary obstruction for high risk patients with *h* < 14 mm and/or *SOVd* < 30 mm.

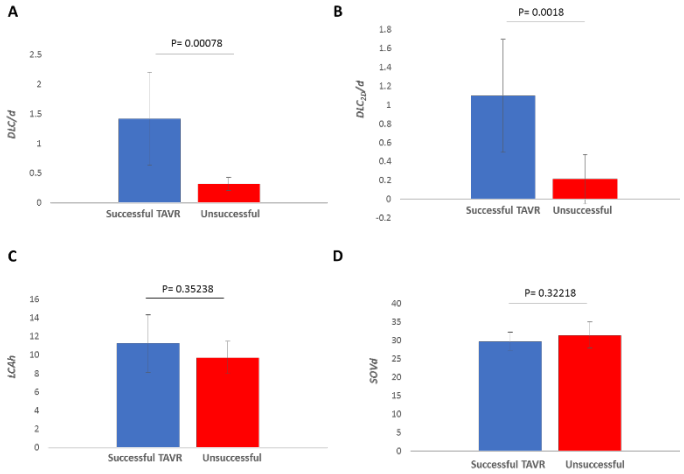

Figure 3: Comparison of means for those who successfully received TAVR and those who did not for (A) DLC_{3D}/d (B) DLC_{2D}/d (C) *LCAh* and (D) *SOVd*

DISCUSSION

We have successfully developed a simple, yet highly accurate 2D model to screen patients for possible coronary obstruction during TAVR based on criteria that can be readily calculated from current pre-TAVR CT angiographic imaging. Through comparison with the more complex and computationally expensive model yielding DLC_{3D}/d, we have validated the 2D model and DLC_{2D}/d as a conservative yet more precise predictor of coronary obstruction than *h* and *SOVd*. Results indicate that a significantly high fraction of patients who have *h* < 14 mm and/or *SOVd* < 30mm can be safely treated with TAVR if assessed with DLC_{2D}/d as compared to the current guidelines using *SOVd* and *h* alone. These findings shed light on a rare but significant potential complication during TAVR, and can assist cardiologists in decision-making process prior to the TAVR procedure.

ACKNOWLEDGEMENTS

The research done was supported by DHLRI TriFit Challenge, The Ohio State University.

REFERENCES

1. Leon, M.B., et al., New England Journal of Medicine, 2016.
2. Masson, J.-B., et al., JACC: Cardiovascular Interventions, 2009.
3. Gökdeniz, T., et al., Heart, Lung and Circulation, 2013.

SB³C2019
Summer Biomechanics, Bioengineering and Biotransport Conference
June 25 -28, Seven Springs, PA, USA

MACHINE LEARNING FOR DISCRIMINATION OF POSTERIOR COMMUNICATING ARTERY ANEURYSM RUPTURE STATUS

F. J. Detmer (1), D. Lückehe (2), F. Mut (1), M. Slawski (3), S. Hirsch (4), P. Bijlenga (5), G. von Voigt (2), J. R. Cebral (1)

(1) Bioengineering Department
George Mason University
Fairfax, VA, US

(2) Computational Health Informatics
Leibniz University
Hannover, Germany

(3) Statistics Department
George Mason University
Fairfax, VA, US

(4) Institute of Applied Simulation
HAW University of Applied Sciences
W denswil, Switzerland

(5) Clinical Neurosciences Department
University of Geneva
Geneva, Switzerland

INTRODUCTION

Aneurysms of the posterior communicating artery (PCOM) account for approximately 25% of all cerebral aneurysms [1]. Their rupture leads to hemorrhagic stroke, which is associated with high mortality and morbidity [2]. Nowadays, an increasing number of unruptured aneurysms is diagnosed as incidental findings. Since the risk associated with treatment to prevent an aneurysm from a future rupture outweighs the natural risk of the rare event of aneurysm rupture [3], deciding whether or not to treat an aneurysm can be particularly challenging. Such treatment decisions could hence be supported by a prediction model for aneurysm rupture. PCOM aneurysms have a higher rupture risk compared to aneurysms at other locations like the middle cerebral artery or other parts of the internal carotid artery [4], however, not all PCOM aneurysms rupture.

To assess which PCOM aneurysms are more likely ruptured, we recently developed and internally validated a logistic regression model discriminating between ruptured and unruptured PCOM aneurysms based on aneurysm morphology, hemodynamics, patient characteristics and PCOM aneurysm angioarchitecture [5]. The aim of this study was to evaluate the model in an external dataset and compare its predictive performance to different machine learning (ML) classifiers.

METHODS

For comparison of the previously developed logistic regression model [5] to the ML classifiers, the same training data of 245 aneurysms (125 ruptured, 120 unruptured, cross-sectional data) characterized by 22 hemodynamic parameters through computational fluid dynamics simulations, 25 shape parameters describing aneurysm size, elongation, and irregularity in shape, patient as and gender, and the PCOM angioarchitectures [6] were used for model training. A detailed description of the training data as well as the parameters can be found in [5] and the references therein.

The logistic regression model had previously been developed using logistic group lasso regression [7]. In the current study, five ML-classifiers that are shown in Table 1 were trained on the data of the 245 aneurysms. For performance evaluation, 33 PCOM aneurysms from two external datasets [8] were used to calculate the accuracy, sensitivity, and specificity for each of the classifiers. Furthermore, for the linear support vector machine (SVM) as well as the SVM with RBF-kernel (RBF-SVM), the area under the receiver operating (ROC) curve (AUC) was computed by using the distances to the separating hyperplane as the varying threshold. To calculate the accuracy metrics for the logistic regression model, a threshold based on the ROC curve was used [5].

RESULTS

Table 1 shows the results of the model evaluation. The largest accuracy in the test data was achieved by the decision tree that had a maximum depth of two determined by 5-fold cross-validation and used the variables size ratio (SizeR), convexity

ratio (CR), and ellipticity index (EI) to classify an aneurysm as ruptured or unruptured.

Table 1: Comparison of performance of different classifiers in test data (n=33). For the decision tree and random forest, the shown values are the mean ± standard deviation obtained from 100 repetitions of training the classifier (kNN=k nearest neighbors).

Classifier	AUC	Accuracy	Sensitivity	Specificity
Lasso	0.59	0.61	0.50	0.68
SVM (linear)	0.63	0.64	0.50	0.74
SVM (RBF)	0.55	0.52	0.43	0.58
kNN	/	0.64	0.50	0.74
Decision Tree	/	0.76±0.000	0.79±0.000	0.74±0.000
Random Forest	/	0.61±0.044	0.52±0.074	0.67±0.053

DISCUSSION

The accuracy of the group lasso model developed based on the 245 PCOM aneurysms decreased from 0.79 in the training to 0.61 in the test data of 33 PCOM aneurysms. Similarly, the AUC decreased from 0.84 to 0.59. These results indicate that the model could have been overfitted resulting from the relatively small sample size. In contrast, the trained decision tree with a maximum depth of two yielded an accuracy of 0.76 in the test data. The sensitivity and specificity of this classifier were 0.79 and 0.74, respectively.

These results indicate that the discrimination of unruptured and ruptured PCOM aneurysms can be increased by using a decision tree as a classifier rather than the group lasso model. This finding could be explained by the fact that the trained decision tree with a maximum depth of two has a comparatively low complexity and consequently a good generalizability with respect to the underlying data, resulting in a good performance in the test data.

Figure 1 illustrates the trained decision tree with eight aneurysms belonging to the two "purest" leaves of the tree. The aneurysms illustrated in group *a* are all unruptured cases with a CR <= 0.877 and SizeR <= 1.429. In contrast, all four aneurysms of the second leave from the left (CR > 8.77) were ruptured. The illustrated geometries show that small aneurysms (SizeR <= 1.429) with a more "conical shape" (group *a*) have a lower chance of being ruptured than small aneurysms with a small neck compared the aneurysm dome (group *b*).

Interestingly, hemodynamic variables were not included in the decision tree. This finding could be explained by the fact that aneurysm shape is related to hemodynamics since the flow is influenced by geometry.

When evaluating an aneurysm rupture probability model trained on aneurysms at different locations [9] with the 33 PCOM test cases, the AUC was reduced even further to 0.54, showing that having a model particularly trained for aneurysms at the PCOM and including additional information about the aneurysm angio-architectures could improve the predictive performance compared to a general model.

At the same time, the number of cases used for model evaluation was comparably low with 33 cases and hence might need to be increased for a more accurate estimation of the model's performance in an external dataset.

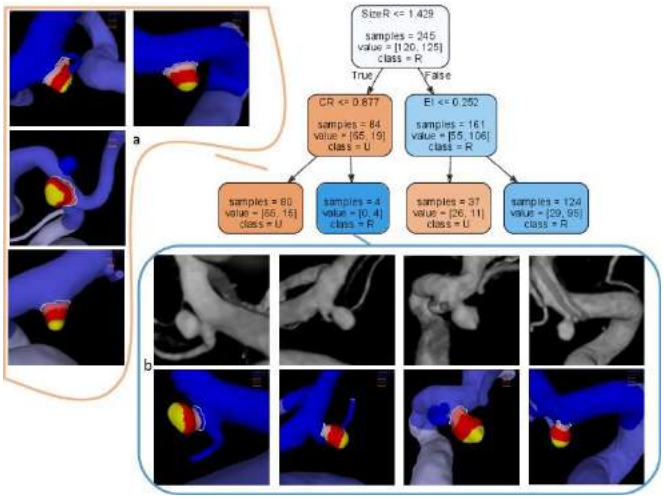

Figure 1: Illustration of trained decision tree. For group *a*, the aneurysms shown in the first row are unruptured cases from the test data, the other two aneurysms unruptured and from the training data. For group *b*, all aneurysms are ruptured aneurysms from the training data

Furthermore, the trained classifiers could vary largely for small changes of the defined tuning parameters (e.g. number of neighbors for the kNN) due to the small training sample size.

All the ML-classifiers were trained and tested using cross-sectional data. Hence, rather than predicting a future rupture, they discriminate between ruptured and unruptured aneurysms at the time when the patient reaches the hospital. To evaluate whether the decision tree or any other classifier could also be used to assess the aneurysm rupture risk, an evaluation in longitudinal data is planned for future work.

In conclusion, the trained decision tree was able to correctly classify 76% of the PCOM aneurysms from the external datasets. Small ruptured aneurysms had a small neck relative to the aneurysm dome, whereas large aneurysms classified as ruptured were less elliptical compared to the unruptured ones.

ACKNOWLEDGEMENTS

The external data were part of the publicly available AneuRisk data and the AneuX data collected and processed in the context of the @neurIST project funded by the EU commission (IST-2004-027703) and AneuX project evaluated by the Swiss National Science Foundation and funded by the SystemsX.ch initiative (MRD 2014/261).

REFERENCES

[1] Golshani K et al., *Surg Neurol Int*., 1:88, 2010
[2] Rivero-Arias O et al., *Cost Eff Resour Alloc*, 8:6, 2010
[3] Wiebers DO et al., *Lancet*, 362:103–10, 2003
[4] Greving, JP et al., *Lancet Neurol*, 13:59–66, 2014
[5] Detmer FJ et al., *Acta Neurochir*, 160:1643–1652, 2018
[6] Chung BJ et al., *AJNR*, 38:2111–2118, 2017
[7] Meier L et al., *J. Royal Stat. Soc*.: Series B, 70:53–71, 2008
[8] Detmer FJ et al., *Acta Neurochirur*, 160:2425–2434, 2018
[9] Detmer FJ et al., *Int J Comput Assist Radiol Surg*., 13:1767-1779, 2018

SB³C2019
Summer Biomechanics, Bioengineering and Biotransport Conference
June 25-28, Seven Springs, PA, USA

A REDUCED ORDER MODELING METHOD FOR CARDIOVASCULAR FLOW

Mehran Mirramezani (1,2), Shawn C. Shadden (1)

(1) Department of Mechanical Engineering
University of California, Berkeley
Berkeley, California, USA

(2) Department of Mathematics
University of California, Berkeley
Berkeley, California, USA

INTRODUCTION

Image-based computational fluid dynamics (CFD) is widely used to simulate blood flow and pressure in arterial networks. These simulations have become increasingly powerful to understand normal and pathological physiology, and improve clinical decisions. However, CFD simulations are computationally expensive and prone to numerical instabilities. These factors have limited the broader adoption of image-based CFD and its use in parametric analyses.

Reduced-order modeling (ROM) of blood flow provides the ability to study global hemodynamics of large cardiovascular networks at a fraction of the computational effort of CFD. This is valuable when multiple simulations are required, such as for data assimilation, optimization, parameter tuning, and uncertainty analysis, or for timely decision support in clinical deployment. We have developed a novel *distributed lumped parameter* (DLP) framework to compute temporal flow and pressure waveforms in cardiovascular applications. To evaluate the accuracy of the proposed DLP methodology, we have applied this framework to diverse range of healthy and diseased patient-specific cardiovascular anatomies including aortic, aorto-femoral, cerebrovascular, coronary, pulmonary and congenital heart disease models (a total of 24, 4 of each type), and have compared the DLP results to those from 3D time-dependent (3Dt) CFD simulations.

METHODS

Here we describe how to construct a DLP model from an image-based 3D geometry by assigning a resistance to each vascular segment considering various sources of energy dissipation.

Viscous and curvature effects: The energy dissipation due to blood viscosity is taken into account by modifying the well-known Poiseuille resistance ($R_v = 8\mu/\pi r^4$). First, an integral form of this equation is used to consider the spatial variation of vessel radius along the vessel length. Next, because secondary flows in a curved vessel cause extra viscous dissipation than for the same flow in a straight vessel, the energy dissipation due to vessel curvature is considered by using an analytical model relating the viscous friction factor of a curved vessel to that of a straight vessel [1]. These two considerations lead to the following formula:

$$R_v = \frac{8\mu}{\pi}\int_0^L 0.1033K^{\frac{1}{2}}\left[\left(1+\frac{1.729}{K}\right)^{\frac{1}{2}} - \frac{1.315}{K^{\frac{1}{2}}}\right]^{-3}\frac{1}{r^4}\,dx \qquad (1)$$

where K is the Dean number.

Sudden expansion effect: The energy loss at sudden expansions is modeled by using a semi-empirical model as [2]:

$$R_s = \sum_{i=1}^{n}\frac{\rho K_t}{2A_{0,i}^2}\left(\frac{A_{0,i}^2}{A_{s,i}^2}-1\right)^2|Q| \quad , \quad K_t = 1.52 \qquad (2)$$

where A_s and A_0 are minimum and nominal cross-sectional areas of the artery, respectively. n is the number of expansions in each artery.

Bifurcation effect: A nonlinear resistance (R_b) is added in series to the resistances due to viscous and sudden expansion effects of a child branch, based on a semi-empirical model [3]:

$$R_b = \frac{\rho}{2Q_j}\frac{Q_{dat}^2}{A_{dat}^2}\left(1+\lambda_j^2\psi_j^2 - 2\lambda_j\psi_j\cos(\theta_j)\right), \quad \lambda_j = \frac{Q_j}{Q_{dat}}, \quad \psi_j = \frac{A_{dat}}{A_j} \qquad (3)$$

where Q_{dat} and A_{dat} are the flow rate and the cross-sectional area of the datum supplier at the bifurcation junction, respectively, and θ_j is the angle between a datum supplier and its child branch.

Pulsatility effect: The effect of changes in velocity profile is considered by changing the viscous resistance based on the Womersley number. This is done by *numerically* calculating velocity profiles from the Womersley solution, and computing the radial

derivative at the vessel wall to obtain a modified viscous friction factor and a modified R_v accordingly.

We developed an *automated* framework (described in **Fig. 1**) to compute flow rate and pressure using the DLP model.

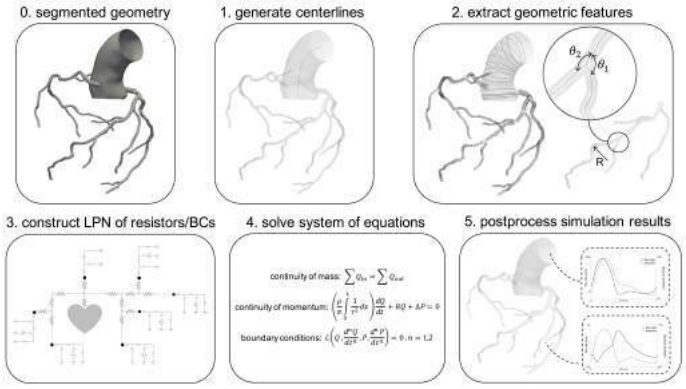

Fig 1. The modeling steps of the automated framework to compute blood flow and pressure in a representative patient-specific coronary model using the DLP method.

RESULTS

To evaluate the proposed DLP framework, we present three comparisons. First, we calculated relative errors between the mean values of the temporal flow rate and pressure from the DLP model against 3Dt CFD simulations at the inlet and outlets of each model. Second, for perspective, we compared the results from the 3Dt CFD with an LP model where a Poiseuille resistance is assigned to each vascular segment by considering the averaged vessel radius and neglecting other sources of dissipation. Finally, the temporal flow and pressure waveforms from the DLP model are compared with their CFD counterparts in several locations. We note that the DLP model is in no way tuned to the CFD results—it is based only on the image segmentation geometry and is fully automated. To ensure a consistent comparison between the DLP and 3Dt CFD modeling, consistent boundary conditions are employed at inlets and outlets. Due to limited space, we only present the results for 4 coronary models, although more models and other vascular domains have been considered.

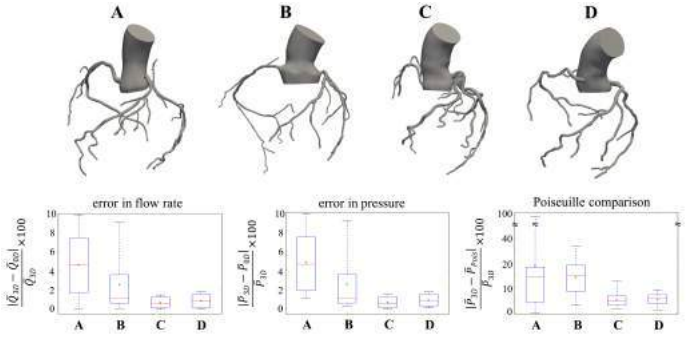

Fig 1. Four coronary models and illustration of errors of mean flow rate (left panel) and pressure (middle panel) between the DLP model ($\bar{Q}_{0D}$, $\bar{P}_{0D}$) and the 3Dt CFD simulation ($\bar{Q}_{3D}$, $\bar{P}_{3D}$). Right panel depicts mean pressure errors between the 3Dt CFD and an LP model assigning a Poiseuille resistance to each vascular segment ($\bar{P}_{pois}$).

Four patient-specific anatomical models of the aorta and major coronary arteries are shown in **Fig. 2**. This set is relatively broad; **Model C** is "healthy" with no stenosis, **Models B** and **D** have mild stenoses in the left and right coronary arteries, respectively, and **Model A** has a severe (~80%) and a mild (~50%) stenosis in a left coronary artery. In all cases, aortic flow was prescribed at the inlet, an RCR Windkessel of the systemic circulation was coupled at the aortic outlet, and coronary-specific LPNs that consider the time-dependent intramyocardial pressure were coupled at the coronary outlets.

As shown in **Fig. 2**, the mean values of the pressure error are 4.9%, 2.6%, 0.7% and 1.0% for **Models A**, **B**, **C**, and **D**, respectively. The maximum error of ~10% is observed for one of the coronary branches of **Model A**. For perspective, the right panel in **Fig. 2** plots error from assigning simple Poiseuille resistances to each vascular segment, which demonstrates significantly higher errors, and hence, the significant improvement of the DLP framework in predicting hydrodynamic effects. **Fig. 3** presents more detailed comparison of the DLP results against those from 3Dt CFD, demonstrating that the DLP model can accurately predict pressure waveforms at different locations of the coronary artery tree of **Model A,** including at **f** and **g** that are downstream branches of the complex stenotic region.

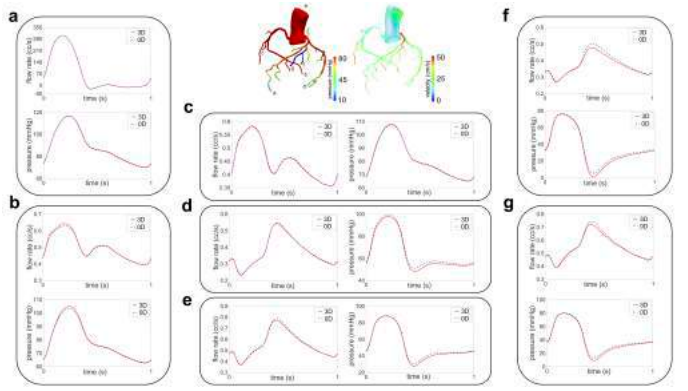

Fig 3. Color contours of early diastolic pressure and velocity of the coronary Model A and examples of comparison of temporal flow rate and pressure waveforms from the DLP model ("0D") and the 3Dt CFD simulations ("3D") at the boundaries

DISCUSSION

We have presented a DLP framework to predict temporal flow and pressure waveforms in 3D vasculature models. This framework is fully automated based on image geometry, and generally requires ~1/1000 of the computational cost compared to 3Dt CFD simulations. Although not shown here due to space, this framework has been applied to a range of vascular models, demonstrating, to the best of the authors' knowledge, one of the most comprehensive comparisons of a ROM to a 3Dt CFD standard. The proposed DLP framework provided consistent prediction with 3Dt CFD simulations with mean errors <7% for all models (including aforementioned non-coronary domains) spanning a reasonably broad range of geometrical and physical characteristics; for example, key parameters such as area reduction ratio ($1 - A_s/A_0$), mean curvature ratio (a/R), Reynolds (Re) and Womersley (α) spanned on the order of ~50-90%, ~0-0.5, ~100-3000 and ~1-20, respectively, in models considered.

To provide more general insight into the contribution of each sources of energy dissipation, we note that the modification due to flow separation at sudden expansions has the highest contribution to accurately predict flow and pressure distributions. Viscous resistance modified by curvature/pulsatility effect has the second highest contribution in energy losses. Finally, the modification introduced by bifurcation effects appears to improve the accuracy of the ROM for cases with more than ~20 junctions such as pulmonary models.

ACKNOWLEDGEMENTS

This work was supported by the NIH (R01-HL-103419).

REFERENCES

[1] Ito, H., J. Appl. Math. Mech., 49, 1969

[2] Young, D.F., Tsa, F.Y., J. Biomechanics, 6, 547-559, 1973.

[3] Mynard, J.P., et al., Int. J. Numer. Meth. Biomed. Engng, 31, 2015.

SB^{3}C2019
Summer Biomechanics, Bioengineering and Biotransport Conference
June 25 -28, Seven Springs, PA, USA

WHOLE BODY HYPERTHERMIA INDUCED INTERSTITIAL FLUID PRESSURE REDUCTION AND ENHANCED NANOPARTICLE DELIVERY TO PC3 TUMORS

Qimei Gu (1), Shuaishuai Liu (3), Arunendra Saha Ray (2), Lance Dockery (2), Marie-Christine Daniel (2), Charles Bieberich (3), Ronghui Ma (1), Liang Zhu (1)

(1) Department of Mechanical Enginneering
University of Maryland Baltimore County
Baltimore, Maryland, USA

(2) Department of Chemistry and Biochemistry
University of Maryland Baltimore County
Baltimore, Maryland, USA

(3) Department of Biology
University of Maryland Baltimore County
Baltimore, Maryland, USA

INTRODUCTION

In recent years, nanotechnology has been implemented in cancer treatment. Nanoparticles can be used as imaging contrast agents, or as absorptive heating generators to confine energy in tumors, or as carriers of therapeutic drugs. For most tumors, drug delivery is often done via intravenous injection. Once the drug reaches the capillaries in the tumor, it has to first pass through pores on the capillary membrane due to pressure difference, then diffuse through the interstitial space, and finally enter into the tumor cells. One challenge is the high tumor interstitial fluid pressure (IFP) that is a major barrier for drug delivery.

In this study, we tested the hypothesis that whole body hyperthermia may lower the tumor IFP to allow more nanoparticles into PC3 tumors after a systemic injection.[1] In vivo experiments were performed to evaluate the effects of whole body hyperthermia on the deposition of nanocarriers in PC3 tumors implanted on mice. Gold nanoparticles coated with ligands that specifically target PC3 tumor cells were developed first, then the nanofluid was injected through the mouse tail vein with or without 1-hour whole body hyperthermia. During the experiments, mouse body temperature and tumor IFP were also measured. MicroCT was used to analyze the total amount of nanoparticle deposition in the resected tumors.

METHODS

Gold nanoparticles were synthesized with citrate stabilization. Through ligand exchange reaction, prepared PPI-CO2H dendrons were coated on the surface of the particles. Finally, DBCO-functionalized Fabs were attached to the dendrons, for enabling targeting of PC3 cells. The finalized nanoparticles were 50 nm in hydrodynamic diameter.[2] The concentration of the nanofluid was 10 mg-Au/mL.

PC3 xenograft tumors were implanted in 8 Balb/c Nu/Nu male mice (~25 g, The Jackson Lab, Bar Harbor, ME), similar to our previous experiments.[3] The tumors are randomized into two groups: the control group without whole body heating and the experimental group with one-hour whole body heating.

Mouse body temperature was monitored by a temperature reader (Bio Medic Data Systems, Seaford, DE) implanted into the mouse peritoneum 48 hours before the experiment. Mouse temperatures were measured using a scanner to activate the temperature sensor and then transfer the reading to a computer. All the mice in the heating group were given an intraperitoneal injection (i.p.) of 1 mL of saline 30 min before heating to prevent dehydration. The mouse was placed in a preheated cage within an incubator set at 39ºC, for one hour.

After the one-hour heating, 200 µL of the prepared nanofluid was injected into the mouse circulatory system via the tail vein. The mouse was later sent back to the animal facility. Twenty-four hours following the nanofluid injection, the mouse was brought back to the lab and euthanized using Na Pentobarbital overdose (160 mg/kg, i.p.). The tumor was resected and immediately scanned by a micro-CT imaging system (Skyscan 1172, Micro Photonics, PA).[3]

During the experiments, tumor IFP was measured by a micro-pressure transducer (Model SPR 524, Millar Instruments, Houston, TX) with a catheter tip size of 0.33 mm. The IFPs were measured at the tumor center and tumor periphery. For each tumor, IFP was recorded four times: before the heating, right after the 1-hour heating, 2 hours after the heating, and 24 hours after the heating. All the measurements were also performed on a tumor in the control group, side by side with the tumor in the experimental group.

RESULTS

The sizes of the tumors in both groups were similar (with heating 667±229 mm^3 vs. without heating 618±122 mm^3). The mice acted normally in the heating chamber and tolerated the one-hour heating well with no observed adverse effects. It was found that the mouse

body temperature increased quickly to 40°C within 15 minutes and was maintained for the rest of the heating duration.

In the tumor group with the 1-hour whole body heating the average IFP decreased approximately 40% from its baseline value right after the 1-hour heating, as shown in Figure 1. Two hours after the heating, the average tumor pressure decreased 52%, and the decrease was more evident at the tumor periphery. 24 hours after the systematic heating, the tumor interstitial pressure rebounded slightly at the periphery location, while decreased further at the center location.

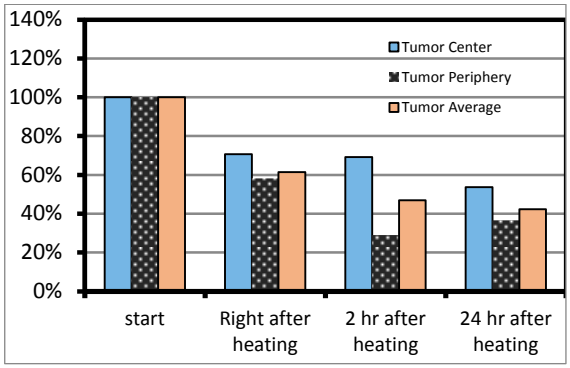

Figure 1. Pressure changes from its baseline value in the experimental group.

IFP was also measured in the tumors of the control group to evaluate whether insertion of the pressure probe alone affects the IFP results. As shown in Figure 2, the average pressure of the two tumor locations does not change significantly in the control group. In the experimental group, the tumor interstitial pressure 24 hours after the whole body heating was 42% of its baseline value. Statistical analyses were performed to evaluate whether the difference between the tumor groups with or without heating is statistically significant. Statistically significance indicated by the *p*-value less than 0.05 is confirmed either 2 hours or 24 hours after the whole body heating.

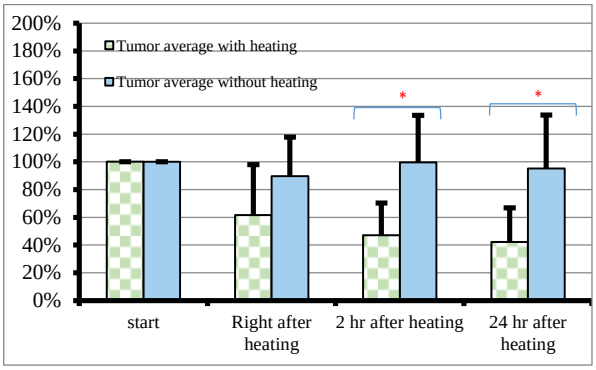

Figure 2. Comparison of pressure changes from its baseline between the two tumor groups, * refers to $p<0.05$.

Imaging analyses were performed to understand the number of microCT voxels in particular grayscale (*GS*) ranges, i.e., 0-9, 10-19, 20-29 … 250-255. It is shown that for a tumor without any nanofluid injection, the average grayscale value is approximately 60, which will be used later as a threshold grayscale value ($GS_{threshold}$) to indicate nanoparticle presence in tumors. As shown in Figure 3, the maximal voxel number in specific grayscale range occurs at the grayscale range of 100-109, shifting it from the scope of 50-60 in tumors without nanoparticle deposition. It is evident that there are more nanoparticles delivered to the tumors after the 1-hour whole body heating, due to the observation that more voxels are in the higher grayscale ranges (grayscale value > 90) than that in the tumors of the control group.

The amount of gold nanoparticles is estimated based on the grayscale values in individual voxels. The threshold grayscale value is selected as 60, thus, in each voxel, the amount of the gold nanoparticles is calculated as $GS\text{-}GS_{threshold}$, one then can add the amounts in all the voxels. The summation is in theory proportional to the gold nanoparticle deposition in tumors, assuming that the gold nanoparticle concentration is directly proportional to the grayscale value exceeding the $GS_{threshold}$ of 60. Figure 4 illustrated that the total amount of the nanoparticles delivered into the tumors in the heating group is 36% larger than that in the tumor group without the whole-body heating. The *p* value equal to 0.044 suggests the positive outcome of 1-hour whole-body hyperthermia on enhancing nanoparticle delivery to PC3 tumors.

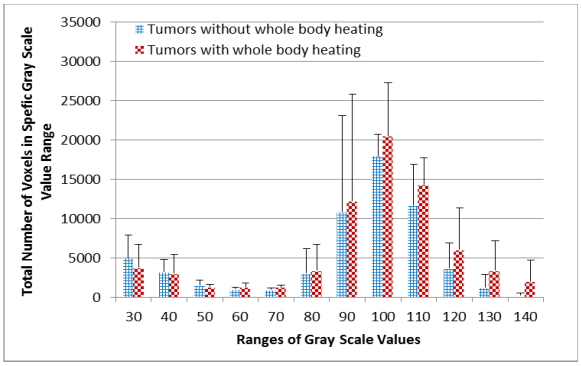

Figure 3. Total number of voxels in specific grayscale value range in both tumor groups

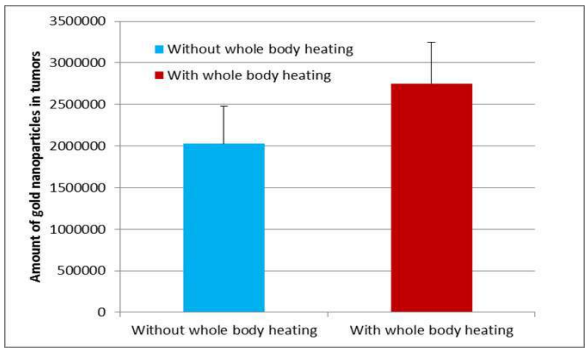

Figure 4. Total amount of gold nanoparticles deposited in tumors

SUMMARY

In this study, we performed *in vivo* experiments on mice to evaluate whether whole body hyperthermia enhances nanoparticle delivery to PC3 tumors. The results illustrate a decrease in IFP after 1-hour whole body hyperthermia treatment, with a statistically significant reduction evident 2 hours after the treatment and the reduction is maintained for 24 hours. The 1-hour whole body hyperthermia leads to 36% more nanoparticle delivery in the experimental group than that in the control group.

ACKNOWLEDGEMENTS

This research was supported by an NSF research grant (CBET-1705538). The research was performed in partial fulfilment of the requirements for the PhD degree by Qimei Gu from University of Maryland Baltimore County, Baltimore, Maryland, USA.

REFERENCES

[1] Wislow et al., *Int. J. Hyperthermia*, , 31(6): 693–701, 2000.

[2] Gu et al., 2018 NEMB conference, Los Angeles, August 21-24, 2018, Paper number NEMB2018-6181, 2018.

[3] Gu et al., ASME *J Heat Transfer*, 141(3):032402, 2019.

SB³C2019
Summer Biomechanics, Bioengineering and Biotransport Conference
June 25 -28, Seven Springs, PA, USA

QUANTIFICATION OF TISSUE ELECTRICAL AND THERMAL RESPONSE DUE TO HIGH FREQUENCY IRREVERSIBLE ELECTROPORATION: A PILOT STUDY IN EX VIVO PERFUSED LIVERS

Melvin F. Lorenzo (1), Tim J. O'Brien (1), Kenneth Aycock (1), Navid Manuchehrabadi (2), Rafael V. Davalos (1)

(1) Department of Biomedical Engineering and Mechanics
Virginia Polytechnic and State University
Blacksburg, Virginia, USA

(2) AngioDynamics
Latham, New York, USA

INTRODUCTION

High Frequency Irreversible Electroporation (H-FIRE) is a minimally invasive ablation modality that utilizes ultrashort duration bursts of bipolar pulsed electric fields to destabilize cell membranes and promote cell death via apoptotic-like cell death pathways [1]. Unlike other ablation modalities, cell death is not dependent on prolonged exposure to increased temperatures. This allows for the application of H-FIRE to tumors near and encasing critical vasculature and other thermally sensitive structures. Preclinical studies with H-FIRE have demonstrated successful ablations for intracranial meningiomas with no adverse effects attributed to the therapy [2]. Additionally, recent studies have demonstrated H-FIRE with no signs of cardiac distress or gross muscle contractions, obviating the need for cardiac synchronization and neuromuscular blockade during surgery [3, 4].

While successful ablation is achievable without generating high thermal energies, clinical application of excessive pulsing and extremely high voltages can lead to unwanted thermal effects. Determining optimal H-FIRE protocols that minimize Joule heating is key to the advancement of this therapy. In this pilot study, we sought to quantify the H-FIRE thermal damage threshold using an Arrhenius damage model and a cumulative equivalent minutes at 43 ℃ (CEM43) model in an *ex vivo* liver perfused organ model. Additionally, we aimed to quantify the dynamic changes in tissue conductivity due to electroporation.

METHODS

An *ex vivo* perfused organ model was used as a testbed for various H-FIRE protocols [5, 6]. Shortly, 3 porcine livers were acquired from a local abattoir within 10 minutes of sacrifice. After cannulating the hepatic artery, portal vein, and hepatic vein with Luer fittings, the liver was gravity perfused with a sucrose-supplemented PBS solution ($\sigma \approx 0.8 \frac{S}{m}$) to prevent coagulation. The liver was placed on a bed of ice and transported to our facilities within a 2 hour span. Upon arrival, the liver was re-perfused at 30 ℃ on a perfusion system according to specifications in [5, 6].

Two 18 gauge monopolar electrodes (AngioDynamics Inc., Latham, NY) were used in the delivery of H-FIRE. These electrodes were set 1 cm apart with a 1.5 cm exposure. H-FIRE was delivered using a custom-built high frequency bipolar pulse generator (Energy Pulse Systems, Lisbon, Portugal) to deliver a 100 μs energized 10-1-10 μs burst scheme as seen in Figure 1. Experimental voltage and current measurements were captured with a 1000× high voltage probe (P5210A; Tektronix) and a 50 MHz current probe (TCP305; Tektronix), respectively, and stored on an oscilloscope (DPO2002B; Tektronix Inc., Beaverton, OR). Three experimental conditions were tested for ablation dimensions. The applied voltage was varied between 1,500 V, 2,250 V, and 3,000 V, and 300 bursts were applied.

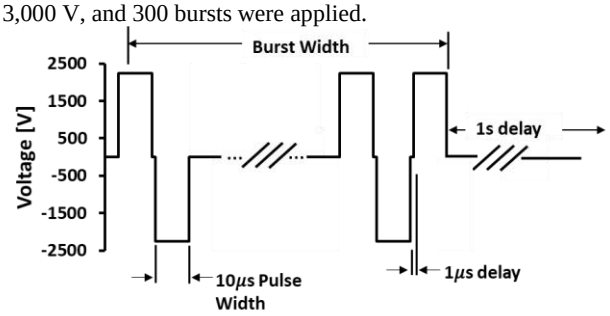

Figure 1. H-FIRE 10-1-10 μs voltage waveform energized for 100μs and delivered at a frequency of 1 Hz.

Numerical simulations were developed in COMSOL Multiphysics v5.4 (COMSOL Inc., Stockholm, Sweden) to capture the electric field distribution and changes in temperature due to Joule heating. First, the electric field distribution was captured by solving the Laplace equation (1) and taking the gradient of the electric potential:

$$0 = -\nabla \cdot (\sigma \nabla \Phi) \quad (1)$$

$$\bar{E} = -\nabla \Phi \quad (2)$$

The changes in conductivity due to electroporation and temperature effects were captured with equation 3:

$$\sigma(|\bar{E}|, T) = \sigma_0 \left(1 + A \cdot flc2hs\left(|\bar{E}| - E_{del}, E_{range}\right)\right) \cdot [1 + \alpha(T - T_0)] \quad (3)$$

where σ_0 is the baseline conductivity, $|\bar{E}|$ is the magnitude of the electric field, E_{del} marks the sigmoid inflection point, E_{range} marks the span of the transition, A determines the final electroporated conductivity, and α is the temperature coefficient of resistance. The parameters $\sigma_0, E_{del}, E_{range}$, and A were determined by matching the numerical and experimental voltage and current in a method similar to [7], taking on values of 0.194 S/m, 650 V/cm, 450 V/cm, and 1.78, respectively (Figure 2). Finally, effects of tissue perfusion were modeled using the Pennes' bioheat equation with a Joule heating term as explained in [6]. All other parameters are listed in Table 1 or are pulled directly from [6].

Two thermal dose models were implemented, an Arrhenius damage model and CEM43 [8]. CEM43 computes equivalent time of exposure to a reference temperature, typically 43 ℃, calculated by:

$$CEM43 = \sum_{i=1}^{N} R_{CEM}^{43-T_i} t_i \quad (4)$$

where R_{CEM} takes on a value of 0.25 when below the break temperature of 43 ℃ and 0.5 when above the break temperature. The Arrhenius damage model is solved from the following equation:

$$\Omega(\tau) = \int_0^{\tau} \xi \cdot e^{-\frac{E_a}{RT(t)}} dt \quad (5)$$

where ξ is the pre-exponential factor, E_a is the activation energy, R is the universal gas constant, and T is the temperature.

Finally, thermal thresholds were determined by matching the dimensions of tissue whitening in the ablation region with those predicted from the model. The numerical values that best captured the long and short axis of the experimental regions of tissue whitening are reported as the thermal threshold values.

Table 1. Numerical modeling parameters

Parameter	Symbol/units	Value	Ref.
Temperature coefficient	$\alpha, \frac{\%}{℃}$	2	[6]
Tissue perfusion	$\omega_b, \frac{1}{s}$	3.575e-3	[6]
Activation energy	$E_a, \frac{1}{s}$	5.51e41	[8]
Pre-exponential factor	$\xi, \frac{J}{mol}$	2.769e5	[8]

RESULTS and DISCUSSION

The experimental voltage/current data were collected at ~250 V (n = 9), ~2,250 V (n = 7), and ~2700 V (n = 11). Figure 2a shows the numerical voltage and current-fitting functions demonstrated for the conductivity curve in Figure 2b. Determination of the relationship between the change in conductivity and the applied electric field is important in modeling the electric field redistribution due to electroporation effects.

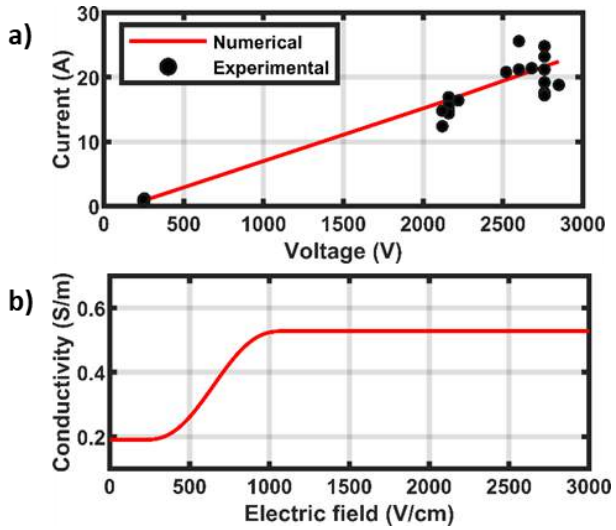

Figure 2. a) Comparison between the experimental and numerically predicted current ($R^2 = 0.94$) and b) resulting conductivity curve fit from the COMSOL simulation.

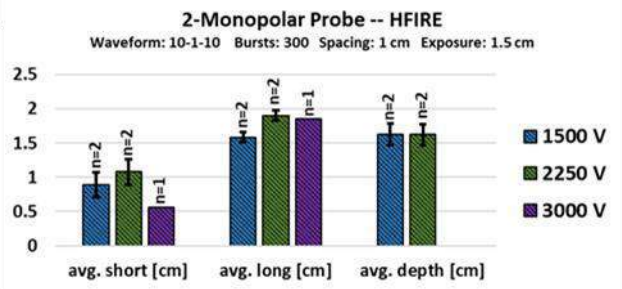

Figure 3. Ablation dimensions 2 hours after treatment.

Our data indicate a slight increase in the ablation as a function of applied voltage. Additionally, measurements (n=2) of the tissue whitening regions from the 1500V data group indicates a CEM43 value of 720 ± 613 and an Ω value of 0.207 ± 0.11. These values best fit our experimental measurements of thermal damage, but future work will be done to (1) increase sample size and (2) definitively verify the presence of thermal damage through histological and pathological analyses. It is important to note that perfusion across the *ex vivo* tissue varied significantly and a higher sample number should provide less variations in the measurement.

ACKNOWLEDGEMENTS

The authors would like to thank AngioDynamics for supporting this project.

REFERENCES

[1] Arena, C et al., *BioMedical Engineering OnLine*, 10(1), p. 102.
[2] Latouche, E et al., *Tech. in Cancer Research & Treay.*, 17, pp. 1-10.
[3] Siddiqui, I et al., *Surgical Innovation*, 24(3), pp. 276-283.
[4] Siddiqui, I et al., *HPB*, 18(9), pp. 726-734.
[5] Bhonsle, S et al., *JVIR*, 27(12), pp. 1913-1922.e2.
[6] O'Brien, T et al., *Int. Journal of Hyperthermia*, 35(1), pp. 44-55.
[7] Sel, D et al., *IEEE TBME*, 52(5), pp. 816-827.
[8] Pearce, John A., International Society for Optics and Photonics.

SB³C2019
Summer Biomechanics, Bioengineering and Biotransport Conference
June 25 -28, Seven Springs, PA, USA

MAGNETIC NANOPARTICLE HYPERTHERMIA FOR PANCREATIC CANCER: A COMPUTATIONAL STUDY

Anilchandra Attaluri (1), Sri Kamal Kandala (2), Robert Ivkov (3)

(1) Department of Mechanical Engineering
The Pennsylvania State University - Harriburg
Middletown, PA, USA

(2) Department of Imaging Physics
University of Texas MD Anderson Cancer Center
Houston, TX, USA

(3) Department of Radiation Oncology and Molecular Radiation Sciences
Johns Hopkins University,
Baltimore, MD, USA

INTRODUCTION

Pancreatic cancer is one of the most lethal forms of malignancy with minimal survival and a mortality rate comparable to its incidence. Due to the lack of specific symptoms and the aggressive nature of this disease, patients present with inoperable locally advanced tumors or metastatic disease at the time of diagnosis. Locally advanced pancreatic cancer (LAPC) patients have a five-year survival rate of < 12% [1]. Concurrent chemo-radiation therapy (CRT) is a standard option for LAPC but has significant toxicity. CRT typically stabilizes tumor progression for a time, and only a small subset of patients (10% to 15%) exhibit an objective response.

Hyperthermia is a well know radiation and chemotherapy sensitizer, that has pleiotropic biologic and physiologic effects to enhance effectiveness of other therapies [2]. Magnetic nanoparticle hyperthermia delivers localized heating by exposing magnetic nanoparticles (MNPs) deposited in the tumor to an alternating magnetic field (AMF). Recent advances in endoscopic ultrasound (EUS) guiding procedures for pancreas facilitate minimally invasive EUS guided delivery of MNPs. Repeated magnetic nanoparticle hyperthermia (MNPH) treatments can be performed by remotely activating MNPs after a single EUS guided delivery of MNPs into pancreatic tumors. Non-overlapping toxicities of MNPH and CRT offer significant potential to enhance therapeutic ratio [2] and may enable reduced dosing of CRT to achieve similar or improved outcomes with reduced toxicity. Local control of large tumors with radiation and chemo-therapies presents challenges, whereas physics of heat deposition and control provides advantages for MNPH.

Both MNPs and human tissue generate heat when exposed to AMF. MNPS generate heat through magnetic hysteresis loss power [3], whereas AMF-coupled tissue heating is a consequence of induced Foucault (eddy) currents [4].

Objective of this computational modelling study was to elucidate the role of tumor volume in treating LAPC with MNPH using finite element bio-heat transfer methods. Preliminary results indicate the need to reduce the non-specific eddy current heating of human tissue when exposed to AMF and large tumors are inherently easy to treat with MNPH.

METHODS

Bio-heat transfer: Penne's bioheat equation was used to model the heat transfer in human tissue.

$$\rho_n c_n \frac{\partial T_n}{\partial t} = k_n \nabla^2 T_n + \rho_b c_b \omega_{b,n} (T_b - T_n) + Q_{m,n} + Q_p \qquad [1]$$

where, n and b represent tissue (tumor, n=1; healthy n=2) and blood parameters, respectively. For either tumor or healthy tissue, ρ_n, c_n, k_n, T_n, $Q_{m,n}$ denote the density, specific heat, thermal conductivity, local temperature, and metabolic heat generation rates. Correspondingly, for the blood ρ_b, c_b, ω_b, T_b denote density, specific heat, perfusion rate, and temperature, respectively.

Eddy current heating: Non-specific tissue heating depends on AMF amplitude (H), frequency (f), and varies along the radial distance (r) of the tissue volume:

$$P_{eddy\ cuurent} \propto \sigma_t (\pi \mu_0 r f H)^2 \qquad [2]$$

where, is σ_t electrical conductivity of the cylinder (idealised tissue) and μ_0 is the permeability of vacuum.

MNPs and heating rate: For modelling, the heating properties of MNPs from a previous experimental study were used [3]. The MNP heating rate is reported as specific loss power (SLP), and for the present effort was fixed at $5 \cdot 10^5 \frac{W}{m^3}$ for AMF having amplitude 10 kA/m at frequency 150 kHz [3]. A uniform distribution of MNPs in half the tumor volume was assumed, representing a volumetric heat

source which presents a realistic simulation of MNPs delivered via a single injection site into a tumor. The total tumor volume determines the maximum injection volume of MNP formulation into the tumor, as previously described [5]. Tumor volume-normalized MNP dose and fixed AMF conditions were used to study the role tumor size on the achievable temperatures in the tumor.

The Pennes bioheat equation was used to model MNP heat transfer in tumor and surrounding tissues. COMSOL Multiphyics® finite element software was used to solve the bioheat equation. The model was verified and validated comparing to the analytical solutions and experimental data available in the literature. The tumor and normal tissue model geometry used for this study is described in the Figure 1. Optimized mesh had 103466 tetrahedral and triangular mesh elements.

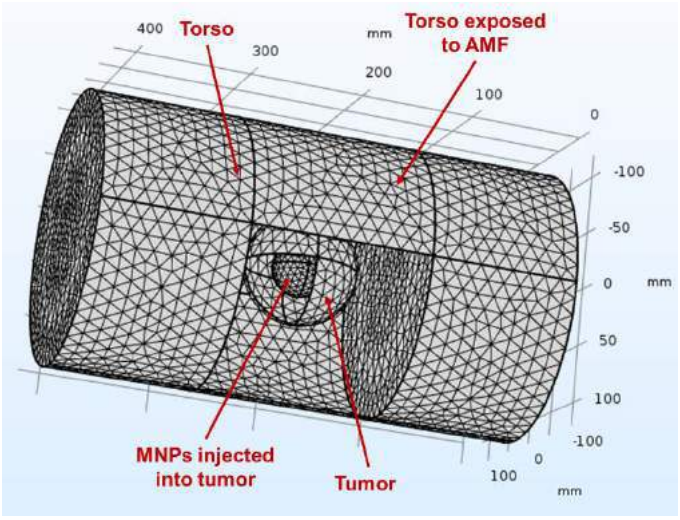

Figure 1: Geometry and the mesh used in the study.

A constant blood perfusion of $6.4 \cdot 10^{-3}\ \frac{1}{s}$ was used for all the tissue types. A treatment duration of 20 min with a time step of 30 s was modeled. Thermophysical properties used in this study were obtained from literature and are reported in Table 1.

Table 1: Thermophysical properties

Property	*Torso*	*Pancreas*
Heat capacity $[J/kg \cdot K]$	3640	4750
Density $[kg/m^3]$	1079	1800
Thermal Conductivity $[W/m \cdot K]$	0.52	0.59
Metabolic Heating Rate $[W/m^3]$	1578	1657

Convective heat flux boundary condition with a convective heat transfer coefficient of $10\ \left[\frac{W}{m^2 \cdot K}\right]$ and an ambient temperature of $20\ [°C]$ was enforced on the cylindrical surfaces of the torso. The circular surfaces for the torso were fixed at a temperature of $37\ [°C]$ to represent nominal body temperature far away from the heating source.

RESULTS

Non-specific eddy current heating is significant at the outer surface of the torso (Figure 2). Temperatures above 40°C in $5-8\ mm$ thick outer layer of the torso is a potential safety concern. Large tumors realized a higher tumor thermal dose compared to small tumors when treated with tumor volume-normalized MION dose and fixed AMF amplitude and frequency (Figure 3).

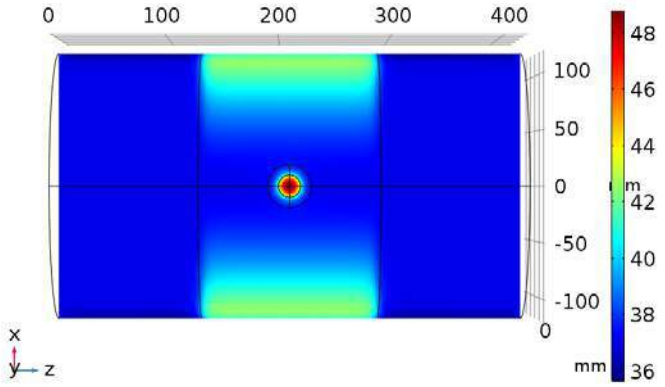

Figure 2: Temperature distribution after exposing tumor volume-normalized MNP dose to AMF for 20 min, for small tumor with a radius of 2 cm shown. Color legend reports temperature in °C. Non-specific eddy current heating on the superficial tissue due to AMF exposure is within the clinically acceptable limits.

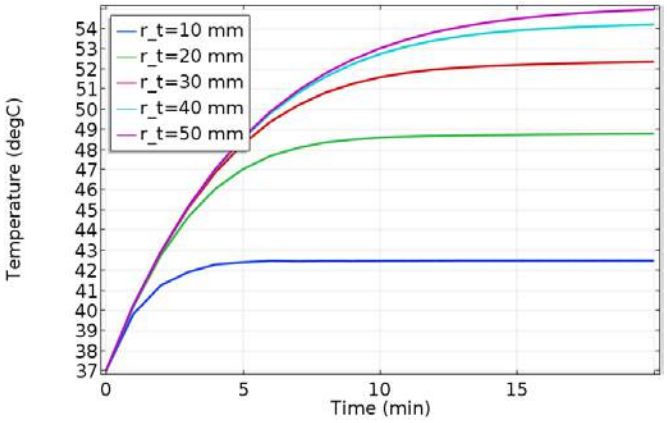

Figure 3: Tumor temperatures as a function of tumor radius, r_t.

DISCUSSION

Simulation results are consistent with previously reported *in vivo* results [6]. Briefly, tumor volume-normalized MNP dose of $5\ \frac{mg\ Fe}{cm^3\ of\ tumor}$ in MiaPaCa-02 subcutaneous human xenograft mouse models exposed to AMF amplitude of 6.5 kA/m (rms) at 160 kHz for 20 min resulted in superficial temperature due non-specific heating 38°C and tumor temperatures of 44°C for large tumors (0.30 cm^3) and 42°C for small tumors (0.15 cm^3). Simulation results follow a similar trend of higher tumor temperatures in large tumors compared to the small tumors. Strategies for reducing the superficial non-specific eddy-current heating will be presented. Future studies will include thermal dose dependent blood perfusion and human voxel models to facilitate development of clinical AMF devices and related technologies to translate MNPH therapy for LAPC to the clinic.

REFERENCES

1. SEER cancer statistics. https://seer.cancer.gov/faststats. Accessed on 01-18-2019).
2. Maebayashi, T et al Oncol Lett. 13(6): 4959–4964, 2014.
3. Attaluri A et al, J. Nanotechnol. Eng. Med. 4(1), 011006, 2013
4. Atkinson, WJ et al, IEEE Trans Biomed. Eng. 31(1):70-75, 1984
5. Attaluri A et al, Int J Hyperthermia. 32(5):543-57, 2016
6. Attaluri, A et al Society for Thermal Medicine Meeting. 2014

SB³C2019
Summer Biomechanics, Bioengineering and Biotransport Conference
June 25 -28, Seven Springs, PA, USA

IN SITU PHOTO-INACTIVATION OF PROTEINS BY MOLECULAR HYPERTHERMIA

**P. Kang (1), XQ. Li (2), S. I. Shiers (2), H. Xiong (1),
T. J. Price (3), Z. Qin (1, 2, 4)**

(1) Department of Mechanical Engineering
University of Texas at Dallas
Richardson, Texas, USA

(2) Department of Bioengineering
University of Texas at Dallas
Richardson, Texas, USA

(3) School of Behavioral and Brain Sciences
University of Texas at Dallas
Richardson, Texas, USA

(4) Department of Surgery
University of Texas at Southwestern Medical Center
Dallas, Texas, USA

INTRODUCTION

Selective and remote manipulation of proteins in living systems with high spatial and temporal resolutions is important to elucidate the post-genome *in situ* protein function and develop precise therapeutics for disease treatment. Though current approaches, including chromophore-assisted light inactivation (CALI)[1], optogenetics[2], and photoswitches[3], made significant developments in optical control of protein function, there are many drawbacks to overcome. Optogenetics requires genetic modification and is limited to light sensitive proteins. CALI utilizes chromophores as photosensitizers to inactivate protein by generation of reactive oxygen species (ROS). However, outcomes of CALI highly rely on ROS generation efficiency, which is dependent on both chromophore selection and cell microenvironment. Photoswitch uses molecules (*i.e.* azobenzene) that switch their conformation during light exposure. However, the working wavelength for photoswitch is narrow in ultraviolet and visible range which limits its further applications *in vivo*. Therefore, it remains challenging to optically control protein activity in live cells without genetic modification and independent of the cellular microenvironment (*i.e.* ROS).

Nanoparticles provide an interface to manipulate protein and cellular activity with high spatial and temporal precision. Physically, it is possible to apply short laser pulses to excite plasmonic nanoparticles and create a nanoscale hotspot, or "thermal confinement" when the pulse duration is less than the heat diffusion[4]. We have recently introduced the possibility of "molecular hyperthermia" (MH), defined as using ultrashort nanosecond laser pulses to excite plasmonic gold nanoparticle (AuNP) to unfold and inactivate targeted proteins with a very well-defined impact zone (in nm size) (Fig. 1). In this report, we demonstrate for the first time that MH can photo-inactivate protease activated receptor 2 (PAR2) in live cells without compromising cell viability. Since MH thermally inactivates protein of interest, it doesn't depend on cellular microenvironment and doesn't require genetic modification. Our results indicate that MH is a promising new approach to manipulate protein activity in live cells.

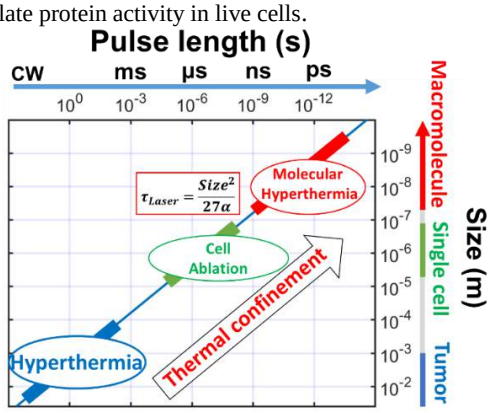

Figure 1. Schematic to illustrate the time and length scales of molecular hyperthermia (MH) compared with hyperthermia.

METHODS

We firstly synthesized AuNP (45 nm) following modified Frens' method[5]. To functionalize AuNPs, we conjugated antibodies (anti-PAR2 antibody MAB3949) onto AuNP by heterobifunctional polyethylene glycol (OPSS-PEG-SVA, 3.4 kDa). Then polyethylene glycol 2-mercaptoethyl ether acetic acid (Thiol-PEG-Carboxyl, 600 Da) was used to backfill and stabilize AuNP. AuNP-PEG was synthesized by stabilizing bare AuNP with Thiol-PEG-Carboxyl and used as the negative control.

Secondly, to monitor PAR2 activity, we cultured HEK293 cells with fluorescence resonance energy transfer (FRET) calcium (Ca^{2+})

indicator TN-XXL transferred [6] in 96 well plate. PAR2 activation was triggered by a PAR2 agonist (2-aminothiazol-4-yl-LIGRL-NH2, 2AT) that leads to Ca^{2+} release and was monitored by plate reader. 2-photon microscope was used to monitor the spatial resolution of PAR2 photo-inactivation by MH. We set excitation wavelength at 436 nm (810 for 2-photon microscope) and collected emission at 485 nm and 527 nm. The FRET ratio (ΔR/R) was calculated with following equation:

$$\frac{\Delta R}{R} = \frac{Fluorescence\ 527}{Baseline\ 527} \Big/ \frac{Fluorescence\ 485}{Baseline\ 485} - 1 \qquad (1)$$

Thirdly, a pulsed nanosecond laser (532 nm, Full width half maximum = 6 ns) was used to create MH *in situ*. Cells were incubated with functionalized AuNP solution to target PAR2. The extra particles were washed away and cells were irradiated with nanosecond laser pulses. PAR2 activity was checked after MH experiments. To investigate the spatial resolution of MH, a multichannel perfusion system was used to load artificial cerebrospinal fluid (ACSF) and 2AT. The 2-photon imaging system was used to monitor the PAR2 inactivation *in situ*. ACSF was perfused to cells for the first 52 seconds to obtain the base line followed by perfusing 2AT for 16 seconds. ImageJ was used to analyze images.

Lastly, WST-1 assay was used to investigate cell proliferation after MH. WST-1 stock solution was diluted 10 times with cell medium. After MH, the medium was replaced with 100 µL WST-1 working solution for each well. Cells were then incubated at 37 °C and 5% CO_2 for 3.5 hours and absorbance was read by plate reader at 450 nm.

RESULTS

Firstly, we tested and confirmed that the engineered HEK293 cells with Ca^{2+} indicator is a robust model to study PAR2 activity. PAR2 is a G-protein coupled receptor (GPCR) that leads to Ca^{2+} signaling upon activation. Incubation of HEK293 cells with 2AT leads to a robust response of ΔR/R increase due to Ca^{2+} release (Fig. 2A). To target PAR2 receptor, antibody modified AuNP was used (AuNP-MAB3949), and AuNP conjugated with polyethylene glycol (AuNP-PEG) was used as the negative control (Fig. 2B).

Next, we tested the effect of MH on PAR2 activity. Comparing PAR2 activity treated by AuNP-MAB3949 and AuNP-PEG under the same laser exposure (532 nm, 100 mJ/cm2, 10 pulses), significant drop (>80 %) in PAR2 activity was observed for AuNP-MAB3949 group at concentrations above 0.32 nM (Fig. 2C), while only 20% for AuNP-PEG group. At the same conditions, there is no significant difference in the cell proliferation between groups using AuNP-PEG and AuNP-MAB3949, suggesting a specific molecular level photo-inactivation by MH (Fig. 2D).

Finally, to demonstrate the precise spatial control of PAR2 by MH, we compared the cellular PAR2 response with and without laser irradiation in the same petri-dish by partially blocking the laser (Fig. 2E). The results suggest that the region without laser irradiation had an obvious Ca^{2+} release after 2AT loading while the region with laser irradiation has a much attenuated Ca^{2+} release (Fig. 2F). This suggests a high spatial control of PAR2 activity with optical manipulation using MH.

DISCUSSION

In this study, we demonstrate a novel method molecular hyperthermia (MH) to optically control protein activity in live cells by showing a GPCR (PAR2) can be photo-inactivated by MH without compromising cell proliferation. PAR2 is implicated in disease conditions including allergic asthma, cancer, arthritis, and chronic pain. Photo-inactivation of PAR2 will help us understand and treat diseases such as chronic pain. Furthermore, to apply MH *in vivo*, gold nanorod could be used with near-infrared laser to manipulate proteins of interest. This promising method overcomes the drawback of current approaches to manipulate protein activity and brings new promises for precise therapeutics of diseases.

In conclusion, we have demonstrated the ability of a newly developed MH technique to manipulate protein activity in live cells. Future works to further understand the underlying mechanism and *in vivo* testing are planned.

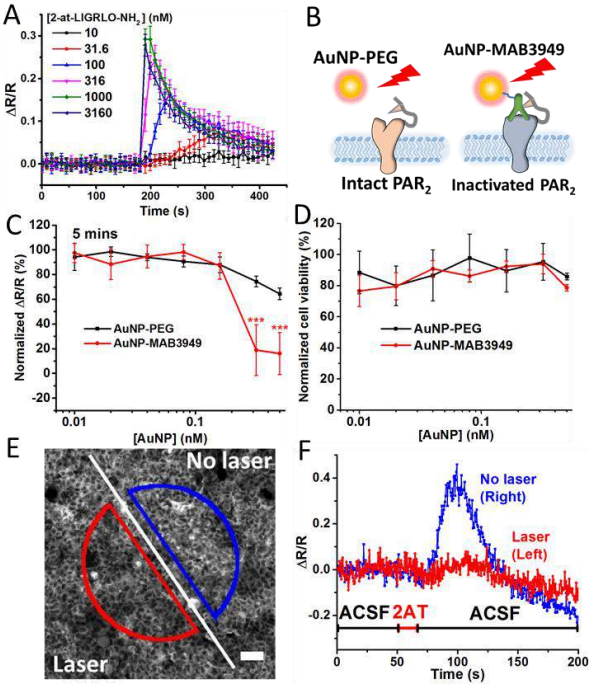

Figure 2. A) The FRET ratio (ΔR/R) signal for different concentrations of 2AT B) Experiment design of MH inactivation of PAR2. C) PAR2 activity after photo-inactivation of MH. D) Cell viability after MH. E) Fluorescence image of cells before and after laser irradiation and ROIs (scale bar: 50 µm). F) Ca^{2+} signals for different ROIs.

ACKNOWLEDGEMENTS

We acknowledge the support of Cancer Prevention and Research Institute of Texas (CPRIT, RP160770, RP180846), National Science Foundation (1631910), and startup fund from The University of Texas at Dallas. We thank Dr. Paul A. Slesinger (Icahn School of Medicine) for providing the HEK293 cell line. We thank Dr. Jamie Moy for helpful discussion for calcium imaging.

REFERENCES

[1] K. Jacobson, *et al.*, Trends Cell Biol 2008, 18, 443.
[2] K. Deisseroth, Nat Methods 2011, 8, 26; R. H. Kramer, *et al.*, Nat Neurosci 2013, 16, 816.
[3] T. Fehrentz, *et al.*, Nat Chem Biol 2018, 14, 764.
[4] G. Huttmann, *et al.*, Therapeutic Laser Applications and Laser-Tissue Interactions 2003, 5142, 88; P. Kang, *et al.*, Small 2017, 13.
[5] G. Frens, Nature Physical Science 1973, 241, 20; C. Ziegler, A. Eychmüller, the journal of physical chemistry C 2011, 115, 4502.
[6] A. Muller, *et al.*, Nat Methods 2014, 11, 1245.

DIFFUSION LIMITED CRYOPRESERVATION OF ARTERIAL TISSUE TO 1.5mm WITH RADIOFREQUENCY HEATED METAL FORMS

Zonghu Han(1), Zhe Gao (1), Anirudh Sharma (1), John C. Bischof (1,2)

(1) Department of Mechanical Engineering
University of Minnesota
Minneapolis, MN, USA

(2) Department of Biomedical Engineering
University of Minnesota
Minneapolis, MN, USA

INTRODUCTION

Recently, we showed that radiofrequency heating of metal forms (i.e. aluminum foil) can improve the warming rate of cryopreserved carotid artery (1 mm thick) tissue systems at rates ≥ 1000 °C/min thereby outrunning damaging ice crystals during warming. This is a significant (i.e. order of magnitude) improvement over rates available from conventional convective approaches. This increased warming rate can in turn be used to either reduce the need for CPA thereby reducing toxicity[1], or increase the thickness of the tissue that can be rewarmed from the cryopreserved state. However, as the thickness of the tissue increases, there will be a diffusive limit for boundary loading where the cryoprotectant (CPA) concentration in the center is insufficient to protect from ice formation even during warming with metal forms. This CPA concentration in the center sets the minimum threshold on the warming rate, which is called critical warming rate (CWR). This work probes that diffusive limit.

METHODS

In this study, we present both modeling and experimental data in arterial tissue (porcine carotid – 1mm to aorta – 2 mm) loaded with a variety of available CPAs (i.e. DP6 - 6M, VS55 - 8.4M, and M22 - 9.3M) and rewarmed with metal forms . In general, using high concentration M22 increases the chance of success and the least concentrated DP6 will be the least promising in terms of viability under the same loading conditions. We use a combination of diffusive CPA loading and estimation of critical cooling and warming rates needed within the tissue to avoid ice crystallization (i.e. failure). We compare these critical warming rates estimated by modelling with rates measured by thermometry, during metal forms rewarming. In general, the CWR to avoid ice crystallization increase dramatically as the CPA concentration is reduced within the tissue. In short, we predicted the CWR needed in the center of the tissue compared to those available from metal forms.

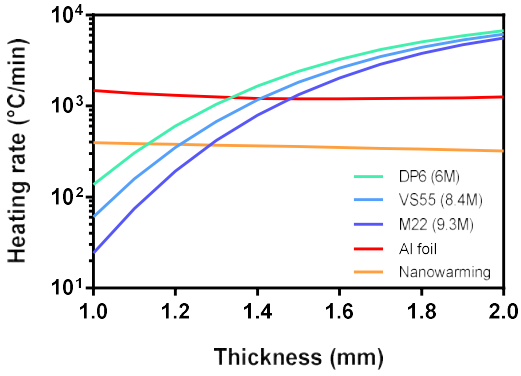

Fig. 1. Theoretical warming rate required at the center of tissue loaded by DP6, VS55 or M22, and the warming rate that can be achieved at the center region if nanowarming (300 °C/min) or Al foil warming (1300 °C/min) technique is applied

RESULTS and DISCUSSION

As we have published [1], the metal forms (i.e. aluminum foils) are placed next to the tissue under an alternating magnetic field (20 kA/m, 360 kHz) to obtain warming rates in excess of 1300 °C/min. Using previously published CPA diffusivity, loading steps and times without toxicity at low temperature [2] we estimate CPA concentrations within the tissue slices and predict CWRs required to successfully rewarm 1.3 mm thick tissue. For instance, DP6 should be successful with 1.3 mm, but fail at 1.5 mm while M22 should be successful at 1.5 mm, but fail at 2 mm as shown in **Error! Reference source not found.**. In short, 1.5 mm-thick iliac arteries are predicted to be the thickest tissues that can be cryopreserved and rewarmed with this approach.

Experiments were then carried out under the same CPA loading conditions as modelled ($n \geq 6$ for each CPA and artery case) to verify the viability predictions. The experimental results in Fig.2 show nearly 100% viability for both the thin carotid arteries (~1 mm) and thick carotid arteries (~1.3 mm) diffused by DP6, over 90% for 1.5 mm-thick iliac diffused by M22, and less than 40% for 2 mm-thick aorta with M22. These experiments are in agreement with the model predictions in Fig. 1, showing 1.5 mm thick tissues as a maximum with this approach.

In general, diffusion of heat (i.e. higher warming rates) and mass of CPA (i.e. higher CPA concentrations in deep tissue without toxicity) are the two keys to successful rewarming cryopreserved tissues at rates above CWR, therefore, avoiding damaging ice. However, this needs to be balanced with the toxicity due to exposure to CPAs. A solution to rewarming thicker arteries (i.e. 2 mm-thick aorta) or organ slices in the future is increased CPA-loading and/or increasing the warming rates. For instance, we can increase the exposure times of tissues to CPA as shown in Fig.3. However, increased exposure times often result in higher toxicity. On the other hand, the predicted warming rate needed at the center of a 2 mm tissue loaded with M22 is approximately 5000^0C/min. Perhaps, these rates and even higher can be achieved through optimal design and material composition of metal forms in the future.

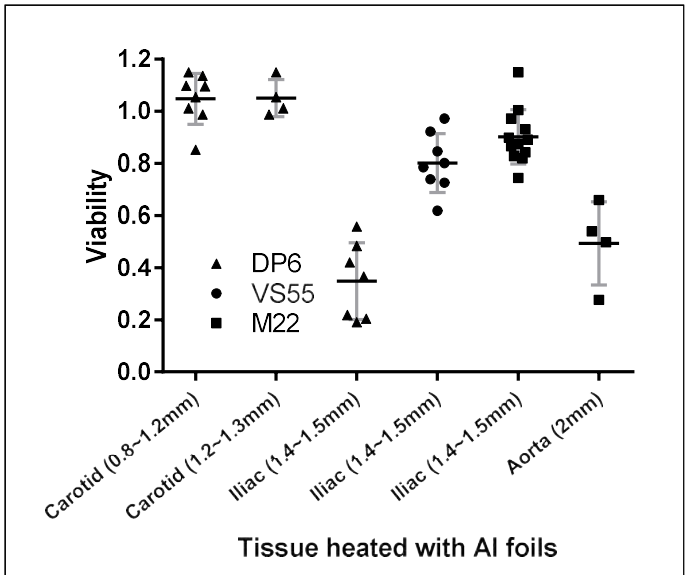

Fig. 3. Experimental results of metal forms heated arterial tissues from 0.8 to 2 mm thickness

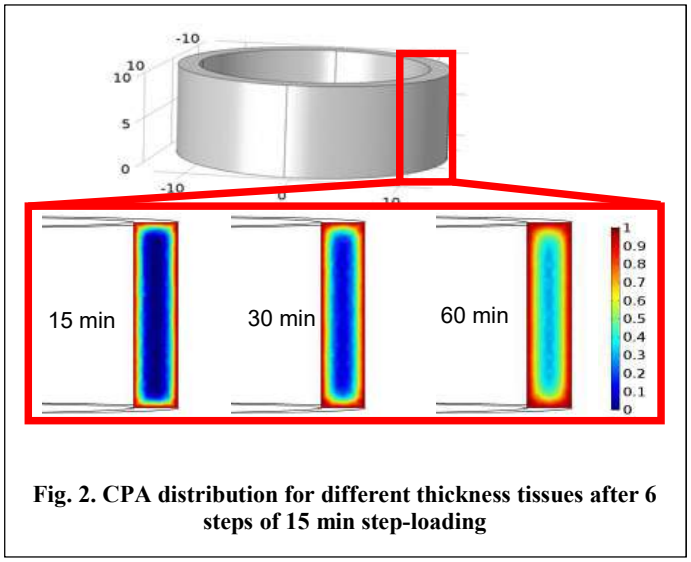

Fig. 2. CPA distribution for different thickness tissues after 6 steps of 15 min step-loading

In summary, diffusive modeling of CPA delivery and heating provided a relatively accurate prediction of the success of metal forms cryopreservation as a function of tissue thickness and CPA type. A key to increasing the thickness of the tissue was either increased CPA loading or increased heating rates from metal forms.

ACKNOWLEDGEMENTS

We thank the Visible Heart Laboratory's C. Soule, A. Deakyne, and T. Healy for access to porcine arteries. Funding: This work was supported by NIH (P41EB015894, R43HL123317)

REFERENCES

[1] Manuchehrabadi N, Shi M, Roy P, Han Z, et al. Ultrarapid Inductive Rewarming of Vitrified Biomaterials with Thin Metal Forms. Annals of Biomedical Engineering. 2018:1-13.

[2] Manuchehrabadi N, Gao Z, Zhang J, Ring HL, Shao Q, Liu F, et al. Improved tissue cryopreservation using inductive heating of magnetic nanoparticles. Science translational medicine. 2017;9(379):eaah4586.

COUNTERINTUITIVE SCALING EFFECTS IN THE DEVELOPING THERMOMECHANICAL STRESS DURING CRYOGENIC COOLING OF THE KIDNEY WITH IMPLICATIONS TO ELECTROMAGNETIC REWARMING FOR ORGAN RECOVERY

Prem K. Solanki and Yoed Rabin

Biothermal Technology Laboratory
Department of Mechanical Engineering
Carnegie Mellon University
Pittsburgh, PA, USA, 15213

INTRODUCTION

The need for long-term preservation of organs and large-size tissue specimens is unquestionable, with vitrification (*vitreous* means *glassy* in Latin) as the most promising method for suspending the biological clock while preserving cell viability and tissue functionality. Vitrification necessitates rapid cooling of the specimen, which is permeated with cryoprotective agents (CPAs), down to the glass transition temperature (T_g) in order to trap it in an amorphous, solid-like state. Unfortunately, the rapid cooling and rewarming rates required for vitrification, coupled with the low thermal diffusivity of the biological material, may yield hazardous effects of thermomechanical stress. Thermomechanical stress might be one of the primary causes of cryopreservation failure, driven by differential thermal expansion (or contraction) and resulting in structural damage, such as plastic deformations and fractures.

The current study investigates thermomechanical effects in rabbit and human kidney models, contained in cylindrical containers and exposed to realistic cryopreservation protocols. The thermomechanical stress is simulated using previously established numerical framework [1], based on finite elements analysis (FEA). Analytical results of simplified cases are also presented to explain counterintuitive observations during stress development.

The onset of rewarming from cryogenic storage has been identified to be the most dangerous to structural failure [2]. Volumetric heating techniques, such as electromagnetic heating in the radiofrequency (RF) range, have been proposed previously to alleviate structural damage during the rewarming phase of the cryogenic protocol. The current study presents a computational framework to simulate the corresponding thermomechanical effects. Furthermore, the computational framework presented in this study can serve as the foundation for optimization of RF heating parameters, including the design of the cooling chamber, the container, and the cryoprotocol.

METHODS

Commercial FEA software packages are employed to solve the coupled electromagnetic, thermal, and solid mechanics fields. The proposed framework starts with a bidirectional-coupled problem of the electromagnetic and thermal fields, to solve for the transient temperature distribution within the specimen. This bidirectional coupling enables the incorporation of temperature-dependent material properties in the electromagnetic model and a heat-generation term dependent on the spatial electric field in the heat transfer model. Next, a unidirectional-coupled problem of the thermal field and mechanical stress distribution is solved, where the specimen is modelled as a Maxwell fluid with temperature-dependent viscosity.

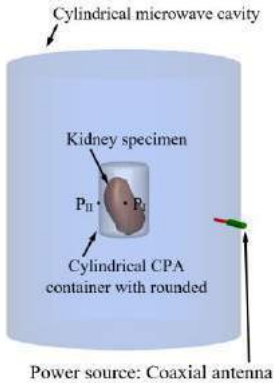

Figure 1: Schematic illustration of the problem geometry (not drawn to scale), where the size of the resonance chamber depends on the specimen and electromagnetic frequency.

The geometric model consists of a cylindrical resonance chamber with a coaxial antenna as the power source (Fig. 1). The kidney models are imported from a previous study [3], where the human kidney model is 21-fold larger than the rabbit kidney. Appropriate curvature is added to the edges of the cylindrical CPA container to avoid thermal runaway.

The dimensions of cylindrical resonance chamber are different for the rabbit kidney and human kidney models, yielding resonance frequencies of 434 MHz and 108 MHz in the TE111 resonance mode, respectively. The TE111 resonance mode is selected to achieve high heating power at the center of the resonance chamber [4].

Electromagnetic model: The spatial distribution of the electric field for a nonmagnetic dielectric material in a resonance chamber is determined by the Maxwell equations in the frequency domain:

$$\nabla \times (\nabla \times \boldsymbol{E}) - \omega^2 \mu_0 \varepsilon_0 \varepsilon_{rc} \boldsymbol{E} = 0 \quad (1)$$

where $\boldsymbol{E}$ is the electric field, f is the frequency, $\omega=2\pi f$ is the angular frequency of the electromagnetic field, ε_0 and μ_0 are the electric and magnetic permeability of free space, respectively, and ε_{rc} is a complex relative permittivity given by $\varepsilon_{rc}=\varepsilon'-j\varepsilon''$, where ε' is the dielectric constant and ε'' is the dielectric loss factor.

The walls of the resonance chamber are assumed to be perfect electric conductors:

$$\hat{n} \times \boldsymbol{E} = 0 \quad (2)$$

where $\hat{n}$ is a unit vector perpendicular to the resonance chamber wall.

Heat Transfer model: Heat transfer within the CPA domain is assumed solely by conduction:

$$\rho C_p \dot{T} = \nabla \cdot (k \nabla T) + \pi f \varepsilon'' |E_{RMS}|^2 \quad (3)$$

where ρ is the density, C_p is the specific heat, T is the temperature, k is the thermal conductivity, and E_{RMS} is the root-mean-square value of the electric field.

A thermal protocol for specimen vitrification consisting of four phases is considered here: convective cooling, storage, RF rewarming, and convective rewarming, Fig. 2.

Solid Mechanics model: The total strain rate in the Maxwell fluid model is calculated as [2]:

$$\dot{\boldsymbol{\varepsilon}}_{total} = \dot{\boldsymbol{\varepsilon}}_{creep} + \dot{\boldsymbol{\varepsilon}}_{elastic} + \dot{\boldsymbol{\varepsilon}}_{thermal} \quad (4)$$

$$\dot{\boldsymbol{\varepsilon}}_{creep} = \frac{\boldsymbol{S}}{2\eta} \quad (5)$$

$$\dot{\boldsymbol{\varepsilon}}_{elastic} = \frac{1}{E_e}[(1+\nu)\dot{\sigma} - \nu \boldsymbol{I} \cdot tr(\dot{\sigma})] \quad (6)$$

$$\dot{\boldsymbol{\varepsilon}}_{thermal} = \beta \dot{T} \boldsymbol{I} \quad (7)$$

where $\boldsymbol{S}$ is the deviatoric stress tensor, η is the viscosity, E_e is the elastic modulus, ν is the Poisson ratio, $\boldsymbol{I}$ is the identity matrix, tr is the trace matrix, and β is the linear thermal expansion coefficient.

Note that although developed by the same famous physicist and mathematician, the Maxwell electromagnetic model and the Maxwell fluid model are completely unrelated.

RESULTS AND DISCUSSION

Figure 2 displays the temperature and stress histories at the center and edge of the specimen, at the locations displayed in Fig. 1. The cooling phase of the protocol for rabbit and human kidney models is consistent with [3]. As the specimen begins to cool below room temperature, the CPA becomes increasingly viscous, and thermomechanical stress development follows. The stress in the specimen reaches a local maximum value as the temperature approaches storage temperature, followed by stress relaxation to insignificantly low level. This is due to the selected storage temperature, which is very close to T_g in order to facilitate stress relaxation [5].

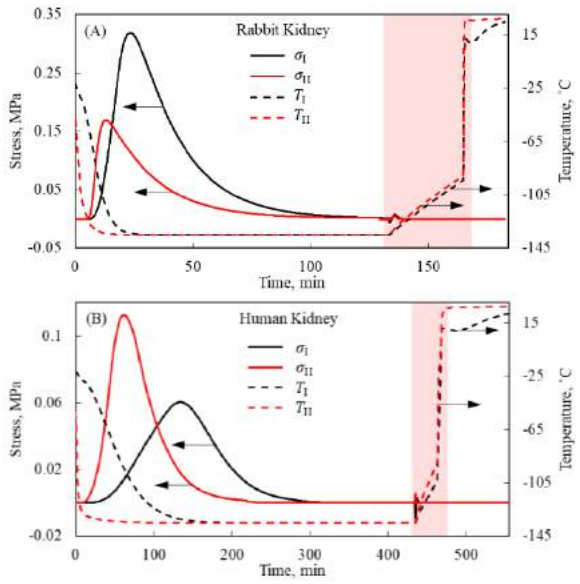

Figure 2: Maximum principal stress and temperature history at points displayed in Fig. 1 for (A) Rabbit kidney and (B) Human kidney. The microwave rewarming section of the thermal protocol is highlighted in red.

The maximum stress at the center of a specimen has been shown directly proportional to the cooling rate at the geometric center of the specimen and to the characteristic dimension of the specimen to second power in simplified cases [5]. In the current study however, the peak stress developed in the rabbit kidney model is found higher than the peak stress developed in the human kidney model despite the former being smaller in dimension.

The above counterintuitive observation is associated with the time variation of the temperature distribution across the specimen while it gains solid-like properties during cooling. It is associated with a 12 orders of magnitude exponential increase in viscosity with the decreasing temperature during vitrification. Due to the underlying principles of heat transfer, the outer region of the larger specimen gains solid-like properties much earlier than the inner region. In general, the corresponding thermal history results in compressive circumferential stress on the outer surface and tensile stress at the center, where tensile stress is the primary cause of fractures in brittle materials. The smaller specimen however becomes a solid-like material subject to a much more uniform temperature, which give rise to a lower compressive stress at the outer surface but to a higher tensile stress at the center. Note that the radial decay in tensile stress and buildup of compressive stress is nonlinear, while other specimen sizes and cryoprotocols may result in different stress distributions. As a result of the parameters tested in this study, the smaller specimen experiences an overall higher tensile stress, which makes it more prone to structural damage.

ACKNOWLEDGEMENTS

This work has been supported by the National Heart Lung and Blood Institute (NHLBI), award R01HL127618.

REFERENCES

[1] Solanki, P. K., and Rabin, Y., *PLoS One*, 13(6), 2018.
[2] Rabin, Y., et al., *Cryobiology*, 53(1): 75–95, 2006.
[3] Ehrlich, L. E., et al., *J. Biomech. Eng.*, 140(1), 2017.
[4] Robinson, M. P., and Pegg, D. E., *IEEE Trans. Biomed. Eng.*, 46(12): 1413–1425, 1999.
[5] Steif, P. S., et al., *Cell Preserv. Technol.*, 5(2): 104–115, 2007.

SB^{3}C2019
Summer Biomechanics, Bioengineering and Biotransport Conference
June 25 -28, Seven Springs, PA, USA

PATIENT-SPECIFIC ESTIMATION OF ASCENDING THORACIC AORTIC ANEURYSIM GROWTH AND REMODELING: FEM BASED CONSTRAINED MIXTURE MODEL

S. Jamaleddin Mousavi, Stéphane Avril

Mines Saint-Etienne, Univ Lyon, Univ Jean Monnet, INSERM, U 1059
Sainbiose, Centre CIS, F - 42023 Saint-Etienne France

INTRODUCTION

Growth and remodeling (G&R) are fundamental mechanobiological processes in normal tissue development and in various pathological conditions. It is suggested that G&R in tissues may be mediated by mechanical stresses. For example, cardiac hypertrophy and normal cardiac growth develop in response to increased hemodynamic loading and altered systolic and diastolic wall stresses [1]. Sustained hypertension is also associated with changes such as increased wall thickness in large arteries [2]. This adaptation ability of soft tissues is related to the existence of a mechanical homeostasis across multiple length and time scales in the vasculature. At the tissue scale, this manifests through continuous mass changes of the components of the extracellular matrix (ECM) such as collagen, elastin and proteoglycans [3].

In the current paper, we are interested in continuum finite-element formulations to simulate G&R in arteries. The first model of mechano-regulated soft tissue growth was presented by Rodriguez et al in the mid-1990s, incorporating the associated growth by multiplicative decomposition of the total deformation gradient into an elastic and inelastic part. Thereafter, this conceptual simplicity has been widely used by others [4]. Although many theories of G&R have modelled the tissue as a homogenized (single-constituent) solid continuum, the constrained mixture model (CMM) has been increasingly employed by a number of authors [3-5], to simulate G&R in arteries, including non-homogenized [3] and homogenized [5] approaches.

Although computational modeling of vasculature G&R has significantly improved our insights of the G&R processes, developing patient-specific models are still a challenging problem (layer specificity, irregular boundary conditions and complex deformations) and an open question. These problems can become extremely challenging in the case of ascending thoracic aortic aneurysms (ATAA) evolution due to the simulateneous and region specific evolution of geometry, material properties, and hemodynamic loads. Therefore, it is interesting to develop a continuum finite-element model (FEM) to simulate G&R of ATAA evolution.

METHODS

According to the CMT, we assume that all constituents (elastin, e, collagen fiber families, c_j, and SMCs, m) in the mixture deform together under the total deformation gradient $\mathbf{F}$ in the stressed field while each constituent has a different "total" deformation gradient resulting from its own deposition stretch of $\mathbf{G}_{\mathrm{h}}^{i}$ with $\{i \in \{\mathrm{e}, c_j, \mathrm{m}\}$ respect to the reference homeostatic configuration. Thus, for each differential mass increment of the ith constituent deposited at time, the total deformation gradient of each constituent ($\mathbf{F}_{\mathrm{tot}}^{i} = \mathbf{F}\mathbf{G}_{\mathrm{h}}^{i}$) may be rewritten by a multiplicative decomposition into an elastic, $\mathbf{F}_{\mathrm{el}}^{i}$, and inelastic (named G&R) parts, $\mathbf{F}_{\mathrm{gr}}^{\mathrm{i}}$, as $\mathbf{F}_{\mathrm{tot}}^{i} = \mathbf{F}_{\mathrm{el}}^{i}\mathbf{F}_{\mathrm{gr}}^{\mathrm{i}}$ [5].

A strain energy density function is defined for the different components of the arterial wall based on the CMT. The intima layer is disregarded here as it is very thin. Based on the mass fractions of each individual component, ρ_t^i, in media and adventitia, the specific strain energy density function may be written as [6]:

$$W = \rho_t^{\mathrm{e}}\left[\frac{\mu_{\mathrm{e}}}{2}(\bar{I}_1^{\mathrm{e}} - 1) + \kappa(J_{\mathrm{el}}^{\mathrm{e}} - 1)\right] + \rho_t^{c_j}\frac{k_1^{c_j}}{k_2^{c_j}}\left(e^{k_2^{c_j}\left(I_4^{c_j}-1\right)^2} - 1\right) + \rho_t^{\mathrm{m}}\frac{k_1^{\mathrm{m}}}{k_2^{\mathrm{m}}}\left(e^{k_2^{\mathrm{m}}(I_4^{\mathrm{m}}-1)^2} - 1\right) \quad (1)$$

with $\bar{I}_1^i = \mathrm{tr}\left(\bar{\mathbf{F}}_{\mathrm{el}}^{i\ (\mathrm{T})}\bar{\mathbf{F}}_{\mathrm{el}}^{i}\right)$, $\bar{I}_4^i = \mathbf{F}_{\mathrm{el}}^{\mathrm{i}\ (\mathrm{T})}\mathbf{F}_{\mathrm{el}}^{i}\colon \mathbf{a}_0^i \otimes \mathbf{a}_0^i$, $\bar{\mathbf{F}}_{\mathrm{el}}^{i} = J_{\mathrm{el}}^{i\ -1/3}\mathbf{F}_{\mathrm{el}}^{i}$ and $J_{\mathrm{el}}^{i} = \det(\mathbf{F}_{\mathrm{el}}^{i})$, where μ_{e}, $k_1^{c_j}$ and k_1^{m} are stress-like material parameters, κ is bulk modulus, $\mathrm{k}_2^{\mathrm{c_j}}$ and $\mathrm{k}_2^{\mathrm{m}}$ are dimensionless material parameters and $\mathbf{a}_0^i$ denotes the corresponding fiber direction in

reference configuration. In the Eq. 1 the two firs terms correspond to the behavior of elastin enforcing incompressibility while third and fourth terms model the behavior of the collagen fiber families and SMCs, respectively.

In CMT–based models, G&R is a conceptual phenomenon during which simultaneous degradation and deposition of different constituents continuously occur. This mass turnover is a stress mediated process during which extant mass is continuously degraded and new mass is deposited into the extant matrix by a stress mediated rate [5, 8, 14]. In this work, in two-layer arterial models, mass turnover of collagen families is mediated by SMC stresses in the media and by collagen stresses in the adventitia (for the latter, it is assumed that fibroblasts of the adventitia would be sensitive to the stresses of collagen, both in intensity and directionality).

The multiplicative decomposition of the inelastic G&R deformation gradient of the ith constituent deposited at different times can be written as $\mathbf{F}_{\mathrm{gr}}^{i} = \mathbf{F}_{\mathrm{g}}^{i}\mathbf{F}_{\mathrm{r}}^{i}$, where $\mathbf{F}_{\mathrm{g}}^{i}$ and $\mathbf{F}_{\mathrm{r}}^{i}$ are inelastic deformation gradients due to growth and remodeling, respectively. The former is related to any change in the mass per unit reference volume and the latter captures changes in the microstructure due to mass turnover. Therefore, having the net mass production rate, the evolution of the inelastic G&R deformation gradient of the ith constituent at time t can be calculated by solving a system of non-linear equations [5]. The proposed model was implemented within the commercial FE software Abaqus through a coupled user material subroutine (UMAT). It is assumed that each element is a mixture of elastin, collagen and SMCs with mass density varying regionally. The deformation of the artery is computed for every time step corresponding to one month of real time.

To demonstrate the applicability of the model to predict patient-specific wall G&R, the model was employed onto the geometry of a real human ATAA. An ATAA specimen and the preoperative CT scan of the patient were obtained after informed consent from a donor undergoing elective surgery for ATAA repair at CHU–SE (Saint-Etienne, France). A 3D structural mesh (the edge of each element was locally aligned with the material directions of the artery) made of hexahedral elements was reconstructed across ATA. 97% of total elastin, 100% of total SMC, and 15% of total axial and diagonal collagen fibers were assigned to the media. Conversely, the rest for each constituent were assigned to the adventitia. Both ends of the ATAA model were fixed in axial and circumferential directions, allowing only radial displacements. For the same patient, 4D flow MRI datasets were also acquired, revealing a jet flow impingement against the aortic wall around the bulge region (downstream the area of maximum dilatation). Guzzardi et al. [7] found that regions with largest WSS underwent greater elastin degradation associated with vessel wall remodeling. Consequently, based on these findings we considered a localized elastin degradation with an exponential on the ATAA G&R.

RESULTS

The G&R response of a patient-specific ATAA to localized elastin degradation is shown in Fig. 1-a, c and e. Due to change of shape, the stress distribution is in continuous adaptation. For all cases, elastin loss induces a transfer of stress to the adventitia in the damaged region. Moreover, an increase of $\mathrm{t_{dam}}$ results in an increase of maximum principal stresses in the arterial wall. It is induced by the related increase of elastin degradation rate. In Fig. 1-b, d and f, the distribution of collagen mass density for different $\mathrm{t_{dam}}$ shows that most of the collagen is deposited in the media where elastin has been lost (recall that ~97% of the elastin is in media), causing finally a thickening of the arterial wall. It is noteworthy that increase of $\mathrm{t_{dam}}$ accelerates collagen deposition and consequently wall thickening.

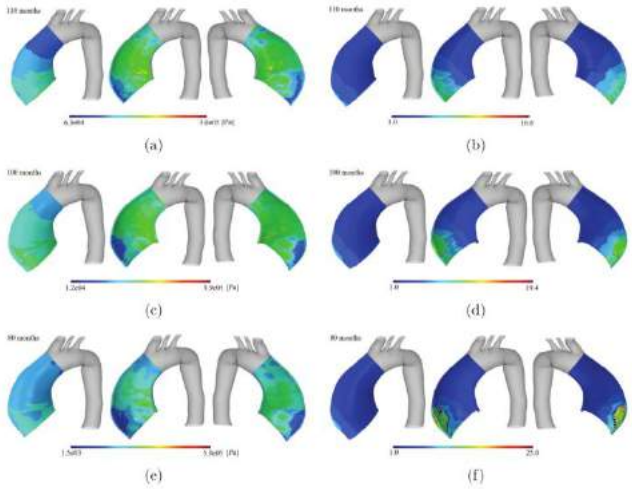

Figure 1: Distribution of the maximum principal stress (first column) and normalized collagen mass density (second column) in a two–layer patient-specific human ATAA responding to localized elastin loss, $\mathrm{t_{dam}}$= 20 (a and b), $\mathrm{t_{dam}}$ = 40 (c and d) and $\mathrm{t_{dam}}$ = 80 (e and f) days. In all cases it is assumed that $\mathrm{k_{\sigma}^{c_j}} = \frac{0.05}{\mathrm{T^{c_j}}}$

DISCUSSION

We considered multiple elastin degradation rate leading to different aneurysm growth rate. Although the global shape of the aneurysm remains similar, the thickening and collagen production rates are different for different cases. Different temporal damage constants showed significant effects on the expansion rate where the higher damage rate delivers the higher G&R rate. In the patient–specific study it also appears that collagen deposition tends to compensate the elastin loss. It is worth noting that as aneurysm grows, principal stress may not necessarily increase in the damaged location. This is observed in AAA growth as well. Moreover, although elastin was degraded locally, dilatation of the ATAA was spread across a larger area due to stress redistribution.

This altogether indicates that the present model has the potential for clinical applications to predict G&R of patient-specific geometries if a realistic rate of elastin loss and collagen growth parameter are available.

ACKNOWLEDGEMENTS

The authors are grateful to the European Research Council for grant ERC-2014-CoG BIOLOCHANICS.

REFERENCES

[1] W. Grossman, Am J Med, vol. 69, pp. 576-84, 1980.
[2] J. Humphrey, Hypertension, vol. 52, pp. 195-200, 2008.
[3] N. Famaey et al., Z Angew Math Mech, pp. 1-19, 2018.
[4] S. Baek et al., J Biomech Eng, vol. 126, pp. 142-9, 2006.
[5] F. Braeu et al., Biomech Model Mechanobiol, vol. 16, pp. 889-906, 2017.
[6] S. Mousavi et al., Int J Numer Method Biomed Eng, vol. 34, p. e2944, 2018.
[7] D. Guzzardi et al., J Am Coll Cardiol, vol. 66, pp. 892-900, 2015.
[8] C. Cyron et al., Biomech Model Mechanobiol, vol. 15, pp. 1389-403, 2016.

MACHINE LEARNING PREDICTION OF RUPTURE STRENGTH OF ASCENDING AORTIC ANEURYSM TISSUE

Xuehuan He (1), Anna Ferrara (2), Yuanming Luo (1), Ferdinando Auricchio (2), Jia Lu (1)

(1) Mechanical Engineering Department
University of Iowa
Iowa City, Iowa, United States

(2) Dipartimento di Ingegneria Civile e Architettura (DICAr)
Universit□ degli Studi di Pavia
Pavia, Italy

INTRODUCTION

Ascending thoracic aortic aneurysm (ATAA), a local dilatation in the aorta, tends to expand gradually and sometimes result in a sudden rupture. When an aortic aneurysm ruptures, the mortality rate is very high [1,2]. From a biomechanical viewpoint, aneurysms rupture when the stress in the wall exceeds its strength. Nowadays finite element method can be used to predict the wall stress on a patient-specific basis, but there is no practical way to obtain the tissue's strength noninvasively. Early studies have shown that there exist relationships between aneurysms strength and prerupture response features. Sugita et al. found that the ATAA strength correlates significantly with a particular stress at a "yield point" before rupture [3]. A recent study found that the ATAA strength has correlation with the tension at the point where the curvature of the total tension strain curve attains maximum [4]. Besides, it was also found that some clinical factors could significantly affect the mechanical properties of the ATAA tissue [5]. Motivated by these findings, a statistical model which could relate ATAA strength to these features is expected to be developed and thus predict the rupture strength. Nowadays, machine learning regression algorithms have earned much importance for the prediction in aneurysm biomechanics [6]. In our work, machine learning regression models are tested to evaluate the feasibility of predicting ATAA strength. The input to the machine learning is certain prerupture response features derived from stress strain curves and some clinical parameters.

METHODS

Dataset used in this study is obtained from Prof. Auricchio's lab as described in [5]. Briefly, 187 specimens of ATAA were excised from 68 patients who underwent elective surgical repair. Stress-stretch curves were obtained from uniaxial tensile tests. Through pre-screening of ATAA ruptures, 30 curves with too much noise are excluded. Principal component analysis (PCA) is applied to the remaining curves to reduce data noise.

Two groups of features are used as the basis for regression. The first is the global parameters (GP) comprised of continuous and categorical clinical parameters. Continuous parameters include age, body mass index (BMI), maximum ATAA diameter (Dmax) and aortic size index (ASI). Values of categorical parameters are obtained through one-hot encoding method: HP: hypertension (1 = hypertensive subject; 0 = no-hypertensive subject), Gender (1=Female; 0=Male), BAV: bicuspid aortic valve (1 = presence of BAV; 0 = no presence of BAV) Zone: (1= Anterior, 0 =Posterior) and Direction (1 = Circumferential, 0 = Longitudinal). The second set of features consists of 8 curve geometric parameters (CG): the curvature, the stress, the strain and the slope of both maximum curvature point and transition point, which are two particular points of stress-stretch curves as shown in figure 1.

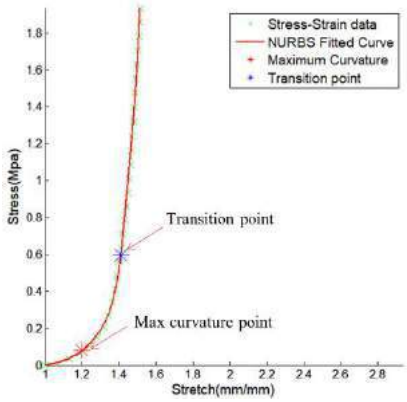

Figure 1: Representative ATAA stress-stretch curve

A typical ATAA stress-stretch curve as shown in figure 1 has a J-shape with a compliant elastin-dominated region at the low stress range turning into a transition phase in the middle and a stiff collagen-dominated region at the high stress range. The maximum curvature of the curve (MC) may reflect how fast the collagen recruitment is, and the stress and strain at this point (MC_stra, MC_stre) may suggest how early the transition occurs and the slope (MC_slope) could be a measurement of the early stiffness. In our work, a transition point is identified based on slope change of the curves. As shown in Figure 1, the slope of a typical stress-strain curve changes significantly in the transition period while becoming stable when it comes to exponential phase. We define the transition point as the point where the rate of change of the curve slope begins to decrease, i.e., the onset of the decreasing of second derivative. The stress and strain (TP_stra and TP_stre) may reflect the end of the transitional phase. The slope (TP_slope) may represent the stiffness of the specimen when collagen fibers fully come into load bearing. The curvature at the transition point (TP_curv) may indicate the change of collagen stiffness when it comes to exponential range.

To facilitate the computation of derivatives, we fit the stress and strain curves to a third-order NURBS function with 3 knot intervals. At the same time, knot positions for each curve are optimized to maintain a smooth change of slope.

Regressions are performed separately over 2 groups of features using a 10-fold cross-validation. A machine learning library, Scikit-learn, is used in the study [7]. The first group is the curve geometric parameters (CG). The second group is the union of curve features (CG) and global features (GP). Ensemble techniques, including ensemble.randomforest regressor (ERF) and ensemble.gradientboosting regressor (EGB) are selected because they can handle mixed input data (continuous data and categorical data). Average mean-square error (AMSE) and average cross-validation score (ACVS) are used to measure the performance.

RESULTS

Table 1 illustrates the regression results on the two groups of features, CG and GP&CG. Note that EGB model shows better performance than EFB model. It can be also seen that global features slightly help to improve the prediction score and reduce AMSE. A good performance of training dataset is observed, as shown the Figure 2.

Table 1: Regression result of training dataset

Features	CG		Union (CG&GP)	
Models Employed	AMSE	ACVS	AMSE	ACVS
ERF	0.0600	0.823	0.0586	0.836
EGB	0.0529	0.840	0.0444	0.858

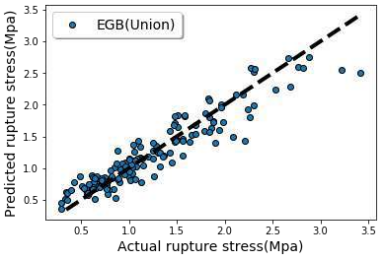

Figure 2: Performance of training dataset

DISCUSSION

In this study, we use machine learning to predict the rupture stress of ATAA. We obtain 0.044 average mean-square error using the union of prerupture geometric features and clinical parameters as input. In overall, the regression results are decent. Figure 3 shows the relative feature importance of each individual feature in the regression model. Note that the stress at the transition point is the most important factor among the curve geometric parameters and age is the most important parameter among clinical parameters. It should be noted that clinical parameters in our work show substantially less contribution when considering two sets of features together.

To evaluate the reliability of the models, we develop a test dataset which consisted of truncated ATAA curves where a tailing segment of arbitrary length is removed. It is worth mentioning that the transition phase of the curves is retained. The truncated curves are subjected to feature harvesting and new curve parameters are generated. We then apply the machine learning models to predict the rupture stress of truncated curves. The R^2 (coefficient of correlation) score and the mean-square error (MSE) are used to evaluate the test dataset performance. Table 2 illustrates the test results, which are very similar to train scores as shown in Table 1. Figure 4 shows the predicted rupture stress vs the rupture stress. The rupture stresses are predicted to within the same level of accuracy as in training. At the same time, we also found that predicted rupture stresses are greater than truncated curve end stress mostly, with only 3 samples slightly lower. This test confirms that the regression result is reasonably trustworthy.

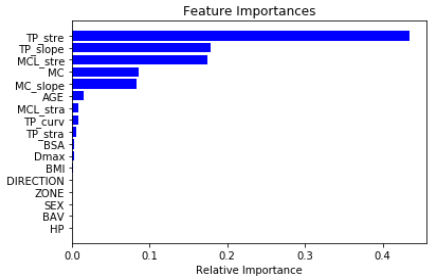

Figure 3: Relative feature importance

Table 2: Regression result of test dataset

Features	CG		Union (CG&GP)	
Models Employed	MSE	R^2	MSE	R^2
ERF	0.0628	0.8395	0.0607	0.8450
EGB	0.0594	0.848	0.0545	0.874

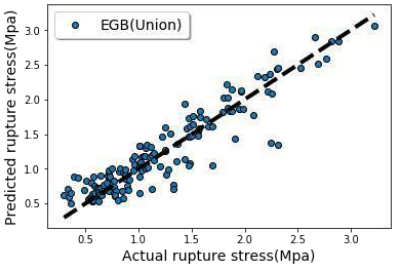

Figure 4: Performance of test dataset

REFERENCES

[1] Evangelista, A. Heart 96(12): 979, 2010. [2] Lavall, Daniel et al. DTSCH ARZTEBL INT.109(13), 227-233,2012. [3] Sugita S, et al. Cardiovasc Eng Technol. 3(1), 41-51,2012. [4] Luo, Y. et al. Int J Numer Method Biomed, 34(6), N/a, 2018. [5] Ferrara et al. J Mech Behav Biomed Mater, 77, 1–11,2018. [6]Liang L. et al. Biomech Model Mechano biol.2017:1-15. [7] Pedregosa F. et al. J Mach Learn Res.2011;12:2825-2830.

SB³C2019
Summer Biomechanics, Bioengineering and Biotransport Conference
June 25-28, Seven Springs, PA, USA

WALL STRESS AND GEOMETRY MEASURES IN ELECTIVELY REPAIRED ABDOMINAL AORTIC ANEURSYMS

Balaji Rengarajan (1), Wei Wu (1), Mirunalini Thirugnanasambandam (2), Shalin Parikh (2), Raymond Gomez (1), Victor De Oliveira (3), Satish C. Muluk (4), Ender A. Finol (1,2)

(1) Department of Mechanical Engineering
University of Texas at San Antonio
San Antonio, TX, U.S.A.

(2) UTSA/UTHSA Joint Graduate Program in Biomedical Engineering
University of Texas at San Antonio
San Antonio, TX, U.S.A.

(3) Department of Management Science and Statistics
University of Texas at San Antonio
San Antonio, TX, U.S.A.

(4) Department of Thoracic & Cardiovascular Surgery, Allegheny General Hospital
Allegheny Health Network
Pittsburgh, PA, U.S.A.

INTRODUCTION

Abdominal aortic aneurysm (AAA) is a vascular disease characterized by the enlargement of the infrarenal aorta by more than 50% and typically a diameter of 5.5 cm is considered aneurysmal. However, smaller AAA are also prone to rupture and severe cases can lead to fatality. Recently, biomechanics-based rupture risk assessment strategies have been postulated as a better measure of the disease severity compared to maximum diameter [1-3]. As computational approaches involve complex finite element models, we aim to utilize geometric predictors of wall stress as part of a rupture risk assessment strategy. In this work, we identify geometric attributes that correlate strongly with wall stress using a cohort of 100 patient-specific AAA models derived from asymptomatic, unruptured, electively repaired AAA.

METHODS

The abdominal computed tomography angiography (CTA) scans of 100 patients who were diagnosed with AAA were obtained from an existing database in the Department of Radiology at Allegheny General Hospital (Pittsburgh, PA). The standard of care images in Digital Imaging and Communications in Medicine (DICOM) format are the input for the in-house segmentation code AAAVasc. A point cloud is generated with the three segmented boundaries along with volumetric binary masks representing the three regions of interest in the aneurysm (lumen, wall, and thrombus) [1]. Surface and volumetric meshes were generated from the masks using the in-house meshing code AAAMesh. Two different volume meshes were generated for each AAA; one with a uniform wall thickness of 1.5 mm and the other with a patient-specific wall thickness distribution (measured from the segmented images).

Using the aforementioned volume meshes, finite element analysis (FEA) was performed with ADINA (Adina R&D Inc., Watertown, MA). A Mooney-Rivlin constitutive model [2] was used to represent the AAA wall material properties while the AAA sac was subject to an intraluminal pressure of 120 mmHg in at least 24 time steps. The results of the simulations were post-processed and visualized using Ansys EnSight (Ansys Inc., Canonsburg, PA) to generate the first principal stress distributions, from which the three biomechanical parameters (peak wall stress: PWS, 99th percentile wall stress: 99thWS, and spatially averaged wall stress: SAWS) were computed.

Using the algorithms described by Shum *et al*., [3] patient-specific geometric indices were calculated that best assess the shape, size, curvature, and wall thickness of each AAA. Forty-five indices were calculated for the non-uniform wall thickness models and 32 for the uniform wall thickness models. The Biquintic Hermite Finite Element (BQFE) method was employed to compute the curvature based indices, as described in Lee *et al* [4]. Point clouds generated from the segmentation were used to calculate the 1D and 2D indices, while the 3D indices were calculated using the volume and surface meshes.

To identify the geometric indices that most correlate with wall stress, a series of tests of hypothesis was carried out. When the p-value was lower than a chosen level of significance, the corresponding geometric index is said to have substantially high correlation with the biomechanical parameter. To account for multiple testing, the Bonferroni correction [5] was applied and the corrected significant level was established at 0.00111 for the non-uniform wall thickness models and 0.00156 for the uniform wall thickness models.

RESULTS

The first principal stress distributions for three exemplary AAA models with non-uniform wall thickness are shown in Fig. 1. The mean and maximum PWS for the non-uniform wall thickness models were 76.9 ± 27.7 N/cm^2 and 183.0 N/cm^2, respectively, while the AAA

models with uniform wall thickness exhibited a mean PWS of 54.5 ± 19.6 N/cm^2 and a maximum of 143.0 N/cm^2. The mean and maximum 99thWS for the non-uniform wall thickness AAA were 49.0 ± 16.6 N/cm^2 and 112.0 N/cm^2, respectively, while for the uniform wall thickness AAA the mean 99thWS was 39.5 ± 9.7 N/cm^2 and the maximum 99thWS was 69.4 N/cm^2. The mean and maximum SAWS were 23.2 ± 8.2 N/cm^2 and 46.3 N/cm^2, respectively, for the non-uniform wall thickness AAA, and 23.0 ± 5.8 N/cm^2 and 46.1 N/cm^2, respectively, for the uniform wall thickness AAA.

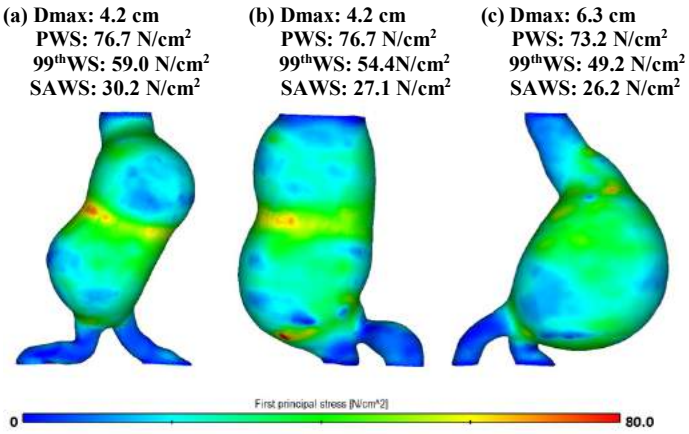

Figure 1: First principal stress map for three exemplary AAA models (non-uniform wall thickness) with (a) small, (b) average, and (c) large maximum diameter. The PWS, 99thWS and SAWS of each model are also indicated.

For all AAA models, the geometric indices significantly correlated with PWS, 99thWS, and SAWS (obtained from the tests of hypothesis) were subject to stepwise regression analysis to identify the most accurate predictors of each of the biomechanical parameters. The outcome of this analysis is shown in Table 1, along with the corresponding regression coefficients and standard errors of the regression residuals. For the non-uniform wall thickness models, minimum wall thickness (TH_{min}), AAA sac volume (V), distal neck diameter ($D_{neck,d}$), and proximal neck diameter ($D_{neck,p}$) were the most significant predictors of PWS. Similarly, TH_{min}, V, and $D_{neck,d}$ were the predictors of 99thWS, while the mean wall thickness at the maximum diameter cross-section (TH_{Dmax}), isoperimetric ratio (IPR), AAA sac length (L), and TH_{min} were the predictors of SAWS. The stepwise regression for SAWS had the highest coefficient of determination (0.67) with a standard deviation of 4.8 N/cm^2. For the uniform wall thickness models, five indices predicted PWS accurately: average diameter (D_{ave}), L2-norm of the mean curvature (MLN), minimum diameter (D_{min}), area averaged Mean curvature (MAA), and maximum compactness (C_{max}). Three indices were predictors of 99thWS: D_{ave}, MAA, and IPR, while five indices were found to be good predictors of SAWS: D_{ave}, MAA, V, $D_{neck,p}$, and IPR. SAWS also had the highest coefficient of determination (0.94) with a standard deviation of 1.4 N/cm^2.

DISCUSSION

The variation of PWS amongst the individual AAA (23.1 - 183.0 N/cm^2 for non-uniform wall thickness and 18.1 – 143.0 N/cm^2 for uniform wall thickness), was greater than the variation of 99thWS (15.9 – 112.0 N/cm^2 for non-uniform wall thickness and 16.3 - 69.4 N/cm^2 for uniform wall thickness) and SAWS' variation (8.1 – 46.3 N/cm^2 for non-uniform wall thickness and 10.8 – 46.1 N/cm^2 for uniform wall thickness).

The outcome of the stepwise regression analyses for the non-uniform wall thickness models revealed that TH_{min} was a strong predictor of all three biomechanical parameters. PWS, 99thWS, and SAWS were negatively correlated with TH_{min}, which can be explained by the fact that rupture (likely where the highest wall stress to strength ratio exists) occurs where the wall is thinnest, as Raghavan and co-workers confirmed in an autopsy study [6]. AAA size also plays a role in predicting wall stress; 1D and 3D size indices $D_{neck,p}$, $D_{neck,d}$, and V were positively correlated with PWS and 99thWS. In the present work, the significant predictors of wall stress did not include D_{max} for any of the biomechanical parameters. We infer from this that, after the effect of the geometric indices listed in Table 1 are accounted for, D_{max} appears to have a lesser influence on wall stress for asymptomatic, unruptured AAA compared to symptomatic, ruptured AAA [5].

For the uniform wall thickness models, D_{ave} and MAA were strong predictors of all three biomechanical parameters. PWS, 99thWS, and SAWS were negatively correlated with MAA, which was also the strongest predictor in the regression models. This is evident by the larger regression coefficients obtained for MAA, MLN, IPR, and C_{max}, in contrast to D_{ave}, D_{min}, V, and $D_{neck,p}$. Such finding is in agreement with the observations by Giannoglou *et al.*, [7] who reported on shape and curvature based indices as metrics for rupture risk assessment.

We infer from this study that wall thickness, size and curvature based indices may act as reliable surrogates of wall stress for asymptomatic and unruptured AAA, and can be used as part of an improved rupture risk assessment strategy compared to D_{max} alone.

Table 1: The significantly correlated geometric indices along with the regression coefficients and standard errors of the regression residual with PWS, 99thWS, and SAWS for the non-uniform and uniform wall thickness AAA models.

Biomechanical parameter	Non-uniform wall thickness		Uniform wall thickness	
	Geometric index and regression coefficient	Standard error [N/cm^2]	Geometric index and regression coefficient	Standard error [N/cm^2]
PWS	TH_{min} (-37.23) V (0.0752) $D_{neck,d}$ (0.264) $D_{neck,p}$ (0.46)	17.6	D_{ave} (0.62) MLN (133.94) D_{min} (0.57) MAA (-640.32) C_{max} (29.44)	11.5
99thWS	TH_{min} (-20.19) V (0.064) D_{neck_d} (0.15)	10.8	D_{ave} (0.62) MAA (-452.30) IPR (2.865)	4.5
SAWS	TH_{Dmax} (-6.27) IPR (-13.66) L (0.2448) TH_{min} (-3.03)	4.8	D_{ave} (0.30) MAA (-172.9) V (0.01) $D_{neck,p}$ (-0.05) IPR (-1.68)	1.4

ACKNOWLEDGEMENTS

This work was supported in part by research funding from National Institutes of Health award R01HL121293.

REFERENCES

1. Shum, J et al., *Med Phys*, 37: 638-48, 2010.
2. Raghavan, ML and DA Vorp, *J Biomech*, 33:475-482, 2000.
3. Shum, J, Carnegie Mellon University: Pittsburgh, PA, 2011.
4. Lee, K et al., *Ann Biomed Eng*, 41:562-576, 2013.
5. Chauan, SS et al., *Ann Biomed Eng*, 45:1908-1916, 2017.
6. Raghavan, ML et al., *J Biomech*, 39:3010-3016, 2006.
7. Giannoglou, G et al., *Angiology*, 57:487-494, 2006.

SB³C2019
Summer Biomechanics, Bioengineering and Biotransport Conference
June 25 -28, Seven Springs, PA, USA

A PARTICLE-BASED MODEL REVEALS AN INSIDIOUS FEED-BACK LOOP BETWEEN AORTIC LAMELLAR DISRUPTION AND CELL APOPTOSIS

Hossein Ahmadzadeh (1), Jay D. Humphrey (1)

(1) Department of Biomedical Engineering,
Yale University,
New Haven, CT, USA

INTRODUCTION

Thoracic aortic aneurysms are often associated with intramural dissection and delamination that start from either an intimal tear or a localized defect within the media. These dissections can propagate and eventually merge with the lumen of the vessel, creating the so-called "false-lumen" which may be filled with blood and develop thrombus over time. Understanding the mechanism by which an aortic dissection grows has remained mostly elusive. Nonetheless, aortas undergoing dissection often exhibit medial degeneration, as characterized by fragmentation of elastic fibers, dysfunction or apoptosis of smooth muscle cells (SMCs), and localized pooling of glycosaminoglycans (GAGs).

To study the biomechanics of aortic dissection, we previously developed a data-driven approach based on a smoothed particle hydrodynamics (SPH) framework (1). Here, we extend our model to include the potential mechanical roles of SMCs dysfunction and apoptosis, degradation of or damage to elastic fibers, and pooling of GAGs on the delamination of the media that may precede dissection. Being a particle-based method, our method allows us to model rupture or and damage to the elastic fibers and to capture the interplay between cellular dysfunction and microstructural defects, as implicated in medial degeneration.

METHODS

We model the aortic wall using our previous formulation for SPH (1). Briefly, we represent the computational domain of the aortic wall with an arrangement of particles that carry information on their surrounding volume and mechanical quantities such as displacement and stress. The domain of the problem is assumed to be a circular cross-section of the descending thoracic aorta of mouse in a passive homeostatic reference configuration with inner and outer radii $R_{\text{in}} = 646.8$ μm and $R_{\text{out}} = 687.0$ μm, for which the luminal pressure is 102 mmHg and the axial stretch is 1.62. The wall is divided into a media that occupies two-thirds and an adventitia that occupies one-third of the wall. The media is further decomposed into repeating layers of elastic fibers (or lamellae) that separate layers of smooth muscle cells (SMCs) and diffuse aggregating GAGs. The adventitia consists primarily of a dense network of fibrillar collagen with some elastin but no SMCs.

Consistently, SPH particles are categorized into three main groups: particles M_{el} (shown red in Fig. 1) primarily model the elastic lamellae of the media, particles M_{int} (blue) represent intra-lamellar SMCs, and fibrillar collagen, and particles A (green) represent the extracellular matrix of the adventitia, which consists primarily of collagen.

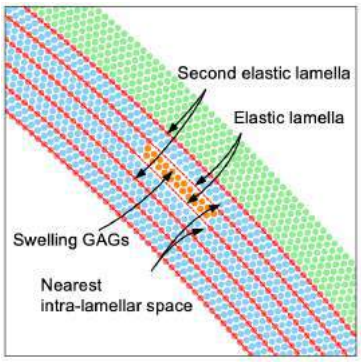

Figure 1: Particle arrangement in the SPH model.

The general form of strain energy function at each particle is

$$W(\boldsymbol{C}_i, \boldsymbol{M}_i^k) = \phi_\Gamma^e \left(\frac{\mu}{2}(I_{1i}^e - 3) - \mu \ln J_i + \frac{\hat{\lambda}}{2}(\ln J_i)^2 \right) + \sum_{k=1}^{4} \phi_\Gamma^{c_k} \left(\frac{c_1^k}{4c_2^k} \left(\exp\left[c_2^k (I_{4i}^k - 1)^2 \right] - 1 \right) \right), \quad (1)$$

where the first term accounts for the neo-Hookean behavior of elastin dominated regions (with μ and $\hat{\lambda}$ as the Lamé constants) and the second term represents the collective behavior of circumferentially-oriented SMCs and collagen fibers which are divided into four families representing locally oriented fiber bundles, namely axial ($k = 1$), circumferential ($k = 2$), and symmetric diagonal ($k = 3,4$) families. The active stress generated by SMC contraction is assumed to act primarily in the circumferential direction. Following (2):

$$\sigma_{\theta,i}^{\text{act}} = \phi_{M_{int}}^{c_2} \, T_{\max} \lambda_{\theta,i} \left[1 - \left(\frac{\lambda_{\max} - \lambda_{\theta,i}}{\lambda_{\max} - \lambda_{\min}} \right)^2 \right]. \quad (2)$$

To model the process of cell apoptosis and replacement with GAGs, a pool of intra-lamellar particles is assumed to undergo the following three steps:

1. *Loss of contractility*: First, the active stress of the designated particles is reduced to zero.
2. *Reduction in stiffness*: Next, the material behavior of the designated medial particles transforms to that of a pure GAG particle (orange in Fig. 1), written as:

$$\boldsymbol{\sigma}_i^{\text{GAG}} = \frac{1}{J_i} \mu^{\text{GAG}} (\boldsymbol{B_i} - \boldsymbol{I}), \quad (3)$$

where the shear modulus (μ^{GAG}) is assumed to be considerably smaller than the shear modulus of the original particles.

3. *GAG swelling*: Finally, the hydrostatic pressure generated by swelling of the negatively charged GAGs is added:

$$\boldsymbol{\sigma}_i^{\text{GAG}} = \frac{1}{J_i} \mu^{\text{GAG}} (\boldsymbol{B_i} - \boldsymbol{I}) - RT \left(\sqrt{(c^{\text{FC}})^2 + (c^*)^2} - c^* \right) \boldsymbol{I}, \quad (4)$$

where c^{FC} is the concentration of GAGs (chosen to be $c^* = 200$ mEq/l, equivalent to ~155 kPa Gibbs-Donnan swelling pressure).

RESULTS

We first examined the bulk response of the aorta, such as the relation between the intraluminal pressure and outer diameter as well as the mean circumferential stress-stretch behaviors. Such comparisons show that the SPH method captures bulk behaviors well while including separate lamellar units that are ignored in the analytical solution. The results also show that SMC contraction constricts the vessel by ~23% in agreement with experimental findings for the murine descending thoracic aorta (3).

We next examined the effect of cell apoptosis and replacement by GAGs on the distribution of the mechanical stresses in the wall. A pool of intra-lamellar particles experienced the three steps of SMC apoptosis and replacement with GAGs. Of particular interest, the change in circumferential stress in the vicinity of a pool, particularly within the nearest and second nearest lamellar and intra-lamellar regions (shown in Fig. 1) is studied. During the first step, loss of contractility within the pool increased the circumferential stress in the nearby regions (Table 1, step I). As SMCs apoptosed and were replaced by GAGs, the reduced tensile stiffness led to an increased circumferential stress experienced by the particles (Table 1, step II).

	Elastic lamella	**Nearest intra-lamellar space**	**Second elastic lamella**
Baseline stress	162 kPa	180 kPa	123 kPa
Step I: Loss of contractility	280 kPa	225 kPa	145 kPa
Step II: Stiffness reduction	282 kPa	228 kPa	148 kPa
Step III: GAG swelling	400 kPa	245 kPa	162 kPa
Step IV: Lamellar disruption	0 kPa	400 kPa	380 kPa

Table 1: Hoop stress concentration near a pool of cells undergoing apoptosis and replacement with GAGs.

Swelling the GAGs within a pool resulted in a much higher circumferential stress on the elastic lamellae surrounding the pool (GAG swelling), but, interestingly, with only a slight effect on stress in the nearest intra-lamellar space, indicating the protective role of elastic lamellae against alterations within their intra-lamellar regions. We then added one additional step (step IV: lamellar disruption) and assumed that the increase in stress in the nearest elastic lamellae causes lamellar rupture. The stress in the disrupted elastic lamellae dropped to zero and the excessive stress transferred to the adjacent intra-lamellar space, substantially increasing circumferential stress in the nearest intra-lamellar region. This result demonstrates how SMC apoptosis and replacement with GAGs in one layer can cause damage in SMCs of the close-by intra-lamellar space through rupture of the shared elastic lamella. Interestingly, following rupture of the elastic lamellae, there was a marked increase in stress in the second nearest elastic lamellae (Table 1, step IV, second elastic lamella), a process that could repeat. This finding suggests that swelling within an intra-lamellar space with subsequent lamellar disruption increases the vulnerability of distant elastic lamellae to rupture and reveals a mechanical mechanism that can explain the transmural propagation of damage. Moreover, this SPH model reveals a two-way feedback loop between cell apoptosis and GAG accumulation with disruption of elastic lamellae. Independent of the triggering event within such a feedback loop, cell apoptosis can induce lamellar disruption, which in return can increase the stress experienced by other SMCs and lead to further cell apoptosis (Fig. 2).

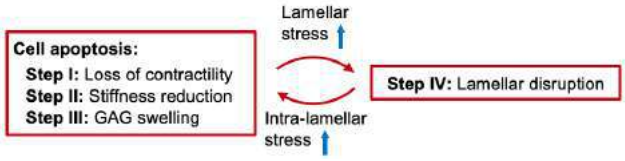

Figure 2: Model predicted two-way feedback loop.

DISCUSSION

In conclusion, our findings reveal key insights into the propagation of damage within the aortic media due to diverse defects, including dysfunction of SMCs and accumulation of GAGs within the intra-lamellar regions and elastic fiber fragmentation across the wall. It appears that there is a strong interplay between cellular dysfunction (cell apoptosis and replacement with GAGs) and microstructural failures (elastic lamellae disruption) that manifests as a feedback loop, thus suggesting that independent of the initiating event, diverse defects can trigger a progressive deterioration of structural integrity (4).

ACKNOWLEDGEMENTS

This work was supported by grants from the US NIH: U01 HL116323, U01 HL142518, and R21 EB020968.

Reference:

[1] Ahmadzadeh et al., J R. Soc. Interface., 15: 20180616., 2018.
[2] Rachev and Hayashi, Ann Biomed Eng. 27: 459–468, 1999.
[3] Murtada et al., J. Biomech. Eng., 138: 051008, 2016.
[4] Ahmadzadeh et al., Biophys. J., under review.

ALTERATIONS IN BIOMECHANICAL PROPERTIES OF AORTIC WALL IN A MOUSE MODEL OF MARFAN SYNDROME

Nazli Gharraee (1), Rahul S. Raghavan (2), Yujian Sun (2), Susan M. Lessner (1,3)

(1) Biomedical Engineering
University of South Carolina
Columbia, SC, USA

(2) Department of Chemistry and Biochemistry
University of South Carolina
Columbia, SC, USA

(3) Cell Biology and Anatomy
University of South Carolina
School of Medicine
Columbia, SC, USA

INTRODUCTION

Thoracic aortic aneurysm (TAA) is a chronic vascular disease and the 13th leading cause of death in the US[1]. TAA can result from a genetic disorder such as Marfan syndrome (MFS)[2]. Mutations of the FBN-1 gene encoding for fibrillin-1 protein are known to give rise to defective elastic fibers and initiation of MFS[3]. Fibrillin-1 is the most abundant component making complex extracellular structures called microfibrils, which are important components in forming the scaffold for elastin fibers. However, the complete sequence of cellular events that links weakening of the elastin fibers to dilation and rupture of the vessel wall remains unclear. It is well accepted that aortic dilation occurs due to the compromised structural integrity, which is caused by unbalanced matrix remodeling, eventually altering passive biomechanical properties of the wall and making it more susceptible to rupture[4]. On the other hand, loss of contractility due to apoptosis and phenotypic switching of the contractile smooth muscle cells is thought to alter the active biomechanics of the wall[5].

Recently, more studies have shown the involvement of SMC progenitor cells in vascular diseases[6]. However, the role of progenitor cells in progression of TAA has not been studied before.

In this work, we studied the cell and extracellular matrix (ECM) alterations as a function of age and related these changes to biomechanical properties of the wall.

METHODS

Animal model: A mouse model of MFS (Fbn1 C1041G/+, Het) was used to study progression of TAA and cellular events over a 3-12 month time course. Wild type (WT) C57Bl/6 mice were used as control groups, with n=5 for each genotype at each time point.

Ultrasound: Vevo 3100 small animal ultrasound was used to image and measure aortic diameters at the proximal and distal ascending aorta and three main points of the aortic root (aortic annulus, Sinus of Valsalva and sinotubular junction).

Immunohistochemistry (IHC): Sections of proximal ascending aorta were stained for specific markers to localize and quantify cellular alterations in aortic adventitia and media. A complete list of primary antibodies used for IHC, their targets, and the relevant aortic layer is presented in Table 1. All images were then used for quantification of the intended marker normalized to the area of the relevant aortic layer using ImagePro Plus software.

Table 1: List of Primary Antibodies Used for IHC.

Target	Aortic layer	Primary antibody
Smooth Muscle Cells (SMCs)	Media	α-smooth muscle actin (α-SMA) smooth muscle myosin heavy chain (SM-MHC)
SMC Progenitor Cells	Adventitia	stem cell antigen-1 (Sca-1)
Proliferating Cells	Media	phospho-histone H3 (PH3)
Apoptotic Cells	Media	Terminal deoxynucleotidyl transferase dUTP nick end labeling (TUNEL)

Second harmonic generation (SHG): SHG microscopy was used to quantitate aortic medial collagen. Quantification was performed similarly to IHC quantification of medial markers.

Wire myography: Active and passive biomechanical responses of the aortic wall under circumferential uniaxial stretch were studied using a wire myograph. Ascending aorta was divided into two sections, proximal and distal, to acknowledge the potential difference in response due to different embryonic origin of the SMCs in each segment.

RESULTS

Ultrasound Data show that aortic diameter significantly increases with time in Het mice. There is a statistically significant difference between genotypes independent of time.

IHC Images demonstrate that while SM-MHC expression in WT mice remains nearly constant, the expression in Het mice at 3 months is comparable to that of WT mice, but it decreases at 6 months and starts to recover to the WT level by 12 months. Expression of α-SMA in both WT and Het mice was nearly constant throughout the time course. Sca-1 expression is significantly higher in het mice vs. WT. Medial cell density showed the same trends for WT and Het over time, where it was significantly higher at 6 months compared to 3 and 12 months. Proliferation and apoptosis were both negligible for all time points. Quantification data for SM-MHC and Sca-1 is presented in Figure 1.

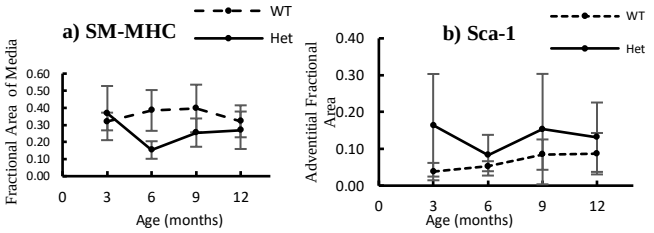

Figure 1: Quantification of fractional area of (a)media and (b)adventitia showing (a)SM-MHC and (b)Sca-1 positive staining from the IHC images over a time course of 3-12 months.

SHG Images show a time-dependent increase in medial collagen expression in Het mice vs. WT indicating the remodeling of ECM.

Myography Biomechanical data show the maximum active force in Het mice is lower than in WT mice at the same age for both proximal and distal ascending aorta. Slope of the toe region of the stress-strain curve, corresponding to elastic behavior of the artery, decreases with time and in aneurysm. There is a similar trend of biomechanical properties for proximal and distal ascending aorta. Figure 2 shows the stress-strain curves demonstrating biomechanical properties of the ascending aorta.

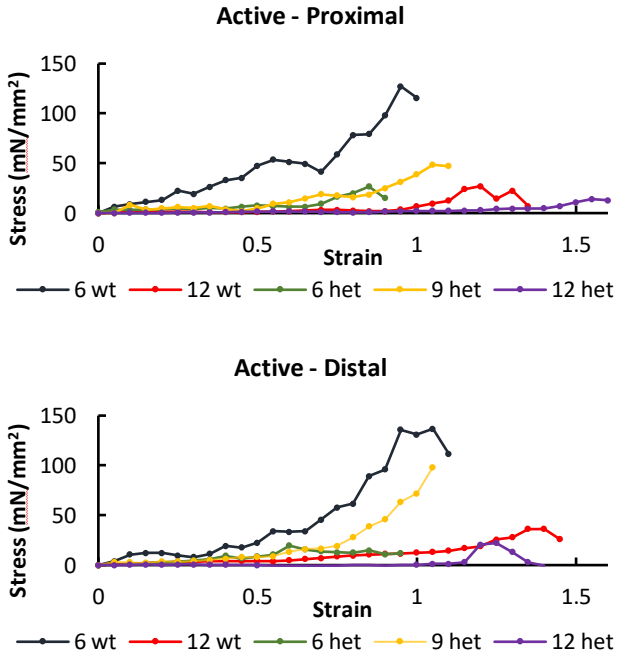

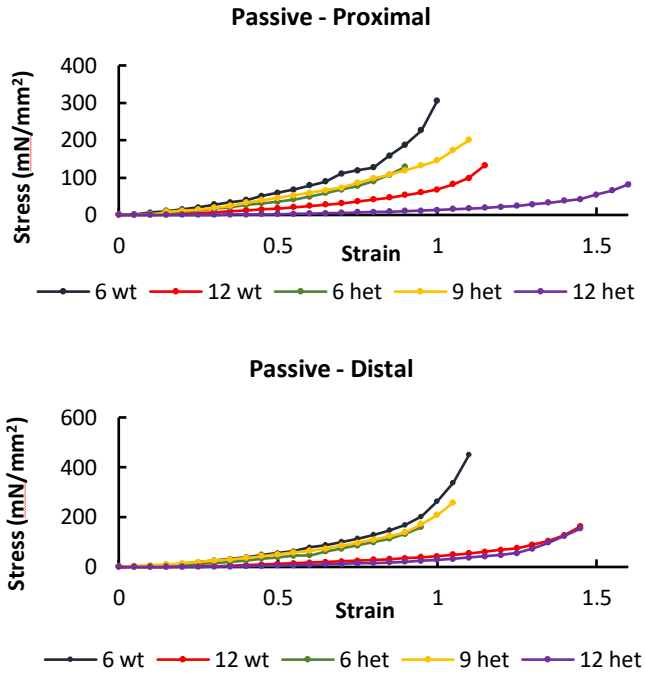

Figure 2: Stress-Strain curves showing the biomechanical properties of the proximal and distal ascending aorta of WT and Het mice at 6, 9 and 12 months.

DISCUSSION

Our results demonstrate that aortic diameter increases most rapidly after 6 months in Het mice in both proximal and distal ascending aorta. At the same age, Het mice show a minimum in SM-MHC expression, suggesting the loss of contractile SMCs. These findings are consistent with the decrease in active force measurements, corresponding to decreased contractility of the wall. The increased Sca-1 expression in Het mice together with the absence of proliferation and apoptosis suggests a role of migration of differentiated SMC progenitor cells in maintaining the medial cell density. Continuous increase in medial collagen deposition from 6 to 12 months reflects the changes in ECM which lead to stiffer walls. These changes are also demonstrated in passive biomechanical measurements, together with the higher distensibility of the arteries as indicated by decreased slope of the stress-strain curves.

ACKNOWLEDGEMENTS

This study was supported by 1R01 HL133662 from NIH/NHLBI and 1R03 EB019663 from NIH/NIBIB. We would like to thank Brooks Lane for his assistance with myography and Joseph Swisher, Joseph Carlucci, Kristian Suarez, and Stephen Smith for their assistance with small animal ultrasound.

REFERENCES

[1] Forte, A. et al., Cardiovasc. Res. 88:395-405, 2010
[2] Kumar, A. et al., Meta gene 2: 96-105, 2014
[3] Dietz, H. et al., Nature 352: 337-339, 1991
[4] Chung, A. et al., Circ. Res:101, 512-522, 2007
[5] Ailawadi, G. et al. Cardiovasc. Surg.,138:1392-1399, 2009
[6] Hu, Y. et al., j. Clin. Invest.,113: 1258-1265, 2004

SB³C2019
Summer Biomechanics, Bioengineering and Biotransport Conference
June 25 -28, Seven Springs, PA, USA

CAN THE ELASTASE INDUCED ANEURYSM MODEL BE USED TO STUDY REMODELING IN SACCULAR ANEURYSMS?

Chao Sang (1), David F. Kallmes (2), Simon C. Watkins (3), Anne M. Robertson (1)

(1) Department of Mechanical Engineering and Materials Science
University of Pittsburgh
Pittsburgh, PA, USA

(2) Department of Radiology
Mayo Clinic
Rochester, MN, USA

(3) Center for Biological Imaging
University of Pittsburgh
Pittsburgh, PA, USA

INTRODUCTION

Cerebral aneurysm (CA) rupture can lead to subarachnoid hemorrhage which is associated with high rates of morbidity and mortality (40-65%) [1]. As risks associated with current treatments of CAs are significant, there is a need for improved treatment and risk assessment. Increased understanding of the temporal development of the disease is essential to meet both these needs. It is commonly accepted that mechanical factors such as abnormal hemodynamics can lead to wall degradation that can in turn alter aneurysm morphology altering the biaxial load state [2]. Ideally, these changes in intramural stress would lead to adaptive collagen remodeling to maintain homeostatic stress. Given the range of CA wall pathology, one would expect a range in capacity for effective remodeling [3].

Although collagen fiber remodeling in CAs is a critical factor in progression, it has received little attention [3]. Unfortunately, in vivo imaging of collagen fibers is not possible and hence such studies must necessarily be done in vitro. While CA tissue can be obtained during surgical clipping, these specimens are typically small and only represent one time point.

Animal models for cerebral aneurysms can address some of these challenges. They provide entire aneurysm domes and can be obtained at selected time points during disease progression. In the present study, an elastase induced rabbit model was used to create saccular aneurysms. The clinical relevance, including geometry, hemodynamics and histology wall types has been previously demonstrated [4, 5]. The objective of the present study is to explore the value of rabbit models in studying wall remodeling in saccular aneurysms.

METHODS

Samples: Twenty-two saccular aneurysms were created in rabbit carotid arteries using vessel ligation and elastase incubation [6]. Aneurysm samples along with control vessels were harvested at four time points (2 weeks, 4 weeks, 8 weeks and 12 weeks) after creation.

Solid Mechanics Simulation: Animal specific 3D models were reconstructed for the aneurysm dome from 3DRA images and the equations of equilibrium were approximated using the finite element method via FEBio Software Suite [7].

Uniaxial Testing and MPM: A custom-built mechanical testing system enabled concurrent imaging under MPM and uniaxial testing [8]. Samples were cut into dogbone shape with long axis aligned in the longitudinal direction [9] such that the specimen length 6 mm and the width at the mid-region was 1.2 mm. Specimens were preconditioned to 20% extension with three cycles and tested quasi-statically to failure.

Constitutive Modeling: The strain energy for each wall layer was modeled as the sum of isotropic and anisotropic contributions

$$W = \frac{\alpha_0}{2}(I_1 - 3) + W_{aniso}$$

Fiber orientation in the medial layer was analyzed in MPM stacks using open source software (CT-Fire) [10]. Adventitial contributions to the anisotropic response were assumed to be negligible as the stretch range was below levels needed for fiber recruitment in that layer. The distribution of collagen fibers was modeled as a planar distribution

$$W = \frac{1}{\pi}\int_0^{\pi} \rho\, w_f\, d\theta$$

where w_f is the normalized fiber train energy function

$$w_f = \frac{\alpha_1}{2}(\lambda_f{}^2 - 1)^2 \cdot H(\lambda_f - 1)$$

λ_f is the fiber stretch which can be obtained from the right Cauchy Green strain tensor for arbitrary fiber direction $\boldsymbol{m_0} = cos\theta \boldsymbol{e_1} + sin\theta \boldsymbol{e_2}$

$$\lambda_f{}^2 = \boldsymbol{C}\colon \boldsymbol{m_0}\otimes\boldsymbol{m_0} = \lambda_1{}^2 cos^2\theta + \lambda_2{}^2 sin^2\theta$$

the Heaviside function *H* is introduced so fibers do not resist loading in compression and ρ is the probability density function (PDF)

$$\rho = \frac{1}{2I_0(\beta_1)} e^{\beta_1 cos2(\theta-\alpha_1)} + \frac{1}{2I_0(\beta_2)} e^{\beta_2 cos\,2(\theta-\alpha_2)}$$

The parameters in the PDF were obtaining as best fits to fiber angle data obtained from MPM images. It then follows that the diagonal components of the Cauchy stress tensor are,

$$\sigma_{11} = \alpha_0 \left({\lambda_1}^2 - \frac{1}{{\lambda_1}^2 {\lambda_2}^2} \right) + \frac{2}{\pi} {\lambda_1}^2 \int_0^\pi \rho \frac{\partial w_f}{\partial {\lambda_f}^2} cos^2\theta \, d\theta$$

$$\sigma_{22} = \alpha_0 \left({\lambda_1}^2 - \frac{1}{{\lambda_1}^2 {\lambda_2}^2} \right) + \frac{2}{\pi} {\lambda_2}^2 \int_0^\pi \rho \frac{\partial w_f}{\partial {\lambda_f}^2} sin^2\theta \, d\theta.$$

For uniaxial testing, $\sigma_{22} = 0$, providing an implicit relation between λ_1 and λ_2. Stress stretch data was used to obtain the material constants from σ_{11}.

RESULTS

Does the collagen structure remodel in response to altered load? Whereas the wall of the control artery is predominantly loaded in the circumferential direction, after the formation of an aneurysm the longitudinal stress increases to approximately half the circumferential stress, Figure 1. Hence, to recover homeostasis the vessel must remodel.

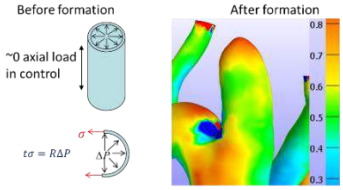

Figure 1. Increased loading in axial direction after IA formation

In the control artery, the media and adventitia contain the majority of the collagen fibers, Figure 2. Collagen is not recruited under axial load in either layer until relatively high stretch (λ=2).

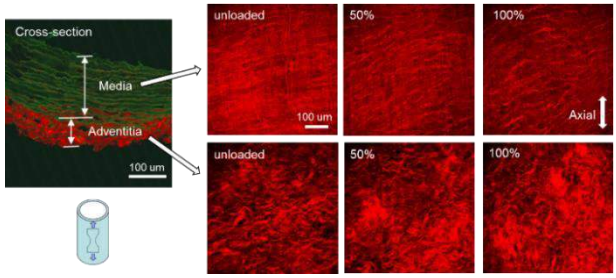

Figure 2. Collagen structure of control artery at different stretch levels

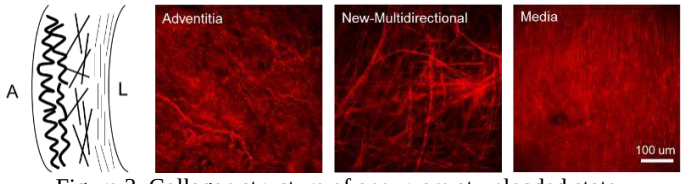

Figure 3. Collagen structure of aneurysm at unloaded state

In the remodeled elastase induced aneurysm, an additional layer developed between the media and adventitia that displayed a stronger SHG signal and a multi-directional distribution of fibers. This new layer was found in 3 out of 5 cases at 2-weeks and all other cases at later time points (n=17). Collagen fibers in this layer reoriented when recruited to load bearing, providing a stiffer response at low stretch, Figure 4. By λ=1.4, all fibers in new layer were aligned in the loading direction.

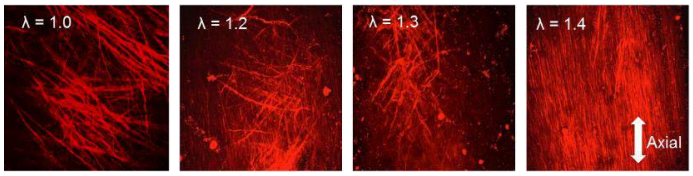

Figure 4. Collagen fibers in new layer reoriented and were recruited to load bearing even at low axial stretch

Does the rabbit model display heterogeneity in strength? As shown in Figure 5, human aneurysms vary in strength: some are weak and others are more robust [3]. Our data for the elastase induced aneurysms also showed two groups: high strength (blue) and low strength (red), Figure 5 suggesting the rabbit model might be useful for evaluating treatment methods that enhance remodeling.

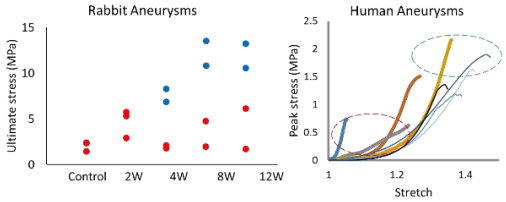

Figure 5. Failure stress of rabbit vs. human cerebral aneurysms [3]

DISCUSSION

This study demonstrated the rabbit model has the capacity to remodel in response to altered load. A new collagen layer with multi-directional fibers was created between the media and adventitia during remodeling in response to altered mechanical loads. This layer was found as early as 2 weeks. The rabbit model can also capture the heterogeneity in strength found in human aneurysms**.** Growth and remodeling theories can be used to interpret this data and provide a tool for better understanding aneurysm evolution. Data for mechanical properties and collagen architecture can be used to inform such models. In ongoing work, we considered two time points-initiation at time zero, corresponding to the control artery and 8 weeks after creation, Figure 6. Mechanical, cellular and fiber data are being used to inform these models, Figure 6.

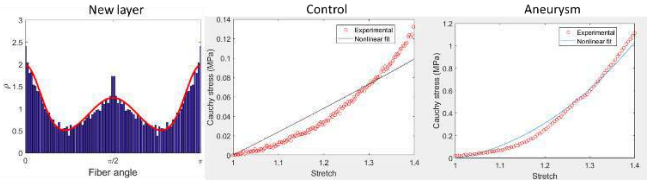

Figure 6. PDF of new layer and nonlinear fit of control and IA data

ACKNOWLEDGEMENTS

The authors are grateful for support from NINDS grant 1R21NS088256.

REFERENCES

[1] Fennell, Vernard S., et al., *Front Surg*, 3:43, 2016.
[2] Frösen, J. et al., *Acta Neuropathologica*, 123(6):773–786, 2012.
[3] Robertson, A. M. et al., *Ann Biomed Eng*, 43(7): 1502–1515, 2015.
[4] Zeng, Z. et al., *Am J Neuroradiol*, 32(3):595–601, 2011.
[5] Wang, S. et al, *J Neurointerv Surg*, neurintsurg-2017, 2017.
[6] Altes, T. A. et al., *Am J Roentgenol*, 174(2): 349–354, 2000.
[7] Maas, Steve A., et al., *J Biomech Eng*, 134(1):011005, 2012.
[8] Hill, M. R. et al., *J Biomech*, 45(5):762–771, 2012
[9] Sang, C. et al., *J Biomech Eng*, 140: 1–10, 2018.
[10] Bredfeldt, J. S. et al., *J. Biomed. Opt.*, 19:016007–016007, 2014.

ADHESION MODELS FOR CELL MIGRATION SIMULATOR ON CONTINUOUS SUBSTRATE

Jay C. Hou[1], Liam Tyler[2], Daniel F. Keefe[2], David J. Odde[1], and Victor H. Barocas[1]

1-Department of Biomedical Engineering,
2-Department of Computer Science & Engineering
University of Minnesota
Minneapolis, MN, USA

INTRODUCTION

Glioblastoma multiforme (GBM) is the most common primary malignant brain tumor, representing 16% of all brain tumors [1]. The prognosis of GBM patients remains poor (median survival of 15 months), and 70% of patients experience recurrence within one year. The lead source of recurrence is the invasive nature of GBM, for which cell migration plays a decisive role [2].

Chan and Odde [3] proposed the motor-clutch model to describe the dynamics of retrograde flow and adhesion force in an F-actin protrusion of a cell. The model assumes that the pulling of myosin motors generates F-actin flow and stretches the adhesion proteins as clutches, which bind and apply force to deform a compliant substrate. The motor-clutch model successfully explains the substrate stiffness sensitivity of F-actin flow and the traction force exerted by the single F-actin bundle of neuron cells. Bangasser et al. [4] extended this approach to a cell migration simulator (CMS) that links together multiple motor-clutch systems as modules, and simulates cell migration by calculating the force balance among all modules. The CMS successfully predicts the stiffness sensitivity of migration, traction force, and F-actin flow of U251 glioma cells.

One of the major limitations of the CMS is the treatment of substrate stiffness via a spring constant for all modules, which assumes implicitly that the effect of the deformation from other modules is negligible, and the link between the spring constant and the Young's modulus of the substrate is unclear. In this study, an elastic isotropic continuous substrate is used to investigate the effect of interactions between modules, and a distributed loading mechanism of modules on the substrate is proposed to describe the link between the spring constant and the stiffness of the substrate.

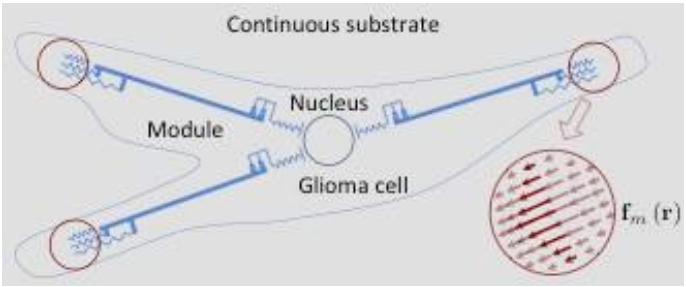

Figure 1: Each module (motor-clutch model [3]) of CMS [4] has a circular adhesion with distributed force ($\mathbf{f}_m(\mathbf{r})$) on the continuous substrate.

METHODS

The CMS adopts the direct Gillespie Stochastic Simulation Algorithm by assuming that all chemical events (e.g. clutch bindings) occur as Markov processes, and each time step can be calculated accordingly [4,5]. The substrate spring constant κ_s is required in the force balance calculation, and the substrate displacement for module m, $\mathbf{x}_{s,m}$, is updated by $\mathbf{x}_{s,m} = \mathbf{f}_m/\kappa_s$, where $\mathbf{f}_m$ is the module force.

In order to link the Young's modulus (E_Y) of the substrate to the spring constant κ_s, we assume that each module applies a distributed force ($\mathbf{f}_m(\mathbf{r})$) on the substrate based on the observation of focal adhesions within a finite area [6] (Fig. 1). According to the Boussinesq solution for a tangential point load on an elastic isotropic half-space [7], the displacement field ($\mathbf{u}(\mathbf{x})$) on the surface of the half-space deformed by $\mathbf{f}_m(\mathbf{r})$ distributed over an area A is

$$\mathbf{u}(\mathbf{x}) = \int_A d\mathbf{r}\mathbf{G}(\mathbf{x}-\mathbf{r})\mathbf{f}_m(\mathbf{r}), \quad (1)$$

where $\mathbf{G}(\mathbf{x}-\mathbf{r})$ is the Green's function for the Boussinesq solution. Assuming that the force, $\mathbf{f}_m(\mathbf{r})$, is linearly decreasing with radial position $\mathbf{r}$ within a circle of radius a, with the total module force F_m, and $\mathbf{f}_m(\mathbf{r})$ can be written by

$$\mathbf{f}_m(\mathbf{r}) = \frac{3}{\pi a^2}\left(1-\frac{|\mathbf{r}|}{a}\right)F_m. \quad (3)$$

Using Eq. 1-3, the spring constant κ_s can be derived by the total force (F_m) divided by central displacement in the area, and is given by

$$\kappa_{\text{sub}} \sim E_Y \cdot a. \quad (4)$$

Now we consider four models to describe the module adhesion:

- **a1**: $a = 1\mu\text{m}$, and $\kappa_{\text{sub}} = E_Y$, which is equivalent to the original CMS.
- **a1(int)**: $a = 1\mu\text{m}$, with the interactive contribution from other modules by updating the module reference position and substrate position with the correction displacement $\mathbf{u}_{\text{other}}$,

$$\mathbf{u}_{\text{other}} = \sum_m^{\text{other}} \int d\mathbf{x}'\mathbf{G}(\mathbf{x}-\mathbf{x}')\mathbf{f}_m(\mathbf{x}'). \quad (5)$$

- **a0.5**: $a = 0.5\mu\text{m}$, and $\kappa_{\text{sub}} = 0.5E_Y$.
- **a(force)**: The radius is proportional to module force ($|\mathbf{f}_m|$),

$$a = 0.5 + 1.5\frac{|\mathbf{f}_m|-50}{150},\ 50\text{pN} < |\mathbf{f}_m| < 200\text{pN}. \quad (6)$$

RESULTS

Simulated cells for model al (original CMS) have maximum migration with random motility coefficient (rmc) ~ $5\text{um}^2/\text{min}$, at the optimal stiffness of 1kPa (Fig. 2, a1), which is consistent with Bangasser et al. [4] (the base parameters with low motor and clutch number in [4] are used). When we account for the contribution from other modules (Model a(int)), the rmc magnitude decreases (Fig. 2, a1(int)). With smaller adhesion radius (Model a0.5), the substrate spring constant becomes half of the Young's modules, $\kappa_{\text{sub}} = 0.5E_Y$, and hence the optimal stiffness shifts to the right (~10kPa) (Fig. 2, a0.5).

When the clutch binding rate, $k_{\text{on}}(1/\text{s})$ increases, the optimal stiffness shifts to softer stiffness for Model a1, and the relation is close to linear in the log-log scale with the slope -2 (log(kPa)/log(1/s)) (Fig. 3, a1). Model a(int) has similar k_{on} sensitivity of the optimal stiffness (Fig. 3, a1(int)). For the smaller adhesion radius (Model a0.5), the k_{on} sensitivity remains similar, but the optimal stiffness shifts to higher values (Fig. 3, a0.5). With the radius proportional to the module force (Model a(force)), the k_{on} sensitivity slope becomes higher, ~ -3 (Fig. 3, a(force)), showing that the optimal stiffness for migration is more sensitive to the parameter k_{on} than in original CMS.

There are ten major parameters having significant effect on the migration results, including the number (n_c), binding force (F_b), binding rate (k_{on}), unbinding rate (k_{off}), stiffness (κ_c) of clutches, the number (n_m) and pulling force (F_{motor}) of motors, polymerization rate (v_{poly}), birth rate (k_{birth}), and capping rate (k_{cap}) of modules. In a complete parameter analysis, it was shown that there are 4 types of parameter groups, and each group shows specific behavior of CMS. For example, the clutch-binding group (n_c, F_b, k_{on}, k_{off}) has a negative effect on the optimal stiffness of migration and F-actin retrograde flow, and a positive effect on the traction force. The effects of different adhesion models are similar for all four groups, and are more significant in migration, and hence the migration of CMS in k_{on} parameter space is shown in this study.

DISCUSSION

This study has investigated the migration response of CMS with various continuum-substrate adhesion models. Model a1 is the original CMS with the radius of adhesion area, $a = 1\mu\text{m}$, and results in the same value of the spring constant and the Young's modulus of the substrate, $\kappa_{\text{sub}} = E_Y$. Model al shows a similar optimal stiffness of migration as in Bangasser et al. [4], and a shift in optimal stiffness with different values of k_{on}, which has not been reported before.

Model al(int) considers the displacement by other modules, resulting in reduced migration coefficient. The correction for displacement is usually along the opposite direction of the module polymerization, and hence reduces the polymerization and the migration (polymerization rate has been shown to promote the migration [8]). Model a0.5 shifts the optimal stiffness of migration to higher stiffness, since the spring constant becomes half of the substrate Young's modulus, $\kappa_{\text{sub}} = 0.5E_Y$. Model a(force) increases the k_{on} sensitivity of the optimal stiffness, which may arise from the change of module force with different k_{on} (data not shown).

In summary, different cell adhesion models show different migration patterns of CMS, but the overall trend of optimal stiffness and parameter k_{on} sensitivity remains similar.

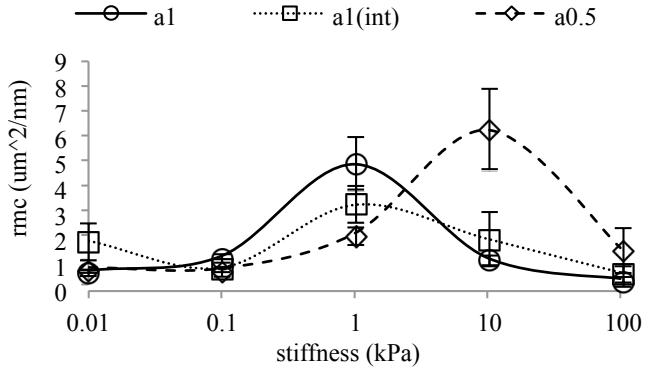

Figure 2: The substrate stiffness sensitivity of random motility coefficient (rmc) of 10 simulated cells by CMS with al, al(int), a0.5 adhesion model (Methods). All error bars are s.e.m.

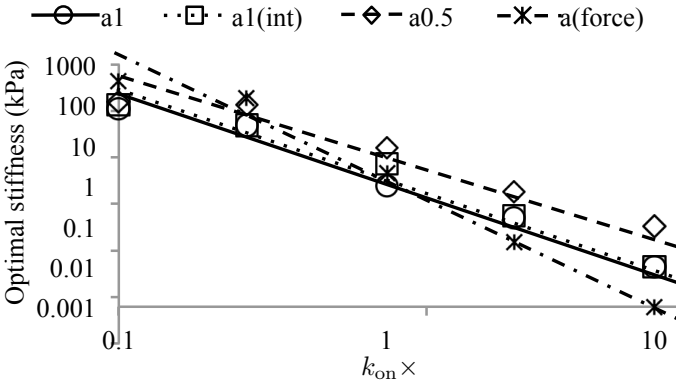

Figure 3: The optimal stiffness of cell migration shifts with various clutch binding rate $k_{\text{on}}(1/\text{s})$ for al, al(int), a0.5, a(force) adhesion model (Methods) with linear regression fits.

ACKNOWLEDGEMENTS

NIH U54 CA210190

REFERENCES [1] Davis, M., *Clin J Oncol Nurs*, 20(5), 2016. [2] S. De Vleeschouwer, *Glioblastoma*, 2017. [3] Chan, C. et al., *Science*, 322(5908), 2008. [4] Bangasser, B. et al., *Nat Commun*, 8(15313), 2017. [5] Keener, J. et al., *Mathematical Physiology*, 2009.
[6] Balaban, N. et al., *Nat Cell Biol*, 3(5), 466, 2001. [7] Butler, J. et al., *Am J Physiol Cell Physiol*, 282(3), 2002.
[8] Prahl et al., *Cell Reports*, 2591(25), 2018.

SB³C2019
Summer Biomechanics, Bioengineering and Biotransport Conference
June 25 -28, Seven Springs, PA, USA

RED BLOOD CELL BIOMECHANICS IN CHRONIC FATIGUE SYNDROME

Amit K. Saha (1), Brendan R. Schmidt (2), Arun Kumar (3), Amir Saadat (4), Vineeth C. Suja (4), Vy Nguyen (3), Justin K. Do (3), Wendy Ho (3), Mohsen Nemat-Gorgani (1), Eric S.G. Shaqfeh (4), Anand K. Ramasubramanian (2), Ronald W. Davis (1)

(1) Department of Biochemistry
Stanford University
Palo Alto, CA, USA

(2) Department of Chemical and Materials Engineering
San Jos□ State University
San Jos□, CA, USA

(3) Department of Biomedical Engineering
San Jos□ State University
San Jos□, CA, USA

(4) Department of Chemical Engineering
Stanford University
Stanford, CA, USA

INTRODUCTION

Chronic Fatigue Syndrome (CFS) is a multi-systemic illness of unknown etiology, affecting millions worldwide [1], with the capacity to persist for several years. It is characterized by persistent or relapsing unexplained fatigue of at least 6 months' duration that is not alleviated by rest. CFS can be debilitating, and its clinical definition includes a broad cluster of symptoms and signs that give it its distinct character, and its diagnosis is based on these characteristic symptom patterns including cognitive impairment, post-exertional malaise, unrefreshing sleep, headache, hypersensitivity to noise, light or certain food items. Although an abnormal profile of circulating proinflammatory cytokines, and the presence of chronic oxidative and nitrosative stresses have been identified and correlated with severity in CFS [2], there are no reliable molecular or cellular biomarkers of the disease.

In the present work, we focus on the pathophysiological changes in red blood cells (RBCs) since CFS is a systemic disease rather than of a particular organ or tissue, and RBCs, comprising ~45% of blood volume, are responsible for microvascular perfusion and tissue oxygenation. RBCs deform and travel through microvessels smaller than their diameter to facilitate the optimal transfer of gases between blood and tissue. The usual shape of a RBC is a biconcave discoid, which is changed to an ellipsoid due to shear flow. This shape gives them a specific surface area-to-volume ratio which facilitates large reversible deformations and elastic transformation [3]. We used a high throughput microfluidic platform to assess the changes in RBC deformability between CFS patients and matching healthy controls. We also performed computational studies to have a better understanding of the cell deformation. In order to explore the mechanisms for observed changes in cell deformability, we explored the membrane fluidity, reactive oxygen species, and surface charge, of RBCs.

METHODS

CFS patients previously diagnosed by physicians using the Canadian Consensus Criteria [4] were selected for the study. Written consent was obtained following Stanford IRB-40146. RBCs were isolated by centrifugation of blood obtained from patients and age-gender matched healthy controls collected in lithium heparin tubes and centrifuged at 250x g for 10 minutes in order to separate blood into the different fractions. All experiments were performed within 3-6 h of blood draw at room temperature.

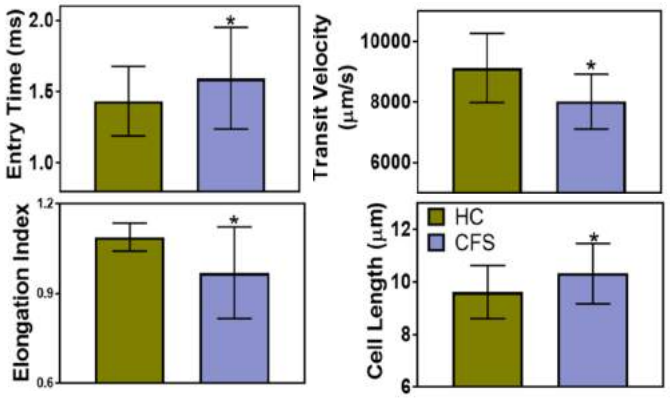

Figure 1. RBC perfusion through microfluidic platform.

To assess deformability of the RBCs, we used a high throughput microfluidic device [5]. 10^7 RBCs/ml were delivered through the microfluidic channels using a custom vacuum-based delivery system at a pressure of -2 psi. The flow of RBCs through the smallest of channels, 5 μm x 5 μm, was visualized at 40X magnification (Leica) and 4000 fps

using a high speed CMOS camera (Phantom VEO 410L), followed by automated image processing using ImagePRO (Media Cybernetics Inc.). For each experiment, at least two microfluidic devices were used per condition, and at least 100 cells were tested per device. Statistical analysis was done using Students' t-test or 2-way ANOVA with Tukey's post hoc test. Since the 5 µm width is smaller than the major diameter of the RBCs, we recorded and analyzed the entry, movement and exit of the cells through these channels.

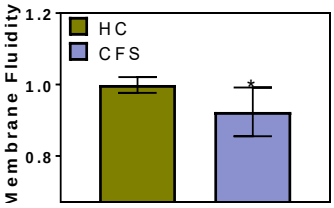

Figure 2. Membrane fluidity of RBCs.

Plasma membrane fluidity was measured using pyrenedecanoic acid (PDA), according to previously established methodologies [5]. The PDA monomers interact with each other and get converted to excimers. This in turn changes the emission spectrum. A ratio of the excimers to monomers gives an estimate of the membrane fluidity.

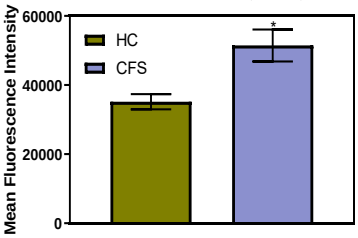

Figure 3. ROS measurement.

The reactive oxygen species (ROS) contents were estimated using Di(Acetoxymethyl Ester) (6-Carboxy-2',7'-Dichlorodihydrofluorescein Diacetate) (Thermofisher Scientific). This non-fluorescent molecule is converted to a fluorescent form due to the removal of acetate groups by ROS activity.

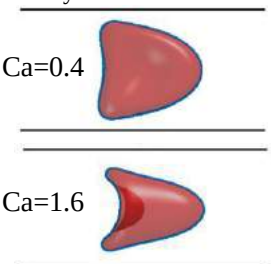

Figure 5. Cell Deformation as a function of Ca.

Our computational approach for solving the motion of deformable, suspended bodies in viscous flows is a modified immersed-finite-element method (IFEM) [6]. The problem is broken into two computational domains: The fluid domain which is Eulerian and the series of particles which are Lagrangian. The fluid solver is a massively parallel, finite volume code which is coupled to the Lagrangian meshes of the particles via an immersed boundary force. A series of interpolation and spreading steps are conducted between the mesh via parallelized stencils so that the forces and velocities of the particle can be communicated between the two domains.

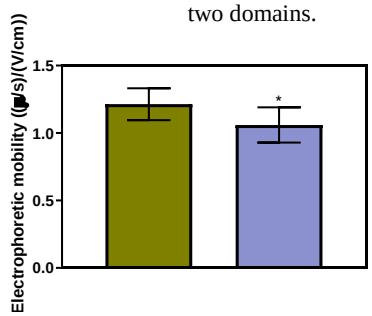

Figure 4. Surface charge of RBCs.

Surface charge was assessed by measuring zeta potential, which is the potential difference between a medium and stationary layer of fluid (interfacial double layer) attached to a particle dispersed in the medium. We tested the zeta potentials of RBC's with the NanoBrook Omni (Brookhaven Instruments Corporation). For this purpose, about 5 µL of whole blood was diluted in 20 mL of 0.9% wt/vol NaCl and the zeta potential of the RBC's in the resulting suspension was measured using Phase Analysis Light Scattering (PALS). The negative charges (mainly sialic acid groups) in the glycocalyx of RBCs and vascular endothelial cells facilitate frictionless blood flow through blood vessels. Loss of charge would correspond to a reduction in zeta potential. In addition to influencing blood flow, charge affects RBC mechanical properties and curvature, and loss of charge would correspond to lower deformability.

RESULTS

RBC deformability. We observed that RBCs from CFS patients had higher entry time, lower average transit velocity and lower elongation index as compared to those from healthy controls (Fig. 1). This collectively implies lower deformability in CFS patients. We also observed significantly different changes in size and fatigue properties of RBCs between healthy controls and CFS patients.

Membrane fluidity. We observed lower membrane fluidity in RBCs from CFS patients as compared to healthy controls (Fig. 2).

Reactive oxygen species (ROS). Higher levels of ROS were detected in RBCs from CFS patients as compared to healthy controls (Fig. 3).

Simulations. We used numerical simulations to determine the quantitative relationship between the cell elasticity, i.e., shear modulus, and the deformation, relaxation, and transient velocity in the microchannels of our microfluidic device. The differences were expressed in terms of the capillary number $C_a = \eta u/\mu_s$, where η is the viscosity of the media, u is the bulk velocity of the fluid inside the channel and μ_s is the shear modulus of the membrane. We use simulation to find the optimal operating conditions for the experiment, such as flow strength and channel dimensions. In addition, a universal curve was constructed based on the simulation results, which relates the deformation to the capillary number. This curve was directly utilized to translate the experimentally measured deformation to the cell elasticity. Fig. 4 shows the different RBC shapes for 2 capillary numbers.

RBC surface charge. We observed a decrease in zeta potential for CFS patients, compared to healthy controls (Fig. 5).

DISCUSSION

Together, the various estimates show that the RBCs in CFS patients are significantly less deformable than those of healthy controls. We speculate that the larger and less deformable RBCs in CFS patients may partly explain the musculoskeletal pain and fatigue in the pathophysiology of CFS due to impaired microvascular perfusion and tissue oxygenation. It has been shown that the quality of life of ME/CFS patients was significantly worse as compared to patients with diseases like sclerosis, cancer (multiple types, such as colon, breast and prostate), type II diabetes, rheumatoid arthritis and chronic renal failure, among others. This work introduces a new paradigm in our understanding of the mechanistic aspects of ME/CFS. It also opens the possibility of a diagnostic platform for ME/CFS using RBC deformability as the biomarker.

ACKNOWLEDGEMENTS

The authors thank the blood donors. The authors thank Dr. Liat Rosenfeld for granting access to the high speed camera. The authors thank Anna Okumu, Julie Wilhelmy and Layla Cervantes for assistance with donor arrangement and sample preparation. The authors thank Open Medicine Foundation for financial support.

REFERENCES

1. Clayton, E.W., JAMA, 2015. **313**(11): p. 1101-2.
2. Montoya, J.G., et al., Proc Natl Acad Sci U S A, 2017. **114**(34): p. E7150-E7158.
3. Kim, J. et al., Journal of Cellular Biotechnology, 2015. **1**(1): p. 17.
4. David S. Bell, M., *The Doctor's Guide to Chronic Fatigue Syndrome.* p. 122-4.
5. Saha, A.K., et al., J Biomech, 2017. **52**: p. 83-88.
6. Saadat, A., et al.,. Physical Review E, 2018. **98**(6).

DEVELOPMENT OF RECOMBINANT INNER-EAR MOTOR PROTEIN PRESTIN EQUIPPED WITH AFFINITY TAG

Michio Murakoshi (1), Hiroshi Wada (2)

(1) School of Frontier Engineering
Kanazawa University
Kanazawa, Ishikawa, Japan

(2) Department of Intelligent Information Systems
Tohoku Bunka Gakuen University
Sendai, Miyagi, Japan

INTRODUCTION

High sensitivity of mammalian hearing is achieved by cochlear amplification. The basis of this amplification is the motility of outer hair cells (OHCs) [1]. This motility is possibly based on the voltage-dependent conformational changes of the motor protein prestin densely embedded in the lateral membrane of OHCs [2-6]. However, the membrane structure of prestin has not yet been clarified. In the present study, to analyze the membrane structure of prestin, the genes of prestin equipped with different affinity tags were transfected into Chinese hamster ovary (CHO) cells and the plasma membrane isolated from this cell was investigated by force spectroscopy using an atomic force microscope (AFM).

MATERIALS AND METHODS

The C-terminal part of gerbil prestin cDNA (*gPres*) was labeled with 3×FLAG tag (3×DYKDDDDK), Avi tag (GLNDIFEAQKIEWHE) or 6×His tag (6×H), and was inserted into a mammalian expression vector. This vector was transfected into CHO cells by lipofection and the cells were subjected to drug selection to generate stable expression cell lines. The prestin RNA expression was confirmed by reverse transcription polymerase chain reaction (RT-PCR) and the protein expression was checked by immunofluorescence staining and by Western blotting.

To confirm the activity of prestin expressed in the generated cell line, the electrophysiological properties of the cell line were measured. Measurements of cell capacitance were performed using the "membrane test" feature of pCLAMP 8.0 acquisition software. To determine the voltage dependence of membrane capacitance, cell potential was swung from -140 mV to +70 mV. After the measurements, the membrane capacitance was plotted versus the membrane potential. The membrane capacitance was fitted to the derivative of a Boltzmann function,

$$C_m(V) = C_{lin} + \frac{Q_{max}}{\alpha e^{\frac{V-V_{1/2}}{\alpha}}\left(1+e^{-\frac{V-V_{1/2}}{\alpha}}\right)^2}, \qquad (1)$$

where C_{lin} is the linear capacitance, $Q_{\max}$ is the maximum charge transfer, α is the slope factor of the voltage dependence of the charge transfer, V is the membrane potential and $V_{1/2}$ is the voltage at half-maximal charge transfer.

Gold-coated atomic force microscopic (AFM) cantilevers were incubated with a drop of mixture of two alkane thiols, i.e., protein resistant oligoethylene glycol (OEG) thiols and biotinylated alkane thiols. After incubation with the mixture, the surfaces were incubated with streptavidin. The cells were then grown on a dish and the inside-out plasma membranes were isolated. Such membranes were incubated with the biotin ligase and prestin was biotinylated so that prestin connects with the streptavidin-coated AFM cantilever via biotin-streptavidin binding. Finally, Avi-tagged prestin was pulled out from the plasma membrane of CHO cell and force curves were obtained. In this study, force peaks detected in the obtained force curves were fitted by the worm-like chain (WLC) model [7, 8]. The WLC model is represented by the following formula:

$$F(z) = \frac{kT}{b}\left(\frac{1}{4(1-z/L)^2} - \frac{1}{4} + \frac{z}{L}\right), \qquad (2)$$

where F is the tensile force, z is the extension length, k is Boltzmann's constant, T is the temperature (in Kelvin) and b is the persistence length, which reflects the polymer stiffness. In this study, the persistence length of 0.4 nm was employed [8]. By using this formula, the contour length L of each force peak, which describes the length of stretched portion of the molecule, was calculated.

RESULTS AND DISCUSSION

To confirm the expression of prestin mRNA, it was extracted from the cell line and the cDNA synthesis was performed. After RT-PCR, the PCR products were subjected to agarose gel electrophoresis. As shown in Fig. 1, bands were observed at around 2200 bp from 6 clones out of 8 clones (FE1:1-3, 1-9, 1-14, 2-2, 2-3, 2-6, 2-9 and 2-14). Since the size of prestin cDNA should be 2235 bp, these bands possibly represent the prestin.

The activity of prestin expressed in the generated cell lines was examined by patch-clamp measurements. The membrane capacitance versus membrane potential measured in a prestin-expressing CHO cell is shown in Fig. 2. As shown in this figure, prestin-expressing cells exhibited bell-shaped nonlinear membrane capacitance (NLC) fitted to Eq. (2), similar to that in OHCs, suggesting that the functional prestin was expressed in the generated cell line.

The relationship between the force applied to the protein and extension distance, i.e., force-extension (FE) curve, was obtained and saw-toothed patterns were observed. The worm-like chain (WLC) model was applied to the FE curve and the force due to the extraction of N domain at 265 amino acid (aa) and that due to the extraction of the loop between N and M domains at 285 aa were detected (Fig. 3).

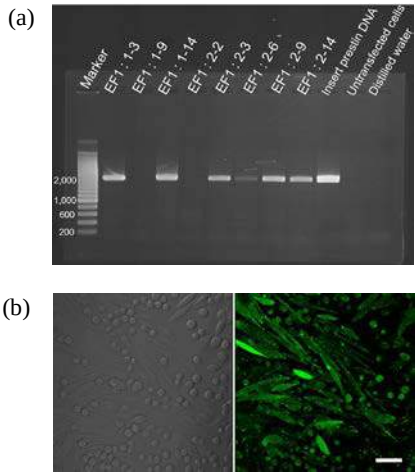

Figure 1: Expression of prestin in the cell lines. (a) RT-PCR analysis of the different clones. (b) A developed CHO cell line expressing prestin with FLAG tag. Left; DIC image, right; GFP image. Scale bar represents 10 µm.

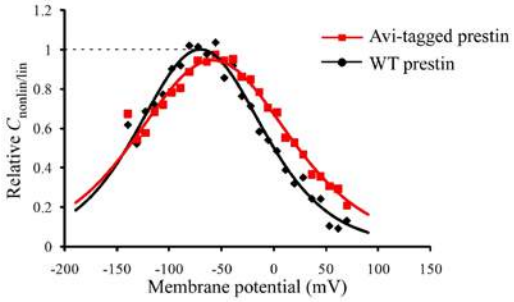

Figure 2: Representative data of patch clamp recording obtained from cells stably expressing Avi-tagged prestin (Red line) and WT prestin (Black line). The cell line which stably expresses Avi-tagged prestin exhibited the nonlinear membrane capacitance (NLC).

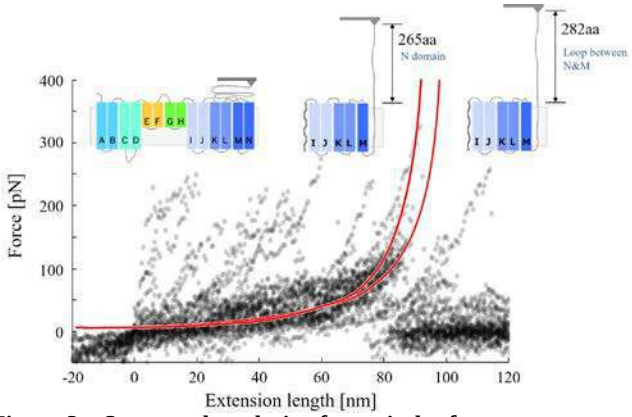

Figure 3: Structural analysis of prestin by force spectroscopy using the AFM. Force-extension (FE) curve was fitted by WLC model.

ACKNOWLEDGEMENTS

This work was supported by JSPS KAKENHI Grant Numbers 23659790, 24791739 and 17H04739, and by JST PRESTO Grant Number JPMJPR13KI.

REFERENCES

[1] Dallos P, Evans BN, Hallworth R, *Nature* 350:155–157, 1991.

[2] Zheng J, Shen W, He DZZ, Long KB, Madison LD, Dallos P, *Nature* 405:149–155, 2000.

[3] Dallos P, Fakler B, *Nat Mol Cell Biol* 3:104–111, 2002.

[4] Murakoshi M, Gomi T, Iida K, Kumano S, Tsumoto K, Kumagai I, Ikeda K, Kobayashi T, Wada H, *J Assoc Res Otolaryngol* 7:267–278, 2006.

[5] Murakoshi M, Iida K, Kumano S, Wada H, *Pflugers Arch* 457:885–898, 2009.

[6] Kumano S, Murakoshi M, Iida K, Hamana H, Wada H, *FEBS Lett* 584:2872–2876, 2010.

[7] Bustamante C, Marko JF, Siggia ED and Smith S, *Science* 265: 1599-1600, 1994.

[8] Rief M, Gautel M, Oesterhelt F, Fernandez JM and Gaub HE, *Science* 276: 1109-1112, 1997.

Inhibition of GSK-3β by LiCl Does Not Affect MSC Differentiation *In Vitro* or Bone Formation *In Situ*

Alyssa G. Oberman, Angela A. Patel, Glen L. Niebur
Bioengineering Graduate Program, Department of Aerospace and Mechanical Engineering, University of Notre Dame
Notre Dame, IN, United States

INTRODUCTION

Osteoporosis is a disease that occurs due to an imbalance in the normal bone remodeling process, resulting in an overall reduction of bone mineral density (BMD) and architectural degradation in trabecular bone. This decrease in BMD ultimately increases fracture risk and poses the potential for more serious repercussions as the disease progresses [1]. Thus it is important to identify potential targets for drug development or other interventions. Current treatment of osteoporosis is limited to the administration of bisphosphonates - drugs that target osteoclasts to prevent bone resorption but do not directly effect bone formation. New drugs or potential targeting pathways that act to stimulate osteogenesis through paracrine signaling to mitigate the effects of aging on osteoblast activity could provide a means to restore BMD, rather than simply mitigating further declines.

Upregulation of factors that initiate osteogenesis can push cells towards an osteogenic fate. The canonical WNT pathway is involved in the control of bone formation by activating transcription factors that control ECM production, and has been identified as a potential target for the treatment of osteoporosis. Recently, drugs that block sclerostin (SOST), a well-known inhibitor of the pathway, have undergone clinical trials. While SOST antibody reduced fracture risk and promoted bone formation [2], the FDA has blocked its release due to adverse cardiovascular events [3]. Other targets in the WNT pathway might have similar efficacy without these effects. One potential target is GSK-3β, which is normally inhibited by WNT signaling to allow β-catenin accumulation.

We attempted to affect GSK-3β activity using lithium chloride (LiCl) which directly affects GSK-3β to inhibit degradation of β-catenin [4] and may be a valuable tool for osteogenesis experiments. An *in vivo* study showed a two-fold increase in bone volume change in an osteoporotic mouse model when the mouse was treated with LiCl [4]. However, *in vitro* studies evaluating the effect of LiCl usage on osteoblast progenitors, mesenchymal stem cells (MSCs), have been inconclusive regarding osteogenic potential.

Because it is still unclear whether LiCl acting on the WNT pathway is sufficient to induce osteogenesis in MSCs, we investigated its effects in two *in vitro* models. First, we applied an *in situ* bone marrow model to evaluate the effects of LiCl on the bone marrow niche, eliminating any potential systemic effects that may present in *in vivo* studies. Secondly, we evaluated the effects of LiCl treatment on MSCs in 2-D culture with and without osteogenic supplements.

METHODS

For the *in situ* experiments, bone explants were harvested from the cervical vertebrae of pigs within 2-3 hours of slaughter. The explants were cultured in a bioreactor for 28 days during which time explants were exposed to normal or drug-treated (5 mM or 12 mM LiCl) media, and static or mechanically stimulated conditions. Mechanical stimulation consisted of sinusoidal vibration with a peak acceleration of ± 0.3 g at 50 Hz which affects the mechanobiological signaling in bone marrow [5]. To investigate the role of cell-secreted factors, we used two media exchange protocols, with the entire volume of media changed once a week or half of the volume changed twice a week. Bone explants were imaged with a μCT scanner before and after culture to measure changes in bone volume (Fig. 1a) [6]. Additionally, media was supplemented with 0.5 mM Alizarin Red and Xylenol Orange for 24 hours on day 6 and day 27, respectively, for dynamic histomorphometry (Fig. 1b).

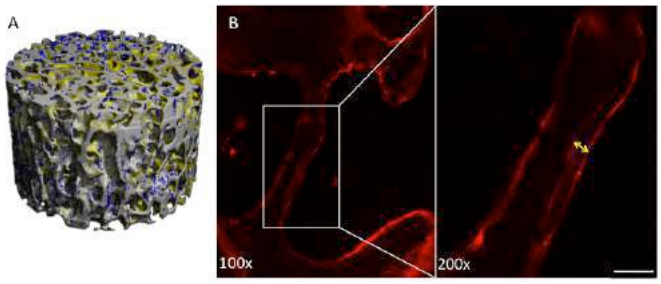

Fig. 1. Changes due to bone remodeling were measured using two techniques. (a) Registered μCT images were compared to identify bone formation (blue) and resorption (yellow) by directly comparing image volumes. (b) Standard dynamic histomorphometry was used to measure bone formation to account for the limited resolution of the μCT scans. Scale bar represents 50 μm.

A 2-D culture study was performed to test the effects of LiCl on differentiation potential of porcine MSCs. Media was supplemented with 5 mM or 12 mM LiCl with or without ascorbic acid 2-phosphate (AA2P) and β-glycerol phosphate (BGP). Standard osteogenic media was used as a positive control and growth media as a negative control [7]. A calcium assay was used to compare calcium deposition as a result of treatment (Stanbio Laboratory, USA).

RESULTS

Neither LiCl treatment nor mechanical stimulation had an affect on bone formation or resorption rates in the *in situ*

culture (Fig. 2a). When media was changed once a week, no changes in bone formation across any groups were seen regardless of drug treatment or loading conditions and bone formation and resorption occurred at the same rate (Fig. 2a). Similarly, bone formation rates measured using dynamic histomorphometry showed no differences between groups (Fig. 2b). However, the rate shifted in favor of bone formation when media changes were modified to reduce the total volume changed at each time point.

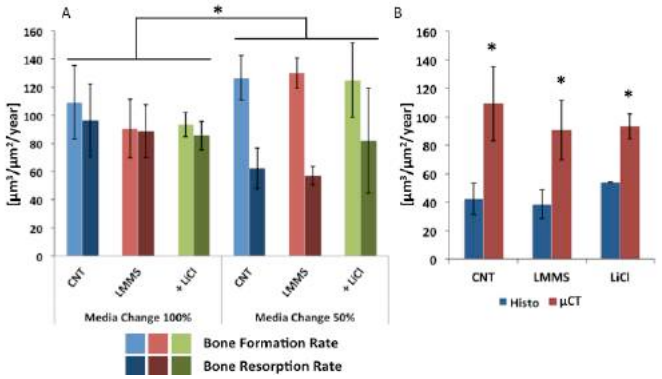

Fig. 2. (a) Bone formation and resorption rates measured via μCT histomorphometry were compared between groups with complete media changes (n = 5, LiCl; n = 10, CNT and LMMS) and partial media changes (n = 4, LiCl; n = 3, CNT and LMMS). Bone formation was higher and resorption rate was lower when half the volume of media was changed. LiCl treatment had no effect (* $p < 0.05$, two-factor ANOVA). (b) Bone formation rates measured via μCT were higher than those measured via dynamic histomorphometry (n = 4) (* $p << 0.01$, Student's t-test).

Two-dimensional cultures showed no change in calcium deposition and MSC differentiation when using LiCl. Addition of AA2P and BGP increased calcium deposition, but were still less than half of that for osteogenic media (Fig. 3).

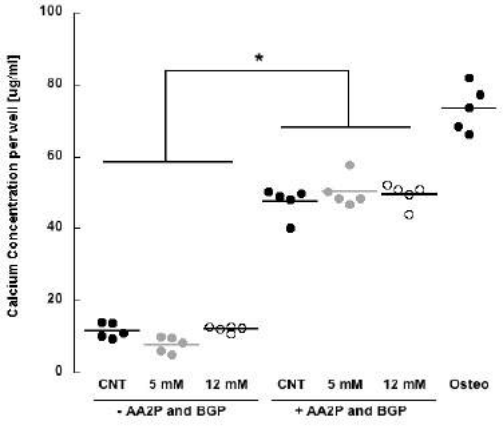

Fig. 3. The effect of LiCl treatment on MSCs was tested in 2-D culture. There were no differences between LiCl treated and negative control groups. Addition of osteogenic supplements increased calcium deposition, which was still lower than standard osteogenic differentiation media (* $p << 0.01$, two-factor ANOVA).

DISCUSSION

LiCl acts as an inhibitor of GSK-3β, which allows β-catenin to accumulate and translocate to the nucleus where a cascade of events increase osteogenesis. However, there have been contradictory results on the behavior of MSCs treated with LiCl. Our data showed that LiCl did not affect calcium deposition in MSC cultures, contrary to previous results where an increase in osteogenic behavior was found [9, 10]. The main difference between our experiment and others is that our treatment groups were not supplemented with dexamethasone, which acts on the glucocorticoid receptor to drive osteogenesis [9-11]. This suggests that GSK-3β inhibition by LiCl alone is not sufficient for MSC differentiation, that it acts on pre-osteoblasts or osteoblasts, or requires systemic hormones.

The combination of *in situ* and 2-D cell culture in this study provided a unique method to assess the effects of GSK-3β on osteogenesis. An important limitation is the small number of samples studied.

The effect of the media changes on bone formation demonstrates that paracrine signaling was essential to bone formation in the bioreactor. Neither LiCl treatment nor mechanical stimulation was able to compensate for the depletion of secreted signaling factors in the media. As a result, bone formation and bone resorption occurred at almost identical rates, which were so low that they may reflect image registration errors. However, when paracrine signaling was maintained, the rates of bone formation increased while resorption decreased.

LiCl had no effect on bone formation *in situ*, even with paracrine signaling, suggesting that bone formation in this system is not rate limited by WNT signaling. This is consistent with our recent findings that bone formation can occur *in situ* without altered SOST expression [5]. Other systemic factors, such as circulating hormones, may have affected bone formation in previous *in vivo* studies [4]. While cell secreted paracrine factors were able to affect bone formation in our bioreactor, systemic hormones such as glucocorticoids that might interact with GSK-3β are likely not present.

ACKNOWLEDGEMENTS

We would like to thank Kimberly Curtis for assistance. This work was supported by the National Science Foundation CMMI-1435467.

REFERENCES

[1] Pisani, P. et al., 2016, World J Orthop, 7(3), pp. 171-181.
[2] Garber, K., 2016, Nat Rev Drug Discov, 15(7), pp. 445-446.
[3] Mullard, A., 2017, Nat Rev Drug Discov, 16(9), p. 593.
[4] Clément-Lacroix, P. et al., 2005, Proc Natl Acad Sci U S A, 102(48), pp. 17406-17411.
[5] Curtis, K. J. et al., 2018, Bone, 107, pp. 78-87.
[6] Birmingham, E. et al., 2014, Annals of biomedical engineering.
[7] Birmingham, E. et al., 2012, Eur Cell Mater, 23, pp. 13-27.
[8] Cohen, P., and Goedert, M., 2004, Nat Rev Drug Discov, 3(6), pp. 479-487.
[9] Yu, Z. et al., 2015, Int J Mol Med, 36(5), pp. 1264-1272.
[10] Tang, L. et al., 2015, Cell Physiol Biochem, 37(1), pp. 143-152.
[11] Langenbach, F., and Handschel, J., 2013, Stem Cell Res Ther, 4(5), p. 117.

SB^{3}C2019
Summer Biomechanics, Bioengineering and Biotransport Conference
June 25 -28, Seven Springs, PA, USA

MECHANICAL FEEDBACK AND COOPERATIVITY IN A THEORETICAL MODEL OF AIRWAY SMOOTH MUSCLE CELL–MATRIX ADHESION

Linda Irons (1,2), Markus R. Owen (1), Reuben D. O'Dea (1), Bindi S. Brook (1)

(1) School of Mathematical Sciences
University of Nottingham
Nottingham, UK

(2) Current address: Department of Biomedical Engineering
Yale University
New Haven, CT, USA

INTRODUCTION

Bronchoconstriction, a narrowing of the airways characteristic of asthma, is regulated by two key processes: the generation of contractile force (via actomyosin crossbridges within airway smooth muscle (ASM) cells) and the transmission of this contractile force to the surrounding extracellular matrix (via integrin-mediated adhesions). In several experimental studies, deep inspirations (DIs) have been observed to reverse bronchoconstriction in healthy subjects, but this reversal was transient or not seen in asthmatics [1–3]. The mechanisms underlying this result are currently unknown. Motivated by these observations, previous research has focussed on understanding how contractile force generation is modulated by oscillatory loading. However, integrins are well-known to respond to environmental fluctuations, and are therefore also an important factor to consider. In this study, we develop a theoretical model to study how both crossbridges and integrins respond to oscillatory loading of the ECM. Using the model, we investigate the mechanical coupling between the two processes and suggest bistability (which arises due to mechanical cooperativity) as a possible mechanism behind differing responses to DIs.

METHODS

The mathematical model (sketched in Fig. 1) consists of three elements in series representing the ECM, integrins and the ASM cell. Within the cell, we consider a passive stiffness as well as parallel contractile units that are governed by the well-established Huxley–Hai–Murphy (HHM) model [4]. The HHM model is an advection–reaction system where myosin crossbridges undergo transitions between four states, accounting for phosphorylation and dephosphorylation of the crossbridges and their attachment and detachment to actin filaments. Transition rate functions are governed by local kinetics, and contractile force is generated by crossbridges in the attached states. Similarly, we consider local binding and rupture kinetics of integrins, adapting a formulation from our previous model of cell–matrix adhesion dynamics [5]. These elements are coupled to, and respond to, mechanical loading, which is applied via an oscillatory displacement condition to the ECM (L'_T, Fig. 1b).

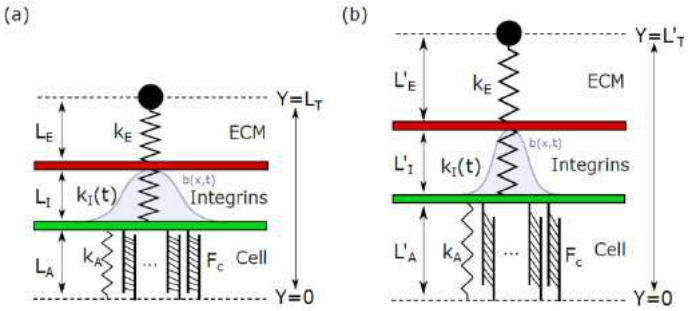

Figure 1: Schematic diagram of the components considered in our model of ASM cell–matrix interactions. Three elements in series represent the ECM, integrins and the cell (consisting of a passive stiffness and parallel contractile units modelled by a 4-state Huxley–Hai–Murphy model [4]). The integrin and crossbridge binding and rupture rates depend on local kinetics and the effective stiffness of the cell and integrin elements evolve in time as binding and deformation-induced rupture occur. The collective integrin spring constant, $k_I(t)$, is determined by an underlying distribution of bound integrins, $b(x,t)$, where x is a coordinate local to each integrin [5].

RESULTS

Due to load-dependent unbinding of integrins and crossbridges, we find that both force transmission and force generation are affected by increasing amplitudes of oscillatory loading (Fig. 2). Moreover, there is a close mechanical coupling between the two processes from which a regulatory mechanism appears to emerge due to negative feedback: integrins and crossbridges have a competing effect on cell deformation, and a decrease in integrin density promotes crossbridge attachment. For intermediate amplitudes of loading we observe a region of bistability where shared loading and cooperativity between integrins can allow an initially high adhesion state to persist. This is analogous to a result reported in our earlier study [5], in which only integrin dynamics were modelled. However, in this fully-coupled model, we observe an additional region (Fig. 3) due to a similar cooperativity between crossbridges. The different regions are attainable as a dimensionless parameter β, which describes the relative strengths of the crossbridges and integrins, varies; for low β, integrin cooperativity is dominant; for high β, crossbridge cooperativity dominates. In both cases, the existence of bistability has interesting consequences. We find that large perturbations in oscillation amplitude (representing DIs) can result in a dramatic reduction in the total contractile force transmitted to the ECM. When bistability is present, this reduction can either persist or recover depending on where the unperturbed oscillation amplitude lies relative to the bistable region. Specifically, if this unperturbed amplitude is bistable, a permanent switch in behaviour is possible. It has been observed that DIs can reverse bronchoconstriction in non-asthmatics but not in asthmatics, and we propose that an underlying bistability could explain this.

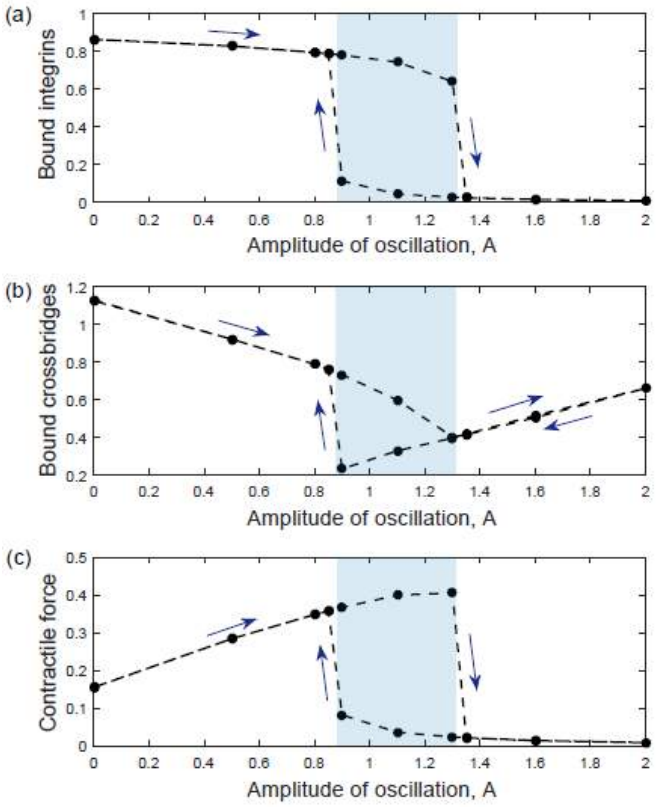

Figure 2: Stable steady states for the densities of (a) bound integrins, (b) attached crossbridges, and (c) total contractile force when oscillations of amplitude A were applied to the ECM. Shading highlights bistability and arrows indicate hysteresis loops.

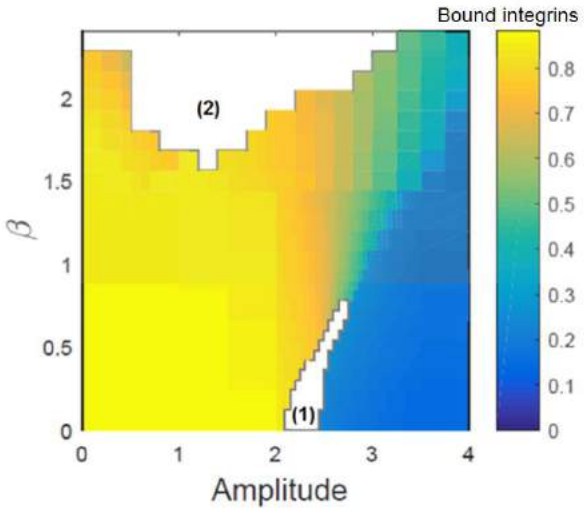

Figure 3: The regions of bistability (white) are from integrin cooperativity (1) and crossbridge cooperativity (2) respectively. Bistable regions shift as the dimensionless parameter β varies, which is a ratio involving the total number and stiffnesses of crossbridges and integrins, describing their relative strength.

DISCUSSION

Motivated by understanding the role of both actomyosin crossbridges and integrins in regulating bronchoconstriction, we developed a mathematical model of their combined responses to oscillatory loading. By coupling local binding kinetics to higher scale relative motion, we demonstrate the existence of mechanical feedback and mechanical cooperativity. To our knowledge, interacting crossbridge and integrin dynamics have not been considered at this level of detail before. A consequence of the mechanical cooperativity is the existence of bistability under certain parameter regimes. In these cases, it is possible to see a permanent switch in qualitative behaviour where large amplitude perturbations lead to reduced levels of total contractile force. Our mathematical model therefore predicts results of clinical significance: we propose that bistability could be a mechanism underlying experimental observations on the bronchodilatory effect of deep inspirations in non-asthmatics. Moreover, the model provides insight into parameters that influence the bistability; for example, we have observed that an increase in passive cell stiffness results in a narrower bistable region, which could be relevant to understanding the ineffectiveness of DIs at reversing bronchoconstriction in asthmatics. In summary, our work highlights the importance of considering both contractile force generation and contractile force transmission, generates hypotheses for the differing responses to DIs in asthmatics and non-asthmatics, and suggests bistability and mechanical cooperativity as important directions for future experimental study.

ACKNOWLEDGEMENTS

R.D.O. and B.S.B. acknowledge support from the Medical Research Council United Kingdom (MR/M004643/1).

REFERENCES

[1] Crimi, E. et al., (2002), *J. Appl. Physiol.*, 93(4):1384–1390.
[2] Kapsali, T. et al., (2000), *J. Appl. Physiol.*, 89(2):711–720.
[3] Scichilone, N. et al., (2000), *Am. J. Respir.Crit. Care Med.*, 162(3):910–916.
[4] Mijailovich, S. et al., (2000), *Biophys. J.*, 79(5):2667–2681.
[5] Irons, L. et al., (2018), *Biophys. J.*, 114(11):2679-1690.

SB³C2019
Summer Biomechanics, Bioengineering and Biotransport Conference
June 25 -28, Seven Springs, PA, USA

EXTRACELLULAR MATRIX STIFFNESS REGULATES CALCIUM OSCILLATIONS IN MULTICELLULAR ENSEMBLES, BUT NOT IN ISOLATED CELLS

Suzanne E. Stasiak (1), Ryan Jamieson (1), Harikrishnan Parameswaran (1)

(1) Bioengineering Department
Northeastern University
Boston, MA, USA

INTRODUCTION

Cellular constriction must be coordinated across multiple length scales for organs to perform vital life processes such as breathing, beating of the heart, maintenance of blood pressure and the peristaltic contractions of the gut. For instance, in order to regulate the flow of air through the airway tree, it is not sufficient that airway smooth muscle (ASM) cells constrict in response to inhaled agonist. These cells need to connect with each other and constrict in a coordinated fashion so as to generate enough force to constrict an entire airway. In the airway, such coordination is achieved by intercellular communication using Ca^{2+} waves. When an airway is exposed to inhaled agonists such as histamine, cytosolic Ca^{2+} oscillations are initialized in the ASM cells. The Ca^{2+}oscillations in adjacent ASM cells are offset in phase such that Ca^{2+} waves appear to move around the circumference of the airway. When the agonist dose increases, the amplitude of the Ca^{2+}oscillations stay the same, but the frequency of Ca^{2+} oscillations increases monotonically with agonist dose. Higher frequency of Ca^{2+} oscillations is accompanied by greater constriction of the airway lumen[1]. While intracellular biochemical pathways that regulate this phenomenon have been subject to numerous studies in the past two decades, the role of extracellular mechanical factors in coordinating cellular contractions is not well understood.

Here, we use a protein-coated silicone substrate of tunable-stiffness to simulate the ECM of soft, healthy airways (Young's modulus E=300 Pa), and stiff, remodeled airways (E=13 kPa). Human ASM cells are cultured either isolated from each other or in patterns that promote cell-cell connections. ASM are subjected to a low dose of agonist (10^{-5}M histamine), and the cell reactivity is measured. Cell reactivity is quantified by imaging the variation in intensity of cytosolic Ca^{2+} with a fluorescent marker over time, and then data processing to obtain a mean oscillation period. We find that ECM stiffness regulates the Ca^{2+} oscillation frequency of ASM in multicellular groups, yet it has no impact on the frequency of individual, isolated cells. Those ASM that are connected to other have an increased oscillation frequency on stiffer substrates, suggesting that they are at a higher tone and more primed to constrict, simply due to the mechanical environment. This has implications for understanding the role of matrix remodeling in the etiology of widespread diseases such as asthma and hypertension.

METHODS

NuSil Gel Fabrication and Photopatterning. Microtissue mimics and isolated cell cultures were developed in order to test the relationship between ECM stiffness and calcium frequency on ASM in different configurations. NuSil (NuSil Silicone Technologies, Carpenteria, CA), a silicone substrate of tunable stiffness[2], was used to mimic the stiffness of healthy and diseased airways. Required volumes of crosslinker were added to the silicone base component in order to create substrates of 0.3 kPa and 13 kPa. Incubating these substrate with 0.1% gelatin allowed protein to coat the surface. In order to create the geometry of the microtissue, only patterned islands on the gel were coated with protein. In order to pattern desired shapes, such as small airway rings, the gel was coated with surface blockers Poly-L-Lysine (PLL; Sigma-Aldrich, St. Louise, MO) and mPEG-SVA (Laysan Bio, Arab, AL), which were then removed by a UV-activatable reagent in specific areas. Protein adhered to the gel in these exposed areas, and the rest of the surface remained blocked from cell adhesion by the PLL-mPEG compound.

Human Airway Smooth Muscle Culture. Human airway smooth muscle cells were obtained through the Gift of Hope Foundation, and used before passage number 7. Cells were seeded onto patterned and unpatterned gels, and allowed to adhere in 10% bovine serum media for

at least 4 hours. The media was then replaced by serum-free media, and incubated for at least 24 hours.

Fluorescent Dye Loading. ASM were incubated with 0.5μM Fluo4-AM for 30 minutes at room temperature, then incubated in dye-free media for an additional 30 minutes to allow the cell esterases to cleave the AM ester. This allows Fluo4 to fluoresce with increasing Ca^{2+} concentration. Cells were imaged immediately after loading the fluorescent dye. A representative image of an ASM microtissue loaded with Fluo4 is shown in Fig 1A, false-colored.

Calcium Imaging. A low dose of histamine (10^{-5} M) was added to the cell media at the start of imaging. ASM were imaged using a Leica DMi8 microscope with a 20x objective. Images were taken at 1 frame per second with a 50ms exposure time, for a total of 5 minutes per sample.

Data Analysis. Each image sequence was opened in Fiji/ImageJ[3]. Regions of interest (ROIs) of 5x5 pixels were hand-selected in the cytoplasm of each cell (Fig 1B). The mean greyscale intensity over the area of the ROI was recorded for each time frame. A custom MATLAB (Mathworks, Natick, MA) code read the intensity values over time and corrected the data for photobleaching. A representative Ca^{2+} oscillation experiencing photobleaching is shown in Fig 1C, with the exponential fit correction dashed line. The bleach-corrected data is shown in Fig 1D. From this data, the peaks of the oscillations were identified, and the average of the time between the peaks was recorded as the mean period for the cell. SigmaPlot (Systat Software, San Jose, CA) was used to run Mann-Whitney Rank Sum tests for statistical analysis of the data.

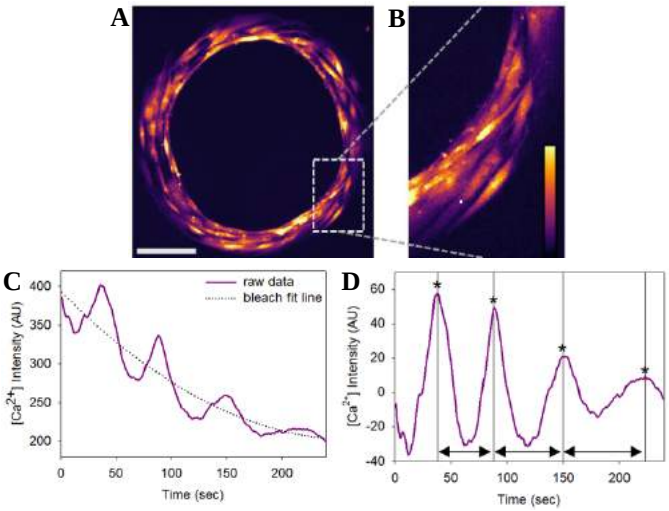

Figure 1: (A) Human airway smooth muscle microtissue on gelatin-coated NuSil (13kPa) with fluorescently labeled Ca^{2+}. Bar = 200μm. (B) Zoomed-in region of the ring to highlight the 5x5 pixel ROI for intensity recordings, shown as a white box. The colorbar represents increasing Ca^{2+} concentration as increasing brightness. (C) Representative raw data calcium signal from an ROI, which must be corrected for photobleaching. Subtracting an exponential fit will accomplish this. (D) Calcium oscillation post bleach correction, with peaks identified and periods measured as the time between peaks.

RESULTS

Our results show that matrix stiffness effects frequency of Ca^{2+} oscillations in multicellular ensembles of HASM cells, like the image of the ASM ring shown in Fig 2A. The mean Ca^{2+} oscillation frequency per cell is significantly lower on the stiffer ECM than on the soft ECM (P=<0.001) (Fig 2B). ASM on stiff matrix oscillated with a mean period

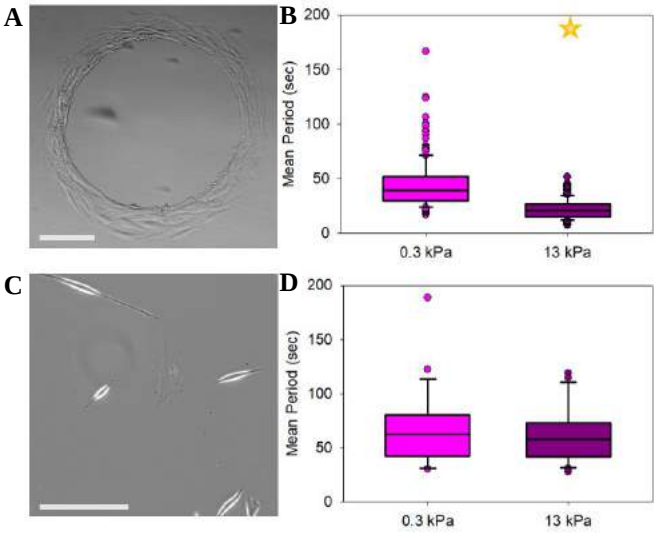

Figure 2: (A) Phase image of multicellular ASM ring. (B) Box plot of mean Ca^{2+} oscillation periods of individual cells within the ASM rings. (C) Phase image of isolated ASM cells. (D) Box plot of mean Ca^{2+} oscillation periods of individual, isolated cells. Bar = 200μm.

of 21.8 seconds (N=172), whereas the ASM on soft matrix had Ca^{2+} oscillation periods averaging at 44.1 seconds (N=195).

Single, isolated cells (Fig 2C) do not show any relationship between Ca^{2+} frequency and ECM stiffness. The mean period data between cells on soft (N=29) and stiff (N=24) ECM is not statistically significant (P=0.668) (Fig 2D).

DISCUSSION

Our study explores the relationship between extracellular matrix stiffening and smooth muscle cell reactivity. With our method of producing these microtissue, we were able to precisely control the mechanical properties to mimic the in vivo environment, while imaging and collecting data. Although photobleaching of the fluorescent dye limited the time series length, we were still able to record enough variations in intensity to measure oscillation periods. We have found that increasing ECM stiffness will increase the frequency of intracellular Ca^{2+} oscillations in the ASM ensembles, but not in isolated ASM cells. The significance of this result is twofold. 1) It provides another example of contrasting behavior between isolated cells and interacting cells to the growing body of research on collective cell dynamics[4,5]. 2) Our data demonstrates that any ECM remodeling that increases the stiffness of the ECM will induce higher frequency Ca^{2+} oscillations in smooth muscle cell ensembles. Since the frequency of Ca^{2+} oscillations is highly correlated with the amount of force generated by the smooth muscle, this suggests that changes in ECM mechanics can be the primary pathway for the development of diseases such as asthma and hypertension.

ACKNOWLEDGEMENTS

This work was supported by NIH grants HL129468 and HL122513 (HP).

REFERENCES

1. Perez JF, Sanderson MJ, *J Gen Physiol*, 125:535-553, 2005.
2. Yoshie H et al., *Biophys J*, 114:2194-2199, 2018.
3. Schindelin J et al., *Nat Methods*, 9:676-682, 2012.
4. Cai D et al., *Cell*, 157:1146-1159, 2014.
5. Potter GD et al., *PNAS*, 113:10334-10339, 2016.

SB³C2019
Summer Biomechanics, Bioengineering and Biotransport Conference
June 25 -28, Seven Springs, PA, USA

ELASTOGRAPHY EVALUATION OF THE ELBOW ULNAR COLLATERAL LIGAMENT IN OVERHEAD THROWING ATHLETES

S. Sadeghi (1), D. Bader (2), D. Cortes (1,3)

(1) Mechanical Engineering Department
Penn State University
State College, PA, USA

(2) Department of Orthopaedics & Rehabilitation, Penn State College of Medicine
State College, PA, USA

(3) Biomedical Engineering Department
Penn State University
State College, PA, USA

INTRODUCTION

The anterior band of the ulnar collateral ligament (UCL) is commonly subjected to repetitive stress in overhead-throwing athletes, causing high sub-failure strain and change in mechanical properties of the ligament [1]. Understanding the effect of repetitive loading in the UCL mechanical properties is essential for diagnosing pathological conditions in the UCL. Additionally, monitoring changes in UCL mechanical properties could potentially quantify the risk of injury and prevent injuries by modifying cycles of throwing and resting and number of throws. Ultrasound shear wave elastography (SWE) is an imaging technique designed to non-invasively measure the shear modulus of soft tissues [2]. The objective of this study was to evaluate the repeatability and to quantify changes in the UCL shear modulus of overhead-throwing athletes over the course of a competitive season. Additionally, a follow-up case study of an injured player is presented. The results of this study show that SWE could be a useful clinical tool for evaluating the health of the elbow UCL.

METHODS

Sixteen healthy non-throwing participants (age = 27.1 ± 4.9; BMI = 22.1 ± 3.2 kg/m^2) were recruited to determine of intra- and day-to-day reliabilities of UCL shear modulus. Five healthy football quarterbacks (age = 19.80 ± 1.30; BMI = 26.60 ± 0.54 kg/m^2) and seventeen healthy baseball players (age = 20.29 ± 1.99; BMI = 26.71 ± 1.46 kg/m^2) including six position players and eleven pitchers were recruited. The protocol quantified changes in shear modulus of the UCL at pre-season and season-end time points for the baseball players and pre-season, mid-season and season-end time points for the football quarterbacks. Additionally, in a case study, one injured baseball pitcher (age=24 and BMI=24.3 kg/m^2) with partial UCL tear was recruited. During the SWE measurement, the participants laid supine with the shoulder at 30^0 of abduction and 90^0 of external rotation and the elbow at 30^0 of flexion [3] (Figure 1(a)). For the statistical analysis, intra-class correlation coefficient (ICC) and Cronbach's alpha reliability coefficient were used to calculate the measurement reliability of the shear modulus in healthy non-throwing participants. A one-way repeated measures ANOVA, followed by post hoc Bonferroni correction, was also employed to evaluate the effect of time on the UCL shear modulus values in overhead throwing athletes.

RESULTS

The B-mode image and shear modulus map of the UCL within the rectangular ROI are shown in Figure 1(b) and 1(c). The ICC and Cronbach's alpha for the intra-day reliability were 0.72 (95% CI = 0.59 - 0.83) and 0.93 respectively, indicating the good reliability. The day-to-day reliability was excellent based on the associated ICC (0.95 with 95% CI = 0.88 - 0.98) and Cronbach's alpha (0.96). There was no significant difference between the dominant and non-dominant arms in the UCL shear modulus (average ± standard deviation) in healthy non-throwing individuals (109.82 ± 43.45 kPa vs. 103.90 ±

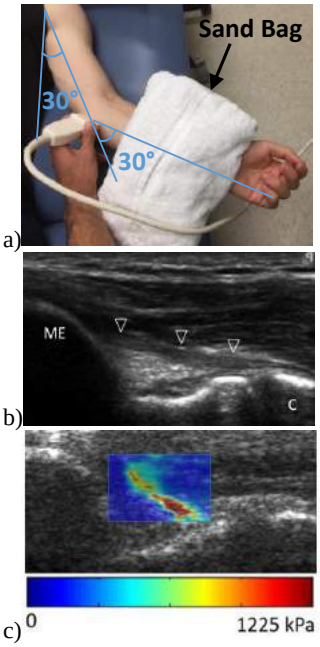

Figure 1: a) Set-up, b) UCL shown with triangles (ME: medial epicondyle, C: coronoid) and c) elastography map

35.61 kPa). The UCL shear modulus values for the dominant arm in baseball players at pre-season and season-end were 347.64 ± 420.05 kPa and 210.83 ± 209.44 kPa respectively; for the non-dominant arm were 503.95 ± 590.59 kPa and 312.67 ± 240.66 kPa, respectively (Figure 2). Additionally, the average UCL shear modulus in both arms of baseball position players was found to be higher than pitchers at the pre-season (i.e. 729.10 ± 596.26 kPa versus 260.36 ± 377.62 kPa) and season-end time points (i.e. 248.16 ± 66.32 kPa versus 205.15 ± 64.87 kPa) (Figure 2a). The shear modulus values for the football quarterbacks for the dominant arm at pre-season, mid-season and season-end were 447.56 ± 339.13, 113.62 ± 52.19 and 207.02 ± 277.88 respectively; for the non-dominant arm were 808.15 ± 578.34, 463.75 ± 190.49 and 491.42 ± 420.03, respectively. Time had a significant effect on UCL shear modulus on the dominant arm in football quarterbacks ($p=0.04$). Additionally, a meaningful difference in shear modulus between the pre-season and season-end time points was obtained ($p = 0.05$). In the case study, the UCL shear modulus of the injured elbow was lower than that of the uninjured elbow, especially within a week after injury (186.45 kPa vs. 879.59 kPa). After 8 weeks of recovery, the shear modulus returned to levels similar to those of the contralateral arm. After 8 weeks, the player progressively resumed throwing activity and he was clear to play at week 25 (Figure 3).

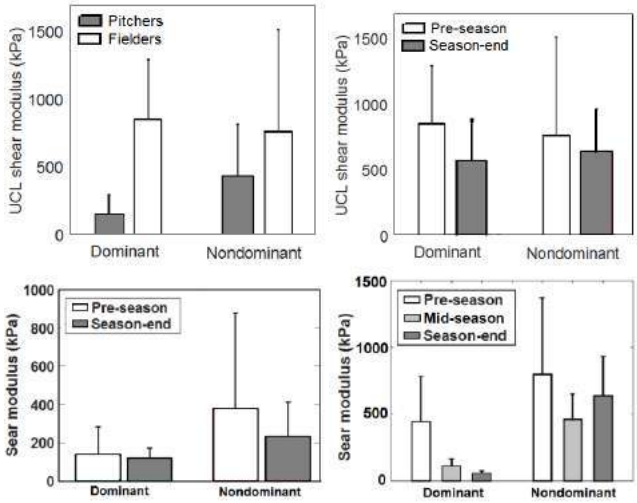

Figure 2: UCL shear modulus of dominant arm is lower in baseball pitchers compared to the fielders (a) the shear modulus changes over the course of a competitive season for fielders (b), pitchers (c), and football quarterbacks (d).

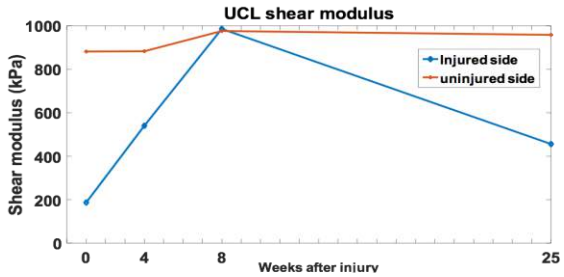

Figure 3: Longitudinal evaluation of torn UCL in the injured baseball pitcher.

DISCUSSION

This study showed that SWE is a reliable tool for the assessment of the shear modulus of the UCL. The shear modulus of the UCL in the dominant arm was pronounced compared to the non-dominant arm in baseball players and football quarterbacks, possibly due to the repetitive loading applied during throwing exercise. The UCL shear modulus in healthy non-throwing individuals was lower than those in both baseball players and football quarterbacks in both arms at all-time points. This might be explained by adaptation and remodeling responses of the ligament to strength training. It was found that the shear modulus of the injured UCL of the baseball pitcher was around 79% lower than that of the healthy one within a week after injury.

The UCL shear modulus in the non-dominant arm of football players was higher than those of the baseball players. This may have been caused by the difference in strength training. The decrease in UCL shear modulus of the dominant arm over the course of the season was higher in the football players compared to the baseball players. This may be explained by differences in the UCL loading because of weight of the balls, kinematics of the arm during throwing, and quantity of throws during training sessions and games. Repetitive loading applied to the dominant arm of throwing athletes may cause a decrease in the shear modulus of that arm. This can be clearly observed in the similarity of the shear modulus of both arms in fielders (Figure 2b) compared to the dissimilar values in the arms of pitchers and quarterbacks (Figure 2c and 2d). These results suggest that the UCL's mechanical properties may uniquely change after repetitive loading in different overhead-throwing sports.

Several studies have investigated the ex-vivo mechanical response of connective tissues to repetitive loading. Rigby et al. [4] reported that if the strain applied to rat tail tendons does not exceed approximately 4%, the specimen can be cycled for a long period of time without damage. Weisman et al. [5] reported a clear relationship between softening (ratio of last cycle peak load to first cycle peak load) and reduction in strength of the ligament as a function of cyclic stress of the medial collateral ligament in rats. Mechanical response of connective tissues to repetitive loading has also been studied in human cadaveric connective tissues. Pollock et al. [6] studied the mechanical response of the inferior glenohumeral ligament to varying sub-failure cyclic strains in 33 fresh frozen human cadaver shoulders. They found that the group of ligaments subjected to higher cycling sub-failure strains demonstrated a significantly greater decrease in load compared to the lower cycling level. To our knowledge, this is the first study to provide information about the UCL shear modulus in overhead-throwing athletes over the course of a competitive season.

Our proposed protocol for evaluating the UCL shear modulus using SWE offers several potential applications for trainers, coaches and practitioners. First, it can be used as a potential tool for evaluating the health status of the UCL and early detection of injury for future sports medicine applications. It could also be applied to evaluate the degree of injury for providing a more accurate diagnosis, and helping medical doctors identify the optimal intervention strategy. The limitation of this study is that our sample for overhead throwing athletes consisted only of college baseball players and football quarterbacks from a single college. In conclusion, SWE could be a reliable tool for quantifying the changes in UCL shear modulus in overhead-throwing athletes over time.

REFERENCES

[1] Ciccotti MG et al., *Am J Sports Med.* 42: 544-551, 2014.
[2] Cortes D et al., *Ultrasound Med Biol*, 41: 1518-1529, 2015.
[3] Atanda A et al., *Am J Sports Med*, 44: 3179-3187, 2016.
[4] Rigby B et al., *J Gen Physiol*, 43: 265-283, 1959.
[5] Weisman G et al., *Am J Sports Med*, 8: 24-30,1980.
[6] Pollock R et al., J Shoulder Elb Surg, 9: 427-435, 2000.

SB³C2019
Summer Biomechanics, Bioengineering and Biotransport Conference
June 25 -28, Seven Springs, PA, USA

ASSESSMENT OF TENDON HYDRAULIC PERMEABILITY USING OSMOTIC LOADING AND BIPHASIC FINITE ELEMENT MODELING

Babak N. Safa (1,2), Ellen T. Bloom (1), Andrea H. Lee (1), Michael H. Santare (1,2), Dawn M. Elliott (1)

(1) Department of Biomedical Engineering
University of Delaware
Newark, DE, USA

(2) Department of Mechanical Engineering
University of Delaware
Newark, DE, USA

INTRODUCTION

Tendon's viscoelastic behavior can be attributed to two mechanisms: fluid flow and intrinsic viscoelasticity [1]. These two mechanisms are difficult to distinguish under tensile loading, and thus their relative contribution is not known. Knowing this is important for evaluation of tendon's inelastic behaviors including viscoelasticity, damage, and plastic deformation. While it is commonly assumed that fluid flow has a small contribution due to tendon's parallel fibril structure, tendon has a large Poisson's ratio ($\nu > 2$) that exceeds the limit of incompressibility ($\nu = 0.5$) [2]. This indicates that tendon experiences volume loss during tensile loading, causing fluid flow which can contribute to the overall viscoelastic behavior of the tissue. Tendon's biphasic parameters, in particular, the permeability, are required to evaluate the fluid flow contribution to tendon viscoelasticity, but these are not well studied and the reported values vary by several orders of magnitude 10^{-16} to 10^{-13} $m^4(N.\sec)^{-1}$ [3], [4].

The objective of this study was to quantify the permeability of tendon using a combination of osmotic loading and finite element (FE) modeling. Changes to tendon's geometry during osmotic loading isolates the effect of fluid flow, which was done using SPEG, a combination of physiological saline and polyethylene glycol (PEG). SPEG controls hydration without diffusion of solutes or changing mechanical properties [5]. The lateral strain over time was fit to a FE model to determine the permeability and other biphasic properties.

METHODS

Tail tendon fascicles were harvested from mature Long-Evans female rats and 60 mm long fascicles were cut in half to obtain paired samples between fresh frozen control and three osmotic loading groups of 1%, 8% and 15% SPEG (n=5 per group), where SPEG solutions were made from polyethylene glycol (PEG 20 kDa) and 0.9% saline. Water content (φ_w) was measured immediately after dissection for the fresh frozen group (as explained previously [5]). The osmotic loading groups were first placed in 8% SPEG for 16 min (which maintains φ_w at the fresh frozen level [5]), then the solution was changed to either 1%, 8% or 15% SPEG, held for 16 min, and φ_w measured (Fig 1A). We performed paired t-tests between fresh frozen and SPEG groups ($p = 0.05$), and Pearson's correlation between φ_w and SPEG concentration ($p = 0.05$). Additionally, the lateral width (a) of the

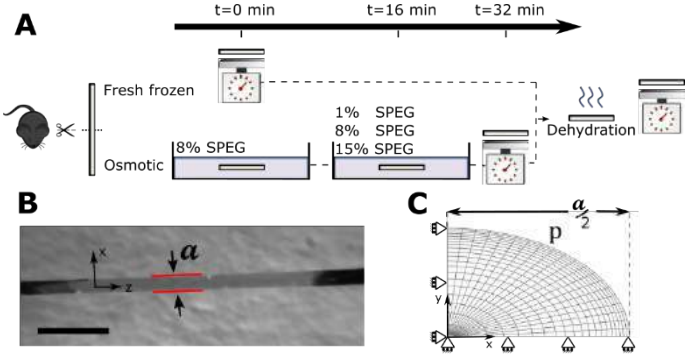

Figure 1: (A) Paired halves of bisected tendons were used as fresh frozen control or equilibrated in 8% SPEG followed by the osmotic loading buffer solution (1%, 8%, or 15% SPEG).) was measured over time in solution (scale = 1 mm). (C) FE analysis included a quarter ellipse with a pressure boundary condition.

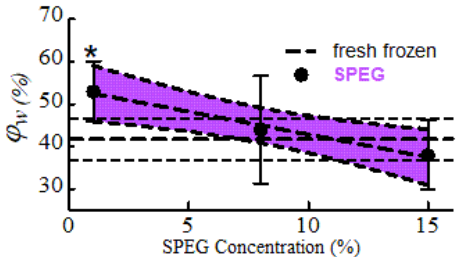

Figure 2: Water content of tissue at the end of osmotic loading. Error bars = 95% CI, * different from fresh frozen (p<0.05)

fascicle was measured throughout the test using a CCD camera (Figure 1B). The lateral strain calculated as $\epsilon_l = a/a_0 - 1$, and the volumetric strain was calculated as $\epsilon_{vol} = 2\epsilon_l$. We compared the magnitude of ϵ_l between 1% and 15% SPEG (t-test $p = 0.05$).

A FE model was developed using FEBio (v2.8 febio.org) to calculate the biphasic properties assuming a plane-strain, symmetric elliptical cylinder cross section (semi major axes 0.14 mm, eccentricity 0.8) (Figure 1C). The pressure boundary condition, calculated relative to 8% SPEG using a phenomenological relation [6], was -63 kPa for 1% SPEG and 146 kPa for 15% SPEG. The solid matrix was modeled using a Holmes-Mow material (modulus E, Poisson's ratio ν, nonlinearity factor β) [7]. Isotropic permeability was modeled with deformation dependency as [7]:

$$k(J) = k_0 \left(\frac{J-\varphi_0}{1-\varphi_0}\right)^{\alpha} e^{\frac{1}{2}M(J^2-1)}. \quad (1)$$

Where, J is the Jacobian of deformation, φ_0 is the reference solid volume fraction ($\varphi_0 = 1 - (\varphi_w)_0$ set to $\varphi_0 = 0.6$); k_0 is the reference permeability, and $[\alpha, M]$ are positive parameters. In summary, the fitted model parameters were: $E, \nu, \beta, k_0, M, \alpha$. For curve-fitting, we used a constrained multivariable nonlinear optimization method with twenty random initial points. The solution with the minimum residual RMSE was taken as the optimal answer.

RESULTS

The water content of fresh frozen samples was φ_w= 42% ± 9%, and correlated with the osmolality of SPEG (r= -0.66, p<0.05) (Fig. 2). The 1% SPEG samples had φ_w = 53% ± 6%, which was 11% higher than the fresh frozen. The φ_w for the 8% SPEG group was not different compared to the fresh frozen group and the φ_w for 15% SPEG was less than 1% SPEG (φ_w= 38% ± 7%) but not different from fresh frozen.

The 1% SPEG caused swelling, which resulted in 0.065 ± 0.025 lateral strain (Fig. 3). Conversely, the 15% SPEG caused a compressive lateral strain of -0.026 ± 0.016, which was 60% smaller in magnitude compared to that of 1% SPEG (p<0.05). By assuming transverse isotropy, these result in 0.132 and -0.056 volumetric strain for 1% SPEG and 15% SPEG, respectively.

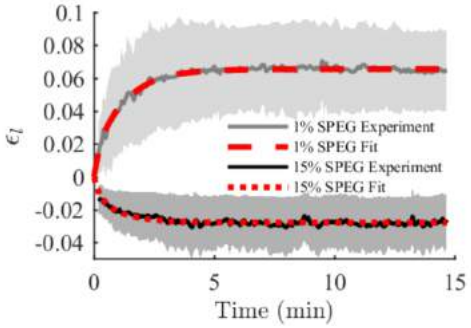

Figure 3: Transverse strain and the model fits. Experiment line is mean ± standard deviation

Table 1: Results of optimization

	E (MPa)	ν	β	$k_0\left(\frac{m^4}{N.sec}\right)$	M	α
1% SPEG	0.14	0.05	2.88	1.70×10^{-16}	2.01	1.92
15% SPEG	0.44	0.28	4.88	1.08×10^{-16}	3.18	2.71

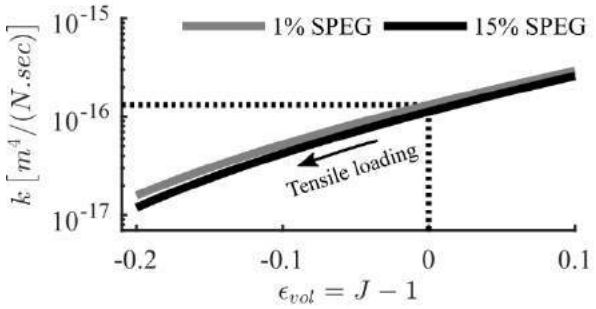

Figure 4: Predicted deformation-dependent permeability.

The FE model fit the experiments extremely well (Fig. 3), where the RMSE was less than 0.0015 for both concentrations, less than 5% of the maximum corresponding lateral strain. Notably, the modulus was 0.14 MPa for 1% SPEG, which was less than a third of 15% SPEG, and the reference hydraulic permeability (k_0) for 1% SPEG was $1.70\times10^{-16}\ m^4(N.\sec)^{-1}$, and similarly $1.08\times10^{-16}\ m^4(N.\sec)^{-1}$ for 15% SPEG (Table 1). By using the fitted permeability parameters (Eq. 1) the permeability was plotted as a function of volumetric strain ($\epsilon_{vol} = J - 1$) (Fig. 4), which indicates permeability is sensitive to deformation and decreases at lower ϵ_{vol}.

DISCUSSION

Using a combination of osmotic loading and biphasic FE modeling, we calculated the reference permeability (k_0) of tendon of ~ $10^{-16}\ m^4(N.\sec)^{-1}$, and showed that it decreases with a decrease to volume, which occurs during tensile loading [2]. These findings agree with the ranges of permeability of similar tissues, such as ligament, and annulus fibrosus [8-9].

An increase of buffer concentration decreased φ_w, as previously reported [5], and the observed changes to φ_w were similar to the estimated ϵ_{vol} in both solutions. This indicates that osmotic loading caused influx and exudation of water. The changes to width (α) were larger with 1% SPEG, despite the smaller relative pressure in the 1% solution, due to the weaker modulus in lateral tension. This indicates that tendon has lateral tension-compression nonlinearity (Table 1).

This study only evaluated transverse permeability and the axial tendon permeability was not studied. In tendon's tensile loading and uniform osmotic loading, axial flow does not occur, because of high aspect ratio and symmetry of sample.

In conclusion, we calculated tendon's deformation-dependent permeability and other biphasic parameters by osmotic loading, which eliminates the effect of axial fibers. Future studies will include these biphasic parameters combined with axial loading to understand the share of different viscoelastic mechanisms and other inelastic behaviors such as damage and plastic deformation in tendon.

ACKNOWLEDGEMENTS NIH-NIBIB R01-EB002425.

REFERENCES

[1] Connizzo *et al.*, *J. Biomech.*, 54: 11–18, 2017. [2] Reese *et al.*, *J. Biomech. Eng.*, 135: 34501, 2013. [3] Yin *et al.*, *J. Biomech.*, 37: 907–16, 2004. [4] Oftadeh *et al.*, *Acta Biomater.*, 2018. [5] Safa *et al.*, *J. Biomech.*, 61: 18–25, 2017. [6] Chahine *et al.*, *Biophys. J.*, 89: 1543–50, 2005. [7] Holmes *et al.*, *J. Biomech.*, 23: 1145–1156, 1990. [8] Weiss *et al.*, *J. Biomech.*, 39: 276–283, 2006. [9] Cortes *et al.*, *J. Biomech.*, 47: 2088–2094, 2014.

SB³C2019
Summer Biomechanics, Bioengineering and Biotransport Conference
June 25 -28, Seven Springs, PA, USA

THREE DIMENSIONAL MORPHOLOGICAL CHANGES IN CARPAL TUNNEL LIGAMENT ARCH IN RESPONSE TO WRIST COMPRESSIVE FORCES

Rakshit Shah (1,2), Zong-Ming Li (1,2)

(1) Hand Research Laboratory
Department of Biomedical Engineering
Lerner Research Institute, Cleveland Clinic
Cleveland, OH, United States

(2) Department of Chemical and
Biomedical Engineering
Cleveland State University
Cleveland, OH, United States

INTRODUCTION

The carpal tunnel is formed by the transverse carpal ligament (TCL) at the volar boundary and the carpal bones at the medial, lateral, and dorsal boundaries. The tunnel serves as a passageway for the median nerve and digit flexor tendons. Prolonged median nerve compression could lead to carpal tunnel syndrome (CTS). The positioning of the median nerve directly beneath the TCL makes it susceptible to compression neuropathy.

Increasing the carpal arch area may potentially provide relief for median nerve compression as a possible treatment for CTS. Carpal arch area has been shown to increase during compressive force application to the carpal bones in modeling and in vitro studies [1, 2]. In vivo compressive force applied in the radioulnar direction across the wrist have been demonstrated as a non-invasive method to increase carpal arch cross-sectional area [3]. With the increase in radio-ulnar wrist compressive force a decrease in TCL-formed ligament arch width and an increase in ligament arch height and area were observed. To date, the change in carpal tunnel morphology with radioulnar compression has only been evaluated in the distal cross-section of the ligament arch. A comprehensive understanding of the volumetric change in ligament arch at the inlet (proximal) and outlet (distal) during application of wrist compressive forces in radio-ulnar direction is still unavailable.

Therefore, the purpose of the current study was to investigate the relative changes in the ligament arch volumes in response to radio-ulnar wrist compression (RWC) forces, at the distal and proximal carpal tunnel regions. For this purpose, a three-dimensional reconstruction of the ligament arch was accomplished. It was hypothesized that an increase in RWC force will lead to an increase in the ligament arch volumes at both regions of the tunnel. The increase in ligament arch volume will be more pronounced at the proximal tunnel region compared to distal tunnel region.

METHODS

Six male cadaveric left hands were used for this study. Change in segmental volume was calculated for the ligament arch at the two tunnel regions (distal and proximal) for three compressive force levels (0N, 10N, and 20N). The contents of the carpal tunnel were excavated from each specimen and a medical balloon along with a catheter ultrasound probe (AcuNav 8F, ACUSON, Siemens Medical Solutions USA Inc.) was inserted inside the tunnel. The balloon was inflated to maintain an elevated pathophysiological intra-tunnel pressure of 60 mmHg. Each specimen was secured on a thermoplastic splint with the hand in a supine and anatomically neutral position (Fig. 1). The four TCL-bone attachment sites were marked and digitized using a 3D MicroScribe digitizer. We used a compressive force application system as decribed in our previous study [3]. The system was positioned and adjusted to either apply no compressive force (0 N) or a transverse compressive

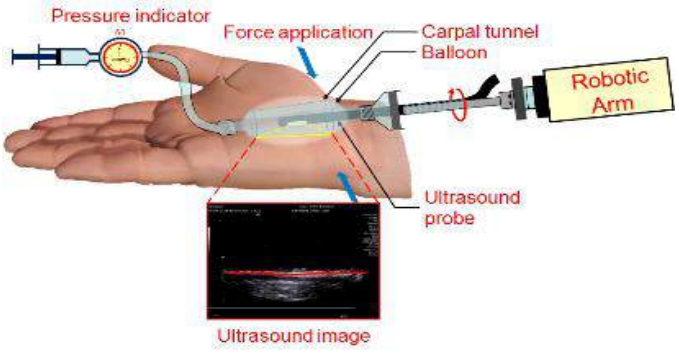

Fig. 1 Experimental Setup

force (10 or 20N). Each trial of compression lasted for 4 minutes with a 4 minutes break between each trial. During each trial, the catheter ultrasound probe driven by a robot arm (Denso Corp.) was rotated circumferentially in increments of 1 degree inside the carpal tunnel to collect ultrasound (US) images in the radial planes. The testing order of the compressive forces (0, 10, and 20 N) were randomized for each specimen.

From each US image, the two-dimensional (2D) image coordinates of the tunnel's internal surface points were extracted using a custom algorithm. The 2D surface points were then transformed into the robot's coordinate system using encoded kinematic transformation to generate three-dimensional (3D) point clouds of each tunnel's inner surface. The proximal and distal boundaries of the carpal tunnel were then determined from the digitized TCL-bone attachment sites. The 3D surface points were trimmed at the boundaries to extract a 3D model of the carpal tunnel (Fig. 2). The generated 3D model was then segmented into the ligament arch based on ligament insertion to the carpal bones, and the arch was further divided into the distal and proximal regions of tunnel. From the segmented regions of the tunnel for each trial, the ligament arch volume (LAV) at each region was calculated.

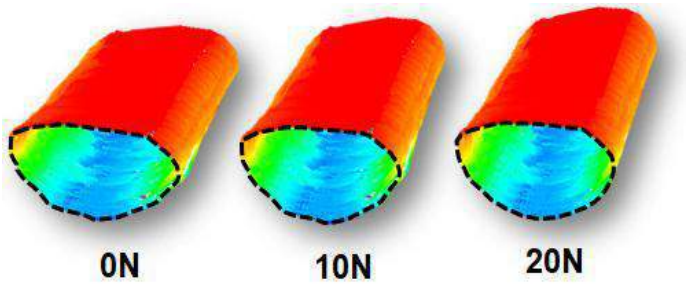

Fig. 2 Reconstructed carpal tunnels during 0N, 10N, and 20N force application

Two-way repeated measures ANOVA was performed to determine whether the LAV varied significantly with the factors of Forces (0, 10, and 20 N) and Regions (distal and proximal). Holm-Sidak's post hoc analysis was performed for pairwise comparisons. Statistical analyses were performed using SigmaStat 4.0 (Systat Software Inc). An α level of 0.05 was considered for statistical significance.

RESULTS

The effects of the RWC on the ligament arch was investigated using a robot-assisted ultrasonography. In general, as the magnitude of compressive force increased, the LAV increased. This was true for both the distal and proximal tunnel regions. At the distal region, LAV during forces of 0, 10, and 20N were 254.1±67.8 mm^3, 308.2±77.3 mm^3, and 322.3±80.8 mm^3 respectively. The proximal region LAV during compressive forces of 0, 10, and 20 N were 737.2±140.4 mm^3, 1052.0±176.6 mm^3, and 1126.3±191.1 mm^3 respectively.

Ligament arch volume (LAV) was significantly affected by the factors of Forces ($P < 0.001$) and Regions ($P < 0.001$). The interaction of the two factors were also significant ($P < 0.001$). Pairwise comparisons showed that LAV significantly increased when the force increased from 0N to 10N and from 0N to 20N at both regions ($P < 0.05$, Fig. 3). LAV did not significantly increase when force increased from 10N to 20N at the distal region ($P = 0.235$) but significantly increased at the proximal region ($P < 0.05$). LAV was significantly smaller in distal region compared to proximal region at all force levels ($P < 0.05$).

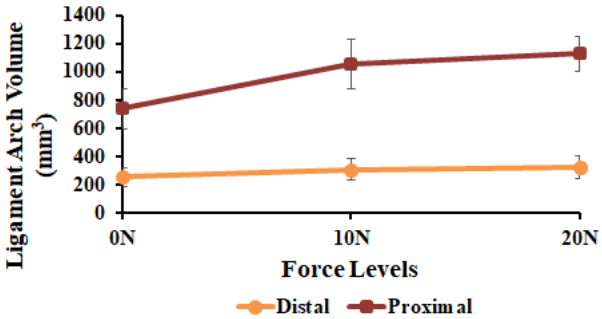

Fig. 3 Ligament Arch Volume at distal and proximal regions at different force levels (0, 10, 20 N)

DISCUSSION

The current study evaluated, using robot-assisted ultrasonography, the effect of radioulnar compressive forces applied across the wrist on the ligament arch volume at the distal and proximal tunnel regions. We found that with the application of compressive forces, the carpal tunnel ligament arch changed in volume at both the inlet and outlet of the carpal tunnel.

The ligament arch increased in volume when a force of 10 N or 20 N was applied compared to no force application. These findings support the findings of a previous study where an increase in distal ligament arch cross-sectional area was observed with the application of wrist compressive forces [3]. LAV showed a more pronounced increase in the proximal region compared to the distal region. The difference in ligament arch volume change between the regions may have been contributed by the distal tunnel being narrower [4], and the TCL being thicker [4] and less elastic distally [5] than the proximal tunnel region.

The study provided a better understanding of the effects of radio-ulnar wrist compressive forces on the TCL-formed ligament arch. The current study observed that the increase in the ligament arch area with compression seen by other studies at the distal region [3], extended to the proximal region of the tunnel. Our previous study showed that the median nerve being housed near the ligament arch showed an increase in circularity distally with RWC [3]. The current findings corroborate a similar beneficial effects of median nerve circularity with an increase in ligament arch volume at both the inlet and outlet of the tunnels. Therefore, the application of external wrist compressive forces could potentially lead to the decompression of the median nerve in patients suffering from carpal tunnel syndrome, relieving their symptoms.

ACKNOWLEDGEMENTS

The study was funded by NIAMS/NIH R01AR068278 and Cleveland State University Graduate Student Research Award 2018-2019. The authors further acknowledge Jeremy Loss and Kishor Lakshminarayanan for their assistance on the project.

REFERENCES

[1] Li, ZM et al., *J Biomech Eng*, 131.8:081011, 2009; [2] Li, ZM et al., *Clin Biomech*, 28.4:402-407, 2013; [3] Marquardt, T et al., *Clin Biomech*, 30.3:248-253, 2015; [4] Rotman, M et al., *Hand clinics*, 18.2:219-230, 2002; [5] Brett, A et al., *Clin Biomech*, 29.6:601-606, 2014.

SB^{3}C2019
Summer Biomechanics, Bioengineering and Biotransport Conference
June 25 -28, Seven Springs, PA, USA

FIBROBLAST-LIKE SYNOVIOCYTES ALTER MATRIX MECHANICS & NEURONAL MMP-1 EXPRESSION UNDER TENSILE FAILURE TO DIFFERENT DEGREES DEPENDING ON CONCENTRATION

Meagan E. Ita (1), Nicholas S. Stiansen (1), Sarah R. St. Pierre (3), Beth A. Winkelstein (1,2)

(1) Department of Bioengineering
University of Pennsylvania
Philadelphia, PA, United States

(2) Department of Neurosurgery
University of Pennsylvania
Philadelphia, PA, United States

(3) Bioengineering Institute
Worcester Polytechnic Institute
Worcester, MA, United States

INTRODUCTION

Abnormal loading of ligamentous joint capsules induces pain cascades by activating the innervating nociceptive fibers [1]. An in vitro neuron-seeded collagen gel system that replicates the capsular ligament's sensory innervation and collagenous microstructure has been used to define relationships between collagen organization and neuronal nociceptive signaling due to macroscale loading [2,3]. But, that model does not include fibroblast-like synoviocytes (FLS), which are abundantly interspersed in the extracellular matrix (ECM) [4,5]. FLS respond to their local environment, but they can also remodel the ECM [4,6]. Although capsule nerves and FLS are mechanosensitive [2-4,6], their interactions with each other and the surrounding network has not been studied in the context of pain due to a lack of in vitro models.

Non-physiologic loading initiates pathological ECM remodeling by fibroblasts, including their secretion of the interstitial collagenase MMP-1 [4,7]. MMP-1 is elevated in joint tissues after trauma and with degeneration [8]. Although MMP-1 has recently been shown to have a role in nociception and ECM degradation in painful joint diseases [8,9], its role in joint pain is unknown. This study tested effects of FLS on collagen gel mechanics and neuronal MMP-1 after stretch. Primary FLS cells were integrated in an in vitro dorsal root ganglia (DRG)-seeded collagen gel system [2,3]. Since capsular ligaments have variable FLS densities regionally [5], and mechanical properties of fibroblast-embedded collagen gels depend on their initial concentration [10], FLS were seeded here at two concentrations. Gel failure properties and stiffness were quantified. Regional strains and collagen organization were measured during loading curve since neurons respond to their local network [2,3]. Collagen fiber alignment maps were captured and fiber orientation angles were quantified by circular variance (CV), with lower CV indicating tighter clustering and more fiber alignment [2]. Because FLS concentration was found to modulate biomechanics, MMP-1 was assessed after gel failure for the low FLS concentration.

METHODS

Cells were harvested from Sprague-Dawley rats, with IACUC-approval. DRGs were harvested from embryonic day 18 rats [3,11] and FLS from adult hind knees [12], cultured, and passaged at 90% confluence. On passage 4, cultures were suspended in Type I collagen solution (2mg/mL; Corning) at concentrations simulating those in the outer ($5x10^4$ cells/mL; low FLS; n=8) or inner ($1x10^5$ cells/mL; high FLS; n=3) layer of the capsular ligament [5]. Gels were cast (1mL/well) and set at 37°C. Because FLS alter gel mechanics that may influence neuron signaling, gels without FLS were included as a control (no FLS; n=8). On DIV1, DRGs (6-10/gel) were seeded on the gel [3,11]. On DIV8, additional collagen (150µL) was added to encapsulate the DRGs.

On DIV9, gels were cut (21mmX8mm) and a grid was drawn on the surface to track elemental strains [2]. Using a planar test machine (574LE2; TestResources; 500g load cells), gels were immersed in a 37°C PBS bath. Testing was integrated with a polarized light imaging system [2] and high-speed cameras (Vision Research) that acquired collagen alignment maps and tracked markers. Force and displacement data (200Hz) were synchronized with images (500Hz). Slack was removed (loading <2mN) and gels were displaced to failure at 0.5mm/s.

Peak force defined failure; stiffness was taken as the slope of the force-displacement curve between 20-80% of maximum force [13]. Marker positions were digitized (Fiji software; NIH) from images before loading (ref), and at 20% of maximum force, 80% of maximum force, and failure. LS-DYNA (LSTC) calculated maximum principal strain (MPS) from marker positions for each grid element and averaged for each gel [2]. CV was quantified from collagen alignment maps taken before loading (ref) and at failure [2] and normalized to reference. Differences in failure force and displacement, stiffness, and reference CV were tested by an ANOVA and Tukey HSD tests. MPS at 20%, 80%

and 100% of failure was compared between groups by a repeated-measures ANOVA. Paired t-tests compared CV changes for each group.

Because low FLS concentration altered strains, a subset of gels (no FLS n=5; low FLS n=4) were immunolabeled after failure for MMP-1 and βIII tubulin. Gels were blocked, incubated overnight with primary antibodies to MMP-1 (1:100) and β III tubulin (1:200), washed, and incubated with secondary antibodies (1:1000). Gels were imaged (Leica TCS SP8 Confocal) with stacks (3-5/gel) of 6 40X images taken at 1µm steps up to 5µm. Equal numbers of images were taken with DRG axons and soma. The maximum intensity projection of each stack was generated using Fiji; the number of positive pixels above that in controls and naïve FLS cultures was quantified. MMP-1 labeling and its co-localization with βIII tubulin (neuronal) were computed, with co-localization normalized to total βIII tubulin. Total and neuronal MMP-1 were separately compared between groups by t-tests.

RESULTS

Although neither the force nor displacement at failure are different (p>0.4) between any group, high FLS concentration has lower force and higher displacement at failure (Fig. 1). The stiffness of the high FLS group is significantly lower (p=0.03) than gels without FLS (Fig. 1). MPS exhibits different increases depending on FLS concentration, with significant differences (p<0.01) between groups at both 80% of failure and failure, and highest strains experienced by high FLS gels (Fig. 2A).

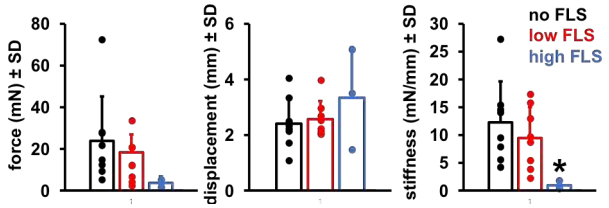

Fig. 1: Failure force and displacement are not significantly different between groups (p>0.4). Stiffness is lower for high FLS (*p=0.03).

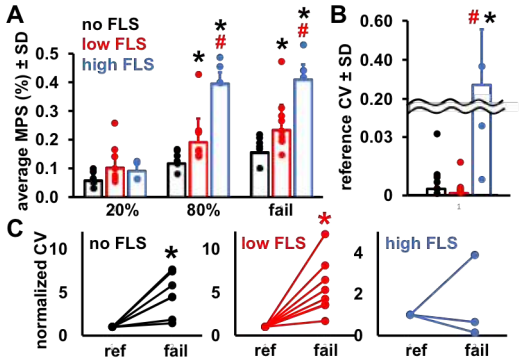

Fig. 2: (A) MPS is different at 80% and 100% (fail) of failure, with high over low (#p<0.01) and both over no (*p<0.01) FLS. (B) Reference CV of high gels is greater (p<0.01) than low (#) and no (*) FLS, (C) but not at failure, unlike no and low FLS (*p<0.01).

Prior to any loading, high FLS gels exhibit significantly higher (p<0.01) CV than the low FLS and no FLS gels (Fig. 2B). Yet, for no and low FLS gels, collagen reorganizes significantly (p<0.01) at failure from its reference state (Fig. 2C). Although the CV of two high FLS gels decreases (Fig. 2C), this change is not significant (p=0.68).

Following strains (Fig. 2A), there is significantly more (p<0.01) MMP-1 in low FLS gels than in gels without FLS (Fig. 3). Positive MMP-1 labeling is observed in both the soma and axons of DRGs in low FLS gels; very little MMP-1 labeling is evident in gels with no FLS (Fig. 3). The co-localization of MMP-1 with βIII tubulin further reveals that *neuronal* MMP-1 is also increased (p<0.01) in the presence of FLS.

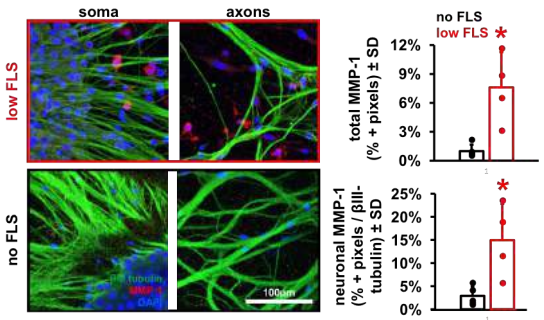

Fig. 3: Images of DRG soma and axons showing MMP-1 labeling for low FLS gel, but scarce labeling in no FLS gel. MMP-1 labeling is greater in the low FLS group (*p<0.01).

DISCUSSION

This is the first demonstration of concentration-dependent effects of primary FLS on collagen gel mechanics and neuronal MMP-1. Although failure properties trend differently, significance was not reached (Fig. 1), likely due to the small size of the high FLS group. The decreased stiffness in that group (Fig. 1) is opposite what is found with dermal fibroblasts at the same concentration [10]. This difference may be due to phenotypic differences or FLS remodeling collagen fibers more since they were cultured longer here [4,6,7]. Since strains directly modulate neuronal neurotransmitters and injury markers [2,3], and FLS increase strains (Fig. 2A), they may lower the threshold for neuronal signaling. Yet, at low loads, MPS was below the pain threshold [1,2], suggesting that may be minor. The higher reference CV of high FLS gels indicates more collagen fiber spread (Fig. 2B), which may also be due to FLS remodeling and can mediate neuronal responses. Low FLS produce similar reorganization of collagen as no FLS (Fig. 2C), which may mean that the difference in MMP-1 labeling (Fig. 3) may not be due to differences in matrix reorganization, suggesting that FLS, either directly or through mechanical effects (Fig. 2A), may regulate neuronal MMP-1 expression (Fig. 3). Studies with these FLS concentrations find they regulate inflammation [12], supporting that notion.

The presence of FLS increases both total and neuronal MMP-1 (Fig. 3). Yet, it is unclear if this is due to FLS or DRGs or both. Both cell types express MMP-1 after a mechanical injury, during pathological remodeling, or in "activated" states like rheumatoid arthritis or spinal cord injury [4,7,14]. Since MMP-1 interacts with neuronal cell surface receptors [9], it is possible that increased neuronal MMP-1 (Fig. 3) is due to neuronal receptor binding of the enzyme. Regardless of source, its elevation after loading is made more relevant by the fact that neurons increase their calcium signaling in the presence of exogenous MMP-1 [9]. Investigating relationships to nociceptive signaling and matrix composition with FLS would clarify FLS-DRG interactions contributing to joint pain.

ACKNOWLEDGEMENTS

Funding from NIBIB (AT010326-07), NIAMS (T32AR00713), and NSF (CMMI15-48571). DRGs were from Penn's MINS.

REFERENCES

[1] Lee K et al *J Neurosci Methods* 137:151-9, 2004 [2] Zhang S et al *J Biomech Eng* 138:021013, 2016 [3] Zhang S et al *JOR* 36:770-7, 2018 [4] Bartok B & Firestein G *Immun Rev* 233:233-55, 2010 [5] Yamashita T et al *Spine* 21:538-43, 1996 [6] Kim S et al *Cell Struct Funct* 27:139-44, 2002 [7] Yang G et al *Gene* 363:166-72, 2005 [8] Kim J et al *Osteoarthr Cart* 23:2242-51, 2015 [9] Allen M et al *Sci Rep* 6:35497, 2016 [10] Evans M & Barocas V *J Biomech Eng* 131:101014, 2009 [11] Cullen D et al *Tissue Eng A* 18:2280-9, 2012 [12] Saravanan S et al *Inflamm Res* 63:451-62, 2014 [13] Lee K et al *J Biomech* 39:1256-64, 2006 [14] Zhou Y et al *Cell Mol Neurobiol* 34:1151-63, 2014.

SB³C2019
Summer Biomechanics, Bioengineering and Biotransport Conference
June 25 -28, Seven Springs, PA, USA

AGING ADVERSELY AFFECTS DIFFERENT RAT ROTATOR CUFF TENDONS SIMILARLY

Joseph B. Newton, George W. Fryhofer, Snehal S. Shetye, Ashley B. Rodriguez, Andrew F. Kuntz, Louis J. Soslowsky

McKay Orthopaedic Research Laboratory
University of Pennsylvania
Philadelphia, PA, US

INTRODUCTION

Rotator cuff tendon tears are a common injury affecting a large portion of the population. Of these rotator cuff tears, 90% involve injury to the supraspinatus tendon, 35% to the infraspinatus, and 25% to the subscapularis [1-6]. Further, advancing age is directly correlated with increased incidence of such tears. However, the age related changes in tendon mechanical properties that may predispose the supraspinatus to injury relative to the other rotator cuff tendons is unclear [7]. Therefore, the objective of this study was to define the age-related alterations in rotator cuff tendon fatigue mechanics to determine whether the supraspinatus is more susceptible to injury due to aging than the infraspinatus and subscapularis. We hypothesized that aging would adversely and preferentially affect supraspinatus tendon fatigue mechanics when compared to the subscapularis and infraspinatus tendons.

METHODS

Experimental design and sample preparation: 7-month juvenile (n=10), 18-month adult (n=10), 27-month old (n=10), and 36-month old (n=10) male F344XBN rats were obtained from the National Institute of Aging (IACUC approved), approximating respective human ages of 18, 43, 63, and 90 years old. After 3 weeks of facility acclimation, all animals were sacrificed. Lower and upper subscapularis (LS & US, respectively [7]), supraspinatus (SS), and infraspinatus (IS), muscle-tendon complexes were then each carefully dissected from the scapula of the right shoulder and removed with the proximal humerus for mechanical testing. Muscle, along with extraneous tissue was removed from each tendon and cross-sectional area of each tendon was measured using a custom laser device [8]. Each humerus was potted in a custom acrylic cylinder secured with polymethyl-methacrylate, leaving the proximal humerus exposed. The head of the humerus was secured using a self-tapping screw to prevent failure at the growth plate. *Mechanical testing:* The LS, US, SS, and IS from each animal were mechanically tested independently on an Instron ElectroPuls E3000. Maximum stresses were calculated from previous ramp to failure testing on contralateral shoulders for each tendon for each group. Mechanical testing consisted of a 0.1N preload, a ramp to 40% maximum load at 1% strain per minute, and cycles to failure (7-40% maximum load at 2Hz). During loading, force and displacement data were acquired and analyzed using MATLAB (Mathworks; Natick, MA). A line was fit to the triphasic peak strain vs. cycles curve, and all fatigue parameters were calculated at breakpoints 1 (BP1) and 2 (BP2) (Figure 1). Cycles to failure, secant modulus and stiffness, peak strain, laxity (resistance of material to elastic deformation), and hysteresis (measure of energy dissipation) were evaluated. A 2-way ANOVA with Bonferroni post-hoc tests was used to compare the different ages for each tendon with significance set to $p<0.05$.

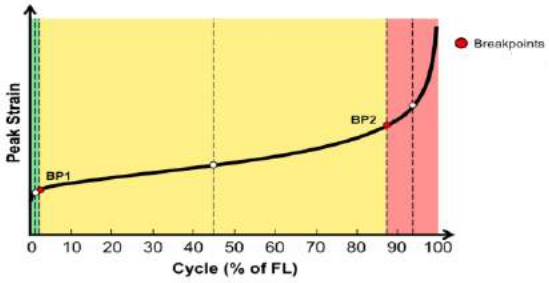

Figure 1: Example peak strain vs. cycles (% of failure) curve. Fatigue parameters were calculated at breakpoints 1 (BP1) and 2 (BP2).

RESULTS

Significant changes in hysteresis at BP2 were seen with aging in all rat rotator cuff tendons tested in fatigue. Secant modulus at BP2 significantly decreased in the LS, SS, and IS in the geriatric group compared to juvenile animals, and in the LS and IS between geriatric and adult rats (Fig. 2). The SS and IS were similar with significant increases in hysteresis in adult, aged, and geriatric animals compared to juvenile (Fig. 3). Peak strain at BP2 was significantly increased in the LS geriatric tendons compared to juvenile and adult, increased in the SS aged tendons compared to juvenile and adult, and in the IS adult tendons from juvenile (Fig. 4). Surprisingly, there were no significant changes in cycles to failure in the LS or SS. The US had increased cycles to failure between juvenile and aged, and the IS had the highest number of cycles to failure in the geriatric group (Fig. 5).

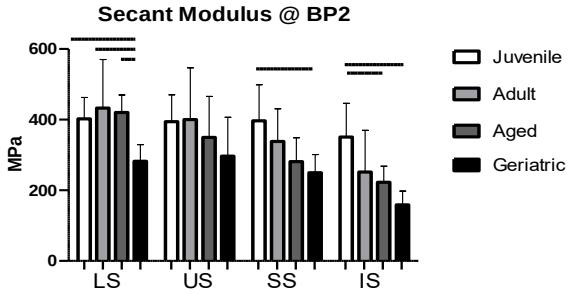

Figure 2: Significant changes in the LS, SS, and IS secant modulus were seen with aging at BP2 between juvenile and geriatric animals.

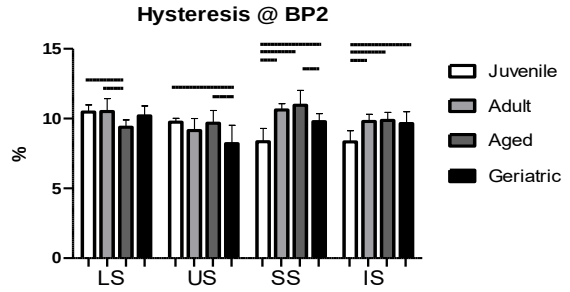

Figure 3: Hysteresis at BP2 increased with aging in SS and IS, and decreased with LS and US.

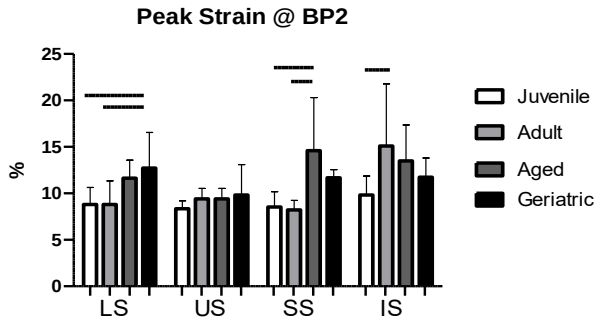

Figure 4: The LS had the highest peak strain in the geriatric group, the SS in the aged group, and IS in the adult group at BP 2.

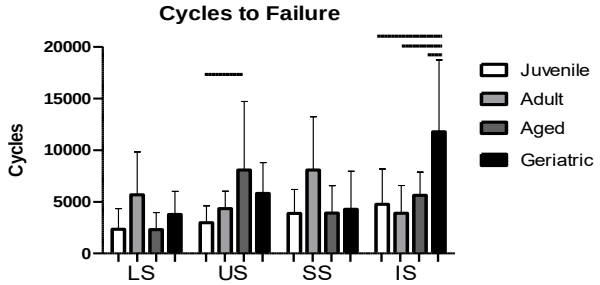

Figure 5: No changes in cycles to failure were detected in the LS and SS. The US had the highest number of cycles to failure in the aged group. The IS had a significant increase in cycles to failure in the geriatric group.

DISCUSSION

Advancing age correlated with significant detrimental changes in the fatigue properties of all rat rotator cuff tendons, supporting that aging, in general, is a factor in the increase of rotator cuff tears seen in humans. Interestingly, supraspinatus fatigue response was not preferentially affected by aging when compared to the other rotator cuff tendons, which is not consistent with tear frequency observed clinically. Significant decreases in secant modulus in the LS, SS, and IS, and changes in hysteresis in all rotator cuff tendons indicate altered load transmission and energy dissipation capacity with aging. Previous literature has shown significant accumulation with aging of advanced glycation end products, cross-linking, and fatty infiltration within the supraspinatus [10]. It has also been shown that the supraspinatus has a decreased fiber alignment response to loading as a result of aging [11]. This altered biochemical and structural environment within the rat rotator cuff tendons may explain the significant changes shown in fatigue mechanical properties in this study. Surprisingly, cycles to failure was highest in the IS in the geriatric group; however, this may be explained by an increase in IS cross sectional area in the geriatric group (not shown). A limitation of this study is that it only analyzes fatigue mechanical properties. It has been shown that significant biochemical compositional, cellular, and structural changes exist with aging in the supraspinatus; however, none of the current studies analyze these changes in reference to the other rotator cuff tendons [10-12]. In summary, this study demonstrates that aging has a significant effect on fatigue properties of the rat rotator cuff, though the supraspinatus was not preferentially affected. Thus, other factors may explain the predominance of supraspinatus tears with age. Future studies will investigate the histological, morphological, and biochemical changes in all rotator cuff tendons in response to aging.

ACKNOWLEDGEMENTS

This study was supported by NIH/NIAMS (R01AR064216) and the Penn Center for Musculoskeletal Disorders (P30AR069619).

REFERENCES

[1] Jempf, JF et al., *Arthroscopy*, 15:56-66, 1999. [2] Minagawa, H et al., *JOR*, 10:8-12, 2013. [3] Muto, T et al., *J Sports Med*, 5476293, 2017. [4] Krishnan, SG et al., *Arthroscopy*, 24:324-8, 2008. [5] Narasimhan R et al. *Int Orthop*, 40:975-9, 2015. [6] Aagaard, KE et al., *Acta Ortho*, 86:558-562, 2015. [7] Svensson, RB et al., *J Appl Physiol*, 121:1237-1246, 1985. [8] Thomas, S et al., *JSES*, 21:1687-1693, 2013. [9] Favata, M et al., *JOR*, 24:2124-32, 2006. [10] Gumucio, JP et al., *JSES*, 23:99-108, 2013. [11] Connizzo, BK et al., *JBME*, 135:0210191–0210198, 2013. [12] Bedi, A. et al., *JSES*, 21:218-227, 2011.

SB³C2019
Summer Biomechanics, Bioengineering and Biotransport Conference
June 25 -28, Seven Springs, PA, USA

COMPARISON OF THE DEFORMATION BEHAVIOR OF THE ANTERIOR CRUCIATE LIGAMENT IN RESPONSE TO VARIOUS EXTERNAL KNEE LOADINGS

Satoshi Yamakawa (1, 2), Richard E. Debski (1), Hiromichi Fujie (2)

(1) University of Pittsburgh, Pittsburgh, PA, USA

(2) Tokyo Metropolitan University, Tokyo Japan

INTRODUCTION

The primary function of the anterior cruciate ligament (ACL) is transmitting tensile forces between the femur and tibia for stabilizing the knee joint. There generally exists a one-to-one relation between stress and strain. Thus, quantitative biomechanical data on the strain behavior of the ACL during physiological knee motions are necessary for a better understanding of the mechanical function of the ACL. Although previous studies determined the strain distribution in the ACL in response to an axial load applied to the ACL, they did not determine the strain distribution in response to external knee loadings [1, 2]. Therefore, the objective of the present study was to determine the strain distribution in the ACL in response to various knee loads.

METHODS

A 6-DOF robotic testing system (FR-2010, Technology Service, Japan) was used to apply loads to knee joints with respect to the knee joint coordinate system [3]. Human cadaveric knees (n=10) were dissected down to the joint capsule and fixed to the robotic testing system. 100 N of anterior tibial load, 5 Nm of internal torque, 5 Nm/10 Nm of internal/valgus torque (simulated pivot shift), and 10 Nm of valgus torque were applied to the intact knee at full extension and 30 degrees of flexion. Afterwards, the medial condyle was removed, and the medial view of the ACL was recorded during the reproduction of the intact knee motion with an HD video camera (HDR-XR500V, SONY). In the recorded image, the medial surface of the ACL was transversely divided into 4 regions from the anterior to posterior fibers and was longitudinally divided into 5 regions: 0-10%, 10-20%, 20-80%, 80-90%, and 90-100% of the length from the femoral attachment (Figure 1). By applying the rotational stereoscopic image method [4] the length changes between each marker were calculated to analyze fiber strains. The reference configuration (zero strain) was defined for the knee at full extension, when 0.5 Nm of extension torque was applied.

Willcoxon signed-rank test was performed to compare the strain values in each region between each external load. P values < 0.05 were considered statistically significant.

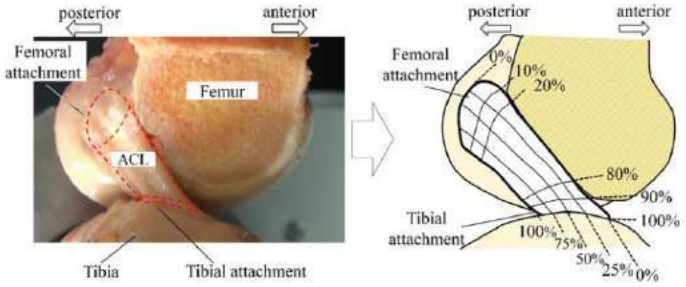

Figure 1 Twenty portions on the ACL surface layer for the strain distribution

RESULTS

Tensile strain occurred in all regions at full extension for all loading conditions. In response to an anterior tibial load, the maximum strain of 6.8% occurred in the femoral insertion site of the most posterior (75-100% of width direction) fibers (Figure 2). In response to an internal torque, the maximum strain of 4.7% occurred at the femoral insertion site of the most posterior fiber (Figure 3). During the simulated pivot shift, the maximum strain of 6.1% occurred at the tibial insertion site in the most anterior (0-25% of width direction) fibers (Figure 4). In response to the valgus torque, the maximum strain of 4.3% occurred at the tibial site in the posterior (50-75% of width direction) fibers. At 30

degrees of flexion, tensile strain did not occur in several regions in the posterior fibers. However, in anterior fibers, tensile strain occurred in almost of all regions.

DISCUSSION

At full extension, the entire ACL was strained in all loading conditions. This result indicated that all medial fibers of the ACL are functional in response to any external knee load at full extension.

At 30 degrees of flexion, unstrained regions occurred in the posterior fibers while the anterior fibers were strained. Unstrained fibers suggests that tensile force was not transmitted to the posterior side of the medial fibers. However, previous studies reported that the posterior fibers (posteromedial bundle) of the ACL were functional in the flexed knee. These results indicate that in the posterior fibers, medial fibers become non-functional in the flexed knee while lateral fibers become more functional. The present results suggested that the load distribution is changing not only width direction but also medial and lateral direction.

The trend that strain was large in the posterior side occurred in response to the anterior tibial load as well as internal and valgus torques at full extension. But, in the simulated pivot shift application, that trend did not occur. This result suggested that in the extended knee, the posterior fibers act mainly against the simple external load such as that applied to along a single axis, but the ACL mobilizes all fibers in response to complex external loads such as the pivot shift.

The present results indicated a complex site- and load-dependent strain distribution of the ACL. The deformation behavior (strain distribution) has a strong relationship to the force transmission of the tissue. Our results suggest that the deformation behavior is important for the improvement and the development of ACL reconstruction procedure. In addition, the deformation behavior of the lateral side of the ACL is important for normal function. In the future, the deformation behavior of the lateral fibers and the entire ACL will be determined.

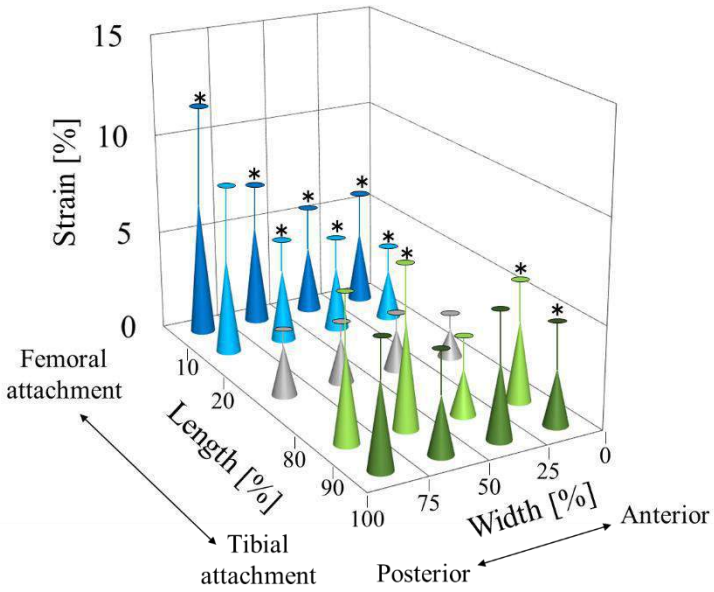

Figure 2 Strain distribution in the ACL in response to 100 N of anterior tibial load at maximum extension (Meas+SD, n=10, *: p<0.05 vs mid-substance)

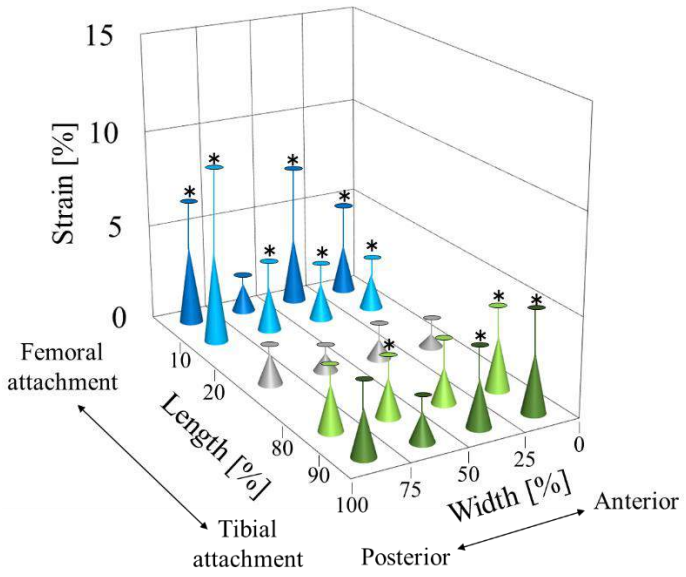

Figure 3 Strain distribution in the ACL in response to 5 Nm of internal torque at maximum extension (Meas+SD, n=10, *: p<0.05 vs mid-substance)

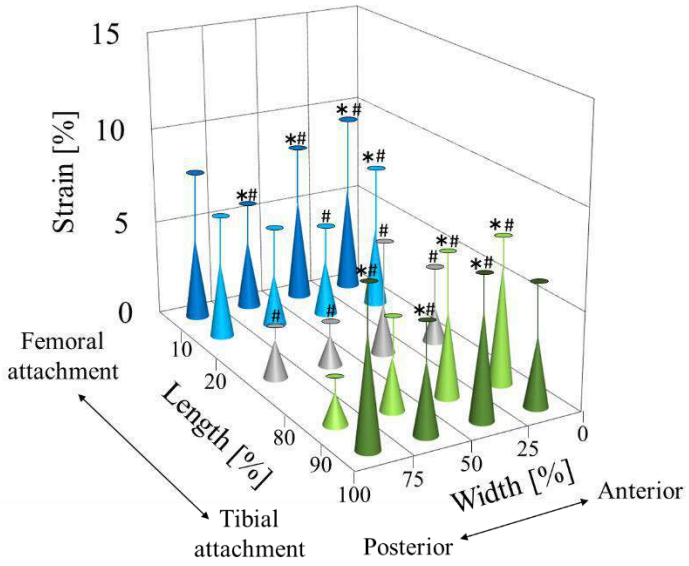

Figure 4 Strain distribution in the ACL in response to 5 Nm/10 Nm of internal/valgus torques at maximum extension (Meas+SD, n=10, *: p<0.05 vs mid-substance, #: p<0.05 vs IR test)

ACKNOWLEDGEMENTS

The present study was supported by JSPS KAKENHI Grant Numbers JP16H03172 and JP16J06537.

REFERENCES

[1] Yamamoto K., et al., Medical Engineering & Physics, 1998
[2] Spalazzi J.P., et al., Wiley InterScience, 2006
[3] Grood, E.S. and Suntay, W.J., J. Biomech. Eng. (ASME), 1983.
[4] Yamakawa S., et al., Proceedings of SB3C, 2017
[5] Fujie H., et al., KSSTA, 2011
[6] Kanamori A., et al., Arthroscopy, 2000

SB^{3}C2019
Summer Biomechanics, Bioengineering and Biotransport Conference
June 25 – 28, Seven Springs, PA, USA

DEVELOPMENT OF FINITE ELEMENT MODEL OF SUBHUMAN PRIMATE BRAIN AND INVESTIGATION OF DIFFUSE AXONAL INJURY THRESHOLDS INDUCED BY HEAD ROTATION

(1) Tushar Arora, (2) Priya Prasad, (1) Liying Zhang

(1) Biomedical Engineering Department
Wayne State University
Detroit, MI, USA

(2) Prasad Engineering, LLC
Plymouth, MI, USA

INTRODUCTION

The National Highway Transportation Safety Administration (NHTSA) uses the Head Injury Criterion (HIC) as a federal rule for frontal and side impact head protection requirements. The advanced finite element (FE) human head model and the simulation of animal brain injury data scaled to the human head model, a new Brain Injury Criterion (BrIC) [1], based on head rotational velocity measure was proposed by the NHTSA to complement the HIC. However, the accuracy of the methods for describing brain injury location, severity and pathology was very limited and the scaling of the animal head rotation motion to the human brain model based on mass information alone is questionable considering the geometrical and neuraxis differences between the animal brain and the human brain. To better correlate model-predicted biomechanical responses with the severity and location of injuries observed in animal experimental models the use of the FE animal brain model is essential. The objectives of the study is 1) to develop an anatomically realistic monkey head model with anatomical structures modeled similar to the latest human head model developed previously [2] to facilitate the translation of the tissue level response parameters; 2) to investigate the effect of angular accelerations of different planes on the severity and pathology of the Diffuse Axonal Injury (DAI) assessed by various biomechanical response parameters in the FE monkey model simulating experimental brain injury. Collectively, the tissue-level injury threshold was established; and 3) by translating the tissue-level injury threshold to the human head model, the real-world injury data was assessed and evaluated. The monkey head model developed can be used directly to simulate a wide range of brain injury types and severities.

METHODS

Development of FE Rhesus monkey head: Reported experimental studies of diffuse axonal injury, subdural hematoma and concussion on the subhuman primates often use Rhesus monkey (Macaca Mulata). The FE model of the Rhesus monkey brain was developed using MRI images [3]. Figure 1 illustrates the process involved in developing the monkey brain model. The MRI images were processed using 3D slicer to generate STL surface and imported to the Hypermesh v13.0 for meshing. The segregation of the various brain structures was performed so that the anatomical boundary can be properly represented. The brain contents were meshed with hexahedral elements using ANSYS ICEM CFD 13.0. The mesh of the white matter was differentiated from the grey matter based on the brain atlas [3]. The FE brain model consisted of grey and white matters, cerebellum, corpus callosum, brainstem, thalamus, pia matter, arachnoid mater, dural mater and dual partition and CSF. In addition, detailed skull, facial bone and flesh mesh were also developed based on data [4] (Figure 2).

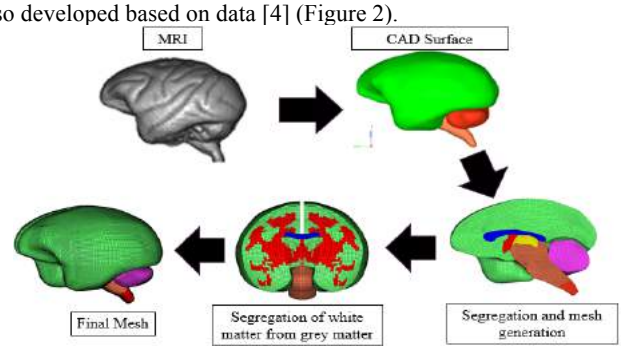

Figure 1: Development of rhesus monkey FE model

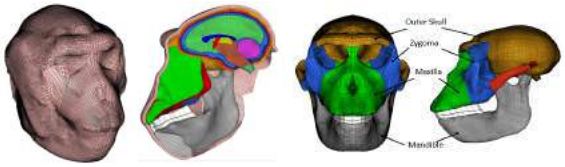

Figure 2: Developed monkey FE head model

The monkey head model has over 500,000 hexahedral and 206,000 quadrilateral shell elements with an average element size at 0.8 mm.

The material models and associated properties defined for the monkey brain, meninges, CSF, skull, facial bones and flesh were the same as the GHBMC 50th percentile male head model (Global Human Body Models Consortium) [2] and updated recently (M50 v5.0).

Simulate head rotational injury experiments and determine the tissue level injury thresholds: The head acceleration time-history measured from the monkey experimental study [5,6] were applied to the FE model. The center of rotation was in the neck at 7.345cm distance from the center of the gravity of the head. The head rotated 60 degrees in the coronal, oblique and sagittal planes of which the overall magnitude were nearly identical. The brain mass of the monkey model (109g) was scaled to the mass of the brain for each test subject. Maximum principal strain (MPS) and Cumulative Strain Damage Measure (CSDM) at 0.5 MPS level were examined in the whole brain, brainstem, white matter and corpus callosum. The localized responses were correlated to the DAI grade sustained in the experimental animals.

Assess the real-world brain injury risk: The two volunteer impact cases [7,8] and three US NCAP cases were simulated by the GHBMC M50 human head model to evaluate predictability of the tissue level thresholds developed from monkey model analysis. BrIC was also used to assess the brain injury risk. All simulations were performed by LS-DYNA MPP R8.1 on a Linux based cluster.

RESULTS AND DISCUSSION

Brain responses correlated to DAI severity: Figure 3 shows a comparison of MPS in the subcortical white matter, corpus callosum and brainstem between the head rotation in the coronal, oblique and sagittal planes. The coronal rotation produced MPS of 45% and 54% higher for brainstem, 8% and 48% higher for corpus callosum, 13% and 22% higher for white matter as compared to those from oblique and sagittal rotations, respectively. Notice that MPS peaked at 13-15 ms, about 5 ms after the angular deceleration peaked, 9 ms after angular velocity peaked and 5 ms after head was stopped at 10-11 ms.

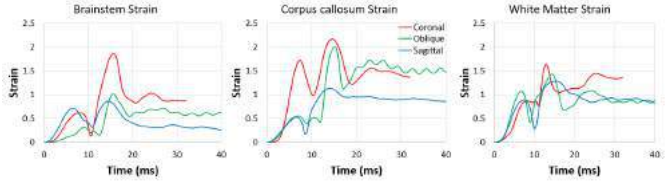

Figure 3: Comparison of MPS in various brain structures due to coronal, sagittal and oblique head rotation

The model predicted high MPS in the brainstem and corpus callosum structure, which suggested that more severe DAI was expected from coronal and oblique rotations as compared to that from sagittal rotation of similar magnitude. This localized tissue response pattern correlated well with the DAI pathological findings that damage to the brainstem and corpus callosum is responsible for the longer duration of coma experienced by the experimental animals than those with damage to the cerebral white matter. Figure4 shows strain contours in the brainstem, corpus callosum and white matter from sagittal, coronal, and oblique head rotations.

The CSDM volume percentage at >0.5 MPS produced by a coronal rotation was 57% and 53% higher in the brainstem and 5% and 49% higher in the corpus callosum as compared to those by the oblique and sagittal rotations, respectively. Again, coronal and oblique loadings resulted in more strained brain tissues in the regions leading to more severe DAI pathology.

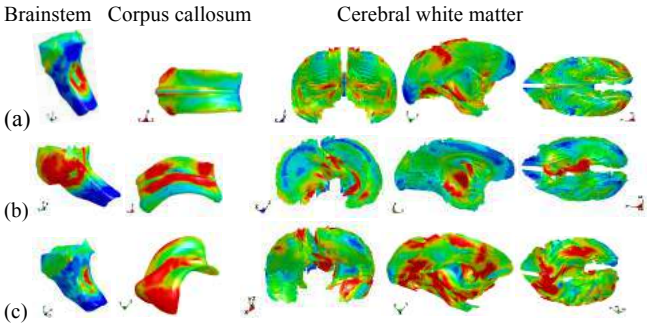

Figure 4: Comparison of MPS contours in various structures due to (a) sagittal, (c) coronal and (3) oblique head rotations

Tissue level thresholds for DAI: The MPS and CSDM analyzed not only clearly differentiated the three DAI grades associated with respective head rotation but also accurately identified the structures associated with each DAI grade level. The MPS and CSDM threshold for predicting DAI 0-1 injury was determined to be 1.3 and 50% (>MPS 0.5) in the brainstem, corpus callosum and cerebral white matte.

Assess the of human brain injury by tissue level thresholds vs. BrIC: The threshold level developed from above study was translated to the GHBMC human head model. Model predicted no injury for the volunteer cases and predict no DAI grade 0-1 for the NCAP cases.

On the other hand, the BrIC predicted 14% and 4% of AIS 4 brain injury, and 67% and 25% of AIS 2 brain injury for frontal and lateral volunteer tests, respectively. The BrIC predicted 8-12% of AIS 4 brain injury, and 46-60% of AIS 2 brain injury for all three NCAP cases.

CONCLUSIONS

The new FE primate head model developed in this study predicted the severity of axonal damages resulted from head rotations in different planes. The specific injury localization pattern was presumably dictated by the anatomy and material properties of the brain and is loading direction sensitive. The tissue-level thresholds established by the direct correlation of the monkey model prediction with the brain pathology found in the experimental animals can be used to assess the injury risk for humans. The human head model accurately predicted real world brain injury risk by using the tissue level thresholds. The BrIC significantly over predicted risk of brain injury and should be refined to improve its predictive capabilities. The rotational brain injury criterion is needed but BrIC needs to be further evaluated.

ACKNOWLEDGEMENTS

The study is funded by the Alliance of Automobile Manufacturers, Inc.

REFERENCES

[1] Takhounts, E. et al. No. 2013-22-0010. SAE Technical Paper, 2013.
[2] Mao, H. et al. Journal of biomechanical engineering 135.11 (2013): 111002.
[3] Rohlfing, T. et al., Frontiers in neuroinformatics, 6: 27, 2012
[4] Digital Morphology Museum, Primate Research Institute, Kyoto University.
[5] Gennarelli, TA. et al. Annals of neurology 12.6 (1982): 564-574.
[6] Mendis, K. Diss. The Ohio State University, 1992.
[7] Ewing, C. SAE Technical Paper, No. 760800, 1976.
[8] Ewing, C. SAE Technical Paper, No. 770927, 1977.

Attestation (1) the majority of the work was completed by Tushar Arora and (2) Tushar Arora conducted the work when he was a student at the corresponding competition level (MS).

PI: Liying Zhang, PhD

SB³C2019
Summer Biomechanics, Bioengineering and Biotransport Conference
June 25 -28, Seven Springs, PA, USA

DEVELOPMENT OF A COMPUTATIONAL BIOMECHANICS MOUSE MODEL FOR TRAUMATIC AXONAL INJURY

C. Bradfield (1, 2), L. Voo (1, 2), K. T. Ramesh (2)

(1) Applied Physics Laboratory
Johns Hopkins University
Laurel, MD, USA

(2) Mechanical Engineering
Johns Hopkins University
Baltimore, MD, USA

INTRODUCTION

This study develops a computational biomechanics model of the mouse brain that can be used to understand mechanisms of Traumatic Axonal Injuries (TAI). Mouse models are commonly used together with blunt impact experiments to understand the pathologies and neurophysiological deficits related to TAI [1,2]. However, the relationship between the motion of the mouse head and the biomechanics of the mouse brain is not well established. Here we develop a Finite Element Model (FEM) of the mouse brain with inclusion of axonal fiber tracts, and use this to compute the strain in the brain tissue in response to a range of head rotational impulse profiles. We then compare the predicted strains in the tissue to the strains observed in specific experiments on mouse brain sections during controlled rotations. This model of the mouse brain will be used in future multiscale efforts examining the relationship between brain biomechanics and TAI.

METHODS

The experimental brain tissue strain responses were obtained using biomechanical experiments on mouse head specimens (n=5) subjected to sagittal rotations. Prior to testing, mice were sacrificed in accordance with a Johns Hopkins University IACUC approved protocol, and their isolated heads were transected in the mid-sagittal plane to expose the intracranial contents. The transected mouse heads were potted in a custom 3D printed mold to control the skull rotation and attached to a drop tower base fixture for experimental testing (Figure 1). A drop mass was released from a predefined height and subsequently impacted a rotary fixture at the tower base. Upon impact, the potted specimen in the rotary fixture achieved a peak angular velocity of 100, 150 or 200 rad/s over a 90-degree rotation. The exposed mid-sagittal surface of the mouse brain was divided into 6 different regions and analyzed to determine the regional tissue response. Digital Image Correlation (DIC) was used to obtain brain surface strains during accelerated and decelerated rotations of the transected mouse heads.

The mouse brain FEM was derived from an average Diffusion Tensor Imaging Atlas [3]. The anatomy of the model was generated by converting fractional anisotropy voxel data to hexahedral elements and white matter tractography to embedded truss elements, which is similar to the modeling approach by Garimella and Kraft [4]. Brain elements were modeled as an Ogden hyperelastic material with shear moduli described through a Prony series to incorporate viscoelasticity. The instantaneous shear moduli and the viscoelastic material properties of the brain tissue were calibrated to align the FEM strains to their experimental match pairs for 150 rad/s tests. Next, using these calibrated properties, simulations were performed at 100 rad/s and 200 rad/s to determine if the model accurately portrayed the experimental strains for separate loading conditions. The percent error between the FEM and experimental peak region-averaged maximum principal strains during the acceleration phase was used for analysis.

RESULTS

The transected mouse brain experiments showed that peripheral tissue regions sustained larger strains than the central regions for all three loading conditions. The left column of figure 2 shows the DIC-based strain profile for a 150 rad/s test in which the peak strains occur from 2.7 ms after rotation was initiated. The higher peripheral strains can also be seen at the same time period. For 150 rad/s tests, the average peak maximum principal strains were 5.7± 2.3 %, 7.6± 2.4 %, 7.9±3.5 % and 8.6±3.7 % for the Rostral Ventral (RV), Caudal Ventral (CV), Rostral Dorsal (RD) and Caudal Dorsal (CD) peripheral regions, while the Rostral Middle (RM) and Caudal Middle (CM) central regions were 4.4±1.7 % and 3.9±1.3 %, respectively (mean ± 1 standard deviation).

Average experimental strain corridors for the three different rostral-based regions are shown in figure 3. Distinct acceleration-based and deceleration-based strains can be seen at t = 2.7ms and t = 13.3ms, respectively.

For the mouse FEM calibration simulations at 150 rad/s, the instantaneous shear moduli of the cerebellum, cerebral cortex, and subcortical model regions were 3.10, 4.65 and 9.30 kPa, respectively. These brain tissue property values are within the published experimental ranges in the biomechanics literature. At 150 rad/s the best and worst fits occurred in the RD and CM regions, with peak strain percent errors of 6.1% and 106.8% during the acceleration phase, respectively. The same regional trends were observed when the calibrated material parameters were used to simulate 100 rad/s and 200 rad/s loading conditions.

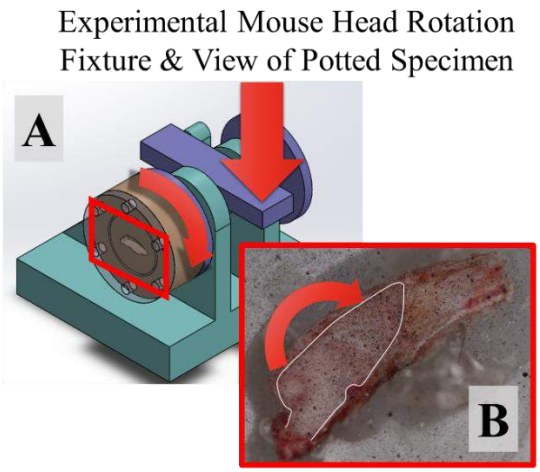

Figure 1: (A) Rotational fixture assembly and (B) high speed camera image of sagittal transected mouse skull & brain undergoing a 150 rad/s rotation

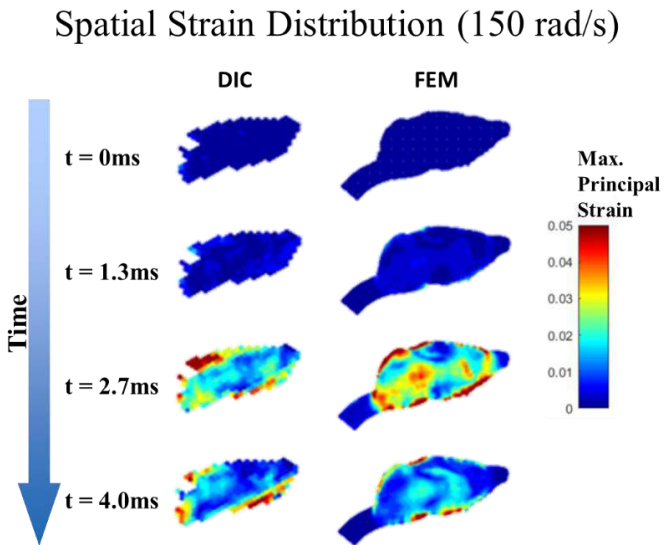

Figure 2: Time evolution of brain strain from DIC measurements and FEM values

DISCUSSION

This research developed a computational biomechanics model of a mouse brain for TAI mechanisms analysis by incorporating white matter fiber tracts and tissue strain validation. This study lays the groundwork for examining the *in-vivo* mechanical response of white matter fiber tracts and their corresponding pathological outcome, which is critical for understanding the link between primary insult and resulting neurophysiological deficits following injury. Future research would include examining various statistical measures for computational and experimental comparisons, FEM prediction of brain deformation under *in-vivo* experimental conditions, and correlation of brain strain responses to axonal injury outcomes [2].

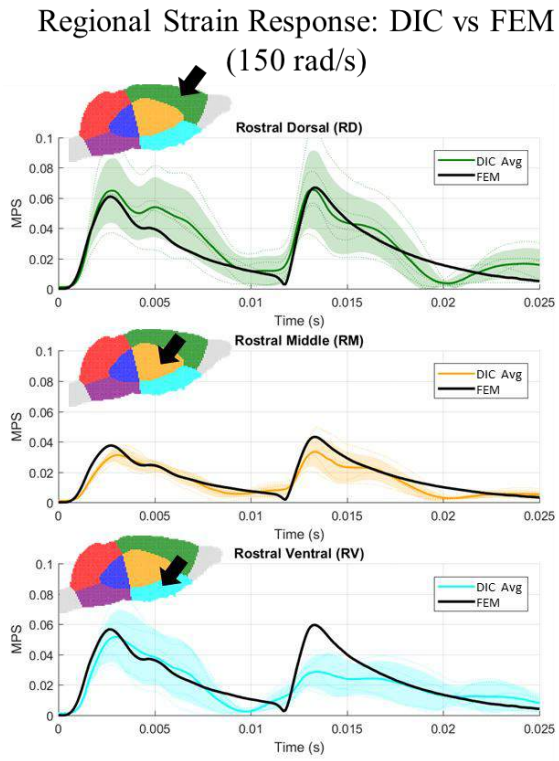

Figure 3: Max. Principal Strain (MPS) during acceleration and deceleration phases for three different brain regions

ACKNOWLEDGEMENTS

Authors gratefully thank Vassili Koliatsos and Nikolaos Ziogas (JHU Department of Pathology) for providing the sacrificed mouse specimen used for mechanical testing, as well as Susumu Mori's research group (JHU Department of Radiology and Radiological Science) for providing the Mouse Diffusion Tensor Imaging Atlas. The National Health Mission Area at the Johns Hopkins Applied Physics Laboratory provided funding for this study as part of an internal research and development project. KTR was supported in part by the Hopkins Extreme Materials Institute during this effort.

REFERENCES

[1] Namjoshi DR, et al. Mol Neurodegener. 2014;9:55.

[2] Ziogas NK, Koliatsos VE. Primary J Neurosci. 2018;38(16):4031-4047.

[3] Aggarwal M, et al., Neuroscience. 2009;162(4):1339-50.

[4] Garimella HT, Kraft RH. Int J Numer Method Biomed Eng. 2017;33(5)

SB³C2019
Summer Biomechanics, Bioengineering and Biotransport Conference
June 25 -28, Seven Springs, PA, USA

A STUDY OF THE BRAIN-SKULL INTERFACE CONDITIONS OF THE WORCESTER RAT HEAD INJURUY MODEL (WRHIM)

Wei Zhao (1), Brian Stemper (2), Songbai Ji (1, 3)

(1) Department of Biomedical Engineering
Worcester Polytechnic Institute
Worcester, MA, USA

(3) Department of Mechanical Engineering
Worcester Polytechnic Institute
Worcester, MA, USA

(2) Department of Biomedical Engineering
Marquette University & Medical College of Wisconsin
Milwaukee, WI, USA

INTRODUCTION

Traumatic brain injury (TBI) remains a leading cause of mortality and morbidity in the United States [1]. Experimental studies of the human head using cadavers [2] or live humans [3] have provided valuable insight into the injury etiology. However, ethical, technical and financial constraints limit the extent to which humans are tested to deduce the underlying injury mechanisms. In addition, individual differences in injury tolerance and concussion history and the relatively unreliable diagnosis could confound the interpretation of findings.

Controlled animal injury models such as rodent avoid these inherent challenges in humans, and they have been extensively used to study injury [4]. Similar to human head models, finite element (FE) models of the rat head also serve as an important bridge to relate impact kinematics, brain responses, and clinical indicators of injury. To date, a number of FE models of the rat head have been developed [5]–[8]. However, they have significant disparities in modeling. In particular, brain-skull interface condition has been defined variously as either sliding contact with [5], [8] or without separation [7], or via a layer of linear elastic material to simulate the cerebrospinal fluid [6]. The diverse brain-skull interface conditions could result in inconsistent brain mechanical responses under the same impact conditions.

In this study, we developed a Worcester Rat Head Injury Model (WRHIM) with high mesh quality to parametrically investigate the significance of brain-skull interface conditions using an *in vivo* rat head rotation impact profile. The results will provide important insights into further model improvement in the future.

METHODS

The Worcester Rat Head Injury Model (WRHIM) was created based on a brain mask segmented from the Waxholm Space Atlas of the Sprague Dawley Rat Brain [9]. The brain mask was imported into Geomagic (Geomagic, Inc., Research Triangle Park, NC) for surface smoothing and further into TrueGrid (version 3.1.3; XYZ Scientific Application, Inc., Livermore, CA) for meshing. Multi-blocks for the cerebrum, cerebellum, brainstem, and spinal cord were created that conformed to the brain geometry (**Fig. 1**). The brain had a mass of 2.5g. Its mesh consisted of 202.6 k high-quality hexahedral elements and 210.6 k nodes with an average element size of 0.22 mm (±0.05 mm). The mesh successfully passed a variety of quality criteria [10]. The brain was modeled by a first-order isotropic Ogden hyper-viscoelastic material derived from porcine brain tension test (strain rate of 30/s [11]).

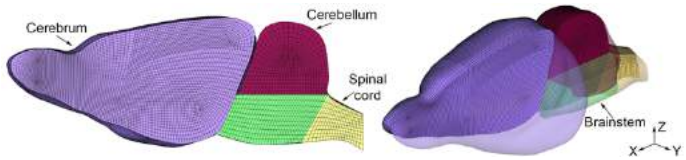

Fig. 1 The Worcester Rat Head Injury Model (WRHIM) with high-quality hexahedral elements of the brain (element and node numbers of 202.6 k and 210.6 k, respectively, with an average element size of 0.22 mm).

Three brain-skull interface conditions were investigated. 1) A layer of cerebrospinal fluid (CSF; thickness of 0.1 mm) was created between the brain and skull by sharing nodes with its surrounding anatomical structures. A linear viscoelastic material identical to that in SIMon [12] was used to allow relative brain-skull tangential motion. 2) The CSF layer was modeled by a softer linear viscoelastic material identical to that of the GHBMC [10], where the initial shear modulus was 0.005 times that of the SIMon counterpart. 3) A sliding contact allowing interface separation with a low friction coefficient of 0.05 was defined between the brain and skull, without CSF.

We simulated a rearward sagittal head rotation by prescribing the angular acceleration profile averaged from three tests on Sprague-Dawley male rats [7]. These experiments measured relative brain-skull displacements at different depths beneath the brain surface, which provided valuable data to validate rat head injury models. Reduced element integration scheme (C3D8R) along with relax stiffness hourglass control (a high scaling factor of 100) [13] was used to preserve simulation accuracy with improved efficiency. For each brain-skull interface definition, relative brain-skull displacements at the reported locations were extracted and compared with the experiment. Element-wise cumulative maximum principal strains over the entire simulation, regardless of time of occurrence, were also compared.

RESULTS

For all interface conditions, relative brain-skull displacements increased with the increase in the depth towards deeper brain (**Fig. 2**). The sliding interface condition and the stiffer CSF led to similar displacements. GHBMC soft CSF matched well with the experiments for locations at 0.5 and 1 mm below the brain surface. In the deeper brain (2 mm below surface), all displacements were overestimated relative to the experiments.

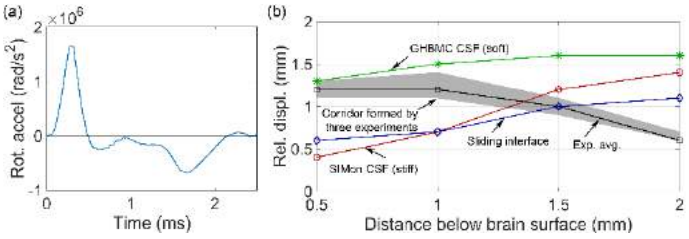

Fig. 2 (a) Rotational acceleration profile used in simulations; (b) Peak magnitudes of simulated relative brain-skull displacement for the three brain-skull interface conditions as compared to the experiments.

When rotational velocity reached its peak (0.5 ms), the patterns of relative brain-skull displacement were largely similar for the three brain-skull interface conditions (**Fig. 3**). However, they differed significantly when the rotational velocity crossed zero (1.8 ms). A soft CSF produced the largest *x*-directional displacement near the neocortex (circles). A soft CSF and the sliding interface produced similar *z*-directional displacement in the central brain larger than that from a stiff CSF (arrows). A stiff CSF also led to larger strains in the cerebrum than a soft CSF or the sliding interface especially near the surface (**Fig. 4**).

DISCUSSION AND CONCLUSION

In this study, we developed the Worcester Rat Head Injury Model (WRHIM) with high mesh quality for the brain. We investigated the significance of brain-skull interface conditions on the relative brain-skull displacement and brain strain using data from an *in vivo* rat head rotation experiment. Our results confirmed that the brain-skull interface conditions played an important role in model behavior.

A softer CSF layer appeared to allow a more reasonable relative displacement near the surface (**Fig. 2**), which may be preferred in subsequent model development. The overestimated large displacement towards the deeper brain regions may be mitigated by further considering material property heterogeneity and the inclusion of white matter anisotropy to provide reinforcement from the white matter fibers. The isotropic material properties used from porcine brain samples may be a limitation in this study, as new data on rat brain material properties [14] are emerging that account for regional brain property heterogeneity. Regardless, this study enhanced our understanding how to further improve the WRHIM in the future.

Finally, the *in vivo* impact accelerations simulated here were much higher than those in a recent rodent injury model simulating human concussion (magnitude of 1640–1730 krad/s^2 vs. 214–364 krad/s^2; impulse duration of 0.5 ms vs. 1.6–3.4 ms for the major acceleration peak [4]). It merits further investigation how the different choices of brain-skull interface conditions and brain material properties affect rat brain strains under these loading conditions that are more relevant to sports-related concussion.

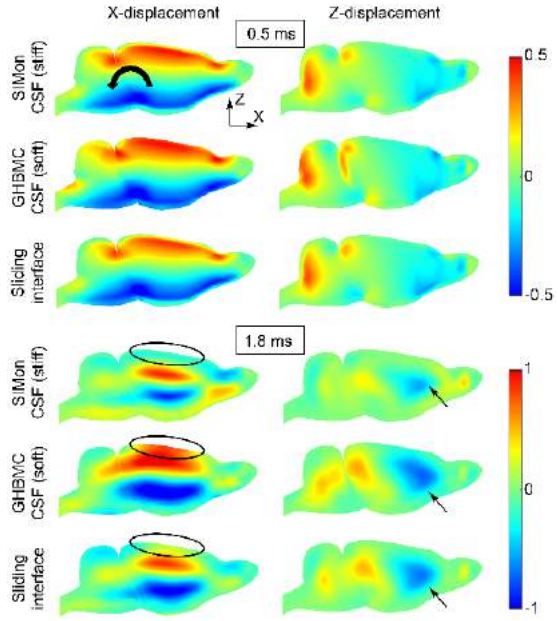

Fig. 3 Patterns of relative brain-skull displacement on a representative sagittal plane for the three brain-skull interface conditions when the rotational velocity reached its peak magnitude (0.5 ms) and crossed zero (1.8 ms).

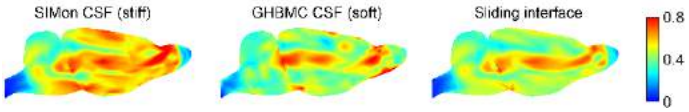

Fig. 4 Patterns of element-wise cumulative maximum principal strain over the entire simulation, regardless of the time of occurrence, on a representative sagittal plane for the three brain-skull interface conditions.

ACKNOWLEDGEMENTS

Funding is provided by the NIH grant R01 NS092853 and the Ford University Research Program (URP).

REFERENCES

[1] Meaney, DF et al., *J. Biomech. Eng*, 136(2):021008, 2014. [2] Hardy, WN et al., *Stapp Car Crash J.*, 51:17-80, 2007. [3] Sabet, AA et al., *J. Biomech.*, 41(2):307-315, 2008. [4] Stempr, BD et al., *Ann. Biomed. Eng.,* 43(5):1071-1088, 2014. [5] Mao, H et al., *Stapp Car Crash J.*, 50:583-600, 2006. [6] Lamy, M et al., *Ann. Adv. Automot. Med*, 55:125-135, 2011. [7] Antona-Makoshi, J et al., *IJAE*, 5:31-37, 2014. [8] Fijalkowski, RJ et al., *Stapp Car Crash J.*, 53:193-213, 2009. [9] Papp, EA et al., *Neuroimage*, 97:374-386, 2014. [10] Mao, H et al., *J. Biomech. Eng.*, 135(11):111002, 2013. [11] Rashid B et al., *J. Mech. Behav. Biomed. Mater.*, 33(1):43-54, 2014. [12] Takhounts, EG et al., *Stapp Car Crash J.*, 52:1-31, 2008. [13] Zhao, W and Ji, *Ann. Biomed. Eng*, 2018. [14] MacManus, DB et al., *Acta Biomater.,* 48:309-318, 2017.

SB^{3}C2019
Summer Biomechanics, Bioengineering and Biotransport Conference
June 25 -28, Seven Springs, PA, USA

PROBABALISTIC ANALYSIS OF INJURY RISK USING HUMAN BODY FINITE ELEMENT MODELS

Travis D. Eliason (1), Matthew L. Davis (2), Derek Jones (2), Daniel P. Nicolella (1)

(1) Musculoskeletal Biomechanics
Southwest Research Institute
San Antonio, TX, USA

(2) Elemance LLC
Clemmons, NC, USA

INTRODUCTION

Computational modeling is an incredibly powerful and widely implemented tool for the analysis of biomechanical systems. Advancements in computational power and software capabilities have allowed researchers to create high fidelity models of the human body capable of modeling the body's response to complex dynamic boundary conditions. These models provide advantages when compared to more traditional experimental methodologies, as it is often difficult and costly to perform cadaver experiments for all potential boundary conditions of interest. With all of their advantages however, computational models still have their caveats. One of these is the fact that a deterministic model only represents a single individual and cannot accurately predict risk of injury across a specific population group.

Across the human population, there exists a great deal of natural variation both in mechanical properties as well as musculoskeletal geometry. Material properties for example can have coefficients of variation (COV) of 80% or higher and these material properties play a critical role in determining if a response was injurious or not. Additionally, overall size of the subject as well as less obvious geometrical differences can have significant effects on the response and corresponding injury prediction. Exercising a computational model within a probabilistic framework helps to the overcome these deficits and allows the model to account for these inherent variabilities. Rather than reporting an injury vs. no injury response as with a deterministic model, the probabilistic model will return a probability of injury relevant to the population of study.

METHODS

In this study we utilized a provided human torso model (Advanced Total Body Model, ATBM) (figure 1) within a probabilistic framework as a proof of concept for quantifying risk of injury due to behind armor blunt trauma. Boundary conditions consisted of 100 gram impactor with an initial velocity of 65.2 m/s centered over the heart. Boundary conditions directly replicated the experimental setup of a whole body PMHS experimental setup. Rib cortical bone strains were output and compared to a threshold [1] for definition of fracture.

Probabilistic analyses were set up for three versions of the model representing a 5th percentile female, 50th percentile male, and 95th percentile male. Material properties of the major structures in the models as well as the boundary conditions were all included in the probabilistic analysis. Distributions were defined for each model parameter to replace the individual values typically defined for a deterministic model. A Latin Hypercube sampling technique was then used to generate 300 random samples of each model size, each with a unique set of material properties and boundary conditions sampled from their respective distributions. Each sample was then run and post processed to export the element by element strains of the rib cortical bone. Combining these responses allows the calculation of the response distribution at each individual element, capturing the response variability that would be expected across a population.

Custom code was then written to take these response distributions and calculate the probability of injury on an element by element basis and produce a probability of injury contour plot (Figure 2). In order to accomplish this strain results for each element of interest in the model were output for every timestep, for every model sample resulting in nearly 1 billion data points. At each element and timestep

a deterministic injury prediction was made for a sample. Then the positive injury predictions were summed across the 300 samples. The percentage of models that predicted an injury for that element at that timestep defines the probability of injury. Rib fracture analysis was completed for all three subject sizes and compared quantitatively as well as qualitatively with the probability of failure contours.

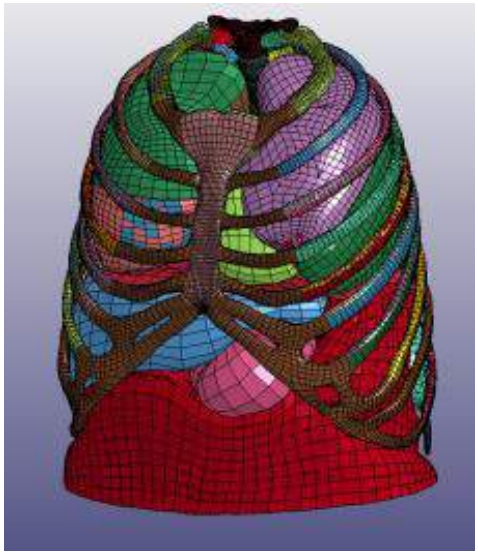

Figure 1: 95% Male ATBM with skin, muscle, and adipose tissue hidden to expose ribs and organ detail

RESULTS

Figure 2 shows a comparison of the predicted rib fracture probabilities for the 5th percentile female and 95th percentile male. The female model had a 34% probability of at least one rib fracture, 1 17% chance of between 2 and 5 fractures, and an 8% chance of 6 or greater fractures. Conversely the 95th percentile male had a 10% chance of at least 1 fracture, a 5% chance of between 2 and 5 fractures, and a 0% chance of 6 or more fractures.

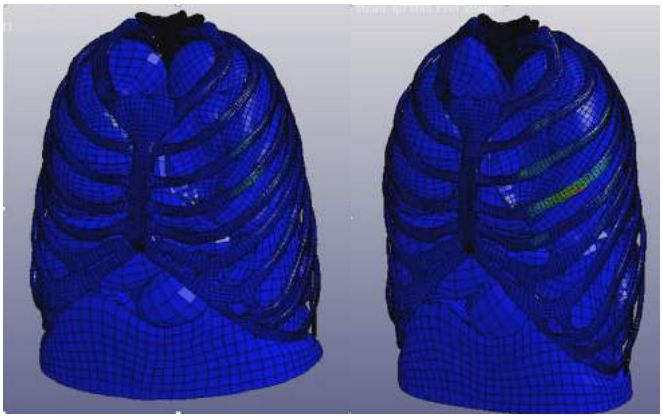

Figure 2: Example probability of injury contour for rib fracture. Contour colors represent the probability of fracture at each element. 95th percentile male results are on the left with 5th percentile female results on the right.

DISCUSSION

While time consuming and technically challenging, we believe that this probabilistic approach to injury prediction gives significant advantages to the traditional deterministic approach. Typically, a deterministic model is used along with a safety factor to determine if a piece of equipment or loading environment is safe. This approach while useful is a blunt tool that ignores the complex interaction human variability has on responses. In order to be sure something is safe large safety factors must be used which result in non-optimal designs which could be improved with a more complete understanding of their interaction with the human system. Additionally, probability of injury prediction results can be directly correlated to military incapacitation scales to convert the probability of injury into an incapacitation level probability. For example, the 5th percentile female results shown in figure 2 correspond to a 34% chance of a MCIS 1 injury, 17% chance of a MCIS 2 injury, and an 8% chance of a MCIS 3 injury. These injury codes offer an actionable interpretation of model results for military decision makers to use. A MCIS score of 1 corresponds to a minor injury with no loss to the mission, MCIS 2 is a moderate injury which leads to slight functional incapacitation but is not life threatening, and MCIS 3 is a serious injury that takes a solider out of a mission but is recoverable [2].

By moving away from the blunt application of safety factors and deterministic models, a more refined understanding of how the human body interacts with the environment can be achieved. This will lead to optimized equipment designs that work across the variability of the human population, that are safer, lighter, and more comfortable. While the work done in this study is a proof of concept, when applied along with rigorous model development, verification, and validation methodologies the probabilistic approach to injury prediction will help better explain the "so what" of modeling results and help users make actionable decisions from those results.

ACKNOWLEDGEMENTS

The authors would like to thank the Office of Naval Research for funding the study and providing the baseline ATBM model.

REFERENCES

[1] Guleyupoglu B. et al., *Traffic Injury Prevention*, 19:S37-S43, 2018.

[2] Lawnick M., et al, *Trauma and Acute Care Surgery*, 75-4:572-581, 2013

SB³C2019
Summer Biomechanics, Bioengineering and Biotransport Conference
June 25 -28, Seven Springs, PA, USA

CHARACTERIZATION OF INJURED BRAIN TISSUE AFTER CONTROLLED CORTICAL IMPACT

S. Qiu (1), W. Jiang (2), C. Lai (1), T. Wang (3), W. Chen (4), L. Tao (4), M. Gao (2), J. Liu (3), J. Zeng (2), Y. Feng (1)

(1) Institute for Medical Imaging Technology, School of Biomedical Engineering Shanghai Jiao Tong University Shanghai, Shanghai, China

(2) Center for Molecular Imaging and Nuclear Medicine, School of Radiological and Interdisciplinary Sciences (RAD-X) Soochow University, Suzhou, Jiangsu, China

(3) Department of Radiology, the Fifth People's Hospital of Shanghai Fudan University Shanghai, Shanghai, China

(4) Department of Forensic Science, Soochow University, Suzhou, Jiangsu, China

INTRODUCTION

Traumatic brain injury (TBI) is one of the leading causes of death and disability of young people in the world [1]. The biomechanical properties of the brain tissue are of great importance to understand the injury mechanism and to improve prognosis of TBI [2]. While most of the brain tissue characterization studies focused on normal tissues [3,4], few studies investigated the injured brain [5].

Many different methods have been used to introduce injury in the animal model, such as lateral fluid percussion (LFP), weight drop closed head model, and controlled cortical impact (CCI) [6]. CCI can control the velocity, depth, duration, and site of impact accurately [7]. Therefore, CCI is one of the mostly used methods in animal models.

Many researchers have investigated the influences of the impact depth, velocity, or the geometry of impactor head [8,9]. They demonstrated that modifying these components influences the location and severity of injury. However, most studies adopted a certain impact angle when inducing the injury to brain and little is known about the viscoelastic properties of the brain tissue after the impact. Understanding the viscoelastic properties of the injured tissue under different impact angles can provide vital information for in-depth knowledge of the injury mechanism.

In this study, we induced brain injury using CCI and characterized the viscoelastic properties of injured tissue. The impact was introduced with 3 different impact velocities and 3 different angles. Viscoelastic properties of the injured region and its contralateral region were characterized and compared. Results could help guide further animal experiments and verify corresponding computer simulation models.

METHODS

A total of 54 adult mice of SPF grade were used in this study. A custom-built CCI device (Figure 1) with a cylindrical impactor head of 3 mm diameter was used to implement injury on the left hemisphere of each mouse. Craniotomy was carried out before introducing injury to the brain. The impact velocities (v) and impact angles (θ) were 0.6 m/s, 0.8 m/s, 1.0 m/s, and 0º, 30º, 50º, respectively.

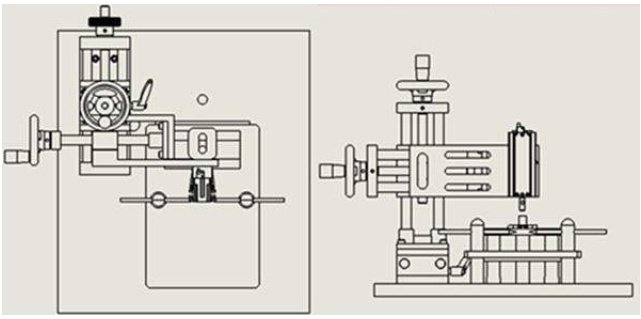

Figure 1. Schematic drawings of the custom-built CCI device.

The mouse brain was taken out immediately for the indentation test after the impact. Coronal slices with a thickness of 3 mm were prepared for testing. With a custom-built indentation device, we conducted indentation test on the impact region and the corresponding contralateral regions on the other uninjured hemisphere. Up to 8% strain of the sample thickness was indented for the ramp-hold test.

We recorded the indentation force and computed viscoelastic properties by fitting the force with 2-term Prony series. A custom-written MATLAB (Mathworks, Natick, MA, USA) code was used for fitting and optimization to estimate the instantaneous shear modulus G_0 and long-time shear modulus G_∞.

One-way and two-way ANOVA tests followed by a Bonferroni test (significance level of 0.05) for the G_0 and G_∞ values were used to evaluate the significances of the impact velocity and angle.

RESULTS

A typical force-time curve is shown in Figure 2(a). G_0 and G_∞ values were estimated by fitting 2-term Prony series. Variations of the experiment data were shown by plotting the 95% confidence interval region (Figure 2(b)).

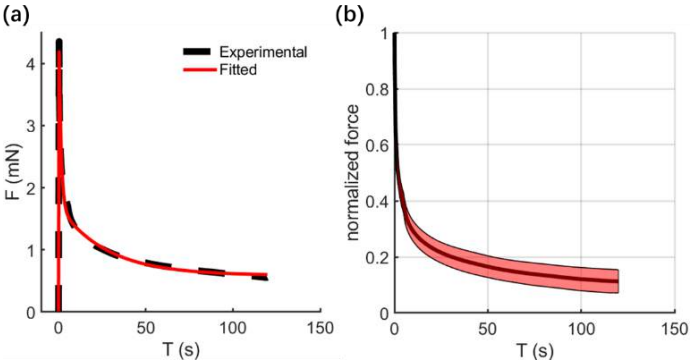

Figure 2: (a) A typical experimental and fitted force-time curve. (b) A typical averaged relaxation curve. The red-shaded area indicates the 95% confidence interval.

Results showed that the average values for both G_0 and G_∞ are lower at impact regions for all impact velocities and angles (Figure 3). For G_0, its average values will increase with the rise of impact angles on the uninjured hemisphere when velocity is low. But for G_∞, we did not observe similar patterns.

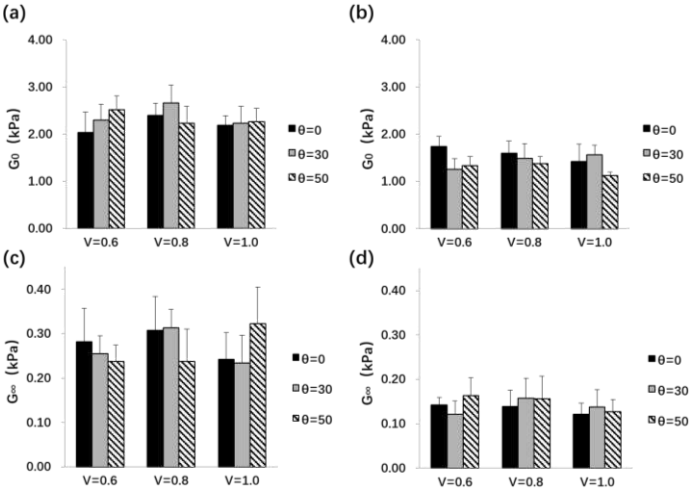

Figure 3: Comparisons of the influence created by different impact angles and velocities in terms of (a, b) instantaneous shear modulus G_0, and (c, d) long-term shear modulus G_∞ with 95% confidence interval. The test areas were (a, c) healthy contralateral regions, (b, d) injured regions.

The one-way ANOVA tests showed that G_0 at the impact region and the contralateral side was influenced significantly with the impact angle changing when velocity was 0.6 m/s. However, no significant differences were observed for G_∞. The two-way ANOVA tests indicated that the impact angle played a vital role in the changing viscoelastic properties of the injured tissue.

DISCUSSION

Many indentation tests have been used to investigate the viscoelastic properties of the mouse brain. Elkin et al. (2011) showed that the average instantaneous shear modulus was ~1 kPa, which is slightly lower than our results [10,11]. Lee et al. (2014) showed that the instantaneous shear modulus for the cerebral cortex and hippocampus region of healthy mouse brain was 3.8 kPa and 1.0 kPa, respectively [12]. Our results for instantaneous shear modulus are around 2.3 kPa for the cerebral cortex and 2.2 kPa for hippocampus regions, respectively. The differences are probably due to the rat model used and a higher strain rate. As for the injured brain tissue region, studies have shown an increased degree of damage with the increase of impact velocities [13]. In this study, we did not observe a significant influence of the impact velocity based on the measured shear modulus. This may be due to the comparatively lower maximum speed we chose.

It is important to highlight that no single animal model of TBI can mimic the entire spectrum of observations of human TBI. Our CCI model was carried out based on the exposed dura that required trephination of the skull. However, latest epidemiological researches have indicated that 85-89% of TBI patients were caused by blunt, closed head trauma [14]. Thus, a future study of the effect of an external impact on the closed animal skull, rather than the exposed dura will be meaningful. In addition, more CCI model configurations, e.g. a larger impact angle and a higher speed of impactor, may provide more information about the biomedical properties of brain tissues.

In this study, we characterized the viscoelastic properties of the injured brain tissue using a mouse CCI model. We observed that the impact angles had a more significant role than the impact velocities. These results showed that the proposed protocol of studying CCI injury using a mouse model is useful in probing the mechanism of brain injury and also provide insights into the influence of impact angle during CCI.

ACKNOWLEDGEMENTS

Funding is provided by grant 31870941 (YF) from National Natural Science Foundation of China (NSFC). Support from Priority Academic Program Development of Jiangsu Higher Education Institutions (PAPD) is also acknowledged. We thank Prof. Philip V. Bayly for helpful discussions.

REFERENCES

[1] Pearn, ML et al., *Cell Mol Neurobiol*, 37:571-585, 2017.
[2] Budday, S et al., *Acta Biomaterialia*, 48:319-340, 2017.
[3] Chatelin, S et al., *Biorheology*, 47:255-276, 2010.
[4] Destrade, M et al., *Int J Nonlin Mech*, 75:54-58, 2015.
[5] Feng, Y et al., *J Mech Behav Biomed*, 71:407-415, 2017.
[6] Flierl, MA et al., *Nat. Protoc*, 4:1328-1337, 2009.
[7] Osier, ND et al., *Front. Neurol*, 7:134, 2016.
[8] Taylor, AN et al., *J. Neurotrauma*, 25:311-323, 2008.
[9] Pleasant, JM et al., *J. Neurotrauma*, 28:2245-2262, 2011.
[10] Elkin, BS et al., *J Biomech Eng*, 133, 2011.
[11] Elkin, BS et al., *J Neurotrauma*, 28:2235-2244, 2011.
[12] Lee, SJ et al., *J Mech Behav Biomed Mater*, 29:213-224, 2014.
[13] Kim, Y et al., *J Neurosci Res*, 96:501-511, 2018.
[14] Myburgh, JA et al., *J Trauma*, 64:854-862, 2008.

SB^{3}C2019
Summer Biomechanics, Bioengineering and Biotransport Conference
June 25 -28, Seven Springs, PA, USA

A MODEL OF TENSION-INDUCED ORGANIZATION OF SUBCORTICAL AXONS DURING CORTICAL FOLDING OF THE BRAIN

Kara E. Garcia (1,2), Christopher D. Kroenke (3), Philip V. Bayly (2)

(1) Department of Anatomy & Cell Biology
Indiana University School of Medicine
Evansville, IN, USA

(2) Department of Mechanical Engineering
Washington University in St. Louis
St. Louis, MO, USA

(3) Department of Behavioral Neuroscience
Oregon Health & Science University
Portland, OR, USA

INTRODUCTION

During fetal development, the human brain forms complex cortical folds and axonal connections (Fig. 1). Abnormalities in cortical folding, as well as disorders including epilepsy and autism, have been linked to abnormal connectivity [3]. However, the physical and biological mechanisms underlying this linkage remain unclear.

Physical and biological evidence suggests that brain folding, or wrinkling, occurs as the outer cortical surface (prospective gray matter) grows faster than the underlying subcortex (prospective white matter) [4], and most computational models of folding approximate subcortical tissue as a passive, nongrowing substrate [5]. However, since axons can elongate in response to tension, several models have hypothesized that the prospective white matter may also grow in response to mechanical feedback [6-7]. These studies elucidated effects of certain subcortical properties (eg. stress-dependent growth rate, anisotropic axon orientations) on folding, but – to date – none have considered the effect of folding on subcortical axon organization.

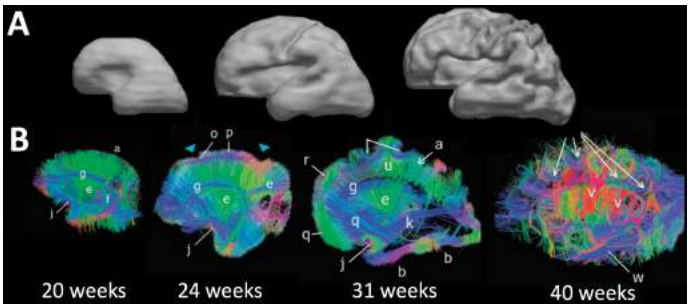

Figure 1: Brain folding and connectivity over development. A. Cortical surfaces from [1]. B. Subcortical tractography from [2].

In this study, we focus on evolution of subcortical axon fibers, which develop during and after the period of brain folding in human. We find that only a model incorporating mechanical feedback, anisotropy, *and* evolving axon density (a novel aspect of our model) accurately predicts axonal organization during early brain development.

METHODS

We developed an axisymmetric model in COMSOL Multiphysics 5.3a, starting from a hollow spherical geometry to approximate the initial curvature and internal lumen of the early brain. We represent brain tissue as a nearly incompressible, modified neo Hookean material with uniform, isotropic stiffness.

As described in [6], we defined the total deformation tensor such that $\mathbf{F} = \mathbf{F}^* \cdot \mathbf{G}$, where $\mathbf{F}^*$ represents elastic deformation and $\mathbf{G}$ represents growth. To account for anisotropic (orthotropic) and stress-dependent growth effects, we defined $\mathbf{G} = G_1\,\mathbf{e_1}\,\mathbf{e_1} + G_2\,\mathbf{e_2}\,\mathbf{e_2} + G_3\,\mathbf{e_3}\,\mathbf{e_3}$ where the growth rate in each direction (i = 1, 2 or 3) at time t is:

$$\dot{G}_i = \left[a f_i(\sigma_i - \sigma_0) + g_{c,i}\right] G_i \qquad (1)$$

For each direction, $\sigma_i = \sigma_i(\mathbf{F}^*)$ is the nondimensionalized Cauchy stress. In this study, we assumed a target stress of $\sigma_0 = 0$ for all cases.

At early stages of development, axons constitute a relatively small proportion of the subcortical tissue. Therefore, we assume stress-dependent growth (axonal elongation) is proportional to both the stress-dependent growth rate (a, units 1/T) and volume fraction of axonal fibers in the i-direction (f_i), which accounts for both orientation and density. Constant growth rate $g_{c,i}$ (units 1/T) is set to zero in subcortical layers and the radial direction (i = 1), while a is set to zero in the cortex.

If stress-dependent growth is primarily growth of axons, but axons only represent a fraction of the total tissue, axon volume fractions must evolve over time as shown for f_1:

$$f_1(t) = \frac{f_{1,0}V + \Delta G_1(t)V}{G_1(t)\,G_2(t)\,G_3(t)V} = \frac{f_{1,0} + (G_1 - 1)}{G_1 G_2 G_3} \quad (2)$$

where V is the initial unit volume and $f_{1,0}$ is the initial volume fraction of axons in the radial direction. A similar equation can be written for axon fractions in tangential direction, f_2. For simplicity, here we do not consider the axisymmetric direction ($f_{3,0} = 0$).

RESULTS

Since the brain exhibits a generally radial orientation prior to folding (Fig. 1B), we first considered the case where $f_{1,0} = 2\,f_{2,0} = 0.2$. As shown in Fig. 2A, we let a small region of cortex grow slightly faster (green) to break symmetry and initiate folding. Folding triggers stress-dependent radial growth beneath gyri and tangential growth beneath sulci, consistent with past models [6]. However, by specifying axon volume fractions, we note that this results in accumulation of radially-oriented axons beneath gyri (projection fibers) and tangentially-oriented axons beneath sulci (short association fibers).

In our hollow model, we also notice accumulation of tangential fibers along the ventricular (inner) surface, similar to long association fibers found deep in the white matter.

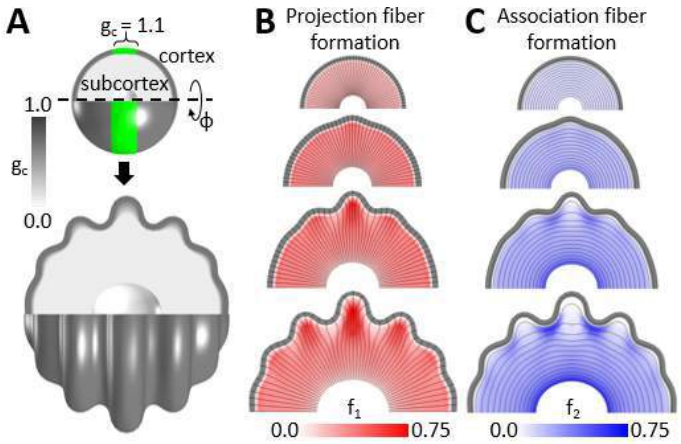

Figure 2: Axisymmetric model of cortical folding and evolving axonal organization. A. Initial and final geometries. B. Evolution of radial axon (projection fiber) density with folding. C. Evolution of tangential axon (association fiber) density with folding.

Subcortical anisotropy can, in turn, influence subcortical growth and patterns of folding [7]. Therefore, we also considered the geometric consequences of an initially isotropic subcortex ($f_{1,0} = f_{2,0} = 0.15$) or constant axon volume fractions ($f_1 = 2f_2 = 0.5$ or $f_1 = f_2 = 0.4$, similar to previous models). Notably, models with constant volume fractions showed less elaborate folding, and models with isotropic subcortical growth showed increased expansion of the ventricle (Fig. 3).

DISCUSSION

In this study, we build upon previous models of cortical folding to understand development of the underlying substrate, the prospective white matter. Consistent patterns in axon organization have been reported for many years [8-9] and represent neural circuits integral to brain functions such as perception, movement, and cognition. Here, we propose a simplified model that generates structures resembling short-range (U-shaped) association fibers, long-range (deep tangential) association fibers, and projection (radial) fibers. Future work will test these concepts on a realistic, 3D geometry for comparison to observed tractography in human, as well as other species (including lissencephalic species, for which U-shaped fibers would not be predicted).

Despite a clear correlation between brain folding and subcortical organization, past theories have failed to resolve the question: Does axon connectivity cause folding, or does fold formation influence axon connectivity? Most studies have focused on the former. Van Essen [3] proposed the well-known axon tension hypothesis, in which axons pull the folds together, but this was shown to be inconsistent with measured stresses in the developing brain [10]. More recently, Holland et al. [7] proposed a mechanical feedback model in which pre-existing axon orientation (eg. U-shaped association fibers) guides folding, but this theory depends on axon orientations measured after folding. Our results do not disprove the possibility of anisotropy-induced folding, but suggest an alternative (or complementary) mechanism of folding-induced anisotropy, consistent with the general trajectory of folding and axon development in human.

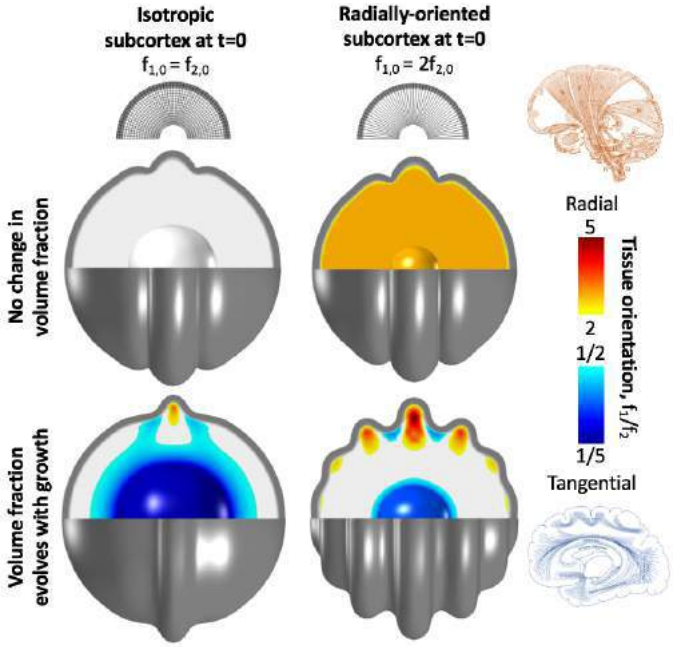

Figure 3: Fractional anisotropy (colorbar) and geometry at t=T under various subcortical conditions. Insets to right: Illustrations of radial (projection) and tangential (association) fibers modified from [8] and [9], respectively.

ACKNOWLEDGMENTS – No funding to declare.

REFERENCES

[1] Wright, R et al., *NeuroImage*, 91:21-32, 2014.
[2] Takashi, E et al., *Cerebral Cortex*, 22(2):455-464, 2012.
[3] Van Essen, DC, *Nature*, 385:313-318, 1997.
[4] Garcia, KE et al., *Phil Trans R Soc B*, 24:373(1759), 2018.
[5] Tallinen, T et al., *Nature Physics*, 12:588-593, 2016.
[6] Bayly, PV et al, *Physical Biology*, 10:016005, 2013.
[7] Holland, MA et al., *Ann Biomed Eng*, 43(7):1640-1653, 2015.
[8] Martin, HN and Martin, EG, *The Human Body*, 1917.
[9] Gray, H, *Anatomy of the Human Body*, 1919.
[10] Xu, G et al, *J Biomech Eng*, 132(7):071013, 2010.

SYNTHESIS AND CHARACTERIZATION OF POROUS SHAPE MEMORY POLYMER MATERIALS FOR USE IN THE DESIGN OF IMPLANTABLE MEDICAL DEVICES

Robert Kunkel (1), Jingyu Wang (1), Jishan Luo (1), Bradley N. Bohnstedt (2), Yingtao Liu (1), Chung-Hao Lee (1,3)

(1) School of Aerospace and Mechanical Engineering
University of Oklahoma
Norman, OK, USA

(2) Department of Neurosurgery
University of Oklahoma Health Sciences Center
Norman, OK, USA

(3) Institute for Biomedical Engineering, Science and Technology
The University of Oklahoma
Norman, OK, USA

INTRODUCTION

Intracranial aneurysms (ICA), or brain aneurysms, are abnormal focal dilations and weakenings of arterial blood vessels in the brain with a prevalence of 0.5-6% in adults [1]. 50-80% of subarachnoid hemorrhage (SAH) cases result from the incidental rupture of an ICA. These rupture events, accounting for 5-8% of all strokes, are most common between ages 40 and 65 and are associated with a mortality rate as high as 40% within the first week [2-4].

Aneurysm treatment therapeutics have evolved quickly with the introduction of Guglielmi detachable coils (GDC) and flow diverting stents. However, challenges still remain for the treatment of both giant and irregularly shaped aneurysms, associated primarily with aneurysmal recanalization and incomplete occlusion [5,6]. One potential way to address these shortcomings is with the use of an expandable shape memory polymer (SMP) foam device. Such devices would take advantage of the shape recovery properties of the SMP and undergo a large, controlled expansion from a compressed state to completely fill the patient's aneurysmal space.

The use of SMP-based devices for the treatment of neurovascular pathologies isn't a new concept. Various SMPs, each with a unique thermomechanical behavior, have been investigated for their use in clot removal, vascular stenting, and aneurysm occlusion [7]. Very few of these investigations, however, detail the process of synthesizing a polymer with desirable characteristics for use in medical device design. In this study, we demonstrated synthesis procedures for both pristine and porous aliphatic polyurethane SMP. By tailoring the ratios between monomer components, a wide range of glass transition temperatures (T_g) and mechanical properties of the SMP could be obtained. We present investigations into the thermo-mechanical properties of a novel SMP foam manufactured using aliphatic polyurethane SMP and a sugar template scarification technique. The results of the investigation are discussed in terms of their efficacy for use in the endovascular embolization treatment of intracranial aneurysms.

METHODS

Twelve different SMP compositions were synthesized by varying the ratios of the three monomers (**Table 1**): (i) Hexamethylene Diisocyanate (HDI), (ii) Triethanolamine (TEA), and (iii) N,N,N0,N0-tetrakis (hydroxypropyl) ethylenediamine (HPED), obtained from Sigma Aldrich without modification. The monomer ratios used during synthesis are summarized in Table 1.

Table 1: Monomer composition table w/ synthesis procedure details

	Monomer Content (%)			Stirring Time (sec)	Heating Rate (°C/hr)
	HDI	HPED	TEA		
SMP1	53.5	46.5	0.0	150	30.0*
SMP2	53.9	44.5	1.6	170	29.6
SMP3	54.3	42.5	3.2	200	29.2
SMP4	55.1	38.4	6.5	225	26.4
SMP5	56.0	34.1	9.9	240	25.2
SMP6	56.9	29.7	13.4	255	23.6
SMP7	57.8	25.1	17.1	270	21.1
SMP8	58.8	20.4	20.8	285	18.5
SMP9	59.7	15.6	24.7	310	15.9
SMP10	60.7	10.6	28.7	330	12.5
SMP11	61.8	5.4	32.8	350	9.6
SMP12	62.3	2.7	35.0	445	8.5

To synthesize pristine SMP, the monomers were combined in a glove box under dry nitrogen atmosphere to prevent moisture uptake. Once combined, the monomers were mixed gently with a magnetic stir bar for the times specified in **Table 1** until optically clear. The mixture was transferred to silicone molds and degassed 5 times in a vacuum oven to -0.8 torr. The molds were then heated at a low vacuum to 130 ºC according to Table 1 and allowed to cure at that temperature for 1 hr.

The glass transition temperature (T_g) of each composition was determined using both differential scanning calorimetry (DSC) and dynamic mechanical analysis (DMA). A desirable T_g (39ºC) was selected from the composition table, and used in the synthesis of foam samples. To create SMP foam, the liquid monomer mixture was cast over a rectangular sugar scaffold with uniform grain size and allowed to cure following procedures for pristine SMP synthesis. After curing, excess SMP was cut away, and the sugar was dissolved out of the solid using water bath sonication at 40 ºC

The mechanical properties of pristine SMP samples were characterized using uniaxial tensile testing at T_g+10 ºC. An Instron uniaxial testing device was used to conduct both failure and cyclic testing. Specimens were tested within a heated environmental chamber and allowed to reach equilibrium with the chamber for 10 minutes before testing. Failure testing was performed first on pristine samples at a rate of 2mm/min. Cyclic tests followed, and consisted of 3 cycles of preconditioning at 25% failure strain and 10 testing cycles at 50% failure strain. The SMP foam samples underwent uniaxial compressive testing, at room temperature, T_g, and T_g+10ºC, also using the Instron uniaxial testing device.

RESULTS

We were able to synthesize pristine SMP samples with T_g's ranging from 87 ºC to 33 ºC. Failure stresses of the pristine SMP samples at T_g+10 ºC ranged from 3.34 MPa to 6.88 MPa, and failure strains ranged from 16.2% to 54.4%. We also demonstrated an SMP foam with good shape recovery within a minute of heating above T_g (**Fig. 2**). Both the pristine and foam samples exhibited a significant reduction in elastic modulus when heated above their respective T_g, as was expected. The measured elastic modulus of the SMP foam was 2.7 MPa at room temperature and 0.23 and 0.18 at 39 ºC (Tg) and 49 ºC (Tg+10 ºC) respectively. The elastic modulus of the pristine samples decreased initially but stabilized after 3-4 loading cycles (**Fig. 1c**). Both pristine and foam samples exhibited a large stress reduction during cyclic loading (**Fig. 1b & Fig. 3**), with the maximum stress decreasing by 7% and 17% over 10 cycles at Tg+10 ºC for the pristine and foam samples respectively.

DISCUSSION

The objective of this project was to conduct a thorough characterization of an aliphatic polyurethane SMP material to evaluate its potential for applications in medical device design, specifically for the treatment of intracranial aneurysms. We showed that we can vary the T_g of the SMP material to achieve a composition which initiates shape recovery between human body temperature (37 ºC) and the threshold for tissue damage (45 ºC), which is ideal for applications in the human body.

For endovascular delivery methods, compressibility is an important factor as it allows large devices to travel through narrow arteries to their target, where they will be deployed. While the pristine form of this material was qualitatively observed to have limited compressibility, we demonstrated that the material can be synthesized as a foam with regular porosity that can withstand much higher compression ratios. Cyclic testing revealed a significant stress relaxation behavior, which is a concern when considering applications where an implanted device is expected to perform a permanent structural role within the body. Future investigations could investigate the relationship between pore size in the SMP foam and the material's mechanical properties with a specific focus on compression ratio. Constrained and unconstrained shape recovery characteristics will also be important topics for future study

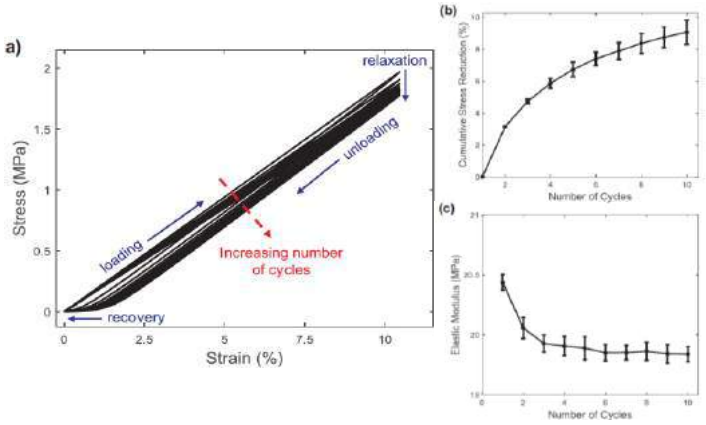

Figure 1: Representative cyclic mechanical testing results (SMP3) when tested at 50% of the observed failure strain (T_g+10 ºC) showing: (a) the relaxation trend in the peak stress with an increasing # of cycles, (b) the increase in the cumulative stress reduction and (c) the convergence of the elastic modulus with an increasing # of cycles.

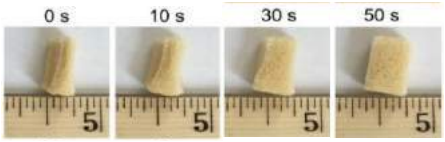

Figure 2: Shape recovery of the porous SMP foam in response to direct heating above the SMP's Tg.

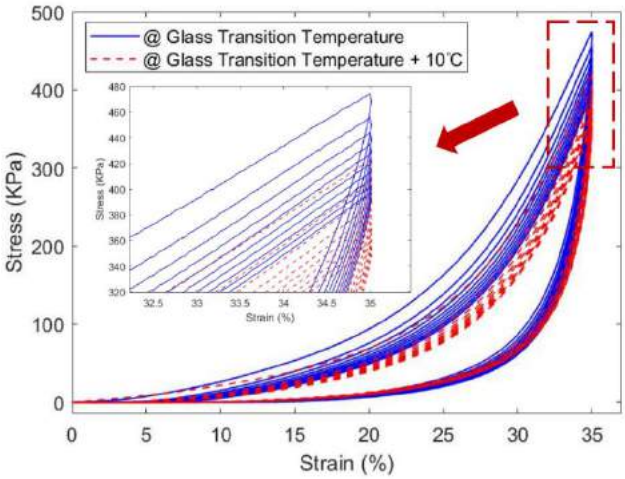

Figure 3: Mechanical characterization of the fabricated SMP foam under cyclic compressive load conditions: mechanical response of the SMP foam at T_g and T_g + 10 ºC under cyclic compressive loading.

ACKNOWLEDGEMENTS

We would like to acknowledge funding from the OCAST Health Research Program (HR-18-002) and the OU IBEST-OUHSC Funding for Interdisciplinary Research.

REFERENCES

[1] Rinkel GJ et al., *Stroke*, 29:251-256, 1998.
[2] Benderson, JB et al. *Stroke*, 40:994-1025, 2009.
[3] Zacharia, BE et al. *Neurosurg Clin*, 21.2: 221-233, 2010.
[4] Wardlaw, JM & White, PM, *Brain*, 123:205-221, 200.
[5] Wehman, CJ et al. *Neurosurgery*, 59:suppl_5, 2006
[6] Roy, D. et al. *Stroke*, 32(9):1998-2004, 2001.
[7] Sokolowski, W. et al. *Biomedical Materials* 2.1 (2007): S23.

DUAL-SUPPORT MECHANICAL ASSISTIVE TECHNOLOGY FOR PEDIATRIC AND YOUNG ADULT PATIENTS

Carson S. Fox MS (1), Randy M. Stevens MD (2), Joseph Rossano, MD (3), Francisco Arabia MD, MBA (4), Amy L. Throckmorton, PhD (1),

(1) BioCirc Research Lab
School of Biomedical Engineering, Science and Health Systems, Drexel University
Philadelphia, PA, USA

(2) Heart Center for Children,
St. Christopher's Hospital Children,
Philadelphia, PA, USA

(3) Division of Cardiology, Pediatric Heart Failure & Transplant Program, The Children's Hospital of Philadelphia,
Philadelphia, PA, USA

(4) Cardiothoracic Surgery, University of Arizona, College of Medicine,
Tucson, A□, USA

INTRODUCTION

Congestive heart failure (CHF) is a progressive disease that affects millions of people worldwide.[1] More than 5 million Americans suffer from CHF and 670,000 new cases are diagnosed each year.[1-3] Health care costs for these patients continues to grow every day and currently amounts to approximately $35 billion annually.[4] In the chronic stages of CHF, treatment consists of pharmacological therapies, intravenous support, and inevitably a heart transplantation, when a patient qualifies and a donor heart becomes available.[1-3] In the U.S., over 3,000 patients are on the waiting list at any given time, however, on average only 2200 transplants take place in a year. Greater than 20% of patients on the heart transplant waiting list die due to lack of available donor hearts. The lack of donor hearts and the increasing need for ventricular support has supported the design and development of alternative methods of support, such as mechanical circulatory devices, including total artificial hearts (TAHs) and ventricular assist devices (VADs) for adults and pediatric patients.[5] As a new invention, we are developing a novel TAH (*Dragon Heart*). This TAH (**Fig. 1**) occupies a space of 50 mm x 50 mm. This new device utilizes the inner hub space of a centrifugal VAD by placing an axial pump through the center. The more compact size of this device has less foreign surface and therefore reduces a risk of infection and an immune response. The impellers of the pumps will be levitated in a magnetic field per 3rd generation technology. Building on a prior design effort[5], we present the computational studies, and prototype testing of the centrifugal and axial flow blood pumps that constitute the *Dragon Heart*.

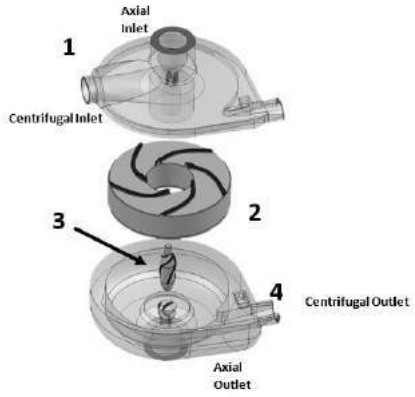

Fig. 1: Continuous Flow Heart Pump. 1) Upper Housing, 2) Centrifugal Left Ventricular Assist Device (LVAD), 3) Axial Right Ventricular Assist Device (RVAD), and 4) Lower Housing. This configuration comprises two separate pump domains that are combined under one pump housing.

METHODS

Design Approach: The axial flow blood pump was designed to support the pulmonary circulation and to generate 3 L/min of flow with a pressure rise of approximately 20 mmHg. The centrifugal flow blood pump was designed to support the systemic circulation and to produce 3 L/min of flow with a pressure rise of greater than 95 mmHg. Both pumps were designed to have an operating rotational speed less

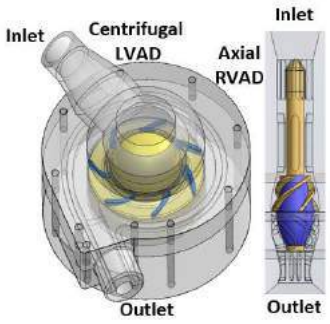

Fig. 2: Centrifugal LVAD and Axial RVAD of the Dragon Heart. Analyzed through computational studies and prototype testing.

than 12000 RPM, a maximum shear stress less than 425 Pa, and a blood damage index less than 2 %.

We used computer aided design (CAD) software to create a 3-D model of the pumps (**Fig. 2**). The geometries were imported into ANSYS workbench, where they were meshed utilizing TurboGrid and ANSYS Mesh. The mesh was refined through grid independence studies and achievement of quality metrics. The mesh was then imported into CFX-Pre where boundary conditions were set. A viscosity of 3.5 centipoise was assigned with a design of 1050 kg/m^3 to represent the fluid properties of blood. The impellers were set in rotating reference frames, while the inlet and outlet volutes, inducer, and diffuser domains were defined in the stationary reference frames. The models were then imported into CFX Solver for simulation. We analyzed the pressure generation, fluid forces on the levitated impellers, particle resonance times and scalar stresses for blood damage studies. In parallel, we used the CAD models to 3-D print prototypes of the pumps for testing. The models were then placed in our hydraulic flow loop using a shaft-driven configuration and evaluated for pressure/flow (P-Q) profiles.

RESULTS

Fig. 3A illustrates the pressure generation from the computational analyses and prototype testing for the centrifugal and axial blood pumps. The prototype of the centrifugal pump slightly outperformed the computational predictions; in contrast, the axial flow computational studies outperformed the prototype. Both design achieved their target performance goals. **Fig. 3B** displays the scalar stress approximations for the centrifugal and axial designs. Higher stress levels were found at the leading edge, blade tip clearance, and the cutwater region in the centrifugal pump. Similarly, higher fluid stress levels were simulated along the blade tip surface, leading and trailing edges of the impellers and in the diffuser region. The scalar stress levels were found to be lower than the target cutoff level. Radial and axial fluid forces were estimated to be less than 0.5 N and 10 N, respectively.

DISCUSSION

In this study, we advanced the design of the *Dragon Heart*. The computational studies revealed that these pumps were able to achieve the pressure and flow requirements to sustain patients with CHF. Both pump demonstrated the ability to impart energy to the blood in the systemic and pulmonary circulations. Computational data trends followed theoretical expectations, whereby faster rotational speeds produced higher pressures and higher flow rates yielded lower pressures. Shear stresses and blood damage estimations were below threshold levels and met requirements. Radial force estimations were low given the axi-symmetry and radially centered position. Similarly, axial force estimations for the axial blood pump remained less than 10 N and followed theoretical trends whereby higher axial forces occurred with higher pressure rises and faster speeds.

When comparing the computational and experimental data, we observed that the centrifugal prototype slightly outperformed the computational data (less than 5% difference). In contrast, the computational predictions for the axial pump significantly outperformed the experimental data for the prototype. Experimental data was both repeatable and reproducible for both prototypes. There are several factors that contribute to the deviation between experimental data and computational modeling. First, there is a geometric mismatch between model and physical prototype. During testing of the axial and centrifugal prototypes, shafts were used to drive rotation, but shafts were not included in the computational study since the device will incorporate a magnetic suspension. Parts of the shafts were always exposed to the analog fluid during experiments and likely contributed to disturbed flow conditions. In particular, a shaft sleeve was employed at the outlet of the axial prototype, which reduces the effective fluid domain and compresses the flow at the outlet, as compared to the computational predictions. Thus, this would have contributed to the lower experimental pressures that were measured. During the manufacturing of the prototypes, rotor clearances were made 15% larger to ensure no impeller touchdown. In addition, the 3-D printing methods have an accuracy of 0.001" per linear inch. All of these factors together contributed to the deviation in computational and experimental findings.

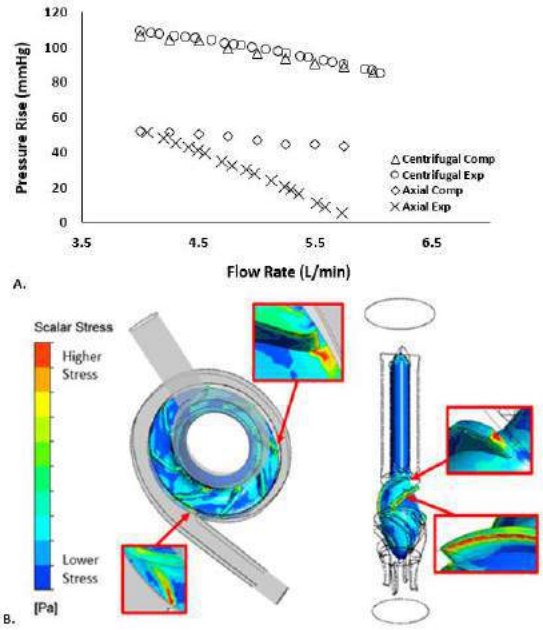

Fig. 3: Centrifugal LVAD and Axial RVAD of the Dragon Heart. Analyzed through computational studies and prototype testing.

CONCLUSIONS

This study describes the next phase of the pump designs in the development of the Dragon Heart. Computational studies and prototype testing revealed that the pump geometries achieved targeted design requirements. Future work will include the design of the motor and magnetic suspension, MRI studies to map the flow of the pumps, hemolytic experiments, and acute animal studies.

ACKNOWLEDGEMENTS

The authors wish to acknowledge the financial support as provided by partial support from a 2018 American Heart Association Predoctoral Fellowship Award (C.S. Fox: #18PRE33990470) and a 2016 Individual Biomedical Research Award from The Hartwell Foundation.

REFERENCES

1. S Westaby and OH Frazier. Long-term biventricular support with rotary blood pumps: prospects and pitfalls. European Journal of Cardio Thoracic Surgery, page ezs256, 2012.
2. AS Go, D Mozaffarian, VL Roger, EJ Benjamin, JD Berry, WB Borden, DM Bravata, S Dai, ES Ford, CS Fox, and et.al. Heart disease and stroke statistics–2013 Update. Circulation, 127(1):e6, 2013.
3. KA Litton. Demystifying ventricular assist devices. Critical care nursing quarterly, 34(3):200–207, 2011.
4. PA Heidenreich, JG Trogdon, OA Khavjou, K Butler, Jand Dracup, MD Ezekowitz, EA Finkelstein, Y Hong, SC Johnston, A Khera, and et.al. Forecasting the future of cardiovascular disease in the US. Circulation, 123(8):933–944, 2011.
5. CS Fox, SG Chopski, N Murad, et al. Hybrid Continuous Flow Total Artificial Heart. Artificial Organs 2018; 42(5): 500-509.

SB^{3}C2019
Summer Biomechanics, Bioengineering and Biotransport Conference
June 25 -28, Seven Springs, PA, USA

DURABLE AND FLEXIBLE SUPERHYDROPHPOBIC AND BLOOD-REPELLING SURFACE WITH SHAPE-CUSTOMIZABLE FEATURES FOR BIOMEDICAL APPLICATIONS

Zhe Li (1), Ba Loc Nguyen (1), Junmin Xue (2), Graeme MacLaren (3),Choon Hwai Yap (1)

(1) Department of Biomedical Engineering, National University of Singapore, Singapore

(2) Department of Material Science and Engineering, National University of Singapore, Singapore

(3) Department of Surgery, Yong Loo Lin School of Medicine, National University of Singapore, Singapore

INTRODUCTION

Blood pumps expose blood to high stresses, causing blood damage (hemolysis and platelet activation), which causes in thrombosis and leads to thrombo-embolic complications and device failure. Blood damage is a serious problem in both centrifugal and roller blood pumps [1,2]. For example, 18% of LVAD patients suffer from hemolysis, which markedly decreased survivability from 89% to 39% at 1 year [2]. In order to reduce the blood damage, the friction force experienced by blood should be reduced. Superhydrophobic (SHP) surfaces have a demonstrated capability of reducing the flow drag [3]. Micro-/nano-scale structures on SHP surface would reduce the liquid-solid contact by trapping a thin layer of air on the surface, and blood flow over a SHP surface would experience a smaller friction force, thus reducing mechanical stress-induced hemolysis and platelet activation. We have recently provided a demonstration that a super-hydrophobic coating can reduce damage to porcine blood in an in vitro flow loop [4].

Here, we report a novel sand-casting technique to prepare SHP surfaces using biocompatible components such as PDMS and silica nanoparticles. The resulted surface is SHP, has enhanced blood repellency, can reduce the water drag forces by up to 72% compared to plain PDMS, has exceptional durability, is flexible and shape-customizable, and can be used on blood pump housing or roller pump tube. Our SHP surface improves on existing SHP surfaces reported in the literature, as they either have durability problem or could not be conveniently shape-customized.

METHODS

The SHP item is prepared in four steps (Figure 1). First, SiO_2 nano particles were functionalized to be SHP. Second, a composite of the SHP SiO_2 & PDMS was prepared. Third, a SHP SiO_2 "nano-sand" mold for casting the final SHP item was fabricated by pressing the prepared composite into a confined cavity under pressure. The mold can have a 3D complex shape. Finally, a SHP item was casted using the prepared mold. Liquid repellence was tested using water and everyday fluids. Porcine blood was used to test the blood repellence property. As blood damage is related with the shear/friction force, friction forces induced by water jetting on our casted sample have been measured. Mechanical durability of the prepared sample was evaluated. Flexibility and 3D shape-customizability have also been demonstrated.

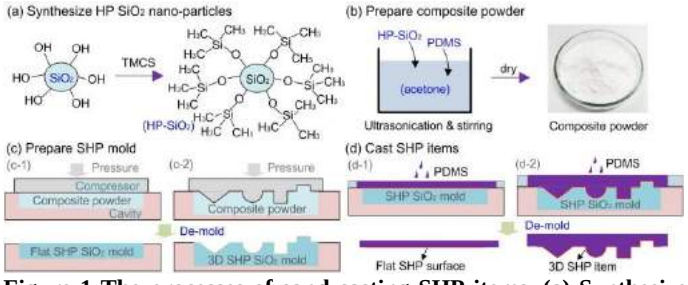

Figure 1 The processes of sand-casting SHP items. (a) Synthesize HP-SiO_2 nano-particles, (b) prepare HP-SiO_2 & PDMS composite powder, (c) prepare the SHP SiO_2 mold, (d) cast SHP items using the prepared SHP mold.

RESULTS

As shown in Figure 2 the casted sample is super-hydrophobic (water contact angle = 158°; sliding angle < 10°), and is blood repellent (blood contact angle = 150.6° ± 1.44°). When a porcine blood droplet was dispensed onto the surface, it rolled off without

leaving any blood stains (Figure 2b). In comparison, on PDMS or PC surfaces, which are common materials in blood pumps, blood would adhere and stain the surfaces (Figure 2c, d). Durability performance of the casted sample are shown in Figure 3a and b, demonstrating superior durability compared to alternative SHP coatings. After 5 hours of high-speed (9.7 m/s) water jetting (Figure 3a), or after 40m worth of abrasion with the #800 grit sandpaper under 10kPa of pressure (Figure 3b), the contact angle maintained above 150°. In contrast, spray-coated and dip-coated SHP samples lost their high contact angle quickly in the same tests. The superior durability was due to the thicker SHP functional layer during the sand-casting, and this thickness could be controlled by varying the sandcasting seepage time. Figure 3c demonstrates that the casted sample is flexible and deformable, and that repeated deformation doesn't compromise its SHP properties. These findings reveal that the casted sample can be durable enough for use as tubings or blood pumps for procedures such as cardiac surgery, which lasts for a few hours.

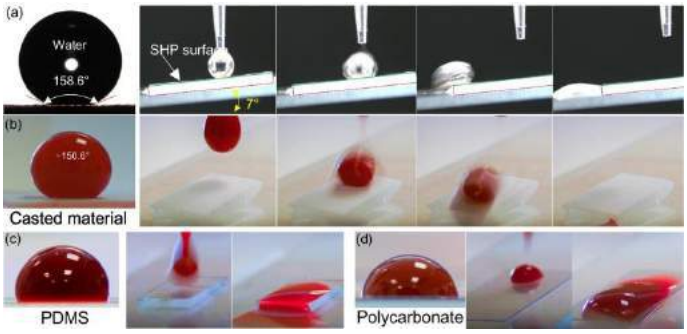

Figure 2 (a) Water contact angle and quick roll-off of a water droplet on the casted SHP sample; (b) blood contact angle of the casted SHP sample, and blood rolling off the casted sample without leaving stains; (c) blood contact angle of PDMS, and blood flowing off PDMS while leaving stains; (d) blood contact angle of polycarbonate, and blood adhered on the surface.

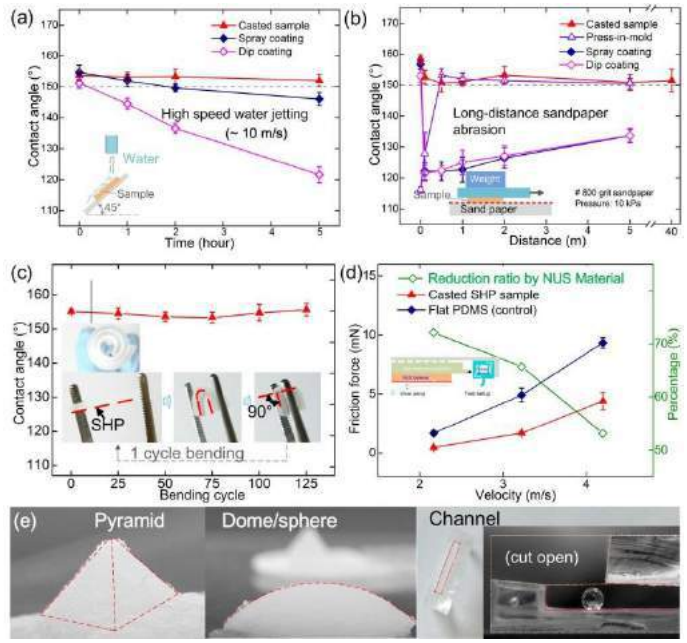

Figure 3 (a-b) High speed water jetting test, and sandpaper abrasion test; (c) demonstration of flexibility and durable SHP after repeated bending; (d) drag reduction test showed that the SHP surface experienced much lower drag forces compared with non-SHP PDMS at water jetting velocities smaller than 4.2 m/s. (e) Casting 3D SHP components of complex geometries.

Moreover, the casted sample can evidently reduce the flow drag by up to 72%, when exposed to water jets of less than 4.2 m/s velocities (Figure 3d). This drag reduction ratio was similar to that for SHP aluminum surfaces [3], but higher than the salinized copper surface [5]. Drag reduction was due to two factors. First, SiO_2 particles functionalized with -CH3 groups had reduced surface energy and repelled water [6,7]. Second, multi-scale micro-structure formed on the casted surface would help generate micro air-pockets on the surface, reducing liquid-solid contact and thus fluid friction. As blood damage is related with the friction induced shear force, the demonstrated SHP and drag reduction capability of the casted surface will be promising in reducing the blood damage for blood pump applications. Also, the developed sand-casting method is versatile and can be customized into 3D SHP items of complex geometries (Figure 3e), which has been demonstrated by prototyping pyramid, dome-shaped, and rectangular SHP items. With these demonstrated advantages, the sand-casting technique developed in this study can be readily scaled up to fabricate a flexible roller pump tube for the heart lung machine or a pumping housing for the centrifugal blood pump applications.

DISCUSSION

The method developed in this study has evident comparative advantages over the reported methods for preparing SHP surfaces. As for the surface modification techniques, such as lithography, nano-/micro-imprinting, etching, spray or dip coating, particle deposition, atomic layer deposition, liquid flame spray et al., they generally prepare coating with a thin SHP layer which would be vulnerable to mechanical damage and thus is not durable. In contrast, the sand-casting method developed in this study can prepare a very durable SHP surface, owing to the high bonding strength of HP-SiO_2 particles on the casted surface and the existence of a sub-surface SiO_2 layer with a controllable thickness. Also, the casted SHP items reported in this study are SHP as prepared, requiring no surface abrasion, and can thus be conveniently customized into complex 3D geometries. Therefore, in this study, a general sand-casting method has been developed to prepare durable, flexible, 3D-geometry customizable, fluorine-free, superhydrophobic and blood-repellent components using bio-compatible materials. With all these features, the developed methods can be readily used to reduce the blood damage in biomedical devices such as the roller blood pump and the centrifugal blood pump.

ACKNOWLEDGEMENTS

This work was supported by Singapore Ministry of Health, National Medical Research Council grant number NMRC/OFIRG/0060/2017 (PI: Yap) and the National Research Foundation (Singapore) Grant number NRF2017-IT002-012 (PI: Yap).

REFERENCES

[1] Roger, VL et al., *Circulation*, 123: e18, 2011.
[2] Mulholland, JW et al., *J Fluids Struct*, 20: 129-140, 2005.
[3] Zhang, H et al., *RSC Adv*, 6: 14034-14041, 2016.
[4] Lai, CQ, et al., *RSC Adv*, 6: 62451-62459, 2016
[5] Wang, Y, et al., *RSC Adv*, 5(24): p. 18909-18914, 2015.
[6] Li, X., et al., *Chem Lett*, 35(1): p. 94-95, 2006.
[7] Zhang, X., et al., *Appl Surf Sci*, 258(20): p. 7907-7911, 2012.

QUANTIFYING THE CAPACITANCE AND RESISTANCE OF A DOUBLE-WALLED AORTIC STENT-GRAFT PROTOTYPE

Shannen B. Kizilski (1), Omid Amili (2), Filippo Coletti (2), Rumi Faizer (3), Victor H. Barocas (4)

(1) Department of Mechanical Engineering
University of Minnesota
Minneapolis, Minnesota, USA

(2) Department of Aerospace Engineering & Mechanics
University of Minnesota
Minneapolis, Minnesota, USA

(3) Department of Surgery
University of Minnesota
Minneapolis, Minnesota, USA

(4) Department of Biomedical Engineering
University of Minnesota
Minneapolis, Minnesota, USA

INTRODUCTION

Arterial stiffening occurs naturally with age as elastin degrades and collagen content increases [1]. Increased stiffness, synonymous with decreased capacitance, can lead to hypertension as well as an overall higher risk of cardiovascular disease (CVD). Over one third of the U.S. population has hypertension, with less than half of patients effectively treated by medical therapy [2]. It is estimated [3] that 25% of all cardiovascular events are attributable to hypertension. Despite the severity of hypertension, treatment options are limited to medication and lifestyle changes.

In this work, we investigate the potential use of a compliant aortic implant, inspired by existing stent-grafts, to therapeutically reduce blood pressure in patients with uncontrolled hypertension. Aortic stent-grafts (SG) offer a minimally invasive, endovascular alternative to open surgery for patients with aortic conditions such as aneurysm or dissection. Although current SGs offer good short-term outcomes, there is growing evidence that the compliance mismatch between SG and native vessel may contribute to complications including new aortic tears, persistent hypertension, and pseudoaneurysm [4-7]. A stent-graft that mitigates these problems by maintaining or increasing aortic capacitance would also have the potential to reduce the risk of hypertension-related conditions.

We have developed a double-walled stent-graft (DWSG) design, which incorporates capacitance through a compressible gas layer within a stiff outer wall. To simulate the effect of the DWSG on blood pressure, a prototype was placed in an experimental flow model of the arterial system. Next, the prototype was isolated and inflated, to quantify the capacitance *C* (Eq. 1) over a range of pressures.

$$\mathbf{C} = \frac{\mathbf{d(lumen\ volume)}}{\mathbf{d(lumen\ pressure)}} \qquad \mathbf{(1)}$$

An axisymmetric finite element (FE) model of the DWSG was developed for comparison to the inflation results. From the FE model, both the capacitance and Poiseuille flow resistance of the DWSG were obtained; these values were put into a lumped parameter model of the flow setup for direct comparison of the pressure profiles.

METHODS

Flow Loop Experiment (FLE): A model of the aorta was built using latex and PVC tubing (Fig. 1a). The DWSG was constructed using thin latex tubing for the inner membrane and a stiff 1" PVC tube for the outer wall. The prototype was placed in the descending aorta section and filled with a known quantity of gas through a valve in the outer wall. A pump provided a pulsatile flow profile at 60 beats per minute, and a needle valve supplied peripheral resistance downstream of the aorta. Pressure was recorded upstream of the stent-graft for cases with different quantities of gas in the DWSG. The pulse pressure was defined as the difference between the peak and minimum pressures in each cycle.

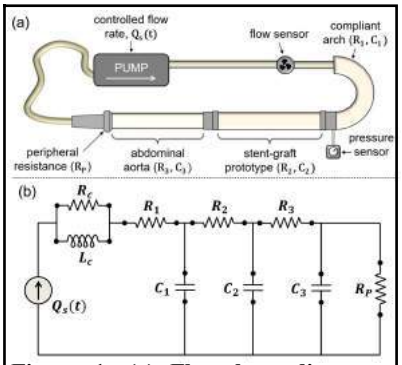

Figure 1: (a) Flow loop diagram; (b) Lumped parameter model: variables correspond to elements labeled in (a). R_c , L_c are from four-element Windkessel model [8].

Inflation Experiment: The DWSG prototype was placed into a rigid, closed test system. After a known charge of gas was added to the membrane layer, the lumen was filled with water through valve-controlled ports. Additional water was added to the lumen in 1mL increments while the pressure was recorded. Six different gas charges from 10 to 70mL were tested, with the specified volumes referring to

the gas volume at atmospheric pressure. Although CO_2 gas would be used in the final device, tests were conducted with ambient air, due to its abundance and the similar behavior of both gases at low pressures. After each test, the lumen was emptied of water, then the gas was removed and measured to confirm that none had escaped during the test.

FE & Ideal Gas Law Model: An axisymmetric model of the DWSG membrane was created (Fig. 2a), to evaluate how it deforms in response to pressure, in the absence of a confined gas. This result was combined with calculations from the ideal gas law to understand how the gas-filled membrane layer should respond to changes in lumen pressure.

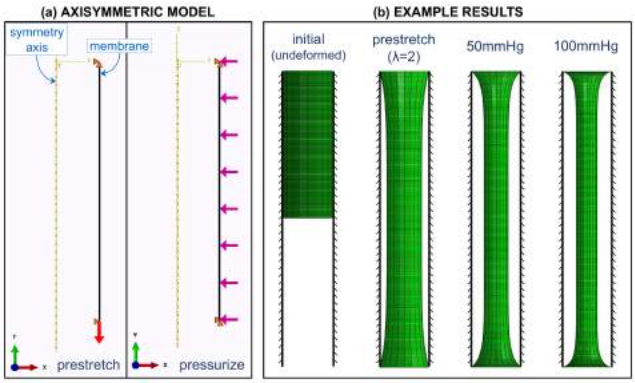

Figure 2: (a) Prestretch and inflation steps of DWSG inflation FE model; (b) Deformed FE mesh at different pressures. Rigid outer wall is not modeled in the simulation but is shown for clarity.

In Abaqus (Dassault Systemes), the elastic membrane was modeled using membrane-type shell elements. An axial prestretch was applied to the membrane, simulating the stretch that is imposed during prototype construction. A series of static pressures was applied to the stretched membrane, with the ends held fixed at their prestretched positions. The resulting volume in the gas layer was calculated in MATLAB (Mathworks) using the deformed membrane coordinates and the fixed position of the outer wall. To account for the effect of the enclosed gas, the intersection points were found between pressure-volume curves for the deformed membrane and for a fixed charge of an ideal gas. The output of this calculation was the relationship between the luminal pressure and the volume of liquid in the DWSG lumen. The derivative of this relationship (dV/dP) was defined as the capacitance of the DWSG. Additionally, the Poiseuille resistance of the DWSG was found by integrating Poiseuille's law over the axial length.

Lumped Parameter Model: A model of the experimental flow loop setup was created (Fig. 1b) to compare pressure profiles from the FLE to those predicted by capacitance and resistance values obtained from the inflation and FE models. The lumped parameter model was based on the four-element Windkessel model [8], but instead of a single capacitor, capacitor-resistor pairs were used to represent three distinct segments of the aorta. A flow rate was prescribed to match pump output from experiments, and peripheral resistance was tuned to match mean pressure from the flow loop with a rigid stent-graft segment. All parameters were held constant across runs, aside from R_2 and C_2, which were specified based on the FE or inflation results. Changes in pulse pressure from the rigid stent-graft case were compared among the models and experiment.

RESULTS

The slope of a linear fit was used to estimate the capacitance in both the FE and inflation data. The fit only considered pressures over 40mmHg, since lower pressures are not physiologically relevant in the aorta. Resistance from the DWSG inflation could not be calculated because membrane buckling inhibited measurement of the lumen radius from photos. Radius of the lumen in the FE model was taken as the x-position of the membrane at each axial position.

Capacitance increased with gas charge in both the inflation and FE model for smaller gas charges (Fig. 3a). The FE model always under-predicted capacitance, and at higher charge it showed a decrease in capacitance, likely as the hyperelastic membrane entered its higher stiffness regime. Resistance increased sharply with charge, due to a decreased lumen radius with higher gas charge (Fig. 2b) and the fact that resistance is proportional to $1/r^4$.

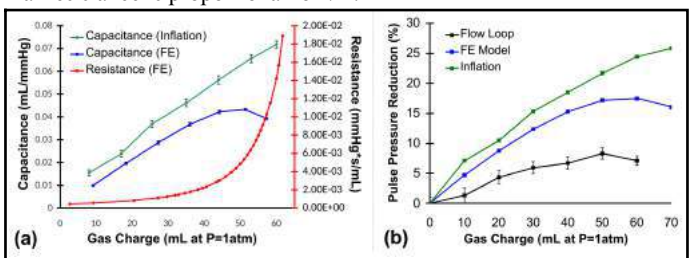

Figure 3: (a) Capacitance and resistance measurements compared for FE and inflation; (b) Reduction in pulse pressure for flow loop measurements and lumped parameter predictions.

Capacitance estimates from the inflation and FE model, and resistance from only the FE model, were put into the lumped parameter model, and the resulting pulse pressures are shown in Figure 3b. Predicted PP followed the same trend as measurements from the flow loop, but the predictions showed a much greater reduction in PP than the flow loop for all gas charges.

DISCUSSION

This work demonstrates the DWSG's potential to reduce lumen pressure when compared to a rigid stent-graft. Static measurements of DWSG capacitance and resistance, when used to predict pressures seen in the flow loop, overestimated the pressure reduction at different gas charges. This result suggests that inertia of the blood and viscosity of the gas, which were neglected by the FE model and inflation, may have significant effect on stent-graft performance.

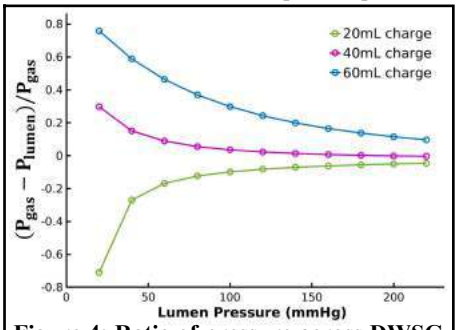

Figure 4: Ratio of pressure across DWSG membrane to gas pressure, for FE model.

One parameter that may be important to investigate in future work is the ratio of pressure change across the membrane to pressure in the gas (Fig. 4). As the ratio decreases toward zero, a change in lumen pressure will cause a larger change in gas volume. Larger gas charge, though exhibiting large capacitance, led to a higher ratio over the relevant range of lumen pressures. A very small gas charge actually led to negative ratio values; at sufficiently small charge, the volume of gas was always below that of the unpressurized, prestretched membrane, so the gas was always experiencing a negative pressure.

ACKNOWLEDGEMENTS

This work was supported in part by NIH grant U01 HL139471 and the Minnesota Supercomputing Institute.

REFERENCES

[1] Yamada, H et al., *J Biomech*, 48(12):3267–3273, 2015.
[2] Muntner, P et al. *Circulation*, 135(10):E146–E603, 2017.
[3] Whelton, PK et al., *J Am Coll Cardiol*, S0735-1097(17)41519-1, 2017.
[4] Spadaccio, C et al., *J Cardiovasc Transl Res*, 9(4):334–342, 2016.
[5] Morris, L et al., *Eur J Vasc Endovasc Surg*, 51(1):44–55, 2016.
[6] Kim, SY et al., *Ann Thorac Surg*, 59:981–989, 1995.
[7] OBrien, T et al., *Med Eng Phys*, 30(1):109–115, 2008.
[8] Stergiopulos, N et al., *Am J Physiol*, 276(1 Pt 2), pp. H81-8.

SB³C2019
Summer Biomechanics, Bioengineering and Biotransport Conference
June 25 -28, Seven Springs, PA, USA

DEVELOPEMENT AND EVALUATION OF AN INTRATRACHEAL AEROSOL DELIVERY DEVICE FOR AVIAN WILDLIFE CONSERVATION EFFORTS

Carlos Abraham Ruvalcaba (1), Susana Ramirez-Perez (1), Stephanie Ortega (1), Lisa Tell (2), Jean-Pierre Delplanque (1)

(1) Mechanical and Aerospace Engineering
University of California, Davis
Davis, CA, USA

(2) School of Veterinary Medicine
University of California, Davis
Davis, CA, USA

INTRODUCTION

The respiratory system's structural complexity makes it difficult to deliver medication to specific locations. Engineers, computational scientists, experimental biologists, and clinicians have been working together to produce devices for precise drug delivery. One such scenario where medication must be delivered to a complex respiratory tract is for the treatment of aspergillosis in avian patients. When brought into captivity or where environmental conditions are suitable, birds are susceptible to fungal infections, specifically with *Aspergillus* spp. This disease can be fatal for the host, as it manifests and grows in several parts of the respiratory system, including the sinus cavities, trachea, and pulmonary parenchyma and air sac membranes [1]. Direct inhalation of the anti-fungal medication amphotericin B has been used as a treatment protocol with limited success [2]. A precise delivery of medication to the lung and air sac membranes of birds is still an open research area.

Additionally, several key device development considerations pose challenges to drug delivery devices. Whole body exposure to aerosolized medication can be toxic, expensive and inefficiency uses of large quantities of drug. In the case of avian patients, patient training to use drug delivery devices is challenging and repeatable treatments in the wild pose greater challenges for dosing accurately. For intratracheal devices, smaller lung geometries also complicate the aerosol flow physics as trachea diameters decrease in size with smaller birds. Liquid versus dry aerosol delivery devices contribute to device complexity and effect aerosol efficacy. Therefore, development of a device for repeatable and efficient drug delivery must make suitable design decisions to address challenges relevant to the species under consideration.

This study presents a new dry aerosol (DA) device to deliver dry amphotericin B in powder form to the lung of an experimental avian species (mallard duck) in order to develop a method for prophylactically treating birds while they are in captivity during oiled-wildlife rehabilitation efforts. The goal was to reduce the asymmetric delivery of medication to the lung, as the liquid spray (LS) device (Penn Century MicroSprayer® Aerosolizer) was found deliver medication unevenly, with medication only reaching one lung lobe [3]. The advantage of using the DA device stems from the ability to prolong the shelf life of the amphotericin B, since it never goes into solution. The new DA device is compared to the previously used LS device. The DA device is evaluated for its left/right (L/R) distribution, drug delivery efficiency, and overall device efficiency.

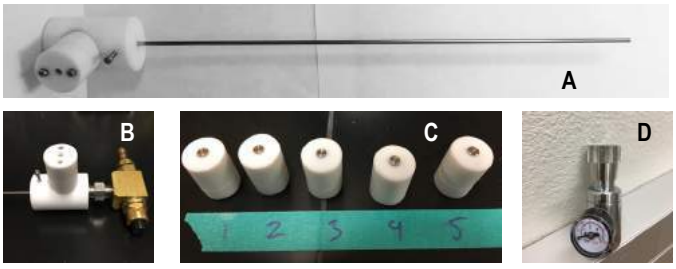

Figure 1: Dry Aerosol Device: (A) Whole device view; (B) Flow control valve; (C) Amphotericin B powder storage capsules; (D) Pressure regulator

METHODS

The DA device was manufactured using traditional subtractive machining, and it is composed the following components: a) interchangeable needle shaft, b) storage capsules for dry powder formulation of amphotericin B, c) device body, d) pressure regulator, e) flow control valve, and f) external air source. Both the device body and the storage capsules are made from Polytetrafluoroethylene (PFTE), and

the device shaft is made of stainless steel. The device body served as the housing for all components and allows for regulated pressure control, with manual valve control for drug insufflation (Figure 1). Each storage capsule is loaded before use allowing for storage ahead of experimental use.

In order to assess device performance metrics, several experimental procedures were conducted to evaluate the differences between the LS device with the DA device. First, a manufactured 3D printed trachea model was tested. Second, explanted chicken tracheas from above the glottis to below the first bifurcation were tested with attached collection reservoirs mimicking the downstream lung physiology. In both cases the shaft of the dry aerosol device was introduced into the tracheal lumen until resistance was met at the bifurcation, then retracted between 2cm-10cm distance. The DA device was loaded with 120 mg dry weight of surrogate powder (sucrose) to emulate the clinically used amphotericin B. The drug delivered efficiency is defined as the percent of total drug found in collection reservoirs from the total drug loaded into the device. The overall device efficiency is defined as percent of total drug minus drug lost to the environment from the total drug loaded into the device.

RESULTS

There was appreciable differences when using the 3D printed model of the trachea compared to the explanted trachea (Figure 2). When using the 3D printed model, the drug delivery efficiency was comparable for both LS and DA devices (73.4% ± 8.9% and 73.9 ± 2.8% respectively). However, when using the explanted trachea, the DA device had a lower drug delivery efficiency (46.4% ± 5.4%) since the tracheal wall is real tissue, and not idealized plastic material. It is important to note that the overall efficiency of the device was not possible to quantify using gross tissue weight due to evaporation of wet tracheal tissue.

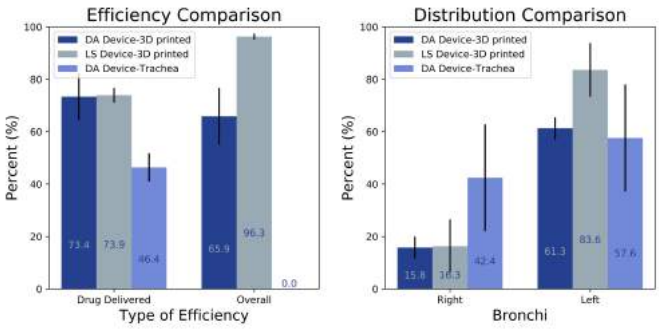

Figure 2: Efficiency (left) and distribution (right) comparisons between LS and DA devices.

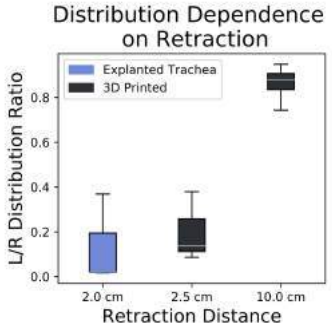

Figure 3: Effect of retraction distance on L/R distribution

The main goal of this study was to regain symmetric distribution by using the DA device in comparison to the LS device. Results show that when using either the DA or LS device with the 3D printed trachea, the L/R distribution remained asymmetric. For the LS device, left bronchi drug delivered was 15.8% ± 2.1% compared to 61.3 ± 2.1%. For the DA device, left bronchi drug delivered was 16.3% ± 5.1% compared to 83.6 ± 5.1%. Inspection of LS device aerosol generation through high-speed imaging showed two interesting findings: 1) the aerosol spray was initially a jet until breakup occurs, dictating the direction of the majority of the stream and, 2) once the aerosol was created, a large droplet aggregate was formed at the tracheal wall leading to dripping of the liquid instead of passive aerosol distribution. The DA device had a similar phenomena occur, but instead, due to the lack of aggregation at the wall, the asymmetry was reduced, but the drug delivery efficiency was also reduced (Figure 2). By increasing the retraction distance, the increase in L/R distribution went from 20.1% to 86.3%, where 100% is perfectly symmetric (Figure 3). In order to mitigate this phenomena for the DA device, the jet momentum must be reduced, and passively carried down the trachea towards the bifurcation.

DISCUSSION

Development of devices for precision delivery of medication for respiratory diseases requires expertise that spans multiple disciplines. In this study, development of a specific device for prophylactic treatment of oiled wildlife birds has shown the complexity of the underlying assumptions when developing and testing devices. By controlling only one specific parameter with a model of the 3D printed trachea proved to be not representative of the *in-vitro* or *in-vivo* usage. Moreover, the flow physics of aerosol generation, driving fluid, and ultimate deposition is an area where much work has left to be done and is currently being pursued by the authors.

Specific to free-ranging birds, current methodologies to treat birds infected with aspergillosis requires intravenous delivery of anti-fungal agents, some of which prove to have systemic toxicity risks. Our proposed method of utilizing dry powder to administer anti-fungal agents directly to the bird trachea lumen have several benefits including reducing systemic toxicity, longer shelf-life and stability of anti-fungal agents, and using water-insoluble drugs. Our focus was to recover symmetric delivery and by understanding the configuration of the device parameters, L/R lung distribution was increased.

ACKNOWLEDGEMENTS

The authors would like to thank the California Department of Fish and Wildlife's Oil Spill Response Trust Fund through the Oiled Wildlife Care Network at the Karen C. Drayer Wildlife Health Center, School of Veterinary Medicine, University of California, Davis for this grant support. Additionally, C.A.R. is funded through the National Center for Advancing Translational Sciences, National Institutes of Health, through grant number UL1 TR001860 and linked award TL1 TR001861. The content is solely the responsibility of the authors and does not necessarily represent the official views of the NIH.

REFERENCES

[1] Olsen, Glenn H. "Avian respiratory system disorders." Association of Avian Veterinarians Proceedings 1989 (1989): 433-435.

[2] Tell, Lisa A., et al. "Study of nebulization delivery of aerosolized fluorescent microspheres to the avian respiratory tract." Avian diseases 56.2 (2012): 381-386.

[3] Phillips, Ashley, et al. "Amphotericin B concentrations in healthy mallard ducks (Anas platyrhynchos) following a single intratracheal dose of liposomal amphotericin B using an atomizer." Medical mycology 56.3 (2017): 322-331.

SB³C2019
Summer Biomechanics, Bioengineering and Biotransport Conference
June 25 -28, Seven Springs, PA, USA

SUPERHYDROPHOBICITY AND VORTEX GENERATORS POTENTIAL TO REDUCE THROMBOGENICITY AFTER PROSTHETIC VALVE IMPLANTATION

Hoda Hatoum (1), David Bark Jr. (2), Hamed Vahabi (2), Sanli Movafaghi (2), Brandon Moore (2), Marcio Forleo (2), Arun Kota (2), Ketul Popat (2), and Lakshmi Prasad Dasi (1)

(1) Department of Biomedical Engineering
The Ohio State University
Columbus, Ohio, USA

(2) Department of Mechanical Engineering
Colorado State University
Fort Collins, Colorado, USA

INTRODUCTION

While mechanical valve designs evolved to improve hemodynamic performance specifically bileaflet ones, blood damage remains a seemingly non-avoidable risk[1]. Blood damage includes platelet activation, thrombosis and hemolysis. Thromboembolism is considered the most common complication affecting 0.1-5.7% of patients after mechanical valve implantation[2]. Due to this, mechanical heart valves require lifelong antithrombotic therapies that may lead to hemorrhage[3]. Turbulent stresses are well established factors contributing to valve related hemolysis and platelet activation[4]. Therefore, minimizing turbulent stresses may help in minimizing the risk of blood damage. Aerospace applications utilize vortex generators (VGs) as a passive flow control technique that delays boundary layer separation[5]. Application of vortex generators on valve leaflets to minimize transvalvular pressure and turbulent stresses may seem effective in-vitro[1], however may also provide optimal geometry for clot formation in between the different slots.

Since the mid-1990s, the so-called "Lotus effect" has been adopted to develop a multitude of surfaces for superhydrophobicity, self-cleaning, low adhesion, and drag reduction in fluid flow, as well as antifouling[6]. Superhydrophobic surfaces are water repellent surfaces. They are characterized by low contact angle hysteresis (less than 10 degrees) along with a self-cleaning effect[6]. In other words, liquid droplets roll off the surface transporting impurities or waste products with them. The objective of this study is to test in-vitro the effect of superhydrophobic valve leaflets with vortex generators on hemodynamics and on the risk of thrombus formation and blood damage.

METHODS

Five different 23 mm bioleaflet mechanical heart valves (BMHV) were 3D printed and designed as follows (Figure 1a-1d): one BMHV was designed without VGs and considered the control case while the four others had different VG configurations mounted on the downstream side of the BMHV: (1) with 4 co-rotating equally distant VGs, (2) with counter-rotating 8 closely spaced VGs, (3) with counter-rotating 4 far spaced VGs, and (4) with counter-rotating 4 closely spaced VGs. VG heights were chosen to be 1 mm, length 2.8 mm, the spacing 5 mm and set at an angle of incidence of 23° based on Bradbury et al.3 Leaflets length is 20 mm. A commercially available superhydrophobic coating - the Ultra-Ever Dry (UltraTech International, Inc.,Jacksonville, FL) - was used in this study. The coating is formed of two layers a bottom coat and a top coat. Both layers were applied as spray to the flat (without vortex generators) 3D printed aortic valve leaflets. After drying the coating, droplets of blood were tested on the surface to check for beading (Figure 1e). Once the coating is proven effective, the valve was hemodynamically tested in a pulse duplicator left heart simulator flow loop under a cardiac output of 5 L/min, a heart rate of 1 beat per second and systolic to diastolic pressures of 120/80 mmHg. In addition, the 4 different configurations of vortex generators along with the one without leaflet generators prior to applying the superhydrophobic coating were hemodynamically tested as well. A 100 different consecutive cycles of pressure and flow data were recorded at a sampling frequency of 100 Hz. Particle image velocimetry was performed to visualize the flow field. Time-resolved PIV images were acquired with a resulting spatial and temporal resolutions of 0.035 mm/pixel and 1000 Hz respectively. Phase locked measurements were recorded for 4 phases of the cardiac cycle (acceleration, peak, deceleration and diastole) repetitively with 250 ensembles each with a spatial resolution of 0.0325 mm/pixel. Refraction was corrected using a calibration in DaVis particle image velocimetry software (DaVis 7.2, LaVision Germany). Principal Reynolds Shear Stresses (RSS) were evaluated.

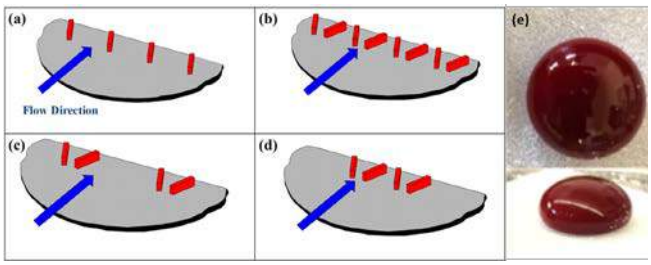

Figure 1: Schematic of the four types of vortex generators used in this study: (a) co-rotating, (b) 8 equally spaced counter-rotating VGs, (c) 4 far spaced counter-rotating VGs and (d) 4 closely spaced counter-rotating VGs; (e) whole blood on a bileaflet mechanical heart valve with a hierarchical coating

RESULTS

Figure 2 displays the Reynolds shear stress contours of the different valve cases at different time points throughout the cardiac cycle. Qualitatively during acceleration, when VGs are far spaced, the distribution of RSS looks different compared to all the other cases irrespective of the magnitude. During mid-systole, more dispersion due to turbulent advection is noted with the 4 far and closely spaced counter-rotating VGs along with the control case without any VG. Decay in RSS is observed in all the cases with increasing distance from the valve. Quantitatively, RSS magnitudes decreased significantly with VGs compared to the control case. At peak systole, RSS magnitudes calculated for the VG cases were also lower than those calculated without VGs. RSS was found to be 38.13 ± 0.89, 12.95 ± 0.32, 15.75 ± 0.71, 24.54 ± 0.84 and 16.33 ± 0.58 Pa for control, co-rotating VGs, 8 counter-rotating VGs, 4 far-spaced VGs and 4 closely-spaced VGs respectively. The co-rotating VGs yielded the lowest RSS magnitudes with statistically significant differences compared with all the other cases ($p < 0.001$).

Figure 3 displays the principal RSS for the control valve and the superhydrophobically coated valve. RSS were higher with the superhydrophobic leaflet valve reaching a maximum of 160±3.5 Pa at peak systole compared with 65±4.2 Pa without the coating.

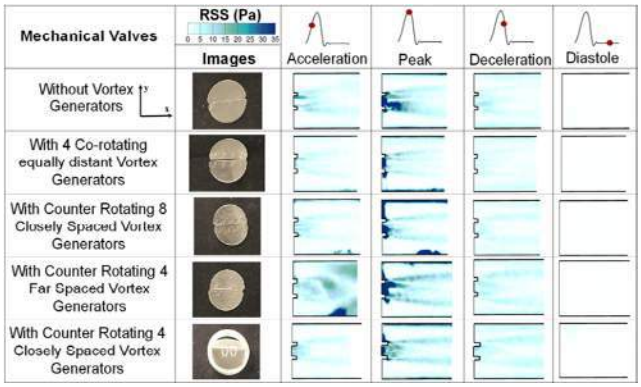

Figure 2: Principal Reynolds shear stresses at different phases in the cardiac cycle. Flow from left to right.

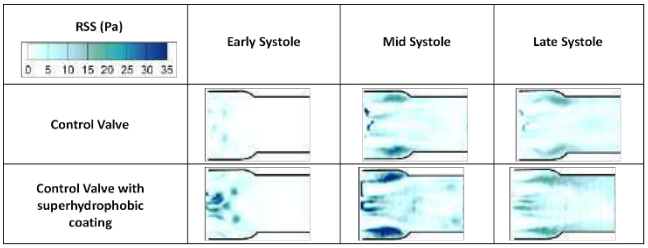

Figure 3: Principal Reynolds shear stresses at different phases in the cardiac cycle for the control valve and the superhydrophobic coated valve. Flow from right to left.

DISCUSSION

RSS is commonly used to predict blood damage, despite the fact it is a statistical measure and not an actual stress experienced by blood cells[7]. Counter-rotating VGs (owing to the geometry) may have enhanced turbulence compared to the co-rotating ones. This may be due to interaction of opposite signed axial vortices. While co-rotating VGs generated same sign axial vortices that helped streamline the flow and maintain a high velocity and a more gradual decay. Without any VGs, the early separation not only leads to stronger turbulence, but also to more energy dissipation.

Superhydrophobic coating leads to skin friction reduction in fluid flow[6]. The addition of the superhydrophobic coating leads to the introduction of "free slip" boundary condition instead of the "no slip" boundary condition. Therefore, for valve case, the tangential component of the velocity is unrestricted instead of being equal to zero. Surface slip is unlikely to improve energy loss performance as shown in the results with the increase of turbulence.

The results of this study indicate that applying the superhydrophobic coating alone on the valve surface may be enough from the low-adhesion standpoint however not sufficient to reduce turbulence. Ongoing studies combining vortex generators and superhydrophobic coatings are currently performed to maximize optimal hemodynamics occurrence.

ACKNOWLEDGEMENTS

The research done was supported by National Institutes of Health (NIH) under Award Number R01HL135505 and the American Heart Association (AHA) under Award Number 19POST34380804.

REFERENCES

[1] Hatoum, H., et al. (2018). *Annals of biomedical engineering*, 1-12.
[2] Murphy, DW., et al. *Journal of biomechanical engineering* 132.7 (2010): 071011.
[3] Cannegieter, SC., et al. *New England Journal of Medicine* 333.1 (1995): 11-17.
[4] Hatoum, H, et al. *The Journal of thoracic and cardiovascular surgery* 156.5 (2018): 1837-1848.
[5] Bradbury, L. J. S., et al. *Journal of Fluid Mechanics* 70.4 (1975): 801-813.
[6] Bhushan, B. *Springer*, 2016.
[7] Ge, L. et al. *Annals of Biomedical Engineering* 36.2 (2008): 276-297.

SB³C2019
Summer Biomechanics, Bioengineering and Biotransport Conference
June 25 -28, Seven Springs, PA, USA

A MULTISCALE MODEL FOR SIMULATING PLATELET AGGREGATION: CORRELATING WITH IN VITRO RESULTS

Peng Zhang (1), Prachi Gupta (2), Jawaad Sheriff (1), Changnian Han (2), Marvin J. Slepian (3), Yuefan Deng (2), Danny Bluestein (1)

(1) Department of Biomedical Engineering
Stony Brook University
Stony Brook, NY, United States

(2) Department of Applied Mathematics
Stony Brook University
Stony Brook, NY, United States

(3) Sarver Heart Center
University of Arizona
Tucson, A□, United States

INTRODUCTION

The coagulation cascade of blood may be initiated by flow-induced platelet activation and aggregation, which prompts clot formation in prosthetic cardiovascular devices and vascular disease processes. Upon activation, platelets undergo complex morphological changes. Activated platelets polymerize fibrinogen into a fibrin network that enmeshes red blood cells. Continuum methods fail to capture subcellular mechanisms such as filopodia formation during platelet activation, while utilizing molecular dynamics is computationally prohibitive. A multiscale approach offers a means to bridge the gap between macroscopic flow and the cellular scales.

We developed a multiscale model for simulating platelet activation and aggregation in viscous blood flows[1]. This model incorporates a Dissipative Particle Dynamics (DPD) model of viscous flow that interfaces with Coarse Grained Molecular Dynamics (CGMD) model of mechanobiology-based platelets[2], to simulate their activation via mechanotransduction pathways[3] and their aggregation by recruitment of flowing platelets by activated platelets deposited onto a blood vessel wall[4]. This model bridges the gap between macroscopic transport flow-induced platelet activation and aggregation scales and the ensuing molecular events, and is further validated through the use of several shear-based techniques that allow observation of platelet shape change and motion over a wide range of shear stresses and exposure durations[3].

METHODS

Our multiple spatiotemporal model employs a modified DPD to describe viscous blood flow in stenoses and microchannels[5], and CGMD to describe the intra-platelet constituents to study the mechanotransduction process[2]. Spatially, the DPD-CGMD is interfaced by imposing a hybrid force field[1]. In this spatial interface, the Lennard-Jones term helps maintain the cytoskeleton-confined shape and the incompressibility of platelets against the applied shear stress of circumfluent flow. The dissipative and random terms maintain the local flow thermodynamic and mechanical properties, and exchange momentum to express interactions between the platelet and the flow. Temporally, an event-driven multiple time-stepping (MTS) scheme[6] is developed as an efficient numeric solver on top supercomputers[7].

The platelet membrane in our model includes 67,004 integrin αIIbβ3 receptors represented by particles and distributed uniformly on the membrane (Fig. 1). The aggregation force field between the receptor particles of different platelets is modeled as:

$$\boldsymbol{F}_{ij} = D_0\left(e^{-2\alpha(r_{ij}-r_0)} - 2e^{-\alpha(r_{ij}-r_0)}\right)\boldsymbol{e}_{ij} + f^A(t_{ij})\left(1-\frac{r_{ij}}{d_c}\right)\boldsymbol{e}_{ij} \quad (1)$$

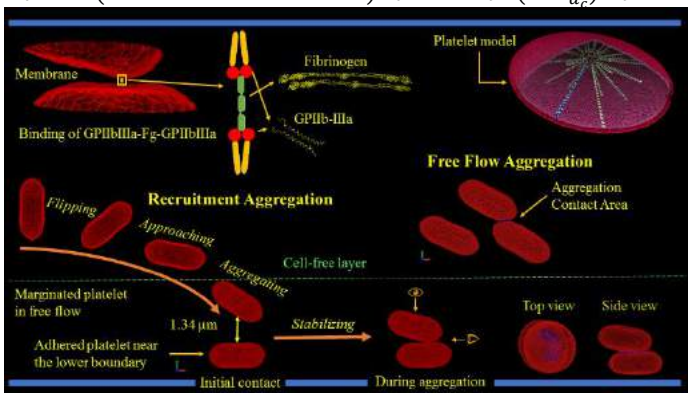

Figure 1: Aggregation of adjacent platelets in shear flows

This molecular-level hybrid force field combines the Morse potential and Hooke force to mimic the binding of αIIbβ3 and fibrinogen (Fg) during platelet aggregation. The simulation setup is in Fig. 1.

We validated our numerical method by correlating numerical simulations and model predictions with in vitro results. For aggregation experiments, purified platelets were prepared as previously described[3], diluted to 100,000/µl, mixed with isolated red blood cells at a hematocrit of 40%, and perfused through 100 µm× 1 mm microchannels (µ-Slide VI$^{0.1}$ Luer, ibidi USA, Inc., Madison, WI) pre-coated with 100 µg/ml von Willebrand factor using a syringe pump (Fig. 2a). This ensured that marginated platelets adhered to the walls of the channel. Then, isolated platelets were diluted to 150,000/µl, treated with 1.5 mg/ml Fg (Enzyme Research Laboratories, South Bend, IN), and perfused over the adhered platelets at shear stresses up to 10 dyne/cm^2 to initiate aggregation. Aggregation events were observed at 100× magnification under a DIC microscope (Ti-E, Nikon, Melville, NY) at 100-420 fps (Neo 5.5 sCMOS, Andor Technology Ltd., Belfast, UK). We measured the length of the bond and contact time between aggregating platelets. (Fig. 2b)

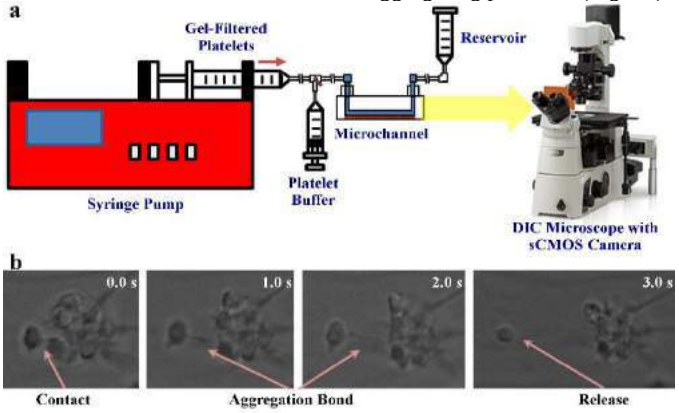

Figure 2: (a) Set-up for aggregation experiments. b) Sequential imaging of platelet aggregation/disaggregation under flow.

RESULTS

Our multiscale model describes the biophysical properties for platelets down to the *nm*-length and *ps*-time scale[2]. Membrane Young's modulus is 31.2 µN/m and shear modulus is 33±9 µN/m. The cytoplasm is modeled by modified Morse potential[8] and its viscosity is 4.1 mPa·s. Actin filament stiffness is 56.3±1.0 pN/nm.

Using this model, we simulated the dynamics of platelet aggregation by recruitment of unactivated platelets flowing in viscous shear flow by an activated platelet deposited onto a blood vessel wall[4], shown in Fig. 1. This simulated the platelet aggregation that is mediated by fibrinogen (Fg) via αIIbβ3 receptors. The binding of αIIbβ3 and Fg is accurately modeled at the molecular scale. This simulation studies a shear stress of 6.7 dyne/cm^2 and a shear rate of 619 s^{-1} with a flow viscosity of 1.07 mPa·s. During the simulation, our multiscale platelet model continuously changes its morphology in response to the dynamic flow stress while flowing and flipping. As platelets are approaching, the receptor αIIbβ3 and the Fg from a bridge (αIIbβ3-Fg-αIIbβ3) which initiates platelet aggregation. With the progress of platelet aggregation, contact area first increases rapidly then stabilizes with time, wherein bond formation becomes more prominent and few bonds are broken. Fig. 3 shows the consistent growth of aggregation contact area, which possesses significant increments as the platelet receptors engage in aggressive bond formation with fibrinogen. Finally, this process leads to an equilibrium phase and forms a stable aggregate. The evolution of contact area through this process demonstrates that aggregation begins with transient bond formation, but as adjustment of contact position concludes, bond formation stabilizes with time, and more permanent bonds are formed, finally leading to a stable aggregate.

In addition, we compared our aggregation model with deformable and rigid platelet models (Fig. 3). We found that a rigid platelet in aggregation led to a very significant underestimation of contact area by 89%, and detaching force by 91~93%. In the final equilibrium state, the deformable model is more stable than the rigid model under shear stress. Hence, rigid platelet aggregates are unstable and more likely to detach.

DISCUSSION

Our approach is the first multiscale numeric method for simulating the platelet activation and aggregation under flow that includes bonding and receptors on the platelet's membrane. Biophysical properties of a platelet are accurately described down to a *nm*-length and *ps*-time scale, and the viscous flow is described at a *µm*-length and *ns*-time scale. Platelets are allowed to continuously deform in response to flow stress. In platelet recruitment aggregation, the microscale properties of the receptor-ligand interactions were precisely modeled at molecular scales and correlated well with in vitro results, including contact area and detaching force. With this improvement, the aggregation model is able to illustrate the microphenomena that have otherwise been missing.

Ongoing experiments have employed this model to study aggregation of multiple platelets in shear flow. Fig. 1 shows a schema for depicting three platelets flowing, deforming and aggregating in free flow. Using numeric simulations, we can then quantify the effect of platelet deformability and flow conditions on platelet aggregation characteristics.

In ongoing studies, a platelet-mediated thrombus growth model under shear was developed. This thrombus model adapts the molecular-scale properties of our current recruitment aggregation model, thus predicting macro-scale properties using micro-scale principles. Such a model has the advantage of reflecting molecular level changes in receptor-ligand bond formation. We expect our model to be adopted by other fields, such as drug delivery, by considering the impact of mechanical events triggering biochemical responses.

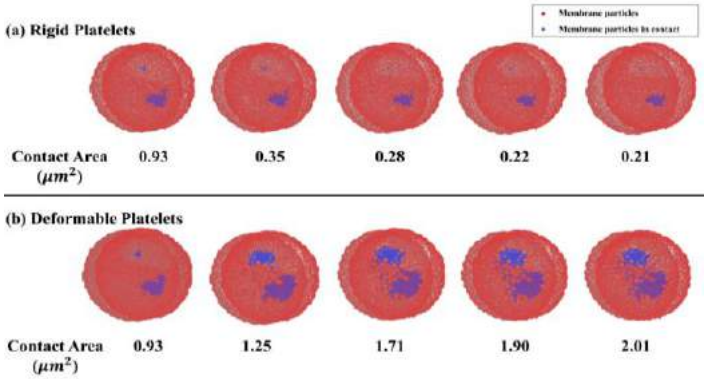

Figure 3: Comparison between aggregation contact area for rigid and deformable models

ACKNOWLEDGEMENTS

This study was made possible by grants from the National NIH U01 HL131052 (PI: D. Bluestein). The simulations in this study used the XSEDE award DMS150011 at SDSC Comet supercomputer (PI: P. Zhang) and LI-Red supercomputer, Stony Brook University.

REFERENCES

[1] Zhang, P et al., *Cell Mol Bioeng*, 7:552-574, 2014.
[2] Zhang, P et al., *J Biomech*, 50:26-33, 2017.
[3] Pothapragada, S et al., *Int J Numer Method Biomed Eng*, 31:1-16, 2015.
[4] Gupta, P et al., *Cell Mol Bioeng*, 2019. (under review)
[5] Gao, C et al., *J Comput Phys*, 335:812-827, 2017.
[6] Zhang, P et al., *J Comput Phys*, 284:668-686, 2015.
[7] Zhang, P et al., *Comput Phys Commun*, 204:132-140, 2015.
[8] Zhang, N et al., *J Comput Phys*, 257(A):726-736, 2014.

SB³C2019
Summer Biomechanics, Bioengineering and Biotransport Conference
June 25 -28, Seven Springs, PA, USA

3D FLEXIBLE NON-NEWTONIAN COMPUTATIONAL FRAMEWORK TO STUDY THROMBOSIS INITIATION

Sabrina R. Lynch (1), Christopher J. Arthurs (2), Zelu Xu (3), Onkar Sahni (3), Jose A. Diaz (4), C. Alberto Figueroa (1,2,4)

(1) Department of Biomedical Engineering
University of Michigan
Ann Abor, Michigan, USA

(2) Department of Biomedical Engineering
King's College London
London, UK

(3) Department of Mechanical, Aerospace and Nuclear Engineering
Rensselaer Polytechnic Institute
Troy, New York, USA

(4) Department of Surgery
University of Michigan
Ann Arbor, Michigan, USA

INTRODUCTION

Thrombosis is a process whereby a blood clot forms *in situ* within a vessel and impedes blood flow. The main three factors contributing to thrombosis can be summarized by Virchow's Triad (Fig. 1). Alone or in combination, hemodynamics, endothelial damage, and blood hypercoagulability all contribute to thrombus formation.

While blood viscosity is known to exhibit a nonlinear behavior, a Newtonian assumption is often employed in computational analyses. This assumption is valid in healthy arteries where shear rates are high and blood recirculation is low. However, in pathological geometries, such as aneurysms, the Newtonian assumption fails, and thus nonlinear viscous effects become exceedingly important. Previous computational models of thrombosis have investigated coagulation through chemistry based formulations focusing on protein dynamics [1-2] but have generally excluded complex 3D hemodynamics. In this work, we developed a computational framework to investigate the interplay between 3D hemodynamics and thrombosis initiation. The salient features of our computational framework are: i) the ability to solve hemodynamics in 3D image based patient-specific vascular models; ii) nonlinear viscous models of blood flow; and iii) a flexible computational framework for non-linear scalar models of protein dynamics that can be easily customized to include an arbitrary number of species and protein interactions. Here, we apply this framework to a human aortic aneurysm model to illustrate non-Newtonian viscous effects and scalar modeling for thrombosis simulation.

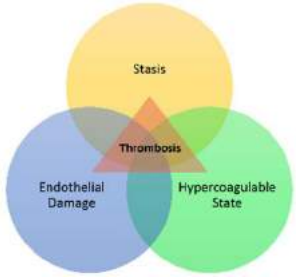

Figure 1: Virchow's Triad

METHODS

A patient-specific thoracic aortic aneurysm geometric model was built from computed tomography angiography image data using the validated software package CRIMSON (www.crimson.software). Blood was modeled as both Newtonian and non-Newtonian fluids with a density of 1060 kg/m^3. Vessel walls were modeled as rigid. A volumetric flow waveform derived from echocardiography data was imposed at the inflow face of the model. Three-element Windkessel models were used to represent the behavior of the distal vascular beds for each outflow face. Numerical values of the Windkessel parameters were tuned to match clinical measurements from duplex Doppler ultrasonography and cardiac catheterization. Mesh independence analysis was completed and a final mesh of ~23 million elements was used for the non-Newtonian analysis (Fig. 2).

Two non-Newtonian constitutive models, Power Law and Carreau-Yasuda (CY), were implemented within CRIMSON and validated against analytical solutions. The CY model, described in Eq. 1, was chosen for all patient-specific studies due to its ability to approximate viscous behavior of blood at low shear rates.

$$\mu(\gamma) = \mu_\infty + (\mu_0 - \mu_\infty)(1 + (\lambda\gamma)^a)^{\frac{n-1}{a}} \quad (1)$$

where μ is blood viscosity, γ is the shear rate and μ_∞, μ_0, λ, n, and a are material parameters. Here, we used μ_∞= 0.0035 Pa, μ_0 = 0.16 Pa s, λ = 8.2s, n = 0.2128, and a = 0.64 kg/m^3 [3].

To model thrombus formation, a staggered finite element approach for solving the reaction-advection-diffusion (RAD) equations was implemented, see Eq. 2. Here, c refers to scalar concentrations, D to diffusivity, R to reaction terms, and $\boldsymbol{u}$ to blood velocity. The reaction terms used can be found in Eqs. 3-6 where k values represent different reaction rates.

$$\frac{\partial c_i}{\partial t} + \nabla \cdot (-D_i \nabla c_i) = R_i - \boldsymbol{u} \cdot \nabla c_i \quad (2)$$

$$\frac{d[IIa]}{dt} = -k_{in}[IIa] + \left(k_{surf} + k_{II}^{AP} \cdot [AP]\right) \cdot [II] \quad (3)$$

$$\frac{d[II]}{dt} = -\left(k_{surf} + k_{II}^{AP} \cdot [AP]\right) \cdot [II] \quad (4)$$

$$\frac{d[AP]}{dt} = k_{AP}^{AP} \cdot [AP] \cdot [RP] + k_{AP}^{IIa} \cdot [RP] \quad (5)$$

$$\frac{d[RP]}{dt} = -k_{AP}^{AP} \cdot [AP] \cdot [RP] - k_{AP}^{IIa} \cdot [RP] \quad (6)$$

These reaction terms represent a previously described 4 scalar reaction model for thrombus formation that has been shown to match patient-specific data [4] and describes thrombin generation via four key players: thrombin (IIa), prothrombin (II), activated platelets (AP), and resting platelets (RP). This RAD was implemented within our non-Newtonian fluid description to develop a framework for investigating thrombus formation in pathological scenarios. RAD simulations were run using the same fluid boundary and initial conditions and the CY model of non-Newtonian viscosity, as described above. A zero Dirichlet boundary condition was applied on the walls for all four scalars, different Dirichlet inflow boundary conditions were applied for each scalar, along with zero Neumann outflow boundary conditions. Initial conditions were chosen to be the same value as the inflow conditions for each scalar.

RESULTS

Fig. 2 shows the impact of viscosity in an aortic aneurysm model. Simulations were run until pressure periodicity was reached, using a Newtonian (left) and CY non-Newtonian assumption (right) (Fig. 2D). Newtonian viscosity was chosen to match the μ_∞ value so that at high shear rates both models produce the same value of viscosity. To investigate the transient effects of non-Newtonian viscosity, three time points in the cardiac cycle are shown: diastole, systole, and transitional (Fig. 2E). The models produced different in-plane flow patterns (Fig. 2B), the Newtonian model showing higher near-wall velocities and gradients compared to the CY model. Lastly, wall shear stress (WSS) was observed to differ both qualitatively and quantitatively between the models (Fig. 2C).

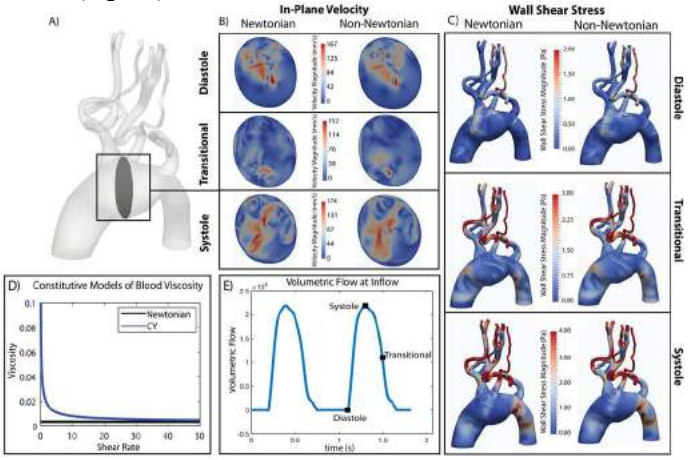

Figure 2: Newtonian and CY results in an aortic aneurysm. A) 2D cross section for velocity contours; B) In-plane velocity for Newtonian and CY viscosity; C) WSS magnitude for Newtonian and CY viscosity; D) Constitutive models for viscosity; E) Definitions of diastole, transitional, and systole.

Fig. 3 shows results from our RAD finite element system. Fig. 3A, D shows a representative 2D cross section of the aortic aneurysm for two given time points along with the velocity profiles. Prothrombin degradation (Fig. 3 B, E) and thrombin generation (Fig. 3C, F) are shown. Thrombin is formed through interaction with prothrombin and activated platelets and propagated through the domain.

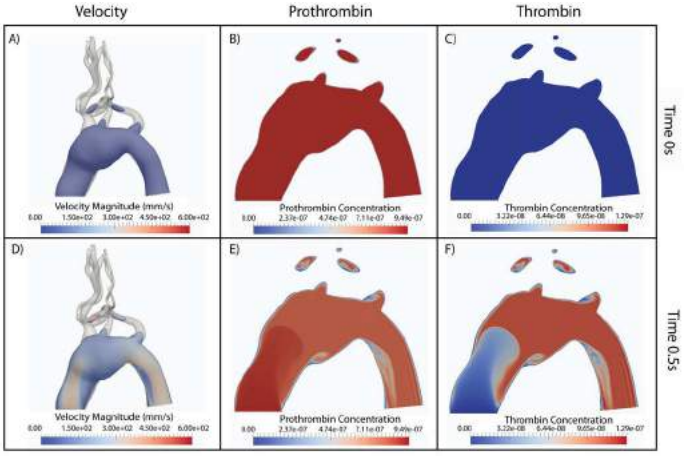

Figure 3: Scalar model of thrombin formation in a patient-specific aortic aneurysm. Velocity field, prothrombin concentration, and thrombin concentration at time t=0s A-C), and t=0.5s D-F), respectively.

DISCUSSION

We have successfully developed a computational framework for investigating nonlinear RAD phenomena involving non-Newtonian hemodynamics in imaged-based cardiovascular models. The combination of these two will for the first time enable the study of thrombus initiation using both a complex description of hemodynamics and biochemistry. We have applied this framework to investigate a patient-specific model of an aortic aneurysm. Results show the successful implementation of the RAD equations with nonlinear reaction terms involving 4 scalars. We were able to solve these equations in conjunction with the Navier-Stokes using one-way coupling between the fluid and scalar problems.

Future investigations will expand the staggered finite element strategy for RAD to include an arbitrary number of scalars using a python interface. This will allow for increased flexibility and user-friendliness enabling users to implement reaction networks on the fly. Our framework will allow for the modeling of thrombosis initiation in complex image-based geometries, using a variety of non-Newtonian descriptions of the fluid. Ultimately, this approach will provide insight into the complex interplay of various blood constituents and potentially reveal new physics of thrombus initiation. Future work will also employ animal models to capture parameters of *in vivo* venous thrombosis to better inform our computational model.

ACKNOWLEDGEMENTS

This work was supported by the NSF GRFP and the American Heart Association Predoctoral Fellowship (18PRE33960252).

REFERENCES

[1] Hockin M.F. et al., *J Biol Chem*, 277(21):18322-18333, 2002.
[2] Bungay S.D. *Math Med Biol*, 20(1):105-129.. 2003.
[3] Biasetti J. et al., *Front. Physiol.*, 3:1–16, 2012.
[4] Papadopoulos K.P. et al., *Med Eng Phys*, 36(2):196-204., 2014.

SB³C2019
Summer Biomechanics, Bioengineering and Biotransport Conference
June 25 -28, Seven Springs, PA, USA

REFINING A NUMERICAL MODEL FOR DEVICE-INDUCED THROMBOSIS

L. Yang (1), S. Deutsch (1), K. Manning (1,2)

(1) Department of Biomedical Engineering
The Pennsylvania State University
University Park, PA, USA

(2) Department of Surgery
Penn State Hershey Medical Center
Hershey, PA, USA

INTRODUCTION

Thrombosis is a common complication resulting from implantation of cardiovascular devices. Computational simulation is a powerful tool to provide predictions on thrombus growth in a given geometry and can be used to evaluate the risk of medical devices after implantation. To accurately predict thrombus growth, simulation in a three-dimensional (3D) geometry is necessary.

Taylor *et al.* developed a thrombosis model that simulates thrombus deposition and growth in a two-dimensional domain, with spatial and time scales relevant to medical devices [1,2]. The model assumes that platelet activation, which depends on wall shear stress, availability of adenosine diphosphate (ADP) and concentration of surface adherent platelets, predominantly contributes to thrombus growth, while the fluid velocity field is affected by the thrombus and coupled to the simulation [1,2]. However, the rate of chemical platelet activation by ADP was assumed to increase linearly with the ADP concentrations once enough ADP accumulated [1,2], which does not match the experimental observations, where the activation is temporary [3,4]. In addition, the thrombus breakdown mechanism, though included in the model, was not activated [1,2]. To describe the device-induced thrombosis procedure more accurately, the current study proposes to modify the existing computational thrombosis model.

Applying the modified thrombosis model, a 3D simulation of thrombus growth was performed to provide a prediction in a time scale relevant to medical devices. The goal is to develop a macroscopic computational thrombosis model that can accurately predict thrombus deposition and growth in a 3D geometry.

METHODS

The velocity ($\boldsymbol{u}$) and pressure (p) fields of laminar fluid flow were solved via the continuity (Eq. 1) and Navier-Stokes equations.

$$\nabla \cdot \boldsymbol{u} = 0 \tag{1}$$

To simulate thrombosis, the Navier-Stokes equation was modified into Eq. 2:

$$\frac{\partial \boldsymbol{u}}{\partial t} + (\boldsymbol{u} \cdot \nabla)\, \boldsymbol{u} = -\frac{1}{\rho}\nabla p + \upsilon\, \nabla^2 \boldsymbol{u} - \upsilon\, F(\varepsilon)\, \boldsymbol{u} \tag{2}$$

where a Brinkman term ($\upsilon\, F(\varepsilon)\, \boldsymbol{u}$) was used to couple the velocity field with thrombus growth and F was a function of the platelet aggregation intensity (ε), whose concentration depends on the following species: activated platelets, non-activated platelets, surface adherent platelets, and ADP. These species were calculated in bulk concentrations to match the scale of the system geometry, through a set of convection-diffusion-reaction equations (Eq. 3):

$$\frac{\partial \mathrm{Q}}{\partial t} + (\mathbf{u} \cdot \nabla)\, \mathrm{Q} = \mathrm{D}\, \nabla^2 \mathrm{Q} + \mathrm{R} \tag{3}$$

where Q is a scalar, D is the diffusion coefficient, and R is a source or sink.

The modified computational model was applied to simulate thrombosis in a backward facing step (BFS), an asymmetric expansion. Prior to simulations, a 3D mesh of the geometry was constructed by SolidWorks (Waltham, MA, USA), with dimensions shown in Figure 1. At the inlet, blood flow was set to be Newtonian, fully developed, steady, and laminar, with a Reynolds number of 490.

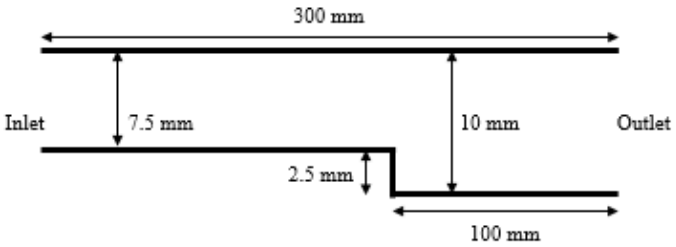

Figure 1: Dimensions of the backward facing step model used for computational studies. Heights of the channel and size of the step match those of the device used in Taylor *et al*. (2014) [5].

The computational thrombosis model was applied using OpenFoam (OpenCFD, Ltd, 543 Bracknell, UK) and thrombus growth was simulated for 30 min. To validate the results, the simulated thrombus growth was compared with *in vitro* measurements obtained from magnetic resonance imaging (MRI). In those experiments, bovine blood was circulated through the BFS model, a thrombus grew within the separation region, and the thrombus size was measured at different time points based on analysis of the MRI scans [5].

RESULTS

The simulation results show that the thrombus is grown right at the step over time, which matches the MRI experimental observations [5]. The volume of the simulated thrombus over time is compared to the *in vitro* MRI data in Figure 2.

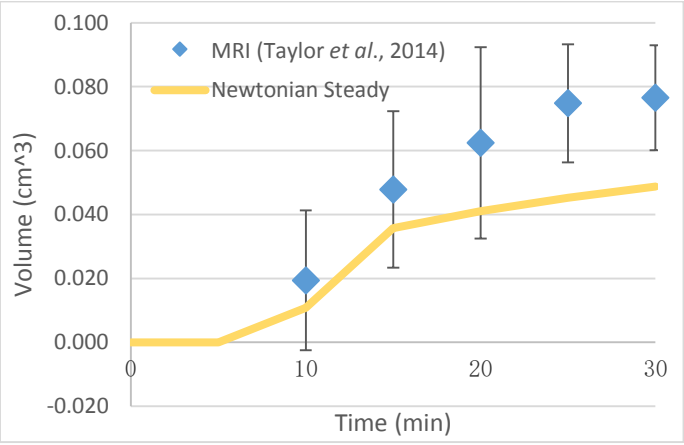

Figure 2: Volume of the simulated thrombus at an asymmetric expansion in comparison to *in vitro* MRI data [5].

The MRI data show that the thrombus volume increases quickly during the first 20 minutes and reaches a constant value after 25 minutes. On the other hand, the simulations predict that the thrombus volume will increase in a similar way and the resultant volumes match the MRI data well during the first 20 minutes of thrombus growth but are lower than the MRI data after that time point.

DISCUSSION

As shown in Figure 2, the rapid increase in thrombus volume at early time points implies rapid thrombus growth. Though the simulation results match the MRI data well during the first 20 minutes, the clot volume is under-predicted at later time points. A possible reason is that the current model only involves ADP as the major platelet activator and effects of the coagulation cascade are not considered. To improve the predictions on thrombus growth, future studies should involve clotting factors that are main contributors to platelet activation and the coagulation cascade, such as thrombin. As thrombin is converted from pro-thrombin and inhibited by anti-thrombin III, both the conversion and inhibition mechanisms should be included as well.

Comparing to the two-dimensional simulations, the three-dimensional simulations are more beneficial as they provide more useful information that is not available in two dimensions (e.g. increase in thrombus volume over time). The current thrombosis model provides prediction on thrombus deposition and growth that match the MRI experimental observations at early time points. However, since the model describes the thrombosis procedure using only four species to reduce the computational cost, the simulation results do not match the MRI data at later time points. The current computational model is limited to predictions for short-term thrombus deposition and growth (i.e. within 20 min). To provide accurate predictions for long-term device-induced thrombosis (i.e. from 20 min to hours), the current model requires modifications so that the thrombosis procedure can be described more accurately, such as including the effects of the coagulation cascade.

ACKNOWLEDGEMENTS

This work is supported, in part, by NIH Grant T32GM108563 and HL13636901.

REFERENCES

[1] Taylor, JO *et al.*, *Biomechanics and Modeling in Mechanobiology*, 15:1713-1731, 2016.
[2] Taylor, JO *et al.*, *J Biomechanics*, 50:114-120, 2017.
[3] Frojmovic, MM *et al.*, *Biophysical J*, 67:2060-2068, 1994.
[4] Chatterjee, MS *et al.*, *Nature Biotechnology*, 28:727-732, 2010.
[5] Taylor JO, *et al.*, *J Biomechanical Engineering*, 136:071012, 2014.

SB³C2019
Summer Biomechanics, Bioengineering and Biotransport Conference
June 25 -28, Seven Springs, PA, USA

Investigation of the interplay between blood and thrombus mechanical properties: A 3D fluid-solid interaction model

F.T. Huda (1), T. Abdel-Salam (1), N.E. Hudson (2), A. Vahdati (1)

(1) Department of Engineering
East Carolina University
Greenville, NC, USA

(2) Department of Physics
East Carolina University
Greenville, NC, USA

INTRODUCTION

Thrombosis is a life-threatening condition, where a blood clot forms within the vasculature and impedes the blood flow to a vital organ. Thrombi can also break apart or become dislodged, leading to life threating conditions such as myocardial infarction and pulmonary embolism. Moreover, thrombi or blood clot can form in blood-contacting medical devices and thwart device functionality. Thus, it's a critical need to understand the mechanical properties of thrombi under blood flow to both enhance clinical diagnoses and develop therapeutic treatments. Previous research has mainly focused on two-dimensional models (2D) of thrombi-blood interaction[1], and clot growth[2].
Fluid-solid interactions (FSI) can play a dramatic effect on the mechanical response of blood clots. The goal of our research was, therefore, to develop a 3D non-linear FSI model that couples clot mechanics with the blood flow to better understand the role of clot and blood mechanical properties on this complex interaction.

METHODS

A 3D model of the blood clot was generated using SolidWorks 2017 (Dassault Systems) and was meshed using Ansys 18.1. Geometric parameters of the murine blood vessel were based on a recent study[1]. We created a FSI model consisting of blood and thrombus using FEBio 2.8 [3]. We utilized a Neo-Hookean constitutive model for the thrombus and assigned a range of stiffness values to the clot. The non-linear stress-strain behavior of the compressible neo-Hookean model is derived from the following hyperelastic strain-energy density function:

$$W = \frac{\mu}{2}(I_1 - 3) - \mu \ln J + \frac{\lambda}{2}(\ln J)^2 \qquad (1)$$

Where I_1 is the first invariant of the right Cauchy-Green strain tensor, J is the determinant of the deformation gradient tensor, μ and λ are Lamé parameters. In our study, μ was assigned different values of 180 Pa, 108 Pa and 36 Pa. We used Preview 2.1 for pre-processing the model. Cyclic pressure boundary conditions were applied representing blood flow at the inlet. It is known that blood behaves like a Newtonian fluid under the high shear rate, while under the low shear rate, it behaves like non-Newtonian fluids[4]. We have considered both Newtonian and non-Newtonian flows for a range of blood clot properties in this study.

We used the Carreau-Yasuda model to represent the non-Newtonian behavior of blood. The dependency of the dynamic viscosity on the shear rate was modeled by the following equation:

$$\mu = \mu_\infty + (\mu_0 - \mu_\infty)((1 + (\lambda\dot{\gamma})^2)^{\frac{n-1}{a}} \qquad (2)$$

where $\dot{\gamma}, \mu, n$ are the engineering shear rate, viscosity, slope of the power law respectively, and a defines the shape of the transition region. The rheological properties of blood were taken from the literature[4].We used the post-processor software, PostView 2.3.2 to visualize our results.

RESULTS

Figure 1 depicts the total displacement state of the clot when inlet pressure is at maximum value for Newtonian versus non-Newtonian flow. The dome of the thrombus encounters the maximum displacement in both cases. Clot under Newtonian blood flow experience 38% higher displacement than the clot under non-Newtonian flow for the same clot stiffness. Figure 2 portrays the shear stress distribution inside the clot, and it can be noticed that shear stress value is higher in the region proximal to the inlet and in immediate vicinity of the vein wall. The clot

under Newtonian flow experienced noticeably higher shear stresses throughout its thickness. Figure 3 shows the maximum shear rate of the fluid at the timepoint corresponding to maximum pressure at the inlet. Newtonian blood model predicts a shear rate that is nearly twice as high as the outcome of the non-Newtonian model near the clot. Figure 4 represents total displacement distribution of the clots having different stiffness values under non-Newtonian flow. Decreasing the shear modulus from 180 Pa to 36 Pa in the Neo-Hookean model results in a 235% increase in maximum total displacement of the clot.

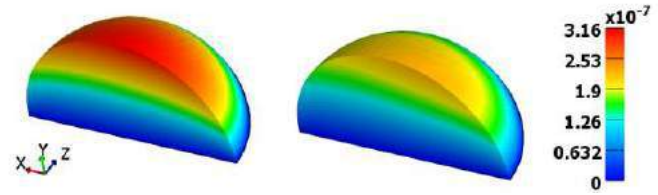

Figure 1: Total displacement distribution of the clot. Left: Newtonian, right: non-Newtonian (unit is in meter and shear modulus of the clot is 180 Pa).

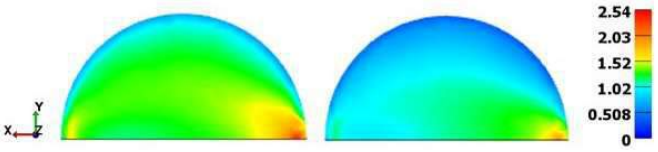

Figure 2: Shear Stress distribution inside the clot. Left: Newtonian, right: non-Newtonian (Fluid flows from negative X to positive X direction. Units are in Pa and shear modulus of the clot is 180 Pa).

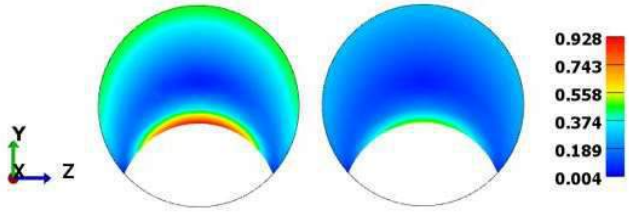

Figure 3: Illustration of maximum fluid shear rate over the clot. Left: Newtonian, right: non-Newtonian (Direction of fluid flow is perpendicular to the view. Units are in 1/s).

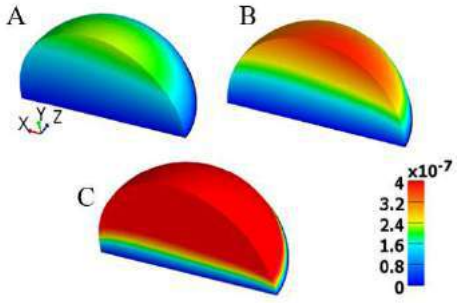

Figure 4: Total displacement distribution of the clot with different stiffness under non-Newtonian flow: (A) 180 Pa, (B) 108 Pa and (C) 36 Pa shear modulus. Units are in meters)

DISCUSSION

The goal of our study was to develop a 3D FSI model of blood-thrombus interaction to study the effect of Newtonian versus non-Newtonian fluid assumption combined with variations in thrombus stiffness. Since red blood cell density and deformability may change with age and different pathological states, including the non-Newtonian behavior of blood in the simulations can lead to more accurate predictions of shear rate particularly near the clot. On the other hand, our results showed that modeling blood as Newtonian can overpredict the shear rate and clot deformation (figures 1, 3). Additionally, blood clots can have different stiffness at different stages of development and different sites in the body. Our results show that the deformation state of the clot can change dramatically because of changes in its mechanical properties (figure 4). Including a deformable blood vessel in the model could further improve the predictive value of our modeling approach.

Furthermore, our study may have important implications for design of mechanical thrombectomy devices[5]. Since these devices directly interact with the clot, the stiffness of the clot and its deformation, strain and stress states could directly impact the removal of the clot by the device. Understanding the complex interaction of the clot with blood for different blood and clot properties can provide more insight into risk predictors for clot dislodgement and embolism. Our results also show that different regions of the clot experience very different states and magnitudes of stress (figure 2). This implies that as blood clots develop over time, different regions of the clot can exhibit region-specific mechanical properties to resist these very different states of stress. Thus, our results lay the groundwork for further computational and experimental investigations into the complex mechanical behavior and properties of developing blood clots.

REFERENCES

1. Xu S, Xu Z, Kim OV, Litvinov RI, Weisel JW, Alber M. Journal of the Royal Society Interface. 2017 Nov 1;14(136):20170441.
2. Yazdani A, Li H, Bersi MR, Achille P, Insley J, Humphrey JD, Karniadakis GE. Scientific reports. 2018 Feb 6;8(1):2515.
3. Maas SA, Ellis BJ, Ateshian GA, Weiss JA. Journal of biomechanical engineering. 2012 Jan 1;134(1):011005.
4. Boyd J, Buick JM, Green S. Physics of Fluids. 2007 Sep;19(9):093103
5. Smith WS. American Journal of Neuroradiology. 2006 Jun 1;27(6):1177-82.

SB³C2019
Summer Biomechanics, Bioengineering and Biotransport Conference
June 25 -28, Seven Springs, PA, USA

NUMERICAL MODELS OF VALVE-IN-VALVE DEPLOYMENT TO EVALUATE THE RISK OF LEAFLETS THROMBOSIS

Halit Yaakobovich (1), Dar Weiss (1,3), Uri Zaretsky (1), Shmuel Einav (1), Gil Marom (2)

(1) Department of Biomedical Engineering
Tel Aviv University
Tel Aviv, Israel

(2) School of Mechanical Engineering
Tel Aviv University
Tel Aviv, Israel

(3) Department of Biomedical engineering
Yale university
New Haven, CT, USA

INTRODUCTION

Valve-in-valve (ViV) placement is an emergent treatment option for degenerated bioprosthetic surgical aortic valves where a transcatheter aortic valve replacement (TAVR) is done inside a failed surgical valve [1]. Reduced leaflet motion as a result of hypoattenuated leaflet thickening (HALT) was recently diagnosed by high-resolution CT scans in bioprosthetic aortic valves in general [2], with highest occurrence after ViV placement [3, 4]. Subclinical leaflet thrombosis was suggested as the reason for the reduced leaflet motion because the phenomenon was resolved in patients receiving anticoagulants [5], medications that are not routinely given to bioprosthetic heart valve patients. Various causes for thrombosis formation have been suggested. One is the hemodynamic factors involved with low blood flow rate and regions of flow stagnation near the leaflets, due to valve confinement [6]. To date, several studies examined the hemodynamic cause of HALT post-ViV by experimental and numerical models. Experimental studies were limited to idealized geometry [7], or could not capture the region of interest in post-ViV procedure [8]. In numerical study, only complete or no confinements, where the TAVR valve is surrounded by surgical leaflets, were accounted for [9]. Our research aims to explore and compare deployments of the latest version of TAVR devices (Medtronic Evolut PRO, Edwards Sapien 3) inside a surgical bioprosthetic valve (Sorin Mitroflow) and to assess the partial confinement influence on the hemodynamics near the ViV's region.

METHODS

The dry modeling of the surgical and TAVR procedures were simulated by finite element analysis in Abaqus Explicit (Simulia, Dassault Systèmes). Three dimensional models of Mitroflow, Sapien 3, and Evolut PRO valves were generated (Figure 1). To model the surgical procedure, an available aortic root anatomy was deformed to the round shape of the surgical valve's suture ring. The Mitroflow valve was investigated because it is more susceptible to early degeneration than other surgical valves [10], while both Sapien 3 and Evolut PRO are the latest FDA-approved TAVR devices and are clinically being used for ViV placement in Mitroflow valves [11,12]. To simulate ViV procedure, TAVR valve deployments inside the surgical valve model were modeled as superelastic expansion and deployment by balloon inflation, for the Evolut and Sapien devices, respectively. The cuff and leaflets were displaced to the deployed stent configuration and the percentage of leaflets confinement was calculated. Post-procedural hemodynamics models were created from the finite elements models results. Computational fluid dynamics (CFD) simulations of the flow through the prosthetic valve with stationary leaflets in the systolic configuration were solved by ANSYS Fluent (ANSYS, Inc.). To validate each valve model, an in-vitro experimental setup was built. Hydrostatic pressure was applied on each valve experimentally and numerically, and their diastolic configurations were compared.

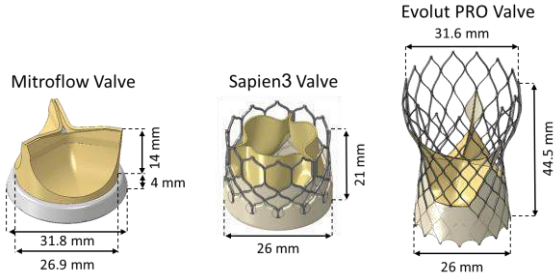

Figure 1: Geometries and dimensions of the bioprosthetic valve models

RESULTS

The mechanical stresses distribution in the surgical valve leaflets and the contact between the leaflets and the deployed stents in ViV configuration were examined. The Evolut stent positioning was not uniform in all direction and the stresses and contact distribution varied among the three leaflets of the surgical valve (Figure 2A). In the Sapien case, the stresses and the contact between the stent and the leaflets were similarly distributed in all the surgical valve leaflets (Figure 2B). The highest stress magnitudes were mainly located at the middle of the surgical leaflets and were higher with the Sapien compared to the Evolut.

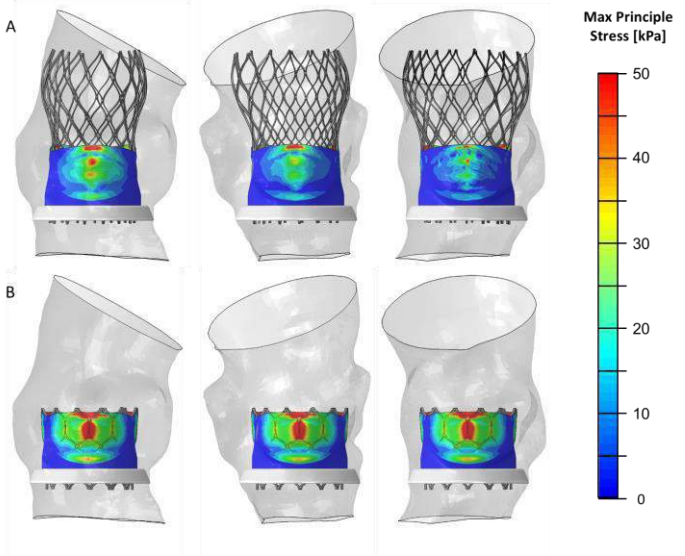

Figure 2: Mechanical stress distribution in the Mitroflow valve's leaflets for (A) Evolut PRO and (B) Sapien 3 deployments

Sapien leaflets were completely confined by the surgical valve leaflets (Figure 3) while the Evolut leaflets were partially confined, creating pockets (neo-sinuses) that cover only 60.3% of the leaflet height (Figure 3). The neo-sinuses in the Sapien case were deeper and narrower than in the Evolut. Preliminary CFD simulation of the systolic flow through the valves has shown a more stagnant flow near the TAVR leaflets in the Sapien valve compared to the Evolut (Figure 3).

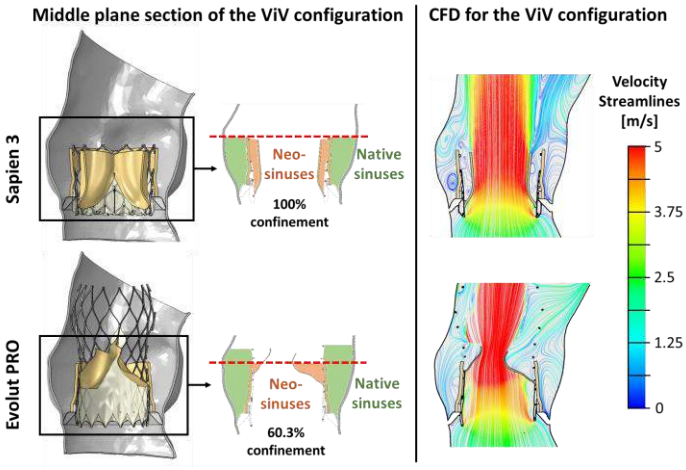

Figure 3: Deployed configurations of Sapien 3 and Evolut PRO inside a Mitroflow valve and the CFD results of the systolic hemodynamics

DISCUSSION

This study evaluated the post-procedural configuration of the latest TAVR devices inside a Sorin Mitroflow valve. Better anchoring of the deployed stent by the surgical valve leaflets was achieved in the Sapien stent compared to the Evolut stent. These differences between the stents can be explained by the balloon inflation deployment of the Sapien and the fact that its deployment is independent of the root anatomy, whereas the Evolut self-expandable stent positioning was influenced by the aortic root geometry. Complete confinement was found after intra-annular deployment (Sapian 3), while partial confinement was found after supra-annular deployment (Evolut PRO). The neo-sinuses, that created in the confined region between the leaflets of the TAVR and the surgical valve, are especially important because they are suspected as regions of flow stagnation that can lead to thrombus formation. Preliminary CFD result has shown stagnating local flow in the neo-sinuses, while the stagnant flow was more dominant in the Sapien ViV configuration compared to the Evolut. These findings can be explained by the ViV configuration for each valve as with the Sapien valve, deeper and narrower neo-sinuses were formed.

Since the lower part of the Evolut stent is wider compared to the middle, a more aortic deployment of the Evolut stent may results in better anchoring of the stent, as well as smaller neo-sinuses, and therefore can help reducing the risks for leaflets thrombosis. These results, of the first numerical simulation of ViV with Evolut or CoreValve, demonstrates the partial confinement that was ignored in previous HALT studies. In the next phase, these hemodynamic models will be solved by fluid structure interaction (FSI) analysis while the TAVR leaflets will be used as the compliant parts in the FSI simulations.

ACKNOWLEDGEMENTS

We thank Prof. Ariel Finkelstein from Sourasky medical center and Prof. Ehud Raanani from Sheba medical center for their assistance.

REFERENCES

[1] Landes, U. et al., *Structural Heart*, 1, (5-6), pp. 225-235, 2017.
[2] Makkar, R. et al., *NEJM*, 373, (21), pp. 2015-2024, 2015.
[3] Jose, J. et al., *JACC: Cardiovascular Interventions*, 10, (7), pp. 686-697, 2017.
[4] Mangione, F.M. et al., *JACC. Cardiovascular imaging*, 10, (1), pp. 82, 2017.
[5] Chakravarty, T. et al., *The Lancet*, 2017.
[6] Nakatani, S. et al., *Heart*, pp. heartjnl-2017-311818, (2017).
[7] Midha, P.A. et al., *Circulation*, pp. CIRCULATIONAHA. 117.029479, 2017.
[8] Hatoum, H. et al., *JTCVS*, 2017.
[9] Vahidkhah, K. et al., *J Biomech*, 58, pp. 114-122, 2017.
[10] Lootens, L. et al., *EACTS*, 52, (2), pp. 272-278, 2017.
[11] Adamo, M. et al., *EuroIntervention: journal of EuroPCR*, 13, (9), pp. e1032-e1039, 2017.
[12] Mosquera, Victor X., et al., *Journal of cardiac surgery*, 2018.

SB³C2019
Summer Biomechanics, Bioengineering and Biotransport Conference
June 25 -28, Seven Springs, PA, USA

ACCURATE DETECTION OF DIFFERENTIAL INTERACTION STRENGTHS IN ENERGY LANDSCAPES USING MACHINE LEARNING

Ahmad Haider (1, 2, 3), Alan Liu (1, 2), Todd Sulchek (1, 2)

(1) G.W. Woodruff School of Mechanical Engineering
Georgia Institute of Technology
Atlanta, GA, USA

(2) Wallace H. Coulter School of Biomedical Engineering
Georgia Institute of Technology
Atlanta, GA, USA

(3) AGCO Corporation
Atlanta, GA, USA

INTRODUCTION

Measurements of free energy landscapes are critical for understanding the basis of many physical, chemical and biological interactions. Boltzmann distribution based energy reconstruction methods, which are used to calculate free energies, are based on the assumption that all possible configurations of the system are sampled [1]. In practice, the limiting factor in accurate free energy reconstructions is the imperfect sampling of a potential field, particularly in the case of interactions with steep gradients and short reaction coordinates [2]. One of the approaches to overcome this limit is to differentially sample the potential landscape to increase sampling times at sharp sections of the landscape. This is possible if we can classify the landscape into regions of differential interaction strengths. The classification can then be used to dynamically vary the probe speed to match the interaction strength and thereby sufficiently sample the entire landscape. The probe would then spend greater time at regions of steep gradients as compared to shallow gradients thereby capturing all possible configurations for the entire system irrespective of potential gradients or length of reaction coordinates. In this paper, we show through cantilever dynamics simulations and application of machine learning algorithms that it is possible to classify an atomic force microscope (AFM) cantilever probe's Brownian excitations within an external force field into regions of differential strength and detect the transitions between these regions.

METHODS

Simulated deflection data was generated using numerical integration of the cantilever dynamics equation used to model the behavior of a fluctuating AFM cantilever probe (k=1000 pN/nm, f_0 =25 kHz, Q = 3) under the influence of an external energy field (6-3 chemical force field) as per equation (1) [3].

$$m.\ddot{z}(t+\Delta t) = F_n + F(\big(z(t)\big) + k.z(t) - b.\dot{z(t)} \quad (1)$$

Where $z(t)$ is the cantilever trajectory in Å, m, k and b are cantilever's mass, spring constant and quality respectively. $F_n = \sqrt{4k_B T b B}$ is thermal force with $T$and B as temperature and bandwidth respectively. The external force field $F(z(t))$ is modeled as per equation (2)

$$F\big(z(t)\big) = 100\left(\frac{0.1}{z}\right)^6 - 0.0006\left(\frac{0.1}{z}\right)^3 \quad (2)$$

The deflections were parsed into multiple small segments and 17 aggregate statistics were computed for each segment, representing features or characteristics of the segments. The computed deflection based features are maximum, minimum, mean, median, mode, skew, kurtosis, variance, standard deviation, fitted gradient, fitted intercept, absolute energy, entropy, number of peaks/valleys, distance between peaks/valleys, percent of observations above mean deflection and percent of observations below mean deflection. The features are then used to group the segments into n distinct clusters or classes using an unsupervised machine learning algorithm (KMEANS) [4]. The clusters can be of different sizes. Each segment's features are iteratively allotted to each cluster until a final configuration is reached in which the centroid of each resulting cluster is maximally distant from the other clusters in terms of Euclidian distances. Since the ideal number of clusters is not pre-determined, hence the above approach is repeated for a range of cluster counts ranging from 1 to 9.

The simulation generated 1 million deflection points which was divided into 1000-point equal size segments. Analysis was performed using Numpy, Pandas and Scikit-learn libraries with custom routines written in Python 3.

RESULTS

An optimal cluster count is determined by minimizing total sum of squared errors (SSE) or distortion for the data points against the cluster centroids. This is also called elbow analysis. The formula for distortion is shown in equation (3) below

$$distortion = \sum_{i=1}^{m} \sum_{j=1}^{n} \left(x_j^{(i)} - \mu_{c(i),j} \right)^2 \quad (3)$$

where x is feature vector of a given segment and μ is the centroid of a cluster. A sharp decrease in distortion across consecutive cluster counts indicates a sharp decrease in SSE which indicates that an optimum is reached. Figure 1 shows two optimal cluster counts corresponding to two (2) clusters and five (5) clusters respectively. Two clusters are not relevant for the analysis since they indicate only general trends, such as probe interaction can be broadly classified as far away from surface and in contact with surface. On the other hand, five clusters captures the complete probe behavior as it samples over the entire energy landscape including short reaction coordinates experienced when the probe instantaneously jumps to the surface. Hence, five clusters are chosen as the optimal configuration for the given interaction.

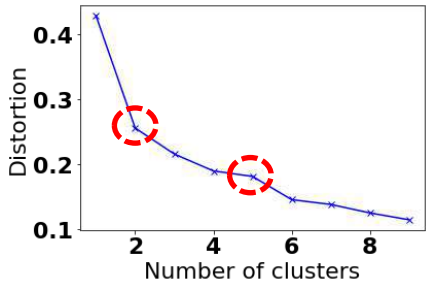

Figure 1: Choosing the optimal number of clusters based on minimization of distortion

The KMEANS model was trained by fitting the segment-based features dataset into five clusters. The fitted model was then used to classify each segment into one of the five clusters/classes. Figure 2 shows the raw deflection data (black) generated using the Brownian simulation with superimposed classes for each of the 1000 segments.

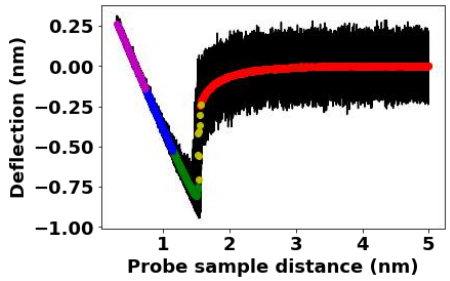

Figure 2: AFM force curve (black) overlaid with machine learning based predictions showing regions of varying interaction strengths

Each class is distinguished by a distinct color and represents a probe location and a corresponding interaction strength. The color coding is described in Table 1 below. As can be seen, interaction strength is strongly coupled to the class predicted by the algorithm. Regions far from the surface and contact have low interactions and are shown in red and purple color respectively. The approach and contact regions have medium interaction strengths and are depicted by yellow and blue regions respectively. Finally, the near contact (or snap in) region has the highest adhesive force and is shown in green color.

Table 1: Probe locations their corresponding interaction strengths as predicted by the machine learning algorithm

Probe Location	Interaction Strength	Color
Far from surface	Weak/None	Red
Approaching surface	Medium	Yellow
Near contact	Strong	Green
Contact	Medium	Blue
After contact	Weak/None	Purple

DISCUSSION

It has been shown that the predicted classes strongly correlate with the strength of interaction and can be used an excellent proxy for the interaction strength. A direct inference of this result is that the segment based features contain sufficient and significant information about the interaction and thus machine learning algorithms can successfully learn and predict differential strengths of the interaction including regions of transition across classes. This method, when integrated into the AFM deflection data collection process, can detect regions in potential landscapes with sharp gradients in real-time and therefore adjust probe speed to increase sampling counts in those regions. This leads to accurate Boltzmann distribution-based energy reconstructions for all subsequently collected datasets, limited only by the hardware of the AFM system in terms of implementing a feedback loop to control the probe speed and direction.

A great advantage of this approach is that we can use the flexibility of the machine learning approach to rapidly experiment with a variety of tunable parameters such as number of classes, segment sizes, types of features, bin widths, classification algorithm choice etc. to identify the best solution spaces to measure any given interaction, before setting up the experiment. This allows to get good reproducible experimental results with lesser expenditure of precious experimental resources, thereby increasing the generalizability of this machine learning based approach.

ACKNOWLEDGEMENTS

The author would like to acknowledge the contribution of PACE, a high performance computing environment at Georgia Institute of Technology, Atlanta for simulation of AFM cantilever probe fluctuations.

REFERENCES

[1] Haider, A. et al., *Proc. Natl. Acad. Sci. U.S.A.*, 113(50):14213-14218, 2016

[2] Haider, A. et al., *J. Phys. Chem. C*, 121(13), 7248-7258, 2017

[3] Ashby, P.D. et al., *J. Am. Chem. Soc.*, 126, 16973-16980, 2004

[4] Hastie, T et al., *Springer Series in Statistics, Springer, NY, USA*, 2001

SB³C2019
Summer Biomechanics, Bioengineering and Biotransport Conference
June 25 -28, Seven Springs, PA, USA

AEROSOLIZED SURFACTANT REPLACEMENT THERAPY IN AN IN VIVO RODENT LUNG INJURY MODEL

Franck J. Kamga Gninzeko (1), Michael S. Valentine (1), Sahil R. Chindal (1), Susan Boc (2), Sneha Dhapare (2), Michael Hindle (2), Dale Farkas (3), P. Worth Longest (3), Rebecca L. Heise (1)

(1) Biomedical Engineering
Virginia Commonwealth University
Richmond, Virginia, USA

(2) Pharmaceutics
Virginia Commonwealth University
Richmond, Virginia, USA

(3) Mechanical and Nuclear Engineering
Virginia Commonwealth University
Richmond, Virginia, USA

INTRODUCTION

Respiratory distress syndrome is a condition that affects all age groups including infants. Premature infants are more prone to this disorder, and in this case it is called neonate respiratory distress syndrome NRDS. To remedy NRDS, patients have to be sedated, intubated and mechanically ventilated while they receive instillation of liquid surfactant replacement therapy [1]. There are multiple surfactant replacement therapy drugs available, including Alveofact®, Curosurf® and Survanta® with Curosurf and Survanta proven to be the best treatments [2]. The most common method of delivery for these surfactant replacement drugs is via instillation of a liquid formulation [3]. However, delivery of surfactant as a dry powder aerosol has not been well explored, and its efficacy is poorly understood.

Using a micrometer-sized excipient enhanced growth (EEG) spray dried powder produced from the Survanta commercial product which is aerosolized using a novel dry powder inhaler (DPI), we can mitigate some of the problems that may arise when using the liquid form of Survanta. The liquid delivery of Survanta does not penetrate all the regions of the lungs and therefore some of the alveolar regions of the lung will not receive any surfactant and may collapse. By changing to an aerosol delivery method, the treatment may penetrate with high efficiency into the distal region of the lung. *We hypothesized that rats that receive EEG Survanta aerosol powder will have improved lung mechanics compared to the ones that received liquid Survanta.* We also did not anticipate any inflammation reaction due to the delivery of surfactant in a powder form.

METHODS

Dispersions containing Survanta, mannitol and leucine in a ratio of 45:33:22 % w/w in a 5%v/v ethanol in water mixture with a solids concentration of 0.125% w/v were spray dried using the Büchi Nano Spray Dryer B-90 HP (Büchi Labortechnik AG, Flawil, Switzerland). Spray drying parameters included an inlet temperature of 70 °C and a gas inlet flow of 120 L/min. Micrometer-sized EEG powders were collected into vials and stored at 2 to 4 °C. Sprague Dawley rats were purchased from Hilltop lab animal, Inc and were housed at Virginia Commonwealth University (VCU) vivarium. The studies performed were approved by VCU Institutional Animal Care and Use Committee and all procedures were performed according to their guidelines.

Rats were surfactant depleted with two warm phosphate buffer saline (PBS) lavages (10 ml/kg). We administered either liquid Survanta at 50 mg/kg using the standard of care instillation method via a 3ml syringe and or EEG Survanta surfactant powder (10 mg) aerosolized and delivered via a novel low actuation air volume dry powder inhaler (Figure 1). After the treatments, the rats were ventilated at 8 ml/kg for a total duration of 10 minutes on a Scireq rodent mechanical ventilator. Ventilation mechanics were measured before the surfactant depletion, after surfactant depletion, and 10 min following treatment. Bronchoalveolar lavage fluid was collected and centrifuged. Supernatant was saved for further analysis, and cytospin was obtained by resuspending and centrifuging the remaining cells onto microscope slides. The slides were then stained. To assess inflammatory response, differential blood cell counts were performed on the lavage.

The statistical analysis was performed via GraphPad Prism using an ANOVA test followed by pairwise comparisons as appropriate.

Fig. 1: Novel low actuation air volume dry powder inhaler used to aerosolize the EEG Survanta powder.

RESULTS

Airway compliance measured after 10 minutes of mechanical ventilation was normalized to the compliance before surfactant depletion and showed that there was a significant improvement with aerosol EEG Survanta compared to instilled liquid Survanta. We also saw a significant increase in normalized compliance of the aerosolized EEG Survanta compared to the normalized compliance after the depletion but before the treatment, however the normalized compliance of the instilled liquid Survanta was not significant from measurements taken after depletion (Figure 2.A). Though there was no significant difference between the normalized resistance of the liquid Survanta treatment compared to the EEG Survanta, the aerosolized powder treatment was closer to the healthy state and significantly different to the normalized resistance taken after the depletion than the liquid Survanta group (Figure 2.B). The normalized elastance also showed a significant decrease in aerosolized EEG Survanta compared to the liquid Survanta (Figure 2.C).

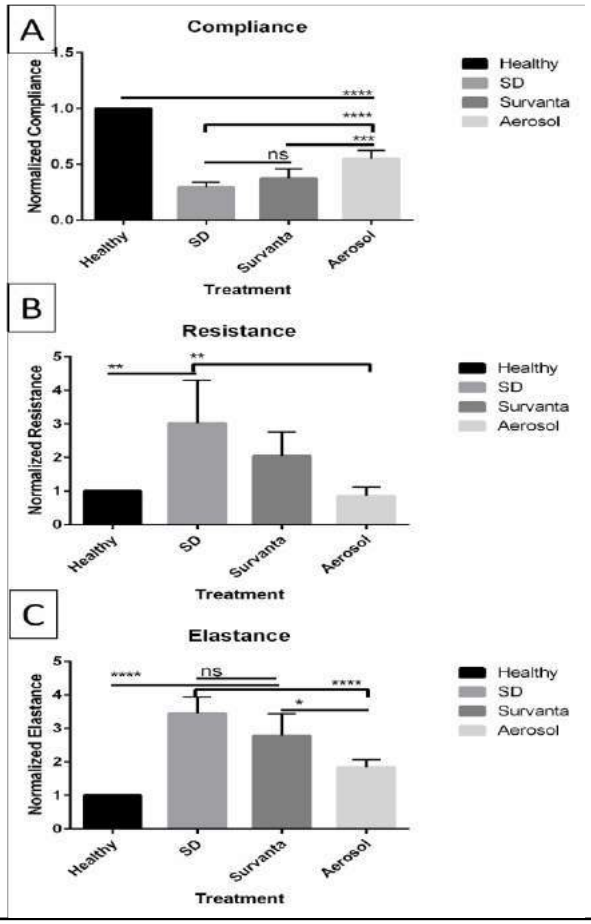

Fig. 2: Ventilation mechanics of healthy rats, after surfactant depletion (SD) and following Survanta instillation and aerosol delivery. * p-value < 0.05, **p-value<0.01, ***p-value<0.001, **** p-value<0.000, ns: non-significant. n=5 for treatments.

Since neutrophils are the first white blood cells to enter a given tissue during inflammation, and accumulation of neutrophils signifies an inflammatory reaction [4], we quantified the number of neutrophils relative to the total of white blood cells present in a 300 cells count. There was no statistical difference between percent neutrophils present following liquid instillation of Survanta compared to following aerosolization of the EEG Survanta powder (Figure 3). Further, the overall low percentage indicated that there was no acute inflammatory response to the Survanta in either form.

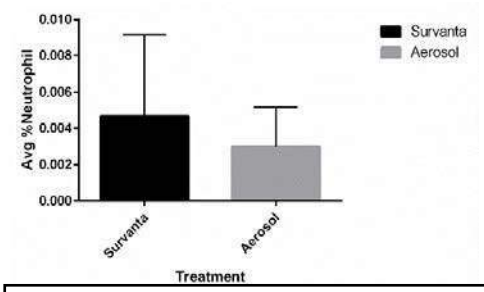

Fig. 3: % neutrophil obtained by number of neutrophils per 300 count of white blood cell count. n=5 per group No statistical differences were observed

DISCUSSION

Lung surfactant is critical to lung function and without it the alveoli will collapse resulting in respiratory distress. For a neonate, it is important to use a surfactant replacement therapy to remedy to NRDS. Current therapy utilizes the invasive instillation of liquid surfactants which although effective is distressing to both the patient and the physician. Alternative methods which are less invasive, such as aerosolized surfactant delivered to lungs should be considered. The results obtained in this study show significant compliance and elastance improvement following aerosol delivery of EEG Survanta compared to liquid instillation of Survanta, and the resistance shows the same trend though not significant. The results suggested that aerosolized spray dried powder Survanta may be more effective than the clinically used liquid Survanta administration for short-term lung mechanics improvements. It is likely that the aerosolized EEG Survanta penetrates and distributes more efficiently inside the lungs, however further studies are ongoing to confirm this. The cytospin data showed no statistical significance between the liquid Survanta and the powder form and a low neutrophil count, indicating that there were no signs of inflammation with either treatment.

In summary, an EEG Survanta powder delivered using a novel DPI is promising method of surfactant replacement therapy. Future studies need to be performed to optimize the delivery system of the EEG Survanta powder and to determine if the efficacy is dose dependent.

ACKNOWLEDGEMENTS

This work was funded by NIH 1R01HL139673-01

REFERENCES

[1] A. Saguil and M. V. Fargo, *Am. Fam. Physician*, vol. 85, no. 4, pp. 352–358, Feb. 2012.

[2] M. Mussavi, K. Mirnia, and K. Asadollahi, *Iran. J. Pediatr.*, vol. 26, no. 5, Jul. 2016.

[3] A. Moen, X.-Q. Yu, R. Almaas, T. Curstedt, and O. D. Saugstad, *Acta Paediatr.*, vol. 87, no. 3, pp. 297–303, 1998.

[4] B. Moldoveanu *et al.*, *J. Inflamm. Res.*, vol. 2, pp. 1–11, Dec. 2008.

SB^{3}C2019
Summer Biomechanics, Bioengineering and Biotransport Conference
June 25 -28, Seven Springs, PA, USA

NUMERICAL ANALYSIS OF DENSE SUSPENSION RHEOLOGY OF RED BLOOD CELLS IN A SHEAR FLOW

N. Takeishi (1), M. Rosti (2), Y. Imai (3), S. Wada (1), L. Brandt (2)

(1) Mechanical Science & Bioengineering
Osaka University
Toyonaka, Japan

(2) Mechanics
Royal Institute of Technology (KTH)
Stockholm, Sweden

(3) Mechanical Engineering
Kobe University
Kobe, Japan

INTRODUCTION

The blood viscosity is a basic biological parameter affecting the blood flow both in large arteries and in microcirculations, and hence it can be used for potential diagnoses of blood-related diseases. Since it is known that elevated blood viscosity is found in blood from patients with diabetes mellitus [1] and other hematologic disorders, a rheological description of the relative viscosity will allow us to precise diagnosis of patients with hematologic disorders. The relative viscosity of a suspension of particles has been modeled as a polynomial function of the volume fraction for suspension of rigid spherical particles [2, 3]. However, a polynomial law in dense suspensions of non-spherical deformable particles such as red blood cells (RBCs) is still missing due to complexity of the phenomenon. We thus numerically investigate the behavior of RBCs in shear flow, and quantify the bulk suspension rheology by the stresslet tensor [3]. Our numerical model has been successfully applied to the analysis of hydrodynamic interactions of blood cells in micro vessels [4-6] and cell adhesion [7]. By using the model, we investigate the effect of the shear rate, volume fraction of RBCs and viscosity ratio between the cytoplasm and plasma on the relative viscosity.

METHODS

We consider a cellular flow consisting of plasma and RBCs with radius a in a rectangular box of size $16a \times 10a \times 16a$ along the stream-wise x, wall-normal y, and span-wise z directions, with a resolution of 8 fluid lattices per radius of RBC. An RBC is modeled as a biconcave capsule, or a Newtonian fluid enclosed by a thin elastic membrane, with a major diameter 8 μm (= $2a$), and maximum thickness 2 μm (= $a/2$). The membrane follows the Skalak constitutive law [8]. The internal and external fluid is solved by the lattice-Boltzmann method (LBM). The load acting on the membrane is solved by the finite element method (FEM). The LBM and FEM are coupled by the immersed boundary method. The precise description of the numerical model and methods are referred to our recent work [9]. The shear flow is generated by moving top and bottom walls, and the problem is characterized by the Capillary number,

$$Ca = \mu_0 \dot{\gamma} a / G_s, \tag{1}$$

where G_s is the membrane surface shear elastic modulus, μ_0 is the plasma viscosity (= 1.2 mPa·s). For the analysis of the suspension rheology, we consider the contribution of the suspended particles to the bulk viscosity in terms of the particle stress tensor $\Sigma^{(p)}$ [6]:

$$\Sigma^{(p)} = \sum_i^N \boldsymbol{S}_i / V, \tag{2}$$

and

$$\boldsymbol{S}_i = \int \left[(\boldsymbol{xq} + \boldsymbol{qx})/2 - \mu_0 (1 - \lambda)(\boldsymbol{vn} + \boldsymbol{nv}) \right] dA_i, \tag{3}$$

where V is the volume of the domain and $\boldsymbol{S}_i$ is the stresslet of the i-th particle, $\boldsymbol{x}$ is the membrane position relative to the center of the RBC, $\boldsymbol{q}$ the load acting on the membrane, $\boldsymbol{n}$ the surface normal vector, λ (= μ_1/μ_0) the viscosity ratio between the cytoplasmic viscosity μ_1 and plasma viscosity μ_0, $\boldsymbol{v}$ the interfacial velocity of the membrane, and A_i the membrane surface area of the i-th RBC. Finally, the relative viscosity can be expressed by

$$\mu_{re} = 1 + \Sigma_{12}^{(p)} / (\mu_0 \dot{\gamma}). \tag{4}$$

RESULTS

Figure 1 shows the example of the numerical results of dense suspension ($\phi = 0.41$) for $Ca = 0.1$ and $\lambda = 5$, which can be assumed as the physiological relevant viscosity ratio. We calculated the relative viscosity μ_{re} in such dense suspension and compare with those reported in previous experimental works [10, 11], where μ_{re} of normal human RBC suspensions for $\lambda = 5$ and $\phi \geq 0.4$ was measured. Out

numerical results of μ_{re} obtained well agree with the experimental results (shear-thinning character) as shown in Fig.2(a). Therefore, our numerical model is able to capture the rheological character of the blood based on the cellular-scale dynamics.

Next, individual RBCs in semi-dilute (ϕ = 0.05) and dense suspensions are investigated, and examples of snapshots of the numerical results are shown in Fig.2(b), where, RBCs subjected to low Ca (= 0.05) in dilute suspension show tumbling or rolling motion, while most of them sifted to swinging motion in dense suspension ϕ (= 0.4). Figure 2(c) shows the numerical results of μ_{re} as a function of ϕ for λ = 5. μ_{re} for each Ca exponentially increases with ϕ, and tends to decrease as Ca increases. In recent our work [9], we showed that a simple polynomial approach cannot be applied to RBC suspensions; this issue cannot be solved by any higher-order expansions, since they necessarily involve particle-particle interactions and thus any higher-order coefficients would depend on the local flow and/or on the local microstructure. Rosti & Brandt (2018) have proposed that the effective volume fraction ϕ_e, which is a collective volume fraction for deformed particles, is able to describe μ_{re} of suspensions of deformable particles [12]. Here, we define ϕ_e with the semi-middle axis of the deformed RBC. The numerical results of μ_{re} successfully collapses on a single non-linear curve at least for $Ca \leq 0.2$. The single non-linear curves are fitted by a general exponential expression based on the Krieger-Dougherty formula [2]:

$$\mu_{re} = \left(1 - \alpha\phi_e\right)^{-\beta}, \qquad (6)$$

where, α = 0.5 and β = 2.2 for λ = 5. The single non-linear master curves for other different λ (= 0.1, 1 and 10) are also displayed in Fig.2(d).

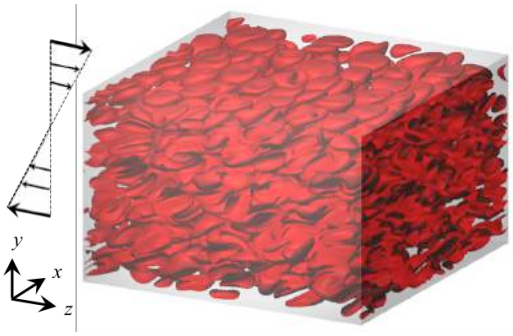

Figure 1: Snapshots of one of the numerical result for dense suspensions (ϕ = 0.41) at Ca = 0.1 and λ = 5.

DISCUSSION

Deformability of RBCs is dependent not only on cytoplasmic viscosity but also on the membrane shear elasticity, plasma protein and membrane viscosity. Although we ignore the membrane viscosity, the previous *in vitro* experiment showed that old RBCs have a higher viscosity without significant difference in membrane shear modulus [13]. Hence it would be interesting to study how the membrane viscosity changes the relative viscosity. In more recent numerical studies modeled sickle RBCs [14] or RBCs in diabetes mellitus [15], and estimated the patient-specific abnormal hemorheology. Those hematologic disorders impair the cell deformability resulting in high blood viscosity. If our proposed master curves especially at high λ (= 10) will be validated with future experimental studies, our numerical results may be able to provide precise diagnosis or drug efficacy for patients with those hematologic disorders.

In summary, the relative viscosity μ_{re} can be well described as a function of an effective volume fraction ϕ_e, defined by the volume of spheres of radius equal to the semi-middle axis of the deformed RBC. μ_{re} successfully collapses on a single non-linear curve as a function of ϕ_e at least for $Ca \leq 0.2$.

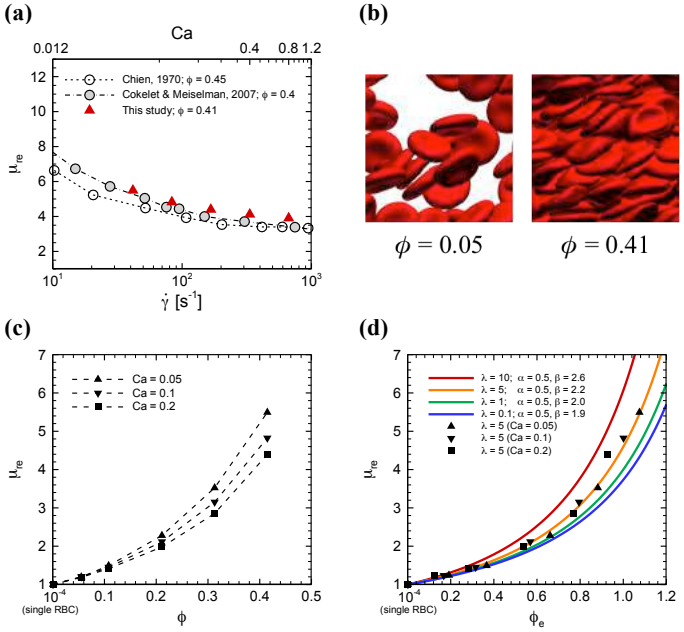

Figure 2: (a) Relative viscosity μ_{re} for ϕ = 0.41 as a function of the shear rate (or Ca). The experimental results of normal human RBC suspension [10, 11] are also displayed. (b) Snapshots of individual RBCs subjected to low Ca = 0.05 in dilute or dense suspension. (c) μ_{re} as a function of ϕ for different Ca. Those results (a-c) are obtained with λ = 5. (d) μ_{re} as a function of the effective volume fraction ϕ_e. The master curves in each λ are also displayed.

ACKNOWLEDGEMENTS

This research was supported by JSPS KAKENHI Grant Numbers JP17K13015, JP18H04100, and by the Keihanshin Consortium for Fostering the Next Generation of Global Leaders in Research (K-CONNEX), established by Human Resource Development Program for Science and Technology.

REFERENCES

[1] Skovborg, F et al., *Lancet*, 287:129-131, 1966.
[2] Krieger, I. M. & Dougherty, T. J. *Trans Soc Rheol*, 3:137-152, 1959.
[3] Batchelor, G. K. *J Fluid Mech*, 41:545-570, 1970.
[4] Takeishi, N et al., *Physiol Rep*, 2:e12037, 2014.
[5] Takeishi, N et al., *Phys Rev E*, 92:063011, 2015.
[6] Takeishi, N & Imai, Y. *Sci Rep*, 7, 2017.
[7] Takeishi, N et al., *Am J Physiol Heart & Circ Physiol*, 311:H395-H403, 2016.
[8] Skalak, R et al., *Biophys J*, 13:245-264, 1973.
[9] Takeishi, N et al., *submitted*, https://arxiv.org/abs/1811.02286.
[10] Chien, S. *Science*, 168:977-979, 1970.
[11] Cokelet, G. R. & Meiselman, H. J, *IOS Press*, 45-71, 2007.
[12] Rost, M. E & Brandt, L, J *Non-Newtonian Fluid Mech*, 262C:3-11, 2018.
[13] Nash, G. B. & Meiselman, H. J, *Biophys J*, 43:63-73, 1983.
[14] Li, X et al., *Interface Focus*, 6:20150065.
[15] Chang, H-Y et al., *Biophys J*, 113:481-490, 2017.

SB³C2019
Summer Biomechanics, Bioengineering and Biotransport Conference
June 25 -28, Seven Springs, PA, USA

DEEP LEARNING ASSISTED LABEL-FREE ON-CHIP SELECTIVE EXTRACTION OF SINGLE-CELL-LADEN DROPLETS FROM OIL INTO AQUOUS SOLUTION WITH DIELECTROPHORESIS

Alisa M. White (1), Yuntian Zhang (1,2), Gang Zhao (2), Xiaoming He (1,3,4)

(1) Fischell Department of Bioengineering
University of Maryland
College Park, Maryland, United States

(2) Department of Electronic Science and Technology
University of Science and Technology of China
Hefei, Anhui, China

(3) Robert E. Fischell Institute for Biomedical Devices
University of Maryland
College Park, Maryland, United States

(4) Marlene and Stewart Greenbaum
Comprehensive Cancer Center
University of Maryland
Baltimore, Maryland, United States

INTRODUCTION

Microencapsulation of single cells has emerged as a powerful tool for accurate diagnosis and more effective disease treatment strategies, such as in single cell diagnostic assays[1,2]. Single cell encapsulation is usually accomplished with the assistance of microfluidic devices, in which cell-laden droplets are generated by shear force between two immiscible fluids. One drawback for this method is that the cell-laden droplets are usually dispersed in oil phase after generation, which is not favorable for cell viability[3,4]. Also, the number of cell-laden droplets is usually small among the generated droplets due to the low cell density essential for one single cell encapsulation (~30 K/mL), which brings a lot of inconvenience to the following applications[5,6].

To sort between cell laden and empty microcapsules, cells can be optically detected after generation, and the cell-laden droplets can therefore be selectively extracted by external forces such as dielectrophoresis (DEP)[7]. However, these methods require labeling of the cells which can be detrimental to future applications, especially in tissue engineering and regenerative medicine due to toxicity[8].

Deep learning has been very efficient in detecting subtle features in images or even surpassing human performance[9]. In this study, we proposed a deep learning-based method for single-cell-laden droplet detection. The detection model takes bright field microscopy graphs as input and does not rely on any extra labeling of the cells. This detection method was further combined with an external DEP force for on-chip real-time extraction of single-cell-laden droplets from oil into aqueous phase. The results indicate this system can achieve considerable high efficiency and purity in extraction of single-cell-laden droplets. Moreover, the cell viability is not compromised after extraction.

METHODS

Experimental Setup. The general system design and experiment setup are shown in Figure 1A and Figure 1B, respectively. Briefly, a microfluidic device is placed on stage of the microscope for observation. The microfluidic device design is shown in Figure 1C. In the extraction region, two needles were used as the electrodes (E1 and E2). These two electrodes are loop connected to a switch which is controlled by a micro-controller. A voltage was applied on the circuit of the electrodes and switch, as illustrated in Figure 1D. The extraction region of the device is monitored using a cell phone which is wirelessly connected to a computer for real-time image capturing and transferring. The deep learning detection model running on the computer then determines whether the droplet in the detection region is empty or cell-laden. If a cell-laden droplet appears in the detection region, the computer program will send a corresponding signal to a micro-controller which activates DEP to extract the cell-laden droplets into the aqueous phase. The wire connection of the microchip is shown in Figure 1E.

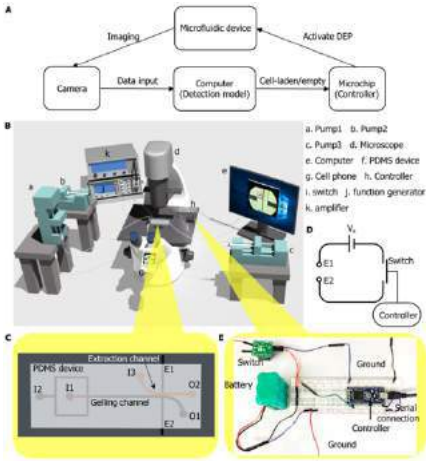

Figure 1. Schematic illustration of the system design. (A) Structure showing the experimental workflow. (B) 3D sketch of the whole experimental setup. (C) Sketch showing the microfluidic device (top view) (D) Circuit connection of the electrodes, switch, and controller. (E) A real picture showing circuit connection of the switch and controller.

Deep Learning Models. The detection model is based on a current state-of-the-art model for object detection, i.e., single shot multiplexer detector (SSD)[10]. Three different backend structures were used in this study for comparison, i.e., MobileNet[11], GoogLeNet (Inception)[12], and Residual-Net (ResNet)[13]. The backend models were first pre-trained on the open source COCO dataset[14]. Then it is further trained with our self-collected droplet images, including both cell-laden and empty (no cell-laden) ones. The fine-tuning was performed using tensorflow[10]. The trained models are evaluated using precision (P) and recall (R) which are defined as following:

$$P = TP / (TP + FP) \quad (1)$$

$$R = TP / (TP + FN) \quad (2)$$

where TP, FP, and FN denotes number of true positives, false positives, and false negatives, respectively.

Statistical Analysis. Statistical analysis is performed in excel using Student's two-tailed t-test assuming equal variance. At least three independent runs were conducted for all experiments.

RESULTS

Generation and Characterization of Droplets. The aqueous solution of 2% (w/v) alginate in saline with MDA-MB-231 cells (30 K/mL) was introduced into I1, oil emulsion was introduced into I2, and the aqueous solution of 1.3 % (w/v) carboxymethyl cellulose in saline with 10 mM calcium chloride was introduced into I3 as the extraction phase (figure 1). Droplets are generated at the flow focusing and gelled into calcium hydrogel by Ca^{2+}. After generation, micrographs of the droplets were captured at the downstream camera region and decided by the detection model whether there are cells in the droplets or not. If the droplets are cell-laden ones, the detection model will send an activation signal to the microcontroller, which controls the switch. DEP force will be applied to the cell-laden droplets consequently, and the droplets will be selectively extracted into the aqueous phase.

Detection Model Training and Characterization. The trained models took images as input and outputted a numerical value (between 0 and 1) indicating the probability that a cell-laden droplet is in the image. This value was then compared with a custom-defined threshold. If the value is greater than the threshold, the detection model takes the image as a positive (with cell-laden droplets). The relation between the model performance and threshold was examined. It was determined that at threshold of 0.9, all three models can achieve precision and recall which are higher than 0.9. Therefore, 0.9 was used as the threshold value in the rest of the study. The model with MobileNet backend achieves the fastest inference time of ~16 ms.

Characterization of Cell Phone Camera. In this study, acquisition speed of 30 fps is used, which means the time interval between two adjacent image frames is about 33 ms. We found that there was some noise in the actual acquisition speed. The actual time interval between two adjacent image frames is about 18-50 ms. For actual real time application at 30 fps, we need the deep learning model to perform single frame inference within 18 ms so we adopted the MobileNet as our backend model for detection for the remainder of the study.

Model Performance on real-time detection. One concern about the detection is that cells might be out of focus when the droplets pass the detection region. The model performs pretty well even for cells which are out of focus. However, due to the small size of single cells (~10 μm), some cells might be inevitably out of focus too much and are not captured in the images. Therefore, we conducted quantitative study by comparing the number of cells flowed into the flow focusing region and the number of cell-laden droplets detected at the downstream (Figure 2). As shown in Figure 2A (top right), the cells before the flow focusing region were observed under phase field. Because the contrast between the cell (shining dot, indicated by the red arrow) and the background is quite obvious, we can get the exact number of cells flowing into the extraction channel. Meanwhile, real-time detection was performed at the downstream under bright field. The quantitative data was shown in Figure 2B. About 80% of the cells can be detected using the detection model under bright field.

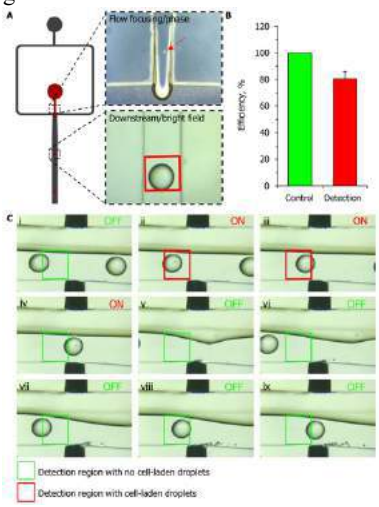

Figure 2. Real-time detection and extraction of cell-laden droplets. (A) Representative images showing the cell appearance before flow focusing junction under phase and detection at the downstream under bright field. (B) Quantitative data showing the detection efficiency of the model. (C) Typical image sequence showing the extraction of the cell-laden droplets from oil into aqueous phase.

Real-time Selective Extraction of Cell-laden Droplets. Then we conducted real-time extraction of cell-laden droplets. Typical graphs showing selective extraction of the droplets from oil into aqueous phase are shown in Figure 2C. When the model decides that a cell-laden droplet is in the detection region, the green box turns to red (which is just for visual effect and not necessary for extraction). The switch is activated, and the cell-laden droplet is extracted from oil into aqueous phase by the DEP force. When an empty droplet passes, the switch stays off and the droplet passes the electrode region without being extracted.

DISCUSSION

Capsules were able to be extracted from an oil to aqueous phase using deep learning-based detection with a high detection rate. More research needs to be conducted to address singles cells that may be out of the plane of focus that cannot be detected. We have demonstrated that high accuracy single cell extraction without harmful labeling is possible. Using a cell phone for detection can allow for a wide range of researchers to utilize this technology in various applications.

ACKNOWLEDGEMENTS

This work is supported by NIH R01 EB023632.

REFERENCES

[1] Collins, D. J. et al., *Lab Chip*, 17: 3439-3459, 2015. [2] Shang, Luoran et al., *Chemical reviews*, 117: 7964-8040, 2017. [3] Choi, J. K. et al., *Biomaterials*, 35: 5122-5128, 2014. [4] He, X. M., *Ann Biomed Eng,* 45: 1676-1684, 2017. [5] Huang, H. et al., *Small,* 11: 5369-5374, 2015. [6] Nam. J et al., *Biomicrofluidics,*6: 024120, 2012. [7] Cao, Z. et al., *Lab on a Chip,* 13:171-178, 2013. [8] Sciambi, A., and Adam R. Abate, *Lab on a Chip,* 15: 47-51, 2015. [9] LeCun, Y et al., *Nature*, 521: 436-444, 2015. [10] Huang, J. et al., *30th Ieee Conference on Computer Vision and Pattern Recognition (Cvpr),* 3296, 2017. [11] Howard, A et al., *arXiv preprint arXiv,*1704.04861, 2017. [12] Szegedy, C. et al., *Proc Cvpr Ieee,* 1-9, 2015. [13] He, K. M. et al., *2016 Ieee Cvpr,* 770-778, 2016. [14] Lin T. et al., *Lect Notes Comput Sc,* 8693:740-755, 2014.

SB³C2019
Summer Biomechanics, Bioengineering and Biotransport Conference
June 25 -28, Seven Springs, PA, USA

BIOTRANSPORT IN THE GLYMPHATIC SYSTEM: MEASURING AND MODELING FLOW THROUGH PERIVASCULAR SPACES

Humberto Mestre (1,2), Jeffrey Tithof (3), Ting Du (1,4), Wei Song (1), Weiguo Peng (1,5), Amanda M. Sweeney (1), Genaro Olveda (1), John H. Thomas (3), Maiken Nedergaard (1,5), and Douglas H. Kelley (3)

(1) Center for Translational Neuromedicine, University of Rochester Medical Center, Rochester, NY 14642, USA.

(2) Department of Neuroscience, University of Rochester Medical Center, Rochester, NY 14642, USA.

(3) Department of Mechanical Engineering, University of Rochester, Rochester, NY 14627, USA.

(4) China Medical University, Shenyang 110122, China.

(5) Center for Translational Neuromedicine, Faculty of Health and Medical Sciences, University of Copenhagen, 2200 Copenhagen, Denmark.

INTRODUCTION

The recently-discovered glymphatic system[1] circulates cerebrospinal fluid (CSF) through the brain, sweeping away proteins and metabolic waste and playing a role similar to the lymphatic system in the rest of the body. Primarily active during sleep[2], the glymphatic system drives CSF through annular perivascular spaces (PVSs) surrounding arteries and veins, from which it accesses deeper brain tissue. The glymphatic system may play a key role in preventing neurological disorders, such as Alzheimer's and Parkinson's diseases, that are associated with accumulation of waste proteins (in these two examples, amyloid-β and tau). The glymphatic system also has potential for drug delivery[3].

However, both the characteristics of biotransport via the glymphatic system and the mechanisms driving that biotransport have been topics of open debate in recent publications. In mice, PVS widths have been estimated from ~nm to ~μm. CSF in PVSs has been said to flow either parallel[2] or anti-parallel[4,5] to the blood in the adjacent vasculature. CSF flow has been suggested to pulse in synchrony with either the respiratory or cardiac cycle.

In results just published,[6] we use *in vivo* particle tracking to measure CSF flow in PVSs surrounding pial arteries in mice, with high resolution in space and time. We show that PVSs surrounding the middle cerebral arteries of mice have characteristic cross-sectional size similar to the artery, 44 μm on average, and smaller size estimates were probably made because PVSs collapse during tissue fixation. We measure typical flow speeds around 20 μm/s, implying laminar flow in which protein transport is dominated by advection (not diffusion). We find that CSF is nearly stagnant near artery bifurcations, possibly explaining why amyloid-β accumulates there in Alzheimer's patients. In results currently under review[7], we show that the elongated, eccentric PVS shapes we observe *in vivo* have lower hydraulic resistance than circular, concentric annuli with the same cross-sectional area. Moreover, we show that hydraulic resistance is minimized when elongation is moderate, and that the elongation we observe *in vivo* nearly minimizes resistance. Thus, PVSs may have evolved their elongated shapes to optimize CSF pumping efficiency.

METHODS

All experiments were approved by the University Committee on Animal Resources of the University of Rochester Medical Center (Protocol No. 2011-023), and an effort was made to minimize the number of animals used. We injected 1-μm tracer particles into the cisterna magnas of male mice, age 8-12 weeks, anaesthetized with ketamine-xylazine to approximate sleep. We also injected intravascular fluorescein isothiocyanate-dextran to make arteries visible. We performed two-photon imaging through a cranial window using a resonant scanner B scope (Thorlabs) with a Mai Tai DeepSee HP Ti:Sapphire laser and a water immersion lens. Typically, we observed flow near the bifurcation of the middle cerebral artery, though we have seen the same phenomena in other pial PVSs as well. Images were recorded at 30 Hz. We used artery images to register the resulting movies during post-processing, removing translations caused by large-scale motions of the mouse with respect to the scope, which would distort flow velocity measurements. We tracked particles using an in-house algorithm written in Matlab, excluding stagnant particles that had apparently adhered to the vessel wall. We calculated hydraulic resistance by solving the Stokes equation numerically, with no-slip boundary conditions, using the Matlab Partial Differential Equation Toolbox. In cases where analytic solutions are known, our results agreed within 1%. Fits to experimental observations were determined by finding the circles and ellipses that have the same normalized second central moments as the corresponding dyed regions.

RESULTS

First, we examined characteristics of CSF flow in PVSs by averaging over time. Figure 1 shows the mean flow measured in one experiment (about 10 minutes long, using about 3 x 10^5 measurements). The mean velocity points in the same direction as blood flow, which proceeds from top-right to bottom-left along the artery shown here. CSF is nearly stagnant in the interior of the arterial bifurcation. The flow is fastest where other arteries and veins come close, narrowing the PVS. A narrower PVS dictates faster flow according to the continuity equation (conservation of mass).

Using the overall root-mean-square particle velocity U, characteristic size L = 44 μm, and viscosity ν = 0.697 x 10^{-6} m^2/s, we calculate the Reynolds number Re = UL/ν ~ 10^{-3}. Its small value suggests laminar flow, consistent with the smooth particle motions we observe. (However, the CSF flows we observe in PVSs do oscillate visibly as the artery walls pulse, as will be discussed in a separate presentation.) Finding Re $\ll$ 1 also implies that the nonlinear term of the Navier-Stokes equation can accurately be neglected in future analyses. We also calculate the Péclet number Pe = UL/D ~ 10^2, where D ~ 10^{-10} m^2/s is the material diffusivity of proteins like amyloid-β. Finding Pe $\gg$ 1 implies that flow dominates diffusion in transporting proteins through this part of the glymphatic system.

The regions where we observe tracer particles have widths similar to the artery, and much larger than the ~nm widths measured in fixed tissue. We confirmed the larger widths by making *in vivo* three-dimensional images (not plotted) with dye in the arteries and dye of another color in the PVSs. By continuing that imaging through fixation, we found that during that process, PVSs collapse and dye infiltrates artery walls, implying that *in vivo* studies are essential.

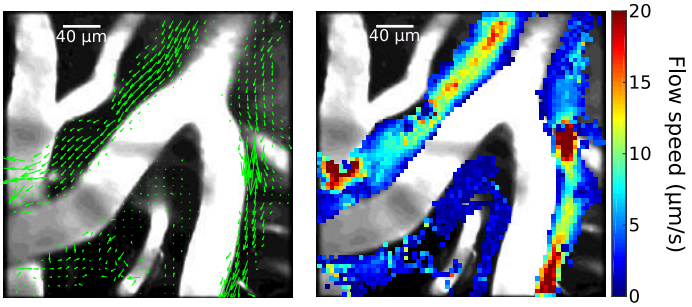

Figure 1: The mean flow of CSF in PVSs, obtained by tracking the motion of 1-μm spheres flowing through the brain of a live mouse. Left: velocity; right: speed. CSF flows in the same direction as the blood and is nearly stagnant in the interior regions of arterial bifurcations. CSF speed varies among animals but is about 20 μm/s on average. Adapted from [6].

We observe particles crossing from one side of an artery to the other only rarely, suggesting that the PVSs is narrow or closed above and below the artery—not a circular annulus. That observation is consistent with cross-sections measured *in vivo*, which show elongated PVSs, as in Figure 2a. We wondered if the elongated shapes might have lower hydraulic resistance (volume flowrate per unit pressure, per unit length) than circular annuli. To test that hypothesis, we considered Stokes flow in straight annuli, assuming the streamlines to be oriented along the annulus. In that case, the momentum equation (Stokes equation) simplifies to a Poisson equation, which together with no-slip conditions at the boundaries of the annulus, fully specifies the flow and the hydraulic resistance. Modeling the PVS as the space between a circular artery and an elliptical outer boundary, we varied the ellipse elongation and PVS area. Figure 2b shows the velocity profile in one of the resulting shapes. Figure 2c shows the hydraulic resistance of many such shapes. Increasing the area reduces the hydraulic resistance, as expected. For a given area, we always find a moderate elongation for which the shape is optimal, in that it minimizes resistance. By fitting circles and ellipses to three published *in vivo* images of PVSs, we calculated the area, elongation, and resistance of each; all are nearly optimal. Thus, PVSs may have evolved their elongated shapes to optimize CSF pumping efficiency.

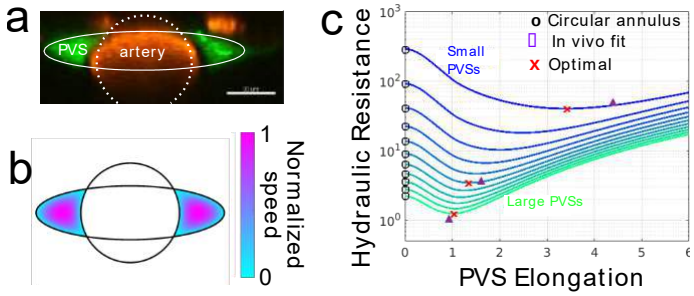

Figure 2: (a) PVSs surrounding pial arteries are elongated, not circular. (b) Velocity profile in a PVS-like shape. (c) Hydraulic resistance of PVS-like shapes. Each curve has a minimum, where pumping efficiency is optimal. Three curves correspond to areas matching real PVSs; their minima are marked in red. The actual shapes, marked in purple, are nearly optimal. Adapted from [7].

DISCUSSION

Our high-resolution measurements of the flow of CSF in PVSs show low-Re, high-Pe flow, parallel to blood flow, that is faster where PVSs narrow and nearly stagnant behind arterial bifurcations. By calculating the hydraulic resistance of a family of PVS-like shapes, we found that over a wide range of parameters, there is always a moderate elongation for which the shape is optimal and maximizes pumping efficiency. The three images of pial PVSs that we found in the literature all have near-optimal shapes. In future work, we hope to perform similar studies on smaller, more distal PVSs. We would also like to consider how artery wall pulsation, which seems to be the primary driver of CSF flow, affects which PVS shapes are optimal for efficient pumping.

ACKNOWLEDGEMENTS

This work was supported by the National Institute of Neurological Disorders and Stroke (R01 NS100366 to M.N.), the National Institute of Aging (RF1 AG057575-01 to M.N., J.H.T., and D.H.K.), Foundation Leducq (FLQ 12CVD01 to M.N.), and the European Union's Horizon 2020 Research and Innovation Programme (SVDs@target) (666881 to M.N.). We would like to thank Dan Xue for assistance with illustrations. HM and JT contributed equally.

REFERENCES

1. Iliff, J. J. *et al. Science Translational Medicine* **4,** 147ra111–147ra111 (2012).
2. Xie, L. *et al. Science* **342,** 373–377 (2013).
3. Plog, B. A. *et al. JCI Insight* **3,** 1188–16 (2018).
4. Morris, A. W. J. *et al. Acta Neuropathol.* **131,** 725–736 (2016).
5. Bakker, E. N. T. P. *et al. Cellular and Molecular Neurobiology* **36,** 181–194 (2017).
6. Mestre, H. *et al. Nat. Comm.* **9:1,** 4878 (2018).
7. Tithof, J. et al. *Under review* (2019). doi:10.1101/522409

SB^{3}C2019
Summer Biomechanics, Bioengineering and Biotransport Conference
June 25 -28, Seven Springs, PA, USA

PREDICTION OF CAROTID RESTENOSIS RISK AFTER ENDARTERECTOMY BY HEMODYNAMIC AND GEOMETRIC ANALYSIS: A 5-YEARS FOLLOW-UP

Diego Gallo (1), Maurizio Domanin (2), Christian Vergara (3), Umberto Morbiducci (1)

(1) Polito^{BIO}Med Lab, Department of Mechanical and Aerospace Engineering
Politecnico di Torino
Turin, Italy

(2) Department of Clinical Sciences and Community Health
Università di Milano
Milan, Italy

(3) Laboratory of Biological Structure Mechanics (LaBS), Department of Chemistry, Materials and Chemical Engineering "Giulio Natta"
Politecnico di Milano
Milan, Italy

INTRODUCTION

Restenosis is the main complication affecting patients outcome after carotid endarterectomy (CEA) [1]. The evidence that late (>5 years) restenosis is similar to primary atherosclerotic lesions [1], for which a key role of low and oscillatory wall shear stress (WSS) is established [2], has led to identify in local hemodynamic disturbances a possible contributor to the development of late restenosis after CEA. Additionally, the clinical translation of the role of hemodynamic disturbances in vascular pathology have motivated the identification of specific geometric attributes of the carotid bifurcation as surrogate markers of the burden of low and oscillatory WSS [3].

The elucidation of the mechanistic processes underlying restenosis development would greatly help clinical decision making about the appropriate CEA closure technique. Clinical debate currently exists concerning closure based on a direct suture (primary closure, PC), or on the interposition of a synthetic graft (patch graft, PG) [4]. To minimize the risk of narrowing of the arterial lumen, the use of PG is recommended for routine use by current guidelines [5]. However, PG involves longer cross-clamping time, higher risk of neurocognitive deficits, infection, pseudoaneurysm development. A selective use for PG based on carotid diameters has also been suggested [4, 5].

Here we aim to establish whether hemodynamics and geometry post-CEA can predict the risk of late restenosis at 5 years in a cohort of 12 real world patients submitted to 13 CEA with two different closure techniques (9 PG, 4 PC). In detail, personalized computational fluid dynamics (CFD) simulations and a geometric analysis were performed and compared with clinical follow up data of intima-media thickness (IMT) at 5 years, to investigate the hemodynamics-driven processes underlying restenosis development and potentially guiding the PG *vs.* PC clinical decision.

METHODS

The study was approved by the I.R.C.C.S. Fondazione Policlinico Ethics Committee and patients provided informed consent.

Patient population data. 13 carotid endarterectomy procedures were performed in 12 asymptomatic patients with diameter stenosis >70%, as defined by a peak systolic velocity (PSV) >200 cm/s measured by Doppler Ultrasound (DUS). According to European guidelines [5], PG angioplasty was performed in 9 cases (PG1-9), PC in 4 cases (PC1-4). All patients were submitted to DUS follow-up at 3 months, 2 and 5 years. Cases with PSV >130 cm/s (indicating a diameter stenosis >50%) were defined as cases of restenosis. No patients presented restenosis at 3 months and 2 years follow ups. Two patients died for myocardial infarction (PG4), and pancreatic carcinoma (PG8) at 3 years. After 5 years, eligible patients were submitted to DUS follow-up for IMT measurements with linear 8 MHz probe and iU22 ultrasound scanner (Philips Ultrasound, USA). IMT values were automatically extracted with Qlab (Philips Ultrasound, USA) at these locations: internal carotid artery (ICA) distal to the carotid bulb (CB); CB; distal end of the common carotid artery (CCA), i.e., the flow divider (FD); CCA at 1 and 2 cm below the flow divider (FD-1cm and FD-2cm, respectively).

Computational hemodynamics. MRI acquisitions (Siemens 1.5T Avanto) were performed within 1 month after surgery and used for 3D geometry reconstruction [6]. The governing equations of fluid motion were solved using P1 bubble-P1 tetrahedral finite elements in the library LifeV (http://www.lifev.org). Patient-specific flow rate waveforms were extracted from echo-color DUS at the CCA and ICA and imposed as boundary conditions [6]. At the external carotid artery (ECA) outlet section, a traction-free condition was imposed [6]. The distributions at the luminal surface of time-averaged WSS (TAWSS), and oscillatory shear index (OSI) were calculated. The bifurcation

region was delimited by sections CCA3, ICA5 and ECA2 (Fig. 1A). Data from all 13 models were pooled to identify the 20th percentile value of TAWSS, and 80th percentile values of OSI. The burden of disturbed WSS was quantified by the surface area exposed to TAWSS, below (OSI above) the corresponding threshold value, and divided by the model surface area [2]. These hemodynamic descriptors are denoted Low Shear Area (LSA) and Oscillatory Shear Area (OSA).

Geometric analysis. Descriptors quantifying the expansion at the bulb (i.e., flare), and the tortuosity of the CCA were considered [3]. Flare was calculated as the ratio between the maximum CCA cross-sectional area (CCA_{max}) and the CCA3 area (Fig. 1A). Tortuosity was calculated between the "inflection point", i.e. the point where the CCA-ICA centerline changes concavity, and the CCA3 centerline point (Fig. 1B) as Tort=L/D-1, where L and D are the curvilinear and Euclidean distance between the two points, respectively.

Statistical analysis. The relationship between the hemodynamic descriptors and the combination of geometric descriptors was quantified by multiple linear regression analysis. The quality of the regression was evaluated with the adjusted coefficient of determination R^2, and the relative contribution of each predictor was determined from the standardized regression coefficients β. Then, linear regression analysis was used to identify relationships between hemodynamic or geometric descriptors with maximum IMT values.

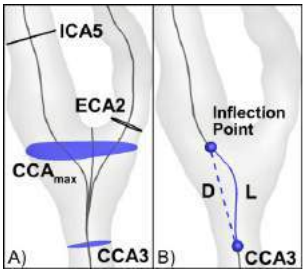

Figure 1: A) CCA_{max} and CCA3 sections, whose ratio defines the flare, are shown in blue. CCA_{max} is normal to the average of the ICA and ECA centerlines. B) The centerline segment between the CCA3 centerline point and the inflection point was used to calculate tortuosity as L/D -1.

RESULTS

Statistically significant differences were observed between the PG and PC groups for LSA and flare (P<0.05), but not OSA nor tortuosity. In detail, PG patients exhibited larger average values of LSA than PC patients (40.85%±19.10% *vs*. 19.42%±10.61%), and higher flare values (2.60±1.42 *vs*. 1.33±0.10). This is not unexpected, since the inserted PG substitutes a portion of the endarterectomized vessel wall which is removed in PC. Notwithstanding the small sample size, a direct relationship emerged between flare and LSA (P<0.05), but not OSA (Table 1). Linear regressions revealed direct associations between maximum IMT at 5 years and both LSA (R^2=0.58, P=0.006), and flare (R^2=0.74, P<0.001) (Fig. 2A), whereas maximum IMT was not correlated with either OSA (R^2=0.15, P=0.241), or tortuosity (R^2=0.25, P=0.116). At 5 years, DUS highlighted the presence of a >70% restenosis in PG1, and >50% restenosis in PG2 (right and left carotid in the same patient), confirmed by magnetic resonance angiography and intra-operatory arteriography (Fig. 2B,C). A clear co-localization emerged between the area exposed to low WSS and the restenosis location (Fig. 2D). This is further confirmed for all cases in Fig. 3, where morphological DUS observations, presented with TAWSS and OSI distributions, allow to appreciate by visual inspection the co-localization between disturbed hemodynamics and observations of myointimal thickening or new atheroma development.

Table 1: Multiple regression of geometry *vs*. hemodynamics.

	Adjusted R^2	β flare	β tortuosity
LSA	0.359*	0.743*	-0.255
OSA	0.132	0.574	-0.200

* P<0.05

DISCUSSION

While the mechanisms leading to restenosis after CEA are still being defined, the establishment of flow disturbances at the bifurcation has been often interpreted by surgeons as an harbinger of complications [4,5]. Here, we successfully linked disturbed hemodynamics after CEA to verified clinical cases of late restenosis, additionally exploring the clinical translation of such a link through surrogate geometric predictors of disturbed hemodynamics. These findings imply that the arteriotomy after CEA should avoid creating a large and sudden expansion, as it is linked to restenosis via the generation of flow disturbances. This is particularly true in obliged PG arteriotomy repair strategies. Our findings suggest also that hemodynamic and geometric analyses hold potential for the stratification of patients at risk for development of late restenosis, providing useful indications about (1) the best arteriotomy repair strategy, and (2) the best follow up strategy. In particular, geometric analysis could be easily integrated in a surgical planning pipeline to virtually explore personalized post-operative scenarios.

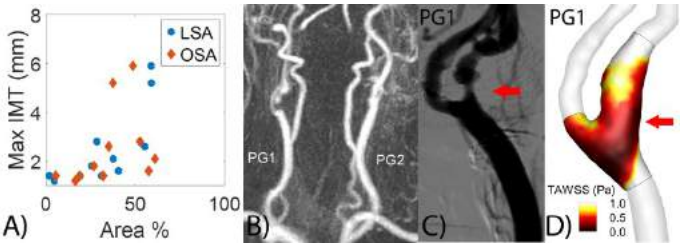

Figure 2: A) Scatter plots of LSA and OSA *vs*. maximum IMT. B), C) Clinical evidence of restenosis for PG1 and PG2. D) The restenosis region was characterized by low WSS (red arrow).

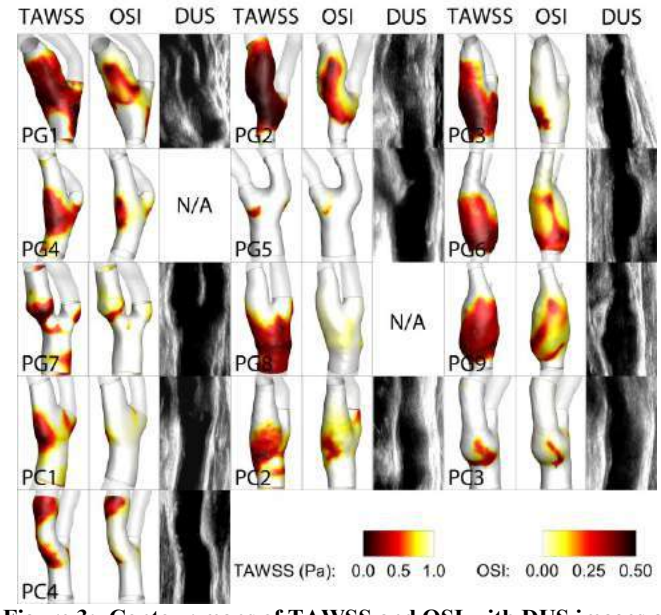

Figure 3: Contour maps of TAWSS and OSI with DUS images at 5 years follow up, showing carotid IMT.

REFERENCES

[1] Hellings, WE et al., *Stroke*, 39:1029-1032, 2008.
[2] Gallo, D et al., *J R Soc Interface*, 15: 20180352, 2018.
[3] Bijari, PB et al., *J Biomech*, 45: 1632-1637, 2012.
[4] Kumar, R et al., *Eur J Vasc Endovasc Surg*, 53(6):776-775, 2017.
[5] Naylor, AR et al., *Eur J Vasc Endovasc Surg*, 55(1):3-81, 2017.
[6] Guerciotti, B et al., *J Biomech*, 49:26-38, 2016.

COMPARISON OF HEALTHY AND PULMONARY HYPERTENSION HEMODYNAMICS

Senol Piskin (1), Ender A. Finol (1,2)

(1) Department of Mechanical Engineering
University of Texas at San Antonio
San Antonio, Texas, USA

(2) UTSA/UTHSA Graduate Program in Biomedical Engineering
University of Texas at San Antonio
San Antonio, Texas, USA

INTRODUCTION

Pulmonary hypertension (PH) is a progressive disease characterized by increased pulmonary artery (PA) and right ventricle (RV) pressure, and elevated pulmonary vascular resistance. It can lead to narrow PA, a thicker RV wall, and eventually RV failure and death [1]. It affects 10 to 52 cases per million with a higher incidence in women [2]. Typically, PH is diagnosed at an advanced stage of development and patients survive three to five years from the time of diagnosis. Clinical diagnosis of PH involves invasive methods such as Right Heart Catheterization (RHC). Several computational studies propose to quantitatively characterize the disease and improve its diagnosis, prognosis, and treatment [3-5]. However, these studies were performed at steady state conditions. The current work aims to improve the computational predictions by performing simulating pulsatile flow conditions with geometries up to the 7th generation of the pulmonary tree and transient resistance boundary conditions. A comparison of normal and diseased (PH) states is performed to establish the differences in flow dynamics between the states.

METHODS

Scanned patient data were reconstructed to obtain 3D patient specific geometries for a healthy subject and a PH subject. Extensions at the inflow and outflow boundaries were integrated into the 3D model to exclude boundary effects from the simulations results. Transient resistances at each outlet were assigned based on the diameter of the outlets to obtain the desired inlet pressure [3-5]. A pulsatile inlet velocity boundary condition was generated using a velocity waveform of a PH patient measured with a Volcano catheter and adjusted based on the patient-specific cardiac output. The pressure waveform, also measured with this catheter, was used to generate an inlet pressure at the proximal main PA (MPA). The resistances at the outlets were iteratively adjusted so that the inlet pressure was matched with the desired MPA pressure at each time step. The Navier-Stokes equations (Equations 1 and 2) were solved using the well validated solver Fluent 19.0 (Ansys Inc., Canonsburg, PA).

$$\nabla . \boldsymbol{u} = 0 \tag{1}$$

$$\frac{\partial \boldsymbol{u}}{\partial t} + (\boldsymbol{u} . \boldsymbol{\nabla}) = -\nabla \mathrm{p} + \nabla . [(\nu)(\nabla \boldsymbol{u} + \nabla \boldsymbol{u}^T)] \tag{2}$$

The simulations were run for at least three cycles for periodic convergence. Figure 1 shows all the steps of the protocol from image segmentation to data post-processing.

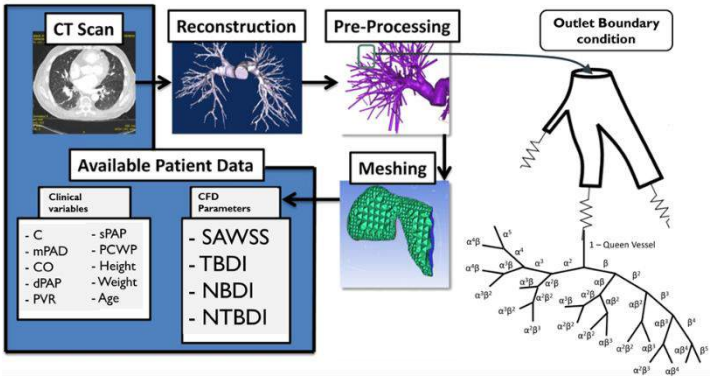

Figure 1: Flowchart of the patient-specific modeling protocol from chest computed tomography image segmentation to computational fluid dynamics (CFD) simulation post-processing.

Figure 2 illustrates the inlet velocity boundary condition and the matched pressure waveform at the proximal MPA.

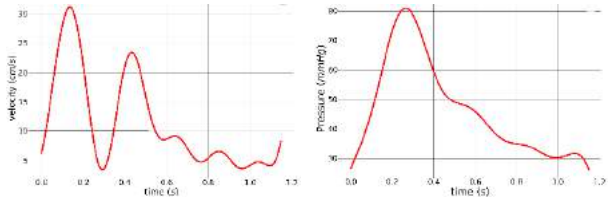

(a) **(b)**

Figure 2: Centerline velocity (a) and pressure (b) recorded at the main pulmonary artery.

The CFD results were post-processed and visualized using Ansys CFD Post (Ansys Inc, Canonsburg, PA) and Paraview (Sandia National Laboratory, Kitware Inc, Los Alamos National Laboratory). Oscillatory shear index (OSI) distributions were obtained using the formulation given in Equation (3). This index shows the variation of WSS in time at each point of the endoluminal wall.

$$OSI = 0.5\left(1 - \frac{\left|\int_0^T \vec{\tau}_w \, dt\right|}{\int_0^T |\vec{\tau}_w| dt}\right) \quad (3)$$

RESULTS

The systolic pressure distribution, illustrated in Figure 3 for the healthy model, shows a high pressure at the proximal MPA and low pressure at the distal PAs. This is expected due to the acceleration phase of the cycle. Figure 3 also shows the WSS distribution for this model with relatively high values of WSS at the bifurcations of the distal PAs.

Figure 4 shows the OSI distributions on the pulmonary artery walls of the healthy and PH subjects for one cardiac cycle. The inlet extensions of the geometry were excluded from the results for the sake of clarity. Both models show relatively high OSI at proximal MPA, left PA, and right PA. However, the PH model has a lower OSI compared to the healthy model throughout most of the PA branches.

DISCUSSION

The blood flow in the pulmonary arteries of a healthy and a PH subject have been simulated using an advanced computational model. In addition, a comparative analysis was performed based on CFD simulations of healthy and PH pulmonary artery models. The preliminary results show clear differences between the two models in terms of their OSI distributions. Prior work from others on PH suggest similar differences in the wall shear stress WSS distributions [6]. The hemodynamic differences between healthy and PH patient models could help diagnose the disease or classify PH severity (e.g. World Health Organization classification). Tang et al. [6] provided evidence for a correlation between PH and WSS and differences in mean WSS between healthy and PH CFD models. We have simulated two patient-specific geometries, which limits the applicability of this study to general clinical outcomes. In addition, other hemodynamic indices could be correlated to clinical variables measured during diagnosis and follow-up of PH patients to obtain meaningful relationships between non-invasive CFD-derived metrics and invasively measured or calculated metrics indicative of PH severity.

ACKNOWLEDGEMENTS

This work was supported in part by National Institutes of Health (NIH) award R01HL121293, American Heart Association (AHA) award 14GRNT19020017 and The Scientific and Technological Research Council of Turkey (TUBITAK) award 2219 – 1059B191501944. The use of ANSYS ICEM, ANSYS Fluent, and ANSYS CFD-Post is gratefully acknowledged through an educational licensing agreement with Ansys, Inc. The use of the Shamu cluster at UTSA is also acknowledged.

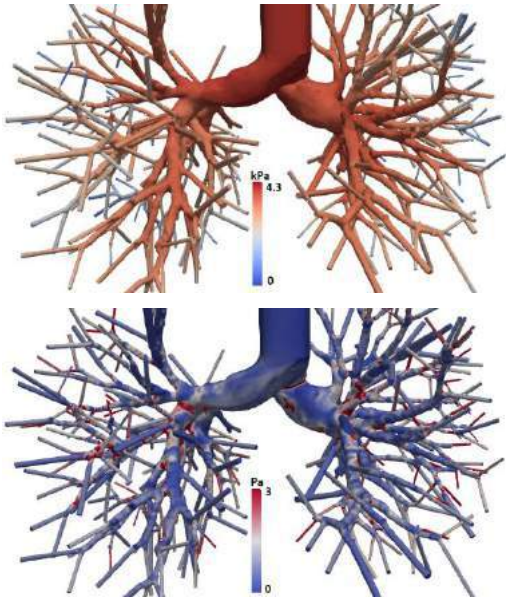

Figure 3: Pressure (top frame, in kPa) and wall shear stress (bottom frame, in Pa) distributions for the healthy model.

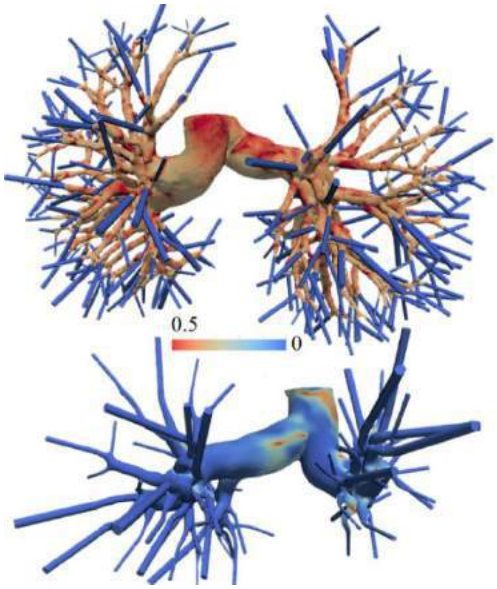

Figure 4: Healthy (top frame) and PH (bottom frame) oscillatory shear index distributions.

REFERENCES

1. Hoeper, MM et al., *Eur Respir Rev*, 23:450-457, 2014.
2. Boucly, A et al., *Eur Respir J*, 50:1700889, 2017.
3. Piskin, S et al., *SES 2017*, Boston, USA, 594, 2017.
4. Piskin, S et al., *WCB 2018*, Dublin, Ireland, O1708, 2018.
5. Kheyfets, VO et al., *Comput Meth Prog Biomed*, 120:88-101, 2015.
6. Tang, TT et al., *Pulm Circ*, 2:470-476, 2012.

FUNCTIONAL CHARACTERIZATION OF ARTERIOVENOUS FISTULA ON SWINE MODELS USING MRI

E. Tubaldi (1), J. A. Rosado-Toro (2), D, Celdran-Bonafonte (2), P. Roy-Chaudhury (2)

(1) Department of Aerospace and Mechanical Engineering, College of Engineering, University of Arizona

(2) Department of Nephrology, College of Medicine, University of Arizona

INTRODUCTION

Approximately one in seven Americans have chronic kidney disease (CKD), of which 1.5% have end stage renal disease and must either begin hemodialysis or receive a kidney transplant. The creation and maintenance of hemodialysis vascular access provides a lifeline to patients reliant on dialysis. Due to its longevity, access-related costs and mortality, arteriovenous fistulae (AVF) is the preferred method of vascular access [1]. Despite its many advantages, AVF can be undermined by early primary failure rates and unsuccessful maturation [2]. These failures are attributed to peri-anastomotic venous segment stenosis [3] which can be quantified by generating three-dimensional (3D) models of the fistula and measuring cross-sectional area (CSA) through the venous segment. To develop patient-specific 3D AVF models we want an operator-independent imaging modality that yields high resolution images without the use of harmful ionizing radiation or contrast agents that may prove toxic to patients with advanced renal failure [4]. For these reasons, we use contrast-free magnetic resonance imaging (MRI) imaging modality. The aim of this study is to generate a set of AVF-specific tools to measure cross-sectional areas in AVF models using MRIs. Analysis was performed in swine, but techniques can be applied into clinical settings.

METHODS

Six male Yorkshire Cross domestic swine were purchased from a USDA-approved vendor and kept at the University of Arizona Animal Care Center. After 7 days of acclimation to the experimental facilities, AVFs were created by joining the external femoral artery and femoral vein (Figure 1(a)). The AVFs are allowed to mature for 28 days [5] and black blood (BB) contrast-free MRIs (parameters shown in Table 1) are performed. To generate the model from BB MRIs, control points should be selected in both the vein and artery are selected (Figure 1(b)). The artery control points should be selected approximately 3 cm proximal and 1 cm distal. One of the vein control points should include the anastomosis plane and the proximal part of the vein, approximately 3cm from the anastomosis plane [6]. Additional control points may be selected in case of complex/non-cylindrical shapes.

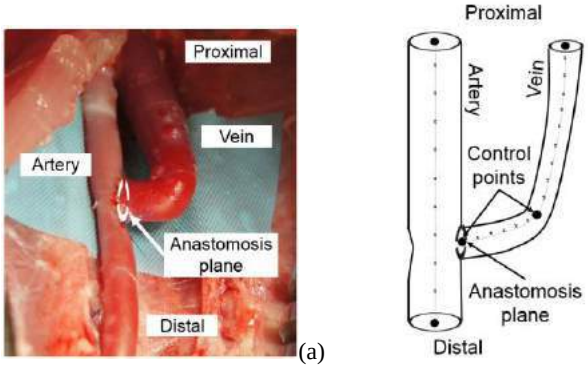

Figure 1: (a) Surgical configuration of AVF, (b) Selection of control points

The control points are then interpolated throughout the vein and artery using a 3D version of dynamic programming (DP) [7]. Given the centerlines, the segmentation is performed using polar DP (Figure 2B) [8]. Given the segmentation, a 3D model is generated (Figure 2C) [9]. The 3D model centerline is refined using a 3D fast marching algorithm [10]. Using the centerline we can acquire CSA at different distances from the anastomosis plane, shown in Figure 2D. The concatenation of all venous CSAs is shown in Figure 2E.

Table 1: Contrast-free MRI parameters.

MR Imaging Parameters	SWINE 1	SWINE 2	SWINE 3	SWINE 4	SWINE 5	SWINE 6
Slice Thickness (mm)	0.75	0.8	0.8	0.8	0.8	0.8
In plane resolution (mm) x (mm)	0.7813 x 0.7813	0.7813 x 0.7813	0.7813 x 0.7813	0.7813 x 0.7813	0.7813 x 0.7813	0.7813 x 0.7813
Matrix Size (pixels)	320 x 320	320 x 266	320 x 266	320 x 266	320 x 266	320 x 266
Echo train length (ms)	60	60	60	60	60	60
Echo time (ms)	11	22	22	22	22	22
Repetition time (ms)	1400	1700	1790	1690	1710	1690

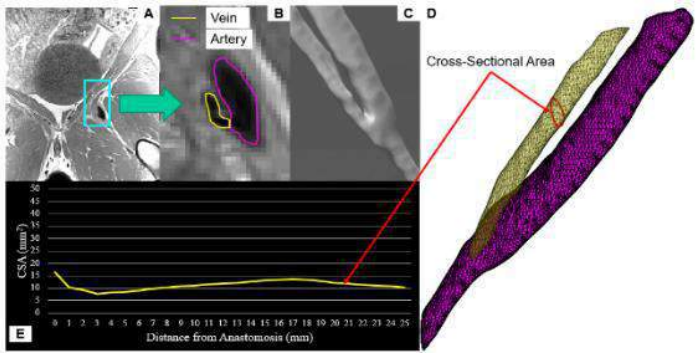

Figure 2: Steps to generate cross-sectional area.

RESULTS

Dividing the artery into three parts allows us to compartmentalize the effects of the fistula on the artery. Table 2 shows that the proximal region of the artery is dilated when compared to its distal counter part; yet both regions are dilated (more than doubled) when compared to their non-AVF arterial CSAs counterparts (Table 3).

Figure 3 shows the heterogeneity of each fistula. Even with standardized surgery procedures, which can be quantified by the small variation in the maximum and mean curvature (Table 4), there is a big variation in not only the functional parameter of each AVF (i.e., minimum CSA) but also the profile of each AVF. Even in cases where the minimum CSA is similar (e.g., Swine 1 and 4), analyzing the CSA profile allows us to get a better understanding of where the stenosis is occurring. This can help physicians localize regions of intervention thus reducing the stress to the AVF.

Table 2: Arterial CSA Analysis.

Mean CSA Region (mm^2):	SWINE 1	SWINE 2	SWINE 3	SWINE 4	SWINE 5	SWINE 6
Proximal	85.1	85.4	74.3	44.7	28.2	86.3
Anastomosis	55.5	81.3	37.8	30.2	22.8	52.8
Distal	60.0	47.2	20.8	18.4	11.3	46.9
Weight (kg)	60.0	75.7	80.0	50.0	63.5	77.1

Table 3: Arterial CSA Yorkshire Cross (No-Fistula) [11].

Mean CSA Region (mm^2):	Weight (kg)
19.6	30-39
20.4	40-49
24.6	50-59
27.3	60-69

Table 4: MRI-derived venous functional parameters.

Functional Parameters	SWINE 1	SWINE 2	SWINE 3	SWINE 4	SWINE 5	SWINE 6
Min CSA (mm^2)	6.9	10.8	11.4	8.6	7.9	26
Curvature (κ)	0.10	0.12	0.13	0.12	0.09	0.10
Maximum Curvature	0.29	0.25	0.23	0.25	0.26	0.26

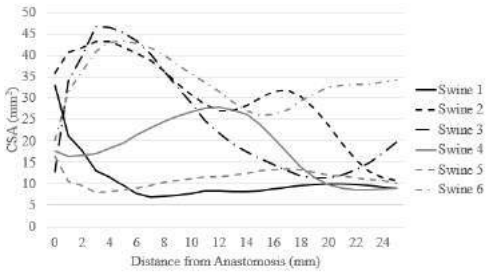

Figure 3: Representation of venous cross-sectional area plotted with respect to the distance from anastomosis.

DISCUSSION

Our findings suggest that differences hemodynamics plays a role in the maturation of the fistula. Future studies will aim to assess the causal relationship between hemodynamic profiles at baseline (3 days after the surgery) and which genomic pathways get activated in order to develop the functional changes seen 28 days after surgery. The ability to find relationship between non-invasive tools and genomics will allow us to intervene before occlusion of AVFs occurs.

ACKNOWLEDGEMENTS

This study is supported through Dr. Prabir Roy-Chaudhury's VA Merit Review I01BX002390 and Prof. Eleonora Tubaldi BIO5 Institute Team Scholars Program.

REFERENCES

[1] Krishanmoorthy MK, Banerjee RK, Wang Y et al., *Int Soc Nephrol*, 81: 745-750, 2012.

[2] Lee T and All on M. Clin *J Am Soc Nephrol*, 12: 865-867, 2017.

[3] Roy-Chaudhury P, Arend L, Zhang J et al., *J Am Soc Nephrol.* 17:1112-1127, 2006.

[4] Haneder S, Kucharczyk W, Schoenberg SO et al., *Top Magn Reson Imag*

[5] Heldnan AW, Cheng L, Jenkins M, et al., *Circ*,103: 2289-2295, 2001.

[6] Wang Y, Krishnamoorthy M, Banerjee R et al. *Nephrol Dial Transplant*, 23:525-533, 2008.

[7] Rosado-Toro JA, Abidov A, Altbach MI, et al., *Comp Med Imag Graph*, 62: 15-25, 2017.

[8] Rosado-Toro JA, Altbach MI, Rodríguez JJ, *IEEE Trans Imag Proc*, 25: 5857-5866, 2016.

[9] Desbrun M, Meyer M, Schröder P et al., *Annual Conf Comput Graph Interact Techn*, 317-324, 1999.

[10] Peyré G, *IEEE Comput Sci Eng*, 13:94-97, 2011.

[11] Lopes-Berkas VC and Jorgenson MA, *JAALAS*, 5:628-634, 2011.

SB³C2019
Summer Biomechanics, Bioengineering and Biotransport Conference
June 25 -28, Seven Springs, PA, USA

IMPACT OF HEMODYNAMICS & ENDOTHELIAL GLYCOCALYX ON CANCER CELL ADHESION TO VASCULAR WALL ENDOTHELIUM

Solomon Mensah (1), Alina Nersesyan (1), Ian Harding (1), Mark Niedre (3), Vladimir Torchilin (4), Eno Ebong (1,2)

(1) Department of Bioengineering
Northeastern University
Boston, MA, USA.

(2) Department of Chemical Engineering
Northeastern University
Boston, MA, USA.

(3) Department of Computer and Electrical Engineering
Northeastern University
Boston, MA, USA

(4) Department of Pharmaceutical Science
Northeastern University
Boston, MA, USA

INTRODUCTION

Cancer metastasis has been identified as one of the major causes of cancer-related deaths [1, 2]. During metastasis, small amounts of primary tumor cells migrate from the parent tumor to other tissues, where they form secondary tumors [3]. The mechanism for secondary tumor homing to new tissues locations remains under investigation, but it is well established that cancer cell migration is enabled largely by circulating cancer cells crossing the vascular endothelial barrier and traveling via the blood vessels [3, 4]. It has been suggested that the migration of cancer cells across the endothelium, in search of locations to colonize for secondary tumor formation, could be due to glycocalyx (GCX) dysfunction, which allows for cancer cell attachment to endothelial cells [4].

Endothelial glycocalyx dysfunction could be a result of multiple factors, and the most common way of GCX dysfunction is through inflammatory stress and enzyme activities which is mostly characterized by the specific loss of GCX components [5]. Currently, evidence is also emerging to suggest that disturbed flow patterns within the vascular system could also result in GCX dysfunction. Harding *et al* recently showed that disturbed flow patterns resulted in the decrease in the expression of GCX in rat cells [6].

We hypothesize that disturbed flow patterns in the vascular system will enhance the attachment of cancer cells to the endothelium due to disturbed flow induced dysfunctions in the glycocalyx. Our results provide evidence to support the fact that hemodynamics and the endothelial glycocalyx, together, play an important role in mediating cancer-endothelial cell interactions relevant to secondary tumor formation.

METHODS

A parallel plate flow chamber [6], was used to to create disturbed flow patterns similar to what is observed *in vivo*. After introducing disturbed and laminar flow patterns to human umbilical vein endothelial cells (HUVEC) for 4 hours at 15 dynes/cm^2, we co-incubated HUVEC monolayers with Red Cell Tracker labeled stage IV breast cancer cell (4T1) or human breast adenocarcinoma cell (MCF7) in circulation, for an hour at 1 dynes/cm^2.

We investigated endothelial cell expression of GCX and the adhesion molecule E-selectin and made correlations to the level of attachment of 4T1 or MCF7 breast cancer cells.

In addition, we confirmed our results *in vivo*, 14 hours after no treatment or intravital treatment of Balb/c mice with 5 units (U) of neuraminidase (an enzyme that

degrades one component of the GCX: sialic acid). Red Cell Tracker labeled 4T1 breast cancer cells were injected into these mice intravitally and allowed to circulate for an hour. Mice were then sacrificed. Endothelial integrity was confirmed. GCX integrity or degradation was confirmed. 4T1 attachment to the blood vessel wall endothelial cells was quantified in the Balb/c mice lungs.

RESULTS

Disturbed flow enhances the attachment of 4T1 and MCF7 breast cancer cells to cultured HUVEC. Labeled 4T1 and MCF7 breast cancer cells were co-incubated, separately, with flow conditioned HUVEC. Compared to laminar flow conditions, 4T1 breast cancer cell attachment to the endothelium in disturbed flow conditions was increased by 2.35±0.29 fold. For MCF7, exposure to disturbed flow resulted in a 2.34±0.42 fold increase in attachment to HUVEC.

Differences in breast cancer cell attachment to HUVEC do not correlate to expression of E-selectin adhesion molecules. In fact, there is non-differential expression of E-selectin adhesion molecules between disturbed and laminar flow regions. We found that no statistically significant difference between the HUVEC expression of E-selectin adhesion molecules in disturbed versus laminar flow regions.

Elevated breast cancer cell attachment to HUVEC coincides with HUVEC glycocalyx degradation in disturbed flow regions, and is a result of glycocalyx degradation. Expression of GCX was assessed by wheat germ agglutinin (WGA) staining and showed an intact GCX on the surface of HUVEC monolayers in laminar flow conditions. After introducing HUVEC monolayers to disturbed flow patterns, the GCX coverage of and thickness on HUVEC were both reduced by about 60%. We attributed the increased breast cancer cell attachment to this reduction in GCX coverage. To confirm the role of the GCX in cancer-endothelial cell adhesion, we degraded the GCX in laminar flow conditions and successfully induced cancer cell attachment in the same region.

In vivo, neuraminidase-induced GCX degradation leads to increased attachment of 4T1 breast cancer cells in the pulmonary blood vessel wall endothelium. When *in vivo* experiments were performed to confirm *in vitro* findings, first we investigated the expression of GCX before and after treating Balb/c mice with 5 U of neuraminidase. We found that there was a statistically significant 20% decrease in the thickness of GCX in neuraminidase treated mice, in comparison with non-treated mice. After treating Balb/c mice with 5 U of Neur, there was also a statistically significant increase in the attachment of 4T1 breast cancer cells to the blood vessel walls in the lungs of neuraminidase treated Balb/c mice, in comparison with non-treated mice. Specifically, we observed a 2.2±0.11 fold increase in the attachment of 4T1 breast cancer cells to the lung blood vessel walls of neuraminidase treated mice, compared to untreated mice.

DISCUSSION

In this study, we showed evidence to support the importance of endothelial cell GCX in regulation of cancer cell attachment to the endothelium. In summary, we found that conditioning endothelial cells in disturbed flow conditions results in an increase in cancer cell attachment to the endothelium, which is independent of E-selectin expression and in correlation with GCX expression. We also confirmed that the increase in cancer attachment occurs as a direct result of decreased GCX expression in in vitro and in vivo. Our results provide new insight into the possible pathway leading to secondary tumor formation during the progression of cancer.

ACKNOWLEDGEMENTS

We appreciate funding from National Institutes of Health (K01 HL125499) and the National Science Foundation (DGE-096843).

REFERENCES:

1. Tian, Q., et al., *Recent perspectives of management of breast cancer metastasis - an update.* J buon, 2017. **22**(2): p. 295-300.
2. Sharma, R., et al., *Breast cancer metastasis: Putative therapeutic role of vascular cell adhesion molecule-1.* Cell Oncol (Dordr), 2017. **40**(3): p. 199-208.
3. Li, J. and M.R. King, *Adhesion receptors as therapeutic targets for circulating tumor cells.* Front Oncol, 2012. **2**: p. 79.
4. Steeg, P.S., *Targeting metastasis.* Nat Rev Cancer, 2016. **16**(4): p. 201-18.
5. Bosmann, H.B. and T.C. Hall, *Enzyme activity in invasive tumors of human breast and colon.* Proc Natl Acad Sci U S A, 1974. **71**(5): p. 1833-7.
6. Harding, I.C., et al., *Pro-atherosclerotic disturbed flow disrupts caveolin-1 expression, localization, and function via glycocalyx degradation.* J Transl Med, 2018. **16**(1): p. 364.
7. Fu, B.M., *Tumor Metastasis in the Microcirculation.* Adv Exp Med Biol, 2018. **1097**: p. 201-218.

SB³C2019
Summer Biomechanics, Bioengineering and Biotransport Conference
June 25 -28, Seven Springs, PA, USA

PULMONARY ARTERY HEMODYNAMIC CHANGES IN PEDIATRIC PATIENTS WITH VENTRICULAR SEPTAL DEFECTS

Melody L. Dong (1), Weiguang Yang (2), Marlene Rabinovitch (2), Jeffrey A. Feinstein (1,2), Alison L. Marsden (1,2)

(1) Bioengineering
Stanford University
Stanford, CA, USA

(2) Pediatric Cardiology
Stanford University
Stanford, CA, USA

INTRODUCTION

Ventricular septal defects (VSDs), the most common type of congenital heart defect (CHD), are characterized by a hole between the two ventricles, resulting in left-to-right shunting and increased flow in the right ventricle and pulmonary artery (PA).[1] The severity of the VSD is often diagnosed by the shunt size, which is measured by the ratio between the pulmonary and systemic flow (Qp:Qs ratio), with small, moderate, and large VSDs having <1.5:1, 2:1, and a 3:1 Qp:Qs ratio, respectively. If the VSD is left untreated or repaired late, it can lead to pulmonary arterial hypertension (PAH) in ~28% of VSD patients.[2] PAH is characterized by elevated PA pressure >25 mmHg and distal PA remodeling. Although previous studies have investigated the hemodynamics and its effect on cellular function in PAH, most have only focused on the disease progression and on the larger PAs.[3,4] Few have investigated the initiation of PAH in the context of small, distal PA hemodynamics, which are most severely affected by the remodeling process in PAH. Difficulties in assessing the hemodynamics in the small, distal PAs include the lack of *in vivo* flow and morphometry measurements, specifically in pediatric patients. We hypothesize that VSDs alter PA hemodynamics and mechanical stimuli on vessel walls, which may initiate cellular dysfunctional pathways in the small PAs and thereby contribute to the initiation of vascular remodeling and PAH.

In this study, we perform computational fluid dynamics (CFD) simulations to study the hemodynamics of the entire PA tree in different sized VSDs to understand the mechanical conditions present at initiation of PAH. We use a patient-specific geometry of the pediatric PA geometry to simulate large PA hemodynamics (>1mm diameter vessels). To model small PAs (<1mm diameter), we develop a preliminary scaling law of the PA morphometry tree based on regression analysis of healthy PA models. With a scaled pediatric PA morphometry tree, we estimate hypothetical hemodynamics in the distal PAs. To our knowledge, this is the first study investigating the hemodynamics at the initiation of VSD-induced PAH that quantifies hemodynamics in the entire PA tree.

METHODS

To model the proximal PAs (>1mm diameter) in a VSD patient, we created a 3D geometric model of the healthy PAs of a 1-year-old male patient (body surface area BSA 0.49m^2, Ht=75.6cm, Wt=11.3kg) from a CT scan using the open-source software package, SimVascular (simvascular.org). For CFD simulations, we used a backflow stabilized 3D Navier-Stokes fluid solver with fluid-structure interaction and variable deformable walls using the coupled momentum method and an elastic modulus of 311kPa.[5,6] At the inlet, we prescribed a generalized normal PA inflow waveform at the main PA, scaled to mean flows of 2.5, 3.75, 5, and 7.5 L/min for control (no VSD), small, moderate, and large VSD conditions. Assuming a cardiac index of 5 L/min/m^2 for our 1-year-old patient, the mean flow rates for the three VSD conditions corresponded to Qp:Qs of 1.5:1, 2:1, and 3:1, respectively.[7] At every outlet, we prescribed a 3-element Windkessel model tuned to match a normal target PA pressure. Outlet boundary conditions were chosen to be consistent for all VSD conditions under the assumption of healthy distal PA vascular resistance and capacitance at the initiation of PAH prior to any remodeling. The 3D PA simulation setup is shown in Figure 1a. From the proximal PA simulation, we extracted pressure, velocity, wall shear stress (WSS), oscillatory shear index (OSI), and strain measurements at 50 random arterial segments throughout the PA model.

Due to the lack of pediatric PA morphometry data, we performed a morphometric analysis of the proximal PAs in different sized patients to extrapolate the distal PA morphometry, which cannot be easily imaged *in vivo*, for any patient size. We used CT/MRA images from a cohort of 12 healthy patients ranging in BSA 0.49-2.01 m^2 to build patient-specific models of the large, proximal PAs (>1 mm diameter, limited by image resolution) in SimVascular. We performed a morphometric analysis of the proximal PAs in the model using the diameter-defined Strahler method to categorize vessels into orders by diameter.[8] Regression analyses of the vessel orders and diameters were performed for each patient. Trends in vessel orders and diameters for a BSA similar to our proximal PA model patient were extrapolated to the small PAs by scaling Huang et al.'s PA morphometry findings.[8] A mathematical distal PA model (<1mm diameter vessels) for a 1-year-old with a BSA of 0.49 m^2 was created according to Spilker et al.'s methods and assuming: (1) the branching pattern of the distal PAs is uniform across all patients, and (2) extrapolation of the proximal PA scaling roughly estimates the distal PA sizes.[9]

We modeled the distal PA hemodynamics by extrapolating the outlet flows from the proximal PA model to the generalized distal PA morphometric model (Fig 1b). To extrapolate flows down to 50μm diameter vessels and calculate wall shear stress (WSS), we apply Poiseuille assumptions with a viscosity power law to account for non-Newtonian effects in the small PAs according to Pries and Secomb's *in vivo* findings.[10]

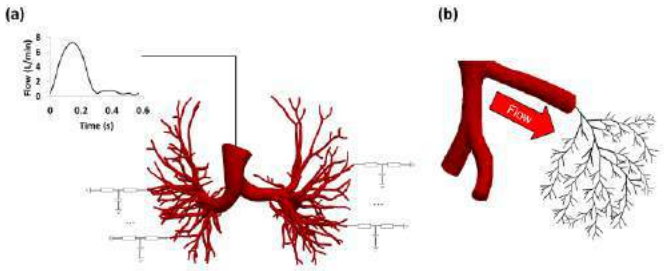

Figure 1: (a) Proximal PA model simulation setup with a prescribed inlet flow waveform and Windkessel outlet boundary conditions. (b) Distal PA mathematical model setup with extrapolated outlet flows from the 3D PA simulation to a BSA-scaled PA morphometry tree

RESULTS

In our proximal 3D model, we found that the average 1st invariant of Green's strain decreased down the PA tree and increased with VSD size (Fig 2a). Local OSI remained the same across different VSD sizes. Pressure waveforms were dampened in the distal PAs and increased in magnitude with larger VSDs. Proximal PA WSS increased with larger VSDs and down the tree with smaller vessels.

Preliminary multi-variable regression analysis of proximal PA morphometry data from pediatric and adult PAs showed logarithmic increases in vessel diameter with BSA. We used regression analyses relating BSA, vessel order, and vessel diameter to predict vessel diameters of the distal PAs for a 1-year-old.

With the 1-year-old scaled distal PA morphometric model, we found that the WSS increased with the smaller, distal PA tree and exceeded 200 dyn/cm^2 in the large VSD conditions. Figure 2b shows increasing WSS from the proximal and distal PA hemodynamics which also increase with VSD size.

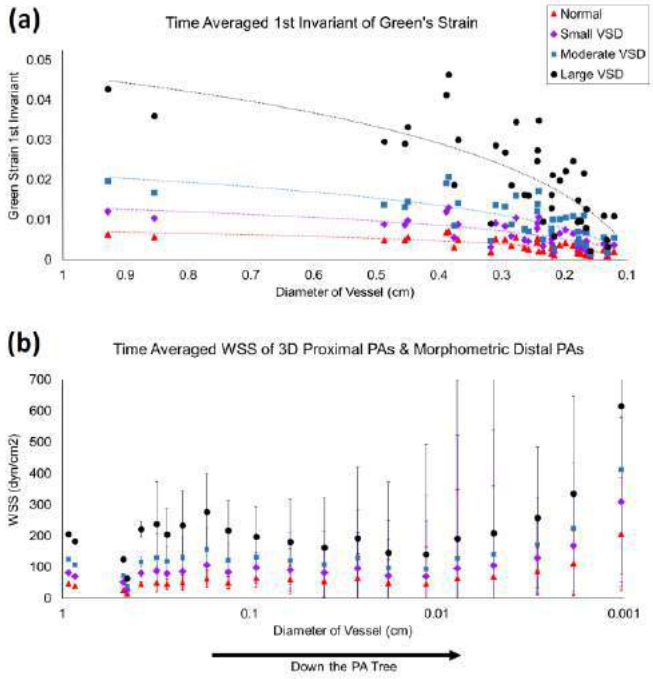

Figure 2: (a) The 1st invariant of Green's strain decreased down the tree and increased with VSD size. (b) WSS increased from the proximal PAs (~1cm-1mm) to the distal PAs (1mm-10μm) and increased with VSD size.

DISCUSSION

Knowledge of the hemodynamics in the small, distal PAs is significant for our understanding of the remodeling process that occurs in PAH. Our study estimates WSS values to be a magnitude higher in the small PAs compared to the large PAs, indicating that remodeling of small PAs may be subject to large hemodynamic differences even before the initiation of PAH. This is significant in informing mechanotransduction studies investigating the initiation of PAH, specifically as a result of the mechanical stimuli involved in untreated CHD patients who later develop PAH. Previous shear stress related gene expression studies on PAH have used much lower WSS values, which correspond mostly to the largest PAs where dilation and remodeling usually occur in late stages of PAH, not initiation or early stages.[3,11]

Furthermore, our preliminary results on the scaling of PA morphometry with patient size provides an initial understanding of how the PAs develop with age. Although morphometric studies have been extensively explored more than two decades ago, questions into how the entire PA tree grows in number and dimensions with age have yet to be answered thoroughly in humans.[12,13] We hope that our preliminary study of *in vivo* PA diameters at different vessel orders will elucidate unknowns into pre-acinar PA morphometry growth. Even with the knowledge of pre-acinar PA growth, which is useful for studying pediatric PAs, assumptions of the intra-acinar vessels must still be made for hemodynamic studies of the small vessels.

This is the first study to estimate the hemodynamics of the entire pediatric PA tree with VSD conditions, showing much higher WSS estimates in the small PAs than previously believed. These results have implications for the design of future biological studies assessing the effects of mechanical stimuli on endothelial cells as well as vascular wall mechanics that may occur during the initiation of PAH.

ACKNOWLEDGEMENTS

This material is based upon work supported by the National Science Foundation Graduate Research Fellowship under Grant No. DGE-1656518. Patient data was obtained from Dr. Jeff Feinstein's cohort of pediatric patients at the Lucile-Packard Children's Hospital. Simulations were performed using Stanford supercomputer resources (Sherlock).

REFERENCES

[1] Uebing, A. and H. Kaemmerer, *Diagnosis and Management of Adult Congenital Heart Disease 2nd ed*, 188-195, 2011.
[2] Engelfriet, P.M., et al., *Heart*, 93(6):682-7, 2007.
[3] Li, M., et al., *J Vasc Res*, 46(6):561-71, 2009.
[4] Tang, B.T., et al., *Pulm Circ*, 2(4):470-6, 2012.
[5] Taylor, C.A., et al., *Comput Methods in Appl Mech Eng*, 158(1-2), 1998.
[6] Figueroa, C.A., et al., *Comput Methods in Appl Mech Eng*, 195(41-43), 2006.
[7] Cattermole, G.N., et al., *Physiol Rep*, 5(6), 2017.
[8] Huang, W., et al., *J Appl Physiol*, 81(5): 2123-33, 1996.
[9] Spilker, R.L., et al., *Ann Biomed Eng*, 35(4):546-59, 2007.
[10] Secomb, T.W., *Annu Rev Fluid Mech*, 49:443-61, 2017.
[11] Szulcek, R., et al., *Am J Respir Crit Care Med*, 193(12), 2016.
[12] Hislop, A., *Paediatr Respir Rev*, 6(1):35-43, 2005.
[13] Davies, G. and L. Reid, *Thorax*, 25:669, 1970.

SB³C2019
Summer Biomechanics, Bioengineering and Biotransport Conference
June 25 -28, Seven Springs, PA, USA

FLUID-SOLID GROWTH MODELING OF PULMONARY VASCULAR TREE: ESTABILISHING A HOMEOSTATIC BASELINE STATE

Hamidreza Gharahi (1), Seungik Baek (1), Vasilina Filonova (2), C. Alberto Figueroa (2,3)

(1) Department of Mechanical Engineering
Michigan State University
East Lansing, MI, USA

(2) Department of Surgery
University of Michigan
Ann Arbor, MI, USA

(3) Department of Biomedical Engineering
University of Michigan
Ann Arbor, MI, USA

INTRODUCTION

Pulmonary arterial hypertension (PAH) is a complex vascular disease associated with a chronically elevated pulmonary arterial pressure. The onset and early progression of PAH can be traced to changes in the morphometry and structure of the distal vasculature tree. The overall goal of this work is to develop a computational model of PAH that couples hemodynamics with a vascular growth model. However, since the present medical imaging modalities are unable to provide accurate information on the downstream blood vessels, we need to establish the geometry of the distal arterial tree, consistent with pulmonary arterial literature. Moreover, modeling the growth and remodeling of the PAH through a fluid-solid growth formulation mandates the definition of the homeostatic baseline state in the distal vessels. The primary objective of the present work is to determine the homeostatic state in the distal arterial tree based on an extension of Murray's law and steady state hemodynamics.

METHODS

The composition and geometry of blood vessels strive to minimize the power consumption and dissipation which includes the metabolic cost of blood supply, power needed to overcome the viscous drag, and cost of maintaining the vessel wall materials. In this study, we assume that the target homeostatic state is governed by such an optimization rule [1]. To this end, the metabolic cost of the arterial wall constituents, C_{wall}, is assumed to be proportional to the mass of each constituent M_R^i with the constants α^i, which are the metabolic cost of each constituent per volume. Here, superscript i indicates each constituent. Similarly, the metabolic power needed for the supply of blood, C_{blood}, is proportional to the volume of blood that needs to be sustained with the constant α^b, which is the metabolic cost of blood per unit volume. Finally, the power per unit length needed to overcome the resistance (viscous drag forces) is computed using Poiseuille equation (C_{drag}).

The vascular wall is assumed to be composed of elastin, collagen fibers, and smooth muscle cell. In addition, a thin-walled model is used for simulating the mechanics of the wall. The total energy cost per unit length in each individual blood vessel can be written as:

$$C\left(M_R^i, R\right) = C_{wall} + C_{blood} + C_{drag} = \frac{2\pi R}{\rho_w}\sum \alpha^i M_R^i + \alpha^b \pi R^2 + \frac{8\mu q^{s2}}{\rho_b R^4} \quad (1)$$

where q^s is the steady state flow rate in the vessel and R is the radius of each vessel. The mechanical equilibrium dictates that the vessel wall must bear the load applied by the intraluminal pressure. Therefore, the mechanical equilibrium as a constraint is applied through

$$p^s R = T_{\theta\theta} \quad (2)$$

where p^s is the intraluminal pressure, and $T_{\theta\theta}$ is the tension in circumferential direction. Finally, a generalization of this minimization to a bifurcating tree involves consideration of the steady state hemodynamics at each bifurcation. This will be achieved by applying the conservation laws for the flow, $q_{d1}^s + q_{d2}^s = q_p^s$, and pressure, $p_{d1}^s = p_{d2}^s = p_p^s$, at the bifurcations. In addition, consistent with the assumption for the cost function, the flow in each vessel is assumed to follow a Poiseuille's solution. The boundary conditions for this problem are either pressure or flow, imposed at the root inlet and terminal vessels outlets (uniformly). Once the geometry and mechanical structure of the arterial tree is defined, an analytical solution based on Womersley's deformable wall theory [2] is applied to simulate the pulsatile hemodynamics in the arterial tree defined as a fractal tree [3].

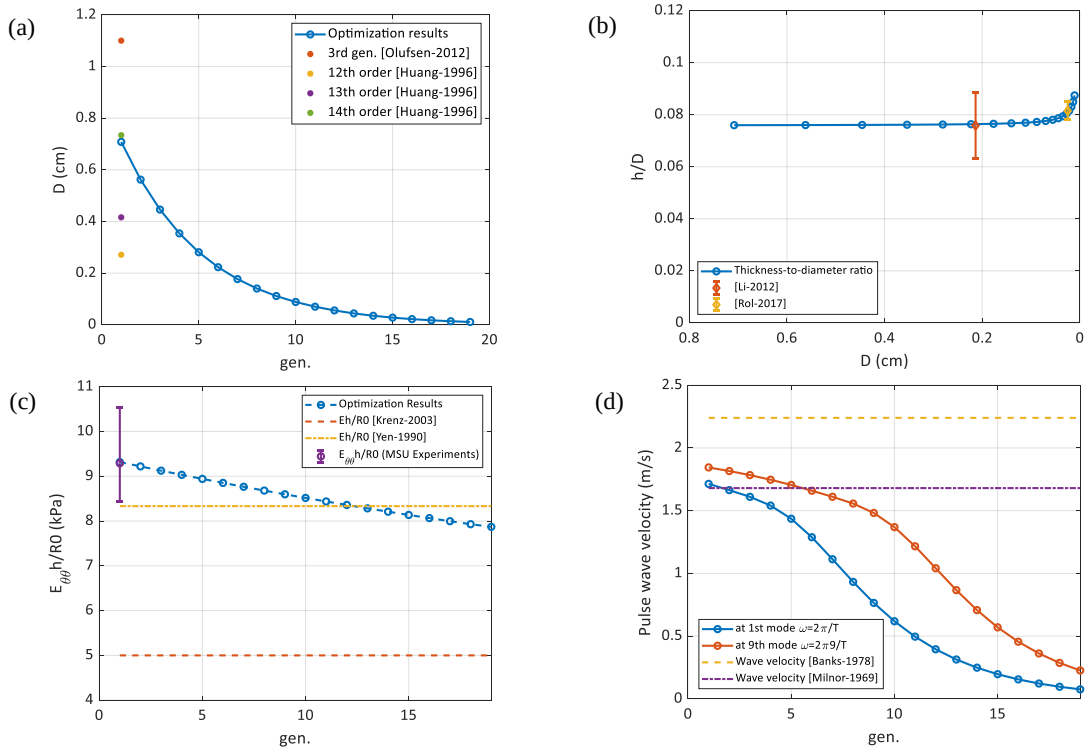

Figure 1 Symmetric tree – homeostatic optimization results: (a) diameter distribution compared to reported data of larger vessels; (b) thickness to diameter ratio distribution versus diameter; (c) ratio of structural stiffness to the unstressed radius versus generation number; (d) pulse wave velocity versus generation number.

RESULTS

Diameters of vessels as a result of optimization are shown in **Fig. 1a**. Our analysis demonstrates that for the linear Womersley theory to be valid, the tree optimization must start from the third bifurcation downstream of the main pulmonary artery. A morphometry study, by Huang and colleagues [4], on the branching pattern and vascular geometry of the human pulmonary arterial trees found 15 orders in the pulmonary arteries using Strahler ordering model. In their study, 1st and 15th orders correspond to precapillary vessels and right/left pulmonary arteries, respectively. A comparison of results obtained in the current study to the results from Huang et al. [4] indicates an agreement between the diameter of our 1st generation and their 14th order pulmonary vessel. **Figure 1b** shows the thickness to diameter ratio of the arteries varying from 7.5% in larger vessels to ~9% in smaller vessels. Using a linearization of the optimization results at the corresponding p^s, structural stiffness ratio to unstressed radius is computed and compared with other studies (**Fig. 1c**). Finally, the results of pulsatile hemodynamics are represented by the pulse wave velocity across different generations of the arterial tree (**Fig. 1d**).

DISCUSSION

We have described a model for identifying homeostatic state coupled with hemodynamics in a network of blood vessels with deformable wall. This model combines a constrained mixture model, which is widely used for modeling growth and remodeling, and a principle of minimum work to identify the otherwise unmeasurable quantities in downstream blood vessels. Applying the framework on a simple fractal tree with 14-19 generations produced physiologically reasonable results. The results compared against experimental data are shown in **Fig. 1**. A comparison with the data from [4] showed a great agreement of the first vessel diameter with what was observed in human pulmonary arterial tree. The wall thickness is obtained from the wall constituents mass resulting from the optimization. The results for thickness show excellent compatibility with limited experimental data in pressurized pulmonary vasculature [5,6]. Experimental studies on the structure of pulmonary vasculature showed a uniform stiffness across the entire pulmonary arteries [7,8]. However, a 15% decrease in the stiffness is observed in the model. It is worth noting that predicted stiffnesses in **Fig. 1c** are linearized at each vessel's estimated *in-vivo* pressure. Another distally unmeasurable but valuable characteristic of pulmonary vasculature is the pulse wave velocity distribution along the tree. The pulse wave velocity depends on a variety of factors including wall stiffness and vessel size. As shown for two harmonics where the 1st is the leading and the 9th is of least contribution **Fig. 1d**, a decrease of the pulse wave velocity across the generations is the result of decrease in the structural stiffness as well as vessel size variability. The pulse wave velocity in larger vessels, however, shows a great agreement with pulse wave velocity measured in large pulmonary arteries in [9,10].

ACKNOWLEDGEMENTS

This work was supported by the National Institute of Health under Grant U01 HL135842.

REFERENCES

[1] Lindström, SB et al. *Biomech. Model. Mechanobiol.*,14:83-91, 2015.
[2] Womersley, JR. *Phys. Med. Biol.*, 2(2):178-187, 1957.
[3] Olufsen, MS et al. *J Fluid Mech*., 705:280-305, 2012.
[4] Huang, W et al. *J. App. Physiol*., 81:2123-33, 1996.
[5] Li, N et al. *Heart Lung Circ*. 21:778-81, 2012.
[6] Rol, N et al. *Pysiol. Rep*. 5:1-9, 2017.
[7] Krenz, GS and Dawson CA. *Circ. Physiol.* 284:2192-2203, 2003
[8] Yen RT et al. *Resp. Biomech*. 109-116, 1990.
[9] Banks J et al. *Clin. Sci. Mol. Med.* 55:477-84, 1978.
[10] Milnor WR et al. *Circ. Res.* 25:637-49, 1969.

SB³C2019
Summer Biomechanics, Bioengineering and Biotransport Conference
June 25 -28, Seven Springs, PA, USA

AN ACTIVE CHEMO-MECHANICAL MODEL PREDICTS ADHESION AND MICROENVIRONMENTAL REGULATION OF 3D CELL SHAPES

Xingyu Chen (1, 2), Veronika te Boekhorst (3), Peter Friedl (3, 4), Vivek B. Shenoy (1, 2)

(1) Department of Materials Science and Engineering
University of Pennsylvania
Philadelphia, PA, USA

(2) Center for Engineering Mechanobiology
University of Pennsylvania
Philadelphia, PA, USA

(3) Department of Genitourinary Medical Oncology
University of Texas MD Anderson Cancer Center
Houston, TX, USA

(4) Department of Cell Biology
Radboud University Medical Center
Nijmegen, The Netherlands

INTRODUCTION

Cells are known to adapt their cytoskeletal structure in response to intracellular signals and changes in the extracellular microenvironment. When cultured on 2D substrates, the cells adopt a more spread and spindle-like morphology with an increase in the stiffness of the substrate [1]. In 3D, cancer cells are known to adapt to the microenvironment by switching between different migration strategies while invading into the surrounding matrix. Each of these migration modes is characterized by unique cell morphologies. Emerging evidence shows that geometric constraints on the cell shape can have an impact on cell stiffness, contractility, cell fate and the ability of the cells to proliferate and differentiate. Therefore, studying the mechanism of cell morphological changes can help understand the fundamental mechanisms of mechanotransduction.

While cell shapes in both 2D and 3D have been considered in many studies, the mechanisms that regulate cell morphological changes remain poorly understood both qualitatively and quantitatively. In this article, we present a chemo-mechanical approach that integrates signaling with free energy associated with mechanical deformation and active contraction to reveal the mechanism of cell morphological adaptation to the microenvironment. Specifically, we modeled the signaling pathways that regulate active recruitment of contractile elements in response to the changes in the prop, the non-linear strain stiffening of the matrix and the engagement of adhesions to obtain the total active potential or free energy of the cell matrix system. We find that different cell shapes are associated with different mechanical stresses and thus have different total energies. We then study how the stress-dependent contributions to the cell active potential due to the cortical actin network and the action fibers that run along the cell body can induce changes in shapes of cells. The role of adhesions which mechanically link the cytoskeleton with the extracellular matrix and regulate mechanotransduction is also studied.

METHODS

To elucidate mechanisms that determine the cell body shape, a chemo-mechanical energy-based model has been developed. The cell-ECM system energy associated with each cell shape is calculated and compared. The energy difference drives the cell shape to evolve from one to another, and the minimum energy determines the equilibrium cell shape. To calculate the system energy, the cell contracted state is considered to be derived from an imaginary quiescent reference state. Myosin motors are not engaged on the actin fibers, and no force or deformation is induced in this state. From the reference state to the contracted state, the energy change is divided into three categories: the cell energy, cell-matrix interface energy, and the matrix energy.

The cell is an active contractile material [2]. It extracts chemical potential energy from myosin motors to actively perform mechanical work. The cell energy thus contains mainly the chemical energy and the motor work. The chemical energy decreases with the increasing amount of myosin motors that are recruited to the cytoskeleton. This energy then converts to the mechanical work done by the myosin motors. The summation of chemical energy and motor work is defined as the cell active potential.

The cell-matrix interface energy characterizes the cell surface tension with originates from the cell membrane tension and cortical tension. This energy increases with the cell surface area.

The matrix energy is the strain energy stored in the matrix as the cell pulls the surrounding collagen fibers. It is calculated using a new constitutive model for collagen networks we have recently developed that accounts for the stiffening of the network along the direction of tensile principal strain directions [3].

RESULTS

When the cell properties are kept the same, and only the aspect ratio increases, the displacement field induced by cell contraction becomes larger and more anisotropic (Fig. 1a). As the cell adopts an elongated shape, the volumetric stress in the cell cytoskeleton increases (Fig. 1a & b). This is because, in the elongated configuration, the cell is less relaxed due to the geometrical constraint. It is as if the elongated cell is in a stiff matrix. The elevated volumetric stress stimulates the mechanosensitive feedback pathways (Rho-ROCK, Ca^{2+}), upregulating the myosin motors recruitment. More myosin motors are recruited with the increased cell aspect ratio (Fig. 1b). This leads to a decreased cell chemical energy, which scales with the motor density (Fig. 1c). Largely determined by the chemical energy, the cell active potential and matrix energy ($U - \Gamma$) decrease as the cell elongates (Fig. 3d). This suggests that the cell actomyosin activity naturally favors an elongated shape. On the other hand, as the cell evolves into an elongated shape with the same volume, the cell surface area increases. This causes the interface energy (Γ) to increase (Fig. 1d). Overall, the competition between the cell energy and the interfacial energy determines a non-monotonic total free energy curve, with the points of local minimum energy indicating the optimal cell shape (Fig. 1d). In some parameter ranges, two minima can be found. In the bistable region, the cell shape can adopt either shape. The cell shape of a cell population exhibits a bimodal distribution.

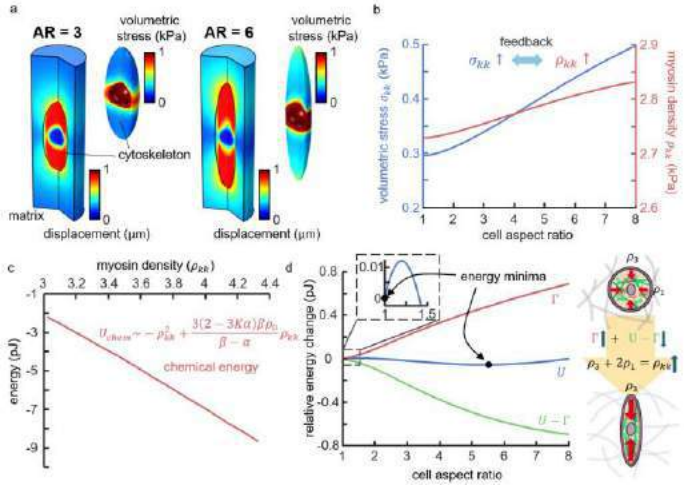

Figure 1: (a) The displacement field induced by cell contraction, and the cytoskeleton volumetric stress field. (b) The average cytoskeleton volumetric stress and myosin motor density with different cell shapes. (c) The relation between the chemical energy and the myosin motor density in (c). (d) The changes in energy as the cell elongates. The local minima of the total energy indicate the preferred cell shapes.

We then predicted that the cell aspect ratio depends on multiple intracellular signaling and extracellular properties (Fig. 2). For example, our model shows that the myosin motor recruitment regulated by feedback is the driving force for cell elongation. If the feedback strength α/β increases, the myosin recruitment from cell elongation further increases. The chemical energy reduction makes the elongated shape more energetically favorable. The model predicts that the cell aspect ratio will increase with the feedback strength α/β as plotted in Fig. 2. Similarly, the impact of the matrix stiffness and the adhesion density are also predicted. The cell aspect ratio increases with increasing matrix stiffness and adhesion density. Here the impact of ROCK inhibitor and integrin inhibitor are qualitatively marked on the phase diagram (Fig. 2). This prediction is consistent with the experimental results. The cells under the treatment of Y-27632 or 4B4 mAb both show rounder morphology compared with the control [4].

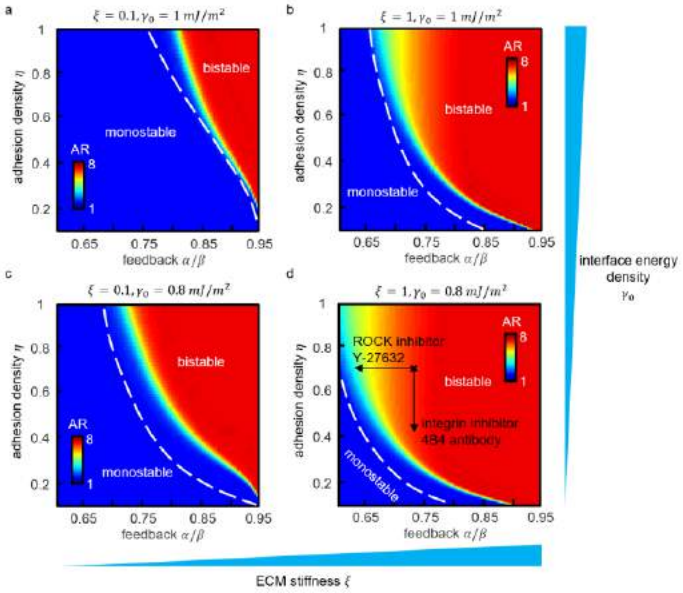

Figure 2: The phase diagram of the cell aspect ratio and stability regions. The adhesion density, feedback strength, interface energy, and matrix stiffness are varied. Here, ξ denotes the scale factor of the ECM stiffness, η denotes the scale factor of adhesion density.

DISCUSSION

Cell morphology evolution is a complicated process that involves crosstalk between intracellular activity and extracellular matrix deformation. Using an energetic approach, our computational model reveals the driving forces underlying the cell shape change and has successfully predicted its dependence on the matrix and the cell biomechanical properties. Specifically, our model identifies that the myosin motor recruitment can lower the system energy as the cell aspect ratio increases, driving the elongation. On the other hand, we found that the cortical tension and the membrane tension increase the system energy when the cell elongates, favoring a round shape which has a minimal surface area. This competition determines a non-monotonic correlation between the cell shape and system energy. The cell shape with the lowest system energy is predicted to be the optimum that the cells should evolve into eventually. The model is applied to predict the shape of cells cultured in collagen with different concentrations under the treatment of Y-27632 and 4B4 mAb. The predictions agree well with experimental results from the literature, validating the model's ability to explain and predict cell shape changes.

ACKNOWLEDGEMENTS

This work was supported by National Cancer Institute awards U01CA202177 and U54CA193417 (to V.B.S.), National Institute of Biomedical Imaging and Bioengineering award R01EB017753 (to V.B.S.) and the NSF Center for Engineering Mechanobiology (CMMI-154857), and NSF grant MRSEC/DMR-1720530.

REFERENCES

[1] Discher, D. E. et al. *Science* 310(5751):1139-1143, 2005.
[2] Shenoy, V. B., et al. *Interface Focus* 6(1):20150067, 2016.
[3] Wang, H. et al. Biophys. J. 107(11):2592-2603, 2014.
[4] Wolf, K. et al. J. Cell. Biol. 201(7):1069-1084, 2013.

SB³C2019
Summer Biomechanics, Bioengineering and Biotransport Conference
June 25 -28, Seven Springs, PA, USA

MYOSIN-INDEPENDENT REGULATION OF CELL AND NUCLEAR STRUCTURES IN WAVY PATTERNS

Bor-Lin Huang (1), Chin-Hsun Huang (1), Richard K. Assoian (2), Pen-hsiu Grace Chao (1)

(1) Department of Biomedical Engineering
National Taiwan University
Taipei, Taiwan

(2) Department of Pharmacology
University of Pennsylvania
Philadelphia, PA, USA

INTRODUCTION

Collagen bundles exist in dense connective tissues, such as tendons and elastic arteries, as parallel wavy fibers [1]. The structure, known as crimp, contribute to the mechanical functionality of the tissue [2]. Cells embedded in this tissue follow the crimp structure and have wavy cytoskeleton and nuclei. We previously demonstrated that fibroblasts in engineered wavy fibrous structures have increased collagen synthesis and altered mechanotransduction compared with aligned straight fibers [3, 4]. Geometric constraints of cell morphology have been shown to control nuclear shape and chromatin dynamics through myosin-mediated cytoskeletal structures [5-7]. To understand how the wavy morphology regulates cell behavior and expression, we hypothesize that actomyosin structures control nuclear shape, which lead to changed chromatin organization.

METHODS

Microfabticaton Fibronectin patterns were printed with the "stamp-off" method [8]. Briefly, PDMS membranes were coated with 50 μg/ml fibronectin and negative regions were removed with PDMS stamps treated with UV/Ozone or air plasma. Positive line patterns were 15 μm in width and the wavy pattern had an inner curvature of 100-133/mm. Pluronic-F127 (0.2 mM) incubation passivated the negative regions before cell culture.

Cell Culture Human bone marrow-derived mesenchymal stem cells or mouse embryonic fibroblasts were seeded on the patterned PDMS membrane for one hour or on the polyacrylamide gel overnight. Myosin activity was inhibited with 50 μM blebbistatin (Bleb) for 30 minutes.

Imaging and Analysis Cytoskeleton organization was examined by fluorescently labeling f-actin with AlexaFlour phalloidin (Invitrogen) and cell nuclei were labeled by DAPI. A custom Matlab program confirmed cell conformity to the patterns and segmented the nucleus to calculate the elliptical Fourier analysis (EFA, [9]) of nuclear perimeter as well as the chromatin condensation index (CCI, [10]).

Traction Force Microscopy (TFM) For TFM, fibronectin patterns were printed on glass and transferred onto polyacrylamide gels (9 kPa) with embedded fluorescent beads (0.2 μm). Cells were seeded on the gel overnight and imaged on a spinning disk confocal microscope (Nikon/Yokogawa) at 20x magnification. Displacement and traction maps were calculated with the ImageJ plugins PIV and FTTC [11].

Statistical Analysis R was used to generate plots and perform one-way ANOVA analysis with post-hot test (α=0.05). All experiments were repeated at least once, with more than 33 cells per group.

RESULTS

Cells conformed to the fibronectin patterns and had actin structures that followed the long axis of the cell. In the wavy pattern, strong actin arcs could be seen in the concave edges, sometimes spanning the pattern (Figure 1A). Fewer, often wavy, actin fibers were found on top of the nucleus in the wavy cells. Nuclear shapes also followed the patterns, with increased deviation from the ellipse in the wavy cells, as seen in the EFA results (Figure 1B). A concomitant increase in chromatin condensation (CCI), as analyzed from the bright DAPI clusters, was seen in the wavy patterns. Since morphology-associated nuclear changes have been attributed to actomyosin tension, we measured cell contractility with TFM. Significant increases (231%) in contractility was found in the wavy cells. Surprisingly, while myosin inhibition with blebbistatin (Bleb) reduced contractility in both groups ($p<10^{-10}$), it did not abolish the differences in contractility or change nuclear shape in the straight and wavy cells (Figure 2, 3A). However, myosin inhibition attenuated the difference in nuclear organization between the straight and wavy shape cells (Figure 3B).

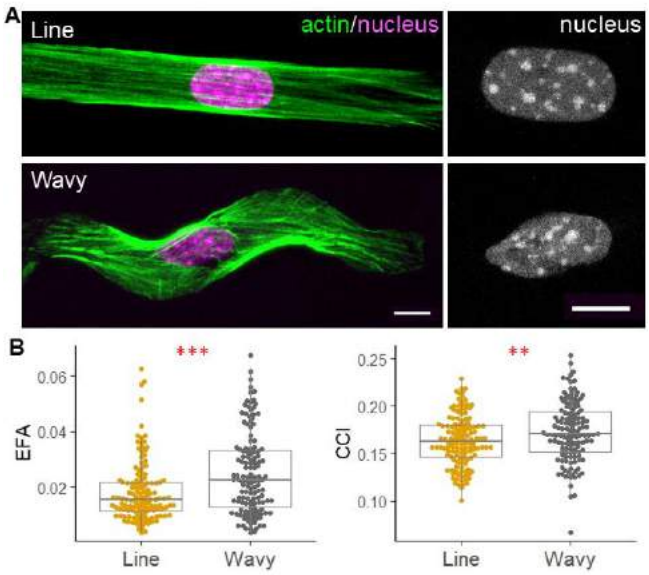

Figure 1: (A) Confocal images of representative cells in the line and wavy patterns. Scale bars = 10 µm. (B) Wavy patterns increase nuclear shape (EFA) and chromatin condensation index (CCI, **p<0.01, ***p<0.001)

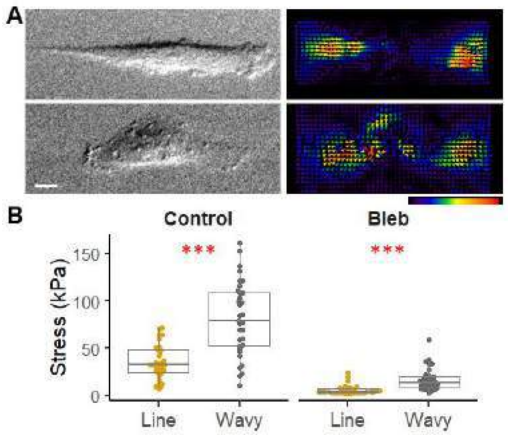

Figure 2: (A) Representative patterned cells on polyacrylamide gels and TFM maps (Scale bar = 10 µm or 1.2 kPa) (B) Wavy cells have higher average cell stress, even with blebbistatin treatment (***p<0.001).

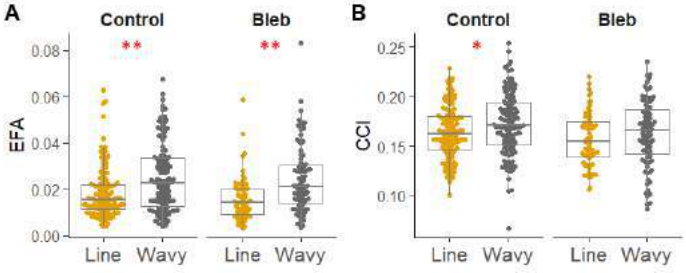

Figure 3: Myosin inhibition had no effects on nuclear shape (A) but reduced changes in chromatin condensation (B) in the wavy cells (*p<0.05, **p<0.01).

DISCUSSION

ECM crimp contributes to the structure-function relationships in elastic dense connective tissues and is disrupted with aging and injury [12-14]. While the mechanical role of the crimp structure is widely reported, few studies have investigated its role in the embedded cells. Using microcontact-printed straight and wavy fibronectin patterns, we demonstrated that cells conform to the line patterns with changed actin cytoskeleton and nuclear structures (Figure 1). Wavy cell morphology enhanced cell contractility, nuclear deformation, and chromatin condensation (Figure 2). Interestingly, the increased nuclear deformation and cell tension did not correspond with increases in projected nuclear area (p=0.31), suggesting curvature-induced nuclear morphological differences are different from cell aspect ratio-related regulations reported previously [15]. Most studies have found the actomyosin cytoskeleton responsible for the cell shape-induced nuclear changes [5, 15] and we confirmed its role in chromatin condensation (Figure 3B, [16]). However, contrary to our hypothesis, myosin-inhibition did not alter nuclear shape or eliminate the differences in curvature-induced cell traction force in our study (Figure 2,3). We have previously demonstrated that curvature-induced nuclear deformation is actin-dependent [17]. Current findings therefore indicate that wavy structures induced myosin-independent mechanisms to regulate traction forces and nuclear organization.

ACKNOWLEDGEMENTS

Funded by the Ministry of Science and Technology (MOST 107-2221-E-002-071-MY2).

REFERENCES

[1] Caves JM, Kumar VA, Xu W, et al. Adv Mater. 2010;22:2041.
[2] Lake SP, Miller KS, Elliott DM, et al. J Orth Res. 2009;27:1596.
[3] Chao P-hG, Hsu H-Y, Tseng H-Y. Biofabrication. 2014;6:035008.
[4] Szczesny SE, Driscoll TP, Tseng H-Y, et al. ACS Biomaterials Science & Engineering. 2017;3:2869.
[5] Jain N, Iyer KV, Kumar A, et al. Proc Natl Acad Sci USA. 2013.
[6] Makhija E, Jokhun DS, Shivashankar GV. Proc Natl Acad Sci USA. 2015;113:E32.
[7] Ramdas NM, Shivashankar GV. J Mol Biol. 2015;427:695.
[8] Desai RA, Rodriguez NM, Chen CS. Chapter 1 - "Stamp-off" to Micropattern Sparse, Multicomponent Features. In: Piel M, Théry M, editors. Methods in Cell Biology: Academic Press; 2014. p. 3.
[9] Lammerding J, Hsiao J, Schulze PC, et al. J Cell Biol. 2005;170:781.
[10] Irianto J, Swift J, Martins Rui P, et al. Biophys J. 2013;104:759.
[11] Tseng Q, Duchemin-Pelletier E, Deshiere A, et al. Proc Natl Acad Sci USA. 2012;109:1506.
[12] Legerlotz K, Dorn J, Richter J, et al. Acta Biomater. 2014;10:4447.
[13] Freedman BR, Zuskov A, Sarver JJ, et al. J Orth Res. 2015;33:904.
[14] Tsamis A, Krawiec JT, Vorp DA. Journal of The Royal Society Interface. 2013;10.
[15] Versaevel M, Grevesse T, Gabriele S. Nat Commun. 2012;3:671.
[16] Spagnol ST, Noel Dahl K. Integrat Biol. 2014;6:523.
[17] Fu K-J, Chao P-HG. Wavy Cells Control Nuclear Morphology through Actin Network. ASCB San Diego, CA2015.

SB³C2019
Summer Biomechanics, Bioengineering and Biotransport Conference
June 25 -28, Seven Springs, PA, USA

MAPPING 3D MECHANICAL STRAINS DURING TISSUE FORMATION WITH A NOVEL FIBRONECTIN-BASED NANOMECHANICAL BIOSENSOR

Daniel Shiwarski (1), Joshua Tashman (1), Alkis Tsamis (1), Quintin Jallerat (1), Malichi Blundon (3), J. Szymanski (1), B. McCartney (3), L. Davidson (4), and A. Feinberg (1,2)

(1) Department of Biomedical Engineering
Carnegie Mellon University
Pittsburgh, PA, USA

(2) Department of Materials Sciences
Carnegie Mellon University
Pittsburgh, PA, USA

(3) Department of Biological Sciences
Carnegie Mellon University
Pittsburgh, PA, USA

(4) Department of Bioengineering
University of Pittsburgh
Pittsburgh, PA, USA

INTRODUCTION

In developing tissue, mechanical forces are integral to a range of processes including cell differentiation, tissue morphogenesis, electrophysiology and contractility, but exact roles remain unknown. When mechanical forces are perturbed by experimental intervention or developmental abnormalities, their disruption can lead to congenital defects and disease. To date, tissue-level mechanical strains have been estimated by computational modeling, or by utilizing oil microdroplets as coarse-grained force sensors (1-2). Both methods lack ideal capabilities, which are (i) direct measurement of strain, (ii) at high spatial resolution over time, and (iii) with minimal perturbation of the system. We hypothesized that an extracellular matrix protein-based mechanical biosensor could measure the magnitude, direction and developmental timing of cell-generated strains within developing tissues and organs. Here we fabricated, calibrated and tested a fluorescently labeled fibronectin (FN)-based nano-mechanical biosensor (NMBS), which when applied to a tissue can deform in 3-D to provide a fluorescence-based strain readout during morphogenesis.

METHODS

To construct the NMBS we engineered a 2-D square-lattice mesh of fluorescent FN using a surface-initiated assembly based approach (Figure 1) (3). Briefly, a micropattern of interest is generated in a computer-aided design program and then transferred to a transparency photomask. The photomask is used in photolithography to expose a photoresist coated glass wafer, and then developed. A polydimethylsiloxane (PDMS) elastomer patterned stamp for microcontact printing is made by casting over the topographically-patterned photoresist-coated glass wafer. PDMS stamps are coated with the desired ECM protein, i.e. fluorescently labeled Alexa Fluor-633 human FN solution. The FN-coated PDMS stamps are stamped onto poly(N-isopropyl acrylamide) (PIPAAm) coated glass coverslips leaving a microcontact-printed fluorescently-labeled FN-based square-lattice mesh, or NMBS, onto the sacrificial PIPAAm surface. PIPAAm is thermoresponsive in water and enables transfer of the FN-mesh to other surfaces. We have NMBS with dimensions of 10 μm lines by 100 μm spacing, 10 μm lines by 20 μm spacing, and 2 μm lines by 2 μm spacing, all 2-5 nm in thickness.

To track tissue strain, the NMBS is transferred to a sacrificial carrier substrate that in turn is used to transfer the NMBS onto a tissue. The NMBS-patterned PIPAAm-coated glass coverslip is placed with NMBS face down onto a Type A gelatin carrier surface. Room temperature ddH2O is added to the glass coverslip causing dissolution of the PIPAAm and subsequent release and integration of the NMBS into the top surface of the gelatin. The NMBS-patterned gelatin gel is then lifted and placed with NMBS face down onto the desired tissue surface. This provides a general approach for transferring the NMBS to a range of tissues and surfaces. Finally, incubation at 37°C for 5 min melts the gelatin, integrating the NMBS onto the tissue surface.

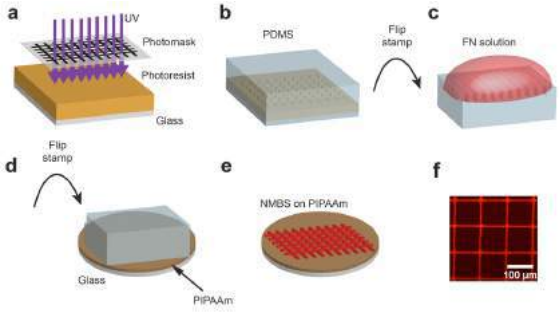

Figure 1: Fabrication of the NMBS via Surface-initiated Assembly

For *ex vivo* experiments, chick skin feather bud explants and Drosophila ovarioles genetically engineered to express Moesin-GFP and Histone-2B-RFP were utilized to create developmental strain maps through live spinning disk confocal microscopy of the NMBS. Stem cell-derived cardiomyocytes were maintained following standardized protocols and were utilized for analysis of cardiac beat frequency and contractile strain via NMBS tracking on a widefield fluorescence microscope in combination with Fluo-4 calcium imaging studies. Quantification and analysis of the NMBS over time was performed through computational image analysis using custom Matlab, Imaris, and ImageJ code following *in vivo* fluorescence imaging studies.

RESULTS

To validate the NMBS as a strain biosensor, FN-NMBS were mechanically calibrated by application onto polydimethylsiloxane (PDMS) "dog-bones" and placed under uniaxial mechanical strain testing. Images of fiduciary marks were utilized to correlate the tensile and compressive macroscopic strain with the FN-NMBS quantified microscopic strain. Following external mechanical deformation, the FN-NMBS exhibited high correlation between microscopic and macroscopic strain verifying its acuracy as a strain sensor (Figure 2).

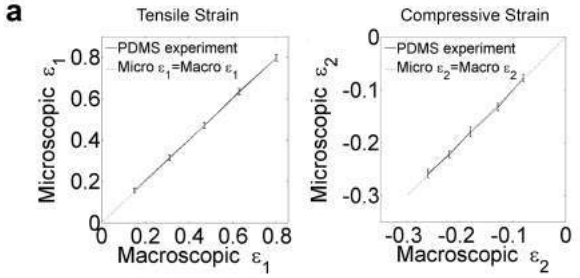

Figure 2: Uniaxial mechanical testing reveals correlation between NMBS microscopic strain and fiduciary macro strain tracking.

Finite element modeling simulations of uniaxial strain testing compared to the fluorescence data obtained via the FN-NMBS, confirmed the accuracy of the NMBS to track tissue level tensile and compressive strain. High-resolution fluorescence imaging of the NMBS applied to developing Drosophila ovarioles (Moesin-GFP, Green, Histone-2B-RFP, Blue, Alexa-633 NMBS, Red) revealed muscular contractions achieving 45% tensile and -46% compression strains every 10 seconds in a biphasic pulsatile fashion (Figure 3a, b).

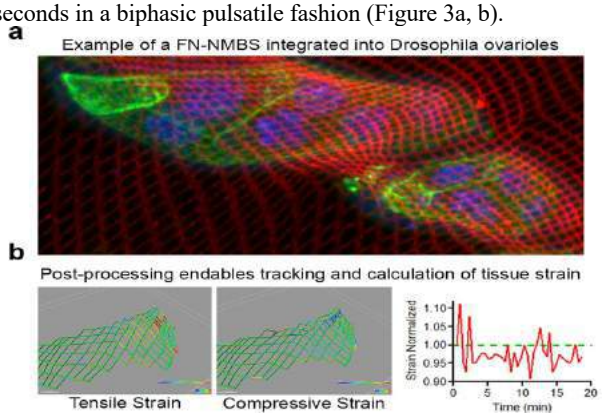

Figure 3: Live imaging and analysis of NMBS demonstrates tracking of *ex vivo* strain in 3D during Drosophila ovariole development.

Additionally, the NMBS was applied to Drosophila ovarioles for 3-D strain mapping during ovariole growth and morphogenesis. Following 3 hours of time-lapse imaging, strain maps were constructed revealing 80% tensile and -60% compression strains throughout the tissue accompanying an ~18% increase in ovariole volume.

Finally, the NMBS was applied to stem-cell derived cardiomyocyte (CM) monolayers to determine CM beat frequency variation and characterize contractile strain. Fluo-4 calcium indicator dyes was used to confirm CM beat frequency and correlate the NMBS data to electrical activity (Figure 4a; NMBS, Red, Fluo-4, Green). By using a Fast Fourier Transform (FFT) of the NMBS signal during CM contraction, we were able to construct a beat frequency map within the field of CMs to uncover 2 primary beat frequencies of 1.18 Hz (Pink) and 0.64 Hz (Grey) (Figure 4b). In addition to the beat frequency quantification, we were able to construct displacement and strain maps for CM contractile cycles showing a maximum displacement of 9 µm per contraction (Figure 4c). Following quantification and imaging of spontaneous CM activity, we electrical stimulated cells at 1, 2, and 3 Hz to validate the accuracy of the NMBS. In all cases, the NMBS beat frequency was an exact match to the stimulation rate.

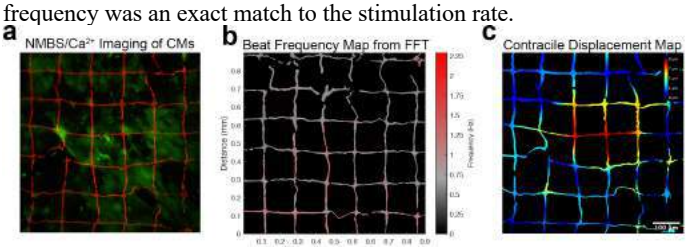

Figure 4: Live imaging of NMBS applied to cardiomyocytes reveals location specific beat frequencies and maps displacement.

DISCUSSION

By using our custom open-source Matlab, Imaris, and ImageJ software, we are able to track a wide range of microscopic tensile strain above 100% and compressive strain below -80% in various biological applications to quantify a variety of dynamic biomechanical properties. In the future, we plan to measure and map cardiac tissue strain in developing Xenopus embryos during heart tube formation and looping. Obtaining a map of the biomechanical strain during cardiac tissue development and utilizing this to improve current engineered cardiac tissues is one of our long-term goals that will bring us one-step closer to realizing the potential of human iPSC-derived cardiac cells for heart regeneration. Importantly, the impact will be even broader, as the tools developed, and knowledge gained are transferable to other cellular, tissue, and organ systems where developmental forces can guide physiology and engineering strategies.

ACKNOWLEDGEMENTS

This project has been funded by a NIH F32 from the National Heart, Lung, And Blood Institute under Award Number F32HL142229.

REFERENCES

[1] Campàs O, et al. Quantifying cell-generated mechanical forces within living embryonic tissues. Nat Meth. 2014 Feb;11(2):183–9.

[2] Polacheck WJ, et al. Measuring cell-generated forces: a guide to the available tools. Nat Meth. 2016 Apr 28;13(5):415–23.

[3] Feinberg AW, et al. Surface-initiated assembly of protein nanofabrics. Nano Lett. 2010 Jun 9;10(6):2184–91.

[4] Jaxckson TR, et al. Spatiotemporally Controlled Mechanical Cues Drive Progenitor Mesenchymal-to-Epithelial Transition Enabling Proper Heart Formation and Function. Current Biology. 2017 May 08, Vol 27, Iss 9, P1326-1335

SB^{3}C2019
Summer Biomechanics, Bioengineering and Biotransport Conference
June 25 -28, Seven Springs, PA, USA

TENDON ENTHESIS CILIUM ASSEMBLY IS DRIVEN BY MECHANICAL LOADING AND HEDGEHOG SIGNALING

Fei Fang (1), Andrea Schwartz (2), Stavros Thomopoulos (1)

(1) Department of Orthopedic Surgery
Columbia University
New York, NY, USA

(2) Department of Orthopaedic Surgery
Washington University in St. Louis
St. Louis, MO, USA

INTRODUCTION

Mechanical forces and hedgehog (Hh) signaling are necessary for the development and maintenance of the tendon enthesis [1]. Loading deprivation of mouse shoulders during postnatal development causes structural, compositional, and functional defects in the tendon enthesis, including reduced collagen fiber alignment, decreased mineral content, and impaired mechanical function [1, 2]. Loss of Hh signaling or Hh-responsive cells leads to significant defects in enthesis formation [1, 3]. Studies in other tissues have shown that both mechano-responsiveness and Hh signaling are regulated by the primary cilium, an antenna-like nonmotile organelle that projects from the cell's surface [4]. However, there is a lack of understanding about the crosstalk between cilium-mediated mechanotransduction and Hh signaling, and whether the cilium controls these processes during tendon enthesis development. Therefore, the current study evaluated the effects of *in vivo* loading on tendon enthesis cilium assembly and related Hh signaling.

METHODS

All animal procedures were approved by the Columbia University Institutional Animal Care and Use Committee. For overloading, 11-week old C57BL/6 male mice were allocated into three groups: treadmill running for 2 weeks, treadmill running for 4 weeks, or cage activity control (N=5 per group). The treadmill protocol consisted of downhill running at 10.2 m/min for 10 min followed by 13.2 m/min for another 40 min each day, 5 days a week, at a decline of 15 degrees. The unloading model followed the protocol from our previous study, which showed that neonatal botulinum toxin (BtxA)-induced paralysis leads to major defects in enthesis formation, and that decreased loading causes an increase in the number of Hh-responsive (i.e., Gli1+) cells [1-3]. To examine the crosstalk among primary cilium, mechanical loading, and Hh signaling, reporter mice were created by crossing Gli1 Cre^{ERT2} mice with Rosa26-mT/mG mice [1, 3]. 0.2 U BtxA in saline was delivered to mouse shoulder muscles twice per week from birth through sacrifice at day 56 (P56). The contralateral limbs were injected with saline and served as controls. To label Gli1+ cells, tamoxifen was dissolved in corn oil and injected subcutaneously at P14 or P28. Conditional knockdown of Ihh signaling. To evaluate whether Ihh hedgehog signaling contributes to primary cilia assembly/disassembly, ScxCre mice were crossed with Smo$^{fl/fl}$ mice. Humerus-supraspinatus tendon complexes from these mice were used for immunohistochemistry to examine cilia [1, 5, 6]. Immunohistochemistry and gene expression. Humerus-supraspinatus tendon complexes were prepared for frozen sections. Immunohistochemistry was used to label primary cilium (acetylated tubulin), Collagen type X, and Gli1 [4]; DAPI was used to visualize nuclei. The percentage of ciliated cells and the percentage of Gli1+ cells (normalized by the total cell number) were determined from histologic sections. Percent ciliation of Gli1+ cells was calculated as the number of cells positive for both primary cilium and Gli1 signaling, normalized by cells only expressing Gli1. For mice from treadmill running and cage activity groups, mRNA was isolated from tendon entheses using TRIzol reagent and Invitrogen PureLink RNA Mini kit [7]. The relative abundance of cilium- and Hh signaling-related genes were evaluated by SYBR-based quantitative RT-PCR. Data are presented as mean ± SD. Paired *t*-tests or unpaired *t*-tests, where appropriate, were used to compare cell percentages and gene expression of control and running groups.

RESULTS

There were more Gli1+/ciliated cells at the tendon enthesis of P7 mice than P28 mice, demonstrating coincident decreases in both Hh signaling and cilium assembly with maturity (Fig. 1). Muscle loading

regulated cilium assembly and Hh signaling. After 2 or 4 weeks of running, fewer cells at tendon enthesis possessed cilia compared to cage activity. However, the percentages of Gli1+ cells and Gli1+ cells with cilia were not affected by treadmill running (Fig. 2A-E). All genes related to cilia and Hh signaling were down-regulated in tendon entheses of treadmill running mice, with statistically significant differences for Ift88, Kif3a, DYNC2H1, and Gli2 (Fig. 2F). Compared to contralateral loaded controls, BtxA-induced unloading led to a significant increase in the number of ciliated cells, but a decrease of Gli+ cells with primary cilia (Fig. 3). ScxCre; $Smo^{fl/fl}$ mice showed significantly increased cilium presence in tendon cells, compared to control (Fig. 4).

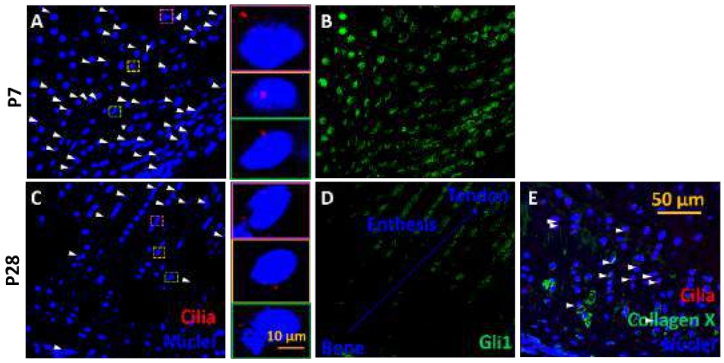

Fig. 1: There were more ciliated (red, arrowheads) and Gli1+ (green) cells in immature (P7; A, B) than mature (P28: C, D) entheses (blue: nuclei). Middle panels are magnified images of the cells highlighted by dotted lines (N=3). Most of cells with cilia (E) were at the fibrocartilage region (green, Collagen X).

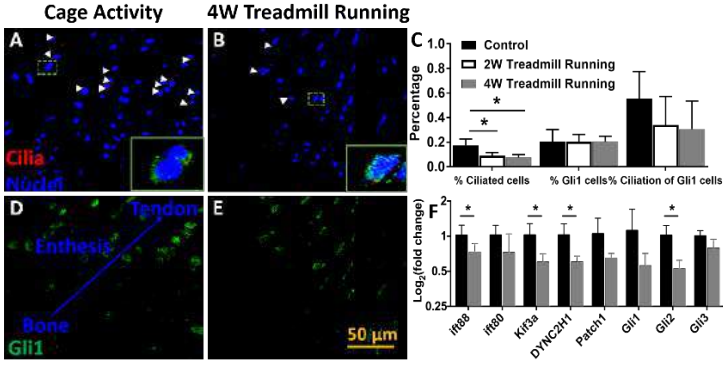

Fig. 2: Overloading via treadmill running led to loss of cilia in tendon enthesis cells. Entheses from cage activity and treadmill running for 4 weeks are shown (A-B, D-E). (C) There was a decrease in cells with primary cilia (red, arrowheads) after treadmill running, but the number of Gli1+ (green) cells was unchanged. (F) Expression of primary cilium and Hh-related genes was similarly downregulated after treadmill running (N=5 *$P<0.05$).

DISCUSSION

Hh signaling was highly co-localized with primary cilium in the postnatal developing enthesis. The presence of cilia and Hh signaling showed reduced trends with tendon maturity, consistent with our previous study [1, 3]. Manipulation of *in vivo* physiological loading of tendon enthesis regulated primary cilium assembly, with unloading causing cilia formation and overloading inducing cilia loss [8]. But the disagreement between an increase of cilium-positive cells caused by unloading and a decrease of the percentage of Gli1+ cells with primary cilium showed that cilium assembly is not fully synchronized with Hh signaling. This difference may also arise due to Gli1- cells forming primary cilia, due to unloading. Conditional knockdown of *Smo* promoted cilium assembly in tendon cells, indicating crosstalk between Hh signaling and cilium. These results indirectly support the idea that the primary cilium acts as both a mechanosensor and a Hh signaling hub at the developing tendon enthesis [7, 8]. To further examine the role of the primary cilium in tendon enthesis function and the influence of Hh signaling on cilium assembly, future work will use transgenic mice to examine structure and function of tendons with inhibited cilium assembly and address whether tendons with dysfunctional primary cilia can respond to mechanical loading and hedgehog signaling.

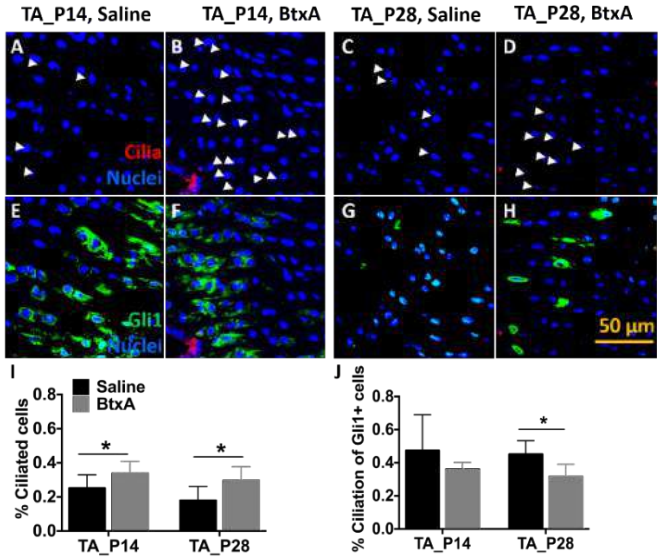

Fig. 3: BtxA unloading caused cilium assembly in the entheses. The entheses of BtxA and saline administration with tamoxifen injected at P14 (TA_P14), or P28 (TA_P28) were examined (A-H). Compared to the saline group, the percentage of ciliated cells (I) in the BtxA group was increased, but the percentage of Gli1+ cells with cilia (J) was reduced (N=4-5 *$P<0.05$).

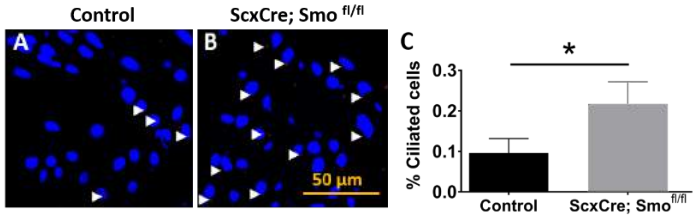

Fig. 4: Conditional knockdown of *Smo* in *Scx*-positive cells caused cilium assembly in tendon entheses. Representative images of control and knockdown mice are shown (A-B). The percentage of cells with primary cilia (C) was increased in knockdown mice.

REFERENCES

[1] Schwartz, A et al., *Development*, 144:1159-1164, 2015.
[2] Tatara, A et al., *PloS One*, 9:e97375, 2014.
[3] Schwarz, A et al., *Development*, 142:196-206, 2017.
[4] Kopinke, D et al., *Cell*, 170:340-351, 2017.
[5] Blitz, E et al., *Dev Cell*, 17:861-873, 2009.
[6] Long, F et al., *Development*, 128:5099-5108, 2001.
[7] Shen, H et al., *FASEBJ,* 31:5466-5477, 2017.
[8] Oliazadeh, N et al., *Sci Rep,* **7**:44260, 2017.

SB³C2019
Summer Biomechanics, Bioengineering and Biotransport Conference
June 25 -28, Seven Springs, PA, USA

SENSING THE CURVATURE: PROTRUSIVE SENSITIVITY OF INVASIVE BREAST CANCER CELLS

Apratim Mukherjee (1), Bahareh Behkam (1), Amrinder S. Nain (1)

(1) Department of Mechanical Engineering
Virginia Tech
Blacksburg, VA, United States

INTRODUCTION

Cancer metastasis requires cells at the tumor boundary to biophysically probe the surrounding extracellular matrix (ECM) fibers through the formation of protrusions prior to detachment and subsequent migration through the ECM [1]. The fibers that the cell protrusions interact with span a wide range of diameters (from tens of nanometers to micrometers) [2], and *in vitro* assays have previously demonstrated that the fiber diameter can strongly influence both cell morphology and focal adhesion arrangements [3,4]. Using non-electrospinning Spinneret based Tunable Engineered Parameters (STEP) platform, we have previously shown that highly metastatic MDA-MB-231 cells form longer protrusions compared to their non-cancerous MCF-10A counterparts [5,6]. We found that the protrusions elongated in a diameter dependent manner by *coiling* (wrapping-around) the fibers. However, our understanding of how fiber curvature regulates *coiling* (protrusion sensitivity) remains limited.

Here, using quantitative high spatiotemporal video microscopy, we interrogate the sensitivity (*coiling*) of individual protrusions to fiber curvature. Specifically, we employ a suspended network of fibers with contrasting curvatures that decouples protrusive dynamics from bulk cell body migration [6]. Our method constrains cell body migration to large diameter (≥2 μm) *base fibers* while allowing studying single protrusions on smaller diameter *protrusive fibers* of different diameters (135, 270, 450, 600 and 1000 nm) (**Fig. 1A**), Interestingly, we find that protrusion tip *coiling* coincides with highly persistent translocation of endogenous granules into the protrusions.

METHODS

The previously reported non-electrospinning Spinneret based Tunable Engineered Parameters (STEP) method [6] was used to spin the protrusive fiber network described above. Polystyrene (PS, Scientific Products, Ontario, NY, MW = 2×10^6 g mol^{-1}) was dissolved in p-xylene (Fisher Scientific, Pittsburgh, PA) at (w/w) concentrations of 7, 8, 10, 12 and 14% to prepare solutions to spin the ~135 nm, ~270 nm, ~450 nm, ~600 nm, and ~1000 nm diameter *protrusive fibers* respectively. The spacing between consecutive *base* and *protrusive fibers* was fixed at ~200 μm and ~75 μm respectively.

MDA-MB-231 mammary ductal adenocarcinoma cells were cultured in Leibovitz's L-15 media (Thermo Fisher Scientific, Waltham, MA) supplemented with 10% Fetal Bovine Serum and 1% penicillin/streptomycin. Prior to seeding the cells, the protrusion scaffolds were incubated with 4 μg/ml Fibronectin (Invitrogen, Carsbad, CA) for 3 hours, followed by cell seeding at a density of ~300,000 cells/ml. Cells were imaged using an AxioObserver Z.1 (with mRm camera) microscope (Carl Zeiss, Germany) at 63× (water immersion objective) magnification with 1 second imaging interval. ImageJ (National Institutes of Health, Bethesda, MD) was used to analyze the images.

At least three independent experiments were conducted for each defined metric and statistical analysis of the data was performed using RStudio (RStudio, Boston, MA). One-way analysis of variance (ANOVA) with the Tukey test was used to test for statistical significance between the different data sets.

RESULTS

Using the STEP platform we investigated MDA-MB-231 protrusive behavior at high spatiotemporal resolution (63× magnification/1 second imaging interval) and found that protrusions extended on suspended fibers by *coiling* around the fiber axis. We defined morphodynamic metrics of protrusion length (L) and eccentricity (E: broadening of protrusion base) to characterize the *protrusive cycle* (growth, maturation and retraction) of a single

protrusion (**Fig. 1A,B**) and the maximum *coil* width (**Fig. 1C,D**) to quantify *coiling* dynamics. We found that the *coiling* occurred in "spurts" synchronously with the growth phase of the *protrusive cycle*. Furthermore, while the fiber diameters at either extreme of the tested range (~135 nm and ~1000 nm) resulted in *coiling* initiation independent of an increase in E, on the intermediate diameters (~270 nm - ~600 nm) a significant increase in E was necessary prior to *coiling* initiation (**Fig. 1E**)**.** Thus, we found that both the average E at *coiling* initiation and the time it takes for *coiling* to be initiated exhibit biphasic relationships with increasing fiber diameter (**Fig. 1F,G**)**.**

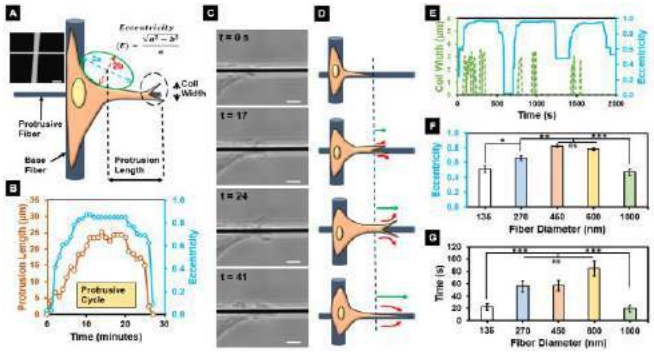

Figure 1: Morphodynamic metrics used to quantitate *coiling* dynamics. (A) Schematic of the protrusion fiber network along with definition of the metrics used to quantitate the protrusive cycle and *coiling* dynamics. Inset shows SEM image of a 2 µm *base fiber* and a 450 nm diameter *protrusive fiber*. **(B)** Representative *protrusive cycle*. **(C, D)** Phase images and schematic showing the temporal evolution of *coiling* on a 600 nm diameter *protrusive fiber*. **(E)** Increase in E is typically required prior to *coiling* initiation (representative profile for a 600 nm fiber diameter case) **(F, G)** Average eccentricity at *coil* initiation and time taken for *coiling* to be initiated as a function of fiber diameter. n values: 21, 21, 23, 20, 20 for the diameters 135, 270, 450, 600, 1000 nm, respectively. All scale bars are 5 µm.

To investigate the dynamics of individual *coiling* events we defined additional metrics of *coil* growth rate (rate at which the *coil* width increases) and the time taken to reach maximum *coil* width. We found that both the maximum *coil* width and *coil* growth rate exhibited an increase with increasing fiber diameter (**Fig. 2A,B**) whereas the time taken to reach the maximum width showed a biphasic response with increasing fiber diameter (**Fig. 2C**).

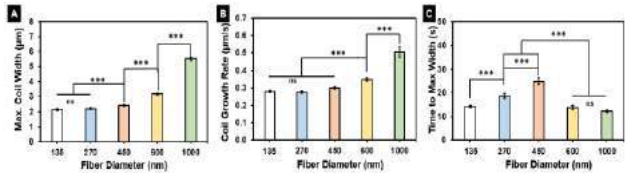

Figure 2: Individual *coiling* dynamics are regulated by fiber diameter. (A) Maximum *coil* width **(B)** *Coil* growth rate and **(C)** Time to reach maximum *coil* width as a function of the *protrusive fiber* diameter. n values: 117, 75, 113, 111, 77 for the diameters 135, 270, 450, 600, 1000 nm, respectively.

We also observed endogenous granules translocating into the protrusions (**Fig. 3A**) during the growth phase of the *protrusive cycle* which coincides with the *coiling* spurts (**Fig. 3B**). Given that fiber diameter regulated *coiling* kinetics, we thus inquired whether the granule dynamics were also influenced by the fiber diameter. We found that similar to the trends shown by the individual *coiling* dynamics, the speed and persistence (ratio of displacement to the total distance) of the granules increased with increasing fiber diameter (**Fig. 3C,D**). Furthermore, mean square displacement (MSD) analysis of the granules trajectory revealed that the granules exhibited superdiffusive motion with the MSD exponent also increasing as a function of fiber diameter (MSD exponent of 1.37 ± 0.07, 1.57 ± 0.05, and 1.77 ± 0.04 on ~135, ~450, and ~1000 nm diameter fibers respectively).

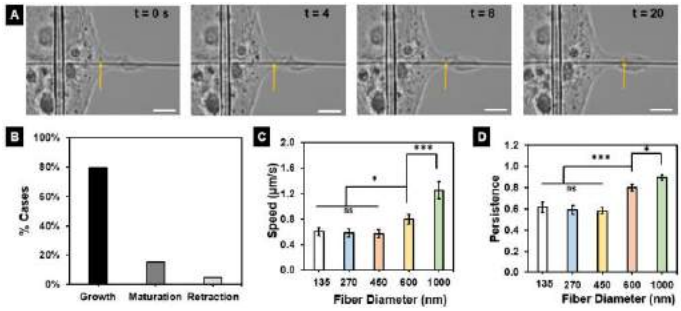

Figure 3: Dynamics of granule translocation into protrusions. (A) Representative time lapse images showing a granule enter into a protrusion (yellow arrows mark granule location; scale bar is 5 µm). **(B)** Percentage of total granule translocation cases during each stage of the *protrusive cycle* (n = 89 granules). **(C, D)** Granule speed and persistence as a function of fiber diameter. n values: 19, 17, 12, 21, 20 for the diameters 135, 270, 450, 600, 1000 nm, respectively.

DISCUSSION

In this study, we quantitatively investigated the dynamics of single protrusion-fiber interactions and found that the fiber diameter plays a significant role in regulating protrusion tip *coiling* dynamics. While both the average E at *coiling* initiation and the time taken to initiate *coiling* exhibit a biphasic response with increasing fiber diameter, the individual *coiling* kinetics (maximum width and growth rate) increases as a function of fiber diameter. The observed differences and similarities in *coiling* dynamics between fibers on either extreme of the investigated range can be potentially explained based on available surface area for the protrusions. The smallest tested diameter fibers (~135 nm) do not provide enough surface area for the maturation of focal adhesions whereas in contrast, the largest examined diameter fibers (~1000 nm) provide sufficient area for cells to attach faster.

In summary, our platform of suspended ECM mimicking fibers allows systematic investigation of how cancer cells biophysically sense fibers of varying diameters, thus allowing us in the future to characterize conditions which either promote or hinder metastatic invasion.

ACKNOWLEDGEMENTS

This work is supported by NSF (1437101 and 1462916) awarded to ASN, NSF CAREER (1454226) to BB. Authors acknowledge the support from Institute for Critical Technologies and Sciences (ICTAS), Virginia Tech.

REFERENCES

[1] Stoletov, K, et al., *Nature Comm.*, 9:1-12, 2018.
[2] Ushiki, T, et al., *Arch Histol Cytol*, 65:109-126, 2002.
[3] Kennedy, K, et al., *Acta Biomater*, 50:41–55, 2017.
[4] Meehan, S, et al., *Biophys J*, 107:2604–2611, 2014.
[5] Nain, A. S, et al., *Macromol Rapid Commun*, 30:1406–1412, 2009.
[6] Koons, B, et al., *ACS Nano*, 11:12037-12048, 2017.
[8] Schliwa, M, et al., *Nature*, 422:759-765, 2003.
[9] Kerber, M, et al., *J Cell Science*, 124:3733-3741, 2011.

SB³C2019
Summer Biomechanics, Bioengineering and Biotransport Conference
June 25 -28, Seven Springs, PA, USA

TOWARDS FIBER-LEVEL TRACTION FORCE MICROSCOPY IN COLLAGEN GELS

Lauren M. Bersie-Larson (1), Jay Hou (1), Victor H. Barocas (1), Paolo P. Provenzano (1)

(1) Department of Biomedical Engineering
University of Minnesota – Twin Cities
Minneapolis, MN, USA

INTRODUCTION

Cell-generated forces drive cell migration and rearrange the surrounding extracellular matrix (ECM). These forces are fundamental to physiological processes such as morphogenesis and wound healing and are altered in disease states such as cancer [1-3]. Quantifying cell-generated forces in 3D, then, is pertinent to better understanding cell migration and matrix remodeling in these contexts. Yet much remains unknown about cell forces in these processes, in part due to the limitations of current methods of measuring cell forces [4].

Traction force microscopy, or TFM, is the most commonly used approach for cell force measurement [1]. Traditional methods of TFM rely on measuring the deformation of 2D substrates to calculate cell forces [2]. However, cells exhibit different migratory modes and focal adhesion dynamics in 3D compared to 2D [5, 6], and these modes are highly dependent on ECM properties; as a result, cell forces measured in 2D may not be representative of the cell forces that would be exerted in a 3D environment [6]. Moreover, the substrates used in classical TFM are linear elastic, while ECM and engineered equivalents have been shown to have nonlinear elastic and viscoelastic properties [7].

In order to improve upon these limitations, 3D approaches have been developed to incorporate more native ECM-like environments such as collagen gels [8]. While these methods address the limitations of traditional 2D techniques, they utilize constitutive models of the ECM to solve for traction forces. In doing so, these methods fail to capture the specific local fiber architecture or account for the fact that as cells migrate and generate forces, they in turn reorganize the surrounding ECM, causing local anisotropy in both fiber alignment and stiffness due to strain stiffening [9].

This work aims to address an unfulfilled need in the field for a method of accurately measuring traction forces in 3D at the fiber level [1, 10].

METHODS

Toward this end, we are developing a method of measuring forces on the fiber level with the following steps: 1) image acquisition of cells deforming 3D matrices using SHG imaging, 2) image analysis of the fiber network architecture from SHG images using a fiber extraction algorithm [11], 3) network deformation tracking using a shape context method [12], and 4) inputting deformations into a discrete network model [13], from which cell forces can be calculated. In order to develop this TFM approach, we must first validate each of these steps. With this in mind, we focus here on the various methods we are using to validate this approach.

Image Analysis: The FIbeR Extraction (FIRE) algorithm [11] has been used in the literature to quantify collagen fiber architecture from SHG image z-stacks. FIRE finds fiber architectures by taking an image stack, flattening it, applying a Gaussian filter, and then binarizing the image using a pixel value threshold. It then utilizes a minimum distance from pixels to the background and traces along the maximal ridges of the distance function. Using an input threshold, the algorithm identifies nucleation points, and then connects these points to local maxima of the distance function, thereby creating a network of nucleation points and branches representing the network architecture.

To test the FIRE algorithm's validity for network architecture extraction, 3 mg/mL collagen gels were created as described in [14] and were imaged at 880 nm using a MaiTai Ti:Sapphire laser to obtain SHG signal for collagen fiber visualization. SHG z-stack images were collapsed using a maximum image projection and qualitatively compared to a z-projection of the extracted network.

Network Deformation Tracking: Once network architectures are extracted from SHG images, deformations of network fibers and nodes (crosslinks within the network) are tracked by registering nodes at each time point based on their so-called shape context, an idea first presented

by Belongie et al. [12]. A shape context, or polar histogram, is constructed for each node in the undeformed and deformed configurations based on the spatial distribution of the other nodes around it. A cost function is constructed based on the match of the shape contexts for each node between images. This cost function is a Chi squared statistic, calculated as follows:

$$C_{ij} = C(p_i, p_j) = \frac{1}{2}\sum_{k=1}^{K}\frac{[h_i(k) - h_j(k)]^2}{h_i(k) + h_j(k)} \quad (1)$$

Where C_{ij} is the cost matrix, a function of points p_i in the initial image and p_j in the deformed image; K is the number of histogram bins; and $h_i(k)$ and $h_j(k)$ are the K-bin normalized histograms at p_i and p_j. Once the cost matrix is created, nodes are matched by minimizing the cost associated with registering nodes using the LAPJV Jonker-Volgenant algorithm for the linear assignment problem in MATLAB [15].

To assess the tracking accuracy, we created networks computationally in MATLAB, deformed them by uniaxially stretching the networks, and then added varying amounts of noise to assess the limits of this method of network deformation tracking.

Force Calculation: Finally, using the tracked network deformations, forces exerted on the network are calculated using a discrete network code [13] where network nodes are modeled as pin joints and fibers are modeled by a nonlinear force-strain equation:

$$f = \frac{AE}{B}[\exp(B\varepsilon) - 1] \quad (2)$$

Where f is the fiber force, A is the fiber cross-sectional area, E and B are material parameters relating to the elastic modulus and nonlinearity, respectively, and ε is the Green strain.

After applying the deformations found by the tracking algorithm to this network model, traction forces may then be found by calculating forces on the interior nodes of the network. Nodes with a resulting nonzero force correspond to those that have an external force applied upon them, and the resulting traction forces can be found accordingly.

To test this portion of the method, simulated cell contractions were applied to networks at a patch of nodes, and the resulting deformation was tracked. Forces calculated from tracking were then compared to the applied forces.

RESULTS

Image Analysis Assessment of the network architecture extraction was performed by visual inspection, and the resulting fiber organization (Fig. 1B) was in good agreement with what was considered the ground truth, the SHG image (Fig. 1A). A 3D view of the resulting reconstructed fiber network is shown in Figure 1C.

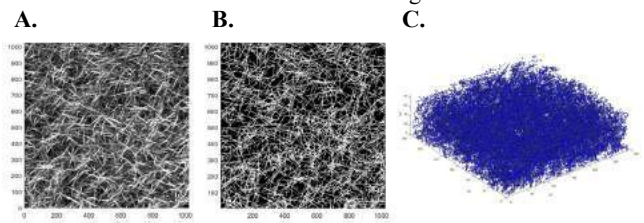

Figure 1: A. Collapsed SHG z-stack of a 3D collagen gel. B. Z-projection of the extracted network architecture from the FIRE algorithm. C. The discrete network model reconstruction.

Network Deformation Tracking Networks were subjected to levels of noise ranging from 0.1% to 5%, and the resulting fiber forces from the tracked deformation were plotted against the fiber forces from the actual deformation (Fig. 2). It can be noted that tracked fiber force measurements start to deviate from exact fiber force values at roughly 4-5% added noise.

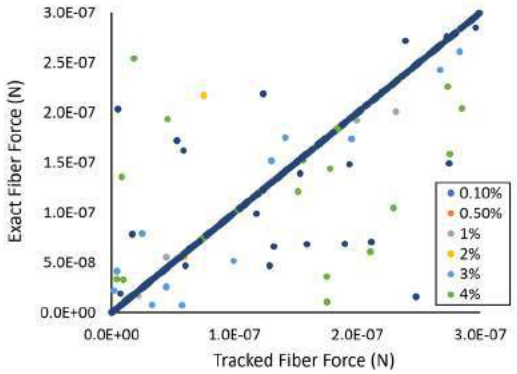

Figure 2: Sensitivity of the tracking algorithm to noise (n= 883).

Force Calculation Results of the validation of the force calculation are shown in Fig. 3. This work demonstrated that the methods do well with low (~100 nN) and medium (~1000 nN) forces, but have a harder time calculating traction force when high forces (~2000 nN) are applied, due to the fact the tracking algorithm is imperfect at larger deformations.

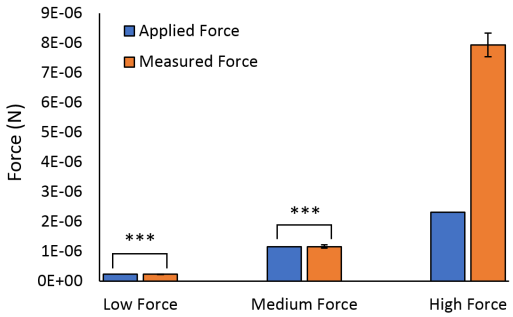

Figure 3: Forces applied to a network versus the measured forces from tracking (error bars= 95% confidence intervals; p < 0.001).

DISCUSSION

We present here the first work towards fiber-level traction force microscopy in collagen gels, which, once complete, can provide better insight into fundamental biological and pathological processes such as development and cancer. The results in our preliminary validation studies hold promise that our approach can accurately calculate traction forces with moderate noise and deformation present, and we are continuing to work on improving our deformation tracking methods for higher noise and deformation levels as we expand into experimental validation techniques.

ACKNOWLEDGEMENTS

This work is supported by NIH grant 5U54CA210190-02.

REFERENCES

[1] Polacheck, W & Chen, C, *Nat Methods*, 13(5):415-23, 2016. [2] Hall, M et al., *Exp Cell Res*, 319(16):2396-2408, 2013. [3] Li, Z et al., *Nanoscale*, 9:19039, 2017. [4] Mulligan, J, et al., *Biomechanics in Oncology*, 319–49, 2018. [5] Petrie, R & Yamada, K, *J Cell Sci*, 125(24):5917–26, 2012. [6] Han, S & Sniadecki, N, *Cellular and Biomolecular Mechanics and Mechanobiology,* 177-200, 2011.
[7] Nam, S, et al., *Proc Natl Acad Sci USA*, 113(20):5492–97, 2016.
[8] Steinwachs, J et al., *Nat Methods*, 13(2):171–76, 2016.
[9] Ahmadzadeh, H, et al., *Proc Natl Acad Sci USA*,114(9)1617–26, 2017. [10] Colin-York, H & Fritzsche, M, *Curr Opin Biomed Eng*, 5:1–5, 2018. [11] Stein, A, et al., *J Microsc*, 232(3):463–475, 2008. [12] Belongie, S, et al., *IEEE Trans Pattern Anal Mach Intell*, 24(4):509–22, 2002. [13] Chandran, P & Barocas, V, *J Biomech Eng*, 128(2):259–70, 2005. [14] Ray, A, et al., *Biophys J*, 112(5):1023–36,. 2017. [15] Jonker, R & Volgenant, A, *Computing*, 38(4):325–40, 1987.

SB^{3}C2019
Summer Biomechanics, Bioengineering and Biotransport Conference
June 25 -28, Seven Springs, PA, USA

INHIBITION OF THE INTEGRIN β1 SUBUNIT INCREASES STRAIN THRESHOLDS FOR PERIPHERAL NEURON DYSFUNCTION AND INJURY

Sagar Singh (1), Beth A. Winkelstein (1,2)

(1) Department of Bioengineering
University of Pennsylvania
Philadelphia, PA, USA

(2) Department of Neurosurgery
University of Pennsylvania
Philadelphia, PA, USA

INTRODUCTION

Injurious-stretch of the spinal facet capsular ligament is a cause of neck pain and supraphysiologic stretch of the innervated capsule induces axonal injury, neuronal hyperexcitability, and upregulation of pain neuromodulators [1-5]. The capsule's extracellular matrix (ECM) is composed of type-I collagen with varying fiber orientations [6,7]. The structural heterogeneity of the capsule leads to complex loading of the innervating afferents, depending on its deformations and matrix organization. Although painful tissue loading, neuronal activation, and collagen reorganization thresholds exist [5,8-12], mechanical thresholds for neuronal dysfunction and/or injury are lacking.

The neuronal cytoskeleton is coupled to the surrounding collagen matrix by the $\alpha_2\beta_1$ integrin subunit and the NR2B subunit of the NMDA receptor, enabling ligament primary afferents to sense microstructural mechanical cues [13-15]. Inhibiting the $\alpha_2\beta_1$ integrin prevents loading-induced substance P increases that are typical with painful loading [16], suggesting that integrin subunit may mediate pain, neuronal dysfunction and/or neuronal injury. Yet, that has not been investigated, partly due to a lack of mechanical thresholds for neuronal dysfunction. This study tested the hypothesis that integrin-mediated ECM-neuron interaction has a role in the strain thresholds for afferent NMDA regulation (a proxy of dysfunction) and/or injury. A previously characterized in vitro neuron-collagen gel model of the capsular ligament [3,5,16] was used to test effects of β_1 integrin inhibition on neuronal responses to macroscopic failure loading. Because extrasynaptic NMDA is increased after neuronal injury and the NR2B subunit is highly expressed in extrasynaptic NMDA receptors that are activated by stretch [15,17], NR2B expression was used as a measure of neuronal dysfunction. ATF3, which is upregulated in neurons within hours after spinal cord and peripheral nerve injuries [18,19], was used as a marker of injury.

METHODS

Gels were made of collagen solution (2mg/mL) derived from rat tails in 12-well plates and incubated at physiological conditions. Dorsal root ganglia were harvested from day 18 rat embryos, dissociated, and plated on gels at $3x10^5$cells/mL. Gels were cultured for 7 days with Neurobasal Media supplemented with 1% FBS, 2% B-27, 0.2% GlutaMAX, 0.25% D-Glucose, 10mM FdU, 10mM uridine, and 2.5S NGF, which was changed every 2-3 days. On day 4, collagen solution (100µL) encapsulated the neurons; on day 7, gels (n=12) underwent biaxial loading in a planar tester (574LE2; TestResources). In a subset of gels (n=4), the integrin β1 subunit inhibitor TC-I15 (100µM; Tocris) [16], was added 36hrs before testing.

Gels were stamped into a cruciform (21mmX8mm) and a grid was drawn on the surface to define elements and calculate strains (Fig. 1). In a 37°C PBS bath, each arm of the gel was secured to microclamps equipped with load cells (500g; ±2mN sensitivity). A camera (Phantom-v9.1; Vision Research) tracked marker positions (500fps; 14.5pixels/mm) while arms were displaced at 3.8mm/s simulating injury rates [20,21]. Force and displacement data (200Hz) were synchronized with imaging, and filtered [3]. A subset of gels (n=8) was put in the bath as unloaded controls for neuronal assays.

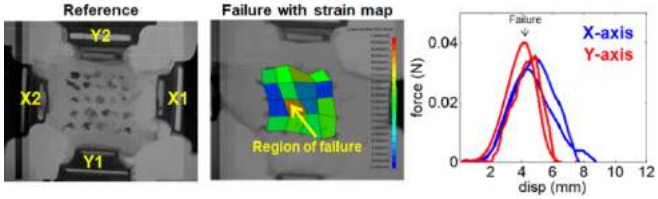

Fig 1: Image of gel in reference unloaded configuration shows its elemental marker grid in the test device with loading axes. Strain map image shows elemental MPS at failure with matching plot.

Failure was defined at the peak force detected on any arm and confirmed visually (Fig. 1). Markers at failure were digitized and their positions relative to unloaded reference were tracked with ProAnalyst (Xcitex). Maximum principal strain (MPS) was calculated with LS-DYNA software (LSTC) [22]. Force, displacement, and MPS were compared between groups by separate t-tests.

After loading, gels were transferred to fresh media supplemented with 1% penicillin-streptomycin for 24hrs and fixed in 4% paraformaldehyde for immunolabeling. Half of each gel was labeled for β_1 integrin and half for NR2B and ATF3; βIII-tubulin labeling was included for all assays. Gels were incubated overnight at 4°C with anti-βIII-tubulin (1:200), either anti-β_1 integrin (1:200) or anti-ATF3 (1:400), and anti-NR2B (1:500), followed by secondary antibodies. Gels were slide-mounted and each element (2100X1800pixels^2) was imaged by a Zeiss 710 confocal microscope. Densitometry quantified each label [23]. The amount of β_1 integrin in loaded gels was normalized to unloaded untreated gels. For each element, neuronal NR2B and neuronal ATF3 was calculated and βIII-tubulin, respectively, and normalized to unloaded control gels. Differences in normalized β_1 integrin for each treatment group were compared by t-tests separately for control or loaded gels. Effects of inhibition on neuronal NR2B and ATF3 were evaluated by two-way ANOVAs.

Strain thresholds for upregulation of NR2B and ATF3 were calculated by logistic regressions of elemental normalized expression of each and MPS [5]. Each element was assigned a value of 1 if the normalized expression was more than in unloaded controls and 0 if it was below control. Elements from unloaded gels were included in the regressions with MPS of 0 since they were not loaded. The 50th-percentile threshold (p50) was defined for each regression and compared by ANCOVA chi-squared goodness-of-fit tests.

RESULTS

Force (29.9±10.5mN), displacement (4.1±1.8mm), and MPS (31.2±19.1%) at failure with inhibition are not different ($p>0.12$) from untreated values (24.9±9.5mN; 4.5±1.1mm; 25.1±13.3%). Integrin inhibition significantly decreases β_1 integrin expression in both unloaded gels (41±14%; $p<0.001$) and failed gels (39±8%; $p<0.001$) (Fig. 2). Both neuronal NR2B ($p<0.049$) and ATF3 ($p<0.008$) increase significantly after loading with and without inhibition (Fig. 2). Yet, the increases in NR2B (2.0±0.8 over control) and ATF3 (1.7±0.7 over control) in inhibitor-treated gels after failure are less robust and not different from the corresponding increases in untreated gels (NR2B 2.2±0.9 over control; ATF 2.5±1.1 over control).

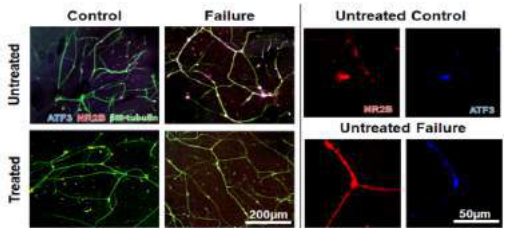

Fig 2: NR2B and ATF3 increase after failure with and without treatment. NR2B is primarily in cell bodies in controls and axonal after failure.

The 50th percentile strain threshold for upregulation of NR2B (15.5%) is significantly ($p<0.001$) higher than that for ATF3 (14.7%) in untreated gels (Fig. 3). Although the p50 for each of NR2B (17.7%) and ATF3 (18.3%) are higher ($p<0.02$) with β_1 integrin inhibition than without (Fig. 3), they are not different ($p=0.43$) from each other.

DISCUSSION

Although inhibiting the β_1 integrin subunit has been shown to regulate neuronal modulation of the neuropeptide substance P [16],

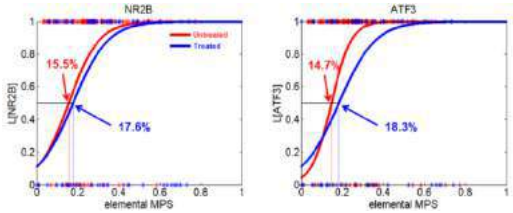

Fig 3: Fits of NR2B and ATF3 against elemental MPS show higher thresholds for NR2B ($p=0.006$) and ATF3 ($p=0.018$) for treated gels than untreated.

this study demonstrates its potential as possibly preventing possible neuronal dysfunction and injury (Figs. 2 & 3). Because the integrin $\alpha_2\beta_1$ mediates binding between the neuronal cytoskeleton and ECM [14], inhibition attenuates the force transfer to the cytoskeleton by collagen fiber deformation and reorientation during macroscopic stretch [3,9]. The collagen heterogeneity of the capsular ligament produces non-uniform local stresses and strains from macroscopic stretch [3]. Although this study did not evaluate local stresses or effects of regional collagen orientation on neuronal injury or dysfunction, microstructural effects likely play a role.

The dose of the integrin inhibitor used in this study matched the lowest dose found to reduce axonal substance P expression after painful stretch and to alter effects between substance P and regional strain [16]. The finding that strain thresholds for NR2B and ATF3 increases change with treatment (Fig. 3) may mean neuronal injury, dysfunction, and nociceptive modulation are mediated in some part by integrin signaling. Substance P expression is mediated by the MAPK and ERK pathways [24], both of which are secondary messengers in integrin-mediated pathways [25], as well as signaling effectors in the cellular stress response that corresponds to ATF3 expression [26]. Although this study suggests stretch-induced integrin activation may be drive the transcriptional changes associated with nociception and neuronal dysfunction, additional studies identifying the specific signaling mechanisms between nociception, neuronal activation and ATF3 expression would provide insight into these pathways and their relationship to mechanical responses at the macro-and micro-scales. Nevertheless, this study demonstrates a possible role of the integrin signaling pathway in mediating stretch-induced neuronal dysfunction and injury.

ACKNOWLEDGEMENTS

Funding from NIH (#AT010326-07) and C. Sharpe Foundation.

REFERENCES

[1] Quinn K et al, *Pain*, 151:414-21, 2010 [2] Kallakuri S et al, *World J Orthop*, 3:10-4, 2012 [3] Zhang S et al, *J Orthop Res*, 36:770-7, 2018 [4] Kras J et al, *Neurosci Lett,* 604:193-8, 2015 [5] Zhang S et al, *J Biomech Eng,* 138:021013, 2016 [6] Zarei V et al, *Biomech Model Mechanobiol,* 16:1425-38, 2017 [7] Ban E et al, *J Biomech Eng,* 139:071009, 2017 [8] Quinn K & Winkelstein B, *J Biomech Eng,* 133:64506, 2011 [9] Quinn K et al, *J Biomech,* 43:1870-5, 2010 [10] Lee K et al, *J Biomech,* 39:1256-64, 2006 [11] Dong L et al, *Brain Res,* 1461:51-63, 2012 [12] Lee K & Winkelstein B, *J Pain,* 10:436-45, 2009 [13] Hynes R, *Cell,* 110:673-87, 2002 [14] Sun Z, *J Cell Biol,* 215:1-12, 2016 [15] Singh P et al, *J Biol Chem,* 287:4348-59, 2012 [16] Zhang S et al, *Ann Biomed Eng,* 45:2813-25, 2017 [17] Petralia R, *Sci World J,* 2012:1-11, 2012 [18] Tsujino H et al, *Mol Cell Neurosci,* 15:170-82, 2000 [19] Hunt D et al, *Front Mol Neurosci,* 5:1-17, 2012 [20] Dong L et al, *Neurosci Lett,* 443:90-4, 2008 [21] Dong L & Winkelstein B, *J Neurotrauma,* 27:163-74, 2010 [22] Zhang S et al, *Biomech Model Mechanobiol,* 17:133-45, 2017 [23] Kras J et al, *Spine,* 39:207-12, 2014 [24] Lallemand F et al, *J Neurochem*, 87:508-21, 2012 [25] Yee K et al, *IET Syst Biol*, 2:8-15, 2008 [26] Lu D et al, *Biochem J*, 401:559-67, 2007.

SB³C2019
Summer Biomechanics, Bioengineering and Biotransport Conference
June 25 -28, Seven Springs, PA, USA

VERTEBRAL ENDPLATE REMODELING REDUCES SMALL MOLECULE DIFFUSION INTO DEGENERATIVE INTERVERTEBRAL DISCS

B. Ashinsky (1,2,3), E. Bonnevie (1,2), S. Mandalapu (1,2), S. Pickup (4), C. Wang (3), L. Han (3), RL. Mauck (1,2), H. Smith (1,2), S. Gullbrand (1,2)

(1) Department of Orthopaedic Surgery
University of Pennsylvania
Philadelphia, PA, USA

(2) Translational Musculoskeletal Research Center
Corporal Michael J. Crescenz VA Medical Center
Philadelphia, PA

(3) School of Biomedical Engineering,
Science and Health Systems
Drexel University
Philadelphia, PA, USA

(4) Department of Radiology
University of Pennsylvania
Philadelphia, PA, USA

INTRODUCTION

Intervertebral disc degeneration is associated with a cascade of cellular, compositional and structural changes to the nucleus pulposus (NP), annulus fibrosus (AF) and boney and cartilage vertebral endplates (EP), and is frequently associated with back pain. Low back pain is the most common cause of disability in the United States, and has a prevalence greater than heart conditions, stroke and cancer combined [1]. Despite this clinical burden, the etiology of disc degeneration remains poorly understood. The disc is the largest avascular structure in the body; cells within the disc therefore rely on diffusive and convective transport via the vasculature in the EP to receive nutrients and eliminate waste products [2]. For this reason, it has long been hypothesized that compromised trans-endplate transport plays a critical role in disc homeostasis, and the initiation and progression of disc degeneration. Despite this critical role, the relationships between endplate structure, function and disc nutrition remain poorly understood. Here, we utilize an *in vivo* rabbit puncture degeneration model to study these interactions, and hypothesize that increasing remodeling of the boney and cartilaginous EP, characterized by increased stiffness and bone density, and reduced vascularity, will reduce small molecule transport into the degenerating disc.

METHODS

Following IACUC approval, 11 male New Zealand white rabbits underwent a surgical procedure to puncture 4 lumbar spine levels per animal. The adjacent, non-punctured levels were utilized as healthy controls. Three animals were euthanized 4 and 8 weeks post puncture, and five animals were euthanized at 12 weeks post puncture. A subset of the punctured discs were utilized in this study. Three animals designated for the 12 week time point received subcutaneous injections of calcein (25 mg/kg) at 6 weeks post-puncture and alizarin (25 mg/kg) at 10 weeks post-puncture to label newly deposited mineral. At the 12 week time point, 3 animals were administered the small molecule, non-ionic MRI contrast agent gadodiamide intravenously, 30 minutes prior to euthanasia [2]. Quantitative MRI T1 mapping of the lumbar spinal levels was performed immediately after euthanasia using an inversion-recovery sequence at 4.7T using a custom solenoid coil. Gadodiamide is a T1 shortening agent, and thus the percent reduction in T1 (discs without gadodiamide versus those with gadodiamide at each time point) provides a measure of small molecule diffusion into the disc. Significant differences ($p<0.05$) in outcomes were assessed via Kruskal-Wallis with Dunn's multiple comparison testing.

Motion segments (n=4-6 per group) were subjected to μCT scanning at 10μm isotropic resolution to quantify bone volume fraction and trabecular morphometry parameters in the vertebral endplate between the growth plate and disc. Following μCT, motion segments were cryosectioned in the sagittal plane using Kawamoto's tape method to 20μm thickness [3]. AFM-nanoindentation (≥12 indents per region, n=3-5 per group) was performed on sections at the AF-EP and NP-EP interfaces using microspherical tips ($R \approx 12.5$ μm, 10 μm/s rate). The effective indentation modulus, E_{ind} (in MPa), was calculated via the finite thickness-corrected Hertz model [4]. Motion segments from animals receiving the calcein and alizarin labels were fixed in formalin, prior to cryosectioning at 20μm using Kawamoto's tape method, and imaged using fluorescent microscopy. Additional motion segments (n=3 per group) were processed for paraffin histology, sectioned to 10μm thickness, and stained with Mallory-Heidenhain trichrome stain to visualize the vasculature in the vertebral endplate, or with alcian blue and picrosirius red to visualize overall degenerative changes to the disc. Second harmonic generation imaging (SHG) was also performed on

paraffin sections to visualize collagen organization at the AF-EP and NP-EP interfaces. Significant differences ($p<0.05$) in quantitative outcomes were assessed via Kruskal-Wallis with Dunn's multiple comparison testing.

RESULTS

In the rabbit puncture model, degeneration progressed with time post-injury, and was characterized by loss of disc height, disorganization of the annulus fibrosus, anterior osteophyte formation, and increases in NP collagen content. SHG showed progressive disorganization of lamellae at the AF-EP interface as well as increases in organized collagen deposition within the cartilage endplate at 4 and 8 weeks, compared to controls. Mallory-Heidenhain staining, which stains erythrocytes in the vasculature orange, revealed a marked reduction in vessel density and size in the vertebral endplate adjacent to the NP at 8 and 12 weeks (Figure 1).

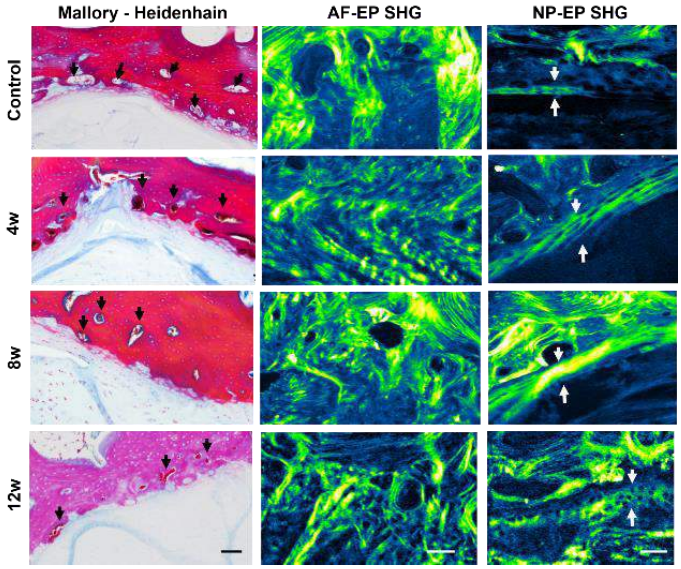

Figure 1: Stain for endplate vasculature (arrows) and SHG of the AF-EP and NP-EP (arrows indicate cartilage EP) interfaces in each group. Scale = 500µm.

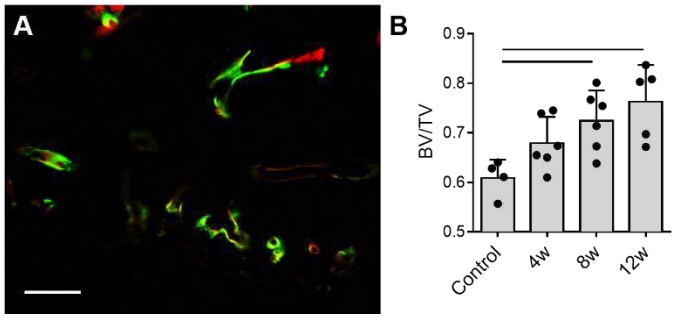

Figure 2: (A) Calcein (green) and alizarin (red) labeling in the vertebral endplate adjacent to the disc 12 weeks post-puncture. Scale = 100 µm. (B) Bone volume fraction of the vertebral endplate for each experimental group. Bars denote p<0.05.

Calcein and alizarin labelling demonstrated increased mineral deposition in the vertebral endplate adjacent to punctured discs, localized to the margins of the marrow and vascular channels (Figure 2A). Bone volume fraction, measured via µCT, was significantly increased in the vertebral endplate adjacent to punctured discs compared to intact controls at 8 and 12 weeks post-puncture (Figure 2B). Trabecular thickness was also significantly increased at 4, 8 and 12 weeks in the vertebral endplate of punctured discs compared to controls.

AFM analysis demonstrated progressive increases in indentation modulus of the AF-EP interface, as well as the cartilaginous endplate adjacent to the NP, with increasing time post-puncture. Finally, gadodiamide diffusion into the NP was reduced in the 12 week puncture-degenerated group compared to healthy controls, while transport into the AF of degenerative discs increased compared to controls.

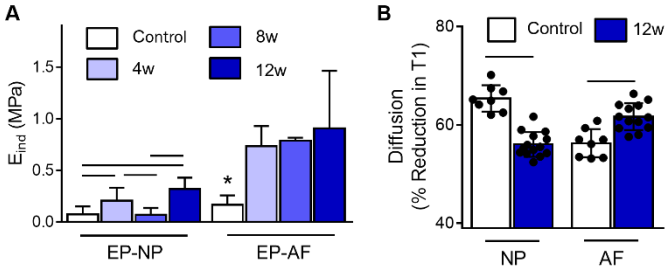

Figure 3: (A) AFM indentation modulus of disc interfaces. Bars denote p<0.05, * = p<0.05 compared with all other time points. (B) Diffusion into the disc measured by post-contrast enhanced T1 mapping. Bars denote p<0.05.

DISCUSSION

The role of small molecule trans-endplate transport in the initiation and progression of disc degeneration is a debated topic in the field. Furthermore, the structure-function relationships governing disc nutrition remain poorly understood. Degeneration of the disc in the rabbit annular puncture model resulted in significant alterations to the adjacent vertebral boney endplate and disc interfaces. *In vivo* calcein and alizarin labelling reveled new mineralization occurring in the vertebral endplate at both 6 and 10 weeks post-puncture, particularly at the borders of the marrow and vascular channels. This bone remodeling led to significant increases in bone volume fraction and reductions in vessel size and density. Disorganization of the AF-EP interface was evident on SHG imaging, as well as increased organized collagen within the cartilage endplate between the NP and boney EP. Furthermore, the interfaces between the bone and disc progressively stiffened with increasing severity of degeneration. These structural and functional changes were concomitant with reductions in small molecule diffusion into the NP. As NP cells rely entirely on diffusive transport for nutrient and waste product exchange, the reduction in disc nutrition may promulgate the progression of degeneration in the NP. Interestingly, diffusion into the AF region increased compared to controls, which may be due to neovascularization in the anterior osteophytes and peripheral annulus fibrosus local to the puncture. This work furthers our knowledge of the role of diffusive transport in disc degeneration, and may be leveraged towards the improved diagnosis and treatment of patients with disc degeneration and back pain.

ACKNOWLEDGEMENTS

This work was supported by the NIH, the Department of Veterans' Affairs, and the Penn Center for Musculoskeletal Disorders.

REFERENCES

[1] Mokdad, A et al., *JAMA*, 319:1444, 2018. [2] Gullbrand, S et al, *Spine*, 40:1158, 2015. [3] Kawamoto,T et al, *Stain Tech*, 61:169, 1986 [4] Han, L, et al *Biophysical J*, 100:1846, 2011.

SB³C2019
Summer Biomechanics, Bioengineering and Biotransport Conference
June 25 -28, Seven Springs, PA, USA

IN-PLANE SHEAR MECHANICAL CHARACTERIZATION OF THE LUMBAR FACET CAPSULAR LIGAMENT

Emily A. Bermel (1), Arin M. Ellingson (2), Victor H. Barocas (1)

(1) Biomedical Engineering
University of Minnesota – Twins Cities
Minneapolis, MN, USA

(2) Rehabilitation Medicine
University of Minnesota – Twins Cities
Minneapolis, MN, USA

INTRODUCTION

The facet capsular ligament (FCL) is a spinal ligament that spans the synovial joint formed by the articular facets [1] on the posterior aspect of the spine (Figures 1A&B). The FCL is composed primarily of collagen fibers and elastin fibers. The FCLs span most of the length f the spine, but the lumbar region is of particular interest to us due to its possible role in low back pain (LBP). LBP is a major public health problem, affecting 80% of adults in the United States and creating a significant burden on society and the health care system [1]. The presence of nociceptive nerves in the lumbar FCL [2,3] suggest that is may be involved in LBP.

Because of the irregular geometry of the FCL, even the simplest body motions can cause complex tissue deformations. We have shown previously [2] that the lumbar FCL undergoes a significant amount of in-plane shear during spinal flexion and extension. The mechanical properties of the lumbar FCL during these types of motion, however, have yet to be characterized in detail. Ianuzzi *et al*. [3], determined the principal strains of the lumbar FCL *in situ* during flexion and extension, but they didn't estimate the tissue stress. The objective of this work was to quantify the mechanical behavior of the lumbar FCL during planar shear testing.

METHODS

Cadaveric lumbar spines, ages 20 – 67 (mean: 53.2 ± 21.7) years obtained through the Minnesota Anatomy Bequest program, and were scanned in a 3T MRI system at the University's Center for Magnetic Resonance Research to grade the health of the facet joints and the intervertebral discs. Discs were graded on the Pfirrmann scale [4], and facet joints were graded on the Fujiwara scale [5]. Spine grading was performed separately by an orthopedic surgeon and a spine research specialist. The facet joints (n = 10, L4-L5 level), were then resected from motion segments (Figure 1A).

To prepare the ligaments for mechanical testing, all posterior musculature was cleared, and the FCL was stripped of its surface membranes (Figure 1B). The curved ligament surface was flattened, and the trabecular bone was removed to facilitate loading of the sample into the testing machine, while still maintaining physiological attachments to the bone.

Figure 1: A.) L4-L5 Motion segment B.) Right facet with FCL C.) Shear testing setup of right FCL. During extension testing the actuator on the right (lateral) moved to stretch the sample. Next, for shear testing, the actuator on the left (medial) moved up or down while the lateral actuator remained fixed.

Mechanical characterization of the FCL was completed on a planar biaxial tester. Two, six-degree-of-freedom load cells were used, with each measuring one normal and two shear forces. Testing (Figure 1C) was completed in two stages. First, a series of uniaxial extension tests were performed to precondition the sample, with the final extension cycle being analyzed. Second, a shear strain was imposed on the ligament as might occur in spinal flexion and extension (10 cycles each

at 0.1 Hz). The ligaments were displaced to 20% strain based on previous research that showed that a 20% strain was a large enough strain to stretch the FCL out of the toe region, but not damage the tissue [6].

The force and displacement data from the load cells and actuators were used to calculate the first Piola-Kirchhoff stress and the engineering strain in the ligament. Surface displacement tracking was performed, following a previously described protocol [6]. Briefly, video data from the cycles of interest were converted in to image stacks, and the undeformed image was imported into Abaqus CAE to generate a planer mesh of the ligament surface, bordered by the bone on the medial and lateral sides. The images were then processed by an image correlation code, and the surface strains were calculated.

A 3D finite element model was developed for each sample geometry using FEBio (2.5.2). The FCL was defined as a Neo-Hookean matrix with a 2D exponential fiber family (Eq. 1)

$$W = C_1(I_1 - 3) + \frac{\xi}{\alpha\beta}\left(exp\left[\alpha(I_n - 1)^{\beta}\right] - 1\right) \quad (1)$$

where C_1 is the neo-Hookean constant, I_1 is the first strain invariant, ξ is the fiber modulus, and I_n is the square of the stretch in the fiber direction. The fiber distribution is defined with a von Mises fiber distribution (Eq. 2).

$$R(\boldsymbol{n}) = \frac{exp[b(2n_1^2 - 1)]}{2\pi I_0(b)} \quad (2)$$

where I_0 is the modified Bessel function of the zeroth order, $\boldsymbol{n}$ is the vector defining the fiber direction, and b is the fiber concentration parameter. The experimental data was fit to the models using a modified *fminsearch* in Matlab (2018b). To visualize the fiber distribution from the FE model fits, a random point cloud was generated from the von Mises distribution using Matlab (2018b) [7].

RESULTS

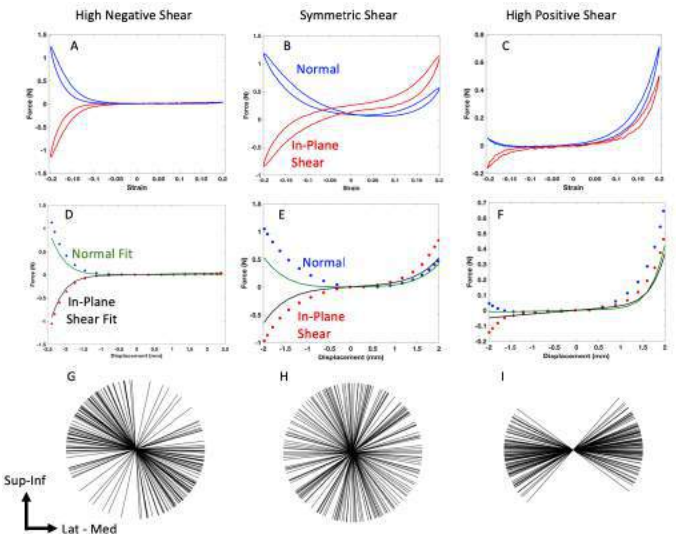

Figure 2: There were three different types of data seen from the mechanical tests (top row) the images shown are from representative samples A.) Asymmetric force during negative shear, B.) Symmetric in-plane shear force, and C.) Asymmetric force during positive shear. The second row is the FE model fit (black and green line) to the data (blue and red dots). The third row is a represented 2D fiber alignment generated from the von Mises distribution fit from the FE model.

Mechanical results for in-plane shear data are shown in Figure 2A-C. All samples (n=10) show one of the three different types, an asymmetric force in either the negative shear direction (Figure 2A, D), the positive shear direction (Figure 2C, E), or a symmetric shear force (Figure 2B, F). The matrix parameter C_1 from Eq. 1, had a an average and 95% confidence interval of 0.018 ± 0.020 MPa, similar to that reported previously [6]. For the fibers, β was 5.71 ± 2.17, ξ was 4.27 ± 2.93 MPa, and α was 1.94 ± 1.02. The fiber parameters were higher in magnitude than those previously reported [6].

The fiber alignment and distribution are represented by Figure 2G-I, which the three different types of data. Figure 2G represents fibers that are aligned (b=3.58) in the direction θ = -31.35° from the horizontal. Figure 2H represents fibers that are not aligned (b < 1). Figure 2I represents fibers are highly aligned (b>4.5, θ = +16.86°). The fiber angle was negative for the 3 samples that showed the high negative shear type response. Similarly, the fiber angle was positive for the samples (n=3) that had high positive shear. The fiber angle and level of alignment had a wide range for the samples (n=4) of the symmetric shear forces. There was not a relationship between the fiber orientation and alignment of FCLs that were taken from the same donor.

DISCUSSION

The ranges of fiber orientation and alignment shown here have a dramatic effect on the shear mechanical response of the tissue. The strain ranges shown in Figure 2A, B, and C for both the positive and negative shear are comparable to what has been reported by Ianuzzi *et al*. [3] for physiological spinal flexion and extension. However, the range of forces and amount of strain at which tissue forces rose sharply varied from sample to sample.

These data indicate that there is more complexity in the fiber orientation and alignment than has been previously suggested and future imaging in combination with mechanical studies could elucidate these complex fiber structures of the lumbar FCLs. Patient-specific FCL models may be necessary to capture individual variation in structure and the resulting effects on spinal kinematics and kinetics.

ACKNOWLEDGEMENTS

Funding for this work was provided by NIH U01-EB016638 and NIH/NICHD K12HD073945. The authors acknowledge the Minnesota Supercomputing Institute (MSI) at the University of Minnesota for providing resources that contributed to the research results reported within this abstract. We would also like to thank Dr. Johnathan Sembrano and Dr. Sharron Yson for grading our specimens and the Anatomy Bequest Program at the University of Minnesota for providing them.

REFERENCES

1. Andersson, G.B.J., *The Lancet,* **354**(9178):581-585, 1999.
2. Claeson, A.A. and V.H. Barocas, *Spine J,* **17**(1):109-119, 2017.
3. Ianuzzi, A., et al. *Spine J*, **4**(2):141-152,2004.
4. Pfirrmann, C.W.A., et al., *Spine*, **26**(17):1873-1878,2001.
5. Fujiwara, A., et al., *Eur Spine J*, **8**:396-401,1999.
6. Claeson, A.A. and V.H. Barocas,. *J Mech Behav Biomed Mater*, **65**:127-136,2016.
7. Chen, Y.-H., et al., *IEEE Signal Processing Letters,* **22**(8):1152-1155, 2015.

SB³C2019
Summer Biomechanics, Bioengineering and Biotransport Conference
June 25 -28, Seven Springs, PA, USA

DIRECT QUANTIFICATION OF INTERVERTEBRAL DISC WATER CONTENT USING MAGNETIC RESONANCE IMAGING

Bo Yang (1), Michael F Wendland (2), Yu Ma (3), Grace D. O'Connell (1)

(1) Mechanical Engineering
University of California, Berkeley
Berkeley, CA, United States

(2) I□BBB - □B3 Institute
University of California, Berkeley
Berkeley, CA, United States

(3) Mathematics
University of California, Berkeley
Berkeley, CA, United States

INTRODUCTION

The intervertebral disc is comprised of the nucleus pulposus (NP) surrounded by the annulus fibrosus (AF). In the healthy disc, both tissues are comprised primarily of water (~85% in the NP, decreasing to ~65% in the outer AF) [1]. Aging and degeneration have been noted by a continuous decrease in NP water content, resulting in altered disc joint mechanics [1]. Previous studies have shown that noninvasive measurements of disc water content, such as T2 mapping, can be used to detect early changes in degeneration [2]. Such detection is important for identifying discs for preventative treatment strategies. However, those techniques largely rely on correlations to biochemical composition and do not directly measure water content. Moreover, water content is an important parameter for computational models that include tissue-swelling behavior [3].

Currently, measuring tissue water content is dependent on destructive techniques (e.g., lyophilization), therefore, is limited to *ex situ* tissues [1]. Alternatively, magnetic resonance imaging (MRI) has been used to estimate disc water content, as signal intensity depends on the proton density within the tissue [4]. However, MRI signal intensity is dependent on scan-parameters and the concentration of free water molecules in the tissue. Even further complications may occur when water molecules that rigidly bound to collagen macromolecules (e.g., ~3% of water in the NP and ~10% of water in the AF) do not appear on MRI due to a short T2 time [5, 6]. The objective of this study was to directly measure tissue water content using MRI. NP and AF water contents were measured noninvasively using T2 imaging and compared with traditional techniques. To generate a range of water content for comparison, healthy discs were mechanically dehydrated.

METHODS

Gravimetric water content (GWC), defined as the fraction of water mass divided by tissue mass, is related to volumetric water content (volume fraction, VWC) through tissue and water mass density (ρ, $\rho_{water} = 1 g/cm^3$, Eq. 1). Although GWC is widely used to report water content, MRI signal intensity (SI) correlates with VWC (SI(echo time =0) $\propto$ VWC) or spin density. Specifically, T2 relaxation times are calculated by curve-fitting MR SI versus echo time to an exponential function ($SI = SI_0 \exp(-TE/T2)$, TE: echo time; relaxation rate, R2 = 1/T2). A known tissue mass density is need to directly compare water content calculated by MRI and traditional techniques.

$$GWC = \frac{V_{water}\rho_{water}}{V_{tissue}\rho_{tissue}} = VWC\frac{\rho_{water}}{\rho_{tissue}} = \frac{VWC}{\rho_{tissue}} \quad (1)$$

Bovine caudal spine sections were obtained from a local abattoir to prepare bone-disc-bone motion segments (n = 20). Before testing, samples were thawed and hydrated in 0.15 M phosphate-buffered saline (150 mmol/L 1x PBS) for 24 hours at 4ºC and equilibrated to room temperature for one hour prior to imaging.

Before scanning, samples were put into a custom-built plastic compression device (Fig. 1a). Images were first acquired with no load applied. To calculate tissue spin density, T2 relaxation was determined for 2.5 mmol/L gadolinium water, which was placed next to the specimen and served as a phantom reference (Fig. 1a). Each sample was imaged using a 3D Fast Low Angle Shot (FLASH) sequence to record 3D geometric information (7T Bruker MRI machine; FOV = 3.2 X 3.2 X 2.8 cm). Then, samples underwent a 2D scan at the mid-disc height using a T2 Rapid Imaging with Refocused Echoes (RARE) sequence to calculate T2 relaxation times (TEs = 7ms, 21ms, 35ms, 49ms, 63ms, FOV = 5 X 5 X 0.12 cm, slice thickness = 1.2 mm, in-plane resolution = 0.39 mm/pixel). TR was set to 8 sec to enable full relaxation from both the gadolinium water and disc [7]. Then, samples were compressed in 1x PBS for 24 hours at 4ºC before re-equilibrating to room temperature to force fluid out of the disc. After dehydration

through mechanical loading, MR imaging was repeated, as described above.

After imaging, samples were quickly unloaded and removed from the device. Explants from the NP center and AF were prepared (6mm in diameter) from a 1-2mm thick transverse slice cut from the mid-disc height. The mass of the hydrated tissue ('wet-mass') was measured on an analytical balance (0.1 mg accuracy). Then, tissue volume was calculated by measuring fluid volume displacement after placing the tissue explant in a bath, according to the Archimedes principle (Fig. 1b) [8] Tissue mass density was calculated by dividing wet-mass over volume. Then, explants were lyophilized for 48 hours to obtain dry mass. GWC was calculated, as defined above.

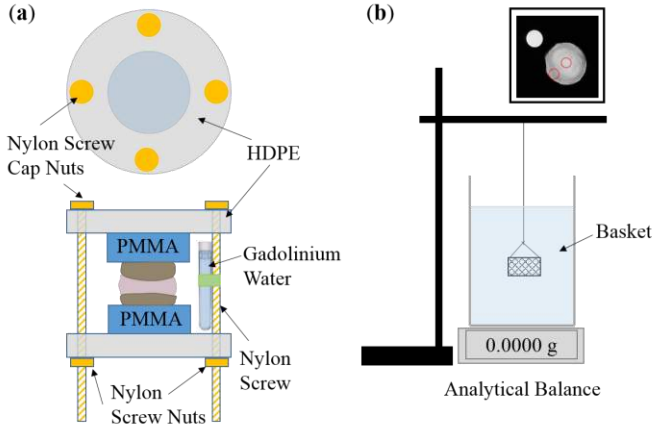

Fig 1: (a) Schematic of plastic compression device with gadolinium water (2.5 mmol/L). HDPE: high-density polyethylene, PMMA: poly (methyl methacrylate). (b) Schematic of tissue volume measurements [12]. Inset: example of T2 scan with circles representing regions of interest for NP and AF.

Exponential models were fit to MR SI versus TE times to calculate T2 and SI_0 on each pixel (*fit* function in Matlab 2018a). Spin density (SD) was calculated by normalizing the tissue SI_0 by SI_0 of gadolinium water. NP and AF region of interest (6 mm in diameter) were selected to calculate averaged SD, T2, and R2 values (Fig. 1 inset). SD and SD normalized by mass density were correlated with GWC. Mass density and R2 were correlated with GWC and SD. Significance was assumed at $p \leq 0.05$.

RESULTS

Three samples were excluded due to damage in the NP (e.g., blood from a fractured endplate). Mechanical compression successfully dehydrated disc samples and generated a wide range of NP GWC (from 0.69 to 0.84). MR spin density was greater than GWC (0.81-0.92) but was positively correlated with GWC ($p < 0.001$; Fig. 2a-open circles). Spin density normalized by mass density (ρ_{tissue}) resulted in a near perfect match with GWC (slope = 1.02, $R^2 = 0.91$, $p < 0.001$; Fig. 2a-black dots). NP mass density (range: 1.07 - 1.17 g/cm^3) and NP relaxation rate (R2) were negatively correlated with both GWC and spin density ($p < 0.001$; Fig. 2b & 2c). NP T2 values (44 – 105 ms) increased with GWC and SD, as expected.

Similar to the NP, AF spin density was positively correlated with GWC ($p < 0.001$; Fig. 2d-circles). Normalizing spin density by mass density resulted in a stronger correlation with GWC ($p < 0.001$), but values were lower than GWC values (Fig. 2d-black dots versus cyan line). Unlike the NP, AF mass density (1.08 - 1.23 g/cm^3) was not correlated with either GWC or spin density ($p > 0.2$, Fig. 2e). AF R2 values were approximately 2X greater than NP R2 values (Fig. 2c & 2f). Correlations between R2 and water content were stronger than correlations with GWC (Fig. 2d vs. 2f).

DISCUSSION

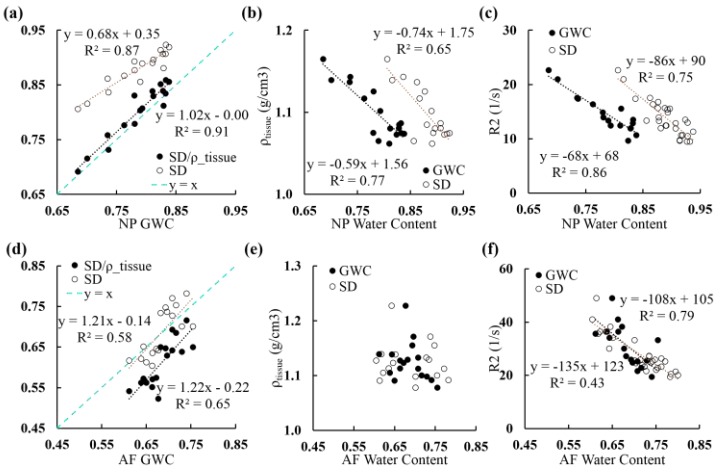

Fig. 2: Results for NP (1st row) and AF (2nd row): (a & d) Spin density (SD) and SD/mass density (ρ_{tissue}) vs. gravimetric water content (GWC). (b & e) Mass density vs. GWC and SD. (c & f) R2 vs, GWC and SD. p< 0.005 for (a)-(d) & (f).

Direct measurements of tissue water content are largely limited to destructive methods that require drying out tissue explants. Fast measurements of water content, on the order of minutes (vs. days), using noninvasive techniques is valuable for tracking tissue hydration with loading, disease progression, or biological repair, as tissue hydration affects joint-level mechanics. Quantitative MR parameters, such as T2 or T1ρ relaxation times, are strongly correlated with water or glycosaminoglycan content [2]. However, the relaxation times represent the behavior during the exponential decay in signal intensity, while the y-intercept should be proportional to the direct water content in the tissue (SD ∝ SI at t = 0 ms). In this study, we demonstrated that normalizing spin density by mass density provided excellent agreement between MR measured water content and water content measured through lyophilization.

However, these findings may be limited to homogenous structures, such as the nucleus pulposus and, potentially, articular cartilage. Agreement between MR measures and lyophilization measurements were not as strong for the AF, a fiber-reinforced tissue. This discrepancy is likely due to a higher concentration of bound water molecules in the AF, compared to the NP (~3% in NP and ~10% in AF) [5], where water molecules bound to collagen fibers have T2 values that are too short to be detected in MR imaging [6]. The greater concentration of bound water molecules partially explains the underestimation in MR-related water measurements (Fig. 2d).

To the best of our knowledge, this is the first study to report disc tissue mass density. NP mass density decreased with an increase in water content, but was always greater than 1.0, resulting in spin density values that were consistently larger than GWC. In conclusion, normalizing quantitative MR parameters with mass density or using the empirical formula (GWC vs SD in Fig. 1a) allow for noninvasive measurements of NP water content.

ACKNOWLEDGEMENTS

This study was supported by Signatures Innovation Fellowship and NSF CAREER grant (1751212).

REFERENCE

[1] Antoniou, J, et al., *J Clin Invest*, 98(4):996-1003, 1996; [2] Kerttula, L, et al., *Acta Radiol*, 42(6):585-91, 2001; [3] Yang, et al., *Biomech Model Mechanobiol*, 2018; [4] Nazari, J, et al., *Magn Reson Imaging*, 33(4):459-64, 2015; [5] Bezci, et al., *Ann Biomed Eng*, 2019 in review; [6] Bydder, M, et al., *J Magn Reson Imaging* 25(2):290-300, 2007; [7] Hwang, D, et al., *Quant Imaging Med Surg*, 6(6):744, 2016; [8] Hughes, SW, et al., *Phys Educ*, 40(5):468, 2005.

LOCATION-WISE FATIGUE DAMAGE PREDICTION FOR THE INTERVERTEBRAL DISC ANNULUS OF THE CERVICAL SPINE

Adhitya V. Subramani (1,4), Phillip E. Whitley (2), Harsha T. Garimella (2), Reuben H. Kraft (1,3,4)

(1) Department of Mechanical Engineering
The Pennsylvania State University
University Park, Pennsylvania, USA

(2) CFD Research
Huntsville, Alabama, USA

(3) Department of Biomechanical Engineering
The Pennsylvania State University
University Park, Pennsylvania, USA

(4) Institute for Cyberscience
The Pennsylvania State University
University Park, Pennsylvania, USA

INTRODUCTION

A significant portion of the military population develops severe neck pain in the course of their duties [1, 2]. It has been hypothesized that neck pain is a consequence of accelerated degeneration of the intervertebral discs of the cervical spine due to the loading from heavy head-supported mass including helmets and accessories worn by military personnel who also experience complex cyclic loading profiles during military missions [3]. In addition, some military operational transportation which includes riding on high speed special operations boats has also been reported to result in high magnitude cyclic loading on cervical spine discs [4].

We present a methodology to computationally predict fatigue damage to intervertebral discs over extended periods of time, by integrating kinematics-based biomechanical models with a continuum damage mechanics-based theory of disc degeneration. In our previous work [5], we made a preliminary assumption of a uniform stress distribution in the disc annulus. In reality this is an over simplification of the complex stress state present. To overcome this approximation, we have developed a validated finite element model of the human cervical spine the offers the complex stress state to be fully modeled. In this study, we explore how the integration of this advanced model improves our insight into the location of damage initiation and pattern of damage progression in the intervertebral disc annulus.

METHODS

In this study, a non-linear, multiaxial fatigue damage model was developed to predict fatigue damage in the intervertebral disc annulus over decade long periods of time. The modeling framework includes four primary components: 1) a non-linear fatigue damage evolution law; 2) ability to capture the effects of aging and damage recovery, accurately mimicing biological phenomena; 3) a fatigue damage model that takes into account the multiaxial stress state in the disc; and 4) correlation with an established clinical grading system for disc degeneration. Figure 1 depicts an overview of the overarching process used to construct the computational framework including model development, model calibration and application.

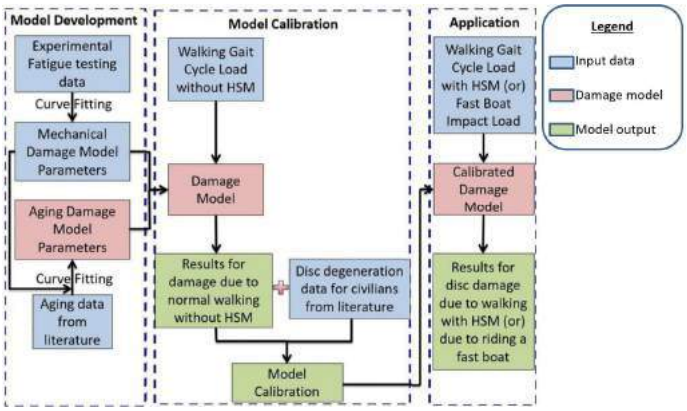

Figure 1: Overview of the computational framework of the damage model.

Nash [6] proposed that the total damage to a biological structure can be segregated based on the cause of damage, according to Equation (1) given below:

$$D_{tot} = D_m + D_a + D_d - H \quad (1)$$

where D_m is the damage due to mechanical loading, D_a is the damage due to aging, D_d is the damage due to disease and H is the recovery of mechanical damage that occurs during rest. Chaboche and Lemaitre [7] proposed a non-linear continuous fatigue damage model for the evolution of mechanical damage, which is described by Equation (2) below:

$$\frac{\delta D_m}{\delta N} = {D_m}^{\alpha} \left[\!\left[\frac{\sigma_a}{M_0(1-b\sigma_{mean})}\right]\!\right]^{\beta} \quad (2)$$

where D_m is the mechanical damage ($0 \leq D_m \leq 1$), N is the number of loading cycles, σ_a is the alternating stress and σ_{mean} is the mean stress of the load cycle. M_0, a, b and β are material parameters which can be determined from non-linear curve fitting processes using stress-life data from fatigue testing experiments on the disc annulus. Integrating the right-hand side of Equation (2) over the number of cycles, we can estimate the total mechanical damage.

The damage model takes into account the multiaxial stress state in the disc. Ion et al. [8] elucidates the use of the signed Von-Mises equivalent stress for multiaxial fatigue calculation in a material, which is the approach we have adopted for our model.

In order to overcome the approximation of uniform stress in the disc annulus, we have developed a validated three-dimensional finite element model of the human cervical spine. This model includes separate mesh regions for cortical bone, trabecular bone, disc nucleus, disc annulus and the major spinal ligaments. By applying the gait cycle loading histories for walking with an Advanced Combat Helmet at the cervical joints of this model (obtained from a rigid full body model [5]), we can obtain the signed Von-Mises stress histories for each element in the disc annuli of the cervical spine. These element-wise stress histories can then be used as input to the fatigue damage model, enabling us to estimate the location-wise damage evolution in the disc annuli. This overcomes the approximation of a uniform stress distribution and enables us to predict the location of damage initiation and pattern of damage progression in the disc annuli. This process of integrating the finite element model and the fatigue damage model has been shown schematically in Figure 2.

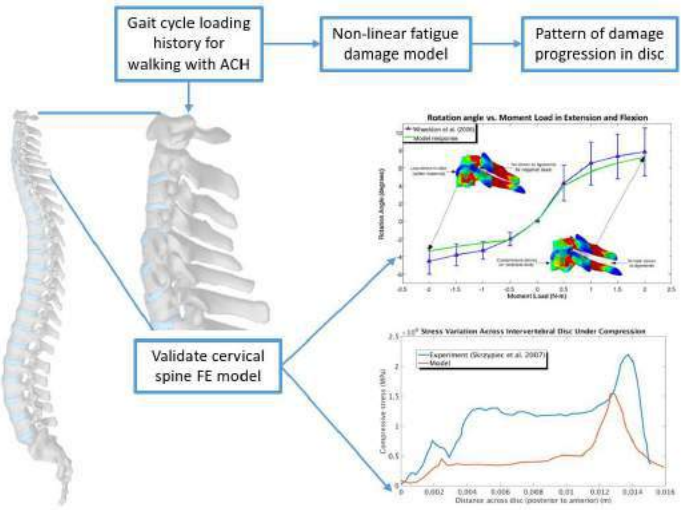

Figure 2: Schematic representation of the integration of the validated finite element model of the human cervical spine with the fatigue damage model.

RESULTS

The various damage model parameters that were obtained from curve fitting processes have been shown in Table 1.

Table 1: Model parameters obtained from curve fitting processes.

Parameter	a	β	M_0 (MPa)	C_a (year^{-1})
Value	9.8865	2.9737	17.8154	0.0030

The gait cycle loading history for walking with an Advanced Combat Helmet was applied to the validated finite element model of the C4-C5 cervical spine segment. Signed Von-Mises stress histories were recorded for each element of the disc annulus and fed as input to the fatigue damage model. Figure 3 shows the Von-Mises stress contours on the disc annulus at simulation times of 0.4 s, 0.8 s and 1.2 s.

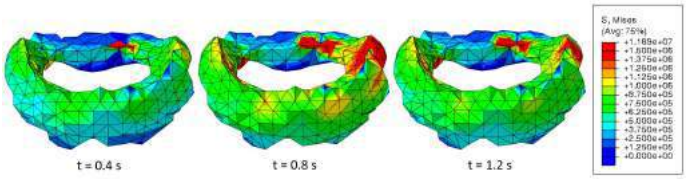

Figure 3: Von-Mises stress contours on the disc annulus at simulation times of 0.4 s, 0.8 s and 1.2 s.

The fatigue damage model was then run for each element in the disc annulus, for a period of 30 years. Figure 4 shows the fatigue damage contours on the disc annulus at times of 10, 20 and 30 years. We continue this process for the entire cervical spine and are currently working to extend to the full spine.

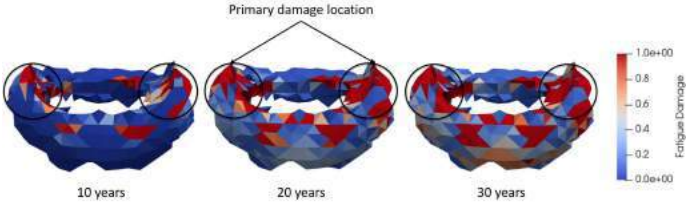

Figure 4: Fatigue damage contours on the disc annulus at times of 10, 20 and 30 years.

DISCUSSION

The location-specific damage evolution predicted by our model conforms to the results obtained by Qasim et al. [9]. Our model has significant real-life implications, including the ability to predict the effect of different spinal postures, loading profiles, etc. on the location-specific fatigue damage evolution in the intervertebral disc annulus.

ACKNOWLEDGEMENTS

This work was partially supported by the US Army under grant W81XWH-14-C-003 and by the National Science Foundation through grant OCI0821527.

REFERENCES

[1] van den Oord, MH et al., *Military medicine*, 175(1):55-60, 2010.
[2] Cohen, SP et al., *Spine*, 35:758-763, 2010.
[3] Mathys, R et al., *Journal of Biomechanics*, 45:2362-2367, 2012.
[4] Ensign, W et al., *NHRC San Diego CA*, NHRC-00-48, 2000.
[5] Subramani, A et al., *AIME*, 10(6):1687814018779494, 2018.
[6] Nash, CD, *New York: ASME*, p.68, 1967.
[7] Chaboche, JL et al., *Fatigue Fract Eng Mater Struct*, 11:1-17, 1988.
[8] Ion, D et al., *Journal of Engg Studies and Research*, 17(2):53, 2011.
[9] Qasim, M et al., *Journal of Biomechanics*, 45(11):1934-1940, 2012.

SB³C2019
Summer Biomechanics, Bioengineering and Biotransport Conference
June 25 -28, Seven Springs, PA, USA

BONE VOLUME FRACTION VS. BONE MASS DENSITY AS A PREDICTOR FOR MECHANICAL PROPERTIES OF THE CANCELLOUS BONE OF HUMAN LUMBAR VERTEBRAL BODIES

F. Travascio (1,2,3), A. Al-Barghouthi (2,3), L. Latta (2,3)

(1) Department of Industrial Engineering
University of Miami
Coral Gables, FL, USA

(2) Max Biedermann Institute for Biomechanics
Mount Sinai Medical Center
Miami Beach, FL, USA

(3) Department of Orthopaedic Surgery
University of Miami
Miami, FL, USA

INTRODUCTION

Mechanical properties, and morphological features of the vertebral cancellous bone play a fundamental role in terms of resistance to fracture and capability of withstanding a specific surgical treatment (e.g., internal fixation vs. bone cement augmentation) [1]. The cancellous bone is a porous solid structure saturated with interstitial fluid, thus its mechanical behavior can be regarded as poroelastic [2]. Previous studies have shown that the elastic modulus (E) of the cancellous bone is associated to its mechanical strength [3]. In addition, the morphology of the solid skeleton (density of pores) relates to how quickly fluids move into the bone, and the physical macroscopic parameter quantifying the ease of fluid motion is the hydraulic permeability (K). Hence, for instance, K may quantify the ease of penetration of bone cement within the vertebral body [4]. Therefore, knowledge of the mechanical properties of the vertebral cancellous bone is highly relevant for both management and prevention of vertebral fractures. However, for practical purposes, such properties should be determined in a minimally invasive fashion.

Bone densiometry (DEXA) and quantitative CT-scan are two mildly invasive diagnostic tools providing information on bone density. Specifically, DEXA provides the bone mass density (BMD), and previous studies attempted to correlate such a measurement with E [3, 4] and K [4] of cancellous bones. Similarly, radiographic density of the CT images have been related to the elastic properties (i.e. E) of bones [5]. Micro-CT technique provides high-resolution images that allow determining bone morphological parameters, such as porosity or bone volume fraction.

The objectives of this study were: (1) to verify whether the vertebral bone volume fraction measured via micro-CT is a good predictor for vertebral mechanical properties; and (2) to compare the predictive capabilities of the vertebral bone volume fraction to those of BMD measured via DEXA.

METHODS

Vertebrae L1, L2 and L3 of were obtained from a 54 y.o. white Caucasian male donor. A schematic of the specimen preparation and the experimental workflow is reported in Figure 1. The vertebral bodies were sliced along the plane orthogonal to the rostral-caudal axis. Each vertebral body yielded 3 slices of ~5mm thickness, for a total of nine vertebral body slices (3 vertebrae x 3 slices => n=9). The BMD of each slice was measured by means of a Hologic QDR 4500 X-ray densitometer (Hologic, Waltam, MA, USA). Subsequently, the slices were tested for indentation to simultaneously yield E and K. Finally, the slices were imaged via micro-CT to determine the volumetric bone fraction.

During the indentation test, the slices were embedded in a phosphate buffer solution, and compressed by a cylindrical indenter (5mm diameter) at the left posterolateral region. The indenter was connected to a servoelectric testing system (Instron E3000, Norwood, MA) with a 5kN load cell. A stress-relaxation test was performed by compressing of 5% (with respect to the initial height of the sample) the vertebral slice at 0.25mm/s rate.

The final displacement was held for 800 seconds, and the time dependent reaction of the sample was measured at a sampling rate of 10Hz. The relaxation of the reaction force of the sample over time was curve-fitted with the solution of a finite element model (FEBio 2.6.2, University of Utah, UT) simulating the indentation test on a vertebral slice. Specifically, the vertebral slice was modeled as a biphasic material; its solid phase was isotropic elastic non-compressible with Young's modulus E; fluid percolation through the vertebral slice was assumed to be governed by Darcy's law with constant hydraulic permeability K. The computational domain changed from slice to slice in order to reflect the geometrical characteristics (shape and size) of the sample tested. A total of ~27,000 tetrahedral elements were used to discretize the vertebral slice and the indenter. The optimization parameters of the curve-fitting were K and E. After indention, a micro-CT (SkyScan1176, Bruker BioSpin Corp., Manning Park, MA) imaged the slices at 50kV with 18μm resolution. The produced images were analyzed via an open source image-processing software (ImageJ, NIH) to yield the bone volume fraction (BV/TV), defined as the ratio of the volume occupied by the bone to the total volume in the indented region. A simple linear regression analysis investigated the correlation between BV/TV and K or E; another regression analysis verified correlations between BMD and BV/TV, K or E.

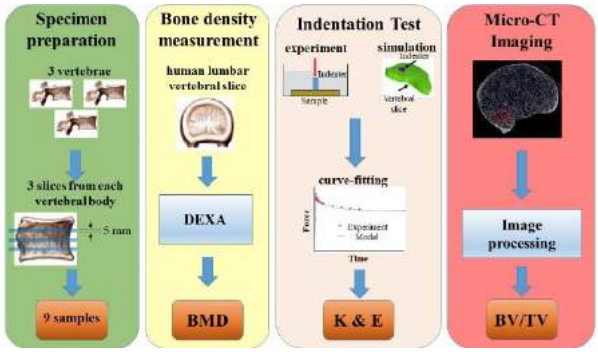

Figure 1 – Specimen preparation and testing workflow

RESULTS

The vertebral slices had BMD ranging form 0.491 to 0.084 g/cm^2. Their K, E and BV/TV ranged from $4.3 \cdot 10^{-3}$ to $3.3 \cdot 10^{-1}$ mm$^4 \cdot$N$^{-1} \cdot$s^{-1}, 3.18 to 18.95MPa, and 0.11 to 0.36, respectively. We found a strong relationships between BV/TV and K ($p < 0.05$; $R^2 = 87.1\%$), and E ($p < 0.05$; $R^2 = 71.9\%$), see Figure 2a-b. When trying to relate BMD to mechanical properties and morphology of the vertebrae, no correlation was found between BMD and either BV/TV or E ($p > 0.05$). However, we found a linear correlation between BMD and K (($p < 0.05$; $R^2 = 73.4\%$), see Figure 2c.

DISCUSSION

The objectives of this study were: (1) verifying whether the bone volume fraction measured via micro-CT image analysis could be a good predictor of fundamental vertebral mechanical properties such as hydraulic permeability and elastic modulus; and (2) compare the prediction capabilities of the bone volume fraction to those of bone mineral density determined via bone densiometry.

The mechanical properties of the vertebrae were measured from analysis of stress-relaxation tests performed via indentation. The magnitude of the measured hydraulic permeability was similar to that previously reported for [6], while the values of the elastic modulus were smaller than those observed in vertebrae [7]. Regression analyses suggest that BV/TV is a strong predictor for K and E. In addition, as previously reported [4], the relationship between BV/TV and K is non-linear.

We found that BMD may represent a good predictor for K ($p < 0.05$; $R^2 = 73.4\%$), in contrast with previous studies showing weak correlation between bone density and hydraulic permeability [4]. However, differently from previous observations [3, 4], BMD was not correlated to either elasticity (E) or morphologic (BV/TV) properties of the vertebrae ($p \sim 0.1$).

In summary, we identified the bone volume fraction, measured via micro-CT, as a strong predictor of the mechanical properties of the vertebral cancellous bone.

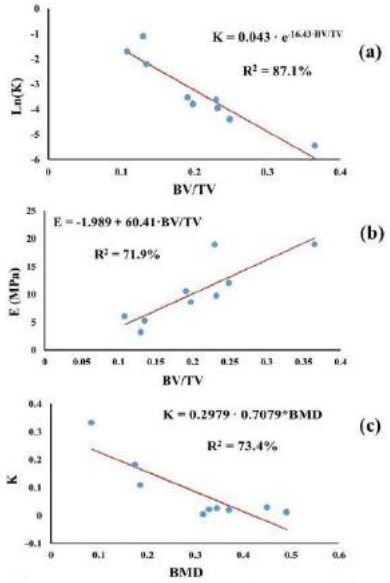

Figure 2 – Morphology (BV/TV) correlates with: (a) hydraulic permeability (K) and (b) elastic modulus (E); (c) bone density (BMD) correlates with permeability (K).

ACKNOWLEDGEMENTS

Supported by Max Biedermann Institute for Biomechanics.

REFERENCES

[1] Hu SS, *Spine*, 22(24):43S-48S, 1997.
[2] Isaksson H, et al., *J Biomech*, 39(8):1507-1516, 2006.
[3] D'Amelio P, et al., *Conn Tiss Res*, 49:99-104, 2008.
[4] Baroud G, et al., *J Biomech*, 37:189-196, 2004.
[5] Zannoni C, et al., *Med Eng Phys*, 20(10):735-740, 1999.
[6] Ochoa and Hillberry, *Proc Ann Meet ORS*, 1992
[7] Hernandez, *Handbook of Biomaterial Properties*, 2016.
[8] Ochia and Ching, *J Biomech Eng*, 124(5):533-537, 2002.

SB³C2019
Summer Biomechanics, Bioengineering and Biotransport Conference
June 25 -28, Seven Springs, PA, USA

MURINE ROTATOR CUFF TENDINOPATHY MODELS: THE ROLE OF MUSCLE LOADING

Adam C. Abraham (1), Fei Fang (1), Mikhail Golman (2), Panagiotis Oikonomou (2), Stavros Thomopoulos (1,2)

(1) Orthopedic Surgery
Columbia University Medical Center
New York, NY, USA

(2) Biomedical Engineering
Columbia University
New York, NY, USA

INTRODUCTION

Over 4.5 million individuals in the US suffer from rotator cuff tendinopathy, leading to lost days from work, occupational challenges, and recreational limitations (1). The pathogenesis of tendinopathy, leading to tendon rupture, is associated with intrinsic (e.g. age, joint laxity, muscle weakness) and extrinsic (e.g. mechanical load, fatigue) factors (2). It is hypothesized that these factors compromise tissue function through the accumulation of micro-damage and/or alterations in cellular metabolism driving poor quality matrix turnover. However, mechanistic studies of tendon lesion etiology are difficult in patients, which typically represent late-stages of disease progression. Therefore, our objective was to establish murine models of rotator cuff tendinopathy based on clinically observed correlates with disease prevalence. Specifically, we examined beneficial through pathologic levels of rotator cuff loading. We hypothesized that muscle overloading or underloading can each drive structural and functional degeneration, increasing the risk of rupture.

METHODS

All procedures were approved by the Columbia University Institutional Animal Care and Use Committee. 12-week old C57BL6/J male mice (n=95) were subjected to one of three rotator cuff tendinopathy models modulating supraspinatus muscle activity. Muscle paralysis was induced by injecting botulinum toxin-A (BtxA) into the supraspinatus muscle. Overuse was achieved using two downhill treadmill running protocols with an initial rate of 17 cm/s for 10 minutes followed by up to 22 cm/s for 40 min each day at a decline of 15 degrees (Overuse +) or 25 cm/s for 30 min each day at a decline of 10 degrees (Overuse ++). Both protocols were performed 5 days a week. Supraspinatus tendon/muscle imbalance was created by surgical excision of the infraspinatus tendon (Tenectomy). All procedures were performed bilaterally, and results were compared to age-matched cage activity control animals. Animals were euthanized at 3 d, 1 wk, 2 wk, and 4 wk time points. Gait function was assessed at 4-week time points for BtxA and treadmill groups (Noldus, CatWalk XT). Mice were placed in a walkway and allowed to freely explore without incentives, footprints of three compliant runs per animals were recorded, and spatiotemporal data was processed for forelimbs. Bone morphometry of the humeral head and tendon cross-sectional area were determined using micro-computed tomography (μCT, Bruker, Skyscan 1272). Supraspinatus tendon-to-bone mechanical properties were assessed using quasi-static uniaxial tension tests to failure (TA Instruments, Electroforce 3230). For histological sections, mouse shoulders were dissected, fixed in 4% paraformaldehyde, decalcified in formic acid (Immunocal, StatLab), and embedded in paraffin using standard techniques. 5 μm sections were obtained and stained with hematoxylin and eosin. Treatment groups were compared using ANOVA and specific differences from control animals were determined using Dunnett's multiple comparisons test; $P<0.05$ was considered significant. All statistical analyses were performed using GraphPad Prism 7. All data shown as mean ± standard deviation.

RESULTS

At 4 weeks, gait analysis demonstrated changes in walking pattern due to overuse, including significant decreases in cadence (Overuse + & Overuse ++, $P<0.0001$, Fig 1) and stride length (Overuse +, $P=0.0097$; Overuse ++, $P=0.0192$), while paralysis resulted in changes in weight bearing, with a lower ratio of forelimb/hindlimb intensity (BtxA, $P=0.013$; n=10/group, Fig. 1). Bone morphometric analysis revealed thickening of the cortical bone due to high-intensity overuse (Overuse ++, $P=0.0005$) and thinning due to muscle paralysis (BtxA, $P=0.0005$, Fig 2). Furthermore, there were significant losses in trabecular bone volume/total volume in the BtxA ($P<0.001$) and tenectomy groups ($P=0.008$), and an increase in the Overuse + group ($P=0.043$,

n=10/group, Fig. 2). These results were driven by local changes in trabecular structure, with BtxA and tenectomy resulting in increased trabecular spacing (P=0.002, P=0.012, respectively), BtxA resulting in decreased trabecular thickness (P=0.010), and treadmill running resulting in increased trabecular thickness (Overuse +, P=0.023; Overuse ++, P=0.0008). Additionally, cortical and trabecular mineral densities were decreased in the BtxA (P<0.001, P <0.001, respectively) and tenectomy (P=0.001, P=0.005, respectively) groups. High-intensity overuse increased cortical mineral density (Overuse ++, P<0.0001). The subchondral bone appeared thinner in BtxA and tenectomy groups and thicker with overuse (Fig. 3). The cross-sectional area of the supraspinatus tendon was significantly decreased due to treadmill running (Overuse +, P=0.007; Overuse ++, P<0.0001; n=10/group, Fig. 4). Tendon-to-bone stiffness was significantly higher in the moderate overuse group (Overuse +, P=0.0016, Fig. 4). Young's modulus and ultimate stress were significantly higher in both overuse groups (Overuse +, P=0.0002, P<0.001; Overuse ++, P<0.0001, P=0.016; n=9-10/group, Fig. 4). Maximum force was significantly decreased in the BtxA group (P=0.004, Fig. 4).

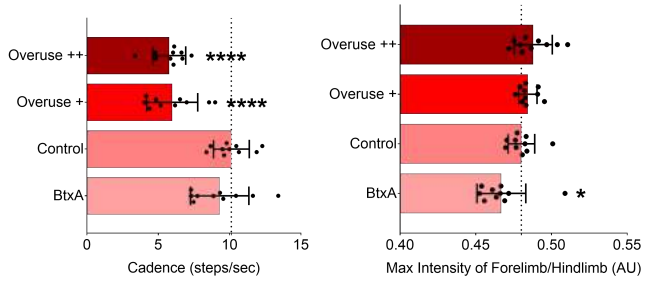

Fig 1. Gait analysis. *p<0.05, **p<0.01, ***p<0.001, ****p<0.0001; sig. diff. than Control.

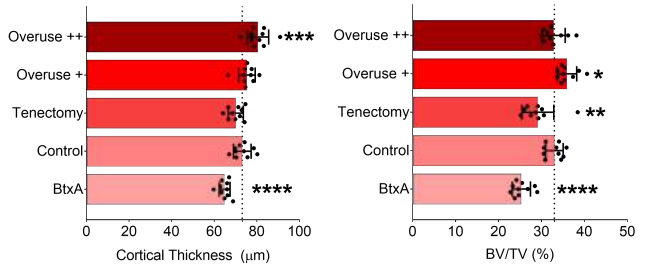

Fig 2. Quantitative bone morphometry from μCT. *p<0.05, **p<0.01, ***p<0.001, ****p<0.0001; sig. diff. than Control.

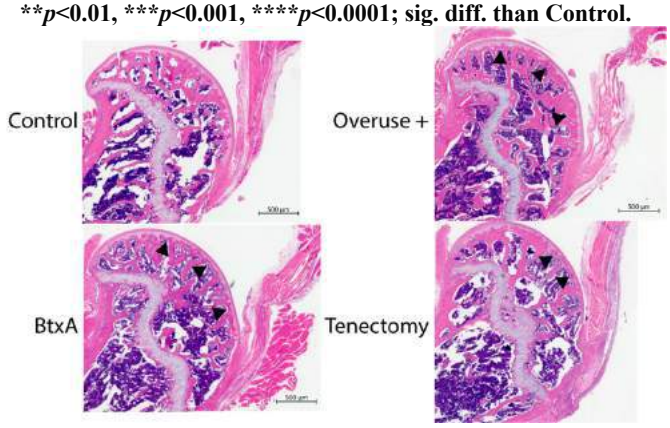

Fig 3. Hematoxylin and eosin staining. Black arrowheads highlight areas of subchondral bone thinning (BtxA, tenectomy) and thickening (Overuse +).

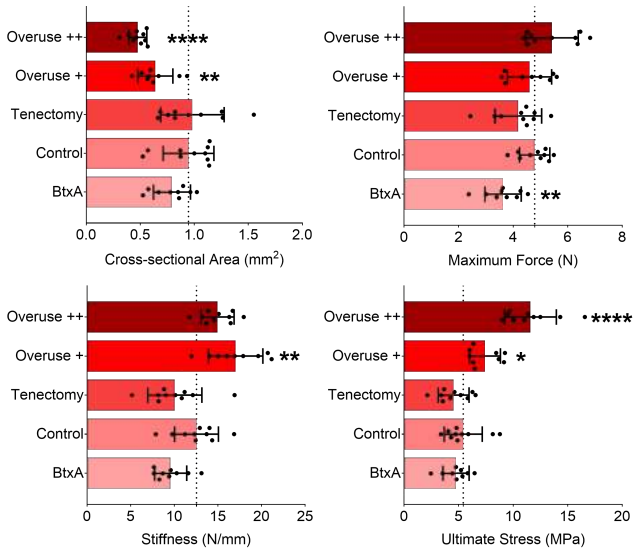

Fig 4. Biomechanical properties. *p<0.05, **p<0.01, ***p<0.001, ****p<0.0001; sig. diff. than Control.

DISCUSSION

Modulating supraspinatus muscle activity had significant impacts on mouse gait as well as the structure and function of the supraspinatus tendon and humeral head. Overuse activity caused changes in walking pattern, driving increased bone mass and tendon stiffness and potentially reducing tissue extensibility and increasing the risk of rupture. Conversely, reduced activity due to BtxA altered animal weight bearing, resulting in decreased bone mass and tendon strength. Surprisingly, surgical destabilization of the rotator cuff with tenectomy primarily affected the bone structure within the humeral head. Similarly, before surgical repair, patients exhibit bone loss at the supraspinatus tendon attachment site of the greater tuberosity (3). However, tendon mechanical properties have been observed to decrease with injury (4) or increase due to ageing (5), suggesting both conditions can increase the risk of rupture. In summary, our results recapitulate clinically observable alterations in rotator cuff structure and function by modulating muscle activity using murine models. Future work will include transcriptomic analyses and immunohistochemistry from each timepoint to determine the biological mechanisms driving functional loss, and how these models overlap with pre-existing clinical evidence at the molecular-scale.

ACKNOWLEDGEMENTS

This work was funded by the National Institutes of Health (R01-AR057386).

REFERENCES

[1] L. S. Oh, et. al., Clin. Orthop. Relat. Res. 455, 52–63 (2007). [2] Y. Xu, G. A. C. Murrell, Clin. Orthop. Relat. Res. 466, 1528–1538 (2008) [3] E. I. Waldorff, et. al., JSES 20, 904–908 (2011). [4] S. Arya, K. Kulig, J Appl Physiol 108, 670–675 (2009). [5] L. K. Wood, E et. al., J Appl Physiol 111, 999–1006 (2011)

SB³C2019
Summer Biomechanics, Bioengineering and Biotransport Conference
June 25 -28, Seven Springs, PA, USA

THE EFFECT OF FATIGUE ON THE IMPACT RESPONSE OF RAT ULNA

C. Yan (1), M. Kersh (2),

(1) Mechanical science and engineering
University of Illinois Urbana Champaign
Urbana, Illinois, United States

INTRODUCTION

Bones are under constant load and impact, so understanding fatigue properties of bones is important in characterizing mechanical properties of bone. Combining fatigue loading and impact, we may understand the effect of fatigue loading on the impact response given different recovery times. Using rats as an animal model, we evaluated the effect of fatigue loading to investigate (1) whether the non-destructive cyclic loading can induce woven bone formation, which is a repairing response to damage, and (2) how would the impact response change given different rest time after cyclic loading.

METHODS

Cyclic fatigue loading was performed on 16 healthy male Sprague-Dawley rats, at 18 weeks of age followed with micro-computed tomography (micro-CT) scan and impact loading test (Fig.1). All protocols were approved by the IACUC at UIUC.

Fatigue loading: Under continuous anesthesia, the rats were placed on a bed between the actuator and the load cell. The right forelimb was positioned with the elbow and volar flexed carpus placed in epoxy-potted aluminum cups [1, 2, 3]. The ulna was loaded axially in compression with a haversine waveform of 0.055N/g at 2Hz across the carpus and the olecranon. Due to the natural shape of the bone, a bending moment was induced along the diaphysis. Loading was stopped when the peak displacement reached 0.75mm± 0.20mm [1]. Pain relief (Meloxicam, 2mg/kg) was given through subcutaneous injection immediately after loading. The left forelimb served as control.

Fixation and CT imaging: Eight rats were euthanized and dissected within 24 hours after loading. The rest were euthanized and dissected 7 days later. All (left and right) ulnae were harvested and potted in customized fixture with epoxy (Fig. 2 A&B). Prior to impact testing, micro-CT scans were acquired for each specimen. Every scan acquired 996 slices of the diaphysis with each containing 996x1016 voxels. Images were binarized and filtered for further analysis.

Impact testing: A drop-tower system (Fig. 2C) was designed for the impact test. The specimen was secured in place during the test and total potential energy from the impact was equal to 17.5% of potential energy of the rat landing from a height of 0.2m. the peak forces of each specimen were recorded.

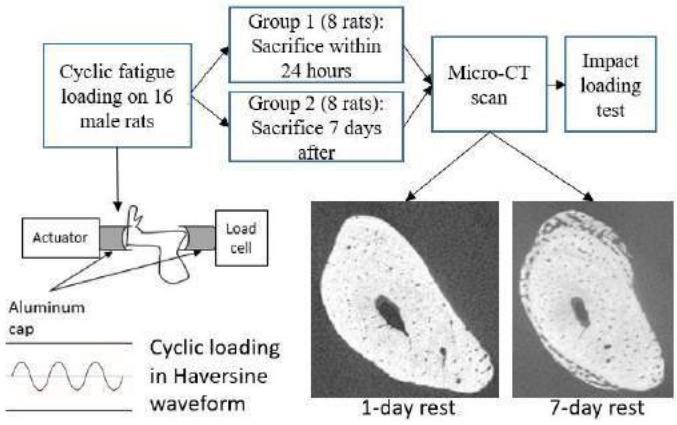

Figure 1: Experimental design for evaluating the effect of cyclic loading on the impact response of the rat ulna.

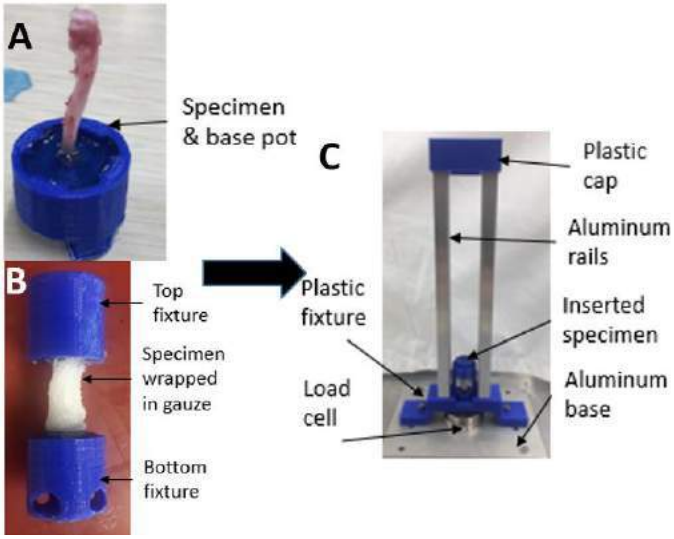

Figure 2: Specimen fixation and impact test apparatus.

RESULTS

There was no relationship found between the body weight and the cycle number needed to reach fatigue. Four rats did not produce useful information and thus were excluded. Ulnae exposed to fatigue loading and rested for 1-day were mechanically more damaged than those had 7-day rest. Of the 6 ulnae that had 1-day rest: 2 were severely damaged before impact loading, 3 of the remaining resulted in full fracture after impact, and 1 stayed intact. However, among the specimens had 7-day rest, only 1 of 6 loaded ulnae fractured after impact, and none of the control ulnae fractured. The fracture rate of the loaded ulnae was five times greater in the 1-day rest group than 7-day (Fig. 3). The peak impact forces were 38.73% higher in the control ulnae than the loaded ($P = 0.0055$) in 7-day rest group and in 1-day rest group. The loaded ulnae with 7-day rest had noticeable woven bone formation, shown as a ring of disorganized bone on the periosteal surface (Fig. 1). Normalized volume with respect to weight (Fig. 4) indicated that the difference between the control and loaded ulnae in 1-day rest group was not significant ($P = 0.27$), but it was in the 7-day rest group ($P = 0.0092$). The controls from both groups were not significantly different.

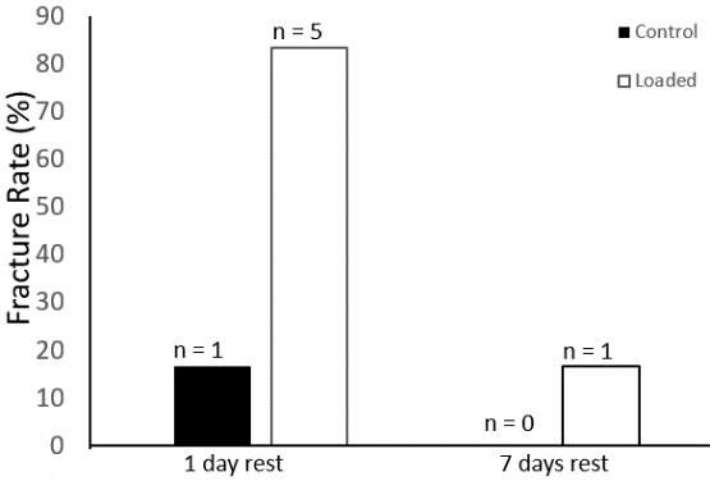

Figure 3: fracture rate of the specimens.

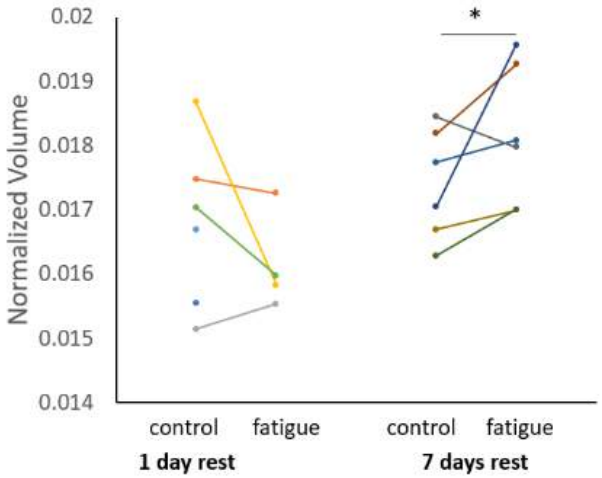

Figure 4: normalized bone volumes with respect to body weight.

DISCUSSION

A single bout of cyclic loading with peak force of 0.055N/g body weight on a rat ulna was enough to induce fatigue damage and cause woven bone formation as a repairing process [4, 5], if rest was given. However, even with 7-day rest, the peak impact forces among loaded ulnae were still significantly lower than the control ($P = 0.0055$), which means the bones recovered partially. Woven bone formation on the periosteal side might have resulted from the higher strain on the periosteal side during cyclic loading. The partial recovery was attributed to the rapid formation of woven bone [6]. The fracture rate indicated that rest time was important in preventing fracture while the bone was fatigued. The difference between the normalized volume among loaded ulnae was attributed to the formation of woven bone as well. However, woven bone did not provide as robust support as healthy cortical bone as shown by the difference between peak impact forces in 7-day rest group loaded and control ulnae.

ACKNOWLEDGEMENTS

The authors would like to thank Beckman Institute for providing the experiment location and animal care.

REFERENCES

[1] B. A. Uthgenannt, M. J. Silva, Use of the rat forelimb compression model to create discrete levels of bone damage in vivo, Journal of biomechanics 40 (2007) 317–324.

[2] V. Bentolila, T. Boyce, D. Fyhrie, R. Drumb, T. Skerry, M. B. Schaffler, Intracortical remodeling in adult rat long bones after fatigue loading, Bone 23 (1998) 275–281.

[3] Y.-F. Hsieh, M. J. Silva, In vivo fatigue loading of the rat ulna induces both bone formation and resorption and leads to time-related changes in bone mechanical properties and density, Journal of Orthopaedic Research 20 (2002) 764–771.

[4] S. H. McBride, M. J. Silva, Adaptive and injury response of bone to mechanical loading, BoneKEy Reports 1 (2012).

[5] J. A. McKenzie, M. J. Silva, Comparing histological, vascular and molecular responses associated with woven and lamellar bone formation induced by mechanical loading in the rat ulna, Bone 48 (2011) 250–258.

[6] B. A. Uthgenannt, M. H. Kramer, J. A. Hwu, B. Wopenka, M. J. Silva, Skeletal self-repair: stress fracture healing by rapid formation and densification of woven bone, Journal of Bone and Mineral Research 22 (2007) 1548-1556.

SB³C2019
Summer Biomechanics, Bioengineering and Biotransport Conference
June 25 -28, Seven Springs, PA, USA

MICROINDENTATION MAPS TWO GRADIENTS IN MECHANICAL PROPERTIES ACROSS THE ZONES OF THE GROWTH PLATE

Kevin Eckstein (1), Karin Payne (2), Virginia L. Ferguson (1)

(1) Department of Mechanical Engineering
University of Colorado at Boulder
Boulder, CO, USA

(2) Department of Orthopedics
University of Colorado at Anschutz
Aurora, CO, USA

INTRODUCTION

The growth plate (*i.e.* physis) is a cartilage tissue that functions to lengthen growing limbs and displays remarkable mechanical characteristics. It is similar to articular cartilage in composition and features zonally varying mechanical properties. However, its structure differs significantly from articular cartilage, especially in the proliferative (PZ) and hypertrophic (HZ) zones (**Fig 1.c**). Notably, the relatively soft physeal cartilage forms strong interfaces to the adjacent epiphyseal and metaphyseal bone. Despite these strong interfaces, ~18% of pediatric fractures occur in the physis.[1]

In some transphyseal fractures, a bony bar forms across the physis and arrests growth or causes an angular deformity. Current methods of resecting bony bars have 18-35% success rates in restoring limb growth.[2] Typically, adipose tissue is implanted after bony bar resection; this tissue is chosen with little consideration to mechanical function and often becomes necrotic, breaks down or dislodges following surgery.[3] In the case of articular cartilage repair, however, mechanical characterization has informed the design of implants that mimic the native tissue properties; likewise, mechanical and chemical characterization of the physis may guide the design of better implants that are mechanically robust, form strong interfaces, and mimic the native mechanical environment to facilitate chondrocyte growth.

The physis, however, is a difficult tissue to mechanically evaluate. Its small dimensions, irregular shape, and confinement between bony tissue has restricted previous work to various compression tests of excised tissues,[4,5] one shear loading study,[6] and one atomic force microscopy (AFM) study.[7] Compression tests have provided valuable results for tissue stiffness, permeability, and anisotropy, but require semi-confinement of the native interfaces to measure spatial variations in properties. Due to the semi-confinement, purely intrinsic properties of the cartilage cannot be measured. Prior results from AFM are only reported for cranial growth plates, which differ in structural organization to limb-lengthening growth plates. The probe size of AFM (R = 20 nm) may also be too small compared to the feature size of physeal cartilage (~20 μm chondrocyte lacunae) and is incapable of capturing the aggregate tissue response. Therefore, a test method that can adequately evaluate the aggregate tissue response and map spatially varying intrinsic mechanical properties is desired.

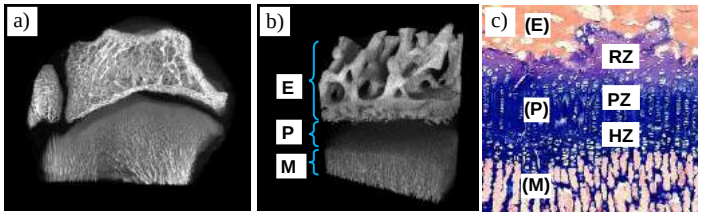

Figure 1: a) X-ray microscopy (XRM) of 9 week old rabbit tibia plateau visualizes mineralized tissue and the absence thereof in the growth plates (arrows). b) cartilage growth plate, *i.e.* physis (P), features strong bone-cartilage interfaces with the epiphysis (E) and metaphysis (M). c) (P) cartilage varies in structure between reserve (RZ), proliferative (PZ), and hypertrophic (HZ) zones.

The objective of this study was to combine microindentation and Raman spectroscopic imaging to characterize the intrinsic mechanical properties and chemistry of the 9 week old rabbit physis. The instantaneous elastic modulus was evaluated across the physis and compared to spatial variations in mineral and protein content previously mapped with Raman spectroscopy.[8] X-ray microscopy (XRM) was also performed to visualize the stochastic interdigitation of the epiphysis-physis interface, which resembles osteochondral interface but is coarser in feature size than the opposite metaphysis-physis interface.

METHODS

A previously frozen femur of a 9-week-old New Zealand white rabbit was sectioned in the sagittal plane and polished (precision polisher; EXAKT 400CS). Microindentation (Hysitron TI 950 TriboIndenter, xZ-500 extended displacement stage) was performed at 164 points across a 1000 × 75μm region (**Fig 2.a**) using a R = 50 μm spherical probe. The probe was lifted off the sample surface, indented to a depth of ~15μm at a rate of 180 μm/s (**Fig 2.b**) and then held for 45 seconds. Hertzian contact and an instantaneous Poisson's ratio ν = 0.5 were assumed to calculate the instantaneous Young's modulus, E_{inst}, at each site. Each row in the map was averaged and plotted against distance across the physis (**Fig 2.c**).

Previous Raman spectroscopy imaging[8] (Renishaw InVia, 785 nm laser, 63× immersion objective, ~1 μm spot size) evaluated peak areas characteristic of mineralization ($\nu_2 PO_4^{-3}$, 415-465cm^{-1}), collagen matrix (amide III, 1215-1300cm^{-1}), and non-collagenous proteins (Phenylalanine, 995-1020cm^{-1}) for 1600 points in a 285 × 1185 μm area (**Fig 2.d**). Peak ratios were plotted with respect to percent distance across the physis for each column of points, then averaged over all samples to reveal trends using Matlab (**Fig 2.e**) (n = 8 samples, 20 columns each). Further imaging was performed using XRM (Zeiss, Xradia 520 Versa; 80kV, 7W, 401 images) to visualize mineralized tissues and their interfaces with the physis.

RESULTS

Microindentation mapping found the instantaneous modulus, E_{inst}, of physeal cartilage to range 0.15 - 1.5 MPa, with the highest stiffness in the reserve zone (RZ) and the lowest in the PZ. Stiffness steadily increased moving from the PZ to the HZ. Across the bone-cartilage interfaces, we found a sharp increase in stiffness to values ranging 750-950 MPa for epiphyseal bone (E), and 60-300 MPa for the more heterogeneous metaphyseal bone (M). Significant relaxation of ~70% was observed in cartilage indents during the 45 second hold time.

We observed an irregular interface between epiphyseal dense bone and physeal cartilage through 3D XRM imaging (**Fig 1.a**), previous 2D Raman spectral mapping (**Fig 2.d**),[8] and microindentation mapping. Raman spectroscopy maps showed a rapid change in mineralization at the epiphysis/physis interface, but a more gradual rise at the heterogeneous metaphyis/physis interface (**Fig 2.e**).

DISCUSSION

Microindentation results revealed two different gradients in mechanical stiffness in the physeal cartilage. First, a sharp gradient was found at the epiphysis-physis interface and across the RZ, where elastic modulus values decreased sharply from 1.5 MPa near the interface to 150 kPa. However, this gradient was sometimes absent in the columns of the heatmap due to the protrusion of epiphyseal bone that extended into the RZ cartilage (**Fig 2.a**). Interestingly, the RZ cartilage appears to be nestled between these bony protrusions, which could contribute to a strong cohesive interface. The RZ was observed to be thin (5-10% of total (P) thickness) compared to other reported physeal zone dimensions;[4] this is likely due to differences in animal model and that the reserve zone thickness is thought to decrease with age. Overall, the RZ was the stiffest of the physeal zones, which correlates with a lack of non-collagenous proteins (NCP) typically found in cells (**Fig 2.d and 2.e**). This indicates the relative modulus of the PZ and HZ is due to their high cellular volume. The second gradient in stiffness occurs across the PZ and HZ, with stiffness steadily increasing from 150 kPa (PZ) to 350 kPa (HZ). This trend agrees with the trend reported by Radhakrishnan.[7] While Raman imaging found that mineral:matrix ratio rises gradually at the physis-metaphysis interface (albeit with high variance), the mechanical properties were observed to rise sharply.

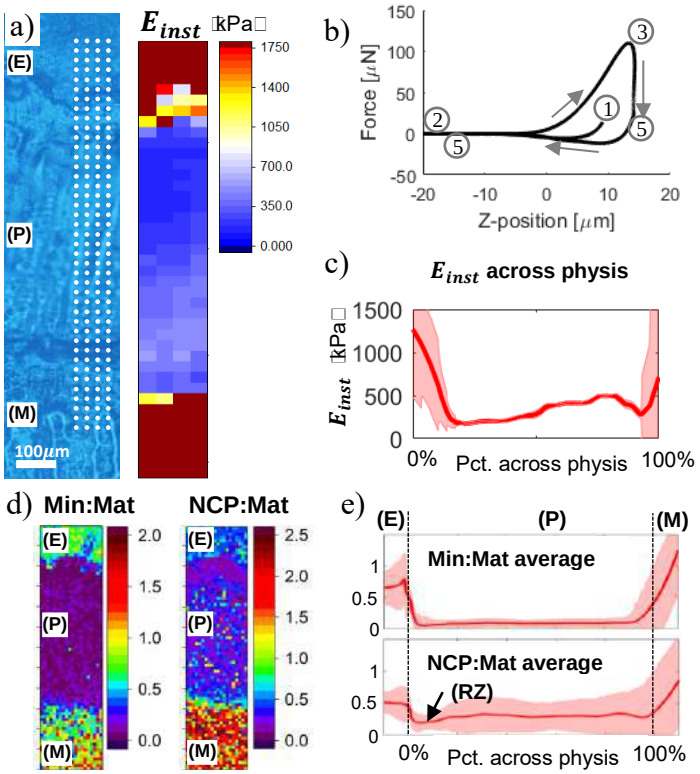

Figure 2: a) Overlay of microindentation map spanning epiphyseal bone (E), physeal cartilage (P), and metaphyseal bone (M); b) Representative loading curve from microindentation; c) Mean stiffness ± SD plotted across % physis (E-P interface at 0%); d) Raman mapping of mineral:matrix (Min:Mat) and non-collagenous protein:matrix (NCP:Mat) peak area ratios; e) Columns of Raman heatmaps plotted with respect to % across physis and averaged ± SD.

The instantaneous modulus results are within range of previously reported equilibrium stiffness values (0.3 - 1.1 MPa),[5] however, the equilibrium response of our tests is significantly lower. One explanation for lower stiffness values may be due to the small-scale indentations being less prone to the stiffening effect of friction, as is present in unconfined compression. Future finite element modeling of indentation may enable us to determine anisotropic properties. Additionally, our relaxation data enables us to fit poroelastic models and characterize the equilibrium response and permeability in future analyses. Beyond this study, 3D XRM images could be used in combination with microindentation data to model the multi-scale mechanics of the physis and its interfaces.

ACKNOWLEDGEMENTS

NIH R21-HD090696-01; NSF CBET 1338154;
NIH NICHD 5R21HD090696-02; NSF CMMI 1726864

REFERENCES

[1] Mizuta, T *et al.*, *J. Pediatr. Orthop.* 7, 518–523 (1987).
[2] Hasler, CC & Foster, BK, *Clin. Orthop.* 242-249 (2002).
[3] Clark, A *et al.*, *BioResearch Open Access* **4**, 65-74 (2015).
[4] Sergerie, K *et al.*, *J. Biomech* **42**, 510-516 (2009).
[5] Villemure, I & Stokes, IAF, *J. Biomech.* **42** 1793-1803 (2009).
[6] Sevenler, D *et al.*, *J. Biomech* **46**, 1597-1603 (2013).
[7] Radhakrishnan, P *et al.*, *Ann. Biomed. Eng.* **32**, 284-291 (2004).
[8] Eckstein, K *et al.*, *8th World Congress of Biomech.* (2018).

FIBROUS NETWORK TOPOGRAPHY REGULATES FIBROTIC PHENOTYPES IN ANNULUS FIBROSUS CELLS

Edward D. Bonnevie (1,2), Sarah E. Gullbrand (1,2), Beth G. Ashinsky (1,2,3), Tonia K. Tsinman (1,2), Dawn M. Elliott (3), Harvey E. Smith (1,2), Robert L. Mauck (1,2)

(1) Orthopaedic Surgery and Bioengineering
University of Pennsylvania
Philadelphia, PA, USA

(2) Translational Musculoskeletal Research Center
CMC VA Medical Center
Philadelphia, PA, USA

(3) Department of Biomedical Engineering
Drexel University
Philadelphia, PA, USA

(4) Department of Biomedical Engineering
University of Delaware
Newark, DE, USA

INTRODUCTION

Cells respond to local mechanical and topographic cues to regulate their phenotype and biosynthetic activities[1-3], with 'stiff' environments driving a fibrotic phenotype[3]. In the context of intervertebral disc injury, loss of nucleus pulposus swelling and release of residual strains in the annulus fibrosus (AF) alter the mechanics and organization of the cellular microenvironment[4]. Here, we used in vivo and in vitro models to test the hypothesis that altered fiber organization in the AF regulates the emergence of fibrotic phenotypes seen in the context of intervertebral disc injury and subsequent degeneration.

METHODS

New Zealand White rabbits were subjected to annulus puncture[5] with a 16-gauge needle to 5 mm depth, with 2-, 4-, and 8-week survival. The annulus fibrosus was assessed via second harmonic generation imaging and staining for alpha smooth muscle actin (αSMA). Fiber environment organization was quantified through an angular spread metric that was calculated as the standard deviation of the fiber angle distribution. Briefly, higher angular spread denotes a more disorganized fiber environment. For in vitro studies, bovine annulus cells were seeded onto electrospun PCL scaffolds, and a tensile stretching device was use to apply prestrain to scaffolds prior to cell seeding (ε = 9% prestrain). Cell-seeded aligned and nonaligned prestrained and free swelling scaffolds (NE, NF, AE, AF) were assessed at 24 hours for fiber organization (angular spread), focal adhesions, YAP/TAZ nuclear localization, αSMA+ stress fibers, and baseline ECM synthesis. For the ECM synthesis assay, methionine was replaced in the cell culture media with L-Azidohomoalanine (AHA), which was incorporated into nascent ECM deposited by seeded cells[6]. Following 48 hour culture, AHA was visualized through

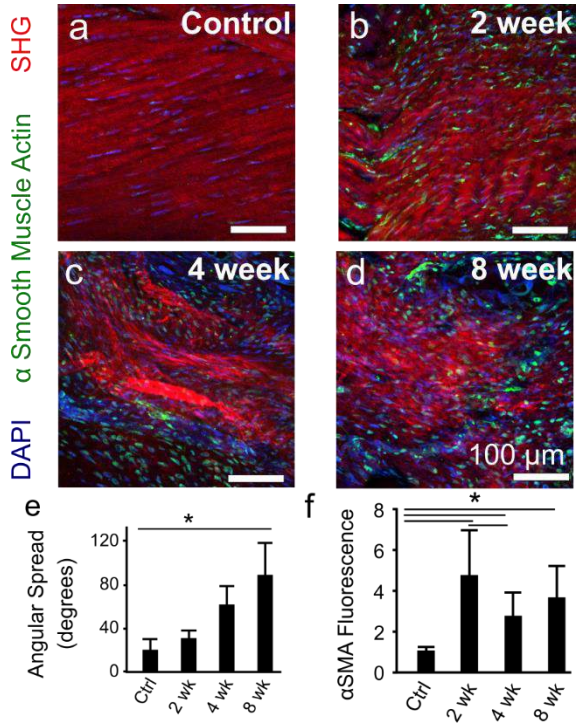

Figure 1: (a-d) Second harmonic generation (SHG) imaging with immunofluorescence revealed that injury leads to (e) progressively more disorganized fibers and (f) the emergence of a fibrotic (alpha smooth muscle actin+, SMA) phenotype (n = 3 animals per group, * p < 0.05).

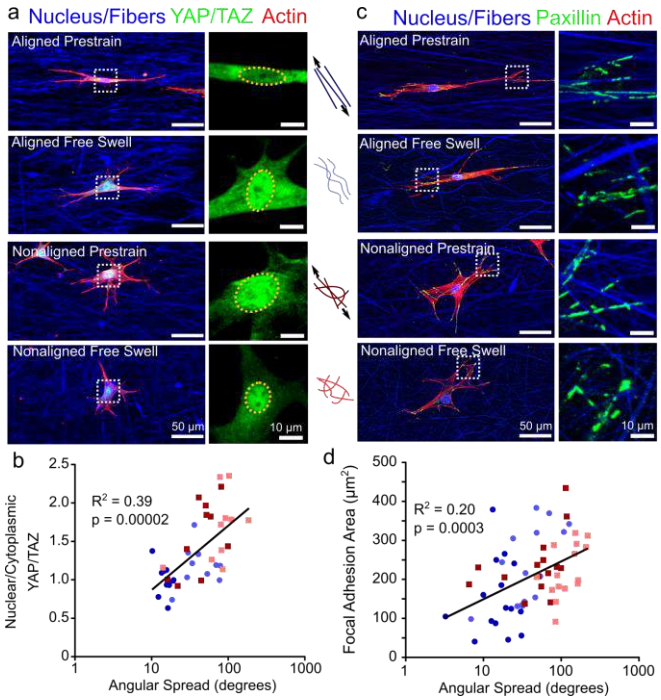

Figure 2: Strain mediated changes in fiber organization modulated the mechanobiologic response of AF cells (n = 40 cells from 8 scaffolds). Local fiber organization correlated with both nuclear/cytoplasmic YAP/TAZ and focal adhesion area (n = 60 cells from 12 scaffolds).

click chemistry and the area of deposition was determined as the AHA-positive area minus cell area.

RESULTS

In the in vivo model, release of residual strains via needle puncture resulted in progressive disorganization of the AF (**Fig 1a-e**) and the emergence of fibrotic phenotypes (i.e., αSMA expressing cells) after 2 weeks; these fibrotic signatures remained elevated through 8 weeks (**Fig 1f**). In the in vitro model, both baseline fabrication parameters (aligned vs nonaligned) and prestrain dictated fiber organization at the cellular length scale (**Fig 2**). This organization had a significant effect on cell spreading (aspect ratio and spread area), with aligned microenvironments promoting elongation and minimizing spread area. These organized, pre-strained fiber environments limited focal adhesion area and maintained nuclear levels of YAP/TAZ at a low level (**Fig 2**). Likewise, incorporation of αSMA into stress fibers depended on the organizational and prestrained state of fibrous environments, with aligned prestrained scaffolds reducing the fibrotic phenotype compared to nonaligned free swelling scaffolds (**Fig 3**). This phenotypic shift was observed in concert with altered cellular synthetic activity, where the deposition of nascent matrix was predicted by local fiber organization (**Fig 3**).

DISCUSSION

Taken together, our data suggest that strain-mediated topography mediated cellular responses, where highly aligned environments curbed cell spreading, nuclear YAP localization, focal adhesion area, αSMA+ stress fibers, and nascent matrix deposition. Our findings also suggest that fibrotic phenotypes emerge with the release of residual strains in the annulus of injured discs (**Fig 1**). This patho-mechanobiologic event was replicated by an in vitro scaffold system, where cellular perception of the local environment was dictated by both baseline and strain-mediated fiber organization. Fiber organization provided cues (contact guidance) in aligned environments to modulate cell shape and size such that YAP/TAZ remained largely cytosolic (**Fig 2**), which in turn, suppressed incorporation of αSMA into stress fibers and the development of a fibrotic phenotype[3] that culminated in lower matrix production (**Fig 3**). Continuing work is focused on using this scaffold-based system to evaluate pharmacologics that might inhibit this fibrotic remodeling response after injury.

ACKNOWLEDGEMENTS

This study was supported by NIH F32AR072478, R01EB02425, T32AR53461, P30AR050950, and VA I01RX002274.

REFERENCES

[1] Engler+ 2005, [2] Dupont+ 2011, [3] Li+ 2017, [4] Michalek+ 2012, [5] Masuda+ 2005, [6] McCleod+ 2016

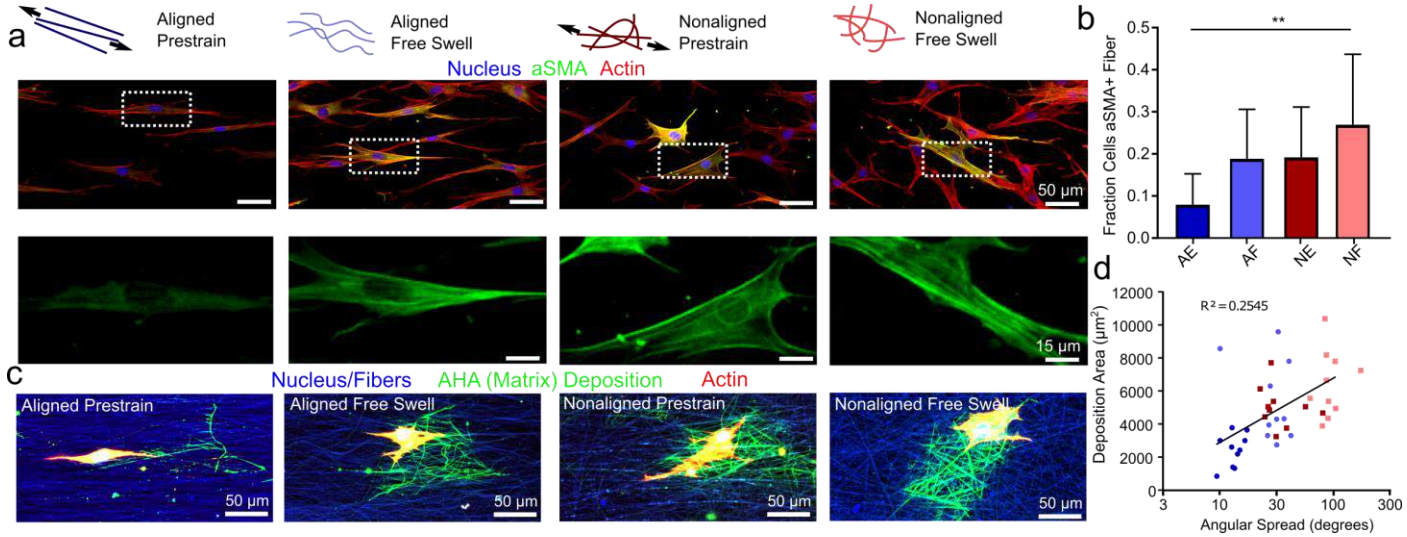

Figure 3: (a-d) Fiber organization modulated αSMA localization to stress fibers (n = 6 scaffolds/group, ** p < 0.01). Local fiber organization predicted matrix formation, where aligned environments reduced nascent matrix deposition. (n = 40 cells from 8 scaffolds).

SB³C2019
Summer Biomechanics, Bioengineering and Biotransport Conference
June 25 -28, Seven Springs, PA, USA

MITOCHONDRIA FUNCTION, STRUCTURAL, AND MECHANICAL OUTCOMES AFTER EXPOSURE TO NEAR-INFRARED LIGHT DURING TENDON MATURATION AND ADULT HEALING

Ryan C. Locke (1), Elisabeth A. Lemmon (1,2), Ellen Dudzinski (1), Sarah C. Kopa (1), Harrah R. Newman (1), Elahe Ganji (1,3), Megan L. Killian (1)

(1) Department of Biomedical Engineering
University of Delaware
Newark, DE, USA

(2) Pre-Vet Medicine and Animal Biosciences
University of Delaware
Newark, DE, USA

(3) Department of Mechanical Engineering
University of Delaware
Newark, DE, USA

INTRODUCTION

Tendon injuries are a major orthopaedic issue that account for significant pain and lost work [1]. Unfortunately, tendon injuries often heal poorly and are difficult to treat [1]. Treatment of tendon injury prior to rupture may reduce disability risk. Currently, injured tendons are primarily treated non-operatively by nonsteroidal anti-inflammatory drugs, physical therapy, electro- or cryo- therapy, orthoses, platelet-rich plasma injections, and photobiomodulation (PBM). Yet many non-operative interventions leave patients with persisting symptoms [2]. Thus, there is a need to improve non-operative treatments of injured tendons. To do so, a better basic science understanding of how non-operative treatments improve tendon health is needed. PBM, the application of low power near-infrared light, has shown promising results in the clinic [3] and with small animal models for adults [4,5]; however, no work has established the influence of PBM on tendon maturation. Additionally, the cellular mechanism of PBM remains elusive, and little work has investigated paired functional outcomes of normal tendon healing compared to tendon healing with PBM.

We hypothesized that the initial response of tendon to PBM results in increased mitochondria metabolism, and we expected this response to be amplified during tendon healing due to an increase in numbers of cells from remodeling. In this study, we aimed to establish the cellular response of tendon to PBM and to measure the effect of PBM on the cellular, structural, and functional properties of tendon 1) during maturation and 2) during adult healing using paired experiments.

METHODS

All experiments were approved by the University of Delaware IACUC. For all experiments, CD1 mice (Envigo) were used. To investigate the cellular mechanisms of PBM during postnatal growth, unilateral Achilles tendons of anesthetized neonatal (P14) littermates were dosed through the skin once (30mW/cm^2 to 2.5J/cm^2). Continuous wave and concurrent near-infrared light (980:810nm, 80:20 power ratio, 1.5cm^2 cross-sectional area, LightForce FXi Laser, LiteCure) was used for all experiments. Mice were euthanized at 4hrs (N=4, 2 males, 2 females) and 24hrs (N=4, 2 males, 2 females) after PBM, and RNA were isolated from control and PBM-dosed tendons using a commercially available kit (PureLink RNA Mini Kit, Invitrogen) following tissue pulverization (MM400, Retsh). Total RNA were reverse-transcribed using Superscript VILO (Invitrogen). Subsequent quantitative Real Time-PCR was performed using a LightCycler 96 System (Roche) and RT^2 Profiler PCR Array for Mouse Mitochondria (330231, Qiagen) with PowerUp SYBR Green (Applied Biosystems). ΔCT values were calculated for each gene using the average of *Actb*, *B2m*, *Gapdh*, *Gusb*, and *Hsp90ab1* as reference genes. To assess the effect of PBM on postnatal maturation of tendon, unilateral Achilles tendons of anesthetized P16 mice were dosed (30mW/cm^2 to 2.5J/cm^2) daily for 4-weeks (N=12, 6 males, 6 females). To assess the effect of PBM on adult tendon healing, bilateral Achilles tenotomy was performed at 6-months (N=4 females, retired breeders) for gene expression studies or at P56 (N=13, 7 males, 6 females) for biomechanical and histological comparisons. For all outcomes, tendons were injured and then healed for 1-week following which unilateral Achilles tendons were dosed (300mW/cm^2 to 2.5J/cm^2) daily for 3 consecutive days (gene expression) or daily for 7-weeks (biomechanics or histology). To investigate the cellular mechanism of PBM during healing, mice were euthanized 4hrs after the third dose of PBM, and the same method of RNA isolation and qRT-PCR described above was followed. For biomechanical testing, mice were euthanized after dosing periods then either frozen in PBS-soaked gauze at -20C for uniaxial tensile testing (N=7-8) or the tendons were dissected and fixed in 4% PFA for histology (N=5). Mice were thawed and tendons dissected prior to

mechanical tests. Uniaxial tensile tests were comprised of a preload of 0.01N, 10 preconditioning cycles from 0.02-0.04N at 0.02mm/s, and ramp to failure at 0.02mm/s (5848, Instron). Cross-sectional areas (CSA) of tendon were assumed as ellipsoidal and gauge lengths (L) were measured using a scaled image after preload. CSA and L were used to measure stress and strain. For histology, tendons were paraffin embedded, sectioned, and stained with picrosirius red, Toluidine Blue, and Hematoxylin & Eosin (H&E). Picrosirius red stained slides were imaged using circular polarized light microscopy (Stemi 2000, Zeiss) to assess collagen alignment and were semi-quantitatively scored by three blinded individuals. H&E sections were used to quantify the gap spacing of healing tissue. Immunolocalization of COL1A2, BCL-2, and COX-1 was performed (N=5) at 1:100 dilutions (COL1A2: sc-393573; BCL-2: sc-19998; COX-1: sc-23960) and detected using a commercially available kit (IHC Select HRP/DAB, Millipore). A repeated measure (control vs. PBM tendon) two-way ANOVA with Sidak's correction for multiple comparisons was performed for the ΔCT of each gene and for mechanical outcomes (Young's Modulus, Ultimate Stress (US), Strain at US, Area Under the Curve (AUC) at US, Stiffness, and Ultimate Load). ΔCT was converted to $2^{-\Delta CT}$, log base-2 transformed, and presented as mean ±95% confidence intervals. Paired t-tests were used to compare collagen alignment and gap space.

RESULTS

In the maturing tendon, *Slc25a24* and *Bcl2l1* were upregulated 4hrs after PBM compared to untreated control (Fig 1A-B), however localization of BCL2, COL1A2, and COX1 was unaffected by daily PBM during maturation (Fig 1C-D, not shown). Genes associated with apoptosis (*Trp53, Hsp90aa1)*, small molecule transport (*Slc25a14, Slc25a24)*, and outer membrane transport (*Tomm34)* were downregulated at 24hrs compared to 4hrs after PBM (Fig 1A). Collagen alignment was semi-quantitatively decreased by PBM during maturation (Fig 1E-G). No changes in mechanics were observed for PBM during maturation (not shown).

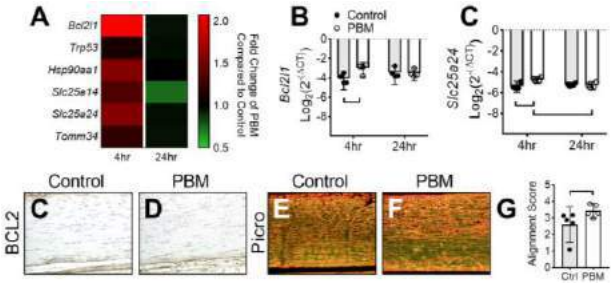

Figure 1: During maturation, one dose of PBM acutely altered mitochondria-related gene expression. (A) Gene expression heat map for fold change of 4hr and 24hr after PBM. (B) *Bcl2l1* and (C) *Slc25a24* were significantly upregulated in PBM groups at 4hrs but not 24hrs after a single dose of PBM. (C-D) After 4wks of PBM dosing, Achilles tendons did not show a noticeable increase in BCL2 immunolocalization. (E-G) PBM treated tendons demonstrated slight decreases in alignment (from picrosirius red staining) compared to control groups. Lines: Significant differences, p<0.05.

During healing, genes associated with membrane translocation of cytochrome c oxidase (*Cox18*) were down regulated after PBM compared to control (Fig 2A-B). *Slc25a13* and *Slc25a19* were down- and upregulated after PBM compared to control, respectively (Fig 2C-D). No differences were observed in gap space, structure (Figure 2E-F), or protein localization (not shown) between control and PBM groups, with fatty and glycan-rich (Figure 2E'-F') regions observed in both groups. Stiffness increased with PBM compared to controls for females (Fig 2G). Young's modulus increased for females compared to males with PBM (Fig 2H). Strain increased for males compared to females with PBM and compared to controls (Fig 2I).

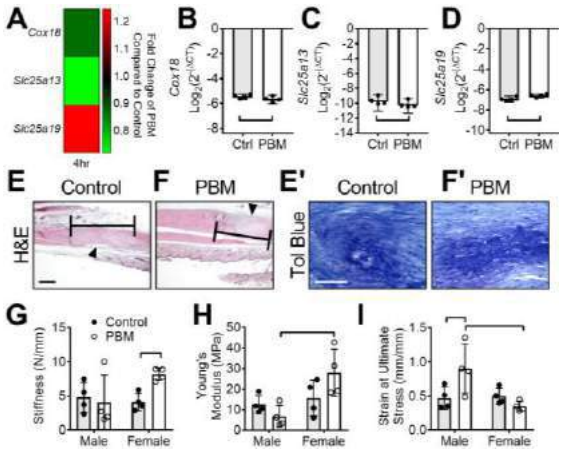

Figure 2: During tendon healing, daily PBM has sex-dependent effects on tendon mechanics. (A) Gene expression heat map for fold change of 4hr after PBM. (B) *Cox18*, (C) *Slc25a13*, and (D) *Slc25a19* were differentially regulated at 4hrs after a single dose of PBM. Lines: Significant differences, p<0.05. (E-F, Scale: 200μm) Gap space, fat infiltration, and (E'-F', Scale: 50μm) proteoglycan presence were not altered by PBM. Bars: Gap space, Arrows: Fat infiltration. (G) Stiffness of female tendons with PBM increased compared to controls, (H) Young's modulus of female tendons with PBM increased compared to males with PBM, and (I) strain of male tendons increased with PBM compared to controls and females with PBM. Mean ±SD.

DISCUSSION

In this study, we found that PBM acutely changes mitochondria gene expression during maturation and healing, yet this effect was not amplified during healing, contrasting our hypothesis. The cellular changes from PBM may have a negligible effect on tendon structure and mechanics during maturation. The effect of PBM on functional outcomes of tendon healing may be sex-dependent [6]. Increased stiffness with PBM compared to controls for females suggests that PBM therapy may be beneficial during healing to improve functional outcomes. It remains unclear if the difference in power of the maturation study (30mW/cm^2) compared to the healing study (300mW/cm^2) may translate to changes in mechanical properties during healing and not influence tendon properties during maturation. A limitation of this study is that sex differences for gene expression were not assessed because of the small sample sizes (N=2).

This was the first study to assess the paired (control vs. therapy) effect of PBM on tendon maturation and healing, and these data warrant further investigation of the effect of power on tendon maturation and the sex-dependent mechanism of PBM during tendon healing.

ACKNOWLEDGEMENTS

Delaware Bioscience Center for Advanced Technology Applied Research Collaboration funding.

REFERENCES

[1] Killian, M. et al., *JSES*, 21:228-237, 2012. [2] Lohrer, H et al., *BMCMD*, 17:207, 2016. [3] Tumilty, S et al., *LSM*, 31:127-135, 2016. [4] Ferreira, R. et al, *PLS*, 33:579-584, 2015. [5] de Jesus, J. et al, *PLS*, 32:345-350, 2014. [6] Pardes et al., *ABME*, 44:2901-2910, 2016.

SB³C2019
Summer Biomechanics, Bioengineering and Biotransport Conference
June 25 -28, Seven Springs, PA, USA

PRIMARY SYNOVIAL FIBROBLAST-COLLAGEN GELS EXHIBIT UNIQUE TENSILE FAILURE PROPERTIES & MICROSTRUCTURE FROM 3T3-COLLAGEN GELS

Meagan E. Ita (1), Harrison R. Troche (1), Beth A. Winkelstein (1,2)

(1) Department of Bioengineering
University of Pennsylvania
Philadelphia, PA, United States

(2) Department of Neurosurgery
University of Pennsylvania
Philadelphia, PA, United States

INTRODUCTION

Fibroblasts are stromal cells with roles in development, repair, wound healing, and extracellular matrix (ECM) remodeling [1]. They remodel their ECM by mechanotransduction mechanisms [2-4]. Fibroblast-collagen interactions studied using 3D fibroblast-populated collagen gels report fibroblast-induced changes in mechanical properties and network microstructure [2,3]. Fibroblasts are defined broadly by their morphology, ability to adhere, and lack of lineage-specific markers, but are functionally and phenotypically diverse [1,4]. Fibroblast-like synoviocytes (FLS) are a unique class of fibroblast-like cells found in the lining and capsular ligament of synovial joints [5,6]. Although FLS have a role in inflammation and degradation, particularly in rheumatoid arthritis [5], little is known about their regulation of matrix mechanics. Defining if, and how, FLS alter matrix mechanics and/or microstructure will help define load-induced cell signaling in tissues, like the capsular ligament, in which FLS reside.

The effect of primary FLS cells on matrix mechanics and microstructure was investigated using a 3D collagen gel system under tensile failure. Since 3T3-collagen interactions in 3D gels are more extensively studied than FLS and are known to exert mechanical forces on their surrounding collagen fibers [7,8], gels with 3T3 also were included and outcomes compared between cell types. Seeding fibroblast concentrations in gels range from $5x10^4$ to $2x10^6$cells/mL, with primary cell lines generally on the lower end due to their eventual senescence and less robust proliferation compared to immortalized cell lines like NIH 3T3 cells [7-11]. To test effects of concentration within the limits of primary FLS growth, two concentrations were used in the low range ($5x10^4$ & $1x10^5$cells/mL). But, these concentrations have differential effects on matrix failure mechanics [9]. Macroscopic gel mechanics were quantified by force-displacement curves and stiffness. Force and regional strains were compared at several displacements during loading. Network microstructure was analyzed using collagen alignment maps at those same displacements, and collagen fiber orientation was quantified using circular variance (CV), with a lower CV indicating a tighter clustering and more fiber alignment [12].

METHODS

FLS were harvested from adult Sprague-Dawley rats by removing the capsular tissue surrounding the hind limb joint [10,11], and cultured in DMEM with 10% FBS and 1% P-S. NIH 3T3 fibroblasts were maintained in the same feeding media. Media was changed every other day and cultures were passaged at 90% confluence. In 2D, FLS are elongated, polygonal and have a branched morphology; 3T3 cells are rounder but still branched (Fig. 1A). On passage 4, cultures were resuspended in Type I collagen solution (2mg/mL; Corning) at a concentration of either $5x10^4$ cells/mL (low FLS n=5; low 3T3 n=4) or $1x10^5$ cells/mL (high FLS n=3; high 3T3 n=4) [7-11]. Collagen was cast in 12-well plates (1mL/well) and allowed to gel at 37°C.

On DIV9, gels were cut (21mmX8mm) and the surface marked for strain tracking [12]. Gels were loaded into a planar test machine (574LE2; TestResources; 500g load cells) and immersed in a 37°C PBS bath. The test setup was integrated with polarized light imaging [12] and high-speed cameras (Phantom-v9.1; Vision Research) to acquire alignment maps and track markers. Gels underwent uniaxial displacement to failure at 0.5mm/s, with force and displacement data (200Hz) synchronized with imaging (500Hz) (Fig. 1B).

Force data were filtered by a 10-point moving average filter [12]. Failure was defined as maximum (peak) force and stiffness was calculated as the slope of the loading curve over 20-80% of peak force [13]. Marker positions in images were digitized at reference, and at 20%, 80% and 100% (failure) of peak force. LS-DYNA (LSTC) calculated maximum principal strains (MPS) for elements defined by the markers (Fig. 1) and elements averaged for each gel [12]. Collagen

alignment maps were generated at the same points during loading as MPS and used to calculate the CV [12]; CV at failure was normalized to reference for each gel. Differences in stiffness and reference CV were tested between cell type and concentration by two-way ANOVA. Force, MPS, and normalized CV were compared between FLS and 3T3 for each concentration using repeated-measures ANOVAs.

RESULTS

Gel contraction is observed with the high FLS concentration causing it to pull away from the well wall during culture, producing shrunken gels with a curled circular edge (Fig. 1C). No contraction was observed for the high 3T3 group or either low concentration group (Fig. 1C). Before loading, collagen organization in the high FLS gels is different from all other groups, with significantly higher CV ($p \leq 0.05$), indicating a larger spread of collagen fibers (Fig. 2).

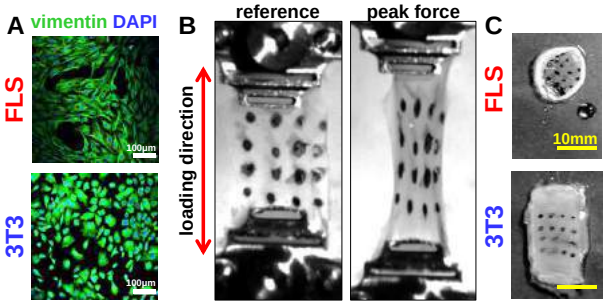

Figure 1: (A) Labeling of the intermediate filament vimentin shows elongated FLS morphology and rounded 3T3s. (B) A low FLS gel before loading (reference) and at failure (peak force). (C) Images with high concentration of FLS or 3T3 show FLS gel contraction.

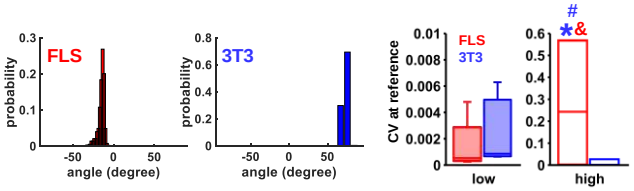

Figure 2: Histograms show the spread of fiber angles for high FLS and low 3T3 gels. High FLS gels exhibit greater CV than low FLS (&p=0.04), low 3T3 (#p<0.05), and high 3T3 (*p<0.05).

Although loading curves are similar for both cell types at low concentration, failure force is consistently higher for 3T3 than FLS gels with the high concentration (Fig. 3A). Forces at both 80% ($p=0.03$) and 100% ($p<0.01$) of peak are significantly higher for gels with 3T3s than FLS at a high concentration (Fig. 3A). Yet, it is not different between cell types at 20% of peak at either concentration (Fig. 3A). Stiffness differences are not significant ($p>0.08$), despite a 10-fold lower value in gels with high FLS than those with low FLS and nearly 20-fold lower value than high 3T3 gels (Fig 3B).

As with force, MPS is different between cell types at the high concentration (Fig. 3C). Although peak force is lower in the high FLS group, MPS in high FLS gels is greater ($p<0.01$) than 3T3 at the same concentration (Fig. 3C). MPS at 80% of peak force is different ($p=0.03$) between cell types at the high concentration. Across all displacements tested, FLS and 3T3 gels are only different at failure for low concentration, with FLS gels having a higher CV (greater disorganization relative to reference) than 3T3 gels ($p<0.01$) (Fig. 3C).

DISCUSSION

At the high concentration, FLS-embedded gels exhibit different macroscopic mechanics, stiffness, and microstructure than gels with embedded 3T3s (Figs. 2 & 3). Although the mechanism by which FLS gels contract was not further investigated here, fibroblast-mediated contraction may occur by cell contraction, traction forces, initial

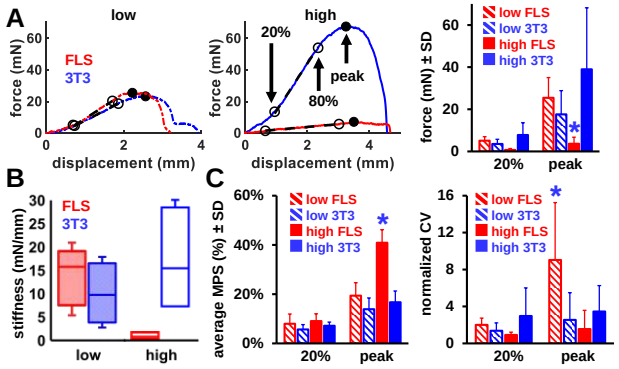

Figure 3: (A) Forces are not different at low concentration, but high FLS gels have lower (*) peak force than high 3T3. (B) Although stiffness of high FLS gels is lower than other groups, it is not significant. (C) MPS is not different at 20% of peak; but at peak, high FLS gels undergo larger MPS than high 3T3 gels (*), and low FLS have higher normalized CV than low 3T3 (*).

elongation and spreading, or by ECM remodeling [2-4], which is supported by the decreased stiffness and initial disorganized matrix (Figs. 1-3). Dermal fibroblasts cultured at the same concentrations used here alter gel modulus by 1.12 (low) and 3 (high) times, respectively, after only DIV1, but increase modulus [9], which is the opposite from the effect of FLS on stiffness (Fig. 3B). Although strain increases with CV in gels without fibroblasts [12], the MPS of high FLS is greater than high 3T3, but the normalized CV is not different (Fig. 3C), possibly due to FLS exerting traction forces [2]. Visualizing cells is needed to define their interactions with the gel matrix.

The concentration-dependent effect of FLS on collagen gel mechanics and microstructure, that differs from 3T3s, is particularly relevant since different regions of synovial joints have different FLS densities [6]. It implies variable mechanosensitive properties may be conferred based on the regional anatomical FLS cell density. In this same collagen gel system absent fibroblasts, pain-related signaling in embedded nerve fibers and collagen network reorganization are induced at strains of similar magnitudes [12]. Given the current findings that both local strains and collagen organization are altered by the presence of FLS (Figs. 2 & 3), it is likely that nerve fibers in FLS-dense regions may be even *more* susceptible to such changes than those in FLS-sparse regions. Including FLS and neurons together will better simulate biologic conditions relevant to trauma and pain. Nonetheless, these findings demonstrate FLS cells exhibit a unique phenotype and action on matrix mechanics and support that primary FLS have distinct behavior at relevant biologic concentrations for systems mimicking the capsular ligaments of synovial joints.

ACKNOWLEDGEMENTS

Funding from NIBIB (AT010326-07), NIAMS (T32AR00713), and NSF (CMMI15-48571). Thanks to Dr. Burdick for the 3T3 cells.

REFERENCES

[1] Rinn J et al *PLoS Genet* 2:e119, 2006 [2] Dallon J & Ehrlich H *Wound Repair Regen* 16:472-9, 2008 [3] Grinnell F & Petroll W *Annu Rev Cell Dev Biol* 26:335-61, 2010 [4] Hinz B *Periodontol 2000* 63:14-28, 2013 [5] Bottini N & Firestein G *Nat Rev Rheumatol* 9:24-33, 2013 [6] Yamashita T et al *Spine* 21:538-43, 1996 [7] Simon D et al *J Mech Behav Biomed Mater* 14:216-26, 2012 [8] Mohammadi H et al *J R Soc Interface* 6:20141074, 2015 [9] Evans M & Barocas V *J Biomech Eng* 131:101014, 2009 [10] Saravanan S et al *Inflamm Res* 63:451-62, 2014 [11] Bing Z et al *Mol Biol Rep* 39:6077-85, 2012 [12] Zhang S et al *J Biomech Eng* 138:021013, 2016 [13] Lee K et al *J Biomech* 39:1256-64, 2006.

CONTACT EXPERIMENTS REVEAL PRESSURE EVOLUTION IN SOFT HYDRATED INTERFACES

Christopher L. Johnson (1), Jiho Kim (1), Alison C. Dunn (1)

(1) Department of Mechanical Science & Engineering
University of Illinois at Urbana-Champaign
Urbana, Illinois, USA

INTRODUCTION

Sliding tissues in the human body such as the blink of the eye or the articulation of the knee joint are critical for sensing and mobility. The slip surfaces are often hydrated, surface-bound extracellular matrix or large hydrophilic molecules, like the mucins and glycoproteins in the tear film, or lubricin in large articulating joints (Figure 1). Their function as low-friction, efficient sliding bearings depends upon how they respond to the pressures in the interface. The mechanics of soft, hydrated tissues are very complex, so we use high-water-content crosslinked hydrogels as a controlled proxy to study the contact mechanics of soft, hydrated surfaces.

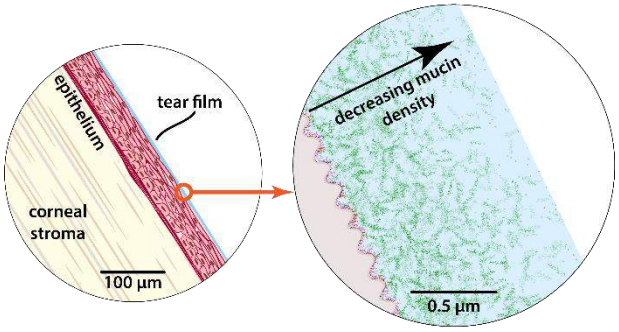

Figure 1: The human tear film is comprised of hydrophilic mucins and glycoproteins which mediate the eyelid/cornea interface.

The standard for indentation and contact measurements is to perform them at moderate indentation rates to both avoid long-term creep but account for quick relaxations that occur due to fluid effects. In addition, recent work has established novel probes both as solid hydrogels [1] and as thin hydrogel membranes which impart a constant-pressure experiment [2]. Those studies have advanced not only contact mechanics but understanding of soft-soft hydrated lubrication, in that the composition of the crosslinked hydrogel inherently controls the interface pressure. While that is true, interfaces in the body are not contacted at moderate timescales, but rather held in contact, such as in the knee joint or the eyelid resting on the cornea when the eye is not blinking. Thus the question we seek to answer is this: Do contact models like the Hertz model [3] or Winkler model [4] describe the behavior of long-duration soft, hydrated contacts? In this study we perform creep relaxation experiments in three contacting configurations such as hard probe-soft substrate, the inverse, and both soft components.

METHODS

Materials

Soft probes and flat substrates were molded either in combination delrin/polyolefin molds or between polystyrene plates, and allowed to equilibrate in water for > 2 hours before testing. The composition was a polyacrylamide of 7.5% acrylamide, 0.3% bisacrylamide, 0.15 % radical donator (APS), and 0.15% initiator(TEMED), all on a weight per total weight basis. This hydrogel was optically transparent and fell in the "ideal" range defined by Pruitt et al [5]. The hard probe was a steel sphere of 1.5 mm diameter (McMaster-Carr) spray-painted black to reduce reflections.

Instrument

A custom, instrumented microindenter was used in force-control mode to apply and hold a light load in the interface (0.50, 0.75, and 1.00 mN). Simultaneously, either particle-exclusion or particle-inclusion microscopy was used to view the contact and record its changes in time up to 10 minutes (Figure 2). Images were recorded with Nikon software on an inverted spinning-disk confocal microscope, using LED

illumination at 470 nm (Ti-E, Nikon Instruments). Particles are 468/508 green fluorescent polystyrene spheres of 1.0 μm diameter (Fisher Scientific). All experiments are submerged in water at 25°C.

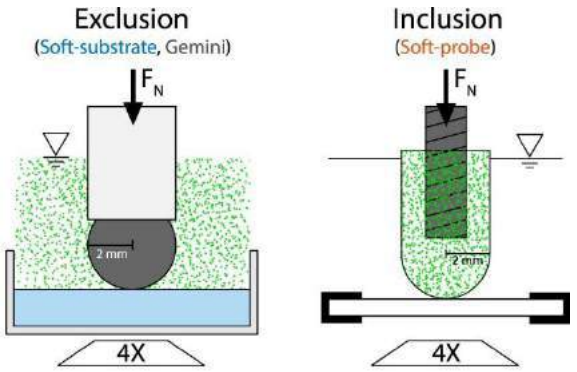

Figure 2: Particle exclusion or inclusion microscopy is used to reveal contact made by an optically-transparent hydrogel.

The viewing area was always constant at 2.3mm x 2.3mm, and the size of the contact are was measured using the known scale in ImageJ software [6]. Finally, the force data and contact areas were anchored together by matching the time at which the force reached its steady-state value. The force was divided by contact area to calculate the average pressure at all time points.

RESULTS

The self-mated, or Gemini contact between the hydrogel probe and hydrogel slab was revealed using particle exclusion microscopy. Contact area increased ~ 20% over 10 minutes (Figure 3, top). This method was also used for a hard probe-on-soft substrate. Particle exclusion had limited success with only a soft probe, so the probe was impregnated with the same particles during polymerization, and the contact area was revealed to increase by only 10% over the same duration (Figure 3, bottom). Each experiment was repeated at least 3X, so these images are representative.

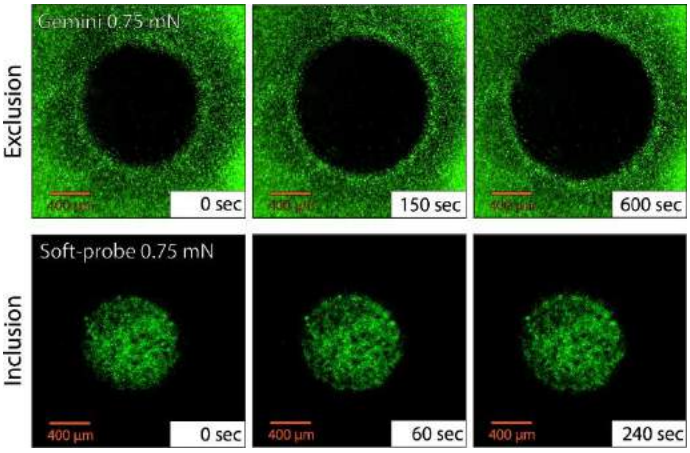

Figure 3: Contact areas increase in time.

All configurations exhibited creep relaxation, manifested as increasing contact area under a constant-load contact experiment. The soft substrate configuration had the greatest extent of contact area growth, the Gemini contact a moderate extent, and the soft-probe the least extent (Figure 4).

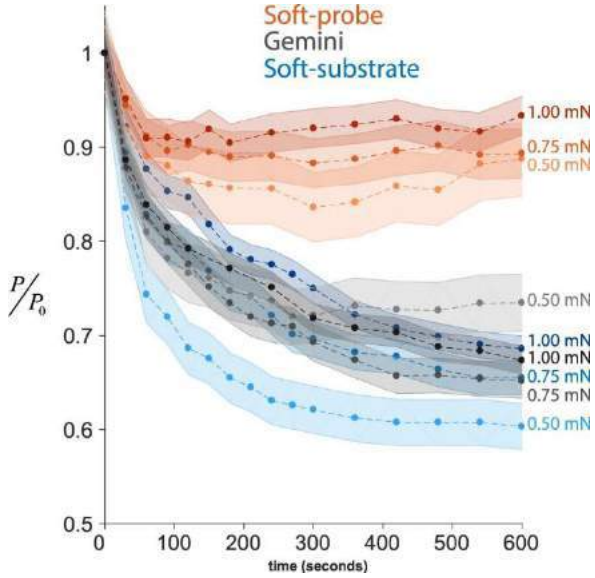

Figure 4: The normalized pressure over time decreases as a function of contact configuration and applied load.

DISCUSSION

These results add a new dimension to contact mechanics of soft materials, moving from quasi-static results that may fit neatly to a Hertz contact or other model to time-dependent responses that evolve if the load is allowed to persist. Preliminary calculations of contact pressure evolution indicate that the Hertz model is only valid over short durations of contact. Our data suggest that for long times, Gemini contact approaches a constant-pressure contact model, which depends upon the equilibrium osmotic pressure of the 7.5 % polyacrylamide material rather than the applied loads. This conclusion supports recent findings on hydrogel lubrication which connect the resistance to slip with the material composition [7,8]. This study is limited in that the same microscopy technique was not used in all measurements, though care was taken to ensure repeatability.

This study provides further understanding of what controls the contact between surfaces of high-water-content hydrogels, with the analogy to compliant and hydrated biological tissue contact, such as the eyelid against the cornea or cartilage against cartilage. Further, it adds to the background knowledge required for materials selection when designing a prosthetic device or coating to contact biological tissues such that it best mimics the natural interaction.

ACKNOWLEDGEMENTS

This work was supported by NSF award #1751945.

REFERENCES

[1] A. C. Dunn et al, *Tribol. Lett*. **54** (2014).
[2] S. L. Marshall et al, *Biotribology* **11** (2017).
[3] K. D. Schulze et al, *Biotribology* **11** (2017).
[4] A. C. Rennie et al, *Tribol. Lett.* **18** (2005).
[5] A. K. Denisin et al, *ACS Appl. Mater. Interfaces* **8** (2016).
[6] C. A. Schneider et al, *Nat. Methods* **9** (2012).
[7] J. M. Urueña et al, *Biotribology* **1**–**2** (2014).
[8] E. R. Reale et al, *Soft Matter* **13** (2017).

SB³C2019
Summer Biomechanics, Bioengineering and Biotransport Conference
June 25 -28, Seven Springs, PA, USA

HARMONIC SHEAR WAVE IMAGING: A NEW ELASTOGRAPHY METHOD TO EVALUATE MECHANICAL PROPERTIES OF SOFT TISSUES

S. Sadeghi (1), D.H. Cortes (1,2)

(1) Mechanical Engineering Department
Penn State University
State College, PA, USA

(2) Biomedical Engineering Department
Penn State University
State College, PA, USA

INTRODUCTION

Ultrasound shear wave elastography (SWE) can be classified as transient or harmonic based on its temporal characteristics. Most transient ultrasound elastography methods use high-intensity ultrasound 'push' pulses that generate a shear wave with a wide frequency spectrum [1]. Several studies have shown biases in the shear wave group velocity measurements of transient methods. These biases can be mitigated by calculating the phase velocity as a function of frequency. However, the energy distribution within the frequency spectrum of transient waves cannot be easily controlled. Therefore, the amplitude of the shear wave may not be optimal at the desired frequency. Conversely, harmonic methods have a narrow frequency bandwidth, which means that the wave energy can be concentrated at the desired frequency. These differences make it difficult to compare measurements obtained with transient and harmonic methods. Several narrowband harmonic imaging techniques have been developed to estimate mechanical properties of tissues. However, all these techniques employ more than one transducer, which may not be optimal for clinical use due to the added complexity to the measurement. The objective of this study was to introduce a narrowband shear wave generation method produced by 'push' pulses with sinusoidally-modulated intensity using a single clinical transducer. In the method, named harmonic shear wave imaging (HSWI), it may be possible to directly compare measurements of wave speed to those obtained using magnetic resonance elastography (MRE). This is desirable for the diagnosis of diseases affecting the stiffness of soft tissues.

METHODS

In HSWI method, the duration of each push pulse was varied sinusoidally with a preset main frequency to modulate the acoustic radiation force for exciting the shear waves (Figure 1). The duration of the push pulse was set to vary between D_{min} = 9.6 µs (50 cycles at 5.208 MHz) and Dmax = 105.6 µs (550 cycles at 5.208 MHz). The duration of the nth push pulse was determined by equation (1):

$$D_n = D_{min} + \frac{(D_{max} - D_{min})}{2}\left[\sin\left(2\pi(n-1)/N_{pp}\right) + 1\right] \quad (1)$$

where n = {1, 2, …, N_{pp}}. One complete excitation cycle was constructed by a preset number of push pulses (N_{pp}). The N_{pp} at each frequency was chosen to produce smooth sinusoidal waves. Plane wave acquisition pulses were transmitted between push pulses to measure shear wave propagation.

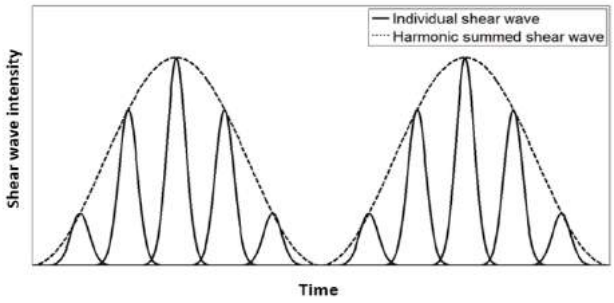

Figure 1: The sequentially excited shear waves with a sinusoidal variation of intensity

The filtered data was processed by using local frequency estimation (LFE) to obtain the 2D quantitative map of shear wave speed. HSWI was validated on a CIRS homogeneous elasticity phantom and agarose gels with different concentrations. HSWI was also performed in the rectus femoris muscle of a healthy male individual to evaluate the HSWI performance in vivo.

RESULTS

Table 1 shows the shear wave speeds measured by HSWI, MRE and SSI from the rectus femoris muscle in vivo, CIRS phantom and agarose gels. In general, the shear wave speeds obtained by the three elastography methods were similar. Figure 2 shows a 2D shear wave

speed map reconstructed by HSWI with a frequency of 500 Hz on the CIRS phantom as an example. Additionally, the comparison between the dispersion curve obtained in CIRS phantom using SSI and shear wave speed obtained using HSWI are shown in Figure 3.

Table 1: Comparison between the shear wave phase velocities of the CIRS phantom obtained by the SSI and HSWI methods.

		Rectus femoris muscle	CIRS	0.4 % agarose	0.5 % agarose	0.6 % agarose
HSWI	100 Hz	2.11±0.04	N/P	1.52±0.09	1.85±0.03	N/P
	200 Hz	2.53±0.09	2.63±0.03	1.51±0.07	1.99±0.04	N/P
	250 Hz	2.71±0.08	2.72±0.06	1.55±0.03	1.97±0.03	2.91±0.05
	450 Hz	3.00±0.19	2.74±0.02	1.55±0.07	1.94±0.04	2.91±0.02
	500 Hz	3.02±0.17	2.79±0.02	1.53±0.06	1.93±0.02	3.00±0.04
	550 Hz	3.06±0.08	2.87±0.01	1.57±0.04	2.00±0.06	2.93±0.05
MRE		N/P	N/P	1.57	1.96	2.94
SSI		2.56±0.07	2.98±0.01	1.72±0.08	2.20±0.02	2.98±0.01

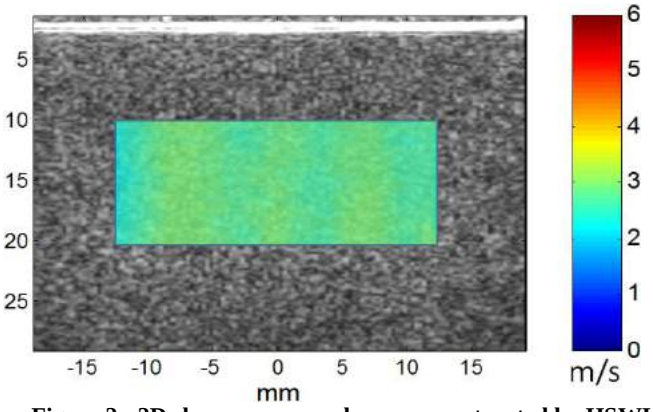

Figure 2: 2D shear wave speed map reconstructed by HSWI.

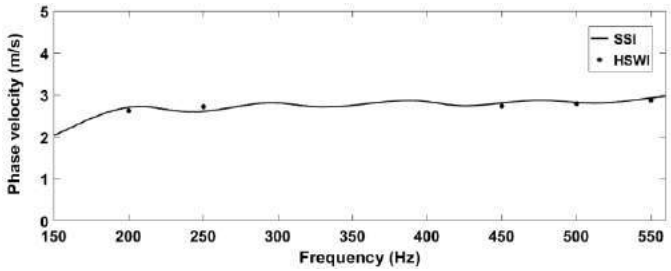

Figure 3: Comparison between the shear wave phase velocities of the CIRS phantom obtained by the SSI and HSWI methods.

Fourier analysis of the sequence of push pulses used in HSWI indicate that the majority of the excitation energy concentrates at the main frequency. The HSWI frequency spectrum is shown in Figure 4. The normalized intensity represents the intensity at the fundamental frequency in HSWI divided by the intensity in shear wave dispersion ultrasound vibrometry (SDUV) method developed by Chen et al. [5] at the same frequency, while the same amplitude was selected for both methods. It can be observed that the intensity of the spectrum at the fundamental frequency is higher in HSWI compared to SDUV. The reason for this difference is that HSWI transmits several push pulses during one push cycle of the excitation while SDUV transmits only one.

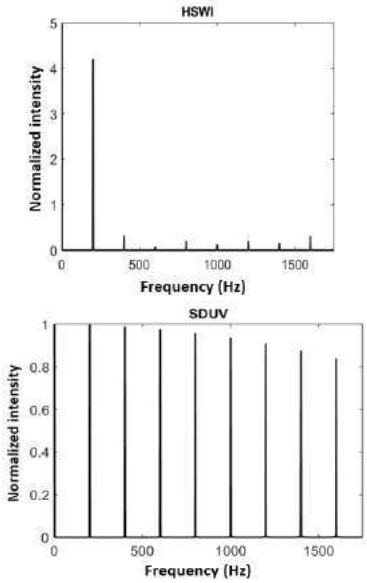

Figure 4: The frequency spectrum in HSWI and SDUV

DISCUSSION

Phantom experiments showed that the shear wave speeds obtained using HSWI and MRE were comparable. The results from HSWI in the rectus femoris muscle of a healthy male individual showed an increase of speed with frequency, as expected, due to the viscoelasticity of the tissue. It can be seen that for lower frequencies, similar to those commonly used in MRE, the wave speed measured by HSWI is lower. Therefore, this represents an example of the difference between HSWI and SSI in vivo. The novelty of our paper is that we introduced a narrowband shear wave generation and shear wave detection technique using a single clinical transducer.

Unlike transient methods, the energy in HSWI is concentrated around a narrow frequency range. Nenadic et al. [2, 3] employed 2D FFT to obtain frequency-dependent shear wave speed for shear wave propagations in bladder wall with viscoelastic properties. However, the application of 2D FFT for obtaining the dispersion curve is limited in the case of in vivo measurements with noisy 2D FFT data [2]. Brum et al. [4] measured the shear wave speed dispersion in the Achilles tendon of ten healthy individuals based on 2D FFT, reporting the maximum shear wave amplitude around 400 Hz. HSWI concentrate most of the energy at the main frequency (Figure 4) that is comparable to MRE, which typically operates at a single frequency between 50-100 Hz. Hence, although no direct comparison between HSWI and SDUV or the mentioned transient methods was made in this study experimentally, it is reasonable to expect that shear waves with higher intensity are generated in HSWI, specially at lower frequencies.

Measurements of shear wave speed by HSWI are, in principle, comparable to MRE because of the use of a single-frequency mechanical excitation. The results in this study showed that the shear wave speeds of the agarose gels measured by HSWI and MRE were comparable. Hence, HSWI might be a useful clinical tool for staging the level of liver fibrosis. In addition, HSWI could also be applied to the differential diagnosis of benign and malignant thyroid nodules, and the evaluation of the stiffness of muscles. The limitation of this study is that, in the LFE algorithm, a higher number of wavelengths of the harmonic shear wave should be present inside the ROI to obtain accurate estimation.

REFERENCES

[1] Palmeri M et al., *Interface Focus, 1:* 553-564, 2011.
[2] Nenadic I et al., *Phys Med Biol*, 58: 2675, 2013.
[3] Nenadic I et al., *IEEE IUS*, 987-990, 2014.
[4] Brum J et al., *Phys Med Biol*, 59: 505, 2014.
[5] Chen S et al., *IEEE UFFC*, 56: 55-62, 2009.

SB^{3}C2019
Summer Biomechanics, Bioengineering and Biotransport Conference
June 25 -28, Seven Springs, PA, USA

STRONG TRIAXIAL COUPLING AND ANOMALOUS POISSON EFFECT IN COLLAGEN NETWORKS

Ehsan Ban (1,2), Hailong Wang (1,2,3), J. Matthew Franklin (4), Jan T. Liphardt (4), Paul A. Janmey (1,5,6), Vivek B. Shenoy (1,2,6)

(1) Center for Engineering Mechanobiology
University of Pennsylvania
Philadelphia, PA, USA

(2) Department of Materials Science and Engineering
University of Pennsylvania
Philadelphia, PA, USA

(3) Department of Modern Mechanics
University of Science and Technology of China
Hefei, Anhui, China

(4) Department of Bioengineering and Chemical Engineering
Stanford University
Stanford, CA, USA

(5) Institute for Medicine and Engineering
University of Pennsylvania
Philadelphia, PA, USA

(6) Department of Bioengineering
University of Pennsylvania
Philadelphia, PA, USA

INTRODUCTION

While cells within tissues generate and sense three-dimensional (3D) states of strain, the current understanding of the mechanics of fibrous extracellular matrices (ECMs) stems mainly from uniaxial, biaxial, and shear tests. Here, we demonstrate that the multiaxial deformations of fiber networks in 3D cannot be inferred solely based on these tests. The interdependence of the three principal strains gives rise to anomalous ratios of biaxial to uniaxial stiffness between 8 and 9 and apparent Poisson's ratios larger than 1. The reconstituted networks [1]–[3] and collagen-rich tissues such as tendons [4] and cartilage [5] exhibit large Poisson effects in stretch tests. These observations are explained using a microstructural network model and a coarse-grained constitutive framework that predicts the network Poisson effect and stress-strain responses in uniaxial, biaxial, and triaxial modes of deformation as a function of the microstructural properties of the network, including fiber mechanics and pore size of the network. We explore the consequences of the multiaxial effects for cell-ECM interactions and rheometry and test our findings using axial-shear rheometry experiments and cancerous mammary acini seeded atop fibrous matrices. We use reconstituted collagen type I networks as a model system for fibrous ECMs.

METHODS

Fiber networks were generated using three-dimensional diluted lattices and Voronoi tesselations. The initial network geometry was created by placing fibers over the edges connecting the first and second nearest neighbors in a body-centered cubic lattice or a three-dimensional Voronoi diagram with random seed points. The pore size of the three-dimensional networks was tuned by changing the number of the seed points. The average nodal coordination number of the network was tuned by randomly detaching fibers from junctions shared by multiple fibers. Fiber waviness was then induced by shaping individual filaments into half-sine waves. Individual fibers were modeled as elastic Timoshenko beams that are flexible in stretching, bending, twisting, and transverse shear. Finite element modeling was performed using the finite element package Abaqus (Simulia, Providence, RI). Mechanical loading was performed by prescribing the displacements of the nodes located on the sample boundaries.

In the rheometry experiments, Collagen type I gels were prepared using collagen isolated from calf skin (MP Biomedicals, Santa Ana, CA, USA), with pH between 7 and 7.5. The gels were polymerized at 37°C. The gels were tested using a Kinexus rheometer (Malvern, Malvern, UK). The shear moduli of the samples were measured by applying a small oscillatory shear strain of 2% at a frequency of 10 rad/sec. Axial strain was applied by changing the gap between the plates.

In the cell-ECM experiments, Rat tail collagen (Corning, Corning, NY) was gelled at concentrations of 1, 2, and 3 mg/mL on pre-chilled glass-bottom imaging dishes (MatTek, Ashland, MA) according to the manufacturer's protocol. MCF10AT acini were cultured and extracted as previously described [6]. Gel deformation was evaluated through measuring displacement field generated by particle image velocimetry using 1-μm Nile-red (535/575) fluorescent beads (Life Technologies, Carlsbad, CA).

RESULTS

The fiber network model showed that in uniaxial tension, the fibers oriented transverse to the direction of loading buckle, leading to a

large Poisson effect, with apparent Poisson's ratios>1. To test the effect of pore size on the Poisson effect, we tuned the density of fibers in the networks by changing the number of the random seeds used to generate the network geometry. The tests indicated increases of apparent Poisson's ratio with increases of pore size (Fig. 1). We then performed biaxial loading of the networks and found anomalous stiffening of the networks in biaxial loading with ratios of biaxial over uniaxial stiffness above 8 (Fig. 1c).

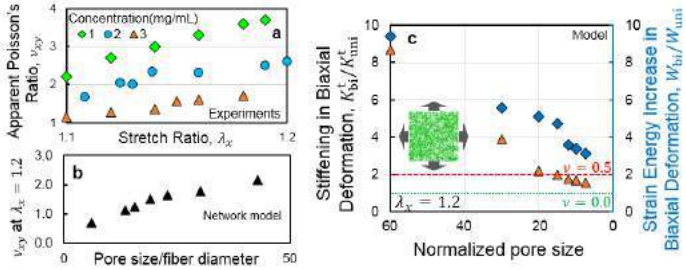

Figure 1: Variation of anomalous apparent Poisson's ratio and biaxial stiffening with polymer concentration and pore size.

Next, we studied the coupling of axial and shear modes of loading. Rheometry experiments combining axial and shear loading (Fig. 2) demonstrated that network shear stiffness changes in proportion to the applied axial stress. Computational results from clamped fiber network models also followed a linear trend (Fig. 2). The fiber network model also showed a quadratic increase of shear stiffness with volumetric strain. (Fig. 2).

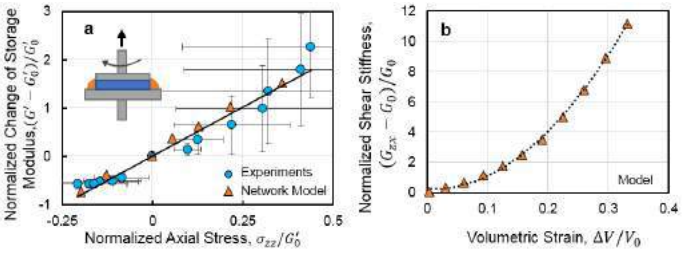

Figure 2: Variation of network shear stiffness against (a) axial stress and (b) volumetric strain.

Using insights from our network model we developed a constitutive model for the multiaxial behavior of the tested networks. This model has the same spirit as our previous models of the long-range force transmission in fibrous networks. The model is governed by the strain energy density function

$$W = W_b + \sum_{i=1}^{3} f(\lambda_i) + g\left(\sum_{i=1}^{3}\sum_{j\neq i} \lambda_i^2 \lambda_j^{2+\alpha}\right). \quad (1)$$

Here, W_b is a neo-Hookean energy describing the strain energy of the isotropic, background fibers. f and g are exponential functions that resemble the strain-stiffening of collagen networks in terms of the principal stretches λ. Finally, α is the parameter coupling the principal stretches. Changing α tunes the apparent Poisson's ratio of the model. Using 6 parameters, this model reproduces the stress-strain curves in uniaxial, biaxial, and triaxial loading, as well as the Poisson effect in uniaxial and biaxial loading. We used the constitutive law to model Poisson effect in the formation of fibrous tracts by a pair of contractile cells.

Our cell-ECM experiments demonstrated a drastic Poisson effect in collagen networks induced by cellular forces (Fig. 3). Densified tracts of aligned fibers formed between a pair of contracting cell clusters, an effect related to the invasion of cancer cells. Measurements of deformation demonstrated that a large Poisson effect is involved in the formation of the fibrous tracts (Fig. 3). The experimentally observed Poisson effect was reproduced by our constitutive model (Fig. 3).

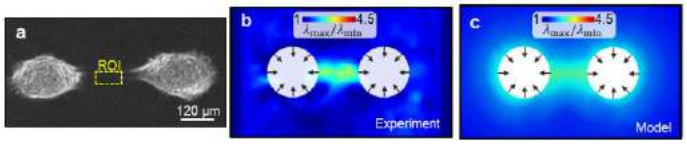

Figure 3: Deformation of collagen networks by a pair of cell clusters

Our models indicate that the anomalous Poisson effect leads to a 100-fold increase of the apparent stiffness of thin samples of collagen in extensional rheometry, and the stiffening effect increases with decreasing gel thickness (Fig. 4).

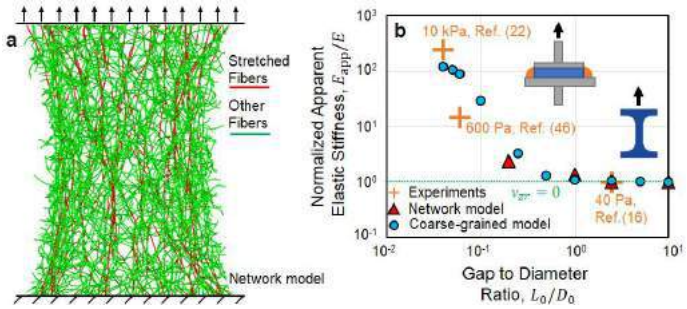

Figure 4: Influence of the Poisson effect on the apparent stiffness of thin collagen networks in extensional rheology.

DISCUSSION

The results of our models also agree with the results of stretch tests [7] and extensional rheology [8], [9] of samples with various aspect ratios gathered from the literature (Fig. 4).

The results of our cell-ECM experiments indicate that in less dense collagen networks, Poisson effect facilitates the densification of fibers and the formation of fibrous tracts, an effect associated with the invasion of acinar cancer cells. We expect that the results of our experiments and the introduced constitutive model aid in the design of new models for cancer invasion and fibrosis.

ACKNOWLEDGMENTS

This work was supported by National Cancer Institute awards U01CA202177 (to V.B.S.) and U54CA193417 (to V.B.S. and P.A.J.), National Institute of Biomedical Imaging and Bioengineering award R01EB017753 (to V.B.S.) and the NSF Center for Engineering Mechanobiology (CMMI-154857), and NSF grant MRSEC/DMR-1720530.

REFERENCES

[1] D. Vader, et al., *PLOS ONE*, 4, 6, p. e5902, Jun. 2009.
[2] R. C. Picu, et al., *J. Biomech. Eng.*, 140:021002–122018.
[3] T. Stylianopoulos and V. H. Barocas, *Comput. Methods Appl. Mech. Eng.*, 196:2981–2990, 2007.
[4] S. P. Reese and J. A. Weiss, *J. Biomech. Eng.*, 135:034501–5, 2013.
[5] D. M. Elliott, et al., *J. Biomech. Eng.*, 124:223–228, 2002.
[6] Q. Shi et al., *Proc. Natl. Acad. Sci.*, 111:658–663, 2014.
[7] B. A. Roeder, et al., *J. Biomech. Eng.*, 124:214–222, 2002.
[8] A. S. G. van Oosten et al., *Sci. Rep.*, 6:19270, 2016.
[9] J. Steinwachs et al., *Nat. Methods*, 13:171–176, 2016.

SB³C2018
Summer Biomechanics, Bioengineering and Biotransport Conference
June 25–28, Seven Springs, PA, USA

FIBER ORIENTATION AND STRUCTURE CHARACTERIZATION OF PREGNANT AND NONPREGNANT HUMAN UTERUS

Shuyang Fang (1), James McLean (2), Christine P. Hendon (2), Joy Vink (3), Kristin M. Myers (1)

(1) Department of Mechanical Engineering
Columbia University
New York, NY, USA

(2) Department of Electrical Engineering
Columbia University
New York, NY, USA

(3) Department of Obstetrics and Gynecology
Columbia University Medical Center
New York, NY, USA

INTRODUCTION

The mechanical function of the uterus is crucial for protection of the fetus in a healthy pregnancy. Throughout gestation, the uterine wall remains in a passive state and accommodates the expanding amniotic sac by growing, unfolding, and stretching. Then—ideally at term (defined as 37 weeks)—the onset of labor triggers a functional change in the uterus: the tissue becomes highly contractile to safely deliver the baby. Early contractile activation of uterine tissue can lead to preterm labor and birth (PTB). In 2014, 9.56 percent of pregnancies ended in PTB; it is also the leading cause of death in children under five years of age [1]. Characterizing uterine muscle, collagen fiber orientation, and dispersion is important for understanding the anisotropic material properties that could lead to mechanical failure of the uterus and cause PTB.

Previous studies using magnetic resonance imaging (MRI) have shown that collagen structure exhibits significant anisotropy across different regions of the uterus and cervix [2]; the fiber architecture was also found to be anisotropic through different layers of the uterine wall, which consists of the perimetrium, myometrium and endometrium [3]; previous optical coherence tomography (OCT) [4] studies determined the alignment and local distribution of collagen fibers within the cervix [5]. Therefore, similar to what has been done for the cervix, the goal of this research is to use OCT to characterize maps of fiber orientation and dispersion within different regions of the uterine wall.

METHODS

Tissue Collection: Three nonpregnant (NP) and two pregnant (PG) term uterine tissue samples were collected from consenting hysterectomy patients. Pregnant patients underwent cesarean hysterectomy due to accreta, a medical condition in which the placenta grows too deeply into the uterine wall. Patient age ranged from 36 to 47 with various recorded obstetric histories. Immediately after hysterectomy, a specimen was collected from each of three uterine locations: the anterior, the posterior, and the fundus, which is the superior-most end of the uterine corpus. All specimens spanned the depth of the uterine wall, which ranged from 15 to 25 mm, and covered a square cross-sectional area with an edge length between 10 and 15 mm. All specimens were flash frozen using dry ice immediately after collection and stored in a –80°C freezer prior to OCT. Fiber directionality data from one nulliparous NP uterus are presented in this abstract. Two more NP uterus samples with parity of one and two and two more PG uterus samples with parity of two and four have been collected and are under analysis to investigate the relationship between parity and uterine fiber structure.

Optical Coherence Tomography (OCT): Three-dimensional volumetric image-sets were obtained from human uterus samples using a commercial spectral domain OCT system, TELESTO (Thorlabs GmbH, Germany), with 6.5 μm axial resolution, 15 μm lateral resolution, and 2.51 mm imaging depth, in air. Each specimen was sliced into five or six slices parallel to the uterine wall. The thickness of each slice ranged from 2 to 4

mm. The slices were numbered from external layer to internal layer with increasing numbers starting from 1. In our experiments, each slice was laid on top of a coarse cork taped to a weighing boat. The bottom of the specimen slice was submerged into phosphate-buffered saline (PBS) to keep the tissue hydrated while the top was dried to avoid reflection. Samples were placed on a linear translation stage underneath the objective. For each slice, both sides were imaged with multiple volumes obtained by moving along the x- or y-axis. Each volume consists of 1375 × 1375 × 512 voxels, corresponding to a tissue volume of 5.5 mm × 5.5 mm × 2.51 mm. Since the surface of the slice was not flat, the axial position of the slice was also adjusted to obtain well-focused images. An overlap of 10% was applied between adjacent volumes for image stitching. A white-light camera image was obtained simultaneously with an OCT image to delineate the field of view of the tissue.

Fiber Direction Characterization: Three-dimensional data was generated by stitching volumes based on OCT data and shift-invariant features within the *en face* plane of the camera image [6]. All volumes were stitched together to form a new complete volume for each specimen slice. Fiber directionality and dispersion analysis was performed by using pixel-wise weighted summation [7]. The fiber direction, α, of a pixel of interest, is determined as:

$$\alpha = \arg\left(\sum_{j=1}^{N} w_j \times \exp(i\alpha_j)\right) \quad (1)$$

For a target pixel, there were multiple fiber direction candidates α_j pointing toward its neighboring pixels. A weight w_j was assigned to each candidate, whose total count was *N*.

A fiber orientation map was generated on one 2D plane parallel to the top surface of the total volume by combining the fiber direction information of each pixel (Fig. 1). A fiber concentration was generated by quantifying the distribution of continuous angles of fiber orientation. Each concentration was then divided by the maximum concentration value to create a normalized histogram (Fig. 2).

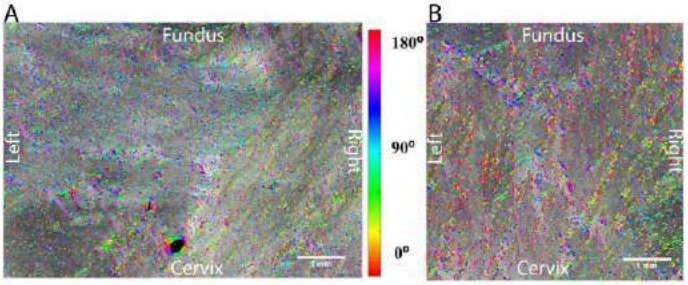

Figure 1. (A) fiber orientation map of anterior specimen slice 5 (innermost layer) with a vertical depth of 560 µm. Black holes are empty regions of no tissue. (B) fiber orientation map of anterior specimen slice 1 (outermost layer) with a vertical depth of 250 µm.

RESULTS

At the inner portion of uterine wall, two major near-orthogonal overlapping fiber groups are characterized with two dominant peaks corresponding to angles of 45° and 150° (Fig 2A), indicating a primarily interweaving bundle structure. Conversely, the outer layer fiber dispersion concentrations are scattered without dominant peaks throughout the entire degree range (Fig 2B), meaning it is comprised of a cluster-like high dispersion arrangement. In the middle layer, the fiber bundles exhibit a structure intermediate to the inner and outer layers, with evident but less pronounced peaks.

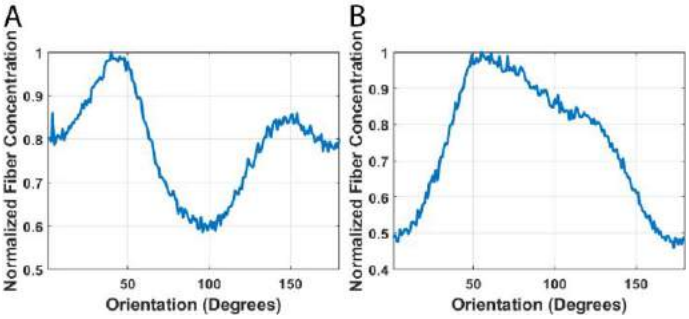

Figure 2. (A) normalized histogram of fiber orientation concentration of anterior specimen slice 5 (innermost layer). (B) normalized histogram of fiber orientation concentration of anterior specimen slice 1 (outermost layer).

Similar characteristics are observed in the posterior specimen; the fundus specimen does not exhibit identifiable local structure.

DISCUSSION

In this study, a workflow of experiments and data processing techniques were used to characterize the architecture of human uterine tissue. The preliminary results show that the internal portion of the uterine wall has a primarily interweaving fiber structure while the external portion consists of more randomly distributed fibers. The same protocol will be applied to four more patient samples with parity varying from zero (nulliparous) to four to investigate the effect of repeated pregnancy on uterine architecture. In addition to *en face* imagery, transverse plane data will be exploited to help us understand the fiber orientation in the direction orthogonal to the uterine wall.

The research and conclusions described in this abstract have the following limitations: due to IRB tissue collection protocol, full uterus sample could not be collected for imaging to perform characterization of global fiber structure; due to time constraints, the data were not analyzed in the transverse plane, though such an analysis could yield valuable information about fiber orientation across layers of the uterine wall.

ACKNOWLEDGEMENTS

Research reported in this publication was supported by the NIH R01HD091153 to KM. The content is solely the responsibility of the authors and does not necessarily represent the official views of the NIH.

REFERENCES

[1] Martin, J. A., et al., *Statistics (Ber).*, 64(1), pp. 1–104, 2015.
[2] Weiss, S. et al., *Anat Rec*, 288A: 84-90, 2006.
[3] Wetzstein, R., et al., *Verh Anat Ges* 64: 461-468, 1970.
[4] Gan, Y. et al., *Biomed Opt Express*, 4 (10): 2150, 2013.
[5] Yao, W., et al., *PLoS ONE*, 11(11): e0166709, 2016.
[6] Gan, Y., et al., *IEEE*, 3873-3876, 2014.
[7] Gan, Y., et al., *Biomed Opt Express*, 6(4): 1090-1108, 2015.

SB³C2019
Summer Biomechanics, Bioengineering and Biotransport Conference
June 25 -28, Seven Springs, PA, USA

CADHERIN-11 REGULATES AORTIC VALVE INTERSTITIAL CELL FORCE GENERATION AND MECHANICAL PROPERTIES

Matthew R. Bersi (1), Meghan A. Bowler (1), W. David Merryman (1)

(1) Department of Biomedical Engineering
Vanderbilt University
Nashville, Tennessee, USA

INTRODUCTION

Calcific aortic valve disease (CAVD) is a degenerative condition that affects 25% of people over 65 and often necessitates total valve replacement in severe cases [1]. With increasing numbers of CAVD patients, there is a need to better understand the biological mechanisms underlying CAVD initiation and progression in order to develop non-invasive pharmacologic therapies for valvular calcification.

Aortic valve interstitial cells (AVICs) are a heterogeneous population of fibroblast-like cells that regulate the structural integrity of the valve. When activated by transforming growth factor beta 1 (TGF-β1), AVICs transition to a myofibroblast phenotype characterized by increased contractility, collagen deposition and expression of smooth muscle alpha-actin (αSMA) and cadherin-11 (CDH11). The resulting increases in intra- and intercellular tensions can cause tearing of the cell membrane leading to cellular apoptosis and calcific nodule formation.

CDH11 was first identified as a potential therapeutic target for CAVD when it was found to be enriched in calcified human aortic valves and required for calcific nodule formation *in vitro* [2]. CDH11 is a mechanosensitive transmembrane protein involved in cell-cell adhesion; homotypic bonds formed by CDH11 are stronger than those of other mesenchymal cadherins – such as cadherin-2 (CDH2) [3]. CDH11 is also the only cadherin known to participate in focal adhesions [4] and has been shown to increase secretion of the proinflammatory cytokine IL-6 by AVICs. Together, these characteristics make CDH11 a unique protein with the potential to sense interactions with the local mechanical environment in order to influence valvular inflammation and matrix synthesis. To better understand CDH11's role in CAVD and AVIC phenotype, we examined how CDH11 influences AVIC force generation and bulk mechanical properties as measured by traction force microscopy and micropipette aspiration, respectively.

METHODS

Isolation of AVICs – Murine aortic valves were excised from *Cdh11*$^{+/+}$, *Cdh11*$^{+/-}$, and *Cdh11*$^{-/-}$ immortalized mice and digested in 2 mg/mL collagenase for 30 minutes at room temperature. Following digestion, valves were seeded on 0.1% gelatin-coated tissue culture treated plates and expanded in DMEM supplemented with 10% fetal bovine serum and 1% penicillin/streptomycin antibiotic to yield AVICs.

Traction force microscopy (TFM) – AVIC traction force generation was quantified for each cell line ($n > 72$ for single cells and $n > 25$ for cell pairs) using standard methods [5]. Briefly, AVICs were seeded on soft (1 kPa), fibronectin-coated polyacrylamide gels with embedded fluorescent microspheres/beads overnight prior to imaging. Comparisons of the bead distributions below each cell before and after detachment from the gel were used to compute gel displacement fields via a subpixel image correlation approach. Combined with polyacrylamide gel material properties, displacements were used to reconstruct traction forces on the surface of the gel using a regularized Fourier transform traction cytometry (reg-FTTC) framework.

Given the reconstructed traction fields, total force generated by each cell $|F|$ was calculated as

$$|F| = \int_{\Omega} |\mathbf{T}(\mathbf{x})| d\mathbf{x} \equiv \iint_{\Omega} \sqrt{T_x(x,y)^2 + T_y(x,y)^2}\, dxdy \qquad (1)$$

where $T_x(x,y)$ and $T_y(x,y)$ denote components of the reconstructed traction vector $\mathbf{T}(\mathbf{x})$ within the cell boundary Ω. Cell-cell interaction forces $\mathbf{F}_{cc}$ were estimated from the traction imbalance that arises when the reconstructed traction field is partitioned at the cell contact border. Values were computed as $\mathbf{F}_{cc} = (\mathbf{F}_1 - \mathbf{F}_2)/2$, where $\mathbf{F}_1$ and $\mathbf{F}_2$ denote the resultant traction force vectors in each cell of the doublet [6].

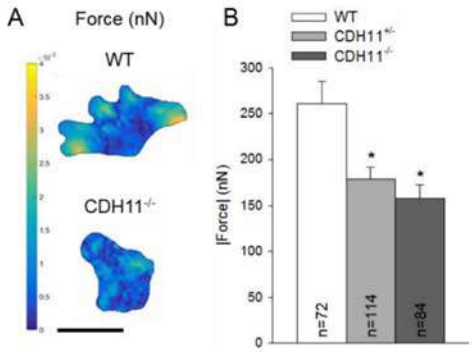

Figure 1: (A) Reconstructed traction force maps from AVIC TFM reveal that (B) CDH11 depletion reduces AVIC force generation.

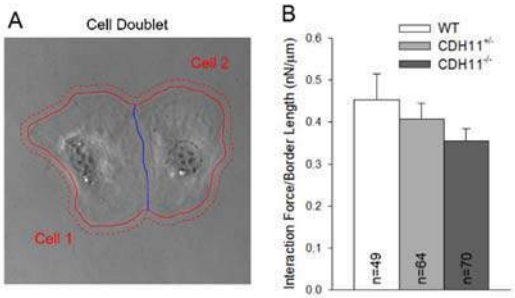

Figure 2: (A) TFM of AVIC doublets reveal that (B) CDH11 depletion reduces AVIC cell-cell interaction forces.

Micropipette Aspiration (MA) – AVICs were gently lifted from tissue culture plates using 0.05% trypsin for no more than 5 minutes and resuspended in DMEM. 100 uL of resuspended cells were then placed in a 35mm dish under a microscope contained within a custom built MA system made up of a precision microfluidic controller, a secondary reservoir, and hand-pulled glass micropipettes fractured to a diameter ~8μm. Upon equilibration of pressures in the MA system, single cells were aspirated at a constant rate of 4 Pa/s for 150 s (maximum aspiration pressure of 600 Pa). Tracking of the cell's leading edge upon aspiration generated characteristic L/a vs. ΔP curves, where L denotes the aspiration distance and a denotes the micropipette radius. From this linear aspiration behavior, the AVIC stiffness E was computed as

$$E = \frac{3\Delta P}{2\phi(\eta)} \frac{a}{L} \qquad (2)$$

where $\phi(\eta) = 2.1$ denotes a wall function accounting for the micropipette wall thickness [7].

Statistical analysis – AVIC traction force and stiffness was compared by one-way ANOVA with post-hoc Tukey HSD tests. Non-parametric statistics were performed when tests for normality and/or equal variance failed. Values of $p < 0.05$ were considered significant.

RESULTS

Cdh11 transgenic AVICs showed a CDH11-dependent reduction in traction force generation (Fig. 1). In particular, reconstructed traction maps revealed an ~40% reduction in average traction force magnitude in *Cdh11*$^{+/-}$ and *Cdh11*$^{-/-}$ AVICs, relative to *Cdh11*$^{+/+}$. Similarly, loss of CDH11 in AVIC cell doublets altered the magnitude of measured cell-cell interaction forces $\mathbf{F}_{cc}$. Accounting for cell size, normalization of $\mathbf{F}_{cc}$ by the border length (blue curve; Fig. 2A) revealed a similar CDH11-dependent reduction, as expected due to impaired adhesion (Fig. 2B).

Single-cell AVIC stiffness measurements also exhibited a CDH11-dependent response. In particular, MA stiffness was increased following loss of CDH11 (Fig. 3B). Western blotting for αSMA (Fig. 3A) revealed a significant increase after CDH11 depletion, suggesting that AVIC contractility is positively correlated with AVIC stiffness.

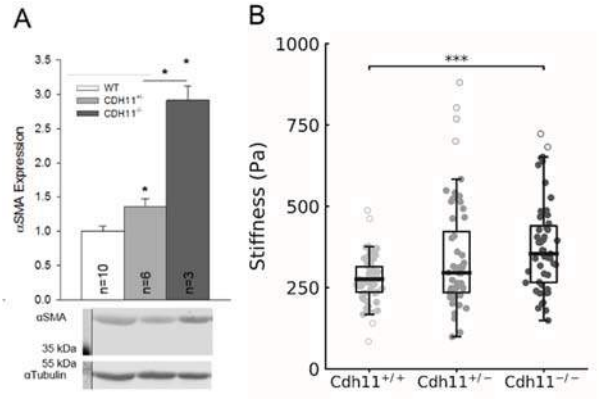

Figure 3: CDH11 depletion (A) increases αSMA expression which correlates with (B) increased AVIC stiffness, as measured by MA.

DISCUSSION

While CDH11 expression regulates AVIC contraction and contributes to disease progression, it is clear that this effect is potentiated by more than cell-cell interactions alone. In particular, AVICs are involved in complex interactions with resident and recruited (immune) cells as well as the local mechanical environment of the valve.

TFM revealed a CDH11-dependent reduction in AVIC force generation that was normalized across genotypes when divided by cell area. This suggests CDH11 alters cell spreading, likely through its interaction with focal adhesion complexes. Indeed, immunostaining for the focal adhesion protein vinculin has shown that *Cdh11*$^{-/-}$ AVICs have fewer, but longer, focal adhesions relative to *Cdh11*$^{+/+}$ [8].

AVIC stiffness, as measured by MA, was found to be increased in CDH11-depleted cells consistent with an increase in αSMA protein expression. That AVIC stiffness positively correlates with AVIC contractility suggests a potential functional adaptation of *Cdh11* transgenic AVICs in response to altered mechanical loading [9].

While targeting CDH11 has shown beneficial effects for CAVD, mechanical analysis of *Cdh11* transgenic AVICs suggests that there is a CDH11-dependent relationship between AVIC mechanobiology, disease progression, and the aortic valve mechanical environment. Further insight into the impact of pharmacologic treatments on the biophysical properties of AVICs is warranted in order to better design therapeutic treatment strategies for CAVD.

ACKNOWLEDGEMENTS

This work was supported, in part, by NIH grants R35 (HL135790), R01 (HL115103), and T32 (HL007411)

REFERENCES

[1] Benjamin, EJ et al., *Circulation*, 137:e67-e492, 2018.
[2] Hutcheson, JD et al. *Arterio Thromb Vasc Biol*, 33:114-120, 2013.
[3] Pittet, P et al., *J Cell Sci*, 121:877-886, 2008.
[4] Langhe, RP et al., *Nat Comm*, 7:1909, 2016,
[5] Butler, JP et al., *AJP Cell Physiol*, 282:C595-605, 2002.
[6] Maruthamuthu, V et al., *Proc Nat Acad Sci*, 108:4708-4713, 2011.
[7] Theret, DP et al., *J Biomech Eng*, 110:190-199, 1988.
[8] Bowler, MA et al., *AJP Heart Circ Physiol*, 315:H1614-1626, 2018.
[9] Merryman, WD et al., *AJP Heart Circ Physiol*, 290:H224-231, 2006

SB^{3}C2019
Summer Biomechanics, Bioengineering and Biotransport Conference
June 25 -28, Seven Springs, PA, USA

A VOLUMETRIC GROWTH MODEL FOR HEALING POST-INFARCTION SCAR

Derek J. Bivona (1), Ana C. Estrada (1), Jeffrey W. Holmes (1,2,3)

(1) Department of Biomedical Engineering
University of Virginia
Charlottesville, VA, USA

(2) Department of Medicine
University of Virginia
Charlottesville, VA, USA

(3) Robert M. Berne Cardiovascular Research Center
University of Virginia
Charlottesville, VA, USA

INTRODUCTION

Following myocardial infarction (MI), the long-term remodeling of the damaged infarct region is a crucial determinant of patient outcome and risk of progression to heart failure [1]. The complex remodeling process involves changes in both the shape and structure of the infarct region, also referred to as infarct scar, that may negatively affect ventricular performance [2]. During the first few weeks after MI, myocytes necrose and their components are resorbed, while myofibroblasts infiltrate the tissue and deposit collagen [3]. The replacement of the necrotic myocytes with collagen results in both an increase in stiffness and a net decrease in tissue volume. By measuring the thickness of the scar along with one or more in-plane scar dimensions, a number of studies have reported changes in scar shape. However, these measurements are typically performed in intact, mechanically loaded hearts, where changes in stiffness could also cause changes in dimensions in the absence of volumetric remodeling.

To better understand the geometric changes that occur during infarct healing, we recently performed an exhaustive review of quantitative studies of infarct remodeling and found that some studies reported in-plane expansion of the healing infarct while others reported in-plane compaction (shrinkage) when dimensions were measured at end diastole in intact hearts [4]. All studies that measured wall thickness reported gradual thinning of the scar, which can aggravate adverse remodeling of the left ventricle (LV) by increasing wall stresses. In order to better interpret these reports and separate the contributions of volumetric growth and remodeling (changes in volume and stress-free shape), infarct stiffening, and elevated LV diastolic pressures typical after infarction, in this study we employed a finite-element model that incorporated prescribed volumetric shrinkage in the infarct scar. We tested whether changes in scar stiffness and loading observed following MI can reproduce observed changes in *in vivo* infarct dimensions if volume loss in the scar occurs isotropically in the unloaded state.

METHODS

A finite-element (FE) model of the diastolic rat left ventricle (LV) was constructed. A rat LV geometry was derived by fitting manually segmented contours from cine-MRI scans, and a representative infarct geometry was derived from late-gadolinium enhancement (LGE) MRI images. A physiologic myofiber structure was assigned, and a transversely isotropic Mooney-Rivlin (TIMR) material was used to model material properties of the normal myocardium. Realistic diastolic pressures were applied to the endocardium to inflate the LV while the displacement of basal surface nodes was fixed longitudinally. In simulations in which the scar was stiffened, the isotropic term of the TIMR material equation was increased to mimic the reported properties of rat infarct scar 6 weeks post-MI [2]. Inflation simulations were run with the FEBio finite element solver [5].

A kinematic growth framework [6] was implemented in a custom FEBio plug-in to simulate isotropic scar volume loss in the initial unloaded state, resulting in 100%, 90%, 80%, 70%, or 60% of the original scar volume remaining prior to the onset of inflation. Then, in-plane scar area on the epicardial surface and average scar thickness were calculated over a range of end-diastolic pressures (EDPs) from 0.75 to 1.5 kPa. Finally, these metrics were normalized to their respective values in the non-remodeled scar at an EDP of 0.75 kPa.

RESULTS

In the absence of scar stiffening, isotropic volume loss (Figure 1A, Left) produced apparent scar compaction or expansion depending on the simulated EDP and the amount of remaining scar volume. With a

doubling of EDP as reported by Fomovsky at some time points following infarction in the rat [2], only the simulations with very limited volume loss (90% or 100% of original volume remaining) fell within the experimentally reported range of in-plane dimensions. All of the simulated cases predicted thinning of the scar at a post-MI EDP of 1.5 kPa (Figure 1A, Right), although the simulations with more volume loss fell closer to the experimental mean.

Simulations of isotropic volume loss accompanied by a physiologic degree of scar stiffening (Figure 1B, Left) predicted in-plane compaction at all diastolic pressures, regardless of the extent of volume loss; these predictions were clearly inconsistent with the experimental data. Moreover, nearly all simulations predicted an increase in scar thickness at end-diastole, due to reduced in-plane stretch (and associated thinning of the incompressible scar) during inflation from the remodeled, unloaded state (Figure 1B, Right). This prediction was also inconsistent with experimental measurements. Overall, these simulations revealed that when previously reported data on post-infarction stiffening and diastolic pressures are incorporated into a finite-element model of the infarcted rat left ventricle, no amount of isotropic volume loss produces dimensional changes consistent with *in vivo* scar dimensions documented in the infarct healing literature.

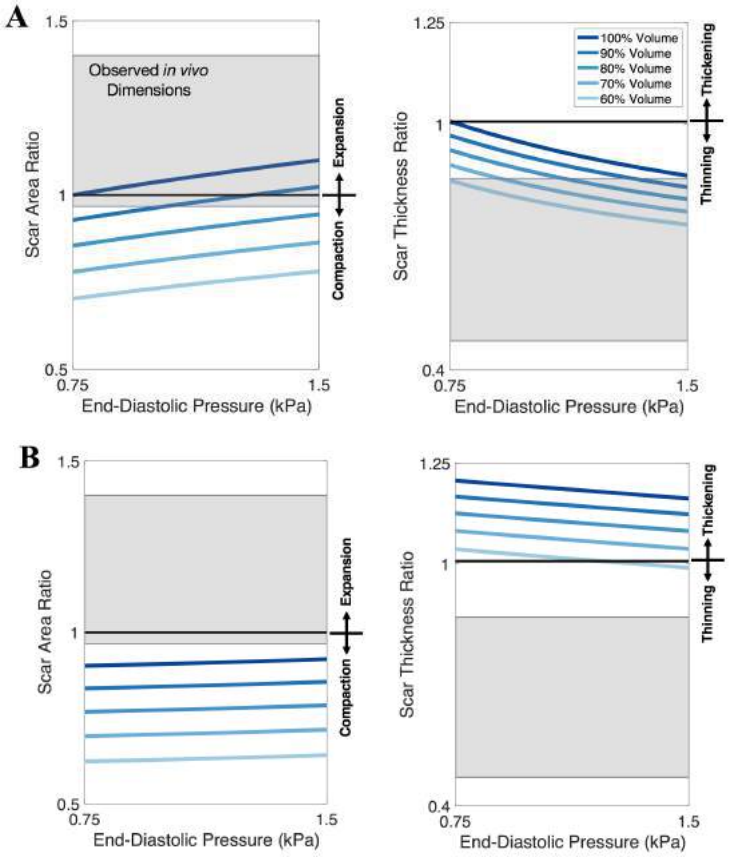

Figure 1. Scar area and scar thickness ratios for (A) non-stiffened infarct and (B) stiffened infarct of varying volumes. Gray boxes indicate the range between the 25th and 75th percentiles of observed *in vivo* dimensions at various times during remodeling [4].

DISCUSSION

The goal of this study was to determine whether a volumetric growth model that assumes isotropic volume loss in the unloaded state could reproduce observed changes in *in vivo* infarct dimensions when appropriately constrained by known changes in scar material properties and loading. The simulations provide strong evidence that the assumption of isotropic volume loss is inconsistent with available data. We believe this finding raises interesting questions about how to model – or even conceptualize – the replacement of muscle by scar in three dimensions. It is not immediately apparent why degrading myocytes and replacing them with collagen and other extracellular matrix should be associated with a change in shape of a region of tissue in its stress-free state. Modeling at the level of the individual proteins and components may be necessary to understand the packing of these elements in the remodeling tissue. These questions have potentially important therapeutic implications, since increasing wall thickness is thought by some to be the primary mechanism by which biomaterial injections limit adverse remodeling of the LV following infarction [7].

The current model still contains several limitations. First, increasing only the isotropic term within the scar material does not allow us to precisely match previously published biaxial testing data on infarct scar; a better match could be achieved by employing a custom strain-energy function as proposed by Fomovsky et al. [2]. Second, only one representative infarct geometry was used in the simulations. Infarcts of different size, location, and transmurality may exhibit different loaded dimension changes. Third, in-plane area ratio is calculated in this study but is compared to normalized in-plane dimension changes from studies that reported a variety of infarct measurements (i.e. absolute circumferential segment length, infarct-containing segment), some of which may contain contributions from the infarct borderzone and remote remodeling. Overall, we consider it very unlikely that any of these factors would alter predicted or measured dimensions enough to invalidate our conclusions.

In conclusion, the present study demonstrates that a volumetric growth model that assumes isotropic volume loss within the scar region in the unloaded LV and accounts for known changes in scar material properties and LV pressures cannot reproduce reported changes in *in vivo* infarct dimensions. The assumption of isotropic volume loss is thus inconsistent with available data, which raises interesting questions about how to envision and appropriately model the replacement of muscle by scar in three dimensions.

ACKNOWLEDGEMENTS

This work was supported by funding from the National Institutes of Health (T32 LM012416, R01 HL116449, U01 HL127654).

REFERENCES

[1] Sharpe, N, *Am J Cardiol*, 70:20-6, 1992.
[2] Fomovsky, G and Holmes, J, *Am J Physiol-Heart C*, 298.1:H221-H228, 2009.
[3] Fishbein, M et al., *Am J Pathol*, 90:57-70, 1978.
[4] Richardson, W and Holmes, J, *J Cardiovasc Transl*, 8.7:421-430, 2015.
[5] Maas, S et al., *J Biomech Eng*, 134.1:011005, 2012.
[6] Rodriguez, E et al., *J Biomech*, 27.4:455-467, 1994.
[7] Kelley, S et al., *Circulation* 99.1:135-142, 1999.

SB³C2019
Summer Biomechanics, Bioengineering and Biotransport Conference
June 25 -28, Seven Springs, PA, USA

A MULTISCALE FLOW-MEDIATED PLATELET ADHESION MODEL AND ITS EXPERIMENTAL VALIDATION

Peng Zhang (1), Jawaad Sheriff (1), Peineng Wang (1), Marvin J. Slepian (2), Yuefan Deng (3), Danny Bluestein (1)

(1) Department of Biomedical Engineering
Stony Brook University
Stony Brook, NY, United States

(2) Sarver Heart Center
University of Arizona
Tucson, A□, United States

(3) Department of Applied Mathematics
Stony Brook University
Stony Brook, NY, United States

INTRODUCTION

Platelet adhesion to blood vessel walls in shear flows is essential in initiating coagulation cascade of blood and prompting clot formation in prosthetic cardiovascular devices and vascular disease processes. In the adhesion process, platelets undergo complex and rapid receptor-ligand binding such as bond association and breakage. Experimental methods have been improved through enhancing the μm-length and ms-time scale results. However, numerical approaches are still very limited. Continuum methods cannot capture the molecular mechanism of vWF-mediated platelet GPIbα binding. Utilizing molecular dynamics (MD), although allowing atomic details, is too computationally prohibitive for large-scale simulations. To bridge this gap, a multiscale model can be developed to depict the platelet's biophysical properties at the cellular scales coupled with macroscopic flows, thus predicting platelet motion under flow conditions.

In this study, we present a novel multiscale flow-mediated platelet adhesion model under viscous blood flow conditions. Following our previous effort[1,2], we adopt a multiscale DPD-CGMD model that combines a Dissipative Particle Dynamics (DPD) for viscous blood flows that interfaces with Coarse Grained Molecular Dynamics (CGMD) for mechanobiology-based platelets[2]. We extended this model by simulating the mechanism of the platelet GPIbα receptor and von Willebrand factor (vWF) binding near a blood vessel wall under shear stress. The platelet GPIbα receptor and the vWF ligand are modeled at a 10-nm length scale. The formation and breakage of the GPIbα-vWF bonds are simulated at a ns-time scale. We validate this numerical model through the use of shear-based experimental techniques that allow observation and measurement of platelet morphological changes and motions over a wide range of shear stresses (0~30 dyne/cm^2) with a ms-time scale image resolution.

METHODS

Employing a modified DPD to describe viscous blood flow in microchannels and stenoses[3], our multiple spatiotemporal scales model employs a unique CGMD approach to describe the intra-platelet constituents in order to model the mechanotransduction processes[2]. Spatially, the DPD-CGMD is interfaced by imposing a hybrid force field[1]. In this spatial interface, the Lennard-Jones term describes the cytoskeleton-confined shape and the incompressibility of platelets against the applied shear stress of circumfluent flow; and the dissipative and random terms maintain the local flow thermodynamic and mechanical properties, and exchange momentum to express interactions between the platelet and the flow.

In the nanoscale, we developed a mechanobiology-based platelet model to describe key constituents and biophysical properties[2]. We modeled a bilayer membrane, an ellipsoid-based discoid shape, rigid filamentous core, gel-like cytoplasm using the Morse potential[4], and actin filaments. An α-helix structure was used to mimic a protrusible actin filament.

The platelet's bilayer membrane has a total of 67,004 particles and its surface area is about 28.6 μm^2. We define the platelet GPIbα with 16,751 copies per platelet, wherein the reported range of GPIbα is between 12,000 to 25,000 per human platelet[5]. Thus, the density of platelet GPIbα in our model is 585 /μm^2. The vWF is fixed on the blood vessel and functions to bind to a platelet GPIbα receptor and initiate platelet adhesion. We define a uniform distribution of vWF at a density of 600/μm^2 on top of blood vessel walls. The force field between the platelet GPIbα receptor and the vWF ligand is described by a hybrid force field combing Morse and Hooke potentials:

$$E_{Adhesion} = E_{Morse} + E_{Hooke} \quad (1)$$

where

$$E_{Morse} = D_0\left(e^{-2\alpha(r_{ij}-r_0)} - 2e^{-\alpha(r_{ij}-r_0)}\right)\boldsymbol{e}_{ij} \quad (r < r_c) \qquad (2)$$

$$E_{Hooke} = k_1(r-r_b)^2 + k_2(r-r_b)^4 \quad (r < r_c) \qquad (3)$$

In Eq (2), D_0 is the well depth of repulsive force, α is the scaling factor, r_0 is the zero-force length. This term is used to keep a certain distance between the receptor and the ligand in adhesion. In Eq (3), k_1 and k_2 are the adhesive coefficients and depends on time duration of adhesion. r_c is the force relaxation distance and is equal to the dissociation and mechanical distance of the GPIbα-vWF bond. Fig. 1 shows the simulation scheme of platelet adhesion to the blood vessel wall under a shear stress of 30 dyne/cm^2. The simulation is conducted in a box of size 18×8×8 μm. No-slip boundary condition is applied on y-axis and periodic boundary condition is used on both x- and z-axis.

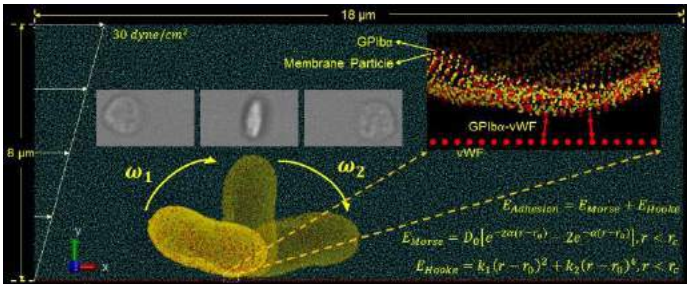

Figure 1: Adhesion of platelet to blood vessel wall in shear flow

We validated our numerical method by correlating simulations and model predictions with in vitro results. In our modeling, we split a whole rotation of an adhered platelet into two periods: period 1 and 2, i.e., ω_1 and ω_2 as indicated in Fig. 1. The period ω_1 is the lift-off period of an adhered platelet from a horizontal position to vertical position wherein the disassociation of the GPIbα-vWF bonds are mimicked. Period ω_2 is the falling period of the platelet from its upright position back to a horizontal position, wherein the GPIbα-vWF bonds form as the platelet re-attaches to the vWF-coated vessel wall. In period ω_1, we adjust the adhesive coefficients of the model to correlate with in vitro measurements. In period ω_2, we tune the force relaxation distance.

For adhesion experiments, purified platelets were prepared as previously described[3], diluted to 150,000/μl and perfused through 100 μm×1 mm microchannels (μ-Slide VI$^{0.1}$ Luer, ibidi USA, Inc., Madison, WI) pre-coated with 100 μg/ml vWF using a syringe pump (Fig. 2a). Perfused platelets were exposed to wall shear stresses of 5-30 dyne/cm^2. Adhesion events, defined as platelets flipping or sliding on the vWF-coated surface, were observed at 100× magnification on a DIC microscope (Ti-E, Nikon, Melville, NY) at up to 1000 fps (Neo 5.5 sCMOS, Andor Technology Ltd., Belfast, UK). We measured platelet major and minor diameters, cross-sectional area, thickness, translational velocity, and angular flipping velocity for each adhesion event (Fig. 2b).

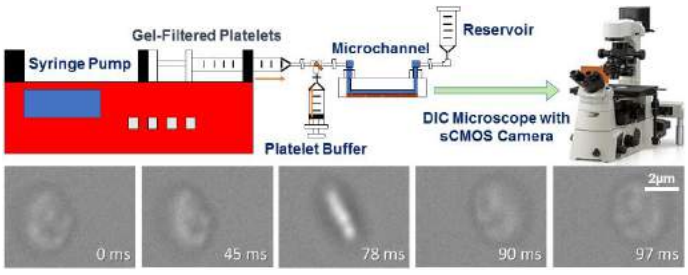

Figure 2: (a) Set-up for adhesion experiments. b) Sequential imaging of platelet adhesion and flipping under flow.

RESULTS

Our multiscale model describes the biophysical properties for platelets down to the *nm*-length and *ps*-time scale[2]. Membrane Young's modulus is 31.2 μN/m and shear modulus is 33±9 μN/m. The cytoplasm is modeled by modified Morse potential[5] and its viscosity is 4.1 mPa·s. Actin filament stiffness is 56.3±1.0 pN/nm.

The experiments indicate two periods, ω_1 and ω_2, during flipping on the vWF surface. The first period describes rotation of the platelet from a horizontal to vertical position, whereby the force exerted by the flow on the platelet lifts it off the vWF substrate and breaks existing GPIbα-vWF bonds. In the second period, the fluid force exerted on the platelet pushes it towards the vWF substrate, thereby allowing GPIbα-vWF bonds to re-form. We observed a difference in the two periods, where $t(\omega_1)$= 16.35±5.14 ms and $t(\omega_2)$= 13.62±4.16 ms (n=30, p>0.05) at 6.7 dyne/cm^2 and 91.5 fps (Fig. 3). Ongoing experiments extend this analysis to shear stresses up to 30 dyne/cm^2, with significant increase in translational and flipping velocities, and reduced discrepancy between the two flipping periods, anticipated with an increase in shear stress. In ongoing experiments, the camera frame rate has been adjusted to 1000 fps to increase temporal resolution to 1 μs/frame, allowing capture of the platelet rotation trajectory in a μs-time scale. Wall shear stress has been increased to 30 dyne/cm^2 to capture a complete rotation of an adhered platelet in approximately 10 ms. We have correlated the rotation angles with the projected platelet areas on the vWF-coated channel surface, thus calculating the angular speed of platelet rotation as a function of adhesion contact area. This relationship will be used to validate the parameters in our model (Eqs. 1-3) and adjust the adhesive coefficients.

DISCUSSION

We developed the first multiscale flow-mediated platelet adhesion model under viscous blood flow conditions. This model can describe the molecular mechanism for the platelet GPIbα and vWF binding. In our model, the receptor-ligand coefficients are determined through correlation with platelet rotation angular speeds measured in vitro. Phenomena of platelet rotating, sliding, and adhering to vWF-coated vessel walls closely follow behavior observed in our experiments. Using this model, we can precisely simulate the formation and breakage of GPIbα-vWF bonds, measure platelet adhesion area, and predict the platelet adhesion force strength that are otherwise difficult to quantify under in vitro flow conditions. In future studies, this model can be extended to study a platelet-mediated thrombus growth model under shear flow. This thrombus model will incorporate our previous platelet flipping, activation and aggregation models[1-3], and coupled with this adhesion model reflecting molecular level changes in receptor-ligand bond formation. We expect our model to be adopted by other fields, such as drug delivery, by considering the impact of mechanical events triggering biochemical responses.

ACKNOWLEDGEMENTS

This publication was made possible by grants from the National NIH U01 HL131052 (PI: D. Bluestein). The simulations in this study used the LI-Red supercomputer, Stony Brook University.

REFERENCES

[1] Zhang, P et al., *Cell Mol Bioeng*, 7:552-574, 2014.
[2] Zhang, P et al., *J Biomech*, 50:26-33, 2017.
[3] Gao, C et al., *J Comput Phys*, 335:812-827, 2017
[4] Zhang, N et al., *J Comput Phys*, 257(A):726-736, 2014.
[5] Michelson, A., *Platelets* (3rd Edition), Page 153. 2012.

DEEP-LEARNING BASED REGION-OF-INTEREST SELECTION IN 3D CEREBROVASCULAR IMAGES

Tatsat R. Patel (1, 2), Prakhar Jaiswal (1), Nikhil Paliwal (1, 2), Adnan H. Siddiqui (2, 3), Rahul Rai (1), Hui Meng (1, 2, 4)

(1) Mechanical and Aerospace Engineering
University at Buffalo, the State University of New York
Buffalo, NY, USA

(2) Canon Stroke and Vascular Research Center
University at Buffalo, the State University of New York
Buffalo, NY, USA

(3) Neurosurgery
University at Buffalo, the State University of New York
Buffalo, NY, USA

(4) Biomedical Engineering
University at Buffalo, the State University of New York
Buffalo, NY, USA

INTRODUCTION

Region-of-interest (ROI) selection has been used for localization of diagnostically relevant regions in medical images [1]. For localized cerebrovascular diseases like intracranial aneurysms (IAs), automated and accurate ROI selection can help enable objective quantitative analyses of the medical images [2]. For example, accurate ROI selection enables accurate image-based 3D morphologic and computational fluid dynamics (CFD) analyses of localized vasculature to study progression, rupture and treatment of IAs [3, 4]. Objective localization of the computational domain helps reduce the inconsistencies in hemodynamics [5]. Furthermore, for efficient transfer and storage of medical images, image compression is required [2]. Automated ROI selection methods can enable use of hybrid techniques for lossless compression of ROI and lossy compression of the remaining regions [2].

For ROI selection in medical images, automated methods have been proposed for purposes such as pancreatic segmentation [6], left ventricular segmentation [7], etc. But these ROI selection methods have not been adopted in cerebrovascular disease localization. Currently, for the ROI selection in cerebrovascular disease, localization relies on manual operation of the image around the site of the vascular disease like IA [3, 5], arteriovenous malformations [8], etc. This manual operation of ROI selection is user-dependent, thereby subjective, inconsistent and inefficient. Furthermore, ROI-based compression techniques require the localization method to be automated [2].

To make ROI selection objective and automated, we developed a deep-learning based technique for ROI selection of major arteries susceptible to cerebrovascular diseases from 3D medical images. As an example, we applied our technique to automatically calculate ROI from 3D digital subtraction angiography (DSA, gold standard for cerebrovascular images [9]) images of intracranial aneurysm patients.

METHODS

Convolutional Neural Networks (CNN) have been used extensively for object detection in computer vision field [10]. Borrowing its concept, we present a novel, computationally efficient 2D parallel CNN for the automated detection and localization of major arteries susceptible to IAs. Our 2D parallel CNN was compared with the traditional 3D serial CNN to compare their performances in terms of accuracy and computational cost. Our methodology uses patient specific 3D DSA images as the inputs, to automatically predict the geometrical features of the cuboidal bounding-box encompassing the major arteries susceptible to IAs to obtain the ROI objectively. This cuboidal bounding-box is defined by 6 scalar geometrical features namely, the coordinates of its center (X_c, Y_c, Z_c) and its dimensions (l_x, l_y, l_z), as shown in Fig. 1. The 6 output parameters are normalized by the length, height and width (512 voxels each) to yield values between 0 and 1.

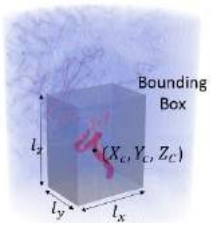

Figure 1: Manual bounding box on representative case.

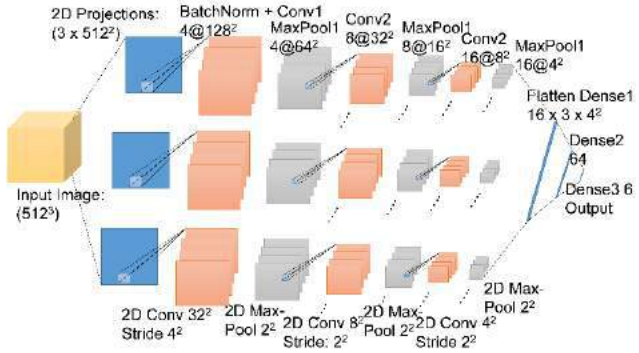

Figure 2: 2D parallel CNN architecture trained to predict geometrical features of the cuboidal bounding box for ROI.

2D Serial and 3D Parallel CNNs

A novel computationally efficient 2D parallel CNN (shown in Fig. 2) and a traditionally used 3D serial CNN (shown in Fig. 3) for object detection in 3D images [10] were built.

As shown in Fig. 2, the 2D parallel CNN takes 3 standard 2D average intensity projections (AIP) of size 512^2 as inputs in 3 parallel encoding paths respectively. The dimensionality of the complete network decreases from 3D to 2D with 2D projections as inputs. This dimensionality reduction saves computational costs and reduces memory requirements.

Contrarily, a 3D serial CNN shown in Fig. 3 uses the complete 3D DSA as an input and the subsequent computations are done in 3D. The internal architecture of the 3D CNN (For eg. Number of convolutional layers, filters, strides, etc.) were kept the same for both the architectures for an objective comparison with the 2D parallel CNN.

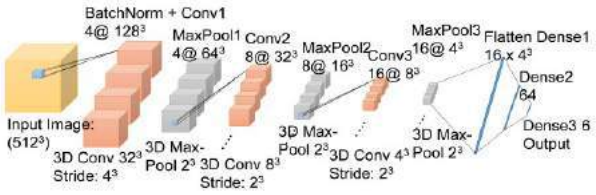

Figure 3: 3D serial CNN architecture trained to predict geometrical features of the cuboidal bounding box.

The networks' parameters were initialized using the Xavier uniform initializer [11] and trained using the Adam's optimizer [12] with a batch size of 16. The Learning Rate (LR) was initially set to 10E-4 with decay coefficients β_1 and β_2 set to 0.99 and 0.9 respectively. Drop-out of 0.4 and a L2 regularization with regularization rate of 0.075 was added at fully-connected layers to ensure models don't over-fit to training data. Mean squared error loss function was used for model training. Mean absolute error was also monitored for evaluating relative performance of the model on the training and validation cohorts for ensuring convergence and avoiding over-fitting.

Patient Database

For model training and evaluation, 225 patient-specific 3D DSA images of the anterior and posterior cerebral arteries with IAs were retrospectively collected from Gates Vascular Institute, Buffalo, NY between 2009 and 2018. The database was randomly divided into training (n=180), validation (n=30) and testing (n=15) cohorts.

Rules for Manual ROI Computation

The bounding box were set up manually for training to encompass the major arteries such that, for images coming from: a) anterior cerebral circulation, the complete internal carotid artery (ICA), posterior communicating artery (PCOM), anterior communicating artery (ACOM) (complete A1, A2 uptill 20D) and mid cerebral artery (MCA) (complete M1, M2 up till 20D) were included, and b) posterior cerebral circulation, the ROI was set up such that the basilar artery (BA) and 40D of posterior cerebral Artery (PCA) were included.

Metrics for Evaluation

To evaluate the trade-off between accuracy and computational cost, both the architectures were compared using the object detection metrics, Intersection Over Union (IoU) and Intersection Over True (IoT), along with the time taken for prediction. With A and B as the region encompassed by the true and predicted labels respectively, IoU and IoT were defined as

$$IoU = \frac{A \cap B}{A \cup B},\ IoT = \frac{A \cap B}{A} \quad (1)$$

Under-prediction might leave out the important vasculature required for further analyses. For the same reason, IoT was also monitored along with IoU as a higher IoT would indicate that the prediction is accurately encompassing the necessary vessels of interest. The acceptable cutoff of IoU for the object detection problem is 0.6 [13].

RESULTS

The performance of the 2D parallel CNN and 3D serial CNN architectures on the training and validation cohorts with progressing epochs while learning the model are shown in Fig. 4. The mean squared loss and the mean absolute error plateau after about ~500 epochs ensuring the convergence of the model trainings. Performance on validation cohorts ensures model was not over-fit to training cohort.

The performance of the 2D parallel CNN and 3D serial CNN architectures in terms of the IoU and IoT on the validation cohort (n=30)

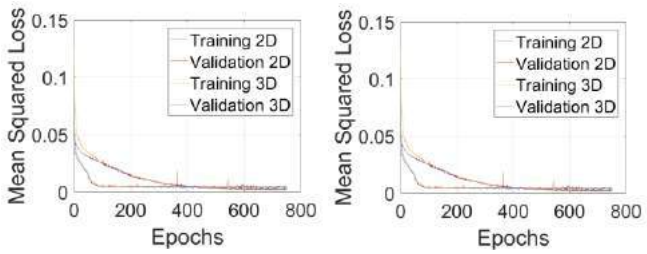

Figure 4: 2D parallel CNN and 3D serial architectures' performance during model training.

post-training can be seen in Table 1. The models predict with an average IoU of 0.68 ± 0.11 and 0.67 ± 0.23 with the 2D parallel and 3D serial CNN models respectively. These predictions meet the cut-off criteria for object detection. Higher IoT further shows safe over-prediction.

The trade-off of both the models in terms of speed for prediction and 'accuracy' are listed in Table 1. The 2D parallel CNN performed ~5 fold faster than the 3D serial CNN, while maintaining the same level of accuracy in terms of the IoU and IoT cut-offs.

The 2D parallel CNN model yielded an IoU of 0.68 ± 0.14 on the testing cohort (n=15), indicating the feasibility of the methodology.

Table 1: Comparison of 2D parallel and 3D serial architecture based on predictions on validation cohort (n=30).

Parameter	*2D Parallel*	*3D Serial*
Time (s)/case	8.13 ± 0.52	42.44 ± 1.35
IoU	0.68 ± 0.11	0.67 ± 0.13
IoT	0.81 ± 0.15	0.82 ± 0.14

DISCUSSION

The accuracy of both the CNNs, measured in terms of IoU and IoT was within the established cut-offs. Moreover, a higher IoT indicated that the models were over-predicting the bounding-boxes. Over-predictions for the bounding-boxes are acceptable whereas severe under-predictions would lead to missing major arteries in the localization. The results on the validation cohort from the novel 2D parallel and traditional 3D serial CNNs show that the architectures are at par in terms of accuracy. But, in terms of the computational cost required for the predictions of the bounding-box parameters with each architecture, the 2D parallel architecture clearly supersedes its counterpart. The results on the independent testing cohort indicated the model was not over-fit to the training and validation cohorts.

CONCLUSIONS

In this study we presented a novel 2D parallel architecture for automated ROI selection in medical images. Comparison of the novel 2D parallel CNN with the traditional 3D serial CNN architecture showed that 2D parallel CNN was the superior choice based on an optimum trade-off between accuracy and computational cost.

ACKNOWLEDGEMENTS

This work was supported by the National Institutes of Health grant R01-NS-091075.

REFERENCES

[1] Jangbari, P., et al., *Int J Comput Appl*,134(10): p. 1-5, 2016.
[2] Janaki, R., et al., *Int J Comput Appl*, 38(2): p. 38-43, 2012.
[3] Xiang, J., et al., Ann Biomed Eng, 44(4): p. 1085-96, 2016.
[4] Meng, H., et al., Am J Neuroradiol, 35(7): p. 1254-1262, 2014.
[5] Steinman, D.A., et al., *J of Biomech Engg*, 135(2): p.021, 2013.
[6] Roth, H.R., et al., *Medical Image Analysis*, 45: p.94-107, 2018.
[7] Kurkure, U., et al., *IEEE TBME*, 56(5): 1360-1370, 2009.
[8] Kumar, K.Y., et al., Advances in Research, 2(1): p.52-57, 2016.
[9] Van Rooij, W.J., et al., *Am J of Neuroradiol*, 29(5): p.976-979, 2008.
[10] Zhao, Z.Q., et al., *preprint arXiv:1807.05511*, 2018.
[11] Glorot, X., et al., *Proc. of 13th Intl. Conf. in AI and statistics*, 2013.
[12] Kingma, D.P., et al., *preprint arXiv:1412.6980*, 2014.
[13] Everingham, M., et al., *Pascal Challenge 2006*, 2006.

SB^{3}C2019
Summer Biomechanics, Bioengineering and Biotransport Conference
June 25 -28, Seven Springs, PA, USA

A FORWARD INCREMENTAL PRESTRESSING APPROACH FOR NONLINEAR FLUID-STRUCTURE INTERACTION HEMODYNAMICS

N. Nama (1), M. Aguirre (2, 3, 4), J. D. Humphrey (5), C.A. Figueroa (1, 6)

(1) Department of Surgery
University of Michigan
Ann Arbor, MI, USA

(2) SaInBioSE, INSERM,
Saint-□tienne, France

(3) Mines Saint-□tienne,
Saint-□tienne, France

(4) Universit□ de Lyon,
Saint-□tienne, France

(5) Department of Biomedical Engineering
Yale University
New Haven, CT, USA

(6) Department of Biomedical Engineering
University of Michigan
Ann Arbor, MI, USA

INTRODUCTION

Computational techniques to simulate cardiovascular flows in three-dimensional models of arteries have attracted significant interest owing to their applications in disease research, medical device design, and surgical planning [1]. To model the fluid-structure interaction (FSI) in compliant arteries, a number of computational methods such as Arbitrary Lagrangian-Eulerian (ALE) methods, immersed methods, Coupled Momentum Method (CMM) etc. have been proposed. Among these, the CMM is particularly attractive since it employs a membrane approach to model the arterial wall, thereby resulting in no additional degrees of freedom compared to a rigid-wall problem [2]. However, the linear membrane model employed in CMM limits its applicability to cases where the arterial wall exhibits small deformations. In this work, we present a nonlinear ALE-FSI extension to CMM that can account for large deformations of arterial wall, while preserving the computational efficiency of CMM to a large degree.

Another important issue concerning the development of patient-specific FSI models is the knowledge of in-vivo state of stress in medically-imaged anatomies. In this work, we adapt a forward incremental prestress approach, proposed for 3D geometries by Gee et al. [3], to a membrane formulation. Through a combination of the membrane prestress algorithm and the nonlinear ALE-FSI formulation, we present an integrated framework to model cardiovascular flows with large wall deformations, while accounting for in-vivo state of stress in medically-imaged vessel geometries.

METHODS

To account for the nonlinear behavior of arterial wall, we employ an ALE approach wherein the fluid is described in ALE configuration, while the arterial wall is modeled as a nonlinear membrane using a Total Lagrangian formulation. The large deformations of the arterial wall are handled via a moving mesh approach using a linear elasticity equation driven by Dirichlet boundary conditions. We utilize a stabilized finite element formulation for Navier-Stokes equation and solve the resulting system of equation in a semi-segregated manner, wherein the fluid-solid equations are solved monolithically as one system while the mesh equations are solved as a separate system.

To obtain the in-vivo state of stress of arterial wall, required for any subsequent FSI simulations, we utilize a forward incremental prestress approach for biological membranes. Referring to Fig. 1, this

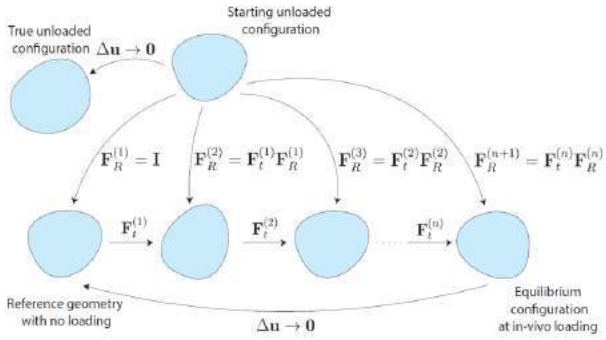

Figure 1: Schematic for forward incremental prestress approach showing various configurations.

algorithm begins with the medically-imaged configuration, albeit without any external loading (corresponding to deformation gradient, F=I). At a given step n, we load this configuration with n^{th} increment of applied pressure and solve for equilibrium. Upon obtaining equilibrium, we update the history deformation gradient, F_R; delete the obtained displacement, and proceed to the next iteration. This approach allows us to eventually obtain a configuration that is in

equilibrium with in-vivo pressure loading, but deviates from the medically-imaged geometry by a non-zero displacement. Therefore, we perform additional load-increment-free iterations to progressively reduce this deviation between the obtained equilibrium and the medically-imaged geometry to a prescribed tolerance.

RESULTS

Fig. 2 shows the velocity distribution and mesh motion in a cylindrical channel with prescribed inlet flow and zero pressure outlet boundary condition at two different time instants. It can be observed that the mesh displacement follows the large deformations of the vessel wall to maintain a good aspect ratio mesh throughout the simulations, thereby confirming the effectiveness of our moving mesh ALE approach.

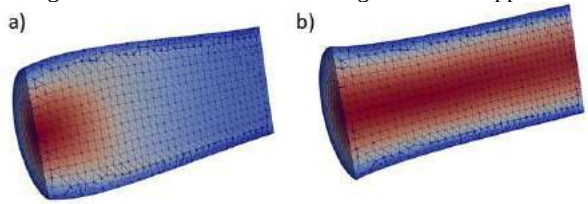

Figure 2: Mesh profile in a cylindrical channel at different time instants.

To model the effect of prestress on arterial wall behavior, we consider a pressure-inflation test on a mouse aortic geometry. Here, the arterial wall is modeled using a Neo-Hookean constitutive model (with c=8 kPa), with fixed ends boundary condition. We consider two cases: (i) the prestress algorithm is used to obtain the state of stress in medically-imaged geometry at p = 80 mmHg; and (ii) the prestress is neglected and the medically-imaged geometry is loaded using a standard forward analysis to obtain the state of stress at p = 80mmHg. The top row of Fig. 3 demonstrates that neglecting prestress results in significant over-estimation of von Mises stress. Moreover, while Fig. 3a shows the state of stress in the medically-imaged geometry; neglecting prestress results in a deformed geometry (Fig. 3b) that deviates from the medically-imaged geometry by a non-zero displacement field. Further loading of these configurations to p = 120 mmHg results in additional overestimation of von Mises stress when prestress is neglected. Notably, neglecting the prestress results in unrealistically large deformations of the vessel geometry (Fig. 3d).

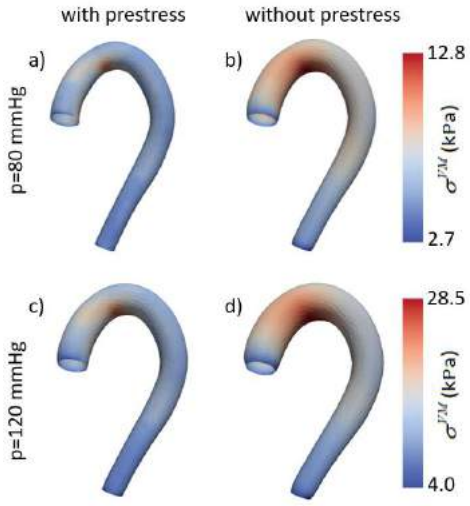

Figure 3: Pressure-inflation test on mice aorta with (a, c) and without prestress (b, d) at p=80 mmHg (top row) and p=120 mm Hg (bottom row)

Next, we consider the effect of inclusion of prestress in an FSI simulation. To this end, we again consider a mice aorta geometry with a prescribed inlet flow (with time period, T = 0.142 s), and RCR outflow boundary conditions [4]. Fig. 4(a) and (b) shows the spatial distribution of pressure at peak systole for cases with and without the inclusion of prestress, demonstrating significantly lower pressure for the case where prestress is ignored. In Fig. 4c, the pulse pressure is higher for the case where prestress is included. This can be attributed to the fact that the presence of prestress makes the vessel wall relatively stiff, resulting in increased pulse pressure.

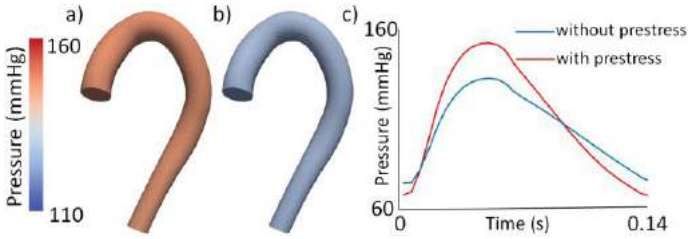

Figure 4: FSI simulation - Spatial distribution of pressure for cases with (a) and without (b) prestress inclusion at peak systole. Corresponding pressure waveform showing increased pulse pressure with inclusion of prestress.

DISCUSSION

The primary contributions of this work are two-fold: (a) development of a novel nonlinear ALE-FSI framework that allows for large deformations of arterial wall, and (b) development of a forward incremental prestress approach for biological membranes. The developed formulation extends the capabilities of CMM by incorporating a moving mesh approach to allow large wall deformations, while employing a nonlinear membrane description of arterial wall for computational efficiency. Our results highlight the importance of including the prestress in cardiovascular simulations. Specifically, ignoring the presence of prestress resulted in significant over-estimation of wall stress and yielded unrealistically large deformations of the arterial wall. Correspondingly, ignoring the prestress in an FSI simulation was found to result in an underestimation of pulse pressure.

The nonlinear ALE-FSI formulation has been implemented within the CRIMSON software (www.crimson.software), which provides a well-established workflow for cardiovascular simulations. This formulation will enhance the capabilities of CRIMSON to allow investigations of cardiovascular flows in cases with large wall deformations, such as ascending thoracic aorta as well as venous hemodynamics. Future work will focus on investigating cases with more complex subject-specific geometries as well as incorporating regionally-varying mechanical properties of arterial wall.

ACKNOWLEDGEMENTS

This work was supported by NIH Grant R01 HL105297.

REFERENCES

[1] Taylor, CA and Figueroa CA, *Annu Rev Biomed Eng.*, 11:109-134, 2009.
[2] Figueroa, CA et al., *Comp Meth Appl Mech Eng.*, 195:41-43, 2006.
[3] Gee, MW et al., *J Biomech*, 42:1732-1739, 2009.
[4] Vignon-Clementel, IE et al., *Comp Meth Appl Mech Eng.*, 195:3776-3796, 2006.

FSI MODELING OF CYCLIC ASPIRATION FOR ACUTE ISCHEMIC STROKE PATIENTS

Bryan C. Good (1), Francesco Costanzo (1,2), Scott Simon (3), Keefe B. Manning (1,4)

(1) Department of Biomedical Engineering
The Pennsylvania State University
University Park, PA, USA

(2) Department of Engineering Science and Mechanics
The Pennsylvania State University
University Park, PA, USA

(3) Department of Neurosurgery
Penn State Hershey Medical Center
Hershey, PA, USA

(4) Department of Surgery
Penn State Hershey Medical Center
Hershey, PA, USA

INTRODUCTION

An estimated 700,000 acute ischemic strokes (AIS) occur annually in the United States [1] due to embolic occlusion of a cerebral artery. Despite improved recanalization rates with new stent retriever devices, over 15% of patients cannot be recanalized with the current technology, and another 17% die within 90 days despite successful recanalization [1]. To date, there is little understanding of why some thromboemboli are successfully removed and others are not. In order to better understand the underlying mechanics of a lodged embolus in a cerebral artery and determine the optimal surgical procedure for its removal, we are developing a continuum-based fluid-structure interaction (FSI) model to predict thromboemboli adhesion and dislodgement under cyclically applied aspiration. The model will allow for patient-specific cerebral artery geometries, blood and thromboemboli mechanical properties, and hemodynamic conditions to be investigated.

METHODS

The modeling framework was developed to simulate a thromboembolus lodged in a cerebral artery, exposed to blood on both proximal and distal surfaces, that is cyclically aspirated by a closely positioned cerebral catheter (**Fig 1A**). The framework combines established thromboemboli and cerebral artery mechanical models with a new model for their interface. The thromboembolus is modeled as an incompressible viscoelastic medium capable of large deformations. The artery will be assumed initially to be rigid but later improved with an anisotropic hyperelastic model for middle cerebral arteries [2]. Although no computational model exists for the thrombus-artery interface, there are models for coarsely ligated biofilms that suggest this interface can be treated using cohesive zone concepts [3] (**Fig. 1B**) where a physical surface with negligible inertia is able to provide traction (**s**) as a function of its opening displacement (δ) and rate ($\dot{\delta}$) (**Eq. 1**):

$$\boldsymbol{s} = f\left(\delta, \dot{\delta}\right)\boldsymbol{e} \tag{1}$$

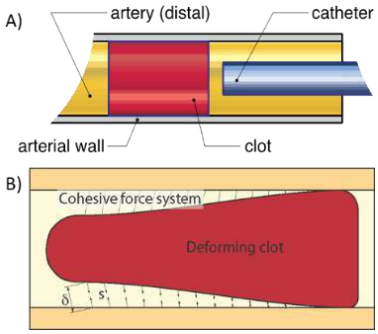

Figure 1: A) Proposed model incorporating a lodged clot in a cerebral artery exposed to cyclic aspiration [4]. **B)** Diagram of the cohesive zone model as the clot pulls away from the arterial wall.

Following the assumptions of a coarsely ligated film, we adopt an Oldroyd-B type rheological model (**Eq. 2**):

$$\delta = \delta_e + \delta_p \tag{2}$$

Where the displacement is a combination of both elastic and viscous components. We then develop the following constitutive equation for the force provided by the cohesive zone (**Eq. 3**):

$$f = k\,\delta_e + \eta_{c1}\dot{\delta} \tag{3}$$

For our AIS application, we assume that the constitutive parameters, which depend on the evolving biochemistry, will vary slowly relative to the external loading imposed during aspiration. Therefore, the constitutive parameters will be treated as constants and determined experimentally. We also hypothesize that a thromboemboli can be removed at lower pressure magnitudes under cyclic versus static aspiration [5] and avoid fracture and distal embolization. To investigate

this hypothesis, all three constitutive models have been implemented into OpenFOAM's finite-volume open-source software in an FSI framework. A previously validated viscoelastic solver for blood [6] is used to simulate local blood flow while a new solid mechanics solver [7] designed for non-linear viscoelastic materials will be used to simulate the thromboembolus.

In brief, the FSI algorithm works by first setting the fluid mesh interface displacement based on interpolation from the solid domain. The solid interface grid-point displacements are interpolated to grid-point displacements of the fluid interface using the AMI approach [8]. Once the displacements have been interpolated to the fluid interface grid-points, they can then be interpolated back to their cell centers before solving for the fluid mesh deformation using a Laplace motion equation. With the updated fluid domain, the fluid governing equations are solved and the resultant pressure and traction forces at the fluid FSI interface are interpolated to the solid interface. Finally, the solid governing equations are solved. Aitken relaxation is used for setting the interface displacement within this inner loop and is then iterated until the FSI residual falls below a predefined tolerance.

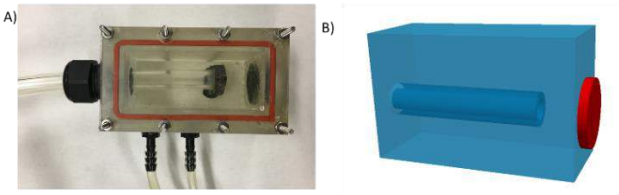

Figure 2: A) Experimental and **B)** computational models of the AIS vessel, catheter and embolus analog used for tracking.

To validate the computational solver, an experimental flow loop and chamber were developed (**Fig. 2A**) to track the displacement of an embolus analog under controlled cyclic aspiration. The flow loop consists of a Cliq Medical aspirator (DHCL Group, Taiwan), a 3-way ASCO solenoid valve (ASCO Valve, Inc) that is controlled by a self-programmed Arduino Uno controller (Arduino AG), an optically clear 3D-printed chamber to mimic a 5x-enlarged middle cerebral artery, and an embolus analog made of neoprene rubber.

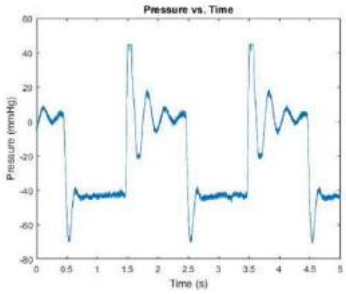

Figure 3: Pressure waveform measured experimentally and applied in computational simulations.

Cyclic pressures were applied at a frequency of 0.5 Hz and with maximum and minimum pressures of approximately 5 And -60 mmHg, respectively (**Fig. 3**). The embolus analogs motion was tracked using a camera and motion analyzed in Matlab. A computational model and mesh were created in Pointwise (Pointwise, Inc) to mimic the experimental setup, imported into OpenFOAM (**Fig. 2B**), and the same pressure waveform applied as a boundary condition on the catheter inlet. FSI coupling boundary conditions were applied at the fluid-solid interface and a traction free condition applied on the downstream surface of the clot.

RESULTS

To validate the full FSI model, extreme cases of both the embolus and cohesive zone properties are being studied both experimentally and computationally: a) deformable embolus with an infinitely stiff cohesive zone (**Fig. 5**) and b) a rigid embolus with a deformable cohesive zone. The viscoelastic properties of the embolus analog material were first determined using cyclic loading in a material testing device and fit to an Oldroyd-B viscoelastic constitutive model. The first case (infinitely stiff cohesive zone) was performed to validate the solid-mechanics model and FSI coupling in order to accurately predict thromboembolus deformation under cyclic aspiration. The predicted displacements were nearly identical with the computational model slightly under-predicting peak displacement at the center of the embolus by 2 and 7% at two time points in **Fig. 4**.

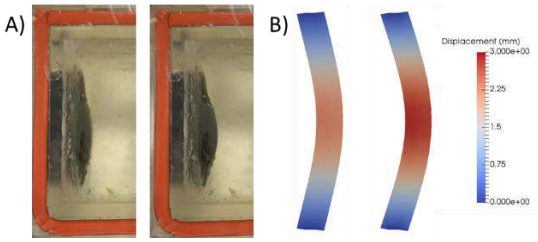

Figure 4: Comparison of **A)** experimental and **B)** computational embolus displacements at two time points during cyclic aspiration.

DISCUSSION

We have developed both an experimental and computational framework for studying the effects of cyclic aspiration on a lodged thromboembolus analog. We will next test our computational solver in another extreme case with a rigid solid and a viscoelastic cohesive zone. We have also collected mechanical testing data for embolus analogs made from bovine blood (**Fig. 5**) and fit the results to the same Oldroyd-B viscoelastic constitutive model and will be incorporating these new parameters into the solid mechanics portion of the FSI solver.

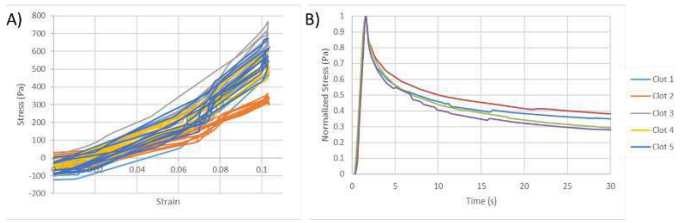

Figure 5: A) Cyclic loading and **B)** stress-relaxation mechanical tests of embolus analogs made from bovine blood.

ACKNOWLEDGEMENTS

AHA Postdoctoral Fellowship 19POST34370040
Undergraduate researchers Connor Foust and Josh Kugel.

REFERENCES

[1] Grech, *et al*. 2015. *The Neuroradiology Journal*.
[2] Kroon and Holzapfel. 2008. *Journal of Biomechanical Engineering*.
[3] Costanzo. 1998. *International Journal of Engineering Science*.
[4] Awadelkarim. Master's thesis, Penn State University. 2017.
[5] Simon, *et al*. 2013. *Journal of Neurointerventional Surgery*.
[6] Good, *et al*. 2016. *Annals of Biomedical Engineering*.
[7] Good. PhD thesis, Penn State University. 2017.
[8] Farrell and Maddison. 2011. *Comput Methods Appl Mech Eng*.

A SYSTEMATIC METHODOLOGY FOR CORRECTING PC-MRI AND CFD INCOMPATIBILITIES

T. Puiseux (1,2), A. Sewonu (2), F. Nicoud (1), S. Mendez (1), R. Moreno (2)

(1) IMAG
Univ. Montpellier, CNRS
Montpellier, France

(2) ALARA Expertise
Strasbourg, France

INTRODUCTION

It is now well established that hemodynamics is associated with the onset and evolution of several cardiovascular disorders such as aneurysms, stenoses, or blood clot formation due to thrombosis. As it provides a comprehensive access to blood flows in-vivo, flow quantification techniques based on time-resolved 3D phase-contrast magnetic resonance imaging (3D PC-MRI) has gained an increasing interest over the last decades [1]. A method to overcome some MRI limitations consists in coupling Computational Fluids Dynamics (CFD) with planar MRI flow measurements as boundary conditions to predict the 3D velocity fields. Nevertheless, a prerequisite to couple CFD to MRI is to ensure that the two techniques converge towards compatible outcomes. Therefore, considerable emphasis has been dedicated to compare and cross-analyze MRI measurements to CFD predictions [2,3]. Despite these efforts, there is still no consensus in the literature on whether or not the two techniques lead to the same outcomes and several limitations are generally pointed out to explain the reported discrepancies. The large variety of possible input options, from the MRI setup (acquisition parameters and post-processing corrections) to the choice of the CFD strategy (numerics, boundary conditions,...) or the framework of the study (in-vivo/in-vitro/in-silico) makes it difficult to draw generalized conclusions.

In this work, we develop a fully controllable, reproducible and MRI compatible experiment designed to generate flow typical of that observed in the cardiovascular system, while removing classical in-vivo sources of discrepancies such as segmentation errors, geometry motions or blood rheology. The flow is predicted by means of high-resolution CFD and compared with velocity data measured by 4D Flow MRI. A quantitative analysis of velocity and Wall Shear Stress (WSS) differences is performed to highlight the potential discrepancies and a generic comparison protocol is proposed to systematically correct for the sources of discrepancies.

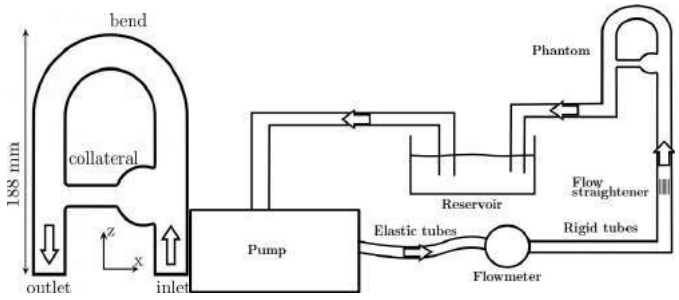

Figure 1: Schematic representation of the flow phantom (left) and the experimental test bench (right).

METHODS

A rigid phantom was designed to mimic the flow through an aortic arch and complemented by a bifurcation in analogy with collateral arteries as well as a protuberance to replicate blood flow patterns in abdominal aortic aneurysms (see Fig. 1). To get a flow split at the bifurcation independent of the outlet boundary condition, and therefore allow a flow distribution purely driven by the fluid mechanics in the domain of interest, a unique outlet was created by merging the collateral segment with the main branch. Several MRI scans were acquired under pulsatile inflow waveform and the measurements were corrected from several types of artifacts (velocity offsets, partial volume effects, image noise). The flow was

simultaneously predicted by means of YALES2BIO, an in-house low-dissipative 4th-order accurate flow solver *(http://imag.umontpellier.fr/~yales2bio/),* already validated in multiple configurations [4,5]. A pixel-based inflow boundary condition was imposed thanks to the velocity profile measured by a time-resolved 2D PC-MRI scan acquired at the inlet of the flow phantom (see [6] for more details).
Several comparisons of velocity fields were performed, varying the level of post-processing adopted for both the MRI and CFD outcomes, using the Pearson's product moment correlation as an indicator of the linearity between the two techniques. The baseline comparison case was defined according to what often appears in the literature, namely to the instantaneous CFD fields compared to the raw MRI measurements. The impact of down sampling the WSS on the correlations was also investigated at peak systole.

RESULTS

As presented in Table 1, velocity correlations may be significantly altered depending on the level of post-processing. The main correlation improvements are obtained either by down sampling the phase-averaged CFD or by correcting for the MRI phase offset artifacts.

$r^2_{\|\mathbf{u}\|}$	$\mathbf{u}_{inst}$	$\mathbf{u}_{HR}$	$\mathbf{u}_{LR}$
Raw MRI	0.63	0.67	0.21
Phase offset corr.	0.81	0.85	0.85
$\mathbf{u}_{wall} = 0$	0.89	0.92	0.96
$\nabla \cdot \mathbf{u} = 0$	0.89	0.93	0.97

Table 1: Magnitude velocity correlation at peak systole, as a function of the level of post-processing. u_{inst} stands for the instantaneous high resolution CFD velocity field of the 40th computed cycle. u_{HR} corresponds to the phase-averaged CFD field and u_{LR} to the phase-averaged velocity down sampled to the MRI spatial resolution. "Phase offset corr." corresponds to the raw MRI dataset corrected from eddy currents and noise artifacts. "u_{wall} = 0" refers to the corrected MRI dataset where a no-slip boundary condition is applied at walls and " $\nabla \cdot u = 0$" refers to the resulting MRI velocity field modified to meet the divergence-free condition.

Phase-averaged CFD velocity fields are qualitatively compared with MRI velocity data corrected from phase offsets (i.e eddy currents and noise masking) in Fig. 2. Removing the first 10th cycles and phase-averaging the CFD velocity over 30 cycles was found to be sufficient to get a reasonable averaged value. Results reveal excellent agreements for the velocity magnitude and highly similar patterns even in the complex flow regions. For example, MRI and CFD capture the recirculation in the aneurysm or back flow in the bifurcation at late diastole.
As presented in Fig. 3, WSS correlations are generally lower than the corresponding velocity correlations. This is mainly due to the sensitivity of the WSS computation to the spatial resolution and residual noise in the near-wall voxels. Moreover, as reflected by the discrepancies observed between WSS computed from u_{HR} (WSS_{HR}) and u_{LR} (WSS_{LR}), down sampling significantly degrades the accuracy of the gradient computation since the intra-voxel averaging smoothens the (strong) velocity gradients present in the wall vicinity.

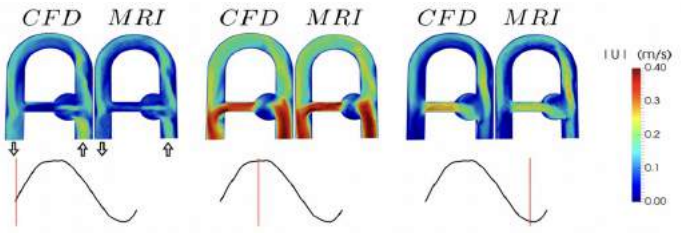

Figure 2: Comparison in the coronal plane of CFD magnitude velocity fields (u_{HR} in Table 1) with MRI measurements (" $\nabla \cdot u = 0$ " in Table 1) at 2 mm resolution at different instants of the cycle indicated by the red lines on the flow rate waveforms below.

DISCUSSION

Since PC-MRI and CFD are drastically different modalities, a direct comparison of their outcomes leads to systematic errors. Results show that the gain obtained by degrading the CFD data is not negligible, yet smaller, compared to the improvement generated by processing, denoising and correcting the raw MRI data. While only poor correlations are obtained when straightforward treatments are applied (r^2 = 63%), a very strong correlation (97% for the velocity, 84% for the WSS) could be reached by carefully post-processing the two datasets. While this methodology was developed under in-vitro conditions, the proposed corrections are also applicable in-vivo.

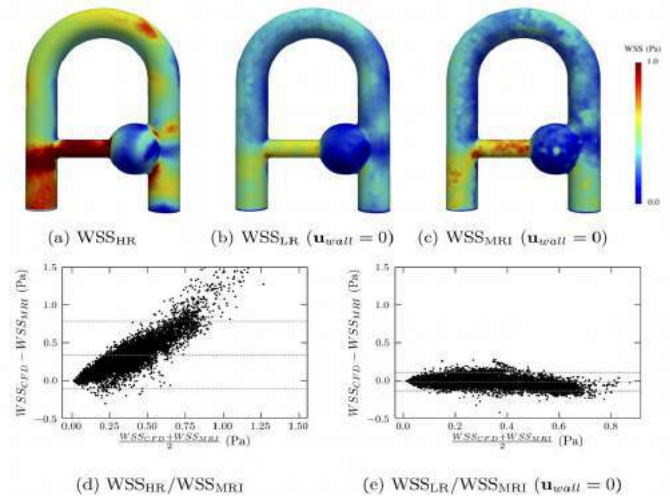

Figure 3: WSS maps on boundary walls at peak systole. (a) WSS calculated from u_{HR}, (b) from u_{LR} (with zero velocity imposed on boundary walls) and (c) from u_{MRI} (third row in Table 1). Bland-Altman plots of the comparison between (d) WSS_{HR} and WSS_{MRI} (corresponding to r^2 = 0.48) and (e) WSS_{LR} and WSS_{MRI} corresponding to r^2 = 0.84.

REFERENCES

[1] Markl, M. et al., *JMRI*, 17:499-506, 2003.
[2] Van Ooij, P. et al., *NMR Biomed,* 25:14-26, 2011.
[3] Kweon, J. et al., *Eur. Radiol.*, 26:3588-3597, 2016.
[4] Chnafa, C. et al., *Ann. Biomed. Eng.*, 44:3346-3358, 2016.
[5] Siguenza, J. et al., *J. Comput. Phys,* 322:723-746, 2016.
[6] Puiseux, T. et al., accepted in *NMR Biomed.*, 2019.

SB³C2019
Summer Biomechanics, Bioengineering and Biotransport Conference
June 25 -28, Seven Springs, PA, USA

Reduced-Order Leaflet Models For Numerical Experiments On Transcatheter Aortic Valves

Shantanu Bailoor (1), Jung-Hee Seo (1), Hoda Hatoum (2), Lakshmi Prasad Dasi (2), Rajat Mittal (1)

(1) Department of Mechanical Engineering
The Johns Hopkins University
Baltimore, MD, USA

(2) Department of Biomedical Engineering
The Ohio State University
Columbus, OH, USA

INTRODUCTION

Transcatheter aortic valve replacement (TAVR) procedures are rapidly becoming the dominant option for aortic valve replacement and are expected to eventually become the standard-of-care for AV replacement. However, prosthetic valves used in TAVR are susceptible to several "malfunctions" such paravalvular regurgitation, leaflet tears, endocarditis and leaflet thrombosis. Since malfunctions like leaflet thrombosis can modify valve motion and downstream hemodynamics, monitoring changes in flow quantities in the valve vicinity might provide insights into potential valve dysfunction. Characterizing the kinematics of, and hemodynamics around healthy and dysfunctional valves is a key first step in such monitoring approaches. This study combines experimental and computational approaches to characterize valve kinematics and transvalvular hemodynamics for healthy and thrombosed TAV models. Imaging data from *in vitro* experiments of prosthetic valves are used to decompose leaflet motion into its principal components and these are used synthesize dynamic leaflet models. We also present data from direct numerical simulation (DNS) for flow through a two-parameter, idealized aortic valve model under healthy and thrombosed conditions. Simulation data is used to explore the detection of leaflet thrombosis using data from embedded sensors.

METHODS

To simulate transvalvular flow, we used an extensively validated, versatile, incompressible flow solver "ViCar3D"[2,3]. This solver has previously been used for DNS of flow through aortic stenoses[4], mitral valves[5] and left ventricles[6]. We performed DNS of transvalvular flow in the aorta with the objective of exploring the use of sensors embedded within the TAV to detect malfunctions such as leaflet thrombosis. We employed an idealized aorta model based on clinical data[7] and included a simple, generic bioprosthetic aortic valve whose motion was governed by a reduced degree-of-freedom (DOF) model. The valve displacement can in general be expressed as a convolution sum of M spatial and temporal modes, as follows:

$$\boldsymbol{d}_v(\boldsymbol{x},t) = \sum_{i=1}^{M} c_i(t)\,\boldsymbol{b}_i(\boldsymbol{x}) \qquad (1)$$

We describe later in this abstract as to how these modes maybe extracted from experimental data. Once the spatial modes have been chosen, the time-coefficient may be obtained by solving a dynamical equation for the leaflets. For a 1-mode (M=1) leaflet model, which is the focus of the current study, an equation for the time-coefficient is obtained by integrating the Newtons second law for a leaflet as follows:

$$\frac{d^2c_i}{dt^2} = \frac{\int \Delta p\, dS}{\int \alpha(\boldsymbol{b}\cdot\boldsymbol{n})dS} - \frac{K}{\alpha}(c_i - c_0) \qquad (2)$$

where Δp is the pressure difference across the leaflet surface obtained from the flow simulation, α is mass coefficient and K is a stiffness coefficient. This simple, ODE based, two-parameter model can be coupled with the full Navier-Stokes' equations and employed in a wide range of numerical experiments.

Mode shapes can be directly extracted from experimental data and here we have extracted this modal information from high-speed imaging data of an in-vitro experiment with a TAV (Figure 1 (a)). Leaflet edges were reconstructed using MATLAB's image processing module by placing marker points along the edge and fitting smooth splines through them (Figure 1 (a)). We use the method of snapshots[1] to extract the principal components associated with the leaflet motion. For each leaflet, the 'n' coordinates of the spline points were recorded along the rows of a matrix, $\boldsymbol{\Delta X}$, while the evolution of each spline point over 'Nt' time levels was ordered along its columns. To obtain the principal components of leaflet motion, singular value decomposition (SVD) of $\boldsymbol{\Delta X}$ was computed, which takes the form: $\boldsymbol{\Delta X} = \mathbf{U\Sigma V}^{\mathrm{T}}$. $\mathbf{V}$ and $\mathbf{U}$ are unitary matrices representing the spatial distribution of orthonormal

basis vectors and their temporal evolution, respectively. $\mathbf{\Sigma}$ is a diagonal matrix containing $r = \min(n,Nt)$ positive entries in descending order, called the singular values of $\mathbf{\Delta X}$. Squares of the singular values represent the fractional contribution of individual modes to the total spatio-temporal information contained in $\mathbf{\Delta X}$.

RESULTS AND DISCUSSION

An example of snapshot PCA implementation is illustrated in Figure 1. For each of the 19 (Nt) snapshot of the prosthetic valve[8] in motion, 20 marker points were manually placed on the leaflet edge and smooth splines, with 100 (n) divisions, were fit through these marker points (Figure 1 (a)). PCA of the spline coordinates was used to create a low-order reconstruction of the leaflet edge, using only the first (Figure 1 (b)) and the first 3 (Figure 1 (c)) out of the possible 19 singular values. A remarkable improvement from using one mode and an excellent edge tracking is observed with the first three modes. This data will eventually be employed in the dynamical model of the leaflets (Eqs. 1 & 2) to synthesize realistic leaflet kinematics in our transvalvular simulations. For now, we employ a simple modal shape $\boldsymbol{b}$ based on visual observation of the leaflets.

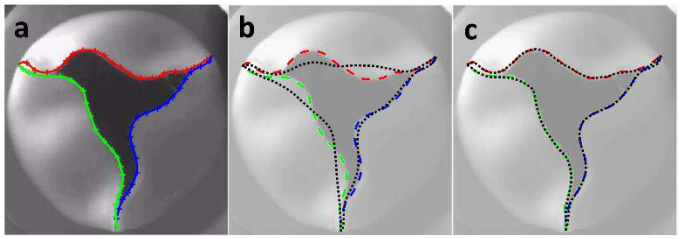

Figure 1: (a) Image of prosthetic valve configuration[8] with spline fits (solid lines) and discrete marker points (+). Reconstruction of (dotted black lines) using PCA (b) mode 1 and (c) modes 1+2+3.

We simulated three transvalvular flow cases, one in which all leaflets of the valve open fully – referred to as the "healthy" case – the next in which one valve leaflet thrombosed (modeled with a higher stiffness) and consequently exhibits reduced leaflet motion (RLM) – referred to as "RLM #1" case. Finally, the third case involved two leaflets with RLM, referred to as "RLM #2" case. The degree of RLM is illustrated in the insets of Figure 2 (b) and Figure 2 (c). A sinusoidal flow-rate was prescribed to drive flow through the aorta and valve. The pressure difference across the leaflet surface and the valve displacement/velocity provide the boundary conditions for the structure and flow solvers, respectively. The stroke volume through the aorta was 60 ml. The simulation Reynolds number with respect to aorta diameter and peak aortic velocity, based on clinical blood flow measurements in patients with prosthetic aortic valves[9], was 4300. Virtual probes were placed at three circumferential locations on the valve skirt (S1, S2, S3) and three corresponding downstream locations on the aorta wall (A1, A2, A3) (Figure 2 (a inset)). Each probe recorded the pressure difference relative to the reference outlet pressure and this information was used to develop a correlation-like metric to distinguish the healthy valve from the dysfunctional one.

The time-varying pressure difference at the six probe locations during one systole are illustrated in Figure 2 for (a) healthy, (b) RLM #1 (Leaflet 1 has RLM) and (c) RLM #2 cases. Leaflet dysfunction may be inferred from azimuthal asymmetry in pressure signals. In the healthy case, the three pressure signals on the valve skirt (S1, S2, S3) are identical and smooth. Pressure downstream of the valve, although jagged, is symmetrical. The jaggedness is attributed to increased flow turbulence resulting from the interaction of blood with the valve leaflets. Both RLM cases, on the other hand, shows azimuthal asymmetry in pressure signals, both upstream and downstream of the valve (Figure 2 (b)). RLM resulted in a greater pressure drop across the valve, indicated by a decrease in A1, A2 and A3 measurements and greater downstream turbulence, as inferred from increased jaggedness. We then computed the normalized pressure cross-deviation, as shown in Eq. (3), and the values for each probe in the two cases are shown in Table 1. The healthy case results in very small q for each probe, indicating high azimuthal symmetry. The RLM cases, on the other hand results in elevated q for each probe but in each case, one azimuthal location recorded significantly larger cross-deviation. For instance, in RLM #1, S1 and A1 recorded larger values than the other probes at corresponding axial locations and particularly, S1 recorded nearly two orders of magnitude larger pressure than S2 and S3. Likewise, in RLM #2 case, A2 and S2 recorded nearly 5 times larger deviations. The metric is thus able to discriminate healthy valves from with leaflet thrombosis. Further, monitoring pressure asymmetry on the valve skirt may be more reliable for detecting valve dysfunction, due to a lack of flow turbulence, as opposed to the aortic wall surface downstream of the valve.

$$q_i = \frac{\overline{\prod_{j=1,j\neq i}^{3} |p_i - p_j|}}{\overline{p_i^2}} \qquad (3)$$

Table 1: Comparison of pressure (x 10^{-4}) recorded by the six probes in the healthy and RLM cases.

	q_{A1}	q_{A2}	q_{A3}	q_{S1}	q_{S2}	q_{S3}
Healthy	17	27	20	0.19	0.32	0.2
RLM #1	**291**	57	68	**148**	5	0.5
RLM #2	76	**646**	109	10	**49**	13

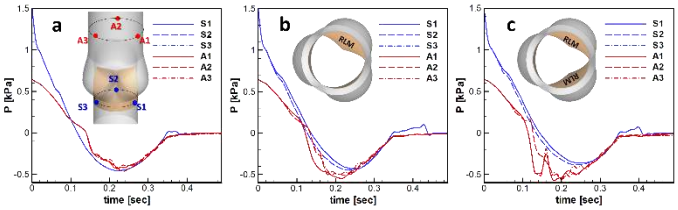

Figure 2: Pressure recorded by the six probes placed in the vicinity of the aortic valve in (a) healthy and (b) RLM #1 case. Probe locations are shown in the insets of (a).

The current study demonstrates the use of reduced-order leaflet models for investigating the coupled biophysics of transcatheter aortic valves. The advantages of such models are that they require limited information for parameterization and they are simpler and more efficient to implement in a computation. Here we have used these models to guide the placement of embedded sensors for detecting leaflet thrombosis. Ongoing work is using these computational models as a basis for a comprehensive study that employs machine learning tools for optimizing sensor configurations for such applications.

ACKNOWLEDGEMENTS

Work supported by NSF grants CBET-1511200 and IIS-1344772.

REFERENCES

[1] Bozkurttas, M et al., *J Fluid Mech*, 631:311-342, 2009.
[2] Mittal, R et al., *J Comp Phys*, 227:4825-4852, 2008.
[3] Zhu, C et al., AIAA 2017-3622, 2017.
[4] Zhu, C et al., *J Fluid Mech*, 851:23-49, 2018.
[5] Seo, JH et al., *Phys Fluids*, 26, 121901, 2014.
[6] Seo, JH and Mittal, R, *Phys Fluids*, 25, 110801, 2013.
[7] Reul, H et al., *J Biomech*, 23(2):181-191, 1990.
[8] Hatoum, H et al., *Journal of Thoracic and Cardiovascular Surgery*, 156:1837-1848, 2018.
[9] Barletta, G et al., *Echocardiography*, 35:329-336, 2017.

SB³C2019
Summer Biomechanics, Bioengineering and Biotransport Conference
June 25 -28, Seven Springs, PA, USA

BIOTRANSPORT IN THE GLYMPHATIC SYSTEM: PULSATION, PERISTALSIS, AND HIGH BLOOD PRESSURE

Humberto Mestre (1,2), Jeffrey Tithof (3), Ting Du (1,4), Wei Song (1), Weiguo Peng (1,5), Amanda M. Sweeney (1), Genaro Olveda (1), John H. Thomas (3), Maiken Nedergaard (1,5), and Douglas H. Kelley (3)

(1) Center for Translational Neuromedicine, University of Rochester Medical Center, Rochester, NY 14642, USA.

(2) Department of Neuroscience, University of Rochester Medical Center, Rochester, NY 14642, USA.

(3) Department of Mechanical Engineering, University of Rochester, Rochester, NY 14627, USA.

(4) China Medical University, Shenyang 110122, China.

(5) Center for Translational Neuromedicine, Faculty of Health and Medical Sciences, University of Copenhagen, 2200 Copenhagen, Denmark.

INTRODUCTION

The recently-discovered glymphatic system[1] circulates cerebrospinal fluid (CSF) through the brain, sweeping away proteins and metabolic waste and playing a role similar to the lymphatic system in the rest of the body. Primarily active during sleep[2], the glymphatic system drives CSF through annular perivascular spaces (PVSs) surrounding arteries and veins, from which it accesses deeper brain tissue. The glymphatic system may play a key role in preventing neurological disorders, such as Alzheimer's and Parkinson's diseases, that are associated with accumulation of waste proteins (in these two examples, amyloid-β and tau). The glymphatic system also has potential for drug delivery[3].

However, both the characteristics of biotransport via the glymphatic system and the mechanisms driving that biotransport have been topics of open debate in recent publications. In mice, PVS widths have been estimated from ~nm to ~μm. CSF in PVSs has been said to flow either parallel[2] or anti-parallel[4,5] to the blood in the adjacent vasculature. CSF flow has been suggested to pulse in synchrony with either the respiratory or cardiac cycle.

In results just published,[6] we use *in vivo* particle tracking to measure CSF flow in PVSs surrounding pial arteries in mice, with high resolution in space and time. We show that the flow pulses in synchrony with the cardiac cycle, consistent with a peristalsis-like "perivascular pumping" in which CSF is driven by the motion of the adjacent artery wall.[7] We alter that motion by inducing high blood pressure to stiffen the wall, and we show that the mean CSF flow speed is reduced ~40%. Perivascular pumping appears to be the primary driver of CSF flow in healthy mice, and its disruption by high blood pressure may relate to the fact that early-onset hypertension is a known risk factor for Alzheimer's disease in humans.

METHODS

All experiments were approved by the University Committee on Animal Resources of the University of Rochester Medical Center (Protocol No. 2011-023), and an effort was made to minimize the number of animals used. We injected 1-μm tracer particles into the cisterna magnas of male mice, age 8-12 weeks, anaesthetized with ketamine-xylazine to approximate sleep. We also injected intravascular fluorescein isothiocyanate-dextran to make arteries visible. We performed two-photon imaging through a cranial window using a resonant scanner B scope (Thorlabs) with a Mai Tai DeepSee HP Ti:Sapphire laser and a water immersion lens. Typically, we observed flow near the bifurcation of the middle cerebral artery, though we have seen the same phenomena in other pial PVSs as well. Images were recorded at 30 Hz. Simultaneously, we measured ECG (at 1 kHz) and respiration (at 250 Hz). To increase blood pressure, we infused Angiontensin-II in 0.9% NaCl into a femoral vein catheter at 5 ng g^{-1} min^{-1} at a volumetric rate of 1 μl min^{-1} using a syringe pump. Control mice received an infusion of NaCl 0.9% instead. We used artery images to register the resulting movies during post-processing, removing translations caused by large-scale motions of the mouse with respect to the scope, which would distort flow velocity measurements. We tracked particles using an in-house algorithm written in Matlab, excluding stagnant particles that had apparently adhered to the vessel wall. The results presented below come from 7 hypertension experiments and 6 control experiments, each involving 19728 ± 4358 tracked particles and 355013 ± 85957 total measurements (mean ± standard error of the mean).

RESULTS

Our videos showed CSF flow in PVSs to be visibly pulsatile, so we set out to study the nature of that pulsation. Using the entire set of

measurements from one control experiment (normal blood pressure), we calculated the root-mean-square flow velocity v_{rms} as a function of time by averaging the squared velocity of all tracked particles in each frame of the video, then calculating the square root of that average. Then we compared v_{rms} to the simultaneous ECG signal, which measured the cardiac cycle, and respiration signal. Specifically, we divided each cardiac cycle into a fixed number of bins and also divided each respiratory cycle into a fixed number of bins. Then, we categorized every v_{rms} measurement, based on the time at which it was made, as falling into a particular cardiac cycle bin and a particular respiratory cycle bin. For example, a measurement might have been made at the moment when 25% of the cardiac cycle had elapsed since the last heartbeat and 45% of the respiratory cycle had elapsed since the last breath; it would be assigned to the (25%,45%) bins. Once all measurements were assigned, we calculated the average for each bin pair. In other words, we calculated the average of v_{rms}, conditioned both on fraction of the cardiac cycle and fraction of the respiratory cycle.

Figure 1 shows the results of conditional averaging. The average speed varies significantly with the cardiac cycle, from ~15 μm/s during much of the cycle to nearly 50 μm/s soon after the heartbeat. The average speed varies much less, however, with the respiratory cycle (~20 μm/s to ~25 μm/s). We have also calculated statistics of the delay time between each peak in v_{rms} and the corresponding peaks in ECG and respiration. The results (not plotted) show that the delay from a heartbeat to a peak in v_{rms} is typically 35 ms and almost never more than 100 ms, whereas the delay from a breath to a peak in v_{rms} is almost equally likely to take values from 0 to 300 ms, with values as large as 500 ms also observed. Thus, our measurements show that CSF flow pulses in synchrony with the cardiac cycle.

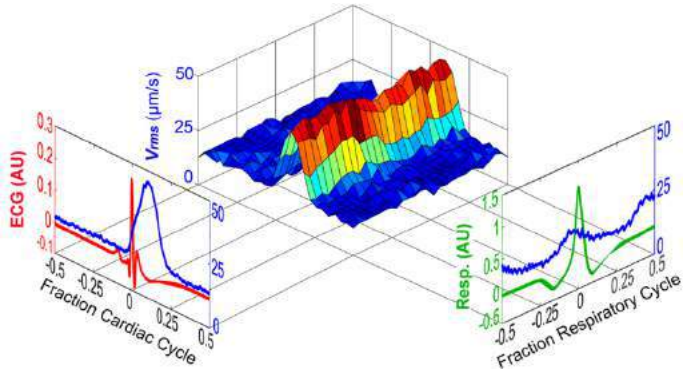

Figure 1: CSF flow pulses in synchrony with the cardiac cycle, not the respiratory cycle. Conditionally averaging the root-mean-square velocity on both cycles shows strong dependence on cardiac activity and weak or negligible dependence on respiratory activity. Protruding plots show averages conditioned on the cardiac (left) or respiratory (right) cycle alone. Adapted from [6].

The observed synchronization between CSF flow and the cardiac cycle supports an existing hypothesis that motion of the adjacent artery walls drives CSF via perivascular pumping[7]. To test that hypothesis, we changed the wall motion by inducing high blood pressure. High pressure causes muscular artery walls to flex harder in order to maintain the same diameter, stiffening the tissue, and presumably changing wave propagation dynamics. We found that Angiotensin-II increases blood pressure in mice from about 80 mmHg to about 135 mmHg in about 2 min, allowing measurements in the same mouse with both normal and high blood pressure. The measured wall deformation and velocity (not plotted) did change significantly, as we expected. The mean flow speed also changed significantly, as Figure 2 shows, dropping on average from 30 μm/s to 18 μm/s. Our measurements further show that when blood pressure is normal, pulsations vary the flow speed between faster and slower, but when blood pressure is high, pulsations typically cause backflow during part of the cardiac cycle, reducing overall pumping efficiency.

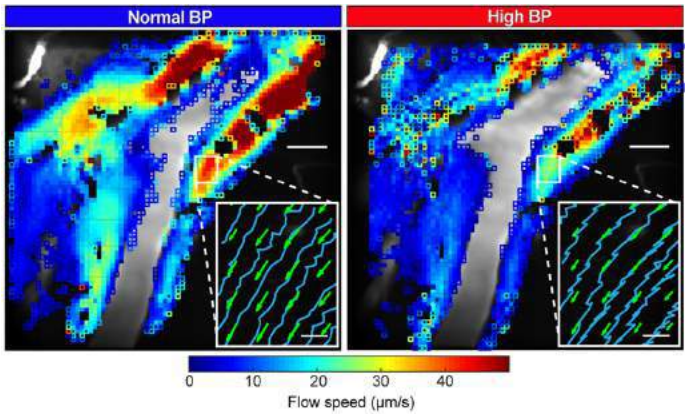

Figure 2: High blood pressure reduces net flow of CSF. CSF flow speed, averaged over all particles observed in the small boxes shown, during ~10 min with normal blood pressure and ~10 min with high blood pressure. Solid boxes contained at least 20 measurements; hollow boxes, less than 20. Scale bars are 40 μm. Insets indicate the mean flow in green and example particle paths in cyan, showing that backflow is common when blood pressure is high. Scale bars are 5 μm. Adapted from [6].

DISCUSSION

Our high-resolution measurements of the flow of CSF in PVSs demonstrate that perivascular pumping is the primary driver of glymphatic flow in healthy mice. Furthermore, the finding that high blood pressure reduces CSF flow significantly may relate to the fact that early-onset hypertension is a known risk factor for Alzheimer's disease in humans. However, that idea should be addressed in future studies, since chronic hypertension in humans and acute hypertension in mice are not the same thing. Future studies could also consider drivers other than perivascular pumping, such as osmotic pressure and vessel volume changes, especially in pathological conditions like traumatic brain injury and stroke.

ACKNOWLEDGEMENTS

This work was supported by the National Institute of Neurological Disorders and Stroke (R01 NS100366 to M.N.), the National Institute of Aging (RF1 AG057575-01 to M.N., J.H.T., and D.H.K.), Foundation Leducq (FLQ 12CVD01 to M.N.), and the European Union's Horizon 2020 Research and Innovation Programme (SVDs@target) (666881 to M.N.). We would like to thank Dan Xue for assistance with illustrations. HM and JT contributed equally.

REFERENCES

1. Iliff, J. J. *et al. Science Translational Medicine* **4,** 147ra111–147ra111 (2012).
2. Xie, L. *et al. Science* **342,** 373–377 (2013).
3. Plog, B. A. *et al. JCI Insight* **3,** 1188–16 (2018).
4. Morris, A. W. J. *et al. Acta Neuropathol.* **131,** 725–736 (2016).
5. Bakker, E. N. T. P. *et al. Cellular and Molecular Neurobiology* **36,** 181–194 (2017).
6. Mestre, H. *et al. Nat. Comm.* **9:1,** 4878 (2018).
7. Hadaczek, P. *et al. Mol. Ther.* **14,** 69–78 (2006).

MICRO PARTICLE IMAGE VELOCIMETRY FOR IN VITRO ASSESSMENT OF PATIENT SPECIFIC WHOLE BLOOD RHEOLOGY

E. Kucukal (1), Y. Man (1), A. Hill (2), S. Liu (1), J. A. Little (2), U. A. Gurkan (1,3)

(1) Department of Mechanical and Aerospace Engineering,
Case Western Reserve University
Cleveland, OH, USA

(2) Division of Hematology/Oncology,
Case Western Reserve University, University Hospitals Seidman Cancer Center,
Cleveland, OH

(3) Department of Biomedical Engineering,
Case Western Reserve University
Cleveland, OH, USA

INTRODUCTION

Blood viscosity is a crucial biophysical parameter implicated in various physiologic and pathophysiologic conditions, including microvascular disease and some hematologic disorders. The primary determinants of blood viscosity are hematocrit, blood cell deformability, plasma viscosity, and cellular aggregation, all of which may individually contribute to an alteration of blood viscosity in response to a range of pathologic scenarios[1]. Therefore, monitoring blood viscosity has a unique potential to assess and monitor circulatory health and disease.

Here, we present a simple microfluidic device for measuring whole blood viscosity (WBV) by means of micro particle image velocimetry (μPIV). Using this micro-platform, we assess the viscosity of whole blood samples obtained from healthy donors as well as individuals with sickle cell disease (SCD). Red blood cells (RBCs) of people with SCD are intrinsically more adhesive and rigid due to a genetic mutation in hemoglobin that results in intracellular polymer, thereby affecting the WBV. Disease severity in SCD has been linked to cellular adhesion, impaired RBC deformability, and increased WBV, wherein the latter has been shown to increase, at least in part, stroke events in children[2]. However, the precise relationship between these parameters has yet to be elucidated. Here, we describe a subject-specific WBV profile among the study group, encompassing a range both above and below a normal level. More importantly, we show an inverse correlation between WBV and RBC adhesion, which may provide a novel insight into the pathophysiologic progression of SCD.

METHODS

The microfluidic system consists of three layers: a microfluidic channel, a constant pressure pump, and an optical microscope as illustrated in Figure 1. The microfluidic channel was fabricated based on a lamination technique as we have previously described[3]. The assembled microchannel was then connected to a reservoir containing 500 ul of whole blood. The pressure pump delivered a constant pressure of 15 mmHg into the reservoir allowing the blood sample to flow across the microchannel. Image acquisition of flowing blood cells was performed at two random fields of view (FOV) at a 4X magnification and at least 500 subsequent images were recorded for each FOV.

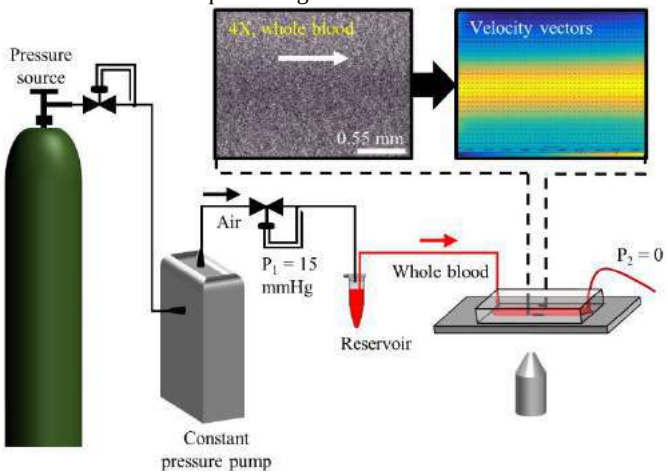

Figure 1. Schematic view of the experimental setup. A constant pressure pump is used to deliver pressurized air into a blood-containing reservoir. The whole blood sample then flows through a microfluidic channel placed on a motorized microscope stage. The velocity vectors within the field of interest are obtained through particle image velocimetry (PIV), where the cellular components of blood are employed as tracing particles.

In this study, blood cells were utilized as tracing particles for the PIV calculations and assumed to provide the average velocity through the microchannel, instead of using additional fluorescent particles, in order to minimize sample manipulation that could alter the hemodynamic properties. Two-image cross correlation method was employed in Matlab using "PIVlab" which produced 250 pairs of velocity fields for each FOV[4]. Time-averaged flow velocities were computed for both FOVs and the mean of those values were assigned as the average velocity of the sample. A calibration curve was generated to link the average velocity to viscosity by using various glycerol/PBS mixtures (0-100%) with known viscosities[5]. A 20 ul solution containing fluorescently labeled 2μm-diameter beads was added into the reservoir prior to the PIV experiments when a glycerol/PBS mixture was tested.

RBC adhesion experiments were carried out in a different microchannel that was functionalized with an endothelium-associated protein, laminin (LN) as we have previously described[3]. Collected blood samples were transferred into two separate tubes dedicated for either the adhesion or viscosity measurements.

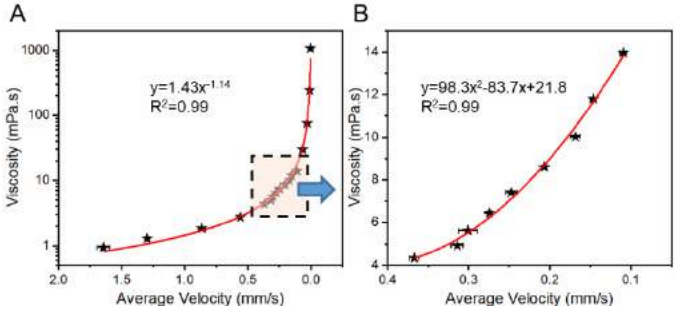

Figure 2. Calibration curves for estimating viscosity based on the average velocity in the microchannel. Glycerol/PBS solutions at varying concentrations between 0% to 100% were mixed with 2 μm-diameter fluorescent beads and flowed through the microchannel at 15 mmHg reservoir pressure. (A) For each glycerol concentration, and thus the known fluid viscosity, an average flow velocity was obtained via PIV. (B) To increase the accuracy, more data points were acquired between average velocities 0.1-0.4 mm/s, since this represented the velocity range for the tested blood samples. N=4 for velocity measurements.

RESULTS

We assessed the viscosity of whole blood samples from healthy donors with no hemoglobin disorders (HbAA) as well as from individuals with homozygous SCD (HbSS) as shown in Figure 3A. We first quantified the average axial velocities via μPIV at a constant pressure within the physiological range (15 mmHg) and then obtained the corresponding estimated viscosity value utilizing the calibration curve (Fig. 2). The measured viscosity values were largely heterogeneous and demonstrated a subject-specific manner in the SCD study population ranging from 4.2 mPa.s to 17.7 mPa.s. We segregated these subjects into two groups: high viscosity group and low viscosity group based on the mean viscosity level (Fig. 3A). Notably, subjects with higher viscosity displayed significantly lower RBC adhesion to LN (Fig. 3B, p=0.02). There was an inverse correlation between RBC adhesion and WBV (Fig. 4, PCC=0.59, p=0.02).

Since both WBV and RBC adhesion are clinically important parameters, we tested whether WBV would correlate with clinical phenotype. Interestingly, subjects with lower WBV tended to have higher lactate dehydrogenase (LDH) levels (Fig. 5) indicative of an ongoing in vivo hemolysis.

DISCUSSION

We present a microfluidic approach to assess WBV via the integration of microfabrication and μPIV. We have shown that viscosity

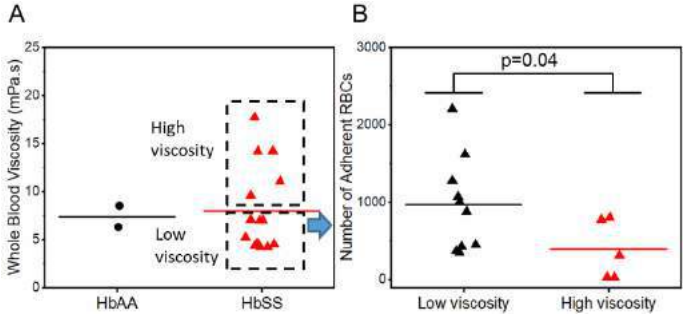

Figure 3. Measured whole blood viscosity and RBC adhesion profiles for healthy (HbAA) and homozygous SCD (HbSS) blood samples. (A) HbSS samples display a significant heterogeneity in WBV. High viscosity and low viscosity groups were identified based on the mean threshold viscosity level of 7.9 mPa.s. (B) Subjects in the low viscosity group (N=10) had significantly greater RBC adhesion to laminin compared to those in the high viscosity group (N=5) *in vitro* (p=0.04, non-parametric Mann-Whitney test).

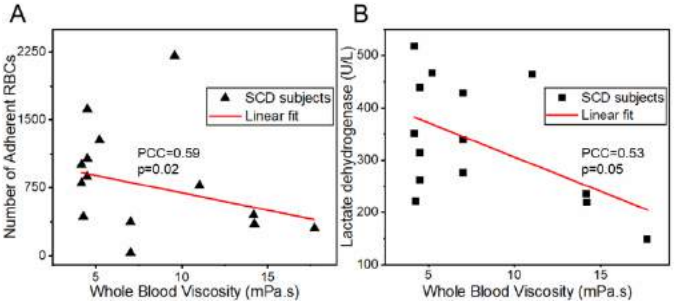

Figure 4. WBV is subject-specific and associates with (A) RBC adhesion to LN and (B) subject LDH level.

of HbSS blood samples varies significantly in a subject dependent fashion and may provide clinically relevant information. For the first time, we have demonstrated a significant (inverse) link between WBV and RBC adhesion wherein subjects with lower WBV displayed greater RBC adhesion. Further, decreasing values of WBV corresponded to higher LDH levels in these subjects, indicating an elevated state of in vivo hemolysis. Notably, these results suggest that subjects with a more severe disease phenotype (increased RBC adhesion and LDH) have lower WBV values. WBV has been implicated in variant sickle disorders, which have a higher Hgb and, in our hands, lower RBC adhesion to LN[6]. This is consistent with the data presented here, in which hemolytic disease has an inverse association with WBV. We speculate that significantly reduced hematocrit levels in subjects with the more severe disease phenotype account for a decreased cellular viscosity. WBV may contribute to a different spectrum of disease, such as variant sickle cell disease, osteonecrosis, and retinopathy.

ACKNOWLEDGEMENTS

This work was supported by National Heart Lung and Blood Institute R01HL133574. U. A. G. acknowledges National Science Foundation CAREER Award 1552782. The authors acknowledge with gratitude the contributions of patients and clinicians at Seidman Cancer Center (University Hospitals, Cleveland).

REFERENCES

[1]. Jun Kang, Y., et al., *Biomicrofluidics,* **7**(5): p. 54111.2013.
[2]. Verduzco, L.A., et al., *Blood,* **114**(25): p. 5117-25.2009.
[3]. Alapan, Y., et al., *Transl Res,* **173**: p. 74-91 e8.2016.
[4]. Thielicke, W., et al., *Journal of Open Research Software,* **2**.2014.
[5]. Volk, A., et al., *Experiments in Fluids,* **59**(75).2018.
[6]. Connes, P., et al., *Blood Rev,* **30**(2): p. 111-8.2016.

SB³C2019
Summer Biomechanics, Bioengineering and Biotransport Conference
June 25 -28, Seven Springs, PA, USA

PATIENT-SPECIFIC METRICS FROM QUANTITATIVE RHEOLOGY OF WHOLE SICKLE BLOOD USING MICROFLUIDICS

José M. Valdez (1), Yvonne Datta (2), John M. Higgins (3), David K. Wood (1)

(1) Department of Biomedical Engineering
University of Minnesota
Minneapolis, MN, United States

(2) Department of Medicine
University of Minnesota
Minneapolis, MN, United States

(3) Department of Systems Biology
Harvard University
Cambridge, MA, United States

INTRODUCTION

Sickle cell disease (SCD) is an inherited hematological disorder resulting from a point mutation in the β-globin gene [1]. The mutated hemoglobin molecule (sickle hemoglobin or HbS) polymerizes under deoxygenated conditions and is associated with decreased red cell deformability as well as damage to the cell membrane and cytoskeleton [2-3]. The result are injured, inflexible red cells and dramatic changes in blood rheology under both normoxic and hypoxic conditions. Clinical complications include the vaso-occlusive crisis, a hallmark event of the disease, where red cells obstruct the vasculature leading to pain episodes, organ damage, and tissue necrosis. In addition to acute complications, patients suffer from chronic pain, anemia, and infections severely limiting their health and lifestyle [4].

Despite improvements in patient clinical care over the past several decades, there is still a critical gap in optimizing treatments based on unique patient phenotypes, which are highly variable. Patient phenotypic diversity is a cause of clinical concern as available treatment options respond differently among patients and few, if any, known clinical parameters predict treatment efficacy [5]. This dearth of effective biomarkers has also severely hampered development of new therapies with only two drugs approved for clinical use in the last 20 years. One promising approach is to quantify the changes in blood rheology under conditions that are relevant in vivo and under treatment. Because the blood rheology is directly linked to the pathophysiology, rheological parameters may provide a set of metrics that is patient-specific to allow for individualized treatments.

In this work, we have developed a microfluidic system to quantify oxygen-dependent rheology for SCD blood. Our microfluidic system incorporates physiologically relevant blood flow velocity, oxygen tension response, and blood pressure, all of which may contribute to pathology in vivo. We present new quantitative metrics that may serve as biomarkers to categorize patient severity, and we demonstrate the application of our platform and metrics to evaluate transfusion therapy.

METHODS

Device Design: We developed a microfluidic platform mimicking physiological features of the vascular microenvironment to investigate SCD blood impairment process. The platform is a trilayer polydimethylsiloxane (PDMS) construct sub-sectioned into a bypass and experimental zone to prevent blood packing. The blood layer consists of an arteriole/venule sized channel with a cross-sectional area of 15 μm by 15 μm. The hydration layer is 100 μm tall and prevents blood dehydration at experimental temperature of 37°C. The gas layer is 150 μm tall and each zone has independent gas control diffusively coupled to the blood layer to control oxygen concentrations (Figure 1).

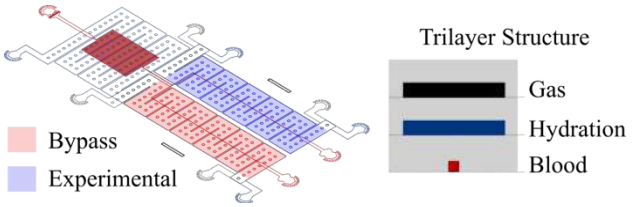

Figure 1: Microfluidic system for studying sickle blood flow consisting of a blood layer (red), hydration layer (blue), and gas layer (black).

Oxygen Transport Modeling and Validation: A COMSOL model was generated to verify oxygen diffusion in the device design. The device was modeled as a PDMS construct with diffusion coefficient of 3.3×10^5 cm²/s and fluid layers using the diffusion coefficient of 4×10^5 cm²/s. Device external walls were modeled as oxygen supply zones at

160 mmHg oxygen tension except the bottom wall which was modeled as a no flux region to represent the glass slide device is bonded to. Model result analysis shows that oxygen tension reached 0 mmHg in experimental zone while bypass section stayed at 160 mmHg (Figure 2A). To experimentally verify oxygen concentrations in the device, a solution with oxygen sensitive dye at 1 mM Ru(bpy)3 phosphate-buffered saline (PBS) was perfused through the blood channel of the microfluidic device. As a 0 mmHg oxygen control, 1 mM Ru(bpy)3 with sodium metabisulfite (SMS) oxygen scavenger at saturating concentrations was used for calibration. Experimental verification revealed similar findings as our modeling results (Figure 2B).

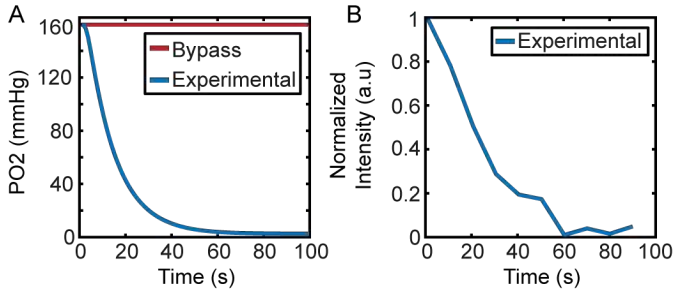

Figure 2: COMSOL oxygen transport modeling (A) and experimental validation (B) shows oxygen temporal response takes approximately 60 seconds to reach 0 mmHg after switching oxygen supply in experimental section while bypass section remains unaltered at 160 mmHg.

Blood Testing Setup: To measure blood rheological properties, microfluidic device was mounted on a microscope setup capable of controlling temperature, oxygen tension, and blood perfusion as previously described [6]. Video data was collected using a high-speed camera and analyzed using a custom MATLAB script.

RESULTS

Flow behavior index reveals a functional change in the blood rheology under hypoxic conditions: We quantified device impedance with whole sickle blood across 9 unique SCD patient samples, 3 oxygen tensions (92 mmHg, 46 mmHg, and 0 mmHg), and a range of pressure biases. Using a circuit model of the device, we extracted apparent viscosity from the impedance data, and we applied a power law fluid model to determine the flow behavior index, which indicates the deviation of the fluid from a Newtonian model. We found that at 92 and 46 mmHg oxygen tension, the flow behavior index is respectively 0.74 ± 0.075 and 0.76 ± 0.049 indicating a shear thinning fluid common for blood (mean ± SD). At 0 mmHg however, a transition occurs were the value goes to 0.87 ± 0.056 indicating a loss of shear thinning behavior (Figure 3A).

Flow behavior index can be used to identify clinical transfusion targets: Transfusion therapy is among the most common treatments for SCD patients and works by diluting SCD red cells with normal, healthy donor cells. A recurring issue with this treatment is that patients can develop alloimmunity and/or iron overload and thus each patient should be transfused to the minimal target for clinical efficacy, but no patient-specific metric exists to predict an effective target. To evaluate the ability of our system to identify clinical targets, we simulated transfusion therapy by mixing type-matched genotype healthy donor blood with SCD at the following ratios (indicated as SS blood percentage/AA blood percentage): 100/0, 70/30, 30/70, 10/90, and 0/100 and evaluated the rheological response of the blood to varying oxygen and blood pressure. We found that at or below a 30/70 mix, the flow behavior index is similar at all oxygen tensions indicating therapeutic efficacy (Figure 3B).

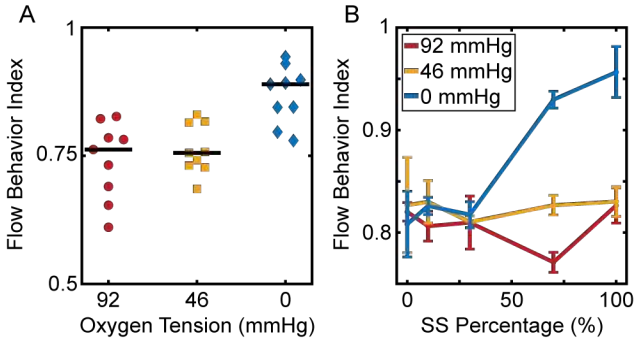

Figure 3: A). Flow behavior index of 9 samples shows sickle blood loses shear thinning behavior as oxygen tension decreases below 46 mmHg. B). Simulated transfusion experiment reveals the potential of using the flow behavior index to identify patient specific transfusion target values.

DISCUSSION

There is a significant need to identify markers which can help predict and understand SCD patient diversity as well as models to better test and characterize therapeutics. In this study, we introduce a new microfluidic platform capable of quantifying SCD blood rheology, and we reveal a rheological metric, the flow behavior index, that is highly sensitive to oxygen tension and putative therapy and appears to be patient specific. We discover that SCD blood undergoes a transition which occurs below 46 mmHg oxygen tension to a fluid that expresses decreased shear thinning behavior. This quantitative metric allows characterization of blood response to oxygen tension and possibly permits identification of patients who are at increased risk to develop complications. In addition to identifying potential clinical markers, our platform was used to characterize a simulated transfusion therapy. We successfully tested and were able to identify target transfusion therapy values that limit the flow behavior index dependency on oxygen tension and potentially predict clinical efficacy. Thus, we have demonstrated the potential to use this assay to predict patient-specific transfusion targets.

Overall, our work has the potential to better address the needs of SCD patients via quantification of blood flow mechanics. The microenvironment where SCD complications occur, however, is complex, and gleaning clinically relevant information from simplified systems remains a challenge. Nonetheless, the model system and metrics presented here show promise to aid in our efforts to understand patient diversity, predict clinical prognosis, and develop new therapies.

ACKNOWLEDGEMENTS

This work was supported by the National Heart, Lung, and Blood Institute (NHLBI) under grants R21HL130818, R56HL132906, and R01HL132906. Portions of this work were conducted in the Minnesota Nano Center, which is supported by the National Science Foundation through the National Nano Coordinated Infrastructure Network (NNCI) under Award Number ECCS-1542202.

REFERENCES

[1] Bunn, FH., *New England Journal of Medicine*, 337:762-769, 1997
[2] Li, X et al., *J. Biomech*, 50: 34-41, 2017
[3] Barabino, GA et al., *Annu Rev Biomed Eng*, 12: 345-367, 2010
[4] Rees, DC et al., *The Lancet*, 376: 2018-31, 2010
[5] Steinberg, MH., *British Journal of Haematology*, 129:465-481, 2005
[6] Lu, X et al., *Biophys. J*, 110: 2751-58, 2016

SB³C2019
Summer Biomechanics, Bioengineering and Biotransport Conference
June 25 -28, Seven Springs, PA, USA

INSTABILITY OF PHOSPHOLIPID BILAYER UNDER SHEAR FLOW: MOLECULAR DYNAMICS SIMULATION

Taiki Shigematsu (1), Kenichiro Koshiyama (2), Shigeo Wada (3)

(1) Global Center for Medical Engineering and Informatics
Osaka University
Suita, Osaka, Japan

(2) Graduate School of Technology, Industrial and Social Sciences
Tokushima University
Tokushima, Tokushima, Japan

(3) Graduate School of Engineering Science
Osaka University
Toyonaka, Osaka, Japan

INTRODUCTION

Biological cells are known to respond to flow fields around them and change their activities in the physiological environment. In contrast, non-physiological high shear flow generated by medical or engineering devices, e.g., ventricular-assisted devices [1], jet injectors [2], and microfluidic cell sorters [3], can induce a rupture of the cell membrane and subsequent cell death. For the development of such the devices, it is essential to understand the mechanism of the membrane rupture and control it. However, as the details of the membrane rupture are elusive in experiments, its mechanism is not fully understood.

Many experiments and numerical simulations have been conducted on biological cells under shear flow [4,5]. These studies have shown that the cells, e.g., red blood cells, are elongated and the membrane tension increases under shear flow. When the tension exceeds the limit of the membrane, the membrane rupture may occur. This is the *common* mechanism of the membrane rupture under shear flow. On the other hand, the molecular dynamics (MD) simulation study [6] has shown that the Kelvin-Helmholtz-like instability of the phospholipid bilayer, which is the fundamental structure of the cell membrane, can occur under high shear flow. This hydrodynamic instability immediately leads to the membrane rupture. Compared to the tension-induced rupture, the details of the hydrodynamic-instability-induced rupture are less understood.

In this study, in order to understand the hydrodynamic-instability-induced rupture of the phospholipid bilayer under shear flow, we performed MD simulations of phospholipid bilayers under high shear flow and explained the underlying mechanism of instability at the molecular level in the frameworks of linear stability analysis.

METHODS

System We employed three dipalmitoylphosphatidylcholine (DPPC) bilayer systems in rectangular simulation box with periodic boundary conditions. To model molecules, we used the MARTINI force field [7], which is a coarse-grained (CG) model suitable for semi-quantitative evaluation of lipid dynamics. The three systems were composed of 256 DPPC and 14,000 water, 512 DPPC and 28,000 water, and 768 DPPC and 42,000 water, respectively. The snapshots of the smallest system are shown in Fig. 1A. The systems were well-equilibrated by at least 1-μs MD simulation at a constant temperature (323 K) and pressure (0.1 MPa). The sizes of the simulation boxes (l_x, l_y, l_z) were 12.8×6.3×25.3, 25.4×6.3×25.3, and 37.9×6.3×25.5 nm^3, respectively.

MD Simulation under Shear Flow In the shear simulation, the systems were divided into 1-nm-bins in the *z*-direction (Fig. 1A). To keep the temperature of the system under shear flow, the temperature of molecules in each bin is separately kept constant (323 K). The velocities of water in the top and bottom bins (shown in red in Fig. 1A) were respectively set to (v_x, 0, 0) and (-v_x, 0, 0) during the shear simulation to express the shear flow. The shear rate $\dot{\gamma}$ was defined as $\dot{\gamma} = 2v_x/(l_z - 2)$. The velocity difference between the bilayer Δu was defined $\Delta u = \dot{\gamma} l_t$, where l_t was the thickness of the bilayer. The shear simulations were performed at a constant temperature and volume condition for 200 ns. Because of the statistical nature of the bilayer rupture [8], we performed three replicates of the shear simulations, starting from different initial configurations, for each system and each shear rate condition.

Linear Stability Analysis Let us consider a water bath divided by an interface consisting of a phospholipid bilayer, which is thin enough to neglect its thickness (see Fig. 1B). We assume a uniform displacement along the *y*-direction and the water as the incompressible inviscid fluid. The velocities and densities of water in the upper and lower regions are constant except on the interface and denoted as u_u, u_l, ρ_u, and ρ_l, respectively. For the deformation energy of the bilayer, we use the Helfrich Hamiltonian *F* [9],

$$F = \int \left\{ \sigma + \frac{1}{2} k_c (c_1 + c_2 - 2c_0)^2 \right\} dA, \quad (1)$$

where σ and k_c are the tension and the bending modulus of the bilayer, respectively. c_1 and c_2 are principal curvatures, and c_0 is the spontaneous curvature. dA is the surface element. As a result of a conventional linear stability analysis with equation (1) [10], we can obtain a stability criterion as

$$|\Delta u| < \sqrt{\frac{4\pi}{\rho}\left(\frac{\sigma}{\lambda} + \frac{4\pi^2 k_c}{\lambda^3}\right)}, \quad (2)$$

where λ is the wave length of bilayer undulation and $\Delta u = u_u - u_l$. Additionally, we assume $\rho = \rho_u = \rho_l$ and $c_0 = 0$. In the MD simulation here, the water density ρ is 986 kg/m^3, and tension σ is 0 mN/m. Because of the considerable variation of the bending modulus k_c reported in previous simulation and experimental studies [11-13], we use various k_c in the range from 4.0×10^{-20} to 12.8×10^{-20} J.

RESULTS

Representative snapshots of the largest bilayer system under shear flow are shown in Fig. 2. When the applied shear rate is below a critical level, the bilayer maintains its continuous structure with undulation during the shear simulation. Conversely, above a critical level, the bilayer undulation suddenly starts to be larger (Fig. 2B-D) and the bilayer is torn (ruptured) (Fig. 2E). The relationship between the velocity difference calculated from the shear rate and the maximum wave length of the bilayer undulation in the system is shown in Fig. 3. The maximum wave length corresponds to the system box length in the flow direction l_x. The critical velocity difference $|\Delta u_c|$, where the bilayer rupture occurs, (which expected to be between green circle and red cross in Fig. 3) tends to decrease with increasing the wave length. The stability criterions calculated from equation (2) with various k_c are also plotted in Fig. 3. The tendency, $|\Delta u_c|$ decreases with λ, obtained from the MD simulations agrees with the theoretical prediction.

DISCUSSION

In our MD simulation, we observed the hydrodynamic instability of the bilayer and subsequent bilayer rupture (Fig. 2) as with the previous MD simulation study [6]. The hydrodynamic-instability-induced bilayer rupture observed here was successfully explained by the linear stability analysis for the macroscopic fluid-fluid interface divided by a thin membrane with the Helfrich Hamiltonian (Fig. 3).

The critical velocity difference $|\Delta u_c|$, where the bilayer rupture occurs, is estimated to be in the range from 10^1 to 10^2 m/s (Fig. 3), which corresponds to the shear rate in the range from 10^9 to 10^{10} s^{-1}. One may think that such the shear flow in the nanometer scale is extremely drastic and the instability might not occur except in highly specific situations. According to the equation (2), the larger λ, the smaller $|\Delta u_c|$. Thus, for example, $|\Delta u_c|$ in the micrometer scale (1-10 μm), which corresponds to the typical length scale of a single cell, is estimated to be about 3-5 orders of magnitude smaller than that in nanometer scale here (~10 nm). This implies that the shear-induced instability might occur in the larger membrane, e.g., the membrane of a single cell, under much lower shear rate. However, it must be noted that great care is required to discuss the instability in the cell membrane in more detail because of some assumptions in the MD simulation and the theory and the difference between the mechanical characteristics of the phospholipid bilayer and actual cell membranes.

ACKNOWLEDGEMENTS

This work was supported by JSPS KAKENHI Grant Number 17K13033.

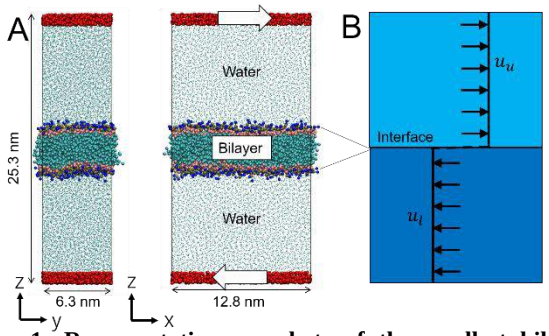

Figure 1: Representative snapshots of the smallest bilayer system (A). Schematic representation of the water bath divided by the bilayer for the linear stability analysis (B).

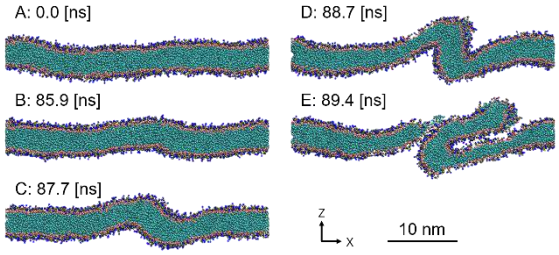

Figure 2: Representative snapshots of the largest bilayer system under shear flow $\dot{\gamma} = 9.0\times10^9$ s^{-1}.

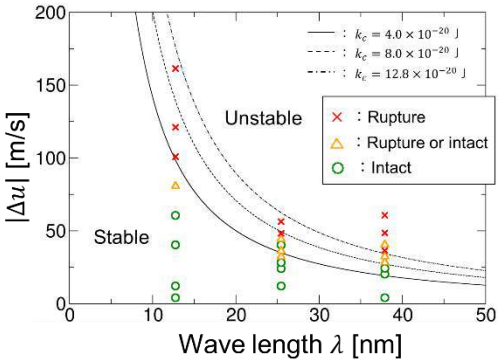

Figure 3: The relationship between the velocity difference and the maximum wave length of the bilayer undulation (system box size). Symbols show the MD simulation results and the curves are calculate from equation (2) with various k_c.

REFERENCES

[1] Deutsch, S. et al., *Annu. Rev. Fluid Mech.*, 38:65-86, 2006.
[2] Cheng, J.H. et al., *J. Control. Release*, 211:37-43, 2015.
[3] Fu, A.Y. et al., *Nat. Biotechnol.*, 17:1109-1111, 1999.
[4] Yaginuma, T. et al., *Biomicrofluidics*, 7:054110, 2013.
[5] Omori, T. et al., *Phys. Rev. E*, 86:056321, 2012.
[6] Hanasaki, I. et al., *Phys. Rev. E*, 82:051602, 2010.
[7] Marrink, S.J. et al., *J. Phys. Chem. B*, 111:7812-7824, 2007.
[8] Shigematsu, T. et al., *Sci. Rep.*, 5:14369, 2015.
[9] Helfrich, W., *Z. Naturfirsch*., 28:693-703, 1973.
[10] Komura, S. and Iwayama, T., *J. Phys. II France*, 7:1331-1335, 1997.
[11] Marrink, S.J. et al., *J. Phys. Chem. B*, 108:750-760, 2004.
[12] Shkulipa, S., Ph.D. thesis, University of Twente, The Netherlands, 2006.
[13] Nagle, J.F., *Chem. Phys. Lipids*, 205:18-24, 2017.

SB³C2019
Summer Biomechanics, Bioengineering and Biotransport Conference
June 25 -28, Seven Springs, PA, USA

COMPUTATIONAL SIMULATIONS OF THROMBOLYTIC THERAPY IN ACUTE ISCHAEMIC STROKE

Boram Gu (1), Andris Piebalgs (1), Yu Huang (1), Dylan Roi (2), Kyriakos Lobotesis (2), Rongjun Chen (1), Simon A. Thom (3), Xiao Yun Xu (1)

(1) Department of Chemical Engineering, Imperial College London, South Kensington Campus, London, United Kingdom

(2) Imaging Department, Charing Cross Hospital, Imperial College Healthcare NHS Trust, London W6 8RF, United Kingdom

(3) National Heart & Lung Institute, Imperial College London, Hammersmith Campus, London, United Kingdom

INTRODUCTION

Acute ischaemic stroke occurs when a blood clot blocks a cerebral artery that supplies nutrient and oxygen to the brain. Thrombolytic therapy is used to dissolve the blood clot, which involves a clot-dissolving drug, such as recombinant tissue-type plasminogen activator (tPA). Although less invasive than mechanical thrombectomy, thrombolytic therapy can be ineffective in certain clinical scenarios and is currently limited to a subset of patients due to the risk of bleeding complications. In order to evaluate the effectiveness of thrombolytic therapy in different clinical settings, we have developed a computational model for thrombolysis in acute ischaemic stroke [1]. Among many factors that influence the effectiveness of thrombolytic treatment, the size and location of the clot are associated with the likelihood of successful recanalisation and clinical outcomes. By using a recently developed computational framework for thrombolytic therapy, we have simulated a number of clinically relevant scenarios to investigate the effects of clot size and location on clot lysis dynamics and recanalization upon intravenous thrombolysis using tPA.

METHODS

Three-dimensional (3D) Patient-specific Geometry A 3D patient geometry is reconstructed from MR images using Mimics 19.0 (Materialise, Leuven). Figure 1 shows the patient-specific geometry used in this study, which includes the internal carotid bifurcation into the A1 segment of anterior cerebral arteries (ACA) and the M1 segment of middle cerebral arteries (M1), as well as the M1 bifurcation into the M2 segments (M2-1 and M2-2). Clot regions numbered 1 to 7 are artificially assigned in the M1 segment and the M2 inferior branch (M2-1). The smallest clot in M1 and M2 is represented by Clot 1 and Clot 5, respectively. By adding the subsequent regions, the clot size in each branch can be increased. Furthermore, a very long clot extending from region 1 in M1 to region 7 in M2-1 can also be simulated by including the region of M1 bifurcation as shown in Figure 1.

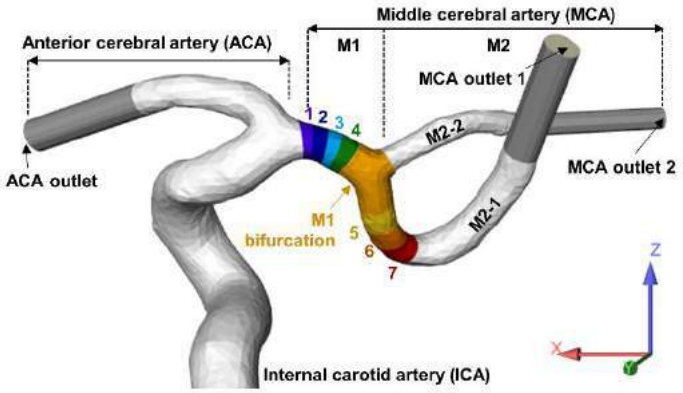

Figure 1: The patient-specific geometry used in this study.

Description of Mathematical Model Our computational model incorporates multiscale physical and biochemical phenomena, including models for (i) blood flow, (ii) species transport, (iii) fibrinolytic reactions and (iv) estimation of clot properties [1]. The macroscopic transport phenomena, i.e., blood flow and species transport of key proteins (tPA, plasminogen, plasmin and anti-plasmin), are described by the modified Navier-Stokes equations with the Darcian momentum source term and the convection-diffusion-reaction equations, respectively. Reaction rates are calculated from the fibrinolytic reaction kinetics, which also affect the clot properties and consequently the Darcian momentum source term. A three-element

Windkessel model is coupled with the Navier-Stokes equations for physiological pressures at each outlet. A compartmental model for systemic concentrations of fibrinolytic proteins is solved to provide inlet boundary conditions for the convection-diffusion-reaction equations. For the estimation of clot properties and reactions kinetics of thrombolysis, the clot is assumed to be composed of a fibrin fibre network alone, ignoring the presence of any cellular components.

These model equations are implemented in an open source computational fluid dynamics (CFD) code, OpenFOAM 4.0. Computations are performed using High Performance Computing (HPC) facilities (Imperial College Research Computing Service [2]).

RESULTS

Here we present flow and clot lysis patterns of two representative scenarios with the largest clot in each occlusion site, when an initial bolus is administered at Time = 60 s. Figure 2 shows flow velocity and clot resistance for the M1 (top) and M2 (bottom) clots at two time points, which correspond to Clot 1-4 and Clot 5-7 in Figure 1, respectively. For both scenarios, there is no visible flow in the occluded branch at Time = 150 s, due to high initial clot resistance of 1.8×10^{13} m^{-2} (= permeability of 5.6×10^{-14} m^2). The clot starts to degrade from its front, followed by gradual reduction in clot resistance and consequently reduced clot volume during clot dissolution. It is noticed in the M2 clot that there is a large stagnation zone between the M1 bifurcation and the clot front at Time = 150 s, unlike in the M1 clot. This is because the M2 clot is positioned distal to the M1 bifurcation, which results in a slower penetration of tPA and hence a delayed degradation of the M2 clot than the M1 clot. A breakthrough path is established at around 360 s and 470 s for the M1 and M2 clots, respectively. This results in a high-velocity jet, allowing convective transport of tPA to become dominant thereafter.

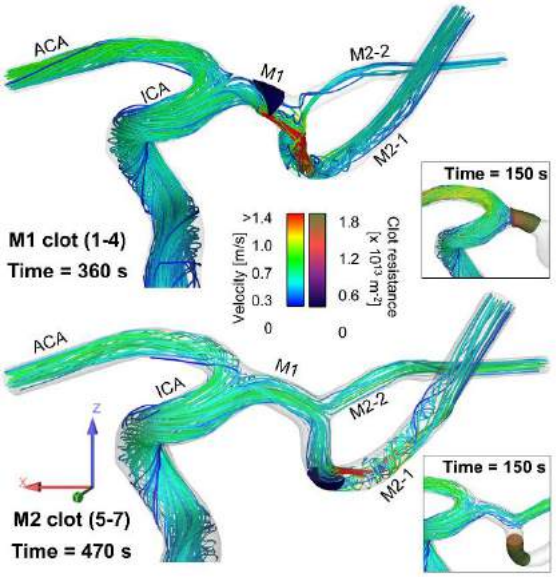

Figure 2: Flow and clot lysis patterns for the largest clots in each occlusion site: M1 clot (top) and M2 clot (bottom).

Simulation results for different clot sizes and locations are compared in Figure 3 in terms of changes in clot volume over time. While reduction in clot volume starts at around 5.5 mins for all clots, complete lysis takes between 5.5 to 9 mins depending on the clot size and location. A general trend is that smaller clots dissolve faster, as expected. When comparing different locations for clots of a similar size, clots in the M2 segment tend to take longer to dissolve than those in the M1 segment, e.g., C1-2 vs C5 and C1-3 vs C5-6. This can be explained by the large stagnation zone initially formed between the M1 bifurcation and the clot front, as in Figure 1, which slows down the transport of tPA in that region.

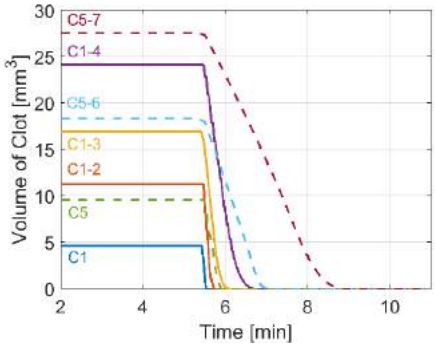

Figure 3: Change in clot volume over time.

DISCUSSION

Our results for lysis patterns show that the lysis front is asymmetric due to the curvature of the blood vessel. Interestingly, faster lysis occurs always from the inner curvature of the vessel due to the presence of recirculation zone and accordingly prolonged residence time of tPA there. As a result, a breakthrough pathway is established at the fast dissolving side, allowing a high-velocity jet to pass through. As clot lysis is accelerated by the convective transport of tPA, flow in the blocked branch is reestablished rapidly before the obstructive clot is completed dissolved.

Comparisons of results for all the simulated scenarios suggest that clots in the M2 segment need a longer time for complete dissolution than those in the M1 segment, mainly due to the presence of a stagnation zone near the front of M2 clots. However, clinical studies reported that distal occlusion is more likely to achieve recanalisation success and a good clinical outcome than proximal occlusion [3]. This is because of the size of distal clots being smaller than proximal ones [3]. Based on our simulation results and clinical observations, we can conclude that recanalisation times are strongly influenced by the size of clots, which is location dependent, and the distance between the clot and its adjacent bifurcation.

In summary, our simulation platform for thrombolysis in ischaemic stroke can offer an in-depth understanding of drug transport and clot lysis under various clinical scenarios. We have validated the predicted temporal concentration profiles for fibrinolytic proteins against available in vitro experimental data, demonstrating satisfactory agreement. However, the predicted recanalization time appears to be shorter than clinical observations [4] due to the assumption of a fibrin only clot with a high initial permeability. Further improvement of the model is underway to incorporate the presence of cellular components in the clot, and to simulate a new tPA delivery system for targeted thrombolytic therapy.

ACKNOWLEDGEMENTS

This research was supported by the National Institute for Health Research (NIHR) Biomedical Research Centre based at Imperial College Healthcare NHS Trust and Imperial College London.

REFERENCES

[1] Piebalgs, A et al., *Scientific Reports* 2018; 8:15810.
[2] Imperial College Research Computing Service, DOI: 10.14469/hpc/2232
[3] Friedrich, B et al., *Stroke* 2015; 46:692–691
[4] Alexandrov, A V et al., *Circulation* 2001; 103:2897–902.

SB³C2019
Summer Biomechanics, Bioengineering and Biotransport Conference
June 25 -28, Seven Springs, PA, USA

COMBINED MICROFLUIDIC-COMPUTATIONAL APPROACH TO QUANTIFY THE EFFECT OF SICKLE-CELL DISEASE ON BLOOD RHEOLOGY

Marisa S. Bazzi (1), José M. Valdez (2), David K. Wood (2), Victor H. Barocas (2)

(1) Department of Chemical Engineering and Material Science
University of Minnesota
Minneapolis, MN, USA

(2) Department of Biomedical Engineering
University of Minnesota
Minneapolis, MN, USA

INTRODUCTION

Sickle cell disease (SCD) is a genetic disorder that affects millions of people around the world. In SCD, hypoxia causes intracellular polymerization of the sickle hemoglobin, leading to increased stiffness and morphological changes in red cells. The changes in red cell biomechanics subsequently cause increased blood viscosity and can even completely obstruct blood flow in the microcirculation. Impaired and occluded flow lead to tissue ischemia and necrosis, chronic infections, severe pain, stroke, and even sudden death in rare cases [1].

Even with this conceptual understanding of the disease etiology, we are still unable to predict which patients will experience the most severe symptoms or which patients will respond best to which treatments. Previous studies have shown that patient clinical outcomes, including response to treatment, are strongly correlated with changes in the apparent viscosity of whole blood under hypoxic conditions [2,3]. Our ability to build predictive models from these data sets is limited, however, because the parameter space of clinical conditions is far too large to sample experimentally.

Mathematical modeling associated with experimental data can provide a reliable way to probe a much larger parameter space with the goal of building a predictive model that is applicable to a broader set of patient-specific variables as well as treatment conditions. Here, we modeled blood as a non-Newtonian fluid, evaluated the changes in apparent viscosity as a function of oxygen tension for a fixed drop in blood pressure, and parameterized the model based on experimental results using a microfluidic blood viscometer.

METHODS

Blood Rheology: Discarded whole blood from patients with sickle cell disease (SCD) and from normal, healthy individuals was collected at the University of Minnesota Medical Center and Massachusetts General Hospital. To characterize the blood's rheological properties, a microfluidic blood viscometer was mounted on a temperature-regulated microscope and blood was perfused using an electronic pressure regulator. Blood oxygen tension was controlled using a previously developed solenoid valve gas mixing setup [4]. Video data were collected using a high-speed camera and analyzed using a custom MATLAB script that implements the Kanade-Lucas-Tomasi feature tracking algorithm. An example data set is shown in Fig. 1.

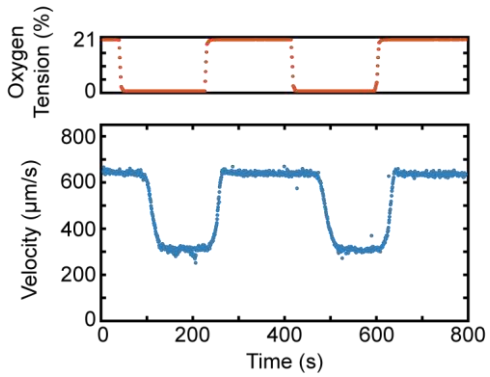

Figure 1: Velocity tracking data of an SCD sample shows response to oxygen tension cyclical modulation between high oxygen (21%) and low oxygen (0%).

Mathematical Flow Modeling: For the mathematical model, the flow is considered to be parallel, fully developed, isothermal, steady flow in a rectangular channel. The momentum conservation law under these assumptions is described by Eq. 1.

$$-\nabla p + \nabla \cdot (\eta \dot{\gamma}) = 0 \quad (1)$$

where p is the mechanical pressure, $\dot{\gamma}$ is the rate of strain tensor, and η is the apparent viscosity of blood.

Blood was expressed as a non-Newtonian fluid by using Carreau-Yasuda model [5]. In this model, the viscosity is a function of the rate of strain as given by Eq. 2.

$$\eta = \eta_\infty + (\eta_0 - \eta_\infty)\left[1 + \left(\frac{\dot{I}I}{\dot{I}I_0}\right)^a\right]^{-\frac{1-n}{a}} \quad (2)$$

Here $\dot{I}I$ is the second invariant of the rate of strain tensor, and η_∞, η_0, $\dot{I}I_0$, a, and n are material parameters that are adjusted based on the experimental data.

Equation 1 was solved using a second-order Finite Difference Method to discretize the spatial derivatives. The resulting nonlinear algebraic system of equations is solved using Newton-Raphson iteration method. Model parameters were adjusted manually to fit the data.

RESULTS

Figure 2 shows the axial (z) velocity profile within the channel for high oxygenation (right) and low oxygenation (left) blood level. As expected, the velocity field was symmetric and had a maximum along the channel centerline.

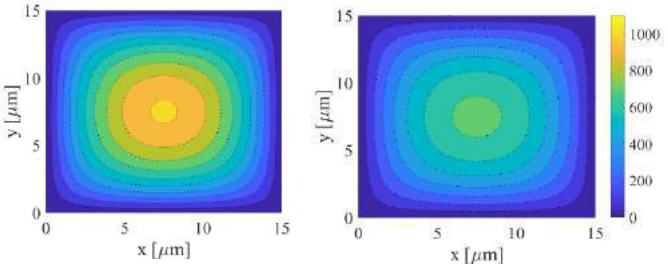

Figure 2: Velocity profile along the transverse direction of the capillary for oxygen tension equal to 21% (left) and 0% (right). Blood is considerably faster in high-O_2 case. Scales has applied to both cases.

Figure 3 compares the numerical simulation results (solid line) with experimental data (open circles) for SCD (right) and healthy (left) blood. The computed velocity $u_z(x, y)$ from Fig. 2 was averaged over y direction to simulate the experimental measurement of y-averaged velocity from the video. As the oxygen tension is reduced, the velocity decreased for SCD blood. Conversely, for the healthy cells the mean velocity shows negligible variation.

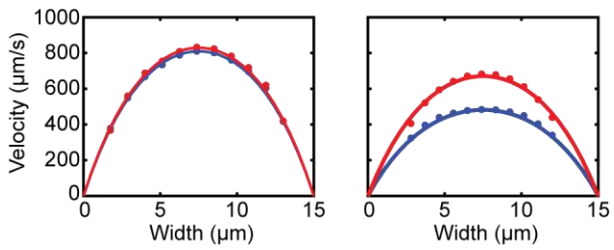

Figure 3: Mean velocity along transversal direction for healthy (left) and SCD (right) blood at 21% (red) and 0% (blue) of oxygen tension. Open circles are experimental data and solid lines are numerical simulations results.

Table 1 shows the parameters values associated with the model results in Fig. 3. Certain features are notable. First, $\dot{I}I_0$was quite large (720+ s^{-1}) when compared with the shear rate in the channel (maximum of 610 s^{-1}), indicating that the flow is close to Newtonian an d the viscosity well approximated by η_0. Second, consistent with the reduced flow rate of SCD blood, η_0 was larger for SCD blood than for healthy blood, and for SCD blood, η_0 increased when oxygen was removed.

Table 1: Parameter values for SCD and healthy blood.

O2 Tension	$\dot{I}I_0(s^{-1})$	$\eta_0\ (cP)$	$\eta_\infty(cP)$	a	n
SCA 21%	720	3.6	1.5	5	0.6
SCA 0%	1200	4.9	2.3	5	0.8
Healthy 21%	10000	2.1	1.1	5	0.5
Healthy 0%	10000	2.05	1.0	5	0.5

DISCUSSION

The dependence of SCD blood viscosity on oxygen tension was studied by correlating mathematical modelling and simulation with experimental data from human SCD blood. Viscosity was described by the Carreau-Yasuda model, where the material parameters were manually adjusted to fit with the experimental data. The velocity profile obtained by Carreau-Yasuda viscosity model shows good agreement with the experimental observation. Results show that deoxygenation increase the viscosity of the SCD blood, leading to the change in the velocity profile observed experimentally. For healthy blood, no significant alteration was observed. Under the conditions studied, it appears that a Newtonian model would have described the flow accurately, but we choose the Carreau-Yasuda model to maintain flexibility and robustness in future studies.

The major contribution of our work is in develop a method that convert experimental data from a well-controlled in-vitro study in a computational model that could be extended to relevant in vivo geometries and conditions. Specifically, the parameters of Table 1 (possibly drawing in more data to define $\dot{I}I_0$, etc.) as a basis for Finite-Element Simulation of non-Newtonian SCD blood flow in the microvasculature.

ACKNOWLEDGEMENTS

Portions of this work were conducted in the Minnesota Nano Center, which is supported by the National Science Foundation through the National Nanotechnology Coordinated Infrastructure (NNCI) Network under Award Number ECCS-1542202. This work was supported by the NHLBI under Grants R21HL130818 and R01HL132906.

REFERENCES

[1] Bunn, FH., *New England Journal of Medicine*, 337:762-769, 1997
[2] Wood, DK et al., *Science Translational Medicine*, 4.123 (2012)
[3] Li, X et al. Interface Focus 6.1 (2016): 20150065.
[4] Lu, X et al. Biophysical journal 110.12 (2016): 2751-2758.
[5] Yasuda, K. Y et al Rheologica Acta 20.2 (1981): 163-178.

MECHANICAL CHARACTERIZATION OF ATHEROSCLEROTIC CORONARY ARTERIES BY EX-VIVO INFLATION TESTING AND INVERSE FINITE ELEMENT MODELING

Su Guvenir (1), Giulia Gandini (1,2), Irene Berselli (1,2), Veronica Codazzi (1,2), Francesco Migliavacca (2), Claudio Chiastra (2), Frank J.H. Gijsen (1), Ali C. Akyildiz (1)

(1) Department of Biomedical Engineering, Erasmus Medical Center, Rotterdam, the Netherlands

(2) Department of Biomedical Engineering, Politecnico Di Milano, Milan, Italy

INTRODUCTION

Atherosclerotic plaque rupture, a major cause of stroke and myocardial infarction [1], was shown to correlate with high structural plaque stresses [2]. Hence, plaque stress analyses are of great value as they can aid plaque rupture risk assessment. Plaque stresses can be obtained with finite element (FE) modeling, where correct representation of the plaque material properties is of great importance for the accuracy of the stress results [3]. However, this essential information on plaque material properties is still majorly lacking [4].

This work aims assessing human coronary plaque material properties. In this study, ex-vivo inflation tests, which mimic the in-vivo loading conditions, were performed with excised atherosclerotic human coronaries, and test results were analyzed with inverse FE modeling (iFEM) for component-wise plaque properties.

METHODS

Ex-vivo inflation testing

Ten atherosclerotic coronary arteries were collected post-mortem at Erasmus Medical Center (MC). The intact atherosclerotic human coronary samples were mechanically tested in an ex-vivo inflation setting, which imposes mechanical loading and boundary conditions closely mimicking the physiological ones. Samples were tested in phosphate buffered saline at 37°C, after ten cycles of mechanical preconditioning of 20% axial stretch and intraluminal pressurization between 0 to 80 mmHg. During the tests intraluminal pressure was increased quasi-statically in increments of 10 mmHg up to 120 mmHg.

During the inflation, the samples were imaged with a high frequency ultrasound (US) system (Vevo 2100, VisualSonics Inc.) using a linear array probe (MS550S) with a center frequency of 40 MHz (Fig. 1). Raw radiofrequency (RF) US data were collected at preselected cross-sections (~ 3 per artery) at each pressure step.

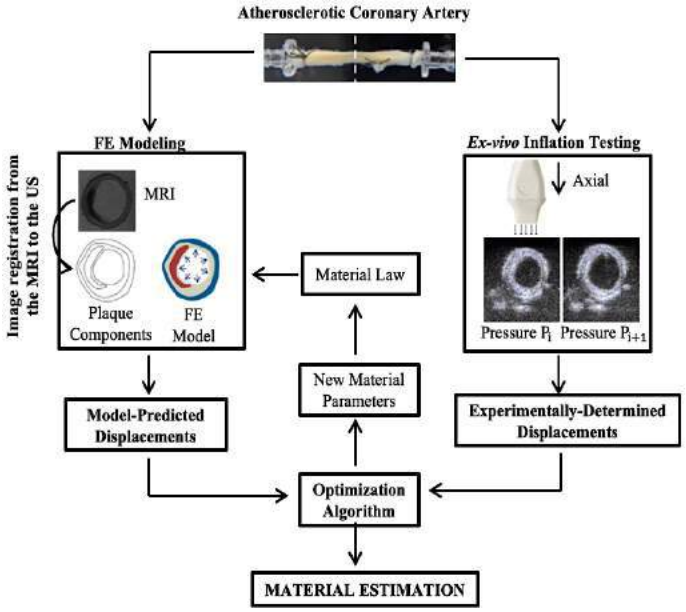

Figure 1: The protocol for plaque mechanical characterization including MRI, inflation testing, US measurements & iFEM.

Full-field plaque deformation measurements

The acquired RF US data was analyzed to assess the full-field deformation on the plaque cross-sections during inflation testing. The in-plane displacements were obtained with a coarse-to-fine 2-D cross-correlation method in three iterations. A median filter of 5 x 5 displacement pixels was applied after each iteration to decrease the

amount of outlying displacement values. The final spatial resolution for the displacement estimates was 15 μm in axial direction (along the US probe) and 55 μm in the lateral direction (across the probe) [5]. This technique was used before for the high-frequency US scanners, for the first time, by our group for porcine iliac arteries [6].

MRI acquisitions

The essential plaque composition and morphology information for the FE models plaque geometry was acquired from high resolution magnetic resonance imaging (MRI) with a 7T, high field scanner (General Electric, Connecticut, USA). MRI scans were performed before the inflation tests and the acquired multi-sequential (T1, T2 and proton density weighted) images were segmented for the arterial wall, fibrous intima, lipid pool and calcifications (Fig. 2). The segmented MRI images were co-registered to US data by using the medical image registration software *elastix* [7] (Fig. 1).

Figure 2: T1, T2 & PD weighted images of a plaque cross-section.

Inverse finite element modeling (iFEM)

A 2-D FE model of each plaque cross-section was created to simulate the ex-vivo inflation testing. All tissue components within the FE model were assumed to be isotropic, and constructed as nearly incompressible Neo-Hookean solids, characterized with a single material parameter constant, C_1. A highly stiff material behavior for calcification and a compliant one for lipid were selected. The iFEM aimed to assess the material properties (C_1 values) of the fibrous intima and the arterial wall, hence they were not predefined. In the FE simulations, three intraluminal pressure steps, 1) from 10-80 mmHg, 2) 80-100 mmHg and 3) 100-120 mmHg were applied to mimic the inflation testing conditions. The simulations were performed in ABAQUS (Dassault Systèmes) under plane strain assumption.

The iFEM approach employed a grid search optimization algorithm, where at each iteration fibrous intima and arterial wall C_1 values were varied, FE model was rerun and root mean square error of the experimentally-measured and model-predicted displacements was calculated (Fig. 1). The C_1 values that resulted in the minimum error were accepted as the optimal estimations of the material properties. The optimization was performed for the three pressure steps (10-80 mmHg, 80-100 mmHg and 100-120 mmHg) separately.

RESULTS

Multi-sequential, high resolution (50 μm in-plane resolution) MRI images were obtained successfully for all 10 coronaries, allowing accurate plaque composition and morphology assessment through component-wise segmentation. Artery segments were successfully prepared for the inflation tests by removing the surrounding connective tissue, cannulation and closing the side branches, even the microscopic ones. The tests and US data acquisition were successfully performed by achieving stabilized pressure for all test samples for each pressure step, by preventing any leakage during pressurization.

In total, 26 cross-sections from the 10 coronary vessels were selected for further material characterization with iFEM. Of the 26 cross-sections, the material characterization of one cross-section has been completed. For the cross-section, iFEM achieved a satisfactory error minimization, where the relative differences between the experimentally-determined and model-predicted displacements were 5.7% for the pressure step (step 1) from 10 to 80 mmHg, 3.3% from 80 to 100 mmHg (step 2) and 2.1% from 100 to 120 mmHg (step 3). Accordingly, the C_1 values derived for the three pressure steps for the fibrous intima were 23,4 kPa, 77,1 kPa and 112.9 kPa, and for the arterial wall 16.7 kPa, 18.5 kPa and 16.7 kPa (Figure 3).

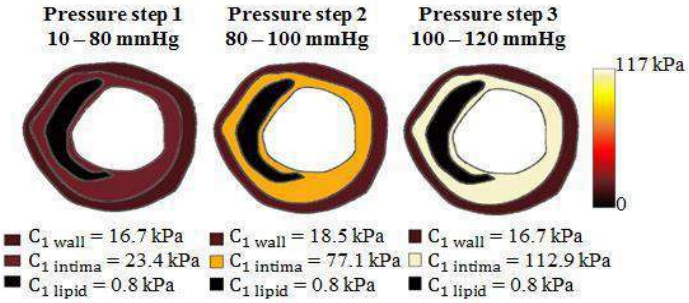

Figure 3: iFEM-estimated material properties of a cross-section.

DISCUSSION

We successfully developed a pipeline to obtain component-wise material properties of atherosclerotic arteries, by utilizing 1) an inflation testing, which employs the most physiological loading conditions ex-vivo and preserves the structural integrity of the artery, 2) high frequency US measurements, 3) high resolution MRI and 4) iFEM. By applying the developed iFEM pipeline successfully for the first vessel, the fibrous intima and the wall mechanical properties were estimated. The results successfully captured the nonlinear stiffening behavior and are in accordance with previously published data on atherosclerotic porcine iliacs [6] and for human arteries [2,8].

The currently-existing limitations of the study are planned to be addressed in the future steps of this work. More advanced hyper-elastic constitutive equations can capture the nonlinearity in a single pressure step simulation and even possibly further reduce the error achieved during the optimization process. Anisotropic constitutive laws can improve the results, which is possible to obtain with the developed pipeline as full-field deformation measurements are acquired. The future work will also include analyzing the remaining 25 cross-sections to obtain mechanical characteristics data of human atherosclerotic coronary plaque from a fairly sized sample population.

Although the developed approach is currently applied for ex-vivo mechanical testing, it holds the great potential to be used for in-vivo characterization as well. The plaque composition and geometry can be obtained similarly from MRI [9] and deformation measurements from US [10]. As such, the developed technique is promising to obtain patient-specific material properties in-vivo and aid rupture risk assessment.

ACKNOWLEDGEMENTS

This project has received funding from the European Commission's Horizon 2020 research and innovation programme under the Marie Skłodowska-Curie grant agreement # 749283.

REFERENCES

[1] Bentzon, J F et a., *Circ Res*, 114:1852-1866, 2014. [2] Cheng G C et al., *Circulation*, 87.4: 1179-1187, 1993. [3] Akyildiz A C et al., *Biomed Eng Online*, 10.1: 25, 2011. [4] Akyildiz A C et al., *J Biomech*, 47.4:773-783, 2014. [5] Lopata, R G P et al., *Ultrasound Med Biol*, 35.5:796-812, 2009. [6] Akyildiz, A C et al., *Ann Biomed Eng*, 44.4:987-979, 2016. [7] Klein, S et al., *IEEE Trans. Med Imaging*, 29:196-205, 2010. [8] Finet G et al., *Coron Artery Dis*, 15.1:13-20, 2004 [9] Yuan C et al., *J Magn Reson Imaging*, 19.6 (2004): 710-719. [10] Hansen HH et al., *Stroke*, 47(11):2770-2775, 2016.

SB³C2019
Summer Biomechanics, Bioengineering and Biotransport Conference
June 25 -28, Seven Springs, PA, USA

HISTOMECHANICAL ANALYSIS OF DECELLULARIZED PORCINE INTERNAL THORACIC ARTERIES

Colton J. Kostelnik (1), Wayne E. Carver (1,2), John F. Eberth (1,2)

(1) Biomedical Engineering Program
University of South Carolina
Columbia, SC, USA

(2) Department of Cell Biology and Anatomy
University of South Carolina
Columbia, SC, USA

INTRODUCTION

Contemporary coronary artery bypass grafting (CABG) uses autologous vessels to circumvent severely occluded regions of the vasculature to restore adequate cardiac perfusion [1]. Often patients with advanced coronary artery disease lack suitable graft tissues and many of these will undergo multiple bypass procedures [1,2]. Thus, a pressing-need exists for the generation of alternative bypass options. Whereas small caliber synthetic grafts experience thrombus formation and restenosis, tissue-engineered blood vessels (TEBVs) could be used to increase long-term graft patency due, in part, to the accurate matching of biochemical and mechanical properties [2,3]. TEBVs success, however, depends strongly on the chosen scaffolding material.

A proven technique for scaffold generation is through the decellularization of native tissues. Decellularization can be achieved via physical, chemical, or enzymatic approaches to completely remove cellular and nuclear material while retaining the native extracellular matrix (ECM). One such approach employs ionic and anionic detergents such as sodium dodecyl sulfate (SDS) and sodium deoxycholate (SDC). Comprehensive studies on how these agents impact the vessel's mechanical properties are currently lacking [5]. Since these mechanical characteristics depend on the abundance of existing ECM components such as collagen, elastin, and ground substances it is important to identify how these may be directly or indirectly altered during decellularization [1-5]. Our previous research identified the native porcine internal thoracic artery (ITA) as a superior candidate for bypass grafting due to its ideal mechanical and histological properties, thus we postulate that the porcine ITA would be an excellent scaffolding material for small diameter TEBVs [2]. The purpose of this study was to compare the ECM integrity and overall mechanical characteristics of porcine ITAs following several chemical detergent concentrations used to remove cellular material.

METHODS

Tissue Preparation. Porcine ITAs, approximately 160 mm in length, were harvested from sows shortly after slaughter at a local abattoir and dissections performed immediately after harvest. Loose perivascular and adipose tissues were removed and arteries were stored in cold 1% phosphate buffered saline (PBS) until decellularization.

Decellularization. Porcine ITAs were rinsed in DI water for 24 hours and then decellularized according to previously identified protocols [5]. All experimental groups were placed in a solution containing the enzyme deoxyribonuclease I (DNase I) to break-down DNA. Vessels were then placed in a solution containing a PMSF antimycotic and an equivalent ratio of SDS to SDC but at varying ratios of total detergents to PBS so that the final concentrations of SDS-SDC in PBS were 6.0, 3.0, 2.0, 1.0, and 0.0% [5]. ITAs undergoing decellularization were then subject to three days of agitation in a specific detergent concentration to ensure complete and homogeneous processing. Other vessels were placed in a separate PBS solution to serve as a time-matched control. After completion of the decellularization treatment, the vessels were rinsed several times with PBS to elute excess detergent and cellular debris. Certain vessels were stained with DAPI and imaged and others used the Quant-iT™ PicoGreen® dsDNA reagent to quantify the residual double-stranded DNA (dsDNA). Western blots of α-smooth muscle actin (α-SMA), a cytoplasmic protein of smooth muscle cells, confirmed DAPI results.

Histology. Movat's Pentachrome staining was employed to identify smooth muscle, elastin, collagen, and glycosaminoglycans (GAGs) as red, black/brown, yellow, and blue colors, respectively [4].

Wiegert's elastic stain (not shown) was used for elastin quantification. Cross-sections of ITAs were paraffin-embedded and cut to approximately 6 µm in thickness. Staining was performed according to the manufacturer's instructions (Poly Scientific R&D Corp).

Mechanical Testing. Biaxial mechanical testing was carried out using a Bose Biodynamic 5270 device as described in [2]. Briefly, ITAs from each detergent concentration were cut into approximately 20 mm sections. Each vessel was then mounted into the testing chamber of the biaxial testing device and the chamber was filled with 1% PBS. The *in vivo* axial stretch ratio from the native ITA was determined when the force value remained pressure invariant. All decellularized vessels were tested at this ratio to facilitate comparisons across groups. Each vessel underwent five cycles of axial stretching and cyclic inflation as preconditioning. For data collection, the pressure was increased from 0 to 120 mmHg while the outer diameter and axial force were measured. Each test was conducted three times.

RESULTS

Decellularization. Porcine ITAs stained with DAPI are shown in Figure 1. Scoring revealed a decrease in cellular and nuclear material as the concentration of detergent increased. Results were largely confirmed with the PicoGreen DNA/RNA quantification kit (Control=21.7±14.2 ng/ml; 0.0% SDS-SDC=14.9±25.7 ng/ml; 1.0 to 6% SDS-SDC=undetectable). Western Blotting revealed the presence of α-SMA only in controls and 0% SDS-SDC.

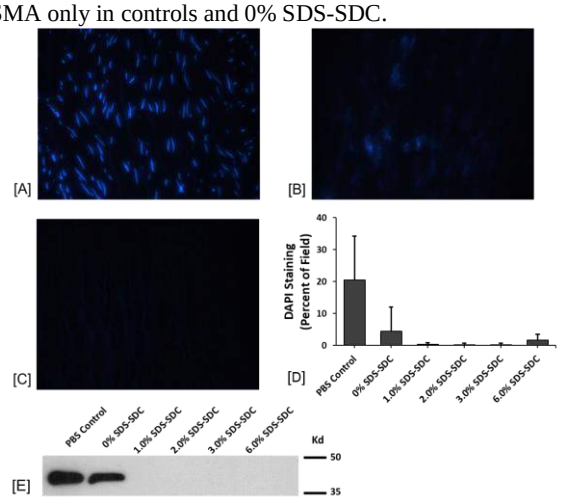

Figure 1: DAPI of decellularized vessels for [A] PBS Control, [B] 0.0% SDS-SDC, [C] 3.0% SDS-SDC, and [D] DAPI quantification (Avg ± STD, n=3 each). [E] Western blot for α- SMA

Histology. Light microscopy of decellularized vessels (Figure 2) confirm the absence of cellular material above 1.0% SDS-SDC. There was a notable decrease in GAG content (blue) that was progressive with detergent concentration. Surprisingly, a strong spatial dependency on anatomical location within the ITA emerged where proximal sections (Figure 2 E & F) have a greater medial thickness and number of elastic lamellae. Wiegert's stain also quantified the percent area of elastic fibers in decellularized vessels and the mean area fraction for the control, 0.0% SDS-SDC, and the 3.0% SDS-SDC vessels were 0.46±0.06, 0.44±0.18, 0.68±0.05, respectively.

Mechanical Testing. All specimens were tested at common axial stretches to facilitate comparisons between groups. Overall, the native and 0.0% vessels exhibited similar mechanical properties and the presence of detergents impacted the stiffness of all vessels in a concentration independent manner (Figure 3). That is, no obvious trends emerged between the varying SDS-SDC concentrations and mechanical properties. Surprisingly, the anatomical location played a greater role in tissue mechanics; a finding that warrants further investigation.

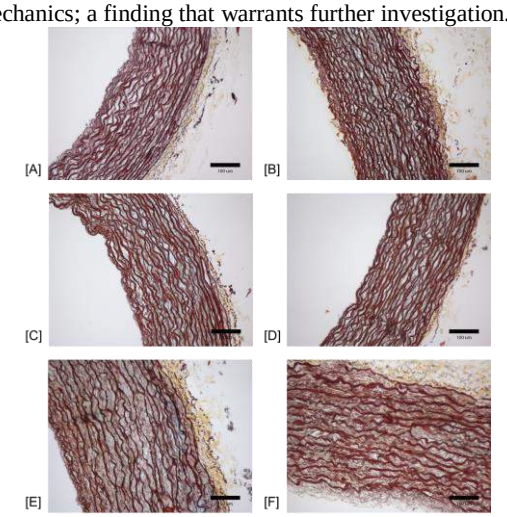

Figure 2: [A] 6.0% [B] 3.0% [C] 2.0% [D] 1.0% [E] 0.0% SDS-SDC, and [F] PBS control. Sections shown from a single sow.

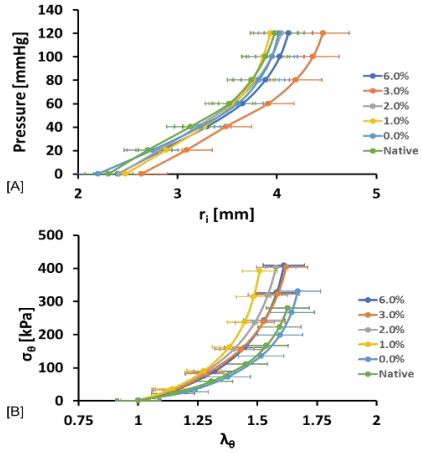

Figure 3: Native and decellularized vessels [A] pressure-radius and [B] circumferential stress-stretch. Avg ± SEM (n=3 each)

DISCUSSION

The histomechanical properties of decellularized vascular scaffolds were investigated. We found that 1.0% SDS-SDC was sufficient for complete removal of cellular material without obvious ECM damage. Biaxial mechanical testing revealed that decellularized vessels were circumferentially stiffer, but stiffness did not depend on SDS-SDC concentration. Likewise, DNase I had no effect on mechanical properties. Ongoing work is being performed to investigate the length-dependent histomechanical properties and the impact of cryopreservation and recellularization.

ACKNOWLEDGEMENTS

NSF EPSCoR OIA-1655740 and NIH R21 EB022131

REFERENCES

[1] Dahl, S et al., *Cell Transplantation*, 12:659-666, 2003.
[2] Prim, D et al., *J Mech Behav Biomed Mater*, 54:93-105, 2016.
[3] Campbell, E et al., *J Mech Behav Biomed Mater*, 14:130-142, 2012.
[4] Pellegata, A. et al., *Biomed Res Int*, 1-8, 2013.
[5] Pu, L et al., *J Biomed Mater Res Part B*, 00B:1-12, 2017.

SB³C2019
Summer Biomechanics, Bioengineering and Biotransport Conference
June 25 -28, Seven Springs, PA, USA

UNDERSTANDING THE TRANSMURAL VARIATION IN EXTRACELLULAR MATRIX FIBER ORIENTATION USING MULTI-PHOTON MICROSCOPY

Anastasia Gkousioudi (1), Jacopo Ferruzzi (2), Yanhang Zhang (1, 2)

(1) Department of Mechanical Engineering
Boston University
Boston, MA, 02215 USA

(2) Department of Biomedical Engineering
Boston University
Boston, MA, 02215 USA

INTRODUCTION

Collagen and elastin fibers are the two major load-bearing extracellular matrix (ECM) components in the arterial wall [1]. The ECM fiber orientation, distribution, and interactions largely define the passive mechanical properties of the arterial wall. Recent studies have provided interesting findings on the contribution of the individual ECM components to arterial mechanics [2, 3, 4]. Collagen and elastin fiber orientation through the arterial wall was characterized using both histological and multi-photon imaging methods. Results indicated that medial collagen fibers were arranged almost symmetrically around the circumferential direction and tended to be closer to the longitudinal direction in the adventitia [4]. Medial elastin fibers were found to have a transmural variation in fiber orientation in the media [3]. Reorientation of both elastin and collagen fibers was observed in to accommodating mechanical loading [2]. However, due to limited laser penetrating depth, sectioning of the tissue is required in order to image the fibers beneath the surface of the tissue.

The goal of this study is to understand the transmural variations in collagen and elastin fiber orientation distribution in intact arteries, and the contributions of ECM fibers to arterial biomechanics. Optical clearing method CUBIC (Clear, Unobstructed Brain/Body Imaging Cocktails and Computational analysis) [5] was adopted in order to increase the imaging depth in intact arterial tissue. Multi-photon microscopy was used to image the elastin and collagen fibers and their transmural variation in fiber orientation in the arterial wall.

METHODS

Sample preparation and optical clearing

Porcine thoracic aorta (12-24 month old) was obtained from a local abattoir. Upon arrival in the laboratory, aorta was carefully cleared from adjacent fat and cut open along the axial direction of the artery. Square samples of approximately 2cm × 2cm were cut with one edge being parallel to the longitudinal direction and the other being parallel to the circumferential direction of the artery.

Samples were then chemically fixed by immersing them into 4% paraformaldehyde (PFA), where they were kept for 24 hours. Samples were then rinsed twice with phosphate-buffered saline (PBS) to washout any remaining PFA. In order to optically clear the samples, they were immersed in CUBIC clearing reagent with gentle shaking at room temperature for two hours. After that, the reagent was replaced every two days for a total duration of six days.

Multi-photon microscopy and image analysis

Samples were kept in the CUBIC clearing reagent while being imaged with a multi-photon microscope. An excitation wavelength of 800nm was used to generate two-photon excitation of fluorescence (525/45nm) from elastin and second harmonic generation (417/80nm) from collagen [2, 3]. Samples were imaged from both the intimal and adventitial side to capture the transmural structural characteristics of collagen and elastin fibers in the media and adventitia, respectively. Both sample sides were imaged to a depth of $210\mu m$ with $1\mu m$ spacing and a field of view of $277 \times 277\mu m$.

Z-stack images of elastin and collagen were acquired and the fiber orientation was extracted for every image using Directionality plug-in in FIJI (http:/Fiji.sc/Fiji, Ashburn, VA). The program uses Fast Fourier Transform (FFT) to obtain the spatial frequencies of the image. The direction of the fibers is extracted by calculating the angle and the intensity of each spatial frequency in the FFT power spectra using edge-detector filters. The distribution functions at each imaging depth were combined into a three-dimensional (3D) image to study the transmural variation in elastin and collagen fiber orientation.

RESULTS

Representative fiber orientation distribution function of medial elastin (Figure 1A) and collagen (Figure 1B) is shown at three imaging depths of $40\mu m$, $100\mu m$ and $140\mu m$. Closer to the intima surface, at imaging depth of $40\mu m$, the two peaks near $\pm 90^o$ indicate that both elastin and collagen fibers are arranged mainly in the longitudinal direction. At imaging depth of $100\mu m$ and $140\mu m$, a peak appears around 0^o which means that the fibers are more circumferentially oriented. Figure 2 shows the transmural variation in elastin and collagen fiber distributions from the reconstructed stacks of images in an imaging depth of $210\mu m$, where imaging depth of $0\mu m$ corresponds to an imaging scan close to the intimal surface. It can be seen that elastin fibers are arranged predominantly in the longitudinal direction closer to the intimal surface and then transitioned rather abruptly towards the circumferential distribution. Although not shown here, the medial collagen follows a similar transmural pattern as medial elastin.

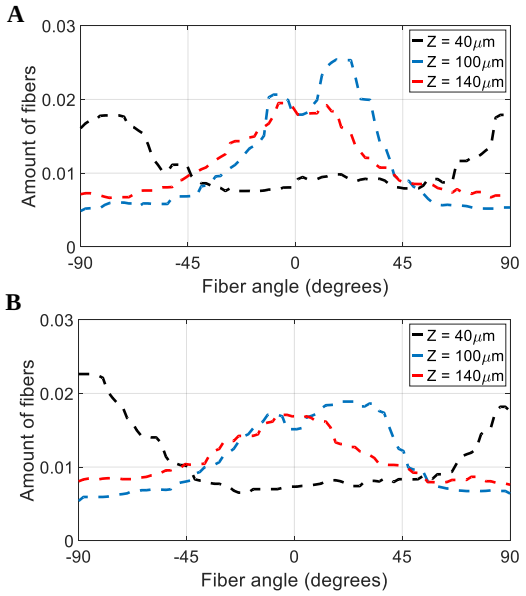

Figure 1: Fiber orientation distribution function of medial elastin (A) and collagen (B) at imaging depths of $40\mu m$, $100\mu m$ and $140\mu m$. 0° corresponds to the circumferential direction and ± 90° corresponds to the longitudinal direction.

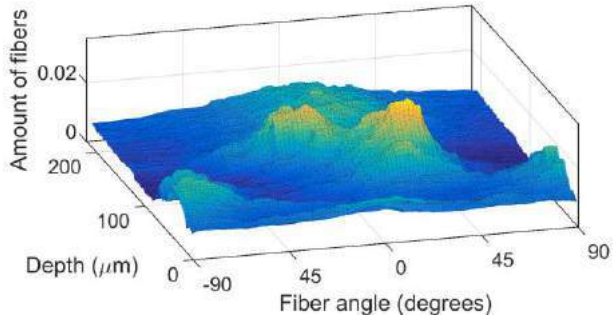

Figure 2. Transmural variation in medial elastin fiber orientation distribution within an imaging depth of $210\mu m$.

In order to further understand the orientation of elastin and collagen fibers as a function of the imaging depth, the circumferential-to-longitudinal fibers ratio was calculated and plotted in Figure 3. This ratio is defined as the amount of fibers in the circumferential direction, A_C, over the amount of fibers in the longitudinal direction, A_L. Specifically, A_C and A_L were defined as the areas under the distribution function from 0 ± 20^o and $90^o \pm 20^o$, respectively [2]. For values less than 1, the fibers follow a longitudinally preferred distribution, while for values greater than 1, fibers are more circumferentially oriented. Our results show that medial elastin and collagen fibers distribution follow a very similar trend through the arterial wall. The fibers transitioned from longitudinally preferred orientation to mainly circumferentially oriented at about $70\mu m$ below the intima surface. Surprisingly, this transition happens rather abrupt, as shown by the steep increase in A_C/A_L. No clear trend was observed in the adventitial elastin and collagen fibers (results not shown).

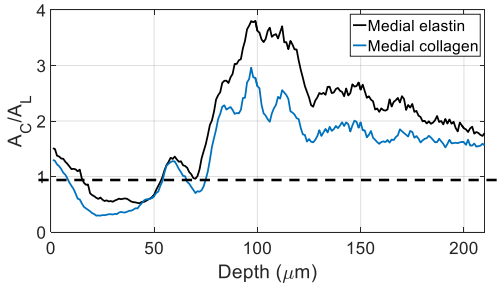

Figure 3. Circumferential-to-longitudinal fibers ratio as a function of the imaging depth.

DISCUSSION

Here we studied the transmural variations in elastin and collagen fiber distributions using optically cleared samples and multi-photon microscopy. Optically cleared samples allowed a nearly fivefold increase in imaging depth from $40-60\mu m$ to more than $200\mu m$ without significant processing of the tissue, which could provide additional structural information of the ECM fibers in deeper layers of the arterial wall.

Our results show that both medial elastin and collagen fibers change their orientation throughout the arterial wall, from a longitudinally to circumferentially preferred orientation. The medial elastin and collagen fiber distributions follow a similar trend indicating the strong correlation of these two major load-bearing components in the arterial wall. The transmural transition in fiber orientation could be attributed to several functional reasons. The lumen surface of the arterial wall is subjected to shear stresses from the blood flow and the corresponding ECM fibers are longitudinally oriented to better accommodate such loading. On the other hand, the fibers in the medial layers of the artery are more circumferentially oriented to bear the large circumferential deformation from the pulsatile blood flow [3,4].

Future studies are underway to study the effect of the optical clearing method on the mechanical and structural properties of the arterial tissue and to understand the transmural variation in ECM fiber distributions with biaxial mechanical loading.

ACKNOWLEDGEMENTS

We acknowledge the funding support R01HL098028 from National Institute of Health (NIH). We would also like to thank Dr. Sun-Joo Jang and Professor Seok-Hyun Yun for their assistance on multi-photon microscopy.

REFERENCES

[1] Humphrey, JD, *Springer Science & Business Media*, 2013.
[2] Chow, MJ et al., *Biophys J*, 106(12):2684-2692, 2014.
[3] Yu, X et al., *J Mech Behav Biomed Mater*, 77:745-753, 2018.
[4] Schriefl, AJ et al., *J R Soc Interface*, 9(71):1275-86, 2012.
[5] Susaki, EA et al., *Nat Protoc*., 10(11):1709-27, 2015.

SB³C2019
Summer Biomechanics, Bioengineering and Biotransport Conference
June 25 -28, Seven Springs, PA, USA

KINEMATIC ANALYSIS OF MURINE CARDIAC HYPERTROPHY USING HIGH-FREQUENCY FOUR-DIMENSIONAL ULTRASOUND

Frederick W. Damen (1), Mauro W. Costa (2), Craig J. Goergen (1)

(1) Weldon School of Biomedical Engineering
Purdue University
West Lafayette, Indiana, USA

(2) The Jackson Laboratory
Bar Harbor, ME, USA

INTRODUCTION

Murine models of cardiac disease have played a crucial role in systematically exploring the contribution of underlying mechanisms toward disease pathophysiology[1-3]. In this effort, *in vivo* imaging techniques have become an invaluable tool for assessing cardiac function, providing clinically-relevant metrics such as: ejection fraction, stroke volume, cardiac output, and left ventricular mass[4, 5]. While high-field cine-MRI is often considered the gold-standard for studying cardiac function in mice due to its ease in imaging complex ventricular morphologies[6-8], our group has recently developed and validated a high frequency four-dimensional ultrasound (4DUS) technique that provides higher spatiotemporal resolution, comparable cardiac volumetric measurements, and faster acquisitions compared to cine-MRI[9, 10].

Here we use our 4DUS data to develop a standard procedure for measuring myocardial deformations from volumetric endocardial and epicardial boundaries across the cardiac cycle, and subsequently use those to compare regional kinematics between animals. We apply this procedure to cohorts of wild-type mice and mice with genetically-induced cardiac hypertrophy and dysfunction, highlighting group-wise differences in temporal circumferential strain patterns.

METHODS

Animal Models: Six male mice with a genetically induced cardiac hypertrophy phenotype (*Nkx2-5*$^{183P/+}$)[11], as well as a cohort of wild-type littermates, had 4DUS data acquired at 8 weeks of age. Following imaging at 8 weeks, mice from each cohort were sacrificed and excised hearts were weighed.

Ultrasound Imaging: All data was collected using the Vevo2100 high-frequency ultrasound system (FUJIFILM VisualSonics Inc, Toronto, Canada) with a 40 MHz center frequency transducer (MS550D) and a linearly translating 3D motor. 4DUS data was created by collecting cardiac- and respiratory-gated planar image data at serial short-axis views across the left-ventricle (LV), and syncing data spatiotemporally in MATLAB (MathWorks Inc., Natick, MA).

Ventricular Boundary Definition: In order to set a standardized paradigm from which ventricular kinematics can be compared between animals, the following procedure was employed to define endocardial and epicardial boundaries:

1. 4DUS data is rotated to have the endocardial and epicardial apices, as well tissue between the aortic and mitral valves, all cross the same axis (Figure 1). This orientation defines the "kinematic axis".
2. The through-plane location of the base, endocardial-apex, and epicardial-apex is manually tracked through the cardiac cycle.
3. Short-axis loops are extracted at positions corresponding to 0, 25, 50, and 75% the distance from the defined base to the endocardial-apex, thus mitigating changes in view due to through-plane motion (i.e. the relative position along the LV is maintained throughout the extracted cine-loop).

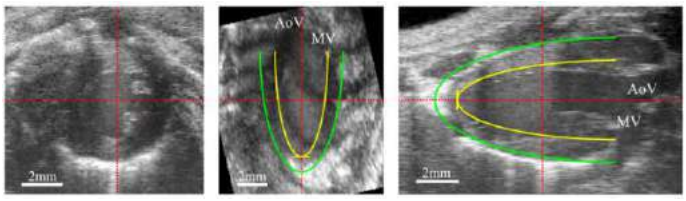

Figure 1. Three orthogonal views of 4DUS data demonstrating standard orientation and contours of the endocardial and epicardial boundaries. Both aortic valve (AoV) and mitral valve (MV) are noted on each long-axis view.

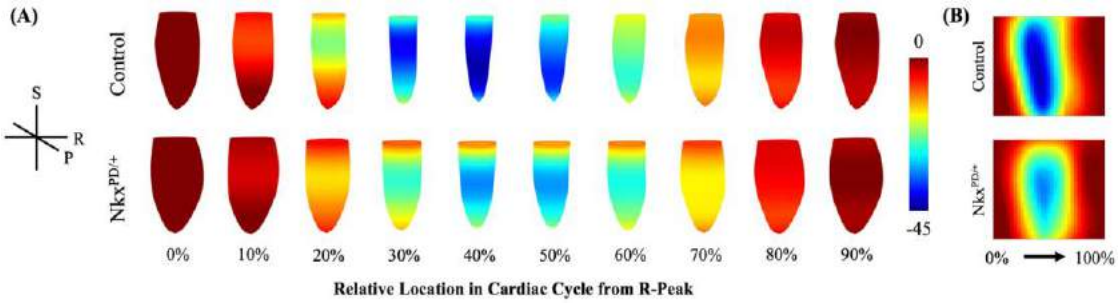

Figure 2. Circumferential strain (A) mapped to mouse-specific left-ventricular geometries across the cardiac cycle, and (B) as time-course plots, shown for a representative (top) control and (bottom) *Nkx2-5*$^{183P/+}$ mouse at 8 weeks of age. All plots are scaled [-45,0] (%).

4. For each cine-loop created in *Step 2*, six points around the kinematic axis (60° apart) are moved temporally to track the radial motion of each boundary (i.e. toward/away from the center of the LV chamber). Hobby-splines are drawn through the tracked points to ensure appropriate border definitions.
5. Points from *Step 3* are then mapped to long-axis views at each 30-degree rotation around the kinematic axis, allowing users to further refine point-placements or spline-parameters.
6. The finalized set of points and splines are used to interpolate a grid of standardized boundary locations for each respective time point: 40 equally-spaced long-axis positions from the LV apex to base by 40 positions circumferentially around the kinematic axis.

Circumferential Strain: For each of the 40 long-axis positions and time point across the cardiac cycle, the cumulative distance between each set of 40 circumferential points (i.e. slice perimeter) is calculated. Cauchy circumferential strain is then defined as:

$$Strain_t = \frac{L_t - L_0}{L_0} \quad [1]$$

where L represents the slice perimeter in millimeters at time point t.

RESULTS

The aforementioned procedure allowed us to quantify differences in circumferential strain between wild-type control and *Nkx2-5*$^{183P/+}$ cohorts, which most notably occurred during systole and early diastole. Figure 2 displays these differences wherein lower magnitude strains (-30% vs. -45%), a less extensive systolic contraction wave from base to apex, and faster relaxation at the base of the heart are observed in the hypertrophic mice versus controls. These same trends are seemingly maintained when comparing time-courses averaged across each cohort (Figure 3). Of note, the differences between cohorts observed at the base of the heart during early diastole are not as prominent at the mid-ventricle or apex levels of the heart.

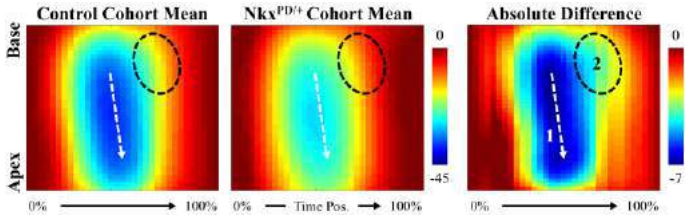

Figure 3. Time-course plots of circumferential strain averaged over (left) control and (middle) *Nkx2-5*$^{183P/+}$ cohorts, respectively, and a plot (right) of the absolute difference between average time-courses (i.e. control – *Nkx2-5*$^{183P/+}$). Plots of averaged time-courses are scaled for circumferential strain [-45, 0] (%), and the absolute difference plot is scaled [-7, 0] (%). Notable differences are highlighted with (#1) a white line representing systole and (#2) a black oval closer to the base of the heart during early diastole.

DISCUSSION

By taking full advantage of information provided in 4DUS cardiac data and establishing a standard procedure for tracking local kinematics in the left ventricle, a comprehensive characterization of cardiac function can be obtained. This study focused on circumferential strain differences in a genetic model of cardiac hypertrophy (*Nkx2-5*$^{183P/+}$) and identified lower magnitude and less extensive systolic contraction waves in the hypertrophic hearts (Figure 3; #1). This is particularly interesting as these findings are from 8 weeks old; prior to when significant differences in global metrics of hypertrophy (e.g. LV mass) have been observed[11]. This suggests that the effects of energy handling deficiency, induced in cardiomyocytes with the *Nkx2-5*$^{183P/+}$ mutation, can be observed prior to significant ventricular hypertrophy and ejection fraction dysfunction[12].

Furthermore, the slower relaxation from peak systole seen at the base of the heart (Figure 3; #2) is suggestive of altered ventricular contractility. As blood flows into the ventricle from the left atrium, the compromised myocardium cannot resist the pressure from the initial inflow as well as wild-type controls. Taken together, the differences between cohorts could help better characterize the hallmarks of hypertrophy observed during disease progression.

Overall, these results show promise for the 4DUS technology and our standardized analysis paradigm to serve as a cost-effective and reliable tool for studying various mouse models of cardiac disease. Future work plans to both extend the breadth of kinematic metrics used and apply these techniques to additional cardiac disease models.

ACKNOWLEDGEMENTS

We would like to acknowledge Arvin Soepriatna and Alycia Berman for their intellectual support in this work. We would also like to acknowledge Brett Hawkins, Andrew Needles, Stephen Buttars, and Kristiina Aasa from FUJIFILM VisualSonics for their technical assistance. This work was supported by the AHA (14SDG18220010). Frederick Damen was supported by a NIH NIDDK T32 Fellowship (DK101001-01).

REFERENCES

[1] Zaragoza, C. et al., *J Biomed Biotechnol*, 2011:497841, 2011.
[2] Patten, R.D. et al., *Circ Heart Fail*, 2:138-44, 2009.
[3] Sheikh, F. et al., *Prog Peditar Cardiol*, 24:27-34, 2007.
[4] Gardin, J.M. et al., *Circ Res*, 76:907-14, 1995.
[5] Pistner, A. et al., *J Vis Exp*, 2010.
[6] Akki, A. et al., *Am J Physiol-Heart C*, 304:H633-48, 2013.
[7] Kober, F. et al., *Magn Reson Mater Phy*, 17:157-161, 2004.
[8] Nahrendorf, M. et al., *Eur Heart J*, 23:202-202, 2002.
[9] Damen, F.W. et al., *Tomography*, 3:180-187, 2017.
[10] Soepriatna, A.H. et al., *Int J Cardiovasc Imaging*, 2017.
[11] Furtado, M.B. et al., *Jci Insight*, 2:e88271, 2017.
[12] Wilmanns, J.C. et al., *Mol Metab*, 2018.

SB³C2019
Summer Biomechanics, Bioengineering and Biotransport Conference
June 25 -28, Seven Springs, PA, USA

SELECTIVE STIFFENING OF A MYOCARDIAL INFARCT IMPROVES PREDICTED SYSTOLIC FUNCTION WITHOUT IMPAIRING FILLING

Kyoko Yoshida (1), Ana C. Estrada (1), Jeffrey W. Holmes (1,2), William J. Richardson (3)

(1) Department of Biomedical Engineering
University of Virginia
Charlottesville, VA, USA

(2) Department of Medicine
University of Virginia
Charlottesville, VA, USA

(3) Department of Bioengineering
Clemson University
Clemson, SC, USA

INTRODUCTION

Roughly 1 million Americans experience a heart attack each year [1]. Although the vast majority of patients survive the event, they are left with reduced cardiac function and an increased risk of heart failure [2]. This reduced cardiac pump performance is due in part to the immediate loss of functioning muscle and is exacerbated by the infarcted region distending and bulging during systole, thereby wasting energy. A wide variety of approaches have sought to mechanically reinforce the infarct zone to limit impairment of systolic function [3]. However, computational models and experimental studies have revealed that reinforcing the infarct also impairs the ability of the left ventricle (LV) to fill during diastole [4-6]. Overall, improvements in systolic function from reinforcement are offset by the reduction in diastolic function, resulting in little change in overall pump function.

As an alternative approach, we hypothesized that appropriately manipulating exponential passive material properties of the infarct could stiffen the infarct only during systole, and thereby improve systolic ejection without impairing diastolic filling. In this current study, we computationally tested this hypothesis using a previously developed finite element (FE) model of an infarcted canine LV.

METHODS

We utilized a previously validated FE model of the normal (baseline) and an acutely ischemic canine LV developed by our lab [7]. Briefly, an average geometry of the canine LV was generated based on CINE MRI scans from sixteen different dogs taken 48 hours post-infarction. A nearly-incompressible transversely isotropic Mooney-Rivlin (TIMR) material was used to simulate normal and ischemic myocardium, with fiber directions ranging from -60° in the epicardium to 60° in the endocardium. Active stress was calculated and generated along the fiber direction using a custom material plug-in. A large anterior infarct was simulated by assigning 30% of the myocardium as an infarct that lacks active contraction. Active and passive material properties in the muscle region and passive material properties in the infarct region were optimized to match previously published experimental data [8], allowing us to simulate full pressure-volume relationships during a cardiac cycle.

To selectively stiffen the infarct during systole, we modified our fitted TIMR material parameters for the infarct region. The passive strain energy density is the sum of an isotropic (F_1), anisotropic (F_2), and penalty term to enforce incompressibility:

$$\Psi = F_1(I_1, I_2) + F_2(\lambda) + \frac{K}{2}[\ln(J)]^2 \qquad (1)$$

where I_1, I_2 are the 1st and 2nd stretch invariants, λ is the fiber stretch, K is the bulk modulus, and J is the determinant of the deformation tensor. In this material model, the anisotropic passive fiber stress is evaluated as:

$$\lambda\frac{\partial F_2}{\partial \lambda} = \begin{cases} 0 & \lambda \le 1 \\ C_3(e^{C_4(\lambda-1)} - 1) & 1 < \lambda < \lambda_m \\ C_5\lambda + C_6 & \lambda \ge \lambda_m \end{cases} \qquad (2)$$

where C_3 and C_4 describe the exponential behavior during the toe region and initial engagement of fibers, C_5 describes the behavior once fibers are straightened and fully engaged, and C_6 enforces stress continuity at λ_m, the transition stretch between these two regimes. In our published model, λ_m was set to 10 so this transition never occurred. Herein, to preferentially stiffen the infarct at systolic pressures, we set $C_5 = 10000$ [kPa] and varied λ_m= [1.2, 1.25, 1.3].

We simulated passive filling to calculate end-diastolic pressure volume relationships (EDPVRs). We generated end-systolic pressure volume relationships (ESPVRs) by applying the average pressure time course from the ischemia experiment and subsequently scaling this

pressure time course by 95% for 5 additional heart beats, corresponding to the expected pressure during occlusion of the inferior vena cava. We used the ED and ESPVRs to generate theoretical cardiac output curves by calculating the stroke volume at a heart rate of 106.7 [beats per sec], a systolic pressure of 85 [mmHg] and a range of filling pressures. All simulations were run using FEBio v.2.6.4 (http://www.febio.org).

RESULTS

Adjusting λ_m allowed us to selectively stiffen the infarct at high fiber stretches (in the range experienced by the fibers during systole) with limited impact on the infarct properties at low fiber stretches (in the range experienced by the fibers during diastole) (Fig.1). Specifically, smaller values of λ_m shifted the fiber stretch at which the stretch-stress curve transitioned into the stiffened region. The chosen value of $C_5 = 10000$ [kPa] led to ~10-fold increase in the maximum stiffness of the scar compared to the properties we previously determined for acutely ischemic canine myocardium.

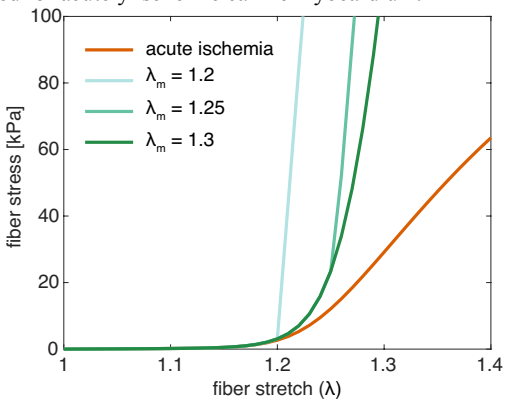

Figure 1: Adjusting λ_m values leads to scar stiffening at high pressures. Plot of fiber stretch vs. stress for the original and new infarct material. Green lines represent varying values of λ_m.

Next, we tested whether changes in the infarct properties led to improved global systolic function without impairing diastolic filling (Fig.2). During passive inflation to 20 [mmHg], decreasing λ_m had little effect on the EDPVR. Conversely, decreasing λ_m shifted the ESPVR towards baseline and smaller end-systolic volumes. These shifts in the ESPVR increased the calculated cardiac output (Fig.3), indicating

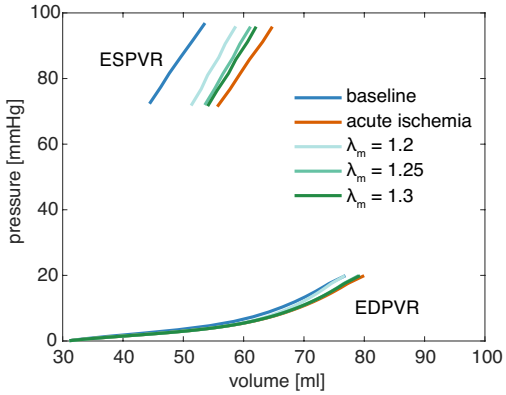

Figure 2: Selectively stiffening the scar decreases end-systolic volumes without affecting end-diastolic volumes. Simulated end-diastolic (EDPVR) and end-systolic pressure volume relationships (ESPVR) for baseline (no scar), acute ischemia, and range of λ_m. Smaller values of λ_m led to bigger shifts towards baseline ESPVR.

enhanced LV function compared to the acute ischemia model. These benefits, however, were less substantial at higher end-diastolic pressures, where infarct stiffening did begin to affect filling.

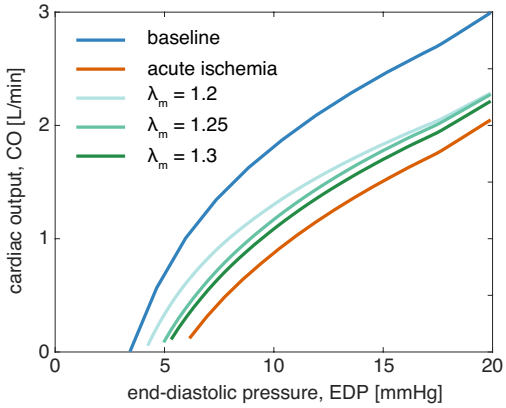

Figure 3: Selective stiffening benefits LV global function. Theoretical cardiac output curves show a shift towards the baseline model, particularly at lower diastolic pressures.

DISCUSSION

In this study, we employed a computational approach to predict whether manipulating the passive material properties of a myocardial infarct could preferentially stiffen the infarct during systole and improve systolic function without impairing diastolic filling. We found that modifying infarct material properties to increase stiffness at high stresses shifted the ESPVRs, but not the EDPVRs, improving global systolic function without impairing filling. The increase in infarct stiffening allowed the remaining myocardium to pump more effectively, as shown by an increased cardiac output at matched diastolic and systolic pressures. This concept might provide a novel basis for designing synthetic patches or injection methods that could overcome limitations of previous attempts to mechanically reinforce infarcts.

One limitation of the simulations presented here is that they do not account for hemodynamic compensation mechanisms that could change in response to infarct stiffening. Constructing cardiac output curves at a fixed end-systolic pressure partially accounts for potential compensation by assuming that reflexes will maintain mean arterial pressure approximately constant. Fully understanding the impact of baroreflex regulation, however, will require coupling the presented FE model to a circulation model to account for compensations such as altered heart rate, systemic resistance, and others.

In conclusion, the computational study employed here suggests that preferentially stiffening the scar during systole is a promising approach for improving LV function following myocardial infarction.

ACKNOWLEDGEMENTS

The authors acknowledge support from the NIH (U01 HL127654).

REFERENCES

[1] Benjamin, E et al., *Circulation*, 137(12):e67-e492, 2018.
[2] Lewis, E et al., *JACC Heart Fail.*, 2(2):159-65, 2014.
[3] Richardson, W et al., *JCTR*, 8(7):421-30, 2015.
[4] Bogen, D et al., *Circ. Res.*, 55(6):805-15, 1984.
[5] Wall, S et al., *Circulation*, 114(24):2627-35, 2006.
[6] Fomovsky, G et al., *JCTR*, 4(1):82-91, 2011.
[7] Estrada, A et al., *Under review*, 2019.
[8] Fomovsky, G et al., *Circ. Heart Fail.* 5(4):515-22, 2012.

SB³C2019
Summer Biomechanics, Bioengineering and Biotransport Conference
June 25 – 28, Seven Springs, PA, USA

HYPERTENSION-INDUCED CHANGES IN THE MECHANICAL BEHAVIOR OF THE LEFT VENTRICULAR WALL

Marissa R. Grobbel (1), Ari Hollander (2), Analeeza Dubay(1), Emma Darios Flood (3), Kibrom M. Alula (3), Gregory D. Fink (3), Stephanie W. Watts (3), Lik Chuan Lee (1), and Sara Roccabianca (1)

(1) Department of Mechanical Engineering
Michigan State University
East Lansing, MI, United States

(2) Department of Chemical Engineering
Michigan State University
East Lansing, MI, United States

(3) Department of Pharmacology and Toxicology
Michigan State University
East Lansing, MI, United States

INTRODUCTION

It is well-known that hypertension induces pathological remodeling in the left ventricle (LV). Specifically, hypertension has been shown to increase collagen volume fraction as well as passive stiffness in the heart [1, 2]. Hypertension is also known to affect the residual stress distribution in the LV—specifically, it decreases the opening angle [3]. Furthermore, we have recently shown that the interaction between myocytes and the collagen fiber network plays a key role in defining LV residual stresses [4]. For this reason, we hypothesize that hypertension also alters the inter-constituent mechanical interaction. To test this hypothesis, we have isolated the LV constituents of healthy and hypertensive rats, performed opening angle tests on them, and used this data to estimate possible forms of the interaction between the constituents in healthy and hypertensive tissue.

METHODS

Opening angle experiment - Whole hearts were extracted from 15 healthy (Sprague-Dawley, fed control diet) and 13 hypertensive (Dahl-Salt sensitive, fed 60% high fat diet) adult male rats. After the LV's were isolated, we obtained ring-shaped samples by cutting lateral slices from the whole heart. Then, the healthy and hypertensive LV's were split into three groups: intact tissue (*n = 5, each*), isolated collagen fibers (*n = 5, each*), and isolated myocytes (*n = 5 healthy, 3 hypertensive*). Samples from the intact tissue group were soaked in a Krebs buffer containing 2,3-butanediome, a myosin inhibitor, to relax the myocytes. Myocytes and collagen fibers were isolated through previously published protocols [4]. Then, classical opening angle tests were performed on all samples. The test consists of introducing a radial cut through the LV free-wall, allowing the sample to open and approach a nearly stress-free configuration. Each sample was allotted 90 minutes to reach equilibrium, during which pictures of the sample were taken, then later used to measure the opening angle.

Modeling of interaction - A constrained mixture modeling framework was utilized to estimate the interaction between myocytes and collagen fibers in both healthy and hypertensive hearts. The inter-constituent interaction was modeled as an isochoric planar deformation—i.e. the collagen fibers "compress" or "stretch" the myocytes in the radial and circumferential directions. Briefly, we describe the interaction introducing a deformation gradient mapping from the unloaded configuration of the isolated constituents to the unloaded configuration of the intact tissue, Equations 1 and 2.

.

$$F^c = diag\left[\frac{1}{\alpha_c}\frac{\partial \rho}{\partial \rho_c}; \alpha_c \frac{\rho}{\rho_c}; \lambda_z\right] \quad (1)$$

$$F^m = diag\left[\frac{1}{\alpha_m}\frac{\partial \rho}{\partial \rho_c}; \alpha_m \frac{\rho}{\rho_c}; \lambda_z\right] \quad (2)$$

The interaction terms α_c and α_m represent the circumferential stretch due to the interaction of the collagen fibers and myocytes, respectively. We employed an isotropic exponential strain energy function to describe the mechanical behavior of each constituent. Then, the strain energy of the intact tissue was evaluated as the mass fraction-weighted average of the two constituents', Equation 3.

$$W^{tot} = \varphi_c\left[c_c\left(e^{k_c(I_1-3)} - 1\right)\right] + \varphi_m\left[c_m\left(e^{k_m(I_1-3)} - 1\right)\right] \quad (3)$$

Parameter estimation - The mechanical parameters, c_c, c_m, k_c, and k_m have been estimated by fitting experimental data from uniaxial ring tests of LV's collected from two healthy rats. Specifically, one ring was decellularized (isolated collagen fiber network), and one was treated

with collagenase (isolated myocytes). The mass fractions φ_c and φ_m were estimated by histological analysis or through literature review [1, 4, 5]. We assumed the mechanical behavior of the constituents is not altered by hypertension. Correspondingly, the only change with hypertension seen by our model will be mass fractions and interaction parameters.

After defining the parameter values in Equation 3, the model was used to find possible solutions for the interaction terms. Solutions were defined as combinations of α_c and α_m that allowed the model to reproduce the experimental results—i.e. to predict the correct experimental opening angle for intact tissue when appropriate tissue composition was considered. Two types of solutions will be presented here: a solution where $\alpha_m = 1$, and a solution where $\alpha_c = 1/\alpha_m$.

RESULTS

We found that the opening angle in the isolated collagen fibers was significantly higher compared to the intact tissue for both (healthy and hypertensive) groups of rats. The opening angle of the isolated myocytes was significantly lower than the intact tissue for the healthy rats ($p < 0.05$). However, this difference was not significant in the hypertensive rats ($p = 0.17$). Additionally, the intact tissue and the isolated collagen fibers of hypertensive LV's had a lower average opening angle than their respective healthy groups, however this difference was significant only in the isolated collagen fibers, Figure 1.

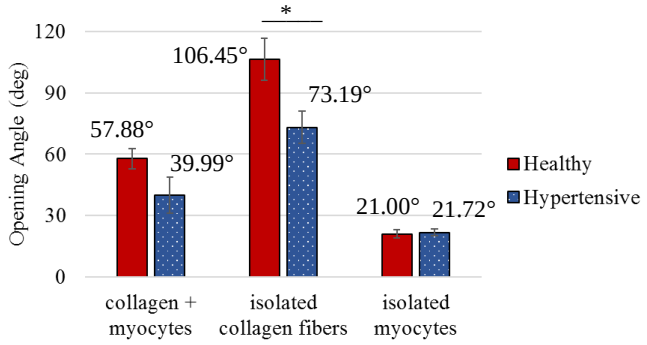

Figure 1. Comparison of opening angle between each experimental group. Error bars showing standard error (* represents $p < 0.05$).

We were able to fit material parameters to the ring test data well; the normalized root mean square deviation of both the isolated collagen fibers and myocytes was less than 5%. Our results show that the isolated collagen fibers were much stiffer than the myocytes, Figure 2.

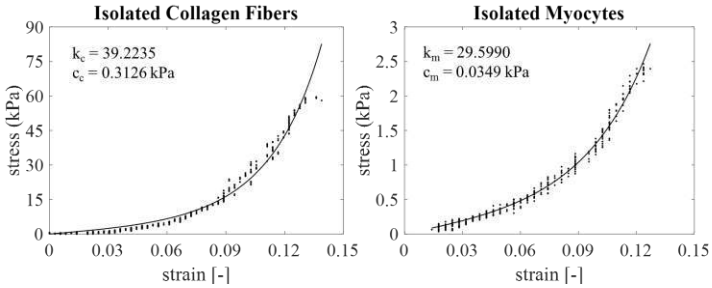

Figure 2. Mechanical data and best-fit material parameters for isolated collagen fiber network and myocytes.

Based on histological analysis, we have determined $\varphi_c = 0.1$ for healthy LV's. However, we do not currently have a measurement for this term in hypertensive LV's. While most studies report an overall increase in collagen area fraction with hypertension [1, 2, 5], there have also been reports of no significant change [6]. For this study, we have used a range between the collagen area fraction measured for healthy rats and an upper limit found in literature, namely within the range $0.1 < \varphi_c < 0.2$.

The "no interaction" ($\alpha_m = \alpha_c = 1$) solution was not valid for either the healthy or hypertensive models. Additionally, no solutions for the healthy and hypertensive were exactly equal. However, for the solution of $\alpha_m = 1$, the value of healthy α_c lies between the high and low values of the hypertensive α_c. For the solution of $\alpha_c = 1/\alpha_m$, though, as φ_c increases, the value for hypertensive α_m strays further away from healthy α_m.

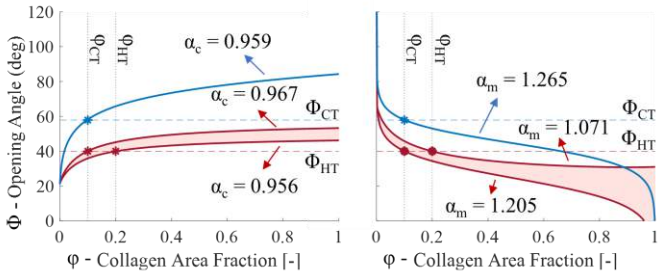

Figure 3. Opening angle as a function of collagen inclusion shows the solutions for interactions of healthy (blue, CT) and hypertensive (red, HT) constituents. Left: solutions of the form $\alpha_m = 1$. Right: solutions of the form $\alpha_c = 1/\alpha_m$. The dots on each curve represent experimental measurements.

DISCUSSION

Our experimental results show that the collagen fibers seem to be the main contributor to residual stress within the LV, both in healthy and hypertensive hearts. However, it has been shown that although the collagen content may increase with hypertension, which might suggest an increase in the opening angle, the residual stress actually decreases. This has been illustrated both in the current study, despite having employed rats from two different strains, as well as a previous study on the intact tissue [3]. In this study, for the first time, we have shown that (1) the opening angle in the isolated collagen fibers also decreases with hypertension, while (2) the opening angle of isolated myocytes seems to not be affected by remodeling. A histological analysis of LV microstructure may help interpret these results.

The model showed that the interaction between myocytes and collagen fibers should not be ignored in either the healthy or the hypertensive LV. None of the solutions for the interactions terms that we have explored were common between the healthy and hypertensive models. Furthermore, it appears that the value of the interaction terms is highly affected by tissue composition. These results strongly suggest that with hypertension-induced remodeling of LV tissue, the interaction between the collagen fibers and myocytes is also changing. In the future, we will work to obtain constituent material parameters and collagen area fraction specific to the hypertensive LV.

REFERENCES

[1] M.A. Rossi. *J Hypertens*, 1998.
[2] J.H. Omens, et. al. *Ann Biomed Eng*, 1995.
[3] J.H. Omens, et. al. *J Mol Cell Cardiol*, 1996.
[4] M.R. Grobbel, et. al. *BMMB*, 2018.
[5] C.W. Doering, et. al. *Cardiovasc Res*, 1988.
[6] K.T. Weber, et. al. *Circ Res*, 1988.

SB³C2019
Summer Biomechanics, Bioengineering and Biotransport Conference
June 25 -28, Seven Springs, PA, USA

BIOPRINTING 3D BREAST EPITHELIAL SPHEROIDS TO STUDY VASCULAR INTERACTIONS IN HUMAN CANCER

Swathi Swaminathan, Alisa Morss Clyne

Mechanical Engineering and Mechanics,
Drexel University, Philadelphia 19104

INTRODUCTION

Conventional 2D *in vitro* cancer cell culture fails to represent the tissue specific architecture, thereby providing a limited physiological model. Animal models recapitulate tissue architecture and whole organism physiology but may not accurately represent human disease. Therefore, physiologically relevant 3D human cancer models are a critical intermediary between conventional 2D *in vitro* culture and human disease. Biofabrication enables cells to be precisely deposited in a 3D structure, allowing improved spatial and temporal control over engineered tissue structure [1]. However, bioprinting based on layer by layer cell-bioink extrusion relies on rapid hierarchal cell self-assembly into 3D tissues. This self-assembly is time consuming and requires complex cellular interactions with extracellular matrix components, heterogenous cell types and growth factors [2].

The objective of this study was to develop an entirely different approach to 3D tissue biomanufacturing. Rather than bioprint individual cells and wait for these cells to form their 3D architecture, we bioprinted multicellular building blocks (e.g., breast epithelial spheroids) to create a model tissue that could be used almost immediately. These pre-formed spheroids were then printed with endothelial cells to study chemotherapy response.

METHODS

Two breast epithelial cell lines were used. MCF-10A, an immortalized non-tumorigenic cell line that organizes into spheroids with a hollow lumen *in vitro*; and MCF10A-NeuN, an MCF10A cell line transfected to overexpress epidermal growth factor (EGF) receptor 2 (Neu/HER2/ErbB2), which yields a poor patient prognosis. Breast cell lines were cultured in DMEM/F12 with 5% horse serum, 20 ng/ml EGF, 10 μg/ml insulin, 10 ng/ml cholera toxin, 500 ng/ml hydrocortisone, and 1% penicillin-streptomycin. Breast cell lines were used to passage 25.

To create 3D breast spheroids, 4,000 breast epithelial cells were resuspended in medium with 20% Matrigel and seeded onto growth factor reduced Matrigel in an 8 chamber BioCoat Falcon Culture slide. Cells formed spheroids in 8 days. To grow endothelial networks, 5-10,000 red cell tracker labelled human umbilical vein endothelial cells (HUVEC) were added to Matrigel-coated wells in Endothelial Basal Medium-2. Cells formed tube-like structures within 6 hours.

3D breast spheroids were co-cultured with endothelial cells in two ways. First, the breast spheroids were carefully pipetted out of their wells and deposited onto the HUVEC networks. Alternatively, the 3D breast spheroids were bioprinted using a multi-nozzle solid freeform fabrication-based computer controlled direct cell writing system [3]. The system consists of three motion arms that allow micron-scale spatial control of material deposition as well as two screw driven motors that deposit biological material. An independent syringe heating enclosure provided temperature control of the bioink within the syringe. The bioink was composed of MCF10A and MCF10A-NeuN cells as either individual cells (200,000 cells/ml) or as spheroids and suspended in either Matrigel or collagen/alginate (3% alginate + 0.025% collagen in 0.9% sodium chloride). Bioink was microextruded using a screw-driven motor (1 mL/min, 25-gauge nozzle).

After 1 to 8 days, samples were fixed with 4% paraformaldehyde, blocked to prevent non-specific binding, and incubated with a primary antibody for integrin α6 (1:100, breast spheroids) or VE-cadherin (1:200, endothelium) overnight at 4°C. Samples were then incubated with an Alexa Fluor 488 secondary antibody (1:200) and Hoescht 33342 (10 μg/ml, nuclei) for one hour at room temperature. After thorough washing, samples were mounted on coverslips in Prolong gold antifade mounting agent and imaged in a Zeiss LSM 700 confocal microscope.

Cell viability in the presence of different doses of paclitaxel was assessed using resazurin. Conditioned medium from bioprinted

structures was transferred to a 96-well plate and incubated with 5% v/v resazurin (0.1 mg/mL) in phenol red-free DMEM medium for two hours at 37°C. Absorbance was measured in a microplate reader and data was collected at 570 nm using the Gen5 software.

RESULTS

We previously found that MCF10A cells killed HUVECs in 2D culture, while HUVECs prevented MCF10A spheroid formation when added into 3D culture. In this study, when pre-formed breast epithelial spheroids were pipetted on pre-formed endothelial networks, the spheroids preferentially attached to the endothelial networks and maintained network viability over 48 hours. Interestingly, over time the breast epithelial cells grew out of the spheroids and migrated along the endothelial networks. While MCF10A spheroids elongated over the endothelial networks after 72 hours of co-culture, MCF10A-NeuN spheroids elongated within 24 hours of co-culture (Figure 1) [4].

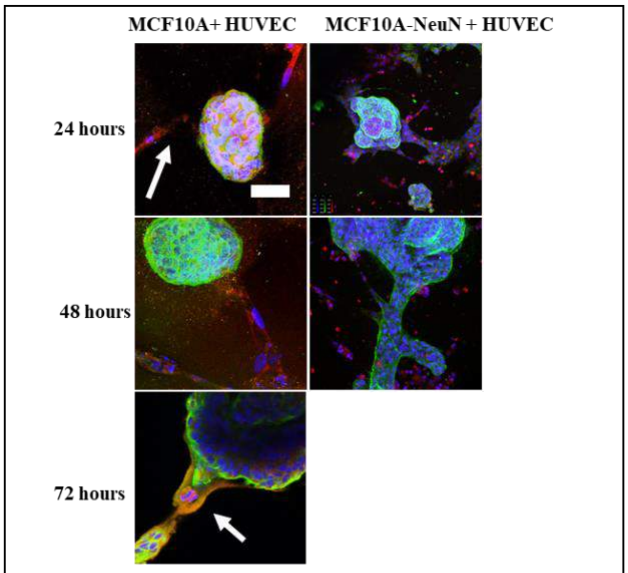

Figure 1: Pre-formed MCF10A spheroids elongated along endothelial networks within 72 hours, whereas MCF10A-NeuN elongated within 24 hours. Blue – nuclei, red – cell tracker(HUVEC), green – integrin α6 (Breast epithelial cells). Scale bar = 20 µm.

While this technique demonstrated successful 3D co-culture of human breast epithelial and vascular endothelial cells, the method was limited in that spheroid location could not be controlled and Matrigel was still used. We therefore tested if the pre-formed breast spheroids could be bioprinted in Matrigel as well as less expensive, temperature insensitive bioinks such as collagen/alginate. We first tested whether individual MCF10A and MCF10A-NeuN cells would self-assemble into spheroids after printing in Matrigel or collagen/alginate. Although cell viability was maintained in both matrices, breast epithelial cells only formed spheroids in Matrigel but not in collagen- alginate bioink.

We then printed preformed breast spheroids in either Matrigel or collagen/alginate using the same printing parameters. After 48 hours, breast spheroids printed in either Matrigel or collagen/alginate maintained their 3D architecture, including the hollow lumen characteristic of MCF10A spheroids (Figure 2, inset in top right shows spheroid center plane). Bioprinted breast spheroids in either bioink maintained their 3D architecture for 96 hours (data not shown) [5].

Finally, we bioprinted both individual breast cells and the pre-formed breast spheroids in a grid structure with HUVECs to determine co-culture viability and chemotherapy response. In both cases, cells and spheroids were more than 80% viable. Interestingly, breast spheroids

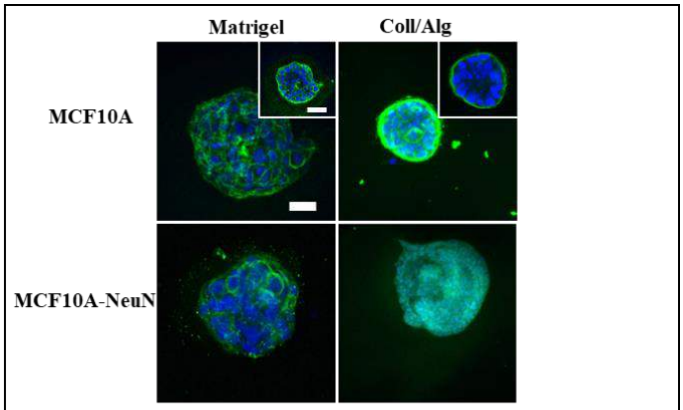

Figure 2: Bioprinted pre-formed spheroids maintained their morphology in both Matrigel and collagen/alginate. Inset (top right) shows hollow center plane of spheroids. Blue – nuclei and green – integrin α6. Scale bar = 100 µm; Inset: Scale bar= 50 µm.

were more resistant to Paclitaxel than individual breast cells, but co-culture with endothelial cells abrogated this effect (Figure 3).

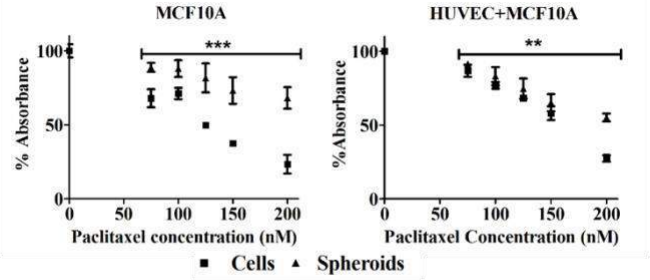

Figure 3: Bioprinted preformed breast spheroids showed increased resistance to paclitaxel in comparison to individual breast cells , but co-culture with endothelial cells abrogated this effect.#p,0.05, ** p < 0.01 , *** p<0.001.

DISCUSSION

In this research, we showed for the first time that 3D cellular structures can be bioprinted while maintaining not only cell viability but also 3D architecture, polarization, and function. We bioprinted the 3D spheroids in alginate-based bioinks, which are largely inert other than the natural matrix proteins that we included. This shows that spheroids could likely be printed in a wide variety of bioinks, both natural and synthetic. We believe that 3D multicellular structure bioprinting has great potential to rapidly create tissue models, perhaps directly from patient cells, which better replicate the structure and function of the *in vivo* tumor microenvironment. Our method decreases the time between bioprinting and experimental assay from weeks to days; increases physiological relevance by allowing the investigator to more precisely control tissue architecture. In the future, we will bioprint breast spheroids onto an endothelial network or with microvascular fragments to create a vascularized breast cancer model.

ACKNOWLEDGEMENTS

We thank Dr. Mauricio Reginato for providing the breast cells.

REFERENCES

[1] Ouyang,L. et al, Biofabrication,8(3):035020, 2016.
[2] Zhao,Y. et al, Biofabrication, 6(3):035001, 2014.
[3] Khalil S, Sun W. J Biomech Eng, 131(11): 111002, 2009.
[4] Swaminathan. et al; ACS Biomater. Sci. & Eng. 3 (11), 2999,2017.
[5] Swaminathan.S, et al, Biofabrication 2019 (In press).

SB^{3}C2019
Summer Biomechanics, Bioengineering and Biotransport Conference
June 25 -28, Seven Springs, PA, USA

FABRICATING 3D CELLUAR AGGREGATES VIA LASER DIRECT-WRITE BIOPRINTING: SIZE- AND SHAPE-CONTROLLED EMBRYOID BODIES AND TUMOR SPHEROIDS

David M. Kingsley (1), Cassandra L. Roberge (1), David T. Corr (1)

(1) Department of Biomedical Engineering
Rensselaer Polytechnic Institute
Troy, NY, USA

INTRODUCTION

Multicellular 3D aggregates, such as embryoid bodies (EBs) and tumor spheroids, provide powerful *in vitro* models to study a wide range of biological processes for diagnostic and regenerative medicine applications. However, control of aggregate size and shape is necessary to recapitulate key *in vivo* parameters. For example, EB size has been shown to influence stem cell lineage specification [1–4], and the size of multicellular tumor spheroids (MCTSs) greatly affects model behavior: small spheroids (100-300 μm diameter) exhibit no gradient-related challenges in cell survival, larger sizes (500-1000 μm) often develop necrotic cores due to lack of sufficient nutrient/waste transport, and medium-sized spheroids (300-500 μm) develop biochemical gradients with discrete radial cell zones (*i.e.*, periphery cells are an active proliferating layer, and most inward are quiescent and/or hypoxic) [5,6].

Beyond size, the shape of cellular aggregates is also an important factor in model development. Size-related heterogeneity is, in part, due to spatiotemporal signaling effects, which are influenced by aggregate shape. Cellular aggregates are typically assumed to take on a spherical morphology, which is approximated by maximum intensity projection (MIP) images in the x-y plane using brightfield microscopy. However, recent evidence suggests that aggregate models can exhibit vastly different sizes and shapes, which can only be appreciated when analyzed in 3D [7]. Thus, both aggregate size and shape are crucial factors that can influence model behavior, with important implications in the development of the desired pathophysiological gradients [8].

Typical aggregate fabrication methods, *e.g.*, liquid overlay, hanging drops, provide modest control of aggregate size, and offer little-to-no control of aggregate shape. Herein, we aim to create size- and shape-controlled cellular aggregates (*e.g.*, EBs, MCTSs) using laser direct write (LDW) bioprinting, by patterning size-controlled cell-loaded microbeads that are then processed into core-shelled structures, within which cells self-assemble to form 3D aggregates that grow to match the geometry of their printed shelled structure.

METHODS

Cell Maintenance. All experiments were conducted with either MDA-MB-231 human breast cancer cells (ATCC, Manassas, VA) or CCE Mouse Embryonic Stem cells (mESCs) (StemCell Technologies, Vancouver, BC, Canada). Tumor cells were cultured in Dublecco's Modification of Eagle's Medium (DMEM) supplemented with 10% fetal bovine serum and 2 mM L- glutamine. Stem cells were grown in standard ES maintenance media with 15% fetal bovine serum, 1mM sodium pyruvate, 100 U mL-1 penicillin/streptomycin, 2 mM L-Glutamine, 0.1 mM MEM non-essential amino acids, 10 ng mL-1 leukemia inhibitory factor (LIF), and 100 μM monothioglycerol in DMEM high glucose. Cells were maintained in T-75 Flasks in a cell culture incubator (37 °C, 95% humidity, and 5% CO2).

LDW Microbeads and Core-Shelled Structure Fabrication. LDW was utilized to 'single-step' fabricate and pattern alginate microbeads into arrays, or as voxels to produce larger continuous structures, as previously described [9]. Briefly, this technique uses two coplanar CAD/CAM controlled motorized stages: a print ribbon above an independently-controlled receiving substrate (**Figure 1a**). To print a bead, a pulse from an ArF excimer laser (193nm) volatilizes a sacrificial film on the underside of the print ribbon, ejecting a droplet of alginate suspending the biopayload (*i.e.*, MDA-MB-231 human breast cancer cells or CCE mESCs) from a transfer layer to the receiving substrate, where it is immobilized and crosslinked *in situ*. The droplet size is controlled by the beam diameter during deposition. For larger multi-bead structures, the between-droplet spacing is adjusted for overlapping voxels, and a continuous alginate structure is formed.

Core-shelled constructs were produced from printed-alginate structures by coating the printed beads with chitosan. This, in turn, created a polyelectrolyte-complexed layer of alginate and chitosan on the outside of the bead. Finally, sodium citrate is used to chelate the calcium crosslinking of the alginate bead, resulting in a polymeric shell surrounding a liquid core containing the cellular payload (**Figure 1b**). The encapsulated cells within these structures were then able to grow over the course of 14 days to produce MCTSs or EBs (**Figure 1c**).

Optical Coherence Tomography (OCT). OCT is a label-free, nondestructive/noninvasive imaging modality that enables 3D structural imaging of biological features with cellular resolution. OCT imaging was performed by a commercial spectral domain system (TEL220C1; Thorlabs Inc.). Cellular aggregates within core-shelled structures were visualized and quantified (*i.e.,* volume and sphericity) using Imaris image analysis software (v9.2, Bitplane USA, Concord, MA) [10].

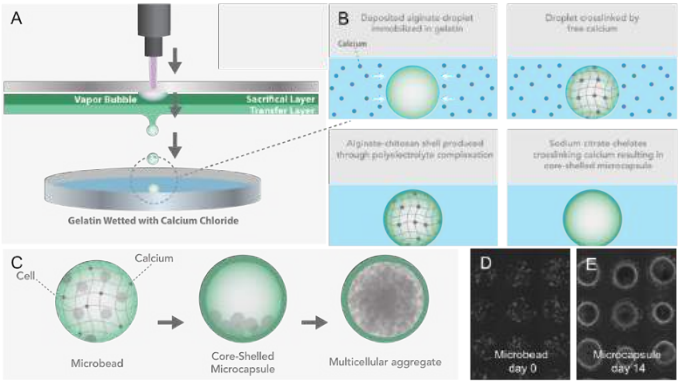

Figure 1: Schematic of microbead LDW (A) , processing into core-shelled structures (B), aggregate formation (C), and time-lapse of an array of alginate microbeads from day 0 (D), to 14-day EB (E).

RESULTS

Laser direct-write successfully fabricated and patterned large (400 µm) and small (200 µ m) microbeads encapsulating cancer and stem cells in patterned arrays (600-µm centroid-to-centroid spacing) (**Figure 1d**). Consistent with prior work, arrays appeared to maintain pattern registry after conversion into core-shelled microcapsules [11]. Importantly, cancer cells and mESCs survived deposition from the print ribbon and processing into core-shelled microcapsule. Furthermore, within capsules, tumor cells and stem cells aggregated and self-assembled to form MCTSs and EBs, respectively, filling the entire capsule volume over 14 days (**Figure 1e**). It appeared that aggregate growth was confined to the geometry of the microcapsule shell, which determined the aggregate volume and shape. Resulting cellular aggregates appeared very densely packed, with a dark region attenuating light at the centroid.

Once LDW's ability to fabricate cellular aggregates from both cancer cells and mESCs was established, this work attempted to quantify the ability to control the size of the aggregate based on the core-shell structure dimensions. Three different core-shelled structures were fabricated (small microcapsule, large microcapsule, and micromat made of overlapping microbeads) and resulting 14 day aggregates were assessed with OCT and analyzed within Imaris (**Figure 2Ai-Aiii**). Core-shelled structures of different sizes produced aggregates of significantly different sizes, however cancer cells and mESCs within microcapsules of similar initial dimensions produced MCTSs and EBs of comparable volume (**Figure 2b**). Sphericity measurements (**Figure 2c**) revealed that both small and large mESC aggregates were highly spherical (0.986 ± 0.006 and 0.917 ± 0.017). Tumor aggregates similarly demonstrated high sphericity in small microcapsules (0.976 ± 0.059), however this was significantly lower in large microcapsules (0.822 ± 0.049), and further reduced in the core-shelled micromats.

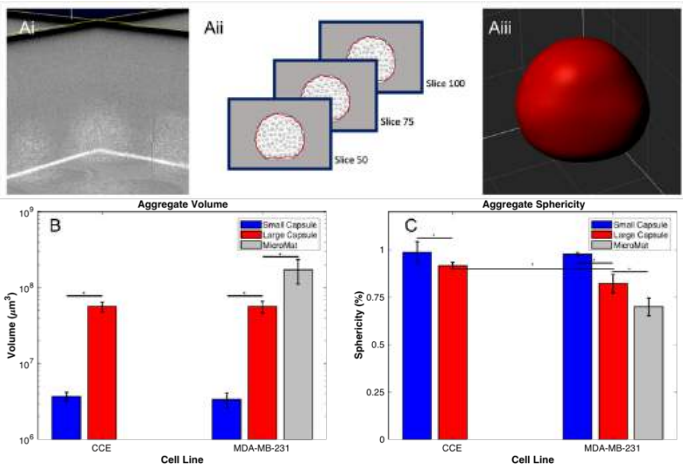

Figure 2: Volumetric scan of a 14-day EB grown in large (400 µm) capsule, collected via OCT and processed using Imaris analysis software (Ai-iii). Volume (B) and sphericity (C) of aggregates grown within small and large microcapsules and micromats, showing the ability to control aggregate size and shape via LDW.

DISCUSSION

For both multicellular tumor spheroids (MCTSs) and embryoid bodies (EBs), the aggregate size plays a key role in the phenotype of the individual cells, and the overall model behavior. This is, at least in part, explained by the development of nutrient (*e.g.,* oxygen and glucose) and cellular-signaling gradients within the aggregates. Thus, specific applications will require control of 3D aggregate size and shape to establish the desired pathophysiological gradients. Moreover, certain applications may demand precise aggregate positioning in the culture/construct to prescribe the desired homotypic/heterotypic cell signaling. Together, this spatial and geometric control is highly desired to create culture models that recapitulate key *in vivo* parameters. Herein, we demonstrate LDW's unique ability to create and spatially pattern size-controlled EBs and MCTSs. Overall, this bioprinting technique offers incredible promise for fabricating idealized *in vitro* models for mechanistic exploration, as well as tissue surrogates for a variety of diagnostic and regenerative medicine applications. Future work in this space will investigate the effects of aggregate size on cellular heterogeneity, a key factor in therapeutic resistance and differentiation.

ACKNOWLEDGEMENTS

This work was supported by the National Institute of Health (NIH) R01 BRG CA20772 (DTC); RPI's KIP seed program (DTC).

REFERENCES

[1] Cha, J et al., *Macromol Res,* 23:245–255, 2015.
[2] Schukur, L et al., *Adv Healthc Mater,* 2:195–205, 2013.
[3] Bauwens, C et al., *Stem Cells*, 26:2300–10, 2008.
[4] Peerani, R et al., *Stem Cells Regen Med*, 21–33, 2009.
[5] Jiang, Y et al., *Biophys J*, 89:3884–3894, 2005.
[6] Lorenzo, C et al., *Cell Div*, 6:1–8, 2011.
[7] Froehlich, K et al., *J Mammary Gland Biol Neoplasia*,89–98, 2016.
[8] Raghavan, S et al., *Oncotarget*, 7:1–26, 2016.
[9] Kingsley, D et al., *Biofabrication*, 5:45006, 2013.
[10] Faulkner, D et al., *Opt InfoBase Conf Pap*,:5–6, 2018.
[11] Kingsley, D et al., *Biotechnol Bioeng*, 113:2264–2274, 2016.

FLUID-STRUCTURE INTERACTIONS AT DROP-DROP INTERFACE DURING DROP-ON-DEMAND PRINTING OF HYDROGEL-BASED SOFT MATERIALS

Cih Cheng, George T.-C. Chiu, Bumsoo Han

School of Mechanical Engineering
Purdue University
West Lafayette, IN, USA

INTRODUCTION

Hydrogel are widely used in numerous applications including healthcare, food, pharmaceutical, and cosmetic products [1], [2]. Moreover, recent advances in polymer sciences enable new emerging applications including smart sensors, stretchable and wearable electronics, and energy storage and conversion devices. To enable these new products as well as to improve current ones, it is crucial for manufacturing equipment and processes to have the capability of integrating these novel materials into three-dimensional (3D) parts with prescribed functional properties. However, hydrogel-based materials are very delicate and fragile to handle with conventional manufacturing methods.

Among various 3D printing techniques, drop-on-demand (DOD) printing shows great potential to address this manufacturing challenge. DOD printing may enable advanced additive manufacturing of functional soft materials by depositing hydrogel droplets with desired functional properties at desired positions with appropriate timing between adjacent droplets. However, it is currently extremely difficult to design DOD printing processes (i.e., when and where adjacent droplets should be deposited) due to limited mechanistic understanding of the behaviors of printed hydrogel droplets during and after deposition, which will eventually determine the functional properties of the printed products. These properties are elastic modulus, hydraulic conductivity and solute diffusivity, which are related to the microstructure of polymer matrix, specifically porosity. In contrast to liquid drop evaporation, gelation-dehydration kinetics of hydrogel ink droplet is poorly understood.

In the present study, we performed a computational study to establish a mechanistic understanding of the behaviors of hydrogel ink droplets during DOD printing processes for manufacturing of hydrogel products. Specifically, we characterized the gelation of printed droplets and their concurrent and/or subsequent dehydration phenomena. This research is based on a hypothesis that a complex interaction between polymer matrix and interstitial water occurs during this dropwise gelation-dehydration as illustrated in Figure 1. The result of this interaction will determine the microstructural characteristics of polymers at intra-, inter-drop and inter-layer scales, ultimately the porosity of the hydrogel printed.

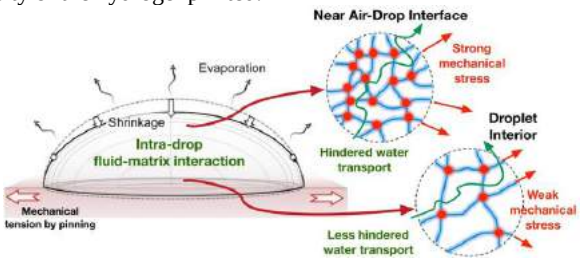

Figure 1: Schematic of intra-droplet fluid-matrix interactions during dehydration of a hydrogel droplet.

THEORETICAL BACKGROUND

Dehydration of two sequentially printed hydrogel droplets were computationally analyzed considering the drop-air and drop-drop interaction. Based on the one-droplet model developed in Han et al.[5], the fluid-matrix interaction in printed droplets were simulated using the consolidation equation and a boundary condition of balancing the vapor flux at the drop-air interface with the interstitial water flux. We assumed that gelation of hydrogel is a rapid process compared to dehydration process, so that gelation occurs instantaneously as droplets are deposited on the substrates. As illustrated in Figure 2, we formulated a

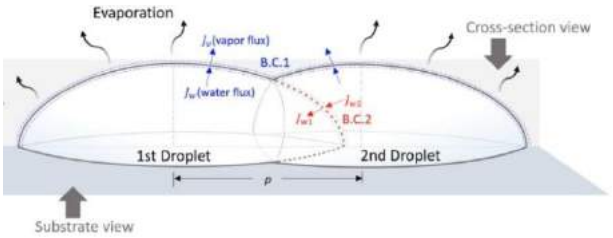

Figure 2: Computational Domain and Boundary Conditions.

boundary condition for the drop-drop interface to consider inter-droplet interaction as below:

$$\rho_w D \frac{\partial e}{\partial \hat{n}}\bigg|_{drop1} = \rho_w D \frac{\partial e}{\partial \hat{n}}\bigg|_{drop2} \quad (1)$$

This boundary condition represents the conservation of interstitial water flux between two droplets. At the interface, the water density and consolidation constant of the two droplets are assumed to be the same. Due to the pinning effect, the droplet diameter is assumed to remain constant during dehydration. These equations were numerically solved using a commercial finite element method (FEM) package (COMSOL Multiphysics). The consolidation equation was solved on the first droplet and subsequently the second droplet. The properties used in the computation are summarized in Table1 [3-9].

Table 1: Summary of the computational model

Parameters	Values
d (diameter of droplets)	500 µm
h (height of droplets)	250 µm
p (pitch)	200 µm
E (elastic modulus)	1000 Pa
K (hydraulic conductivity)	1×10^{-3} m^2/Pa·s
v (Poisson's ratio)	0.3
h_m (mass transfer coefficient)	0.01 m/s

RESULT

Figure 3 shows the dilatation contours and interstitial water flux vectors during dehydration of printed droplets. After a single droplet is printed (i.e., Step 1), a relatively high shrinkage (i.e., negative dilatation) is localized at the periphery of the droplet similar to the "coffee ring effect", as shown in Figure 3(a). Dilatation increases from the periphery to the center. This implies interstitial water transports from the center to the periphery. Figure 3(b) shows the dilatation after deposition of the second droplet.

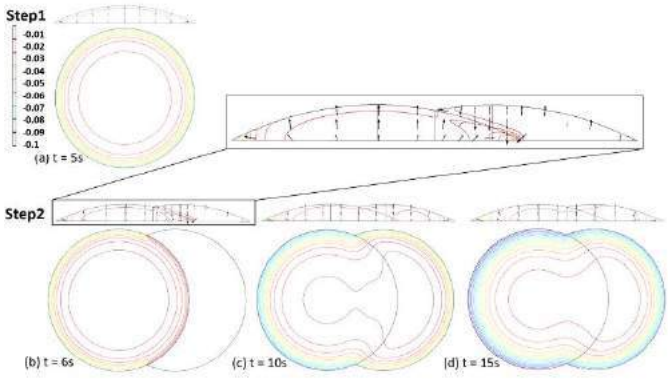

Figure 3: Droplet-dilatation and water flux during dehydration of printed droplets. (Contour plot at the substrate surface and cross-section contour plot with deformation gradient, i.e. water flux.).

The dilatation of the first droplet at the drop-drop interface significantly increases immediately after deposition of the second droplet. This suggests localized rehydration of the first droplet by the hydrated second droplet. A high degree of deformation is observed in the region of the drop-drop interface, indicating that rapid water transport occurs at the boundary of the two droplets. This change is thought to be caused by the large dilatation difference between a partly dehydrated droplet (1st one) and a fully hydrated droplet (2nd one). Accordingly, it is anticipated that high residual stress will be built up at the interface and may cause potential defects of the printed products. After the initially dehydrated drop has rehydrated, the interstitial water transport between two droplets is diminished at later time points (i.e., Figure 3 (c) and (d)). Evaporation becomes dominant in the 2nd droplet inducing outward water transport. Finally, the two droplets coalesce and dehydrate together like a single-drop case. The resulting two drops are not expected to have the same microstructural properties.

DISCUSSION

The present results suggest spatiotemporal variation of dilatation during curing (i.e., drying) of printed hydrogel, which is directly related to the porosity of polymer matrix, in printed drops. This variation could be explained by considering fluid-matrix interactions at the drop-drop interface. The drying process of droplets of various solutions, such as water, polymer suspension, blood, etc. has been well studied previously [10]. However, the most studies of droplet evaporation only focuses on one sessile droplet, which are not relevant to drop-drop interactions during DOD printing of hydrogels. The present computational model can provide a mechanistic explanation of the drop-drop interaction, and enable the prediction of spatiotemporal porosity, ultimately functional properties, of printed hydrogels.

ACKNOWLEDGEMENTS

This study was partially supported by a Program Grant from Purdue Institute of Drug Discovery, and a grant from NSF (CMMI-1449358).

REFERENCES

[1] Kirillova et al (2017) "4D Biofabrication Using Shape-Morphing Hydrogels," *Adv. Mater.*, pp. 1–8.
[2] Shiblee et al (2018) "3D Printing of Shape Memory Hydrogels with Tunable Mechanical Properties," *Soft Matter*.
[3] Oyen et al (2014) "Mechanical characterisation of hydrogel materials," *Int. Mater.*, pp. 44–59.
[4] Lee et al (2009) "Characterization of an anisotropic hydrogel tissue substrate for infusion testing," *J. Appl. Polym. Sci.*, pp. 1992–2002.
[5] Han et al (2016) "Dropwise gelation-dehydration kinetics during drop-on-demand printing of hydrogel-based materials," Int. J. Heat Mass Transf., pp. 15–25.
[6] Ghosh et al (2010) "Freezing-Induced Changes of Extracellular Matrix and Functional Properties of Engineered Tissues".
[7] Teo et al (2011) "Effects of freezing-induced cell-fluid-matrix interactions on the cells and extracellular matrix of engineered tissues," *Biomaterials.*, pp. 5380–5390.
[8] Biot (1941) "General Theory of Three-Dimensional Consolidation," *J. Appl. Phys.*, pp. 155–164.
[9] Kays et al (1980) "*Convective Heat and Mass Transfer"*.
[10] Park (2015) "Preservation of tissue microstructure and functionality during freezing by modulation of cytoskeletal structure," *J. Mech. Behav. Biomed. Mater.*, pp. 32–44.

SB³C2019
Summer Biomechanics, Bioengineering and Biotransport Conference
June 25 -28, Seven Springs, PA, USA

DIRECTED SELF-ASSEMBLY OF 3D IN VITRO TISSUE MODELS USING DROPLET MICROFLUIDICS

Jasmine Shirazi (1), Michael J. Donzanti (1), Jason P. Gleghorn (1)

(1) Department of Biomedical Engineering
University of Delaware
Newark, DE, USA

INTRODUCTION

Vasculogenesis occurs in the developing embryo and results in a disorganized vascular network known as a plexus. By harnessing the cells' innate ability to self-assemble into vascular networks, we are able to fabricate large scale vascularized constructs of arbitrary geometries, allowing for a wide range of shapes and sizes and thus making this process ideal for various types of grafts or constructs [1]. A key feature of vascular self-assembly is that it closely recapitulates the *in vivo* processes of vasculogenesis and angiogenesis [2], especially in comparison to patterned models [3]. Physiological vascularized tissues display inherent heterogeneity in vessel size and extracellular matrix (ECM). We combined our bulk vasculogenesis-based method with a droplet-based 3D culture to achieve directed self-assembly whereby the cells are able to self-assemble in a quasi-deterministic manner based on environmental cues (Figure 1).

As a proof-of-concept of our customizable vascularized constructs, we have generated a 3D *in vitro* "minimal bone marrow niche." The bone marrow is a complex, heterogenous structure that relies heavily on vascular signaling. It is the primary site of hematopoiesis, and in disease conditions, leukemogenesis. The architecture of the bone marrow is divided into two niches: the endosteal niche and the vascular niche [4]. Whereas it is tempting to consider these niches separately, there is evidence that a single hematopoietic stem cell (HSC) or leukemic stem cell (LSC) can be simultaneously regulated by cells of different niches [5]. We have developed an *in vitro* model that recapitulates both bone marrow niches. This minimal bone marrow niche incorporates osteoblasts and endothelial cells as each of these cells influence hematopoiesis and leukemogenesis. This platform allows for the assessment of cellular interactions and ECM properties in a complex pseudo-structured microenvironment. This directed self-assembly-based approach allows for assembly of vascularized microdomains with deterministic cell populations and defined matrix properties. The stiffness and size of each droplet can be tuned to capture the heterogeneity of the *in vivo* tissue. Collagen is an ideal material for this application as it is the most abundant ECM protein in the bone marrow [6]. Accounting for the multifactorial influence of the bone marrow microenvironment will provide a more comprehensive understanding of HSC/LSC differentiation in the presence of stromal and vascular cells. As such, our model overcomes the limitations of single cell studies to investigate how the cells of the bone marrow niche work in concert to regulate hematopoiesis. These techniques can also be applied to the create large scale vascular networks.

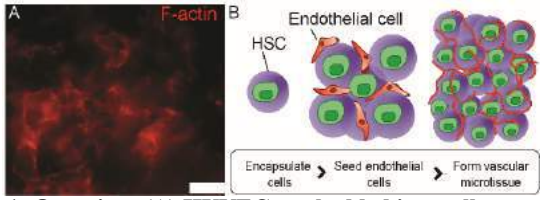

Figure 1: Overview. (A) HUVECs embedded in a collagen gel self-assemble into a large scale vascular network called a plexus. (B) Seeding HSC/LSC-laden droplets with HUVECs results in a vascular bone marrow model. (scalebar= 200 μm)

METHODS

Human umbilical vein endothelial cells (HUVECs) were cultured in EGM2, KG-1a (a leukemic stem cell line) were cultured in IMDM, and Saos-2 (osteoblast cell line) were cultured in McCoy's 5A. Collagen was freshly isolated from rat tails [3]. Each cell type was stained with a specific lipophilic membrane dye (Vybrant). KG-1a cells were encapsulated in collagen droplets using a flow-focusing droplet generator. Droplet size was modulated based on the flow rates of the dispersed and continuous phase. Microfluidic droplet generators were fabricated using standard photolithography approaches to generate SU-

8 silicon masters [7]. Replica molding and oxygen plasma treatment protocols were used to produce polydimethylsiloxane (PDMS)-glass microfluidic devices [8]. 3 mg/mL collagen was perfused as the dispersed phase, while Novec7500 fluorinated oil (3M) supplemented with 0.1125% Krytox 157 FSH oil (DuPont) served as the continuous phase. Droplet generation was imaged using a Fastec IL5 high speed camera. Collagen droplets were moved into media through solvent transfer and incubated overnight with the appropriate cells (HUVEC or Saos-2). Samples were imaged with a Zeiss confocal LSM880.

RESULTS

Using droplet microfluidics, we generated collagen droplets dispersed in a continuous phase of fluorinated oil (Figure 2). The flow-focusing device allowed for the creation of a range of droplet diameters by altering the flow rates. Resulting droplets were transferred from oil into media for cytocompatibility and subsequent culture.

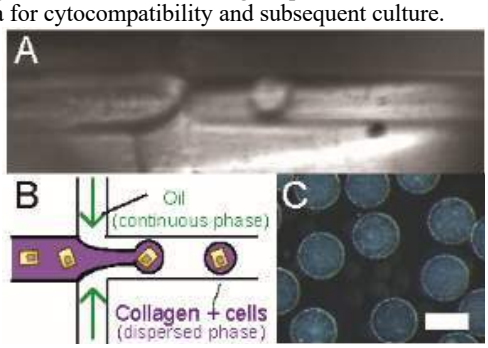

Figure 2: Collagen droplets were generated through flow-focusing. (A) Droplet formation was captured using a high-speed camera (acquisition rate = 991 fps). (B) Cell-laden collagen droplets are formed in oil. (C) Droplets are monodisperse. (scalebar= 200 µm)

For initial studies in vascular self-assembly, collagen droplets were coated with HUVECs that were labeled with a lipophilic membrane dye. After individual droplets were coated with cells, the droplets were combined to aggregate them into larger constructs (Figure 3). This enabled the endothelial cells to proliferate and self-assemble a vascular network around the individual collagen droplets. The vascular lumens of the self-assembled constructs ranged in size, demonstrating that this method is effective at generating vessels at a variety of length scales.

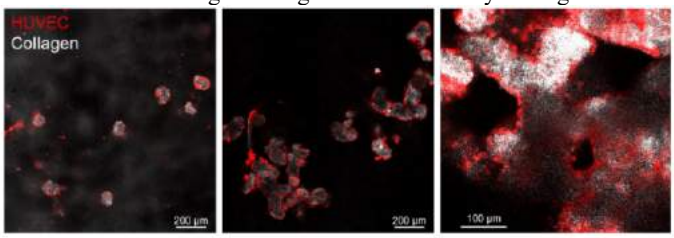

Figure 3: HUVEC-coated collagen droplets form vascularized microtissues. Individual collagen droplets are coated with membrane dye-stained HUVECs (left). The droplets form aggregates leading to microtissues (center). The aggregates result in larger constructs containing lumens of varying sizes (right).

To generate a complex bone marrow tissue with microdomains consisting of vascular and endosteal niches, collagen droplets with an LSC line (KG-1a) encapsulated within were generated in the same fashion and coated with either HUVECs to mimic the bone marrow vascular niche or an osteoblast cell line (Saos-2) to mimic the endosteal niche. Cells were labeled with membrane dye prior to tissue generation, and confocal imaging confirms that the HUVEC and osteoblast-coated droplets containing the LSCs remained intact in culture (Figure 4).

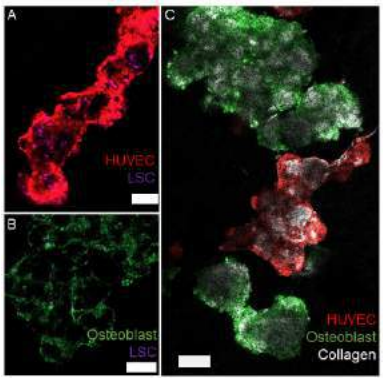

Figure 4: Collagen droplets were used to generate a "minimal bone marrow niche." (A) The vascular niche was modeled by coating LSC-laden droplets with HUVECs, and the (B) endosteal niche was modeled by coating LSC-laden droplets with osteoblasts. (C) Reflectance microscopy confirmed both niches formed surrounding the collagen droplets. (scalebars= 100 µm)

DISCUSSION

By harnessing the directed self-assembly of a droplet-based vascular network, we demonstrated a straightforward model that captures the heterogeneity of the bone marrow in an *in vitro* system. Existing *in vitro* bone marrow models are relatively straightforward and generally include two cell types (typically HSC/LSCs and osteoblasts) without accounting for the bone marrow vasculature. Given the important role the vasculature plays in the regulation of HSCs, models that do not incorporate vascular endothelial cells are missing critical soluble factors important for proper differentiation. 3D bone marrow models are proven to be superior to 2D models because soluble factors are prone to local accumulation [9]. Our 3D co-culture model consisting of LSCs, osteoblasts, and endothelial cells will recapitulate the complex interactions among the various bone marrow niches and can provide a mechanistic understanding of how neighboring cell-secreted chemokines impact LSC behavior.

This method can extend to the development of other vascularized tissue models by including other cell types. By incorporating defined regions of varying phenotypes, we can simultaneously capture multiple aspects of a heterogeneous tissue with regard to the vascular networks and the mechanical properties experienced by the cells. By exploiting and further controlling endothelial cells' tendency to self-assemble into networks, we are able to create networks of unprecedented size to study phenomena on varying length scales through vasculogenesis. Ongoing studies are focused on incorporating more stromal cells and expanding to other endothelial cell types.

ACKNOWLEDGEMENTS

Funding for this research was provided in part by the National Science Foundation (OIA1537256), the University of Delaware Research Foundation Strategic Initiatives Grant, and the National Institutes of Health (P30GM110759, R01HL133163).

REFERENCES

[1] Morgan, JT et al., *Biomaterials*, 189:37-47, 2019.
[2] Davis, GE et al., *Int Rev Cell Mol Biol*, 288:101-65, 2011.
[3] Bersini S et al., *Biotechnol Adv*, 34(6):1113-30, 2016.
[4] Choi, JS et al., *Biotechnol J*, 10(10):1529-45, 2015.
[5] Wang, LD et al., *Nat Rev Mol Cell Biol*, 12(10):643-55, 2011.
[6] Klamer, S et al., *Cell Adhes Migr*, 8(6):563-77, 2014.
[7] Bremond, N et al., *Phys Rev Lett*, 100(2):024501, 2008.
[8] Gleghorn, JP et al., *Lab Chip*, 10(1):27-9, 2010.
[9] Cuddihy, MJ et al., *Small*, 9(7):1008-15, 2013.

ENGINEERING A 3D MODEL OF DUCTAL CARCINOMA IN SITU USING MULTI-MATERIAL FRESH 3D BIOPRINTING

Joshua Tashman (1), Thomas Hinton (1), Daniel Brown (2), Daniel Shiwarski (1), Andrew Lee (1), Andrew Hudson (1), Adrian Lee (1), Adam Feinberg(1,3)

(1) Department of Biomedical Engineering
Carnegie Mellon University
Pittsburgh, PA, USA

(2) Magee-Women's Research Institute
University of Pittsburgh
Pitsburgh, PA, USA

(3) Department of Materials Science and Engineering
Carnegie Mellon University
Pittsburgh, PA, USA

INTRODUCTION

Ductal carcinoma in situ (DCIS) is an abnormal proliferation of premalignant luminal epithelial cells into the breast duct. Only 10-20% of DCIS cases progress from premalignant to malignant; however, there is no clinical tool to determine the likelihood of this transformation [1]. An *in vitro* ductal model of DCIS recapitulating *in vivo* progression to malignancy, by providing a clinical predictive tool, would significantly decrease morbidity and cost associated with prophylactic surgeries. Such a model has been difficult to create via conventional fabrication techniques. To address this, we use our previously developed Freeform Reversible Embedding of Suspended Hydrogels (FRESH) to 3D bioprint collagen-based scaffolds in in complex, 3D geometries. Specifically, we FRESH printed full scale mammary ductal trees based on anatomical imaging data, as well as subcomponents of the ductal network to investigate cellular infiltration and remodeling of the engineered breast tissue constructs.

METHODS

Collagen scaffolds were FRESH bioprinted and then seeded with mammary cells. Briefly, FRESH works by embedding hydrogel bioink in a gelatin microparticle hyrogel support bath with yield stress behavior (fig. 1) [2]. Here, alginate and collagen type I bioinks were prepared as concentrated solutions of pre-polymers. For the hydrogel support bath, we utilized a gelatin microparticle slurry (20 μm mean particle size) washed with $CaCl_2$ and Na-HEPES. 3D models were either generated or derived from optical projection tomography imaging of mouse breast duct trees. Printing instructions were generated using the open-source slicing program Slic3r. 3D printing was carried out with a commercial desktop 3D printer fitted with custom open source syringe pump extruders. To extract printed constructs from the support bath, prints were released at 37°C to melt the gelatin microparticles and washed in a $CaCl_2$ Na-HEPES solution. All printing was conducted in sterile conditions or post-print sterilized with ethanol. Constructs were seeded with

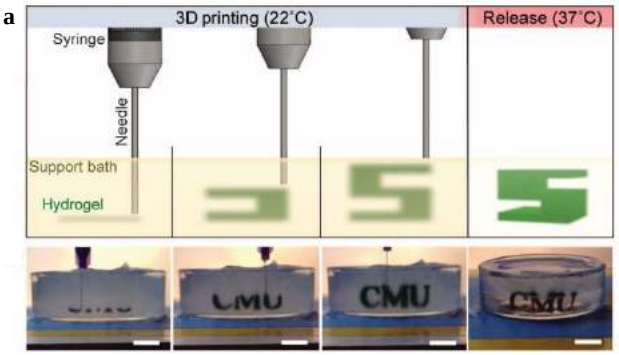

Figure 1: Freeform embedding of suspended hydrogels 3D (FRESH) bioprinting. a) Cartoon demonstrating the Freeform Reversible Embedding of Suspended Hydrogels (FRESH) process. At 22 °C a hydrogel ink is extruded into a gelatin support bath and allowed to gel. After printing the support bath is thermoreversed at 37° C and the print can be retrieved.

MCF10A or primary human breast cells (from prophylactic mastectomies provided by collaborators at Magee-Women's Research Institute) and cultured for 14 days, after which they were fixed, stained, cleared with benzyl alcohol benzyl benzoate, and imaged using confocal fluorescence microscopy.

RESULTS

To demonstrate our ability to reproduce the full complexity of a breast ductal tree we printed a full-scale model generated from tomographic projection imaging (fig. 2a). This ductal tree had a collagen type I inner lumen surrounded by an alginate support structure. Reflectance confocal microscopy of the print surface showed geometric fidelity with the digital files (fig. 2b). To recapitulate a non-malignant breast duct, we printed a tubular construct from collagen type I and seeded it with healthy primary human breast cells (fig. 2c). Whole mount confocal imaging of these constructs reveals spreading and self-assembly into a confluent luminal and myoepithelial bilayer (fig. 2d, e). To assess interactions of cancerous cells with our constructs, we printed an alginate reinforced collagen type I ductal end bud and seeded it with MCF10A cells (fig. 2f, g). Seeded cells produced confluent monolayers coating the end bud lumen (fig. 2h).

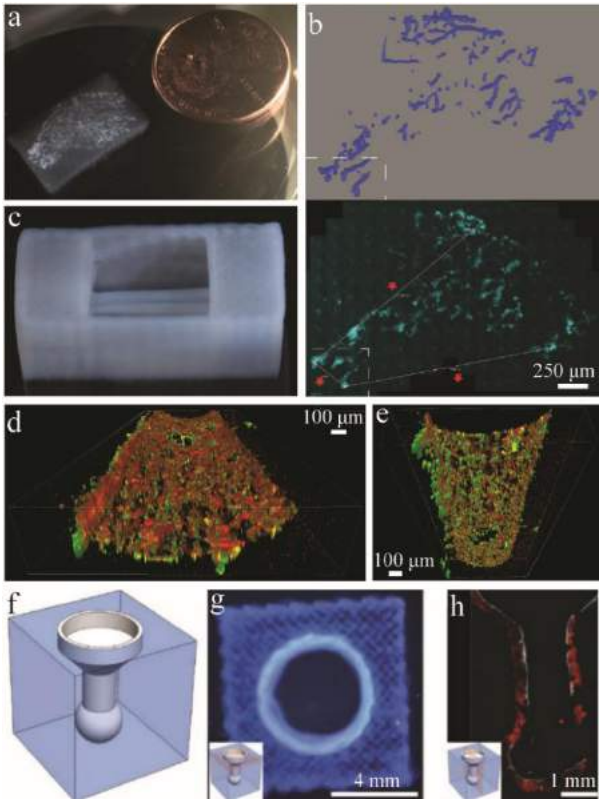

Figure 2: Development of an *in vitro* ductal carcinoma in situ model using freeform embedding of suspended hydrogels. a) A collagen type I and alginate FRESH print of the ductal tree next to a U.S. penny. b) Digital model and reflectance confocal microscopy of the ductal tree. c) A ductal tube model printed in collagen type I. d), e) Surface generated from confocal imaging of seeded tube stained with luminal (red) and myoepithelial (green) markers (d luminal, e exterior). f) A funnel-shaped epithelium design with alginate (blue) supporting a collagen epithelium (white). g) A top-down view of the funnel. h) A cross-section of the entire collagen epithelium (red) with a confluent monolayer of MCF10A cells (cyan).

DISCUSSION

We have shown that we can utilize multi-material FRESH 3D bioprinting to produce complete ductal trees in full physiological detail. We have also demonstrated the printing of essential structural subcomponents of ductal trees, namely a ductal tube, and an end bud at relevant sizes compatible with cell seeding and whole mount fluorescence imaging. Additionally, we developed normal and malignant models by seeding constructs with either healthy human primary breast (from prophylactic mastectomies provided by collaborators at Magee-Women's Research Institute) or MCF10A cells. Together these steps move us closer to producing an *in vitro* model for studying progression of DCIS from premalignancy to malignancy that recapitulates the *in vivo* process.

ACKNOWLEDGEMENTS

This work was funded by the Congressional Directed Medical Research Program (CDMRP) Breast Cancer Research Program under award W81XWH-16-1-0018.

REFERENCES

[1] Special Section: Breast Carcinoma In Situ. ACS, 2015.
[2] Hinton TJ, et al. Three-dimensional printing of complex biological structures by freeform reversible embedding of suspended hydrogels. Sci Adv., 2015.

SB³C2019
Summer Biomechanics, Bioengineering and Biotransport Conference
June 25 -28, Seven Springs, PA, USA

INTEGRATING IN VITRO AND IN SILICO TECHNOLOGIES: DEVELOPMENT OF A PERFUSION BIOREACTOR AND ITS DIGITAL TWIN

Liesbet Geris (1,2,3), Mohammad Mehrian (1,2), Sebastien de Bournonville (1,3), Toon Lambrechts (1,4), Jean-Marie Aerts (1,4), Frank P. Luyten (1,5), Ioannis Papantoniou (1,5)

(1) Prometheus, R&D Division for Skeletal Tissue Engineering, KU Leuven
Leuven, Belgium

(2) Biomechanics Research Unit, GIGA In silico medicine, University of Liège
Liège, Belgium

(3) Biomechanics Section
KU Leuven,
Leuven, Belgium

(4) M3BIORES
KU Leuven
Leuven, Belgium

(5) Skeletal Biology & Engineering Research Center
KU Leuven
Leuven, Belgium

INTRODUCTION

One of the major bottlenecks and cost drivers of cell-based therapies at this point is the manufacturing process that all too often is a scaled out version of the cumbersome manual laboratory procedures established during product development. Bioreactors have been adopted as an enabling technology for tissue engineering construct production, both for single cells and tissue culture. In contrast to static 2D culture in flasks or cell factories, bioreactors can incorporate sensors, allowing the identification and control of critical culture parameters such as temperature, pH, dissolved oxygen or the fluidic pattern (i.e. perfusion, mixing or agitation).

Integrating this information in order to monitor, control and optimize the bioreactor process requires the ability to combine different data sources, historic information as well as the already identified mechanisms of action of 3D tissue growth. In silico models (i.e. computer models) provide such a framework.

In this study, we describe the development of a perfusion bioreactor for cell expansion along with its digital twin, allowing for a precise monitoring, modeling and control of the cell culture process.

METHODS

A perfusion bioreactor was developed previously in our group, allowing for culture of cells in 3D printed scaffolds [1]. Seeding, harvesting, cell identity preservation and extracellular matrix production were investigated under various culture regimes (flow speed & refreshment regimes) [1-2]. A compact, benchtop version of the perfusion bioreactor set-up was recently developed [3], including connections for electronic and optical sensors at the chamber in- and outlet for environmental monitoring and control (Fig. 1). Scaffold filling, life/dead characterization, DNA content, overall glucose consumption and lactate production were tested to show the similarity between the benchmark and compact system. All experiments were carried out with human Periosteal Derived Cells (hPDCs) seeded on 3D printed Titanium scaffolds (6mm ø, 6mm height) with either a diamond-shaped unit cell or a triple period minimal surface unit cell.

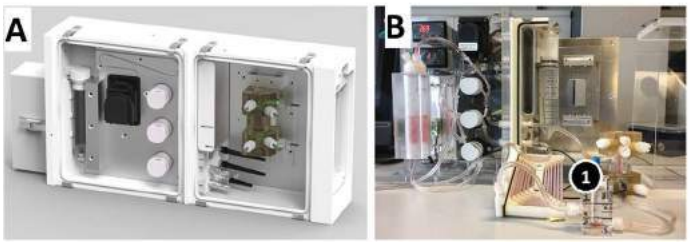

Figure 1: compact benchtop bioreactor. A: Illustration of the bioreactor housing with sensorized bioreactor chamber (right). B: Prototype of the bioreactor, highlighting the fluidic components of the recirculation loop and the internal configuration of the oxygenator

Based on observations made in a suite of experimental results obtained with a pilot version of the perfusion bioreactor set-up, a mechanistic computer model of the neotissue (cells + extracellular matrix) growth was developed [4]. The speed of neotissue growth (Vg) was observed to be influenced by local curvature ($g(\kappa)$), flow-induced shear stress ($f(\tau)$), oxygen ($h_1(C_o)$), glucose ($h_2(C_g)$) and lactate concentrations ($h_3(pH)$).

$$V_g = A_g \cdot f(\tau) \cdot g(\kappa) \cdot h_1(C_o) \cdot h_2(C_g) \cdot h_3(pH) \quad (1)$$

Neotissue growth was modeled in FREEFEM++ by means of the level set method whereby the neotissue growth was simulated by advecting the interface between neotissue and void space in the scaffold with the speed *Vg* defined as in Eq (1). Flow-induced shear stress was calculated from the Computational Flow Dynamics results. The other model variables were calculated based on Michaelis-Menten kinetics describing the spatio-temporal evolution of metabolic variables. Model convergence studies were executed to determine appropriate numerical implementation settings. The different model components were calibrated using in-house experimental data. Predictions on neotissue growth for two different triply periodic minimal surfaces (Gyroid, Dcup) were verified in a dedicated experimental set-up.

Finally, a reduced and reparametrized version of the model was developed (in MATLAB®) by homogenizing the equations over the scaffold volume. A reduction by 10^5 in computation time was obtained, allowing for rigorous single- and multiple objective optimization studies to determine bioreactor settings for maximal neotissue growth [5]. For this study, various evolutionary algorithms were used to perform the optimization.

RESULTS

Online monitoring of oxygen, glucose and lactate is now possible in the newly developed benchtop set-up. Comparing the results from the benchtop bioreactor and the benchmark showed no significant differences in terms of cumulative glucose consumption and lactate production (Fig. 2A), DNA content (Fig. 2B), Gene expression analysis showed similar gene signatures of the expanded populations in both systems.

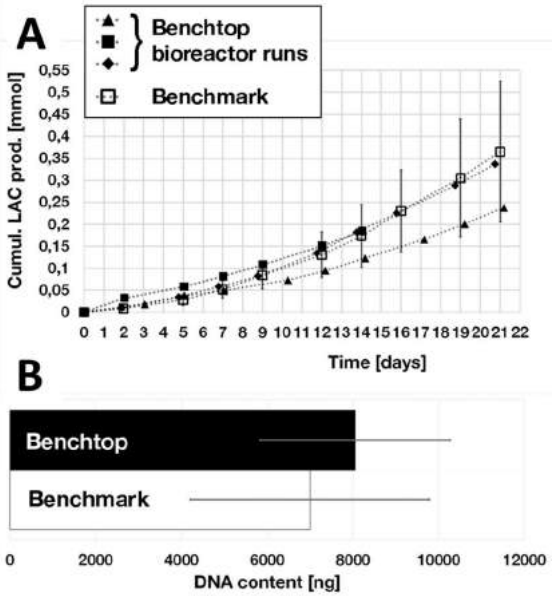

Figure 2: Comparison compact benchtop bioreactor and benchmark. A: Cumulative lactate production over culture time. B. DNA quantification after 21 day culture.

Model predictions showed enhanced neotissue formation and lactate production for Gyroid scaffolds compared to Dcup scaffolds (Fig. 3A). Experimental results (Fig 3B) were quantified in 3D by contrast enhanced nanoCT imaging, confirming model predictions.

The reduced model results (Fig. 3C) showed increased neotissue formation for frequent replacement of the bulk of the medium in the bioreactor. Taking into account the cost of culture (medium & labor costs) shifted the optimal settings towards lower replacement frequencies and medium fractions.

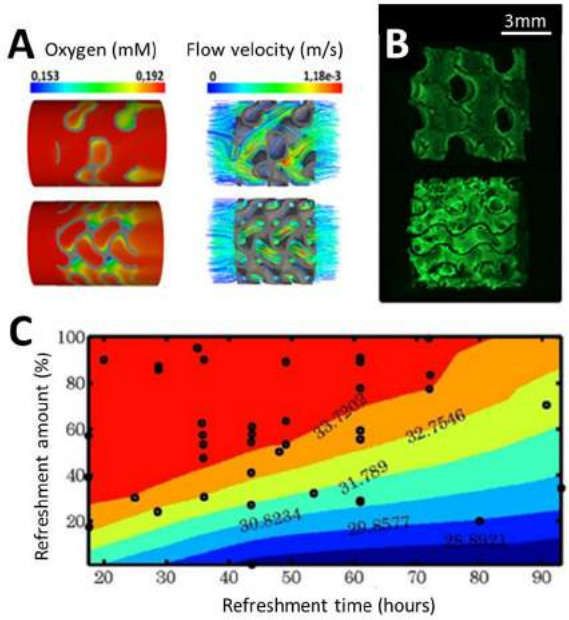

Figure 3: Simulation results and model validation experiments. A: Simulation results for local oxygen concentrations and perfused fluid flow velocity in a Dcup (top) and Gyroid (bottom) titanium scaffold after 3 weeks of bioreactor culture. B: Life-dead staining of human periosteal cells cultured in the bioreactor for 3 weeks. C: Bayesian optimization of culture regime for maximum scaffold filling (color scale with red highest filling perentage) at 1 week.

DISCUSSION

The integrated development of a compact benchtop bioreactor along with its digital twin will provide, on the one hand, additional experimental read-outs for model credibility building and, on the other hand, the necessary real-world data for the development of real-time model-based monitoring and control algorithms for the culture process. This, in turn, will allow for the precise prediction and follow-up of neotissue formation in a 3D perfusion environment, which is an important step towards automation of cell expansion in the context of tissue engineering therapies.

ACKNOWLEDGEMENTS

This work received funding from the European Commission (FP7 ERC StG 279100 & H2020 ERC CoG 772418), the Belgian fund for national research (FNRS; T.0256.16) and the Regenerative Medicine Crossing Borders initiative (www.regmedxb.com) powered by EWI-Vlaanderen. SdB is funded by an FWO-SB scholarship, TL by a VLAIO innovation mandate.

REFERENCES

[1] Sonnaert M. et al. *J Tissue Eng Regen Med*, 11(2):519-530, 2017.
[2] Sonnaert M. et al. *PLoS ONE*, 10(8):e0136875, 2015.
[3] Guyot Y. et al. *BMMB*, 15:169-80, 2016.
[4] Mehrian M. et al. *Biotech Bioeng*, 115(3):617-29, 2018.
[5] de Bournonville S. et al., *Biotech J.*, Prov. Accepted, 2019.

SB³C2019
Summer Biomechanics, Bioengineering and Biotransport Conference
June 25 -28, Seven Springs, PA, USA

SEX-DEPENDENT ORIENTATION AND SIZE OF THE ANTERIOR CRUCIATE LIGAMENT THROUGHOUT SKELETAL GROWTH IN THE PORCINE STIFLE JOINT

Danielle Howe (1), Stephanie G. Cone (1), Jorge A. Piedrahita (2), Lynn A. Fordham (3), Jeffrey T. Spang (4), Matthew B. Fisher (1,4)

(1) Department of Biomedical Engineering
North Carolina State University and
University of North Carolina- Chapel Hill
Raleigh, NC, USA

(2) College of Veterinary Medicine
North Carolina State University
Raleigh, NC, USA

(3) Department of Radiology
University of North Carolina- Chapel Hill
Chapel Hill, NC, USA

(4) Department of Orthopaedics
University of North Carolina- Chapel Hill
Chapel Hill, NC, USA

INTRODUCTION

Pediatric anterior cruciate ligament (ACL) injuries are on the rise, increasing by 74% from 2001 to 2015 [1]. Concerningly, reinjury rates are 4-6 times higher in this population than in adults [2]. Additionally, there are differences in injury rates between sexes. Interestingly, females are at a higher risk of ACL tear than males during adolescence, but not during childhood [3]. Still, data is limited regarding the differences in maturation of the ACL between males and females throughout skeletal growth. In terms of orientation, data suggest increases in ACL-tibial plateau angle from birth to skeletal maturity in humans [4]. Sagittal and coronal ACL-tibial angles were significantly larger in females than in males (by ~2°) from 1 to 20 years of age, but no significant differences between sexes within individual age groups were found. ACL length has been shown to increase similarly in males and females through skeletal growth, diverging at adolescence where the ACL in males becomes longer than in females [5]. ACL cross-sectional area (CSA) has been found to be larger in males than females at skeletal maturity [6], but little data exists comparing the ACL CSA between males and females during growth. Little data is available investigating mid-substance CSA of the individual bundles (anteromedial (AM) and posterolateral (PL)) of the ACL during growth.

The porcine model is a common large animal model to study the musculoskeletal system, particularly the knee joint, and has been used to study the effects skeletal growth [7]. Our group has previously examined ACL orientation and size in female Yorkshire pigs [8]. Therefore, the objective of this study was to examine the orientation and size of the male porcine ACL throughout growth, and to compare these findings to previous data on the geometry and orientation of the female ACL throughout growth. We hypothesize that there are differences in ACL maturation between sexes, specifically that tissue orientation and size will diverge between males and females at adolescence.

METHODS

Hind limbs were collected from a total of 30 male Yorkshire pigs at 0 (newborn), 1.5 (early juvenile), 3 (juvenile), 4.5 (early adolescent), and 6 (early adolescent) months of age (n=6 per age group). Data was previously collected from the same number of female animals at the same ages [8]. All animals were cared for by the North Carolina University Swine Educational Unit, and all experimental protocols were approved by the North Carolina State University Institutional Animal Use and Care Committee. Hind limbs were harvested and the stifle joint was isolated from the animals immediately after euthanasia and prepared for magnetic resonance imaging (MRI). 0-month old limbs were imaged in a 9.4-Tesla Bruker BioSpec 94/30USR machine (Bruker BioSpin Corp, Billerica, MA) using a 3D fast low angle shot scan sequence (3D-FLASH, voxel size=0.1x0.1x0.1 mm). All other age groups were imaged in a 7.0-Tesla Siemens Magnetom machine (Siemens Healthineers, Erlangen, Germany) using a double echo steady state scan sequence (DESS, voxel size=0.42x0.42x0.4 mm). All joints were imaged at full extension.

Images were processed using commercial software (Simpleware). The angle of incidence of the ACL relative to the tibial plateau was calculated in the sagittal and coronal planes [8]. The AM and PL bundles of the ACL were segmented from all images, and exported as 3D models for size analysis using a custom MATLAB code. Bundle lengths were calculated as the length between the midpoint of the femoral and tibial insertions. Bundle CSA values were calculated as the average CSA of the middle 50% of each model. Statistical testing was performed using two-way ANOVA with age and sex as main effects and Tukey's post-hoc tests (JMP, α=0.05).

RESULTS

MR images showed a general increase in size of the stifle joint and changes in the soft tissues within the joint (Fig. 1). Cartilage thickness and growth plate size greatly decreased relative to the size of the joint with increasing age.

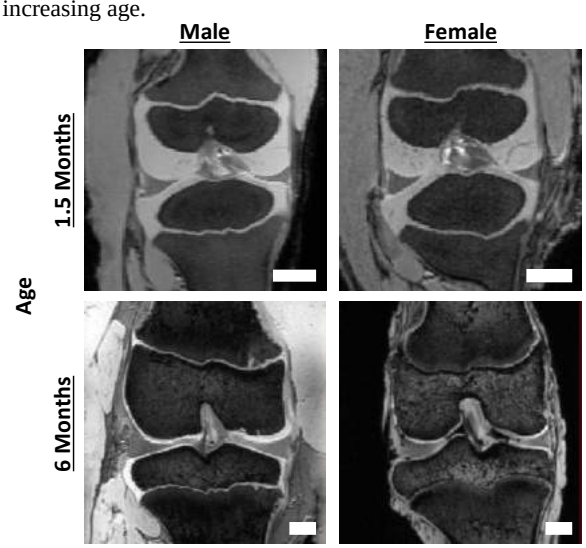

Figure 1: Magnetic resonance images of male and female porcine stifle joints in the coronal plane at 1.5 and 6 months of age. Scale bars are 10 mm.

For both the coronal and sagittal angle of the ACL, statistically significant effects due to age, sex, and age-sex interaction were found ($p<0.05$) (Fig. 2). Coronal angle increased by 18° and 28° from 0 to 6 months of age in males and females, respectively, and sagittal angle increased by 19° and 17° from 0 to 6 months of age in males and females, respectively ($p<0.05$). Overall, coronal angle was 6° higher in females than males, pooled across ages ($p<0.05$), and sagittal angle was 2° higher in males than females, pooled across ages ($p<0.05$). Comparing data at specific age groups using post-hoc analyses, the coronal angle was 7° and 14° higher in females relative to males at 4.5 and 6 months, respectively ($p<0.05$).

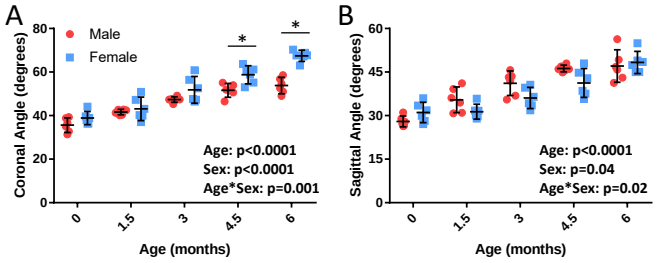

Figure 2: The orientation of the ACL relative to the tibial plateau in the coronal (A) and sagittal (B) planes. Statistical results of main effects shown in corner. Significance ($p<0.05$) between sexes within an age group indicated (*). No age specific significance between sexes was detected in post-hoc analyses for sagittal angle.

Age, sex, and age-sex interaction also had statistically significant effects on CSA and length of both AM and PL bundles of the ACL ($p<0.05$) (Fig. 3). Overall, all metrics increased with age ($p<0.05$) and were larger in males than in females ($p<0.05$). Comparing data at specific age groups using post-hoc analyses, AM length was 35% larger in males than females at both 1.5 and 3 months of age ($p<0.05$). PL length was 52%, 39%, and 19% larger in males at 1.5, 3, and 4.5 months of age, respectively ($p<0.05$), and PL CSA was 41% greater in males at 6 months of age ($p<0.05$).

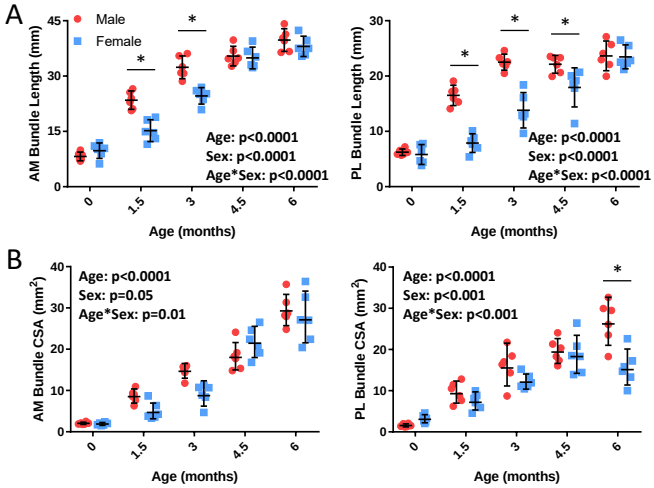

Figure 3: Length (A) and CSA (B) of the AM and PL bundles of the ACL. Statistical results of main effects shown in corner. Significance ($p<0.05$) between sexes within an age group indicated (*). No age specific significance between sexes was detected in post-hoc analyses for AM CSA.

DISCUSSION

In this study, we measured ACL orientation and geometry throughout growth in male and female pigs. Overall, all metrics increased with age, coronal ACL angle was higher in females than males, and ACL bundles were larger in length and CSA in males than females. The coronal angle and PL CSA data at the later age groups matched the literature describing steeper and smaller ACLs in human females than males after adolescence [4-6], partially confirming our hypothesis. However, we did not see a clear divergence in all metrics, particularly length, between males and females at early adolescence as originally hypothesized. This may be because the age range in this study is not broad enough to capture the differences in length between sexes throughout adolescence, since the oldest group is only at early to middle adolescence. In future work, we will study an additional age group to study late adolescence (18 months). The significant interaction between age and sex seen in nearly all metrics indicates that the manner in which the ACL grows with age is sex-dependent. Ongoing work will assess how sex-specific tissue properties may be related to differences in ACL injury rate between sexes during adolescence. Specifically, future work will be done to investigate this possibility by studying the biomechanical function of the ACL in males and females throughout growth.

ACKNOWLEDGEMENTS

We would like to thank the Swine Education Unit (NC State) and the Biomedical Research Imaging Center (UNC-CH) for their contributions to this work. Funding provided by NIH (R03-AR068112, R01 AR071985) and NSF (DGE-1252376).

REFERENCES

[1] Zbrojkiewicz, D., *Med J Aust*, 208:354-358, 2018. [2] Webster, K.E. and Feller, J.A., *Am J Sports Med*, 44:2827-32, 2016. [3] LaBella, C.R. et al, *Pediatrics*, 133:1437-50, 2014. [4] Kim, H.K. et al, *Radiology*, 247:826-835, 2008. [5] Edmonds, H.E. et al., *J Pediatr Orthop*, 35:712-20, 2015. [6] Whitney, D.C. et al., *Am J Sports Med*, 42:1796-805, 2014. [7] Cone, S.G. et al., *Tissue Eng Part C Methods*, 23:763-780, 2017. [8] Cone, S.G. et al., *J Orthop Res*, 35:2725-2732, 2017.

SB³C2019
Summer Biomechanics, Bioengineering and Biotransport Conference
June 25 -28, Seven Springs, PA, USA

DECORIN, ALONE AND IN TANDEM WITH BIGLYCAN, ALTERS VISCOELASTICITY IN AGED TENDONS

Ryan J. Leiphart, Snehal S. Shetye, Stephanie N. Weiss, Louis J. Soslowsky

McKay Orthopedic Research Laboratory, University of Pennsylvania, Philadelphia, PA, United States

INTRODUCTION

Risk of tendon injury increases with age, yet the age-associated changes to tendon tissue that lead to increased injury risk have yet to be elucidated [1]. Decorin (Dcn) and biglycan (Bgn) are small, leucine-rich proteoglycans (SLRPs) present in the tendon extracellular matrix that regulate collagen fibrillogenesis [2,3]. Both SLRPs are highly expressed during development, and conventional knockouts of either molecule impact tendon mechanical properties [4]. While knockout of decorin protects against age-associated reductions in tendon mechanical properties, acute deletion of biglycan or both SLRPs in mature tendons reduces mechanical and structural properties [5,6,7]. These results demonstrate that these SLRPs play a role in tendon homeostasis in addition to their role in development. However, the differential roles of these molecules in aged tendon homeostasis is unknown. Therefore, the objective of this study was to determine the effect of acute deletion of decorin, biglycan, or both SLRPs on aged tendon mechanics. Due to the negative impact of decorin during tendon aging and the positive impact of biglycan in tendon homeostasis, we hypothesized that acute deletion of biglycan would reduce tendon mechanical properties more than acute deletion of decorin, and that acute deletion of both SLRPs would result in similar mechanical properties to biglycan-deficient tendons.

METHODS

Animals: Female wild-type (WT) (n=6) and bitransgenic $Dcn^{flox/flox}$ (n=11), $Bgn^{flox/flox}$ (n=9), and $Dcn^{flox/flox}$/ $Bgn^{flox/flox}$ (n=15) mice with a tamoxifen (TM) inducible Cre were used in this study (IACUC approved). At 485 days old, mice received three consecutive daily TM injections (4mg/40g body weight) for Cre-mediated excision of targeted genes. Mice were sacrificed 30 days later (515 days of age). Patella-patellar tendon-tibia complexes were harvested from the left hind limb and prepared for mechanical testing as described [5].

Mechanical Testing: Uniaxial, viscoelastic testing was performed with an Instron 5848. The testing protocol consisted of 10 cycles of preconditioning, followed by stress relaxations at 3%, 4%, and 5% strain for 10 minutes. Following each stress relaxation, frequency sweeps of 10 cycles at 0.1, 1, 5, and 10 Hz were performed. A ramp-to-failure followed the final stress relaxation. Percent relaxation, dynamic modulus (E*), and phase shift (δ) were computed for each stress relaxation and frequency sweep. Stiffness, modulus, maximum load, and maximum stress were quantified from the ramp-to-failure data.

Statistics: For all mechanical properties, one-way ANOVAs with Bonferroni post-hoc tests were used to compare across genotypes. Significance was set at $p<0.05$, and trends were set at $p<0.10$.

RESULTS

Quasi-Static Mechanics: No differences in CSA were observed between genotypes (data not shown). No differences in stiffness or maximum load were observed between genotypes (Fig 1). No differences in insertion or midsubstance modulus were observed between genotypes (Fig 2). $Dcn^{-/-}/Bgn^{-/-}$ tendons had larger maximum stresses than $Dcn^{-/-}$ tendons (data not shown).

Stress Relaxation: $Dcn^{-/-}/Bgn^{-/-}$ tendons exhibited larger stress relaxations than WT and $Bgn^{-/-}$ tendons at 3% and 4% strain (Fig 3). $Dcn^{-/-}$ tendons exhibited a larger stress relaxation than WT tendons at 4% strain, and $Dcn^{-/-}/Bgn^{-/-}$ tendons trended towards more stress relaxation than $Bgn^{-/-}$ tendons at 5% strain.

Dynamic Mechanics: No differences in dynamic moduli were observed between genotypes at any strain level or frequency (data not shown). At 3% strain, $Dcn^{-/-}/Bgn^{-/-}$ tendons had larger tan(δ) values than WT tendons at all frequencies (Fig 4). $Dcn^{-/-}/Bgn^{-/-}$ tendons had larger tan(δ) values than $Bgn^{-/-}$ tendons at 0.1Hz and 1Hz and trended towards larger tan(δ) values at 5Hz. $Dcn^{-/-}$ tendons trended towards larger tan(δ) values than WT tendons at 5Hz and 10Hz. At 4% strain, $Dcn^{-/-}/Bgn^{-/-}$ tendons had larger tan(δ) values than WT tendons at 0.1Hz, 5Hz, and 10Hz (Fig 5). $Dcn^{-/-}/Bgn^{-/-}$ tendons had larger tan(δ) values than $Bgn^{-/-}$ tendons at 0.1Hz and 5Hz and trended towards larger tan(δ) values at 10Hz. $Dcn^{-/-}$ tendons had larger tan(δ) values than WT tendons at 1Hz and 10Hz, had larger tan(δ) values than $Bgn^{-/-}$ tendons at 1Hz, and trended towards larger tan(δ) values than WT and $Bgn^{-/-}$ tendons at 5Hz. At 5% strain, $Dcn^{-/-}/Bgn^{-/-}$ tendons had larger tan(δ) values than $Bgn^{-/-}$ tendons at 0.1Hz and 1Hz (data not shown). $Dcn^{-/-}$ tendons trended towards larger tan(δ) values than $Bgn^{-/-}$ tendons at 0.1Hz and 1Hz.

DISCUSSION

Induced knockout of decorin, biglycan, or both molecules in aged tendons did not impact quasi-static mechanical properties compared to WT tendons. Dynamic mechanical properties were also unaffected by genotype. Viscoelastic properties were most affected by both decorin knockouts, especially at low (3%) and intermediate (4%) strains. Deficiency of both decorin and biglycan led to increased viscoelasticity compared to WT and biglycan-deficient tendons at 3% and 4% strain. Deficiency in decorin alone led to some increases in viscoelasticity at the intermediate strain level compared to WT and biglycan-deficient tendons. The viscoelastic effects of decorin or decorin/biglyan deficiency were largely lost at the high (5%) strain level. These results run contrary to our hypothesis that deletion of biglycan would lead to

larger reductions in mechanical properties than decorin deletion and that double knockout tendons would have similar mechanical properties to biglycan-deficient tendons. Instead, knockout of both molecules led to large increases in viscoelastic properties, and some of these properties were increased with decorin deficiency alone.

Results demonstrate that decorin plays a larger role than biglycan in aged tendon mechanics. While no differences were observed between WT and *Bgn*$^{-/-}$ tendons, *Dcn*$^{-/-}$ tendons had increased viscoelastic properties compared to control tendons. While biglycan has been shown to impact mechanics in mature tendons, biglycan expression decreases with age [6,2]. This decreased expression may explain the negligible effect of biglycan deletion in aged tendons.

The structure-function role of decorin within the tendon matrix remains controversial. Conventional knockout of decorin impacts both quasi-static and viscoelastic properties of the patellar tendon [4,8]. Depletion of SLRP GAG chains in tail tendon fascicles, however, does not affect quasi-static and viscoelastic properties [9,10]. Results of this study support previous findings that decorin deficiency alters tendon viscoelastic properties at the tissue level.

The viscoelastic changes seen in decorin-deficient tendons were enhanced with the dual deletion of decorin and biglycan. Biglycan expression has been shown to increase in response to induced deletion of decorin [11]. The *Dcn*$^{-/-}$/*Bgn*$^{-/-}$ genotype eliminates this potential compensatory mechanism, which may explain the observed increases in viscoelastic properties in these tendons.

A limitation of this study is the small sample size used across groups, which may lead to certain parameters being underpowered. In addition, the mechanical changes observed lack a mechanistic explanation at this time. Future studies will analyze differential gene expression between these genotypes to better understand how decorin and biglycan together influence aged tendon mechanics.

This study reveals the role of decorin in the viscoelastic properties of aged tendons and demonstrates that biglycan may offset changes in these properties following the loss of decorin. These results provide further understanding of the role of SLRPs in the mechanical properties of aging tendons.

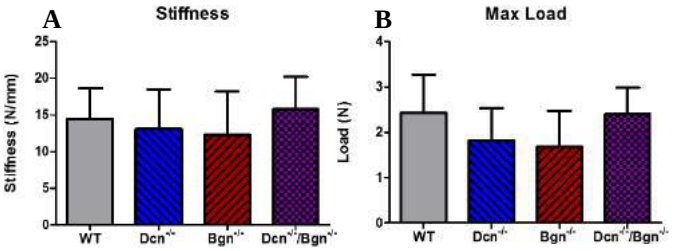

Figure 1. Quasi-static mechanical properties. No differences in stiffness (A) or maximum load (B) were observed between genotypes.

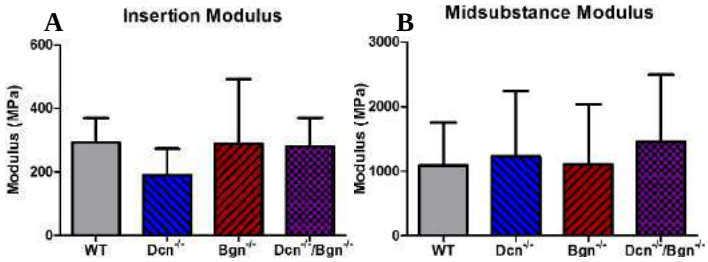

Figure 2. Quasi-static material properties. No differences in insertion (A) or midsubstance (B) modulus were observed between genotypes.

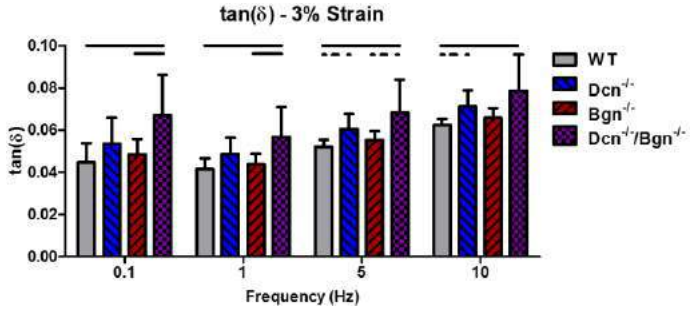

Figure 4. tan(δ) at 3% strain. *Dcn*$^{-/-}$/*Bgn*$^{-/-}$ tendons had a larger phase shift than WT tendons at all frequencies and *Bgn*$^{-/-}$ tendons at 0.1Hz and 1Hz. Solid lines indicate p<0.05, dashed lines indicate p<0.10.

ACKNOWLEDGEMENTS

This work was supported by the NIH (P30AR069619, R01AR068057) and the NSF GRFP. The authors thank Dr. David Birk and Mei Sun for providing the mice for this study.

REFERENCES

[1] Birch, HL et al., *Adv Exp Med Biol*, 920:247-260, 2016. [2] Zhang, G et al., *J Cell Biochem*, 98:1436-1449, 2006. [3] Ameye, L et al., *FASEB*, 16:673-680, 2002. [4] Robinson, PS et al., *J Biomech Eng*, 127:181-185, 2005. [5] Dunkman, AA et al., *Matrix Biol*, 32:3-13, 2013. [6] Beach, ZM et al., ORS, 0237, 2018. [7] Robinson, KA et al., *Matrix Biol*, 64:81-93, 2017. [8] Elliott, DM et al., *Ann Biomed Eng*, 31:599-605, 2003. [9] Fessel, G & Snedeker, JG, *J Theor Biol*, 268:77-83, 2011. [10] Fessel, G & Snedeker, JG, *Matrix Biol*, 28:503-510, 2009. [11] Dunkman, AA, et al., *Matrix Biol*, 35:232-238, 2013.

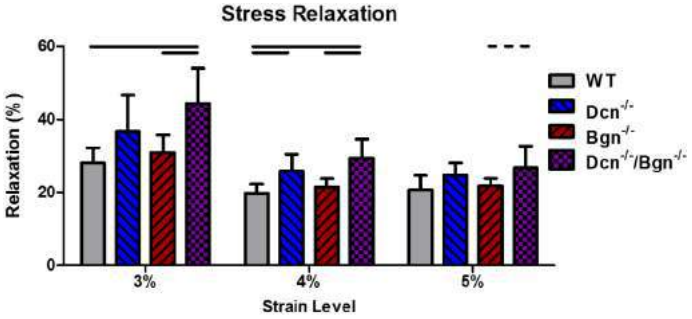

Figure 3. Stress relaxation. *Dcn*$^{-/-}$/*Bgn*$^{-/-}$ tendons exhibited larger stress relaxations than WT and *Bgn*$^{-/-}$ tendons at 3% and 4% strain. Solid lines indicate p<0.05, dashed lines indicate p<0.10.

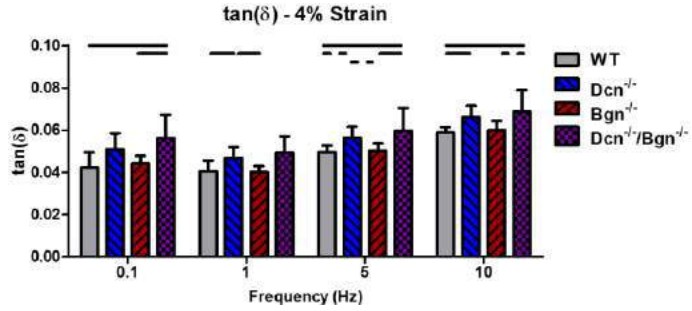

Figure 5. tan(δ) at 4% strain. *Dcn*$^{-/-}$/*Bgn*$^{-/-}$ tendons had a larger phase shift than WT tendons at 0.1Hz, 5Hz, and 10Hz and *Bgn*$^{-/-}$ tendons at 0.1Hz and 5Hz. Solid lines indicate p<0.05, dashed lines indicate p<0.10.

SB^{3}C2019
Summer Biomechanics, Bioengineering and Biotransport Conference
June 25 -28, Seven Springs, PA, USA

BATH OSMOLARITY ALTERS MULTISCALE MECHANICS AND DAMAGE IN TENDON

Ellen T. Bloom (1), Andrea H. Lee (1), Dawn M. Elliott (1)

(1) Department of Biomedical Engineering
University of Delaware
Newark, Delaware, USA

INTRODUCTION

Phosphate buffered saline (PBS) is a common choice for bathing solution in mechanical testing of biological tissue; however, even at physiological concentrations, the PBS bath causes increased hydration and decreased modulus in tendon and other tissues [1-3]. The physiological PBS bath also causes microstructural changes in tendon, by increasing collagen fibril diameter and interfibrillar spacing [3]. Beyond these observations, it remains unknown how a PBS bath solution may alter tendon multiscale mechanical behavior and damage. Our group has quantified tendon multiscale mechanics and damage, showing that microscale strain and sliding are related to tissue-level parameter changes after mechanical loading [4,5]. We hypothesize that increased tendon swelling and microstructural changes due to swelling in physiological PBS alter microscale sliding and increase tendon damage during tensile loading and that these effects can be mediated with a bath osmolarity that maintains fresh tendon hydration. We have recently shown that by altering the osmolarity of the bath using a combination of Tris-buffered saline (S) and 8% polyethylene glycol (PEG), which we defined as SPEG, the hydration and macroscale modulus of tendon is conserved compared to fresh tendon [2]. The objective of this study was to compare the effects of PBS and SPEG incubation on multiscale tendon mechanics and damage. The effect of bath solution on tissue mechanical behavior is critical knowledge that is necessary to interpret past work and design future studies.

METHODS

Sample Preparation: Rat tail tendon fascicles were harvested from 4-7 month-old female Long-Evans rats and tested in either physiological 0.15M PBS (n=8) or in 8% SPEG (n=7). Previous work showed that 8% SPEG maintains tendon's fresh frozen hydration and tensile modulus [2]. Following dissection, each sample was stained with 10 μg/ml 5-DTAF (Life Technologies).

Multiscale Mechanical Testing: Testing used an established protocol on a uniaxial device mounted on an inverted confocal microscope [4,5]. After gripping, a 0.1 N preload was used to define the reference length, 4 photobleached lines were made on the midportion, and each sample was preconditioned with 5 cycles to 2% grip strain. Testing included ramping each sample to 6% grip strain (baseline, i.e., pre-damage, Fig. 1A), holding for a 15-min relaxation, unloading to the initial length for a 40-min rest, then loading to failure (diagnostic, i.e., post-damage). All loading and unloading rates were 0.1%/s. Tissue-level parameters were calculated using displacement of ink markers measured via CCD camera (Fig. 1B, arrow).

Data Analysis: Tissue-level parameters were calculated via digital image correlation from the CCD images and included transition point, inflection point, and linear region modulus (Fig. 1A). The stress-strain curve from zero to the inflection point, here defined as the point where the curve shifts from strain-stiffening to strain-softening behavior [5],

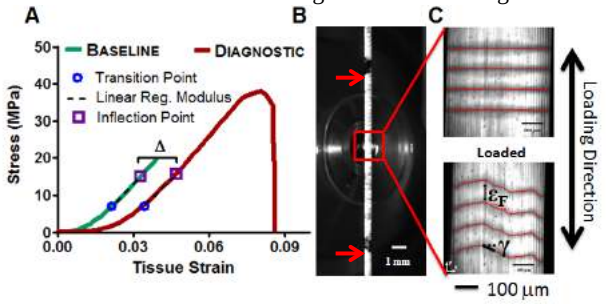

Fig 1. (A) Representative loading curve showing Δ and tissue-level parameters; (B) configuration of sample in tester showing ink markers (arrows) and (C) photobleached lines during reference and deformed with loading.

was fit with a nonlinear constitutive model which optimized the transition strain and stress (end of the toe region) and linear region modulus [6]. These parameters were calculated for baseline and diagnostic ramps. Transverse strain was calculated from confocal images. To test the effect of bath osmolality between PBS and SPEG, a two-tailed t-test was used (p=0.05). To test for damage following mechanical loading (the difference between baseline and diagnostic) in each test (Fig. 1A), a two-tailed t-test was used (p=0.05).

Microscale parameters were measured using confocal images, from the deformation of photobleached lines, and included microscale strain (ε_f) and microscale sliding (γ) (Fig. 1C). Microscale strain was measured as the distance between the pairs of photobleached lines, and microscale sliding as the averaged tortuosity of the lines [4,5]. Non-recoverable sliding, a measure of microscale damage, was defined as the residual sliding that remained at the end of the 40-min rest period. An exponential decay function was fit to the microscale sliding recovery to quantify a time constant for sliding recovery.

RESULTS

Tissue-level Mechanics: At baseline, the SPEG group had a higher modulus compared to the PBS group (Fig. 2C), consistent with a previous study [2], and there was no difference between SPEG and PBS for transition and inflection point (Fig. 2A,B). At diagnostic, the modulus decreased compared to baseline for both SPEG and PBS, providing evidence that damage had occurred [4], however the modulus was no longer different between the two groups (Fig. 2C). At diagnostic, the transition strain was higher in SPEG compared to PBS. At diagnostic the inflection point strain increased for both groups compared to baseline, but there was no difference between SPEG and PBS. The transverse strain, measured from confocal images throughout the test, was significantly higher in SPEG compared to PBS immediately after loading (t=0), (Fig. 2D), however, there was no difference between the groups throughout the remainder of the test.

Microscale Mechanics: The microscale strain in the SPEG group was higher than PBS throughout loading, and was lower than PBS after unloading and throughout the recovery (Fig. 3A). Microscale sliding was not different between the SPEG and PBS groups and only partially recovered for both (Fig. 3B). Interestingly, the rate of the sliding recovery was significantly faster for SPEG (Fig. 3C), and the amount of non-recoverable sliding, a measure of microscale damage, was significantly lower for SPEG compared to PBS (Fig. 3D).

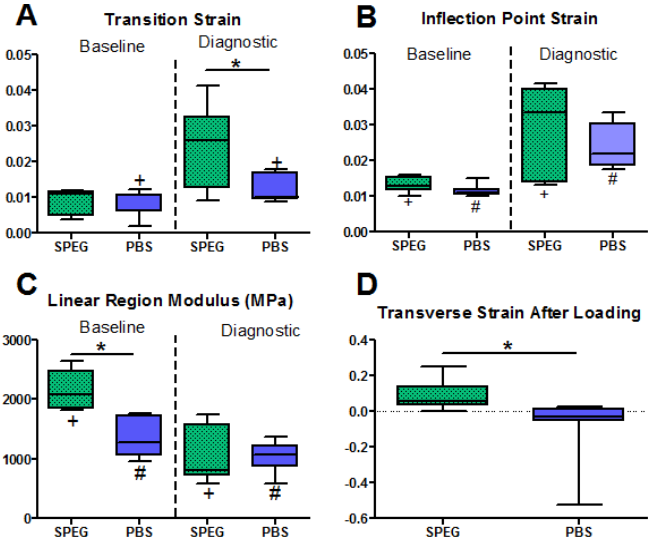

Fig 2. (A-C) Tissue-level parameters during baseline and diagnostic. (D) Transverse strain fully recovered in both groups. Error bars show 95% CI and * # and + represent p<0.05, # and + between baseline and diagnostic within a group.

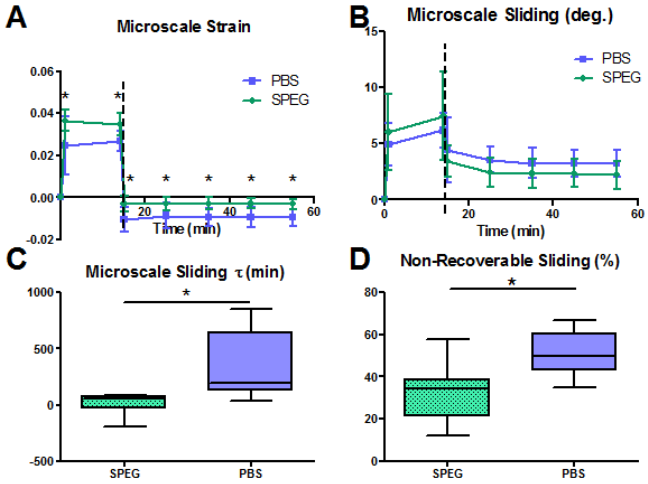

Fig 3. (A) Microscale strain and (B) sliding only partially recovered for both groups. (C) Time constant for sliding (SPEG n=6) and (D) non-recoverable sliding were smaller in SPEG samples. Error bars show 95% confidence interval and * represents p<0.05.

DISCUSSION

This study investigated the effect of bath solution on multiscale mechanics and damage in tendon by comparing PBS and SPEG, where the SPEG maintains fresh-frozen tissue hydration and physiological PBS swells the tissue. The tissue-level mechanical changes were consistent with previous work [1-3], as were the PBS group's tissue and microscale mechanics [4,5]. Importantly, we observed differences between PBS and SPEG in the tissue-level damage and the microscale mechanics. The increased ability of SPEG samples to recover microscale strain and sliding compared to PBS, suggests that swelling increases microscale damage. When tested in SPEG the sliding recovery is also faster (lower time constant) compared to PBS, suggesting that microscale viscoelasticity is affected by swelling. Whether this is due to fluid flow or intrinsic viscoelasticity is not yet known. Overall, these findings suggest that testing in PBS, where swelling is induced, not only affects the tissue-scale properties, but also affects the microscale mechanics, viscoelasticity, and damage.

This study shows that the osmolarity of bath solution, which changes the sample hydration and tissue-scale mechanics, is important in tendon mechanical testing and also affects the microscale loading and mechanical damage. These tests were about 1 hour in duration and included a ramp, hold, and recovery. Previous work that has used physiological PBS as a bathing solution therefore likely swelled the tissue (depending on test duration), and those study results should be considered in light of the potential swelling effect. However, as long as appropriate controls were used to investigate the study hypotheses, reported findings are relevant. Future mechanical testing, particularly long duration tests such as cyclic fatigue, should consider using a SPEG bath solution with an osmolarity that maintains fresh tissue water content.

ACKNOWLEDGMENTS

The NIH R01 EB002425 and NIH INBRE grant PG0GM103446.

REFERENCES

[1]Han *et al.*, *Ann. Biomed. Eng.*, 40:1610–1621, 2012. [2]Safa *et al.*, 2017.[3]Screen *et al.*, *Acta Biomater.*, 2:505–513, 2006. [4]Lee *et al.*, *Ann. N. Y. Acad. Sci.*, 1409:85–94, 2017.[5]Lee *et al.*, *Acta Biomater.*, 57:363–372, 2017.[6]Tanaka *et al.*, *J. Biomech. Eng.*, 133:074502, 2011.

SB^{3}C2019
Summer Biomechanics, Bioengineering and Biotransport Conference
June 25 -28, Seven Springs, PA, USA

MAGNETIC RESONANCE ELASTOGRAPHY OF THE HUMAN FOREARM DURING ISOMETRIC CONTRACTIONS

Daniel R. Smith (1), Andrea Zonnino (1), Peyton L. Delgorio (1), Raymond Duda (1), Fabrizio Sergi (1), Curtis L. Johnson (1)

(1) Department of Biomedical Engineering
University of Delaware
Newark, DE, USA

INTRODUCTION

Redundancy in the neuromuscular system enables humans to perform skilled motor tasks [1], though it is mostly unknown how the central nervous system manages and exploits redundancy, especially for fine motor tasks. Quantifying and analyzing the muscle co-activation could help in better understanding the mechanisms of fine motor control in neuromotor impairment. 40% of stroke survivors, or about two million United States citizens [2], are affected by upper motor neuron syndrome, which commonly leads to "abnormal coupling" of different muscle groups [3]. We propose to use magnetic resonance elastography (MRE) to study the coordinated action of multiple forearm muscles. MRE is a magnetic resonance imaging technique in which an external actuator generates shear waves that propagate through soft tissue. The wave motion is imaged with MRI, and then an inversion algorithm is used to solve for the tissue viscoelastic mechanical properties [4]. Other studies have shown the promise of using MRE to quantify the viscoelastic mechanical properties of skeletal muscle [5], including examinations of bicep muscle [6] and thigh muscle [7] stiffness with load or contraction, though forearm muscles and wrist torque contractions have yet been studied with MRE. Because viscoelastic properties of muscles are related to muscle force, as described by the short-range stiffness model [8], it may be possible to use MRE to ultimately estimate muscle force from viscoelastic properties. The purpose of this work is to quantify the mechanical changes to the forearm flexors and extensors measured via MRE in different isometric loading conditions (rest, flexion, extension).

METHODS

Subjects: We examined three healthy participants (2/1 M/F Age: 21-27) with a Siemens 3T Prisma scanner. Subjects laid headfirst and prone in the bore of the scanner with their right arm in a forward posture in a custom device (Figure 1).

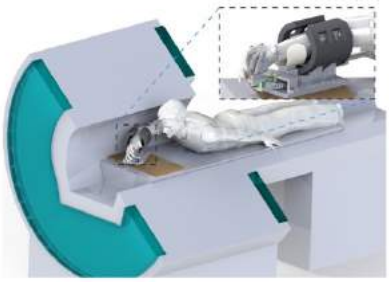

Figure 1: Experimental setup for the forearm MRE experiments

The custom device has three points of contact with the arm and hand: the passive driver for MRE under the belly of the forearm muscles; a strap to restrain the forearm; and a hand constraint against which force is applied during the experiments. A flexible MRI coil is constrained between the base of the device and the passive driver and then wrapped around the proximal forearm for imaging.

Imaging Protocol: MRE scans used an echo-planar imaging (EPI) MRE sequence with 3.0 mm isotropic resolution. Imaging parameters included: TR/TE = 1127/33 ms, FOV = 144 x 240 mm, 48 x 80 matrix, slices = 15. During MRE scans, vibrations were generated at 80 Hz using a pneumatic actuator (Resoundant) with a passive driver built into the custom forearm device. MRE scans were performed at three isometric contraction conditions (rest, flexion, and extension) with three repetitions of each series of contraction conditions. Two auxiliary isotropic T1-weighted anatomical scans (one acquired sagittally and one

acquired axially) were included for anatomical localization of individual muscles.

A follow-up experiment was performed on a single subject to observe muscle stiffness differences based on contraction intensity. MRE data was acquired with the participant instructed to perform wrist flexion and extension at both high and low torque levels. In this experiment we used a higher-resolution MRE scan with 2.0 mm isotropic resolution. Imaging parameters included: TR/TE = 2629/44 ms, FOV = 144 x 240 mm, matrix = 72 x 120, slices = 30. The higher resolution scans required three separate interleaved acquisitions to sample the entire displacement field necessary for mechanical property estimation, with the subject instructed to rest between contractions.

Analysis: We used a non-linear inversion algorithm (NLI) [9] to estimate the viscoelastic shear stiffness from the measured displacement fields (Figure 2). The stiffness in calculated from the complex shear modulus, $G = G' + iG''$, as $\mu = 2|G|^2/(G'+|G|)$. The shear stiffness describes the resistance of a viscoelastic solid to a harmonic shear forcing at the actuation frequency (80 Hz in this experiment).

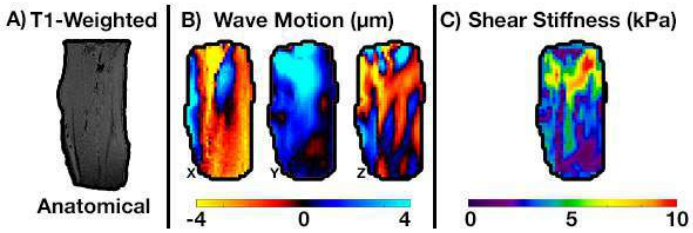

Figure 2: A) Single slice of a T1-weighted anatomical scan of the forearm; B) the x, y, and z components of the wave motion in the same forearm slice; and C) the corresponding forearm stiffness map.

The T1-weighted anatomical scans were used to create regions-of-interest (ROIs) for each of the individual muscles with four flexors (flexor carpi radialis, flexor carpi ulnaris, flexor digitorum profundus, and flexor digitorum superficialis) and five extensors (brachioradialis, extensor carpi radialis brevis, extensor carpi radialis longus, extensor capri ulnaris, extensor digitorum). We examined differences in muscle stiffness with contraction used a paired *t*-test after averaging each of the repetitions for each subject. We excluded MRE scans with low SNR from this analysis.

RESULTS

In the first experiment, we observed differences in the complex shear stiffness of the extensor muscles between rest (5.64 kPa) and both contraction conditions. The extensors significantly increased during extension (7.81 kPa; +38.5%; p = 0.009), and also increased during flexion, though this was not significant (6.65 kPa; +17.9 %; p = 0.173) across the subjects. We did not observe significant differences in the flexors between rest (5.91 kPa) and flexion (5.07 kPa; -16.5%; p = 0.178) or extension (5.21 kPa; -13.4%; p = 0.122) across the subjects.

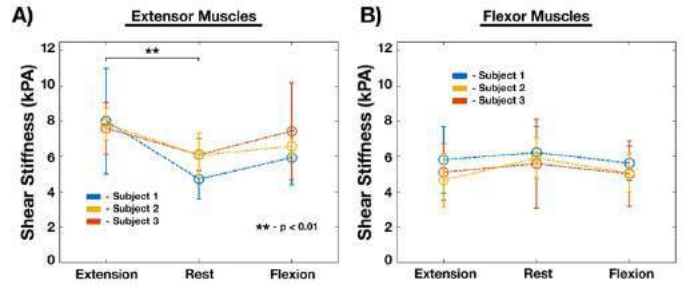

Figure 3: Muscle stiffness changes at different contraction conditions: rest, extension, and flexion. A) Mean and standard deviation of stiffness across all extensor muscles for each subject and condition, and B) mean and standard deviation of stiffness across all extensor muscles for each subject and condition.

In the second experiment, multiple levels of contraction intensity resulted in an increased stiffness based on level of muscle activation (Figure 4). Both extensor and flexor muscles stiffened during agonist contraction, with greater stiffening at high torque. They also stiffened during antagonist contraction though to a lesser degree. These results are consistent with the previous experiment and revealed that flexor muscles likely behave similarly as extensor muscles, but with less overall stiffening during these contraction tasks.

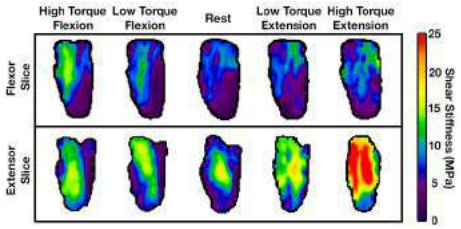

Figure 4: A comparison of forearm MRE stiffness data from single slices through the flexor (top) and extensor (bottom) muscles during five activation states: high torque flexion, low torque flexion, rest, low torque extension, and high torque extension.

DISCUSSION

In this study, we observed stiffening in extensors whether they were acting as agonists or antagonists, though there appeared to be a higher stiffness, and therefore higher activation, during their agonist function. In this case, the extensor muscles act as we hypothesized: with increased stiffness during contraction, and more activation as agonists. Stiffening during antagonist function likely indicates co-contraction for stability during flexion. However, in the flexor muscles, we did not observe a significant change whether they were acting as agonists or as antagonists. The second experiment with multiple levels of contraction revealed that flexor muscles likely behave similarly as extensor muscles but with less overall stiffening. This observation is likely due to the use of higher imaging resolution for more accurate and reliable stiffness mapping. Additionally, this experiment indicated that stiffness during contraction is related to activation intensity, and likely force output. However, these scans took almost twice the time for data collection during each contraction state, which could introduce experimental challenges, such as muscle fatigue, due to the sustained contractile state. Future work will include exploring this possible limitation and counteracting it with accelerated data acquisition, as well the use of an MR-compatible force/torque sensor and visual feedback to control the level of contraction and correlate the levels of muscle stiffness to measurements of joint torque.

REFERENCES

[1] Guigon, E., et al. Journal of Neurophysiology 97.1:331-347. 2007
[2] Mozaffarian, D., et al. Circulation. 133.4: e38-360. 2016
[3] Dewald, J. P. A., et al. Brain 118.2: 495-510. 1995
[4] Manduca, A., et al. Medical Image Analysis, *5*.4: 237–254. 2001
[5] Mariappan, Y. K., et al., Clin. Anat., 23.5: 497–511. 2010
[6] Dresner, M. A., et al., J. Magn. Reson. Imaging, 13.2: 269–276. 2001
[7] Barnhill, E., et al. Physiological Measurement 34.12: 1675. 2013
[8] Rack, P. and Westbury, D.R., The Journal of Physiology 240.2: 331-350. 1974
[9] McGarry, M. D. J., et al., Medical Physics. 39.10: 6388-6396. 2012

SB³C2019
Summer Biomechanics, Bioengineering and Biotransport Conference
June 25 -28, Seven Springs, PA, USA

SEX-RELATED DIFFERENCES IN CARPAL ARCH MORPHOLOGY

Kishor Lakshminarayanan, Rakshit Shah, Zong-Ming Li

Hand Research Laboratory
Department of Biomedical Engineering
Cleveland Clinic
Cleveland, OH, USA

INTRODUCTION

Carpal tunnel syndrome (CTS) occurrence has a sex propensity with women being 3 times more likely to develop the condition [1]. One possible cause proposed for the higher incidence is that women have smaller wrist size than men [2]. The smaller wrist size in women also extends to a relatively smaller carpal tunnel cross-sectional area in women compared to men [3,4]. However, there was no sex-related differences in the relative carpal tunnel contents area [5]. Specifically, the relative median nerve cross-sectional area was not significantly different between the sexes [6]. The reduced available space for the tunnel contents in women could increase the likelihood of the median nerve getting compressed against the TCL. With median nerve being in close proximity to the TCL, investigating the sex-related differences in TCL-formed carpal arch morphology could provide insight into the higher incidence of CTS in women.

In addition to sex-related differences in carpal tunnel area, women have less compliant carpal tunnels compared to men [7]. Moreover, women have been shown to have a less elastic TCL than men [8] which may contribute to the reduced carpal tunnel compliance in women. Based on these evidences, it is possible that women have a predisposition for a reduced palmar bowing of the TCL compared to men. A less elastic TCL might not be able to palmarly bow adequately to accommodate for any reduction in available space for contents within the tunnel. Consequently, a reduced palmar bowing in women could make them more susceptible to median nerve compression by the TCL. However, to date, little is known about the differences in palmar bowing of the TCL between the sexes.

The purpose of this study was to determine whether the TCL-formed carpal arch would be different between healthy women and men at the distal and proximal carpal tunnel. The carpal arch was quantified by palmar bowing (carpal arch height-to-width ratio). It was hypothesized that women would have smaller palmar bowing, especially in the distal tunnel.

METHODS

Twenty healthy young adults (10 women and 10 men) were recruited for the study. Subjects signed a written informed consent form approved by the Institutional Review Board before participating in the study. Subjects were asked to sit next to a testing table and place their right hand on the testing table with the shoulder abducted 30° and the elbow flexed 90°. The hand and wrist were then stabilized by a thermoplastic splint in a supine and anatomically neutral position (Fig. 1). Velcro® straps were used to secure the forearm, stabilize the four fingers in extension, and position the thumb in a naturally abducted position. An ultrasound system with a 18L6 HD linear array probe (Acuson S2000, Siemens Medical Solutions USA, Mountain View, CA, USA) was utilized for data collection. Ultrasound images were collected at the distal or proximal tunnel region. Three trials of ultrasonographic image collection were conducted at each tunnel level for each subject.

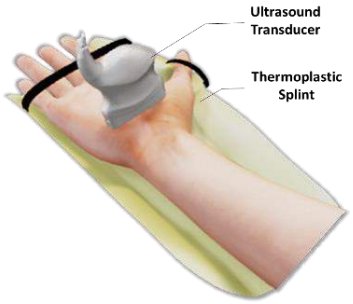

Fig. 1. Experimental setup for ultrasound imaging

For each distal and proximal tunnel ultrasound image, the volar boundary of the TCL was manually traced along with the osseous attachment points (ridge of the trapezium and hook of the hamate at

distal tunnel and pisiform and scaphoid at proximal tunnel) using a custom LabVIEW program (Fig. 2). The traced TCL boundary and osseous insertion points were exported as calibrated image coordinates in mm for calculation of carpal arch width, and height. Arch width at distal or proximal tunnel was defined as the distance between the respective osseous attachment points of the TCL, and arch height was obtained as the maximal perpendicular distance of the TCL boundary points to the line along the arch width. The arch height was normalized with respect to the arch width as a palmar bowing index (PBI). The TCL tracing on the same image were performed three times and associated outcome data were averaged for statistical analyses.

Two-way mixed ANOVAs were used to determine the effect of sex (female and male) and location (distal and proximal) on the dependent variables of the arch height, width, and PBI. Post-hoc Bonferroni t-tests were used for all pairwise comparisons. Statistical analyses were performed using SigmaStat 4.0 (Systat Software Inc, San Jose, CA, USA). An α level of 0.05 was considered for statistical significance.

RESULTS

Arch height was significantly affected by the factors of sex ($p<0.001$) and location ($p<0.001$) (Fig. 3a), and their interaction was not significant ($p=0.918$). Females had significantly smaller arch height compared to men at both locations ($p<0.05$). At the distal tunnel, the arch height (0.9±0.2 mm) for females was significantly smaller than the arch height (1.8±0.4 mm) for males ($p<0.05$). At the proximal tunnel, females had an arch height of 4.3±0.7 mm, which was significantly smaller than the arch height of 5.1±0.6 mm for males ($p<0.05$).

Arch width was significantly affected by the factor of sex ($p<0.05$) but not location ($p=0.172$) (Fig. 3a). The interaction between sex and location also significantly affected the arch width ($p<0.05$). The arch width at the distal level (22.8±1.1 mm) for females was not significantly different from the arch width (24.1±2.3 mm, $p=0.09$) for males. At the proximal level, females had significantly smaller arch width compared to men (21.2±1.4 mm vs. 24.4±1.6 mm, $p<0.05$).

PBI as the arch height normalized with respect to the arch width was found to be significantly affected by the factors of sex ($p<0.05$) and location ($p<0.001$) (Fig. 3b), and their interaction was not significant ($p=0.154$). PBI was significantly smaller in females compared to males at the distal tunnel ($p<0.05$) but not the proximal tunnel ($p=0.465$). At the distal tunnel, females had a significantly smaller PBI of 0.04±0.01 than the PBI for men which was 0.08±0.01 ($p<0.05$). At the proximal tunnel, the PBI was not significantly different between the sexes (0.20±0.03 for females and 0.21±0.03 for males, $p=0.465$).

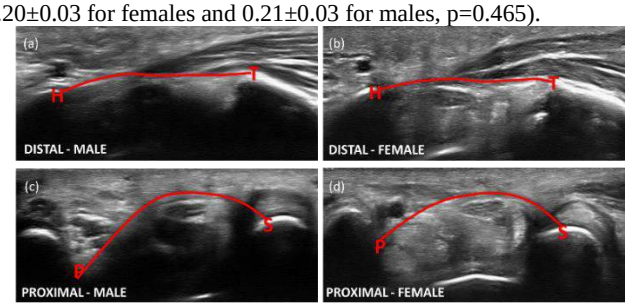

Fig. 2. Ultrasound images at each tunnel level (distal and proximal) for a representative male and female subject. The images reflect the selection for the traced TCL (solid line) and the landmark of interest - hook of hamate (H), ridge of the trapezium (T), pisiform (P), and scaphoid (S)

DISCUSSION

The evaluation of the TCL-formed carpal arch, and their differences between the sexes at the distal and proximal tunnels has

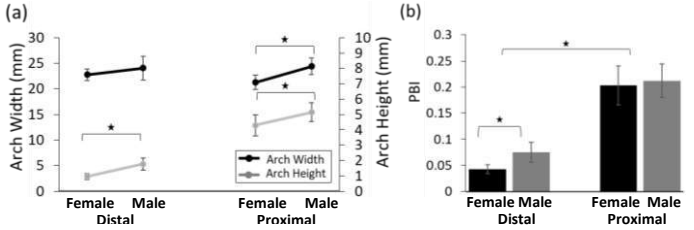

Fig. 3. The (a) arch width and height, and (b) palmar bowing index at the two tunnel levels (distal and proximal) for the two sexes (female and male)

delivered several key findings. The most significant of the findings is that females had a smaller palmar bowing than men. The palmar bowing (arch width-to-height ratio) had a pronounced reduction in females at the distal tunnel compared to the proximal tunnel. These findings support the findings of Monagle et al. [6] who reported a reduced palmar bowing in females compared to men at the distal tunnel level, but not at the proximal tunnel.

The reduced palmar bowing in females observed in our study could possibly be caused by the less compliant carpal tunnels in women compared to men observed by Li et al. [7]. The TCL being less elastic [9] but of similar thickness in women compared to men [9] may have contributed to the reduced tunnel compliance and consequently a reduced palmar bowing in women than men. Additionally, the pronounced reduction in palmar bowing at the distal tunnel compared to the proximal may have been contributed by the distal tunnel being narrower than the proximal [10], with the TCL being thicker distally [9-11] and less compliant than at the proximal tunnel [12].

The pronounced reduction in palmar bowing only at the distal tunnel in females compared to males show that women have a small and disproportionate TCL-formed arch. The small and disproportionate carpal arch observed in our study counter the debate that the females' naturally smaller wrists may predispose them to the development of CTS. The findings show that not just size difference but also sex-related differences inherent to the female anatomy makes women more susceptible to CTS than men.

Although women had smaller carpal tunnel area than men at both distal and proximal tunnels, the median nerve area at the distal tunnel was not different between the sexes [4]. In our study, the pronounced reduction in palmar bowing of the TCL in females could reduce the available space for the carpal tunnel contents including the median nerve at the distal tunnel. With median nerve being near the TCL and having no sex-related difference in nerve area at the distal tunnel, the reduced palmar bowing in females could predispose the median nerve to compression against the TCL. In conclusion, females having reduced palmar bowing than men, especially at the distal narrower end of the carpal tunnel might play an important role in higher incidence of CTS in women.

ACKNOWLEDGEMENTS

The study was funded by NIAMS/NIH R01AR068278

REFERENCES

[1] National Institutes of Health, 2017; [2] Farmer, JE+, J Hand Surg Eur, 33:445-8, 2008; [3] Sassi, SA+, J Hand Surg, 41E(6):638-642, 2016; [4] Kim, HS+, J Ultrasound Med, 31:23-9, 2012; [5] Bower, JA+, Clin. Biomech, 21:816-825, 2006; [6] Monagle, K+, Am. J. Roentgenol, 6:1581-1586, 1999; [7] Li, ZM+, J. Musculoskeletal Res, 9:153-159, 2005; [8] Lin, R+, Hand, 15:305-309, 1983; [9] Brett, AW+, Clin. Biomech, 29.6: 601-606, 2014; [10] Cobb, TK+, Hand Surg Am, 22: 635-639, 1997; [11] Pacek, CA+, Hand, 5:135-140, 2010; [12] Xiu, KH+, Clin. Biomech, 25:776-780, 2010

SB³C2019
Summer Biomechanics, Bioengineering and Biotransport Conference
June 25 -28, Seven Springs, PA, USA

Utilizing ARFI Imaging to Predict Linear Region Modulus of Tendons from Toe Region Data

**Gerald A. Ferrer (1), Waqas Khalid (1),
Volker Musahl (1,2), Kang Kim (1,3), Richard E. Debski (1,2)**

(1) Department of Bioengineering
University of Pittsburgh
Pittsburgh, PA, USA

(2) Department of Orthopaedic Surgery
University of Pittsburgh
Pittsburgh, PA, USA

(3) Department of Medicine
University of Pittsburgh
Pittsburgh, PA, USA

INTRODUCTION

Ultrasound is becoming a more popular tool for clinicians to diagnose musculoskeletal injuries (ie. tendon and ligament injuries). Currently, evaluation of tissue quality based on ultrasound images is mostly qualitative and depends on the user. Quantifying mechanical properties of tendons with ultrasound remains difficult [1]. Acoustic Radiation Force Impulse (ARFI) imaging is an ultrasound technique that generates a localized force onto the tissue of interest at a precise location and the resulting tissue displacement is measured [2]. Information about the resulting tissue displacement could lead to insights about the tissue's mechanical properties. ARFI imaging is primarily utilized for compliant, isotropic biological tissues such as the breast and liver to detect the presence of tumors [2,3]. However, the utility of ARFI imaging is not well understood for stiff, anisotropic biological tissues such as a tendon (tendon modulus in linear region: ~100s of MPa vs breast/liver ~kPa). Due to the high stiffness of tendons, ARFI imaging may only be possible at low loading levels, corresponding to the toe region of a stress-strain curve. However, to differentiate between damaged and un-damaged tendons, understanding the tendon modulus in the linear region is important. Furthermore, quantifying the mechanical properties of tendons with ultrasound techniques has not been established. Therefore, the objective of this study was to predict the tendon modulus in the linear region from ARFI data collected in the toe region of a stress-strain curve.

METHODS

Nine fresh-frozen cadaveric biceps tendons (55 ± 5 years) were harvested and prepared for tensile testing and ARFI imaging of the tendon midsubstance. The cross-sectional area of the tendon midsubstance was determined using a laser scanner (Next Engine, Desktop 3D Scanner, Santa Monica, CA, USA). For tensile testing, each tendon underwent 1N preload, 1-10N preconditioning (10 cycles) and loaded to 30N. The ends of the tendon were clamped with custom soft tissue clamps and aligned for tensile loading in the materials testing machine (Instron, Model 5965, Norwood, MA, USA) and tendon midsubstance strain was measured with an optical tracking system (DMAS, Spica Technology, Kihei, HI, USA). The stress-strain data, representing the mechanical properties of the toe region, from loading the tendon to 30N was utilized for analysis.

For ARFI imaging, the tendon was loaded into a custom tensioning jig immersed in distilled water. For each tendon, ARFI images were acquired at 3 low stress levels within the toe region of the stress-strain curve (<1MPa and <20N) using a research ultrasound platform (Verasonics, VDAS V-1 Model, Redmond, WA, USA) and commercial linear array transducer (ATL L7-4). A localized radiation force at the tendon midsubstance was generated using a full-frame ARFI push (spatial resolution = 148 μm) at the elevation focus of the transducer (25mm) for 1000 cycles at 5.2MHz. ARFI tendon displacement was tracked from post-ARFI push images and measured at the center area of the tendon to minimize boundary effects and used for analysis.

To predict the linear region modulus from toe region data, 4 steps needed to be accomplished. 1) Use ARFI tendon displacement data to predict the strain in the tendon. 2) Use predicted strain values and fit to the exponential approximation of a stress-strain curve to determine best fit model parameters. 3) Use model fit parameters to predict toe region modulus. 4) Use toe region modulus to predict linear region modulus. To validate our predictions, 6 of the 9 specimens were randomly chosen to establish the relationships. The remaining 3 specimens were used to validate predictions with experimental results.

Predict tendon strain from ARFI data: A linear regression was performed to determine the linear relationship between the measured strain acquired during tensile testing and ARFI tendon displacement

data. Equation 1 estimates tendon strain (ARFI strain) by describing the relationship between ARFI displacement data with increasing stress.

$$\text{ARFI Strain} = 1 - \frac{ARFI\ Displacement_{Applied\ Stress}}{ARFI\ Displacement_{Lowest\ Applied\ Stress}} \qquad (1)$$

Similar to the classic strain equation (change in length divided by original length), Equation (1) evaluates the change in ARFI displacement with increasing stress with respect to ARFI displacement at the lowest applied stress.

Stress-strain curve model fit and relationship to toe region modulus: Using the estimated tendon strain from ARFI data (ARFI strain), equation 2 was utilized to approximate the stress-strain (σ-ε) relationship. Parameter A*B approximates initial stiffness [4]. A linear regression was then performed to relate A*B to the toe region modulus calculated from tensile testing. Toe region modulus was determined with a linear fit of the data up until 1% strain, maximizing the number of data points such that $r^2 > 0.9$.

$$\sigma(\varepsilon) = A(e^{B\varepsilon} - 1) \qquad (2)$$

Predict linear region modulus: The mechanical testing protocol for the 9 specimens did not reach the linear region of the stress-strain curve (strain <3%). Therefore, a dataset of 16 previously tested fresh-frozen cadaveric biceps tendons were utilized to determine the relationship between the toe region modulus and linear region modulus. All specimens were non-destructively tested in tension and the tendon midsubstance reached the linear region of the stress-strain curve (strain >3%). Linear region modulus was determined with a linear fit from the end of the stress-strain curve, maximizing the number of data points such that $r^2 > 0.9$. A linear regression was used to establish the linear relationship between toe and linear region modulus. Significance was set at $p < 0.05$ for all relevant analyses.

RESULTS

Significant linear relationships were found for all steps in the process of predicting linear region modulus from toe region ARFI data. ARFI strain (defined in equation 1) was linearly related to the measured strain from tensile testing by a factor of 0.02 ($p < 0.05$, $r^2 = 0.562$). Average error between predicted ARFI strain and measured tendon strain was 63.6 ± 45.9%. The toe region modulus was linearly correlated to parameter A*B by the relationship *y = 1.22x + 19.1* (Figure 1). Predicting the linear relationship between the linear region modulus from the toe region modulus was also significant (*y = 4.5x + 14.7*, Figure 2). Comparing experimental results and predictions from the derived relationships, the magnitude of error for predicting model fit parameter A*B was 11.3 ± 10.9% and toe region modulus was 18.7 ± 10.2% (Table 1). Predicted linear region moduli ranged from 195.5 MPa to 299.7 MPa.

Table 1: Experimental data and model predictions from ARFI tendon displacement data

Tendon	A*B (MPa)		Toe Region Modulus (MPa)		Linear Modulus (MPa)
	Predicted	Actual	Predicted	Actual	Predicted
#1	34.8	38.8	63.7	91.4	273.9
#2	20.9	21.1	46.4	40.5	195.5
#3	39.4	50.9	69.4	78.1	299.7

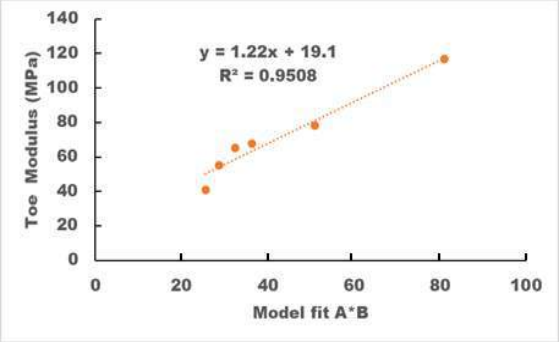

Figure 1: Relating parameter A*B and toe region modulus ($p < 0.05$, $r^2 = 0.951$)

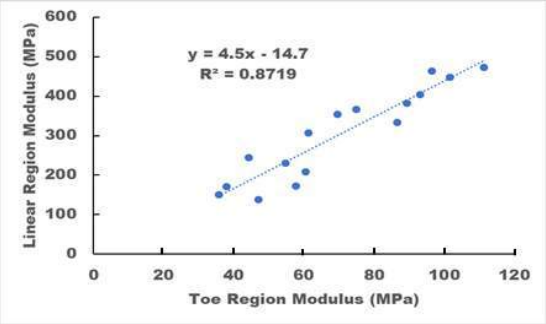

Figure 2: Linear relationship between linear region modulus and toe region modulus ($p < 0.05$, $r^2 = 0.872$)

DISCUSSION

The results of this study demonstrate the feasibility of predicting the linear region modulus of tendons from ARFI imaging data collected in the toe region using only linear relationships. Specifically, a strong relationship was found for predicting the linear region modulus once the toe region modulus is determined. Other ultrasound techniques such as shear wave elastography have only been able to describe relative changes in tendon stiffness [1,5]. All predicted values of toe and linear region moduli were physiologically reasonable. Preliminary tests indicated that ARFI imaging at stress levels in the linear region is not feasible since the tendon is too stiff for the acoustic radiation force to generate any measurable displacement.

Predicting tendon strain from ARFI displacement data was the limiting factor in terms of achieving the most accurate predictions (Equation 1). The equation chosen to estimate tendon strain (ARFI strain) from ARFI displacement data was chosen since it closely resembles the classic strain equation. Additionally, a linear relationship between ARFI strain and the measured tendon strain during mechanical testing was assumed. However, non-linear relationships may be needed to relate stress-strain with stress-ARFI displacement data since tendons are non-linear, viscoelastic, and transversely-isotropic. Nonetheless, errors less than 20% of the measured values for both model fit parameter A*B and toe region modulus are an encouraging first step.

This study serves as the foundation for future work in developing more sophisticated relationships to improve the accuracy of relating ARFI displacement data and tendon strain. With further development, ARFI imaging may be a viable approach to evaluate the linear region mechanical properties of tendons non-invasively and ultimately serve as a diagnostic tool for tendinopathies.

ACKNOWLEDGEMENTS

Support from the University of Pittsburgh Swanson School of Engineering, Department of Bioengineering, Orthopaedic Surgery, and NSF-GRFP No. 1247842 is gratefully acknowledged.

REFERENCES

[1] Baumer, TG et al., *J Biomech*, 53: 201-204. 2017.
[2] Nightingale, K et al., *Curr Med Imaging Rev*,7(4): 328-339. 2011.
[3] Fahey, BJ et al. *Ultrasound Med Biol*, 31(9): 1185-1198. 2005.
[4] Abramowtich, SD et al., *Ann Biomed Eng*, 32(3): 329-335. 2004.
[5] Slane, LC et al., *Eur Radiol*, 27:474-482. 2017.

SB³C2019
Summer Biomechanics, Bioengineering and Biotransport Conference
June 25 -28, Seven Springs, PA, USA

Shear wave propagation and estimation of material parameters in a nonlinear, fibrous material

Z. Hou (1), R. J. Okamoto (1), P. V. Bayly (1,2)

(1) Mechanical Engineering and Materials Science
Washington University in St. Louis
St. Louis, MO, United States

(2) Biomedical Engineering
Washington University in St. Louis
St. Louis, MO, United States

INTRODUCTION

Elastographic techniques, including both ultrasound elastography and magnetic resonance elastography (MRE) have great potential for non-invasive evaluation of the properties of soft tissues. MRE has been used to estimate parameters of linear elastic or viscoelastic material models in diverse tissues including skeletal muscle [1], liver [2, 3], and brain [4]. However, many biological tissues are nonlinear and anisotropic. Here we consider the use of MRE to estimate parameters of the Holzapfel-Gasser-Ogden (HGO) model, a simple and widely used nonlinear material model for fibrous biological soft tissues [5, 6].

MRE is based on MR imaging and analysis of shear waves in tissue excited by external vibrations. Typically, this tissue is assumed to be stress-free. For nonlinear materials, superimposing vibrations on a pre-deformed configuration alters the shear wave speeds due to changes in the linearized tissue stiffness. In this study we derived closed-form expressions for the relations between shear wave speeds and HGO model parameters in the reference (stress-free) and several pre-deformed configurations. These expressions were verified by analysis of displacement fields from numerical simulations. We demonstrate how these relationships can be used to estimate HGO model parameter values from MRE measurements of shear wave speeds.

METHODS

Theoretical values for wave speeds are found from the eigenvalue problem

$$\rho c^2 \boldsymbol{m} = \boldsymbol{Q}(\boldsymbol{n}) \cdot \boldsymbol{m}, \tag{1}$$

where $\mu = \rho c^2$ is the eigenvalue of acoustic tensor $\boldsymbol{Q}$, c is shear wave speed, $\boldsymbol{n}$ is the propagation direction, and $\boldsymbol{m}$ is the polarization direction vector of the wave. The acoustic tensor $\boldsymbol{Q}$ can be expressed in Cartesian coordinates as:

$$Q_{ij} = A_{piqj} n_p n_q, \tag{2}$$

where $\boldsymbol{A}$ is the (tangent) elasticity tensor which relates incremental strain and incremental stress.

In transversely isotropic fibrous materials, shear wave speed depends on both material properties and directions of propagation and polarization relative to fibers. For a given propagation direction, distinct eigenvalues of (1) correspond to speeds of "slow" and "fast" shear waves with different polarization directions. The slow and fast shear wave polarization directions in the reference configuration are:

$$\boldsymbol{m_s} = \frac{\boldsymbol{n} \times \boldsymbol{a}}{|\boldsymbol{n} \times \boldsymbol{a}|} \qquad \boldsymbol{m_f} = \boldsymbol{n} \times \boldsymbol{m_s} \tag{3}$$

where $\boldsymbol{a}$ is the fiber direction, $\boldsymbol{m_s}$ and $\boldsymbol{m_f}$ are the slow and fast polarization directions.

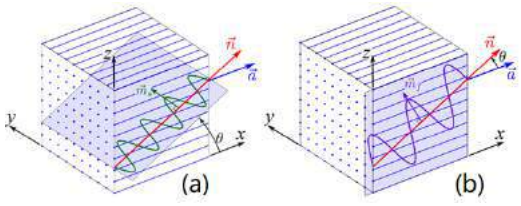

Figure 1 Waves of different polarization directions in transversely isotropic materials. (a) A "slow" wave involves displacements in the slow polarization direction, $\boldsymbol{m_s}$. (b) A "fast" shear wave involves displacement in the fast polarization direction, $\boldsymbol{m_f}$.

The HGO model is described comprehensively in [7]. It is defined by a strain energy density function containing volumetric (W_{vol}), isochoric (isotropic Neo-Hookean, W_{iso}, and anisotropic, W_{aniso}) terms:

$$W_{vol} = \frac{K}{2}(J-1)^2, \quad W_{iso} = \frac{\mu}{2}(\bar{I}_1 - 3) \tag{4}$$

where K is the bulk modulus and μ is the shear modulus for small deformations. Many biological soft materials have shear moduli between 10^2-10^5 Pa, spanning acellular collagen and fibrin gels [8, 9] and muscle [10]. The anisotropic term can have different forms depending on fiber arrangement. The formulation proposed by Gasser et al. [11] accounts for the effects of fiber stretch in a single family of slender fibers with nonlinear properties and a distribution of orientations:

$$W_{aniso} = \frac{k_1}{2k_2}\{\exp[k_2(\kappa\bar{I}_1 + (1-3\kappa)\bar{I}_4 - 1)^2] - 1\}, \text{for } \bar{I}_4 > 1 \quad (5)$$

We did not model the bi-linearity between fiber tension and compression ($I_4 < 1$) in the HGO model.

Cauchy stress and (tangent) elasticity tensors in the HGO material are found by differentiating the strain energy density function:

$$A_{piqj} = F_{p\alpha}F_{q\beta}\frac{\partial^2 W}{\partial F_{i\alpha}\partial F_{j\beta}} \quad (6)$$

These tensors may be obtained in the reference or pre-deformed configurations; in general they depend on parameters μ, κ, k_1, k_2, fiber angle ϕ, and pre-deformation (shear γ, e.g.). In each configuration, the acoustic tensor, $\boldsymbol{Q}$, may be found and used to determine wave speeds and directions from Eq. (1). These in turn also depend on the parameters of the model. Thus, in principle, shear wave speeds can be used to estimate HGO parameters.

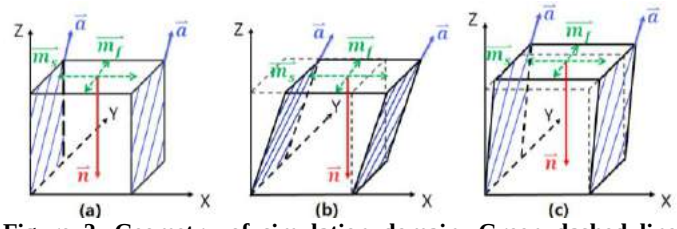

Figure 2. Geometry of simulation domain. Green dashed lines represent vibrations in two perpendicular directions (X or Y). Red arrows show propagation direction along the negative Z-axis. Blue solid lines show fiber direction, where $\phi = 45°$. One fiber family in (a) reference configuration and pre-deformed configuration of simple shear in the (b) XZ plane or (c) YZ plane.

For insight and efficiency of iterative parameter estimation methods, closed-form expressions that relate wave speeds to model parameters are highly desirable. Such expressions were determined from symbolic analysis of the eigenvalue problem (Eq. 1) for the pre-deformed configurations of Fig. 2b, 2c. Symbolic solutions were obtained with Matlab Symbolic Toolbox (Mathworks, Natick, MA).

$$c_{s_{xz}} = \sqrt{\frac{\mu}{\rho} + 2\frac{k_1}{\mu}\gamma_{xz}^2 M^2 \exp(M^2 k_2 \gamma_{xz}^4)} \quad (7)$$

$$c_{f_{xz}} = \sqrt{\frac{\mu}{\rho} + \frac{k_1}{\mu}\left(N^2 + 6\gamma_{xz}^2 M^2 + 2\gamma_{xz}^4 k_2 M^2 (N^2 + 4\gamma_{xz}^2 M^2)\right)\exp(M^2 k_2 \gamma_{xz}^4)}\,. \quad (8)$$

$$c_{s_{yz}} = \sqrt{\frac{\mu}{\rho} + 2\frac{k_1}{\mu}\gamma_{yz} M (\gamma_{yz} M + N)\exp\left((\gamma_{yz} M + N)^2 k_2 \gamma_{yz}^2\right)} \quad (9)$$

$$c_{f_{yz}} = \sqrt{\frac{\mu}{\rho} + \frac{k_1}{\mu}\left(N^2 + 6\gamma_{yz}^2 N^2 + 6\gamma_{yz} MN + 2\gamma_{yz}^2 (2\gamma_{yz} M + N)^2 (\gamma_{yz} M + N)^2\right)\exp\left((\gamma_{yz} M + N)^2 k_2 \gamma_{yz}^2\right)} \quad (10)$$

where ($c_{s_{xz}}$ $c_{f_{xz}}$) and ($c_{s_{yz}}$ $c_{f_{yz}}$) are the slow and fast shear wave speeds for pre-deformations γ_{xz} and γ_{yz} respectively. The terms M and N are combinations of the dispersion parameter κ and the angle ϕ between the fiber and the propagation direction:

$$M = 2\left((1-3\kappa)\cos^2\phi + \kappa\right); \quad N = (1-3\kappa)\sin 2\phi. \quad (11)$$

To verify analytical results, finite element (FE) simulations of shear wave propagation were performed using finite element software (COMSOL Multiphysics, Burlington, MA). Static pre-deformation and frequency-domain perturbation steps were performed in a cubic domain ($5 \times 5 \times 5$ mm^3). The HGO model was implemented in COMSOL to model elastic behavior; an isotropic loss factor of 0.1 was used to provide a small amount of viscoelastic damping. Frequency of excitation was 200 Hz, in order to provide multiple wavelengths in the domain. The domain was discretized into 5000 hexahedral elements. To demonstrate convergence, results were confirmed at higher resolution.

RESULTS

FE simulation results and theoretical predictions from the closed-form formulas for wave speed were compared for three conditions (no pre-deformation, simple shear in the XZ plane, and simple shear in the YZ plane). In Fig.3 below, the top row (panels a-e) displays c_f/c_0, the normalized ratio between the fast wave speed and the isotropic, linear, shear wave speed $c_0 = \sqrt{\mu_0/\rho}$. Similarly, the bottom row (panels f-j) depicts the ratio c_s/c_0. Parameters $\mu, k_1, k_2, \kappa,$ and γ_{yz} affect these ratios. Simulation results agree well with analytical predictions.

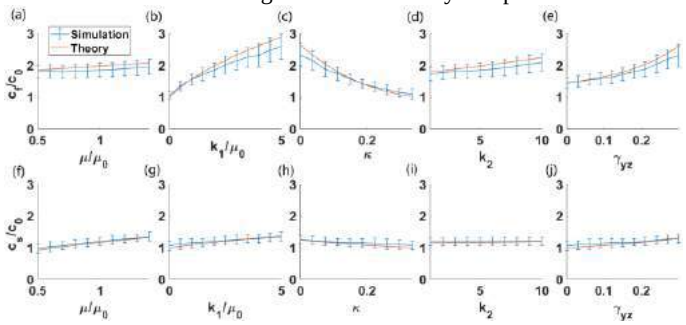

Figure 3. Relationships between fast and slow wave speeds and HGO model parameters (μ, k_1, κ, k_2) with simple shear γ_{yz}. Blue bars denote results from simulation; orange curves show analytical results. Default parameters are: $\mu_0 = 1000$ Pa, $\mu/\mu_0 = 1$, $k_1/\mu_0 = 2$, $\kappa = 1/12$, $k_2 = 5, K/\mu_0 = 10^4, \gamma_{yz} = 0.2$.

DISCUSSION

In materials that can be modeled as anisotropic, nonlinear, and nearly incompressible, slow and fast wave shear speeds can be measured from MRE and used to estimate parameters of the material model. In nonlinear anisotropic materials, unlike linear materials, pre-deformations in different directions may play an important role. Closed-form expressions for shear wave speeds in an HGO material, as functions of pre-deformation and material parameters, were derived and confirmed by numerical simulation. Wave speeds in different conditions (reference, or pre-deformation in simple shear in the XZ plane or YZ plane) showed excellent agreement between analytical predictions and simulation results. These results provide a new approach to parameter estimation for nonlinear material models of fibrous soft tissues.

ACKNOWLEDGEMENTS

NSF Grant CMMI-1727412 and NIH Grant R01/R56 NS055951.

REFERENCES

[1] Bensamoun et al., *IRBM*, 4:4-9, 2015.
[2] Chamarthi et al., *Magnetic Resonance Imaging*, 32:679–683, 2014
[3] Yang et al., *Magnetic Resonance Imaging*, 44:92-95, 2017
[4] Kolipaka et al., *Clinical Imaging*, 51:114–122, 2018
[5] Volokh, *J Mech Behav Biomed Mater*, 4:1582-1594, 2011
[6] Shearer, *Journal of Biomechanics*, 48:290-297, 2015
[7] Holzapfel et al., *J. Elast*, 61:1-48, 2000
[8] Namani et al., *J Biomech Eng*, 134:061004, 2012;
[9] Sundararaghavan et al., *J Biomed Mater Res A*, 87:308-320, 2008
[10] Okamoto et al., *J Biomech Eng* 122:479-487. 2000
[11] Gasser et al., *Interface*, 3:15-35, 2006

SB³C2019
Summer Biomechanics, Bioengineering and Biotransport Conference
June 25 -28, Seven Springs, PA, USA

SHOCK WAVE PROPAGATION IN BRAIN TISSUE

D. Keum, S. Assari, K. Darvish

Biomechanics Laboratory
Department of Mechanical Engineering
Temple University
Philadelphia, PA, USA

INTRODUCTION

While Traumatic Brain Injury (TBI) continues to be the leading cause of accidental fatality [1], over the past decade, there has been a significant increase in the number of TBI incidents among military combat personnel [2] as a result of prominent use of Improvised Explosive Devices (IEDs). Previous studies have shown that brain tissue behaves like a nonlinear viscoelastic material. However, proposed material models were primarily developed for sports or motor vehicle injury applications [3]. Considering the nonlinearity and viscoelasticity observed in brain tissue, there has been an increasing need for better understanding of the material properties of brain tissue in higher loading rates.

The goal of this study was to enhance our understanding of the mechanical behavior of brain tissue at loading rates that resemble that of blast-induced TBI (BINT). A custom-designed high-rate shear test setup (HRS) was used to apply high-rate displacement rates that can cause a shear shock wave in brain tissue samples. The propagation of the shear shock wave was investigated and compared with gelatin gel samples.

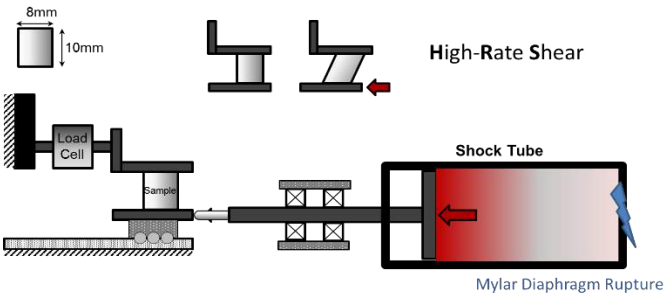

Figure 1. Schematic of the high-rate shear (HRS) test setup.

METHODS

Fresh bovine brains were used as test specimens because of their availability, having similar material properties as human brain [3], and their large size which makes extracting homogeneous samples more practical. The specimens were obtained from a local slaughter house with no visible damage to the brains. For maintaining their ionic balance and water content, the brains were kept in PBS solution immediately after purchase and kept at 5ºC before testing that was conducted 3 to 6 hours post-mortem.

Cylindrical samples (n=6) were excised from 2 brain specimens from the corona radiata region approximately along the direction of axon fibers using an 8-mm diameter boring tool. Homogeneous samples with mainly white matter were selected for this study with approximately 10 mm height.

As it is schematically shown in **Figure 1.**, the test apparatus consisted of an actuator (piston) that was driven by a 2-in diameter shock tube with peak over pressure levels ranging from 150 kPa to 250 kPa. The sample was placed between two parallel plates (fixed with super glue) with the lower plate being pushed by the actuator. The top plate was connected to a 250 gram load cell (model 11, Honeywell) recorded at 50k samples/s and the sample deformation was recorded by a high speed camera at 10 kfps (Phantom v4.2, Vision Research).

Samples were tested with strain rate of bottom plate between500 to 1000 s^{-1} to investigate the shear wave propagation along the length of the sample. The deformation of the sample was captured using the high-speed video and quantified by tracking the markers placed along the length of the sample after image processing. Then the shear wave front was identified by a sharp change in angle of the markers with respect to

the vertical line. The effective shear wave velocity was calculated as the velocity of propagation of that sharp angle along the sample length.

The effective shear wave velocity was also calculated from the travel time of the shear force from the bottom plate to the top plate. This time period was measured in the recorded force-time history.

Gelatin gel has previously been used as a brain surrogate material. 5% and 10% gelatin gel samples with the same size as the brain samples were also tested to compare the characteristics of the shear wave propagation and their dependence on the material properties.

RESULTS AND DISCUSSION

The propagation of shear wave in a representative brain sample is shown in **Figure 2 top**. The corresponding force time history is given in the bottom figure, which shows the shear wave travel time, followed by a rapid rise in the force (about 0.5 ms) and then reducing to zero as a result of the sample failure.

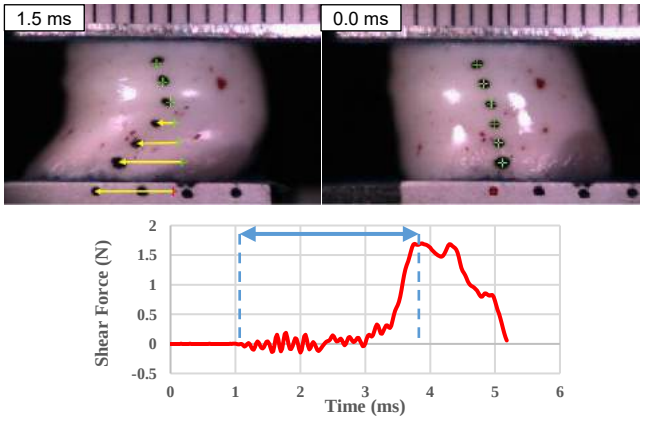

Figure 2. (Top) Bovine brain tissue sample under high-rate shear deformation. The shear wave front propagating from the bottom plate to the top plate can be observed using high speed imaging. (Bottom) A representative shear force measurement is shown. The travel time of shear force from bottom plate to the top plate that is connected to the load cell is shown in this graph.

The shear wave speed is calculated at each marker location on the sample. **Figure 3 top** shows how the shear wave speed is changing as it propagates along the sample from bottom to top. As it can be seen, the shear wave speed is decreasing from about 4 m/s as it propagates along the sample and after about 50% distance it travels with an almost constant speed of about 2 m/s. The reported range of shear modulus for brain tissue, based on low to medium rate tests [4] is in the range of 2 to 4 kPa which corresponds to the shear wave velocity of 1.5 to 2 m/s. This range agrees with the constant elastic wave velocity obtained in this study. One possible explanation for reduction of the shear wave velocity could be that the wave is in the form of a shock wave at the initiation point and is therefore propagating faster than the elstic shear wave speed. The shear shock wave could have been generated because of the high rate loading input. The minimum displacement input velocity was about 6 m/s which is 3 times higher than the highest expected speed of elastic shear waves in brain tissue. The shock wave later disperses into elastic waves and its speed reduces. These results show that brain tissue is highly rate sensitive at strain rates that occur during BINT. Generation of shear shock waves could be crucial in causing injury in the tissue and further study is needed to investigate if the existing brain tissue material models can model such behavior in high rate loading conditions.

The results of gel tests showed that material properties not only affect the elastic shear wave velocity, they also affect the shear shock wave velocity (**Figure 3 bottom**). In the stiffer gel, the shear wave velocities were higher throughout the sample. The shock wave characteristics of 10% gel was very similar to brain.

In summary, the results of this study showed that shear shock waves can be produced in high loading rates that are experienced in brain tissue during BINT. The shockwave initial velocity and reduction of the velocity are properties of the material that need to be further characterized.

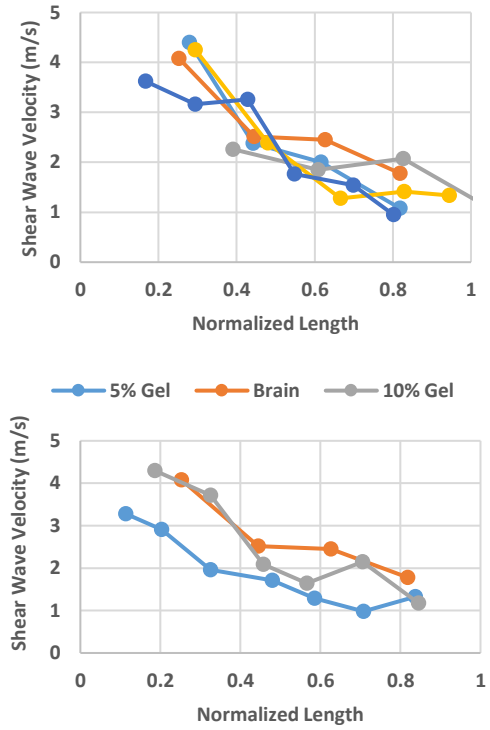

Figure 3. (Top) Calculated shear wave speed at different locations along the sample are shown for 5 representative bovine brain samples. (Bottom) Shows how the shear wave velocity can be different for different materials, here 5%, 10% gelatin gels in comparison with a bovine brain sample.

ACKNOWLEDGEMENTS

This work was partially supported by the Army Research Lab cooperative agreement W911NF-18-2-0269.

REFERENCES

[1] CDC, N.C. for I.P. and C., 2017. Traumatic Brain Injury Facts. Available at: https://www.cdc.gov/traumaticbraininjury/get_the_facts.html.

[2] Tanielian, T. & Jaycox, L.H., 2013. Invisible Wounds of War: Psychological and Cognitiv e Injuries, Their Consequences, and Services to Assist Recovery. Journal of Chemical Information and Modeling, 53(9), pp.1689–1699.

[3] Takhounts, E.G., Crandall, J.R. & Darvish, K.K., 2003. On the importance of nonlinearity of brain tissue under large deformations. *Stapp car crash journal*, 47, pp.79–92. Available at: http://www.ncbi.nlm.nih.gov/pubmed/17096245.

[4] Laksari, K., Assari, S. & Darvish, K., 2010. Modeling linear head impact and the effect of brain-skull interface. In *SBEC Proceedings*. pp. 437–439.

EFFECT OF CORPUS CALLOSUM DEMYELINATION ON MURINE BRAIN INJURY MECHANISM

Javid Abderezaei (1), Gloria Fabris (1), Zachary Lopez (1), Cassandra Gologorsky (1,2), Johannes Weickenmeier (1), Mehmet Kurt (1,3)

(1) Department of Mechanical Engineering, Stevens Institute of Technology, Hoboken, NJ, USA.

(2) Department of Biomedical Engineering, Cornell University, Ithaca, NY, USA.

(3) Translational and Molecular Imaging Institute (TMII), Mount Sinai Hospital, New York, NY, USA.

INTRODUCTION

Traumatic brain injury (TBI) is a recurring health concern, affecting as many as 2.8 million people each year in the US [1] and about 50% more especially amongst young athletes when unreported cases are considered [2]. Despite substantial research efforts in recent years, our physical understanding of how various brain substructures affect the progression of injury remains rather limited. Corpus callosum (CC), which is comprised of myelinated fibers is one of the regions of interest in mild TBI that has been poorly understood [3]. Hulkower *et al.* implemented diffusion tensor imaging (DTI) to identify fractional anisotropy (FA) abnormalities in the brains of TBI patients. They observed that white matter (WM) tracts such as CC, fornix, thalamus and hippocampus are among the most common brain regions with abnormal FA in the patients who suffered from TBI [4]. Hernandez *et al.* identified peak principal strain in the CC as one of the predictors of mTBI following a head impact [5]. Other studies also showed large amounts of strain near CC during impact, which hints at the importance of analyzing the link between the microstructural and mechanical properties of CC [6]. Myelin has been previously shown by Weickenmeier *et al.* to be a prominent factor in changing the WM stiffness [7]. Taking into account the importance of mechanical properties of the brain and how it affects the progression of injury, here we developed an experimental animal study in which the stiffness of CC in mice was decreased through local demyelination to investigate its role in response to mTBI. In the next step, we utilized a finite element (FE) simulation to further analyze how mechanical stiffness variance of WM affect the strain patterns in the mice brain model

METHODS

Experimental animals and surgical procedures: In this study, we used young adult C57BL6/J mice (male; n=8; Jackson Laboratory) weighing between 25 and 30 g. All animal care, surgical and post-surgical procedures were IACUC-approved.

The animals were anesthetized with 3% sevoflurane and a midline incision was made at the top of their head. Stereotaxic equipment (calibrated relative to bregma) was used to drill a 2 mm hole into the skull. 1 μL of a 1% lysolecithin solution - a toxic which has been previously shown to cause demyelination [8] – was injected into the CC of the first group of mice (n=4). In a similar procedure also 1 μL PBS was injected into the CC of the second group of mice (n=4, control group). 3 days after the injection, mTBI was induced on the animals.

A modified weight drop (WD) impact acceleration model was used to induce mTBI [9]. A rod with a diameter of 3 mm and mass of 317 g raised to a height of 2.5 cm, was dropped at 1 mm rostral of coronal suture and 2 mm left of sagittal suture (Fig. 1A) of the mice which was anesthetized with sevoflurane and subcutaneously injected with lidocaine.

Mice were transcardially perfused 24 h after the WD. Dissected brains were incubated in formalin (24 h) then transferred to sucrose (48 h). Coronal brain sections (40 µm) were obtained using a cryostat. Samples were stained with GFAP primary antibody (GFAP: Z0334, Dako) coupled to appropriate

secondaries in order to visualize damage localization and patterns of cell death. Fluorescent images were acquired and analyzed in ImageJ to quantify GFAP staining via a custom-made masking algorithm.

Finite Element Simulations: In order to replicate the effect of the change of stiffness on the patterns of injury in the mice brain, we utilized a murine FE model based on the atlas from the National High Magnetic Field Laboratory [10,11]. In this model a New Hookean material model using the properties in [12,13] was chosen. The brainstem and the bottom of the cortex of the FE model were pinned and a pressure of 10 N/mm^2 at 1 *mm* rostral of coronal suture and 2 *mm* left of sagittal suture was applied to the brain model. The responses for various k_{WM}/k_{GM} (white matter/ grey matter stiffness) were simulated and the strains developed in various regions of the brain were quantified.

RESULTS

We analyzed n=8 mouse brains and excluded one of the outliers from PBS injected group due to the issues with staining and fluorescence imaging. We observed a 27.1% increase in astrocyte activation in the body region of CC (*i.e.*, injection site) of subjects that experienced both the PBS injection and WD (p=0.01; Fig. 1B). Analyzing the regions above CC and near grey matter (GM), we did not observe substantial increase in astrocyte count of lysolecithin injected group (12.4% increase compared to the PBS injected group, p=0.72), which signals that more subjects are needed to be studied.

To further understand this phenomenon, we analyzed the strain patterns simulated in the FE model (Fig. 2). We observed that by varying k_{WM}/k_{GM} from 3.0 to 0.3 there is a significant change in the strain response (ε) pattern of the brain, from $\varepsilon = 1.55 \times 10^{-1}$ to 1.93×10^{-1}, respectively.

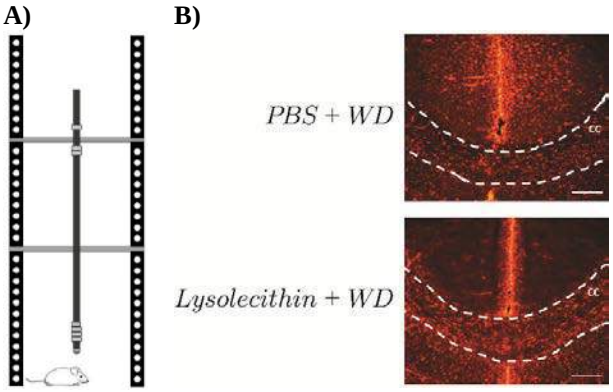

Figure 1: Schematics of WD device and the inflammatory response of the mice brain. 1A) A modified WD model was implemented to induce a mild impact on the mice head. B) Immunofluorescent staining of the area surrounding the CC in coronal slices adjacent to the injection site (Red: reactive astrocytes (GFAP). Scale bar: 200 µm).

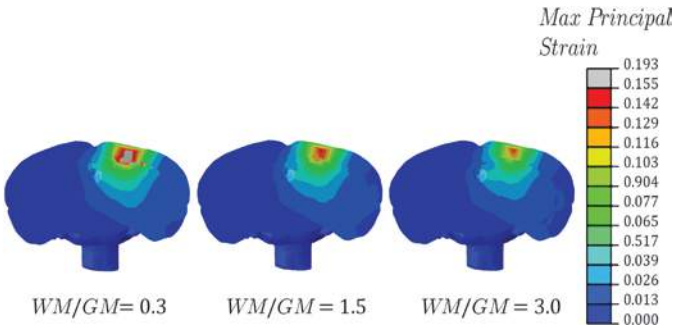

Figure 2: Finite element simulation of the weight drop for various WM and GM stiffness ratios.

DISCUSSION

A comprehensive study into how varying mechanical properties of different brain sub-structures can affect TBI mechanism is crucial to better understand the role of each sub-region in injury mechanism. Here, we decreased the stiffness of CC thorough local demyelination, and observed significantly less astrocyte activation in the body of CC. Since the pediatric brain undergoes significant microstructural changes, including myelination [14], understanding the shielding effect of myelin in TBI could be crucial in understanding the injury mechanisms. Additionally, considering the vulnerability of CC to TBI especially amongst the children [15], this study further hints at the importance of understanding this region in injury patterns.

To further analyze our findings, we simulated this experiment with FE models. We observed that in the softest k_{WM}, the strain pattern is more diffuse, penetrating deep into the brain. This is in agreement with our experimental results, where we observed more diffuse astrocyte activation in demyelinated cases (Fig. 1B).

Our preliminary study further emphasizes the importance of studying how CC can affect injury metrics and hints that myelin in the CC acts as a mechanical shield to protect the brain from damage during mTBI.

ACKNOWLEDGEMENTS

This research was supported by NSF Grant No. CMMI-1826270 and CMMI-1728186. We also like thank Dr. George McConnell and Dr. Brian O'Neill for training on animal surgeries.

REFERENCES

[1] Taylor, A et al., *MMWR, 66*(9), *2017.*
[2] McCrea, M et al., *CJSM*, *14*(1), 13-17, 2004.
[3] Giordano, C., et al., *SAE Technical Paper*. 2014-22-0002, 2014.
[4] Hulkower, M. B et al., *AJNR*, *34*(11), 2064-2074, 2013.
[5] Hernandez, F et al., *Ann Biomed Eng*, *43*(8), 1918-1934., 2015.
[6] Zhao, W., & Ji, S., IRCOBI Conf, 208–220, 2015.
[7] Weickenmeier, J et al., *JMBBM*, 84: 88-98, 2017.
[8] Yazdi, A et al., *Neuroscience*, *311*, 34-44, 2015.
[9] Flierl, A et al., *Nat. Protoc.*, 4(9): 1328-1337, 2009.
[10] Ma, Y et al., *Neuroscience*,135(4):1203-15, 2005.
[11] Ma, Y et al., *Front. Neuroanat., 2*, 1. 2008.
[12] MacManus, D et al., *JBiomech*, *48*(12), 3213-3218, 2015.
[13] Clayton, E et al., *Phys. Med. Biol*, *56*(8), 2391, 2011.
[14] Kim, G et al., *Neuroradiology*, *59*(10), 1043-1051, 2017.
[15] Wilde, A et al., *J Neurotrauma*, *23*(10), 1412-1426, 2006.

SB³C2019
Summer Biomechanics, Bioengineering and Biotransport Conference
June 25 -28, Seven Springs, PA, USA

HIGH-RATE ANISOTROPIC AND REGION-DEPENDENT PROPERTIES IN HUMAN INFANT CRANIAL BONE

Robert M. Metcalf (1), Jessica M. Comstock (2), Brittany Coats (1)

(1) Mechanical Engineering
University of Utah
Salt Lake City, Utah, USA

(2) Pediatric Pathology
University of Utah
Primary Children's Hospital
Salt Lake City, Utah, USA

INTRODUCTION

Skull fracture is a common occurrence in both abusive head trauma and accidental trauma in children, but little is known about the intrinsic dynamic material properties of infant and toddler cranial bone. Early studies investigated quasistatic material properties of human infant bone and reported anisotropic and region-dependent results [1]. We previously evaluated infant and toddler skull at high strain-rates, but only tested specimens perpendicular to the dominant fiber direction [2]. In this study, we evaluate the dynamic material properties of the pediatric skull in the dominant fiber direction, and test the hypothesis that infant skull is a viscoelastic material.

METHODS

All human subject protocols were reviewed and approved by the Institutional Review Boards at the University of Utah and Primary Children's Hospital. Human cranial bone specimens were collected through autopsies performed by the Pathology Department at Primary Children's Hospital. Criteria for acceptance into the study were subjects ≤ 3 years old of age with no prior history of skull fracture, skull malformations, HIV, or hepatitis. Two cranial specimens, occipital and parietal, with the trabecular fibers oriented along the long axis of the specimen (parallel) were removed according to Figure 1 and frozen from each subject.

On the day of testing, frozen cranial samples were thawed to room temperature (25°C) in a phosphate buffered saline (PBS) solution. Samples were lightly machined under a constant drip of saline to produce a uniform thickness and shape, and tested within 1 hour of thawing.

Previously, we designed and validated a drop tower load frame to perform high-rate three-point flexural tests [2]. For this study, the drop tower was modified to reduce inertial effects, integrated with a higher resolution laser displacement sensor (LK-G152, Keyence, Osaka, Japan), and instrumented with a new 25-lb load cell (Honeywell, Morris Plains, NJ) and amplifier (IAA100, Futek, Irvine, CA). The testing protocol and analysis were the same as previously reported [2], which were based on ASTM standard D790. Previously, we evaluated impact heights from 1, 2 and 3 feet. No significant differences with drop height were noted. Due to the limited number of specimens, only drops from 2 feet were used in this study. Per the ASTM standard, a minimum span to thickness ratio of 14:1 was maintained throughout the study.

Displacement (δ) and force (F) data were collected via laptop (MSI, New Taipei City, Taiwan) using a data acquisition system (Labview Signal Express 2015, National Instruments, Austin, TX) sampled at 10,000 Hz. A fourth order Butterworth low pass filter with a cut-off frequency of 800 Hz was used on each data set.

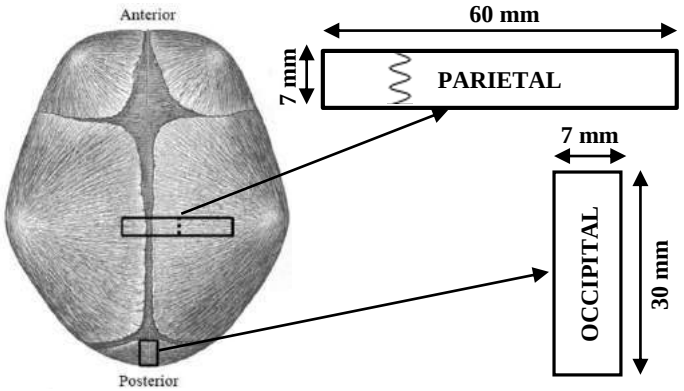

Figure 1: Specimen location and trabeculae fiber orientation. Original skull image by Mikael Häggström, used with permission.

Elastic modulus (E) was calculated using the Bernoulli-Euler equation (1). Where $\left(\frac{F}{\delta}\right)$ is the force-displacement ratio during the linear elastic region of the three-point flexure test (Fig. 2), L is the span of the test, and I is the moment of inertia of the rectangular cross section of the specimen [3].

$$E = \left(\frac{F}{\delta}\right)\frac{L^3}{48I} \quad (1)$$

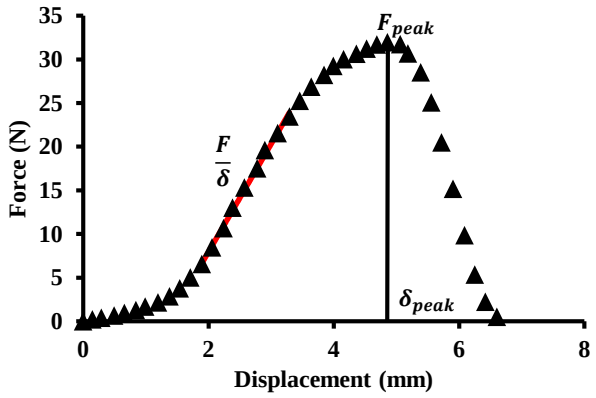

Figure 2: Force-displacement curve of a 4 week-old infant. F_{peak} and δ_{peak} are the maximum values for force and displacement, respectively. The diagonal red line represents the linear approximation used to calculate the bending modulus.

In-plane stress (σ_{xx}) was calculated using Timoshenko's corrected beam theory equation (2) which accounts for the radial tensile forces within the beam as a result of an applied concentrated load to the center of the beam [3].

$$\sigma_{xx} = \frac{3FL}{8wc^3}y - 0.133\frac{F}{wc} \quad (2)$$

In this equation, F is the measured force, w is the specimen width, c is half the specimen thickness, and y is the location of interest on the outer surface of the specimen ($y = \pm c$). Ultimate stress (σ_{ult}) was calculated by using the maximum force (F_{peak} in Fig. 2) for F in equation (2).

Flexural strain (ε_f) for three-point bending was calculated from the relationship given by the ASTM standard D790.

$$\varepsilon_f = \frac{5t\delta}{L^2} \quad (3)$$

Where δ is the deflection of the specimen, t is the thickness of the specimen. Ultimate strain (ε_{ult}) was selected as the flexural strain corresponding to the ultimate stress.

A correlation analysis was used to identify significant increases in E, σ_{ult}, and ε_f with age. A paired Student's t-test identified significant differences in material properties with region (parietal/occipital). A two-way ANOVA was used to identify significant differences in orientation (parallel vs. perpendicular) and region (parietal/occipital) when combined with data from our previous study [2]. Finally, parietal bone material properties were extracted from Kriewall and McPherson [1], Coats and Margulies [2], and the present study to evaluate the effects of rate and anisotropy on the material properties of human infant cranial bone. Significant differences were defined as $p < 0.05$.

RESULTS

Sixteen human pediatric cranial bone specimens were collected from 9 infant donors ranging from 32 weeks gestation to 10 months of age (Ave±SD: 9.053±17.78 weeks). Bending modulus (E) significantly increased with donor age ($p = 0.008$). Ultimate stress (σ_{ult}) also increased with age, but variation was large and it did not reach significance ($p = 0.067$). E and σ_{ult} were generally higher in the parietal bone (E: 4807±2976 MPa; σ_{ult}: 108.5±42.28 MPa; Fig. 3) compared to the occipital bone (E: 3884±3016 Mpa; σ_{ult}: 84.54±36.09 MPa), but this was not significant. E in infants < 1 month old was 10 times greater and σ_{ult} 8 times greater when tested parallel to the dominant fiber direction (E:3471±1834 MPa; σ_{ult}: 90.12±23.70 MPa) compared to perpendicular to the fiber direction (E: 259.0±197.7 MPa; σ_{ult}: 17.65±21.27 MPa).

When data was combined with [1] and [2], E along the fiber direction was significantly greater than perpendicular to the fiber direction. This significant effect was stronger in infants < 1 month old ($p < 0.0001$) than in infants ≥ 1 month old ($p = 0.025$). Strain-rate had a significant effect on E for infants ≥ 1 month of age ($p < 0.026$), but not for infants < 1 month of age.

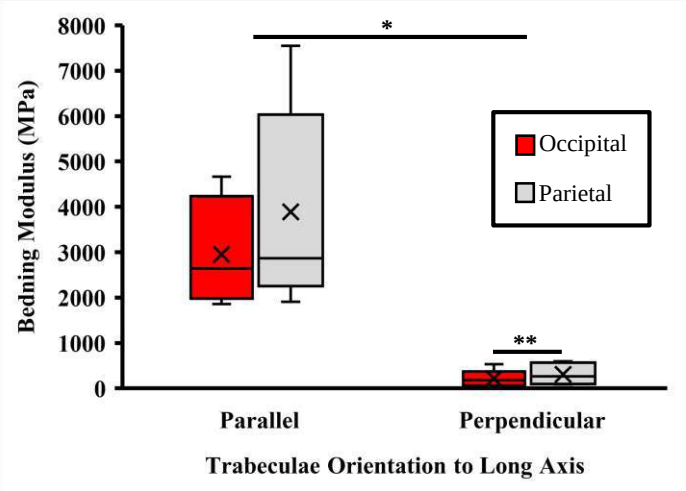

Figure 3: Bending modulus of parietal and occipital bones in infants < 1 month of age. Parallel data is from the present study and perpendicular is from [2]. * $p < 0.0001$ ** $p = 0.038$

DISCUSSION

In this study, bending modulus significantly increased with age. This is in agreement with other studies [1-2] and further supports the use of age-specific data when investigating pediatric head injury. The effect of specimen location when tested parallel to fiber orientation was not significant and differs from the effect of region (parietal/occipital) when tested perpendicular to fiber orientation [2]. This may be due to the low power from a small number of occipital specimens in the present study. Interestingly, strain-rate had no significant effect on modulus for infants < 1 month old, but modulus was significantly increased with increasing strain-rates for infants ≥ 1-month-old. Adult skull exhibits a significant rate-dependence, and our findings may indicate the beginning of associated developmental changes from birth to adulthood.

Previous quasistatic studies report modulus is 3 times greater parallel to the trabeculae compared to perpendicular [1]. At high strain-rates, we found modulus was 10 times larger, signifying a rate-dependent effect on the anisotropy of the infant skull.

ACKNOWLEDGEMENTS

This research was supported by a DOJ grant (2016-DN-BX-0160).

REFERENCES

[1] McPherson, G et al., *J Biomech*, 13:9-16, 1980.
[2] Coats, B et al., *J Neurotrauma*, 23:1222-1232, 2006.
[3] Timoshenko, S., *Theory of Elasticity*. McGraw-Hill, 1970.

SB^{3}C2019
Summer Biomechanics, Bioengineering and Biotransport Conference
June 25 -28, Seven Springs, PA, USA

BILATERAL SKULL FRACTURES DUE TO CONTROLLED HEAD DROPS IN INFANT PORCINE SPECIMENS

Patrick E. Vaughan (1,2), Alexis Goots (3), Todd Fenton (3), Roger C. Haut (1,4), Feng Wei (1,2,4)

(1) Orthopaedic Biomechanics Laboratories
Michigan State University
East Lansing, MI, USA

(2) Department of Biomedical Engineering
Michigan State University
East Lansing, MI, USA

(3) Department of Anthropology
Michigan State University
East Lansing, MI, USA

(4) Department of Mechanical Engineering
Michigan State University
East Lansing, MI, USA

INTRODUCTION

During cranial impact with a large, rigid flat surface, the cranial point of contact bends inwards while the surrounding bone area bends outwards in a wave-like motion, resulting in cranial out-bending. Due to this globalized response of the skull, fracture location does not have to correspond to the place of contact [1] as demonstrated by Gurdjian et al. [2,3] in their pivotal stress coat and human head impact studies. This wave-like response of the head has more recently been observed by Fujiwara et al. [4] on occipital impacts of an anthropomorphic head model, demonstrating simultaneous cranial contractions of the occipital and frontal bones, with the parietal and temporal bones experiencing expansion, or out-bending. Interestingly, Griffen et al. [5] using case-based data demonstrates that occipital and frontal impacts result in transverse bilateral fractures of the temporal bone, with fractures perpendicular to the sagittal suture. Additionally, Weber et al. [6] using pediatric human specimens (0-8.2 months) demonstrates similar transverse bilateral fractures from a parieto-occipital impact in 1/15 impacts.

Bilateral fracture, i.e. symmetric fracturing over contralateral bones, is typically classified as a complicated skull fracture that is an indicator for child abuse [1]. The cause of these injuries is generally believed to be due to a crush scenario, or as a result of multiple impacts [1]. However, a detailed account of a therapist who witnessed an incident where a 6-week-old child fell backwards out of a stroller impacting the posterior midline (top) of the head on a stair, resulted in symmetric longitudinal bilateral fractures across both parietal bones, with fractures running parallel to the sagittal suture [7]. This case marks the first reliably reported instance of a single accidental impact resulting in bilateral fractures. Other cases attribute crush head injuries from being squeezed between two rigid surfaces such as a boot and the ground, or a body and a door resulting in similar bilateral fractures [8]. It is possible that a child's body weight can act as the opposing force in a crush-type injury from a head-over-heels fall.

As there are no known experimental studies that have consistently generated bilateral skull fractures, the purpose of the current study was to collect experimental evidence using infant porcine head specimens to test the hypothesis that cranial out-bending can produce direction-dependent bilateral fractures from top of the head impacts, back of the head impacts, and parieto-occipital impacts.

METHODS

A total of 30 infant porcine specimens (Sus scrofa domesticus) from 1-22 days (4.0 ± 4.9 days) of age were collected from a local farm and frozen within 12 hours of death at -20°C. While frozen, the heads were removed from the body by cervical dislocation, labeled with age/head mass/specimen number, and remained at -20°C until testing. The specimens were thawed in room temperature 24 hours prior to the tests. All heads were screened by palpation of the scalp for pre-existing head trauma before each experiment. An approved IACUC exemption was obtained for the current study.

A custom drop tower was used in the current study to generate a single impact of the isolated heads against a flat aluminum plate (Figure 1) in three distinct locations of interest. The porcine head was impacted on top of the head at the posterior midline between both parietals (N=10), on the posterior right parietal bone as a parieto-occipital impact (N=10), and on mid-occipital (N=10) (Figure 2, row 1). From a preliminary study, the minimum drop height to produce fracture was 75.5 ± 5.3cm for the parietal-occipital and top of the head impacts, and 116.8 ± 2.5cm for the occipital impacts. These heights were therefore used in the current study. A single impact was performed for all specimens tested.

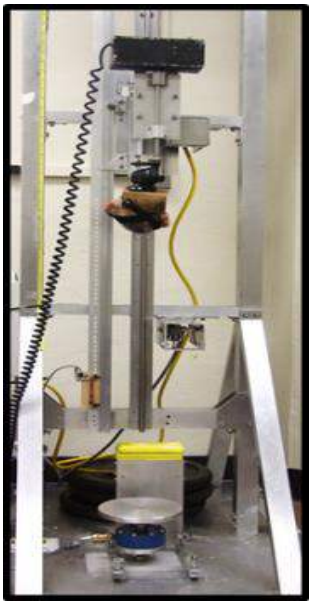

Figure 1: Experimental setup for infant porcine head impacts onto a flat plate.

The impact force generated by contact between the porcine skull and the impacting interface was measured over time with a 2500-lbf load transducer (model 1010AF-2.5K, Interface; Scottsdale, AZ) which was mounted below the fixed impact surface. The contact forces versus time were recorded at a sample rate of 10,000 Hz by a personal computer.

Following impact, the skull was palpated for fracture, and a viewing window was cut for photo documentation of the fracture patterns prior to heat maceration and cranial reassembly. All remaining soft tissues were removed by heat maceration of the skull in a mixture of water and laboratory detergent for four hours. After air-drying the bones, they were re-assembled and glued back together.

General Linear Model ANOVA in Minitab 16 (State College, PA) was used to analyze the impact energy, the overall peak contact force, the time to reach overall peak contact force, and the duration of impact time for each study group (top of the head impact, parieto-occipital impact, and mid-occipital impact). Statistical results were considered significant with $p<0.05$.

RESULTS

Top of the head impacts generated 90% (9/10) longitudinal bilateral fractures (approximately parallel with the sagittal suture) in a mixed combination of both parietal and frontal bones (Figure 2, column 1, row 2). In contrast, back of the head impacts generated 60% (6/10) transverse bilateral fractures (approximately perpendicular to the sagittal suture) in both parietal bones and 20% (2/10) longitudinal fractures in both parietal bones. Of the occipital impacts 100% (10/10) had minor to extensive occipital fractures (Figure 2, column 3, row 2). The Parietal-occipital impacts produced 90% (9/10) fractures in non-impacted bones on both the impacted and non-impacted sides of the skull (Figure 2, column 2, row 2). Of these impacts, 78% (7/9) fractures into other bones were contiguous in nature, while 33% (3/9) were deflected diastatically along the suture and then continued into non-impacted bones. These patterns were similar to those from center-parietal impacts documented previously by this research team [9].

For the mechanical parameters of interest, the overall peak force (628.4 ± 227.9 N), time to overall peak force (4.9 ± 2.1 ms), and contact duration (13.7 ± 3.3 ms) were not statistically significantly different between impact locations. As the required drop height to produce fracture was greater for occipital impact, the impact velocity (4.79 ± 0.05 m/s) and kinetic energy (7.7 ± 1.7 J) was greater for occipital impacts than those for the other impact locations. Parieto-occipital and top of the head impacts were not significantly different in terms of impact energy (5.1 ± 0.9 J) and drop velocity (3.85 ± 0.14 m/s).

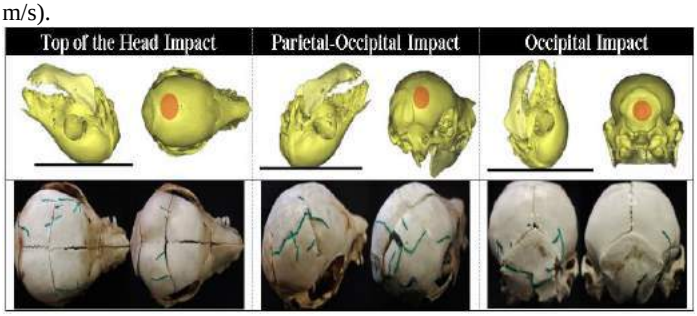

Figure 2: Each column has its representative model of the porcine head orientation in contact with the flat plate (left), with the targeted impact location (red dot, right), and two representative skull reconstructions (with fracture lines in green) below.

DISCUSSION

The objective of the study was to determine if top of the head impacts, back of the head impacts, and parieto-occipital impacts onto a large, flat plate could produce bilateral cranial fractures consistently under a controlled, experimental setting using the infant porcine head specimens. The results of the current study showed that the head drop tests not only consistently produced bilateral skull fractures, but the fracture orientations also demonstrated a directional dependency to the impact location. Impacts to the top of the head consistently produced longitudinal bilateral fractures, as demonstrated in the Arnholtz et al.' case [7], while impacts to the back of the head as well as a small number of parietal-occipital impacts produced transverse bilateral fractures, supporting those observed in the Weber study [6] and Griffen et al. study [5].

It is important to note that this experimental fixture simulated a single-impact crush injury of the head where the weight of the guide trolley was included into the impact mass of the head. This study provides convincing evidence that a single head impact can produce symmetric cranial fractures in multiple bones, and that while bilateral fractures can be diagnostic of an abusive event, it may also be a symptom of an accidental head-over-heels fall that may result in a crush-type injury. Caution should be taken in interpreting these results for the pediatric subject, as the overall geometry, cranial thickness, and material properties specific to the infant porcine skull may influence the resulting fracture patterns.

ACKNOWLEDGEMENTS

The authors would like to thank Clifford Beckett for technical support on the project.

REFERENCES

[1] Bilo, P.A.C., et al, *Head Ch2*. 15-47, 2010.
[2] Gurdjian, ES, et al., *AM J Surg*, 78(5):736-42, 1949.
[3] Gurdjian, ES, et al., *Radiology*, 54(3):313-39, 1950.
[4] Fujiwara, S, et al., *Forensic Sci Int*, 43:159-169, 1989.
[5] Griffen, JE, et al., *Laryngoscope*, 89 (9 part 1):1432-5, 1979.
[6] Weber, W, *Z Rechtsmed*, 92:87-94, 1984.
[7] Arnholtz, D, et al., *J Trauma*, 45:172, 1998.
[8] Hiss, J and Kahana, T, *J Trauma*, 38(1):32-4, 1995.
[9] Powell, BJ, et al., *J Forensic Sci*, 58(3):678-83, 2013.

ESTIMATES OF HIGH-RISK SINGLE AND CUMULATIVE HEAD IMPACT DOSES IN AMERICAN FOOTBALL

Adam Bartsch PhD PE (1), Vincent Miele MD (2), Edward Benzel MD (3), Jay Alberts PhD (3), Alok Shah (4), John Humm (4), Brian Stemper PhD (4), Michael McCrea PhD (4)

(1) Chief Science Officer
Prevent Biometrics
Minneapolis, MN, USA

(2) Department of Neurosurgery
University of Pittsburgh Medical Center
Pittsburgh, PA, USA

(3) Neurological Institute
Cleveland Clinic
Cleveland, OH, USA

(4) Medical College of Wisconsin, □ablocki VA
Center and Marquette University
Milwaukee, WI, USA

INTRODUCTION

In 2011, after reviewing scalar on-field kinematics data leading concussion clinicians concluded *"Recenti studies suggest that a concussive injury threshold is elusive, and may, in fact, be irrelevant when predicting the clinical outcome*".[1] In 2014 the Institute of Medicine concluded that "*Available studies of head injury biomechanics have identified the importance of linear and rotational movements of the head in injury causation...*" and "*there are currently inadequate data to define thresholds for linear and rotational acceleration specifically associated with concussions*…".[2]

It is likely that higher fidelity estimates of spatial and temporal impact parameters will clarify the currently unclear impact dose-response relationship.

The aim of this study was to investigate spatial and temporal estimates of head impact doses collected with a laboratory-calibrated impact monitoring mouthguard (IMM) system in American football. We first calibrated the IMM system in n=751 laboratory American football tests against instrumented Reference headforms. Next, we analyzed time-synchronized video and IMM data collected during n=445 player-games of high school and collegiate American football. Summary statistics on all impacts were synthesized. Cases where a player sustained impacts during a single play, or during a cumulative game's-worth of plays, and on video was demonstrably witnessed to meet the NFL's "No-go" criteria were analyzed in-depth.

METHODS

The IMM is an impact monitor that is instrumented with twelve channels of linear acceleration measurement at 3.2kHz ("12a", **Figure 1**) and has been described elsewhere.[4,5] Each IMM has an embedded flexible circuit board contained within FDA-grade mouthguard material. The IMM also includes a microprocessor, battery, wireless charging, onboard storage and wireless data offload.

Figure 1. The Impact Monitoring Mouthguard (IMM) System.

To evaluate the quality of IMM impact estimates, we compared their spatial and temporal outputs versus instrumented Reference headforms in the laboratory for all tested directions/locations combined. For this comparison we used published head impact dosimeter validity specifications[3-6].Laboratory calibration tests (n=751) generated first harmonic frequency content in the range of 20-100Hz, like what is seen on the field of play.[4] Impacts were delivered using a linear pneumatic impactor and Hybrid III headform with fixed mandible (n=434) or articulating mandible (n=132), as well as using a pendulum with NOCSAE headform and fixed mandible (n=185).

After calibrating the IMM system against Reference in the laboratory, a total of 2851 video-verified head impacts were retrospectively identified from 445 player-games. Players with zero

head impacts during a game were not included in this analysis. Each event was time-synchronized to 30fps video collected of each game. Any events collected when the athlete was not being impacted in the head were identified as false positives and discarded. The remaining true positive events were scrutinized based on published methods to confirm a head impact occurred in the video and the computed motion was physically realistic and matched the video.[7]

RESULTS

In the laboratory testing, head impacts for IMM versus Reference fit a linear model close to the ideal form; IMM=0.97*REF+1g, R^2=0.97 (**Figure 2**). Non-trivial processing algorithm, adequate IMM coupling to dentition, knowledge of sensor positions and orientations with respect to Reference, and calibration of individual sensor outputs were required to achieve this level of accuracy.

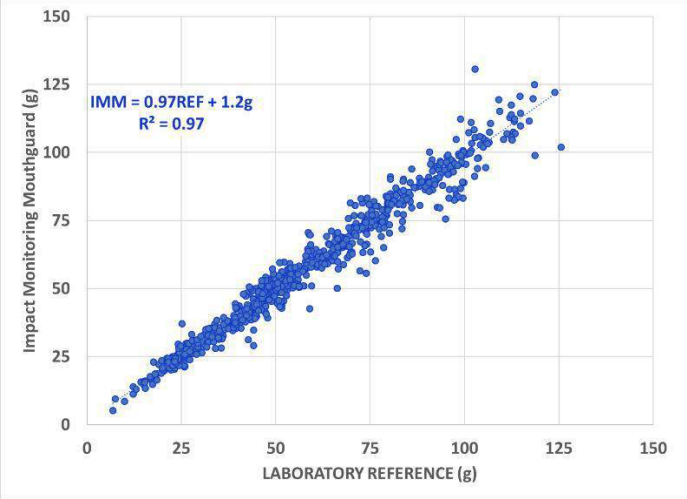

Figure 2. Comparison of IMM versus Reference in Laboratory.

During on-field data and video analysis, there were approximately 13,000 triggering events captured, with n=2851 true positives confirmed after hardware and software filters were applied, along with the time synchronized video (**Table 1**).

# Video-verified Impacts	# Player-games	Average # Impacts/game		Impact Location[8]	
2851	445	6.4		58% to Front, 30% to Sides	
Median PLA (g)	**Median PAA (rad/s^2)**	**Median PLV (m/s)**	**Median PAV (rad/s)**	**Median KE Transfer (J)**	**Median RWE**
21	1600	1.5	12	6	0.00002

Table 1. Summary from n=2851 Video-Verified Head Impacts

There were four (4) players with coronal plane impacts during a single play, three (3) players who sustained cumulative sagittal plane impacts during a game identified as "No-Go" candidates[9]

DISCUSSION

We found an average of 6 to 7 video-verified head impacts per player-game in this study, which is in line with published video-verified studies[10] and approximately one order of magnitude lower than published studies without video verification.[11]

For the four players with "No-go" single play impacts, all impacts were to the side of the players' heads. Coronal plane impact sensitivity has been a hypothesized clinical injury mechanism[12] and our results support that hypothesis. However, other studies have pointed to top and front of head impacts as being the most dangerous.[1]

The single play computed kinematics were in the top 5% of all impacts. We did not see high PLA/PAA impacts without obvious player "No-go" observations. This finding disagrees with other studies that have reported high PLA/PAA impacts without any demonstrable "No-go" observations[13].

Also observed in single play "No-go" impacts, the kinetic energy transfer (40J to 110J) was an order of magnitude higher than the median (6J). This makes sense, as computational models predict substantially higher brain stress and strain when kinetic energy transfer is high in an impact[14, 15]. On the contrary, the RWE metric[16] was low for three of the four "No-go" single play impacts. This also makes sense as RWE values increase exponentially on a logistic regression above critical PLA and PAA values of ~120g and 6000rad/s^2. The PLA/PAA values in our analysis were generally lower than RWE critical values.

For the three players with "No-go" cumulative impacts, 75% of cumulative impacts were to the front of the players' heads. The total KE transfer, 100J to 320J, was 1-2 orders of magnitude higher than the median value of 6J. Although the number of subjects is modest, this result could point to a spatial and temporal – within one gameday - tolerance to head impact in the frontal direction. It was interesting that the cumulative RWE was low for the "No-go" cumulative players. This can be explained by the fact that most of the cumulative impact doses had negligible RWE since only 15% of cumulative impacts were above 40g PLA or 3000rad/s^2 PAA.

ACKNOWLEDGEMENTS & DISCLOSURES

Daniel Brett, DDS of Sportsguard Laboratories (Kent, OH) and Djamil Abiyev of Partners Dental Studio (Minneapolis, MN) manufactured custom mouthguards used in this study.

AB is an employee of Prevent Biometrics. Cleveland Clinic has a license agreement for IMM on which AJB, ECB and VJM are inventors and have potential for fee-for-service payments, royalties and/or equity. AB, JA, EB, AS, JH, MM and BS receive research support from the United States Department of Defense, National Institutes of Health and/or Department of Transportation. Cleveland Clinic, Medical College of Wisconsin and University of Pittsburgh IRBs (CC13-899, MCW PRO00022950, UPMC 10/30/2018). Opinions, interpretations, conclusions and recommendations are those of the authors and are not necessarily endorsed by the NIH, DOT or DOD.

REFERENCES

[1] Guskiewicz KM, Mihalik JP: Exer Sport Sci 2011; 39: 4-11.
[2] IOM & NRCC. Washington, DC, National Academies Press, 2014.
[3] Siegmund GP et al. Ann Biomed Eng 2016; 44: 1257-74.
[4] Bartsch AJ et al. STAPP Car Crash Journal 2014; 58: 1-28.
[5] Hedin DS et al. IEEE Medicine and Biology 2016.
[6] https://www.helmet.beam.vt.edu/sensor-ratings.html
[7] Kuo C et al. PLoS ONE 2018; 13(6): e0199238.
[8] Greenwald RM et al. Neurosurgery 2008; 62: 789-798.
[9] https://www.playsmartplaysafe.com/wp-content/uploads/2018/08/
[10] Duma SM et al. Clin J Sport Med 2005;15:3–8.
[11] Broglio SP et al. Med. Sci. Sports, 42, 11, 2064-2071, 2010.
[12] Fijalkowski RJ et al. J. Neurotrauma 24:1387-1398, 2007.
[13] Stemper BS et al. Annals Biomed. Engr., Vol. 46, 2018.
[14] McAllister TW et al. Ann Biomed Eng 2012; 40: 127.
[15] Zhang L et al. Trans ASME, Vol. 126, April 2004, pp 226-236.
[16] Rowson S & Duma SM. Annals Biomed. Engr., Vol. 41, No. 5, May 2013 pp. 873–882.

SB^{3}C2019
Summer Biomechanics, Bioengineering and Biotransport Conference
June 25 -28, Seven Springs, PA, USA

STENT INTERVENTION IMPROVES FLOW DISTRIBUTION AND VASCULAR GROWTH IN PORCINE PULMONARY ARTERY STENOSIS

Ryan Pewowaruk[1], Klarka Mendrisova[2], Carolina Larrain[3], Chris Francois[4], Luke Lamers[5], Alejandro Roldán-Alzate[1,2,4]

(1) Biomedical Engineering
University of Wisconsin - Madison
Madison, WI, USA

(2) Mechanical Engineering
University of Wisconsin - Madison
Madison, WI, USA

(3) School of Medicine & Public Health
University of Wisconsin - Madison
Madison, WI, USA

(4) Radiology
University of Wisconsin - Madison
Madison, WI, USA

(5) Pediatrics – Cardiology Division
University of Wisconsin - Madison
Madison, WI, USA

INTRODUCTION

Most complex forms of congenital heart disease (CHD) require surgical repair during infancy [1]. A common post-operative complication of these early surgeries is branch pulmonary artery stenosis (PAS) [2-6] which is associated with both acute and chronic morbidity and mortality [7-9]. Catheter interventions with intravascular stenting are a first line therapy for post-surgical PAS in older patients and with technological advances this therapy is now being used in infants and small children. Little is known about the acute and chronic consequences of early stent therapy for treatment of post-surgical PAS occurring early in life or the capabilities of 4D Flow MRI to longitudinally define consequences of stent interventions with serial dilations in a porcine PAS model. We hypothesize that early stent interventions will allow for normal pulmonary vascular and lung parenchyma growth and normal branch PA flow distribution.

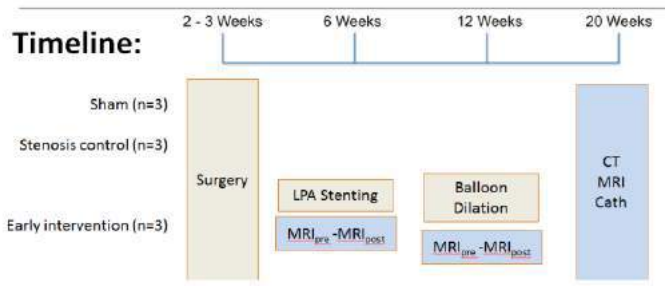

Figure 1: Experimental timeline showing stenosis surgery, LPA stenting, balloon dilation and final imaging for the early intervention group. Sham and stenosis controls only have imaging at 20 weeks.

METHODS

Isolated left PAS was created in neonatal piglets (n=6, 5. 4 kg) by suturing a short segment of 4.0mm Gore-Tex tube graft around the proximal left PA (LPA). Cardiac catheterizations with pre and post intervention MRI occured at 6 (LPA stent), 12 (LPA stent dilation) (n=3). At 20 weeks all animals (n=9) had catheterization and imaging. From cone-beam CT angiography (Dyna CT) data sets the pulmonary arteries were segmented. Areas from centerlines were calculated for the RPA, LPA and six similar first order branch arteries. MRI was performed on a 3. 0T scanner using the 4D Flow MRI sequence PC-VIPR (Phase Contrast Vastly Under sampled Projection Imaging) [10]. 4D Flow MRI quantitatively and qualitatively assessed cardiac and vascular blood flow. Analysis planes and streamlines are shown in Fig2D. Cardiac index (CI) is cardiac output (CO) normalized by bodyweight. LPA flow percentage equals LPA flow divided by CO measured in the MPA. Alveoli counts were obtained from R and L lung tissue samples. Statistical analysis is performed using ANOVA with post hoc hypothesis testing correcting for multiple comparisons.

RESULTS

RV, MPA and LPA pressures where similar in the interventions and sham controls while the stenosis controls had increased RV and MPA pressures with lack of pulsatility in the LPA (Table 1).

Figure 2A is a representative Dyna CT image the pulmonary vasculature of the three study groups. LPA 1st order branch artery areas (Fig 2B) were similar in sham and interventions, both of which were larger than the stenosis controls. RPA 1st order branch areas demonstrate the opposite trend (Fig 2C).

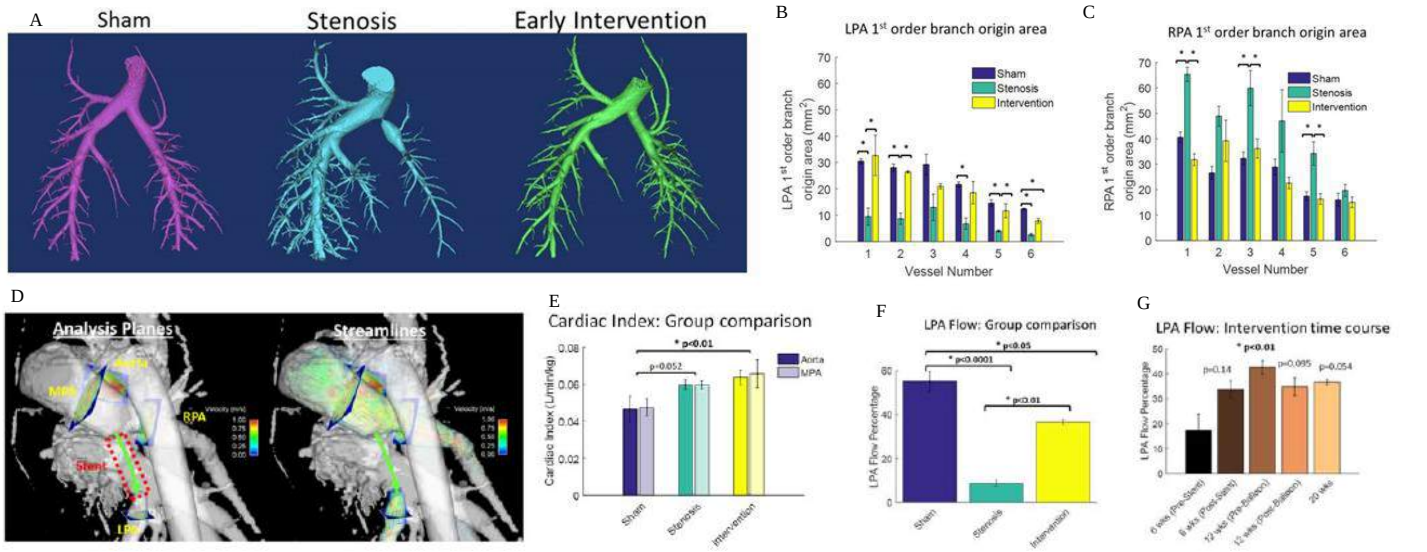

Figure 2: 3D renderings of the pulmonary vasculature show altered stenosis morphology, **B.** Stenosis decreases the LPA 1st order branch areas and intervention increases the LPA 1st order branch areas to normal, **C.** Stenosis increases the RPA 1st order branch areas and intervention decreases the RPA 1st order branch areas to normal , **D.** 4D Flow MRI data is lost in the stent, but flow is still able to be analyzed proximal and distal to the stent, **E.** CI is greater in intervention animals than sham, **F.** Stenosis decreases LPA flow and intervention increases LPA flow, but not to normal levels, **G.** Longitudinal LPA flow percentage shows intervention improves LPA flow initially, then LPA flow remains constant.

Table 1: Pressure catheterization measurements

	Sham	Stenosis	Intervention
RV Pressure (mmHg)	29/8	40/10	29/6
MPA Pressure (mmHg)	30/15	39/18	29/14
LPA Pressure (mmHg)	29/17	15/13	23/14

The mean number of L lung alveoli were similar in sham and interventions and both were increased compared to stenosis controls. No differences were noted for the R lung alveolar counts (Fig3). Abnormal bronchiolar arterioles with significant medial hypertrophy and lack of normal pulmonary arterioles were present in the stenosis controls.

CI is greater in the intervention group than the sham group (Fig2E). Intervention improves LPA flow percentage compared stenosis controls, 37% vs 9% ($p<0.01$) (Fig2F). Intervention LPA flow percentage is still impaired compared to sham controls, 37% vs 54%. The initial intervention increase LPA flow percentage from 17% to 34%, then remains relatively constant (Fig2G) despite stent dilation at 12 weeks and additional time for growth.

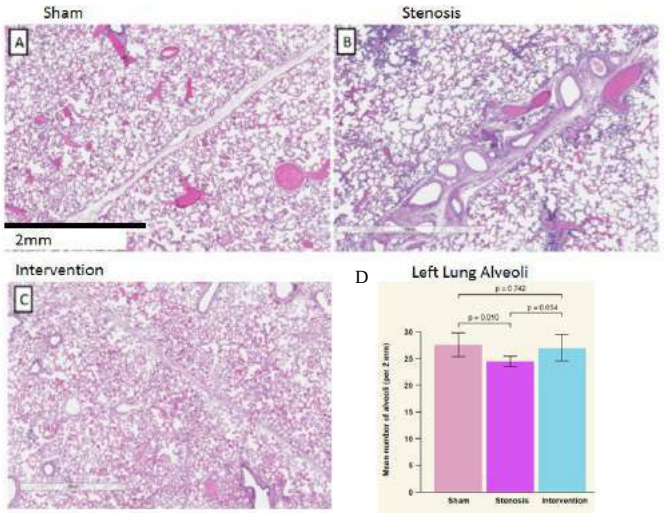

Figure 3: Representative lung histology for **A**. Sham, **B**. Stenosis, **C**. Intervention, showing that **D**. intervention preserves left lung alveoli

DISCUSSION

In this animal model of surgical PAS, early stent intervention normalized R heart pressures, was associated with a trend towards improved growth of the first order branches of the LPA and allowed for improved pulmonary development, as demonstrated by normal L lung alveolar counts and normal appearing pulmonary arterioles. Despite "successful interventions" percentage of L lung pulmonary blood flow was significantly decreased compared to sham controls. This persistent flow discrepancy did not compromise cardiac output as estimated by MRI imaging.

More broadly, this study demonstrates the capability of 4D-flow MRI to comprehensively examine the acute and chronic effects of minimally invasive interventions. While MRI signal is lost due to the stent material artifact, flow can still be quantified proximal and distal to the stent. For longitudinal studies looking at the time course of an intervention, 4D flow MRI is non-invasive unlike heart catheterization and provides greater information than other non-invasive modalities like ultrasound and nuclear medicine perfusion scans.

Future work will include additional PA stenting animals (n=10 total) compared to sham and untreated stenosis controls and analyze ventricle function using 4D flow metrics of kinetic energy and vorticity.

ACKNOWLEDGEMENTS

This investigation was supported by the UW Cardiovascular Research Center T32 HL 007936, the UW Clinical and Translational Science Award program UL1TR000427 and the UW department of radiology.

REFERENCES

[1] Hoffman J, et al. *Am J Cardiol* 1978;42:641-47.]
[2] Hirsch J, et al. *Ann Surg* 2000;232:508-14.
[3] Parry A, et al. *J Am Coll Cardiol* 2000;36:2279-83.
[4] Groh M, et al. *Circulation* 1991;84:III206-12.
[5] Kim H, et al. *J Thorac Cardiovasc Surg* 2014;148:2597-601.
[6] Wilder T, et al. *Ann Thorac Surg* 2016;101:996-1004.
[7] Gatzoulis M, et al. *Lancet*;356:975-81.
[8] Harrison D, et al. 1997;30:1368-73.
[9] Rhodes J, et al. *Am J Cardiol*. 1998;81:1217-9.
[10] Wieben O, et al. *Eur J Radiol*, 2008. 65(1):15-28.

SB³C2019
Summer Biomechanics, Bioengineering and Biotransport Conference
June 25 -28, Seven Springs, PA, USA

SHEAR STRESS MODULATES CARDIOMYOCYTE PROLIFERATION VIA ENDOTHELIAL CELL-CARDIOMYOCYE SIGNALING

Matthew C. Watson (1,2), Lauren D. Black III (2,3), Erica M. Kemmerling (1)

(1) Mechanical Engineering
Tufts University
Medford, MA, USA

(2) Biomedical Engineering
Tufts University
Medford, MA, 02143

(3) Cellular, Molecular, and Developmental Biology
Sackler School for Graduate Biomedical Sciences
Tufts University School of Medicine
Boston, MA, 02111

INTRODUCTION

Congenital Heart Defects (CHDs) occur in approximately 1% of all live births and are the leading cause of mortality in infants and small children[1]. Malformations of the left ventricle are among the most serious of CHDs. It has been established that altered hemodynamics can lead to the development of CHDs, especially malformations of the left ventricle such as Hypoplastic Left Heart Syndrome (HLHS); however, the specific mechanism by which hemodynamics affects ventricular growth is still poorly understood [2, 3]. The fetal heart grows primarily through proliferation of cardiomyocytes (CMs) [4]. Endothelial secreted neuregulin-1 (NRG) has been suggested as a potential therapeutic target to promote CM proliferation [5]. Recently, it has been shown that ECs secrete NRG in response to mechanical and biochemical cues [6]. *We hypothesized that fluid shear stresses may modulate communication between endothelial cells (ECs) and CMs, and that altered shear stress in congenital pathologies may affect CM proliferation.*

METHODS

To assess the proliferative effects of NRG on cardiomyocytes we exposed neonatal rat cardiomyocytes (NRCMs) cultured on either tissue culture plastic or tissue culture plastic coated with solubilized fetal cardiac extracellular matrix (ECM) to exogenous NRG. NRCMs were cultured with serum-free media containing either 200 ng/mL of NRG, 100 ng/mL of NRG, or no NRG. After 24 hours and 5 days, cells were fixed with 4% paraformaldehyde, labeled with anti-cardiac α-actin and anti-Ki67 (a proliferative marker), and imaged using an Olympus IX81 fluorescent microscope. Custom pipelines developed in CellProfiler (Broad Institute, Cambridge, MA) assessed proliferation of cells.

We then assessed shear effects on ECs alone, using a custom-built macroscale cone-plate shearing device, capable of applying controlled, pulsatile flow to human endothelial cells. ECs were seeded on glass coverslips 48 hours prior to device installation. The device was filled with endothelial cell growth medium 2 (EGM-2) (Lonza Inc., Basel, Switzerland), and ECs were exposed to steady, oscillatory, and physiological (healthy and unhealthy) pulsatile shear stress. After shear exposure, media was collected, and coverslips were removed. ECs were fixed in 4% paraformaldehyde and labeled with either anti-VE-Cadherin or anti-neuregulin-1. Images of VE-Cadherin stains loaded into custom pipelines developed in CellProfiler (Broad Institute, Cambridge, MA) were used to assess EC eccentricity, spread area, aspect ratio, and orientation with respect to the flow.

As a preliminary experiment to assess communication between ECs and CMs, we utilized a transwell assay. Human ECs seeded were seeded on transwell membranes positioned above NRCMs seeded on TCP. ECs were placed on an orbital shaker and exposed to shear stress for 24 hours. CMs were fixed in 4% paraformaldehyde, stained with anti-cardiac α-actin and anti-Ki67, and imaged using an Olympus IX81 fluorescent microscope. Custom pipelines developed in CellProfiler (Broad Institute, Cambridge, MA) assessed proliferation of cells.

In a separate experiment, we generated 3D printed models of patient specific geometries. We used these 3D models to more accurately replicate the flow inside a complicated, patient-specific left ventricle geometry. As a proof of concept, we first used an adult left ventricle geometry extracted from a patient specific CT scan. Models were modified to include cutouts for the installation of engineered tissue constructs. Constructs, seeded with human adult cardiac fibroblasts, were installed in the 3D printed model and cultured for 24 hours in serum containing medium. Currently, we are working on applying realistic flow waveforms to cells installed in the models to more accurately replicate flow inside a ventricle.

Technical Presentation #321

RESULTS

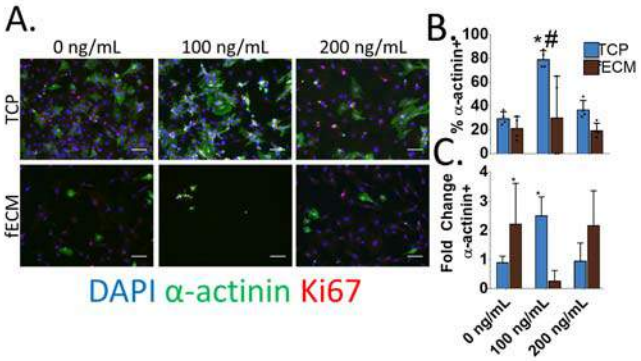

Figure 1: (A) Representative images of cells stained with DAPI for nuclei (blue), α-actinin for CMs (green), and the proliferation marker Ki67 (red). (Scale Bar = 100 µm). (B) The percentage of α-actinin+ cells. (C) Fold change of α-actinin+ cells with respect to cells fixed after 24 hours. (n = 4 per group). * = p < 0.01 compared to TCP at 0 ng/mL. # = p < 0.01 compared to fECM at 100 ng/mL.

First, we assayed the proliferative effects of NRG-1 on NRCMs seeded on either solubilized fetal cardiac extracellular matrix, or tissue culture plastic (Figure 1A). We observed a significant increase in positive staining for cardiac α-actin in NRCMs treated with 100 ng/mL of NRG1 cultured on TCP compared to NRCMs treated with no NRG on TCP (Figure 1C). We did not see significant changes in positive stains cardiac α-actin in NRCMs cultured on solubilized cardiac fetal ECM.

We then sought to expose monolayers of ECs to controlled physiological levels of shear stress to better quantify EC phenotype and protein expression. A custom-built cone-plate shearing device (Figure 2A-B) exposed monolayers ECs to pulsatile shear stresses. Eccentricity measurements (Figure 2C) and immunofluorescent images (Figure 2D-E) verify that our device can successfully culture ECs under sheared conditions. Additionally, positive stains for NRG (Figure 2E) verify the ECs are expressing NRG under sheared conditions. We then used a transwell experiment to assess how CMs may respond to ECs exposed to shear stress. We observed trends in proliferation of NRCMs in response to ECs in a transwell exposed to shear stress (Figure 3A-B).

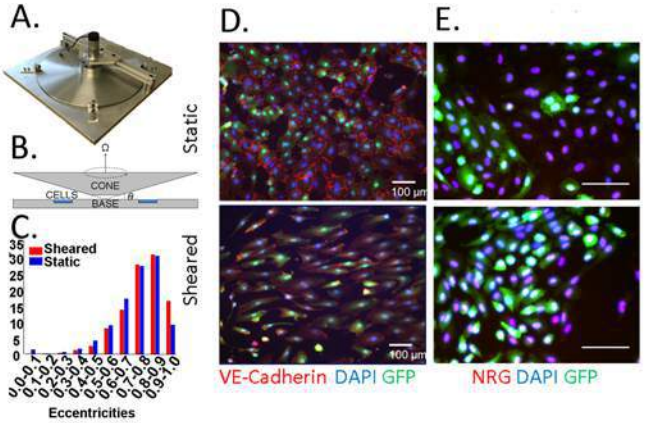

Figure 2: Photograph (A) and schematic (B) of cone-plate viscometer. (C) Percentages of ECs in each eccentricity range under static or shear stress culture conditions. (D-E) Representative images of ECs after 24 hours of static culture or shear stress culture. (D) VE-Cadherin (red). (E) NRG expression (red). Direction of flow is left to right (Scale Bars = 100 µm).

We have started preliminary experiments to address complicated flow-induced shear stresses that arise from patient specific geometries. Patient specific ventricle geometries extracted from CT scans were 3D printed. Engineered tissue constructs containing cardiac fibroblasts (CFs) were installed into the 3D printed models and cultured for 24 hours. For future studies, engineered constructs containing CMs, ECs, and CFs installed in 3D printed ventricle models will be connected in a pulsatile flow loop to assess how specific flow patterns may modulate cellular communication. Results from these studies will be presented.

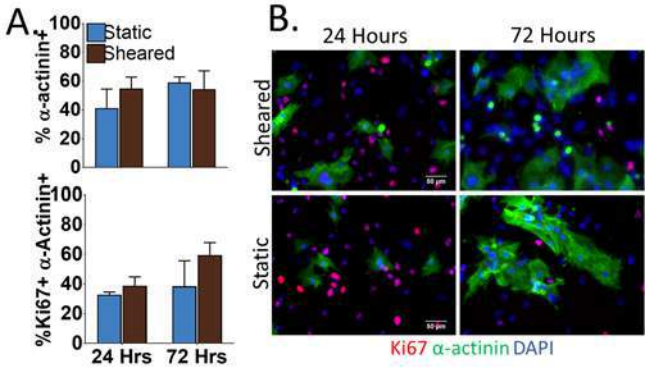

Figure 3: (A) Percent of CMs that are proliferating in response to ECs in a transwells under either static culture of sheared culture (n=2 per group). (B) Representative images of CMs staining for Ki67, alpha-actinin, and DAPI. (SB = 50 µm).

DISCUSSION

The significant increase in cells expressing cardiac α-actin observed in cells on TCP treated with exogenous NRG (Figure 1C) suggests that NRG expression is important for understanding CM proliferation, and thus fetal ventricular growth. We have designed a cone-plate shearing device capable of culturing ECs under sheared conditions. Under sheared conditions, these ECs are expressing NRG (Figure 2E). Furthermore, increased trends in cells expressing cardiac α-actin in response to ECs exposed to shear stress (Figure 3) suggest that there is communication between ECs and CMs that is modulating CM proliferation; however, additional studies with controlled shear stresses are necessary to evaluate significance and to elucidate the mechanism of EC-CM communication. Finally, we have manufactured a patient-specific ventricular model with cell cutouts for the installation of 3D engineered tissues. This model is capable of culturing cells in static conditions and culturing cells in a pulsatile flow loop.

ACKNOWLEDGEMENTS

We thank Dr. Sitaram Emani and Boston Children's Hospital for their expertise on congenital heart defects and for providing us with MRI images of fetal hearts.

REFERENCES

1. Rozmiarek, A.J., et al., J Pediatr Surg, 2004. **39**(6): p. 821-4; discussion 821-4.
2. Axt-Fliedner, R., et al., Ultrasound in obstetrics & gynecology, 2006. **28**(1): p. 106-109.
3. Mäkikallio, K., et al., Circulation, 2006. **113**(11): p. 1401-1405.
4. Soonpaa, M.H. and L.J. Field, Circ Res, 1998. **83**: p. 15-26.
5. Polizzotti, B.D., et al., Sci Transl Med, 2015. **7**(281): p. 281ra45.
6. Hedhli, N., et al., Circulation, 2011. **123**(20): p. 2254-2262.

SB³C2019
Summer Biomechanics, Bioengineering and Biotransport Conference
June 25 -28, Seven Springs, PA, USA

COMPUTATIONAL SURGICAL PLANNING FOR PERIPHERAL PULMONARY ARTERY STENOSIS IN CHILDREN WITH ALAGILLE AND WILLIAMS SYNDROMES

Ingrid S. Lan (1), Weiguang Yang (2), Jeffrey A. Feinstein (1,2), Alison L. Marsden (1,2)

(1) Bioengineering
Stanford University
Stanford, CA, USA

(2) Pediatric Cardiology
Stanford University
Stanford, CA, USA

INTRODUCTION

Peripheral pulmonary artery stenosis (PPAS) is a relatively rare form of congenital heart disease (CHD) found in < 1% of CHD patients, but frequently found in association with Alagille and Williams syndromes. PPAS is characterized by stenoses in the central and peripheral pulmonary arteries (PAs) and results in disparity in left vs. right lung perfusion, right ventricular (RV) hypertension, and ultimately RV failure [1]. Since the stenoses are frequently distal and complex, most centers favor catheter-based interventions despite unfavorable outcomes, including unchanged RV pressures, risks of vessel dissection, aneurysm formation, rupture, and even death [2, 3, 4]. Furthermore, the pathophysiologic features of the PAs, including medial thickening, nonparallel arrangement of smooth muscle cells, and elastin deficiency, place these patients at a uniquely high risk of in-stent stenosis and thus reintervention [5, 6]. More recently, comprehensive surgical reconstruction of PPAS, or patch augmentation of all stenoses in the main, branch, lobar, and segmental arterial levels, has been shown to significantly reduce RV pressures with low morbidity and mortality [1].

To our knowledge, no studies have investigated hemodynamic conditions following catheter-based angioplasty and/or stenting in Alagille or Williams patients. While previous computational fluid dynamics (CFD) studies have modeled the post-operative hemodynamics following surgical reconstruction of PPAS in Alagille patients [7, 8], they lacked validation against post-operative PA and RV pressures, the primary indicators of success in PPAS repair. In this study, we aim to investigate the hemodynamics enabling surgical reconstruction to outperform stent placement for PPAS repair in Alagille and Williams patients, and further, to provide patient-specific predictions of stenoses that should be surgically patched in order to achieve normal RV pressures and balanced lung perfusion. We hypothesize that unlike surgical reconstruction, catheter-based interventions fail to reduce the large resistance associated with diffuse stenoses in the distal pulmonary vascular bed and therefore fail to reduce the PA and RV pressures.

METHODS

Using the open-source software SimVascular (simvascular.org) and computed tomography (CT) scans, we generated 3D anatomical models of the pre-operative PAs of a 13-year-old male Alagille patient and a 7-month-old male Williams patient, both of whom underwent surgical reconstruction at Lucile Packard Children's Hospital at Stanford. A healthy adult PA inflow waveform scaled to each patient's cardiac output was prescribed at the inlet, and a 3-element Windkessel model was prescribed at each outlet to model the downstream vasculature not resolved by CT. Hemodynamic simulations were performed with a backflow-stabilized 3D Navier-Stokes solver. Fluid-structure interaction was incorporated via the coupled momentum method [9] with an elastic modulus of 1.5 x 10^6 dyn/cm^2 for the PAs.

An automated tuning framework was developed to iteratively identify all boundary conditions (BCs) necessary to achieve patient-specific pre-operative systolic, diastolic, and mean pressures at the main PA (MPA), left main PA (LPA), and right main PA (RPA) measured via cardiac catheterization—a total of 9 target pressures. In particular, a 0D lumped parameter circuit was designed as a surrogate model of the 3D fluid domain. In each iteration, Nelder-Mead optimization was first performed on the 0D surrogate model parameters and 3D outlet BCs to match the CFD-simulated and catheterization-measured pressures, respectively (Figure 1), before another CFD simulation was run using the newly optimized 3D outlet BCs. The log barrier method (Equation 1) was implemented to ensure physiological tuning ranges:

$$\tilde{\phi}(\vec{x}) = \phi(\vec{x}) - K\sum_{i=1}^{m} \ln[-g_i(\vec{x})] \qquad (1)$$

where $\phi(\vec{x})$ and $\tilde{\phi}(\vec{x})$ are the original and modified cost functions, K is a scalar multiplier, m is the total number of inequality constraints, and each $g_i(\vec{x}) \leq 0$ is an inequality constraint. The optimized 3D outlet BCs were distributed to all outlets with the assumptions that all downstream vessels in the RPA or LPA form parallel circuits, and that each outlet resistance is inversely proportional to the outlet area [10].

Surgeon-guided virtual surgery will be performed to reconstruct post-operative anatomies, and simulated post-operative outcomes will be validated against cardiac catheterization data as well as available lung perfusion data. Finally, virtual stent placement will be performed on the pre-operative models, and simulated outcomes will be compared to those of virtual surgical reconstruction. In either case, adaptive outflow boundary conditions [7] will be determined using a structured tree model [11, 12] and the assumption that arteries respond to flow perturbations by maintaining wall shear stress levels [13].

RESULTS

The automated tuning framework successfully minimized the cost function in all tuning iterations for the 0D surrogate model parameters

and 3D outlet BCs (Figure 2). Correspondingly, the severe pre-operative PA pressure drops across proximal stenoses in both patients were accurately captured: $\Delta P_{MPA\text{-}RPA}$ = 29 / 3 m16 mm Hg (systolic/ diastolic, mean) and $\Delta P_{MPA\text{-}LPA}$ = 39 / 0 m17 mm Hg in the Alagille patient (Figure 3A); $\Delta P_{MPA\text{-}RPA}$ = 106 / 21 m48 mm Hg and $\Delta P_{MPA\text{-}LPA}$ = 98 / 11 m38 mm Hg in the Williams patient (Figure 3B). No pre-operative lung perfusion scan was available for the Williams patient, but the highly skewed PA flow distribution was accurately captured in the Alagille patient: 68% R / 32% L. Post-operative results will also be presented.

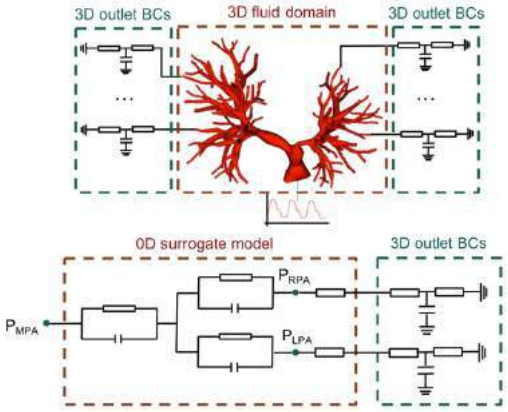

Figure 1: 0D lumped surrogate model for the 3D fluid domain in series with the 3D lumped outlet BCs.

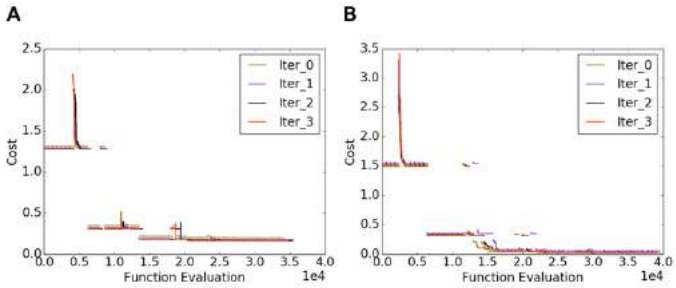

Figure 2: Nelder-Mead function evaluations in all tuning iterations for (A) 0D surrogate model parameters and (B) 3D outlet BCs for the Alagille patient.

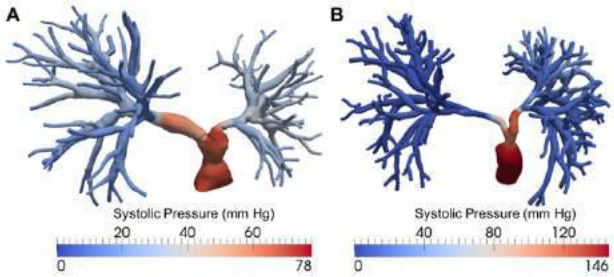

Figure 3: Pre-operative systolic PA pressures in the (A) Alagille and (B) Williams patients.

DISCUSSION

Given the severely stenotic and hypoplastic PA morphology, drastic pressure drops across stenoses, and skewed lung perfusion in Alagille and Williams patients, outlet BCs for hemodynamic simulations are particularly challenging to identify such that all patient-specific clinical targets are achieved. In this study, an automated tuning framework was designed to tune outlet BCs of PA hemodynamic simulations to patient-specific systolic, diastolic, and mean MPA, RPA, and LPA pressures. While automated tuning has previously been performed for coronary hemodynamic simulations [14], our framework is easily generalizable to different 0D lumped parameter circuit designs and even other non-PA vascular physiologies. Importantly, it also allows for tuning to hemodynamic quantities within arbitrary regions of the 3D domain rather than the outlets alone.

The outcomes of PPAS repair vary widely from complete repair to early or late mortality associated with complications such as vessel dissection, aneurysm formation, and rupture. CFD simulations provide a unique platform for computational patient-specific surgical planning, in which patient-specific anatomical models are altered to represent different interventional cardiology techniques, and the post-interventional hemodynamics are assessed in each case. Previous studies investigating hemodynamic conditions following surgical reconstruction of PPAS in Alagille patients were only validated against post-operative lung perfusion scans [7, 8]. Our ability to accurately predict post-operative outcomes would suggest the potential to identify all stenoses that need to be addressed in order to achieve normal PA pressures and balanced lung perfusion. Such predictions would prove particularly valuable to cardiothoracic surgeons by providing a model-based tool and possibly improving surgical outcomes.

While our study investigates the immediate post-interventional PA hemodynamic conditions following catheter-based angioplasty and surgical reconstruction of PPAS, arteries are known to respond to flow perturbations through acute adaptation as well as chronic growth and remodeling [13]. One limitation is therefore the inability to assess the long-term growth and remodeling processes in the pathophysiologic vascular wall that underlie in-stent stenoses in Alagille and Williams patients. Other limitations include the lack of post-operative CT scans for anatomical validation and the small patient cohort. Nonetheless, our study is the first to lend insight into the post-interventional hemodynamics enabling surgical reconstruction to outperform stent placement for PPAS repair in both Alagille and Williams patients.

ACKNOWLEDGEMENTS

This study is supported by the National Science Foundation Graduate Research Fellowship and the Stanford Graduate Fellowship in Science and Engineering. CFD simulations were performed using Stanford Research Computing Center's Sherlock cluster and the Extreme Science and Engineering Discovery Environment (XSEDE), which is supported by National Science Foundation grant number ACI-1548562.

REFERENCES

[1] Monge, MC et al., *J Thorac Cardiovasc Surg*, 145(2):476-481, 2013.
[2] Stamm, C et al., *J Thorac Cardiovasc Surg*, 120(4):755-763, 2000.
[3] Geggel, RL et al., *Circulation*, 103(17):2165-2170, 2001.
[4] Cunningham, JW et al., *Circ Cardiovasc Interv*, 6(4):460-467, 2013.
[5] Hallbergson, A et al., *Am J Cardiol*, 113(3):541-545, 2014.
[6] Zussman, M et al., *Congenit Heart Dis*, 10(4):310-316, 2015.
[7] Yang, W et al., *Biomech Model Mechanobiol*, 15(5):1345-1353, 2016.
[8] Yang, W et al., *Congenit Heart Dis*, 13(2):241-250, 2018.
[9] Figueroa, CA et al., *Comput Methods in Appl Mech Eng*, 195(41-43):5685-5706, 2006.
[10] Troianowski, G et al., *J Biomech Eng*, 133(11):111006, 2011.
[11] Olufsen, MS, *Am J Physiol*(1 Pt2):H257-268, 1999.
[12] Olufsen, MS et al., *Ann Biomed Eng* 28(11):1281-1299, 2000.
[13] Kamiya, A and Togawa T, *Am J Physiol*, 239(1):H14-21, 1980.
[14] Tran, JS et al., *Comput Fluids*, 142:128-138, 2017.

SB³C2019
Summer Biomechanics, Bioengineering and Biotransport Conference
June 25 -28, Seven Springs, PA, USA

FLUID-STRUCTURE ANALYSIS OF A COLLAPSIBLE AXIAL IMPELLER AND PROTECTIVE CAGE FOR DYSFUNCTIONAL FONTAN PHYSIOLOGY

Matthew D. Hirschhorn MS (1), Evan A. Bisirri MS (1), Randy M. Stevens MD (3), Joseph W. Rossano MD (2), Amy L. Throckmorton PhD (1)

(1) BioCirc Research Lab
School of Biomedical Engineering, Science and Health Systems, Drexel University
Philadelphia, PA, USA

(2) Division of Cardiology, Pediatric Heart Failure & Transplant Program, The Children's Hospital of Philadelphia, Philadelphia, PA, USA

(3) Heart Center for Children, Cardiothoracic Surgery,
St. Christopher's Hospital for Children,
Philadelphia, PA, USA

INTRODUCTION

There are 1.3 million people in the United States who survived into adulthood who were born with with congenital heart defects. Single ventricle physiolgies account for 9-12% of congenital heart anomolies[1]. Single ventricle patients undergo a series of palliative procedures during the early years of life, resulting in a reconstructed cardiac circuit known as Fontan physiology. In these patients the single fully-formed ventricle actively drives blood through systemic circulation and passively draws blood through pulmonary circulation[2]. These patients commonly encounter numerous long-term complications, such as early-onset congestive heart failure, thrombosis, arrhythmias, and protein losing enteropathy[2]. The complications in this cohort of patients results in an annual clinical treatment and management cost in excess of $1 billion[3]. Improvements to surgical techniques have brought the post-operative mortality rate to under 5%[2] but the 10-, 20-, and 30- year survival rate is only 74%, 61% and 43%, respectively[4]. Pharmaceutical and surgical advances have slowed for Fontan patients. Heart transplantation is the best option if the patient can survive the waiting period.

It has theorized a pressure boost of 1-5mmHg in the pulmonary arteries is adequate to alleviate many of these complications, and there is a growing interest in the use of blood pumps as a bridge to therapy or transplant[2,5]. Currently available blood pumps have limited utility for these patients because they are large and primarily designed to support systemic circulation in adults. A major constraint of current pumps that limits their usefulness for Fontan patients are designs with rigid blades that have a fixed diameter. The rigid blade designs prevent minimally invasive insertion and require off-design operation to adapt the pump to the unique pressure generation needs of the Fontan circuit. Off design use leads to irregular flow patterns, inefficient performance, and blood damage. The presented study investigates the use of flexible blade, cage, and diffuser designs to begin working toward the design of a minimally invasive blood pump with blade pitch adjusting capabilities. The design in development will be inserted into the surgically created Fontan connection and have an impeller with three raised blades, a protective cage with four helical fibers, and a diffuser. A rigid version of the design, seen in Figure 1 below, has been optimized through computational modeling and benchtop experimental testing.

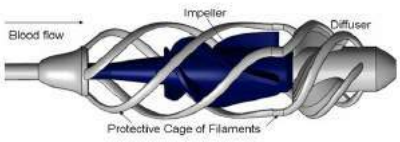

Figure 1 Fontan Blood Pump in Development

METHODS

Using one-way fluid-structure interaction (FSI) computational studies completed in ANSYS 15.0, the implications of blade deformation on blood damage and pump performance were investigated. For the flexible impellers, we considered biocompatible materials of construction of nitinol, polyurethane, and silicone. We investigated operating conditions of flow rates between 2.0-4.0 L/min and rotational speeds of 3000-9000 RPM. Blood was defined as a Newtonian fluid with a density of 1050 kg/m^3 and a dynamic viscosity of 3.5 cP. The shear stress transport turbulence model was used when solving the physics of the fluid domain. Material constants for the biocompatible impeller and cage materials investigated were found in the scientific literature. In the one-way studies, the fluid pressure on the surface of the impeller was calculated using computational fluid dynamics (CFD). Next, the surface pressure was exported and used to determine impeller deformation using finite element analysis (FEA).

Finally, the deformed impeller geometries were exported from the FEA software package and imported back into the CFD software to assess the impact of deformation on pressure generation, blood damage index, and fluid streamlines. The results for the undeformed and deformed cases were compared.

In another set of one-way FSI studies, the level of predicted deformation was calculated for cages and diffuser made of steel, nitinol and polyurethane at flow rates of 2.0 and 4.0 L/min at rotational speeds of 2000, 3000 and 4000 RPM. These studies were completed both with and without a rotating impeller at the center of the model.

To ensure the meshes used for all computational studies were of high quality, mesh independence studies were completed for all domains and the standard mesh quality metrics of skewness, aspect ratio, Jacobian ratio, and element quality were used. Blood damage index was predicted using an experimentally derived power law relationship, seen in Equation 1 below, that relates the shear stresses experienced by red blood cells and the residence time within the pump domain[6].

$$BDI = \int_{inlet}^{outlet} 1.8x10^{-6} \cdot \tau^{1.991} \cdot dT^{0.765} \qquad (1)$$

RESULTS

It was found that rotational speed, and not flow rate, is the largest determinant of impeller deformation. The maximum deformation occurred at the blade trailing edge. The models predicted the maximum impeller deformation for nitinol to be 40nm, Bionate 80A polyurethane to be 106um, and silicone to be 2.8 mm, all occurring at 9000 RPM from 15 kPa of fluid pressure on the trailing edge of the impeller blade. Figure 2 shows impeller deformation as a function of rotational speed for the three materials investigated. Figure 3 is a visual representation of silicone impeller deformation at 9000 RPM. The undeformed impeller is represented by a wireframe outline. Blade deformation is largest at the trailing edge blade tip. Blood flow is left to right in the image.

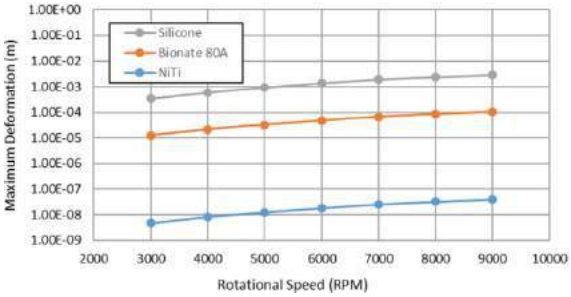

Figure 2 Impeller deformation by rotational speed

The effect of silicone deformation on pump performance was significant, particularly at rotational speeds above 5000 RPM where a decrease in pressure generation of more than 10% was observed for all rotational speeds. Despite the loss in pressure generation, the calculated pressure increase exceeded the level required to alleviate Fontan complications. The estimated blood damage observed for all materials tested at all operational conditions remained below the level that is acceptable for blood pumps.

When analyzing cage and diffuser deformation, steel deformed less than a millimeter, nitinol deformed on the millimeter scale and polyurethane deformed on the centimeter r scale. The steel and nitinol models retained their shape despite deformation and polyurethane became highly distorted.

DISCUSSION

These studies began to illuminate the effects of flexible material deformation on pump performance, with the goal of developing an intravascular, collapsible, pitch adjusting blood pump for Fontan physiology. Pump collapsibility will allow minimally invasive percutaneous deployment. Pitch adjustment will allow the operating conditions of the pump to be matched with specific patient needs so optimum operating conditions can be maintained to increase efficiency and decrease irregular flows and blood damage.

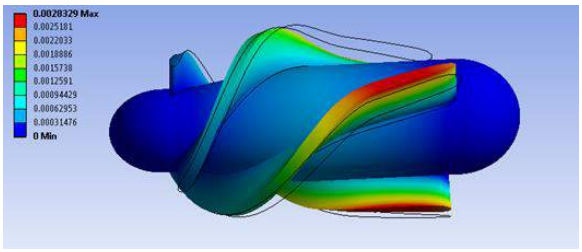

Figure 3 Silicone impeller deformation at 9000 RPM.

When analyzing impeller deformation, nitinol deformed on the nanometer scale, polyurethane deformed on the micrometer scale and silicone deformed on the millimeter scale. An increase in rotational speed had the greatest impact on the level of deformation. This information will be leveraged in future composite designs to select the optimal materials to ensure collapsibility and pump performance. More flexible materials, like silicone, allow increased collapsibility but also have deleterious effects on pump performance at high rotational speeds.

Blood damage was predicted to be below the acceptable threshold for all materials and operating conditions. The effect of significant impeller deformation on blood damage was inconsistent and requires additional investigation. The calculated impeller deformation reduced blood damage metrics in some circumstances and the reduction could be leveraged in the future with additional investigation to full characterize the system. These results support the continued development of an axial-flow, mechanical assist device as a new clinical therapeutic option for patients with dysfunctional or failing Fontan physiology

ACKNOWLEDGEMENTS

The authors wish to acknowledge the financial support for this work provided by the Philadelphia-TriUniversity Consortium for Innovation in Pediatric Research (Grant number: 250596) and the U.S. Department of Education Graduate Assistance in Areas of National Need (GAANN) Doctoral Training Grant, "Interdisciplinary Collaboration and Research Enterprise (iCARE) for Healthcare" Fellowship (M.D. Hirschhorn).

REFERENCES

1. Pike, N. A. *et al.* Clinical profile of the adolescent/adult fontan survivor. *Congenit. Heart Dis.* **6,** 9–17 (2011).
2. Kanter, K. R. *Management of Single Ventricle and Cavopulmonary Connections*. *Sabiston and Spencer Surgery of the Chest* **8,** (Elsevier Inc., 2013).
3. Go, A. S. *et al. Heart Disease and Stroke Statistics - 2014 Update: A report from the American Heart Association*. *Circulation* **129,** (2014).
4. Pundi, K. N. *et al.* 40-Year Follow-Up after the Fontan Operation Long-Term Outcomes of 1,052 Patients. *J. Am. Coll. Cardiol.* **66,** 1700–1710 (2015).
5. Chopski, S. G., Moskowitz, W. B., Stevens, R. M. & Throckmorton, A. L. Mechanical Circulatory Support Devices for Pediatric Patients With Congenital Heart Disease. *Artif. Organs* **41,** E1–E14 (2017).
6. Fox, C. *et al.* Hybrid Continuous-Flow Total Artificial Heart. *Artif. Organs* **42,** 500–509 (2018).

SB³C2019
Summer Biomechanics, Bioengineering and Biotransport Conference
June 25 –June 28, Seven Springs, Pennsylvania, USA

MECHANICS AND EFFICIENCY OF THE ZEBRAFISH EMBRYONIC HEART TUBE

Alireza Sharifi (1), Alex L. Gendernalik (2), Deborah Garrity, David L. Bark Jr. (1,2)

1) Department of Mechanical Engineering
Colorado State University
Fort Collins, CO, United States

(2) School of Biomedical Engineering
Colorado State University
Fort Collins, CO, United States

(3) Department of Biology
Colorado State University
Fort Collins, CO, United States

INTRODUCTION

The heart is the first organ to function in vertebrates, initiating contractions shortly after heart tube fusion. Immediately after formation, the valveless heart tube is able to drive blood forward throughout the embryonic body through a series of contractions initiated by a confluent monolayer of myocardial cells. This layer compresses a layer of cardiac jelly that is sandwiched by the myocardium and endocardium. The valveless pumping mechanism at this stage has received significant attention over the past decade where studies have investigated the potential of peristalsis or impedance pumping, by studying contractile mechanics and blood flow. However, mechanical properties of this stage are rarely considered, limiting the ability to identify the pumping mechanism. Here, we have developed a computational Multiphysics model to study the interplay between mechanical properties, contraction, and blood flow. We validate our results through experiments involving a zebrafish heart (30 hpf).

METHODS

In the simulation, the heart-like model was developed to represent the zebrafish heart at stage 26-30 hpf. This heart tube model consists of two-layers, myocardium and cardiac jelly, with the assumption that the endothelium is relatively compliant and can be neglected. The heart tube diameter is defined as 0.05mm with a length of 0.18mm. The cardiac jelly thickness is 10-15 μm and the myocardial thickness is 3-4 μm.

Arbitrary Lagrange Eulerian formulation is used to simulate the Navier–Stokes equations. Five different pumping mechanisms were studied: 1,2) peristaltic with exponential and sinusoidal contraction function, 3,4) impedance with exponential and sinusoidal contraction function, and 5) the biological pumping based on muscle contraction. Myocardial contraction was implemented by imposing an external load function. No-slip boundary conditions were applied at the fluid–structure interface. The outlet pressure is a 0D model, involving a function of flowrate and peripheral vascular resistance. Pressure at the inlet of the fluid domain was set to zero.

The range of model parameters were found from published studies. Yet, there is a severe deficiency of reliable data due to accessibility and experimental limitations. Therefore, a sensitivity analysis was performed to find the dependence of cardiac output on the model parameters. Sensitivity analyses for each parameter were conducted to narrow the range of values to have a 0.04 mm^3/min cardiac output. Parameters are shown in table 1. To assess the ideal pumping mechanism, we also calculated the efficiency for each type.

In the experiment, heart wall motion was characterized at the following cycle (T) fractions; .2T, .4T, .6T, .8T, and T. Blood velocity was also computed through spatiotemporal kymographs. All experiments on embryonic zebrafish are approved by IACUC at CSU. Selected embryos were dechorionated and placed in a solution of E3 egg maintenance media for holding. Individual embryos were moved to a glass bottom coverslip and embedded in 1.5% low-melt agarose to arrest movement for imaging, performed on an inverted microscope system (Olympus IX73 with 20X objective and the optical resolution of 0.37-0.45 microns) using a high-speed camera (Photron Fastcam Mini UX100) at 1600 frames per second and 45 μm/pixel.

RESULTS

To validate the pumping mechanisms, the experimental velocity measurement is compared with the three defined pumping mechanisms (peristaltic, impedance and biological). The biological pumping mechanism is based on the calcium flux in the mouse cardiac muscle and within agreement with mouse muscle isotonic contractions [1, 2]. The motion is also shown in Fig. 1 and the pattern of contraction agrees best with experimental patterns in a zebrafish.

Table1. The parameters values for the sensitivity analysis

Parameter	Unit	Value	Range
Myocardium thickness	µm	3.5	3-4
Cardiac jelly thickness	µm	12	10-15
Heart length	µm	180	-
Diameter	µm	50	-
Blood density	kg/m^3	1035	1035-1045
Blood viscosity	Pa.s	0.004	0.003-0.004
Wave speed	mm/s	0.4	0.1-0.8
vascular resistance	$Pa.s/m^3$	2×10^{12}	$1\text{-}4\times10^{12}$
Wave length	µm	180	0.1L-1.5L

The velocity is compared between simulations and experiments to assess which pumping mechanism flow best matches experimental flow. Simulations of impedance and peristaltic pumping mechanisms divert from experiments by 31% and 26%, respectively. Alternatively, there is good agreement between the biological mechanism and experimental results (11%, which is within the experimental measurement error). In biological pumping, contraction starts near the inlet, traveling as a wave to the middle of the heart when the contraction is still occluding near the outlet.

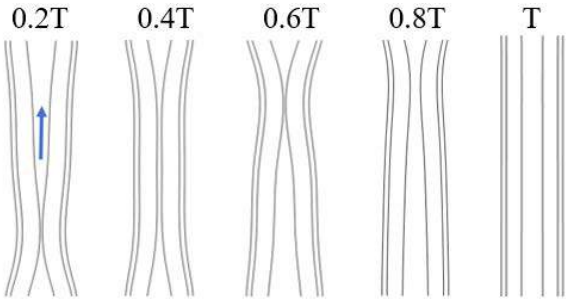

FIGURE 1: Heart wall motion (myocardium and cardiac jelly) during one cardiac cycle for biological pumping

As the mechanical properties of the zebrafish embryonic heart are unknown in early development, the stiffness of each wall layer was also studied, assuming a Hookean material as a first order approximation. Values are assumed to be reasonably estimated when the simulation cardiac output matches experiments. As shown in Fig. 2(a) the valid range for the cardiac jelly elastic modulus is 10-30 pa. Increasing the elastic modulus 3 times, decreases the cardiac output by 17% for biological pumping and 28% for impedance and peristaltic pumping. Fig. 2(b) shows the modulus of the myocardium is larger than the cardiac jelly with a value of 25 to 40 Pa Increasing the myocardium elastic modulus by 60% decreases the cardiac output by almost 22%.

Energy loss is further calculated to determine what pumping mechanism is most efficient. Peristaltic pumping has the highest energy loss which is 3.2 times larger than impedance pumping. The biological pumping mechanism can provide sufficient cardiac output with the least energy for the wall motion. The energy loss in biological pumping is higher than in impedance pumping but lower than in peristaltic. Impedance pumping mechanisms have the least energy loss but also their cardiac output is not as high as the two other pumping mechanisms.

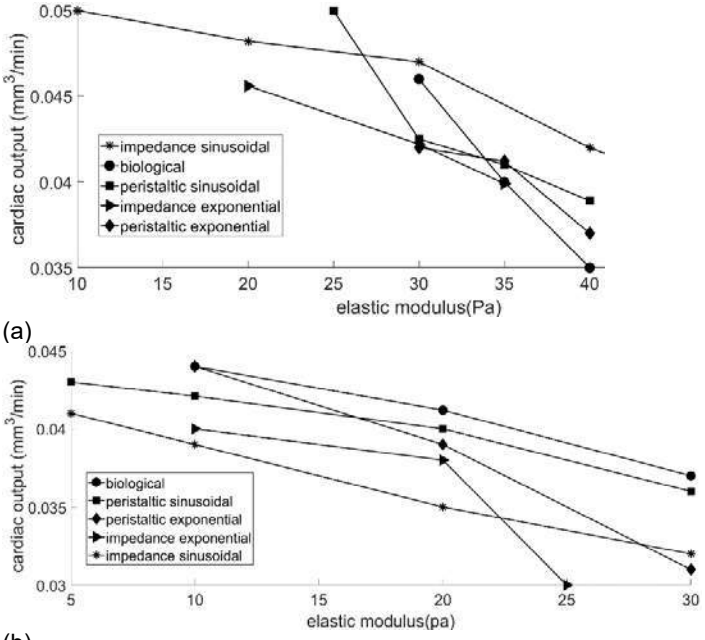

FIGURE 2: Elastic modulus of (a) myocardium (b) cardiac jelly for different pumping mechanisms

DISCUSSION

In the present work, we used experimental and numerical methods to study the mechanics and efficiency of the zebrafish embryonic heart tube (30hpf). We found that the elastic modulus of the cardiac jelly is lower than the myocardium. Our values are close to those measured in the chicken embryonic heart tubular stage (stage HH 10/11), where Zamir et al. found 6-24 Pa for cardiac jelly and 30- 120 Pa for the myocardium [3-6]. We studied different pumping mechanisms and introduced the biological pumping mechanism which is not necessarily an impedance or a peristaltic pump. The energy efficiency of each mechanism is also studied to find the most efficient pumping mechanism. When subjected to peristaltic pumping, the heart tube produces a proper cardiac output, but the wall motion is not valid and is also inefficient. Velocity changes in time for impedance pumping is not in agreement with the experimental results. The impedance pump also does not provide the necessary cardiac output. As compared to peristaltic and impedance pumping, our proposed biological pumping produced the highest cardiac output with the least amount of energy loss, indicating that it accurately describes pumping seen in the embryonic heart tube. Through an understanding of pumping mechanics and material properties, it is possible to quantify the complex stresses that exist during embryonic heart development and to determine how these stresses contribute to normal morphological development or to cardiac malformation in the form of a congenital heart defect.

REFERENCES

[1] De Vita, R., et al. *Journal of theoretical biology*, 425:1-10, 2017.
[2] Stuyvers, B., et al. *The Journal of physiology*, 544:817-830, 2002.
[3] Zamir, E., et al. *J Biomech Eng*, 126:823-830, 2004.
[4] Latacha, K., et al. *Dev Dyn*, 233: 1272-1286, 2005.
[5] Kozlovsky, P., et al. *Ann Biomed Eng*, 44:3069-3083, 2016.
[6] Männer, J., et al. Developmental Dynamics, 239(4), 1035-1046.

WHOLE EMBRYONIC HEART ULTRASOUND IMAGING, MOTION TRACKING AND FLOW SIMULATIONS REVEAL HEMODYNAMIC ROLE OF EMBRYONIC ATRIA

Sheldon Ho (1, 3), Wei Xuan Chan (1), Nhan Phan-Thien (2), Choon Hwai Yap (1)

(1) Department of Biomedical Engineering
National University of Singapore
Singapore

(2) Department of Mechanical Engineering
National University of Singapore
Singapore

(3) NUS Graduate School for Integrative Science and Engineering
National University of Singapore
Singapore

INTRODUCTION

Past investigation found that fluid mechanical forces influenced cardiovascular development and abnormal flow conditions could lead to congenital heart malformations, [1] which is clinically a leading cause of birth defect related deaths.[2] We utilized a previously established 4D high-frequency imaging technique [3] on HH25 chick embryos (just before septation), tracked the cardiac motion with a novel motion tracking algorithm, which could enable wall strain calculations, and performed flow simulations to understand the hemodynamics.

METHODS

3 embryonic hearts were studied. Cine-ultrasound images were obtained at multiple planes spaced evenly. Images for more than 20 cardiac cycles were averaged into 1 cardiac cycle via quadratic mean to create contrast between tissue and blood (none was naturally present), in accordance to our previously established imaging technique. [3] A novel cardiac motion tracking algorithm was utilized, where a cyclic motion model was curve-fitted to displacement fields calculated by pair-wise 3D image registration for all consecutive time points. Dynamic mesh computational fluid dynamic (CFD) simulations were then performed to obtain flow fields and flow stresses. Doppler velocity measurements were obtained at the outflow tract and used to determine boundary conditions. From the motion tracking algorithm, the cardiac wall strains could be calculated. From the flow simulations, wall shear stresses (WSS) characteristics were determined. Systolic ejection work done was also calculated, using embryonic cardiac pressure values reported in the literature. [4]

RESULTS

Figure 1A demonstrate that the cardiac motion tracking algorithm worked very well, and tracked ventricular volume matched manual segmentations in a test case very well. At HH25 (4.5 days old), the embryonic hearts had a single primitive ventricle and two joined primitive atria with atrial appendages (figure 1B).

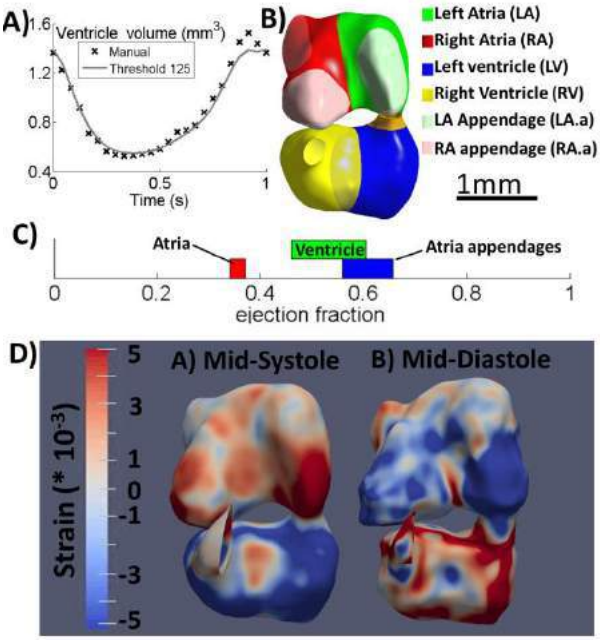

Figure 1: (A) Ventricular volume vs time, comparing manual segmentation and automatic tracking. (B) Ventral view of embryonic heart. (C) Ejection fraction of cardiac structures. (D) Cardiac wall strain rate at two time points.

The atria were found to have lower stroke volume and ejection fraction than the ventricle. Interestingly, however, the atrial appendages were found to be highly contractile, having higher ejection fraction than even the ventricles. The appendages occupied only about 15.7% of the atria's diastolic volume but contribute about 27.0% to the total atrial stroke volume. Strain mapping in Figure 1D demonstrates that the atrial appendages underwent the highest strains within the atria, and had strain magnitudes comparable to the ventricle. Ejection work done calculations in figure 2 further demonstrated that the atrial appendages accounted for 40% of work done by atria. These suggested that the embryonic atrial appendage might have the role of fluid pumping in the embryonic heart.

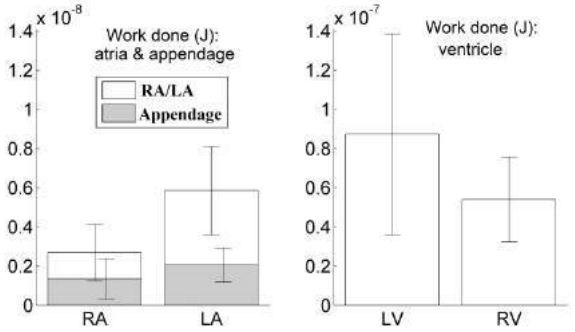

Figure 2: The Work done by the different chamber of the heart.

Analysis of the CFD flow fields demonstrated that during late ventricular diastole (atrial systole) the ventricle could directly drew inflow from the veins, without the aid of the atria (figure 3). Further, Figure 2 demonstrated that the ejection work done by the ventricle was 1 order of magnitude higher than that of the atria, most likely because the ventricle pumped against high pressures but the atria did not. This suggested that the atria pumping function was not essential for providing circulatory energy. Instead, we propose that the atria pumping would be important for creating flow and WSS stimuli to ensure normal heart development. This was supported by literature evidence where surgical manipulation of the atria was shown to cause abnormal remodeling of the ventricle, [5] and knocking out contractile function of the atria was found to be embryo-lethal, due to the failure of the cardiac cushions, heart valves and septation to form properly [6].

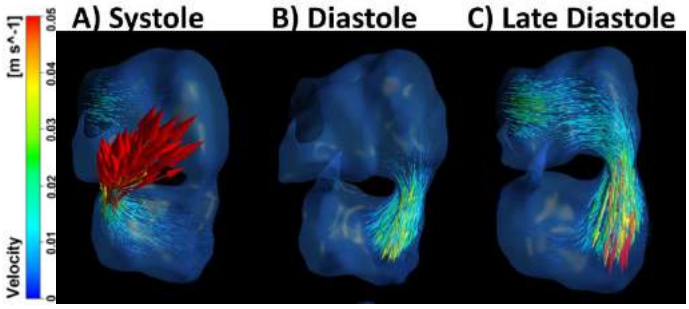

Figure 3: CFD flow field results. (A) Ventricle systole and ejection via the outflow tract, and atria diastole and filling. (B) Ventricular diastole and atria systole, resulting in high flow through the atrioventricular junction. (C) At late atria systole / ventricular diastole, direct atrial inflow towards the ventricle occurred.

Consequently, it would be important to understand flow WSS in the embryonic heart. Figure 4 shows the WSS waveforms and spatial patterns for a typical embryonic subject. Significant spatial temporal variations were found, and the atria and ventricle experienced elevated WSS during different times of the cardiac cycle. The highest WSS were observed at the ventricular outlet, the atrioventricular junction, and the septating mid-line between the two atria and the two ventricles. High WSS were thus imposed on the locations where the cushions and developing septum were, and could be important stimuli required for proper valve and septum development.

Interestingly, the right atrial appendages were found to have a high retention of blood fluid, as could be demonstrated by particle tracking analysis. Blood in this appendage merely moved in cyclic linear motions within the length of the appendage and were seldom washed out. Due to this phenomenon, significant oscillatory shear index is found in the right atria as well.

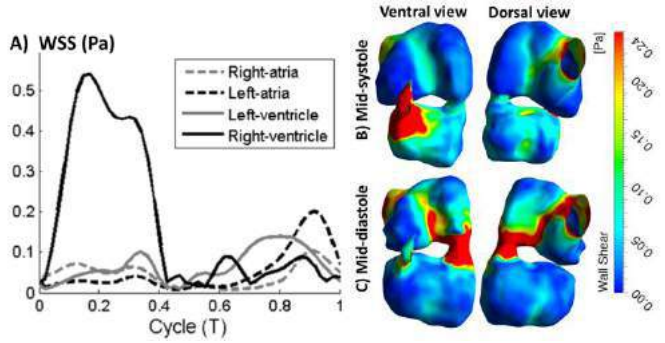

Figure 4: (A) Averaged WSS across a cardiac cycle. (B) WSS during mid-systole. (C) WSS during mid-diastole. High WSS at sites where valvulogenesis and septation will occur.

DISCUSSION

Our study results suggested that the atrial appendage were interestingly highly contractile in the embryonic heart, and played out-sized role in contributing to atrial blood pumping, both in terms of stroke volume and energy contributions. To date, the function of the atrial appendages were not known, although in adults with fibrillation, they have a high tendency to experience blood clots. Surgical ablation or occlusion of the appendages in these adults have resulted in no harmful effects on patients. It was thus interesting to find the embryonic atrial appendage taking up the fluid pumping role.

However, our flow field and flow energy study has pointed out that the atria do not have substantial contribution towards circulatory energy. The ventricle seemed to be capable of drawing flow directly in from the veins, bypassing the atria. We thus hypothesize that the atria pumping would be important to provide the suitable flow mechanical force stimuli for proper development in the heart. As discussed above, there are literature evidence that disruption of atrial pumping would cause abnormal ventricular, [5] and cushions development, [6] supporting our hypothesis. Our WSS investigations demonstrated that the atrioventricular junction and septating tissues protruding into the cardiac lumen has higher WSS, and this could be an important stimuli for their development, leading to valvulogenesis and septation.

ACKNOWLEDGEMENTS

National University of Singapore Young Investigator award 2015, (PI: Yap) for funding.

REFERENCES

[1] Hoffman JIE, et al. *J Am Coll Cardiol.* 2002;39(12):1890-1900.
[2] Yang Q, et al. *Birth Defects Res A.* (2006) 76(10):706-713.
[3] Ho S, et al. *Ann Biomed Eng* (2017) 45: 2309
[4] Keller BB, et al. Circ. Res (1991) 68(1):226.
[5] Huang C. *Development* (2003) 130:6111-6119
[6] Tobita K. *Am J Physiol – Heart and Circ Physio* (2000) 279:H959

SB³C2019
Summer Biomechanics, Bioengineering and Biotransport Conference
June 25 -28, Seven Springs, PA, USA

ASSESSMENT OF PULMONARY ARTERIAL STRUCTURE AND ITS ASSOCIATION WITH RIGHT VENTRICULAR FUNCTION IN PULMOINARY ARTERIAL HYPERTENSION

Frank Servin (1), Jose A Rosado (2), Rajesh Janardhanan (2), Jason X.J. Yuan (3), Franz P Rischard (4), Rebecca R Vanderpool (1,3)

(1) Department of Biomedical Engineering
The University of Arizona
Tucson, Arizona, United States

(2) Department of Medical Imaging
The University of Arizona
Tucson, Arizona, United States

(3) Division of Translational and Regenerative Medicine
The University of Arizona
Tucson, Arizona, United States

(4) Division of Pulmonary, Allergy, Critical Care and Sleep Medicine
The University of Arizona
Tucson, Arizona, United States

INTRODUCTION

Pulmonary Hypertension (PH) is a progressive pathophysiological condition that emerges as high blood pressure in the pulmonary vasculature and ultimately results in right ventricular failure [1]. Symptoms of pulmonary hypertension are vague and can include shortness of breath, fatigue, weakness, angina, and syncope [2]. PH is categorized into 5 groups, and the focus of this study is group 1- Pulmonary Arterial Hypertension (PAH).

Significant remodeling and narrowing of pulmonary arteries results in increased mean pulmonary arterial pressure (mPAP) and pulmonary vascular resistance (PVR) [3]. Pulmonary arterial hypertension is diagnosed based on a mean pulmonary arterial pressure (mPAP) $\geq$ 25 mmHg and a pulmonary arterial wedge pressure (PAWP) $\leq$ 15 mmHg measured during a right heart catheterization (RHC) [1]. Other measurements include: systolic and diastolic PA pressure (sPAP, dPAP) and cardiac output (CO). Parameters of RV function include end-systolic elastance (Ees), arterial elastance (Ea), and RV-PA Coupling [4]. Additional testing can include an echocardiogram, a chest CT and a Magnetic Resonance Angiogram (MRA) [3].

Current clinical assessments of vascular structure from CT imaging are labor intensive and have not been directly related to RV function. The aim of this study is to 1) develop methods to quantify pulmonary vascular structure from cardiac MRAs and 2) to investigate associations between vascular structure and RV function in patients with PAH.

METHODS

Patients with a clinical MRA were retrospectively selected from the University of Arizona's PH registry. The final analysis was performed on patients that had undergone both a RHC and a clinical MRA. Patients were categorized into two groups: PAH (mPAP $\geq$25mmHg and a PCWP $\leq$ 15 mmHg) and Control (mPAP $\geq$25mmHg).

Exported DICOMS MRA Images were imported into SimVascular (2018.05.23), an open source software package for cardiovascular modeling [5]. The principal artery, anterior artery, anterior basal artery, and medial basal artery were segmented (Figure 1) as previously described [4]. Branches were modeled from their origin to their end, following the path of the largest diameter.

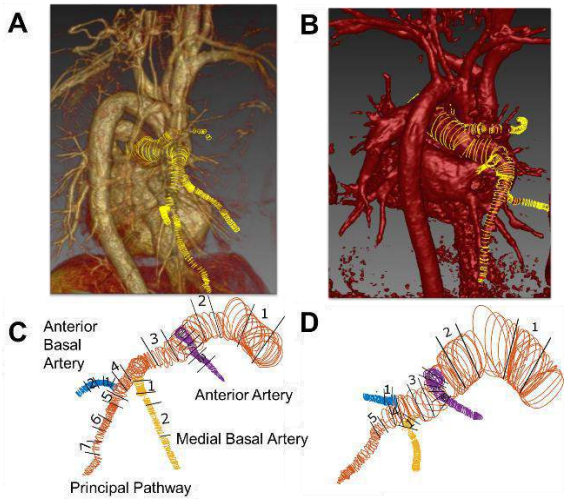

Figure 1: Volume renderings of the pulmonary vasculature in a representative A) Control and B) PAH patient. C) and D) Wire representations of the principal pathway, anterior artery, anterior basal artery, and medial basal artery.

Once the arteries were segmented based on volume renderings (Figure 1A, B; yellow-segments), the raw data was exported and analyzed using a custom code in MATLAB (v2018). The custom code determined the diameter, and cross-sectional area (CSA) of each segmentation along each artery. To get a representative diameter for segments along each artery, the measured diameters were averaged for the region between each branch (Figure 2A, segments 1 to 7). The pathlength of each artery was determined as the sum of the distance between each of segmentations along the artery.

Hemodynamic Equations

$$PVR = (mPAP - PAWP)/CO$$
$$stroke\ volume\ (SV) = (mPAP - PAWP)/CO$$
$$PA\ Ca = SV/(sPAP - dPAP)$$
$$Ees = (Pmax\ iso - sPAP)/SV$$
$$Ea = sPAP/SV$$

Pulmonary vascular resistance and PA compliance (PA Ca) were calculated as measures of functional changes in the pulmonary circulation. Single-beat analysis were used to measure RV function with Eea, Ea, and the ratio Ees/Ea (RV-PA coupling). Data are presented as mean ± standard deviation and an Analysis of Variance test with a Tukey HSD post hoc analysis were used to determine the difference in PA diameters between patient groups. Linear regressions were used to determine the correlation coefficients. Correlations were considered significant when the p-value is less than 0.05.

RESULTS

Twenty patients were selected for analysis (10 controls and 10 PAH) but three patients were excluded from the final analysis due to missing RHC data (Control N=2) or poor quality MRA images (PAH: N = 1).

The pulmonary arteries in both patient groups were segmented using the same segmentation and visualization settings (Figure 1). The average diameter from each of the segments in the principal pathway was compared between groups (Figure 2). Patients with PAH had significantly larger diameters in the first three segments of the principal pathway compared to control patients (Figure 2B). The average pathlength for the principal pathway was the same for both controls (201.31 mm ± 30.87 mm) and PAH (208.87mm ± 34.10 mm) patients. There were no significant differences in diameter or pathlengths in the anterior artery, anterior basal artery, and medial basal artery between groups (Data not shown).

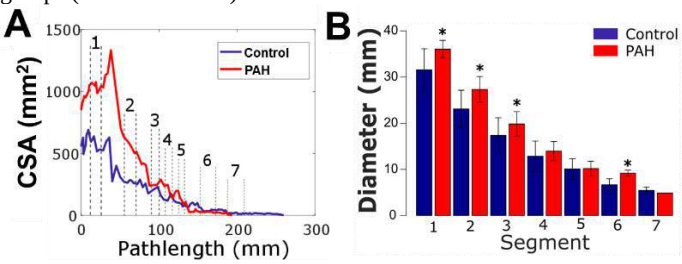

Figure 2: A) Cross sectional area (CSA) as a function of the pathlength in control and PAH. B) Comparison of the average diameter in each segment between groups. * p < 0.05 vs Control

As expected, patients with PAH have increased mPAP, increased PVR and decreased PA Ca compared to control patients (Table 1). RV function is significantly reduced in patients with PAH with increased arterial afterload and decreased RV-PA coupling. Patients with PAH have a significant increase in mPAP, PVR, pulse pressure (PP), Pulmonary arterial compliance (PAC), arterial elastance (Ees), and arterial elastance (Ea). However, PAH Patients experienced a significant decrease in RV-PA Coupling. There was a non-significant correlation between PVR and the MRA measured (r^2 = 0.16, p = 0.07) and no correlation between PA Ca and the MRA measured (r^2 = 0.01). Right ventricular afterload had no correlation with PA diameter (r^2 = 0.1) but Ees/Ea had a non-significant correlation and RV-PA coupling also significantly correlate with the average PA diameter (r^2=0.16, p = 0.07).

Table 1: Hemodynamic Results. Data presented as mean ± standard deviation.

RHC Data	Control	PAH	p-value
	N = 8	N = 9	
mPAP (mmHg)	17 ± 4	52 ±7	<0.001
PAWP (mmHg)	7 ± 2	7 ± 4	0.871
CO (L/min)	5.5 ± 1.5	4.9 ± 1.2	0.345
PVR (mmHg)	1.9 ± 0.6	9.9 ± 0.3	<0.001
PA Ca (ml/mmHg)	4.9 ± 1.3	1.3 ± 0.6	<0.001
Ees (mmHg/ml)	0.8 ± 0.5	0.9 ± 0.4	<0.001
Ea (mmHg/ml)	0.4 ± 0.1	1.4 ± 0.4	<0.001
Ees/Ea	2.1 ± 1.0	0.7 ± 0.3	<0.001

DISCUSSION

It is feasible to use clinical MRA images to quantify pulmonary vascular structure in patients with and without pulmonary hypertension. Patients with PAH having increased PVR and PA diameters compared to control patients. These results are in keeping with previous findings that have found increased PA diameters in PAH patients from CT scans [6]. MRA imaging has lower resolution than traditional CT imaging but provides the benefit of allowing for the quantification of the dynamic motion of the right ventricle and RV volumes in the same scan as the pulmonary vascular structure. Limitations in imaging resolution is a potential reason for why there were no significant differences in the length of the principal pathway between control and PAH patients.

Increased pulmonary vascular resistance in patients suggest that there is a decrease in the diameter of the vasculature. Our results show PAH patients have increased PA diameters that is likely due to the increased operating pressure (mPAP: 52 ± 7 mmHg) compared to control patients (mPAP: 17 ± 4 mmHg). There were no detectable differences between patient groups in the anterior artery, anterior basal artery, and medial basal arteries. We are limited in our ability to detect changes in smaller distal pulmonary vessels due to the resolution of MRA images.

Previous studies have found increased PA diameters significantly associate with mortality [6,7]. Our data suggests there is potentially a correlation between PA diameter and PVR and RV-PA coupling. Our data suggests pulmonary vasculature structure in combination with RV function could be used to further investigate the development and progression of RV failure.

ACKNOWLEDGEMENTS

Funding: NIH MARC Training Grant T34 GM08718 (FS), ABRC NIA ADHS18-198871 (RRV).

REFERENCES

[1] Lai Y-C, *et al, Circulation Research* 1:115-30, 2014.
[2] Galie N, *et al, European Heart Journal*. 903-934, 2015.
[3] Wang Z, and Chesler NC. *Pulmonary Circulation*. 2:212-220, 2011
[4] Vanderpool RR, *et al, Journal of Applied Physiology*. 110,1: 180-198, 2011
[5] Updegrove A, *et al, Ann Biomed Eng*, 525–541, 2017
[6] Tonelli AR, et al. *Respirology*, 8:1649-1655, 2017
[7] Demerouti EA, *et al. Respiratory Care*, 7: 1246-54, 2013

SB^{3}C2019
Summer Biomechanics, Bioengineering and Biotransport Conference
June 25 -28, Seven Springs, PA, USA

QUANTITATIVE ANALYSIS OF FLOW DISTRIBUTION WITHIN THE FETAL HEART USING IN-VITRO 4D FLOW MRI

Lucille E. Anzia (1), Katrina L. Ruedinger (2), Shardha Srinivasan (3), Barbara Trampe (4), Timothy Heiser (4), J. Igor Iruretagoyena (4,5), Alejandro Roldan-Alzate (1,2,6)

(1) Mechanical Engineering
University of Wisconsin-Madison
Madison, WI, USA

(2) Biomedical Engineering
University of Wisconsin-Madison
Madison, WI, USA

(3) Pediatric Cardiology
University of Wisconsin-Madison
Madison, WI, USA

(4) Obstetrics and Gynecology
University of Wisconsin-Madison
Madison, WI, USA

(5) Maternal and Fetal Medicine
University of Wisconsin-Madison
Madison, WI, USA

(6) Radiology
University of Wisconsin-Madison
Madison, WI, USA

INTRODUCTION

Fetal cardiac anomalies are diagnosed through fetal echocardiography (echo) and are among the hardest fetal anomalies to characterize *in utero*. It has been suggested that these defects may originate from blood flow patterns through the developing heart or from a genetic basis[1]. Therefore, visualizing the intra-cardiac flow distributions during gestation may be helpful to understand fetal cardiac anomalies. *In vitro* four dimensional flow magnetic resonance imaging (4D Flow MRI), a technique that combines patient-specific 3D printed geometries with MRI, has been successful in children and adults to model specific hemodynamic states to improve surgical techniques as well as study system efficiency[2,3]. Recently, we showed the success of applying 4D Flow MRI to fetal life by using patient-specific 3D printed heart models at two gestational ages, 28 and 30, to visualize intra-cardiac flow profiles[4]. This previous study was the first to 3D print geometry from a fetal echo, and was the second reported 3D printed model from an echo[5]. The purpose of this study was to validate this modeling technique for intra-cardiac flow analysis by quantitatively comparing in vitro patient specific fetal flow distributions measured with 4D Flow MRI with those reported in literature.

METHODS

One fetal echo, deemed to be developing normally at 32-weeks' gestation was analyzed with IRB approval. The ultrasound was segmented and designed in Mimics/3-Matic (Materialize, Leuven, Belgium) to represent the cardiac lumen (Figure1a,b). Any unclear valve or heart anatomy, likely due to acoustic shadowing or fetal movement, were created based on the mean fetal measurements from literature at 32-weeks' gestation. Multiple 2D cross section measurements from Mimics were compared with the 3D volume (Figure 1b) created in 3-Matic to minimize error due to smoothing and model post-processing. A wall and connectors were added (Figure 1c) leaving a cavity representing the flow lumen and the life size model was 3D printed (Form 2, Formlabs Inc, Somerville, MA).

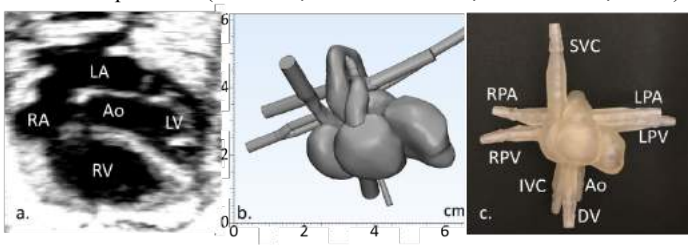

Figure 1: a) Fetal echo of the normal fetus at 32 weeks gestational age. b) Right anterolateral view of the segmented fetal heart model (cm). Cylinders added to the segmented vasculature represent average vessel size at the given age. c) 3D printed model of (b).

For *in vitro* assessment the heart model (Figure 1c) was connected to a positive displacement pulsatile pump at 1 L/min of water (BDC PD-1100, BDC Laboratories,Wheat Ridge,CO) and imaged using a clinical 1.5T MRI scanner with a head coil (Signa HDxt,GE Healthcare,Waukesha,WI). Appropriate resistance was applied to the outlet pulmonary arteries[6]. Post-processing of the 4D Flow MRI data was done and the intra-cardiac flows were visualized and quantified by placing planes in the vessel of interest in EnSight (CIE,Apex,NC). Intra-cardiac flow distributions (Aorta (Ao), pulmonary artery (PA), ductus arteriosus (DA), foramen ovale (FO), left and right pulmonary arteries (LPA+RPA)), were compared against percent flow distributions found in literature[7,8]. All flows were measured with planes with the following exceptions: DA flow was calculated by

subtracting Ao flow before and after the DA; FO flow was calculated by subtracting PA flow from inlet flows (IVC+SVC+Ductus Venosus (DV)). All literature values represented the mean for that gestational age.

RESULTS

The fetal echo successfully incorporated the heart anatomy. The following vessel and valve diameters were slightly modified based on dimensions reported in literature: LPA, RPA, LPV, RPV, FO, DV and mitral, tricuspid, aortic and pulmonary valve diameters[9-13]. Segmentation, post-processing, and 3D printing were successful to create a physical model of a patient-specific 32-week fetal heart (Figure 1c).

In-vitro analysis with 4D Flow MRI produced consistent flow patterns throughout the whole anatomy and conserved mass (Figure 2a). There is evident flow through the other fetal shunt, the DA (insert) to bypass the pulmonary vessels, as illustrated in the insert of Figure 2a. Significant flow can also be seen passing from the RA to the LA through the FO, as denoted by the white arrow (Figure 2b), consistent with the normal shunting of blood through the fetal heart.

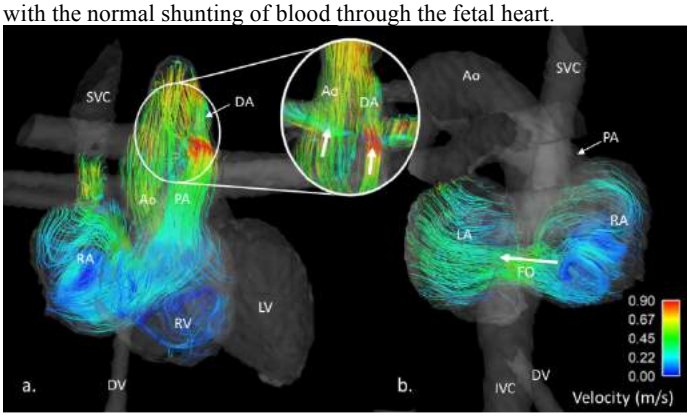

Figure 2: a) Velocity streamlines (m/s) from *in-vitro* 4D Flow MRI. Blood enters the RA from the SVC and IVC (not pictured), followed by the RV, then accelerates out the (PA). Flow exiting the PA joins the Ao via the ductus arteriosus (DA). Peak velocity is observed approaching the DA (insert). b) Visualization of blood flow across the (FO) is illustrated and denoted by the white arrow.

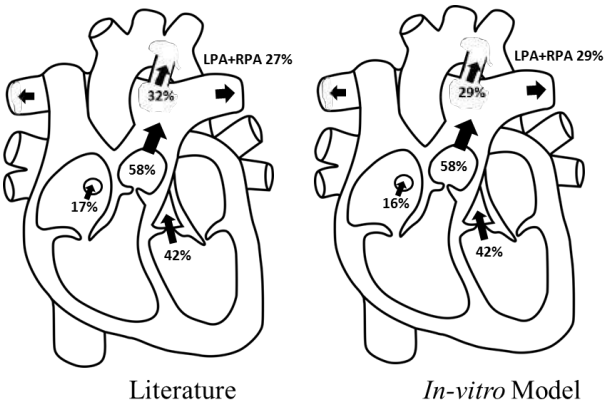

Figure 3: Illustration of intra-cardiac flow distributions from literature [7,8] and the *in-vitro* 3D-printed fetal heart model.

Quantitative analysis of flow distributions were consistent with flows reported in literature (Figure 3). Aortic and pulmonary valve flow are an average of two values reported in literature (41.4% and 42.6%, and 58.6% and 56.9% respectively), the other distributions were only reported by one source[7,8].

Flow values are reported as percentage of total cardiac output. These flows were found to be 16% through the FO, 58% through the PA, 42% through the Ao, 29% through the DA and 29% through the PA. Internal consistency of 4D Flow MRI measurements has been previously determined as 8%[14]. Therefore, no significant differences were found between intra-cardiac flows in literature and those from the *in-vitro* assessment of the 3D printed patient-specific fetal heart.

DISCUSSION

Results from this study in conjunction with our previous study suggest that the presence of the DV plays a key role in the intra-cardiac blood flow across the FO, consistent with literature [4,6].

Since *in-vivo* values were unavailable for this patient, literature values of the 50th percentile flow distribution at 32-weeks' gestation were chosen. Therefore, a potential limitation of this study is if modeled heart was not the 50thpercentile, and future work will take the growth percentile into account.

Although this heart model is a passive representation of the fetal heart, it has shown to provide reliable intra-cardiac flow distributions. Other limitations such as estimating the exact sizes of the anatomy and using water instead of blood are present but are not believed to be significant. Future work will include analysis of more normally developing hearts at various gestational ages to determine the consistency of this modeling technique to estimate flow patterns *in-vivo.* Additionally, the continued advancement of new flexible materials with 3D printing will allow for more flexible materials to be used to better represent the beating heart.

As mentioned by Ruedinger et al., this modeling technique can be helpful for parents to better understand the fetal anatomy, especially when a fetal cardiac anomaly is present. This study supports the use of 3D printing a patient-specific fetal heart as well as *in-vitro* 4D Flow MRI to analyze intra-cardiac flow distributions in fetal life. This information, in conjunction with diagnostic routine could be valuable to physicians and parents to better understand complex flow regimes, such as in cases of fetal cardiac anomaly.

ACKNOWLEDGEMENTS

This work was funded by the National Institutes of Health Grant, 4K12-DK100022-04 (Dr. Roldán-Alzate).

REFERENCES

[1] Donofrio, MT et al., Circulation,129:2183–2242,2014.
[2] Rutkowski, DR et al.,Comput Methods Biomech Biomed Eng Imaging Vis,6(5):545-555,2018.
[3] Roldan-Alzate, A et al., AJR Am J Roentgenol, 207:58-66,2016.
[4] Ruedinger, K et al., Circulation,11:e007705, 2018.
[5] Samuel, BP., J Digit Imaging,28:459-461, 2015.
[6] Rudolph, AM., Hepatology, 71:1047-1061, 1983.
[7] Rasanen, J et al., Circulation, 1;94(5):1068-73, 1996.
[8] Mielke, G & Benda, N., Circulation,103(12)1662-8, 2001.
[9] Sharland, GK & Allan, LD. Ultrasound Obstet. Gynecol,2:175-181, 1992.
[10] Ruano, R et al., J Ultrasound Med,26:309-316,2007.
[11] Dong, FQ et al., Ultrasound Obstet Gynecol,38:652-657, 2011.
[12] Pokharel, P & Ansari,MA, J Nepal Med Assoc,56(202):124-31,2017.
[13] Feit, LR et al., Ultrasound Obstet Gynecol, 1:313-319, 1991.
[14] Frydrychowicz, A et al., Eur Radiol,27(12):5316-5324, 2017.

SB³C2019
Summer Biomechanics, Bioengineering and Biotransport Conference
June 25-28, Seven Springs, PA, USA

ON THE USE OF PENTAGALLOYL GLUCOSE FOR MECHANISTIC SUPPRESSION OF ABDOMINAL AORTIC ANEURYSM

Vangelina Osteguin (1), Sourav S. Patnaik (2), Alycia G. Berman (3), Craig J. Goergen (3), Ender A. Finol (2)

(1) Department of Biomedical Engineering
The University of Texas at San Antonio
San Antonio, TX, U.S.A.

(2) Department of Mechanical Engineering
The University of Texas at San Antonio
San Antonio, TX, U.S.A.

(3) Weldon School of Biomedical Engineering
Purdue University
West Lafayette, IN, U.S.A.

INTRODUCTION

Abdominal aortic aneurysm rupture is a major health concern and is associated with significant mortality. At the extracellular matrix (ECM) level, an increase in elastase and collagenase levels eventually make the aortic wall weak. Ultimately the wall ruptures when the forces applied exceed the material strength of the vessel. In this study, we investigated the application of an organic polyphenolic compound called pentagalloyl glucose (PGG), which has shown beneficial cardiovascular effects in humans [1], can assist in stabilizing the arterial tissue by crosslinking the extracellular matrix proteins (i.e. elastin), and can potentially assist in suppression of aneurysm growth. To assess PGG interaction with arterial tissue ECM, we evaluated murine abdominal aortic specimens treated with or without PGG through pressure-inflation testing. We hypothesized that the application of PGG *in vivo* will improve the biomechanical characteristics of the abdominal aorta wall and will prevent further damage from enzymatic actions.

METHODS

Aneurysm Mouse Model – Animal studies were performed following IACUC approval at Purdue University. Eleven male C57BL/6 mice at 8-10 weeks of age underwent laparotomy under sterile conditions and the abdominal organs were retracted outside the abdomen to expose the aorta. To induce aneurysms, 5.0 mg/mL pancreatic porcine elastase (PPE) was topically applied to the infrarenal aorta for 5 minutes while 0.2% beta-aminoproprionitrile was continuously administered via drinking water beginning 2 days prior to surgery and extending the length of the study. After elastase treatment, 7 of the 11 animals received a PGG (0.06%) topical treatment on the abdominal aorta as an aneurysm preventive measure and the 4 remaining mice received a saline solution (control). Aortic expansion was monitored via high frequency ultrasound (Vevo2100, FUJIFIM VisualSonics) on a weekly basis (prior to surgery and post-surgery up to 4 weeks). Animals were sacrificed four weeks post-surgery and their abdominal aortas were dissected and utilized for pressure inflation testing.

Figure 1: Experimental setup for pressure-inflation testing. The inset shows the specimen view from the top.

Pressure Inflation Testing – Pressure inflation tests were performed using the free-end technique to analyze the deformation of the vessels when subjected to intraluminal pressures [2]. The experimental set up (Fig. 1) consisted of a high-resolution camera (Basler Inc., Germany) mounted on an inverted microscope (Olympus, Center Valley, PA), while the specimens were mounted on 500-µm-diameter stainless steel cannulas with machined grooves placed in a vessel chamber (LSI, Burlington, VT). Specimens were secured at both ends with 6-0 sutures and the chamber was filled with clear PBS

(Sigma-Aldrich Inc., MO). A syringe pump (Chemyx, Stafford, TX) was utilized to pressurize the specimens at room temperature and the syringe filled with food dye + PBS for detecting rupture or leaks in the specimen. Pressure changes were recorded using a digital pressure transducer (Omega Inc., Norwalk, CT).

Data Collection & Analysis – As shown in Fig. 2, the undeformed configuration of each specimen was captured by dissecting a small segment of the infrarenal aorta. From the captured images, wall thickness (t) and outer and inner radii (r_i) were measured. A perfusion rate of 0.5 mL/min was used until burst pressure was achieved. Simultaneous pressure data and images were recorded via a custom LabVIEW® program. Using the Vision Assistant® package from LabVIEW®, suture to suture distances (axial deformation) and external diameter changes (circumferential deformation) of the specimens were measured.

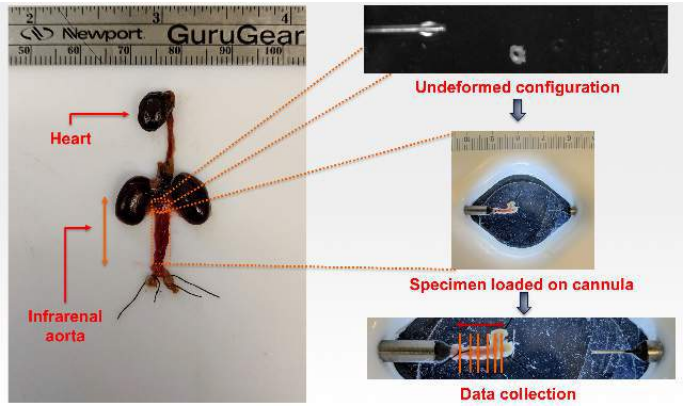

Figure 2: Schematic of experimental protocol and data collection procedure.

Mean circumferential and axial Cauchy stresses, along with Green strains for finite deformation, were calculated using Eqs. (1) - (4),

$$\sigma_\theta = \frac{Pr_i}{t} \quad (1)$$

$$\sigma_z = \frac{Pr_i}{2t} \quad (2)$$

$$E_\theta = \frac{1}{2}(\lambda_\theta^2 - 1) \quad (3)$$

$$E_z = \frac{1}{2}(\lambda_z^2 - 1) \quad (4)$$

where P is the applied transmural pressure. From the stress-strain curves, biomechanical parameters such as the elastic modulus (slope of the linear portion of the curve), maximum stress, and maximum strain were recorded for each specimen orientation (i.e. axial or circumferential).

Statistical Analysis – Data were expressed as mean ± std. deviation for all biomechanical parameters. To test for significant differences, unpaired t-tests were applied across the groups (saline vs. PGG). Data was considered significant at $p < 0.05$.

RESULTS

Biomechanical analysis of the murine abdominal aorta specimens revealed a stiffer response from PGG-treated specimens compared to the controls. There were no significant differences in the biomechanical parameters in the circumferential orientation. In the axial orientation, the elastic modulus of the control specimens was lower, but non-significant, than the PGG treated specimens (Fig. 3A; $p = 0.11$). The maximum stress achieved by PGG treated specimens (88.6 ± 18.0 kPa) was nearly 3.43 times greater than the control specimens (25.8 ± 4.8 kPa) (Fig. 3A; $p < 0.001$). However, the maximum strain was lower in the specimens from the PGG group compared to the saline group (Fig. 3C) (0.110 ± 0.018 mm/mm vs. 0.078 ± 0.008 mm/mm; $p < 0.001$).

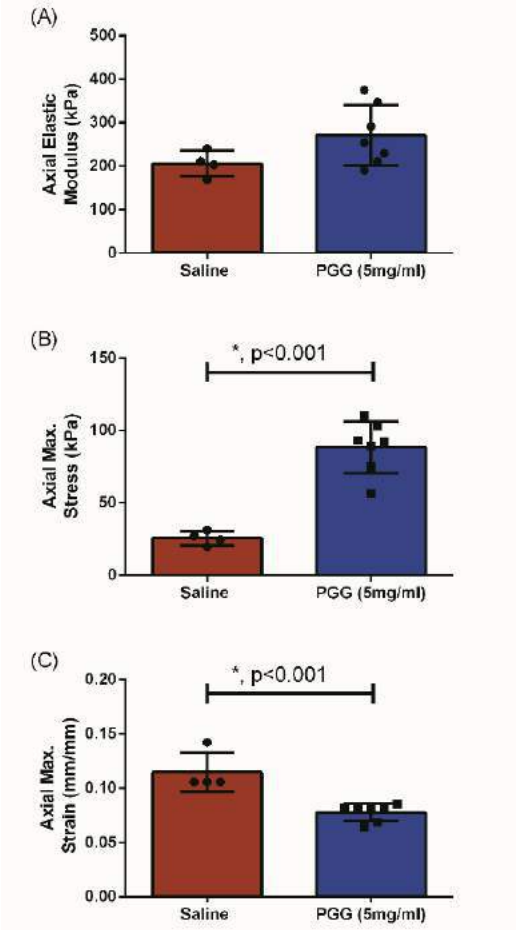

Figure 3: Biomechanical parameters derived from the axial direction of the murine abdominal aorta specimens. *denoted level of significance at p < 0.001.

DISCUSSION

In this investigation, we utilized a peri-adventitial application of PGG to the murine abdominal aortas as a preventive measure prior to elastase-induced pathological changes. The observed biomechanical changes in the PGG-treated specimens may be due to the crosslinking activity of the polyphenol *in vivo*. PGG forms cross-links across ECM proteins, especially elastin and collagen, and forms a stabilized arterial matrix that enhances its biomechanical strength. Future studies are needed to determine if (i) a topical application is the best method for suppressing aneurysm growth, (ii) the increase in stiffness due to PGG treatment is dose dependent, and (iii) the PGG will be effective in suppressing small diameter aneurysms in a clinical setting.

ACKNOWLEDGEMENTS

This work was supported by a U.S. National Institutes of Health Award (R01HL121293) and an American Heart Association Collaborative Sciences Award (16CSA28480006).

REFERENCES

[1] Patnaik, SS et al., *Ann Biomed Eng*, 47(1): 39–59, 2019.
[2] Lee, AY et al., *Cardiovasc Eng Tech,* 1(4):282-9, 2010.

SB³C2019
Summer Biomechanics, Bioengineering and Biotransport Conference
June 25 -28, Seven Springs, PA, USA

NOVEL METHOD OF DETECTING THE EFFECT FROM INHALED ANESTHETICS ON PERIPHERAL VENOUS PRESSURE WAVEFORMS

Kaylee R. Henry (1), Ali Z. Al-Alawi, BS (1), Md Abul Hayat, BS (2), Patrick C. Bonasso, MD (3), Hanna K. Jensen, PhD, MD (3), Jingxian Wu, PhD (2), Kevin W. Sexton, MD (4), and Morten O. Jensen, PhD (1)

(1) Department of Biomedical Engineering
University of Arkansas
Fayetteville, Arkansas, USA

(2) Department of Electrical Engineering
University of Arkansas
Fayetteville, Arkansas, USA

(3) Division of Pediatric Surgery
University of Arkansas for Medical Sciences
Little Rock, Arkansas, USA

(4) Department of Surgery
University of Arkansas for Medical Sciences
Little Rock, Arkansas, USA

INTRODUCTION

Analysis of peripheral venous pressure (PVP) waveforms is a novel method of monitoring intravascular volume, especially in cases of hemorrhage. [1][2] However, the PVP signal can potentially be confounded by parameters other than volume status, such as anesthetic agents. We hypothesized that inhaled anesthetics may have an impact on the PVP signal in the pediatric patient undergoing elective surgery for craniosynostosis, where isoflurane is used as an anesthetic agent.

During craniosynostosis surgery, prematurely closed sutures on the skull are opened, and moderate to severe hemorrhage from scalp vessels occurs routinely. The depth of the patient's anesthesia both in the hemorrhagic and non-hemorrhagic portion of the surgery is controlled by altering the minimum alveolar concentration (MAC) of isoflurane, where a higher MAC corresponds to a higher dosage of the anesthetic. This study determines if MAC influences the PVP waveform, and then utilizes machine learning to predict MAC given an arbitrary PVP waveform.

METHODS

Data Acquisition: Data were collected at Arkansas Children's Hospital from ninesequential patients undergoing surgery for craniosynostosis. PVP waveforms were continuously collected from patients using a 24-gauge Insyte N-Autoguard peripheral intravenous (PIV) catheter (Becton Dickinson Infusion Therapy Systems) which was connected to a Deltran II pressure transducer (ADInstruments) through a 48-inch arterial pressure tubing. [1] Two patients were discarded due to missing data relating between real operation time and its equivalent *LabChart* time.

Algorithm Development: Due to interference in the PVP waveform from device motion, system set-up error, PIV location, and sensitivity to movement, incisions, and breathing, an algorithm was developed using *MATLAB* to pre-process the data and remove unwanted parts of the waveforms.

First, the entire PVP waveform was sampled at a rate of 100Hz from *LabChart* for each patient. After sampling the waveform, the PVP data was exported into a custom *MATLAB* program along with the corresponding MAC value for every PVP value. The program allows the user to select the time period in which to analyze the data with the algorithm, and the number of standard deviations from the mean waveform value that will serve as the upper and lower bounds of the cleaned data. The algorithm takes sections of the PVP data at a user-selected length of time to analyze. For every section of the PVP waveform signal, the mean value of the data in that section was calculated, and if any data points in that time section exceeds above or below the user-defined number of standard deviations, then the entire section of data is removed. This method is illustrated in Figure 1below. The algorithm goes through the entire PVP waveform, which can be up to 4 hours long, removing sections of the data that are unwanted. After cleaning the data, the final waveform is exported, and transformed into the frequency domain before statistical analysis.

Poster Presentation #P004

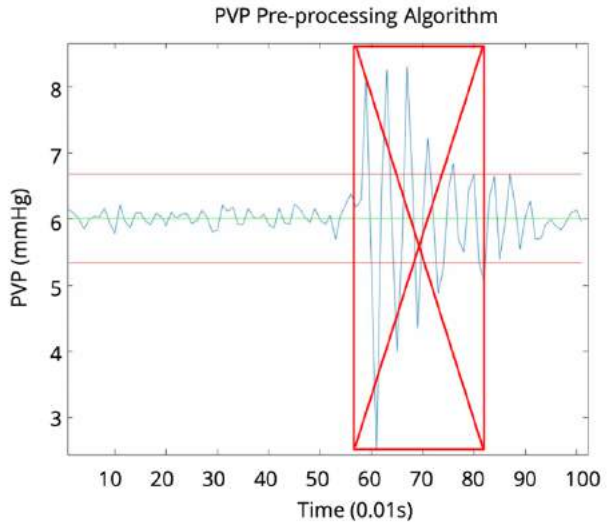

Figure 1: Data Pre-processing algorithm.

Statistical Analysis: Before performing the statistical analysis, the PVP waveform was separated into 10-second segments based on which MAC group they fell into. There were *n* MAC groups that were assigned a group number *n>0* when MAC fell between *n-1* and *n-0.1*. For example, if MAC ranged between [0-0.9], then it would be classified as MAC group 1. In Table 1 below, the MAC groups for each patient are listed.

Table 1: MAC groups for each patient.

	MAC group #
Patient 3	1, 2, 3
Patient 4	1, 2, 3
Patient 5	1, 2
Patient 6	1, 2
Patient 7	1, 2, 3, 4
Patient 8	1, 2, 3, 4, 5, 6
Patient 9	1, 2, 3, 4

After grouping the PVP waveforms, a multivariate analysis of variances (MANOVA) test was applied using *R Studio* for each patient. The independent variable for the test was MAC group and the dependent variable was the PVP waveform, with 50 frequency variables.

Finally, each patient's PVP data was loaded into the machine learning system, which utilized a k-nearest neighbor test to predict if the PVP data was from MAC group 1 and 2. For the test, k=1 and 70% of the patient's data was used for training, and 30% was used for testing the system.

RESULTS

Because of its robustness, the Pillai's Trace was utilized as the test statistic for the MANOVA test, with α=0.05. The results of the test are shown in Table 2 below.

Table 2: MANOVA results.

	df	*df error*	*F*	*partial* η^2	*p-value*
Patient 3	50	231	4.60	0.499	*<0.01*
Patient 4	50	221	3.02	0.406	*<0.01*
Patient 5	50	249	2.79	0.359	*<0.01*
Patient 6	50	571	17.30	0.602	*<0.01*
Patient 7	50	101	2.86	0.586	*<0.01*
Patient 8	50	110	7.26	0.768	*<0.01*
Patient 9	50	226	3.71	0.450	*<0.01*

The results from the k-nearest neighbor test are shown below in Table 3. The correct and incorrect predictions are shown as fractions out of the total number of 10-second segments.

Table 3: K-nearest means prediction results.

	Correct Prediction	Percent Correct	Incorrect Prediction	Percent Incorrect
Patient 3	66/82	80%	16/82	20%
Patient 4	55/67	82%	12/67	18%
Patient 5	89/90	98%	1/90	2%
Patient 6	143/186	77%	43/186	23%
Patient 7	27/35	77%	8/35	23%
Patient 8	23/28	82%	5/28	18%
Patient 9	64/82	78%	18/82	22%

DISCUSSION

Our study found that there is a significant relationship between the dosage of inhaled anesthetic and the PVP waveform. The PVP waveform increases as the MAC increases. We were also able to show that the machine learning system was able to accurately distinguish between the PVP waveforms of each MAC group and predict the correct MAC for an arbitrary PVP at least 77% of the time. Isoflurane is a known potent vasodilator, and our results indicate that the subsequent changes in vascular resistance are reflected in the venous circulation and thus PVP signal as well. Future research in PVP waveforms should take into account any anesthetic agents the patient has received, and this clear relationship should be considered in any future application of PVP signal technology. These results are also useful for the development of a novel anesthesia monitor for children, as the only current device of this kind is a bispectral index monitor which only assesses the depth of anesthesia.

REFERENCES

[1] Hocking, KM, et al., *Shock*, 46(4):447-452, 2016.
[2] Sileshi B, et al., *Journal of Intensive Care Medicine,* 41(6):1147-1148, 2015.
[3] Bonasso, P et al., *Journal of Clinical Monitoring and Computing,* 32:1149-1153, 2018.

SB³C2019
Summer Biomechanics, Bioengineering and Biotransport Conference
June 25 -28, Seven Springs, PA, USA

FLUVASTATIN DECREASES ENDOTHELIAL NITRIC OXIDE SYNTHASE O-GLCNACYLATION

Danika E. Meldrum (1), Sarah Basehore (1), Alisa Morss Clyne (2)

(1) School of Biomedical Engineering, Science, and Health Systems
Drexel University
Philadelphia, PA, USA

(2) Mechanical Engineering and Mechanics
College of Engineering
Drexel University
Philadelphia, PA, USA

INTRODUCTION

Pulmonary hypertension (PH) is a fatal disease that has an incidence of 15-50 people per million with a median survival of 2.8 years [1]. PH is characterized by endothelial dysfunction, including reduced vasodilation and increased inflammation in blood vessels partially due to decreased nitric oxide (NO) bioavailability [1]. In addition, PH lungs show increased glucose uptake and glucose-mediated protein post-translational modifications such as protein O-GlcNAcylation [2,3].

NO is produced by activation of endothelial nitric oxide synthase (eNOS) through eNOS phosphorylation at the Ser-1177 site [4]. eNOS activity can also be modified at this same site by O-GlcNAcylation [5]. eNOS O-GlcNAcylation may decrease eNOS phosphorylation and consequently decreased endothelial NO bioavailability [5,6]. Protein O-GlcNAcylation occurs through the hexosamine biosynthetic pathway (HBP), which produces the critical substrate UDP-GlcNAc. The addition and removal of O-GlcNAc from target proteins is performed by O-GlcNAc transferase (OGT) and O-GlcNAcase (OGA), respectively [5].

Statins have shown positive effects in many cardiovascular diseases via improved endothelial cell function and anti-inflammatory effects [7]. Animal studies using statin treatment have shown success in reversing pulmonary vascular remodeling but the exact mechanism responsible is unknown and human studies have been inconclusive [8-10]. *In vitro*, statins increase endothelial cells eNOS and reduce cell glucose metabolism via glycolysis [9,11]. We hypothesized that statins reduce eNOS O-GlcNAcylation to promote eNOS phosphorylation and NO bioavailability. To investigate this hypothesis, we treated HUVEC with fluvastatin *in vitro* at varying concentrations and time durations and measured total and GlcNAcylation eNOS by Western blot.

METHODS

Human umbilical vein endothelial cells (HUVEC) were cultured in Endothelial Growth Medium-2 (EGM-2) supplemented with 10% fetal bovine serum, 1% penicillin-streptomycin, and 1% L-glutamine. 300,000 cells/mL were seeded on collagen coated plates. Experimental treatment began when samples reached confluency 48 hours later.

HUVEC were treated with supplemented EGM-2 with or without 500 nM fluvastatin for 24 or 48 hours. In some cases, 100 µM ATP in PBS was added for 1-minute following fluvastatin treatment to investigate eNOS phosphorylation. Following treatment, samples were analyzed via Western Blot. Samples were washed with cold PBS and scraped off in ice-cold lysis buffer (20 mM EDTA, 2 mM $NaVO_4$, 2 mM PMSF, 50 mM NF, 10% glycerol, complete protease inhibitor (Roche), pH 7.4). Next, samples were needle lysed, and centrifuged in 4°C at 13,000 RPM for 10 minutes. Supernatant was collected and the protein content of all samples was normalized via BCA assay. Sample proteins were separated by SDS-PAGE on a 4-12% Bis-Tris gel (Life Technologies) and transferred to nitrocellulose membranes using the Invitrogen iBlot system. Membranes were blocked with a 5% BSA in PBS-T solution for 1 hour. Membranes were incubated overnight with primary antibodies for protein O-GlcNAcylation, p-eNOS, eNOS, OGT, OGA, and βactin, followed by a horseradish peroxidase conjugated secondary antibody for 2 hours at room temperature. Protein bands were detected using an enhanced chemiluminescence kit (Western Lightning, PerkinElmer) and visualized with a Fluorchem digital imager (Alpha Innotech). Protein band intensities were quantified using AlphaEase FC software. Student's t-test was used to compare experimental groups (*$p<0.05$, **$p<0.01$, ***$p<0.001$).

Poster Presentation #P005

RESULTS

We first measured eNOS quantity and protein O-GlcNAcylation in HUVEC exposed to fluvastatin at varying doses (Figure 1) and for increasing times (Figure 2). eNOS O-GlcNAcylation significantly decreased (*p<0.05) while total eNOS significantly increased (*p<0.05) when HUVEC were treated with 5 µM and 10 µM fluvastatin (Figure 1A and 1B, respectively).

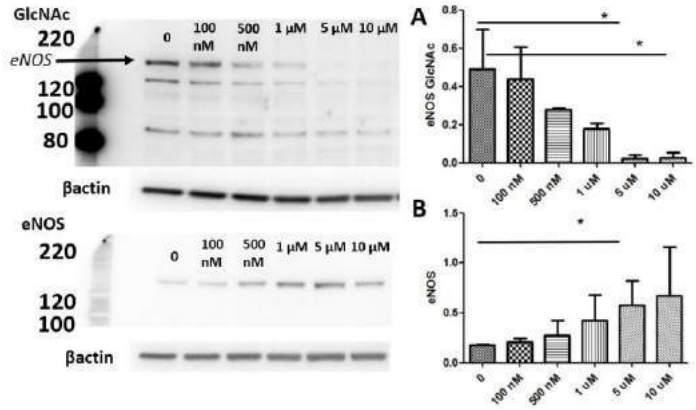

Figure 1: Endothelial cells treated with higher fluvastatin concentrations showed a significant decrease in eNOS O-GlcNAcylation (A) and increase in eNOS (B) as compared to untreated cells. HUVECs were treated with 0, 100 nM, 500 nM, 1 µM, 5 µM, or 10 µM fluvastatin for 24 hours. (*p<0.05, **p<0.01, ***p<0.001).

We next tested whether a lower fluvastatin dose (500 nM) would affect eNOS at longer time points, since concentrations only up to 1 µM are possible in human circulation after standard drug dosage [10]. eNOS O-GlcNAcylation, normalized to either βactin or total eNOS, decreased (***p<0.001) after both 24 hours and 48 hours of fluvastatin treatment (Figures 2A and 2B, respectively). Total eNOS also increased (**p<0.01) after both 24 hours (**p<0.01) and 48 hours (*** p<0.001) of fluvastatin treatment (Figure 2C).

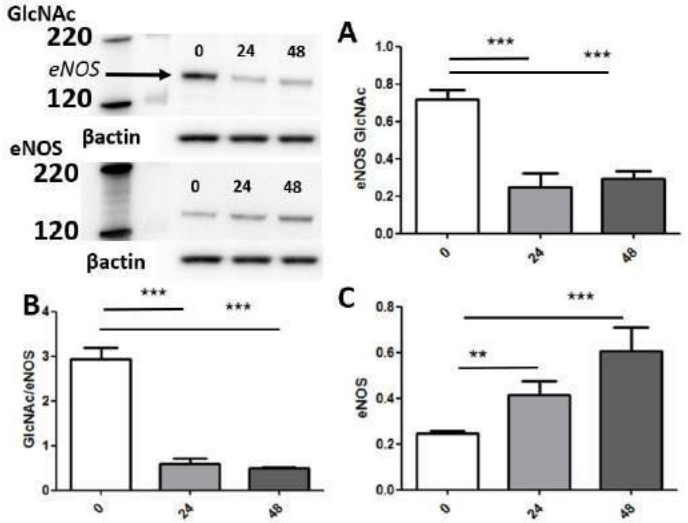

Figure 2: HUVEC treated with 500 nM fluvastatin for 24 and 48 hours showed a significant decrease in eNOS O-GlcNAcylation and increase in eNOS as compared to untreated cells (*p<0.05, **p<0.01, ***p<0.001).

We next investigated whether the decrease in eNOS O-GlcNacylation due to fluvastatin treatment increased eNOS phosphorylation (Figure 3). HUVEC treated with fluvastatin and then stimulated with ATP showed a significant increase in peNOS compared to HUVEC that were not treated with fluvastatin when samples were normalized to βactin (3A, *p<0.05). However, the effect was not significant when samples were normalized to total eNOS (3B, p>0.05). This suggests that the increased peNOS in fluvastatin treated cells is due to increased eNOS expression and that eNOS O-GlcNAcylation may not affect ATP-induced eNOS phosphorylation.

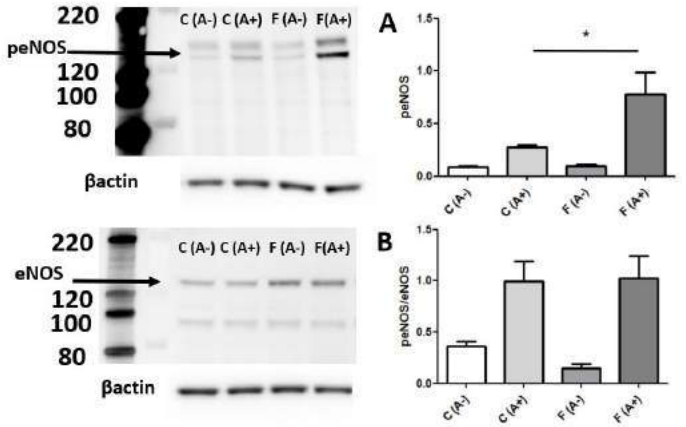

Figure 3: HUVEC treated with 500 nM fluvastatin for 24 hours and stimulated with 100 µM ATP (F(A+)) showed a significant increase in peNOS compared to controls stimulated with ATP (C(A+)) when normalized to βactin but not when normalized to eNOS (*p<0.05, **p<0.01, ***p<0.001).

DISCUSSION

We now show that fluvastatin decreases eNOS O-GlcNAcylation, which may contribute to its positive effects in cardiovascular disease. Our results do not suggest that reducing eNOS O-GlcNAcylation via fluvastatin increases eNOS phosphorylation. However, whether reduced eNOS O-GlcNAcylation restores eNOS function and NO bioavailability in diseases such as PH warrants further investigation. The effect of statins on other diseases with increased O-GlcNAcylation, such as hyperglycemia in diabetes, should be explored in the future.

ACKNOWLEDGEMENTS

This research was supported by NIH 1R01HL140239-01.

REFERENCES

[1] Chester, A.H. et al., *Glob Cardiol Sci Pract*, 2017 (2).
[2] Lima, V. V. et al., *J Am Soc Hypertens*, 2009 3(6): 374–387.
[3] Ohira, H. et al., *J Am Coll Cardiol*, 2015 65(10S): 1135-015.
[4] Barnes J. W. et al., *Circulation*, 2015 131(14): 1260–1268.
[5] Musicki, B. et al., *Proc Natl Acad Sci U.S.A.*, 2005 102(33): 11870-11875.
[6] Du, X.L. et al., *J Clin Invest*, 2009 108(9): 1341–1348.
[7] Brault, M. et al., *Metab: Clin Exp*, 2014 63: 735 – 745.
[8] Murata, T. et al., *Arterioscler Thromb Vasc Biol*, 2005 (25)11: 2335-2342.
[9] Laufs, U. et al., *Circulation*, 1998 97(12): 1129-35.
[10] Carlin, C. M. et al., *Am J Respir Cell Mol Biol*, 2007 37: 447–456.
[11] Wang, W. et al., *J Cell Mol Med*, 2010 (88)3: 309-317.

SB³C2019
Summer Biomechanics, Bioengineering and Biotransport Conference
June 25 -28, Seven Springs, PA, USA

INVESTIGATIONS OF THE CHORDAE TENDINEAE'S MECHANILCAL PROPERTIES OF PORCINE ATRIOVENTRICULAR HEART VALVES

Colton J. Ross (1), Devin W. Laurence (1), Yan D. Zhao (2), Ming-Chen Hsu (3), Ryan D. Baumwart (4), Yi Wu (1), Chung-Hao Lee (1)

(1) Biomechanics and Biomaterials Design Laboratory
School of Aerospace and Mechanical Engineering
The University of Oklahoma
Norman, OK, USA

(2) Biostatistics Core Stephenson Cancer Center
The University of Oklahoma
Health Sciences Center
Oklahoma City, OK, USA

(3) Department of Mechanical Engineering
Iowa State University
Ames, IA, USA

(4) Center for Veterinary Health Sciences
Oklahoma State University
Stillwater, OK, USA

INTRODUCTION

The two atrioventricular heart valves (AHVs), the mitral valve (MV) and tricuspid valve (TV), facilitate proper cardiac blood flow through opening and closure of soft tissue leaflets. These soft tissue leaflets are supported during closure by the chordae tendineae (CT), preventing prolapse of the leaflet into the atria. However, when the chordae tendineae fail to prevent leaflet prolapse regurgitation can occur. Currently surgical methods include chordal replacement using an expanded polytetrafluoroethylene (ePTFE) suture. However, the materials used in the chordal replacement have a higher elastic modulus than the native CT which can lead to regurgitation recurrence [1]. Refinement of these surgical procedures can be informed through characterizations of the native CT's mechanics.

Previously studies have performed quantifications of the CT's stress-stretch response as an *individual* segment, rather than as a functioning *group* [2-3]. In *individual* CT testing, the CT were separated from the leaflet and papillary muscles points of attachment before mechanical testing. However, by analyzing the chordae mechanics as a *group* structure by preserving the points of attachment, a mechanical characterization may be made which better represents how the CT operates *in vivo*. Further, limited information exists on the mechanics of the CT of the TV. This study addresses the need for mechanical characterizations of the CT as a *group* structure, which will be useful in computational modeling and therapeutics refinement.

METHODS

Tissue Preparation: Healthy porcine hearts (80-140 kg, 1-1.5 years of age) were retrieved from a local slaughterhouse. For group CT testing, the thickest, strut CT of the mitral valve anterior leaflet (MVAL) and tricuspid valve anterior leaflet (TVAL) were excised with their papillary muscles and leaflet points of attachment preserved, obtaining one group from the left (LG) and right (RG) of the leaflet apex (**Fig. 1a**).

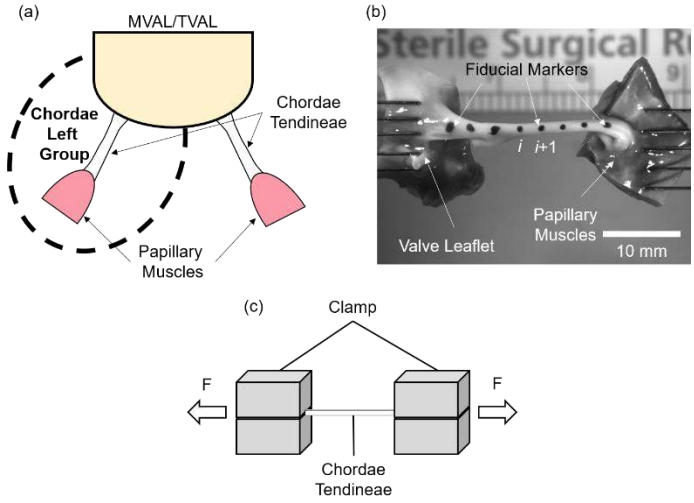

Figure 1: (a) The CT group was excised from the valve, preserving leaflet and papillary muscle points of attachment and tested (b) using a tine-based approach, as opposed to (c) schematic of the clamping mechanism used in the individual CT testing [2-3].

Mechanical Testing: In group CT testing, specimens (n=7 for each group) were mounted to a commercial biaxial testing system (BioTester – CellScale Biomaterials Testing) using tines which pierced the papillary muscles and leaflet sections (**Fig. 1b**). This tine-based testing

method allows for freedom of movement for the chordal points of attachment at the papillary muscles and leaflet, as opposed to a clamping-based method (**Fig. 1c**) where those interactions are not adequately considered. Fiducial markers were placed on the CT segment for data image correlation (DIC)-based strain calculation.

CT groups were mechanically tested by: (i) a preconditioning step of 15 loading and unloading cycles, targeting a force of 1.4N and 1.2N for the MVAL and TVAL CT tissue groups, respectively, and (ii) a mechanical testing step of 15 additional loading and unloading cycles. The preconditioning step was performed to exercise the tissue to its *in vivo* configuration [4]. The testing forces employed were used due to their similarity to physiologic loading in the respective valves [5-6]. Chordal diameters were measured using a microscope.

Data Analyses: For calculating stress chordal diameters were used assuming a circular, uniform cross-sectional area. Tissue stretch was quantified using DIC techniques to obtain time-dependent fiducial marker positions. Marker positions were used to find the three components of CT stretch: (i) the preconditioning stretch (λ_0^1), (ii) the total tissue stretch (λ_0^2), and (iii) the mechanical stretch (λ_1^2).

Statistical Analyses: Physical quantities were determined for statistical significance using SAS 9.4. One-way ANOVA was used to determine significance between CT groups of the same valve. Two-way ANOVA was used to determine significance between left and right CT groups, and MVAL and TVAL CT groups, with the interaction term also considered. A p-value <0.05 was considered statistically significant, while a p-value <0.10 was deemed nearly statistically significant.

RESULTS

The diameters of the MVAL CT tissue groups were found to be 30-60% thicker than the TVAL CT tissue groups. Specifically, the MVAL-RG diameters were nearly significantly higher than the MVAL-RG (p=0.059). Also, the MVAL CT diameters were found to be significantly higher than the TVAL CT thicknesses (p<0.001).

CT tissue groups followed the non-linear, exponential force-displacement trend expected of soft tissues (**Fig. 2**) [7]. The mean preconditioning stretches (**Fig. 3a**) of the MVAL CT tissue groups were found to be significantly higher than the TVAL CT tissue groups (p=0.014). The RG was found to have a nearly significantly higher preconditioning stretch than the LG (p=0.068). Additionally, the mean preconditioning stretches of the MVAL RG were found to be nearly significantly higher than the MVAL LG (p=0.081).

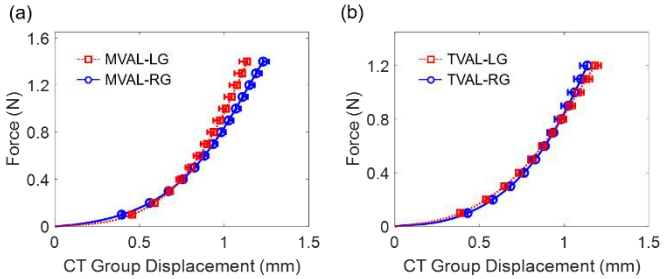

Figure 2: The force-displacement responses of the (a) MVAL-CT tissue groups (n=6) and (b) TVAL-CT tissue groups (n=7).

From the total tissue stretches (**Fig. 3b**), the MVAL CT tissue groups experienced significantly higher total tissue stretch than the TVAL CT groups (p=0.018). Nearly significant difference was found between the LG and RG (p=0.083). From mechanical stretches, no statistically significant differences were found (**Fig. 3c**).

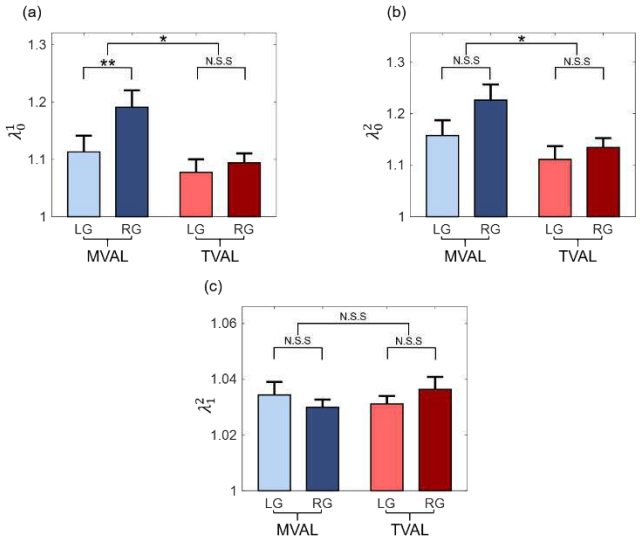

Figure 3: The (a) preconditioning stretch, (b) peak stretch, and (c) mechanical stretch of the CT group. Values are reported as the mean ± SEM. Notation: *, statistical significance; **, near statistical significance; N.S.S, not statistically significant.

DISCUSSION

This study provides a unique characterization of the MVAL and TVAL CT which considers the effects of the points of attachment on observed CT mechanical properties, rather than characterizing *individual* CT segments. Further, this study contributes to the limited research of the right-side CT. In a previous study [3] testing *individual* strut CT of the MV and TV to a 1MPa stress it was found that the MV CT had an approximate 6.5% strain and the TV CT had an approximate 1.5% strain. In our study testing CT *groups*, at a 1MPa testing stress the MV and TV CT were found to have an average strain of 13.1±3.2% and 20.7±3.0%, respectively. Comparing to previous studies it can be seen the preservation of the chordal points of attachments provides new, unique information about the chordal mechanics.

This study has some limitations. For instance, there was some CT shear/torsional stress in uniaxial mechanical testing due to improper planar alignment of the specimen. However, this stress can be considered negligible as the CT segment recovered its *in vivo* functional state after approximately 10 loading/unloading cycles where axial stretch was the dominant stretch mode. Using the information found in this study, computational models of the AHVs may be refined to inform therapeutic refinement using characterizations which represent CT function *in vivo*, as compared to characterizations of *individual* CT.

ACKNOWLEDGEMENTS

This work is supported by the American Heart Association Scientist Development Grant (SDG) Award (16SDG27760143), and the Mentored Research Fellowship & the Undergraduate Research Opportunities Program at the University of Oklahoma.

REFERENCES

[1] Cochran, RP et al., *J Cardiac Surgery*, 6:508-13, 1991.
[2] Casado, JA et al., *JMBBM*, 13:1-13, 2012.
[3] Pokutta-Paskaleva, A et al., *Acta biomater.*, 85:241-52, 2019.
[4] Fung, Y et al., *Am J of Phys-Heart Circ. Phys.*, 237:H620-31, 1979.
[5] Jimenez, JH et al., *Annals of biomed. eng.*, 31:1171-81, 2003.
[6] LeBlanc, NL et al., *American J of Vet. Research*, 79:404-10, 2018.
[7] Yamada, H et al., *Strength of Biological Materials*, 1970.

SB³C2019
Summer Biomechanics, Bioengineering and Biotransport Conference
June 25 -28, Seven Springs, PA, USA

RELATIONSHIP OF PLATELET ADHESION WITH SURFACE TOPOGRAPHY IN THE PENN STATE PVAD

Cecilia A. Richardsen (1), Ashlyn S. Mueser (1), Branka Lukic (1,2), Christopher A. Siedlecki (1,2), William J. Weiss (1,2), Keefe B. Manning (1,2)

(1) Department of Biomedical Engineering
The Pennsylvania State University
University Park, PA, USA

(2) Department of Surgery
Penn State Hershey Medical Center
Hershey, PA, USA

INTRODUCTION

From 2010 to 2017, 439 children, among the 4,731 children on the transplant list, died while waiting for a heart. [1] There is a clear shortage of hearts available for transplant and a need for a pediatric bridge-to-transplant device.

To meet this need, a pneumatic, pulsatile pediatric ventricular assist device (PVAD) has been developed by Penn State and is shown in Figure 1. While animal studies have been encouraging, thrombus formation has been observed, which remains a problem in ventricular assist devices. Previous studies have shown that surface roughness of the segmented poly-(ether polyurethane urea) (SPEUU) seamless blood sac can lead to the aggregation of platelets in a fibrin matrix.

Figure 1: The Penn State pediatric ventricular assist device developed at the Penn State College of Medicine. [2]

The goal of this research is to study surface irregularities in relation to the presence of platelet and fibrin deposits, which will provide insight into why thrombosis occurs here.

METHODS

Twelve ovine studies have been completed at the Penn State Hershey Medical Center with the PVAD implanted in the animal for a target of 4 to 6 weeks. An explanted blood sac was characterized for each study. Immunofluorescent labeling and confocal microscopy were used to identify the presence of platelets and fibrin on the surface of the blood sac. These structures were confirmed with environmental scanning electron microscopy (ESEM). Biological structures were enzymatically degraded from the surface, and optical profilometry was used to characterize the surface topography of each blood sac. All images were taken in a snake-like pattern shown in Figure 2.

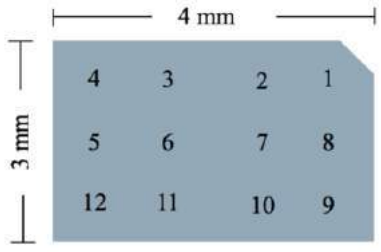

Figure 2: Samples from each blood sac were cut to a size of 4 mm by 3 mm. The microscopy and profilometry images were correlated using the numbering scheme presented. [3]

The roughness average (Ra), an average of all values on the roughness profile, the root mean squared (RMS), an average deviation from the roughness average center line, and the Swedish height (H), a roughness average of the middle 90% of the data, were collected for each sample. An overview of these methods is shown in Figure 3. A non-implanted SPEUU blood sac was used as the control and was analyzed with the same methods. Images taken from confocal, ESEM, and optical profilometry were correlated for each sample, as shown in Figure 4. Based on these images and the surface roughness parameters, the relationship between thrombus deposition and surface topography was determined.

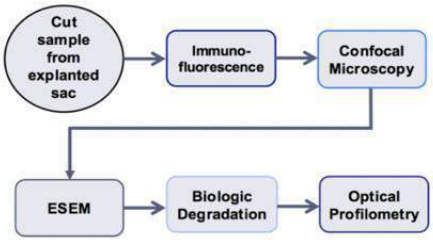

Figure 3: Overview of explanted sac protocol. [3]

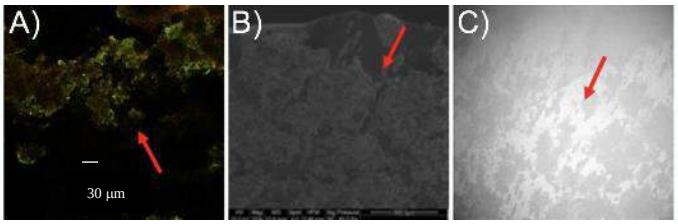

Figure 4: (A) Sample confocal microscopy, (B) ESEM, and (C) optical profilometry images taken from a macroscopic clot on the surface of the Penn State PVAD blood sac. [3]

RESULTS

Explanted sacs were analyzed by studying the correlated images. In total, 5 macroscopic deposits were found on 4 of the 12 sacs studied. There were also 26 microscopic deposits found across all of the 12 sacs studied. Macroscopic deposits were visualized without the use of a microscope, where the microscopic deposits were revealed upon use with the confocal microscope.

A diagram of the PVAD is shown in Figure 5, with locations for all deposits identified and later analyzed.

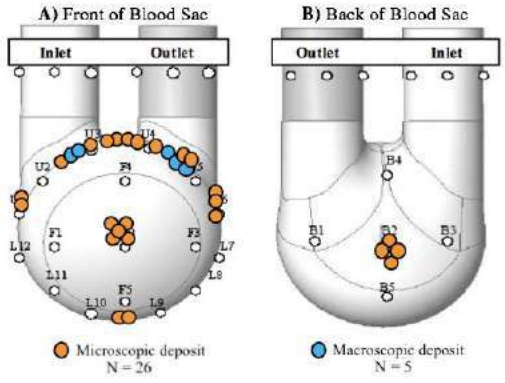

Figure 5: Map of all deposits found across the 12 sacs analyzed. In total, (A) there were 22 microscopic deposits with 5 macroscopic deposits found on the front of the sac, and (B) 4 microscopic deposits found on the back of the blood sac.

The topography of each sac was analyzed by the size of the deposit to compare the roughness in regions of macroscopic deposits, microscopic deposits, and the control. The RMS value for the five macroscopic deposits observed was 16% greater than that of the 26 microscopic deposits and 76% greater than the control. Similar trends were observed for the roughness average (Ra) and Swedish height (H).

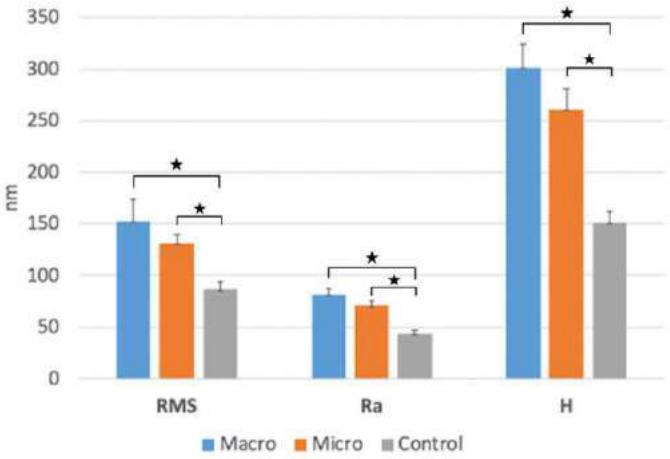

Figure 6: Comparing average RMS, Ra, and H values for macroscopic clots, microscopic clots, and a control sac.

DISCUSSION

There was greater sac surface roughness in regions of larger thrombus deposition. The majority of the deposits were found in the transition from the inlet and outlet ports to the main body of the sac.

The surface roughness parameters are higher for macroscopic and microscopic clots than for the control samples. A two-factor t-test (α = 0.05) was conducted to determine the significance of the findings. The difference between the macroscopic deposits and the control was significant for RMS, Ra, and H. The difference between the microscopic deposits and the control was also significant for RMS, Ra, and H. The differences between macroscopic and microscopic deposits were not statistically significant for any surface roughness parameter.

These data provide a procedure for determining the relationship between thrombus deposition and surface topography in the Penn State PVAD. Areas of higher surface roughness on the SPEUU seamless blood sacs could promote deposition of platelets and fibrin. Future studies could add more statistical significance to the results found for these 12 sacs and provide a more complete map of deposit locations.

ACKNOWLEDGEMENTS

Partially supported by NIH HL108123 and HL131921.

REFERENCES

[1] Organ Procurement and Transplantation Network. US Department of Health and Human Services: Health Resources and Services Administration. https://optn.transplant.hrsa.gov/

[2] Vogler, E.A., Siedlecki, C.A. 2009. Contact activation of blood-plasma coagulation. *Biomaterials.* 30*:*1857–69.

[3] Mueser, A. 2017. Relationship of platelet adhesion with surface topography in the Penn State pediatric ventricular assist device. MS Thesis at The Pennsylvania State University.

[4] Zygo Corporation: MetroPro Surface Texture Parameters *www.zygo.com*: 1–20, 2013.

SB³C2019
Summer Biomechanics, Bioengineering and Biotransport Conference
June 25 -28, Seven Springs, PA, USA

MOUSE AORTIC MECHANICAL PROPERTIES FROM FINITE ELEMENT MODEL OPTIMIZED TO MATCH RING-PULL EXPERIMENTS

Carl T. Schoephoerster (1), Ryan R. Mahutga (1), Victor H. Barocas (1)

(1) Department of Biomedical Engineering
University of Minnesota
Minneapolis, MN, USA

INTRODUCTION

The vascular system plays the essential role of delivering oxygenated blood to tissues throughout the body, and when it fails dire consequences are seen. For example, aortic aneurysms that rupture kill more than 15,000 people per year[1]. Even more troubling, the incidence of aortic aneurysm has tripled in the U.S. during the past 30 years[1]. Aortic dissections discovered after they occur are deadly (~20% of patients die before reaching hospital). Both aneurysm and dissection are aberrant mechanical events, and understanding of how and why they happen is crucial to prevention, diagnosis, surgical interventions, and therapeutic development. While aortic dissections can occur in different regions of the aorta, there is a disparity in the prevalence of where they happen, with the most common starting in the ascending thoracic aorta and extending to or beyond the aortic arch[2]. Thus, we hypothesize there are characterizable regional differences in the mechanics of the aorta.

The goal of this study was to determine the properties of the wild-type (WT) mouse aorta along its entire length through the excision and uniaxial testing of ring specimens. A finite element (FE) model of a ring-pull test was regressed to experimental data to determine mechanical properties. In the past, ring-pull experimentation could not be used to elucidate mechanical properties directly because the ring pulls had to be treated as uniaxial tests, which they are not. With improved methods for solving FE problems, however, particularly for contact problems, it is now possible to use inverse methods to solve for mechanical properties in such systems. The overall questions addressed by this work were whether aortic mechanical parameters could be reliably ascertained from ring-pull experiments, how they change in different regions, and how they affect macroscopic behavior under *in vivo* like conditions (i.e., inflation with physiologic pressures).

METHODS

Sample Preparation

The heart and attached aorta were dissected from adult WT mice (age 8 -16 months) between the iliac bifurcation and top of the arch. The aorta was cut at its root away from the heart and sectioned into alternating ~0.5mm and ~2mm wide rings (Figure 1). Samples 0.5 mm in width were used to establish the average wall thickness and inner/outer diameter of rings. Rings 2mm in width were measured and used for the ring-pull tests. Ring inner diameters varied between 0.97 and 1.19mm.

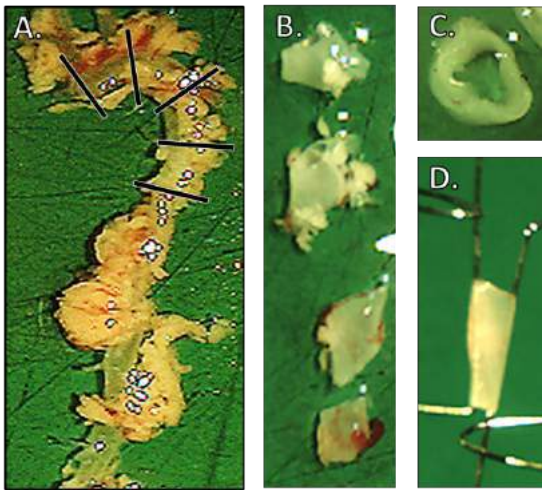

Figure 1: A. Aorta and approximate cut locations; B. Cut rings; C. Top-view of ring; D. Side-view of ring on pulling apparatus

Ring-Pull Test Protocol

The 2mm wide rings were placed onto a custom fixture, consisting of a pair of thin wires (0.5mm in diameter) inserted through the lumen of the aorta sample[4]. Each fixture was attached to a load cell and oriented so that the pull was uniaxial. Rings were preloaded to an elliptical shape to keep them from moving on the fixture. Rings were pulled at a rate of 2mm/min until failure[3]. Figure 2 shows the dimensions used and a schematic of the test.

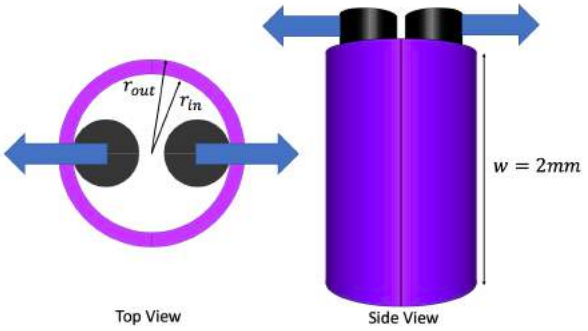

Figure 2: Ring-pull test geometry and schematic

FE Ring-Pull Simulation and Parameter Optimization

A computational model of the ring-pull experiment was created in FEBio. The wire rod in the test was treated as a rigid body, and the tissue ring was treated as an uncoupled solid mixture, with neo-Hookean behavior and an exponential power law to account for two different fiber populations—located at +45 and -45 degree orientation in the circumferential-axial plane (1)[3,5,6].

$$W = c_1(I_1 - 3) + \frac{\xi}{2\alpha} * (e^{0.5\alpha(\lambda^2-1)^2} - 1) \quad (1)$$

W is the total strain energy density function of the tissue; c_1 the constant for the neo-Hookean nature of the tissue; I_1 is the first invariant of the deformation gradient; ξ is the fiber bundle modulus; α is the exponent representing non-linearity; and, λ is the stretch of the tissue. A custom code was developed that used the Nelder-Mead simplex algorithm to optimize the parameters c_1, ξ, and α to match experimental force/displacement data.

Because the simulation involves a contact problem, more setup was required to get the correct results. At the start of the simulation, the tissue was placed precisely in contact with the wire. This requirement added a layer of complexity to the problem, and a custom code was created to take a template FE model file, filter out the tissue nodal positions, scale them to the dimensions of the specific ring used in the experiments, shift them into exact contact with the rod, and output a correct simulation file specific to each ring sample. The contact was specified to be a sliding interface between the rod and the inner ring surface, neglecting friction between the surfaces. The augmented Lagrangian method with two-pass automatic penalty was used with a penalty factor of 2 and a gap tolerance of 0.01.

RESULTS

The optimized parameters from ring-pull simulation are shown in Figure 3 along with a representative fit. The constant scaling the neo-Hookean portion (c_1) dominates in low-strain regions, as fiber stretch has not yet come into play. Parameters α and ξ govern the behavior of fibers, and come into play in larger strain regions where non-linear stress/strain relationships are present. The general trend of the data shows increasing fiber stiffness and nonlinearity as we move around the arch from the aortic root toward the upper portion of the thoracic aorta. Parameters were also determined from a uniaxial fit to the experiment data, which yielded α values two orders of magnitude larger (0.585 to 1.338), c_1 values decreasing from nearly the same values for the first two rings (0.0145, 0.00747 MPa) to nearly zero for the last two rings, and ξ values an order of magnitude smaller (0.00724 to 0.0507 MPa) than those determined from the optimization shown in Figure 3b.

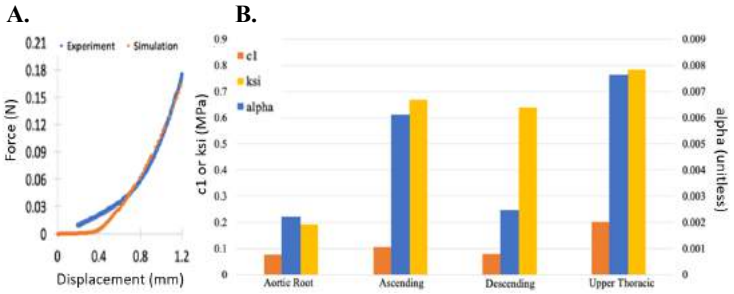

Figure 3: A. Representative fit of FE force-displacement with experimental data B. Optimized parameters for ring-pull tests

Figure 4 shows a heat map of the 1st principle stress for a representative simulation. The stress tends to concentrate on the luminal side just past the contact point of the rod. The geometry along the rod and just beyond the contact patch becomes wider along the luminal surface, as has been observed in experiments.

Another important aspect of this simulation is the implementation of contact. The contact gap was maintained to be less than 5% of the initial wall thickness with typical values <1%. The contact pressure along the surface increased from zero to ~2.5MPa under large strains.

Figure 4: Stress concentration in tissue during ring-pull

DISCUSSION

The optimization of model parameters using the simplex method provided a reasonable fit to the experimental data (average RMSE of 4mN). This is significant because the simulation does not make the uniaxial assumptions made when one simple curve fits the constitutive model. This is highlighted in Figure 4, where stress concentrates along the tissue surface in contact with the wire rod, which is something not accounted for in uniaxial extension. The uniaxial fit to the data predicted much different parameters compared to the optimization done in this study, typified by much more nonlinear fibers and very little influence of the neo-Hookean ground substance. Thus, determining model parameters through FE optimization is more appropriate than treating these experiments as uniaxial extension.

It is clear that different regions have different behavior (i.e., have different model parameters) (Figure 3b). A general trend is seen where the fiber parameters become more prominent and nonlinear as we move along the aorta, whereas the neo-Hookean component (elastin matrix, ground substance) remains relatively constant. It is hard to draw conclusions, however, based on the limited sample size.

Future work on this project will include adding to the dataset of WT mouse aortas to distinguish behaviors between groups (e.g., male vs. female, old vs. young). The results from this study will serve as the basis for a new FE model of mouse aorta expansion during inflation, accounting for the regional variation measured here.

REFERENCES

1. *Circulation*. 2013; 127; 2. *Merck Manual: Aortic Dissections* 2017; 3. SB3C, 2017, Tucson, AZ; 4. *Cardiovascular solid mechanics*; 2002; 5. *FEBio Theory Manual*, 2016; (v2.5); 6. *J. BME,* 2004; 12.

SB³C2019
Summer Biomechanics, Bioengineering and Biotransport Conference
June 25 -28, Seven Springs, PA, USA

A COMPUTATIONAL STUDY OF THE ROLE OF THE PERICARDIUM ON CARDIAC FUNCTION IN NORMAL AND HYPERTENSIVE HEARTS

Emilio A. Mendiola (1), Huan Nguyen (1), Reza Avaz (1,2), Michael S. Sacks (1,2)

(1) Willerson Center for Cardiovascular Modeling and Simulation, Institute for Computational Engineering and Sciences, The University of Texas at Austin, Austin, USA

(2) Department of Biomedical Engineering, The University of Texas at Austin, Austin, USA

INTRODUCTION

The heart and lungs operate as a single functional unit [1]. Efficient operation of the cardiopulmonary system requires coordinated performance of the left (LV) and right ventricles (RV). Pulmonary arterial hypertension (PAH) causes an increase in pressure and subsequent growth and remodeling in the RV. While the pericardium has been shown to impact LV and RV interdependence, the effect of the pericardium on ventricular interaction and organ-level cardiac function in a hypertensive heart remains unexplored [2]. We recently developed finite-element (FE) rat heart models (RHM) of both normal and hypertensive specimens using extensive imaging and pressure-volume datasets [3]. In this work, we extended our biventricular RHMs to account for the effect of pericardial sacs and used the models to investigate the alterations in systolic and diastolic ventricle interaction and function from a normal to hypertensive state. We used the extended models to test the hypothesis that the gradual dilation of the RV throughout the development of PAH compromises the integral of the pericardium, which is to act as a mechanical constraint against pathological changes is heart size [4].

METHODS

We developed two implementations of the FE biventricular RHM based on extensive datasets from normal and post-hypertensive rat hearts in order to simulate and understand the local and organ-level remodeling of the RV in response to PAH. Additionally, we implemented model-specific pericardia to investigate the role of the pericardium with respect to ventricular function in both normal and hypertensive hearts.

PAH Animal Model

A total of 8 male Fischer-344 rats were used in this study. The hypertensive group (PAH, n=4) received a moderate dose of monocrotaline (MCT) by subcutaneous injection to induce PAH. The control group (n=4) received an equivalent volume of saline. At four weeks post MCT injection, terminal pressure-volume (P-V) measurements were collected and the harvested hearts were imaged by a cardiac MRI scan. FE biventricular RHMs (Fig. 1) were constructed and validated using imaging datasets and in-vivo hemodynamic measurements collected at the Texas Heart Institute.

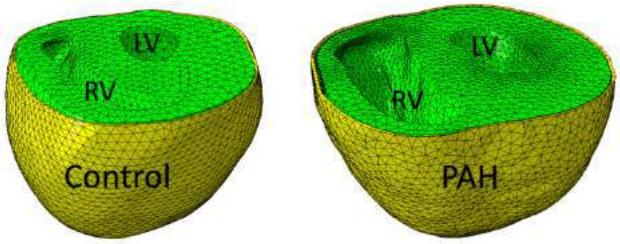

Figure 1: FE models of control (left) and PAH (right) murine hearts (green) and pericardia (yellow).

Finite Element Model

An anisotropic hyperelastic constitutive model was used for both myocardium and pericardium. Myofiber direction was mapped to the FE mesh from reconstructed diffusion tensor imaging. The fibrous structure of the pericardium was assumed to have a similar distribution as that of the epicardium of the heart.

$$\mathbf{S} = \mathbf{S}^{passive} + \mathbf{S}^{active} \quad (1)$$

A stress decomposition approach to was used to describe the passive and active behaviors of the tissue (1), where

$$\mathbf{S}^{passive} = \frac{\partial W^{dev}}{\partial \bar{\mathbf{E}}} + \mathbf{S}^{vol}$$
$$\mathbf{S}^{active} = T_{Ca^{+2}}(t)\frac{1+\beta(\lambda-1)}{\lambda^2}\mathbf{N}\otimes\mathbf{N} \quad (2)$$

and where T_{Ca} is the contractility parameter, **N** is the fiber direction, and β is a constant. W^{dev} is the deviatoric strain energy.

Inverse Modeling

The RHM passive and active behavior was determined through an inverse modeling approach to match the organ-level hemodynamic measurements. Passive stiffness was determined by matching the end-diastolic point in the model to in-vivo measurements. The active contraction parameter, T_{Ca}, was determined by minimizing the error between model behavior and the acquired pressure-volume (PV) loop.

Addition of the Pericardium

Pericardia were modeled as hyperelastic thin FE shells adjacent to the epicardium. Interaction between the pericardium and the epicardium is modeled as a frictionless sliding contact.

Several numerical experiments were conducted with the RHMs with and without pericardium in both control and hypertensive states and the following relationships were evaluated: (i) RV and LV volumetric inflation to assess the diastolic function of each ventricle, (ii) the influence of a varying chamber size in one ventricle on the end-diastolic pressure and peak-systolic pressure of the other to assess diastolic and systolic ventricular interdependence, (iii) complete P-V loops over one cardiac cycle to assess change in organ-level cardiac function.

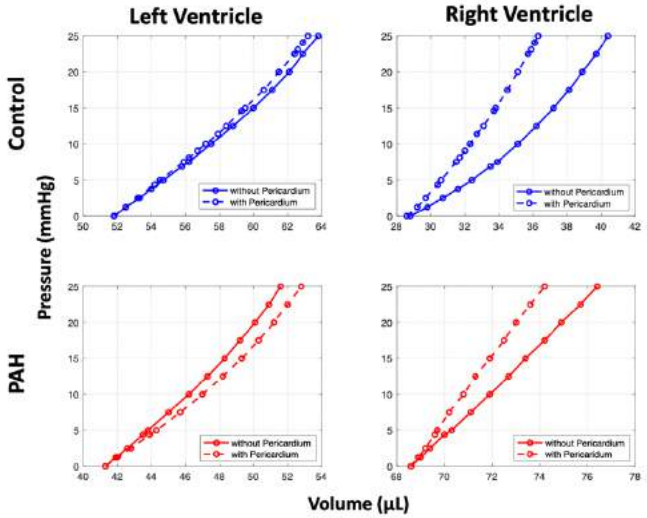

Figure 2: RV and LV end-diastolic pressure-volume relationship in control and PAH hearts with (dashed) and without (solid) pericardium.

RESULTS

We found that the addition of the pericardium does not have a significant impact on the stroke volume (SV) of the control RHM, while it decreased the SV of the RV in the hypertensive heart. Addition of the pericardium resulted in a slight decrease in the contractility of the RV necessary to maintain cardiac output in the normal heart, whereas a significant increase in contractility was noted in the PAH model (Fig. 3). This may be due to the overall decrease in RV diastolic filling that we observed in the comparison of RV diastolic filling with and without pericardium. In addition, we found a significant lack of biventricular interaction during systole in the PAH heart with pericardium.

DISCUSSION

Results for the normal heart were consistent with previous studies of the functions of the pericardium and effects of pericardiectomy [2]. Notable changes in the end-diastolic volume are present in the RV with the addition of the pericardium in both control and PAH hearts. The slight decrease in the contractility of the control RV with pericardium and a significant increase of contractility seen in the PAH RV suggest that the major role of the pericardium, which is to act as a mechanical constraint to pathological variations in heart size, has been chiefly compromised in the hypertensive heart [4]. Results show little change in the LV function in both models, implying the presence of the pericardium does not biventricular interaction in either diastole and systole.

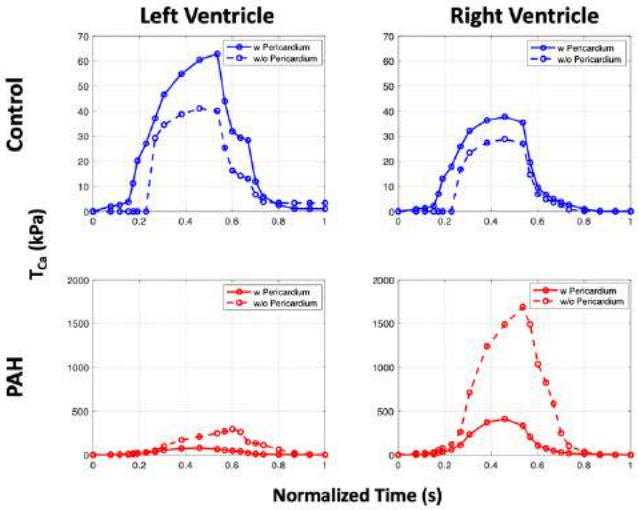

Figure 3: RV and LV contractility over the cardiac cycle of control and PAH hearts with (dashed) and without (solid) pericardium.

Further investigation in to the adaptation of the pericardium in hypertension are necessary to conclusively determine changes in the pericardium's adaptive function. The major assumption of this work was that the pericardium itself does not undergo remodeling due to PAH. Our investigation was limited by the lack of tissue experimentation examining fibrosis in the pericardium in response to PAH; future work will address these restrictions.

The presence of the pericardium is understood to impact cardiac output and ventricular interaction. Models such as those used in this study could inform the development of therapies for complex comorbidities in structural heart disease.

ACKNOWLEDGEMENTS

We would like to thank Dr. Richard A. F. Dixon and all at the Molecular Cardiology Research Lab at the Texas Heart Institute for their help implementing the animal model and collecting experimental data.

REFERENCES

[1] Lu, L. et al, *Am. J. Physiol. Heart Circ. Physiol.*, 281: H2661-K2679, 2001.
[2] Janicki, J. et al, *Physiology*, 238: H494-H503, 1980.
[3] Avazmohammadi, R. et al, *Ann. Biomedical Eng.*,47:138-153, 2018.
[4] Holt, J.P. *Am. J. Cardiol.,* 26: 455-465, 1970.

SB³C2019
Summer Biomechanics, Bioengineering and Biotransport Conference
June 25 -28, Seven Springs, PA, USA

ESTIMATING THE CONTRIBUTION OF THE ENDOVASCULAR CATHETER ON CEREBRAL HYPOPERFUSION DURING MECHANICAL THROMBECTOMY

Christina S. Ngo (1), Jeffrey D. Pyne (2), Jaiyoung Ryu (3), Shawn C. Shadden (2)

(1) Department of Bioengineering
University of California, Berkeley
Berkeley, CA, United States

(2) Department of Mechanical Engineering
University of California, Berkeley
Berkeley, CA, United States

(3) Department of Mechanical Engineering
Chung-Ang University
Seoul, South Korea

INTRODUCTION

With recent clinical evidence showing the immense benefit of endovascular treatment for acute ischemic stroke (AIS) with proper patient selection, a need has emerged to further optimize this procedure to minimize patient harm[1]. While the primary goal of the AIS endovascular catheter treatment is to reestablish bulk flow to the occluded artery, it is unknown whether the catheter introduces additional cerebral hypoperfusion during deployment. With sensitive cerebral tissue already in an ischemic state (also known as penumbra zones) due to inadequate oxygen and glucose levels to sustain neuronal survival, additional hypoperfusion, even for a small duration, could impact long-term brain tissue recovery in localized regions. The purpose of this computational study is to quantify endovascular catheter induced hypoperfusion across patient populations during middle cerebral artery (MCA) thrombus removal procedures.

A 1D-lumped parameter network (LPN) cerebrovascular model[2], designed with cerebral autoregulation, CO_2 reactivity, cerebral spinal fluid (CSF) generation/reabsorption, and intracranial pressure dynamics can be used to study the hypoperfusion effects of an endovascular device, specifically catheters used for thrombus retrieval, on arterial blood flow in the brain. The 1D portion of the model is built upon the cross-sectionally averaged Navier-Stokes equations coupled to elastic arteries. The LPN represents the intracranial vascular bed dynamics through an electrical circuit model design. Static vascular beds are characterized through constant resistors to influence blood flow distribution as well as CSF generation/reabsorption, venous resistance, and cortical collateral vessels. Cerebral active flow compensation such as autoregulation and CO_2 reactivity utilizes dynamic resistances that model physiological behavior based around myogenic vasodilation or vasoconstriction. Overall, the LPN represents the intracranial space, and is constrained by the fixed volume balance of the Monro-Kellie doctrine between blood flow, CSF, brain tissue compliance, and intracranial pressure. Ultimately, after a characteristic analysis and two-step Adams-Bashforth numerical solve, the cerebrovascular model outputs average arterial area, flow velocity, and pressure across the entire arterial network. The 1D-LPN model design facilitates aorta to cerebral circulation coverage, specializes in rapidly capturing flow rerouting and systemic flow dynamics, and can actively account for physiologic cerebral flow disruptions that deviate from baseline flow with autoregulation compensation. Additionally, the model has the ability to evaluate the hypoperfusion influence of both patient-specific and surgical parameters within an endovascular procedure, making it a reasonable model to study endovascular device hypoperfusion effects across a wide spectrum of parametric possibilities[3]. Understanding the influence of these parameters has implications for endovascular device design in ischemic stroke and works towards quantifying the potential undesired cognitive impact of endovascular device deployment.

METHODS

In order to study the effects of the catheter on blood flow within the cerebral network, the 1D-LPN model was first tuned to account for the change in arterial area where the catheter is present during surgery. The model areas were first tuned along specific vessels according to clinically-relevant catheter sizes (catheter diameter: 3mm, microcatheter diameter: 0.9mm)[4]. As shown in **Figure 1a**, for an occlusion in the right middle cerebral artery (RMCA), the catheter takes the path indicated by the blue line. The catheter pathways represent the typical endovascular routes neurointerventionalists take to reach the left or right middle cerebral arteries. To properly capture the flow effects of the endovascular device placement within the 1D vessel framework, an annular area-reduced vessel equivalent was calculated. Here, it is assumed that the catheter is positioned within the center of an artery to form an annular geometry producing a different flow effect from a general reduction of vessel area. For the equivalent area-reduction

calculation, **Eq. (1)**, target vessel radii were calculated by equating flow between the standard and annular section Poiseuille's Law.

$$R_{target} = \sqrt[4]{\left| R_{artery}^4 - R_{catheter}^4 - \frac{(R_{artery}^2 - R_{catheter}^2)^2}{\ln(R_{artery}/R_{catheter})} \right|} \quad (1)$$

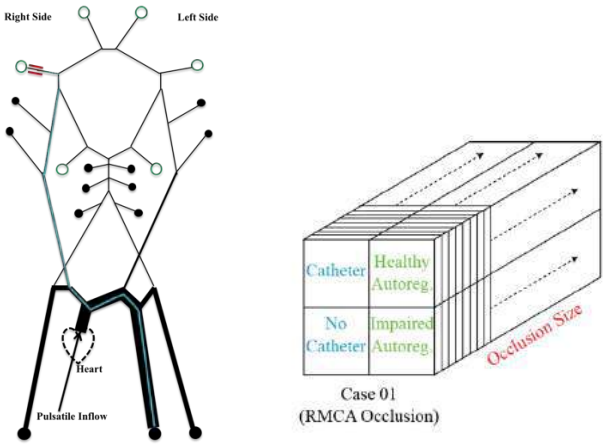

(a) (b)

Figure 1: a) Visual representation of endovascular device path (in blue) within the 1D portion of the cerebrovascular model[2]. b) Breakdown of the simulation scenarios for one endovascular pathway. Colors correspond to parameters varied in the study.

To provide unpressurized target areas to the cerebrovascular model, the percent difference between an artery's simulation area and its target area was used as a measure of tracking the artery's tuning progress. Along the way, visualization and data collection methods were implemented to track the progress of each artery through iterations, and a conditional gain system was created to make the updates between each iteration more robust.

Once the model was fully tuned to account for the presence of the catheter, parametric simulations were run. Specifically, 160 parametric simulations were run for each endovascular pathway, accounting for 40 different levels of MCA occlusion, endovascular catheter presence, and cerebral autoregulation ability (see **Figure 1b**). The 40 difference occlusion sizes ranged from 0 to ~100% (2.5% apart), with 0 representing a non-occluded artery and ~100% being the most extreme case. The catheter was treated as a binary parameter - it was either present or not present. Autoregulation was also treated as a binary parameter; either indicative of healthy young autoregulation or completely impaired global autoregulation ability. Looking at autoregulation ability as healthy (complete autoregulation ability) and completely impaired (no autoregulation ability) offers the best- and worst-case autoregulation abilities. From these simulations, flow values were extracted and averaged after steady-state (periodicity) was reached. These values were then compared against the flow value of the occlusion-free and catheter-free simulation case in order to determine the percent blood flow loss.

In an ischemic event, there is a reduction of blood flow in a localized area of the brain. By considering clinically determined flow thresholds for defining selective neuronal loss (between baseline and underperfused), penumbra (significantly underperfused and at-risk), and infarct (dead) tissue, rough approximations for tissue damage at particular occlusion sizes can be determined[5]. While these zones are highly dependent on ischemic duration, they provide context for the hypoperfusion degree needed for observable ischemic damage.

RESULTS

Overall, the presence of the catheter was found to decrease flow in the RMCA across all occlusion sizes and autoregulation abilities as shown by the difference in the dashed and solid lines in **Figure 2**. For occlusion sizes of approximately 45-75%, the catheter resulted in a significantly greater hypoperfusion effect than completely impaired autoregulation. However, for occlusions that were predicted to cause tissue to be in the upper penumbra region (75-90%), the flow effects of the catheter and autoregulation were comparable. Lastly, for occlusion sizes associated with infarct (≥90%), the loss of autoregulation had a more devastating effect than the presence of a catheter, but the greatest hypoperfusion effect here is due to the occlusion itself. In addition to looking at flow within the RMCA, flow values for the other major cerebral arteries were investigated. Within the occlusion hemisphere, the neighboring right posterior cerebral artery (RPCA) flow was unaltered and the right anterior cerebral artery (RACA) experienced increases (+6%) or decreases (-15%) in flow depending on autoregulation ability and presence of the catheter.

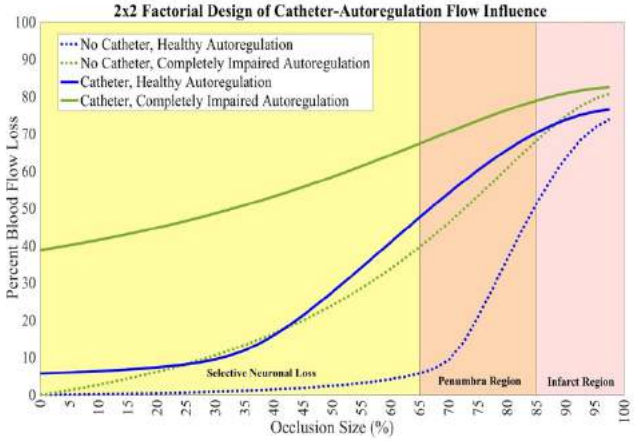

Figure 2: Comparing RMCA percent blood flow loss due to catheter presence and autoregulation ability across occlusion sizes.

DISCUSSION

The endovascular catheter considered does contribute to MCA vascular bed hypoperfusion by decreasing MCA baseline flow by an additional 6 - 42% depending on the degree of MCA occlusion and autoregulation ability. Additionally, for MCA occlusion size of 42 - 90%, blood flow decrease due to the endovascular catheter is stronger than the impact of completely impaired autoregulation ability. While this study provides evidence that endovascular devices do significantly impact vascular bed perfusion during MCA thrombus removal, the cognitive consequence is unknown. Future work will focus on incorporating variations in cerebral circle topology, cortical collateralization ability, and various catheter sizes into the parametric study. Additionally, the authors plan to consider the neurological cost of this flow decrease by approximating the relationship between hypoperfusion degree, hypoperfusion duration, and subsequent neurological injury.

ACKNOWLEDGEMENTS

The authors graciously acknowledge the Bakar Fellows Program for the funding of this research.

REFERENCES

[1] Albers, Gregory et al., *New England J of Medicine,* 378(8), 2018.
[2] Ryu, Jaiyoung et al., *J Biomech Eng*, 137(10), 2015.
[3] Pyne, JD et al., *Heart and Brain Symposium*, 2018.
[4] Stryker Neurovascular Interventions: Merci™, Trevo™ , 2014.
[5] Latchaw, RE et al., *Stroke,* 34(4), 2003.

SB³C2019
Summer Biomechanics, Bioengineering and Biotransport Conference
June 25 -28, Seven Springs, PA, USA

ALTERATION OF THE MECHANICAL RESPONSE OF PORCINE TRICUSPID VALVE ANTERIOR LEAFLETS FOLLOWING EXPOSURE TO DE-IONIZED WATER

Margaret M. Clark, Samuel D. Salinas, Rouzbeh Amini

Department of Biomedical Engineering
The University of Akron
Akron, OH, USA

INTRODUCTION

The biomechanical properties of the tricuspid valve (TV) leaflets have been quantified previously [1,2]. To minimize the effects of osmotic pressure on the mechanical responses of the tissues, in the abovementioned studies, isotonic phosphate buffer saline (PBS) were used for tissue storage and during the course of the experiments. While the effects of hypo- and hyper-osmolarity have not been particularly studied in cardiac valves, the mechanical response of other soft tissues has been shown to be sensitive to the osmotic pressure [3-5]. As such, our laboratory and many other investigators have used isotonic solutions whenever conducting experiments on cardiac valves.

In a recent published experiment, however, pulsatile flow of de-ionized (DI) water was used in ex-vivo hearts to stimulate cardiac valve motion [6]. Interestingly, the authors did not find any significant differences in the study outcomes using DI water. The objective of our study was to further examine the effects of DI water on the mechanical response of TV leaflets using a more controlled bench-top method, i.e. the biaxial mechanical testing approach. We *hypothesized* that the mechanical response of the porcine TV anterior leaflets obtained from biaxial tensile loading experiments will be different when the samples are immersed in DI water as compared to those immersed in PBS.

METHODS

Fresh porcine hearts were obtained from a local slaughterhouse and transported in chilled PBS solution. Upon arrival of the samples in our laboratory, the TV anterior leaflet was dissected (n=9). The average thickness of the leaflet was measured before it was trimmed to a custom 3D printed phantom [1]. While the sample was lined up in the anatomical radial and circumferential directions and placed in the custom phantom, suture lines were attached to the leaflet to be mounted on a biaxial loading machine according to previously established methods [1]. Four fiducial markers were glued on the leaflet in order for the biaxial testing machine to track the deformation of the tissue. For the control test, five loading protocols were conducted while the tissue is immersed in PBS. The five protocols were performed similar to our previous published work [1], with a maximum stress of 127 kPa which roughly represented right ventricular pressure of 30 mmHg. The loading machine software reported the forces applied to the tissue, from which the stresses were calculated according to the following equations

$$\sigma_{rr} = \frac{F_r}{A} \quad (1)$$

$$\sigma_{cc} = \frac{F_c}{A} \quad (2)$$

where σ_{rr} and σ_{cc} are the normal stresses in the radial and circumferential directions, respectively; F_r and F_c are the tensile forces exerted on the tissue in the radial and circumferential directions, respectively; and A is the cross-sectional area of the trimmed square-shape TV leaflet specimen. The specimen was then removed from the biaxial machine and placed in DI water for 2 hours. The leaflet was trimmed again to the custom phantom before biaxial loading protocols, in which DI water was used as the immersing solution. For this study only the equibiaxial stress-strain data were used and analyzed. However, data from the other four protocols were stored properly for future analysis. For the equibiaxial cases, strain values were calculated from the positional data of the fiducial markers using an internally-developed MATLAB script as described previously [1]. To determine the changes in the tissue samples following DI water exposure, the circumferential and radial strains of the control experiments at the 85 kPa equibiaxial stress were compared to their post-DI-exposure values using paired Student's t-tests ($p<0.05$ indicating significant difference).

Poster Presentation #P011

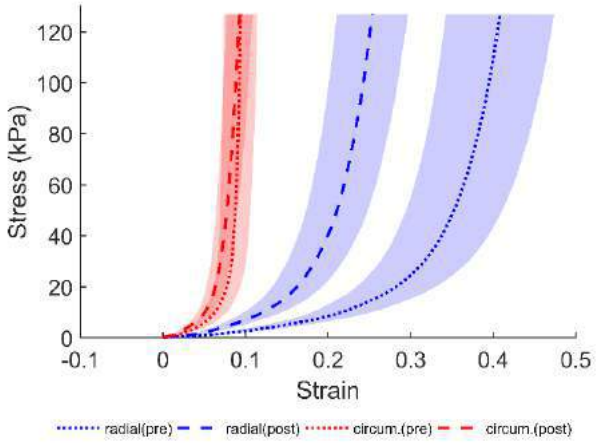

Figure 1: The average radial and circumferential mechanical responses for pre- and post-DI exposure of the TV anterior leaflet for the equibiaxial loading protocol. Shaded regions represent standard error (n=9).

RESULTS

Visual examination of the equibiaxial stress-strain data (Fig. 1) shows that the average tissue strain decreased following exposure to DI water in the radial direction. The leaflet strain in the circumferential direction, however, appeared to be only slightly different from pre- to post-DI water exposure (Fig. 1).

We further examined the strain values at 85 kPa equibiaxial stress, which is an estimation for the physiological right ventricular pressure value of 25 mmHg (previously approximated using the law of Laplace [1]). As shown in Fig. 2, we found a significant difference between the values of strains in the radial direction for the samples that only immersed in the PBS and those of the same samples after exposure to DI water. However, no significant difference was observed in pre- and post-DI exposure strains in the circumferential direction.

It is noteworthy that the immersion in the DI water resulted in the tissue physically expanding due to osmotic swelling. As such, the samples had to be trimmed to the controlled size before biaxial mounting as shown in the visual representation in Fig. 3.

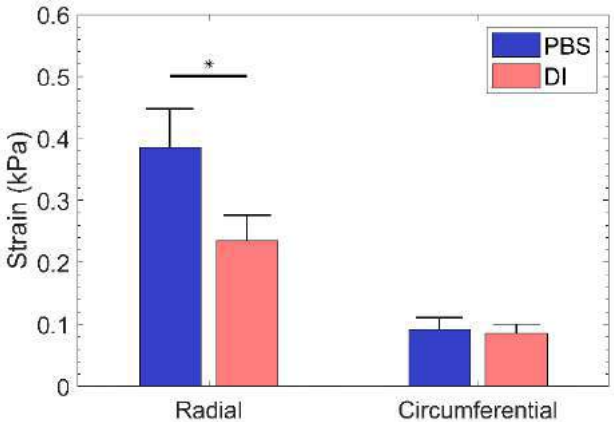

Figure 2: The comparison of the strain of the TV anterior leaflet immersed in PBS compared to that of the same samples after exposure to DI water at a stress level of 85 kPa. The error bars represent standard error (n=9). The asterisk represents significant difference.

Figure 3: Swelling of a representative anterior TV leaflet specimen following submersion in DI water. For comparison, the custom-made phantom used for trimming the sample is included. The upper left extension of the leaflet is used to reference the radial from the circumferential direction.

DISCUSSION

In this study we examined whether the DI water would be an acceptable alternative for storage and handling of heart valve tissues before and during biomechanical testing, as compared to commonly used isotonic PBS. Not only did we observe physical changes (i.e. expanding and thickening) in tissues due to swelling, we also found out that the mechanical response of the tissue significantly changed after exposure to DI water. In our strain examinations, we only observed significant changes in the radial direction. Nevertheless, due to the tensorial nature of the strain, any significant change in only one of the components of the strain tensor indicates a significant difference in the overall state of the deformation.

In their recent study [6], Pierce et al. measured the indentation response of the mitral valve annulus and its surrounding tissues in two sample groups: one submerged in DI water for three hours and one submerged in isotonic saline solution for the same amount of time. Unlike our observations, they did not find any significant difference between the two groups. One should be cautious in extending the conclusions of our multiaxial testing of heart valves to uniaxial indentation of the annular tissue. Nevertheless, we suspect that a small sample size, and consequently a large variability in the measured values of the indentation forces might have led to the conclusion of Pierce and colleagues.

In summary, consistent with our initial hypothesis, we found out that DI water immersion significantly impacted the biomechanical properties of the TV anterior leaflet. As such, isotonic solutions, such as PBS, are more suitable mediums for storage and handling of valvular tissues in experiments in which the biomechanical response of the leaflets plays an important role.

ACKNOWLEDGEMENTS

Funding was provided in part by a grant from the American Heart Association (Grant No. 16SDG27770088).

REFERENCES

[1] Khoiy, KA and Amini R., *J Biomech Eng*, 138(10):104504, 2016.
[2] Laurence, D et al., *J Biomech*, 83:16-27, 2019.
[3] Lanir, Y et al., *Amer J Physio-Heart and Circulatory Physio*, 270(5):H1736-43, 1996.
[4] Guo, X et al., *Amer J Physio-Heart and Circulatory Physio*, 293(4):H2328-34, 2007.
[5] Lanir, Y, *J Biomech*, 45(5):780-9, 2012.
[6] Pierce, EL et al., *Ann Biomed Eng*, 47(2):381-391, 2018.

SB³C2019
Summer Biomechanics, Bioengineering and Biotransport Conference
June 25 -28, Seven Springs, PA, USA

ON THE DISTRIBUTION OF AORTIC VALVE CUSP CALCIFICATION

Varshini Guhan, Megan Heitkemper, Dr. Lakshmi Dasi

(1) Department of Biomedical Engineering
The Ohio State University
Columbus, Ohio, United States

INTRODUCTION

Aortic valve stenosis is the buildup of calcification in the cusps of the aortic valve, which limits valve mobility and function. This disease has a high mortality rate in the elderly population and can become severe over the course of one year, thus taking the patient's life before an aortic valve replacement can be performed. In one study, aortic valve stenosis had a significantly low first-year survival rate, at only 60% [1]. The exact mechanism of calcification formation in a stenotic aortic valve is unknown and explanations for the disease have varied in the past few years [2]. It is important to understand the root cause of this condition to better treat aortic stenosis patients.

The Right Posterior Sinus (RNS) is the sinus in the aortic valve, which does not have a coronary artery stemming from it, thus interchangeably referred to as the non-coronary cusp. The other sinuses, the Left Posterior Sinus (LPS) and the Anterior Aortic Sinus (AAS), have the left and right coronary arteries stemming from the cusps respectively. These areas are also referred to as the left coronary region and right coronary region respectively. Towards the goal of better understanding and treating aortic stenosis, the objective of this study is to identify areas of high deposition of calcification, and which sinuses if any, have a higher tendency to collect calcium on its cusps. Thus, this research aims to explore the distribution of calcification volume present on the cusp of each region.

METHODS

The study population included 29 senior patients (> 64 yrs.) with average age of 80 years old at The Ohio State University Wexner Medical Center between January 2014 and September 2018. The pre-procedural patient specific aortic root, calcium nodules and cusps were segmented for each of the 29 patients from computed tomography (CT) images using Mimics Research 18.0 (Materialise, Belgium). The calcification nodules of each patient were then identified as attached to one cusp (LCC, RCC, or NCC) and the volume of calcium deposited on the cusps was determined. Each cusp was assigned a colour during the modeling process to help easily distinguish the calcification lesions visually (as shown in Figure 1). The mean and standard deviation of the calcification volume for each cusp was used to determine if there were any significant differences between two particular regions. A Mann-Whitney U-test was carried out to compare mean calcification volume between two different regions and identify significant differences between each pairing; p-values were calculated between the left- and right-coronary regions, the left- and non-coronary regions, and right- and non-coronary regions. The p-values identified how calcification buildup was distributed among the three leaflets (LCC, RCC, or NCC).

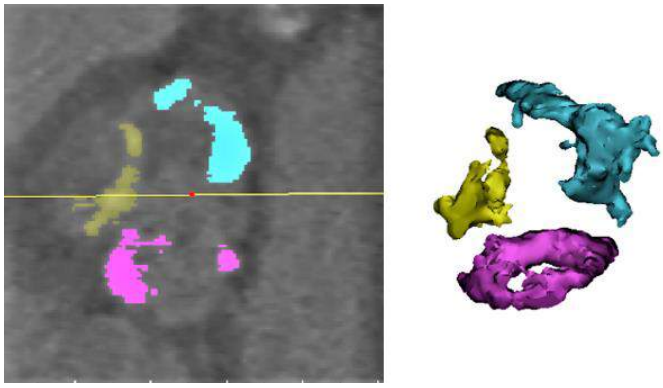

Figure 1: Constructed Calcification Geometries on Native Aortic Valve Cusps Using Mimics Research 18.0

RESULTS

The average volume of calcification was found to be significantly higher for the Right Posterior Sinus than the Left Posterior Sinus or the Anterior Aortic Sinus. As shown in Figure 2, the average of the calcification on the Left-Coronary Cusp is 29.10 cm^3 higher in amount than the calcification found on the Right-Coronary Cusp. The NCC had an average of 228.26 cm^3 of calcium, while the LCC and RCC had 107.95 and 137.05 cm^3 respectively (Figure 2). The calculated standard deviation of calcification on the NCC, LCC, and RCC is 184.39, 116.52, and 150.71 cm^3 respectively. The p-value analyzing the LCC and RCC data was 0.36393 (Figure 2), which is larger than the significance factor of 0.05, thus showing that there is no significant difference between the measurements taken in the LCC and in the RCC. Between the regions with the presence of a coronary artery (AAS and LPS) and the Right Posterior Sinus, the p-values were shown to 0.0183 for the LCC and NCC and 0.00233 for the RCC and NCC (Figure 2). Both p-values of 0.0183 and 0.00233 were under the significance factor of 0.05, which indicated that there was a significant difference between the calcification found in the left-/right- coronary regions and the non-coronary region. These results show that NCC collects a higher amount of calcifications than the RCC and LCC.

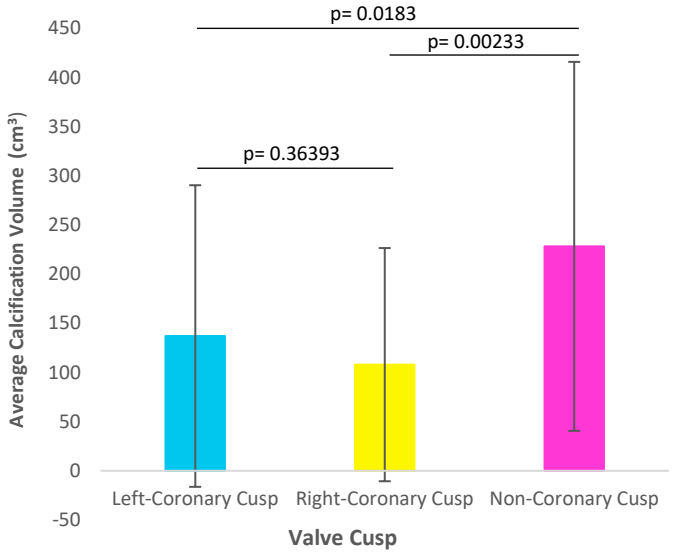

Figure 2: Average calcification volume on Left-Coronary Cusp, Right-Coronary Cusp, and Non-Coronary Cusp

DISCUSSION

The results show that the Non-Coronary Cusp has a significantly higher volume of calcification than the Left- and Right-Coronary Cusps. The results had high standard deviations and the standard deviation of the calcification volume on the NCC was higher than the other two standard deviations, as shown with the overlapping error bars in Figure 2. However, both the p-values for the difference in calcification between left- and non- coronary regions and right- and non-coronary regions were less than the significance level of 0.05, indicating that there is a significant distinction between calcification present in the left- and right-coronary regions and the non-coronary region. This follows the widely accepted notion that the non-coronary region has a more stagnant blood flow due to the absence of a coronary artery, which allows for a greater amount of unwanted calcification.

The experiment and process of data imaging clearly showed the tendency of calcium to deposit in the Right Posterior Sinus over the two sinuses (Anterior Aortic and Left Posterior) that gave rise to a coronary artery. There is more flow present in the sinuses which have an outlet through which the blood would move. An increase in flow rate leads to lower calcium deposition, since the constant motion of the blood does not allow the calcium to adhere to the cusps. Thus, we can consider the idea that the blood flows through the Anterior Aortic Sinus and the Left Posterior Sinus without depositing as much calcium on the cusps due to the presence of the coronary arteries emerging from these sinuses, as opposed to the higher amount of calcification build up in the right posterior sinus, which lacks a steady flow of blood through the sinus.

This data analysis focuses on the averages of the calcification in each region for the patient population as a whole, rather than focusing on the differences in calcification volumes between the non-coronary region and the left- and right-coronary regions for an individual patient. This allows for a better depiction of the scale in which the data was collected; the amount of calcification in each individual case varies significantly, so it is important to understand the size difference in relation to how much calcification was present. In the future we will calculate the calcific ratio between each of the three leaflets for individual patients, which could eliminate possible discrepancies between the average trend portraying the calcification on the NCC to be higher than the buildup on the LCC and RCC.

In the future, the images of the patients' aortic valves in the mid-systolic position could be used to collect observations and form patterns about the regions of the cusps in which calcium is deposited. This can be used in future research correlating the amount of calcification with the shape of the calcium formation in the aortic sinuses. These measurements can also be used to predict the risks of calcification and the way in which calcium deposits for future cases of aortic valve stenosis.

In sum, we have shown that the regions in which the cusps are located has a significant effect on the amount of calcification formation. This knowledge could be used towards further understanding and treating aortic stenosis.

ACKNOWLEDGEMENTS

The aortic valve geometries were constructed by both Amirsepehr Azimian and the author.

The research in this grant was supported by the DHLRI Tri-fit challenge.

REFERENCES

[1] Turina J., Hess O., Sepulcri F., Krayenbuehl H. P.; Spontaneous course of aortic valve disease, *European Heart Journal*, Volume 8, Issue 5, Pages 471–483, 1 May 1987

[2] Steinberg D. H., *Journal of the American College of Cardiology*, 73 (3) 315-316, Jan 2019

SB³C2019
Summer Biomechanics, Bioengineering and Biotransport Conference
June 25 -28, Seven Springs, PA, USA

AN INVESTIGATION OF LAYER-SPECIFIC TISSUE BIOMECHANICS OF PORCINE ATRIOVENTRICULAR VALVE ANTERIOR LEAFLETS

Cortland H. Johns (1), Katherine E. Kramer (1), Anju R. Babu (1), and Chung-Hao Lee (1)

(1) Biomechanics and Biomaterials Design Lab
School of Aerospace and Mechanical Engineering
The University of Oklahoma
Norman, OK, USA

INTRODUCTION

The atrioventricular heart valves are located between the atria and the ventricles and facilitate blood flow between the chambers. Valvular heart diseases are one typical example of cardiovascular lesions, such as valve regurgitation (blood backflow), stenosis (narrowed valves due to hardening of leaflets) and atresia (completely blocked blood flow). These conditions can be fatal and often require valve repair or replacement. Comprehension of these valvular diseases is reliant on thorough characterization of heart valve structures for use in computational models. Our lab has focused on computational modeling of heart valves, specifically the tricuspid valve, to simulate how various pathological scenarios typically associated with regurgitation affect the biomechanical function. A thorough materials characterization of valve leaflet tissue is crucial to facilitate a more precise model.

Previous models and studies of mechanical behavior of heart valves have only examined the stress distribution throughout the entire thickness of intact leaflets [1]. However, it has been shown the leaflets have four layers that contribute in different ways to the mechanics of the whole leaflet. Previous studies determined that different layers of aortic valve tissue possessed different mechanical behavior because of their distinct microstructure constituents [2]. The objective of this research is to determine if the atrioventricular heart valves possess similar layer-specific variance to the aortic valve. We will accomplish this by micro-dissecting atrioventricular valve leaflets and subjecting the tissue samples to various loading ratios. We ultimately aim to improve our computational model of heart valves to better patient-specific treatment methods and save lives.

METHODS

Tissue Preparation: Porcine hearts are dissected to obtain the mitral valve anterior leaflet (MVAL) and tricuspid valve anterior leaflet (TVAL). The leaflets are then placed in a freezer for 24 hours. A micro-dissection procedure is then used to dissect the MVAL into the atrialis/spongiosa, fibrosa, and ventricularis layers and the TVAL into the atrialis/spongiosa and fibrosa/ventricular layers. These combinations result from the spongiosa and ventricularis layers being too thin to separate from the other leaflet layers. In brief, the tissue (MVAL or TVAL) is first placed on a wax plate, with the ventricularis facing upwards, and stretched to its full size using surgical pins. Then, a scalpel is used to make a small incision separating the atrialis/spongiosa (A/S) layers from the remaining tissue. Thin-pointed tweezers are then used to peel the A/S layer away from the tissue with an ophthalmic scissor also used to sever any significant connections between the two layers (**Fig. 1**). The MVAL tissues are then flipped over with the ventricularis side facing upwards to also remove the ventricularis layer. Then, samples are labeled and briefly stored in phosphate-buffered saline before mechanical characterization.

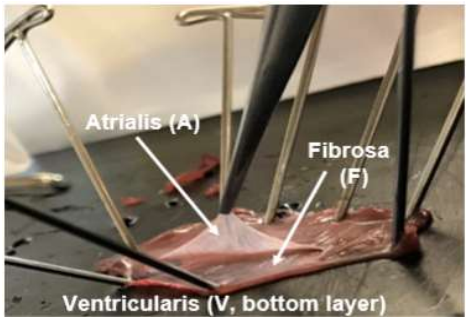

Figure 1: Microdissection of the Atrialis/Spongiosa and Fibrosa/Ventricularis layers of tissue

Biaxial Mechanical Characterization: The tissue sample is then removed from the container, the thickness is measured three times, and then it is mounted to the biaxial testing machine (Cellscale Biomaterials Testing,). A surgical pen is then used to create a four-node fiducial marker array for subsequent image-based strain calculations. Finally, the tissue undergoes various loading ratios (**Fig. 2**) for mechanical characterization.

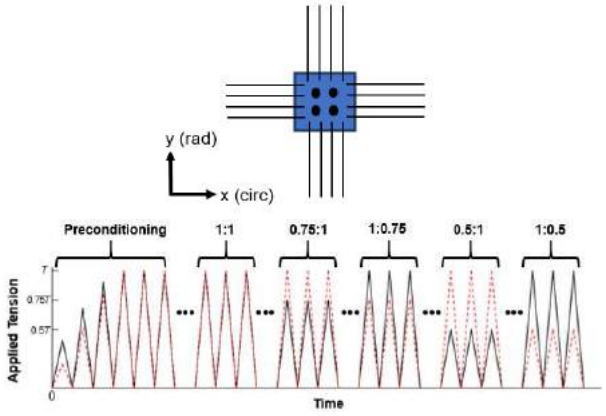

Figure 2: (top) a mounted tissue sample with markers applied, (bottom) a sample of the set of force protocols for layer specific tests

RESULTS

Results for the peak total tissue stretches of the two TVAL layers and three MVAL layers are presented in **Fig. 3**. Due to increased peak total tissue stretches of the atrialis/spongiosa layer compared to other layers in both the TVAL and MVAL, this study suggests that the atrialis/spongiosa layer is this most extensible layer of tissue in both mitral and tricuspid valve tissue. According to previous studies of mechanical behavior of tricuspid valves, the intact TVAL exhibits fewer peak total tissue stretches than the atrialis/spongiosa, but greater peak total tissue stretches than the fibrosa/ventricularis layer [1].

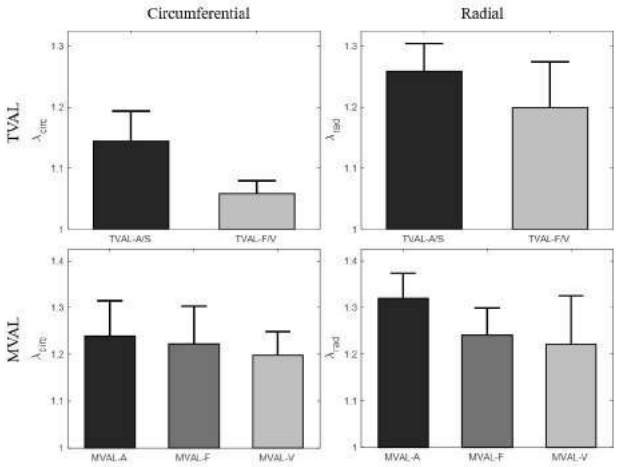

Figure 3: Circumferential and radial peak total tissue stretches in the layers of the TVAL and MVAL

Results for stress versus stretch of the two TVAL layers and three MVAL layers are presented in **Fig. 4**. The atrialis/spongiosa layer exhibited greater anisotropic behavior in both the TVAL and MVAL compared to other layers. While the atrialis/spongiosa layer exhibits a great deal of anisotropy, the mechanical behavior of the other layers of both TVAL and MVAL tissue appear to be nearly isotropic.

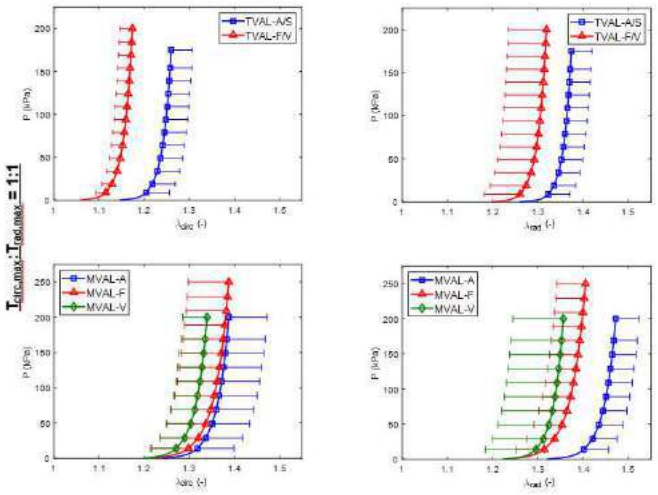

Figure 4: Circumferential and radial stress versus stretch curves for the layers of the TVAL and MVAL under 1:1 force loading

DISCUSSION

This study is the first of its kind to quantify the mechanical response of the different layers of the atrioventricular heart valves. With other studies having supported the anisotropic nature of intact heart valve leaflets, the results of this study indicate that the atrialis/fibrosa layer of tissue contributes significantly to the anisotropy of heart valve tissue [1]. However, considering that the intact TVAL was more compliant than the fibrosa/ventricularis layer and stiffer than the atrialis/spongiosa layer, it is evident that all three tissue layers influence the valve's mechanical behavior.

According to histology performed on our tissue samples, the atrialis/spongiosa layer of the TVAL was made up of similar portions of collagen and elastin (45% and 43%, respectively.) Additionally, the atrialis/spongiosa and ventricularis layers in the MVAL were made up of over 50% elastin. In order to understand how these microstructural components contributed to the differing mechanical behavior of the layers of valvular tissue, a study should be performed on tissues with elastin and collagen removed.

Altogether, the mechanical data obtained in this study can be used to improve existing computational models of heart valves. This will contribute to better treatment options, thus improving prognoses, increasing patient quality of life, and ultimately saving lives.

ACKNOWLEDGEMENTS

This work was supported by the American Heart Association (16SDG27760143), IBEST Seed Funding, and the OU Vice President for Research Faculty Investment Program, and the Undergraduate Research Office's Mentored Research Fellowship. We'd also like to thank all of the BBDL lab members who were not mentioned for their constant support.

REFERENCES

[1] Jett, S., et. al., *JMBBM*, 87:155-171, 2018.

[2] Sacks, M., and Yoganathan, A., *Phil. Trans. R. Soc. B*, 362:1369-1391, 2007.

SB³C2019
Summer Biomechanics, Bioengineering and Biotransport Conference
June 25 -28, Seven Springs, PA, USA

A STUDY OF PRESSURE DYNAMICS ACROSS A STENOTIC ORIFICE

Tori Burton (1), Hoda Hatoum (1), and Lakshmi Prasad Dasi (1)

(1) Department of Biomedical Engineering
The Ohio State University
Columbus, Ohio, USA

INTRODUCTION

Aortic stenosis (AS) affects approximately 2% of people over the age of 65 and is classified as the narrowing of the aortic valve often caused by calcium buildup on the leaflets of the valve[1]. This stenosis causes a substantial pressure drop across the aortic valve which means the heart has to work harder to pump blood to the entire body. The two common methods of characterizing the severity of AS are echocardiography or cardiac catheterization[2]. Catheterization gives direct pressure measurements but is a highly invasive procedure, so echocardiography is the clinically accepted approach. Unlike catheterization, an echocardiogram is only able to quantify the pressure gradient across the valve indirectly using the simplified Bernoulli equation and is not able to capture the recovery of pressure that occurs downstream in the aorta. Accurate assessment of the workload is crucial towards better timing of intervention and management of patients with AS[2]. Most recent efforts to develop better models still utilize the Bernoulli's principle[2-4]. In Bernouilli's equation, velocity and pressure are related in terms of kinetic and potential energy, respectively. So as fluid velocity increases at the stenosis as a result of a narrowed cross-sectional area, static pressure decreases. As the velocity decreases again, the reverse is true, and pressure is restored. The pressure of the fluid will theoretically recover as the diameter of the conduit increases distally to the vena contracta; however, energy loss due to friction makes it impossible to fully recover. It is therefore important to examine the limitations of Bernoulli's principle as it pertains to unsteady effects, as well as frictional effects before sophisticated models may be developed. The objective of this study is to assess the spatio-temporal variations of static pressure along a streamline through a stenotic orifice under physiological aortic conditions.

METHODS

The hemodynamics were assessed across an orifice chamber of area 0.6cm^2 placed upstream and in series with a 21mm Medtronic Hancock II surgical aortic valve (SAV) in the aortic position of a left heart simulator flow loop. The working fluid used in the experiment was a mixture of water and glycerin with viscosity and density similar to those of blood. A Millar catheter was inserted axially into the orifice chamber in order to take pressure measurements at various longitudinal distances from the insertion point. The flow loop was run continuously under physiological pressure and flow conditions (cardiac output = 5 L/min; heart rate = 60 beats per minutes; systolic to diastolic pressures = 120/80 mmHg) while data were recorded for 50 cycles per measurement location. Measurements were taken every 0.5 cm, starting at 14cm and moving back to 0cm. Distances of 0-3cm represent the measurement points upstream of the orifice and 3.5-14cm lie downstream, as shown in Figure 1 below.

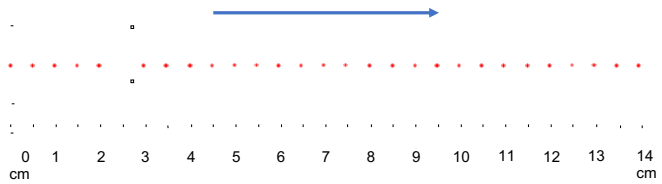

Figure 1: Schematic side view of orifice chamber; red dots represent points of measurement; blue arrow represents direction of flow.

RESULTS

Figure 2 shows pressure versus time for three different positions: before the stenotic orifice, immediately after, and about 10cm downstream. Both systole and diastole are included in order to observe the entire cardiac cycle. The pressure upstream of the orifice at position

1cm is exceptionally higher than both 5cm and 13cm and remains higher for the duration of systole; however, all points in the chamber experience similar pressure changes during diastole.

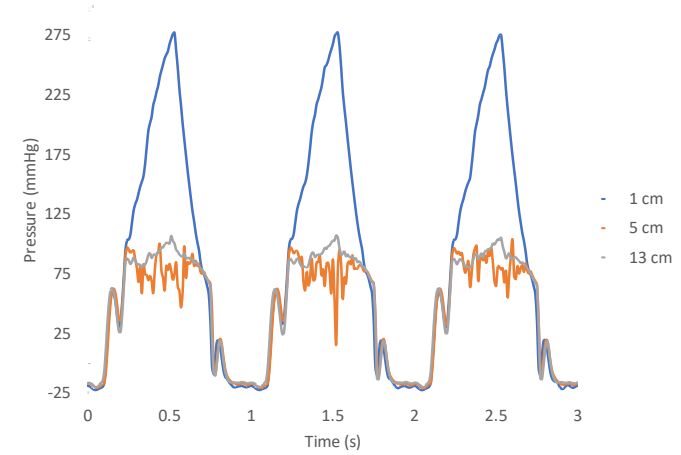

Figure 2: Variation of pressure with time over 1 full cardiac cycle.

Pressure versus longitudinal position is depicted in Figure 3. The times shown are every 0.05 seconds for the duration of systolic flow in order to isolate positive flow conditions. Static pressure is high before the orifice (located at 3.0cm) and drops immediately after. Pressure is then recovered slightly, but never reaches its initial value. The data shown in Figure 3 is a comparison of pressure and position using an ensemble average of individual pressure values per point in time.

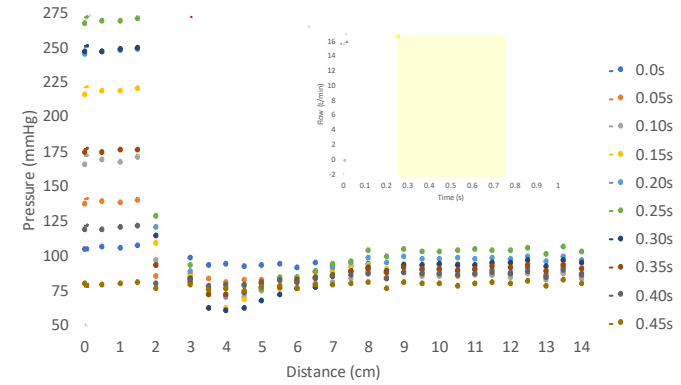

Figure 3: Variation of pressure with distance from stenotic orifice; red dashed line denotes the mid-orifice location; yellow contour in the inset figure highlights area of data (systolic flow).

DISCUSSION

Figure 3 reveals a fair amount of information regarding pressure based on distance from a stenotic orifice. At the start of systole (0 seconds), the pressure measurements are relatively low and remain low throughout the duration of systolic flow. This can be attributed to the fact that the velocity has only begun to increase following diastolic flow. At the very end of systole (0.45 seconds), pressure is even lower than at the onset of systole and follows an almost completely linear curve with little to no changes in pressure throughout the length of the chamber. In contrast, the intermediate times (0.15-0.30 seconds) possess a disparate curve with an extremely high initial pressure (>200 mmHg) that drops below 75 mmHg immediately distal to the stenotic orifice and finally slightly recovers to less than half its initial pressure (~100 mmHg). These results are reasonable based on the understanding of the direct relationship between velocity and orifice area which causes the fluid velocity to increase significantly at the orifice. Again, Bernoulli's equation explains the relationship between velocity and pressure— as velocity increases, static pressure decreases. The pressure recovery that occurs downstream from the stenotic orifice is the result of velocity slowing as the area of the conduit is increased and it does not continue to recover fully to the initial pressure because the velocity plateaus approximately 5cm after the valve; consequently, the static pressure reaches its maximum recovery value. Focusing only on these intermediate time points, the vena contracta is an important piece of data to analyze and there are very slight discrepancies between its location based on the data; however, the majority of the intermediate time point curves place the vena contracta at ~4 cm.

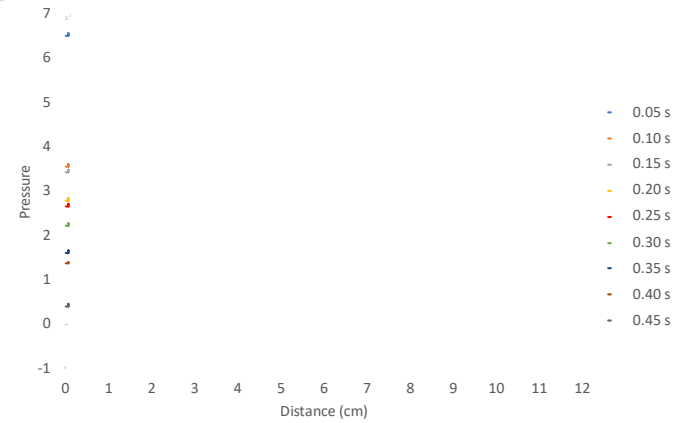

Figure 4: Normalized Pressure vs Distance Curves

Figure 2 is a depiction of 3 full cardiac cycles at 1, 5, and 13 cm. During systole, the pressure at a point just before the orifice (1cm) increases significantly. The pressure at a point further downstream from the orifice (13cm) stays relatively low, increases a tiny bit, and decreases once again. In contrast significant turbulent fluctuations may be observed at 5cm position. In order to verify the validity of the Bernoulli's principle, the normalized pressure drop was plotted (Figure 4). Figure 4 reveals several important points when normalized with respect to the velocity at the orifice (V_o) and pipe (V_p). Firstly, the pressure at the orifice is significantly different from that predicted from Bernoulli and this may be attributed to the flow acceleration in time as well as non-insignificant energy losses. Further pressure never recovers to a normalized pressure difference less than 1.0 except at the end of systole. This may indicate that even simplified Bernoulli may be severely under-predicting the true pressure drop across the orifice. The implications of these findings need to be further explored in a stenotic aortic valve model. Further studies are necessary to develop new empirical models that can capture the true severity of workload without being limited to the evident limitations of the Bernoulli equation when applied even to an idealized orifice.

ACKNOWLEDGEMENTS

The research reported was supported by National Institutes of Health (NIH) under Award Number R01HL119824.

REFERENCES

[1] Czarny M.J. et al. Clin Med Insights Cardiol. 2014; 8(Suppl 1): 15–24

[2] Otto C.M. Journal of the American College of Cardiology, 2006. 47(11): p. 2141-2151

[3] Garcia D. et al. Journal of biomechanics, 2005. 38(6): p. 1303-1311.

[4] Garcia D. et al. Journal of biomechanics, 2006. 39(16): p. 3036-3044

SB³C2019
Summer Biomechanics, Bioengineering and Biotransport Conference
June 25 -28, Seven Springs, PA, USA

A STUDY OF THE EFFECTS OF AN INCREASED BEAT RATE ON THE PENN STATE PEDIATRIC VENTRICULAR ASSIST DEVICE

Brady L. Houtz (1), Sailahari V. Ponnaluri (1), Maureen B. Gallagher (1), Charlee Dawson (1), Bryan C. Good (1), Steven Deutsch (1), Keefe B. Manning (1,2)

(1) Department of Biomedical Engineering
Pennsylvania State University
University Park, PA, USA

(2) Department of Surgery
Penn State Hershey Medical Center
Hershey, PA, USA

INTRODUCTION

Congenital heart disease is the leading cause of infant death annually, with nearly 40,000 cases in the United States alone [1]. A heart transplantation is often the only treatment option for these patients, despite the high average organ transplant waiting list mortality rate of 13% [2]. Ventricular assist devices (VADs) have proven to be effective in treating heart failure in adult patients. The growing success of VADs lead to the design of pediatric ventricular assist devices (PVADs) which were adapted for the smaller anatomical features of pediatric patients. Therefore, the Penn State 12cc pneumatic, pulsatile PVAD (Figure 1) was developed. This device can be used as bridge-to-transplantation by reducing the mechanical load experienced by the heart while increasing the cardiac output.

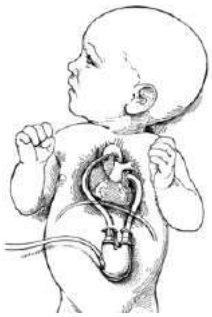

Figure 1: Schematic for the implantation of the Penn State PVAD in an infant [3]

One of the major issues surrounding cardiac assist devices is the development of thrombosis. Flow visualization techniques can be used to assess the risk of clotting in certain regions of low flow or shear. Prior *in vitro* studies of the Penn State PVAD have examined hemodynamic parameters with a beat rate of 75 bpm [4], however, infant heart rates typically range from 100 to 180 bpm [5]. This study aims to examine the effects of an elevated beat rate on the Penn State PVAD by quantifying the fluid dynamics using particle image velocimetry (PIV).

METHODS

An acrylic model of the Penn State PVAD was used in order to provide an optically clear surface for visualization. This model was placed in a mock circulatory flow loop (Figure 2) consisting of compliance and resistance components to obtain physiologically relevant conditions.

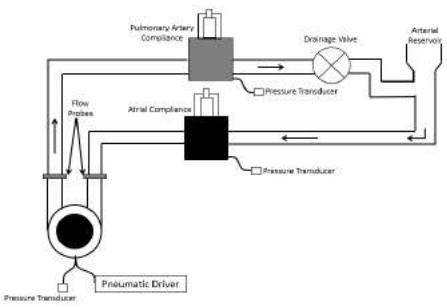

Figure 2: Mock circulatory loop for PVAD [6]

Poster Presentation #P015

A 40% hematocrit, non-Newtonian blood analog was created to mimic the viscoelastic behavior of blood by matching the nonlinear kinematic viscosity and elasticity. The flow and pressure waveforms for the 75 bpm and 125 bpm were matched to mimic flow in a healthy infant. To ensure complete ejection and filling, the systolic duration was set to 43% for the 75bpm case and 47.5% for the 125bpm case. The outlet pressure in the vessel corresponds to an aortic pressure of 90/60 mmHg. For both cases, the flow rate was set to 1.0 L/min.

PIV was used at three different planes (7, 8.2, and 11 mm) within the PVAD (Figure 3). The 0 mm reference plane started at the furthest edge of the inlet valve. Data were collected for 16 time points, including the complete systole and diastole of the PVAD.

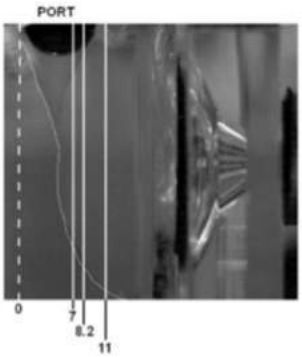

Figure 3: Parallel planes used for flow analysis [4]

RESULTS

In both cases, the cycle begins with a strong inlet jet which transitions into a solid body rotational flow (Figure 4A). Two jets can be observed, one for the major orifice and one for the minor orifice of the tilting disk valve. The velocity of the major and minor inlet jets, during the 125 bpm case, was higher than the jets at the 75 bpm case. The 125 bpm case has a maximum velocity of 1 m/s, whereas the 75bpm case only reaches 0.7 m/s.

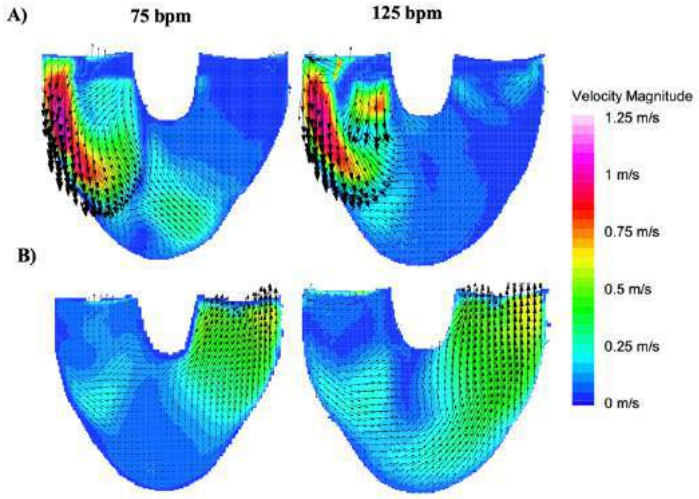

Figure 4: Comparison between the 75 and 125 bpm conditions during A) pump filling (33% diastole) and B) ejection (71% systole)

The strong inlet jet creates recirculation within the device. This recirculation is stronger at the higher beat rate and lasts for an extra 20% of diastole. As the pressure within the sac increases, the recirculation region transitions towards the outlet valve and an outlet jet forms (Figure 4B). The outlet jet for the 75 bpm case is slightly stronger than the 125 bpm case.

DISCUSSION

At a higher beat rate, there was an overall increase in the strength of the inlet jet. This resulted in a stronger recirculation region that lasted for a longer percentage of diastole. The strong recirculation reduces stagnation and washes the walls of the device to prevent clotting. By increasing the beat rate, the flow within the device creates more favorable conditions for reducing clotting.

These results are consistent with previous studies showing that an elevated beat rate reduces the risk of thrombosis in the Penn State PVAD. The data support the claim that the device could be used as a bridge-to-transplant in pediatric patients, as it has favorable conditions under varying, pediatric heart rate, flow rate and pressures.

CONCLUSION

The comparison of flow within the Penn State 12cc PVAD at a higher beat rate can help to predict how the device will behave under normal conditions, considering pediatric heart rates typically range from 100 to 180 bpm. The stronger inlet jet and recirculation region suggests that the PVAD is less susceptible to clotting when operated under normal pediatric conditions. Future studies could examine the effects of increased beat rate on flow with the PVAD, confirming some of the flow observed in this study.

ACKNOWLEDGEMENTS

This study was supported by NHLBI HL108123 and NSF EEC-1560064.

REFERENCES

[1] Hoffman, J.I. *Journal of the American College of Cardiology*. 39(12): 1890-1900. 2002.
[2] Jayaprasad, N. *Heart Views,17*(3), 92. 2016
[3] Baldwin, J.T. *Circulation*, 3(10): 153. 2006.
[4] Roszelle, B. N. *Annals of Biomedical Engineering*. 38(2): 439-455.
[5] Vorvick, L.J. *Medline Plus*. 2017.
[6] Manning, K. B. *et al. Artificial Organs,* 32(6): 442-452. 2008.

SB³C2019
Summer Biomechanics, Bioengineering and Biotransport Conference
June 25 -28, Seven Springs, PA, USA

HEMODYNAMICS OF CORONARY ARTERIAL ANEURYSMS IN KAWASAKI DISEASE — AN IDEALIZED ANEURYSM MODEL

A. Lu (1), N. Grande Gutierrez (2), A. Marsden (1,2,3)

(1) Department of Bioengineering
Stanford University
Stanford, CA, USA

(2) Department of Mechanical Engineering
Stanford University
Stanford, CA, USA

(3) Department of Pediatric Cardiology
Stanford University
Stanford, CA, USA

INTRODUCTION

Kawasaki disease (KD), a vasculitis of unknown etiology typically occurring in infants and young children, is the leading cause of acquired heart disease in childhood in developed countries. Approximately 20-25% of patients may eventually develop coronary artery aneurysms (CAAs) if not treated within ten days of disease onset. Unlike cerebral or abdominal aorta aneurysms, which pose a risk of rupture, CAAs are threatening in their potential for inducing thrombus formation, resulting in myocardial infarction and sudden death [1].

Current American Heart Association (AHA) guidelines for risk stratification rely on aneurysm size alone as the criterion for initiating systemic anticoagulation; however, studies suggest risk may also depend on hemodynamic parameters such as time averaged wall shear stress (TAWSS), residence time (RT), and oscillatory shear index (OSI), which are not available through image data alone [2,3]. Indeed, CAAs' complex geometries, as well as aneurysm shape, number, and location, may all contribute to abnormal hemodynamics and correlate with patient outcome.

Patient-specific hemodynamic simulations can non-invasively supply informative hemodynamic parameters for better thrombotic risk assessment; however, existing studies have been limited in patient cohort size and struggle to quantify effects of aneurysm shape on local hemodynamics. With such limitations in mind, existing patient-specific models can be augmented by introducing artificial aneurysms of specified length and diameter, to achieve a systematic evaluation of relationship between CAA shape, size, and position on local hemodynamics. Ultimately, elucidating the relationship between hemodynamics and aneurysmal shape characteristics may underlie more powerful risk stratification methods to support clinical decision-making regarding initiation of anticoagulation therapy.

METHODS

Idealized Aneurysm Models

Existing AHA aneurysm classification for small, medium, and giant CAAs serves as a guide to proceed from body surface area-normalized Z-score to an estimated maximal diameter for a given coronary vessel [4]. Using aneurysmal shape index (ASI), defined as the ratio of aneurysmal length to maximal lumen diameter,

$$ASI = \frac{L}{d_{max}} \quad (1)$$

we produce a set of aneurysms according to a range of lengths and diameters. Beginning with an existing patient-specific model of the aorta and coronary vasculature, we prescribe length and diameter to guide smooth, radially symmetric deformations to generate idealized artificial aneurysms at specific positions (examples in **Figure 1b**). This aneurysm generation pipeline and simulation post-processing rely on functionality from the Visualization Toolkit Package (VTK) package.

Computational Hemodynamics

Each new generated aneurysm model is processed in Simvascular [5], an open source software enabling patient-specific cardiovascular simulation. Using Tetgen [6], an open source package for mesh generation included in Simvascular, we generate a tetrahedral finite element mesh. The Simvascular solver then computes a numerical solution to the time-dependent Navier-Stokes equations governing blood flow. Blood is modeled as an incompressible Newtonian fluid (density=1.06 g/cc, dynamic viscosity=0.04 dynes/cm^2) and walls are assumed to be rigid in all cases.

Systolic myocardial contraction increases intra-myocardial pressure, transiently increasing distal coronary resistance substantially and causing coronary flow to be out of phase with systemic flow. Specialized boundary conditions coupling intra-myocardial pressure to coronary flow are required to replicate this complex physiology in the

Poster Presentation #P016

numerical model. We achieve this with a closed-loop, Lumped Parameter Network (LPN) modeling the heart and distal vasculature, which imposes boundary conditions with tunable parameters to produce physiologically accurate cardiac output, heart rate, blood pressure, and flow distributions. For idealized models described in this work, LPN parameters are kept constant to better isolate the effects of aneurysmal geometry on hemodynamics. **Figure 1** shows the full pipeline, proceeding from baseline model to artificial aneurysms and simulation results over isolated aneurysm regions.

RESULTS

Idealized aneurysms of 3 representative shape index values (ASI = 2, 4, 6) were generated for 5 diameters (z-score = 6, 8, 10, 12, 14) at positions along the right coronary artery (RCA) and left anterior descending (LAD). Hemodynamic simulation results were isolated over aneurysmal regions to identify the effects of shape, size, and position on local hemodynamic conditions. Idealized aneurysm models show consistent variation in distribution of hemodynamic parameters as Z-score increases, as seen in **Figure 1c**. TAWSS distribution varies consistently with ASI while holding Z-score constant. As in **Figure 2**, percentage of area exposed to low TAWSS increases with ASI at all Z-scones. Similar trends are observed in aneurysm cases in the LAD.

DISCUSSION

It has been shown that TAWSS over aneurysmal regions is associated with risk of thrombosis, and that a decision boundary based on percentage of aneurysm surface area exposed to low TAWSS is more predictive of thrombosis than aneurysm diameter for KD patients [7]. Thus, we assess the distribution of TAWSS over the surface as one potential surrogate for hemodynamic behaviors that may underlie thrombosis. Results exemplified by **Figure 2** show that aneurysm diameter alone may not be sufficient to predict local hemodynamic variables such as TAWSS. We observe that aneurysms similar in diameter but with different aspect ratios can furnish substantially different hemodynamic environments. In some cases, smaller diameter aneurysms with higher ASI (fusiform shape) even produce lower TAWSS values than more saccular aneurysms with larger maximum diameter. We show that a combination of aneurysm shape and length, in addition to other potential factors such as vessel curvature and aneurysm position, may contribute to local hemodynamic behaviors. Correlation between aneurysm hemodynamic and geometric features suggests potential to link clinical measurements easily obtained from echocardiography or other routine imaging modality, with patient outcome. Such approaches may form the basis for more sophisticated geometry-based risk stratification methods supporting clinical decision-making in assessment of KD patients.

ACKNOWLEDGEMENTS

I am deeply thankful for Professor Marsden. Her supervision and support have allowed me to grow and explore my passion. I am also thankful for my mentor, Marsden lab graduate student Noelia Grande Gutiérrez, for her guidance and mentorship, which have allowed me to develop this independent work. This work used software from SimVascular open source project (www.simvascular.org)

REFERENCES

[1] Kato H, et al. *Circulation*. 1996;94:1379-1385. [2] Ohkubo T, et al. *Pediatr Int*. 2007:49:1-7. [3] Sengupta D, et al. *Biomech Model Mechanobiol*. 2014;13:1261-1276. [4] McCrindle BW, et al. *Circulation*. 2017;135:e927-e99 [5] Updegrove A, et al. *Ann. Biomed. Eng.*, 45 (2017), pp. 525-541 [6] H. Si. *Math. Softw.*, 41 (11) (2015) [7] Grande Gutierrez N, et al. *International Journal of Cardiology,* 2019.

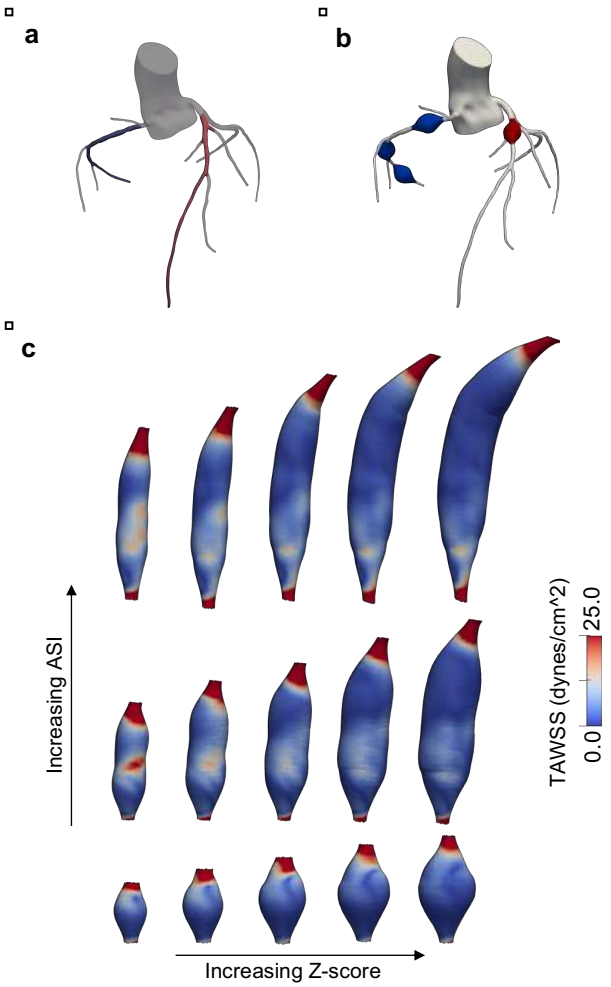

Figure 1: *a,* Baseline model of aorta, coronary vasculature with RCA and LAD highlighted. *b,* Idealized aneurysms in the RCA and LAD with ASI = 2, overlaid. *c,* Isolated results from proximal RCA. Z-score = 6, 8, 10, 12, 14 with ASI=2, 6, 8

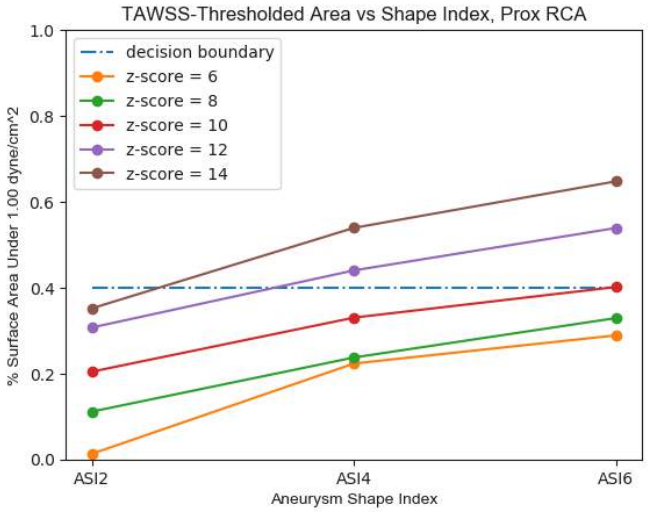

Figure 2: Fractional aneurysm surface area exposed to less than 1.00 dynes per sq. cm. of TAWSS as a function of ASI, grouped by aneurysm z-score.

SB³C2019
Summer Biomechanics, Bioengineering and Biotransport Conference
June 25 -28, Seven Springs, PA, USA

FLUID DYNAMICS STUDY OF AN IMPLANTABLE BLOOD PUMP FOR PATIENTS WITH A FAILED FONTAN CIRCULATION

Cody J. Kubicki (1), Bryan C. Good (1), William J. Weiss (1,2), Keefe B. Manning (1,2)

(1) Department of Biomedical Engineering
The Pennsylvania State University
University Park, PA, USA

(2) Department of Surgery
Penn State Hershey Medical Center
Hershey, PA, USA

INTRODUCTION

Approximately 1 out of every 10,000 children are born with a single ventricle congenital heart disease [1]. The Fontan operation palliates the effects of this disease and allows these children to live long into adulthood. The operation allows systemic venous blood to bypass the non-functional right ventricle and provide blood directly to the pulmonary circulation. With new preoperative methods and procedure improvements, the survival rates for Fontan patients has increased to over 85% at 20 years post-operation [2]. This means there is an increasing patient population entering adulthood and beginning to experience a pathology known as Failing Fontan. This chronic disease can be divided into three categories of symptoms: (1) ventricular dysfunction, (2) systemic complications of Fontan physiology, and (3) chronic Fontan failure [3]. All three decrease the quality of life for the many patients suffering from this disease.

The goal of this project is to investigate the fluid dynamics in an implantable blood pump that will provide mechanical support for patients with failed Fontan circulation. The flow will be quantified using particle image velocimetry (PIV).

METHODS

To study the fluid dynamics within the pump a flow loop was constructed to obtain pressure head versus total flow rate (HQ) curves and to image specific flow regions under steady flow conditions. The loop consisted of a single inlet, single outlet reservoir and tubing that connects the reservoir to the two inlets and single outlet of the acrylic Fontan Pump model (shown in Figure 1). Pressure transducers (Merit Medical, Jordan, UT) were inserted near each of the inlets and at the outlet to monitor pressure within the system and calculate the pressure drop across the pump. An external flow probe (Transonic Medical, Ithaca, NY) was used to determine total flow rate through the system and through each inlet. A 60-40 flow split was maintained between the inlets representing the inferior vena cava (IVC) and superior vena cava (SVC), respectively, by varying resistance on the SVC tubing. This flow split mimics the physiological conditions the pump would experience after implantation. A Newtonian blood analog composed of water, glycerin, and sodium iodide replicated the viscosity of 40% hematocrit blood and the refractive index of acrylic, producing a kinematic viscosity of 3.57 cSt.

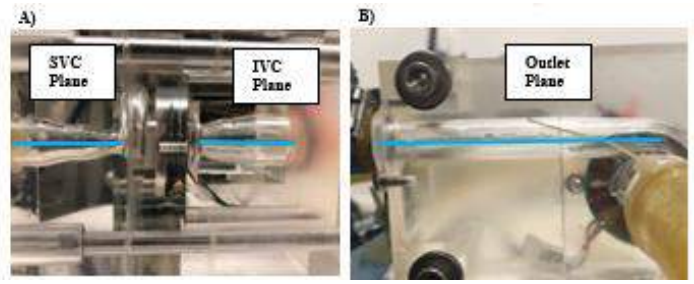

Figure 1: A) Side view of Fontan pump for the SVC and IVC inlets. B) Top view of the Fontan pump for the outlet, both denoting the centerline PIV plane of interest.

Next, we established pump operating conditions for PIV using the blood analog properties, properties of blood, and the HQ curves (Figure 2). The point of interest highlighted in Figure 2 represents ideal operating conditions for the model, an axial speed of 4000 RPM, total flow rate of 5 LPM, and a pressure head of 30 mmHg.

Poster Presentation #P017

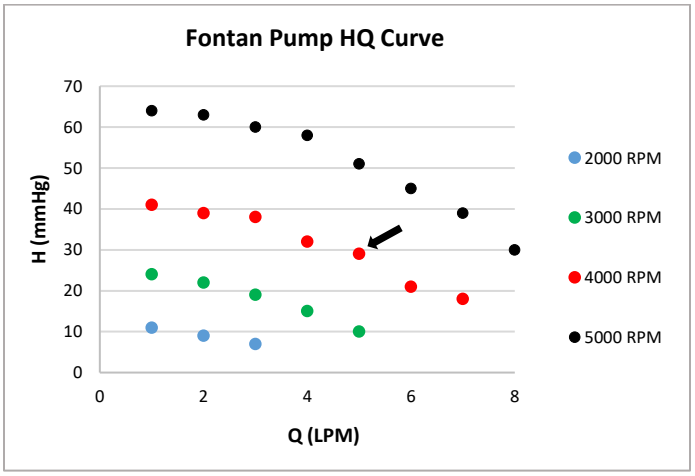

Figure 2: HQ curves of the implantable Fontan pump (optimal operating condition designated by arrow).

Non-dimensional parameters were used for proper comparison of pump flow fields. The parameters used to determine operational conditions for the acrylic model were the pump Reynolds number (Equation 1) and flow coefficient (Equation 2):

$$\mathrm{Re}_{pump} = \frac{\rho \omega D^2}{\mu} \quad (1)$$

$$C_v = \frac{Q}{\omega D^3} \quad (2)$$

Where ρ is density, ω is rotational velocity of the rotor, μ is dynamic viscosity, D is characteristic diameter, and Q is flow rate. To match these non-dimensional parameters to the target operating condition, the pump was operated at 4282 RPM and at a total flow rate of 5.35 LPM. This non-dimensionalization was carried out for each operating point along the HQ curves in Figure 2.

Finally, a camera (TSI, Inc., Shoreview, MN) and PIV laser (Quantel, Bozeman, MT) were mounted orthogonally above and parallel to the pump, respectively, to visualize the PIV planes perpendicular to the camera through the centerline of the two pump inlets and the outlet (Figure 1). PIV data were collected at the extreme operating conditions of the HQ curves. The outlet plane required two sets of images to capture the entire region, one near the rotor blades at the volute exit and one further downstream. One thousand image pairs were collected in each region and processed using Insight 4G (TSI, Inc., Shoreview, MN) and Tecplot Focus (Tecplot, Bellevue, WA).

RESULTS

The PIV data show standard flow fields expected from the pump operating under steady inlet conditions. As demonstrated in Figure 3, the flow was 2D axisymmetric through the centerline of the SVC inlet. The velocity increased significantly from an average of 0.18 m/s at the entrance to 0.54 m/s as it tapered to the rotor blade passage region and pump volute

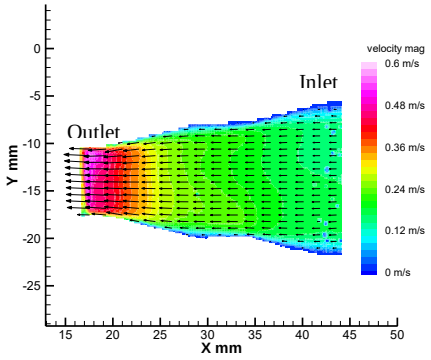

Figure 3: Mean PIV flow data at the centerline of the SVC inlet for 4280 RPM and 2.14 LPM.

The velocity field was relatively constant throughout the outlet. However, there was a region at the top of the flow field in Figure 4 that shows near zero velocity flow. This may have been a result of the 3D flow at this point with the fluid exiting the rotor passage region moving out of the 2D PIV plane.

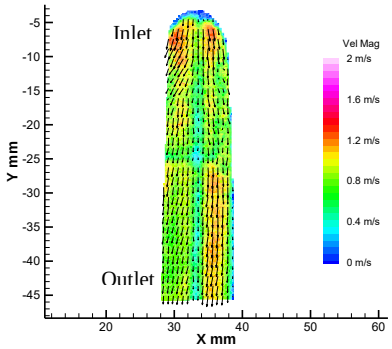

Figure 4: Mean PIV flow data at the centerline of the outlet for 4280 RPM and 5.35 LPM.

DISCUSSION

These preliminary results provide an initial understanding of the hemodynamics within the Fontan pump. The experimental data will also be used to help validate CFD simulations. Mean velocities observed in the PIV data approximately match calculations based on average flow rate and geometry. A seam in the acrylic model at the center of the outlet (X = 33 mm) may have caused the inconsistency observed in this part of the flow field. Future data collection in the pump will include planes offset from the centerline to gain a better understanding of flow through the entire 3D geometry. Finally, this study was limited to steady boundary conditions, which may not be accurate for predicting how the pump will perform *in vivo*.

ACKNOWLEDGEMENTS

Research supported by the Department of Defense W81XWH-16–1-0536. We would also like to thank our collaborators at the Hershey Medical Center for developing the Fontan acrylic pump model.

REFERENCES

[1] Hoffman, J *et al. Journal of the American College of Cardiology*, 39:1890-1900, 2002
[2] Iyengar, AJ *et al. Circulation*, 116:157-164, 2007
[3] Goldberg, D *et al. Expert Review of Cardiovascular Therapy*, 9:785-793, 2014

SB³C2019
Summer Biomechanics, Bioengineering and Biotransport Conference
June 25 -28, Seven Springs, PA, USA

HETEROGENEITY AND ANISOTROPY IN THE MICROSCALE ENERGY DISSIPATING PROPERTIES OF THE KNEE MENISCUS

Kevt'her Hoxha (1), Chao Wang (1), Biao Han (1), Robert L. Mauck (2), Lin Han (1)

(1) School of Biomedical Engineering, Science and Health Systems
Drexel University
Philadelphia, PA, United States.

(2) Department of Orthopaedic Surgery
University of Pennsylvania
Philadelphia, PA, United States.

INTRODUCTION

The synovial joint of the knee is essential for shock absorption and joint lubrication during locomotion. For high frequency activities, such as running and jumping, the shock absorption function is governed by the fluid flow-induced poroelasticity of cartilage [1], in which, the interstitial fluid pressurization arises due to the densely packed, highly negatively charged aggrecan in the cartilage extracellular matrix (ECM) [2]. Besides articular cartilage, the meniscus is also a key functional unit of the knee joint, enhancing congruency, providing direct load transmission to the cartilage [3] and increasing joint stability [4]. Like cartilage, the meniscus also exhibits pronounced time-dependent mechanical properties [5]. However, the meniscus ECM has a distinctive structure and composition, marked by a type I collagen-dominated outer region that gradually transitions into a type II collagen and aggrecan-rich inner region [6]. Our recent studies suggested that the structure and mechanical behavior of the meniscus ECM is highly heterogeneous and anisotropic [5]. It is unclear, however, if or how, the meniscus contributes to the poroelastic energy dissipation of the joint in a region- and orientation-specific manner. Such knowledge is important, given that meniscus injury often occurs during high frequency activities, and is a common cause of post-traumatic osteoarthritis. Thus, a more in-depth understanding of meniscus biomechanics will provide new benchmarks for documenting disease progression and developing regenerative strategies. The objective of this study was to investigate and detail the microscale energy dissipating mechanical behavior of the meniscus, with a focus on the tissue structural heterogeneity and anisotropy.

METHODS

Sample preparation. Medial menisci were harvested from adult bovine (18–30 months old) knees. The outer one-third (outer region) and inner one-third (inner region) were dissected and embedded in O.C.T. Blocks from both regions were cryo-sectioned in the transverse or coronal plane at the thickness of 10-μm to produce both horizontal and vertical sections from the outer and inner zones.

Histology. Safranin-O/Fast Green staining was applied to assess tissue-level collagen structure and the distribution of sulfated glycoaminoglycans (sGAGs, mostly from aggrecan).

AFM Nanorheometric testing. The microscale energy dissipating mechanical properties were determined using a custom-built AFM-nanorheometer with microspherical tips ($R \approx 12.5$ μm, $k \approx 2$ N/m) and a Dimension Icon AFM, followed by our established procedures [7]. Specifically, a 2-3 nm random binary sequence displacement was superimposed onto the ~ 1 μm static compression during a 100-sec ramp-and-hold. The dynamic force, F^*, and depth, D^*, as a function of frequency (1-1000Hz) was extracted via discrete Fourier transform. The complex dynamic modulus magnitude, $|E^*|$, and phase angle, δ, were derived via the Taylor expansion of Hertz model [8]. The self-stiffening ratio was obtained by the ratio of $|E^*|$ at high (900-1000 Hz, E_H) versus low (1-3 Hz, E_L) frequencies.

sGAG Depletion. Enzymatic removal of chondroitin-sulfate GAGs (CS-GAGs) via 1 U/ml incubation in chondroitinase ABC for 30 min was performed to observe the role of GAGs in the inner vertical region.

Statistical test. One-way ANOVA followed by Tukey-Kramer post-hoc analysis was used for statistical testing, with $\alpha = 0.05$.

RESULTS

Histology showed the more fibrous nature of the meniscus outer zone, marked by the prevalence of circumferentially aligned collagen fibers. The inner zone had apparently higher staining for the sGAGs, signifying a higher concentration of aggrecan (Fig. 1a). AFM nanorheometric testing detected substantial heterogeneity and anisotropy in the microscale properties, marked by the distinctive frequency spectra of $|E^*|$ and δ among test regions and orientations (Fig. 1b). As a result, the moduli, E_L and E_H, self-stiffening ratio, E_H/E_L, and maximum phase angle, δ_m, varied significantly between inner and outer zones, and between horizontal and vertical sections. Overall, the moduli and phase angles were higher on the vertical sections than horizontal sections (Fig. 1c). For the vertical sections, while the moduli, E_L and E_H, were both higher in the outer region, the inner region showed higher E_H/E_L and δ_m, indicating a greater contribution of energy dissipating behavior in those regions. Removal of CS-GAGs resulted in a significant reduction of E_H/E_L, maximum phase angle, δ_m, and both E_H and E_L illustrating the contribution of CS-GAGs to the overall energy dissipative properties in the inner region (Fig. 2).

DISCUSSION

This study highlights the distinct microscale energy dissipating mechanical properties of the meniscus ECM. In particular, greater time-dependence was found in the vertical sections. According to the literature, at the deformation length scale of the AFM-nanorheometric test (contact radius ~ 2 μm), the time-dependence and energy dissipation are primarily governed by poroelasticity [9]. On the vertical sections, the loading axis is parallel to the collagen fiber axis, resulting in compression of collagen fibrils with lateral confinement from adjacent fibrils and proteoglycans residing in the interfibrillar space [6]. In comparison, in the horizontal section, the loading axis is perpendicular to the fiber axis, which leads to local uncrimping or sliding of the fibrils. Therefore, given that proteoglycans are more confined by laterally constrained compression, indentation in the vertical direction allows for a higher degree of fluid pressurization, and thus, more pronounced energy dissipating time-dependent behavior (Fig. 3).

For vertical sections, while the outer region was stiffer due to the more organized collagen fibers, the inner zone exhibited a higher degree of energy dissipation. Such contrast shows the importance of aggrecan in the microscale energy dissipation of the meniscus. This contrast possibly suggests that the collagen fibers have limited contributions to the poroelastic energy dissipation. It also indicates that, during high frequency loading, the meniscus mainly dissipates energy in its aggrecan-rich, compressive load-bearing inner zone. On the other hand, the highest δ_m (16 ± 2°, mean ± S.E., measured in the IV region), was much lower than bovine cartilage (36 ± 2°, [2]), indicating that the contribution of the meniscus to knee shock absorption is secondary to that of cartilage.

ACKNOWLEDGEMENTS

This work was supported by the National Science Foundation Grant CMMI-1751898.

REFERENCES

[1] Mow, VC et al., *J Biomech* 17:377-394, 1984. [2] Nia, HT et al., *ACS Nano* 9:2614-2625, 2015. [3] Sweigart, MA et al., *Proc Inst Mech Eng H* 219:337-347, 2005. [4] Fithian, DC et al., *Clin Orthop Relat Res* 19-31, 1990. [5] Li, Q et al., *Acta Biomater* 54:356-366, 2017. [6] Sanchez-Adams, J et al., *J Appl Physiol (1985)* 111:1590-1596, 2011. [7] Han, B et al., *Trans ORS*, 2017. [8] Mahaffy, RE et al., *Biophys J* 86:1777-1793, 2004. [9] Nia, HT et al., *Biophys J* 101:2304-2313, 2011.

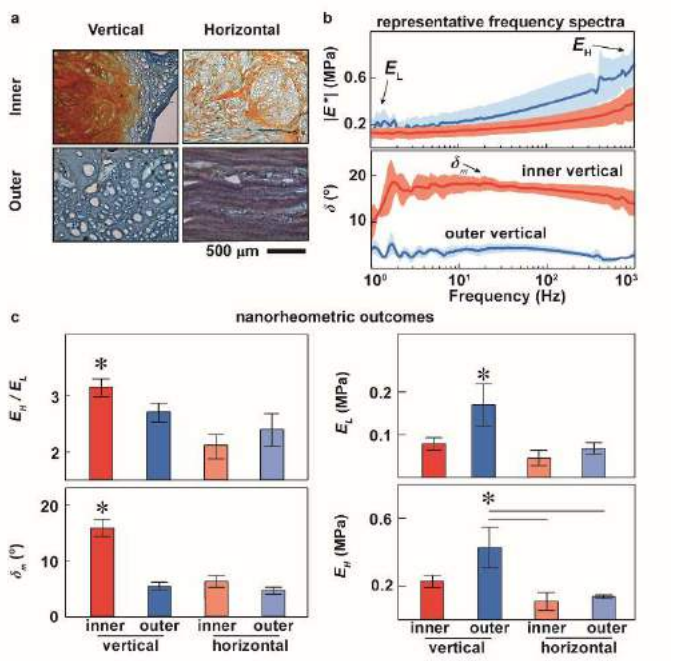

Figure 1: Saf-O/Fast Green histology and frequency-domain time-dependent nanorheometic test by AFM. a) Histology showed sGAG distribution on inner and outer regions of bovine meniscus horizontal (transverse) and vertical (coronal) sections, respectively. b) Representative frequency spectra of dynamic modulus and phase angle (mean ± S.E., $n \geq 3$ animals). c) Time-dependent micromechanical properties of the four tested regions/orientations.

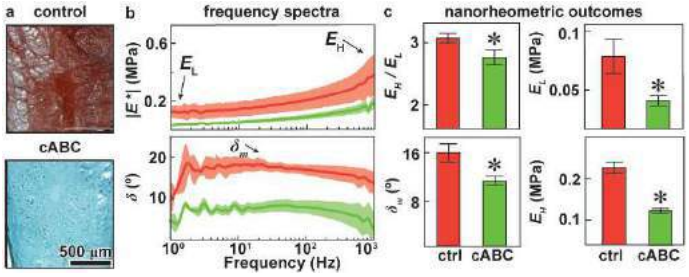

Figure 2: Effect of sGAG removal on the time-dependent micromechanics of the meniscus inner zone. a) Saf-O/Fast Green histology showed the reduction of sGAG staining. b) Representative frequency spectra of dynamic modulus and phase angle. c) Time-dependent micromechanical properties (mean ± S.E., $n \geq 3$ animals).

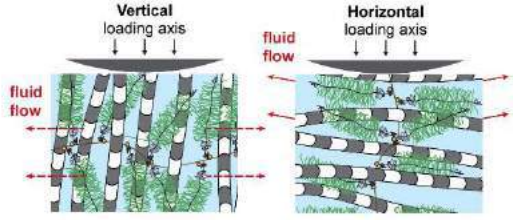

Figure 3: Schematics illustrate the relationship of indentation loading axis to meniscus ECM fibrils and fluid flow directions.

SB³C2019
Summer Biomechanics, Bioengineering and Biotransport Conference
June 25 -28, Seven Springs, PA, USA

2D OR NOT 2D;
COMPARING 2D AND 3D MEASUREMENTS OF COLLAGEN MICROSTRUCTURE

**Gosia Fryc (1), Bin Yang (2), Alexandra Gogola (2),
Bryn Brazile (2), Yi Hua (2),
Tian Yong Foong (3), Ian A. Sigal (2,3)**

(1) Department of Chemistry
University of Pittsburgh
Pittsburgh, PA, USA

(2) Department of Ophthalmology
University of Pittsburgh
Pittsburgh, PA, USA

(3) Department of Bioengineering
University of Pittsburgh
Pittsburgh, PA, USA

INTRODUCTION

Collagen is central to many soft tissues, and it is therefore of great interest to characterize and understand its microstructure [1]. Substantial efforts have been devoted to this endeavor by us [2,3] and others [4,5]. Many of these studies have analyzed collagen microstructure based on histological sections [1,2,5]. Sections have several benefits, such as the specificity afforded by labels and stains, the opportunity to easily isolate the tissues of interest, and the potential to share materials with pathology labs. Sections, however, have an important limitation: they provide only 2D information of the 3D collagen microstructure. Some have proposed to address this limitation by applying the 2D techniques in stacks of sections [6]. Although better, these are still not truly 3D.

We recently introduced a 3D analysis technique based on polarized light microscopy (3D-PLM) that allows quantifying both in-plane and out-of-plane angles of collagen fibers on a thin histological section [7]. Our goal in this study was to demonstrate the use of 3D-PLM to quantify collagen microstructure in 3D. Specifically, we focus on two aspects of microstructure that are of great importance to eye tissue mechanics and development, namely, collagen fiber crimp tortuosity and lamellar layering in the limbal region. To demonstrate the power of this technique, we compare measurements of microstructure between eyes of young and old eyes. We then also compare the 3D measurements with those obtained using the more traditional measures in 2D.

METHODS

3D fiber orientation quantification –We utilized the 3D-PLM technique described in detail elsewhere [7]. Briefly, tissue sections were imaged using polarized light under 4 different polarization states. Analyzing the changes in pixel intensity between the four polarization states, we calculated both in-plane and out-of-plane fiber orientation.

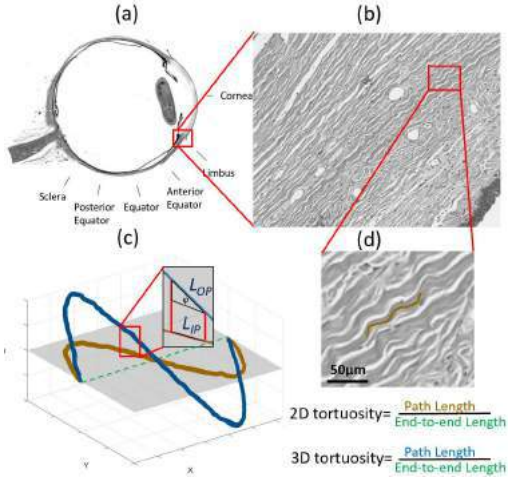

Figure 1 (a) Example longitudinal section of a normal human eye; (b) Close-up of the limbus region to illustrate collagen fiber organization. (d) Further close-up showing fiber waviness or crimp and lamellar structure. (c) Schematic of the analysis of a collagen fiber (blue line) in 3D or 2D projection (brown line).

Collagen fiber tortuosity – The tortuosity was calculated as the ratio of the path length along a tortuous fiber and the straight end-to-end length between two endpoints. For a small segment of a fiber, the length is calculated as $L_{OP}=L_{IP}/\cos(\varphi)$, where L_{OP} is the true (or out-of-plane) length of a fiber segment, L_{IP} is the projected (or in-plane) length in X-Y plane, φ is the out-of-plane fiber orientation. For the 2D tortuosity was calculated using only in-plane fiber path lengths, (Fig 1d, brown). For the 3D tortuosity, we used out-of-plane fiber orientation to estimate the length along a tortuous fiber (Fig. 1c, blue).

3D fiber structure measurement in limbus of human eyes – We performed both 2D and 3D tortuosity measurements in the limbus region of sagittal sections of a young eye (9-month-old) and an old eye (97-year-old). The de-identified human eye sections were prepared in accordance with the tenets of the Declaration of Helsinki and the Health Insurance Portability and Accountability Act. The limbus regions of both human eye sections were imaged with a 10X strain-free objective, and the images were analyzed with 3D-PLM. We traced manually the collagen fibers following the fiber bundles to include at least two crimp periods (brown line in Fig. 1d). We performed a 2-sample t-test to test for a significant difference between the crimp tortuosity in limbus of young and old eyes. Fiber tortuosity measurements were then used to calculate a stretch-based collagen recruitment curve.

RESULTS

Fig. 2 shows example color-coded in-plane and out-of-plane fiber orientation maps in limbus of both young and old eyes. Collagen fibers in the young eye are more tortuous and show more crimp than in that of the old eye. The line profile of the out-of-plane angle revealed that the young eye has thinner lamellae, as discernible by the higher frequency of the angle oscillations.

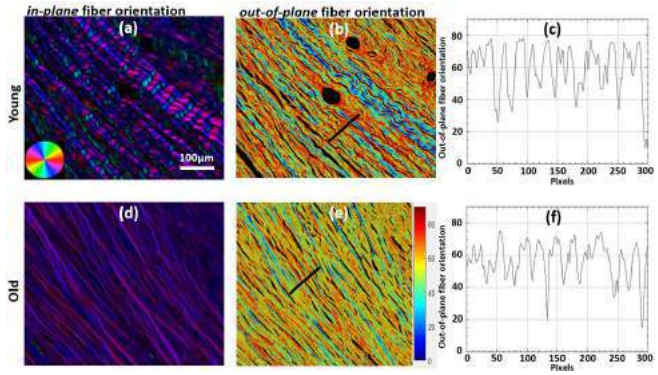

Figure 2 Example in-plane and out-of-plane fiber orientation maps of young and old eyes. Colors and brightness represent local fiber orientation and retardance, respectively. Profiles of out-of-plane orientation (c and f) along the black lines in b and e show that the young eye had thinner lamellae .

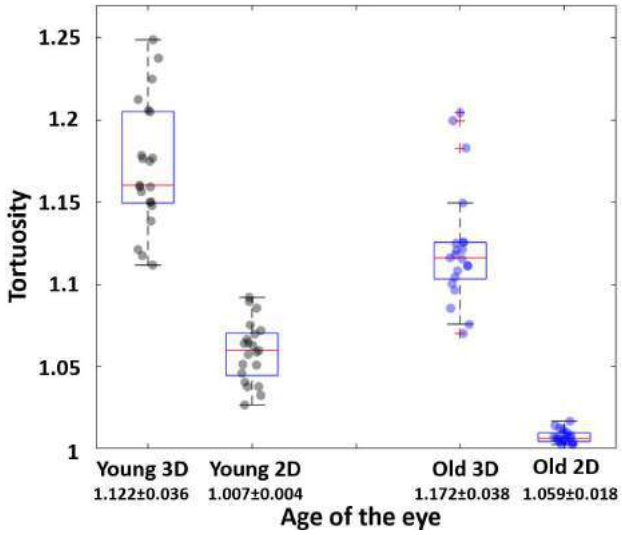

Figure 3 Tortuosities in both eyes, in 2D and 3D. Below each label are shown the mean and SD. Tortuosities decreased with age and were underestimated by 2D analysis.

Tortuosities measured in 3D were 11.4% and 11.1% larger than in 2D for young and old eyes, respectively (Fig 3). As expected, tortuosity decreased substantially and significantly with age ($P<0.0001$) [8]. Though the change was larger in 2D measurements (5.2%) than in 3D (4.5%). Tortuosity had a larger spread in young eyes and in 3D measurements, than in old eyes and 2D measurements. Fig. 4 shows the predicted stretch-induced collagen fiber recruitment in the limbus region.

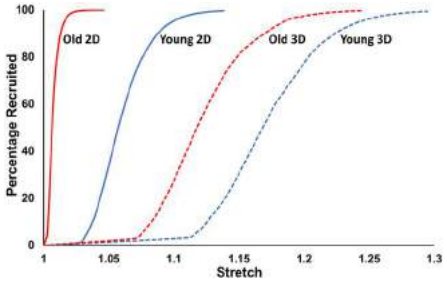

Figure 4. Stretch-induced collagen fiber recruitment in the limbus region. All cases exhibited sigmoid-shaped curves, but recruitment rates varied substantially. In both young and old groups, 3D crimp measures predict that the collagen fibers would be fully recruited at a substantially higher level of stretch than the 2D measures.

DISCUSSION

We have demonstrated that the application 3D-PLM to quantify collagen fiber microstructure from histological sections produces substantial and significant differences in the measurements. The results show that more conventional 2D tortuosity measurements underestimate 3D tortuosity by about 10%. This difference, while apparently small, should not be misunderstood as being negligible. Predicted fiber recruitment curves show that the difference will have a very substantial impact on the tissue mechanics. Collagen fiber crimp is the basis for the nonlinear mechanical behavior at the macroscale, in a process of stretch-induced stiffening called fiber recruitment [1].

Our results also show that the overall trend of age-related differences in collagen fiber tortuosity previously reported [8] still holds. This suggests that while 2D tortuosity measurements may underestimate 2D values, they may still capture the essence of the parameter, at least for limbus crimp. Similarly, both 2D and 3D measures predict a lower stretch level for full fiber recruitment in the old eyes. Using the out-of-plane angle analysis, we confirmed that the density of lamellae (or the number of lamellae per unit thickness) is higher in younger than in older eyes. We suspect that this is because young lamellae are developing and have not reached full thickness.

Overall, we have shown that the imaging and analysis technique of 3D-PLM provides valuable information on collagen crimp and lamellae layering. The technique can be applied to measure other aspects of microstructure, and for other collagenous tissues.

ACKNOWLEDGEMENTS

NIH R01-EY023966, R01-EY028662, and P30-EY008098

REFERENCES

[1] Fratzl, P., *Springer Science & Business Media*, 2008.
[2] Jan, NJ., et al. *Invest. Ophthalmol. Vis. Sci.* 58.9, 2017
[3] Brazile, B., et al. *Invest. Ophthalmol. Vis. Sci.* 59.11, 2018
[4] Grytz, R., et al. *J Mech Behav Biomed Mater,* 2.5, 2009
[5] Liu, X., et al. *Invest. Ophthalmol. Vis. Sci.* 55.4, 2014
[6] Liuzzi, M., *J. Biol. Chem.*, 260.9,1985
[7] Yang, B, et al., *J Biophotonics,* 11(8):e201700356, 2018
[8] Gogola, A., et al., *Invest. Ophthalmol. Vis. Sci.* 59(7), 2018

SB³C2019
Summer Biomechanics, Bioengineering and Biotransport Conference
June 25 -28, Seven Springs, PA, USA

The Effect of a Cannabinoid Receptor 2 Agonist on Motor Function after Blast-Induced Neurotrauma

B. Alturkestani, S. Assari, O. Sharaf. I. Hendricks, S.J. Ward[1], R.F. Tuma[1], K. Darvish

Biomechanics Laboratory
Department of Mechanical Engineering
Temple University
Philadelphia, PA, USA

1) Center for Substance Abuse Research
Lewis Katz School of Medicine
Temple University
Philadelphia, PA, USA

INTRODUCTION

Blast-induced traumatic brain injury (bTBI) present complex challenges to the military. Such injury can cause multisystem, life-threatening injuries, and blast survivors suffer a range of acute and chronic negative health consequences. The emphasis of our research is on harnessing the neuroprotective and anti-inflammatory properties of non-psychoactive cannabinoids for the treatment of blast injury with or without concomitant hemorrhage. Previous studies have shown that activation of the cannabinoid receptor type 2 (CB2) may have neuroprotective effects [1]. In this study we investigated whether administration of O-1966, a CB2 receptor agonist, before injury has any effect on the recovery of the motor functions of rats after mild bTBI.

METHODS

A compressed-gas driven shock tube was used to replicate bTBI in rats **(Figure 1)**. The test apparatus consisted of a small tube diameter (50 mm) opening that allowed targeting only the head of the animal [2]. It was verified that the overpressure in thorax and abdomen were negligible. Prior to the blast exposure, animals were anesthetized with isoflurane and the head was secured and oriented for dorsal exposure in a custom holder. A rapid overpressure of 270 kPa was applied for a duration of 1.6 ms to induce mild bTBI [3]. The animals were exposed to either single blast or triple blast exposures. In the multiple exposure case, there was a 3-hour wait time between each exposure.

Sprague-Dawley wild-type rats (male, average 300 grams), were used for this study and divided randomly into three test groups of Treatment with O1966 (injury+medication), Sham (only anesthesia), and Vehicle (injury+non-therapeutic injection). O-1966 was administered at 5.0 mg/kg IP.

The motor function of rats was assessed using the rotarod experiment [4]. A commercial rotarod (LE8500, PanLab Harvard Apparatus) was used for four rats at a time. The testing was divided into two phases of baseline training and post injury evaluation. The baseline training was done for 5 days that are indicated as days -7 to -3. The animals were then allowed to rest for two days (weekend, days -2 and -1). Any drug injection and then the bTBI test was done in day 0. The Post-injury phase of the rotarod test was done on the animals for 4 days after the injury (days 1 to 4). Th e tests result is given as the speed in revolutions per minute (rpm) at which the animal falls off the rotating rod (Speed at Fall or SAF). The rotarod device was used in the accelerating mode that

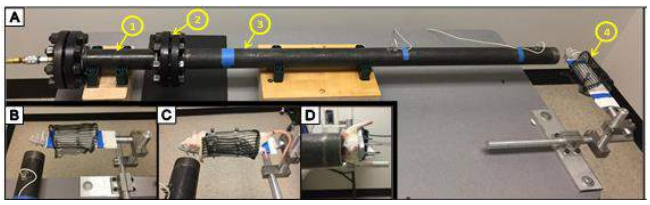

Figure 1. The Compressed-Gas Driven Shock Tube **(A)** showing the driver section (1), diaphragm location (2), driven section (3), and the animal holder (4). The custom-made animal holder **(B)** minimizes the acceleration induced brain injuries and allows for different exposure orientations **(C & D).**

changed the speed gradually from 4 rpm to the maximum of 40 rpm. The animals that did not show any training, i.e., their SAF value did not increase during the 5-day baseline period, were excluded from further data analysis.

The number of animals that are reported in this study are n=8 for treated with O1966 (5 single and 3 triple hits), n=9 for Sham (3 single and 6 triple anesthesia), and n=11 for Vehicle (6 single and 5 multiple hits).

RESULTS AND DISCUSSION

The results are summarized in **Figure 2** which show the mean SAF values with standard error of the mean as error bars. As can be seen, in the training period, the animals started at about 10 rpm and reached to about 30 rpm. The training pattern is generally increasing asymptotically, which indicates that the 5-day training period was enough. This is consisted with previous studies [4].

The post-injury data shows that there is almost no difference in Sham SAF, as expected, but there is reduction of SAF in injured animals (both O1966 and Vehicle) in days 2 and 3 followed by recovery in day 4. Based on these preliminary observations, quantitative comparisons were made between day 2 (maximum effect of injury) and day -3 (maximum training before injury).

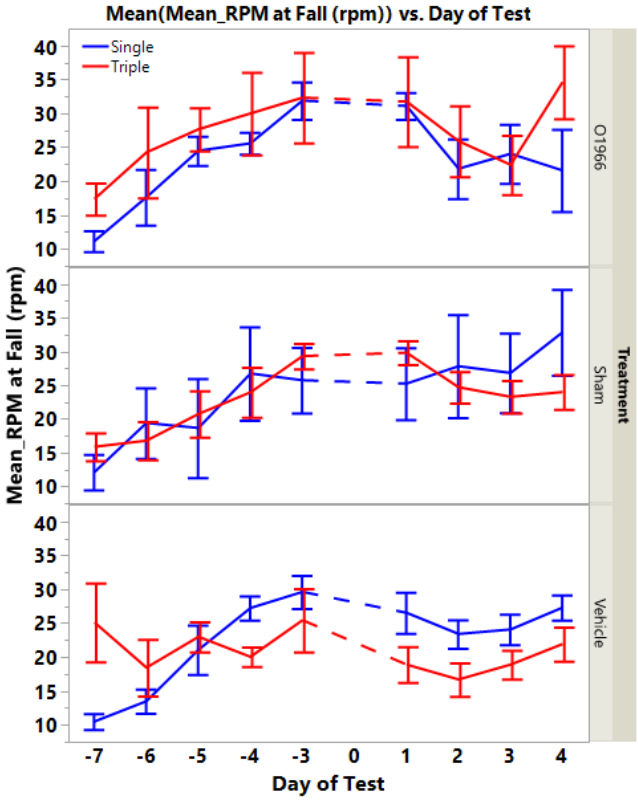

Figure 2: Rotarod performance for all groups. **Top:** bTBI and treated with O-1966. **Middle:** Sham control group that were anesthetized only. **Bottom:** Vehicle group with bTBI and non-therapeutic injection. Both drug and Vehicle animals were exposed to either a single (blue) and triple (red) shock waves.

For quantitative comparison, *t* test was used with 5% probability as the threshold of statistical significance. When comparing the effect of injury, there is reduction in SAF **(Figure 2, bottom)** for both single (p=0.08) and triple (p=0.14) hit cases although they are not statistically significant. For treated animals **(Figure 2, top)**, the difference is almost the same for single hit case (p=0.09) but it is much closer to pre-injury for the triple hit case (p=0.49).

Based on the observation mentioned above, a comparison was made between single and triple hit cases at day 2 after injury. The results showed that the difference is more in the Vehicle case with triple hit resulting in 7 rpm less (p=0.07). This difference in the O-1966 case is less (4 rpm) with p=0.57 and is close to sham (3 rpm) with p=0.70.

In summary, the result of this study shows that treatment with O1966 can improve recovering from multiple blast exposures but was not effective in mild blast TBI with single hit. Multiple exposure resulted in more severe injury and made CB2 receptors more responsive to O1966. In the future, the effect of O1966 dosage on injury severity needs to be investigated.

This study showed that rotarod results were sensitive to indicate the effect of the injury and the drug. The effect of injury was maximized at 2 days after the injury and the animal almost recovered fully recovered after 4 days. Since statistical significance could not be achieved with the number of samples used here, more data is needed to improve the statistics of this work and verify the preliminary conclusions.

ACKNOWLEDGEMENTS

This work was partially supported by a PA-CURE grant from The Pennsylvania Department of Health.

REFERENCES

[1] Ronca, R. D., Myers, A. M., Ganea, D., Tuma, R. F., Walker, E. A., & Ward, S. J. (2015). A selective cannabinoid CB2 agonist attenuates damage and improves memory retention following stroke in mice. Life sciences, 138, 72-77.

[2] Assari, S., Laksari, K., Barbe, M., & Darvish, K. (2013, November). Cerebral blood pressure rise during blast exposure in a rat model of blast-induced traumatic brain injury. In ASME 2013 International Mechanical Engineering Congress and Exposition (pp. V03AT03A016-V03AT03A016). American Society of Mechanical Engineers.

[3] Panzer MB, Wood GW, Bass CR, Scaling in neurotrauma: how do we apply animal experiments to people? Exp.Neurol. 2014; 261 120-6

[4] Hamm, R. J., PIKE, B. R., O'DELL, D. M., LYETH, B. G., & JENKINS, L. W. (1994). The rotarod test: an evaluation of its effectiveness in assessing motor deficits following traumatic brain injury. Journal of neurotrauma, 11(2), 187-196.

SB³C2019
Summer Biomechanics, Bioengineering and Biotransport Conference
June 25 -28, Seven Springs, PA, USA

DRONE BLADE INDUCED SKIN LACERATION AND EYE INJURY RISK; AN INVESTIGATION OF SKIN AND EYE SURROGATE MODELS

Lauren A. Duma, Mark T. Bergonia, Barry Miller, Stefan M. Duma

Institute for Critical Technology and Applied Science
Virginia Tech
Blacksburg, Virginia, United States

INTRODUCTION

As the use of drones becomes increasingly popular and more widespread, the number of drone related injuries has the potential to increase. Drone accidents have caused a variety of injuries, including skin lacerations, open globe eye lacerations, and head injuries leading to unconsciousness. [1]

Possible skin surrogates that can be used to test drone injuries include cadaver skin, porcine skin, porcine eyes, and chamois. Frozen cadaver skin has proven to be ineffective, due to ice crystal formation and rapid decay. [2] This limits cadaver skin from displaying realistic biomechanical properties. Human volunteers have been used; however, given extreme injury risk, this is not a viable option. [3] Porcine skin has been used in other experiments and has shown similar structure to human skin. [2] Chamois, or synthetic skin, has also been shown to represent qualities similar to human skin. [4]

The objective of this study is to assess and analyze the ability of drones to cause laceration injuries, and to study and compare the effectiveness of skin and eye surrogates, including porcine skin, porcine eyes, and chamois, as viable and appropriate replacements.

METHODS

A total of eight experiments were performed. Two drones were selected for testing: the Phantom 4 Advanced and the Air Hogs Axis 200. For the Phantom 4 Advanced, each surrogate type, chamois, porcine skin, and porcine eye, was tested twice. For the Air Hogs Axis 200, the porcine eyes were tested twice.

The Phantom 4 Advanced had blades 9.42 inches long (total length) and 1.221 inches wide, with the thickest point on the blade being 0.1005 inches. The blade tip was 0.454 inches wide, and 0.0410 inches thick. The Air Hogs Axis 200 had blades 6.278 inches long (total length) and 0.7085 inches wide, with the thickest point on the blade being 0.0280 inches. The blade tip was 0.437 inches wide and 0.0250 inches thick. Blade velocity was calculated using rotational velocity and blade length at the tip.

High speed video was used to record the blades of each drone at maximum throttle coming into contact with chamois, porcine skin, and porcine eyes. The video camera model was the Phantom Miro LC321S with 768 x 576 resolution, recording at 6,100 frames per seconds, and 20 microsecond exposure for skin tests or 40 microsecond exposure for eye tests. A custom slider table was used to preform each test. Each drone was secured to a platform, while the skin or eye surrogate was moved into the blades a measured distance and for a specific amount of time (Figures 1 and 2). The surrogates were each mounted to ballistic gelatin. The condition of the skin surrogate was recorded before and after the experiment.

Figure 1: Aerial view of the skin laceration tests. The chamois skin surrogate (shown), mounted to ballistic gelatin, was moved into contact with the Phantom 4 blade at maximum speed.

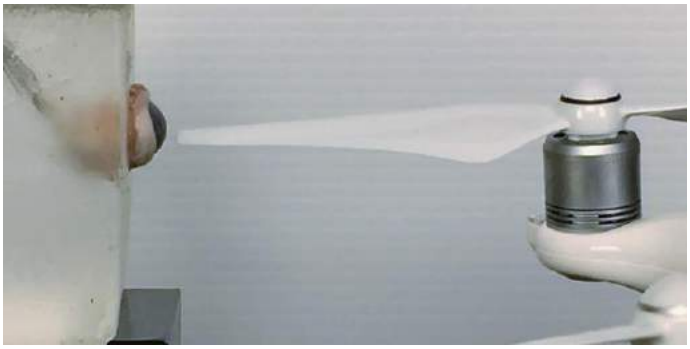

Figure 2: Side view of the testing setup for the eye impact tests. The porcine eye surrogate (shown), mounted to ballistic gelatin, was moved into contact with the Phantom 4 blades at maximum speed.

RESULTS

The rotational velocities for the Phantom 4 in tests 1 through 6 ranged from 7944 rpm to 8423 rpm (Table 1). The Air Hogs Axis 200 had a rotational velocity of 2181 rpm, significantly less than the Phantom 4. This corresponded to a similar difference in blade tip speed with the Phantom 4 ranging between 3,118 ft/s to 3,306 ft/s compared to the Air Hog blade tip speed of 571 ft/s.

Table 1: Rotational blade velocity of each test performed.

Test Number Drone Surrogate Type Rotational Velocity

Test	Drone	Surrogate	Rotational Velocity	Blade Tip Speed
1	Phantom 4	Chamois	7944 rpm	3118 ft/s
2	Phantom 4	Chamois	8209 rpm*	3222 ft/s
3	Phantom 4	Porcine skin	8115 rpm	3185 ft/s
4	Phantom 4	Porcine skin	8209 rpm*	3222 ft/s
5	Phantom 4	Porcine eye	8423 rpm	3306 ft/s
6	Phantom 4	Porcine eye	8354 rpm	3279 ft/s
7	Air Hogs	Porcine eye	2181 rpm	571 ft/s
8	Air Hogs	Porcine eye	2181 rpm*	571 ft/s

***Average rotational velocity was taken from matched experiments if not enough video frames were available.*

The chamois and porcine skin surrogates displayed similar results when coming into contact with the Phantom 4 blades. In tests 1 through 4, both surrogates had a minor scrape with no laceration (Table 2). For example, in test two, the chamois had a visible scrape after coming into contact with the Phantom 4 blade (Figure 3). The porcine eye surrogates had varied results when impacted with the Phantom 4 and Air Hogs Axis 200 blades. The porcine eyes hit by the Phantom 4 blades displayed far more extreme injuries. For example, in test 5, the porcine eye had a total globe rupture (Figure 4). The porcine eyes impacted by the Air Hogs Axis 200, however, only experienced partial corneal abrasions.

Table 2: Observed injury results of each test performed.

Test	Observed Injury
1	No laceration, minor scrape
2	No laceration, minor scrape
3	No laceration, minor scrape
4	No laceration, minor scrape
5	Total globe rupture within 6 strikes
6	Full thickness corneal laceration, no globe rupture
7	10% corneal abrasion
8	20% corneal abrasion

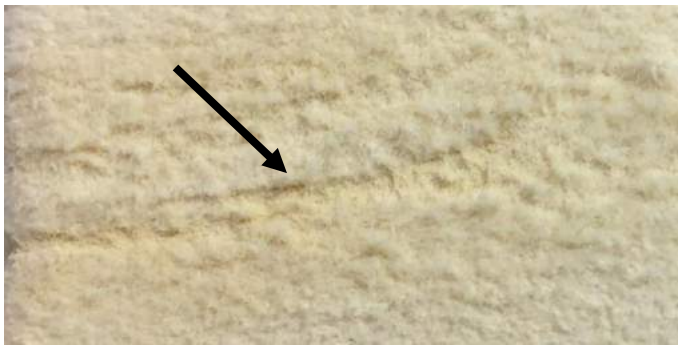

Figure 3: The chamois skin surrogate after making contact with the Phantom 4 blade in test 2. A minor scrape with no full thickness laceration was observed.

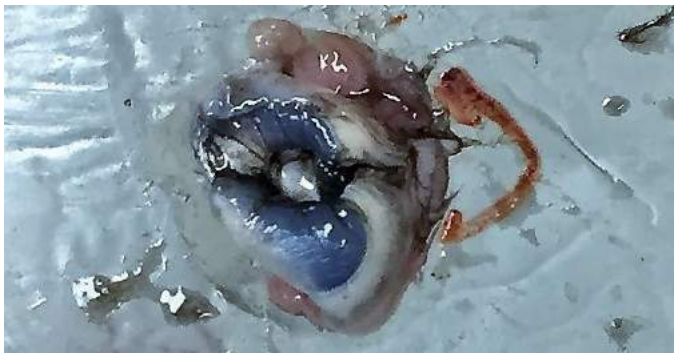

Figure 4: The porcine eye surrogate after making contact with the Phantom 4 blade in test 5. After 6 strikes, there was a total globe rupture.

DISCUSSION

The chamois and porcine skin did not prove to be viable skin surrogates. The Phantom 4 Advanced drone has caused severe skin lacerations that have required stitches, while no lacerations. The porcine skin and chamois did not reflect this, as only minor scrapes were observed.

In contrast, the porcine eye proved to be a viable eye surrogate. For the Phantom 4 Advanced tests full globe rupture was observed as was also seen in the field. Also, the Air Hogs Axis 200 tests resulted in minor corneal abrasions and no full lacerations. This is to be expected from the smaller toy drone.

The total globe rupture that results from the Phantom 4 coming into contact with someone's face has lifelong consequences. Because recovery from a total globe rupture is unlikely, this injury would result in permanent blindness.

Future work with drone blade injury risks should include more variables such as speed, diameter, and blade thickness. Future testing could also include experimentation with different skin models that might have thinner epidermises.

ACKNOWLEDGEMENTS

I would like to acknowledge and thank ICTAS for their support of this research project.

REFERENCES

[1] Moskowitz, E.E. et al, *Am J of Ophthalmology*, 10, 35-37, 2018.
[2] Ranamukhaarachchi, S.A. et al., *Nature*, 6:32074, 2016.
[3] Reed, Matthew P. et al., *SAE*, paper number 942217, 1994.
[4] Papy, Alexandra et al., *IRCOBI*, 2012.

SB^{3}C2019
Summer Biomechanics, Bioengineering and Biotransport Conference
June 25 -28, Seven Springs, PA, USA

DIRECT MEASUREMENT OF COLLAGEN FIBER ORIENTATION ALONG THE SURFACE OF LIGAMENTS AND TENDONS OF THE KNEE IN A PORCINE MODEL

Emily P. Lambeth (1), Stephanie G. Cone (1), Matthew B. Fisher (1,2)

(1) North Carolina State University and
University of North Carolina-Chapel Hill
Department of Biomedical Engineering
Raleigh, NC, USA

(2) Department of Orthopaedics
University of North Carolina-Chapel Hill
Chapel Hill, NC, USA

INTRODUCTION

More than 100,000 anterior cruciate ligament (ACL) injuries [1] and approximately 74,000 collateral ligament injuries [2] occur each year in the United States alone. Recently, the incidence of ligament injuries has been increasing at a higher rate in children and adolescents than in their adult counterparts [3], but treatments for these young patients continue to be based upon research in skeletally mature subjects [4]. Previous studies have found that graft rotation during ACL reconstruction surgeries has an immediate effect on biomechanical function [5]. Our group has previously found differences in the shape of the ACL bundles between different age groups and bundles using magnetic resonance imaging (MRI) [6]. However, it is unclear whether these changes in tissue morphometry also correspond to changes in the orientation of the individual highly-aligned collagen fiber networks within the tissue. In order to tease out such changes, an *in situ* analysis of collagen fiber behavior within ligaments and tendons is needed. This work is further motivated by previous studies, which have assessed the orientation of the anteromedial (AM) and posterolateral (PL) bundles of the ACL at their femoral and tibial insertion sites by dividing the tissues into small bundles [7]. While this previous study directly measured the fibrous bundles of the ACL and found orientation changes at the insertion sites based on anatomical location, it did not characterize the behavior of the fibers in the midsubstance of the ligaments. The objective of our study was to directly analyze the collagen fibers in major ligaments and tendons along their length in the porcine stifle joint, and to compare the fiber paths between tissues and at two joint flexion angles: full extension (~40° in the pig) which is the flexion angle from our MRI scans, and 60° of flexion which is a more common position in previous literature reporting ACL rotation [8]. In order to do so, we collected points along surface collagen fibers in the patellar tendon (PT), medial collateral ligament (MCL), lateral collateral ligament (LCL), and the AM and PL bundles of the ACL in a juvenile porcine model at both 40° and 60° knee positions. We plan to measure the difference in orientation of the fibers relative to the bulk tissue. We are continuing this work by developing a curve fitting system to quantify fiber orientation relative to the bulk tissue.

METHODS

Hind limbs from juvenile (2.5 month old) female Yorkshire cross-breed pigs (n=6) were collected. Tissue was removed from the femur and tibia up to the joint space and a fiberglass epoxy was applied to the bones in order to interface with clamps on a biomechanical robotic system. Testing was performed using a 6 degree-of-freedom universal force sensing robotic system (KUKA, SimVitro). Additionally, we took MRI scans of juvenile porcine stifle joints (7T Siemens MRI scanner, double echo steady state scan sequence, 0.42x0.42x0.4 mm voxels) and created 3D models of all tissues of interest using commercial software (Simpleware, Synopsys) (Fig. 1A). These 3D models were analyzed to obtain measures of bulk tissue rotation [6].

For the *in situ* testing, a passive path was determined from full extension (~40° of flexion) to 60° of flexion. 5-7 fibers were identified on the PT, MCL, and LCL and 8-12 points along each fiber were recorded (Fig. 1B, 1C) with a 3D point digitizer (MicroScribe) at both 40° and 60° of flexion. All remaining soft tissue other than the ACL as well as the medial femoral condyle were removed, and the digitization procedure was performed on 4-6 fibers within the AM bundle of the ACL in both positions. Lastly, the AM bundle was removed and the procedure was repeated for approximately 4-6 fibers on the PL bundle of the ACL at 40° and 60° of flexion.

Fiber points were imported into MATLAB as isolated points which were translated into 3D scatterplots (Fig. 1D). These plots were created

for individual fibers and all fibers from an individual tissue we superimposed into plots for further analysis.

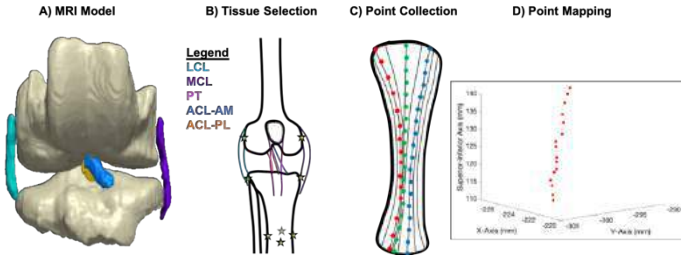

Figure 1: 3D renderings were created of porcine stifle joints featuring soft tissues of interest (A). Diagram of the tissues of interest and anatomic points that were collected in this experiment (B). Points were collected running along several collagen fibers on the tissue surfaces (C). Points from individual collagen fibers were plotted in 3D space (D).

RESULTS

In the LCL, MCL, and PT, fibers were relatively linear in nature and there was little to no overlap in the tracks created by the individual fibers (Fig 2). In comparison, the fibers within the AM and PL tissues appeared less linear than those in the other tissues (Fig 2). The fibers from the AM and PL bundles were more irregular, in that the paths created by the fibers varied in the planes normal to the primary axis of the ligament. Additionally, there was more variance in the paths created between digitized points for the AM and PL bundles in comparison to the paths created in the LCL, MCL, and the PT. The LCL, MCL, and PT tissues were made of fibers that were aligned to the primary direction of the tissue, with little crossover between fibers and little variance from a straight line (Fig. 2).

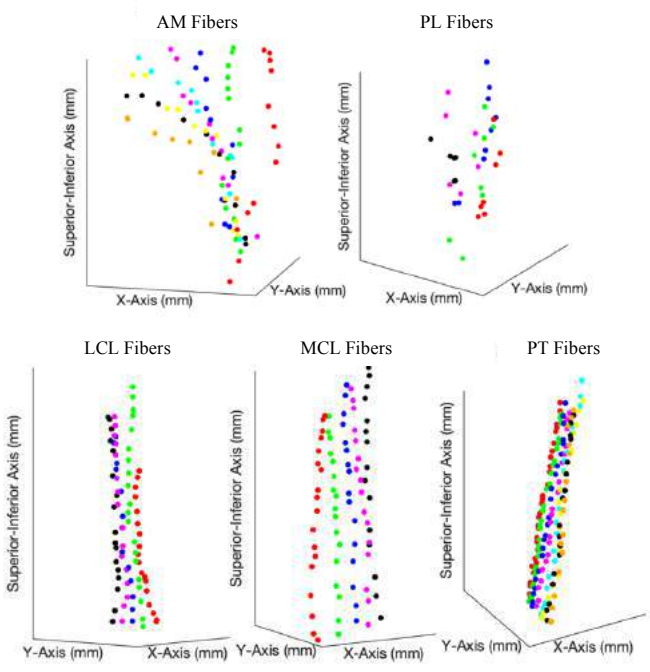

Figure 2: Fibers for the tissues of interest from a representative joint at full extension (40° of flexion in the pig) after rotation onto the anatomical longitudinal axis. Dots indicate points digitized along the fibers with separate fibers depicted as different colors.

DISCUSSION

In this study, we were able to use an *in situ* approach to assess the rotation of collagen fibers along the surface of several ligaments and tendons in the porcine stifle joint at multiple flexion angles. For the LCL, MCL, and PT, the fibers followed similar paths within a single tissue, although small fiber-to-fiber variation could be seen. For the AM and PL bundles of the ACL, we observed much higher degrees of fiber-to-fiber variation. This matches visual observations of fiber orientation noted during the digitization process. These observations are further strengthened by a preliminary analysis in which fiber points were fit to second degree polynomial curves. Although we have been able to model the fibers using this approach with high correlation coefficients (R^2>0.992) across tissues, the fit was better in tissues such as the LCL, MCL, and PT where less fiber rotation occurred. Interestingly, in our initial analysis, flexion and extension of the joint did not have a noticeable impact on fiber orientation, despite previous studies reporting both fiber and morphometric changes due to knee flexion angle changes in both human and porcine joints [6-8]. This discrepancy may be due to differences in the ranges of flexion angles studied [6-8].

Ultimately, our goal is to develop a non-invasive MRI-based method to assess fiber rotation within ligaments and tendons. To do so, we will compare the pitch and angles of fiber rotation via MRI and our direct *in situ* method using a single set of joints, allowing direct comparison of the methods. Ongoing efforts will involve developing a method to fit points onto MRI-based surfaces in order to track the rotation of both fibers and bundles in a 3D coordinate system. These measurements will be validated using our direct *in situ* method. Interestingly, the non-linear appearance of point maps for the AM and PL bundles of the ACL found in the current study correspond with our early MRI-based findings, where we found ~57° rotation of the primary axis of the AM bundle and ~55° rotation of the primary axis in the PL bundle. Additionally, a future direction involves dividing the tissues into regions and comparing regional fiber patterns. We also plan to expand this study to include early juvenile and late adolescent groups in order to assess potential differences in fiber alignment during growth. Overall, this work represents an initial step toward a method to noninvasively assess fiber rotation, which may better inform surgical interventions and enhance our understanding of ligament and tendon structure.

ACKNOWLEDGEMENTS

We would like to thank Powered Research for their support. Funding provided by NSF (DGE-1252376) and NIH (R03-AR068112, R01-AR071985).

REFERENCES

[1] Gordon, MD et al., *Am Acad Orth Surg,* 169, 2004; [2] Daniel, DM et al., *Dan Knee Injuries*, 2, 2003; [3] LaBella, C et al., *Pediatrics*, 133:1437-1450, 2014; [4] Mall, NA et al., *Am J Sp Med*, 42:2363-2370, 2014; [5] Elmans, L et al., *Clin Orth Rel Res*, 278-284, 2003; [6] Lambeth, EP et al., *BMES Ann Meet*, 2018; [7] Hara, K et al., *Am J Sp Med*, 37: 2386-2391, 2009; [8] Zhang, X et al., *IEEE EMBS Conf*, 2008.

SB³C2019
Summer Biomechanics, Bioengineering and Biotransport Conference
June 25 -28, Seven Springs, PA, USA

ELASTASE TREATMENT INCREASES AND ACCELERATES STRESS RELAXATION IN TENDON.

James A. Abraham (1), Jeremy D. Eekhoff (2), Spencer P. Lake (1,2,3)

(1) Department of Mechanical Engineering and Materials Science
Washington University in St. Louis
St. Louis, MO, USA

(2) Department of Biomedical Engineering
Washington University in St. Louis
St. Louis, MO, USA

(3) Department of Orthopaedic Surgery
Washington University in St. Louis
St. Louis, MO, USA

INTRODUCTION

Tendons act as one of the most important parts of a human's musculoskeletal system, as they are the connectors between bone and muscle. The compositional and organizational properties of tendons determine their ability to provide adequate mechanical function. While the collagen matrix is known to provide high tensile strength, relatively little is known about how the non-collagenous components of a tendon, and more specifically elastic fibers, influence its mechanical properties [1-3]. Elastic fibers are composed of elastin deposited onto a microfibrillar scaffold and exist predominantly in the interfascicular matrix (IFM), which is located between collagen fascicles and may link them together [1, 4]. Elastic fibers have been suggested to provide important mechanical roles in tendon; for example, they may allow a tendon to recoil after being loaded. Clinically, understanding the effect of elastic fibers on the mechanical properties of tendon could facilitate future research on diseases such as Marfan Syndrome and Williams Syndrome, both of which stem from mutations to elastic fiber-related genes [5]. More in-depth understanding would allow clinicians to help patients with elastic fiber deficiencies in a more informed and effective manner.

However, there is little experimental evidence on how elastic fibers affect the tensile mechanics of tendon. Previous research using genetically modified mouse models has suggested that elastin has an effect on a tendon's mechanical properties, but the effect was less than initially anticipated. Because of the vast difference in tendon size between mice and larger animals, the distribution of the elastin within the tendon and IFM may also be quite different [3]. Therefore, comparing the contribution of elastin in larger tendons with a prevalent IFM may better elucidate how elastin functions under tensile load in tendon.

In order to isolate the mechanical effect of elastic fibers, comparisons can be made by testing tendons, with and without enzymatic elastin degradation treatment, under the same loading conditions. Previous studies have used elastase to determine the effects of elastin digestion on the quasi-static mechanical properties of tendon and ligament; however, no studies to date have investigated changes to viscoelastic properties in tension with elastase treatment [3,6]. In this study, bovine long digital extensor tendon (LDET), which is functionally analogous to the human tibialis anterior tendon, was used as a representative tendon for large species. The purpose of this study was to utilize mechanical testing before and after elastase incubation to determine the role of elastin on the viscoelastic mechanical properties of tendon.

METHODS

Bovine LDETs were acquired from a local abattoir and frozen at -20° C until use. Before testing, samples were thawed at room temperature for 30-60 minutes. Cross-sectional area of each tendon was measured using a non-contact laser scanning device. Samples were loaded in custom clamps gripped between pieces of sandpaper to ensure minimal slipping occurred. Clamps were placed in an Instron 5542 Testing Machine, a 0.5 MPa preload was applied, and the gauge length was then measured using calipers. Once the gauge length and preload were determined, samples were preconditioned using ten cycles to 6% strain and subsequently tested in stress relaxation for ten minutes at 6% strain followed by triangular loading waveforms to 2, 4, and 6% strain to assess hysteresis (Figure 1). Following testing, the clamps were removed and incubated in either PBS (controls) or 3.5-4 units/mL elastase solution for 24 hours while maintaining a constant gauge length. Both control and test solutions contained 0.1 mg/mL soybean

trypsin inhibitor to prevent digestion of collagen. Following incubation, the clamps were reloaded into the Instron and the tendon was loaded using the same protocol as the pre-incubation test. Changes in mechanical parameters after PBS or elastase incubation are reported.

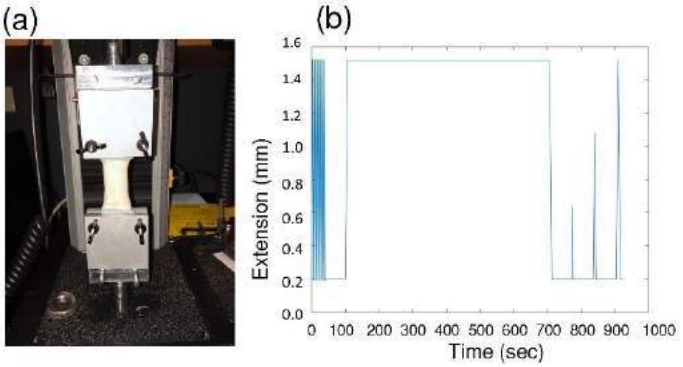

Figure 1: (a) A LDET sample loaded in the custom-made clamps. Samples were loaded in tension in the Instron 5542. (b) A time versus displacement graph for the testing protocol. The protocol for the pre and post incubation tensile testing protocol included 10 cycles of preconditioning at 6% strain, followed by a 10-minute stress relaxation at 6% strain and hysteresis curves to 2, 4 and 6% strain.

In between experiments, the enzyme solution was filtered using a hollow fiber filter with a maximum pore size of 0.1 μm to remove released tendon fragments and prevent bacterial growth in the solution. For elastase-treated samples, the activity of the elastase solution was measured daily [7] and additional elastase was added as necessary to ensure constant activity across all samples.

RESULTS

Elastase treatment altered the viscoelastic and quasi-static mechanical properties of LDETs compared to PBS treated controls (Figure 2). In control samples, peak stress, equilibrium stress, and relaxation time (i.e., time to reach 50% of total relaxation) values remained relatively constant after incubation, while percent relaxation decreased after incubation (Figure 2d). In contrast, both the peak and equilibrium stress significantly decreased after elastase treatment (Figure 2b,c). Moreover, the relaxation time significantly decreased (Figure 2e), and percent relaxation remained slightly closer to the pre-incubation values following elastase incubation (Figure 2d).

Hysteresis at 2% strain and linear modulus values also decreased after elastase treatment relative to controls (not shown). The transition strain increased after both PBS and elastase incubation, although the effect was significantly great in elastase treated samples (not shown).

DISCUSSION

Our preliminary results show that digestion of elastin significantly altered the viscoelastic properties of tendon. despite making up only 1-2% of tendon weight [4]. These changes were likely due to the fact elastin is a protein in elastic fiber in tendon. Although it makes up a small percentage of a tendon's dry weight, its function is unique and quite different than collagen, the major component of tendon [4]. When the elastin is digested the tendon's structural mechanisms relaxe, hence the change in viscoelastic properties. Elastin-dependent results are also intriguing when considering the function of the LDET in bovine hooves.

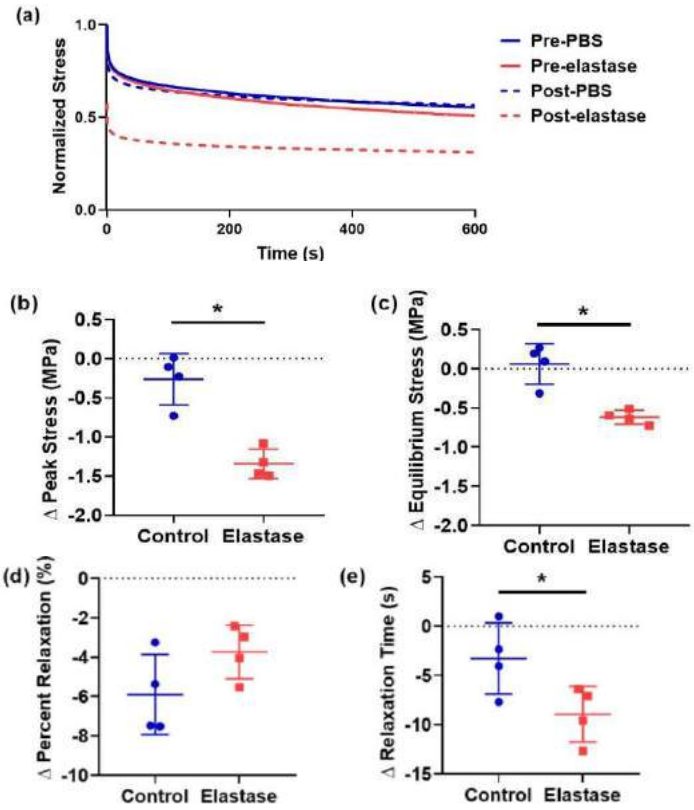

Figure 2: (a) A plot of stress normalized to pre-incubation values during the stress relaxation period versus time. (b) The change of peak stress during the stress relaxation period. (c) A plot of the change of equilibrium stress before and after incubation. (d) Difference in percent relaxation during stress relaxation. (e) Change in relaxation time which is time to reach 50% relaxation.

Like the tibialis anterior tendon in humans, the LDET is a positional tendon, meaning the tendon is not strained with the same magnitude or as frequently as a more energy-storing tendon [8]. This difference in function has previously been shown to relate to differences in mechanical properties and elastin content in functionally distinct tendons [8]. However, significant changes were still observed after elastase incubation, which suggests that elastin plays a significant role in the positional tendon's function. Further research will determine if elastase incubation has a larger effect in energy-storing tendons.

ACKNOWLEDGEMENTS

We thank the National Science Foundation (1562107) and the National Institutes of Health (T32EB018266) for funding.

REFERENCES

[1] Fang F et al, *J Biomech*, 47: 2869-2877, 2014.
[2] Eekhoff JD et al, *J Biomech Eng*, 139: 1115-1122, 2017.
[3] Fang F et al, *J Mech Behavior Biomed Mats*, 63: 443-455, 2016.
[4] Grant T et al, *J Anatomy*, 222: 573-579, 2013.
[5] Curran, M et al, *Cell Press*, 73: 159-168, 1993.
[6] Henninger H et al, *J Ortho Res*, 31: 1226-1233, 2013.
[7] Bieth J et al, J Biomech Medicine, 11: 350-357, 1974.
[8] Screen R et al, *J Ortho Res*, 33: 793-799, 2015.

SB^{3}C2019
Summer Biomechanics, Bioengineering and Biotransport Conference
June 25 -28, Seven Springs, PA, USA

Ultrasound shear wave Elastography of the Anterior Cruciate Ligament

G. Schwartz (2), R. Heller (1), S. Sadeghi (1), D.H. Cortes (1,2)

(1) Mechanical Engineering Department
Penn State University
State College, PA, USA

(2) Biomedical Engineering Department
Penn State University
State College, PA, USA

INTRODUCTION

About 250,000 Anterior Cruciate Ligament (ACL) reconstructions are performed every year in the US, resulting in an annual health care cost exceeding $2 billion [1]. ACL injury typically occurs in the physically-active young population. The incidence of ACL injury is greater in males due to greater exposure to physical activity, however, the relative risk of injury per exposure is 2 to 8 times greater in females [2]. Long-term effects of ACL rupture include strength asymmetries, residual pain, and osteoarthritis. Specifically, 50% of individuals who continue playing competitive sports, will develop OA after an ACL repair [3]. ACL ruptures occur when forces, sometimes within physiological limits, exceed the strength of the ACL, which may be compromised due to micro-damage caused by repetitive loading, hormonal effects, genetic factors, or cell-driven abnormal processes. Therefore, in-vivo measurement of changes in the mechanical properties of the ACL can provide valuable information for the evaluation of risk of injury and prevention of ACL injuries. Evaluation of ACL is commonly done using MRI [3], which is expensive and only provides information about size and structure. Ultrasound shear wave elastography (SWE) is an imaging technique designed to non-invasively measure the shear modulus of soft tissues [4]. The objective of this study was to evaluate the repeatability of SWE for quantifying the ACL shear modulus in healthy individuals.

METHODS

To compare the ability of ultrasound of localizing the ACL, a comparison between MRI and B-mode ultrasound was performed in a healthy individual (male, 29 years old). A T2-weighted MR image (Siemens Prisma, 3T, TE: 60 ms, TR: 2000 ms) with fat saturation was performed with the knee bent at 90 degree flexion. B-mode ultrasound images (Verasonics, Vantage 128, L7-4) were obtained from the same individual with the knee also at 90 degree flexion.

The ultrasound elastography method was implemented in a research scanner (Verasonics, Vantage 128). Unique characteristics of our elastography method, compared to commercial scanners, are the ability of precisely locating the push pulses at the insertion of the ACL to create a mechanical wave that propagates along the ACL and the ability of measuring the wave speed when the wave is propagating in a diagonal direction rather than horizontally.

To evaluate the repeatability of the SWE technique and the effect of knee flexion, fifteen healthy patients (Mean age ± SD, 21.13±1.25; Mean BMI ± SD, 22.14±5.06) were recruited in this study. All subjects had a dominant right leg. During the measurement, the participants were asked to lie supine with the knee joint in three different positions: 90 degree flexion in the knee, 120 degree flexion in the knee, and fully flexed knee posture, where the tibia is perpendicular to the patient bed (Fig 1). An angle adjustable knee brace was used to secure the knee. The ultrasound transducer was placed between the patella and the tibia plateau and the measurements were performed in both knees. To evaluate day-to-day reliability, the same procedures were repeated on two different days with an interval of at least two days.

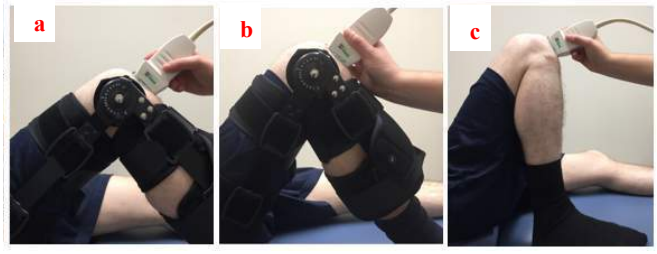

Figure 1: Experimental setup for the ACL SWE when the participant is at: (a) 90 degree of flexion in the knee (b) 120 degree of flexion in the knee (c) fully flexed knee posture.

Poster Presentation #P024

RESULTS

The comparison between the knee MRI and ultrasound images shows that it is possible to the distal portion of the ACL using ultrasound.

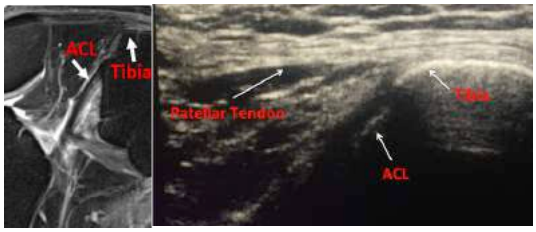

Figure 2: MRI image of the ACL (left), Ultrasound image of the ACL (right)

The shear wave propagation within ACL is shown in Fig. 3. There was not a significant difference between the shear wave speed in dominant and nondominant leg. The shear wave speed increased with increasing the knee flexion and putting more tension on the ACL.

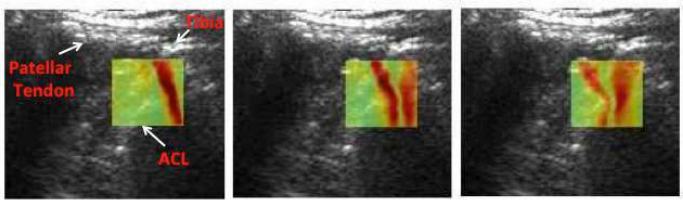

Figure 3: The shear wave (red) propagation of the ACL at different time steps: (a) 5 ms, (b) 20 ms, (c) 40 ms, after transmitting push pulses.

The shear wave speeds within ACL at each posture are shown in Figure 4. The Between-days intraclass correlation (ICC) (95% CI) for the ACL shear wave speed was 0.83 (0.74-0.89), suggesting excellent reliability. The standard deviation and standard error of the mean at each posture is shown in Table 1.

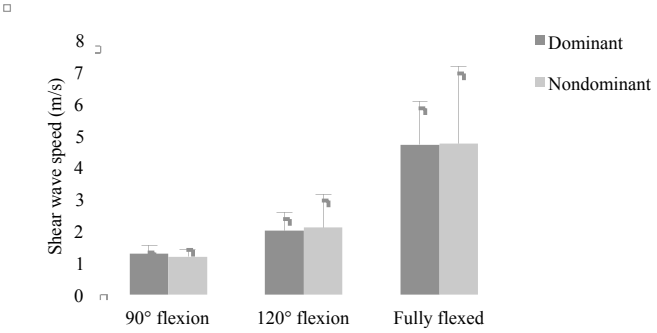

Figure 4: Shear wave speed within ACL increased with increasing of the knee flexion (mean ± standard deviation)

Table 1: Standard deviation (SD) and error of the mean (SEM) at different postures for the ACL measurements.

Flexion angle	SD, SEM (m/s)
90 degree	0.23, 0.09
120 degree	0.91, 0.37
Fully flexed	1.63, 0.67

DISCUSSION

The present study investigated the reliability of the SWE technique for evaluating ACL shear modulus in healthy individuals. The results suggest that ultrasound SWE could be a repeatable tool for quantifying the change in ACL shear modulus. The shear wave speed within ACL is increased with increasing the flexion of the knee, suggesting that ultrasound SWE is sensitive to the loading of the ACL. The correlation is significant because it provides the changes in mechanical properties of the ACL in motion. Studies have shown that the ACL provided more than 80% of anterior restraining force from 30° to 90° of knee flexion, while other ligamentous structures such as the medial joint capsule, the iliotibial tract, and the medial and lateral collateral ligaments provided no relevant secondary restraint to this motion [5].

There are several mechanisms responsible for change in the mechanical properties of ACL. Jones et al. [6] found a correlation between the mechanical properties of the ACL and stiffness, bodyweight, and physiological loading. Ultimate failure load was found to have a significant correlation with bodyweight whereas there was no statistical difference of stiffness at different ages. Non-contact modes of failure, such as tensile or torsional ruptures and tears, are also important in decisions for surgical reconstruction of the ACL [6]. SWE can be used to track these mechanisms that alter the mechanical properties of the ACL.

Our proposed protocol for evaluating the ACL shear modulus using SWE offers several potential applications for trainers, coaches and practitioners**.** It may also potentially improve ACL reconstruction surgery and current rehabilitation protocols. This method is safe and non-invasive, which allows evaluation of the ACL directly in patients. This technology opens new avenues of research for evaluating the different tissues used as ACL grafts, and their adaptation after surgery. First, it can be used as a potential tool for evaluating the health status of the ACL and early detection of injury for future sports medicine applications. For example, it could be used to routinely monitor the ACL of athletes during a season in order to understand if an ACL is injured or if it has a higher risk of injury. Second, it could also be applied to evaluate the degree of injury. Several studies have shown that allografts are more likely to fail at the points of insertion compared to autografts [7]. Third, there is controversy regarding the choice of hamstring verses patellar tendon autographs [7]. SWE may help medical doctors identify the optimal intervention strategy, monitor the recovery process and the effect of the treatment. This may potentially reduce the probability of patients who develop OA and minimize the costs of procedures and rehabilitation. This information can also be carried into other injuries and ligament repairs for further impact on society.

The limitation of this study is that our sample for healthy individuals consisted only students under the age of 25 with a normal BMI. Future studies will focus on evaluating patients with a ruptured ACL and ACL reconstructions. In conclusion, SWE could be a reliable tool for quantifying the changes in ACL shear modulus.

ACKNOWLEDGEMENTS: Penn State Start-Up Funds.

REFERENCES

[1] Buller LT, et, al. Orthopaedic journal of sports medicine. 2014 Dec 26; 3(1):2325967114563664.
[2] Renstrom P, et al. Br J Sports Med. 2008;42(6):394-412.
[3] Norris, R., et, al. The open orthopaedics journal. 2012 6, 506-10.
[4] Cortes DH, et, al. Ultrasound in medicine & biology. 2015 Jun 1;41(6):1518-29.
[5] Dargel J, et, al. *Strategies Trauma Limb Reconstr*. 2007;2(1):1-12
[6] Jones, RS et al. Clinical Biomechanics, 10(7): 339 – 344
[7] Wasserstein D, et, al. Sports Health. 2015;7(3):207-216. doi:10.1177/1941738115579030.

SB³C2019
Summer Biomechanics, Bioengineering and Biotransport Conference
June 25 -28, Seven Springs, PA, USA

EXTRACELLULAR MATRIX STIFFNESS ALTERS CHONDROCYTE PHENOTYPE THROUGH TRPV4 REGULATION

Ryan C. Skinner (1), Mallory Griffin (1), Nicholas S. Trompeter (1), Cindy Farino (1), Omar Banda (1), John H. Slater (1), Randall L. Duncan (1,2)

(1) Department of Biomedical Engineering
University of Delaware
Newark, Delaware, USA

(2) Department of Biological Sciences
University of Delaware
Newark, Delaware, USA

INTRODUCTION

Osteoarthritis (OA) is the most common joint disorder in the United States, affecting over 27 million adults (1). Risk factors for OA include age, obesity, previous injury, and genetic predisposition. The prevalence of OA is predicted to increase as the US population grows older, potentially affecting 25% of adults by the year 2020 (1). The cellular mechanisms of OA progression are poorly understood and current treatments for OA involve joint replacement and pain management. OA is characterized by the degradation of articular cartilage. During the development of OA, the stiffness of the extracellular matrix (ECM) of cartilage decreases due to a degradation of both collagen type 2 and proteoglycans (2). This progression involves a shift in the balance of anabolic factors, that buildup the ECM, and catabolic factors that break down the ECM. The mechanosensitive Transient Receptor Potential Vanilloid 4 (TRPV4) channel conducts calcium and responds to mechanical force, osmolarity, and chemical stimulation. The TRPV4 channel has been shown to play a crucial role in the development and function of cartilage (3). While altering matrix stiffness changes the function and phenotype of mesenchymal stem cells, few studies have investigated the role of altering matrix stiffness on chondrocyte phenotype and function. Therefore, I postulated that the loss of cartilage ECM stiffness would alter the function and phenotype of chondrocytes. The goal of this project was to determine how ECM stiffness influences TRPV4 activity, chondrocyte cytomechanics, and function. Here we show that decreasing the ECM stiffness, modeled by poly(ethylene-glycol) (PEG) hydrogels, reduces the ability of the TRPV4 channel to respond to osmotic challenge.

METHODS

PEG-DA/RGDS Hydrogels: Polyethylene-glycol diacrylate (PEG-DA) was used as the polymer for the hydrogel; Hank's Balanced Salt Solution (HBSS) with calcium and magnesium was used as the buffer; Lithium phenyl-2,4,6-trimethylybenzoylphosphinate (LAP) was used as the photoinitiator. Peptide H-Arg-Gly-Asp-Ser-OH (RGDS, Bachem, Torrance CA), a fibronectin derived cell adhesion peptide, was used for cell attachment. Varying weight percentages of PEG-DA were added into solution to alter the stiffness of the polymerized gel. Hydrogels were made by the Slater Lab at University of Delaware. Hydrogels were tested compressively on an Instron Single Column Tabletop Model Testing System (Model 5943, Norwood MA) to determine the Young's Moduli at different weight percentages of PEG-DA. Weight percentages of 14.1% PEG-DA represents a healthy cartilage stiffness of 350kPa, 9.8% PEG-DA an intermediate model at 175kPa, and 5.2% an osteoarthritic stiffness model at 35kPa were used in these studies.

Cell Culture: Chondrocytes, murine ATDC5 chondrogenic cells (Sigma Aldrich) were cultured on the hydrogel surface. Chondrocytes were grown in DMEM/F-12 50-50 media supplemented with 10% Fetal Bovine Serum (FBS) (Atlas Biologicals) and 1% Penicillin/Streptomycin (Hyclone).

Calcium Imaging: Experiments were conducted as previously describes (4,5). All experiments were conducted at room temperature to avoid temperature-sensitive spontaneous TRPV4-mediated calcium oscillations. Cells were loaded with Fluo-4 (Life Technologies) before being recovered in either HBSS or in 100nM GSK2193874 (GSK219), a TRPV4 antagonist. Cells were challenged with 50% Hypotonic Swelling (HTS) after a 1-minute baseline was recorded.

Poster Presentation #P025

Cytoskeletal Immunostaining: ATDC5 cells were cultured for 48 hours and then serum starved for 24 hours, as previously described. Actin was stained with Phalloidin-iFluor 488.

Statistical Analysis: One-way or Two-way ANOVAS were used to determine significance, with Tukey-Kramer's post-hoc test used to compare between groups. p-values < 0.05 were considered significant.

RESULTS

Graham et al. have shown that compressive and tensile moduli decreases in OA cartilage explants (4). However, how this decrease in mechanical properties of cartilage alters osmosensation of chondrocytes has yet to be studied. TRPV4 is a key osmosensor in chondrocytes, as knock-out of the channel significantly attenuates the response of chondrocytes to osmotic pressure and dynamic load (5). Thus we investigated how altering ECM stiffness changed TRPV4 channel activity. Studies from our lab indicate that polymerization of the actin cytoskeleton can regulate TRPV4 activity. Additionally, decreasing the stiffness of the ECM leads to decreased actin polymerization in cells. Here, we confirm that a decrease in stiffness of the ECM leads to the formation of fewer actin stress fibers (Fig. 1). As the stiffness of the gels was decreased, the intensity of the stain and actin stress fiber formation diminish.

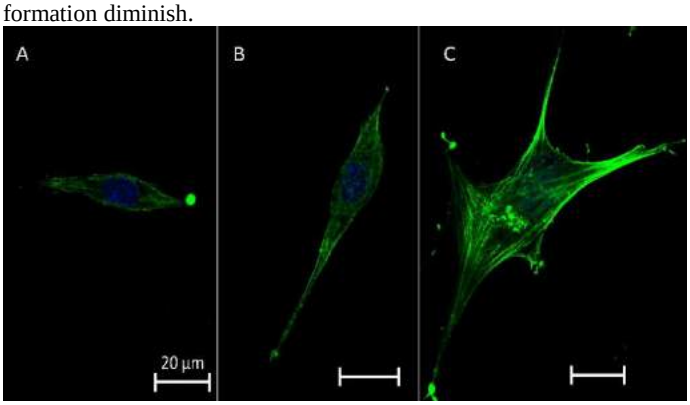

Figure 1: Immunofluorescent staining of ATDC5 cells on PEG hydrogels. A.) 5.2% Osteoarthritic stiffness model with low actin stress fiber formation and low levels of staining, B.) 9.8% Intermediate stiffness model, C.) 14.1% Healthy stiffness model with increased actin fiber formation and high intensity of the stain. n= 1.

Previous results from our lab indicate that increasing actin stress fiber formation attenuates TRPV4 mediated calcium influx. However, the decrease in actin polymerization on the lower PEG-RGDS gels significantly lessened the response of ATDC5s to hypotonic challenge (Fig. 2). To confirm the role of TRPV4 in altered chondrocyte calcium response to changes in stiffness, GSK219 was used to inhibit TRPV4 on the PEG-DA models. When intracellular calcium influx was normalized to the baseline, significant differences between the models materialize (Fig. 2A). Cells grown on the 350kPA gels, representative of healthy cartilage, show significantly higher responses to HTS when compared to cells grown on both the 175 kPa (intermediate) and 35 kPa (OA) gels (Fig. 2B). Additionally, ATDC5 cells grown on the 175 kPA gels show a significantly greater response to HTS when compared to cells grown on the 35kPA gels. Interestingly, inhibition of TRPV4 with GSK219 significantly suppressed the response of cells to HTS when they were seeded on the healthy and intermediate gels, only. When the area under the curves were analyzed, a similar trend to the peak over baseline responses is seen. Chondrocytes grown on the healthy and intermediate gels have a trend of GSK219 inhibiting the responsiveness of the cells to HTS.

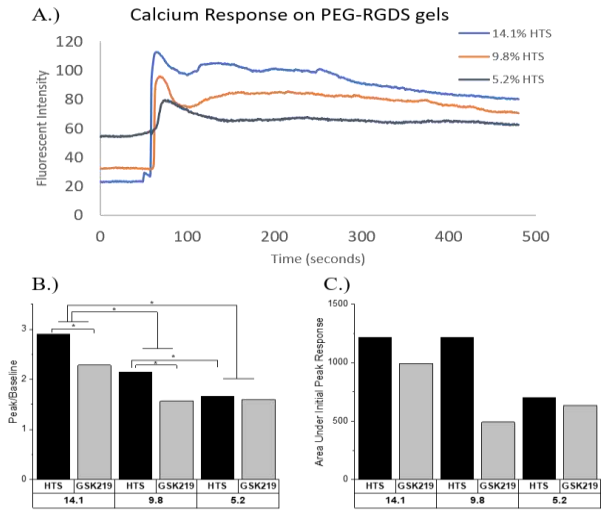

Figure 2: Calcium imaging representative traces on PEG hydrogels. A.) ATDC5 cells stimulated with HTS on 14.1%, 9.8%, and 5.2% gels. B.) Peak/baseline response on gel models with TRPV4 inhibitor GSK219. C.) Area under the curve on gel models. n= 3.

DISCUSSION

Our findings show how ECM stiffness alters TRPV4 activity in chondrocytes. Cytoskeletal staining demonstrated that cells displayed higher actin stress fiber formation on the healthy stiffness model than on both the intermediate and the osteoarthritic stiffness models. Actin stress fibers contribute to the mechanosensitive ability of the TRPV4 channel, with our results indicating that as the stiffness of the ECM decreases, the response of chondrocytes to HTS is suppressed in a TRPV4-depedent mechanism. Han et al have shown that proteoglycan rich microdomains have lower ECM strain, which corresponded to a higher calcium baseline (2). Here, our data confirms that the calcium baseline of ATDC5 chondrocytes is significantly increased as the matrix loses stiffness. Furthermore, cell morphology was altered depending on matrix stiffness, with the appearance of increased cell spreading and cytoskeleton organization on the higher stiffness gels.

Although previous studies from our lab indicate that actin stress fiber formation attenuates calcium influx, our hydrogel models may provide a more physiologically accurate model of chondrocyte behavior. The results suggest that there is an optimal range of calcium stimulation which promotes healthy chondrocyte function, and deviations above or below this range can have adverse effects. Our data indicates that ECM stiffness contributes to the regulation of calcium stimulation and cytoskeletal organization. The balance of TRPV4 activity may play a key role in the progression of OA, as other studies indicate ablation or over-activation of TRPV4 both cause deleterious effects on the phenotype of chondrocytes (2,5). Further studies will explore the role of ECM stiffness on TRPV4 and chondrocyte function through investigating the role of TRPV4 stimulation on these gels and the role of modulating the stiffness on anabolic and catabolic gene expression. This information could provide new ways to target OA progression and improve therapies for OA patients.

REFERENCES

[1] Lawrence, R et al., *Arthritis Rheum*, 58(1): 26-35, 2008.
[2] Han, W et al., *Nature Material.* 15(4): 477-84., 2016.
[3] Hurd, L et al., *Am J Med Gen, Part A*, 165:2286-2293, 2015.
[4] Graham, B et al., *J Orthop Res*, 36(12):3256-3267, 2018.
[5] O'Conor, CJ et al., *PNAS*, 111(4):13-16-1321, 2014.

SB³C2019
Summer Biomechanics, Bioengineering and Biotransport Conference
June 25 -28, Seven Springs, PA, USA

ASTHMATIC AND HEALTHY AIRWAY MORPHOLOGY MEASURED FROM CT-BASED GEOMETRIES

Irina Pyataeva (1), Kamran Poorbahrami (2), Ellesse Cooper (3), Ben Piperno (2), David Mummy (4), Sean Fain (4,5,6), Jessica M. Oakes (1)

(1) Department of Bioengineering, Northeastern University, Boston, MA, USA

(2) Department of Mechanical and Industrial Engineering, Northeastern University, Boston, MA, USA

(3) Department of Biology, Northeastern University, Boston, MA, USA

(4) Departments of Biomedical Engineering, (5) Medical Physics, and (6) Radiology, University of Wisconsin-Madison, WI, USA.

INTRODUCTION

Asthma, characterized by chronic airway inflammation, airway obstruction, and lung remodeling, is one of the most prevalent chronic lung diseases in the US [1]. Lung remodeling causes an increase of the airway wall thickness and a decrease in lumen size in severe asthmatics [2]. The changes in geometry due to remodeling or obstruction result in alteration of airway resistances and respiratory patterns [3]. Due to the high variance in airway geometry of asthmatic patients, it is important to develop a framework to quantify the morphometric differences between asthmatic and healthy patients and correlate these findings to clinical and inflammatory metrics. Understanding the changes in morphology due to asthma may be a key factor to better diagnostics [4]. The main goals of this study are to develop and test a framework to quantify lung morphometry in healthy and asthmatic patients and to compare severe, mild to moderate, and healthy groups to each other. We extract airway lengths, radii, and bifurcation/gravitational angles from 3D realistic CT-based airway models and then study the inter subject variability between each severity group.

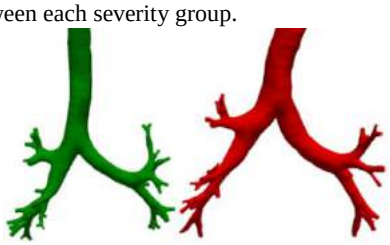

Figure 1. ***Model rendering for the healthy subject (green) compared to the severe asthmatic subject (red).***

METHODS

Our group created airway geometries for 3 healthy, 5 mild-moderate, and 6 severe asthmatic patients from high-resolution CT scans acquired at Total Lung Capacity (TLC) (Fig. 1). The demographic information is presented in Table 1. Centerlines for each model were extracted in SimVascular [5] in form of discrete points in space with minimum inscribed sphere radius associated with each point.

Table 1. ***Demographic information in form of mean ± standard deviation.***

	Gender	Height (cm)	TLC volume (ml)
Healthy	1 m, 2 f	167.7±8.4	4697±1894
Moderate	3 m, 2 f	175.8±9.9	6333±928
Severe	5 m, 1 f	180.0±4.1	7304±310

Next, centerline data was imported in Matlab to reconstruct and analyze the geometry (Fig. 2). Data exported from SimVascular were in the form of discrete points in a list format. For each point, we obtain the XYZ coordinate location and the minimum inscribed sphere radius. The developed Matlab code separates the points into individual branches and connects them together to form a complete lung geometry.

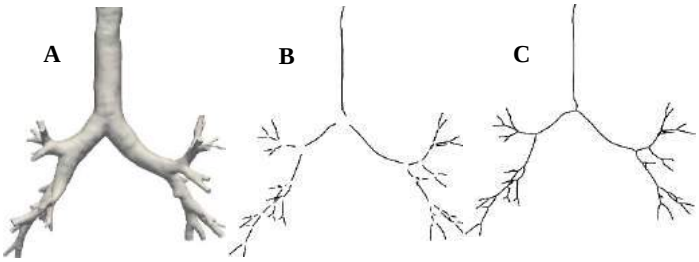

Figure 2. ***The process of reconstructing centerline geometry for a moderate asthmatic subject. A. 3D rendering of the model. B. Centerline points extracted and assigned to branches. C. Branches are joined together.***

After the geometry is fully reconstructed, the algorithm computes the total length of each airway branch. Next, we determine the average, maximum, and minimum radius for each branch from the minimum inscribed sphere radius associated with each point. We identify the key anatomical regions of interest and recorded and compared values for these regions.

Finally, we compute the main bifurcation angle at the location where the trachea splits into the main right and left bronchi (Fig. 3). To do this, we determine the best fit lines through the centerline points in all three dimensions, using a total least squares analysis for the left main bronchi, the right main bronchi, and the trachea. From these lines, we find the total angle of bifurcation (angle α) and the bifurcation angle between the trachea and main right and left bronchi (angles β and γ).

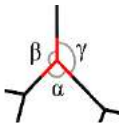

Figure 3. ***Angle of bifurcation measurements*.**

RESULTS

We found the average airway radii for healthy, moderate, and severe asthmatic groups. Radii data was normalized by subject's lung volume to account for differences in lung size between subjects and is plotted in Fig. 4. Error bars represent inter-subject variability. We choose to plot the radii by anatomical region to correlate results with defects measured with HP ^{3}HE MRI data in future studies.

We observed a higher variability in healthy subjects due to a limited sample size and an outlier in form of a female subject with a low TLC lung volume of 2487 ml. The variability of height is also greater in the healthy subjects, and height is known to correlate with lung dimensions, increasing radii range.

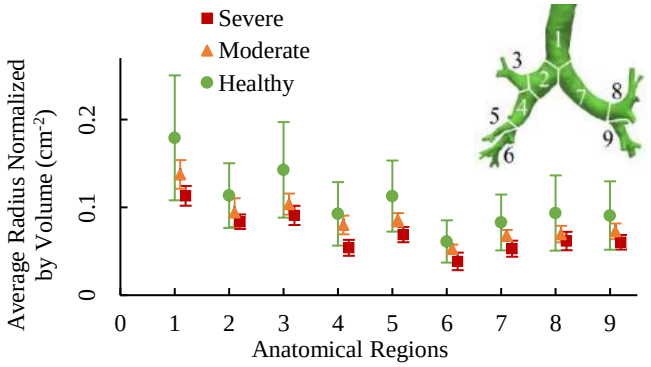

Figure 4. ***The average airway radii normalized by volume at different anatomical regions. Region definitions: trachea (1), right main bronchus (2), right superior lobar bronchus (3), right superior to middle conducting bronchus (4), right middle lobar bronchus (5), right inferior lobar bronchus (6), left main bronchus (7), left superior lobar bronchus (8), and left inferior lobar bronchus (9).***

We also found the average airway length for the same key anatomical regions with an exception of trachea for the three groups in Fig. 5. Trachea is excluded from the length analysis because only the lower portion of the trachea geometry was modelled for this study. We observed that the airway average length and variability doesn't seem to change significantly with asthma progression.

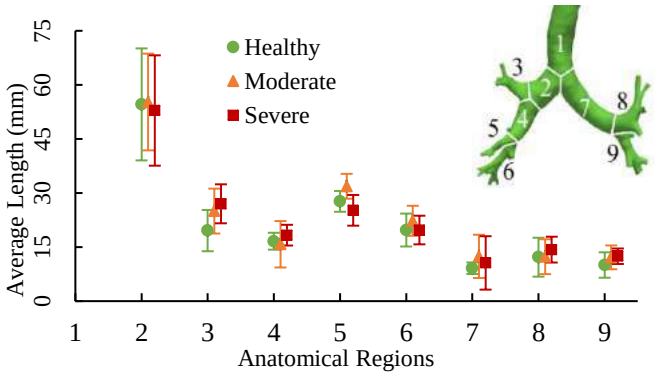

Figure 5. ***The average airway length measured at different anatomical regions of the models.***

For the given models we also obtained bifurcation angles, as illustrated in Fig. 3 for the three groups. We observed an increase in variability of the total angle of bifurcation with asthma progression. There is also an increase in average total bifurcation angle for the moderate group compared to the healthy group.

Table 2. ***Angles of bifurcation across three groups in form of mean ± standard deviation.***

	α (degrees)	**β (degrees)**	**γ (degrees)**
Healthy	87.99±5.55	145.02±21.85	125.58±20.14
Moderate	102.56±13.39	119.32±13.33	135.91±11.99
Severe	87.68±16.25	129.53±13.93	143.08±8.28

DISCUSSION

Using the framework described above, we successfully acquired length, as well as average, maximum, and minimum radius for the key airways of 6 severe, 5 moderate, and 3 healthy patients. We determined that the average airway radius normalized over volume appears to decrease with asthma progression. However, the airway length between the groups doesn't seem to change significantly with asthma progression. The total angle of bifurcation and its variability seem to increase with asthma progression. Our findings align well with previously documented airway constriction and increase of bifurcation angle in severe asthmatic patients [6]. We plan to increase our sample size and analyze correlations with physiological parameters in future studies.

ACKNOWLEDGEMENTS

This work is supported by NIH/NHLBI R21 HL140436-01. Human data collected was facilitated by: NIH/NHLBI R01 HL069116; R01 HL080412; U10 HL109168; NIH/NCATS UL1TR000427.

REFERENCES

[1] Akinbami, L et al., *National Center for Health Statistics*, 2011.

[2] Choi, S et al., *The Journal of Allergy and Clinical Immunology*, vol. 140, no.3, pp. 690–700.e8, 2017.

[3] Fehrenbach, H et al., *Cell and tissue research*, 367, 3:551-569, 2017.

[4] Montesantos, S et al., *PLOS ONE*, 12(7), p.e0182052, 2017.

[5] Updegrove, A et al. *Annals of biomedical engineering* 45.3 (2017): 525-541

[6] Choi, S et al., 2014. *American Journal of Respiratory and Critical Care Medicine*, Vol.189, 2014.

SB³C2019
Summer Biomechanics, Bioengineering and Biotransport Conference
June 25 -28, Seven Springs, PA, USA

CONTRIBUTIONS OF COLLAGEN II, LAMININ, AND FIBRONECTIN TO VITREORETINAL ADHESION IN HUMAN EYES

Joseph D. Phillips (1), Christopher J. Creveling (1), Brittany Coats (1)

(1) Mechanical Engineering
University of Utah
Salt Lake City, Utah, USA

INTRODUCTION

Vitreoretinal adhesion plays an important role in ocular health and pathologies. In aging eyes, the vitreous undergoes syneresis and gradually separates from the retina, often resulting in posterior vitreous detachment (PVD). In an incomplete PVD, lingering vitreoretinal attachments exert tractional forces on the retina, causing sight-threatening damage such as macular holes and edema [1]. However, vitreoretinal adhesion mechanisms are not well understood. Previous research suggests that collagen as well as non-collagenous proteins, such as laminin and fibronectin, are critical components of the vitreoretinal interface modulating adhesion, and are often the targets of pharmacologic vitreolysis to induce a full PVD [2]. However, proteins have not been quantified, nor do we know their contribution to vitreoretinal adhesion. The objectives of this study were to (1) quantify collagen II, fibronectin, and laminin at the vitreoretinal interface and identify differences by region and with age, and (2) identify correlation of each protein density with regional vitreoretinal adhesion. These data will, for the first time, provide quantitative data regarding the regional mechanisms of adhesion at the vitreoretinal interface.

METHODS

A custom rotational peel test system was used to measure the adhesive strength between the vitreous and retina in human eyes (n=26) as described in [3] and shown in Figure 1. Maximum and steady state peel force were measured in the equator and posterior regions of each eye. After the peel test, specimens of unpeeled retina were collected from regions adjacent to the peeled retina. The vitreous was collected with each specimen to ensure an intact vitreoretinal interface. The specimens were then placed into a fixative solution of 1% buffered formaldehyde and 1.25% glutaraldehyde.

Following fixation, 3-4 micron sections were cut from each specimen and stained for collagen II, laminin, and fibronectin using immunohistochemistry (IHC). Digital images of each stained vitreoretinal specimen were acquired on an automated slide scanner (ZEISS Axio Scan, ZEISS, Oberkochen, Germany) and processed by a custom MATLAB program (The MathWorks, Inc., Natick, Massachusetts). The custom program segmented the image by color based on a k-means clustering algorithm, and the user identified the protein in the image. The protein density was calculated as a unitless pixel ratio by dividing the total number of stained pixels in the image by the geometric pixel length of skeletonized retina. An example image showing the segmented protein pixels and the skeletonized retinal length is shown in Figure 2.

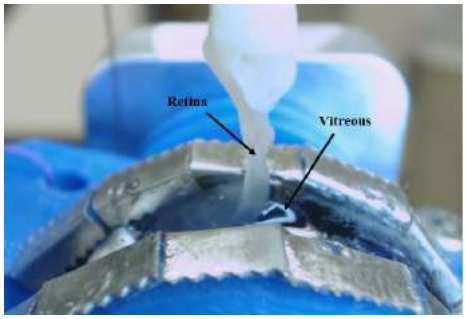

Figure 1: Image of the custom peel test system described in [3]. The retina is peeled from the vitreous as the device rotates.

Collagen II, laminin, and fibronectin are known to be present at the vitreoretinal interface [2]. Stained pixels were only accounted for in the density calculation if they were considered part of the vitreoretinal interface. Images with no stain were assumed to be due to processing artifacts and excluded from the analysis.

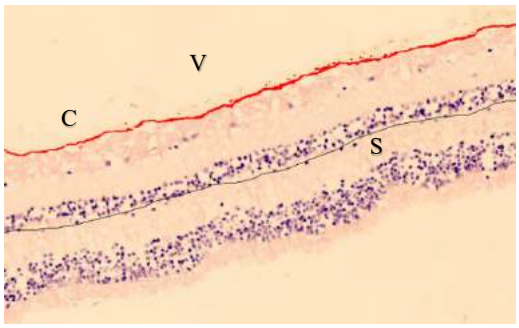

Figure 2: IHC image of a human retina from the posterior of a 70-year old donor. Collagen II (C) is shown in red at the vitreoretinal interface separating the retina from the vitreous (V). The retina is converted into a skeletonized line (S) to estimate retinal length.

Paired Student's t-tests were used to determine significant differences in protein density between regions of the eye (equator and posterior pole). We previously reported a significant decrease in equatorial and posterior pole adhesion after 60 years of age [3], so these analyses were performed first with all ages combined, and then repeated for individuals ≤60 years of age and those >60 years of age. Finally, collagen II, laminin, and fibronectin density were statistically correlated with the maximum peel force measured adjacent to each specimen. A p-value <0.05 was considered significant.

RESULTS

Collagen II was significantly greater in the equator (9.22±5.53) than in the posterior pole (4.24±1.71, p=0.024), and did not significantly change with age. Laminin and fibronectin exhibited interesting age- and region-dependent trends. Specifically, there was no difference in laminin density between the equator or posterior pole until after 60 years of age (Figure 3A). At this age, laminin in the posterior pole (3.69±2.23) decreased to levels lower than the equator (5.10±2.36). Conversely, fibronectin in the posterior pole was greater than the equator (5.51±2.50 vs 3.31±1.46), but decreased after 60 years of age in the posterior pole to equal density in the equator (Figure 3B). The trends with laminn and fibronectin were not statistically significant due to limited specimens in some groups.

Collagen II significantly increased with increasing maximum peel forces (p=0.02, Figure 4A,B), but only in the posterior pole. Interestingly, laminin significantly increased with increasing maximum peel forces (p=0.01, Figure 4C,D), but only in the equator. Fibronectin had a positive correlation (r=0.50) with maximum peel force in the posterior pole, but this trend was not significant (p=0.25).

DISCUSSION

In this study we quantified collagen II, laminin, and fibronectin at the vitreoretinal interface, and identified age and region-dependent differences. Further, we found significant region-dependent correlations of proteins with adhesion force that suggest different mechanisms of adhesion between the equator and the posterior pole.

Collagen II was significantly greater in the equator compared to the posterior pole and did not change with age. This corroborates observations made in previous studies [4]. Interestingly, collagen II correlated with vitreoretinal adhesion in the posterior pole, but not the equator. This supports theories of differing mechanisms of adhesion between the equator and posterior pole. In the posterior pole, collagen fibers running anterior to posterior may penetrate the inner limiting membrane (ILM) to tether the vitreous to the retina. This is corroborated by the data in the present study and from our previous study [3] which

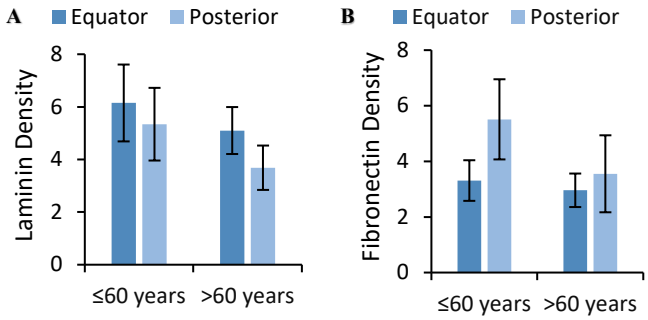

Figure 3: (A) Laminin and (B) fibronectin density by age for each region. Error bars represent standard error.

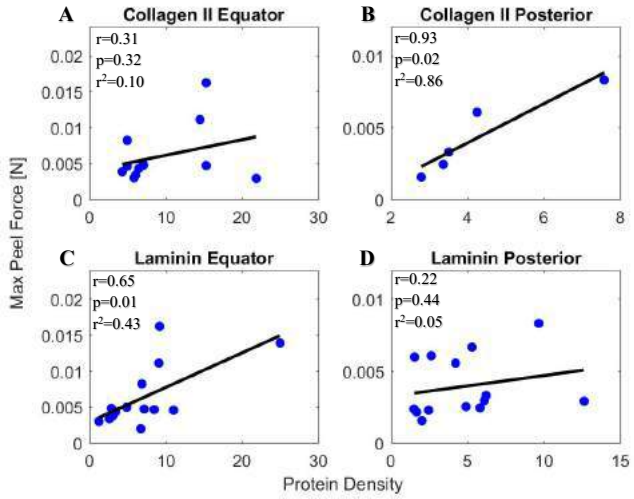

Figure 4: Correlation of collagen II (A,B) and laminin (C,D) density to maximum vitreoretinal peel force in the equator and posterior pole.

found ILM rupture was significantly higher in the posterior pole after peeling compared to the equator, despite requiring lower adhesive forces for failure. We believe the increased ILM rupture is due to collagen fiber pull-out.

In the equator, only laminin density was significantly correlated to vitreoretinal adhesion, even though this region had higher amounts of collagen II compared to the posterior pole. This suggests sheet-forming adhesive proteins, such as laminin, create adhesion between the vitreous and the retina in the equator. Fibronectin also increased with maximum peel force in the equator, but the trend was not significant. Therefore, fibronectin, and potentially other proteins, may also contribute to vitreoretinal adhesion in the equator.

ACKNOWLEDGEMENTS

Support for this work was provided from the National Eye Institute with the National Institutes of Health award no. R21EY025813. The authors thank the Utah Lions Eye Bank, and donor families for providing human donor eyes.

REFERENCES

[1] De Smet et al., *Ophthalmologica*, 230:165–178, 2013.
[2] Bu et al., *PLoS One*, 10:1–23, 2015.
[3] Creveling et al., *Front. Bioeng. Biotechnol.*, 6:1–11, 2018.
[4] Bishop, *Prog. Retin. Eye Res.*, 19:323-344, 2000.

SB³C2019
Summer Biomechanics, Bioengineering and Biotransport Conference
June 25 -28, Seven Springs, PA, USA

RAPID QUANTITATIVE ASSESSMENT OF POSTURAL CONTROL FUNCTION FOR MILD TRAUMATIC BRAIN INJURY: EVALUATION OF A PORTABLE FORCE PLATE DEVICE

Jonathan P. VanPaepeghem, Kunal Dave, Liying Zhang

Biomedical Engineering
Wayne State University
Detroit, MI, United States

INTRODUCTION

As reported by the Center for Disease Control and Prevention (CDC), concussions, also known as a mild traumatic brain injury (mTBI), are a major public health disorder.[1] A recent report estimated between 1.6–3.8 million sports-related mTBIs occur annually in the U.S. alone, but this number is likely greater due to underreported mTBIs arising the failure of injury recognition.[2] It is reported nearly 250,000 U.S. military service members were diagnosed with a mTBI since 2000, yet this number is also believed to be underestimated due to underreporting.[3] Unfortunately, those with acute mTBIs often have subjective, nonspecific complaints and only undergo a routine physical exam. The only way such mTBIs can be diagnosed is through expensive testing and/or subjective clinical evaluation. In a military environment, mTBI results are interpreted by relatively small numbers of highly trained health care providers, resulting in delays in diagnoses and treatment. Currently there is no effective measurement tool that can be administered quickly and accurately by a broad range of medical staff in multiple environments to assist in diagnosing mTBIs and help provide consistent, objective evidence-based care.

The Balance Error Scoring System (BESS) is the most commonly used postural control evaluation tool for sports-related mTBIs. It assesses an individual's ability to maintain balance based on information from the vestibular systems and somatosensory signals that the brain receives from the muscles and joints. The BESS is an emerging tool for sideline mTBI evaluation, as it allows for postural assessment in the absence of instrumented balance devices.[4] When conducting a BESS test, the subject is asked to position themselves in three stances: double-leg stance, single-leg stance, and a tandem stance in a heel-to-toe fashion. All three stances are performed on both a firm surface and again on a foam surface, with the eyes closed during a 20-second trial. During each trial, the test administrator will count each of the six errors that may occur and a final score is provided at the end of the six trials (errors include opening of the eyes, lifting hands off the iliac crests, stepping or stumbling and falling out of position, lifting the forefoot or heel, abducting the hip > 30º, or failing to return to the test position in more than 5 seconds.[5]

While it has been reported that the BESS has moderate to good reliability to assess static balance, it faces multiple limitations when administered independently.[6] The test is extremely subjective with high test-variability, and is subject to the skill of the observer administering the test.[5,7] In addition, discerning a false positive from an intentioned act is difficult for the observer to detect with the naked-eye. The SiM – 1000 Portable Force Plate[8], is a computerized balance assessment device designed for athletic teams and health care professionals to quickly and objectively diagnose a mTBI. It is a FDA Class 1 balance assessment medical device. The SiM – 1000 utilizes accurate, durable, and reliable automotive sensor technology to detect weight sway through various mechanical measures, and is also robust and portable, weighing only 35 lbs. Previous studies have reported that the SiM – 1000 provides objective balance data with a high correlation to the visual BESS.[8] This portable device has the potential to provide quick, objective early identification of mTBIs on the sideline and in a military setting. However, sufficient research is needed to establish its utility. The current study was conducted to further verify the accuracy of the balance score obtained between the SiM – 1000 device and the visual BESS on a healthy population.

METHODS

Research was conducted on a total of twenty-six university students between the ages of 19 and 33 years (mean ± SD = 23.8 ± 3.56) who volunteered to perform the test. Before each test, subject sex (23 male, 3 female), weight (71.6 ± 13.3 kg), height (173.9 ± 7.34 cm), and known medical conditions relating to postural instability were recorded for potential use in future research. Subjects were fully informed of the

proper positioning for each stance of the BESS test and instructed to remove their shoes for each of the trials. Each test subject completed all six 20-second trials of the BESS test while standing on the SiM – 1000 Portable Force Plate. Each subject was video recorded with an iPhone 7 for the duration of the six trials.

After the completion of all trials, the overall BESS and individual stance scores output by the SiM program were recorded. The recorded video for each subject was analyzed and the number of errors were manually counted and recorded in compliance with the BESS protocol.[5] The total and individual stance scores output by the SiM program were then correlated with the associated manual scores from each video in order to determine the efficacy of the SiM program. Linear regression analysis was used to correlate the SiM program and manual scores for each of the six individual stances and total scores from all subjects.

Trials were also completed in which a subject intentionally committed errors during each stance to determine if the SiM program can discern between intentional and legitimate errors. The SiM program output parameters including Lateral Sway Length, Anterior-Posterior Sway Length, Vector Sway Length, and Vector Sway Velocity were also analyzed to determine how the program defines errors.

RESULTS

The total SiM scores and manual scores for each of the twenty-six subjects is shown in Figure 1. The coefficient of determination of the linear regression was $R^2 = 0.6005$. When plotting the SiM scores and manual scores for the individual stances, it was found that the single-leg foam test score had the poorest R^2 value of the six stances ($R^2 = 0.3715$, individual stance avg. $R^2 = 0.6226$). The SiM score for the single-leg foam tests were found to be consistently lower than the manual scores.

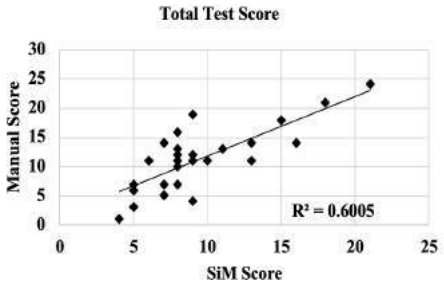

Figure 1: Correlation of Total BESS Score (SiM vs. Manual)

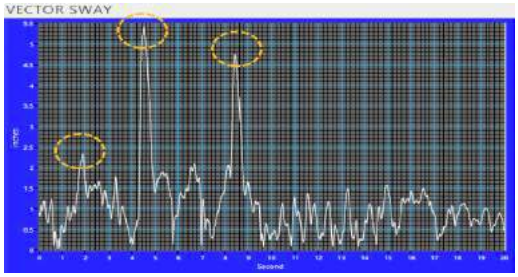

Figure 2: Vector Sway Length Plot with Indicated Peaks

Figure 2 shows the peaks of the Vector Sway Length plot of the single-leg foam stance that occurred at the same instant manual errors were recorded from the video analysis. The initial peak present at 2-seconds correlated with a minor sway in which the subject abducted the hip > 30º, and the two prominent peaks occurring at 5- and 8-seconds correlated with foot taps on the platform. It was found that among all of the output parameters, the peaks and timing of the Vector Sway Length plot correlated well with when a subject came out of position and tapped the platform with their foot.

When the intentional errors of opening the eyes, lifting the hands off the iliac crests, and abducting the hip > 30º were committed in each of the stances, the SiM program usually did not award an error. This was verified by the Vector Sway Length measure. When the intentional errors of stepping or stumbling and falling out of position, lifting the forefoot or heel, or failing to return to the test position in more than 5-s were committed, the SiM program did award an exact number of errors.

DISCUSSION

The findings suggest that the correlation between the total BESS score automatically reported by the SiM program and total score recorded manually via video analysis is sufficient. In general, the SiM program can effectively detect the errors of stepping or stumbling and falling out of position, lifting the forefoot or heel, or failing to return to the test position in more than 5-seconds, regardless of whether or not a trained administrator was conducting the test.

When the errors of opening of the eyes, lifting hands off the iliac crests, and abducting the hip > 30º were committed deliberately by the test subject, an error score was likely to be awarded by the manual BESS method. When using the SiM, the Vector Sway Length measured by the load cell effectively detects the stability or minimal sway that was present during the act and does not usually award what would be considered an intentional error. This demonstrates that the SiM can provide a more accurate and consistent evaluation of postural imbalance.

When analyzing the SiM program scores for the individual stances, a discrepancy was found with the detection of "simultaneous" errors. When two detectable errors are committed within one-second or less from another, the SiM program only awards one error, while the manual scoring protocol would award two discrete errors.[5] Thus, it is evident that the SiM program defines "simultaneous" as any number of errors that occur within one-second or less from another. According to the BESS manual, "simultaneous" errors are only counted as a single error, but no time interval limit between the two consecutive errors was specified.[5] The interval between "simultaneous" errors in BESS tests requires further clarification. It is feasible that the Vector Sway Length history analyzed by the SiM can assist medical professionals with improving the definition of "simultaneous" errors.

The peaks of the Vector Sway Length plot were a strong indicator of errors in most trials, but it is unclear how the SiM program specifically assigns those errors (the threshold level is unreported). For the single-leg foam stance, the SiM consistently underpredicted the scores, suggesting the error threshold setting for this case should be improved.

The SiM – 1000 Force Plate device is unique in that it is portable, durable, weather resistant, and produces consistent objective BESS scores. Future studies are required to verify the SiM using a large sample population and research should investigate the correlation between SiM BESS scores, symptoms, and clinical history data following mTBIs.

ACKNOWLEDGEMENTS

Naval Medical Logistic Command Contract N6264518C401.

REFERENCES

[1] Centers for Disease Control and Prevention (CDC) Report, 2003.
[2] Langlois, JA. et al. (2006). J. Head Trauma Rehabilitation 21(5): 375–378.
[3] Helmick, KM. et al. (2015). Brain Imaging and Behavior 9(3):358-366.
[4] Bell, DR. et al. (2011). Sports health. 3(3): 287-95.
[5] Balance Error Scoring System (BESS). University of North Carolina's Sports Medicine Research Laboratory, Chapel Hill, NC 27599-8700.
[6] Kelly, KC. et al. (2014). Journal of Athletic Training 49(5): 665-673.
[7] Finnoff, JT. (2009). *PM & R*, 1(1): 50-54, doi:10.1016/j.pmrj.2008.06.002.
[8] *Safety in Motion*, www.sim-technologies.com.

SB³C2019
Summer Biomechanics, Bioengineering and Biotransport Conference
June 25 -28, Seven Springs, PA, USA

MECHANICAL INFLUENCE OF GRAPHITIC CARBON NITRIDE FILLER ON POLY(VINYL ALCOHOL) THIN FILM HYDROGELS FOR WOUND HEALING

Bradley S. Henderson (1), Katelyn F. Cudworth (1), Andrew Clifford (2), Dylan Quintana (2), John Thurston, Ph.D. (2), Trevor J. Lujan, Ph.D. (1)

(1) Department of Mechanical and Biomedical Engineering
Boise State University
Boise, ID, USA

(2) Department of Chemistry
College of Idaho
Boise, ID, USA

INTRODUCTION

Poly(vinyl alcohol) (PVA) hydrogels are often used in wound healing due to their biocompatibility, biodegradability, and their hydrophilic nature. Their unique ability to absorb a substantial amount of water in comparison to their dry weight allows for elevated nutrient transport, controlled fluid exchange, and possible pain relief. Graphitic carbon nitride (g-C_3N_4), a photo-responsive biomaterial, can be used as a filler in PVA hydrogels to create a non-toxic electrostatic polymer that promotes an antimicrobial solution at the injury site and accelerates the healing process. The selection of an ideal concentration of g-C_3N_4 will depend on how this filler influences the mechanical properties of the film. A film that is too strong will cause atrophy of surrounding tissues from stress shielding, while a film that is too weak may result in mechanical failure.

The objective of this study is to determine the mechanical effect of adding varying amounts of g-C_3N_4 filer to PVA based films. It is expected that increases in the filler concentration will increase the film's stiffness, strength, and durability.

METHODS

Thin films were fabricated by combining 1.5 g of PVA with 15 mL of H_2S0_4 (0.5 M), which was then stirred at 95 °C until dissolution of the material occurred. Different weight percentages of carbon nitride filler (0, 0.67, 3.33, and 6.67%) were then added to 4.5 mL of dH_2O and sonicated for 15 minutes resulting in four test groups. These percentages were selected because they demonstrate antimicrobial activity. The g-C_3N_4 mixture was added to the PVA solution and stirred. The resulting mixture was then processed and casted forming the final product. Relative crystallinity of the PVA films was quantified by using Fourier transform infrared spectroscopy to measure the area ratio of two vibrational modes (A_{1140}/A_{1127}).

Uniaxial tensile experiments were performed on the thin films using a mechanical testing system (Fig. 1A). The films were submerged in 0.9% saline solution at room temperature for 24 hours prior to punching the specimens into dog bone shaped coupons (Fig. 1B, left). Coupon dimensions were based on industry standards for polymer films (ISO 527-3),[1] and emery cloth tabs were applied to the coupons using cyanoacrylate to prevent slipping. Tabbed specimens were loaded into an E10000 mechanical test system (Instron, Norwood, MA) with an average grip-to-grip length of 16.2 ± 1.0 mm (Fig 1A).

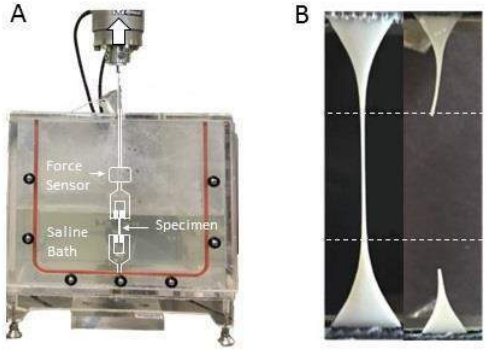

Figure 1: Mechanical testing setup and analysis. A) Specimens were immersed in a saline bath and pulled in tension (white arrow). B) Each specimen was punched in a left) dog bone shape to right) promote failure in the midsubstance of narrow gauge region (within the white dashed lines).

A preload of 0.05 N was applied, and front and side images were taken with a digital camera. The test chamber was filled with 0.9% saline solution at room temperature (21.8 ± 0.3 ℃) and the coupon was allowed to equilibrate in the saline bath for ten minutes before being pulled to failure at 1% strain/s. All analyzed specimens failed in the midsubstance (Fig 1B, right), except for four specimens in the 0% group that failed near a grip. Eight specimens were tested in each group (0, 0.67, 3.33, and 6.67%), for a total of 32 tests.

The experimental data was analyzed with a custom MATLAB script. Image processing methods[2] were used to calculate specimen width (0.35 ± 0.05 mm) and thickness (0.26 ± 0.04) in the narrow-gauge region. Engineering stress and engineering strain curves were generated for all tests (Fig. 2). Tensile strength and failure strain were calculated at the ultimate tensile stress, energy density to failure, which is a measure of durability, was calculated as the area under the stress-strain curve, and tensile modulus, a normalized measure of stiffness, was calculated as the linear slope of the stress-strain curve. The effect of carbon nitride filler on tensile strength, failure strain, energy density to failure, and tensile modulus was determined using a MANOVA, followed by Bonferroni post-hoc tests for multiple comparisons.

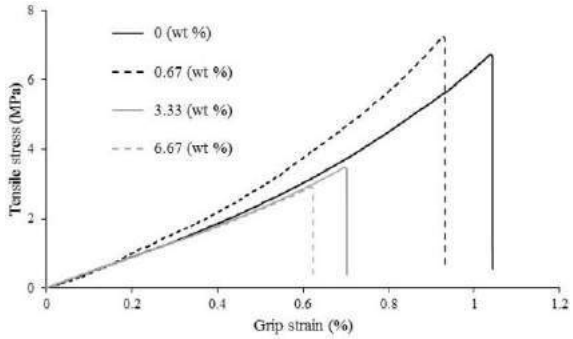

Figure 2: Stress-strain curves of representative specimens from each group with different percentages of carbon nitride filler.

RESULTS

The 0.67% group had an average increase in tensile strength, failure strain, and energy density to failure of 67%, 45%, and 130%, respectively, when compared to the 6.67% group. ($p < 0.05$) (Fig. 3A, 3B, 3C).

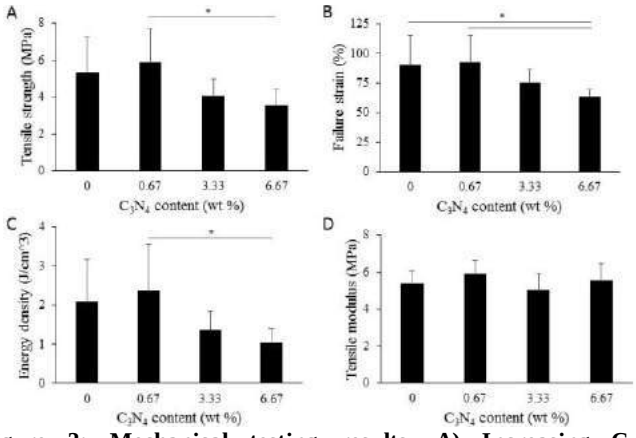

Figure 3: Mechanical testing results. A) Increasing C_3N_4 concentration decreased tensile strength, B) decreased failure strain and C) decreased energy density to failure. D) Increasing C_3N_4 concentration had no significant effect on tensile modulus. * = significant difference between C_3N_4 content.

Linear modulus and linear stiffness showed no significant differences between sample groups (Fig. 4D) ($p < 0.05$).

Changes in tensile strength at each concentration level of C_3N_4 were reflected by similar changes in relative crystallinity (Fig. 4).

DISCUSSION

The mechanical properties of thin film PVA hydrogels were influenced by the concentration of C_3N_4 filler. Specimens with increased filler concentrations exceeding 0.67% had reductions in tensile strength, failure strain, and energy density to failure while tensile modulus remained unchanged (Fig. 3). Structural changes in crystallinity were followed by functional changes in mechanical behavior, suggesting that mechanical properties can be controlled by adjusting the ratio of crystalline and amorphous regions during film fabrication (Fig. 4).

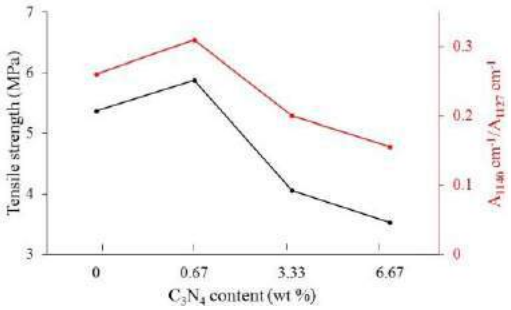

Figure 4: Comparison of the relative crystallinity and tensile strength at each weight percent of carbon nitride filler.

The results from this study did not support our hypothesis, as mechanical integrity was decreased when adding filler above a threshold of 0.67%. One explanation is that above a threshold the filler may cause material disorganization and plane slippage[3,4]. The average tensile strength of the pure PVA films in the present study was 5.4 MPa, which is comparable to human skin tissue (2–15 MPa)[5], but is considerably less than studies by Wang et al. and Liang et al. that reported tensile strengths of 20 MPa and 50 MPa, respectively[6,7]. This may be due to variations in PVA fabrication methods and mechanical testing techniques. For instance, unlike previous studies, the present study tested specimens in a saline bath to more closely simulate physiological conditions. Another distinction of our mechanical test protocol was the reporting of failure location (i.e. midsubstance vs. grip). In the present study, all analyzed specimens failed in the midsubstance, except four specimens in the pure PVA group. This indicates that the tensile strength and failure strain of the pure PVA specimens may be slightly underestimated relative to the specimens with carbon nitride filler added to the PVA. In summary, this study developed and applied an accurate test methodology to determine the mechanical influence of graphitic carbon nitride filler on PVA films.

ACKNOWLEDGEMENTS

This study was funded by the National Institute of General Medical Sciences (P20GM109095).

REFERENCES

[1] [ISO527-3: 1995IEI] [2] Creechley, J et al., *J Mech Behav Biomed Mater*, 69:185-192, 2016. [3] Kouser, R et al., *Mat Sci Eng C-Mater*, 84:168-179, 2018. [4] Zhang, L et al., *J. Mater. Chem*, 21:10399-10406, 2011. [5] Dunn, M et al., *Connect Tissue Res*, 12:59-70, 1983. [6] Wang, J et al., *Sep. Purif. Technol*, 188: 24-37, 2017. [7] Liang, J et al., *Adv. Funct. Mater*, 19:2297-2302, 2009.

A NOVEL WORKFLOW FOR GENERATION OF PATIENT-SPECIFIC 3D ASTHMATIC AIRWAY MODELS FROM CT DATA

Ellesse Cooper (6), Kamran Poorbahrami (1), Ben Piperno (1), David G. Mummy (2), Sean Fain (2,3,4) Jessica M. Oakes (5)

(1) Department of Mechanical and Industrial Engineering, Northeastern University, Boston, MA, USA.

(2) Departments of Biomedical Engineering, (3) Medical Physics, and (4) Radiology, University of Wisconsin-Madison, WI, USA.

(5) Department of Bioengineering Northeastern University, Boston MA, USA.

(6) Department of Biology Northeastern University Boston MA, USA.

INTRODUCTION

Asthma is a chronic airway disorder that causes physical and conformational changes within the airways of affected subjects [1]. Factors including ventilation heterogeneity, airway remodeling, and mucus plugging make it difficult to deliver therapeutics to obstructed airways, resulting in inadequate dose concentrations in some patients. The prescription of dose concentrations based on generalized data has led inhaled drug therapies to be ineffective for 10-15 percent of patients, leading to uncontrolled asthma [1]. Patient-specific data must be taken into consideration. To better understand respiratory mechanics and the deposition of inhalant therapy particles throughout the airway tissues a unique work flow was developed to generate 3D airway models for computational simulations, reflecting realistic and patient-specific geometry. Following our previously-developed simulation pipeline [2], these models will be employed to investigate airflow and particle disposition patterns and to optimize regional drug targeting.

METHODS

CT scans at two lung states, Total Lung Capacity (TLC) and Functional Residual Capacity (FRC) were collected, and a Hyperpolarized (HP) ^{3}He MRI scan was conducted at FRC + 14% TLC. Models were created in TLC because narrowing of airways in FRC prevented successful selection of all the necessary branches needed for simulation.

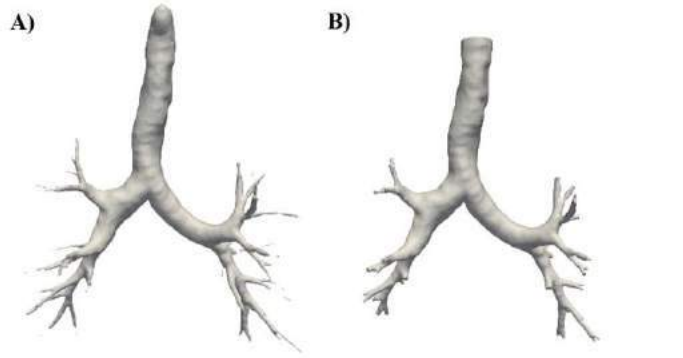

Figure 1. *Initial geometry obtained in SimVascular* ***(A)*** *and model after airways have been trimmed and extruded in Blender* ***(B)*** *of a patient with severe asthma.*

To create patient-specific models, thoracic CT scans at TLC were uploaded as DICOM data into the program Slicer, where the images were compounded and saved as a VTK file. The VTK was then loaded into an open source software SimVascular [3]. In SimVascular, the airways were selected using the 3D region growing function. A seed was placed in an open airway, and the program grew the region to find nearby airways based on a defined threshold. We aimed to select a minimum of 38 branches. From the HP ^{3}He MRI data, segmental volume defect percentages (SVDPs) were calculated for 19 lung segments in total, 9 in the left lung and 10 in the right lung. For each segment, we needed the segmental feeding airway (SFA) to have two subsegmental daughter branches in order to couple the SVDPs with the SFAs.

Selecting the 38 necessary branches, between 60 and 90 segment selections were created and then unioned together to form the geometry of the initial model (*Figure 1A*). The selection process was particularly challenging in patients with severe asthma due to the extreme narrowing of branches and the presence of mucous plugs and fully collapsed airways. Patient CT data was referenced to confirm the location of plugs and collapses, allowing us to create an accurate model of the patient's remodeled airway tree.

After the initial geometry was established, the 3D model was cleaned and trimmed in the modeling program Blender. Disconnected airways, excess generations, and sharp edges were removed. The remaining branches were trimmed to have flat faces perpendicular to the airway (*Figure 1B*). These faces were then extruded outward to resolve the effect of the SVDP outlet boundary conditions for the simulations.

The simulations required a high-quality mesh, which Blender was incapable of providing as it decreases the mesh quality of the model. Therefore, we choose to use the 3rd party software, OpenFlipper, to improve the surface remesh, generating a higher-quality model with more elements from which a volume mesh could then be extracted.

Next, the models were moved into the program Paraview where they were scaled down to the size of the equivalent models in FRC based on a calculated scalar factor γ (1).

$$\gamma = \sqrt[3]{\frac{V_{FRC}}{V_{TLC}}} \quad \textbf{(1)}$$

where V_{FRC} and V_{TLC} are the volumes of the lung at FRC and TLC, measured from the CT scans. The scaling step allowed us

to use HP ^{3}He MRI data collected in FRC for simulation analysis.

Back in SimVascular, the model was labeled based on the 19 established segmental feeding airways. Patient models often differed in location and size of branches, as well as in number of bifurcations. Once labeled, the final mesh was created. A total surface and volume mesh resulted in a final model with between 9 and 14 million elements, which could then be used for airflow and particle deposition simulations.

RESULTS

Models were successfully created in TLC for 17 patients. Of the 17 patients, 7 were severe asthmatics, 7 were mild or moderate, and 3 were healthy. Between the severe asthmatics there was visible variety in morphometric features. Differences were present in airway size, ellipticity, bifurcations, and gravitational angles, likely due do the remodeling that occurs as a result of the chronic respiratory illness (results not shown here). There was noticeably less variety in the airway structures of healthy and moderately affected patients. The scaling step of the workflow was evaluated by airflow simulation comparisons. A full model at FRC was created for one severe asthmatic subject. Due to the extreme narrowing of relaxed-state airways, this could only be achieved for one subject.

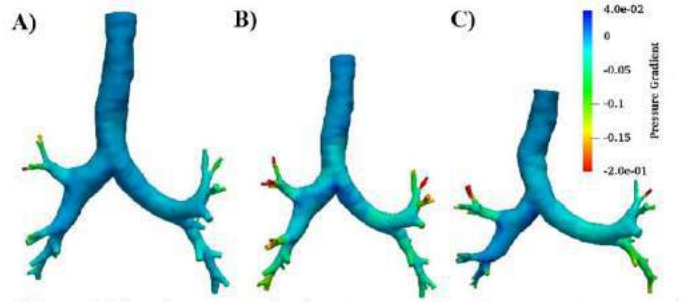

Figure 2. *Simulation results for pressure distribution in airways of models in TLC (**A**), TLC scaled to FRC (**B**), and FRC (**C**) for one patient with severe asthma. Pressure gradient in cm H_2O.*

For this subject, fluid dynamics simulations were performed at TLC, FRC, and TLC scaled to FRC ($\gamma = 0.8$, *Figure 2*). The boundary conditions for all three gas flow simulations were set based upon the SVDPs calculated from the HP ^{3}He MRI data. Because the MRI data was most reflective of the FRC state, the FRC model simulations were viewed as the control. When the airway resistances in the unscaled TLC model were compared to the FRC model, the 3D resistance in FRC was more than twice the resistance in TLC (Table 1). However, the scaled model matched the FRC resistance much more closely, suggesting that the simulation on the scaled model is more representative of normal breathing conditions. The greatest improvement was seen for the left upper, right upper, and right middle segments (Fig. 2), while scaling resulted in less change in the left and right lower segments.

In reality, the airways should not scale uniformly from TLC to FRC, particularly with disease presence. Therefore, it will be impossible to model FRC with high accuracy, as demonstrated by the regional differences in pressure gradients (Fig. 2). Considering this limitation, the scaling step of our workflow is justified because we achieve values closer to those found for the FRC simulations, specifically the measures that are most important in the clinic (e.g. airway resistance and dosimetry).

Table 1. *Airway resistance in airflow simulation for models in TLC, FRC, and scaled to FRC. Models were generated from data of one severe asthmatic with SVDP 17.17 ± 15.34*

Model	3D Resistance (cm H_2O-s/ml)
TLC	**1.90 E-03**
FRC	**4.60E-03**
SCALED TO FRC	**4.40E-03**

DISCUSSION

Asthma is typically controlled by direct delivery of therapeutics to the lung via inhalation. Due to airway remodeling, many patients with severe asthma may not respond to prescribed dosages. With the ultimate goals of predicting lung mechanics and optimizing drug delivery and dosage, a novel workflow was developed to generate airway models with patient-specific geometry which could then be utilized for airflow and particle deposition simulations. The progress in accurate modeling is considered the first step towards our goal of understanding how asthma affects patients in unique ways.

The number and quality of airways that could be achieved for each model were limited by the resolution of the initial CT scans. Many of the outer airways were only a few pixels wide and could not be detected by the semi-automated 3D region-growing functions. As MR imaging and CT resolutions advance, it may become possible to measure defects and produce models that extend beyond the segmental areas, better capturing the realistic patient-specific geometry of the airways. We are also interested in including extra-thoracic airways in future studies, as that would allow us to capture the laryngeal jet and associated turbulence in the simulations.

By creating a database of realistic 3D airway models from individuals of different ages, genders, and asthma severities, we will have the means to test deviation from expected respiratory variations in the future. A database of models and simulation results would provide insight into pathological flow characteristics and airway mechanics in asthmatics, which could improve disease classification and lead to more successful treatment options for treatment-resistant asthmatics. So far, we have successfully created 17 models from patient CT scans in TLC and performed simulations using HP ^{3}He MRI data. We aim to create a database of 60 models.

ACKNOWLEDGEMENTS

This work is supported by NIH/NHLBI R21 HL140436-01. Human data collected was facilitated by: NIH/NHLBI R01 HL069116; R01 HL080412; U10 HL109168; NIH/NCATS UL1TR000427.

REFERENCES

[1] Global Asthma Network, Auckland, New Zealand, Tech. Rep., 2014.

[2] Oakes J. M. et al. IEEE Transactions on Biomedical Engineering, in press, 2018.

[3] Updegrove, Adam, et al. Annals of biomedical engineering 45.3 (2017): 525-541.

SB³C2019
Summer Biomechanics, Bioengineering and Biotransport Conference
June 25 -28, Seven Springs, PA, USA

WATER SPORT HEAD INJURIES; ABILITY OF HELMETS TO REDUCE HEAD IMPACT ACCELERATIONS

Brock G. Duma, Mark T. Begonia, Abigail M. Tyson, Casey L. Charron, Stefan M. Duma

Institute for Critical Technology and Applied Science
Virginia Tech
Blacksburg, Virginia, USA

INTRODUCTION

As watersport popularity grows, the number of head injuries, including concussions, is increasing.[1] Each year there are over 7,000 tubing related injuries treated in a hospital, of those nearly 2,000 are head injuries .[2] For participants under 20 years old, the leading head injury mechanism is contact with another person (Figure 1). Head injury risk could potentially be lowered, if the participants utilized a helmet. The purpose of this study was to evaluate the biomechanical performance of watersport helmets and to investigate the potential of watersport helmets to reduce head injury risk in tubing.

Figure 1: Watersport activities with multiple people can result in head injuries from contact with participants.

METHODS

Ten helmets were selected as a representative subset of all available watersport helmets, and two samples of each helmet were tested. A total of 28 tests were performed with 24 helmeted, and four controls at 2 m/s and 4 m/s with impacts to the side and rear for each speed (Figure 2). The helmets are from wakeboarding, kayaking, water skiing, and women's lacrosse. A custom impactor was used to test the helmets under head-to-head conditions which are known to be associated with the highest risk of concussion in tubing. The impactor consists of two NOCSAE head and Hybrid III neck configurations on 16 kg sliding masses to represent the head, neck and torso of 50th percentile participants. The struck head was instrumented with a triaxial angular rate sensor and three linear accelerometers. For each testing configuration, both rotational and linear head accelerations were recorded.

Figure 2: Side view of the testing configuration for the 2 m/s rear impact with the Pro-Tec helmet as the subject matter.

RESULTS

All of the tests with helmets resulted in lower head accelerations compared to the control tests that simulated bare head impacts. For example, in the 2 m/s side impact condition the control test resulted in 71g and 5,595 rad/sec^2 while the ten helmeted tests resulted in 15 +/- 3 g (range 11 to 22), and 1221 +/- 297 rad/sec^2 (range 780 to 1,864). In the 2 m/s rear impact condition, the control test resulted in 66g and 4,395 rad/sec^2 while the ten helmeted tests resulted in 14 +/- 4 g (range 8 to 18.9), and 1,090 +/- 204 rad/sec^2 (range 624 to 1,430).

In the 4 m/s side impact condition, the control test resulted in 180g and 12,746 rad/sec^2 while the ten helmeted tests resulted in 67 +/- 23 g (range 31 to 109), and 5641 +/- 1,759 rad/sec^2 (range 2,494 to 7,912) (Figure 2 and Figure 3). In the 4 m/s rear impact condition, the control test resulted in 169g and 10,896 rad/sec^2 while the ten helmeted tests resulted in 42 +/- 16 g (range 23.2 to 79), and 3,158 +/- 839 rad/sec^2 (range 1,605 to 4,752).

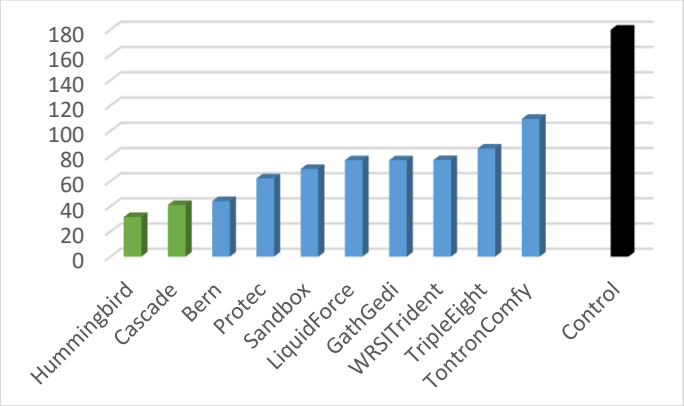

Figure 2: Peak resultant linear acceleration values (g) for the top speed of 4 m/s in the side impact direction.

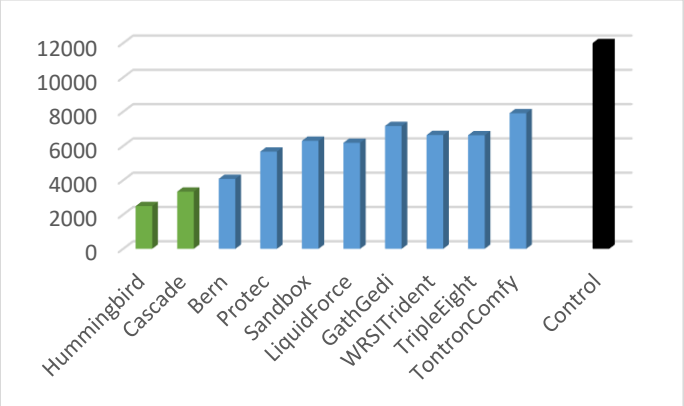

Figure 3: Peak resultant rotational acceleration values (rad/s^2) for the top speed of 4 m/s in the side impact direction.

DISCUSSION

The women's lacrosse helmets had the lowest linear and rotational accelerations in every configuration tested (Figure 4). In the 4 m/s side impact tests, their accelerations were more than 50% less than the average for the watersport helmets, and less than 20% of the control impact accelerations.

Figure 4: Hummingbird (left) and Cascade (right) women's lacrosse helmets were the best performing helmets.

All watersports helmets reduced both linear and rotational accelerations for all test configurations. In the 4 m/s control tests, very high accelerations were observed and would most likely result in head injury as they correspond to a 99% risk of concussion [3]. Although the 2 m/s helmet tests resulted in very low acceleration values, the control values for the unhelmeted tests were high and underscore the importance of both a low speed and higher speed test configuration. But in particular, the Hummingbird utilized a unique soft shell design which helped it perform the best in every configuration that we tested, except the 4 m/s rear impact in which the Cascade performed the best. The Cascade helmet had an unusually large rear pad, which allowed for the lower accelerations. Because of the results gained from the Hummingbird tests, this type of soft shell helmet might be recommended for use in watersport activities in particular tubing activities with multiple participants on a tube.

Interestingly, the price of a helmet was not correlated to performance, with the most expensive helmet resulting in the highest accelerations for the helmeted tests. This trend has been observed in other helmeted sports as well. Data from these tests can help consumers make informed decisions.

A limitation of this study is that not all water sport helmets were tested. A sample of eight types of water sport helmets were tested based on the most popular purchased helmets from Amazon. It is possible that other helmets would test differently, but wearing helmets while performing watersports will dramatically reduce head impact accelerations.

ACKNOWLEDGEMENTS

The authors thank our good friend Brett Stoner and his unfortunate water sport head injury for motivating this study.

REFERENCES

[1] Baker, JI et al., *J Sports Science and Medicine* 9:92-97, 2010.
[2] Heisimer, KR et al., *J Physical Activity and Health* 10(2):45-49, 2013.
[3] Rowson, S et al., *Annals of Biomedical Engineering* 41(5), 8873-882, 2013.

SB³C2019
Summer Biomechanics, Bioengineering and Biotransport Conference
June 25 -28, Seven Springs, PA, USA

THE INFLUENCE OF RADIOGRAPHIC PROJECTION ANGLE ON VISUALIZATION OF THE SUBTALAR JOINT

Kalebb Howell (1), Nicola Krahenbuhl (2), Rich Lisonbee (1), Beat Hintermann (2), Charles L. Saltzman (1), Andrew E. Anderson (1), Alexej Barg (1), Amy L. Lenz (1)

(1) Orthopaedics
University of Utah
Salt Lake City, UT, USA

(2) Orthopaedics
Kantonsspital Baselland
Liestal, Switzerland

INTRODUCTION

A thorough understanding of subtalar joint morphology is needed to diagnose hindfoot pathology, to develop pre-operative plans for reconstructive surgeries, and to evaluate the success of treatment [1,2]. Recently-published data suggest that the posterior facet of the subtalar joint has a major impact on the evolution of hindfoot disorders, including planovalgus deformities and ankle osteoarthritis [3]. Thus, there is a clinical need to evaluate the appearance of the posterior facet and the orientation of the subtalar joint relative to other anatomic landmarks of the hindfoot. Recently, the general appearance of the posterior facet as well as the subtalar inclination angle (SIA) and calcaneal slope (CS) were assessed on weightbearing CT scans [3]. The SIA and CS measurements were measured in three coronal slices of weightbearing CT scans within the anterior, middle, or posterior regions of the posterior facet [4,5]. Although weightbearing CT scans have become common for assessment of foot and ankle disorders in recent years, conventional radiographs are still the standard for imaging the hindfoot [6]. A formal consensus regarding normative values for these measurements on conventional radiographs has not yet been reached, which has slowed progress towards standardizing diagnoses based on evaluation of plain film radiographs. Furthermore, current radiographic measurement methods are shown to be sensitive to intra- and inter-observer agreement. The subtalar joint is arguably more complex in shape than the tibio-talar joint, and thus, even subtle changes in the position of the foot and ankle and X-ray equipment are likely to alter the general appearance of this structure as well as affect measurements of the SIA and CS. However, studies have not assessed how foot position and orientation of the X-ray equipment affect measurements of the subtalar joint in a systematic manner. The purpose of this study was to determine how changes in the radiographic equipment beam projection angle from horizontal (tilt) and axial rotation of the foot influenced subtalar joint measurements. In addition, the subtalar joint line was projected on three-dimensional (3-D) models of the calcaneus to investigate whether the visible area of the posterior facet changes across different foot positions. We hypothesized that the position of the foot and X-ray equipment impacts the assessment of the subtalar joint.

METHODS

Participants

Informed consent was provided by a total of 27 healthy volunteers. Inclusion criteria included individuals 40 to 70 years of age that did not have any previous medical history of foot or ankle injury and/or surgery.

Computed Tomography Collection and Image Processing

Each participant underwent a weight bearing CT scan (Planmed Verity, Planmed Oy, Helsinki, Finland; 0.2 mm slice thickness, 1 mm slice interval) of their foot and ankle with their calcaneus aligned in reference to the second metatarsal for a parallel alignment relative to the scanner's anterior-posterior axis. The CT images were segmented to generate 3-D surfaces representing the tibia, fibula, talus and calcaneus bones (Amira, v6.0.1, Visage Imaging, San Diego, CA, USA). Surfaces were smoothed and decimated to reduce segmentation artifact. Next, digitally reconstructed radiographs (DRRs) were generated of each bone surface by projecting the CT image data to a plane representing the desired view. A total of 25 DRRs were created to represent views with different positions of the foot and radiographic projection angle. Here, we began with an antero-posterior (AP) view, defined by no rotation of the foot and no simulated downward tilt of the X-ray beam. Iterative combinations of internal rotation of the foot and simulated downward tilt of the X-ray beam ranging from 0 to 40° (10-degree increments) yielded 25 possible permutations, resulting in 675 DRRs for the cohort.

Radiographic Measurements of the Subtalar Joint

The SIA was measured on each DRR and was defined as the angle between the surface of the talus and the posterior facet of the calcaneus [1]. The CS was also calculated and was defined as the angle between a line from the medial to the lateral boarder of the posterior facet to a vertical line [5]. A custom MATLAB script (Version R2017b, MathWorks, Natick, MA, USA) loaded DRR views individually and guided the reader through measurements of SIA and CS, automatically calculating angles based on the user-defined line defining the joint lines. The SIA and CS were measured at two different times, separated by 2 weeks, to assess intra-observer agreement. Measurements obtained by an orthopaedic surgeon were compared to those made by a scientist to establish an estimate for inter-observer reliability.

Projection of the Posterior Facet Relative to the Joint Line

The joint line visualized on the DRR views was projected onto the posterior facet and was evaluated by defining virtual anatomical landmarks around the perimeter of the articular surface (Fig.1). First, six anatomic landmarks of the posterior facet of the subtalar joint (calcaneal side) were defined in the CT image data as virtual beads and included the: (1) antero-medial point, (2) medial point, (3) posterior point, (4) superior point, (5) lateral point, and the (6) antero-lateral point. The positions of these virtual beads were defined mathematically using the second principle of curvature to isolate the perimeter of the posterior facet (PostView, v2.1.0, FEBio, Salt Lake City, UT). Once the bead locations were established, their placement was used to quantify direction and magnitude of anatomical bead locations relative to the visualized joint line in each of the 25 DRR views (Fig 1A). A rotation sequence for the appropriate internal rotation and simulated downward

tilt of the X-ray equipment was applied to each 3-D calcaneus model containing the defined anatomical beads in MATLAB (Fig 1C). The custom MATLAB script used the points to perform a curve fit of the joint line in that projection view and sequentially calculated the six anatomical beads' direction and magnitude from the joint line within the calcaneal articular surface based on nodes within the 3-D surface model.

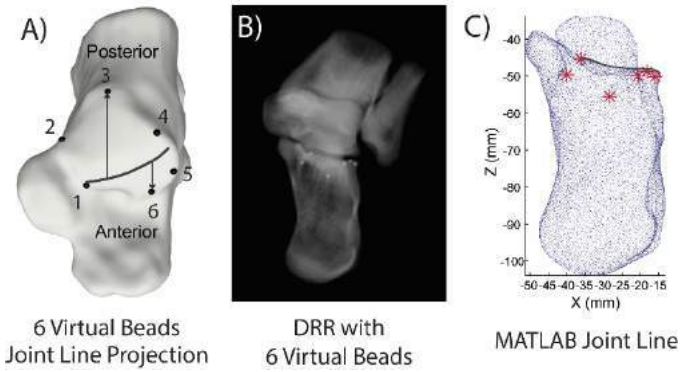

Figure 1: (A) Six virtual landmark beads and projected joint line. (B) DRR projection (30° of ankle internal rotation and 40° of simulated downward tilt of the X-ray beam) with six virtual beads. (C) MATLAB figure of calcaneus rotated into the 30/40-degree position; the black joint line was defined as a curve fit with the red stars representing six virtual bead locations.

Statistical Analysis

Inter- and intra-observer agreement was assessed using the two-way random intraclass correlation coefficient (ICC) and presented with a 95% confidence interval (95% CI) for SIA and CS measurements. Agreement was considered very good for an ICC > 0.80; good with an ICC = 0.61 – 0.80; moderate with an ICC = 0.41 – 0.60; fair with an ICC = 0.21 – 0.4; and poor with an ICC < 0.20 [7].

RESULTS

Radiographic Measurements of the Subtalar Joint

Across the 25 DRR viewing perspectives, SIA measurements ranged on average from 3.8 to 20.9° (Table 1) and CS measurements ranged on average from 54.8 to 105.8°. Simulated downward tilt of the X-ray beam decreased the mean SIA. The mean SIA and CS also changed when the foot was internally rotated when compared to a constant simulated beam tilt. The lowest ICC values were evident at the AP view of the foot without any downward tilt or rotation (SIA inter-observer agreement 0.368, CS inter-observer agreement 0.184). For the other views, the reliability ranged from 0.416 to 0.967 (SIA) and from 0.586 to 0.996 (CS).

Table 1: SIA Measurement of the Subtalar Joint Posterior Facet

SIA		Internal Rotation				
		0°	10°	20°	30°	40°
		Mean (SD)	Mean (SD)	Mean (SD)	Mean (SD)	Mean (SD)
Tilt	0°	12.0 (6.1)	14.0 (6.3)	18.2 (5.6)	20.5 (5.5)	20.9 (5.3)
	10°	9.9 (5.9)	12.4 (6.0)	14.4 (5.1)	15.3 (4.7)	15.2 (4.9)
	20°	8.7 (5.3)	9.0 (5.8)	9.2 (5.1)	9.5 (4.8)	9.9 (5.3)
	30°	4.4 (2.7)	4.5 (3.3)	4.4 (3.1)	5.0 (3.4)	5.5 (4.7)
	40°	3.8 (3.4)	3.6 (2.8)	3.8 (3.1)	4.4 (3.5)	4.3 (3.3)

Projection of the Posterior Facet Relative to the Joint Line

The visible area where the joint line was projected onto the posterior facet changed between the different viewing perspectives (Fig 2). While on an AP view of the foot and ankle the posterior area of the posterior facet was visible, a slightly more anterior area was visible when the foot was internally rotated. Simulated downward tilt of the X-ray beam also changed the visible area of the posterior facet from a posterior (without downward tilt) to more anterior (40° downward tilt).

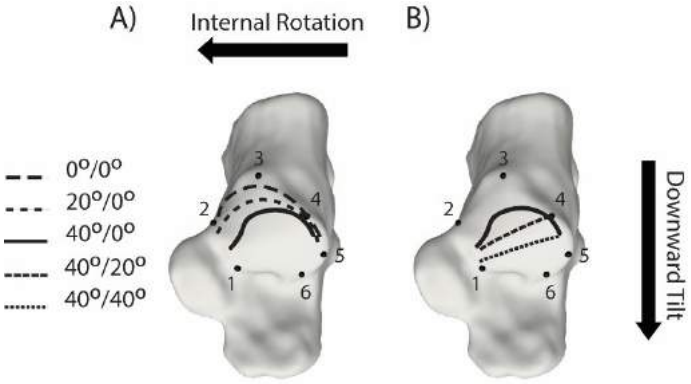

Figure 2: Projection of the posterior facet on 3D models of the calcaneus. (A) Internal rotation (without downward tilt of the X-ray beam) demonstrates a curved joint line projected onto the posterior facet, the visualized joint line begins posteriorly and moves anteriorly. (B) Simulated downward tilt (at 40° internal rotation) of the X-ray beam shows a more anterior aspect of the posterior facet of the subtalar joint.

DISCUSSION

This study assessed the influence of various DRR projection views with different internal rotations of the foot and simulated downward tilt of X-ray equipment on the visualization of the subtalar joint. The major findings were a) measurements describing the alignment of the subtalar joint (SIA and CS) changed between different viewing perspectives, and b) changes in DRR projection visualized a joint line on different aspects of the posterior facet articulating surface. Understanding the radiographic appearance of the posterior facet in healthy individuals on DRRs is important to identify pathologic changes among symptomatic, diseased ankles. Studies using weightbearing CT scans have shown that the configuration of the posterior facet may have an impact on the evolution of ankle osteoarthritis [2,5]. To our knowledge, DRRs generated from weightbearing CT scans have not been assessed for the purpose of evaluating how changes in the alignment of the X-ray equipment could affect visualization of the subtalar joint. Use of DRRs is advantageous because it allows for computer-controlled projections, thus preventing errors that would otherwise be present if standard X-ray equipment was used for this study.

Based on our results, we recommend 20° of internal rotation of the foot to assess the posterior aspect of the posterior facet, while a combined 20° internal rotation of the foot and 40° downward tilt of the X-ray beam is likely best for assessing the anterior aspect of the posterior facet. With a better understanding of the projection of the subtalar joint, clinicians will be better-equipped to make meaningful interpretations of the morphology of hindfoot on conventional radiographs, thus providing reliable diagnoses for their patients.

ACKNOWLEDGEMENTS

Funding from the National Institutes of Health (Grant No. R21AR063844), LS-Peery Discovery Program in Musculoskeletal Restoration, the Swiss National Science Foundation (SNF; P2BSP3_174979) and the Swiss Orthopaedic Society (Swiss Orthopaedics) are greatly acknowledged.

REFERENCES

[1] Krahenbuhl, N et al., *EFORT*, 2(7):309-316, 2017.
[2] Cody, EA et al., *Foot Ankle Int*, 73(8):874-881, 2016.
[3] Wang B et al., *Clin Orthop Rel Res*, 473(1):318-325, 2015.
[4] Colin, F et al., *Foot Ankle Int*, 35(10):1057-1062, 2014.
[5] Krahenbuhl, N et al., *Foot Ankle Surg*, 10(18), 2017.
[6] Lopez-Ben R, *Foot Ankle Clin*, 20(2):223-241, 2015.
[7] Yeung TW et al., *Skeletal Radiol*, 44(6):823-829, 2015.

SB³C2019
Summer Biomechanics, Bioengineering and Biotransport Conference
June 25 -28, Seven Springs, PA, USA

EFFECTS OF VOLUMETRIC BOUNDARY CONDITIONS ON THE COMPRESSIVE MECHANICS AND MODELING OF PASSIVE SKELETAL MUSCLE

Anurag J. Vaidya (1), Benjamin B. Wheatley (2)

(1) Biomedical Engineering
Bucknell University
Lewisburg, PA, USA

(2) Mechanical Engineering
Bucknell University
Lewisburg, PA, USA

INTRODUCTION

For over two decades, computational models of human body—such as the Toyota THUMS model— have been used in automobile safety [1]. These models rely on accurate material properties for each tissue. However, the compressive behavior of skeletal muscle is not fully understood, particularly regarding the differences in muscle response to *in vivo* loading conditions [2]. It is likely that *in vivo* muscle experiences a variation between confined and unconfined volumetric boundary conditions, but nearly all previous studies investigating passively compressed tissue have focused on muscle in unconfined compression (UC) [2, 3]. One study has investigated muscle under anisotropic semi-confined compression [4], however none have studied muscle in fully confined compression (CC). Thus, we have investigated the effects of volumetric boundary conditions (UC and CC) on the stress relaxation of skeletal muscle. Moreover, a finite element model simultaneously characterizing muscle behavior in both boundary conditions is explored.

METHODS

Using an impermeable steel well, transverse oriented plugs (ø = 6.4mm) of porcine tibialis anterior (TA) from six animals were subject to CC stress relaxation tests. Two testing configurations were employed with n=8 for each: fast-compression (strain rate = 15%/s $\epsilon = 15\%$) and slow-compression (strain rate = 1.5%/s,$\epsilon = 1.5\%$). Similarly, transverse oriented cubes (thickness = 7.9 ± 0.5 mm) of TA from six animals were exposed to stress relaxation tests under UC in two testing configurations with n=8 for each: fast-compression (strain rate = 40%/s,$\epsilon = 40\%$) and slow-compression (strain rate = 5%/s,$\epsilon = 5\%$). All samples relaxed for 400s after compression. Data was collected by a 10N Instron load cell at 100 Hz. Testing was completed within eight hours of sacrifice to reduce the effects of rigor mortis. Muscle samples were hydrated by physiological buffer solution. First Piola-Kirchoff stress and nominal strain were determined through post-hoc analysis of initial specimen dimensions.

Three-dimensional finite element models of UC and CC geometries were developed in Abaqus (Dassault Systèmes). The UC geometry was reduced to a quarter of the sample by symmetry with 175 first-order 8-node hexahedral elements (type C3D8RH). This model was compressed by rigid platen and reaction force on platen was divided by initial area to acquire first Piola-Kirchhoff stress. The CC geometry was reduced to a two-dimensional axisymmetric model of cylinder with 96 first-order 4-node quadrilateral elements (type CAX4RH). Displacement was prescribed for top surface and as no lateral expansion occurred, first Piola-Kirchhoff stress was determined directly from model output. Displacements in both fast compression models simulated the slight experimental overshoot applied by the Instron.

A quasi-linear hyper-viscoelastic material formulation was chosen to model the behavior of skeletal muscle subject to both CC and UC. The model utilized third degree Yeoh form [5] of a polynomial hyperelastic strain energy density function ($\Psi(\mathbf{C})$) (Equation 1).

$$\Psi(\mathbf{C}) = \sum_{i=1}^{3} C_{i0}\,(\bar{I}_1 - 3)^i + \sum_{i=1}^{3} \frac{1}{D_i}(J-1)^{2i} \qquad (1)$$

Here C_{i0} and D_i are material parameters, $\bar{I}_1$ is defined as $\bar{I}_1 = \bar{\lambda}_1 + \bar{\lambda}_2 + \bar{\lambda}_3$ where $\bar{\lambda}_i = J^{-\frac{1}{3}}\lambda_i$ (λ_i are the principle stretches), and J is the volume ratio. A Prony series viscoelastic model (Equation 2) was applied to the shear ($\bar{I}_1$) and volumetric (J) responses in Equation 1.

$$K(\tau) = K_\infty + \sum_{i=1}^{4} K_i e^{-\tau/\tau_i^K} \qquad G(\tau) = G_\infty + \sum_{i=1}^{4} G_i e^{-\frac{\tau}{\tau_i^G}} \qquad (2)$$

Poster Presentation #P033

Here $K(\tau)$ is the time dependent bulk modulus and $G(\tau)$ is the time dependent shear modulus. K_∞ and G_∞ model long-term bulk and shear modulus respectively. τ_i^K and τ_i^G are time constants ($\tau_1^G = \tau_1^K = 0.05s$, $\tau_2^G = \tau_2^K = 1s$, $\tau_3^G = \tau_3^K = 20s$, $\tau_4^G = \tau_4^K = 400s$). A power law model ($y = Ax^{-B}$) was also fit to all relaxation data to characterize and compare relaxation behavior between testing groups.

The finite element model consisted of fourteen parameters (6 hyperelastic, 8 viscoelastic). Parameter identification was achieved by a nonlinear least-squares deterministic optimization (*lsqnonlin* in MATLAB). The error function (Equation 3) was minimized to simultaneously fit experimental UC and CC fast-compression data (t_{peak} is time of peak experimental stress). UC and CC slow-compression data was then predicted by this optimized model.

$$error = \sum_{t=0}^{t_{peak}} t * (\sigma_{model} - \sigma_{exp}) + \sum_{t=t_{peak}}^{401} \frac{(\sigma_{model} - \sigma_{exp})}{t} \qquad (3)$$

RESULTS

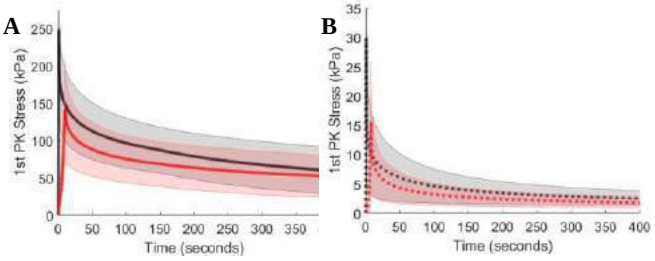

Figure 1: Average stress relaxation curves for (A) CC fast and slow compression (B) UC fast and slow compression with standard deviation

Figure 1 shows that despite lower strain levels, muscle was stiffer in CC than in UC (p-value<0.001). In both UC and CC, muscle stiffness increased with strain rate (p=0.02 for CC, p=0.03 for UC), which is consistent with previous studies [2]. Fitting the power law model ($\bar{R}^2$=0.96) shows that relaxation behavior differed with boundary condition at both strain rates (p<0.001 for slow compression, p=0.042 for fast compression). Relaxation was independent of strain rate in UC (p=0.47), whereas it depended on strain rate in CC (p=0.030) (Table 1). The FEA model provided excellent simultaneous fits to CC and UC fast-compression data (Figure 2 A-B) (Table 2). Optimized parameters (Table 3) were used to calculate initial shear modulus (0.044 kPa) and initial bulk modulus (42.6 kPa). Approximately two thirds of muscle instantaneous shear and bulk moduli relaxed with the first time constant (0.05s) for both CC and UC (Table 3). The model showed acceptable validation for UC and CC slow-compression (Figure 2C-D, NRMSE UC 10.65%, CC NRMSE 9.02%).

Table 1: Power law B-parameter values ± SD for different groups

	CC Fast	CC Slow	UC Fast	UC Slow
B value	0.23 ± 0.06	0.15 ± 0.07	0.32 ± 0.08	0.35 ± 0.04

Table 2: Error values for model-experiment comparisons

Error Type	UC	CC
Peak error	0.05%	4.72%
NRMSE	1.71%	0.85%

Table 3: Optimized finite element model parameters

Parameter Type	Parameter	Optimized value
Hyperelastic (MPa)	C_{10}, C_{20}, C_{30}	2.22e-5, 1.32e-4, 3.16e-5
Hyperelastic (MPa^{-1})	D_{10}, D_{20}, D_{30}	46.99, 1.29, 10e10
Shear Coefficients	G_1, G_2, G_3, G_4	0.68, 0.13, 0.097, 0.077
Bulk Coefficients	K_1, K_2, K_3, K_4	0.62, 0.091, 0.093, 0.17

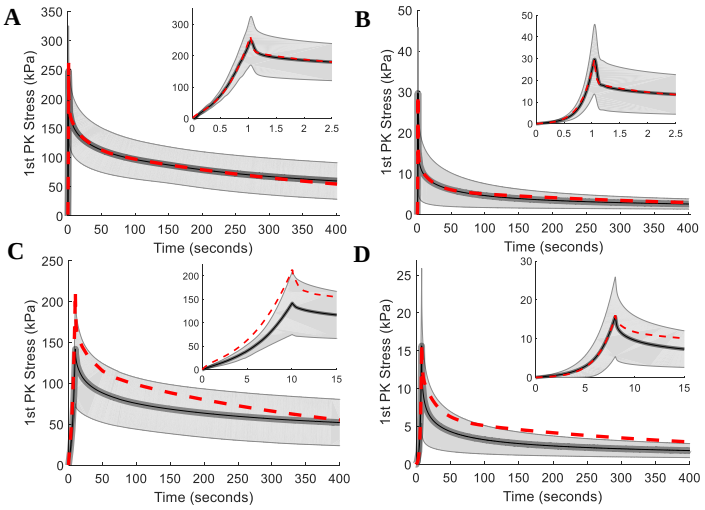

Figure 2: Average fast-compression experimental data (solid black) and optimized model (dashed red) with SD for **(A)** CC and **(B)** UC. Average slow-compression experimental data (solid black) and model predictions (dashed red) with SD for **(C)** CC and **(D)** UC.

DISCUSSION

This study presents new data of passively compressed muscle under different volumetric boundary conditions (UC versus CC) along with a quasi-linear hyper-viscoelastic finite element analysis. While a previous viscoelastic approach successfully modelled stress relaxation of muscle in UC [3], this study simultaneously fit stress relaxation data of muscle in CC and UC, thus providing greater accuracy for the volumetric behavior of skeletal muscle.

Since muscle's bulk modulus is three orders of magnitude larger than its shear modulus, muscle shows great resistance to volumetric deformations. This supports previous findings of near incompressibility of muscle [2, 4]. The validation for CC slow compression suggests that there may be a mechanism in addition to viscoelasticity that dictates muscle stiffness and stress relaxation under volumetric deformations. The impermeable walls of the CC testing well may trap intramuscular fluid within the muscle. This boundary condition— along with previous studies showing non-negligible permeability of skeletal muscle [6]— suggests that pressurization of incompressible fluid may contribute to the stiffness of muscle in CC. Such a model may induce non-linearity in the relaxation behavior of muscle in compression.

It is not yet entirely clear how differences in strain level and rate attribute to data presented in Figure 1. Studies at higher strain levels are required, nevertheless this study provides a robust model that effectively characterizes compressive behavior of skeletal muscles in different volumetric boundary conditions.

ACKNOWLEDGEMENTS

The authors thank Program for Undergraduate Research at Bucknell University for funding this study.

REFERENCES

[1] Toyota Motor Europe. "Toyota THUMS." *Toyota Motor Europe*
[2] Moh., M., *J Mech Behav Biomed Mater* 62 (2016): 468-480.
[3] Van Loocke, M., *Journal of biomechanics* 41.7 (2008): 1555-1566.
[4] Böl, M., *J Mech Behav Biomed Mater* 63 (2016): 115-124.
[5] Yeoh, H., *Rubber Chemistry and technology* 66.5 (1993): 754-771.
[6] Wheatley, B., *Comput Meth Biomech Biomed Eng Imaging* 20.6 (2017): 598-601.

SB³C2019
Summer Biomechanics, Bioengineering and Biotransport Conference
June 25 -28, Seven Springs, PA, USA

THE EFFECT OF *IN VIVO* IONIZING RADIATION ON THE MICROMECHANICS OF MOUSE VERTEBRAE

TONGGE WU (1), MEGAN M. PENDLETON (1), NOAH B. BONNHEIM (1), JOSHUA S. ALWOOD (2) TONY M. KEAVENY (1,3)

(1) Department of Mechanical Engineering
University of California, Berkeley
Berkeley, CA, USA

(2) Space Biosciences Division,
NASA Ames Research Center,
Moffett Field, CA, USA

(3) Department of Bioengineering
University of California, Berkeley
Berkeley, CA, USA

INTRODUCTION

Deep space flight or cancer treatment can expose bone tissue to a high dose of ionizing radiation, which has been linked to increased fracture risk [1], [2]. However, the mechanisms leading to increased risk are not well understood. For example, experiments on mice exposed to ionizing radiation *in vivo* have shown altered bone micro-architecture in the mouse vertebral body without altered strength [3]. Since mechanical behavior is expected to correlate with micro-architecture, such discordance suggests that ionizing radiation *in vivo* may uniquely alter the vertebral body micro-mechanics [4]. To gain insight into this issue, we investigated how local deformation, load transfer mechanisms, and initial failure location in the mouse vertebra are altered following *in vivo* exposure to a whole-body clinically-relevant dose (5Gy) of ionizing radiation. In addition to providing insight into *in vivo* radiation effects, this study can illustrate the structure-function relationship within the vertebral body, in particular the role of changes in micro-architecture on whole-vertebra mechanical behavior.

METHODS

Twenty-seven 17-week-old male mice (C57BL/6J) were randomly divided into two groups. One group (N=14) was not exposed to any radiation (control) and the other (N=13) was irradiated by acute 5Gy γ-radiation (^{137}Cs source). Both groups were sacrificed after 11 days. The L4 and L5 vertebrae were excised from all mice and the vertebral bodies were isolated. The L4 vertebral bodies were then subjected to a uniaxial compressive monotonic mechanical test to measure whole-vertebral body stiffness and ultimate force (strength). The L5 vertebral bodies were scanned with micro-computed tomography (μCT) at an isotropic resolution of 10 μm after which trabecular and cortical tissue were manually segmented for each μCT slice. Those images were then analyzed for various micro-architectural parameters. (L5 vertebral bodies were also subjected to fatigue mechanical test, data not reported.)

The μCT images were also analyzed by 3D linearly elastic finite element analysis. Each voxel-based finite element model (10 μm element size, 8-noded cubic elements; bone tissue Young's modulus 10 GPa, Poisson's ratio 0.3 [5]) was subjected to a 0.5% apparent compressive strain (FEAP Ver8.3). Three major outcomes were defined: 1) the 90th percentile of the maximum and minimum principal strains in the trabecular and cortical compartments as well as the whole vertebral body; 2) the trabecular load fraction, defined as the ratio of axial force in the trabecular bone to the whole vertebral body, calculated at each transverse slice; and 3) the ratios of high-risk cortical bone to total cortical bone, of high-risk trabecular bone to total trabecular bone, and the high-risk cortical bone to high-risk trabecular bone. The high-risk tissue was quantified by first normalizing the maximum and minimal principal stresses of each element by its tensile (61 MPa) or compressive (150 MPa) yield stress, respectively, then taking the higher absolute value. Elements within the top 10% of values were classified as "high-risk", and were further classified either in tension or compression [5].

For statistical analysis, we compared results between the control and irradiated groups using unpaired t-tests (JMP Pro Ver14.0); significance was assumed at $p<0.05$.

RESULTS

For uniaxial compression testing (on L4), there was no significant effect of ionizing radiation on either vertebral strength ($p=0.55$, Fig.1a) or stiffness ($p=0.97$, Fig.1b).

By contrast, there was a significant effect of ionizing radiation both on measurements of trabecular micro-architecture ($p<0.01$) and on the 90th percentile values of the principal strains ($p<0.01$). Following radiation, the trabecular bone volume fraction and (Fig.1c) the connectivity density decreased (Fig.1d), and the trabecular separation (Fig.1e), thickness, and SMI (not shown) increased. These difference in

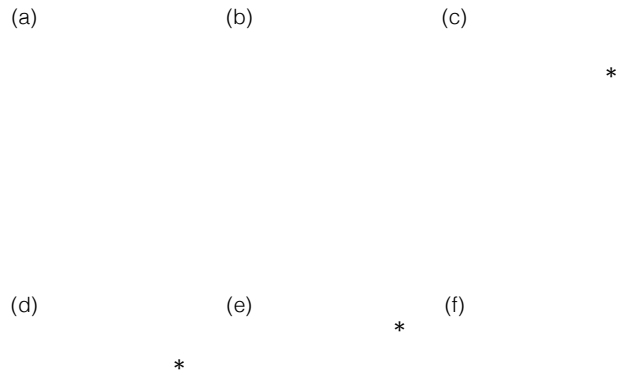

Figure 1: (a-b) Whole-bone mechanical testing and (c-f)

Mean ± 95% CI (confidence interval) (*: p<0.01)

trabecular micro-architecture indicated a transformation from a well-connected plate-like structure towards a sparser rod-like structure. The 90th percentile of principal strains in the trabecular bone (Fig.3a and 3b) were lower for the irradiation group, implying that the trabecular tissue was less likely to fail after exposure to radiation. On the other hand, cortical thickness (Fig.1f) and the 90th percentile of principal strains in the cortical compartment were not altered by radiation (p>0.5).

With respect to the trabecular load fraction, at all transverse sections of the vertebral body the trabecular load fraction was lower following irradiation (p<0.05) (Fig.2). While the overall load sharing behaviors before and after radiation exposure were similar, the load fraction was significantly lower at each transverse section following radiation exposure.

Consistent with these trends, the high-risk cortical fraction (ratio of high-risk cortical bone to total cortical bone) was significantly higher following irradiation (p<0.01) (Fig.3c), but the high-risk trabecular fraction was significantly lower following irradiation (p<0.01) (Fig.3d). Since the high-risk tissue was defined with consideration of asymmetric

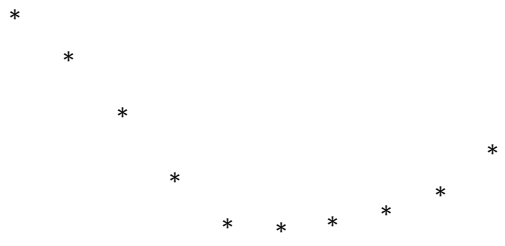

Figure 2: Load fraction of trabecular bone along caudal

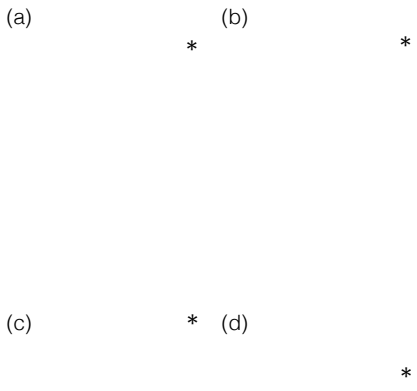

Figure 3: (a-b) Principal strains in the trabecular bone and

Mean ± 95% CI (*: p<0.01)

failure criteria, the location of high-risk tissue should indicate where the initial failure would occur when the whole vertebral body was overloaded. Prior to irradiation, around 6% of trabecular bone and 16% of cortical bone were subject to initial failure, and these values were found to be 4% for trabecular bone and 20% for cortical bone after irradiation. Therefore, it can be inferred that the radiation shifted the initial failure region from the trabecular bone to the cortical shell.

DISCUSSION

These results indicate that clinically-relevant doses of ionizing radiation altered the morphology of the trabecular bone in the mouse vertebral body — and the micro-mechanics throughout the vertebral body — without altering overall stiffness or strength. These morphological changes are likely attributed to effects of radiation on osteoclast and osteoblast activity, which can alter the trabecular micro-architecture [2]. Given changes in the micro-architecture of trabecular bone, the vertebral body reduced the maximum and minimum principal strains in the trabecular bone and shifted more load and initial failure risk to the cortex. Such changes in the micro-mechanics after radiation treatment effectively preserved the whole-bone level stiffness and strength. Thus, we have demonstrated how the mouse vertebral body can adapt its micro-architecture for biomechanical preservation.

ACKNOWLEDGEMENTS

This research was partially supported by a NASA Science and Technology Research Fellowship (NSTRF) NNX14AM56H to MMP. Experimental resources were provided through NASA Space Biology PECASE to Dr. Joshua S. Alwood. Computational resources were made available through the Savio computational cluster resource, provided by the Berkeley Research Computing program at the University of California, Berkeley.

REFERENCES

[1] Baxter, N. N. *et al.*, *J. Am. Med. Assoc.*, 294, 20, 2587–2593, 2005.
[2] Willey, J. S. *et al.*, *Clin. Rev. Bone Miner. Metab.*, 2011.
[3] Kondo, H. *et al.*, *Radiat. Res.*, 171, 3, 283–289, 2009.
[4] Alwood, J. S. *et al.*, *Bone*, 47, 2, 248–255, 2010.
[5] Bevill, G. *et al.*, *Bone*, 39, 6, 1218–1225, 2006.

SB³C2019
Summer Biomechanics, Bioengineering and Biotransport Conference
June 25 -28, Seven Springs, PA, USA

INVESTIGATING SEX-SPECIFIC ACCURACY OF PROXIMAL FEMUR COORDINATE SYSTEMS DERIVED FROM STATISTICAL SHAPE MODELS

C. Winsor (1), X. Li (2), J. Zhang (3), C.R. Henak (1), H. Ploeg (4)

(1) Mechanical Engineering
University of Wisconsin - Madison
Madison, WI, USA

(2) Mechanical Engineering
University of Sheffield
Sheffield, UK

(3) Auckland Bioengineering Institute
University of Auckland
Auckland, N□

(4) Mechanical and Materials Engineering
Queen's University
Kingston, ON, CAN

INTRODUCTION

Retrospective analysis of computed tomography (CT) scans via CT-based patient-specific finite element analysis (FEA) is proposed for increased accuracy of fracture risk prediction. Patient CT scans are frequently limited to the proximal femur. However, full femur anatomy more accurately defines the patient-specific femoral coordinate system (PSFCS) than proximal femur anatomy [1]. Statistical shape modelling (SSM), based on cadaveric databases, can be used to estimate full femur anatomy [1]; and therefore; PSFCS can be defined for CT scans of the proximal femur. Using this approach has been shown to result in increased predictive accuracy [1]; however, this technique is not recommended when surface errors exceed 1.5 mm in the proximal region [2]. Sex differences in femoral angle are well documented [3] and may be relevant for increasing the accuracy of PSFCS estimates. The aim of this study was to quantify the accuracy of the estimated PSFCS for a previously untested cadaveric dataset by sex.

METHODS

Materials and CT Scanning: This study was conducted on 24 cadaveric femurs from 7 women (aged 43-61) and 5 men (aged 55-63). CT scans were captured on a GE Discovery CT750 HD CT scanner at the Wisconsin Institute for Medical Research. Scan settings were 120 kVp, 1.25 mm slice thickness, 0.625 mm slice spacing, variable current, and monochrome2.

Segmentation and Statistical Shape Modeling: Femurs were segmented using Mimics v19.0 (Materialise, Leuven, Belgium). Two geometries were created: a full femur model (Fig. 1a), and a proximal 1/3 femur model (Fig. 1b). SSM was conducted using MAPClient software [4]. An iterative closest point algorithm aligned the center of the segmented mesh of the proximal 1/3 model (yellow) with an averaged left or right SSM femur mesh (red) (Fig. 1c). The averaged proximal femur was replaced with the full femur (red) from the cadaveric database (Fig. 1d) and a full femur shape (yellow) was estimated via SSM (Fig. 1e). The actual full femur (grey) and the estimated full femur (yellow) can be visually compared (Fig. 1f).

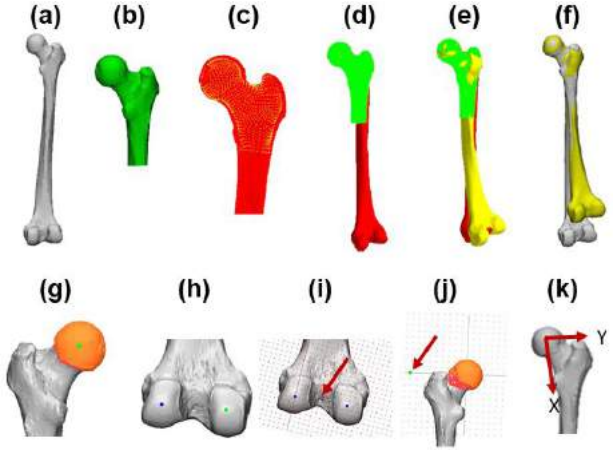

Figure 1: Full femur estimate from the proximal 1/3 femur for PSFCS definition: (a) Specimen full femur; (b) specimen proximal 1/3 femur; (c) aligned specimen proximal femur (yellow) and statistical shape cloud from MapClient cadaveric database (red); (d) specimen proximal femur (green) and averaged full femur (red); (e) specimen full femur estimate (yellow) with specimen proximal femur (green) and averaged full femur (red); (f) specimen full femur (grey) and full femur estimate (yellow); (g) center of femoral head; (h) posterior condyle surfaces; (i) knee center estimate; (j) lateral coordinate; (k) PSFCS.

Poster Presentation #P035

Coordinate System Definition: The PSFCS was defined for actual and predicted full femurs using the same process in 3-Matic v13 (Materialise, Leuven, Belgium) [1]. The origin was defined at the center of the femoral head, using the analytical fit tool with a sphere (Fig. 1g). The coordinates of the most posterior surface of the two condyles were visually identified (Fig. 1h). The knee center was estimated as their midpoint (Fig. 1i). The x-axis was defined along the unit vector through the origin and the knee center estimate. The y-axis was defined as the laterally directed (Fig. 1j) unit vector, orthogonal to the x-axis and co-planar with the origin, the knee center, and the posterior condyles. The z-axis was defined by the cross product of the x- and y-axes (Fig 1k).
Vectoral Analysis and Statistics: Vectoral analyses of the PSFCS for the actual and the predicted femurs were conducted in MATLAB 2018b (Mathworks, Natick, MA, USA). The distance vector between the femoral head center and the knee center estimate was calculated for the PSFCS of each femur. The angle, K, between the two resulting distance vectors (x-axes) was determined for each patient (Fig. 3). Additional distance vectors (y-axes) between the femoral head center and the lateral coordinate were determined and the angle, L, between them was calculated (Fig. 3). The Euler angles were calculated between the actual femur predicted femur coordinate systems. A Student's one-sided t-test was conducted on the angles.

RESULTS

The distance between the center of the femoral head and the knee center estimate was under-predicted and poorly correlated with the actual distance (men: slope 0.16, $R^2 = 0.017$; and, women: slope 0.43, $R^2 = 0.020$, Fig. 2). Angle K was less than 10° for all femurs, while angle L ranged from 7° to 60° for all femurs (Fig. 3). These and Euler angles are summarized in Table 1. Angle L ($p = 0.051$) and Euler angle Θ_X ($p = 0.028$) for women were larger than for men.

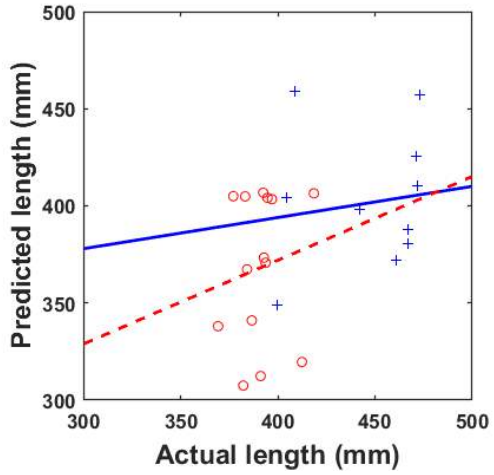

Figure 2: Correlation between the predicted versus the actual femur length from the center of the femoral head to the center of the knee. Male femurs are blue plus signs and female femurs are red circles, dashed line.

Table 1: Mean and standard deviation for K, L, and Euler angles

Group	Men	Women	Combined
Angle K	4.48° ± 2.47°	4.19° ± 2.16°	4.16° ± 2.24°
Angle L	12.0° ± 8.89°	20.2° ± 14.6°	16.3° ± 12.6°
Θ_X	0.5° ± 9.2°	8.7° ± 16.3°	9.4° ± 18.4°
Θ_Y	0.3° ± 2.2°	0.8° ± 2.0°	1.2° ± 3.0°
Θ_Z	-0.3° ± 2.3°	0.2° ± 2.8°	-0.2° ± 3.6°

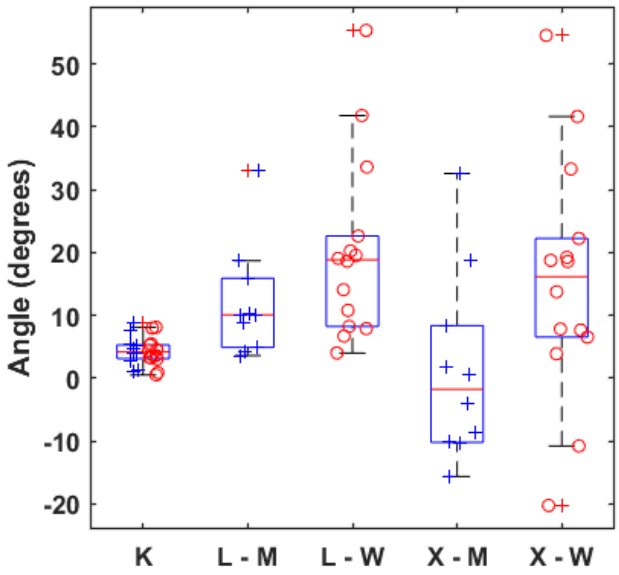

Figure 3: Angle K, between the actual and predicted femur length vectors for all specimens (x-axes). L – M and L – W, reflect the difference between the actual and predicted y-axis for men and women, respectively. Euler angle Θ_X (X – M and X - W). Male femurs are blue plus signs and female femurs are red circles.

DISCUSSION

This study quantified the accuracy of the estimated PSFCS for this dataset. The combined Euler angles for these femurs are comparable with prior studies (Table 2); however, this dataset does display more variation in Θ_X. The largest errors were found in the y-axis estimates (angle L), especially when differentiating by sex (Table 1). The errors in y-axis estimates and the larger Θ_X for women demonstrate a need for further investigation on additional patients.

Table 2: Euler Angle Comparison between Studies

Euler Angle	Qasim et al. [1] n = 95, all female	Zhang et al. [2] n = 13	Current n = 24
Θ_X	12° ± 7°	7.7° ± 4.0°	9.4° ± 18.4°
Θ_Y	7° ± 3°	2.6° ± 1.0°	1.2° ± 3.0°
Θ_Z	3° ± 3°	7.5° ± 4.2°	-0.2° ± 3.6°

Further study for determining a more accurate method for deriving PSFCS for use in patient-specific FEA is necessary. PSFCS estimates from the proximal femur may be improved by using: (a) sex-specific averaged SSM femur mesh; (b) the closest femoral match from the cadaveric database; or (c) additional proximal femur anatomical landmarks. In summary, SSM provides an important and promising start towards deriving PSFCS for the retrospective study of CT scans for femur strength prediction.

ACKNOWLEDGEMENTS

The authors thank the Whitaker Foundation and the Institute for International Education. The authors acknowledge helpful discussions with Alexander Teague.

REFERENCES

[1] Qasim, M et al., Osteoporos Int, 27:2815, 2016.
[2] Zhang, J et al., CMBBE, 5:566-576, 2017.
[3] Yoshioka, Y et al., JBJS, 69-A 6:873-880, 1987.
[4] Zhang, J et al., CMBBE, 2:176-185, 2014.

SB³C2019
Summer Biomechanics, Bioengineering and Biotransport Conference
June 25 -28, Seven Springs, PA, USA

EFFECTS OF COLLAGENASE AND ELASTASE ON THE MECHANICAL PROPERTIES OF PORCINE ABDOMINAL AORTA

C. Blum (1), C. Korenczuk (1), V. H. Barocas (1)

(1) Department of Biomedical Engineering
University of Minnesota- Twin Cities
Minneapolis, MN, USA

INTRODUCTION

Elastin, collagen, and smooth muscle cells are primary components that comprise the microstructure of arteries and contribute to the vessel mechanical behavior. During the course of the cardiac cycle, varying loading configurations are imposed on the vessel wall, causing each microstructural component to experience different amounts of combined loading. While macroscopic mechanical behavior, such as anisotropy, has been observed in vessel studies [1], the contribution of each individual constituent to the overall vessel mechanics is still relatively unclear. Selectively removing components via enzymatic digestion allows demarcation between constituent contributions to various loading configurations. Previous studies have presented a wealth of uniaxial data [2], but a deficiency in shear testing. Testing shear loading configurations is highly important, as many disease etiologies begin between the artery layers [3]. Despite much progress in understanding vessel mechanics, there remains a need to explore the role of each arterial component, in order to grasp the underlying mechanisms behind important vascular diseases. Here, we use enzymatic digestion to explore the role of collagen and elastin on the mechanical composition of porcine abdominal aortas in uniaxial and shear lap loading configurations. These two test protocols were chosen to evaluate both normal and shear stress effects on the tissue.

METHODS

Tissue samples were dissected from porcine abdominal aortas obtained from pigs sacrificed as part of separate, IACUC-approved studies at the UMN Visible Heart Laboratory.

Collagenase and elastase solutions were prepared (500 U ml−1, Type IV, Worthington Biochemicals, NJ, USA, and 10 U ml-1, porcine pancreatic elastase, Worthington Biochemicals, NJ, USA, respectively) in 1X Dulbecco's phosphate-buffered saline solution (Quality Biological, MD, USA). Samples were thoroughly cleaned and incubated at 37 ◦C for 1, 3, 5, 7, or 9 hours [4]. Tissue was completely submerged in buffered-media and thoroughly washed in 1X PBS following treatments. Small samples from each artery segment were collected after each study for later histological review.

Tissue thickness was measured using calipers by taking six measurements at different positions along the artery and calculating an average thickness. All cylindrical arteries were cut open along their lengths to produce planar sections. Once oriented in the circumferential (θ) and longitudinal, 'axial' (z), directions, these were then dissected into uniaxial and lap samples (Figure 1).

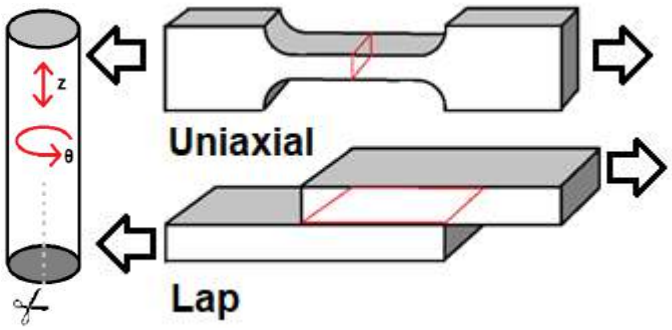

Figure 1: Uniaxial and Lap test geometries.

Uniaxial and lap data were collected using a Microbionix Uniaxial Tester (University of Minnesota, Tissue Mechanics Lab) with a 5 N load cell. After samples had been mounted, the load cell was zeroed, and the

actuator arm was moved so reach an 0.2 N pre-load. Samples were then pulled to failure at a constant rate of 0.045 mm/s. To maintain tissue hydration during the experiments, samples were placed in a 1X PBS bath at room temperature.

Stress and strain of uniaxial samples were calculated by finding the force over the original cross-sectional area of the neck and by the displacement divided by the original sample length, respectively. For lap samples, the average shear stress was calculated as the force divided by the original overlap area of the sample.

RESULTS

Control data (Figure 2) was used to establish baseline stress and strain values in the absence of matrix degradation enzymes and validate the testing methods. As expected, the circumferential direction showed greater stiffness in both the uniaxial and the lap tests. In the subsequent examination of the digested samples, we focused on the failure point, defined as the maximum stress, and we calculated the average failure stress and failure strain.

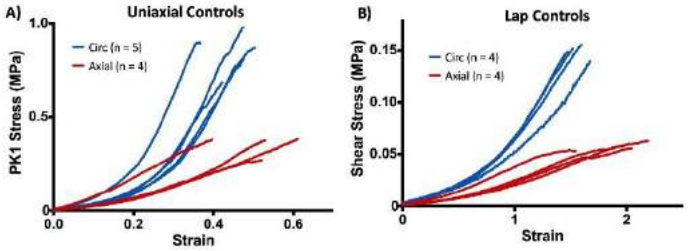

Figure 2: A) Uniaxial and B) Lap tests on control samples.

The average failure stresses and strains are shown in Figure 3. After an initial rise in failure stress at the 1-hour time point, especially in the uniaxial tests, further digestion led to a gradual decline in failure stress indicative of a degraded collagen matrix. The early strengthening can be attributed to a preliminary cross-linking of amino acids located near the enzyme binding sites in the collagen [5]. This effect was most notable in the circumferential direction. The failure strain showed little effect of digestion except for a rise in failure strain for the axial lap tests following long-time elastase digestion (Fig. 3D).

An additional observation, whose significance is not clear, is that while control lap samples in both orientations, as well as digested lap samples in the circumferential direction, failed in the overlap region, but digested samples failed in the sample arms. Since the arms of a lap sample are in extension during the test, this shift in the location of the failure point may be driven by weakening of the tissue in uniaxial extension as seen in Figure 3A. Similarly, the drop-in failure stress during lap testing (Figure 3C) is not an indication of weakening in shear but rather a consequence of extreme weakening of the arms.

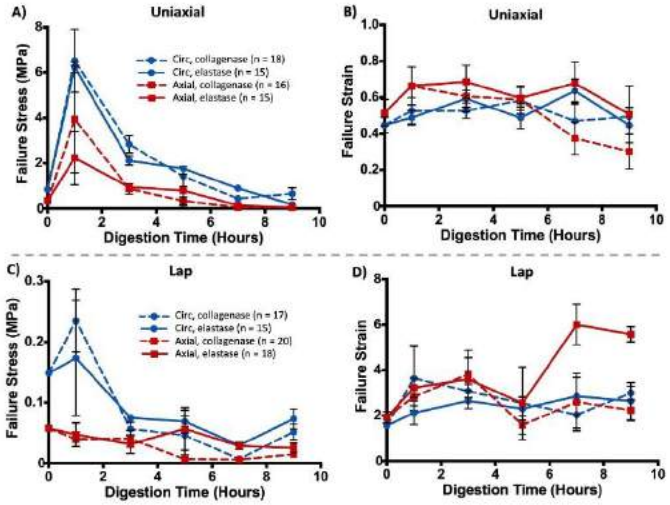

Figure 3: A) Failure stress and B) Failure strain in uniaxial tests. C) Failure stress and D) Failure strain in lap tests. Points are mean ± 95 confidence interval.

DISCUSSION

Much is understood about the biological and biomechanical mechanisms that contribute to vascular disease progression, but much also remains unknown. There is a lack of available tissue from the onset of vascular disease to its end stages, making ex-vivo digestion experiments a critical substitute. This study examined the contributions of collagen and elastin to the failure behavior of the tissue in both shear and uniaxial extension.

Collagen and elastin degradation for uniaxial testing showed very similar results for circumferential direction, but a failure stress of half for axial when using elastase. Failure strains remained similar for the two. There is an opposite trend for lap samples, with a decrease in circumferential failure stress for elastase, but no measurable trend for the axial tests.

There are, of course, other biomacromolecular and cellular components that contribute to vascular mechanics. Future mechanical testing will focus on cell contributions to artery microstructure by decellularization testing and incorporating computational models to improve understanding of microstructure behavior.

ACKNOWLEDGMENTS

The authors acknowledge the University of Minnesota Tissue Mechanics Lab for the use of their uniaxial equipment, and the Visible Heart Lab for porcine tissue. This material is based upon work supported by the National Science Foundation Graduate Research Fellowship Program under Grant No. 00039202 (CEK) and NIH grant U01 HL139471. CEK is a recipient of the Richard Pyle Scholar Award from the ARCS Foundation.

REFERENCES

[1] Ferruzzi, J., Vorp, D. A., & Humphrey, J. D. (2010). Journal of the Royal Society, Interface.

[2] Macrae, R. A., Miller, K., & Doyle, B. J. (2016). Strain.

[3] Mazurek, R., et al. Advances in Pharmacology Vascular Pharmacology - Smooth Muscle, 2017.

[4] Namrata Gundiah et al 2013 Physiol. Meas.

[5] Snedeker JG, Gautieri A. Muscles Ligaments Tendons J. 2014.

FINITE ELEMENT SIMULATION FRAMEWORK FOR INVESTIGATING PATHOLOGICAL EFFECTS ON ORGAN-LEVEL TRICUSPID VALVE BIOMECHANICAL FUNCTION

Devin W. Laurence (1), Emily Johnson (2), Ming-Chen Hsu (2), Arshid Mir (3), Harold M. Burkhart (4), Yi Wu (1), and Chung-Hao Lee (1,5)

(1) Biomechanics and Biomaterials Design Laboratory
School of Aerospace and Mechanical Engineering
University of Oklahoma
Norman, OK, USA

(2) Department of Mechanical Engineering
Iowa State University
Ames, IA, USA

(4) Department of Pediatrics
University of Oklahoma
Health Sciences Center
Oklahoma City, OK, USA

(3) Department of Surgery
University of Oklahoma
Health Sciences Center
Oklahoma City, OK, USA

(5) Institute for Biomedical Engineering, Science, and Technology
University of Oklahoma
Norman, OK, USA

INTRODUCTION

The tricuspid valve (TV), located in the right side of the heart, has been historically under-treated in the clinical setting due to assumptions that functional tricuspid regurgitation (FTR) will regress after treatment of left-sided lesions [1]. Recent studies have contradicted these assumptions and demonstrated that FTR often continues to progress after the repair, worsening the overall prognosis [2]. In addition to left heart disease, TR may result from right heart dilation in congenital heart disease, primary pulmonary hypertension as well as an increased pressure-volume load seen in single ventricle patients. Thus, the TV has become of great focus in the past 5-10 years with emphases on more accurate assessment of FTR and determination of the optimal treatment time. However, proper assessment of FTR can be difficult, especially for patients who have less than moderate FTR [3-4]. Furthermore, current methods utilize various medical imaging modalities for these assessments, such as 2D/3D echocardiography, that provide key information regarding the TV geometry but no information regarding the TV mechanical environment. Therefore, the objective of this study is to develop a finite element framework for the TV to address these limitations. Specifically, this framework will provide enhanced information about key geometrical and mechanical quantities associated with pathological valves to assist clinicians in the assessment of FTR.

METHODS

Finite Element Model Geometry: The finite element (FE) model geometry was generated in two steps. First, the TV annulus and chordae tendineae geometries were obtained from micro-CT image data of an ovine TV fixed in the closed position. Second, the leaflet geometry was created using a previously-published parametric model for the TV [5], represented by cubic B-spline surfaces and curves [6]. These geometries were then combined (**Fig. 1**) using the ABAQUS CAE interface.

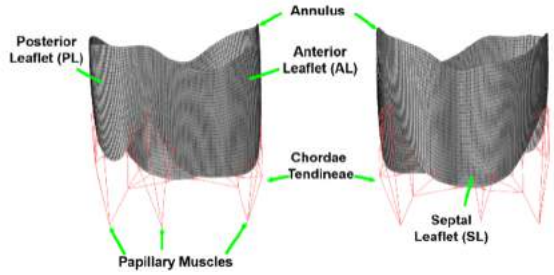

Figure 1: Schematic of the finite element geometry.

FE Simulations: FE simulations were performed using the ABAQUS explicit dynamic solver. Both the valvular annulus and papillary muscles were assumed to be fixed to prevent rigid body motion. Transvalvular pressure of 25 mmHg (40 mmHg for the pulmonary hypertension scenario) was applied to the ventricular side of the leaflets for 0.4 seconds, which is the approximate duration of systole, to simulate systole. The leaflets were represented by a simplified isotropic material model:

$$\psi = c_0(I_1 - 3) + c_1(e^{c_2(I_1-3)^2} - 1) \quad (1)$$

wherein c_0, c_1, and c_2 are the material model constants, and I_1 is

the first invariant of the right Cauchy-Green deformation tensor. The chordae tendineae were assumed to be nonlinearly elastic with a Young's modulus of 40 MPa and Poisson's ratio of 0.30.

A series of numerical studies were performed to investigate the effect of various pathologies typically associated with FTR on quantitative values described in the next sub-section. The specific scenarios were pulmonary hypertension (PH) and annulus dilation (AD) with a flattened annulus.

Simulation Results Post-Processing: Results from the different scenarios underwent extensive post-processing to quantify key geometrical and mechanical quantities. The geometrical quantities of interest were those typically quantified in the clinical setting, specifically the leaflet tenting height, tenting area, and coaptation height (**Fig. 2**). For the mechanical quantities, the von Mises stress and maximum in-plane Green-Lagrange Strain (MIPE) were averaged for all elements of the leaflet geometry, and qualitative comparisons were made between the contours.

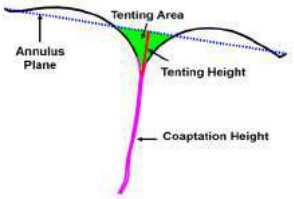

Figure 2: Schematic of the geometrical metrics.

RESULTS

FE simulation results presenting the von Mises stress and MIPE contours for the healthy, PH, and AD scenarios are provided in **Fig. 3**. The von Mises stress was observed to increase in the central area of the leaflets from ~75 kPa in the healthy scenario to ~125 kPa in the PH scenario, while the AD scenario remained around ~75 kPa with differences in the contour. Similar trends were observed for the MIPE.

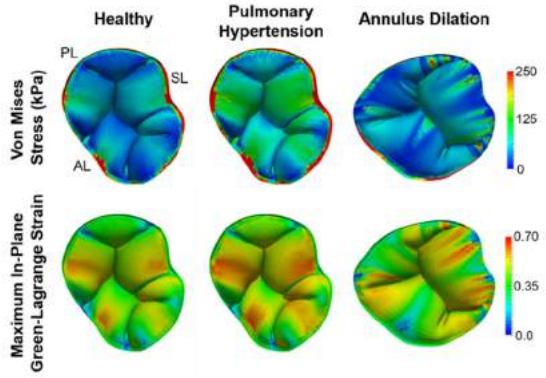

Figure 3: Simulation results of the healthy, pulmonary hypertension (PH), and annulus dilation (AD) scenarios.

Results for the geometrical and mechanical quantities are provided in **Fig. 4**. The geometrical quantities generally varied between the coaptation considered. The PH scenario showed a consistent decrease in the tenting height and increase in the coaptation height when compared to the healthy simulation. Moreover, the AD scenario resulted in an increase in all geometrical quantities for the AL-SL and PL-SL coaptations. The PH scenario had a larger increase in mechanical values compared to the AD scenario.

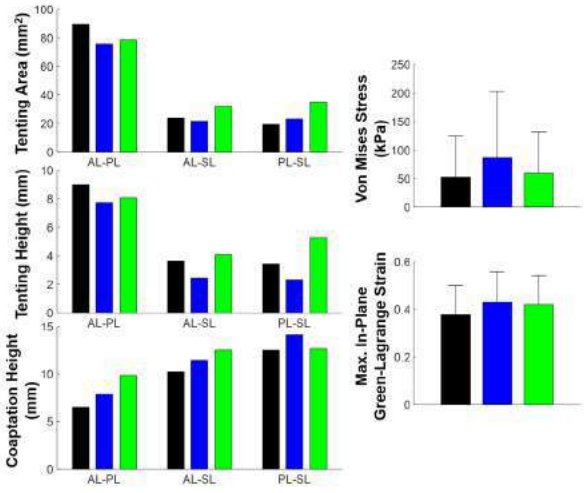

Figure 4: Geometrical and mechanical quantities from the study scenarios. The x-axis labels stand for different leaflet coaptations (e.g., AL-PL is the coaptation between the anterior and posterior leaflets). Black: Healthy; Blue: PH; Green: AD.

DISCUSSION

This study is *the first of its kind* to determine the effects of PH and AD using an FE framework. However, a previous study by Casa et al., [7] determined the individual and combined effects of PH and AD *in-vitro*. The trends observed in the geometrical quantities are comparable to the previous *in vitro* study with differences in the effect of PH on the PL-SL coaptation. Overall, the numerical changes for PH and AD were larger in the *in-vitro* study but were within the same order of magnitude. Differences between the two studies could stem from the choice of valve. The *in-vitro* study used excised porcine valves whereas this study used a parametric representation of the TV leaflets with real annulus and chordae geometry.

Our findings could improve the understanding of how PH and AD affect TV function. TV coverage index (TV leaflet length / TV tenting area) is currently used as a marker for PH [8] and this could be expanded. Moreover, the developed framework opens new avenues for patient-specific *in-silico* modeling, which could significantly benefit the clinical setting. For example, the framework could use a patient's geometry to aid with the assessment of the valve's status. This would be of great value when making decisions about the need for TV repair at the time of cardiac surgery for other lesions. Furthermore, the framework could also be used to guide patient-specific therapeutics.

ACKNOWLEDGEMENTS

This work was supported by the American Heart Association Scientist Development Grant (16SDG27760143) and the OU VPR Faculty Investment Program.

REFERENCES

[1] Braunwald, N. et al., *Circulation*, 35(suppl):I63-I69, 1967.
[2] Carpentier, A. et al., *J. Thorac. Cardiovas. Surg.*, 67:53-65, 1974.
[3] Dreyfus, G. et al., *J. Am. Coll. Cardiol.*, 35:2331-2336, 2015.
[4] Lancellotti, P. et al., *Eur. J. Echocardiography*, 11: 307-332, 2010.
[5] Stevanella, M. et al., *Med. Eng. & Physics*, 32:1213-1223, 2010.
[6] Kamensky, D. et al., *CMAME*, 330:522–546, 2018.
[7] Casa, L. et al., *Annals of Biomedical Engineering*, 41(4): 709-724.
[8] Medvedofsky et al., *Eur. Heart J Cardiovasc Imaging*, 18(1): 86-94.

SB³C2019
Summer Biomechanics, Bioengineering and Biotransport Conference
June 25 -28, Seven Springs, PA, USA

AN INTEGRATED OPTO-MECHANICAL SYSTEM FOR QUANTIFICATION OF DYNAMIC MICROSTRUCTURE AND MECHANICS OF HEART VALVE TISSUES

Samuel V. Jett (1), Zachary V. Schuermann (1), Arshid Mir (2), Harold M. Burkhart (3), and Chung-Hao Lee (1,4)

(1) Biomechanics and Biomaterials Design Laboratory
School of Aerospace and Mechanical Engineering
The University of Oklahoma
Norman, OK, USA

(2) Division of Pediatric Cardiology
Department of Pediatrics
University of Oklahoma Health Sciences Center
Oklahoma City, OK, USA

(3) Division of Cardiothoracic Surgery
Department of Surgery
University of Oklahoma Health Sciences Center
Oklahoma City, OK, USA

(4) Institute for Biomedical Engineering, Science and Technology
The University of Oklahoma
Norman, OK, USA

INTRODUCTION

Many biomechanical diseases, such as heart valve stenosis, tendon tears, and arterial aneurysms, cause impairment in organ function via alterations and remodeling in tissue microstructure. Consequently, prior studies have examined the microstructure of healthy and diseased tissues [1]. Methodologies for microstructural analysis include histology, small angle light scattering (SALS), polarized light microscopy (PLM), and second-harmonic generation (SHG) imaging, among others. However, these techniques are incapable of capturing the *dynamic* nature of tissue microstructure and the collagen fibers therein. In collagenous tissues, such as the tendon and heart valves (HVs), the orientations and dispersion of the load-bearing collagen fibers dynamically adjust in response to mechanical loading [2]. In this study, we developed and validated a novel integrated system consisting of a biaxial tester and a polarized spatial frequency domain imaging (pSFDI) device to quantify load-driven changes to collagen microstructural architecture in tissues.

METHODS

Birefringent Microstructural Scattering Theory: Collagen fibers exhibit birefringence, i.e., a polarization-dependent refractive response. For a single fiber with coplanar polarization, the refractive index depends upon the fiber orientation (θ_f) relative to the polarization of the light (θ_p). The reflected light intensity (I) of the fiber under co-polarized illumination and capture is described by Eq. (1).

$$\mathrm{I} = a_0 + a_2 \cos\left(2\left(\theta_p - \theta_f\right)\right) + a_4 \cos\left(4\left(\theta_p - \theta_f\right)\right) \quad (1)$$

This birefringent relation between I, θ_f, and θ_p is further visualized in **Figure 1** with an example fiber angle of 90° and typical fitting Fourier series coefficients (a_0, a_2, a_4) as observed for collagen fibers.

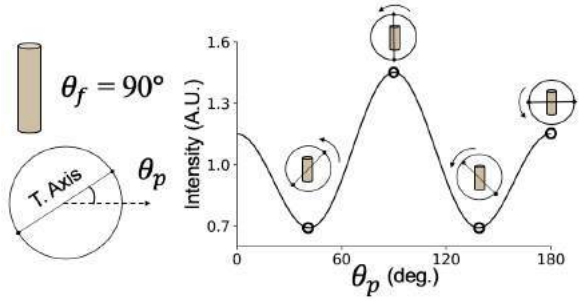

Figure 1: Schematic of the reflected intensity response of a collagen fiber at $\theta_f = 90°$ under co-polarized illumination and capture (T. Axis ~ Transmission axis of the polarizer).

This reflected intensity response holds for clusters of collagen fibers as well. In brief, the average orientation of a group of collagen fibers (θ) can be calculated as the θ_p where the reflected intensity is at its maximum. Additionally, the spread of the group of fibers can be represented via the degree of anisotropy (DOA) metric [3]:

$$\mathrm{DOA} = 1 - \left[\frac{a_0}{(a_0 + a_2 + a_4)}\right] \quad (2)$$

pSFDI System Theory: In pSFDI, a projector generates patterned images, according to spatial frequency domain imaging (SFDI) theory, and projects these images through a polarizer and onto a sample. The reflected light then passes through the same polarizer and is captured by a camera. To acquire the intensity response of the sample, the polarizer is incrementally rotated through 180° with an image captured at each increment. The pixelwise θ and DOA can be calculated by fitting Eq. (1) to the intensity response at each pixel and applying the fit coefficients to Eq. (2) (**Fig. 2a**).

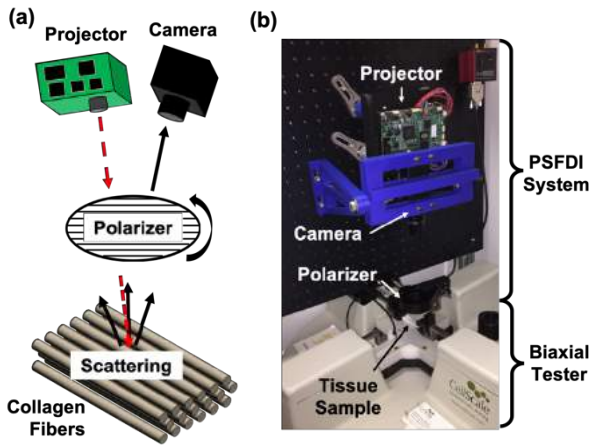

Figure 2: (a) Schematic showing the passage of light through the fundamental components of the pSFDI system, and (b) image of our integrated pSFDI and biaxial testing systems.

The Integrated System: Our group integrated a commercial biaxial tester (CellScale Biomaterials Testing, Canada) with a vertically-mounted pSFDI system to produce a combined opto-mechanical testing system (**Fig. 2b**). The testing sequence is controlled by in-house LabView programs and data/image analyses were performed in Python.

RESULTS

Tendon Tissue Testing: For validation, we performed uniaxial mechanical testing on a strip of bovine tendon with a 50° preferred fiber orientation, a width of 18 mm, and a thickness of 0.75 mm (**Fig. 3**).

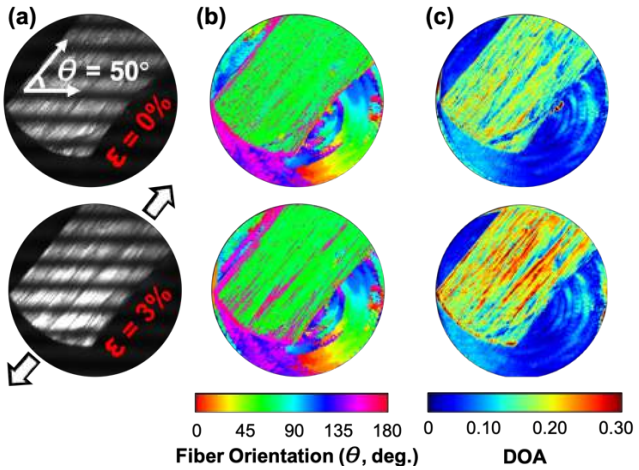

Figure 3: (a) Raw testing images, (b) θ predictions, and (c) DOA predictions for a tendon sample under 0% and 3% strains.

The θ prediction of 50° was accurate for both unloaded and loaded states, despite the appearance of some bands associated with 150° false predictions in the loaded tendon (**Fig. 3b**). On the other hand, the DOA predictions exhibited substantial load-dependency, with the domain-average DOA increasing from 0.145 for the unloaded tendon to 0.188 for the loaded tendon (**Fig. 3c**).

HV Leaflet Testing: We also used our system to examine the dynamic collagen microstructural architecture within a porcine mitral valve anterior leaflet (MVAL) with a thickness of 0.87 mm. We conducted a standard biaxial mechanical preconditioning protocol to restore the tissue's *in-vivo* behavior, then characterized the MVAL microstructure without loading (**Fig. 4c**) and under equibiaxial loading of 1.0 N (**Fig. 4d**).

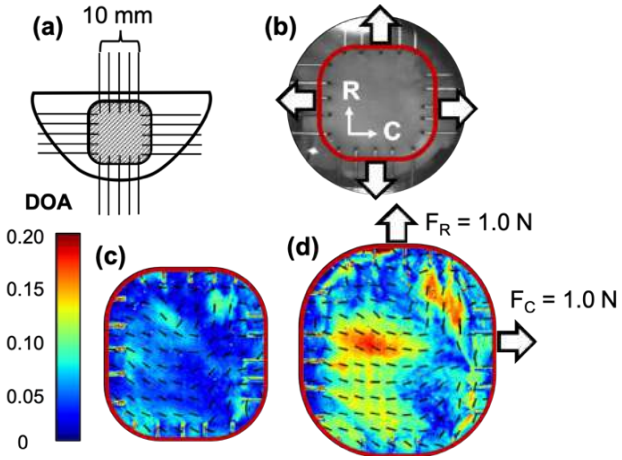

Figure 4: (a) Schematic of the MVAL testing region, (b) image of the mounted MVAL with directions marked (R: radial, C: circumferential). Predicted θ (dashed lines) and DOA: (c) without loads and (d) under an equibiaxial load of 1.0 N.

The fiber orientation predictions showed a strong bias toward the circumferential tissue direction but minor load-dependency, with domain-averaged θ of 177.1° prior to loading and 176.4° after loading. This bias manifested in the non-uniform dilation of the loaded tissue, with stretch of 29.7% in the radial direction but only 18.6% in the circumferential direction. In constrast to θ, the DOA showed a substantial response to external loads, with domain-averaged DOA increasing from 0.045 to 0.085 with applied loading. We also found subtle spatial variance in both the fiber orientation and DOA predictions.

DISCUSSION

The highly-uniform collagen orientation predicted in bovine tendon agrees with the known longitudinal fiber architecture. The increase in DOA we observed in the loaded tendon confirms intuition and suggests potential uncrimping of the collagen fibers with applied loads. For the HV leaflet tissue, our findings suggested that the loaded fibers: (i) are predominantly oriented in the circumferential direction and (ii) exhibit substantial spatial heterogeneity are supported by a mechanical study that found spatial differences and an increased circumferential stiffness in the MVAL mechanical response [4]. Although our study is the first to examine the fiber architectural changes in the full HV leaflet under biaxial loading, a prior study utilized SHG imaging and found microstructural load-dependency in the superficial layer [5]. Our study provides richer information to establish that MVAL load-dependency extends through the leaflet thickness. The similarity of tendon and MVAL microstructural predictions from this study to prior results validated the systemic capacity and opens doors to new research explorations, including: (1) novel applications in structural constitutive modeling, (2) understanding of the impacts of connective tissue disease on microstructure dynamics, and (3) improved microstructural analysis of fibrous biomaterials and engineered tissues.

ACKNOWLEDGEMENTS

This work is supported by the American Heart Association Scientist Development Grant 16SDG27760143 (CHL).

REFERENCES

[1] Jeffery, A et al., *J Bone and Joint Surgery*, 73(5):795-801, 1991.
[2] Driessen, N.J. et al., *J Biomech Engr*, 127(2):329-336, 2005.
[3] Goth, W et al., *Opt. E. and Tissue Biomechanics III*, 9710, 2016.
[4] Laurence, D et al., *J Biomech*, 34:859-871, 2018.
[5] Alavi, S et al., *Amer. J of Phys-H and C,* 309(2):276-284, 2015.

SB³C2019
Summer Biomechanics, Bioengineering and Biotransport Conference
June 25 -28, Seven Springs, PA, USA

COMPUTATIONAL ANALYSIS OF UNHELMETED BICYCLE ACCIDENTS THROUGH MULTI-BODY AND FINITE ELEMENT SIMULATIONS

Lise Gheysen (1), Michel Woering (2), Markos Kapeliotis (2), Jos Vander Sloten (2)

(1) IbiTech – BioMMeda
UGent
Ghent, Belgium

(2) Biomechanics Section
KU Leuven
Leuven, Belgium

INTRODUCTION

Head injuries commonly occur after bicycle accidents, with rates up to 2/3 for severely injured cyclists [1]. Appropriate head protection could contribute in the prevention of these head injuries. To determine the requirements for appropriate head protection, knowledge about the injury mechanisms is needed. Much effort has already been done to establish head injury criteria for multiple injury types, commonly using finite element head models (FEHM) [2]. However, no consensus about a good predictor with a corresponding threshold has been found.

At the same time, within the framework of accident reconstruction, real-life accidents are a potential source of valuable information, as they allow to study severe human head injuries in realistic situations. In order to investigate the head response in these real-life accidents, a work-flow based on validated multi-body (MB) models and a FEHM has already been used [3]. The available information about the true situation in these accidents has a varying accuracy. Besides, the pedestrian and bicycle MB models have many variables [4, 5]. Both aspects lead to uncertainty on the reliability of the outcome of the MB simulations. No quantification of the uncertainty introduced by the reconstruction of real-life bicycle accidents without car collision was found in literature.

Therefore, it is the aim of this study to assess the added value of using the validated MB models and FEHM to study real-life bicycle accidents. Two topics will be discussed in particular. The first one is the quantification of the uncertainty introduced by the use of MB software, which is used to obtain the head kinematics from real-life unhelmeted bicycle accidents without car-collision. The second part considers the possibility to correctly predict the diagnosed Acute Subdural Hematoma (ASDH) and brain contusions, based on finite element analysis (FEA), with the MB head kinematics as input, and the current knowledge about injury predictors and their corresponding thresholds.

METHODS

Parametric study of MB simulations For five real-life bicycle accidents, whereof the accident and injury description was collected at the University Hospital of Leuven, an initial simulation was set up based on a validated 50th percentile male MB model in MADYMO [5]. A trial and error approach was used. It was required that the impact place of the simulations corresponded to the description. Thereafter, two types of parametric studies, based on six input variables (see table 1), were performed. The peak resulting angular acceleration ($\alpha_{Peak,Res}$) was taken as output variable, as it was found to be linked to the injury mechanisms [2]. The influence of each input variable was investigated for three cases by considering the maximal change in $\alpha_{Peak,Res}$ per variable and per case, with respect to the initial simulation, and univariate linear regression. A methodology based on an orthogonal array and multivariate linear regression was applied to the other two cases. Besides, based on the subset of simulations leading to the correct impact place, the uncertainty on $\alpha_{Peak,Res}$ was quantified. The head kinematics with the minimal and maximal $\alpha_{Peak,Res}$ were selected for each case as input for the FEA, together with those of the initial simulation.

Head impact FEA The KTH FEHM, adapted to study brain contusion and ASDH due to ruptured bridging veins (BV), was used to perform the analysis in LS Dyna based on the obtained head kinematics. The maximal engineering strain of all BV and the relative motion damage measure (RMDM) were investigated as predictors of ASDH [6]. For brain contusion, the maximal principal compressive and tensile true strain were assessed using strain injury thresholds of 0.20 and 0.25 [7, 8]. After comparing the results of the predictors to each other, they were compared to the medical information in a qualitative way. The ability to distinguish injured and uninjured cases was assessed and the correctness of the predicted locations was considered.

Poster Presentation #P039

Table 1: Input variables of the parametric study and the corresponding ranges. Feet-pedals and Hands-handlebars indicate the strength of the connection between the feet and the pedals and between the hands and the handlebars, respectively.

Parameter	Range	Step
Position pedal hub	-20° to 20° w.r.t. initial position	10°
Position upper body	Ca. 25° to 60° w.r.t. vertical line	8.64°
Speed	60% to 140% of initial speed	20%
Saddle height	-6 cm to 6 cm w.r.t. initial height	3 cm
Feet-pedals	60% to 140% of initial strain	20%

RESULTS

Parametric study of MB simulations Although the maximal change in input variable differed often strongly from case to case, there was at least one case with a maximal change larger than 70% in $\alpha_{Peak,Res}$ for each input variable (see table 2). The number of significant univariate linear relations and the number of significant terms in the multivariate relations were limited and the variables leading to the significant relations and terms were case dependent. Next, based on the subset of simulations leading to the reported impact place, the smallest maximal change on $\alpha_{Peak,Res}$ was ca. 30%.

Table 2: Overview of the maximal changes for $\alpha_{Peak,Res}$ per input variable. The maximal change per case from the subset of simulations with the correct impact place is given as well.

Case	Upper body	Pedal hub	Feet-pedals	Hands-handlebars	Speed	Saddle height	Correct impact
1	60%	72%	8%	96%	42%	60%	72%
2	64%	26%	0%	43%	51%	63%	42%
3	81%	38%	80%	92%	84%	83%	52%
4	NA	NA	NA	NA	NA	NA	33%
5	NA	NA	NA	NA	NA	NA	232%

Head impact FEA For ASDH due to ruptured BV, the predicted injury locations and distinction between injured and uninjured cases of the maximal BV strain and RMDM were similar. The predicted brain contusion locations for the strain measures were comparable on a general level as well. The comparison with the medical information suggested for both head injury types that using the head kinematics of the initial simulations led to a correct distinction between injured and uninjured cases, with a true strain threshold of 0.20 for brain contusions. This was no longer true when looking to the simulations based on the minimal and maximal $\alpha_{Peak,Res}$. While the predicted location of ASDH agreed well with the medical information, the brain contusion locations had a limited agreement.

DISCUSSION

Parametric study of MB simulations The high maximal change for each input variable in at least one case, indicated that all input variables had a relevant importance. That small changes in the input variables can imply large maximal changes in the rotational head acceleration, was also noticed before [4]. However, the relevance of the input variables for a particular bicycle accident varied and it is not ensured that all important variables were taken into account.

Next, with the considered sample size, no general trends in the influence of the uncertainty on the initial situation and the relative importance of the input variables could be established using uni- or multivariate linear regression. One study that performed regression based on a parametric study of MB simulations was found [9]. However, as the linear velocity instead of $\alpha_{Peak,Res}$ was used as output, the results of the study are not transferrable. It is, therefore, suggested that more cases should be considered in order to gain further insight.

Besides, the smallest maximal change in $\alpha_{Peak,Res}$ was ca. 30% for the subset of simulations with the correct impact place, implying a minimal uncertainty of 30% on $\alpha_{Peak,Res}$. However, this uncertainty indicates a minimum and is only valid for the considered cases and ranges of variables, so caution is warranted. Including more cases is needed to expand the insight in the uncertainty that could be expected in general.

Other limitations related to the parametric studies, next to the limited number of cases, are the user-dependence of the simulation set-up, the assessment of the estimated impact place and the use of a 50th percentile male model for all cases.

Head impact FEA Based on the medical information, the injured cases could be separated well from the uninjured ones for ASDH due to BV rupture and brain contusions, based on the head kinematics of the initial simulations. The threshold distinguishing the victims diagnosed with BV rupture from those without, i.e. a maximal BV strain of ca. 0.14, is situated at the lower boundary of the experimentally determined BV rupture strains [10]. This implies that the threshold might be realistic. However, the threshold should be interpreted as upper boundary of the safe region, rather than as an indication of BV rupture. For brain contusions, the maximal principal strain threshold of 0.20, situated within the range of thresholds proposed before, allowed to correctly distinct the victims with and without brain contusion for the initial simulations [7, 8].

For BV rupture, the injury locations were predicted quite well. Caution should, however, be taken, as the reliability of the location prediction with the FEHM was questioned before [11]. Considering brain contusions, the locations were determined in a suboptimal way, due to the lack of CT scans. Moreover, the correspondence with the medical information was limited.

Besides, the dependence of the ability to distinct harmed from unharmed victims on the use of the minimal, initial or maximal MB simulation, stresses the risk of the uncertainty related to using MB software for the reconstruction of real-life bicycle accidents.

Conclusion By using the head kinematics from the initial MB simulations as input for the FEA, the presence of ASDH due to ruptured BV and brain contusion was correctly predicted for the five real-life accidents, despite the uncertainty on the initial situation and the lack of consensus on the injury predictors and thresholds. The work-flow, therefore, has the potential to contribute in head injury research. However, further improving the characterization of the uncertainty and the use of CT scans to assess the injury locations, is required to improve the insight in the reliability of the results obtained with this work-flow.

ACKNOWLEDGEMENTS Not applicable.

REFERENCES

[1]Amoros, E. et al., *BMC public health,* 11:653, 2011.
[2]Kleiven, S., *Stapp Car Crash Journal,* 51:81-114, 2007.
[3]Bourdet, N. et al., *International Journal of Crashworthiness,* 19:222-232, 2014.
[4]Verschueren, P., K.U.Leuven. Faculteit Ingenieurswetenschappen, 2009.
[5]MADYMO, "Human body manuals," TASS International 2017.
[6]Takhounts, E. et al., *Stapp Car Crash Journal,* 47:107-133, 2003.
[7]Shreiber, D. I. et al., *Proceedings: Stapp Car Crash Conference,* 41:277-291, 1997.
[8]Mao, H. et al., *International Journal for Numerical Methods in Biomedical Engineering,* 27:357-366, 2011.
[9]Bourdet, N. et al., *Proceedings of the Institution of Mechanical Engineers Part P-Journal of Sports Engineering and Technology,* 226:282-289, 2012.
[10]Monea, A. G. et al., *Journal of the mechanical behavior of biomedical materials,* 32:155-165, 2014.
[11]Cui, Z. Y. et al., *Computer Methods in Biomechanics and Biomedical Engineering,* 20:530-539, 2017.

SB³C2019
Summer Biomechanics, Bioengineering and Biotransport Conference
June 25 -28, Seven Springs, PA, USA

REPEATED NON-INJURIOUS LOADING INDUCES CHANGES IN LOCAL MECHANICS & COLLAGEN FIBER ORGANIZATION THAT MAY BE INJURIOUS

Travis M. Kotzur (1), Beth A. Winkelstein (1,2)

(1) Department of Bioengineering
University of Pennsylvania
Philadelphia, PA, United States

(2) Department of Neurosurgery
University of Pennsylvania
Philadelphia, PA, United States

INTRODUCTION

Neck and back pain have high incidence and costs, and the spinal facet joint and its capsular ligament have roles in pain [1-3]. Yet, how mechanical signals are transduced to painful ones is still unclear. Previously considered non-injurious loading [4,5] is increasingly being shown to induce mechanical and biologic dysfunction, including ligament laxity and pain responses. Studies of effects of such loading on the microstructural scale report collagen disorganization [6,7], suggesting the possibility for injury and/or dysfunction at the cellular level. Further supporting that hypothesis, repeated loading even below thresholds for pain and injury produces pain and changes in ligament structure [6,8]. Because collagen organization is dictated by macroscopic ligament stresses and strains, and mediates neuronal responses [9,10], defining microstructural effects of macroscale loading applied after an otherwise non-injurious exposure is needed to define pain mechanisms.

This study used a collagen gel system [7] to study effects of repeated stretch on mechanics and collagen organization. All gels underwent stretch that has been previously defined to be non-injurious, inducing strains (~8%) below the threshold for pain and lasting structural damage [7]. To test whether the collagen microstructure is disorganized or damaged, a second stretch was applied either at the same non-injurious magnitude or at a magnitude (~17% strain) known to activate neurons [7]. During loading, force, strain and circular variance (CV) were measured to define macromechanics, regional kinematics and collagen organization with fiber alignment maps [7,11,12].

METHODS

Gels underwent repeated non-injurious stretches, or a non-injurious stretch followed by an injurious one. Gels were made using a solution (2mg/ml) of rat tail Type I collagen (Corning), formed in a 12-well plate [7], and incubated at physiological conditions to set overnight and then cut into a 21mmx8mm strip. A matrix of markers was placed on the surface to define elements and track deformations (Fig. 1) [6]. Gels were submerged in a PBS bath and clamped in a planar test machine (574LE2; Test Resources). Each gel underwent a uniaxial stretch (1.5mm; non-injurious; NI) at 0.5mm/s, was held for 2s, returned to its reference unloaded state (AfterNI) and held for 10s (Fig. 1). A

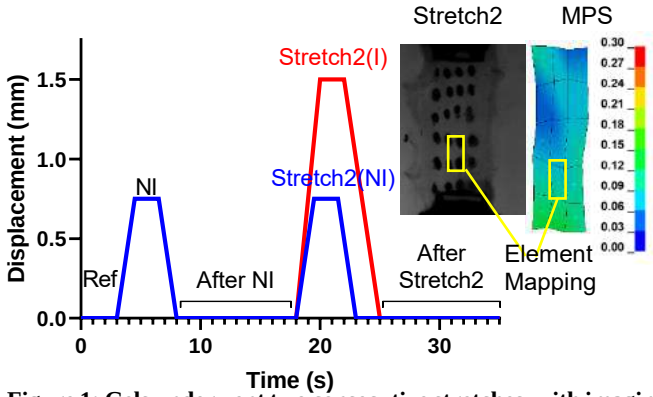

Figure 1: Gels underwent two consecutive stretches, with imaging data analyzed at designated events. The image shows a gel at Stretch2(I) with grid, element and corresponding MPS.

Poster Presentation #P040

set of gels (n=5) received a second NI stretch (Fig. 1); another set (n=5) underwent a second stretch (3mm; injurious; I) at the same rate (Fig. 1). Force and displacement data (200Hz) were synchronized with imaging (Phantom v9.1; Vision Research; 500fps; 568x568pixels^2) that tracked the markers. Polarized light imaging acquired fiber alignment maps [7,11] at: unloaded (ref), Stretch1 (NI), AfterNI, Stretch2, and after Stretch2 (Fig. 1).

From the imaging data, maximum principal strain (MPS) and CV were calculated to define changes in local kinematics and collagen fiber organization during the stretches and holds. Using marker displacements and the LS-DYNA software (LSTC), elemental MPS at each event was calculated [12]. CV at each element also was calculated from the alignment maps at each event. Separate paired t-tests compared force, strain, and CV between each matched event for each group.

RESULTS

Imaging data were unavailable for a gel in each group. For all gels, the force (11.46±8.93mN), strains (7.96±3.43%) and CV (0.087±0.19) at the first NI stretch are not different ($p>0.2$). Both force and MPS at the second NI stretch are significantly lower ($p<0.05$) than at the first NI stretch (Fig. 2). In contrast, force and MPS at the higher (3mm) injurious Stretch2 are both increased significantly ($p<0.03$) over matched Stretch1 values (Fig. 2).

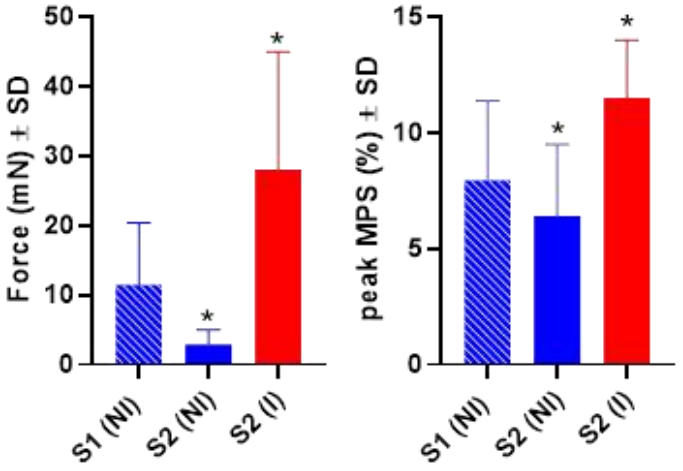

Figure 2: Peak force and MPS for groups at each event show both are significantly increased for injurious Stretch2 (S2(I)) (*$p<0.03$) and decreased (*$p<0.05$) for non-injurious Stretch2 (S2(NI)).

The CV at the injurious Stretch2 (0.003±.003) is also significantly higher ($p<0.01$) than its corresponding Stretch1 (0.002±0.001), indicating that the collagen fibers are becoming more disorganized as the fibers are becoming less aligned with each other (Fig. 3). In addition, the CV for a non-injurious Stretch2 (0.185±0.25) is significantly different ($p<0.05$) from corresponding CV values at the first NI stretch (0.23±.30). Taking all gels together, there is no difference ($p>0.2$) in CV at the first NI stretch (0.087±0.19) from the corresponding reference CV value (0.084±0.20).

DISCUSSION

The fact that CV at the first NI stretch is not different from the corresponding reference CV value implies that a single non-injurious stretch is not enough to cause microstructural changes. This is supported by the finding that Stretch1 induces strains (Fig. 2) below the threshold for unrecoverable strain, laxity and collagen disorganization [4,6,7]. However, a second similar stretch does change the collagen network microstructure, which is evidenced by compromised load capacity and increased deformations and fiber disorganization (Figs. 2 & 3). In the context of ligament pain, changes in collagen fiber organization directly mediate and align with neuronal activation and signaling [4,6,7,13]. Although effects of repeated loading on neurons was not evaluated here, comparable non-painful facet capsule stretch exposures *do* induce pain when repeated within 2 days in vivo [8]. Further, the fact that the second NI stretch produces collagen disorganization, which is known to occur at the same strains as neuronal pERK upregulation [7], suggests the possibility for pain generation, despite strains at that second stretch (6.4±3.1%) being decreased compared to the first stretch (7.9±4.1%) (Fig. 2). Since pERK can be induced through cellular deformation [14,15], it is possible that such activation occurs even at lowered strains. Future studies incorporating neurons is these collagen gels will help with direct assessment of their mechanical and physiological responses and the relationships between these and physiologic preconditioning or sensitization that may occur as a result of repeated exposures.

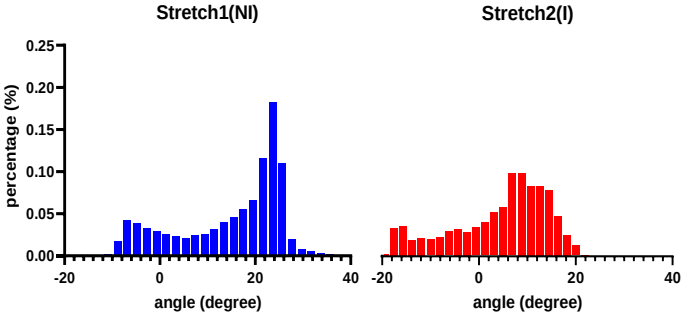

Figure 3: Histograms of fiber alignment for the gel in Fig. 1 showing tighter fiber angle clustering at non-injurious Stretch1, but more disorganization (larger spread of angles) at Stretch2.

ACKNOWLEDGEMENTS

This project was funded by the NIH (AT010326-07), Thanks to Meagan Ita for assistance with experimental design and testing advice.

REFERENCES

[1] Strine T et al *Arth Rheum* 57:656-65, 2007 [2] Cohen S et al *Anes* 106:591-614, 2007 [3] Jaumard N et al *J Biomech Eng* 133:071010, 2011 [4] Lee K et al *Stapp Car Crash J* 48:373-96, 2004 [5] Dong L et al *Brain Res* 1461:51-63, 2012 [6] Quinn K et al *Stapp Car Crash J* 51:169-87, 2007 [7] Zhang et al *J Biomech Eng* 138:021013, 2016 [8] Kartha S et al *J Biomech Eng* 14:10.1115, 2018 [9] Lake S et al *J Mech Behav Biomed Mater* 13:25-35, 2012 [10] Khalsa P et al *J Neurophys* 76:175-87, 1996 [11] Quinn K & Winkelstein B *J Biomed Opt* 14:054010, 2009 [12] Miller K et al *Ann Biomed Eng* 40:1102-10, 2012 [13] Zhang S et al *JOR* 36:770-7, 2018 [14] Samarakoon R et al *J Cell Physiol* 195:411-20, 2003 [15] Neary J et al *J Neurosci* 23:2348-56, 2003.

SB^{3}C2019
Summer Biomechanics, Bioengineering and Biotransport Conference
June 25 – 28, Seven Springs, PA, USA

INVESTIGATION OF SCALING TECHNIQUES USED FOR DEVELOPING BRAIN INJURY CRITERION BY FINITE ELEMENT MODELS OF THE PRIMATE AND HUMAN MODEL SIMULATING HEAD ROTATION

(1) Tushar Arora, (1) Kunal Dave, (2) Priya Prasad, (1) Liying Zhang,

(1) Biomedical Engineering Department
Wayne State University
Detroit, MI, USA

(2) Prasad Engineering, LLC
Plymouth, MI, USA

INTRODUCTION

Biomechanical analysis of human injury response and injury tolerance data may require the use of normalization or scaling method due to the variability between the human test subjects. For most biomechanical testing, data are scaled to the 50th percentile adult male. Scaling techniques based on equal stress-equal velocity technique were often used to scale these experiments done on human surrogates (e.g. volunteers, cadavers) to human population of different ages and genders, to establish injury thresholds. The equal stress-equal velocity method assumes a constant mass density and constant modulus of elasticity between subjects and a scaling factor is determined by assuming geometric similarity [1]. The development of Brain Injury Criteria (BrIC) [2] was based on human head finite element (FE) modeling of the experimental brain injury in animals by scaling the head kinematics of the animals (rhesus monkeys, baboons and miniature pigs) to the FE human head model. The accuracy of equal stress-equal velocity scaling method used in above process is questionable as it solely based on the mass difference without considering the anatomical, geometrical differences between the heads and brains of the animals. It was reported that scaling law works for elastic material but not for viscoelastic materials of the brains of similar geometry [3]. The objective of the current study was to evaluate and demonstrate the issues of not considering geometrical and anatomical differences between human and animal head with the use of the mass scaling method in the development of human brain injury criterion. To achieve the goal, both primate FE head model and human head model were used to simulate the experimental data directly or using scaling method to scale the head kinematics from the monkey to the human and from the monkey to the monkey with different brain mass in order to assess the geometric effect on the resulting brain responses and potential injury severity predicted by the models.

METHODS

FE head models: Evaluation of scaling techniques was studied by comparing the brain tissue response predicted between three head models simulating animal test conditions based on mass scaling method. Model 1 was a detailed rhesus monkey (macaca mulata) head model developed recently and scaled to the brain of the monkey subject used in each of the three experiments. Model 2 represented a large size monkey by scaling the Model 1 to approximate the brain mass of the Global Human Body Models Consortium (GHBMC) 50th percentile adult male head model [4] that was recently updated. Model 3 was the GHBMC M50 head model. Figure 1 shows the three models used for the evaluation and comparison of the resulting brain responses.

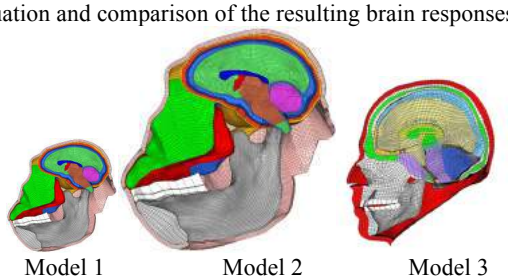

Figure 1: Models used for evaluating the scaling techniques based on mass of the brain

Scale factors and scaling the head rotational loading: The scaling factor to scale the Model 1 mesh to Model 2 was determined based on

mass scaling method and the factor is 1.95. The mass of the rhesus monkey brain model was 109 g. The experimental case simulated was based on reported monkey head rotational experiments on diffuse axonal injury [5,6]. The head rotational acceleration used for the input to Model 1 was the unscaled original monkey experimental loading. For model 2, the input used for Model 1 was scaled based on the mass of brain of the Model 2 which has a similar mass as the GHBMC M50 head model. For Model 3, the input was the same as that used for the Model 2. The Ommaya's mass scaling method to scale the rotational acceleration was applied [7]. To scale the input 1 to the input 2, the magnitude of the angular acceleration of the monkey test data was scaled by 0.263 while the time duration was by 1.95. Figure 2 shows the angular acceleration, velocity and calculated angular displacement for the two inputs.

The material models and associated properties for monkey models were based on the GHBMC M50 head model (v5.0). Maximum principal strain (MPS) and Cumulative Strain Damage Measure (CSDM) were examined between the models for subcortical white matter, corpus callosum (CC) and brainstem structures, the common structures observed for Diffuse Axonal Injuries (DAI) in experimental models. All simulation was performed using LS-DYNA MPP R8.1.

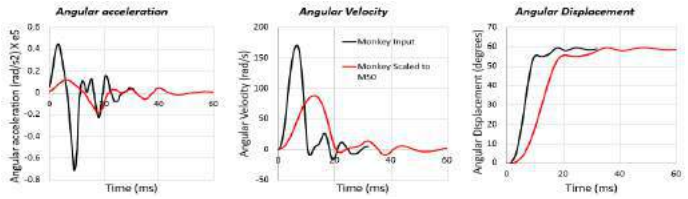

Figure 2: Input profiles: Input 1 for Model 1 and input 2 for Model 2 and Model 3

RESULTS AND DISCUSSIONS

Maximum principal strain: The monkey model with monkey experimental input (Model 1, Input 1) and scaled monkey model with scaled original input to brain similar to the human (Model 2, Input 2) yielded similar MPS results for the structures involved in DAI with a variation of 8%, 1% and 0% respectively, for the brainstem, the corpus callosum and the subcortical white matter. The GHBMC M50 model (Model 3, Input 2) with scaled input from monkey to M50 yielded much different MPS with 48%, 48% and 45% variations respectively at the corresponding three brain structures, as compared to the Model 1 as shown in Figure 3. The peak strain in the monkey model occurred earlier than that in the scaled monkey model. It is due to the input of shorter duration used for the monkey model and a longer duration input for the scaled monkey model due mass scaling applied to scale the peak rotational acceleration and associate duration.

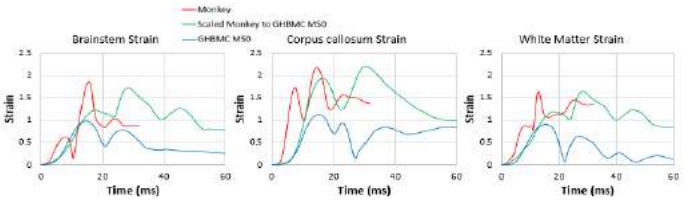

Figure 3: Comparison of MPS resulted from the three models

MPS contours predicted for the brainstem, CC and subcortical white matter from three models are depicted on Figure 4. The strain distribution, location and patterns in the same structure were nearly identical between the monkey brain and the scaled monkey to the mass of human brain, because the two models had the identical geometry while the mass scaling is valid. In contrast, the human head model exhibited different response pattern and strain localization than the monkey model and scaled monkey when compared to that of human brain mass model.

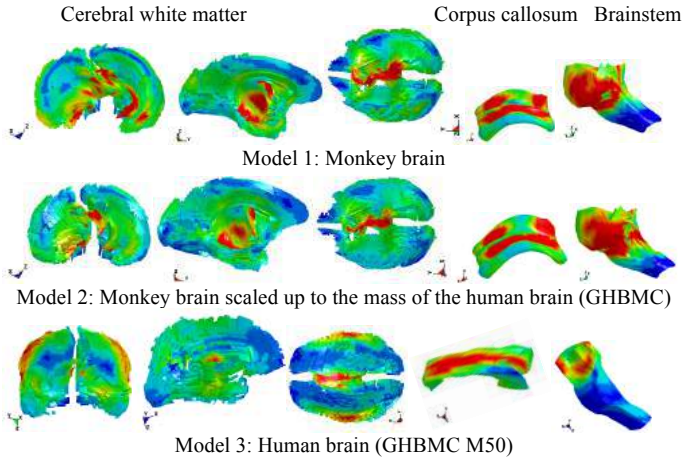

Figure 4: MPS contours predicted from the three models

Cumulative strain damage measure: The peak CSDM volume percentages at 0.5 MPS predicted by the scaled monkey model showed slight deviation at 6%, 10%, 4% and 12% more or less than those predicted by the monkey model in the whole brain, brainstem, corpus callosum and white matter, respectively. The GHBMC model predicted 50%, 50%, 33% and 67% less CSDM than the monkey model at the corresponding structures, respectively using the input that was scaled from animal experimental data.

CONCLUSIONS

The similarities in biomechanical responses (MPS and the CSDM) experienced by the brain of various structures from the monkey model and the scaled monkey model demonstrate that mass scaling technique works well within the species of identical anatomy and geometry. The profound differences in MPS and CSDM results found when using scaled experimental data simulated by the human head model and the experimental data simulated by the same animal model suggests that the scaling method used in the development of new brain injury criterion [2] is unreliable owing to the geometrical, shape and neuraxis differences between the two species. The primate model developed for this study can be applied to develop tissue-level response correlates for various brain injury severities and be translated to the human head model such as the GHBMC head model in order to improve its capability of establishing reliable brain injury criteria.

ACKNOWLEDGEMENTS

The work is supported by the Alliance of Automobile Manufacturers, Inc. and the Global Human Body Models Consortium, LLC.

REFERENCES

[1] Eppinger, RH. et al. No. 840885. SAE Technical Paper, 1984
[2] Takhounts, E et al. No. 2013-22-0010. SAE Technical Paper, 2013.
[3] Firoozabakhsh KK and DeSilva, CN. J Biomechanics 8 (1975): 65-73.
[4] Mao, H et al. Journal of Biomechanical Engineering 135.11 (2013): 111002
[5] Gennarelli, TA., et al. Annals of neurology 12.6 (1982): 564-574.
[6] Mendis, K. Diss. The Ohio State University, 1992.
[7] Ommaya, A. K., DAVID W TAYLOR NAVAL SHIP RESEARCH AND DEVELOPMENT CENTER BETHESDA MD STRUCTURES DEPT.

SB^{3}C2019
Summer Biomechanics, Bioengineering and Biotransport Conference
June 25 – 28, Seven Springs, PA, USA

DETERMINATION OF TISSUE LEVEL INJURY THRESHOLD FOR OCULAR TRAUMA BY FINITE ELEMENT ANALYSIS

Kunal Dave, Liying Zhang

Biomedical Engineering Department
Wayne State University
Detroit, MI, USA

INTRODUCTION

There are over 2.5 million traumatic eye injuries that occur each year in the United States. Ocular injuries can occur from sports related impacts, in automobile crashes and by high speed projectiles from fireworks and BB guns. With the increase in use of weapons releasing fragments, the rate of eye injuries has increased to higher level as compared to total military injuries. The improved understanding of mechanism of ocular injury in blunt impact may help design improved protective device for eye protection. A number of blunt impact tests have been conducted on human eye specimens but the reported injury was limited to globe rupture. The experimental studies on porcine eye reported anatomical and pathological injury to the cornea, lean and retina tissues in blunt and blast loading conditions. The morphological and anatomical features of the porcine eye were very similar to those of the human eye. Finite Element (FE) modelling of traumatic event can serve as a powerful tool to study biomechanical process and tissue response of ocular injury at various conditions. In earlier studies, kinetic energy was reported as an injurious parameter for globe rupture. However, kinetic energy is incapable of providing information on the responses of various ocular tissues to injury and the injury localizations. The objectives of this study were to 1) develop and validate a detailed FE porcine eye model, 2) simulate a number of experiments to quantify the local tissue response parameters for various types of ocular injury including corneal abrasion, lens dislocation, retinal damage and globe rupture, and 3) develop injury threshold risk curves for various ocular trauma.

METHODS

FE eye model development: The geometric information of the porcine eye was taken from the literature [1-3]. The finite element mesh of the porcine eye was developed using Hypermesh 13 (Altair Engineering, MI). The model consists of all essential components of the eye including the cornea, sclera, aqueous humor, iris, lens, zonules, ciliary body, retina, choroid, and vitreous humor (Figure 1). The cornea and sclera tissue were modeled as non-linear elastic materials. The aqueous humor, vitreous humor and retina were modelled as viscoelastic materials. The iris, lens, zonules, ciliary body, and choroid were modelled as linear elastic materials. The FE eye model was constructed with over 12,500 solid hexahedral elements and over 850 shell elements with an average resolution being 0.6 mm. All simulations were carried out using LS-DYNA MPP Version 971 R8.1 (LSTC, CA).

FE eye model validation: The FE eye model was first subjected to a validation against corneal displacement measurement from BB (0.345-gram, 4.5-mm diameter, v=62.3 m/s) impact experiments [4]. The model predicted corneal indentation, equatorial variation, and longitudinal variation of the globe were compared with test results. The objective rating software CORA was used to assess the correlation [5]

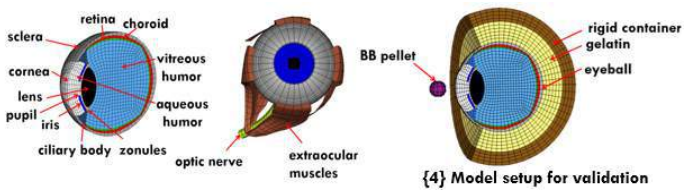

Figure 1: FE eye model

Ocular injury predictor and risk function development: The mode was applied to simulate a total of 86 tests reported in the literature using different blunt impact projectiles as mentioned in Table 1 [6-8].

The biomechanical response parameters predicted by the model were related to the observed injuries. The maximum principal stress predicted at the cornea-sclera junction component and at corneal apex along with the pressure in the central vitreous were monitored for globe rupture. The displacement, strain rate and product of strain and strain rate were calculated at corneal apex for predicting corneal abrasion. Maximum principal stress and maximum principal strain predicted at retina in macular region was monitored for retinal damage. For lens dislocation, strain rate and product of strain and strain rate were predicted at the center of lens just behind aqueous humor. Logistic regression analysis was performed to assess various tissue-level response predictors for predicting risks of globe rupture (86 cases), lens dislocation (N =15), retinal damage (N =15) and corneal abrasion (N =13). The Area Under the Receiver Operating Characteristic (ROC) Curves (AUC) were used to evaluate relative predictability, sensitivity and specificity of the regression models for predicting various ocular trauma.

Table 1: Blunt impact simulations

Type of Injury	Number of Cases Simulated	Type of Projectile	Diameter of Projectile(mm)	Mass of Projectile(gm)	Velocity Range(m/s)
Globe Rupture (86 cases) {6}, {7}, {8}	11	Airsoft Ball	6	0.12-0.2	67-115
	20	Paintball	17.3	3.2	68-108
	4	Delrin Impactor	19.9	112.55	8-9
	5	Plastic Rod	7.62	0.35	5-20
	19	Foam	4.5-12.5	0.04-0.50	16-149
	4	Aluminium Rod	9.25-11.16	3.57-5.19	28-37
	8	BB Pellet	4.37-4.5	0.345	62-96
	15	Steel Projectile	6.35-45.5	2.6-45.5	4-38
Lens Dislocation & Retinal Damage {6}	15	Steel Projectile	6.35-45.5	2.6-45.5	4-38
Corneal Abrasion {7}	13	Foam	12.5	0.15-0.50	18-87

RESULTS

Validation results: The corneal displacement calculated by the FE eye model from BB pellet impact was 8.2 mm matching the experimental value reported by Delori et al 1969 (Figure 2). The CORA rating was 0.84 which implied a good correlation of the temporal response of the corneal displacements between the model prediction and experimental measurement.

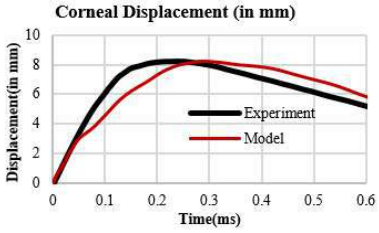

Figure 2: Experimental validation of FE eye model

Logistic regression for determining ocular injury thresholds: For cases of globe rupture, the pressure in the vitreous humor and maximum principal stress in the sclera and cornea were predicted to be constantly higher in the case with globe rupture than that without globe rupture. The prediction of high stress location was consistent with the experimental observation where the limbus region (cornea-scleral junction) was the common site of failure in globe rupture cases. For the logistic regression models, the AUC values based on cornea maximum principal stress, vitreous pressure and normalized impact energy were 0.995, 0.876, and 0.986, respectively for predicting globe rupture. The AUC value based on the principal strain rate, product of strain and strain rate in the lens and the impact energy were 0.94, 1, 1 for lens dislocation. For the retinal damage, the AUC values based on retina stress, retina strain and impact kinetic energy were 1, 1 and 0.97, respectively (Figure 4). The AUC values based on cornea displacement, product of strain and strain rate and impact kinetic energy were 0.925, 0.925, 0.95, respectively, for predicting corneal abrasion.

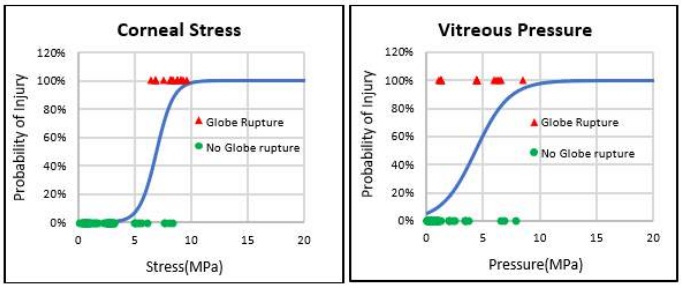

Figure 3: Injury risk curve for globe rupture

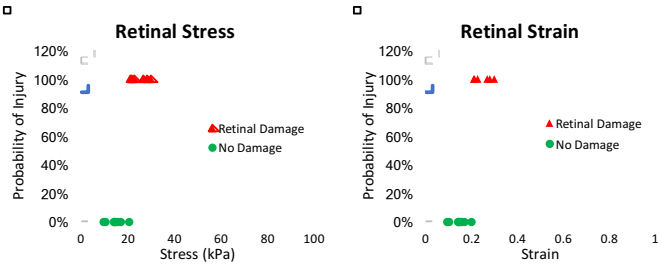

Figure 4: Injury risk curve for retinal damage

DISCUSSION

An anatomically detailed finite element porcine eye model with all essential intraocular tissues has been developed and validated against corneal displacement response. The model has been used to simulate 86 blunt ocular impact experiments. The direct correlations between the biomechanical response parameters predicted by the model and the pathological damage location observed in experiments can help improve our understanding of the mechanism of various ocular injury types based on local tissue responses. The injury predictors and associated damage threshold functions have been established to predict the risk of corneal abrasion, retinal damage, lens dislocation and globe rupture from blunt impacts. The corneal abrasion and globe rupture (100%) would occur when the maximum principal stress exceeds 1.2 MPa in cornea and 10 MPa in limbus, respectively. The retinal damage would occur when the maximum principal stress or maximum principal strain exceeds 19 MPa or 0.2. The future work will apply the FE porcine eye model to understand the mechanism of blast-induced ocular trauma and develop tissue level threshold for blast induced ocular injury.

ACKNOWLEDGEMENTS

This research was supported in part by MRMC Contract No. W81XWH-12-2-0038, US Army.

REFERENCES

[1] Woo, S., et al. Annals of biomedical engineering 1.1 (1972): 87-98
[2] Olsen, T., et al. Invest. ophthalmology & visual sci. 43.8 (2002): 2529-2532.
[3] Reilly, M., et al. Experimental eye research 88.3 (2009): 483-494.
[4] Delori, et al. , Invest. Ophthalmology & Visual Sci. 8.3 (1969): 290-301.
[5] Gehre C., The 22nd Int ESV, Washington, DC. 2011
[6] Scott, W. Association for the Advancement of Automotive Medicine, 2000
[7] Duma, S., Journal of Trauma and Acute Care Surgery 48.4 (2000): 786-789
[8] Kennedy, E., No. 2006-22-0026. SAE Technical Paper, 2006

SB³C2019
Summer Biomechanics, Bioengineering and Biotransport Conference
June 25 -28, Seven Springs, PA, USA

COMPUTATIONAL ANALYSIS OF LISFRANC SURGICAL REPAIRS

M. Tyler Perez (1), John R. Owen (2), Robert S. Adelaar (3), Jennifer S. Wayne (1)

(1) Department of Biomedical Engineering
Virginia Commonwealth University
Richmond, Virginia, United States

(2) Department of Orthopaedic Surgery
Virginia Commonwealth University
Richmond, Virginia, United States

(3) Orthopaedic Surgical Specialty Care
McGuire VA Medical Center
Richmond, VA, United States

INTRODUCTION

Lisfranc injuries of the mid-foot are challenging to identify during initial evaluations because the common measurements to indicate their presence are small and the mechanism of injuries often include other injuries in the foot. Untreated Lisfranc injuries result in severe discomfort and pain (1). When the diastasis (separation) between the medial cuneiform and second metatarsal is greater than 2 mm, surgery to repair the joint is indicated. However, historically, these surgeries have a low satisfaction rate with patients (2). Recent literature has compared a range of surgical repairs with conflicting recommendations on which procedure provides the optimal environment to promote healing and avoid implant failures (2-4).

This study applies computational modeling, both rigid body and finite element analyses, to compare the stability and stress contours associated with three different repair procedures: open reduction and internal fixation (ORIF) with endobuttons, ORIF with cortical screws, and arthrodesis with cortical screws. The focus is to identify the procedure that results in the most stable joint after the surgery, which has been related to better outcomes (5). The use of computational models allow for a common anatomy to be used for the different procedures and provide more extensive measurements without having to rely on cadaveric or patient studies. The ultimate purpose of this work is to help practitioners in selecting the optimal procedure for patients.

METHODS

Computerized tomography scans of a healthy foot were used to generate 3D solid models of the individual bones. The bones were imported into the 3D design software SolidWorks (Dassault Systemes, Waltham MA) and positioned in 30˚ plantar flexion, the position believed to put maximal stress on the Lisfranc joint (3). Ligaments were modeled as tension only elements across the bones and were provided with *in situ* strain in the original rigid body of this injury (6). Using a previous cadaver study that was loaded with axial compression of 343 N (7), the model validated the cadaver results for a healthy foot and a foot with a ligamentous Lisfranc injury (cut Lisfranc and intercuneiform ligaments).

With the computational rigid body model validated on cadavers, the three repair procedures were simulated. For the ORIF with endobuttons case, two tension only elements were added to represent the fiberwire spanning from the medial cuneiform and the second

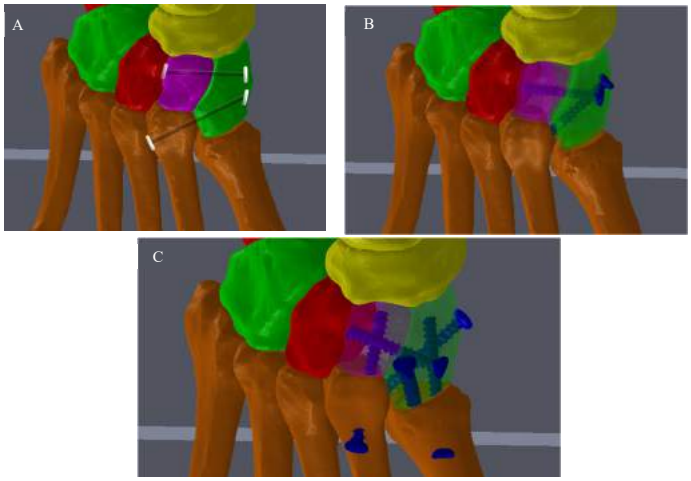

Figure 1: A) AP view of endobutton (illustrative) tension only elements. B) AP view of two screws used for ORIF with screws. C) AP view of arthrodesis fixation

metatarsal as well as the medial cuneiform and the intermediary cuneiform (Figure 1A). The ORIF with screws model used rigid bodies for the screws which were placed in a similar orientation as the endobuttons (Figure 1B). The arthrodesis case used five screws and was based on that used in previous clinical studies (Figure 1C) (4). Screw-bone interfaces were treated as bonded contacts. For all these simulations, muscle forces were incorporated in the rigid body model to simulate muscle activation for standing in 30° plantar flexion (8,9). Each model was loaded with the same axial compression of 343 N after which three diastasis measurements were recorded. From each rigid body simulation, contact forces and ligament/muscle forces were extracted in order to perform a finite element analysis (FEA) in ANSYS Workbench (ANSYS, Canonsburg PA) for the stresses generated during the loading (Figure 2).

All three surgical repair models tracked the dorsal, interosseous, and plantar separation (diastasis) between the medial cuneiform and second metatarsal, relative to the healthy, unloaded foot. These separations were compared to both a healthy and injured model that have previously been validated to determine the ability of the surgery to reverse the excessive instability in the joint after injury.

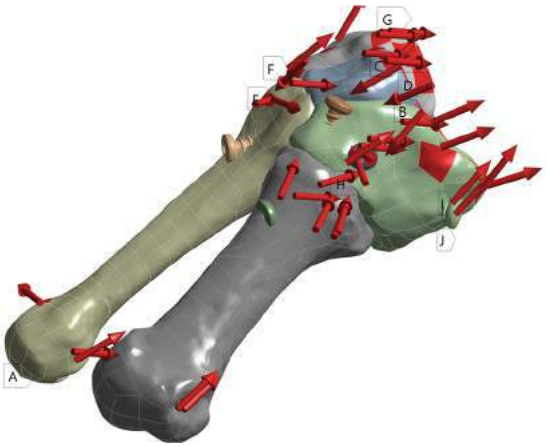

Figure 2: ANSYS FEA study of the arthrodesis procedure with forces applied shown with red arrows.

RESULTS

When comparing the diastasis measurements throughout the Lisfranc joint (Figure 3), the endobutton procedure reduced the plantar and interosseous diastasis seen in the injured model; however, the dorsal aspect of the joint closed while the plantar aspect opened relative to the healthy foot. The screws and arthrodesis repairs greatly reduced the amount of diastasis and provided values closer to a healthy model.

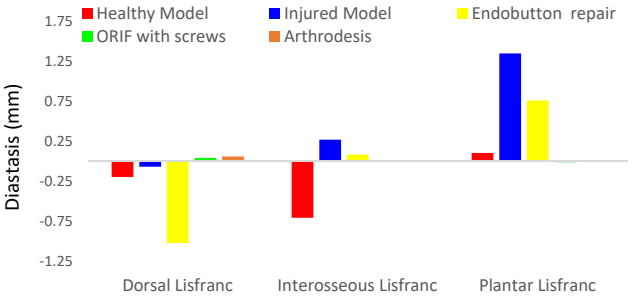

Figure 3: Diastasis measurements of the Lisfranc joint for the healthy, injured, and three repair models

The stresses in the bone and hardware for the ORIF repair showed one area of yielding in the screw spanning the Lisfranc joint. The arthrodesis procedure did not show any areas of yielding though stresses were high in similar regions as for the ORIF repair. In the ORIF case, the yielding was isolated to a small region of the screw threading. Other regions of the screw shaft showed high stresses.

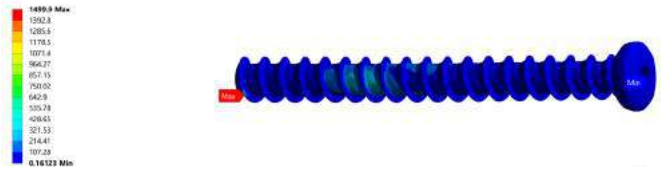

Figure 4: von-Mises stress contour (MPa) on screw spanning the Lisfranc joint in the ORIF procedure

DISCUSSION

A major indicator of successful Lisfranc surgical repairs is the ability for the procedure to reduce movement in the joint following surgery (5). This study demonstrated how screw fixation techniques are better in preserving joint diastasis between the medial cuneiform and the second metatarsal when weight bearing. While the endobutton procedure exhibited some improvements over an injured foot, the non-rigid nature of the wires and their placement allowed separation along the plantar portion of the joint. Some studies that have recommended endobutton fixation have praised that the non-rigid fixation technique allows for earlier mobilization and full weight bearing (10).

One concern with screw fixation is implant failure. The finite element analysis for ORIF screw fixation procedures showed a region of yielding in the screw threads (stress greater than 827 MPa for Ti-6Al-4V screws). Both ORIF and arthrodesis procedures exhibited other regions of high stress which could be susceptible to fatigue failure. However, these stresses may be caused by the bonded contact condition set between the screws and bone which may be overly restrictive to motion.

Based on the need to re-establish anatomical fixation after a Lisfranc injury (either temporarily with ORIF or permanently with arthrodesis), screw fixation provides the best stability. Weight bearing and activities should be controlled however, because of the potential for implant failure during initial healing. As fusion occurs in the arthrodesis case or as tissue healing occurs for ORIF with screws, the risk of implant failure should reduce. Ultimately, this computational approach supports previous clinical studies that show less diastasis with screw fixation techniques (3,11) and points to reasons for implant failure (12). This study shows the ability of computational models to help inform on outcomes of different surgical procedures in a cost effective manner. It also demonstrates the flexibility of these types of studies where variations in patient anatomy is controlled.

REFERENCES

[1] Myerson: J Bone Joint Surg 81:1999. [2] Desmond: Foot Ankle Int. 27:2006. [3] Marsland: Foot Ankle Surg. 19:2013. [4] Cochran: Foot Ankle Int. 38:2017. [5] Kuo: J Bone Joint Surg 81:1999. [6] Perez: Trans ORS, Poster#1987: 2019. [7] Bansal: Trans ORS. Podium#0153: 2018. [8] Fukunaga: J App Physiol 80:1996. [9] Spratley: PhD Dissertation, VCU 2013. [10] Brin: Foot Ankle Int. 31:2010. [11] Ahmed: Foot Ankle Int. 31:2010. [11] Alberta Foot Ankle Int. 26:2005.

SB³C2019
Summer Biomechanics, Bioengineering and Biotransport Conference
June 25 -28, Seven Springs, PA, USA

mcDESPOT QUANTITATIVE MRI CORRELATES WITH ARTICULAR CARTILAGE MATERIAL PROPERTIES

Matthew M. Grondin (1), Fang Liu (2), Michael F. Vignos (3), Richard Kijowski (2), Corinne R. Henak (1,3)

(1) Department of Biomedical Engineering
University of Wisconsin-Madison
Madison, Wisconsin, United States

(2) Department of Radiology
University of Wisconsin-Madison
Madison, Wisconsin, United States

(3) Department of Mechanical Engineering
University of Wisconsin-Madison
Madison, Wisconsin, United States

INTRODUCTION

Osteoarthritis (OA) is a degenerative disease of the articular cartilage (AC). During OA, the structural constituents of AC, proteoglycans (PGs), sulfated glycosaminoglycans (sGAGs) and collagen, are lost. This results in decreased fluid retention, reduced modulus, and reduced energy dissipative capacity [1-4].

Quantitative magnetic resonance imaging (qMRI) techniques can distinguish healthy from osteoarthritic cartilage by identifying altered cartilage composition or structure. Commonly used techniques include delayed gadolinium-enhanced MRI of cartilage (dGEMRIC) and transverse T_2 relaxation. dGEMRIC is a contrast-enhanced method that produces longitudinal relaxation (T_{1Gd}) maps sensitive to sGAG content [5-9]. T2 maps do not require contrast [4, 5, 10-13]. Multi-component Driven Equilibrium Single Shot Observation of T_1 and T_2 (mcDESPOT) is a contrast-free method that provides measurements of both bound water fraction (F_{PG}) and T_2, with relatively short scan times [14]. mcDESPOT has been shown to have high sensitivity for detecting cartilage degeneration in human knees [14], suggesting its utility in predicting material properties for computational modeling [14].

Given that both qMRI metrics and material properties are governed by AC structure and composition, qMRI may allow for non-invasive estimates of material properties. However, previous studies have revealed confounding results with correlations between commonly measured qMRI metrics (i.e., T_{1Gd} and T_2) and cartilage material properties varying widely from weak to strong [4,5,10-12]. Thus, more recently developed qMRI techniques may allow for more accurate estimates of cartilage material properties. Given the promise of mcDESPOT, the aim of this study is to evaluate the association between mcDESPOT metrics (i.e., F_{PG} and T_2) and macroscale AC material properties.

METHODS

In this study, location-specific F_{PG} and T_2 values were correlated with AC mechanical properties (Fig. 1). Acquired tissue samples underwent mechanical testing for macroscale mechanical properties. The associations between material properties and qMRI mapping values

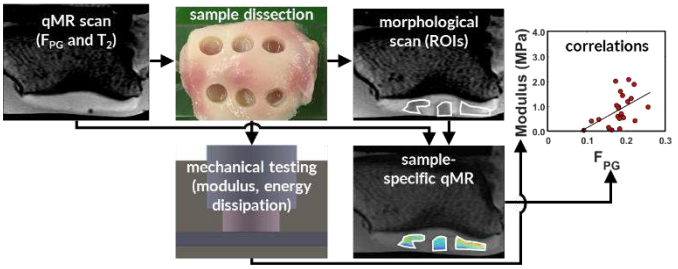

Fig. 1. Overview of methods to correlate qMRI parameters with material properties.

were evaluated using Pearson correlation coefficients.

TISSUE ACQUISTION. Frozen human cadaveric knees were obtained through Science Care, Inc. (Phoenix, AZ) with selection criteria including individuals less than 60 years of age; body mass index less than 25 kg/m^2; no prior history of knee injuries, pain, or arthritis; and no prior knee surgeries. After acquisition, specimens were frozen at -20°C. Samples were thawed and patellae were removed for imaging.

QUANTITATIVE MR IMAGING. Baseline scans of cadaveric patellae were acquired using the mcDESPOT sequence on a 3.0 T scanner (Discovery MR750; GE Healthcare, Waukesha, WI) using an

Invivo MRI Precision 8 Channel Wrist Array Coil (GE Healthcare, Waukesha, WI). Patellae were submerged in DPBS with protease inhibitors throughout imaging. F_{PG} and T_2 were calculated [14]. Following sample dissection, patellae were reimaged to determine regions of interest (ROIs). MatrixUser (Fang Liu, University of Wisconsin-Madison, Madison, WI) was used to first segment bone from AC in baseline MR images. This mask was used to register the baseline qMRI and post-dissection morphological MR images using Elastix (University Medical Center Utrecht and contributors). ROI-specific qMRI values were found by segmenting plug ROIs on the qMRI maps.

MECHANICAL TESTING. Cylindrical samples (6 mm diameter) were removed from the resected cartilage surfaces and frozen at -20°C. Sample thickness was measured using a current-based micrometer. Mechanical testing was conducted on a tabletop test machine with a 1000 g load cell (TA Instruments 3230-AT, New Castle, DE). Twenty-three samples from 5 human cadaveric patellae were tested. Samples were loaded between two glass platens. Samples were tare loaded to 3 g for 5 minutes, then axially loaded at 1 Hz to 10% engineering strain for 10 cycles. Data were processed using MATLAB (MathWorks, Natick, MA). The loading stress-stretch curve was fit to an exponential (Eq.1), with the derivative providing the tangential modulus at zero strain (Eq. 2):

$$\sigma = A\left(e^{B(\lambda-1)} - 1\right) \quad (1)$$

$$d\sigma/d\lambda\,|_{\lambda=1} = AB \quad (2)$$

Where A and B are material constants, σ is 1st Piola-Kirchhoff stress, and λ is stretch. Dissipated energy per cycle was calculated as the area between the loading and unloading stress-strain curves using trapezoidal numerical integration.

STATISTICAL ANALYSIS. Pearson correlation coefficients were calculated between the material properties and mcDESPOT metrics with statistical significance defined as $p < 0.05$. Correlations were split into the following groups: strong (0.5<|R|<1.0), moderate (0.3<|R|<0.5), weak (0.1<|R|<0.3), and very weak or none (0<|R|<0.1).

RESULTS

High-resolution T_2 and F_{PG} maps were acquired for patellar cartilage (Fig. 2). Mechanical properties and qMRI were correlated (Fig. 3). F_{PG} was strongly correlated with both initial modulus and dissipated energy (Fig. 3A, C). T_2 was moderately correlated with both initial modulus and dissipated energy (Fig. 3B, D).

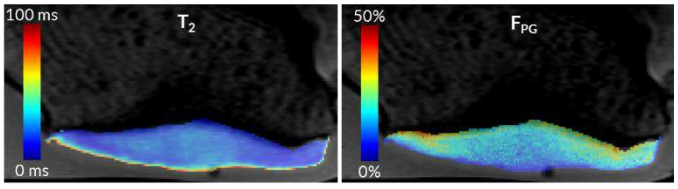

Fig. 2. Representative qMRI maps across patellar AC. The articular surface is down, lateral is to the left.

DISCUSSION

The purpose of this study was to evaluate correlations between mcDESPOT metrics and bulk mechanical properties. The strength of correlations between qMRI and mechanical properties in this study was consistent with previous literature. Our findings indicate improved correlations between qMRI mapping values and mechanical properties over previous non-contrast methods, but weaker correlations compared to contrast-enhanced MRI. Correlations between T_2 and mechanical properties have varied from poor to strong strengths. While some studies found weak to moderate strength correlations between various mechanical properties such as Young's, equilibrium, and instantaneous

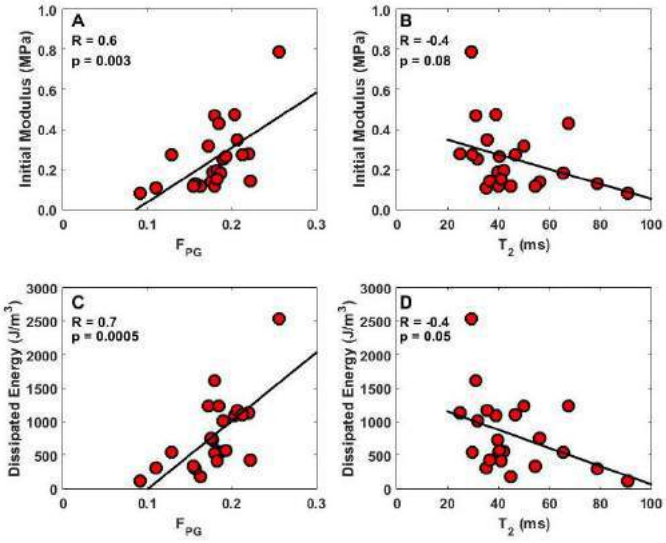

Fig. 3. Correlations between mechanical properties and qMRI for initial modulus versus F_{PG} (A), initial modulus versus T_2 (B), dissipated energy versus F_{PG} (C), dissipated energy versus T_2 (D).

moduli (0.1<|R|<0.5) [5,10,11], others found strong correlations with Young's modulus (0.70<|R|<0.80) [4,12]. The correlations in the present study between material properties and T_2 are consistent with these previous studies. In comparison to T_{1Gd}, the strength of correlations with both T_2 and F_{PG} indicates that contrast-enhanced imaging may provide more accurate estimates of AC material properties as compared to non-contrast enhanced MRI. T_{1Gd} correlations range from weak to strong between Young's, equilibrium, and instantaneous moduli (0.03<|R|<0.81) [4,5,10,12], stronger than correlations with non-contrast enhanced parameters.

Interestingly, correlations between F_{PG} and material properties were stronger than correlations between T_2 and material properties. Previously, F_{PG} has been shown to be strongly related to PG content [15,16]. Thus, the strong correlations likely reflect the influence of PGs on both the modulus and dissipative capacity of cartilage. Overall, these results suggest that mcDESPOT offers an improved method versus T_2 alone for contrast-free estimation of cartilage material properties.

In conclusion, this study successfully leveraged a novel non-contrast enhanced MR modality that correlates well with mechanical properties. Correlations can be used to provide mechanical context for mcDESPOT-based evaluation of cartilage health, or for computational modeling with subject-specific cartilage material properties.

ACKNOWLEDGEMENTS

Funding from CTSA through NCATS (UL1TR002373), NIAMS (R01-AR068373), GE Healthcare, and NSF GRFP (DGE-1747503).

REFERENCES

[1] Tang+, *J. Orthop. Res*, 2011; [2] Goldring+, *HSS J.*, 2012; [3] Lakin+, *Annu. Rev. Biomed. Eng.*, 2017; [4] Nissi+, *Osteoarthr. Cartil.*, 2007; [5] Juras+, *J. Magn. Reson.*, 2009; [6] Trattnig+, *J. Magn. Reson. Imagin*, 2007; [7] Bashir+,*Magn. Reson. Med.*, 1999; [8] Bashir+, *Magn. Reson. Med.*, 1996; [9] Williams+, *AJR Am. J. Roentgenol.*, 2004; [10] Nieminen+, *J. Biomech.*, 2004; [11] Lammenausta+, *J. Orthop. Res.*, 2006; [12] Nissi+, *Magn. Reson. Med.*, 2004; [13] Keenan+, *Osteoarthr. Cartil.*, 2011; [14] Liu+, *Radiology*, 2015; [15] Reiter+, *Magn. Reson. Med.*, 2009; [16] Reiter+, *Magn. Reson. Med.*, 2011.

SB³C2019
Summer Biomechanics, Bioengineering and Biotransport Conference
June 25 -28, Seven Springs, PA, USA

CHARACTERIZATION OF SHEAR WAVE SPEED-STRESS RELATIONSHIP IN COLLATERAL LIGAMENTS

Jonathon L. Blank (1), Joshua D. Roth (1), Darryl G. Thelen (1,2)

(1) Department of Mechanical Engineering
University of Wisconsin-Madison
Madison, WI, USA

(2) Department of Biomedical Engineering
University of Wisconsin-Madison
Madison, WI, USA

INTRODUCTION

Dissatisfaction rates after total knee arthroplasties (TKAs) exceed 18%, amounting to 700,000 patients per year [1][2]. Overly tight collateral ligaments, which can contribute to pain and stiffness, are often linked with patient dissatisfaction [3][4]. Therefore, collateral ligament tension is an important mechanical variable that affects surgical outcomes. Surgeons are currently reliant on indirect subjective approaches, e.g. laxity testing, for balancing collateral ligaments in the operating room. We are investigating the use of shear wave tensiometry to directly assess ligament tension, and thereby enable surgeons to more objectively position TKA components.

Shear wave tensiometry is a non-invasive approach for gauging axial stresses in soft tissues. Our prior work has shown that shear wave speed squared is proportional to applied stress in tendons [5]. The purposes of this study were to (1) determine if the shear wave speed-stress relationship extends to ligaments, and (2) compare load-dependent wave speeds between the lateral and medial collateral ligaments (LCL and MCL), which exhibit substantially different geometries.

METHODS

Three lateral and three medial collateral ligaments were collected from large (>120 kg) pigs. Collateral ligaments from large pigs have been previously shown to have an axial loading response similar to that of human collateral ligaments [6]. Each ligament was isolated by removing proximal and distal bone blocks, with ligament-bone insertions left intact. Once secured in aluminum cups using a potting material, the ligaments were subjected to a cyclic load using an electrodynamic testing system (MTS Systems Corporation, Eden Prairie, MN). After pre-conditioning (50 seconds of cyclic loading between 30 and 300 N at 1 Hz), the specimens underwent 10 loading cycles from 30 to 300 N at 1 Hz. During loading, shear waves were excited in each ligament using a piezoelectric actuator to impulsively tap the ligament. Transverse tendon velocity was measured using laser vibrometers (Polytec, Inc., Irvine, CA) at two points spaced 5 mm apart (Fig. 1). Ligaments were kept moist and intact during the testing

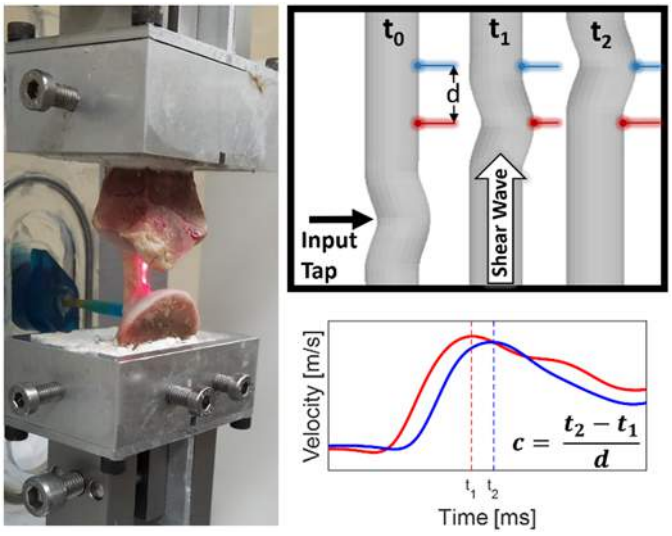

Figure 1: Shear wave speeds were captured using laser vibrometers and a piezoelectric tap applied transversely to the ligament (left). Shear wave speed (c) is measured using the time delay between two successive laser vibrometer velocity signals.

Poster Presentation #P045

procedure. Three cyclic loading trials for each specimen were analyzed for the purpose of this study, accounting for a total of nine trials for each type of collateral ligament.

For each tap, the induced shear wave speeds were computed by measuring the time delay between arrival of the wave at the two successive laser points (Fig. 1) [5]. Average axial stresses during the loading were computed by approximating the cross-section of the LCL as an ellipse and the cross-section of the MCL as a rectangle. The average cross-sectional areas were 13.6 mm^2 for the LCL and 19.4 mm^2 for the MCL.

Stress and wave speed data were grouped according to ligament type (i.e. LCL or MCL) for analysis. For each ligament type, linear regression was conducted with the stress as the independent variable and the squared wave speed as the dependent variable. A follow-up regression was performed to determine whether the intercept and slope of the squared wave speed-stress relationship were different between ligament types. This follow-up regression included data from both ligament types (Y_i, X_i), an indicator variable for ligament type (D_i), and an interaction term ($X_i D_i$) (Eq. 1).

$$Y_i = \alpha + \beta X_i + \gamma D_i + \delta(X_i D_i) + \varepsilon_i \quad (1)$$

RESULTS

The average squared wave speed of both the LCL and MCL increased monotonically as the axial stress in the ligament was increased (Fig. 1). There were moderately strong linear relationships between squared shear wave speed and stress in both the LCL and MCL (R^2 = 0.67 and 0.65, respectively). The slope of the linear fit was significantly greater in the MCL (2.15 $m^2/s^2/kPa$) than in the LCL (1.87 $m^2/s^2/kPa$), ($p < 0.0001$). However, there was not a significant difference between the intercepts of these two regression fits ($p = 0.7$).

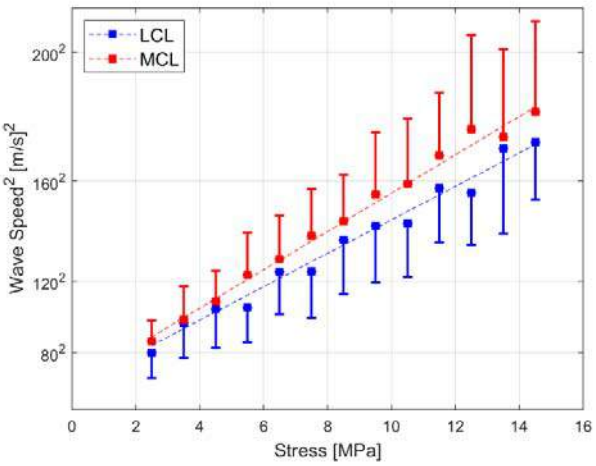

Figure 2: Squared wave speed and stress relationship for the lateral and medial collateral ligaments (LCLs and MCLs). Plotted are the mean (±1 s.d.) wave speeds within 1 MPa bins. The dashed lines indicate the linear fits determined from each regression that included data from all three LCL/MCLs.

DISCUSSION

Our study shows that ligament shear wave speed increases with axial stress in a predictable manner. This observation suggest it may be feasible to use shear wave tensiometers [5] to gauge ligament tension, and thereby enable surgeons to more objectively balance ligament loads in TKA procedures.

We did observe a slight difference in the slope of the squared wave speed-stress relationship between the LCL and the MCL, with the MCL exhibiting higher wave speeds at a given stress. This difference may be attributable to the differing cross-sectional geometries of the ligaments. The MCL has a sheet-like cross-section which can give rise to a non-uniform distribution of axial stress across its width. This non-uniformity creates local regions of fibers that are at a higher axial stress than the average axial stress used in this study. Therefore, it is possible that the higher wave speeds measured in the MCL were indicative of this higher localized stress. In contrast, the LCL has a rope-like cross section, which should lead to a relatively uniform axial stress across its width and a local stress similar to that of the average stress.

Shear wave speeds at low loads were similar between the two ligaments. This result might be attributable to the direct dependence of wave speed on material properties (specifically the tissue shear modulus and effective density) in an unloaded state [5]. Both the LCL and MCL are ligamentous bundles of collagen fibers oriented in the direction of loading, and thus may be expected to have consistent material property values across different specimens.

The precise nature of the wave speed-stress relationship in ligaments did differ from that previously seen in tendons. In particular, we observed higher wave speeds in ligaments than tendons at a given stress. This result may, in part, be attributable to different wave speed measurement approaches. Our prior study used high frame rate ultrasound to measure the vibration frequency of standing waves in axially loaded tendons [5]. In contrast, this study used laser vibrometry to measure the arrival time of transient waves in ligaments. There were also slight differences in boundary conditions. Tendons were isolated and fixed in clamps [5], whereas this study retained the ligament-bone insertions to better reflect *in situ* conditions. We are continuing to investigate how these experimental factors may influence the measurement of wave propagation in tissues.

The findings of this study suggest that human collateral ligaments with dissimilar geometries may exhibit different shear wave speeds, and thus stresses, under the same axial load. Moving forward, results from this study can be used to better interpret stresses in collateral ligaments from *in situ* shear wave speed measurements. Overall, these findings motivate the further development of an intraoperative sensor to guide ligament balancing in total knee arthroplasties with the ultimate goal of improving surgical outcomes and patient satisfaction.

ACKNOWLEDGEMENTS

This project was funded with continued support from NIH (EB024957 and 2 T32 AG 213-27) and specimens were procured from the University of Wisconsin-Madison Department of Animal Sciences.

REFERENCES

[1] Bourne, R et al., *Clin. Orthop. Relat. Res.*, 468: 57–63, 2010.
[2] Kurtz, S et al., *J. Bone Jt. Surg.*, 89–A: 780–785, 2007.
[3] Babazadeh, S et al., *Orthop. Rev. (Pavia).*, 1: 70–78, 2009.
[4] Elmallah, R et al., *J. Arthroplasty*, 31: S102–S105, 2016.
[5] Martin, J et al., *Nat. Commun.*, 9: 2–10, 2018.
[6] Germscheid, N et al., *J. Biomech.*, 44: 725–731, 2011.

SB³C2019
Summer Biomechanics, Bioengineering and Biotransport Conference
June 25 -28, Seven Springs, PA, USA

TRIBOCORROSION BEHAVIOUR OF METALLIC IMPLANTS: A COMPARATIVE STUDY OF COCRMO AND TI6ALV4

Mihir V. Patel, Edward Cudjoe, Jae Joong Ryu

Mechanical, Industrial & Manufacturing Engineering Department
Youngstown State University
Youngstown, OH 44555 USA

INTRODUCTION

Prosthetic implantation has been successful to restore mobility and increase the function of the diseased joints [1]. Modular design of joint replacements are most widely used due to ease of anatomic customization [2]. However, the modular interface such as stem-head interface of total hip joint replacements (THR) as shown in Figure 1 is continually subjected to wear and corrosion. The bearing components of THR are usually made out of polymers, metals, and ceramics. Metal alloys such as titanium-alloys (Ti6Al4V) and cobalt-chromium-alloys (CoCrMo) have manifested their long useful life due to superior mechanical strengths and electrochemical stability during active articulations in human bodies [3].

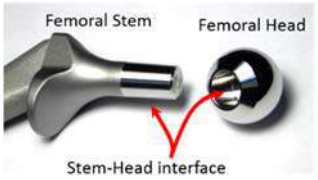

Figure 1. Modular Total Hip Joint Replacement (THR)

Ti6Al4V has been chosen for an orthopedic implant material owing to its inertness in the biochemical environment with mechanical strengths. CoCrMo alloys exhibit its good chemical stability with superior mechanical properties as summarized in Table 1. The grater hardness of CoCrMo results in desirable wear resistance and the oxide layer effectively protect the surface from corrosion attack. However, previous clinical studies and in vitro simulations of tribocorrosion presented the contrary results, i.e. cobalt chromium implant surface showed higher wear rate than the titanium implant surface, despite higher hardness of cobalt chromium surface than titanium surface [3-4].

Table 1. Mechanical Properties of Ti6Al4V and CoCrMo

Materials	Yield Strength (MPa)	Ultimate strength (MPa)	Hardness (HRC)
Ti6Al4V (F136)	924	1000	33
CoCrMo (F1537)	958	1338	45

This tribocorrosion damage mechanism is a multifactorial process involving mechanical properties, loading conditions, and environment. Tribocorrosion of orthopedic implants is a crucial issue and has been found to significantly limit the useful life of the implants. Wear and fretting corrosion in artificial joints result in the formation of soluble and particulate debris that can migrate in locally or systemically and induce a cascade of inflammatory events that may ultimately result in bone loss (osteolysis) and subsequent implant failure [5]. It is evident that enhancing the durability and reliability of total joint replacements is a critical engineering problem that affects society and the economy. In spite of the widely appreciated magnitude of this problem, there remains a critical gap in the knowledge base that centers on the complex multifactorial damage mechanism of modular interfaces of implants. The current article reports the tribocorrosion of Ti6Al4V and CoCrMo to compare and understand the complicated process of the alloys. Findings from this research will help predict the overall life-cycle of metallic orthopedic implants under fatigue loadings at the modular joint replacements for the vast application for biomedical devices.

METHODS

Cyclic reciprocation of a 3mm-diameter spherical alumina pin (Nanovea, CA) was employed on the smooth implant alloys to simulate fretting fatigue motions at the modular interfaces. Reciprocating motion was performed at 1 Hz and 1800 cycles. The implant alloys were fabricated into rectangles to the final dimensions of W1.0mm x H2.54mm x L22.95mm using the electric discharge machining. The

1.0mm x 2.54mm surface was polished to the average roughness R_a = 13.8 nm and R_a = 17.5 nm for Ti6Al4V and CoCrMo, respectively. The alloys were exposed to phosphate buffer saline solution (PBS) during fretting contact to observe surface damage response accelerated by environmental corrosion. A custom-built liquid cell was manufactured and placed on the high resolution stage of Mechanical Tester (Nanovea, CA) to control reciprocating motions. Two different normal loads were applied to simulate elastic range fatigue contact at 143 mN and 300 mN. Open circuit potential (OCP) changes were monitored during cyclic reciprocations of the alumina sphere. Potentiodynamic polarization resistance (PPR) were measured to identify corrosion responses without mechanical stimuli through the potential range from -1 V to 1.5 V with a slow scan rate 0.2 mV/s. Saturated calomel (reference) electrode was immersed in the PBS electrolyte. The alloy sample (working electrode) and platinum wire (counter electrode) were connected to potentiostat controller (Gamry Instruments, PA). The experimental apparatus was represented in Figure 2.

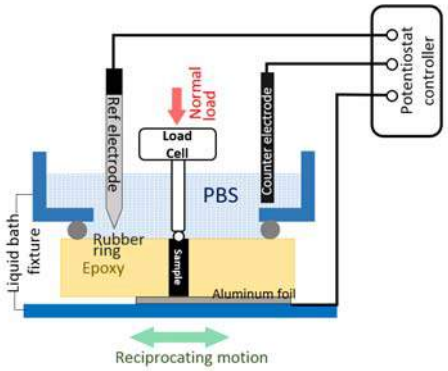

Figure 2. Schematic of the fretting corrosion test system

RESULTS

Open circuit potential measurements were performed in a sequence of (1) dwell: exposure in PBS for 10 min without fretting; (2) fretting corrosion: rubbing in PBS for 30 min; and dwell: again exposing in PBS after fretting was ceased. Ti6Al4V surface showed two stages of oxide recovery. Shortly after sliding contact was initiated, the potential decreased sharply and in the midrange of the sliding potential was gradually decreased at both high and low normal loads. However, CoCrMo potentials continuous increased and the oxide recovery finally began after the fretting was ceased. Ti6Al4V presented the more load sensitive behaviors. The potential change with the greater normal load at 300 mN was doubled compared to potential change with 143 mN, while CoCrMo fretting corrosion responses depicted the comparable potential change with both levels of normal loads. Therefore, it described that the electrochemical enhancement of titanium oxides would be superior to that of chromium oxides.

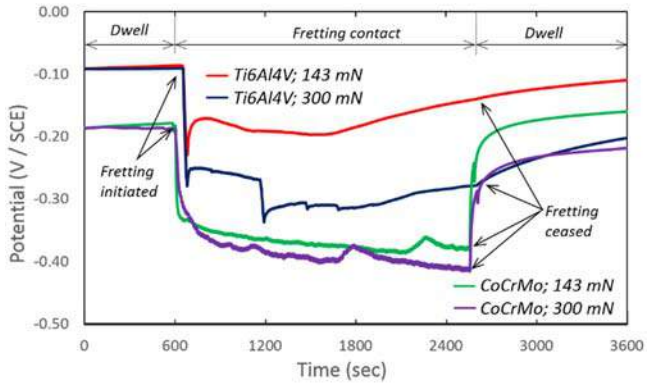

Figure 3. OCP measurement for Ti6Al4V and CoCrMo at different contact normal loads

Table 2 summarized the parameters from dynamic polarization curves presented in Figure 4. The higher current density of CoCrMo would indicate rapid initiation of corrosion process of CoCrMo in the most of the potential. The lower corrosion current (I_{corr}) of Ti6AL4V indicates that the corrosion rate of the surface without fretting is less than corrosion rate of CoCrMo. Therefore, it was elucidated that Ti oxide provides more protection than Cr oxide from corrosion attack [6].

Table 2. Parameters from potentiodynamic polarization curves

Materials	I_{CORR} (A cm^{-2})	E_{corr} (V)
Ti6Al4V (F136)	3.10E-7	–0.40
CoCrMo (F1537)	2.09E-6	–0.332

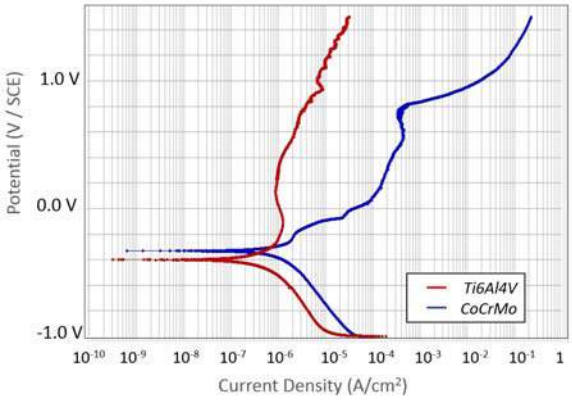

Figure 4. Potentiodynamic Polarization scan at 0.2 mV/s

DISCUSSION

The oxide layer on Ti6Al4V is more noble and lesser prone to corrosion when mechanical stimulus was combined with corrosion attack compared to CoCrMo surface. Ti6Al4V surface actively enhances the corrosion resistivity. Although CoCrMo possesses the superior mechanical properties with greater hardness and ductility, when the surface is exposed to a corrosive environment, the electrochemical damage was accelerated. However, the rapid passivation of Ti6Al4V illustrated the fast oxide layer reformations even during the active fatigue sliding contact. The greater normal contact loads would induce more significant electrochemical damage on Ti6Al4V. Figure 5 summarizes that the damage process would be by the competition between deteriorative mechanical abrasion and atomic dissolution and beneficial enhanced passivation by residual strains [7].

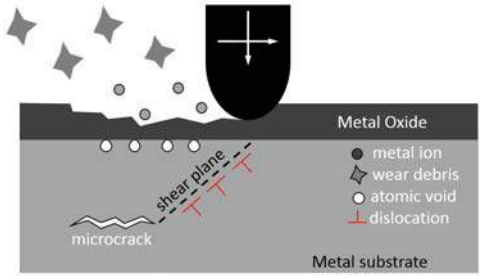

Figure 5. Tribocorrosion process: stress-enhanced dissolutions

ACKNOWLEDGEMENTS

Authors are gratefully acknowledge the financial support of University Research Council and Center for Excellence program at Youngstown State University.

REFERENCES

[1] Villanueva, J., Trino, L., Thomas, J. et al., *J Bio Tribo Corros*, 3:1, 2017.

[2] Liao, Y., Hoffman E., Wimmer, M. et al., *Phys Chem Chem Phys*, 15:746-756, 2013

[3] Moharrami, N., Langton, D.J., Sayginer, O. et al., *Thin Solid Films*, 549: 79-86, 2013

[4] Langton D.J., Sidaginamale, R., Lord, J.K. et al. *Bone Joint, Res.* 56:1, 2012.

[5] Christiner, T., Pabbruwe, M.B., Kop, A.M. et al. *J Bone Jt Surg*, 3: 4, 2018

[6] Alemón, B., Flores, M.,Ramírez, W. et al., *Tribology International*, 81:159-168, 2015

[7] Chandra, A. Ryu, J.J., Karra P. et al. *CIRP Ann Manuf Technol*, 58: 499-502, 2009

SB³C2019
Summer Biomechanics, Bioengineering and Biotransport Conference
June 25 -28, Seven Springs, PA, USA

AN AGE-AWARE CONSTITUTIVE MODEL FOR HUMAN SCLERA INCORPORATING EXPERIMENTALLY-MEASURED COLLAGEN FIBER TORTUOSITY

Tian Yong Foong (1,2), Yi Hua (1), Alexandra Gogola (1), Rouzbeh Amini (3), Ian A. Sigal (1,2)

(1) Department of Ophthalmology
University of Pittsburgh
Pittsburgh, PA, United States

(2) Department of Bioengineering
University of Pittsburgh
Pittsburgh, PA, United States

(3) Department of Biomedical Engineering
University of Akron
Akron, Ohio, USA

INTRODUCTION

Sclera biomechanics are intimately tied with diseases such as glaucoma and myopia [1, 2]. Hence, there has long been an interest in developing constitutive models of ocular tissues [3, 4]. These models, however, do not explicitly incorporate some key aspects of the tissue microstructure, such as the fiber waviness or crimp (Figure 1). As collagenous tissues, their biomechanics are dependent on the underlying fibers, and in particular their waviness or crimp [1, 5]. Using polarized light microscopy, we recently reported that collagen crimp tortuosity in human sclera decreases significantly with age [1]. It is important to understand how the decreased crimp tortuosity influence the mechanical response of the eye to elevated IOP.

Our goal was to incorporate the microstructural information of collagen fibers into a constitutive model and to derive the stiffness of collagen fibers and the surrounding matrix. We subsequently examined the effects of aging on the derived mechanical properties.

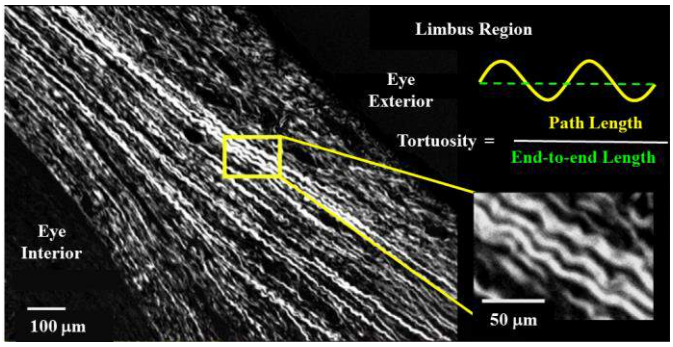

Figure 1: Wide-field view of the limbus region using polarized light microscopy (adapted from Jan et al. [1]). The wavy pattern of the collagen fibers is clearly discernible. The close-up images show the periodic waviness analyzed in this work.

METHODS

Overall method strategy: using polarized light microscopy, we imaged axial whole-globe sections of human eyes. Collagen crimp morphology in the posterior sclera was quantified through tortuosity. The tortuosity was incorporated into a microstructure-based constitutive model. By fitting the experimentally measured stress-stretch curve in the same scleral region [6], we then derived the age-dependent stiffness of collagen fibers (C_5) and the surrounding matrix (C_1).

Age-dependent collagen crimp in the posterior sclera: following Jan et al. [1], we analyzed 7 axial whole-globe sections from 3 normal eyes of 3 human donors, with 40, 72 and 97 years old, respectively. Sections were imaged using polarized light microscopy at a resolution of 0.73 µm/pixel. We quantified collagen fiber tortuosity in the posterior sclera. The distribution of crimp tortuosity for all three age groups is shown in Figure 2.

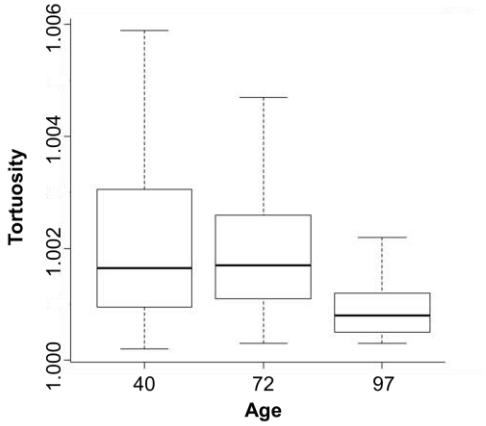

Figure 2: Boxplots of collagen crimp tortuosity in the posterior sclera of the three human eyes donors analyzed.

Collagen microstructure-based constitutive model: the mechanical response of the sclera were modeled using a fiber-based constitutive equation of the form

$$W = W_{fiber} + W_{matrix} \quad (1)$$

where W is the total strain energy density, W_{fiber} is the strain energy density of the collagen fibers, and W_{matrix} is the strain energy density of the surrounding matrix.

The strain energy density equation for the collagen fibers was modeled using the form [3]

$$\lambda \frac{\partial W_{fiber}}{\partial \lambda} = \begin{cases} 0 & \lambda \leq \lambda_m \\ C_5(\lambda - \lambda_m) & \lambda > \lambda_m \end{cases} \quad (2)$$

where λ_m is the collagen crimp tortuosity, λ is the fiber stretch, and C_5 is the stiffness of the straightened fibers.

The strain energy density equation for the surrounding matrix was modeled as a Mooney-Rivlin solid which has the form

$$W_{matrix} = C_1(I_1 - 3) + C_2(I_2 - 3) \quad (3)$$

where C_1 and C_2 are material constants defining the stiffness of the matrix and I_1 and I_2 are the first and second invariants of the right Cauchy-Green deformation tensor (non-directional measures of material deformation). In this work, C_2 was set to zero which is analogous to a neo-Hookean formulation.

RESULTS

Figure 3 shows the age-dependent stress-stretch curves of the posterior sclera predicted by our collagen microstructure-based constitutive model and by the inflation test experiments reported by Coudrillier and colleagues [6]. The derived stiffness of the collagen fibers and of the surrounding matrix with aging are shown in Figure 4.

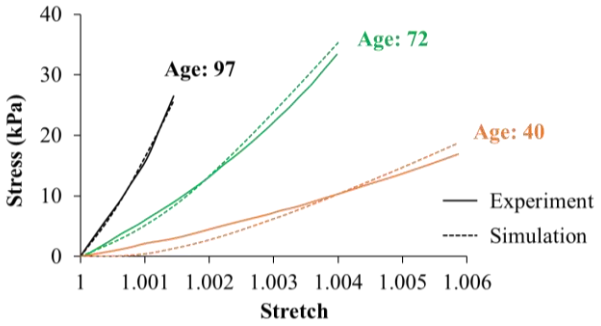

Figure 3: Age-dependent stress-stretch curves of the posterior sclera predicted by our collagen microstructure-based constitutive model simulation (dashed lines) and by the inflation tests (solid lines) [6]. The measured nonlinear stress-stretch behavior of the posterior sclera and the stiffer response with aging were captured well by our collagen microstructure-based constitutive model.

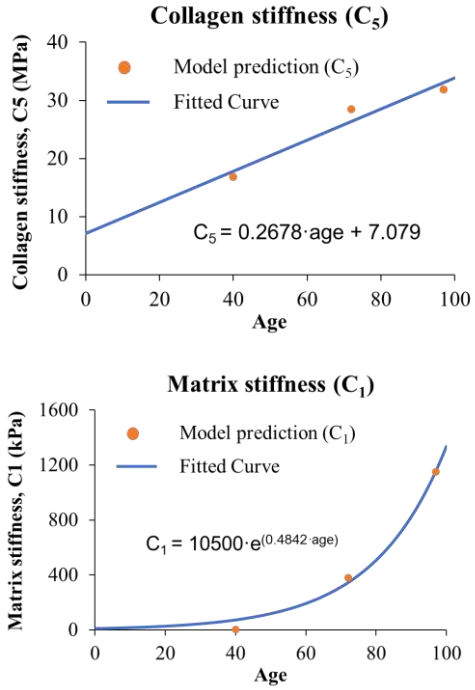

Figure 4: Model-predicted stiffness of collagen fibers (top) and the surrounding matrix (bottom) with aging. With aging, the stiffness of the collagen fibers increased linearly, and the stiffness of the matrix increased exponentially.

DISCUSSION

Our goal was to incorporate the experimentally-derived microstructural information of collagen fibers into a constitutive model and to derive the stiffness of collagen fibers and the surrounding matrix. We then further examined the effects of aging on the derived mechanical properties.

Our collagen microstructure-based constitutive model predicted a nonlinear stress-stretch behavior of the posterior sclera at three ages, consistent with the experimental measures [6]. Note that the fiber stiffness is at least one order of magnitude larger than the matrix stiffness. As a result, the tissue-level stiffness should be dominated by the stiffness of collagen fibers. Importantly, in our constitutive models, the collagen fibers were assumed as linear elastic. The predicted nonlinear stress-stretch behavior of the posterior sclera is caused by the process of fiber recruitment based on the tortuosity. To the best of our knowledge, this is the first report of the use of microstructural properties to derive a nonlinear stress-stretch behavior of scleral tissue.

We also found that the stiffness of collagen fibers increased linearly, and that of the matrix increased exponentially with aging. Similar stiffening effects of collagen fibers with age have been reported in the literature for the cornea [7] and the sclera [8, 9] using various experimental techniques. However, the effect was attributed to the accumulation of nonenzymatic glycation-type cross-links with aging [10]. Inverse models have also been used to suggest age-related changes in sclera properties, including compliance and fiber crimp.[11] Those findings, however, were based on experimental measurement of deformations, without direct measurements of crimp. Unfortunately, no studies yet have measured the stiffness of the matrix and its changes with aging. Further studies are necessary to elucidate the causes for matrix stiffening and its potential role in eye physiology and pathology.

In summary, we incorporated the experimental microstructural information of collagen fibers into a constitutive model and then derived the age-dependent stiffness of collagen fibers and the surrounding matrix of the posterior sclera. Findings from this work can help reveal the role of microstructure on eye physiology, in aging, and in biomechanic-related diseases, such as glaucoma.

ACKNOWLEDGEMENTS

Supported by National Eye Institute of Health Grants R01-EY023966, and P30-EY008098; Research to Prevent Blindness; and Eye and Ear Foundation (Pittsburgh, PA, USA).

REFERENCES

[1] Jan, N.J. et al., *Exp Eye Res*, 172: 159-170, 2018
[2] McBrien, N.A. et al., *Optometry and Vision Science*, 86: E23, 2009
[3] Girard, MJA. et al., *j Biomech Eng*, 131: 051011, 2009
[4] Pandolfi, A. et al., *Bio mech Model Mechanobiol*, 5: 237, 2006
[5] Jan, N.J. et al., *Invest Opthalmol Vis Sci.*, 58: 735-744, 2017
[6] Coudrillier, B. et al., *IOVS*, 53: 1714-1728, 2012
[7] Jue, B. et al. *J Biomech*, 19(10):847-53, 1986
[8] Keeley, F.W. et al., *Exp. Eye Research*, 39: 533-542, 1984
[9] Avetisov,E.S et al,*Metab Pediatr Syst Ophthalmol*, 7(4):183-8, 1983
[10] Verzijl, N. et al., *Arthritis Rheum*, 46(1):114-23, 2002
[11] Grytz, R. et al., *Invest Ophthalmol Vis Sci*., 55:8163-72, 2014.

SB³C2019
Summer Biomechanics, Bioengineering and Biotransport Conference
June 25 -28, Seven Springs, PA, USA

STOCHASTIC MODEL FOR PLATELET SPREADING UNDER FLOW

Iain Macleod Briongos(1), Peter M. Hammes(1), David L. Bark(1,2,3)

(1) School of Biomedical Engineering
Colorado State University
Fort Collins, CO, USA

(2) Department of Mechanical Engineering
Colorado State University
Fort Collins, CO, USA

(3) Department of Pediatrics Division of Hematology,
Oncology, and Bone Marrow Transplant
University of Colorado Anschutz Medical Campus
Aurora, CO, USA

INTRODUCTION

Platelets are fundamental to maintaining the integrity of the cardiovascular system. Despite and/or because of their efforts, cardiovascular-related disease is the leading cause of death in the developed world, through heart attack and stroke often resulting from platelet responses to non-physiological hemodynamic environments. Limited understanding of the mechanisms behind platelet biophysics that lead to binding, activation, and spreading further limits the ability design blood-contacting devices without inducing a thrombotic response. To mitigate these risks, patients with current generation blood-contacting devices are treated with systemic anticoagulant and antiplatelet therapies that must be carefully modulated to avoid bleeding complications. Under high flow, however, these therapies exhibit limited efficacy, and can have serious side effects leading to drug-related deaths. Lastly, platelet function is tightly linked to bleeding disorders, e.g. Gray platelet syndrome, of which the cause of many have yet to be explained. Overall, platelets play a key role to the health of our cardiovascular system.

At the core of these platelet responses, is an ability to sense and respond to their mechanical environment through chemical signaling. This ability, known as mechanotransduction, is critical to many fundamental cell functions. However, unlike many other cells, the area of platelet biophysics has received limited attention, with most focus on the study of platelet-surface interactions and the proteins are involved. However, these studies do not provide an explanation for how platelets respond under flow or how they actively respond to mechanical forces. In our recent work, we found a decision-making process in platelets that appears to be force dependent, where platelets choose to both bind and spread or to detach.

By developing a computational model of platelet biophysics, combined with key experiments, it will be possible to identify dominant biophysical pathways that platelets use to sense surrounding forces in the context of flow and their binding substrate. Results may help in the design of medical devices like blood pumps, artificial heart valves, stents, et cetera. Better understanding of when and how platelets bind can lead to discovery of currently unused targets in biophysical pathways, which can be used for the development of novel antiplatelet therapies, while possibly helping us to understand and treat unexplained bleeding disorders.

METHODS

Model - A stochastic model was made to show platelet binding to a stiff surface. The model is a modified version of the one proposed by Bangasser et al. 2017 [1]. The model has been modified to more accurately depict the activation of integrin $\alpha_{IIb}\beta_{III}$ and subsequent platelet spreading. Additional forces were added to the model simulating flow conditions. Parameters for the model were collected from the literature and through platelet experiments described below. Finally, a sensitivity analysis was performed to determine what characteristics of a platelet play a key role in force sensing

Platelet Isolation - Whole blood was collected with written consent and IRB approval into 5ml Monoject blood collection tubes with 0.5ml 3.5% buffered sodium citrate (Covidien LLC, Mansfield, MA). Acid-Citrate-Dextrose and Apyrase (New England Biolabs Inc., Ipswich, MA) was further added. Platelets were resuspended into Tyrodes-Albumin Buffer (TAB) after 2 centrifugation steps with PGI2 (Cayman Chemical Company, Ann Arbor, MI). The final platelet concentration was checked using a Hemavet hemocytometer (Drew Scientific, Miami Lakes, FL) and was adjusted to 3*10^8 with the addition of more TAB.

Retrograde Flow - Actin retrograde flow is the flow of actin towards the granulomere, which is caused by elastic resistance of the

cell membrane to the extension of the actin fiber. This value is measured for a more complete picture of the internal forces acting on a platelet as it spreads. This was determined by allowing washed platelets to spread on a fibrinogen (an $\alpha_{IIb}\beta_{III}$ counterreceptor) coated surface, with the subsequent addition of a solution containing fibrinogen-coated 1 micron diameter beads (Invitrogen). The rate at which a bead moved along the platelet body was determined.

Spreading Validation - To confirm rate of $\alpha_{IIb}\beta_{III}$ usage, and quantify actin polymerization and filopodial growth, isolated platelets were placed on glass coverslips with and without fibrinogen at different concentrations of fibrinogen. Image series were taken covering the full length of spreading, from the landing of the platelet on the surface until spreading had completed. The spread time was calculated, and the rate of spreading found.

Flow in Whole Blood - Once the model was validated for static conditions an additional force was added to simulate flow conditions. This was subsequently verified experimentally by flowing whole blood at a known shear rate in a microfluidic device containing a strip of fibrinogen. The created tether was monitored to determine growth rate and break point or time to fully spread, depending on the applied shear.

RESULTS

Platelets spread at a rate of 14.6 ± 3 nm/s, reaching a fully spread state at 296 ± 8 s. This spreading rate validates actin polymerization and $\alpha_{IIb}\beta_{II}$-fibrinogen kinetics. Total internal reflection fluorescence microscopy (TIRFm) was used to assess separation distance, Fig. 1. Beads on a spread platelet had a speed of 7.7 ± 1.7nm/s and 7.7 ± 1.6nm/s. Rate of retrograde flow increased in the presence of CK666, an inhibitor of actin assembly by actin-related protein Arp2/3 complex, and decreased in the presence of blebbistatin, which inhibits myosin II. In both cases, variability of retrograde flow increased. These results incorporate the rate of myosin contraction and retrograde actin polymerization, which are used to validate parameters in our model.

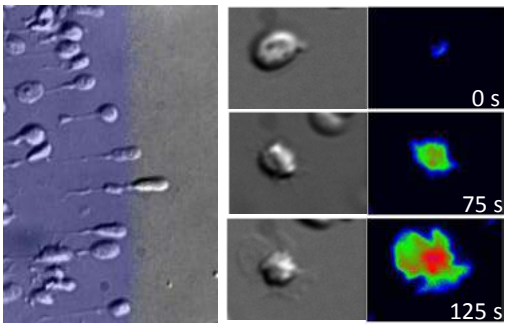

Figure 1: Left: Platelets binding to 100 μg/ml fibrinogen (labeled in purple) under flow with a wall shear rate of 600 s^{-1}. Middle: Platelets spreading with TIRFm images. Right: Retrograde flow bead tracks.

The rate of spreading as seen in the model was very similar to the found rate of spreading for platelets. With the additional force added to the model, the model spread rate and time were found to be like the median range of shear rates. At very high and very low shear rates the model did not match the experimental times.

DISCUSSION

Here, we present a model for platelet spreading under flow on elastic surfaces, with experimental validation. Based on parameters such as force of fluid flow, wall shear rate, actin extension rate and myosin contractile forces, we can predict platelet activity, including clutch engagement rate. The combined results tell us net spreading forces, total platelet body movement per time point, and allow us to gain insight into overall platelet responses in static or flow conditions.

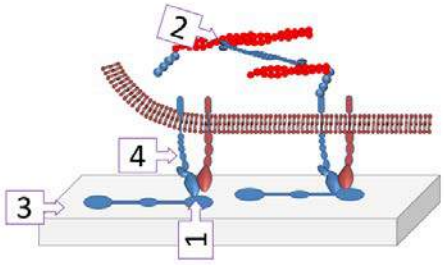

Figure 2: Model of actin cytoskeleton extension. 1) On and off rate of a2bb3 binding fibrinogen. 2) Myosin motor force, actin polymerization, and motor stall force. 3) Surface stiffness. 4) A2bb3 material properties, number of integrins, and bond rupture force.

Under static conditions, platelets attach and spread. However, under flow, platelets react differently, perhaps in a force dependent manner. Under flow, after initial binding via a discrete adhesion point, the platelet body will pull away in the direction of the flow, after which, they sometimes spread and sometimes detach. This model is designed to look at how flow changes adhesion based on forces acting on the platelet, and should work in both constant and pulsatile flows conditions.

Previous work has shown that under static conditions, as surface stiffness increases, so do the platelet contractile forces [2]. Our research supports this and suggests that the same principle is occurring under flow. However, flow can overcome these contractile forces, resulting in the extension of a platelet body into the flow direction, as a result of slipping 'biological clutches.'

This work is a preliminary assessment of a model for platelet spreading on surfaces. It will need to be expanded to incorporate more initial parameters, with the aim of giving us more complete output data, such as rate of spreading found from actin extension rate, platelet motility, found from platelet adhesion strength and surface stiffness.

Overall, we have developed a model that is providing insight into platelet active responses to changes in force based on kinetic binding rates, actin polymerization rates, and myosin contraction rates. Combined, this model and experiments provide a first step toward elucidating complex platelet responses under flow. Identification of these processes will provide new insight into potential targets for antiplatelet therapies to prevent heart attacks and stroke. They may also give us new insight into still unexplained bleeding disorders.

ACKNOWLEDGEMENTS

The authors gratefully acknowledge funding from the American Heart Association (Award# 18CDA34110134). We also acknowledge funding from National Science Foundation (Award# 1762705), program director Dr. Michele Grimm.

REFERENCES

[1] Bangasser, Benjamin L., et al. "Shifting the Optimal Stiffness for Cell Migration." *Nature Communications*, vol. 8, 2017, p. 15313., doi:10.1038/ncomms15313.

[2] Lam, Wilbur A., et al. "Mechanics and contraction dynamics of single platelets and implications for clot stiffening." *Nature materials* 10.1 (2011): 61.

SB³C2019
Summer Biomechanics, Bioengineering and Biotransport Conference
June 25-28, Seven Springs,PA, USA

EVALUATING SINGLE MUSCLE CONTRACTION USING ELECTRICAL STIMULATION AND SHEAR WAVE ELASTOGRAPHY

H. Patel (1), S. Sadeghi (2), D. Cortes (1, 3)

(1) Mechanical Engineering Department
Penn State University
State College, PA, USA

(2) Mechanical Engineering Department
Penn State University
State College, PA, USA

(3) Biomedical Engineering Department
Penn State University
State College, PA, USA

INTRODUCTION

Measurement of the force produced by individual muscles is critical for understanding muscle physiology, how body motion is produced and controlled, how injuries affect muscle function, and how body function is affected by muscle pathologies. However, measuring the force produced by individual muscles non-invasively remains an unmet challenge in biomechanics. The motion of most joints in the body is produced by the simultaneous action of several muscles. The resultant force (or torque) from the action of all the muscles crossing the joint can be measured using dynamometers (i.e.,Biodex) or calculated from motion capture data. However, there are an infinite number of combinations of individual muscle forces that can result in the measured torque. Current attempts to estimate individual muscle force often require convoluted combinations of additional experimental modalities, theoretical models, and assumptions that may be valid only for specific muscle groups under specific conditions. Surface electromyography (sEMG) may be used to measure the activation of an individual muscle. However, calculating force from sEMG measurements requires the measurement of many other parameters and frequent calibration due to low signal-to-noise ratio, differences in tissue electrical properties among individuals, and surrounding conditions [1].

A major challenge in the study of the relationship between shear modulus and muscle force is the ability of measuring the force from a single muscle at the time. This cannot be done by voluntary muscle contraction since joint motion is typically produced by the simultaneous contraction of several muscles. Neuromuscular electrical stimulation (NMES) has been previously used to induce contraction of single muscles in-vivo [2]. NMES can be delivered using surface electrodes or acupuncture needles. The advantage of surface electrodes is the non-invasive nature of the procedure, while needles have a more localized effect. The objectives of this is study are to evaluate changes in the shear modulus of the *Tibialis anterior* (TA) muscle and the surrounding muscle in the lower leg when the TA is stimulated using NMES and to compare the two delivery methods (surface and needle electrodes). Results from this study can help determine whether the combination of NMES and Shear wave elastography can be used to analyze single muscle contraction.

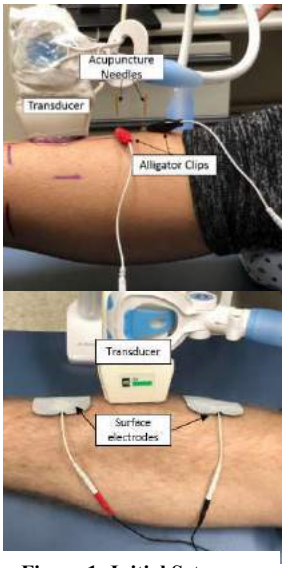

Figure 1: Initial Setup on the lower leg

METHODS

Six healthy participants (Four male and two female; Age 22.5 ± 1.378; BMI 24.85 ± 5.57) were recruited for this study. They were asked to lie down in a natural position on their back with their legs extended out. From the proximal end of the tibia, approximately 4 inches (~10.2 cm) and 6 inches (~15.2 cm) were measured and marked with a marker. Two acupuncture needles of 30 gauge and 30 mm in length were inserted at the marked spots. Similarly for the surface NMES procedure, two electrode pads were placed at the same location. The pads and needles were attached to the Electrical Muscle Stimulator (Quattro 2.5) device via NMES leads. The ultrasound transducer (Verasonics) was placed on the lower leg using the fixture. Figure 1 shows the initial setup for needle and surface NMES.

Poster Presentation #P049

Five unstimulated baseline values of shear wave speed for the top layer of the TA muscle were collected through the SWE method. The NMES device was then slowly ramped up to the maximum tolerable intensity (1 mA for needle and 40 mA for surface NMES) to contract the muscle at a frequency of 50 Hz and the duration of 300 μs on a constant mode. Once stimulated, five shear wave speed values were collected once again from the top layer of the TA muscle. The procedure was repeated for the lower layer of the TA muscle. Additionally, the change in shear modulus of the *Peroneus Longus* (PL) muscle, the *soleus* muscle, and the *Tibialis Posterior* muscle was also collected during stimulation to verify that the surrounding muscles are not being contracted in this procedure by changing the position of the transducer on the lower leg and keeping the needles in at the same position. A short break was given between contractions to allow the patient to rest in order to avoid fatigue in muscles.

RESULTS

In the case of surface electrodes, the shear modulus of the TA and surrounding muscles increased as plotted in Figure 4. On average, the values of shear modulus increased from 11.96±8.01 to 65.04±122.37 (average of both upper and lower TA), while the change of shear modulus of the surrounding muscles was very significant. Figure 3 shows the dramatic increase in the shear modulus of all surrounding muscles during sEMG. When using needle electrodes, the values of shear modulus increased from 7.207±3.44 to 17.08±1.97 (average of both upper and lower TA), while the change of shear modulus of the surrounding muscles was not significant. The increase in shear modulus of the TA was not uniform; the upper portion of the TA had a higher value of shear modulus during stimulation (23.013±4.02) than that of the lower region (11.06±4.001). The color map in figure 2 confirms the increase in the shear wave speeds through the TA muscle during contractions and shows little to no change in the *Soleus* and the *Peroneus Longus* muscles, respectively, during NMES.

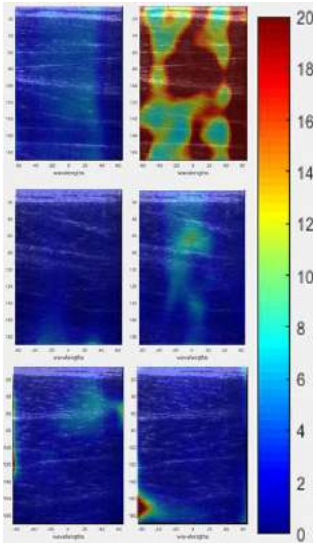

Figure 2: B-mode and shear modulus color map (kPa) of the TA muscle (top), Soleus Muscle (middle), and the PL Muscle (bottom), before (left) and during (right) NMES

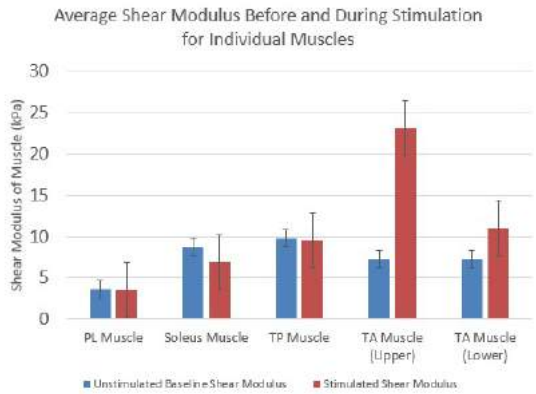

Figure 3: Graphical representation of the changes in shear modulus in the muscles using needle electrodes

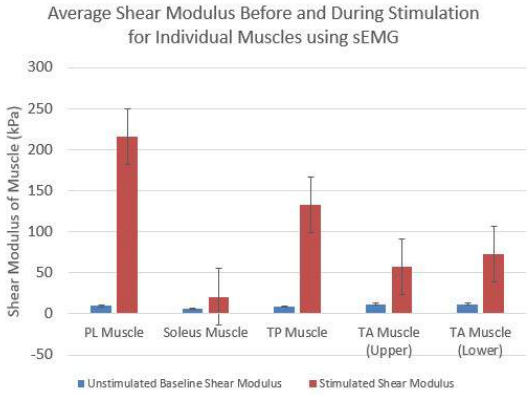

Figure 4: Graphical representation of the changes in shear modulus in the muscles using surface electrodes

DISCUSSION

The results suggest that it is possible to stimulate a single muscle using needle electrodes. Conversely, the use of surface electrodes resulted in the stimulation of surrounding muscles, which is possible due to the larger surface area of the electrode pads. In the case of needle electrodes, the variability in the results could arise from factors, such as the depth of the needle and the placement of the needle. As it can be seen in Fig. 3, the lower (deeper) portion of the TA muscle experienced a smaller increase in shear modulus during electrical stimulation. This could be caused by inconsistent needle depth. Needles where placed following the typical protocol for electroacupuncture. However, the variability could still be present because the size of the TA muscle differs from person to person. Surface NMES produced a more intense contraction of muscle (higher modulus) probably due to the larger electrical current applied.

Several recent studies have suggested a linear relationship between individual muscle force and its shear modulus (F-μ relationship) during isometric muscle contraction. These measurements have been performed in the Abductor Digiti Minimi muscle, which is the only muscle producing little finger abduction torque. The Abductor Digiti Minimi is one the few examples in the body of joint motion controlled by a single muscle. Therefore, the ability of experimentally measuring forces from individual muscles is instrumental for evaluating F-μ relationships in other muscles. Additionally, the mechanistic principles behind the F-μ relationship are presently unknown. For this reason, it is unknown why the proportionality constant of the F-μ relationship varies across muscles and across individuals, preventing *a priori* estimation of individual muscle force. F-μ relationship may be modulated by muscle pennation angle and muscle volume, which are important muscle properties playing a role in force production. The effect of muscle pennation angle and muscle volume on the F-μ relationship will be evaluated in future studies.

In conclusion, needle stimulation is a technique that allows studying the contraction of individual muscles using shear wave elastography. However, it seems to produce a lower intensity of muscle contraction.

ACKNOWLEDGEMENTS: NIH UL1 TR002014.

REFERENCES

[1] E. F. Shair, S. A. Ahmad, M. H. Marhaban, et al., "EMG Processing Based Measures of Fatigue Assessment during Manual Lifting.," *Biomed Res. Int.*, vol. 2017, p. 3937254, 2017.

[2] S. A. Riewald and S. L. Delp, "The action of the rectus femoris muscle following distal tendon transfer: does it generate knee flexion moment?," *Dev. Med. Child Neurol.*, vol. 39, no. 2, pp. 99–105, Feb. 1997.

SB³C2019
Summer Biomechanics, Bioengineering and Biotransport Conference
June 25 -28, Seven Springs, PA, USA

IMPLEMENTING REAL-TIME EXTRINSIC MUSCLE CONTROL IN A ROBOTIC GAIT SIMULATOR FOR INVESTIGATING LOWER EXTREMITY FUNCTION

W. Spivey (1), C. O'Cain (1), B. Gepner (1), E. Spratley (1), J. Kerrigan (1)

(1) Mechanical Engineering
University of Virginia
Charlottesville, VA, USA

INTRODUCTION

Recent studies have demonstrated high incidences of poor outcomes and implant failure in total ankle replacement patients [1]. Currently, no test methodology exists to sufficiently quantify the degree to which these implants replicate normal ankle mechanics during the dynamic activities of daily living. Quantifying these responses are key to understanding how these implants affect foot and ankle function, and how future implants can be improved. Biomechanics research on living subjects is limited to what can be measured non-invasively. Consequently, post mortem human surrogates (PMHS) remain the gold standard for human biomechanical measures. Nevertheless, PMHS lack the passive tone and muscle activation that drive the torque-generating muscle tension across the joints of the foot and ankle during gait. In an effort to address this shortcoming, several research groups have developed robotic gait simulators that allow dynamic muscle forces to be applied to the foot during gait [2,3]. This study demonstrates the capability of a six degree-of-freedom robotic gait simulator design capable of applying full body weight (BW) at near-normal gait speeds with real-time extrinsic muscle control, as well as its potential utility for investigating biofidelic foot and ankle dynamics.

METHODS

The major components of the robotic gait simulator are the serial robot, tendon actuators, coordinate digitizing arm, motion analysis system, and a six degree-of-freedom load cell (6-DoF) (Figure 1).

The 6-DoF position and force/torque controlled serial robotic test system was used to drive previously collected in vivo tibia kinematics. The PMHS specimen was affixed to the end-effector of the robot through rigid urethane potting at the proximal tibia. Prior to testing, multiple points on the PMHS limb were digitized and used to generate a specimen-specific ankle coordinate system with respect to the robot's coordinate system.

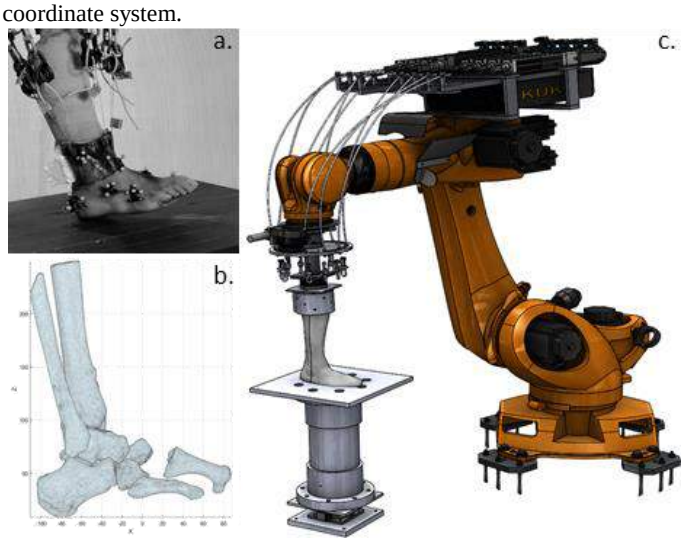

Figure 1. a-c: a. Specimen before toe-off. b. Motion tracking data applied to simulate foot motion. c. Model of entire system.

Nine linear actuators were used to pull tension in each the following nine tendons: (1) Achilles, (2) Tibialis Anterior, (3) Tibialis Posterior, (4) Flexor Hallucis Longus, (5) Flexor Digitorum Longus, (6) Extensor Hallucis Longus, (7) Extensor Digitorum Longus, (8) Peroneus Longus, and (9) Peroneus Brevis. These tendons represent the largest contributors to gross foot and ankle motion, especially with regards to Plantarflexion and Dorsiflexion [4]. Muscle force time-

histories were generated based on percent activation and physiological cross sectional area.

The single PMHS right lower extremity used for the study was disarticulated at the knee from a 46-year-old donor (99.3 kg, 175.3 cm). Approximately 150mm of the proximal tibia was denuded to allow for connection to the end of the robot. Additionally, a 50 mm window of skin was removed from around the circumference of the ankle just above the medial malleolus in order to expose the tendons of each of the extrinsic muscles inserting in foot. Each actuator was then affixed to its respective tendon using polyester surgical thread by means of a Krakow stitch. By virtue of the very high tension required, the Achilles was attached using a custom aluminum cryoclamp. Retroreflective motion tracking arrays were attached to the following bones: tibia, fibula, calcaneus, talus, navicular, cuboid, first metatarsal, and fifth metatarsal.

Four body weight (BW) conditions were tested: 25%, 50%, 75%, and 100%. For each BW, a target ground reaction force (GRF) time-history was used to optimize the tibialis anterior force during heel strike, superior position of the tibia during midstance, and Achilles force during toe-off. Each BW condition had 8-12 optimization runs, with 3 experimental runs each. Testing took place over the course of 4 days.

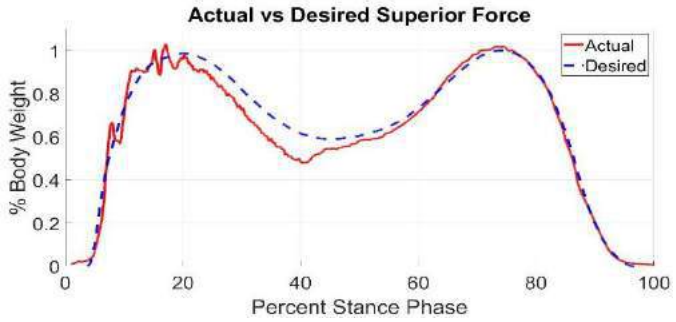

Figure 2. Actual and Desired GRF Target

Data collected can be separated into two main categories, force and moment data from the walking platform, and bone kinematics from the motion tracking arrays. Platform load cell data is reported in the ankle coordinate system and did not require substantial post processing.

Marker arrays were digitized in a pretest CT scan along with the rest of the specimen in order to establish a rigid body transformation between each marker array and its respective bone. During testing, a laboratory reference frame was established using motion-tracking targets attached to the plane of the walking platform. All of the motion capture data is reported in this lab reference frame, with the anterior direction being +X, medial direction being +Y, and superior direction being +Z. Using the established transformations, motion-tracking trajectories are applied to all of the marker arrays and their bones, respectively.

RESULTS

The robotic gait simulator imposed known tibia kinematics from previous human volunteer gait data, as well as estimated extrinsic muscle force time-histories [3] on a PMHS lower extremity. Vertical displacement was modulated according to observed GRF to represent the effects of different body weights during gait.

The system was able to trace the GRF approximately within 10% of the input target (Figure 2). Increasing body weight led to observed changes in global foot kinematics. The calcaneus everted 6 degrees under 100% BW versus only 2 degrees for the 25% BW trial. Likewise, the navicular was observed to compress 18 mm inferiorly toward the ground plate during the 100% BW, while only compressing 15 mm under 25% BW (Figure 3).

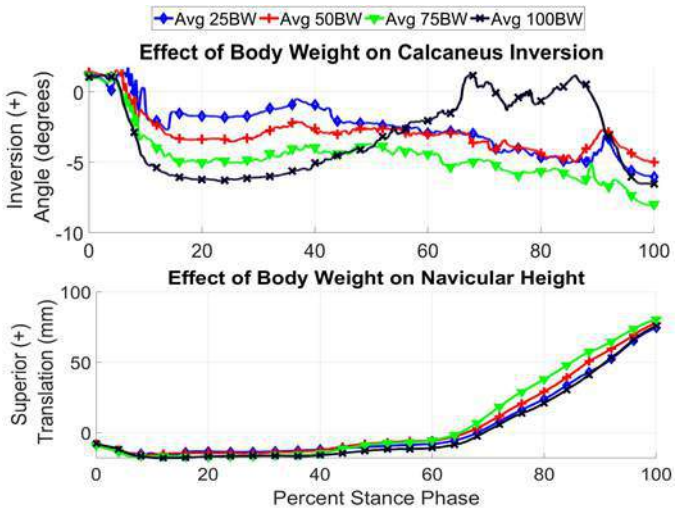

Figure 3. [TOP] Drop in longitudinal arch height as measured by Z excursion of the navicular. [BOTTOM] Change in hindfoot varus/valgus as measured by rotation about calcaneus x axis.

DISCUSSION

The robotic gait simulator was able to reproduce gait-like motions of a PMHS lower extremity. Ground reaction forces and tibia kinematics from living subject 3D motion tracking were accurately reproduced. Further, the gross motion of the foot was consistent with translations and rotations reported in the literature [5]. As we were interested in understanding the effect of body weight on foot function, the relative motions of the calcaneus and navicular were of particular interest. For increasing levels of axial load, it was observed that the hindfoot had increasing amount of valgus tilt (negative rotation about the x-axis). Likewise, increasing load led to the centroid of the navicular moving inferior (negative translation in the z-axis). These trends are consistent with those reported previously for living subjects and are characteristic of the longitudinal arch of the foot spreading and compressing with every larger amounts of axial loads [5].

The 100% BW trials deviated during toe-off from the expected trends. This was due to the foot sliding posteriorly during toe-off, suggesting that the imposed anterior-posterior (AP) and medial-lateral (ML) tibia kinematics needs to be tuned during optimization runs to match human volunteer gait data.

Further specimens are needed to investigate whether or not these trends are consistent. Additionally, further investigation into mitigating shear AP and ML sliding of the foot, as well as improving the optimization scheme to reduce the approximately 10% model error.

In order to improve clinical outcomes, implants must be better at replicating the complex characteristics of the dynamic activities of daily living. This system represents the first step towards integrating all necessary components, muscle effects, positional effects, and dynamic effects to replicate precise in vivo bony kinematics.

ACKNOWLEDGEMENTS

Funding for the project was provided by the University of Virginia through the Research and Innovation Award program and the Engineering and Medicine initiative.

REFERENCES

[1] Gougoulias, N et al. *Clin Orthop Relat Res*, 468:199. 2010
[2] Aubin PM. Doctoral Dissertation. University of Washington. 2010.
[3] Noble LD. Doctoral Dissertation. Cleveland Clinic. 2011.
[4] Perry J. Gait Analysis. 1992
[5] Lundgren P. *Gait and Posture*. Karolinska Insititue. 2007

SB³C2019
Summer Biomechanics, Bioengineering and Biotransport Conference
June 25 -28, Seven Springs, PA, USA

EVALUATION OF ACCURACY OF FOUR MUSCLE MODELS USING INTRAMUSCULAR PRESSURE – A SURROGATE FOR MUSCLE FORCE

G. Boggess (1), M. Shourijeh (1), F. Ates (2), W. Litchy (3), K. Coleman-Wood (2), K. Kaufman (2) B. Fregly (1)

(1) Department of Mechanical Engineering
Rice University
Houston, TX, USA

(2) Department of Orthopedic Surgery
Mayo Clinic
Rochester, MN, USA

(3) Department of Neurology
Mayo Clinic
Rochester, MN, USA

INTRODUCTION

Muscular impairments are at the heart of numerous orthopaedic and neurological conditions. However, rehabilitation protocols for these conditions are generally not subject-specific and the results of the protocols can be mixed [1]. Neuromusculoskeletal (NM) models may improve rehabilitation effectiveness by allowing researchers and clinicians to evaluate the proposed intervention on a computational model of the subject prior to beginning rehabilitation. Neuromusculoskeletal models' accuracy have traditionally been evaluated on their ability to match calculated joint inverse dynamics loads. However, due to the muscle redundancy problem (more muscles than degrees of freedom), there are infinite combinations of muscle forces that produce the same joint moments. Therefore, matching inverse dynamics moments does not guarantee that the individual muscle force predictions are accurate. This is a challenge if muscle force predictions are to be used to make rehabilitation decisions.

Intramuscular pressure (IMP) is the interstitial fluid pressure within a muscle. Animal studies have shown IMP to have high correlations with muscle force [2]. Therefore, IMP provides a minimally invasive opportunity to verify muscle force predictions from neuromusculoskeletal models.

This study examined the effect of four muscle models on the correlation between predicted muscle force and IMP. These muscle models were included in a subject-specific neuromusculoskeletal optimization. This study is one of the first studies in humans to assess the accuracy of muscle force predictions from musculoskeletal models.

METHODS

Prior to participation in this study, the subject signed informed consent documents approved by the Mayo Clinic Institutional Review Board. The subject was a 26-year old female (height: 174.3 cm, weight: 62.8 kg). The subject laid on her back with her foot secured to a custom torque cell dynamometer. In order to isolate ankle plantar/dorsiflexion as the single degree of freedom the subject's ankle axis was aligned with the axis of the dynamometer. Additionally, a wooden block was inserted under the subject's foot to invert the subject's foot 20º. This isolated the subject's tibialis anterior as the sole plantarflexor by reducing other plantarflexor muscles' ankle flexion moment arm. Surface EMG electrodes were placed over the tibialis anterior, soleus, medial gastrocnemius, and lateral gastrocnemius. A fine-wire EMG electrode was inserted into the tibialis anterior. Finally, a fiber-optic IMP sensor was inserted into the tibialis anterior parallel to the muscle fibers. The subject performed 21 total trials. The trials were three dorsiflexion Maximum Voluntary Contractions (MVCs) in each of three positions: with the foot dorsiflexed 5º-10º, in a neutral position, and plantarflexed 20º; three ramp to max effort trials in the same three positions; and finally, three plantarflexion MVC trials in the neutral position. The plantarflexion MVC trials were necessary to calibrate ankle plantarflexor muscles in the neuromusculoskeletal model. Each trial was cut to reflect the time from 250 ms before the onset of ankle torque to the maximum torque. The 250 ms buffer was added to account for the electromechanical delay. Trials were removed from consideration if there was a significant negative region in the IMP (possibly indicating cavitation) or if there was a sudden spike in the IMP greater than the max in any other trial.

The neuromusculoskeletal model used in this study is a modified version of a previously published EMG-driven model can optimize parameters for subject-specificity. The optimizable parameters are EMG to activation parameters, tendon slack length, ideal fiber length, muscular geometry, and tendon compliance if a compliant tendon model was used. The model's cost function encourages agreement with measured joint inverse dynamics loads and generic moments generated

Poster Presentation #P051

by passive muscle force as reported in literature. Finally, a term that encouraged agreement between muscle force predictions and measured IMP could be turned off and on. The model was reduced to nine muscles and two degrees of freedom (ankle plantar/dorsiflexion and subtalar rotation). To avoid local minima in the optimization, six optimizations were performed alternating between optimizing the EMG to activation parameters; tendon slack length, ideal fiber length, and tendon stiffness in the compliant tendon case, and muscle geometry. Finally, all parameters were adjusted at once to conclude the optimization.

Four muscle models were used in this study: rigid tendon with one fiber type, rigid tendon with fast and slow twitch fibers, compliant tendon with one fiber type, compliant tendon with fast and slow twitch fibers. Compliant tendon models were based on Millard et al [2]. Models with fast and slow twitch fibers were based on Wakeling et al [3].

RESULTS

Tables 1-3 present the results of the four optimizations. In general, subject-specific parameters led to higher force predictions-IMP correlations than the initial generic neuromuscular parameters. Additionally, important features of the IMP curves were captured in the predicted forces (Figure 1).

Two-fiber type muscle models had higher correlations with the measured IMP than their matched single fiber muscle models. However, two fiber type models had worse moment matching results than their matched single fiber type models. Results were mixed when comparing rigid tendon muscle models to compliant tendon models. The rigid tendon model performed better when a single fiber was used while the compliant tendon model led to significant improvement when two muscle fibers were used.

Adding a term to the cost function that encouraged higher correlation between predicted muscle force and measured IMP predictably led to higher correlations. However, this optimization also improved moment matching results. While the improvements were minor for rigid tendon models, significant improvement was observed for compliant tendon models.

Table 1: Performance of Muscle Models Blinded to IMP

	Initial R^2	Final R^2	RMS (Nm)	MAE (Nm)
Rigid Single Fiber	0.8307	0.8518	4.196	3.1527
Rigid Two Fiber	0.8524	0.8707	5.9331	4.3889
Compliant Single Fiber	0.8317	0.8211	4.6499	3.7353
Compliant Two Fiber	0.8542	0.8689	5.0139	3.7977
Performance of Muscle Models are Aware of IMP				
Rigid Single Fiber	0.8307	0.8621	4.1765	3.1509
Rigid Two Fiber	0.8524	0.8769	5.925	4.349
Compliant Single Fiber	0.8317	0.8556	4.3351	3.2713
Compliant Two Fiber	0.8542	0.8747	4.9922	3.752
Percent Improvement in IMP-Aware vs. IMP-Blind Case				
Rigid Single Fiber	-	1.2%	0.5%	0.1%
Rigid Two Fiber	-	0.71%	0.1%	0.9%
Compliant Single Fiber	-	4.2%	6.8%	12.4%
Compliant Two Fiber	-	0.7%	0.4%	1.2%

DISCUSSION

All muscle models had high average correlations between predicted force and measured IMP. This indicates that while there are infinitely many muscle force solutions, EMG-driven neuromusculoskeletal models can accurately predict muscle forces.

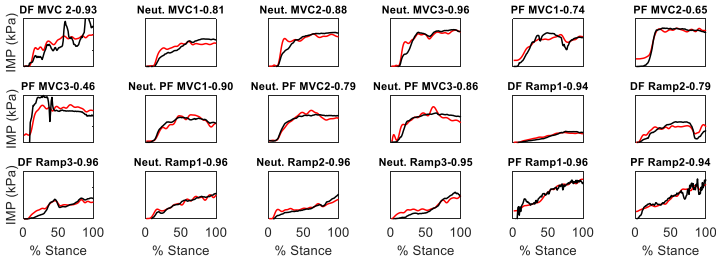

Figure 1: Agreement between scaled predicted tibialis anterior force (red) and measured IMP (black)

This work presents evidence that a two-fiber type model more accurately reflects muscle force production than a single fiber type model. Two-fiber type models had 4% higher correlations with IMP than single fiber type models. This is remarkable because the only difference between the single-fiber and two-fiber models were that the fast and slow twitch fibers in the two-fiber models had separate activations and maximum contraction velocities. These led the two fibers to operate at different points on the force-velocity curve. This provides strong evidence that treating the electromyographic signal as a single signal is not bio-fidelic. Even small changes like assigning two maximum contraction velocities to the high and low frequency components of the EMG signal yielded significant improvements in muscle force matching. However, despite better muscle force matching, two-fiber type models had worse moment matching results than single fiber type models. This may be a result of EMG scaling problems. A single EMG scale term was used to scale both activations in the two-fiber models. At low levels of activation, like those in the antagonist movements used here, fast twitch fibers should be preferentially activated because of the low muscle force required. However, currently both EMGs are proportionally scaled up, leading to an underestimation of the joint moment. Future work will give each fiber separate EMG scaling factors. It is expected that at that point two-fiber models will have better moment matching than their matched single fiber models.

The higher correlations from the two-fiber type models suggest that for muscle producing significant force, a two-fiber type model more accurately represents muscle force production.

Finally, the table shows that adding a cost function term that encourages muscle force predictions to match IMP not only increases force-IMP correlations, but also improves moment matching. This improvement is most significant for compliant tendon models. This supports the idea that IMP is a good surrogate for muscle force predictions because predictions more similar to IMP also yield more realistic moments.

ACKNOWLEDGEMENTS

Funding provided by Cancer Prevention Research Institute of Texas Grant RR170026, NIH grant R01HD31476, and NSF Graduate Research Fellowship Grant No. (1842494)

REFERENCES

[1] Kristensen J, Franklyn-Miller A, *Br J Sports Med*, 46:719-726, 2012
[2] Go, S, et al., *Ann Biomed Eng*, 45:739-46, 2017
[3] Millard M, et al. J. Biomech Eng, 135: 0210051-02100511
[4] Wakeling J, et al. *Ann Biomed Eng* 40:1708-1720, 2012

SB³C2019
Summer Biomechanics, Bioengineering and Biotransport Conference
June 25 -28, Seven Springs, PA, USA

THE EFFECTS OF ANKYLOGLOSSIA ON THE TONGUE MOTILITY OF INFANTS DURING BREASTFEEDING

Yiela Saperstein (1), David Elad (1,2), Andrew F. Laine (1), Scott A. Siegel (3), Catherine Watson Genna (4)

(1) Department of Biomedical Engineering
Columbia University
New York, NY, USA

(2) Department of Biomedical Engineering
Tel Aviv University
Tel Aviv, Israel

(3) School of Medicine/School of Dental Medicine
Stony Brook University
Suffolk County, NY, USA

(4) International Board Certified Lactation Consultant, 8315 98th Street,
Woodhaven, NY, USA

INTRODUCTION

Breastfeeding is universally accepted as being beneficial for infants. During initiation of breastfeeding, the infant latches onto the mother's nipple and areola, and the nipple extends as far as the infant's hard-soft-palate junction (HSPJ). The infant moves his tongue and mandible in an up and down motion to extract milk. As previously reported by our lab, the anterior tongue moves as a stiff body while the posterior tongue exhibits peristaltic motion [1]. Ankyloglossia, also known as tongue-tie, is a condition where the lingual frenulum, that connects the tongue to the bottom of the mouth, is thicker, shorter, or stiffer than usual. This limits the motion of the tongue and can impede feeding. Tongue-tie is currently treated with a frenectomy, a surgical intervention where the lingual frenulum is slightly cut to allow for better motion of the tongue. However, the use of frenectomies for the treatment of tongue-tied infants has been controversial due to the absence of objective measures to indicate the need for a frenectomy. While frenectomies are not highly invasive or risky surgeries, they do cause slight injury and discomfort to infants and should not be performed unless necessary and beneficial [2]. The goal of this study was to objectively quantify tongue kinematics for evaluation of potential parameters that may detect changes and improvements in breastfeeding due to frenectomy.

METHODS

We recruited 6 mothers with tongue-tied infants scheduled for frenectomies. Ultrasound videos were taken with an ultrasound transducer placed under the infant's chin. Mid-sagittal ultrasound clips were recorded for about 10 seconds immediately before and after frenectomy. The experimental protocol has been approved by the IRB committee and mothers signed informed consent. Follow-up surveys were given to caregivers to help assess effectiveness of the frenectomy.

The analysis was conducted on the clearest of the ultrasound video segments from before and after frenectomy using the MATLAB code developed in our lab [1]. First the videos were separated into frames. The palate and tongue were tracked on each frame using the active contours method (i.e., snake). Reduction of noise due to breathing of the mother, infant, and technician was done using registration with respect to the hard palate as the hard palate does not deform during breastfeeding. Polar coordinates were placed on the registered images to allow tracking of the local motion of the tongue along each polar line. This resulted in a time dependent signal of local tongue motility during breastfeeding (i.e., distance vs. time). Then we applied Fast-Fourier transform (FFT) to explore the dominant frequencies, and auto-covariance to analyze the periodicity of tongue motility.

RESULTS

The ultrasound video clips were analyzed using MATLAB. Computation of the infant's tongue-motility about the polar lines was used to represent the local dynamics of the tongue in the mid-sagittal plain. The results shown are from breastfeeding immediately before and after the frenectomy procedure. The time dependent local motility for a representative subject is shown for the anterior (Figs. 1a,b) and the posterior tongue (Figs. 1c,d). The frequency spectrum obtain by FFT is depicted in Figs. 1e, f and the periodicity characteristics obtained by the auto-covariance of the time-dependent motility signal at each tongue location is shown in Figs. 1g, h. The dominant frequencies from both the pre- and post-frenectomies were 2.34 Hz. It can be seen that there was more of a periodic motion evident post-frenectomy in both the anterior and posterior tongue motion and the dominant frequency was more defined post-frenectomy. The representative data shown in Fig. 1 demonstrated improvement after the frenectomy. However, improvements were not seen in all the analyzed scans.

Poster Presentation #P052

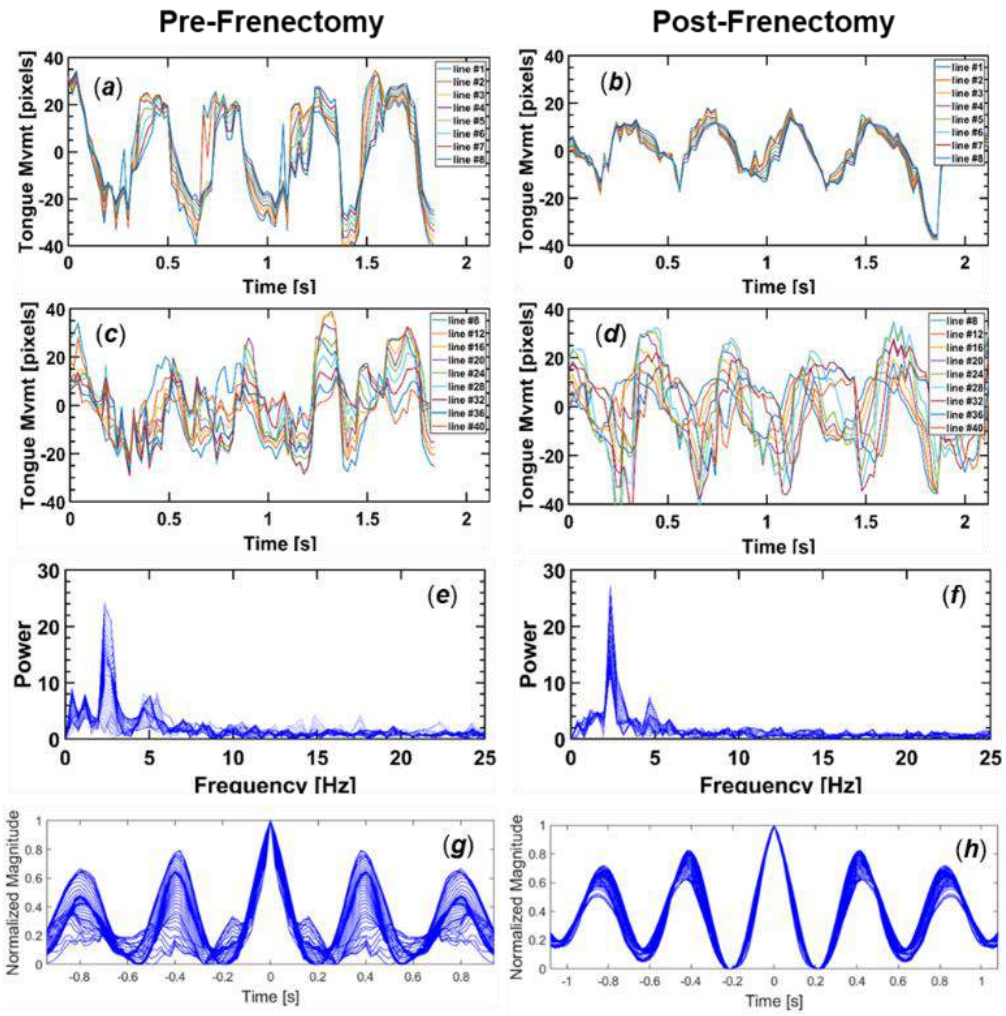

Figure 1: (a, b, c, d) Time dependent signals of tongue motion before and after frenectomy. (a) and (b) Motion of the anterior tongue; (c) and (d) Motion of the posterior tongue; (e) and (f) FFT of the tongue motion; (g) and (h) Auto-covariance of tongue motion.

DISCUSSION

The present study is based on objective analysis of ultrasound video clips recorded during breastfeeding to explore the periodicity of the tied tongue before and after frenectomy. While breastfeeding has been studied through the use of ultrasound in the past [3], the method used here is one of the first to utilize registration with respect to the hard palate in order to reduce the noise and mitigate errors from movement of the ultrasound videos. The hope was that by using a reproducible, quantifiable method of analysis, this would allow us to get closer to objectively answering the long controversial questions: Are there significant differences seen in the tongue motion of tongue-tied babies versus non-tongue-tied babies and if there are differences, is the frenectomy effective in treating these differences?

Other studies have shown improvements due to frenectomies in adults or babies using visual images [4] or by visually analyzing ultrasound videos [3]. This study is different in that it uses a quantifiable and reproducible procedure to analyze the ultrasound videos. However, while the results presented here showed an improvement after frenectomy, this was not apparent in all of the analyzed videos. It is unclear if this is due to the method itself, due to the fact that the post-frenectomy videos were taken immediately after surgery when there may have still been an open wound, or because the frenectomies themselves were unsuccessful. To answer this question, we will use the responses from surveys completed by parents about the improvements in feeding a few weeks after the surgery. This way we can determine if the computational results match the anecdotal evidence.

REFERENCES

[1] Elad, D. Proceedings of the National Academy of Sciences of the United States of America 111 (14), 5230-5235, 2014.
[2] Kummer, A. W. The ASHA Leader 10 (17), 6-30, 2005.
[3] Geddes, D. T Pediatrics. 122. (1), 2007-2553, 2008.
[4] Marchesan, I. Journal da Sociedade Brasileira de Fonoaudiologia, 24(4), 409-412, 2012.

SB³C2019
Summer Biomechanics, Bioengineering and Biotransport Conference
June 25 -28, Seven Springs, PA, USA

DEVELOPMENT OF A COMPUTATIONAL MODEL OF BRAIDED STENT FOR CEREBRAL ANEURYSM TREATMENT

S. Shiozaki (1), T. Otani (1), S. Wada (1)

(1) Department of Mechanical Science and Bioengineering,
Graduate School of Engineering Science, Osaka University,
1-3 Machikaneyamacho, Toyonaka,
Osaka, Japan

INTRODUCTION

The cerebral aneurysm is an abnormal ballooning of the cerebral artery and its rupture causes subarachnoid hemorrhage. In the process of intravascular treatment for the cerebral aneurysm, stent deployment into parent artery of aneurysm is one of popular approaches. There are two types of stents for treatment; laser-cut stent and braided stent, and both of them are mainly used to assist coil embolization to prevent the coil removal to the parent artery. In particular, the braided stent consisting of multiple metallic wires is one recently proposed for expecting high flexibility. Furthermore, it is widely known that deployment of the braided stent can act to divert blood flow in the parent artery from the aneurysm [1].

In clinical use, however, there is a critical issue of the braided stent deployment that incomplete stent expansion often occurs especially in the cases that the deployment into the aneurysm with curved parent arteries [2][3]. This under expansion induces blood flow stagnation in the gap between the stent and the arterial wall, which may promote thrombosis and embolization of the parent artery. Conversely, over expansion of the stent to avoid the stent malfunction brings abnormal contact force to the arterial wall, which might induce arterial inflammation and changes of the arterial shape. To assist surgeons to achieve complete stent expansion with appropriate contact force in each clinical case, understanding of the mechanical characteristics of the braided stent with considering mechanical properties of wires constituting the stent and these mechanical interactions is hopeful.

The present study develops a mechanically-consistent computational model of braided stent. Mechanical behavior of the wires constituting the stent are expressed by a set of beam elements in finite element manner and these multiple contacts with friction are treated in computation. Numerical example demonstrates two cases of the stent deployment simulation with different arterial geometries.

METHODS

Computational stent modeling Here we consider mechanical model of the wire constituting the braided stent. The wire was assumed as a thin slender beam which obeys Kirchhoff's rod theory [4], and thus the elastic energy of the wire per unit length, U is derived by integrating the stretching, bending and torsional elastic energies, given by

$$U = \frac{1}{2}[k_s\varepsilon^2 + k_t(\kappa_1 - {}^0\kappa_1)^2 + k_b(\kappa_2 - {}^0\kappa_2)^2 + k_b(\kappa_3 - {}^0\kappa_3)^2] \qquad (1)$$

where k_s, k_t and k_b is the stretching, torsional and bending stiffness, ε is the axial strain, κ_1, κ_2 and κ_3 is the degree of twist and curvatures and ${}^0\kappa_1$, ${}^0\kappa_2$ and ${}^0\kappa_3$ is those in the reference state. Internal forces of the wire were obtained from eq. (1) based on the minimum energy principle. Each wire was discretized to be a set of two-node beam elements and these deformation including finite rotations was treated by the corotational beam element formulation [5]. Multiple contacts between wire-arterial wall, catheter and wire itself were detected by the method of our previous study [6] and treated by expressing repulsive force in normal direction and tangential frictional force based on [4]. Note that the arterial wall and catheter were assumed to be rigid.

Following these internal and contact forces, algebraic form of the equation of motion of the stent is finally given by

$$\mathbf{M}\ddot{\mathbf{U}} + \mathbf{C}\dot{\mathbf{U}} + \mathbf{F}_{\text{int}}(\mathbf{U}) = \mathbf{F}_{\text{ext}}(\mathbf{U}, \dot{\mathbf{U}}), \qquad (2)$$

where $\mathbf{U}$ is the displacement vector of all nodes of wires, $\mathbf{M}$ is the mass matrix, $\mathbf{C}$ is the damping matrix, $\mathbf{F}_{\text{int}}$ is the internal forces and $\mathbf{F}_{\text{ext}}$ is the contact forces. Stent motion during deployment into arteries was expressed by solving eq. (2) iteratively by explicit Newmark-type predictor-corrector scheme with adaptive time stepping [7].

Poster Presentation #P053

Setup for numerical examples Numerical example of the stent deployment simulation into arteries was conducted. We constructed the braided stent consisting of 24 wires with the diameter of 0.04 mm. Outer dimeter and total length of the stent were set to 5mm and 22.7 mm, respectively, and assumed wires are made from Co-Cr alloy with Young's modulus of 225 GPa and shear modulus of 95 GPa. Each wire was discretized by 100 nodes. An initial state of the braided stent for the numerical simulation is shown in Fig. 1. We set a wire shape at the reference state to the single helical shape with constant curvatures and torsion.

Two cases of stent deployment into arteries were conducted using different arterial geometries with the radius of 4 mm. Idealized arterial geometries of the straight and 2-D curved shapes with the curvature radius of 12 mm were constructed. The catheter was set to be a straight tube with a diameter of 0.7 mm.

The stent was packed into the straight catheter by the method of [8] and this catheter with the stent was set on the centerline of each artery. In case of the 2-D curved artery, the catheter with the stent was quasi-statically deformed to fit the centerline of the catheter to that of the 2-D curved artery. The stent was deployed into each artery by gradually pulling the catheter.

RESULTS

Snapshots of the deployment process of the braided stent into the straight and curved arteries are demonstrated in Fig. 2. The stent was deployed around the arterial wall from the distal end as the catheter was pulled in both cases. In the case of the straight artery, the stent expanded uniformly to the arterial wall from the distal end (Fig. 2 left). On the other hand, in the case of the curved artery, the stent expanded along the inside of the artery and contacted on the inside of arterial wall (Fig. 2 middle-right). After deployment, a gap between the stent and the arterial wall locally occurred outside the curved artery (Fig. 2 bottom-right).

Figure 3 shows the spatial distribution of the contact forces between the stent and the arterial wall. In the case of straight artery, contact forces were distributed locally in the longitudinal direction whereas uniformly in the circumferential direction. On the other hand, in the case of curved artery, contact forces concentrated on the inside of the curved artery. Magnitude and deviations of the contact force in each case was evaluated by box plot (Fig. 4) and these differences were assessed by Mann–Whitney U test. Magnitudes of the contact forces were same order in both cases, whereas that in the case of curved artery was significantly higher than those in the case of straight artery.

SUMMARY

The present study proposed the computational model of the braided stent taking into account of the mechanical characteristics of wires constituting the stent and these mechanical interactions. Two cases of numerical examples of stent deployment in a straight and a curved artery were conducted. Results exhibited that the stent expanded uniformly in the circumferential direction in case of the straight artery whereas located on inside in the case of the curved artery and relatively strong contact force was generated inside of the artery. These results successfully demonstrated that the present computational model of the braided stent is capable to represent mechanical behavior of the stent during deployment into arteries. Moreover, because mechanical properties of the wire can be handled in the present model, the present model has a potential to evaluate effects of number of wires and wire mechanical properties on the mechanical characteristics of the braided stent. For this perspective further numerical experiment may be helpful to improve design of the braided stent and its performance assessment.

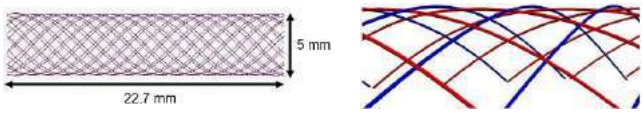

Figure 1: A state of the braided stent. Left: An initial state of the braided stent for the numerical simulation. Right: Braiding details (Red, right-handed helical wires; Blue, left-handed helical wires).

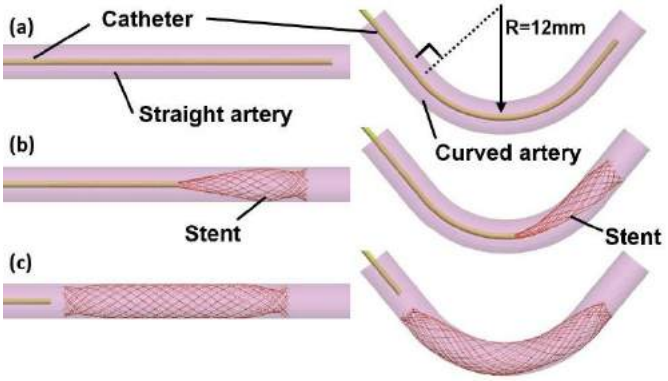

Figure 2: Snapshots of the stent deployment into the straight artery (left) and the curved artery (right).

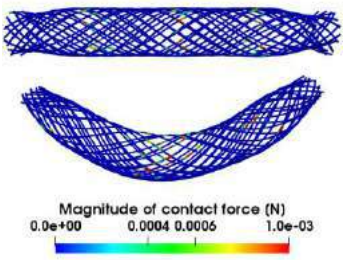

Figure 3: Spatial distribution of the contact force between the stent and arterial wall.

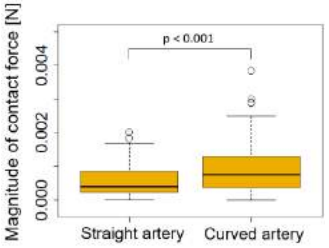

Figure 4: Box plots of the magnitude of contact force.

ACKNOWLEDGEMENTS

We thank Hiroyuki Takao and Soichiro Fujimura for clinical input. This work was supported by research grants from JSPS Grants-in-Aid for Scientific Research (18H18367 to Otani) and MEXT as a Priority Issue (Integrated computational life science to support personalized and preventive medicine) to be tackled by using post-K computer (hp180202 to Wada).

REFERENCES

[1] Mut F and Cebral JR, *Am. J. Neuroradiol.*, 33:2010–2016, 2012.
[2] Heller RS and Malek AM, *J. Neurointerv. Surg.*, 3:340–343, 2011.
[3] Valdivia M, *Neurosurgery*, 64:130–134, 2009.
[4] Vetter R et al., *Epl*, 112:1–6, 2015.
[5] Battini J and Pacoste C, *Comput. Methods Appl. Mech. Engrg.*, 191: 1755–1789, 2002.
[6] Otani T et al., *J. Biomech. Eng.*, 140:041013, 2018.
[7] Zienkiewicz OC and Xie YM, *Earthq. Eng. Struct. Dyn.*, 20:871–887, 1991.
[8] Ma D et al., *J. Biomech.*, 45:2256–2263, 2012.

SB³C2019
Summer Biomechanics, Bioengineering and Biotransport Conference
June 25 -28, Seven Springs, PA, USA

ACCELEROMETERS USED TO MEASURE MAGNITUDE AND FREQUENCY OF HAND MOVEMENT FOR CHILDREN WITH CEREBRAL PALSY DURING CONSTRAINT INDUCED MOVEMENT THERAPY

Brianna M. Goodwin (1), Emily K. Sabelhaus (2), Ying-Chun Pan (3), Kristie F. Bjornson (4), Kelly L. D. Pham (5), William O. Walker (2), and Katherine M. Steele (1)

(1) Department of Mechanical Engineering
University of Washington
Seattle, WA, USA

(2) Rehabilitation Medicine
Seattle Children's Hospital
Seattle, WA, USA

(3) Department of Bioengineering
University of Washington
Seattle, WA, USA

(4) Department of Pediatrics
University of Washington
Seattle, WA, USA

(5) Physical Medicine & Rehabilitation
University of Washington
Seattle, WA, USA

INTRODUCTION

Cerebral palsy (CP) is a non-progressive neurologic disorder of movement and posture that affects approximately 2 in every 1000 children in the United States [1]. Of these children, 40% have unilateral or hemiplegic CP, with abnormal tone, decreased strength, dystonia, and other muscle impairments impacting movement on one side of the body [2].

Constraint-Induced Movement Therapy (CIMT) is an evidence-based treatment for children with hemiplegic CP [3]. CIMT uses a constraint, typically a rigid cast, to restrict motion of the unimpaired hand, forcing the child to use their impaired hand during therapy and daily life. While CIMT has been shown to improve hand function, the protocols are often variable and results are only measured in the clinic [4, 5]. CIMT is both time and resource intensive for the children, their families, and providers. Understanding the extent to which casting influences hand use both in therapy and in daily life, as well as the outcomes after therapy are critical to optimizing treatment protocols.

Wearable technology, including accelerometers, has been used to quantify hand movement and evaluate hand function for both children with CP and adult stroke survivors [6, 7]. The goal of this research was to use accelerometry metrics to quantify hand use in clinical and home environments before, during, and after CIMT for children with CP and compare it to typically-developing (TD) peers.

We hypothesized that (1) impaired hand use would increase during CIMT, both at home and in the clinic, and (2) that increased impaired hand use during CIMT would be associated with enhanced bimanual use in daily activities after CIMT.

METHODS

We recruited seven children with hemiplegic CP undergoing CIMT (age: 6 – 10yr, 5 boys/2 girls) and seven TD children (age: 6-11yr, 1 boy/6 girls) from a pediatric tertiary care facility.

Per the institution's CIMT protocol, the unimpaired hand of each child in the CP cohort was placed in a cast for three weeks. Unilateral hand training of the impaired hand occurred in the clinic for 2 hours/day, 4 days/week. On Fridays, the cast was removed and the children received bimanual training for 2 hours before replacing the cast. The CP cohort wore ActiGraph GT9X Link (*ActiGraph Corp*., Pensacola, FL) tri-axial accelerometers on both wrists for 3 consecutive days during three time periods: 1-week before, during, and 6-8 weeks after CIMT. Functional tests (grip strength, lateral pinch strength, and Box & Blocks) and the Canadian Occupational Performance Measure (COPM) were completed before and after CIMT. Box & Blocks was used to test manual dexterity and the COPM is a ten-point scale, used to assess how satisfied each child felt he/she was meeting their self-identified goals. The TD cohort did not receive therapy, but wore the Actigraph accelerometers on both wrists for three consecutive days at home, on three occurrences temporally aligned with the CP cohort time periods.

Accelerometry data were downloaded using 1-second activity counts and analyzed using the use ratio (UR) and magnitude ratio (MR) [6, 7]. The UR is the amount of active time of the impaired hand divided by that of the unimpaired hand (eqn. 1); it is used to assess frequency of hand use. A UR of one indicates the same frequency of movement between each hand, a number greater than one is indicative of more impaired hand use, and a number less than one indicates more unimpaired hand use. The MR is the natural log of the impaired hand

vector magnitude of acceleration in the three directions (i.e., $x^2 + y^2 + z^2$) divided by that of the unimpaired (eqn. 2). Values outside of the range ±7 were set to ±7 to constrain the range of values, similar to prior research [6]. MR is a metric used previously to describe magnitude of hand use in individuals recovering from neurologic injury [6]. Results were compared using paired t-tests between CIMT subjects and unpaired t-tests to compare between cohorts.

$$UR = \frac{Hours\ of\ Non{-}Dominant/Impaired\ Hand\ Use}{Hours\ of\ Dominant/Unimpaired\ Hand\ Use} \quad (1)$$

$$MR = ln[\left(\frac{Non{-}Dominant/Impaired\ Magnitude}{Dominant/Unimiapred\ Magnitude}\right)] \quad (2)$$

RESULTS

The UR or MR were similar across time periods for the TD cohort, averaging 1.0 +/- 0.0 and -0.3 +/- 0.3, respectively. Before therapy children with CP used their impaired hand less (UR = 0.87 +/- 0.2, p=0.27) and with a lower magnitude (MR = -1.2 +/- 1.2, p=0.19) compared to the TD cohort first data collection (Figure 1).

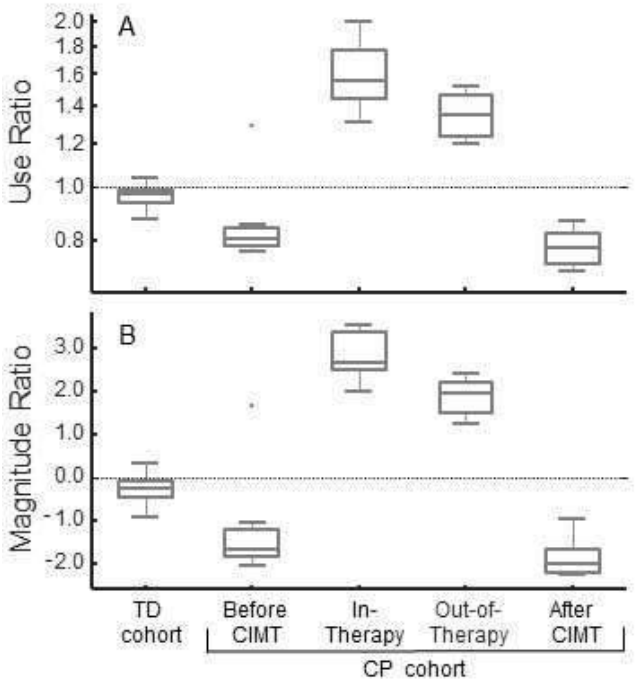

Figure 1: Use ratio (A) and magnitude Ratio (B) for the typically developing (TD) cohort and cohort of children with cerebral palsy (CP), before, In-Therapy (during CIMT while working with a therapist), Out-of-Therapy (during CIMT while doing activities outside of therapy, i.e. school), and after CIMT. The dashed lines represent equal hand use; 1 for the use ratio and 0 for the magnitude ratio.

During CIMT while working with a therapist (in-therapy), frequency and magnitude of movement of the impaired hand compared to the unimpaired hand increased significantly compared to pre-CIMT values, with average in-therapy UR of 1.6 +/- 0.2 (p=0.0003) and MR of 2.8 +/- 0.5 (p=0.0001). Children with CP also significantly increased these values during CIMT while out-of-therapy, with average UR of 1.4 +/- 0.1 (p=0.0004) and MR of 1.9 +/- 0.4 (p=0.0006). However following CIMT, children fall back to baseline values for both frequency (0.8 +/- 0.1, p=0.32) and magnitude (-1.9 +/- 0.4, p=0.30) of impaired hand use.

After CIMT, the CP cohort scored higher on impaired hand functional measures: grip strength increased by 8.3 +/- 7.3 (p=0.05), lateral pinch increased 5.2 +/- 3.5 (p=0.03) and the number of blocks transferred in 60 seconds increased by 4.3 +/- 5.1 (p=0.11) blocks. Furthermore, children rated their performance on being able to reach their self-identified goals by 3.7 +/- 2.4 (p=0.00005) points higher following CIMT (measured by the COPM).

DISCUSSION

The combination of increased UR and MR levels during therapy with increased functional gains following CIMT suggests that children are gaining unimanual skills as a result of CIMT. However, the subsequent drop to baseline values in the accelerometry metrics after CIMT suggests that these gains are not maintained outside of the clinic.

Similar to this study, other studies have shown improved functional scores measured in the clinic [8]. Coker-Bolt and colleagues (2017) performed a similar study, where children with CP wore two accelerometers before and after a 1-week, 30-hour CIMT intervention. The study reported that five of 12 children showed gains in accelerometry values one to two weeks after CIMT [7]. In the present study, all participants returned to baseline values 6-8 weeks after CIMT. These results may suggest that immediately following CIMT there is an opportunity to employ new strategies to help children transfer unimanual skills gained in CIMT into greater impaired hand use outside of the clinic, such as remind-to-move therapy, bimanual interventions, or other interventions.

ACKNOWLEDGEMENTS

We thank the Seattle Children's Hospital Academic Enrichment Fund, Seattle Children's Hospital Occupational Therapists, and the CIMT team for their help integrating this research into clinical care.

REFERENCES

[1] Cans, C et al,. *J Pediatr Child Health*, 18:393-398, 2008.
[2] Holmeffur, M et al., *Dev. Med. Child Neurol*, 41:886-891, 2009.
[3] Novak, I et al., *Dev. Med. Child Neurol*, 55:885-910, 2013.
[4] DeLuca , S C et al., *Pediatr Rehabil*, 10:37-46, 2017.
[5] Brauers, L et al., *Pediatr Rehabil*, 10:11-17, 2017.
[6] Lang, C E et al., *JoVE*, 122, 2017
[7] Coker-Bolt, P et al., *Pediatr Rehabil*, 10:27-36, 2017.
[8] Stearns, G E et al., *NeuroRehabilitation*, 24:95-108, 2009.

SB^{3}C2019
Summer Biomechanics, Bioengineering and Biotransport Conference
June 25 -28, Seven Springs, PA, USA

A Novel Design for Shear Rate Optimization of the Venous-End Anastomosis of an Arteriovenous Graft

Dillon C. Williams (1), Guy M. Genin (2), Mohamed A. Zayed (3), Eric C. Leuthardt (4)

(1) Vascular Surgery Biomedical Research Laboratory
Washington University in Saint Louis
Saint Louis, MO, United States

(2) NSF Science and Technology Center for Engineering Mechanobiology
Washington University in Saint Louis
Saint Louis, MO, United States

(3) Vascular Surgery Biomedical Research Laboratory
Washington University in Saint Louis
Saint Louis, MO, United States

(4) Center for Innovation in Neuroscience and Technology
Washington University in Saint Louis
Saint Louis, MO, United States.

INTRODUCTION

Gradual loss of kidney function typically progresses to end stage renal disease, in which the kidneys are no longer able to filter out excess waste and fluids. To combat the accumulation of toxic levels of waste, electrolytes, and fluids in the body, hemodialysis is performed, in which blood is removed from the arterial system, filtered externally by a dialyzer, then reintroduced into the venous system.

Hemodialysis often requires an arteriovenous graft, a synthetic tube connecting an artery to a vein, as an access site for removal and return of blood. These grafts have relatively high rates of morbidity because they trigger thrombus formation at the venous anastomoses by perturbing blood flow fields beyond the physiological range of vessel wall shear strain rates [1-5]. Wall shear strain rates below the healthy physiological range (<50 1/s) can lead to thrombus formation by allowing coagulation factors to accumulate, while rates above the physiological range (>1000 1/s) can do so by allowing platelet aggregation [6]. Despite these major patient care issues, the role of graft shaping and placement on flow fields has not been quantified, and the possibility that graft design could be tuned to improve these flow fields has not been explored.

We hypothesized that the placement of and shaping of an arteriovenous graft affects the flow fields at the venous anastomosis. We performed a series of computational fluid dynamics simulations that supported this hypothesis. Results revealed ways that arteriovenous graft design can be optimized to reduce risk factors.

METHODS

We estimated the pulsatile flow field of blood in an arteriovenous system with a graft in place through pressure-based, transient computational fluid dynamics (CFD) simulations. A back of the envelope estimate of the Reynolds number, prompted us to use a viscous, laminar model. A series of idealized, straight arteriovenous grafts were constructed in commercial CAD software (DesignModeler, ANSYS, Canonsburg, PA) based upon the typical arterial and venous presentations. The venous attachment was simulated at 90º, 60º, 45º, 30º, 15º and 13º. Additionally, a tailored venous anastomosis was developed, with geometry designed to constrain wall shear rates in the vein to stay within physiological ranges. This was done by modifying the shape on the distal insertion to manipulate the entering arterial blood to have similar dynamics to the venous blood.

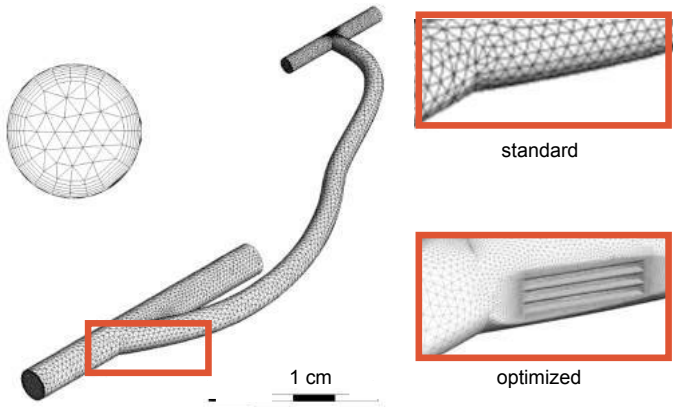

Figure 1: Meshing of the simple arteriovenous graft model

A computational mesh was generated using ANSYS Fluent (ANSYS, Canonsburg, PA). Care was taken to ensure that discretization was not distorted in regions of high curvature and at

edges. For each simulation, mesh size was refined until convergence was reached, following standard procedures [7]. An inflation mesh was set at the wall to ensure complexities at the boundary layer could be resolved. Figure 1 shows the geometry and meshing of the arteriovenous graft model.

Blood was modeled as a non-Newtonian fluid following the Navier-Stokes equation. The Bird-Carreau constitutive law was used to represent the non-Newtonian, pseudo-plastic nature of blood, as is appropriate for oscillatory flow with high Wormersley number. The inlet condition for the artery was based on velocity wave forms measured in the radial and brachial arteries [8] [9]. For the arterial and venous outlets an outflow boundary condition was used to model the. downstream effects that are present in the circulatory [10] [11].

RESULTS

Blood entering a vein from an arteriovenous graft perturbed the venous flow fields. These perturbations varied with anastomosis. For severe angles, boundary layer separation occurred immediately distal to the anastomosis, This lead to pathologically low shear rates at the location on the vein wall. Elevated shear strain rates were evident near the distal end of the graft insertion. The incidence of pathological flow fields could be modulated by altering the anastomosis entry angle (Figure 2), including undesirable features such as high shear rate at the distal end of the graft and boundary layer separation on the vein wall.

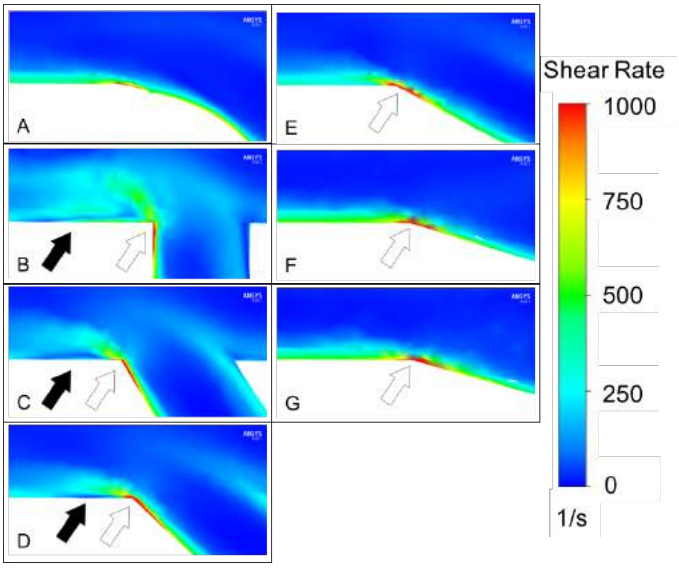

Figure 2: Cross sectional view of the various venous anastomoses showing the blood shear strain rate fields 30%of the way through the cardiac cycle. (a) Graft following optimization. (b) 90°, (c) 60°, (d) 45°, (e) 30°, (f) 15°, and (g) 13°. White arrows, peak shear strain rates on the wall; black arrows, flow separations

To quantify the degree to which blood flow was perturbed pathologically over one heart beat, the shear strain rate was recorded at each of the mesh cells on the vein wall for each time point, normalized with respect to area, and visualized on a histogram (These normalized distributions revealed an important role for the insertion angle in determining the fraction of the vein wall that experienced pathological shear strain rates. As evident from the logarithmic representation of area fraction in Figure 3, a, the small fraction of blood flow that was outside of the physiological range increased as the venous anastomosis insertion angle increased to 90º.

The analysis of standard venous anastomoses indicated that standard graft design cannot introduce arterial blood into the venous system without creating areas of excessively low and excessively high wall shear rate. We studied an optimized anastomosis. For this design, an intact boundary layer was maintained. Data in Figure 3 suggested that the optimized anastomosis reduced instances of shear rate outside the physiological range.

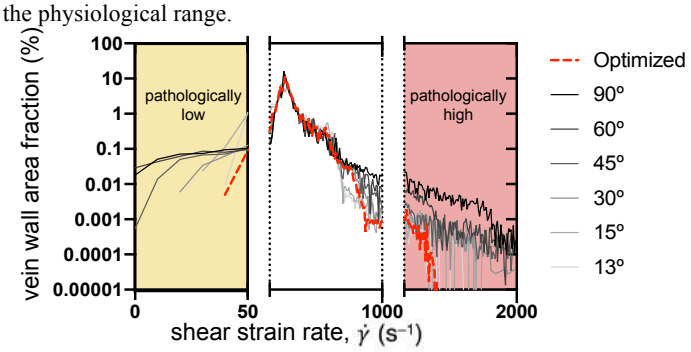

Figure 3: Shape optimization ameliorates pathological flow fields.

DISCUSSION

The shear strain rate fields at the vein wall play an important role in maintaining vessel health. Prior work has shown that shear rate above and below the physiologically healthy range can lead to thrombosis. The implantation of a foreign artifact such as a graft creates an environment that is at risk for wall shear strain rates in the pathological range. We showed here that the passage of arterial blood flow could be controlled by the specific geometry of an anastomosis to reduce the prevalence of pathological wall shear strain rate. These results are important as they show that anastomosis insertion angle, an aspect of graft implantation that a physician typically has control over, has a direct impact on shear environment. Insertion angle optimization can reduce the incidence of pathologically high and low shear rates on the venous walls

Even following anastomosis insertion angle optimization, the flow fields could not be tailored to eliminate all unhealthy shear. The unique optimized anastomosis, however, maintained the boundary layer across the threshold from the graft to the vein wall, and substantially reduced the vein wall area over which pathological shear strain rates were observed. Results support the idea that relatively minor changes to graft design can make substantial progress towards achieving safer grafts.

ACKNOWLEDGEMENTS

This work was supported in part by the US National Science Foundation through the NSF Science and Technology Center for Engineering MechanoBiology, grant CMMI 1548571.

REFERENCES

[1] Akoh, J. A., 2009. *J Vascular Access,* 10(3), 137–147.
[2] Bell, D. D.,1988. *Archives of Surgery,* 123(9), 1169–1172.
[3] Shen, F., 2008 *Arterio Thromb Vasc Bio,* 28(11), 2035–2041.
[4] Neeves, K., 2010. *Biophys J,* 98(7), 1344–1352.
[5] Ruggeri,Z.M.,2007. *Thrombosis Research,*120, S5–S9.
[6] Stalker, T. J., 2014. *Current Opinion in hematology,* 21(5), 410.
[7] Inc., A., 2009. *Fluent User's Guide*. Canonsburg, PA: Ansys Inc.
[8] Azhim, A., 2008. *J Biomed Pharmaceutical Eng,* 2(1), 1–6.
[9] Hughes, A. D., , 2008. *Hypertension,* 51(6), e45–e46.
[10] Vignon-Clementel, I. E.,2010. *Copm Meth Biomech* B*iomed Eng,* 13(5), 625–640.
[11] Van Canneyt, K2013. *J Biomech,* 46(2), 345–353.

SB³C2019
Summer Biomechanics, Bioengineering and Biotransport Conference
June 25 -28, Seven Springs, PA, USA

FLOW THROUGH SOFT TISSUE EQUIVALENTS: MEASURING THE HYDRAULIC PERMEABILITY OF COLLAGEN GELS

Christopher S. Vidmar, Brittany L. Fisher, Victor K. Lai

Department of Chemical Engineering
University of Minnesota-Duluth
Duluth, MN, USA

INTRODUCTION

Interstitial flow is a vital phenomenon in physiology. Interstitial flow helps the transport of nutrients and wastes between cells [1], helps lymphatic regeneration [2], and affects the production rates of vascular smooth muscle cells [3]. Understanding the roles and processes of interstitial flow will aid in drug delivery and can be used in the advancement of tissue engineering, where the permeability of these tissue equivalents affects the transport of nutrients through the tissues. Despite this significance, little is understood about fluid flow through the interstitium. Specifically, fibrous materials in the interstitium create a high resistance to hydraulic flow [3]. Collagen is one of the primary fibrous materials in the interstitium. There are many models that estimate the permeability of collagen gels, such as the Carmen-Kozeny equation [4], Happel's model [5], and more complex computational models [6]. However, there are very few reported experimental values of collagen permeability. One such example is [7], where the hydraulic permeability of collagen was measured as a function of collagen concentration. To our knowledge, however, such permeability studies have not been extended to investigate other variables such as collagen fiber alignment or other fiber types (e.g. fibrin, collagen-fibrin co-gels). Here, we present a method for measuring the hydraulic permeability of a collagen gel. This experimental setup can be modified to account for other variables, such as collagen densities, fiber alignments and pressure dependence.

METHODS

Apparatus: Figure 1 shows the experimental setup made of a 30" long, ½" diameter PEX tubing calibrated to measure the change in height. A valve controls the volumetric flow rate through the sample. A smaller piece of PEX tubing holding the sample is connected to the bottom of the valve. The top of the apparatus is filled with water.

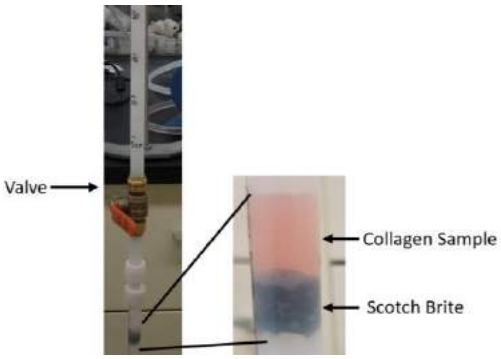

Figure 1. Apparatus used to determine permeability. Full length of the PEX tubing is not shown for clarity

Collagen Type I Preparation: 4 mL of 1.98 mg/mL collagen type 1 was prepared. In a 15 mL centrifuge tube, 816 µL of 1M HEPES buffer solution, 104 µL of 1M NaOH, 400 µL 10x of Minimum Essential Medium Eagle (MEM), and 40 µL of 200 mM L-Glutamine. 2640 µL of 3mg/mL collagen I rat tail (ThermoFisher Scientific, Waltham, MA) was added with a frozen pipette. The solution was mixed and transferred to a 4", ½" diameter PEX tube with parafilm one on end. The gel was incubated at 37ºC for 30 minutes before testing.

Permeability measurement: A piece of Scotch-Brite™ is rolled up and placed in the bottom tube. Water flows through the apparatus as the change in height versus time is measured. To find hydraulic permeability (κ), the hydraulic resistance (R) of the Scotch-Brite™ is determined using Darcy's Law (eq. 1):

$$Q = -\frac{\kappa A}{\mu L}\Delta P = \frac{1}{R}\Delta P = \frac{1}{R}\rho g \Delta h \quad (1)$$

Where Q is the volumetric flow rate, μ is the viscosity of water, A and L is the cross-sectional area and length of the sample respectively, ΔP is the pressure change, $\rho$is the density of water, g is gravitational acceleration, and Δh is the change of the water height. The volumetric flow rate can be written as the change in height per unit time (eq. 2):

$$Q = \frac{dV}{dt} = A\frac{d(\Delta h)}{dt} = \frac{1}{R}\rho g \Delta h \quad (2)$$

Combining eq. (1) and (2), this differential equation can be solved to give eq. (3):

$$\Delta h = \Delta h_0 \exp\left(\frac{-\rho g t}{R*A}\right) \rightarrow \ln(\Delta h) = \frac{-\rho g}{R*A}t + \ln(\Delta h_0) \quad (3)$$

Once the resistance of the Scotch-Brite™ is determined, the Scotch-Brite™ is transferred to the PEX tube containing the collagen sample. The collagen is moved to sit above the Scotch-Brite™ to hold the collagen in place. The height of the collagen sample is measured. Water is run through the sample, compressing the collagen sample until the collagen reaches a steady height. The collagen is then measured before and after the tests to ensure there is negligible compressive effect during the tests. Nine total runs are done for the collagen sample. The hydraulic resistance acts in series, allowing for the calculation of the hydraulic resistance of the collagen ($R_{collagen}$) from the resistance of the Scotch-Brite™, $R_{Scotch\text{-}Brite}$:

$$R_{series} = R_{scotch\ brite} + R_{collagen} \quad (4)$$

Comparison with Happel's model: The calculated permeability is compared to Happel's model for flow through an array of cylinders using the following equations [5]:

$$\kappa = \frac{2}{3}k_{\perp} + \frac{1}{3}k_{\parallel} \quad (5)$$

$$k_{\perp} = \frac{a^2}{8}\left[\frac{1}{\sigma}ln\left(\frac{1}{\sigma}\right) - \frac{1}{\sigma}\frac{1-\sigma^2}{1+\sigma^2}\right] \quad (6)$$

$$k_{\parallel} = \frac{a^2}{8}\left[4 - \sigma + \frac{1}{\sigma}\left\{2ln\left(\frac{1}{\sigma}\right) - 3\right\}\right] \quad (7)$$

Where $k_{//}$ is the flow through parallel cylinders, $k_{\perp}$ is flow through perpendicular cylinders, a is the collagen fibril radius of 50 nm and σ is the solid volume fraction. The compressed collagen was estimated to have a concentration of 9.9 mg/mL, and a σ value of 0.007 was found using a bulk collagen density of 1.41 g cm^{-3}.

RESULTS

Permeability Measurements: A representative plot of ln(Δh) versus time is shown in Figure 2 below. The data is fitted with a linear trendline according to Eq. (3). The slope from the Figure 2a (left) is combined with equation 4 to calculate flow resistance of Scotch-Brite™, allowing for the permeability to be found, which was 2.1651×10^{-10} m^2. The slope from Figure 2b (right) is used to calculate the total hydraulic resistance. The resistance due to the collagen sample can then be found through equation 4, and the permeability of the collagen sample was found to be $9.49 \times 10^{-11} \pm 2 \times 10^{-11} m^2$.

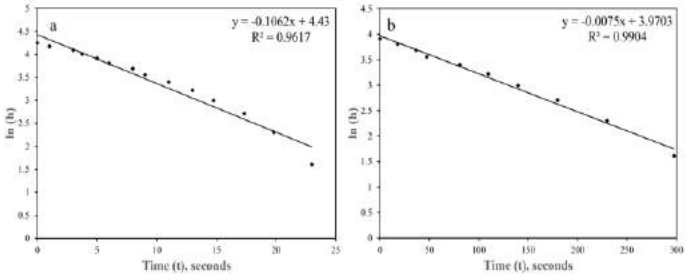

Figure 2. ln(height) versus time for a sample of just Scotch-Brite™ (left) and of one containing both Scotch-Brite™ and collagen (right). The permeability of the collagen gel, $9.49*10^{-11}$ m^2 is calculated from the slope of the right graph.

Comparison with Happel's Model and Other Works: Figure 3 shows a large discrepancy between all three methods, as the permeability values are orders of magnitudes away from each other.

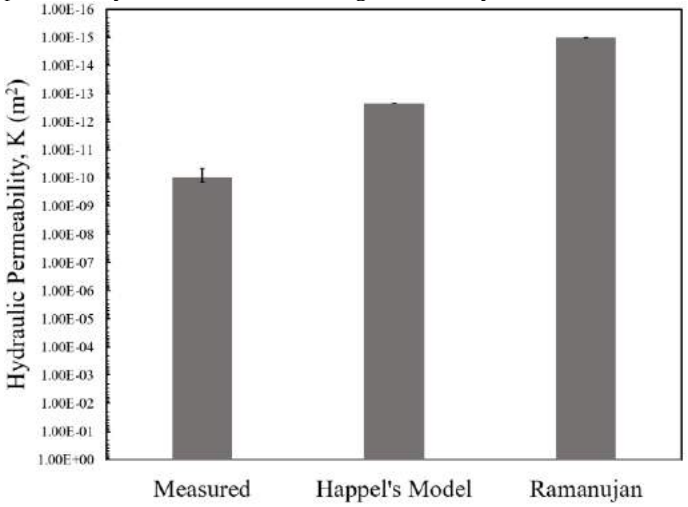

Figure 3. Graph comparing permeability values. The measured value reported here is higher than both Happel's Model and the one reported by Ramanujan, et al. [7]

DISCUSSION

The permeability of Scotch-Brite™ was calculated to be $2.16 \times 10^{-10} m^2$, which is on the same order of magnitude as the literature value of 5.03×10^{-10} m^2 [8]. It is unknown how tightly wound the Scotch-Brite™ was while in the apparatus, which could lead to some variations with the permeability values.

The discrepancy with the Happel model could be due to the assuming that the collagen fibers are an array of rigid cylinders, which does not accurately replicate the collagen network. In addition, the Happel model does not account for molecular interactions between the collagen fibers and the fluids. The discrepancy seen with the value reported in Ramanujan, et al. could be due to different gel preparation techniques, which may drastically alter the network morphology (e.g. connectivity, fiber diameter, etc.). For the experimental set-up described here, near-wall flow likely contributed to a higher permeability. The major discrepancies seen in Figure 3 suggest the need for more accurate methods to experimentally determine collagen permeability to validate the various predicated values from theoretical models.

ACKNOWLEDGEMENTS

This work is supported by the University of Minnesota-Duluth Chancellor's Faculty Small Grant.

REFERENCES

[1] O'Brien F, et al., *Technology and Health Care.* 15(1):3-17, 2007.
[2] Boardman KC, et al., *Circ Res.* 92:801-808, 2003.
[3] Wang S, et al., *Arteriosceler Thromb Vasc Biol.* 20:2220-2225, 2000
[3] Levick JR., *Q J Exp Physiol.* 72(4):409-437, 1987.
[4] Swartz MA, et al., *Annu. Rev. Biomed. Eng.* 9:229-256, 2007
[5] Serpooshan V, et al., *Acta Biomaterialia* 6:3978-3987, 2010.
[6] Stylianopoulos T et al. *Phys Fluids.* 20(12):123601, 2008.
[7] Ramanujan S, et al., *Biophys.* 83:1650-1660, 2002.
[8] Okonkwo K. *University of Delaware.* 1-96, 2010.

SB³C2019
Summer Biomechanics, Bioengineering and Biotransport Conference
June 25 -28, Seven Springs, PA, USA

EFFECT OF DIFFERENT INLET VELOCITY PROFILES ON PATIENT-SPECIFIC CFD SIMULATIONS OF HEALTHY TRACHEA

Bipin Tiwari (1), Tarun Kore (2), Sandeep Bodduluri (3), Surya P. Bhatt (3), Vrishank Raghav (1)

(1) Department of Aerospace Engineering
Auburn University
Auburn, Alabama, USA

(2) Department of Chemical Engineering
Auburn University
Auburn, Alabama,USA

(3) UAB Lung Imaging Core and Division of
Pulmonary, Allergy and Critical Care Medicine,
University of Alabama at Birmingham,
Birmingham, Alabama, USA

INTRODUCTION

Expiratory central airway collapse (ECAC), defined by >50% collapse of large airways during expiration, resulting from either cartilaginous weakening or redundancy of the posterior membranous wall of the trachea, is an increasingly recognized disorder associated with cigarette smoking and chronic obstructive pulmonary disease (COPD) [1]. Pathophysiology of ECAC is multifactorial and the biomechanics of airflow in the trachea could be an important factor resulting in the progression of the disease. With improving our understanding of ECAC as the motivation, this study aims to establish a computational methodology to comprehensively investigate the biofluid mechanics in healthy and diseased patient-specific trachea.

Studying the airflow characteristics in human airways has gained a renewed interest in recent years due to potential patient treatment options. Understanding fluid mechanics of airflow remains a challenge due to the complexity of human lungs and their individual characteristics. Computational fluid dynamics (CFD) simulation is one way to study and understand the flow through complex airways [2]. While earlier CFD investigations adopted engineering simplifications such as idealized geometry, advancement in computational efficiency and noninvasive technology now allow researchers to study respiratory flows in a patient-specific manner [3]. Previous studies have utilized patient-specific trachea models with various mesh sizes, use of flow extensions, and a wide range of inlet and outlet boundary conditions [2,3,4]. However, none of the studies have conducted the assessment and comparison of CFD simulations of respiratory flow with the use of different velocity profiles as the inlet boundary condition.

In this study, we specifically explore the effects of different idealized inlet flow assumptions on CFD simulations using patient-specific trachea models. We aim to ascertain if the velocity profile affects the CFD-derived wall shear stress (WSS) results from the trachea. We compare the simulations in patient-specific tracheas to discern the differences in the wall shear stress parameters with different flow conditions at the inlet. Thus, the objective of the present study is two-fold, to simulate 1) nominal tidal flow (tidal breathing) as shown in Figure 1a and 2) steady flow both using the different inlet velocity conditions of a flat profile as seen in Figure 1b and a parabolic profile as seen in Figure 1c. We aim to compute flow field metrics such as wall shear stress variations along with Time-Averaged Wall Shear Stress (TAWSS) and Oscillatory Shear Index (OSI) from these simulations.

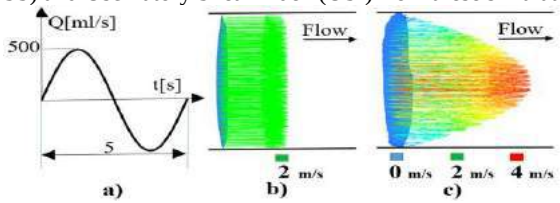

Figure 1: a) Tidal flow; b) Flat profile; c) Parabolic Profile

METHODS

Geometry Extraction and Processing: The 3D geometry of five patient-specific healthy tracheas obtained from the computed tomography (CT) scans were smoothed and clipped with 3D slicer (V4.8.1; www.slicer.org) as shown in Figure 2a. The processed model was saved into Standard Tessellation Language (STL) format. Then, Solidworks (solidworks corp., Waltham, USA) was used to simplify the inlet and outlet boundaries of the trachea model as shown in Figure 2b.

CFD Methodology and Boundary Conditions: The trachea model was imported to ICEM CFD (ANSYS Inc.,Pennsylvania,USA) where an unstructured mesh was generated with a mixture of prism and tetrahedral elements using the octree mesh method as shown in Figure 2c. The prism boundary layer having 6 concentric rows with a growth

factor of 1.11 was used. Depending on the size of the trachea model, the number of elements varied from 600,000 to 1,000,000 and the element size was set around 1% of the inlet diameter. The file from ICEM CFD was exported to fluent format for use in flow simulations.

ANSYS-Fluent (ANSYS Inc.,Pennsylvania,USA) flow solver was used for steady and transient laminar flow model simulations. The boundary condition for the inlet portion which is near the mouth was given a velocity boundary condition using a user defined function (UDF) and an outlet condition was prescribed with a pressure of 1 atm. The velocity boundary condition was selected from the healthy adult data having tidal volume of 500ml with 12 breaths per minute [5]. From this data from a healthy adult, a blunt (flat profile) and a parabolic profile velocity boundary condition was formulated and implemented for two different simulations in both steady and transient case. A pressure-based solver with a simple pressure-velocity coupling scheme and a second order spatial discretization of pressure and momentum was used for each simulation in ANSYS-Fluent. Continuity and velocity residuals values were set to $1 \times e^{-3}$ as a convergence criterion.

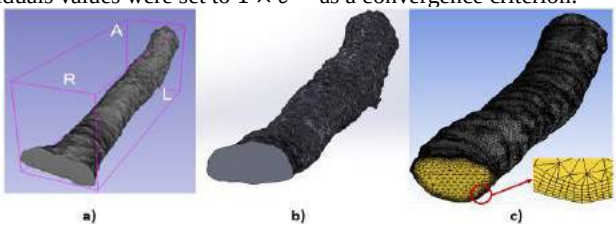

Figure 2: a) Smoothed and clipped trachea geometry with 3D slicer; b) Simplified geometry with Solidworks; c) Mixture of prism and tetrahedral elements with details of prism layers

Metrics Evaluated: WSS and TAWSS parameters were calculated using the definitions shown below and the spatial average was obtained for each case. After, all of the 5 patient case values were averaged for comparison between steady flow and tidal flow. The overall distribution of OSI through the trachea wall was used to qualitatively assess the oscillatory nature of the flow.

$$\vec{\tau}_w(\mathrm{WSS}) = \mu \frac{\partial u}{\partial y} \quad (1)$$

$$\mathrm{TAWSS} = \frac{1}{T}\int_0^T |\vec{\tau}_w| dt \quad (2)$$

$$\mathrm{OSI} = 0.5\left(1 - \frac{\left|\int_0^T \vec{\tau}_w \, dt\right|}{\int_0^T |\vec{\tau}_w| dt}\right) \quad (3)$$

RESULTS

Figure 3 below illustrates the steady flow simulation of the wall shear stress variation in a flat and parabolic inlet velocity profiles for one of the five cases. The spatial average of the WSS over the trachea was calculated to be 0.05 Pa (flat profile) and 0.08 Pa (parabolic profile) for the case shown in Figure 3, which is a 60% difference in average wall shear stress between the inlet conditions.

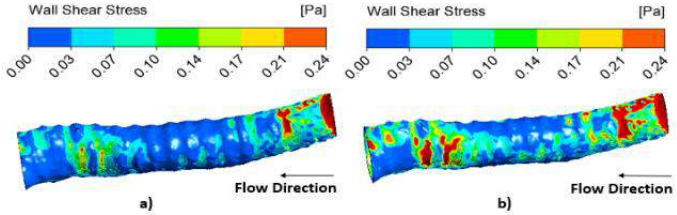

Figure 3: Wall shear stress variation in steady flow simulation a) Flat Profile; b) Parabolic Profile

Figure 4 illustrates the time-averaged wall shear stress (TAWSS) and oscillatory shear index (OSI) variation for a flat and a parabolic velocity inlet boundary condition for the same case as in Figure 3. The spatial average of TAWSS over the trachea was calculated to be 0.03 Pa (flat profile) and 0.05 Pa (parabolic profile) for the case shown in Figure 4, which is a 67% difference between the inlet conditions. Qualitatively, it was observed that the OSI was higher for the parabolic inlet conditions (Figure 4b) than for the flat inlet conditions (Figure 4a).

The spatially averaged WSS and TAWSS for all 5 cases were averaged and tabulated in a bar graph as seen in Figure 5. Furthermore, the overall results of steady flow WSS is greater than the tidal flow TAWSS for both flat and parabolic profile velocity inlet conditions.

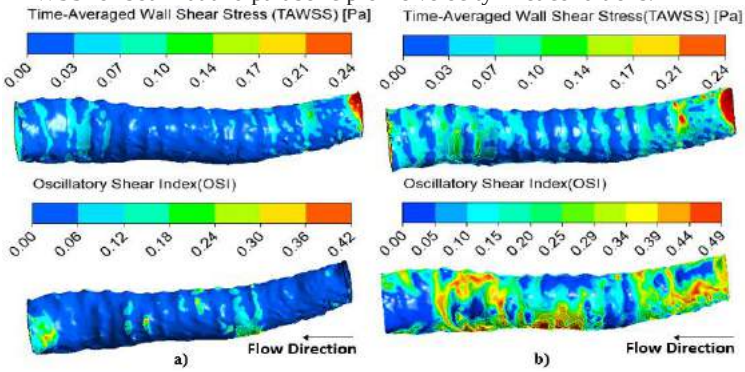

Figure 4: TAWSS and OSI variation in tidal flow simulation a) Flat profile; b) Parabolic profile

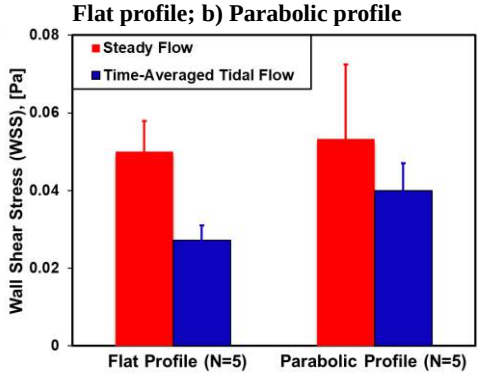

Figure 5: Comparison showing TAWSS and WSS averaged over 5 healthy tracheas

DISCUSSION

In this study, it is observed that the use of a simplified velocity profile influences the WSS, TAWSS and OSI results for both steady and tidal flow cases. Using different inlet profiles as boundary conditions, produces variations in the wall shear stress distribution (Figure 4 and 5) which could prove important for understanding patient breathing flow dynamics. The current study distinguishes the flow metrics like WSS, TAWSS and OSI for different inlet conditions and distribution patterns from those described in previous studies [3]. This type of study where processing medical imaging and integrating with CFD analysis for derivation of flow field metrics will help improve the better understanding of airflow dynamics through patient-specific tracheas. While this study is a good first step, there are some limitations. First, the bifurcation at the carina was not considered and it could have an influence on the results obtained. Second, the compliant nature of the trachea was not modeled and a rigid trachea was used for this study.

REFERENCES

[1] Carden, KA et al. Chest, 127:984-1005, 2005
[2] Sul, B et al., Comput Biol Med, 52:130-143, 2014
[3] Malve, M et al., Comput Methods Biomech 16:198-216, 2013
[4] Horsefield, K et al., J Appl Physiol, 31:207-217, 1971
[5] Qi, S et al.,Comput Math Methods Med, 2017

SB³C2019
Summer Biomechanics, Bioengineering and Biotransport Conference
June 25 -28, Seven Springs, PA, USA

QUANTIFYING DISTORTION ENERGY IN COLLAGEN MATRICES SUBJECTED TO COMPLEX LOADS USING A BIAXIAL BIOREACTOR

Katherine A. Hollar, Danielle N. Siegel, John B. Everingham, Abdullah Ahmad, Alvaro Morfin, Dr. Gunes Uzer, Ph.D., Trevor J. Lujan, Ph.D.

Department of Mechanical & Biomedical Engineering
Boise State University
Boise, ID, USA

INTRODUCTION

Mechanical loads, such as tension, compression, and shear, can stimulate growth and remodeling in musculoskeletal soft tissues. In order to test and validate theories that describe this mechanobiological response, bioreactors have been designed to apply various loading conditions to cellularized constructs during an *in vitro* culture period. Conventional bioreactors are limited to applying mechanical loads along one preferred axis [1, 2], but biaxial bioreactors can simultaneous apply tensile and compressive loads, which mimic the physiological loading environment of connective tissue. A novel application of biaxial bioreactors is to apply controlled states of planar stress in order to study the effect of strain energy, which is the stored energy from deformation, on cellular behavior. Furthermore, strain energy can be decomposed into hydrostatic and distortion (deviatoric) energy, which is related to volume change and material distortion, respectively. Tissue distortion has been linked to changes in the structure and function of tendon and ligament [3], yet the specific impact of distortion energy on tissue remodeling has not been quantified due to challenges in applying targeted levels of strain energy to cellular constructs. Therefore, a need exists to develop an experimental methodology that can apply varying levels of distortion, while maintaining a constant strain energy density, to understand how distortion specifically influences the cellular activity, matrix structure, and mechanical function of cellularized constructs. By identifying the specific mechanical mechanisms that trigger cells to remodel and repair, scientists and physicians will be better able to treat and prevent connective tissue disorders.

The objective of this research is to validate a novel method of subjecting 3D collagen constructs to differing magnitudes of distortion energy while maintaining a targeted strain energy density. We hypothesize that combined loads will increase distortion energy relative to single tensile or compressive loads.

METHODS

Setup. The biaxial bioreactor consists of a horizontal and vertical actuator to apply tensile and compressive forces, respectively, a culture chamber to contain specimens of varying lengths, and a camera housed at the base of the bioreactor for tracking localized specimen deformation (Fig. 1). To control the applied tensile and compressive forces, a custom LabVIEW program was previously developed using a force feedback control loop to dynamically regulate the position command sent to the bioreactor actuators [4].

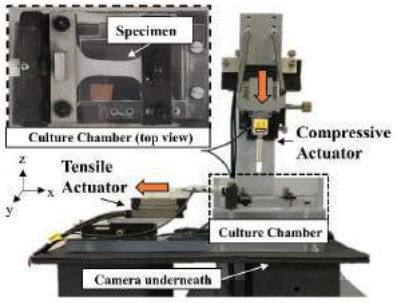

Figure 1: Biaxial bioreactor.

Construct Preparation and Applying Complex Loads. Type-I collagen sponges (DSM, Exton, PA) were speckled with water insoluble black ink using a commercially available DIC stamp (Correlated Solutions, Irmo, SC). The sponges (n = 3) were then cut into dog-bone shaped specimens using a custom designed punch and hydrated in water overnight. Once fully hydrated, the specimens were subjected to five different loading conditions: only tension (*T*), only compression (*C*), equal tension and compression (*T/C*), compression with low magnitudes of tension (*LT/C*), and tension with low magnitudes of compression (*T/LC*) applied by the bioreactor. Before testing, specimen dimensions were measured. Preloads of 0.05 N in tension and 0.025 N in compression were applied, depending on the loading condition. Friction was reduced between the tissue platform of the bioreactor and the

specimen interface by applying a clear, biocompatible lubricant (Miller-Stephenson Chemical Company, Danbury, CT). Engineering stress, σ, was calculated along the x- and z- axes using force sensor data (σ_y=0). Engineering strain, ε, was calculated along the x- and y-axes by tracking the speckle patterns on the specimens using digital image correlation (DIC; Fig. 2), while strain along the z-axis was determined based on encoder values from the compressive actuator.

Specimens were preconditioned in tension for ~900 cycles to apply tensile strains between 6-8%. At the end of preconditioning, the tensile elastic modulus was calculated as the stress-strain slope, where the average strain was calculated from DIC in the region of interest (ROI; Fig. 2). Strain energy density was determined as the area under this stress-strain curve (Fig. 3A). Next, the compressive loading condition was applied to the same specimen and the compressive modulus was measured. Using the compressive modulus, a compressive force was selected to apply the targeted strain energy density measured in tension. For the combined loading *T/C* group, the tensile modulus and compressive modulus were used to select tensile and compressive forces that each applied half of the total targeted strain energy density. In addition, the tensile and compressive forces for the *T/LC* group were selected to equal 2/3 and 1/3 of the total targeted strain energy density, respectively. Similar calculations were then conducted for the *LT/C* group. The loading conditions for these tests can be plotted with respect to principal planar stresses, σ_A and σ_B (Fig. 3B). For all loading conditions, additional tests were performed to minimize the percent error between the actual and targeted strain energy density by adjusting the applied forces. To calculate distortion energy, total strain energy density, *W,* was decomposed into hydrostatic and distortion components (Eq. 1). A one-way ANOVA with a Tukey-Kramer post-hoc test was used to detect differences in distortion energy between the five loading conditions. A paired samples t-test was used to determine whether test iterations reduced the error in applying targeted strain energy values.

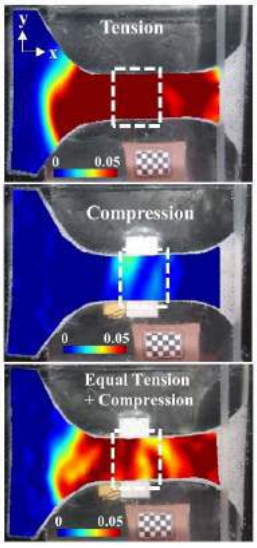

Figure 2: Strain maps for three types of loads (white dashed line = ROI).

$$W = \frac{1}{2}(\boldsymbol{\sigma}:\boldsymbol{\varepsilon})_{hydrostatic} + \frac{1}{2}(\boldsymbol{\sigma}:\boldsymbol{\varepsilon})_{distortion} \quad (1)$$

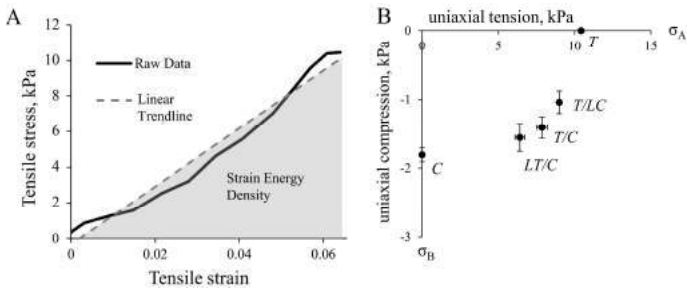

Figure 3: Bioreactor methods. A) Representative stress-strain plot. B) Principal planar stresses (σ_A, σ_B) for all loading conditions.

RESULTS

The bioreactor was able to accurately apply a single magnitude of strain energy density to specimens that were subjected to various loading conditions (Fig. 4A). The average error in applying a targeted strain energy density was reduced from 11 ± 4% to 4 ± 3% when using an iterative approach (Fig. 4A; p = 0.002). The combined loading conditions experienced the greatest distortion energy, where these groups were on average 53% and 160% greater than the only tension and compression group, respectively (Fig. 4B). However, only the compression group was determined to be significantly different than the combined loading conditions ($p < 0.05$).

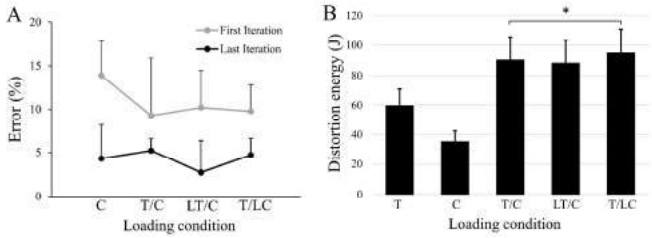

Figure 4: Bioreactor results. A) Error in applying the targeted strain energy density determined from only tension tests to four other loading conditions. B) Distortion energy (* = significantly greater than compression).

DISCUSSION

In this study, strain energy density was successfully controlled in collagen matrices subjected to different loading conditions in a biaxial bioreactor. These results demonstrate that the bioreactor can be used to accurately control the application of planar stress for varying amounts of distortion while maintaining a constant strain energy density (Fig. 3B). Distortion energy was largest for combined planar loads, which supports our hypothesis and is consistent with mechanical theory. However, there was little variation in matrix distortion between the combined loading conditions, which suggests that distortion is insensitive to varying magnitudes of simultaneously applied tensile and compressive loads.

To our knowledge, this is the first experimental study to 1) control total strain energy density in a localized region of a 3D construct and 2) measure distortion energy in 3D constructs. This required the novel implementation of an algorithm to predict the strain energy density being applied in a ROI based on moduli values. In order to measure the actual strain energy density in the ROI, where planar stresses were applied, a camera was inserted under the bioreactor. Using DIC, we were thus able to confirm that tension was homogenously transferred through the gauge region of the construct while compression was simultaneously applied (Fig. 2). This study gives us confidence that we can apply controlled levels of shear (i.e. distortion) throughout the volume of a ROI in a 3D matrix. More importantly, these results will allow us to test new mechanobiology theories based on strain energy, which can potentially unify existing theories that only account for single directional loads (i.e. only tension, only compression) [5]. A future experiment will use this newly validated method to investigate the effect of dynamic distortion on fibroblast-seeded constructs during culture.

ACKNOWLEDGEMENTS

Funding kindly provided by grant NIGMS #P20GM109095.

REFERENCES

[1] Nirmalanandhan, V.S. et al., *Tissue Eng Part A*, 14:1883-1891, 2008. [2] Juncosa-Melvin, N. et al., *Tissue Eng*, 12:2291-2300, 2006. [3] Ko, K.S. et al, *J. Biol. Chem.*, 276:35967-35977, 2001. [4] Everingham, J.B. et al., *WCB*, 2018. [5] Peterson, A. et al., *Tissue Eng Part A,* 18:1804-1817, 2012.

SB^{3}C2019
Summer Biomechanics, Bioengineering and Biotransport Conference
June 25 -28, Seven Springs, PA, USA

AN INTERCALATING CROSSLINKABLE AND BIOCOMPATIBLE HYDROGEL SYSTEM FOR RESURFACING DAMAGED CARTILAGE

Brian C. Wise (1,2), Jay M. Patel (2,3), Claudia Loebel (1), Jason A. Burdick (1), Robert L. Mauck (1,2,3)

(1) Department of Bioengineering
University of Pennsylvania
Philadelphia, Pennsylvania, United States

(2) McKay Orthopaedic Research Laboratory
University of Pennsylvania
Philadelphia, Pennsylvania, United States

(3) Corporal Michael J. Crescenz VA Medical Center
Philadelphia, Pennsylvania, United States

INTRODUCTION

Cartilage injuries represent one of the most common intra-articular knee injuries [1]. Focal lesions jeopardize normal fluid pressurization, altering strains, and initiating a vicious chemo-enzymatic and mechanical cycle of cell dedifferentiation/death and degradation of adjacent ECM, propagating the defect area and concluding in joint-wide osteoarthritis [2]. Prior attempts have sought to restore mechanical integrity of damaged cartilage via genipin cross-linking or material-based resurfacing [3-4]. While showing some promise, these options present concerns regarding toxicity and durability of the engineered interface, respectively. In this study, we developed a modified hydrogel system (methacrylated hyaluronic acid) that intercalates within the cartilage ECM and can undergo photo-induced crosslinking following diffusion into the tissue (**Fig 1A**). The purpose of this study was to optimize the delivery system, focusing on the effect of material concentration, application time, and degree of crosslinking on the ability of the biomaterial to infiltrate into defected cartilage surfaces and restore cartilage mechanical function.

METHODS

Material Synthesis: Hyaluronic acid (HA; 75kDa) was methacrylated (~50% modification) and conjugated with fluorescent peptides (FITC) for tracking. The material was oxidized with sodium periodate to introduce aldehydes (~30% substitution), which can form covalent linkages with exposed amines in damaged tissue [5].

Assessment of UV Penetration: The ability of UV light to penetrate into cartilage tissue was first investigated. Juvenile bovine trochlear cartilage plugs (12mm diameter) were sectioned parallel to the articular surface at thicknesses ranging from 10µm to 300µm. Samples were placed on glass slides and hydrated with phosphate buffer solution (PBS). A UV lamp was positioned above a radiometer and set to an initial irradiance of ~10 mW/cm^2. Cartilage samples of varying thickness were placed between the radiometer and the UV lamp, and irradiance was measured.

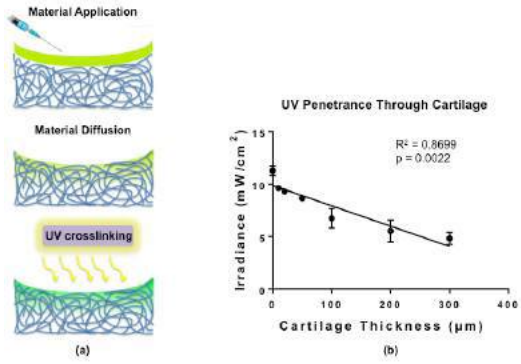

Figure 1. (a) Schematic showing the application of material to the defect surface, diffusion into the cartilage, and UV-mediated cross-linking to form an intercalated network within the tissue. (b) Irradiance as a function of cartilage thickness. n=5-10 per thickness.

Material Infiltration: Juvenile bovine trochlea plugs (6mm diameter) were excised, and the superficial zone of these samples was removed to represent a focal defect. Material solution (1%, 4% or 10%) was applied for 1, 5, or 10 minutes, followed by 10 minutes of UV-crosslinking and serial rinsing in PBS. In addition to these fresh "focal defects," material penetrance into degenerated defects was evaluated by digesting additional plugs in 0.1% collagenase at 37°C for 30 minutes. Digested plugs were subjected to a 1% material

solution for 1, 5 or 10 minutes, followed by UV crosslinking. All plugs were sectioned perpendicular to the articular surface to obtain axial cross-sections (20μm thick). Chondrocyte nuclei were visualized with DAPI, and biomaterial was visualized via the covalently linked FITC peptide. Fluorescence intensity was quantified as a function of cartilage depth. The cartilage surface was defined as the point at which fluorescence intensity reached 20% of maximum, and the infiltration depth was determined as the point at which fluorescence intensity fell below 20% of the maximum value (**Fig 2** – red lines).

Surface Mechanics: Finally, the ability of the intercalated material to alter the mechanics of the cartilage surface was investigated. Juvenile bovine trochlear cartilage plugs were retrieved and the superficial zones were removed. Half of these plugs were digested in 0.1% collagenase for 30 minutes, while the remainder were maintained in their naïve state. A 1% material solution was applied to the surface of plugs for 5 minutes, followed by 10 minutes of UV crosslinking and PBS-rinsing. Surface mechanics were evaluated by atomic force microscopy (AFM) to obtain elastic moduli. Borosilicate glass colloidal tips (5μm diameter) attached to cantilevers (k ~ 1.5 nN/nm) were used to generate force maps (~16 sites per region, ~10 μm/s) at various locations along each surface of the sample. Indentation curves were sampled at 1.5 Hz, with a force trigger of 750 nN and were fit to the Hertz model to extract elastic moduli (E).

Statistical Analysis: Irradiance versus cartilage thickness data was analyzed with a linear regression fit. Infiltration and AFM data were analyzed by two-way analysis of variance (ANOVA) with post-hoc Tukey's tests ($p < 0.05$).

RESULTS

Radiometer readings as a function of cartilage sample thickness are depicted in **Fig 1B**. The baseline irradiance without cartilage (11.29 mW/cm^2) steadily decreased with increasing sample thickness, falling below 50% of the initial intensity at a cartilage thickness of 300μm (4.83 mW/cm^2). Extrapolating a linear fit of irradiance versus cartilage thickness (R^2 = 0.8699, $p<0.0022$) suggests that irradiance will completely dissipate at a cartilage depth of 509.1 μm.

Biomaterial application and cross-linking showed that material infiltrated and intercalated within the cartilage matrix (**Fig 2A**).

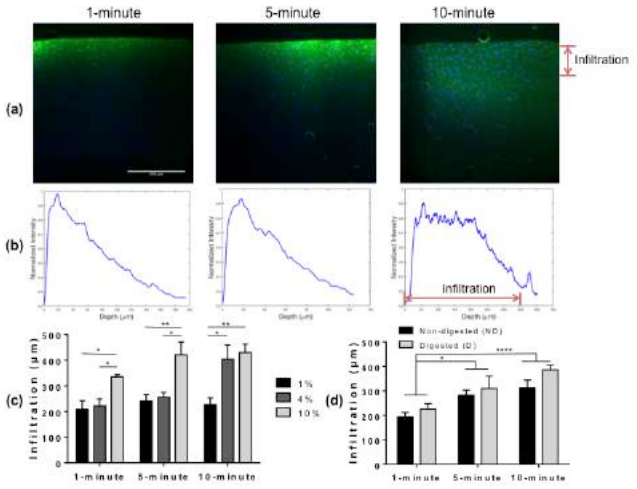

Figure 2. (a) Fluorescence imaging of non-digested samples with 4% material solution applied for 1, 5 and 10 minutes. (b) Normalized fluorescence intensity as a function of depth. (c) Material infiltration data for non-digested samples for 1, 4, 10% solutions for application times of 1, 5, 10 minutes (n=5). (d) Material infiltration into digested and non-digested samples for 1% material solution (n=10).

Furthermore, intensity peaked at approximately 25 μm in the 1-minute and 5-minute application groups, followed by a gradual decline (**Fig 2B** – left/middle). Conversely, for the 10-minute application, intensity remained elevated to depths approaching 200 μm (**Fig 2B** – right). Average penetration depth for non-digested samples (**Fig 2C**) showed a general trend of increasing depth of penetration with increasing application time, with the exception of the 1% solution. Overall, two-way ANOVA indicated a statistically significant impact of both material solution percentage ($p < 0.0001$) and application time ($p=0.004$), with infiltration increasing with both variables. All application combinations showed infiltration greater than 200 μm (**Fig 2C**). Infiltration also increased with application time for the digested samples (**Fig 2D**), and digestion increased infiltration by 9.9-24.1% across the three application times ($p=0.07$).

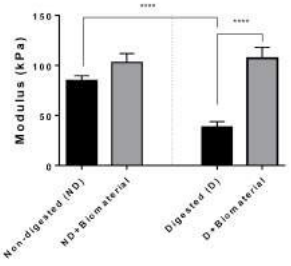

Figure 3: Elastic moduli from AFM analysis of non-digested and digested samples without material and with 1% material solution.

Elastic modulus of non-digested cartilage without material was 84.4 +/- 29.2 kPa, and showed a 54.1% decrease in modulus following digestion ($p < 0.0001$; **Fig 3**). Biomaterial application and crosslinking provided a 22.1% increase ($p=0.07$) in non-digested samples. This enhancement was more pronounced in digested cartilage, with a nearly 3-fold increase in elastic modulus (33.9 to 94.3 kPa, $p<0.0001$).

DISCUSSION

The results of this study demonstrate the ability of our HA hydrogel to intercalate and incorporate into both defected (nondigested) and degenerated (digested) articular cartilage. Crosslinking of the hydrogel is likely governed by the penetrance of UV light into the tissue, as well as material concentration and application time, impacting the depth of retained material. More importantly, this system displayed effective fortification of the damaged interface, restoring degenerated samples to mechanical properties matching native tissue. These findings may have implications for the treatment of both focal and degenerated cartilage defects, both mechanically for load support, and biologically for chondrocyte health. While these biological implications have not been studied here, future experiments will elucidate the impact of material application on cellular and tissue response.

ACKNOWLEDGEMENTS

This work was supported by the National Institutes of Health, the Department of Veterans Affaris, and the NSF-sponsored Center for Engineering MechanoBiology.

REFERENCES

[1] Hjelle, K et al. Arthroscopy, 18:730-734, 2002.
[2] Guilak, F., *Best Pract. Res. Clin. Rheumatol.*, 25:815-823, 2011.
[3] McGann, M.E. et al., *J. Ortho. Res*., 33(11):1571-79, 2015.
[4] Grenier, S. et al., *J. Biomech*., 48:122-29, 2015.
[5] Wang, D. et al., *Nature Materials*, 6:385-92, 2007.

SB³C2019
Summer Biomechanics, Bioengineering and Biotransport Conference
June 25-28, Seven Springs, PA, USA

ENGINEERING SPATIAL GRADIENTS OF DIAMAGNETIC PARTICLES AND CELLS IN HYDROGELS USING NEGATIVE MAGNETOPHORESIS

Hannah M. Zlotnick (1, 2, 3), Andy T. Clark (4), Xuemei M. Cheng (4), Robert L. Mauck (1, 2, 3)

(1) Department of Bioengineering
University of Pennsylvania
Philadelphia, PA, USA

(2) Department of Orthopaedic Surgery
University of Pennsylvania
Philadelphia, PA, USA

(3) Translational Musculoskeletal Research Center
Philadelphia VA Medical Center
Philadelphia, PA, USA

(4) Department of Physics
Bryn Mawr College
Bryn Mawr, PA, USA

INTRODUCTION

Cell and bioactive molecular gradients are critical for tissue development, maturation, and function. In articular cartilage, cell number decreases from the superficial zone (SZ) to the deep zone (DZ). Cell shape, orientation, and biologic activity also vary through the depth, and contribute to the depth dependent mechanical properties of cartilage [1]. To recapitulate this zonal cell distribution and matrix properties, studies have layered hydrogels of different stiffnesses [2] or containing different zonal chondrocyte subpopulations [3, 4]. While such layered scaffolds are an improvement over homogenous scaffolds for cartilage tissue engineering, the sharp transitions in these constructs are not physiologic and may be susceptible to failure under physiologic loading.

Towards the development of engineered cartilage with continuous spatial variation in cellular composition, this study developed and validated a method to spatially pattern particles and/or cells in *a single* hydrogel. To do so, hyaluronic acid (HA) hydrogel precursor solutions were supplemented with a clinically used paramagnetic contrast agent, Gadodiamide, to increase the magnetic susceptibility of the fluid. Based on previous literature [5-8], we hypothesized that diamagnetic particles (i.e. cells) suspended in the HA solution would be repelled from a nearby permanent magnet and would accumulate in areas of lower magnetic field strength in a computationally predictable manner.

METHODS

Experimental setup. The magnetic cell positioning setup included (i) one permanent magnet (15/16" diameter x 1/2" thick, B_{rmax} = 13,200 Gauss; K&J Magnetics, Inc.), (ii) a glass slide, (iii) a polydimethylsiloxane (PDMS) ring with an inner 4 mm diameter, and (iv) a PDMS cover (**Fig. 1**). The PDMS ring was positioned 3.8mm above the central axis of the magnet on the glass slide.

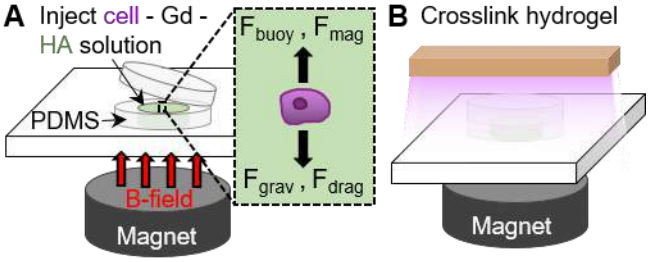

Figure 1. Schematic of permanent magnetic setup and gel fabrication. (A) A solution containing particles/cells, Gadodiamide, and hyaluronic acid is injected into a PDMS ring. (B) UV light is used to crosslink the hydrogel and stop movement of particles/cells.

Gel fabrication. A 1% w/v methacrylated hyaluronic acid (MeHA) solution [9] with 0.05% photoinitiator (Irgacure) was combined with 200 mM Gadodiamide (Gd; Omniscan) and fluorescent polystyrene microspheres (10 μm diameter; 250,000 beads/mL). 20 μL of MeHA – beads – Gd solution was pipetted into the PDMS ring and covered. After either 1 minute, 3 minutes, 5 minutes, or 10 minutes of magnetic field exposure, the solution was crosslinked with UV light (λ = 365 nm; intensity: 10 mW/cm^2) for 10 minutes. Gels fabricated with cells used juvenile bovine mesenchymal stem cells (2 million/mL) labeled with CellTracker Far Red. Samples were cut diametrically after UV exposure and were imaged with an inverted fluorescent microscope.

Modeling and simulation. The magnetic field throughout a 2D cross section of the hydrogel (R: 0-2mm, Z: 0-1.3mm) was computed at each point on a 20 μm spaced rectangular grid in COMSOL. Magnetic field values and their respective derivatives were exported into a custom

MATLAB script to plot the movement of polystyrene beads (10 μm in diameter, 1.05 g/mL density) over ten minutes with a time step of 5 seconds. The molar magnetic susceptibility of gadolinium-based paramagnetic solutions is 3.2 x 10^{-4} M^{-1} [7]. The following equations were solved in MATLAB with the variables defined in Table 1.

Governing equations – adapted from Durmus et al. [7].

$$\boldsymbol{F_{mag}} + \boldsymbol{F_{drag}} + \boldsymbol{F_{bouyant}} + \boldsymbol{F_{grav}} = m\boldsymbol{a} \quad (1)$$

$$\boldsymbol{F_{mag}} = (\frac{V\Delta\chi}{\mu_0}\boldsymbol{B}\cdot\boldsymbol{\nabla})\boldsymbol{B} \quad (2)$$

$$\boldsymbol{F_{drag}} = 6\pi R\eta f_D\boldsymbol{v} \quad (3)$$

$$\boldsymbol{F_{bouyant}} = V\rho_f\boldsymbol{g} \quad (4)$$

$$\boldsymbol{F_{grav}} = V\rho_c\boldsymbol{g} \quad (5)$$

Table 1. Variables used in model.

Var	Description	Units	Value
V	Bead volume	μm^3	523.6
$\Delta\chi$	Magnetic susceptibility of bead – Magnetic susceptibility of fluid	none	$\chi_c = 0$ $\chi_f = 6.4\ x\ 10^{-5}$
B	Magnetic induction	T	Calculated from COMSOL
μ_0	Mag permeability of free space	NA^{-2}	1.2566 x 10^{-6}
r	Radius of bead	μm	2.5-20
η	Dynamic viscosity of uncrosslinked hydrogel	Pa•s	$10^{-2} – 10^{1}$
f_D	Drag coefficient	none	1 [7]
v	Velocity of bead	m/s	Calculated
m	Mass of bead	g	5.5 x 10^{-7}
a	Acceleration of bead	m/s^2	Calculated
ρ_f	Density of fluid	g/mL	1.081 (measured)
ρ_c	Density of polystyrene bead	g/mL	1.05
g	Gravitational acceleration	m/s^2	9.8

RESULTS

The stray B-field was modeled in COMSOL across half of the 2D cross section of the hydrogel (**Fig. 2A**). As expected, the field strength decreased along the Z-direction and was relatively constant along the R-direction, given that the gel was significantly smaller in diameter than the magnet. Overall the field strength ranged from 0.28T to 0.34T through the depth of the gel.

Using the MATLAB particle movement model, a parameter sweep was carried out for particle radius (r: 2.5 μm-20 μm) and fluid viscosity (η: 10^{-2}-10^{1} Pa·s) (**Fig. 2B**). Increasing radius increased drag force, while also increasing magnetic force, such that particles with a greater radius were more responsive to the applied field. Increases in viscosity slowed particle movement. To validate the model, polystyrene beads of uniform size and density were used. The model output (**Fig. 2C**) was strikingly similar to the experimental data acquired (**Fig. 2D**). As predicted, particles moved away from the magnet placed underneath the Gd-meHA solution. After 3 minutes of magnetic field exposure, there was a clear gradient of particles within the hydrogel. After 10 minutes, most beads had reached the top of the gel, similar to the model.

After validating the computational model, fluorescently labeled cells were mixed into the Gd-meHA solution and subjected to the same magnetic field as in Figure 2. In control gels, the cells were evenly dispersed throughout the depth, as expected (**Fig. 3**). After applying the magnetic field for 5 minutes before crosslinking, there was a clear gradient from the top to the bottom of the constructs, as shown in the fluorescence intensity plot.

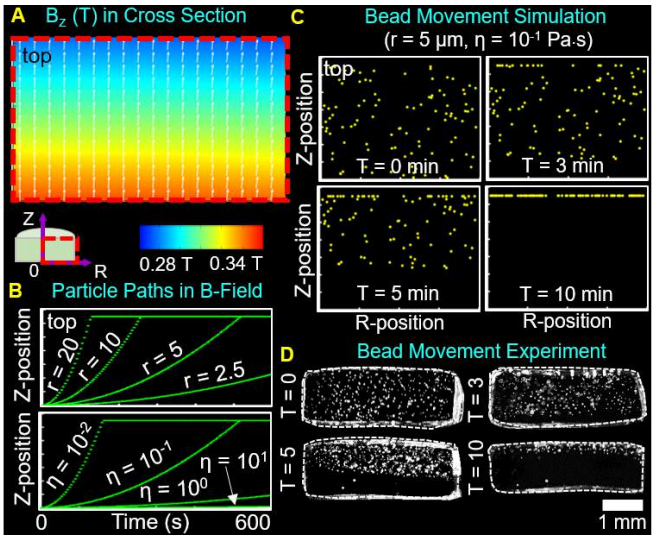

Figure 2. B-field modeling and particle movement. (A) COMSOL model of the magnetic field in a 2D cross section of the hydrogel. (B) Path of particle over 10 minutes in B-field based on radius or viscosity of fluid. (C) Simulation of polystyrene bead movement. (D) Experimental data of polystyrene bead movement.

DISCUSSION

These data demonstrate that negative magnetophoresis may be used to pattern cells in 3D space for potential interface tissue engineering applications. A wide array of stray B-fields can be designed with additional permanent magnets. This technique is advantageous over other magnet-based methods that require iron oxide particles to be tethered to or phagocytosed by cells, since iron particles can negatively affect cell differentiation [8]. Additionally, the computational model may be used to expedite experimental work focused on patterning objects of known density and diameter in a paramagnetic fluid. This work lays the foundation for future studies focused on long-term culture of engineered constructs with spatial cell gradients to investigate how cell density influences tissue mechanics and cell-cell interactions.

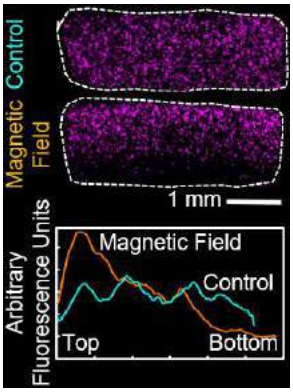

Figure 3. Label-free magnetic cell patterning in a hyaluronic acid gel. Fluorescent intensity was averaged across the width of a ROI from the top to the bottom of the sample cross section.

ACKNOWLEDGEMENTS

This work was supported by the Department of Veterans' Affairs, the Penn Center for Musculoskeletal Disorders, and the Center for Engineering MechanoBiology (CEMB), CMMI: 15-48571.

REFERENCES

[1] Klein, TJ et al., *JOR*, 40:182-190, 2007. [2] Zhu, D et al., *Tissue Eng Part A*, 24:1-10, 2018. [3] Kim, M et al., *Acta Biomat*, 58:1-11, 2017. [4] Ng, KW et al., *Tissue Eng*, 15(9): 2315-2324, 2009. [5] Anil-Inevi, M et al., *Sci Rep*, 8:1-10, 2018. [6] Shen, F et al., *Analyt Chem*, 84:3075-3081, 2012. [7] Durmus, NG et al., *PNAS*, 112:E3661-E3668, 2015. [8] Kostura, L et al., *NMR Biomed*, 17:513-517, 2004. [9] Burdick, JA et al., *Biomacromol*, 6:386-91, 2005.

SB³C2019
Summer Biomechanics, Bioengineering and Biotransport Conference
June 25 -28, Seven Springs, PA, USA

COMPUTATIONAL HEMODYNAMICS & COMPLEX NETWORKS INTEGRATED PLATFORM TO STUDY INTRAVASCULAR FLOW IN THE CAROTID BIFURCATION

Karol Calò (1), Diego Gallo (1), Valentina Mazzi (1), Stefania Scarsoglio (1), Muhammad O. Khan (2), David A. Steinman (3), Luca Ridolfi (1), Umberto Morbiducci (1)

(1) PolitoBIOMed Lab, Department of Mechanical and Aerospace Engineering, Politecnico di Torino, Turin, Italy

(2) Cardiovascular Biomechanics Computation Lab, Department of Pediatrics, Cardiology, Stanford University, Stanford, California, US

(3) Biomedical Simulation Lab, Department of Mechanical & Industrial Engineering, University of Toronto, Toronto, Ontario, Canada

INTRODUCTION

The well-established role of hemodynamics in cardiovascular disease [1] makes the study of cardiovascular flows of wide interest. Here we apply for the first time a method based on complex networks (CNs) theory [2] to investigate and characterize quantitatively the complexity of cardiovascular flows. The rationale lies in the ability of CNs to explore the complexity of physical systems, such as 4D cardiovascular flows, in a synthetic and effective manner. CN-based approaches have already proven useful for data-driven learning of dynamical processes that are hidden to other analysis techniques. In detail, a dataset of 10 patient-specific computational hemodynamics models of human carotid bifurcation (CB) is considered here. Quantitative metrics derived from CNs theory are applied to two fluid mechanics quantities describing the intricate intravascular hemodynamics. These are (1) the so-called axial velocity, i.e. the blood velocity component aligned with the main flow direction, as identified by the vessels centerline, and (2) the kinetic helicity density, a measure of pitch and torsion of the streaming blood. The obtained results suggest the potency of CNs in unveiling fundamental organization principles in cardiovascular flows.

METHODS

Ten patient-specific computational hemodynamics models of CB from the Vascular Aging-The Link That Bridges Age to Atherosclerosis (VALIDATE) study are considered. An overview of the methods is provided in **Figure 1**. Briefly, vascular geometries and flow rates at inflow and outflow boundaries were acquired from contrast-enhanced angiography and phase-contrast MRI. The common carotid artery (CCA) geometry was reconstructed from the thoracic segment, where possible, to well above the bifurcation. On the reconstructed models, uniformly discretized tetrahedral computational grids were generated, and unsteady-state computational fluid dynamics (CFD) simulations based upon the finite elements method were carried out [3-4]. Additional details are provided elsewhere [3-4].

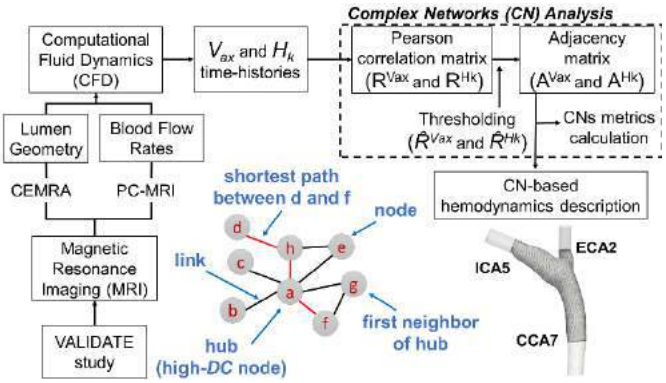

Figure 1: Schematic diagram of the proposed integrated CFD/CNs approach and explanatory example of a CN.

The full-length models were then truncated normal to the branch axis at sections located 7, 2 and 5 radii along respectively the CCA, the external (ECA) and internal (ICA) carotid artery (CCA7, ECA2 and ICA5 sections, respectively, in **Figure 1**), to ensure a consistent spatial extent across all cases [4]. To describe the complexity of intravascular hemodynamics, two fluid mechanics quantities are considered, axial velocity (V_{ax}) and kinetic helicity density (H_k). In detail, V_{ax} is representative of the main flow direction and was calculated by projecting the velocity vector field along the local vessel centerline [5]. The pseudoscalar H_k, defined as the internal product between velocity and vorticity vectors, is considered here due to the recognized

atheroprotective significance of helicity in the CB [4] and, in general, in the evolution and stability of both turbulent and laminar flows. Here CNs are applied to the time-histories of these quantities at each grid node along the cardiac cycle to unveil fundamental organization principles in the CB hemodynamics. In graph theory, a CN is a network with significant patterns of connection between its elements and nontrivial topological features (an explanatory example is presented in **Figure 1**). The CN is defined by a set of nodes $V = 1,...,N$ and a set of links E between nodes $\{i, j\}$. In this study the nodes of each CN are represented by the grid points of the finite element mesh used to perform the CFD simulations. For each CB model, the network is built by applying a correlation criterion [6-7]: for each pair of nodes $\{i, j\}$ of the discretized fluid domain, the linear Pearson correlation coefficient R_{ij} is calculated between time-histories of V_{ax} and H_k. Then, the corresponding network is built up based upon the constraint that a topological link between nodes i and j does exist if and only if R_{ij} is greater than a threshold value $\hat{R}$. The threshold values are set equal to the median of the overall R_{ij} distributions ($\hat{R}^{V_{ax}}$=0.55, $\hat{R}^{H_k}$=0). The obtained network is represented by its adjacency matrix:

$$A_{ij} = \begin{cases} 0, \ if \ \{i,j\} \notin E \ or \ i = j, \\ 1, \ if \ \{i,j\} \in E. \end{cases} \quad (1)$$

A_{ij} contains all the information about node connectivity: A_{ij}=1 if a link does exist between node i and node j ($R_{ij} > \hat{R}$); A_{ij}=0 elsewhere. On the built up networks, we calculated the following several CNs metrics: (1) the *degree centrality* (DC_i) of node i, defined as the fraction of nodes of the network directly connected to node i (the so-called first neighborhood of node i); (2) the *diameter D* of the network, defined in terms of number of links as the maximum value of the shortest path length between nodes i and j (**Figure 1**, in red); (3) the *Average Euclidean Distance* (AED_i) [6] of node i from all its first neighbors *n(i)*. *AED* provides a quantitative evaluation of the length of persistence of the correlation of hemodynamic structures inside the vascular domain, and their main direction of propagation. Intravascular structures characterized by high *AED* keep their correlation high within a large spatial distance, on the other hand for low *AED* structures the correlation vanishes within a shorter distance.

RESULTS

The volumetric maps of the V_{ax} degree centrality *DC* are presented in **Figure 2** for all the investigated CB models. In general, for V_{ax} high *DC* values characterize the nodes in the CCA, while nodes located at the carotid bulb present lower *DC* values. In most cases, high correlation among V_{ax} time-histories is restored distally to the flow divider, in ECA and ICA. On average, the value of the network diameter *D* is equal to 4 (range 3-5) for the ten investigated cases. Notably, the models presenting the highest and the lowest value for *D* are the same presenting respectively the highest and lowest value of carotid flare, a measure of the geometric expansion of the carotid bulb and known trigger of flow disturbances. The volumetric map for *AED* metric for a representative model is also displayed in **Figure 2**. In detail, *AED* map reveals that V_{ax} time-histories of nodes located close to CCA7 and ICA5 sections are characterized by a neighborhood that expands on a distance equivalent to 3 CCA7 diameters (*dCCA7*) or more, while shorter *AED* characterize nodes located in the carotid bulb. The CN-based analysis on H_k highlighted in all the models that two balanced, distinguishable positively/negatively correlated regions emerge from the distribution of *DC* values, which represent the detailed picture of those counter-rotating helical flow structures visualized and described in terms of integral quantities in previous studies [4]. All H_k networks are characterized by D = 2, i.e. the most distant nodes are separated only by a two-links path. Lastly, from the *AED* results, it emerged that H_k time-histories with the largest *AED* (equal to 3.5 *dCCA7*) are located close to the CCA7 and ICA5 sections. Interestingly, in general helical flow structures exhibit shorter *AED* values, i.e., shorter length of persistence of the correlation, in the bulb region, similarly to what was observed for V_{ax}.

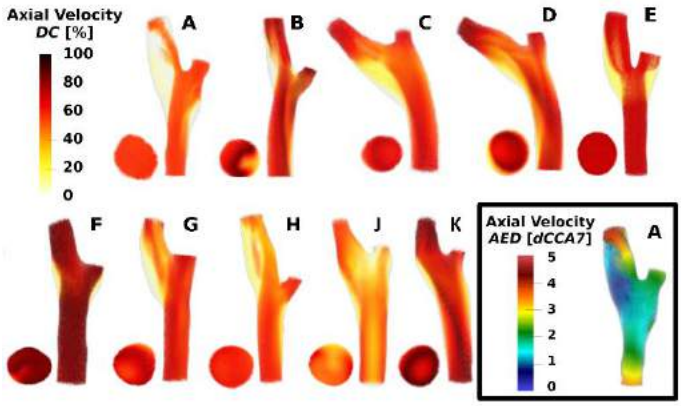

Figure 2: Volumetric maps of *DC* for all the ten V_{ax} networks, and volumetric distribution of *AED* for one representative model.

DISCUSSION

The CNs analysis on V_{ax} allows one to isolate two distinct regions, i.e., an "undisturbed" hemodynamic region vs. a "disturbed" hemodynamic region. The former presented high *DC* and *AED* values, physically implying that in that region forward flow dominates and V_{ax} time-histories are highly correlated, and this correlation is kept for large distances. The "undisturbed" hemodynamic region represents the largest fraction of the nodes, as *DC* values are >80%. On the other hand, the "disturbed" hemodynamic region corresponds to the carotid bulb, where the propensity to plaque formation is stronger. There, only a smaller fraction of nodes is highly correlated (lower *DC* values), expanding for an *AED* of about one CCA7 diameter. The observed correspondence between metric *D* and the carotid flare suggests that the expansion at the bifurcation, markedly contributing to break up the topological links of the network, is the putative mechanism of correlation dispersion of V_{ax}. As far as H_k is concerned, CNs analysis emphasizes the presence of two distinguishable, balanced counter-rotating helical structures [4] as an emergent feature in CB hemodynamics, showing that in the bulb helical patterns maintain correlation on a much shorter distance than elsewhere. This aspect confirms (in such a way that can be measured in terms of persistence length of the correlation within the fluid domain) the role of the carotid sinus in promoting complex flow structures. In conclusion, the proposed integrated CFD-CNs-based approach has the potential to provide a more complete picture of the intravascular flow complexity/disturbances, quantifiable in terms of persistence length of correlated hemodynamic quantities.

REFERENCES

[1] Morbiducci, U et al., *Thromb Haemost*, 115:484-92, 2016.
[2] Boccaletti, S et al., *Phys Rep*, 424:175-308, 2006.
[3] Hoi, Y et al., *Physiol Meas*, 31:291-302, 2010.
[4] Gallo, D et al., *Ann Biomed Eng*, 43(1):68-81, 2015.
[5] Morbiducci, U et al., *J Biomech*, 48(6):899-906, 2015.
[6] Scarsoglio, S et al., *Int J Bifurcation and Chaos*, 26(13), 1650223:1-12, 2016.
[7] Iacobello, G et al., *Phys Rev E*, 98(1), 013107, 2018.

SB³C2019
Summer Biomechanics, Bioengineering and Biotransport Conference
June 25 -28, Seven Springs, PA, USA

AUTOMATIC TECHNIQUES FOR DETERMINING BOUNDARY CONDITION PARAMETERS IN COMPUTATIONAL HAEMODYNAMICS

Christopher J. Arthurs (1), C. Alberto Figueroa (1,2)

(1) Imaging Sciences and Biomedical Engineering
King's College London
London, United Kingdom

(2) Biomedical Engineering
University of Michigan
Ann Arbor, MI, United States of America

INTRODUCTION

In order for personalized computational models to have predictive or diagnostic value for the individual, it is essential that real-world data describing the individual case are assimilated into the model. In the field of 3D computational haemodyanics (CH), data can be obtained on a range of different aspects of the individual in question, in various modalities. These data vary in terms of the difficulty involved in their assimilation into the model; this is primarily due to the differences in the available state-of-the-art assimilation technologies available in each case.

For example, in personalized CH, accurate representation of an individual's blood vessel geometry and structure – via segmentation from 3D medical image volumes – is relatively advanced, accurate and fast, and is supported by specialized tools such as CRIMSON [1]. Similarly, the imposition of data such as known volumetric blood flow waveforms on CH models is well-supported. The reason for these is that these categories of data can be imposed directly upon our model. These directly-imposable data types can be considered to constitute a first class of data.

In the present work, we are interested in values which can be measured, but which represent emergent properties of the model, rather than values which can be imposed directly. These represent a second class of data; one which must be assimilated indirectly, by adjusting other aspects of the model until they are reproduced by the model, rather than by direct imposition. This second class is much more difficult to deal with, it is not clear in advance how a model should be adjusted in order to achieve the reproduction of the data in question. General principles may be known (if X is increased then Y will get closer to the desired value), but the exact magnitude of the necessary adjustments to X are much more difficult to determine.

In general, an educated trial-and-error approach can be taken, guided by general principles, but more systematic – and ideally, automated – methods are required.

In the present work, we discuss some methods for data assimilation which can be applied to patient-specific CH models, in order to determine appropriate parameters for the model's boundary conditions. These are described by zero-dimensional lumped parameter network (LPN) models, which have a number of electronic-circuit-analogous component parameters which must be determined, so the parameterization procedure fundamentally amounts to making patient-specific estimates of the properties of the zero-dimensional vascular bed representations (see the electrical circuit models in Figure 1 or 2). The Class II data that we will make use of will be blood pressure and flow measurements recorded within the domain of the model, and we will know that the parameters are appropriate when the simulated results reproduce this target data. We have a particular interest in Kalman filtering based approaches [2, 3].

METHODS

We developed a novel Kalman filtering based approach for determining the appropriate boundary condition parameters in a variety of cases. Our approach was to create a CH model geometry, determine some physiologically-appropriate LPN boundary condition parameters, and perform a "forward" simulation in order to generate some target pressure and velocity waveforms within the domain; this is Class II data. We then reset the model boundary condition LPN parameters to some generic, incorrect values, and run the data assimilation procedure, filtering for these parameters, and assess how well the filtering approach manages to: 1) recover the original parameters, and 2) reproduce the data observed in the forward simulation.

Poster Presentation #P062

Our novel techniques as part of the Kalman filtering process were required in order to filter the complex LPN models that modern CH studies necessitate. For example, in the present work we made use of the arbitrary boundary condition model toolbox present in CRIMSON [1], which allows users to assemble custom arbitrary LPNs from a toolbox of circuit components. In order to support the arbitrary nature of such circuits, a novel mathematical approach was required.

Specifically, Kalman filtering in this context proceeds by generating a series of perturbations of the current LPN parameter state. Each member of this series is called a *particle*, and each particle represents a complete copy of the whole simulation state, differing only in terms of the perturbed parameters. Each particle is then advanced forward in time by one time-step, under the time evolution described by the incompressible Navier-Stokes equations, the produced pressure and flow values compared with the target data, and then the particles are recombined to create an *a posteriori* estimate of the model state, including a best new estimate of the target LPN parameters.

The requirement for a novel mathematical approach as part of this is due to the arbitrary nature of the LPN models. Unlike classical three-element Windkessel models, which have been determined using Kalman filtering previously [3], an arbitrary LPN model will have internal, time-dependent pressure states which are not directly determinable from the pressure at the 3D model's boundary. These states require careful consideration in the context of the filter, because each particle must contain internal an LPN state which is compatible with the perturbed parameters. If this is not the case, then the particles will exhibit inconsistent behavior over time, as if a series of shocks or discontinuities are delivered to the model, and the Kalman filtered estimates will not converge.

For this reason, after the generation of each particle, we introduce an update step to the filtering procedure, in which we update the LPN's internal state so that it is self-consistent, before it is stepped forward in time. However, because the pressure and flow at the 3D interface are both known variables at this point in time, the linear system representing the LPN circuit is overdetermined, and therefore solutions generally do not exist, and the internal LPN state cannot be found. Therefore, we "deconstrain" the values of the internal LPN pressures from the previous time-step, which are state variables in the presence of capacitance units due to the dP/dt term which occurs in the capacitor equation. This is philosophically justified because the particle has no true previous time-step, as the parameters have just been generated, and the available internal state belongs to what is really a different model, with a different parameter set.

In general, this approach leads to an underdetermined linear system. The solution to this problem is to make use of both the overdetermined and underdetermined linear systems simultaneously, by finding a least-squares solution to the overdetermined linear system, constrained by the requirement that it must satisfy the equations of the underdetermined system, too. Filtering can then proceed as normal for CH models [3].

RESULTS

Results are shown for the filtering of a single Windkessel (Figure 1), and for a coronary model (Figure 2). We see that the filter does a good job of finding appropriate values for the parameters, with some discrepancies which will be discussed later. Not shown is the fact that the target pressure and flow waveforms (one of each) are well recovered by the model with the final parameters found by the filter.

DISCUSSION

It is worth noting that the parameters are not necessarily recovered precisely. This is due to two factors. The first is that there may be multiple possible parameter sets which explain the observed input

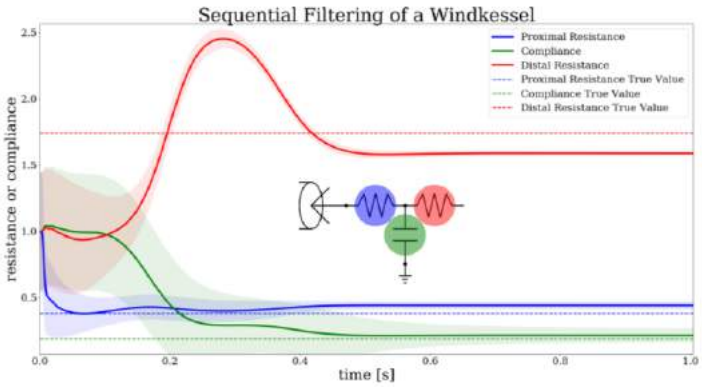

Figure 1: Filtering a 3-element Windkessel model. Standard deviations for the estimate of each parameter are shown shaded.

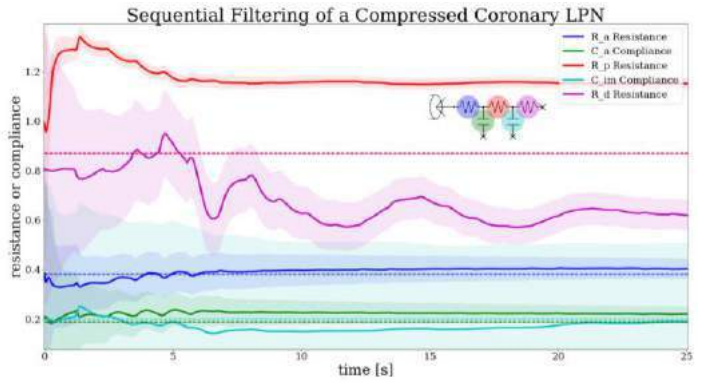

Figure 2: Filtering a 5-element coronary model. Standard deviations for the estimate of each parameter are shown shaded. Target values are shown as dashed lines of the appropriate color.

data, indicating that the parameters are not all directly identifiable, at least not without more data. This may have implications for LPN design, or for the data requirements for creating an accurate model. The second is that the model may end up in a state where the data is no longer achievable, regardless of the parameters, because of the current location of the system in pressure-velocity state space. To overcome the latter problem, it is sometimes sufficient to terminate the filtering procedure, save the final parameter estimates, then restart the whole filtering approach (resetting the state space), but this time starting with the saved parameter estimates.

The outcome of this work shows, for the first time, the automatic determination of parameters in some complex lumped parameter network models in CH. This required the development of a new mathematical and philosophical approach to the internal state of the LPNs within each particle, and will support automatic parameter determination in real-world models.

ACKNOWLEDGEMENTS

This work was supported by the European Research Council under the European Union's Seventh Framework Programme (FP/2007-2013) [ERC Grant Agreement No. 307532]

REFERENCES

[1] CRIMSON website. www.crimson.software.
[2] Moireau, P et al., D, ESAIM: Contr Opt Var, 17:380-405, 2010.
[3] Xiao, N PhD Thesis, Stanford University. December 2013.

DEVELOPING A SCALABLE OPEN-SOURCE SOLVER TO SIMULATE HEMODYNAMICS IN THE HUMAN PULMONARY VASCULATURE

Narasimha R. Pillalamarri (1), Senol Piskin (1), Ender A. Finol (1)

(1) Department of Mechanical Engineering
University of Texas at San Antonio
San Antonio, TX, USA

INTRODUCTION

Employing computational methods to simulate pulmonary blood flow permits the assessment of complex multivariate interactions between the arterial wall, blood stream, and the right ventricle. Characterizing patient-specific pulmonary hemodynamics can possibly aid in devising novel custom-made treatments for pulmonary diseases. Moreover, simulation-based diagnosis presents a promising approach to circumvent invasive diagnostic procedures such as right heart catheterization. However, a dependable scalable software platform is imperative in this regard. This work elucidates the conception and development of a scalable in-house computational fluid dynamics (CFD) solver undertaken to simulate patient-specific hemodynamics in the pulmonary vasculature. The CFD solver contributes toward our long-term goal of characterizing aberrant hemodynamics and blood-tissue interactions engendered by pulmonary hypertension (PH).

METHODS

The CFD solver was developed using open-source C++ libraries available in OpenFOAM – v5.0 distribution. OpenFOAM works on the collocated finite-volume formulation for numerical representation of the equations governing fluid motion and the message passing interface (MPI) method for parallel computing. The open-source toolbox features a range of numerical schemes, methods and turbulence models. Our code follows the PIMPLE algorithm to evaluate the conservative form of three-dimensional Navier-Stokes equations. The PIMPLE algorithm is an combination of Issa's [1] Pressure-Implicit with Splitting of Operators (PISO) algorithm and Patankar's [2] Semi-Implicit Method for Pressure-Linked Equations (SIMPLE). At its core, the PISO algorithm is used, which decouples the pressure and velocity fields, and linearizes the convection term. SIMPLE contributes by allowing under-relaxation to ensure convergence within each time step. OpenFOAM's hierarchical structure allows us to switch off the contribution from SIMPLE by setting the relaxation factors to 1; this option is availed in our simulations. The governing equations are the Navier-Stokes equations for isothermal incompressible flows, i.e. Eqs. (1) and (2),

$$\nabla . \boldsymbol{u} = 0 \tag{1}$$

$$\frac{\partial \boldsymbol{u}}{\partial t} + (\boldsymbol{u} . \boldsymbol{\nabla})\boldsymbol{u} = -\nabla \mathrm{p} + \nabla . [(\nu)(\nabla \boldsymbol{u} + \nabla \boldsymbol{u}^T)] \tag{2}$$

where $\boldsymbol{u}$ is the fluid velocity vector, p is the density-normalized or kinematic pressure, and ν is the kinematic viscosity of the fluid.

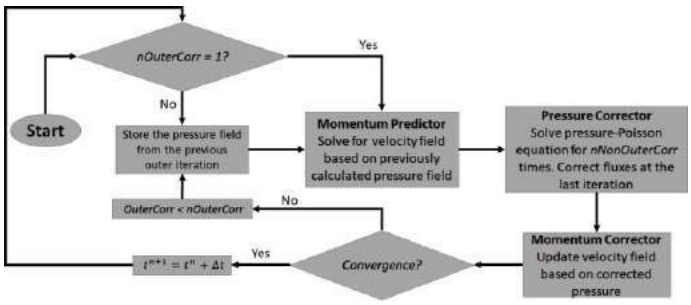

Figure 1: Flow chart of PIMPLE solution procedure used in OpenFOAM. nOuterCorr is the number of outer corrector loops; and nNonOrthoCorr is the number of non-orthogonal pressure corrector loops.

Equations (1) and (2) are evaluated using the pressure–velocity coupling methodology, which can be described in three steps: (1) momentum predictor, (2) pressure solver, and (3) momentum corrector.

The solver performs multiple iterations within a given time step and equation under-relaxation between each iteration is allowed for stability. The algorithm (see Figure 1**Error! Reference source not found.**) allows automatic time step adjustment to maintain a stipulated CFL number.

Velocity and pressure data were recorded with a Volcano catheter in eight PH patients at Allegheny General Hospital (Pittsburgh,). The data was normalized with respect to the mean of the distributions. Inlet centerline velocity adjusted with the cardiac output and mean pulmonary arterial pressure ($mPAP$) were used as dimensional factors to generate quasi patient-specific waveforms. A resistance structured-tree outflow boundary condition, proportional to the outlet radius, was applied at each outlet cross-section. The outlet resistances were dynamically adjusted to achieve the patient-specific pressure waveform at the inlet. This transient resistance boundary condition ensured the time lag between velocity and pressure waveforms typical of the human circulation in large arteries.

The iterations were conducted on a parallel architecture using Intel's Knight Landing (KNL) nodes on Stampede-2 at Texas Advanced Computing Center (TACC), University of Texas at Austin. It is a Linux environment with Omni-Path network with a fat tree topology and a 100 GB/s bandwidth disk system. Each node comprises of 68 cores, 96 GB of DDR RAM, and 16 GB of high speed MCDRAM. Static mapping library, SCOTCH, was used to decompose and distribute the simulation domain among the processors, while ensuring minimum inter-processor boundaries. To ensure accurate flux evaluation at the inflow/outflow boundaries, all mesh elements belonging to a single boundary surface were constrained to be allocated to a single processor. This constraint obviated the occurrence of inter-processor boundaries at the inlet/outlet faces.

RESULTS

The total run time for simulating pulsatile blood flow through a patient-specific vasculature was approximately 200 hours on 32 cores. The run time was reduced to 48 hours when the same simulation was run on 128 cores. Beyond this point, increasing the number of cores ensued insignificant changes to the run time (see Figure 12). The hemodynamics were simulated under a Newtonian fluid assumption [3]. We observe a decreasing pressure distribution from the inlet to the outlet during the accelerating phases of the cycle ending at peak systole. Subsequently, a reversed pressure gradient is observed until the end of diastole. The pressure distribution obtained between peak systole and end diastole are the outcome of a prevailing decelerating incompressible flow. The PIMPLE algorithm evaluates pressure by substituting the velocity field into the pressure-Poisson equation. Thus, the pressure field is obtained as a product of the existing velocity distribution. In transient situations, this protocol is indeed expected to yield a pressure gradient reversal. Moreover, geometric influences occurring on account of the simulation domain also impact the velocity and pressure fields. These effects are articulated in the form of spatially oscillating pressure gradients.

DISCUSSION

There are several commercial and open-source software available for simulating large artery hemodynamics. ANSYS provides a reliable and highly validated infrastructure; however, the economics of software licenses poses a critical bottleneck. Open-source software is, to a large extent, custom made for specialized applications. To this end, a third-party user experiences a steep learning curve working with the available boundary conditions, computational models, numerical schemes, and their optimal combinations. Limited documentation and material models for the fluid domain limits universal applicability. In this work, we utilized the widely validated OpenFOAM C++ libraries whose community-based support has evolved over the years to provide basic to advanced levels of troubleshooting. The next phases of this work involves conducting hemodynamic simulations on multiple patient-specific pulmonary vasculatures. Correlations obtained between simulation-based indices and clinical data will contribute towards our long-term goal of identifying non-invasively detectable biomarkers of a developing PH condition.

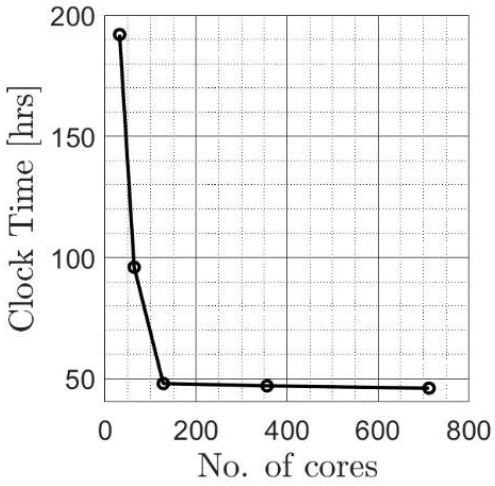

Figure 2: Speed up obtained in simulating pulsatile blood flow in the pulmonary vasculature discretized with 8 million grid points.

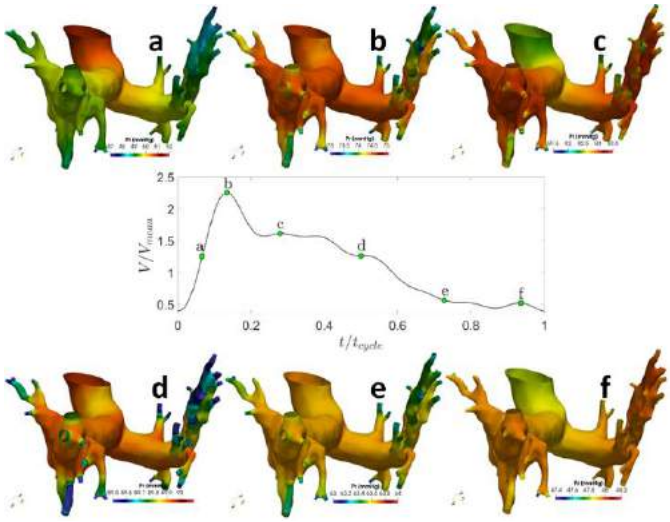

Figure 3: Pressure fields experienced by patient-specific vasculature during a complete cardiac cycle.

ACKNOWLEDGEMENTS

This work was supported by National Institutes of Health award No. 1R01HL121293. Code development and testing took place on Stampede-2 at Texas Advanced Computing Center (TACC), University of Texas at Austin.

REFERENCES

1. Issa, RI, *J Comp Phy*, 62:40-65, 1986.
2. Patankar, S et al., *Heat exchangers: design and theory sourcebook*, 1974.
3. Arzani, A, *J Roy Soc Int*, 15:20180486, 2018.

SB^{3}C2019
Summer Biomechanics, Bioengineering and Biotransport Conference
June 25 -28, Seven Springs, PA, USA

SOLUTION ADAPTIVE REFINEMENT OF CUT-CELL CARTESIAN MESHES IMPROVES MECHANICAL HEART VALVE SIMULATION PERFORMANCE

Ryan J. Pewowaruk (1), Tim Ruesink (2), Yanheng Li (3), David Rowinski (3), Alejandro Roldán-Alzate (1,2,4)

(1) Biomedical Engineering
University of Wisconsin - Madison
Madison, WI, USA

(2) Mechanical Engineering
University of Wisconsin - Madison
Madison, WI, USA

(3) Convergent Science
Madison, WI, USA

(4) Radiology
University of Wisconsin - Madison
Madison, WI, USA

INTRODUCTION

Computational fluid dynamics (CFD) analysis of biomedical systems is often performed with stationary boundaries due to the complexity. However, significant boundary motion is observed in the majority of anatomies (blood vessels, ventricle, heart valve, cerebrospinal fluid, etc) and medical devices (artificial heart valves, ventricular assist devices, etc) that are studied with CFD. In most commercial CFD solvers using boundary fitted tetrahedral meshes, the additional complexity of moving boundaries is due to deformation of the initial CFD mesh as the boundary moves, which deteriorates mesh quality and requires remeshing which is both computationally expensive and induces additional numerical error [1]. Immersed boundary (IB) methods are another common approach to moving boundaries and don't require remeshing [2]. In IB and other Eulerian methods the grid size is limited which is also not ideal as the solution may not be fully converged [1]. A third approach to moving boundaries is the use of cut-cell meshes, in which the cells at the boundary are cut into polyhedra to match the shape of the boundary. With cut-cell meshes, remeshing moving boundaries is very efficient as the Cartesian interior mesh remains the same and only the boundary mesh is altered [1]. Cell faces will remain orthogonal, resulting in greater numerical stability than a mesh with skewed cells.

Another benefit of cut-cell meshes is that solution adaptive mesh refinement (AMR) may be applied every time step due to efficient remeshing. Cut-cell meshes have been used in a small number of aortic valve and mechanical heart valve (MHV) simulations [3]. AMR has been used extensively for internal combustion simulations [4] but has not yet been used on a biomedical system. Additionally, the performance of cut-cell meshes compared to other methods and the effectiveness of AMR has not been investigated for biomedical flows with moving boundaries.

This study focuses on flow in a MHV, a medical device used to treat heart valve disease. MHVs are long lasting but known to have high rates of thrombus formation [5]. MHVs are frequently studied with CFD as thrombus formulation is highly related to fluid-dynamics within the valve. We aim to compare the performance of MHV CFD using 1. tetrahedral meshes, 2. cut-cell meshes and 3. cut-cell meshes with AMR. We hypothesize that cut-cell meshes perform more efficiently than tetrahedral meshes and that AMR will improve the efficiency of cut-cell meshes.

METHODS

We simulate flow in a 19mm bi-leaflet MHV (CryoLife, Kennesaw, GA) using experimentally measured flowrates and pressures as boundary conditions (BCs) from an *in vitro* flow loop. Leaflet motion is imposed using measurements from video recordings. Only systole is simulated as leaflet motion is obscured by the valve ring during diastole. The fluid is an incompressible 60-40 gycerol-water mixture with a viscosity of 0.0146 Pa sec and a density of 1167 kg/m^3.

Cut-cell mesh CFD is performed with CONVERGE (Convergent Science, Madison, WI) using a PISO algorithm. An adaptive time-step algorithm uses a CFL like condition to prevent a boundary moving more than half a cell length in a single time step. Cell sizes range from 4mm to 250μm.

Tetrahedral mesh CFD was attempted with FLUENT (ANSYS Inc, Canonsburg, PA) using a SIMPLE algorithm as PISO was found to be unstable in simulations with stationary leaflets. In FLUENT simulations with moving leaflets could not be performed due to poor mesh quality (cell skewness > 0.99) in regions of the valve with 10-100μm gaps.

AMR is implemented with CONVERGE. Refinement is based on

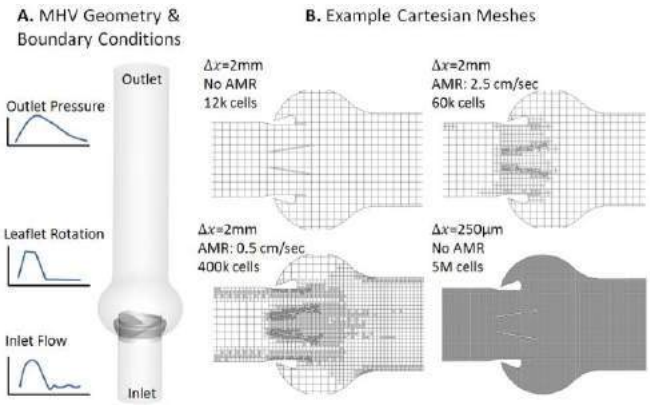

Figure 1: A. Geometry of 19mm MHV and aortic root with BCs for inflow, outlet pressure and leaflet rotation. **B.** Meshes at different resolutions and AMR settings. 2.5 cm/sec sub-grid AMR refines within the valve while 0.5 cm/sec AMR also refines distal to the valve.

the sub-grid field (ϕ') or difference between the actual field (ϕ) and resolved field ($\overline{\phi}$) [6]

$$\phi' = \phi - \overline{\phi}. \quad (1)$$

The sub-grid field is defined by an infinite series,

$$\phi' = -\frac{dx_{[k]}^2}{24}\frac{\partial^2\overline{\phi}}{\partial x_k \partial x_k} + \frac{1}{2}\frac{dx_{[k]}^2}{24}\frac{dx_{[l]}^2}{24}\frac{\partial^4\overline{\phi}}{\partial x_k \partial x_k \partial x_l \partial x_l} + \cdots, \quad (2)$$

however in practice only the first term is used to approximate the sub-grid field as an infinite series cannot be evaluated

$$\phi' \approx -\frac{dx_{[k]}^2}{24}\frac{\partial^2\overline{\phi}}{\partial x_k \partial x_k}. \quad (3)$$

When the sub-grid field is above a specified level a cell is refined into 8 identical cells and if the sub-grid field below $1/5^{th}$ the specified level the embedding is released. The refinement level is an integer determining how many times a cell can be refined. Velocity is chosen as the variable to monitor for refinement and sub-grid field values of 2.5cm/sec and 0.5cm/sec are both analyzed. A variety of base grid sizes are simulated from 8mm-2mm and using a refinement level of three.

CFD accuracy is evaluated at a point between the leaflets (Fig2B, red circle) and in the valve wake (Fig2B, black square) using the L_1 norm of the axial velocity over time. Total error (Fig2A) is the average error at these two points. The 250μm mesh without AMR is considered the converged solution. CPU-time is calculated by taking the simulation wall time and multiplying by the number of cpus used in the calculation. A numerical method is more efficient if the performance curve (error vs cpu time) is shifted to the left, i.e. greater accuracy for the same cpu time.

RESULTS

Performance curves for cut-cell mesh simulations show that the 0.5 cm/sec sub-grid AMR is the most efficient (Fig2A). For simulations using approximately 10^4 sec cpu time, 0.5 cm/sec sub-grid AMR simulation (2mm base grid) has an L1 error six times less than a simulation not using AMR (500μm base grid). The 2.5 cm/sec sub-grid AMR performs worse than no AMR.

The reason for the poorer performance of the 2.5 cm/sec sub-grid AMR can be seen when looking at meshes At a 2.5 cm/sec sub-grid the AMR algorithm refines cells along the valve leaflets (Fig1B). Looking at error within the valve leaflets (Fig2B), 2.5 cm/sec sub-grid AMR outperforms no AMR simulations, and at comparable cpu times has similar error to 0.5 cm/sec sub-grid AMR. 2.5 cm/sec sub-grid

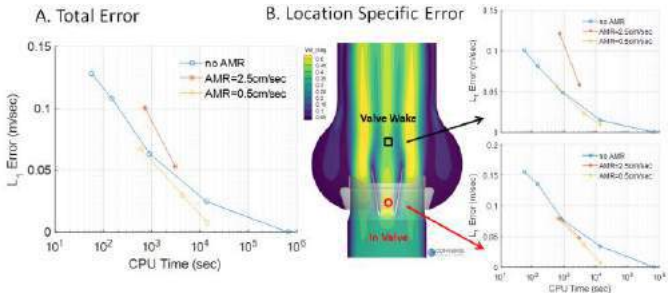

Figure 2: A. The performance curves for total error show that an AMR sub-grid of 0.5 cm/sec is the most efficient. **B.** Within the valve both AMR sub-grids perform more efficiently than no AMR. In the valve wake, 0.5 cm/sec is more efficient than no AMR while 2.5cm/sec is less efficient than no AMR.

AMR does not refine cells in the valve wake (Fig1B) and performs worse than simulations without AMR in this location (Fig2B).

DISCUSSION

Heart valve simulations have used cut-cell meshes [3] but not AMR. These simulations did use boundary layer mesh refinement which could be used with AMR to further improve performance. AMR has been used in tetrahedral mesh simulations [7] but these simulations had rigid boundaries. In previous tetrahedral studies, AMR was only performed at the end of a simulation, not at every time step which decreases the potential benefit of AMR. It is important to note that performance depends on AMR settings.

A key limitation is that leaflet motion was prescribed instead of solved with fluid-structure-interaction (FSI). Future work will investigate AMR using FSI. We were also unable to perform tetrahedral mesh CFD so a comparison of tetrahedral and cut-cell meshes cannot be made. Others have reported increasing gap sizes in heart valve geometries to preserve mesh quality [8] and while this is a solution, the nonlinear response of flow to gap-size ($O(h^3)$) makes this approach undesirable unless a porous media or other approach is used to limit flow.

We found that AMR can improve CFD performance in a MHV with moving leaflets. A 400k cell simulation with AMR can be run on a desktop computer and has error less than 0.5cm/sec (70cm/sec peak velocity) compared to a 5M cell simulation run on a cluster. In addition to FSI, future work will investigate AMR performance in other anatomies and medical devices as well as the performance of cut-cell mesh AMR compared to tetrahedral meshes and IB methods. We also look to validate MHV CFD and 4D Flow MRI of MHVs against particle image velocimetry.

ACKNOWLEDGEMENTS

This investigation was supported by the UW Cardiovascular Research Center T32 HL 007936. CONVERGE was provided by a partnership between Convergent Science and the University of Wisconsin – Madison.

REFERENCES

[1] Marom, G et al., *Arch Computat Methods Eng*, 22:595-620, 2015.
[2] Peskin, C. *J Comput Phys*, 25(3)220-52, 1977.
[3] Marom, G et al., *Med Biol Eng Comput*, 50:173-182, 2012.
[4] Pal, P et al., *J Energy Resour Technol*, 140(10), 2018.
[5] Pibarot, P et al., *Circulation*, 119(7): 1034-1048, 2009.
[6] CONVERGE v2.4 Manual, Ch. 10.3 "Adaptive Mesh Refinement"
[7] Sahni, O et al., *Eng with Computers*, 24:267, 2008.
[8] Gosh, R et al., *J Biomech Eng*, 140(12), 2018.

SB³C2019
Summer Biomechanics, Bioengineering and Biotransport Conference
June 25 -28, Seven Springs, PA, USA

UNCETRAINTY QUANTIFICATION OF OUTFLOW BOUNDARY CONDITIONS ON PRESSURE QUANTIFICATION IN AORTORENAL ARTERY SYSTEM

Huidan (Whitney) Yu[1,2], Monsurul Khan[1], Hao Wu[1], Xiaoping Du[1], Alan P. Sawchuk[2]

(1) Department of Mechanical and Energy Engineering
Indiana University-Purdue University, Indianapolis (IUPUI)
Indianapolis, Indiana, USA

(2) Department of Surgery
School of medicine, Indiana University
Indianapolis, Indiana, USA

INTRODUCTION

Image-based computational hemodynamics (ICH) has emerged as a new method for noninvasive quantification of a full wealth dynamic information of blood flow in human vessels. Such a capability gives rise to a promising patient-specific aid in clinic to either diagnose the true degree of hemodynamic abnormality or predict the therapeutic/surgical benefits to patients for various cardiovascular diseases. In recent years, a unique computational platform [1], named *InVascular*, as schematized in Fig. 1, has been developed, validated, and applied for the assessment of true severity of renal arterial stenosis (RAS) [2] and the prediction of

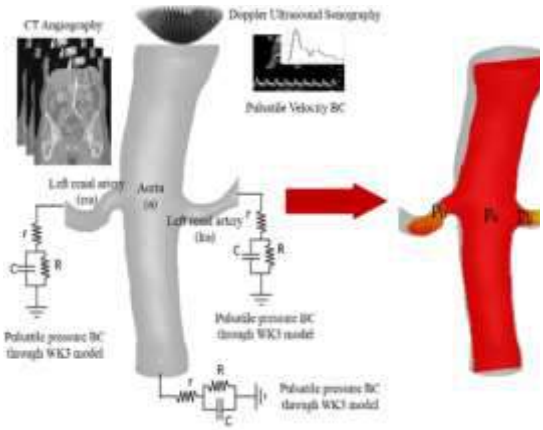

Fig. 1 Schematics of InVascular from CT and DUS, together with WK3 model to 4-D dynamic pressure in aortorenal artery system.

optimal implant of left ventricle assist device [3] utilizing patient's CT angiography (CTA) and Doppler ultrasonography (DUS) data. Integrating unified lattice Boltzmann method [1, 4] for both image segmentation and computational hemodynamics through a seamless connection with GPU (Graphic Processing Unit) parallel computing technology [5], *InVascular* enables exceptionally fast computation to establish correlation between trans-stenotic pressure gradient and volumetric reduction of renal artery, from which the hemodynamic severity contributing to the blood flow resistance in the diseased renal artery can be determined [2]. Such data are not readily available from the current standard clinical measurements. While it is encouraging that the non-invasive computational pressure has a good agreement with the invasive pressure measurement in aortic, left, and right renal arteries, referred to p_a, p_{lr}, and p_{rr}, of five clinic cases, the reliability of the computational results needs to be further addressed noticing that there exist various uncertainties in the entire process from image acquisition to 4-D hemodynamics (Fig. 1). Since only a segment of a vessel anatomy can be included in ICH due to the limit of computational power, boundary conditions (BCs) at inlets and outlets play critical roles to achieve reliable computational results. In *InVascular*, we choose 3-element WindKessel (WK3) model as outflow BCs. Three parameters, representing vessel compliance (C), proximal resistance (r), and distal resistance (R), form a lumped vessel network to close the blood flow loop. Due to lack of patient-specific data, the three parameters are determined empirically based on the physiological hemodynamics in aortorenal artery system. It is well known that uncertainty always exist in any modeling and simulation process [6]. Uncertainties due to the inaccurate data of local blood flow rate, vessel hardness, blood viscosity, etc. can affect the accurate determination of the three parameters. We therefore treat the parameters as random variables and quantify their effects on the output variables, i.e. the blood pressure values of p_a, p_{lr}, and p_{rr}, through uncertainty quantification (UQ).

METHODS

A patient case (male, 64) with existing CTA and DUS image data is selected from a previous research project [2] that was for the validation of *InVascular* to quantify 4-D pressure in aortorenal artery system (Fig. 1). The computed pressure waves in one cardiac cycle of p_a, p_{lr}, and p_{rr}

Table 1. WK3 model parameters (r, R, C) for out BCc at the exits and validated systolic pressure of aorta, left and right renal arteries.

Values / Vessel	r ($dynes \cdot s/cm^5$)	R ($dynes \cdot s/cm^5$)	C ($cm^5/dynes$)	Systolic pressure (mmHg)
Aorta (a)	108.12	3386.38	1.0e-5	155.80
Right renal artery (rr)	3306.39	8505.96	4.8e-6	141.72
Left renal artery (lr)	2879.76	7386.06	5.4e-6	144.61

have been compared to the corresponding invasive measurement with very good agreements, demonstrating the reliability of *InVascular* for the non-invasive pressure quantification. Table 1 shows the three parameters (r, R, and C) used in the WK3 model for outflow BCs as well as the validated systolic pressure in the aortic, right renal, and left renal arteries. In this study, we quantify the effects of the uncertainty of the outflow BCs on the *in vivo* systolic pressure quantification for this patient case. The input and output variables are the three parameters at three exits and systolic pressure values, denoted by x_i (i=1-9) and y_j (j=1-3), respectively. We assume that the input variables are independently and normally distributed. Their means are shown in Table 1. Their standard deviations are determined by coefficients of variation of 3%. This means that the standard deviations of the input variables are 3% of their means. Since the uncertainty in the input variables is not significant, we use the FOSM (First Order Second Moment) method [7, 8], which is accurate when the standard deviations are small. The required derivatives, $\partial y_{ij}/\partial x_j$ with i=1-3 and j=1-9, are computed using the finite difference method.

RESULTS

FOSM uses a linear approximation and all input variables are normally distributed. Thus, the three output variables are also normally

Table 2 95% confidence intervals of model predictions

U Results / Outputs	Mean (μ_y)	Standard deviation (σ_y)	95% confidence Interval
y_1 (p_a)	155.80	1.3743	[153.05,158.55]
y_2(p_{rr})	141.72	1.1149	[139.49,143.95]
y_3(p_{lr})	144.61	1.1224	[142.37,146.86]

distributed. The distribution parameters of the output variables are shown in Table 2. For a normal distribution, the 95% confidence interval is approximately determined by the mean plus and minus two standard deviations [9]. The 95% confidence intervals of the pressure values of p_a, p_{rr}, and p_{lr} quantified via *InVascular*, are therefore [153.05, 158.55], [139.49, 143.95], and [142.37, 146.86], in mmHg, respectively, given the uncertainty in the outflow BCs. The coefficients of correlation between the three pressure values are $\rho_{a\text{-}rr} = 0.8969$, $\rho_{rr\text{-}lr} = 0.8497$, and $\rho_{a\text{-}lr} = 0.9474$. The correlations are positive and strong. This means that if any pressure value increases, it is likely that the other two pressure values will increase. With the means, standard deviations, and coefficients of correlation, the joint probability density of the three output variables is also fully defined.

The UQ analysis indicates the following.

- The pressure values of p_a, p_{rr}, and p_{lr} are random variables because they depends on random WK3 parameters.
- UQ produces a family of output variables (predictions) instead a point prediction. For this case study, the complete joint distribution of the pressure values is obtained.
- The joint distribution provides not only the average pressure values, but also their standard deviations, which are a measure of uncertainty.
- The three pressure values are strongly correlated, and the correlation is positive.
- The 95% confidence levels of the pressure values provide the likelihood that the actual values could occur. This can help us make more reliable decisions based on the simulation result.

DISCUSSION

Computational quantification of trans-stenotic pressure gradient using non-invasive ICH is a promising new means to replace the invasive catheter-based measurements currently in clinic practice. Such a new capability is significantly meaningful for more quantitatively determining the severity of arterial stenosis and the necessity of interventional therapy to avoid the patient's discomfort and to reduce the medical cost. It is inherently patient-specific thus expected to impact on precision medicine for cardiovascular diseases as stenosis can occur in all the major vessels, not only renal arteries in the current study but also coronary, cerebral, and iliac arteries that are being investigated. However, due to the existence of various uncertainties in medical image acquisition, image segmentation, computational models, and inflow and outflow BCs, the reliability of the computational quantification has been a big concern. Little knowledge about how the variability of key data and models due to unavoidable uncertainties would affect the accuracy of the ICH outcomes has been gained so far. As the very first step, we have focused on how the systolic pressure in aorta and renal arteries are affected by the uncertainties in the outflow BCs through the variations of the parameters representing the proximal and distance resistance and vessel compliance in WK3 model. Our study has demonstrated the benefits of considering uncertainty in the process of modeling and simulation. We have moved to the next step of the study, in which around 10 patient cases with different degrees of RAS observed from CTA are studied. We will investigate more sources of uncertainty and obtain more accurate uncertainty information about the model input variables. More advanced and more accurate UQ methods, such as Saddle-point Approximations, are being introduced.

ACKNOWLEDGEMENTS

The research is supported by the University Fellowship of IUPUI.

REFERENCES

[1] Yu, H *et al*, *US Patent Application Publication*, US 2017-0337327 A1, Pub. Date: Nov. 23, 2017

[2] Sawchuk, AP *et al*, *J Vas Surg*, 68(3), e64–e65, 2018

[3] Yu, H *et al*, *Circul Res.*, 121, A221, 2017

[4] Yu, H *et al*, *Phys Rev E*, 89, 063304, 2014

[5] Wang, Z *et al*, *Computer & Fluids*, 115(2015)192-200, 2015

[6] Du, X, *ASME J Mech Des*, 130(9), 091401-1 - 091401-10, 2008.

[7] Hu, Z, and Du, X, *Struct Multidis Optim*, 51(1), 1-21, 2015.

[8] Haldar, A and Mahadevan, S, Probability, *Reliability, and Statistical Methods in Engineering Design*. John Wiley & Sons New York/Chichester, UK, 2000.

[9] Abernethy, R et al, *J Fluids Eng*, 107(2) , 161-164, 1985

SB^{3}C2019
Summer Biomechanics, Bioengineering and Biotransport Conference
June 25 -28, Seven Springs, PA, USA

MODELING PULSE WAVE PROPAGATION FOR IDEALIZED AND PHYSIOLOGICAL ARTERIES WITH FLUID-STRUCTURE INTERACTIONS IN FEBIO

Jay J. Shim (1), Vittorio Gatti (2), Pierre E. A. Nauleau (2), Grigorios M. Karageorgos (2), Elisa E. Konofagou (2, 3), Gerard A. Ateshian (1)

(1) Department of Mechanical Engineering
Columbia University
New York, NY, USA

(2) Department of Biomedical Engineering
Columbia University
New York, NY, USA

(3) Department of Radiology
Columbia University Medical Center
New York, NY, USA

INTRODUCTION

Cardiovascular disease (CVD) accounted for more deaths in the United States every year than any other cause of death since 1918, and was the underlying cause for 30.8% of all deaths in the United States in 2013 [1]. With regards to CVD, arterial stiffness is of clinical significance as an independent predictor of cardiovascular morbidity and mortality in hypertensive patients, type 2 diabetes, end-stage renal disease, and in elderly populations [2]. Arterial stiffness can be measured using noninvasive methods that obtain the arterial pulse wave velocity (PWV), which has been traditionally related to arterial stiffness using the Moens-Korteweg equation (MKE) [3]. However, the MKE assumes that the vessel is infinitely long, straight, isolated, and cylindrical with a wall that is elastic, isotropic, linear, homogeneous, and thin, which contains a homogenous, incompressible, and nonviscous fluid [3, 4]. While the qualitative relationship between stiffness and PWV in the MKE is useful, these assumptions are not realistic *in vivo* as arteries are highly curved, branched, and surrounded by adjacent tissue, and the vessel wall and blood are non-linear, viscoelastic, and heterogeneous [4]. As a result, there is a need for modeling software that can accurately calculate the PWV under physiological conditions.

FEBio is a free, open-source finite element software (febio.org), that was developed specifically for the biomechanics and biophysics communities [5]. It already offers many constitutive relations suitable for biomechanics such as nonlinear, anisotropic, heterogeneous, hyperelastic, and viscoelastic materials that may undergo remodeling, damage, chemical reactions, and solute transport. Recently we formulated and implemented a novel 3D fluid-structure interaction (FSI) solver in FEBio based on mixture theory where the FSI domain was described as a mixture of fluid and solid constituents that have distinct motions [6]. Our FSI formulation did not require stabilization methods to achieve good convergence, producing a compact set of equations and robust code implementation that was validated and verified against a wide range of problems.

This study illustrates how the FEBio FSI solver can be utilized to accurately measure PWV of models of varying complexity and assumptions. A PWV benchmark problem of a flexible tube was compared with FEBio results to show accuracy in idealized cases [7]. The PWV for same model was solved for at different values for the wall stiffness to compare with expected values. Finally, the PWV was calculated for a realistic carotid artery problem with non-Newtonian blood, heterogeneous, nonlinear, and anisotropic thick wall, with surrounding adipose tissue.

METHODS

For the flexible tube problem [7], the model consisted of a cylinder with length L=100 mm, inner diameter D=20 mm, and wall thickness t=2 mm. Both ends have a symmetry boundary condition. The inlet is prescribed a step pressure of 5 kPa to initiate the pulse wave. The wall is Neo-Hookean with E=1 MPa, ν=0.3, and ρ_s=1000 kg/m^3. The fluid is Newtonian with bulk modulus K_f=2.2 GPa, ρ_f=1000 kg/m^3, and viscosity μ=0.004 Pa·s. The tube was modeled as a quarter cylinder with 20,520 linear elements and 23,111 nodes.

Then using the same model, different values for E were used in order to observe how the PWV from FEBio correlated with the MKE, which is shown in Eq. 1 [4].

$$\mathrm{E} = \frac{2R\rho_f}{t} PWV^2 \quad (1)$$

PWV was also compared to a more accurate equation that allows for thick walls and compressible fluid. In-house Matlab code plotted fluid pressure along the center axis onto a spatiotemporal map, where the PWV was then calculated at the half-height of the pressure increase.

Finally, the PWV was calculated in a realistic bifurcated carotid artery example, originally used as a FSI example problem [6]. In this model, the arterial wall was an anisotropic, heterogeneous, multi-layered, and fiber-reinforced composite described by Holzapfel's material model with material parameters obtained from carotid arteries from cadavers [8], and the blood was a non-Newtonian Carreau fluid [9]. Adipose tissue was assumed to be a neo-Hookean material [10]. To initiate the pulse wave, the outlet pressure and inlet velocity were raised to physiological levels representing diastole (10.6 kPa and 0.1 m/s respectively) and allowed to equilibrate before a step increase in the velocity, representing systole (0.5 m/s). The PWV was calculated before the bifurcation. This model had 271,933 linear elements and 59,673 nodes.

RESULTS

The comparisons of the results for the PWV test problem between FEBio and literature are shown in Fig. 1, where centerline pressure values were taken at 5 different time points [7,11]. Overall there was good agreement between FEBio and literature results.

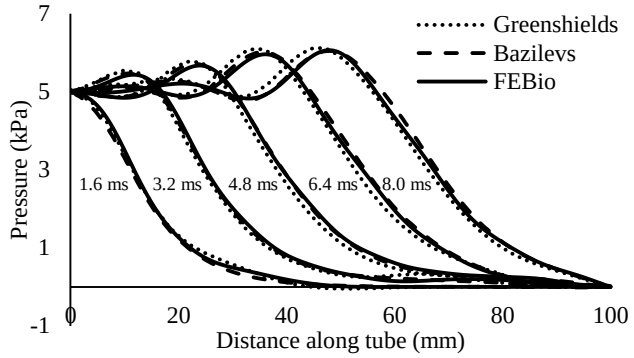

Figure 1: Centerline pressure of flexible fluid-filled tube.

The PWV of same models at different stiffness values were compared with the MKE and equation from Greenshields (GE) [7]. The results are documented in Table 1. FEBio PWV showed good agreement with GE, and followed the expected trends with MKE.

Table 1: PWV at different E for flexible fluid-filled tube.

Stiffness (MPa)	FEBio (m/s)	MKE (m/s)	Error (%)	GE (m/s)	Error (%)
0.5	6.432	7.071	9.03	6.204	3.68
1	8.802	10.000	11.98	8.774	0.32
2	12.416	14.142	12.20	12.408	0.07
4	17.541	20.00	12.29	17.547	0.03
10	27.473	31.623	13.12	27.741	0.97

Finally, the PWV was calculated from the realistic bifurcated carotid artery. The artery mesh and the surrounding subcutaneous adipose tissue, is shown in Fig. 2. The pulse wave propagated through the carotid artery before the bifurcation and then reflected as it hits the junction, which is illustrated in Fig. 3. The PWV of the artery (calculated before the bifurcation) was 13.59 m/s. Clinically, the PWV of the carotid artery was 9.84±3.86 m/s and 10.68±3.29 m/s for geriatric people (average age ~69) without and with carotid atherosclerosis respectively [12].

DISCUSSION

This study illustrates how FSI in FEBio can be used to accurately calculate PWV both in idealized and realistic artery models. With the fluid-filled elastic tube model, FEBio was in agreement with literature results (Fig. 1), which verified that FEBio can be used to model the propagation of the pulse wave in simple cases. Observing the PWV change at different E for this model (Table 1), the good agreement with the GE demonstrates that FEBio PWV behaved as expected under different conditions. FEBio and MKE did not agree as well most likely due to unacceptable simplifying assumptions, although FEBio followed anticipated trends. For the physiological artery model, the incident pulse wave was observed to both reflect at the junction and be transmitted to the two branches as expected (Fig. 3) [4]. The calculated PWV was within range, although at the higher end of the clinical PWV for elderly patients with and without carotid arthrosclerosis. However, this was reasonable as the wall material properties were obtained from donors who were older than those in the clinical study (76.8 average age), most of whom had varying degrees of arthrosclerosis [8]. Thus, from these results, in addition to its many material models and features, FEBio can be a powerful and versatile tool for modeling pulse wave propagation in arteries. Future potential applications include, for example, patient-specific studies and artery wall material characterization. Currently, studies are ongoing that use FEBio to model PWV in phantoms to complement experimental results obtained using ultrasound to observe the effect of stenosis formed by plaque.

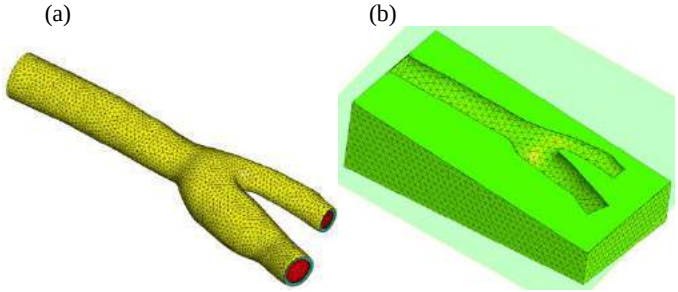

Figure 2: Mesh for (a) carotid artery, with the fluid in red, media in cyan, and adventitia in yellow and (b) surrounding tissue.

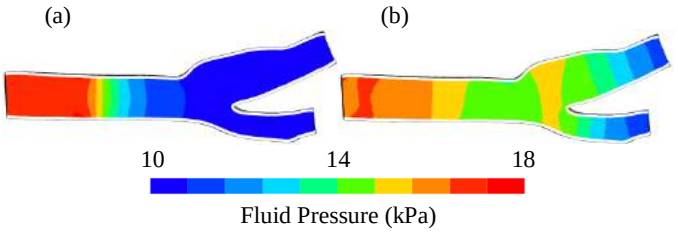

Figure 3: Pulse wave (a) before and (b) after bifurcation.

ACKNOWLEDGEMENTS

National Science Foundation (Grant No. NSF GRFP DGE-16-44869).

REFERENCES

[1] Mozaffarian D et al., *Circulation*, 133:e38-e360, 2015.
[2] Cecelja M et al., *J R Soc Med Cardiovac Dis*, 1(11):1-10, 2012.
[3] Shahmirzadi D et al., *J Biomech Eng*, 131(11):114502, 2012.
[4] Fung YC, 1997, Springer-Verlag, New York, NY.
[5] Maas SA et al., *Annu Rev Biomed Eng*, 19:279-99, 2017.
[6] Shim JJ et al., *J Biomech Eng*, In Review.
[7] Greenshields CJ et al., *Int J Numer Meth Engng*, 64:1575-93, 2005.
[8] Sommer G et al., *J Mech Behav Biomed Mater*, 5(1):116-28, 2012.
[9] Cho YI et al., *Biorheology*, 28(3-4):241-62, 1991.
[10] Alkhouli N et al., *Am J Physiol End Metab*, 305:E1427-35, 2013.
[11] Bazilevs Y et al., *Comput Mech*, 38:310-22, 2006.
[12] Shen L et al., *Cerebrovasc Dis*, 32(suppl 1):16-20, 2011.

SB³C2019
Summer Biomechanics, Bioengineering and Biotransport Conference
June 25 -28, Seven Springs, PA, USA

IN VITRO VOLUMETRIC LAGRANGIAN PARTICLE TRACKING AND 4D PRESSURE FIELD IN A LEFT VENTRICLE MODEL

Hicham Saaid[1], Matteo Novara[2], Jason Voorneveld[3], Christiaan Schinkel[4], Jos Westenberg[5], Frank Gijsen[3], Patrick Segers[1], Pascal Verdonck[1], Johan Bosch[3], Sasa Kenjeres[4], Daniel Schanz[2], Sebastian Gesemann[2], Andreas Schröder[2], Tom Claessens[6]

(1) BioMMeda, Institute Biomedical Technology
Ghent University
Ghent, Belgium

(2) Institute of Aerodynamics and Flow Technology
German Aerospace Center (DLR)
Gottingen, Germany

(3) Thoraxcenter Biomedical Engineering
Erasmus Medical Center
Rotterdam, The Netherlands

(4) Department of Chemical Engineering
Delft University of Technology
Delft, The Netherlands

(5) Department of Radiology
Leiden University Medical Center
Leiden, The Netherlands

(6) Department of Materials, Textiles And Chemical Engineering
Ghent University
Ghent, Belgium

INTRODUCTION

The intraventricular flow structures generated during the diastolic phase are believed to facilitate the filling of the heart, mass transport and momentum by keeping the blood moving throughout the diastolic phase and smoothly redirecting the flow towards the outflow tract [1]. The intraventricular flow dynamics are influenced by structural/anatomical alterations of the left ventricle (LV) cavity and changes in cardiac physiology [2]. Consequently, researchers are highly interested in the effect of the adaptation of the LV to the flow dynamics. The LV flow has an intrinsic complex three-dimensional and unsteady structure. However, in vivo imaging methods are still limited in terms of temporal and/or spatial resolution and are often complemented and/or validated by *in vitro* or *in silico* methods. Until now, in vitro flow investigations were primarily performed in 2D or pseudo-3D, where the volumetric flow was reconstructed from a series of planar measurements. We believe, however, that LV flow analyses would highly benefit from the application of an instantaneous volumetric measurement technique.

The goal of our present work is to investigate the evolution of the 3D intraventricular flow structures downstream of a biological valve mounted in a compliant LV model. The flow is investigated by means of a truly volumetric particle-based imaging technique; a 3D multi-camera imaging system is used to record time-resolved images of tracer particles within the investigated volume. The Shake-The-Box (STB [3]) Lagrangian Particle Tracking (LPT) algorithm is employed to reconstruct individual particle tracks during the cardiac cycle. The FlowFit data assimilation algorithm [4] allows for the interpolation of the scattered LPT results onto a regular grid and for the extraction of the 4D relative pressure field.

METHODS

An anatomically realistic LV is mimicked by means of a flexible membrane driven by a programmable pump (Vivitro Systems, Inc., Victoria, BC, Canada). The 0.5 mm thick membrane was manufactured by painting silicone layers onto a 3D printed mold; the geometry of the mold was based on the mean shape of 150 computed tomography patient segmentations [5]. The LV membrane is immersed in a Plexiglas ten-sided polygon tank and connected via the valve holders (figure 1a), where the aortic and the mitral valve are placed. The atrial and aortic chambers are connected via an adjustable resistance and fixed to the tank lid. The tank is connected to a pulsatile pump that generates semi-sinusoidal volumetric changes in the tank and consequently induces a loop of inflow and outflow in the LV.

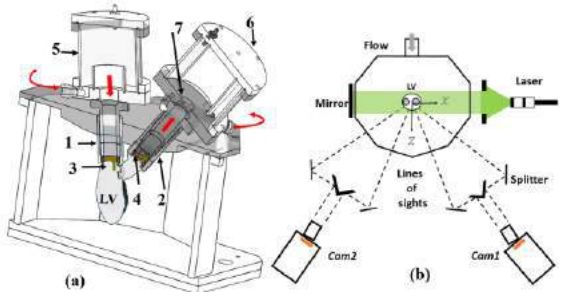

Figure 1: (**a)** CAD view of the nine-sided tank. 1-2: valve holders, 3-4: mitral and aortic valve position, 5-6: atrium and aortic blocks, 7: aortic pressure catheter. (**b)** Sketch of the 3D imaging system (top view).

To minimize optical distortion, a fluid mixture with the same refractive index as the silicone membrane was used (table 1). The fluid was seeded with Fluorescent Rhodamine-B coated particles. The 3D

imaging system was designed to simultaneously acquire four different views of the LV model using only two high-speed cameras (Imager Pro HS 4M, PCO, Kelheim, Germany) with a custom-made image splitter that was placed in front of each camera (figure 1b). A volume of approximately 80x110x70 mm^3 was illuminated by a double-cavity Nd:YLF laser. A long-pass filter was mounted in front of a macro lens (100 mm, Samyang Optics co Ltd., Korea) to selectively capture the fluorescent light scattered by the particles. The calibration of the camera system was performed by imaging a 3D calibration target located at the center of the investigated domain along the viewing direction (Z axis). The target calibration yielded an average error of 0.2 pixels; the volume self-calibration [6] technique was employed to reduce the residual calibration error down to less than 0.02 pixels. The measurements were performed during two consecutive cardiac cycles of 857 ms at a sampling rate of 2 kHz, resulting in 1714 recordings.

The recording sequence was processed using the Shake-The-Box algorithm [3]. STB enables the reconstruction of single particle tracks in 3D over long time-resolved sequences of recordings from a multi-camera imaging system. The method makes use of the Iterative Particle Reconstruction (IPR [7]) to reconstruct the 3D particle locations. An initial phase where tracks are identified over the first few realizations is followed by the prediction of the particle location at subsequent recordings; the predicted location is then corrected by means of an image matching scheme. Subsequently, the scattered position, velocity and acceleration measurement provided by the STB are interpolated onto a regular 3D grid by the FlowFit data assimilation algorithm [4] where a system of cubic B-splines is used to represent the velocity and pressure fields. By leveraging physical constraints derived from the Navier-Stokes equations, the spatial resolution is increased beyond the sampling offered by the tracked particles. The spatial gradients (such as vorticity, Q-criterion and viscous stress) can be evaluated analytically from the B-spline functions.

LV silicone membrane	Thickness: 0.5 mm
	Refractive index: 1.413
Mitral and aortic valves	25 and 19 mm biological valve
Hydraulic settings	Pseudo-sinusoidal -70 BPM
	Stroke volume: 50 ml
Fluid: 60% glycerol 40% water	η=17,7$mPa{\cdot}s$ ρ=1160 kg/m^3
Seeding: Rhodamine-B	Diameter: 20-50 µm
Imaging system	CMOS 4MP camera sensor
	Laser: 30 mJ/pulse (per cavity)

Table 1: Relevant setup and processing parameters

RESULTS

Figure 2 (a-b) shows approximately 7000 individual particle tracks during the inflow (a) and outflow phase (b); the tracks are visualized in the 3D domain by plotting the velocity vectors (color-coded by the vertical velocity) at the instantaneous particle locations along 18 subsequent recordings. The biological valve induces a strong trans-mitral jet directed towards the anterior wall of the LV, with a vertical velocity (V_y) of up to 1.3 m/s. The topology of the inflow jet is characterized by a crossed flow path, where the outflow fluid crosses the inflow path during the ejection phase (fig 2c). In physiological conditions the intraventricular flow path is looped [8] as shown in (fig 2d). The vortical structures induced in the LV cavity are visualized by iso-surfaces of Q-criterion (fig 2e). Multiple vortices are formed during the filling phase, similar to the vortices generated from a cylinder with an inclined exit. Figure 2f depicts the iso-surface of velocity magnitude colored by the pressure field relative to an offset P_0. In further processing P_0 is estimated via direct pressure measurement inside the LV model via a thin catheter.

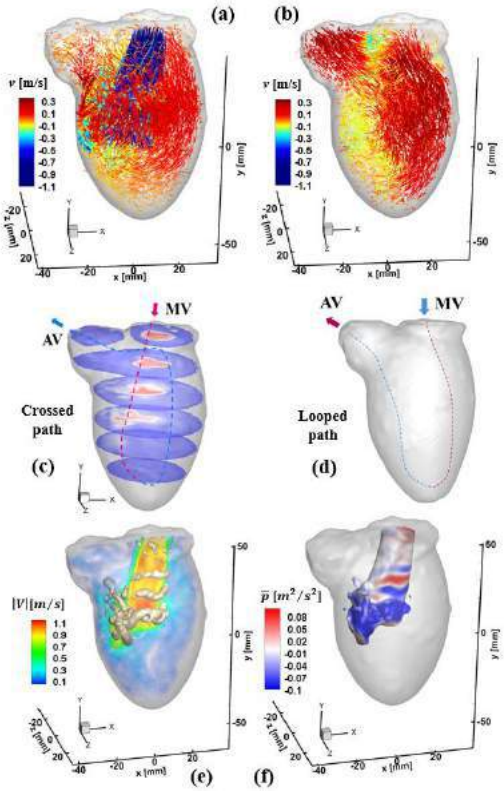

Figure 2: **(a-b)** Particle tracks over 18 recording during the diastolic and systolic phase, respectively, colored by vertical velocity component(along the Y axis). **(c)** Transversal cross-section colored with velocity magnitude. MV mitral valve, AV aortic valve. The dashed line depicts the crossed flow path. **(d)** Looped flow path in a healthy heart. **(e)** Vortex structures: iso-surface of Q-criterion (at 9350 s^{-2}) and contours of velocity magnitude in the XY plane at Z= -5 mm. **(f)** Iso-surface of velocity magnitude color-coded with the relative pressure.

DISCUSSION AND CONCLUSION

To the best of our knowledge, this is the first in vitro study to provide time-resolved Lagrangian 3D intraventricular flow patterns and relative pressure within a flexible LV model downstream of a biological valve. The preliminary results showed the formation, evolution and dissipation of the vortical structures during the diastolic phase. Considering that the implemented 3D imaging setup provides time-resolved access to the full velocity gradient tensor, we consider that this setup is an ideal tool for validation of numerical simulations and medical imaging.

REFERENCES

[1] Kilner, PJ et al., *Nature*, 404(6779), 2000
[2] Bermejo, J et al., *Annu Rev Fluid Mech*, 47:315–342, 2015
[3] Schanz, D et al., *Exp Fluids*, 57, 70, 2016.
[4] Gesemann, S et al., 18th *Lisbon symposium*, July 4-7, 2016.
[5] Metz, CT et al., IEEE Trans Med Imaging 31:1311-1325, 2012
[6] Wieneke, B et al., *Exp Fluids*, 45(4), 549-556, 2008
[7] Wieneke, B, *Meas Sci and Technol*, 24, 024008, 2012
[8] Pedrizzetti, G et al., *Ann Biomed Eng*, 38:769–773, 2010

SB³C2019
Summer Biomechanics, Bioengineering and Biotransport Conference
June 25 -28, Seven Springs, PA, USA

IMPACT OF DIFFERENT BIFURCATION STENTING TECHNIQUES ON ENDOTHELIAL SHEAR STRESS WITHIN A PHERIPHERAL BIFURCATION

Azadeh Lotfi (1), Tracie J. Barber (2)

(1) Department of Mechanical and Manufacturing Engineering, UNSW Australia Sydney, NSW, Australia

(2) Department of Mechanical and Manufacturing Engineering, UNSW Australia Sydney, NSW, Australia

INTRODUCTION

In the lack of information on the preferred method of bifurcation stenting in peripheral arterial disease (PAD) patients, further experiences with hemodynamic analysis are required to gain understanding of the underlying mechanisms implicated in ISR formation using different bifurcation stenting arrangements in peripheral arteries.

The aim of this study is to quantify altered hemodynamics due to virtual implantation of the most commonly used double-stent bifurcation stenting techniques including T, Culotte (CUL) and Crush (CRU) in a model of a below-the-knee bifurcation. The model of popliteal bifurcation generated from representative vascular dimensions is used for subsequent computational fluid dynamics (CFD) analysis. Time averaged wall shear stress (TAWSS) and oscillatory shear index (OSI), were quantified as hemodynamic indicators of disturbed flow responsible for ISR formation. The results of this study can help endovascular interventionalists in the selection of a suitable strategy for PAD treatment.

METHODS

For bifurcation models, the geometry of the popliteal artery which branches into anterior tibial artery and tibio-peroneal trunk is used to construct different configurations of stenting techniques. The geometric characteristics used for creating these models are given in **Error! Reference source not found.**. For virtual stent implantation, the Bx Velocity device (Johnson & Johnson Interventional System, Warren, NJ, USA), was selected due to their major application in the treatment of below the knee arteries. The stent geometry information was reconstructed from optical microscopy images [1] as well as available manufacturer's product catalogue most of which can be find in [2].

All grid discretization were generated using ICEM 14.5 (ANSYS Inc., Canonsburg, PA, U.S.A). The geometric models were meshed using the hybrid tetrahedral-prismatic layer elements with regards to the information provided in our previous study [3].Convergence testing was first carried out on mesh density, and then continued to time step size and residual level for all models through transient simulation to ensure the reliability and stability of the grid solutions. The robust GCI methodology is used to evaluate the uncertainties involved in each solution in accordance with our previous study [3]. After all, a total number of 8683951, 8301933 and 7915173 elements were used to discretize the model of CUL, CRU and T techniques, respectively. A time step of 0.001s was deemed most feasible to sufficiently resolve the complex hemodynamic flows yielding the average courant number less than 1. RMS residual level equals to 10^{-4} was used as a convergence criteria. Simulations were run for 3 consecutive cycles and only the results from the third cycle were used for analysis to avoid transient start-up effects.

The blood was assumed to be a Newtonian and homogeneous fluid with a density of 1060 kg/m^3 and a viscosity of 0.0035 Pa.s. The peak Reynolds number for all flows ensures a laminar fluid model for all cases. The walls were assumed to be rigid, nonporous and smooth as the arterial wall thickens due to calcified atherosclerotic plaque accumulation. A physiological triphasic flow waveform obtained from the proximal segment of popliteal bifurcation was imposed as an inlet MB boundary condition while the flow rate profile through the anterior tibial artery was applied at the distal MB outlet. A zero static pressure

condition was imposed at the SB outlet to meet flow continuity. ANSYS CFX 16.2 (Canonsburg, PA, USA) was utilized for simulation.

Table 1: Design characteristics used for regenerating 3D digital models of stented bifurcated popliteal artery.

Geometric Characteristics	
Proximal MB diameter (mm)	4.5
Distal MB diameter (mm)	3.9
SB diameter (mm)	2.5
Bifurcation angle	60°
Oversize ratio	10%
Stent strut width × thickness (mm) (fully embedded strut protrusion)	0.013 × 0.14
Stent Profile	Rectangular

RESULTS

TAWSS was considered to capture the significant difference between the models. The fluctuations in WSS was evaluated through the use of OSI. The results on using these two metrics to address the adverse hemodynamics within these three models are displayed in Figure 1. Looking at the distal MB and the SB, similar patterns for low TAWSS and high OSI were observed for all models, mainly confined to the near-stent strut and over the outer wall of the SB proximal to the ostium.

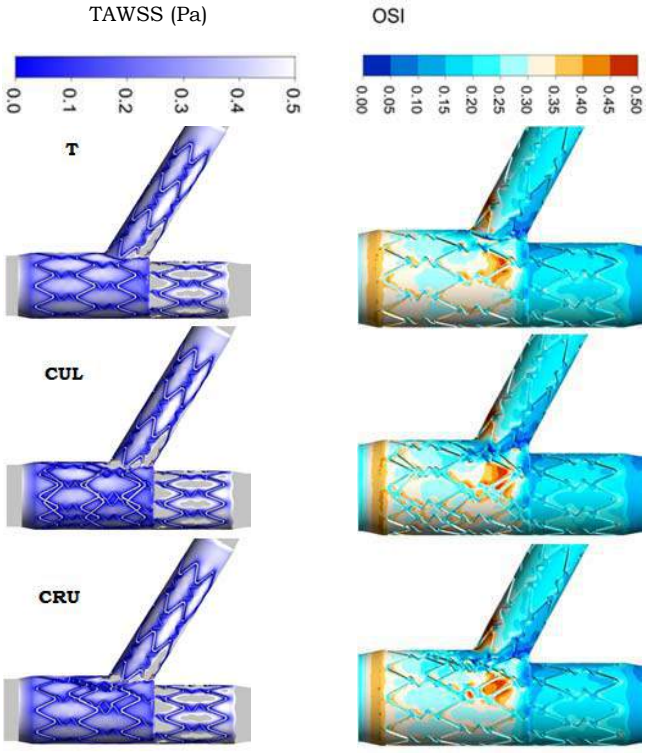

Figure 1: (Left column) Adverse TAWSS and (Right column) OSI contour plots along the arterial wall for T, CUL and CRU models.

The noticeable difference in distribution of these two hemodynamic indices is observed at the PM segment varying depending on the different insertion of additional stent into the artery. In the proximal MB, increasing areas of low TAWSS and high OSI are noted for CUL as compared to CRU. This is due to the in-stent recirculation caused by the presence of the additional layers of struts, more pronounced in CUL where the second layer localised all around the PM segment. Another distinct difference obtained was that the low OSI value localised at the location of carina in T model, is extended to the lateral walls at the ostium of CUL and CRU, indicating minimal variation in WSS throughout the cycle.

DISCUSSION

The results of this study indicated that each bifurcation stenting technique has distinct impact on the flow patterns shown through adverse TAWSS and OSI metrics, known to influence ISR. The deleterious interaction of additional layers of struts in CRU or CUL provided some disadvantages, most notably the highest risk of ISR in CUL followed by a less significant one in CRU. However, CUL and CRU demonstrated the most favourable results in preserving the bifurcation ostium patency as the least adverse events and thus ISR was obtained for this region due to the better SB ostial coverage provided by multiple layers of struts.

In this study, due to the marked difference in the diameter of PM and DM segments, the geometric variation in the PM and SB segments resulting from the concentration of one or multiple layers of struts for T, CUL and CRU, did not appear to impact the near-wall flow condition in the DM segment. Thus, all stented models seem to expose to adverse hemodynamic condition similar to each other. This indicates the same chance of the exposure of this segment to the likely mild ISR across all techniques. However, a more pronounced difference is observed in the results of [4] in a model of the coronary artery throughout the SB and DM segment between T, CUL and CRU techniques, emphasizing different performance of these techniques in terms of ISR formation in coronaries and peripheries when the major geometrical configuration such as the lumen dimeter and the bifurcation angle and the inflow properties differs between the two arteries.

Among all considered double-stent models, T showed to provide a balanced haemodynamic environment that eliminated the adverse effect of multiple layers of struts within the PM segment while maintaining the flow condition throughout the SB and DM segment similar to the other techniques However, as the coverage of the SB ostium in this technique is not as good as CUL or CRU, more of the ostial area can exposed to potential restenosis, also shown through the localisation of adverse TAWSS and high OSI within more of the ostium section. Therefore, this technique is not suited to lesions which involve the ostium and the proximal SB.

REFERENCES

[1] Migliavacca, F. et al., Med. Eng. Phys. 27:13–18, 2005.
[2] Gundert, T.J. et al.,. J. Med. Device 7, 011004, 2013.
[3] Lotfi, A. et al., J. Biomech. Eng, 138:31005, 2016.
[4] Katritsis, D.G. et al., Circ. Cardiovasc. Interv, 5:530–539, 2012.

SB³C2019
Summer Biomechanics, Bioengineering and Biotransport Conference
June 25 -28, Seven Springs, PA, USA

IMPROVEMENT AND IN VITRO VALIDATION OF A FINITE ELEMENT BASED VIRTUAL COILING METHOD FOR INTRACRANIAL ANEURYSM

Robert J. Damiano (1,2), Saeb Ragani (1,2), Adnan H. Siddiqui (1,2,4), Jason M. Davies (1,2,4), Hui Meng (1,2,3,4)

(1) Department of Mechanical and Aerospace Engineering
University at Buffalo
Buffalo, NY, USA

(2) Canon Stroke and Vascular Research Center
University at Buffalo
Buffalo, NY, USA

(3) Department of Biomedical Engineering
University at Buffalo
Buffalo, NY, USA

(4) Department of Neurosurgery
University at Buffalo
Buffalo, NY, USA

INTRODUCTION

Embolic coils treat intracranial aneurysms (IAs) by inducing blood stasis inside the IA, leading to its thrombotic occlusion, but 20.8% of coil-treated IAs are incompletely occluded at treatment follow-up [1]. Computer simulation of coiling and aneurysmal flow could help predict treatment outcomes *a priori*, but it requires accurate modeling of coils and their deployment. We previously developed a finite element method (FEM)-based virtual coiling technique to investigate effects of different treatment strategies on aneurysmal hemodynamics [2]. Here, we (1) improved the pre-shape and mechanical properties of modeled coils and (2) tested how coiling simulations compared with experimental coil configurations. Being highly dynamic, actual coil configurations are practically irreproducible in simulation, which makes validating coiling simulations challenging. Thus, we developed a new experimental approach for validating coiling simulations. We fabricated 4 physical phantoms based on two patient-specific IAs and deployed 1 or 2 coils in each phantom. To characterize coil configuration, each treated phantom was solidified into a block and sanded down into 5 sequential cross-sections, on which we measured coil density and lacunarity (spatial uniformity). In order to compare our original and improved virtual coiling methods, we simulated the experimental deployments 9 times with different initial conditions in the simulations, using our original and then the improved method in each phantom geometry. The resulting 72 virtually treated phantoms were sectioned into planes to match the experimental phantom cross-sections. Results from both methods agreed well with experiments, with the improved method having better agreement.

METHODS

Improvements to Coil Pre-Shape and Mechanical Properties Coils have a multiscale geometry with three levels: primary wire, secondary spring-like structure, and tertiary pre-shape [3]. As in our original coiling method, we simplified the coil's complex geometry in the improved method in this study: the coil's primary wire was not modeled and its secondary spring-like structure was modeled as a series of linked, tubular finite element beams. In our original coil method, "random", three-dimensional parametric curves were adopted as the coil's tertiary pre-shape, as demonstrated in Figure 1A. In our improved coil model, we improved the modeling of the coil's pre-shape. Coil pre-shapes are proprietary, but coil patents are publically available, which contain illustrations of pre-shapes. As the basis for our pre-shape model, we selected the pre-shape in Figure 5A of U.S. Patent No. 6,322,576 24 (here, Figure 1B) and modeled it in Soldiworks [4]. In our original coil model, we assumed that the coil's beam elements' elastic moduli (E_b, G_b) were the same as the coil's platinum primary wire (E_w and G_w). In the improved coil model, we considered the influence of the coil's spring-like structure and calculated spring-inspired beam properties (E_b and G_b) by equating beam stiffness to spring stiffness (i.e. compressive, shearing, and flexural) to calculate "effective" beam properties [5].

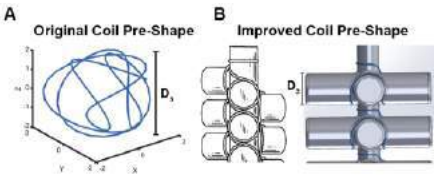

Figure 1: Original and improved coil pre-shape models. A. The original pre-shape model was a "random" spherical 3D curve generated by parametric equations. The improved pre-shape model was created by virtually mimicking the mechanical winding of the coil's secondary structure around a complex-shaped mandrel (the "tree-like" structure).

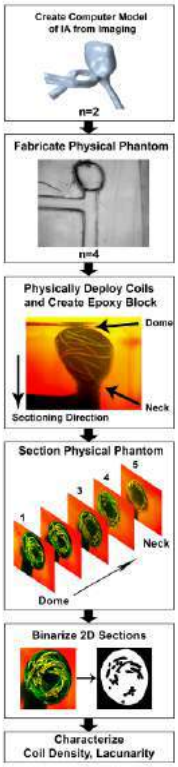

Figure 2: Overview of the experimental approach to extract and characterize coil configuration from the coiled phantoms.

Experimental Approach to Evaluate and Validate Coiling Methods In order to experimentally validate our virtual coiling methods, as well as determine if the improved method had better accuracy than the original method, we developed an *in vitro* approach to extract and characterize the geometry of coil configurations in patient-specific IA phantoms. To obtain real coil configurations to validate our coiling method, we deployed one or two coils in two phantoms each of two patient-specific IAs. These 4 coiled phantoms were solidified in epoxy and sanded to extract 5 intra-aneurysmal cross-sections from which coil configuration was characterized and quantified. Specifically:

1. *To create physical phantoms of the aneurysm models*, we 3D printed plastic molds (positive) of their *stl* files and created optically clear silicone phantoms (negative) from them, using our previously developed phantom fabrication technique [6].
2. *To obtain coil configuration from the coiled IA phantoms*, we extracted 2D cross-sections by solidifying the phantoms in epoxy, sanding them down sequentially in planar cross-sections, and stepwise imaging the coil containing cross-sections [7].
3. *To characterize coil configurations*, we binarized the 2D cross-section images and quantified coil distributions on them using coil density (CD) and lacunarity (L) (spatial uniformity) [8].

A flowchart summarizing this experimental approach is shown in Figure 2.

To compare and validate our virtual coiling methods, we modeled each physical phantom and in each phantom, we modeled the physical coil deployments 9 times using both our original and improved modeling methods. The virtually treated phantoms were sectioned into 5 planes matching those extracted from the experiments, and virtual coil distributions were quantified. To compare the simulation results with experiments, coil distribution quantifications were plotted together and analyzed. To obtain a "volumetric" (or 3D) representation of coil configuration resulting from each deployment, we summed the values of CD and L of each deployment over the 5 cross-sections. To quantify distances between the volumetric experiment and simulation points in order to compare the accuracy of the both simulation methods, we standardized CD and L such that they were on the same scale. Then, we calculated 3 Euclidean distances, namely d_{Min}, d_{Max}, and d_{Avg}.

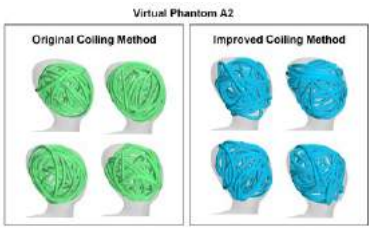

Figure 3: Examples of virtual coiling results from the original (green) and improved (blue) methods in virtual Phantom A2. Only 4 of the 9 virtual deployments are shown for each method.

RESULTS

As an example of physically deployed coils in an IA, treated Phantom A2 is shown in the middle of Figure 3. Images of the 5 cross-sections – the result of sanding this coiled phantom – are also shown. For virtual coiling results in the virtual phantoms, Figure 3 shows 4 of the 9 simulated deployments by both modeling techniques in Phantom A2. The top row of Figure 4 shows binarized images of cross-section 2 (S2) of Phantoms A1 and A2, together with the CD-L graphs for this cross-section. The bottom row of Figure 4 shows volumetric CD and L. The graphs show that the improved method produced volumetric realizations closer to the experimental realizations in the four phantoms. Figure 6 shows the results of the Euclidean distance calculations. Figure 6A illustrates the concepts of the 3 Euclidean distances, using the results of Phantom A2 as example. Figure 6B plots bar graphs of these distances resulting from the 2 virtual coiling methods for the 4 phantoms.

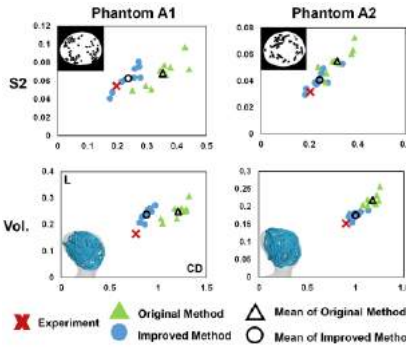

Figure 4: Quantification of coil experimental and computational results in Phantoms A1 and A2. Graphs S1-S2 show the raw values for lacunarity vs. coil density measured on cross-sections 1-2, and the graphs labeled Vol. show the summed "volumetric" values of CD and L for both phantoms. The binarized image of each experimental cross-section is shown in its corresponding graph.

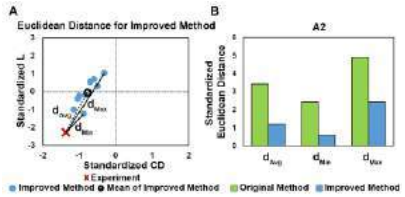

Figure 5: Euclidian distances from experiment to the computational results of both methods in the standardized, "volumetric" dataspace. A. An illustration of the three Euclidean distances evaluated. B. Bar graph of the three standardized Euclidean distances calculated for the original and improved methods in Phantom A2. All three distances were smaller for the improved method than for the original method.

It is clear from Figure 6B that d_{Min}, d_{Max}, d_{Avg} are consistently smaller for the improved method than for the original method. This result was the same in the other 3 phantoms. In other words, regardless of what distance is considered, the improved method better captures the physical reality than the original method.

DISCUSSION AND CONCLUSION

In this study, we improved the coil model in our FEM-based virtual coiling method and developed a validation approach to test if the improvements led to more accurate coiling simulations compared to experiment. Our results indicate that while both the original and improved methods agreed well with experiments, the improved method had consistently better agreement. This suggests that the model improvements were necessary to increase the accuracy of the virtual coiling method.

ACKNOWLEDGEMENTS

The National Institutes of Health (R01 NS 091075) supported this study.

REFERENCES

[1] Ferns, S. P. et al., *Stroke*, 40:e523-529, 2009.
[2] Damiano, R. J. et al., *J Biomech*, 48:3332-3340, 2015.
[3] White, J.B. et al., *AJNR*, 29:1242-1246, 200
[4] Wallace, M.P. et al., *United States: Target Theraputics Inc*, 2001.
[5] Wahl, A. M., *Mechanical springs*, Penton Publishing, 1944.
[6] Paliwal, N. et al., *J Biomech Eng*, 139:12, 2017.
[7] Sadasivan, C. et al., *Cardiovasc Eng Technol*, 4:63-74, 2013.
[8] Chueh, J.Y. et al, *J Neurointerv Surg*, 7:676-681, 2015.

SB³C2019
Summer Biomechanics, Bioengineering and Biotransport Conference
June 25 -28, Seven Springs, PA, USA

AUTOMATED SEGMENTATION OF CEREBRAL ARTERIES FROM PATIENT-SPECIFIC 3D CEREBROVASCULAR IMAGES USING DEEP-LEARNING AND GROUP MORPHOLOGY

Tatsat R. Patel (1, 2), Nikhil Paliwal (1, 2), Prakhar Jaiswal (1), Adnan H. Siddiqui (2,3), Rahul Rai (1), Hui Meng (1, 2, 4)

(1) Mechanical and Aerospace Engineering
University at Buffalo, the State University of New York
Buffalo, NY, USA

(2) Canon Stroke and Vascular Research Center
University at Buffalo, the State University of New York,
Buffalo, NY, USA

(3) Neurosurgery
University at Buffalo, the State University of New York
Buffalo, NY, USA

(4) Biomedical Engineering
University at Buffalo, the State University of New York,
Buffalo, NY, USA

INTRODUCTION

Image-based computational tools have helped gain insights into clinical diagnosis and treatment decisions for cerebrovascular diseases like intracranial aneurysms (IAs) [1]. However, these tools have failed to translate into the clinical workflow to aid the clinicians in decision-making. One of the big bottlenecks for the lack of translation is the segmentation of patient's medical image to create 3D vascular model. Currently, the segmentation processes in the computational tools are either manual or semi-automatic [2-5]. In both these segmentations, it is necessary to clean-up the final 3D model, and correctly distinguish between vasculature and imaging artifacts during the processing. This manual interaction with the image is highly time-consuming and subjective, which makes segmentation a big bottleneck in the computational tools. Therefore, if computational tools are to be translated into the clinic, the segmentation has to have the following features: automated, objective, efficient and anatomically accurate. To that end, in this study we propose an automated workflow for segmentation of 3D medical images using group morphology and convolution neural networks (CNN). Furthermore, with digital subtraction angiography (DSA) being the gold standard for IA examinations [5], we show the application of our workflow, by training and validating our model on 45 patient-specific 3D DSA images of aneurysm patients. We quantified dice similarity coefficient (DSC) of our model on an independent test dataset (n=5), which quantifies the similarity of our workflow's predictions as compared to the ground truth (manual segmentation).

METHODS

The flowchart of the proposed automated segmentation workflow is shown in Figure 1. The workflow consists of four steps: (1) pre-processing, (2) patch-extraction and CNN predictions, (3) image-binarization, and (4) post processing. In the first step, we take the complete (512^3 voxels) or partial (localized to major arteries susceptible to aneurysms) 3D cerebrovascular image, and use group morphological erosion-dilation process to eliminate erroneous imaging artifacts. In step 2, smaller patches are extracted from the cleaned image and a pre-trained CNN predicts the probability of each voxels in the patch being part of vasculature. In step 3, these predictions are binarized into either 1 (vessel) or 0 (background). This binarized image is further cleaned up

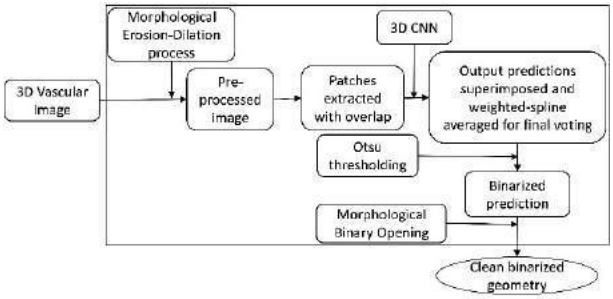

Figure 1: Workflow for automated segmentation of 3D vascular images, combining 3D CNN with group morphology operations.

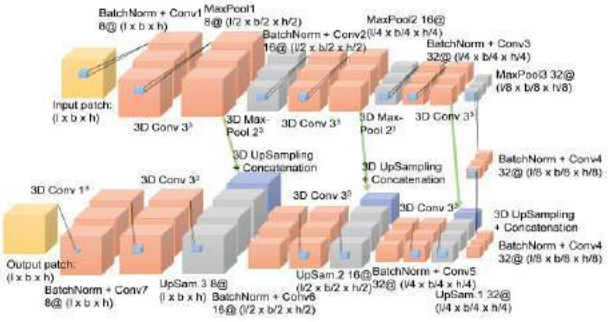

Figure 2: Proposed 3D U-Net for predicting vessels and background.

to get rid of any disconnected branch to give a fully connected network of desired vasculature. The following section provides details on the methods used in each step.

Pre-processing using erosion-dilation

We used group morphological opening (erosion followed by dilation) to remove erroneous imaging artifacts. This method first 'erodes' the objects smaller than the structuring element and then dilates to restore the shape of the remaining objects for artifact removal.

Patch extraction and CNN architecture

For training, the pre-processed image was divided into smaller patches with 50% overlap. Overlap amongst patches helps maintain continuity in data [6] and increases the number of training samples. For prediction, repeated values in overlapping patches were weighted-spline averaged for patch fusion [6]. As shown in Fig. 2, U-Net architecture is

used for the CNN, which is a well-established 3D CNN for biomedical image segmentation [7].

Image binarization based on Otsu's thresholding

The predictions from the CNN network are real numbers between 0 and 1, separating background from vasculature. To binarize these predictions a generalizable Otsu's thresholding method [8] is employed, which objectively maximizes the between-class variance of the classes.

Post-processing using morphological binary area opening

Morphological area opening was used to remove unattached artifacts in the CNN predictions to yield cleaner final segmentation.

Proof of concept study

Steps 1 and 3 in our automated workflow were derived mathematical formulations, which have been established and tested in other applications [9]. However, step 2 involves a 3D CNN, which required training to test the feasibility of our complete segmentation workflow. To that end, we collected 3D DSA images of 50 aneurysm patients to train (n=40), validate (n=5) and test (n=5) the feasibility of the computational workflow.

For this study, from the collected images we used only the regions encompassing the major arteries susceptible to aneurysms from the collected images. For showing feasibility of the workflow, a pipeline without the pre-processing step was implemented and tested. Moreover, the patch fusion for predictions were done by simple averaging.

Training & testing of the CNN model

For the CNN training and testing, first, the patient specific 3D DSA were manually segmented inside the pre-extracted ROI. The segmented surface were voxelized using the open-source mesh voxelization algorithm [10] and converted to binarized 3D volumes.

The CNN model was trained using the patches pre-extracted from the ROI. Different patch sizes were tested to evaluate the trade-off between accuracy and memory requirements. The percentage overlap for predictions was also varied to evaluate the trade-off between accuracy and the computational cost. For the model training, a hybrid of binary cross-entropy and Dice Similarity Coefficient (DSC) was used as the loss function [6]. As DSC was used as one of the contributor of the loss function, only patches with atleast one '1' label in the ground truth were used for the training [6]. The models trained for varying patch sizes and % overlaps were evaluated by comparing the DSC.

PRELIMINARY RESULTS

The performance of the models' training using 16^3, 32^3 and 64^3 sized voxel patches with 50% overlap on the training and validation cohort is shown in Fig. 3. The convergence of the models in the training and testing cohort can be observed from the progression of the loss function and DSC towards a plateau after ~700 epochs.

Optimum patch-size and overlapping voxels

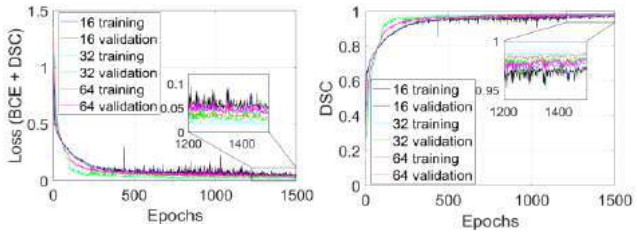

Figure 3: Loss and dice similarity coefficient for different patch of training models. Results showed that a patch size of 32 voxels provided best training.

The performance of the models on complete images of the validation cohort can be seen in Fig. 4. The graphs indicate the sensitivity analysis of the model to patch size and % overlap used for the predictions. A patch-size of 64 incrementally yields the highest DSC. Overlap of 87.5% yielded the highest DSC for varying % overlap. But considering the time taken to predict results at such high overlap %, an overlap of 50% is ideal. A higher % overlap results in incremental difference in the performance, but exponentially increases the time required for the prediction.

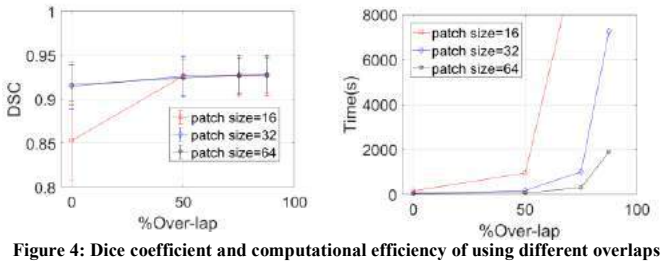

Figure 4: Dice coefficient and computational efficiency of using different overlaps of the patch size during training.

With an ideal patch-size of 64 and ideal % overlap of 50% along with post-processing, the model yielded a DSC of 0.919 ± 0.0342 on the testing cohort (n=5). A representative case from the testing cohort has been shown in Fig. 5. With only 40 cases used for training, the model was able to segment the major arteries but misses out on some minor arteries as can be seen in Fig. 5.

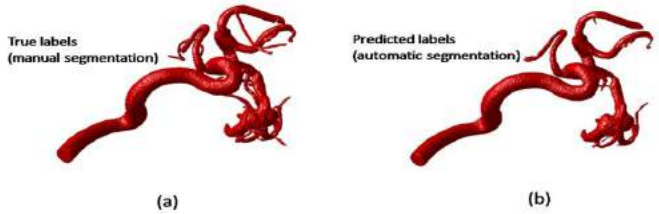

Figure 5: Comparison of automatically segmented image from the proof of concept study (training n=40) with manual segmentation for a representative 3D DSA

DISCUSSION

This proof of concept study for automated segmentation of cerebral vasculature from 3D DSA images produces a DSC of 0.919 ± 0.0342 on the independent testing cohort, when trained and validated on 40 and 5 cases, respectively. Furthermore, for predictions on the testing cohort, we found that optimum path-size of 64 and % over-lap of 50% gave the best trade-off between accuracy and computational cost. We found that our model missed smaller arteries during the predictions, which might due to the limited number of cases available for training (n=40). With a higher number of cases, we believe that our workflow would be able to capture these smaller arteries and be more robust. Thus, out tool has the ability to be potentially used in a clinical setting to provide reliable and quick segmentation for further analyses.

CONCLUSIONS

This work gives a feasibility study of the concept of using group morphological operations along with deep learning on the major cerebral artery segmentation to achieve automatic, objective, computationally efficient and accurate segmentation that can be used for accurate analysis downstream of the analysis pipeline.

ACKNOWLEDGEMENTS

This work was supported by the National Institutes of Health grant R01-NS-091075.

REFERENCES

[1] Xiang, J., et al., *Ann Biomed Eng*, 44(4): p.1085-96, 2016.
[2] Bogunovic, H., et al., *Med Phys*, 38(1): p.201-222, 2011.
[3] Tetteh, G., et al., *arXis preprint*, arXiv: 1803.09340, 2018.
[4] Chen, L., et al., *arXiv preprint*, arXiv:1712.07194, 2017.
[5] Phellan, R., et al., arXiv preprint, arXiv: 1803.09340v2, 2018
[5] van Rooij, W.J., et al., *Am J Neuroradiol*, 29(5): p.976-979, 2008.
[6] Hashemi, R., et al., *IEEE Access*, 7: p.1721-1735, 2018.
[7] Ronneberger, O.P, et al., *Med Image Comput Assist Interv*, 2015.
[8] Otsu, N., *IEEE Trans Syst Man Cybern Syst*., 9(1): p.62-66, 1979.
[9] Sreedhar, K., et al., *arXiv preprint*, arXiv: 1203.25143, 2012.
[10] Karabassi, E.A., et al., *J Graph Tools*, 4(4): p.5-10, 1999.

SB^{3}C2019
Summer Biomechanics, Bioengineering and Biotransport Conference
June 25 -28, Seven Springs, PA, USA

FABRICATION OF A FLEXIBLE IDEALIZED 3D PRINTED AORTIC DISSECTION FOR IN VITRO ANALYSIS

S. García-Rodríguez (1), A. Holtz (2), H. Zhou (2), R. Medero (2), A. Roldán-Alzate (1,2,3)

(1) Department of Radiology
University of Wisconsin-Madison
Madison, Wisconsin, USA

(2) Department of Mechanical Engineering
University of Wisconsin-Madison
Madison, Wisconsin, USA

(3) Department of Biomedical Engineering
University of Wisconsin-Madison
Madison, Wisconsin, USA

INTRODUCTION

In aortic dissection (AD), an aortic wall tear results in a false lumen formation, leading to complications such as aneurysm growth, rupture, end-organ malperfusion and hypertension [1]. Hemodynamics are highly complex, with a wide range of velocities and chaotic flow. Thus, the study of this pathology can be greatly benefitted by numerical and physical modeling, the latter relevant in CFD validation studies. However, despite great advances in patient-specific physical models [2-4], representation of wall mechanical properties is still a challenge. The purpose of this study was to present the feasibility of a flexible AD model fabrication and in vitro testing for flow assessment.

METHODS

Model Design and Fabrication

A virtual 3D geometry was created by extruding the cross-section of an AD taken from medical data (Mimics, 3-matic; Materialise; Leuven, Belgium) (Fig. 1A). Connectors were added at the inlet and outlets. The inlet section was combined into a single channel while each outlet was kept isolated (Fig. 1B).

The geometry was 3D printed (fused deposition modeling) using polyvinyl-alcohol (PVA) and placed in a PMMA casting box [2]. Sylgard 184, a PDMS silicone (The Dow Company; Midland, MI), was used as the model material, due to its refractive index and material properties, loosely comparable to common cardiovascular tissues [4]. Sylgard components were mixed (10:1 ratio) and degassed in a vacuum chamber (-80 kPa, 45 minutes) to remove air bubbles before pouring into the mold to cure. The PVA core was then manually removed after softening by soaking in hot water. The final model is shown in Fig. 1C.

Optical Imaging

A high-speed camera system (Phantom v341, Vision Research, Wayne, NJ), equipped with 60 mm f/2.8D lenses (Nikon Inc., Melville, NY), was set up to visualize model walls [5]. A 42% water-58% glycerol solution (ρ = 1.14 g/cm^3, μ = 0.01017 Pa-s) was used to match Sylgard 184 refractive index (n = 1.41), and was circulated using a pulsatile flow pump (BDC Laboratories, Wheat Ridge, CO). The model walls were imaged for approximately 1 s.

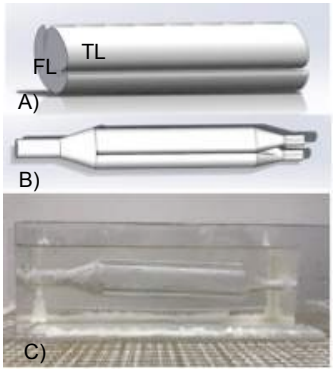

Figure 1: A) Virtual 3D geometry of the extruded AD cross section; B) idealized AD model as a casting insert; C) finalized silicone AD model.

Images were used to measure the length of both the true and false lumens (TL, FL) from a lateral view (Fig. 2). Change in length was recorded at several time points, using in vitro peak systole as the reference.

4D Flow MRI

MRI scanning was performed in a clinical 3T scanner (Discovery MR 750, GE Healthcare, Waukesha, WI) using a 5-pt phase contrast vastly undersampled isotropic projection (PC-VIPR) [6] sequence. Scanning parameters were FOV 320 x 320 mm, TR/TE = 6.15/2.0 s, FA 8, slice thickness 1.25 mm, Venc = 80 cm/s. Cardiac gating was used to align the data acquisition with the pulsatile flow profile. The data was reconstructed with 14 time steps and corrected for motion and noise.

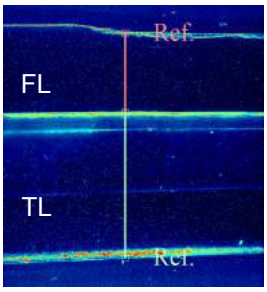

Figure 2: Lateral view of AD model from high-speed camera, indicating length measurements.

MR images were processed (EnSight; CEI Inc, Apex, NC) to visualize velocity distribution at cross planes, velocity streamlines and vectors. Time-resolved magnitude images were used to measure area of FL and TL at a plane located at the longitudinal center of the model along the cardiac cycle (ImageJ; public domain, NIH).

RESULTS

Opical Imaging

Resulting length measurements from high-speed camera images show some change in length of the lumens (mean strain 3.22% for FL and 0.1% for TL), thus demonstrating some flexibility or flap movement, represented especially on the FL.

4D Flow MRI

Fig. 3A shows velocity magnitude distribution throughout the model. Velocities were higher in the TL compared to the FL. Furthermore, velocity streamlines show completely retrograde flow in the FL; some of the flow exits the FL through the inlet bifurcation to enter into the TL (Fig. 3B). Velocity vectors show high magnitudes in the TL, exhibiting a non-parabolic profile (Fig. 4).

Area measurements in time-resolved magnitude images throughout the pumping cycle show variations that resulted in a mean strain of 3.50% for the FL and 3.20% for the TL.

DISCUSSION

The fabrication methods in this study show the feasibility of a 3D printed model with flexible walls. Several manufacturing process aspects can be optimized to achieve in vitro wall properties appropriately representing cardiovascular pathologies. Modifications of the flap and surrounding silicone block geometry could allow more deformation. Future work will also focus on a more patient-specific geometry. The fabrication methods here described provide a model with the transparency apt for particle image velocimetry, allowing highly accurate CFD and 4D Flow MRI validation.

This study was successful in using a pulsatile in vitro system in combination with the flexible model, which contrary to other flexible resin models, was able to withstand working pressures and flow conditions. Existence of a FL produces chaotic and retrograde flow, usually present in ADs. The use of 4D Flow MRI allows the study of velocities throughout the model. With geometries and wall properties that more closely represent in vivo tissues, models can be used to systematically study FL hemodynamics in vitro.

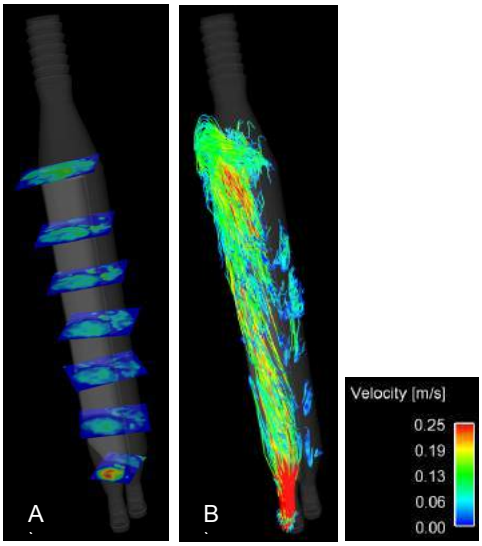

Figure 3: A) Velocity distribution along the AD model; B) velocity streamlines.

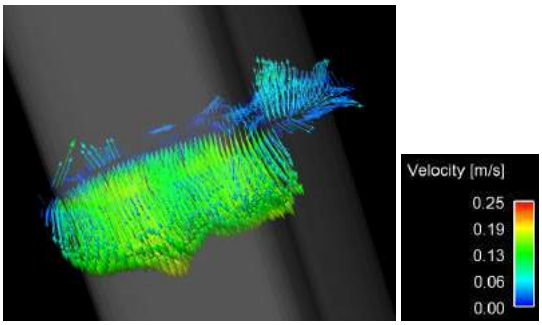

Figure 4: Velocity vectors at the longitudinal center of the AD model, at in vitro peak systole.

Both optical imaging and magnitude image measurements demonstrate transverse change in area of the lumens. The FL exhibits a higher strain. The lower resolution in MRI magnitude images is a limiting factor, as well as some subjectivity in contouring and measuring boundary definition. The TL strain measured in optical images was low compared to magnitude image measurements. This could indicate bulk movement along with the flap towards the FL or deformation in the other dimension of the cross plane. However, both techniques resulted in evidence of in vitro wall movement.

ACKNOWLEDGEMENTS

GE Healthcare provides MRI research support at UW-Madison.

REFERENCES

[1] Khan, IA et al., *Chest*, 122:311-328, 2002. [2] Yazdi, SG et al., *Ann Biomed Eng*, 46:1697-1721, 2018. [3] Usmani, AY et al., *Exp Fluids*, 57:186, 2016. [4] Geoghegan, PH et al., *Exp Fluids*, 52:1331-1347, 2012. [5] Medero R et al., *Ann Biomed Eng*, 46:2112-2122, 2018. [6] Johnson KJ et al., *Magnet Reson Med*, 63:349-355, 210.

EXPERIMENTAL EVALUATION OF TWO FAST VIRTUAL STENTING ALGORITHMS FOR MODELING FLOW DIVERTERS IN PATIENT-SPECIFIC INTRACRANIAL ANEURYSMS

Saeb R. Lamooki (1,2), Vincent M. Tutino (1,3,4), Nikhil Paliwal (1,2), S.V. Setlur Nagesh (1), Robert J. Damiano (1,2), Adnan H. Siddiqui (1,4,5), Hui Meng (1,2,3,4)

(1) Canon Stroke and Vascular Research Center Buffalo, NY, USA

(2) Department of Mechanical & Aerospace Engineering, University at Buffalo Buffalo, NY, USA

(3) Department of Biomedical Engineering, University at Buffalo Buffalo, NY, USA

(4) Department of Neurosurgery, Jacobs School of Medicine and Biomedical Sciences, University at Buffalo Buffalo, NY, USA

(5) Department of Neurology, Jacobs School of Medicine and Biomedical Sciences, University at Buffalo Buffalo, NY, USA

INTRODUCTION

Flow diverter (FD) is a self-expanding, densely woven stent mesh implanted across the neck of an intracranial aneurysm (IA) as an effective endovascular treatment device. By diverting the blood flow away from the aneurysm and into the parent artery, the FD aims at inducing stasis inside the IA, which causes thrombotic occlusion of the aneurysm and thus excludes it from the circulation. Despite the unique effectiveness of FD in treating challenging IAs such as giant, wide-necked and fusiform aneurysms, approximately 25% of FD-treated aneurysms do not occlude within 6 months of treatment.[1] For such unoccluded cases, persistent blood flow in the aneurysm may expose it to thrombotic complications and latent risk of rupture.[2]

Studies have shown that residual filling of the FD-treated IAs reflects ineffective flow diversion of FD in the unoccluded cases.[3,4] Paliwal et al. have found that FD treatment outcome is dependent on the post-treatment hemodynamics [3], which in turn depends on the geometrical parameters of the implanted FD. Therefore computer modeling of FD implantation using "virtual stenting" techniques along with computational fluid dynamics (CFD) could potentially aid clinicians in treatment planning.[5-8]

For a virtual stenting algorithm to be integrated into the clinical workflow, it needs to be able to accurately and rapidly simulate the FD treatment in patients. Previously, we developed an FEA-based high fidelity virtual stenting (HiFiVS) technique, which accurately captures the physics of FD deployment processes.[5,6] However, the computational cost associated with this method is high.

Recently we developed two fast virtual stenting techniques—virtual stenting workflow (VSW) and ball sweeping (BS). The VSW is a dynamic algorithm based on pseudo-physical forces for expansion of a generic simplex mesh in the parent artery.[7] Although it has been used in many clinical studies, [3,9] the modeling technique has not been properly validated. The only validation of VSW was a comparison of post-treatment CFD results for a porous Enterprise stent—not FD—in a patient-specific IA, against CFD results of post virtual stenting using the HiFiVS technique. The HiFiVS technique itself was rigorously validated in terms of deployed FD geometry [6]. Since FDs are composed of a much larger number of braided wires than the Enterprise stents, the VSW simulations of FD deployment still have to be geometrically and hemodynamically validated against experiments.

To further reduce computation, the BS technique takes a very different approach by skipping expansion and collision detection.[8] Being a static algorithm, BS sweeps a maximally inscribed sphere along the parent artery to directly generate a stent surface. However, since BS completely lacks the physics, it is unclear whether it can accurately represent the actual FD deployment. Thus, it is imperative to validate BS to investigate whether it can still provide accurate FD deployments in patient-specific IAs.

Clearly, there is a need to validate the accuracy of both VSW and BS algorithms for simulating FD deployment against experimental data. This was the purpose of this study.

METHODS

We employed VSW and BS algorithms to simulate the deployment of pipeline embolization device (PED) in three representative patient-specific aneurysm models: two internal carotid artery (ICA) aneurysms (one 7 mm and one 17 mm) and one anterior cerebral artery (ACA) aneurysm (10 mm). We physically deployed a PED in each of the phantoms of these IAs and evaluated the accuracy of the virtually deployed PED geometry against the experimental results. We also validated the CFD-derived post-treatment flow in the virtually treated IAs against particle image velocimetry (PIV) measurements in the phantoms.

Validation Workflow – As shown in Fig.1 we segmented the DICOM images of the selected IAs. Next, we 3D printed Vero models of these IAs and used them to fabricate silicone phantoms using the lost wax technique.[10] One PED (ev3, Chestnut Medical, Menlo Park, CA) was deployed in each phantom by an experienced neurointerventionalist. We captured the geometry of the deployed PEDs in the silicone phantoms using bright field imaging and performed image processing to calculate the porosity and pore density. Furthermore, to measure post-treatment hemodynamics, we performed PIV experiments on the treated phantoms and measured the IA velocity on a 2D plane. Next, we imaged the phantoms to obtain their 3D geometrical models and modeled the FD deployment using VSW and BS algorithms. The porosity and pore density of the virtually implanted devices were calculated and compared against the experimental results. We also performed CFD on the virtually treated IAs to obtain the velocity field in each aneurysm and compared them against PIV measurements.

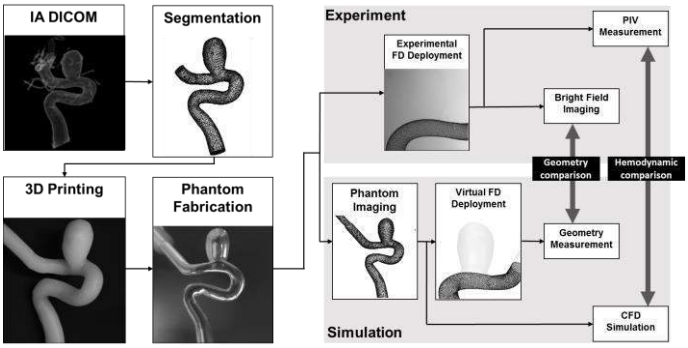

Figure 1 Validation workflow

Geometric and Hemodynamic Parameters – We captured the experimental and virtual deployed PEDs (for both VSW and BS) from sagittal and transverse views and divided each one to 3 zones: "proximal", "neck", and "distal." We further divided each zone to 4 patches, totaling 12 patches for each IA. These patches matched between experiments and virtual models. We calculated porosity and pore density for each patch, and quantified the absolute errors in these metrics between experiment and both VSW and BS. These errors were averaged over all the patches across all 3 IAs in each zone, which resulted in a single average error for each algorithm at each zone. A student's t-test was performed on the errors to determine whether there was a statistical difference between the two algorithms at each zone.

In addition to geometrical parameters, we calculated the post-treatment average IA velocity at the PIV plane from both CFD and PIV velocity fields. We also calculated the average 2D inflow velocity at the neck. For each of the hemodynamic metrics, we calculated the error between PIV and CFD for each algorithm and performed student's t-test to determine if there was statistical difference between them.

RESULTS

Geometrical Accuracy – Figure 2 shows the deployed PED in the 3 IA models from experiments and the two virtual stenting modeling techniques. Qualitatively, the VSW results match experiments better than BS. In particular, the virtual FDs simulated by BS show large and irregular bulges at the IA neck, which are absent in the physically deployed FDs. To quantify the accuracy of the algorithms in recapitulating the FD geometry, we calculated the porosity and pore density of the PED patches. As shown in Fig. 3, VSW had lower average porosity errors (p=0.589 at proximal, p=0.593 at neck, p=0.692 at distal) with smaller standard errors, and lower average pore density errors (p=0.003 at proximal, p=0.049 at neck, and p=0.004 for pore density) with smaller standard errors, compared to BS.

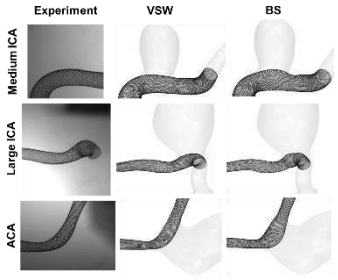

Figure 2 Experimental and virtual deployments in 3 IA models

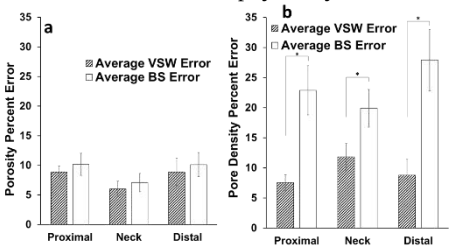

Figure 3 Average errors in porosity (a) and pore density (b) at the 3 zones for VSW and BS deployment. * indicates p<0.05

Hemodynamic Accuracy – We compared the CFD-calculated flow fields on virtually treated IA models against the PIV measurements on a representative plane in each PED-treated phantom. Figure 4 shows that CFD flow field on both VSW- and BS-treated IAs qualitatively captured the PIV measurements basic flow patterns in terms of the inflow jet location, the number and location of the vortices in the aneurysm, and the overall flow pattern. However, quantitative comparison of IA average velocity (Fig. 5-a) and 2D inflow velocity (Fig 5-b) shows higher accuracy for VSW in all IAs, albeit not statistically significant (p=0.167 for IA velocity and p=0.105 for 2D inflow velocity).

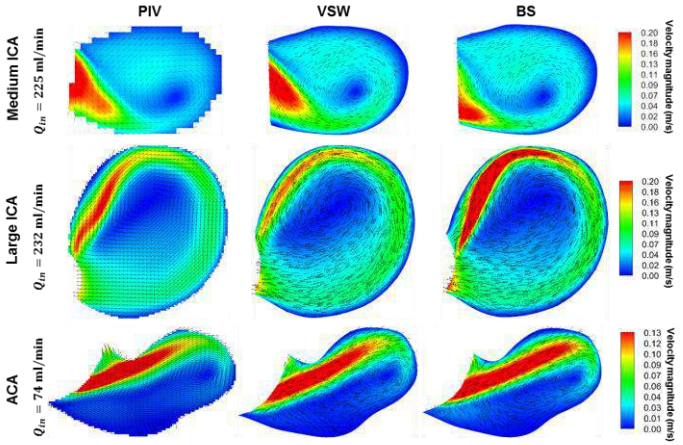

Figure 4 Post-treatment flow fields from PIV experiment and simulations

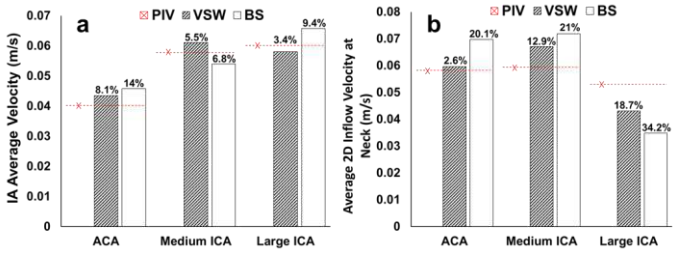

Figure 5 IA average velocity and average 2D inflow velocity calculated from CFD and experiment. Percent errors are shown on top of the bars.

DISCUSSION AND CONCLUSION

The VSW algorithm outperformed BS in capturing the PED geometry. Pore density from VWS had significantly less error compared to BS. Porosity from VWS was also smaller albeit not significantly. Moreover, in terms of hemodynamics, VSW-treated IAs had average less error than BS-treated cases IA velocity and 2D neck inflow velocity, calculated from CFD, but these did not reach statistical difference. The computational time performance of the two algorithms need to be evaluated in the future.

ACKNOWLEDGEMENTS

This work was supported by the National Institutes of Health grant R01-NS-091075 and Canon Medical System Corporation. We would like to thank Robert J. Damiano, Hamidreza R. Oghaz, and Sanyasi S. Veeturi for helpful discussions.

REFERENCES

[1] Brinjikji W. et al., Stroke, 44(2): 442-4277, 2013.
[2] Ikeda H. et al., J peritherapeutic neuroradiology, 21: 674-683, 2015.
[3] Nikhil P. et al., Neurosurgical Focus, 45(5): E7, 2018.
[4] Mut F. et al., J Neurointerv Surg, 7(4): 286-90, 2015.
[5] Ma D. et al., J Biomech, 45(13): 2256-2263, 2012.
[6] Ma D. et al., Ann Biomed Eng, 41(10):2143-56, 2013.
[7] Paliwal N. et al., CMBBE, 19(13): 1423-1431, 2016.
[8] Zhao L. et al., SPIE Int Soc Opt Eng, 9786, 2016.
[9] Zhang Q. et al., J Neurointerv Surg,10(3): 252-257, 2018.
[10] Paliwal N. et al., J Biomech Eng, 139(12), 2017.

SB³C2019
Summer Biomechanics, Bioengineering and Biotransport Conference
June 25 -28, Seven Springs, PA, USA

ADHESION EFFECT ON LOCALIZATION OF DEFORMABLE MICRO-PARTICLES IN BLOOD FLOW

H. Ye (1), Z. Shen (2), Y. Li (1,2,3)

(1) Department of Mechanical Engineering
University of Connecticut
Storrs, CT, USA

(2) Department of Mechanical Engineering
University of Connecticut
Storrs, CT, USA

(3) Department of Mechanical Engineering
University of Connecticut
Storrs, CT, USA

INTRODUCTION

The margination and adhesion of micro-particles (MPs) have been Margination, defined as the migration of a particle in blood flow towards the periphery of the blood vessel, allows the particle to come close to the endothelium, and then adhere to the vessel wall [1]. It is of significant importance to understand such physiological processes for curing relevant diseases. For example, in the inflammation process, margination of leukocytes towards the vessel wall is the precondition for an organism to perform defence functions, such as adhering to vascular endothelium and transmigrating into the tissues. In atherosclerosis, the thrombosis, formed by the clot, is caused by the margination and accumulation of numerous platelets responding quickly to events on the vessel wall, e.g. injury. Additionally, margination has extensive applications in microfluidic devices for the removal of pathogens and the separation of cells [2].

METHODS

We use the lattice Boltzmann method and molecular dynamics to solve the fluid dynamics and particle dynamics (including red blood cells (RBCs) and elastic MPs) in blood flow, respectively. Additionally, a stochastic ligand–receptor binding model is employed to capture the adhesion behaviours of elastic MPs on the vessel wall. The schematic is shown in Figure 1.

RESULTS

Margination probability is used to quantify the localization of elastic MPs at the wall. Two dimensionless numbers are considered to govern the whole process: the capillary number Ca, denoting the ratio of viscous force of fluid flow to elastic interfacial force of MP, and the adhesion number Ad, representing the ratio of adhesion strength to viscous force of fluid flow. We systematically vary them numerically and a margination probability contour is obtained. We find that there

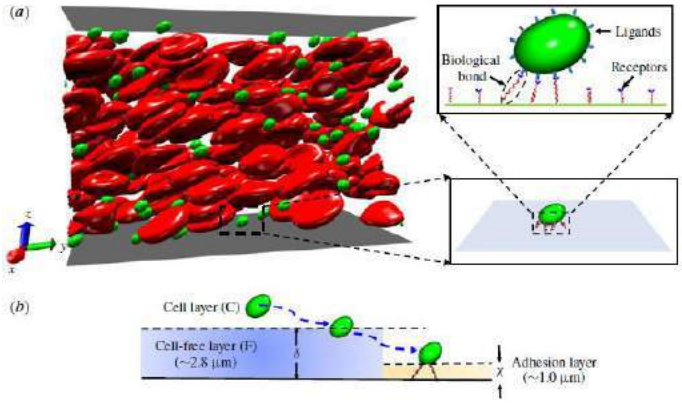

Figure 1 Transport of elastic MPs in blood flow. (a) Computational model of margination and adhesion of elastic MPs in blood flow. The zoomed panels give the detailed adhesion behaviour of an elastic MP under a stochastic ligand–receptor binding effect. (b) Schematic of transport process of an elastic MP from the centre of the bloodstream (denoted (C)) to the cell-free layer (F), and then reaching the adhesion layer.

exist two optimal regimes favouring high margination probability on the plane Ca–Ad. The first regime, namely region I, is that with high adhesion strength and moderate particle stiffness; the other one, region II, has moderate adhesion strength and large particle stiffness (see Figure 2).

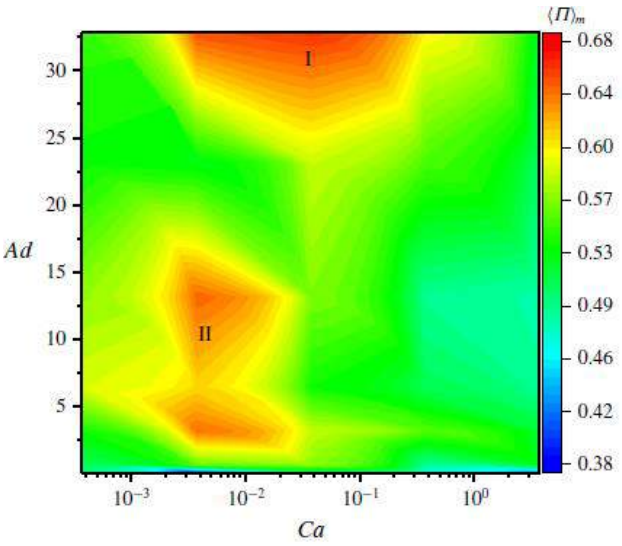

Figure 2 Contours of margination probability on the Ca–Ad plane

DISCUSSION

We conclude that the existence of optimal regimes is governed by the interplay of particle deformability and adhesion strength. The corresponding underlying mechanism is also discussed in detail. There are three major factors that contribute to the localization of MPs: (i) near-wall hydrodynamic collision between RBCs and MPs; (ii) deformation-induced migration due to the presence of the wall; and (iii) adhesive interaction between MPs and the wall. Mechanisms (i) and (iii) promote margination, while (ii) hampers margination. These three factors perform different roles and compete against each other when MPs are located in different regions of the flow channel, i.e. near-wall region. In optimal region I, adhesion outperforms deformation-induced migration; and in region II, the deformation-induced migration is small compared to the coupling of near-wall hydrodynamic collision and adhesion [3].

ACKNOWLEDGEMENTS

This work was supported by the National Science Foundation (OAC-1755779). Z.S., H.Y. and Y.L. are all grateful for the support from the Department of Mechanical Engineering at the University of Connecticut. Z.S. and H.Y. acknowledge partial financial support from the GE Fellowship for Innovation. This research benefited in part from the computational resources and staff contributions provided by the Booth Engineering Center for Advanced Technology (BECAT) at the University of Connecticut. Part of this work used the Extreme Science and Engineering Discovery Environment (XSEDE), which is supported by the National Science Foundation grant no. ACI-1053575.

REFERENCES

[1] KOUMOUTSAKOS, P., PIVKIN, I. & MILDE, F. 2013 The fluid mechanics of cancer and its therapy. *Annu. Rev. Fluid Mech*. 45 (1), 325–355.

[2] HOU, H. W., BHAGAT, A. A. S., CHONG, A. G. L., MAO, P., TAN, K. S. W., HAN, J. & LIM, C.T. 2010 Deformability based cell margination – simple microfluidic design for malaria-infected erythrocyte separation. *Lab on a Chip* 10 (19), 2605–2613.

[3] Ye, H., Shen, Z., & Li, Y. (2019). Interplay of deformability and adhesion on localization of elastic micro-particles in blood flow. *Journal of Fluid Mechanics*, 861, 55-87.

SB^{3}C2019
Summer Biomechanics, Bioengineering and Biotransport Conference
June 25 -28, Seven Springs, PA, USA

4D FLOW MRI DETERMINATION OF WINDKESSEL PARAMETERS FOR PATIENT SPECIFIC CARDIOVASCULAR SIMULATION

Ryan J. Pewowaruk (1), Alejandro Roldán-Alzate (1,2,3)

(1) Biomedical Engineering
University of Wisconsin - Madison
Madison, Wisconsin, USA

(2) Mechanical Engineering
University of Wisconsin - Madison
Madison, Wisconsin, USA

(3) Radiology
University of Wisconsin - Madison
Madison, Wisconsin, USA

INTRODUCTION

Image based computational fluid dynamics (CFD) has the capability to enhance medical imaging outcomes, investigate complex biomechanics phenomena and improve clinical decision making [1-4]. Image based CFD has been applied to many cardiovascular diseases like coronary artery stenosis [1], congenital heart defects [2,3] and cerebral aneurysms [4]. Numerical and computational resource advances allow the use of patient specific vessel wall stiffness in fluid-structure interaction (FSI) [5] and patient specific reduced order modeling of the distal vasculature [6] not directly available from medical imaging. Using FSI with patient specific vessel stiffness is important for accuracy as CFD simulations assuming rigid walls have been shown to overestimate wall shear stresses and fundamentally alters the physics of pulsatile flow as waves will be propagated at infinite speed. Reduced order modelling of the distal vasculature has been shown to improve velocity field accuracy. While patient specific vessel wall and distal vasculature properties are important for accuracy, previous methods to define these patient specific boundary conditions (BCs) are based on pressure measurements [7,8]. Tonometry can be used to measure pressure in the carotid and iliac arteries for estimating pressures in aortic simulations but invasive catheterization is required to measure pressure in other cardiovascular.

The goals of this abstract are: 1. Describe a method for defining patient specific BCs from non-invasive 4D Flow MRI, 2. Validate this method for an *in vitro* model, 3. Demonstrate the feasibly of defining patient specific BCs from 4D Flow MRI *in vivo*.

METHODS

Our noninvasive method to determine patient specific BCs from 4D flow MRI is motivated by cardiovascular physics and physiology (Fig1). First, pulse wave velocity (*PWV*) is used to determine the vessel stiffness (*Eh*, *E* is elastic modulus and *h* is wall thickness).

$$Eh = \frac{PWV^2}{\rho D} \quad (1)$$

PWV is calculated as the slope of flow versus area in early systole [9]. This is derived from wave intensity analysis (WIA) where flow rate (*Q*) and vessel cross-sectional area (*A*) are decomposed into forward and backwards travelling waves. It can be derived from conservation laws that *PWV* is equal to the ratio of incremental changes in either forward or backward traveling waves. The difficulty is that to decompose waves into forward and backward travelling components *PWV* must be known. Fortunately, in early systole it is appropriate to assume that there are only forward travelling waves and thus *PWV* is calculated as the ratio of incremental changes in *Q* and *A*.

$$PWV = \pm\frac{dQ_{\pm}}{dA_{\pm}} \approx \frac{dQ}{dA}\Big|_{t \in early\ systole} \quad (2)$$

Once stiffness is known from PWV, the pulse pressure in the vessel can be calculated from the systole to diastole artery area change using the Law of Laplace [10]. Distal compliance (*C*) can then be calculated from *Q* and the pulse pressure (ΔP).

$$\Delta P = \frac{\sigma_{\theta\theta} h}{R_{dia}} = \frac{E\epsilon_{\theta\theta} h}{R_{dia}} = \frac{Eh}{(1-\nu^2)R_{dia}}\left(1 - \sqrt{\frac{A_{dia}}{A_{sys}}}\right) \quad (3)$$

$$C = \frac{\Delta V}{\Delta P} = \frac{(Q_{sys} - Q_{dia})(t_{sys} - t_{dia})}{\Delta P} \quad (4)$$

Lastly, an exponential decay is fit to vessel area during diastole. The exponential time constant (τ) is assumed to be the distal vasculature time constant and used to calculate resistance $R = \frac{\tau}{C}$.. While τ for area will not be the same as τ for pressure, vessel area is a function of pressure and should provide an estimate of τ.

FSI is performed for half a cardiac cycle to rapidly estimate stiffness as PWV is not affected by initial transients. Vessel stiffness is

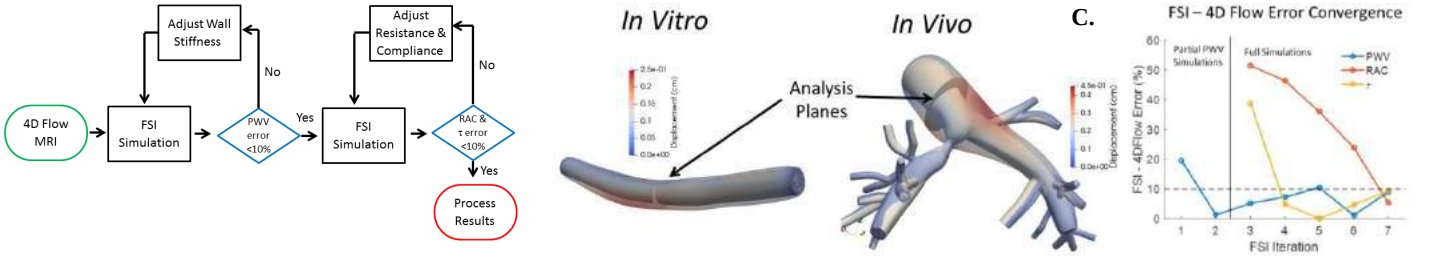

Figure 1: A. Flow chart describing the algorithm to determine patient specific conditions from 4D Flow MRI. An initial iterative loop is used to rapidly match PWV, then a second loop matches RAC and τ, **B.** Geometric models of the *in vitro* phantom and the *in vivo* PAS. Original geometry is opaque while the deformed geometry is shown as transparent. **C.** Error plots of the *in vivo* PAS showing the convergence of PWV, RAC and τ over the course of 7 FSI simulation iterations. The simulation is considered to match 4D Flow MRI when error is less than 10%.

Table 1: FSI Validation Against Benchtop Measurements

Measurement	Benchtop [11]	FSI	Error
PWV (cm/sec)	93 ± 2	102	10%
Max Disp (mm)	1.73 ± 0.02	1.98	15%

modulated until error between measured and simulated PWV is less than 10%. Next, four heartbeats are simulated to reach a periodic solution. Compliance and resistance are modulated until relative area change (RAC) and τ error is less than 10%.

The method is applied to an *in vitro* phantom of pulsatile flow in a latex tube (Fig1B) [11] and validated compared to benchtop measurements. MRI is obtained on a 3.0T scanner using 4D Flow MRI PC-VIPR (Phase Contrast Vastly Under sampled Projection Imaging) [12]. Flow rates are calculated from velocity fields and vessel areas from complex difference images. FSI is performed with the open source software Simvascular [5, 13]. After validation an *in vivo* subject specific simulation of a porcine pulmonary artery stenosis (PAS) (Fig1B) is performed. BCs from the PAS are then applied to the same anatomy with a virtually placed stent to simulate catheter based intervention. The results of the virtual intervention are compared to 4D Flow MRI measurements taken immediately before and after intervention in the porcine PAS.

RESULTS

FSI displacements (Fig1B) agree with MRI measurements. FSI and 4D flow measurements for *in vivo* PAS (Fig1C) converge to the 10% error criterion for PWV at the second iteration, τ at the fourth iteration and RAC at the seventh iteration. This is a comparable number of total iterations to methods using pressure [7,8]. FSI shows reasonable agreement with benchtop measurements (Table 1). Virtual intervention accurately predicts post-intervention LPA flow percentage 9% error versus 4D Flow MRI. There is error between FSI and 4D Flow MRI for the stenosis which could be due to difficulty segmenting an accurate stenosis geometry.

DISCUSSION

Using 4D flow MRI to determine FSI BCs enables implementing advantages of patient specific simulation in enhancing information from medical imaging, surgery and intervention planning, and basic science research without the risks associated with catheterization. Realistically, a cardiologist will only perform invasive catheterization when necessary for treatment or diagnosis. For patient specific simulation to be widely applicable, methods for non-invasively determining BCs need to be developed and validated.

This method may not give as accurate of simulated pressures, particularly mean pressure, as approaches which use pressure catheterization to determine BCs. For an incompressible liquid such as blood, only pressure gradients drive flow not the mean pressure. For applications looking at local flow quantities such as velocity, wall shear stress or pressure gradients fitting BCs to vessel wall motion could provide more accurate results as the flow will now be solved for more accurate time resolved geometry. For other applications such as quantifying ventricular afterload in a closed-loop simulation, accurate mean pressures are important.

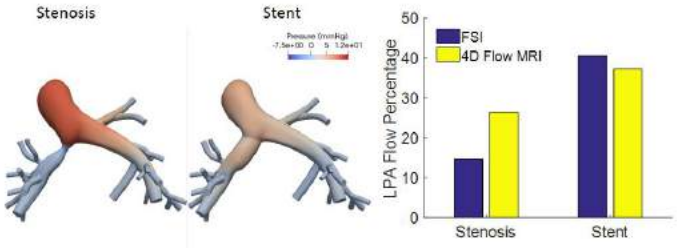

Figure 2: A. Virtual intervention predicts stenting decreased MPA pressure and **B.** accurately predicts LPA flow percentage.

Flow and areas measured from 4D Flow MRI can determine vessel wall stiffness and distal vasculature bed resistance and compliance. The ability to determine BCs for patient-specific simulations without invasive catheterization increases the ability to couple FSI and 4D Flow MRI for translational and basic science studies of cardiovascular disease and eventually clinical decision making. Future work will validate this method in additional *in vitro* phantoms against high speed camera strain measurements [15] as well as apply this technique to other vascular anatomies.

ACKNOWLEDGEMENTS

This investigation was supported by the UW Cardiovascular Research Center T32 HL 007936 and used UW Center For High Throughput Computing resources.

REFERENCES

[1] Taylor C, et al., *J Am Coll Cardiol*, 61(22):2233-41, 2013.
[2] Marsden A, et al., *Appl Mech Reviews*, 67, 2015.
[3] Roldán-Alzate A, et al. *J Biomech*, 48(7):1325-30, 2015.
[4] Liang L, et al. *J Neurointerv Surg* 2018.
[5] Figueroa C, et al *Comp Meth Appl ME*, 195(41):5685-705, 2006.
[6] Moghadam M, et al. *Comp Mech*, 48(3)277-91, 2011.
[7] Xiao N, et al. *Int J Numer Meth Biomed Eng*, 30:204-31, 2014.
[9] Zambrano B, et al. *J Biomech*, 68:84-92, 2018.
[9] Quail M, et al. *AJP Heart Circ Physiol*, 308(12):1603-11, 2015.
[10] Olufsen M. *Am J Physiol*, 276:H257-68, 1999.
[11] Ruesink T, et al. *Cardiovasc Eng Technol* 2018.
[12] Wieben O, et al., *Eur J Radiol*, 65(1):15-28, 2008.
[13] Updegrove A, et al. *Ann Biomed Eng* 45(3):525-41, 2017.

SB³C2019
Summer Biomechanics, Bioengineering and Biotransport Conference
June 25 -28, Seven Springs, PA, USA

DIFFERENCES IN PARENT ARTERY GEOMETRY BETWEEN ACOM AND MCA ANEURYSMS

F. Mut (1), M. Lawson (1), J. R. Cebral (1)

(1) Bioengineering Department
George Mason University
Fairfax, Virginia, USA

INTRODUCTION

Understanding the mechanisms of aneurysm formation and evolution towards rupture or stabilization is important to improve patient selection for treatment or conservative observation as well as for improving procedures and devices [1].

Hemodynamics is thought to be involved in the process of aneurysm formation, and in particular high flows and wall shear stress have been implicated in the initiation of intracranial aneurysms [2]. Although hemodynamics is also thought to influence the progression and rupture of cerebral aneurysms, its role in these mechanisms has not been clearly established [3].

It is well known that aneurysms selectively form at arterial bifurcations in or around the circle of Willis and that aneurysms at different locations have different rupture risks and may rupture at different sizes [4].

Aneurysms at the anterior communicating artery (ACOM) are fed by the A1 segments of the anterior cerebral artery (ACA), while aneurysms at the middle cerebral artery (MCA) bifurcation are fed by the M1 segment of the MCA. Both, the M1 and A1 branches are supplied by the internal carotid artery (ICA), which at its terminus bifurcates into the ACA and MCA. Thus, if hemodynamics influences aneurysm formation (and subsequently aneurysm evolution), it is reasonable to hypothesize that the ICA bifurcation of patients with ACOM aneurysms may be different from those of patients with aneurysms at the MCA bifurcation.

Therefore, the aim of this study was to compare the geometric characteristics of the ICA bifurcation between patients harboring aneurysms at the ACOM and patients with aneurysms at the MCA bifurcation, and between ruptured and unruptured aneurysms at these two locations.

METHODS

Aneurysm Data

Patients with aneurysms in the anterior communicating artery or the middle cerebral artery were selected from our database of patient-specific computational fluid dynamics (CFD) models. The requirement for inclusion was that the entire segments of the internal carotid artery from the ophthalmic artery to the ICA terminus, the M1 segment of the MCA from the ICA terminus to the MCA bifurcation, and the A1 segment of the anterior cerebral artery from the ICA terminus to the ACOM origin were included in the vascular model. A total of 66 patients with MCA aneurysms (46 unruptured, 21 ruptured) and 55 patients with ACOM aneurysms (24 unruptured, 32 ruptured) were included in the study.

Vascular Data

Patient-specific vascular models previously constructed from 3D rotational angiography images and stored in our database [5] were used to quantitatively characterize the geometry of the M1, A1 and ICA ophthalmic-terminus arterial segments, as well as the ICA bifurcation.

Vessel skeletons are automatically constructed using an advancing front method that starting from the vascular model inlets and outlets iteratively places maximally inscribed spheres along the vessel axes until no more spheres can be placed, or the skeleton connects to another skeleton node. In a subsequent step arterial branches containing no skeleton nodes are identified and new starting points are automatically added, and the advancing front process is repeated. With this approach, it is possible to automatically skeletonize branches such as the ACOM or PCOM connecting independent arterial trees into an arterial network. Skeletons are oriented from the vascular model inlets towards the

outlets (the orientation of communicating arteries is arbitrary). In a second step, the vascular model and the network skeleton are loaded into a graphical tool that allows the user to manually edit the skeletons to correct any topological defects, create new branches if missing, delete undesired branches, split or join branches, re-orient the skeletons, and finally label different anatomical arterial branches and bifurcations, such as the M1, A1 and the ICA ophthalmic-terminus branch and ICA bifurcation.

Arterial Characterization

Once the arterial branches have been skeletonized and labeled, their geometries are characterized by computing the following quantities: a) length – pathline or geodesic length along the branch, b) diameter – mean diameter of the inscribed spheres along the branch skeleton, c) tortuosity – ratio of geodesic length and Euclidean distance between end points, d) tapering – mean rate of change of arterial diameter along arterial branch, and e) eccentricity – average of maximum over minimum diameter of cross sectional cut normal to the branch. Similarly, arterial bifurcations (ICA in this case) are characterized by computing the angles between the parent branch (ICA) and each of the daughter branches (M1 and A1), and between the daughter branches; as well as ratios of the branch characteristics a-e) of A1 segments over M1 segments of each ICA bifurcation.

Data Analysis

Geometrical characteristics of A1, M1 and ICA segments and the ICA bifurcation were statistically compared using the Mann-Whitney test between patients harboring ACOM aneurysms versus patients harboring MCA bifurcation aneurysms, as well as between ruptured and unruptured aneurysms of these two groups of patients. The p-values were adjusted for multiple comparisons using the Benjamini-Hochber (BH) method. Differences were considered significant if $p<0.05$. Statistical analysis was carried out using R.

RESULTS

Comparisons between the mean values of the geometrical characteristics of the ICA bifurcation branches between patients with ACOM and MCA aneurysms are graphically summarized in Fig. 1. This figure shows the ratio of the mean values computed over the ACOM aneurysm group over the mean values computed over the MCA aneurysm group.

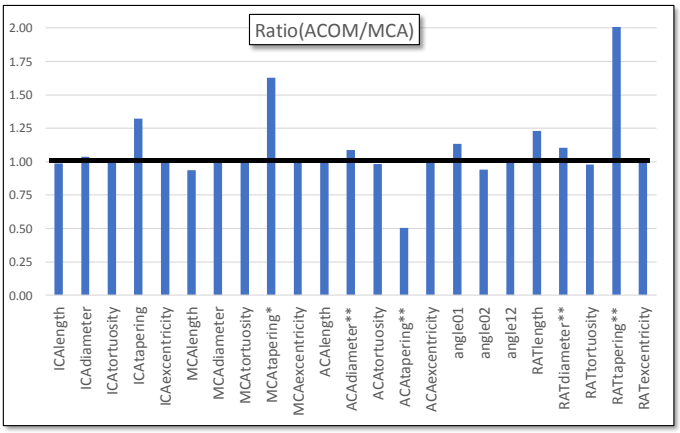

Figure 1: Comparison of geometric characteristics of the ICA bifurcation between patients with ACOM vs MCA aneurysms.

These results indicate that patients harboring aneurysms at the ACOM tend to have larger A1 diameters ($p=0.0374$), lower tapering of the A1 ($p<0.0001$), and larger tapering of the M1 segment. Conversely, patients with aneurysms at the MCA bifurcation tend to have larger tapering of the A1 ($p<0.0001$) and smaller A1 diameters ($p=0.0374$), and smaller tapering of the M1, although this latter association was not significant after adjustment for multiple testing ($p=0.0201$, before adjustment; $p=0.0925$, after adjustment).

No significant differences were found between ruptured and unruptured ACOM aneurysms, while ruptured MCA aneurysms had marginally shorter A1 segments than unruptured MCA aneurysms ($p=0.0506$).

DISCUSSION

In summary, the findings of this study indicate that the aneurysm feeding branch (A1 for ACOM aneurysms; M1 for MCA aneurysms) tends to be of larger diameter and with less tapering than the opposite branch of the ICA bifurcation (M1 for ACOM aneurysms; A1 for MCA aneurysms), which also tends to have larger tapering. These findings seem to confirm our expectations that anatomical configurations and geometries of the ICA bifurcation favor increased flows towards the side where the aneurysms formed compared to the opposite side of the ICA bifurcation.

This observation could explain why aneurysms tend to from at one location in one patient and at a different location in other patients, i.e. perhaps the patient's anatomical characteristics favor the creation of adverse hemodynamic environments due to changes in the systemic circulation which could result in wall damage at one location in some patients and in other patients at other locations.

No major differences were found between the ICA bifurcation characteristics of ruptured and unruptured aneurysms at each location, which suggests that the geometry of the parent artery likely influences the location where aneurysms form, but not whether they rupture or not. After formation, the evolution of the aneurysms is likely influenced by the intra-aneurysmal hemodynamics (studies have shown differences between ruptured and unruptured aneurysms, or between stable and unstable aneurysms [6]), which is largely determined by the aneurysm shape and its exact location on the parent artery but not so much of the geometry of the proximal parent artery.

ACKNOWLEDGEMENTS

This work was partially supported by NIH grant R01 NS076491.

REFERENCES

[1] Weir, B, *J Neurosurg*, 96:3-42, 2002
[2] Meng, H et al. *Stroke*, 38:1924-1931-42, 2007
[3] Meng, H et al., *Am J Neuroradiol*, 35(7):1254-1262, 2014
[4] Cebral, JR and Raschi M, *Ann Biomed Eng*, 41(7):1366-1383, 2013
[5] Detmer, F et al., *Int J Comp Assist Radiol Surg*, 13:1767-1779, 2018
[6] Chung, BJ et al., *Am J Neuroradiol*, 39(10):1860-1866, 2018

SB³C2019
Summer Biomechanics, Bioengineering and Biotransport Conference
June 25 -28, Seven Springs, PA, USA

PREDICTING ANEURYSMAL DEGENERATION IN THE DISSECTED THORACIC AORTA: A COMPUTATIONAL FLUID DYNAMIC APPROACH

Arianna Forneris (1), Alina Ismaguilova (1), Giampaolo Martufi (2), Jehangir J. Appoo (3), Elena S. Di Martino (2,3).

(1) Biomedical Engineering Graduate Program, University of Calgary, Calgary, Canada

(2) Schulich School of Engineering, University of Calgary, Calgary, Canada

(3) Libin Cardiovascular Institute of Alberta, University of Calgary, Calgary, Canada

INTRODUCTION

In patients surviving the acute period after aortic dissections (AD), the dissected descending aorta may progress to aneurysm formation (20-50% within 1-5 years[1]). Understanding which patients are likely to develop aneurysms can affect early disease management and long-term clinical outcomes.

Disturbed fluid dynamics is known to be a key factor in the onset and progression of vessel wall pathological remodeling that leads to decreased wall strength behind AD pathogenesis[2].

Purpose of this study is to analyze flow patterns and assess blood-vessel interactions by mean of computational fluid dynamics (CFD)-based indices and geometric features as potential risk factors for aneurysmal degeneration of the dissected descending aorta.

METHODS

Multidimensional non-linear growth analysis, assessed on multiple planes across aortic length, was carried on follow-up images of 22 patients with residual dissected descending thoracic aorta after surgery for type A. Patients with a rapidly expanding aorta (maximum growth > 5mm/year[3]) were compared to patients with a stable aortic size. CFD simulations were performed on patient-specific geometries obtained from CTA images early after surgery for type A aortic dissection.

Time-Averaged Wall Shear Stress (TAWSS), Oscillatory Shear Index (OSI) and Relative Residence Time (RRT) (equations 1,2,3), were computed to quantify local hemodynamic disturbances[4] and correlated with aortic growth. Flow entering the FL at peak systole was evaluated as a percentage of the total flow in the thoracic aorta.

$$TAWSS = \frac{1}{T}\int_0^T |WSS(s,t)|dt \qquad (1)$$

$$OSI = 0.5\ [1 - \left(\frac{|\int_0^T WSS(s,t)dt|}{\int_0^T |WSS(s,t)dt}\right)] \qquad (2)$$

$$RRT = \frac{1}{(1-2\cdot OSI)\cdot TAWSS} \qquad (3)$$

RESULTS

CFD simulations indicate that flow patterns in the dissected aortas are very complex and disturbed, presenting flow separation and recirculation affected by the entry tear size and location

All patients showed low velocities in the false lumen (FL) and higher values in the true lumen (TL), especially in the narrowed region distal to the entry tear.

The TAWSS is uniformly low (< 0.4Pa) in the ascending aortas and the outer surface of the FL, with a region opposite to the tear presenting elevated TAWSS (> 1.5Pa) as consequence of flow impingement on the wall (figure 1). High TAWSS were mostly located at the tear edge, with rapidly growing dissections showing higher peak TAWSS over an increased area combined with larger diameter at first scan and higher FL flow rate (figure 1). Patients with rapid growth also presented an increased tortuosity of the aorta.

Slow recirculating flow associated with prolonged RRT was found in the retrograde expansion of the FL favoring thrombus formation.

The pressure distribution on the aortic wall was also evaluated from CFD results at different times during the cardiac cycle (figure2). The higher systemic pressure in the FL causes the true lumen to collapse during diastolic peak. The systolic phase (systolic peak and mid-systolic

deceleration) presents the opposite situation showing higher pressure in the TL. Patients prone to rapid aortic growth, however, exhibit a different trend, with higher pressure in FL compared to the TL also during mid-systolic deceleration and consequently for most of the cardiac cycle. Red circles in figure 2 highlight the contours showing higher pressure in the vessel region that was subject to enlargement (at the level of the inferior left pulmonary vein on axial view).

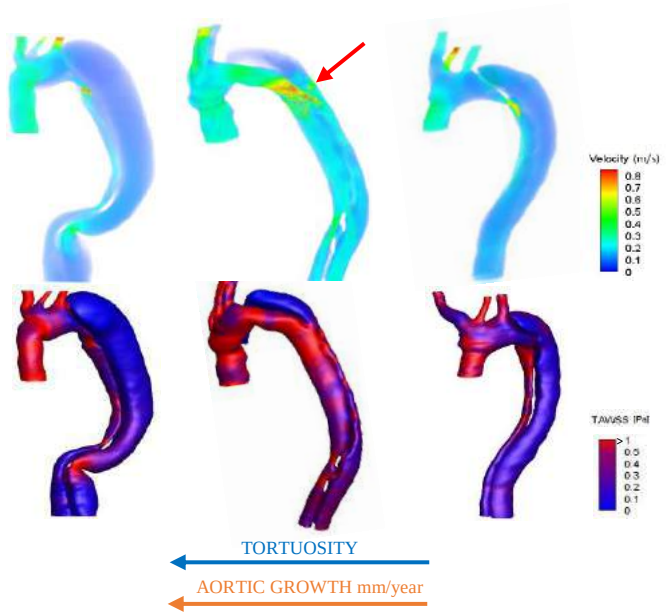

Figure 1: CFD-based analysis is reported for three of the patients in the population. Velocity profiles are reported at systolic peak in the top row with the red arrow pointing at flow impingement on the FL wall. TAWSS luminal distribution is shown in the bottom row. Bottom arrows indicate increasing tortuosity and aortic growth.

DISCUSSION

The management of aortic dissection disease is restrained by our understanding and ability to predict each patient's clinical course. Current clinical practice and several studies have indicated the FL patency to be a risk factor for long-term complications and aneurysmal degeneration, but there is no patient-specific criterion that can reliably predict rapid aortic growth. Our results suggest that CFD-based hemodynamic indices help the characterization and quantification of local flow disturbances, with high shear stress patterns correlating with rapid growth. Flow rate and pressure differences between the lumens maintain a patent FL promoting aortic expansion associated with worse long-term outcomes.

CTA images used in the study represent a limitation: they don't provide patient-specific flow information and they were not electrocardiographically gated, showing the dissection flap position as a time-weighted average of the configuration during diastolic and systolic phase.

Local hemodynamics and the characterization of flow patterns are critical factors that may help understand which flow features promote changes in the vessel patho-physiology. The employment of CFD may be a valuable tool to investigate which flow conditions play a role in the progressive weakening of dissected aortas and provide a rationale for risk stratification by identifying a subgroup of patients that may benefit from early intervention.

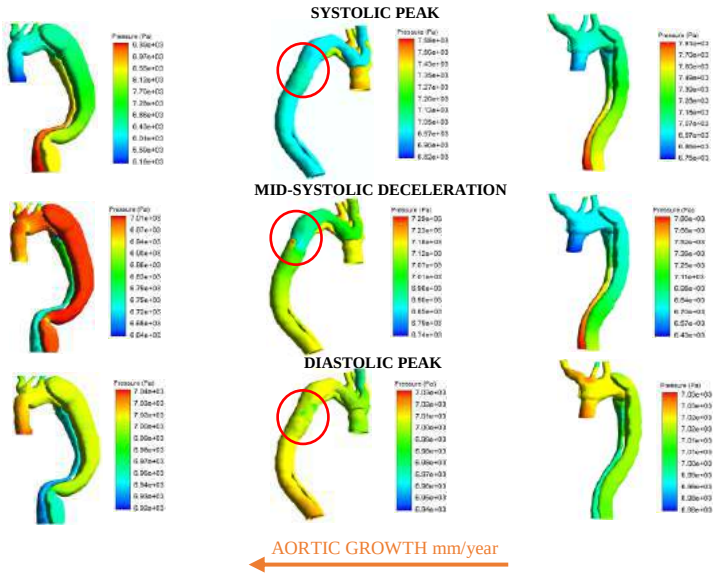

Figure 2: Pressure distribution on the aortic wall for three of the patients during three phases of the cardiac cycle, namely systolic peak, mid-systolic deceleration and diastolic peak (from top to bottom). The red circles highlight the pressure contours in the area subject to enlargement for this specific patient.

ACKNOWLEDGEMENTS

This research was supported by the Werner Graupe International Fellowships in Engineering and the NSERC CREATE I3T Program. We thank the Circle CVI Cardiovascular Imaging Inc. for providing their imaging software.

Special thanks to Dr. Eric Herget for his expertise and help with patients' images, and to Kevin Chung for his help with image segmentation.

REFERENCES

[1] Khan IA et al., *Chest*, 122(1):311-28, 2002.

[2] Davies MJ et al., *Heart*, 75: 434–435, 1996.

[2] Boodhwani M et al., *Can J Cardiol*, 30(6): 577-589, 2014.

[4] Gallo D et al., *Visualization and Simulation of Complex Flows in Biomedical Engineering*, 12: 1-24, 2014.

SB³C2019
Summer Biomechanics, Bioengineering and Biotransport Conference
June 25 -28, Seven Springs, PA, USA

PATIENT-SPECIFIC EVALUATION OF POST-TEVAR HEMODYNAMIC PERFORMANCE IN AORTIC DISSECTION

Selene Pirola (1), Claudia Menichini (1), Baolei Guo (2), Simone Saitta (1), Weiguo Fu (2), Zhihui Dong (2), Xiao Yun Xu (1)

(1) Department of Chemical Engineering
Imperial College London
London, UK

(2) Department of Vascular Surgery
Fudan University
Shanghai, China

INTRODUCTION

Type B aortic dissection (TBAD) is a serious clinical emergency which can lead to complications such as aortic aneurysm, rupture or malperfusion syndromes. Thoracic endovascular repair (TEVAR) can effectively treat this disease. Image-based computational fluid dynamics (CFD) has been widely used to evaluate hemodynamics in dissected aortas and after TEVAR. However, most computational models used simplified inlet and outlet boundary conditions, due to the lack of patient-specific flow and pressure measurements, and validation of computational results against *in vivo* measurements is scarce.

The aim of this work is to evaluate TEVAR hemodynamic performance by making use a newly developed CFD methodology for patient-specific analyses based on 4D flow magnetic resonance imaging (MRI) and pressure measurements acquired pre-TEVAR. Results for pre- and post-TEVAR hemodynamics were compared and validated against available *in vivo* measurements.

METHODS

The study was conducted on a TBAD patient (59-year old, female) who presented aneurysmal dilatation in the thoracic false lumen (FL) and was treated with TEVAR in chronic phase [1]. Doppler wire (DW) pressure measurements were taken during TEVAR procedure, before and after stent deployment. CT (computed tomography) images were acquired before and 3 months after TEVAR and were used to reconstruct the pre- and post-TEVAR geometries. The 12-month CT follow-up of this patient was also available. The geometric models included the supra-aortic branches, the superior mesenteric, celiac, renal and iliac arteries, and were discretized into unstructured meshes of about 6 (pre-TEVAR) and 4 (post-TEVAR) million elements.

For both pre- and post-TEVAR models, a full set of patient-specific boundary conditions was obtained using the pre-TEVAR 4D flow MRI data and DW pressure measurements. Through-plane time-varying velocity profiles were extracted from the pre-TEVAR 4D flow MR images and mapped onto the 3D global coordinates of the computational model inlet using an in-house Matlab tool [2]. 3-element Windkessel models were used at each model outlet, with their parameters being tuned using the pre-TEVAR DW pressure measurements, and flow distribution obtained from the 4D flow MRI data [3]. Simulations were run in ANSYS CFX, where the described boundary conditions were implemented via user-defined profile data and FORTRAN subroutines. Blood was modelled as an incompressible Newtonian fluid, and flow was assumed to be laminar.

RESULTS

CFD results were validated against 4D flow velocities and *in vivo* DW pressure measurements, showing good qualitative and quantitative agreement, with a maximum difference between CFD-predicted and DW-measured pressures of 11 mmHg. Fig. 1 shows comparisons between pre- and post-TEVAR pressure distributions. In the Pre-TEVAR model, FL and true lumen (TL) pressures were comparable in the aortic arch and started to differ from mid-descending aorta, with FL pressure being higher. After TEVAR only a small percentage of flow entered the abdominal FL. Hence, TL pressure was higher than in the FL at mid-systolic acceleration and deceleration. Overall, CFD results predicted a reduction in pressure after TEVAR, which was consistent with the *in vivo* pressure measured by DW (see comparisons in Fig.1). Flow in the pre-TEVAR thoracic FL was characterized by stagnation and recirculation, particularly at the first entry tear level where a large persistent recirculation region was present. On average 56% of the aortic flow

Poster Presentation #P077

entered the thoracic FL, of which 26% re-entered the TL through the re-entry tear. Post-TEVAR, the thoracic FL was completely thrombosed with only a small percentage of flow entering the abdominal FL. Overall, the aortic flow was well organized. 40% of the aortic flow entered the FL, of which only 10% entered the abdominal FL, while most of it was diverted to the right renal artery. The reduced FL flow post-TEVAR caused an increase in TL velocity, with a substantial increase in flow eccentricity and vorticity. In addition, FL enlargement caused a local narrowing in the TL which persisted after TEVAR and resulted in high velocities and elevated WSS there.

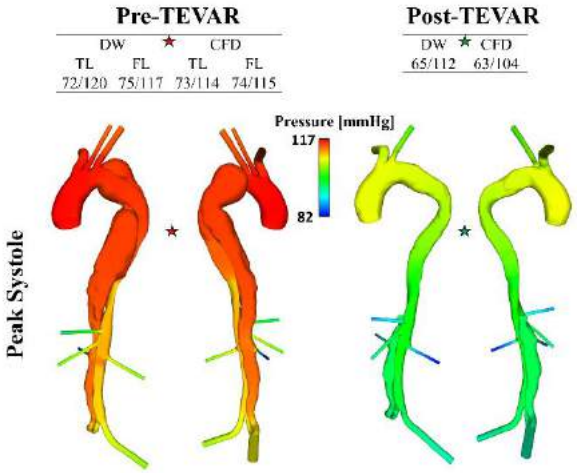

Figure 1: Comparison of pre- and post-TEVAR peak systolic pressure distributions. At the top, *in vivo* DW pressure measurements (in mmHg) are reported, along with CFD-predicted pressures. Stars mark the level where pressures were measured.

To highlight dominant flow features, Fig. 2 shows cycle-averaged velocity contours. At the re-entry tear pre-TEVAR flow is directed from the FL to TL, this is reverted after TEVAR, due to occlusion of the first entry tear by the stent-graft. At T8-9 level, a dominant anticlockwise vortical structure is observed in the pre-TEVAR FL, while the TL presents an almost uniform velocity profile. At this level, the post-TEVAR aorta shows complete thrombosis of the FL and considerable remodeling of the TL with a highly eccentric velocity profile. At T12-L1, the pre-TEVAR aorta presents an almost uniform velocity distribution in the FL, while the TL shows considerable spatial variation, with distinct high and low velocity regions. The post-TEVAR TL is significantly remodeled with a relatively uniform velocity distribution. At L3-4, flow in the pre-TEVAR TL and FL shows dominant vortical structures. While the FL is still patent in the post-TEVAR aorta, velocities in the TL are higher than those in the pre-TEVAR TL, and significantly higher than those in the post-TEVAR FL.

DISCUSSION

Hemodynamics has a fundamental role in the development and progression of TBAD, and in TEVAR outcomes and complications. Computational methods have been widely employed to study hemodynamics in aortic dissection. However, the limited availability of patient-specific flow data led to the common use of idealized boundary conditions, particularly post-TEVAR, when 4D flow cannot be used due to artefacts caused by the metal stent-graft. In this study a 4D flow MRI-based methodology was developed for detailed analysis of post-TEVAR hemodynamic performance using 4D flow and DW pressure data acquired before TEVAR. To validate the proposed methodology, CFD results were compared against 4D flow MRI data and *in vivo* DW-measured pressures, demonstrating a good agreement. Particularly, the pressure decrease after TEVAR was well captured by the CFD model. This suggested that boundary conditions extracted from pre-TEVAR data could be used for post-TEVAR hemodynamic assessment. This allowed for comparison of pre- and post-TEVAR hemodynamics.

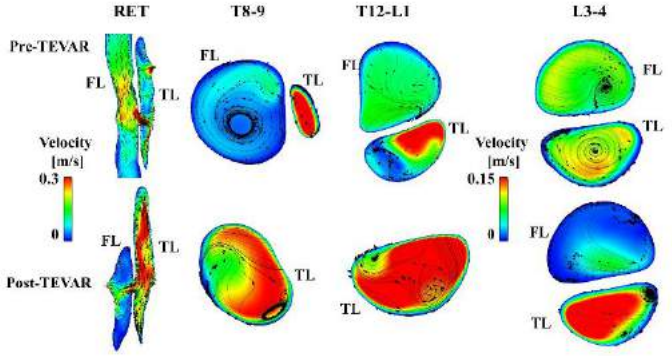

Figure 2: Mean velocity contours for a sagittal section at the re-entry tear (RET) level and at three different cross-sections along the aorta. T8-9, T12-L1, and L3-4 are the levels of the spine (T=thoracic, L=lumbar). For the sagittal view, velocity vectors are shown; while for the cross-sections the projection of the velocity streamlines is shown, with arrows indicating the flow direction.

Pressure distribution plays a key role in aortic dissection, determining FL expansion and rupture, and being crucial for TEVAR outcome. Pressure analysis showed that TEVAR successfully reduced the absolute mean and maximum pressures, along with the central pulse pressure, suggesting that TEVAR could decrease the workload for the heart. Large recirculation regions were observed in the FL at the first entry tear (pre-TEVAR) and re-entry tear (post), suggesting the possibility of further FL thrombosis at these locations. Results also showed that flow through the re-entry tear was strongly affected by TEVAR, with only 10% of thoracic FL flow entering the abdominal FL post-TEVAR, while the rest was diverted to the right renal artery. This raised concerns about the distal organ and limb perfusion, as the dissection extended to the right iliac artery. Indeed, the 12-month follow-up CT scan showed FL thrombosis with partial occlusion of the right iliac artery [1]. In addition, a substantial increase in TL flow eccentricity and vorticity was observed post-TEVAR. Despite these features are common in healthy aortas, high values have been linked to atherosclerosis. Therefore, this finding should be further investigated.

Overall, our methodology allowed for detailed comparison of pre- and post-TEVAR hemodynamics in a TBAD patient. The comparison highlighted several changes in the TL hemodynamics and predicted the possibility of further thrombus formation and distal organ malperfusion, which were confirmed by clinical follow-ups.

ACKNOWLEDGEMENTS

This work was supported by the European Commission within the Horizon 2020 Framework MSCA-ITN-ETN (642458), National Natural Science Foundation of China (81470573, 81371648, 81770474, 81770508), Shanghai Committee of Science and Technology, China (16410722900), and the Royal Society (IE161052), UK.

REFERENCES

[1] Menichini, C et al., *J Endovasc Ther*, 25:571-577, 2018.
[2] Pirola, S et al., *APL Bioengineering*, 2:026101, 2018.
[3] Pirola, S et al., *J Biomech*, 60:15-21, 2017.

SB³C2019
Summer Biomechanics, Bioengineering and Biotransport Conference
June 25 -28, Seven Springs, PA, USA

IMAGE-BASED ASSESSMENT OF THE HEMODYNAMIC PERFORMANCE OF SURGICAL AND TRANSCATHETER AORTIC VALVE REPLACEMENTS

Selene Pirola (1), Omar A. Jarral (2), Mohammad Y. Salmasi (2), Declan P. O'Regan (3), John R. Pepper (4), Thanos Athanasiou (2), Xiao Y. Xu (1)

(1) Department of Chemical Engineering
Imperial College London
London, UK

(2) Department of Surgery and Cancer
Imperial College London
London, UK

(3) Department of Clinical Science
Imperial College London
London, UK

(4) Royal Brompton and Harefield NHS
Fundation Trust
London, UK

INTRODUCTION

Aortic valve (AV) diseases are a leading cause of heart failure, and a significant risk factor for thoracic aortic aneurysm and dissection. Surgical AV replacement (SAVR) and transcatheter AV implantation (TAVI) can relieve cardiovascular symptoms, but have also been linked to negative wall remodeling [1]. Despite the long recognized role of local hemodynamic factors in wall remodeling [2], computational studies of patient-specific hemodynamics after AV replacement are rare [3]. Even fewer studies compared the hemodynamics before and after valve replacement, or SAVR with TAVI.

The aim of this work is to present a comprehensive evaluation of the hemodynamic function of different aortic valve replacement procedures, in comparison with healthy and pathological aortic hemodynamics.

METHODS

The study cohort included: a healthy volunteer, 3 patients with severe aortic valve stenosis who underwent SAVR with two-leaflet mechanical (MV1 and MV2) or biological (BV) valves, and a TAVI case. For the two MV cases, pre-operative data were available and analyzed (P1 and P2, respectively). Ethical and institution approvals were obtained (Wales REC, 14/WA/1225 and 16/NI/0160) for this study and all patients gave their informed consent.

Magnetic resonance (MR) imaging and phase-contrast MR images (PC-MRI) were acquired with a 1.5T Philips Achieva system. PC-MRI data were acquired at two transverse sections, with one located in the aortic root and another in the proximal descending aorta. Patients' central pressure was measured 30 min prior to the MR scan. Patient-specific models of the thoracic aorta and aortic branches were reconstructed from MR images by using Mimics (Materialise). Geometric models were discretized using structured meshes (0.9-2.7 million elements). Three-directional velocity profiles were extracted from the PC-MRI measurement in the aortic root, and were mapped to the inlet of the computational model for each patient [4], allowing for a patient- and valve-specific representation of the inlet boundary condition. 3-elements Windkessel models were applied at all the model outlets, with model parameters adjusted to fit each individual patient [5]. These boundary conditions were implemented in ANSYS CFX for flow simulations, which assumed the flow to be laminar and blood as a Newtonian fluid.

RESULTS

Inlet velocity profiles extracted from PC-MRI data were analyzed to obtain maximum flow velocity in a cardiac cycle, and to calculate flow displacement (FD) at peak systole [6]. Table 1 reports a summary of the obtained quantitative results. Comparison of inlet velocity maxima shows that all cases except TAVI present higher values than HV, with the highest peak velocity found in AV stenosis (P2). SAVR reduced the maximum flow velocity in MV1 and MV2. All patients had higher levels of flow displacement than the healthy control (HV), indicating moderate or marked flow eccentricity in the ascending aorta.

Fig.1 shows instantaneous velocity streamlines at two time intervals. Compared to the well-organized streamlines in HV, flow in P1 and P2 was highly asymmetric especially in P2 where a strong jet developed from the AV and impinged on the outer curvature of the ascending aorta. After AV replacement, both MV1 and MV2 showed an overall improvement in flow patterns, with reduced maximum velocity and flow eccentricity, although a weakened flow jet could still be seen along the outer curvature, together with flow recirculation at the inner wall. Similarly, BV was characterized by eccentric flow and a prominent flow jet from the inlet, mainly due to asymmetric valve

Poster Presentation #P078

opening. Amongst all the analyzed cases, TAVI hemodynamics showed the most similarity to that of HV.

Table 1: Quantitative results obtained from PC-MRI and CFD analyses. V_{max} = maximum inlet velocity; FD = flow displacement; TAWSS = time-averaged wall shear stress (values given for mean and maximum in the ascending aorta); HFI = helicity flow index.

Subject ID	V_{max} (m/s)	FD	TAWSS mean (Pa)	TAWSS max (Pa)	HFI
HV	1.06	0.05	1.51	4.31	0.47
P1/MV1	2/1.8	0.11/0.1	3.5/2.5	11.2/8.3	0.42/0.42
P2/MV2	2.8/1.7	0.13/0.11	3.4/2.5	10.4/14.3	0.31/0.44
BV	2	0.19	2	7	0.29
TAVI	0.8	0.09	1.3	3.3	0.36

Mean and maximum values of time-averaged wall shear stress (TAWSS) in the ascending aorta are reported in Table 1, while distributions are shown in Fig.2. Compared to HV, all cases except TAVI showed more spatial variations in TAWSS. Comparisons of pre- and post-operative TAWSS values for the MV patients suggested a reduction in the mean TAWSS in the ascending aorta (-29% for MV1, -27% for MV2), but an increase in the max TAWSS in MV2 (+38%). All cases had lower helicity flow index (HFI) values compared to HV (Table 1). In addition, MV cases showed a normalization of HFI which increased by 42% in P2 before and after operation.

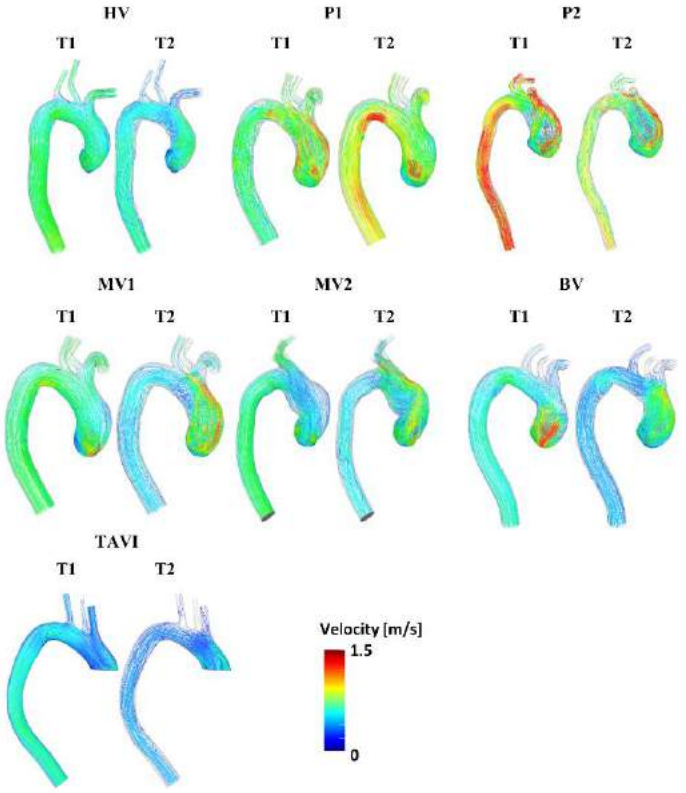

Figure 1: Comparison of instantaneous velocity streamlines at peak systole (T1) and mid-systolic deceleration (T2).

DISCUSSION

In the present work, state-of-the-art image-based patient-specific CFD was used to study aspects of aortic hemodynamics after different aortic valve replacement procedures, SAVR and TAVI. Our results showed that some degree of normalization in aortic hemodynamics was achieved in all patients, regardless of the procedure employed. Nevertheless, flow eccentricity was more pronounced and maximum velocities and WSS were higher in the SAVR than the TAVI cases and normal control. Overall, it is clear that hemodynamic features are patient and prosthesis dependent.

The observed high velocity jet along the ascending aorta outer curvature may increase the risk of aneurysm formation and dissection, while the marked flow recirculation might cause valve thrombosis [7]. Reduced HFI values with respect to the healthy control also suggest increased lipid penetration and reduced oxygen transport at aortic wall [8], which could promote aortic wall disease. In addition, it is likely that deviations from normal will lead to increased ventricular afterload, which could delay ventricular remodeling.

Overall, our results confirm that abnormal flow features are a key contributor to the fact that after aortic intervention patients continue to be at higher risk of aortic events, despite correction of their valve pathology.

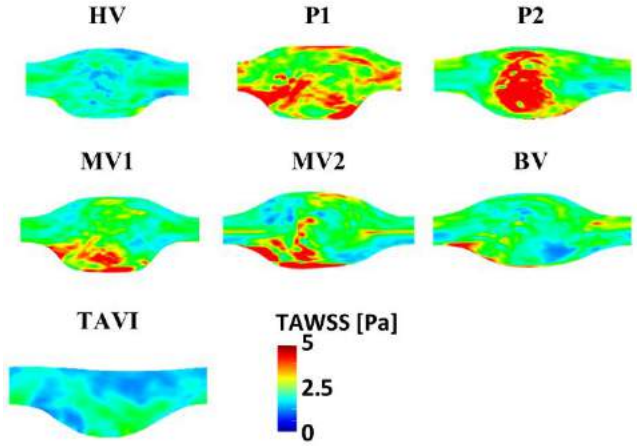

Figure 2: TAWSS maps in the ascending aorta. The ascending aorta (from the model inlet to the root of the first branch) was cut along the inner curvature and unfolded.

ACKNOWLEDGEMENTS

This work was supported by the European Commission within the Horizon 2020 Framework through the MSCA-ITN-ETN European Training Networks (Project No. 642458). MR images were acquired as part of a project supported by the National Institute for Health Research (NIHR) Biomedical Research Centre and the NIHR Cardiovascular Biomedical Research Unit.

REFERENCES

[1] Hope, MD et al., *JACC Cardiovasc Imaging*, 4:781-7, 2011.
[2] Bollache, E et al., *J Thorac Cardiovasc Surg*, 156:2112-20, 2018.
[3] Tan, FPP et al., *CEVT*, 3: 123-35, 2011
[4] Pirola, S et al., *APL Bioengineering*, 2:026101, 2018.
[5] Pirola, S et al., *J Biomech*, 60:15-21, 2017.
[6] Sigovan, M et al., *J Magn Reson Imaging*, 34:1226-30, 2011.
[7] Vahidkhah, K et al., *Eur J Cardiothorac Surg*, 51:927-35, 2017.
[8] Liu, X et al., *Ann Biomed Eng*, 38:917-26, 2010.

SB³C2019
Summer Biomechanics, Bioengineering and Biotransport Conference
June 25 -28, Seven Springs, PA, USA

Hemodynamic Characteristics Associated with Cerebral Aneurysms Evolution

Seyedeh Fatemeh Salimi Ashkezari (1), Fernando Mut (1), Juan R. Cebral (1)

(1) Bioengineering Department
George Mason University
Fairfax, VA, USA

INTRODUCTION

A cerebral aneurysm is an abnormal dilation of a cerebral artery in the brain. It is estimated that approximately 2-5% of the general population have at least one cerebral aneurysm [1, 2].

While many studies have identified aneurysm growth as a strong risk factor for prospective rupture, the pathophysiology by which aneurysms evolve is poorly understood. Hemodynamics is thought to be an important factor in the progressive degeneration and remodeling of the aneurysm wall. However, the specific changes in the aneurysm flow conditions during its evolution are not yet fully understood [3].

As a matter of fact, to determine the growth rate of unruptured aneurysms it is necessary to follow-up the aneurysms for a long period of time so that significant growth could be observed. However, many clinicians recommend treating aneurysms that have enlarged during follow-up observations, which leads to fewer longitudinal follow-up imaging data being available to study the aneurysms' evolution and possible associated hemodynamic variables.

The objective of this work was to study the changes in hemodynamic characteristics of cerebral aneurysms during their evolution and to investigate whether those changes are different between aneurysms in different locations.

METHODS

A total of 66 cerebral aneurysms at three locations, anterior communicating artery (ACOM), posterior communicating artery (PCOM), and middle cerebral artery (MCA) were selected from our databased and studied with image-based computational fluid dynamics (CFD).

For each aneurysm, two synthetic sequences approximating the aneurysm geometry at three earlier stages were generated by (a) shrinking the aneurysm sac with a Laplacian smoothing function while keeping the aneurysm neck fixed (Fixed Neck), and (b) shrinking the aneurysm sac and diminishing the aneurysm neck size at each stage (Growing Neck). CFD simulations were carried out for each aneurysm and each simulated evolution stage in the generated sequences under similar flow boundary conditions.

A total of 19 hemodynamic parameters were computed to characterize and compare the hemodynamic environment, flow intensity, spatial complexity, and temporal stability at different stages and between different aneurysms. Wall shear stress (WSS) distributions in two aneurysms, one with a fixed neck and another with a growing neck are illustrated in Figure 1.

RESULTS

The main findings of this study are summarized in Figure 2. This figure presents the average rate of change of different hemodynamic variables for aneurysms with growing and fixed necks in the three locations considered. Statistical analysis (Paired t-test) was performed to explore differences in the rates of change between the two modes of evolution. For each parameter, a p-value less than <0.05 signifies that growing neck

had a greater average rate of change than the fixed neck (indicated with a "*" in Fig. 2).

As aneurysms enlarged, the inflow rate (Q) increased in aneurysms with growing necks, and decreased in aneurysms with fixed necks. The concentration of the inflow jet (ICI) increased in both, but increased faster in aneurysms with growing necks. On the other hand, the mean velocity (VE), and wall shear stress (WSS Mean) decreased as the aneurysms enlarged in both fixed neck and growing neck simulations, but they decreased faster for fixed neck cases. In addition, the mean oscillatory shear index (OSI Mean), corelen (a measure of flow complexity), and podent (a measure of flow instability) increased as the aneurysms enlarged, but their rate of change were not significantly different between growing and fixed neck cases. Similar overall hemodynamic changes were observed for aneurysms at all three locations considered.

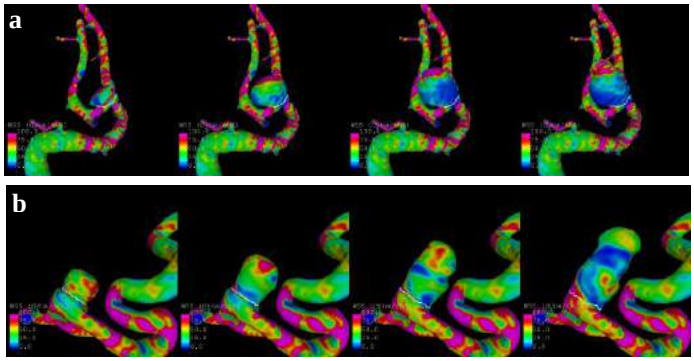

Figure 1: WSS distributions in aneurysms and arteries resulted from simulating the aneurysm evolution. Figures show (a) fixed neck, meaning shrinking aneurysm and keeping the neck fixed and (b) growing neck, shrinking both aneurysm and the neck.

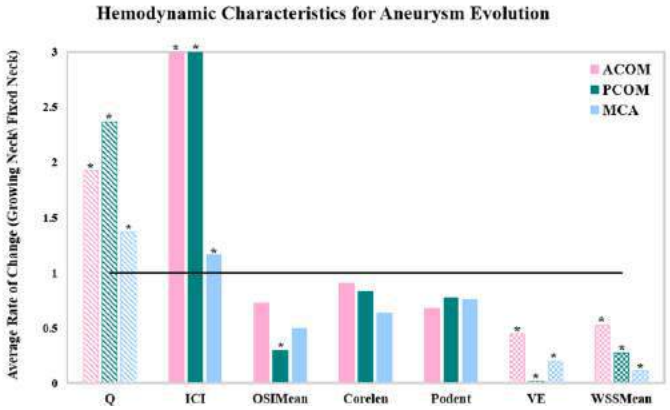

Figure 2: Ratios of rates of change of hemodynamic variables of growing neck over fixed neck aneurysms. Statistically significant differences (P < .05) are indicated with an asterisk. Bars with diagonal patterns show positive average rates of change in growing neck and negative average rates of change in fixed neck. Bars with solid fills present positive average rates of change in both fixed and growing neck cases, and checked bars illustrate negative average rates of change in both modes of evolution.

DISCUSSION

Hemodynamics is believed to play a driving role in the pathogenesis of cerebral aneurysms. The goal of this work was to study the changes in the aneurysm flow condition that take place as the aneurysm evolves. We focused on three locations, and observed differences in the evolution of flow characteristics of aneurysms with fixed and growing necks. We found that similar changes occurred in most hemodynamic characteristics (except for aneurysm inflow rate) but these changes occurred at different speeds depending on whether the neck of the aneurysm was fixed or enlarging.

In a previous study Chung et al. [4] found that compared to stable unruptured aneurysms, ruptured aneurysms had faster flows, more complex flow patterns, and more concentrated and oscillatory shear stress distributions, when controlling for aneurysm location.

In our study, we observed that as the aneurysm grows, the flow velocity and wall shear stress tend to decrease, and this decrease occurs faster in aneurysms with fixed necks. The flow complexity, instability, and oscillation tend to increase, but there was no significant difference in the speed of increase between aneurysms with growing and fixed necks. Additionally, the inflow rate increased in aneurysms with growing necks and the inflow jet became more concentrated as the aneurysm enlarged. These observations suggest that aneurysms with fixed necks may evolve towards a flow environment characteristic of stable aneurysms faster than aneurysms with growing necks, thus perhaps placing aneurysms with growing necks at a higher risk of destabilization and rupture.

REFERENCES

[1] Rinkel, Gabriel JE, et al. "Prevalence and risk of rupture of intracranial aneurysms: a systematic review." *Stroke* 29.1 (1998): 251-256.

[2] Sadasivan, Chander, et al. "Physical factors effecting cerebral aneurysm pathophysiology." *Annals of biomedical engineering* 41.7 (2013): 1347-1365.

[3] Sforza, Daniel M., Christopher M. Putman, and Juan Raul Cebral. "Hemodynamics of cerebral aneurysms." *Annual review of fluid mechanics* 41 (2009): 91-107.

[4] Chung, B. J., et al. "Identification of hostile hemodynamics and geometries of cerebral aneurysms: a case-control study." *American Journal of Neuroradiology* 39.10 (2018): 1860-1866.

SB³C2019
Summer Biomechanics, Bioengineering and Biotransport Conference
June 25 -28, Seven Springs, PA, USA

INTENSITY OF STENOSIS-INDUSED FLOW INSTABILITIES OF THE INTERNAL CAROTID ARTERY: A COMPUTATIONAL APPROACH

Viviana Mancini (1), Aslak W. Bergersen (2), Kristian Valen-Sendstad (2), Patrick Segers (1)

(1) IBiTech – bioMMeda
Ghent University
9000 Ghent, Belgium

(2) Department of Computational Physiology
Simula Research Laboratory
1364 Fornebu, Norway

INTRODUCTION

Carotid stenosis is the leading cause of ischemic stroke [1]. Carotid auscultation is routinely used in the clinical practice to screen for the presence of bruit as a marker for asymptomatic carotid stenosis. The carotid bruit stems from unstable flow downstream of the stenosis. However, auscultation is strongly operator dependent. Carotid bruit also presents itself as skin vibrations, due to the propagation of stenosis-induced instabilities as mechanical waves. A Laser Doppler Vibrometer (LDV) would hence potentially allow us to infer the presence of flow instabilities by measuring skin vibrations. The aim of this study is to evaluate the proof-of-principle of LDV–based stenosis detection in a patient-specific model of a stenosed carotid artery, yet accounting for the varying flow rate, flow split and degree of stenosis that one may encounter *in-vivo*. We applied a computational fluid dynamics (CFD) strategy and then compared our findings with *in-vitro* LDV recordings, previously performed on a replica of a stenosed bifurcation [2], for validation purposes.

METHODS

Computer tomography angiography images of a 75-year old patient with severe stenosis (76%) in the internal carotid artery (ICA) were segmented to obtain a model of the carotid bifurcation. Later, manipulation of the geometry allowed to reconstruct the healthy lumen [3] and to obtain four additional stenotic models with varying degree of stenosis (56%, 66%, 86%, 96%) [4]. The six models were meshed using VMTK with a spatial resolution of $\Delta x_{mean} = 1.92 \cdot 10^{-4}$ m, previously found to be adequate [5]. The common carotid artery (CCA) flow rate and the ICA flow split boundary conditions (BCs) were set according to clinical data [6, 7]. Including only plausible scenarios, a total of 19 simulations were run. As such, Q_{CCA} varied from 145 to 529 ml/min, and Q_{ICA}/Q_{CCA} flow split from 11.9 to 70.8%. Blood was modeled as Newtonian fluid with $\nu = 3.3 \cdot 10^{-6}\, m^2/s$. We ran the simulations for three cardiac cycles with time step $\Delta t = 5 \cdot 10^{-5}\, s$ using the 2nd order finite-element CFD solver *Oasis* [8]. The pressure traces of the last two cycles were extracted from the centerline point located one CCA diameter downstream of the stenosis throat. The traces were then high-pass filtered to retrieve only its fluctuating components [9]. The logarithm of the time integral of their power was used as measure of the intensity of flow instabilities I_{FI}, as shown in equation (1).

$$I_{FI} = Log_{10}\left(\int_{0\,Hz}^{10\,kHz} Power_{high-pass\ filtered\ pressure}\right) \quad (1)$$

We evaluated the impact of Q_{CCA}, Q_{ICA}/Q_{CCA}, Q_{ICA}, $Area_{stenosis}$, $Velocity_{stenosis}$ and $Reynolds_{stenosis}$ on I_{FI} of the stenosed models by means of linear regression analysis.

Furthermore, the Q-criterion, defined as in equation (2), was used to visually identify vortexes in the simulations run on the six models with average degree-specific Q_{CCA} and Q_{ICA}/Q_{CCA}.

$$Q = \frac{1}{2}\left[\left|\vec{\Omega}\right|^2 - \left|\vec{S}\right|^2\right] > 0 \quad (2)$$

The experimental data were LDV recordings of the displacement of the skin-mimicking foil put on top of the ultrasound gel (mimicking the neck's soft tissues) in which the compliant replica of the stenosed bifurcation was embedded. The flow conditions applied to the *in-vitro* model were in the same range as the boundary conditions of the subset of CFD simulations for which Q_{ICA}/Q_{CCA} was kept constant while Q_{CCA} varied between 145 and 529 ml/min. To ease the comparison, the same post processing was applied to the experimental (EXP) data.

Poster Presentation #P080

RESULTS

All factors have a positive relationship with I_{FI}. The poorest predictor for the presence of flow instabilities was the stenosis severity, which could only account for 12% of the variation in the data. The Reynolds number at the stenosis throat was the best predictor for I_{FI} (Figure 1).

Although the magnitude of CFD data is not is the same range as the EXP data, since we are comparing two different physical quantities, the trend is remarkably consistent.

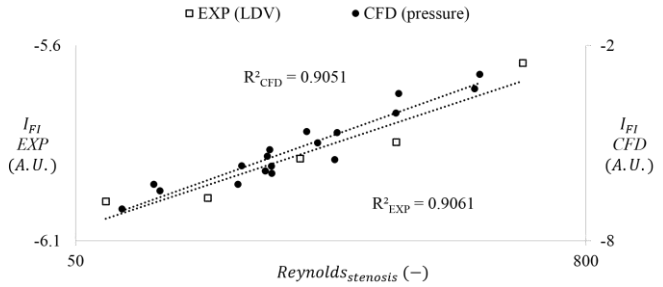

Figure 1. The positive relationship between I_{FI} and $Reynolds_{stenosis}$ holds for CFD as well as for EXP data.

A qualitative comparison of the vortical structures of the several degrees of stenosis is provided in Figure 2. The 56% to 76% stenoses harbor more intense flow instabilities than the 86% stenosis. The extremely severe 96% stenosis, on the other hand, does not harbor any instability, and neither does the healthy subject model.

Despite the $Reynolds_{stenosis}$ of the healthy-subject model is comparable to the one of the 86% stenosis and 20% larger than the 56% stenosis, no unstable flow can be detected in the ICA.

DISCUSSION

The aim of this study was to explore the relationship between the degree of stenosis, inlet flow rate, and flow split with the intensity of the downstream flow instabilities. Our validated CFD methodology allowed us to identify vortexes in the moderate and severe stenoses (56% – 86%), which quickly dissipated further downstream. Of note is that the 96% stenosis did not harbor any flow instabilities because of the extremely low, but physiological, $Reynolds_{stenosis}$. This suggests that an absence of flow instabilities does not imply the absence of a stenosis. Similar conclusions were drawn by a clinical study on asymptomatic carotid patients, where they found the sensitivity and specificity of auscultation for extreme stenoses to be only 26% and 49%, respectively [10].

Given the high comparability of the CFD and EXP data, we expect the LDV to behave similarly to the routinely used clinical methodology (auscultation), but with tool-aided consistency. Naturally, the absolute values of I_{FI} did not match when comparing the data from *in-vitro* and computational setup since they are from two different physical quantities. Nonetheless, our finding is that the pressure from the rigid-wall CFD simulations can be used as a surrogate measure for wall vibrations. That being said, pressure traces from fluid structure interaction simulation (FSI) would perhaps have been even better correlated. Of note is also that intra-arterial pressure measurements were available from *in-vitro* recordings. The catheter was, however, found to affect the downstream-stenosis flow field, thereby making the comparison with CFD data unfeasible.

Furthermore, from the *in-vitro* experiments we observed that the LDV also detected changes in flow rate. For extreme severe stenosis the flow is expected to redistribute to the remaining vessels. Therefore, by comparing the LDV inferred flow rate on both carotid arteries, it could be possible to detect unilateral stenosis and hence improve the sensitivity of the technique.

Currently running clinical studies will provide data to verify our findings.

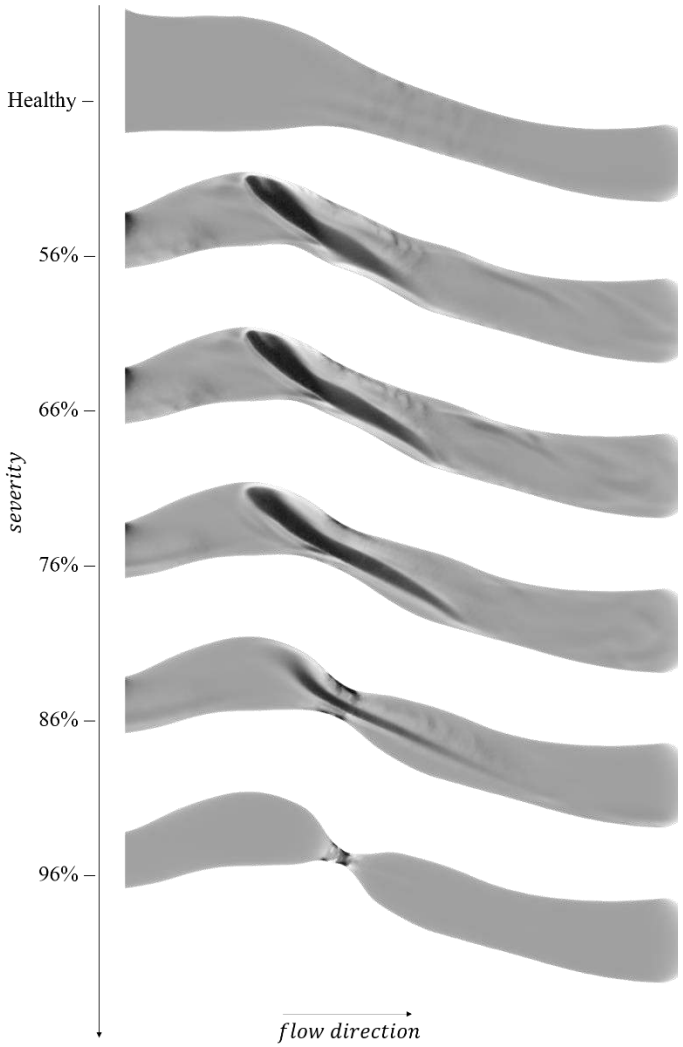

Figure 2. The healthy model and the 96% stenoses do not harbor flow instabilities, whereas the moderate and severe stenoses do.

ACKNOWLEDGEMENTS

H2020 European funded 644798 CARDIS project.

REFERENCES

1. Moomaw C. J., *Neuroepidemiology* 40, 36–41 (2013).
2. Mancini V., *PLoS One* (submitted in 2018).
3. Iannaccone F., *Int. J. Artif. Organs* 37, 928–939 (2014).
4. Kjeldsberg H. A., *J. Open Source Softw.* (submitted in 2018).
5. Mancini V., *Cardiovasc. Eng. Technol.* (submitted in 2018).
6. Likittanasombut P., J. *Neuroimaging* 16, 34–38 (2006).
7. Groen,H. C., *J. Biomech.* 43, 2332–2338 (2010).
8. Mortensen M., *Comput. Phys. Commun.* 188, 177–188 (2015).
9. Khan M. O., *J. Biomech.* 52, 179–182 (2017).
10. Johansson E. P., *BMC Neurol.* 8, 1–8 (2008).

SB³C2019
Summer Biomechanics, Bioengineering and Biotransport Conference
June 25 -28, Seven Springs, PA, USA

PREDICTING THROMBOSIS RISK IN THE LEFT ATRIAL APPENDAGE OF HUMAN HEART

Breandan A.B. Yeats BS (1), Hoda Hatoum, PhD (1), Thura T. Harfi, MD,MPH (2), Lakshmi P. Dasi, PhD (1)

(1) Department of Biomedical Engineering
The Ohio State University
Columbus, Ohio, USA

(2) Department of Internal Medicine
The Ohio State University
Columbus, OH, USA

INTRODUCTION

The left atrial appendage (LAA) is a pouch that is extruded laterally from the left atrium[1]. Atrial fibrillation (AF) decreases the contractility of the left atrial appendage (LAA). The rapid fluctuation of electrical pulses caused by AF leads to decreased blood velocities that result in stagnation of blood in this area leading to conditions that are associated with thrombosis. If the formed thrombus embolizes, it can lead to stroke that currently affect over three million people in the United States[2]. Normal blood flow at the apex of the LAA, the most lateral portion, allows blood to fill and empty out of the apex each cycle. However, this also worsens over time due to the weakening of surrounding muscle fibers[1].

Patients with AF are frequently treated by cardioversion, a procedure where electrical shock is administered to the heart to restore sinus rhythm. However, cardioversion is contraindicated if the patient already has a thrombus formed in the LAA for risk of systemic embolization. Currently, to identify if the patient has LAA thrombus, transesophageal echocardiography (TEE) and cardiac computed tomography (CT) are performed. TEE is a semi-invasive procedure where an ultrasound probe is run through the esophagus to collect real time images of the LAA as well as velocity measurements throughout the cardiac cycle. CT is used by injecting a contrast agent in the patient and identifying regions of low contrast indicating low blood flow or thrombus that does not allow diffusion of the contrast agent.

Blood velocity in the LAA has been shown to be strongly related to thrombus formation[3]. However, it is still not considered a factor sufficient to prescribe anticoagulants and is only measured using the invasive test of TEE. The aim of this study is to develop a computational framework to non-invasively predict the risk of thromboembolism through assessing flow stasis in the LAA.

METHODS

As a part of an IRB approved study, high resolution cardiac CT images of four patients (3 with AF and 1 without AF) were collected throughout the cardiac cycle. Patients 1-3 were in sinus rhythm and patient 4 was in atrial fibrillation at the time of the scan. Patients 3 and 4 showed signs of blood stasis/thrombosis on CT images as evident by the presence of LAA filling defect (lack of contrast opacification) in the apex of the LAA that was dense in patient 4 and mild in patient 3. Figure 1 shows CT images of each patient indicating this evidence.

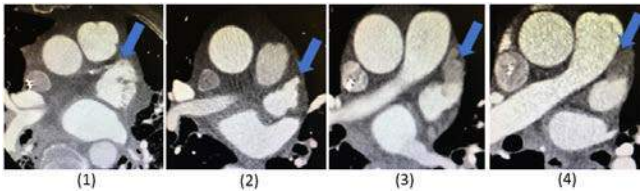

Figure 1: (1-2) No filling defect suggesting no blood stasis/thrombus, (3) soft filling defect suggesting moderate blood stasis/thrombus, (4) dense filling defect suggesting severe stasis/thrombus.

4D CT reconstructions were created using Mimics Research 18.0 (Materialise, Belgium). Each LAA was then discretized in 3-Matic Research 13.0 (Materialise, Belgium). The 4 segmented LAAs are shown in Figure 2. 1-2 are LAAs that had no detection of blood stasis or thrombus formation from CT scan analysis and 3-4 showed signs

blood stasis/thrombus formation. CFD analysis was then performed using Ansys CFX 17.1 Academic (Canonsburg, PA) to create a velocity map within each LAA. Each LAA 1-4 had the following number of tetrahedral volume elements respectively: 376056, 197617, 429434, and 519839. The boundary conditions consisted of an inlet velocity at the orifice that was measured using the 4D CT volume change. Each simulation used blood material properties with density of 1060 kg/m^3 and dynamic viscosity of 0.00278 kg/m-s.

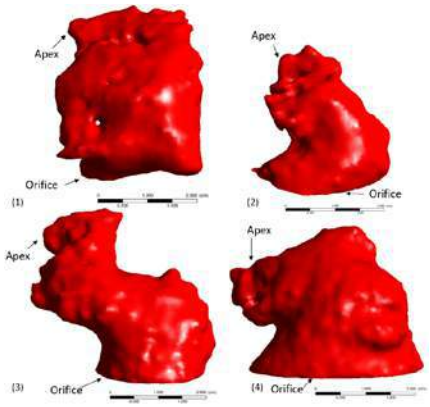

Figure 2: LAA segmented geometry of all four patients.

RESULTS

Figure 3 shows the velocity contour maps for all four LAAs. The colors range from red to blue, red being the maximum velocities and blue being the lowest velocities. Areas that show gray coloring indicate zero velocity. LAAs 1 and 2 show minimal areas with low blood velocities. LAAs 3 and 4 have large areas at the apex with very low or zero blood velocities and had evidence of blood stasis or thrombus formation. Table 1 shows the apex and maximum velocity measurements and maximum shear stresses for each LAA from the CFD analysis. LAA 1 did not have AF and showed the highest maximum velocity and shear stress of 64.4 cm/s and 3.20 Pa respectively. LAA 2 did have AF but did not show signs of thrombus formation or blood stasis and had a lowered maximum velocity of 39.7 cm/s. LAA 3 had AF and showed signs of thrombus formation or blood stasis and had an even lower maximum velocity and shear stress compared to LAA 2. LAA 4 was in AF during the CT scan and showed signs of thrombus formation and blood stasis. It also showed the lowest velocities of 0 cm/s at the apex and maximum of 1.96 cm/s with the lowest maximum shear stress of <0.01 Pa.

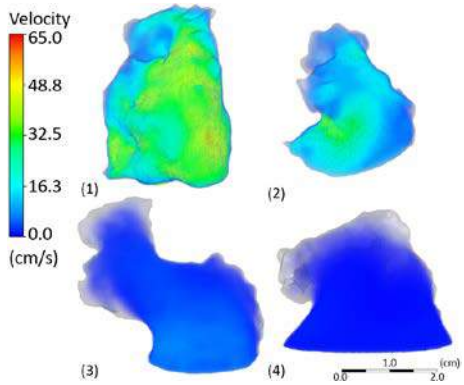

Figure 3: LAA velocity map results of four patients, (1-2) no stagnation or thrombus detected, (3-4) detected stagnation/thrombus with low blood velocities.

Table 1: LAA apex velocity and maximum shear stress measurements for each patient.

LAA Number	History of AF	Heart rhythm at time of scan	Stagnation/ Thrombus	Apex Velocity (cm/s)	Max Velocity (cm/s)	Max Shear Stress (Pa)
1	No	Sinus	No	3	64.4	3.20
2	Yes	Sinus	No	3	39.7	0.79
3	Yes	Sinus	Yes	0.2	13.6	0.11
4	Yes	AF	Yes	0	1.96	<0.01

DISCUSSION

The average LAA outflow velocities in normal subjects ranging from 80 ± 23 cm/s to 63 ± 29 cm/s and inflow velocities ranging from 61 ± 18 cm/s to 54 ± 17 cm/s both decreasing with age[4]. LAAs with peak velocities of <35 cm/s are considered to be at high risk of thrombus formation[5]. Our CFD analysis shows data consistent with the clinical profile of the study subjects. LAA 1 shows velocity levels with a low risk of thrombus formation (maximum >35 cm/s). This result is expected since no stagnation or thrombus was detected from the CT data and this patient did not have AF. LAA 2 shows velocity levels that are low normal and indicates less risk of thrombus formation. LAA 3 shows low velocities which agree with CT finding of soft filling defect/stasis. Finally, LAA 4 shows very low velocities which match with the detection of dense filling defect consistent with severe blood stasis/thrombus. These low flow velocities show how regressed blood velocities can become while a patient is experiencing AF. Furthermore, LAAs 3 and 4 also showed very low shear stresses. Nesbitt et al.[6] has shown that platelet aggregates can form in locations with low shear, this coupled with low velocities could be why there was a detection of blood stasis/thrombus in these LAAs. It is important to note that although subject 2 and 3 have similar clinical profile (both has history of AF and both are in normal sinus rhythm during the CT scan), their CFD profiles are quite different with high risk of thrombosis in subject 3 and low in subject 2.

The use of CFD in this application allows for the non-invasive measuring of blood velocities while using only routine CT scans. It can be used as an alternative for predicting the potential of thromboembolism in patients intended for cardioversion. It also constitutes a first step towards integrating blood flow into the decision of anticoagulation pharmaceutical prescription in atrial fibrillation patients. The ability to analyze shear stresses is also beneficial since it can play a large role in platelet activation and the development of thrombi – which with the current clinical tools, is not possible. The use of CFD can be utilized to further study shear stress and its impact specifically within the LAA.

ACKNOWLEDGEMENTS

Research was supported by National Institutes of Health (NIH) under Award Number R01HL135505.

REFERENCES

[1] Beigel, R et al., *Journal of the American College of Cardiology*, vol. 7, No. 12, 2014.
[2] Naccarelli, G et al., *The American Journal of Cardiology*, vol. 104, issue 11: 1534-1539, 2009.
[3] Markl, M et al., *Circulation: Cardiovascular Imaging*, vol. 9, no. 9, 2016.
[4] Agmon, Y et al., *The American Journal of Cardiology*, vol. 86, issue 7: 769-773, 2000
[5] Fatkin, D et al., *The American Journal of Cardiology*, vol. 23, issue 4: 961-969, 1994.
[6] Nesbitt, W et al., *Nature Medicine*, vol. 15, no. 6: 665–673, 2009.

SB³C2019
Summer Biomechanics, Bioengineering and Biotransport Conference
June 25 -28, Seven Springs, PA, USA

EFFECTS OF SUBJECT-SPECIFIC, SPATIALLY REDUCES, AND IDEALIZED BOUNDARY CONDITIONS ON THE PREDICTED HEMODYNAMIC ENVIRONMENT IN THE MURINE AORTA

Kelly A. Smith (1), Samer S. Merchant (1), Edward W. Hsu (1), Lucas H. Timmins (1,2)

(1) Department of Biomedical Engineering
University of Utah
Salt Lake City, UT, USA

(2) Scientific Computing and Imaging Institute
University of Utah
Salt Lake City, UT, USA

INTRODUCTION

Genetically manipulated murine models for atherosclerosis (e.g., apolipoprotein-E-null knock out; ApoE$^{-/-}$) have become valuable tools for understanding the disease pathogenesis [1]. As data have convincingly demonstrated the role of hemodynamics in atherosclerosis development [2], these animal models have been used to extensively investigate the relationship between wall shear stress (WSS) and mechanosensitive cellular mechanisms. As a result, image-based modeling techniques have been established to predict the *in vivo* hemodynamic environment and associate distinct flow patterns to changes in gene and protein expression [3]. Recent advancements in medical imaging [e.g., velocity phase-contrast magnetic resonance (PCMR) imaging] have become effective tools to advance these computational models. For example, PCMR imaging provides highly resolved, quantitative data on blood flow patterns that can serve as boundary conditions (BC) for subject-specific models to predict WSS distributions in complex geometries. However, the acquisition of 3D flow patterns at all inlet and outlets of interest can be tedious and costly, with no data having demonstrated the essential imaging data required to accurately predict the *in vivo* hemodynamics. Furthermore, application strategies for BC can greatly vary, leading to possible differences in the predicted hemodynamic environment and WSS distributions.

Thus, the aims of this study were to (i) examine the effects of variations in applied BC on predicted flow rates and (ii) quantitively compare the effects of idealized, spatially reduced, and comprehensive subject-specific BC on predicted WSS distributions, both in the murine aorta.

METHODS

Animal Model Male ApoE$^{-/-}$ mice (n = 3; C57BL6 background; 12, 14, and 16 weeks of age) on an atherogenic from 8 weeks of age were utilized in this study. Animals were house and cared for according to according to guidelines proposed by the NIH, and all experimental procedures were approved the IACUC at the University of Utah prior to study execution.

Image Data Collection Under anesthesia (isoflurane in oxygen), animals were connected to physiologic monitoring system (ECG, temperature, respiration) and placed in 7T MR scanner (Bruker BioSpec). Velocity-encoded PCMR imaging data were acquired in planes perpendicular to the aorta at the root and the three major branches off the aortic arch. Three-dimensional (3D) PCMR imaging data were acquired at the aortic root (through-plane VENC = 50 cm/s, in-plane VENC = 25 cm/s), and only through-plane data were collected at the three major branches off the aortic arch (VENC=13 cm/s). All scans were ECG-gated with an in-plane resolution of 118 μm.

Anatomic data were obtained by micro-computed tomography (μCT) scanning of the vasculature following perfusion with an iodine-based contrast agent (BrightVu®, Scarlet Imaging). Briefly, animals were injected with 100 units of heparin immediately following MRI acquisition. After 30 minutes, the animals were euthanized via CO_2 inhalation, and a thoracotomy was performed to expose the heart. Animals were exsanguinated via cardiac puncture and a saline flush, followed by contrast agent perfusion. Upon completion of perfusion, specimens were place in an ice bath to solidify the contrast agent and stored in a 10% neutral buffered formalin solution. Animals underwent μCT imaging (Quantum GX μCT, PerkinElmer) to acquire high-resolution data of the aorta at an isotropic voxel resolution of 78 μm. Volumetric data were segmented (Seg3D), and the aortic region from the root to the suprarenal aorta, including 12 mm of the root branching vessels, were isolated (Geomagic; Geomagic, Inc.).

Computational Modeling Flow extensions were added to the outlets, and the isolated volumes were discretized with hexahedral

elements (ICEM, Ansys, Inc.), including an 8-element boundary layer. The mesh was imported into the FEBio software suite for computational fluid dynamics (CFD) analysis [4]. PCMR data were processed to map velocity information onto the computational mesh. Briefly, circular grids were assigned to corresponding PCMR- and μCT-derived inlets. The deformation gradient to map the PCMR grid to the μCT grid was calculated and applied to the PCMR velocity data. Finally, velocity values were interpolated at the mesh element centroids.

To assess sensitivity of predicted hemodynamics to the applied BC, five finite element models were created for each aortic geometry: A) temporal 3D velocity profile at inlet, temporal mass flow split at outlets (i.e., the % of inlet flow exiting each outlet varied over time); B) temporal 1D (through plane PCMR data) velocity profile at inlet, temporal mass flow split outlets; C) temporal 3D velocity profile at inlet, steady mass flow split outlets (i.e., a constant % of inlet flow exited each outlet); D) temporal 3D velocity profile at inlet, traction free outlets; E) steady plug profile (velocity was average of through plane pulsatile waveform) at inlet, traction free outlets. The descending aorta outlet was always assumed to be traction free. For all models, the fluid was assumed to be an incompressible Newtonian fluid ($\rho = 1060$ kg/m^3, $\mu = 3.5$ cP), the arterial walls were assumed rigid, and a no-slip BC was applied at the wall.

Following solution convergence, predicted outlet flow rates in the traction free models were determined. Furthermore, data were post-processed to generate time-averaged WSS (TAWSS) magnitude maps. TAWSS values were extracted from distinct regions (superior and inferior aortic arch; medial and lateral descending aorta) to evaluate anatomic differences in the predicted hemodynamics.

RESULTS

Significant differences were observed between PCMR-measured and predicted outlet flow rates for all three aortic arch branching vessels. For example, measured flow rates in the brachiocephalic (BCA), left common carotid (LCCA), and left subclavian (LSA) arteries of the 12 week old animal were 0.16 ± 0.006, 0.0035 ± 0.001, and 0.00042 ± 0.0002 mL/s, respectively, while predicted values under temporal flow conditions (model D) were 0.018 ± 0.008, 0.021 ± 0.009, and 0.00042 ± 0.0002 mL/s ($p < 0.05$ across all). Furthermore, maximum measured flow rates were 12%, 83%, and 98% smaller than predicted values in the BCA, LCCA, and LSA, respectively. Similar trends were detected when comparing PCMR-derived flow rates to predicted flow rates under steady flow conditions (model E). For example, predicted flow rates in the BCA, LCCA, and LSA in model E were 0.022 ± 0.009 (41% lower than measured), 0.0055 ± 0.002 (38% lower), and 0.00061 ± 0.0003 (32% lower) mL/s ($p < 0.05$ for BCA and LCCA). Regardless of age, similar trends in flow rates were observed.

Variations in applied BC resulted in appreciable differences in predicted TAWSS distributions throughout the aortic territory, including the aortic arch, branching vessels, and descending aorta (Fig. 1). However, despite differences in TAWSS values across models,

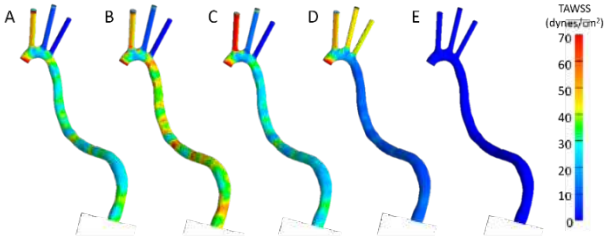

Figure 1: Time-averaged wall shear stress (TAWSS) distributions across models for 12 week old animal.

relative trends were apparent in all models. Specifically, TAWSS values in the inferior aortic arch were lower than values on superior arch and values on the medial side of the descending aorta were similar to values on the lateral side. For example, in model A (pulsatile 3D velocity profile applied at the inlet, temporal mass flow split applied at the outlets), TAWSS values in the inferior and superior arch were 14.9 ± 1.5 and 40.9 ± 7.6 dynes/cm^2, respectively (174% difference), and values were 34.2 ± 2.9 and 28.7 ± 1.2 dynes/cm^2 in the medial and lateral descending aorta, respectively (16% difference).

Quantitative comparisons across the five models revealed significant differences in predicted TAWSS values at the evaluate anatomic regions as compared to model A, which was defined as the most comprehensive animal-specific model (Fig. 2). For example, application of temporal mass flow split at the outlets, but a temporal 1D profile at the inlet (model B) resulted in significantly higher TAWSS values in the inferior arch and descending aorta (16.6 ± 0.9 and 12.1 ± 1.1 dynes/cm^2, respectively) as compared to model A ($p < 0.05$). Likewise, application of a temporal 3D profile at the inlet, but temporal mass flow split at the outlets (model C) led to significant differences in the inferior arch (16.7 ± 0.9 dynes/cm^2) when compared to model A ($p < 0.05$). Most notably, application of traction free BC at the outlets resulted in significant differences in TAWSS values in the superior arch and descending aorta even when a temporal 3D profile was applied at the inlet and significant differences in all anatomic regions if a steady plug inlet velocity profile was applied (model E). Regardless of age, similar trends in TAWSS anatomic differences were observed.

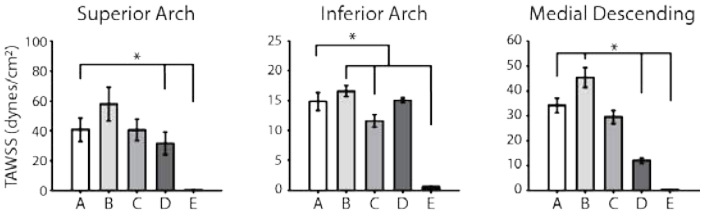

Figure 2: TAWSS values at anatomic regions of the murine aorta across models for the 12 week old animal; *p < 0.05.

DISCUSSION

The presented study highlights the effects that variations in BC have on the predicted hemodynamics in the murine aorta. We demonstrated that application of traction free or steady mass flow splits at model outlets resulted in significantly overestimated outlet flow rates when compared to PCMR-measured *in vivo* values. Furthermore, we identified that while all models had similar relative TAWSS distributions, variations in inlet and outlet BC significantly affected TAWSS magnitudes. While only murine aortic hemodynamics were examined, our findings agree with previously reported data in the human aorta [5]. These data further highlight the importance of judiciously identifying a BC strategy to ensure predictive accuracy in hemodynamic models across animal and patient-specific models.

ACKNOWLEDGEMENTS

The authors gratefully acknowledge the assistance of Prof. Gerard Ateshian (Columbia Univ.) with the CFD analysis in FEBio.

REFERENCES

[1] Breslow, J.L., *Science*, 272(5262):685-688, 1996.
[2] Ku, D.N. et al., *Arteriosclerosis*, 5(3):293-302,1985.
[3] Suo, J. et al., *Arterioscler. Thromb. Vasc. Biol.*, 27:346-351, 2007.
[4] Maas, S.A. et al., *ASME J. Biomech. Eng.*, 134(1):011005, 2012.
[5] Morbiducci, U. et al., *J. Biomech.*, 46(1):102-9, 2013.

SB³C2019
Summer Biomechanics, Bioengineering and Biotransport Conference
June 25 -28, Seven Springs, PA, USA

PRE-PROCEDURAL PATIENT-SPECIFIC IN-SILICO DEPLOYMENT OF SAPIEN AND EVOLUT TRANSCATHETER AORTIC VALVES

Sri Krishna Sivakumar[1], Hoda Hatoum[2], Jennifer Dollery[3], Scott Lilly[3], Lakshmi Prasad Dasi[2]

(1) Department of Mechanical Engineering
The Ohio State University
Columbus, Ohio, USA

(2) Department of Biomedical Engineering
The Ohio State University
Columbus, Ohio, USA

(3) Department of Cardiovascular Surgery
The Ohio State University
Columbus, Ohio, USA

INTRODUCTION

Transcatheter aortic valve replacement (TAVR) is a new and exciting approach to treat aortic valve stenosis in patients who are considered to be high-risk for open heart surgical aortic valve replacement (SAVR)[1]. Due to the minimally invasive approach of TAVR, it has a strong appeal to becoming the standard of care for low-risk patients as well [1]. However, TAVR also has complications associated with it such as coronary obstruction (CO) [2], paravalvular leakage (PVL), thrombosis among others. In particular, coronary obstruction is the cause of mortality of about 1.5% of the patients undergoing TAVR [3]. The current predictive models of CO involve measurement of coronary artery height (h) and the Sinus of Valsalva diameter (SOVd) to compare with criteria developed on the basis of clinical observations. Despite the efficiency of these models, there are about 1% of TAVR patients that still suffer from coronary obstruction [3]. Therefore it is necessary to accurately predict and determine the possibility of occurrence of such adverse effects as part of pre-procedural planning. The most commonly used and commercially available TAVs are the balloon expandable Edwards SAPIEN characterized by a short profile (height) and the self-expandable Medtronic Corevalve/Evolut valve characterized by a long profile. The selection parameters between SAPIEN and Evolut are not yet completely established for different coronary obstruction cases, however it is possible that valve selection can play an important role in mitigating the occurrence of coronary obstruction [4]. The objective of this study is to predict and compare the deployment behavior of Edwards SAPIEN and Medtronic Evolut transcatheter aortic valves in the context of coronary obstruction by using patient specific 3D computational modelling.

METHODS

This study utilized computational modelling of TAVR for a set of 5 patients considered to be at risk of coronary obstruction based on predictive guidelines of SOVd > 30mm and h < 12mm. Patient specific 3-D geometries of the aortic root, leaflets and calcification were reconstructed from pre-procedure 2-D computed tomography (CT) images. Using Mimics Research 21.0, (Materialise NV, Leuven, Belgium) a threshold mask was applied onto the CT images and by highlighting the corresponding regions of interest, the 3D models of the root, leaflets and the calcification were generated. The generated 3D models were exported to 3-Matic Research 13.0 where the models were meshed with triangular elements of size 1.0 mm. The number of elements generated in each model was of the order ~50000 triangle elements. Post-processing was done to ensure anatomical correctness of the models. The final geometry was then exported to ABAQUS Explicit 6.14 (SIMULIA, DS Corp., Providence, RI, USA) for finite element analysis to simulate the deployment of the Evolut and SAPIEN valves. To allow for positioning of the Evolut and SAPIEN stents during deployment, the leaflets were pre-expanded using a model cylinder expanding radially. The Evolut and SAPIEN stents were created using Solidworks (DS Corp., Waltham, MA, USA) and the bio-prosthetic leaflets were ignored in the making of the stent to cut down computational time. The stent is modelled as elasto plastic with ρ = 8.2 x 10^{-9} tonn/mm^3 and E = 241316 MPa with v = 0.3 and σ_y = 585 MPa and σ_y = 1035 MPa. The aortic root is modelled as a hyperelastic material with ρ = 1.0 Kg/m^3 and Neo Hookean coefficients C10 = 0.5, D1 = 5; the calcium is modelled as an elastic material with ρ = 1.2 ·Kg/m^3, E = 2.5MPa and v = 0.475. A self-expanding stent deployment method was used to simulate the behavior of the Evolut valve. The stent

was crimped using a funnel and holder cylinders and the holder was then moved to the intra-annular position where the stent was released for self-expansion. The SAPIEN valve was deployed using a balloon. A crimped balloon and the SAPIEN stent were situated at the intra-annular position and fluid is injected to inflate the balloon with a fluid cavity pressure of 0.48MPa. The deployment of the Evolut and the SAPIEN valve were also simulated at the supra-annular and sub-annular positions.

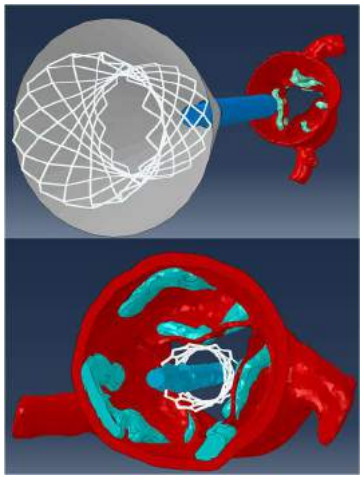

Fig. 1: Visualization of the assembly to deploy Evolut(top) and SAPIEN(bottom) valves

RESULTS

Fig. 2 shows the cross-sectional view of the deployed valve and the left coronary artery comparing the Evolut and SAPIEN valve deployment behavior. It is observed that the deformation of the leaflets is different between the two valves. Fig. 3 compares the valve deployment of the Evolut and SAPIEN in supra-annular, intra-annular and sub-annular positions.

DISCUSSION

The difference in the stent geometry is the reason for the difference in the deformation seen in Fig.2 between the valves. Since the SAPIEN valve is balloon expanded, the valve deforms according to each patient's aortic geometry while Evolut maintains its shape across all deployments. Due to the shorter profile of the SAPIEN valve, the depth at which the valve is deployed affects the leaflet deformation caused by the valve whereas in the case of the Evolut, the leaflet deformation remains the same across all the 3 positions of deployment. The approach presented here can be used as a predictive procedural planning tool to achieve better clinical outcomes.

ACKNOWLEDGEMENTS

The research done was partly supported by National Institutes of Health (NIH) under Award Number R01HL119824.

REFERENCES

[1] Dasi, L. P., et al. Ann. Biomed. Eng. 45:310–331, 2017

[2] Dvir D. et al. Circulation: Cardiovascular Interventions. 2015;8:e002079.

[3] Ribeiro HB et. al., *ColliCardiol* 2013;62(17):1552–62.

[4] Noorani A**, et al.** Interv Cardiol. 2014 Apr; 9(2): 121–125.

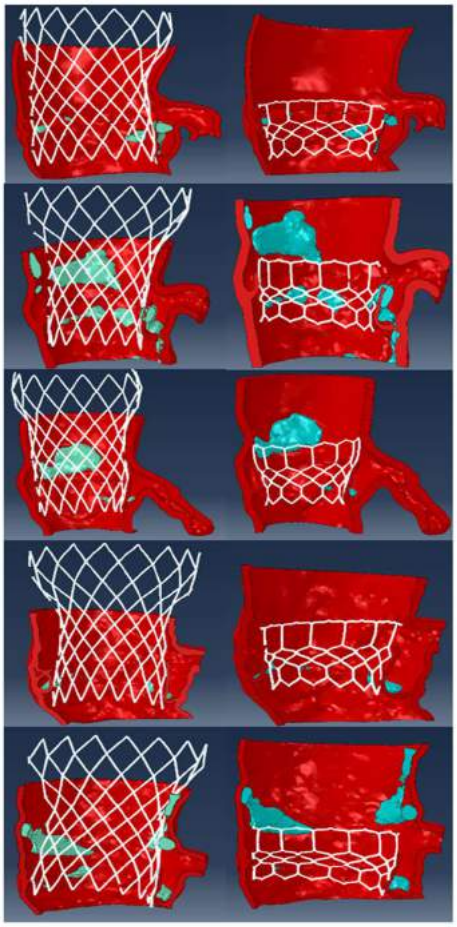

Fig. 2: Comparison of the 3D geometry of the aortic root and leaflets post simulation for Evolut (left) and SAPIEN (right) valves.

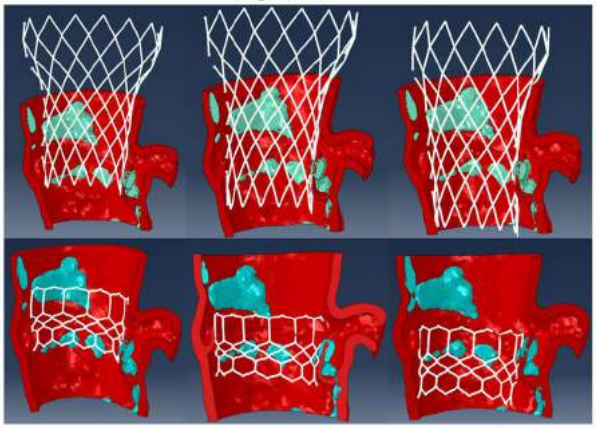

Fig.3: Comparison of the effect of depth of deployment in Evolut(top) and SAPIEN(bottom) valves in supra-(left), intra-(center) and sub-annular(right) positions

SB³C2019
Summer Biomechanics, Bioengineering and Biotransport Conference
June 25 -28, Seven Springs, PA, USA

EFFECTS OF RESOLUTION AND DYNAMIC RANGE OF DUAL-VENC 4D FLOW MRI ON FLOW MEASUREMENTS IN CEREBRAL ANEURYSMS: IN VITRO 4D FLOW STUDY IN A SCALED MODEL

Sean M. Rothenberger (1), Melissa C. Brindise (2), Joseph C. Muskat (1), Susanne Schnell (3), Pavlos P. Vlachos (1,2) and Vitaliy L. Rayz (1,2)

(1) Weldon School of Biomedical Engineering
Purdue University
West Lafayette, IN, USA

(2) School of Mechanical Engineering
Purdue University
West Lafayette, IN, USA

(3) Feinberg School of Medicine
Northwestern University
Evanston, IL, USA

INTRODUCTION

Within the adult population, approximately 3.2% of individuals have an unruptured intracranial aneurysm (UIA) [1]. Advancements in medical imaging resulted in an increasing number of (UIAs) discovered incidentally. Current clinical procedures for risk-stratification of cerebral aneurysms have been shown to be unreliable [2]. This has resulted in the over-treatment of patients with UIAs through potentially risky surgical or endovascular procedures. Recent studies indicate that local hemodynamic factors, e.g. wall shear stress (WSS) and oscillatory shear index (OSI), relate to aneurysm progression [3]. Consequently, these hemodynamic factors may help predict the stability of UIAs and assist clinicians in decision-making and management of UIA patients. Intra-aneurysmal hemodynamics can be acquired in vivo with three-directional phase-contrast MRI (4D Flow MRI) or with patient-specific modeling techniques, which include in vitro measurements or Computational Fluid Dynamics (CFD). 4D Flow measurements in cerebral vasculature can be affected by limited spatiotemporal resolution and velocity dynamic range of the technique. The range of velocities that can be measured with 4D Flow depend on a "venc" (velocity encoding) parameter, typically set above the expected maximum velocity. In measuring complex flows with a large dynamic range, velocities exceeding the venc would cause image aliasing, while a venc set too high results in low velocity-to-noise ratio (VNR) for slow flow. Schnell et al. has introduced dual-venc 4D Flow MRI which has a higher dynamic range and lower noise in its measurements [4]. Dual-venc 4D Flow MRI combines two acquisitions with different venc values, a smaller venc tailored to slow flow regions and the larger one for high velocities observed in jets.

Compared to in vivo 4D Flow, in vitro techniques can provide higher resolution which can improve the accuracy of calculated hemodynamic metrics. Currently, almost all modeling studies rely on CFD for the calculation of intra-aneurysmal velocity fields. While providing superior resolution, CFD results may be affected by image segmentation errors and the many modelling assumptions, such as flow boundary conditions, wall compliance, fluid material properties, etc. Experimental studies can serve as a separate modality providing validation to both in vivo and in silico approaches. This study aims to investigate the effects of increased resolution and dynamic range of 4D Flow MRI on resulting flow metrics, by conducting in vitro flow measurements in a scaled cerebral aneurysm model.

METHODS

Collaborators at Northwestern University provided 4D Flow MRI and time-of-flight (TOF) MR angiography data which was acquired for an internal carotid artery (ICA) aneurysm. TOF data of the aneurysm with the proximal and distal arteries were segmented and a flow phantom was fabricated through 3D printing. A 1-to-1 and a 2-to-1 scaled models were printed (Figure 1). Extensions were added to the inlet of the flow models to ensure

Figure 1: Cerebral aneurysm flow phantoms a) 1-to-1 model b) 2-to-1 model

fully developed flow. These aneurysm models were connected to a flow loop which pumped a gadolinium enhanced water-glycerine fluid through the models at a steady flow rate. The density and viscosity of this working fluid matched those of blood. The Reynolds number of the fluid flow in both models was 313, matching that calculated for the in vivo flow conditions at peak systole. The inlet flow rate for the 1-to-1 and 2-to-1 models was 4.45 and 8.90 mL/s, respectively, matching that of in vivo measurements. Velocity measurements in both models were acquired with both dual and single-venc 4D Flow MRI. This resulted in a total of four datasets. MRI studies were performed on a Siemens 3T PRISMA scanner at a spatial resolution of 0.8x0.8x0.8 mm^3. The low and high vencs for the 1-to-1 model were 30 and 60 cm/s, while the low and high vencs for the 2-to-1 model were 15 and 30 cm/s, respectively. The reported high venc values were the vencs used for the standard single-venc 4D Flow MRI measurements. The acquired phase-contrast MRI images were post-processed using software developed at Northwestern and the flow fields were visualized using Paraview software. The resulting velocity distributions were used to compare 4D flow resolution in low velocity regions and to calculate the velocity divergence for each model.

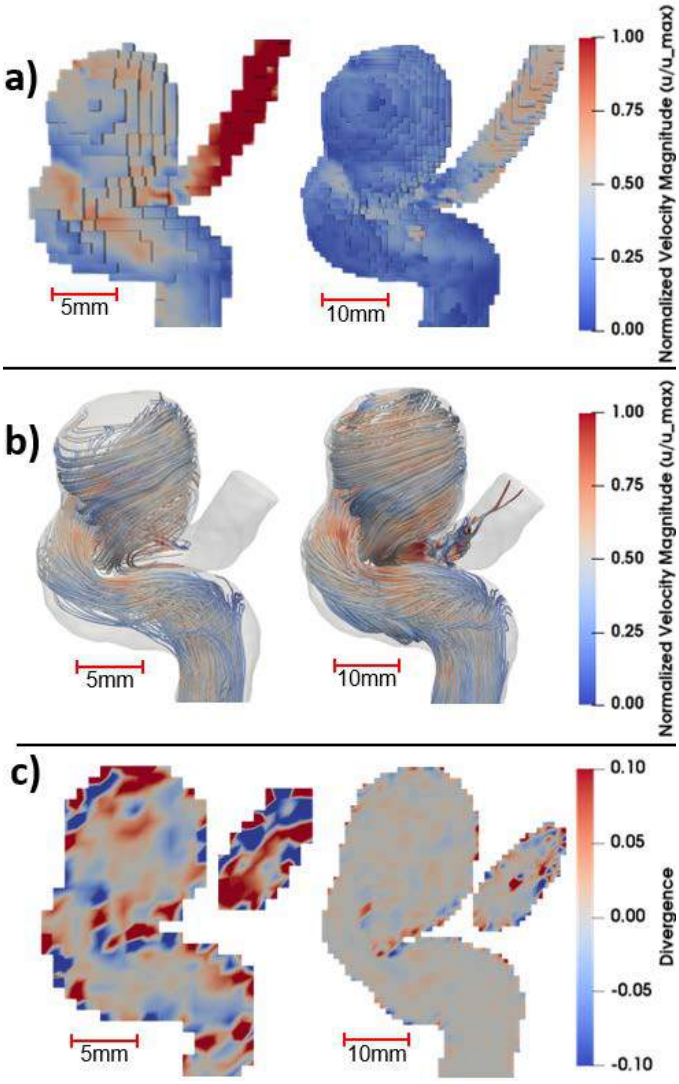

Figure 2: 1-to-1 (left) and 2-to-1 (right) scaling comparisons a) resolution b) streamlines c) divergence

RESULTS

Two 4D flow techniques used in two models of different scale resulted in a total of four cases representing the same flow conditions. Figure 2a displays the increased spatial resolution of 4D Flow as a result of scaling the model. Additionally, the observed velocities at the surface of the 2-to-1 model are noticeably lower than that of the 1-to-1 model. Flow streamlines obtained in all four cases were compared. Figure 2b demonstrates that the scaled model provided a better depiction of recirculating flow within the dome of the aneurysm and in the ICA bend. Regardless of scale, dual-venc results provided denser streamlines and a better flow visualization within the near-wall regions and areas of secondary flow (e.g. ICA bend). Figure 2c displays the divergence results comparing the unscaled and scaled models at a cross section of the aneurysm. These results show that mass conservation was not maintained with 4D Flow measurements, which leads to errors in other flow-derived metrics. Most notably, the divergence was observed to decrease by two orders of magnitude within the scaled model. In all four cases, divergence increased along the walls, where the velocities were comparable to image noise.

DISCUSSION

This study experimentally investigated the advantages of using dual-venc 4D Flow MRI technique along with increased relative resolution on measured intra-aneurysmal hemodynamics. Dual-venc measurements provided better assessment of low velocity regions due to its lower noise and increased dynamic range. In particular, these better represented flow features near the wall and within the ICA bend. Additionally, the measured velocity fields in the 2-to-1 scaled model were more consistent with the laws of physics. With a higher relative resolution, each voxel better captures local velocity profiles, thus increasing the accuracy of calculated velocity gradients. This results in a substantially lower local and global divergence, i.e. mass conservation. Additionally, Figure 2a shows that the 2-to-1 model provides an improved assessment of near-wall velocities. Due to the higher relative resolution, the low velocities in the voxels adjacent to the wall were not averaged with the higher velocities farther away.

The findings of this study demonstrate that dual-venc 4D Flow MRI and a scaled model improved the accuracy of the measured intra-aneurysmal hemodynamics. In particular, the scaled model measurements resolved the flow near the wall and reduced the divergence. Furthermore, this experiment suggests that the use of dual-venc 4D Flow MRI will provide a more accurate assessment of slow flow features. This suggests that the resolution of in vivo 4D Flow MRI in cerebral vessels should be substantially increased in order to accurately assess intra-aneurysmal hemodynamics These improved measurements are crucial to providing reliable calculations of flow-derived metrics such as WSS and, therefore, predictions of aneurysm progression.

ACKNOWLEDGEMENTS

Funding for this study was provided by NIH R21 NS106696.

REFERENCES

[1] Thompson, G et al., *Am. Stroke Assoc.*, 2015.
[2] Jeong, YG et al., *J. Korean Neurosurg.*, 45:11, 2009.
[3] Meng, H et al, *Am. J. Neurorad.*, 35:1254–1262, 2014.
[4] Schnell, S et al, J. Mag. Res. Img., 46:102–114, 2017.

IN-SILICO CHARACTERIZATION OF PATIENT-SPECIFIC PULMONARY HYPERTENSION HEMODYNAMICS

Narasimha R. Pillalamarri (1), Senol Piskin (1), Sourav S. Patnaik (1), Alifer D. Bordones (2), Vitaly O. Kheyfets (3), Ender A. Finol (1)

(1) Department of Mechanical Engineering
University of Texas at San Antonio
San Antonio, TX, USA

(2) Department of Biomedical Engineering
University of Texas at San Antonio
San Antonio, TX, USA

(3) Department of Bioengineering
University of Colorado Denver
Denver, CO, USA

INTRODUCTION

Deciding on the course of treatment for pulmonary hypertension (PH) requires multiple sessions of a six-minute walk test, transthoracic echocardiography, and right heart catheterization (RHC). These invasive procedures, particularly RHC, substantially limits the clinicians' ability to safely diagnose and monitor disease progression. Multiple imaging and simulation-based studies have indicated that patient-specific pulmonary hemodynamics can potentially identify a developing PH condition [1-4]. Moreover, computational methods facilitate the assessment of complex multivariate interactions between the arterial wall, blood stream, and the right ventricle. Spatiotemporal localization can possibly identify individual contributions of the proximal and distal pulmonary vasculature (PPV and DPV) towards disease progression. Our research aims to identify the deviations from regular flow phenomenon and simulation-based metrics that can potentially contribute towards developing non-invasive diagnostic procedures.

METHODS

Following IRB approval, patient-specific geometries of the pulmonary vasculatures were reconstructed from chest computed tomography angiography images obtained from PH patients at Allegheny General Hospital (Pittsburgh, PA). The surface reconstruction procedure is described in detail by Kheyfets et al [5]. The computational model for each patient extends from the proximal main pulmonary artery (MPA) up to six generations of branching pulmonary arteries. Each geometry was discretized with 5 to 8 million tetrahedral mesh elements in ANSYS ICEM (Ansys Inc., Canonsburg, PA).

The CFD solver was developed using open source C++ libraries available in OpenFOAM v5.0 distribution. The governing equations were evaluated using the pressure–velocity coupling method which can be described in three steps: (1) momentum predictor, (2) pressure solver, (3) momentum corrector.

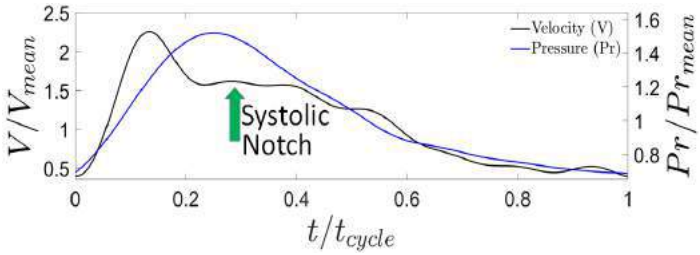

Figure 1: Pressure and velocity waveforms obtained from averaging the data collected from eight PH patients via a Volcano catheter. The velocity profile possesses a systolic notch typical of PH patients [6].

Velocity and pressure data was recorded with a Volcano catheter in eight PH patients at Allegheny General Hospital. The data was normalized with respect to the mean of the distributions. Cardiac output derived peak inlet velocity and mean pulmonary arterial pressure ($mPAP$) were used as dimensional factors to generate quasi patient-specific waveforms, as seen in Fig. 1. A resistance structured-tree outflow boundary condition, proportional to the outlet radius, was applied at each outlet cross-section. The outlet resistances were dynamically adjusted to achieve the patient-specific pressure waveform at the inlet. This transient resistance boundary condition ensured the time lag between velocity and pressure waveforms typical of the human circulation in large arteries.

Following the simulations, multiple hemodynamic metrics were evaluated. For brevity, only the computation of wall shear stress (WSS)

is covered in this abstract. For the complete cardiac cycle, spatially averaged wall shear stress (SAWSS) was evaluated using Eq. (1).

$$SAWSS = \frac{1}{A}\int_A \mu \frac{\partial u}{\partial n}\, \partial A \quad (1)$$

Power regression correlations were evaluated between SAWSS and pulmonary vascular resistance (PVR), which is a clinically derived metric evaluated using Eq. (2),

$$PVR = \frac{mPAP - PCWP}{HR \times SV} \quad (2)$$

where PCWP is the pulmonary capillary wedge pressure, HR is the heart rate, and SV is the stroke volume. The correlations were reported at four time instants representing the pre-systole (t/t_{cycle} = 0.06), peak systole (t/t_{cycle} = 0.11), systolic notch (t/t_{cycle} = 0.33), and diastole (t/t_{cycle} = 0.9) phases of the cardiac cycle.

RESULTS

SAWSS increased tenfold, from approximately 1.5 dyn/cm^2 to 15 dyn/cm^2 from the beginning of the cardiac cycle to peak systole, as shown in Figure 2. Neglecting the high WSS values close to the outflow boundaries, spatially, a maximum WSS of 18 dyn/cm^2 was obtained for an exemplary patient-specific vasculature (see Figure 3 for patient P1). Figure 4 illustrates the power law correlations between SAWSS and PVR at the aforementioned four instants of the cardiac cycle. The lowest R^2 value was observed at peak systole (0.7686), while the highest R^2 value was obtained at diastole (0.8936). This is in close agreement with the steady-state analysis conducted at mid-systole by Kheyfets et al [5]. It must be noted that Kheyfets and colleagues reported on a 20-patient dataset compared to the five-patient dataset presented in this work. The pressure distribution obtained for patient P1 is in agreement with the prevalent velocity distribution of an incompressible fluid flow, as seen in Figure 5.

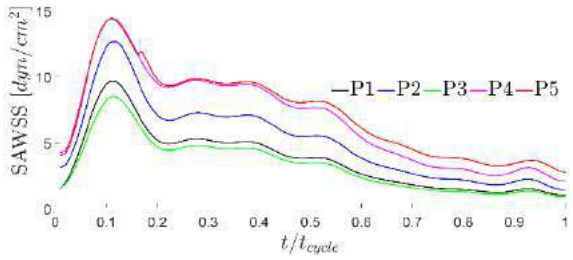

Figure 2: Spatially averages wall shear stress obtained for five PH patient-specific geometries for a complete cardiac cycle.

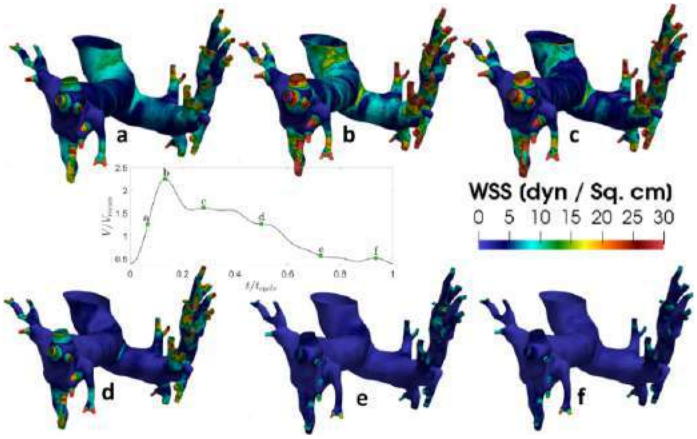

Figure 3: Wall shear stress (WSS) distributions at selected time instants during one cardiac cycle for patient P1.

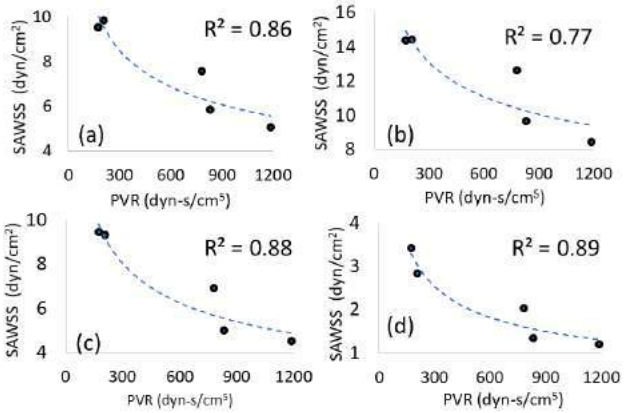

Figure 4: Power law regression correlations between SAWSS and PVR at t/t_{cycle} = a) 0.06, b) 0.11, c) 0.33, and d) 0.9.

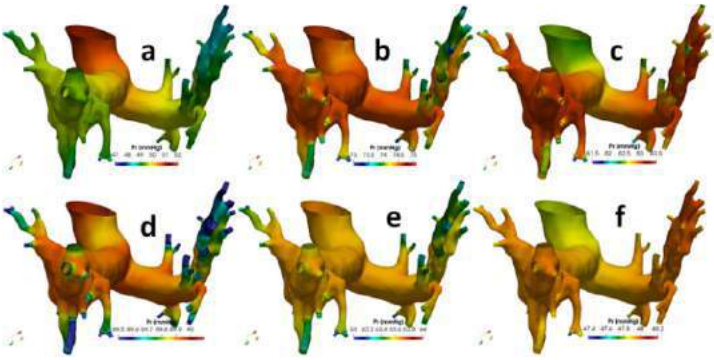

Figure 5: Pressure distribution in patient P1 at selected time instants during the cardiac cycle. The temporal locations are the same as those identified in Figure 3.

DISCUSSION

Efforts to non-invasively identify PH markers have rendered substantial significance to computational flow analysis. The onset mechanisms of abnormal flow patterns can be linked to signs and symptoms of a developing PH condition. For example, in pulmonary arterial hypertension, the narrowing of arteries and low radius of curvature of the left/right pulmonary artery surfaces contribute to flow separation and shear layer instability. A major limitation of this study is the small pool of patient-specific data. In addition, we lack precise knowledge of the individual inlet velocity and pressure waveforms at the proximal MPA. Nevertheless, applying spatiotemporal localization on computationally derived indices is expected to gage the relative contributions of the PPV and DPV for diagnosis and progression of PH.

ACKNOWLEDGEMENTS

This work was supported in part by National Institutes of Health award 1R01HL121293. The simulations are conducted on Stampede - 2 at the Texas Advanced Computing Center (TACC). The use of ANSYS software was possible through an educational licensing agreement.

REFERENCES

1. Barker, AJ et al., *Magn Reson Med*, 73:1904-1913, 2015.
2. Tang, BT et al., *Ann Biomed Eng*, 39:347-358, 2011.
3. Kheyfets, V et al., *J Biomech Eng*, 135:061011, 2013.
4. Piskin, S, *WCB 2018*, Dublin, Ireland, 2018.
5. Kheyfets, V et al., *Comput Meth Prog Biomed*, 120:88-101, 2015.
6. Kitabatake, A et al., *Circulation*, 68:302-309, 1983.

SB³C2019
Summer Biomechanics, Bioengineering and Biotransport Conference
June 25 -28, Seven Springs, PA, USA

DEVELOPMENT OF AN EXPERIMENTAL SYSTEM EXPLORING THE EFFICACY OF CYCLIC ASPIRATION ON CLOT DISPLACEMENT IN A CEREBRAL THROMBECTOMY MODEL

Joshua F. Kugel (1), Connor C. Foust (1), Bryan C. Good (1), Keefe B. Manning (1,2)

(1) Department of Biomedical Engineering
The Pennsylvania State University
University Park, PA, USA

(2) Department of Surgery
Penn State Hershey Medical Center
Hershey, PA, USA

INTRODUCTION

Embolic occlusion of the cerebral artery causes an acute ischemic stroke (AIS) in an estimated 700,000 patients every year [1]. Removal of the thromboembolus requires surgical intervention involving a catheter-based thrombectomy. Advancements in clot removal techniques have led to recanalization rates of up to 85% in cases studied [2], but 17% of patients deemed successful will still die within 90 dies after the procedure [1]. Successful recanalization rates in all patients cannot be achieved without more of an understanding to the mechanics of thromboemboli removal. Current methods of catheter-based thrombectomy involve the release of anticoagulant drugs at the clot site (catheter-directed thrombolysis) and mechanical intervention. Mechanical thrombectomy is based upon stent retrieval and static aspiration methods. Previous research done by Simon *et al.* on aspiration-based thrombectomy demonstrated the effectiveness of an alternative method, cyclic aspiration [3]. The study showed promise in potentially increasing recanalization rates based on the speed and clearance rates of the clots tested. However, further validation is needed for cyclic aspiration thrombectomy to be considered as an alternative surgical procedure. This study will look at the development of an experimental model to predict the deformation, adhesion and dislodgement of thromboemboli under induced cyclic loading. The goal of this study is to track the displacement of an embolus analog under controlled cyclic aspiration.

METHODS

The system was modeled to represent a thromboembolus lodged in a cerebral artery in which cyclic aspiration is introduced by a cerebral catheter. An optically clear, hollow chamber was designed and 3D printed to represent the inside of a cerebral artery (**Fig 1**). Neoprene rubber was inserted into the chamber to represent an embolus analog and clear PVC tubing to represent a cerebral catheter. The parameters of this chamber were determined using physiological reasoning, and the chamber was scaled up 5x. Therefore, the embolus analog was determined to have a diameter of 0.7" (5x-enlargement of the middle cerebral artery diameter [4]) and the tubing was determined to have an inner diameter of 5/16" (5x-enlargement of the Penumbra Ace 68 Reperfusion Catheter).

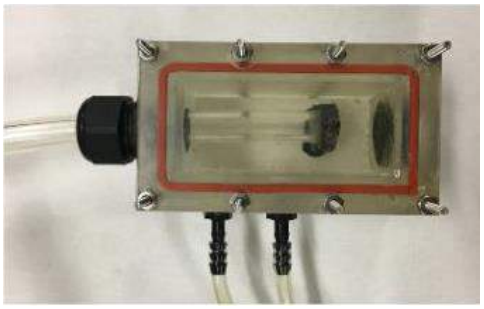

Figure 1. Model of the chamber representing cerebral artery, catheter, and embolus analog.

An experimental flow-loop was designed and created to model the cyclic aspiration (**Fig 2**). A Roscoe Medical Cliq Aspirator was used to introduce a constant aspiration pressure to the system. In order to create cyclic aspiration rather than static aspiration, the model required the use of an ASCO 3-way solenoid valve that was controlled through a self-programmed Arduino microcontroller to open and close between ports 1 and 2 at a frequency of 1 Hz. Additional ports were added to the artery chamber to allow for monitoring of the locally applied pressure and connection to a fluid reservoir.

Poster Presentation #P086

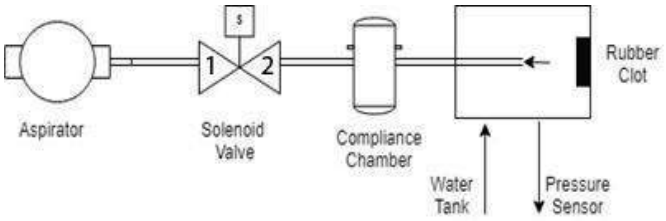

Figure 2. Schematic of the experimental flow loop.

Initial pressure waveforms contained maximum and minimum pressures of approximately 40 and -60 mmHg, respectively. This waveform contained unwanted sharp peaks and rebounding due to very rigid tubing (Durometer 95A) (**Fig 3A**). A second design iteration included softer tubing (Durometer 65A) and the addition of a compliance chamber to control the effect that the tubing had on the pressure signal. The newly obtained pressure waveform had maximum and minimum pressures of approximately 0 and -40 mmHg, respectively (**Fig 3B)**. The newer design provided results that were more physiologically relevant compared to the first and were deemed to be ideal for the goal of gradually dislodging an embolus without causing clot fracture.

A)

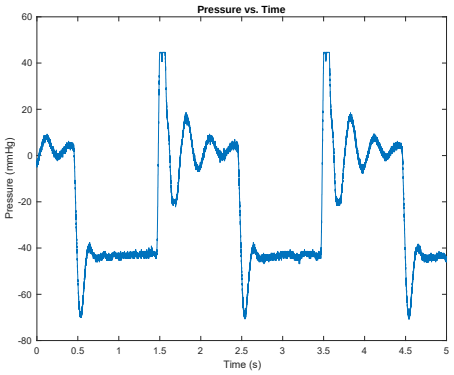

B)

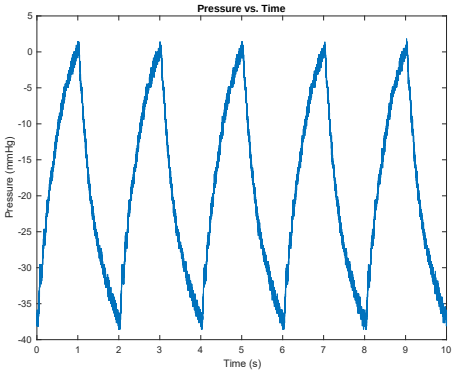

Figure 3. A) Pressure waveform measured experimentally with the first design iteration. **B)** Pressure waveform measured experimentally with the second design iteration.

The 2D motion and displacement of the embolus analog were tracked using a video camera with specifications of 1080p HD at 30 frames per second. Individual frames were extracted from the video using MATLAB, and the clot displacement in each frame was measured using ImageJ.

RESULTS

The 2D displacement of the embolus analog was measured in each image. By performing these measurements, the clot was able to be tracked as it displaced outward due to the applied negative aspiration pressure (**Fig 4**). The maximum displacement of this embolus analog was measured to be approximately 1.06 mm at the maximum aspiration pressure of -40 mmHg.

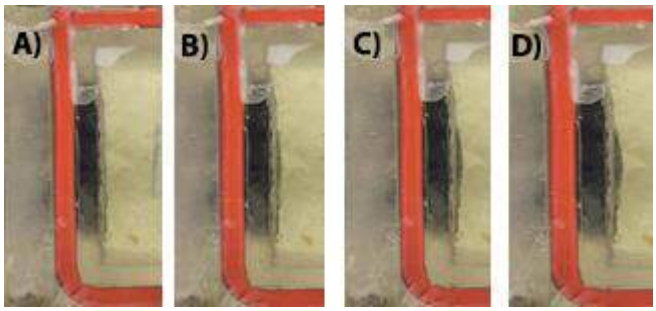

E)

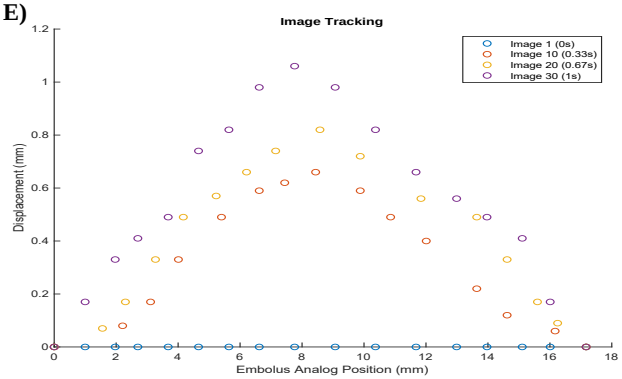

Figure 4. A) Image 1 at time=0 seconds. **B)** Image 10 at time=0.33 seconds. **C)** Image 20 at time=0.67 seconds. **D)** Image 30 at time=1 second. **E)** Tracking of the embolus analog's 2D displacement over 1 second.

DISCUSSION

This study developed an experimental model of embolic occlusion of the cerebral artery that can be used as a baseline for further testing of cyclic aspiration conditions. In comparison with previous tests [3], the similarities in the pressure waveforms collected add confidence in the data. Pressure and displacement data from this experiment will be used to validate future computational models of cyclic aspiration in cerebral arteries. Further testing on the effects of changing frequency, pressure magnitude, and clot material need to be conducted in order to design a more physiologically relevant model using synthetic clots and catheters in the future.

ACKNOWLEDGEMENTS

This work is supported partially by AHA Postdoctoral Fellowship 19POST34370040.

REFERENCES

[1] Grech, R *et al*., Neuroradiol J, 28(2):152-71, 2015.
[2] Dávalos, A *et al*., Stroke, 43:2699–705, 2012.
[3] Simon, S *et al*., J NeuroIntervent Surg, 6:667-683, 2014.
[4] Pai S B, Varma R G, Kulkarni RN., Neurol India, 53:186-90, 2015.

PENNSTATE

Keefe B. Manning, Ph.D.
Department of Biomedical Engineering
The Pennsylvania State University
205 Hallowell Building
University Park, PA 16802
(814) 863-6318
kbm10@psu.edu

February 14, 2019

Dear Review Committee:

I attest that (1) the majority of the work was completed by the first/presenting author and (2) the first author conducted the work when they were a student at the corresponding competition level.

Sincerely,

Keefe B. Manning, Ph.D.
Professor of Biomedical Engineering and Surgery
Associate Dean for Academic Affairs, Schreyer Honors College

SB³C2019
Summer Biomechanics, Bioengineering and Biotransport Conference
June 25 -28, Seven Springs, PA, USA

ASSESSING FEMORAL IMPLANT FAILURE RISK BY APPLYING CONTROLLABLE TORQUE WITH ROBOT MANIPULATOR AND 6 DOF SENSOR

M. Gudauskis (1, 2), A. Pietros (1), B. L. Davis (1), B. Jonard (3)

(1) Department of Biomedical Engineering
The University of Akron
Akron OH, USA

(2) Institute of Mechatronics
Kaunas University of Technology
Kaunas, Lithuania

(3) Department of Orthopaedics
Summa Healthcare System
Akron OH, USA

INTRODUCTION

Assessment of femoral implant failure risk requires customizable testing and measurement systems, particularly for situations where the interactions between multiple orthopaedic implants are of interest. An increasing number of individuals are obtaining total knee arthroplasties, with a subset also requiring surgery for a subsequent fracture, months or years following the knee replacement procedure. By the American Joint Replacement Registry, AJRR, the incidence rates of periprosthetic fractures is 0.3–5.5% for over 600,000 primary Total Knee Arthroplasty not including revision.

Robotic systems are widely used in industry and research. Their advantages lie in the ability to apply precise moments and forces to the object(s) being tested.

This study focuses on risk of femoral shaft fracture using a dual approach; (i) computational modeling, and (ii) experimental validation using an industrial robot manipulator (KUKA KR 5 Six R650 CR2) coupled with a 6DOF sensor. The integration of these technologies is used to assess the response of surgically-repaired femurs to physiologically-appropriate external loads. The aims of this study are to evaluate/validate computational model results by means of the robot manipulator and 6 DOF sensor.

METHODS

A computational model of a femur implanted with a TKR and Introchanter Antegrade Nail (Smith and Nephew models Genesis II femoral component size 5 and Intertrochanter Antegrade nail sizes 5213 to 5227) was created in Abaqus and modeled using a volumetric tetrahedral mesh. Regions of interest (ROI's) were identified for each model, corresponding to the anatomical areas between the TKR that are considered at risk for fracture. Loading conditions included (i) axial forces of 1.7kN, and (ii) torques of 5 to 15 Nm that were applied to the proximal end of the femur with the distal end being fixed. Material conditions for bone ranged from 17 GPa to 11.56 GPa, corresponding to Young's moduli for normal and osteoporotic bone, respectively.

Figure 1: Femur with ipsulateral implant model

A synthetic bone specimen from Sawbones (3403) was utilized for testing as an analogue representation of an actual bone. A set of rosette strain gauges (WA-06-060WR-120) were applied with each ROI, corresponding with peak strain results in the Abaqus simulation. The exact position was verified with a Microscribe G2 instrument.

In order to evaluate stresses within the ROI, a clamp was attached to the femoral head and connected to the distal end of the KUKA robot. All loading was applied by way of torsion from the KUKA linkage to the head of the femur. These loading conditions were applied with the distal femur being fixed in dental cement. The position of the femur was set at a 0° in abduction and 0° in flexion. The kinematics scheme of the testing system are shown in Figure 2.

A LabView program was designed to control the testing parameters. The software collects and saves force and torque sensor data and the robot's kinematics. In this case, the torque was set to 5 Nm and rotations about the robot axis (along the femoral neck) were incrementally increased by 0.1 degree. This was done because the LabView cannot control a KUKA robot directly, and can only execute the program which is stored in robot controller.

Poster Presentation #P087

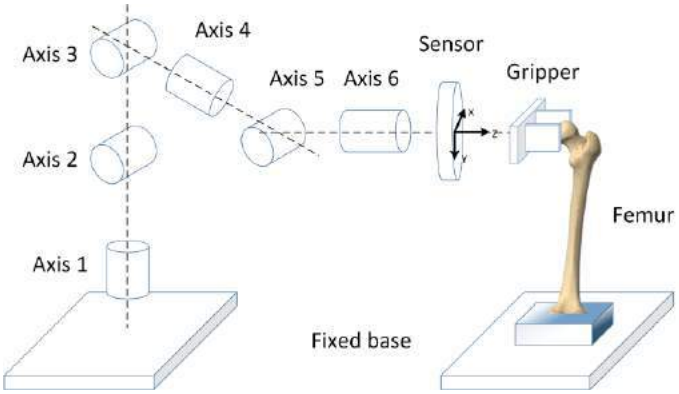

Figure 2: Kinematics scheme of testing system

Since the LabView software cannot control the robot's continuous motion, and can only execute the program in the controller, all testing was performed in a quasi-static manner. Sensor values were measured periodically until such time that the trial was concluded.

RESULTS

For each loading condition there were significant effects due to both bone quality and loading conditions. At 5 Nm torque (Figure 3), normal bone density, and an interprosthetic gap of 8 cm, fracture risk increased by 14% (compared to a situation with a TKR alone). With bone density reduced to 1.6 gm/cm3, the fracture risk increases 19%. The fracture increases dramatically when applying osteoporotic bone instead of non-osteoporotic bone.

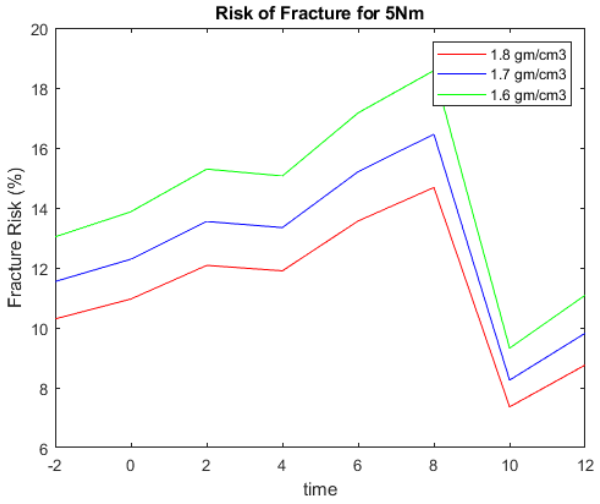

Figure 3: Risk of Fracture for 5 Nm

After the controllable torque test, the results of sensors Z axis torque (Tz) exhibited a step-type incremental process. This graph is similar to the graph of strain gauge measured values of the bone torque (Figure 4). This figure shows the step increments of deformation in the synthetic femur along the anterior surface. These results can be correlated with the applied torque from axis 6 of KUKA robot. In case the software are made to run as an infinity loop, the test results shows three trials in which the robot created torques of 5 Nm.

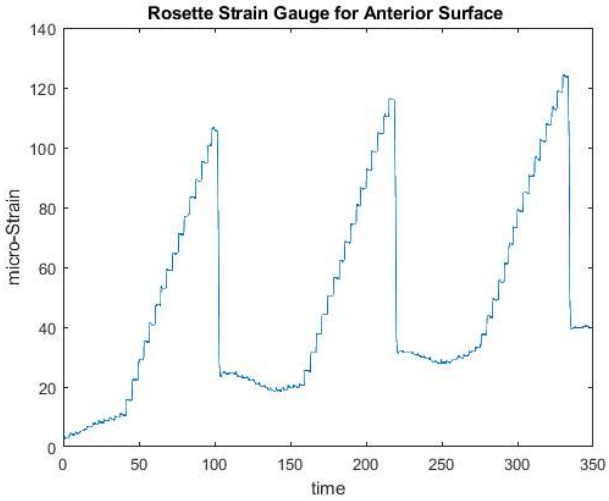

Figure 4: Rosette Strain Results for 45 degrees

DISCUSSION

The results highlight the dependence of fracture risk on both inter-prosthetic distances as well as bone quality. A gap length corresponding to a 2-cortical diameter margin shows a limited stress-riser effect. The results highlight that the careful consideration in nail length is necessary for reducing stress risers by nearly 30% for both non- and osteoporotic femurs with ipsilateral implants.

The controllable torque with robot manipulator and 6DOF sensor test validates the approach of incrementally rotating the robot arm while measuring sensors data. In the future, different sawbone models will be assessed to further validate the results of placing both intramedullary and total knee implants in a femur.

REFERENCES

[1] Hamidreza Farhoudi et al., *J Materials*, 9:982, 2016.
[2] Bono, James V. et al. Revision Total Knee Arthroplasty. Springer, 2018.
[3] American Joint Replacement Registry. "Third AJRR Annual Report on Hip and Knee Arthroplasty Data." AJRR. American Joint Replacement Registry, 2016. Web. 14 June 2017.
[4] Basso, Trude, et al. *Journal of Biomechanics*, vol. 47, no. 16, 2014, pp. 3898–3902.
[5] Samiezadeh, Saeid, et al. *J Mechanical Behavior of Biomedical Materials*, vol. 56, 2016, pp. 87–97.
[6] Bougherara, Habiba, et al. *Medical Engineering & Physics*, vol. 33, no. 1, 2011, pp. 121–128.
[7] Chapman, J. R. *J Biomechanical Engineering*, vol. 118, no. 3, Jan. 1996, p. 391.
[8] Viceconti, M. Medical Engineering & Physics, vol. 22, no. 5, 2000, pp. 379–380.
[9] Mcnamara, Brian P., et al. *J Biomechanics*, vol. 30, no. 6, 1997, pp. 621–630., doi:10.1016/s0021-9290(97)00003-1.
[10] Bates, Nathaniel A., et al. Clinical Biomechanics, vol. 30, no. 1, 2015, pp. 1–13.

SB³C2019
Summer Biomechanics, Bioengineering and Biotransport Conference
June 25 -28, Seven Springs, PA, USA

DRILL PLUNGE IN ORTHOPEDIC SURGERY DEFINED

S. Baskerville (1), T. Conway (1), S. Schultz (1)

(1) Biomedical Engineering
Florida Institute of Technology
Melbourne, Florida, USA

INTRODUCTION

Although *drill plunge* is commonly mentioned within orthopedic surgical studies, there has been minimal effort to define the phrase. The clinical relevance of orthopedic *drill plunge* is undeniable, as plunging can damage neurovascular and connective tissues near the drilling site (3,6). Further complications may arise as a result of iatrogenic *drill plunge* injury, including enhanced post-operative pain and the possibility of additional corrective surgeries. One of the studies evaluated showed that even experienced orthopedic surgeons plunge past the opposite cortical boundary of the drilling site by 5.1mm on average (1). The objective of this research is to define *drill plunge* clearly and its detrimental effects.

METHODS

The major process involved in the development of a quantifiable definition for *drill plunge* required the compilation of as many references and attempted descriptions in the literature as possible. These definitions were pulled from patents and research papers as far back as the 1980s. Some authors provide a short, vague definition while others do not attempt to define it, and instead assume that references to *drill plunge* are common knowledge. Once all of the definitions of *drill plunge* were gathered, similarities and discrepancies were found and evaluated.

Additionally, the geometry and mechanics of a drill bit were studied. The goal was to determine how much of the drill bit needs to go completely through the bone for optimal placement of the screw or pin in ideal cases. It is necessary to study the drill bit to define *drill plunge* properly. The proposed definition seeks to address the shortcomings of previous references to *drill plunge*, as well as provide a quantifiable metric, which can be normalized across all bit geometries.

RESULTS

Papers dating back to the early 1980s were reviewed. They mentioned *drill plunge* as a prevalent source of error in commonly implemented orthopedic surgical methods. Many of these papers provide unclear definitions, while others make poor attempts at describing *drill plunge* or providing a standardized measurement descriptor or methodology. The definitions provided are similar to each other, but none describes completely what qualifies as *drill plunge*. Additionally, *drill plunge* is mentioned in patents for devices that help to prevent plunging, but they do not provide any definition of plunging (8, 9). Various select definitions from the reviewed papers can be found in Table 1.

Research papers studying the average *drill plunge* in a variety of scenarios explain how the plunge was measured. There have been a number of methods used to measure *drill plunge*, most involving measurement of the indent in spongey material caused by the plunging of the drill bit (4). Another method involved placing a cover over the drill bit and measuring the amount of drill bit exposed after drilling (1).

Poster Presentation #P088

Table 1: References to *drill plunge* and available definitions.

Date(s)	Definition
2004	"length of drill protruding after the bone has been drilled" (2)
2012, 2017	"soft tissue penetration" (1,7)
2009	"amount of drill bit penetration into the underlying soft tissues" (5)
2018	"distance a drill bit obtrudes the far cortex during the process of drilling through a bone" (4)

In order to understand the placement of the drill bit needed, figure 1 shows a diagram of a typical drill bit. This illustrates the key features of drill bit geometry. In order for the drilled pilot hole to have uniform diameter equivalent to the major diameter of the drill bit, the flutes of the drill bit must differentially approach the opposite cortical boundary of the drilled bone. Therefore, the drill bit does not fully drill through the bone until the leading edges of the bit are completely through the bone.

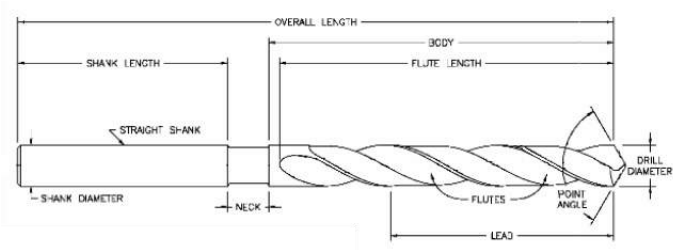

Figure 1: Drill bit diagram.

Through observation, discussion, and literature review, a new formal and quantitative definition of *drill plunge* is proposed. *Drill plunge* can be classified as the measured length of fully-fluted drill bit that travels beyond the opposite cortical boundary of the bone. This metric excludes any length of the drill bit which must theoretically move past the opposite cortical boundary in order for a full and complete pilot hole to be formed. This excluded length is typically referred to as the drill bit tip. Manipulating the geometry of the drill bit, the tip can be taken into consideration when measuring *drill plunge* by using the following equation:

$$T = \frac{D}{2\tan(\frac{\emptyset}{2})} \quad (1)$$

Where T is the drill bit tip length that should be taken into account when measuring plunge depth. D is the diameter of the drill bit and ∅ is the point angle on the drill bit. The calculated drill bit tip length should be subtracted from the amount of measured plunge to provide the true plunge depth of the full functional geometry of the bit. As the drill bit becomes dull, the length of the drill bit tip will decrease. Therefore, there will be a small amount of error the longer the drill bit is in use. This definition of *drill plunge* is not to be limited to cases exclusively involving soft tissue penetration.

DISCUSSION

Anytime a bone is drilled during surgery, the soft tissues on the opposing side of the bone are at risk for serious damage (3). Many surgeons do not want to address that they plunge when drilling, but it is almost inevitable with the tools currently available. Therefore, many studies have been completed on *drill plunge* and ways to minimize it. Even with the harmful effects, literature lacks a proper definition explaining what qualifies as *drill plunge*.

There is a real necessity for a thorough definition of *drill plunge*, as the definitions provided by the papers reviewed do not fully classify *drill plunge* with a universally useful level of detail. The studies that measured the *drill plunge* as the depth of the hole created in a spongey material past the bone is inaccurate because it does not account for the geometry of the tip of the drill bit. The tip of the drill bit needs to go completely through the entire bone so the implant can be properly anchored. Therefore, the end of the fluted length of the bit should be flush with the far side of the drilled bone. The exclusion of drill bit tip length in *drill plunge* measurements allows for normalization in experimental data across all drill bit geometries.

ACKNOWLEDGEMENTS

This research was supported and funded by Smart Medical Devices and Dr. John Perry.

REFERENCES

[1] Alajmo G, Schlegel U, Gueorguiev B, et al., *J Orthop Trauma*, 26:8, 2012.

[2] Dubrowski A, Backstein D, *Journal of Bone and Joint Surgery*, 86-A: 2778, 2004.

[3] Hart N, Clark J, Krause W, et al., *Journal of Shoulder and Elbow Surgery*, 22:814-820, 2013.

[4] Kazum E, Dolkart O, Rosenthal Y, et al., *Journal of Surgical Education*, 00:1-5, 2018.

[5] Khokhotva M, Backstein D, Dubrowski A, *Association médicale canadienne*, 52: 98-102, 2009.

[6] Lavernia C, Cook C, Hernandez R, et al., *The Journal of Arthroplasty*, 22:124-132, 2007.

[7] Ruder J, Turvey B, Hsu J, Scannel B, *Journal of Surgical Education*, 74:472-476, 2017.

[8] Hendel, Phillip M. Guided Osteotome for Harvesting Cranial Bone Graft. US: Patent 4,600,005. 15 Jul. 1986.

[9] Wang E, Kung G. Drill Guide for Precise Drilling. US: Patent 4,961,673. 9 Oct. 1990.

SB³C2019
Summer Biomechanics, Bioengineering and Biotransport Conference
June 25 -28, Seven Springs, PA, USA

A PRELIMINARY STUDY ON CORRELATIONS BETWEEN MICROARCHITECTURAL PARAMETERS OF HUMAN TRABECULAR BONE

Pengwei Xiao (1), Joel Gomez (1), Matthew Kirby (1), Ed Guo (2), Xiaodu Wang (1)

(1) Department of Mechanical Engineering
The University of Texas at San Antonio
San Antonio, Texas, United States
(2) Department of Biomedical Engineering
Columbia University
New York, United States

INTRODUCTION

Microarchitectural features have a direct effect on the mechanical behavior of trabecular bone. In the past, morphological parameters are usually used to characterize microarchitectural features of trabecular bones, which at best provide average measures of trabecular bone microarchitecture. Recent studies have shown that trabecular bone can be decomposed into individual trabecular plates and rods by using Individual Trabecula Segmentation (ITS) techniques [1,2,3]. This advanced technique allows for accurate characterization of microarchitectural features based on information of individual trabeculae, which could help improve patient-specific prediction and prevention of bone fragility fractures. Our previous study indicates that there exists a commonality in the underlying probabilistic distributions of individual microstructural features of trabecular bones [4,5]. However, it is still unknown regarding the correlations between the microarchitectural parameters obtained from the individual trabeculae, which may provide further details about the interplay of these microarchitectural parameters. In this study, the correlations between microarchitectural parameters were analyzed based on data from sixty-six trabecular bone specimens, which were obtained from donors of different age and sex and from different anatomic locations (femoral neck, vertebral body, proximal tibia, and greater trochanter) [6]. The results of this study showed that the correlations between trabecular microarchitectural parameters followed similar patterns irrespective of anatomic locations. This finding is important for understanding the natural design of trabecular microstructures.

METHODS

Trabecular bone specimens from twelve femoral neck (N_{FN} =12), eleven lumbar 1 vertebral body (N_{VB} =11), twenty-two proximal tibia (N_{PT} =22) and twenty-one greater trochanter (N_{GT} =21) trabecular structures were analyzed to determine if the microarchitectural parameters of trabecular bone were correlated. The sixty-six trabecular bone samples were cored from the center of their respective anatomic locations and the longitudinal axis of each specimen was aligned with the principal axes of trabecular orientations. The specimens were imaged using μCT at a resolution of 21μm voxels and digitally reconstructed. The digitized models were then decomposed using Individual Trabecula Segmentation (ITS) software to determine the size, orientation, and spatial arrangement of individual trabeculae. Eight microstructural parameters were defined from ITS data, including plate area (PA), plate thickness (PT), plate nearest neighbor distance (PS), plate orientation (PO), rod length (RL), rod diameter (RD), rod nearest neighbor distance (RS) and rod orientation (RO). Finally, pairwise quantile-quantile regression was performed to determine the correlations among the microstructural parameters.

RESULTS

The pairwise quantile-quantile regression analyses indicated that correlations might exist between the pairs of trabecular bone microarchitectural parameters (*i.e.* PA vs PT, PA vs PO, PA vs Ps, PT vs PO, PT vs PS and RL vs RD, RL vs RO, RL vs RS, RD vs RO, RD vs RS) at different anatomic locations (**Fig. 1**). Due to the missing data, the results for the correlations between plate or rod spatial parameter and other microarchitectural parameters for greater trochanter were not available. The results indicated that the quantile-quantile regression patterns between the microstructural features of trabecular bone were similar irrespective of anatomic locations. In addition, some correlations were observable between the trabecular size, orientation, and spatial arrangements. For instance, it appeared that larger and thicker plates tended to orient parallel to the major principal axis of trabecular bone specimens. The plate area vs. plate thickness and rod

length vs. rod diameter were following a similar pattern at difference anatomic locations.

DISCUSSION

First, the results of this study indicate that the correlations between most microarchitectural parameters are similar irrespective of anatomic locations (*i.e.* femoral neck, vertebral body, proximal tibia and greater trochanter) and donor ages and sexes, except for trabecular sizes vs. trabecular orientations showing some different patterns at different

Figure 1: Correlations between microarchitecture parameters

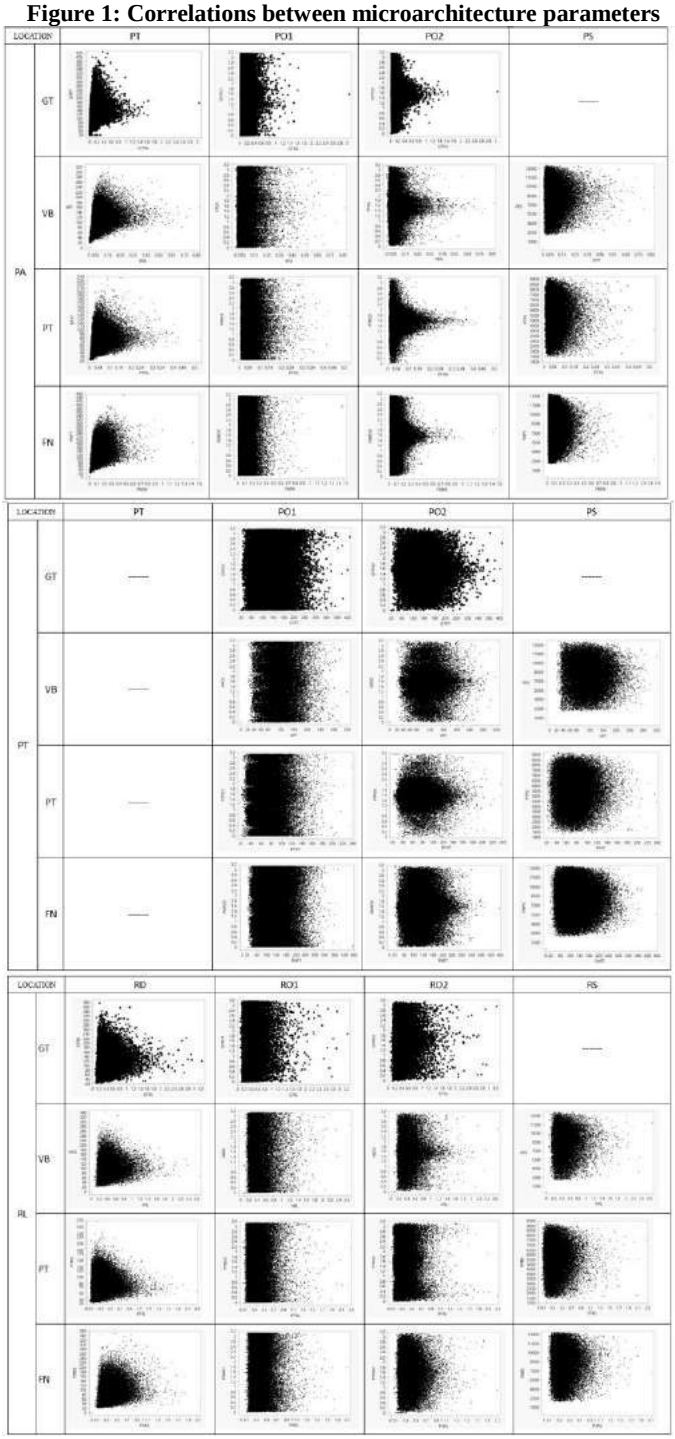

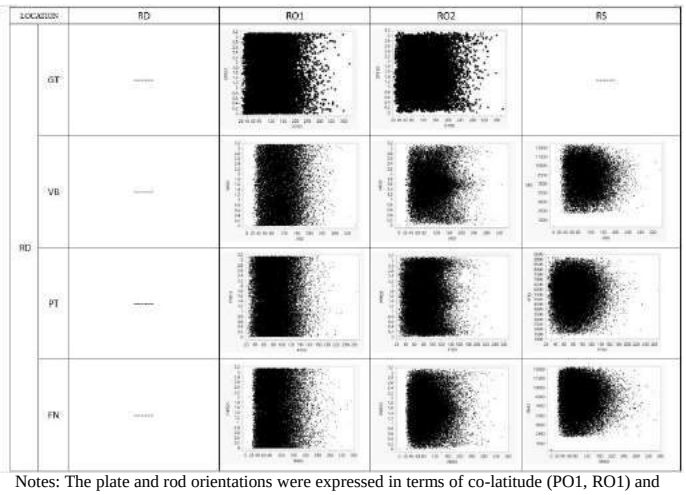

Notes: The plate and rod orientations were expressed in terms of co-latitude (PO1, RO1) and Longitude (PO2, RO2).

anatomic locations. This implies that the size of trabeculae is correlated with their orientations differently at the different anatomic locations.

Secondly, the pairwise quantile-quantile regression between PA and PT, RL and RD exhibits a similar pattern of triangular shape, suggesting that the plate area has a weak correlation with plate thickness. In addition, the pairwise quantile-quantile regression between PA and PO2, PT and RO2 illustrates a peaked pattern around the major principal direction of the bone samples. This suggests that larger and thicker plate are preferentially oriented parallel to the principal direction of the bone specimens. Moreover, the pairwise quantile-quantile regression between PA and PS, PT and PS, RL and RS, RD and RS follows a similar pattern of semi-circular shape, indicating a weak correlation between the parameters.

Finally, no correlation between PA and PO1, PT and PO1, RL and RO1, RD and RO1, and RD and RO2 appears to exist since no distinguishable patterns could be observed (rectangle shape).

In summary, the results of this study indicate that some of the microstructural parameters may be correlated, thus giving rise to more insights into the underlying organization of individual trabeculae for trabecular bones.

ACKNOWLEDGEMENTS

Acknowledge grant or other funding support or the assistance of others as appropriate.

REFERENCES

[1] X Sherry Liu, et al., *J Journal of Bone and Mineral Research*, 23:223-235, 2008.
[2] X Sherry Liu, et al., *J Journal of Bone and Mineral Research*, 25:1496-1505, 2010.
[3] Bin Zhou, et al., *J Journal of Biomechanics*, 47:702-708, 2014.
[4] Feng Zhao, et al., *J Bone*, 111:59-70, 2018.
[5] Morshed, A.H.M.M, *Master of Science in Mechanical Engineering*, University of Texas at San Antonio, 2015.
[6] Matthew Lyle Kirby, *Master of Science in Mechanical Engineering*, University of Texas at San Antonio, 2017.

SB³C2019
Summer Biomechanics, Bioengineering and Biotransport Conference
June 25 -28, Seven Springs, PA, USA

THREE-DIMENSIONAL ANISOTROPIC RESIDUAL STRESSES IN THE ABDOMINAL AORTA

Taisiya Sigaeva (1), Gerhard Sommer (2), Gerhard A. Holzapfel (2,3), Elena S. Di Martino (1,4)

(1) Department of Civil Engineering
University of Calgary
Calgary, Canada

(2) Institute of Biomechanics
Graz University of Technology
Graz, Austria

(3) Department of Structural Engineering
Norwegian University of Science and Technology
Trondheim, Norway

(4) Centre for Bioengineering Research and Education
University of Calgary
Calgary, Canada

INTRODUCTION

It is known that residual stresses have a strong effect on the homeostatic stress state in arteries and should be accounted for in biomechanical models. The conventional approach of modelling residual stresses is the opening angle method. In this method, the circumferential residual deformations are measured by simple ring cutting experiments, and the corresponding residual stresses are then mathematically derived. However, it has been demonstrated that the three-dimensional residual stress model, introduced in [1], is more accurate in capturing not only the circumferential residual deformations, but also the axial ones, which are found to be essential in preventing arterial buckling. Moreover, accounting for the individual layers' residual deformations as proposed in [1] is very important considering the non-homogeneous nature of arteries. In this work, we extend the model from [1] to the anisotropic case using the recently introduced material model from [2]. This allows us to study the influence of anisotropy and microstructure on the residual stresses.

METHODS

In this work, we focus on residual stresses of the abdominal aorta. The axial and circumferential residual deformations of individual layers of the healthy abdominal aorta are estimated from the experimental study conducted in [3] – see Figure 1. To describe the anisotropic response of an aortic layer and account for both in-plane and out-of-plane collagen fibre alignments, the material model from [2] is employed. The strain-energy function (SEF) Ψ can be split into an isotropic term Ψ_1 and an anisotropic term Ψ_2, i.e.

$$\Psi = \underbrace{\frac{c}{2}(I_1 - 3)}_{\Psi_1} + \underbrace{\sum_{i=4,6} \frac{k_1}{2k_2}[\exp(k_2 E_i^2)) - 1]}_{\Psi_2}. \qquad (1)$$

Here, I_1 is the first invariant of the right Cauchy-Green tensor, E_4 and E_6 are Green-Lagrange quantities, and c, k_1, k_2 are mechanical material parameters. In addition, E_4 and E_6 depend on the microstructural material parameters κ_{ip} and κ_{op} describing in-plane and out-of-plane fibre dispersions.

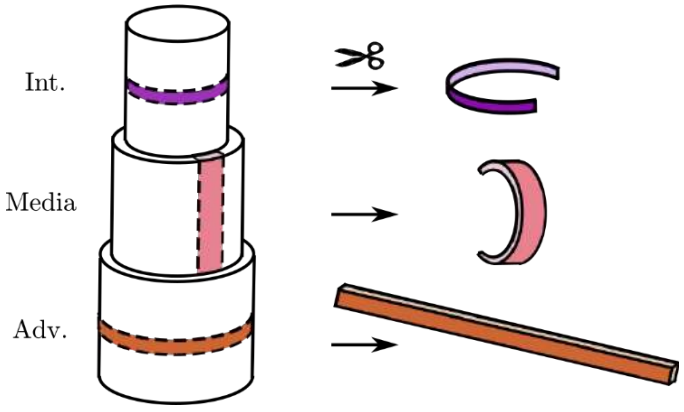

Figure 1: Dominant axial (for the medial layer) and circumferential (for intimal and adventitial layers) residual deformations, as measured for the healthy human abdominal aorta.

Material parameters for this model must be determined from both microstructural analysis and mechanical testing of individual layers - the corresponding data for the healthy abdominal aorta were taken from [4].

Kinematics of the residual deformations together with the anisotropic SEF (1) $\Psi = \Psi_1 + \Psi_2$, and its "isotropic" version $\Psi = \Psi_1$, were used to derive expressions for isotropic and anisotropic residual stresses in individual aortic layers. The equilibrium equations, boundary conditions of zero-stress on the surfaces of the aorta and interface conditions of continuous radial stresses across the layers form boundary-value problems that were solved to determine all the unknows of the problem. This allows a comparison of isotropic and anisotropic residual stresses of a quantification and investigation of the contribution of the anisotropic term Ψ_2 in the SEF (1), which is associated with the fibrous structure of the aorta.

SELECTED RESULTS

Residual stresses for the healthy abdominal aorta are shown in Figure 2 for the isotropic ($\Psi = \Psi_1$) and the anisotropic ($\Psi = \Psi_1 + \Psi_2$) SEFs. As can be seen, that the intimal layer of the aorta behaves rather isotropically, while the effect of the anisotropic term Ψ_2 in the adventitia is minimal. In contrast, the anisotropy seems to have a significant contribution in the media.

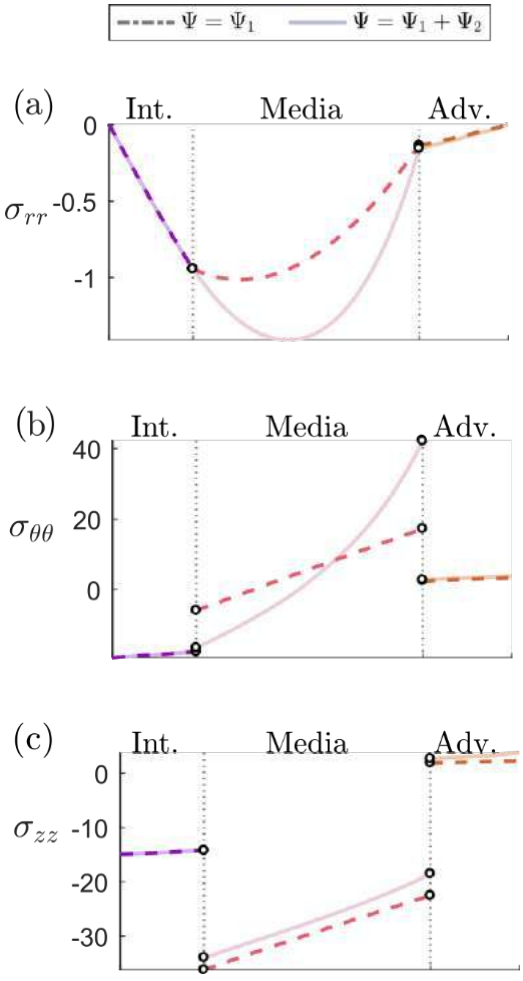

Figure 2: Influence of the anisotropic term Ψ_2, in the SEF (1) on the residual stresses: (a) radial; (b) circumferential; (c) axial.

DISCUSSION

The different layers of large arteries such as the aorta have been shown to exhibit residual deformations in both the axial and circumferential directions. Modeling this complex behaviour requires a consideration of the heterogeneous material properties of the different layers, as well as the micro-structural differences. We achieved this by using an anisotropic SEF. Because residual strains are present in the absence of loads the presence of anisotropy has often been neglected in the computation of stresses derived from such residual strains. Our results show that this is legitimate for the intimal layer, which is highly compressed when unloaded and therefore any fibers present can be assumed to be unloaded. However, this is not the case for the other two layers. The adventitia is a highly collagenous layer, and while many fibres are most likely in a "non-activated" state at low strains, some effects due to the anisotropy of the structure were noted (see Figure 2). On the other hand, the media has a large fraction of elastin fibres, which appear to play a role on the residual stresses, together with any medial collagen fibres, if present. The model developed captures the most relevant effects of residual deformation in all three layers of a healthy abdominal aorta considering their unique mechanical and structural properties.

ACKNOWLEDGEMENTS

This research has been made possible by a James M. Flaherty Research Scholarship from the Ireland Canada University Foundation, with the assistance of the Government of Canada/avec l'appui du gouvernement du Canada. Contributions from National Science and Engineering Research Council of Canada (NSERC) Discovery Grant and the Heart and Stroke Foundation of Canada are gratefully acknowledged.

REFERENCES

[1] Holzapfel GA et al. (2010). Journal of the Royal Society Interface, 5; p. 20090357.
[2] Holzapfel GA et al. (2015). Journal of the Royal Society Interface, 12(106); p. 20150188.
[3] Holzapfel GA et al. (2007). Annals of Biomedical Engineering, 35(4); pp. 530–545.
[4] Niestrawska JA et al. (2016). Journal of the Royal Society Interface, 13(124); p. 20160620.

SB^{3}C2019
Summer Biomechanics, Bioengineering and Biotransport Conference
June 25 -28, Seven Springs, PA, USA

A BIOMECHANICS-BASED RISK PREDICTION METRIC FOR THORACIC AORTIC DISSECTION

Spandan Maiti (1), James R. Thunes (1), Leonid Emerel (2), Thomas G. Gleason (1,2), David A. Vorp (1,2)

(1) Department of Bioengineering
University of Pittsburgh
Pittsburgh, PA, USA

(2) Department of Cardiothoracic Surgery
University of Pittsburgh
Pittsburgh, PA, USA

INTRODUCTION

Type A Aortic Dissection (TAAD) is a life-threatening condition involving delamination of aortic media layers. Current clinical guidelines recommend prophylactic surgical replacement of the ascending aorta at an aneurysm diameter >5.5cm to mitigate the risk of TAAD. However, large retrospective series and data from the international registry of acute aortic dissection (IRAD) has shown that as high as 62% of patients with TAAD have aortic diameters distinctly less than 5.5 cm [1], indicating the need of improved evidence-based risk prediction metrics. From a mechanics perspective, dissection is the biomechanical failure of the aortic wall that occurs when ascending aortic aneurysm wall stress exceeds wall strength; thus, wall stress may serve as a reasonable predictor of dissection. Both maximum wall stress and stretch based risk prediction metrics have been recently suggested in the literature. However, the lack of the clinical knowledge of whether a dissection actually ever occurred restricts the accuracy and validity of these models. We hypothesized that patients sustaining TAAD exhibit abnormal aortic wall stress in the longitudinal direction prior to the development of dissection. Our objective in this work was to establish the dissection potential index (DPI), a metric for early adjudication of TAAD risk based on longitudinal component of the wall stress. Towards that end, we constructed pre-dissection aortic images of the dissected as well as non-dissected patients from our clinical database, and created wall stress maps for each patient utilizing patient-specific wall tissue biomechanical properties. These maps were used to create patient specific dissection potential index.

METHODS

Aortic dissection patients with pre-dissection CT imaging ($n = 10$) were chosen as the study group. A control set of patients without aortic dissection ($n = 9$) was also chosen for comparison. A number of clinical data including age, gender, weight, height, body mass index, body surface area and blood pressure were matched for these two cohorts. Scans were collected with patient consent and IRB approval. Mimics (Materialize, Leuven, Belgium) and Geomagic (3D Systems, Rock Hill, SC) were used to 3D reconstruct a solid model of the thoracic aorta from the scans. Finite element meshing was performed using Trelis (csimsoft, American Fork, UT) resulting in meshes with 30,000-50,000 3-noded triangles. Systolic (AoS) and diastolic (AoD) aortic diameters for each patient was assessed using the parasternal long axis window of two-dimensional transthoracic echocardiography, measured 3 cm above the aortic valve. AoD was obtained at the peak of the R wave in the simultaneously recorded electrocardiogram, while AoS was measured at the initiation of the T wave. Patient specific aortic stiffness was estimated from these diameter measurements and knowledge of corresponding systolic and diastolic blood pressure [2]. A two- parameter isotropic constitutive model, previously developed for abdominal aortic tissue [3], was calibrated in a patient-specific manner to match imaging obtained aortic stiffness.

The aortic models were loaded to an internal pressure of 200 mmHg using a custom membrane dynamic finite element program. Displacements at all the boundaries of the resulting aortic model were restrained to zero to prevent rigid body motion during finite element simulation. Convergence of the computational results was ensured by decreasing the pressurization rate if the change in maximum stress exceeded 5% under a 2x increase in load steps. DPI $= \sigma_{LONG}/S_{LONG}$, relating the stress and the strength of the tissue in the longitudinal direction, was plotted over the entire aorta. Proposed dissection potential is based on longitudinal wall stress and strength inspired by our recent work on biomechanical pathways of TAAD [4]. Population-relevant longitudinal strength was measured from uniaxial tensile

experiments [5]. Locations of dissection origin were identified by direct evaluation of perioperative contrast CT scans by clinicians blinded to the dissection potential mapping, and compared to the regions of high dissection potential.

RESULTS

There was significant difference ($p < 0.005$, Student's t-test) in the peak dissection potential of the control set ($\mathrm{DPI} = 0.30 \pm 0.04, \mathrm{mean} \pm \mathrm{std}$) and the dissection set ($\mathrm{DPI} = 0.49 \pm 0.06$). Interestingly, longitudinal trend of the DPI (Figure 1), obtained from multiple CT scans taken over a period for each dissection patient, revealed a monotonic increase. Moreover, we found that DPI was >0.30 in regions of clinically observed dissection for 8 patients (Figure 2). In general, there was elevated dissection potential on the greater curvature of the ascending thoracic aorta compared to the rest of the aorta (red regions in Figure 2).

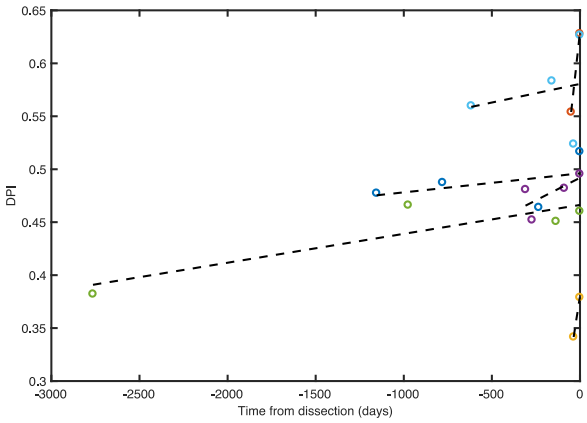

Figure 1: Evolution of DPI with time for dissected patients. Data for individual patients are denoted by different colored circles.

DISCUSSION

We found that peak longitudinal wall stress for the dissected patients is significantly different than the control patients. This finding corroborates previous investigations that identified aberrant imaging-based aortic wall biomechanics in patient populations with known increased dissection risk. Finite element simulation and associated biomechanical analysis as a means to assess aortic dissection risk have been previously posited. However, these prior studies focused on the maximum circumferential stress or stretch as the limiting factor, and the dissection-risk metrics discussed in these studies were devoid of clinical data validation. Our proposed dissection potential, based on longitudinal wall stress and strength, is consistent with the surgical observation of dissection initiation from primarily circumferentially oriented intimal tears, and appears to be capable of stratifying patients with aortic dissection from those without. The locations of dissection initiation fell within the regions of elevated risk (DPI>0.3) for 8 of the 10 patients.

The presented study has the following limitations. The number of patients for whom we had multiple pre-dissection CTAs and echocardiograms among a consecutive series of TAADs was small (n=10), and consequently may not be representative of the entire TAAD population. Our future study will include more dissected patients as well as patients with stable aneurysms. For the computational simulations, we assumed that the stiffness in the longitudinal direction was similar to that in the circumferential direction thus motivating our use of an isotropic material model. Our future work will include other methods of image based distensibility measurements so that both longitudinal and circumferential stiffness can be separately assessed.

Our findings support using a new, biomechanically-based approach to predicting aortic dissection potential using multiple patient-specific imaging data points. A biomechanically-based paradigm using patient-specific metrics will likely improve our ability to predict aortic dissection potential and thus better direct appropriate elective aortic intervention relative to the current guidelines that are based on maximal orthogonal aortic dimensions.

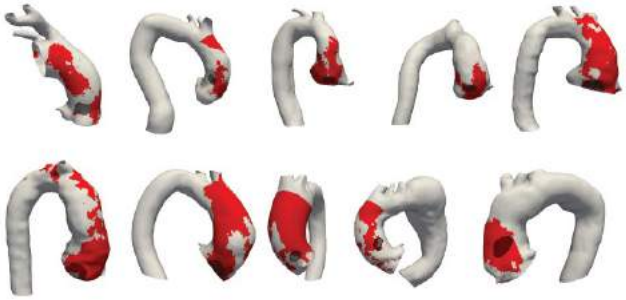

Figure 2: Regions indicating dissection potential, DPI, greater than 0.30 (red) and location of aortic dissection initiation as determined by surgical notes (black highlighted regions) for the dissected cohort (n = 10).

ACKNOWLEDGEMENTS

Research reported in this work was partly supported by the National Science Foundation award number CBET 1511504 and National Institutes of Health under award number HL109132. The content is solely the responsibility of the authors and does not necessarily represent the official views of the National Science Foundation or National Institutes of Health.

REFERENCES

[1] Erbel, R et al., *Euro Heart J*, 35:2873-926, 2014.
[2] Sen, T et al., *J Cardiology*, 62:236-40, 2013.
[3] Raghavan, ML and Vorp, DA, *J Biomech*, 33:475-82, 2000.
[4] Emerel, L et al., J *Thorac Cardiovasc Surg*, In Press, 2019.
[5] Pichamuthu, JE et al., *Ann Thorac Surg*, 96:2147-54, 2013.

SB^{3}C2019
Summer Biomechanics, Bioengineering and Biotransport Conference
June 25 -28, Seven Springs, PA, USA

PHYSIOLOGIC STRENGTH OF ASCENDING THORACIC AORTIC TISSUE DEPENDS ON STRESS BIAXIALITY

James R. Thunes (1), Ronald N. Fortunato (1), Thomas G. Gleason (1,2), David A. Vorp (1,2), Spandan Maiti (1)

(1) Department of Bioengineering
University of Pittsburgh
Pittsburgh, PA, USA

(2) Department of Cardiothoracic Surgery
University of Pittsburgh
Pittsburgh, PA, USA

INTRODUCTION

Type A Aortic Dissection (TAAD), initiated from an intimal tear in the ascending thoracic aorta, is a major health concern. Current clinical practice for the prediction of patient-specific dissection risk, based on maximum orthogonal diameter of the aorta [1], is not adequate. However, as high as 62% of patients with TAAD have aortic diameters distinctly less than the clinical guideline of 5.5 cm [2], strongly suggesting the clinical need for improved evidence-based dissection risk prediction metrics. As dissection ultimately involves biomechanical failure of the vessel wall, construction of such metrics will require fundamental knowledge of the aortic wall tissue strength under physiologic loading conditions.

Uniaxial as well as equibiaxial tissue strength of healthy and aneurysmal human aortic tissue specimens have been reported in the literature. Under physiologic loading conditions, however, the ascending thoracic aortic wall is subjected to a wide range of stress biaxiality. To quantify the aortic tissue failure behavior under such physiologic loading conditions, the tissue strength under the entire plausible spectrum of physiologic stress biaxiality must be evaluated. In this work, we present an experimentally-informed structural model of the aortic wall media to estimate the physiologic tissue strength under general biaxial loading conditions. Extensive biaxial simulations were then performed on the experimentally validated model to estimate physiologic tissue strength for a feasible range of biaxiality ratio.

METHODS

We created a finite element-based representative volume element (RVE) of the lamellar structure of the aortic media for two clinically relevant patient populations: patients with normal (tricuspid) aortic valve with and without aortic aneurysm. The RVE was constructed of two elastic lamellae (EL) separated by an interlamellar (IL) space, all modeled as isotropic neoHookean materials. For symmetry reasons, the thickness of the EL were taken as 0.75 μm (half their physiological thickness) and the thickness of the IL was taken as 11 μm. Two planar collagen networks were created within the IL space and adjacent to the EL. The networks were constructed of discrete collagen fibers 3 μm in diameter and were modeled as linear elastic rods active only in tension beyond their recruitment stretch. Previously determined network parameters: mean fiber diameter (γ), orientation index (OI), and areal density (AD) were used as inputs to a custom Matlab (R2016b, Mathworks, Natick, MA) script to construct the collagen networks. Mean fiber direction was $+\gamma$ for one of the networks and $-\gamma$ for the other. For the control (and aneurysmal) patient population, $\gamma = \pm 11^\circ$ ($\gamma = \pm 35^\circ$) and $OI = 0.67 \pm 0.01$ ($OI = 0.60 \pm 0.01$) [3]. Based on the literature, there are no significant difference in collagen content between aneurysmal and non-aneurysmal populations [4]; thus an areal fiber density of 0.48 for both patient populations was used. For each cohort, five different collagen fiber networks with the same target OI were constructed to minimize the effect of individual network artifacts on the final result for the aortic media.

Finite element simulations were performed using a custom non-linear embedded-fiber finite element method [5,6] in which the collagen fibers are explicitly modeled within the simulation. All RVEs were loaded biaxially with physiologically plausible tractions σ_{CIRC} and σ_{LONG}. Per convergence studies, the final RVE consisted of 15,000 8-noded hexahedral elements. The biaxiality of the stress state was quantified by biaxiality ratio $B = \sigma_{LONG}/\sigma_{CIRC}$, where B=0 and ∞ represents uniaxial CIRC and LONG loading, respectively, and B=1 is equibiaxial loading scenario. A drop in stress in either direction indicated tissue failure, and corresponding peak stress was recorded as the physiologic tissue strength. Visualization of the finite element

Poster Presentation #P092

mesh and the simulated network were performed using Paraview (v5.6, Kitware, Clifton Park, NY).

RESULTS

Aortic tissue strength exhibited a dependence on the biaxiality ratio (Fig. 1, left column) for both non-aneurysmal and aneurysmal tissue. Both circumferential (CIRC, B=0) and longitudinal (LONG, B=∞) uniaxial strength matched experimental data [7]. There was a transition from failure in the CIRC to LONG direction at B_{trans}=0.68 and 0.69 for non-aneurysmal and aneurysmal tissue, respectively. Below B_{trans} (blue shaded region), the overall tissue failure was governed by the failure of circumferentially oriented fibers. In contrast, tissue failure was caused by the failure of longitudinally oriented fibers beyond B_{trans} (pink shaded region). Evolution of fiber stress leading to aneurysmal tissue failure for two representative values of B from each regime are shown in Fig 2 (similar trend seen for non-aneurysmal tissue, not shown). Physiologic tissue strength, the maximum stress at which the tissue failed under biaxial loading condition, varied linearly with *B* in both regions remaining within 10% of the respective uniaxial strength. Fig. 1 (right column) presents the comparison of physiologic strength and corresponding experimentally observed uniaxial strength both above and below B_{trans}. For both populations, physiologic strength was statistically similar to uniaxial CIRC strength for biaxiality ratios below transition, and to uniaxial LONG strength above B_{trans}.

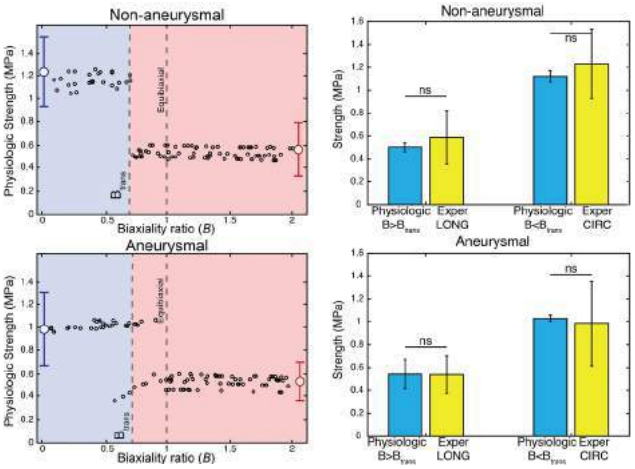

Figure 1: Physiologic strength under different biaxiality ratios for control and aneurysmal tissues (left column). Large open circles with error bars denote the mean and standard deviation for uniaxial tensile experiments in either the CIRC (blue) or LONG (red) directions. Comparisons of physiologic strength (blue bars) and experimentally derived uniaxial strength (yellow bars) are also shown for both populations (right column).

DISCUSSION

We found that physiologic tissue strength is dependent on the biaxiality ratio of the applied loading. Importantly, the critical physiologic strength, defined by its lowest magnitude over the entire range of stress biaxiality, is statistically similar to the uniaxial longitudinal strength of the tissue. This fact suggests that critical physiologic strength can be estimated from the uniaxial testing of the aortic tissue in LONG direction. A non-aneurysmal aorta (B≅0.5 for idealized cylindrical geometry) is expected to fail at a stress in excess of uniaxial circumferential strength, explaining why this event is extremely rare. B increases in aneurysmal aortas due to localized bulging, often noted in TAAD patients [8]. This geometric change in turn may cause a dramatic decrease in physiologic tissue strength at locations with $B>B_{trans}$, providing a potential rationale for higher susceptibility to dissection for aneurysmal patients.

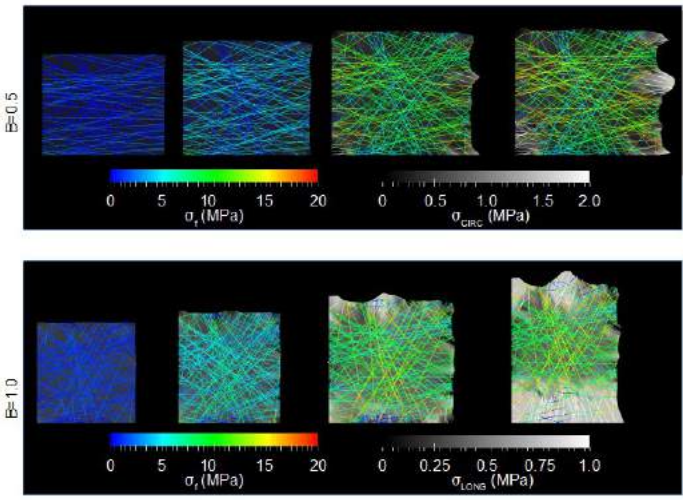

Figure 2: Stress contours in the fibers (color, failed fibers white) and matrix (greyscale) for a representative aneurysmal aortic tissue RVE for B=0.5 (top row) and B = 1.0 (bottom row). The CIRC component of the matrix stress is shown in the upper panels and the LONG component of the matrix stress in the lower panels.

In conclusion, using a structural finite element model of the aortic media, we have estimated the physiologic aortic tissue strength under the entire range of plausible biaxial loading conditions. Our work extends the current experimental knowledge of uniaxial and equibiaxial tissue strength. The work presented herein is an important first step towards understanding the failure biomechanics of aortic dissection under physiologic loading conditions. An important future direction will be the non-invasive estimation of patient-specific tissue physiologic strength from the experimentally assessed population-specific uniaxial tissue strength.

ACKNOWLEDGEMENTS

Research reported in this work was partly supported by the National Science Foundation award number CBET 1511504 and National Institutes of Health under award numbers HL109132 and T32-HL076124.

REFERENCES

[1] Erbel, R et al., *Euro Heart J*, 35:2873-926, 2014.
[2] Pape, LA et al., *Circulation*, 116:1120-27, 2007.
[3] Pasta, S et al., *Med Eng Phys*, 38:121-30, 2016.
[4] Iliopoulos, DC et al., *Med Eng Phys*, 31:1-9, 2009.
[5] Thunes, JR et al., *J Biomech*, 49:1562-69, 2016.
[6] Thunes, JR et al., *J Biomech*, 71:84-93, 2018.
[7] Pichamuthu, JE et al., *Ann Thorac Surg*, 96:2147-54, 2013.
[8] Emerel, L et al., J *Thorac Cardiovasc Surg*, In Press, 2019.

SB³C2019
Summer Biomechanics, Bioengineering and Biotransport Conference
June 25 -28, Seven Springs, PA, USA

INVERSE MIXED STRAIN METHOR FOR ANEURYSM STRESS ANALYSIS

Yuanming Luo, Jia Lu

Department of Mechanical Engineering
The University of Iowa
Iowa City, IA, USA

INTRODUCTION

Inverse finite element method, which solves problems of which a deformed state is given at the onset, has demonstrated its utility in stress analysis of vascular systems structures [1]. However, the pure displacement formulation is known to suffer from volumetric locking in the impressibility limit and shear locking in bending-dominated deformations. To overcome the issue, mixed and enhanced formulations have been developed for forward finite element analysis [2, 3]. These methods have been widely used and demonstrated the effectiveness in resolving the locking issues in forward analysis. Recently, we introduced inverse formulations of the mixed and enhanced strain methods for large deformation analysis of hyperelastic material. The methods draw on existing forward formulations [4] and are designed in such a way that the deformation predicted by forward elements can be exactly reverted. In this presentation, we discuss the importance of using the inverse mixed method for abdominal aortic aneurysm (AAA) stress analysis. It will be demonstrated that the mixed formulation can provide trustworthy stress solution in the limit of incompressibility. Moreover, the abdominal aortic aneurysms can be thought as statically determined structure in that the wall stress depends primarily on the deformed geometry. However, when using the pure displacement formulation, this feature may not be sharply captured because of the presence of numerical noise in the computed pressure field in the incompressibility limit. It will be shown that the inverse mixed method can effectively resolve this issue.

METHODS

In the pure displacement finite element approach, the discrete balance equations are developed from the weak form:

$$\int_{\Omega} \delta \mathbf{F} : \mathbf{F}\mathbf{S} dV + \delta \Pi_{ext}(\boldsymbol{u}) = 0 \tag{1}$$

The proposed inverse mixed method is based on $\bar{\mathbf{F}}$ projection. $\bar{\mathbf{F}}$ is defined as Equation (2):

$$\bar{\mathbf{F}} = \left(\frac{\theta}{J}\right)^{\frac{1}{3}} \mathbf{F} \tag{2}$$

$J = \det \mathbf{F}$, and θ is an additional field variable representing the volumetric strain, constructed as the least square projection of the volume ratio J on a lower dimensional space. Replacing $\mathbf{F}$ with $\bar{\mathbf{F}}$, the weak form can be expressed as in the current configuration Ω :

$$\int_{\Omega} \delta \bar{\mathbf{F}} : \bar{\mathbf{F}}\mathbf{S} j dv + \delta \Pi_{ext}(\boldsymbol{u}) = 0 \tag{3}$$

Here $j = 1/J$ is the inverse volume ratio. The equation is now understood as one solving the inverse deformation $\boldsymbol{\Phi} : \Omega \to \Omega_0$. To obtain the finite element equation, the weak form is linearized with respect to the increment of the inverse displacement $\mathbf{U} = \mathbf{X} - \mathbf{x}$, where $\mathbf{X}$ is reference configuration and x is the current configuration.

RESULTS

Some illustrative results of the proposed mixed method are presented in this section. An abdominal aneurysm model is used to examine the stress solution as the material approaches the incompressibility limit and the sensitivity of stress to material parameters. The geometry of the abdominal aneurysm is shown in Figure 1. The aneurysm is meshed with a single layer of 8-node solid elements which has 4112 elements. The top and bottom edges of the mesh are fixed. A pressure of 120 Hgmm is applied to the inner surface of the aneurysm. The compressible neo-Hookean model in [5] is used.

For convenience, the Lame parameters μ and λ are converted to Young's modulus E and Poisson ratio ν .

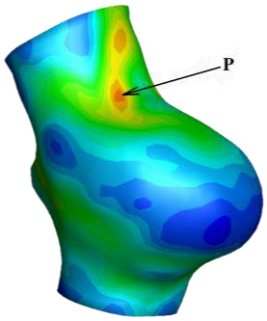

Figure 1 An AAA model with the peak stress point

(1) Stress at the incompressibility limit

Six material sets: ν = 0.3, 0.4, 0.45, 0.49, 0.499, 0.4999 with the same E = 1.0E5 MPa are used to investigate the performance of the method at the incompressibility limit in terms of the value of the peak stress. To compare, the same analyses are conducted using the pure displacement formulation. The peak stresses are presented in Figure 2. As can be seen from the figure, the stress values from the mixed formulation (in black) are insensitive to the value of the Poisson's ratio. For the pure displacement method (in blue), the von Mises stress reduces significantly when ν approaches 0.5. The magnitude of displacement becomes significantly smaller when ν approaches 0.5, indicating numerical locking.

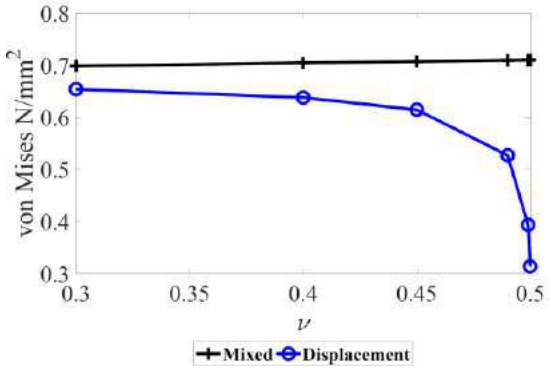

Figure 2 Peak stress vs Poisson's ratio

(2) Sensitivity of stress to material parameters

To investigate sensitivity of stress prediction to the material parameters, analyses with two material sets: E = 1.0E5 MPa, ν = 0.3 and E = 1.0E8 MPa, ν = 0.4999 are conducted. The stress distributions are compared with those from the pure displacement method. The contours of von Mises stress from the two formulations are shown in Figure 3 and 4. It can be observed that, for the mixed formulation, the stress contours from the two material sets are very close to each other (Figure 3 (a) and Figure 3 (b)). In contrast, the solutions from the displacement method differ significantly (Figure 4 (a) and Figure 4 (b)). The results show that, in this case, the mixed formulation is insensitive to the material parameters while the displacement formulation is not.

DISCUSSION

This study shows that the mixed formulation can significantly improve the performance of 8-node solid element when the material approaches the incompressibility limit. Considering that almost all biological soft tissues are incompressible or nearly incompressible, the mixed formulation appears to be indispensable for accurate stress prediction in tissue structures. In particular to the AAA, it is known that typical AAAs are statically determined structures wherein the wall stress depends minimally on the wall material and that the inverse method helps to capture this property [1]. However, for the displacement formulation, this property could be compromised numerically due to the treatment of the incompressibility constraint. We have shown that the mixed method can pointedly address the numerical issue and provide stress solutions that are insensitive to material parameters even at the incompressibility limit. For *in vivo* stress analysis, since the material parameters are impossible to know on a patient-specific basis, it is prudent to employ methods that can produce material-insensitive stress solution if/when the physics dictates so. The inverse mixed formulation appears to fit this goal. Convergent studies with different mesh levels are also conducted. The results show that, when the mesh level is refining to a certain level, the displacement and stress results converge nicely to stable values. Due to the page limits, these results are omitted here.

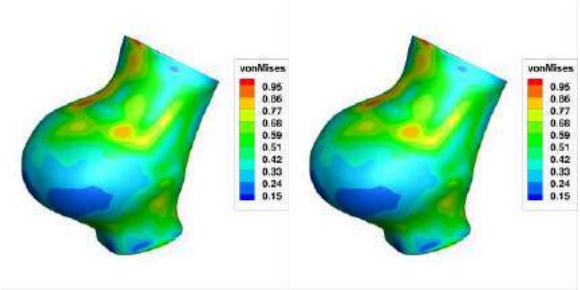

(a) E = 1.0E5 MPa, ν = 0.3 **(b) E = 1.0E8 MPa, ν = 0.4999**

Figure 3 Mixed formulation

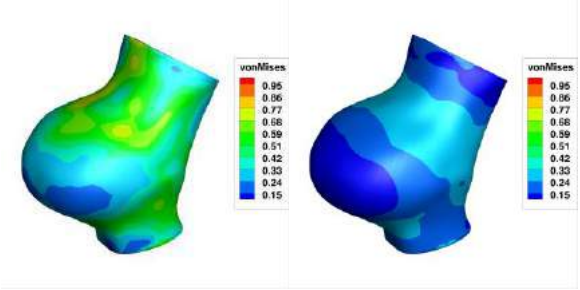

(a) E = 1.0E5 MPa, ν = 0.3 **(b) E = 1.0E8 MPa, ν = 0.4999**

Figure 4 Displacement formulation

REFERENCES

[1] Lu, J. et al., *J Biomech*, 40(3), pp.693-696.
[2] Simo, J.C. et al., *Computer Methods in Applied Mechanics and Engineering*, 51(1-3), pp.177-208.
[3] Simo, J.C. et al., *International Journal for Numerical Methods in Engineering*, 33(7), pp.1413-1449.
[4] Govindjee, S. et al., *Computer Methods in Applied Mechanics and Engineering*, 136(1-2):47-57, 1996.
[5] Elguedj, T. et al., *Computer Methods in Applied Mechanics and Engineering*, 197(33-40), pp.2732-2762.

SB³C2019
Summer Biomechanics, Bioengineering and Biotransport Conference
June 25 -28, Seven Springs, PA, USA

MICROSTRUCTURAL CHARACTERIZATION OF INTRALUMINAL THROMBUS IN ABDOMINAL AORTIC ANEURYSMS

Pete H. Gueldner (1, 2), Sourav S. Patnaik (1), Senol Piskin (1), Mirunalini Thirugnanasambandam (1), Satish C. Muluk (3), and Ender A. Finol (1)

(1) Department of Mechanical Engineering
University of Texas at San Antonio
San Antonio, Texas, USA

(2) Department of Biomedical Engineering
University of Texas at San Antonio
San Antonio, Texas, USA

(3) Department of Vascular Surgery
Allegheny General Hospital
Pittsburgh, Pennsylvania, USA

INTRODUCTION

The exact cause of abdominal aortic aneurysm (AAA) is still unknown and damage to the structural proteins of the extracellular matrix (ECM) has been postulated as one of the chief etiologies for aneurysm development. As the arterial ECM primarily comprises elastin and collagen fibers, these proteins have been the focal point of studies related to pathological origins of AAA and their resultant changes in tissue biomechanics. The formation of intraluminal thrombus (ILT), complicates the overall understanding and interplay of the ECM protein's structure-function relationship. Glycosaminoglycans (GAGs) are one such class of proteins that is directly linked with the elasticity of arterial ECM [1]; however, its role in AAA mechanics is still not entirely understood. In this study, we aim to find an association between patient-specific AAA wall mechanics and geometric indices with region-based aneurysmal tissue protein quantifications (GAGs).

METHODS

Patient Data – Five human AAA underwent surgical repair at Allegheny General Hospital - AGH (Pittsburgh, PA) and their computer tomography angiography (CTA) images were obtained upon approval by the AGH Internal Review Board. These images were further utilized for biomechanical quantification and geometric characterization. The surgical procedure involved removal of the ILT and its associated wall tissue from the left anterolateral potion of the AAA. These specimens were subsequently classified into abluminal, medial and luminal ILT regions, and wall tissue sections, and utilized for histological characterization.

Biomechanical Analysis and Quantification of Geometric Indices – The CTA images were segmented using an in-house image segmentation and geometry quantification tool (AAAVASC) [2, 3] (Fig. 1). The Matlab© (Mathworks, Natick, MA) based package allowed us to segment the AAA into their respective domains: lumen, ILT, and outer wall.

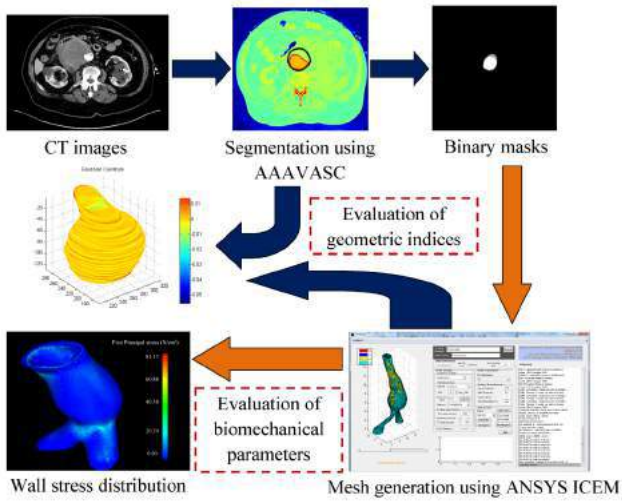

Figure 1. Steps involved in post-processing CTA images to generate masks (AAAVASC) and for calculation of geometric indices [3].

The two-dimensional images were reconstructed utilizing surface meshing to recreate the 3D AAA model. This model was then utilized for geometric calculations and the geometry used to generate tetrahedral volume meshes using ANSYS ICEM (Ansys Inc., Canonsburg, PA). Finite element analysis (FEA) was performed using the ADINA (Adina R&D Inc., Watertown, MA) solver with an intraluminal pressure of 120

mmHg. Results of the FEA simulations were post-processed to quantify the first principal stress distribution on the AAA wall using ANSYS Ensight, from which the peak wall stress (PWS) was computed. 1D, 2D, 3D size and shape, and wall thickness geometric indices were calculated as a part of the morphometric analyses.

Histology – The AAA specimens underwent routine histological processing while the slides (5-7 µm thick sections) were stained with Alcian Blue for GAGs, imaged on an Olympus CX41 microscope at 4x magnification and the images stitched using Microsoft Image Composite Editor. The stitched images were then quantified using the Fiji (GitHub, San Francisco, CA) extension of ImageJ (National Institutes of Health, Bethesda, MD), which was used to semi-automatically perform GAG distribution in each image (in luminal, abluminal, medial, and wall tissue sections). All image based-quantifications were performed in triplicate.

Statistical Analysis – Patient-specific data obtained from FEA, geometric indices, and histology were expressed as mean ± std. deviation. To test the differences in GAG distribution across the locations, one-way ANOVA was applied with Tukey's pairwise comparison. Next, to evaluate the inter-relationship between the tissue GAG expressions and PWS or geometric indices, Pearsons' correlation was performed. Data was considered significant at $\alpha = 0.05$.

RESULTS

GAG distribution in the ECM across the four regions were found to be significantly different from the ILT luminal to the wall tissue regions ($p < 0.001$). More specifically, GAG content of luminal, medial, and abluminal regions was found to be lower than the wall tissue region (11.8 ± 1.6 % vs. 12.7 ± 1.7% vs. 14.7 ± 2.9% vs. vs. 18.7 ± 2.2%; $p = 0.0006$) (Fig. 2).

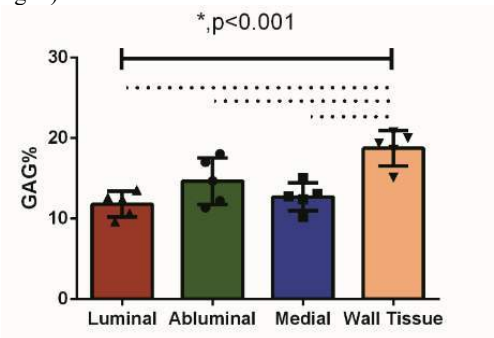

Figure 2: GAG distribution across the ILT and wall tissue regions. *denotes significant differences at $\alpha < 0.001$.

PWS exhibited a strong negative association with the medial GAG distribution (r = -0.9836, p = 0.0025) (Fig. 3, Table 1). Conversely, AAA asymmetry (β; given by 1 – ratio of the distance between the lumen centroid and the centroid of the cross section where maximum AAA diameter is located, to the max AAA diameter) exhibited a strong positive association with the GAG distribution in the aforementioned ILT location (r = 0.9425, p = 0.0164). Further, the correlation of abluminal GAG distribution was strongly associated with the following wall thickness indices: (i) positively with $t_{w,skew+;}$ and negatively with $t_{w,skew-}$ (skewness indicates whether the distribution of wall thickness is normal, positively skewed, or negatively skewed); (ii) negatively with $t_{w,modeVar}$ (mode of the variance of wall thickness), $t_{w,minVar}$ (minimum variance of the wall thickness), $t_{w,median}$ (median of the wall thickness), and $t_{w,mode}$ (mode of the wall thickness), respectively (see Table 1). Wall tissue GAG distribution exhibited a strong association with the 3D size index γ, which is the ratio of AAA ILT volume to vessel volume (r = 0.8825, p = 0.0475).

DISCUSSION

Contrary to previous literature, GAGs were observed in the AAA wall and ILT. Pooling of GAGs between the elastic lamellae has been postulated as the prime cause of thoracic dissecting aneurysms [4], which is uncommon in AAA. However, the phenomenon of increased PWS with lowered GAG expression (Fig. 3) is a clear evidence that their role is more mechanical (contractile and elastic) in nature. Removal of GAGs from the arterial ECM has been shown to increase stiffening of the tissue and induce loss of viscoelasticity [1]. In addition, higher amounts of GAGs in the ECM of the wall compared to the ILT regions suggests the notion that oxygen is limited in the ILT. The interaction between ILT and the aortic wall is complex, and the increase in GAG expression in the AAA wall, but not in ILT, suggests a possible elasticity gradient from the adventitial to the luminal surface of the aneurysmal aorta (Fig. 2).

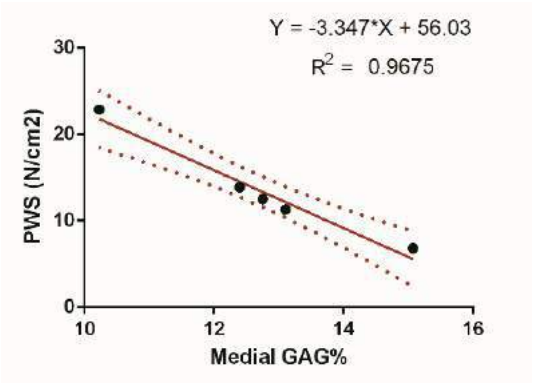

Figure 3: Strong negative association of PWS with medial GAG distribution.

Table 1: Correlation of region-wise GAG distribution with PWS and geometric indices.

Parameters	Luminal GAG%	Abluminal GAG%	Medial GAG%	Wall Tissue GAG%
PWS (N/cm²)	ns	ns	-0.9836 (0.0025)	ns
β	ns	ns	0.9425 (0.0164)	ns
Percent thickness above average thickness ($t_{w,skew+}$) (%)	ns	0.9152 (0.0293)	ns	ns
Percent thickness below average thickness ($t_{w,skew-}$) (%)	ns	-0.9152 (0.0293)	ns	ns
$t_{w,modeVar}$ (mm)	ns	-0.9044 (0.035)	ns	ns
$t_{w,minVar}$ (mm)	ns	-0.9044 (0.035)	ns	ns
$t_{w,median}$ (mm)	ns	-0.9462 (0.0149)	ns	ns
$t_{w,mode}$ (mm)	ns	-0.9404 (0.0173)	ns	ns
γ	ns	ns	ns	0.8825 (0.0475)

ACKNOWLEDGEMENTS

This work was supported by NIH award No. 1R01HL121293. Pete Gueldner was supported by a National Science Foundation (NSF) Undergraduate Research Scholarship.

REFERENCES

[1] Mattson, JM. et al., *Biomech Model Mechanobiol*, 16 (1): 213-225, 2018.
[2] Shum, J. et al., *Ann Biomed Eng*, 39(1):277- 286, 2011.
[3] Chauhan, SS. et al., *Ann Biomed Eng*, 45(8)1908-16, 2017.
[4] Roccabianca, S., et al., *Biomech Model Mechanobiol*, 13(1):13-25, 2015.

The University of Texas at San Antonio
Department of Mechanical Engineering

February 16, 2019

To whom it may concern:

Concerning the attached abstract, which Mr. Pete Gueldner is submitting to the ASME Student Paper Competition at the BS level, I attest that (1) the majority of the work was completed by the first/presenting author (Pete Gueldner), and (2) the first author conducted the work when he was a student at the corresponding competition level (during his junior year).

Should you require additional information regarding this attestation, please feel free to contact me. I can be reached at (210) 458-8058 or via e-mail at ender.finol@utsa.edu.

Sincerely,

Ender A. Finol, Ph.D.
Professor
The University of Texas at San Antonio (UTSA)
Department of Mechanical Engineering (ME)
Program Faculty of the UTSA/UTHSCSA Joint Graduate Program in Biomedical Engineering (BME)
Director, Vascular Biomechanics and Biofluids Laboratory (VBBL)
One UTSA Circle
San Antonio, TX 78249-0670
USA
Office: EB 3.04.08, +1-210-458-8058
Lab: BSE 2.230, +1-210-458-8591
Fax: +1-210-458-6504
ME: http://engineering.utsa.edu/mechanical/team/ender-finol-ph-d/
VBBL: http://www.vascularbiomechanics.org
Email: ender.finol@utsa.edu, finole@vascularbiomechanics.org
Faculty Member, NSF/CREST Center for Simulation Visualization and Real-Time Prediction: http://sivirt.utsa.edu/
Member of the Editorial Board for **Annals of Vascular Surgery**: http://www.journals.elsevier.com/annals-of-vascular-surgery
Associate Editor for **Annals of Biomedical Engineering**: http://www.springerlink.com/content/0090-6964/

SB^{3}C2019
Summer Biomechanics, Bioengineering and Biotransport Conference
June 25 -28, Seven Springs, PA, USA

MATERIAL CHARACTERIZATION OF ATHEROSCLEROTIC PLAQUES WITH VIRTUAL FIELDS METHOD

Ronald D. van den Berg (1,2), Stephane Avril (3), Frank J.H. Gijsen (1), Ali C. Akyildiz (1)

(1) Dept. of Biomedical Engineering
Erasmus Medical Center
Rotterdam, the Netherlands

(2) Dept. of Biomechanical Engineering
Delft University of Technology
Delft, the Netherlands

(3) Centre for Biomedical and Healthcare Engineering
Mines Saint-Etienne
Saint-Etienne, France

INTRODUCTION

Fatal cardiovascular events such myocardial infarction and stroke are majorly caused by atherosclerotic plaque rupture (1). Plaque rupture is a biomechanical event that occurs when local plaque stresses exceed strength. Plaque stresses can be assessed with computational techniques, such as finite element (FE) modelling. Accurate representation of the plaque material behavior is a must for correct plaque stress assessment (2).

Atherosclerotic plaque tissue is highly heterogeneous, composed of various structural components. For accurate regional stress assessment, it is of great importance to measure the component-wise material properties of atherosclerotic plaques. However, mechanical properties data of atherosclerotic plaques is scarce and mainly limited to gross properties of plaques (3). Recent studies did component-wise material characterization of plaques using inverse FE approach (4,5). However, this technique is computationally expensive as it requires FE updating iteratively. Hence, faster techniques are required, especially for in-vivo characterization and clinical use in the future.

A fast approach for material characterization is the virtual fields method (VFM), which is based on the principle of virtual work (6). Since the date VFM was established, it was employed by various engineering applications and also recently in the cardiovascular biomedical field for healthy arteries (7). The current study applies the VFM to material characterization of heterogeneous atherosclerotic plaque tissue, for the first time. Here we present the derived virtual fields for the particular application of intraluminal pressurization of atherosclerotic arteries and the validation of the approach using synthetically generated experimental data.

METHODS

VFM principle and derivation of the virtual fields

VFM employs the virtual work principle, which can be for a given solid of volume V in the absence of body forces and for a (pseudo-)static loading written as follows:

$$-\int_V \sigma : \varepsilon^* + \int_S \boldsymbol{t} \cdot \boldsymbol{u}^* = 0 \qquad (1)$$

where σ is the Cauchy stress tensor, ε^* is the virtual strain (small strain definition) tensor derived from the virtual displacement vector $\boldsymbol{u^*}$, and $\boldsymbol{t}$ is the distribution vector of the traction loads exerted on the surface S. VFM utilizes full-field deformation measurements of the investigated structure. Together with a predefined constitutive law, the deformation fields are used to obtain the Cauchy stress tensor σ. In case of an incompressible hyperelastic material description with a strain energy density function ψ, the stress tensor σ is obtained from:

$$\sigma = -pI + 2 \cdot \frac{\partial \psi}{\partial F} \cdot F^T \qquad (2)$$

where p is the hydrostatic pressure term enforcing incompressibility constraint, I is the identity tensor, and F is the deformation gradient tensor obtained from full-field deformation measurements. The material parameters to be determined with VFM are integrated in the strain energy density function ψ.

VFM principle (Eqn 1) requires describing kinematically admissible virtual displacement fields $\boldsymbol{u^*}$. Choosing the fields smartly is a key issue as the final analytical equation(s) obtained from Eqn 1 must enable the evaluation of the unknown material constants in the strain energy density function ψ.

In an ideal case of homogeneous full-field deformation, same number of virtual fields, and hence analytical equations derived from Eqn 1, as the number of unknowns would be sufficient to solve the

system of the equations. However, in case of heterogeneous full-field deformation measurements, noise in the measurements and nonlinearity of the material properties the identification strategy requires use of a minimization technique and virtual displacement fields more than the number of equations. For this study, trust region reflective technique integrated in a custom-developed MATLAB code was utilized as the minimization algorithm and the system of the analytical equations obtained from Eqn 1 by prescribing multiple virtual fields is used in the minimization to identify the unknown material parameters. The first phase of the study included finding appropriate virtual fields for the specific application of intraluminal pressurization of atherosclerotic plaques.

Validation study

As this is the first study applying VFM to the intraluminal pressurization of atherosclerotic plaques, the derived virtual displacement fields and the VFM approach required validation. Therefore, synthetic full-field displacement measurements of atherosclerotic plaques for physiological intraluminal pressure of 100 mmHg were computed with FE modelling. The ten FE models were based on ten realistic plaque morphology obtained from histology segmentation of human carotid plaques (Figure 1). Incompressible Neo-Hookean material models, described by a single material constant *C*, were assumed for the plaque components. The *C*-values for the four components were: fibrous tissue=120 kPa, calcified tissue=423 kPa, lipid rich tissue=5 kPa, and the arterial wall=250 kPa (8,9). In the end, the VFM-estimated values were compared against these "ground-truth" values.

Sensitivity analysis

The sensitivity of the employed VFM approach to the number of the prescribed virtual fields and on the initial guesses for the *C*-values of the four plaque components was investigated. Ten initial guesses were generated randomly within the range of 1-1000 kPa for the four components.

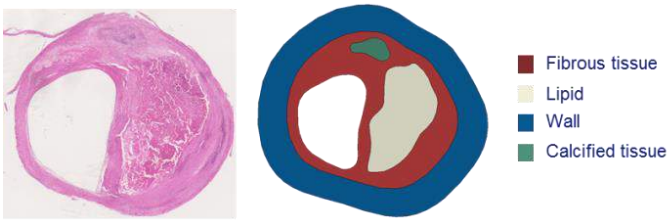

Figure 1: FE models for validation analysis were obtained from segmented carotid plaque histology images

RESULTS

Because of the incompressibility condition a strong requirement in the search of the virtual fields was that the trace of the virtual strain fields was equal to zero, but resulting in non-zero integral evaluations in Eqn 1 at the same time. We identified a smart choice of an in-plane displacement field fulfilling these requirements to be $\boldsymbol{u}^*=[x/(x^2+y^2), y/(x^2+y^2), 0]$. Multiplying this field by $\cos^n(\Theta)$ and $\sin^n(\Theta)$, where $\Theta=y/x$ and n defines the order, and rotating the field m-times with increments of π/m, new virtual displacement fields were acquired. In the end, the number of equations obtained equaled to m-times-n.

As expected, the maximum relative error of the VFM-estimated *C*-values compared to the ground truth decreased by increasing the number *m* and/or *n*. The error values for the fibrous tissue component are illustrated in Figure 2. Approximately 120 virtual fields were sufficient to achieve an error of < 5%.

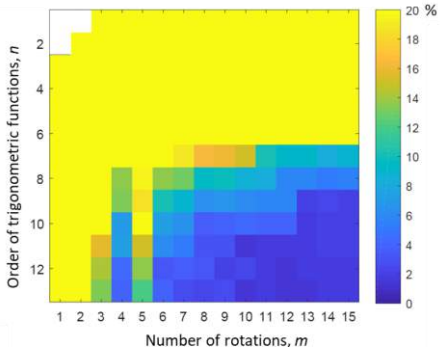

Figure 2: Dependency of the relative error for fibrous tissue component between VFM-derived *C*-values and "ground truth" on number of rotations, *m* and order of trigonometric functions, *n*.

An illustrative case of m=12 and n=12 showed an excellent estimation of the *C*-values by VFM. The median error for all VFM evaluations of 10 plaque cases and 10 initial guesses (in total 100 evaluations) combined resulted in VFM-derived *C*-values for fibrous tissue as 122 kPa, for wall as 258 kPa, for lipid as 7 kPa and for calcified as 457 kPa (Table 1). The highest absolute error was for the calcified tissue (34 kPa) with a relative error of 8%. The VFM evaluation for this illustrative case took <10 min using the developed MATLAB code in a decent PC (Intel i7, single core, RAM=16GB).

Table 1: VFM-results of an illustrative case

	C-value (kPa)	
Component	**Ground truth**	**VFM estimate**
Fibrous tissue	120	122
Lipid	5	7
Calcified tissue	423	457
Arterial wall	250	256

DISCUSSION

In this study, VFM was used for the first time for atherosclerotic plaque mechanical characterization. The validation analysis showed high accuracy of the VFM approach for the particular application, demonstrating the great potential of VFM for heterogeneous plaque characterization from full-field deformation data. In-vivo full-field plaque deformation can be acquired from MRI and ultrasound. Moreover, the computational time required for the VFM approach was in the order of minutes, much shorter than e.g. inverse FE approach, which might take hours or days. Hence, the developed VFM technique has great potential to be used for in-vivo plaque characterization.

ACKNOWLEDGEMENTS

This project is funded by the European Commission under the Marie Skłodowska-Curie grant agreement # 749283.

REFERENCES

[1] Falk E et al., *Circulation*, 92:657, 1995. [2] Akyildiz, A et al., *Biomed Eng Online*, 10:25, 2011. [3] Akyildiz, A et al., *J Biomech*, 47:773, 2014. [4] Akyildiz, A et al., *Annals Biomed Eng*, 44(4):968, 2016. [5] Le Floc'h, S et al., *Ultrasound Med & Biol*, 38(12):2084, 2012. [6] Pierron, F; Grediac,M, *Springer*, "The virtual fields method", 2012. [7] Bersi, M et al., *J Biomech Eng*, 138, 2016. [8] Nieuwstadt, H et al., *Med Eng Phys*, 37(8): 801, 2015. [9] Ebenstein, D et al., *J Biomed Mater Res A*, 91A(4): 1028, 2009

SB³C2019
Summer Biomechanics, Bioengineering and Biotransport Conference
June 25 -28, Seven Springs, PA, USA

MICROSTRUCTURE-BASED FINITE ELEMENT MODELING FRAMEWORK FOR SIMULATING PASSIVE INFLATON OF THE LEFT VENTRICLE

Ce Xi (1), Ghassan S. Kassab (2), Lik Chuan Lee (1)

(1) Department of Mechanical Engineering
Michigan State University
East Lansing, MI, USA

(2) California Medical Innovations Institute
San Diego, CA, USA

INTRODUCTION

Quantifying the individual role of microstructural features in affecting organ-level heart function and tissue-level ventricular mechanics requires a validated and efficient finite element (FE) implementation of a microstructural-based constitutive model. To the best of our knowledge, such a microstructural-based FE modeling framework is currently lacking. To address this gap, we developed and experimentally validated a microstructural FE model of the left ventricle (LV) with a realistic 3D geometry and muscle fiber architecture to describe the passive mechanics of myocardial tissue during inflation. The model was implemented using an open-source FE library FEniCS.

METHODS

Microstructural Constitutive Model Formulation. A microstructure-based constitutive model was developed to describe the passive mechanical behavior of the myocardium. The total strain energy function (SEF) of the myocardium W_{total} is assumed to be represented by the volume-weighted sum of that of its constituents, i.e.,

$$W_{total} = \phi_g W_g + \phi_m W_m + \phi_c W_c - p(J-1) \ . \qquad (1)$$

where (ϕ_g, W_g), (ϕ_m, W_m) and (ϕ_c, W_c) are the (volume fraction, SEF) of the ground matrix, muscle fibers and collagen fibers, respectively, with $\phi_g + \phi_m + \phi_c = 1$. In Eq. (1), J is the determinant of deformation gradient tensor and p is the Lagrange multiplier to enforce incompressibility. The SEFs W_g and W_m are prescribed to be an isotropic Neo-Hookean and an exponential function of the muscle fiber stretch, respectively. Taking into account the collagen fibers waviness and spatial arrangement (**Fig. 1**) in a stochastic manner [1], the SEF of the collagen matrix is given by

$$W_c = \frac{C_4}{2}\int_0^{2\pi}\int_0^{\pi}\left[\int_0^{\epsilon_c(\theta,\phi)} D(x)\frac{(\epsilon_c(\theta,\phi)-x)^2}{1+2x}dx\right]R(\theta,\phi)d\phi d\theta \qquad (2)$$

where $D(x)$ is a prescribed waviness distribution function, $R(\theta,\phi)$ is the spatial distribution function, C_4 is the elastic modulus of the collagen fiber and ϵ_c is the uniaxial strain of the individual collagen fiber.

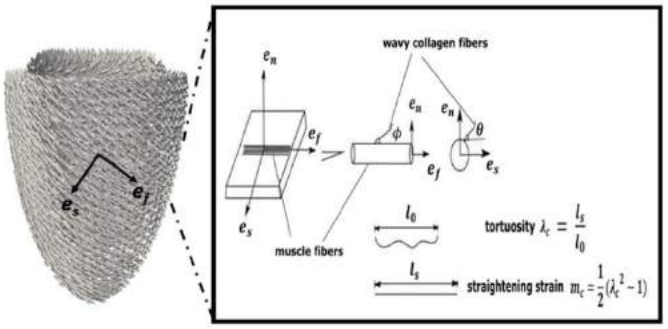

Fig. 1. Schematic of microstructural model showing muscle fiber orientation with a linear transmural variation from 70º (endocardium) to -40º (epicardium) and the local arrangement the collagen fibers with respect to the local muscle fiber.

Parameter Estimation. We used the biaxial mechanical test data obtained from 6 specimens of the canine mid-wall myocardium from a previous experiment [2] to estimate the constitutive model's parameters. A nonlinear programming solver "fmincon" in MATLAB was used to find optimal parameters that minimize the sum of squared residuals between the model predictions and measurements of the stress-stretch relations. These fitted model parameters were then prescribed in the FE framework to simulate passive filling of the LV.

Poster Presentation #P096

FE Simulation of LV Passive Filling. Based on experimental measurements, a truncated ellipsoidal LV geometry with unloaded volume of ~20 ml and a linear transmural variation of muscle fiber helix angle (**Fig. 1)** is prescribed in the FE framework. We computed pressure-volume relationship as well as strains to compare with an independent set of measurements made in the intact LV. The load taken up locally by individual tissue constituent in the LV was also computed.

RESULTS

Biaxial Fitting. The microstructural constitutive model shows very good fit to the biaxial measurements (**Fig. 2**). The fitted structural parameter values are also within the range of microscale measurements made on individual tissue constituents (e.g., collagen fiber stiffness and tortuosity as well as cardiac muscle elastic modulus) [3].

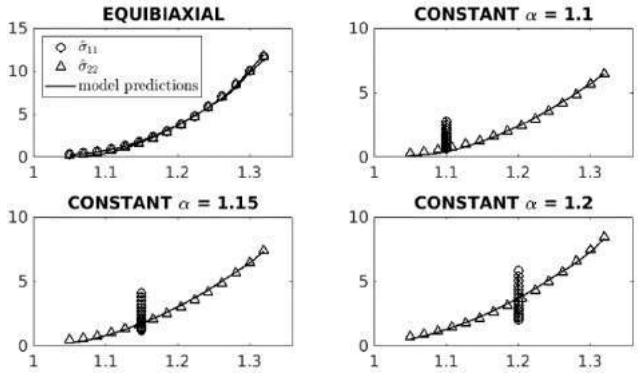

Fig. 2. Comparison of the fitted and experimental Cauchy stress-stretch data for a representative specimen.

FE model predictions. The pressure-volume curves predicted by the FE LV model using the 6 sets of parameter values framework all fell within the measurements range [4]. Tortuosity-pressure relationship of the collagen fibers computed from the fitted parameter values are also largely in agreement with the measurements [5] (**Fig. 3**).

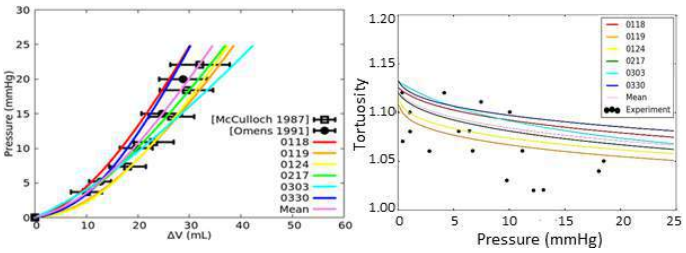

Fig. 3. Comparison of the inflation pressure-volume and tortuosity-pressure curves derived from 6 sets of fitted model parameter values and their mean values with measurements.

Effects of collagen ultrastructure. The global LV stiffness is very sensitive to the collagen fiber waviness and spatial orientation as measured by the collagen fiber azimuthal angle ϕ. Decreasing the mean collagen fiber waviness and increasing ϕ lead to a reduction in the LV volume at a fixed pressure (**Fig. 4**).

Myocardial Stress. The simulation results show that the contribution of cardiac muscle fiber is substantial at all transmural locations, accounting between 40 – 70% of the total stress. The contribution of collagen fibers to the total stress increases from 22% at the epicardium to 96% at the endocardium. Interestingly, the results also show that at 60% transmural depth, the contribution of collagen fibers starts to exceed that of the muscle fibers (**Fig. 5**).

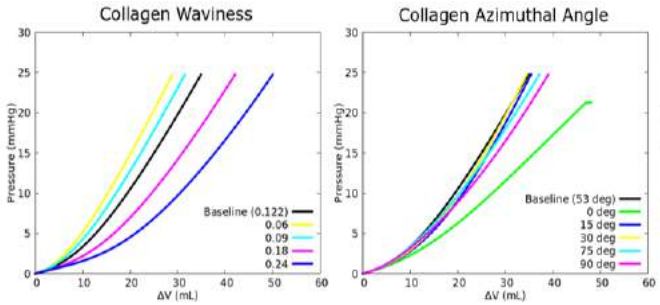

Fig. 4. Sensitivity of LV function to collagen network ultrastructure.

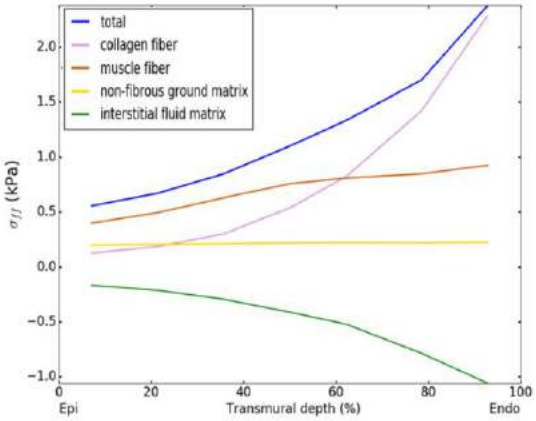

Fig. 5. Transmural variation of the contribution of individual constituent to the total muscle fiber stress at 8 mmHg.

DISSCUSSION

We have developed and validated a microstructure-based constitutive model of the passive myocardium in a three-dimensional FE modeling framework with measurements made across multiple scales; i.e., at the constituent, tissue and organ levels. Calibrated against the tissue-level biaxial test data derived from the mid-wall of the canine myocardium, the fitted parameter values are consistent with microscale measurements made on individual cardiac tissue constituents and the FE model predictions using these values are in agreement with independent measurements from experiments on the intact canine LV.

We found that the LV function is sensitive to the collagen fiber network ultrastructure and the load taken up by tissue constituents varies with LV location. The latter finding has implications on pharmaceutical therapies that target specific tissue individual constituent; e.g., attenuating myocardial fibrosis and reducing myocyte titin stiffness in heart failure with preserved ejection fraction. Specifically, this finding suggests that reducing LV passive stiffness by altering collagen fiber network is most effective if applied to the sub-endocardial region. Conversely, altering myocyte stiffness to reduce LV stiffness is most effective when applied to the sub-epicardial region.

ACKNOWLEDGEMENT

This work is supported by NIH (R01 HL134841, U01 HL133359-01A1), NSF 1702987, AHA 17SDG33370110.

REFERENCES

[1] Horowitz, A et al. *J Biomech Eng.* 110: 200-207, 1988.
[2] Humphrey, JD et al. *J Biomech Eng.* 112: 340-346, 1990.
[3] Brady AJ. *Am J Physiol.* 260: H1062-1071, 1991.
[4] McCulloch AD et al., *Am J Physiol.* 252: H233-241, 1987.
[5] MacKenna, DA et al. *Basic Res Cardiol.* 91:111-122, 1996.

SB³C2019
Summer Biomechanics, Bioengineering and Biotransport Conference
June 25 -28, Seven Springs, PA, USA

A THERMODYNAMICALLY MOTIVATED CROSS-BRIDGE CYCLING FRAMEWORK TO PREDICT MYOFIBRIL REMODELING UNDER CONDITIONS ASSOCIATED WITH LV HYPERTROPHY

Eoin McEvoy (1), Patrick McGarry (1)

(1) Discipline of Biomedical Engineering,
National University of Ireland Galway,
Galway, Ireland

INTRODUCTION

Heart failure is a global pandemic affecting over 25 million people worldwide. This inability of the heart to sufficiently perfuse the body may follow from cardiac eccentric hypertrophy, a medical condition whereby the ventricle becomes thinner and longer, often onset by an increased diastolic blood volume. Cardiomyocytes undergo longitudinal cell growth and addition of sarcomeres in-series [1]. The contractility of this thin ventricle wall is dramatically reduced, and, consequently, the volume of blood ejected during systole is reduced. While there have been significant advances made in the field of cardiac modelling in recent years [2,3] the cell-level mechanisms that drive hypertrophy have yet to be uncovered. In this study, we investigate the effects of pathological loading conditions on contractility and remodeling of cardiac myofibrils.

MODEL DEVELOPMENT

Contractility and remodeling: Transient force generation in cells is governed by cycling of myosin heads within the sarcomere, with an attachment transition rate

$$k_a = k_d \exp([1/kT]\{\delta\mu_a - \phi + F\Delta\}) \quad (1)$$

obtained from equilibrium [4]. Here, the myosin strain energy ϕ is generated by hydrolysis of ATP and depends on the sarcomere strain rate $\dot{\tilde{\varepsilon}}_n$ (Fig. 1(a)). The local concentration of parallel myofibrils $\hat{\eta}$ is governed by equilibrium between bound and unbound contractile proteins, with the thermodynamically consistent rate equation for fibre formation/dissociation [5] given as:

$$\dot{\hat{\eta}} = \frac{\widehat{N}_u}{\hat{n}}\omega_n \exp\left(-\frac{\hat{n}(\mu_{ab} - \mu_u)}{k_B T}\right) - \hat{\eta}\omega_n \exp\left(-\frac{\hat{n}(\mu_{ab} - \mu_b)}{k_B T}\right), \quad (2)$$

where μ_b and μ_u are the free energies of the bound contractile proteins in a myofibril and unbound proteins, respectively, μ_{ab} is an activation barrier. $\widehat{N}_u$ is the protein availability, whereby the total number of available contractile proteins, bound and unbound, is a conserved quantity. ω_n is the collision frequency of unbound molecules, k is the Boltzmann constant, and T is the absolute temperature. $\hat{n}$ is the number of actin-myosin sarcomeres along the length of a myofibril, with the kinetic remodeling law as follows:

$$\dot{\hat{n}} = -\frac{1}{\hat{n}}\left(\frac{\widehat{N}_u}{\hat{\eta}}\right)^2 \left[\psi(\tilde{\varepsilon}_n) - \frac{\partial\psi}{\partial\tilde{\varepsilon}_n}(1 + \tilde{\varepsilon}_n)\right]\frac{\alpha_n}{\mu_{b0}}, \quad (3)$$

where ψ is the internal sarcomere energy which increases with increasing strain $\tilde{\varepsilon}_n$, and α_n is a rate constant. As shown in Fig. 1(b) the model dictates that the remodeling process is initiated to achieve an optimal overlap of the actin/myosin filaments (e.g. more sarcomeres are added in-series when the filaments become highly stretched).

Tissue modeling: The active molecular/cell framework is combined with a passive hyperelastic myocardium model [6], with the anisotropic stress component given by:

$$\boldsymbol{\sigma}_{aniso} = \sum_{m=f,s} 2a_m(I_{4m}-1)\exp[b_m(I_{4m}-1)^2]\ \boldsymbol{a}_m \otimes \boldsymbol{a}_m + a_{fs}I_{8fs}\exp\left(b_{fs}I_{8fs}^2\right)(\boldsymbol{a}_m \otimes \boldsymbol{a}_m + \boldsymbol{a}_m \otimes \boldsymbol{a}_m), \quad (4)$$

where I_{4f}, I_{4s}, and I_{8fs} are anisotropic invariants and $\boldsymbol{a}_m$ $(m = f, s)$ is a unit vector indicating the myofibre or sheet orientations in the deformed configuration. The operator $\otimes$ is the dyadic product of vectors resulting in a second-order structure tensor. a_m and b_m $(m = f, s,\ fs)$ are anisotropic material parameters for each contribution. An idealized left ventricular geometry is developed (with fibre directions varying spatially across the heart wall) and active beating is simulated. Physiological boundary conditions are applied to the tissue for (i) blood volume in a healthy state (V_h), and (ii) increased diastolic blood volume (V_p). Cell remodeling following the application of pathological loading conditions is investigated.

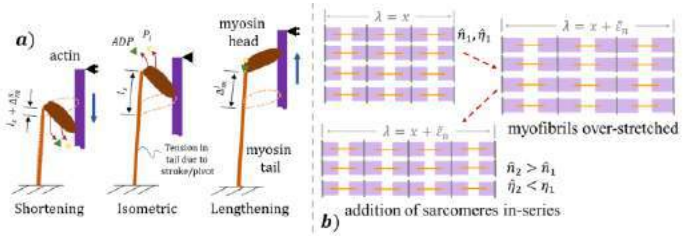

Figure 1: (a) Schematic of actin-myosin cross-bridge cycling under shortening, isometric, and lengthening boundary conditions; (b) Remodeling of myofibrils subjected to over-stretching (reduced actin/myosin overlap). Sarcomeres are added in-series and the parallel concentration of myofibrils is reduced.

RESULTS

The predicted ventricle pressure for healthy conditions is shown in Fig. 2(a), and the Cauchy stress in the fibre (*f*) direction in Fig. 2(b). The cell tension that develops is not instantaneous, but transient due to the dynamic attachment of myosin heads (as motivated by calcium signaling and the tissue strain state). The influence of altered diastolic blood volume $\Delta\hat{V}_d$ on the number of in-series sarcomeres $\hat{n}$ is shown in Fig. 2(c). Higher applied $\Delta\hat{V}_d$ translates to an increased ventricle wall strain (thereby increasing the internal sarcomere strain $\tilde{\varepsilon}_n$). The consequent reduction in actin/myosin overlap lowers the availability of myosin heads and therefore the active contractility (increasing the sarcomere free energy). Simulations predict that the steady state values of $\hat{n}$ will thus increase with increased $\Delta\hat{V}_d$. However, due to the constraint on the number of contractile proteins, the parallel concentration of myofibrils $\hat{\eta}$ is lowered (Fig 2(d)) and the overall contractility of the tissue is reduced.

DISCUSSION

In this study a thermodynamically motivated model for cell contractility is implemented to simulate the behaviour of the myocardium during the cardiac cycle, predicting correct patterns of ventricle pressure. We demonstrate that eccentric hypertrophy is initiated by a higher wall stretch associated with an increased venous return, to restore an optimal overlap of the actin/myosin filaments. Such a fundamental understanding of the mechanisms that drive remodeling could facilitate the development of advanced diagnostic models to predict if and when heart failure will occur.

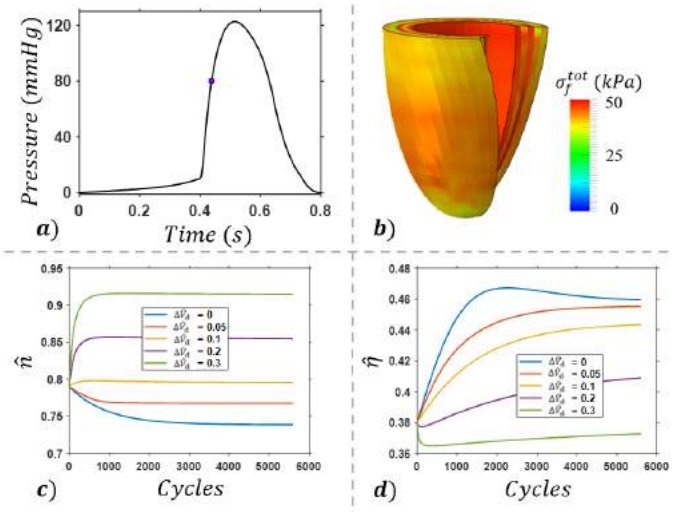

Figure 2: (a) Predicted ventricle pressure over cardiac cycle; (b) Cauchy stress σ_f^{tot} in fibre (*f*) direction at peak systole; Predicted (c) number of in-series sarcomeres $\hat{n}$ and (d) parallel concentration of sarcomeres $\hat{\eta}$ following application of increased diastolic blood volume $\Delta\hat{V}_d = V_p/V_h - 1$.

ACKNOWLEDGEMENTS

The authors acknowledge funding from Science Foundation Ireland (18/ERCD/5481), the Irish Research Council (GOIPG/2015/2954) and the NUI Galway Hardiman Scholarship.

REFERENCES

1. Dorn *et al.* (2003). 'Phenotyping Hypertrophy'. *Circ Research.*
2. Rausch *et al.* (2011). 'Computational Modeling of Growth: Systemic and Pulmonary Hypertension in the Heart'. *Biomech Model Mechanobiol*
3. Baillargeon *et al.* (2014). 'The Living Heart Project: A Robust and Integrative Simulator for Human Heart Function'. *European Journal of Mechanics-A/Solids*
4. McEvoy *et al.* (2019). 'Transient Active Force Generation and Stress Fibre Remodelling in Cells under Cyclic Loading'. *Biomech Model Mechanobiol* (*in review*)
5. Vigliotti *et al.* (2015). 'A Thermodynamically Motivated Model for Stress-Fiber Reorganization'. *Biomech Model Mechanobiol*
6. Holzapfel *et al.* (2009). 'Constitutive Modelling of Passive Myocardium: A Structurally Based Framework for Material Characterization'. *Philos Trans A Math Phys Eng Sci*

SB³C2019
Summer Biomechanics, Bioengineering and Biotransport Conference
June 25 -28, Seven Springs, PA, USA

CONTRACTILITY MODELLING TOWARDS PREDICTING ECCENTRIC HYPERTROPHY IN A PATIENT-SPECIFIC HEART MODEL

Ryan J. Coleman (1), Eoin McEvoy (1), Patrick McGarry (1)

(1) Biomedical Engineering
National University of Ireland, Galway
Galway, Ireland

INTRODUCTION

Eccentric hypertrophy is a medical condition whereby the ventricle wall becomes thinner and longer, typically onset by an increased diastolic blood volume. At the cell-level, this is characterized by longitudinal cell growth and addition of sarcomeres in-series [1]. As the disease progresses, the contractility of the thin-walled structure is reduced and, therefore, the pumping ability of the heart is impaired. While there have been several advances in patient-specific finite element simulations of the heart [2], previous models implemented phenomenological representations of tissue contractility [3]. In contrast, the current study implements a thermodynamically motivated model for actin-myosin cross-bridge cycling in cardiac myocytes [4]. Predictions of contractility for this thermodynamic cross-bridge cycling model are compared to results for widely used phenomenological models. In particular, the influence of pathological increases to diastolic blood volume on tissue contractility and remodeling is investigated.

METHODS

A linearized form of myocyte strain during a cardiac cycle is implemented in a 1D framework, to simulate the effect of pathological boundary conditions on active force generation of myofibrils. Contractility is simulated via the phenomenological model of Walker *et al.* [3], and the thermodynamically motivated model of McEvoy *et al.* [4]. The Walker model for myofibril stress is given as:

$$\sigma_{af}\left(t, E_{ff}\right) = \frac{T_{max}}{2} H(E_{ff}) \left[1 - \cos\left(\omega\left(t, E_{ff}\right)\right)\right], \quad (1)$$

where t is the cycle time, E_{ff} is the myocyte strain in the fibre direction, and T_{max} is the maximum isometric tension generated by a sarcomere. The function $H\left(E_{ff}\right)$ describes the influence of stretch mediated calcium signaling, such that

$$H\left(E_{ff}\right) = \frac{{Ca_0}^2}{C\,{a_0}^2 + {ECa_{50}}^2\left(E_{ff}\right)}, \quad (2)$$

where C_{a0} is the peak intercellular calcium concentration, and ECa_{50} is the length-dependent calcium sensitivity. ω is a time-dependent relation, given by:

$$\omega\left(t, E_{ff}\right) = \begin{cases} \pi \frac{t}{t_o} & 0 \le t \le t_o \\ \pi \frac{t - t_o + t_r(l)}{t_r} & t_o \le t \le t_o + t_r(l) \\ 0 & t \ge t_o + t_r(l) \end{cases}, \quad (3)$$

$$t_r(l) = ml + b, \quad (4)$$

$$l\left(E_{ff}\right) = l_r\sqrt{2E_{ff} + 1}, \quad (5)$$

where t_o is the time to reach peak tension, m and b are constants, and l_r is the stress-free sarcomere length. Material parameters are consistent with those reported by Baillargeon *et al.* [2].

In the thermodynamically motivated model for actin-myosin cross-bridge cycling developed by McEvoy *et al.* [4], the attachment of myosin is dependent on molecular-level boundary conditions. The active myofibril stress caused by cell contractility is given by:

$$\sigma_f\left(t, E_{ff}\right) = \sigma_{iso}\,\frac{T_s\left(t, E_{ff}\right)}{T_{s0}}. \quad (6)$$

Here, σ_{iso} is the maximum isometric stress of a myofibril, T_{s0} is isometric sarcomere tension, and T_s is the current sarcomere tension.

$$T_s\left(t, E_{ff}\right) = \hat{m}_a\left(t, E_{ff}\right)\kappa_m\,\Delta_m, \quad (7)$$

where $\hat{m}_a$ is the normalised number of attached myosin heads, κ_m is the myosin tail stiffness, and Δ_m is a distribution of tail extensions. The evolution of $\hat{m}_a$ is described by a kinetic equation, with

$$\frac{d\hat{m}_a}{dt} = -k_d\hat{m}_a + k_a\hat{m}_d, \quad (8)$$

where $\hat{m}_d$ is the normalised number of detached myosin heads, and k_a and k_d are rate coefficients derived from steady state equilibrium.

Poster Presentation #P098

Furthermore, the McEvoy framework computes the steady state concentration of sarcomeres in-parallel and in-series, which depend on the strain state and myofibril/sarcomere stress σ_f. The (normalized) number of sarcomeres in-series is given by:

$$\dot{\hat{n}} = \begin{cases} -\frac{1}{\hat{n}}\left(\frac{\hat{N}_u}{\hat{\eta}}\right)^2\left[\psi(\tilde{\varepsilon}_n) - \frac{\delta\psi}{\delta\tilde{\varepsilon}_n}(1-\tilde{\varepsilon}_n)\right]\frac{\alpha_n}{\mu_{b0}} & if\ \frac{\delta\psi}{\delta n} \le 0 \\ -\frac{\hat{n}}{4}\left[\psi(\tilde{\varepsilon}_n) - \frac{\delta\psi}{\delta\tilde{\varepsilon}_n}(1+\tilde{\varepsilon}_n)\right]\frac{\alpha_n}{\mu_{b0}} & else \end{cases}, \quad (9)$$

where $\hat{N}_u$ is the normalized number of unbound proteins, ψ is internal sarcomere energy, α_n is a rate constant, and μ_{b0} is the sarcomere energy in its ground state. The internal strain within a sarcomere is given by

$$\tilde{\varepsilon}_n = \frac{1+E_{ff}}{\hat{n}} - 1. \quad (10)$$

The (normalized) concentration of sarcomeres in-parallel is determined from:

$$\dot{\hat{\eta}} = \frac{\hat{N}_u}{\hat{n}}\omega_n \exp\left[-\hat{n}\,\frac{\mu_{ab}-\mu_u}{k_B T}\right] - \hat{\eta}\omega_n \exp\left[-\hat{n}\,\frac{\mu_{ab}-\mu_b}{k_B T}\right], \quad (11)$$

where ω_n is the collision frequency of unbound molecules, μ_{ab} is the an activation barrier, μ_u is the standard enthalpy of unbound cytoskeletal proteins, μ_b is the standard enthalpy of n^R bound cytoskeletal proteins, k_B refers to Boltzmann's constant, and T is absolute body temperature. Material parameters implemented are consistent with those reported by McEvoy *et al.* [4].

RESULTS

The computed active contractile stress is shown in Fig. 1, for both the Walker *et al.* [3] model and the thermodynamically motivated model of McEvoy *et al.* [4]. These models present a level of conformance in the active stress generated at physiological strains (Fig. 1(a,b)). With an increase in strain (associated with increased diastolic venous return), the Walker *et al.* [3] model predicts a reduced relaxation rate due to the dependence on E_{ff} (Fig. 1(c,d)). However, the McEvoy *et al.* [4] model predicts a reduction in peak stress due to myofibrillar remodeling onset by a reduced actin-myosin overlap, consistent with progression of eccentric hypertrophy [1].

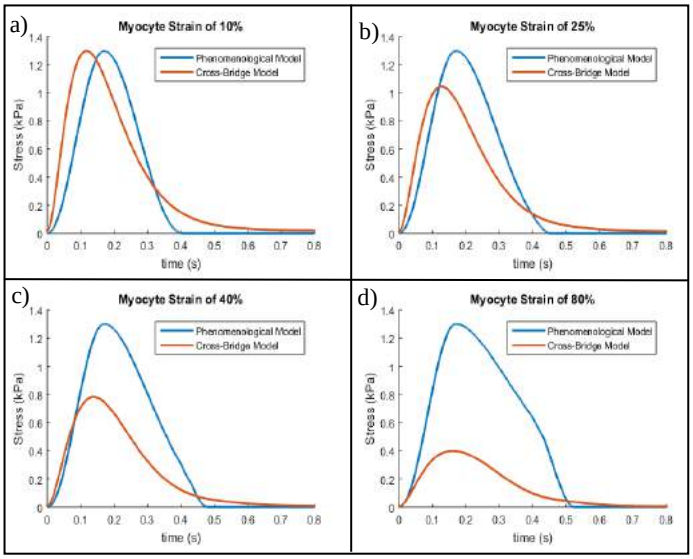

Figure 1. Myofibril stress modelled from both the Walker et al. phenomenological model [3], and the McEvoy et al. cross-bridge model [4]. Stress is calculated from a myocyte strain cycle of (a) $E_{ff}^{max} = 10\%$, simulating normal physiological myocyte contraction. (b) $E_{ff}^{max} = 25\%$, simulating mild pathological myocyte contraction. (c) $E_{ff}^{max} = 40\%$, simulating pathological myocyte contraction. (d) $E_{ff}^{max} = 80\%$, simulating severe pathological myocyte contraction.

Fig. 2(a) shows the evolution of the area concentration of sarcomeres in parallel, $\hat{\eta}$. Fig. 2(b) shows the evolution of the axial concentration of sarcomeres in series, $\hat{n}$. At steady state $\hat{\eta}$ is predicted to decrease with increasing myocyte strain. In contrast, $\hat{n}$ increases with increasing myocyte strain. This indicates a high myocyte strain (due to a high diastolic ventricular blood volume) leads to in-series addition of sarcomeres. This necessitates a reduction of the area concentration of sarcomeres in parallel, leading to thinning and elongation of the ventricle wall.

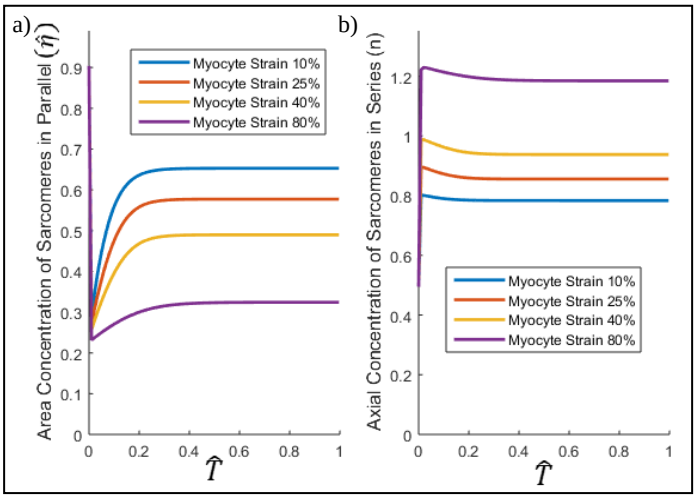

Figure 2. Thermodynamic cross-bridge cycle model predictions of the evolution of (a) area concentration of sarcomeres in parallel $\hat{\eta}$, and (b) axial concentration of sarcomeres in series $\hat{n}$.

DISCUSSION

In eccentric hypertrophy a reduction in wall thickness is accompanied by a reduction in actively generated myocardium contractility [1]. In this study we demonstrate that our thermodynamically motivated cross-bridge cycle model correctly predicts a decrease in sarcomere concentration and contractility following volumetric overload. Our prediction that diastolic blood volume overload results in increased axial concentrations of sarcomeres in-series and decreased area concentration of sarcomeres in parallel provides a sub-cellular explanation for the development of eccentric hypertrophy. In contrast to our cross-bridge cycle model, the phenomenological contractility model of Walker *et al.* [3] incorrectly predicts that peak myofibril contractility is independent of the myocardium strain.

Our thermodynamically motivated cross-bridge cycle model has the potential to provide patient specific diagnosis of hypertrophy and impaired cardiac function.

ACKNOWLEDGEMENTS

The author would like to acknowledge Science Foundation Ireland (grant 18/ERCD/5481) for funding this work.

REFERENCES

[1] Dorn, G., et al. Circulation Research, 92(11), pp.1171-1175, 2003. [2] Baillargeon, B., et al. European Journal of Mechanics - A/Solids, 48, pp.38-47, 2014. [3] Walker, J.C., et al., American Journal of Physiology, Heart and Circulatory Physiology 289: H692–H700, 2005. [4] McEvoy, E., et al., Biomechanics and Modelling in Mechanobiology (in review)

SB³C2019
Summer Biomechanics, Bioengineering and Biotransport Conference
June 25 -28, Seven Springs, PA, USA

CARDIAC GROWTH AND REMODELING: USING MACHINE LEARNING TO CORRELATE CELL AND ORGAN SCALES

M. Peirlinck (1), F. Sahli Costabal (2), K.L. Sack (3,5), J.S. Choy (4), G.S. Kassab (4), J.M. Guccione (5), M. De Beule (1), P. Segers (1), E. Kuhl (2)

(1) Biofluid, Tissue and Solid Mechanics for Medical Applications (IBiTech, bioMMeda), Ghent University, Ghent, Belgium

(2) Departments of Mechanical Engineering & Bioengineering, Stanford University, California, USA

(3) Department of Human Biology, University of Cape Town, Cape Town, South Africa

(4) California Medical Innovations Institute, Inc., San Diego, California, USA

(5) Department of Surgery, University of California at San Francisco, San Francisco, California, USA

INTRODUCTION

Cardiovascular disease is the single leading cause of death worldwide with an estimated 17.3 million deaths in 2016, representing 31.5% of all global deaths [1]. With a 5-year mortality rate of 50%, heart failure remains (and will remain in the foreseeable future) one of the most common, costly, disabling and deadly medical conditions. In a traditional biomechanical sense, cardiac growth and remodeling can be considered a protective and reparative homeostatic mechanism. Combined with chronic alterations in the heart's hemodynamic loading conditions however, these mechanisms can lead to pathological anatomical and physiological changes that depress cardiac performance and eventually lead to heart failure. Hypertrophy is often progressive, but the time course and extent of progression is highly patient-specific. The most pertinent clinical question tends to be prognostic where anticipation of the rate of progression is essential for treatment planning [2]. The mechanobiological factors regulating the hypertrophic response of the heart have been the subject of extensive research throughout the past decades [3], and still remain up for debate. Consequently, cardiac growth models have the potential to provide mechanical insights in disease onset and progression, which can aid clinical decision-making or the design of emerging therapies. Considerable debate remains as to which stimuli are necessary to include in mechanistic growth laws. Most evidence, both at tissue and cellular levels, points to mechanical factors as mediating stimuli. In eccentric hypertrophy, end-diastolic wall stress was initially considered as a stimulus, but later studies opposed this hypothesis and implied that end-diastolic strain at the tissue level may be a more realistic stimulus [3]. In this study we investigate this hypothesis and assess the ability of the corresponding growth law to capture experimentally observed trends in a unique animal study where eccentric hypertrophy was characterized across multiple scales at once.

METHODS

The progress of eccentric hypertrophy was studied over a period of 8 weeks in six Yorkshire domestic pigs. At the start of the study, moderate to severe mitral valve regurgitation was created in the left ventricle by disrupting one or more chordae. To characterize changes on the organ level, bi-weekly echocardiograms were taken to compute the left ventricular end-diastolic and end-systolic volumes (EDVs and ESVs), stroke volumes, ejection fractions, and wall thicknesses. For the cell level characterization, endomyocardial biopsy samples were collected at the day of mitral valve chordae disruption and at bi-weekly follow-ups. These biopsy samples were histologically prepared and examined to characterize myocyte width (MW) and length (ML). The changes and uncertainty in measured organ and cell level variables across different subjects were analyzed using Bayesian inference, where it was postulated that the measurements are drawn from log-normal distributions that evolve linearly over time. To take into account the variability between subjects and, at the same time, take advantage of the entire acquired dataset, we postulate a hierarchical model, i.e., that the measurements between subjects are related. We assumed that the different parameters that describe the log-normal means of a measurement at a certain time and their log-normal standard deviations are respectively drawn from a normal distribution and a Half-Cauchy or Lewandowski-Kurochiwa-Joe distribution. Using a Hamiltonian Monte Carlo method, we performed a statistical inference which results in statistically predictive posterior distributions of the measured quantities of interest [4].

To correlate changes in end-diastolic volume to changes in myocyte morphology, we adopted a transversely isotropic kinematic-based growth model where the overall deformation is given by $\boldsymbol{F} = \boldsymbol{F}^e \cdot \boldsymbol{F}^g$ [5]. Here, the growth deformation $\boldsymbol{F}^g$ maps the original reference state to an intermediary unstressed grown state. The elastic

deformation, $\boldsymbol{F}^e$ maps the intermediary state into the intact, loaded state. Only $\boldsymbol{F}^e$ contributes to the stress state of the tissue. The growth tensor was defined as $\boldsymbol{F}^g = \boldsymbol{I} + (\vartheta^{\parallel} - \boldsymbol{1})\, \boldsymbol{n} \otimes \boldsymbol{n}$ where the eccentric growth multiplier $\vartheta^{\parallel}$ is updated if the elastic stretch in the fiber direction, λ^e, exceeds a critical physiological threshold value λ^{crit}, which was assumed to be equal to the local fiber stretch at the end of diastolic filling:

$$\dot{\vartheta}^{\parallel} = \tau^{-1}\langle \lambda^e - \lambda^{crit} \rangle \qquad (1)$$

Left-ventricular finite element models were created for each animal based on the echocardiography images at the minimum cavity volume of the cardiac cycle, which was assumed to be a stress-free state. The tissue's elastic response of the myocardial tissue was characterized by the classical Holzapfel-Ogden model [6] and calibrated for each subject specifically in accordance to our previous studies [7, 8]. The complex myocardial fiber architecture was incorporated using a rule-based method where the myofibers's helical angle varies transmurally from +60° (endo) to -60° (epi). Next, the uncertainty in end-diastolic volumes for each pig, quantified using Bayesian inference as described earlier, was introduced into the growth models. We achieved this by considering 500 samples of each pig's end-diastolic volume evolution distribution. For each sample, the corresponding evolution in end diastolic volume was used to simulate the tissue's growth response. Instead of performing a forward growth simulation (see Figure 1) for each of these 500 samples for each pig, we trained a subject-specific Gaussian process regression using 20 training and 10 validation simulations to predict the median longitudinal growth multiplier based on the imposed changes in end-diastolic volume due to mitral regurgitation. For each pig, the 500 medians of the simulated longitudinal growth multipliers were then compared to 500 samples of the posterior myocyte length measurement distributions and the overlap was quantified.

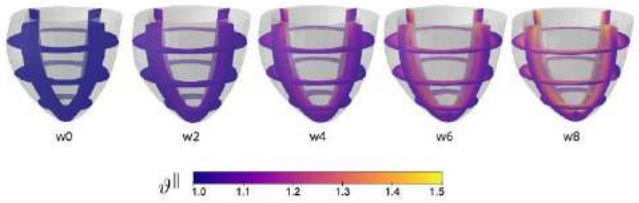

Figure 1: Simulated stretch-driven fiber growth evolution in the volume-overloaded pig #6 heart. Time evolution of the simulated regional longitudinal growth multiplier for pig #6 over a time span of 8 weeks.

RESULTS

Based on 28 echocardiography measurements and the Bayesian inference analysis, the average end diastolic volume (EDV) and end systolic volume (ESV) increased from 67.9 ± 20.6ml and 30.2 ± 9.5ml at baseline to 100.2 ± 17.9ml and 51.3 ± 9.0ml at week eight, which lead to a decreased ejection fraction. On a weekly basis, this meant an EDV increase of +5.95%/week, with a rapid increase between weeks 6 and 8 (see Figure 2 for the EDV evolution of pig #6). Based on 460 histological myocyte width and length measurements and the Bayesian inference analysis, the ML increased on average from 85.45 ± 22.30µm to 107.75 ± 26.57µm while the average MW remained relatively constant at 13.55µm. On a weekly basis, this translates into an average ML increase of +3.26 %/week with a steeper increase between weeks 6 and 8 (see Figure 2 for the ML evolution of pig #6).

Propagating the quantified uncertainty on volume overload through the six different subjects resulted in a quantified uncertainty of the computationally predicted endocardial myocyte lengths (500 simulations for each pig). Comparing these simulation results with the 500 predicted samples from the Bayesian inference uncertainty of the measured myocyte lengths for each pig, the average agreement between simulation and experiment was 52.7%, ranging from an excellent agreement of 85.7% for pig #5 to a poor agreement of 6.0% for pig #2 (see the agreement of 67.7% for pig #6 in Figure 1). Knowing that pig #2 was the largest pig of the study, and considering this pig as an outlier, the average agreement for the remaining pigs was 62.0%.

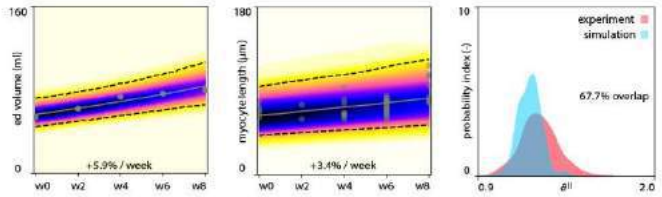

Figure 2: Changes in end diastolic volume and myocyte length in response to left ventricular volume overload for pig #6 (left & mid). Gray dots represent individual measurements of EDVs and MLs respectively, solid gray lines represent the medians computed using Bayesian inference and dashed black lines the corresponding 95% confidence intervals. Color contours from black to white highlight the probability density from high to low. **Simulation and experiment of chronic myocyte lengthening across endocardial wall in response to left ventricular volume overload for pig #6 (right).** Blue and red probability density functions represent computationally simulated MLs in the endocardial wall and experimentally measured MLs respectively, both with uncertainty.

DISCUSSION

Predictive cardiac growth models are a potentially important clinical tool to assess disease progression and optimize treatment in heart failure patients. To quantify the predictive power of these models, this study proposed a systematic experimental and computational approach to correlate how hemodynamic changes lead to changes in myocyte morphology. Using machine learning tools, the individual organ scale and cell scale behavior of each animal was interpreted in view of the collective behavior of all animals, which allowed us to quantify the uncertainty on our experimental and computational results. For each pig, we created and calibrated a finite element model of the left ventricle, to simulate the hypertrophic tissue reaction to volume overload based on a stretch-driven eccentric growth law. Subsequently, the uncertainty on end-diastolic volume overload was propagated through each of these subject-specific cardiac models, which resulted in a quantified uncertainty on predicted myocyte morphology changes. Considering pig #1, #3, #4, #5 and #6, the considered growth law alone predicts the changing myocyte morphology with an accuracy of 62.0%.

ACKNOWLEDGEMENTS

This work was supported by a Flanders Innovation and Entrepreneurship Agency strategic research grant (M. Peirlinck), by a Becas Chile-Fulbright Fellowship (F. Sahli Costabal) and by the National Institutes of Health grant U01 HL119578 (J.M. Guccione, G.S. Kassab, E, Kuhl).

REFERENCES

[1] Townsend, N., et al., *European Heart Journal*, 37(42): 3232-3245, 2016.
[2] Witzenburg, C.M. and J.W. Holmes, *J. Elast.* 129(1): 257-281, 2017.
[3] Omens, J.H., *Prog. Biophys. Mol. Bio.*, 69(2-3): 559-572, 1998.
[4] Sahli Costabal, F., et al., *Acta Biomat.*, 2019. doi:10.1016/j.actbio.2018.12.053.
[5] Göktepe, S., et al., *Journal of Theoretical Biology*, 265(3): 433-442, 2010.
[6] Holzapfel, G.A. and R.W. Ogden, *Phil. Trans. Royal Soc.A* 367: 3445-3475, 2009.
[7] Peirlinck, M., et al., *Int. J. Num. Meth. Biomed. Eng.*, 35(1): e3151, 2019.
[8] Sack, K.L., et al., *Front. Physiology*, 9(539)2018.

SB³C2019
Summer Biomechanics, Bioengineering and Biotransport Conference
June 25 -28, Seven Springs, PA, USA

CHANGES IN THE ANISOTROPIC AND VISCOELASTIC PROPERTIES OF THE OVINE RIGHT VENTRICLE UNDER CHRONIC PRESSURE OVERLOAD

Wenqiang Liu (1), Michael Nguyen-Truong (1), Elisabeth Gray (1), Jeremiah Easley (3), Eric Monnet (3), Christian Puttlitz (1,2), Zhijie Wang (1,2)

(1) School of Biomedical Engineering
Colorado State University
Fort Collins, Colorado, United States

(2) Department of Mechanical Engineering
Colorado State University
Fort Collins, Colorado, United States

(3) Department of Veterinary Medicine and Biomedical Sciences
Colorado State University
Fort Collins, Colorado, United States

INTRODUCTION

Right ventricle failure (RVF) is a fatal disease and contributes significantly to the morbidity and mortality in a variety of cardiovascular diseases[1]. The mechanical behavior of the RV (e.g., stiffness) is closely related to its physiological function[2]. However, the understanding of the mechanical property changes in failing RVs is still limited. Most previous studies have assumed the RV to be orthotropic but ignored the viscoelastic behavior. It is known that the ventricle is an anisotropic and viscoelastic tissue[3]. Therefore, the changes in RV anisotropic and viscoelastic properties during pressure overload remains a key knowledge gap.

The goal of the study is to investigate the changes of the RV anisotropic and viscoelastic properties under chronic pressure overload. Using a newly revised model of pulmonary artery constriction (PAC) in adult sheep, we established RV failure and performed *ex vivo* biaxial mechanical tests to determine RV mechanical properties. We hypothesize that the remodeling in failing RVs leads to changes in anisotropic and viscoelastic properties compared to the healthy controls. Our findings of the RV biomechanical changes will assist with the understanding of the biomechanical mechanisms of RV failure secondary to chronic pressure overload.

METHODS

All procedures were approved by IACUC at Colorado State University. RV failure was established by chronic pressure-overload using a newly revised PAC method in ovine. Briefly, patient specific, graded PAC was performed on week 0 and 4 in 8-month-old male sheep and the animals were euthanized 11 weeks after the initial PAC (N=3). Age-matched male healthy sheep were used as controls (N=3). Hemodynamic measurements were obtained prior to euthanasia. Then, RV tissues were harvested and the equibiaxial mechanical tests (at stretch rate of 15 mm/min) were performed. We failed to obtain the mechanical data in one PAC RV. The RV outflow tract direction was marked as the longitudinal direction. Cauchy stress (σ) and Green's strain (ε) were calculated from the experimental data as done previously[4]. Elastic moduli (E) were obtained as the slopes of the loading curve in the last cycle in three different strain ranges (low: 0-0.04, middle: 0.04-0.08, high: 0.08-0.12). The hysteresis loop was obtained from the last cycle of

loading and unloading curves. Then, the stored energy (W_s) and viscosity (a) were quantified by the area beneath the loading curve and the width of the loop at the mid-stress, respectively (Fig. 1). Finally, histology analysis was performed for RV collagen content using Picrosirius red staining. Student's t-test was performed and $p \leq 0.05$ was considered significant.

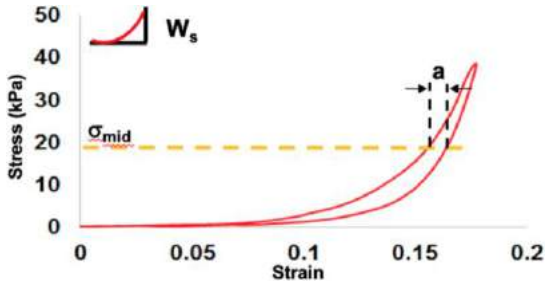

Figure 1. Measurement of the viscosity using the width of the hysteresis loop at middle stress (σ_{mid}).

RESULTS

The 11-week patient-specific, graded PAC led to the development of RV failure, which was evidenced by significant increases in RV systolic pressure (RVSP) and Fulton Index and reduction in stroke volume (Table 1). Accumulation of collagen occurred in the RVs (Table 1, p=0.07 control vs. PAC).

Table 1. Hemodynamic and biological changes of the ovine RVs under chronic pressure overload. *p<0.05.

	Control	PAC
RVSP (mmHg)	22.7±1.1	43.6±8.2 *
Stroke Volume (mL)	108.2±19.2	72.4±9.6 *
Fulton Index (%)	28.4±1.3	43.0±3.5 *
Total Collagen Content (%)	3.6±1.0	6.1±1.4

In terms of the mechanical changes, we found that in general, the RV elastic moduli (E) tended to increase in the longitudinal direction (Fig. 2A) in all strain ranges (Table 2). But there were no changes in E in the circumferential

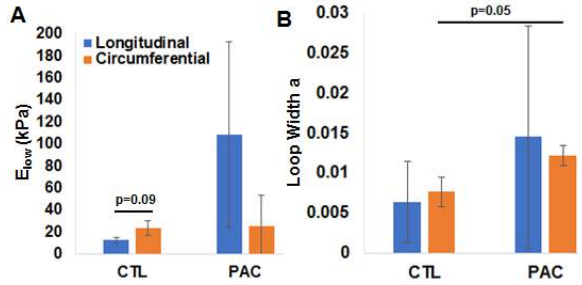

Figure 2. Changes of low strain elastic modulus (A) and viscosity (B) of the RV in different directions.

Table 2. Measurements of E in the longitudinal direction (L) and Ws in both directions (L, C) in the RVs.

	Control	PAC
E_{low}, L (kPa)	12.7±2.8	108.9±84.4
E_{mid}, L (kPa)	23.4±7.1	257.6±249.9
E_{high}, L (kPa)	210.3±132.0	1065.3±1170.4
W_s, L	2.1±0.8	3.6±0.3 †
W_s, C	2.9±1.8	2.3±0.6

direction (data not shown). Similar trends were seen in the stored energy (Ws) (Table 2; †p=0.08), which is an indicator of the elasticity of the tissue. These data suggest a change in the anisotropic property under pressure overload. The RV tended to be stiffer in the circumferential direction (Fig. 2A; p=0.09) in the baseline (which is consistent with our unpublished data); however, after PAC, it tended to be stiffer in the longitudinal direction. Lastly, we quantified the viscosity by the width of the loop at the mid-stress. We observed increased viscosity in the PAC RV in the circumferential direction (Fig. 2B; p=0.05).

DISCUSSION

This study is the first to investigate the anisotropic and viscoelastic mechanical properties of adult ovine RVs and their changes under pressure overload. In this pilot study (with small Ns), we obtained novel findings in the biomechanical changes of the failing RVs: 1) A strong trend of change in RV anisotropic behavior was observed after the pressure overload. The RV was stiffer in the circumferential direction initially and became stiffer in the longitudinal directions after PAC. This may be related to the accumulation of collagen as well as the change in the collagen fiber angle (data not shown). 2) An increased viscosity of the RV was observed in the circumferential direction. This indicates more energy loss over a cardiac cycle in the diseased RV. Future study will recruit more animals and include functional analyses of the RV. Our study will bring more insights into the mechanism of the development of RV failure.

REFERENCE

[1] Haddad, F et al., *J Circulation*, 117, p1717, 2008.

[2] Jang, S et al., *J Am Heart Assoc*, *25*(4), p175, 2017.

[3] Nguyen, M et al., *Ad Exp Med and Bio*, 1098, p1, 2018.

[4] Labus, M et al., *J Me Be of Bm Mat*, *62*, p195, 2016.

SB³C2019
Summer Biomechanics, Bioengineering and Biotransport Conference
June 25 -28, Seven Springs, PA, USA

MECHANICAL CHARACTERIZATION OF BOVINE EMBOLUS ANALOGS FOR INVESTIGATING ACUTE ISCHEMIC STROKE RECANALIZATION

Gretchen E. Hiller (1) Bryan C. Good (1), Keefe B. Manning (1, 2)

(1) Department of Biomedical Engineering
The Pennsylvania State University
University Park, PA, USA

(2) Department of Surgery
Penn State Hershey Medical Center
Hershey, PA, USA

INTRODUCTION

An estimated 700,000 acute ischemic strokes (AIS) occur each year in the Unites States, as a result of embolic occlusion of a cerebral artery. In spite of the improved recanalization rates of cerebral arteries, by means of novel stent retriever devices, 15% of patients' arteries still cannot be recanalized. In addition, 17% of patients with successful arterial recanalization die within 90 days [1]. Currently there is little understanding as to why some thromboemboli are successfully removed, and others are not. In order to improve our understanding of thromboemboli adhesion and removal in AIS, we must first be able to characterize the mechanical properties and accurately model the behavior of thromboemboli. Therefore, we are developing embolus analogs from bovine whole blood to mimic the properties of human thromboemboli in AIS patients. Since most biological tissues are stored in paraformaldehyde (PFA), this study seeks to characterize the mechanical properties of bovine embolus analogs fixed in 4% PFA solution to those unfixed, in order to develop relationships to the behavior of thromboemboli *in vivo*.

METHODS

Bovine embolus analogs were created using a 1:1 ratio, of platelet rich plasma (PRP) and red blood cells (RBC). Calcium chloride ($CaCl_2$) was then added, in a 1:50 $CaCl_2$ to PRP ratio, in order to reverse the effects of CPDA in blood collection bags and restore the blood's coagulation properties. The mixture of PRP, RBC and $CaCl_2$ was injected into 3D printed cylindrical blood clot molds (**Fig 1A**) via a syringe, and left over night to form cylindrical bovine embolus analogs, with approximate diameters of 7 mm. Exact embolus analog dimensions were measured and recorded, using calipers for later stress and strain calculations. Of the 10 fully developed bovine embolus analogs, half were tested right away while the other half were stored for another 24 hours in a 4% PFA solution, for fixation similar to clinically obtained samples. To determine the mechanical properties of the bovine embolus analogs, both cyclic compression and stress-relaxation tests were performed. The incremental loads were applied and measured using a Lloyd Tensile Testing (AMETEK Inc., Largo, FL) device and 3D printed compression pieces designed to connect to the device (**Fig 1B**).

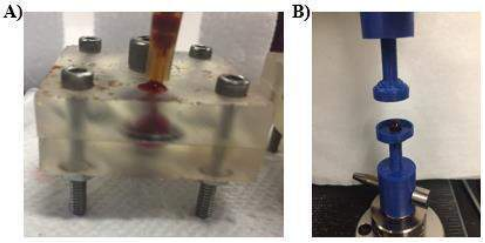

Figure 1: A) 3D printed cylindrical blood clot molds, with bovine blood clots, and B) uniaxial tensile device attachment pieces, holding a bovine embolus analog.

For compression testing, the analogs were loaded to a strain of 10% at a rate of 1 Hz to replicate the expected loading conditions of cyclic aspiration. Ten fixed and ten unfixed embolus analogs were loaded for each mechanical test (cyclic loading and stress-relaxation) and stress-strain hysteresis and stress-relaxation curves were extracted. Using in-house MATLAB code, the average curves were determined for each of the loading conditions and embolus analog types. Lastly, we fit the stress-relaxation data to a 3-term Prony series (**Eq. 1**):

$$g(t) = g_\infty + g_1 \cdot e^{-\frac{t}{z_1}} + g_2 \cdot e^{-\frac{t}{z_2}} \qquad (1)$$

Where g_∞, g_1, and g_2 are the characteristic amplitudes, z_1 and z_2 are the characteristic relaxation times, and t is the time.

RESULTS

The average cyclic loading data set for both the fixed and unfixed bovine blood clots (**Fig 2**).

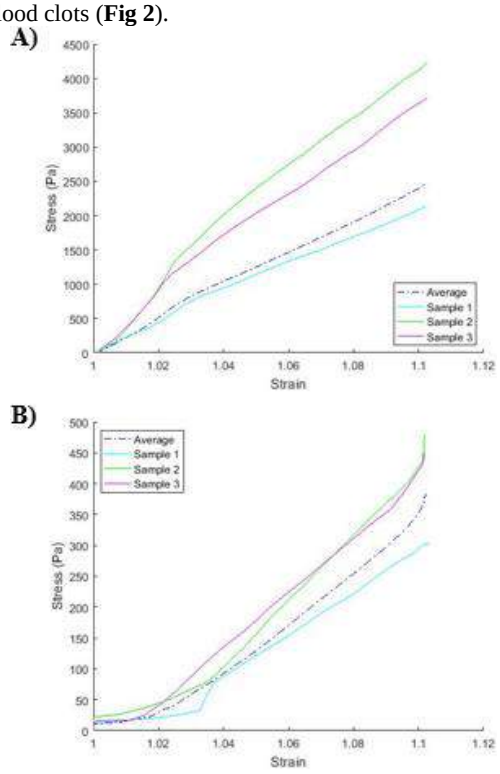

Figure 2: A) Fixed and B) unfixed bovine embolus analog loading data.

Lastly, the average stress-relaxation data sets for both the fixed (**Fig 3**) and unfixed (**Fig 4**) bovine blood clots were fit to 3-term Prony series.

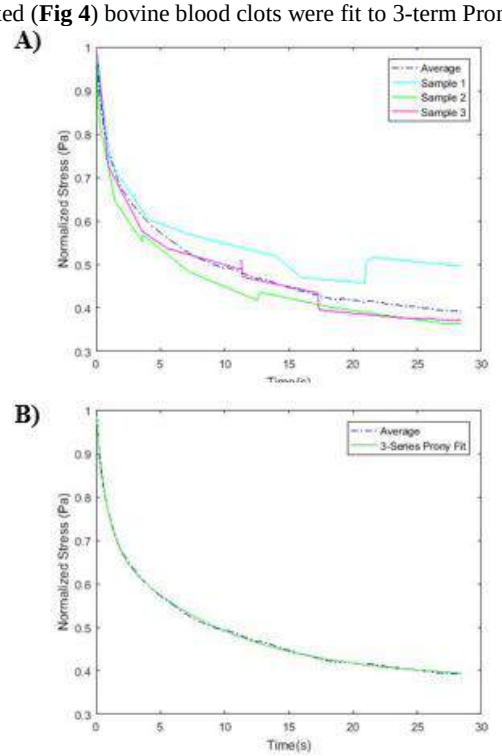

Figure 3: A) Fixed bovine embolus analog stress-relaxation data and B) average data fit to a 3-term Prony series.

For the fixed embolus analogs, referring to (**Eq.1**) the characteristic amplitudes were determined to be 0.3795, 0.2715, and 0.3343 and the relaxation times were 0.8206 and 9.1753.

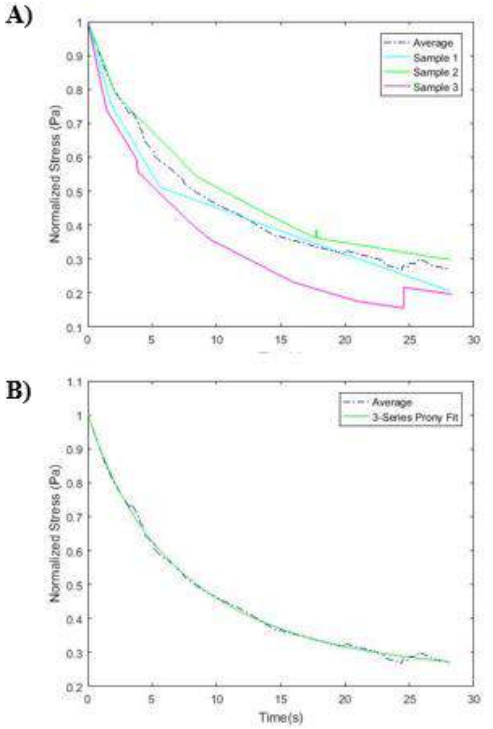

Figure 4: A) Unfixed bovine embolus analog stress-relaxation data and B) average data fit to a 3-term Prony series.

For the unfixed embolus analogs, referring to (**Eq.1**) the characteristic amplitudes were determined to be 0.2376, 0.5847, and 0.1796 and the relaxation times were 10.0076 and 3.0877.

DISCUSSION

This experiment outlines a developed procedure to create bovine embolus analog and a method to characterize the mechanical properties of these analogs, both unfixed and fixed in 4% PFA. Specifically, the stress-strain curves representing the cyclic loading, show the difference in the measured stress between the fixed bovine embolus analogs and those unfixed is about an order of magnitude, with the fixed being stiffer. However, the average cyclic loading data sets have very similar curve shapes. In addition, by fitting the stress-relaxation curves to the 3-term Prony series, respectively, the experimenter can compare between the two sets, as well as compare to future human thromboemboli retrieved from AIS patients. The stress-relaxation curves are very similar, looking at the curves they both decrease to about 0.4, or 60% relaxation, in approximately 20 seconds. In future work, histology will be performed on both sets of embolus analogs.

ACKNOWLEDGEMENTS

This work is supported partially by AHA Postdoctoral Fellowship 19POST34370040. We would also like to acknowledge the contribution of Michael Buzas.

REFERENCES

[1] Grech, *et al.* 2015. *The Neuroradiology Journal.*

PENNSTATE

Keefe B. Manning, Ph.D.
Department of Biomedical Engineering
The Pennsylvania State University
205 Hallowell Building
University Park, PA 16802
(814) 863-6318
kbm10@psu.edu

February 14, 2019

Dear Review Committee:

I attest that (1) the majority of the work was completed by the first/presenting author and (2) the first author conducted the work when they were a student at the corresponding competition level.

Sincerely,

Keefe B. Manning, Ph.D.
Professor of Biomedical Engineering and Surgery
Associate Dean for Academic Affairs, Schreyer Honors College

SB³C2019
Summer Biomechanics, Bioengineering and Biotransport Conference
June 25 -28, Seven Springs, PA, USA

ASSESSMENT OF ASCENDING AORTIC WALL STRESSES FOR NONDISSECTED PATIENTS WITH BICUSPID AORTIC VALVE AND DISSECTED PATIENTS WITH TRICUSPID AORTIC VALVE

S. Ravi (1), D. A. Vorp (1), S. Maiti, PhD., (1)

(1) Department of Bioengineering
University of Pittsburgh
Pittsburgh, PA, United States of America

INTRODUCTION

Acute ascending aortic dissection, also known as Type A dissection, or TAAD, is a life-threatening condition in which a tear in the intimal layer of tissue of the aortic wall allows blood to collect within the tear site and delaminate the vessel wall, often propagating the dissection in antegrade or retrograde fashion. As fluid continues to fill within the vessel wall, the wall becomes pressurized and flow is compromised by constriction of the aortic vessel while aneurysmal volume increases. Once it becomes too large, TAAD patients are at risk for blockages in the vessel and/or a rupture of the vessel itself [1]. Typically, the aortic valve is a tricuspid valve (TAV), but bicuspid aortic valves (BAV) are the most common congenital heart condition that occurs in approximately two percent of the population. According to clinicians, it is of common opinion that BAV patients are of greater risk for dissection than TAV patients [2].

Currently, surgical repair of ascending aorta is based upon having an aneurysmal diameter greater than 5.5 cm, and even lower for BAV patients [4]. However, data from the international registry of acute aortic dissection (IRAD) has shown that approximately 62% of patients with TAAD have aortic diameters distinctly less than 5.5 cm, demonstrating the necessity for an improved metric in characterizing aneurysms [1]. From a biomechanical perspective, dissection is caused by the mechanical failure of the aortic wall, when the wall stress exceeds the wall strength. Thus, quantification of aortic wall stress has the potential to provide additional dissection risk indicator. In this study, two cohorts of patients – one of BAV patients with stable aneurysms, one of dissected TAAD patients with TAV phenotype – were examined to quantify the longitudinal and circumferential stresses of each group while providing insight into how the biomechanics of BAV patients may differ from those of TAAD patients.

METHODS

Patient scans were collected by the University of Pittsburgh Medical Center in Shadyside from the Cardiovascular Department. Scans were collected with patient consent and IRB approval. CT scans of patient chest cavities were taken, and GE proprietary segmentation software within the Volume Viewer was used to isolate the aorta, generating a 3-dimensional image. The images were exported as DICOMs within a new set of aorta-specific axial slices. Any artifacts in the resulting surface model were removed in Mesh Mixer version 4.0 (Autodesk). Additionally, the surface models were smoothened to ensure that they contained one surface and contained enough details to capture the shape of the aorta. The smoothened engineering model was then meshed with 3-noded triangular elements in Trelis (Sandia National Labs). The resulting finite element meshes for the aortic models contained 30,000-50,000 elements to be used for computational model formation. Once processed through Trelis, a custom nonlinear finite element software was used to pressurize the model to 200 mm Hg (approximately 26.67 kPa). The material of the aorta wall was taken to be isotropic and hyperelastic relevant to BAV patients [2]. The material model considered is described in [2]. The finalized models were viewed through Paraview (Kitware, STATE) to display the map of longitudinal and circumferential stresses across the aortic surface model. Nodal stresses across the map were exported in an Excel document, in which mean and standard deviation (SD) were calculated to find the maximum at the 95th percentile of stresses to exclude noise. The results were plotted in a box and whisker plot created in IBM SPSS Statistical Software.

RESULTS

A total of nine BAV and eight TAAD patients were included in this study. Stress analyses for TAAD patients were taken from a

Poster Presentation #P102

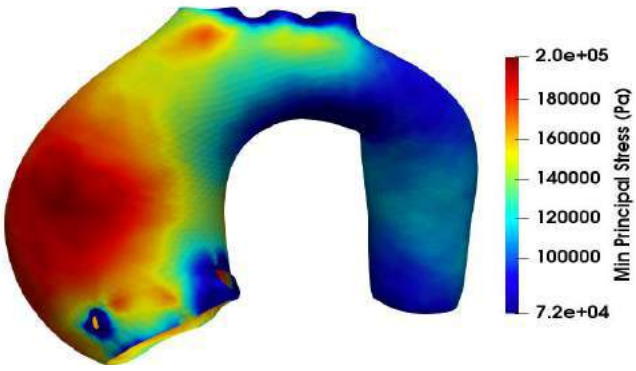

Figure 1A: Representative stress map of BAV patient showing longitudinal stress when aortic model pressurized to 200 mm Hg

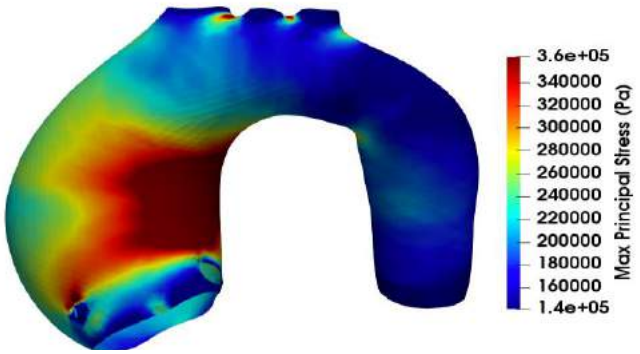

Figure 1B: Representative stress map of BAV patient showing circumferential stress when aortic model pressurized to 200 mm Hg

previous publication from our group [1]. The average peak longitudinal stress maximum was 209.2 ± 11.7 kilopascals for BAV patients versus 172.3 ± 36.6 kPa for those of TAAD patients (Figure 2A). On the other hand, the average peak circumferential stress maximum was 382.6 ± 21.2 kPa for BAV patients versus 492.3 ± 138.7 kPa for those of TAAD patients. The difference between the two groups (BAV and TAAD) circumferential stresses is significant (p=0.001, student's t-test) as are the longitudinal stresses (p=0.001).

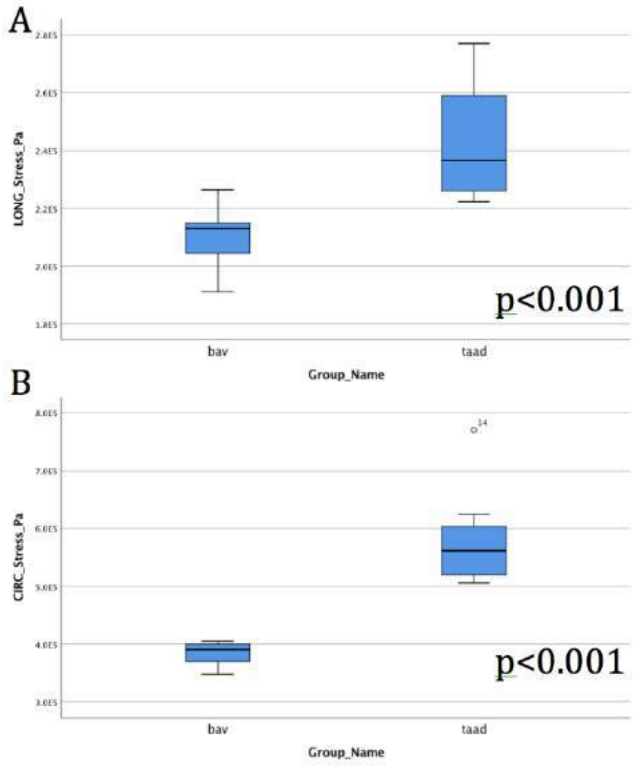

Figure 2A-B: Box and Whisker Plots for (A) Longitudinal Stress and (B) Circumferential Stress for both groups

DISCUSSION

From the study, it is evident that peak longitudinal and circumferential wall stress for the BAV patients are significantly different than those of the TAAD patients. From analysis, it is evident that BAV patients with stable aneurysms display lower peak longitudinal and circumferential stress than TAAD patients who dissected. Because both aortic models were pressurized to the same magnitude, the lower longitudinal stress of BAV patients demonstrates lower risk of failure for BAV patients' aortic walls. From a biomechanics perspective, these results are contrary to some published literature. Although, clinically, BAV patients are thought to be more vulnerable to dissection than other patients with aneurysms, the results of this study show that biomechanically BAV may not be as high of a risk as previously thought [1,3].

There were a few limitations that can be improved upon in future works. The necessity of smoothening the model to run finite element analysis could may have compromised the accuracy of the aortic surface from the CT scans. As meshes move through the different smoothening software utilized, it may have been slightly altered in geometry and thickness before being pressurized. Furthermore, during the analysis, by using an isotropic constitutive model it is assumed that stiffness is similar in both the longitudinal and circumferential stresses. Future methods can investigate other methods of analysis that may separately analyze both stiffnesses. Furthermore, during the calculation of the 95th percentile max, it was assumed that the stresses were distributed normally.

These findings support the use of biomechanics-based paradigms to predict aortic dissection event. Investigating multiple patient groups, we can continue to create a patient-specific metric based on biomechanics rather than aortic dimensions that will improve our ability to classify aneurysms and predict dissection patterns. By delving into this new approach, physicians can have a better method in determining whether intervention is required to treat aneurysms more accurately.

ACKNOWLEDGEMENTS

I would like to thank Dr. Spandan Maiti for allowing me to conduct research under him. I would also like to thank Drs. Leonid Emerel and Thomas Gleason from the University of Pittsburgh Medical Center for providing patient aortic geometries for this research endeavor. Finally, I would like to thank Ronald Fortunato for teaching me the background biomechanics and software used to successfully complete this project.

REFERENCES

[1] Emerel, L et al. *Journal in Thoracic and Cardiovascular Surgery*. 10.1016/j.jtcvs.2018.10.116.
[2] Pichamuthu, J et al. *The Society of Thoracic Surgeons*. 96:2147-54, 2013.
[3] Borger MA, et al. J Thorac Cardiovasc Surg. 2018; 156:473-480.
[4] Anagnostopoulos CE, et al. *American Journal of Cardiology*; 30(3):263-73.

University of Pittsburgh

Swanson School of Engineering
Department of Bioengineering

306 Center for Bioengineering
300 Technology Drive
Pittsburgh, PA 15219
412-383-9713
Fax: 412-383-8788
www.engr.pitt.edu/bioengineering

To
Whomever it may concern
Dated: 02.17.2019

I, the PI of the presented work hereby attest that
(1) Majority of the presented work has been completed by S. Ravi, the first and presenting author of this work, and
(2) He is currently an undergraduate student in our department. He performed this work as an undergraduate student researcher in my lab.

Thanking you,
Sincerely,

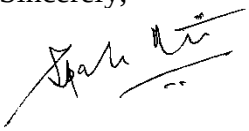

Spandan Maiti
Assistant Professor
Department of Bioengineering
University of Pittsburgh
207 CNBIO, 300 Technology Drive
Pittsburgh, PA 15219

SB³C2019
Summer Biomechanics, Bioengineering and Biotransport Conference
June 25 -28, Seven Springs, PA, USA

APPLICATION OF DIGITAL IMAGE CORRELATION TO THE LOCAL STRAIN ANALYSIS OF MOUSE AORTAS: NOVEL METHOD TO CREATE SPECKLE PATTERN

Liya Du (1), Brooks A. Lane (1), John F. Eberth (1,2), Susan M. Lessner (1,2)

(1) Biomedical Engineering Program
University of South Carolina
Columbia, SC, USA

(2) School of Medicine
University of South Carolina
Columbia, SC, USA

INTRODUCTION

Digital image correlation (DIC) is a non-destructive and non-contact optical technique to measure deformation and strain of materials. The method is based on optically tracking the displacements of a speckle pattern created on the material surface. In the case of soft tissues such as mouse aorta, there are several advantages to using DIC since it can provide local, rather than global, deformations and it is suitable for large strain measurements, typical of soft tissues taken to failure [1] [2].

For the optimal use of DIC, several requirements should be met for speckle patterning: 1) randomness, 2) high contrast, 3) appropriate size of speckle in the field of view (3-5 pixels), and 4) firm attachment of speckle to specimen during deformation. In previous DIC studies of soft tissues, the methods employed to create a speckle pattern include the use of an airbrush to spray dye or paint on the specimen, or coating the sample with toner powder. However, biological samples must be partially dehydrated before applying paint which may affect the mechanical properties of the specimen, and toner powder is too hydrophobic to adhere well on specimens when submerged in aqueous solution during mechanical testing. In addition, it is difficult to evenly distribute paint or toner powder on the surface of a hydrated biological specimen [2]. Therefore, a novel method utilizing colloidal gold particles to create a speckle pattern on mouse aorta is proposed in this work. Based on their unique surface chemistry, chemical inertness and stability in aqueous environments, colloidal gold particles are a promising new candidate for speckle patterning for DIC strain measurements of mouse aorta and similar small biological specimens [3].

METHODS

Colloidal gold particles were synthesized by reducing chloroauric acid ($HAuCl_4$) in ascorbic acid solution. In this method, 250 μl of 0.1 M chloroauric acid was added into 10ml of 0.3M ascorbic acid solution with vigorous stirring for 15 min. The solution was then incubated at room temperature for at least 96 h. Gold nanoparticles start to aggregate, and eventually the size of aggregated gold particles can be tuned in the range of 1-10 μm. The suspension was centrifuged (5000 rpm/2min) to remove acidic supernatant, and the remaining precipitated gold particles were resuspended in phosphate-buffered saline (PBS) solution. The mouse aorta samples were soaked in the colloidal gold particle suspension. Due to coordinate covalent and hydrophobic interactions, spontaneous adsorption of gold particles onto the mouse aorta surface occurs to form a random speckle pattern. The patterned sample was mounted on a Bose mechanical test bed to conduct uniaxial tensile tests with CCD camera tracking the displacement of the speckle pattern on the mouse aorta samples. Strain fields were analyzed using VIC-2D software. Image acquisition and DIC settings include 2 MP Point Grey camera, 25 mm macro lens, 35 x 35 subset for VIC-2D.

Ten consecutive images of a stationary speckled mouse aorta in the Bose set-up were captured and analyzed in VIC-2D for system error analysis.

RESULTS

Figure 1 shows a random speckle pattern created on the mouse aorta specimen. The size of a typical random speckle covers 3-5 pixels in each direction. In Figure 2, the intensity histograms of patterned specimens had greyscale values in the range 60-255, indicating a sufficient level of contrast between the mouse aorta and the speckle pattern for reliable image matching by DIC. Figure 3 demonstrates that after the sample has been submerged in PBS for 1 hour, the random speckle pattern is still stable in an aqueous environment.

In Figure 4, strain measurement of speckle patterned mouse aorta was compared over the whole specimen (a) and in the central region (b) in the y-direction during a uniaxial mechanical tensile test. In Figure 4a, ε_{yy} is not uniform on the sample due to bending and friction at the mounting arms during deformation. Thus, the local strain of mouse aorta in uniaxial tension can be obtained from the central region as illustrated in Figure 4b.

For system error analysis, the corresponding pseudo-strain measurements (mean, median and standard deviation) for ε_{xx}, ε_{yy} and ε_{xy} are summarized in Table 1.

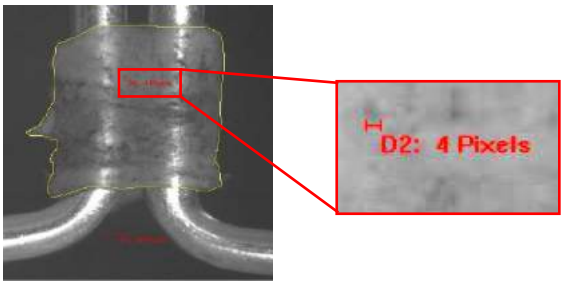

Fig. 1. Patterned mouse aorta mounted on Bose set-up

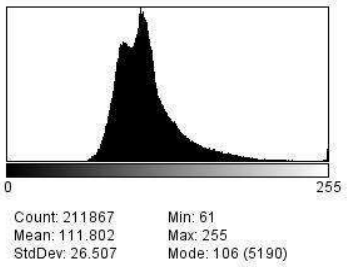

Fig. 2. Intensity histogram analysis of region of interest illustrated in Figure 1

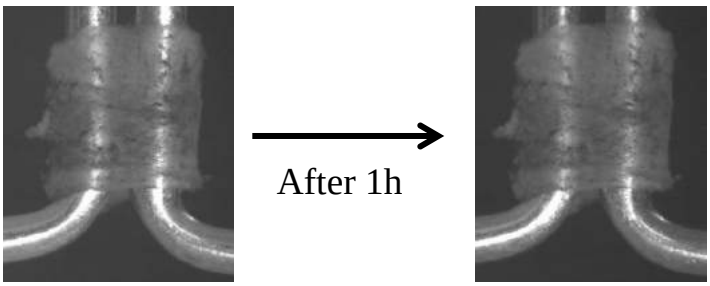

Fig. 3. Patterned mouse aorta submerged in PBS for 1 hour

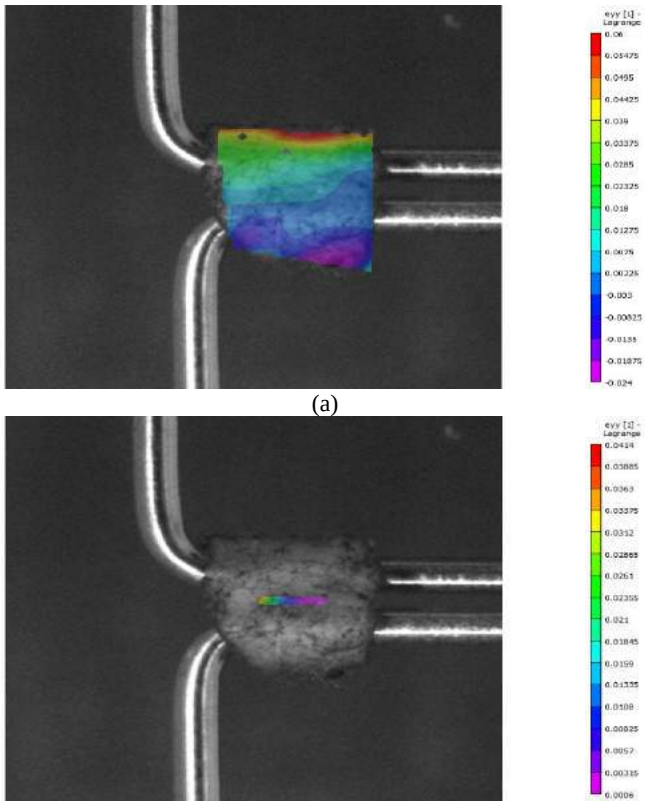

(a)

(b)

Fig. 4. Strain analysis of mouse aorta in y-direction (a) over the whole specimen; (b) in the central region;

Table 1. System error analysis: pseudo-strain data in different directions

	ε_{xx}	ε_{yy}	ε_{xy}
Mean	0.00228	-0.00065	-0.00435
Median	-0.00357	0.0043	-0.00643
Standard deviation	0.01134	0.01254	0.00666

DISCUSSION

The novel method utilizing colloidal gold particles to create a speckle pattern on mouse aorta shows promising results compared to previous patterning methods. The colloidal gold particles can form random, stable, high contrast, suitable sized speckles on mouse aorta suitable for DIC analysis to track the specific pattern before and after deformation to measure local strain of mouse aorta. Thus, it can be considered as an efficient patterning method for future application of DIC strain measurements in soft biological tissues.

ACKNOWLEDGEMENTS

This work was funded in part by NSF CMMI-1760906 and NIH R01 HL133662.

REFERENCES

[1] Lessner, S.M. et al., *Provisional Patent Application US 62/743,874* filed 10/10/2018, USC Disclosure ID No.1370

[2] Ning, J. et al, *Microsc Microanal* ,17, 81–90 , 2011

[3] Aaron, J. et al., *Optics Express* 16, 2153–2167, 2008

SB³C2019
Summer Biomechanics, Bioengineering and Biotransport Conference
June 25 -28, Seven Springs, PA, USA

TOWARDS AN ULTRASOUND IMAGING FRAMEWORK FOR TRANSMURAL EVALUATION OF RIGHT VENTRICULAR MYOCARDIAL FIBER ORIENTATION UNDER LOADING

Danial Sharifi Kia (1), Marc A. Simon (1,3,4,5), Kang Kim (1,2,3,4,5)

(1) Department of Bioengineering, University of Pittsburgh, Pittsburgh, PA, USA

(2) Center for Ultrasound Molecular Imaging and Therapeutics, University of Pittsburgh and UPMC, Pittsburgh, PA, USA

(3) Division of Cardiology, School of Medicine, University of Pittsburgh, Pittsburgh, PA, USA

(4) Heart and Vascular Institute, University of Pittsburgh Medical Center (UPMC), Pittsburgh, PA, USA

(5) McGowan Institute for Regenerative Medicine, University of Pittsburgh and UPMC, Pittsburgh, PA, USA

INTRODUCTION

Myocardial fiber orientation plays an important role in cardiac systolic and diastolic function, distribution of cardiac wall stress and electrical propagation [1]. Structurally, the myocardium is a layered composite made of myofibers, collagen and an amorphous ground matrix with 69%, 29% and 2% volume fractions respectively [2]. Myocardial fibers are stacked with counterclockwise rotations throughout the heart wall. Transmural variation of fiber orientation in myocardial tissues leads to unique structural and biomechanical properties. Remodeling of myofibers and alterations in transmural fiber orientations can lead to drastically different tissue properties in diseased conditions such as pulmonary hypertension (PH), in which the right ventricle (RV) experiences increased tissue stiffness and anisotropy due to fiber remodeling [3]. Knowledge of the kinematics of myocardial fibers helps understanding the contribution of fiber-level myocardial structure to tissue function and tissue-level mechanical properties. However, myocardial wall thickness often complicates the study of fiber kinematics transmurally.

Albeit very high resolution and sensitivity, the depth limit of optical techniques such as confocal (100 µm limit) or multi-photon microscopy (1600 µm limit) prevents practical applications of these technologies for analyzing intact myocardial architecture. In order to study the 3D static architecture of myocardial fibers, several studies have employed diffusion tensor magnetic resonance imaging (DTMRI) techniques [4]. Even though DTMRI provides detailed information on the static architecture of myofibers, this process is time consuming and effects of exposure to ionizing radiation, cost-effectiveness and restrictions on MRI-safe materials limit its applicability for benchtop and clinical applications for a larger population. On the other hand, ultrasound imaging is a cost-effective technique that has been widely used for real-time cardiac diagnosis. However, detecting myofibers require ultrasound imaging at a much higher frequency than conventional applications, which leads to increased speckle noise and lower signal to noise ratio [5]. In the current study, we aim to employ an enhanced mathematical framework to analyze high-frequency ultrasound images for effective quantitative assessment of 3D myofiber orientations in the RV wall under loading conditions.

METHODS

Square specimens were harvested from the R2 zone [4] of fresh-frozen porcine right ventricular myocardiums. Specimens were then embedded in a 6% gelatin gel (Sigma-Aldrich, St. Louis, MO) and scanned under static conditions for algorithm development and verification purposes. RV specimens were scanned at 40 MHz using a high-frequency ultrasound scanner (Vevo 2100, FUJIFILM-VisualSonics, Toronto, Ontario, Canada). 3D scans of the RV wall were generated by a stack of 2D images at 32 µm increments throughout the tissue thickness (acquired using an electrical servo stage). Since the high frequency of ultrasound scans results in a significant speckle noise level in the acquired images, similar to previous studies [5], a nonlinear anisotropic diffusion filter (NLADF) was used to reduce the noise levels using the anisotropic diffusion equation [6]:

$$I_t = div(c(x,y,t)\nabla I) = c(x,y,t)\Delta I + \nabla c \,.\, \nabla I \qquad (1)$$

here, I is the image intensity in 2D space, and c is the anisotropic diffusion tensor. The NLADF filtering framework is based on the diffusion equation and helps reducing the noise levels while keeping the main features of the image and their respective orientations [6] (Fig. 1). Filtering was performed using a previously developed multi-scale decomposition framework for myocardial tissues [5]. The resulting image was then denoised and masked using Otsu's threshold . Despite considerably reduced noise levels, the high speckle noise in the original image leads to myofibers represented in interrupted pieces. In order to

establish connectivity between different fiber segments, a coherence enhancing diffusion filter (CEDF) was used [7]. The CEDF filtering framework functions similar to the NLADF algorithm , except that *c* is replaced by a tensor with similar eigenvectors, but with eigenvalues chosen in a way that diffusion happens along the highest coherence direction and helps completing disconnected segments while keeping the orientation of image features (Fig. 1). At this stage, instead of performing a multi-scale decomposition on the CEDF resulting image (as employed in previous studies [5]), the filtered image via NLADF is fed to the CEDF algorithm and then directly masked and thresholded for fiber detections. The resulting image is denoised and myofibers are detected via skeleton extraction. The result was then converted to a binary format from which myofibers were detected and quantified using the Hough transform. Fiber distributions were plotted in a histogram and a probability density function (PDF) was fitted to the distribution at each section throughout the RV thickness. Finally, histological staining (H&E) was performed on the tissue specimen for comparison purposes. Fiber orientation of histological scans were detected using Image J (imagej.nih.gov).

Following algorithm verification, RV specimens were loaded using a custom-built uniaxial loading device that allows real-time ultrasound imaging of the tissue. Transmural fiber orientation of the tissue was analyzed before and after 10% strain loading.

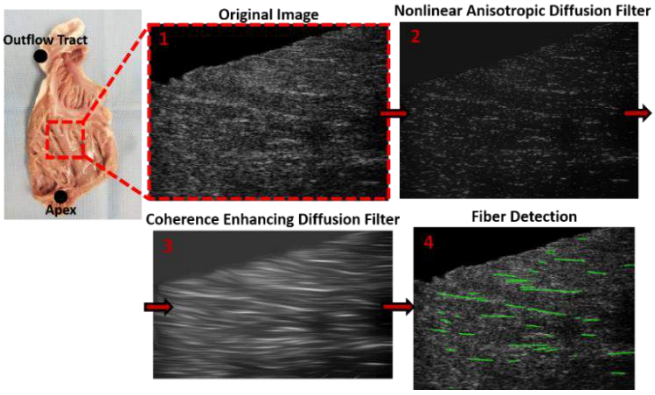

Figure 1: The framework used to detect myofiber orientations

RESULTS

The developed method shows acceptable estimations of the transmural variation of myofiber orientation in the RV wall (Fig. 2). A combination of NLADF, CEDF, image denoising techniques and quantitative line detection algorithms are able to estimate the orientation of myofibers with less than 5% error (representative results: 86 vs 89.6 deg at 2% thickness and 157.2 vs. 159.3 deg at 25% thickness; 0% thickness defined at epicardium).

Analyzing the orientation of myofibers under loading (Fig. 3) reveals fiber remodeling in the loading direction as well as increase in the alignment (orientation index) of myofibers as a result of the applied strain (representative result: fiber remodeling from 5.6 deg to 3.7 deg under 10% stain at 65% thickness).

DISCUSSION

In this study, a framework was developed for quantitative assessment of transmural myocardial fiber kinematics under loading conditions. Fiber orientations detected via processed high-frequency ultrasound images demonstrated acceptable accuracy compared to histological staining. Displacement controlled loading resulted in reorientation of myofibers along the loading direction with increased orientation index. This is in agreement with previous computational studies on the effects of loading on soft tissue fiber remodeling [8].

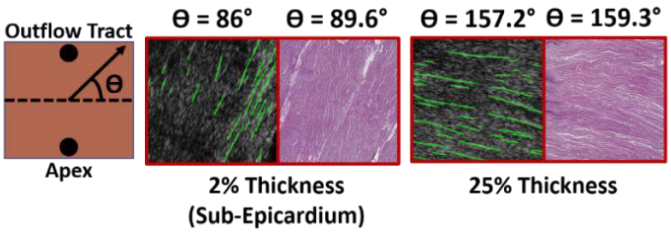

Figure 2: Representative orientation estimations using ultrasound imaging and the developed framework vs. histological staining

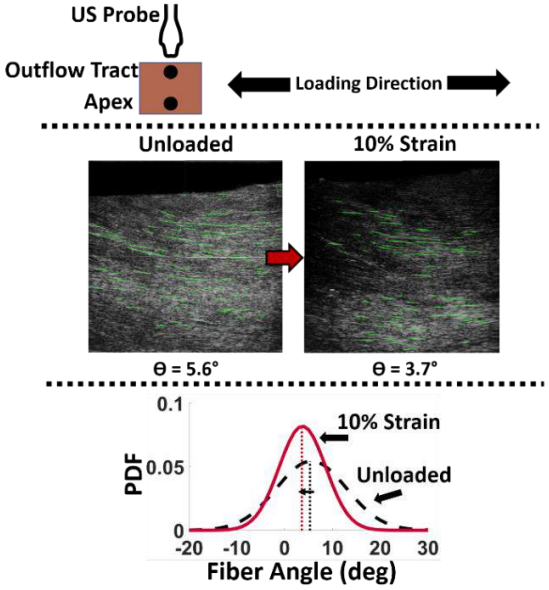

Figure 3: Representative myofiber reorientation detection using a custom uniaxial testing device and the developed framework

In the current setup, investigating biaxial fiber kinematics is limited due to restrictions on ultrasound attenuation that requires ultrasound scans being performed from at least one free side of the tissue. Custom loading grippers equipped with ultrasound probes will be developed for future studies to enable real-time high-frequency ultrasound scans during biaxial testing.

Nevertheless, the developed framework demonstrates promising capabilities in analyzing 3D myocardial fiber orientations under loading. This can help better understanding the underlaying connection between myofiber architecture and tissue-level RV mechanical behavior and has potential applications for RV failure diagnostics in pulmonary hypertension as well as applications to the left ventricle and general cardiac function assessment.

ACKNOWLEDGEMENTS

The high frequency small animal ultrasound scanner is supported by NIH Shared Instrument grant (NIH 1 S10 RR027383-01, K. Kim).

REFERENCES

[1] Vetter, F et al., Circ Res, 96(2):244-251, 2005.
[2] Avaz, R et al., Biomech Model Mechanobiol, 16(2):561-581, 2017.
[3] Hill, M et al., Ann Biomed Eng, 42(12):2451-2465, 2014.
[4] Agger, P et al., J Cardiovasc Magn R, 19(1):93, 2017.
[5] Qin, X et al., Phys Med Biol, 59:3907-3924, 2014.
[6] Perona, P et al., IEEE Trans Pattern Anal Mach Intell, 12(7), 1990.
[7] Weickert, J, Int J Comput Vis, 2:111-127, 1999.
[8] Thunes, J et al., J Biomech, 71:84-93, 2018.

SB³C2019
Summer Biomechanics, Bioengineering and Biotransport Conference
June 25 -28, Seven Springs, PA, USA

IMPROVED STRAIN ANALYSIS OF LEFT VENTRICULAR FUNCTION POST MYOCARDIAL INFARCTION IN MICE

Danielle S. Wilson (1), Zhen Zhu (1), Stephanie M. George (1) Jitka A. I. Virag (2)

(1) Department of Engineering
College of Engineering and Technology
East Carolina University
Greenville, NC, USA

(2) Department of Physiology
Brody School of Medicine
East Carolina University
Greenville, NC, USA

INTRODUCTION

Cardiovascular disease is the leading cause of death globally and remains the number one cause of death in the United States [1]. A myocardial infraction (MI) is caused by an arterial blockage preventing blood from flowing to a part of the heart, thus restricting tissue oxygenation and resulting in myocardial cell death. Approximately every 40 seconds an American will have a MI, resulting in 114,023 citizens killed in 2015 [1]. In 2013, MI was one of the 10 most expensive medical conditions treated in hospitals [1]. Therefore, there is a huge need to improve treatment efficacy to reduce the number of Americans killed by this awful disease and alleviate the socioeconomic burdens.

When the flow of blood is blocked to an area of the myocardium, the cardiomyocytes downstream of the occlusion become necrotic as the cells are no longer provided with oxygen [2]. Therefore, the contractility of the heart is compromised, resulting either in sudden death, or leading to ventricular remodeling and eventually heart failure [1-3]. Echocardiography is the standard cardiac imaging technique for humans and small animals as it is noninvasive, inexpensive, widely available, and has a short imaging and post-processing time [4-7]. The standard measurements obtained from M-mode echocardiography to assess left ventricle (LV) function are chamber dimensions, wall thickness, ejection fraction (EF), and fractional shortening (FS), which, as indices of global cardiac function, lack the sensitivity to detect subtle changes in regional LV performance at the early stages of disease progression [4,8-9].

Speckle tracking techniques with strain analysis overcomes this issue by tracking the movement of the myocardium, based on the speckles generated from the reflection and scattering of the ultrasonic beam which varies according to the tissue density [4-7,9]. Commercially developed algorithms have been used to calculate the circumferential, radial, and longitudinal strain and strain rate globally or regionally across 6 anatomical segments of the LV, after injury of the left anterior descending (LAD) artery in murine models [4-5,9].

Since 1986, the standard of care for acute MI is reperfusion therapy to reduce injury, preserve LV function, and decrease mortality; however, it must occur within hours of the ischemic event and, although it can reduce the extent of injury, it does not completely restore normal cardiac function [3,10]. EphrinA1-Fc (EA1) intramyocardially administered at time of injury has been shown to significantly decrease ischemic damage of the myocardium post-MI [2,10]. The EA1 treatment is delivered to the anterior wall to the right of the occlusion, leading to decreased injury and preservation of global function. The impact on damage and function in the specific region affected by this treatment relative to regions that don't receive the treatment are unknown. Therefore, being able to analyze strain in more regions would reveal earlier detection of LV dysfunction, and determine specifically where EA1 is affecting the contractile function of the LV.

The purpose of this study is to develop a methodology to analyze the strain and strain rate in mice post-MI and treatment at 12 equal segments along the myocardium and compare these results to the VevoStrain software (VisualSonics, Toronto, Canada) strain values. This methodology will be used to determine the LV function and effectiveness of the treatment. In the future this will optimize the treatment process by determining the location being treated and extent of treatment to the infarct and remote regions of the heart.

METHODS

This study was approved by the East Carolina University Institutional Animal Care and Use Committee (IACUC AUP#Q228d) and conforms to the guidelines by the National Institute of Health for the Care and Use of Laboratory Animals. Data was collected in Greenville, NC.

Poster Presentation #P105

Experimental Protocol. Mice (10-14 weeks) were anesthetized with an intraperitoneal injection of 20 µl/g body weight of tribromoethanol (20 mg/ml) and mechanically ventilated. The LAD coronary artery was temporarily ligated using an 8-0 suture. Sham controls were performed with the suture pulled through the heart without ligation. Within 1 minute of coronary ligation, an intramyocardial injection of either 6 µg IgG-Fc or 6 µg EA1 (both in 6µl) was given.

Image Acquisition and Commercial Processing. Echocardiography was performed blindly to surgical procedure and injection with the Vevo 3100 (VisualSonics, Toronto, Canada) diagnostic ultrasound with a 30MHz linear-array transducer used. All acquisitions were performed on conscious, restrained mice in supine position at 24 hours post-MI. Standard parasternal long-axis and short-axis 2D gray-scale echocardiographic images were obtained. M- and B-mode images were acquired at a frame rate of >300 frames/second. Mice were then anesthetized with lethal intraperitoneal injection of 0.1 mL pentobarbital (390mg/ml). To detect LV remodeling, 3-4 consecutive cardiac cycles were manually selected with the VevoStrain software. The endocardium was manually traced by selecting points along the endocardial border at a frame between systole and diastole. The epicardium was then automatically traced. The software then calculated the strain and strain rate for the 6 standard segments along the LV with the embedded code.

Novel Image Processing Protocol. Echocardiographic images obtained in Digital Imaging and Communications in Medicine (DICOM) format were analyzed offline using MATLAB (MathWorks Inc., Natick, Massachusetts). The speckles were averaged across 3-4 consecutive cardiac cycles which were manually selected. To quantify strain, a region of interest was selected where the motion of the speckles in this area were tracked. The region of interest is the area between the epicardial and endocardial of the LV. The contours of the epicardium and endocardium were semi-automatically traced. Perpendicular lines were then generated connecting these contours. To determine strain and strain rate of the LV, a block-matching method will be used to track blocks containing the same speckle pattern in the defined search area frame-by-frame for the previously selected cardiac cycles. Displacement of the generated lines will be calculated from the starting location to end location. This will be used to calculate strain with Equation 1.

$$\varepsilon = \frac{(L-L_0)}{L_0} \quad (1)$$

The LV will be divided into 12 equal segments. The peak strain values across the region of interest will be averages for the 12 segments. Radial and circumferential strain are determined from short-axis images, and radial and longitudinal strain are determined from long-axis images. To measure strain rate, the shift in the displacement will be divided by the time between frames, using Equation 2.

$$\varepsilon\ rate = \left[\frac{(L-L_0)}{L_0}\right] \times sec^{-1} \quad (2)$$

To validate the results, the novel strain analysis will be compared to the VevoStrain software data. The results from the novel method will be averaged into the six segments to get comparative values. In addition, these strain measurements will be averaged across the six segments to get global values.

Statistical Analysis. A one-way ANOVA was used to determine statistical significance between experimental groups for longitudinal strain rate and global strain values.

RESULTS

To-date strain in 6 segments has been calculated using commercial code. The longitudinal strain rate for the EA1 treated mice exhibits similar results to the sham mice compared to IgG-Fc treated mice (Figure 1). EA1 mice produces intermediary global strain.

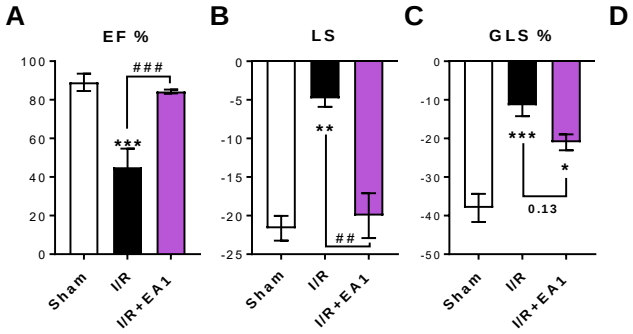

Figure 1: Longitudinal strain rate (1/s) and global strain (%) results from VevoStrain software.

Thus far, the contours of the defined region of interest have been traced (Figure 2) using the novel processing code, with perpendicular lines connecting these contours. The speckle tracking is currently being developed.

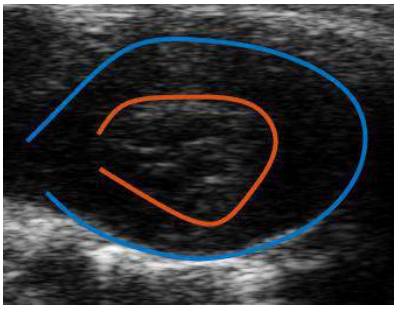

Figure 2: Epicardial and endocardial contour tracing with novel processing code

DISCUSSION

Cardiac dysfunction lessened in mice treated with EA1 after 30 minute infarct and 24 hour reperfusion. LV dyssynchrony, represented by strain rate, decreased in EA1 mice compared IgG-Fc mice, signifying EA1 hearts experienced uniform contractions, similar to that of sham hearts. The global strain results indicate that LV remodeling is minimized with EA1, leading to improved contractile performance. Current challenges being faced with the development of the novel code are poor image quality resulting in lost speckles, and the small size of a mouse heart, making it difficult to analyze the LV in smaller regions.

ACKNOWLEDGEMENTS

This work was supported by the Department of Engineering at East Carolina University and funding under 1RH15HL124483-01A1.

REFERENCES

[1] Benjamin, E et al., *Circulation*, 137:e67-e492, 2018.
[2] Dries, J et al., *J Physiology*, 589:1725-1740, 2011.
[3] O'Neal, W et al., *Medical Hypotheses*, 80:738-744, 2013.
[4] Bauer, M et al., *Circulation Research*, 108:908-916, 2012.
[5] Andrews, T et al., *Echocardiography*, 31:375-384, 2013.
[6] Ram, R et al., *Am J Physiol Heart Circ Physiol*, 301:H1765-H1780, 2011.
[7] An, X et al., *Plos One*, 11:e0149155, 2016.
[8] Theodoropoulos, C et al., *VisualSonics*, White Paper: Strain Analysis, 2008.
[9] Ferferieva, V et al., *European Heart J – Cardiovascular Imaging*, 14:765-773, 2012.
[10] DuSablon, A et al., *Plos One*, 12:e0189307, 2017.

SB³C2019
Summer Biomechanics, Bioengineering and Biotransport Conference
June 25 -28, Seven Springs, PA, USA

STRUCTURAL CHANGES IN THE PROGRESSION OF PULMONARY ARTERIAL HYPERTENSION

Erica R. Pursell (1), Daniela Valdez-Jasso (1)

(1) Bioengineering
University of California San Diego
San Diego, CA, USA

INTRODUCTION

Pulmonary arterial hypertension is a disease characterized by elevated blood pressure in the pulmonary system. Traditionally, increases in pressure are thought to be due to increased resistance from the peripheral lung vasculature. However, proximal vascular remodeling has been shown to be a predictor of risk for cardiovascular events such as pulmonary arterial hypertension [1].

While changes in the mechanical response of tissues can be indicative of vascular remodeling, quantification structural changes can better describe the vascular response to elevated loads. A study by Pursell *et al* indicated that in a monocrotaline rat animal model of PAH, the axial elastic modulus of the left pulmonary artery (LPA) initially decreases followed by an increase at the late stage of the disease [2]. While the study also indicated fibers become aligned in the axial direction, the circumferential stiffness increased in both LPA and RPA segments with significant changes in the RPA. Inconsistencies in mechanical and structural changes may be due to the manual tracing of the fibers. Therefore, this study aims to determine a more robust method of characterizing structural and organizational modifications of collagen fibers.

METHODS

Proximal LPA segments were harvested from male Sprague-Dawley rats (Charles River Laboratories). At 8 weeks of age, rats in hypertensive groups were treated with a subcutaneous monocrotaline (MCT) injection to induce PAH and left for 1 week (MCTW1, n = 3), 2 weeks (MCTW2, n = 6), 3 weeks (MCTW3, n = 5), and 4 weeks (MCTW4, n = 6) to reach varying stages of disease. Rats in the normotensive group were randomly injected with a saline solution (n = 2) or not given any treatment (n = 2). Hemodynamic measurements indicated no difference in the normotensive animals. The segments were then stretched to their *in-vivo* ($\lambda_z = 1.4$) length and imaged under a multiphoton microscope (MPM) via second harmonic generation to capture the collagen fibers.

A custom MATLAB code was used to identify collagen fibers in the MPM images and determine their individual fiber orientations (Figure 1) and tortuosities (Equation 1). First, noise was removed from images with a Weiner filter using neighborhoods of 10x10 pixels. Edges were then isolated with a canny edge detection method and the fibers were skeletonized using the MATLAB function, bwmorph. Fiber endpoints were identified, and pixels were traced from each endpoint until another endpoint was reached to determine the length of the fiber. The Pythagorean theorem was then used to determine the straight path between endpoints and this segment was used in determining the fiber orientation. Duplicate fibers and fibers with length less than 50 pixels or tortuosity over 2 were discarded as visual inspection indicated these were fragments of fiber tracings. The fiber tracing code was verified with fabricated fiber images and manual tracings of fibers with FIJI.

$$\tau = \frac{L}{C} \tag{1}$$

Here, L is the length of the curved fiber and C is the distance between the two ends of the fiber. As fibers become straighter, L and C become closer in value and tortuosity approaches a value of 1.

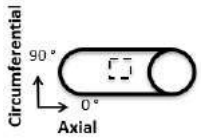

Figure 1: Depiction of fiber orientations. Fibers aligned in the axial direction have an angle of 0° and circumferential fibers, an angle of ± 90°.

The probability density functions of tortuosity and fiber orientation were determined and fitted with a Burr (Equation 2) and normal distribution (Equation 3), respectively.

$$f_\tau = \frac{\frac{kc}{\alpha}\left(\frac{\tau}{\alpha}\right)^{c-1}}{\left(1+\left(\frac{\tau}{\alpha}\right)^{c}\right)^{k+1}} \quad (2)$$

$$f_\theta = \frac{1}{\sigma\sqrt{2\pi}} \exp\left(-\frac{(\theta-\mu)^2}{2\sigma^2}\right) \quad (3)$$

In the Burr distribution (f_τ), k and c are shape parameters while α is a scale parameter. For the normal distribution (f_θ), μ is the mean and σ is the standard deviation. The average distribution for each group was then plotted for comparison.

RESULTS

Our code was able to identify the edges of collagen fibers (Figure 2) and determine the tortuosity and fiber angle of collagen fibers imaged via multiphoton microscopy.

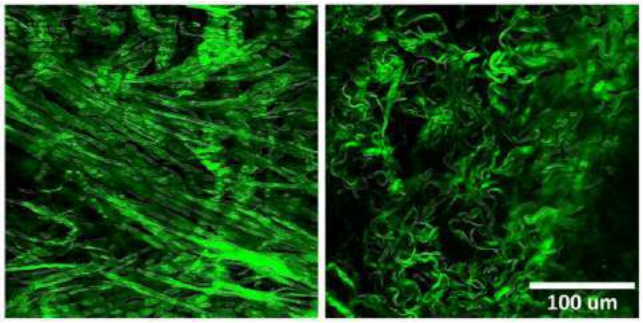

Figure 2: Representative MPM fiber tracing with collagen fibers (green) and the detected edges (red) taken from a hypertensive animal (left), and normotensive animal (right).

Probability densities of tortuosity were created for each sample and fitted with a probability density function (Figure 3, right). The averages of the probability density function parameters were then used to compare the tortuosity distribution of each group (Figure 3, left).

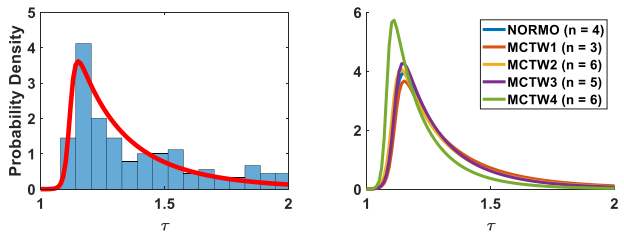

Figure 3: Probability density function fitted to the distribution of tortuosity measurements from a normotensive vessel (left). Average tortuosity distributions for normotensive animals in blue, MCT week 1 in orange, MCT week 2 in yellow, MCT week 3 in purple, and MCT week 4 in green (right). Note: tortuosity shifts to the left for MCT week 4.

The distributions of the tortuosity values were similar for normotensive through MCTW3, though the peak for MCTW1 was slightly lower than that of the normotensive group. The distribution for MCTW4 shifted to the left, indicating that the fibers are becoming straighter. Furthermore, the fiber orientation became more aligned in the late stage of disease

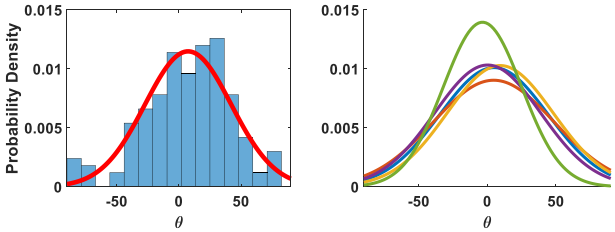

Figure 4: Probability density function fitted to the distribution of angle measurements from a normotensive vessel (left). Average angle distributions for normotensive animals in blue, MCT week 1 in orange, MCT week 2 in yellow, MCT week 3 in purple, and MCT week 4 in green (right). Note: fibers are more axially aligned in MCT week 4, indicated by the tighter distribution.

DISCUSSION

In this study, structural changes in proximal left pulmonary arterial segments were quantified via a fully automated custom MATLAB code. Edges of fibers were traced and used to determine fiber orientation. Here, the average distribution of tortuosity and fiber orientation was similar between normotensive and MCTW1-3, except for a slightly wider distribution in the MCTW1 group. Interestingly, Pursell *et al* found that vessels the axial Young's modulus decreased from the normotensive to early disease stage (MCTW1), though the modulus increased in the advanced stage of the disease (MCTW4) [2]. This is consistent with our finding that fibers have both a tighter distribution in the axial direction and decreased tortuosity the late stage of PAH (MCTW4). While this work was able to determine structural changes in pulmonary arteries via analysis of multiphoton images, these methods are very time consuming and costly. Therefore, future studies aim to determine mechanical models that can incorporate structural parameters such as the GOH model which incorporates the probability density function of fiber orientations to determine the mechanical contribution of groups of fibers [3].

ACKNOWLEDGEMENTS

Funded by the American Heart Association Scientist Development Grant 16SDG29670010 and the UCSD NHLBI training program. We would also like to acknowledge Julian Ho for his assistance in MATLAB coding.

REFERENCES

[1] Drexler, ES et al., *J of Research of the National Institute of Standards and Technology*, 113:239-249, 2008.
[2] Pursell, ER et al., *J Biomech. Eng.* 138, 2016.
[3] Gasser, TC et al., *JR Soc. Interface*, 3:15-35, 2005.

SB³C2019
Summer Biomechanics, Bioengineering and Biotransport Conference
June 25 -28, Seven Springs, PA, USA

DYNAMIC MECHANICS OF CYCLICALLY STRETCHED VASCULAR SMOOTH MUSCLE CELLS

Taylor M. Rothermel (1), Patrick W. Alford (1)

(1) Department of Biomedical Engineering
University of Minnesota – Twin Cities
Minneapolis, Minnesota, USA

INTRODUCTION

Vascular smooth muscle cells (VSMCs) are the most prevalent cell type in arteries, and loss of function of VSMCs is implicated in cardiovascular disease, which is a leading cause of death globally. VSMCs exist in a dynamic mechanical environment characterized by cyclical stretching in which they are able to rapidly adapt to maintain vessel integrity [1]. Cellular microbiaxial stretching (CμBS) has previously been used to measure the mechanical properties of cells in response to applied strain [2]. Here, we investigate the mechanical behavior of human VSMCs when exposed to cyclical stretching.

METHODS

CμBS constructs were constructed as described by Win et al [2]. Briefly, polyacrylamide (PA) gels with elastic modulus of 13.5 kPa were adhered on top of elastomeric PDMS membranes fixed between custom brackets. The gel was microcontact printed with aspect ratio 4 rectangular islands of fibronectin with dimensions 32 μm x 128 μm.

Human umbilical artery VSMCs were cultured according to standard methods and were seeded onto the micropatterned gel constructs at a density of approximately 5000 cells/ construct (Fig. 1(a)). The cells were serum starved for 24 hours before experiments. All experiments were conducted in serum free media at 37 C° and 5% CO_2.

Constructs were loaded into the biaxial stretcher (Fig. 1(b)) and cyclically stretched parallel to their long axes. An initial set of images of the cell and fluorescent bead layer were taken. A cyclic square-wave-form stretch with peaks of 0% and 15% strain, each held for 3 minutes, was then performed (Fig. 1(c) and Fig. 1(d)). Cells were imaged at 1 Hz for 24 minutes. Cells were then lysed and cell free images of the bead layer were taken at each strain.

A similar stretching protocol was implemented to find the stresses at the end of the relaxation cycle. Bright field and fluorescent images

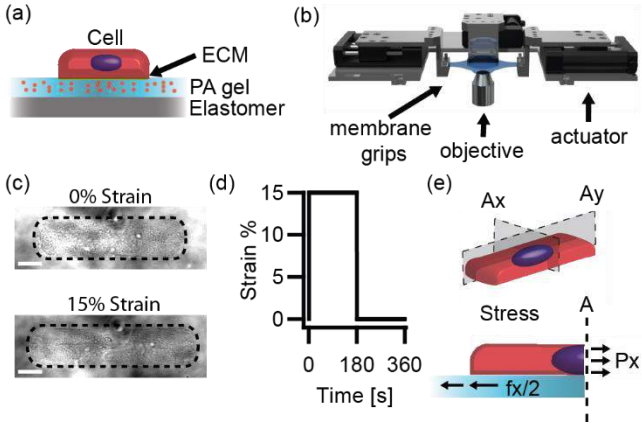

Figure 1: (a) Schematic of cell on fibronectin patterned on polyacrylamide gel [2], (b) the CμBS device [2], (c) representative bright field images of VSMCs at 0% and 15% strain, (d) stretching protocol, and (e) schematic detailing the relationship between the cell traction stresses, cross sectional area, and first Piola-Kirchhoff stress. Scale bar: 20 μm.

were taken of the cell and bead layer shortly before the end of the 3 minute time period at each strain. This was repeated for 10 cycles.

CμBS microscopy was used to measure material properties of the cells before and after cyclical stretching. Equibiaxial strains were incrementally stepped from 0% applied strain to 15% applied strain and then back down to 0% applied strain in intervals of 5% applied strain. At each interval bright field and fluorescent bead images were acquired.

Particle image velocimetry was used to compare relative substrate displacement between cell and cell free image pairs. Traction stress

vector fields were determined from the deformation fields using an unconstrained Fourier transform traction cytometry algorithm [3]. The vector field of size n was composed of substrate traction stress vectors, $\boldsymbol{T^n} = T_x^n \boldsymbol{e_x} + T_y^n \boldsymbol{e_y}$, where $\boldsymbol{e_i}$ is the unit vector in the i direction. Substrate traction forces were defined by $\boldsymbol{T^n} a^n$ where $\boldsymbol{T^n}$ is the vector acting on the area, a^n, of the discrete surface n. Substrate traction forces are balanced by cell forces at their interface. Cell forces were defined as $\boldsymbol{f^n} = f_x^n \boldsymbol{e_x} + f_y^n \boldsymbol{e_y} = -T_x^n a^n \boldsymbol{e_x} - T_y^n a^n \boldsymbol{e_y}$. Forces oriented away from the cell midline were denoted as positive and tensile. The total tensile force $f_x = \sum_n f_x^n \, r_x^n / |r_x^n|$ and $f_y = \sum_n f_y^n \, r_y^n / |r_y^n|$, where $\boldsymbol{r^n} = r_x^n \boldsymbol{e_x} + r_y^n \boldsymbol{e_y}$ is the vector that described the location of surface n with respect to the cell center. The first Piola-Kirchhoff (PK1) stresses, represented by $P_x = f_x/(2A_x)$ and $P_y = f_y/(2A_y)$, can be calculated at the midplane of the cell using the total tensile force and the undeformed cross sectional area of the cell (Fig. 1(e)).

Immunofluorescent staining was done according to a standard protocol for nuclei (DAPI), actin (phalloidin), and paxillin.

RESULTS

When VSMCs were exposed to square-wave stretching, we observed that the stress decreased over time when held at a constant 15% strain. When returned to 0% strain, the stress dipped below the initial stress before increasing with time though not recovering fully to the initial stress (Fig. 2(a)). To examine if this behavior continued over multiple cycles, cells were cyclically stretched and the stresses normalized to the initial stress at 0% strain. The same behavior was demonstrated during each cycle (Fig. 2(b)). The stress that the cell relaxed to at each step appeared to change with each cycle, so we examined the stress every three minutes for 10 cycles. With each cycle, the stresses generated by the cell appeared to decrease and at a faster rate for the 15% strains than the 0% strain (Fig. 2(c)).

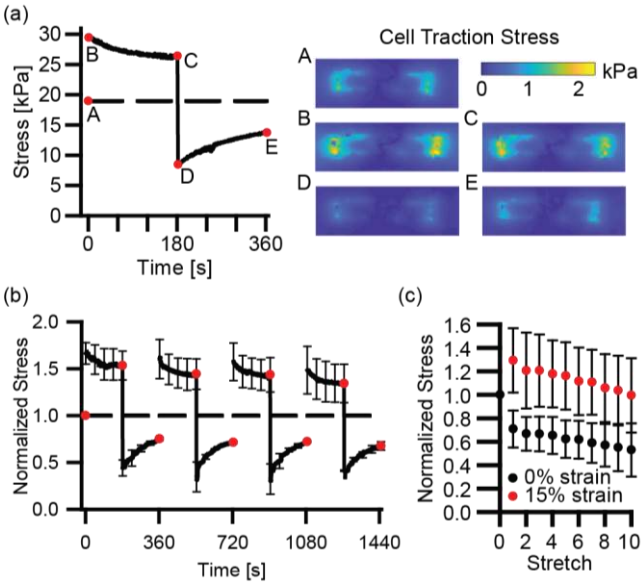

Figure 2: (a) Trace of the stresses over time (solid line) during one stretching cycle with initial stress (dashed line) for a representative cell and corresponding traction fields for the points marked by lettered red circles, (b) temporal stresses (solid line) for cyclically stretched VSMCs normalized to initial stress (dashed line) (n = 3) (mean ± standard deviation), (c) stress at the end of each cycle (as indicated by red dots in (b)) for ten stretching cycles at 0% and 15% strain (n = 27) (mean ± standard deviation).

To determine the effect of cyclical stretching on the mechanical properties of the cell, the stress during equibiaxial stretching was compared between cells that were and were not cyclically stretched. The cyclically stretched cells appeared to demonstrate less hysteresis in the direction of the long axis compared to the unstretched cells (Fig. 3(a)). To investigate any change in the cellular structure as a result of the cyclical stretching, fluorescent images of cells stained for nuclei and actin were acquired (Fig. 3(b)). The actin alignment was analyzed and showed that actin in the unstretched cells were slightly more aligned than the in stretched cells (Fig. 3(c)).

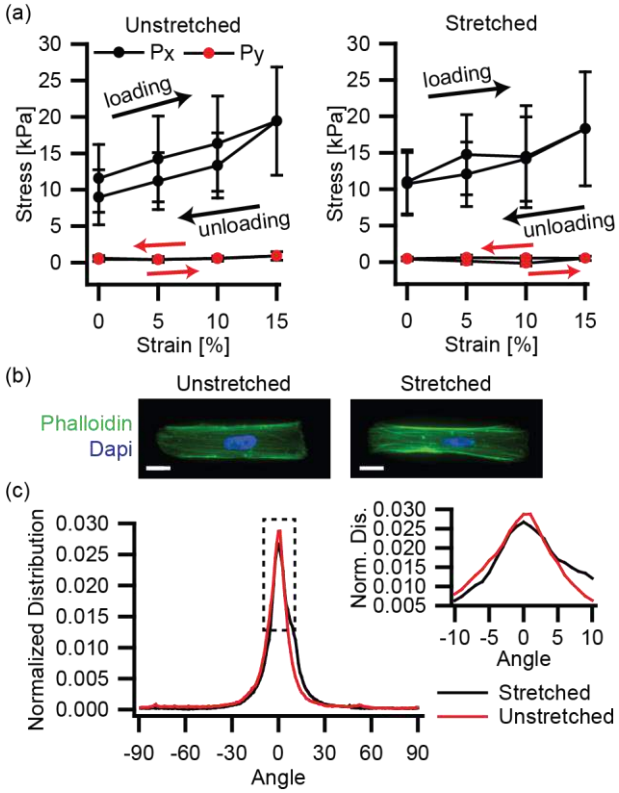

Figure 3: (a) Cell stress-strain curves under biaxial stretching for cells before and after cyclical stretching (n = 9, 13) (mean ± standard deviation), (b) representative fluorescent images of VSMCs stained for nuclei (blue) and actin (green), (c) actin orientations of VSMCs before and after cyclical stretching for 10 cycles (n = 7, 8) with inset showing detail of the peak of the orientation distribution. Scale bar: 20 μm.

DISCUSSION

Previous studies have shown that VSMCs remodel and adapt to their mechanical environment [1]. Here, we describe how VSMCs react to cyclical stretching in a dynamic mechanical environment. The cells demonstrate remodeling during cyclical stretching that alters stresses generated by the cell and the actin structure of the cell. This knowledge can be used to form more robust mechanical models of cell behavior.

ACKNOWLEDGEMENTS

We acknowledge financial support from National Science Foundation (NSF) CMMI-1553255 and CMMI-1563198 (P.W.A).

REFERENCES

[1] Steucke, K et al, *J Biomech Engr*, 139(7): 071005, 2017.
[2] Win, Z et al, *J Biomech Engr*, 139(7):071006, 2017.
[3] Tseng, Q et al, *PNAS*, 109:1506-1511, 2011.

SB³C2019
Summer Biomechanics, Bioengineering and Biotransport Conference
June 25 -28, Seven Springs, PA, USA

MECHANICS OF THE BULBUS ARTERIOSUS IN ZEBRAFISH: WHY THE SHAPE OF THE P-D LOOP IS CRUCIAL

Matthias Van Impe (1), Patrick Sips (2), Julie De Backer (2,3), Patrick Segers (1)

(1) IBiTech-bioMMeda
Ghent University
Ghent, Belgium

(2) Center for Medical Genetics
Ghent University Hospital
Ghent, Belgium

(3) Department of Cardiology
Ghent University Hospital
Ghent, Belgium

INTRODUCTION

The zebrafish (*Danio rerio*) is a growingly popular animal model in fundamental cardiovascular research. Low maintenance costs, ease of genetic manipulation and fast generation times are a few advantages of this vertebrate model organism. So far, the overwhelming majority of the conducted studies have focused on embryonic and larval zebrafish, taking advantage of their transparency for imaging purposes and their tractability for higher throughput applications. Nevertheless, adult zebrafish can also be very useful to evaluate progressive diseases, such as post-injury ventricular remodeling, and to validate hypotheses generated in embryonic or larval models [1]. Despite some obvious major anatomical differences, the essential cardiovascular physiology of humans and zebrafish is highly similar. Many human cardiovascular drugs have been shown to have similar or even identical effects on zebrafish physiology and zebrafish genetic models have already recapitulated numerous human cardiovascular disorders [2]. What is less well understood, however, are biomechanical aspects of the zebrafish circulation. Given the increased awareness of the role of mechano-biology in cardiovascular (patho)physiology, a better understanding of the biomechanical factors of the zebrafish circulation may be equally important as our understanding of its biological functions. While computational models play an important role in human cardiovascular biomechanic research, finite element models covering the cardiovascular biomechanics of either developing or adult zebrafish are, to the best of our knowledge, non-existent.

The cardiac anatomy of zebrafish consists of the sinus venosus, one atrium, one ventricle, the bulbus arteriosus and ventral aorta. Paired vessels starting from the ventral aorta provide blood flow to the gills and rejoin at the dorsal aorta [3]. The blood pumped by the ventricle passes the bulbus arteriosus, which functions as a non-contractile elastic reservoir, before it enters the ventral aorta. The functioning of the bulbus as an elastic reservoir has several advantages as it smoothens the effect of systolic pressure, which is necessary because of the delicate vasculature of the gills, and also helps to maintain the pressure during diastole. Furthermore, the elastic recoil of the bulbus results in an extended, i.e., more continuous, flow into the gills and ensures adequate gas exchange this way. The aims of this study are to (i) develop a 3D finite element model of the bulbus arteriosus and (ii) to assess the constitutive material law that allows us to mimic the pressure-diameter relation of the bulbus.

METHODS

Basics of the bulbus arteriosus

The bulbus is pear-shaped, tapering towards the ventral aorta, and has three distinct layers (Figure 1, left): the adventitia, outer media and inner media. A small layer of endothelial cells forms the intima [3,4]. As in arteries, mainly elastin, collagen and smooth muscle cells determine the mechanical behavior of the bulbar wall. Fibers in the inner and outer media are orientated longitudinally and circumferentially respectively. Whereas arteries have J-shaped pressure-diameter (P-D) loops, the bulbi of teleost fish (including the zebrafish) have r-shaped P-D loops. The r-shape arises from a steep initial rise in pressure followed by a compliant plateau phase [4]. The steep initial pressure rise is due to the very small lumen dimensions at low pressures, and the longitudinal elements almost completely occlude the bulbus at zero pressure. The stiffness of a bulbus is much lower than that of an artery, and this, together with the high extensibility, explains the efficient recoil and compliant plateau phase. All this allows the bulbus to maintain ventral aortic pressures and flows over a large volume range [5].

Finite Element model of the bulbus arteriosus – constitutive models

Version 5.4 of COMSOL Multiphysics® was used to study the mechanical behavior of the bulbus. A 2D axi-symmetric model was

sufficient to capture the mechanical behavior and allowed for a reduction in computational effort. We implemented and compared different (hyperelastic) material models to check whether or not the unique and unusual r-shape of the bulbar P-D loop could be obtained. Note that for all hyperelastic materials, the stress-strain relation can be derived from a strain energy density function as explained in [6].

Neo-Hookean and Mooney-Rivlin model The classical example of a hyperelastic material model is the Neo-Hookean model. The Mooney-Rivlin model is another hyperelastic material model which has proved to give good results for modeling certain types of biological tissue. Both material models are isotropic, and furthermore will assume that the bulbus is incompressible. The strain energy density functions for the Neo-Hookean and Mooney-Rivlin model are then, respectively:

$$W = \frac{c}{2}(I_1 - 3) \quad (1)$$

and

$$W = \frac{c_1}{2}(I_1 - 3) + \frac{c_2}{2}(I_2 - 3) \quad (2)$$

where c, c_1, c_2 are stress-like material parameters and I_1, I_2 are invariants of the right Cauchy-Green tensor. Both the Neo-Hookean and Mooney-Rivlin model are built-in in COMSOL Multiphysics 5.4®.

Holzapfel-Gasser-Ogden (HGO) model Whereas the two models just described are purely phenomenological, (parts of) the histology of the bulbus can be included with the HGO model. The strain energy density function is now split into two parts:

$$W = W_{isotropic} + W_{anisotropic} \quad (3)$$

where for the isotropic part for example equation (1) or (2) can be used. In this case, we will use the classical Neo-Hookean model. The anisotropic part accounts for the fibers and their orientation within the bulbar wall, treating the bulbus as a fiber-reinforced material. The anisotropic part of the strain energy density function can be written as the sum of the following expressions [6]:

$$W_4 = \frac{k_1}{2k_2}(\exp(k_2(I_4 - 1)^2) - 1) \quad (4)$$

$$W_6 = \frac{k_1}{2k_2}(\exp(k_2(I_6 - 1)^2) - 1) \quad (5)$$

where k_1 is again a stress-like material parameter, k_2 is a dimensionless material parameter and I_4, I_6 are the fourth and sixth invariants of the same tensor as before. These invariants depend on the fiber directions and introduce another parameter, β, which describes the angle between the spiraling fibers. Figure 1 (right) provides a visualization of the anisotropic part of the strain energy density throughout the bulbar wall. Note the circumferential and longitudinal direction in the outer and inner media respectively. The right image presents the bulbus at zero pressure, which explains the very small lumen (diameter of 0.05 mm).

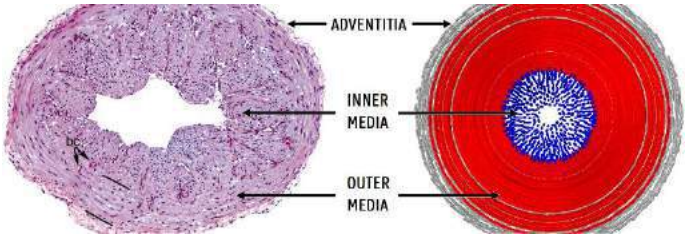

Figure 1: Left-a cross section of the bulbus clearly visualizing the three layers, separated by bars. Copyright left image: Hu et al. [3]. Right-a visualization of the anisotropy of the strain energy density function throughout the bulbar wall of our COMSOL model.

We implemented the HGO model in COMSOL Multiphysics® as a user-defined hyperelastic material model, and looked at the bulbus as a three-layered structure which leaves 12 material parameters to be defined (summarized in Table 1 - IM: inner media, OM: outer media, A: adventitia).

Table 1: material constants for the constitutive models

Neo-Hookean			Holzapfel-Gasser-Ogden										
c	265	Pa	c_{IM}	250	Pa	$k_{1,IM}$	50	Pa	$k_{2,IM}$	0.8	-	β_{IM}	90 deg
Mooney-Rivlin			c_{OM}	50	Pa	$k_{1,OM}$	10	Pa	$k_{2,OM}$	0.1	-	β_{OM}	0 deg
c_1, c_2	44	Pa	c_A	10	Pa	$k_{1,A}$	10	Pa	$k_{2,A}$	0.7	-	β_A	60 deg

RESULTS

The P-D loop was generated for the different material models by simulating the inflation of the bulbus. The comparison experimental data was based on [3],[4] and [5]. Note that due to the r-shape of the P-D loop, a large difference in diameter is observed over the physiological pressure range (which is approximately 0.8-2.2 mmHg [3]). The curves in blue, green and purple indicate the best fit for the Neo-Hookean, Mooney-Rivlin and HGO model respectively. Taking into account the observed fiber directions, the β-parameter in the HGO model was set to 90º (i.e., longitudinal), 0º (i.e., circumferential) and 60º in the inner media, outer media and adventitia respectively. As depicted in Figure 2 for the inner media (IM), changing the β-parameter from the observed (longitudinal) value resulted in a bad fit of the P-D loop.

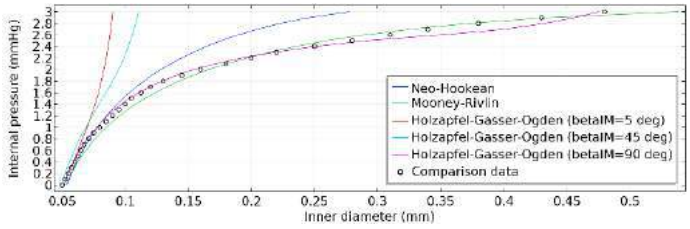

Figure 2: Simulation of the pressure-diameter (P-D) loop with the different material models. For each case, the best fit is depicted.

DISCUSSION

The COMSOL Multiphysics® simulations show that the typical r-shape of bulbar P-D loops can be obtained with the proposed material models. Both the P-D loop of our Mooney-Rivlin and HGO model agree well with the comparison data. We consider the fact that the HGO model can include (parts of) the histology of the bulbus as a crucial advantage compared with the purely phenomenological Mooney-Rivlin model, although, based on these first results, the (possible) superiority of the 3-layered HGO model is far from clear. More simulations are necessary, but we hypothesize that the 3-layered HGO model will provide more plausible stress distributions within the bulbar wall. Furthermore, at pressures above the physiological range, it is reported that the stiffness of the bulbus increases again [4], something which is impossible to obtain with the Mooney-Rivlin model. Experimental data is necessary and will lead to a more correct tuning of the different parameters. All findings in this study contribute to the search for a physical and physiological model of the mechanics of the bulbus, a key component in the cardiovascular system of the zebrafish. We can conclude that this study provides a strong basis for a mechanical model of the bulbus and once this model is completely validated, the step towards a Fluid-Structure Interaction (FSI) model of the bulbus can be taken.

ACKNOWLEDGEMENTS

This project was funded by an interdisciplinary research project grant from Ghent University (special research fund).

REFERENCES

[1] Wang, L. et al., *Dis Models Mech*, 10:63-76, 2017.
[2] MacRae, C. et al., *Nat Rev Drug Discov*, 14:721-731, 2015.
[3] Hu, N. Et al., *Anat Rec*, 264:1-12, 2001.
[4] Braun, M. et al., *J Exp Biol*, 206:3311-3326, 2003.
[5] Braun, M. et al., *J Exp Biol*, 206:3327-3335, 2003.
[6] Holzapfel, G. et al., *J Elast*, 61:1-48, 2000.

SB³C2019
Summer Biomechanics, Bioengineering and Biotransport Conference
June 25 -28, Seven Springs, PA, USA

THE EFFECTS OF LEAFLET RESIDUAL STRAINS ON AORTIC VALVE DYNAMICS

Rana Zakerzadeh (1), Ming-Chen Hsu (2), Michael S. Sacks (1)

(1) James T. Willerson Center for Cardiovascular Simulation, Institute for Computational Sciences and Engineering, Department of Biomedical Engineering, University of Texas at Austin
Austin, Texas, USA

(2) Department of Mechanical Engineering
Iowa State University
Ames, Iowa, USA

INTRODUCTION

The aortic valve (AV) tissue exhibits highly nonlinear, anisotropic and heterogeneous material behavior due to its complex microstructure. A thorough understanding of AV functional characteristics can shed light on its function in health and disease. In this work, we highlight a previously unexplained aspect of AV function: the role of leaflet residual strains. Leaflet residual strains are defined as the remaining strains in the intact AV after all external forces have been removed. Presence of residual strains indicates that a stress–free state does not exist in–vivo. Therefore, to be able to make accurate stress estimations of AV and determine their effects on AV dynamic behavior, it is important to quantify these residual strains by determination of AV stress-free configuration.

Yet, in spite of its importance, to date, the effect of residual strains on in–vivo dynamics of AV has never been quantified or simulated systematically. In a recent study the existence of substantial residual strains in human AV using 3D echocardiographic (3DE) imaging and excised leaflet geometry was demonstrated [1]. However, since determination of the effects of all states (stress-free, in-situ, etc.) by direct measurement in humans is not possible, we took a computational modeling approach. However, the leaflet residual strains measured in [1] (**Figure 4.a**) have not been incorporated in current simulations of the AV. Thus, in the present work we developed a computational framework to determine the residual strains in the AV leaflets and to investigate its influence on AV dynamics based using the human in-vivo results obtained in [1].

METHODS

We first define the kinematic state β_0 as the excised unloaded state where AV leaflets were removed from the heart. We define β_1 as the in–vivo configuration of the AV when the transvalvular pressure is zero, just before leaflets contact. In order to introduce residual strains in our finite element model, we developed a two-step protocol (**Figure 1**). First, we created the ex-vivo configuration β_0. Starting with the known unloaded configuration β_1, with an estimated non-uniform deformation gradient $\boldsymbol{F}$ we shrink the geometry of the valve.

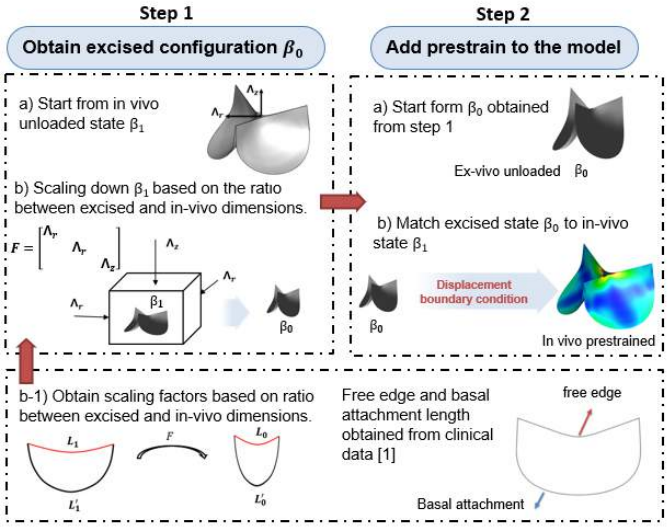

Figure 1: Implementation of residual strains in AV model.

The appropriate scaling factors are obtained from the ratio between excised and in–vivo key dimensions (i.e. free edge and attachment edge length ratio) clinical data provided in [1]. We use the results of Fig.5 in the aforementioned paper to estimate the behavior of the leaflet in–vivo

and ex–vivo and design our objective function for the optimization purpose. For this process, we used the function *fminsearch* in the Optimization Toolbox of MATLAB. Second, we recreated the in–vivo unloaded configuration β_1. Starting with the virtually created ex–vivo configuration β_0, we applied a Dirichlet displacement boundary condition along the edges of the leaflets to solve for the leaflet deformation which returns AV to its in–vivo geometry. For this purpose, we used a thin shell isogeometric structure dynamic finite element solver developed in [2] and implemented the constitutive material model described in [3] as a subroutine into our solver where the material parameters are determined by fitting the predicted stress-strain curves to the corresponding experimental data set of native human AV. We then calculated the resulting strains. Following this step, we applied physiological loading taken from [2] to simulate the in–vivo loaded configuration where the duration of the cardiac cycle is 0.76 s.

RESULTS

The predicted AV dynamics with and without residual strains were first compared in the fully opened and fully closed states (**Figure 2**). The model that considered residual strains, captures triangle opening behavior. Conversely, for the model without residual strains the material behaves less stiff, results in twists at the fully closed stage and also it fails to capture accurate opening behavior.

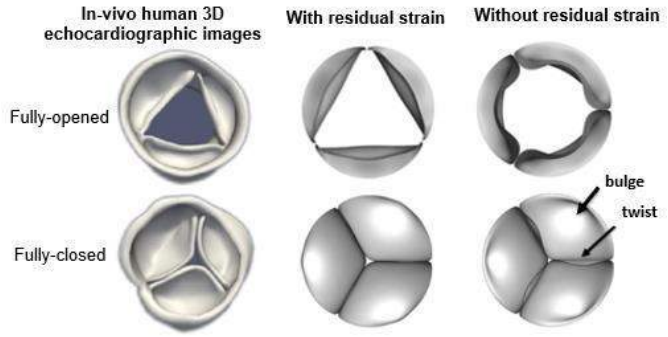

Figure 2: Comparison of AV dynamics for 2 cases with clinical imaging data: with and without including residual strain.

We also examine the effect of changing residual strains level on valve dynamics by adjusting radial shrinkage scaling factor $\boldsymbol{\Lambda_r}$. The strain distribution for different levels of $\boldsymbol{\Lambda_r}$ is obtained (**Figure 3**). Decreasing $\boldsymbol{\Lambda_r}$ corresponds to increasing the level of residual strains which causes the material to behave stiffer, therefore, strain gradient reduces within the leaflet (i.e. more uniform strain distribution).

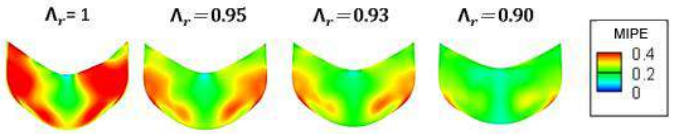

Figure 3: Total strain distribution at the fully-closed state for different levels of residual strains (from left to right more residual strain is induced to the model), deformation of the valve colored by maximum in-plane principal Green-Lagrange strain (MIPE).

We compared our results with some previous studies. In particular with regional principal stretch variation presented in [1] when the valve is fully closed. In general, the results are in good agreement with previous studies. For example, the radial stretches have been reported to be higher than the circumferential ones. Moreover, circumferential stretches are close to one over the leaflet (**Figure 4.a**). However, a direct comparison of stretch values is not possible. We also simulated the coupling of the aortic root, AV, and the surrounding blood flow through several cardiac cycles using our immersogeometric fluid-structure interaction (FSI) methodology (**Figure 4.b**).

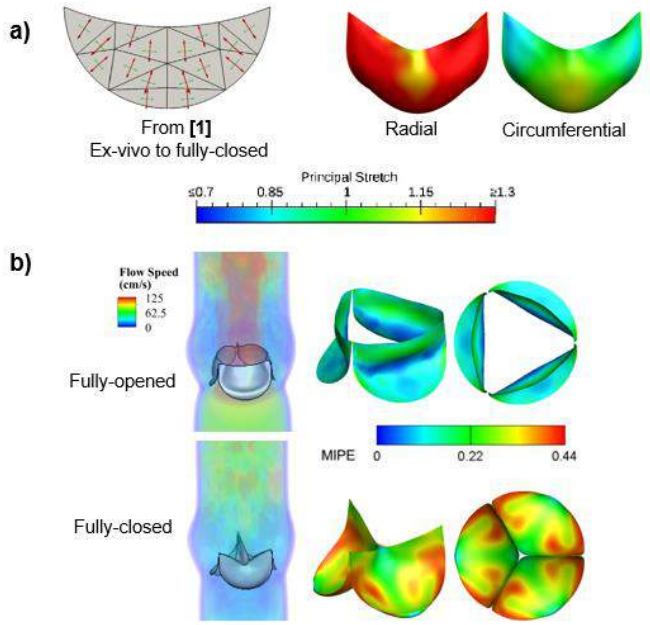

Figure 4: (a) Comparing principal stretch contours at fully-closed configuration to [1], (b) Residual strains incorporated in FSI framework for simulation of blood flow velocity and maximum in-plane principal Green-Lagrange strain (MIPE) in a cardiac cycle.

DISCUSSION

In general, we observed that including residual strains had a substantial influence on overall leaflet dynamics. Specifically, it had the largest effect on the shape of the AV leaflet in the fully-opened (maximum forward flow) configuration. During the leaflet deformation from just-coapted (zero transvalvular pressure) to fully-loaded (maximum transvalvular pressure), the circumferential strains was close to unity over the leaflet. This difference in functional geometry might also influence flow in the sinus and aortic root interactions. Interestingly, we also noticed that even though the AV did not support any measurable pressure gradient in the just-coapted state, the leaflets were significantly strained with respect to the excised state. Higher strains near the commissures and lower strains in the coaptation zone is observed as the region near commissures experiences the highest stress concentrations and the coaptation area is where leaflets come in contact. Moreover, we observed that including the residual strains decreases the strain gradient within the leaflet, and increases the apparent tissue stiffness; therefore, decreases the range of valve deformation.

Functionally, we and others have shown that residual strains in heart valves and other soft tissue (i.e. arteries) depends primarily on elastin fibers. Therefore, consideration of residual strains in AV takes charge of the elastic part of the leaflet mechanical response and causes the collagen fibers to become stiffer at higher stresses. A deeper study on this issue constitutes an important aspect for future research.

ACKNOWLEDGEMENTS

This work has been supported by NHBLI grant R01 HL129077.

REFERENCES

[1] Aggarwal, A., et al., J Biomech., 2016, 49(12), pp.2481-2490.
[2] Hsu, M.-C., et al. Comput. Mech., 2015. 55(6): p. 1211-1225.
[3] Zhang, W., et al. J Mech Behav Biomed Mat, 2019. 89: p. 168-198.

SB³C2019
Summer Biomechanics, Bioengineering and Biotransport Conference
June 25 -28, Seven Springs, PA, USA

EFFECTS OF -80°C FREEZING ON THE BIOMECHANICAL RESPONSE OF TRICUSPID VALVE LEAFLETS

Samuel D. Salinas, Margaret M. Clark, Rouzbeh Amini

Department of Biomedical Engineering
The University of Akron
Akron, OH, USA

INTRODUCTION

The short-term storage of frozen soft tissues is advantageous from the standpoint of tissue availability and the amount of time needed to conduct experiments. A plethora of tissue types have been tested previously, indicating that there is negligible effect on the mechanical response of tissues due to freezing [1-3]. On the other hand, a number of studies, focusing on tissues such as arteries, aortas, tendons, ligaments, and cartilage offer insights that may contradict with the abovementioned studies [1,4]. Such opposing results suggest that freezing-induced changes in mechanical properties may be tissue-dependent.

Our research team is interested in biomechanical studies of the tricuspid valve (TV), an atrioventricular valve on the pulmonary side of the heart. The TV apparatus is composed of three leaflets: anterior, posterior, and septal leaflets. We have previously conducted biaxial mechanical testing on freshly excised TV leaflets. However, to the best of our knowledge, the effect of freezing on the mechanical response of TV leaflets has not yet been determined [5]. As such, the aim of this study was to examine the feasibility of using frozen porcine TV when fresh TV is unavailable. We hypothesized that the biaxial mechanical response of porcine TV leaflets does not change following storage in phosphate buffered saline (PBS) at -80°C and subsequent thawing.

METHODS

Fresh porcine hearts were collected from a local slaughterhouse and transferred to our research laboratory in chilled PBS. The three TV leaflets ($n = 9$ for anterior and posterior, $n = 8$ for septal) were then isolated and kept in PBS at room temperature. Careful attention was given to align the direction of biaxial stretching with the radial and circumferential directions of the leaflet as defined previously [5]. Once mounted on our custom-built biaxial testing machine, five loading protocols with radial-to-circumferential stress values (in kPa) of 127:127 (equibiaxial), 95.25:127, 127: 95.25, 63.5:127, and 127:63.5 were applied. Nine preconditioning cycles were applied to each sample. The maximum stress of 127 kPa in this study was approximated based on a right ventricular pressure of 30 mmHg. The sample was then removed and placed in a six-well plate filled with PBS and promptly stored in a -80°C freezer. The same specimens were re-tested between one to three days later with the same procedure described above.

Positional data of the fiducial markers were analyzed with an in-house MATLAB (Nantick, MA) script, as described previously [5]. Briefly, the Green-Lagrangian strain tensor **E** was defined as

$$\mathbf{E} = \frac{1}{2}(\mathbf{C} - \mathbf{I}) \quad (1)$$

where **I** was the identity matrix, and **C,** the right Cauchy-Green deformation tensor, was defined as $\mathbf{F^T F}$. The deformation gradient tensor **F** was obtained from the positional data of four fiducial markers at each deformation state. The normal components of the first Piola-Kirchoff stress (i.e., P_{11} and P_{22}) were defined as

$$P_{(ii)} = \frac{f_i}{A_o} \quad (2)$$

where f_i was the force applied in the i^{th} direction and A_o is the corresponding undeformed cross-sectional area. The resulting stress-strain responses were then averaged for each protocol. Since deformation values were calculated in tensorial quantities and mechanical tests were conducted in a number of different loading conditions, the invariants of the right Cauchy-Green deformation tensor were used as scalar metrics for comparison between fresh and frozen samples. In particular, I_C, the first invariant of **C** was defined by

$$I_C = tr(\mathbf{C}) \quad (3)$$

and II_c , the second invariant of **C** was defined by

$$II_c = \frac{1}{2}[(tr\ \mathbf{C})^2 - tr\ \mathbf{C}^2] \quad (4)$$

Statistical analysis was performed using the Kruskal-Wallis test for I_C and II_c at identical stress levels between fresh and post-frozen for all

five protocols and leaflets, with significance level set as p-value < 0.05. Utilizing the law of Laplace and a physiological right ventricular pressure of 25 mmHg, we estimated an equibiaxial stress level of 85 kPa for comparison of fresh and post-frozen samples. We similarly adjusted the stress levels across the other four protocols to 72:96, 96:72, 54:108, and 108:54 (circular points in Fig. 1A) for comparison.

RESULTS

Across all protocols, visual examination of the average responses collected before and after freezing showed a *slight* increase in compliance for all three leaflets post-freezing, as shown in Fig. 1 for the equibiaxial protocol (127:127). However, analyzing the first and second invariants of the right Cauchy-Green strain tensor, we found no statistically significant difference between pre- and post- freezing samples. Figure 2 demonstrates the average first and second invariants pre- and post-freezing across all 5 protocols for the anterior leaflet. Data for the other two leaflets were similar (not presented), i.e., no significant difference was observed.

DISCUSSION

The aim of this study was to determine whether the mechanical response of TV leaflets could be maintained after storing specimens at -80°C. When comparing the deformation of the frozen leaflets at predefined stress levels with those of the fresh leaflets, we found no significant differences. For this study, we have conducted statistical comparisons of the deformation values only for a few selected values of the stress tensor. Similar comparison at other stress levels can provide further evidence of the similarity of the tissue responses before and after freezing. We expect no significant differences at *other* stress levels since visual examination of the stress-strain response (Fig. 1) demonstrate overlapping values and similar trend at any stress level.

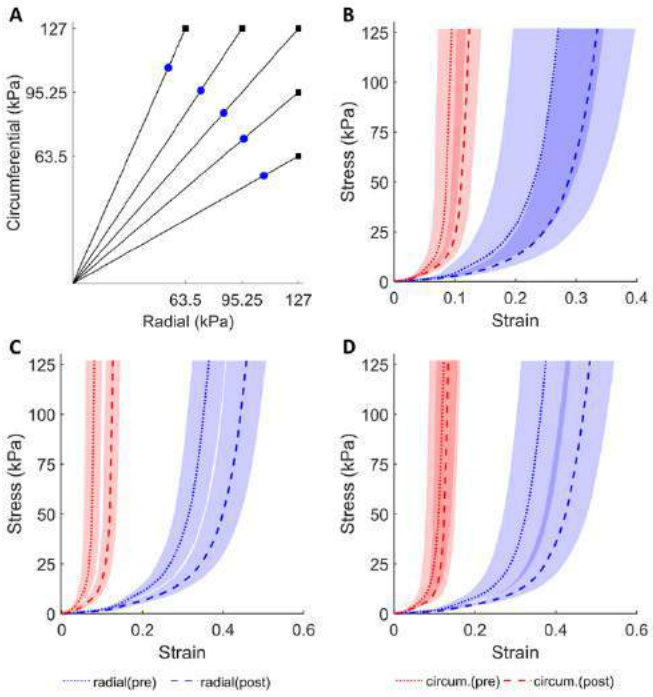

Figure 1: (A) Circumferential versus radial stress values of five testing protocols; the circular markers show the stress levels used for comparison of the strain invariants between pre- and post-freezing samples. Average response curves for (B) the anterior, (C) posterior, and (D) septal leaflets for the equibiaxial test. Shaded regions are standard errors.

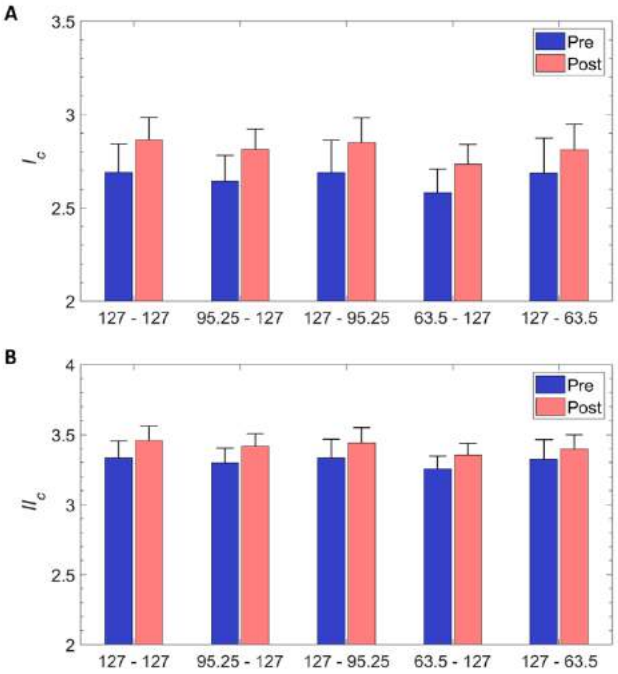

Figure 2: (A) the first and (B) second invariants of the right Cauchy-Green deformation tensor for the anterior leaflet. Error bars are standard error ($n = 9$).

The similarity in mechanical responses pre- and post-freezing suggest that the extracellular matrix (ECM) architecture, particularly that of collagen, did not deviate much from its initial pre-freezing alignment. Although not significant, the increase in compliance (both in radial and circumferential directions) may be attributed to a disruption in ECM fiber alignment due to the movement of water as ice crystals were formed. Further imaging analysis of the microstructure (e.g. similar to analysis of ocular tissues conducted by Gogola et al. [6]) could provide insights as to how microstructural parameters such as ECM fiber orientation and/or crimp could be affected by freezing.

In summary, consistent with our initial hypothesis, we observed no significant difference in mechanical response of TV leaflets induced by short term storage at -80°C. Such an outcome is advantageous as the fresh tissues may not be always readily available on the day of experiments. In addition, while one should be cautious in extending the outcomes of animal studies to their human counterparts, the lack of difference between fresh and previously frozen samples is of particular importance for human tissues. In particular, access to fresh donor tissues are scarce and requires strong ethical arguments for usage in mechanical testing experiments.

ACKNOWLEDGEMENTS

The help of Nicholas Hann and Evan Clark, summer high school research students is acknowledged. Funding was provided in part by the American Heart Association (Grant No. 16SDG27770088).

REFERENCES

[1] Venkatasubramanian, RT et al., *Ann Biomed Eng*, 34:823-832, 2005.
[2] Szarko, M et al., *BMC Musculoskelet Disord*, 11:231. 2010.
[3] Moon, DK et al., *J of Biomechs*, 39:1153-1157. 2006.
[4] Clavert, P et al., *Surg Radiol Anat*,*23*:259-262, 2001.
[5] Khoiy, K et al., *J Biomech Eng*, 138:104504. 2016.
[6] Gogola, A et al, *Invest Ophthalmol Vis Sci*. 59:2987-2998, 2018.

SB³C2019
Summer Biomechanics, Bioengineering and Biotransport Conference
June 25 -28, Seven Springs, PA, USA

ROLE OF GLYCOSAMINOGLYCANS IN BIAXIAL MECHANCAL BEHAVIORS OF PORCINE ATRIOVENTRICULAR HEART VALVE LEAFLETS

Chung-Hao Lee (1), Colton Ross (1), Devin Laurence (1), Lauren Evans (1), Jacob Richardson (1), Anju Babu (1), Ean Beyer (1), Yi Wu, (1), Gerhard A. Holzapfel (2), Arshid Mir (3), Harold M. Burkhart (4)

(1) Biomechanics and Biomaterials Design Laboratory
School of Aerospace and Mechanical Engineering
The University of Oklahoma
Norman, OK, USA

(2) Institute of Biomechanics
Graz University of Technology
Graz, Austria

(3) Division of Pediatric Cardiology
Department of Pediatrics
The University of Oklahoma Health Sciences Center
Oklahoma City, OK, USA

(4) Division of Cardiothoracic Surgery
Department of Surgery
The University of Oklahoma Health Sciences Center
Oklahoma City, OK, USA

INTRODUCTION

The mitral valve (MV) and the tricuspid valve (TV), also named the atrioventricular heart valves (AHVs), are responsible for regulating unidirectional blood flow from the atria into the ventricle via proper cyclic closing and opening of the valve leaflets. Proper leaflet function relies on the valve leaflet tissue's microstructural components (e.g., collagen fibers, elastin, and glycosaminoglycans (GAGs)) [1]. Maintaining valvular function utilizing surgical reparative techniques is associated with a survival benefit. Previously, the clear zone portions of both the MV and TV leaflets have been characterized, and the mechanical testing results revealed an anisotropic, nonlinear mechanical response [2-3]. These studies provided insight into the mechanical characteristics of the respective tissue layers: the collagenous fibrosa being the major load-bearing layer, and the elastin-rich layers being responsible for the tissue's low-stress elasticity.

In addition, studies [5-6] have quantified the biomechanical role of the GAGs in aortic valve leaflets. Despite these earlier investigations in aortic valve tissue biomechanics, quantifications of the GAGs' contributions to leaflet mechanical behavior have not been made for the AHVs. Thus, there is a need for comprehensive investigations of the GAGs' biomechanical role in the AHV leaflet function, which will lead to greater refinement of AHV leaflet microstructure knowledge and have implications with regard to surgical valve preservation versus replacement. The goal of this study is to fill this gap in knowledge through biaxial mechanical characterization of AHV leaflet tissues before and after enzymatic treatment to remove the GAG constituent.

METHODS

Tissue Preparation: Healthy porcine hearts (80-140 kg, 1-1.5 years of age) were obtained from a local abattoir (Country Home Meat Co., OK) on the same day as animal slaughter. The central portions of the excised leaflets were sectioned into 10 x 10mm specimens (**Fig. 1a**), and three measurements were averaged to obtain the tissue thickness.

GAG-Degradation Procedure: To examine the GAG contributions to AHV leaflet tissue mechanics, force-controlled biaxial mechanical tests were performed prior to and after an enzyme-based GAG degradation procedure previously developed for the aortic valve leaflets [6]. In brief, an enzyme solution consisting of 30 Units/mL of enzyme Hyaluronidase type VI-S and 0.6 Units/mL of enzyme Chrondroitinase ABC from Proteus vulgaris in 100 mM Ammonium Acetate Buffer Solution (AABS) was prepared with an adjusted pH of 7.0. The MVAL/TVAL tissue specimen was placed in a 1.5 mL vial tube filled with the prepared GAG-degradation solution and continuously shaken for 100 minutes at 37 °C, with which enzyme-treatment time was determined by histology-based GAG content quantification (**Fig. 1b**).

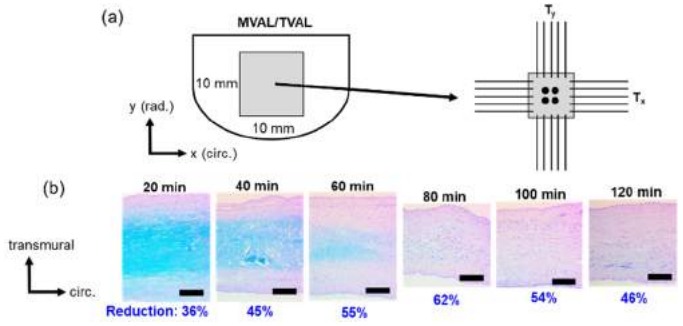

Figure 1. **(a)** Dissection of the MV and TV anterior leaflets into 10 x 10mm specimens, and the experimental setup for biaxial mechanical testing. **(b)** Alcian blue-stained histological images, demonstrating the progression of the GAG constituent removal associated with various enzyme treatment durations. Scale bar = 200 μm.

Poster Presentation #P111

Biaxial Mechanical Testing: For biaxial mechanical testing the prepared MVAL or TVAL specimen was mounted using a set of 4 BioRake tines to a commercial biaxial testing system (BioTester–CellScale, Canada) equipped with a 1.5N capacity load cell. The tissue's circumferential direction, with which the majority of collagen fibers are oriented, was aligned with the testing x-direction while the radial direction was aligned with the testing y-direction (**Fig. 1a**).

For quantification of the GAG contribution to the overall leaflet's mechanical behavior, a sequential biaxial mechanical testing procedure was performed, including: *(i) control testing* — untreated (control, C) MVAL or TVAL specimen (effective testing size 7 x 7mm); *(ii) GAG degradation* — enzymatic removal of glycosaminoglycans; *(iii) post GAG-removal testing* — enzyme-treated specimen (denoted by -T; effective testing size 5.5 x 5.5mm). Biaxial mechanical testing performed before and after GAG removal consists of a previously developed force-controlled biaxial mechanical testing protocol [3], with a preconditioning step, followed by 10 cyclic loading cycles at various membrane tension ratios (T_x:T_y = 1:1, 0.5:1, and 1:0.5).

Biaxial Data Analyses: The DIC functionality of the BioTester system was used to obtain time-dependent positions of the four fiducial markers. The time-dependent marker positions were then used to compute the deformation gradient **F**, and subsequently the principle stretches in the circumferential and radial directions (λ_{circ} and λ_{rad}). The membrane tensions (T_x and T_y) associated with each deformation gradient were computed using the load cell's force reading and each specimen's effective testing region edge length.

Statistical Analysis: Results are represented as the mean ± SEM (standard error of the mean). To determine the statistically significant differences between the control and enzyme-treated groups of both the MVAL and TVAL a two-tail Student's *t*-test was performed. A p-value < 0.05 was considered to be statistically significant, and a p-value < 0.1 was deemed nearly statistically significant.

RESULTS

Comparing the control and enzyme-treated groups with regard to the equi-biaxial loading ratio (T_x:T_y= 1:1), it was observed that the GAG-degraded specimens experienced greater stretches than the control specimens in both the circumferential and radial directions. In the circumferential direction, this difference was 5.4% for the MVAL and 4.7% for the TVAL, while for the radial direction the difference was 5.3% for the MVAL and 7.6% for the TVAL (**Fig. 2**). These differences were determined to be statistically significant (MVAL, $p<0.007$; TVAL, $p<0.034$). Similar trends in stretch and statistical significance were observed for the non-equibiaixal loading protocols.

The tissue stretch values for the equi-biaxial protocol (T_x:T_y= 1:1) were further used to compare the anisotropic index (AI = $\lambda_{rad}/\lambda_{circ}$) for the MVAL and TVAL. The MVAL tissues demonstrated minimal change between the control and treated AI values (1.055 ± 0.022 vs. 1.052 ± 0.022; p = 0.910), whereas the TVAL tissues revealed a slight, statistically insignificant, increase in AI (1.031 ± 0.017 vs. 1.059 ± 0.028; p = 0.148).

In addition, the preconditioning stretches (λ_{circ}^{PPC} and λ_{rad}^{PPC}), *defined as the tissue deformations between the tissue mounting configuration and the post-preconditioning configuration primarily due to the preconditioning effect*, were shown to be greater post-treatment for both the circumferential and radial directions. Specifically, the circumferential direction preconditioning stretch was 2.1% greater for the MVAL (p = 0.128) and 2.7% greater for the TVAL (p = 0.111). The radial direction preconditioning stretch was 3.9% greater for the MVAL (p = 0.039, statistically significant) and 4.8% greater for the TVAL (p = 0.072, nearly statistically significant).

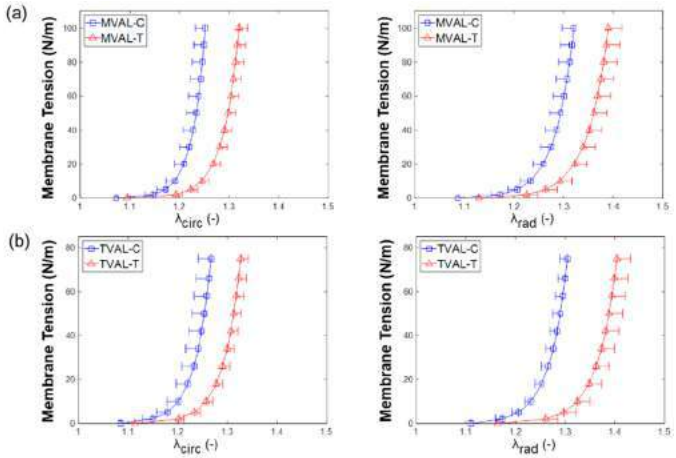

Figure 2. Mean ± SEM of the tissue stretch responses of the control (C) and enzyme-treated (T) groups for the **(a)** MVAL tissue specimens (n=7), and **(b)** TVAL tissue specimens (n=6): T_x:T_y = 1:1.

DISCUSSION

From biaxial mechanical testing, it was found that the removal of the GAGs from the AHV leaflet resulted in a statistically significant difference in leaflet peak tissue stretch, with greater extensibility observed in each direction after GAG removal. Previous studies of GAG contribution to heart valve leaflet function have been performed primarily on the aortic valve leaflets [5-6]. In these studies, it was found that GAG removal from the AV leaflets resulted in a greater buckling behavior, a greater flexural rigidity, and differences in tensile viscoelastic properties. In contrast, in our study, it was found that a removal of GAGs from the MVAL and TVAL resulted in statically significant changes in extensibility. One possible explanation may be that the greater contribution of GAGs could be attributed to the difference in the AV and AHV leaflet structures, as the AV does not contain the atrialis layer present in the AHV leaflets.

This study has successfully provided insight into the previously uninvestigated mechanical contribution of the glycosaminoglycans to AHV leaflet function. The findings of this study suggest that GAGs are responsible for regulating the extensibility of the tissue, acting as a mediator between the atrialis and fibrosa layers. Study limitation may warrant future examinations: the effective testing area for the tissues being different before and after enzyme treatment and no investigations been made on the effect of the testing size on the observed mechanical properties. Nevertheless, findings from this study will be useful in enhancing the understanding of the leaflet microstructure that would be essential to the refinement of AHV computational models. In addition, these results could help guide development of therapeutics for valvular heart diseases, including medical therapy, valve repair techniques and replacement prostheses.

ACKNOWLEDGEMENTS

This work is supported by the American Heart Association Scientist Development Grant (SDG) Award (16SDG27760143).

REFERENCES

[1] Sacks, MS & Yoganathan, AP, *Philos Trans R Soc Lond B Biol Sci*, 362:1369-1391, 2007.
[2] Grashow, JS et al., *Ann Biomed Eng*, 34:315-325, 2006.
[3] Jett, S et al., *J Mech Behav Biomed Materi*, 87:155-171, 2018.
[4] Stella, JA & Sacks, MS, *J Biomech Eng*, 129:757-766, 2007.
[5] Lovekamp, JJ et al., *Biomaterials*, 27:1507-1518, 2006.
[6] Eckert, C.E., *Acta Biomater*, 9:4653-4660, 2013.

SB³C2019
Summer Biomechanics, Bioengineering and Biotransport Conference
June 25 -28, Seven Springs, PA, USA

STATE OF THE ART SIMULATION OF THE EARLY STAGES OF BIOPROSTHETIC HEART VALVE FATIGUE

Will Zhang (1), Rana Zakerzadeh (2), Michael S. Sacks (2)

(1) Biomedical Engineering
The University of Michigan
Ann Arbor, MI, USA

(2) Willerson Center for Cardiovascular Modeling and Simulation
Institute of Computational Engineering and Sciences
The University of Texas at Austin
Austin, TX, USA

INTRODUCTION

The most popular replacement heart valves continue to be bioprosthetic heart valves (BHV) fabricated from xenograft biomaterials. While these devices have many benefits such as immunogenicity and better flow dynamics, failure due to structural deterioration mediated by fatigue and/or tissue mineralization continues to be the central issue plaguing the current designs [1]. Even moderate improvements to its current 10–15 years lifespan can have significant impacts for many patients. However, despite decades of clinical BHV usage and growing popularity, evaluating the durability of BHV design remain very empirical, and the mechanisms underlying their failure remains poorly understood. For example, in vitro accelerated wear testing (AWT) is the only device-level method for evaluating durability. Yet only visible structure damages are used for analysis. Thus, there is a profound need for the development of novel simulation technologies for better understanding and predicting of the changes in the mechanical properties of BHVs at the tissue level.

The dominant fatigue mechanism during the initial stages of cyclic loading is permanent set. Permanent set occurs in BHVs due to the use of glutaraldehyde to suppress the immunogenic response to the xenograft tissue, where the crosslinks formed are reversible at room and body temperature. However, this also has profound effects on the mechanical properties of the tissue, including allowing the microstructure and stress-free configuration of the tissue to gradually change without inducing structural damage. We have shown through the structural constitutive model we developed that permanent set alone can explain all structural and mechanical changes in the BHV biomaterial in the first 50-70 million cycles of testing, and that this process eventually seizes, and the final stress-free geometry depends on the collagen fiber architecture of the tissue [2]. In this work, we developed a numerical framework for simulating the time evolving properties of BHVs at the device level based on the structural constitutive model [2] and attempt to predict the geometric and structural change that occurs with long-term cyclic loading. We will use this framework to evaluate some initial BHV designs and how they affect the unloaded geometry, collagen fiber architecture, and how the BHVs deform.

METHODS

Permanent set model. Consider the simplest case for permanent set, the 1-D model held at a fixed stretch. The original material is in the reference state Ω_0 and is deformed to the configuration Ω_t. The spontaneous breaking and reforming of the glutaraldehyde allow some of the tissue to break from Ω_0 and reform in Ω_t. The resulting changes in the reference configuration of the convect the collagen fibers architecture and change the mechanical properties of the tissue (Fig. 1) [2]. The stress of the tissue can be described using a structural model incorporating the changing collagen fiber architecture [3], where the strain energy is given by

$$\Psi = \Psi_{matrix} + \Psi_{collagen} + \Psi_{interactions}. \quad (1)$$

In the general case, the mass fraction of tissue in the original reference configuration can be described as a function of time, $b(t)$, and the mass fraction of materials formed in the new configuration, $a(t, \Omega(s))$, needs to be extended to be a function of both time and the loaded configuration at time s, $\Omega(s)$, in other words the strain history. The stress of the crosslinked tissue is thus given by

$$\mathbf{S}(t) = b(t)\mathbf{S}_{\Omega_0} + \int_0^t a\big(t, \Omega(s)\big)\mathbf{S}_{\Omega(s)} ds. \quad (2)$$

Effective model framework. One major challenge hindering time evolving simulations incorporating structural information is the large

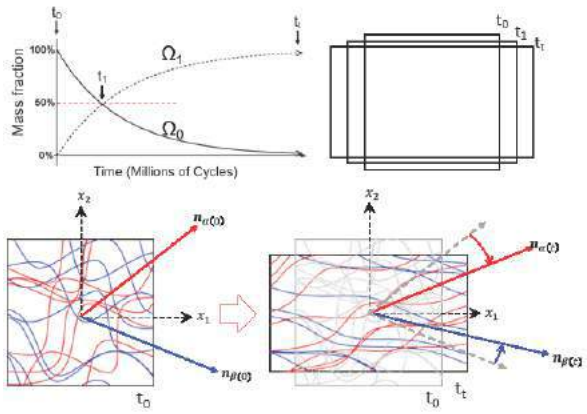

Figure 1: A representation of permanent set in a 1D case held at constant strain. The mass fraction of tissue gradually changes to the loaded state (Ω_t), changing the reference configuration (Top) while convecting the collagen fiber architecture (Bottom)

computational cost. We estimate the computational cost of the structural model [2] is five magnitudes higher due to the quadruple integral involved. It is for this reason that we developed an effective constitutive model approach to improve the efficiency of such simulations [4]. The form of this effective constitutive model is

$$\Psi_{eff} = c_0(e^Q - 1). \tag{3}$$
$$Q = b_1E_{11}^2 + b_2E_{22}^2 + b_3E_{12}^2 + b_4E_{11}E_{22} + b_5E_{11}^4 + b_6E_{22}^4 + b_7E_{11}^3E_{22} + b_8E_{11}^2E_{22}^2 + b_9E_{11}E_{22}^3 + b_{10}E_{12}^4 + b_{11}E_{11}^2E_{12}^2 + b_{12}E_{22}^2E_{12}^2 + b_{13}E_{11}E_{22}E_{12}^2.$$

This form both can fully capture the response of the structural model and has similar computational costs to other phenomenological approaches. Equation 3 is used for the quasi-static simulations, whereas the structural model (Eqn. 1) is used to determine the model parameters c_0 and b_i (Fig. 3).

Numerical Simulation Framework. The numerical simulation can be divided into 3 main stages. (1) Setting up microstructure, material properties and geometry in the initial uncycled state, 2) perform quasi-static simulation to find the current loaded state, 3) updating the material properties of the structural constitutive model at the local material level, and 4) updating the new post cycling reference geometry at the device-level and changes in the local microstructure. Step 2-4 are repeated for each time subsequent time step until the last time step (Fig. 2).

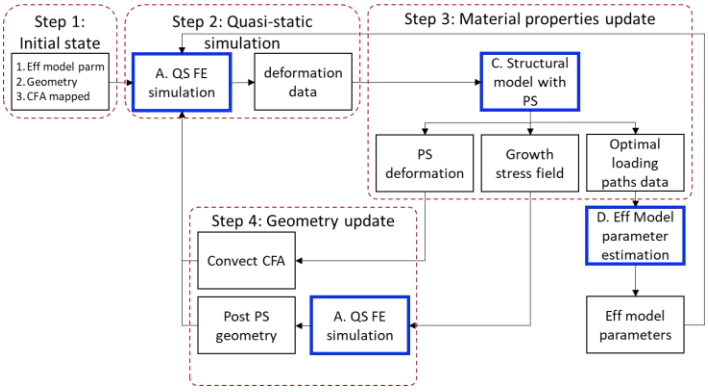

Figure 2: Implementation for the permanent set (PS) simulation divided in to four main stages.

RESULTS

BHVs undergoes significant changes in geometry in response to permanent set, especially in the first 25 million cycles. This process gradually stops after around 40-50 million cycles. The regions that undergo most permanent set are the belly region, the center of the free edge, and the regions near the commissures, where the leaflets initial make contact (Fig. 3). The belly region and the center of the free edge have the least support from the surrounding two leaflets which causes them to deform more. The regions near the commissures are the points where the leaflets initially meet during the closing motion. These regions are also the most common regions of failure in BHVs. We were also able to predict the change in the collagen fiber architecture and found that the belly region and the free edge undergoes the greatest degree of realignment, causing the fibers to spread.

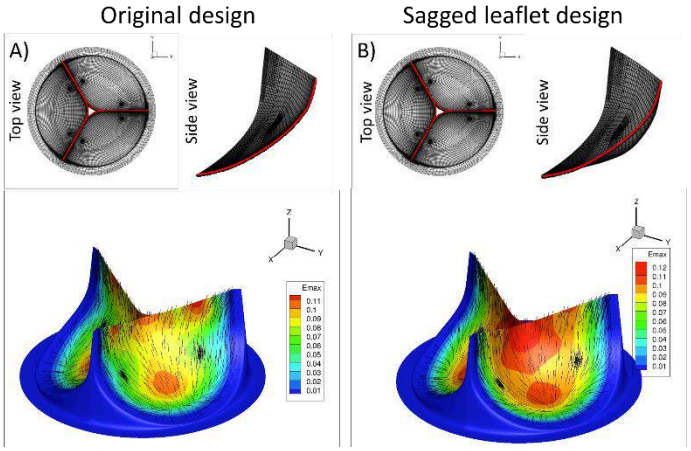

Figure 3: Simulations of BHVs with initial geometries is based on A) the Edward pericardial valve, and B) altered to have greater belly region curvature. The color shows the maximum principal component of the local change in reference configuration.

DISCUSSION

We have developed a complete time-dependent framework for the numerical simulation of BHVs in response to permanent set under long-term cyclic loading. This simulation utilizes the predictive mechanism based constitutive model for the permanent set effect in exogenously crosslinked soft tissues that we previously developed. We have shown that we can use this simulation to predict how the evolving geometry, microstructural and material property changes. This framework opens the possibility of optimizing the initial BHV design to the final geometry after permanent set has seized, where it will operate for its remaining 9- to 14-year lifespan. These results can then be extended to predict regions with increased likelihood of structural damage, where the collagen fibers are over-stretched or held in a constant extended state. Thus, accounting for the permanent set effect is especially important in the design of BHVs to better improve their performance and durability.

ACKNOWLEDGEMENTS

This work is supported by NIH grants HL119297, HL108330, HL073021, and HL063064.

REFERENCES

[1] Sacks, M.S. & Schoen, F.J. *Ann Thorac Surg.* 79(3):1072-80, 2005.
[2] Zhang, W., et al. *J Mech Behav Biomed Mater.* 75:336-50, 2017.
[3] Sacks, M.S. et al. *Interface Focus.* 6(1):20150090, 2016.
[4] Zhang, W., et al. *J Mech Behav Biomed Mater.* 89:168-98, 2019.

SB³C2019
Summer Biomechanics, Bioengineering and Biotransport Conference
June 25 -28, Seven Springs, PA, USA

IMAGE-BASED SIMULATION OF THE MITRAL VALVE REPAIR SURGERY IN ISCHEMIC MITRAL REGURGITATION PATIENTS

Amir H. Khalighi (1), Bruno V. Rego (1),
Robert C. Gorman (2), Joseph H. Gorman, III (2), Michael S. Sacks (1)

(1) Willerson Center for Cardiovascular Modeling and Simulation
Institute for Computational Engineering and Sciences
Department of Biomedical Engineering
The University of Texas at Austin
Austin, TX, USA

(2) Gorman Cardiovascular Research Group
Department of Surgery
Perelman School of Medicine
University of Pennsylvania
Philadelphia, PA, USA

INTRODUCTION

Hear valve disease is striking the western world with an ever-increasing prevalence rate [1]. Among the most common valvular lesions, ischemic mitral regurgitation (IMR), appears within one month of infarction in the growing population of patients who have suffered cardiac arrest [2]. While two major surgical solutions for IMR (repair and replacement) have improved significantly over the past three fFirate of success with a high mortality rate [3]. Consequently, there is an eminent need for improving treatment options to help patients who suffer from MV disorders, especially IMR.

It is widely believed that to achieve better patient outcomes, MV treatments need to be tailored to each patient's conditions. Image-based computational modeling of the MV provides a promising approach to this issue by allowing for quantitative assessment of different treatment options through simulating the valvular response to repair on a patient-specific basis. However, the clinical application of MV *in silico* simulations has always been hindered by the fact that imaging MV in the clinic cannot resolve the complete geometry of the valve with sufficient spatiotemporal resolution for computational modeling. In the present study, we addressed this issue through developing functionally equivalent models of the chordal structure to build high-fidelity image-based models of the complete MV and in turn simulate MV repair surgery. Our methodology uses only the information that is available prior to surgery and successfully showcases how image-based computational models of the MV can be used to provide additional insight into patient-specific response to annuloplasty repair of the valve.

METHODS

Three patients were randomly selected from the Cardiothoracic Surgical Trial Network (CTSN) for this study. We processed real-time 3D echocardiographic (rt-3DE) images for these patients from before and after undergoing the annuloplasty surgery to extract patient-specific leaflet geometries (Figure 1). For each patient, the pre-operative open valve model was converted into a 3D triangulated mesh using Poisson disk resampling and ball pivoting algorithms. The acquired mesh was then morphed to the closed leaflet geometry through a hyperelastic shape-warping technique that enforced the closed leaflet shape through a level-set penalization.

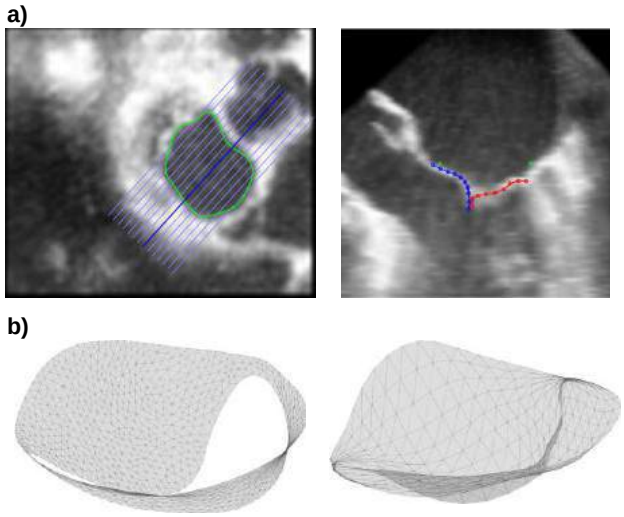

Figure 1, (a) rt-3DE images of the MV were interactively processed to develop patient-specific geometric representations of the MV leaflets for both end-diastolic and end-systolic states (b).

Briefly, in this method the ventricular side of the leaflet geometry is first pressurized till the reference open shape transforms to the vicinity of target closed shape. Then, a locally corrective pressure field enforces the final adjustments such that the morphed leaflet mesh from the open state matches the closed leaflet image data. The details of our shape-matching technique including the image processing pipeline, leaflet constitutive relation, and finite element analysis framework can be found in Rego et al. [4].

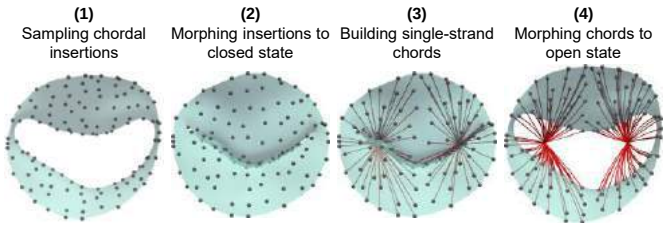

Figure 2, the pipeline to develop functionally equivalent chordal models is shown from surgeon's view.

As mentioned above, the chordal part of MV apparatus cannot be fully resolved via *in vivo* imaging modalities. We have addressed this issue in detail in our previous studies on the MV chordae tendineae (MVCT) by analyzing the micron-resolution characteristics of the chordal anatomy [5] and more recently developing functionally equivalent chordal models [6]. In the present study, we followed the same approach to build patient-specific synthetic chords that can reproduce the effect of native MVCT on the closing behavior of the MV apparatus (Figure 2). To build functionally equivalent chords, at first the open leaflet mesh was uniformly sampled in 3D to acquire a point cloud of the chordal insertions on the leaflet. This point cloud was then mapped to the closed state using the computed registration field, *vide supra*. Next, the average papillary muscle (PM) locations also extracted from rt-3DE imaging data were connected to the morphed insertion locations to build single strand chords. The constructed chordal model was then merged with the leaflet geometry, morphed back to the open state, and calibrated to the pre-operative state to build a complete model of the MV apparatus.

To predict the effects of annuloplasty repair surgery on each patient, the post-operative valvular configuration was simulated by applying the displacement boundary conditions on the annulus and PM heads (Figure 3). We used the commercial Finite Element software package Abaqus explicit to perform the closing simulations using a non-linear quasi-static solver with direct time integration and automatic time-stepping. The constitutive relation to model the mechanical behavior of the leaflets and chords and details of our finite element models can be found in Rego et al. [4] and Khalighi et al [6].

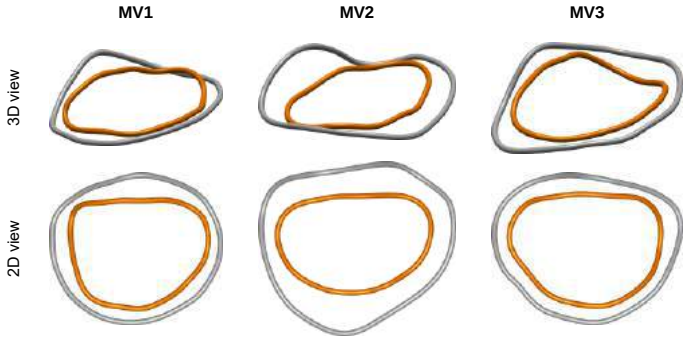

Figure 3, the gray and golden curves respectively correspond to pre- and post-operative annular shapes.

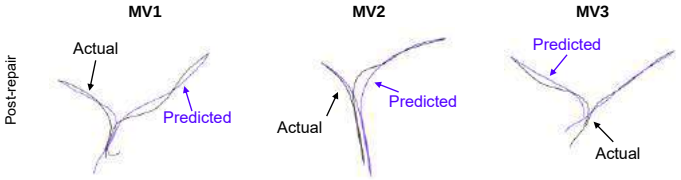

Figure 4, the simulation results show a high level of fidelity in predicting post-operative closed valvular geometry

RESULTS

The simulation results showed that our modeling approach can be used to reliably predict the closing behavior of the MV following annuloplasty surgery using pre-operative imaging data (Figure 4). In addition, we computed the leaflet deformation fields in the local surface directions which demonstrated the effects of undersized annuloplasty ring on the entire leaflet (Figure 5). Interestingly, the comparison of pre- and post-operative deformation patterns revealed that the circumferential strain and stress decreased significantly in the entire leaflet while radial components of the strain and stress remained mostly the same before and after the annuloplasty repair surgery.

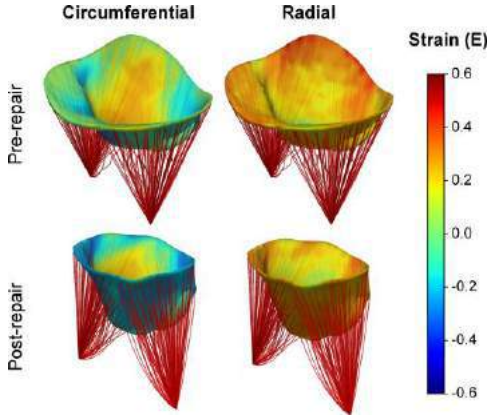

Figure 5, the directional strain fields computed for a representative patient in pre- and post-operative states are shown.

DISCUSSION

Simulating the MV response to surgery from clinical imaging data allows for refinements to treatment planning and optimization of repair surgery procedures. In this study, we presented a pipeline that allows for patient-specific modeling of the MV to predict the valvular response to annuloplasty repair with high predictive power. Our framework only relies on the clinically obtainable imaging data prior to the MV repair operation and thus can be extended into a virtual surgery tool that provides surgeons with additional insight into the patient-specific valvular response to different treatment options.

ACKNOWLEDGEMENTS

This material is based upon work supported by the NIH (grant no. R01-HL119297), the NSF (grant no. DGE-1610403), and the AHA (grant no. 18PRE34030258).

REFERENCES

[1] Benjamin, EJ et al., *Circulation*, 135:146-603, 2017.
[2] Bursi, F et al., *Circulation*, 111:295-301, 2005.
[3] Acker, MA et al., *N Engl J Med*, 370:23-32, 2014.
[4] Rego, BV et al., *Int J Numer Method Biomed Engng*, 34:e3142.
[5] Khalighi, AH et al., *Ann Biomed Eng*, 45:378-393, 2017.
[6] Khalighi, AH et al., *Ann Biomed Eng*, 47:60-74, 2019.

SB^{3}C2019
Summer Biomechanics, Bioengineering and Biotransport Conference
June 25 -28, Seven Springs, PA, USA

A NON-INVASIVE METHOD TO QUANTIFY AORTIC VALVE LEAFLET DEFORMATION

Bruno V. Rego (1), Samuel T. Potter (1), Alison M. Pouch (2), Robert C. Gorman (2), Michael S. Sacks (1)

(1) Willerson Center for Cardiovascular Modeling and Simulation
Institute for Computational Engineering and Sciences
Department of Biomedical Engineering
The University of Texas at Austin
Austin, TX, USA

(2) Gorman Cardiovascular Research Group
Department of Surgery
Perelman School of Medicine
University of Pennsylvania
Philadelphia, PA, USA

INTRODUCTION

The potential clinical benefit of patient-specific biomechanical models of cardiovascular disease remains an unrealized goal, often due to difficulties in non-invasively acquiring necessary kinematic data. This is particularly true in assessing bicuspid aortic valve (BAV) disease, the most common cardiac congenital defect in humans which leads to premature and severe aortic stenosis/insufficiency (AS/AI) [1]. However, assessment of BAV risk for AS/AI to determine treatment on a patient-specific level is hampered by large anatomic variations that remain largely unquantified. There is thus a need for simulation techniques that can directly integrate individualized BAV geometry and deformation data from *in vivo* imaging modalities. Towards this goal, we have extended an approach developed for human mitral valve (MV) [2] to determine tri-leaflet aortic valve (TAV) and BAV leaflet deformations based on clinically obtained *in vivo* imaging data.

METHODS

Data acquisition. Data was acquired from multiple individuals at several points in the cardiac cycle and segmented using previously developed methods [3]. Imaging data was collected on a patient-specific basis for individuals with TAV and for those with BAV. During segmentation, the Raphe labels were applied to BAV data sets on leaflets where a Raphe existed (Figure 1).

Spline surface fitting. The segmented imaging data was fit with a Non-uniform Rational B-Spline (NURBS) surface as follows. First, a closed NURBS curve was fit to the leaflet boundaries and converted into an open NURBS surface. The surface was matched to the segmented image data by least squares error minimization between the surface and segmented data points. In areas of data sparsity, Sobolev regularization was used to stabilize the least squares fit [4].

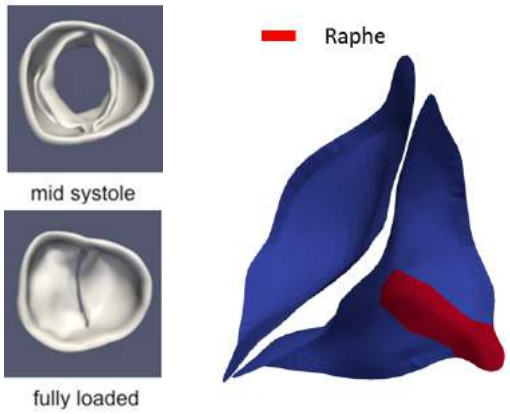

Figure 1. Representative segmented image of a BAV.

Strain estimation. To acquire diastolic deformation fields across the entire aortic valve (AV) leaflet surface non-invasively, we utilized a previously validated image-based strain estimation method developed by our group [2], which yields local strain information directly from clinical-quality *in vivo* images. An essential feature of our approach is that it does not rely on physical markers to extract surface deformations; we thus did not assume any material point correspondence between open-state and closed-state images when estimating diastolic strains. Instead, we exploited the fact that the gross

subject-specific closed-state geometry of the leaflets can be precisely acquired from diastolic scans, and developed the following method to enforce this closed shape during a finite element (FE) simulation of AV closure: While pressurizing the open-state valve mesh, we penalized any mismatch between the simulated and true (i.e. imaged) closed shapes of the leaflets using a local corrective pressure field (LCPF), which was at any instance and location linearly proportional to the shortest distance between the FE mesh and the true AV medial surface. In this way, the LCPF locally "pushed" regions of the AV so that the imaged closed-state geometry was matched (Figure 2). In addition to the LCPF, data points along the basal attachment of the AV were mapped from the open to the closed state by matching points using the NURBS surface parameterization.

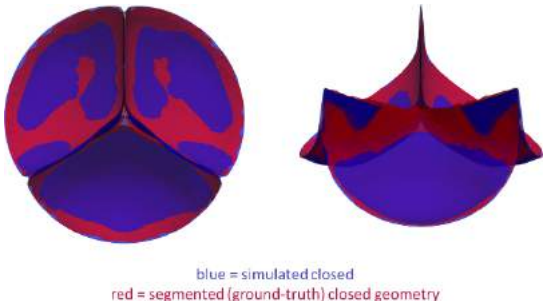

Figure 2. Image-derived and simulated diastolic AV geometries. The LCPF yielded a geometry that was within 0.5 mm of the true geometry at all points.

To further validate our method, we applied the strain estimation method to a computationally generated NURBS geometry of a bioprosthetic TAV implant, with locally prescribed collagen fiber orientation distributions and material properties (Figure 3). This validation approach had the distinct advantage of allowing for the comparison of our estimated stretch fields to ground-truth local stretch maps for the modeled TAV, which were obtained via isogeometric analysis.

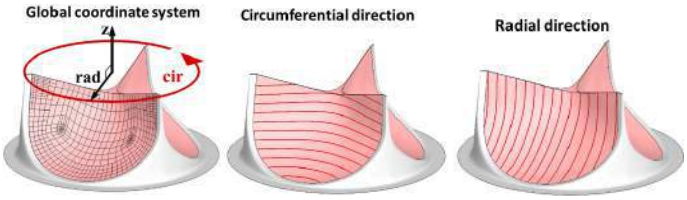

Figure 3. Definition of local material directions in the TAV.

RESULTS

The technique was able to capture the complex, heterogeneous leaflet deformation field of the AV. Moreover, our non-invasive method was able to yield strain estimates within 5% of their ground truth value over the entire leaflet surface (Figure 4). Resulting strain fields also corresponded well with results of structural simulations based on population-averaged fiber structural data and *in vivo* measurements from previous studies [5]. Based on the observed spatial resolution of the observed resultant strain field, this approach is sufficiently sensitive to capture the effects of variations in Raphe geometry as well as patient-specific heterogeneity in the in-plane deformations of both TAV as well as BAV leaflets.

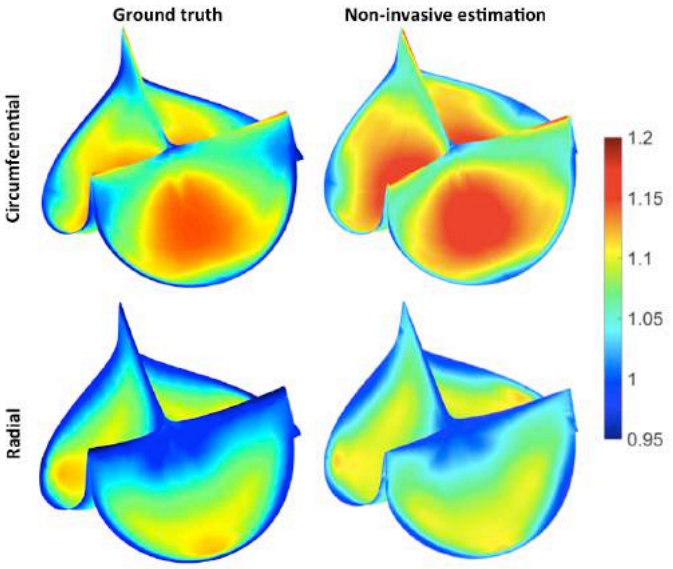

Figure 4. In-plane stretch in the normal TAV, showing the capability of the method to capture substantial regional heterogeneity as well as directional differences in strain.

DISCUSSION

We demonstrated the ability of our approach to non-invasively capture the deformation of an individual's TAV or BAV from *in vivo* imaging data with high sensitivity and regional detail. Deformation is a key parameter in the clinical assessment of valvular function, and serves as a direct means to determine regional variations in structure and function. This study is an essential step toward patient-specific assessment of BAV based on correlating leaflet deformation and AS/AI progression, as it provides a means for assessing patient-specific strain patterns.

ACKNOWLEDGEMENTS

This material is based upon work supported by the National Institutes of Health (grant no. R01-HL119297 to JHG and MSS), the National Science Foundation (grant no. DGE-1610403 to BVR), and the American Heart Association (grant no. 18PRE34030258 to BVR).

REFERENCES

[1] Brown JM et al. (2009) *J Thorac Cardiovasc Surg*, 137(1):82–90.
[2] Rego BV et al. (2018) *Int J Numer Meth Biomed Engng*. e3142.
[3] Pouch, AM et al. (2015) *Med Image Anal*, 26:217-231
[4] Smith, DB et al. (2000) *Ann Biomed Eng*. 28:598-611
[5] Aggarwal A et al. (2016) *J Biomech*, 49(12):2481-2490.

SB³C2019
Summer Biomechanics, Bioengineering and Biotransport Conference
June 25 -28, Seven Springs, PA, USA

COLLAGEN ARCHITECTURE, CELLULARITY, AND BIAXIAL MECHANICS OF OVINE TRICUSPID VALVE LEAFLETS

William D. Meador (1), Mrudang Mathur (2), Marcin Malinowski (3), Tomasz Jazwiec (3), Tomasz A. Timek (3), Manuel K. Rausch (1,4)

(1) Department of Biomedical Engineering
The University of Texas at Austin
Austin, TX, USA

(2) Department of Mechanical Engineering
The University of Texas at Austin
Austin, TX, USA

(3) Cardiothoracic Surgery
Spectrum Health
Grand Rapids, MI, USA

(4) Department of Aerospace Engineering and Engineering Mechanics
The University of Texas at Austin
Austin, TX, USA

INTRODUCTION

The three leaflets of the tricuspid heart valve (TV) function in a demanding and dynamic mechanical environment. Specifically, leaflets undergo tension, shear, and flexure with every heartbeat. To maintain their function under those conditions, the leaflets have evolved into structurally and biologically complex tissues. The stress environment, tissue structure, leaflet mechanics, and valve function are all interrelated. In fact, the leaflets of the left atrioventricular valve, the mitral valve (MV), have been shown to be able to grow and remodel in response to changing stress environments, in order to adapt to disease for example. Despite a mature understanding of the biomechanics of MV leaflets, little is known about TV leaflets. For instance, it is not clear how TV leaflet constituents influence their host's mechanical behavior. Toward elucidating the structure-function relationship of the TV leaflets, Amini Khoiy et al. characterized the biaxial anisotropic nonlinear behavior of porcine TV leaflets [1]. Additionally, Pham et al. quantified the mechanical properties and structural properties of human TV leaflets with biaxial testing and histology, respectively [2]. Most recently, Jett et al. used biaxial testing and histology to elucidate the material properties and gross biological structure of porcine TV leaflets [3]. However, there remains a need to understand how mechanosensing constituents (i.e. resident cells) influence the biological structure of TV leaflets and may thus, regulate their mechanical behavior. As such, the objective of this work is to elucidate the structure of mechanosensitive constituents (i.e. cells) and their micro-mechanical matrix (i.e. extracellular proteins, collagen), and its effect on tissue mechanics in ovine TV leaflets. This knowledge may have important implications for our understanding of TV behavior in altered stress environments, such as disease states, and developing TV-specific surgical techniques and devices.

METHODS

Toward this objective, we excised three tricuspid valves from six month-old healthy Dorset sheep. We excised 7x7 mm tissue samples from all three leaflets' (i.e. anterior, posterior, septal) belly region. Using a digital thickness gauge, we measured their average thicknesses. We applied four marker dots to each sample and photographed the stress-free reference configuration. We then mounted, preconditioned, and tested each sample in five biaxial configurations using a biaxial tension device. Simultaneously, we imaged the four marker dots to acquire in-plane strains. After biaxial testing, we prepared the same samples for two-photon microscopy. To this end, we applied a cell-permeant nuclear counterstain. To ensure full thickness image acquisition, we then applied a glycerol optical clearing solution under sonocation. We imaged three locations in 10μm z-step increments, through the entire thickness. At each imaging site, we epicollected the second harmonic generation of collagen and the fluorescence of the nuclear stain.

We isolated and analyzed the downstrokes of all biaxial loading configurations. We informed deformation gradients via strain image tracking, and calculated membrane tensions from raw force and displacement data. To account for mounting strain, we applied the additional deformation gradient from the stress-free state to the end of the downstroke. To analyze the preferential collagen fiber distributions, we used the ImageJ plugin, Directionality, and fit von Mises functions to the fiber distribution data at all locations and depths. For each sample, we normalized and averaged all location's von Mises distributions into a single distribution at each depth. We then averaged and interpolated the von Mises distributions by leaflet, through the thickness. Lastly, we utilized an in-house MATLAB code to analyze cell nuclei morphology at all locations and depths. We analyzed these parameters via similar averaged and interpolated histogram approaches described above.

Poster Presentation #P115

RESULTS

Results for equibiaxial loading are presented in Figure 1. We found that all leaflets exhibit similar behavior in the circumferential direction. When contrasting circumferential with the radial direction, the posterior leaflet exhibits strong anisotropy, while anterior and septal leaflets behave similar to one another with less degrees of anisotropy.

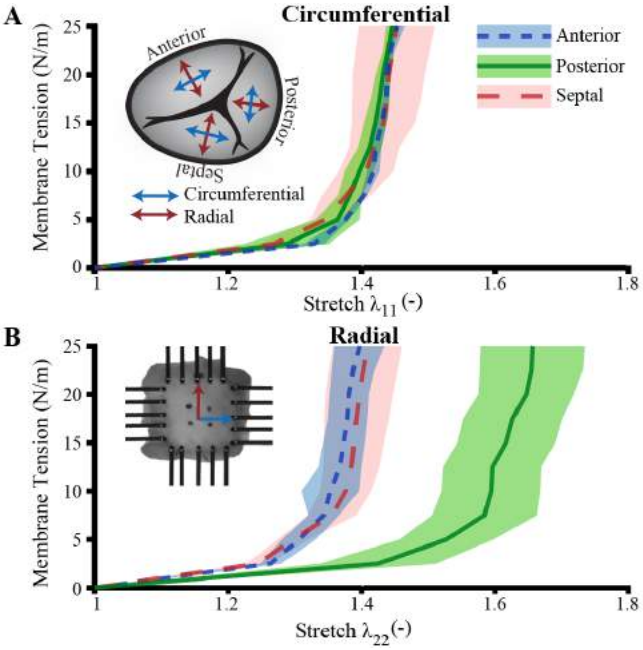

Figure 1: (A) Circumferential and (B) radial equibiaxial behavior of anterior, posterior and septal leaflets. Insets: (A) Definitions of circumferential and radial directions for tricuspid valves. (B) Biaxial sample as mounted for testing.

The collagen distribution and cell nuclei morphology analyses are presented in Figure 2. We found that the mean collagen fiber direction for anterior ($\mu = 74.2 \pm 4.5°$), posterior ($\mu = 72.7 \pm 1.8°$) and septal ($\mu = 72.5 \pm 1.2°$) leaflets is similar at all depths, while fiber orientation dispersion ($\kappa = 1.45 \pm 0.20$, $\kappa = 1.62 \pm 0.12$, and $\kappa = 1.23 \pm 0.31$, respectively) vary by leaflet and depth. Additionally, we found that cell nuclei orientation vary by depth and leaflet, preferentially aligning in the circumferential direction. Specifically, nuclei orientation of the posterior leaflet is less dispersed than anterior and septal leaflets. Eccentricity is similar among all leaflets by depth.

DISCUSSION

In this study we explored the tissue mechanics and constituent structure in healthy ovine TV leaflets using biaxial tension testing and two-photon microscopy. Specifically, we investigated and compared the structure and distribution of cell nuclei and their collagen matrix through the depths of all three TV leaflets, and analyzed these with respect to the tissue biaxial behavior.

All samples showed a classic nonlinear J-shaped curve. We found that the posterior leaflet exhibits the most anisotropic behavior of the leaflets, agreeing with the findings of both Amini Khoiy et al., and Jett et al. However, in our study, the anterior and posterior leaflets showed limited degrees of anisotropy, in disagreement with Amini Khoiy et al., Pham et al., and Jett et al. Possible reasons for the disagreement may arise from our use of a truly stress-free reference configuration, as opposed to the other studies that measure strain from the mounted state. Moreover, Amini Khoiy et al. and Jett et al. studied porcine TV leaflets, and Pham et al. studied human TV leaflets.

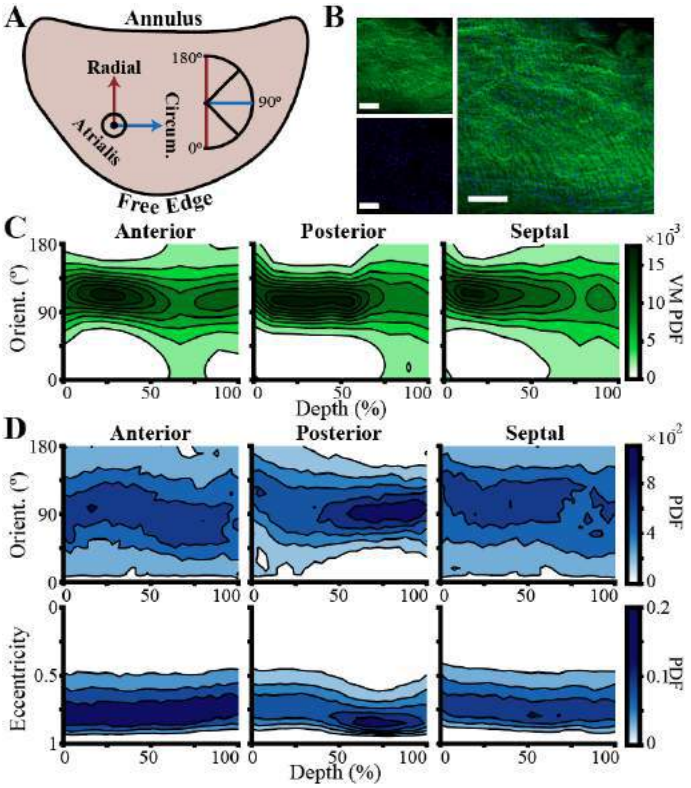

Figure 2: (A) Coordinate system and orientation map. (B) Composite image of collagen fibers (green) and cell nuclei (blue) (scale bar = 100 μm). (C) Collagen orientation distributions and (D) cell nuclei morphological distributions.

The mean collagen orientation is consistent between leaflets and through the leaflet thickness, with slight deviations toward the radial axis at the atrialis (~0-10%). The most interesting finding is how collagen fiber dispersion varies both by leaflet and depth. For all three leaflets, collagen orientation is mostly uniform through depth, but is widely dispersed in fibrosa/ventricularis layers (> 60%). Additionally, the posterior leaflet has the largest region of low dispersion, which may explain its large anisotropic behavior compared to the other leaflets. We also found that the cell orientations for all three leaflets agree with the orientation profiles of collagen, suggesting that the cells and collagen are aligned, potentially for mechanical reasons. The posterior leaflet cells had the lowest orientation dispersion among leaflets, similar to the posterior leaflet's collagen profile. Cell nuclei eccentricity was similar among leaflets by depth, but may be indicative of certain cell phenotypes (i.e. endothelial v. mesenchymal/interstitial). An additional analysis of cell membrane morphology would complement our study.

These data are necessary for understanding TV behavior in normal stress environments. They also provide the platform for comparison among altered stress environments, such as disease states.

ACKNOWLEDGEMENTS

We would like to acknowledge Matthew Bersi, PhD, for his assistance in analyzing cell nuclei morphology.

REFERENCES

[1] Amini Khoiy, K et al., *J Biomech Eng*, 138(10):104504, 2016.
[2] Pham, et al., *Acta Biomater*, 54:345-355, 2017.
[3] Jett, S et al., *J Mech Behav Biomed Mat*, 87:155-171, 2018.

SB³C2019
Summer Biomechanics, Bioengineering and Biotransport Conference
June 25 -28, Seven Springs, PA, USA

QUANTIFICATION OF SIMULTANEOUS STRUCTURE, STRAIN, AND STRESS BEHAVIORS IN LAYERED SOFT TISSUES

Samuel T. Potter (1), Will Goth (2), James W. Tunnell (2), Michael S. Sacks (1)

(1) Willerson Center for Cardiovascular Modeling and Simulation
Institute for Computational Engineering and Sciences
Department of Biomedical Engineering
The University of Texas at Austin
Austin, TX USA

(2) Biophotonics Laboratory
Department of Biomedical Engineering
The University of Texas at Austin
Austin, TX USA

INTRODUCTION

It has long been recognized that collagen fiber architecture (CFA) plays the key role in the mechanical behavior of collagenous soft tissues. However, a barrier to deeper understanding of the biomechanical behavior of collagenous soft tissues is the lack of methods for rapidly collecting CFA data in a non-destructive, non-contacting, full field manner. Typical transmitted light techniques e.g. small angle light scattering are too slow to be able to capture near real-time data on CFA dynamics and require modification to clear tissue. Polarized Spatial Frequency Domain Imaging (pSFDI) is a recently developed reflectance imaging modality that can rapidly obtain high-resolution fiber architecture data over wide fields of native tissues with controlled transmural measurement extent without the need for specimen optical clearing or sectioning [1]. Moreover, the CFA information can potentially be used as a form of texture for Digital Image Correlation (DIC) to create full-field, pixel resolution displacement fields without the need to apply some form of visual texture. Furthermore, while both the CFA and DIC deformation data can be represented and stored in various ways, Non-uniform Rational B-Splines (NURBS) surfaces represent a convenient and compact way of representing both types of data as smooth, continuous fields with a single, unified set of basis functions.

In the present study, we have combined pSFDI and NURBS based DIC into an experimental/computational system that can rapidly collect soft tissue specimen structure, strain, and stress information from a single experimental setup without specimen alteration. This combined approach allows us to investigate collagen fiber kinematics, particularly the affine kinematic model, which is widely used in computational models of fibrous tissues, with high spatial resolution.

METHODS

pSFDI system Our pSFDI imaging system has been previously described [1,2]. Briefly, a digital micro-mirror device (DMD) projected spatial frequency patterns through a linear polarizer (LP) onto the soft tissue specimen. The image of this spatial frequency pattern was captured through the same LP by a CMOS camera (Figure 1). This system was able to collect the pSFDI image data for a single spatial frequency over the full 2 cm x 2 cm field of view in approximately 5 seconds.

Data acquisition. The pSFDI imaging system was integrated with our planar biaxial testing device [3]. Native bovine pericardium (BP) specimens were presorted by their fiber preferred direction (PD) and then mounted onto the biaxial testing system with the fiber PD aligned with the test system's X1 axis. The specimens were then tested to an equibiaxial stress level of 225 kPa in a stepped loading protocol. pSFDI imaging data was collected at each step in the loading protocol. After the pSFDI images were collected over the stepped load protocol, the protocol was repeated with standard DIC speckle texture in order to compare deformation fields computed using the pSFDI texture versus the standard texture. Standard DIC speckle texture in the form of acrylic paint was applied to

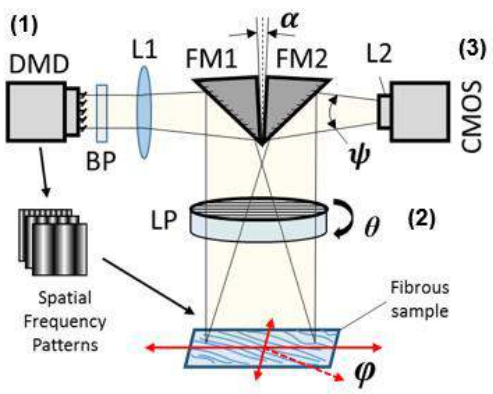

Figure 1. Schematic of pSFDI system detailing major components.

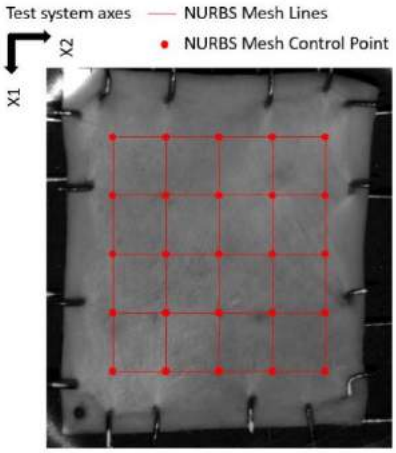

Figure 2. Specimen mounted on test device. NURBS mesh overlaid

the specimen using an airbrush (Figure 2). The stepped loading protocol was repeated with grayscale images of the speckle texture captured at each load step. The raw pSFDI images were processed with a custom Matlab program (MathWorks, Natick, MA) to produce maps of the CFA of the pericardium specimen which included information on fiber prefered direction (PD) and the degree of anisotropy (DOA), which correlates with the normalized orientation index (NOI) of the CFA orientation distribution function (ODF).

DIC. The processed pSFDI image data was converted to grayscale images. A custom Python program was used to perform a NURBS based DIC analysis [4] on the grayscale images to produce full field maps of the sample in-plane deformation (**F2D)**. An advantage to the NURBS based approach is that it enforces global continuity on the computed deformation field, thus eliminating non-physical deformations that can sometimes occur with traditional window based DIC analysis methods. First, a NURBS mesh is superimposed over the reference image (Figure 2). A trial deformation field is then created by displacing the control points of the mesh. Then the zero normalized sum of squares difference (ZNSSD) is computed between the pixels in the reference image mesh and corresponding pixels in the deformed image mesh. The L-BFGS-B algorithm is used to minimize the scalar ZNSSD value over mesh control point displacements. The minimizing control point displacement values are interpolated with the NURBS basis functions to create the full field deformation map.

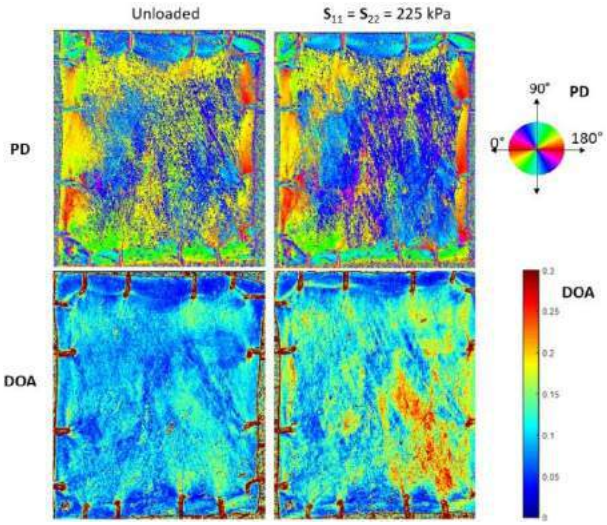

Figure 3. Changes to specimen fiber preferred direction (PD) and degree of anisotropy (DOA)

Affine kinematics. The affine kinematic model states that the total number of collagen fibers in a volume element of a tissue remains constant under deformation. The relationship between the fiber PD vectors in the reference **N** and deformed **n** configurations is given by

$$\mathbf{n} = \mathbf{F_{2D}N} \quad (1).$$

The orientation distribution function between the reference and deformed configurations, $\Gamma(\theta)$ and $\Gamma(\beta)$, respectively are related via

$$\Gamma(\beta) = \frac{\lambda_{\mathbf{N}}^2}{\det(\mathbf{F_{2D}})}\Gamma(\beta) \quad (2)$$

where $\lambda_{\mathbf{N}}^2$ is the square of the stretch in the fiber direction. Measured fiber PD data from the specimen reference configuration was used in conjugation with the computed **F2D** in this affine relationship to predict the value of the fiber PD in the deformed configuration. This predicted value was compared with the actual measured fiber PD.

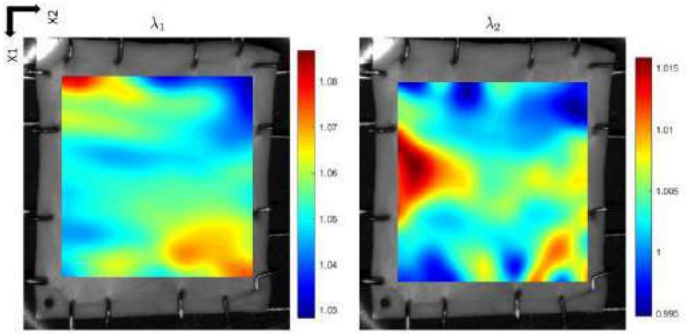

Figure 4. Deformation fields shown as stretch in the two biaxial test axis direction.

RESULTS

CFA. The pSFDI system captured the complex changes to the fiber PD and DOA with high spatial resolution (Figure 3). As expected, the CFA showed increased alignment under load as evidenced by the increase in DOA value. The DOA measurement also showed evidence of the CFA rearranging around the suture hook attachments used to mount the specimen to the biaxial testing device.

Deformation. The CFA data collected by pSFDI was shown to be a viable form of texture for DIC and the resulting deformation fields (Figure 4) showed regional variability in agreement with deformation fields computed from the standard DIC texture. Mean percent error for stretch in X1 was 2.5e-3 $\pm$ 1.1e-5 and 1.8e-3 $\pm$ 8e-6 for X2.

DISCUSSION

Our pSFDI system was able to capture the changes to bovine pericardium CFA over the full specimen in near real-time without the need to do any specimen preparation. This CFA data in turn was a viable texture for NURBS based DIC to compute the full field deformation map for the specimen. This combined experimental/computational approach represents an integrated way to simultaneously collect data on specimen CFA, strain, and stress in a single setup in near-real time. While the initial results are promising, we will continue to validate the approach for other types of soft tissues and biomaterials. We will also validate our deformation measurements computed using the pSFDI data as the DIC texture to measurements made using the traditional powder speckle texture approach. Finally, we have used the computed strain fields in combination with the CFA information to validate the affine kinematic model (1,2) and showed good agreement between the measured data and the affine model.

ACKNOWLEDGEMENTS

Supported by NIH NHLBI R01 HL142504, R01 HL129077

REFERENCES

[1] Yang, B. et al. *Biomed Opt Express* 6, 1520–1533 (2015)
[2] Goth, W. et al. *Ann Biomed Engr*, In Revision
[3] Zhang, W. et al., *J Biomech Engr*, 137 (2015)
[4] Elguedj, T. et al., *Comp Meth Appl Mech Engrg*, 200 (2011)

SB³C2019
Summer Biomechanics, Bioengineering and Biotransport Conference
June 25 -28, Seven Springs, PA, USA

THE ROLE OF SCLEROSTIN IN CALCIFIC AORTIC VALVE DISEASE

J. Ethan Joll (1) and W. David Merryman (1)

(1) Biomedical Engineering
Vanderbilt University
Nashville, TN, U.S.A.

INTRODUCTION

Calcific aortic valve disease (CAVD) is the most common disease of the cardiac valves and is an increasing concern in ageing populations. 1.5 million patients suffer from the disease and half of all untreated severe cases of CAVD result in death within two years [1]. Progression of the disease is characterized by the aortic valve becoming fibrotic and calcified, reducing valvular compliance and limiting blood flow into systemic circulation. This process - termed aortic stenosis – causes pressure overload, which leads to heart failure and death if left unchecked. Recent work investigating sex differences in CAVD show that women experience a larger degree of fibrosis while men preferentially experience calcification, indicating a potential difference in disease progression [2].

Currently, the only effective treatment for CAVD is valve replacement. There are no available pharmaceutical treatments. This is due to the unclear molecular mechanisms that govern the initiation and propagation of the disease. CAVD is known to be an actively regulated bioprocess involving a number of resident and invading circulating cells and various aberrant molecular pathways [3]. Sclerostin has recently been identified as a key regulator of bone homeostasis, playing a key role in the bone resorption axis. Sclerostin acts as a Wnt antagonist, which reduces the production of new bone matrix [4]. In addition, it facilitates the production of RANKL in osteocytes which causes osteoclastogenesis, increasing the resorption of bone [5].

Recent work has shown that sclerostin is produced in the aorta as well as the calcified aortic valve [6-7]. A recent phase III clinical trial for Romosozumab, a sclerostin blocking antibody, showed strong effects in bone, but was flagged for an increase in cardiovascular events. To date, there is only one direct study of the effect of sclerostin in cardiovascular disease, with Krishna et al. showing a protective effect in the development of angiotensin-II induced aortic aneurysm and atherosclerosis [8]. Based on the increasing amount of interest in sclerostin in cardiovascular disease and its potential as a drug target, this study aims to determine the role of sclerostin on the development of calcific aortic valve disease in cells and mice in order to more fully understand the implications of targeting this protein for treatment of disease.

METHODS

To generate mouse aortic valve interstitial cell lines (mAVIC), mice carrying the Immorto gene aged 4-6 weeks were sacrificed and the aortic valve leaflets were isolated. Tissue was digested using collagenase and cells were allowed to adhere to gelatin-coated tissue culture dishes. Aortic valve interstitial cells were confirmed by positive staining for α-smooth muscle actin and morphological characteristics. Nine cell lines were generated.

The direct effect of sclerostin on mAVIC's was assessed using a recombinant mouse protein at 1 ng/mL (R&D Systems). Cells were treated with control media or media supplemented with sclerostin for 6 hours. RNA was harvested and isolated using the Trizol method (Thermo Fisher Scientific). Expression of pro-CAVD RNA markers was assessed using quantitative polymerase chain reaction (qPCR).

A genetic mutant model was utilized to assess the role of sclerostin in the development of CAVD in a mouse model. Wild-type and mice carrying a heterozygous or homozygous deletion of the SOST gene were generated. At 10 weeks they were transitioned to a high-fat/high-cholesterol chow (Test Diet). The mice were aged for twelve months with echocardiography of the aortic valve performed at 2.5, 4, 6, 9, and 12 months. Long-axis velocity waveforms were measured using a custom Matlab script to assess changes in peak aortic velocity and mean gradient to characterize the development of CAVD.

Poster Presentation #P117

N=9 cell lines were used in this study. N=20 mice were used in each genotype divided evenly between male and female sex. D'Agostino- Pearson normality test was performed to assess data distribution. Student's t-test was used to test for significance between two groups. One-way analysis of variance was used to test for differences between multiple groups. Two-way analysis of variance was used to test the effects of sex, mutation, and their interaction in the animal study. For non-normally distributed data, the non-parametric variants of these tests were utilized.

RESULTS

Administration of recombinant sclerostin protein caused an increase in expression of Col1a1 in female cell lines but a corresponding decrease in male cell lines indicating a different mechanism of action. α-SMA expression increases in both male and female cell lines at a similar level (fig. 1).

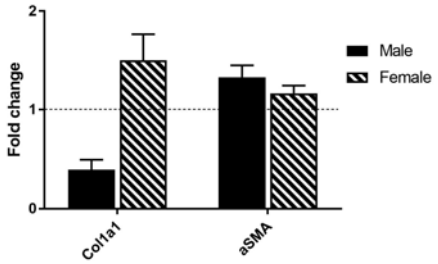

Figure 1: Sclerostin protein causes differential expression of collagen-1, increasing in females and decreasing in male cell lines.

Sclerostin causes the expression of RANKL in osteocytes which regulates osteoclastogenesis. However, this is a pro-disease factor in the development of CAVD [1]. Interestingly, an increase in expression of RANKL non-significantly (p=0.1271) correlated with α-SMA (fig 2, left) and significantly (p=0.0191) correlated with collagen (fig 2, right). Additionally, RANKL expression increased in males and decreased in females, indicating a potential sex-dependent regulation of this factor.

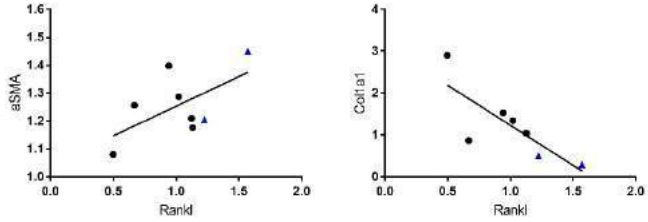

Figure 2: Pro-disease factor, RANKL, correlates positively with α-SMA expression (left) but negatively with Col1a1 (right). Triangles correlate with cell lines derived from male mice.

Echocardiographic parameters of CAVD were measured at 4 months of age in sclerostin mutant mice (fig. 3). Male and females differed significantly. With deletion of sclerostin, male mice had increased peak systolic velocity (fig. 3, top left) and mean gradient (fig. 3, top right) trending toward significance (p=0.2 and p=0.07 respectively) indicating a potential protective effect of the sclerostin on valve health. The opposite was true in females with a trending improvement of velocity (fig. 3, bottom left) and gradient (fig. 3 bottom right) with removal of sclerostin gene, indicating it is potentially a negative regulator of disease in this sex (p=0.08 and p=0.07 respectively).

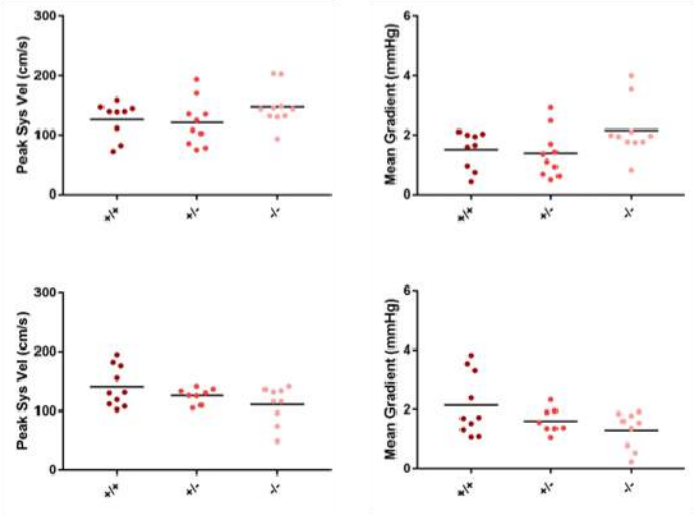

Figure 3: Deletion of the SOST gene diminishes valve function in males (top) and improves function in female (bottom).

DISCUSSION

CAVD is a disease that currently affects a significant number of people and will continue to be a public health concern in ageing populations. The lack of an available pharmaceutical treatment due to a poor understanding of the disease process is a major barrier in treating this disease.

This study begins to elucidate the role of sclerostin in CAVD. Sclerostin protein causes a potential shift to a disease phenotype in mAVIC's *in vitro*. There appear to be sex-differences at the cellular level. In human CAVD, females have shown to develop fibrosis while men tend toward calcification. This is supported by the data presented here with sclerostin causing collagen expression increases in female mAVIC's and the opposite for male. RANKL could be a potential regulator as male cells increased expression and females decreased. This tracked positively with α-SMA expression but negatively with collagen, indicating possible involvement of multiple pathways that interact with sclerostin in CAVD. In mice, female aortic valve performance improves with deletion of sclerostin while the opposite is true for males, providing more evidence for potential sex differences.

There are several limitations to this study that lend to future work. RANKL as a mediator of the sclerostin cellular effect is only correlation and needs to be directly investigated. Mouse data is currently not statistically significant. However, four months being relatively early for a full phenotype makes a stronger phenotype at later time points likely.

The role of sclerostin in cardiovascular disease remains unclear. However, this research reveals that this protein may be involved in the sex-dependent initiation or progression of calcific aortic valve disease.

ACKNOWLEDGEMENTS

NIH R35HL135790 and T32EB021937.

REFERENCES

[1] Yutzey KE et al., *ATVB,* 34 (11): 2387-2393, 2014.
[2] Simard L et al., *Circ research,* 120 (4): 681-691, 2017.
[3] Rajamannan NM et al., *Circulation,* 124 (16), 1783-1791, 2011.
[4] Delgado-Calle J et al., *Bone,* 96: 29-37, 2017.
[5] Wijenayaka AR et al., *PLoS One,* 6 (10). 2011.
[6] Moester MJC et al., *Calcif Tissue Int,* 87 (2): 99-107, 2010.
[7] Koos R et al., *J Heart Valve Dis,* 22 (3): 317-325, 2013.
[8] Krishna SM et al., *ATVB,* 37 (3): 553-566, 2017.

SB³C2019
Summer Biomechanics, Bioengineering and Biotransport Conference
June 25 -28, Seven Springs, PA, USA

A SPATIAL MEAN CURVATURE MAP OF THE AORTIC VALVE - RELEVANCE TO CALCIFICATION

Amanda Barreto, Asad M. Mirza, Sharan Ramaswamy

Department of Biomedical Engineering
Florida International University
Miami, Florida, United States

INTRODUCTION

Critical calcific aortic valve disease (CAVD) is a health condition which will require prosthetic valve replacement. The disease is expected to increase from 2.5 million cases in 2000 to 4.5 million in 2030 worldwide [4].

Calcification in the aortic valve is a highly regulated process which may be linked to early elastin degradation. For example, the expression of the MMP-12 gene activates inflammation in the valves leading to the fragmentation of elastin in the valve extracellular matrix (ECM), which in turn, may contribute to an increase in calcium deposits, hence leading to critical CAVD [3].

Functionally, the aortic valve is made up of three leaflets that facilitate unidirectional blood flow during systole. Subsequently, in the diastolic period, the leaflets close, thereby preventing blood regurgitation [1]. The deformation of the leaflets leads to a complex mechanical stress distribution through the course of the cardiac cycle, which is difficult to readily monitor.

Here, we hypothesized that tracking of aortic valve leaflet shape could be readily achieved via its time-dependent curvature during the cardiac cycle. The leaflet curvature changes could subsequently be used as a biomarker to assess abnormal valve extracellular matrix (ECM) remodeling activity, a potential precursor to CAVD. As a first step, the objective of the present study was to identify the mean anatomical spatial curvature distribution in an aortic valve without calcified deposits.

METHODS

A 3-dimensional model of a calcific aortic valve was acquired commercially (Materialise Inc, Plymouth, MI). The valve possessed calcific nodules, which were computationally removed to model a healthy valve (Fig 1A. and 1B.). The 3D model of the valve depicted a temporal position corresponding to the early diastolic period, when it was still slightly open.

Meshlab (ISTI-CNR, Pisa, Italy) was used to subdivide the mesh wherein every edge was split in its midpoint (Fig 1C and 1D). Duplicate vertices were removed and then a Laplacian function was used to smoothen any unevenness in the mesh. The normal values for vertices of the mesh were then calculated using the average of the nearest 10 neighbor vertices. The mesh was then saved in the polygon file format (PLY) for further processing.

An in-house script (MATLAB, Mathworks, Natick, MA) was used to import this mesh and calculate the mean leaflet curvature. The x,y,z data was parametrized to u, v and their respective normal were input into equation (1) below and solved for the principle curvatures (k_{min} , k_{max}) given by Meusiner's theorem [5].

$$k(\varphi) = \frac{e\varphi^2 + 2f\varphi + g}{E\varphi^2 + 2F\varphi + G} \quad (1)$$

where, φ is $\frac{du}{dv} = \tan(\theta)$, (e, f, g) and refers to the inner product of either u, v and their respective normal vector. Similarly, (E, F, G) refers to the inner product of points u, v with themselves. The mean curvature was then calculated as

$$k_{mean} = \frac{k_{min} + k_{max}}{2} \quad (2)$$

Mean curvature quantification was computed along the three cusps of the aortic valve geometry. Specifically, three points were extracted from each leaflet's: free edge, belly region, and close to the aortic wall. This process was performed on both the inflow (ventricularis) and outflow (fibrosa) sides of the valve.

RESULTS

The mean curvature for the ventricularis (A) and fibrosa (B) sides of the aortic valve was computed (Fig. 2). The nearest 50 vertex points at the

center of the region of interest were averaged together to report the curvature values (Table 1) for the various regions of the leaflet (free edge, belly, and aortic wall).

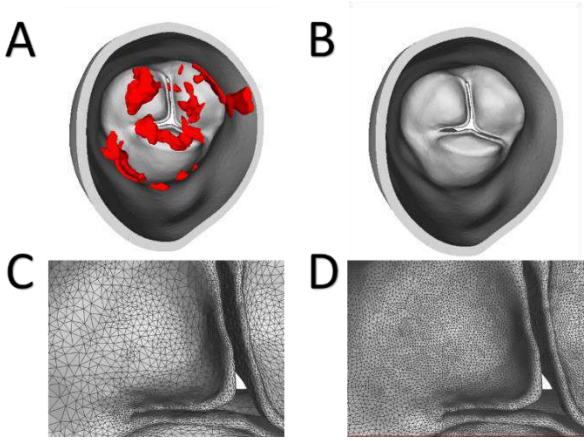

Figure 1: (A) Aortic valve with calcific nodules. (B) Aortic valve after computational removal of calcific nodules. (C) Default mesh. (D) Subdivided by midpoint scheme mesh.

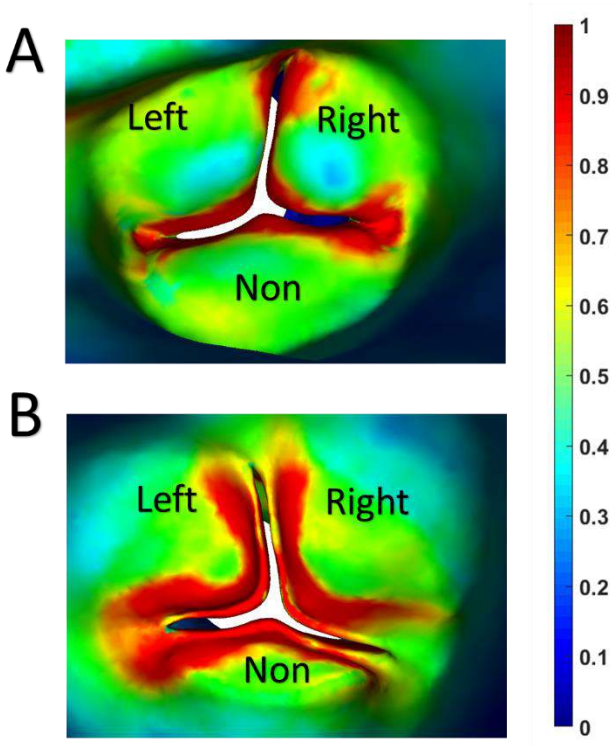

Figure 2: Mean curvature maps across all three leaflets (A) Ventricularis and (B) Fibrosa sides of the aortic valve.

DISCUSSION

The increasing rate of patients experiencing critical CAVD each year demands earlier diagnosis of the disease, to enable more effective patient management. Elastin protein is a key component of the valve's ECM and plays an important role in its function. The degradation of elastin has been associated with CAVD [3,8]. Since elastin content and structure contributes towards the leaflet temporal shape during the cardiac cycle, a measure of the valve's elastin status may be possible via the leaflet curvature, a potential bio-marker for early CAVD detection.

Table 1: Mean Curvature Across Aortic Valve Leaflets of the Ventricularis and Fibrosa Path

Ventricularis

	Free Edge	Belly Region	Wall
Non	.98	.41	.59
Right	.99	.25	.53
Left	1	.32	.51

Fibrosa

	Free Edge	Belly Region	Wall
Non	1	.55	.37
Right	1	.65	.33
Left	1	.49	.35

Our results showed that the mean curvature was relatively high along the free edges of the leaflet on the fibrosa-side (Fig. 2). Our preliminary observations (unpublished) associate much higher mean curvatures with loss of elastin in aortic valve tissues. In addition, the non-coronary cusps exhibited higher mean curvatures compared to the left and right coronary cusps (Fig. 2). The non-coronary cusp has previously been shown to be more susceptible to calcification [7]. Collectively, the current findings suggest that the non-coronary cusp may be a specific leaflet that may be monitored for longitudinal mean curvature tracking, as a measure of elastin content. Particularly, the free edge may be a specific anatomical location that could be targeted, as the current results indicate that its elastin content is relatively low, potentially making it vulnerable to calcification.

While our results give some evidence to the importance of using curvature as a predictive marker for CAVD there were various limitations to our study. We only examined a single early diastolic time-point for the aortic valve geometry. Therefore, an immediate next step in this work will be the evaluation of dynamic curvature changes in the aortic valve leaflets over the cardiac cycle, utilizing an *a priori* identified curvature metric that co-relates strongly with elastin content in the aortic valve.

ACKNOWLEDGEMENTS

A Coulter Seed Grant in the Department of Biomedical Engineering, College of Engineering and Computing, support of the Honors College, and the CURE program, Florida International University are gratefully acknowledged.

REFERENCES

[1] Fallahiarezoudar, E., et al. Procedia Manufacturing 2: p. 135-140. 2015

[2] Moses, D.A., et al. *Magn. Reason. Med*., 52: p. 154-163. 2004

[3] Perrotta, I., et al. *Histopathology*, 59(3): p. 504-513. 2011

[4] Yutzey, K.E., et al. *Arterioscler Thromb Vasc Biol*, 34(11): p. 2387-93. 2014

[5] do Carmo MP. Differential geometry of curves and surfaces. Englewood. Cliffs, NJ: Prentice Hall; 1976.

[6] Ayari R, et al. *Journal of Computers* vol. 9, no. 7, pp. 1572-1576, 2014.

[7] Cujec B., et al. *J. Am. Soc. Echocardiogr*. vol. 1, no. 6: p.430-2. 1988

[8] Bailey, M. T., et al. Journal of Biomedical Materials Research, 66(1): p. 93-102. 2003

SB³C2019
Summer Biomechanics, Bioengineering and Biotransport Conference
June 25 -28, Seven Springs, PA, USA

MATCHING MATERIAL AND CELLULAR TIMESCALES MAXIMIZES CELL SPREADING ON VISCOELASTIC SUBSTRATES

Ze Gong (1), Spencer E. Szczesny (2), Steven R. Caliari (3,4), Elisabeth E. Charrier (5), Ovijit Chaudhuri (6), Xuan Cao (1), Yuan Lin (7), Robert L. Mauck (2), Paul A. Janmey (5), Jason A. Burdick (3) and Vivek B. Shenoy (1)*

(1) Department of Material Science and Engineering
University of Pennsylvania
Philadelphia, Pennsylvania, USA.

(2) Department of Orthopaedic Surgery
University of Pennsylvania
Philadelphia, Pennsylvania, USA.

(3) Department of Bioengineering
University of Pennsylvania
Philadelphia, Pennsylvania, USA.

(4) Department of Chemical Engineering
University of Virginia
Charlottesville, Virginia, USA.

(5) Institute for Medicine and Engineering
University of Pennsylvania
Philadelphia, Pennsylvania, USA.

(6) Department of Mechanical Engineering
Stanford University
Stanford, California, USA.

(7) Department of Mechanical Engineering
University of Hong Kong
Hong Kong, China

INTRODUCTION

Tumor invasion, as a critical step in cancer progression and metastasis, requires tumors cell spreading on extracellular matrix (ECM) *in vivo*. Mounting evidence has demonstrated that the physical properties of the ECMs play a key role in cell migration and spreading [1, 2]. It is commonly believed that focal adhesions (FAs), which anchor the cell to the ECM as well as serve as hubs for the exchange of biological and mechanical stimuli [3, 4], are responsible for such mechano-sensitivity of cells.

Cells probe the stiffness of their surroundings by gauging the resistance of FAs to actin retrograde flow generated by intracellular myosin contractions [4, 5]. FAs, acting like molecular clutches, alter the movement of actin intracellular structures by providing a tunable connection to the ECM [5]. Based on this picture, the well-known motor clutch model [5, 6] was developed, which successfully predicted the dependence of cell adhesion traction (and consequently cell spreading) on ECM rigidity.

Beyond substrate rigidity, most natural ECM materials such as collagen, fibrin and tissues are viscoelastic in nature and exhibit a strong frequency-dependent mechanical response. Interestingly, it was reported recently that cell spreading can be enhanced by stress relaxation of a cell culture substrate (e.g., alginate, polyacrylamide), which was dependent on the elastic modulus of the ECM [2, 7]. This was explained by local remodeling (leading to increased ligand density) of the matrix during deformation [2], which corresponds to a plastic rather than viscous response. On the other hand, our own experiments suggest that viscosity has a negligible effect on how cells spread. However, it is unclear how a purely viscoelastic substrate can have different effects on cell spreading. By modifying the motor clutch model, we developed a theoretical model capable of revealing the physical mechanisms governing the cellular response to viscoelasticity.

METHODS

Model description: myosin motors pull the actin filament bundle towards the cell center, generating retrograde flow of actin. The molecular bonds/clutches, connecting the F-actin with the substrate, were assumed to be able to randomly break or re-engage with a dissociation or association rate of $r_{off,i}$ or r_{on} respectively. The master equation describing the evolution of the state of each clutch can be written as:

$$dP_{b,i}/dt = \left(1 - P_{b,i}\right)r_{on} - P_{b,i}r_{off,i} \quad (1)$$

Engagement of the clutches leads to slowing down of the retrograde flow allowing the polymerization at the leading edge to push the cell membrane forward resulting in the spreading of the cell. Based on the Bell's model, the dissociation rate is expected to increase exponentially with $F_{c,i}$, that is

$$r_{off,i} = r_{off}^{0} \cdot \exp\left(F_{c,i}/F_b\right), \quad (2)$$

where F_b is a characteristic force and r_{off}^{0} represents the breaking rate of clutches in the absence of any force. Recent experiments demonstrated that FAs grow on stiff substrates through the recruitment of integrin to the adhesion complex via talin unfolding [8, 9]. Following the model developed by Elosegui-Artola *et al* that describes such FA reinforcement [9], the association rate r_{on} is replaced by

$$r_{on} = r_{on}^{0}\left(1 + \alpha\left(F_a - F_{cr}\right)\right), \quad (3)$$

once the average clutch force F_a has surpassed a force threshold F_{cr}. For viscoelastic ECMs, we modeled as a standard linear viscoelastic solid material, and the force-displacement relation is given by

$$(k_a + k_l)\eta\, dx_s/dt + k_a k_l x_s = k_a F_s + \eta\, dF_s/dt. \quad (4)$$

Here k_a and k_l are the additional and long-term stiffness of substrate respectively, while η represents the viscosity for dashpot (Fig. 1a). We use both Kinetic Monte Carlo based on Gillespie algorithm and

analytical solution by solving ordinary differential equation (ODE) to simulate the process of cell spreading. All simulations and analysis were carried out in MATLAB.

Fabrication method: Viscoelastic polyacrylamide gels are fabricated by integrating viscous linear polyacrylamide (5%) in the structure of an elastic cross-linked polyacrylamide network (8%). Viscoelastic hyaluronic acid gels are fabricated by combining covalent and supramolecular crosslinking hyaluronic acid. More details can be seen in the work of Gong *et al.* [10].

RESULTS

By treating the substrate as a standard linear viscoelastic solid (Fig. 1a), we found that an intermediate level of viscosity can promote cell spreading when the ECM rigidity is relatively low. As for high rigidity, the large tension borne by the clutches triggers an increase in their binding rates as well as an increase in the integrin density (clutch reinforcement), which saturates the cell response to substrate stiffness and eliminates any role of viscosity. These data are presented in heat maps of spreading response in the parameter space spanned by the substrate and cellular timescales (Fig. 1b).

The competition between extracellular timescales (ECM relaxation timescales) and intracellular timescales (focal adhesion lifetime and clutch binding timescale) leads to the viscoelastic regulation (Fig. 1a). For low ECM rigidity, maximum cell spreading is achieved at an optimal level of viscosity, where the substrate relaxation time τ_s falls between the timescale for clutch binding τ_b and the characteristic binding lifetime τ_l (Fig. 1c regime II). This is because viscosity stiffens soft substrates on a timescale faster than the clutch off-rate, which enhances cell-ECM adhesion and subsequent cell spreading. Conversely, for stiff substrates (Fig. 1b reinforcement regime), talin unfolding triggers integrin recruitment and viscosity does not influence cell spreading since the number of bound clutches is saturated.

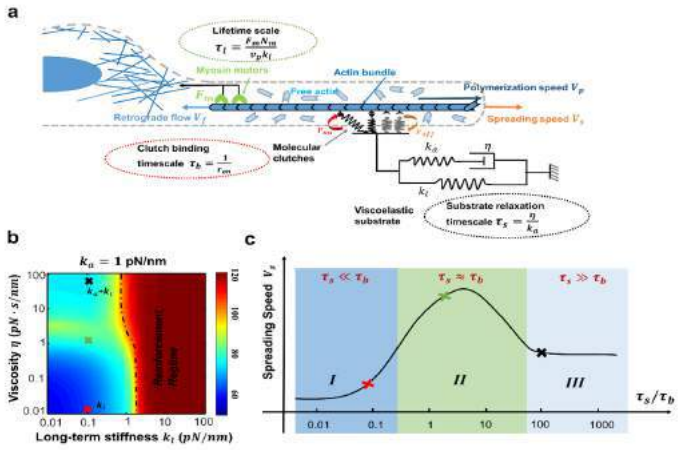

Figure 1 (a) Schematic of the motor clutch model of a cell attached to a viscoelastic ECM modeled as a standard linear solid. (b) Heat map of spreading speed, V_s, plotted as a function of the long-term stiffness, k_l, and viscosity, η, for $k_a = 1$ pN/nm. (c) Schematic of three regimes for effect based on relaxation timescales: I) when $\tau_s \ll \tau_b$, the viscoelastic ECM has the same effect on cell spreading as an elastic ECM with long-term stiffness k_l. II) when $\tau_s \approx \tau_b$, maximum spreading is observed on viscoelastic ECMs. III) when $\tau_s \gg \tau_b$, the viscoelastic ECM gives the same spreading speed as an elastic ECM with the initial stiffness $k_a + k_l$.

To further verify the predictions of our model, we performed cell spreading experiments on viscoelastic ECMs synthesized by different methods. Our model successfully explains the viscoelastic regulation of cell spreading for three completely distinct types of hydrogels (HA, polyacrylamide, alginate) with different ways of imparting viscoelasticity (supra-molecular interactions, semi-interpenetrating network, ionic crosslinking), different stiffness (range from $10^{-1} - 10^{1}$ pN/nm), and different cell types (human MSCs, 3T3 fibroblasts, U2OS osteosarcoma line). By capturing the mechanism by which substrate viscoelasticity affects cell spreading across a wide range of material parameters, our model provides a useful tool for designing biomaterials that optimize cellular adhesion and mechano-sensing.

DISCUSSION

Most viscoelastic ECMs possess multiple relaxation timescales. To determine which relaxation timescale is most significant, we also developed a practical way to calculate the effective relaxation timescale of viscoelastic ECM regarding their influence on cell spreading. First, relaxation time spectra were obtained from stress relaxation data of viscoelastic substrates. Then, we picked the most significant timescale (i.e., the highest peak for $\tau_s \geq \tau_b$) from relaxation spectrum as the effective timescale. Explicit simulations with multiple timescales confirmed that our choice of the effective timescale faithfully describes the dynamic cell spreading on viscoelastic substrates [10]. In cases where there are multiple prominent relaxation times beyond the binding timescale, simulations show that the resulting cell spreading is approximately a weighted average of the effect for each timescale.

Previous studies suggested that the effects of substrate viscoelasticity on cell spreading are due to local substrate densification and plastic flow [2]. However, these experimental results can be reproduced by our model, demonstrating that viscoelasticity alone is capable of explaining their findings. Overall, we have developed an analytical model that incorporates the viscoelastic relaxation time spectrum and successfully explains the effects of substrate viscoelasticity on cell spreading. It can also help predict cell spreading over the full parameter space for viscoelastic substrates, which will enable the rational design of biomaterials.

ACKNOWLEDGEMENTS

This work is supported by the National Cancer Institute awards U01CA202177 and U54CA193417 (to V.B.S.), National Institute of Biomedical Imaging and Bioengineering award R01EB017753 (to V.B.S.), and the NSF Center for Engineering Mechanobiology (CMMI-154857).

REFERENCES

[1] V. B. Shenoy, H. Wang, & X. Wang, *Interface focus,* 6(1):20150067,2016.
[2] C. Ovijit, *et al.*, *Nat Commun,* 6:6365, 2015.
[3] X. Cao, et al., *Biophys J,* 109(9):1807-1817, 2015.
[4] J. T. Parsons, K. H. Martin, J. K. Slack, J. M. Taylor, & S. A. Weed, *Oncogene,* 19(49):5606-5613, 2000.
[5] C. E. Chan & D. J. Odde, *Science,* 322(5908):1687-1691, 2008.
[6] B. L. Bangasser & D. J. Odde, *Cell Mol Bioeng,* 6(4):449-459, 2013.
[7] A. R. Cameron, J. E. Frith, & J. J. Cooper-White, *Biomaterials,* 32(26):5979-5993, 2011.
[8] A. Elosegui-Artola, et al., *Nat Cell Biol,* 18(5):540-548, 2016.
[9] A. Elosegui-Artola, et al., *Nat Mater,* 13(6):631-637, 2014.
[10] Z. Gong, et al., *Proc Natl Acad Sci,* 115(12): E2686-E2695, 2018.

SB³C2019
Summer Biomechanics, Bioengineering and Biotransport Conference
June 25 -28, Seven Springs, PA, USA

EXTRACELLULAR MATRIX MICROSTRUCTURE MODULATES MYOFIBROBLAST DIFFERENTIATION WITHIN 3D FIBROUS MICROENVIRONMENTS *IN VITRO*

Daniel L. Matera (1), Brendon M. Baker (2)

(1) Department of Chemical and Biological Engineering, University of Michigan, Ann Arbor, MI.

(2) Department of Biomedical Engineering, University of Michigan, Ann Arbor, MI.

INTRODUCTION

Fibrosis is a central component of several untreatable interstitial lung diseases including idiopathic pulmonary fibrosis (IPF), which possesses an average expected patient survival of 3–5 years post-diagnosis [1]. Our current understanding of the progression of fibrosis involves a stepwise cascade whereby tissue damage leads to macrophage accumulation and cytokine release, which in turn triggers the proliferation and differentiation of resident fibroblasts into an expansive myofibroblast (MF) population. Considered the major cellular drivers of fibrotic diseases [2], MFs cause eventual organ failure through excessive extracellular matrix (ECM) secretion, remodeling and crosslinking. The differentiation of fibroblasts into MFs is known to be influenced by both biochemical and physical cues from the tissue microenvironment [3–5]. In particular, it has been suggested that a sufficiently stiff matrix is a prerequisite to MF differentiation; below a threshold matrix stiffness, fibroblasts fail to activate into MFs even in the presence of potent fibrotic soluble cues such as transforming growth factor β1 (TGF-β1) [6]. These studies implicate matrix mechanics as a required signal for MF induction, however, previous *in vitro* studies primarily employed 2D elastic culture surfaces to model healthy vs. fibrotic tissues [7]. In contrast, fibroblast-macrophage interactions and MF differentiation occur within the lung interstitium, the fibrous 3D tissue spaces surrounding lung parenchyma. To provide a synthetic model of the interstitium for studying the dynamics of fibrosis, we have developed fiber-reinforced hydrogel composites (FHC) with controllable fibrous microstructure. These materials which support fibroblast and macrophage culture can be degraded and remodeled by cells over time. Using this system, we examined the effect of 3D fibrous microstructure on myofibroblast differentiation *in vitro*.

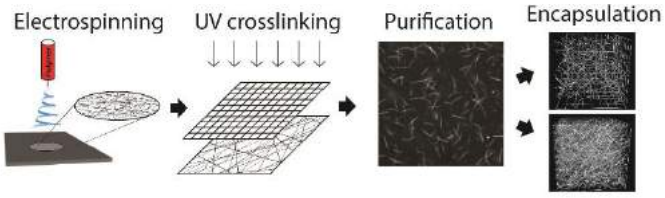

Figure 1: Fiber-reinforced hydrogel composite fabrication technique. DexVS fibers are electrospun, UV crosslinked under a photomask used to define fiber length, collected, and encapsulated in user-defined 3D hydrogels at varying fiber

METHODS

Fiber fabrication: Dextran vinyl sulfone (DexVS) was dissolved at 60% w/v in 1:1 water:dimethylformamide with 0.015% Irgacure 2959 photoinitiator and electrospun into a thick fibrous mat. A photomask was used to photopolymerize fiber segments of defined lengths. These fibers were then hydrated,purified by centrifugation, and coupled with cell adhesive ligand RGD at a concentration of 2mM. Hydrogel encapsulation: Fibers were resuspended in 5% w/v gelatin methacrylate (GelMA) hydrogel solutions containing cells and 0.02% LAP photoinitiator. Cell culture: Human dermal fibroblasts (HDF) and normal human lung fibroblasts (NHLF) were cultured in DMEM with 10% FBS and murine bone marrow derived macrophages (BMDMs) were cultured in RPMI with 10% FBS and 10 ng/ml M-CSF. Cells were encapsulated in GelMA fiber reinforced hydrogels and cultured for 7-14 days with or without 5ng/ml TGF-β1. Media was

changed every 2 days. Visualization: 3D cultures were fixed with 4% paraformaldehyde and immunostained for YAP (Abcam ab52771) and αSMA (Sigma A5228) with counterstaining for cell nuclei (DAPI) and F-actin (phalloidin). 3D image stacks were collected on a Zeiss LSM800 confocal microscope.

RESULTS

To model ECM microstructural changes during the transition from healthy to fibrotic lung interstitium, we generated 3D matrices with a tunable input density of DexVS fiber segments encapsulated in a bulk GelMA hydrogel (**Figure 1**). We cultured human dermal fibroblasts in non-fibrous controls, low (FD 0.5% vol.) and high (FD 1% vol.) fiber density matrices for 7 days in the presence of TGF-β1, and then stained for F-actin and yes-associated protein 1 (YAP), a transcriptional co-activator previously associated with MF differentiation. Cells in fibrous composites exhibited higher spread area compared to non-fibrous controls, and YAP nuclear localization was nearly two-fold higher at high fiber density (FD 1% vol.) compared to controls **(Figure 2a,b).** Potentially due to YAP-induced proliferation, we also noted increased cell density and multicellular clusters with high fiber density **(Figure 2b)**, similar to the fibroblastic foci observed histologically in fibrotic tissues. When culturing normal human lung fibroblasts (NHLFs) for 14 days in the presence of TGF-β1, we observed significantly greater staining for the MF marker αSMA in fiber-reinforced (FD 1% vol.) compared to control conditions **(Figure 2c,d)**.

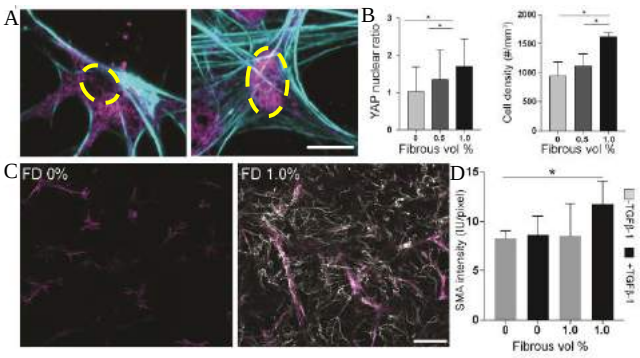

Figure 2: A) Representative images of HDFs in control or fiber-reinforced hydrogels (day 7) stained for YAP (magenta) and F-Actin (cyan). Cell nuclei outlined in yellow; scale bar: 10 µm. B) Corresponding quantification of YAP and cell density. C) Images of NHLF αSMA (magenta) expression (day 14) in control and fiber-reinforced hydrogels in the presence of TGF-B1. DexVS fibers depicted in white; scale bar: 50 µm. D) NHLF αSMA quantification. * indicates significant difference with p-value < 0.05.

To examine if hydrogel composites could support fibroblast-macrophage interactions that lead to MF differentiation, we performed 3D co-culture experiments with NHLFs and mouse macrophages. After 7 days of co-culture, we noted nearly a 200% increase in αSMA staining in co-cultures as compared to fibroblast monocultures lacking TGF-β1 supplementation (**Figure 3a,b**). Interestingly, NHLF differentiation into MFs due to macrophage co-culture was more pronounced and occurred faster than in monoculture conditions supplemented with 5ng/ml TGF-β1 **(Figure 3b)** – the established concentration used *inivitro* to model a soluble profibrotic stimulus.

DISCUSSION

This work introduces fiber-reinforced hydrogels to model the interstitial tissue spaces where fibrotic changes unfold. These composites can be fabricated with a bulk hydrogel of choice,

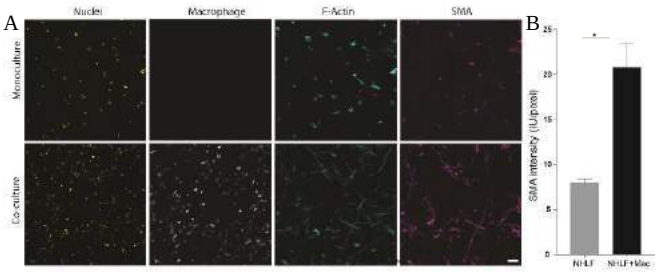

Figure 3: A) Fibroblast (monoculture, top) and fibroblast-macrophage (co-culture, bottom) encapsulated within FHCs at day 7, showing maximum projections of nuclei (yellow), macrophages (white), F-actin (cyan), and αSMA (magenta); scale bar: 50 µm. B) Quantification of αSMA staining intensity. * indicates significant difference with p-value < 0.05.

while presenting cells with a highly tunable fibrous topography. Initial findings with dermal and lung fibroblasts are in line with numerous *inivivo* studies correlating fibroblast proliferation and MF differentiation with an increasingly dense fibrous microstructure in the interstitium. In composites with lower fiber density, significant differences in spread area, YAP activity, and cell density relative to non-fibrous controls were not observed **(Figure 2b)**. As healthy interstitial tissue is naturally fibrous, low fiber density may reflect a homeostatic ECM architecture. Although only fiber density was explored in this work, future studies employing this model could allow for a more extensive investigation into how 3D fibrous microstructure influences fibroblast and macrophage phenotypes.

While fibroblast monoculture studies have improved our understanding of MF differentiation, previous clinical trials targeting solely MFs were largely unsuccessful in halting disease progression and reducing patient mortality [9,10]. Recent efforts have shifted toward the role of supporting cell types such as macrophages; the first FDA approved drugs for IPF, Pirfenidone and Nintedanib, target innate immunity in addition to fibroblasts [11,12]. The intricacies of how fibrotic ECM affects innate immunity, and how immune cells directly influence resident fibroblast population is not fully understood. This approach enabling long term co-culture of macrophages and fibroblasts in a structurally relevant matrix will support future studies examining dynamic interactions between these cells mediated by the ECM. In summary, this work establishes a biomimetic model of fibrotic interstitial tissue, where physical and soluble fibrotic cues from the microenvironment can be modeled via fibrous ECM and macrophage incorporation, respectively. This model will provide further insight into fibroblast- and macrophage-ECM interactions, and would be a suitable platform for drug screening applications and high-resolution time-lapse microscopy.

ACKNOWLEDGEMENTS This work was supported in part by the NIH (HL124322) and from the NSF GRFP (DGE1256260).

REFERENCES

[1] Farkas J et al., Am. J. Respir, 2011 (45(1):1-15); [2] Wynn T Nat. Med. 2012 (1028–40); [3] Darby, O et al., Lab. Invest,1990 (63(1):21-29); [4] Singer AJ et al., N. Engl. J. Med, 1999 (341(10):738-746); [5] Gabbiani G et al., J. Pathol, 2003 (200(4):500-503); [6] Goffin JM et al, J. Cell Biol, 2006 (172(2):259-268); [7] Balestrini JL et al., Integr. Biol, 2012 (4(4):410-421); [8] Varga, J et al., Curr. Opin. Rheumatol, 2008 (20(6):720-728); [9] Vittal, R et al., Pharmacology, 2007 (321(1):35-44); [10] Distler, J et al., Rheumatology, 2009 (48(2):98-103); [11] Schaefer, C et al., Eur. Respir. Rev, 2011 (20(120):85-97); [12] Wollin, L et al., J. Pharmacol. Exp. Ther, 2014 (349(2):209-220).

SB³C2019
Summer Biomechanics, Bioengineering and Biotransport Conference
June 25 -28, Seven Springs, PA, USA

ARCHITECTURE AND FUNCTION OF CHICK EMBRYONIC HEART CELLS ARE MEDIATED BY GEOMETRIC ECM PATTERNING CUES

Bernard L. Cook III (1), Patrick W. Alford (1)

(1) Department of Biomedical Engineering
University of Minnesota
Minneapolis, MN, USA

INTRODUCTION

Heart formation begins with migration of bilateral pre-cardiac cell populations towards the embryo's midline (Fig. 1A-1B), a process driven by germ layer sheet folding and cell movements along protein gradients. At the midline, these populations merge to form the primitive linear heart tube (Fig. 1C). Subsequent morphogenesis, or shape change, of the heart tube involves symmetry breaking and bending (Fig. 1D) to eventually produce a functional heart. Disruption of these processes can result in congenital heart defects (CHDs), the leading cause of death in infants younger than one year [1]. Morphogenesis is a fundamentally mechanical process. Extracellular matrix (ECM) protein gradients and cell contractility gradients direct proper migration of and fusion of bilateral pre-cardiac cell populations to fuse at the embryo's midline to form the primitive linear heart tube, respectively [2,3], while actin polymerization is necessary to drive bending of the linear heart tube to adopt a C-shape [4]. Notably, F-actin arrangement of heart tissue varies between the inner and outer curvature of the heart (Fig. 1E-1G) and disrupting this native arrangement can reverse left-right asymmetry decision for heart looping suggesting that local cytoskeletal changes might drive global shape changes [5,6]. Here, we culture embryonic heart cells explanted from chicken embryos onto ECM micropatterns to determine how ECM architecture influences both F-actin arrangement and active force generation.

METHODS

Construct preparation. Custom constructs used for micropatterning cells were prepared. Dow SYLGARD™ 527 polydimethylsiloxane (PDMS) was spin-coated onto glass coverslips.

Micropatterning constructs. PDMS stamps were prepared using standard photolithography techniques. Stamps with aspect ratio 1

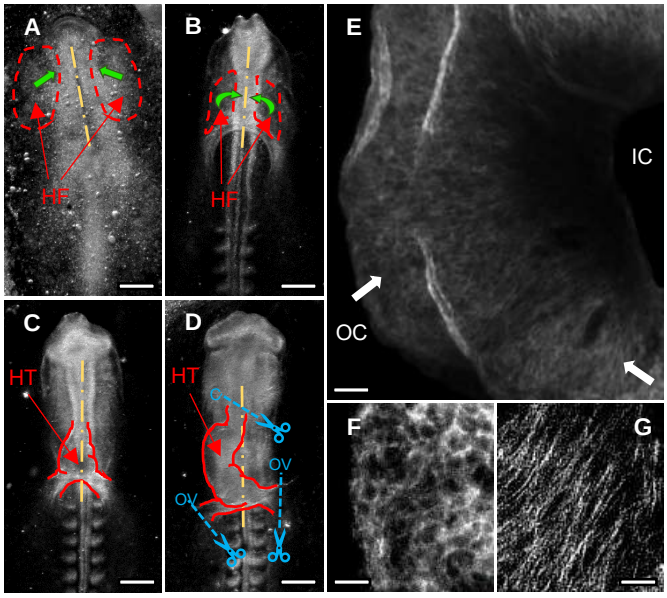

Figure 1: A) Pre-cardiac cells ("heart fields" (HF), dotted red) migrate (green) towards embryo midline (yellow). B) HFs fold out of plane, continue towards midline. C) HFs fuse to form the primitive linear heart tube (HT, red). D) HT bends and rotates to form a C-shape. E) Whole-heart explant stained for F-actin, depicting both inner and outer curvature (IC and OC, respectively). White arrows on left and right highlight F-actin structure at F) OC of heart and G) IC of heart, respectively. Scale: A=600 μm, B-D=300 μm, E=30 μm, F-G=10 μm.

(AR1) and aspect ratio 4 (AR4) "islands" with areas of 4000 μm^2 (AR1: 63 μm × 63 μm, AR4: 127 μm × 32 μm) were incubated feature-side-up with 50 μg/mL fibronectin in deionized water for 1 hr at room temperature. Excess fibronectin solution was removed from the stamps, and then stamped onto UV-treated custom constructs. Constructs were blocked with 1% pluronics for 5 min.

Preparation of chicken embryos & heart explants. Fertilized White Leghorn chicken eggs were incubated on their side in a humidified, 38.5°C environment for 46-56 hrs to yield embryos at Hamburger & Hamilton stages 9-14. Filter paper hole-punched with a "figure-8" pattern was gently set on top of the vitelline membrane surrounding the embryo and allowed to adhere. Then, cuts through the vitelline membrane were made around the filter paper to remove the embryo and vitelline membrane attached to the filter paper. The embryo was rinsed in PBS and placed in a 35 mm tissue culture dish with 1 mL of ice-cold PBS for further dissection. Hearts were explanted under a Lumar dissection scope. To remove hearts, microdissection scissors were used to make incisions through the omphalomesenteric veins and the primitive conus (Fig. 1B, labeled "OV" and "C," respectively; cut lines shown in blue). All explanted hearts were placed in 4°C Dulbecco's Modified Eagle's Medium (DMEM) in a microcentrifuge tube before further processing.

Heart cell extraction & seeding constructs. Heart explants were further digested prior to seeding cells onto stamped constructs. Explants in DMEM were centrifuged, media removed, and resuspended in 0.25% trypsin-EDTA warmed to 37°C for further digestion. Heart cells were then seeded onto stamped constructs in DMEM supplemented with 10% chick serum and 1% penicillin-streptomycin. Cell-seeded constructs were incubated at 37°C in a humidified, 5% CO_2 environment until they were ready to be assessed.

Immunohistochemistry & cell structure quantification. Cell structure on both AR1- and AR4-stamped constructs was assessed at both 4 and 24 hrs post-seeding. Cells were fixed with 4% PFA and stained with phalloidin and DAPI to asses F-actin structure and nuclei, respectively. Cell islands were imaged on an inverted fluorescent microscope. F-actin alignment for individual micropatterned islands was determined by applying a custom MATLAB code to F-actin fluorescent images.

Traction force calculation. Cell traction forces were determined using standard traction force microscopy (TFM) techniques [7]. Briefly, fluorescent nanoparticles were embedded in custom PDMS constructs. Constructs were stamped with ECM micropatterns and seeded with cells as described. Using an inverted fluorescent microscope, fluorescent bead layers beneath cell islands were imaged with cells and without cells to capture with-cell and cell-free bead images. Particle image velocimetry (PIV) and Fourier transform traction cytometry (FTTC) plugins in ImageJ were applied to with-cell and cell-free bead images for individual islands to determine cell traction forces.

RESULTS

Heart explant cells remained viable in culture for 24 hrs as observed by beating of patterned islands (data not shown). Cells cultured for 4 hrs possessed interconnected F-actin "rings" surrounding individual nuclei (Fig. 2A, first column) on both AR1 and AR4 fibronectin islands, characteristic of epithelial cells and evident in stained whole-hearts (Fig. 1C). However, cells cultured for 4 hrs often did not span the entire area of ECM islands. Cells cultured for 24 hrs had less-apparent F-actin rings surrounding individual nuclei. Moreover, cell islands appeared to more thoroughly adopt the fibronectin island shape and possessed F-actin filaments spanning over nuclei, suggesting out-of-plane growth and remodeling.

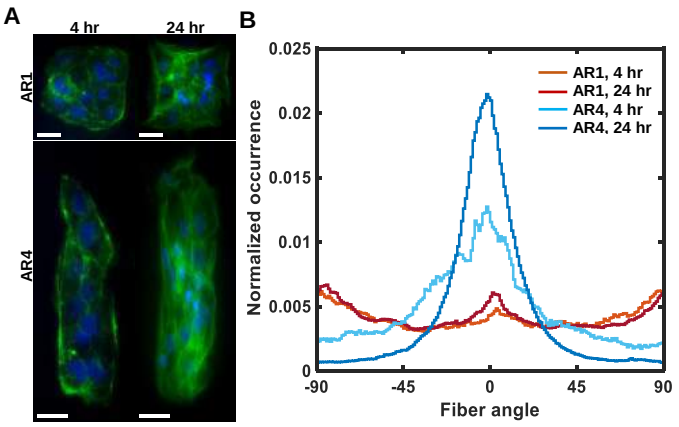

Figure 2: A) Embryonic heart cells cultured on aspect ratio 1 (AR1, top row) and aspect ratio 4 (AR4, bottom row) ECM islands stained for F-actin (green) and nuclei (blue) after 4 and 24 hours in culture (left and right columns, respectively). B) F-actin alignment of cell islands. Scale in A) = 20 μm.

Alignment data suggests that AR4 cell islands undergo F-actin remodeling between 4 and 24 hrs in culture, while AR1 cell islands undergo little to no remodeling (Fig. 2B). Cells patterned on AR1 islands have nearly isotropic alignment and undergo little remodeling in the plane of the cells. F-actin in cells patterned on AR4 islands is primarily aligned with the long-axis of the island after 4 hrs in culture and undergoes substantial remodeling to align more strongly with the long axis of the ECM island after 24 hrs in culture.

DISCUSSION

Here, we found that embryonic chick heart cells cultured on fibronectin ECM islands adopt F-actin alignment and remodel F-actin dependent on ECM island shape. Cytoskeletal structure responds to ECM shape, and informs active cell-generated forces. Studies show that extracellular architecture influences cytoskeletal structure and active force generation in individual cells and embryos [8,9]. Taken in context of such studies, our results suggest that ECM geometrical constraints influence F-actin alignment and may influence cell-generated forces and morphogenetic behavior of the heart. Understanding how ECM shape cues guide F-actin structure and cell-generated forces may help explain heart morphogenesis phenomena like existence of endodermal contraction gradients responsible for fusion of cardiac fields and actin-driven C-bending of the linear heart tube. Future work seeks to determine how differences in ECM shape influence cell-generated forces.

ACKNOWLEDGEMENTS

We acknowledge financial support from the National Science Foundation CMMI-1563198.

REFERENCES

[1] Roger, V. et al., *Circulation*, 123:e18-e209, 2011.
[2] Linask, K., and Lash, J., *Dev Biol*, 129:315-323, 1988.
[3] Shi, Y. et al., *Phys Biol*, 12:016012, 2015.
[4] Shi, Y. et al., *J Biomech Eng*, 136:081002-1, 2014.
[5] Itasaki, N. et al., *Anat Embryol*, 180:413-420, 1989.
[6] Itasaki, N. et al., *Anat Embryol*, 183:29-39, 1991.
[7] Tseng, Q. et al., *PNAS*, 109(5):1506-1511, 2012.
[8] Shao, Y. et al., *Integr Biol*, 6:300-311, 2014.
[9] Chanet, S. et al., *Nat Commun*, 8:15014, 2017.

THREE-DIMENSIONAL CT MORPHOMETRIC IMAGE ANALYSIS OF THE CLIVUS AND SPHENOID SINUS IN CHIARI MALFORMATION TYPE I

Blaise S. T. Nwotchouang (1), Maggie S. Eppelheimer (1), Paul Bishop (1,2), Dipankar Biswas (3), Janna M. Andronowski (4), Jayapalli R. Bapuraj (5), David Frim (6), Rick Labuda (7), Rouzbeh Amini (1,3), Francis Loth (1,3)

(1) Department of Biomedical Engineering
University of Akron
Akron, OH, US

(2) Department of Vascular Surgery
Cleveland Clinic
Cleveland, OH, US

(3) Department of Mechanical Engineering
University of Akron
Akron, OH, US

(4) Department of Biology
University of Akron
Akron, OH, US

(5) Department of Radiology
University of Michigan Health System
Ann Arbor, MI, US

(6) Department of Neurosurgery
University of Chicago
Chicago, IL, US

(7) Conquer Chiari
Wexford, PA, US

INTRODUCTION

Chiari malformation type 1 (CMI) is a neurological syndrome that is diagnosed when the tonsillar position (TP) is below the foramen magnum [1]. Individuals with CMI are known to experience a wide range of symptoms, notably occipital headaches, neck pain, sleep apnea, dysphagia, dropping attacks, dizziness, photophobia and balance problems [2]. While a TP below the foramen magnum is considered to be radiological evidence for CMI, recent studies have shown that TP alone may not be sufficient to identify individuals with symptomatic CMI. Smith et al. reported 1–2% of individuals with TP greater than 5 mm but no CMI symptoms [3]. Strahle et al. found 10 times more asymptomatic individuals with a TP greater than 5 mm than symptomatic CMI individuals [4]. Due to inconsistencies between TP and identification of symptomatic CMI, several studies have examined various brain morphometrics in an effort to find additional markers that are unique to CMI subjects [5,6].

In this study, we assessed the dysmorphism and volumetric differences in the 3D morphology and spatial position of the clivus and sphenoid sinus in CMI and control subjects. We hypothesized that 3D clival parameters are significantly smaller in CMI subjects as compared to control subjects. In addition, we explored the aeration of the sphenoid sinus and the area of the sella turcica for CMI subjects and controls.

METHODS

Computed tomography (CT) images of 30 adult females diagnosed with CMI (age = 34.4 ± 7.9 yrs. [mean ± standard deviation], BMI = 33.5 ± 9.4) and 30 control subjects matched by age and BMI (age = 35.3 ± 9.2 yrs., BMI = 34.5 ± 7.1) were evaluated. All patient information including demographic data, health-related data, and CT scans were voluntarily submitted by the CMI subjects through the *Chiari1000* project [5]. All the CT scans were de-identified and void of patient data. An OsiriX DICOM PACS server (Pixmeo SARL, Geneva, Switzerland) was used to store and process the CT scans at The University of Akron. Control CT scans were received from the Cleveland Clinic (Cleveland, Ohio) after Institutional Review Board (IRB) approval (#18-250).

Due to variations in head orientation during the CT image acquisition, image registration was performed on each image set such that skull position and orientation were in the same 3D plane with respect to a reference image set (Fig. 1). By aligning the images in the same 3D plane before comparison, any differences in the position of the clivus or sphenoid sinus that were due to head orientation during the CT image acquisition were eliminated. The clivus and sphenoid sinus were manually segmented on the registered 3D CT image sets using the open source software ITK-SNAP (see Figure 2).

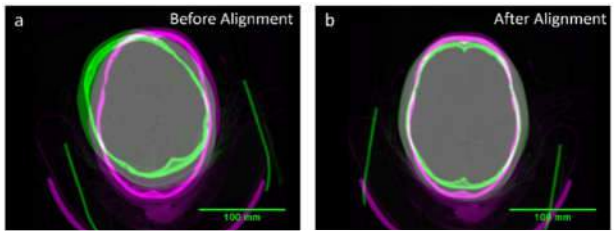

Figure 2. A typical image: (a) before and, (b) after registration.

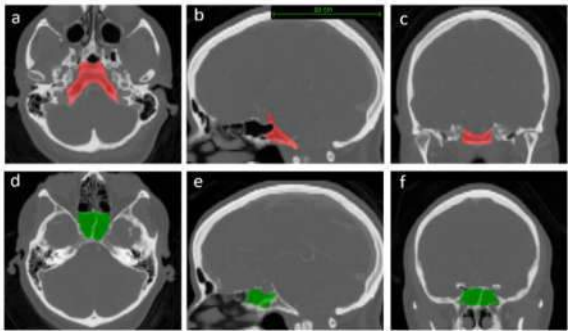

Figure 1. Screenshot from ITK-SNAP during segmentation of the clivus and sphenoid sinus: a) axial view of the clivus bone, b) sagittal view of the clivus, c) coronal view of the clivus, d) axial view of the sphenoid sinus, e) sagittal view of the sphenoid sinus, and f) coronal view of the sphenoid sinus.

A total of 18 parameters were measured for the clivus, sphenoid sinus, and sella turcica. Nine parameters were measured for the clivus (i.e., volume; surface area; difference in spatial position of the centroid (x-, y-, and z-axis) for CMI subjects compared to the centroid of the controls; width; thickness; height; and length). Clivus length was measured using *ITK-SNAP*. The other eight measurements of the

clivus—which included volume; surface area; spatial position in the x-, y-, and z-axis; width; thickness; and height—were conducted using the *regionprops3* function in MATLAB (MathWorks, Natick, MA) and an in-house software developed in MATLAB.

Measurements for the eight parameters of the sphenoid sinus were conducted in a manner similar to those for the clivus. The final parameter examined was the area of the sella turcica. The sella turcica—identified as the area that extends from the base of the pituitary fossa up to the line connecting the tuberculum sella and the dorsum sellae—was traced in the midsagittal plane as shown in Figure 3.

RESULTS

Of the 18 parameters analyzed, 11 parameters were found to be significantly different in CMI subjects as compared to controls: six for the clivus, four for the sphenoid sinus, and one for the sella turcica (as shown in Table 1). A consistent trend was noticed for the clivus, where the size of the clivus in CMI subjects was smaller overall. This trend can be clearly seen in Figure 3, which shows a side-by-side visual comparison of the clivus of a typical CMI subject and that of a control with a similar age and BMI. The opposite trend was seen for the sphenoid sinus, where the sphenoid sinus was larger in CMI subjects. Most notably, our measurements revealed the clivus volume to be 31% smaller in CMI subjects as compared to controls. In contrast, the sphenoid sinus was found to have a 38% larger volume in CMI subjects as compared to controls. In addition, the sella turcica area was found to be 27% smaller in CMI subjects compared to controls.

Table 1. Morphometrics for CMI subjects and controls (differences are reported as mean values for CMI subjects subtracted from those of controls).

	Chiari	Controls	
Parameters	Mean (SD)	Mean (SD)	p
Clivus volume (cm^3)	9.7 (2.3)	14 (2.9)	< 0.01
Clivus surface area (cm^2)	5.2 (0.8)	7.2 (1.1)	< 0.01
Clivus length	42.1 (4.3)	46.6 (3.7)	< 0.01
Clivus width (mm)	44.3 (3.2)	47.2 (2.9)	< 0.01
Clivus thickness (mm)	37.4 (4.9)	46.8 (9.4)	< 0.01
Clivus height (mm)	36.3 (4.9)	39.1 (3.2)	0.01
Sphenoid sinus volume (cm^3)	9.3 (3.0)	6.7 (1.9)	< 0.01
Sphenoid sinus surface area (cm^2)	4.0 (1.0)	3.2 (0.7)	< 0.01
Sphenoid sinus thickness (mm)	33.7 (5.7)	28.9 (4.9)	< 0.01
Sphenoid sinus height(mm)	23.4 (3.4)	20.3 (2.1)	< 0.01
Area of sella turcica (mm^2)	69.7 (22)	95.1 (24)	< 0.01

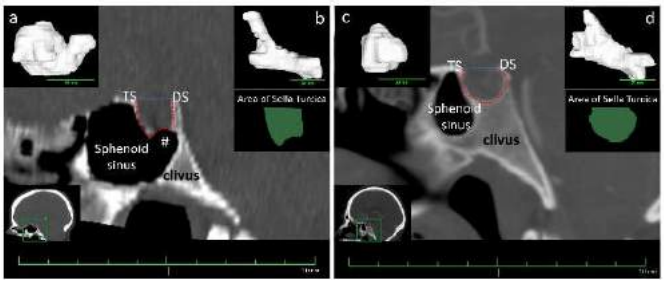

Figure 3. Side-by-side comparison of CT sagittal view of the sphenoid sinus in a CMI subject (left) and an age- and BMI-matched control (right): Lateral view of (a) sphenoid sinus and (b) clivus for the CMI subject. Lateral view of (c) sphenoid sinus and (d) clivus for the control. The red dashed line shows the trace line used to determine area of the sella turcica: TS, tuberculum sella; DS, dorsum sella; the area labeled as # in the image at the left represents invagination of the clivus in the CMI subject.

DISCUSSION

This study identified osseous morphometric differences in several cranial structures (the clivus, sphenoid sinus, and sella turcica) between CMI subjects and controls. The first significant finding from our analysis was a smaller clivus volume in CMI subjects. This finding of a reduced clivus volume in CMI has not been reported in the literature to date. The importance of such a finding is unclear, although it does follow the trend of previous reports of underdeveloped osseous structures in CMI subjects such as shorter clivus length and a smaller posterior cranial fossa [1]. Although previous studies have not quantified clivus volume in CMI subjects, there is evidence that the abnormally small PCF in CMI implicates cranial constriction as the most likely cause for the extension of the cerebral tonsils below the foramen magnum [7]. Clivus length was also found to be significantly smaller in CMI subjects (4.5 mm shorter) compared to controls in the present study; this result is supported by previous reports in the literature [1,5]. While a shorter clivus length in CMI subjects is well established, some studies reported no statistical differences [8]. Based on the 3D morphometric analysis, we found the clivus to have a significantly reduced width in CMI subjects as compared to controls. Milhorat et al. also reported a smaller clival width in CMI subjects [7].

During the analysis of the clivus, a consistent trend was visualized in CT images of CMI subjects: invagination of the anterior clivus was observed, which increased the pneumatization of sphenoid sinus anterior to the clivus. To quantify the increased pneumatization, the sphenoid sinus 3D morphology was evaluated in the present study. Interestingly, the volume and surface area of the sphenoid sinus were found to be 38 and 24% larger, respectively, in CMI subjects as compared to controls. The sphenoid sinus volume of 6.7 cm^3 for the controls in our study is similar to the value of 7 cm^3 reported by Yonetsu et al. [9]. Overall, the results herein are novel, as no studies in the literature have reported the clivus volume, sphenoid sinus volume, and sella turcica area differences for CMI subjects as compared to controls. These findings can serve as additional diagnostic criteria for CMI.

In conclusion, 3D morphology of the clivus and sphenoid sinus is significantly smaller in CMI subjects when compared to controls. In addition, the centroid position of the clivus and sphenoid sinus were shown to be similar in CMI subjects and controls. These results confirm our hypothesis that 3D clival parameters are significantly smaller in CMI subjects as compared to controls. Future work should focus on investigating how the 3D morphology of osseous structures can further our understanding of the pathophysiology of CMI.

ACKNOWLEDGEMENTS

The authors acknowledge Conquer Chiari for support of this work.

REFERENCES

[1] Milhorat T. H., et al., *Neurosurgery* 44: 1005-1017, 1999.
[2] Fischbein R., et al., *Neurol Sci* 36: 1617-1624, 2015.
[3] Smith B. W., et al., *J Neurosurg* 119: 812-819, 2013.
[4] Strahle J., et al., *J Neurosurg Pediatr* 8: 214-221, 2011.
[5] Houston J. R., et al., *J Neuroradiol* 45: 23-31, 2018.
[6] Karagoz F., N. et al., *Acta Neurochir (Wien)* 144: 165-171; discussion 171, 2002.
[7] Milhorat T. H., et al.,*Acta Neurochir (Wien)* 152: 1117-1127, 2010.
[8] Nishikawa M., et al., *J Neurosurg* 86: 40-47, 1997.
[9] Yonetsu K., et al., *AJNR Am J Neuroradiol* 21: 179-182, 2000.

SB³C2019
Summer Biomechanics, Bioengineering and Biotransport Conference
June 25 -28, Seven Springs, PA, USA

CONTROLLED RELEASE FROM MECHANICALLY-ACTIVATED MICROCAPSULES IN DEVELOPING TISSUE MICROENVIRONMENTS

Ana P. Peredo (1,3,4), Yun Kee Jo (2), Daeyeon Lee (2), George R. Dodge (1,3,4), Robert L. Mauck (1,3,4)

(1) Department of Bioengineering
University of Pennsylvania
Philadelphia, PA, USA

(2) Department of Chemical and Biomolecular Engineering
University of Pennsylvania
Philadelphia, PA, USA

(3) McKay Orthopaedic Lab
Department of Orthopaedic Surgery
University of Pennsylvania
Philadelphia, PA, US

(4) Translational Musculoskeletal Research Center
The Corporal Michael J. Crescenz VA Medical Center
Philadelphia, PA, USA

INTRODUCTION

Tissues in the musculoskeletal system are continuously subjected to mechanical forces that regulate homeostasis during normal tissue function [1-3] and in degeneration and regeneration after injury [4-5]. We recently posited that this same mechanical environment could be used to control drug release and enable the therapeutic delivery of molecules when needed, leading to improved outcomes and faster healing. To that end, we developed mechanically-activated microcapsules (MAMCs) for on-demand drug delivery using a custom micro-fabrication system [6]. Here, we extended the application of this new technology by developing a suite of MAMCs with different mechano-activation and degradation profiles, and probed the stability of their mechano-activation after culture in physiologic environments, including residence *in vivo* (subcutaneous implantation) and in the context of maturing tissue engineered constructs.

METHODS

Spherical MAMCs were fabricated using a glass capillary microfluidic device [5]. An inner solution of bovine serum albumin (BSA) (with Alexafluor488-BSA for visualization) was used as a model drug while the middle phase contained 85:15 poly (lactic co-glycolic) acid (PLGA) (with Nile Red for visualization). MAMCs were collected in various molar solutions of NaCl. This was done to increase collecting solution osmolarity and cause capsule shrinkage during hardening (osmotic annealing) (**Fig. 1A**). After hardening, MAMC diameter and shell thickness were measured using confocal microscopy (**Fig. 1B-C**). To evaluate microcapsule mechano-activation, MAMCs were subjected to compression between parallel plates at 0.5% strain/sec. to loads of 0.25-5N, with rupture assessed via confocal microscopy (**Fig. 1D**).

To probe MAMC mechano-activation in a 3D 'repair'/tissue maturation model, small (D: 30.7μm, t: 2.8μm) and large (D: 54.5μm, t: 1.6μm) MAMCs (at $1.2x10^5$ MAMCs/mL per type) were embedded into a 2% agarose hydrogel along with bovine MSCs ($60x10^6$ cells/mL). Cylindrical constructs (⌀=4mm, t=2.25mm) were cultured for 5 weeks in chondrogenic media (+TGF-β3) (**Fig. 2A**). At 1 and 5 weeks, constructs were subjected to Live/Dead staining, sectioned and stained for glycosaminoglycan (GAGs, Alcian Blue) and collagen (Picrosirius Red) content, and tested for mechanical properties [6]. Additional samples were dynamically compressed between parallel plates (from 2-20% strain at 5Hz) for 1 or 5 hrs. and subsequently imaged to determine mechanically-induced release of MAMC contents (**Fig. 2B-F**).

In another study, MAMC stability was analyzed in basal media (with 10% FBS) and bovine synovial fluid *in vitro* for up to 28 days at 37°C (**Fig. 3A-B**). To investigate MAMC stability in a physiological environment, small or large MAMCs were embedded in 500kPa PEGDA hydrogels at 0.2% v/v and implanted subcutaneously in athymic rats for up to 28 days (**Fig. 3C**). At day 7 and 28, rats were sacrificed and hydrogels were extracted and imaged, after which they underwent dynamic compression as previously described (**Fig. 3, C-D**) to probe their retention of mechano-activation.

Normally distributed data was analyzed by one-way or two-way ANOVA followed by Tukey's post-hoc; non-normally distributed data was analyzed via Kruskal-Wallis test with Dunn's Multiple Comparison or Bonferroni post-hoc.

RESULTS

MAMCs of different thickness and diameter were prepared through controlled osmotic annealing. Those with thicker shells and smaller diameters (i.e. higher t/D ratio) had an increased resistance to rupture (**Fig. 1C-D**). MSC-laden constructs matured over time, as illustrated by an increase in GAG and collagen staining around encapsulated MAMCs (**Fig. 2C**). The construct equilibrium modulus

increased from 17.8 ± 4.7kPa at week 1 to 149.2 ± 20.5kPa at week 5. This increased matrix stiffness resulted in greater activation of MAMCs within constructs when subjected to 5 hrs. of dynamic loading on day 28, with larger MAMCs remaining more sensitive to load (**Fig. 2E**) compared to smaller MAMCs (**Fig. 2F**). Large MAMCs were less stable over time *in vitro* in synovial fluid, while small MAMCs remained patent (and retained their inner contents) over a 28-day period in all solutions (**Fig. 3A-B**). A similar trend was observed with MAMCs implanted subcutaneously, yet by 28 days, a greater percentage of MAMCs of both sizes had lost patency compared to *in vitro* incubation (**Fig. 3C**). However, large MAMCs continued to rupture more than small ones after 5 hrs. of dynamic compression (**Fig. 3, E**).

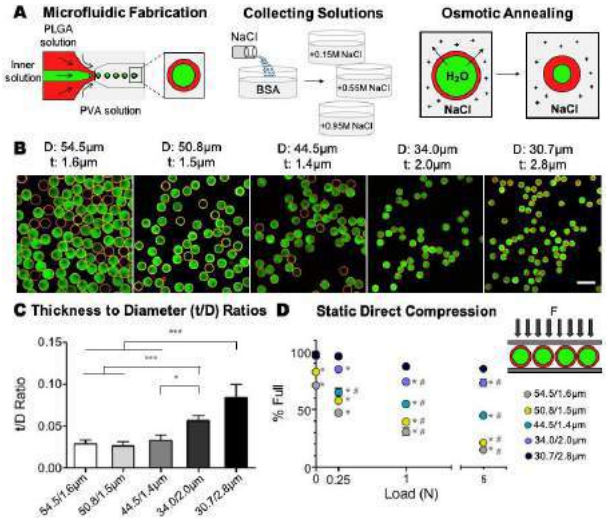

Figure 1: MAMCs were fabricated and collected in solutions +/- NaCl for osmotic annealing (A). This generated MAMCs with differences in diameter (d) and shell thickness (t), which were observed via confocal microscopy (B) (scale bar = 100µm) and quantified (C). Direct compression of MAMCs showed an increased resistance to rupture under load with increasing t/D ratios (D). (* p≤0.05 vs. 0 hrs, # vs. 30.7/2.8µm)

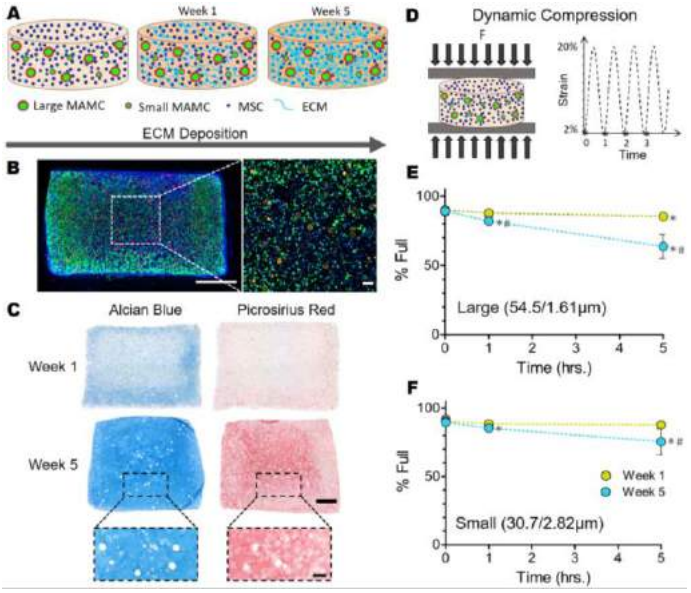

Figure 2: Large and small MAMCs were embedded in MSC-seeded hydrogels and cultured for 5 weeks (A). Cells remained viable at 5 weeks (live cells = green, nuclei=blue, MAMC shells = red) (B). Constructs matured with time, as evidenced by increased GAG and collagen staining (C). With dynamic compression (D), large MAMCs (E) were more susceptible to rupture than small MAMCs (F) in mature constructs. (Scale bar of full gel =1mm, zoom in =100µm; * p≤0.05 vs. 0 hrs, # vs. Week 1)

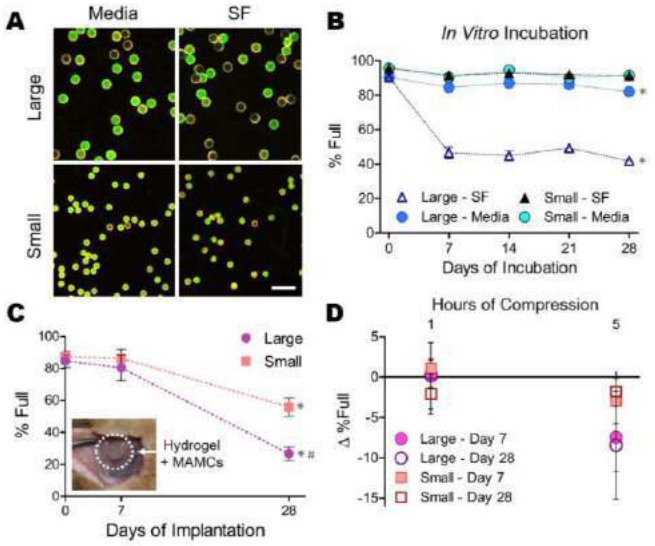

Figure 3: Small MAMCs remained stable over time while large MAMCs were less stable in synovial fluid (SF) incubation by day 28 (A-B). In the same manner, after subcutaneous implantation for up to 28 days (C, inset), small MAMCs were more stable over time *in vivo* than larger MAMCs (C). Large MAMCs ruptured more with increased dynamic loading than small MAMCs (D). (* p≤0.05 vs. Day 0 or 0 hrs, # vs. Media, 30.7/2.8µm)

DISCUSSION

In this study, we expanded the range of microcapsule dimensions that could be produced, creating a suite of MAMCs with a wide range of mechano-sensitivity and stability profiles. Furthermore, we demonstrated the utility of MAMCs in a healing, matrix growth and maturation setting by showing higher activation of MAMCs upon sufficient matrix deposition (compared to little activation before matrix production). MAMCs in cell-laden constructs did not alter cell viability or hinder matrix production, and these co-encapsulated MAMCs retained their contents throughout culture. We also evaluated, for the first time, MAMC stability in an *in vivo* setting. Varying MAMC size and shell thickness resulted in different MAMC stability profiles with *in vivo* incubation, with higher t/D MAMCs demonstrating higher stability both *in vitro* and *in vivo*. Taken together, these data demonstrate the potential of this MAMC technology for on-demand mechanically-mediated drug delivery. Utilizing MAMCs with different rupture profiles could enable the sequential delivery of different therapeutic molecules necessary at different stages of healing and regeneration, providing improved tissue repair and more rapid return to function.

ACKNOWLEDGEMENTS

This work was supported by the National Institutes of Health (R01 AR071340) and the Penn Center for Musculoskeletal Disorders.

REFERENCES

[1] Felsenthal, N et al., *Dev*, 144: 4271-4283, 2017. [2] Szczesny, SE et al., *Am J Orth*, 39: 525-30, 2010. [3] Sanchez-Adams, J et al., *Cur Rheu Rep*., 16: 451, 2014. [4] Mohanraj, B et al., *Adv Func Mat*, 29, 2019. [5] Tu, F et al., *Lang*, 28: 9944-52, 2012. [6] Mauck et al., *Osteo Car*, 11: 879-90, 2003.

SB³C2019
Summer Biomechanics, Bioengineering and Biotransport Conference
June 25 -28, Seven Springs, PA, USA

FINITE ELEMENT MODELING TO STUDY MUSCULOSKELETAL GROWTH: A COMPARISON OF NODE AND ELEMENT-BASED APPROACHES

Danielle Howe (1), Nikhil N. Dixit (2), Katherine Saul (2), Matthew B. Fisher (1, 3)

(1) Department of Biomedical Engineering
North Carolina State University and
University of North Carolina- Chapel Hill
Raleigh, NC, USA

(2) Department of Mechanical and Aerospace Engineering
North Carolina State University
Raleigh, NC, USA

(3) Department of Orthopaedics
University of North Carolina- Chapel Hill
Chapel Hill, NC, USA

INTRODUCTION

Understanding growth and changes in tissue morphology over time is useful for designing treatments and therapies after injury of mechanically loaded tissues. Finite element (FE) modeling offers one way to simulate 3D musculoskeletal tissue growth and study how it is affected by biological and biomechanical conditions. Tissue growth has been simulated using node-based (e.g. thermal expansion [1,2]) and element-based approaches (e.g. osmotic swelling [3]) as mechanisms to serve as surrogates to model biological processes such as cell division. Despite the usefulness of both approaches, it is unclear how to directly relate the coefficients governing node- and element-based growth. To develop comparable models and aid in interpretation across models, it would be useful to determine the mathematical relationship between the two approaches. According to thermal expansion theory, the volumetric thermal expansion coefficient (α_V) is equal to 3x the linear thermal expansion coefficient (α_L) for a given isotropic material [4]. We propose that this principle will hold, such that the coefficient implemented in the element-based (volumetric) model must be 3x the coefficient used in the node-based (linear) model to cause similar growth. Additionally, existing element-based approaches implement growth within a constitutive model [3] while the existing node-based approach does not [1]. Correspondingly, we hypothesize that tissue material properties will affect comparisons across models, with stiffer materials restricting growth in the element- but not the node-based model. Therefore, the objective of this study was to determine under what conditions existing element- and node-based growth approaches produce comparable results and to assess the impact of modulus on these comparisons.

METHODS

Element-based FE models of tissue growth based on existing literature were developed in FEBio (v.2.6.4) [5] via osmotic swelling [3] using Equation (1), in which an increased ratio of internal (C_r) to external solute concentration (C_E) with constant solid volume fraction (φ) causes an expansion (ΔV) of elemental volume (V).

$$\Delta \mathrm{V} = \mathrm{V} * (C_r/C_E - \varphi - 1) \quad (1)$$

Node-based FE models were developed in Abaqus (v.6.13) via the mechanism of thermal expansion [1,2] using Equation (2), in which increased temperature (ΔT) with linear thermal expansion coefficient (α_L) causes expansion (ΔL) of the distance (L) between nodes.

$$\Delta \mathrm{L} = \mathrm{L} * \alpha_L * \Delta \mathrm{T} \quad (2)$$

To relate the models, Equation (1) was equated to the volumetric thermal expansion as shown in Equation (3), with volumetric thermal expansion coefficient (α_V).

$$\Delta \mathrm{V} = \mathrm{V} * \alpha_V * \Delta \mathrm{T} \quad (3)$$

The system was solved for C_r with $\varphi = 0$, and the relationship shown in Equation (4) was derived and implemented in the element-based model.

$$C_r = \mathrm{C_E}(\alpha_V * \Delta \mathrm{T} + 1) \quad (4)$$

In both models, a rudiment composed of a cylinder with a hemispherical end was used as the initial geometry (Fig. 1). Growth stimulus was applied as a linear function of normalized distance along the rudiment (Fig. 1), and implemented through Equations (1) and (4) as a temperature differential (ΔT).

To compare node-based to element-based growth, the element-based model was run with expansion coefficients, α_V, equal to 1x, 2x, 3x, 4x, and 5x the α_L (0.08) of the node-based model, with modulus of 1 kPa. To evaluate the effect of material properties, elastic modulus was varied from 1kPa to 1GPa, using the conversion ratio from the prior simulations resulting in the minimum difference between the element- and node-based models.

Poster Presentation #P124

All simulations were iterated through 10 growth cycles. Maximum height and width of the rudiment were recorded after each cycle, and percent differences were calculated between the models.

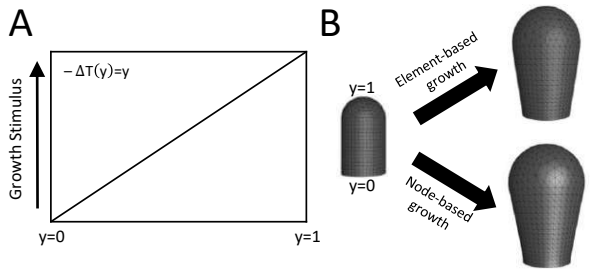

Figure 1: (A) Growth stimulus (ΔT(y)) was implemented as a linear function of normalized distance along the rudiment. (B) A simple rudiment geometry was simulated through element-based and node-based growth for 10 cycles of growth.

RESULTS

Rudiment heights in element- and node- based models were most similar in simulations when the element-based growth coefficient was 3x the node-based growth coefficient (Fig. 2). Element-based predictions were 14%, 4%, and 8% different in height compared to node-based simulations for 2x, 3x, and 4x coefficients, respectively (Fig. 2B). Rudiment widths were also most similar between the two models for simulations when the element-based growth coefficient was 3x the node-based growth coefficient. However, widths were nearly as similar between the models when the element-based growth coefficient was 4x the node-based coefficient. Element-based predictions were 20%, 7%, and 8% different in width compared to node-based simulations for 2x, 3x, and 4x coefficients, respectively (Fig. 2C).

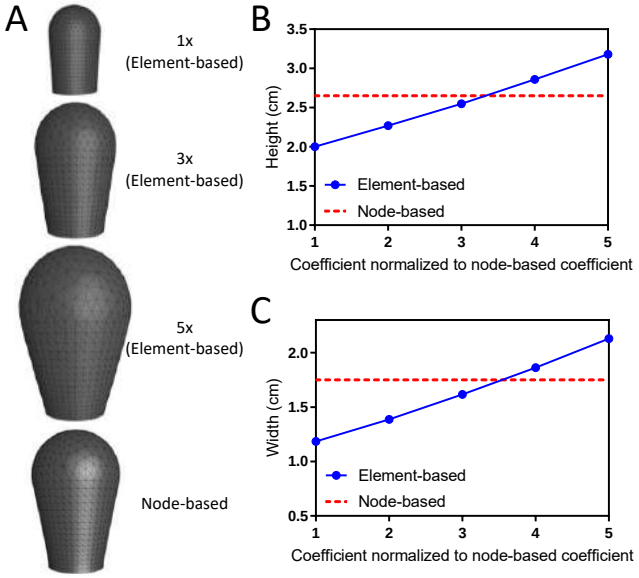

Figure 2: (A) Rudiment geometry after 10 cycles of growth. Rudiment height (B) and width (C) after 10 cycles of growth with element-based growth coefficient equal to 1x, 2x, 3x, 4x, and 5x the node-based growth coefficient.

Over the tested modulus range of 1 kPa to 1 GPa using a 3x coefficient, element-based growth decreased in a sigmoidal manner as modulus was increased, with growth decreasing most from 0.1 MPa to 10 MPa (Fig. 3). Node-based growth was unaffected by modulus. Predictions between models were most similar at low modulus (E=1kPa), with 4% and 7% differences in height and width, respectively, after 10 cycles (Fig. 3B-C).

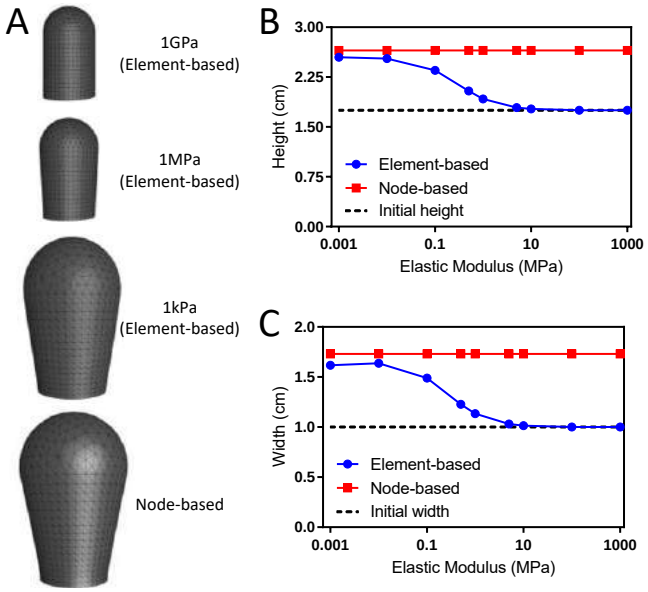

Figure 3: Modulus influenced growth in element but not node-based models. (A) Rudiment geometries after 10 cycles of growth. Rudiment height (B) and width (C) after 10 cycles of growth for varying modulus values.

DISCUSSION

In this study, we simulated musculoskeletal tissue growth using existing element- and node-based approaches, compare growth between the two approaches, and studied the effect of material properties on growth. We found that to create comparable element- and node-based models of growth, osmotic swelling should use an expansion coefficient that is approximately 3 times the expansion coefficient for linear (node-based) thermal expansion. This is consistent with volumetric versus linear thermal expansion theory [4]. The element-based model experiences slightly less growth than the node-based model at this coefficient value, likely because elements are additionally constrained by growth of adjacent elements while nodes move independently.

Further, we found that high tissue modulus restricted growth in the element-based, but not node-based, model, since the element-based approach implements growth within a constitutive model relating stress and strain, while the node-based approach does not. This allows growth in the element-based approach to be influenced by local and neighboring tissue stiffness. Thus, care must be taken to use low modulus values during growth simulations if comparisons are to be made to node-based approaches. Future work will extend these computational approaches to study growth of biological tissues and investigate how growth of musculoskeletal tissues is affected by mechanical stimulation.

ACKNOWLEDGEMENTS

Funding provided by National Center for Simulation in Rehabilitation Research (Stanford University, NIH P2C HD065690) and National Institutes of Health (R01 AR071985).

REFERENCES

[1] Giorgi, M. et al., *J Ortho Res*, 47:989-995, 2014. [2] Heegaard, J. H. et al., *J Ortho Res*, 17:509-517, 1999. [3] Ateshian, G. A. et al., *J Biomech*, 131:101001, 2009. [4] ASM International. *ASM Ready Reference: Thermal Properties of Metals*, 9-10, 2002. [5] Maas, S.A. et al., *J Biomech Eng*, 134:011005, 2012.

SB³C2019
Summer Biomechanics, Bioengineering and Biotransport Conference
June 25 -28, Seven Springs, PA, USA

MITRAL VALVE LEAFLET REMODELING FOLLOWING MYOCARDIAL INFARCTION

Bruno V. Rego (1), Amir H. Khalighi (1), Eric K. Lai (2), Robert C. Gorman (2), Joseph H. Gorman, III (2), Michael S. Sacks (1)

(1) Willerson Center for Cardiovascular Modeling and Simulation
Institute for Computational Engineering and Sciences
Department of Biomedical Engineering
The University of Texas at Austin
Austin, TX, USA

(2) Gorman Cardiovascular Research Group
Department of Surgery
Perelman School of Medicine
University of Pennsylvania
Philadelphia, PA, USA

INTRODUCTION

Each year, more than 40,000 people in the United States undergo surgery for mitral valve (MV) repair, frequently as a treatment for mitral regurgitation brought on by myocardial infarction (MI) [1]. Currently, the preferred method for repairing the MV is through the insertion of an annuloplasty ring, which constricts the mitral annulus sufficiently for the leaflets to coapt and thus for valve function to be restored. Long-term efficacy of this repair procedure remains a major challenge, however. A full 30% of patients experience recurrence of ischemic regurgitation within 6 months of surgery, and more than 60% have regurgitation within five years [2]. Repair failure is primarily attributed to changes in the geometry of the MV annulus, whose shape is severely altered post-MI and during ring implant, as well as to permanent displacement of the papillary muscles, which coincides with post-MI left ventricular distention [3]. These dramatic changes cause stress overload throughout the valve apparatus, leading to irreversible leaflet tissue damage, and ultimately the return of ischemic regurgitation [4].

In addition to altered loading, growth and remodeling in the MV following MI and after surgery undoubtedly also play a major role in determining the success or failure of repair. Recent work has uncovered evidence of significant cell activation and matrix turnover in the MV leaflets following MI [5]. Due to the established causal link between tissue strain and cell-driven remodeling mechanisms [6], a detailed account of tissue-level deformation patterns in the post-MI MV can provide substantial insight into the current biosynthetic state of the valve. In the present study, we examined how the *in vivo* diastolic and systolic geometry and deformation patterns of the MV change after MI, in an effort to gain a deeper understanding of the driving factors behind post-MI valvular remodeling. This foundation is an essential prerequisite for future efforts to design, optimize, and simulate novel MV repair devices and surgical strategies on a patient-specific basis.

METHODS

Following established protocols [7], real-time three-dimensional echocardiography (rt-3DE) images were acquired from eight non-diseased adult Dorset sheep. Each subject was imaged pre-MI, immediately post-MI (t = 0 wk), four weeks post-MI (t = 4 wk), and eight weeks post-MI (t = 8 wk). At each time point, representative end-diastolic and end-systolic images of each subject were traced in parallel cross-sections spanning the MV from commissure to commissure, with the annulus, individual leaflets, and coaptation zone labeled separately. Starting from the segmented end-diastolic rt-3DE image of each MV, we constructed subject-specific meshed geometries of the entire leaflet surface, including both the annular and leaflet free-edge boundaries. The end product of this processing step was a complete subject-specific leaflet geometry for each specimen (Figure 1). Circumferential and radial material directions were then defined as in Rego et al. [8].

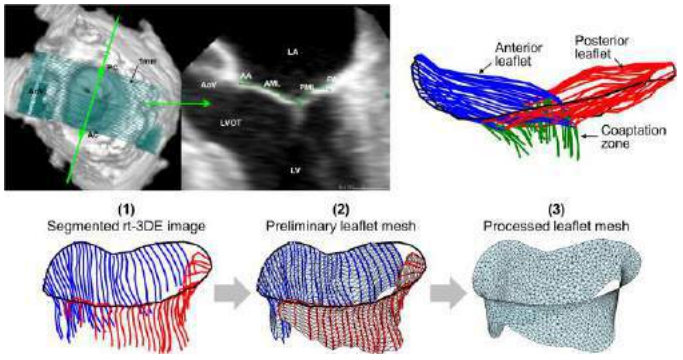

Figure 1: Pipeline for MV geometric modeling, starting from non-invasive rt-3DE images of the valve.

Poster Presentation #P125

To determine systolic deformation fields across the entire MV leaflet surfaces non-invasively, we utilized a previously validated image-based strain estimation method developed by our group [8], which yields local strain information directly from clinical-quality *in vivo* images (Figure 2). Essential features of our approach are that it does not require knowledge of the MV chordal structure nor exact mechanical properties, which cannot be extracted from rt-3DE. Moreover, our method does not rely on physical markers to extract surface deformations; we thus did not require any material point correspondence between open-state and closed-state images when estimating systolic strains. Instead, we exploited the fact that the gross subject-specific closed-state geometry of the leaflets can be precisely acquired from systolic scans, and developed the following method to enforce this closed shape during a finite element (FE) simulation of MV closure: While pressurizing the open-state valve mesh, we penalized any mismatch between the simulated and true (i.e. imaged) closed shapes of the leaflets using a local corrective pressure field (LCPF), which was at any instance and location linearly proportional to the shortest distance between the FE mesh and the true MV medial surface (Figure 2). In this way, the LCPF locally "pushes" regions of the MV so that the imaged closed-state geometry was matched.

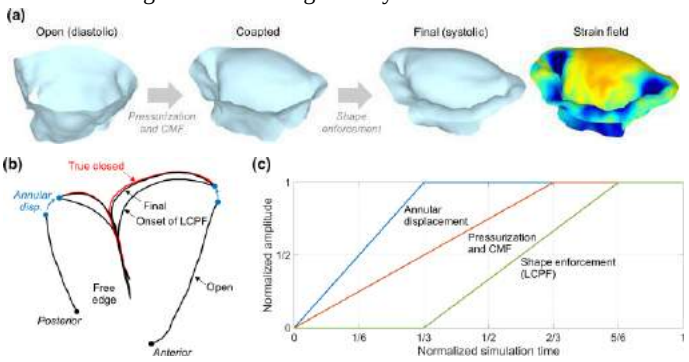

Figure 2: (a,b) Snapshots of a simulated valve throughout a FE simulation with shape enforcement, in 3D and 2D. (c) Coordination of boundary conditions and loads that are applied to ensure proper closure and shape enforcement.

To estimate strains between two subject-specific diastolic scans (from different time points), the same strain estimation method was applied, only without atrioventricular pressurization. To allow for both biomechanical and clinical interpretations, all systolic strain fields were then expressed with respect to both pre-MI and current diastolic states.

RESULTS

Analysis of rt-3DE images showed that the MV annulus is substantially dilated post-MI, consistent with previous findings [9]. Moreover, both leaflets were severely tethered post-MI, causing them to exhibit greater tenting in closure (Figure 3). Paired t-tests revealed that at t = 4 wk and t = 8 wk, both annular orifice area and leaflet surface area were significantly greater than their pre-MI values, with average increases of 20% and 16% respectively ($p < 0.05$ for all).

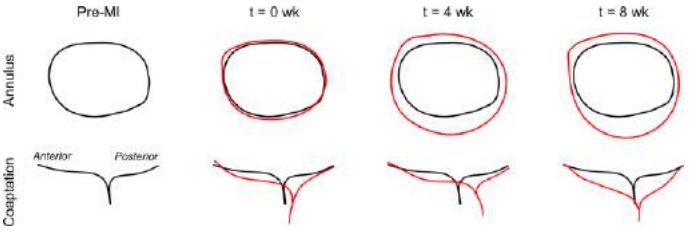

Figure 3: Post-MI changes in annulus and leaflet shape over time.

These MI-induced effects propagated throughout both leaflets to yield substantial changes in strain patterns. Following MI, *diastolic* stretches in both circumferential and radial directions changed substantially, though with significant regional heterogeneity, and mostly stabilized by t = 4 wk (Figure 4). In *systole*, when referenced to the pre-MI diastolic configuration, directional stretches remained largely unchanged over much of the leaflet (Figure 5, top). Referenced to the current time's diastolic configuration, however, systolic stretches became time-dependent (Figure 5, bottom), suggesting that the MV's post-MI remodeling is driven mostly by alterations in diastole.

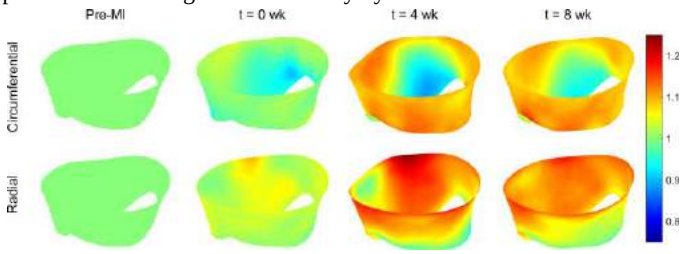

Figure 4: Diastolic directional stretch fields over time.

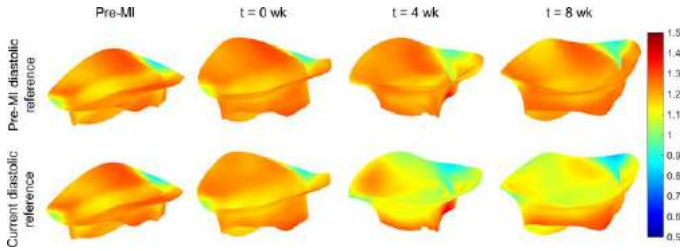

Figure 5: Systolic radial stretch, with respect to both pre-MI and current diastolic configurations.

DISCUSSION

Our results shed significant light on the post-MI state of the MV. Interestingly, while the valve underwent drastic changes in both geometry and mechanical behavior following MI, most of these appear to stabilize over about four weeks. Mechanistically, the results suggest that the MV mostly responds passively to MI over this initial period, undergoing a permanent deformation induced by altered boundary conditions. Further investigation is required, however, to establish whether remodeling occurs over longer time scales post-MI. In our ongoing work, we are building upon the present study to investigate how fiber architecture, tissue composition, and biosynthetic activity in the MV change following MI, which will allow us to draw connections between tissue-level deformations and cellular behavior *in vivo*.

ACKNOWLEDGEMENTS

This material is based upon work supported by the National Institutes of Health (grant no. R01-HL119297 to JHG and MSS), the National Science Foundation (grant no. DGE-1610403 to BVR), and the American Heart Association (grant no. 18PRE34030258 to BVR).

REFERENCES

[1] Glower, DD et al., *J Am Coll Cardiol*, 64:172-181, 2014.
[2] McGee, EC et al., *J Thorac Cardiovasc Surg*, 128:916-924, 2004.
[3] Gorman, JH et al., *Ann Thorac Surg*, 77:544-548, 2004.
[4] Go, AS et al., *Circulation*, 129:28-292, 2014.
[5] Dal-Bianco, JP et al., *J Am Coll Cardiol*, 67:275-287, 2016.
[6] Ayoub, S et al., *J R Soc Interface*, 14:20170580, 2017.
[7] Jassar, AS et al., *Ann Thorac Surg*, 91:165-171, 2011.
[8] Rego, BV et al., *Int J Numer Method Biomed Engng*, 34:e3142.
[9] Daimon, M et al., *Echocardiography*, 27:1069-1077, 2010.

SB³C2019
Summer Biomechanics, Bioengineering and Biotransport Conference
June 25 -28, Seven Springs, PA, USA

A MACHINE LEARNING MATERIAL MODEL FOR SOFT TISSUE REMODELING

Wenbo Zhang (1), Tan Bui-Thanh (2), Michael S. Sacks (1)

(1) Willerson Center for Cardiovascular Modeling and Simulation
Institute for Computational Engineering and Sciences
Department of Biomedical Engineering
The University of Texas at Austin
Austin, TX, USA

(2) Department of Aerospace Engineering and Engineering Mechanics
Institute for Computational Engineering and Sciences
The University of Texas at Austin
Austin, TX, USA

INTRODUCTION

When complex mechanical behaviors are involved, the high-fidelity mesoscale/multiscale methods for soft tissue constitutive models are attractive and predictive but are also computationally very demanding. Traditional phenomenological models have simple forms based on physical insight, but they often lack the ability to be predictive. For example, for remodeling of the bioprosthetic heart valve (BHV), predictive structural constitutive models have been developed for time independent and time evolving properties of exogenously crosslinked collagenous soft tissues under cyclic loading [1,2]. To simulate novel BHV designs or further identify underlying mechanism, efficient computational methods are crucial.

Neural networks approaches are an attractive alternative attention because of their high representation capability, flexible designs, and high speed when properly trained. To this end, we investigated possible approaches to build a neural network (NN) model that can replicate the responses of detailed structural models for soft tissue with manageable computational costs. The fact that the NN model was trained on analytical model instead of experimental data helped to implicitly impose proper regularization so that the fitting problem was well-defined. In this paper, we considered a particular analytical model, i.e. a recently developed full structural model for cross-linked soft tissue [2].

METHODS

The structural model for cross-linked tissues [1,2] has three contributions from the matrix, the collagen fibers, and the fiber-fiber interaction,

$$\Psi_{cro} = \Psi_{\text{mat}} + \Psi_{\text{col}} + \Psi_{\text{int}}. \tag{1}$$

The matrix term is a modified Yeoh model. The collagen term is an ensemble average over the fiber orientation distribution function (ODF) Γ_n, and the recruitment distribution function (RDF), Γ_s,

$$\Psi_{\text{col}} = \phi_{\text{col}}\eta_C \int_\theta \Gamma_n(\theta) \int_1^{\lambda_n} \Gamma_s(\lambda_s) \left(\frac{\lambda_n}{\lambda_s} - 1 \right)^2 \mathrm{d}\lambda_s \mathrm{d}\theta. \tag{2}$$

where, ϕ_{col} is the mass fraction of matrix, η_C is the modulus of the collagen fibers, $\lambda_n = \sqrt{n \cdot \mathbf{C} \cdot n}$ is the stretch in $n = n(\theta)$ direction, λ_s is the slack stretch, λ_n / λ_s is the true stretch after collagen fibers are straightened. The interaction term, Ψ_{int}, is more computational costly since it involves a quadruple integral. To accurately compute the quadruple integral with tensor product quadrature rule, it requires $21^4 = 194481$ quadrature nodes. This gives rise to the need of an efficient surrogate model that can replicate the behavior of the structural model while respect the fundamental physical principles.

To be physically meaningful, Ψ needs to be non-negative everywhere. The tangential stiffness matrix $\mathbf{C} \in \mathbb{R}^{3\times3}$, is symmetric and positive definite everywhere $\mathbf{C}(\mathbf{E}) \in \mathbb{S}^3_{++}$, $\forall \mathbf{E}$. Also, the material frame indifference is automatically satisfied as long as we are using $\mathbf{E}$, which is defined on the reference configuration.

Then, this becomes a function approximation problem. Since the stress-to-strain map is continuous and we can restrict its support to a compact set in $\mathbb{R}^3$, it is feasible to use the single/multi-layer perceptron for function approximation by the universal approximation theorem.

Poster Presentation #P126

$$\text{find} \quad \tilde{\mathbf{S}}(\mathbf{E}),$$
$$\min \quad \frac{1}{|I_{\text{tr}}|}\sum_{i\in I_{\text{tr}}}\left(\tilde{\mathbf{S}}(\mathbf{E}^{(i)})-\mathbf{S}^{(i)}\right)^2. \tag{3}$$

The design of the NN model is shown in Figure 1. We use one hidden layer with 21 neurons with the sigmoid function as activation function and post-multiply the third component of the output by the shear strain to control the oscillation effect.

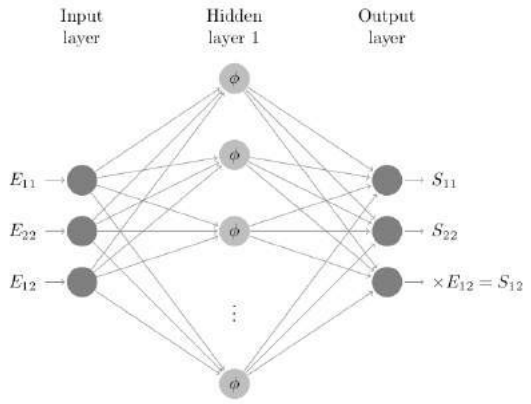

Figure 1: The neural network for strain-to-stress mapping.

The data set for training and validation, $D=\{(\mathbf{E}^{(i)},\mathbf{S}^{(i)})\}_{i=1}^{n}$, are generated by the structural model. We can restrict our attention to a bounded range of strains, defined as component-wise inequality $\mathbf{E}_{lb}\le\mathbf{E}\le\mathbf{E}_{ub}$, instead of the whole space $\mathbb{R}^3$, because large strains/stresses are of little interest for real-world applications. Denote the index set as I_{tr} for the training part, and I_{val} for the validation part. The validation data are 2.5 times denser than the training one.

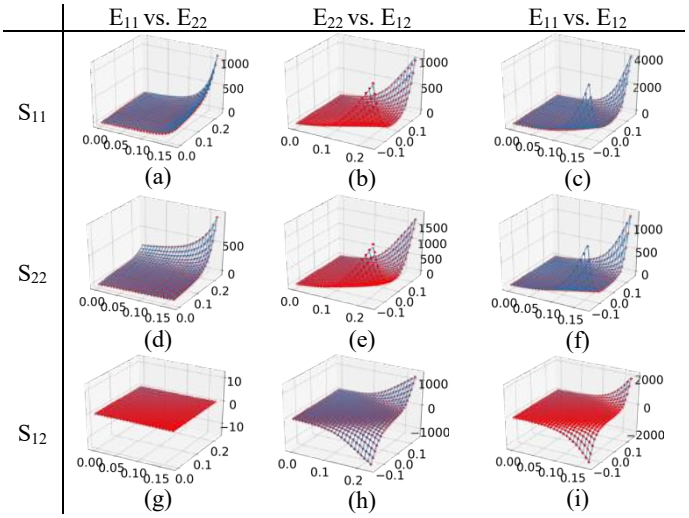

Figure 2: Validation results for the NN model.

RESULTS

We used Adam [3] for training, even though Adam does not guarantee convergence for some convex optimization problems [4]. We found the algorithm converges for our cases. Since the function is continuous, we use the maximum norm of the discrepancy between $\tilde{\mathbf{S}}(\mathbf{E}^{(i)})$ and $\mathbf{S}^{(i)}$ for all i,

$$\max_{i\in I_{val}} \|\tilde{\mathbf{S}}(\mathbf{E}^{(i)})-\mathbf{S}^{(i)}\|_{\infty}, \tag{4}$$

to calibrate the validation error.

In Figure 2, we show the fitting results in comparison with validation data for $E_{11}-E_{22}$ plane, $E_{22}-E_{12}$ plane and $E_{11}-E_{12}$ plane. As it shows, all the cases give good fitting results. The validation error for this neural network is 27.6851 kPa. In Figure 2 (g), the error is comparable to the rounding error. If we use the third output of the hidden layer as the shear stress without post-multiplying the shear strain, the validation error for the trained neural network is 92.8646 kPa and the shear stress S_{12} oscillates when the shear strain E_{12} is zero as shown in Figure 3.

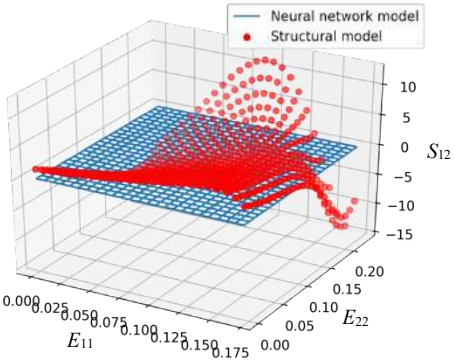

Figure 3: Shear stress oscillation for E_{12}=0.

DISCUSSION

In this work, we have for the first time examined building a NN model as a surrogate constitutive model for a high-fidelity but computationally costly soft tissue model. We show results for the NN model to fit the data, i.e., the strain-to-stress mapping, and it shows reasonable convergence results. The present NN with only 21 neurons can serves as an efficient surrogate model for detailed structural model. We also introduce a scheme to control the numerical oscillation in the fitting results. Therefore, the present work serves as a proof-of-concept for the use of neural networks in replicating the same response as the predictive structural model with improved efficiency. Thanks to the flexibility of the NN model, it paves the way for applying machine learning methods for simulation of soft tissues and identification its mechanical properties to much broader applications. We are currently extending it to time dependent models that include fatigue and growth for simulating the long-term behavior of soft tissues.

ACKNOWLEDGEMENTS

The authors gratefully acknowledge support of this work by NIH R01 HL142504 and R01 HL129077.

REFERENCES

[1] Sacks, MS et al., *Interface Focus*, 6(1):20150090, 2016.
[2] Zhang, W et al., *J Mech Behav Biomed Mater* 75:336-350, 2017.
[3] Kingma, DP et al., *ICLR*, 2015
[4] Reddi, SJ et al, *ICLR*, 2018.

SB³C2019
Summer Biomechanics, Bioengineering and Biotransport Conference
June 25-28, Seven Springs, PA, USA

BIOMECHANICAL RESTORATION POTENTIAL OF PENTAGALLOYL GLUCOSE AFTER ARTERIAL EXTRACELLULAR MATRIX DAMAGE

Sourav S. Patnaik (1), Narasimha Rao Pillalamarri (1), Senol Piskin (1), Mirunalini Thirugnanasambandam (2), Vangelina Osteguin (2), Gladys P. Escobar (3), Eugene Sprague (3), Ender A. Finol (1)

(1) Department of Mechanical Engineering
University of Texas at San Antonio
San Antonio, TX, USA

(2) Department of Biomedical Engineering
University of Texas at San Antonio
San Antonio, TX, USA

(3) Department of Medicine
University of Texas Health San Antonio
San Antonio, TX, USA

INTRODUCTION

Aortic aneurysm-related deaths have increased by 52% globally in the last two decades [1] and, more precisely, abdominal aortic aneurysm (AAA) is one of the leading causes of death in men [2]. In AAA patients, the risk of aortic vessel rupture increases with increasing aneurysm size and growth rate; but to date the exact etiology is not clearly understood. Increases in elastase and collagenase activity, leading to the loss of mechanical tissue strength, has been postulated as one of the primary causative factors of AAA-related ruptures [3]. Naturally, anti-inflammatory or matrix metalloproteinase inhibiting chemicals are the primary choice for stabilizing the aortic extracellular matrix (ECM). Pentagalloyl glucose (PGG) is one such polyphenolic compound known to bind with elastin and collagen, and stabilizes the ECM [4, 5]. In this study, we evaluated the ability of PGG to restore simulated AAA enzymatic damage (elastase + collagenase) to porcine abdominal aortic tissues.

METHODS

Biomechanical testing – Three porcine abdominal aorta tracts were obtained from a local abattoir, with six specimens each per group (n = 18). The specimens, of approximate size 7 x 7 mm, were divided into groups as native (N), elastase digested (E) (1 hour in enzyme solution of 1.5 mg/mL elastase and 0.5 mg/mL collagenase), and PGG treated (P) (12-hour incubation in 0.6 mg/mL PGG [2-4] after enzymatic treatment). Testing was performed in a 37ºC saline bath with a CellScale© Biotester (Waterloo Instruments Inc., Ontario, Canada) with metallic clamps securing the specimens with the orientation shown in Fig. 1. Specimens were preloaded up to 2 g, preconditioned ten times in the physiological range, and stretched under tensile strain up to ~30%. Force and extension data were recorded, from which engineering stress and strain were calculated to generate stress-strain curves.

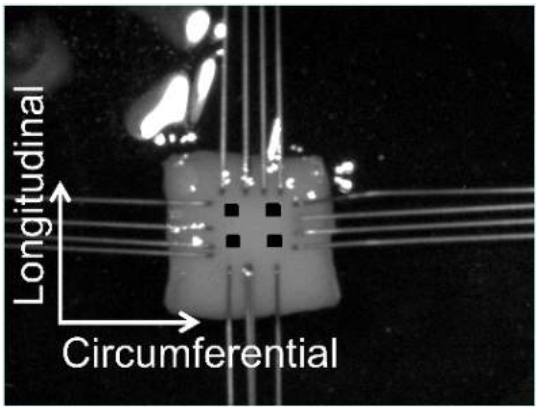

Figure 1: Experimental setup for biaxial tensile testing of porcine abdominal aorta specimens. The specimen shown belongs to the native tissue group (N). n = 18 specimens were tested using CellScale BioTester® submerged in saline solution at 37°C.

Mechanical parameters such as stretch ratio (λ_θ), given by Eq. (1), and ultimate Cauchy stress (σ_{ult}), given by Eq. (2), were calculated.

$$\lambda_\theta = \frac{l}{l_0} \quad (1)$$

$$\sigma_{ult} = \frac{F_{ult} * \lambda}{A_i} \quad (2)$$

Green-Lagrange strain was calculated from the stretch ratios and parameters such as tensile modulus and anisotropy index were subsequently computed. The tensile modulus (slope of the curve) for the circumferential and longitudinal directions, and the anisotropy index, were calculated for each group at different strain levels (33%, 66%, and

95%). The strain energy density was also evaluated for each group by calculating the area under the stress-strain curve (AUC) for both tissue orientations.

Constitutive Modeling – To characterize the material behavior of these porcine aortic tissues, a Holzapfel-Gasser-Ogden (HGO) multilayer material model (Eq. 3) was fitted to the experimental stress-strain data,

$$\Psi = \frac{c}{2}(I_1 - 3) + \sum_{\substack{layer=media,\\ adventitia}} \sum_{i=4,6} \frac{k_1}{2k_2}\left[\exp\left(k_2\left(I_i^{layer} - 1\right)^2\right)\right] \qquad (3)$$

where c, k_1, k_2 are model parameters, I_i^{layer} are the ith invariants of the Cauchy stress tensor per artery layer, and α_M and α_A are the angles of the collagen fiber bundles in the arterial tissues. A Levenberg-Marquardt algorithm was utilized to generate the best subset of material constants that can minimize the differences of the sum of squares between the experimental data and the model.

Statistical analysis – Differences between the biomechanical data obtained from the three groups (N, E, and P) were analyzed by ANOVA using SPSS (IBM Corp., Armonk, NY). Pairwise comparisons were performed using Tukey's tests with results considered significant when $p < 0.05$.

RESULTS

Using the HGO model, the phenomenological behavior of the specimens was captured for the N, E, and P groups (an exemplary curve is shown in Fig. 2), with their respective material constants described in Table 1. The tensile modulus of the P group was greater than the N and E groups at 33% strain in both circumferential (0.0681 ± 0.0392 MPa > 0.0273 ± 0.0129 MPa > 0.0214 ± 0.0116 MPa) and longitudinal directions (0.0628 ± 0.0435 MPa > 0.0222 ± 0.0205 MPa > 0.0181 ± 0.0097 MPa) (Figs. 3A-B; $p < 0.05$). Similarly, AUC was found to be greater for the P group than the N and E groups for the circumferential (0.0093 ± 0.0049 MPa > 0.0033 ± 0.0013 MPa > 0.0033 ± 0.0015 MPa) and longitudinal directions (0.0086 ± 0.0055 MPa > 0.0023 ± 0.0014 MPa > 0.0026 ± 0.0014 MPa) (Figs. 3C-D; $p < 0.05$). The tensile modulus at 66% and 95% strains for both directions, and the anisotropy index, were not significant ($p > 0.05$).

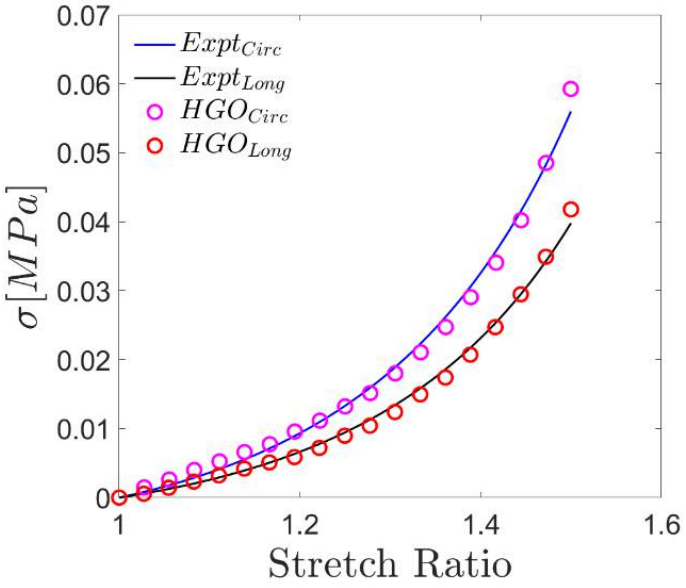

Figure 2: HGO model fitting with exemplary stress-strain curves from the native group (N).

Table 1: HGO material model constants for the three experimental groups.

Groups	c (MPa)	k_1 (Pa)	k_2 (-)	α_M (degrees)	α_A (degrees)
Native	0.033	0.493	0.889	23.834	18.288
Enzyme	0.024	0.620	0.982	19.455	20.882
PGG	0.054	0.528	0.681	50.859	31.813

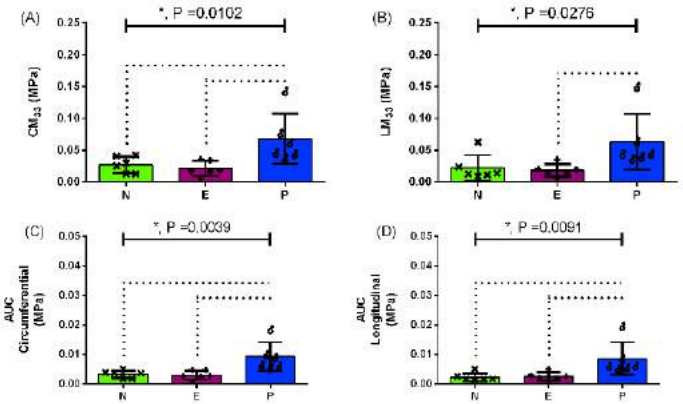

Figure 3: Biomechanical parameters for the native (N), elastase-digested (E), and PGG-treated (P) porcine abdominal aorta specimens. Circumferential modulus at 33% strain – CM_{33} (A), longitudinal modulus at 33% strain – LM_{33} (B), and area under the curve for circumferential (C) and longitudinal (D) directions were significant across the groups ($p < 0.05$; denoted by *).

DISCUSSION

The aforementioned three types of specimens in this study were chosen to represent healthy, aneurysm pathology, and PGG-treated-aneurysm tissue conditions, respectively. By using a mixture of enzymes (collagenase and elastase), we successfully compromised the porcine abdominal aorta extracellular matrix (ECM), evident from the reduced biomechanical strength. The addition of PGG after enzymatic degradation led to a recovery of the arterial biomechanical properties (Figs. 2 & 3). This restoration of mechanical integrity stems from the intricate bonds forged by PGG, which specifically crosslinks arterial elastin and collagen [4, 5]. Currently, there are limited non-surgical treatment options for AAA patients, and hence, it is important to understand the changes that are introduced by administration of PGG locally (as in this study), and perhaps in future systemic administration for treating AAA. Forthcoming investigations will focus on the microstructural changes in the tissue due to PGG treatment and potential translation of this work toward *in vivo* applications.

ACKNOWLEDGEMENTS

This work has been supported by a U.S. National Institutes of Health Award (R01HL121293) and an American Heart Association Collaborative Sciences Award (16CSA28480006).

REFERENCES

1. Naghavi, M et al., *Lancet*, 385:117-71, 2015.
2. Anderson, RN et al., *Natl Vital Stat Rep,* 50:1–85, 2002.
3. Diehm, N et al., *Prog Cardiovasc Dis,* 50:209-17, 2007.
4. Isenburg, JC et al., *Circulation,* 115:1729-1737, 2007.
5. Patnaik, SS et al., *Ann Biomed Eng*, 47:39-59, 2019.

SB³C2019
Summer Biomechanics, Bioengineering and Biotransport Conference
June 25 -28, Seven Springs, PA, USA

LOW-ENERGY MECHANICAL IMPACTS TO ARTICULAR CARTILAGE INCREASE AT LEAST ONE ANABOLIC PROTEIN IN CHONDROCYTES

S. Santos (1), K. Richard (2), M. C. Fisher (3,4), C. N. Dealy (3,4,5), D. M. Pierce (1,6)

(1) Department of Biomedical Engineering
University of Connecticut
Storrs, CT, USA

(2) Department of Global Health
University of Connecticut
Storrs, CT, USA

(3) Center for Regenerative Medicine and Skeletal Development
UConn Health Center
Farmington, CT, USA

(4) Department of Reconstructive Sciences
UConn Health Center
Farmington, CT, USA

(5) Department of Orthopedic Surgery
UConn Health Center
Farmington, CT, USA

(6) Department of Mechanical Engineering
University of Connecticut
Storrs, CT, USA

INTRODUCTION

Acute joint trauma resulting from accidents or sports injuries may trigger a cascade of degenerative events within cartilage leading to post-traumatic osteoarthritis (PTOA), a significant cause of morbidity in aging populations[1]. Many studies link PTOA to increases in collagen and proteoglycan degradation[2], decreases in protein synthesis, changes from collagen type II to type I synthesis[3], and apoptosis and necrosis of chondrocytes[4], among other mechanotransducive responses. Such changes result from deleterious responses from either chondrocytes (mature cells in articular cartilage) or chondroprogenitor cells (multipotent cells capable of chondrogenic differentiation)[5].

We used genetic markers to observe activity of both chondrocytes and progenitor cells. In particular, we observed chondrocyte proliferation using the protein Ki67[6], which marks active phases expressed during the cell cycle[7]. We also observed changes in the pivotal transcription factor Sox9, which serves as a master regulator of cartilage formation and differentiation, and is a widely accepted marker of chondrocytes and chondrogenic progenitor cells[8]. We also studied activation of phosphorylated Epidermal Growth Factor Receptor (pEGFR), which is a tyrosine kinase receptor with multiple roles in development, homeostasis, and disease[9].

It is well established in the current literature that mechanical impact or compression injury of articular cartilage results in changes in gene expression that lead to matrix degradation and catabolic cellular responses; however, many of these studies generate visible macroscale damage to the articular surface of cartilage[10,11]. Especially in early disease stages, when damage may not be visible and when microcracks in the network of collagen[12] likely form, how mechanical factors affect cell function remains unknown. In this study, we aimed to determine the mechanotranducive response of chondrocytes to low-energy impacts to cartilage.

METHODS

In total we tested 98 full-thickness cylindrical specimens (Ø 3 mm) with both cartilage and subchondral bone intact from two bovine medial femoral condyles, received on ice within 48 hours from slaughter (Animal Technologies, Inc., Tyler, TX). We assigned specimens to one of three impact groups (none, 1.5 mJ/mm^3, 3.2 mJ/mm^3) and measured the time-course (0, 24, 48, 72 hours post-impact) localization of Sox9, Ki67, and pEGFR via immunohistochemistry.

Mechanical Impact Test: We impacted the articular surface of specimens from the 1.5 mJ/mm^3 and 3.2 mJ/mm^3 impact groups in unconfined compression using a drop tower with a flat metal platen (Ø 12.4 mm)[12]. We impacted samples at 0.5 m/s[12]. We calculated the actual impact energy density (E_{imp}) applied to each specimen using

$$E_{\text{imp}} = \frac{m v_{\text{imp}}^2}{2\pi r^2 t}, \quad (1)$$

where m is the total mass applied, v_{imp} is the velocity of the load carriage at the moment of impact, r is the specimen radius, and t is the specimen thickness. We measured the acceleration and force at a sampling rate of 100,000 Hz. Post-impact we rinsed samples in PBS. For the control group, the specimens rested in PBS for the duration of the test.

Cell Culture and Fixation: We placed the specimens in the 0-hour time-course groups in 4% paraformaldehyde (Sigma, St. Louis, MO). We placed the remaining specimens in 1 mL of sterile media comprised of DMEM/F12 (Gibco, Gaithersberg, MD), 0.05 mg/mL ascorbic-acid-2-phosphate (Sigma), 0.1% bovine serum albumin (Sigma), 10% fetal bovine serum (Atlanta Biologicals, Flowery Branch, GA), 100 units/mL penicillin (Gibco), and 100 µg/mL streptomycin (Gibco) for culture at 37˚C and 5% CO_2 for 24, 48, or 72 hours post-impact and changed this daily. Once we removed these specimens from culture, we fixed them

in 4% paraformaldehyde (Sigma) for four days, and decalcified using 14% EDTA with NH_4OH (Sigma) for four days at 4 ˚C with rocking.

Histology and Immunohistochemistry: We stained matrix proteoglycans with 1% aqueous Safranin O (Sigma) counterstained with Weigert's Iron Hematoxylin (Poly Scientific, Bay Shore, NY) and 0.02% aqueous Fast Green (Fisher Scientific, Hampton, NH). For immunohistochemistry, we de-paraffinized, rehydrated, and incubated a subset of slides with citrate antigen retrieval buffer followed by 3% hydrogen peroxide, blocking solution, and overnight incubation with primary antibodies in blocking buffer[13]. We diluted the following primary antibodies to 1:1000: rabbit anti-Ki67 (Abcam, Cambridge, MA); rabbit anti-Sox9 (Abcam); and rabbit anti-pEGFR (Abcam). We incubated slides with a biotinylated anti-rabbit secondary antibody which we detected using a Vectastain Elite ABC kit (Vector Laboratories) and chromogenic detection with DAB (Vector)[13].

Imaging and Image Analysis: We imaged slides using a Nikon Eclipse E800 light microscope and obtained full cross-sections using a 4x objective, and three to five images of central regions of the immunohistochemically stained slides with 0-600 pixels of overlap using a 20x objective. We excluded sample edges. We used images from specimens stained with Safranin O to qualitatively assess the integrity of the articular surface. We recreated full-thickness cross-sections from the 20x images using Fiji's Grid/Collection Stitching Plugin[14] for ImageJ (NIH, Bethesda, MD), and determined boundaries for the superficial (SZ), middle (MZ), and deep zones (DZ) using morphology of the lacunae and the cellular arrangement. For each antibody, we quantified positive and negative cellular staining within each zone, and calculated the percent positive cells.

Statistical analyses: We tested for normal distributions of the percent positive cells for each antibody using the Shapiro-Wilk Test for normality. We used separate two-way ANOVAs to evaluate the effects of impact and time on the percent positive cellular localization of each antibody within each zone and included impact level and time as fixed effects, and both the thickness of each specimen and the cow identifier as covariates. We used post-hoc tests to evaluate significant differences among treatment combinations for interactions, and used separate linear regressions to investigate interactions between impact energy density, first Piola-Kirchhoff stress, and engineering strain with the percent positive cells.

RESULTS

In Fig.1, we show distributions of the percent positive cells for each antibody separated by through-thickness zone and time in culture. We found no significant differences in the interaction of impact group and time as predictors for zonal response of percent positive cells for Ki67 and pEGFR. However, we found that positive cellular localization of anti-Sox9 in each zone varied with respect to time. For anti-Sox9, we found statistically significant differences ($p < 0.05$) in SZ at 48 hours, and MZ and DZ at 0, 24, and 72 hours. We did not find statistically significant differences in the total number of cells for any antibody and zone at any time. We also found significant inverse relationships between Sox9 localization in the MZ and DZ for all three predictors.

DISCUSSION

This study is the first to demonstrate changes in Sox9, a master regulator of chondrogenesis, in response to low-energy impact loading. We used low-energy impacts that are below the threshold that induces cell death, which can be as low as 5 mJ/mm^3 [15]. We selected 1.5 and 3.2 mJ/mm^3 as non-injurious, low-energy impacts that have 25% and 40% probability of microcracking the network of collagen[12]. Alternatively, we found mechanical stimuli that positively influence mechanotransducive responses. Here mechanotransduction refers to the processes through which cells sense and respond to mechanical stimuli by converting them to biochemical signals that elicit specific cellular responses. We identified mechanical impacts that upregulated Sox9, and determined that impact energy density is a better predictor of positive cellular Sox9 than first-Piola-Kirchoff stress or engineering strain. Additionally, our low-energy impacts did not alter cell proliferation or pEGFR signaling.

Although there are no definitive cellular markers for chondroprogenitors, they express Sox9 among other markers and migrate towards damaged articular cartilage matrix. We distinguished between chondroprogenitors and mature chondrocytes by migration inferred by comparing proliferation with the total number of cells in each through-thickness zone. Since the number of cells present in any zone did not change with increased Sox9, the changes we observed may come from mature, non-migratory chondrocytes. Thus, low-energy impacts may have no effect on chondroprogenitor cells, but may affect mature chondrocytes.

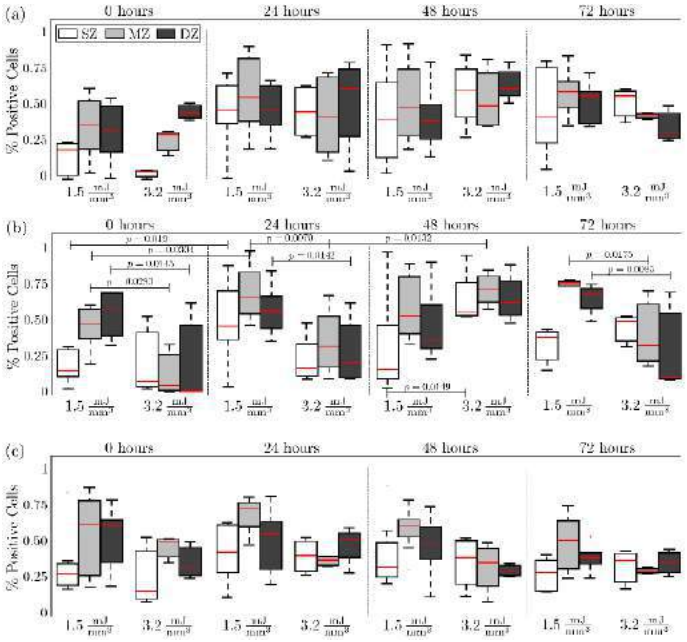

Figure 1: Distributions of the percent positive cells in the SZ, MZ, and DZ of (a) Ki67, (b) Sox9, and (c) pEGFR.

ACKNOWLEDGEMENTS

We thank the NSF CAREER 1662429, NSF 1662429, and the Ford Fellowship Foundation. We thank Caitlyn Monterosso for assistance processing and staining a portion of specimens analyzed in this study.

REFERENCES

[1] Ryan, J et al., *J Tissue Eng Regen Med*, 3:107-16, 2009. [2] Setton, L et al., *J Orthop Res*, 13:473-82, 1995. [3] Lahm, A et al., *Arch Orthop Trauma Surg*, 130:557-64, 2010. [4] Chen, C et al., *J Orthop Res*, 19:703-11, 2001. [5] Seol, D et al., *Arthritis Rheum*, 64:3626-37, 2012. [6] Muinoz-Lopez, E et al., *Open Orthop J*, 6:150-9, 2012. [7] Scholzen, T et al., *J Cell Physiology*, 182:311-22, 2000. [8] Healy, C et al., *Dev Dyn*, 215:69-78, 1999. [9] Seol, D et al., *Arthritis Rheum*, 64:3626-37, 2012. [10] Lee, JH et al., *Arthritis Rheum*, 52:2386-95, 2005. [11] Chan, PS et al., *J Orthop Res*, 23:1146-51, 2005. [12] Kaleem, B et al., *Osteoarthritis Cartilage*, 25:544-53, 2017. [13] Fisher, M et al., *Bone*, 37:741-50, 2005. [14] Preibisch, S et al., *Bioinformatics*, 25:1463-5, 2009. [15] Duda, G et al., *Clin Orthop Relat Res*, 393:302-9, 2001.

SB³C2019
Summer Biomechanics, Bioengineering and Biotransport Conference
June 25 -28, Seven Springs, PA, USA

ALPHA SMOOTH MUSCLE ACTIN-EXPRESSING BONE MARROW PROGENITOR CELLS CONTRIBUTE TO TUNNEL INTEGRATION FOLLOWING ACL RECONSTRUCTION

Timur B. Kamalitdinov (1), Keitaro Fujino (1), Yaping Ye (1), Xi Jiang (1), Snehal S. Shetye (1), Ashley B. Rodriguez (1), Andrew F. Kuntz (1), Miltiadis H. Zgonis (1), Nathaniel A. Dyment (1)

(1) Department of Orthopaedic Surgery,
University of Pennsylvania, Philadelphia, PA, USA

INTRODUCTION

The coordinated events that give rise to zonal tendon/ligament insertions into bone (i.e., enthesis) during development are well established. These mechanisms are less known in the adult because traditional reattachment surgeries of avulsed tendon to bone result in disorganized scar and do no re-establish a zonal enthesis. Ligament injuries, such as the anterior cruciate ligament (ACL), are often reconstructed by passing a tendon graft through a bone tunnel, which does yield zonal attachments. Therefore, ligament reconstructions can serve as a test platform to better understand the mechanisms that drive adult zonal tendon-to-bone repair. Tunnel integration following ACL reconstruction is driven by cells outside the graft [1], presumably from the bone marrow stroma. However, markers that define this progenitor population and the signaling pathways that regulate the repair response are not established. Quiescent resident mesenchymal progenitor cells expressing α-smooth muscle actin (αSMA) have been shown to contribute to new bone formation and fracture repair [2]. Moreover, αSMA expression is increased in the amplifying progenitor population following injury. The objective of this study was to label αSMA amplifying progenitor cells to determine their relative contribution to tendon-to-bone attachments and surrounding bone during tunnel integration following ACL reconstruction.

METHODS

Institutional IACUC approved all relevant procedures in this study. Experimental Design. Inducible Cre mice driven by αSMA ($SMACre^{ERT2}$) were crossed with Ai9-tdTomato Cre reporter mice resulting in double positive mice (SMACre;tdTom). These mice were then crossed with transgenic Col1a1(3.6kb)-CFP mice. The triple positive mice were used to trace the contribution of αSMA-expressing cells in the bone marrow to Col1a1-expressing cells within attachments formed during the tunnel integration process. ACL reconstruction surgery was performed in 3-4 month old mice (20 total). Anterior drawer tests were performed on a subset of mice just after surgery (N=5-6/group) while remaining mice were assessed histologically at 1, 2, and 4 weeks post-surgery (N=3-5/group). Tamoxifen was injected on either post-surgery days 0, 3, and 6 (Early Injection Group) to target the original amplifying progenitor pool or days 7, 10, and 13 (Late Injection Group) to target αSMA-expressing cells after the initial expansion. All mice were injected with demeclocycline (DEM) one day before sacrifice to demarcate regions of active mineral deposition in the tunnel and surrounding bone. ACL Reconstruction. All surgical procedures were performed under a microscope. The right knee joint of each mouse was subjected to surgical transection of the ACL followed by reconstruction (ACLR). Three 3-4 cm long tail tendons were harvested, sutured at both ends with 7-0 nylon, and maintained in PBS during surgery. The ACL was transected with a 27G needle. After confirmation of significant anterior drawer and intact PCL, 27G needles were used to drill tunnels originating at the ACL femoral and tibial footprints through the femur and tibia. The tendon graft was passed through the tunnels and fixated to the external cortices of the femur and tibia with metal washers. At 1, 2, and 4 weeks post-surgery, mice were euthanized via CO_2 asphyxiation and both hindlimbs were harvested. Stability of the knee joint was confirmed macroscopically, and the reconstructed limb was processed for histology. Biomechanical Testing. Following sacrifice on the day of surgery, left hindlimbs were isolated and removed of all extraneous soft tissue. All capsule ligaments, including the cruciates and collaterals, along with the menisci were left intact. The distal half of each tibia was potted in PMMA. The potted tibial end was fixed in a custom fixture on the material testing machine that allowed for adjustment of tibial plateau angle. The distal end of the femur was lowered into another custom fixture that could control knee flexion by rotating the femur around the joint center of rotation. The knee joint was tested for anterior and posterior stability by cyclic loading between

±0.4N for 10 cycles and the 10th cycle was used to quantify stability. Samples are defined as: Intact – intact left knee, ACLT – ACL transected left knee (transected on testing machine after testing intact), ACLR – ACL reconstruct right knee, ACLRT – ACLR graft transected right knee (transected on testing machine after testing ACLR). Multiplexed Mineralized Cryohistology. Reconstructed hindlimbs were fixed in formalin and embedded in OCT. Tape-stabilized, frozen mineralized sagittal sections of the knee were collected and each section was subjected to four rounds of imaging including 1) fluorescent GFP reporters and mineralization label, 2) tartrate-resistant acid phosphatase (TRAP) fluorescent staining, 3) alkaline phosphatase (AP) fluorescent staining, and 4) toluidine blue (TB) staining. Layered composite images of these rounds were made in image editing software. Histological Analysis. Labeling efficiency (% tdTom+ cells) of mineralized fibrocartilage of attachments and osteocytes in newly formed bone was quantified using Fiji. Statistical Analysis. One-way ANOVA with state of ACL (α = 0.05, Bonferroni post-hoc) was used to compare biomechanical parameters. Mann-Whitney U test ($p < 0.05$) was used to compare differences in tdTom+ labeling efficiencies.

RESULTS

Biomechanical Analysis. Anterior drawer test showed that reconstruction restored 47% of anterior stability compared to ACL transected limbs (Fig 1D). ACL Reconstruction. By 2 weeks post-surgery, SMACre;tdTom+ cells infiltrated the graft (Fig. 2B), anchored collagen fibers to underlying bone (Fig. 2C), and expressed AP (Fig. 2D) near the tidemark (Fig. 2 dotted line) as they mineralized the fibrocartilage to create a zonal attachment. Fate Mapping of SMACre;tdTom+ Bone Marrow Progenitor Cells. SMACre;tdTom+ cells contributed to 30-50% of all cells within the mineralized fibrocartilage of the attachments with no statistical difference between groups ($p > 0.05$, Fig. 3A). Mineralized fibrocartilage was not present at 1 week post-surgery. SMACre;tdTom+ cells expressed high levels of Col1a1(3.6-kb)-CFP within the remodeling tendon graft. CFP intensity decreased with time with lowest intensities at 4 weeks. One week post-surgery, SMACre;tdTom+ cells formed woven bone adjacent to the tunnel interface. After 1 week, most of the stromal expansion was over and the SMACre;tdTom+ cells began forming new bone or attachments. Two weeks post-surgery, bone surrounding the tunnels was more organized (B in Fig. 2A) which continued to 4 weeks post-surgery. Labeling the original amplifying progenitor pool during the first week of repair resulted in significantly higher labeling efficiency of osteocytes in newly formed bone at D28 ($p < 0.05$, Fig. 3B). Interestingly, there was a significant drop in labeling efficiency with time in the late injection group (D14 vs D28) but not the early injection group (D7 vs D28) (Fig. 3B).

DISCUSSION

Recreating the spatiotemporal events needed to create a functional zonal tendon-to-bone attachment are critical to producing a functional repair. The murine ACL reconstruction model in this study can serve as a test platform to specifically target cells, genes, and pathways that regulate zonal tendon-to-bone repair. Overall, the SMACre;tdTom mouse model is efficient at targeting cells that contribute to tunnel integration and the targeting can be tuned temporally. While αSMA-expressing bone marrow progenitor cells have been shown to produce new bone during repair [2], this study demonstrates that they also have the potential to produce fibrocartilage within bone tunnel attachments. A limitation of this study was that not all cells within newly formed bone at 1 week post-surgery can be confirmed to be osteocytes. Future studies will use the SMACre^{ERT2} mice to target specific genes and pathways involved in enthesis development to determine their functional role in adult tendon-to-bone repair.

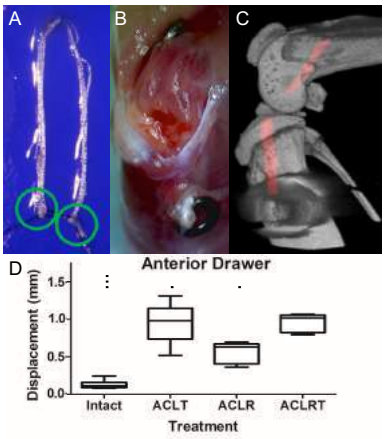

Figure 1. ACL reconstruction procedure and anterior drawer test. Tail tendon autografts (A) were used to reconstruct the ACL via external cortical fixation (metal washer in B-C) leading to femoral and tibial bone tunnels originating near the native ACL footprints (red in C). Anterior drawer measurements of intact, ACLT, ACLR, and ACLRT groups (D). Bars denote $p < 0.05$.

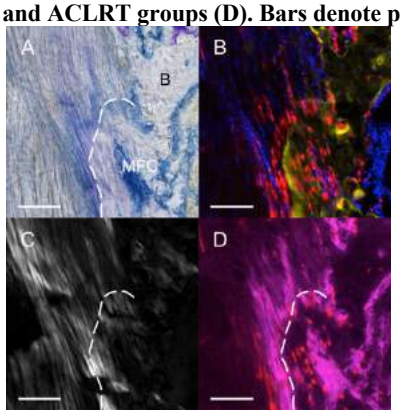

Figure 2. Mineralized fibrocartilage tendon-to-bone attachments form in tunnels 2 weeks post-surgery. A) Toluidine blue, B) nuclei (blue), tdTom+ cells (red), and mineral label (yellow), C) collagen via polarized light, D) AP activity (magenta) and tdTom+ cells (red). Scale = 100μm. MFC – mineralized fibrocartilage, B – bone.

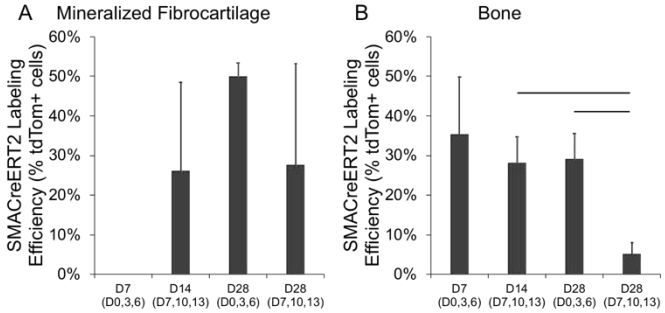

Figure 3. Fate mapping of SMACre;tdTom+ bone marrow progenitor cells reveals spatiotemporal contributions to tunnel integration. A) Mineralized fibrocartilage labeling, B) Bone labeling. Error bars: SD. Lines denote $p < 0.05$.

ACKNOWLEDGEMENTS

Study supported by NIH R00 AR067283 and P30 AR069619.

REFERENCES

[1] Kobayashi, M et al., *Am J Sports Med,* 33(12):1892-1897, 2005.
[2] Grcevic, D et al., *Stem Cells*, 30:187-196, 2012.

SB^{3}C2019
Summer Biomechanics, Bioengineering and Biotransport Conference
June 25 -28, Seven Springs, PA, USA

IN SILICO MODELING OF SOFT TISSUE FAILURE FROM SUBFAILURE DAMAGE TO COMPLETE RUPTURE

Ronald N. Fortunato (1), Anne M. Robertson (1,2), Chao Sang (1), Spandan Maiti (1,2)

(1) Department of Mechanical Engineering and Material Science
University of Pittsburgh
Pittsburgh, PA, USA

(2) Department of Bioengineering
University of Pittsburgh
Pittsburgh, PA, USA

INTRODUCTION

Biomechanical failure of the extracellular matrix in cerebral aneurysm wall tissue can lead to loss of biomechanical integrity culminating in catastrophic rupture of the wall. The fatality rate associated with rupture of intracranial aneurysms is 45% and long term disability rate is 64% [1]. Thus, there is a pressing need to understand failure behavior of the arterial wall. Studies of the pre-failure biomechanics of the artery wall are common in the literature, and more recently, our group and others have analyzed tissue failure as a progression from the pre-failure response to complete failure in an attempt to understand the role of tissue structure in failure. However, the sub-tissue level biomechanical mechanisms governing overall wall tissue failure are still not fully understood. In this abstract, we present a cohesive volumetric finite element (CVFE) modeling approach that incorporates tissue failure properties as model parameters, and assesses their role in governing overall tissue failure behavior. Our model is capable of simulating spontaneous initiation, propagation, and coalescence of multiple tears within the tissue leading to complete specimen level mechanical failure. Using this model, we simulated experimental uniaxial stress-stretch experiments on human and sheep arterial tissues while simultaneously recapitulating image-derived data on overall tissue failure behavior. We also quantified the spatially heterogeneous sub-tissue level damage evolution using this model. We found tissue damage initiates before the peak of the stress-stretch curve is achieved, and the peak is correlated with the intrinsic tissue strength. We also found that tissue fracture toughness controls the post-peak biomechanical behavior.

METHODS

We utilized the CVFE approach to model the evolution of tissue damage and ultimate tissue failure. In this method, the mechanical response of the bulk (volumetric) domain is governed by a hyperelastic constitutive response while a separate failure constitutive law, defined by the potential tear interface, governs the tissue failure response. A generalized structure tensor (GST) based model including fiber dispersion [2] was employed to simulate the anisotropic behavior of the fibrous soft tissue. Following earlier works on material failure behavior [3,4], we postulated that tissue failure is a gradual and irreversible process localized within a process zone. Potential failure sites were placed at the edges of the finite elements, and were prescribed with a cohesive failure law relating traction and separation across the evolving tear [5].

The cohesive failure law in opening mode and shearing mode relates tractions t_n and t_t in normal and tangential directions, respectively with corresponding normalized displacement jumps $\bar{\Delta}_n$ and $\bar{\Delta}_t$ as:

$$t_n = \frac{S}{1-S}\frac{\sigma_{max}}{S_{init}}\bar{\Delta}_n\,, \qquad t_t = \frac{S}{1-S}\frac{\tau_{max}}{S_{init}}\bar{\Delta}_t \tag{1}$$

where the displacement jumps are normalized by critical displacement jumps Δ_{nc} and Δ_{tc} in corresponding directions. Further, $S \coloneqq min[S_{init}, \max(0,1-\bar{\Delta})]$, an internal damage parameter that depends on the normalized displacement jump $\bar{\Delta} \coloneqq \left({\bar{\Delta}_n}^2 + {\bar{\Delta}_t}^2\right)^{1/2}$, in the process zone, thus coupling these two modes of failure. σ_{max} and τ_{max}, the intrinsic tissue tensile and shear strength, respectively, were set equal and were estimated from the peak of the experimental stress-strain curve for arterial tissue [6]. Fracture toughness for two modes, denoted as G_I and G_{II}, were set equal, where fracture toughness is defined as the energy per unit area required to create a new tear. This property was used as a free parameter of the model, and was calibrated to recapitulate experimentally observed modes of failure reported in [6]. Critical displacements Δ_{nc} and Δ_{tc} were calculated from $G_I = \frac{1}{2}\sigma_{max}\Delta_{nc}$ and $G_{II} = \frac{1}{2}\tau_{max}\Delta_{tc}$.

Multiphoton microscopy of the organization of collagen fibers within human and sheep arteries were reported in a previous publication from our group [6]. Based on this data, we modeled the collagen fibers using two fiber families with mean directions of ±5° about the circumferential direction, and with a small planar fiber dispersion ($\kappa = 0.05$). Other GST model parameters representing fiber and matrix stiffness were calibrated by performing nonlinear regression of the model predicted stress-strain curves against the experimental ones reported in [6] using Matlab (R2018a, Mathworks, Natick, MA).

We simulated both rectangular and dogbone specimens of equal length (7.1mm), grip to grip length (3.5 mm), width at clamp (2 mm), and thickness (250 μm). The steel clamp used to fix the tissue, being of much higher stiffness than the tissue and the insert material layer

was idealized as rigid and not explicitly modeled. Rather its effect was modeled as a uniform gripping pressure on the contact surface of the insert material between the grip and tissue specimen. The insert layer between the clamp and specimen was modeled as a cuboid with a thickness of 0.787 mm and a contact surface of 1.8 mm by 2 mm.

To mimic the experimental loading conditions, we first applied a uniform clamping pressure of 12.5 kPa then stretched the tissue uniaxially until failure. Reaction forces at each load step were used to calculate the average Cauchy stress, approximated as the reaction force divided by the current cross-sectional area was computed mid-specimen. The R Factor was defined as the area under the post-peak Cauchy stress versus stretch curve divided by the area under the total curve.

All statistical analyses were conducted using SPSS (IBM Corp., Armonk, NY). For the comparison of two groups with normally distributed data, a two-sample independent t-test was conducted. If the data were not normal, a Mann-Whitney test was conducted. Comparison between two or more groups was performed using a one-way independent ANOVA followed by a Bernoulli post hoc test. Results of the correlation analysis were reported in terms of non-parametric Spearman's correlation coefficient (r). The alpha level of significance for all statistical tests was set at $\alpha<0.05$.

RESULTS

Figure 1 presents the stress-stretch curves along with the axial stress contours on the specimen surface for three different uniaxial simulations with cases of increasing stiffness and a constant fracture toughness combination of 2 kJ/m^2 in the medial layer and 4 kJ/m^2 in the adventitial layer. To investigate the micromechanics of the failure process, we monitored the evolution of the internal damage parameter of the cohesive failure law, S. In particular, we superimposed the evolution of the internal parameter S on the stress-stretch curves in the top panels of Figure 1. Consistent with our experimental study of uniaxial failure in human cerebral and sheep carotid arteries [6], the peak stress (Point B) in Figure 1 was not associated with complete tissue failure or a large change in cross section for these cases. Rather, various degrees of material softening due to distributed tissue damage could be observed at the peak stress. This finding held for the entire cohort of specimens tested in our study that covered a wide range of material properties, two specimen geometries, and boundary conditions. In agreement with experiments [6], the post-peak response of the simulations varied from abrupt to gradual failure. In abrupt failure cases, the media and adventitia both failed together, Figure 1(a,c), whereas in the gradual failure case the medial and adventitial layers fail sequentially Figure 1(b). Black arrowheads in Figure 1 designate the locations of complete failure (S=0) in the tissue.

For all specimen shapes and insert materials considered here, the magnitude of peak stress was statistically similar to the intrinsic tissue strength, though the peak stress was consistently higher. For example, the average peak stress for the low and high strength cases were 16.01% (p=0.95) and 13.56% (p=0.98) greater than their respective input intrinsic strengths. We also did not find statistically significant differences in peak stress due to varying fracture toughness (G11-G48) for low (p=0.08) or high (p=0.05) strength tissue except between the lowest and highest toughness cases G11 and G48 (p=0.02). However, the post-peak (peak stress to complete failure) stress-stretch curve transitioned from abrupt to gradual with increasing fracture toughness. This was quantified by a positive correlation between R Factor and fracture toughness for all parametric studies with varying parameters of strength, protocol, and stiffness.

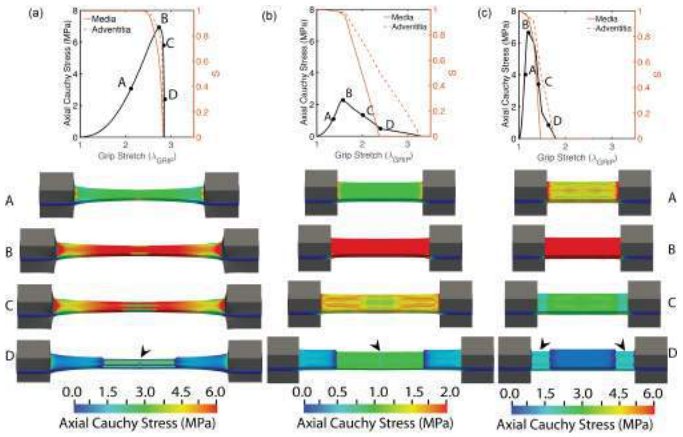

Figure 1: Stress distributions during uniaxial loading to failure. (a) and (c) represent high cohesive strength cases while (b) represents the low cohesive strength case. A dogbone specimen is shown in (a), while (b) and (c) are rectangular samples.

DISCUSSION

Prior to this work, there was very limited data on the relationship between tissue failure progression and the tissue failure properties. Our analysis demonstrates that tissue failure is a continuous process starting from localized softening followed by initiation, propagation and coalescence of multiple tears leading to complete separation of the specimen. It is of importance that uniaxial peak stress corresponds to localized tissue softening and partial damage in the highly stressed regions, rather than complete tissue failure. For example, peak stress was always associated with the reduction of the internal damage parameter, S, from its initial value, indicating onset of material softening. This is consistent with the experimental observations in [6].

We found that for low strength tissues, the higher tissue fracture toughness consistently resulted in a gradual post-peak response. However, for tissues with high strength, the fracture process tends to be abrupt for all combinations of media and adventitia fracture toughnesses studied. High strength tissues can absorb substantial amounts of strain energy prior to the onset of failure. As a result, there is a buildup of mechanical energy released during fast tear propagation. In contrast, lower pre-failure strain energy enables the tissue to absorb additional post-peak energy before the complete failure. Our work reveals how intrinsic material failure properties, namely strength and fracture toughness, control the specimen scale tissue mechanical failure behavior including the post-peak failure response. In summary, our parametric study shows the post peak response in failure testing deserves greater attention than it currently receives, as it provides information about the failure process that could have substantial consequences for living tissues.

ACKNOWLEDGEMENTS

Research reported in this work was supported by the National Institutes of Health under award numbers 1R01NS097457-01 and T32-HL076124.

REFERENCES

[1] Kelly, P et al., *Stroke*, 32(2):530-534, 2001
[2] Gasser, T. C. et al., *J R Soc Interface*, 3:15-35, 2006.
[3] Dugdale,D et al., *J of Mech. Phy. of Solids*, 8(2):100-104, 1960.
[4] Barenblatt, G et al., *Adv. in Applied Mechanics*, 7:55-129, 1962.
[5] Maiti, S et al., *Acta Materialia*, 53(3):823-834, *2005*.
[6] Sang, C et al., *J of Biomech. Eng.*, 140(6): 061010, *2018*.

SB³C2019
Summer Biomechanics, Bioengineering and Biotransport Conference
June 25 -28, Seven Springs, PA, USA

MYOFIBROBLAST ACTIVATION IN SYNTHETIC FIBROUS MATRICES COMPOSED OF DEXTRAN VINYL SULFONE

Christopher D. Davidson, Danica Kristen P. Jayco, Daniel L. Matera, William Y. Wang, Brendon M. Baker

Department of Biomedical Engineering
University of Michigan
Ann Arbor, MI, USA

INTRODUCTION

Cellular interactions with the surrounding extracellular matrix (ECM) guide fundamental behaviors such as spreading, migration, and proliferation, and thus play an important role in tissue homeostasis and disease pathogenesis [1,2]. In particular, cells can interrogate diverse physical aspects of their microenvironment and respond accordingly over various timescales. As biophysical properties of native tissue ECMs and natural biomaterials (such as collagen and fibrin gels) are challenging to experimentally modulate, synthetic materials such as polyacrylamide or poly(ethylene glycol) have been crucial in investigating the role of matrix properties in cell behavior. While these synthetic materials offer controllable and modular design, they fail to mimic the complex mechanical and topographical properties of fibrous tissues. We have previously demonstrated the cell's ability to physically remodel matrix fibers influences initial cellular mechanosensing events such as cell spreading and adhesion formation [3], but how these initial responses impact the longer-term cell response has not been explored.

Fibrosis is one context where a deeper understanding of mechanosensing in fibrous microenvironments would be invaluable. A central component of many diseases, fibrosis has been implicated in 45% of all deaths in the developed world [4]. The principal cells that drive this disease are myofibroblasts (MFs). Differentiated from hyper-proliferative fibroblasts, MFs contribute excessive ECM synthesis and contractile forces that cause tissue stiffening and eventual organ failure. However, due to a lack of biomaterial platforms that accurately capture the fibrous structure and mechanical behavior of the stromal tissue spaces where fibrotic processes take hold, we lack an understanding of how properties of fibrous ECM influence cell proliferation and MF differentiation. In this work, we developed a novel fibrous material composed of electrospun of dextran vinyl sulfone (DexVS) with tunable mechanical properties that supports long-term culture of fibroblasts to examine MF activation as a function of matrix stiffness.

METHODS

DexVS Synthesis: Dextran was reacted with divinyl sulfone following a previously described procedure [5]. Briefly, dextran (5 g) was dissolved in 250 mL of sodium hydroxide (100 mM) solution under vigorous stirring before addition of divinyl sulfone (12.5 mL). The reaction proceeded for 3.5 minutes before termination by addition of hydrochloric acid. Product was dialyzed against milli-Q water for 3 days and then lyophilized. DexVS was characterized by H-NMR and a vinyl sulfone/dextran repeat unit ratio of 0.4 was determined. Electrospinning: DexVS was dissolved at 0.7 g ml^{-1} in a 1:1 mixture of milli-Q water and dimethylformamide with 0.6% (w/v) LAP photoinitiator. This solution was electrospun and crosslinked via UV light and LAP photoinitiator. Fibers were collected on poly(dimethylsiloxane) (PDMS) arrays of circular wells produced by soft lithography. DexVS matrices were then functionalized with cyclo [Arg-Gly-Asp-D-Phe-Lys(Cys)] (cRGD) to facilitate cell attachment. Cell Culture: Normal human lung fibroblasts (NHLF) were cultured in DMEM containing 1% penicillin/streptomycin, L-glutamine, and 10% fetal bovine serum. To induce MF differentiation, NHLFs were cultured for 7 days and supplemented with transforming growth factor beta (TGF-β1, 10 ng/ml). Mechanical Testing: Young's moduli of suspended DexVS fiber matrices were measured by microindentation with an SU8 cylindrical indentor affixed to a tungsten filament following a previously described method [3]. Staining and Microscopy: Cells were fixed in 4% paraformaldehyde for 10 min at room temperature. To stain the actin cytoskeleton and nuclei, cells were permeabilized, blocked in 1% bovine serum albumin, and stained simultaneously with phalloidin and DAPI. For α-SMA immunostaining, samples were permeabilized,

blocked for 1 h in 1% fetal bovine serum, and incubated with α-SMA antibody (1:2000, Abcam #7817) for 1 h at room temperature. Fixed samples were imaged on a Zeiss LSM 800 laser scanning confocal microscope. Statistics: Statistical significance was determined by ANOVA or Student's t-test where appropriate, with significance indicated by $p<0.05$.

RESULTS

Fibrous matrices were fabricated by electrospinning DexVS onto collection substrates such that fibers were suspended over an array of microfabricated wells (Fig. 1a). Exposure to UV light in the presence of photoinitiator (LAP) crosslinks DexVS, enabling control over the Young's moduli of individual fibers and bulk matrices. Crosslinking proved sensitive to the concentration of LAP photoinitiator during UV exposure, duration of UV exposure, and LAP concentration within the electrospinning solution. Through these means, the Young's moduli of matrices were tunable between 0.6 and 4.02 kPa (Fig 1b,c). To confirm that DexVS matrices require functionalization for cell adhesion and do not passively absorb serum-borne ECM proteins, the adhesive peptide cRGD was coupled to substrates at variable concentrations. Cell spreading proved highly sensitive to the amount of cRGD, with no spreading noted in the absence of cRGD. As cell spreading was maximal at 100 μM, this concentration was utilized for all subsequent studies (Fig. 1e). Cell viability on DexVS matrices was confirmed via live/dead assay, demonstrating negligible cell death on both soft (0.6 kPa) and stiff (3.8 kPa) matrices (Fig 1d).

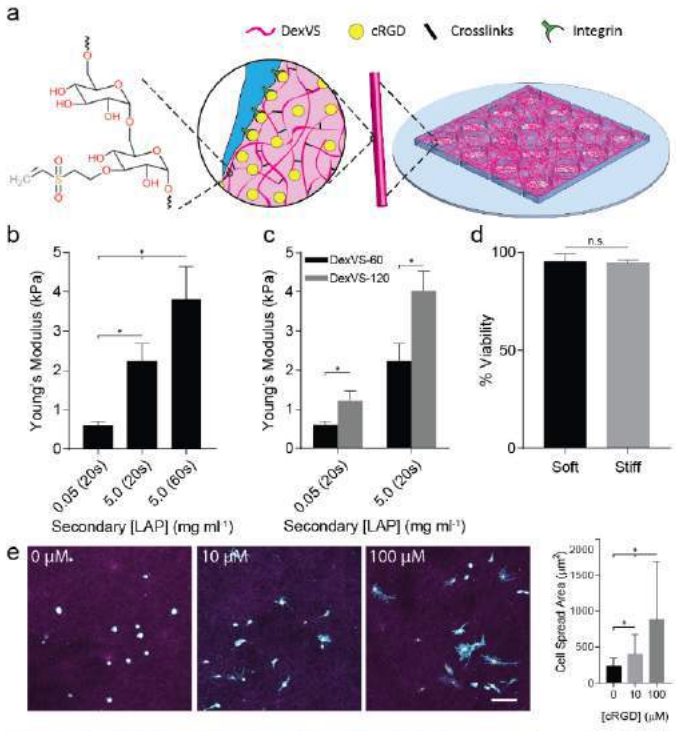

Figure 1. a) Schematic of multi-well substrate supporting suspended matrices of DexVS fibers coupled with cRGD. Young's modulus of DexVS matrices as a function of (b) LAP concentration, duration of UV exposure, and (c) LAP concentration within the electrospinning solution. d) Soft and stiff DexVS networks are biocompatible and have no affect on cell viability. e) Cell spreading as a function of cRGD concentration. Scale bar: 100 μm. All data presented as mean ± std.

We next utilized DexVS fibrous matrices to examine the influence of ECM stiffness on MF activation. Previous studies on polyacrylamide hydrogels have shown that stiff matrices are required for MF activation [6]. We cultured NHLFs for 7 days in the presence of TGF-β1, a potent soluble mediator of MF activation. Cells seeded on soft matrices revealed high levels of matrix reorganization and fiber recruitment as compared to those on stiff matrices (Fig 2a, DexVS). Interestingly, higher levels of proliferation (as quantified by EdU assay) and MF activation (as quantified by positive α-SMA immunostaining) were noted on soft DexVS matrices (Fig 2a-c) as compared to non-deformable stiff matrices.

DISCUSSION

In this work, we established a new synthetic fibrous material to study longer-term cell responses. DexVS was synthesized and processed into suspended fiber matrices with tunable stiffness that support long-term (7+ days) cell culture. We utilized this system to study the influence of fibrous matrix stiffness on MF activation, an important step in the fibrotic cascade. Contrary to previous results with hydrogels, decreased matrix stiffness led to increased proliferation and α-SMA expression, two hallmarks of fibrotic tissues. We hypothesize that this is due to fiber recruitment in softer matrices, as this has previously been shown to increase local ligand concentration and promote focal adhesion maturation and resulting signaling [3]. Future work will more rigorously investigate the relationship between MF activation and physical remodeling of the matrix. Furthermore, DexVS matrices may be a valuable setting to study cell-ECM interactions during other long-term processes such stem cell differentiation, tissue homeostasis, and disease pathogeneses.

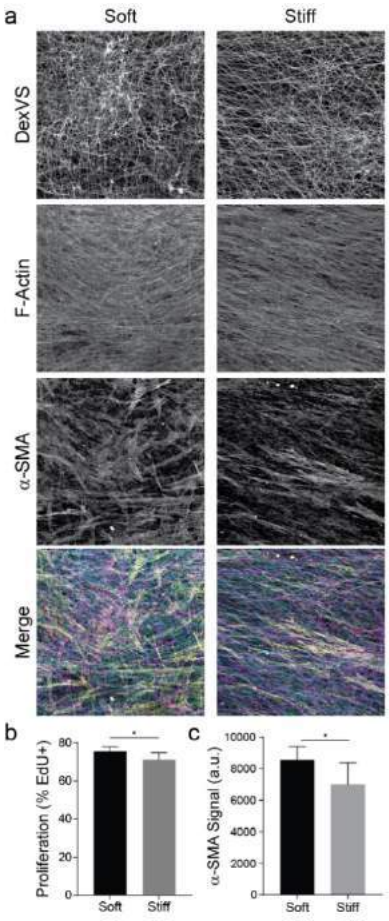

Figure 2. a) Confocal fluorescent images of phalloidin and α-SMA stained NHLFs after 7 days of culture with TGF-β1 on soft and stiff DexVS matrices. Merged images (bottom) showing fibers (magenta), actin (cyan), and α-SMA (yellow). Quantificaiton of proliferation (b) and total α-SMA fluorescent intensity (c). Scale bar: 100 μm. All data presented as mean ± std.

ACKNOWLEDGEMENTS

This work was supported in part by the National Institutes of Health (HL124322). C.D.D., D.L.M, and W.Y.W. acknowledge financial support from the National Science Foundation Graduate Research Fellowship Program (DGE1256260).

REFERENCES

[1] Vogel, V et al., *Nat Rev Mol Cell Biol*, 7:265-275, 2006. [2] Discher, DE et al., *Science*, 310:1139-1143, 2005. [3] Baker, BM, et al. *Nat Mater*, 14:1262-1268, 2015. [4] Wynn, TA, *Nat Rev Immunol* 4:583-594, 2004. [5] Yu, Y et al., *Biomacromolecules*, 13:937-942, 2012. [6] Liu, F et al. *J Cell Biol*, 190:693-706, 2010.

INTERACTION OF PENTAGALLOYL GLUCOSE WITH THE MICROVENVIROMENT OF MACROPHAGES

Sourav S. Patnaik (1), Vangelina Osteguin (2), Tina Rodgers (2), Rohini T.G. Vishwanath (2), Craig J. Goergen (3), Dan Simionescu (4), Gabriela R. Uribe (2), Ender A. Finol (1)

(1) Department of Mechanical Engineering
University of Texas at San Antonio
San Antonio, TX, USA

(2) Department of Biomedical Engineering/Chemical Engineering Program
University of Texas at San Antonio
San Antonio, TX, USA

(3) Weldon School of Biomedical Engineering
Purdue University
West Lafayette, IN, USA

(4) Department of Bioengineering
Clemson University
Clemson, SC, USA

INTRODUCTION

Pentagalloyl Glucose (PGG) is a naturally occurring polyphenolic compound that has a variety of biological effects, including several cardiovascular health benefits [1, 2].

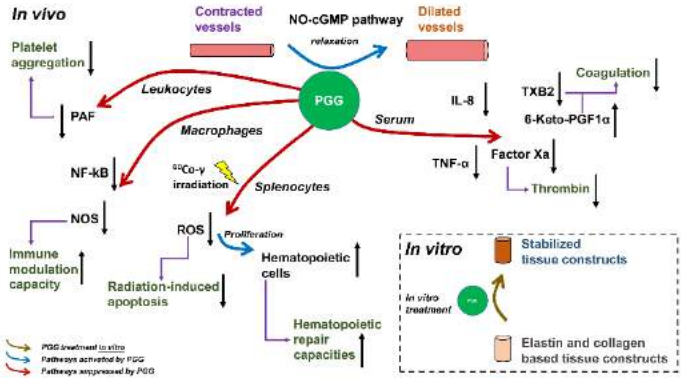

Figure 1: PGG-mediated activation and suppression of molecular pathways with relevance to vascular health. The inset illustrates in vitro PGG-based tissue treatment for extracellular matrix (ECM) stability. Adapted from Patnaik et al. [2]

PGG works as an antioxidant in the body and reduces reactive oxygen species (ROS) buildup in arterial tissues, which is potentially damaging to DNA, proteins, etc.. Prior to evaluating the antioxidant potential of PGG, it is important to establish its toxicity level. In this study, we aim to investigate the *in vitro* toxicity effects of PGG on murine macrophages (MP).

METHODS

MP cells were routinely cultured in a 96-well cell culture plates with a density of 1 x 10^3 cells using DMEM culture media supplemented with 10% FBS and 1% antibiotics at 37°C, 5% CO_2 environment. After 24 hours, these cells were subjected to dose-dependent PGG treatments (0.1% w/v; Sigma-Aldrich, MO, USA) of 0, 250, 500, 750, and 1000 µL. 4% paraformaldehyde fixation of the cells was performed as a positive control. Cell viability was assessed using a MTT assay for each treatment group – control, PGG-treated (250, 500, 750, and 1000 µL), and fixative-treated (n = 6 each). Absorbance of each well was quantified at 570 nm using a plate reader (BioTek® Instruments Inc., Winooski, VT) and results were reported as mean ± standard deviation. Microscopic images (10x) of the MP cells were obtained for each group (Leica Microsystems) and their 3D surface analysis was performed using ImageJ (National Institutes of Health, Bethesda, MD). Statistical analysis (ANOVA with Dunnet's for comparison with control) was performed using GraphPad® 5.0 to analyze differences in the MTT assays across the groups. All experiments were repeated six times. Data was considered significant at $\alpha = 0.05$.

RESULTS

After a 24-hour incubation period, we found that the highest dosage of PGG (1000 µL) was not cytotoxic to MPs and did not show any extracellular matrix (ECM) crosslinking compared to fixed cells. Cells treated with PGG showed morphological characteristics similar to the control cells, as shown in Figs. 2a-e. There was no cross-linking observed in the control and PGG-treated groups (Figs. 2a-e). Further, the surface plot features of MPs treated with 1000 µL of PGG resembles the control condition closely, compared to the fixed group (see Figs. 3a-c).

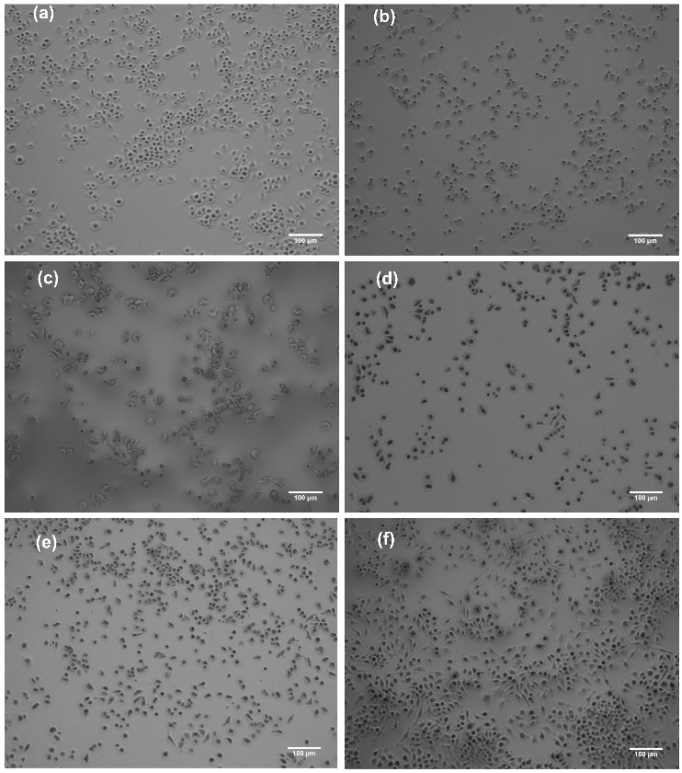

Figure 2: Microscopic characteristics of MP cells. (a) Control sample of MP cell with no PGG, (b) MP cells with 250 µL of PGG, (c) MP cells with 500 µL of PGG, (d) MP cells with 750 µL of PGG, (e) MP cells with 1000 µL of PGG and lastly, (f) MP cells that were fixed with 4% paraformaldehyde. Each scale bar represents 100 microns.

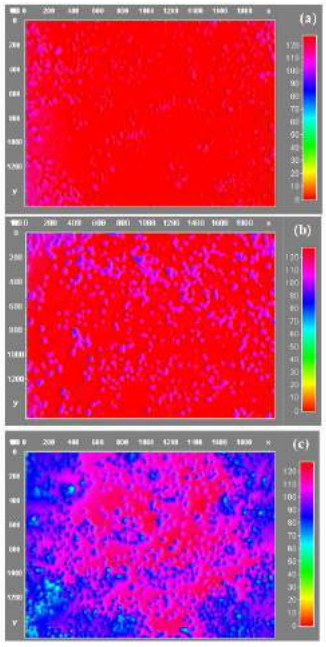

Figure 3: 3D surface plot of MP cells in (a) control, (b) 1000 µL of PGG, and (c) fixative conditions (4% paraformaldehyde). Blue denotes a more compact topography, which is indicative of a more cross-linked ECM.

From the MTT assay, dose-dependent increases in PGG concentration did not exhibit any change in cell viability. There was significant difference in cell viability between the control and fixed groups, as illustrated in Fig. 4. However, there were no pairwise differences observed between the control and PGG groups.

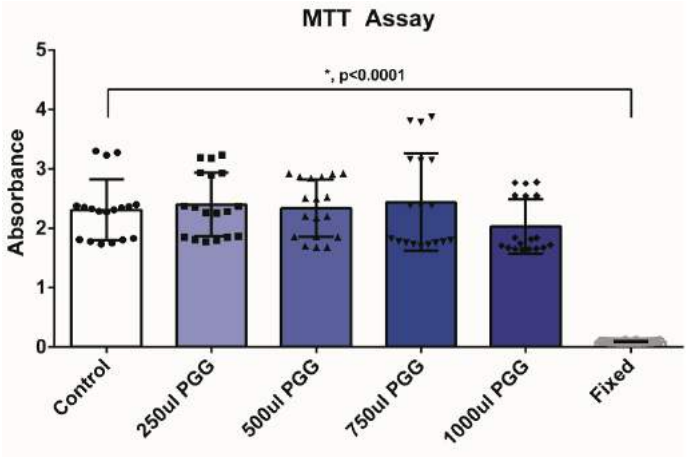

Figure 4: PGG toxicity analysis using MTT assay. * denotes significant difference across the groups and the bars indicate the pairwise differences in the data.

DISCUSSION

There are concerns about PGG being a strong cross-linking agent, which may lead to stiffening of arteries [3]. For the application of PGG to arterial aneurysmal tissues, PGG-mediated crosslinking can be beneficial to restore the extracellular matrix integrity [1] and enhance its biomechanical properties (which are otherwise compromised due to inflammatory secretions from macrophages and other sources [2]). It is critical that in addition to the extracellular matrix (ECM) stabilization, PGG should not affect the native cells. In our investigation, we found that after a 24-hour incubation with MP cells,

- the highest dosage of PGG (1000 µL) was not cytotoxic, and
- PGG did not show any ECM cross-linking compared to the fixed cells.

The present work supplements the several beneficial elasto-regenerative potential of this natural polyphenolic compound. The ultimate goal for the use of PGG in pathological conditions is to reduce inflammation by lowering the ROS levels.

Further investigation is needed to evaluate changes in secretory protein profile that can directly influence the oxidative stress developed in the cellular environment. Next, we aim to evaluate the ROS activity of these cells by using CellRox® deep red reagent and flow cytometry analysis. The results from such study will help us translate the application of PGG into animal models, and can potentially assist in formulating a pharmacological intervention for vascular diseases such as aortic aneurysms, atherosclerosis, etc.

ACKNOWLEDGEMENTS

This work has been supported by a U.S. National Institutes of Health Award (R01HL121293) and an American Heart Association Collaborative Sciences Award (16CSA28480006).

REFERENCES

1. Isenburg, JC et al. *Cirulation*, 115:1729-1737, 2007.
2. Patnaik, SS et al. *Ann Biomed Eng*, 47:39-59, 2018.
3. Kloster, BO et al. *Ann Med Surg (Lond)*, 7:65–70, 2016.

SB³C2019
Summer Biomechanics, Bioengineering and Biotransport Conference
June 25 -28, Seven Springs, PA, USA

RAPID ACTUATION AND TUNABLE CONTROL OF DNA MACHINES

Alexander E. Marras (1), Stephanie Lauback (2), Ze Shi (3), Gaurav Arya (4), Ratnasingham Sooryakumar (5), Carlos E. Castro (6)

(1) Institute for Molecular Engineering
University of Chicago
Chicago, IL, USA

(2) Department of Physics
Juniata College
Huntingdon, PA, USA

(3) Department of NanoEngineering
University of California San Diego
La Jolla, CA, USA

(4) Department of Mechanical Engineering
and Materials Science
Duke University
Durham, NC, USA

(5) Department of Physics
Ohio State University
Columbus, OH, USA

(6) Department of Mechanical
and Aerospace Engineering
Ohio State University
Columbus, OH, USA

INTRODUCTION

Precise robotic motion is ever-present within our cells in dynamic proteins like ATP synthase and kinesin. Functioning much like macroscopic machines, these proteins have multiple components and defined motion paths. Engineers across many disciplines use inorganic- and bio-materials to create nano- and micro-robots with similar functionality. Structural DNA nanotechnology, pioneered by Nadrian Seeman [1] and Paul Rothemund [2], enables researchers to design and fabricate DNA-based structures with nanometer-scale spatial control by employing well understood DNA base pairing and nucleic acid synthesis methods. This attractive technology has produced structures with controllable size, shape, and flexibility and has recently been expanded to kinematic mechanisms [3] and modular structures [4]. As the aspiration of biocompatible programmable machines moves closer to reality, a requirement for control over these devices arises.

Recent advances have demonstrated controlled motion of DNA devices, primarily using DNA handles and strand invasion to bind or displace reconfigurable components [3, 5, 6] with timescales of minutes or longer. Here, we present two strategies for actuating DNA-based mechanical devices in near real time. First, we demonstrate an approach using a simple modification to existing devices that adds a network of weak binding sites on complementary components for environmentally controlled rapid actuation [7]. A network of weak DNA handles is activated by increasing cation concentration, which raises the avidity of the network to join the two components. Likewise, reconfiguration is quickly reversible in decreased salt conditions. Second, we present an innovative method for real-time actuation using a magnetic stimulus [8]. Micron-scale rigid arms couple magnetic beads to nanoscale devices for direct manipulation through an externally applied magnetic field. This level of spatiotemporal control over DNA devices can serve as a foundation for real-time manipulation of molecular systems.

METHODS

DNA devices were constructed following procedures from Castro et al. [9]. Briefly, ~8000 nt viral DNA was mixed with ~200 synthetic oligonucleotides designed to self-assemble into predetermined geometries in a buffered solution with 18 mM $MgCl_2$. The solution was subjected to rapid heating to 65 °C then slowly cooled in a thermal annealing ramp over ~2 days to 25 °C. Structures were purified using polyethylene glycol precipitation with buffer exchange. Structure characterization primarily involved imaging on a FEI Tecnai G2 Spirit transmission electron microscopy (TEM) and a Bruker AXS Dimension Icon atomic force microscope (AFM). Bulk actuation response for cation-activated hinges was measured using Förster resonance energy transfer (FRET) calculations from ensemble

fluorescent intensity in a Horiba FluoroMax-4 spectrofluorometer. Kinetic studies for both systems involved single-molecule fluorescent imaging performed on a Nikon TiE inverted total internal reflection fluorescence (TIRF) microscope with a Dual-View light-splitting cube for FRET calculations. External magnetic fields were applied using four orthogonal electromagnets, which provided in-plane magnetic fields and a central solenoid which provided out-of-plane magnetic fields. All experiments were performed at room temperature.

RESULTS

In order to demonstrate two rapid actuation methods, we modified DNA origami hinges as example mechanisms. Figure 1 shows two 18-helix rectangular bundles with flexible single-stranded DNA connections forming a hinge axis. Extending specific DNA strands to include short binding sequences (blue and green overhangs), allows us to program these hinges to change conformation under the presence of certain ionic conditions. By defining specific sequences on each arm, we can program the actuation pathway. For instance, the sequence of blue overhangs in Figure 1 is weakly complementary to that of the green overhangs on the opposite arm. Increasing cation concentration strengthens DNA base-pairing interactions, closing the hinge. Lowering the cation concentration through buffer exchange promptly reverses this reconfiguration. We studied four design variables that modulate the actuation response of our devices: the number of overhang connections, the strength of these connections, the torsional stiffness of the hinge, and the cation used, exhibiting the ability to precisely tune actuation response. A key advantage of actuating DNA devices using ion-mediated control of localized overhangs is the potential for fast response. To investigate the opening and closing kinetics of our ion-activated hinges, we used a single-molecule FRET assay to show transitions occurring on millisecond time scales as buffers are exchanged every few seconds (Figure 1, right).

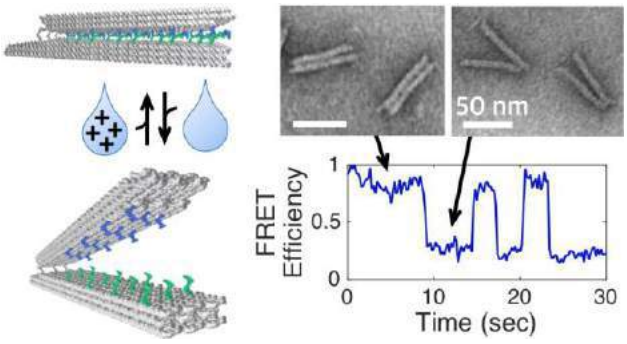

Figure 1: Ion-activated actuation uses weakly complementary sequences on opposing surfaces to trigger reconfiguration under the presence of increased cation conditions. Single-molecule FRET studies show that these transitions occur on millisecond (≲ 200 ms) time scales. Scale bars = 50 nm.

To demonstrate our magnetic actuation method, we built a DNA origami rotor and hinge, which both use nanoscale components to assemble micron-scale filaments. The DNA origami filaments have a cross section of 56 helices for enhanced rigidity. Figure 2 shows a hinge with a magnetic bead attached to the end of one arm with the other arm immobilized (not shown). Using a rotating magnetic field, the mechanisms are rotated with precision of ~±10°, varying slightly with the different systems being controlled. The strength and frequency of rotation of the magnetic field can be adjusted to tune actuation response. This system couples micron-scale control systems with nano-scale engineering for real time actuation of rotational devices.

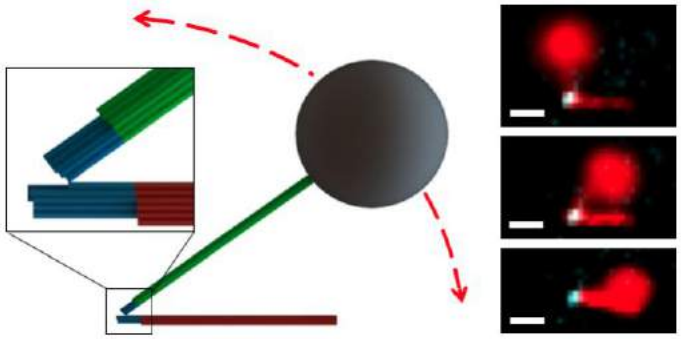

Figure 2: Control of DNA origami assemblies via externally applied magnetic fields using a low-cost platform that enables actuation into many distinct configurations with sub-second response times. Scale bars = 1 μm.

DISCUSSION

Given recent advances in structural DNA nanotechnology, the rapid manipulation capabilities established here could bring nanodevices for nanomanufacturing and biosensing closer to reality. Both approaches are amenable to a variety of complex devices, which we envision can serve as a foundation for nano- or micro-scale robotic systems based on DNA origami assemblies. Importantly, our actuation strategies can be carried out using low-cost platforms with simple DNA modifications or off-the-shelf electromagnets and could be applied to new and existing devices to enable low-cost real-time manipulation of a wide range of dynamic DNA assemblies.

ACKNOWLEDGEMENTS

This work was supported by NSF awards CMMI-1536862 and CBET-1351159, and the U.S. Army Research Office under Contract No. W911NF-14-1-0289. We thank the Campus Microscopy and Imaging Facility and NanoSystems Laboratory at Ohio State University. A.E.M. was partially supported through a Presidential Fellowship from Ohio State University.

REFERENCES

[1] Seeman, N.C., *J Theor Biol*, 99:237-247, 1982.
[2] Rothemund, P., *Nature* 440:297, 2006.
[3] Marras, A.E., et al., *Proc Natl Acad Sci*, 112:713-718, 2015.
[4] Gerling, T., et al., *Science*, 347:1446-1452, 2015.
[5] Lunds, K., et al., *Nature*, 465:206, 2010.
[6] Zhou, L., et al., *Small*, 14:47, 2018.
[7] Marras, A.E., et al., *ACS Nano*, 12:9484-9494, 2018.
[8] Lauback, S., et al., *Nat Commun*, 9:1446, 2018.
[9] Castro, C.E., et al., *Nat Methods*, 8:221, 2011.

SB³C2019
Summer Biomechanics, Bioengineering and Biotransport Conference
June 25 -28, Seven Springs, PA, USA

HIGH-THROUGHPUT CELL MECHANICAL PROPERTY MEASUREMENTS FROM CREEP EXPERIMENTS IN AN EXTENSIONAL FLOW MICROFLUIDIC DEVICE

Huda Irshad (1), Safwa Ali (1), Gwendolyn M. Cramer (2), Jonathan P. Celli (2), and Joanna B. Dahl (1)

(1) Department of Engineering
University of Massachusetts Boston
Boston, MA, USA

(2) Department of Physics
University of Massachusetts Boston
Boston, MA, USA

INTRODUCTION

Cell mechanical behavior measured at the single-cell-level is a high-level indicator of complex and integrated molecular changes that occur during physiological and pathophysiological processes. Due to the label-free nature of intrinsic cell mechanical properties, mechanical phenotyping, or grouping of cells based on mechanical behavior, has promising applications for fundamental cell biology research and in clinical settings for disease diagnostics and therapeutics.

The high-throughput capabilities of microfluidics have made possible exciting mechanical phenotyping studies of large populations of cells [1-4]. However, while extremely high-throughput mechanical phenotyping devices have significant clinical applications, the platforms sacrifice simplicity of modeling that would allow for measurement of intrinsic cell mechanical properties that is independent of the microfluidic device. For these existing devices, the deforming force is dependent on cell size and for some, pressure fluctuations due to transient occlusion of parallel channels. We have taken another strategy to deform cells with steady viscous forces that only depend on channel geometry and fluid parameters, avoid contact with device walls, and obtain a symmetric cell deformation so that we can achieve close agreement with modeling conditions, and therefore obtain more accurate mechanical property measurements.

The objective of this work is to introduce an extensional flow microfluidic platform that measures the mechanical properties of suspended cells and rigorously accounts for the full set of field equations and boundary conditions. To demonstrate a measurement capability of this device, we utilized a creep measurement technique to extract mechanical properties of cell-sized alginate hydrogel microparticles. We also present preliminary differential mechanical measurements of pancreatic cancer cell sub-lines with established drug resistant phenotype, an emerging component of our on-going project to understand the mechanisms that make rare subpopulations of tumors drug resistant and more invasive.

METHODS

A microfluidic extensional flow device, commonly called a cross-slot, consists of two channels that intersect at 90 degrees, generates a linear planar extensional flow field. The initially spherical cells or microparticles focused to the center streamline elongate into prolate ellipsoids in the extensional flow region that has a uniform extensional strain rate (Figure 1). Devices were made of polydimethylsiloxane (PDMS) and fabricated using standard soft lithography techniques. Channel dimensions are 100 µm deep and 500 µm wide.

Alginate microparticles were fabricated using an emulsion technique from 0.5% (w/v) sodium alginate and suspended in aqueous 0.5% (w/v) methylcellulose (μ = 15 mPa·s). Sphere sizes were 10-50 µm. Cultured cells were trypsinized and suspended in 0.5% (w/v) methylcellulose with an approximate density of 1M cells/mL.

To perform mechanical property measurements, the microparticle or cell suspension were infused with a syringe pump into both cross-slot inlet channels (flow rate 1050 µL/hr, extensional strain rate 35 s^{-1}, channel average flow velocity 5.8 mm/s). Sphere deformation in the extensional flow region was imaged using an inverted microscope (Zeiss Axiovert 200M) with a 10x objective under brightfield (alginate microparticles) or phase contrast (cells) microscopy. For alginate particles, movies were captured with a Phantom VEO-E 340L high-speed camera at 8000 frames/s, and cell movies were capture with a Photometrics Prime95B sCMOS camera at ~80 frames/s.

The time evolution of strain for a single microparticle or cell as it passes through the extensional flow region was quantified from a sequence of 4 - 15 images (cells) or 60-100 images (alginate particles). Mechanical property parameters were obtained through linear

Poster Presentation #P134

regression on the observed strain ε vs. time t data on a linear (alginate) or log-log (cells) plot applying the appropriate model (models in Results). Microparticle strain was defined as $\varepsilon = (a-b)/(a+b)$, where a and b are the long and short axes, respectively, of an ellipse fitted to the outer edge of the microsphere/cell. The custom image processing and modeling fitting was performed in MATLAB.

RESULTS

Our mechanical model is a single analytic equation that relates the time-dependent sphere deformation to suspending fluid flow because we chose experimental parameters such that both the flow field and the deformable viscoelastic sphere can be described by linear theories (Stokes flow and linear viscoelasticity, respectively) Using the viscoelastic correspondence principle [5], the Laplace-transformed viscoelastic solution is obtained directly from the corresponding elastic solution [6]. The final result for a Kelvin-Voigt viscoelastic solid (spring and damper in parallel, creep compliance $J(t) = J_0(1 - e^{-t/\tau})$) is obtained upon inversion:

$$\varepsilon(t) = \frac{5}{2}\mu\Omega J_0\left(1 - e^{-t/\tau}\right) \qquad (1)$$

where the suspending fluid parameters are viscosity μ and extensional strain rate Ω and the sphere Kelvin-Voigt parameters creep compliance J_0 and retardation time τ.

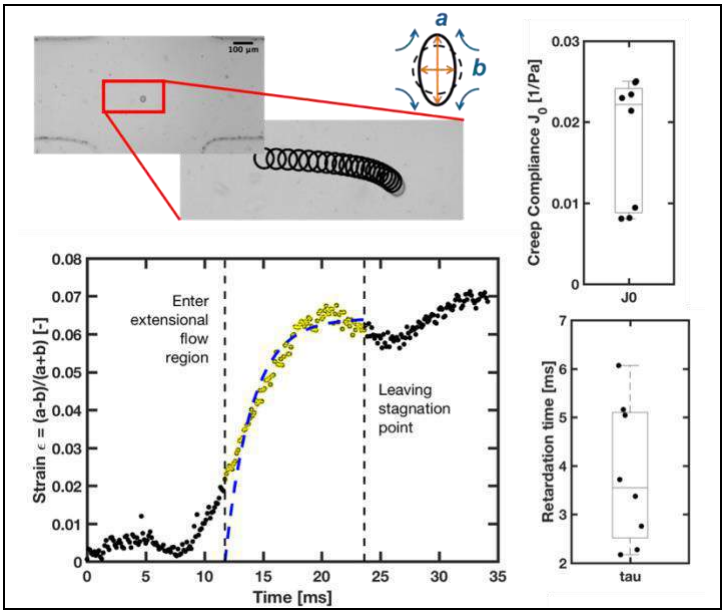

Figure 1: Alginate microparticle deforming in cross-slot device and results of Kelvin-Voigt fit to strain data (n = 8).

Cells have been shown to obey the power-law [7] under many conditions, and this constitutive law (relaxation modulus $G(t) = G_0(t/t_0)^{-\alpha}$) yields the model:

$$\varepsilon(t) = \frac{5}{2}\frac{\mu\Omega}{G_0}\left(\frac{t}{t_0}\right)^{\alpha}\frac{\sin(\pi\alpha)}{\pi\alpha} \qquad (2)$$

where G_0 is the reference stiffness at an arbitrary time t_0 and $0 < \alpha < 1$ is the fluidity parameter (0 for Newtonian fluids, 1 for elastic solids).

DISCUSSION

We have demonstrated a new microfluidic measurement technique that performs high-throughput creep measurements to obtain the time-dependent shear modulus of any viscoelastic sphere. By observing cells/spheres over 10-20 ms, we capture the creep curve plateau, not just the initial rapid increase in strain. The advantages of our measurement technique compared to previous designs include no need to calibrate the deforming force due to lack contact with walls, a simpler deformation shape that is easier to accurately capture in recorded images, and the measurement of time-dependent (viscoelastic) as opposed to time-independent (elastic, after initial transients have died out) properties. Our platform has the potential to be a repeatable, precise, and accurate technique. The data here are preliminary, and we are in the process of validating the alginate microparticle data with bulk rheometer and AFM measurements. The quality of data will also improve once our analysis code is robust enough to process thousands of cells.

Our alginate particles are softer than previous reported alginate measurements, but that is expected considering alginate is known to degrade in water and we used older microparticles that sat in water for two months. The equivalent frequency range of our platform is limited to about one decade, compared to ~8 decades for a rheometer. This is a drawback the specific materials use to make our microfluidic device.

The PANC1 and PANC1OR pancreatic cancer cell sublines are genetically matched yet possess contrasting invasive potential, chemoresistance, cellular architectures, and also viscoelastic mechanical properties according to these preliminary data. Our forthcoming work could be particularly informative since the drug sensitive/resistant cells here come from a common lineage thus allowing for the first time a direct correlation of mechanical phenotype and drug responsiveness.

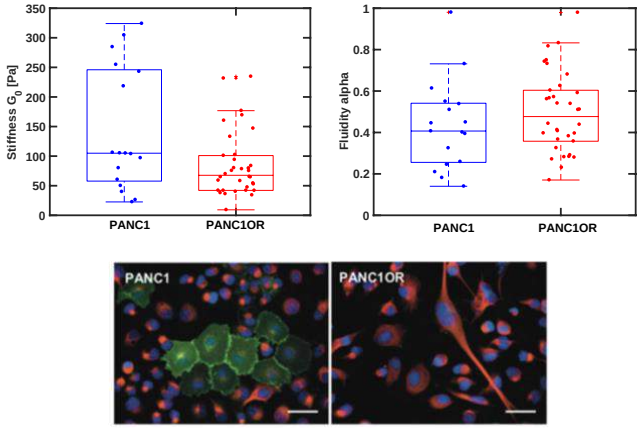

Figure 2: Power-law mechanical properties for PANC1 cells (n = 17) and PANC1OR cells (n = 34). The chemoresistant, more invasive PANC1OR cells are softer (smaller G_0) and more fluid (larger α). Cell staining from our collaborator's earlier work [8] demonstrates the different subline mechanical phenotypes.

ACKNOWLEDGEMENTS

The PANC1/PANC1OR cells were provided by our collaborator Jon Celli (Physics, UMB). The project was funded by the University of Massachusetts Boston Healey Research Grant Program.

REFERENCES

[1] Gossett, DR et al., *PNAS*, 109(20):7630-7635, 2012. Lin, J. et al, *Microsyst Nanoeng*, 3:17013, 2017.
[2] Lange, JR et al., *Biophys J*, 112(7):1472-1480, 2017.
[3] Mietke, A et al., *Biophys J*, 109(10):2023-2036, 2015. Mokbel, M et al., *ACS Biomater Sci Eng*, 3(11): 2962-2973, 2017.
[4] Nyberg, KD et al., *Biophys J*, 113(7):1574-1584, 2017.
[5] Christensen, RM, *Theory of Viscoelasticity*, New York: Academic Press, Inc. 1982.
[6] Murata, T., *J Phys Soc Jpn*, 50(3):1009-1026.
[7] Fabry, B et al., *PRL*, 87(14):148102, 2001.
[8] Cramer, GM et al., *Mol Cancer Res*, 15(1):15-25, 2017.

SB³C2019
Summer Biomechanics, Bioengineering and Biotransport Conference
June 25 -28, Seven Springs, PA, USA

A COMPUTATIONAL APPROACH FOR OPTIMAL DESIGN OF TISSUE ENGINEERED VASCULAR GRAFTS

Jason M. Szafron (1), Abhay B. Ramachandra (1), Christopher K. Breuer (2), Alison L. Marsden (3), Jay D. Humphrey (1,4)

(1) Department of Biomedical Engineering
Yale University
New Haven, CT, USA

(2) Center for Regenerative Medicine
Nationwide Children's Hospital
Columbus, OH, USA

(3) Departments of Pediatrics and Bioengineering
Stanford University
Stanford, CA, USA

(4) Vascular Biology and Therapeutics Program
Yale School of Medicine
New Haven, CT, USA

INTRODUCTION

Our prior work has demonstrated acceptable outcomes for porous polymer scaffolds implanted as inferior vena cava interposition grafts in SCID/bg mouse models with no evidence of catastrophic failure because of extensive neotissue deposition prior to complete polymer degradation [1]. Yet, the long-term behavior of these grafts remains different from that of native vessels, suggesting a need for improvements in implant design. Computational models of vascular graft growth and remodeling (G&R) can both describe and predict neovessel formation [2,3], and recent studies have incorporated key scaffold parameters such as microstructure and degradation behavior within the G&R framework. Furthermore, formal optimization methods have been used computationally to identify parameter values in vascular G&R, suggesting that a coupling of these computational models can yield parameter values that lead to a particular G&R outcome [4], which depends of course on the objective function minimized by the optimization procedure. Herein, we examine a G&R framework coupled to an optimization procedure with the aim of optimizing graft design parameters.

METHODS

A constrained mixture model of vascular growth and remodeling was adapted to include mass production due to the immune response associated with implantation of a polymeric scaffold and from mechanobiological principles suggesting that cells seek to promote mechanical homeostasis [5]. Immuno-driven matrix production was parameterized in terms of the scaffold microstructure such that mass production was sensitive to changes in the pore size and fiber diameter of the construct. Mechano-mediated matrix production occurred as the stiff polymeric constituents degraded and the inflammatory response resolved, leading to increased loading of mechano-sensitive constituents. Changes in graft constituent mass densities were computed throughout the G&R time course with different times treated as a series of quasi-static equilibrium states. Such a model allowed output of relevant metrics of evolving graft behavior that were then compared to native properties to identify the scaffold microstructure and degradation profile that minimized differences in native and graft behavior throughout the G&R time course.

An objective function that promotes optimal graft behavior not only prevents catastrophic failure, but also promotes native-like neovessel behavior. Minimizing the deviation in graft radius from the native venous radius represents a correlate for dilatation and stenosis, which can occur as a result of a blunted or an exuberant inflammatory response, respectively. Graft compliance, that is, the change in graft diameter for a given change in pressure, can be used as a metric of structural stiffness that considers both geometric and material effects in determining graft mechanical behavior, which modulates the loading of adjacent vessels. Material stiffness has been shown to be an important indicator of vessel microstructural health, with changes in stiffness linked to disease processes [6]. Therefore, the chosen objective function sought to minimize

the root mean squared deviation in graft radius, compliance, and material stiffness from that of the native vessel. Numerical optimization was performed with the Surrogate Management Framework (SMF) [4,7], which is a non-intrusive, derivative-free method that enables an easy coupling with the G&R framework.

RESULTS

The coupled G&R/SMF model produced a graft design with improved matching of radius, compliance, and material stiffness relative that of the native vein throughout much of the G&R time course, which is to be contrasted with the current state-of-art empirically determined graft (Fig. 1A-C). While matching was particularly close for radius, with less than a 1% deviation from native at the end of G&R over 100 weeks, compliance and material stiffness continued to deviate by more than 10% and 40%, respectively, at the end of G&R (Fig. 1D). Additional simulations showed that closer matching of either compliance or material stiffness required a tradeoff in matching for the other metric due to an inverse correlation.

Optimal graft microstructure was found to differ from that used in the experimental grafts, with larger fibers necessary to promote robust matrix production in the immuno-compromised SCID/bg mice. Additionally, rapid degradation of the scaffold material was found to be favorable as it allowed the evolving neovessel to more quickly match the native radius, while the more robust immune response prevented dilatation (Fig. 1A).

DISCUSSION

Numerous studies have attempted to experimentally identify improved scaffold properties for tissue engineering scaffolds via an iterative (trial and error) design process. Such studies provide valuable data on the cellular response to specific changes in scaffold design, such as the effect of fiber diameter on cellular infiltration [8]. However, experimentally determining an optimal graft design is costly, both in terms of resources and time. We suggest here that computational models can be used to identify improved candidate scaffold designs, which could accelerate the design process for tissue engineered constructs. Furthermore, the G&R framework allows us to look beyond catastrophic failure and attempt to match functionally significant vessel properties, such as compliance and material stiffness.

Of course, in vivo experiments examining graft outcomes with the candidate scaffold will be necessary to validate the model prediction. Such validation experiments will also provide additional data, which can then be used to inform and refine the modeling framework. Such feedback between experiment and simulation highlight the complementary nature of these tools to enable rational tissue engineering design.

ACKNOWLEDGEMENTS

This work was supported, in part, by grants from the US National Institutes of Health (R01 HL098228, R01 HL128602, R01 HL128847) and a Graduate Student Research Fellowship from the National Science Foundation (NSF DGE1122492).

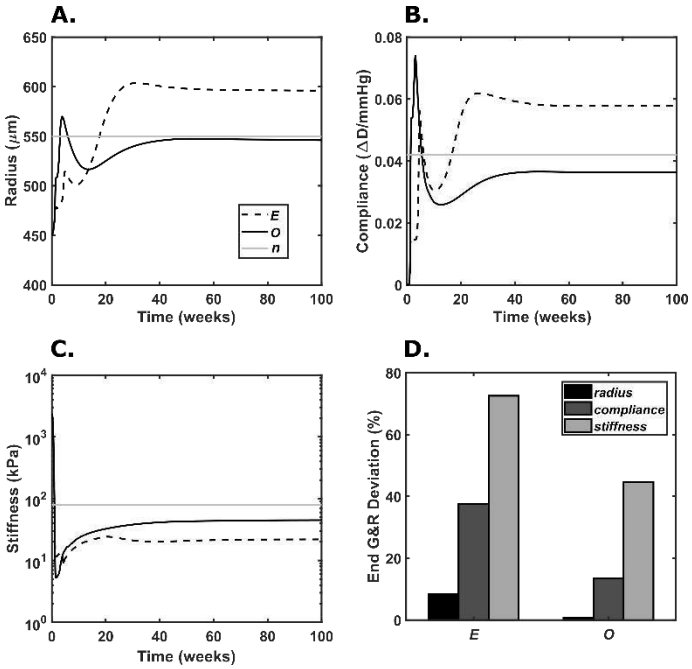

Figure 1. (A) Evolving inner graft radius for the experimental case (*E*, dashed line), the optimized case (*O*, solid line), and the native target (*n*, gray line). (B) Evolving compliance for each case. (C) Evolving material stiffness for each case. (D) Absolute deviations from the native value for each metric at the end of the G&R time course for the experimental and optimal cases.

REFERENCES

[1] Naito, Y, et al., *Tissue Eng Part A*, 20(1-2), 346-355, 2013.
[2] Miller, K.S., et al., *J Biomech*, 47(9), 2080-2087, 2014.
[3] Khosravi, R., et al., *Tissue Eng Part A*, 21(9-10), 1529-1538, 2015.
[4] Ramachandra, A. B., et al., *J Biomech Eng*, 137(3), 031009, 2015.
[5] Szafron, J. M., et al., *Ann Biomed Eng*, 46(11), 1938-1950, 2018.
[6] Bellini, C, et al., *J R Soc Interface*, 14(130), 20161036, 2017.
[7] Audet, C., Dennis Jr., J.E. *SIAM J Optim*, 17(1), 188-217, 2006.
[8] Balguid, A., et al., *Tissue Eng Part A*, 15(2), 437-444, 2008.

SB³C2019
Summer Biomechanics, Bioengineering and Biotransport Conference
June 25 -28, Seven Springs, PA, USA

CURLING ANGLE MEASUREMENT OF LV BI-LAYERED SURFACE STRIP REVEALS RESIDUAL STRESS IN THE EPICARDIUM

Xiaodan Shi (1,3), Yue Liu (2), Katherine Copeland (1), Sara McMahan (1), Song Zhang (3), Ryan Butler (3), Yi Hong (1), Michael Cho (1), Pietro Bajona (4), Huajian Gao (2), Jun Liao (1,3)

(1) Department of Biomedical Engineering
University of Texas at Arlington
Arlington, TX, United States

(2) School of Engineering
Brown University
Providence, RI, United States

(3) Collage of Engineering and Veterinary Medicine
Mississippi State University
Mississippi State, MS, United States

(4) Department of Cardiovascular and Thoracic Surgery
University of Texas Southwestern Medical Center
Dallas, TX, United States

INTRODUCTION

Omens and Fung showed that, if a radial cut is applied to an equatorial slice of a rat heart, the rat's left ventricle (LV) exhibits an open angle-like morphology, revealing residual stress in the LV wall [1]. However, the heart's epicardial layer, with elastin as the dominant component, has not been well investigated, specifically on how it contributes to ventricular biomechanics. During our dissection of tissue samples from the heart surface with the epicardial layer and heart muscle, we noticed this bi-layered surface strip always curls towards the epicardial side. This surface curling reveals the existence of residual stress in the epicardial layer. In this study, we developed a curling angle measurement technique to prove and characterize the residual stress in the LV epicardial layer.

METHODS

Fresh porcine hearts (~ 6-month old, Yorkshire) were obtained from a local abattoir. Both circumferential (CD) and longitudinal (LD) LV surface strips (~15 mm×5 mm×1.5 mm) were dissected from seven locations (**Figure 1A**). The epicardial strip dimensions were determined to achieve optimal curling behavior (**Figure 1B**). The intact native hearts were fixed in 10% buffered formalin, and the fixed LV surface strips were then dissected to accurately capture the natural surface curvature of the heart as a reference. Each dissected tissue strip was immersed in 1X PBS to achieve free-floating and stress-free status, and the side-view digital pictures were taken after the full occurrence of curling (~1 minute). ImageJ was then used to analyze the curly-enclosed angle ($\theta_{curly\text{-}enclosed}$) from the native strip and the natural angle ($\theta_{natural}$) from the formalin-fixed strip. The total curling angular change (θ_{Δ}) was defined and calculated as: $\theta_{\Delta} = 360° - \theta_{natural} - \theta_{curly\text{-}enclosed}$ **(Figure 1C**).

RESULTS

We successfully used the heart surface strip curling as a means to reveal and characterize the residual stress of the epicardial layer (effect of epicardial elastin in essence). Heart surface strips showed various degrees of curling in different anatomical locations. Circumferentially (**Figure 2A**), θ_{Δ} revealed that (i) the larger curling happened in the lateral locations (B2, M2) when compared to the anterior l (B1, M1) and posterior locations (B3, M3); (ii) the apex location had the largest circumferential curling. Longitudinally (**Figure 2B**), (i) the curling was larger in the anterior locations (B1, M1) when compared to the lateral (B2, M3) and posterior locations (B3, M3); (ii) again, the curling in the apex location was dramatically large.

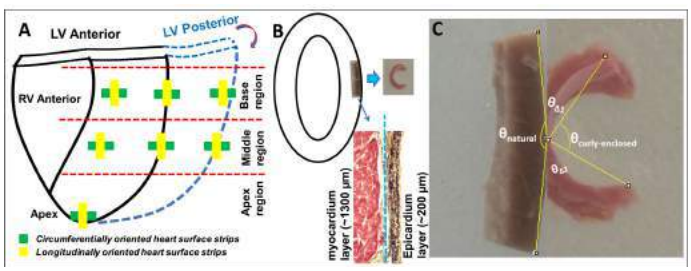

Figure 1: (A) Sample preparation plan for circumferentially and longitudinally dissected LV surface strips. (B) Illustration showing the curling phenomenon of the heart surface strips. (C) Calculation of total curling angular change.

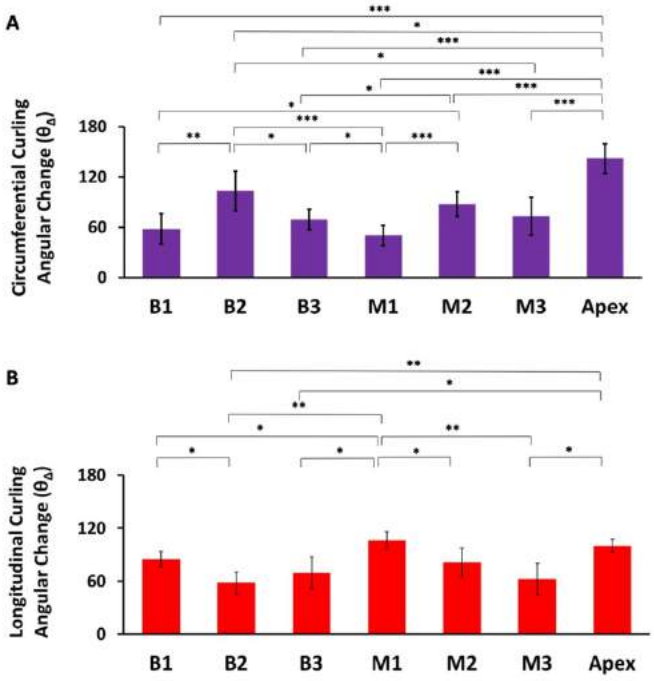

Figure 2: Measurements of total curling angular change in the circumferentially-dissected (A) and longitudinally dissected (B) heart surface strips at seven anatomical locations.

CONCLUSION

The observed heart surface curling clearly reveals the existence of residual stress in the epicardial layer. In other words, the epicardial layer is under tension when it covers the unpressurized intact heart. However, after a strip is dissected out from the heart, the boundary condition that restricts the elastin network from contraction does not exist anymore. As a result, the contraction of the epicardial layer bends the tissue strip and then a curling morphology occurs.

ACKNOWLEDGEMENTS

This study is in part supported by1R01EB022018-01 from NIH, 13GRNT17150041 from AHA, and UT STARS.

REFERENCES

[1] J.H. Omens, Y.C. Fung, Circulation Research, 1990, 66(1) 37-45.

SB³C2019
Summer Biomechanics, Bioengineering and Biotransport Conference
June 25 -28, Seven Springs, PA, USA

EFFECTS OF MICROGRAVITY ON 3D BIOPRINTED CONSTRUCTS TO ASSESS CARDIOVASCULAR DISORDERS

Likitha Somasekhar (1), Prabhuti Kharel (1), Kenia Nunes (1), Paul Gatenholm (2), Kunal Mitra (1)

(1) Department of Biomedical and Chemical Engineering and Sciences
Florida Institute of Technology
Melbourne, Florida, United States

(2) Department of Chemistry and Chemical Engineering
Chalmers University of Technology
Gothenburg, Sweden

INTRODUCTION

The need for three-dimensional (3D) culture models in research and medical applications has become increasingly important due to their ability to mimic in vivo tissues along with its extracellular matrix (ECM). 3D bioprinted models will help us understand the effects of microgravity on cellular organization of the cytoskeleton, intracellular signalling mechanisms and gene expression and on cellular apoptosis [1]. Over the past two decades, research has shown that exposure to microgravity in space leads to post flight orthostatic intolerance in astronauts and cardiovascular dysfunction is a key mechanism responsible for this occurrence [2]. Microgravity-induced adaptive alterations in vascular structure and function contributes to vascular dysfunction, the main component responsible for cardiovascular problems. Endothelial cells (ECs) which cover the entire inner surface of blood vessels, play a crucial role in maintaining the functional integrity of the vascular wall and little is known on the effects of microgravity on ECs. There is limited research data available about vascular dysfunction during and post spaceflight. Researchers have been trying to interpret the role of oxidative stress in cardiovascular related disorders. Reactive oxygen and nitrogen species are thought to contribute to pathogenesis of many cardiovascular disorders (CVD) including atherosclerosis, hypertension and congestive heart failure [3]. Because reactive oxygen species (ROS) are capable of rapidly inactivating nitric oxide (NO) and since endothelial function is characterized by nitric oxide bioavailability, it is an important indicator of vascular health. NO is an important protective molecule in the vasculature and endothelial NO synthase (eNOS) is responsible for most of the vascular NO produced. A variety of enzymatic and non-enzymatic processes can generate ROS and NO in mammalian cells. ROS are highly dependent on their concentration in the tissue, when present in moderate and high levels it triggers oxidative damage. There is still limited understanding about the pathways involved with vascular dysfunction in microgravity and is the focus of this research.

METHODS

3D Bioprinted Cellular Construct

Hydrogel is prepared using sodium alginate (Fischer Scientific) and gelatin (Sigma-Aldrich) that is dissolved respectively in DI water and 10X PBS solution under constant stirring to make a 5% (w/v %) solution. Human Umbilical Vein Endothelial Cells (HUVECs) (PromoCell) are maintained in fresh endothelial cell growth medium and are then used to bioprint cellular constructs at a range of $2.216x10^6$ cells/ml - $8.38\ x10^6$ cells/ml using the syringe-based extrusion (SBE) system. The cellular construct is then crosslinked with 0.5M calcium chloride (Fischer Scientific). The channels present in the construct as shown in Figure 1A allow transport and diffusion of oxygenated perfused media to the cellular environment to maintain cell viability. The cellular construct is then placed in the microgravity simulator system a 3-D clinostat Gravite available at NASA KSC as shown in Figure 1B. After exposure to microgravity, the tissue constructs are embedded in Tissue-tek and sectioned (5-mm-thick slices).

DHE Assay

Dihydroethidium (DHE) is a cell-permeable compound, it enters the cells and interacts with $O^{\bullet-}$ to form oxyethidium, which in turn interacts with nucleic acids to emit a bright red color detectable qualitatively. Each sample is washed with PBS before staining at a conc. of 5 μM reconstituted in Krebs solution. After 30-min incubation, imaging is performed using a Nikon C1 Confocal fluorescence microscope. Nikon EZ-C1 Freeviewer (V 3.90) software is used for image acquisition. Five different fields were counted for each sample. ImageJ software is then used for measuring exposure of red

fluorescence to evaluate ROS production in the construct as shown in Figure 2.

Nitric Oxide Assay

Nitric oxide released by the cells is measured using a fluorescence probe 4-Amino-5-Methylamino-2',7'-Difluorofluorescein Diacetate (DAF-FM) at 5 µM conc. diluted in 1X PBS which produces a green fluorescence (488nm) after exposure to simulated microgravity as shown in Figure 3. After 30-min incubation, imaging is performed using a Nikon C1 Confocal fluorescence microscope. Nikon EZ-C1 Freeviewer (V 3.90) software is used for image acquisition. Five different fields are counted for each sample. ImageJ software is then used for measuring and evaluating NO production in the construct.

RESULTS

Two factors, space radiation and microgravity are prominently involved in ROS and NO generation in biological systems. ROS production is facilitated in specific organs and tissues including neuronal and cardiovascular systems. Results from simulated microgravity demonstrates increased ROS production and reduced NO bioavailability as shown in Figures 4 and 5 respectively. The tissue constructs that are not exposed to microgravity (ctrl) yields higher NO production and decreased ROS when compared to the constructs exposed to microgravity. This shows an increase in oxidative stress, which is due to the decrease in NO production and increase in ROS production, resulting in endothelial dysfunction, and thus can lead to CVD during spaceflight. Statistical analysis of NO and ROS revealed a significant decrease in the microgravity samples ($p < 0.05$).

Figure 1: A. 3D bioprinted cellular constructs. B. 3D clinostat Gravite available at NASA KSC.

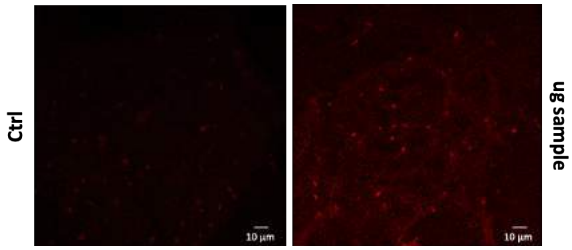

Figure 2: Fluorescence confocal microscopy images of ROS released by the cells.

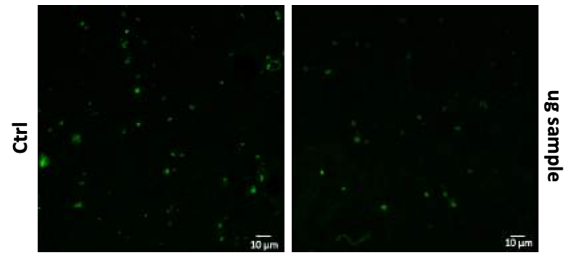

Figure 3: Fluorescence confocal microscopy images of NO released by the cells.

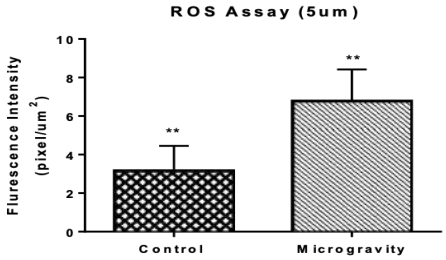

Figure 4: Fluorescence intensity measurement of ROS obtained from the cellular constructs.

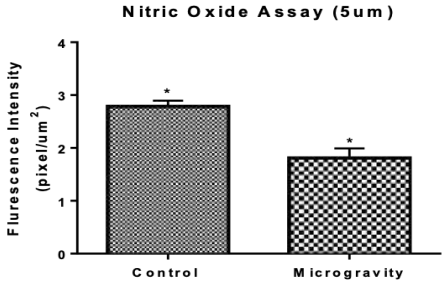

Figure 5: Fluorescence intensity measurement of NO obtained from the cellular constructs.

DISCUSSION

The architectural design of the cellular construct bioprinted is optimized to improve the diffusion limitation in the 3D constructs and test for mechanical stabilization. Despite all the advances, there isn't a model to investigate vascular dysfunction under the influence of microgravity. It is anticipated that 3D cell culture models will provide significant advantages including more physiologically relevant representations of cell morphology, proliferation gradients, response to drugs, gene expression, and overall cell behavior. Many studies have reported that cells can sense mechanical stresses, including variation of gravitational forces due to the changes in the forces that are transmitted across transmembrane adhesion receptors which link the cytoskeleton to the ECM and to other cells [4]. The results presented in this study demonstrates that exposure to microgravity affects the endothelial cells by increasing production of ROS as shown above by uncoupled eNOS which in turn causes further production of superoxide anion rather than NO which contributes markedly to this pathophysiology. Further experimentation based in simulated microgravity can advance our knowledge of the relationship between altered cellular mechanisms and on the vasculature of the tissue. Understanding oxidative stress in the space environment may help us understand the pathophysiological process and contribute to solving the problems caused due to exposure to microgravity and radiation.

ACKNOWLEDGEMENTS

We acknowledge partial funding from NASA Florida Space Grant Research Program and assistance from Dr. Ye Zhang from NASA KSC for providing microgravity simulator access.

REFERENCES

[1] Claassen, Dale E and Brian S. Spooner., *International review of cytology*, Vol. 156. Academic Press, 301-373, 1994.

[2] Griffoni, C., et al., *J Cell Biochem,* 112(1): p. 265-72, 2011.

[3] Cai, Hua et al., *Vascular Biology Protocols*, Humana Press, 293-311, 2007.

[4] Ingber, Donald., *The FASEB Journal,* 13.9001: S3-S15, 1999.

SB^{3}C2019
Summer Biomechanics, Bioengineering and Biotransport Conference
June 25 -28, Seven Springs, PA, USA

PATIENT SPECIFIC, IN VITRO STUDIES OF PATHOLOGIES CAUSED BY HEART DISEASE ASSOCIATED LAMIN A/C MUTATIONS

M. Mehrabi (1), R. Tran (1), H. Widyastuti (3), C. Nguyen (3), M.V. Zaragoza (3), A. Grosberg

(1) Department of Biomedical Engineering and the Edwards Lifesciences Center for Advanced Cardiovascular Technology, University of California, Irvine, Irvine, California, USA

(2) Center for Complex Biological Systems, University of California, Irvine, Irvine, California, USA

(3) UCI Cardiogenomics Program, Department of Pediatrics, Division of Genetics & Genomics and Department of Biological Sciences, School of Medicine, University of California, Irvine, Irvine, California, USA

INTRODUCTION

The nuclear lamina protein, Lamin A/C (LMNA), mutations can cause pathologies in multiple organs [1]. For example, the progeria disease is associated with a mutation to the LMNA gene, and it leads to a devastating early aging and death. In contrast, other LMNA gene mutations do not cause early aging, but instead have a subtler effect with patients presenting only with heart disease symptoms [2-4]. However, the mechanisms by which the LMNA mutation emerges exclusively in the heart muscle are unknown. One important avenue that needs to be explored is the unique mechanical environment of the heart, which could trigger pathological changes. We aimed to study the mechanisms that lead to these differences in vitro with patient specific cell-lines.

METHODS

Here we will present a study of 10 cell-lines negative for mutations or with four different types of LMNA mutations: 1) Hutchinson-Gilford progeria syndrome LMNA gene mutation, 2) LMNA splice-site mutation (c.357-2A>G , p.N120Lfs*5), 3) LMNA nonsense mutation (c.736 C>T, p.Q246X), and 4) LMNA missense mutation c.1003C>T (p.R335W) in exon 6 [5]. Fibroblasts from each of these cells lines were cultured and subject to a variety of mechanical stimulation akin to those experienced by cells in the myocardium. The cells were then fixed and stained to visualize the nuclei, actin fibrils, and the underline remodeled fibronectin. To analyze this data, we applied existing algorithms to quantify the re-organization of actin in response to mechanical stimulation by calculating both the actin orientational order parameter. Additionally, we analyzed the nuclei population in each sample for the number, defective percentage, nuclear area, and eccentricity. Furthermore, some of the fibroblast cell-lines were used to create patient specific iPS-derived cardiomyocytes. PATIENT's and CONTROL's fibroblasts (from skin biopsy) were reprogrammed to iPSCs (Fig. 1A) and differentiated to cardiomyocytes (Fig 1B-C). The PATIENT and CONTROL iPSC-derived cardiomyocytes were cultured and immunostained for Nuclei, actin fibrils, and Sarcomere (Fig 1B: blue, green, and red, respectively). The tissues were imaged with a confocal microscope, and the stained architectures were quantified. The presence of sarcomeres was used to confirm proper differentiation. Moreover, for the functional assay, iPSC- derived cardiomyocytes were evaluated by the "Heart-on-a-Chip" device based on the muscular thin film (MTF) technology. The cardiomyocytes can either contract spontaneously or they can be paced using a myopacer at 0.5-2 Hz by field stimulation electrodes. The dynamics of the tissue constructs were recorded and analyzed using ImageJ and Matlab software. Data for PATIENTs and CONTROLs chips were collected and analyzed for frequency and stress as a function of time for all conditions tested.

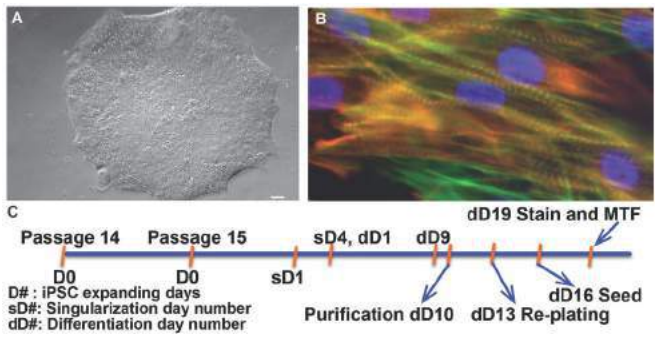

Figure 1: Time-line of differentiation. (A) iPSC colony; (B) Sarcomeres (red) in iPSC-derived cardiomyocytes; (C) time line.

RESULTS

It was found that mechanical stimulation alone applied to fibroblasts results in almost no significant differences (Fig. 2) between PATIENT and negative CONTROL lines for either tissue organization (Fig. 2) or nuclear morphology (Fig. 3).

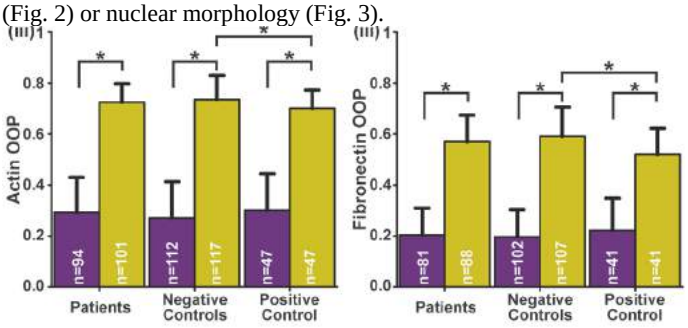

Figure 2: Organization of Actin Fibrils and extracellular matrix for PATIENTs, Negative CONTROLs, and a progeria cell line (positive control). Purple – no stretch, yellow – stretch at 1 Hz.

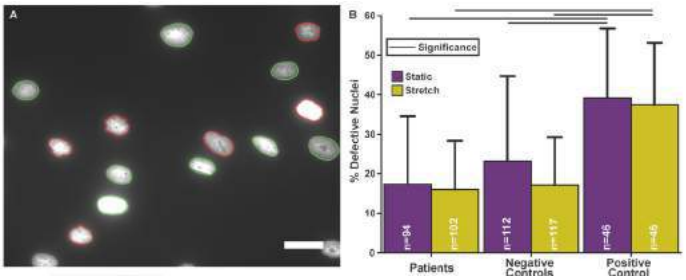

Figure 3: (A) Nuclei identified as defective (red) or normal (green). (B) The percent of nuclei as defective in each sample for all cell-lines.

There are some minor family specific variations (Fig. 4). However, it is unlikely that such minor changes could lead to major pathological responses.

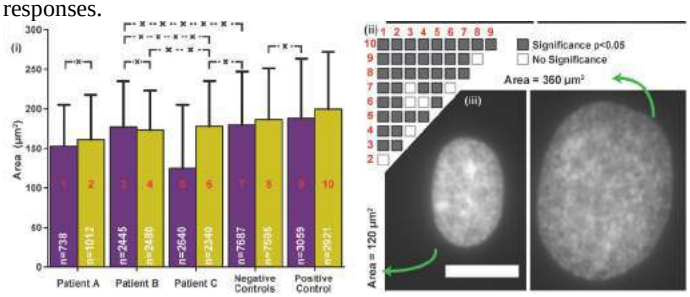

Figure 4: An example of subtle differences between the families of PATIENTS: (i) Nuclear area for static (purple) and stretch (yellow) conditions; lines with x's indicate no significance. (ii) A significant matrix referencing the red labels on (i). (iii) Examples of small and large nuclei.

In contrast, our data shows significant differences between iPSC-derived cardiomyocytes of PATIENTs and CONTROLs in frequency and active stress (Fig. 5). When the CONTROL tissues are paced, the measured frequency matches the induced frequency (Fig. 5A – black line trend on blue points). In contrast, when PATIENT tissues are paced, the actual frequency does not match the pacing frequency, which can be due to LMNA mutation and could be a cause of heart disease initiation. It is also interesting to note that the variation in measured frequency for paced tissues is much greater for PATIENTS than CONTROLS. The active stress was measured as the difference between the systolic and diastolic stresses (Fig. 5B). For negative CONTROLS tissues, the active stress increased when the tissues were paced. In PATIENTS, the active stress does not increase, which is another indication that the cells from the PATIENTS lines do not respond to pacing. Moreover, negative CONTROLS tissues have significantly higher active stress than the PATIENTS (Fig. 5B).

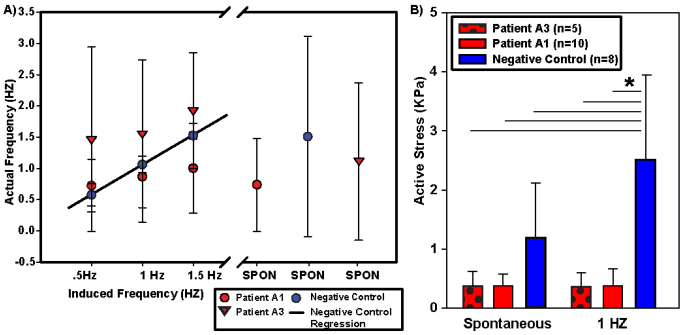

Figure 5: (A) Frequency response of PATIENT (red) and CONTROL (blue) tissues; right side of plot shows the results of no pacing – i.e. the spontaneous contraction. (B) Generated stress by the cardiac tissues.

DISCUSSION

Our cardiomyocyte results demonstrate that it is possible to construct an iPSC-derived cardiomyocyte in vitro model that differentiates between CONTROL and PATIENT populations. This is significant because the PATIENTS do not develop heart disease until they are at youngest in their 30s and sometimes in their 60s. With this work, we demonstrated that it is possible to see the consequences of this mutation within a reasonable lab experiment time frame.

Our stretcher results, in contrast, do not show that simple mechanical perturbation (which exists in contracting cardiomyocytes) is sufficient to cause significant differences in fibroblast morphology. There are two possible explanations for this – mechanical and biological. In terms of mechanics, it is possible that the stretch regime chosen for our experiments does not sufficiently recapitulate the cardiac tissue environment to trigger the mutation pathology. Alternatively, it is possible that the biological differences between fibroblasts and cardiomyocytes are dictating the location of the pathology. This will need to be further investigated.

ACKNOWLEDGEMENTS

This study was funded by NIH 1 R01 HL129008-01 (Grosberg, Zaragoza) and NIH T32 HL 116270 (Hughes).

We are thankful for Linda McCarthy's assistance with fibroblast cell lines.

REFERENCES

1. Parnaik, V.K.2008, Academic Press. p. 157-206.
2. Zaragoza, M.V., et al., PLoS ONE, 2016. **11**(5).
3. Zaragoza, M.V., et al., Clinical Genetics, 2017. **91**(3): p. 499-500.
4. Zaragoza, M., et al., Cells, 2017. **6**(4): p. 40.
5. Core, J.Q., et al., PLoS ONE, 2017. **12**(11): p. e0188256.

SB³C2019
Summer Biomechanics, Bioengineering and Biotransport Conference
June 25 -28, Seven Springs, PA, USA

ADIPOSE STROMAL CELL-DERIVED EXTRACELLULAR VESICLES INDUCE ELASTIN AND COLLAGEN DEPOSITION BY AORTIC SMOOTH MUSCLE CELLS

Eoghan M. Cunnane (1,2,3), Aneesh K. Ramaswamy (1), David A. Vorp (1,2,4,5,6), Justin S. Weinbaum (1,2,7)

(1) Dept of Bioengineering
University of Pittsburgh
Pittsburgh, PA 15261

(2) McGowan Institute for Regenerative Medicine
University of Pittsburgh
Pittsburgh, PA 15219

(3) Tissue Engineering Research Group
Dept of Anatomy
Royal College of Surgeons in Ireland
123 St Stephen's Green, Dublin 2, Ireland

(4) Dept of Surgery
University of Pittsburgh
Pittsburgh, PA 15213

(5) Dept of Cardiothoracic Surgery
University of Pittsburgh
Pittsburgh, PA 15213

(6) Dept of Chemical and Petroleum Engineering
University of Pittsburgh
Pittsburgh, PA 15261

(7) Dept of Pathology
University of Pittsburgh
Pittsburgh, PA 15261

INTRODUCTION

Aortic aneurysm (AA) is a chronic inflammatory disease of the aortic wall whereby degeneration of healthy tissue triggers progressive dilation of the vessel. Approximately 5 million people >50 years present with abdominal AA in the US [1,2] and over 200,000 new abdominal AAs are diagnosed annually [3]. AA rupture occurs when the aortic wall tissue can no longer bear the load induced by physiological forces due to advanced degeneration. This event is responsible for 15,000 high-mortality events annually in the US alone [4]. Wall degeneration can be attributed to changes in structural macromolecules, specifically, elastin degradation coupled with disorganization of the collagen network [5].

Currently, surgical intervention is the only option available to AA patients and the decision to intervene is primarily governed by aortic diameter measurements. Adult patients are recommended for surgery once their AA exceeds a "critical diameter" of 5.5cm. However, no non-surgical treatment option is available to patients who fall below the threshold despite the pronounced risk of rupture in this cohort. A targeted treatment to arrest degeneration and/or induce regeneration of functional elastic and collagen fibers could offer a viable non-surgical therapeutic option for patients with sub-critical AA dilations.

Work by our group has shown that periadventitial delivery of adipose-derived stromal stem cells (ASC) to a growing elastase-induced mouse aneurysm slows dilation and preserves elastic lamellae [6]. More recent unpublished work by our group has linked this elastin inducing effect to the products secreted by ASC. Specifically, we have shown that ASC conditioned media (CM) can stimulate elastic fiber assembly by healthy adult SMCs using a multi-level elastogenesis analysis. However, it is currently unknown if this elastogenic effect is caused by free factors within the CM or factors packaged within extracellular vesicles (EVs). EVs are cell-derived phospholipid membrane based nano-particles that present with functional surface/membrane proteins and contain protein and RNA species that can replicate the therapeutic effects of their parent cell [7]. Determining the specific fraction of the ASC CM that induces elastogenesis is critical to developing a well-defined and translatable treatment option. This study therefore tested if ASC derived EVs induce deposition of elastin and collagen fibers by aortic smooth muscle cells (SMCs) within three-dimensional *in vitro* fibrin gel constructs and if these fibers are mechanically functional. We compared the effect of ASC derived EVs to ASC CM and ASC CM that has been depleted of EVs (dEV CM) in order to de-couple the effects of free and encapsulated factors.

METHODS

Healthy adult human SMCs were purchased from ATCC and loaded within 3D fibrin gel constructs. Fibrin gel constructs were fabricated as previously described [8] using 200μL of fibrin and a SMC seeding density of $5x10^5$ cells/mL. A fibrinolysis inhibitor (12mM aminocaproic acid) was used to halt construct breakdown. Gels were plated on either stiff (tissue culture plastic) or soft (Flexcell plates) substrates. Culture media was changed every 48-72 hours for 30 days.

ASC CM was generated by culturing primary ASCs in two T175 tower flasks (5 layers in each) for 48 hours. ASCs were cultured in 1:1 DMEM:F12 supplemented with Pen-Strep, Fungizone and 10% FBS that had been depleted of EVs via 18 hours of ultracentrifugation at 120,000g. EVs were isolated from ASC CM using differential ultracentrifugation. Specifically, the CM was centrifuged at 250g to remove cells, 2500g to remove debris, filtered through 0.2 um to remove apoptotic bodies and then pelleted via ultracentrifugation at 100,000g for 70 minutes. EVs were characterized using transmission electron microscopy (TEM) to determine morphology, dynamic light scattering (DLS) to examine size and bicinchoninic acid assay (BCA) to quantify EV protein content before and after lysis using 2% SDS.

Treatments applied to the gels included: (1) No Treatment (NT): SMC growth-supplemented media; (2) Non-Conditioned Media (NCM): a 1:1 combination of SMC growth-supplemented media and fresh ASC culture media, (3) ASC CM: a 1:1 combination of SMC growth-supplemented media and ASC conditioned media; (4 and 5) 1x and 3x EV: a 1:1 combination of SMC growth-supplemented media and fresh ASC culture media supplemented with two different concentrations of EVs, and (6) dEV CM: a 1:1 combination of SMC

growth-supplemented media and ASC CM that has been depleted of EVs via differential ultracentrifugation.

Ninhydrin (insoluble elastin) and hydroxyproline (collagen) protein assays were used to quantify macromolecule deposition as a percentage of total protein within the stiff and soft substrate gels [9]. Uniaxial tensile testing of soft gels was performed using an Instron #5543A device. Mechanical properties are reported as the modulus of the response curves in the low and high stretch regions.

RESULTS

Characterisation of EVs demonstrates that (1) the particles are spherical and cup-like in appearance which is typical of EVs, (2) there are two distinct populations of particles that represent exosomes (~70nm) and microvesicles (~300nm) and (3) total protein content is increased upon lysis of the EVs indicating that protein is encapsulated within the EV's phospholipid membrane (**Figure 1**).

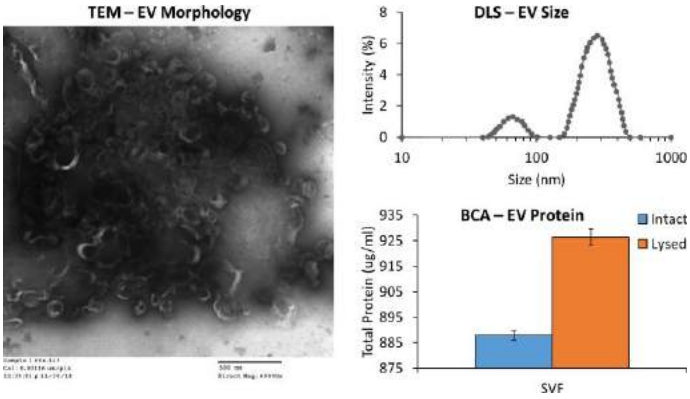

Figure 1: Morphology, size and total protein content of EVs isolated from ASC CM.

Both EV groups and the ASC CM group show similar levels of elastin deposition after 30 days in stiff substrate gels that are greatly increased compared to dEV CM, NT and NCM (0.07±0.07% NT, 0.03±0.04% NCM and 0.04±0.04% dEV CM, vs 0.27±0.12% ASC-CM, 0.25±0.1% 1x EV and 0.22±0.1% 3x EV) (**Figure 2A**). The EV groups also generated a greater level of collagen deposition after 30 days in stiff substrate gels compared to ASC CM (0.04±0.05% NT, 0.13±0.06% NCM and 0.1±0.3% dEV CM, vs 0.16±0.03% ASC-CM, 0.23±0.09% 1x EV and 0.31±0.03% 3x EV) (**Figure 2B**).

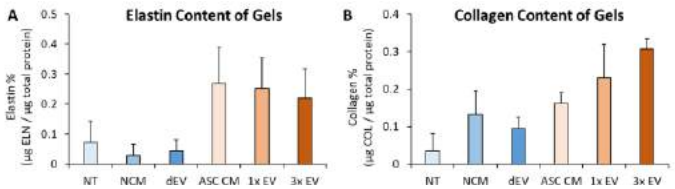

Figure 2: Insoluble elastin and collagen generated by SMCs within stimulated stiff substrate fibrin gels.

There was no significant difference between ASC CM or EV groups and control groups regarding insoluble elastin deposition after 30 days in soft substrate gels (0.23±0.14% NT, 0.24±0.07% NCM, and 0.29±0.26% dEV CM, vs 1.25±2.72% ASC-CM, 1.45±2.19% 1x EV and 0.41±0.32% 3x EV) (**Figure 2A**). Similarly, there was no significant difference between ASC CM or EV groups and control groups regarding collagen deposition after 30 days in soft substrate gels (0.19±0.19% NT, 0.2±0.06% NCM and 0.2±0.15% dEV CM vs 0.34±0.15% ASC-CM, 0.3±0.1% 1x EV and 0.28±0.12% 3x EV) (**Figure 2B**).

Tensile testing of the same soft substrate gels following 30 days of culture revealed that the low elastic modulus of the gels was largely unchanged (**Figure 3C**). There is an apparent trend regarding high modulus whereby the EV groups display a greater high modulus compared to the remaining groups. However, the standard deviation is large across all examined parameters for the soft substrate gels (0.05±0.3kPa NT, 0.1±0.04kPa NCM and 0.13±0.07kPa dEV CM vs 0.12±0.08kPa ASC-CM, 0.15±0.16 1x EV and 0.21±0.24kPa 3x EV) (**Figure 3D**).

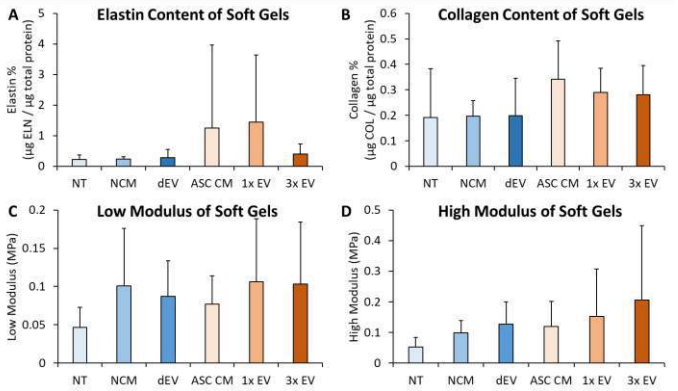

Figure 3: Insoluble elastin and collagen within stimulated soft substrate fibrin gels and mechanical properties of the gels.

DISCUSSION

Our analysis shows that stimulating SMCs with ASC derived EVs in fibrin gels plated on stiff substrates results in greater insoluble elastin and collagen deposition compared to NT, NCM and dEV CM. This demonstrates the potentially wide-ranging vascular extracellular matrix regenerative capabilities of ASC EVs.

Experiments conducted in soft substrate gels demonstrate larger standard deviations then stiff substrate gels, therefore limiting the conclusions that can be drawn regarding the mechanical functionality of EV stimulated elastin and collagen.

We conclude that ASC EV treatment of SMCs stimulates elastin and collagen deposition. This could potentially lead to an effective non-surgical regenerative therapy for treatment of AA. Future work will perform qPCR to examine SMC elastin chaperone protein transcription and gel imaging to examine fiber diameter and intersection density.

ACKNOWLEDGEMENTS

This work was supported by the European Union's Horizon 2020 Research and Innovation Program under the Marie Sklodowska-Curie grant agreement 708867 (E.M.C.), the Leonard H. Berenfield Graduate Fellowship in Cardiovascular Bioengineering and National Institutes of Health T32 HL094295 (A.K.R.), the National Institutes of Health grants HL129066 and HL130784 and McCune Foundation Pediatric Device Initiative (D.A.V.), and University of Pittsburgh Competitive Medical Research Fund (J.S.W.).

REFERENCES

[1] C. Fleming, et al., Annals of Internal Med., 142:3, 203-211, 2005.
[2] E. Gillis, et al., Circ Res, vol. 113, no. 3, pp. 327-40, 2013.
[3] K.C. Kent et al., J Vasc Surg, vol. 52, no. 3, pp. 539-48, 2010.
[4] K.C. Kent, N Engl J Med, 371: 22, 2101-8, 2014.
[5] D.M. Basalyga, et al., Circulation, 110 (2004), 3480-3487
[6] K.J. Blose, et al., Regenerative Medicine, 9:6, 733-741, 2014.
[7] E.M. Cunnane, et al., Frontiers Cardiovascular Med., 5, 86, 2018
[8] J.S. Weinbaum, et al., Tis. Eng. Part C, 16: 3, 459-467, 2010.
[9] B. Starcher, Analytical Biochemistry, 292:1, 125-129, 2001.

SB³C2019
Summer Biomechanics, Bioengineering and Biotransport Conference
June 25 -28, Seven Springs, PA, USA

TISSUE-ENGINEERED INTRA-ARTERIAL BARRIER FOR MECHANOBIOLOGY STUDIES

Sara Ben Saadon (1), Mark Gavriel (1), Ruth Gotlib (1), Uri Zaretsky (1), Ariel J. Jaffa (2), Dan Grisaru (3), David Elad (1)

(1) Department of Biomedical Engineering, Tel-Aviv University, Tel-Aviv, Israel

(2) Department of Obstetrics and Gynecology, Lis Maternity Hospital, Tel-Aviv Medical Center, Tel-Aviv, Israel

(3) Gynecological Oncology Unit, Lis Maternity Hospital, Tel-Aviv Medical Center, Tel-Aviv, Israel

INTRODUCTION

The arterial wall intima is composed of endothelial cells and fenestrated elastic lamina adjacent to the smooth muscle cells of the tunica media. This intra-arterial barrier is subjected to the physical stresses imposed by the flowing blood. Biological cells can rearrange their cytoskeleton as they grow, divide and adapt to the physical environment. Actin filaments, microtubules and intermediate filaments are the major components of the cytoskeletal structure and play dominant roles in various cellular events, including cell proliferation, migration, differentiation and apoptosis. They also determinate the mechanical properties and shape stability of cells and contribute to cell-to-cell and cell-to- extracellular matrices physical interactions. The cell regulates the length and stability of its cytoskeletal filaments by converting information received through signaling pathways [1].

Many models have been developed in permeable supports in culture dishes, lacking the ability to disassemble the co-coculture complex for insertion in test chambers for mechanobiology studies. The knowledge of the mechano-behavior of the cells under physical forces can contribute to tissue engineering studies. For instance, the study of how different physical loads can contribute during cellular growth to successfully engineer artificial tissue and organs that mimic the *in vivo* biological characteristics and biophysical environment. It will also help to accelerate the development of three-dimensional (3D) tissue engineer techniques for pre-programming functional biological characteristics with mechanical viability. In addition, the development of *in vitro* platforms can replace human or animal experiments for basic studies and testing medications or hazardous materials.

We developed a multi-layer tissue-engineered model that mimics the inner *in vivo* architecture of the arterial intima to allow for *in vitro* mechanobiology studies. This model will be tested in flow systems that generate fluid flow wall shear stresses (WSS) on the endothelial cells in order to explore the biological response to different physical environments.

METHODS

A co-culture of endothelial and smooth muscle cells has been developed on a collagen-coated Polytetrafluoroethylene (PTFE) synthetic membrane. We developed a custom-designed well equipped with a PTFE membrane that can be disassembled for insertion of the co-culture model in flow chambers. The collagen coated membrane was also coated with human fibronectin and then seeded with human umbilical arterial smooth muscle cells (HUASMC). After 24 hours we coated the HUASMC with collagen and seeded human umbilical vein endothelial cells (HUVEC). After one more day, the tissue engineered model was ready for application of WSS induced by steady flow. In addition, we also cultured a monolayer of HUVEC for evaluation of differences in cytoskeleton changes between HUVEC of monolayer and HUVEC on co-culture due to provocations of WSS. Immunofluorescent staining and confocal imaging were utilized to confirm that the *in vitro* model was composed of a multi-layer structure of HUVEC on top of HUASMC. We used antibodies that depicted the VE-cadherin of the HUVEC and the HUASMC actin.

The flow circuit for applying WSS on top of the HUVEC cells was composed of a flow chamber with a rectangular cross-section which can hold 6 well bottoms with the tissue-engineered vascular wall model and a peristaltic pump was used to generate steady uniform flow of medium [2]. Since the height (h=1 mm) of the flow chamber is much smaller than either its length (l=100 mm) or its width (b=35 mm), the fluid flow characteristics within the flow chamber can be described as a parallel plate flow. Thus, the WSS is given by,

Poster Presentation #P140

$$\tau = \frac{-6\mu Q}{bh^2} \qquad (1)$$

where μ is the fluid viscosity and Q is the fluid flow rate.

RESULTS

We generated a 3D *in vitro* model of HUVEC cultured on top of HUASMC similar to the *in vivo* organization of the arterial inner barrier. Confocal images of the *in vitro* model with the two layers of different cells is shown in Figure 1. This model was cultured in the custom-design wells and 90% confluency for both HUVEC and HUASMC was observed after 1 day of cultivation. The average height of the intra-arterial barrier 3D model was about 22 μm.

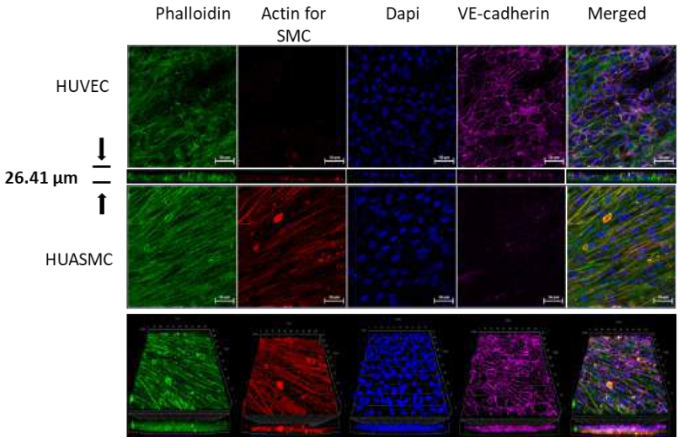

Figure 1: Confocal images of the arterial co-culture. The top row shows the HUVEC - positive for VE-cadherin (pink). The bottom row shows HUASMC - positive alpha-actin (red). At the middle Z-stack projection from the side. F-actin stained with phalloidin (green), and nuclei with DAPI(blue) (n≥20).

We carried out experiments in which steady flow WSS were applied on top of the HUVEC for 60 min. These in *vitro* experiments were conducted with a monolayer of HUVEC as well as with a co-culture of HUVEC on HUASMC. Confocal images of the HUVEC cytoskeletal components of the monolayer of HUVEC is depicted in Figure 2, for control without flow (τ=0) and after exposure to WSS of τ=24 dyne/cm^2. The F-Actin in HUVEC cultured as monolayer was more visible in samples exposed to WSS than in the control. Moreover, the VE-cadherin appears to be more solid in the control than in the well under WSS. The confocal images for the HUVEC cultured on top of the HUASMC are depicted in Figure 3, for control without flow (τ=0) and after exposure to WSS of τ=24 dyne/cm^2. In the samples with flow, HUVEC began to acquire an elongated shape as is well known that the endothelial cells align themselves with the flow.

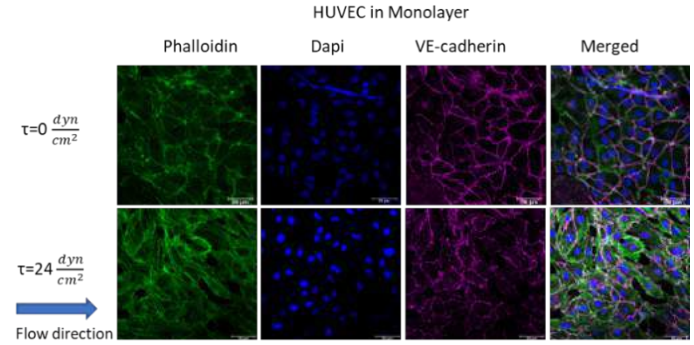

Figure 2: Confocal images of monolayer of HUVEC – control and after exposure to WSS (n≥5). VE-cadherin (pink). F-actin stained with phalloidin (green) and nuclei with DAPI(blue) (n≥20).

Figure 3: Confocal images for *in vitro* co-culture model with and without WSS (n≥5). VE-cadherin (pink). F-actin stained with phalloidin (green), and nuclei with DAPI(blue) (n≥20).

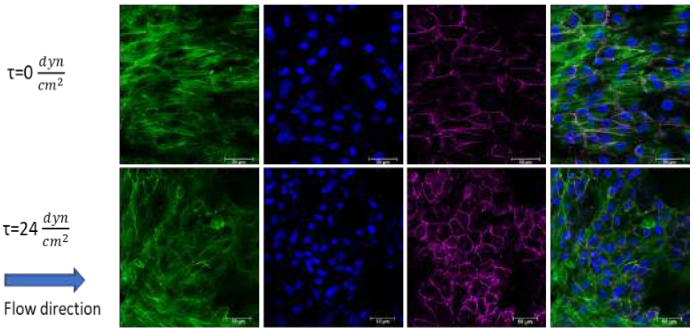

DISCUSSION

A 3D *in vitro* model of the intra-arteria wall was developed in custom-wells and was exposed to different WSS. The HUVEC cells expressed more F-actin in models under strong WSS and the cells began to align themselves towards the flow direction. This new co-culture model of the arterial inner barrier will be useful to study the contribution of adjacent cell layers to the biological response to environmental physical provocations. The results can be useful for mechanobiology studies such as different flow types, static and dynamic pressures. Furthermore, examination with this *in vitro* model may be helpful in advanced studies of tissue engineering.

ACKNOWLEDGEMENTS

This work was supported by a grant # 2505/16 from the Israel Science Foundation (ISF-NSFC Joint Scientific Research Program).

REFERENCES

[1] Johnson, A. et al., *Molecular biology of the cell* (6th ed.), Taylor & Francis Group, NY, 2015.

[2] Shav, D. et al., *PLoS ONE*, 9(2): e88304, pp:1-13, 2014

SB³C2019
Summer Biomechanics, Bioengineering and Biotransport Conference
June 25 -28, Seven Springs, PA, USA

THE ROLE OF PRESTRESS IN CALCIFICATION OF HUMAN CORONARY ARTERY SMOOTH MUSCLE CELLS *IN VITRO*

Amirala Bakhshian Nik (1), Daniela Medina (1), Manuel Garcia Russo (1), Walter Heatherly (1), Joshua D. Hutcheson (1)

(1) Biomedical Engineering Department,
Florida International University
Miami, FL, USA

INTRODUCTION

Vascular calcification is the leading indicator of cardiovascular morbidity and mortality [1]. Recent studies have shown that vascular calcification is initiated through specific calcifying extracellular vesicles (EVs) released by cells in the vascular wall. Once released from cells, calcifying EVs aggregate and fuse to form microcalcifications, which serve as building blocks for larger calcifications [2]. Calcifying EV formation begins with endocytosis of caveolae, small invaginations in the cell membrane [3].

Caveolae endocytosis and intracellular trafficking integrates tissue non-specific alkaline phosphatase (TNAP) into smooth muscle cell-derived EVs. TNAP mediates atherosclerotic mineral deposition through hydrolysis of calcification inhibitors and generation of free phosphate ions [2]. Caveolae are also known mechanosensors that respond to changes in cell membrane tension; however, the relationship between cell mechanics and the formation of calcifying EVs remains unknown. Previous studies have shown that increased cell contraction is required for calcification [4], and increased contraction leads to elevated cell prestress according to tensegrity models [5]. We hypothesize that increased human coronary artery smooth muscle cell (HCASMC) contraction and prestress is required for the caveolae-dependent formation of calcifying EVs and pathological calcification.

METHODS

Glucose has been shown to increase cell contractility, and the stiffness of the extracellular environment resists cell contraction. HCASMCs were cultured under three glucose concentrations (0, 1.5 g/L, and 4.5 g/L) in two conditions: control media or media supplemented with pro-calcific (PC) reagents (0.1 mM L-ascorbic acid, 10 mM β-glycerophosphate, and 10 nM dexamethasone). Extracellular calcification was measured with alizarin red S staining. Phalloidin staining assessed actin filament length and cell area as a measure of HCASMC contractility. Nanoindentation was used to investigate changes in HCASMC stiffness (an indicator of tensegrity prestress). To study the effect of prestress on calcification, HCASMCs were treated with jasplakinolide (50nM), which promotes actin filament elongation.

To study the effect of growth substrate stiffness on vascular calcification, HCASMCs were cultured on two substrates with stiffness of 1 and 100 MPa and treated by either control (4.5 g/L glucose) or PC media for 21 days. Furthermore, to investigate the influence of cytoskeleton alterations, HCASMCs were treated for 21 days under control and PC media, where either actin filaments or microtubules were disrupted by cytochalasin D or nocodazole, respectively. After collecting conditioned media at day 14, EVs were isolated using ultracentrifugation at 100,000×g. TNAP activity colorimetric assay was performed to assess the activity level of this enzyme in released EVs.

Poster Presentation #P141

RESULTS

The average surface area (Figure 1A) of phalloidin-stained HCASMCs cultured in 0g/L glucose, 1.5 g/L glucose, and 4.5 g/L glucose (Figure 1C) was determined using a custom MATLAB image analysis script. After 3 days in culture, 1.5 g/L glucose resulted in a 26% decrease in HCASMC area, and 4.5 g/L glucose treated HCASMCs exhibited a 42% decrease in area with short, thick actin stress fibers compared to cultures with 0 g/L glucose (Figure 1A, 1C). Relative to cultures with no glucose, 4.5 g/L glucose treatment for 3 days resulted in a 1.3-fold increase in HCASMC stiffness, and the addition of PC components increased HCASMC stiffness by 3.4-fold (Figure 1B). The decrease in HCASMC area correlated with a dose-dependent increase in calcification after 21 days in culture as shown by alizarin red S staining (Figure 1C, inset images). The addition of jasplakinolide inhibited the decrease in HCASMC area following 3 days in 4.5 g/L glucose media and mitigated calcification in these cultures after 21 days (Figure 1C). Our results suggest that glucose-mediated increases in HCASMC contractility and prestress is required for calcification.

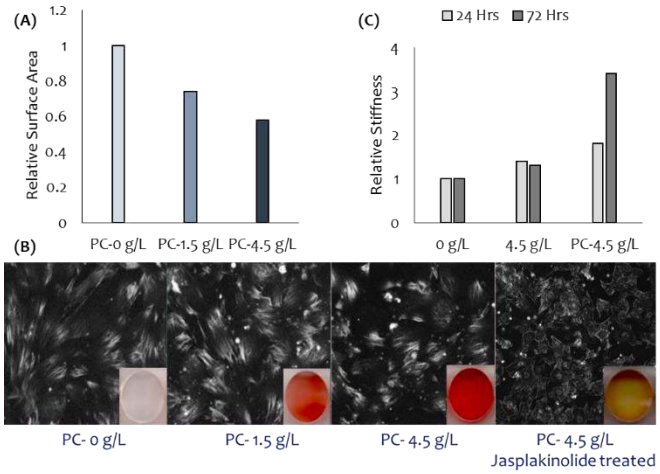

Figure 1: (A) Average areas of HCASMCs in PC media with 0, 1.5, or 4.5 g/L glucose for 3 days; (B) Nanoindentation measurement of HCASMC stiffness in response to 4.5 g/L glucose in control and PC media compared to cultures with 0 g/L glucose; (C) Representative images of phalloidin-stained HCASMCs in PC media with 0, 1.5, 4.5 g/L glucose, and 4.5 g/L glucose Jasplakinolide treated for 3 days. Inset images of alizarin red S staining after 21 days.

Culturing HCASMCs on a lower stiffness substrate yielded a 1.8-fold increase in EV TNAP activity in control media compared to tissue culture plastic controls (Figure 2A). HCASMCs cultured in PC media on a lower stiffness substrate exhibited a 7.6-fold increase in EV TNAP activity compared to HCASMCs cultured in normal media on tissue culture plastic (Figure 2A). Disruption of actin filaments and microtubules led to a 30% and 10% decrease in EV TNAP activity, respectively (Figure 2B).

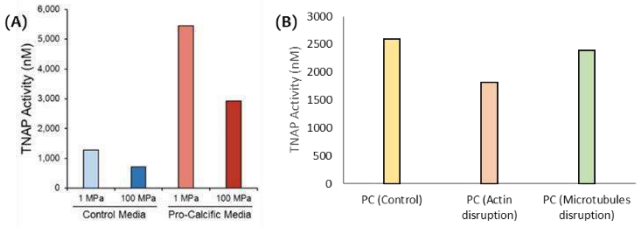

Figure 2: TNAP activity in EVs from (A) different ECM stiffness, and (B) cytoskeleton disruption.

DISCUSSION

The data indicate that elevated prestress or reduced substrate stiffness enhance the calcification potential of HCASMCs. Tensegrity models predict that either of these changes could lead to plasma membrane compression. This compression may induce caveolae endocytosis and the initiation of calcifying EV formation. Subsequent deposition of mineral stiffens the extracellular matrix, resisting the compression. Therefore, the mechanisms identified in this study may indicate caveolae trafficking as a rheostat that allows cells to sense and direct changes in extracellular stiffness. Future works will address this proposed mechanism and potential related therapeutic interventions for vascular calcification.

ACKNOWLEDGEMENTS

JDH is funded by the American Heart Association.

REFERENCES

[1] Hutcheson, JD et la., *Nat. Mater.*, 15:335-343, 2016.
[2] Goettsch, C et al., *J. Clin. Investig*, 126(4):1323-1336, 2016.
[3] Schwenke, C et al., *Cardiovasc Res*, 68(1): 128-135, 2005.
[4] Xu, J et al., *FASEB J*, 31(1 Supplement): 1080.20, 2017.
[5] Ingber, DE, *J. Cell Sci*, 116(7): 1157-1173, 2003.

SB³C2019
Summer Biomechanics, Bioengineering and Biotransport Conference
June 25 -28, Seven Springs, PA, USA

REGULATION OF NUCLEAR ARCHITECTURE, MECHANICS AND NUCLEO-CYTOPLASMIC SHUTTLING OF EPIGENETIC FACTORS BY CELL GEOMETRIC CONSTRAINTS

F. Alisafaei (1,2), D. S. Jokhun (3), G. V. Shivashankar (3,4), V. B. Shenoy (1,2)

(1) Department of Materials Science and Engineering, School of Engineering and Applied Science, University of Pennsylvania, Philadelphia, PA, USA

(2) Center for Engineering Mechanobiology, University of Pennsylvania, Philadelphia, PA, USA

(3) Mechanobiology Institute and Department of Biological Sciences, National University of Singapore, Singapore

(4) FIRC Institute for Molecular Oncology (IFOM), Milan 20139, Italy

INTRODUCTION

Cells sense mechanical signals from their microenvironment and transduce them to the nucleus to regulate gene expression programs. To elucidate the physical mechanisms involved in this regulation, we developed an active chemo-mechanical model to describe the three-way feedback between the adhesions, the cytoskeleton, and the nucleus. The model shows how cell geometric constraints affect the three-way feedback and induce cytoskeleton-mediated alterations in the properties of the nucleus such as nuclear lamina softening, chromatin stiffening, nuclear lamina invaginations, increase in nuclear height and shrinkage of nuclear volume. We predict how the disruption of cytoskeletal components impacts the feedback and subsequently induce alterations in the properties of the nucleus. The predictions are experimentally validated by studying the properties of nuclei of fibroblasts on micropatterned substrates with different shapes and areas.

METHODS

We develop a chemo-mechanical model that accounts for all the key cellular components involved in the transmission of mechanical stimuli from the cell-matrix interface to the nucleus including (i) the cytoskeleton, (ii) the nucleus, and (iii) the focal adhesions.

The cytoskeletal model is composed of the myosin motors, the microtubule network, and the actin filament network [1]. We model the nuclear envelope (NE) as a filamentous network material which stiffens along the tensile principal axes of the stress tensor to capture the fact that lamin A,C increases with tension in NE. We combine our mechanical model with reaction-diffusion equations for the transport of epigenetic and transcription factors. With the average contractility at hand from our mechanical model simulations, the signaling model enables us to quantitatively predict the contractility dependent translocation of these factors such as HDAC3 and MKL.

RESULTS

NIH 3T3 mouse fibroblast cells are cultured on fibronectin-coated micropatterned substrates with two extreme geometries (Figs. 1A and 1B): a rectangle with an aspect ratio of 1:5 and a substrate surface area of 1600 μm^2 (large and elongated substrate geometry), and a circle with a substrate surface area of 500 μm^2 (small and circular substrate geometry). Cells on the rectangular substrate have higher and polarized contractility, cytoskeletal tension, and cytoskeletal stiffness leading to a flattened and elongated nuclear morphology (Fig. 1C). As a result, tension is generated in the nuclear envelope lamina of rectangular cells correlated with their higher levels of lamin A,C and nuclear envelope stiffness (Fig. 1D).

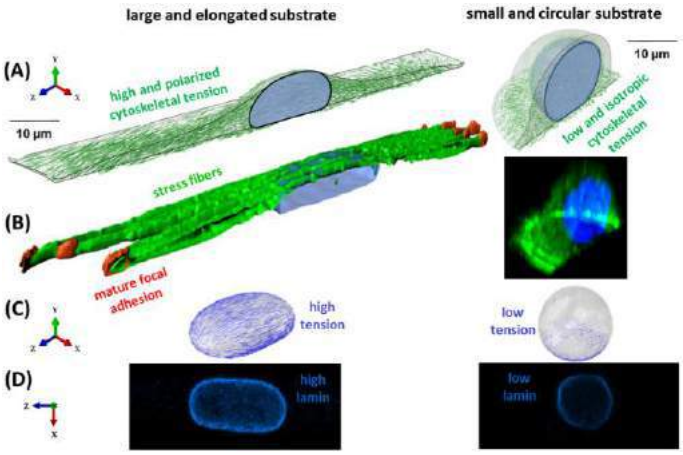

Figure 1: Cell geometric constraints regulate cell contractility, actin organization, and nuclear envelope lamina stiffness.

Poster Presentation #P142

Next, fibroblasts are cultured on fibronectin-coated micropatterned substrates with the same substrate surface area of 1600 μm^2 but various aspect ratios 1:1 (Fig. 2A), 1:3 (Fig. 2B), and 1:5 (Fig. 2C) [2]. Formations of apical and lateral stress fibers lead to flattening (Fig. 2E) and elongation (Fig. 2F) of the nucleus in the rectangular substrate geometries (1:3 and 1:5 aspect ratios) compared to the square substrate geometry (1:1 aspect ratio) as actomyosin contractility increases with anisotropy in tensile stresses (Fig. 2D). We also find that stress fibers (Fig. 2G) are formed in the direction of the maximum principal stress (Fig. 2H).

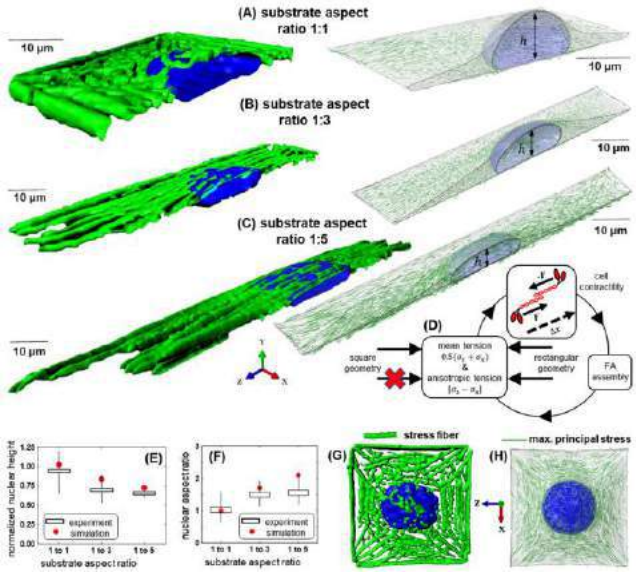

Figure 2. Substrate aspect ratio induces alterations in prenuclear actin organizations and nuclear morphology.

We next show that microtubules in large and elongated cells buckle without being able to significantly indent the nucleus as the MTOC is pushed toward the cell boundary by the nucleus (Figs. 3A and 3C). In contrast, cells on small and circular substrates exhibit crescent-shaped nuclear morphologies as the MTOC pushes against the nucleus and forms a local indentation in the nucleus (Figs. 3B and 3D). Similar to the circular cell, the nucleus is indented by the MTOC when actin filaments are depolymerized in the rectangular cell (Fig. 3E). We finally show that overexpression of lamin A,C rescues nuclear invagination in circular cells (Fig. 3F).

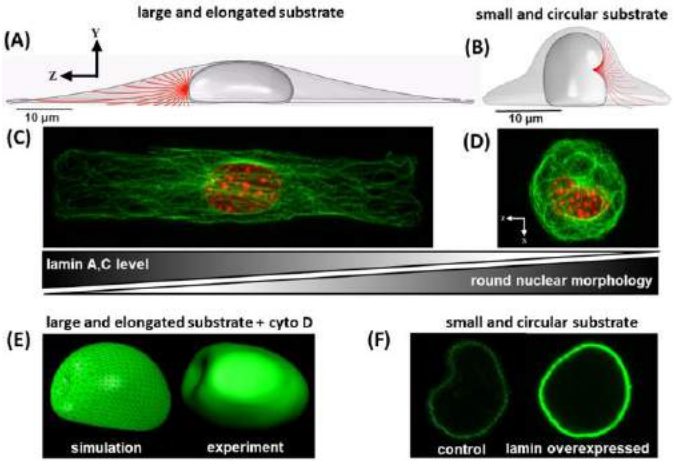

Figure 3. Nuclei with low levels of lamin A,C and round morphologies are indented by the MTOC.

We also report that the level of contractility regulates nucleo-cytoplasmic translocations of epigenetic and transcription factors (Fig. 4A) [3]. Cells on large and elongated substrates have higher contractility (compared to small and circular cells) and higher levels of polymerized F-actin (Fig. 4B). As G-actin is polymerized into F-actin, MKL unbinds from G-actin and shuttles to the nucleus leading to higher nuclear accumulations of MKL in large and elongated cells (Fig. 4C). On the other hand, decreasing contractility by constraining cells on smaller and unpolarized substrates (Fig. 4D) or by using actomyosin inhibitors (Figs. 4E-G) leads to translocation of HDAC to the nucleus and subsequently chromatin condensation.

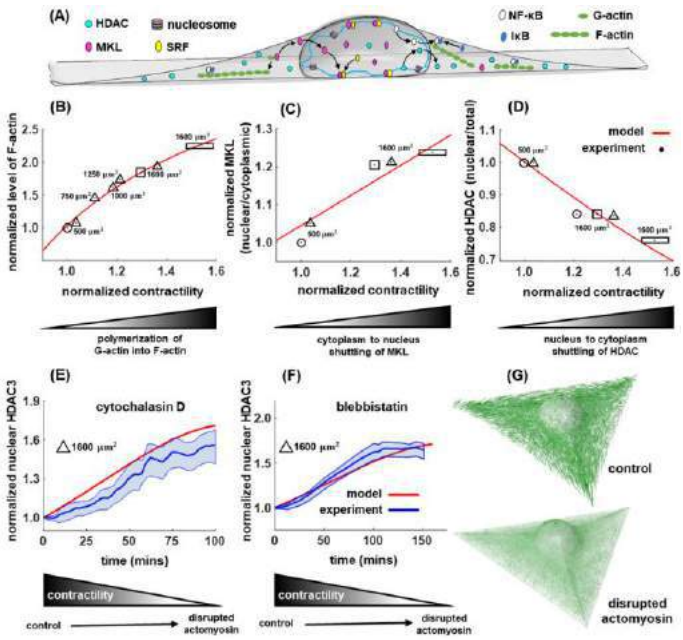

Figure 4. Cell geometric constraints induce nuclear translocation of HDAC driven by decreases in actomyosin contractility.

DISCUSSION

Using a chemo-mechanical model, we showed how the physical properties of the microenvironment, including cell substrate area, shape, and stiffness, impact the properties of both cytoskeleton and nucleus by regulating the dynamic reciprocities between tension-dependent formation of focal adhesions, phosphorylation of myosin motors, polymerization of actin filaments, stiffening of the nuclear envelope lamina network, and nucleo-cytoplasmic shuttling of epigenetic factors. Given the predictive power of the model as illustrated by extensive experimental tests, it can potentially be used to describe abnormal nuclear morphology in diseases like progeria, cancer, fibrosis, and dilated cardiomyopathy.

ACKNOWLEDGEMENTS

This work is supported by the National Cancer Institute awards U01CA202177 and U54CA193417 (to V.B.S.), National Institute of Biomedical Imaging and Bioengineering award R01EB017753 (to V.B.S.), and the NSF Center for Engineering Mechanobiology (CMMI-154857).

REFERENCES

[1] Damodaran, K et al., *MBoC*, 29:3039-3051, 2018.
[2] Li, Q et al., *Biomaterials*, 35:961-969, 2014.
[3] Jain, N et al., *PNAS*, 110:11349-11354, 2013.

SB³C2019
Summer Biomechanics, Bioengineering and Biotransport Conference
June 25 -28, Seven Springs, PA, USA

COMPUTATIONAL MODELS OF ENDOTHELIAL CELL BIOCHEMICAL RESPONSE TO SHEAR STRESS

Jonathan Garcia (1), Alisa Morss Clyne (2)

(1) School of Biomedical Engineering, Science, and Health Systems
Drexel University
Philadelphia, PA, USA

(2) Mechanical Engineering and Mechanics
College of Engineering
Drexel University
Philadelphia, PA, USA

INTRODUCTION

Endothelial cells respond both morphologically and biochemically to the mechanical environment. The cell response is highly complex, with protein expression, activation, and cellular localization changing as the cell responds to mechanical stimuli [1]. Current experimental techniques cannot simultaneously measure all of these factors in real time, even in simplistic 2D cell culture models. Therefore, computational models are needed to predict cell mechanobiology responses and thereby direct future experimental studies.

Computational cell models come in many forms. Mass action kinetic models require reaction kinetic parameters but can simulate the cell response over time. These models can also directly couple the mechanical environment, for example fluid flow, to mass transport and binding kinetics [2]. Stoichiometric models require less information since they rely on reaction stoichiometry. These models account for all genetic and biochemical components and their reactions (e.g., genome-scale); however, they are limited to steady state conditions [3].

In this study, we developed two computational models of endothelial cell response to fluid shear stress. First, we created a mass action kinetics model of endothelial growth factor binding in cells adapted to either static conditions or fluid flow. Second, we created a stoichiometric model of endothelial glucose metabolism and analyzed pathway changes associated with shear stress response. In both cases, the models were developed and validated with experimental data.

METHODS

Mass action kinetics model of growth factor binding in flow

The mass action kinetics model was created in Comsol for fibroblast growth factor-2 (FGF2) using Glycotech parallel plate flow chamber dimensions (6 cm long x 1 cm wide x 0.0127 cm high). The fluid was defined as incompressible Newtonian fully developed laminar flow with no-slip boundary condition at the walls. The standard convection–diffusion mass balance equation was used to define FGF2 concentration with respect to location and time:

$$\frac{\partial [F]}{\partial t} + \nabla \cdot (-D\nabla[F] + [F]\vec{u}) = 0 \qquad (1)$$

where [F] is FGF2 concentration, D is the FGF2 diffusion coefficient and u is the velocity vector. Reactive species included FGF2, the FGF receptor (FGFR) and heparan sulfate proteoglycans (HSPG). Possible reactions are shown in Figure 1.

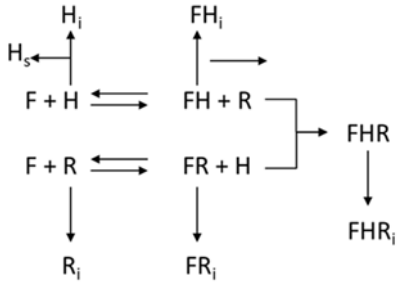

Figure 1: Model schematic showing species, reactions, and bound complexes. F = FGF2, R = FGFR, H = HSPG, FR = FGF2-FGFR, FH = FGF2-HSPG, FHR = FGF2-HSPG-FGFR. i indicates internalized species.

For example, FGF2-HSPG (FH) complexes were defined to change with time based on association, dissociation, and internalization rates:

$$\frac{d[FH]}{dt} = \alpha k_{on,FH}[F][H] - k_{off,FH}[FH] - k_{on,FHR}[R][FH] - k_{i,FH}[FH] \qquad (2)$$

For experimental validation, endothelial cells were exposed to shear stress in a Glycotech flow chamber. After 24 hours, medium was changed to binding buffer with 0 or 10 ng/mL FGF2 for an additional two hours of flow. Cell surface HSPG-bound FGF2 was first extracted using a salt buffer, after which FGFR-bound FGF2 was extracted using an acid buffer. FGF2 was quantified in all extracts using an FGF ELISA.

Stoichiometric model of glucose metabolism in flow

The stoichiometric model was built using Recon3D, a genome-scale model that represents a human cell metabolic network [3]. In this model, the coefficients for metabolites and reactions were represented in a stoichiometric matrix, while fluxes were represented as the flux vector, which contained upper and lower flux bounds. The FASTCORE algorithm was then used to remove reactions that are not expressed in endothelial cells based on human endothelial gene arrays (ArrayExpress; E-GEOD-21212). The final model contained roughly 1000 unique metabolites and 1500 biochemical reactions.

The model was validated with $^{13}C_6$-glucose mass spectrometry experimental data. Endothelial cells were exposed to either static culture or steady laminar flow (20 dynes/cm^2 shear stress) for 24 hours in a custom cone and plate device. Cells were then cultured with 5 mM $^{13}C_6$-glucose for 24 hours to ensure steady state. Metabolites in cells and media were extracted using 80:20 methanol:water and analyzed using ultra high-performance liquid chromatography (UHPLC). The human metabolome database (HMDB) was used for metabolite identification.

RESULTS

Mass action kinetics model of growth factor binding in flow

We first experimentally measured FGF2 binding to endothelial cells adapted to shear stress. As shear stress increased from 0 to 20 dynes/cm^2, FGF2 binding to cell surface HSPG increased five times and then decreased 40 dynes/cm^2 shear stress. FGF2 binding to cell surface FGFR did not change with shear stress. Both flow rate and receptor effects were statistically significant, as was their interaction ($p < 0.001$).

We then used the computational model to predict what might contribute to biphasic FGF2 binding to cell surface HSPG under flow. The computational model run under varied flow rates did not reproduce the experimental results. Instead, FGF2 bound to cell surface HSPG remained constant at all shear stress levels, suggesting that it is not flow itself but cell adaptation to flow that alters FGF2 binding.

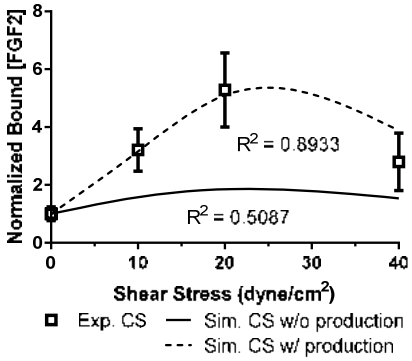

Figure 2: The computational model closely matched experimental data only when HSPG production was included along with availability and dissociation. [FGF2] = 10 ng/mL (5.56 x 10^{-5} μM); [HSPG] =2.16 x 10^{-10} mol/m^2; [FGFR] = 4.15 x 10^{-12} mol/m^2

We therefore investigated cell changes that could increase or decrease cell surface HSPG binding. HSPG production rate and binding availability, both of which are suggested to change with flow, had large effects on FGF2-HSPG but not FGF2-HSPG-FGFR, suggesting that these are FGF2 storage rather than signaling complexes. FGF2 dissociation from HSPG, which has been proposed to demonstrate slip-bond characteristics, also had a large effect on FH complexes. We then estimated how HSPG production, availability and FGF2 dissociation would change with flow based on our prior data and the literature. When we added these flow-induced changes into our computational model, it matched our experimental data well (Figure 2) [4].

Stoichiometric model of glucose metabolism in flow

Since stoichiometric models do not have unique solutions, we first ran the model with an objective function of maximizing ATP production. Since endothelial cells primarily use aerobic glycolysis rather than the TCA cycle, we shuttled 98% of pyruvate to secreted lactate. The model successfully produced 2 ATP from glycolysis and 32 ATP from oxidative respiration.

We then simulated fluid flow in the model by blocking PFK1, a critical enzyme in glycolysis that has been shown to be decreased by increased KLF2 in laminar shear stress [5]. Interestingly, glycolysis blockade at this rate limiting enzyme did not affect ATP production. Instead, glucose proceeded through a glycolysis side branch, the pentose phosphate pathway, at the blockade and then rejoined glycolysis as glyceraldehyde 3-phosphate (Figure 3). These data show that metabolic inhibition is complicated by the high incidence of pathway side branches and re-entrant loops. Thus a computational model validated with experimental data is critical to understanding metabolic changes in endothelial cells adapted to fluid shear stress.

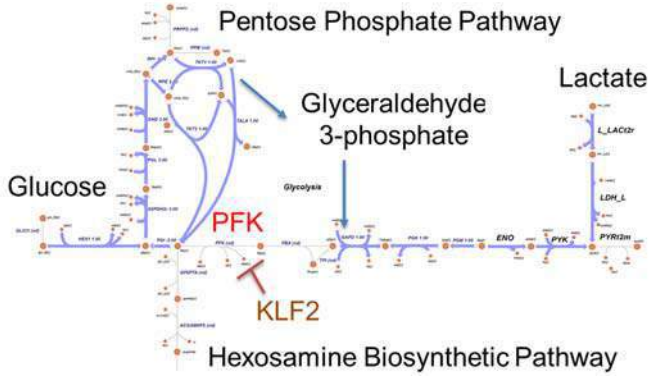

Figure 3: When glycolysis is inhibited in endothelial cells exposed to laminar shear stress, the cell uses the pentose phosphate pathway to bypass the blockade and produce ATP.

DISCUSSION

These two different models demonstrate the power of computational tools to integrate multiple data sets, generate of hypotheses by running experiments in silico, explore mechanisms to explain experimental results, and interpret high throughput/high dimensional data. These models can then be used to predict responses to other mechanical stimuli and inhibitors, include parenchymal cell interactions, and be incorporated into human organismal models.

ACKNOWLEDGEMENTS

We thank NSF CBET-0846751 & NIH 1R01HL140239-01 for funding.

REFERENCES

[1] Davies, P., *Nat Reviews Cardiology*, 6:16-26, 2009.
[2] Patel, N *et al*., *Ann Biomed Eng*, 41(1):154-171, 2013.
[3] Brunk, E *et al*., *Nat Biotech*, 36:272-281, 2018.
[4] Garcia, J *et al*., *Ann Biomed Eng*, in press.
[5] Doddaballapur, A *et al*., *ATVB*, 45:137-145, 2015.

SB³C2019
Summer Biomechanics, Bioengineering and Biotransport Conference
June 25 -28, Seven Springs, PA, USA

PERLECAN DEFICIENCY IMPAIRS THE INTRACELLULAR CALCIUM SIGNALING IN MECHANICALLY LOADED BONE AND OSTEOCYTES

S. P. Pei (1), S. Parthasarathy (1), A. Parajuli (1), J. Martinez (1), M. X. Lv (1), S. D. Jiang (1), D. Wu (2), S. Wei (1), X. L. Lu (1), M. C. Farach-Carson (2), C. B. Kirn-Safran (1), L. Y. Wang (1)

(1) University of Delaware
Newark, DE, USA

(2) University of Texas Health Center
Huston, TX, USA

INTRODUCTION

Perlecan (*Hspg2,* a large linear proteoglycan) is found within the pericellular matrix of osteocytes [1]. It can serve as a critical component of the mechanosensing tethers in the lacunar-canalicular system [2], allowing osteocytes to sense and respond to mechanical signals [3]. Deficiency in perlecan is associated with profound musculoskeletal disorders, such as the Schwartz-Jampel syndrome with reduced stature and skeletal abnormalities [4]. Previously we demonstrated marked attenuation of bone formation under mechanical loading in a perlecan deficient mouse model [5]. However, the underlying molecular mechanisms remain unclear. Intracellular calcium is a ubiquitous messenger that controls numerous cellular processes, including proliferation, development, and differentiation [6]. Intracellular calcium peaks are one of the earliest cellular responses of osteocytes (within seconds) following mechanical stimulation in vitro and in situ [7,8]. In this study, we aimed to test ***the hypothesis*** that perlecan deficiency impairs the intracellular calcium signaling pathway in mechanically loaded bone and the encased osteocytes.

METHODS

(1) RNA sequencing: 19-week-old perlecan deficient mice (Hypo) and WT controls (C57BL/6J, n = 3 /genotype) were subjected to unilateral tibial loading for 7 days on the left tibia (5 min/day, 4Hz, 8.5N) [5]. The contralateral right tibia served as non-loaded control. Total RNA samples were collected from freshly isolated tibiae (with marrow) 24h after the last loading session, and sequenced similarly as [9]. Differentially expressed genes (DEGs: Hypo vs. WT) were identified (FDR < 0.05 and cutoff fold-change of 2) and submitted to DAVID (version 6.8) for enriched KEGG pathways analysis [10] (**Fig.1 A**). (2) In situ osteocyte intracellular calcium imaging: 18-21-week-old male mice (8 WT; 4 Hypo) were used. Tibiae were harvested, incubated for 2 h, loaded with Fluo-8 AM calcium indicator for 0.5 h, and imaged with a confocal microscope under cyclic loading as in our previous study [8] (**Fig.1 B**). Student's t test and Mann-Whitney *U* tests were used to compare the percentage of responsive cells (with normal distribution) and the other measures (without normal distribution), respectively, between WT and Hypo, and the Chi-square test was used to compare the percentage of responsive cells with multiple peaks between WT and Hypo, with $p < 0.05$ as statistical significance.

RESULTS

(1) RNA sequencing: Regarding the calcium signaling pathway, relative to WT, Hypo mice showed 6 and 7 DEGs (all with decreased transcription levels), resulting in a trend ($p = 0.07$) and a significant ($p = 0.006$) enrichment of the pathway in the non-loaded and loaded tibiae, respectively. Detailed analysis of the loaded tibiae (**Fig. 2**) clearly demonstrated an overall down-regulation of the calcium signaling pathway, as seen in the 4-8 fold decrease in the transcripts of the L-type calcium channel (*Cacna1s*), ER Ca^{2+} releasing receptor (RYR/ *Ryr1*), ER Ca^{2+} refilling pump (SERCA/ *Atp2a1*), and some downstream genes (myosin light chain kinase 2/ *Mylk2*; myosin light chain kinase 4/ *Mylk4*; Troponin C/ *Tnnc2*; Phosphorylase Kinase Catalytic Subunit Gamma 1/ *Phkg1*). The decreasing fold changes of *Atp2a1* and *Ryr1* in Hypo vs. WT were also validated with RT-qPCR results. (2) Intracellular calcium response: Perlecan deficient mice showed more than 58% lower responding rate (% osteocytes with at least one calcium peak over the total number of cells: WT 15.7%; Hypo 6.6%, $p = 0.04$, **Fig. 3B**). The responding Hypo osteocytes, in average, exhibited fewer number of peaks (WT 2.4; Hypo 1.6, $p = 5 \times 10^{-6}$) and lower percentage of multiple responding peaks (1+ peaks, WT 53%; Hypo 25%, $p = 3 \times 10^{-6}$, **Fig. 3B**) during the 8-min recording. The dynamic measures of the first peaks in Hypo, relative to WT, showed a

Poster Presentation #P144

trend of lower magnitude (WT 1.49; Hypo 1.41, $p = 0.09$), longer arising time (WT 7.88 sec, Hypo 8.70 sec, $p = 0.04$), and longer relaxation time (WT 5.34 sec, Hypo 7.15 sec, $p = 0.0004$, **Fig. 3C**). Pooling all the peaks together, similar differences were observed in Hypo relative to WT in the peak magnitude (-6.8%, $p = 0.001$) and relaxation time (+23%, $p = 0.0007$), but no change in arising time (+0.4%, $p = 0.5$, **Fig. 3D**). Overall, the calcium response in Hypo osteocytes was impaired with fewer responsive cells, lower peak magnitude, longer arising time, and delayed return to baseline from the peak.

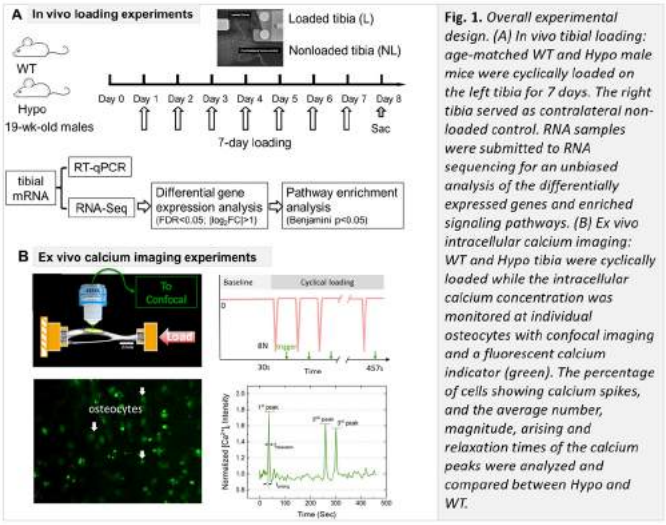

Fig. 1. *Overall experimental design. (A) In vivo tibial loading: age-matched WT and Hypo male mice were cyclically loaded on the left tibia for 7 days. The right tibia served as contralateral non-loaded control. RNA samples were submitted to RNA sequencing for an unbiased analysis of the differentially expressed genes and enriched signaling pathways. (B) Ex vivo intracellular calcium imaging: WT and Hypo tibia were cyclically loaded while the intracellular calcium concentration was monitored at individual osteocytes with confocal imaging and a fluorescent calcium indicator (green). The percentage of cells showing calcium spikes, and the average number, magnitude, arising and relaxation times of the calcium peaks were analyzed and compared between Hypo and WT.*

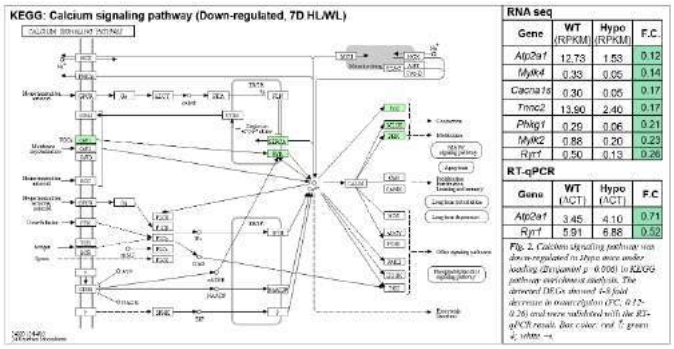

RNA seq

Gene	WT (RPKM)	Hypo (RPKM)	F.C.
Atp2a1	12.73	1.53	0.12
Mylk4	0.33	0.05	0.14
Cacna1s	0.30	0.05	0.17
Tnnc2	13.90	2.40	0.17
Phkg1	0.29	0.06	0.21
MylK2	0.88	0.20	0.23
Ryr1	0.50	0.13	0.26

RT-qPCR

Gene	WT (ΔCT)	Hypo (ΔCT)	F.C
Atp2a1	3.45	4.10	0.71
Ryr1	5.91	6.88	0.52

Fig. 2. Calcium signaling pathway was down-regulated in Hypo mice under loading (Benjamini p < 0.008) in KEGG pathway enrichment analysis. The affected DEGs showed 0.5-fold decrease in transcription (FC: 0.12-0.26) and were validated with the RT-qPCR results. Bar color: red ↓, green ↑, white →.

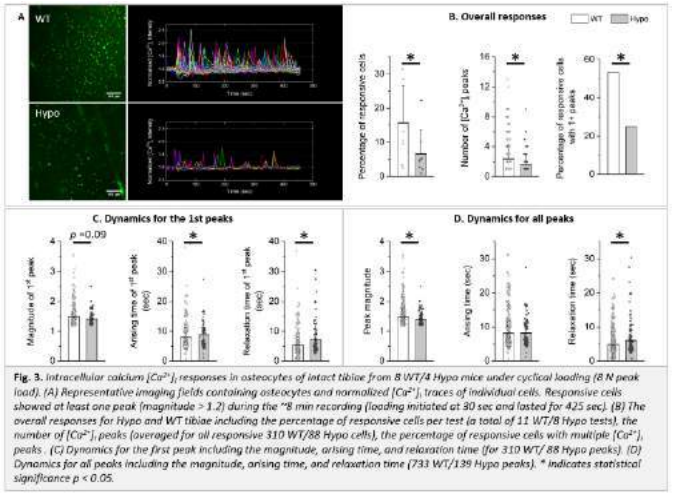

Fig. 3. *Intracellular calcium [Ca²⁺]ᵢ responses in osteocytes of intact tibiae from 8 WT/4 Hypo mice under cyclical loading (8 N peak load). (A) Representative imaging fields containing osteocytes and normalized [Ca²⁺]ᵢ traces of individual cells. Responsive cells showed at least one peak (magnitude > 1.2) during the ~8 min recording (loading initiated at 30 sec and lasted for 425 sec). (B) The overall responses for Hypo and WT tibiae including the percentage of responsive cells per test (a total of 11 WT/8 Hypo tests), the number of [Ca²⁺]ᵢ peaks (averaged for all responsive 310 WT/88 Hypo cells), the percentage of responsive cells with multiple [Ca²⁺]ᵢ peaks. (C) Dynamics for the first peak including the magnitude, arising time, and relaxation time (for 310 WT/ 88 Hypo peaks). (D) Dynamics for all peaks including the magnitude, arising time, and relaxation time (733 WT/139 Hypo peaks). * indicates statistical significance p < 0.05.*

DISCUSSION

Perlecan deficient mice showed downregulation of the calcium signaling pathway in RNA sequencing, which was validated with reduced intracellular responses under mechanical loading in situ. These results support our hypothesis and elucidate the mechanisms underlying the attenuated anabolic response to loading in Hypo [6].

ACKNOWLEDGEMENTS

The study was supported by NIH grants (P30GM103333, RO1AR054385). The RNA sequencing work was partially supported by a core access award through NIH NIGMS IDeA Program rant (P20GM103446). We acknowledge the excellent consulting and technical support from Dr. Brewster Kingham, Director of UD's DNA Sequencing & Genotyping Center, and helpful discussion with Dr. Jian Wang from U Delaware.

REFERENCES

[1] W. R. Thompson, J. Bone Miner. Res., 2011.
[2] S. S. Wijeratne, Matrix Biol., 2016.
[3] L. Wang, Curr. Osteoporos. Rep., 2018.
[4] K. D. Rodgers, Hum. Mol. Genet., Jan. 2007.
[5] B. Wang, J. Bone Miner. Res., 2014.
[6] M. J. Berridge, Nat. Rev. Mol. Cell Biol., 2000.
[7] X. L. Lu, J. Bone Miner. Res., 2014, 2012.
[8] D. Jing, FASEB J., 2014.
[9] N.H. Kelly, Bone, 2016.
[10] D. W. Huang, Nat. Protoc., 2009.

SB³C2019
Summer Biomechanics, Bioengineering and Biotransport Conference
June 25 -28, Seven Springs, PA, USA

A MODIFIED BIOREACTOR CONFIGURATION TO STUDY EFFECTS OF LOW INTENSITY PULSED ULTRASOUND TREATMENT

Abdolrasol Rahimi (1), Zach Pittz (1), Nicholas Weaver (1), Natasha Case (1)

(1) Biomedical Engineering Program
Saint Louis University
Saint Louis, MO 63103

INTRODUCTION

Long-term application of a low intensity pulsed ultrasound (LIPUS) regimen has been shown to enhance bone healing for a subset of patients with nonunions. Preclinical and *ini vitro* studies have suggested that LIPUS contributes to bone healing by stimulating early synthesis of extracellular matrix proteins and by activating bone formation pathways. For the clinical regimen, LIPUS is delivered as a pulsed signal (1.5MHz frequency with 20% duty cycle and pulse repetition frequency of 1KHz) for a treatment time of 20 m daily.

US bioreactors are common platforms that have been used in *ini vitroi* studies to investigate effects of LIPUS treatment under well-controlled conditions. To more effectively interpret the results of *ini vitro* US experiments, a thorough understanding of US wave propagation and the acoustic pressure field in the bioreactor is needed, and this can be achieved by using computational modeling. Studying how changes in design parameters affect the acoustic pressure in US bioreactor experimentally is challenging and often impractical. However, computational modeling is a reliable and cost-effective approach to complement experimental data, enabling the assessment of how a change in a design parameter affects the acoustic pressure in various regions of the US bioreactor. A current complication of US bioreactors is the presence of an air interface, which results in high variability in the acoustic pressure field because of the near complete wave reflection at the interface. The first objective of this study was to analyze effects of an air interface and resulting wave reflections on the acoustic pressure in the US bioreactor. The distance that the US transducer is positioned above the dish surface where the cell monolayer is located is a major factor that determines the pressure magnitude delivered to cells. Therefore, the second objective was to determine the transducer position that would support development of the maximum pressure level at the cell layer.

METHODS

A multi-physics finite element model of the US bioreactor was developed (COMSOL, V5.3) and included the piezoelectric US transducer immersed in culture medium contained within a circular culture dish, water. The US transducer model was composed of a three-layered cylinder including a matching layer, a piezoelectric disk (25 mm diameter), and a backing layer surrounded by a stainless-steel casing. The bottom surface of the culture dish was either contacted by air or by a water layer coupled with a non-reflecting boundary that represented an acoustic absorbent material (Figure 1). The Helmholtz wave equation was developed to simulate wave propagation in the culture medium and water. Frequency domain simulations were conducted to evaluate the acoustic pressure within the US bioreactor and to estimate the acoustic pressure experienced by the cell layer. For pressure at the cell layer, the acoustic pressure in the fluid layer contacting the upper surface of the culture dish was spatially averaged over the center area of the dish (25 mm diameter) and will be referred to as the pressure at the dish surface. For direct pressure measurements, the transducer (25 mm active element diameter, Precision Acoustics) was placed in the center of the culture dish in contact with the medium to deliver US at 1.5 MHz center frequency, 30 mW/cm^2 spatial-average temporal-average intensity, and a pulse repetition frequency of 1KHz (Figure 1). A water layer bounded by an acoustic absorbent material (Precision Acoustics) was placed in contact with the bottom portion of the dish to remove the air interface. The acoustic pressure in the culture medium was measured by a needle hydrophone with an active element diameter of 400 μm connected to a pre-amplifier. The output signal of hydrophone was collected by an oscilloscope.

The MC3T3-E1 cell line was used as a pre-osteoblast model. Cells were cultured in MEM with 10% FBS and 1% penicillin/streptomycin

Poster Presentation #P145

and seeded at 40-50 x 10^3 cells/cm^2. After 2-3 days, cultures were incubated with medium containing 0.5% FBS overnight and LIPUS stimulation was applied the next day. Western blotting was performed on whole cell lysates of stimulated and control samples to evaluate phosphorylation levels of ERK1/2 Map kinase, P38 Map kinase, AKT kinase, and Focal Adhesion Kinase (FAK) followed by densitometry.

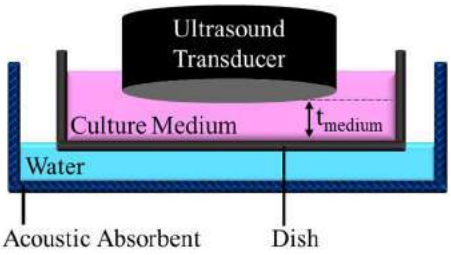

Figure 1. In-well ultrasonication configuration. The US transducer was placed in a cell culture dish in contact with the culture medium. To remove the air interface and minimize the reflection, a water layer and an acoustic absorbent material were added under the dish.

RESULTS

Simulations were conducted to both explore effects of the air interface at the lower dish surface on the acoustic pressure field and to determine the placement of the US transducer above the culture dish to deliver the maximum pressure. Thus, the thickness of the culture medium layer between the US transducer and the upper surface of culture dish (denoted t_{medium}) was varied from 1.5 to 4.5 mm and the acoustic pressure was evaluated (Figure 2.A). In the original in-well bioreactor configuration, the US waves travel from the transducer through each consecutive layer of the model until reaching the bottom surface of the culture dish in contact with air, where near complete reflection of the acoustic wave occurs (>99.9%). When the water layer and acoustic absorbent material are placed under the dish, US waves will travel into the water and eventually will be damped by the acoustic absorbent. As t_{medium} increased from 1.5 to 4.5 mm, the acoustic pressure at the dish surface experienced repetitive minimum and maximum pressures, observed in both configurations. This showed the importance of the US transducer distance from the upper dish surface. The averaged ratio between six consecutive maximum and minimum pressures was 5.3 when the air interface was present (Figure 2.A). This ratio dropped to 1.2 in the modified bioreactor configuration. Simulations showed that a 100 µm deviation in the transducer position away from a location where the pressure was maximum caused a69% decrease in acoustic pressure if air contacted the lower dish surface, but only a 7% decrease with the modified configuration removing the air interface. To evaluate the acoustic pressure field in the culture medium, the volume average of the acoustic pressure in the medium was calculated. The volume-averaged acoustic pressure at maximum was 4.8- and 1.1-fold higher than minimum for the original and modified bioreactor configurations, respectively. These findings revealed that by making a simple modification of adding a water layer and an acoustic absorbent material, the pressure variability could be substantially decreased. This reduced pressure sensitivity to t_{medium} provided an experimental system that would support improved reproducibility across experiments.

When incoming and reflected waves interfere, the pressure amplitude at a given location can increase if constructive interference occurs or can decrease if destructive interference occurs. The higher level of wave reflections due to the presence of the air interface led to increased constructive and destructive interference, as demonstrated by the maximum pressure in the presence of the air interface being 2.4-fold higher than the maximum pressure in the modified configuration (Figure 2.A). To validate the computational model, acoustic pressure at the dish center for both configurations was measured using a needle hydrophone (Figure 2.B). Results showed that acoustic pressure at the dish center when the air interface was present was 2.2-fold higher than the pressure when the air interface was removed by using the acoustic absorbent material. Overall, the normalized acoustic pressure from the hydrophone measurement was in close agreement with the computational modeling results.

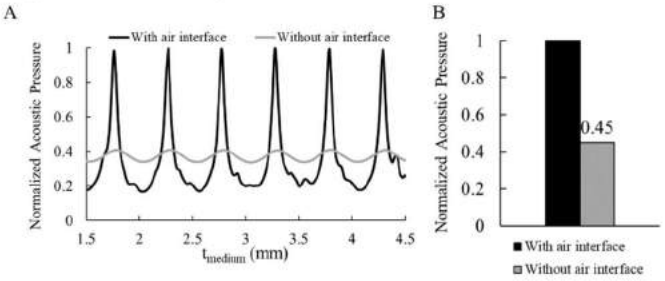

Figure 2. (A) Normalized acoustic pressure at the dish surface as the culture medium layer thickness changed. Results are normalized to the maximum spatially averaged acoustic pressure at the dish surface. (B) Normalized acoustic pressure at the dish center using a needle hydrophone.

Cellular responses to the US treatment were studied using the modified bioreactor configuration. Cell monolayers were lysed after 20 min incubation following US treatment and western blotting analysis was performed. Densitometry analysis on immunoblot images indicated that signaling pathways were responsive to the stimulus of US waves in the modified bioreactor configuration. Results showed 2.5-, 2.3-, 1.7-, and 1.9-fold increase in phosphorylation level of FAK, AKT kinase, ERK1/2 Map kinase, and P38 Map kinase, respectively, in the stimulated cell monolayers compared to control untreated samples. This finding confirmed that this modified bioreactor configuration can be used effectively to conduct *inivitro* cellular experiments.

DISCUSSION

Using computational modeling, the effects of the air-dish interface on the acoustic pressure at the dish surface for ultrasonication within a culture dish were investigated. Including an acoustic absorbent layer to remove the reflection from the air interface decreased the pressure variability as the thickness of the culture medium varied. Moreover, simulations showed careful consideration should be given to the relative location of the US transducer from the dish. Experimental results showed that LIPUS applied using the modified bioreactor configuration with an acoustic absorbent layer could activate signaling pathways in MC3T3-E1 cells, consistent with previous studies using the original bioreactor configuration. These signaling pathways are known to be involved in bone fracture healing. Overall, this work demonstrated that computational modeling is a robust tool to characterize the acoustic pressure in US bioreactor and understand how changes in design parameters may affect the acoustic pressure. Although this study was limited to evaluations of the pressure field for a 2D *inivitro* experimental setup, future studies will investigate the acoustic pressure field for LIPUS applied to cell-seeded scaffolds.

ACKNOWLEDGEMENTS

Funding, including a graduate fellowship, was provided by the Parks College of Engineering, Aviation and Technology.

SB³C2019
Summer Biomechanics, Bioengineering and Biotransport Conference
June 25 -28, Seven Springs, PA, USA

DESIGN AND COMPUTATIONAL MODELING OF AN ULTRASOUND BIOREACTOR FOR STIMULATION OF CELL-SEEDED SCAFFOLDS

Jacob Crapps (1), Abdolrasol Rahimi (1), Natasha Case (1)

(1) Biomedical Engineering
Saint Louis University
St. Louis, MO, USA

INTRODUCTION

Daily application of a low intensity pulsed ultrasound (LIPUS) regimen has been shown to have positive effects on bone fracture healing [1]. However, the underlying mechanisms are not well understood. While most *in vitro* studies have focused on US stimulation of two-dimensional (2D) cell monolayers, a fracture site requires treatment of a three-dimensional (3D) volume and US propagation within such a space is complex. Therefore, *in vitro* studies using 3D models, such as cell-seeded scaffolds, are needed to investigate the bioeffects of LIPUS under well-controlled conditions. A limitation of commonly used US bioreactor designs is the presence of an air-liquid or air-solid interface in the direct path of US wave propagation, which causes wave reflections and formation of standing waves [2]. These effects increase variability in the pressure delivered to cells within the bioreactor, thereby reducing reproducibility across experiments. To provide a well-controlled environment for ultrasound stimulation of cell-seeded scaffolds, an ideal bioreactor configuration would eliminate air interfaces along the US wave transmission path and allow for the central positioning of the scaffold.

The purpose of this study was to develop and characterize a novel bioreactor configuration for US stimulation of cell-seeded scaffolds using a design that eliminated all air-fluid and air-solid interfaces intersecting the wave propagation path. In the bioreactor configuration, an enclosed sample holder filled with culture medium was combined with an acoustic absorbent (AA) material. The US transducer was submersed in water and positioned below the sample holder. The acoustic pressure in the fluid domains of the US bioreactor was evaluated by developing a finite element model and conducting multiphysics simulations in the frequency domain. Effects of individual configuration parameters, including thickness of the water layer, presence of the AA material, and radius of the inner well, on the spatially-averaged acoustic pressure over the surface that a scaffold would occupy were analyzed.

METHODS

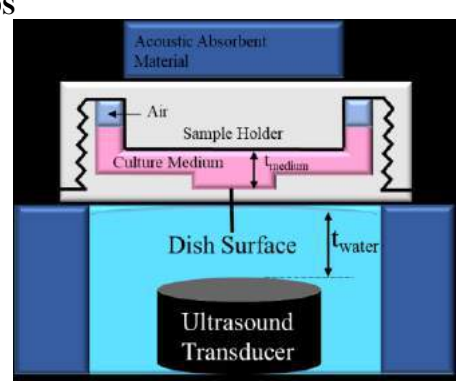

Figure 1: A bioreactor was developed for ultrasonication from below the sample, with 3D printed sample holder for containment of a cell-seeded scaffold, an ultrasound transducer submersed in water, and an acoustic absorbent material.

A novel sample holder was designed and fabricated (Figure 1) using a stereolithography technique (Form 2, Formlabs) with a durable resin. Two pieces were designed to screw together creating a central horizontal channel filled with culture medium through which US waves would pass and an outer vertical cylindrical channel to trap air bubbles. The base of the holder had a central inner well for positioning a scaffold at the center of the US pathway.

A model of the configuration was developed in COMSOL Multiphysics software (V5.3**,** COMSOL). A solid mechanics interface

was used to model the sample holder, transducer components, and AA material (Aptflex F28, Precision Acoustics) as isotropic, linear elastic materials. An electrostatics interface was used to model the charge distribution in the piezoelectric disc component of the transducer, and an acoustic pressure module was used to model the acoustic pressure in the water, air, and culture medium. The spatially-averaged acoustic pressure at the inner well surface was then analyzed under various conditions.

RESULTS

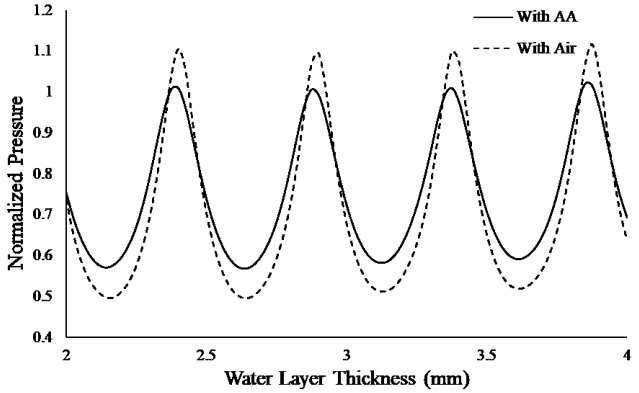

Figure 2. The spatially-averaged acoustic pressure at the inner well surface was analyzed with variation in the thickness of the water layer between the sample holder and transducer. Simulations were conducted with either the AA material (solid line) or air (dashed line) contacting the top of the sample holder. All pressure values were normalized to the maximum acoustic pressure in the presence of AA.

A sample holder consisting of two solid components was designed and fabricated to eliminate the air-culture medium interface that would be present with the use of a standard tissue culture dish. Frequency domain simulations of the US bioreactor using this sample holder were conducted. As the thickness of the water layer beneath the sample holder was increased from 2 to 4 mm, the spatially-averaged pressure at the inner well surface varied in a repetitive pattern, moving first to a point of minimum pressure (node) and then to a point of maximum pressure (antinode). This repetitive pattern was observed when either the AA or air contacted the top of the sample holder, indicating that this variance was due in part to weak standing waves formed from reflections at sample holder-liquid interfaces (~5.6% reflection at each). The acoustic pressure increased 1.75-fold from the node (N) to antinode (AN) position with the AA layer present. This difference was increased with air contacting the top of the holder (2.72-fold from N to AN), due to the additional contribution of reflections at this air-solid interface on wave interactions within the bioreactor. To further investigate the importance of eliminating air-fluid boundaries in the US bioreactor, a similar simulation was conducted with the entire top portion of the sample holder modeled as air, which would be comparable to using a tissue culture dish for a sample holder. In this simulation, the average pressure at the well surface increased 4.19-fold from node to antinode position.

To assess the impact of the inner well on pressure developed within the bioreactor, a simulation was conducted to compare two inner well radii for effects on the radial pressure pattern at the inner well surface, and a water thickness corresponding to an AN position was used. In the original configuration with an inner well radius of 7.5 mm, the pressure pattern was irregular, with radial pressures being an average of 39% of the maximum pressure and dropping as low as 18% of the maximum. When the radius was increased to 15 mm to be larger than the active element of the transducer, there was less radial variation, with pressure values being an average of 50% and dropping as low as 36% of its maximum pressure. However, the maximum pressure at the well surface was only 77% of the maximum with a radius of 7.5 mm. This simulation indicated a potential flaw in the original design of the sample holder, as the geometry of the smaller inner well produced a less uniform radial pressure pattern. Based upon the differences in radial pressure variation, the simulation in Figure 2 was repeated using an inner well radius of 15 mm. The results showed that the inner well radius had a minimal effect on wave interactions within the bioreactor, as the difference in pressure between the N and AN position was 1.74-fold with the AA layer and 2.49-fold with air.

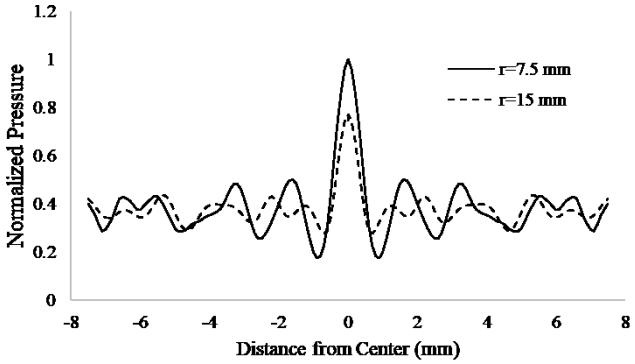

Figure 3. Acoustic pressure across the surface of the inner well with simulations conducted for inner well radii of 7.5 mm and 15 mm and an AN position for the water layer thickness. All radial pressures were normalized to the maximum pressure for r = 7.5 mm.

DISCUSSION

Overall, this study showed that the proposed novel bioreactor design provided an environment with less experimental variability for the US treatment of a cell-seeded scaffold. It effectively removed all air-liquid interfaces using a uniquely designed sample holder and an acoustic absorbent material, which reduced wave reflections and resultant wave interference within the bioreactor. However, multiple solid-liquid boundaries in the bioreactor contributed to the formation of weak standing waves, with the positioning of the transducer below the sample holder being shown to be an important parameter influencing pressure developed at the inner well surface. Additionally, this study showed that the radius of the inner well of the sample holder influenced pressure variations in the region where cell-seeded scaffolds would be located. Future work will include the addition of scaffolds as porous solids to the computational model.

ACKNOWLEDGEMENTS

Funding was provided by the Parks College of Engineering, Aviation and Technology

REFERENCES

[1] Padilla, F et al., *Ultrasonics*, 54:1125-1145, 2014.

[2] Leskinen, J. et al, *Ultrasound in Medicine and Biology,* 38:777-794, 2012

SB³C2019
Summer Biomechanics, Bioengineering and Biotransport Conference
June 25 -28, Seven Springs, PA, USA

PULSATILE ELECTROMAGNETIC FIELDS REGULATE BONE INTEGRITY THROUGH ACTIVATION OF VOLTAGE SENSITIVE CALCIUM CHANNELS

A. Dela Paz (1), C.T. Gregory (2) R. Duncan (1, 2), M. Mirotznik (3)

(1) Department of Biomedical Engineering
University of Delaware
Newark, DE, USA

(2) Department of Biological Sciences
University of Delaware
Newark, DE, USA

(3) Department of Electrical & Computer Engineering
University of Delaware
Newark, DE, USA

INTRODUCTION

Osteoporosis is a debilitating bone condition, affecting nearly 54 million Americans, in which the body loses excessive amounts of bone, produces too little bone, or both. This results in fragile bones that are at greater risk for fracture. Bone is sensitive to mechanical loads, and loss of mechanical load, such as in extended bed rest or microgravity, results in significant bone loss. Voltage sensitive calcium channels (VSCC) are the channels responsible for regulating the osteoblasts that secrete and mineralize the bone matrix. They are divided into two primary types: L-types and T-types. L-type VSCCs, or Ca_v 1.2 L-type channels are long lasting and require a higher voltage for activation whereas T-type VSCCs, or Ca_v 3.1 T-type channels/Ca_v 3.2 T-type channels are activated with lower voltages and primarily open during membrane depolarization. The Duncan lab has previously shown that the in vitro and in vivo inhibition of LVSCC, and TVSCC in vitro, significantly reduces the mechanical response of bone at both the cellular and tissue levels. Although past research has shown that pulsed electromagnetic fields (PEMF) promote osteoblastic proliferation, exact mechanisms are unknown. I hypothesize that VSCCs can be stimulated by PEMF and in turn can stimulate bone formation.

METHODS

Osteoblast Cell Culture

MC3T3-E1 pre-osteoblasts (American Type Culture Collection) were cultured in Minimum Essential Medium Eagle Alpha Modification (MEM-α, Sigma-Aldrich) and supplemented with 10% Fetal Bovine Serum and 1% Penicillin and Streptomycin. Media was changed every 2-3 days and cells were passaged at 80% confluence with 0.25% Trypsin.

Creating a Pulsed Electromagnetic Field Generator

Equation 1, as shown below, is a derivation from the Biot-Savart law to define the magnitude of the uniform magnetic field between Helmholtz coils. It has been rearranged to solve for current, *I*, as shown in equation 2.

$$B = \frac{4^{\frac{3}{2}}}{5}\frac{\mu_0 \eta I}{R} \qquad (1)$$

$$I = \frac{BR}{\frac{4^{\frac{3}{2}}}{5}\mu_0 \eta} \qquad (2)$$

Where $\mu_0 = 4\pi \times 10^{-7} (T \cdot m/A)$
η = # of turns of wire
I = current of coil (A)
R = radius of coil (m)

The PEMF generator was developed using a 33220A Arbitrary Waveform Generator from Agilent as a voltage source, a Lepai LP-2020A+ Hi-Fi Stereo Amplifier to amplify the source signal, and the Agilent Intuilink Waveform Editor application to create a pulsed square wave. A pair of 3B Scientific 51000611 Helmholtz coils were used to create the EMF, and a PCE MFM 3000 AC/DC Magnetic Meter from PCE instruments was used to measure the strength of the produced magnetic field. The pulsed waveform was designed to have a burst width of 5 ms, a pulse width of 0.2 ms, a pulse wait of 0.02 ms, and a burst wait of 15 ms repeated at 45 Hz. In order to produce a uniform magnetic field, the coils were placed away from each other at a distance equal to their radii. A base for the coils and the platform for the culture dishes was designed using Solidworks and machines out of acetal plastic in the College of Engineering Student Machine Shop.

Methods for Proliferation Studies of PEMF Exposed Osteoblasts

An MTS assay was used to determine cell proliferation. MC3T3-E1 cells were seeded on collagen I coated 96-well plates at a density of 2,500 cells/cm^2. Two rows of wells were treated with MEM-α media, two rows were treated with MEM-α with 5μM nifedipine, an L-VSCC inhibitor, and two rows were treated with MEM-α with 5μM NNC-55, a T-VSCC inhibitor. Media was changed just before cells were exposed to a PEMF at a magnitude of 2.2 ± 0.5mT for two hours a day for four days. At 24, 48, 72, and 96 hours, the CellTiter96™ AQueous One Cell Proliferation assay was used, and absorbance values were then recorded using the Synergy™ H1 plate reader from Biotek.

Methods for Fluorescent Microscopy of Osteoblasts

MC3T3-E1 cells were seeded at a density of 4000 cells/mL on 35mm MatTek petri dishes with 14mm microwells. Two days later, the cells were incubated in a 25μM Quinacrine (QAC), a fluorophore that binds to ATP, for 30 minutes. Cells were then exposed to PEMF for 0, 1, 2, 3, 4, or 5 minutes and rinsed twice with Hank's Balanced Salt Solution with Calcium and Magnesium (HBSS with Ca^{2+} and Mg^{2+}, Sigma-Aldrich). Then, 1mL of HBSS with Ca^{2+} and Mg^{2+} was added to each dish and imaged using an Axioscope (Zeiss).

RESULTS

MC3T3-E1 cells that were exposed to PEMF at 2.2 ± 0.5mT showed significantly greater proliferation than the non-stimulated controls after two days of exposure. Cells treated with either L-VSCC or T-VSCC inhibitors showed significantly reduced proliferation, regardless of exposure to PEMF at 2.2 ± 0.5mT, as shown in Figure 1.

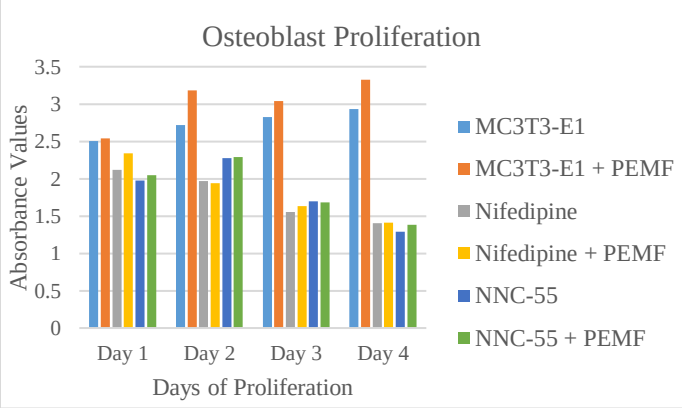

Figure 1: Graph of the relative absorbance values with respect to the recorded baseline at Day 0. The MC3T3-E1 cells ± PEMF exposure proliferation whereas those treated with VSCC inhibitors ± PEMF exposure show reduced proliferation (n=16).

Preliminary data in figure 2 has shown that ATP is released from intracellular stores in MC3T3-E1 cells. The average fluorescent light intensity was measured and shown to drastically decrease once the cells were exposed to PEMF.

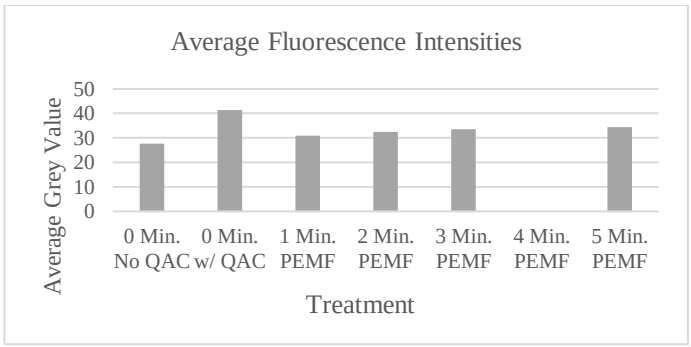

Figure 2: Graph of the fluorescence intensities of MC3T3-E1 osteoblast-like cells at several treatments including 0 minute exposure without Quinacrine, 0 minute exposure with Quinacrine, 1 minute exposure, 2 minute exposure, 3 minute exposure, and 5 minute exposure to PEMF.

DISCUSSION

We propose that PEMF stimulates osteogenesis through activation of L-VSCC and T-VSCC- previous data in our lab suggests this is through activation in the L-VSCC. The proliferation studies indicate that VSCCs may be activated by PEMF to further stimulate proliferation, as inhibition of these channels attenuates proliferation. The ATP studies indicate that ATP is stored within intracellular vesicles prior to PEMF exposure, and VSCCs are activated to release ATP their stores once exposed to PEMF. Future work includes: additional studies to determine the effects of PEMF on ATP release, testing other magnitudes of PEMF to determine the optimal field for osteogenesis, running apoptosis studies to determine if cells are dying or if they are phasing into a senescent stage, developing a small, wearable, cuff-like device to implement these tests in mice.

ACKNOWLEDGEMENTS

This work was supported by a grant from the National Institutes of Health (NIDCD DC014461). We would also like to thank the University of Delaware's Undergraduate Research Program for additional funding of this project, and Scott Nelson and Jeff Ricketts for assistance in the Student Machine Shop.

REFERENCES

[1] National Osteoporosis Foundation. (n.d.). Learn What Osteoporosis Is and What It's Caused by. Retrieved from https://www.nof.org/patients/what-is-osteoporosis/

[2] PharmacyPedia. (2016, July 01). How can Vitamin D help those with Osteoporosis? Retrieved from https://pharmacypedia.org/can-vitamin-d-help-osteoporosis/

[3] Jing, D.(2014), Pulsed Electromagnetic Fields Partially Preserve Bone Mass, Microarchitecture, and Strength by Promoting Bone Formation in Hindlimb-Suspended Rats. J Bone Miner Res, 29: 2250-2261. doi:10.1002/jbmr.2260

[4] Thompson, W. R. (2011), Association of the α2δ1 subunit with Cav3.2 enhances membrane expression and regulates mechanically induced ATP release in MLO-Y4 osteocytes. J Bone Miner Res, 26: 2125-2139. doi:10.1002/jbmr.437

[5] Li, J. (2002), L-Type Calcium Channels Mediate Mechanically Induced Bone Formation In Vivo. J Bone Miner Res, 17: 1795-1800. doi:10.1359/jbmr.2002.17.10.1795

[6] Genetos, D.(2010), Fluid Shear-Induced ATP Secretion Mediates Prostaglandin Release in MC3T3-E1 Osteoblasts, J Bone Miner Res, 20:41-49

2019 Summer Biomechanics, Bioengineering, and Biotransport Conferecne (SB³C)
SB³C and the National Science Foundation (NSF)
June 25 – June 28, Seven Springs, Pennsylvania

CREATING THE STORKEL: A WATER OCCLUDING DEVICE FOR ACCIDENTAL SUBMERSION WITH A TRACHEOSTOMA

Claire M. Chaisson
Clarkson University
Potsdam, New York, USA

Samantha K. Denning
Clarkson University
Potsdam, New York, USA

Kelli E. Grimes
Clarkson University
Potsdam, New York, USA

William J. Pelowski
Clarkson University
Potsdam, New York, USA

Michael A. Valleau
Clarkson University
Potsdam, New York, USA

Faculty Advisor
Byron D. Erath, Ph.D.
Clarkson University
Potsdam, New York, USA

INTRODUCTION

In the human throat, the hypopharynx houses the larynx, which allows for vocal function. In certain instances, such as irreversible damage from laryngeal cancer or severe throat trauma, a laryngectomy may be necessitated. During a laryngectomy, the larynx may be completely or partially removed from the hypopharynx. Following surgical removal, a hole (stoma) is created in the throat to allow air to enter the lungs.

Post operation, individuals permanently breathe through the stoma. In the year 2018, about 13,150 new cases of laryngeal cancer were discovered, with ~50,000~60,000 laryngectomy patients (i.e. laryngectomees) currently living in the United States [1-2].

With the stoma being a direct passageway to the lungs, laryngectomees are at significantly higher risk of drowning through accidental submersion while around open bodies of water. This can deprive laryngectomees of participating in popular, water-based activities, an important part of social interaction and engagement, as 61.3% of Americans participate in swimming activities, 36.2% in boating activities, and 33.9% in fishing activities annually [3]. The inability to participate in social activities such as those listed can have severe psychological impacts, particularly for laryngectomees, as approximately 22.2% suffer from a psychiatric disorder after their operation [4]. Maintaining social contacts and participating in regular activities can help prevent the development of these disorders.

While two commercially-available products exist, which allow laryngectomees to safely swim, they are not comfortable for long term wear and, most importantly, require anticipation of submersion by the user. As such, they do not function for accidental/unanticipated water submersion as may occur while boating, fishing, etc. [5]. The purpose of this project is to develop a product which allows a laryngectomee to participate in aquatic activities, where accidental submersion is a risk, without risk of personal safety.

PRODUCT DESIGN

The stoma snorkel (Storkel) is designed to fulfill the following objectives: (1) passively occlude water from the stoma when submerged at any angle, (2) maintain comfortable respiratory function while above water, (3) allow for comfortable long-term usage of equipment and (4) enable uninterrupted speech while equipped. The three most common mechanisms of speech for a laryngectomee are tracheoesophageal (TEP), esophageal, and usage of an electrolarynx. While the Storkel will not interfere with esophageal and electrolarynx speech, to use TEP speech it must be possible to temporarily occlude the stoma to redirect air from the trachea, through an implanted prosthesis, and into the esophagus.

Figure 1 displays the prototype. A stoma attachment (1) extends slightly into the stoma and provides an attachment point for the rest of the Storkel. A silicone pad interface (2) ensures that the attachment is comfortable, and an adhesive dressing (3) makes a water-tight seal around the stoma. A plastic junction (4) connects to the stoma attachment and splits into two directions. One downward to the drainage valve (5) to expel any water that may incidentally enter the system, and one to the flexible tubing (6). A small spring (7) and button valve (8) are embedded within the plastic junction and can be used to momentarily block the airway within the plastic junction, allowing for TEP speech (see inset). In order to keep the entire apparatus stable and more comfortable for long periods of use, a neck strap (9) and head band (10) hold the tubing firmly in place.

A float valve mechanism (13-16) is incorporated to occlude the airway during submersion, while automatically reopening upon surfacing. The float valve consists of a hollow shell, such that the positive buoyancy force produced during submersion due to the air pocket inside is the same magnitude as the opposing force due to gravity when not submerged. Figure 2 illustrates how, in an upright position, this causes the valve to remain open, but when submerged, the moment arm of the buoyancy force (X_B) is larger than that of the force of gravity (X_g) thereby lifting the weight and closing the airway.

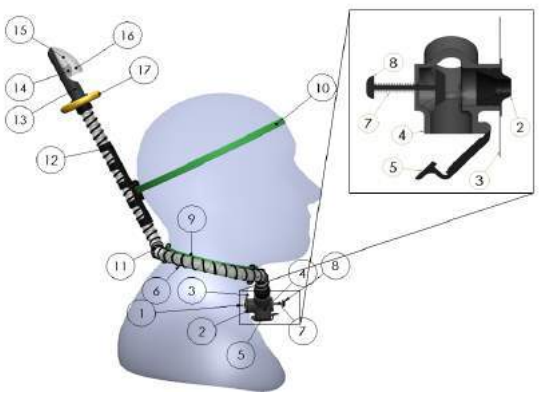

Figure 1: Fully-assembled Storkel

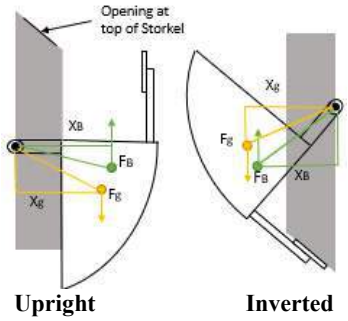

Figure 2: Proof of float weight concept

In the inverted orientation, the gravitational force holds the valve closed regardless of whether it is submerged or not. To ensure that the float valve functions correctly regardless of the angle of submersion (i.e., such that the axis of rotation is normal to the water surface), a flotation ring (17) is added to the tubing. This flotation ring ensures the housing of the float valve is in a semi-upright position so that the float valve actuates properly. It is recommended that this product is used in conjunction with a life-jacket to minimize time submerged.

To ensure that the tubing will not restrict respiratory function, the pressure drop within the tube must be less than what the lungs can comfortably produce during normal respiration. This pressure drop is calculated through the energy equation in equation 1.

$$\left(\frac{\Delta p}{\rho g} + \alpha \frac{\Delta V^2}{2g} + \Delta z\right) = \left(\sum f_i \frac{L}{D} + \sum K_L\right)\frac{V^2}{2g}, \quad (1)$$

where ρ is density, p is pressure, V mean velocity, g is gravity, and z is height. The right side of the equation accounts for the losses due to friction and bending in the tube. The tubing in the Storkel is smooth and the flow is laminar so a modified equation for friction losses can be used. The Storkel will have three 90-degree bends that will constitute the minor losses. The K value for a 90-degree bend is 0.3.

A person participating in moderate exercise produces an airflow rate around 75 L/min or 0.00125 m^3/s [6]. Using that flow rate and a range of diameters from 0.01 m - 0.028 m the pressure drop can be calculated. During normal respiration the average lung pressure is 784 Pa [7]. Comparing the average lung pressure to the calculated pressure drops, the Storkel diameter must be greater than 0.02 m to enable sufficient airflow.

Prototype evaluation will be carried out to ensure the following: (1) the connection interface fits comfortably with the stoma, (2) the collar will provide sufficient stabilization, (3) the method of speech is not interrupted, and (4) the float valve actuates appropriately following submersion. The fitting test, comfort tests, and speech performance tests will be performed in conjunction with Utica, NY Laryngectomee support group. The float valve will be tested by submerging the apparatus in a multitude of scenarios, while varying multiple parameters such as angle of entry to surface and depth of submersion.

BUDGET & MARKET ANALYSIS

The target market for the Storkel is individuals with a stoma who desire a safe method of enjoying water activities. This market encompasses both laryngectomy and tracheostomy patients, both of whom utilize stomas. In addition to laryngectomees, there are upwards of 100,000 tracheostomies performed each year [8, 9], although many are temporary, performed during in-patient hospitalization. The combination of these populations will represent the core of potential consumers and will create a total market size estimated to be just over 110,000 individuals. Noting that not all may be interested in water activities, market analysis indicates this will result in a more realistic market size currently estimated at 48,000.

The first year market share is conservatively predicted to be 3.0%, and to grow by 1.0% annually thereafter, until achieving a steady-state market capture of 7.0% in year 5.

The current Storkel prototype is projected to be produced at a per unit cost of $27.96. The cost breakdown of each component is shown in Table 1. Most components will be produced in house with a 3D printer (Stratasys F270). The remaining parts (tubing, adhesive, neck strap and headband) can all be purchased directly from retailers. Including shipping costs, each unit is expected to cost a total of $32.96. The projected sales price is $110, yielding a per unit profit of $77.04.

Expenses include the 3D printer, which will be purchased for $20,000, as well as salary and benefits for one full-time employee ($100,000.00). Overhead costs will be minimized by partnering with the Peyton Hall Incubator, associated with Clarkson University, which will function as the manufacturing and distribution facility as this space is available at no cost. A loan for $45,000 at 5% interest rate for 60 months will be taken out to cover start-up costs (purchase of the 3-D printer) as well as marketing expenses and unanticipated costs in the first 5 years. In year 1, a net annual revenue is predicted to be $-4,500. However, by year six the revenue will grow to $153,800, ensuring a profitable endeavor.

Table 1: Parts List and Production Costs

Part Number	Part Name	Price ($)
1	Stoma Attachment	$0.06
2	Silicone Pad	$0.08
3	Adhesive Dressing	$1.00
4	Junction	$0.39
5	Drainage Valve	$0.08
6	Tubing	$10.52
7	Spring	$0.88
8	Button Valve	$0.05
9	Neck Strap	$9.80
10	Head Band	$4.00
11	Clip 1	$0.10
12	Clip 2	$0.23
13	Float Casing	$0.43
14	Float Weight	$0.02
15	Float seal	$0.01
16	Float Cover	$0.17
17	Flotation Ring	$0.14
	Total	**$27.96**

ACKNOWLEDGEMENTS

This work was supported by the National Science Foundation under grant NSF-CBET 1510367. Thank you to the Clarkson University Shipley Center and the Utica, NY Laryngectomee Support Group for their help and advice.

References

[1] Brook, I "The Laryngectomee Guide" 1-5, 2013

[2] Maddox, P. et al, American Academy of Otolaryngology—Head and Neck 147: 85-90

[3] National Survey on Recreation and the Environment (NSRE): 2000-2002

[4] Bussian, C. "Mental health after laryngectomy and partial laryngectomy: a comparative study" 267:261 2010

[5] Karamzadeh, A et al., Otolaryngology-Head and Neck Surgery 125:528-532, 2001

[6] University of Michigan, Physiological Support Systems and Exercise. Exercise Physiology. 3-6

[7] Notre Dame University, Physics of breathing. Medical Physics. 100-101.

[8] American Cancer Society "Key Statistics for Laryngeal and Hypopharyngeal Cancers", 2019

[9] Cheung N. et al, *Respiratory Care,* 59:895-919, 2014

SB³C2019
Summer Biomechanics, Bioengineering and Biotransport Conference
June 25 -28, Seven Springs, PA, USA

DYNAMIC TRACKING OF FLUORESCENTLY LABELED TYPE I COLLAGEN MOLECULES; DIRECT QUANTIFICATION OF MOLECULAR ASSOCIATION WITH NATIVE FIBRILS

Seyed Mohammad Siadat, Jeffrey W. Ruberti

Department of Bioengineering, Northeastern University, Boston, MA, USA

INTRODUCTION

Collagen is the most abundant protein in vertebrate animals, found in tissues that regularly experience tension, compression, and shear forces. Although connective tissue has been the subject of investigation for more than 100 years[1], there are currently no widely accepted mechanistic models of growth and remodeling of collagenous connective tissue. It has been suggested that fibril growth is the result of linear and lateral fusion of immature intermediate fibrils[2]. It has also been shown that placement of collagen is a function of the local tissue micro-mechanical environment[3], that fibroblast traction can rearrange collagen fibrils[4], and in some cases, that actin filaments align with fibripositors and intracellular fibrils[5]. However, the detailed mechanism by which the actual collagen molecules (and microfibrils) are added (or subtracted) from the resident collagen fibrils is not known. It is highly probable that the mechanism that drives growth and remodeling will operate independently of the cell surface or at some nominal distance from it[6]. Unlike early development[7], when connective tissues are highly-cellular, much of growth and remodeling occurs when the matrix-to-cell volume ratios are relatively high.

To explore the possible mechanisms that govern homeostasis at the fibril surface, it is important to be able to observe directly, the motion of individual collagen monomers entering and exiting the fibril. Our goal was to fluorescently label and track collagen monomers, while minimizing the effect of labelling on fibrillogenesis of collagen. Our approach was to achieve a labeling ratio of 2-3 fluorophores per collagen molecule to minimize disrupting the functionality of collagen, while still permitting us to determine the orientation of the tagged molecules on a fibril surface. Such a tool has the potential to not only track individual molecular associations in a complex biological system but also the directionality with respect to the fibril axis. This will permit us to determine if the associations are functional or non-specific.

METHODS

Collagen Labeling. Type I bovine collagen solution was diluted to 1 mg/ml using 10 mM hydrochloric acid, and then mixed 1:1 with 0.2 M sodium carbonate–bicarbonate buffer containing 1 M sodium chloride. Alexa Fluor 488 was dissolved in dimethyl sulfoxide to a concentration of 0.5 mg/mL and added to collagen solution to achieve 1-10 fluorophores per collagen molecule. The reaction mixtures were stirred for 3 hours at room temperature. (Figure 1)

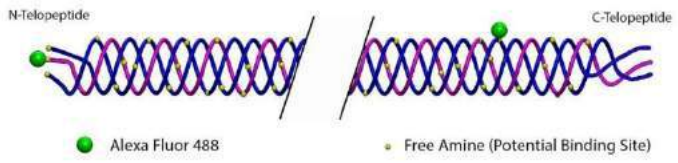

Figure 1: Schematic of collagen molecule labeled with 2 fluorophores.

Molecular Association of Labeled Monomers with Native Fibrils Experiment. A glass bottom, ITO coated Delta-T dish and a perfusable coverglass lid were plasma cleaned and coated with 1% BSA at 4 °C overnight. The dish was placed on the microscope stage and 1 mL of sclera fibril suspension was added. Then 5 mL of 2 µg/mL labeled collagen was added at 1 ml/h to maintain constant concentration inside the chamber. The collagen concentration was kept at 2 µg/mL (sub-threshold for new fibril formation) to prevent self-assembly and formation of new fibrils. DIC and fluorescent images were taken every 10 minutes for 6 hours using 60x oil objective.

Poster Presentation #P149

RESULTS

Labelling 100% of the collagen monomers with this small molecular weight probe affected the self-assembly kinetics for new fibrils (figure 2), but produced little discernible effect on assembled fibril morphology (D-banding) as confirmed by transmission electron microscopy. Reducing the relative number of labeled monomers to below 5% of the total number of monomers restored the self-assembly kinetics suggesting that the effect of the label can be taken into account via calibration.

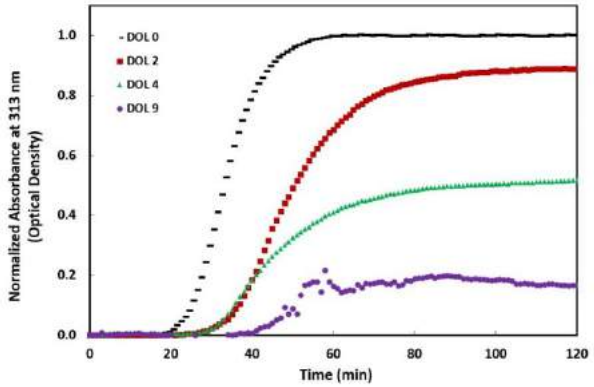

Figure 2: Turbidity of 50 µg/mL labeled collagen at 37 °C. DOL is the degree of labelling.

We then exposed native, young bovine scleral collagen fibrils, extracted from 1-10 day old animals, to a small concentration of labeled monomers. The incorporation rate and total accumulation (to reach saturation) of labeled collagen into the scleral fibrils (predominantly type I collagen) was measured as 2.8 ± 1.2 and 4.0 ± 1.5 molecules/(µm^2.minute) and 114.3 ± 26.8 and 207.1 ± 55.4 molecules/µm^2 at 25 and 30 °C, respectively. The reaction of the monomers with the fibril surfaces produced a kinetic signature similar to *de novo* collagen assembly, with an activation energy of 12.6 kcal/mol. The results suggest that our labeled, exogenous collagen molecules dynamically associate with and incorporate into young native collagen fibrils (figure 3).

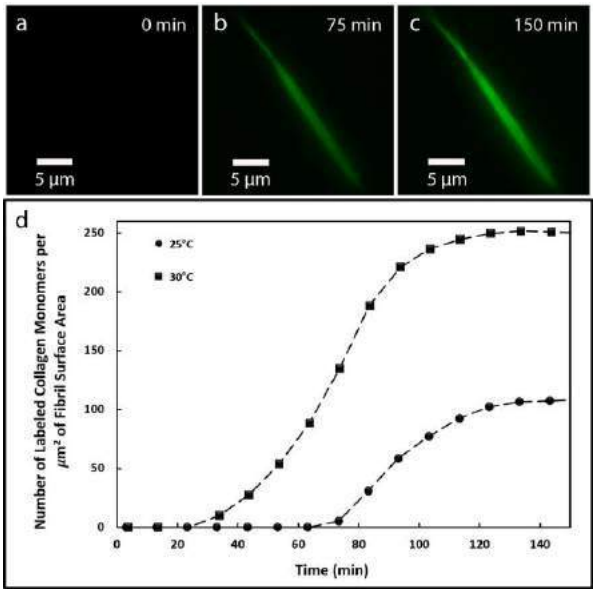

Figure 3: Incorporation of labeled collagen into native fibrils.

DISCUSSION

Part of the difficulty in establishing k_{on} and k_{off} is the insoluble nature of the collagen fibrils and the uncertainty of the nature of their association with soluble monomers/microfibrils. While estimation of the rate constants for collagen fibril surface erosion and adsorption requires relatively simple quantitative fluorescence microscopy, determining whether or not collagen monomers are incorporating functionally into extant fibrils is more difficult. The goal of this study was to develop methods which enable us to ask quantitative questions about the dynamics of molecular assembly and disassembly at the collagen fibril surface.

The activation energy of 12.6 kcal/mol calculated in the present study was lower than values reported in the literature for collagen assembly *in vitro* (27 – 58 kcal/mol)[8-10], suggesting that the activation energy for growth of a native fibril is less than formation and growth of a reconstituted fibril *in vitro*. Moreover, it has been shown that proteoglycans can be removed from collagenous tissue by trypsin treatment[11,12]. Therefore, the lateral growth of our proteoglycans-free scleral fibrils and the lower activation energy can be attributed to the absence of proteoglycans. Therefore, the presence of proteoglycans on the scleral fibrils in our study might inhibit the incorporation of collagen monomers and guide the equilibrium fibril diameter[13,14].

The lag time during initial fibrillogenesis (figure 2) is due to the lack of pre-existing nucleation sites that must be established. However, this is not the case in figure 3 where monomers are incorporating into the already extant native fibrils. The lag time we observe might be due to formation of microfibrils and their lateral association with the native fibrils. The plateau region of a turbidity experiment (figure 2) is partially due to consumption of the reactant, while our monomer/fibril association experiment (figure 3) had a constant supply of monomers. Saturation of scleral fibrils by labeled monomers shows that besides proteoglycans, there must be other inhibiting factors that arrest the fibril's growth. We suspect that collagen fibrils reside in a state of dynamic equilibrium with the local extracellular milieu and that this equilibrium can be altered by mechanical strain, shifting the molecular association rates, k_{on} and k_{off}, between fibrils and molecules.

REFERENCES

[1] Mall, F. P., *Developmental Dynamics* **1**, 329-365 (1902).
[2] Birk, D. E. *et al*., *Dev Dyn* **202**, 229-243 (1995).
[3] Beloussov, L. & Dorfman, J., *American Zoologist* **14**, 719-734 (1974).
[4] Stopak, D. & Harris, A. K., *Dev Biol* **90**, 383-398 (1982).
[5] Canty, E. G. *et al.*, *J Biol Chem* **281**, 38592-38598 (2006).
[6] Stopak, D. *et al.*, *Proc Natl Acad Sci U S A* 82, 2804-2808 (1985).
[7] Canty, E. G. & Kadler, K. E., *J Cell Sci* **118**, 1341-1353 (2005).
[8] Williams, B. R. *et al.*, *J Biol Chem* 253, 6578-6585 (1978).
[9] Kadler, K. E. *et al.*, *J Biol Chem* **262**, 15696-15701 (1987).
[10] Silver, F. H. & Birk, D. E., *Collagen and related research* **3**, 393-405 (1983).
[11] Bergmann, M. & Stein, W. H., *Journal of Biological Chemistry* 128, 217-232 (1939).
[12] Schmitt, F. O. *et al.*, *Journal of Cellular and Comparative Physiology* **20**, 11-33 (1942).
[13] Brown, A. I. *et al.*, *Soft Matter* 10, 8500-8511 (2014).
[14] Cameron, S. *et al.*, *Soft Matter* **14**, 4772-4783 (2018).

2019 Summer Biomechanics, Bioengineering, and Biotransport Conferecne (SB^{3}C)
SB^{3}C and the National Science Foundation (NSF)
June 25 – June 28, Seven Springs, Pennsylvania

MECHANICAL ADVANCES IN CARDIOPULMONARY RESUSCITATION

Jeffrey S. Stransky
Rowan University
Glassboro, New Jersey, USA

Morgan Dean
Rowan University
Glassboro, New Jersey, USA

Faculty Advisor(s)

Thomas L. Merrill
Rowan University
Glassboro, New Jersey, USA

Jennifer A. Kadlowec
Rowan University
Glassboro, New Jersey, USA

INTRODUCTION

Every year, 475,000 cardiac arrests occur; 45% of out of hospital cardiac arrests lead to death due to failure in cardiopulmonary pulmonary resuscitation (CPR) [1]. Less than 1 in 6 people can perform CPR properly [2]. To correct areas of common failure, such as depth of chest compression and rate of compressions, assistive CPR devices are being implemented among emergency medical staff (EMS). Regardless of innovations, assistive CPR devices provide no statistical increase in survival over manual CPR [3].

Clinical immersion through the Bioengineering Scholars Summer Program allowed undergraduate engineering and medical students hands-on discovery of medical problems [4]. A list of problems derived from recorded observations were filtered to find the most heavily weighted problem. Observations of a failed usage of an automatic CPR machine produced the following need statement: "There is a need to address CPR in out-of-hospital adult cardiac arrest patients, prior to EMS arrival that optimizes layperson compressions and reduces fatigue".

The goal of this work is to develop a mechanically assistive CPR device to be used in home by family members of cardiac arrest victims prior to EMS arrival. The absolute design criteria is to be a mechanical device that optimizes bystander's performance of CPR. Optional criteria would be to increase bystander reaction rates and reduce user fatigue. The majority of this work focused on need validation and preliminary design of a solution; solid specifications and manufacturability were not within the scope of this project.

NEED VALIDATION AND REQUIREMENTS

The defined need statement was validated through 50 surveys and 7 interviews of professionals varying from Rowan University EMS, Gloucester County EMS, and Cooper University Hospital. Here, surveys were flagged for statistics, uncommon problems and stories, and solidification to researched facts. This research is limited to locational trends; further research is required before implementing to other regions. Some major takeaways include: the importance of compression location and bystander CPR prior to EMS arrival. Improper compression location could result in puncturing the heart or lungs which significantly increases risk of death. Bystander CPR is often low quality due to fatigue and lack of training; it is also often not performed at all. The interviews confirmed the patient population as individuals who are in the age range of 40-60 years old [5]. Interviewees expressed lack of confidence in performing CPR on obese victims suggesting a solution be tailored towards larger body types.

Requirements were established through 3 primary resources: AHA and FDA standards, the surveys and interviews, and existing products. Functional requirements include: harnessing the victim in place and performing compressions. Performance requirements include: force application to the body between 100-125 pounds, minimum compression frequency of 100 beats per minute (BPM) with a depth of 2-2.5 inches [6, 7]. Depth may vary depending on the chest bust of the individual. Interface requirements include: compressions located between the sternum tip and the nipple line beginning at a maximum of 45-60 seconds after cardiac arrest begins [8].

PRODUCT DESIGN

The assistive CPR machine is comprised of an alignment harness, a dual linkage system for variable compression depth, and a crank handle.

To address an immense spectrum of possible body sizes, from 5th percentile female to 95th percentile male profiles, two harness sizes will need to be produced. These percentile dimensions were defined using published resources from NASA and the US Anthropometry Survey [9, 10]. The scope of this design focused on the 95th percentile male due to the comments on obesity from the surveys. To apply the harness, the victim must be lying down face up. The harness will be "forklifted" over the victim's head and encompass the upper torso as shown in Figure 1. Compression straps will be used to deform the harness frame and fix itself to the victim's body. A forklift approach reduces time by eliminating the need to roll the victim onto a compression tray.

The dual linkage system consists of a crank-rocker assembly and rocker-slider assembly. The crank is a hand powered input. The slider is a cylindrical, compressive piston. The two assemblies share the rocker linkage. Three variable pivot holes along the rocker linkage allow for adjustable compression depth. This variability is useful for larger patients who require a deeper compression to overcome additional chest bust. This linkage system is shown in Figure 2.

A custom written Excel-Visual Basic (VBA) code was used to parametrically alter linkage sizes to find possible permutations validated by the Grashof Condition [11]. These linkages were manually filtered by stroke length, by overall size, and with mechanical design intuition. Since the required compression force and frequency are given as requirements, these were used as inputs to solve for crank handle torque and angular velocity. The results of the VBA provided near instant insight on the performance of every linkage permutation.

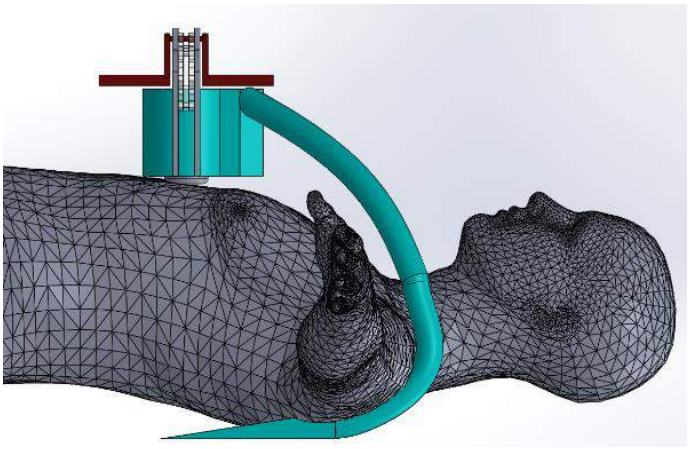

Figure 1: Side view of harness and linkage system applied to laying victim. Compression straps not shown.

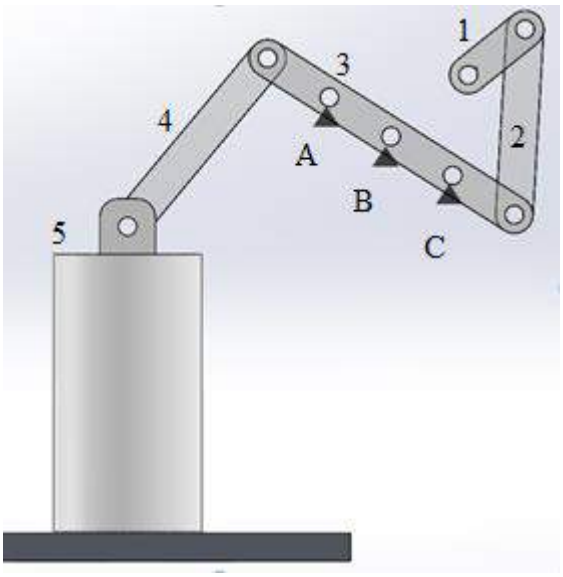

Figure 2: Front view of the dual linkage system. Link 1 is connected to the input crank handle. Link 2 and 4 are connecting links of the first and second assembly. Link 3 is the dual rocker linkage. Link 5 is the slider which acts as the compressive piston for CPR. Nodes A, B, and C are pivot point options.

Prior to EMS arrival, compression feedback will be given by use of a tachometer on the crank handle linkage. The machine will measure the compression frequency and alert the user of variance from the optimal frequency based on the performance requirements. Flashing LEDs will correspond to labels "Too Slow", "Good", or "Too Fast".

BUDGET & MARKET ANALYSIS

Based on the need statement, the primary customers are individuals and families with a history of cardiac arrest or other heart-related health complications. Secondary customers are EMS personnel and other healthcare providers. The total estimated cost for developing a functional prototype is $107 as compiled in Table 1.

Table 1: Primary component summary bill of materials to build functional prototype [12].

Part(s) per machine	Cost [$]
Linkages	47.75
Crank Handle	13.00
Harness	46.25
Total	107.00

SUMMARY

There is a validated need for mechanically assistive CPR machine outside of the hospital for laypersons. This work has produced a design template for a harness, a variable linkage system, and crank handle.

Future work will include material simulations on the harness and linkage. The harness design will be solidified to ensure correct compression alignment. A verbal feedback system will be added to supplement the LEDs and include instructions of use. Instructions will include dialing 9-1-1, the harnessing the victim, and beginning compressions.

ACKNOWLEDGEMENTS

Our work was supported by NIH NIBIB Grant Number: 5R25EB014782. The content is solely the responsibility of the authors and does not necessarily represent the official view of NIH. This work was also supported by the Rowan University Mechanical Engineering Department. We are grateful for this support.

We would like to thank Robert Phillips for his significant contribution to development of VBA codes for linkage simulation and selection. We would like to thank Chris Iapicco, Collier Tonkin, Maciej Miodunka, and Jake Nugent for their contributions to design. We would like to thank Jason Sood and the other medical professionals for their contributions in validating this need.

REFERENCES

[1] "How CPR is changing Lives." Internet: https://cpr.heart.org/AHAECC/CPRAndECC/AboutCPRECC/CPRFactsAndStats/UCM_475748_CPR-Facts-and-Stats.jsp [September, 2018].
[2] "What are the most serious problems with CPR?" Internet: You Can Save a Life Anywhere. http://www.sca---aware.org/blog/bob---trenkamp/what-are-the-most-serious-problems-with-cpr. [July, 2018].
[3] Gates, S et al, *J Resuscitation*, 94:91–97, 2015
[4] Sood S, Short M, Hirsh R, Kadlowec J, Merrill T. (2015) "Biodesign Through Clinical Immersion", *VentureWell Conf.*, Washington, DC
[5]Ewy, G, *J Acute Med Surg*. 5(3):236–240, 2018.
[6] Mayo Clinic, "Cardiopulmonary resuscitation: First aid". Internet: https://www.mayoclinic.org/first---aid/first---aid---cpr/basics/art---20056600. [July, 2018].
[7] ACLS, "Chest Compressions: Best Practices." Internet: https://acls.com/free-resources/knowledge-base/bls-articles/chest-compressions-best-practices [September 2018].
[8] Platenkamp, M et al. J *Netherlands Heart*. 22(9):404-407, 2013.
[9] NASA. Man-Systems Integration Standards. 1(3):32-79.
[10] Gordon, C et al, "Anthropometric Survey of U.S. Personnel: Summary Statistics Interim Report". March 1989.
[11] Constans, E et al. Introduction Mechanism Design Computer Applications. 2018
[12] McMaster-Carr. Online: https://www.mcmaster.com/. [December 2018].

SB³C2019
Summer Biomechanics, Bioengineering and Biotransport Conference
June 25 -28, Seven Springs, PA, USA

THERMAL ANALYSIS OF PARTIAL VITRIFICATION WITH APPLICATION TO LARGE-SIZE CRYOPRESERVATION

Purva Joshi and Yoed Rabin

Biothermal Technology Laboratory
Department of Mechanical Engineering
Carnegie Mellon University
Pittsburgh, PA, USA, 15213

INTRODUCTION

Despite advances in medicine and biotechnology, concurrently with an increased awareness of the benefits of organ donation and transplantation, an everlasting gap exists between organ demand and supply [1]. According to the Global Observatory on Donation and Transplantation, only 10% of the worldwide demand for organ transplantation is being met [2,3]. Organ cryopreservation is a promising technique which can successfully increase the availability of organs for transplant medicine by improving both logistics and outcomes of transplantation [3,4].

A typical cryopreservation protocol includes loading the specimen with a cryoprotective agent (CPA) solution, cooling to cryogenic temperatures, storage for an indefinite period of time, rewarming, and washing out the CPA, all while minimizing injury to cells and damage to the tissue structure. Vitrification is a cryopreservation protocol where the cooling and rewarming rates are rapid enough in order to prevent ice crystallization—the cornerstone of cryoinjury (*vitreous* in Latin means *glassy*). Given the virtually infinite combinations of parameters that affect cryopreservation success, it is prudent to precede experimental cryobiology by computer simulations of the process, in order to facilitate a robust analysis and optimization of the protocol, thereby preserving resources and potentially accelerating progress. Consistently, the current study focuses on adverse phase-change effects occurring in attempts to vitrify CPA solutions.

This study proposes a framework for thermal analysis of the partial vitrification in large specimens. This framework concerns a simplified scenario where the thermal field and the kinetics of crystallization are unidirectionally coupled, where the crystal formation is assumed to behave similarly to a quasi-steady phase-change process once a critical cooling rate is surpassed. Essentially, this study represents a practical, first-order approach, which is appropriate for high-concentration CPA solutions, typical to whole organ vitrification. The computation framework represents an expansion of the so-called enthalpy approach [5], where the unique contribution of this study comes about. This computational framework is materialized with the finite elements analysis (FEA) commercial code ANSYS, while integrating recently developed differential scanning calorimetry (DSC) data on physical properties of relevant CPAs.

METHODS

The geometry analyzed in this study is of a cylindrical container, consisting of two subdomains: CPA solution and solid walls. No tissue sample is included in the current proof-of-concept analysis, which would be permeated with the same concentration CPA solution, and which may have similar properties [6]. Heat transfer in the container and the CPA undergoing vitrification is assume solely by conduction while a combined convection and radiation heat transfer coefficient is assumed between the outer surfaces of the walls and the cooling chamber [7].

The enthalpy approach [5,8] is based on an effective specific heat, representing the combined effects the intrinsic specific heat and the temperature-dependent effect of latent heat:

$$h_{12} = \int_{T_1}^{T_2} C_{eff}\, dT = \int_{T_1}^{T_2} C_p\, dT + L_{12} \qquad (1)$$

where, h_{12} is the enthalpy changes between the onset of crystallization at T_1 and the termination of crystallization at T_2, C_{eff} is the effective specific heat, C_p is intrinsic specific heat, and L_{12} is the latent heat absorbed between the corresponding temperatures. Consistently, the thermal conductivity within the phase-transition temperature range is

Poster Presentation #P151

temperature-dependent and calculated as a mixture of amorphous and crystallized materials [9].

RESULTS AND DISCUSSION

Cooling-Rate Effect: Figure 1 displays the crystallization amount and the temperature field for four representative cooling rates: 4.5°C/min, 7.5°C/min, 15°C/min and 30°C/min, where the former is below the critical cooling rate of 5°C/min. Data in Fig. 1. refers to the temperature below which significant phase-transition during cooling is negligible, -75°C, when the sample is cooled from an initial temperature of -25°C to a storage temperature of -120°C.

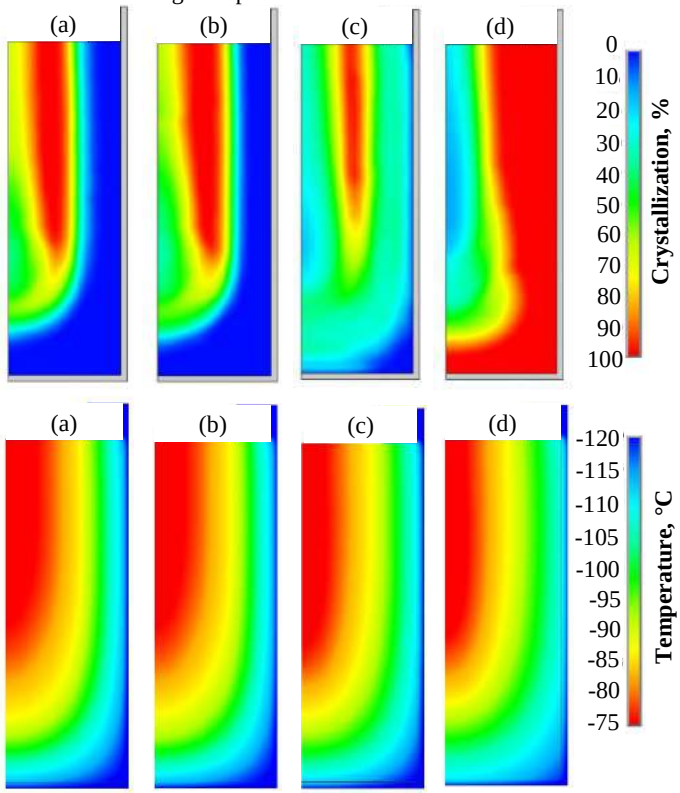

Figure 1: Crystallization amount and temperature field after completion of phase transition subject to the following cooling rate: (a) 30°C/min (t = 1060s), (b) 15°C/min (t = 1157s), (c) 7.5°C/min (t = 1308s), (d) 4.5°C/min (t = 1638s).

Unexpectedly, crystallization at the center of the container happens even when the outer surface is cooled at 30°C/min, Fig. 1(a)., which is higher that the critical cooling rate, due to the decay of heat transfer rate towards the center of the container. When the cooling rate at the outer surface is decreased to 15°C/min, Fig. 1(b)., the amount of vitrification close to the container wall decreases, but so is the portion of crystallization at the center of the container. However, this reduction in complete vitrification is merely 3% of the entire domain as compared to the change in the cooling rate which was reduced by half.

Only 3% of the entire domain vitrifies when the external cooling rate is set to 7.5°C /min, Fig. 1(c)., while the overall crystallization portions is 1%. This means that 96% of the domain is partially vitrified to a varying degree. The trend of crystallization described above is very difficult to trace from the temperature field alone, as displayed in the lower portion of Fig. 1., which signifies the importance of the proposed detailed analysis.

Counterintuitively, while complete crystallization is observed near the container wall at a subcritical cooling rate, Fig. 1(d)., partial vitrification is also found near the center of the container. In fact, the lowest amount of crystallization is observed in the latter case near the center of the container, despite the lower external cooling rate. This can be explained by an accelerate cooling rate at the center of the domain when the so-called "thermal wave" reaches there. Here the speed of propagation of thermal information is proportional to the thermal diffusivity and inversely proportional to the specific heat of the material.

Initial Temperature Effect: To study the effect of initial temperature on crystallization, two temperature values were considered: 0°C and -25°C, while the cooling rate was kept constant at 7.5°C/min. Counterintuitively, the case with the highest initial temperature resulted in a lower portion of overall crystallization, which can be explained by the longer period of time available for the thermal wave to reach the center of the domain, before the entire domain reaches the phase transition temperature range.

Container Size Effect: The dimensions were increased by two folds to study the crystallization trends in a volume required for cryopreservation of a human kidney [9]. Keeping the initial temperature and storage temperature consistent with the other studied cases (-25°C and -120°C, respectively), cooling rates as high as 100°C/min did not result in partial vitrification at the center of the larger container.

CONCLUSIONS

This study proposes a simplified model and a computation framework to explore effects of partial crystallization in cryopreservation processes. This study focused on the effect of cooling rate, initial temperature and container size on the extent of vitrification obtained in the container. Results of this study demonstrate that the extent of vitrification obtained in the specimen is highly dependent on the initial temperature as well as the storage temperature. Results also suggest a non-linear relationship between the cooling rate at the outer surface of the domain and the vitrification potential. For example, doubling the cooling rate resulted in an increase in complete vitrification in only by 3% of the domain. Counterintuitively, cooling rates lower than the critical cooling rate do not always result in complete crystallization in the specimen. Lower cooling rates resulted in complete crystallization at the boundaries but only partial crystallization at the center. While increasing the cooling rate increases the extent of vitrification close to the container wall, it may have adverse effect on the extent of crystallization at the center of the domain, depending on the specific size of the container and thermal protocol. In a broader perspective, this study demonstrates the value of thermal design and analysis of cryopreservation protocols using computer simulations.

ACKNOWLEDGEMENTS

This work has been supported by the National Heart Lung and Blood Institute (NHLBI), award R01HL127618.

REFERENCES

[1] Organ Procurement and Transplantation Network. (n.d.). Retrieved from https://optn.transplant.hrsa.gov/. Date retrieved: 1/14/2019.
[2] Giwa, S et al., *Nature Biotechnology*, 35:530-542,2017.
[3] Jones, B et al., *Bull. World Health Organ*, 90:718-719, 2012.
[4] Lewis, J.K et al., *Cryobiology*, 72:169-182, 2016.
[5] Rabin, Y et al., *Int. J. Heat and Mass Transfer*, 36: 673–683,1993.
[6] Ehrlich, L et al., *J.Biomech. Eng.*, 140: 011005-011005-8,2018.
[7] Feig, J. S. G et al. *Cryobiology*, 73(2): 272–281,2016.
[8] Rossi, M.R et al. *Comput. Methods Programs in Biomed.*, 85(1):41-50, 2007.
[9] Ehrlich, L et al., *Cryobiology*, 73(2):196-202, 2016.

SB³C2019
Summer Biomechanics, Bioengineering and Biotransport Conference
June 25 -28, Seven Springs, PA, USA

POINT-OF-CARE DIAGNOSIS OF RESPIRATORY SYNCYTIAL VIRUS BY DIGITAL NANOBUBBLE DETECTION

Y. Liu (1), V. Godakhindi (2), R. Levitz (3), J. Kahn (3), Z. Qin (1,2,4)

(1) Department of Mechanical Engineering
University of Texas at Dallas
Richardson, TX75080, U.S.

(2) Department of Bioengineering
University of Texas at Dallas
Richardson, TX75080, U.S.

(3) Department of Pediatrics
University of Texas Southwestern Medical Center
Dallas, TX75390, U.S.

(4) Department of Surgery
University of Texas Southwestern Medical Center
Dallas, TX75390, U.S.

INTRODUCTION

Respiratory syncytial virus (RSV) is among the leading causes of pediatric death secondary to pneumonia worldwide and to date there is no effective vaccine available or antiviral therapy. Early and point-of-care (POC) diagnosis of RSV is critical to isolate infection reservoirs and inform treatment decisions. Current diagnostic methods for RSV detection, including laboratory-based tests such as polymerase chain reaction (PCR, i.e., respiratory panel for FILMARRAY multiplex PCR system, >$1400 per test) or rapid diagnostic tests such as lateral flow immunoassay (LFI, i.e., Alere RDT), are either costly and time consuming or lack of sufficient sensitivity.

Colorimetric assay can detect intact viruses in a simple step, without the need of extracting and amplifying RNA. The antibody functionalized Gold nanoparticles (GNPs) are used to target the viruses surface protein. The adjacent plasmonic GNPs on the virus are coupled, leading to a color change (Figure 1A). However, one major limitation of the colorimetric detection is the large amount of coupled GNPs required to yield a substantial and detectable color change. Inspired by recent developments of digital assays [1-2], we report a novel digital nanobubble detection as a read-out method to significantly improve the limit of detection (LOD) of the colorimetric plasmonic coupling assay by 2-3 orders of magnitude. The sample-to-answer diagnosis can be achieved within 30 minutes by minimal additional time to the already rapid GNP-based aggregation assay. The proposed method is generally applicable to detect a broad range of viral infections.

METHODS

Antibody and GNP conjugation: Synagis (Palivizumab) was chosen as the RSV-specific monoclonal antibody. Synagis provides passive immunity against RSV by binding the RSV envelope fusion protein on the virus surface and blocking a critical step in the membrane fusion process. GNPs (15 nm/30 nm/45 nm) were synthesized on the basis of the standard citrate reduction technique with slight modifications, and GNP concentration is calculated according to their optical properties. To conjugate Synagis onto GNPs surface, we tested passive absorption, PEGylated method, and DTSSP method reported earlier [3-5] to create GNP-Syn probes. The probes were characterized by dynamic light scattering (DLS) using Malvern Zetasizer Nano (Malvern Instruments Ltd., UK).

GNP aggregation assay: RSV and other closely related respiratory viruses such as Human metapneumovirus (hMPV), Parainfluenza viruses (PIV), and Influenza Virus A (IVA) were then incubated with GNP-Syn probes for at least 30 min at room temperature in the presence of 5% sucrose and cell debris in 1×PBS. The optical spectrum was measured using a Beckman Coulter UV-Vis spectrophotometer (model DU800), and the GNPs targeted viruses samples were observed by transmission electron microscopy (TEM JEOL JEM 2100). Each of the GNP samples was spotted onto a thin carbon film coated Cu grids (300 mesh, Pacific Grid Tech) and air-dried for TEM characterization.

Digital nanobubble detection: To selectively detect coupled GNPs, which indicate the presence of the RSV, ultrashort laser pulses were applied to activate the coupled GNPs and create transient cavitation bubbles, i.e. nanobubbles, at a laser intensity threshold well below the threshold required for single nanoparticle cavitation [6]. The nanobubbles can be readily detected due to the high refractive index mismatch and scattering (Figure 1B). Basically, a syringe pump is used to flow the sample (GNP-syn + RSV) through a simple micro-capillary channel (ID=400 um). Then a short laser pulse (532 nm, pump laser) was applied while simultaneously monitoring with a continuous low-power probe laser beam (633 nm).

Poster Presentation #P152

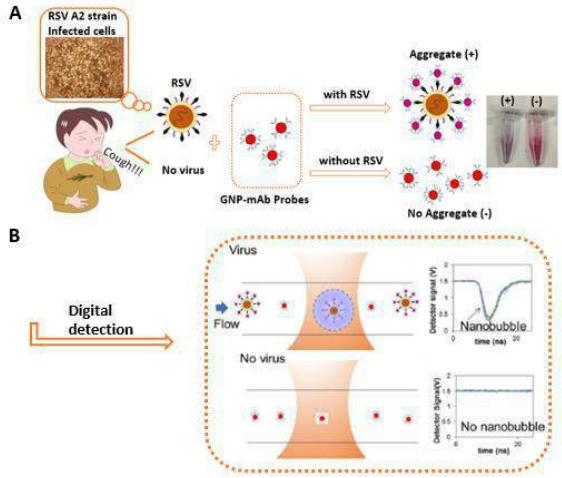

Figure 1: Schematic of (A) analog colorimetric detection and (B) digital nanobubble detection.

RESULTS

For analog detection, 45 nm GNP-Syn probe was first tested. GNP-Synagis conjugation leads to plasmon resonance peak shift from 532 to 538 nm and hydrodynamic diameter increase by 23 nm (Figure 2A). Polyethylene glycol (PEG) has a nonspecific affinity to viruses and has been used to concentrate viruses. Thus, using PEG does not show the specific detection of viruses. Passive absorption has some limitations for long term storage of GNP-syn probes. We explore another decent method using DTSSP bifunctional crosslinker to modify GNPs surface and create more stable GNP-DTSSP-syn probes, which can distinguish crude stocks of RSV from other respiratory viruses (Figure 2B, C). This colorimetric detection results suggest that the LOD of the analog assay is about 10^4~10^5 PFU/mL, which is below the mean nasal viral load on day 1 of infection. RSV targeted by GNP-DTSSP-syn probes was confirmed by TEM imaging (Figure 2D).

For digital nanobubble detection, we have tested the nanobubble probability over a wide range of laser energy using 15 nm GNPs (Figure 3A). The results suggested that the presence of the viruses will lower the energy threshold for nanobubble generation. By analyzing the nanobubble probability versus the virus's titer at the laser fluence of 500 mJ/cm^2, we can differentiate RSV at the titer of 10^0~10^6 PFU/ml from the control group (Figure 3B).

DISCUSSION

In this study, we developed a novel digital nanobubble diagnosis technique based on the colorimetric immunosensor to detect RSV in a simple step. The results from analog detection assay suggest GNPs aggregation is a promising method in POC diagnosis of RSV. Digital nanobubble detection can provide about 2-3 orders of magnitude improvement in the limit of the detection (LOD) compared with the colorimetric detection. This work will have a broader impact on addressing the scientific challenge for rapid and ultrasensitive diagnosis in the biomedical community and contributing to infectious disease management which eventually reduced morbidity, mortality, and healthcare costs. Future work is needed to enhance the dynamic range and the sensitivity by optimizing the size or the concentration of the GNP probes.

ACKNOWLEDGEMENTS

This research is partially supported by UT Dallas startup fund and National Institute of Health (R21AI140462).

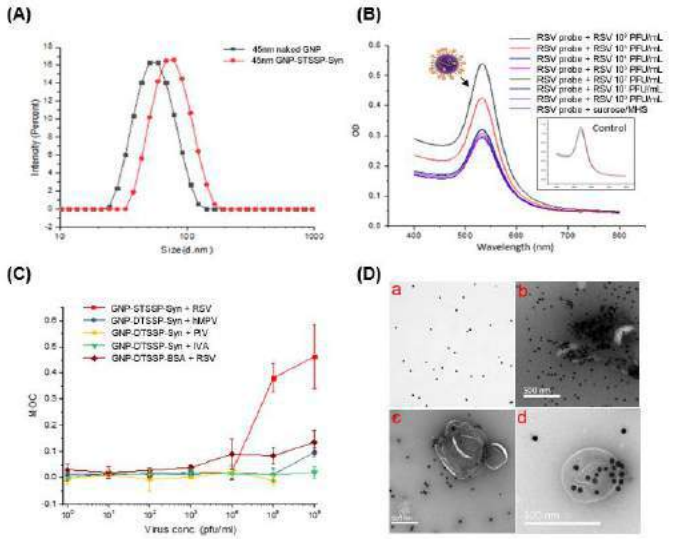

Figure 2: Analog detection of RSV. (A) Dynamic light scattering of naked GNP and GNP-DTSSP-syn probes. (B) UV-Vis measurements of the colorimetric assay. (C) Preliminary results of differentiating crude stocks of RSV from Human metapneumovirus (hMPV), Parainfluenza viruses (PIV), and Influenza Virus A (IVA). (D) TEM imaging of (a) GNP-DTSSP-Syn probes and (b, c, d) GNP-DTSSP-Syn probes incubate with RSV.

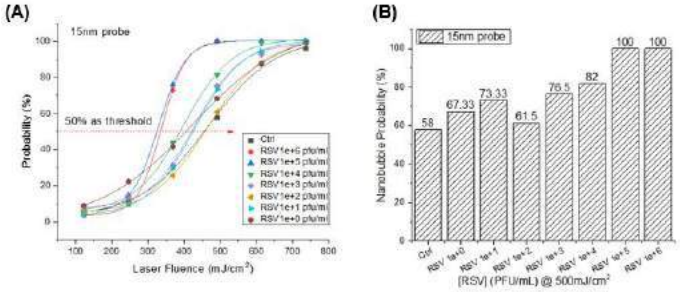

Figure 3: Digital nanobubble detection of RSV. (A) Nanobubble probability as a function of Laser fluence. (B) Nanobubble probability as a function of RSV titer at 500mJ/cm^2.

REFERENCES

[1] Gansen A, et al., Digital LAMP in a sample self-digitization (SD) chip. Lab Chip. 2012 Jun 21; 12(12): 2247-2254.

[2] Rodriguez-Manzano, J., et al. Reading Out Single-Molecule Digital RNA and DNA Isothermal Amplification in Nanoliter Volumes with Unmodified Camera Phones. ACS Nano 10, 3102-3113 (2016).

[3] Y. J. Liu, et al., Colorimetric detection of influenza A virus using antibody-functionalized gold nanoparticles. Analyst, 2015, 140, 3989–3995.

[4] Dai, Q., Walkey, C. & Chan, W.C. Polyethylene glycol backfilling mitigates the negative impact of the protein corona on nanoparticle cell targeting. Angew Chem Int Ed Engl 53, 5093-5096 (2014).

[5] Driskell J. D., Jones C. A., Tompkins S. M., Tripp R. A. (2011). One-step assay for detecting influenza virus using dynamic light scattering and gold nanoparticles. Analyst 136, 3083.

[6] Lukianova-Hleb, E., et al. Plasmonic Nanobubbles as Transient Vapor Nanobubbles Generated around Plasmonic Nanoparticles. Acs Nano 4, 2109-2123 (2010).

SB^{3}C2019
Summer Biomechanics, Bioengineering and Biotransport Conference
June 25 -28, Seven Springs, PA, USA

SAFE DURATION OF A PERSON SOAKING INSIDE A HOT TUB: THEORETICAL PREDICTION OF TEMPERATURE ELEVATIONS IN HUMAN BODIES USING A WHOLE BODY HEAT TRANSFER MODEL

Myo Min Zaw, Manpreet Singh, Ronghui Ma, Liang Zhu

Department of Mechanical Engineering
University of Maryland Baltimore County
Baltimore, Maryland, USA

INTRODUCTION

Soaking in hot tubs has become a popular relaxation activity during all seasons. Unfortunately, hot tub related emergency visits increase in recent years. Based on a New York Times article, approximately more than 6000 emergency visits in 2007 are related to hot tube injury. Although most of the injuries were due to slips or falls, still more than 10% of those visits were heat stroke related. People often mistakenly assume a sense of safety since the head is typically not soaking inside the hot water. Understanding how high the body temperature especially the brain temperature will rise is crucial to educate the public to prevent heat stroke from happening when using hot tubs.[1]

In this study, we first develop a whole body model based on measurements of a human body, with realistic boundary conditions incorporated before and after a person jumps into a hot tub. For the transient heat transfer simulation, the initial condition is the established steady state temperature field of the human body with appropriate clothing layer to ensure thermal equilibrium of the body with its surroundings. Once the person is inside a hot tub, the Pennes bioheat equation[2] is used to simulate the transient temperature elevations of the body, and the rising of the arterial blood temperature is solved by an energy balance equation modeling thermal exchange between body tissue and the blood in the body.[3] The safe duration of soaking in hot tubs is then determined as affected by the hot tub water temperatures.

METHODS

A physical whole body model based on realistic measurements of a human body was generated. As shown in Figure 1, the body (81 kg, 1.82 m tall) consists of three components: the hemispherical brain, the rectangular column of the internal organ, and the muscle for the rest of the body. Each component has its own thermal and physiological properties. The Pennes bioheat equation[2] is used to model the transient temperature field of the body as

$$\rho_t c_t \frac{\partial T_t}{\partial t} = k_t \nabla^2 T_t + \omega_t \rho_b c_b (T_b(t) - T_t) + Q'''_{met,t} \qquad (1)$$

where ρ is density, c is specific heat, k is thermal conductivity, ω is local blood perfusion rate, and Q'''_{met} is volumetric heat generations rate. Initially, the body is exposed to an ambient environment, and the thermal resistances due to clothing layers and convection/radiation with the air are lumped as an overall heat transfer coefficient U_{air}. Once the body is soaking inside a hot tub with water, the overall heat transfer coefficient is same for the head surface, however, a new overall heat transfer coefficient U_{water} is calculated based on free convection in water. The boundary condition can be written as

$$-k_t \left.\frac{\partial T_t}{\partial n}\right|_{surface} = U_{air,or,water}(T_t - T_{air,or,water}) \qquad (2)$$

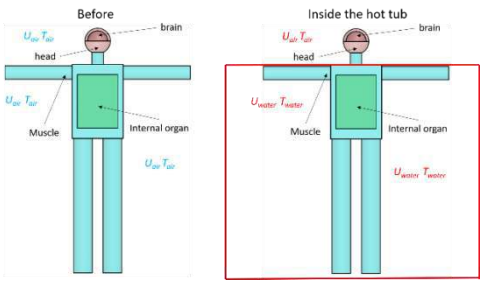

Figure 1: Schematic diagrams of the whole body model and its boundary conditions before and after the body inside a hot tub.

In Eq. 1, the arterial temperature T_a that is initially prescribed as 37°C rises with time. One can model the blood in the body as a lumped system that only varies with time.[3] The increase or decrease in the arterial blood temperature is due to its heat exchange with the surrounding tissue in the body, described by the Pennes perfusion

source term in Eq. 1. The following equation is developed for determining the time-dependent arterial temperature $T_a(t)$ as

$$\rho_b c_b V_b \frac{dT_a(t)}{dt} = Q_{tissue-blood}(t) = \rho_b c_b \bar{\omega} V_{body}\left[\bar{T}_t(t) - T_a(t)\right] \quad (3)$$

where V_b is the blood volume and V_{body} is the body volume, $\bar{\omega}$ is the average blood perfusion rate, and $\bar{T}_t(t)$ is the weighted average tissue temperature of the body, they are defined as

$$\bar{\omega} = \frac{1}{V_{body}} \iiint_{bodyvolume} \omega \, dV_{body}, \quad \bar{T}_t(t) = \iiint_{bodyvolume} \omega T_t(x,y,z,t) dV_{body} \Big/ \iiint_{bodyvolume} \omega dV_{body} \quad (4)$$

Eq. 1 and Eq. 3 are solved simultaneously to demonstrate thermal exchange between the arterial blood and tissue. Numerical simulations are carried out by ANSYS 19.2 Fluent.

RESULTS

Table 1 gives the physical and physiological parameters used in the heat transfer simulation. Note that the local blood perfusion rate of the internal organ region is adjusted so that the cardiac output of the body is equal to 5.5 liter/min, while the other two blood perfusion rates are obtained from literature.[4] The overall heat transfer coefficient U_{air} = 4.4 W/m^{2}K is determined so that the body establishes a thermal equilibrium with the surrounding air before the person is inside the hot tube. U_{water} is calculated as 61.93 W/m^{2}K, however, its value would be much bigger if the water is actively stirred to move around. Three water temperatures (40°C, 43°C, and 46°C) are prescribed to evaluate the temperature elevations in the body.

Table 1 Physical and physiological properties[4]

	Brain	Internal organ	Muscle	Blood
k, W/mK	0.52	0.52	0.52	0.50
ρ, kg/m^3	1050	1050	1050	1050
c, J/kg K	3800	3800	3800	3800
ω, 1/s	0.0087	0.0021	0.00052	-----
Q'''_{met} W/m^3	9225	2198	554	-----

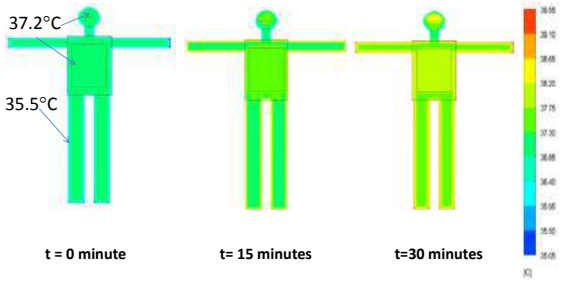

Figure 2: Contours of the temperature field of the body in a hot tub for 30 minutes, T_{water} = 40°C.

Figure 2 shows the temperature contours of the body for the beginning, 15 min, and 30 min inside the hot tub. The initial temperature field is reasonable.[5] Once the person is soaking inside a hot tub at 40°C, one can see the skin surface temperature rises from 35.5°C initially to that of the water, and the brain has the highest temperature in the body during the soaking from 37.2°C initially to 38.2°C after 30 min.

The weighted average tissue temperature (Eq. 4) and the arterial temperature T_a during the soaking are plotted in Figure 3. Initially they are the same as 37°C, due to the prescribed thermal equilibrium before the hot tub soaking. Once the body is immersed in hot water, heat conduction from the skin to the body tissue elevates the body temperature, making the right side of Eq. 3 positive, thus, resulting in an increase in the arterial blood temperature. The warmer arterial blood then further elevates the tissue temperature, shown in the perfusion source term in Eq. 1, continuing positive feedbacks between T_a and the weighted average tissue temperature. The shoulder by shoulder temperature rises in Figure 3 are consistent with our previous studies of a human body subject to harsh environment or during heavy exercise.[5] If one follows the recommendation of hot tub manufactures to soak in water at 40°C for up to 30 min, the maximal body temperature is less than 38.1°C. However, the threshold of body temperature at 38.5°C is reached after soaking for 25 or 18 min when T_{water} is 43°C or 46°C, respectively. Body temperature can rise to 39.4°C when staying in a 46°C hot tub for 30 min.

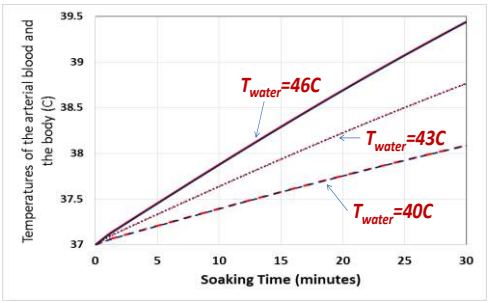

Figure 3: Temperature increases during soaking (red: weighted average tissue temperature, blue: T_a).

Table 1 lists temperatures of individual components in the body with time. Initially, the brain and internal organ have almost the same temperatures, which are higher than the muscle temperature. The brain maintains the highest temperature during most of the soaking time even if it is exposed to ambient air. However, the muscle temperature surpasses the temperature of the internal organ first, then the brain temperature once the soaking time is long. An increase in muscle temperature would divert more blood flow to the muscle region. If the cardiac output can't catch up, it may lead to reductions of the blood flow to vital organs, particular to the brain, and may also cause a decrease in systemic pressure to a dangerous level.

Table 1: Temperatures of individual components, °C

T_{water}		0 min	10 min	20 min	30 min
40°C	Brain	37.234	37.518	37.8704	38.204
	Internal organ	37.228	37.404	37.7297	38.071
	Muscle	36.684	37.357	37.7597	38.082
43°C	Brain	37.234	37.694	38.2664	38.809
	Internal Organ	37.228	37.511	38.0423	38.598
	Muscle	36.684	37.78	38.4348	38.951
46°C	Brain	37.234	37.862	38.6567	39.410
	Internal organ	37.228	37.611	38.3485	39.119
	Muscle	37.484	38.198	39.1055	39.832

SUMMARY

In this study, a whole body heat transfer model is developed to simulate temperature rises in individual body components when the body is soaking in hot water. The Pennes equation is coupled with an energy balance equation to determine both the temperature field of the body and the arterial temperature rises during the soaking. The recommended hot tub water of 40°C by manufactures is safe when the soaking time is less than 30 minutes. However, the soaking time should be limited to 25 minutes or 15 minutes when the hot water is 43°C or 46°C, respectively. Actively stirring the water in hot tubs would lead to shortening of the predicted soaking time, especially in adults with cardiac conditions.

ACKNOWLEDGEMENTS

This research was supported by an NSF research grant (CBET-1705538).

REFERENCES

[1] Bartlett and Braun, *Am. J. Phys.*, 51(2):127-132.
[2] Pennes, *Journal of Applied Physiology*, 1:93–122, 1948.
[3] Zhu et al., *Advances in Numerical Heat Transfer*, 3:97-219, 2009.
[4] Lebrun et al., *Journal of Thermal Biology*, 62:129-137, 2016.
[5] Paul et al., *Numerical Heat Transfer*, 68(6):598-618, 2015.

SB³C2019
Summer Biomechanics, Bioengineering and Biotransport Conference
June 25 -28, Seven Springs, PA, USA

CREATING A DISTINCT CAPTURE ZONE IN MICROFLUIDIC FLOW GREATLY ENHANCES THE THROUGHPUT AND EFFICIENCY OF CANCER DETECTION

Jiangsheng Xu[1,2], Xiaoming He[1,2*]

(1) Department of Biomedical Engineering,
The Ohio State University,
Columbus, OH, USA

(2) Fischell Department of Bioengineering,
University of Maryland
College Park, MD, UAS

INTRODUCTION

Cancer is a major public health problem worldwide and is the second leading cause of death in the United States. In 2018, 1,735,350 new cancer cases and 609,640 cancer deaths are estimated by the American Cancer Society [1]. Cancer progression ends in metastasis in critical organ such as the lungs, liver, bone and brain, which is the major cause of cancer death [2]. Therefore, early detection of the disease may result in the disparities in cancer survival if timely treatment is conducted. One of the major steps that cancer cells undertake to establish the metastatic tumor is that the primary cancer cells invade the surrounding parenchyma and intravasate into blood to circulate and spread [3]. These rare circulating tumor cells (CTCs) are considered to be a valuable target for early detection and characterization of cancers [4].

We developed a microfluidic device with distinct capture and flow zones (ZonesChip) for highly efficient antibody-based capture of CTCs from human blood. The cells are moved from the flow zone into the capture zone by applying an external force (dielectropheresis or DEP force in this study). The flow speed in the capture zone is low, which not only facilitates the binding between CTCs and antibody on the microposts, but also reduces the possibility of the captured cells being washed away by the flow-induced force. Our results indicate that at high flow speed, this separation of the flow and capture zones can improve the efficiency of capturing spiked cancer cells from <1.5% to ~100% for devices without engineered flow and capture zones. In these devices, the injected cells stay dominantly in the flow zone, limiting their likelihood of being captured.

METHODS

Fabrication of microfluidic device. Photoresist SU-8 2025 (MicroChem, Westborough, MA, USA) was spin-coated on the surface of a 4-inch silicon wafer with a thickness of 100 μm. PDMS (Dow Corning, Midland, MI, United States) pre-polymer and its crosslinking agent were poured over the photoresist mold, and cured at 72 °C for 3 h. Then, the PDMS surface modification with antibody was performed according to a previously reported method with slight modification.[5]

Experimental setup. As show in Fig. 1a, inlet 1 was connected to a syringe filled with DEP buffer (10% (w/v) sucrose and 0.3% (w/v) glucose in deionized water). Cells suspended in DEP buffer were introduced into the device via inlet 2 and collected from the outlet. The diameter of the microposts was 100 μm, and the gap between two adjacent microposts was 50 μm. The height of the channel was 100 μm. Electrodes 1 and 2, made of copper (Pololu, Las Vegas, NV United States), were inserted into the space between the sidewall and the microposts immediately next to the sidewall in the main channel on both sides of the device, for applying the patterned electric voltage on the device. The microcontroller was programmed to turn the switch on (for 3 s) and off (for 3, 3, 1, 0.5, 0.25 s when the flow rate was 0.1, 0.5, 1, 2, and 4 mL/hr, respectively).

RESULTS

Design of the ZonesChip with distinct capture and flow zones. The ZonesChip microfluidic device system (Fig. 1a) consists of two major components: (1) parallel patterned microposts modified with anti-EpCAM antibody for capturing the CTCs, and (2) electrodes placed against the inner sidewalls of the channel for generating DEP force that can move the cells and increase the cell-micropost contact frequency. More importantly, by taking advantage of the parallel design of the microposts (Fig. 1b), two distinct zones can be created in the main channel: (1) a capture zone (green in Fig. 1b) with low flow speed (< 0.2 mm/s, see Fig. 1c) for capturing cancer cells, and (2) a flow zone (yellow in Fig. 1b) with high flow speed (> 0.2 mm/s) (see Fig. 1c) for samples to flow through the microfluidic device. And cells will experience a positive DEP force, and be driven from the flow zone with low electric field towards the capture zone with strong electric field

Poster Presentation #P154

(Fig. 1d). In a device without antibody modification, nearly all cells move in the flow zone in the absence of an electric field (i.e., switch off, Fig. 1e, left). When the switch is on, and an electric voltage (V_p = 200 V) is applied on the device (i.e., switch on), nearly all the cells are moved by the DEP force into the capture zone from the flow zone, and contact with the microposts (Fig. 1e, middle). When the switch is off again and the voltage is removed, nearly all the cells are dragged away from the capture zones and move back into the flow zones (Fig. 1e, right).

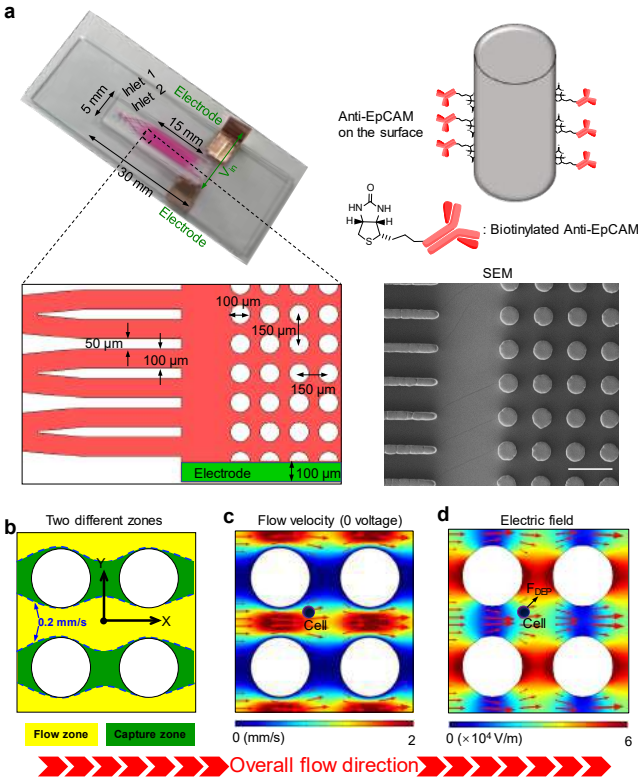

Figure 1: Microfluidic device with distinct capture and flow zones.

As shown in Fig. 3a, the captured PC-3 cells are all in the capture zone, and most of them are in the middle of the capture zone. This further confirms the aforementioned force and cell movement analyses. Typical high-magnification light and scanning electron microscopy (SEM) images of a captured PC-3 cell are shown in Fig. 3a and b, respectively. The capture efficiency of PC-3 cells spiked into the DEP medium is further quantified under various conditions to assess the importance of separating the capture and flow zones. As shown in Fig. 3c, with both DEP and surface modification with antibody, the capture efficiency reached ~100% at all the flow rates of 0.1, 0.5, and 1 mL/hr. Additionally, the capture efficiency of PC-3 cells spiked in DEP medium with both DEP and antibody modification at various flow rates (0.5-4 mL/hr) is shown in Fig. 3d. At the flow rate of 1 mL/hr, the capture efficiency can reach 98.1%, as the flow rate increases from 1 to 4 mL/hr, the capture efficiency decreases. To further test the universality of the ZonesChip for capturing EpCAM+ cancer cells, six types of cancer cells with positive EpCAM expression (PC-3, HCT-116, SK-MES-1, OVCAR-3, MCF-7, and CAPAN-2 cells) spiked in WBC suspensions (5×10^6 WBCs /mL) are studied and the data are shown in Fig. 3e. For all the cancer cells, the capture efficiency can reach more than 91%, suggesting this device works efficiently for all the EpCAM+ cancer cells. Furthermore, the capture of PC-3 cells spiked at various numbers in WBC suspensions is conducted, and the capture efficiency can be ~92% (i.e., the slope of the fitting line in Fig. 3f) on average when the spiked cell number is over a range of 2 to 1300 cells per mL (Fig. 3f). This data suggest this device has the capacity to work effectively over a large concentration range of cancer cells in blood samples.

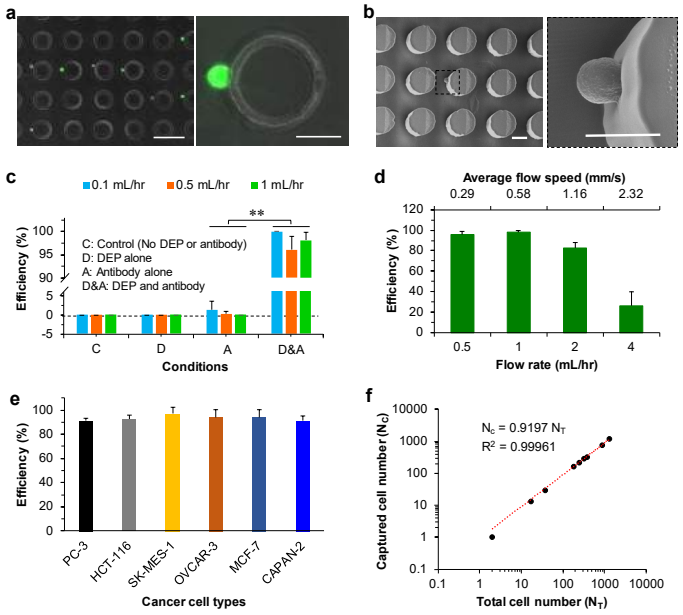

Figure 2: Capture of cancer cells spiked in medium.

DISCUSSION

we developed an antibody-based microfluidic approach for CTC detection with distinct capture and flow zones to greatly enhance the throughput with high detection efficiency. This is achieved by minimizing the flow speed and thus flow-induced force in the capture zone even at flow speeds that are ~4 times higher than that commonly used in the literature, and by using DEP force to move cells from the flow zone into the capture zone. This idea of separating the flow zone from the capture zone has an immense potential to enhance microfluidics-based disease detection.

ACKNOWLEDGEMENTS

This work was partially supported by grants from American Cancer Society (ACS #120936-RSG-11-109-01-CDD) and NIH (R01CA206366) to X.H., and a Pelotonia post-doctoral Fellowship to J.X.

REFERENCES

[1] Cristofanilli, M. et al., *N Engl J of Med,* **351:**781-791, 2004.
[2] Plaks, V., et al., *Science,* **341**:1186-1188, 2013.
[3] Sasportas, et al., *PLoS One,* **9:**105079-105090, 2014.
[4] Rawal, S., et al.,. *Annu Rev Anal Chem* **10**:321-343, 2017.
[5] Shim, S. et al.. *Biomicrofluidics* **7:**011807-011812, 2013.

FUNDAMENTAL ASPECTS OF PAPER-BASED MICROCHIP ELECTROPHORESIS – pH GRADIENT

M. N.Hasan (1), R. An (1), A. Akkus (1), D. Akkaynak (2), A. Minerick (3), U. A. Gurkan (1,4,5)

(1) Mechanical and Aerospace Engineering Department
Case Western Reserve University
Cleveland, OH, USA

(2) Department of Ecology & Evolutionary Biology
Princeton University
Princeton, NJ, USA

(1) Department of Chemical Engineering
Michigan Technological University
Houghton, MI, USA

(4) Biomedical Engineering Department
Case Western Reserve University
Cleveland, OH, USA

(5) Orthopedics Department
Case Western Reserve University
Cleveland, OH, USA

INTRODUCTION

Microchip electrophoresis provides a compact, rapid, and streamlined means for complete diagnostic workflow for disease detection, which is the essence of any point-of-care (POC) technology [1]. Capillary electrophoresis (CE) based microchips have been widely implemented for various analytical applications. We previously presented the first mass-producible, paper-based microchip electrophoresis (HemeChip) platform (Fig. 1) [2-4]. HemeChip is a point-of-care technology that uses a strip of cellulose acetate (CA) as the separation medium for the electrophoretic separation process. It performs electrophoretic separation of hemoglobins in whole blood and can detect, identify, and quantify the hemoglobin types present in a blood sample. In traditional microchip systems, extensive studies have been performed on system electrochemical behaviors such as ion migration, electrochemical reaction and pH change. However, this information is missing for paper-based microchip systems since they are mostly based on passive capillary flow or pressure driven flow instead of electric or electrochemical driving forces. This knowledge discrepancy may affect diagnosis accuracy and precision for paper-based microchip electrophoresis system, such as HemeChip. Because, hemoglobin separation in CA electrophoresis takes place based on charge to mass ratio, which can be affected by the pH. In this work, we present a method to investigate dynamic pH variation and gradient within paper-based microchips. A new electrophoresis buffer was developed to manifest run-time pH change based on colorimetric analysis (Fig. 2). Using an image analysis technique, spatial and temporal change in pH was quantified in CA electrophoresis. The dynamic change in pH was quantified (Fig. 3) using calibrated digital time-lapse imaging.

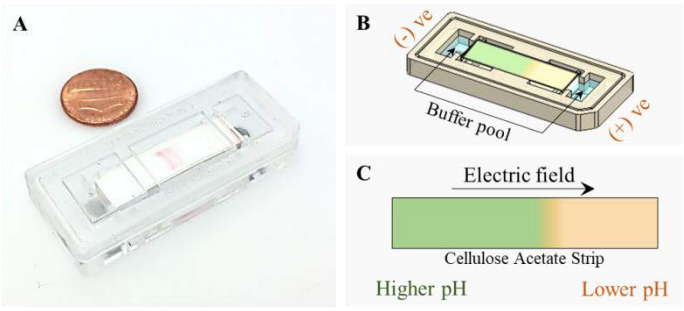

Figure 1: HemeChip pH measurement: (A) HemeChip cartridge with separated hemoglobin bands. **(B)** Overview of run-time pH gradient during the electrophoresis process. **(C)** A representative illustration of the pH gradient along the CA paper after the HemeChip test is completed.

METHODS

The design and development of HemeChip technology as well as the HemeChip test process has been described previously [2, 3]. The HemeChip cartridge contains a strip of CA paper, which acts as the separation medium. For a standard HemeChip test, 10x concentrated

TBE (Tris/Borate/EDTA) buffer is diluted to 1x, pH 8.4, using ultrapure water. In this presented method of pH measurement, a modified TBE buffer solution was developed. The modified buffer is the 10x concentrated TBE buffer diluted to 1x buffer, using a 50:50 mixture of ultrapure water and pH-indicator solution (pH 4-10).

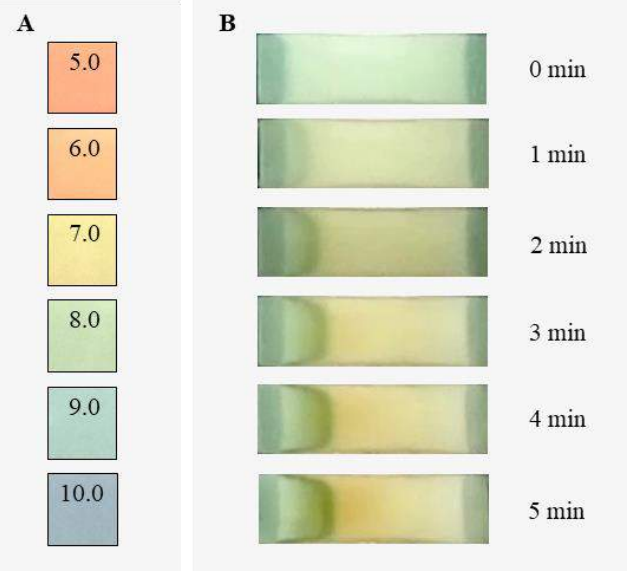

Figure 2: pH gradient across the CA paper strip during electrophoresis process. (A) A custom color map developed for the dynamic pH change tracking for the electrophoresis process. **(B)** A time lapse of the HemeChip test with the modified pH buffer. Time lapse shows the change in pH and its distribution across the CA strip.

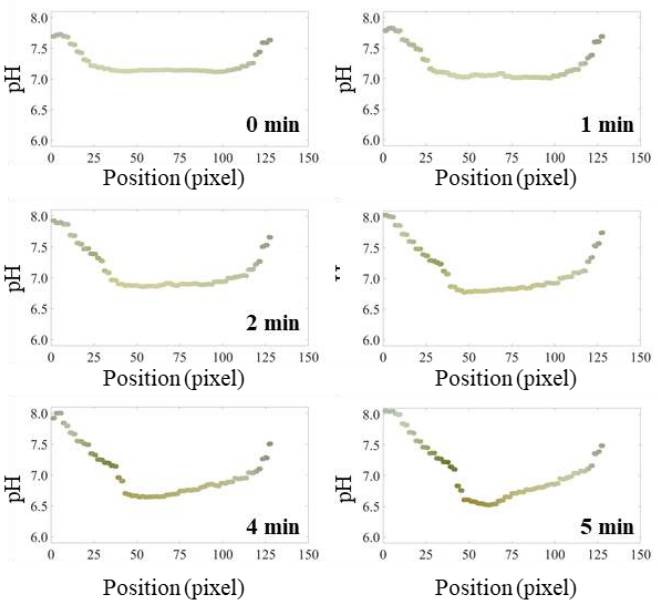

Figure 3: Dynamic pH tracking along the length of the CA paper. The figure shows the change in pH along the length of the CA paper at different times during an electrophoresis test.

For the dynamic measurement of pH, the CA paper strip is soaked and the buffer pools are filled with the modified buffer and a HemeChip test is run (without blood sample) following the standard test protocol [3]. The process is imaged using a Raspberry Pi 3B+ unit. A custom developed color map has been developed (Fig. 2A) using standard pH solutions in CA paper (pH: 5 - 11). The captured images (Fig. 2B) are later analyzed compared with the color map to quantify the dynamic pH change (Fig. 3).

RESULTS

The pH gradient in the CA paper can be obtained by fitting color change data into a customized pH-calibration curve. During the HemeChip electrophoresis process, electric potential was applied and color change, thus the pH gradient was observed. Through color calibrated time-lapse imaging, the change in average hue due to pH change was captured, and was converted into pH value (Fig. 3) based on the pH color dictionary that was derived using the same color calibration procedure (Fig 2A). Figure 2B shows a gradient of pH from both ends towards mid-section of the CA paper strip, which changes over time as the electrophoresis process is run. Figure 3 shows the pH across the CA paper strip in 0-5 minutes. As the time passes, the pH near the cathode end (left) of the CA increase, while the pH at anode end (right) does not change noticeably (Fig. 1C&3), while the pH at the mid-section of the CA paper shifts into acidic range (pH: 6.5).

DISCUSSION

We presented a dynamic pH change tracking method for measuring pH change within CA paper-based microchip electrophoresis system. Through color calibrated digital images, we quantified pH change within the separation medium and found it to be in the range of 6.5-8 (Fig. 3). This result suggests that instead of a uniform and constant pH value at 8.4 (TBE buffer), a pH gradient emerges and persists during electrophoresis process within CA paper. This pH gradient may lead to a hemoglobin charge to mass ratio variation during the separation process, which may lead to hemoglobin mobility affected temporally and spatially. This may affect separation efficiency, band resolution, and hence may impact detection accuracy. Future work will focus on minimizing pH gradient in CA electrophoresis through strategies, including electrode modification to control electrochemical reactions, and modification of the separation medium.

ACKNOWLEDGEMENTS

Development of this technology has been supported by National Institutes of Health Fogarty International Center (R21TW010610), and National Heart Lung and Blood Institute Small Business Innovation Research Program (R44HL140739). This article's contents are solely the responsibility of the authors and do not necessarily represent the official views of the National Institutes of Health.

COMPETING INTERESTS

MNH, JAL, and UAG are inventors of intellectual property (HemeChip technology) licensed by Hemex Health Inc. for commercialization. These inventors have financial interest in Hemex Health Inc., including licensed intellectual property, stock ownership, and consulting. Competing interests of Case Western Reserve University employees are overseen and managed by the Conflict of Interests Committee according to a Conflict of Interest Management Plan.

REFERENCES

[1] Wuethrich, A et al., Anal Chim Acta. 1045: p. 42-66, 2019.
[2] Hasan, M N et al. *2017 IEEE Healthcare Innovations and Point of Care Technologies (HI-POCT)*, 2017.
[3] Hasan, M N et al., Blood. 130(Suppl 1): p. 3519, 2017.
[4] Hasan, M N et al., Blood. 132(Suppl 1): p. 1095, 2018.

SB³C2019
Summer Biomechanics, Bioengineering and Biotransport Conference
June 25 -28, Seven Springs, PA, USA

ROBUSTNESS OF CONVOLUTIONAL NEURAL NETWORKS FOR MALARIA PARASITE IDENTIFICATION IN THIN BLOOD SMEAR IMAGES WITH ADVERSARIAL IMAGE NOISE

Bill Sun (1) and Liang Liang (2)

(1) Walton High School
Marietta, Georgia, United States

(2) Department of Computer Science
University of Miami
Coral Gables, Florida, United States

INTRODUCTION

Malaria is a serious and sometimes fatal disease caused by a single-celled protozoan parasite in the *Plasmodium genus*, the most lethal of which is *P. falciparum*. The most common biological vector for the parasite is the female Anopheles mosquito. As the malaria parasites infect the red blood cells (RBCs), through blood transfusions, organ transplants, or contaminated needles, the disease can be spread from person to person. Thus, the prompt detection of malaria is essential for a patient to receive timely treatment and for preventive measures to be implemented to prevent further spread of infection from mosquitoes.

Two commonly used mechanisms of detecting malaria include rapid diagnostic tests (RDT), in which test kits are able to detect the presence of malarial antigens, and "blood smears," where a drop of a patient's blood is spread out on a microscope slide. This technique of microscopic diagnosis remains the gold standard for laboratory confirmation of malaria. However, the results depend on the quality of the staining reagents, the resolution and magnification of the microscope, and the experience of the laboratorian, all of which can be lacking tropical and sub-tropical regions where malaria is the most prevalent.

Convolutional neural networks (CNNs) are a type of deep neural networks that have achieved excellent performance in the field of computer vision. Studies have demonstrated that CNNs can be effectively used for malaria parasite identification. In particular, Rajaraman, *et al.* 2018[1] investigated the accuracy of six pre-trained CNNs, for example accuracy of 95.7% from the ResNet-50 was obtained, and developed a customized CNN which achieved an accuracy of 94.0%. These excellent results demonstrate the strong potential of CNNs for the clinical applications. Compared to the pre-trained CNNs, the customized CNN has a much smaller size, suitable to be used in mobile devices.

However, studies have shown that CNNs are not robust to small input perturbations, known as adversarial attacks[2], which work effectively on the images of a wide range of objects such as handwritten digits, animals, human faces, vehicles, and even traffic signs. A recent study[3] shows that adversarial attacks can cause many state-of-art CNNs to make wrong classifications of medical images: by adding small perturbation to the input image, the output of a CNN could flip from the correct classification to a wrong one. Medical images often contain noises[4] or artifacts[5] from imaging process. Such noises and artifacts can be considered as perturbations on clean images, which could also cause CNNs to output wrong results. Until today, there does not exist a general solution to this robustness problem.

The objective of this study is to investigate and improve CNN robustness for the application of malaria parasite identification. We choose the customized CNN from the work of Rajaraman, *et al* [1] as the base model, and new CNN models are derived from it by changing the structure and/or adding a constraint to the loss function. To add perturbations to images, the Fast Gradient Sign Attack (FGSA)[6] algorithm was used. The experiments show that the new CNN models are very robust to FGSA perturbations, whereas the base model suffers significantly from the perturbations.

METHODS

In this study, we utilized the public dataset provided by Rajaraman, *et al.* 2018 of the NIH[1]. The dataset consisted of Giemsa-stained thin blood smear slides from 150 de-identified *P. falciparum*-infected and 50 de-identified healthy patients. In total, there were 27,558 cell images with equal numbers of parasitized and uninfected cells. To evaluate the base and new models, the images were split randomly into a training set and a testing set at the patient level. The training set contains infected and uninfected images from 160 patients; the testing set contains the remaining images. Pixel values were normalized in the range of 0 to 1.

Poster Presentation #P156

Data argumentation using random image rotation was applied to increase the amount of training data, reducing overfitting.

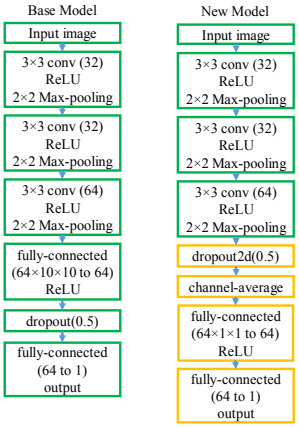

Figure 1. The base and new CNN models

Fig.1 shows the structures of the base and new CNN models. The new model includes a sigmoid output layer, a 2D-dropout[7] layer, and a channel-average layer which computes the average value of each feature channel. In additional to the binary cross entropy (BCE) loss, another loss term is added as a constraint on the magnitude of the derivative of BCE loss with respect to the input image[8].

RESULTS

We performed evaluations on: the base model (CNN-B), base-model with the constraint (CNN-BC), the new model (CNN-N), and the new model with the constraint[8] (CNN-NC). Fig. 2 shows the accuracies of the models on the testing set during the training epochs. The models were implemented using Pytorch. At the end of each epoch, FGSA perturbation noises (parameter ε=0.01) were added to the testing images, and the accuracies were re-evaluated on the noisy data, shown in Fig. 3. Some examples are shown in Fig. 4. (More examples will be shown during the conference)

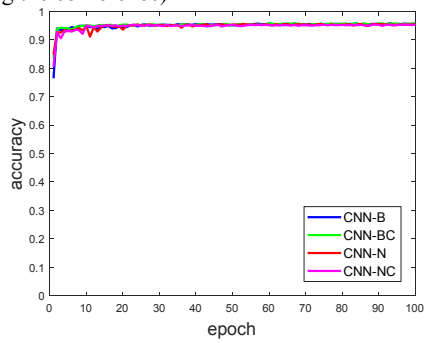

Figure 2: Accuracy vs Epoch for the CNNs on original data

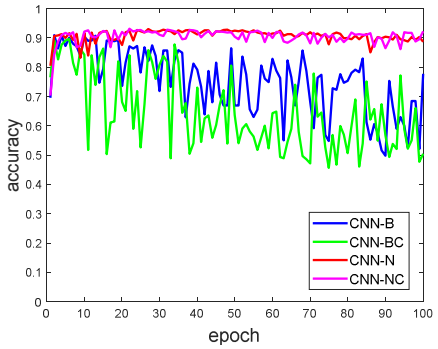

Figure 3: Accuracy vs Epoch for the CNNs on noisy data

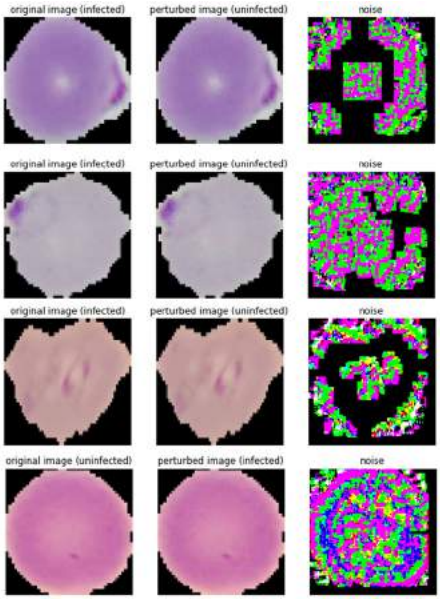

Figure 4: left panel: original images (CNN output), middle panel: noisy images (CNN output), and right panel: noise distribution.

DISCUSSIONS

The results show that all models have similar accuracies on the original testing data. But, the base model is not robust to noisy data, which suggests that it may not be safe to use it in clinical applications. The constraint[8] was not very helpful for improving the robustness of the base model. The new model shows high robustness even without the constraint, which is attributed to the channel-average layer: averaging will remove noise. It may be noticed that the accuracy of the base model on the noisy data is relatively high during the early training stage, and then it decreased and oscillated, which may suggest overfitting. Thus, early stopping could be a simple strategy to maintain robustness. However, in practice, it is difficult to set up a criterion to determine at which epoch the training process should stop.

In our future work, we will explore more new structures and learning strategies. We will test the models against imaging noises, image artifacts, and all of the adversarial attack algorithms in the literature. We believe the robustness issue will be eventually resolved.

REFERENCES

[1] Rajaraman S, Antani SK, Poostchi M, Silamut K, Hossain MA, Maude RJ, Jaeger S, Thoma GR: Pre-trained convolutional neural networks as feature extractors toward improved malaria parasite detection in thin blood smear images. PeerJ 2018, 6:e4568.

[2] Akhtar N, Mian A: Threat of Adversarial Attacks on Deep Learning in Computer Vision: A Survey. IEEE Access 2018, 6:14410-30.

[3] Finlayson SG, Chung HW, Kohane IS, Beam AL: Adversarial Attacks Against Medical Deep Learning Systems. arXiv:180405296 2018.

[4] Gravel P, Beaudoin G, Guise JAD: A method for modeling noise in medical images. IEEE Transactions on Medical Imaging 2004, 23:1221-32.

[5] Barrett JF, Keat N: Artifacts in CT: Recognition and Avoidance. RadioGraphics 2004, 24:1679-91.

[6] Goodfellow IJ, Shlens J, Szegedy C: Explaining and Harnessing Adversarial Examples. arXiv:14126572 2014.

[7] Tompson J, Goroshin R, Jain A, LeCun Y, Bregler C: Efficient object localization using Convolutional Networks. 2015. pp. 648-56.

[8] Ross AS, Doshi-Velez F: Improving the Adversarial Robustness and Interpretability of Deep Neural Networks by Regularizing their Input Gradients. AAAI Conference on Artificial Intelligence 2018.

SB³C2019
Summer Biomechanics, Bioengineering and Biotransport Conference
June 25 -28, Seven Springs, PA, USA

TOWARDS PATIENT SPECIFIC VASCULAR NAVIGATION OF THERAPEUTICS

Luke Puller (1), Matthew Charles (1), Darien Perez (1), Scott Anderson (1), Anilchandra Attaluri, Ph.D.

(1) Mechanical Engineering
Pennsylvania State University
Harrisburg, Pennsylvania, USA

INTRODUCTION

Hepatocellular Carcinoma (HCC) has a 5-year survival rate of 11%. It is the 5th most common cause of cancer related death in men and the 8th in women [1]. Despite significant advances during the past two decades, high rates of tumor recurrence and disease progression following treatment of locally advanced liver cancer remain unresolved issues, urging the need for development of novel approaches. Transarterial Chemoembolization (TACE) exploits the preferential hepatic arterial blood supply of liver tumors to selectively deliver high concentrations of drugs via the intraarterial route [2,3,4]. Use of gradient magnetic fields and magnetic drug carriers (MDC) for TACE is a promising approach to improve drug targeting to the tumor and reduce systemic toxicity [2,3,4]. Previous approaches included a simple placement of an external magnet over the tumor location [2] and using an expensive MRI for vascular navigation of the MDC [3,4]. Herein we propose an external electromagnet to steer the MDC at the bifurcation using the patient images to create a robust, low-cost patient specific magnetic navigation system (Figure 1).

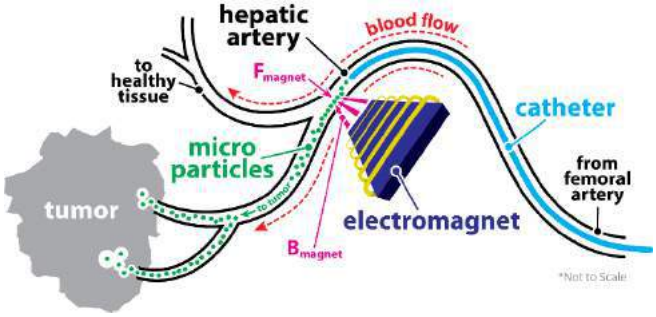

Figure 1: Illustration of using an electromagnet to direct microparticles through the hepatic artery.

This study investigated the possibilities of using an external magnet to navigate MDC to cancerous tissue in the liver. Using patient image-based vascular models, an optimum route for the drugs could be determined which would reduce systemic toxicity. Magnetic steering of the drugs requires drug-loaded magnetic microspheres and a device to generate a gradient magnetic field. To test these theories, a patient image-based computational fluid modeling approach was used in this study in addition to a simplified physical model to compare the results.

METHODS

Simulation: The first step in making this a patient specific treatment was to obtain an image of the hepatic artery and make it compatible with commercially available finite element simulation software. Once in the simulation software we were able to run flow simulations and input a concentration of particles into the flow. Pressure values were found from literature that could be inputted into the simulation to then calculate flow velocities. Below is a flow chart of these steps (Figure 2).

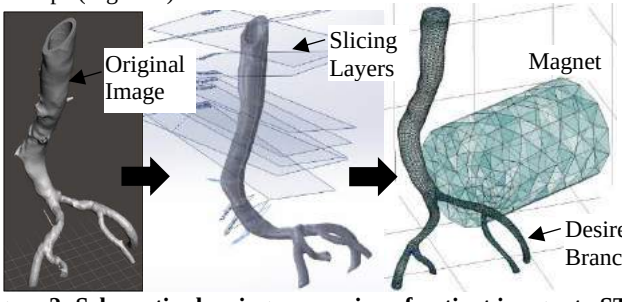

Figure 2: Schematic showing conversion of patient images to STL file and final geometry imported to simulation software.

Poster Presentation #P157

We could then observe the effect of and applied magnetic field on the flow of magnetically sensitive particles. Due to the image having multiple flow pathways, we were able to determine the ideal distance of the magnet from the artery to direct most of the particles down the desired branch.

The modeling variables were determined using average pressure values at the inlet of the hepatic artery from literature and then calculating outlet pressures for each of the exit points using Poiseuille's Law:

$$Q = \frac{\pi \Delta P r^4}{8 \eta L} \quad (1)$$

Experiment: A physical flow model was made using a 3D printed bifurcation. This allowed us to get a general idea of how a magnet effects the flow of particles. It also helped us to determine inputs for our simulation model. Magnetic microspheres (12-00-304, Micromod, Rostock, Germany) were injected into a closed-loop circulating water network exposed to a magnetic field gradient at the bifurcation using an N52 neodymium permanent magnet (127 lb pulling force, 1.46 T magnetic flux density). The magnet was positioned at different intervals throughout the study. An open-source pixel counting software (ImageJ) was used to analyze images of the particles. The efficiency was found using these pixel counts from before and after the bifurcation.

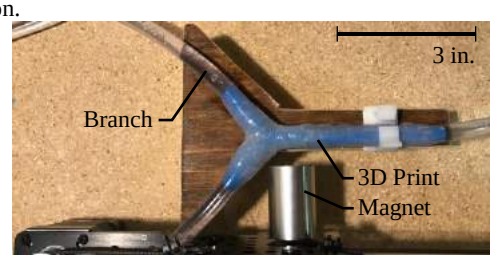

Figure 3: A 3D-printed test piece and flow loop used to compare with our simulation results.

RESULTS

Simulation: Figure 3 below shows the results from the patient image-based model simulation. The highest efficiency (~72%) of directing particles into the desired branch was found at a magnetic flux density of 248 mT. Higher magnetic flux lead to an agglomeration of the particles to the vessel walls. The microparticles agglomerated to the walls of the model when subjected to a greater flux density, resulting in a lower efficiency. Due to the small strength of the magnet used, the position had to be very close (10 mm) to the bifurcation to direct the microparticles.

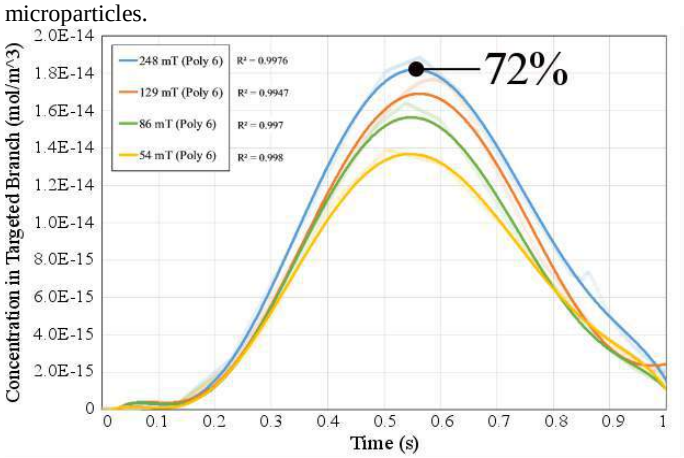

Figure 4: Plot shows the concentration of MDC's entering and leaving the target artery as a function of particle injection time.

Experiment: The experimental model was limited to a single 3D-printed bifurcation. The results from the experiments showed that a 248 mT flux density provided an efficiency of 78%, and the agglomeration on the walls of the vessel at higher flux densities was seen in this model as well as in the simulation.

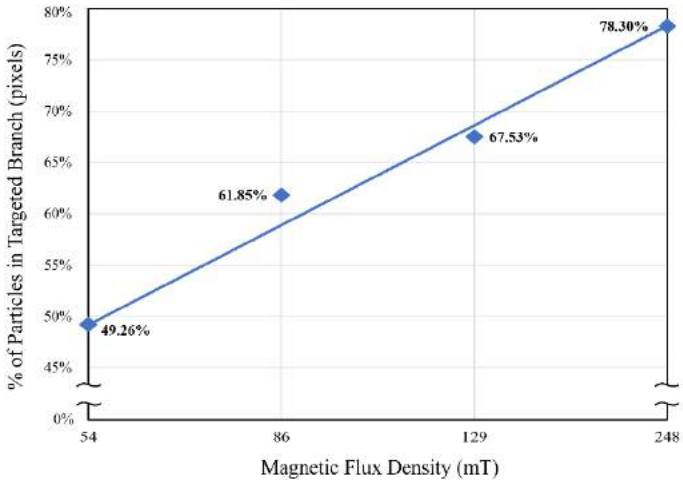

Figure 5: Concentration of particles in the upper branch of the bifurcation (physical model).

DISCUSSION

The magnet was positioned at different intervals throughout the study to hone the steering of the microspheres into one branch of a bifurcation, while avoiding agglomeration near the walls of the vessel. Results show that there is a dependence on the magnetic field strength and geometrical characteristics as the effective magnetic force on the concentration of particles is sensitive to the governing magnetostatic equations. The steering efficiency of the concentration is therefore dependent on the magnet being used and an optimized position of a static magnetic field is to be found in the future as well as the introduction of an electromagnet.

Future studies should introduce an electromagnet in place of the permanent magnet, then design an electromagnet magnet with a larger spatial gradient to accommodate larger distances of operation. Another means of improvement would be to allow for movement of the magnet to 'follow' the particles and allow for more precise targeting.

ACKNOWLEDGEMENTS

We would like to thank Dr. Brian Maicke, Dr. Ma'Moun Abu-Ayyad, Mitch Spear, and Dr. Christopher Melani at the National Cancer Institute for their unwavering support.

REFERENCES

[1] American Cancer Society. *Liver Cancer: Statistics*. 2018.
[2] Kobeiter H, Georgiades CS, Leakakos T, Torbenson M, Hong K, Geschwind JF. *Anticancer Research*. 27:755-760, 2007.
[3] Pouponneau P, Leroux JC, Martel S. *Biomaterials*. 30:6327-6332, 2009.
[4] Pouponneau P, Leroux JC, Soulez G, Gaboury L, Martel S. *Biomaterials*. 32:3481-3486, 2011.

SB^{3}C2019
Summer Biomechanics, Bioengineering and Biotransport Conference
June 25 -28, Seven Springs, PA, USA

THEORETICAL EVALUATION OF TEMPERATURE ELEVATION, THERMAL DAMAGE, TRANSPORT POROSITY ENHANCEMENT, AND MAGNETIC NANOPARTICLE MIGRATION IN TUMORS DURING LOCAL HEATING

Manpreet Singh, Ronghui Ma, Liang Zhu

Department of Mechanical Engineering
University of Maryland Baltimore County
Baltimore, Maryland, USA

INTRODUCTION

Recent microCT imaging study[1] has demonstrated different patterns of nanoparticle distribution by local heating. A much larger nanoparticle distribution volume in tumors after heating was observed than that in tumors without localized heating, suggesting possible nanoparticle redistribution/migration during heating. It is unclear what kinds of mechanisms resulted in the nanoparticle migration from high concentration region to low concentration region. It has been speculated that an increase in nanoparticle diffusion coefficient may play an important role here. It is possible that the intracellular solution is released from the dead cells after cell membrane raptures. The relationship between diffusion coefficient and porosity of tumors suggest a 3.5 fold increase in nanoparticle diffusion coefficient if the porosity is elevated from 20% to 60%.

In this study, we develop a 1-D model to evaluate to what extent the enhanced nanoparticle diffusion coefficient leads to an increase in the nanoparticle distribution volume in tumors after local heating. The Pennes bioheat equation is used to simulate temperature elevations in a tumor with magnetic nanoparticle deposition, when it is subject to an alternating magnetic field. The blood perfusion rate and metabolism in tumors, and local tumor porosity are coupled with local thermal damage using the Arrhenius integral. Finally, the diffusion equation is implemented to simulate possible spreading of nanoparticle, providing a dynamic volumetric heat generation rate distribution in the heat transfer simulation. Results from the 1-D model may be extended to 3-D situations of nanoparticle redistribution in magnetic nanoparticle hyperthermia based on realistic microCT scans of tumors.

METHODS

A spherical tumor (10 mm in radius, initial porosity φ_0=0.2) is proposed for this study. The tumor is exposed to a convection environment (h=10 W/m^{2}K, T_{air}=25°C), and magnetic nanoparticles originally injected occupy a smaller spherical region (4 mm in radius) at the tumor center. The volumetric heat generation rate distribution Q'''_{MNH} was initially uniformly distributed in the small spherical region as 1.38*10^6 W/m^3. The Pennes bioheat equation[2] in 1-D spherical coordinates used to simulate the transient temperature field during magnetic nanoparticle hyperthermia:

$$\rho c\frac{\partial T}{\partial t}=\frac{k}{r^2}\frac{\partial}{\partial r}\left(r^2\frac{\partial T}{\partial r}\right)+\frac{\omega_0}{e^{\Omega}}\rho_b c_b(37-T)+\frac{Q'''_{m,0}}{e^{\Omega}}+Q'''_{MNH} \quad (1)$$

All the thermal properties in Eq. 1 such as density ρ (1000 kg/m^3), specific heat c (3500 J/kgK), thermal conductivity k (0.64W/mK), blood perfusion rate ω_0 (0.00083 1/s) and metabolism $Q'''_{m,0}$ (2708 W/m^3) are the same as that in Lebrun et al.[3] In Eq. 1, both the blood perfusion rate and metabolism decrease as the increase in the local thermal damage, defined by the Arrhenius integral Ω:

$$\Omega(r,t)=A\int_0^t \exp\left[-E_a/R_u T(r,\tau)\right]d\tau \quad (2)$$

Q'''_{MNH} in Eq. 1 is directly proportional to the local volume-averaged nanoparticle concentration C (mol per unit volume of tissue) as:

$$Q'''_{MNH}(r,t)=2266.67*C(r,t) \quad (3)$$

Thermal damage to tissue also results in an increase in the porosity φ from its original value φ_0 as:[4]

$$\varphi(r,t)=\varphi_0+(100\%-\varphi_0)(1-e^{-\Omega(r,t)}) \quad (4)$$

The governing equation for nanoparticle diffusion is written as

$$\frac{\partial C}{\partial t}=\frac{1}{r^2}\frac{\partial}{\partial r}\left(\varphi D_n r^2\frac{\partial(C/\varphi)}{\partial r}\right) \quad (5)$$

where the diffusion coefficient D_n is a function of the interstitial space fraction (porosity) φ:[4]

$$D_n=D_{n,f}\left[2\varphi/(3-\varphi)\right] \quad (6)$$

where $D_{n,f}$ is the nanoparticle diffusion coefficient in interstitial fluid.

The initial temperature field in the tumor is assumed uniform as 37°C, and the initial nanoparticle concentration C_0 in the small sphere is 608.899 mol/m^3. Heating duration is set as 25 minutes (1500 seconds). The coupled equations (Eqs. 1-6) are solved simultaneously using COMSOL software.

RESULTS

Figure 1 shows temperature and thermal damage contours at various time instants during heating. The maximal temperature occurs at the tumor center and reaches 57°C after heating of 25 minutes. The thermal damage defined as $\Omega \geq 4$ with the dark red color. Thermal damage region occupies a sphere with a radius of 3.3 mm after 1000 seconds of heating. At the end of 1500 seconds of heating, tumor cell within a spherical region with a radius of 4.8 mm are permanently damaged.

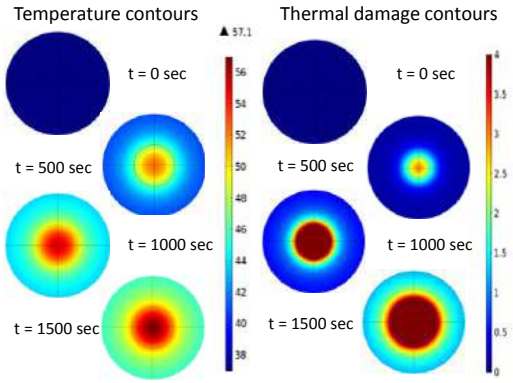

Figure 1: Temperature distribution (left) and thermal damage region (right) in the tumor during heating

The results of the spatially and temporally varying porosity and nanoparticle diffusion coefficient are updated during the heating, shown in Figure 2. Initially, the porosity is uniform everywhere as 20%, and it gradually increases as thermal damage spreads from the tumor center to its periphery. After 1000 seconds of heating, the porosity at the center increases to 93%. At the end of the heating session the porosity of most tumor region is 100%, suggesting permanent thermal damage. The change of the effective nanoparticle diffusion coefficient due to increase in porosity follows a similar trend (Figure 3) and the diffusivity at center increases from its initial value of $9.57*10^{-12}$ to $6.59*10^{-11}$ (m^2/s) after 1500 seconds of heating.

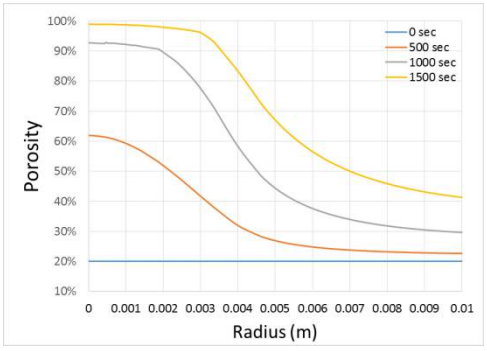

Figure 2: Tumor porosity distribution during heating

The nanoparticle distribution has been re-simulated based on the updated porosity and nanoparticle diffusion coefficient and the results are shown in Figure 4. The initial nanoparticle concentration profile is assumed as a quasi-step function. Once the thermal damage spreads towards the tumor periphery, significant nanoparticle diffusion occurs in the region with the maximum concentration gradient. As a result, it is observed that nanoparticles have diffused to the tumor periphery, expanding the tumor region containing nanoparticles from a spherical regions with a radius of 4 mm (t=0) to that with a radius of 4.7 mm at the end of the heating session. If one defines the nanoparticle distribution volume as a region containing a nanoparticle concentration ≥5% of the maximal nanoparticle concentration, a heating of 1500 seconds results in a nanoparticle distribution volume increase by approximately 62%.

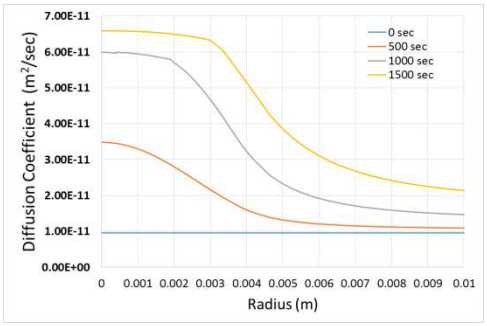

Figure 3: Distribution of the enhanced nanoparticle diffusion coefficient during heating

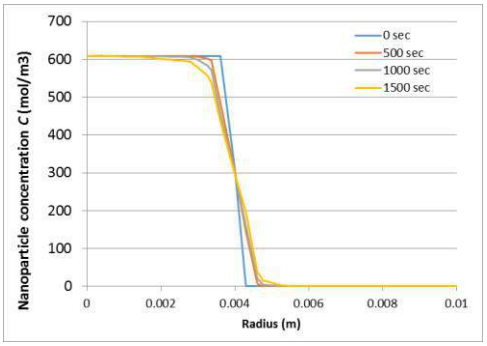

Figure 4: Nanoparticle concentration redistribution due to change in the tumor structure during heating

SUMMARY

In this study, a theoretical framework is developed, consisting of a nanoparticle diffusion model and a heat transfer model to address possible nanoparticle redistribution. Their dynamic interactions during magnetic nanoparticle hyperthermia treatment are evaluated via modified tumor porosity and diffusion diffusivity of nanoparticle concentration in porous tumors. The simulation results have shown that thermal damage induced nanoparticle redistribution has increased the tumor volume containing nanoparticles by 62%. This study demonstrates the feasibility of enhancing nanoparticle dispersion from injection sites using targeted thermal damage.

ACKNOWLEDGEMENTS

This research was supported by an NSF research grant (CBET-1705538). The research was performed in partial fulfilment of the requirements for the PhD degree by Manpreet Singh from the University of Maryland Baltimore County, Baltimore, Maryland, USA.

REFERENCES

[1] Gu et al., ASME *J Heat Transfer*, in press, 2019.
[2] Pennes, *Journal of Applied Physiology*, 1:93–122, 1948.
[3] Lebrun et al., *Journal of Thermal Biology*, 62:129-137, 2016.
[4] Zhang et al., ASME *J Heat Transfer*, 131(4):043209, 2009.

SB³C2019
Summer Biomechanics, Bioengineering and Biotransport Conference
June 25 -28, Seven Springs, PA, USA

ALOE-ALGINATE HYDROGELS FOR CERVICAL CANCER TREATMENT: ANTIOXIDANT AND DRUG RELEASE ACTIVITY

Sierra N. McConnell (1), Patrick N. Charron (2), Rachael A. Oldinski (1,2)

(1) Electrical and Biomedical Engineering
University of Vermont
Burlington, Vt, United States of America

(2) Mechanical Engineering
University of Vermont
Burlington, Vt, United States of America

INTRODUCTION

Cervical carcinoma is the second most prevalent cancer affecting women today. The human papilloma virus (HPV) is a common precursor to cervical carcinoma, and greatly increases a woman's risk of developing cervical cancer if contracted. The current state of the field relies heavily upon screening and pre-clinical testing to prevent cervical carcinoma and detect it as early as possible. When cervical cancer develops treatment is limited; patients undergo a hysterectomy followed by both local radiation and systemic chemotherapeutic treatment. Localized chemotherapeutic delivery greatly reduces adverse effects of chemotherapy and may be employed as radiation sensitizers are adjuvant therapies. For non-traditional therapy, aloe vera (*barbadensis miller*) is investigated for medicinal purposes: it is an antioxidant, beneficial for the natural vaginal biome, and promotes re-epithelization of the cervix. Alginate is studied as a drug delivery vehicle for its non-toxic cross-linking ability. The current study aims to develop an aloe/alginate hydrogel for the localized delivery of a chemotherapeutic to the cervix. It was hypothesized that the natural-based hydrogels will exhibit appropriate mechanical properties and anti-cancer biological activity based on antioxidant level [1,2, 3] and drug encapsulation and release.

METHODS

Aloe extraction

Aloe gel was harvested from aloe leaves. The gel within the aloe vera leaf was extracted by gentle scraping, then blended until homogenous using a standard blender, followed by lyophilization.

Aloe/alginate hydrogel fabrication and characterization

Three % (w/v) polymer hydrogels were formed from non-modified alginate, a 1:1 weight ratio of aloe and alginate, and a 2:1 weight ratio of aloe and alginate. The polymer solutions were placed in Teflon molds, then crosslinked using 0.5M $CaCl_2$ solution. Once formed, hydrogels were frozen at -80 ºC and lyophilized. Hydrogels were chemically characterized via Fourier-transform infrared (FTIR) spectroscopy. Rheological data was collected using an AR2000 stress-controlled rheometer (TA Instruments). An oscillatory time sweep was performed at 10 Hz and 1% stain at room temperature; storage moduli (G′) were collected after the addition of 0.5M $CaCl_2$.

Swell ratio and degradation

Two groups of aloe-alginate were prepared, ratios of 1:1 and 2:1. Cylindrical hydrogel specimens (6mm x 3 mm) were formed via $CaCl_2$ crosslinking, frozen at -80 ºC and then lyophilized. The dehydrated specimens were weighed, then placed in 500 µL of simulated vaginal fluid (SVF), consisting of: 3.51 g NaCl, 1.40 g KOH, 0.22 g $Ca(OH)_2$, 0.018 g bovine serum albumin, 2.00 g lactic acid, 1.00 g acetic acid, 0.16 g glycerol, 0.4 g urea, and 5.0 g glucose. [4] The pH was then adjusted to 4.2 using HCl. Samples were rehydrated for 24 hours at 37 ℃ in a shaker incubator. A wet weight of each sample was measured. Equilibrium water content was calculated as the percentage of wet weight divided by initial dry weight. The samples were lyophilized for 24 hours. The weight loss was calculated as the final mass subtracted from the initial mass, divided by the initial mass. To determine the polymer loss due to hydration and diffusion of non-crosslinked molecules, the mass of the dry sample after the crosslinking process was performed was measured.

Antioxidant assay

The reaction medium (7mM ABTS+ stock solution with 2.45 mM potassium persulfate (1/1, v/v)) was prepared, mixed overnight, then diluted with ethanol to an absorbance of 0.700 ± 0.05 at 734 nm. A photometric assay was conducted on 0.9 mL of ABTS+ solution and 0.1 mL of experimental samples (100 and 200 ug/mL of hydrogel eluent, i.e., SVF) and mixed for 45 seconds. The measurements were taken after 1 and 15 minutes at 734 nm. The antioxidant activity of the tested samples was determined by the decrease in absorbance at different concentrations. [2,3]

Drug encapsulation and release

A set of the 1:1 and 2:1 aloe:alginate solutions (10 mL) were mixed with 80 µL and 50 µL of 10% doxorubicin hydrochloride (DOX). The solutions were placed in molds and crosslinked. Six mm diameter hydrogel samples were suspended in 500 µL of SVF, and incubated at 37 ℃. At 2, 4, 6, 8, 12, 24 h, and daily up to 7 days, 100 µL of SVF was

removed for analysis, and replaced with 100 µL of fresh SVF to maintain the total volume. The samples were analyzed at 480 nm the values were compared to a standard curve DOX concentration was determined by using an absorbance assay and generating a standard curve. Cumulative DOX (µg) release over time was calculated by adding the mass of DOX released at each time point per mass of the hydrogel samples.

RESULTS

The aloe:alginate hydrogels retained each component after crosslinking, verified via FTIR spectra (data not shown). The hydrogel exhibited appropriate stiffness and high swelling ratios, which maintained structural integrity while releasing chemotherapeutic. In addition, the degradation products from control aloe:alginate hydrogels demonstrated high antioxidant activity compared to the alginate control.

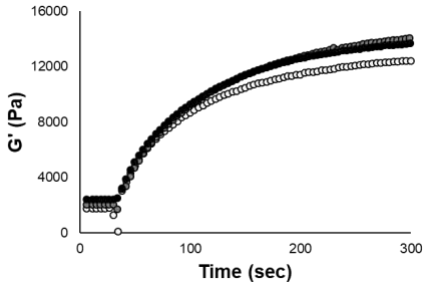

Figure 1. Storage moduli (G′) of aloe:alginate hydrogels after crosslinking with 0.5M $CaCl_2$. The hydrogels demonstrate appropriate integrity as an implantable hydrogel.

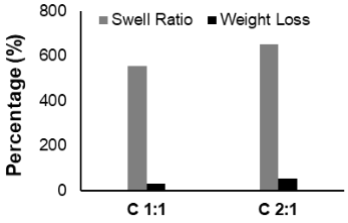

Figure 2. Swell ratio and weight loss of various weight ratios of aloe:alginate hydrogels after incubation in simulated vaginal fluid for 24 hours.

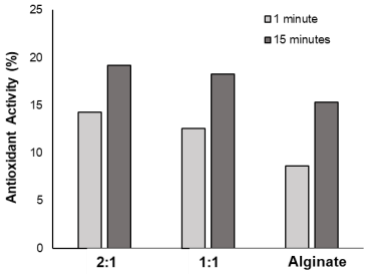

Figure 3. Antioxidant activity of various aloe:alginate hydrogel, with different weight ratios, compared to alginate controls. The assay was performed on the degradation products of the hydrogels after swelling in simulated vaginal fluid for 24 hours.

DISCUSSION

The anti-oxidant behavior of the aloe-alginate hydrogels may have applications in the treatment of cervical cancer exhibiting the ability to quench reactive oxygen species. Additionally, the gelation behavior and sustained release a chemotherapeutic are also promising for a device for localized cervical drug delivery. The hydrogel exhibited structure integrity appropriate for adhesion to the vaginal canal, and the material also swelled, lost little weight, and sustained antioxidant properties in simulated vaginal fluid. In summary, the material will allow for a new form of treatment for cervical cancer, using a sustainable plant-based product further protecting healthy cervical tissue. One limitation of this study is the cross-linking techniques of $CaCl_2$. However, there are other possibilities for crosslinking, either via pH or temperature, using various salts or chemically modified alginate. Furthermore, DOX was used in this study to reveal the kinetics of the drug release from the hydrogel, which was selected due to its solubility and detection via absorbance. This study demonstrates that aloe-vera has great potential to enhance cancer treatment and may also succeed in a multitude of applications related to women's health. For further investigation into the potential uses of the aloe:alginate drug delivery hydrogel ongoing *in vitro* study are investigating the cytotoxicity towards cervical carcinoma cells, in addition to the encapsulation of various pharmaceuticals.

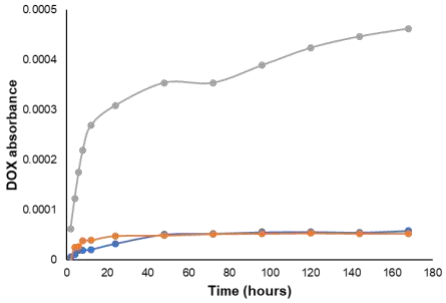

Figure 4. DOX release from aloe:alginate hydrogels. Two concentrations of DOX were encapsulated in the hydrogels, and release took place in simulated vaginal fluid at 37 ℃.

ACKNOWLEDGEMENTS

Funding for the project was provided in part by NIH Grant R01 EB020964 (Oldinski) and a Barrett Foundation Scholarship (McConnell).

REFERENCES

Each reference should include the last name of at least the first author followed by his/her initials, the journal name, volume, pages and year. You may include more detailed reference information if space allows.

1. Cano, A., et al. Arnao *Phytochemical Analysis* 9, no. 4 (July 1998): 196–202.
2. Cao, G., et al, *Free Radical Biology and Medicine* 14, no. 3 (March 1993): 303–11.
3. Amin, I. M., et al, *Science and Technology* 25, 31-40 (2017)
4. Owen, D. H., et al. *Contraception* 59, no. 2 (February 1999): 91–95.

SB³C2019
Summer Biomechanics, Bioengineering and Biotransport Conference
June 25 -28, Seven Springs, PA, USA

MODELLING LYMPH PROPULSION IN A SERIES OF PUMPING LYMPHANGIONS

G. Adeli Koudehi (1), M. Van Impe (1), C. Alejandro Silvera Delgado (1), C. Debbaut (1), C. Casteleyn (2), P. Cornillie (2), P. Segers (1)

(1) IBiTech – BioMMeda
Ghent University
Ghent, East Flanders, Belgium

(2) Department of Morphology
Ghent University
Ghent, East Flanders, Belgium

INTRODUCTION

The lymphatic system is a unidirectional vessel network maintaining the fluid balance by transporting the excess fluid from the interstitium and ultimately returning it to the venous circulation. Despite the adverse pressure gradient, lymph propulsion is possible due to the presence of the contracting collecting vessels that actively push the fluid forward and the valves which inhibit backflow. Impairment of the lymphatic transport leads to a variation of pathologies including lymphedema which is characterized by swelling of the limbs, high susceptibility to infection, and tissue fibrosis. Lack of a proper understanding about the mechanisms of fluid transport during lymphedema has in part lead to the absence of effective treatments.

Since the lymphatic system does not have a central pump, transport of lymph along the lymphatic system is mainly dependent on the synchronized contraction of the lymphangions, the small units that make up lymphatic collecting vessels. Most of the models describing the lymphatic system are either lumped or one-dimensional [1]. As far as we know, the only three-dimensional model of a lymphangion was the work of Rahbar and Moore [2] excluding the valves. The purpose of this study was to computationally model the propulsion of lymph in a series of lymphangions by means of active contraction of the lymphangions and one-way valve implementation.

METHODS

Our model describes a series of three pumping lymphangions immersed in the interstitium and was defined using COMSOL Multiphysics. The 2D axisymmetric geometry (500 µm by 3320 µm) includes 3 different domains being the inner volume of the collecting vessel (3 lymphangions each with a diameter of 100 µm and length of 1000 µm), the lymphatic vessel wall (10 µm thickness) and the interstitium (Figure 1). Lymph and interstitial fluid were modelled as a free fluid phase with a density of 997 kg/m^2 and a viscosity of 1.5 mPa·s. The lymphatic wall was considered as a linear elastic material. The valves were implemented as a porous medium, yet with a pressure dependent permeability ranging between 10^{-10} and 10^{-25} m², which prevents lymph backflow whenever the pressure gradient over a valve is negative. At the boundaries of the interstitium, a sinusoidal pressure with a magnitude of 3.5 mmHg and a frequency of 0.4 Hz was chosen [3]. At the inlet and outlet of the vessel, open boundaries with zero pressure were imposed so that the lymph propulsion would be only the result of pumping lymphangions. At the vessel wall of each lymphangion, a boundary load, with the maximum magnitude of 5 N/m^2, was applied with a contraction delay of 0.5 s between the lymphangions [4].

Poster Presentation #P160

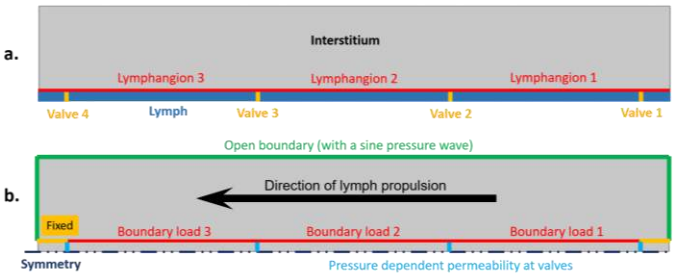

Figure 1: (a) Geometry and different domains of the model; (b) boundary conditions implemented in the model.

RESULTS

The results showed that we were able to model the simultaneous contraction along the length of the lymphangion leading to a maximum of 1.2 μm compression in radius (Figure 2c). With each contraction, the following lymphangion is initially expanded before its own contraction starts (Figure 2b). The graph of velocity magnitude in time (Figure 3) highlights the closed and open states of the valves. As each lymphangion contracts, its proximal valve closes while the distal valve stays open. Lymph velocity also proved to be very sensitive to the force applied at the vessel wall: changing the load from 5 N/m^2 to 10 N/m^2 lead to doubling of the maximal lymph velocity magnitude. Peak permeability of the valves was changed from 10^{-10} to 10^{-9} elevating both average lymph velocity magnitude and backflow. Altering the minimum permeability with a factor of 10 had no impact on the results.

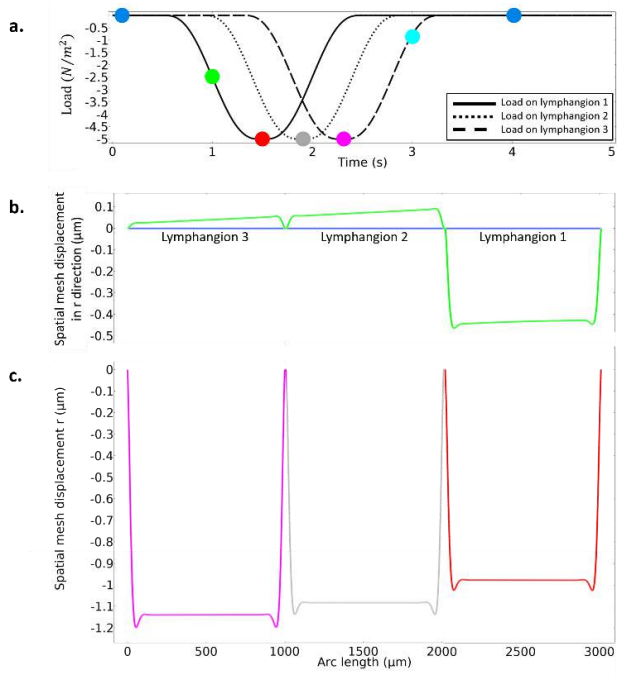

Figure 2: Panel (a) presents the load applied as a boundary load at each lymphangion wall; (b) shows the spatial deformation of the vessel wall for two time points of 0 s (blue) and 1 s (green); (c) compares the deformation of the 3 lymphangions at different time points of 1.5 s (red), 1.9 s (grey), and 2.3 s (purple) when they have their maximum deformation.

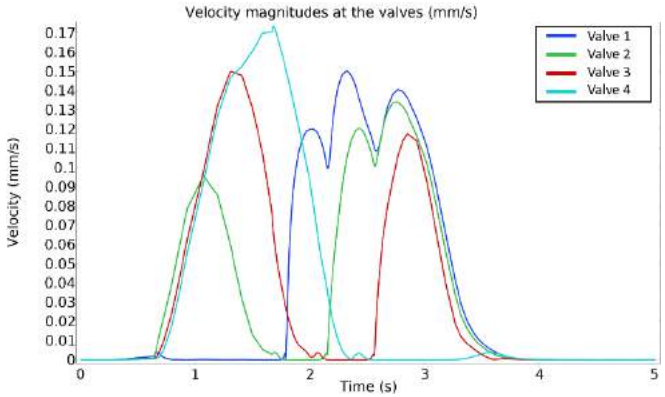

Figure 3: Velocity magnitude (mm/s) of the lymph as it passes through the valves. In the instances where the valves are closed, velocity magnitude of lymph is recorded as zero mm/s.

DISCUSSION

These initial computational results illustrate the ability of our approach to model the unidirectional valves and the pumping mechanism of the lymphangions. Our model showed more sensitivity to the high value of valve permeability (10^{-10}; minimum resistance) than to the low value of valve permeability (10^{-25}; maximum resistance), similar to the behavior of the lumped parameter model of Jamalian et al. [5]. In the next steps, we will perform a parameter study, incorporate a poroelastic interstitium and increase the topological complexity to better match anatomical reality. To extend this model, we can also incorporate the initial lymphatics and study lymphatic uptake in multiple scales. We will also set up validation experiments in mice by which we will collect morphological and physiological data of the lymphatic system.

ACKNOWLEDGEMENTS

This work is supported by the Research Foundation Flanders through project funding (FWO-project G022117N) and a post-doctoral grant (C. Debbaut; 1202418N).

REFERENCES

[1] Margaris KN and Black RA, *Journal of the Royal Society Interface*, 9:601-612, 2012.
[2] Rahbar E, Moore Jr JE, *Journal of biomechanics*, 44:1001-1007, 2011.
[3] Galie P, Spilker RL, *Journal of biomechanical engineering*, 131:111004, 2009.
[4] Bertram CD, Macaskill C, Davis MJ, Moore Jr JE, *American Journal of Physiology-Heart and Circulatory Physiology*, 310:H847-H860, 2016.
[5] Jamalian S, Bertram CD, Richardson WJ, Moore Jr JE, *American Journal of Physiology-Heart and Circulatory Physiology*, 305:H1709-H117, 2013.

SB³C2019
Summer Biomechanics, Bioengineering and Biotransport Conference
June 25 -28, Seven Springs, PA, USA

A 2D AXISYMMETRIC COMPUTATIONAL MODEL FOR THE STUDY OF MASS TRANSPORT INTO LYMPHATIC CAPILLARIES AND PRE-COLLECTOR VESSELS

Carlos A. Silvera Delgado (1), Ghazal A. Koudehi (1), Matthias V. Impe (1), Charlotte Debbaut (1), Patrick Segers (1)

(1) IBiTech-bioMMeda, Ghent University, Belgium, Ghent

INTRODUCTION

The lymphatic system is a unidirectional vessel network expanding throughout the body, evacuating interstitial fluid back into the circulation. Main components are lymphatic capillaries (initial or terminal lymphatics), collecting lymphatics and lymph nodes. Lymphatic capillaries, composed of a single layer of endothelial cells, are the sites where interstitial fluid (IF) enters the system, where it forms lymph. Primary one-way valves (endothelial flaps) along the length of the capillaries prevent retrograde flow towards the interstitium in normal physiological conditions. Lymphatic capillaries coalesce into the larger pre-collector and collector vessels and trunks. Lymph is returned to the central circulation both at lymph nodes and by the collecting lymphatics which propel the lymph by active contraction and external input from the surroundings. Impairment of lymph formation and evacuation can lead to lymphedema (swelling of extremities), high susceptibility to infection, and tissue fibrosis. The aim of this study was to develop a computer model for the study of lymph mass transport, particularly focusing on lymphatic clearance during lymphedema. Existing models of lymphatic capillaries are 2D models and do not include the pre-collector region. Furthermore, they most often focus on single valves, rather than the overall capillary function.

MATERIALS AND METHODS

A 2D axisymmetric model of a single capillary and a pre-collector is proposed. The model includes three the lymphatic capillary (80 µm diameter, length 310 µm), the tapering pre-collector (minimal diameter 80 µm, maximal diameter 120 µm, length 310 µm) and the interstitium (500x920µm²). The interstitium was considered as a poroelastic medium (which can thus change its volume). The vessel was assumed to be a linear elastic solid (Young's Module of 0.5 kPa) with a 10 µm thickness. The model geometry was designed to be consistent with values found in literature [1]. The lymph and interstitial fluid were assumed to have the same density (1000 kg/m^3) and viscosity (1.5 cP) [2]. The fluid along the domains was assumed to be Newtonian. The

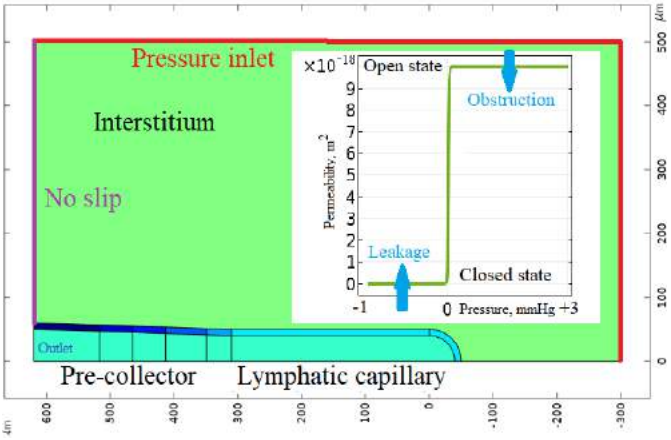

Figure 1: 2D model geometry with applied BCs. The subpanel shows how wall permeability changes to mimic primary valves.

physiological values of the permeability and Young's Modulus of the interstitium were assumed to be 7.6e-14 m^2 and 5 kPa, respectively.

Primary lymphatic valve function was mimicked by implementing a wall permeability that depends upon the transendothelial pressure difference (see Figure 1). To mimic lymphedema, different combinations of wall permeability (from $1x10^{-18}$ m^2 to $1x10^{-27}$ m^2) and Young's Modulus for the interstitium (from 5 kPa to 10 kPa) were implemented. Computational simulations were performed using COMSOL Multiphysics® 5.4, Free and Porous Medium package. Since lymph formation is an unsteady mechanism, transient simulations have been performed.

I. Governing equations

The classical Biot theory of poroelasticity treats a porous material as a linear elastic solid governed by Hooke's law, while the flow inside the porous domain is described by Darcy's law. In this model, Brinkman's equations that are an extension of the Darcy's law have been applied. The equations ensure a continuous velocity and pressure field at the interface of the two domains (the endothelial layer and the lymph channel) because the equations are valid for low and high permeability values.

II. Fluid dynamics and solid mechanics boundary conditions (BCs)

As lymph formation relies on the cyclic nature of the interstitial pressure, a sinusoidal pressure (peak-to-peak from 3 to -1 mmHg; 1Hz) was applied at the external edges of the interstitium (Figure 1, red line) [3]. Pressure at the outlet of the pre-collector vessel was set to 0 mmHg. No slip conditions were applied elsewhere. The external edges of the interstitial space were free to move, but the lymphatic vessels were fixed (no active/passive contraction). These BCs lead to a time-dependent pressure difference between the interstitial space and the lymphatics and hence a pressure-dependent permeability of the wall (Figure 1).

III. Modelling lymphedema and pathology

Lymphedema was reproduced in two ways: first, an initial lymphatic obstruction was reproduced by decreasing the permeability of the lymphatic valves with constant values imposed for open and closed state (from $1x10^{-18}$ m^2 to $1x10^{-20}$ m^2); second, lymphatic leakage was modelled by increasing the permeability of the wall during the closed state (from $1x10^{-27}$ m^2 to $1x10^{-18}$ m^2) keeping the open state in the normal value ($1x10^{-17}$ m^2). Modelling fibrotic conditions in lymphedema was done by increasing the Young's Modulus of the interstitium (from 5 kPa to 10 kPa).

RESULTS

Figure 2 shows the characteristic interstitial swelling (together with Von Mises stresses) when modeling lymphedema in response to lymphatic leakage. For the assumed parameter values, maximum swelling reached a 10% increase in volume compared to the resting condition. Increasing the Young's Modulus of the interstitium decreases the amount of fluid that enters the lymphatic capillary. Figure 3 illustrates how the flow rate of the capillary is critically dependent on the permeability, since a decrease of it reduce flow rates.

Figure 4 displays the maximum backflow at the outlet when varying the permeability of the wall, mimicking lymphatic leakage.

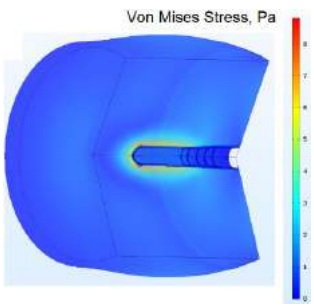

Figure 2: Interstitial swelling and Von Mises stress when mimicking secondary lymphedema.

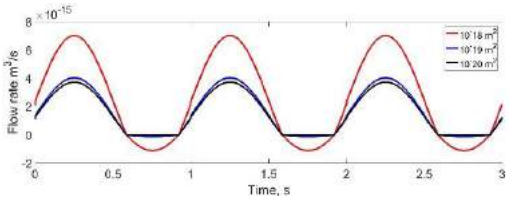

Figure 3: Flow rate at the outlet in case of lymphatic obstruction for three wall permeability values.

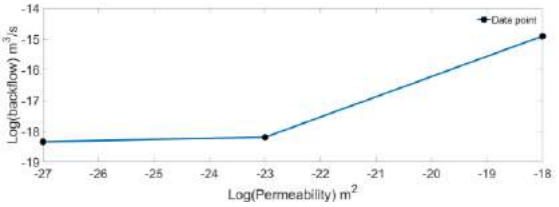

Figure 4: Maximum backflow in case of lymphatic leakage as a function of wall permeability. The values for the x-axis and y-axis have been presented in logarithmic scale.

DISCUSSION

Despite its geometric simplicity, this 3D computational model of the poroelastic interstitial space and initial and secondary lymphatics allowed us to replicate lymphedema in response to impaired lymphatic clearance, leading to an increase of interstitial fluid volume and swelling of the tissue (Figure 2). Lymphatic leakage (increased permeability) has two consequences: (i) fluid is being cleared from the tissue less efficiently than under normal physiological conditions; (ii) the presence of backflow provokes an imbalance in the water content of the interstitium, leading to tissue swelling.

We circumvented addressing primary valve malfunctioning at the level of the individual valves by modelling valve function via a pressure (and space) dependent wall permeability. Furthermore, the time dependent pressure boundary conditions imposed at the boundary of the interstitial domain lead to a pressure dependency of permeability and a functional pumping of the primary lymphatics (Figure 3). The computed flow rates are in good agreement with literature [2].

The novelty of our approach is that it is highly straightforward to represent different levels of impairment of the pre-collectors and the lymphatic capillaries, from a total obstructed capillary (zero wall permeability at all times) to a leaking one (high permeability at all tiles) and any intermediate situation (and this in space-dependent manner). Further research will focus on further extension of the model, coupling it to pumping lymphangions, and extensive validation.

ACKNOWLEDGEMENTS

This work is supported by Research Foundation Flanders through project funding (FWO-project G022117N) and a post-doctoral grant (C. Debbaut; 1202418N).

REFERENCES

[1] C. Heppell et al. *Bull. Math. Biol.*, vol. 77, no. 6, pp. 1101–1131, 2015.

[2] J. B. Dixon et al. *J. Biomed. Opt.*, vol. 10, no. December, p. 64016, 2005.

[3] A. Moriondo et al. *Am. J. Physiol. Circ. Physiol.*, vol. 289, no. 1, pp. H263–H269, 2005.

MICROFLUIDIC ASSESSMENT OF RED BLOOD CELL DEFORMABILITY AND MICROVASCULAR OCCLUSION RISK IN MALARIA AND SICKLE CELL DISEASE

Y. Man (1), E. Kucukal (1), Q. D. Watson (2), J. Bosch (3), J. A. Little (4), P. A. Zimmerman (2), U. A. Gurkan (1)

(1) Department of Mechanical and Aerospace Engineering, Case Western Reserve University Cleveland, OH, USA

(2) Center for Global Health and Disease, Case Western Reserve University Cleveland, OH, USA

(3) Division of Pediatrics Pulmonology and Allergy Immunology, Case Western Reserve University, Cleveland, OH, USA

(4) Division of Hematology/Oncology, Case Western Reserve University, University Hospitals Seidman Cancer Center, Cleveland, OH, USA

INTRODUCTION

The ability of red blood cells (RBCs) to undergo extensive reversible deformation when passing through narrow blood vessels and capillaries is critical for the continual blood flow and adequate perfusion in microcirculation. However, within the context of various hematological disorders, such as malaria and sickle cell disease (SCD), obstruction of small blood vessels is frequently induced by abnormal RBCs due to their altered deformability. Here, we demonstrate a functional microfluidic device that is composed of a series of micropillar arrays embedded into the microchannel (**Fig. 1A**). We designed the microfluidic device such that abnormal RBCs with significantly reduced deformability are retained by the upstream micropillar arrays containing coarse constrictions, while those with moderately reduced deformability by the downstream micropillar arrays containing finer constrictions. We further report a new parameter, namely RBC Occlusion Index (RBI), computed based on the overall occlusions induced by abnormal RBCs within the device, correlated to subject-specific clinical phenotypes. Our results indicated that the developed microfluidic device and the measured RBI values may serve as a promising universal tool to assess deformability and associated microvascular occlusion risk of RBCs within the context of microcirculatory health and disease.

METHODS

The microfluidic platform was designed and produced using established polydimethylsiloxane casting protocols and bonded to microscope slides (**Fig. 1B**). The masters of PDMS channels were fabricated with silicon wafers using standard photolithography techniques and followed with 2-h surface passivation using fluorinated saline vapor.

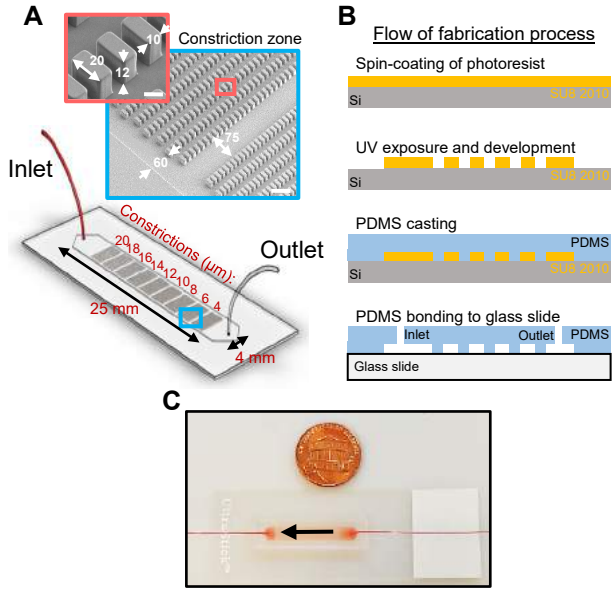

Figure 1. The microfluidic device: design and fabrication. (A) Each microfluidic device is composed of 9 micropillar arrays containing narrow constrictions from 20 μm to 4 μm. Inset: SEM images showing the inspection of the fabricated PDMS micropillar arrays (all indicated dimensions are in microns). Scale bars represent a length of 100μm and 10μm, respectively. (B) Flow of the fabrication process of the device. (C) Macroscale view of the microfluidic device. Arrow indicates flow direction.

Prior to introducing RBC samples into the device, the channel was rinsed with pure ethanol and PBS, and then incubated with 2% BSA overnight to reduce non-specific cell adhesion. A 20%-hematocrit RBC suspension was injected into the microchannel at a constant inlet pressure of 60cm H_2O for 20 minutes (**Fig. 1C**). Non-retained RBCs were washed off with PBS. Serial quantitative evaluation of occlusions induced by abnormal RBCs and calculation of the corresponded RBI values were carried out under standardized protocols on 5 healthy subjects, 15 subjects with homozygous HbSS (SCD), and 5 cultured malaria (*Plasmodium falciparum*)-infected blood samples.

RESULTS

We observed significantly elevated numbers of occlusions in the channel induced by RBCs from SCD and malaria-infected samples, compared to RBCs from healthy subjects, as expected. To assess the extent to which individual RBC subpopulations induced vaso-occlusive events in capillary bed within different micropillar arrays, we defined and calculated the RBI of an individual sample based on the numbers of occlusions induced in each micropillar array ($RBI = \sum Number\ of\ occlusions\ within\ the\ unit \times \frac{The\ unit\ number}{4}$).

Our results (**Fig. 2**) show that the RBI was heterogeneous in blood from SCD subjects, varying between 271 and 16,310 (mean ± standard error of the mean (SEM); 2,727.7 ± 1,005.8), which is significantly greater compared to healthy subjects (115.1 ± 24.4) (**Fig. 2**, p=0.001, Mann-Whitney U test). Additionally, the RBI of malaria-infected RBCs ranged between 1,906.5 and 6,487 (3,232.7 ± 838.6), which is also significantly greater compared to healthy subjects (**Fig. 2**, p=0.012, Mann-Whitney U test). These results indicate that within the context of malaria and SCD, RBC deformability is significantly altered, which directly leads to increased microvascular occlusion risk.

Because the RBI scores of SCD subjects were very heterogeneous (271-16,310), the SCD subjects were categorized into two groups (RBI < and > 1,000 (**Fig. 3A**). The SCD subjects with RBIs >1,000 exhibited significantly higher white blood cell (WBC) counts (**Fig. 3B**, p=0.032, Mann-Whitney U test), lactate dehydrogenase (LDH) levels (**Fig. 3C**, p=0.028, one-way ANOVA), and reticulocyte counts (**Fig. 3D**, p=0.023, Mann-Whitney U test), but lower platelet counts (**Fig. 3E**, p=0.043, Mann-Whitney U test) and fetal hemoglobin (HbF) levels (**Fig. 3F**, p=0.043, Mann-Whitney U test).

DISCUSSION

We present a microfluidic approach that allows quantitative analysis of RBC deformability and microvascular occlusive risk within the context of malaria and SCD. We have shown that RBCs from subjects with SCD and malaria-infected samples are significantly less deformable compared to RBCs from healthy subjects, based on the size-dependent occlusions within our micropillar arrays. These subject-specific RBI values have been demonstrated to correlate with subjects' clinical phenotypes. When RBCs travel from arterioles through capillary bed to venules, the dimension of the blood vessels exhibit a wide range of variations from nearly 100 μm to 4 μm [1]. Therefore, our microfluidic device can be utilized to monitor RBC-capillary bed interactions and help in understanding the dynamic pathophysiology of various circulatory diseases.

REFERENCES

[1] Picot, J., et al., *A biomimetic microfluidic chip to study the circulation and mechanical retention of red blood cells in the spleen.* Am J Hematol, 2015. **90**(4): p. 339-45.

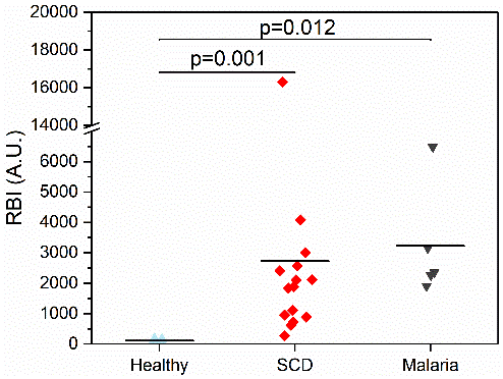

Figure 2. Assessment of RBI values of RBCs from healthy subjects, SCD subjects, and malaria-infected samples. The RBI generated by RBCs from subjects with SCD and malaria-infected samples are significantly greater compared to the RBI generated by RBCs from healthy subjects (p=0.001 and p=0.012, Mann-Whitney U test). Data point cross bars represent the mean.

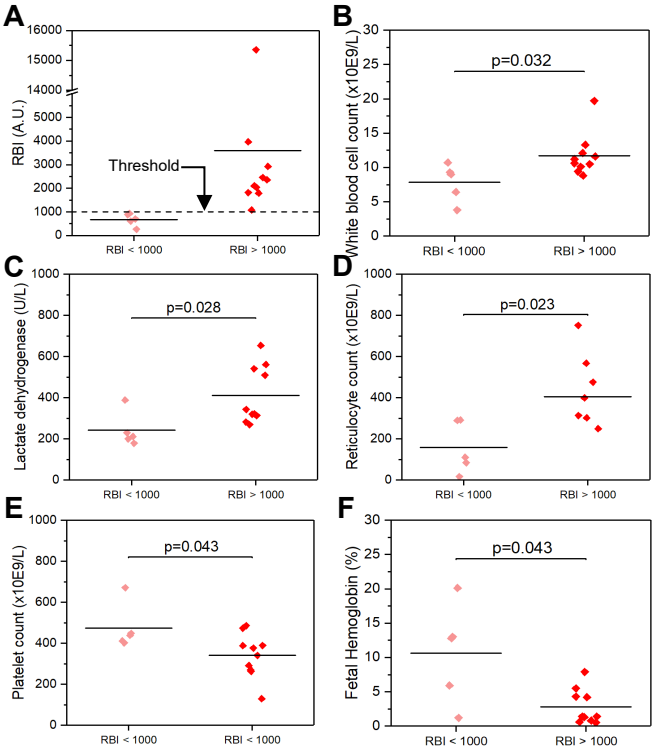

Figure 3. RBI is associated with clinical phenotypes in SCD. The RBI generated by subjects with SCD >1,000 (A) exhibited significantly higher WBC counts (B), LDH levels (C), and reticulocyte counts (D), but lower platelet counts (E), and HbF levels (F) compared to those with RBI <1,000. Data point cross bars represent the mean.

ACKNOWLEDGEMENTS

U. A. G. and J. A. L. acknowledge National Heart Lung and Blood Institute R01HL133574, which supported this study in part. U. A. G. acknowledges National Science Foundation CAREER Award 1552782, which supported this study in part. The authors acknowledge with gratitude the contributions of patients and clinicians at Seidman Cancer Center (University Hospitals, Cleveland).

SB³C2019
Summer Biomechanics, Bioengineering and Biotransport Conference
June 25 -28, Seven Springs, PA, USA

MICROFLUIDIC ASSESSMENT OF RED BLOOD CELL DETACHMENT IN SIMULATED MICROVASCULAR FLOW

U. Goreke (1), S. Iram (2), G. Singh (2), J. A. Little (3), M. Hinczewski (2), U. A. Gurkan (1)

(1) Mechanical and Aerospace Engineering Department
Case Western Reserve University
Cleveland, OH, US

(2) Department of Physics
Case Western Reserve University
Cleveland, OH, US

(3) Department of Hematology and Oncology
Case Western Reserve University
Cleveland, OH, US

INTRODUCTION

Vaso-occlusive crises (VOCs) are one of the most important pathophysiological manifestations of Sickle Cell Disease (SCD). Number of studies suggest that one of the key mechanisms which contribute to the VOCs is the adhesion of sickle RBCs to activated vascular endothelial cells in microvasculature [1, 2]. The essential reason for such abnormal adhesion to endothelial wall is the polymerization of abnormal hemoglobin molecule when deoxygenated, predisposing sickle RBCs to hemolysis [3]. In addition, emergence of anti-adhesive therapies targeting adhesion proteins on sickle RBCs claim reduction of the VOCs in vivo, supporting the hypothesis that adhesion of sickle RBCs is a key component in VOCs [4, 5]. Although the adhesion events are well studied, detachment of sickle RBCs, which might be key to understanding of survival of RBC adhesion under shear, is underexplored.

Our purpose was to experimentally examine the RBC detachment process using microchannels by gradually increasing the shear force acting on the adhered RBCs (Figure 1). We captured the sickle RBCs on a surface immobilized laminin-1 using technology described by Alapan *et al.*[6], then, collected videos of the adhered RBCs while gradually increasing the flow rate of buffer. Shear rate was ranged from 50 s^{-1} to 950 s^{-1}, such that it was kept in physiological range of capillary venules in microcirculation [7]. Timing of each RBC detachment was quantified by an image analysis algorithm that tracks the motion of RBCs in the video outputs. We described detachment characteristic of each blood sample tested by plotting ratio of number of adhered RBCs at time t to initial number of adhered RBCs by analyzing each RBC detachment event. Then we analyzed data further to understand survival rates of RBCs under different flow conditions.

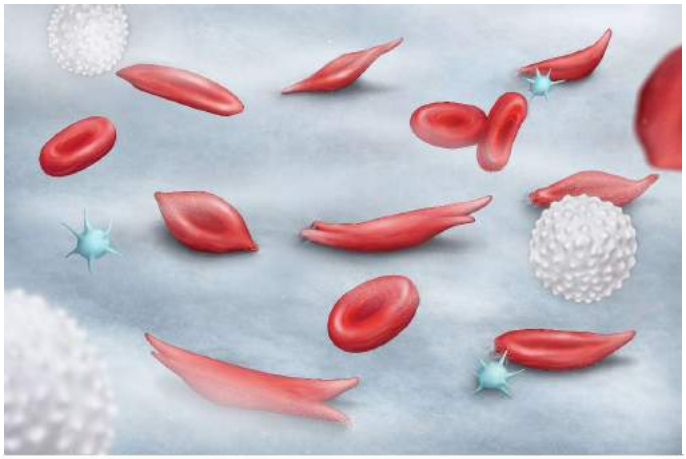

Figure 1: Red blood cells are illustrated during their detachment from the protein surface.

METHODS

Microfluidic Chip Fabrication. The microchannels were fabricated by assembling a double sided adhesive (DSA) film on a rectangular polymethyl methacrylate (PMMA) piece and fixing the PMMA onto a APTS (3-aminopropyl triethoxysilane) functionalized microscope glass slide through the DSA. The microchannel height was determined by the DSA thickness, which was approximately 50 mm and which mimicked the scale of post capillary venules.

Surface functionalization. A cross-linker agent GMBS was used in order to covalently immobilize the proteins to the microchannel surfaces. After GMBS treatment and wash, 22.5 µL of protein working solutions (100 mg×µL^{-1}) were injected into the microchannels and

incubated for 1.5 hours at room temperature. Then, 30 µL of BSA solution was added into the microchannels, and held at 4°C overnight.

Blood processing and data acquisition. The microchannels were placed on an inverted motorized microscope stage for visualization and connected to a programmable syringe pump. Whole blood samples were tested within 24h after drawing. Blood flow rate was kept at 18.5 mg×µL^{-1} until residual BSA was completely removed. Afterwards, 15 µL of blood perfused at 1.85 mg×µL^{-1}, corresponding to an approximate shear stress of 1 dyne×cm^{-2} throughout the microchannel. In order to wash the non-adherent cells off of the microchannel surfaces, wash buffer containing 1% BSA and 0.09% sodium azide was connected to the device and the buffer was pumped starting at a flow rate of 5 µL×min^{-1} for 100 µL to ensure that most of non-adherent cells were completely removed. Next, the flow rate of the wash buffer was increased gradually at linear rates while the videos of the microchannel surface were recorded at 10 fps and at 10X magnification. The duration of each video was set to be 20 minutes.

Analysis algorithm. A MATLAB© based code for automated processing of the experimental video data was developed. The pre-processing for identification of sickle RBCs adhered to functionalized surface was performed. This ensured the removal of spurious and non-specific adhesions that would interfere with the tracking algorithm. Then the pre-processed data was fed into the tracking algorithm specifically designed for microfluidic assays, to generate temporal detachment counts. The tracking kernel tackled issues like discarding mobile cells flowing into the frame of view, and being able to identify onset of rolling (as opposed to complete detachment). Trial runs tested against manual analysis yielded robust agreement.

RESULTS

Results are obtained through the tracking algorithm. Detachment events were recorded as the moment cells left their initial position. 17 blood samples were tested in these experiments at four different rates of gradual increase of shear force, which are defined as 'shear rate ramps' in this context. Fractions of initial population still attached at time t was represented by S(t) and are presented in Figure 2 for each sample at different ramps.

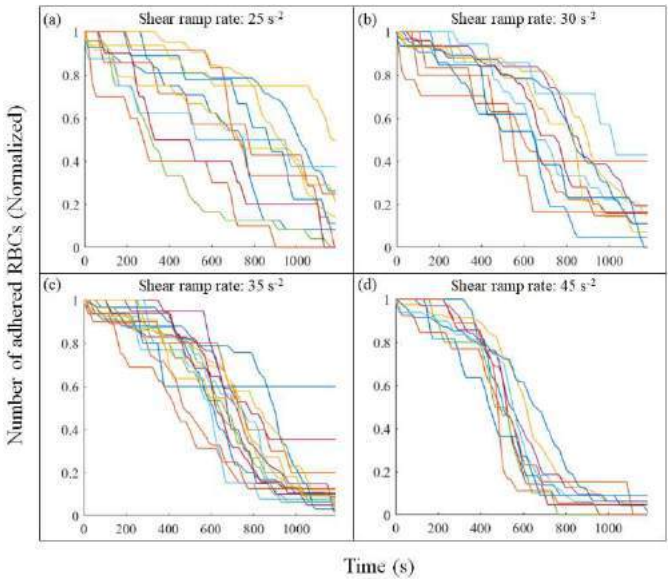

Figure 2. Number of adhered sickle RBCs with time. At a force ramp rate of (a) 2.5 µL/min^2, (b) 3 µL/min^2, (c) 3.5 µL/min^2, (d) 4.5 µL/min^2. Each sample has the same color across plots.

Theoretically, area under the temporal detachment curve gives us average time to detachment, t_{avg}, of RBCs in that population which is calculated as;

$$t_{avg} = \int S_{(t)}\, dt \qquad (1)$$

Average time to detachment of samples of sickle RBCs under different ramp rates are depicted in Figure 3. Coefficient of variation decreases with the increasing force ramp rates.

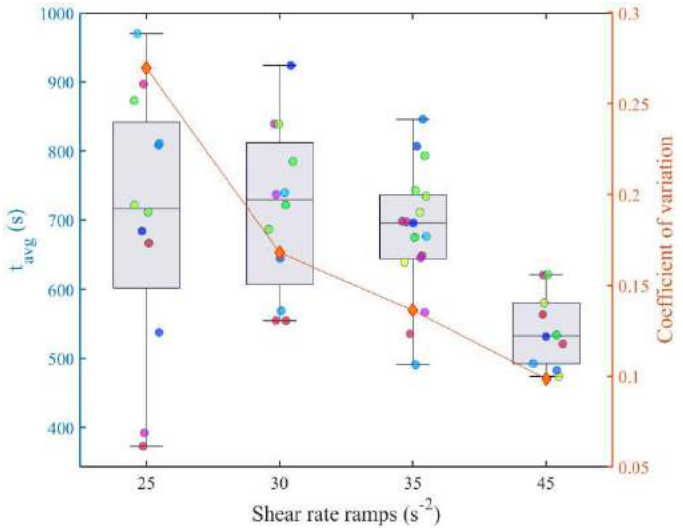

Figure 3. Average time to detachment with corresponding ramp groups. Each sample has the same color across plots.

DISCUSSION

Observing and analyzing detachment of sickle RBCs unveiled many interesting features of sickle RBCs. One of these features is that both sickle RBCs and SCD itself, exhibits heterogeneous adhesion characteristics. S(t) curves revealed that as the ramp rate increases, the average time to detachment of sickle RBCs gets shorter, however, considerable portion of sickle RBCs managed to stay at its initial position at even high flow rates giving a hint of underlying mechanism. Samples also showed considerably different S(t) curves across different ramp rates. S(t) curves at higher ramp rates are less dispersed than the curves at lower ramp rates. These new insights might play a key role in understanding and treating long and painful episodes of VOCs.

ACKNOWLEDGEMENTS

This work was supported by grants, National Heart Lung and Blood Institute R01HL133574, and National Science Foundation CAREER Award 1552782.

REFERENCES

[1] Alapan, Y., et al., *Scientific Reports*. 4,2014.
[2] Telen, M.J., *ASH Education Program Book*. 2007(1):84-90,2007.
[3] Gladwin, M.T., et al., *N. Engl. J. Med.* 350:886-895,2004.
[4] Ataga, K.I., et al., *Br. J. Haematol.* 170:768-780,2015.
[5] Zennadi, R., *PLoS ONE*. 9:e110306,2014.
[6] Alapan, Y., et al., *Transl. Res.* 173:74-91.e8,2016.
[7] Lipowsky, H.H., *Microcirculation*. 12(1):5-15,2005.

SB³C2019
Summer Biomechanics, Bioengineering and Biotransport Conference
June 25 -28, Seven Springs, PA, USA

EFFECTS OF LEAKY TUMOR VASCULATURE ON TISSUE STRESS AND POROSITY IN A BIPHASIC MODEL OF BRAIN GLIOMA

J. Rey (1), M. Sarntinoranont (1), J. Ewing (2)

(1) Mechanical and Aerospace Engineering
University Florida
Gainesville, FL, USA

(2) Department of Neurology
Henry Ford Health System
Detroit, Michigan, USA

INTRODUCTION

The mechanical forces present within a tumor and its surrounding normal tissue affect tumor progression and therapies. These forces can influence the growth and metastatic potential of cells directly or indirectly by compressing tumor blood vessels [1]. The resulting hypoxic conditions stimulate the formation of leaky vasculature that elevate interstitial fluid pressure and drive extracellular fluid out of tumors, posing a challenge for targeted drug delivery [1].

Past tumor mechanical models have focused on stresses resulting from tumor growth within host tissue and the role of extracellular matrix fibers [2] [3]. However fluid exuded by tumor blood vessels can also exert forces on cells and matrix components. A better understanding of how this can influence the stress state of tumors is needed, especially in brain gliomas given brain parenchyma lacks lymphatic vessels to clear away exudate. These tumors also tend to be softer than the surrounding normal tissue making their growth more difficult to explain.

Previous tumor models have used biphasic theory to account for the interplay of fluid and solid components in tissue [4]. In this study, a spherical biphasic finite element tumor model was developed to predict interstitial fluid and solid phase stresses caused by vascular exudation and its effect on tissue porosity. This is the foundation for future models with MRI-based geometries that account for blood vessel heterogeneity and collapse.

METHODS

A biphasic finite element model of a spherical tumor embedded within brain tissue was developed using the FEBio software suite [5]. In the biphasic formulation the solid phase includes cells and extracellular matrix while the fluid phase consists of the interstitial fluid. The leaky tumor vasculature was modeled as a distributed fluid source governed by Starling's law.

$$\dot{V}_f/V = L_p(p_v - p) \tag{1}$$

The left hand side is the ratio of fluid volume produced per unit time, $\dot{V}_f$, and tissue volume, V. This ratio varies directly with the difference between vascular pressure, p_v, and interstitial fluid pressure, p, where L_p is a vascular leakiness parameter.

The solid phases of both the tumor and host tissue were modeled as Neo-Hookean materials. The porosity of the solid phase, ϕ, was derived in terms of the Jacobian of deformation, J, and porosity in the reference configuration, ϕ_0.

$$\phi = 1 - \frac{1}{J}(1 - \phi_0) \tag{2}$$

Interstitial fluid obeyed Darcy's law with hydraulic conductivity, k, which coupled to tissue deformation by a Holmes-Mow formulation

$$k = k_0 \left(\frac{J - (1 - \phi_0)}{\phi_0}\right)^{\alpha} e^{\frac{1}{2}M(J^2 - 1)} \tag{3}$$

where α and M are fitting parameters and k_0 is hydraulic conductivity in the reference configuration [6].

The modeled geometry consisted of a 3 mm radius tumor and surrounding host tissue that extended at least five radii beyond the tumor boundary. Because of spherical symmetry, only an octant of the sphere was considered while prescribing symmetry boundary conditions on the internal surfaces and free fluid flux through the tumor boundary. The model was implemented on a rectilinear mesh with 21,952 elements with elements becoming coarser with distance from the tumor boundary.

Tissue vascular leakiness, stiffness, porosity and hydraulic conductivity were assumed uniform within tumor and host tissue except a smoothly varying transition region at the tumor boundary. To achieve this smooth variation, material properties were assigned to the finite

element mesh on an element by element basis in a set of custom MATLAB scripts. Baseline material properties were estimated from previous studies in our labs.

RESULTS

Fluid exuding through leaky tumor vasculature resulted in elevated interstitial fluid pressure within the tumor and a steep pressure decline near the tumor boundary (Figure 1). The pressure field within the tumor generated the lowest fluid velocity near the tumor center and the highest velocity near its boundary.

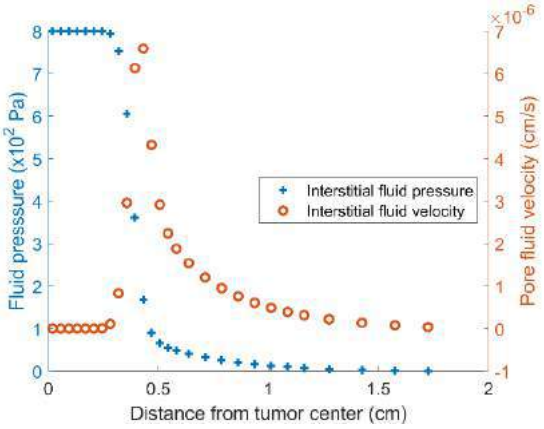

Figure 1: Interstitial fluid pressure and velocity produced by fluid sources obeying Starling's law distributed within tumor tissue

Another consequence was an increase in tumor tissue volume that strained the solid matrix of the tumor and surrounding host tissue. The solid matrix of the host tissue experienced radial compression and hoop tension whereas that of the tumor experienced radial and hoop tension (Figure 2).

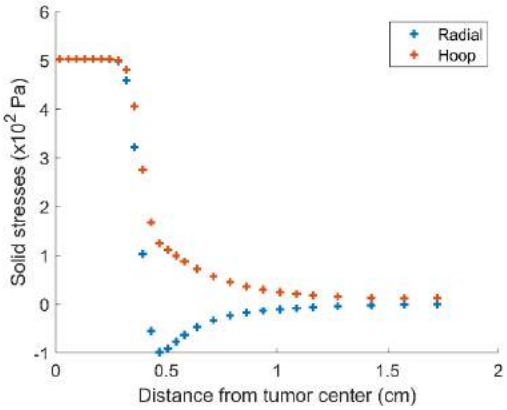

Figure 2: Radial and hoop stresses produced by fluid sources obeying Starling's law distributed within tumor tissue.

The increase in tumor tissue volume had the effect of increasing the porosity of the solid matrix. Beginning with a smoothly varying porosity curve in the reference configuration characterized by low porosity within the tumor because of elevated cell density, the deformed configuration predicted a reduction in porosity just beyond the tumor boundary (Figure 3).

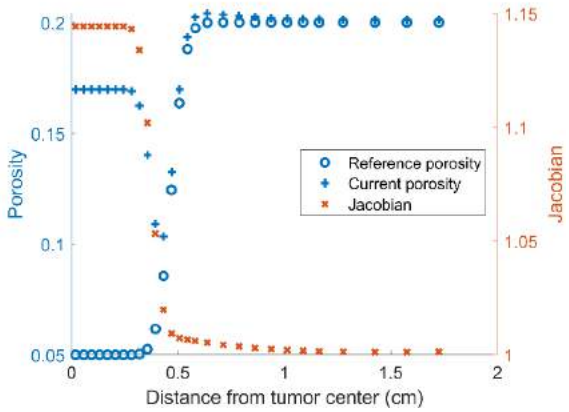

Figure 3: Radial variation of tissue expansion and porosity

DISCUSSION

A biphasic finite element model of a spherical brain glioma was develop to study how fluid production by tumor vasculature affects the stress state and porous properties of tumor and host tissues. The fluid pressure and velocity magnitude were greatest in the center and rim of the tumor, respectively, in agreement with past theoretical and animal models [1] [4] [7]. The solid stress state of the surrounding host tissue was radial compression and hoop tension as is expected for growth induced stress, but stress in the tumor interior was radial and hoop tension which is opposite that induced by growth [2]. The tension in the tumor's solid phase balances the outwardly directed interstitial pressure drop produced by its leaky vasculature. The presence of leaking vessels could potentially alleviate compressive growth stresses and promote further growth since compression appears to inhibit cell proliferation [1].

Porosity measurements for rat gliomas taken with DCE-MRI have indicated slightly lower porosity within the tumor center and even lower porosity at its boundary relative to the host tissue [8]. The tissue deformation expected from fluid production transformed a uniformly low porosity within the tumor to a profile that matches more closely with these measurements [8]. The mechanical forces that accompany leaking vessels likely play an important role in the growth of brain gliomas given they are appear to be softer than the surrounding tissue which is at odds with previous theoretical tissue stiffness predictions [9]. Future work will account for tumor growth to compare its contribution to the overall stress state with that of vascular leakiness.

ACKNOWLEDGEMENTS

This work is funded via a subcontract of NCI/NIH R01-CA218596 (Ewing, James and Brown, Stephen) *MRI Signatures of Response to High-Dose Radiotherapy in Rat Models of Cerebral Tumor*.

REFERENCES

[1] Jain R, et al., *Ann Rev Biomed Eng*, 16:321–46, 2014
[2] Stylianopoulos T, et al., *Proc Natl Acad Sci*, 109:15101-8, 2012
[3] Iranmanesh F, et al., *J Biomech Eng Trans ASME*, 139:10, 2017
[4] Sarntinoranont M, et al., *Ann Biomed Eng*, 31:327-35, 2003
[5] Maas SA, et al., *J Biomech Eng*, 134(1):011005, 2012.
[6] Holmes M, *J Biomech*, 23(11):1145–56, 1990.
[7] Elmghirbi R, et al., *Magn Reson Med*, 80:2040-52, 2018
[8] Ewing J, et al., *NMR Biomed*, 28:1557-69, 2015
[9] Voutouri C, et al., *PLoS One*, 9(8): e104717, 2017

SB³C2019
Summer Biomechanics, Bioengineering and Biotransport Conference
June 25 -28, Seven Springs, PA, USA

MODELLING ADVECTION-BASED NANOPARTICLE DRUG DELIVERY TO THE LEFT VENTRICLE USING A SPLITTING METHOD FOR ADVECTION-DIFFUSION-KINETICS

Alexandra K. Diem (1), Kristian Valen-Sendstad (1)

(1) Department of Computational Physiology
Simula Research Laboratory
Fornebu, Norway

INTRODUCTION

The use of nanoparticles (NP) target drug delivery directly to the heart for treatment of diseases via nanoparticles (NP) has been a major goal of cardiovascular research since the early 2000s. Recently, such NP delivery systems based on non-invasive administration via inhalation have successfully been developed and shown to reduce heart failure in mice [1]. However, the transition of such innovative technology to larger animals and subsequently humans, requires careful optimisation of physico-chemical parameters of the NP, in order to achieve efficient distribution throughout the tissue.

We address this challenge by presenting a finite-element model of NP delivery via perfusion through the myocardium in the left ventricle (LV), which presents its own unique challenges: The discrepancy of scales between the size of the LV, blood vessels perfusing the LV, and NP requires the development of efficient averaging methods to effectively reduce simulation times. To achieve this, perfusion is represented by a three-compartment porous media continuum model based on Darcy's law [2], while NP delivery is approximated by splitting advection and diffusion kinetics across compartments.

Using these methods we demonstrate efficient simulation of NP delivery to the myocardium.

METHODS

We model the myocardium of the LV (domain Ω) as a three-compartment porous media continuum model, where a compartment represents artery, arteriole and capillary beds, respectively. Denoting different compartments using index i,

$$-\nabla \cdot (\boldsymbol{K}_i \cdot \nabla p_i) + \sum_{k=1}^{3} \beta_{i,k}(p_i - p_k) = s_i \qquad \text{in } \Omega \quad (1)$$

with $\boldsymbol{K}$ permeability of the porous medium, p pressure, and $\beta_{i,k}$ exchange coefficient between compartments i and k, and s source/sink terms. We use Neumann boundary conditions to model the inflow of blood from the coronary arteries via volumetric inflow

$$(-\boldsymbol{K}_i \cdot \nabla p_i) \cdot \boldsymbol{n} = \Psi_i \qquad \text{on } \Gamma_N \quad (2)$$

on boundaries Γ_N.

NP distribution is modelled using standard advection-diffusion (AD) kinetics for each compartment i

$$\partial c_i/\partial t = \nabla \cdot (D_i \nabla c_i) - \nabla \dot{(}\boldsymbol{w}_i c_i) + \sum_{k=1}^{3} \gamma_{i,k} c_i + s_i \qquad \text{in } \Omega \quad (3)$$

with c NP concentration, D diffusion coefficient, $\boldsymbol{w}$ advection velocity, $\gamma_{i,k}$ exchange coefficients between compartments i and k, and s source/sink terms.

Splitting Method for NP Deposition

Deposition of NP into myocardial tissue can only occur within the capillary bed. The non-linear advection-diffusion equation is time consuming to solve and thus we introduce the following splitting method: We model a *bolus of NP* as a collection of NP using Lagrangian particle tracking in the artery and arteriole bed (compartments 1 and 2)

$$\partial \boldsymbol{x}_{1,2}/\partial t = \boldsymbol{w}_{1,2} \qquad (4),$$

while modelling diffusion in the capillary bed (compartment 3)

$$\partial c_3/\partial t = \nabla \cdot (D_3 \nabla c_3) + \gamma_{2,3} c_2 + s_3 \qquad (5)$$

The equations are solved using the finite element Python package FEniCS [3]. Time discretisation is achieved using a Crank-Nicolson scheme.

RESULTS

The efficiency of the splitting method was tested on a unit square geometry over 3.0 s using a prescribed sinusoidal velocity profile (Figure 1) before application of the new method to a human LV geometry.

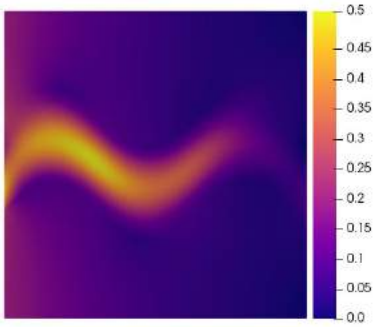

Figure 1: Velocity field in the unit square test geometry.

The equations were solved over 0.2 s on the test geometry with 5k, 20k, 40k and 80k dofs, respectively and a time step size of 0.005 s. Using the conventional AD equations the solution time increases exponentially from 26 s to 660 s, while the splitting method solves in 6 s to 66 s. Errors were measured by calculating the total mass over the geometry. In the case of the AD equations the error decreases linearly from 2.7×10^{-5} to 2.1×10^{-5}, while it stays roughly constant around 1.2×10^{-5} for the splitting method. Figure 2 shows the an example solution over 3 s using the splitting method. An example solution for the human LV geometry using 10k dofs is shown in Figure 3.

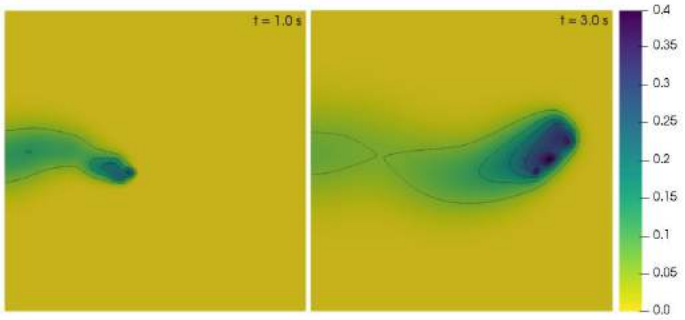

Figure 2: Concentration in the capillary compartment of the test geometry with isocontours.

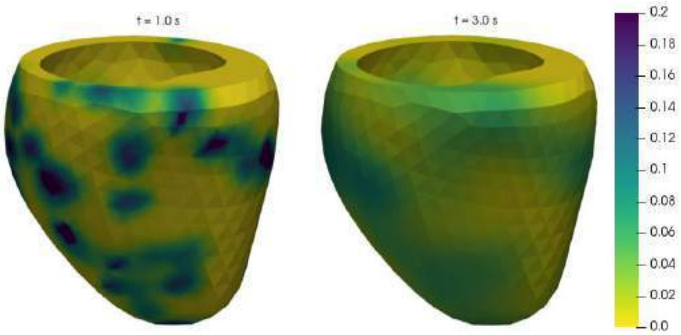

Figure 3: Concentration in the capillary compartment in the myocardium of a human LV geometry.

DISCUSSION

Interest in using NP for the non-invasive, targeted delivery of drugs to the heart tissue has been growing over the last twenty years. Experimental research currently focusses on rodents and simulations possess the potential to accelerate the transition of the technology to testing in large animals. However, the conventionally used advection-diffusion equations are computationally expensive. Here, we present an efficient method to track NP in the LV via a combination of Lagrangian particle tracking and diffusion. This method leads to a speedup of the simulations by reducing both the required mesh size and number of time steps.

ACKNOWLEDGEMENTS

The authors acknowledge the European Community for its financial support in the framework of the project CUPIDO (www.cupidoproject.eu) H2020-NMBP2016 720834.

REFERENCES

[1] Miragoli, M et al., *Sci Transl Med*, 10:424, 2018.
[2] Michler, C et al. *Int J Numer Method Biomed Eng*, 29:217-32, 2013.
[3] Alnaes, M et al. *Archive Numer Soft*, 3, 2015.

SB³C2019
Summer Biomechanics, Bioengineering and Biotransport Conference
June 25 -28, Seven Springs,PA, USA

COMPARISON OF PRINCIPAL COMPONENT ANALYSIS AND NON-NEGATIVE MATRIX FACTORIZATION IN PREDICTION OF UNMEASURED MUSCLE EXCITATIONS

Di Ao (1), Mohammad S. Shourijeh (1), Carolynn Patten (2),Benjamin J. Fregly (1)

(1) Department of Mechanical Engineering
Rice University
Houston, Texas, USA

(2) Department of Physical Medicine and Rehabilitation
University of California
Davis, California, USA

INTRODUCTION

To drive the computational models of musculoskeletal systems to estimate muscle forces and joint moments during a variety of dynamic motor tasks, electromyography (EMG) signals have been traditionally focused on. Surface EMG signal is non-invasive to record. However, it is unable to reliably record activity of the deeply located muscles that highly contribute to the generation of joint moments. Even though intramuscular recording--as one alternative to surface EMG, is able to pick up less surrounding muscle activities and capture more accurate deep muscle excitation, there are still potential complications of patient discomfort and pain. Additionally, there is also the risk in having the EMG fine wire electrodes to penetrate pathological tissue. One example, which is one of the long-time interests of this study, is the tumor developed in the hip region of the pelvic sarcoma patients, and that iliopsoas muscle group cannot tolerate a fine wire.

One strategy for the neural motor system to interact with the highly complex environment and to accomplish the multidimensional dynamic motor tasks is to identify the operation regularities [2]. A common hypothesis is that muscle synergies that are extracted from muscle excitations may be able to represent these regularities in the motor system. The muscle synergies extracted from a group of muscle excitations have been shown to be able to reconstruct the excitations of the other muscles [3], which can also demonstrate the coordination of these muscle synergies underling behaviors. Taking the advantages of extrapolative property of muscle synergies, we may rebuild the unmeasured muscle excitations by investigating of the control strategy of muscle synergies in measured muscles.

Matrix factorization algorithms have been widely used to decompose a large number of experimental EMG signals into a smaller number of time-varying synergy commands, along with time-invariant synergy weights. However, the performance of each algorithm can be affected by specific assumptions and signal processing methodologies [1, 4].One of the intrinsic defects of EMG is the challenge in attaining true maximum local muscle excitation for normalization. As a popular matrix factorization and data compression algorithm, principal component analysis (PCA)can capture the most important features of the large dimensional dataset, which may not be as sensitive as non-negative matrix factorization (NMF)to scaling scheme of muscle excitations and may provide us benefits in finding quick, unique and reliable synergies without ‘truly’ normalizing the data. In this study, a comparison is presented between PCA and NMF to investigate the performance of each on reconstruction of the unnormalized measured muscle excitations and extrapolation to predict unnormalized unmeasured muscle excitations.

METHODS

In this study, we compared the performance of the synergies extracted from normalized measured EMG data by PCA and NMF in fitting unnormalized measured and unmeasured muscle excitations. Data from previously published work was used in which EMG of 16 muscle groups were recorded from a stroke patient walking at different speeds, including self-selected speed (0.5 m/s; 3 trials) [4]. To test our hypothesis, the EMG of iliopsoas, collected by fine wire electrodes, was taken out as ‘unmeasured’ EMG signal, and the remaining 15 EMG signals were assumed to be ‘measured’. All the measured EMGs were processed by band-pass filtering, full-wave rectifying and low-pass filtering. The resulting linear envelopes were normalized with

Poster Presentation #P166

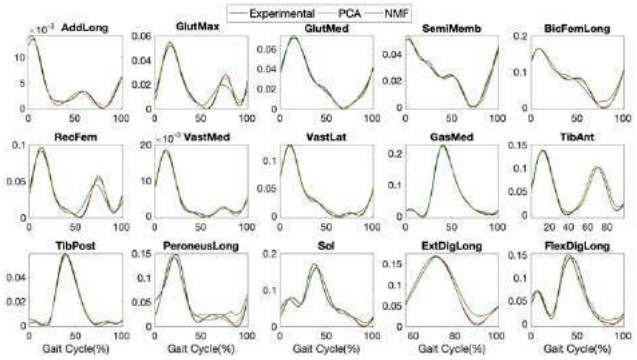

(A)

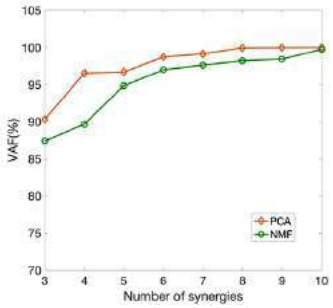

(B)

Figure1. (A) The 15 reconstructed unnormalized measured muscle synergies (at 5 synergies); (B) The average VAF values at each number of synergies between experimental and reconstructed original unnormalized measured muscle excitations.

respect to the peak processed EMG values observed across the entire set of recorded trials. We applied NMF on normalized measured muscle excitations and PCA on the demeaned normalized measured muscle excitations to extract synergy excitation commands. The synergy weights corresponding to all unnormalized muscle excitations were found via linear algebra. The similarity in the shape and amplitude between experimental and reconstructed muscle excitations was quantified by Variance Account For (VAF) and Pearson correlation (r).

RESULTS

With the 5 synergies from PCA and NMF extracted from the 15-channel normalized measured muscle excitations (normalized to max values over all trials), the original unnormalized measured muscle excitations were reconstructed fairly accurately (Fig.1A). For both PCA and NMF, the VAF values showed a rising trend by increasing the number of synergies. However, across all selected number of synergies, the VAF values with PCA were higher than those with NMF (Fig.1B).

The ability in reconstruction of the unnormalized missing muscle excitation (iliopsoas) by the synergies extracted using PCA and NMF from normalized measured muscle excitations was also compared, as shown in Fig. 2A for 5 synergies. Except for 3 synergies, all the VAF values with PC were greater than those with NMF. For PCA, the VAF values reached above 95%with 4 synergies. Pearson correlation values r between the reconstructed excitation and experimental PCA were higher than those with NMF at all the numbers of synergies above four (Fig.2C).

DISCUSSION

By increasing the number of synergies, the synergies extracted from normalized measured muscle excitations with both PCA and NMF resulted in better fitting both unnormalized measured and unmeasured muscle excitations. In other words, by appropriately optimizing synergy vectors (e.g. via EMG-driven model based optimization [Meyer et al. or who?]), we can rebuild original unnormalized muscle excitations that agree with the experimental signals using the PCA or NMF synergies extracted from normalized measured muscle excitations. However, PCA did a noticeably better and more reliable job than did NMF.

PCA is a linear decomposition approach that leads to the unique solution of PCs instead of multiple solutions as in NMF, which may allow us to perform synergy extraction repeatedly on rescaled version of muscle excitations through optimization process. Another advantage of PCA is that the synergies extracted from the normalized muscle excitations-- to the maximum values across all trials in the current study--can be applied to predict the original unnormalized missing muscle excitation more accurately compared to NMF. Hence, PCA-based synergy analysis could be performed before the start of the calibration process of missing synergy vectors and muscle specific parameters, while NMF may need to perform on rescaled-muscle excitations over and over again through optimization. Finally, the issue with finding the true normalized muscle excitations to derive synergies would not exist anymore if PCA is applied.

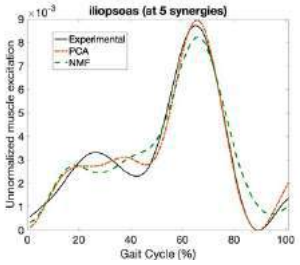

(A)

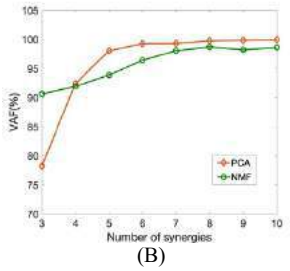

(B)

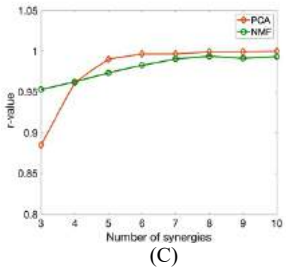

(C)

Figure 2. (A) The reconstructed unnormalized unmeasured iliopsoas muscle excitation (at 5 synergies); (B) The average VAF values for reconstruction of original unnormalized measured excitations; (C) The average r-values at each number of synergies between experimental and reconstructed original unnormalized measured muscle excitations.

ACKNOWLEDGEMENTS

Cancer Prevention Research Institute of Texas (CPRIT) funding RR170026.

REFERENCES

[1]M, Sartori, et al., *J Biomech*, 47:3613-3621, 2014.
[2]M. C. Tresch, et al., *J Neurophysiol* 95: 2199-2212, 2006.
[3] N. A Bianco, et al., *J Biomech Eng*, 140:011011, 2018.
[4] C. Banks, et al., *Front Comput Neurosc*, 11: 78, 2017

SB³C2019
Summer Biomechanics, Bioengineering and Biotransport Conference
June 25 -28, Seven Springs, PA, USA

VARIANCE IN SWIMMER SYMMETRY DUE TO EFFORT AND FATIGUE

C. Main, C. Goehler

Department of Mechanical Engineering and Bioengineering
Valparaiso University
Valparaiso, Indiana, USA

INTRODUCTION

The current methods for quantifying human motion in swimmers are not as advanced as those implemented for other athletes. While runners have a variety of sensors that can be attached to their body to measure joint flexure and gait, it is increasingly difficult to measure parts of the swim stroke due to the lack of waterproof sensors, and some sensors that are waterproof tend to be invasive in that they affect the stroke of the swimmer. The most common method for evaluating swimmers is qualitative observation from the pool deck and timing with a stopwatch [1], which is heavily influenced by refraction of light from the water and very unreliable. Current quantitative methods of measuring the biomechanics of swimmers include the use of Computational Fluid Dynamics to measure drag coefficients [2], tether cords to measure force [3], waterproof EMGs for muscle activation [4] and inertial magnetic measurement units for joint flexion [5], and accelerometers [6] in wearable technology to count strokes and laps.

The main objective of this study was to use a minimally invasive sensor to analyze basic "gait" patterns of swimmers swimming the front crawl at various intervals of effort, and then measure the average path of the stroke throughout each trial and how each stroke varies from the average. By determining how much a swimmer can vary in their stroke while fatigued, it may be possible to determine a threshold of safety for swimmers. If swimmers spend too much time continuously swimming outside of a certain threshold of safety for position of stroke and variance in stroke, they will be more likely to be injured from the repetition of incorrect swimming mechanics. These injuries that stem from repetitive motions are often career-ending and can greatly affect athletes in their daily life outside of the pool, even with treatment. Understanding where this threshold of safety exists will then help coaches create more effective practices that can help their swimmers improve technique and efficiency in water without risking injury.

METHODS

A GaitUp Physilog®5 motion sensor was clipped to the back of the swimsuit on two female collegiate swimmers. These sensors measure acceleration in Cartesian coordinates along with gyration about each axis, pressure, and temperature. The swimmers then swam eight trials, the first four at 70% effort, 80% effort, 90% effort, and 100% effort respectively, and the last four in reverse order. The first swimmer, a sprinter, completed trials 100 yards in length, the other swimmer, a distance swimmer, completed trials that were 200 yards in length.

The data from these sensors was then uploaded to a program in MATLAB. In the program, the data was filtered, position was derived from acceleration using kinematic equations, and each stroke was averaged together to identify the average stroke pattern for each trial. Then, each stroke was compared to the average to determine the variance of each stroke and the total variance of every stroke in a trial compared to the average. Finally, three parameters were calculated. The variance per trial was calculated using Eq. (1), the average amplitude of each trial was calculated using Eq. (2), and the change in amplitude between right and left strokes was calculated using Eq. (3), where *s* signifies position in all three equations. These values were compared to the percent effort of each trial to see trends in how effort and fatigue may influence the symmetry and consistency of stroke.

$$variance = \Sigma(s_{stroke} - s_{average}) \quad (1)$$

$$average\ amp = \frac{1}{2}\left(\frac{\Sigma\, s_{max}}{\#\ strokes} - \frac{\Sigma\, s_{min}}{\#\ strokes}\right) \quad (2)$$

$$\Delta amp = \frac{\Sigma\, s_{max}}{\#\ strokes} + \frac{\Sigma\, s_{min}}{\#\ strokes} \quad (3)$$

Poster Presentation #P167

RESULTS

Each swimmer's data was run through a MATLAB program that plotted the position vs. time of each of her strokes and determined her average stroke pattern as shown in Figure 1. This allowed qualitative observation of the variance in each stroke throughout the trial.

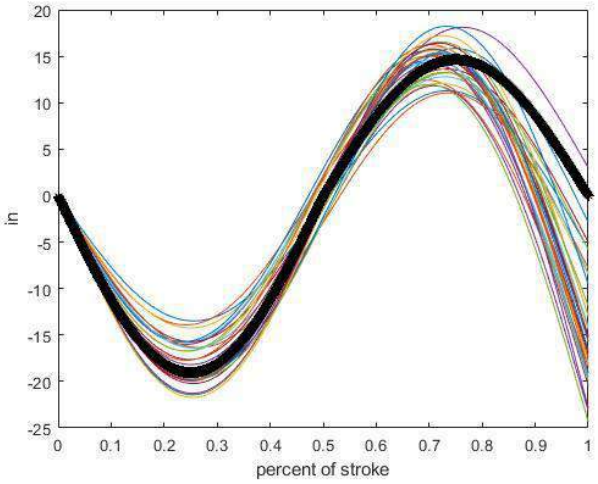

Figure 1: Each stroke swam by the sprinter in her 5th trial compared to her average stroke pattern.

The average amplitude of each stroke was determined by taking the absolute values of the maximums and minimums of each stroke and averaging them. Then, for each trial, all of the average amplitudes of the strokes are averaged together and plotted in Figure 2. In both swimmers, as effort increased to 100% in trials 4 and 5, the average amplitude of rotation actually decreased 33.3% and 21.7% in the sprinter and the distance swimmer respectively as compared to their first trial.

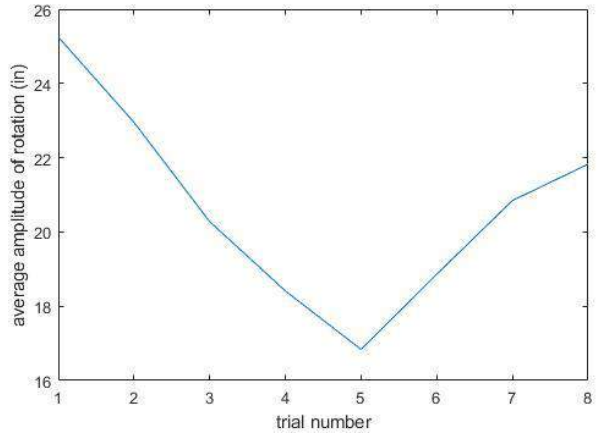

Figure 2. The change in the average amplitude of rotation of the sprinter for each trial.

The variance of each stroke was measured as each data point's distance from the average stroke line. The total variance of each trial was determined and plotted in Figure 3. In both swimmers, the variance tended to become less negative as effort increased.

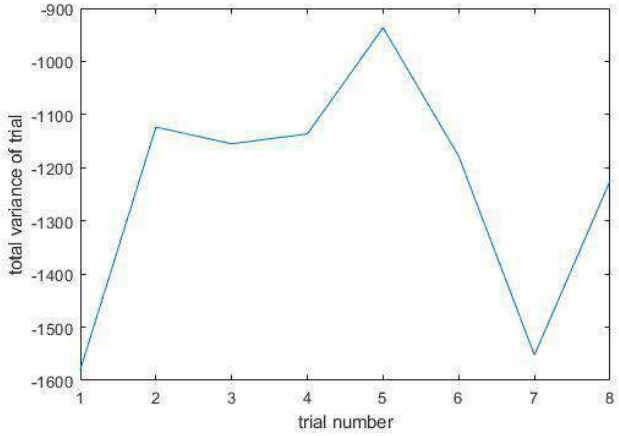

Figure 3. The change in the stroke variance of the sprinter for each trial.

The change in amplitude between left and right strokes did not vary significantly based on effort in either the sprinter or distance swimmer. When the change in amplitude from side to side was divided by the average stroke amplitude to find percent change in symmetry, there was also no significant correlation with effort or fatigue.

DISCUSSION

The data shown aligns with qualitative data often reported by coaches. As swimmers become more fatigued they tend to swim "shorter" or with less length in each stroke and less rotation. This also follows intuition that as swimmers try to swim faster, they will move their arms faster, and have less time to rotate fully to the side for each stroke. The decrease in amplitude of rotation from Figure 2 depicts a "shorter" stroke in trials 4 and 5, which are both at an intensity of 100%.

However, the variance becoming less negative does not seem intuitive. As the swimmer goes faster, he or she will be paying less attention to stroke mechanics, so it may be thought that the variance would be greater. Contrarily, it seems that as the average amplitude gets smaller, there is less room for error from the swimmer, so the overall variance decreases.

Finally, the absence of significant change between left and right strokes shows that neither of these swimmers seem to favor one arm more when they are tired. If the swimmer favors one arm when she is swimming at a normal pace, fatigue does not greatly impact this habit.

Future work would investigate swimmers' amplitudes and variances for longer periods of time along with taking qualitative observations from the swimmers. This will allow for the beginnings of a threshold of safety to be created for symmetry, stroke position, and variance of swimmers in order to prevent future injuries.

ACKNOWLEDGEMENTS

I would like to thank the Valparaiso University Women's Swim Team for their assistance and participation, and Dr. Craig Goehler for his support on this project.

REFERENCES

[1] Strzala M. et al, *Journal of Human Kinetics*, **60**(1), 51-62, 2017
[2] Barbosa T. et al, *Journal of Sports Sciences*, **36**(5), 492-498, 2018
[3] Gatta G. et al, *Journal of Sports Sciences*, **36**(5), 506-512, 2018
[4] Yamakawa K. et al, *Human Movement Science*, **54**, 276-286, 2017
[5] Mangia A. et al, *Sensors*, **17**(4), 927, 2017
[6] Lecoutere and Puers. *Procedia Engineering*, **147**, 627-631, 2016

SB³C2019
Summer Biomechanics, Bioengineering and Biotransport Conference
June 25 -28, Seven Springs, PA, USA

JOINT STIFFNESS MODULATION OF GAIT VARIABILITY IN A STROKE PATIENT DURING GAIT

Geng Li (1), Di Ao (1), Mohammad S. Shourijeh (1), Marleny Arones (1), Carolynn Pattern (2), Benjamin J. Fregly (1)

(1) Department of Mechanical Engineering
Rice University
Houston, Texas, USA

(2) Department of Physical Medicine & Rehabilitation
University of California, Davis
Davis, California, USA

INTRODUCTION

Individuals who become hemiparetic post-stroke demonstrate higher-than-normal gait variability [1]. Increased gait variability impairs stability [2], elevates the risk of falling [3], and hence makes individuals post-stroke more prone to injury during walking. It is therefore important to understand how the gait variability is modulated in the stroke-affected individuals so that effective treatments can be designed to reduce gait variability and improve stability during walking.

Previous studies used either temporal (stride-to-stride time) or spatial (stride length and width) metrics to describe gait variability. This study used joint position variability to address the gait variability in both temporal and spatial sense. This study attempted to investigate whether the joint stiffness, defined as the elastic response created by actuating muscles at the joints to the changes in joint kinematic, had been the modulator of joint position variability.

METHODS

The subject for this study was a right-side paretic chronic stroke survivor. The subject walked on an instrumented treadmill while motion, force, and electromyography (EMG, for 16 leg muscles groups) were collected. The subject's self-selected walking speed was 0.5 m/s. A previous study built a musculoskeletal model of the subject and calibrated the model through an EMG-driven framework until the model-predicted joint moments matched well with those from inverse dynamics [4].

The muscle parameters and forces extracted from the calibrated model were substituted into an analytical formulation to solve for joint stiffness, defined as

$$k_j = -\frac{\partial M_j}{\partial \theta_j} = \sum_{i=1}^{n_M} \left(r_{ij}^2 \frac{\partial F_i^T}{\partial l_i^{MT}} - \frac{\partial r_{ij}}{\partial \theta_j} F_i^T \right) \quad (1)$$

where i represents the i^{th} muscle among the 35 muscles in the model, and j represents the j^{th} degree of freedom (DoF, used interchangeably with joint) among the 6 DoFs in each leg: hip flexion-extension (Hip FE), hip abduction-adduction (Hip AA), hip rotation (Hip Rot), knee flexion-extension (Knee FE), ankle flexion-extension (Ankle FE), and subtalar inversion-eversion (Subtalar IE). r_{ij} is the moment arm for the i^{th} muscle about the j^{th} joint, F_i^T is the tendon force and l_i^{MT} is the length of the muscle-tendon unit for the i^{th} muscle.

In the calculation of the joint position variability, the time between two subsequent heel-strikes of the same foot was defined as a full gait cycle. There were 101 uniformly spaced time points within the gait cycle to represent each percentage of the gait cycle. A full gait cycle was divided into the following five phases: 1st double support (DS1), single support (SS), 2nd double support (DS2), initial-to-mid swing (SW1) and mid-to-terminal swing (SW2). The onset of each phase was determined by detecting foot lifting or landing events from the ground force data for each trial and taking the averages across a total of 10 trials for each leg. For each phase in the gait cycle, only the joint angle data at the center of the phase (removing the first and final 5 time points to avoid outlier data at the transition between two phases) were selected for the calculation of joint position variability (JPV). At each selected time points of the gait phases, the standard deviation of joint angles across different trials was defined as JPV and calculated.

For the same selected time points, the mean of joint stiffness at each point across different trials was also calculated. The Pearson correlation coefficient r between JPV and mean joint stiffness were computed to determine the relationship between JPV and mean joint stiffness.

RESULTS

The phases in each trial determined by the event detection were fairly consistent as the standard deviation of phase boundaries was typically between 2 – 3 % gait cycle. The paretic side had shorter DS1

but longer DS2 phases than the non-paretic side had (22.4 vs 27.4 for DS1 and 22.4 vs 25.5 for DS2), as shown in Table 1.

Table 1: The bound of gait phases expressed as mean (std) in gait cycle %, and selected data points for each phase

	Non-paretic Side		Paretic Side	
Phase	Bound	Selected	Bound	Selected
DS1	27.4 (2.3)	5 – 22	22.4 (1.9)	5 – 17
SS	52.4 (2.2)	32 – 47	48.8 (1.7)	27 – 44
DS2	74.8 (3.1)	57 – 70	74.3 (2.1)	54 – 69
SW1	87.4 (2.1)	80 – 85	87.2 (2.0)	80 – 85
SW2	100.0 (0.0)	90 – 95	100.0 (0.0)	90 – 95

In general, JPV is lower and mean joint stiffness range was paretic side compared to the ones on the non-paretic side. Exceptions were the small stiffness range of Hip FE joint on the non-paretic side during SS phase and large JPV of Subtalar IE joint on the paretic side during SS and DS2 phase (Figure 1 and 2). JPV within SS and the DS2 phases were tightly controlled at most joints except at knee and subtalar joints.

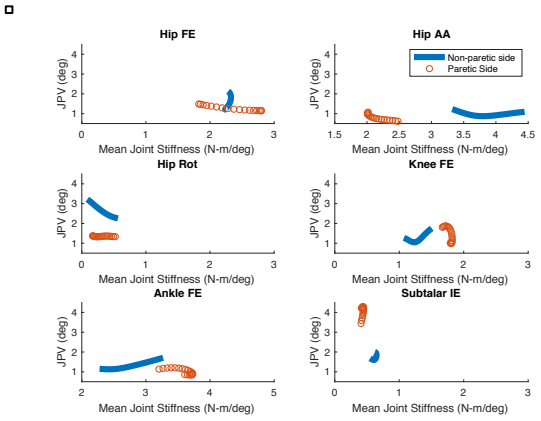

Figure 1: JPV vs mean joint stiffness during SS phase

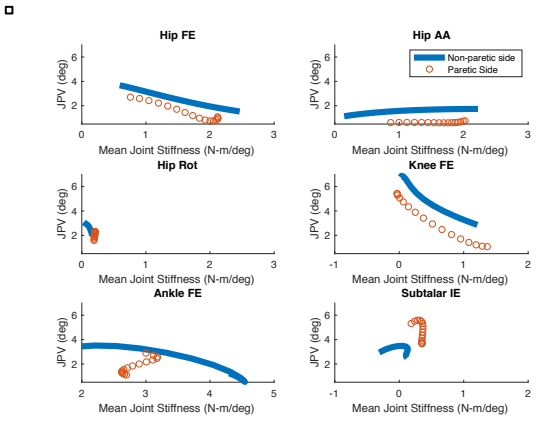

Figure 2: JPV vs mean joint stiffness during DS2 phase

A large proportion of Pearson correlation coefficients that measure linearity in the relationship between JPV and mean joint stiffness were either greater than 0.9 or less than -0.9 (bolded values in Table 2). This indicated that there was strong linear relationship between JPV and mean joint stiffness on during various phases of gait. Majority of the strong linear relationship could be observed on the non-paretic side.

Table 2: Correlation coefficient between JPV and joint stiffness

Non-paretic side at walking speed = 0.5 m/s						
Phase	Hip FE	Hip AA	Hip Rot	Knee FE	Ankle FE	Subtl. IE
DS1	-0.14	**0.94**	**0.97**	**-0.99**	-0.78	0.32
SS	0.75	-0.19	**-0.99**	0.76	**0.96**	0.51
DS2	**-0.99**	**0.94**	**-0.95**	**-0.98**	**-0.95**	-0.18
SW1	-0.77	0.74	**0.96**	**0.95**	**-0.98**	0.44
SW2	**0.94**	**0.99**	**0.99**	**-0.97**	**-0.96**	**0.96**
Paretic side at walking speed = 0.5 m/s						
Phase	Hip FE	Hip AA	Hip Rot	Knee FE	Ankle FE	Subtl. IE
DS1	0.10	**-1.00**	**0.90**	0.77	-0.82	0.32
SS	**-0.98**	**-0.90**	-0.13	-0.74	-0.75	0.51
DS2	**-0.97**	0.45	0.86	**-0.98**	**0.92**	-0.48
SW1	**-0.98**	**-1.00**	0.67	**-0.96**	**1.00**	**-0.91**
SW2	**1.00**	**0.99**	**-0.99**	**1.00**	0.43	**-0.90**

DISCUSSION

Join stiffness could be considered as the response provided by muscles to modulate gait variability. Ideally, a strong negative linear relationship ($r < -0.9$) should be expected as it showed that joint stiffness was modulating gait variability effectively, i.e. decreased JPV when increasing joint stiffness. However, a positive linear relationship did not necessarily mean ineffective modulation of the gait variability. It could mean that the joint still maintained the required level of stability while allowing some freedom in motion. The key criteria in determining the effectiveness of the gait variability modulation should be how much variation was allowed. For instance, during the SS phase, the stiffness of knee and ankle on the non-paretic side increased, but the variability gained minimally (Figure 1, less than 0.5 degree). This could still be considered as effective modulation of joint position variability.

For the three joints (Hip FE, Knee FE and Ankle FE) that governed the motion in the sagittal plane, the ones on the non-paretic side demonstrated more effectiveness in modulating JPV than the ones on the paretic side during the SS phase (Figure 1) where most amount of stability was required and least amount of gait variability was desired. The joints on the non-paretic side operated in lower-stiffness region while allowing the same JPV as the joints on the paretic side did in the higher-stiffness region. The muscles on the paretic side had to exert more effort to generate higher joint stiffness to control the variability.

During the DS2 phase, the paretic side showed lower JPV in all joints except Subtalar IE than the non-paretic side did for same or higher mean joint stiffness (Figure 2). This could be due to that the joints in the paretic side had limited range of freedom. However, this result pointed out that the subject had sufficient stability in the paretic leg during double support stance. Treatment should focus on improving stability during other gait phases when stability was lacking.

The limitation of this analysis was the low number of walking trials (10 trials for each leg) usd. Error in processing the data for one trial could cause the data to be out of sync with data from the other trials and distort variability. The single trial anomaly could be remedied by having large number of trials to minimize the distorting effect. However, calculating joint stiffness of large number of trials could be computationally expensive.

ACKNOWLEDGEMENTS

This work is supported by Cancer Prevention Research Institute of Texas (CPRIT) funding RR170026.

REFERENCES

[1] Balasubramanian, CK et al., *Gait Posture*, 29(3):408-414, 2009.
[1] Tawy, GF et al., *Gait Posture*, 59: 272-277, 2018.
[2] Hausdorff, JM et al., *Arch Phys Med Rehabil*, 82(8):1050-, 2001.
[4] Meyer, AJ et al. *PloS ONE*, 12(7), 2017

SB³C2019
Summer Biomechanics, Bioengineering and Biotransport Conference
June 25 -28, Seven Springs, PA, USA

ANALYTICAL CALCULATION OF MUSCULOSKELETAL JOINT STIFFNESS

Mohammad S. Shourijeh (1), Di Ao (1), Carolynn Patten (2), Benjamin J. Fregly (1)

(1) Department of Mechanical Engineeri
Rice University
Houston, TX, USA

(2) Department of Physical Medicine & Rehabilitation
University of California
Davis, CA, USA

INTRODUCTION

Estimation of muscle forces during human movement could facilitate the development of improved interventions for disorders such as osteoarthritis, stroke, cerebral palsy, and Parkinson's disease [1]. Optimization methods have been often used to predict muscle forces. However, it is well known that these approaches lead to minimized antagonistic coactivation and therefore joint stiffness. During gait, the human body not only varies the forces generated by the lower limbs but also the limb stiffness to control stability or to absorb impacts [2]. While joint stiffness has been identified as a crucial factor in joint stability, many studies have discussed stiffness without clearly describing how to define it. Although many studies have defined stiffness as the slope of the joint moment-angle curve--quasi-stiffness, this quantity does not account for how the system is controlled, i.e., whether the moment is coming from a muscle-actuated or a torque-actuated system. While the majority of studies use quasi-stiffness, few studies have shed light on how to compute stiffness in a muscle-actuated system, e.g. [2], [3]. However, published studies do not provide the complete derivation of their joint stiffness equation.

This study 1) formulates muscle and joint stiffness analytically from musculotendon kinematics and kinetics, 2) verifies the analytical stiffness calculations with a numerical perturbation method, and 3) compares the analytic stiffnesses with the formulation used in previous studies [2], [3].

METHODS

This study used previously collected data from a male chronic stroke survivor with significant walking dysfunction. Motion, ground reaction, and electromyography (EMG; from 16 lower extremity muscles) data were collected simultaneously from the subject as he walked on an instrumented treadmill at 0.4, 0.5, 0.6, 0.7, and 0.8 m/s.

A modified OpenSim ([4]) model with 31 degrees of freedom (DoFs) and 35 muscles was used for the initial musculoskeletal analysis, including detailed scaling, inverse kinematics, and inverse dynamics. An EMG-driven framework was used to calibrate musculotendon parameters based on Meyer et al. [5].

Muscle stiffness was calculated analytically using a custom Hill muscle model with rigid tendon. The stiffness of each joint was calculated using analytical relationships derived from the muscle model. In brief, for any joint j possessing generalized coordinate θ_j and joint moment M_j, joint stiffness k_j was defined as

$$k_j = -\frac{\partial M_j}{\partial \theta_j} = \sum_{i=1}^{n_M} \left(r_i^2 \frac{\partial F_i^T}{\partial l_i^{MT}} - \frac{\partial r_{ij}}{\partial \theta_j} F_i^T \right) \quad (1)$$

where $r_{ij} = -\partial l_i^{MT} / \partial \theta_j$. In contrast, Refs. [2], [3] used the following joint stiffness formulation:

$$k_j = \sum_{i=1}^{n_M} \left(r_i^2 \frac{\partial F_i^T}{\partial l_i^{MT}} + \frac{\partial r_{ij}}{\partial \theta_j} F_i^T \right). \quad (2)$$

In both equations, r_{ij} is the moment arm for muscle i (from 1 to the total number of muscles n_M) about DoF j, F_i^T is the tendon force for muscle i, and l_i^{MT} is the length of the muscle-tendon unit.

For the numerical part, DoFs were perturbed one at a time at each walking joint angle θ_j for a small step of $-\delta\theta$ and $+\delta\theta$. Then the corresponding joint moments (M^- and M^+) were computed using the musculoskeletal equations. Next, using centered finite difference, numerical stiffness was computed as $k_j^{Num} = ({M_j}^+ - {M_j}^-)/2\delta\theta$. Perturbation size (finite difference step size) was varied between 10^{-2} to 10^{-16} to assure finding accurate derivatives.

RESULTS

By decreasing the perturbation step size to $\delta\theta = 10^{-12}$, the analytical and numerical joint stiffnesses matched perfectly, as shown

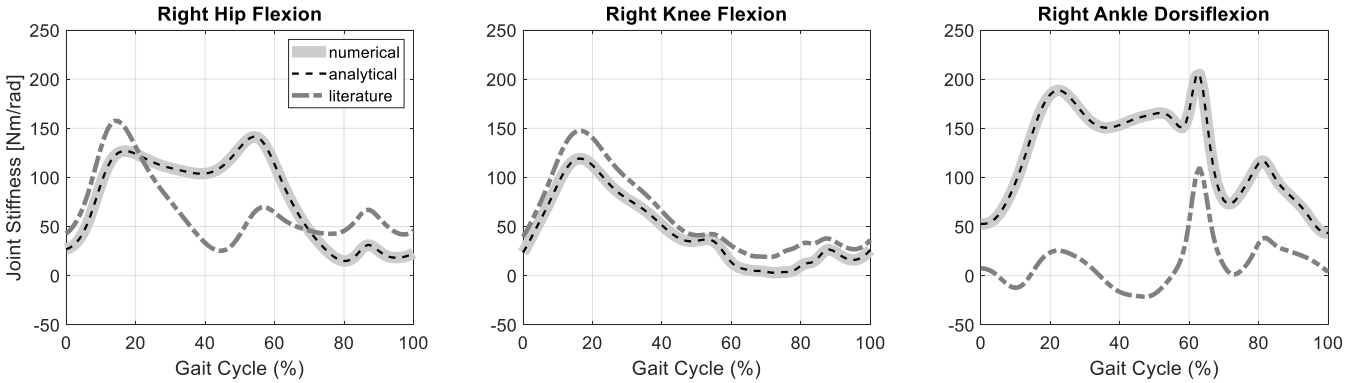

Figure 1) Analytical (dashed black line) versus numerical perturbation (solid thick grey line) and literature (dashed grey line) joint stiffness for hip flexion, knee flexion and ankle dorsiflexion of the right (paretic) side

in Figure 1 for one trial of the patient's self-selected speed (0.5 m/s; as an example) for three representative DoFs: right (paretic) hip flexion, right knee flexion, and right ankle dorsiflexion. Further reduction of the perturbation step size led to jagged results due to truncation errors.

DISCUSSION

Although Pfeifer et al. [2] reported good agreement between their stiffness formulation and experimental joint stiffness data, our study showed that their results differ from the numerical perturbation method. Since our analytical formulation produced identical results to those from the perturbation method, future investigation is warranted to understand the source of the disagreement.

This study introduced an analytical muscle stiffness formulation. The analytical derivation of muscle stiffness was possible due to the use of a custom musculotendon model and parameterization of musculotendon length as a function of generalized coordinates. An analytical expression for muscle stiffness may be useful for many different human-centered applications, such as in biomechanics, rehabilitation, and human-robot interaction. Another benefit of this study's stiffness formulation is the ability to examine the stiffness contribution of individual muscles.

Prediction of muscle forces is crucial in the design of treatments, such as assistive devices and implants. Current biomechanical models result in minimized antagonistic coactivation and therefore joint stiffness levels. Joint stiffness could play an important role in computational algorithms of muscle force prediction. Antagonistic muscles could be recruited to change joint stiffness while the net muscle moment stayed the same. Furthermore, stiffness seems to be correlated with the stability of joints and overall human body movement. Therefore, correctly formulating muscle and joint stiffness may be valuable.

ACKNOWLEDGEMENTS

Cancer Prevention Research Institute of Texas (CPRIT) funding RR170026

REFERENCES

[1] A. Erdemir *et al.*, "Model-based estimation of muscle forces exerted during movements," *Clin. Biomech.*, vol. 22, no. 2, pp. 131–154, 2007.

[2] S. Pfeifer *et al.*, "Model-based estimation of knee stiffness," *IEEE Trans. Biomed. Eng.*, vol. 59, no. 9, pp. 2604–2612, 2012.

[3] M. Sartori *et al.*, "Modeling and simulating the neuromuscular mechanisms regulating ankle and knee joint stiffness during human locomotion," *J. Neurophysiol.*, vol. 114, no. 4, pp. 2509–2527, 2015.

[4] S. L. Delp *et al.*, "OpenSim: open-source software to create and analyze dynamic simulations of movement," *Biomed. Eng. IEEE Trans.*, vol. 54, no. 11, pp. 1940–1950, 2007.

[5] A. J. Meyer *et al.*, "Lower extremity EMG-driven modeling of walking with automated adjustment of musculoskeletal geometry," *PLoS One*, vol. 12, no. 7, p. e0179698, 2017.

SB³C2019
Summer Biomechanics, Bioengineering and Biotransport Conference
June 25 -28, Seven Springs, PA, USA

IDENTIFYING POSTURAL INSTABILITY USING TOPOLOGICAL DATA ANALYSIS

Kyle W. Siegrist (1), James R. Chagdes (1), Amit Shukla (1), Ryan M. Kramer (2), Michael E. Cinelli (3)

(1) Mechanical and Manufacturing Engineering
Miami University
Oxford, Ohio, USA

(2) Air Force Research Laboratory
711th Human Performance
Wright-Patterson Air Force Base, Ohio, USA

(3) Kinesiology and Physical Education
Wilfrid Laurier University
Waterloo, Ontario, CA

INTRODUCTION

Falls are common across a wide range of populations ranging from older adults to individuals with neurological impairments [1,2]. Each year falls lead to injuries in millions of people and accounts for 10-15% of all emergency department visits [3]. In the population of people over 65 years of age, falls are the underlying cause of more than 50% of injury-related hospitalizations and 40% of all nursing home admissions. The financial fallout is a major burden to the United States healthcare system, costing over $31 billion in direct costs alone in 2015 and only expected to continue to increase [1]. Globally this problem is expected to grow significantly because by 2030 the number of people aged 65 and more will have tripled to 1.5 billion [4] and those suffering from neurological impairments will have exceeded 1 billion [5].

Finding effective methods capable of detecting a manifestation of impaired balance when there are no apparent signs of instability can thus improve the quality of life of billions of people while reducing the economic cost. One of the fundamental limitations is that postural instability is rarely identified before a fall occurs, and only then does a patient receive appropriate attention for improving balance control. While prior research has tried to address this by looking for subtle changes in postural sway, there is a lack of connection between these changes and their root cause. An ability to identify the mechanisms responsible for instability and in turn to provide personalized balance training would improve the efficiency of rehabilitation, ultimately reducing the substantial economic cost associated with falls.

To address these limitations Chagdes et al. [6] developed a method for identifying an oscillatory instability predicted by a mathematical model of upright balance when neurological delay is long. While this study successfully identified this instability in over half of the individuals with neurological impairment, the method was unable to distinguish differences between the remaining individuals with neurological impairment and healthy control participants. Furthermore, the method was unable to identify a second instability predicted by the model resulting in a leaning posture when feedback gain was too low.

In this study, we present a novel approach for detecting manifestations of impaired balance and identify the likely mechanism of instability using topological data analysis (TDA) and the inverted pendulum model of Chagdes et al. [6]. TDA uses techniques from topology mathematics to provide a reduction in the dimensionality of datasets and is robust to noise. Using TDA we explore not only the region of oscillatory instability but also the regions of leaning instability and upright stable balance. This is accomplished through a data mapping technique where data is group based on proximities between the data generated by the mathematical model and experimental data of Chagdes et al. [6].

METHODS

Experimental Data: The experimental data consisted of the de-identified center of pressure (CoP) data used in Chagdes et al. [6] of 12 individuals with multiple sclerosis (MS), 12 age-matched healthy controls, and 12 healthy older adults. Participants completed three trials with their eyes-open and three trials with their eyes-closed. Data were collected at 50 Hz for 30 seconds.

Simulation Data: Time series realizations were generated by simulating the mathematical model of Chagdes et al. [6] for 1,500 different combinations of neuromuscular feedback gain and time delay equally spaced across the stability region shown in Figure 1. Time series realization were sampled at 50 Hz for a duration of 30 seconds.

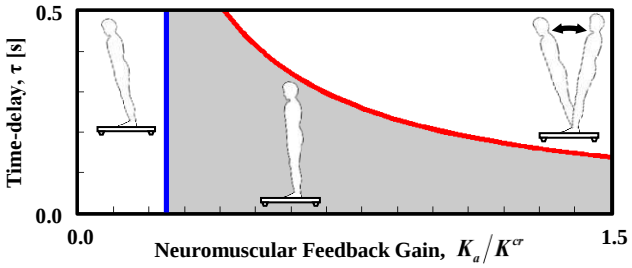

Figure 1: Upright balance stability boundaries predicted by mathematical model showing (left) leaning instability region, (center) stable region, and (right) oscillatory instability region.

Data Transformation and Model Mapping: In their current states the data sets offer a low dimensional comparison in a TDA space as the only variable linking the simulated and experimental dataset was the anterior-posterior CoP. To increase the dimension of comparison we decomposed CoP using the continuous wavelet transform for 128-scales of the Mexican Hat wavelet. All except for the first four of the 128 vectors of wavelet coefficients were then used to create the model mapping between the simulated and experimental dataset. The first four scales were ignored as they were related to frequency ranges above 6.25 Hz beyond the capacity of upright quiet stance.

To accomplish the mapping process, two models were created using the Ayasdi workbench platform: (1) a mapping model, and (2) a classifier model. The mapping model was created using both simulated and experimental data to link experimental behavior to the mathematical model. The link between datasets was created by generating families of related simulation data points based on their proximity to their experimental counterparts. Following this linking, stability of experimental data was quantified by identifying occurrences of this data in the classifier model, which was created from only simulated data. All models were created using the neighborhood lens one and two, a resolution of 70, and a gain of two.

RESULTS

The classifier model (Figure 2) shows three distinct regions. The region highlighted in red corresponds to the stable region and the blue regions to the left and right correspond to the oscillatory instability and the leaning instability respectively.

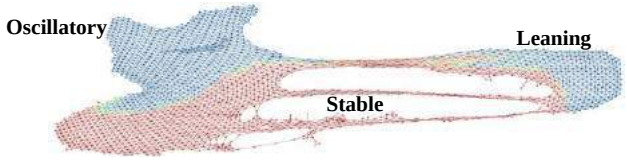

Figure 2: Classifier model constructed from simulation data using the normalized correlation metric.

The subsequent mapping models (Figure 3) show the information density by coloration of the mapping a participant with MS and their healthy counterpart. Red nodes represent data nodes dominated by the subject's experimental data and blue nodes represent nodes saturated by the simulation data. Family grouping of simulation data points from the non-saturated nodes were constructed to map between the simulation and experimental data. These groupings were then mapped back to the original classifier model for both the MS subject (Figure 4) and their healthy counterpart (Figure 5). Classification of upright stability was indicated by coloration with red nodes indicating a large rate of occurrence in a region, blue a low rate, and grey if no occurrence.

Figure 3: Mapping model of (left) a participant with MS, and (right) a healthy MS control participant.

Upon mapping of the MS participant's data back to the classification model (Figure 4), we identified a high correlation to the oscillatory instability region as well as to the boundary between the stable and leaning states. Over all the trials, roughly 56% of this participant's mapped experimental data fell within the stable region, 30.5% fell within the oscillatory region, and 13.5% fell within the leaning region of our classification model.

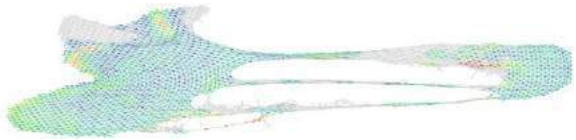

Figure 4: Mapping of experimental data onto the classifier model for a participant with MS.

Similarly, mapping of the healthy MS control participant's data back to the classification model (Figure 5), we identified that the highest correlation was with the stable and leaning regions. Over all trials, about 54.1% of this participant's mapped experimental data fell within the stable region, 36.9% fell within the leaning region, and 9% fell within the oscillatory region of our classification model.

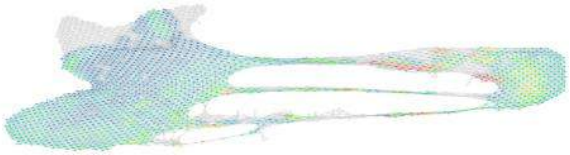

Figure 5: Mapping of experimental data onto the classifier model for a healthy MS control participant.

DISCUSSION

Our analysis shows that the MS participant had a larger amount of data correlated to the oscillatory instability region than their healthy counterpart indicating instances of impaired balance. Furthermore, the large percentage of the MS participant's data falling within the stable and oscillatory instability region supports the findings of Chagdes et al. [6] which identified intermittent instability in this participant.

A limitation of this work is the low number of participant data analyzed. While future studies will aim to analyze the entire data set of Chagdes et al. [6] the current study demonstrates the power of TDA in quantifying postural stability. The framework developed has the potential to not only quantifying postural stability but to identify progression toward impairment, to identify the mechanisms of instability, to provide insight into personalized rehabilitation plans, and to provide feedback on the effectiveness of rehabilitation.

REFERENCES

[1] Burns, ER et al., *J. Safety Res.*, 58 99–103, 2016.
[2] Tinetti, ME et al., *N. Engl. J. Med.*, 331 (13): 821–827, 1994.
[3] Scuffham, P et al., *J. Epidemiol. Community Heal.*, 57 (9): 740–744, 2003.
[4] Suzman, R et al., *NIH Publ. No 117737*, 1 (4): 273–277, 2011.
[5] WHO, *Medicine (Baltimore).*, 229, 2006.
[6] J.R., C et al., *J. Biomech.*, 49 (7): 1170–1179, 2016.

A novel strategy for concurrent reduction of fluid reduction of fluid drag and protein adsorption for cardiovascular medical devices.

Yi-Chih Cheng (1), Yeong Yuh LEE (1), Yi Hui TAN (3), Fung Ling YAP (2), Koon Gee NEOH (3), Choon Hwai Yap (1)

(1) Department of Biomedical Engineering, National University of Singapore, Singapore

(2) Institute of Materials Research and Engineering (IMRE), Agency for Science, Technology and Research (A*STAR), Singapore

(3) Department of Chemical and Biomolecular Engineering, National University of Singapore, Singapore

INTRODUCTION

Cardiovascular medical devices such as blood pumps and blood contacting tubings are important life-saving devices, but are associated with blood damage, which occurs due to two mechanisms. In devices with high flow rates such as blood pumps, high fluid stresses lead to hemolysis and subsequently thrombosis [1], and on almost all artificial surfaces, protein adsorption occurs leading to foreign surface thrombosis reactions [2]. One of the methods recently proposed to decrease hemolysis risk is to reduce fluid shear stresses via surface drag reduction with superhydrophobic coatings [3]. Superhydrophobic surfaces trap a thin layer of air in a micro-/nano-structured surface to enable fluid slip, and is known to reduce drag forces of flowing liquids [4]. However, hydrophobic surfaces are more susceptible to protein adsorption [5], and this can remove the Cassie-Baxter state of the coating and remove slip-flow characteristics. Here, we propose a novel strategy to utilize superhydrophobic surfaces to reduce drag forces and at the same time ensure good functional durability via additional grafting of anti-adsorption material on the surface. To demonstrate the feasibility of this strategy, we grafted polyethylene glycol (PEG) onto PDMS surfaces with micro-patterns (obtained via micro-imprinting), and showed that the resulting surface could concurrently reduce drag and protein adsorption

METHODS

Micro-structured polydimethylsiloxane (PDMS) substrates were prepared using the micro-imprinting technique, at the Institute of Materials Research and Engineering, A*STAR, Singapore. The imprinted PDMS substrate had a regular surface pattern of micro-pillars which were 2 μm in length, width, height and gap spacing (denoted as PDMSμ). SEM images of these patterns are shown in Figure 1. Two methods were used to graft PEG onto the micro PDMS samples, namely, the plasma activation method and silanization activation method. Both methods endowed functional groups (silanol for plasma activation, and epoxy group for silanization activation) on the otherwise inert PDMS surface to enable PEG molecule attachment. Comparing with the plasma activation method, the silanization method allows us to limit the activated area to the top of the pillars since it is difficult for aqueous solutions to penetrate the air pocket between the pillars.

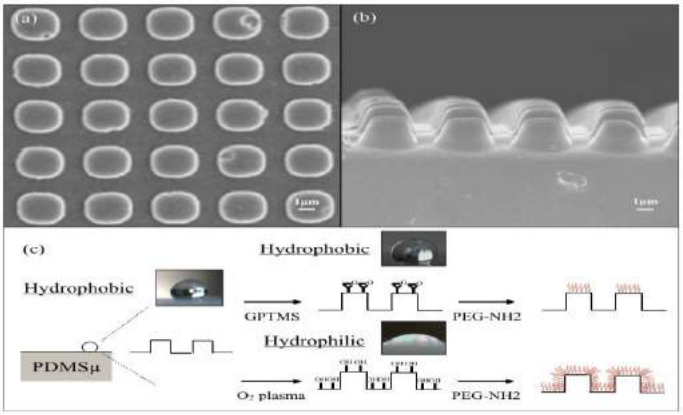

Figure 1 SEM images of (a) top view and (b) side view of PDMSμ. (c) Schematic illustration of the modification of PDMSμ via silanization activation method, and oxygen plasma activation method.

RESULTS

The SEM images in Figure 2 shows the morphology of PDMSμ, and how the morphology evolves over time during incubation in PEG solution. For plasma activation method, the width and the height of the

pillar structures reduced as the PEG-reaction time increased due to PEG deposition at all locations on the surface, both on the pillar and in the depressions between pillars. As deposition advanced, the new pillar structures, composed of PEG alone, would gradually adopt narrower, sharper and shorter pillar shapes. With silanization activation on the other hand, PDMS could only be deposited on the tips of the pillar structures, since wet chemistry was employed for the deposition, and the water-based solutions could not get into the depressions between pillars due to the Cassie-Baxter state of the surface. To obtain more quantitative measurements of the morphology, AFM measurements were taken (Figure 2 c-d). The results showed that PDMSμS had more uneven pillar tip surfaces, demonstrating PEG deposition. Figure 2e shows the contact angle characteristics for both PDMSμS and PDMSμP. With more advanced PEG deposition, PDMSμS showed a small gradual reduction in contact angle. PDMSμP on the other hand, demonstrated a drastic decrease initially, but regained higher contact angle with longer reaction times.

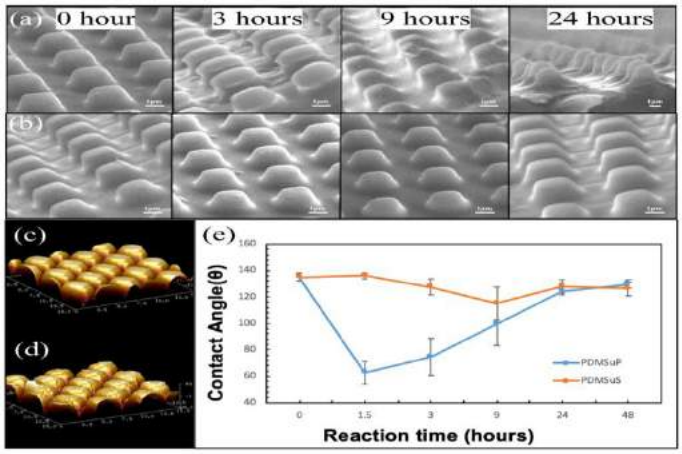

Figure 2 SEM images of oblique view of (a) PDMSμP and (b) PDMSμS after immersion in PEG solution for different durations; AFM images of (c) pristine PDMSμ, (d) PDMSμS-24; (e) contact angle trend of PDMSμP (blue line) and PDMSμS (red line) after immersing for different reaction time.

To evaluate its anti-fouling ability and drag reduction performance, we did series of experiment. In Figure 3., protein adsorption on PDMSμ decreased by 25% compared to plain PDMS. This could be due to the smaller contact area between surface structures and the protein solution, due to the Cassie-Baxter state of PDMSμ. For PEG-modified PDMSμ surfaces, both activation methods decreased the protein adsorption dramatically, with over 80% decrease for the plasma activation method. PDMSμP performed better than PDMSμS most likely because it was more thoroughly coated with PEG. The results of the water jetting test are shown in Table 1. The PEG-modified flat PDMS (PDMSP) does not show an increase in drag force compared to flat PDMS, suggesting that no-slip flow condition was found in both, and either surface could be used as control. Comparing PDMS and PDMSμ, it can be seen that addition of microstructures to PDMS resulted in significant decrease of flow drag forces, which is consistent with the literature on how the Cassie-Baxter state can enable drag reduction, especially at lower jetting velocities. In the case of the PEG-coated samples, the drag reduction was observed as well, which shows that the surface maintains the Cassie-Baxter state even though hydrophilic polymer was deposited on the surface. At the higher jetting velocities, the dynamic pressures imposed by the jet increases fluid pressure on the sample surfaces, and could be suppressing the Cassie-Baxter state to reduce slip flow.

Table 1 Friction drag reduction percentage of pristine PDMSμ and modified PDMSμ under different water flow velocity.

flow rate(m/s)	PDMSP-24	Pristine PDMSμ	PDMSμS-24	PDMSμP-24
3.61	1%	16%	5%	7%
3.99	1%	9%	6%	10%
4.29	0%	7%	5%	9%
4.67	0%	11%	5%	9%
Average	0%	11%	5%	9%

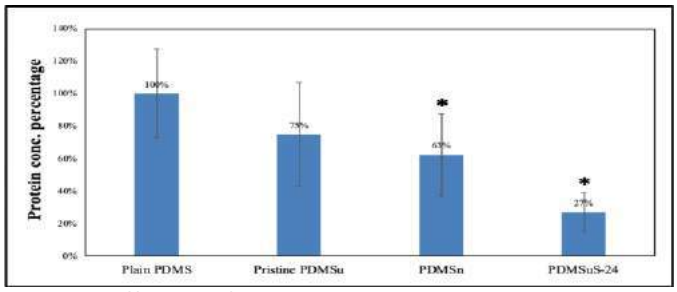

Figure 3 Difference of the protein adsorption amount under static environments (immersing in 1mg/ml BSA solution for 4 hours). Significant differences compared to the plain PDMS surface ($p < 0.05$) are marked *.

DISCUSSION

Test results showed that both PEG grafted surfaces reduced protein adsorption compared to untreated PDMS surfaces, and both retained some drag reduction capabilities. Further, PDMSμP was more successful than PDMSμS at reducing flow drag and protein adsorption, and was more functionally durable when fouled with protein. Recently, there has been substantial interest in using superhydrophobic surfaces for medical tubings and conduits to tap into their drag reduction capabilities [6], and such tubings were observed to repel blood and reduce coagulation [7]. This approach can be used on medical conduits with low pressure, such as venous blood tubings, drug and saline tubings, and venous catheters, where there is an absence of high pressure to breach the Cassie-Baxter state. The PEG-modified PDMS microstructured surfaces in the current study will be very suitable for such applications as well, given their anti-fouling and drag-reduction properties. The present work thus validated the strategy of grafting anti-adsorption polymer to slip-flow material to retain benefits of both anti-fouling and drag reduction. However, the materials investigated were not yet optimized, and other anti-fouling polymers and substrates might be able to enhance the extent of anti-fouling and drag reduction. Future work to investigate and optimize this is thus much warranted.

ACKNOWLEDGEMENTS

This work was supported by Institute of Materials Research and Engineering (IMRE), Agency for Science, Technology and Research (A*STAR), Singapore (PI: Yap) and the National Research Foundation (Singapore) Grant number NRF2017-IT002-012 (PI: Yap).

REFERENCES

[1] L. B. Leverrtt, et al., *Biophysical Journal*, 12:257, 1972.
[2] I. H. Jaffer, et al., *J Thromb Haemost*, 13(2): S72–S81, 2015.
[3] C. Q. Lai, et al., *RSC Advances*, 6(67): 62451–62459, 2016.
[4] H. Park, et al., *J Fluid Mech*, 747: 722–734, 2014.
[5] L. Santos, et al., *Cont Lens Anterior Eye*, 30(3):183–188, 2007.
[6] J. H. Jeong, et al., *Colloids Surf B Biointerfaces*, 371–379, 2000.
[7] P. Harder, et al., *J Phys. Chem. B*, 102(2):426–436, 1998.

SB³C2019
Summer Biomechanics, Bioengineering and Biotransport Conference
June 25 -28, Seven Springs, PA, USA

INTEGRATED SWITCHABLE VENTRICULAR ASSIST DEVICE FOR PEDIATRIC PATIENTS

Harut Sarkisyan MS (1), Randy Stevens MD (2,3), Amy Throckmorton PhD (1)

(1) Biomedical Engineering
Drexel University
Philadelphia, PA, USA

(2) Pediatrics, College of Medicine,
Drexel University
Philadelphia, PA, USA

(3) Heart Center for Children
St. Christopher's Hospital for Children
Philadelphia, PA, USA

INTRODUCTION

Each year, thousands of pediatric patients develop premature congestive heart failure (CHF) due to exposure to bacteria or viruses that attack the heart's muscle tissue or due to being born with congenital heart defects.[1,2] Most severe cases require heart transplantation or the use of short or long-term mechanical circulatory support (MCS) systems, such as ventricular assist devices (VADs). VADs have demonstrated success as a bridge-to-transplant and bridge-to-recovery in a small number of pediatric patients.[3,4] VADs specifically for children, continue to lag behind those developed for adults. In addition, there is no heart pump with the design innovation to support the dysfunctional states of heart failure and the range of the anatomic and physiological heterogeneity in pediatric patients from one stage of development to another. To address this unmet clinical need, the BioCirc Lab is developing a dual-configured mechanical pumping device that has an axial pump parallel in configuration with a centrifugal pump, as shown in **Figure 1** below.

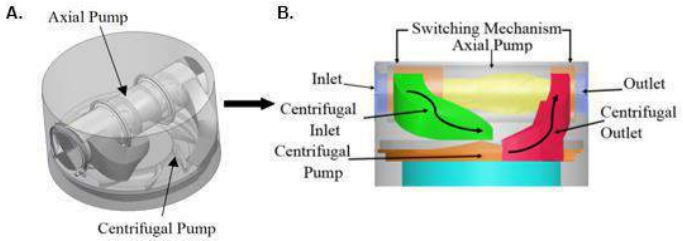

Figure 1: A. Orientation of the two pumps in a single housing. B. Blood flow path within the VAD

This innovative new medical device will have the ability to switch from the axial pump to the centrifugal pump, as the patient ages or as the pressure/flow demands increase. The pumping system is being designed to be able to deliver flows of 1 - 5 L/min and pressure rises of 50 - 120 mmHg at 2,000 - 14,000 RPM. The impellers of these blood pumps are levitated using magnetic bearings and rotated by motor magnets. In this study, we focus our efforts on the initial design of the centrifugal and axial blood pumps for this new medical device.

METHODS

The design of the centrifugal pump was performed based on the Taguchi optimization method, which allowed us to find the optimal parameters. The axial pump was previously designed. Computational fluid dynamics simulations was conducted in order to find the optimal parameters for both an axial and a centrifugal pump. ANSYS CFX computational fluid dynamics software was used to generate the mesh and model for simulation. The axial pump is divided into the following sections: inducer, impeller, diffuser, and straightener. Each section was iteratively improved, while modifying the length, height, thickness, inlet and outlet angles, and twist angle. Grid independence and mesh quality studies were performed for each pump design. The axial pump was evaluated at operational speeds of 10,000 RPM to 14,000 RPM. The axial pump is being designed to generate 50-80 mmHg at 1 to 3 LPM for 10,000 to 14,000 RPM. The design goal was to meet the pressure-flow requirements for a pediatric patient, while also maintaining the scalar stress below 425 PA, radial force below 1 N, residence time below 600 ms, blood damage index below 2%, and axial force below 10 N. The centrifugal pump is being designed to generate 80-120 mmHg at 3 to 5 LPM for 2,500 to 3,500 RPM. The following centrifugal pump parameters and levels were considered for

optimization; shroud clearance (0.15mm, 0.25mm, 0.35mm), blade number (4, 5, 6), twist angle (30º, 60º, 90º), and angle difference between the top and bottom of the blade at the trailing end (3º,5º,8º). Four parameters with 3 levels in each results in Taguchi matrix based on **Equation 1** below.

$$N = 1 + \sum_{i=1}^{IndVar} (Levels(i) - 1) \qquad (1)$$

IndVar represents the number of impeller parameters, Level represents how many values for each parameter are being considered, and N represents the minimum number of designs needed. The 9 centrifugal designs were then analyzed by simulation to predict pressure generation, scalar stress, axial and radial fluid forces on the surfaces of the impellers, fluid residence time, and blood damage levels.

RESULTS

The axial pump has an overall length of 50 mm. The impeller is designed to have 4 blades. **Figure 2** shows that the axial pump is able to provide 50-80 mmHg for 1 to 3 LPM for operating speeds of 11,000 to 14,000 RPM.

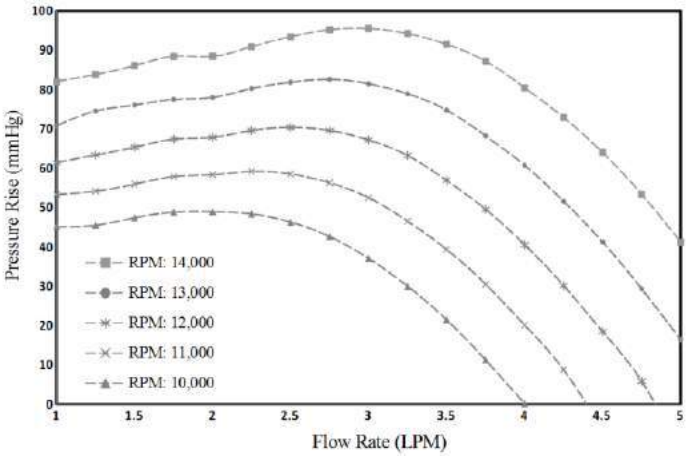

Figure 2: Pressure generation profile of the axial pump

The scalar stress, blood damage indices, fluid residence time, radial and axial forces were all within the target limits for the axial pump. However, at the highest rotational speed and lowest flow rate, we did estimate a higher than expected scalar stress level. The optimal centrifugal design obtained through the Taguchi Optimization method has an overall diameter that is less than 50 mm with 6 blades, shroud clearance of 0.15mm, twist angle of 90º, and angle difference of 8º. **Figure 3** illustrates that the centrifugal pump is able to provide 80-120 mmHg for 3 to 5 LPM while running at 2,500 to 3,500 RPM.

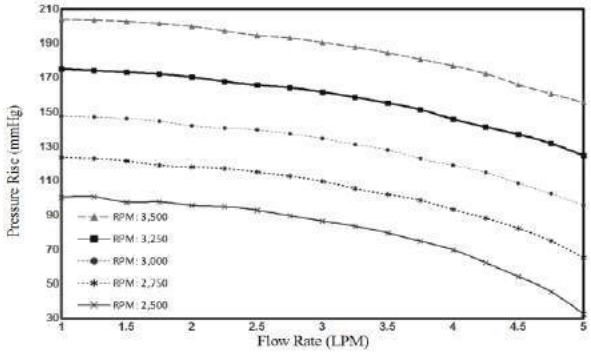

Figure 3: Pressure generation profile of the centrifugal pump

The average scalar stress, blood damage index, residence time, radial forces were all within the desired limits. For the axial pump the maximum axial and radial forces were 0.7N and 0.04N and for the centrifugal pump the maximum radial force was 0.75N. The resulting conceptual design of the axial and centrifugal pumps are shown in **Figure 4**. An axial and a centrifugal pump are positioned in parallel with respect to one another in a single housing.

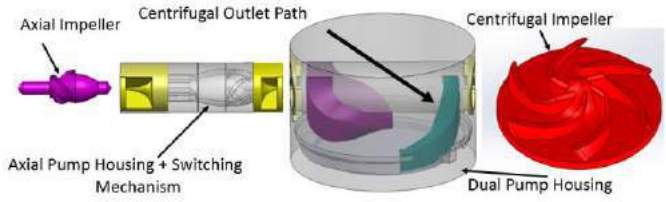

Figure 4: Exploded view of the blood pump

DISCUSSION

The parameters and values chosen for the Taguchi Optimization Method led to a centrifugal pump design that met the target performance values required to support pediatric patients. The axial pump was iteratively improved until recirculation was virtually illuminated within the impeller and diffuser regions. The centered position of the impeller and the height of the blades for both the axial and the centrifugal pump lowered the axial and radial forces below the threshold values. For centrifugal pumps the distance between the shroud and blades added with the distance from the blade trailing end to the edge of the hub had a substantial impact on scalar stress and blood damage index. In case of the axial pump, the distance between the leading edge of the impeller blades and the straightener blades combined with the distance between the trailing edge of the impeller blades and diffuser blades had a significant impact on scalar stress and blood damage index. Scalar stress values of each blood particle were low in magnitude, thus maintaining the blood damage index near 2%. Results of the CFD studies shows that the Taguchi Optimization method is a beneficial tool for designing a blood pump for pediatric patients. All the computational simulations were conducted at steady state conditions. In order to better predict the performance of the pumps next stage would be to carry out further computational simulations using quasi-steady flow and transient flow. We also seek to experimentally verify through prototype testing using a water-glycerin mixture.

ACKNOWLEDGEMENTS

The authors wish to acknowledge the financial support as partially provided by a 2016 Individual Biomedical Research Award from The Hartwell Foundation.

REFERENCES

[1] Schultz, A.H. et al., *The Journal of thoracic and cardiovascular surgery*, *154*(1), 273-281.

[2] Benjamin, E. J., et al. "American Heart Association Statistics Committee and Stroke Statistics Subcommittee." *Heart disease and stroke statistics-2017 update: a report from the American Heart Association. Circulation* 135.10 (2017): e146-e603.

[3] Kirlin, J. et al., *INTERMACS Quality Assurance Quarterly Report (2016 Q4) - Cumulative*. 4th ed. [ebook] Interagency Registry for Mechanically Assisted Circulatory Support, pp.1-116.

[4] Kirklin, J. K. et al., Sixth INTERMACS annual report: a 10,000-patient database. *The Journal of Heart and Lung Transplantation*, *33*(6), 555-564.

SB³C2019
Summer Biomechanics, Bioengineering and Biotransport Conference
June 25 -28, Seven Springs, PA, USA

EXPERIMENTAL MODELING OF CORONARY INTERVENTION: TOWARDS COMPUTATIONAL SIMULATION

Maxwell J. Bean (1), David Jiang (2), Sam E. Stephens (1), Megan E. Laughlin (1), Hanna K. Jensen (1), Barry Uretsky (3), Lucas H. Timmins (2), Morten O. Jensen (1)

(1) Dept. of Biomedical Engineering
University of Arkansas
Fayetteville, AR, USA

(2) Dept. of Biomedical Engineering
University of Utah
Salt Lake City, UT, USA

(3) Interventional Cardiology
Univ. of AR for Medical Sciences
Little Rock, AR, USA

INTRODUCTION

Bifurcation lesions are the most frequent complex coronary lesion encountered in everyday interventional practice. Accounting for up to 20% of all coronary disease treated by percutaneous coronary intervention, they pose a significant challenge to present stenting techniques, resulting in lower success and higher complication rates compared to non-bifurcation lesions [1,2]. Current coronary artery bifurcation stenting techniques entail a high level of operative complexity as the main and side branches of the bifurcation must be treated separately. Further, certain contemporary techniques leave areas of the bifurcation exposed outside of the stent, creating a predisposition to turbulent flow and restenosis. Additional techniques utilize overlapping or adjoining stents, which can create a high amount of stress on the arterial wall leading to vascular neointimal growth and restenosis [3].

Current information on the flow and stresses that coronary artery stents are exposed to, especially in a bifurcation, is limited. This project aims to establish an experimental model of coronary stent implantation to advance optimal stent design through evaluation of post-deployed stent and lesion geometry, as well as provide an approach to produce input and validate future finite element modeling techniques. The overall goal is to determine the forces that stents encounter in the bifurcation along with providing indications for optimal stent designs to treat a bifurcation lesion using coronary intervention.

METHODS

To investigate the biomechanics of stented coronary arteries, experimental data from the Cardiovascular Biomechanics Laboratory at the University of Arkansas are summed into three major components: the artery, the stent and the balloon. The artery is evaluated at specific lesion geometries with a pre-defined Medina classification, consisting of the main branch, distal branch, and side branch with predetermined divergent angles. Specific parameters are being investigated and will be ready for presentation at the 2019 SB3C conference. A novel method of creating tissue mimicking phantoms has been developed in collaboration with industry (Humimic Medical, Ft. Smith, AR).

Geometry data was gathered from a 2.25 mm diameter cobalt chromium Mini Vision Multi-link stents (Abbott Laboratories) using a Nikon XT H 225 ST μCT system in both the crimped and deployed states. The deployed stent was expanded with 9 atmospheres of pressure using the polyethylene terephthalate balloon included with the device from the manufacturer.

RESULTS

A successful scanning of the stents was completed, and the acquired data was converted to a 3D Computer Aided Design model using a custom developed MATLAB script. The files were reconfigured and prepared for future use in a Finite Element Modeling simulation of a deployed stent in the bifurcation. Said scanned files are displayed in Figure 1.

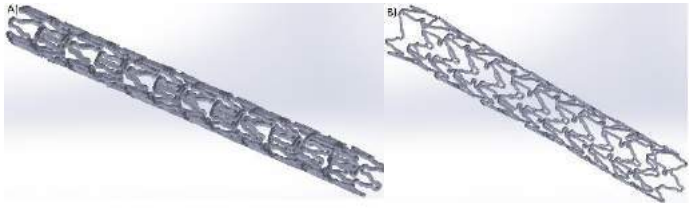

Figure 1: 3D scans of a commercially available Multi-link stent in the crimped (left) and deployed (right) states

Provided a three-dimensional model of the coronary artery geometry, an artery exhibiting stenosis can be fabricated using the tissue mimicking gel. The tissue mimicking phantoms with

blood vessels can be utilized for in vitro testing of medical devices, such as coronary stents. (Fig 2).

Figure 2: Example of gel phantom containing an artery

The mechanical and acoustic properties of the human tissue mimicking gel and blood vessels can be closely matched to that of in vivo cardiac and surrounding tissues, including arteries. This provides an ideal in vitro model for validating future computational simulations, and will be used for the bifurcation lesion experimental setup. Three-dimensional models of the bifurcation exhibiting various degrees of stenosis were successfully created, two of which can be seen in Figures 3A and 3B. While deployed in the phantom, the crimped and deployed stents will be scanned using the μCT machine as is shown in the exploded view of Figure 3C.

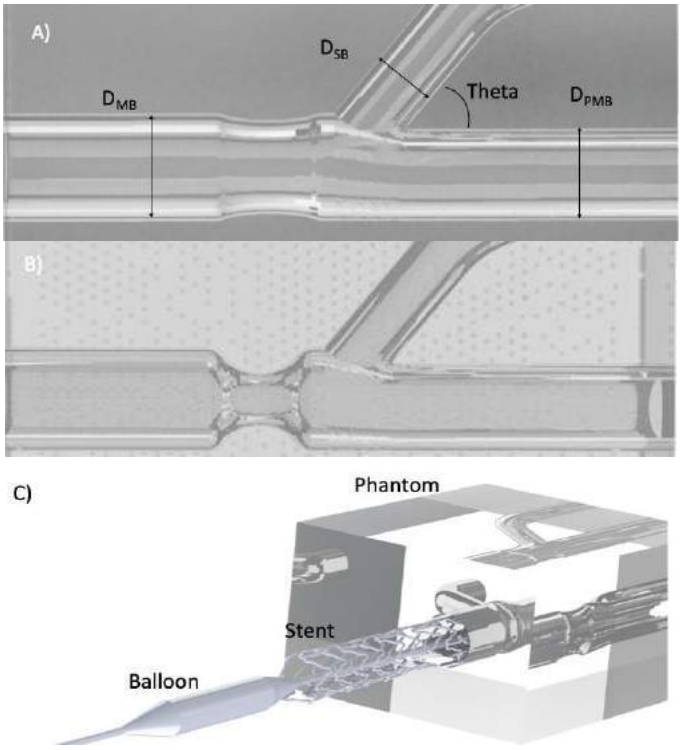

Figure 3: 3D models of bifurcation lesion phantoms at two different stenosis percentages (A & B); C) stenosis induced phantom with a Multi-link stent and a standard sized 10mm diameter balloon

DISCUSSION

Currently, stents used in treating bifurcations create a predisposition to high rates of in-stent-stenosis, thrombosis, and adverse clinical events. By clarifying the stresses and strains exerted on the stented vessel, this study can contribute to enhanced understanding of the unique therapeutic requirements for coronary bifurcation lesions.

Data from the crimped stent experiments will provide a parametrical basis and boundary conditions for future computational simulations, while the deployed stent will be used for validating these simulations. The results can provide a platform for the development of novel stent designs that will decrease stress on the arterial wall, thus reducing the risk of long-term complications. Additionally, the future framework of this study utilizing the Finite Element software will decrease development time and testing of superior stenting devices and procedures to reduce current efforts in optimizing stent design and pave the way for innovative technology to improve clinical outcomes for those suffering from coronary artery disease [4].

ACKNOWLEDGEMENTS

This work was supported by American Heart Association Grant #18AIREA33960590 and the Arkansas Research Alliance.

REFERENCES

[1] M. Michael *et al.*, "Acute procedural and six-month clinical outcome in patients treated with a dedicated bifurcation stent for left main stem disease: the TRYTON LM multicentre registry," *Eurointervention Journal*, vol. 8, no. 11, Mar. 2013.

[2] A. Latib and A. Colombo, "Bifurcation Disease: What Do We Know, What Should We Do?," *JACC: Cardiovascular Interventions*, vol. 1, no. 3, pp. 218–226, Jun. 2008.

[3] L. H. Timmins, M. W. Miller, F. J. Clubb Jr, and J. E. Moore Jr, "Increased artery wall stress post-stenting leads to greater intimal thickening," *Laboratory Investigation*, vol. 91, no. 6, pp. 955–967, Jun. 2011.

[4] N. Li, H. Zhang, and H. Ouyang, "Shape optimization of coronary artery stent based on a parametric model," *Finite Elements in Analysis and Design*, vol. 45, no. 6–7, pp. 468–475, May 2009.

SB³C2019
Summer Biomechanics, Bioengineering and Biotransport Conference
June 25 -28, Seven Springs, PA, USA

AGONIST / ANTAGONIST CONTROL COMBINING MIXED SENSITIVITY DESIGN AND ITERATIVE LEARNING

Patrick J. Schimoler (1,2), Jeffrey S. Vipperman (2), Mark Carl Miller (1,2)

(1) Department of Orthopaedic Surgery
Allegheny General Hospital
Pittsburgh, PA, 15212

(2) Department of Mechanical Engineering
and Materials Science
University of Pittsburgh
Pittsburgh, PA, 15261

INTRODUCTION

Cadaveric experimentation provides orthopaedic researchers with the ability to make invasive measurements and apply multiple test conditions to the same specimen but is without active, internal actuation. Researchers have overcome this shortcoming by developing cadaveric testbeds known as joint motion simulators (JMSs). JMSs typically actuate a joint specimen by rigidly supporting one side of the specimen while leaving the other side free to be actuated by a motor driven, cable system that connects to muscle insertion sites along physiologic lines of action. Paralleling a joint's natural structure, a JMS's cable actuation often works in opposing agonist / antagonist (AA) arrangements.

JMS control is complicated by the uni-directional nature of cable actuation, geometric nonlinearities, specimen variation, and specimen degradation. An ideal JMS control system would be stable and have accurate joint position and tendon tension control with the potential for small cable tensions and without the need for specimen specific adjustments. Cable actuated AA systems, possessing all but the biological complications, have been studied in robotics and controlled with mixtures of position and tension control [1, 2]. Mixtures of position and tension control have also been applied in JMS control [3].

Our hypothesis is that the position / tension control paradigm can be extended with a combination of mixed sensitivity robust control, tendon tension source switching, and iterative learning control (ILC) to form an ideal JMS control system. Nonlinearities and specimen variation can be lumped into the uncertainty accounted for in the robust control framework which provides stability and decoupling. Tendon tension source switching allows small tendon tensions and prevents slack, alleviating many of the cable actuation complications. ILC, its prerequisites met by the robust closed loop system, adapts feedforward inputs for each specimen to accurately track commanded joint position and tendon tension trajectories.

As a first step in validating this approach, this control combination was applied to a simple AA system consisting of a single degree of freedom (DOF) joint actuated by two opposing actuators (Figure 1).

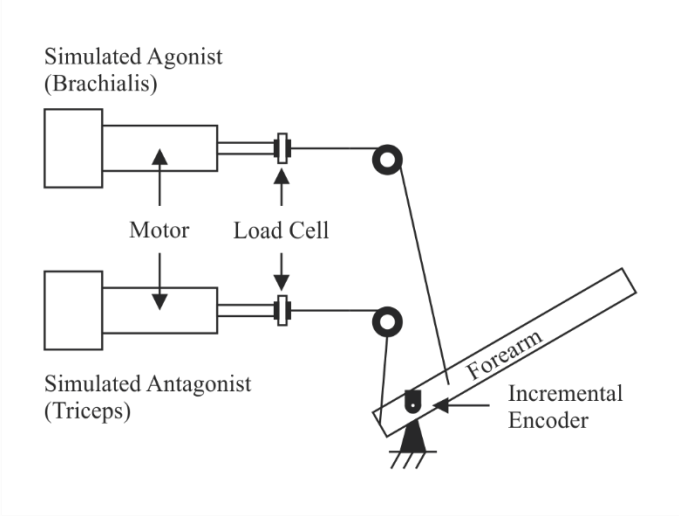

Figure 1: Elbow flexion as an agonist / antagonist pair.

METHODS

The control approach was applied to and tested on an existing elbow JMS validated to have physiologic geometry [4]. The motors and pulleys designed to simulate the brachialis and triceps were connected to a mechanical elbow whose motion was restricted to flexion /

extension (FE) to form an AA system. A linear decoupling matrix, designed as a function of moment arms and stiffnesses in the middle of the elbow's FE range, was inserted prior to the brachialis and triceps velocity inputs giving approximate joint position and tendon tension decoupling. Using a stepped sign approach, transfer functions were identified at 60°, 90°, and 120° of flexion from inputs of joint position velocity and tendon tension velocity to outputs of joint position and tendon tension. A nominal model and uncertainty models were assembled from these identified transfer functions. A mixed sensitivity robust controller was designed using the nominal model, desired performance, input voltage limitations, and plant uncertainty [5]. If the original decoupling was not accurate, the robust design decoupled the system based on the identified transfer functions. Tendon source switching was accomplished with logic that closed the tension control loop with the smaller of the brachialis and triceps tensions. With the approximate decoupling of joint position and tendon tension control; independent, proportional ILCs were designed to generate and update tracking references for joint position and tendon tension [6].

The system was commanded to track a 90° flexion cycle in 5s. Antagonist tension was to be maintained at 3N. The ILC was iterated 20 times. The maximum and RMS joint position and tendon tension errors were calculated for each trial.

RESULTS

Over the course of 20 trials, maximum joint position error was reduced below 0.25° and RMS joint position error was reduced to 0.10° (Figure 2). Over the same trials, maximum tendon tension error was reduced to 0.50N and RMS tendon tension error was reduced to below 0.15N (Figure 3). All error reductions were approximately monotonic.

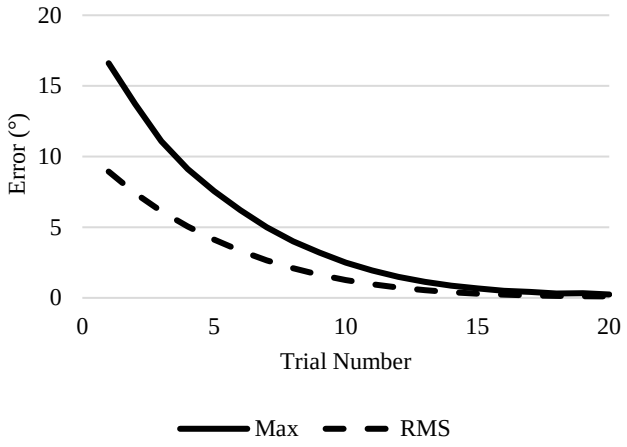

Figure 2: Max and RMS joint position error as a function of trial number.

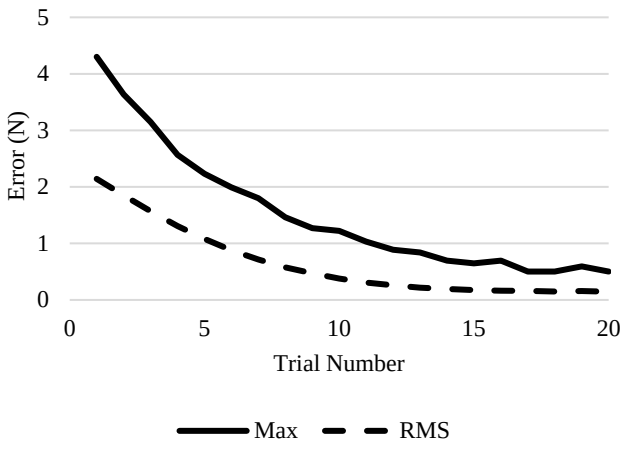

Figure 3: Max and RMS tendon tension error as a function of trial number.

DISCUSSION

A combination of mixed sensitivity robust control, tendon tension source switching, and ILC successfully reduced joint position and tendon tension errors in an AA system performing a common motion in JMS related testing. Oscillations at the FE natural frequency of the system prevented further reductions in error. The work was limited in that it tested only a single degree of freedom system. Additionally, only one elbow specimen, a mechanical analog, was tested. Further work will extend the approach to 2 DOFs adding pronation / supination to FE as well as test the approach across a range of cadaveric elbows.

REFERENCES

[1] SC Jacobsen et al., Control Systems Magazine, 10(2): 23-28, 1990.
[2] V Potkonjak et al., Int. J. Adv. Robotic Sy., 8(5): 143-155, 2011.
[3] L Ferreira, U. Western Ontario, PhD, 2011.
[4] L Kuxhaus et al., J. Med. Devices, 3(3): 031002/1-7, 2009.
[5] S Skogestad and I Postlethwaite, Multivariable Feedback Control, 2007.
[6] K Moore, Iterative Learning Control for Deterministic Systems, 1993.

SB³C2019
Summer Biomechanics, Bioengineering and Biotransport Conference
June 25 -28, Seven Springs, PA, USA

ANALYSIS OF A POLY(ETHYLENE GLYCOL) DIACRYLATE (PEGDA) OPTICAL SENSOR-BASED WHISPERING GALLERY MODE SHIFT SUBJECTED TO SHOCK WAVE IMPACT

Ling Zhang (1), Maurizio Manzo (2), Sarah A. Bentil (1)

(1) Department of Mechanical Engineering
Iowa State University
Ames, Iowa, USA

(2) Photonics Micro-Devices Fabrication Lab (PMDF)
Department of Engineering Technology
University of North Texas
Denton, TX, USA

INTRODUCTION

Hydrogel based polymers are usually applied in tissue engineering and drug delivery applications, due to characteristics that include non-fouling behavior and tunable density. Microscale pressure sensors, based on whispering gallery mode, have been used to measure steady state and unsteady wall pressure in fluid mechanics and biomedical applications [1-3]. A microscale resonator, spherical, dome-shaped, and disk shape, made with polymer is embedded in soft materials [1-3]. What remains unknown is whether this type of sensor, embedded in soft materials, can be used to measure shock wave pressures caused by improvised explosive devices (IED). This study applies finite element methods to quantify the diametral deformation of microspherical resonators based whispering gallery mode (WGM) sensor, embedded in a soft material and subjected to shock wave impact. The diametral deformation can be correlated to the shift of optical resonances; the optical resonances shift is then correlated to the pressure variation. The sensing element is made with poly(ethylene glycol) diacrylate, known as PEGDA. The results of this work will provide design guidelines for manufacturing PEGDA sensors to measure dynamic pressure in soft materials and brain tissue.

METHODS

Finite element (FE) analysis of PEGDA embedded in polydimethylsiloxane (PDMS) was performed. The aim of this analysis is to quantify the diametral change of the PEGDA sensor embedded in PDMS during shock wave loading [4].

A hemispherical-shaped PDMS, simulating a simplified brain geometry, is used to study shock wave impact, while the geometry of the PEGDA sensor is spherical. The diameter of the hemispherical PDMS is 50 mm and the diameter of the spherical PEGDA sensor is 13 μm, which is 0.26% of the PDMS. Simplification of the FE simulation was made by considering a small region around the spherical sensor. Thus, the geometry of the PDMS is a brick (Figure 1). The size of the bricked-shaped PDMS is $0.1 \times 0.1 \times 0.04\ mm^3$. However, future simulations will consider a larger brick dimension to determine the optimal brick size.

The spherical PEGDA sensor is halfway embedded into the PDMS and the two contact faces were set with a bonded boundary condition. The top-half surface of the spherical PEGDA sensor is a free surface, and the bottom-half are internal surfaces. For the brick-shaped PDMS, not all faces are free surfaces. Rather, the four edges of the PDMS shown in Figure 1 are fixed, which allow the deformation to be symmetric.

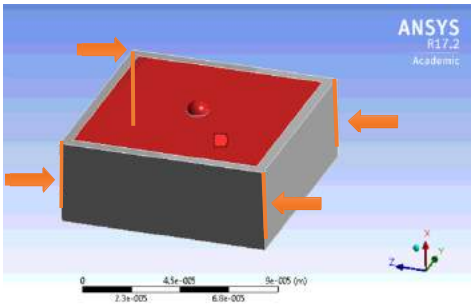

Figure 1: Geometry of spherical PEGDA sensor and PDMS brick in the FE simulation. Edge fixed support locations are depicted by the orange arrows. The pressure (red) applied to the top surface of the PEGDA sensor and PDMS are also shown.

Pressure load data was taken from shock tube experiments conducted in the laboratory. In these experiments, a pressure transducer

(PCB 113B22) was placed at the end of a custom-built shock tube to measure the pressure applied on the sample. This pressure was applied on the surfaces of the PEGDA and PDMS shown in Figure 1. The pressure measured from the dynamic pressure transducer is shown in Figure 2. To avoid conflict with the fixed support boundary condition placed on the PDMS, the pressure was not applied on the edge of the surface.

An isotropic elastic model was applied for both the brick-shaped PDMS and the PEGDA pressure sensor. The Young's modulus of PDMS is $3 \times 10^6\ Pa$, while the Young's modulus of PEGDA is $1 \times 10^5\ Pa$, which is much softer than PDMS [3, 4]. Poisson's ratio for both PDMS and PEGDA is 0.49, since an incompressible assumption was made. A tetrahedral mesh was applied. The total number of elements was 450,000, which was chosen after a mesh independence study.

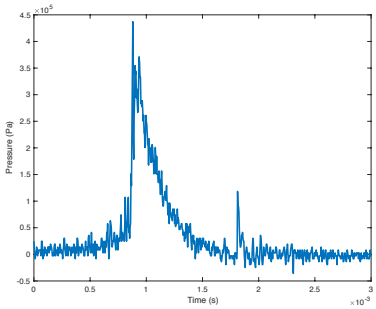

Figure 2: The pressure captured with dynamic pressure sensor located at the end of shock tube.

RESULTS AND DISCUSSION

The radial deformation of the micropspherical PEGDA sensor can be correlated with the shift of the optical resonances thorough the equation $\Delta\lambda/\lambda=\Delta R/R+\Delta n/n$, where $\Delta\lambda$ is the optical shift, λ is the light wavelength in vacuum, ΔR is the radial variation of the microsphere, R is the radius of the microsphere, Δn is the refractive index variation of the microspherical PEGDA material, and n is the index of refraction; $\Delta n/n$ can be neglected as showed in [1-3]. For a microsphere made with PEGDA (~n=1.46) of a diameter of 13 µm and assuming a wavelength light of 600 nm, a free spectral range (FSR), which is the distance between optical modes of the same order, of ~6 nm is calculated.

The maximum deformation of the PEGDA pressure sensor is provided using the equivalent elastic strain result shown in Figure 3. The maximum strain location is near the interface of PEGDA and PDMS. Three locations (Figure 3) on the surface of the PEGDA sensor were chosen near the interface.

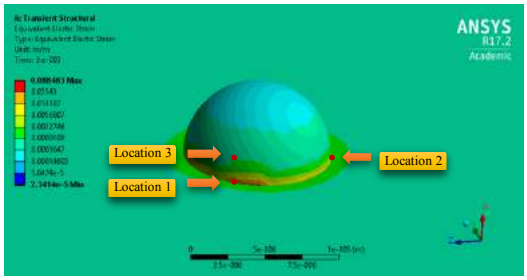

Figure 3: The equivalent elastic strain result on the surface.

Radial displacement results are shown in Figure 4, for the three locations considered. The maximum deformation ranges from 0.3 µm to 0.19 µm. The maximum deformation is 14.6% of the diameter. Thus, the maximum diameter decrease is 29.2% of the sensor diameter. The maximum deformation leads to a FSR of ~8.7 nm. Therefore, a smaller PEGDA microsphere should be used (larger FSR) or a slightly stiffer hydrogel should be employed for the fabrication of the sensor. The FE simulation results show that a PEGDA sensor with a Young's modulus of $1 \times 10^5\ Pa$ will yield a maximum diameter change of 29.2%, when compared with the sensor's original diameter. Future studies will vary the stiffness of PEGDA and PDMS, to investigate the influence on diametral change.

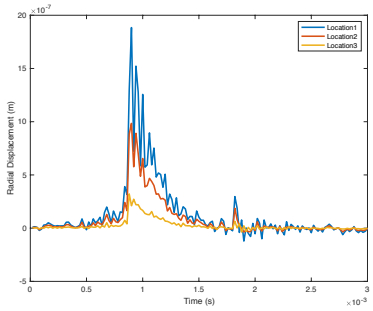

Figure 4: The radial displacement at the three locations.

This study provides insight into the deformation of a soft pressure sensor embedded into soft materials, for quantifying the mechanical response of the soft material's surface following shock wave impact. Embedding rigid pressure transducers in PDMS will influence this soft materials' dynamic response to shock wave impact. However, utilizing micron-sized spherical PEGDA sensor is a viable solution to measure the dynamic pressure on the surface of PDMS, without affecting the deformation response. Manzo et al. [5] have encapsulated a dome shaped sensor made with mixture of Trimethylolpropane Tri(3-mercaptopropionate), commercial name THIOCURE and PEGDA into a 1:10 PDMS slab and it was used as pressure gauge sensor; the resolution exhibited was ~50 kPa. In the future, shock wave experiments will be conducted on embedded PEGDA sensors on the surface of soft materials, to validate the FE results.

ACKNOWLEDGEMENTS

This research was financially supported by the Roy J. Carver Charitable Trust under Grant #18-5021 and is acknowledged gratefully.

REFERENCES

[1] M. Manzo, "Temperature compensation of dye doped polymeric microscale lasers," *J. of Polym. Sci.: Part B,* vol. 55, no. 10, pp. 1099-0488, 2017.

[2] M. Manzo and O. Cavazos, "A wireless photonic intraocular pressure sensor," *ASME International Mechanical Engineering Congress and Exposition,* vol. 3, pp. V003T04A053-V003T04A053, 2017.

[3] M. Manzo, T. Ioppolo, V. LaPenna, U. Ayaz and V. Otugen, "A photonic wall pressure sensor for fluid mechanics applications," *Rev. Sci. Instrum.,* vol. 83, no. 10, p. 105003, 2012.

[4] S. A. Bentil, K. T. Ramesh and T. D. Nguyen, "A Dynamic Inflation Test for Soft Materials," *Experimental Mechanics,* vol. 56, no. 5, p. 759–769, 2016.

[5] M. Manzo and T. Ioppolo, "Untethered photonic sensor for wall pressure measurement.," *OSA Publishing,* vol. 40, no. 10, pp. 2257-2260, 2015.

SB³C2019
Summer Biomechanics, Bioengineering and Biotransport Conference
June 25 -28, Seven Springs, PA, USA

EXERCISE THERAPY AFFECTS GLENOHUMERAL JOINT STABILITY IN PATIENTS WITH ISOLATED SUPRASPINATUS TEARS

Luke T. Mattar (1), Camille C. Johnson (2), Tom H. Gale (2), Adam Popchak (3), James J. Irrgang (3,2), William J. Anderst (2), Volker Musahl (2,1), Richard E. Debski (1,2)

(1) Department of Bioengineering, University of Pittsburgh, Pittsburgh, PA, USA

(2) Department of Orthopaedic Surgery, University of Pittsburgh, Pittsburgh, PA, USA

(3) Department of Physical Therapy, University of Pittsburgh, Pittsburgh, PA, USA

INTRODUCTION

Rotator cuff tears are a prevalent and serious clinical issue with an incidence as high as 20-30% in the general population[1,2]. High treatment failure rates have been reported for non-operative treatment and can result in substantial pain and disability emphasizing the need to improve upon current treatment methods[3]. Current studies have observed poor kinematics and range of motion loss in rotator cuff tear patients during various activities[4,5]. However, internal and external rotation at 90° of humerothoracic abduction is not well understood in-vivo, which is relevant for activities of daily living. Rotator cuff tears commonly occur in the supraspinatus tendon[1], an active compressor of the humeral head into the glenoid when performing external rotation in the abducted position. Thus, it is important to understand the effect an isolated supraspinatus tear has on the efficacy of the internal and external rotators of the rotator cuff to stabilize glenohumeral translations within the joint during this task. The objective of this study is to determine the effects of a 12-week exercise therapy program on glenohumeral kinematics in subjects with isolated supraspinatus tears during internal and external rotation at 90° of humerothoracic abduction.

METHODS

Ten subjects (mean age 58.7 ± 5.6 years, mean BMI 27.5 ± 3.8) with a symptomatic degenerative rotator cuff tear isolated to the supraspinatus tendon were recruited for the study after providing IRB-approved written informed consent. Exclusion criteria included asymptomatic tears, previous shoulder injury, or presence of severe capsule tightness. Each subject underwent computed tomography (CT) of the affected shoulder and the images were segmented to create a 3-dimensional (3D) subject specific surface model of the humerus and scapula using Mimics 20 software package. The glenohumeral joint was imaged using biplane radiography[6]. Three trials of the motion were captured over 2 seconds per trial, starting in maximum internal rotation and ending after maximum external rotation was reached. The subjects were seated with their back straight and the affected arm at 90° of humerothoracic abduction for all trials. A stand was positioned at the distal end of the humerus to support the arm and to maintain the humerothoracic abduction angle. Digitally reconstructed radiographs from each subject and the captured biplane radiograph images were matched frame by frame using a custom model-based tracking technique (accuracy ±0.4mm and ±0.5°)[6]. Local coordinates systems for the humerus and scapula were based on a glenoid modified variation of the International Society of Biomechanics (ISB) standards[7]. Outcome measures included anterior/posterior (AP) and superior/inferior (SI) translation of the humerus with respect to the glenoid, contact center of the humerus on the glenoid, and maximum external rotation. AP and SI contact positions were normalized to glenoid width and height respectively. The normalization of the glenohumeral contact data results in the total contact path length normalized to glenoid size. Due to the variation in the amount of internal and external rotation between subjects, comparisons between pre- and post-therapy were made on an individual basis using the largest shared range of motion between data collection sessions. For all kinematic data, the trial containing the maximum external rotation angle was used for all analyses. Strength of the glenohumeral internal and external rotators were measured pre- and post- exercise therapy using a handheld dynamometer (Lafayette Manual Muscle Testing System). Paired sample t-tests were used to determine the difference in maximum external rotation, contact path length, and glenohumeral external rotation strength pre- and post-therapy with significance set as $p<0.05$.

Poster Presentation #P176

RESULTS

All subjects successfully completed the 12 weeks of exercise therapy. A significant reduction in contact path length of 12.6% ± 14.3% of glenoid size occurred post-exercise therapy (Table 1, p=0.02). Eight subjects showed a decrease in contact path length with the largest decrease in contact path length being 38% (Table 1). A non-significant increase in maximum external rotation of 4.0° ± 9.2° occurred post-exercise therapy (Table 1, p=0.20). Six subjects showed an increase in maximum external rotation, with the largest change being 18.1° (Table 1). Nine subjects experienced a significant increase in glenohumeral external rotation strength at 90° of humerothoracic abduction post-exercise therapy with an increase of 18.8N ± 8.6N (Table 1, p=0.001). Glenohumeral external rotation strength post-exercise therapy was not obtained for Subject 2.

Table 1: Individual Differences in Kinematics Post-Exercise Therapy Program

Subject	Max. ER Angle (°)	Contact Path Length (%glenoid size)	ER Strength (N)
1	-4.7	-4.2	5.6
2	13.6	-14.4	-
3	10.4	-13.4	26.5
4	-3.1	-38.0	29.4
5	-7.4	-19.6	12.4
6	18.1	-24.0	29.4
7	-7.1	13.7	12.1
8	10.3	-7.2	13.1
9	3.6	-19.4	18.0
10	5.9	0.6	22.6

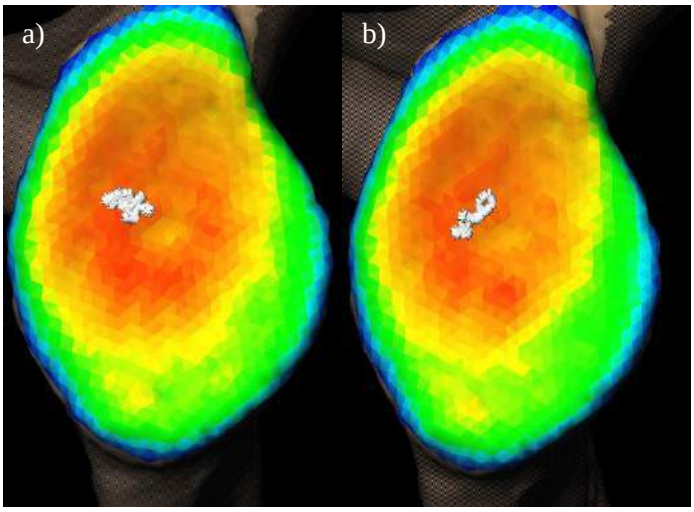

Figure 1: Representative contact path kinematics for a single subject during the internal and external rotation task. a) Pre-exercise therapy and b) post-exercise therapy. The contact path is represented by the white line.

DISCUSSION

Our data shows that a structured exercise therapy program that focuses on restoring range of motion and strength overall successfully reduced the contact path length and increased glenohumeral external rotation strength and maximum external rotation range of motion (although only contact path length and strength were found to be significant). A significant decrease in contact path length post-therapy is indicative of greater joint stability during external rotation at 90° of humerothoracic abduction. The observed improvement in stability may be due to improvements in compensatory rotator cuff and scapular stabilizing muscles such as the force couple created by the infraspinatus and subscapularis post-therapy as shown by the improved measures of glenohumeral external rotation strength in clinic. A non-significant increase in maximum external rotation of 4.0° ± 9.2° was observed. These findings were similar with ranges of 7.3°-15.2° reported in other studies determining the efficacy of conservative treatment in patients with full-thickness rotator cuff tears[8,9]. In the referenced studies, conservative treatment occurred for either 2 or 6 months and goniometers were used to measure external rotation ranges of motion. Other studies have tested the effects of exercise therapy in internal and external rotation with the arm by the side[10]. It was found that exercise therapy had no effects on the contact path length demonstrating that improvements in glenohumeral kinematics may be task dependent. These findings are clinically significant as specific exercise therapy programs may need to be developed to address task specific rehabilitation needs.

Limitations of the study include the lack of cartilage on the glenoid and humerus in the model tracking technique. This may lead to overestimation of contact path length. However, because the primary objective was to determine the effects of a 12-week exercise therapy program on glenohumeral kinematics within the same subject, lack of cartilage in the model should not have affected the quantitative comparisons.

Further studies should be done that analyze the effects of exercise therapy on glenohumeral kinematics longitudinally in subjects with isolated supraspinatus tears to determine if joint motion and stability is maintained over time. This may potentially be used to determine factors that lead to success or failure of structured exercise therapy programs and help to improve upon current treatment methods.

ACKNOWLEDGEMENTS

Support from the National Institutes of Health grant 5R01AR069503 is gratefully acknowledged.

REFERENCES

[1] Minagawa, H et al., *J Orthop*, 10:8-12, 2013.
[2] Yamamoto, A et al., *J Shoulder Elbow Surg*, 19:116-120, 2010.
[3] Kuhn, JE et al., *JSES*, 18:138-160, 2009.
[4] McCabe, RA et al., *JOSPT*, 35:130-135, 2005.
[5] Kolk, A et al., *Clinbiomech*, 45:43-51, 2017.
[6] Bey, M et al., *J Biomech Eng*, 128:604-609, 2006.
[7] Wu, G et al., *J Biomech*, 38:981-992, 2005.
[8] Baydar, M et al., *Rheumatol Int*, 29:623-628, 2009.
[9] Krischak, G et al., *J Shoulder Elbow Surg*, 22:1173-1179, 2013.
[10] Ferrer, G et al., *KSSTA*, 26:267-274, 2018.

SB³C2019
Summer Biomechanics, Bioengineering and Biotransport Conference
June 25 -28, Seven Springs, PA, USA

BICEPS VOLUNTARY ACTIVATION: METHOD TO CALCULATE PRE-STIMULUS MOMENT AFFECTS MAGNITUDE BUT NOT REPRODUCIBILITY

Thibault Roumengous (1), Paul A. Howell (1), Carrie L. Peterson (1)

(1) Department of Biomedical Engineering
Virginia Commonwealth University
Richmond, VA, USA

INTRODUCTION

The technique of superimposing electrical stimulation during a voluntary contraction, termed the interpolated twitch technique, has been used to assess voluntary activation (VA). VA quantifies the degree of voluntary drive to a muscle during maximal effort. Measured in the non-impaired elbow flexors, VA is reproducible within an individual from day to day [1]. VA may be beneficial for understanding changes in voluntary drive in patient populations due to injury or disease progression, or to assess the efficacy of rehabilitation. Towards our long-term goal to assess the reproducibility of VA of the biceps in individuals with spinal cord injury to direct rehabilitation, we first aim to standardize methods used to calculate VA.

In order to measure VA, participants must reach and maintain a perceived maximal effort until the superimposed stimulus is delivered [2]. The pre-stimulus moment is used to compute the amplitude of the interpolated twitch. The method to quantify the pre-stimulus moment varies across the literature, contributing to difficulties when comparing results [3]. Two main approaches can be identified: the mean moment of a short period before the stimulus onset [4-6], or the maximal moment reached any time prior to the stimulus onset [7]. Additionally, several studies do not report the exact method to determine the pre-stimulus moment. The objective of this study was to determine whether the method to calculate the pre-stimulus moment affects VA and/or the inter-session reproducibility of VA in non-impaired individuals.

METHODS

Experimental Set-up: Ten healthy participants (ages 19 to 27; 7 males, 3 females) were seated in a chair in an upright position with their dominant arm supinated in a cast attached to a force-moment transducer. The forearm was immobilized such that a 90º elbow angle was maintained during the experiment. After a short familiarization phase and a warm-up, participants were instructed to perform a set of 3 maximum voluntary contractions (MVCs). Participants were provided visual feedback of their effort relative to their average MVC, and were asked to perform 10 additional MVCs during which they would receive two stimuli per trial; one stimulus superimposed during the maximum moment, and another stimulus at rest, five seconds after the MVC to elicit a potentiated twitch. A visual moment feedback and verbal encouragements were provided during effort. Each participant completed three sessions separated by at least a day.

Stimulation Parameters: Stimulation electrodes were positioned over the biceps (anode) and anterior face of the elbow joint (cathode). Optimal stimulation intensity was found by increasing the stimulus intensity until the moment response reached a plateau. 120% of this intensity was then used during the protocol to ensure that a supramaximal stimulus was delivered.

Moment Data Processing: For each trial, the pre-stimulus moment was computed with three different methods as follows:
1) The average moment maintained for 50 ms prior to the stimulus.
2) The instantaneous maximal moment within a 500 ms window prior to the stimulus after application of a 10 ms moving average smoothing filter.
3) The instantaneous maximal moment within a 500 ms window prior to the stimulus with a 50 ms moving average smoothing filter.

For each of the three methods, the twitch moment was computed for each trial as the difference between the maximum moment occurring within 150 ms after the superimposed stimulus and the pre-stimulus moment. The potentiated twitch occurring at rest was computed as the difference between the maximal moment within 200 ms after the

Poster Presentation #P177

stimulus and the mean resting moment prior to stimulus. VA was calculated as a percentage given by equation (1).

$$\%VA = 1 - \left(\frac{Superimposed\ twitch\ moment}{Potentiated\ twitch\ moment} \right) \times 100 \quad (1)$$

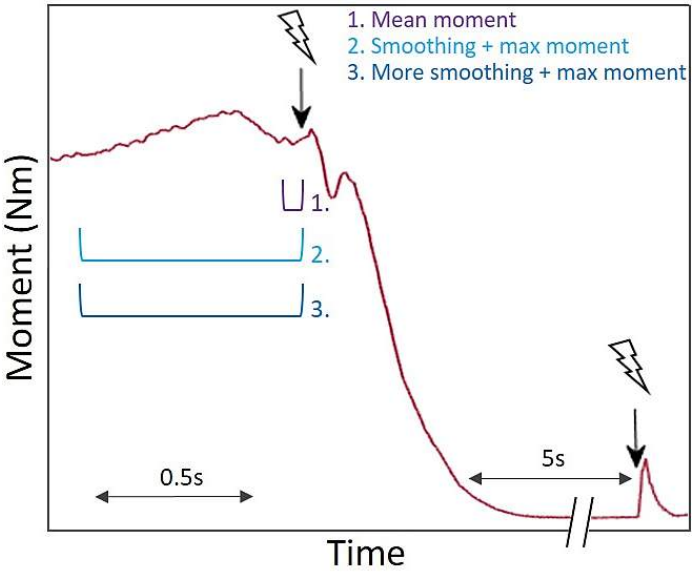

Figure 1: MCV trial example. The three methods used to calculate the pre-stimulus moment are illustrated. In red; moment trace with arrows indicating electrical stimulation, first superimposed to MVC then at rest, potentiated.

Data and Statistical Analysis: VA was calculated for each trial with all three methods then averaged per subject. In order to test the null hypothesis that the mean estimates of VA are equal between the three methods, a one-way ANOVA was performed on the dataset. The Intraclass Correlation Coefficient in a two-way random effects model with repeated measures (ICC 2, k), following Shrout and Fleiss [8] was computed as a measure of the inter-session reproducibility. Here, the ICC is a reflection of the reproducibility of the average per-subject measure of VA across the entire set of three sessions.

RESULTS

For each of the three methods, we observed no differences in VA estimates between sessions. The following ICC (2,k) values (Shrout-Fleiss reliability; random set mean k scores) were calculated for each of the three methods: Method 1: 0.931; Method 2: 0.926; Method 3: 0.928. VA values estimated using Method 1 were significantly lower than Method 2: -2.804% with a 95% confidence interval of [-3.626% ; -1.981%] (P adj. < 0.0001) and Method 3: -2.581% with an 95% confidence interval of [-3.4038% ; -1.7585%] (P adj. < 0.0001). No statistical differences were found between VA calculated with Method 2 and 3 (P adj. = 0.8005) (Table 1).

Table 1: Average voluntary activation across subjects for each method of determining the pre-stimulus moment (mean ± standard deviation in percent).

	Method 1	Method 2	Method 3
Session 1	95.82 ± 4.62	98.62 ± 2.83	98.33 ± 3.24
Session 2	95.46 ± 4.25	98.45 ± 3.34	98.19 ± 3.52
Session 3	94.89 ± 4.44	98.03 ± 3.19	97.83 ± 3.28

DISCUSSION

We aimed to determine whether the method used to calculate the pre-stimulus moment affects VA and/or the inter-session reproducibility of VA. High ICCs calculated for all three methods suggest that regardless of method, VA is highly reproducible between sessions. In non-impaired subjects who are not fatigued, VA should theoretically approach 100% in most MVCs collected in proper experimental conditions [9]. We found that the more aggressive smoothing filtering of Method 3 had no effect on the estimation of VA compared to Method 2. Additionally, we found that measuring the pre-stimulus moment right before the onset of the superimposed stimulus (i.e., Method 1) leads to a slight but significant underestimation of VA compared to the other two methods. One possible explanation for this observation is that the subject might reach a higher moment output during their MVC that does not occur within the 50 ms window. In other words, the superimposed stimulus does not coincide with the maximum moment, which causes a larger twitch response. Despite familiarization, most subjects–especially those not physically trained–exhibit a moment drift after reaching maximal effort rather than maintaining a plateau. It is possible to mitigate this mismatch effect by measuring the maximal pre-stimulus moment after filtering the signal to discard moment spikes.

A limitation of the approach represented by Methods 2 and 3 is that it results in an indirect or delayed measure of the superimposed twitch. Specifically, the pre-stimulus moment subtracted from the twitch peak moment can be measured any time before the stimulus onset rather than directly at the base of the twitch as with Method 1. Therefore, Methods 2 and 3 rely on the assumption that VA can be estimated using a non-instantaneous measure of the superimposed twitch amplitude.

In conclusion, the method used to calculate the pre-stimulus moment does affect VA and should be taken into consideration when using the interpolated twitch technique; however, it does not alter the reproducibility of VA.

ACKNOWLEDGEMENTS

This work was supported by VCU's CTSA (UL1TR000058 from the National Center for Advancing Translational Sciences) and the CCTR Endowment Fund of Virginia Commonwealth University.

REFERENCES

[1] Allen, G.M., Gandevia, S.C., and McKenzie, D.K., *Muscle Nerve*, 18:593–600, 1995.
[2] Shield, A. and Zhou, S., *Sports Med*., 34:253–267, 2004.
[3] Horstman, A.M., *J. Appl. Physiol.*, 107:359–366, 2009.
[4] Peterson, C. L et al., *PLOS ONE*, 12:e0171141, 2017.
[5] Allen, G.M., McKenzie, D.K., and Gandevia, S.C., *Muscle Nerve Off. J. Am. Assoc. Electrodiagn. Med*, 21:318–328, 1998.
[6] Luc, B.A et al., *J. Electromyogr. Kinesiol*. 26:73–81, 2016.
[7] Cadigan, E. W et al., *Front. Physiol*., vol. 8, 2017.
[8] Shrout, P.E., and Fleiss, J.L., *Psychol. Bull.* 86:420, 1979.
[9] Herbert, R.D. et al., *J. Neurophysiol.* 82,:2271–2283, 1999

SB³C2019
Summer Biomechanics, Bioengineering and Biotransport Conference
June 25-28, Seven Springs, PA, USA

EFFECTIVENESS OF AN EXTENSIVELY ACTIVE AND AUTHENTIC LEARNING ENVIRONMENT IN AN UNDERGRADUATE BIOMEDICAL ENGINEERING MODULE – A CASE STUDY IN A SOUTH-EAST ASIAN COHORT

Vivek Vasudevan, Alberto Corrias, Martin L. Buist, Leo Hwa Liang, Choon-Hwai Yap

Department of Biomedical Engineering
National University of Singapore
Singapore

INTRODUCTION

There is extensive literature on the effectiveness of active learning in the context of engineering courses [1-2]. When students construct their own understanding of concepts through carefully designed activities, they assimilate the contents better, obtain better understanding and retain more lasting impressions of the concepts. Similar evidence for an authentic learning environment is found in literature [3], wherein learning based on authentic real-life scenarios elevates the status of class material from inconsequential textbook concepts to practical and useful real-world knowledge. This motivates students to learn, and engages them better. We designed an extensively active and authentic learning module in the context of South-East Asian biomedical engineering education and tested its effects on learning effectiveness and learning motivation on two consecutive years (Fall Semesters of 2017/18 and 2018/19).

METHODS

The course that was implemented was known as Engineering Principles and Practice, which is a foundational first year module that aims to equip students with fundamental engineering knowledge such as energy and mass balances, and foundational mechanics, as well as introduces them to engineering skills such as back-of-envelope calculations, block diagrams, and CAD drawings. The module was designed to have 25% lecture and 75% activity time. Lectures were conducted in the flipped classroom format, which prepared students for two 3-hour active learning sessions in the same week. Each active learning session involved a number of small groups of students (8 groups of 5 students), paired to a lecturer and two teaching assistants, for a more interactive instructional setting. The active learning sessions were carefully designed to scaffold students' learning, and involved an elaborate new laboratory setup to enable this scaffolding. These sessions forced students to actively assimilate technical content by putting them into practical scenarios where they needed to use principles taught in the lectures to solve their problems. Time was spent on a selected real world scenario that exposed the students to an actual application of theory, thereby introducing an authentic learning paradigm to course design. For example, students investigated the working principles and technical issues involved in the use of a real-life Emergency Room (ER) medical device, namely, an extra-corporeal centrifugal blood pump. Activities involving actual centrifugal blood pumps of various designs were incorporated into the active learning sessions to enhance the authentic learning component. Additional authentic learning components were included by inviting industry experts to give talks to students on topics related to their class activities.

In the final form, the module was implemented with (1) extensive active and collaborative learning, (2) a highly authentic learning environment, (3) flipped classroom for most of the class. The module structure is summarized in Fig. 1.

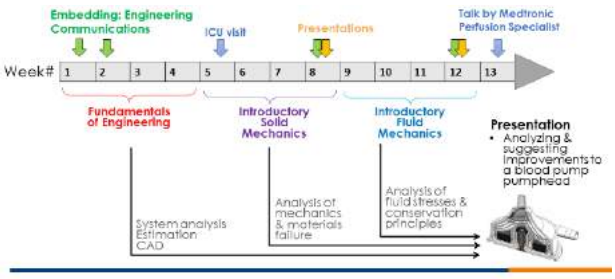

Figure 1: Module Structure for BN1101

RESULTS

Efficacy of learning environment was assessed through triangulation of student's survey, two focus-group discussions, and assessments. The data is summarized in Figs. 2a – e based on the responses to students' survey, with scores between **Strongly Disagree** (0) to **Strongly Agree** (5). Data suggested that active learning approach led to a better engagement of students, enhanced learning and made deeper impressions of concepts taught (Fig. 2a). The collaborative learning approach increased peer-to-peer learning among students and efficiently utilized lecture time for a broader understanding of differing viewpoints (Fig. 2b). The authentic learning component helped correlate theoretical principles with real life applications and demonstrated the utility of concepts taught (Fig. 2c). The flipped components of the module (in the form of online video lectures) were found to be effective as the students' could learn the materials at their own customized pace (Fig. 2d). Finally, the module increased passion among the students toward their major, and facilitated a slight shift from emphasis on performance-orientated goals towards learning-oriented goals (Fig. 2e).

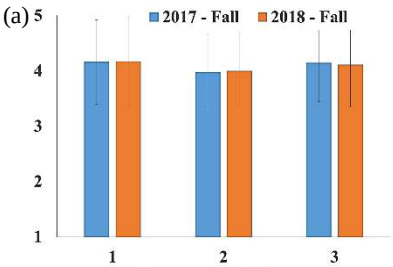

Active learning
1 – I **like the active and hands-on** components
2 – I **learnt much** from activity sessions
3 – Hands-on component facilitates a **deeper impression** of concepts

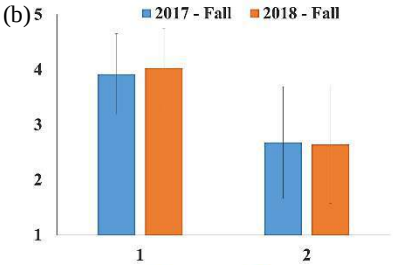

Collaborative learning
1 – During activity sessions, I **learnt from my classmates**
2 – Activities take **too much time** for little learning. I feel I can learn more if I studied myself

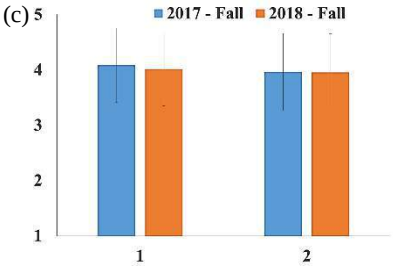

Authentic learning
1 – Module showed that engineering **principles are very useful in real world** Biomedical Engineering applications
2 - The concepts I learnt in this module could be **useful to my future career**

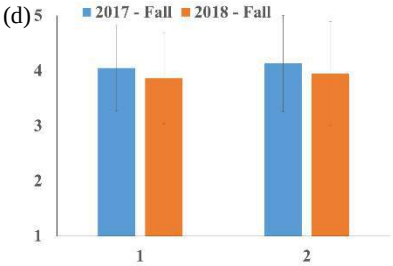

Flipped classroom
1 – Online lectures were **effective**
2 – I **prefer online video lectures** compared to traditional classroom lectures

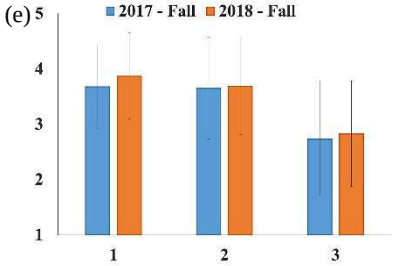

Learning motivation
1 – Module **increased my passion** for Biomedical Engineering
2 – I am **motivated to learn beyond my class** requirements
3 - Module **changed my view on importance of grades**

Figure 2: Summary of responses to students' survey for BN1101. (2017 – Fall: n = 131; 2018 – Fall: n = 138)

DISCUSSION

Although the profession of Biomedical Engineering has a relatively recent emergence of approximately 15 years ago, it has grown rapidly undergoing drastic changes, and has been projected to continue growing rapidly [4]. Such a dynamic environment requires enhanced pedagogy, to train students to be adaptable, flexible, and resourceful. An extensively active and authentic learning approach would therefore be appropriate to prepare students for this rapidly growing field.

Active learning brings about constructivist learning, with a better assimilation of technical content due to a practical need to use these knowledge to solve problems [1]. Our case study results demonstrated an agreement with literature, that this approach could lead to a deeper understanding and more lasting impression of concepts learnt [2, 5]. We believe that active learning must be supplemented with authentic learning, so that the enhanced learning effectiveness from active learning can be paired with improved learning motivation and student engagement. Authentic learning gives real-world relevance to class material so that students' perception of their value will be elevated [3]. Our results suggested that this design has been successful.

Apart from these outcome, there were also encouraging albeit moderate signs of improvement in students' interest for their course of study, as were their motivation for learning outside the classroom. This suggested a moderate shift in students' learning motivation away from one that over-prioritizes grades.

Other minor pedagogical enhancements included a flipped classroom and collaborative learning. Flipped classroom shifted the presence of the lecturer from a low cognitive phase of learning (during lecture) to a higher cognitive phase of learning (during problem solving activities) to enhance learning [6]. Our results demonstrated that most students welcomed this approach. They also liked the web videos as they conferred learning flexibility, allowing control over their own pace of learning. Finally, the extensive small group activities were found to enhance collaborative learning [7], and peer instruction [8], and most students were found to welcome this interaction.

ACKNOWLEDGEMENTS

Funding by the Learning Innovation Fund – Technology (LIFT) grant from the National University of Singapore (2017, PI: Yap)

REFERENCES

[1] Freeman, S., *P Natl Acad. Sci USA*, 111:8410-8415, 2014.
[2] Prince, M., *J Eng Educ*, 93:223-231, 2004.
[3] Herrington, J., *ETR&D-Educ Tech Res*, 48:23-48, 2000.
[4] U.D.o.L. Bureau of Labor Statistics, Employment outlook for engineering occupations to 2024, 2016.
[5] Laws, P., *UniServe Science News* 13:14-19, 1999.
[6] Bishop JL, *ASEE Natl. Conf. Proc.* 30:1-18.
[7] Stump GS, *J Eng* Educ, 100:475-497, 2011.
[8] Crouch CH, *Am J Phys*, 69:970-977, 2001.

SB³C2019
Summer Biomechanics, Bioengineering and Biotransport Conference
June 25 -28, Seven Springs, PA, USA

INJURY PREVENTION VIA COMPUTER MODELING OF STUD TRACTION

Justin L. Rittenhouse (1), Peter A. Gustafson (1,2)

(1) Mechanical and Aerospace Engineering
Western Michigan University
Kalamazoo, MI, USA

(2) Homer Stryker MD School of Medicine
Western Michigan University
Kalamazoo, MI, USA

INTRODUCTION

The majority of NFL injuries transpire to the foot and ankle region, accounting for 26% of all reported injuries [1], of which a significant but unknown number are related to excessive traction. Injuries related to foot traction are ubiquitous ranging from insufficient traction (slip and fall) to excessive traction (failure to release causing fracture or soft tissue damage). The existing literature on computational modeling of the footwear/ground interaction is limited and focused primarily on musculoskeletal dynamics simulation (i.e., the load transfer through the body) rather than on transfer into the body (through the ground/foot interface). Hence, there is opportunity to develop and/or enhance techniques for modeling footwear traction to reduce injury.

METHODS

The first part of this research was obtaining experimental data for comparison. In this case, three football studs were torqued to slip on artificial turf in a laboratory setting to provide validation data (see Figure 1). The studded assembly was turned at 1 degree per second in artificial grass alone, rubber infill alone, and grass+infill artificial turf on a servo hydraulic load frame for 60 seconds. The bench results were used to calibrate a discrete element model (DEM) of three studs. Subsequently, a series of simulations were run to determine the effects of stud geometry and pattern. The models applied 1 degree per second for 60 seconds or 2.58 meters per second for .4 seconds, as with published literature [2, 3]. Each model evaluated the torque/rotation load history and the force/translation history in two directions. The three load scenarios were repeated on four common stud shapes and three unique stud patterns. Filtered torque, force, and kinetic energy were evaluated as indicators of stud grip. A third order Butterworth low pass filter with a cutoff frequency of 20 Hz was used on the collected data to assist in the reduction of noise.

Figure 1: Set up for Laboratory experiments.

RESULTS

Results for round studs within infill alone via a DEM simulation were within the expected range (see Figure 2). The load path mimicked experimental data. However, this was not true for round studs in grass+infill (see Figure 3). The grass+infill load path is only similar to experimental data for the first half second, at best. Thus, more research is required. Noting, once the experimental data was post-process it was clear artificial grass alone has a negligible effect on the studs. This was intuitive but was done for completeness.

Round, square and hex shape studs were compared via computer simulations in infill alone. Peak torque increased 17% and 0.9% for the square and hex stud compared to the round studs. Mean torque over time increased 22% and 0.4%, respectively.

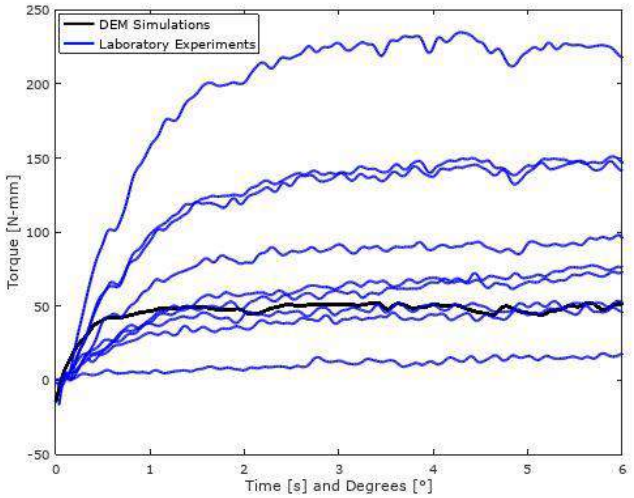

Figure 2: Laboratory experiments compared to DEM simulations, infill alone.

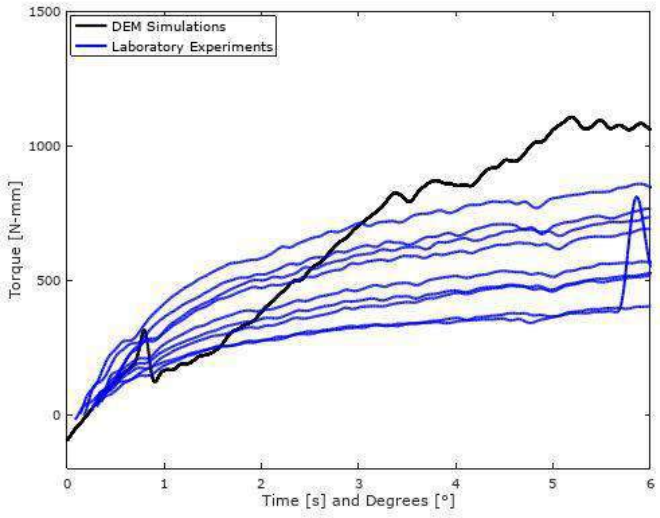

Figure 3: Laboratory experiments compared to DEM simulations, grass+infill.

DISCUSSION

Admittedly, the grass+infill model is inapt and does not model the complexities associated with artificial turf. This was believed to be due to software limitations. Hence, a change to - what appears to be – a more feature rich software has been made. Research is still on-going in this area but appears promising

Stud geometry appears to play a significant role in torque generation in infill alone. Clinically, the results suggest that round studs may limit torque transfer and thus might reduce injury. However, the optimal balance between traction and release has not been established. Based on these preliminary results, the discrete element method appears to provide effective dynamic stud/turf interaction modeling and may be useful in a broader set of studies.

ACKNOWLEDGEMENTS

We would like to thank Nicolas Aumonier and FieldTurf for donating all the turf necessary for this research.

REFERENCES

[1] Berkowitz, A et al., *Washington Post*, Washingtonpost.com [Accessed 15 Nov. 2017], 2013.

[2] Da Corte, D., *UPCommons*, Online, [Accessed 6 Oct. 2017], 2018.

[3] Krik, R et al., *Sports Engineering*, 10:129-144, 2007.

SB³C2019
Summer Biomechanics, Bioengineering and Biotransport Conference
June 25 -28, Seven Springs, PA, USA

AN ECG ANALYSIS DETERMINING THE IMPACT OF MOTHER'S METABOLIC EQUIVALENT VALUE IN PREGNANCY ON INFANT HEART RATE VARIABILITY

Alexandra J. Williams (1), Colby M. Jolly (2), Dr. Christy M. Isler (3), Dr. Kelley E. Haven (4), Dr. Edward J. Newton (3), Dr. Linda E. May (5), and Dr. Stephanie M. George (1)

(1) Department of Engineering
East Carolina University
Greenville, NC, USA

(2) Department of Kinesiology
East Carolina University
Greenville, NC, USA

(3) Department of Obstetrics and Gynecology
East Carolina University
Greenville, NC, USA

(4) Department of Family Medicine
East Carolina University
Greenville, NC, USA

(5) School of Dental Medicine
East Carolina University
Greenville, NC, USA

INTRODUCTION

Participation in exercise is important in all stages of life. Moderate exercise during pregnancy has shown to have positive consequences for the mother as well as the fetus [1-2]. Regular exercise during pregnancy for the mother is associated with improved maternal cardiovascular function, limited weight gain and fat retention, improved insulin resistance and metabolic control, preventing the onset of gestational diabetes mellitus, reduced delivery time, and decreased depressive symptoms after giving birth [1-2]. For the fetus, improved fetal stress tolerance, reduced neonatal fat mass, and advanced neurobehavior maturation have been shown through maternal exercise [1-2].

Previous research has reported that regular maternal aerobic exercise during pregnancy to be associated with lower fetal heart rate (HR) and higher heart rate variability (HRV) at 36 weeks gestation, and this trend continues to be seen in infants at one month of age [1-2]. HRV is the beat to beat variation in the duration of the R-R interval (RRi) and is a noninvasive tool able to assess cardiac autonomic function [1-4]. In developing fetuses and infants, HRV can demonstrate how well the central and peripheral nervous system are working together [1-2].

Metabolic equivalent (MET) value is a technique used by exercise experts to measure physical activity for a varied population [5]. One MET is the amount of oxygen required by the body in a resting state, which equals 3.5 ml O_2/kg/min [5]. Less than 3.0 METs is considered light exercise, between 3.0-6.0 METs is considered moderate exercise, and greater than 6.0 METs is considered vigorous exercise [5]. Based on the associations between HR and the intensity of maternal exercise and HRV and the duration of maternal exercise found in [1-2], this study aims to determine the impact of average MET values of the mother throughout the entire pregnancy on infant HR and HRV at 1 month of age. Infants born to mothers with higher MET values will have lower HR and higher HRV.

METHODS

The study population was comprised of infants born to women enrolled in a randomized, blinded, prospective study designed to determine how exercise affects the infant's health outcomes [1-2, 6]. Forty-seven mother-infant pairs were enrolled in this study. If participants met the specified requirements, they were randomly assigned to exercise intervention (aerobic, circuit, resistance) or no intervention (control).

A continuous ECG recording was obtained for infants at one month of age by using a Hexoskin Shirt-Junior's (Carre Technologies Inc, Montreal, QC). The recordings were taken when the infants were in a quiet but alert state. The software used to analyze the ECG signals and the RRi signals was Kubios HRV Premium (Kubios Oy, Kuopio, Finland). Before the files were processed through Kubios, two MATLAB (The MathWorks, Inc., Natick, MA) scripts were used. One extrapolated the RRi signal files between four and five minutes to five minutes, added 10 seconds to the beginning of each file, and converted the excel files into text files, an acceptable input file type for Kubios. The other script converted the wav files, which contain the ECG signal, into text files.

Five minutes is needed to calculate the time and frequency parameters of HRV. Files between four and five minutes were extrapolated to five minutes, but files less than 4 minutes were discarded. Two files were rejected for not having adequate time/RRi. Thirteen files were discarded due to the signal being more than half artifact/noise. In these files, the infants were either moving around or the electrodes became unattached. It should be noted that nine of the 47 infants had two recordings. This is done to verify the variability. The best file of the two recordings was used, and the other was discarded.

One file was loaded into Kubios at a time. Once the artifacts were removed, the file was saved to a .CSV batch file, which allowed all 32

files to be saved to one excel file. For statistical analysis, t-tests were used to compare infant HR, root mean square of successive differences (RMSSD), standard deviation of normal-to-normal intervals (SDNN), low frequency (LF), high frequency (HF), LF/HF ratio, and the MET values for the entire pregnancy between the exercise and control group.

RESULTS

Forty-seven participants were enrolled in the study. After exclusion criteria was met, the analysis included 32 participants: 15 aerobic exercisers, 4 resistance exercisers, 5 circuit exercisers, and 8 non-exercisers (control). A MET value of 6, 5.5, 8, and 3 was assigned to the groups list above, respectively, but the average MET was calculated by multiplying the compliance of the mother to her exercise regime to her assigned MET value. Due to the size of the resistance and circuit group, the three exercise groups were combined and referred to as the exercise group. Mothers whose compliance to her specified exercise regime was less than 75% (n=5) were not accounted for in Table 1 but were accounted for in Figure 1. The mean, standard deviation, and p value of HR, SDNN, RMSSD, LF, HF, and LF/HF ratio between the exercise and control group were displayed in Table 1.

Table 1: Results for Exercise vs. Control Group

	Mean±SD		p value
	Exercise (n=19)	Control (n=8)	
HR (bpm)	151±14.6	160±19.4	0.115
SDNN (ms)	24.2±9.36	21.1±5.71	0.151
RMSSD (ms)	14.9±10.2	11.4±5.26	0.132
LF (ms^2)	160±107	213±171	0.223
HF (ms^2)	78.8±77.1	60.8±60.0	0.261
LF/HF	3.16±2.08	4.82±4.67	0.181
MET	5.93±1.16	3±0.00	1.01E-09

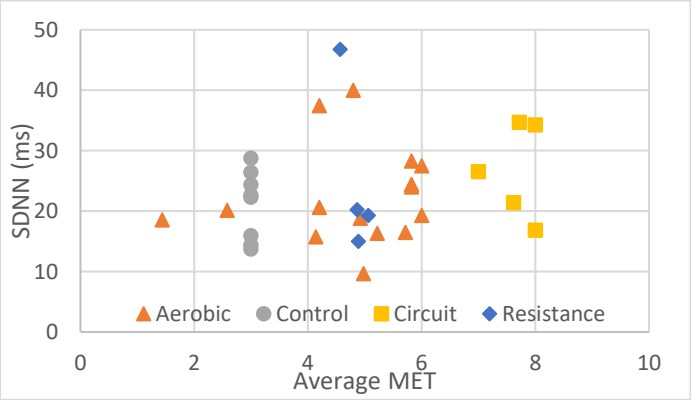

Figure 1: SDNN vs. Average MET with a correlation coefficient of 0.202

No statistical significance was seen for the HR, SDNN, RMSSD, LF, HF, or LF/HF between the exercise and control group. Infant HR was lower (151 vs. 160 bpm, *p value* = 0.115) and overall HRV (SDNN) was higher (24.2 vs. 21.1 ms, *p value* = 0.151) in the exercise group when compared to the control group, but neither variable reached significance. Infant short term HRV (RMSSD) was higher (14.9 vs. 11.4 ms, *p value* = 0.132) and only HF was higher (LF; 160 vs. 213 ms^2, *p value* = 0.223) (HF; 78.8 vs. 60.8 ms^2, *p value* = 0.261) when comparing the exercise group to the control, but none of these variables reached significance either.

To find the correlation between the average MET and HRV, the average MET value was plotted against SDNN, and a linear regression line was used. SDNN was the chosen time domain parameter since SDNN assess overall HRV.

DISCUSSION

The results observed in this study for the exercise group compared to the control group corresponded closely to the findings in [1] for HR, SDNN, RMSSD, and HF but not for LF and LF/HF. In [1], the final sample size was 43 mother-infant pairs, 16 more participants than the current sample size of mothers compliant to their exercise regime (n=27). In [1], the HR was lower and SDNN was higher for infants exposed to maternal exercise compared to the control, but the HR and SDNN in did not reach statistical significance. The p values produced in this study for HR and SDNN were more statistically significant than the p values seen for HR and SDNN in [1].

For the RMSSD, LF, and HF in [1], statistical significance was found for each parameter, and the infants exposed to maternal exercise had higher RMSSD, LF, and HF than the control. But in this study, infant exposed to maternal exercise only had higher RMSSD and HF when compared to the control. The LF was higher for the control than the exercise group, and this contradicts the findings in [1-2]. The lower LF for the exercise group could be a result of the small sample size of this study or the software used to calculate HR and HRV.

A weak correlation was seen between the average MET and HRV. This can be attributed to the small sample size. Also, having all the control subjects assigned a MET of 3 could be skewing the results.

Overall, the results found in this study support the findings in [1] demonstrating that the effects of maternal exercise, lower HR and higher HRV, can be seen at one month of age. The findings support that maternal exercise produces positive, lasting effects on infant cardiac autonomic control. Regular maternal exercise, aerobic, circuit, or resistance, may be the earliest step available to improve cardiovascular health and outcomes in future generations.

In this study, the RRi signal was mainly used to calculate the HR and HRV. Further research will be done to compare the ECG signal results to the RRi signal results. Artifacts can be manually corrected when the ECG is uploaded. This will eliminate the risk of identifying normal beats as abnormal.

Two limitations are acknowledged for this study. First, a small sample size was used. Only 19 of the 24 exercise participants were in compliance with their specified exercise regime, and the control group consisted of eight participants. Second, potential correlations between pre/pregnancy activity/fitness level, maternal resting HR, maternal age, gestational weight gain, or infant sex were not considered.

ACKNOWLEDGEMENTS

This project was supported by an Undergraduate Research and Creativity Award (URCA) grant from the Division of Research Economic Development, and Engagement at East Carolina University and a grant from the American Heart Association's (AHA) Innovative Project Award.

REFERENCES

[1] May, L et al., *Early Human Development*, 90:33-38, 2014.
[2] May, L et al., *Early Human Development*, 86:213-217, 2010.
[3] Gustafson, K et al., *Early Human Development*, 88:539-546, 2012.
[4] Murray, N and Russoniello, C, *Applied Psychophysical and Biofeedback*, 37:219-227, 2012.
[5] Franklin, B et al., *The American Journal of Cardiology*, 121:382-387, 2018.
[6] Moyer, C et al., *BMC Pregnancy Childbirth*, 15:133, 2015

SB³C2019
Summer Biomechanics, Bioengineering and Biotransport Conference
June 25 -28, Seven Springs, PA, USA

FOR YOUR INFORMATION: STUDENT EVAULATIONS OF TEACHING ARE BIASED AGAINST WOMEN AND FACULTY OF COLOR

Naomi C. Chesler (1), Dante Fratta (2), Elizabeth Harris (3), Wayne Pferdehirt (4), Heidi L. Ploeg (5), Barry Van Veen (6)

(1, 2, 3, 4) Biomedical Engineering, Civil and Environmental Engineering, Collaborative for Engineering Education and Teaching Effectiveness, and Engineering Professional Development
University of Wisconsin-Madison
Madison, WI USA

(5) Mechanical and Materials Engineering
Queen's University
Canada

(6) Electrical and Computer Engineering
University of Wisconsin-Madison
Madison, WI USA

INTRODUCTION

Many universities exclusively rely on student evaluations of teaching (SET) for assessment of teaching by faculty and use these ratings in tenure and promotion decisions. However, SET have significant systemic bias with respect to gender, race, and sexual orientation. Moreover, they are not a good measure of either teaching or learning in many contexts. These biases and limitations indicate that SET should not play a significant role in promotion processes or be used to revise instructional practices. Instead, detailed strategies for peer evaluation could improve formative feedback for faculty and assessment of engineering instruction.

LITERATURE REVIEW

Student feedback is a critical component of course and instructor evaluation. A common method of collecting feedback from students is via anonymous surveys on course and instructor demands, accessibility, and quality. The compiled numerical data is then used to evaluate the performance of faculty, staff and student instructors. Recent studies call this use of student evaluations of teaching (SET) into question. Multiple studies have shown that SET results are biased with respect to gender [1], to sexual orientation and gender identity [2], and to race [3]. Even purportedly objective metrics, such as how quickly homework are graded and returned, are affected by student understanding of gender [1]. Moreover, evidence has shown that numerical SET results do not reflect either the effectiveness of instruction or of learning [4,5]. As a result, changes to teaching practices in response to SET scores may not improve teaching or learning. For all of these reasons, SET are problematic when used in merit, tenure and promotion decisions.

Because they are an efficient way to gather student feedback, SET are unlikely to be eliminated on today's college campuses. Also, despite their limitations, SET can yield useful information. For example, very poor evaluations can be indications of problems that must should be addressed [6]. In addition, SET can be used by individual instructors teaching the same course in subsequent years to track student response to instructional changes. Also, SET can be a useful tool to gather feedback on students' expectations [1] and the individual student comments from SET can guide course and instructor improvement.

RECOMMENDATIONS FOR USE OF SET

Stark and Freishtat [4] provide a set of recommendations on appropriate use of SET:

- effectiveness and value of courses should not be used as evaluation items,
- averages of scores should be de-emphasized while score distribution and number of responses should be reported,
- results from a low number of responses should not be used,
- comments from students should be considered only after understanding their limitations, and
- SET comparisons between different courses' content, types, sizes and areas of studies should be avoided - e.g., departments should not compare individual instructors against departmental averages

Regarding averages of scores in particular, disadvantages as compared to distributions include that:

- They presume the differences between values at the lower end of the scale (e.g., a 1 and a 2) is the same as that between values at the higher end of the scale (e.g., a 4 and a 5);
- They presume that the difference between numerical ratings (e.g., 3 and 4) mean the same to different students;

- They presume that a given numerical rating (e.g., 4) means the same thing to different students;
- They presume a rating of 5 balances a 3 to be equivalent to two ratings of 4; and
- At least half the faculty in any department will have average scores below the median average score.

In summary, the use of averages promotes simplistic judgement of a complex, nuanced activity.

PEER EVALUATION OF TEACHING

One frequently used tool for assessing teaching effectiveness is observation by peers [7]. In Peer Evaluation of Teaching, a peer of the instructor observes one or several classes and provides oral and written feedback. The systematic collection of peer evaluations of teaching are then documented in dossiers used for promotion and tenure decisions. One of the limitations of peer evaluation is that it takes a significant effort to obtain useful information. For example, [8] summarizes a set of recommended practices needed for effective peer evaluation. These include:

- Peers need to be trained for the effective use of the technique.
- A single class observation is not enough to obtain reliable indicators of teaching/learning effectiveness. At least three observations are recommended.
- Contextual information regarding the classroom activity, such as learning objectives, must be provided to the observer.
- A checklist must be provided to help the peer assess specific areas of the learning/teaching activity.
- The peer should be a strict observer. Participation of the peer in the teaching/learning activity – even their presence in the room – may distract the instructor or students from their activity.
- The peer should observe entire class periods.
- A written review should be provided right after the observed session.

SELF-ASSESSMENT

One opportunity for continuous improvement that is not typically included in evaluations of teaching is a formal self-assessment. Reflection is key to learning in many professional domains, including teaching [9]. As instructors become more experienced, self-assessment and self-reflection – for example through journaling, watching videos of themselves in the classroom or other evaluations – become useful forms of ongoing professional development [10]. To guide self-assessment and reflection in mathematics and science instruction, Wieman and Gilbert developed a Teaching Practices Inventory (TPI) [11]. The authors argue that teaching effectiveness can be measured by characterizing the use of best practices. In developing this inventory, Weiman and Gilbert sought to address the following objectives: validity–the result of the assessment must be strongly correlated with achievement; meaningful comparisons–the instructor should be able to be compare their performance against peers; fairness–the tool should be widely applicable and valid across curricula; practicality–implementation should be inexpensive for instructors and institutions; and improvement–the results could be used by instructor to improve their teaching. Currently, the TPI is available in multiple formats including an anonymous Qualtrics survey that takes ~10 min: www.cwsei.ubc.ca/resources/TeachingPracticesInventory.htm. Unlike a grading system in which 100 is the best and 0 is the worst, scores of 100% would indicate that all best-practices are used in a single course, which is not encouraged by the authors. In a single high-performing department, the distribution of scores ranged from 10 to 50 with a median in the low 30s [6]. Indeed, the numerical score is not the emphasis; rather the value of this inventory is that the instructor reflects on their current practice and considers how best-practices may be incorporated to improve teaching and learning.

SUMMARY

Teaching and learning are complex activities. Thus, it is no surprise that they are difficult and time-consuming to assess properly. When gathering student feedback, SET are an alluring tool: there is an automated process for obtaining them and they can distill assessment of teaching to a single number. However, significant gender, race, and sexual orientation bias in SET and evidence that SET do not measure learning raise serious concerns about continued reliance on them for merit and promotion decisions. MacNell et al. [1], among other researchers, suggest that universities consider phasing out SET for tenure and promotion decisions "but still use them to get feedback on what students want and expect from their courses."

Use of research-proven best practices for teaching should also be considered for promotion and tenure decisions given their correlation with teaching effectiveness [11].

We recommend that departments encourage their instructors, particularly probationary faculty, to take advantage of the wide range of institutional resources for improving teaching. Appropriate use of research-proven best practices will improve the quality of teaching and learning. It will also the increase the success and job satisfaction of instructors.

REFERENCES

[1] MacNell, Driscoll, and Hunt, (2015), What's in a Name: Exposing Gender Bias in Student Ratings of Teaching, Innov High Educ, 40: 291-303.
[2] Ewing, Stukas, and Sheehan, (2003). Student Prejudice Against Gay Male and Lesbian Lecturers. J Sov Psych, 143(5): 569-579.
[3] Ho, Thomsen, and Sidanius, (2009), "Perceived Academic Competence and Overall Job Evaluations: Students' Evaluations of African American and European American Professors." J of App Soc Psych 39(2): 389-406.
[4] Stark and Freishtat, (2014), An Evaluation of Course Evaluations, Science Open Research.
[5] Boring, Ottoboni, and Stark, (2016), Student evaluations of teaching (mostly) do not measure teaching effectiveness, Science Open Research.
[6] Wieman, (2015), A Better Way to Evaluate Undergraduate Teaching. Change, The Magazine of Higher Learning, January-February 2015.
[7] Hill and Grossman, (2015), Learning from Teacher Observations: Challenges and Opportunities Posed by New Teacher Evaluation Systems, Harvard Educational Review. 83(2): 371-384.
[8] Weimer, (2010), Guidelines for Effective Classroom Observations, URL: http://www.facultyfocus.com/articles/faculty-evaluation/guidelines-for-effective-classroom-observations/ [Accessed on March 23, 2017].
[9] Schön, (1983) *The Reflective Practitioner: How professionals think in action*, Temple Smith
[10] Zeichner and Liston, *Reflective teaching: An introduction*, 2013 Routledge
[11] Wieman, C. and Gilbert, S. (2014), The Teaching Practices Inventory: A New Tool for Characterizing College and University Teaching in Mathematics and Science, CBE—Life Sciences Education, 13: 552–569.

SB³C2019
Summer Biomechanics, Bioengineering and Biotransport Conference
June 25 -28, Seven Springs, PA, USA

INCORPORATING NATIONAL BIOMECHANICS DAY INTO BIOMECHANICAL ENGINEERING COURSES

Sara E. Wilson (1,2)

(1) Mechanical Engineering
University of Kansas
Lawrence, Kansas 66045

(2) Bioengineering
University of Kansas
Lawrence, Kansas 66045

INTRODUCTION

National Biomechanics Day (NBD) was started in 2016 by Paul DeVita as past-president of the American Society of Biomechanics.[1] It has occurred in early April each year since 2016 and is schedule for April 10, 2019. The primary goal of NBD is to introduce the field of biomechanics to K-12 students and their teachers, particularly those in high schools. Participating biomechanists come from institutions across the United States as well as internationally. International participants in 2018 came from 52 nations including Australia, Brazil, Chile, the Czech Republic, New Zealand, Portugal, Singapore, Iran, Pakistan, and the United Kingdom.[2] Participating biomechanists come from a variety of fields including engineering, kinesiology and sports science aligning with the membership of the American Society of Biomechanics. The topic areas that have been the focus of NBD include sport biomechanics, clinical biomechanics, animal biomechanics, human locomotion, modeling and robotics, imaging and material testing, and biomechanical technology, but the event is not restricted to these topics. Other areas of activity include an Art in Biomechanics competition, biomechanical interpretations of famous movies, and a two-minute video tweet competition. While participants are encouraged to schedule activities on the scheduled day, the event allows for alternate scheduling to accommodate needs.

NBD is an example of a service learning activity that can be used in a classroom setting. Service learning (a form of experiential learning) integrates meaningful community service with instruction to enhance learning while strengthening communities and teaching civic responsibility.[3] In service learning, the instructor becomes the facilitator of knowledge rather than the controller of knowledge.[3] Effective service learning should include reflection on the experience in order to link knowledge and concepts to the service learning activities.[3] Important in successful service learning projects is assessing partnerships to ensure that activities benefit both the learner and the community served.[3]

METHODS

Prior to NBD, my initial efforts at bringing a service learning component to my class involved having student teams participate in a locally run engineering expo. Engineering expo is hosted by the University of Kansas School of Engineering and brings K-12 children from around the region to campus for engineering demonstrations as well as K-12 engineering competitions including a Rube Goldberg, egg drop, and balsa wood bridge competitions. This event is hosted in the last week of February or first week of March, making it feasible only for Spring semester courses. The early timing during the semester also presented challenge in incorporating activities into the curriculum. The activities by the students typically involved demonstrating motion capture.

Because the early timing of this event proved to be a challenge, this project was changed to having students develop a demonstration for a subsequent year's engineering expo. While this allowed for greater development of learning objectives, the

Poster Presentation #P182

students were not able to successfully utilize their efforts in a service learning environment.

In Spring 2019, we are working with a local elementary school to bring demonstrations to three kindergarten classrooms on National Biomechanics Day. This activity has been made possible by the formation of relationships with the teachers cultivated through community connections.

All of these projects have been done in teams of 3-5 students. I have also used several types of demonstration projects for these efforts that can be broadly divided into two classifications: open-ended and prescribed.

The prescribed projects, in the senior/graduate course ME 757 Biomechanical Systems, have involved the development of a computational and physical passive-dynamic walker and demonstration of passive-dynamic walking mechanics (Fig. 1). In this project, students were asked to work with provided MATLAB code to develop an animation of passive dynamic walking and to build a physical passive dynamic walker out of any materials.[4] The physical walkers have been constructed out of a diverse range of materials including wood, PVC pipe, rubber bands, dowels, binder clips, and rapid prototyped parts. There is a wide array of videos and materials on the internet for students to use to support this effort and the project closely aligns with the course materials.

Open ended projects have been used in several courses including ME 757 Biomechanical Systems, ME 882 Advanced Control Systems and ME 758 Physiological Systems. In Spring 2019, the students have been assigned an open ended project for the NBD day presentations to kindergarteners. The guidelines for this project are that the teams need to identify one to two key concepts about an organ system (musculoskeletal, respiratory, cardiovascular, renal, etc.) and create a 10-minute demonstration that will convey that concept to kindergartners. The open ended nature of this type of project requires the students to figure out the key concepts rather than having those defined. It also leaves room for variability in the quality and extent of the work. To manage some of this variability, the project requirements include a proposal phase (in which teams identify three target demonstrations and receive feedback) and an early classroom demonstration and feedback one month prior to the kindergarten demonstration. Students will be evaluated by not only the instructor but also their teammates, classmates, the kindergarten teachers and the children. The teachers will be asked to evaluate the teams not only on the quality of the presentation but also the usefulness of the presentation for their students. The teachers are included in both the development of the specifications of the project as well as feedback on the overall exercise.

RESULTS

The past efforts to utilize the late February/Early March University of Kansas Engineering Expo date proved to be a challenge for incorporation of a meaningful experience into the curriculum. Projects in other courses that were developed, but never presented to children lacked the impact a true service learning project can have to both the engineering students and the community. National Biomechanics Day is well suited for service learning due to its timing as well as the integration with an international biomechanics community. For the course described here, National Biomechanics Day is not a perfect match as much of NBD activities focus on sports and human motion while this activity is taking a broader view of biomechanics to include other physiological systems (respiratory, cardiovascular, renal, etc.). NBD has also been primarily focused on the high school level. We chose the elementary level due to community connections. Requiring the teams to present to kindergartners also requires they focus and simplify their presentation in ways that could be very powerful in reinforcing the concept with the engineering students. The elementary school selected is an ESL school with a diverse, multilingual student population with 62% participating in free/discounted lunch program (an indicator of low income diversity).

DISCUSSION

Service learning has the potential to not only reinforce classroom learning but to also provide benefit to the community at large. National Biomechanics Day is an opportunity to incorporate service learning projects into biomechanical engineering classrooms. The timing of NBD is well suited to a semester long project and allows for students to have covered much of the course before interacting with K-12 students. Prescribed projects have the advantage of clear education objectives and metrics, but open-ended projects can allow students to explore and develop ideas on their own and create a greater range of materials for the target K-12 students. Open-ended projects do require greater intermediate assessment and feedback to be successful.

Figure 1. Examples of passive dynamic walkers constructed for educational demonstrations.

REFERENCES

[1] "National Biomechanics Day" (2019, January 22). Retrieved from http://nationalbiomechanicsday.asbweb.org/

[2] DeVita, P. "National Biomechanics Day April 11, 2018" Retrieved January 22, 2019 from http://nationalbiomechanicsday.asbweb.org/wp-content/uploads/sites/3/2018/09/National-Biomechanics-Day-2018-Summary.pdf.

[3] Seifer SD and Connors K. , Eds. Community Campus Partnerships for Health. Faculty Toolkit for Service-Learning in Higher Education. Scotts Valley, CA: National Service Learning Clearinghouse, 2007.

SB³C2019
Summer Biomechanics, Bioengineering and Biotransport Conference
June 25 -28, Seven Springs, PA, USA

DEVELOPING THE COMPONENTS OF A MULTISCALE COMPUTATIONAL PLATFORM IN THE DESIGN OF A GEOMETRICALLY TUNABLE BLOOD SHUNT FOR NORWOOD RECIPIENTS

Ellen E. Garven MS (1), Kara L. Spiller PhD (2), Randy M. Stevens MD (3), Amy L. Throckmorton PhD (1)

(1) BioCirc Research Laboratory, School of Biomedical Engineering, Science and Health Systems, Drexel University Philadelphia, PA, USA

(2) Biomaterials and Regenerative Medicine Laboratory, School of Biomedical Engineering, Science and Health Systems, Drexel University Philadelphia, PA, USA

(3) Cardiothoracic Surgery St. Christopher's Hospital for Children Philadelphia, PA, USA

INTRODUCTION

Infants with single ventricle physiology are born with a range of complex cardiac malformations resulting in an underdeveloped left or right ventricle. The incidence of these defects, including hypoplastic left heart syndrome, is approximately 2-4 per 10,000 births [1]. Patients undergo a series of palliative surgeries to reconfigure their anatomy, the first of which—the Norwood procedure—is completed within days after birth. In the Norwood, a systemic-pulmonary shunt is implanted to connect the functional ventricle to both circulations. This shunt remains in place until the second-stage procedure, completed at approximately 6 months of age [2]. Despite advancements in overall patient care, mortality rates have stagnated in recent years, remain the highest among congenital heart procedures, and remain elevated even after hospital discharge [3,4]. These rates indicate an inherent treatment issue.

The Norwood results in a circulation that mixes oxygenated and deoxygenated blood. This is adequate to sustain life given that the oxygenation ratio is properly balanced. Given that the shunt is solely responsible for the pulmonary perfusion, this balance is highly dependent on shunt conditions. Many variables can alter that balance during the months the shunt is in place, including normal developmental changes in vessel geometry, cardiac output, and pulmonary vascular resistance. Although some of these effects can be managed pharmacologically, a fixed shunt theoretically cannot maintain adequate blood oxygenation during the numerous changes during infancy.

The design of a new geometrically tunable hydrogel-based blood shunt would address the limitations of a static shunt, by adjusting in geometry in proportion to the patient's growth. This shunt (Figure 1) offers an innovative solution to balance the blood oxygenation ratio.

Computational fluid dynamics (CFD) has been shown to be valuable for patient-specific modeling, surgical planning, and is regularly incorporated into multiscale models where the anatomical region of interest is coupled to a lumped parameter model. The overarching goal of this project is to create a multiscale model to be used in the design and development of the tunable shunt. This specific investigation lays the groundwork for that model, by developing and verifying the CFD component (Figure 2, left). This study is the first step in establishing that computational framework, and creates a valuable resource to complement the anticipated materials-based research.

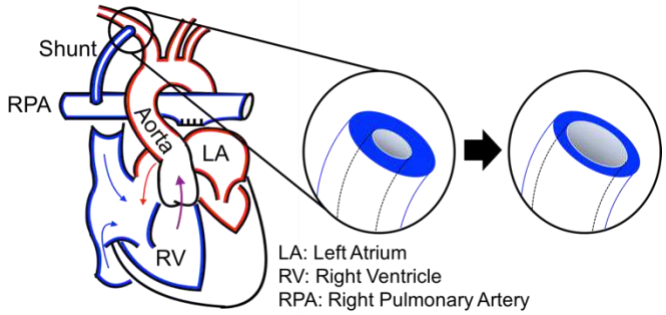

Figure 1 The blood shunt with an inner lumen diameter expandable over time in proportion to growth.

METHODS

A model of the aortic arch region was developed from imaging data. The geometry was scaled to match typical neonatal dimensions and a Modified Blalock-Taussig Shunt (MBTS) was added based on surgical sketches. The MBTS was selected as the initial geometry for verification purposes, as it has a wide body of computational literature, and because the innovative shunt design would be arranged similarly.

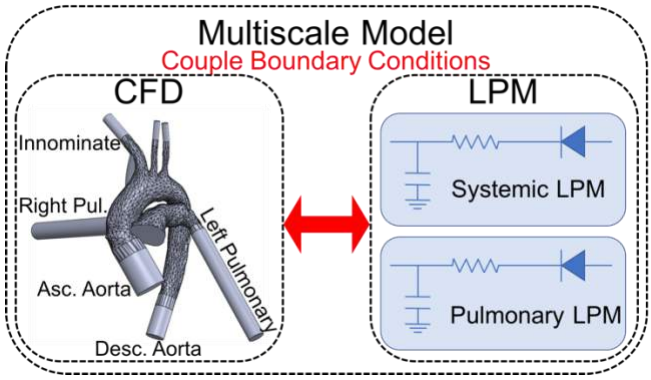

Figure 2 The components of the multiscale model include CFD simulations of the aortic arch (developed in this study) coupled to lumped parameter models (LPM).

ANSYS was used to conduct the CFD studies under steady state conditions while varying shunt diameter, hematocrit, and cardiac output. Studies were performed to determine appropriate boundary conditions, to create a high-quality, grid-independent mesh, and to select an appropriate model of turbulence. Unless specified, blood was assumed to be Newtonian with a dynamic viscosity of 3.5 cP and density of 1050 kg/m^3. The shunt diameter was varied over a range of diameters (3, 3.5, 4, and 5mm), the results of which would provide comparison to other literature. Cardiac output was varied as a measure of sensitivity to developmental changes, over a reasonable range expected clinically (0.5-1.5 LPM). The blood fluid physics was studied because blood is a non-Newtonian fluid. However, it is frequently assumed Newtonian in computational literature, an assumption safe to make when shear strain rates are above 100 s^{-1}[5]. A non-Newtonian model was implemented that covered the range of expected hematocrits (20-60%) [5].

The results of these simulations were used to select parameters in future modeling efforts and to verify its behavior. Streamlines were qualitatively assessed for vortices and eddies. The ratio of pulmonary-to-systemic flow, Qp/Qs, was calculated. The average and maximum velocities, shear rates, and shear stresses were gathered for further comparisons.

RESULTS

A grid-independent mesh was found to include approximately 6 million elements. The turbulence model comparison revealed the streamlines of the $\kappa - \omega$ model showed more complex flow patterns in the pulmonary arteries than the $\kappa - \epsilon$ model, so the $\kappa - \omega$ model was selected for all remaining studies. A baseline model was confirmed to have the desired Qp/Qs of 0.8, representing the non-ideal flow distribution typically observed in Norwood patients.

Larger shunt diameters allowed for larger pulmonary flow rates, increasing the Qp/Qs ratio and decreasing the average velocity in the shunt. The Qp/Qs ratios were found to vary between 0.6 with the 3mm shunt, to 2.6 with the 5mm shunt (Figure 3a). As the cardiac output increased, the Qp/Qs ratio decreased, demonstrating the rate limiting effect of the shunt diameter at increased inflow rates.

Three discrete hematocrits were implemented with the non-Newtonian model of blood physics: 20, 40 and 60%. The Qp/Qs ratio was found to decrease with increasing hematocrit, as an increasing percentage of blood was distributed to the descending aorta. The shear strain rates were found to be below 100 s^{-1} at several locations in the model, including the ascending aorta, however, the entirety of the shunt was sufficiently above that threshold. Consequently, the dynamic viscosity was higher at the aortic inlet than in the shunt (Figure 3b).

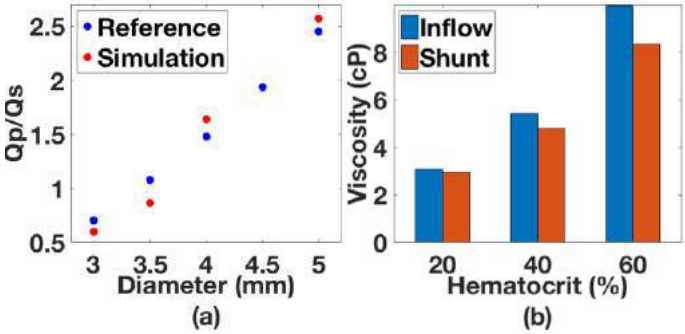

Figure 3 (a) Shunt diameter increased the Qp/Qs ratio in agreement with literature [6] (b) At each hematocrit, the viscosity was higher at the aortic inlet than in the shunt.

DISCUSSION

The Qp/Qs ratios in the shunt diameter study were found to agree with the relationships and magnitudes widely reported, as compared in Figure 3a [6]. This agreement supports the validity of the fundamental ability of the model to reproduce basic relationships. The cardiac output study showed a rate-limiting effect of the shunt, as an increased amount of fluid flow to the system was not evenly distributed due to the resistance of the narrow diameter shunt. Even with relatively minor changes of 0.1 LPM resulted in sub-optimal changes to the Qp/Qs ratio. This analysis could be extended in future time-variant studies to further analyze the heart rate, a significant variable for the cardiac output.

The results of the fluid physics studies indicated a non-Newtonian model was successfully implemented. As seen in the difference in viscosity between the aortic inflow and the shunt, different viscosities were observed in regions with shear strain rates below 100 s^{-1}. Even though strain rates above that threshold were observed in the shunt, rates below the threshold were seen in the aortic arch, meaning that the non-Newtonian behavior of that fluid could have a downstream effect on the behavior in the shunt. While many use the Newtonian assumption, this data supported the use of the non-Newtonian model going forward [5]. However, this is just a single model of blood behavior, and it should be evaluated against the many others that exist in the literature.

Overall, the model developed was observed to be consistent with literature at precise steady-state conditions, providing evidence for the validity of these methods. These preliminary analyses are relevant to the overall goal. The effect of a diameter change will be impactful for the study of the degree to which the shunt geometry should be tuned, and the cardiac output study will inform the sensitivity of the ideal shunt diameter to day-to-day changes in heart rate or stroke volume. This model is the first major component in the creation of the computational platform to study the dynamic diameter changes for the tunable shunt. Future work will include the implementation of a lumped parameter model to be coupled with this work into a multiscale model. This model will serve as the foundation to inform and investigate many physiological hypotheses and design questions in the future of the design and development of this new innovative device.

REFERENCES

[1] Reller, M et al., *J Pediatrics*, 153:807-813, 2008.
[2] Dirks, V et al., *Euro J Cardio-Thorac Surg*, 44:1096-1102, 2013.
[3] Ohye, R et al., *N Engl J Med*, 362: 1980-1992, 2010.
[4] Petrucci, S et al., *Ann Thorac Surg*, 92: 642-652, 2011.
[5] Good, B et al., *Ann Biomed Eng*, 44:1019-1035, 2016.
[6] Migliavacca et al., *Am J Physiol Heart Circ Physiol*, 280: 2076-2086, 2001

SB³C2019
Summer Biomechanics, Bioengineering and Biotransport Conference
June 25 –June 28, Seven Springs, Pennsylvania, USA

QUANTIFYING HEMODYNAMICS IN HYPOPLASTIC LEFT HEART SYNDROME

Banafsheh Zebhi. (1), Hadi Wiputra(2), Lisa Howley (3), Bettina Cuneo (3), Dawn Park (3), Hilary Hoffman (3), Lisa Gilbert (3), Choon Hwai Yap (2), David Bark (1,4)

(1) Department of Mechanical Engineering Colorado State University Fort Collins, CO, USA

(2) Department of Biomedical Engineering, National University of Singapore, Singapore

(3) Department of Pediatrics Cardiology, Children's Hospital Colorado, Aurora, CO, USA

(4) School of Biomedical Engineering, Colorado State University, Fort Collins, CO, USA

INTRODUCTION

Congenital Heart Defects (CHD) occur in nearly 1% of all births per year in the United States [1]. Among these, Hypoplastic Left Heart Syndrome (HLHS) is responsible for about 9% [2]. HLHS is a complicated disease in which the left ventricle is underdeveloped. The common treatment for HLHS is a multistep postnatal surgical procedure which has a high mortality rate; even when it is successful, it leaves patients with lifetime complications. Therefore, there is a need for better and more successful treatment options.

To find better clinical interventions, we first need to get insight into the hemodynamics inside the heart; as numerous animal studies have shown that the intracardiac flow patterns in embryonic heart play a significant role in cardiovascular development [3]. This signifies the importance of understanding the relationship between blood flow (hemodynamics), structural development, and remodeling of the human fetal heart. Therefore, here, we quantify the hemodynamics during cardiac development in normal fetal hearts and fetuses diagnosed with HLHS to identify if a correlation exists between specific flow patterns and the heart malformations.

METHODS

We used Computational Fluid Dynamics (CFD) based on non-invasive patient-specific human fetal ultrasound scans to quantify intracardiac flow in the right ventricle in both normal and HLHS cases. 9 fetal hearts, including 4 normal (22-35 weeks of gestation) and 5 HLHS (22-37 weeks of gestation), were studied using 4D patient-specific spatio-temporal image correlation (STIC) ultrasound. Scans were collected using a RAB6 probe on a GE Voluson E10 system (GE Healthcare, USA). 4DView software (GE Healthcare, USA) was used to convert the 4D volume data to series of 2D images at multiple time points. These images were semi-automatically segmented using a lazy snapping algorithm using a custom-written C++ code. Segmented slices were then converted to a 3D model using VMTK software. The surface of the reconstructed 3D geometries was smoothed using Geomagic software (3D Systems, Morrisville, NC). Ventricular wall motion was modeled using a Spherical Harmonic Transform algorithm created in MATLAB (MATLAB, Natick, MA) along with Doppler velocity waveform from ultrasound data, and measured volumes from the reconstructed 3D geometries using:

$$r_{model}(\theta, \phi, t) = \alpha(\theta, \phi)\Omega(t) + r_0(\theta, \phi) \quad (1)$$

where $\Omega(t)$ is the characteristic waveform which was obtained by taking the cube root of the ventricular volume over time, $\alpha(\theta, \phi)$ is amplitude of displacement waveform, and $r_0(\theta, \phi)$ is the initial radius. The wall motion was modeled as a function of volume at each time point of the cardiac cycle and radial displacement in θ and ϕ directions, where θ probes from 0 to 180 and ϕ probes from 0 to 360. The wall motion was incorporated into a user defined function (UDF) utilized in a computational fluid dynamics (CFD) simulation (ANSYS Inc., Canonsburg, PA). Hemodynamic parameters such as wall shear stress (WSS), transverse wall shear stress (transWSS), interventricular pressure gradient (IVPG), kinetic energy (KE), work done (Wd) and the energy loss were computed. Statistical analyses were performed using SAS software (SAS Institute Inc., Cary, NC, USA) between HLHS and normal groups, and between mid-stage and late-stage of development. Wilcoxon test was performed with 80% confidence interval at significance level (α) of 0.2.

RESULTS

Overall, the fetal heart rate decreases and CO increases with gestational age for all hearts, while all hemodynamic parameters, i.e.

CO, WSS, transWSS, and IVPG, are larger in HLHS cases relative to normal cases.

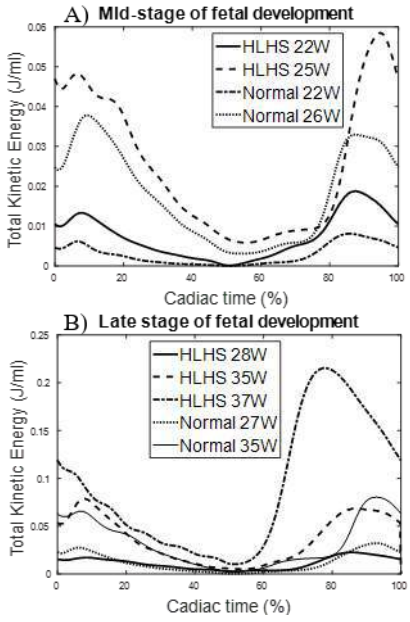

FIGURE 1: Kinetic energy in the control volume during systole and diastole at (A) mid-stage and (B) late-stage of cardiac development.

Fig. 1 shows the KE with systole shown during the first ~50% of the cardiac cycle and diastole for the second half of the cardiac cycle. KE in HLHS is about 3 times more than that of normal hearts. Trends further show that KE in the ejection phase is similar for normal and HLHS hearts. However, more KE is produced during the filling phase for HLHS. Correspondingly, we found that the right ventricle thicker and stiffer for HLHS cases.

The maximum systolic Wd in HLHS is higher than normal hearts by 40%, Fig.2. In HLHS the average energy loss is approximately 2.4 times more that the average energy loss in normal, demonstrating that HLHS hearts are less efficient than normal hearts.

DISCUSSION

Our CFD results provide unique and detailed insight into flow for a highly complex congenital heart malformation involving a single ventricle defect for the first time. With this effort, we can begin to identify changes in required effort from the right ventricle when the left ventricle loses any useful function.

Our results show that all studied hemodynamic parameters in HLHS were higher when compared with normal, which indicates the right ventricle in HLHS compensates for left ventricule dysfunction as an adaptive response to provide enough blood supply for the body. As a result, the HLHS right ventricle works harder to eject the blood out, with more energy loss, leading to ineffecient pumping [4]. The high blood velocity in HLHS leads to the formation of strong vortices and high WSS, along with high transWSS. The increased effort from the right ventricle leads to a thicker, less compliant wall. Although, we can only correlate these results, it's likely that the thickened, stiff wall may demonstrate a hypertrophic cardiomyopathy that may pertain to an adaptive response to high pressure in HLHS, which can be sensed by myocardial cells through mechanotransduction [5].

The patterns of normal and HLHS cardiac development demonstrates that as fetuses grow, the filling phase of the ventricle for HLHS results in a slightly higher KE than its ejecting phase, while in normal hearts, the ejecting phase becomes stronger than the filling phase to meet the increased demand as the body grows. It is likely that the HLHS right ventricle can't sufficiently compensate through the ejection phase, and therefore, the filling phase aids in the production of a necessary CO, possibly through increased atrial contraction. Also, HLHS diastolic KE is higher than normal by 7% at mid-stage, and changes to 2.3 times at late-stage. In the other words, the more HLHS fetus grows, the more the right ventricle loses its ability to eject the blood, and to meet the demand. The presence of a high blood flow velocity in HLHS at an early stage of development contributes to generation of high WSS and high flow momentum, and consequently production of a highly multidirectional flow which may be linked to HLHS.

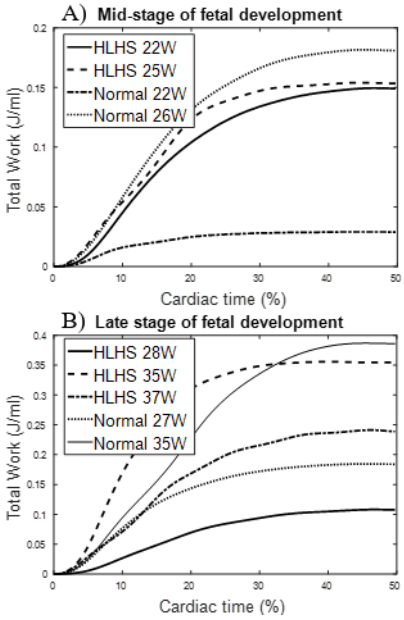

FIGURE 2: Systolic work done by HLHS and normal right ventricle at (A) mid-stage and (B) late-stage of cardiac development.

This work provides insight into the blood flow hemodynamics in normal and diseased fetal hearts. It is a first step toward characterizing hemodynamics in a disease state to determine how to better correct congenital heart defects like HLHS. Additional work needs to be performed to uncover the potential treatments that have better outcomes.

ACKNOWLEDGEMENTS

The authors gratefully acknowledge funding from National Institutes of Health (NIH) under Award Numbers UL1 TR001082.

REFERENCES

[1] Hoffman et al., JACC 39.12: 1890-1900, 2002.
[2] Norwood et al., *Ann. Thorac. Surg.* 52.3: 688-695, 1991.
[3] Hove et al., *Nature* 421.6919: 172, 2003.
[4] Wiputra et al., *Am J Physiol Heart Circ Physiol* 311.6: H1498-H1508, 2016.
[5] Bogaard et al., *Chest* 135.3: 794-804, 2009.

SB³C2019
Summer Biomechanics, Bioengineering and Biotransport Conference
June 25 -28, Seven Springs, PA, USA

ON THE QUANTIFICATION OF HEMODYNAMICS IN THE ASCENDING AORTA TO PREDICT PATHOGENESIS IN BICUSPID AORTIC VALVE (BAV) DISEASE

Tejas Canchi (1), Sargon A. Gabriel (1), Mustafa Gok (1, 2), David F. Fletcher (3), Stuart M. Grieve (1, 4)

(1) Sydney Translational Imaging Laboratory, Heart Research Institute, The University of Sydney, NSW, Australia

(2) Department of Radiology, Faculty of Medicine, Aydin Adnan Menderes University, Aydin, Turkey

(3) School of Chemical and Biomolecular Engineering, The University of Sydney, NSW, Australia

(4) Department of Radiology, Royal Prince Alfred Hospital, Sydney, NSW, Australia

INTRODUCTION

Bicuspid aortic valve (BAV) disease is the most common congenital anomaly of the heart valves and occurs in 2% of the population. BAV patients are predisposed to aortic dilations and dissections and abnormal secondary flow that results in elevated wall shear stress on the arterial wall. There are several types of BAV; the most common being fusion of the right and left coronary cusp (RL-BAV), and fusion of the right and non-coronary cusps (RN-BAV). These morphotypes contribute to the variation of hemodynamics in the ascending aorta. Blood flow in RL-BAV and RN-BAV aortas has been observed to be helical in nature (as compared with predominantly streamlined flow in healthy patients). Hope et al. [1] observed that the helical flow is markedly different in the two morphotypes; with the RL-BAV showing right-handed helical flows from right anterior flow jets, and the RN-BAVs showing left-handed helical flow from left posterior flow jets. Such changes in the hemodynamics of the aorta is expected to directly influence its biomechanical properties. This includes principally, the influence of helical flow on the arterial wall, resulting in elevated wall shear stress (WSS), and hence clinical complications.

The hemodynamics of BAV disease can be directly quantified using 4D-flow MRI measurements of the flow field in the ascending aorta [2]. Much of what is known about BAV hemodynamics comes from studies that involve 4D-flow MRI and tools such as computational fluid dynamics (CFD). Using such tools, Meierhofer et al. [3] and Saikrishnan et al. [4] compared the hemodynamics of healthy tricuspid aortic valves (TAV) with a set of BAV types to determine flow variations and resulting WSS. A prospective study showed that the cumulative net WSS and circulatory WSS were significantly increased in individuals with BAV compared with individuals with TAV in the mid-ascending aorta (main pulmonary artery level) [3]. However, the axial component of the WSS was significantly reduced in the BAV patients compared with the TAVs. This led the researchers to conclude that flows in the ascending aorta of TAV individuals was mostly streamlined while those of BAV patients were helical in nature. Saikrishnan et al. [4] reinforce these findings in an *in vitro* study conducted using Particle Image Velocimetry (PIV) on both types of valves. The study included stenosed BAVs, as well as those with regurgitation. The researchers observed systolic jets in BAV patients. The structural setup of BAVs resulted in delayed vortex formation in early systole as opposed to the normal flow behaviour of TAV patients. This was also reported by Hope et al. [1], but in a cohort that did not include patients with stenosis or regurgitation.

BAVs confer a considerable burden of morbidity and mortality. Despite this, there is no clear mechanistic understanding of the abnormal flow behaviour associated with this condition. In this study, 4D-flow MRI imaging of the flow conditions generated by BAV cases (with normal valvular functions, and without concomitant stenosis or regurgitation) is used to generate realistic CFD models of flow and WSS. This approach is applied in healthy aortas in order to better understand the interplay between abnormal flow at the valve level in RL-BAV and RN-BAV compared with normal TAV flow.

METHODS

A cohort of five healthy ascending aortas was chosen to perform the analysis. Inlet flow boundary conditions were drawn from healthy TAV and three types of BAV pathologies, to be applied to the cohort. Participants provided written informed consent in accordance with the ethical guidelines of the respective institutional review boards. MRI scans were generated using a GE Medical Systems 3T 750W MRI scanner including MR angiographies and 4D-flow data. An in-house semi-automated segmentation to simulation pipeline was used to perform CFD analysis, using ANSYS CFX v18.2. Inlet velocity

Poster Presentation #P185

boundary conditions were obtained from 4D-flow MRI measurements. To remove the influence of vessel shape, the five healthy TAV aortas were used as the common vessel wall boundaries for each type of BAV inlet case studied. Blood flow was assumed laminar and incompressible, with blood having a non-Newtonian viscosity governed by the Carreau-Yasuda (modified Cross) formulation [5]. The outlet flow boundary conditions were estimated using physiological flow division based on Murray's Law, and by a zero-gauge pressure outlet boundary at the descending aorta.

RESULTS

The average age of the cohort of normal aortas was about 50 years. The BAV inlet flows were drawn from patients that were age-matched with the healthy aortas. The WSS, Oscillatory Shear Index (OSI) and the velocity streamlines for the subject cohort were processed at peak systole in the sixth cardiac cycle to remove the effect of initial conditions. Figure 1 shows the velocity streamlines of a representative healthy aorta when the three different BAV inlet flow conditions are applied. The helical vortex development in the ascending aorta in the RN-BAV is significantly stronger than the other BAV morphotypes.

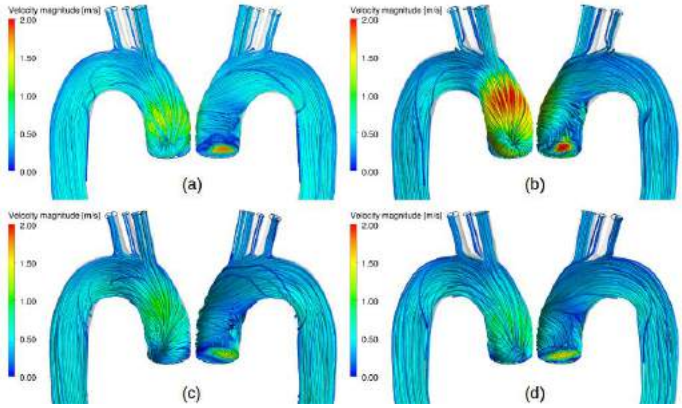

Figure 1. Velocity streamlines in a normal aorta with (a) TAV, (b) RN-BAV, (c) RL-BAV and (d) 0AP-BAV inflow conditions.

Figure 2 shows the WSS distribution within a representative healthy aorta when the three types of BAV inlet flow conditions are applied. The peak WSS is highest in the RN-BAV with a value of 25.9 Pa, as compared with the normal TAV aorta showing a peak WSS of 15.8 Pa. Figure 3 shows the OSI for the set of normal and BAV inlets on the healthy aorta.

DISCUSSION

This is the first known work on modeling healthy aortas by introducing pathology to propose a generalizable model for flow dysfunction in BAV patients. The aim of the study was to use 4D-flow MRI to apply measured flow fields of BAV and TAV subjects at the sinotubular junction and to use CFD to quantify hemodynamic parameters that will result in providing a comprehensive diagnostic model to predict complications in BAV patients.

As seen in Figure 1, the streamlines show the flow development to be markedly different in each of the three types of valve physiologies with the BAV inlet aortas showing strong helical vortices in the ascending aorta. The progression of the helical vortex has been deemed to be a significant biomarker in the assessment of risk for aortic dilatation and dissection. In addition, quantification of WSS as shown in Figure 2 will provide a basis for comparison of healthy TAV patients with those having aortic valve disease. The RN-BAV shows markedly higher WSS and this is attributable to the high velocity systolic jets impinging on the aortic wall. These jets originating in the valve are dependent on the morphotypes. The flow in the ascending aorta with RN-BAV is right-hand helical and lasts spatially longer along the ascending aorta compared to a healthy TAV. The OSI, which is a hemodynamic parameter, does not show significant variation amongst the cases, indicating that it is more influenced by the geometry of the aorta which is controlled in this study. The use of 4D-flow MRI based CFD methods to quantify flow in aortic valve disease can provide valuable information to the clinician in the assessment of progression towards complications like aortic dilatation and dissections.

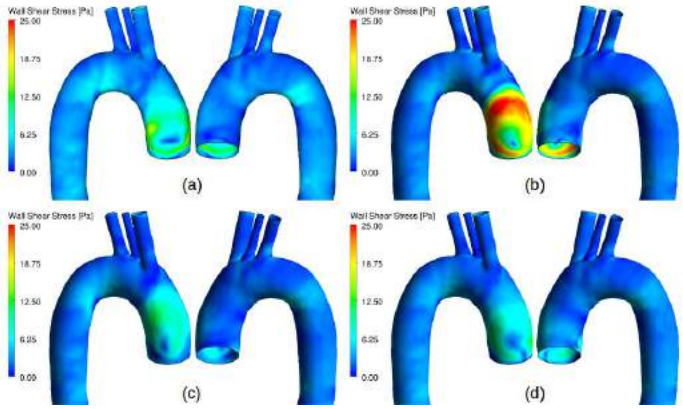

Figure 2. Distribution of WSS in a normal aorta with (a) TAV, (b) RN-BAV, (c) RL-BAV and (d) 0AP-BAV inflow conditions.

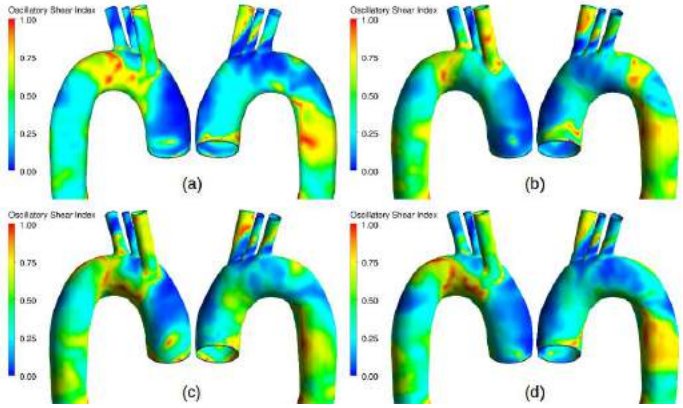

Figure 3. Distribution of OSI in a normal aorta with (a) TAV, (b) RN-BAV, (c) RL-BAV and (d) 0AP-BAV inflow conditions.

ACKNOWLEDGEMENTS

The authors acknowledge the Heart Research Institute, the Sydney Medical School Foundation, the Parker Hughes bequest, the National Health and Medical Research Council (NHMRC), and the Frecker Family Trust for funding support.

REFERENCES

[1] Hope DM et al., Radiology, 255(1): 53-61, 2010.
[2] Callaghan FM et al., JMRI, 43(2):352-363, 2016.
[3] Meierhofer C et al., Eur Heart J Cardiovasc Imaging,14(8):797-804, 2013.
[4] Saikrishnan N et al., Ann Biomed Eng., 40(8): 1760-1775, 2012.
[5] Leuprecht A and Perktold K, Comput Methods Biomech Biomed Engin., 4(2), 149-163, 2001.

SB³C2019
Summer Biomechanics, Bioengineering and Biotransport Conference
June 25 -28, Seven Springs, PA, USA

MULTIPLE MITRACLIPS: THE BALANCING ACT BETWEEN PRESSURE GRADIENT AND REGURGITATION

Shelley Gooden (1), Hoda Hatoum (1), Konstantinos Boudoulas (2), Lakshmi Dasi (1,2)

(1) Department of Biomedical Engineering
The Ohio State University
Columbus, Ohio, US

(2) Division of Cardiac Surgery
The Ohio State University
Columbus, Ohio, US

INTRODUCTION

Mitral regurgitation (MR) is quite prevalent, present in 1.7% of the general population and 9.3% of those age 75 and older [1]. Unfortunately, surgical treatment is not suitable for high-risk patients. Instead, transcatheter therapies can be used, such as Abbott's MitraClip NT, which can benefit symptomatic Degenerative MR (DMR) and functional MR patients with high MR grades and ventricles that aren't severely dilated [2,3,4]. One issue is sufficiently maintaining reduced MR while avoiding an elevated transmitral pressure gradient that creates mitral stenosis (MS), as patients with procedure related MS of pressure gradient > 5 mmHg have poorer long-term outcomes than those with residual MR [3,4]. This issue is more important when clinicians consider a second or third MitraClip when intra-procedural MR continues. Together, this leads to the question of when more than one MitraClip should be deployed, since more clips can further decrease MR but also cause pressure gradient to further increase [4]. The objective of this study is to understand how multiple MitraClips effects the hemodynamic performance of the mitral valve (MV) for various DMR severity levels, with a specific focus on increases in pressure gradient. The hypothesis of this study is that though MitraClip increases pressure gradient, the valve benefits by reducing regurgitation.

METHODS

Experiments were performed using an in vitro left heart simulator with full ventricular and atrial function. A custom MV chamber was designed to hold the valve, with a system to hold the papillary muscles (PMs) in place, as function is vital to valve competence. The working fluid was a 60-40 water-glycerin mixture to achieve the density (1060 kg/m^3) and kinematic viscosity of blood (3.88 cSt), and the valve in the aortic position was a 21 mm Medtronic Hancock II valve. The setup also allowed for high fidelity pressure and flow hemodynamic measurements of the valve to quantify parameters, including effective orifice area (EOA), pressure gradient, and mitral regurgitant fraction (MRF) defined as the ratio of regurgitant volume to stroke volume.

A porcine mitral valve with septolateral and intercommissural dimensions of 20 mm and 32 mm was sutured to a plate, as shown in Figure 1A. The valve was modeled in native (unaltered) and pathophysiological states with MR severities defined as mild, moderate, and severe, with MRFs of < 0.30, < 0.50, and ≥ 0.50, respectively [5,6]. This valve was tested under a systolic ventricular pressure of 120 mmHg and heart rate of 60 beats per minute, where systole composed one-third of the cardiac cycle. The cardiac output was set to 3 L/min appropriate for the valve size. 12 configurations were created, which included the number of clips (0, 1, and 2) and valve state (native and mild, moderate, and severe MR).

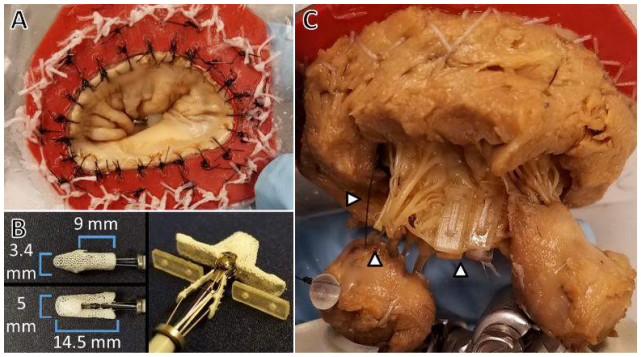

Figure 1: Mitral Valve and MitraClip

A MitraClip analog was created to mimic the footprint MitraClip has on the leaflets while allowing removal of the device such that the same valve can be assessed for all configurations. A comparison of the

analog with the MitraClip is shown in Figure 1B. For clipped cases, clips were sutured to the center of the leaflets (Figure 1C).

Severe DMR was induced via cutting all chordae tendineae connecting the posterior leaflet to the anterolateral PM, and moderate and mild MR was achieved via placing suture(s) to restore select connections (Figure 1C).

Flow and pressure were recorded for at least 50 cycles for each configuration. EOA, pressure gradient, and MRF were calculated and compared between each clip case for each valve state using Tukey tests.

RESULTS

Hemodynamic data for the native valve is shown in Figure 2. For the native case, there was a statistically significant difference for each parameter between clipping configurations.

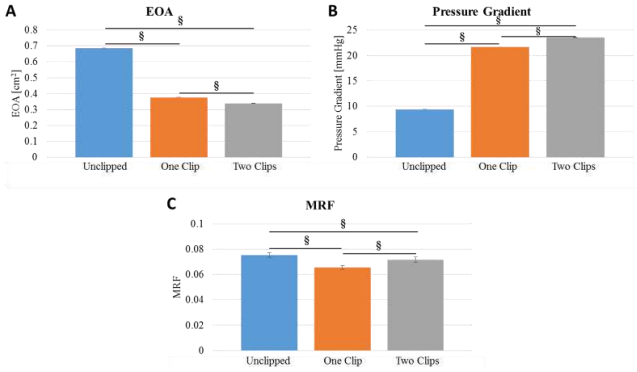

Figure 2: Native Valve Hemodynamics

Data for the mild and moderate MR cases are shown in Table 1 while that for the severe case is shown in Figure 3.

Table 1: Mild and Moderate MR Hemodynamics

	Configuration	EOA [cm²]	Pressure Gradient [mmHg]	MRF
Mild	Unclipped	0.75	8.57	0.146
	One Clip	0.51	15.60	0.142
	Two Clips	0.50	16.04	0.139
Moderate	Unclipped	0.90	10.76	0.395
	One Clip	0.70	9.32	0.150
	Two Clips	0.46	19.58	0.150

For the mild case, there was a statistically significant difference for each parameter between clipping configurations ($p < 0.0001$, except MRF in unclipped vs one clip – $p < 0.001$).

Clipping the native and mild MR valve did not decrease MRF to a degree clinically relevant. However, EOA and pressure gradient were impaired.

For the moderate case, there was a statistically significant difference for each parameter ($p < 0.0001$), except for MRF in one vs two clips (NS). Clipping the moderate MR valve greatly improved MRF, reducing severity to mild. EOA and pressure gradient also decreased. However, the use of two clips instead of one gave no added benefit to MRF but continued to decrease EOA, while pressure gradient doubled.

For the severe case (see Figure 3), there was a statistically significant difference for each parameter between clipping configurations. MRF decreased drastically with clips for the severe case. The use of one clip decreased MR to moderate. However, EOA was halved to 0.54 cm^2 and pressure gradient almost doubled to 22.1 mmHg. Two clips decreased MR to mild, and EOA continued to decrease to 0.42 cm^2 while pressure gradient continued to increase to 27.3 mmHg.

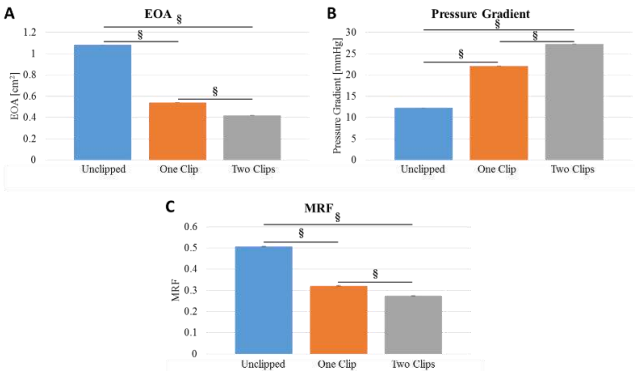

Figure 3: Severe MR Hemodynamics

DISCUSSION

MRF did not change in the native and mild cases, as MRF was not high enough for the clip to impact when restricting leaflet motion. These results were as expected, as the MitraClip is intended for treating higher grades of MR. As a result, the pressure gradient sufficiently increased to 20+ mmHg for the native case and 15+ mmHg for the mild case. A study by Katz et al [7] demonstrated a 50% decrease of the mitral valve area after the first clip and a further decrease of 30-40% after the second, which explains the elevated pressure gradients. This great elevation is harmful, especially because MRF was not reduced. Clipping the moderate valve decreased MR severity to mild. It is interesting to note the unexpected decrease of pressure gradient with one clip in the moderate case. This decrease may be attributed to the decrease of forward flow. Two clips being unable to further reducing MRF may be due to clip location, as the second centered clip was unable to impact MRF. A study by Magruder et al specified that multiple clips may only be efficient for a wide regurgitant jet of diameter exceeding 7.5 mm [8]. This shows that though lowering MR is the goal, adding clips can elevate pressure gradient and may not help MRF.

Clipping greatly reduced MRF for the severe case. One clip decreased severity to moderate while two decreased severity to mild. However, MRF did not significantly decrease with two clips compared to one but further impaired EOA and pressure gradient. Similar to the moderate case, MRF not further decreasing may be due to clip placement. Again, this shows that though MR can be further reduced to an even lower severity, pressure gradient can be further elevated.

This study shows that validated in vitro models can be used to explore the full effect of MitraClip. Ongoing studies are currently performed to optimize MitraClip usage.

ACKNOWLEDGEMENTS

This research was supported by National Institutes of Health (NIH) under Award Number R01HL119824.

REFERENCES

[1] Benjamin, E.J. et al., *Circulation*, 137:e67-e492, 2018.
[2] Juillière, Y, *Arch. Cardiovasc. Dis.*, 2018.
[3] Neuss, M. et al., *JACC Cardiovasc Interv*, 10:931-939, 2017.
[4] Giordano, A. et al., *J Cardiol Ther*, 1:133-137, 2014.
[5] Nishimura, R.A. et al., *AHA*, 64:e57-e185, 2014.
[6] Grayburn, P.A. et al., *Ann Biomed Eng*, 64:2792-2801, 2015.
[7] Katz, W.E. et al, *Cardiovasc Diagn Ther*, 7:616-632, 2017
[8] Magruder, J.T. et al, *Med Devices (Auckl)*, 9:53-60, 2016.

SB³C2019
Summer Biomechanics, Bioengineering and Biotransport Conference
June 25 -28, Seven Springs, PA, USA

BASILICA-TYPE LEAFLET LACERATION TO REDUCE RISK OF THROMBOSIS IN TRANSCATHETER AORTIC VALVE REPLACEMENT

Hoda Hatoum (1), Pablo Maureira (2), Scott M. Lilly (3) and Lakshmi P. Dasi (1)

(1) Department of Biomedical Engineering
The Ohio State University
Columbus, Ohio, USA

(2) Department of Cardiac Surgery
Centre Hospitalier Universitaire de Nancy
Nancy, France

(3) Department of Medicine
The Ohio State University
Columbus, Ohio, USA

INTRODUCTION

Subclinical leaflet thrombosis following transcatheter aortic valve (TAV) replacement (TAVR) and valve-in-valve (ViV) has been correlated in literature to neo-sinus and sinus flow stasis[1, 2]. Therefore, it is possible to reduce the risk of leaflet thrombus if not eliminate it, if the washout in the sinus and neo-sinus regions tremendously improves. Recently, the bioprosthetic or native aortic scallop intentional laceration to prevent iatrogenic coronary artery obstruction also known as BASILICA has been introduced as a technique to help mitigating coronary obstruction through lacerating the bioprosthetic leaflet[3]. Despite being used in the context of solving potential coronary obstruction, BASILICA as previously explained, introduces a laceration to the leaflet that opens a narrow but direct flow pathway between the sinus and the neo-sinus, and thus potentially altering flow dynamics in both sinus and neo-sinus. The objective of this study is to assess neo-sinus and sinus flow washout with and without leaflet laceration in the context of leaflet thrombosis.

METHODS

A 23mm Edwards SAPIEN 3 and a 26mm Medtronic Evolut were deployed in a 23mm transparent surgical aortic valve model (See Figure 1) pre and post-leaflet laceration with and without coronary flow. The neo-sinus and sinus hemodynamic were evaluated under pulsatile flow conditions ensured by a left heart pulse duplicator yielding physiological flow and pressure curves and including a left coronary loop[1]. Briefly, the left coronary flow is controlled by a Starling resistor that was collapsed or expanded during specific intervals to match the changes in coronary flow during myocardial contraction or relaxation respectively. Base hemodynamics for all conditions were maintained with a systolic to diastolic pressure of 120/80mmHg, 60 beats per minute heart rate, a systolic duration of 33% and a cardiac output of 5l/min. The working fluid in this study is a mixture of water-glycerin producing a density of 1080 Kg/m^3 and a kinematic viscosity of 3.5 cSt similar to blood. Particle image velocimetry was performed in order to quantify sinus flow hemodynamics and leaflet washout.
Using Lagrangian particle tracking, sinus and neo-sinus washout was

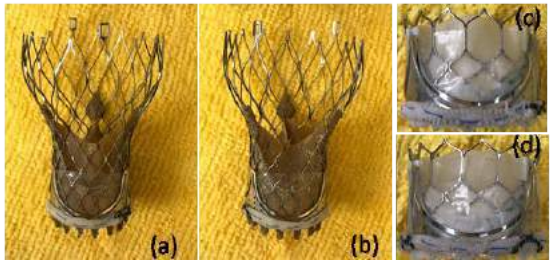

Figure 1: Valve-in-valve deployment in a transparent surgical valve model with (a) Evolut and (c) SAPIEN 3 pre-leaflet laceration and (b) Evolut and (d) SAPIEN 3 post-laceration.

evaluated. Briefly, particles were seeded as a uniform grid of 0.0003mx0.0003m cell size over the sinus region at the beginning of the cardiac cycle. Each particle's trajectory was computed by integrating its velocity with respect to time based on:

$$\frac{d\vec{x}}{dt}(t) = \vec{u}((\vec{x}), t)) \quad (1)$$

With:

$$\vec{x}(\mathrm{t} = 0) = \vec{x}_0 \quad (2)$$

After every cardiac cycle only the particles that remained in the sinus were re-seeded based on their last positions and their trajectory over the subsequent cardiac cycle was calculated. This process continued until

all particles exited. Once all the particles exited the sinus, a histogram of the time spent by the particles was generated and then converted to a cumulative distribution function representing the particles' survival probability as a function of time. This procedure is repeated over 6 cycles for every valve combination. The resulting curves represent the sinus washout characteristic for all cases.

RESULTS

Fig.2 shows the velocity fields of the sinuses without coronary flow. It is clear that higher velocities (expressed by larger vectors) exist at the interface between sinus and neo-sinus after BASILICA. Washout results in the neo-sinus are shown in Fig.3a.

Without coronary flow: Without coronary flow, total washout (0% particles remaining in the neo-sinus) with Evolut TAV laceration, total washout was achieved by the end of the first cardiac cycle. 65% of the particles exited by 0.5s. With a SAPIEN 3 TAV without coronary flow, total washout was achieved after 3.5s progressively with 90% of the particles exiting by the end of the second cardiac cycle. With leaflet laceration, total washout was achieved at 0.8s almost immediately.

With coronary flow: With coronary flow, total washout with Evolut was achieved after 2.75s, 80% before the end of the first cardiac cycle and the remaining 20% gradually over the remaining 2s. After leaflet laceration, total washout was achieved at 0.54s. With a SAPIEN 3 TAV

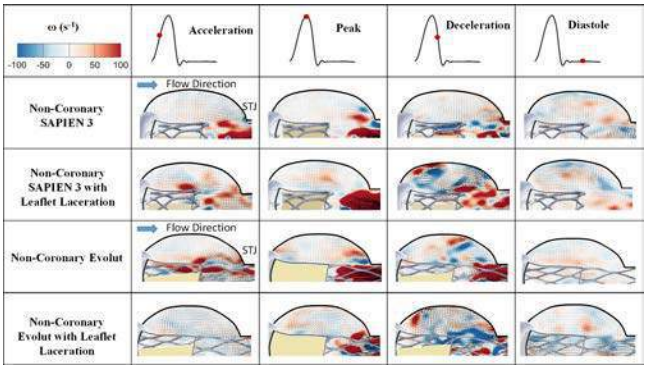

Figure 2: Vector fields in the sinuses without coronary flow.

without coronary flow, washout occurs progressively and total washout is completed after 3.5s. After leaflet laceration, total washout was achieved at 0.8s. With coronary flow, total washout with SAPIEN 3 was completed before the end of the 3rd cycle at 3.93s. 80.5% were washed out before the end of the 1st cycle. After leaflet laceration, total washout was achieved at 1.3s with 96.1% already washed out by 0.5s.

Fig.2b shows the washout in the sinus of the 8 different ViV combinations with and without coronary flow with Evolut and SAPIEN 3 TAVs.

Without coronary flow: total washout was achieved with Evolut ViV after 1.4s. Before the gradual decrease to 1.4s, 90% of the particles were already out of the sinus by 2/3rd of the first cycle. After leaflet laceration, total washout was completed at 0.8s. SAPIEN 3 ViV without coronary flow leads to a total gradual washout after 2.09s while after leaflet laceration, total washout was completed after 2s with steeper and less gradual phases.

With coronary flow: total washout with Evolut ViV was achieved after 0.79s while after leaflet laceration, total washout was immediately completed by 0.26s. SAPIEN 3 ViV with coronary flow yields a total washout by 0.85s, while after leaflet laceration total washout was completed at 0.99s.

DISCUSSION

Implementing a laceration to the leaflet of the surgical valve in ViV is simply allowing the flow to exit a cavity (neo-sinus) more freely from two sides now instead of one: forward and upward toward the sinus. Without laceration, the connection between sinus and neo-sinus is nonexistent directly. This "trans-leaflet" flow explains the increased velocity observed at the intersection of the sinus and the neo-sinus compared to the cases without leaflet laceration. In the presence of coronary flow, the influx from the neo-sinus is almost directly and fully

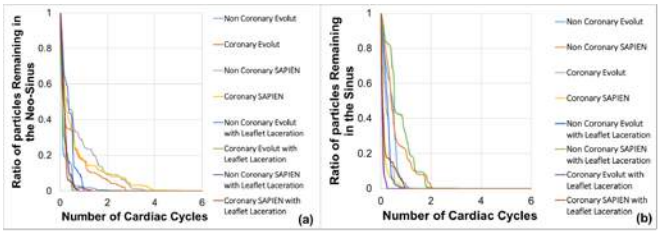

Figure 3: (a) Washout curves in the (a) neo-sinus and (b) the sinus.

absorbed by the coronary ostium. Leaflet laceration adds new flow features because of the new trans-leaflet flow and enhances the flow in the sinus particularly in the area towards the annulus where stagnation is most likely to occur[4,5]. In addition, the presence of laceration alters the typical flow features in the sinus. The aortic sinus vortex is pushed further towards the sinotubular junction (STJ) and the flow is forced to exit the sinus faster with the new flow influx. Several studies have shown the impact of coronary flow on sinus hemodynamics in ViV[1,4]. The results presented in this study show that leaflet laceration may provide the sinus (if it is non-coronary) the same advantage that coronary flow presents in terms of enhanced fluid motion and increased velocities in the sinus[1,4]. Thrombosis occurs most likely in low flow regions characterized by longer particle or cell residence time[6] and poor washout is believed to be one of the reasons that lead to bioprosthetic valve thrombosis[7,8]. Allowing the flow to have more degrees of freedom and to stop being partially confined in the neo-sinus explains why washout was tremendously improved by at least a factor of two between pre and post-laceration. Washout in the sinus was also improved post-laceration only the differences were not as important as those obtained in the neo-sinus. The extra momentum brought into the sinus from the neo-sinus as previously explained creates vortices in the sinus back adjacent to the annulus side that help in pushing the fluid outside the sinus into the STJ side. With coronary flow, this mechanism is much more enhanced[1].

ACKNOWLEDGEMENTS

The research done was partly supported by National Institutes of Health (NIH) under Award Number R01HL119824.

REFERENCES

[1] Hatoum, H et al., *ATS*, 2018.
[2] Midha, PA et al., *CirculationAHA*, 2017.
[3] Dvir, D et al., *EuroIntervention*, 2018. 14(AB): p. AB74-AB82.
[4] Hatoum, H et al., *JTCVS*, 2017.
[5] Mangione, FM et al., *JACC: Cardiovascular Imaging*, 2017. 10(1): p.82-85.
[6] Rayz, V et al., *ABME*, 2010. 38(10): p. 3058-3069.
[7] Jahen, SE et al., Interactive cardiovascular and thoracic surgery, 2018. 27(1): p. 108-115.
[8] Hatoum, H et al., *JTCVS*, 2018.

SB³C2019
Summer Biomechanics, Bioengineering and Biotransport Conference
June 25 -28, Seven Springs, PA, USA

EARLY DIAGNOSIS OF REDUCED LEAFLET MOBILITY AFTER TRANSCATHETER AORTIC VALVE REPLACEMENT

Hoda Hatoum (1), Jung-Hee Seo (2), Shantanu Bailoor (2), Scott Lilly (3), Rajat Mittal (2) and Lakshmi Prasad Dasi (1)

(1) Department of Biomedical Engineering
The Ohio State University
Columbus, Ohio, USA

(2) Department of Mechanical Engineering
Johns Hopkins University
Baltimore, Maryland, USA

(3) Department of Internal Medicine
The Ohio State University
Columbus, Ohio, USA

INTRODUCTION

Transcatheter aortic valve (TAV) replacement (TAVR) has emerged as an alternative to surgical aortic valve surgery[1]. Recently, leaflet thrombosis – mainly recognized by reduced leaflet mobility - was identified as an adverse effect of TAVR[2]. Leaflet thrombosis is sub-clinical thus cannot be identified with routine clinical tools, in addition to not being always accompanied by direct symptoms[3]. With the increasing number of TAVR procedures performed annually, the likelihood of adverse effects is also going to increase. Therefore there is a need to predict or identify the early onset of the occurrence of these adverse effects. Miniaturized pressure biosensors, if incorporated in the valve at different locations, can convey information once any abnormality in the valve function occurs[4]. In order to determine configuration of these biosensors to monitor various hemodynamic signals in the vicinity of the valve there is need to understand localized variations in pressure along the stent frame and distal to the valve with and without reduced leaflet mobility (RLM). The objective of this study is to identify the impact of RLM due to leaflet thrombosis on the pressure at different selected points on the TAV frame and distal to the frame.

METHODS

A 26mm Edwards SAPIEN 3 TAV was hemodynamically assessed in a pulse duplicator left heart simulator flow loop under physiological pressure and flow conditions (cardiac output = 5 L/min; heart rate = 60 beats per minutes; systolic to diastolic pressures = 120/80 mmHg). Reduced leaflet mobility was simulated by manually obstructing the leaflet (corresponding to point 5 in Figure 1) which prevented the leaflet from opening during systole. Pressure was recorded using a Millar catheter at various locations. Locations 1, 2 and 3 (shown in Figure 1) are at the sinotubular junction (STJ) plane and locations 5, 6 and 4 are behind the valve leaflets in the order of locations 1, 2 and 3 respectively. In addition, measurements of pressure at different points in the outflow region (at valve leaflets, at STJ line and at 5 cm from the valve orifice) along with a measurement of the ventricular pressure were also performed. Figure 1 summarizes the locations of these points.

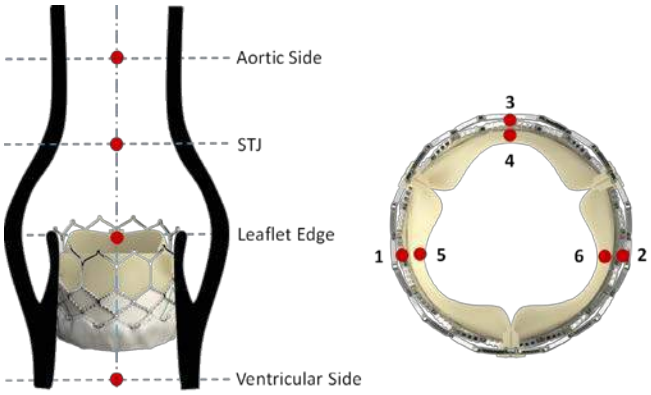

Figure 1: Measurements locations of the different pressure points.

One hundred consecutive cardiac cycles of pressure at each location, and flow rate data were recorded at a sampling rate of 100 Hz. Fluctuating pressure was obtained by subtracting the ensemble averaged pressures from the instantaneous pressures signals. Total and fluctuating pressure signal two point correlations as well as individual power spectral density functions were calculated to assess the impact of RLM on the local dynamics of the pressure field.

Poster Presentation #P188

RESULTS

Figure 2 shows the ensemble averaged pressure over the cardiac cycle at the points indicated in Fig.1. The figure shows that there exists a pressure loss (Fig.2a, b and c) with RLM at all points distal to the valve and not necessarily only at the one point where the leaflet immobility is applied. The ventricular pressure does not show significant change in magnitudes with and without RLM (Fig. 2d). Figure 3 shows the power spectrum of the fluctuating pressure (i.e. instantaneous minus ensemble averaged) at pts. 1, 2, 3, 5, 6 and 4. The figure highlights pt.1 with RLM (dotted blue line) and pt. 5 (located behind 1) that show the lowest peaks at primary and all harmonic frequencies (1Hz, 2Hz, 3Hz etc). Table 1 shows the two point correlation coefficients between points 1, 2 and 3 for the different cases. When the valve is fully open, RLM increases the correlation coefficient between the points, keeping a lower value between 2 and 3. During all the cardiac cycle, correlation coefficients varied non-monotonically between the 3 points and between pre-RLM and post-RLM. Looking only at the fluctuating component of the pressure during all the cardiac cycle, RLM led to low correlation coefficients that subsequently decrease with the lowest being between 2 and 3. Also, the correlation coefficients were negative for some cases pre and post RLM showing that as the pressure at Pt 1 increases, that at Pt 2 and 3 decreases pre-RLM. The same applies between Pts 1 and 3 and 2 and 3 post-RLM.

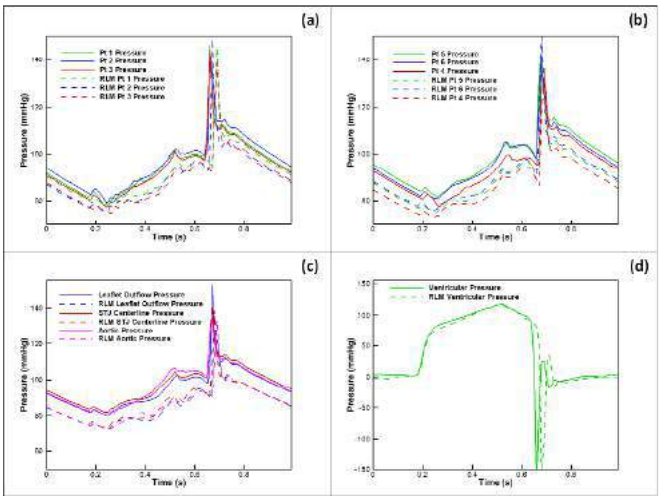

Figure 2: Recorded pressure at points (a) 1, 2 and 3, (b) 5, 6 and 4, (c) along the longitudinal axis of the aorta and (d) in the ventricular side.

Correlation Coefficients		Pts 1 and 2	Pts 1 and 3	Pts 2 and 3
Open Valve Phase	Pre-RLM	0.944	0.944	0.935
	Post-RLM	0.978	0.972	0.952
All Cardiac Cycle	Pre-RLM	0.967	0.972	0.965
	Post-RLM	0.791	0.973	0.800
All cardiac cycle – fluctuating pressure	Pre-RLM	-0.180	-0.185	0.046
	Post-RLM	0.041	-0.045	-0.034

Table 1: Correlation coefficients between Pts 1, 2 and 3 pre- and post- RLM for different cases.

DISCUSSION

As expected reduced leaflet mobility has been shown to cause an increase in pressure gradient (additional ~15mmHg in this experiment) across the valve compared with healthy subjects [5]. Results of this study show a drop in the pressure at and around the outflow of the valve. The severity of pressure gradient throughout the progression of leaflet thrombosis thus could be captured and identified with embedded pressure sensors. From the power spectrum analysis (Fig.3), the leaflet that was forced to stay closed during valve opening phase (pt.1 and pt.5 located behind 1 at the leaflet level) displayed the lowest power spectrum densities at both primary and harmonic frequencies compared with the other points, which made it easily identifiable. Therefore, the temporal pressure fluctuation behavior of the RLM subjected leaflet is not only different compared with the other leaflets but also could be predicted with a sufficiently high sampling frequency.

Because of probably the effect of pressure variation occurs mostly there, the results demonstrate that the correlation coefficients are higher between the point where RLM is induced and the other 2 points (1 and 2; 1 and 3) compared with the other points (2 and 3).

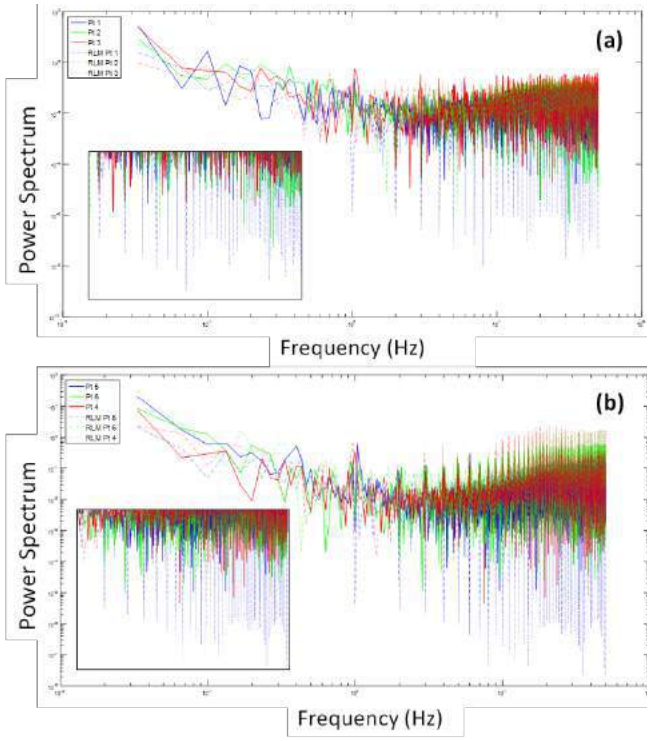

Figure 3: Power Spectrum of fluctuating component of pressure versus frequency in log-log scale for points (a) 1, 2 and 3 and (b) 5, 6 and 4. Insets show power spectrum for frequencies exceeding 1 Hz.

ACKNOWLEDGEMENTS

The research done was partly supported by National Institutes of Health (NIH) under Award Number R01HL119824.

REFERENCES

[1] Dasi, LP., et al. *Annals of biomedical engineering* 45.2 (2017): 310-331.

[2] Makkar, R., et al. *New England Journal of Medicine* 373.21 (2015): 2015-2024.

[3] Chakravarty, T., et al. *The Lancet* 389.10087 (2017): 2383-2392.

[4] Matilla, MA. *Environmental microbiology* 20.1 (2018): 141-144.

[5] Marwan, M., et al. *Journal of cardiovascular computed tomography* 12.1 (2018): 8-13.

HEMODYNAMICS, IN ADDITION TO MORPHOLOGY, PREDICTS LONG-TERM OUTCOME OF INTRACRANIAL ANEURYSMS TREATED WITH FLOW DIVERTERS

Nikhil Paliwal (1, 2), Jason M. Davies (2, 3), Adnan H. Siddiqui (2, 3), Hui Meng (1, 2, 3)

(1) Mechanical and Aerospace Engineering
University at Buffalo
Buffalo, NY

(2) Canon Stroke and Vascular Research Center
University at Buffalo
Buffalo, NY

(3) Neurosurgery, University at Buffalo, Buffalo, NY

INTRODUCTION

Flow diverters (FDs) have emerged as an alternative paradigm to traditional coil embolization for treatment of intracranial aneurysms (IAs), especially for wide-neck and fusiform aneurysm morphologies. [1] The densely woven mesh of FDs aim to induce flow stasis in the aneurysmal sac, while promoting thrombotic conditions and eventual occlusion of the IA. Despite its recent success in treatment of IAs, approximately 25% of FD-treated IAs fail to reach complete occlusion after 6 months of treatment. Patients with persistent residual filling in the aneurysm sac after FD-treatment are at risks of thromboembolic complications and aneurysm rupture. *A priori* assessment of FD-treatment outcome could aid the clinicians in treatment optimization and lead to better outcomes.

We recently developed a computational workflow that uses neural network to predict the 6-month clinical outcome of FD-treated aneurysms with 90% accuracy, as shown in Figure 1. [2] Our computational workflow includes aneurysmal morphology assessment, device modeling and CFD simulations to obtain relevant morphological, FD-related and pre- and post-treatment hemodynamic parameters (Figure 1). [3, 4] These parameters are imported into a machine-learning algorithm, which could predict the 6-month clinical outcome of FD-treated aneurysms. Although shown to be highly accurate in our preliminary testing, the computational analysis workflow involves modeling the FD device and image-based CFD simulations, which are time consuming (~24 hours). This could make it difficult to be adopted into the clinical setting.

In this study, we investigated whether device modeling and subsequent hemodynamic analysis are truly necessary to make accurate FD-treatment outcome predictions. In particular, if morphology alone could provide similar prediction accuracy, this would drastically reduce the computational cost and make transition into the clinic more straightforward. To that end, we applied the computational workflow on FD-treated aneurysm patients to develop two predictive models using: (1) morphological parameters only and (2) both morphological and hemodynamic parameters.

METHODS

Patient Selection

Patients treated using the commercial FD—Pipeline embolization device (PED, Medtronic)—at the Gates Vascular Institute between 2009-2018 were retrospectively collected for this study. The inclusion criteria was: (1) sidewall aneurysm located at the internal carotid artery (ICA), (2) treated using a single PED, (3) availability of 6-month follow-up angiographic image and (4) pre-treatment 3D digital subtraction angiography (DSA) image. For cases that satisfied the inclusion criteria, 3D DSA images before treatment, clinical outcome at 6-months and clinical and

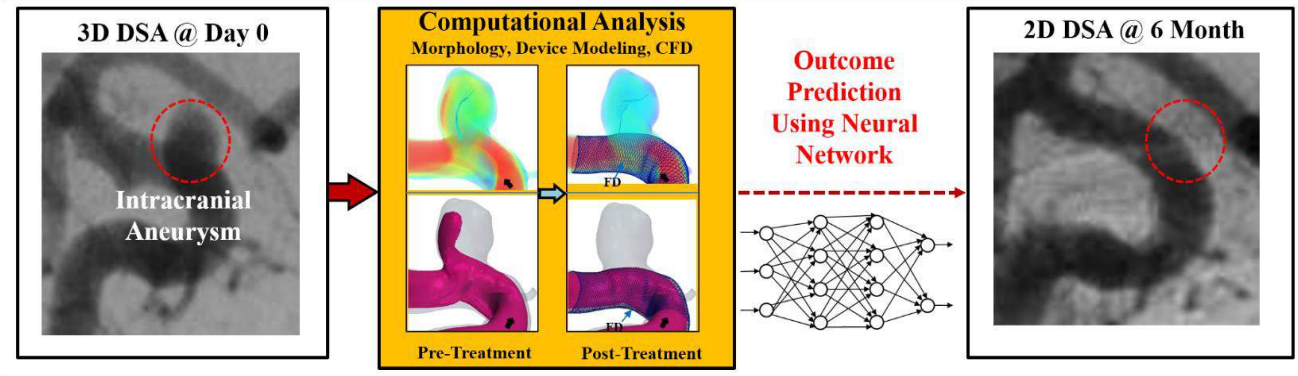

Figure 1: Schematic of the computational analysis workflow. The 3D DSA prior to treatment are taken as input, and computational analysis is performed that includes morphology analysis, device modeling and CFD simulations. These analyses provide the parameters/features for each case, which are used in a neural network to predict the 6-month occlusion outcome.

demographic data were collected. Based on their angiographic outcome at 6-month follow-up, aneurysms were divided into two groups: occluded (complete occlusion) or residual (contrast filling at the aneurysmal neck/dome). The 3D DSA images were segmented using the open-source software virtual modeling toolkit (www.vmtk.org).

Virtual Device Modeling and CFD Simulation Setup

We used an in-house virtual stenting workflow to model the clinical deployment of FDs in the 3D aneurysm models. [2] After virtual device deployment, we used STAR-CCM+ (v11.02, Siemens PLM, Plano, TX) to perform the volumetric meshing and subsequent CFD simulations. Pulsatile flow simulations were performed for each case, with blood assumed to be Newtonian and rigid wall assumption at the arterial walls. The density and dynamic viscosity was set as 1056 kg/m^3 and 0.0035 Pa-s. For each aneurysm case, 2 simulations were performed: one untreated and one treated with the FD.

Parameters Quantified: Morphology and Hemodynamics

Based on the segmented 3D aneurysm model, and pre- and post-treatment CFD simulations, morphological and hemodynamic parameters were calculated. Morphological parameters included aneurysm size, neck diameter, size ratio, aspect ratio, neck ratio and ostium ratio. In terms of hemodynamics, pre- and post-treatment hemodynamic values of inflow rate, aneurysm averaged velocity, shear rate and turnover time were quantified. [2, 3] A total of 14 parameters were calculated for each FD-treated aneurysm case: 6 morphological and 8 hemodynamic parameters.

Training Neural Network Algorithm

Supervised machine algorithms with binary classification were used to train neural network (NN) algorithm, which is inspired by human brain that uses system of interconnected neuronal layers to generate non-intuitive combinations of input features to enhance the classification model for accurate predictions.

Model Training and Testing

Using NN algorithm, we trained two models on the same dataset: (1) using morphological features alone and (2) using both morphological and hemodynamic features. Before training the models, we randomly divided the database into training and testing cohorts roughly at a 3:1 ratio. The parameters were then normalized dataset to a zero mean and a standard deviation of 1. For each model, the training loss function was observed to enable the convergence of each trained model.

To quantify the training performance of each model, receiver operating characteristic (ROC) curves were plotted, and the area under the ROC curve (AUC) was calculated. To quantify the predictive accuracy of each model, the correct predictions of both models on the independent testing samples was divided by the total number of testing samples.

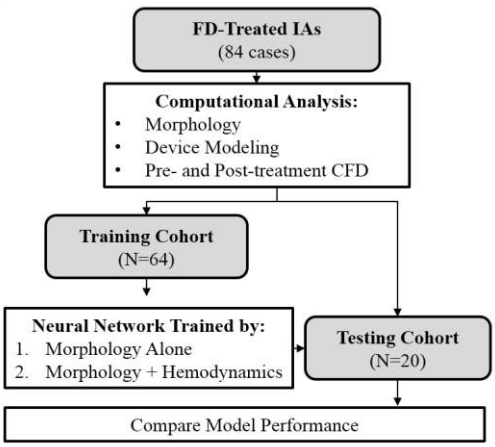

Figure 2: Flowchart for training and testing neural network models. Two models were trained: (1) using morphological parameters only and (2) using morphological and hemodynamic parameters.

RESULTS

Patient Database

Based on the selection criteria, 84 aneurysms in 80 patients were included in this study. Based on the 6-month clinical outcome, 63 aneurysms were completely occluded (occlusion group) and 21 had residual contrast filling at neck/dome of the aneurysm (residual group).

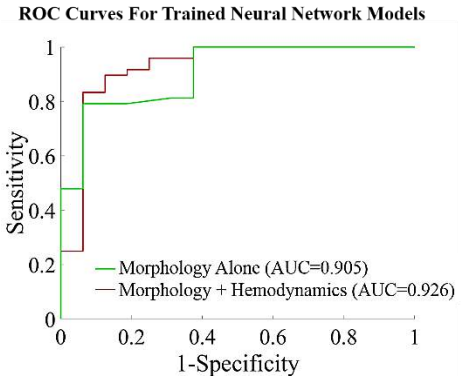

Figure 3: ROC curves for the trained neural network models. Green indicated the model trained with morphological features and red indicates the model trained using morphological and hemodynamic features. AUCs for both models are also provided.

Randomization of the data resulted in 64 cases (48 occluded, 16 residual) in the training cohort and 20 cases (15 occluded, 5 residual) in the testing cohort.

Training Performance and Testing Accuracy of Predictive Models

The ROC curves of the two trained models on the training data is shown in Figure 3. Model trained using both morphology and hemodynamic parameters (AUC=0.926, 95% CI: 0.685, 0.982) had better performance than morphology-only model (AUC=0.905, 95% CI: 0.797, 0.978).

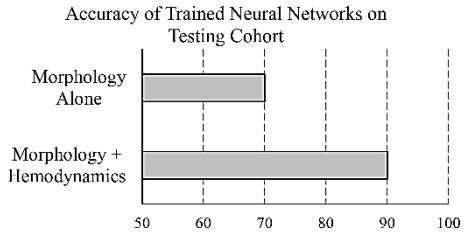

Figure 4: Accuracy of the two neural network prediction models on the independent testing cohort.

Figure 4 shows accuracy of the two models on the independent testing cohort. Prediction model trained using both morphological and hemodynamic parameters outperformed the model trained using morphology by 20%.

DISCUSSION & CONCLUSIONS

Our results show that including hemodynamic features along with morphological features during training of the neural network model slightly improved the AUC, but the accuracy in testing cohort was drastically increased for predicting FD-treatment outcome. This suggests that model trained using morphology alone was overfitting to the training data. The importance of pre- and post-treatment hemodynamics in accurate predictions also suggest that hemodynamics might play a bigger role than morphology alone in the healing of FD-treated aneurysms. In future studies, we will train another model using clinical parameters to compare its performance with these models.

ACKNOWLEDGEMENTS

This study was supported by NIH grant R01-NS-091075 and Canon Medical System Corporation. We thank Dr. Vincent Tutino and Robert Damiano for helpful discussions and Center for Computational Research for providing computational resources.

REFERENCES

[1] Brinjiki et al., Stroke, 442-447, 2013
[2] Paliwal, N et al., *Neurosurg Foc*, 45:E7, 2018.
[3] Paliwal, N et al., *AJNR Am J Neuroradiol*, In Press
[4] Mut et al., *J Neurointerv Surg*, 286-290, 2014

SB³C2019
Summer Biomechanics, Bioengineering and Biotransport Conference
June 25 -28, Seven Springs, PA, USA

CORRELATION OF COMPUTATIONAL INSTANTANEOUS WAVE-FREE RATIO WITH FRACTIONAL FLOW RESERVE IN THE CASE OF MULTIPLE INTERMEDIATE CORONARY ARTERY STENOSES IN A LEFT MAIN BIFURCATION

Arash Ghorbanniahassankiadeh (1), David S. Marks (2), John F. LaDisa, Jr. (1,2,3)

(1) Department of Biomedical Engineering
Marquette University and the Medical College of Wisconsin
Milwaukee, Wisconsin, United States

(2) Department of Medicine
Medical College of Wisconsin
Milwaukee, Wisconsin, United States

(3) Departments of Physiology and Pediatrics
Medical College of Wisconsin
Milwaukee, Wisconsin, United States

INTRODUCTION

Cardiovascular disease (CVD) is the leading cause of mortality in the U.S. and leads to ~8M inpatient procedures annually. ~86M Americans have some form of CVD and a substantial portion suffer from coronary artery disease (CAD) [1]. Whether or not to treat a particular coronary stenosis is often debated among interventional cardiologists, with hemodynamic criteria from fractional flow reserve (FFR) [2] and its computational counterpart, (FFR_{CT}) [3], growing in popularity over image-based criteria. However, in cases of multiple stenoses in the left main coronary artery (LMCA) bifurcation, FFR may yield inaccuracies [4]. In practice, invasive FFR can be costly and requires potentially uncomfortable vasodilator agents. Park et al. offered an integrated FFR and IVUS method for better lesion classification [5]. However, the cost of implementation, procedural time and availability of trained personnel are potential limitations. FFR_{CT} also uses computational fluid dynamics (CFD) analysis with non-linear lumped parameter boundary conditions that require careful tuning under several applicable flow conditions [6].

A wave-free period in diastole when coronary resistance is constant and minimum affords the possibility of performing pressure-derived stenosis severity assessment without a pharmacological agent. The instantaneous wave-free ratio (iFR) is an index derived to quantify severity using this method. iFR is defined as the ratio of the mean instantaneous pressure distal to a coronary stenosis relative to that in the aorta during the wave-free period. iFR has been correlated to FFR with values from 0.83 to 0.92 reported as equivalent for FFR 0.8, which is the putative standard for percutaneous coronary intervention [7]–[9].

The computational counterpart of iFR (iFR_{CT}), derived from coronary CTA, is a strong tool for integrated evaluation of a coronary stenosis. However, in cases of multiple intermediate coronary stenoses near the LMCA bifurcation when the FFR is in its clinically important range (0.6-0.9), the effect of downstream lesions on iFR is not clear. The objective of the current work is to computationally assess the accuracy of the current iFR threshold in an idealized case consisting of multiple lesions near the LMCA bifurcation and determine the correlation between iFR_{CT} and FFR_{CT}. The independency of iFR to hyperemia is also debated [8], which is further studied here.

METHODS

Computational model creation. Segmentation and model construction was performed using a normal CTA data set on the SimVascular website (Documentation, Coronary Normal). Models of stenoses in the LMCA, LAD, and LCX were then created. Clinically representative minimum lumen areas (MLA) of 6 and 4.5 mm^2 [2] for the LMCA and 4 and 3 mm^2 for the two branches [10] were compared to study the effect of multiple lesions on iFR and FFR (Figure 1).

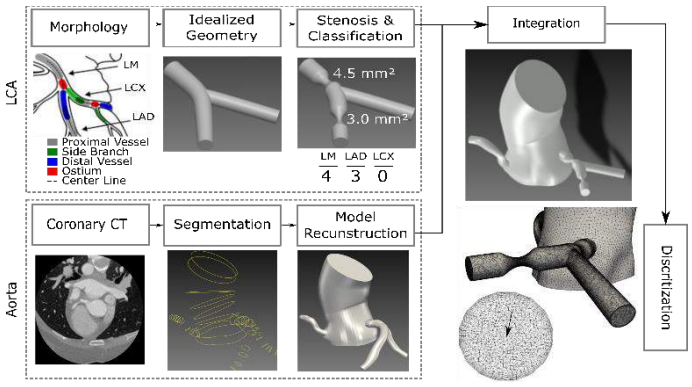

Figure 1: Model creation, classification, integration, discretization

Simulations and boundary conditions. Parameters for CFD simulations were implemented using SimVascular (simtk.org). A five-element non-linear model was used at coronary outlets. The model consists of small artery resistance (R_a), micro-circulation resistance (R_m), venous resistance (R_v), arterial capacitance (C_a) and myocardial capacitance (C_m) [11]. The flow distribution to each coronary outlet was calculated based on a generalization of Murray's law (radius ratio to the 2.6 power) [12]. In the autoregulatory range (Figure 2), flow was assumed constant and 4% of cardiac output (CO) [13] at rest. Similarly, for the pharmacological stress condition, flow was assumed to be 7% of CO [14]. According to literature, CO of 5 and 8.6 L/min, systolic blood pressure (SBP) of 120 and 78 mmHg, diastolic blood pressure (DBP) of 80 and 56 mmHg and heart rate (HR) of 60 and 96 bpm were considered for rest and stress condition, respectively [15]. Depending on the severity of a coronary stenosis, hemodynamics may fall into the autoregulatory or maximum vasodilation range [16] (Figure 2).

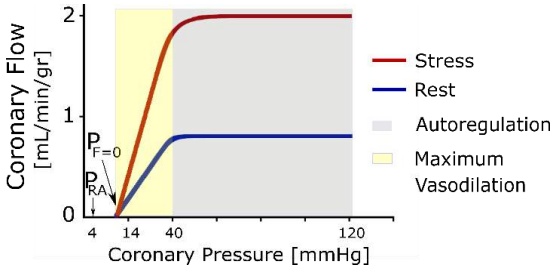

Figure 2: Autoregulatory relation under rest and pharmacological stress conditions (i.e. 140 µg/kg/min adenosine).

RESULTS

From rest to stress in the normal case, the cardiac cycle decreased from 1 to 0.625 s, the average coronary flow increased from 3.4 to 10.1 mL/s, and its range increased from 4.2 to 14.1 mL/s. In the stenoses models, the range of coronary flow decreased substantially with the severity of stenosis. The FFR_{CT} was between 0.68 and 0.98. In the stress condition, a significant drop in iFR_{CT} was observed yielding a value <0.7 for models with multiple lesions. During rest condition, however, it results in values above 0.94. For cases with two lesions the iFR_{CT} ranged from 0.94 to 0.97 suggesting significant epicardial pressure drop (Table 1) when related to FFR_{CT}.

Table 1: Computed FFR_{CT} and iFR_{CT} for all cases

Class	MLA [mm^2]		% of Stenosis		iFR_{CT}		FFR_{CT}
	LM	LAD	LM	LAD	Rest	Stress	
Normal	-	-	0	0	1.00	0.96	0.98
400	4.5	-	79	0	0.97	0.69	0.80
600	6	-	72	0	0.98	0.81	0.89
430	4.5	3	79	83	0.94	0.51	0.68
440	4.5	4	79	78	0.95	0.61	0.75
630	6	3	72	83	0.95	0.59	0.73
640	6	4	72	78	0.96	0.70	0.81

DISCUSSION

According to the results, during rest condition, an iFR_{CT} of 0.96 corresponds to FFR_{CT} 0.81 showing a correlation between lack of suggested treatment for iFR_{CT} and FFR_{CT} in the case of multiple stenoses. For multiple lesions, iFR_{CT} varies within a limited range and values of 0.94-0.95 suggest treatment when interpreted relative to FFR_{CT}. Results also suggest that the iFR_{CT}, which is independent to hyperemia by definition, does depend on pharmacological stress conditions. This fact is also reported in VERIFY clinical trial [8].

REFERENCES

[1] M. Dariush *et al.*, "Heart Disease and Stroke Statistics—2016 Update," *Circulation*, vol. 133, no. 4, pp. e38–e360, Jan. 2016.

[2] Park, S.J. *et al.*, "Intravascular Ultrasound-Derived Minimal Lumen Area Criteria for Functionally Significant Left Main Coronary Artery Stenosis," *JACC Cardiovasc. Interv.*, vol. 7, no. 8, pp. 868–874, 2014.

[3] Douglas, P. S. *et al.*, "Clinical outcomes of fractional flow reserve by computed tomographic angiography-guided diagnostic strategies vs. usual care in patients with suspected coronary artery disease: the prospective longitudinal trial of FFR(CT): outcome and resource impacts study," *Eur Hear. J*, vol. 36, no. 47, pp. 3359–3367, 2015.

[4] Fearon, W. F. *et al.*, "The impact of downstream coronary stenosis on fractional flow reserve assessment of intermediate left main coronary artery disease: human validation," *JACC Cardiovasc Interv*, vol. 8, no. 3, pp. 398–403, 2015.

[5] Park, S. J., "Unprotected left main percutaneous coronary intervention: integrated use of fractional flow reserve and intravascular ultrasound," *J. Am. Heart Assoc.*, vol. 1, no. 6, p. e004556, 2012.

[6] Zarins, C. K. et al., "Computed fractional flow reserve (FFTCT) derived from coronary CT angiography.," *J. Cardiovasc. Transl. Res.*, vol. 6, no. 5, pp. 708–714, Oct. 2013.

[7] Sen, S. *et al.*, "Development and validation of a new adenosine-independent index of stenosis severity from coronary wave-intensity analysis: results of the ADVISE (ADenosine Vasodilator Independent Stenosis Evaluation) study.," *J Am Coll Cardiol*, 2012.

[8] Berry, C et al., "VERIFY (VERification of Instantaneous Wave-Free Ratio and Fractional Flow Reserve for the Assessment of Coronary Artery Stenosis Severity in EverydaY Practice): A Multicenter Study in Consecutive Patients," *J. Am. Coll. Cardiol.*, vol. 61, no. 13, pp. 1421–1427, 2013.

[9] Jeremias, M. A., "Multicenter Core Laboratory Comparison of the Instantaneous Wave-Free Ratio and Resting Pd/Pa With Fractional Flow Reserve: The RESOLVE Study," *J. Am. Coll. Cardiol.*, vol. 63, no. 13, pp. 1253–1261, 2014.

[10] Oviedo, C. *et al.*, "Intravascular ultrasound classification of plaque distribution in left main coronary artery bifurcations: where is the plaque really located?," *Circ Cardiovasc Interv*, vol. 3, no. 2, pp. 105–112, 2010.

[11] Sankaran, S. at al., "Patient-specific multiscale modeling of blood flow for coronary artery bypass graft surgery," *Ann Biomed Eng*, vol. 40, no. 10, pp. 2228–2242, 2012.

[12] Zhou, G Y. et al., "On the design of the coronary arterial tree: a generalization of Murray's law," *Phys Med Biol*, vol. 44, no. 12, pp. 2929–2945, 1999.

[13] Kim, H. J. et al., C. A. Figueroa, K. E. Jansen, and C. A. Taylor, "Patient-Specific Modeling of Blood Flow and Pressure in Human Coronary Arteries," *Ann. Biomed. Eng.*, vol. 38, no. 10, pp. 3195–3209, 2010.

[14] Bottcher, M. et al., "Effect of caffeine on myocardial blood flow at rest and during pharmacological vasodilation," *J Nucl Med*, vol. 36, no. 11, pp. 2016–2021, 1995.

[15] LaDisa Jr., J. F. *et al.*, "Stent implantation alters coronary artery hemodynamics and wall shear stress during maximal vasodilation," *J. Appl. Physiol.*, 93(6), pp. 1939–1946, 2002.

[16] Duncker, D. J. et al., "Regulation of coronary blood flow in health and ischemic heart disease," *Prog Cardiovasc Dis*, vol. 57, no. 5, pp. 409–422, 2015.

SB³C2019
Summer Biomechanics, Bioengineering and Biotransport Conference
June 25 -28, Seven Springs, PA, USA

THE EFFECTS OF OSCILLATORY SHEAR REGULATION ON PARACRINE SIGNALING BETWEEN VASCULAR ENDOTHELIAL CELLS AND VASCULAR SMOOTH MUSCLE CELLS

CP. Hsu (1), A. Tchir (1), J.D. Hutcheson (1)*, S. Ramaswamy (1)*

*Co-advised principal investigators

(1) Department of Biomedical Engineering
Florida International University
Miami, FL, USA

INTRODUCTION

The vascular wall consists of a layer of endothelial cells (VasEC) that are directly in contact with blood flow, and a sublayer of vascular smooth muscle cells (VasSMC). Vascular remodeling often involves paracrine signaling between VasECs and VasSMCs, and diseases such as atherosclerosis can result from improper communication between these cells.

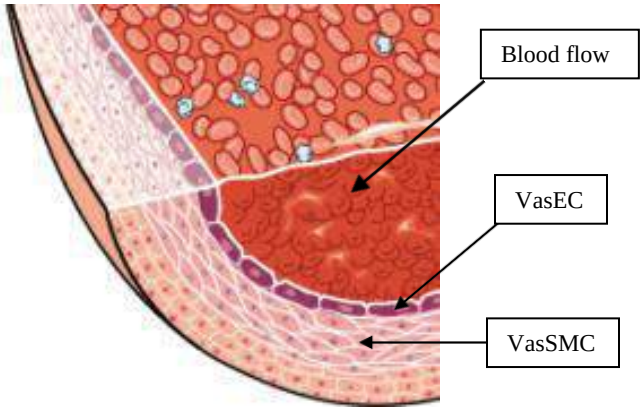

Figure 1: Vascular Endothelial Cells (VasECs) and Vascular Smooth Muscle Cells (VasSMCs)

VasECs are known to respond to hemodynamic stimuli, and VasEC dysfunction in atherosclerosis occurs preferentially at regions exposed to oscillatory flow. Studies have demonstrated development of cardiovascular tissues under dynamic environments such as flow, flexure, and stretch, in which have significant impact on cell phenotype [1]. In this regard, there may be a range of oscillations that maintains vascular tissue integrity. In the current study, we conditioned VasECs under various specific oscillatory flow profiles, which can be quantified by the oscillatory shear index (OSI) parameter. It is widely accepted that biomechanical cues are critical in maintaining vascular tissue homeostasis; however, oscillation dependent changes in cell communication and molecular regulation has not been thoroughly investigated. We therefore examined the paracrine signaling of biochemical end-products between VasEC and its sublayer, VasSMC, through the biochemical environment resulting from physiologically relevant oscillations.

METHODS

Oscillatory shear index (OSI; Equation 1) is a parameter that quantifies the change in direction and magnitude of wall shear stresses [2]. The following OSI magnitudes were applied to the VasECs: static (no flow), steady flow (OSI = 0), 0.25 OSI, and 0.5 OSI.

OSI is defined as:

$$OSI = \frac{1}{2}\left(1 - \frac{\left|\int_0^T \tau_\omega dt\right|}{\int_0^T |\tau_\omega| dt}\right) \quad (1)$$

Where τ_ω = wall shear stress, T = duration of cycle, t = time

VasECs were seeded for 24 hours at 2.0 x 10^5 cells per channel in 24-well Bioflux plates, consisting of 8 microfluidic channels per plate (Fluxion Biosciences, San Francisco, CA). VasECs were later

conditioned for 48 hours using a shear stress cell assay system (Fluxion Biosciences) at a magnitude of 1 dyne/cm^2 [3].

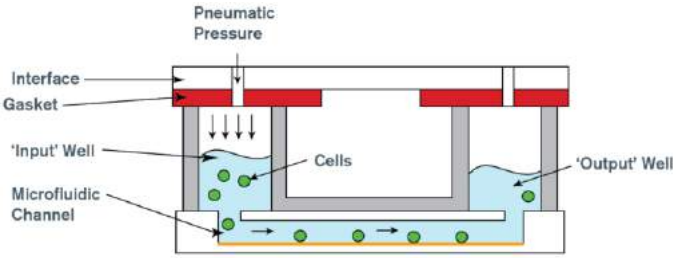

Figure 2: Schematic of microfluidic channels

The conditioned media from VasECs for each flow group were collected. These media were subsequently used to culture VasSMCs for 48 hours using 8 x 10^5 cells in 6-cm dishes. After exposure to the conditioned media of the various flow groups, key phenotypic markers expressed by VasSMC were assessed using RT-qPCR at three replicates per target gene per flow sample group. Data from RT-qPCR consisted of cycle threshold, or C_T values, which were analyzed using the Livak method, $\Delta\Delta C_T$ [4], to compute fold change with the static (no flow) sample group as control.

RESULTS

Three VasSMC samples (n=3) at three replicates per target gene were analyzed. Higher expression of smooth muscle alpha-actin (alpha-SMA) was observed in VasSMCs exposed to non-static VasEC conditioned media compared to those exposed to the static media (Figure 3). Alpha-SMA expression was highest in VasSMCs exposed to steady flow (OSI = 0). Compared to the steady flow group, alpha-SMA expression decreased with increasing levels of OSI.

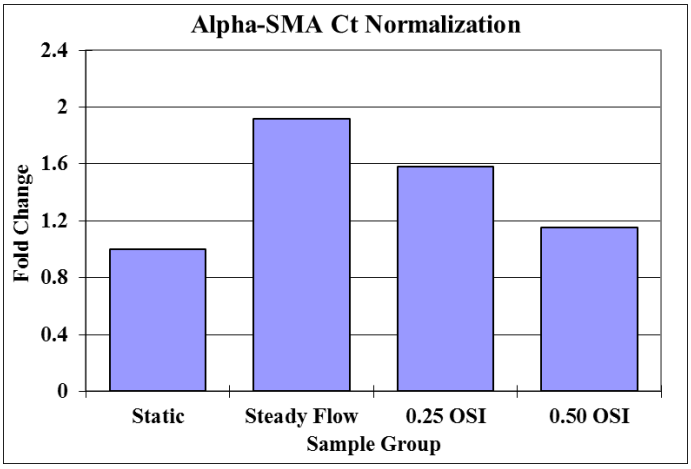

Figure 3: Expression of Alpha-SMA from Vascular Smooth Muscle Cells

DISCUSSION

We observed that various oscillatory flow profiles alter cell responses to its immediate environment via both cell-to-cell paracrine and autocrine communication. A higher expression of alpha-SMA from VasSMC in non-static groups of conditioned media may indicate that fluid motion promotes paracrine signaling for fibrotic development. As alpha-SMA is a marker for contractile phenotype of adult smooth muscle cells, non-static flow groups experienced by VasEC may have led to the secretin of factors then enabled paracrine regulation of VasSMC phenotype.

It is known that VasSMCs exhibit a less proliferative and more contractile phenotype with abundant alpha-SMA [5]. The VasSMCs exposed to steady flow conditioned VasEC media expressed the highest level of alpha-SMA amongst all sample groups. As oscillatory flow was introduced to the system, the expression of alpha-SMA decreased. This supports previous observations of vascular remodeling in regions of oscillatory flow.

Previous studies have shown the role of disturbed flow in VasEC physiology and pathogenesis of vascular diseases. However, in this study, we have further verified that through OSI-initiated paracrine signaling, the biochemical end-products released from VasECs under disturbed flow is also transmitted to the sublayer cells, or the VaSMCs, thereby potentially affecting their phenotype.

REFERENCES

[1] Rath S, Salinas M, Villegas AG, Ramaswamy S. Differentiation and Distribution of Marrow Stem Cells in Flex-Flow Environments Demonstrate Support of the Valvular Phenotype. PLoS One 2015;10(11):e0141802.

[2] He X, Ku DN. Pulsatile Flow in the Human Left Coronary Artery Bifurcation: Average Conditions. ASME. *J Biomech Eng*. 1996;118(1):74-82.

[3] Chiu JJ, Chien S. Effects of disturbed flow on vascular endothelium: pathophysiological basis and clinical perspectives. *Physiol Rev*. 2011;91(1):327-87.

[4] Livak K, Schmittgenj TD. Analysis of Relative Gene Expression Data Using Real-Time Quantitative PCR and the $2^{-\Delta\Delta C_T}$ Method. *Methods*. 2001;25(4):402-408.

[5] Chen L, DeWispelaere A, Dastvan F, et al. Smooth Muscle-Alpha Actin Inhibits Vascular Smooth Muscle Cell Proliferation and Migration by Inhibiting Rac1 Activity. *PLoS One*. 2016;11(5):e0155726. Published 2016 May 13. doi:10.1371/journal.pone.0155726.

SB³C2019
Summer Biomechanics, Bioengineering and Biotransport Conference
June 25 -28, Seven Springs, PA, USA

NON-LINEAR CD31 EXPRESSION IN VASCULAR ENDOTHELIAL CELLS IN RESPONSE TO INCREASING OSCILLATORY FLOW CONDITIONS

Alexandra G. Tchir, Chia-Pei Hsu, Sharan Ramaswamy

Biomedical Engineering
Florida International University
Miami, Florida, USA

INTRODUCTION

Cardiovascular disease is one of the leading causes of death worldwide. As the overall population ages, rates of heart disease and stroke are continuing to rise at alarming rates. Proper function of vascular endothelial cells is a critical underlying factor in the prevention of arterial disease. Specifically, the vascular endothelium has several functions including maintaining hemostatic balance, regulating vascular tone and angiogenesis, initiating wound healing responses when needed as well as paracrine signaling with vascular smooth muscle cells [1]. The endothelial cells in the vascular system receive signals from both intrinsic and extrinsic factors and responds in different ways to maintain homeostasis [1]. Hemodynamic forces are a major regulator of the vascular endothelium. Endothelial cells have mechanoreceptors which sense the blood fluid-induced biomechanical signals which are then used to maintain the vascular phenotypic [2]. Pulsatile blood flow generates oscillatory patterns at different sites in the vascular system, resulting in oscillatory shear stresses. Many studies have shown the correlation between regions of oscillatory flow and atherosclerosis. A parameter used to quantify oscillatory flow is the oscillatory shear index (OSI). Oscillatory shear index is defined as [3]:

$$OSI = \frac{1}{2}\left(1 - \frac{abs\left(\int_0^T \tau dt\right)}{\int_0^T abs(\tau) dt}\right) \qquad \text{(Eq.1)}$$

A zero OSI is indicative of unidirectional flow while 0.5 would represent maximum temporal oscillatory flow conditions [4]. High OSI is said to correspond with regions where atherosclerotic plaque will eventually form [5]. In the current investigation, we speculated that there is a specific range of OSIs that leads to pathology which is distinct from an OSI range necessary to maintain arterial homeostasis. Hence, we exposed vascular endothelial cells to different oscillatory flow conditions in *in vitro* culture and subsequently assessed their phenotypic responses.

METHODS

Vascular endothelial cells were commercially obtained. The cells were plated to a size of 2 X 10^5/channel for a total of 8 channels/experimental group in a commercially available shear stress cell assay system (Bioflux 200, Fluxion Biosciences, San Francisco, CA) in our laboratory. Three OSI profiles based on pulsatile flow waveforms (Fig. 1) were applied for a period of 48 hours as follows: 0 (steady flow), 0.25 and 0.5. An accompanying no flow control (static) group consisting of roughly 80,000 cells per channel was also cultured for the 48 hour period. Note that prior to cell-plating the microfluidic channels were pre-coated with gelatin for proper cell adhesion and were subsequently primed with fresh media. The time-averaged shear stress in the flow experiments was in the order of 1 dyne/cm^2, with the steady shear stress group set to a constant value of 1 dyne/cm^2. After 48 hours of culture, RNA was extracted from the cells using TRIzol (Invitrogen, Carlasbad, CA), and *Power* SYBR Green RNA to CT *1-step* kit (Applied Biosystems, Waltham, Massachusetts) utilized to perform RT-PCR (Applied Biosystems, Waltham, Massachusetts). Target genes were as follows: *B-actin* and *CD31*. Using the CT values from the RT-PCR, the normalized gene expression for each flow profile was performed using the ΔΔCT/Livak method [7].

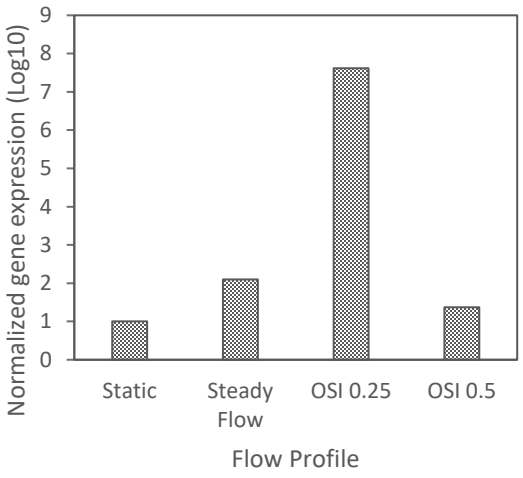

Figure 1: The 0.25 and 0.5 OSI flow profiles.

RESULTS

The average cyclic threshold values for gene expression were summarized (Table 1) and were subsequently used to calculate fold changes between the groups. The Preliminary results showed substantial up-regulation of the CD31 gene under an OSI of 0.25 (Fig 2). On the other hand, the lowest expression of *CD31* was at the highest an OSI of 0.5 OSI.

Table 1: The average CT values of the four different flow profiles for the genes B-actin and CD31.

Gene	Static	Steady	0.25 OSI	0.5 OSI
B-actin	22.09	21.43	24.9	24.58
CD31	28.94	27.21	28.82	30.97

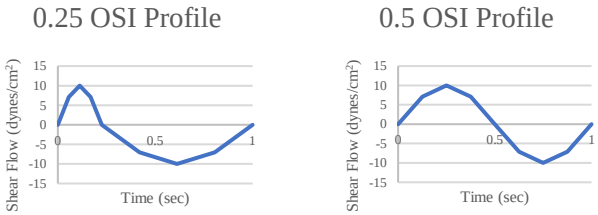

Figure 2: Gene expression from porcine valvular endothelial cells of the vascular endothelial phenotypic marker, CD31.

DISCUSSION

CD31 is a widely used endothelial cell marker, that is relatively sensitive and specific to endothelial cell differentiation [7]. Its upregulation at an OSI of 0.25 opposes conventional theory that higher OSI are adverse while steady flow conditions (OSI = 0) are ideal, in the context of atherosclerosis. The preliminary findings here point towards a non-linear, parabolic-type, rather than linear relationship between CD31 gene up-regulation and OSI, with a peak gene expression occurring at OSI = 0.25.

In conclusion, maintaining the shear stress magnitude while systematically modifying localized OSI conditions, may help towards delineating distinct ranges of oscillatory blood fluid-induced biomechanical stimuli that may play a critical role in normal versus abnormal vascular tissue remodeling. Further experimentation would thereby necessitate establishing greater resolution in OSI and its association with multiple healthy/diseased vascular endothelial cell gene markers.

ACKNOWLEDGEMENTS

A.T. was supported by NIH/NIGMS T34 GM083688.
The following student training programs at Florida International University are also gratefully acknowledged: MARC U*STAR and QBIC.

REFERENCES

[1] Widmer, R J, et al., *Global cardiology science & practice*, 3:291-308.
[2] Chistiakov, D, et al., *Acta Physiologica*, 219:382-408.
[3] He, X, Ku D N, *J Biomech Eng*, 118:74-82.
[4] Salinas, M, Ramaswamy, S, *J of Biomechanics*, 47: 3517-3523.
[5] Ku, D N, et al., *Arteriosclerosis*, 5(3):293-392, 1985.
[6] Schmittgen, T, Livak, K, Nature Protocols, 3:1101-1108, 2008.
[7] Hornick, J, *Practical Soft Tissue Pathology: a Diagnostic Approach*, 1-7, 2019.

SB³C2019
Summer Biomechanics, Bioengineering and Biotransport Conference
June 25 -28, Seven Springs, PA, USA

INTRA-VALVULAR PRESSURE DYNAMICS AND VALVE SPECIFIC PRESSURE RECOVERY IN TRANSCATHETER AORTIC VALVE REPLACEMENT: IMPLICATION ON VALIDITY OF ECHO DERIVED GRADIENT

Hoda Hatoum (1), Maurice Alston (2), David Orsinelli (2), Gregory Rushing (3), Susan O'Neil (3), Nancy Matre (3), Konstantinos D. Boudoulas (3), Scott M. Lilly (2) and Lakshmi Prasad Dasi (1)

(1) Department of Biomedical Engineering
The Ohio State University
Columbus, Ohio, USA

(2) Department of Internal Medicine
The Ohio State University
Columbus, Ohio, USA

(3) Department of Cardiovascular Surgery
The Ohio State University
Columbus, Ohio, USA

INTRODUCTION

Transcatheter aortic valve (TAV) replacement (TAVR) has emerged as an alternative to surgical aortic valve surgery. The assessment of TAV function post-implantation is routinely performed using standard echocardiography[1]. Another method of measurement of transvalvular pressure gradient is the cardiac catherization[1]. Both measurement techniques yield different results with the echo providing measurement at the vena contracta (VC) whereas catherization provides measurement distally from the VC. Therefore, cardiac catherization takes into consideration pressure recovery as well as true losses which are not reflected in the modified or simplified Bernoulli equation. Briefly, as the jet expands, its velocity decreases and pressure is recovered depending on several factors such as turbulence. In a retrospective study between January 2017 and March 2018 at the Ohio State University medical center, a total of 204 patients of which 86 had TAVR with SAPIEN TAV and 118 with Medtronic Evolut were studied. Transvalvular pressure gradients (PG) were measured by echocardiography and cardiac catherization. The mean PG with SAPIEN TAVs was 12.3 and 3.9 with echo and catherization respectively. The mean PG with Evolut TAVs was 9.1 and 3.6 mmHg with echo and catherization respectively. It seems from this cohort of patient that SAPIEN yields higher pressure gradients with echo and higher pressure recovery compared to Evolut. Several studies demonstrated the contributions of the stent and valve cusps to flow acceleration inside the valve and total valve gradient of the Edwards SAPIEN valve[2]. The objective of this study is to elucidate on the physical mechanics behind the flow acceleration and recovery variations between the SAPIEN 3 and Evolut TAVs through the measurements of precise axial pressure profiles.

METHODS

A 26mm Edwards SAPIEN 3 TAV was hemodynamically assessed in a pulse duplicator left heart simulator flow loop under physiological pressure and flow conditions (cardiac output = 5 L/min; heart rate = 60 beats per minutes; systolic to diastolic pressures = 120/80 mmHg). Experiments on the Evolut TAV are currently ongoing. Pressure was recorded using a Millar catheter that was inserted longitudinally along the centerline of the aortic valve chamber. Measurements were obtained upstream of the valve (ventricular), at the entry of the valve stent, inside the valve and distal. Measurement were taken at intervals of 0.5cm. Position 0 corresponds to the upstream measurement, position 0.5 cm corresponds to the point at the valve entry, positions 2.0 to 3.5 cm correspond to locations inside the valve and 5.5 cm and above correspond to downstream of the valve. A hundred consecutive cardiac cycles pressure and flow rate data were recorded at a sampling rate of 100 Hz. Particle image velocimetry (PIV) was performed with the 26mm SAPIEN 3 along with a 26mm Evolut under the same hemodynamic conditions. Time-resolved PIV images were acquired with resulting spatial and temporal resolutions of 0.0723 mm per pixel and 1000 Hz, respectively. Phase locked measurements were recorded for 4 phases of the cardiac cycle (acceleration, peak,

deceleration, and diastole) repetitively 250 times with a spatial resolution of 0.0723 mm per pixel. Reynolds shear stress (RSS) was computed as follows:

$$RSS = \rho\sqrt{\left(\frac{\overline{u'u'}-\overline{v'v'}}{2}\right)^2 + \left(\overline{u'v'}\right)^2} \quad (1)$$

Where ρ is the blood density and u' and v' are the instantaneous velocity fluctuations in the *x* and *y* directions respectively.

RESULTS

Figure 1 shows the variations of pressure versus axial position along the centerline shown for every 50 ms for the full cardiac cycle. The valve is open (systole) from time 0 to 0.34 s. During systole, a highly non-monotonic pressure profile with respect to axial position can be appreciated. Localized adverse

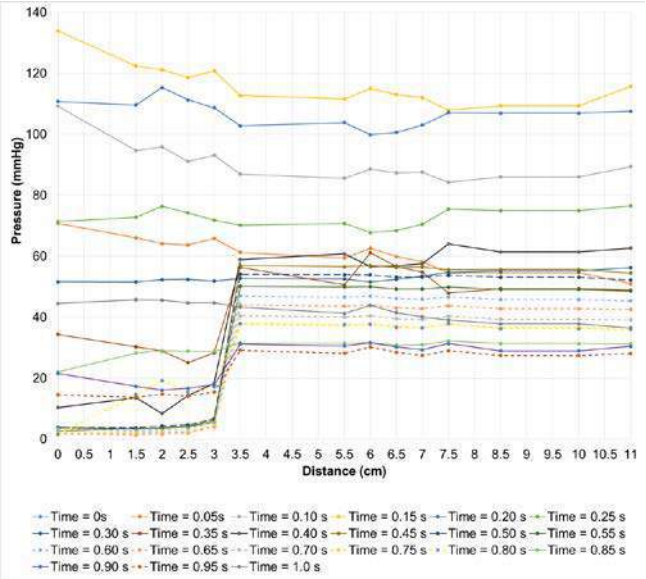

Figure 1: Variation of ventricular pressure with distance downstream of the SAPIEN 3 valve.

pressure gradients are seen within the valve as well as beyond the 5.5 cm position corresponding to pressure recovery. During diastole (time>0.34s), pressure downstream of the valve (beyond 3.0 cm) is higher than that upstream consistent with valve closure.

Figure 2 shows the principal Reynolds shear stresses at different phases in the cardiac cycle. Peak principal RSS was equal to 337.22Pa and 157.91Pa with the Evolut and SAPIEN respectively.

DISCUSSION

Two important physical mechanisms concerning flow acceleration within the valve and pressure recovery emerge from the results. With respect to flow acceleration, it can be appreciated that the pressure varies non-monotonically between locations corresponding to 2.0 to 3.5 cm with local adverse pressure gradients occurring inside the valve during acceleration as well as deceleration phases of systole. From a classical standpoint, the pressure is expected to simply decrease monotonically in this region. These adverse pressure gradients may be attributed to the SAPIEN skirt particularly its dynamic effects (potentially local flow acceleration and separation within the valve). Based on a previous study highlighting a mechanism of flow separation at valve inflow due to obstruction of the inlet[4], it seems that the SAPIEN 3 skirt may allow for this mechanism to happen thus influencing the variations in pressure inside the valve.

With respect to pressure recovery, Figure 1 illustrates pressure recovery seen from measurement locations 5.0 cm through 11 cm. In this region, there appears to be a phase dependent behavior of pressure recovery. Interestingly, during acceleration phases (time 0.05s, 0.10s, and 0.15s) the net pressure rise between x=3.5cm and 11.0cm is negligible and even negative at earlier (e.g. at 0.05s). During deceleration phases (time 0.20s and 0.25s) there appears to be a clear pressure recovery signal. We anticipate this characteristic to be different for the Evolut TAV currently being characterized as evident from the starkly differing turbulence characteristics shown in the RSS fields (Figure 2).

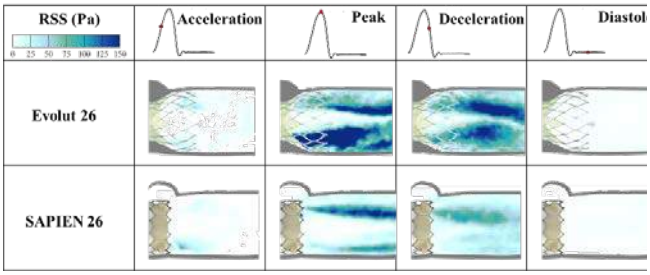

Figure 2: Principal Reynolds shear stresses at different phases in the cardiac cycle.

RSS measures the shear stress (acting on the mean field) between fluid layers when fluid particles decelerate or accelerate while changing direction[3]. The higher the RSS magnitude the higher the turbulence, thus the overall pressure drop. The clinical results obtained with SAPIEN 3 showed a higher pressure drop at the VC yet a higher pressure recovery compared with the Evolut. The differences seen in turbulence levels (Figure 2) corroborate these clinical observations as more turbulence is obtained with Evolut (by almost a factor of two) than with SAPIEN. Clinical and in-vitro studies comparing these two valves are necessary to compare and evaluate pressure drop and recovery in both TAVs and are parts of currently ongoing studies.

ACKNOWLEDGEMENTS

The research done was partly supported by National Institutes of Health (NIH) under Award Number R01HL119824.

REFERENCES

[1] Otto, CM. *Journal of the American College of Cardiology* 47.11 (2006): 2141-2151.

[2] Shames, S. et al. *Journal of the American Society of Echocardiography* 25.6 (2012): 603-609.

[3] Gunning, PS. et al. *Annals of biomedical engineering* 42.9 (2014): 1989-2001.

[4] Hatoum, H et al. *J of Biomechanics.* 74 (2018): 171-179.

SB³C2019
Summer Biomechanics, Bioengineering and Biotransport Conference
June 25 -28, Seven Springs, PA, USA

DESIGN OF A COST-EFFECTIVE CARDIAC FLOW LOOP FOR TESTING TAVR PLACEMENT IN PATIENT-SPECIFIC ANATOMY

Christine M. Buffinton (1), Benjamin S. Conser (1), M. Laura Beninati (1), Shikhar Agarwal (2)

(1) Department of Mechanical Engineering
Bucknell University
Lewisburg, PA, USA

(2) Interventional Cardiology and Structural Interventions
Geisinger Medical Center
Danville, PA, USA

INTRODUCTION

Aortic stenosis is a disease in which the aortic valve (AV) connecting the left ventricle and aorta narrows, resulting in restricted blood flow to the body and subsequent complications that can end in heart failure. The mortality rate is more than 50% at 2 years with untreated, symptomatic disease [1]. The incidence of aortic stenosis in the population rises with age to reach 10% of those in the 80s [2].

A leading cause of aortic stenosis in younger patients is bicuspid aortic valve, where two leaflets of the normal tricuspid valve are congenitally fused. Bicuspid AV occurs in 1-2% of the population. Other abnormalities usually accompany the defect, such as increased risk of aortic aneurysm and dissection (5-9 times the general population incidence), tissue changes in the aorta, and larger aortic root dimensions [3]. In an 11-year study of 932 sequential replacements for stenotic aortic valve without evidence of mitral stenosis, 49% had bicuspid valve, with an additional 5% unicuspid [4]. Patients with bicuspid AV typically have surgery for AV replacement at an earlier age [3].

The traditional surgical aortic valve replacement (SAVR) procedure involves sternotomy and bypass. A newer, minimally invasive procedure, transcatheter aortic valve replacement (TAVR), involves delivering an initially collapsed replacement valve by catheter. When expanded within the aortic root, it pushes the existing valve leaflets to the side without removing the existing valve. TAVR is approved for intermediate or high-risk surgical patients for standard valve replacement surgery, but not for bicuspid aortic valve, which involves higher risks of difficulty in the valve-in-valve insertion and variable aortic root anatomy, leading to improper seating and leakage.

The goal of this project was to create a tabletop flow loop modeling blood flow through the human aorta to allow testing of existing TAVR valves in bicuspid AV anatomy. The system was designed to reproduce fluid flow rate, pressure, and timing across the AV (Fig. 1). It was also designed for insertion of interchangeable 3D-printed sections of human anatomy reconstructed from national databases of bicuspid defects that could then be implanted with a commercial valve, and for accessibility by ultrasound. This project began as a student design project with a funding cap. The requirements of ability to test in real patient anatomy and minimal cost preclude use of a commercial system. The long-term goal is to help determine the feasibility of TAVR in cases of bicuspid AV.

METHODS

The system was first modeled with the traditional 3-element Windkessel model, implemented in MATLAB and Simulink. The Windkessel model uses electrical analogies to represent fluid quantities: charge, current, and voltage for volume, volumetric flow rate, and pressure; electrical resistance for fluid resistance, and capacitance for system compliance. This analysis showed reasonable values for lumped resistance and compliance elements. The effects on the system of varying their magnitude was also clear: increasing the resistance shifted the entire pressure trace upward, while increasing the compliance increased the difference between systolic and diastolic pressures.

The fluid pump is a crucial element of the system. A piston pump was first designed and fabricated, but later discarded because of the difficulty in maintaining a tight piston seal while keeping friction at a manageable level. The piston pump was replaced by a bellows pump (Dynatest bellow, Thermiseal cover, 2" ID, 3" OD), with bellows collars fastened to custom aluminum blocks. Both pumps were driven by a custom cam-follower mechanism designed with MATLAB and Solidworks and analyzed with Working Model. The aluminum cams, manufactured in-house, reproduced a cycle of 40% contraction and 60% relaxation. A

Poster Presentation #P194

motor (Leeson M1125004.00, 1/17 hp, 36 lb-in torque) and motor controller (Leeson Speedmaster 174308.00) drove the cam at a set rotation speed, representing heart rate. Separate cams produced stroke volumes of 60 mL, 70 mL, and 80 mL.

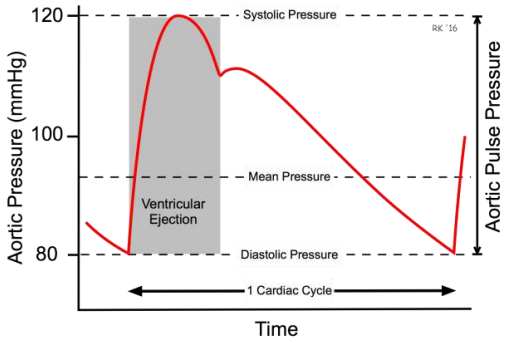

Figure 1: The target aortic pressure waveform (reproduced from [5]). Systolic pressures to 180 mmHg were achieved by Arduino-controllable ball valve, while the pulse pressure was controllable with fluid column and air pressure in the compliance tank.

Fluid was pumped within a closed system through valves, sensors, and lumped compliance and resistance elements (Fig. 2). Commercial check (one-way) valves regulated the intake and outtake of the pump, although the outtake valve was only used during design and testing to avoid damage to an expensive, implantable TAVR valve. The blood analog fluid was produced by adding glycerin to distilled water to reach 1.0501 specific gravity and 3.3 cSt viscosity. The fluid flowed through 3/8-in I.D. amber gum and copper tubing.

A compliance tank representing the lumped compliance of the aorta and peripheral circulation was inserted at the location shown (Fig. 2). In this position, it mainly reflects aortic compliance, defined as change in blood volume due to change in pressure. The compliance chamber is a sealed polycarbonate container with a fluid inlet and outlet. A column of fluid contained within the chamber rises and falls with the system pressure. The compliance was controlled by adjusting the air pressure above the fluid with an attached air bladder pump.

To reduce cost and keep the system user accessible, sensors were chosen that interfaced with an Arduino Uno board. An in-line, flow-rate sensor (Adafruit, Liquid Flow Meter - Plastic ½" NPS threaded) verified output from the pump. Pressure transducers were placed both before the 3D print with TAVR valve and after the compliance tank (Honeywell HSCDANT005PG2A5). A voltage-controlled ball valve (Belimo B218B+TR24-SR US) located downstream from the compliance chamber was Arduino-controlled to maintain system pressure as measured by the pressure transducer after the compliance tank.

A closed-loop PD feedback control system with user interface was implemented to control the system mean pressure. The control system gains were chosen to optimize the ball valve's response time based on the system beats per minute, pressure sensor sampling rate (nominally 30 Hz), operating speed of the ball valve's motor, and minimizing overshoot of the target pressure, all dependent on the compliance existing in the system. A GUI allowed the user to easily set the target system pressure and view a real-time pressure vs. time trace.

RESULTS

Replacing the piston pump with a bellows significantly reduced the motor power needed. System pressures of 80 – 180 mmHg and flow rates of 5 – 18 L/min could be obtained. An unwanted side effect was occasional warping of bellows path, later corrected with a sleeve. On start-up, the control system and ball valve required less than one minute to reach desired pressure, and pressure was maintained within 2% afterward. The motor and controller were the most expensive part of the system, but the total of all purchased parts was less than $1000. Investments not reflected in this total include in-house expertise (student, faculty, and technician) and existing materials.

The 3D-printed section is crucial in achieving the project goal. Prototypes were printed in transparent, flexible material (Agilus 30 or TangoPlus by Stratasys) and designed to include the aortic root and approximately 3-4 cm each of left ventricle and aorta on either side of the valve location. The sections achieved the desired result of water-tight interchangeability and ultrasound permeability.

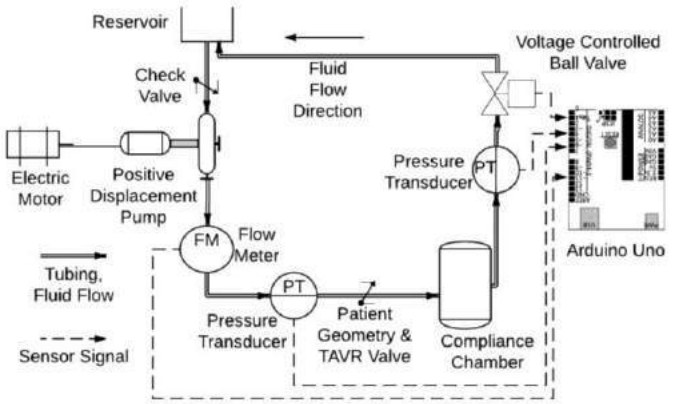

Figure 2: Schematic of the cardiac flow loop designed to test replacement valves positioned in 3D-printed sections reproduced from bicuspid aortic valve anatomy.

DISCUSSION

Some important questions remain about the printed section geometry, such as the importance of mimicking the actual tissue elasticity, and how much of left ventricle and aorta need to be incorporated. Further experimentation will attempt to answer these questions.

This system provides an *in vitro* means to test valves designed for TAVR placement in anatomical models constructed from patients with bicuspid aortic valve. Aortic regurgitation is currently the bane of TAVR. Unlike SAVR, where the artificial valve is sutured in, minimizing the risk of leakage, TAVR can be complicated by aortic regurgitation around the valve prosthesis. Unfortunately, there is not a good tenable solution for treatment of aortic regurgitation. This problem is magnified in the cases of bicuspid aortic valve, where the valve leaflets are often asymmetrical, leading to an overall non-circular annulus, which leads to a greater chance of aortic regurgitation.

With respect to TAVR, there are several different kinds of prostheses available. These include balloon expandable valves, self-expandable valves, and mechanically expanded valve prostheses. Obviously, their expansion characteristics afford unique deployment mechanics rendering them useful in different valve morphologies and geometries. It remains unclear, which of these prostheses are most suitable for bicuspid valve anatomy. The system described here will help ascertain the degree of aortic valve regurgitation in a closely simulated condition, which will help with the choice of the valve in a real human being.

REFERENCES

[1] Otto CM and Prendergast DM, *NEJM 371*, 744-56, 2014.
[2] Zakkar M, Bryan AJ, Anglini GD, *BMJ 355*, 2016.
[3] Lewin MB and Otto CM, *Circulation 111*: 832-4, 2005.
[4] Roberts WC and Ko JM, *Circulation 111*:920-5, 2005.
[5] Klaubunde RE, www.cvphysiology.com, accessed Jan. 18, 2019.

SB³C2019
Summer Biomechanics, Bioengineering and Biotransport Conference
June 25 -28, Seven Springs, PA, USA

EFFECT OF LEAFLET OPENING GEOMETRY ON TURBULENT CHARACTERISTICS FOR PROSTHETIC AORTIC VALVE APPLICATIONS

Megan Heitkemper (1), Hoda Hatoum (1), Jun Kim (1), Lakshmi P Dasi (1)

(1) Department of Biomedical Engineering
The Ohio State University
Columbus, Ohio, USA

INTRODUCTION

While thrombotic proclivity of heart valve prostheses is often related to material characteristics, thrombogenic potential is also highly dependent on flow conditions, which are significantly influenced by valve design. Increased turbulent stresses are associated with increased thrombogenic potential, and therefore it is important to investigate turbulent stresses in characterizing prosthetic valve function. Turbulent stress levels, and especially Reynolds shear stress, are well known to be an indirect measure of the shear stresses experienced by blood cells and platelets in a turbulent flow environment[1]. Therefore, an ideal prosthetic valve design would yield the least turbulent effects and decreased levels of Reynolds stress while exhibiting surface hemocompatiblity. While the effect of geometric orifices on turbulent jet flows has been studied extensively, no study has investigated the effect of prosthetic valve opening geometry on turbulent stress levels [2]. Previous studies have indicated that valve opening geometry can vary, especially in investigational valve designs with novel materials [3]. In this study, we aim to characterize in-vitro the hemodynamic function and turbulent flow characteristics of two distinct leaflet opening geometries modeled after known prostheses to determine how the leaflet geometry will affect flow turbulence and thus thrombogenic potential.

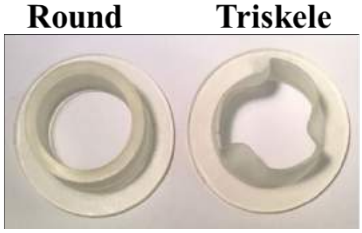

Figure 1: Leaflet opening geometries

METHODS

Leaflet opening geometries modeled after commercially available valves (round) and a polymeric valve previously introduced (triskele-like) [3] of the same area were 3D printed. The 3D printed geometries were implanted in the aortic position of a pulse duplicator left heart flow simulator and hemodynamic performance was evaluated under physiological pressure (120/80 mmHg), heart rate (60 bpm), and cardiac output (5 L/min). A working fluid of 60/40 water to glycerin was used to provide density and kinematic viscosity comparable to blood, at 1060 kg/m^3 and 3.5 $\cdot 10^{-6}$ m^2/s respectively. Aortic and ventricular pressures as well as flow rates were collected at a sampling frequency of 100 Hz for 60 consecutive cardiac cycles. From these data, mean transvalvular pressure gradient (ΔP) and effective orifice area (EOA), were computed for each of the orifices.

Particle Image Velocimetry (PIV)

Particle image velocimetry (PIV) was performed to visualize and evaluate the flow velocity field through the leaflet opening geometriess and to identify turbulence characteristics. Briefly, the flow of interest was seeded with florescent PMMA-Rhodamine B particles and illuminated by a thin laser sheet created with a double pulsed neodymium-doped yitrium lithium fluoride (Nd-YLF) solid state laser. Time-resolved recordings were acquired at spatial and temporal resolutions of 0.037 mm/pixel and 1000 Hz respectively. 250 repetitions of phase locked measurements were recorded for acceleration, peak systole, deceleration, and mid-diastole phases of the cardiac cycle.

DaVis PIV software (DaVis 7.2; Lavision, Göttingen, Germany) was used for all image post processing.

Principal RSS is a statistical quantity that measures the shear stress between fluid layers when particles decelerate or accelerate while changing direction [4] and is calculated as:

$$RSS = \rho \sqrt{\left(\frac{\overline{u'u'} - \overline{v'v'}}{2}\right)^2 + \left(\overline{u'v'}\right)^2} \quad (1)$$

where ρ is the density of the working fluid (Kg/m^3) and $u'$and v' are the instantaneous velocity fluctuations in the x and y directions respectively (m/s). Equation (1) implicitly assumes no out-of-plane component of instantaneous velocity, *w'*, and can be considered as a 2D surrogate of the principle RSS [4].

RESULTS

Phase averaged velocity vector fields and corresponding vorticity contours for the two 3D printed leaflet opening geometries are shown in Figure 1 at four time points in the cardiac cycle, namely, acceleration, peak systole, deceleration and diastole, which are denoted by a red dot along the representative aortic flow curve. Bright red and blue contours represent the vorticity within the shear layers which correspond to the jet boundaries. The distance between the shear layers represent the width of the jet at a distance downstream from the valve.

Velocity Vector Field and Vorticity Contours

At peak systole, the triskele leaflet opening geometry produced lower velocities than the round leaflet opening geometry at the valve

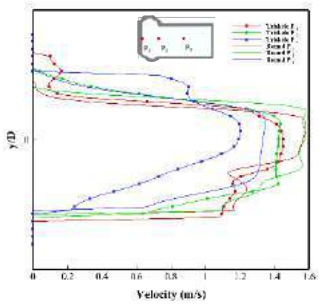

Figure 1: Velocity profile in m/s; at the valve opening (P_1); at the STJ (P_2); at one diameter from the STJ (P_3); where y/D is the position indexed by the valve diameter

opening, the sinotubular junction (STJ), and one valve diameter from the STJ (Figure 1). For both geometries, peak velocity was approximately the same at the STJ as it was one valve diameter from

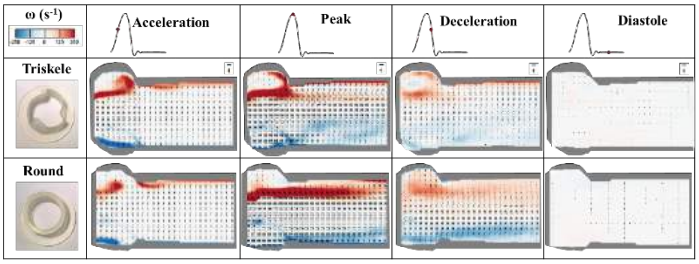

Figure 2: Phase averaged velocity vectors and vorticity contours throughout the cardiac cycle

the STJ, reaching a peak of approximately 1.4 m/s for the triskele geometry and 1.6 m/s for the round geometry. At peak systole, the shear layers are less pronounced with the triskele leaflet configuration compared to the round leaflet configuration, and attached to the aortic chamber approximately 16 mm from the outlet. There is a significantly larger region of flow separation for the round leaflet configuration, with flow attachment not occurring until approximately 42 mm from the outlet. At the deceleration phase, the presence of shear layers has diminished for the triskele configuration, and only very slightly for the round configuration. In the triskele configuration, the shear layers are significantly diminished at approximately the STJ of the aortic root chamber, much before the shear layers are diminished for the round configuration.

Reynolds Shear Stress

Figure 2 shows the principal Reynolds shear stress (RSS) at acceleration, peak, deceleration and diastolic phases of the cardiac

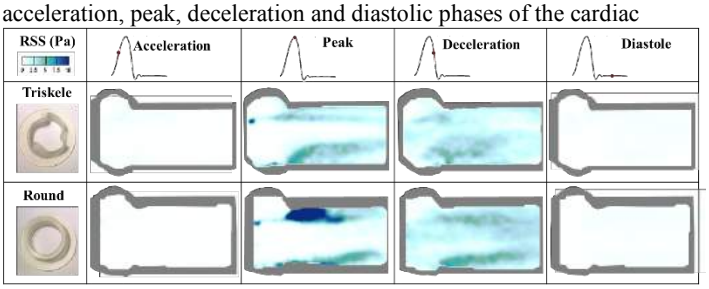

Figure 3: Phase averaged Principal Reynolds shear stresses (RSS) throughout the cardiac cycle

cycle for each valve. For each leaflet opening geometry, the highest values of RSS were present at peak systole, with 11.3 Pa in the triskele leaflet configurationand 30.9 Pa in the round leaflet configuration. In comparison to the round leaflet opening geometry, the triskele had a significantly smaller region in which higher RSS values were present.

DISCUSSION

The decrease in vorticity fluctuation seen for the triskele leaflet opening geometry is indicative of a decrease in turbulence (and therefore energy loss). The decreased velocity and vorticity fluctuation during peak systole and deceleration phases as compared to the round configuration is likely due to the 3D curved surfaces that induce a radial and azimuthal velocity component of the flow as it exits the valve opening, leading to sooner flow reattachment. RSS magnitudes have an important role in determining the biocompatibility of a valve prosthesis because they can indicate regions of probable platelet activation from turbulent fluctuations of the blood velocity[2,5-6]. All current valve designs studied to date have mean turbulent shear stresses in excess of 20 Pa [7], which is comparable to the round leaflet opening geometry as expected. Therefore, while a round leaflet opening configuration for a valve prosthesis is often desirable, the results presented here show that it may not be the most optimal choice to limit turbulence. In order to mitigate the durability issues that are caused by blood damage, an appropriate leaflet opening geometry should be considered during the design and development of novel valve prostheses.

ACKNOWLEDGEMENTS

The research reported was supported by National Institutes of Health (NIH) under Award Number R01HL119824.

REFERENCES

1. Dasi, L.P., et al., Clin Exp Pharmacol Physiol, 2009.**36**(2): p. 225-37.
2. Afriyie, Y., Univeristy of Manitoba, Winnipeg. 2017. p. 1-21.
3. Yousefi, A., et. al., Ann Biomed Eng, 2016. **45**(2):p. 464-475.
4. Hasler, D. and D. Obrist, PLOS ONE, 2018. **13**(3): p. e0194384.
5. Nygaard, H., et al., J Biomech, 1992. **25**(4): p. 429-40.
6. Schoephoerster, R.T, et al., J Biomech, 1991. **24**(7): p. 549-562.
7. Yoganathan, a., et. al., Annu. Rev. Biomed. Eng. 2004.. **6**: p. 331-362

SB³C2019
Summer Biomechanics, Bioengineering and Biotransport Conference
June 25 -28, Seven Springs, PA, USA

IN VITRO FORWARD FLOW PERFORMANCE OF THE KONECT™ RESILIA ™ AORTIC VALVED CONDUIT

Vahid Sadri (1), Immanuel David Madukauwa-David (2), Ajit P. Yoganathan (1)

(1) The Wallace H. Coulter School of Biomedical Engineering Georgia Institute of Technology Atlanta, GA, USA

(2) George W. Woodruff School of Mechanical Engineering, Georgia Institute of Technology, Atlanta, GA

INTRODUCTION

Thoracic aortic aneurysms (TAA) occur in an estimated 6 per 100,000 person-years [1], and typically involve the aortic root or the ascending aorta. Complications associated with TAA include intramural hematoma, aortic dissection, and aortic rupture [2]. In order to prevent these complications, consensus guidelines recommend surgical correction for patients that meet necessary criteria. One of the surgical options for aortic root aneurysm includes aortic root replacement with a valved-conduit where both the aortic wall and valve are replaced.

Edwards Lifesciences recently developed a bioprosthetic valved conduit featuring a valve along with incorporated sinuses of Valsalva. The inclusion of sinuses of Valsalva has been postulated to be advantageous, as it more closely mimics patient anatomy (At the time of this writing, this product is not yet approved for human use). However, the hemodynamic and physiological benefits of this design are yet to be investigated. Hence, the purpose of this study was to characterize the *in vitro* flow characteristics the design of the KONECT™ RESILIA ™ Aortic Valved Conduit (AVC), which features a sinus section. The performance of this AVC was compared with the same AVC model but without a sinus section (the control group) to show that there are improved hemodynamic effects to the function of the valve portion of the device associated with valve/graft interface.

METHODS

Test Section Flow Models.

There were two testing chambers used in this study. The KONECT RESILIA valved conduit (AVC_{Sinus}) was used as the test group, and the same aortic valved conduit model without a sinus section, $AVC_{No\ sinus}$, was used as the control group. Particle image velocimetry (PIV) experiments require optical access to the region of interest. Hence, transparent versions of the grafts (milled acrylic blocks) were used. These chambers were designed to approximate the internal dimensions of an annular size 25 mm KONECT RESILIA aortic valved conduit that pressurized at 100 mmHg. The pressurized graft diameter was measured by laser micrometer.

Pulsatile Flow Loop.

These models were placed in pulsatile simulators for hemodynamic studies. The pulsatile experiments were conducted using the Georgia Tech left heart simulator at nominal hemodynamic conditions: cardiac output of 5 LPM, heart rate of 70 beats per minute, and a mean arterial pressure of 100 mmHg (120/80 mmHg). This experimental setup is described in detail in previous publication [2] and conforms to ISO 5840-2 testing guidelines for surgically implanted heart valves[3]. The working fluid used in these experiments was a water-glycerin mixture (36% glycerin), which was used to mimic the kinematic viscosity of blood.

Bulk Hemodynamic Characterization

Hemodynamic performance of the valves was evaluated using transvalvular pressure gradient (TVPG) and effective orifice area (EOA). TVPG values were calculated as the mean pressure gradient (ΔP_{mean}) across the valve during systole, while EOA values were calculated as the root mean square of the measured flow (Q_{rms}) per the following equation.

$$EOA = \frac{Q_{rms}}{51.6\sqrt{\frac{\Delta P_{mean}}{\rho}}} \quad (1)$$

For calculating EOA, the positive systolic gradient period was used as the duration for Q_{rms} and ΔP_{mean}. All values were acquired over 50 cardiac cycles and then averaged to get representative data both for the rapid deployment and control valves.

Poster Presentation #P196

Planar particle image velocimetry (PIV)

PIV was used to quantitatively assess flow field characteristics of the valves at acceleration (75 ms), peak systolic (175 ms), and deacceleration (250 ms) phases of the cardiac cycle (856 ms). The flow was seeded with fluorescent particles, and a pulsed Nd:YAG laser source was used to create a thin laser sheet using appropriate optics in the center plane of the test sections (Figure 1). At each acquisition time point, 200 image pairs were acquired to enable averaging of flow fields. Details on these techniques have been described in a previous publication[4].

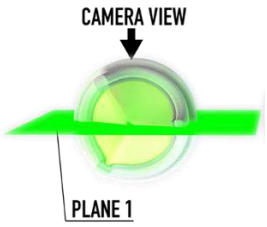

Figure 1: Acquisition plane for PIV testing

Statistical Analysis

All bulk hemodynamic data were analyzed for normality using Shapiro Wilk's test. Differences between groups were identified using independent samples t-test for normally distributed variables or Mann Whitney U-test for non-normally distributed variables. P values of 0.05 or below were considered significant.

RESULTS

A summary of hemodynamic results for the AVC models is given in Figure 2 for cardiac output of 5 liter per minute. Mean TVPG (mmHG), EOA (cm^2), and closing volume (mL) increased with increasing cardiac output. AVC_{Sinus} showed lower mean TVPG than $AVC_{No\ sinus}$ (Figure 2). A similar trend was seen in EOA; AVC_{Sinus} had a higher EOA than $AVC_{No\ sinus}$. No differences were found in valve closing volume between AVC_{Sinus} and $AVC_{No\ sinus}$.

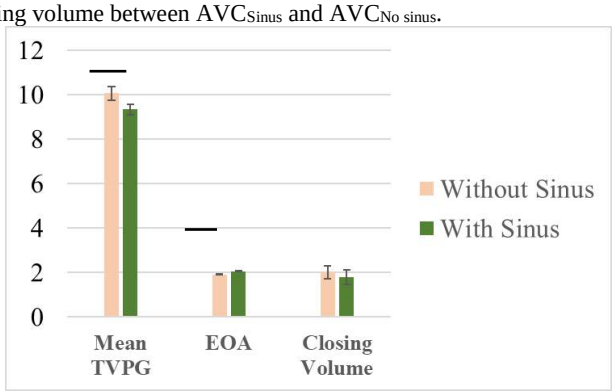

Figure 2: Bulk hemodynamic comparison between the two AV conduit models, Bars: p < 0.05.

A comparison of PIV results for the AVC models is given in Figure 3. During the acceleration phase, the maximum velocity for $AVC_{No\ sinus}$ was lower than AVC_{sinus}. The maximum velocities observed for $AVC_{No\ sinus}$ and AVC_{sinus} were 1.62 m/s and 1.73 m/s, respectively. At peak systole, the maximum velocities observed for $AVC_{No\ sinus}$ and AVC_{sinus} were 2.26 m/s and 2.23 m/s, respectively.

During the deceleration phase, higher velocities were observed in the $AVC_{No\ sinus}$ compared to the AVC_{sinus} model. The maximum velocities observed were 1.42 m/s and 1.2 m/s for the test sections, respectively.

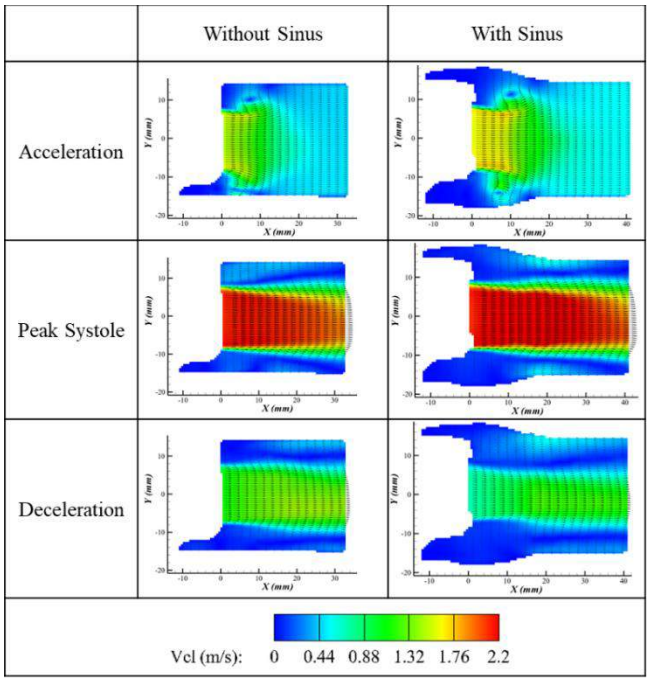

Figure 3: Velocity vector fields in Plane 1 under 5LPM cardiac output for the AV conduit with a sinus and without a sinus during the acceleration, peak systolic, deceleration, and diastolic phases

DISCUSSION

In this study, the *in vitro* flow characteristics of the KONECT RESILIA AVC were investigated to highlight the benefits of an AVC with a sinus of Valsalva compared to one without a sinus. Major findings included the following:

The AVC model with a sinus had lower pressure gradients and 10 percent higher EOA compared to the AVC without a sinus. This suggests that the presence of an additional amount of space and fluid behind the leaflets in AVC_{Sinus} contributed to less constraint on the AVC leaflets.

AVC_{Sinus} had lower velocities during the peak systolic phase of the cardiac cycle than $AVC_{No\ sinus}$. Due to the wider opening of the AVC_{Sinus} leaflets, at the same flow rate, lower velocities are expected.

Our particle image velocimetry results revealed a vortical structure hits the aortic wall during the acceleration phase. This phenomenon shows that when no Valsalva sinus is present, the fluid has insufficient space to retreat upon leaflet opening, potentially causing energy dissipation and momentum loss. In turn, a back pressure is generated on the leaflet that leads to lower EOA, and a higher transvalvular pressure gradient.

The KONECT RESILIA conduit reproduces the bulged section of the native aortic root corresponding, to the sinuses of Valsalva. The importance of the sinuses of Valsalva in regulating aortic valve motion during the cardiac cycle has been extensively studied [5]. By using this Valsalva-type conduit, it was possible to obtain more physiologically accurate valve motion characteristics that leads to more durability for the valve. Furthermore, a drawback of excluding a sinus from AVC design could be reduced valve durability due to the non-physiologic flow characteristics of the valve.

ACKNOWLEDGEMENTS

This study was funded by a research grant from Edwards Lifesciences.

REFERENCES

[1] Kuzmik GA et al., J Vasc Surg 2012; 56: 565–571.
[2] Midha PA et al., Ann Biomed Eng 2017; 45: 405–412.
[3] International Organization for Standardization. ISO 5840-3: 2013,
[4] Gunning PS et al., Ann Biomed Eng 2014; 42: 1195–1206.
[5] Grande-Allen KJ et al., J Thorac Cardiovasc Surg 2000;119:753-756

SB³C2019
Summer Biomechanics, Bioengineering and Biotransport Conference
June 25 -28, Seven Springs, PA, USA

AUTONOMOUS PUMPING IN A PHYSICAL MODEL OF A MULTI-LYMPHANGION SYSTEM

John Montani (1), Luke E. Riexinger (1), Lance L. Munn (2), James W. Baish (1)

(1) Biomedical Engineering Department
Bucknell University
Lewisburg, PA, USA

(2) Steele Laboratory
Harvard Medical School and
Massachusetts General Hospital
Boston, MA, USA

INTRODUCTION

The lymphatic system is responsible for managing the balance of interstitial fluid, but unlike blood flow that is driven by a central pump, the lymphatic system consists of a series of units called lymphangions that serve as both pump and conduit. Each lymphangion consists of a segment of vessel surrounded by lymphatic muscle cells with each end bounded by valves that limit backflow [1,2]. Lacking a central pacemaker like the heart, the lymphangions contract in response to mechanical and electrochemical signals from the fluid within and from neighboring lymphangions. In particular, Ca^{2+} ions and NO have been shown to affect the contraction and relaxation of the lymphatic muscle cells while their concentrations are influenced by the transmural pressure and fluid shear stress [3].

While much has been learned about the dynamics of lymphatic pumping from intravital microscopy, ex vivo preparations and computational modeling, networks of multiple lymphangions have been found to be particularly complex and challenging to study. As an adjunct to these existing approaches we have explored the use of a physical model that mimics many of the essential features of the living system. In earlier studies, we studied the dynamics of the system under pre-programmed pace-making patterns. The purpose of this study is to determine what conditions lead to autonomous pumping. That is, what combination of vessel wall stretch, fluid shear stress, cell signaling and valve behavior can trigger self-sustaining contractions without an artificial pace-maker?

METHODS

Our physical model of a multi-lymphangion system consists of three units constructed from a compliant ½ in. ID PVC tube inside a rigid chamber that can be pressurized by air admitted under computer control from a high pressure manifold (Fig. 1). As changes in the air pressure are used to compress and relax the tubing, water flow is directed downstream by one-way valves at the end of each unit. Sensors are placed throughout the system to monitor pressure and flow. Matlab® programs and a National Instruments® interface manage the air flow (contraction and relaxation) and data collection. The lymphangion units can be assembled into a variety of series, parallel or tree-like configurations that can be oriented horizontally or vertically to introduce gravity effects. While the tubing is much larger than even the largest lymphatic vessels, we have found that the flow is dominated by the resistance of the valves and the compliance of the tubing with little evidence of significant inertial effects much like the situation in vivo. Measured values for the resistance and compliance of each element provide a scaling relationship between our physical model and its anatomical counterpart.

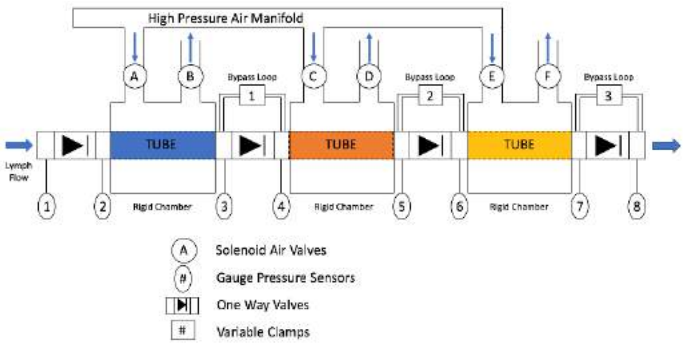

Figure 1. Schematic of the multi-lymphangion model. Bypass loops on check valves allow some backflow

In this study we introduced two features that support autonomous operation. First, we modified the control program to use feedback from the measured pressures and flow throughout the system to determine the next actions of each lymphangion (Fig. 2). The lymphangions were programmed to contract briefly when their internal pressure exceeded a fixed threshold, mimicking a stretch response. In addition, the duration of the interval between contractions could be extended during periods of high flow, mimicking a shear stress-NO response. The second modification was to add bypass loops around the one-way valves (Fig. 1). These loops permit a controlled amount of flow to leak backward between the lymphangions to simulate the bias toward being open that has been observed in real lymphatics [4].

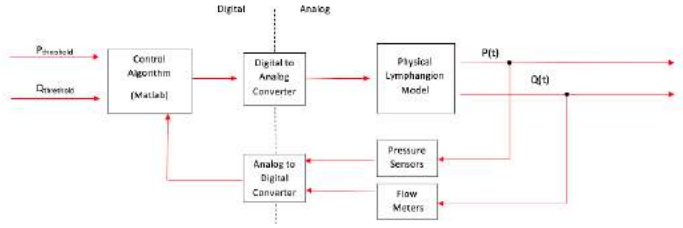

Figure 2: Schematic of feedback controlled multi-lymphangion model.

RESULTS

We first programmed the system to retain the first lymphangion as a preprogrammed pace-maker with all downstream units programmed to react to the pressure and flow conditions within their respective units. The downstream units were programmed to contract after their internal pressure exceeded a pre-set threshold. Initially, we did not include bypass loops on the valves. In this configuration the downstream units followed the lead of the upstream unit. However, when the upstream unit was switched from programmed timing to the same reactive algorithm as the downstream units, all contractions soon stopped throughout the system. While many variations on this algorithm were tried, we found none that could sustain contractions.

We then added the bypass loops on the valves. The backflow in each loop could be adjusted independently. With the bypass loops open between the units we found that fully autonomous pumping could be readily sustained (Fig 3). An initial series of contractions needed to be programmed into the first unit, but once the downstream units were pumping the first unit could be switched to the same reactive algorithm and would continue pumping.

The effects of shear stress were introduced by programming the units to have a longer interval between contractions or a higher threshold for the transmural pressure necessary to trigger a contraction. When the flow rate and accompanying shear stress are sufficiently high, contractions can cease as would be advantageous when the vessels are oriented so that gravity assists flow.

DISCUSSION

The mechanism by which autonomous pumping occurs is as follows. When a downstream unit contracts, most of the flow is forced further downstream, but the bypass loops allow a small amount of fluid to move upstream. In doing so the pressure in the upstream unit will increase slightly, thus stretching the vessel wall making it more likely to contract. The resulting contraction of the upstream unit will then force

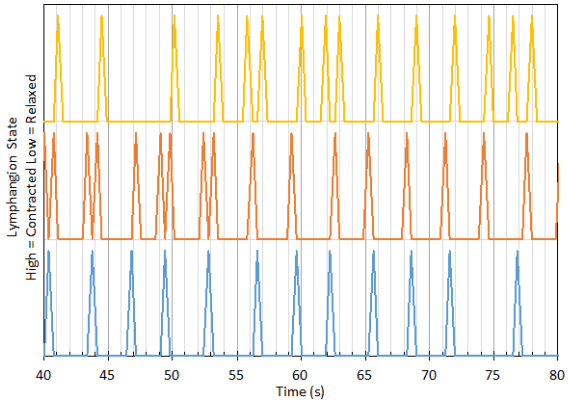

Figure 3: Self-sustained, autonomous contraction sequence of the first (blue), second (orange), and third (yellow) lymphangion units with backflow at each valve.

fluid downstream to initiate a new contraction downstream that can feed pressure back upstream and so on. Our results cannot rule out the possibility that other mechanism could support self-sustained pumping, but here we found that the leakage of fluid upstream between units was necessary. This result is consistent with the bias of lymphatic valves toward the open condition seen in vivo [4].

Careful examination of the contraction patterns in Fig. 3 shows that the sequence of contraction can be either retrograde or orthograde relative to the flow even though the time averaged flow remains downstream in all cases. This result is also consistent with observations in vivo [5].

We have found that our physical model is useful for studying the dynamics of complex pump-conduit systems similar to lymphatic vessels. While not a complete substitute for existing methods, our model provides a unique mix of visual, tactile, audible and quantitative feedback to the user.

ACKNOWLEDGEMENTS

This work was supported by NIH grant RO1-HL128168 to JWB and LLM.

REFERENCES

[1] Margaris, K. N. and Black, R. A., *Royal Soc. Interface* 9(69), 601-612, 2012.
[2] Breslin, J. W. et al, *Comprehensive Physiology*, 9, 207-299, 2019.
[3] Padera, T. P., et al, *Annual. Rev. Biomed. Eng.*, 18, 125-158 2016.
[4] Bertram, C. D., et al, *Am J Physiol Circ Physiol* 310, H847-H860, 2016.
[5] Kunert, C. et al, *PNAS*, 112, 10938-10943, 2015.

SB³C2019
Summer Biomechanics, Bioengineering and Biotransport Conference
June 25 -28, Seven Springs, PA, USA

CULTURE OF LYMPHATIC ENDOTHELIAL CELLS IN A CUSTOM BIOREACTOR FOR STUDIES COMBINING STRETCHING AND FLUID SHEAR STRESS

Caleb A. Davis (1), Walter Cromer (2), David C. Zawieja (2), Michael R. Moreno (1,3)

(1) Biomedical Engineering
Texas A&M University
College Station, TX, USA

(2) Medical Physiology
Texas A&M Health Science Center
Temple, TX, USA

(3) Mechanical Engineering
Texas A&M University
College Station, TX, USA

INTRODUCTION

The lymphatic vessels perform vital transport functions, including return of excess fluid from the tissues to the circulatory system. Inadequate fluid transport can lead to edema, a common and debilitating condition in both the developed and developing world. Lymphatic transport relies on both intrinsic and extrinsic contractions, but the mechanoregulatory mechanisms responsible for intrinsic contraction are not fully understood. Lymphatic endothelial cells (LEC) likely play a role, being sensitive to local fluid shear stress (FSS) and the wall strain caused by contraction [1]. The effects of these mechanical forces have been studied extensively in vascular endothelial cells [2], but considerably less so for LEC [1]. Importantly, to our knowledge, no studies applied simultaneous FSS and stretching to LEC in vitro, through these occur concurrently in vivo.

We therefore developed a custom bioreactor to apply both types of forces (FSS and stretch) simultaneously to cultured LEC, attempting to verify the levels of FSS and strain through analytical, computational, and optical measurement techniques. Studies applying controlled levels of mechanical forces should help illuminate the endothelial role in mechanoregulatory mechanisms of intrinsic lymphatic contraction.

Maintaining cell attachment in such a bioreactor is nontrivial; in addition to moderate and widely varying levels of FSS, lymphatic vessels can experience high dynamic circumferential strains of >50%, compared to 5-10% in arteries [3]. We therefore conducted studies to determine which treatments most effectively promote LEC attachment to the silicone membranes we plan to use in the bioreactor, including under conditions involving FSS and high dynamic strain. Additionally, we used a fluorescence Live/Dead assay to investigate whether live cells were maintained in culture inside the experimental chamber.

METHODS

Bioreactor Design: Cells in the bioreactor are cultured on a flexible silicone membrane. The sealed culture module containing the membrane acts as a standalone culture system until the cells have reached sufficient confluency. The module contains viewing ports for transmitted-light imaging for easy monitoring of cell status. This chamber can then be integrated into the stretch and flow bioreactor without disrupting the cells. To achieve dynamic stretch, the membrane is stretched uniaxially in-plane over a pair of steel rollers; this is controlled by the movement of a step-motor-actuated shaft (Fig. 1).

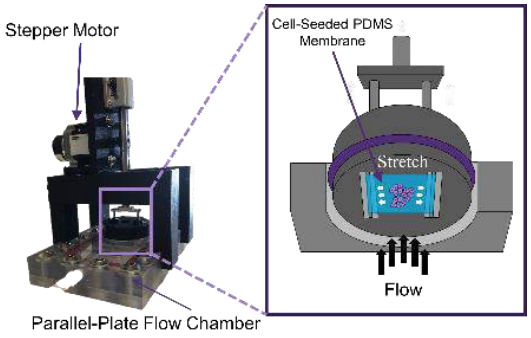

Figure 1: Custom Flow-Stretch Bioreactor

FSS is applied by placing the cultured membrane in an adapted parallel-plate flow channel in a circulating flow loop with a pump circulating media at a given flow rate. Importantly, the FSS and stretching on the LEC are independently controlled, meaning any number of flow, stretch, or combined flow/stretch scenarios could be simulated in the same device. Computational Fluid Dynamics (CFD) studies in ANSYS Fluent were performed to calculate wall shear stress

at the cell culture region of interest using a custom meshed model of the chamber. Boundary conditions were flow rate at the channel input and pressure at the output. Materials for all potentially cell-contacting components of the device were selected for biocompatibility and autoclavablity.

LEC Attachment Studies: Rat mesenteric LEC were cultured on silicone (PDMS) membranes treated with various substrates (gelatin, Poly-D-Lysine [PDL], fibronectin). Phase contrast images at 24 and 72 hr post-seeding were processed with ImageJ to identify and count cells in 3 different locations on each membrane, and the cell count was compared between treatments. In a second experiment, fibronectin-treated LEC-seeded membranes were stretched to 20% and back 3 times at 1%/sec. One membrane was exposed to FSS via an orbital rocker for 12 hr before testing. Phase contrast images pre-test and at 0 and 24 hr post-test were analyzed with ImageJ and compared as before. Finally, cell-seeded fibronectin-treated membranes were mounted into the custom parallel-plate flow chamber. Cells were exposed to ~5 dynes/cm^2 steady FSS for 16 hr. Phase contrast images pre- and post-test were analyzed with ImageJ and compared as before. Significance testing was Student's t-test (for FSS study) and ANOVA with Tukey HSD post-hoc testing.

Strain Measurement: A random dot pattern was applied to silicone membranes using spray paint. Mounted in the system, the membranes were stretched by manually inputting step values into the stepper motor. Images were taken via digital camera every 100 steps. The Digital Image Correlation (DIC) software GOM-Correlate was used to map the strain values on the membrane surface.

RESULTS

Bioreactor Design: In the assembled bioreactor, stretch and flow were applied at experimental rates without leakage or mechanical failure. Cells were cultured in the standalone culture module which was then able to be integrated into the stretch/flow system. The viewing ports included in the culture module allowed phase contrast images to be taken on an inverted microscope without disrupting the cells or unsealing the culture area (Fig. 2).

Figure 2: (Left) Culture module being imaged on inverted microscope. (Right) Phase contrast images of 3t3 fibroblasts imaged in the culture module

LEC Attachment Studies: Significantly more LEC were attached to the fibronectin-treated membranes than PDL after 72 hr. Fibronectin on silicone was the most effective treatment observed, providing attachment equal to or better than that seen on gelatin-treated glass controls. On silicone membranes stretched to 20%, there was a significant decrease in number of cells attached after 24 hours, but the decrease was not significant for a membrane exposed to FSS before stretching (Fig. 3, Left). Qualitative assessment of morphology suggested that morphology changed less after stretching for pre-stressed cells. In the FSS study, LEC-seeded membranes showed no significant decrease in number of cells attached after 16 hr at 5 dynes/cm^2 steady FSS (Fig. 3, Right).

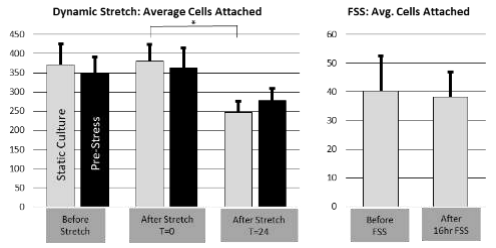

Figure 3: (Left) LEC counted before and after dynamic stretch. (Right) Cell count before and after steady FSS.

Strain Measurement: Green Strain in the direction of stretch was averaged over the membrane cell culture region of interest (Fig. 4, error bars ±SD). Within the range of movement of the motor, this reached 30-40% strain. A linear model assuming 0 strain at 0 motor steps found a slope of 3.74×10^{-5} strain units per motor step, with a correlation coefficient (R^2) of 0.94.

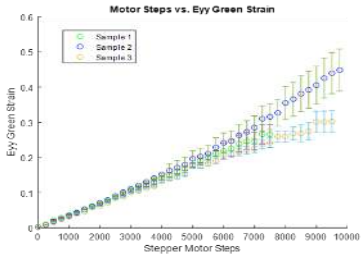

Figure 4: Steps vs. mean Green strain in the silicone membrane.

DISCUSSION

We have developed a custom bioreactor designed for novel in vitro studies with simultaneous stretching and FSS applied to LEC. Strain measurements on the membrane in the device indicate average strain values similar to those that could plausibly be encountered in vivo, with a highly linear relationship between motor movement and membrane strain, FSS levels on the cells cannot be directly measured, but can be calculated via CFD or analytically given the flow rate and various assumptions. However, validation of the FSS will require more future work, such as demonstrating the elicitation of known shear stress responses in the LEC (e.g. altered morphology and mRNA expression).

Preliminary results indicate that LEC can be cultured on the flexible silicone membranes to be used in future experiments, and remain attached under conditions of fluid shear stress and dynamic strain. Fibronectin has proven to be a useful substrate to facilitate cell attachment to the silicone. It appears attachment during a stretching experiment can be encouraged through application of FSS during culture as a pre-stress. Additionally, future validation will include Live/Dead analysis of cells cultured in the bioreactor.

The work presented here represents a proof of concept of the bioreactor, with the goal of facilitating experiments which will combine flow and stretch. By studying LEC response in a controlled environment to FSS and stretching, we aim to investigate how these forces and the LEC affect the mechanoregulation of intrinsic lymphatic pumping.

ACKNOWLEDGEMENTS

Research supported by NIH U01 Grant #23-463934-00001

REFERENCES

[1] Jafarnejad, M et al., *Am J Physiol Heart Circ Physiol*, 308(7):H697-H706, 2015.
[2] Davis, CA et al., *J Biomech Eng*, 137(4):040801, 2015.
[3] Dixon, JB et al., *Microcirculation*, 13:597-610, 2006.

IN VITRO ANTROPHOMORPHIC MODEL OF THE CEREBROSPINAL FLUID SYSTEM: APPLICATION TO SUBARACHNOID HEMORRHAGE FILTRATION

Lucas R. Sass[1], Mohammadreza Khani[1], Gabryel Conley Natividad[1], Elliott Marsden[1], Shavaine Byass[1], Omolola Bangudu[1], Aaron R. McCabe[2], Laura M. Zitella Verbick[2], Shivanand P. Lad[3], Bryn A. Martin[1]

(1) Department of Biological Engineering
The University of Idaho, Moscow, ID, USA

(2) Minnetronix Neuro, Inc.
St. Paul, MN, USA

(3) Department of Neurological Surgery
Duke University, Raleigh, NC, USA

INTRODUCTION

Complications such as delayed cerebral ischemia, vasospasm and hydrocephalus account for the poor prognosis and death of many patients following subarachnoid hemorrhage (SAH)[1]. Primarily caused by ruptured aneurysms and trauma, SAH releases blood into the cerebrospinal fluid (CSF) exposing the surrounding tissue to inflammatory clotting byproducts[2]. Removal of blood via lumbar drain has been shown to positively impact clinical outcomes and the rapid removal of blood from the CSF is the target of a new device aimed at improving patient outcomes. The presented work outlines the assembly and testing of an in vitro platform (**Figure 1a**) modeling active clearance of SAH using a dual lumen catheter-based CSF Filtration device[3][4] (Neurapheresis™ System; Minnetronix Neuro, St. Paul, MN). This device introduces a flow loop aimed at improving particle clearance from the CSF. The resultant model allows parametric testing of therapies and devices such as Neurapheresis therapy that would otherwise be prohibitively difficult and costly to perform in vivo. Additionally, the in vitro model provides known boundary conditions that allow validation of computational analogs for iterative optimization schemes.

METHODS

A complete geometry of the craniospinal CSF system was constructed from our previously published spinal anatomy[5] and segmentation of additional high-resolution subject specific magnetic resonance imaging (MRI) of the complete cranial volume (**Figure 1b** and **c**). The highly complex geometry of cortical surface and ventricular CSF system was smoothed and simplified such that total cranial CSF volume remained congruent with the original model. This was achieved by offsetting the cranial arachnoid and pial surfaces by a uniform gap of ~2.0 mm. The falx cerebri and tentorium cerebelli were modeled as impermeable divisions between the left and right hemisphere as well as the cerebral and cerebellar compartments respectively. Additional geometry for access and flow ports was also added. Final digital geometry was submitted for stereolithographic 3D printing with a layer and in-plane resolution of 127 μm and 500 μm respectively for the cranial volume and 127 μm and 250 μm in the spinal column (**Figure 1**). The caudal end of the model was connected to a custom-built CSF flow pump imparting a waveform based on in vivo CSF flow waveform measured at C2/C3 via phase-contrast MRI (**Figure 2b**). The dual lumen neurapheresis catheter was inserted through an access port such that aspiration and return flow occurred at L2/L3 and T2/T3 respectively (**Figure 1d**). An aqueous solution of fluorescein sodium (15 μM) was used to fill the model initially and represented a uniform distribution of blood. In the case of Neurapheresis therapy, flowrates for aspiration of the fluorescein solution and return of clean deionized water (DIH_2O) were set at 2.0 ml/min and 1.8 ml/min, respectively. A net volume of 0.2 ml/min was discarded, per design, by the system and replaced by an equal flowrate of DIH_2O into the lateral ventricles to maintain a constant system volume. For comparison, a lumbar drain was simulated with an aspiration rate of 0.2 ml/min at L2/L3 with ventricular production of DIH_2O at 0.2 ml/min. All experiments were conducted with the model at 30 degrees from horizontal. Time-lapse imaging was collected, and digital image subtraction of maximum and minimum background intensity images were applied to normalize the data and obtain spatial-temporal fluorescein concentration (**Figure 2a**).

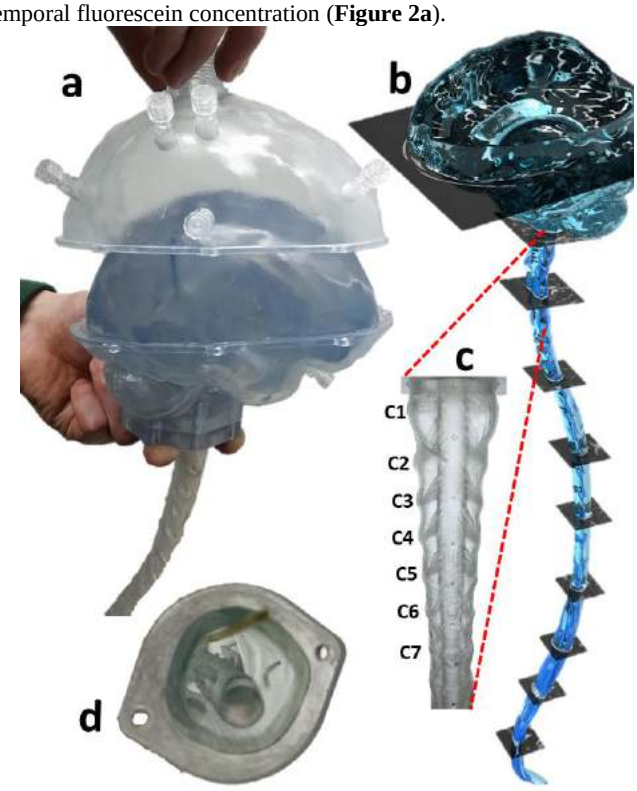

Figure 1: (a) 3D printed Cranial CSF phantom with upper arachnoid shell removed showing cortical surface. (b) Digital reconstruction of the complete CSF system from MRI. (c) Cervical spine detail showing 3D printed nerve roots included in the spinal model. (d) T9 looking caudally, catheter insertion was posterior to the spinal cord.

RESULTS

The final model included realistic spinal nerve root detail and a subject specific ventricular system including the lateral, third and fourth ventricles, sylvian cisterns, cisterna magna, pontine cistern as well as foramen Monro, Magendie, Luschka and Sylvian aqueduct. Final cranial and spinal volumes were 215.0 ml and 97.0 ml, respectively with a total CSF system volume of 312.0 ml. Spatial-temporal tracer concentration revealed Neurapheresis therapy to dramatically decreased tracer concentration compared to lumbar drain (**Figure 3**). The difference in concentration decrease was strongest within the upper thoracic spine. At 24 hours, tracer conentration 20 cm below the foramen magnum (FM) had decreased to 1.5% for Neurapheresis therapy and 8.5% for lumbar drain from the intial unform distribution of 10%.

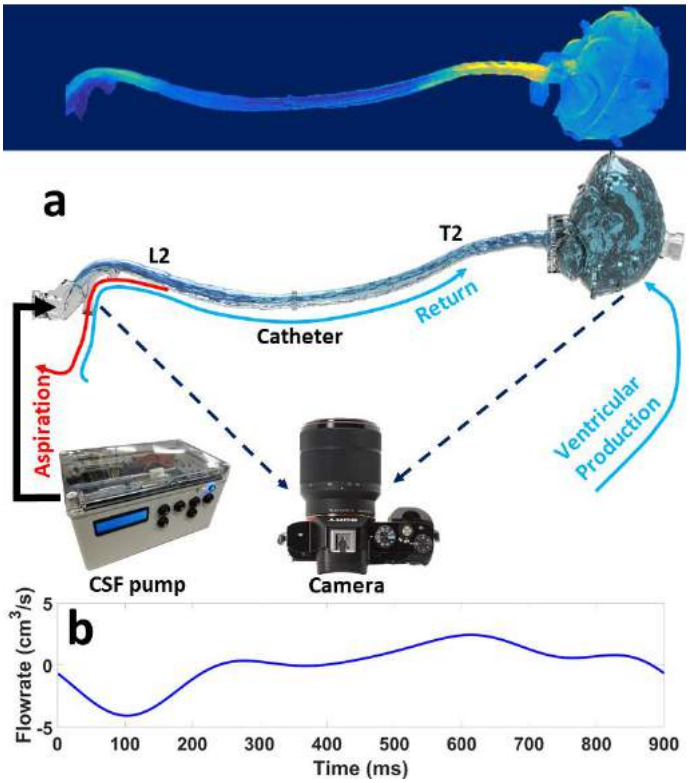

Figure 2: Schematic of the in vitro system. (a) CSF with tracer was removed at L2 and clean water returned at T2 and in the lateral ventricles. (b) Oscillatory CSF flow was delivered by a custom-built pump programmed with an idealized waveform measured with phase-contrast MRI at C2/C3.

DISCUSSION

The developed anthropomorphic in vitro model and imaging system allowed parametric evaluation of CSF tracer clearance for a subject specific geometry and physiologic conditions. In comparison to lumbar drain, Neurapheresis therapy at the flow rate analyzed increased tracer clearance to a greater degree at all time points after ~10 minutes (**Figure 3**). These changes were most pronounced within the dual-lumen catheter flow-loop region and also extended to the cortical subarachnoid space. Distribution of tracer concentration was relatively uniform around the spinal cord for the duration of the experiment. CSF production stemming from the 4th ventricle outlets decreased local tracer concentration near that region (cisterna magna).

Several anatomic simplifications were necessary in the cranial model due to limitations in 3D printing capabilities and MR image resolution. These included cortical and ventricular surface smoothing and a rigid CSF space geometry (non-compliant) that resulted in a constant CSF flow rate throughout the model. CSF pulse was assumed to be cardiac related only with no impact from respiration. Digital imaging was obtained as a projection of the model (2D). Thus, it was not possible to obtain the exact 3D spatial distribution of tracer concentration over time. Lastly, CSF production, aspiration, and return rates resulted in a total CSF volume drift of <20 mL over the 24-hour period (<6%).

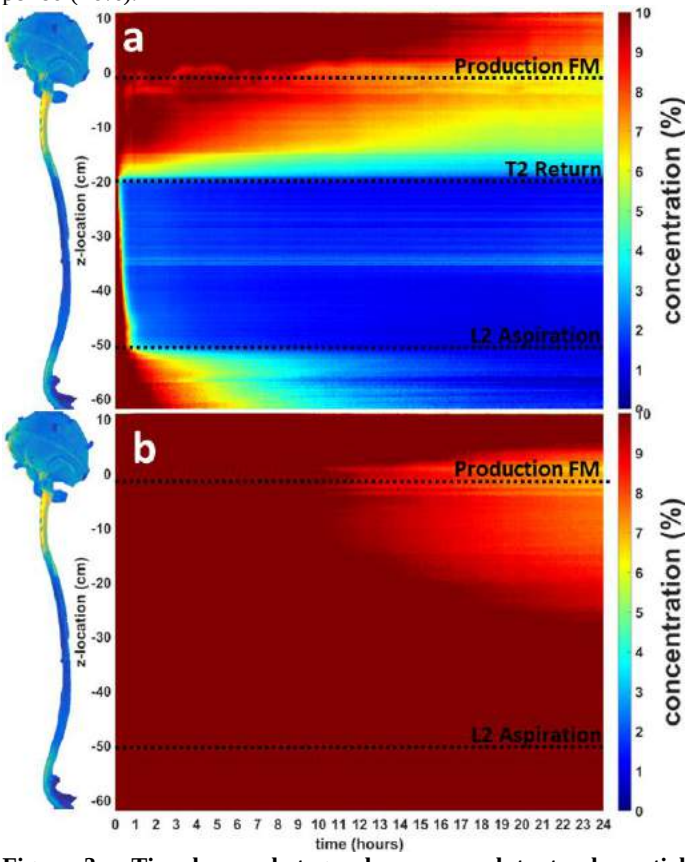

Figure 3: Time-lapse photography was used to track spatial temporal tracer distribution. (a) Experiment conducted with neurapheresis therapy set to an aspiration rate of 2 ml/min, return rate of 1.8 ml/min, and ventricular CSF production rate of 0.2 ml/min. (b) Experiment conducted with a lumbar drain rate of 0.2 ml/min and ventricular production of 0.2 ml/min.

ACKNOWLEDGEMENTS

This work was supported by Minnetronix Neuro, Inc., an Institutional Development Award (IDeA) from the National Institute of General Medical Sciences (NIGMS) of the National Institutes of health (NIH) under Grants #P20GM1033408, #4U54GM104944-04TBD, and #1R44MH112210-01A1, and University of Idaho Vandal Ideas Project.

REFERENCES

[1] H. Lantigua, *et al.*, *Critical Care*, vol. 19, Aug 31 2015.
[2] J. Bardutzky, e*t al.*, *Trials*, vol. 12, p. 203, Sep 14 2011.
[3] G. J. Smilnak, *et al.*, *J Infect Dis*, vol. 218, pp. 1147-1154, Aug 24 2018.
[4] S. L. Blackburn, *et al.*, *Oper Neurosurg (Hagerstown)*, Jun 5 2018.
[5] L. R. Sass, *Fluids Barriers CNS*, vol. 14, p. 36, Dec 19 2017.

SB³C2019
Summer Biomechanics, Bioengineering and Biotransport Conference
June 25 -28, Seven Springs, PA, USA

IMPACT OF CEREBROSPINAL FLUID FILTRATION ON SUBARACHNOID HEMORRHAGE CLEARANCE: A COMPUTATIONAL FLUID DYNAMICS STUDY

Mohammadreza Khani (1), Lucas R. Sass (1), M. Keith Sharp (2), Aaron R. McCabe (3), Laura M. Zitella Verbick (3), Shivanand P. Lad (4), Bryn A. Martin (1)

(1) Department of Biological Engineering
The University of Idaho
Moscow, ID, USA

(2) Department of Mechanical Engineering
University of Louisville
Louisville, TN, USA

(3) Minnetronix Neuro, Inc.
St. Paul, MN, USA

(4) Department of Neurological Surgery
Duke University
Raleigh, NC, USA

INTRODUCTION

Subarachnoid hemorrhage (SAH) is a severe and often-fatal event [1] in which blood is released into the cerebrospinal fluid (CSF) due to intracranial insult, ruptured intracranial aneurysm, and/or other head trauma. It has been hypothesized that early and rapid filtration of blood and blood breakdown byproducts (e.g., hemoglobin and other inflammatory mediators) post-SAH may reduce the incidence of stroke, cerebral vasospasm [2] and hydrocephalus, and shorten hospital stay. A computational model of CSF filtration could help understand blood clearance from the CSF system. The present study objective was to formulate such a model to evaluate the Neurapheresis™ System (Minnetronix Neuro, St. Paul, MN), which consists of a dual-lumen intrathecal catheter, a filtration assembly, and a controller (Figure 1a) [3] designed to accelerate blood clearance from the subarachnoid space. In brief, Neurapheresis therapy involves aspiration of CSF from the lumbar spinal subarachnoid space (SSS), filtration of blood and/or other pathogens specific to the malady, and then return of filtered CSF to the SSS at the thoracic spine, via redundant fenestrations (to avoid clogging or blockages) in the dual-lumen catheter. The impact of the Neurapheresis system on CSF flow velocities, steady-streaming, and subarachnoid blood clearance was investigated by comparing it to a case with lumbar drain only.

METHODS

A multiphase computational fluid dynamic (CFD) model of the SSS was built using ANSYS Fluent 19.1 (ANSYS Inc., version 19.1, Canonsburg, PA, USA). Model geometry was defined by our previously developed anatomically realistic open-source 3D intrathecal space [4-6]. A dual-lumen catheter geometry was added to the posterior SSS at the T2-L2 level and positioned at the midline (**Figure 1b**). The final computational mesh comprised 14.8 M cells. Flow boundary conditions

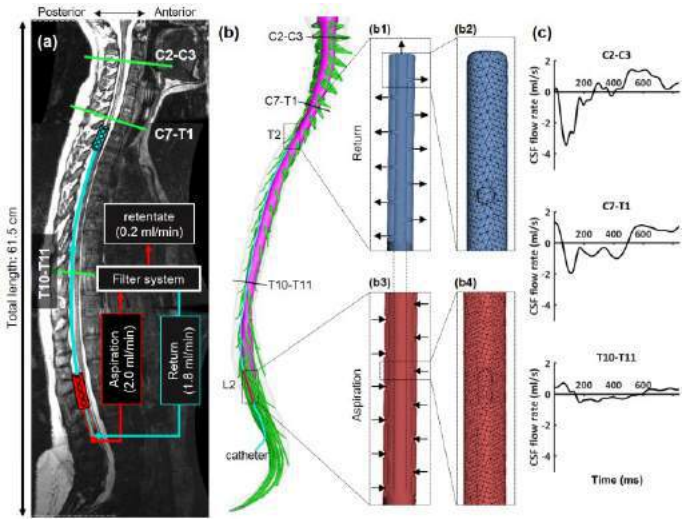

Figure 1: (a) Schematic of the Neurapheresis system catheter. (b) Overview of 3D CFD model. (b1-b4) Magnified view of the Neurapheresis catheter return and aspiration ports, surface mesh, and flow direction. (c) Subject-specific CSF flow along the SSS.

reproduced subject-specific non-uniform CSF flow along the spine (**Figure 1c**) by imposing non-uniform dura deformation [4, 5]. CSF was considered to be incompressible with a density of 993.8 kg/m3 and Newtonian with a viscosity of 0.693 mpa·s. Velocity results were obtained for the second flow cycle with a time-step size of 0.01 s (total cardiac cycle = 0.85 s) [4]. CSF flow was quantified in terms of axial distribution of Reynolds number and CSF velocity contours. To visualize steady-streaming along the spinal axis due to convective

acceleration of oscillatory flow within an eccentric annulus, the cyclic mean sagittal velocity, $U_{z\text{-}mean}$, at each node was calculated. This steady-streaming velocity field [7] was then held constant (''frozen flow field'') to compute hemorrhage clearance. Blood was modeled as a passive species advected in the bulk fluid phase (CSF). An initial uniform blood concentration of 10% was assumed. Neurapheresis system aspiration flow was set at 2.0 ml/min and return to 1.8 ml/min, for retentate of 0.2 ml/min (**Figure 1a**). Simulated blood concentration was plotted spatially and temporally at multiple spinal levels over 24 hours for Neurapheresis therapy and a lumbar drain with 0.2 ml/min CSF removal.

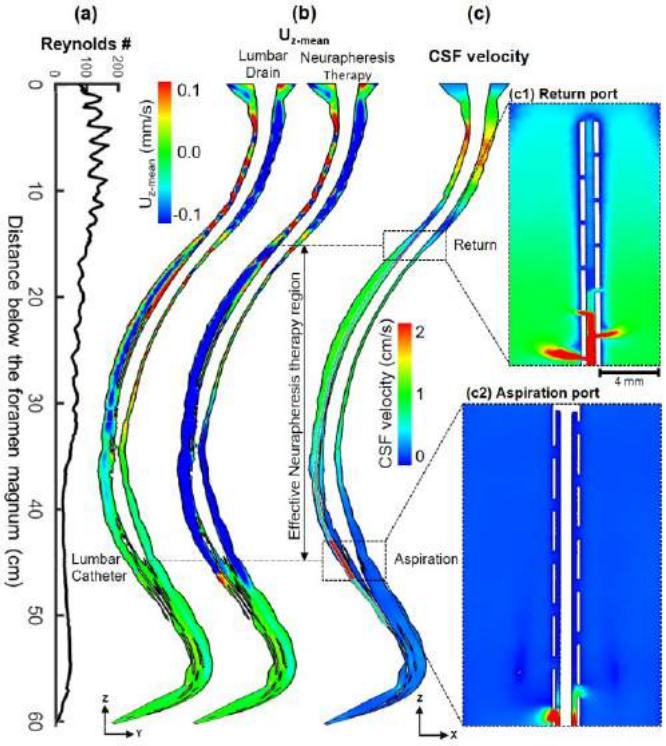

Figure 2: (a) Reynolds number distribution computed along the spine. (b) Sagittal visualization of cyclic mean velocity, $U_{z\text{-}mean}$, and (c) Sagittal visualization of CSF velocity magnitude profiles. (c1-c2) Magnified coronal view of the return and aspiration ports.

RESULTS

Maximum Re was 180 and located within the cervical spine (**Figure 2a**). The sagittal $U_{z\text{-}mean}$ velocity profiles showed a region of caudally directed (↓) steady-streaming in the posterior SSS in the middle thoracic spine and in the anterior SSS in the cervical spine (**Figure 2b**). Average steady-streaming velocity for Neurapheresis therapy and lumbar drain was 0.19 and 0.09 (mm/s), respectively. Visualization of unsteady CSF velocity contours in the sagittal plane showed that peak CSF velocities occurred in the cervical spine (**Figure 2c**). CSF velocity profiles near the aspiration and return ports showed that most of the flow into and out of the domain originated from the first two holes at the return and the aspiration port (**Figure 2c1-2**).

Blood concentration contours demonstrated that the lumbar and thoracic SSS were largely cleared of blood after 24 hours of Neurapheresis therapy (**Figure 3a-b**). The average blood concentration plots showed relatively rapid removal of blood from the thoracic SSS after 1 hr of filtration (**Figure 3b**). 24 hours after Neurapheresis therapy, less than 10% of the initial blood concentration remained in the lumbar and thoracic spine and more than 70% was cleared from the cervical spine (**Figure 3c**). In comparison, lumbar drain had a much lower impact on blood concentration reduction. After 24-hours of lumbar drain, blood concentration in the thoracic spine decreased to ~7% compared to <1% under neurapheresis therapy (**Figure 3c**).

DISCUSSION

Neurapheresis therapy was found to have little impact on CSF velocities in comparison to normal cardiac-induced physiologic CSF movement. Therefore, it is not expected that these alterations to CSF velocities would, on their own, have ramifications to the normal physiology. Previous research has shown that peak cardiac-induced CSF velocities in healthy people range from 2-4 cm/s within the intrathecal space [8]. Our findings show that Neurapheresis therapy-induced CSF velocities ($U_{z\text{-}mean}$) do not exceed 0.08 cm/s for Neurapheresis flow of 2.0 ml/min (**Figure 2**).

The Neurapheresis therapy drastically reduced blood concentration within the intrathecal space within a relatively short period of time in comparison to a lumbar drain with a typical CSF removal rate of 0.2 ml/min. The reduction in blood concentration was most evident within the flow-loop region introduced by the dual-lumen catheter.

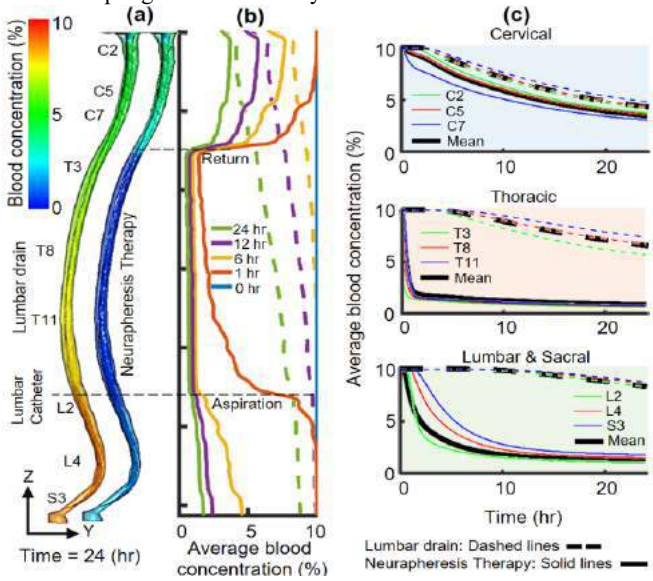

Figure 3: (a) Sagittal profile of average blood concentration after 24 hours with lumbar drain (left) and Neurapheresis therapy (right). (b) Average axial blood concentration for different time points with Neurapheresis therapy (solid lines) versus lumbar drain (dashed lines). (c) Temporal average blood concentration at different SSS levels.

ACKNOWLEDGEMENTS

This work was supported by Minnetronix Neuro, Inc., an Institutional Development Award (IDeA) from the National Institute of General Medical Sciences (NIGMS) of the National Institutes of health (NIH) under Grants #P20GM1033408, #4U54GM104944-04TBD, and #1R44MH112210-01A1, and University of Idaho Vandal Ideas Project.

REFERENCES

[1] Lantigua, H., et al., Critical Care, 19, 2015.
[2] Bardutzky, J., et al., Trials, 12, 2011.
[3] Blackburn, S.L., et al., Oper Neurosurg, 151, 2018.
[4] Khani, M., et al., J Biomech Eng, 140(8), 2018.
[5] Khani, M., et al., J Biomech Eng, 139(8), 2017.
[6] Sass, L.R., et al., Fluids Barriers CNS, 14(1): p. 36, 2017.
[7] Kuttler, A., et al., J of Pharmacokinetics and Pharmacodynamics, 37(6): p. 629-644, 2010.
[8] Bunck, A.C., et al., Eur Radiol, 22(9): p. 1860-70, 2012.

SB³C2019
Summer Biomechanics, Bioengineering and Biotransport Conference
June 25 -28, Seven Springs, PA, USA

TOWARDS PHYSIOLOGICALLY-RELEVANT VOCAL FOLD MODELS FOR VOICED-SPEECH INVESTIGATIONS

Mohsen Motie-Shirazi (1), Natalie I. Jagelski (1), Byron D. Erath (1)

(1) Department of Mechanical and Aeronautical Engineering
Clarkson University
Potsdam, New York, USA

INTRODUCTION

Human voice is produced as air is driven from the lungs through the larynx, producing self-sustained oscillation of the vocal folds (VFs). Oscillations are achieved due to a combination of geometry and material properties of the VF structure. Due to their relative inaccessibility, in vivo VF investigations focused on the diagnosis and remediation of VF pathologies are severely limited. As such, synthetic models that replicate the anatomical, aerodynamic and acoustic properties of voice production show significant promise as VF surrogates.

Initial attempts at reproducing synthetic VF oscillations were achieved with simplistic single-layer, homogeneous, isotropic models that utilized a generalized VF geometry;[1] a significant simplification of the complex layered structure of the VFs that is comprised of the thyroarytenoid muscle, lamina propria, and epithelium.[2] Subsequent attempts at developing synthetic VF models have produced more realistic VF dynamics through the implementation of multi-layered approaches.[3] Nevertheless, shortcomings that prevent broader deployment of these models still exist, including; (1) unnaturally high onset pressure (the minimum pressure at which the VFs soscillate), (2) abnormally low closed quotient (CQ) (the ratio of closed phase to oscillation period), and (3) the lack of a robust mucosal wave, which is a hallmark of healthy and normal vocal fold oscillations.

The objective of this work is to revisit the underlying assumptions related to synthetic VF model development to develop more physiological VF surrogates that address current shortcomings and, as such, provide a viable alternative platform for performing scientific investigations of voiced speech.

METHODS

The VFs are commonly modeled as a three-layer structure consisting of a body, cover, and epithelium. To overcome existing model shortcomings, histological images of the VFs[2] (Fig.1) were revisited to identify key features that have been neglected in prior modeling attempts. These include: (1) an undercut on the superior surface, (2) inclusion of a layer of adipose tissue (AT) that fills the paraglottic space[4] (the space between VF and thyroid cartilage), (3) a ligament membrane within the VF (the conus elasticus), and (4) a longer medial contact length. Including the undercut is expected to reduce the onset pressure as the structure will have less support under the superior edge, while also creating a more pronounced divergent state that leads to a better mucosal wave. AT provides a more flexible substrate for the VF and is also expected to lower the onset pressure due to the added mass, but may also lead to increased abnormal motion in the inferior-superior direction. However, the inclusion of a thin and stiff conus elasticus layer should counteract this unwanted motion by increasing the stiffness in the inferior-superior direction.[5] In addition, extending the medial length should result in better VF closure and improve both the CQ and the robustness of the mucosal wave.

The reported dimensions for an excised human VF are the basis for the peripheral geometry in the anterior-posterior cross section of the newly-developed models used in this study (Fig.2). [5] Furthermore, by

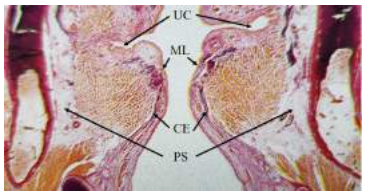

Figure 1: Coronal section of the vocal folds showing the Undercut (UC), Medial Length (ML), Conus elasticus (CE), and Paraglottic space (PS)

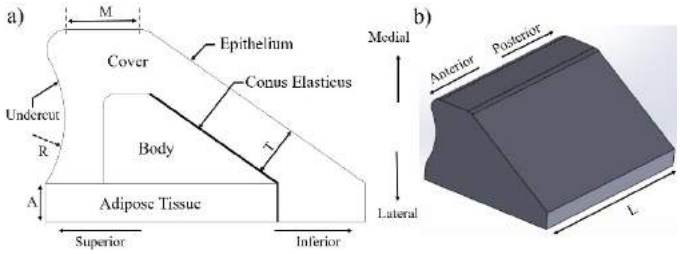

Figure 2: Vocal fold shape and geometry a) Anterior-Posterior cross section, b) 3D view

using histological images, the geometry and dimensions of the inner layers are estimated. As can be seen in Fig.2(a), the newly proposed model consists of 5 layers: (1) an AT layer that separates the VF from the thyroid cartilage, (2) a body layer, (3) the conus elasticus, (4) the cover layer, and (5) the epithelium.

Synthetic models are manufactured using Smooth-OnEcoflex 00-30™ and Dragon Skin™ 10 silicone rubber and adding different ratios of silicone thinner to create the desired stiffness. A mold is created for each layer and the models are fabricated by sequentially adding and curing each layer of silicone. The modulus of elasticity for each silicone ratio is found by performing dynamic mechanical analysis, to ensure physiological relevance. Table.1 lists the range of physiological values for the corresponding in vivo VF tissues layers.

Table 1: Model and physiological stiffness values for the different layers of the vocal folds

Layer	Physiological Stiffness Range (kPa)
Adipose Tissue	1 – 10
Body	7 – 30
Cover	2 – 8

The model variables (see Fig. 2) were parametrically varied to assess their impact on the model VF dynamics; namely, (1) adipose tissue thickness (A), (2) adipose tissue stiffness, (3) superior surface undercut radius (R), (4), length of the medial surface (M), (5) thickness of the cover (T), (6) anterior-posterior length (L), and (7) the amount of static contact pressure along the medial surface.

The self-oscillatory dynamics of each model is tested in a laryngeal flow facility. The facility consists of a large plenum supplied by regulated, compressed air, with a 15 cm long, 2.89 cm^2 cross-section area exiting it, which represents the lung volume and tracheal airway, respectively. Synthetic VFs are mounted into two opposing brackets, and positioned such that the medial surfaces are in contact. The amount of compression between the models can be adjusted, and is recorded. In this manner, air passes from the lung chamber, through the tracheal tube, and then through the VF models, driving the models into self-oscillation. The mean flow rate is measured by a Dwyer flow meter that is positioned before the plenum. A Dwyer manometer, which is connected to static pressure tap, measures the mean subglottal pressure, while the unsteady pressure is recorded with a Kulite XCS-063 pressure transducer. A Photron high-speed camera records the VF vibration at frame rates of 20 kHz.

For each test, the kinematics of the model VF oscillations are acquired from the high-speed video. The glottal area (the space between the VFs) is determined by defining a threshold filter such that the VF boundaries are detected. A known reference length in the images, the VF length, is used to calibrate the images. By computing the glottal area, it is possible to then compute the CQ as well as the lag between the inferior and superior edges of the VFs, which provides a benchmark for evaluating the robustness of the mucosal wave. In addition to the video acquisitions, the onset pressure, flow rate, and fundamental oscillation frequency are recorded and compared to physiological measures. The experimental procedure includes changing one parameter each time and studying its effect on the VF motion to achieve a model that best conforms to the aforementioned physiological characteristics.

RESULTS

For each investigation, the medial compression pressure was held constant by using shims between the mounting brackets that hold the VF models. Adding the AT layer reduced the onset pressure, which is one of the major shortcomings of synthetic VF models, with optimal results found at the lower limit of AT stiffness. At this lower limit of AT stiffness, the effect of the superior undercut was studied by changing its radius. The undercut had a significant effect on reducing the onset pressure and creating a more pronounced convergent-divergent motion (increase inferior-superior phase lag) in the mucosal wave. For short lengths of the medial VF surface, complete closure of the VFs was rarely achieved, and the oscillation mode resembled that of falsetto, as opposed to normal, or chest-register motion. Increasing the length increased the phase lag between the inferior and superior margins of the VFs, which enhanced the mucosal wave quality, but increased the onset pressure as well. Hence, there is a trade-off between achieving a lower onset pressure and increased convergent-divergent glottal motion, indicative of a more pronounced mucosal wave. For this reason, the shortest medial length that lies within the physiological range was chosen for subsequent investigations. With the cross sectional geometry specified, the effect of thickness and stiffness of the various tissue layers was investigated, where it was found that the stiffness of the cover layer had the greatest influence on the frequency of oscillation, onset pressure, and CQ. Finally, the role of medial compression was studied. Low medial compression resulted in the inability to achieve good VF closure and a healthy mucosal wave, while excessively high compression deformed the VF and produced irregular oscillations.

DISCUSSION AND CONCLUSIONS

It was shown that the shape and material properties of each layer play an important role in synthetic VF vibration dynamics. In this study, the geometry, stiffness, and medial compression of synthetic VF models were methodically improved to generate a physiologically-relevant surrogate for VF investigations. The synthetic model was shown to generate a more robust mucosal wave with a CQ that is similar to physiological measures while keeping the glottal area, fundamental frequency, and onset pressure within an acceptable range.

Synthetic VF model investigations are highly repeatable and provide a low-cost approach. Moreover, the ability to tune them to match particular phonatory behaviors (e.g. model pathologies) is highly attractive. The new model proposed in this study was found to be a valuable tool for experimental VF modeling approaches that show very good agreement with generalized clinical measures of aerodynamic and kinematic VF performance.

ACKNOWLEDGEMENTS

This research was supported by the National Institute on Deafness and Other Communication Disorders through grant P50DC015446.

REFERENCES

[1] Thomson, S, L. *Acoust. Soc. Am*, 118(3), 1689-1700, 2005.
[2] Hirano, M. *Histological Color Atlas of the Human Larynx*, 1993.
[3] Murray, P. R., *J. Acoust. Soc. Am*, 132(5), 3428-3438, 2012.
[4] Sato, K. *Ann Otol Rhinol Laryngol,* 102(12), 930-934, 1993.
[5] Sidlof, P, *J. Biomech*, 41(5), 985-995, 2008.

SB³C2019
Summer Biomechanics, Bioengineering and Biotransport Conference
June 25 -28, Seven Springs, PA, USA

COMPUTATIONAL METHODOLOGY TO ESTIMATE RESISTANCE TO CEREBROSPINAL FLUID MOTION IN THE SPINAL CANAL FOR CHIARI PATIENTS WITH SPECIFIC AND NONSPECIFIC SYMPTOMS

Alaaddin Ibrahimy (1), Rafeeque A. Bhadelia (2), Abraham F. Bezuidenhout (2), Francis Loth (1,3)

(1) Department of Mechanical Engineering
The University of Akron
Akron, OH, USA

(2) Department of Radiology
Beth Israel Deaconess Medical Center
Boston, MA, USA

(3) Department of Biomedical Engineering
The University of Akron
Akron, OH, USA

INTRODUCTION

Chiari malformation type 1 (CMI) is a structural abnormality of cerebellum at the craniospinal junction, the part of brain which is primarily responsible for motor control. This malformation was radiologically described in 1985 by Aboulezz et al.[1] as a greater than 5 mm caudal displacement of the cerebellar tonsils below the foramen magnum (FM). However, cerebellar tonsillar position (CTP) does not always correlate with the symptom severity. The conundrum arises because some individuals who meet the MR imaging criteria are asymptomatic, while individuals with less than 5 mm CTP have CMI symptoms[2]. Hence, researchers have been seeking different measurement parameters to quantify CMI severity.

An alternative method to quantify the impact of CTP is longitudinal impedance (LI), a scalar parameter used to quantify impedance or fluid flow blockage per unit length of a conduit such as the spinal canal. In this study we used LI as a parameter to determine the cerebrospinal fluid (CSF) flow blockage at the foramen magnum (FM). CMI patients report different types of symptoms and these symptoms have been shown to be related to the percentage change in CSF stroke volume [3]. We hypothesized that LI will also be different for specific and nonspecific symptomatic CMI patients.

METHODS

Thirteen symptomatic CMI patients with a mean age of 38.6 ± 6.7 years and CTP greater than 5 mm were studied. Two board-certified neurosurgeons with more than fifteen years of experience in Chiari developed a grading scale for symptom severity and divided patients into two groups blinded to MR images: 1) Nonspecific CMI (NS-CMI) (5/13) – CMI patients with nonspecific symptoms like non-coughing-related or mild occasional cough-related headache, neck pain, dizziness, paresthesia, and/or dysphagia. 2) Specific-CMI (S-CMI) (8/13) – CMI patients with symptoms like severe cough-related headache, myelopathy, syringomyelia, and muscle atrophy, as described in a previous study [3].

The cervical spine of each patient was imaged with 3D T2-weighted MR imaging on a 3T scanner [Achieva; Philips Healthcare, Best, the Netherlands]. A semi-automatic active contour segmentation aka "Snake"[4] was used to segment the inner and outer boundaries of cervical spinal subarachnoid space (SAS) between FM and 6 cm caudal to FM using ITK-SNAP [UPenn, PA]. The boundaries were smoothed and reconstructed by two commercial software MeshLab [ISTI-CNR, Pisa, Italy] and Maya 2018 [Autodesk Inc, San Rafael, CA] and both ends (FM & caudal end) of the 3D model was extruded 4 cm to allow the flow to be nearly fully developed inside the model.

An unstructured tetrahedral mesh was created using two different Tetra/Mixed mesh methods (Robust {Octree} & Quick {Delaunay}) for computational fluid dynamics (CFD) using ICEM 18.2 [Ansys Inc, Canonsburg, PA]. Finite volume solver software Fluent [Ansys Inc, Canonsburg, PA] was utilized to run the fluid simulation, modelling CSF as water at 37 °C, 1.0 g/cm3, and $\mu = 0.001$ P. The 3D segmented model outer and inner surfaces were assumed to be a rigid wall with no slip condition applied. The caudal end of the model was treated as the INLET with an unsteady velocity inlet boundary condition (IBC), which represented cardiac cycle and CSF flow. The cranial end was treated as the OUTLET with a constant pressure boundary condition (CPBC). Each case was evaluated using two cycles to avoid cycle independency. Figure 1 shows the 3D model construction steps of the cervical spinal SAS.

The unsteady average pressure change with respect to time was evaluated as the difference between pressure at FM and 2.5 cm below the FM. The resulting pressure drop waveform and the flow waveform were used to calculate LI at each waveform harmonic for all subjects.

Poster Presentation #P202

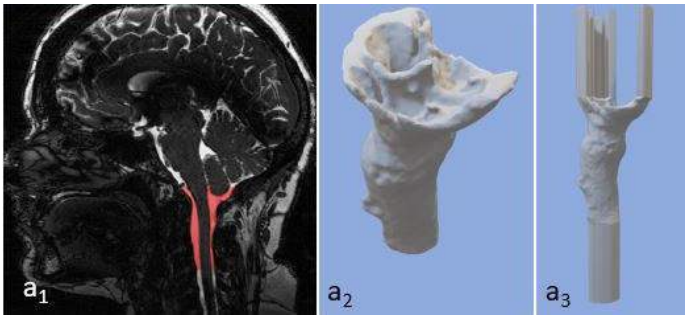

Figure 1: 3D model construction steps of cervical spinal SAS (a_1-MR Image, a_2-3D segmented model, a_3-3D model with extensions)

Each frequency component of the pressure and flow waveforms were extracted using fast Fourier transform. Next, LI was integrated from 1 to 8 Hz to obtain a characteristic value to compare each case (Equation 1). Statistical significance was evaluated as $p < 0.05$.

$$LI = \int_{1\ Hz}^{8\ Hz} \left| \frac{fft(\Delta P)}{fft(Q)} \right| df \quad (1)$$

RESULTS

Mean average values of integrated LI and CTP for S-CMI and NS-CMI subjects are listed in Table 1.

Table 1: Mean Average Integrated LI and CTP

	S-CMI	NS-CMI
Integrated LI (dynes/cm^5)	1056.7 ± 599.2	645.7 ± 484.6
Average CTP (mm)	17.5 ± 7.4	12.2 ± 6.2

Although statistical analysis revealed no significant difference between integrated LI magnitude for S-CMI and NS-CMI patients, the mean average values of S-CMI patients was 64% larger than NS-CMI patients (1056.7 ± 599.2 and 645.7 ± 484.6, $p = 0.2$ respectively).

Integrated LI is plotted as a function of CTP in Figure 2. NS-CMI patients have lower average integrated LI compared to S-CMI, and integrated LI for NS-CMI increased in a linear fashion with respect to CTP (r = 0.99, $p = 0.001$). However, the integrated LI for S-CMI patients is scattered and is not significantly correlated with CTP (r = -0.11, $p = 0.80$).

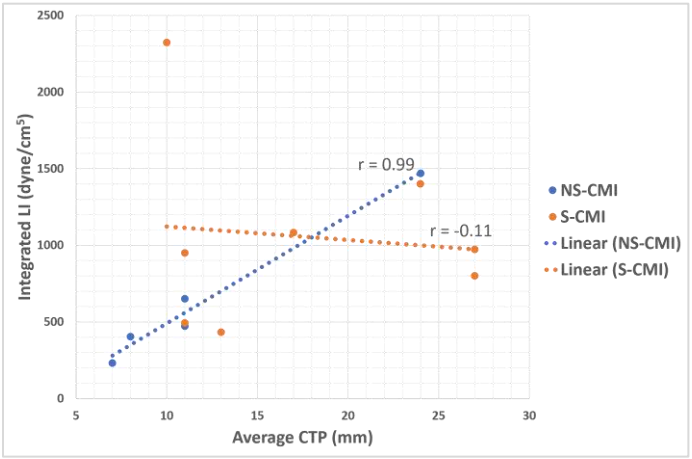

Figure 2: Integrated LI as a function of CTP

DISCUSSION

In this study, we evaluated integrated LI for two groups of symptomatic CMI patients. We found out that the average integrated LI for CMI patients with specific symptoms and objective finding, that is more severe disease, was 64% larger than those with nonspecific symptoms. However, it was not statistically significant. This might be due to small sample size and large standard deviation. In addition, Figure 2 shows an exception where the NS-CMI patient with CTP of 24 mm had an integrated LI magnitude of 1470 dyne/cm5, which is larger than the average integrated LI for S-CMI.

Furthermore, Figure 2 implies that larger CTP does not always follow the trend of greater resistance to flow. For example, the largest integrated LI (2323 dyne/cm^5) was measured for a S-CMI patient, who had a CTP of 10 mm. On the other hand, two S-CMI patients with the largest CTP of 27 mm had almost 3 times smaller integrated LI magnitudes (973 and 799 dyne/cm^5). Therefore, it indicates that the CTP may be a poor indicator of CSF flow impedance, which was also shown by Shaffer et al.[5]. This is expected since Bezuidenhout et al.[3] found no statistically significant relationship between CMI severity and anatomical measurements.

Several limitations were present in our study. First, the small sample size restricts us from recommending our method as an objective evaluation for disease severity in CMI until further patient data are collected in a larger study. However, this small group demonstrated statistically different LI values for the two groups (S-CMI and NS-CMI patients) and shows potential as a metric to assess CMI patients. Second, due to small sample size, the patients were only divided into two groups as was done by a previous study[3]. However, due to a wide range of symptoms and clinical findings, it would be better to divide the patients into more groups based on symptoms. If this methodology is to be used in future studies, these limitations must be considered and improved.

In conclusion, this study shows that LI appears to be a useful geometric parameter in quantifying CMI symptom severity by comparing S-CMI and NS-CMI patients. While these results support the prior studies that CTP may not be related neurological symptoms[3,5], these results also show that CTP does not necessarily have a linear relationship with CSF flow blockage. A larger and more controlled study population is needed to fully understand the clinical relevance, if any, of LI.

ACKNOWLEDGEMENTS

We acknowledge the support for this work from Conquer Chiari.

REFERENCES

[1] A. O. Aboulezz, K. Sartor, C. A. Geyer, and M. H. Gado, "Position of Cerebellar Tonsils in the Normal Population and in Patients with Chiari Malformation: A Quantitative Approach with MR Imaging," *J. Comput. Assist. Tomogr.*, vol. 9, no. 6, 1985.

[2] R. Voelker, "Chiari Conundrum : Researchers Tackle a Brain Puzzle for the 21st Century," vol. 301, no. 2, pp. 1–3, 2009.

[3] A. F. Bezuidenhout *et al.*, "Relationship between cough-associated changes in CSF flow and disease severity in chiari i malformation: An exploratory study using real-time MRI," *Am. J. Neuroradiol.*, vol. 39, no. 7, pp. 1267–1272, 2018.

[4] P. A. Yushkevich *et al.*, "User-guided 3D active contour segmentation of anatomical structures : Significantly improved efficiency and reliability," vol. 31, pp. 1116–1128, 2006.

[5] N. Shaffer, B. Martin, and F. Loth, "Cerebrospinal fluid hydrodynamics in type I Chiari malformation," *Neurol. Res.*, vol. 33, no. 3, pp. 247–260, 2011.

SB³C2019
Summer Biomechanics, Bioengineering and Biotransport Conference
June 25 -28, Seven Springs, PA, USA

MULTIPHASE FLUID DYNAMICS OF SHEAR-THINNING DROPLETS IN A MICROFLUIDIC FLOW-FOCUSING DEVICE

Ali Bozorgnezhad (1), Jason Gleghorn (1,2)

(1) Department of Mechanical Engineering
University of Delaware
Newark, Delaware, USA

(2) Department of Biomedical Engineering
University of Delaware
Newark, Delaware, USA

INTRODUCTION

Shear-thinning hydrogels are interesting materials because they can be used as injectable cellular and drug delivery platforms. Their unique chemistry often produces materials that self-heal and re-gel after removal of shear stress. In addition to being used to deliver biological molecules and cells within a bulk gel via injection [1–3], shear-thinning droplets have been proposed to be used in tissue engineering and multi-stage drug delivery applications [4–6].

Despite the fact that there are many microfluidic droplet studies and a significant focus on shear-thinning hydrogels in biological systems [7], the fluid dynamical mechanisms of non-Newtonian shear-thinning droplet formation have not been fully determined. Davidson and Cooper-white [8] studied the dynamics of shear-thinning pedant drop formation in air from a circular orifice. Qiue et al. [9] numerically studied formation of Newtonian droplets from an aperture in the continuous phase of a shear-thinning fluid. Ren et al. [10] numerically studied Newtonian droplet generation in a continuous phase of shear-thinning fluid in a co-flow device. These studies concluded that the viscosity of a shear-thinning fluid has a significant impact on the control of droplet size. Additional studies innovated on the computational methods used to study droplet formation in T-junctions using the Lattice Boltzmann Method (LBM) [11,12].

Whereas, much progress has been made in understanding droplet formation in T-junctions, there is a significant lack of understanding on the mechanisms of droplet formation of shear-thinning fluids in flow-focusing geometries. The flow focusing droplet generators are used to generate smaller droplets with higher control of size and frequency of droplet generation compared to two other passive methods of droplet generation including co-flows and cross-flow (T-junction) [13]. Furthermore, most of the investigations to date have examined droplet formation in systems with a non-Newtonian continuous phase rather than a shear-thinning dispersed phase. In the current study, we focus on the formation of shear-thinning droplets in a Newtonian continuous phase using a passive flow-focusing droplet generator. We modeled a shear-thinning hydrogel with a Power-law model and studied the effects of flow behavior index, flow consistency index and interfacial tension on the mechanism and mode of droplet generation.

METHODS

The VoF (Volume of Fluid) in ANSYS FLUENT 19.0 was used for simulation of multiphase flow of shear-thinning flow-focusing droplet generator shown in Fig. 1. Droplets were generated in silico using a flow focusing geometry and a Newtonian continuous phase (HFE-7500 oil) and non-Newtonian dispersed phase (shear-thinning hydrogel), Figure 1.

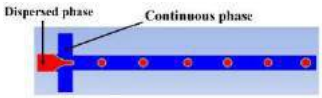

Figure 1: Flow focusing droplet generator

A Power-law model (equation 1) was used to describe the non-Newtonian shear-thinning hydrogel.

$$\tau = K(\dot{\gamma})^n \quad (1)$$

Where τ, $\dot{\gamma}$, K and n are shear stress, shear rate, flow consistency and flow behavior indices, respectively. The flow behavior index (n), is less than 1 for a shear-thinning fluid.

The continuum surface force (CSF) model developed by Brackbill et al. [14] was used to model the interfacial tension (σ). The interfacial

tension term was added as a source term to the momentum equation (equation 2).

$$\vec{F}_{Vol}=\sigma\left(\frac{\rho_d \kappa_d \nabla \alpha_d}{1/2\,(\rho_d+\rho_c)}\right) \quad (2)$$

Where α_d, ρ_d, ρ_c are the volume fraction of dispersed phase, density of dispersed phase and density of continuous phase, respectively. The surface curvature, κ_d, of the droplet defined as divergence of unit normal $\vec{n}_d$, given by equation 3.

$$\kappa_d = \nabla \cdot (\vec{n}_d) \quad (3)$$

Wall adhesion effects were considered by adjusting the surface curvature near the wall using Youngs method [15]. The boundary value for the inlets of continuous and dispersed phases were constant velocity and outflow. It is assumed that there is a no-slip condition at the walls.

RESULTS

We studied the effects of flow behavior index, flow consistency index and interfacial tension on the mechanism and mode of droplet generation (Table 1, 2 and 3, respectively). All simulation variables are held constant across these in silico studies except the parameter that is studied.

Table 1: Effect of *n* (*K*=0.01, σ=0.03 N/m)

n	Contour of multiphase flow	*n*	Contour of multiphase flow
0.75	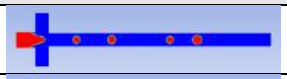	0.85	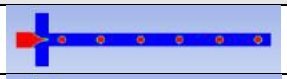
0.8	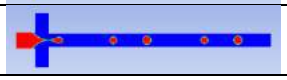	0.9	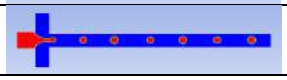

Table 2: Effect of *K* (*n*=0.9, σ=0.03 N/m)

K	Contour of multiphase flow	*K*	Contour of multiphase flow
0.005	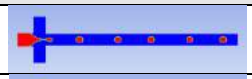	0.015	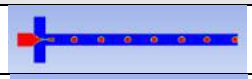
0.01	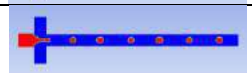	0.02	

Table 3: Effect of interfacial tension (*K*=0.01, *n*=0.9)

σ (N/m)	Contour of multiphase flow	σ (N/m)	Contour of multiphase flow
0.02	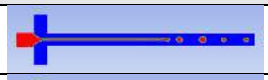	0.04	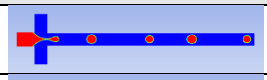
0.03	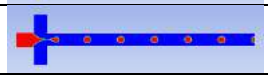	0.05	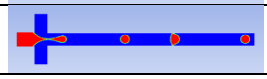

DISCUSSION

We investigated the role of the flow behavior index (*n*), the flow consistency index (*K*) and the role of interfacial tension (s) on droplet formation of a shear-thinning fluid in computational multiphase fluid dynamics studies. It is observable from Table 1 that at a fixed operating condition, the droplet generation mode changes from the bimodal (pairs of droplets with different sizes for *n* = 0.75 and 0.8) to monodispersed (*n* = 0.85 and 0.9) with increasing flow behavior index (*n*). Increasing this parameter also decreases droplet size; however, the mechanism of droplet formation is insensitive to *n* as for all values tested, a dripping mode of droplet formation was observed. In contrast, when the flow consistency index was varied, significant changes to the droplet generation mechanism and size polydispersity were observed. At low *K*, droplets are formed via dripping in a monodisperse size range, but at larger *K*, droplet generation is unstable, shifting to a polydisperse population owing to a change in droplet formation mechanism due to a shift into a jetting mode. Likewise, droplet size decreases with increasing *K*.

Alterations in the interfacial surface tension, σ, in our model have primary effects on the jetting to dripping transition and thus the overall polydispersity and mode (e.g. bimodal, monodisperse, etc). Low σ results in jetting of the shear-thinning material into the continuous oil phase with minimal droplets formed. When the interfacial tension is increased to the 0.03 N/m, then the droplet generation mechanism and mode are changed to dripping and-monodispersed. Interestingly, when the interfacial tension is increased (0.04 N/m), the droplet generation mode is changed to dripping-bi-modal. Further increases in σ (0.05 N/m), result in occasional plug flow of the droplet within the channel in a non-periodic manner due to an instability in droplet generation due to a consequent pressure drop. The droplet generation is shown to be very sensitive to the interfacial tension. Whereas we haven't included the addition of surfactants as are commonly used in these systems, these data do highlight the non-intuitive results of including surfactants in shear-thinning dispersed phase systems to prevent collescnec and aggregation of dispersed phase droplets. Surfactant use, which lowers interfacial surface tension, should be carefully used as lowering σ, can result in an unstable dripping-to-jetting transition and a polydispersed droplet population in shear-thinning droplet generators.

ACKNOWLEDGEMENTS

Funding for these studies was provided by the National Science Foundation (OIA1736030).

REFERENCES

[1] M. Guvendiren, H.D. Lu, J.A. Burdick, Soft Matter 8 (2012) 260–272.
[2] Q. Wang, J. Wang, Q. Lu, M.S. Detamore, C. Berkland, Biomaterials 31 (2010) 4980–4986.
[3] Z. Liu, P. Yao, RSC Adv. 5 (2015) 103292–103301.
[4] C. Loebel, C.B. Rodell, M.H. Chen, J.A. Burdick, Nat. Protoc. 12 (2017) 1521–1541.
[5] Y. Wang, L. Li, Y. Kotsuchibashi, S. Vshyvenko, Y. Liu, D. Hall, H. Zeng, R. Narain, ACS Biomater. Sci. Eng. 2 (2016) 2315–2323.
[6] L. Zhang, J. Wu, N. Sun, X. Zhang, L. Jiang, J. Mater. Chem. A 2 (2014) 7666–7668.
[7] M. Guvendiren, H.D. Lu, J.A. Burdick, Soft Matter 8 (2012) 260–272.
[8] M.R. Davidson, J.J. Cooper-White, Appl. Math. Model. 30 (2006) 1392–1405.
[9] D. Qiu, L. Silva, A.L. Tonkovich, R. Arora, Microfluid. Nanofluidics 8 (2010) 531–548.
[10] Y. Ren, Z. Liu, H.C. Shum, Lab Chip 15 (2015) 121–134.
[11] Y. Shi, G.H. Tang, Commun. Comput. Phys. 17 (2015) 1056–1072.
[12] S.G. Sontti, A. Atta, Chem. Eng. J. 330 (2017) 245–261.
[13] P. Zhu, L. Wang, Lab Chip 17 (2017) 34–75.
[14] J.. Brackbill, D.. Kothe, C. Zemach, J. Comput. Phys. 100 (1992) 335–354.
[15] D. Youngs, in: Num. Method Fluid Dyn., 1982, pp. 273–285.

SB^{3}C2019
Summer Biomechanics, Bioengineering and Biotransport Conference
June 25 -28, Seven Springs, PA, USA

FRACTURE PATTERNS IN CONCENTRATED 4-POINT BENDING OF THE OVINE FEMORA: THE EFFECTS OF AGE AND RATE OF LOADING

Patrick E. Vaughan (1,2), Feng Wei (1,2,3), Roger C. Haut (1,3)

(1) Orthopaedic Biomechanics Laboratories
Michigan State University
East Lansing, MI, USA

(2) Department of Biomedical Engineering
Michigan State University
East Lansing, MI, USA

(3) Department of Mechanical Engineering
Michigan State University
East Lansing, MI, USA

INTRODUCTION

The current literature associates bending failure of a long bone with butterfly fracture, in which fracture initiates transversely at the tensile side of a bent bone and branches in a Y-shape as it propagates toward the compression side, resulting in a wedge fragment known as a tension wedge [1]. Thus, the orientation of the resulting wedge fragment is often considered diagnostic of impact direction [2]. However, numerous experimental studies indicate that bending of a long bone does not always produce butterfly fracture, and the produced wedge fragments also vary in tension or compression. Martens et al. [3] report that 4-point bending of posterior-loaded human femora produces compression wedge fracture in 85% specimens and oblique fracture in 15% specimens. In 3-point bending experiments using ovine femora, Reber and Simmons [4] report butterfly fractures in approximately half the sample, in which 60% are tension wedges and 40% are compression wedges. Recently, a study from our laboratory using 3-point bending on unembalmed human femora shows the complete fracture types being transverse, oblique, and comminuted fractures, with patterns of the incomplete fracture being comparable to a tension wedge [5].

While long bone fractures are a common injury in adults as well as in the pediatric population and the rate of loading has also been shown to significantly influence fracture morphology [6], the effects of age and rate of loading on failure patterns of long bone fracture due to bending remain largely unknown. In addition, the application of the standard 3-point bending configuration commonly used in studies investigating bending failure of a long bone may put restrictions on the evaluation of fracture data due to potential local stress concentrations that may form under the central loading point, decreasing the overall bending strength of the bone [3].

The purpose of the current study was to perform controlled, concentrated 4-point bending (similar to that of Martens et al. [3]) impact experiments on skeletally immature and mature fresh ovine femora with two different rates of loading. It was hypothesized that fracture patterns, as well as mechanical failure parameters, would be different between the two age groups and between the two rates of loading.

METHODS

Skeletally immature (1-7 days old, n=20) and mature (1-2 years old, n=20) ovine femora were collected from animals that died of natural causes in a local farm. An approved IACUC exemption was obtained for the current study. The whole femoral bone was dissected, cleaned of soft tissues, wrapped in saline-soaked gauze, and frozen at -20°C. The femoral specimens were thawed overnight at room temperature prior to testing. All tests were performed within 24 hours of thawing.

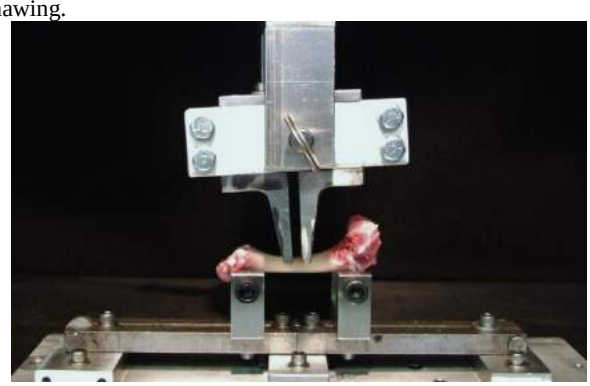

Figure 1: Experimental setup with a femur in 4-point bending.

Poster Presentation #P204

A custom-built bending fixture was utilized to load the specimen in a servo-hydraulic testing machine (Instron, Norwood, MA). Concentrated 4-point bending, similar to that used in Martens et al. [3], was applied to specimens through a pin-supported fulcrum that uniformly loaded the asymmetric bone surface throughout failure (Figure 1). The two inner supports were set to 10% of the femoral length, while the outer supports were set to 60% of the length. All femora were loaded posteriorly, assuming no difference in fracture patterns between anterior and posterior impacts [5]. The anterior surface of the femur was rested on free-rolling pin supports.

In each age group, unpaired specimens were randomly separated into a low rate group (test in 2 Hz or 0.25 s to peak, n=10) and a high rate group (test in 10 Hz or 0.05 s to peak, n=10). After a preload of 20 N was applied for 5 s, bending impacts were performed in displacement-control, with a maximum displacement set to 5 mm. For each impact the force-displacement data were collected by a personal computer via a load cell (Interface, Scottsdale, AZ). Failure force of each specimen was documented and the slope of the force-displacement curve was defined as the bending stiffness. Following impact, bone fragments were collected and any remaining adhering soft tissues were removed using heat maceration techniques. Each specimen was subsequently reconstructed from its constituent bone fragments to allow for photographic documentation of fracture outlines. Medial and lateral views were recorded to account for potential asymmetry.

Two-way ANOVA with Tukey post hoc test in Minitab (State College, PA) was used to compare the differences in failure force and bending stiffness between the immature and mature specimens (factor one) and between low and high rates of loading (factor two), with $p<0.05$ considered significant.

RESULTS

Force-displacement curves showed a linear response of each bone with a sudden drop in load indicating an abrupt fracture in all cases. While failure forces in the low rate tests were not statistically different from those in the high rate tests for either the immature (585.1±187.7 N versus 586.8±117.7 N, respectively, $p=0.995$) or the mature bones (4376.4±1169.0 N versus 3909.1±1348.8 N, respectively, $p=0.958$), it required significantly higher force to fracture the mature bone than that required to fracture the immature bone in either rate of loading ($p<0.001$). Similarly, bending stiffness was significantly higher ($p<0.001$) in the mature bones than that in the immature ones for either rate of loading (1892.0±333.4 N/mm versus 180.2±97.2 N/mm for the low rate and 1843.0±692.5 N/mm versus 208.3±66.6 N/mm for the high rate of loading). No statistical differences in bending stiffness were observed between the low and high rate of loading for either age group.

Upon visual inspection of the gross fracture patterns of the femora in both the medial (M) and lateral (L) views, it became clear that the fracture patterns under a concentrated 4-point bending scenario were dependent on both the age of development and the loading rate. Specifically, the immature bone produced transverse (4/10 (40% M), 8/10 (80% L)) and partial butterfly fractures (2/10 (20% M), 2/10 (20% L)) at the low loading rate (Figure 2, left), while the mature bone produced compression wedges (15/20 (75% M), 15/20 (75% L)) and oblique fractures (3/20 (15% M), 2/20 (10% L)) of the proximal third of the bone at both low and high rates of loading (Figure 2, right). Interestingly, the immature bones at the high loading rate produced variant fractures (6/10 (60% M), 6/10 (60% L)) that transitioned from a partial tension wedge to a partial compression wedge, or a combined tension and compression wedge (Figure 2, left). In mature specimens loaded at the high rate, a unique 2-tailed compression wedge pattern was observed (3/10 (30% M), 1/10 (10% L)) (Figure 2, bottom right).

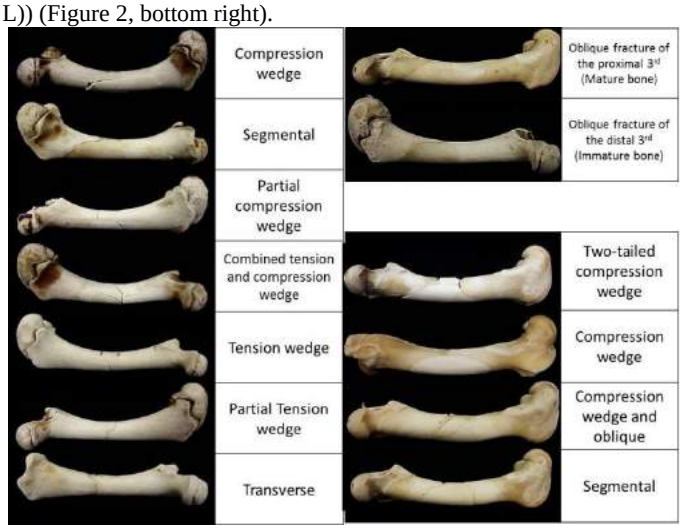

Figure 2: Typical fracture patterns in the immature (left) and mature (bottom right) bones, and oblique fractures (top right).

DISCUSSION

The results of the current study demonstrated that for the mature femora, compression wedge fracture can be generated consistently under a concentrated 4-point bending configuration, further supporting the findings of Martens et al. [3] where a compression wedge is produced in 85% adult human femora due to 4-point bending. It is therefore suggested that the traditionally accepted determination of impact direction in a long bone based on the orientation of the produced wedge fragment, i.e. tension versus compression wedge, may be questionable. The concentrated 4-point bending configuration used in the current study, in addition to being more appropriate than a 3-point bending configuration from a mechanics point of view [3], may also be more forensically relevant, as impacts involving car bumpers or even flat plates with proper dimensions might be more accurately simulated by this 4-point than the traditional 3-point loading configuration. This may also explain the variations in long bone fracture patterns observed in various experimental studies using the traditional 3-point bending configuration [4,5].

While in the current study the effect of loading rate on the mechanical failure parameters (failure force and bending stiffness) was not found to be significant, the results on fracture patterns showed that the immature femora were rate sensitive. At the low loading rate, immature femora primarily failed in transverse fractures and partial tension wedge fractures, while at the high rate of loading a combined tension and compression wedge fracture emerged in immature bones.

The current study has shown that age and rate of loading can play important roles in the ovine femoral fracture patterns. The forensic community and medicolegal professionals should take cautions in interpreting impact direction from long bone fracture patterns.

ACKNOWLEDGEMENTS

The authors thank Mr. Clifford Beckett for technical assistance.

REFERENCES

[1] Kress, TA, *University of Tennessee* (dissertation), 1996.
[2] Emanovsky, P, In: *Skeletal Trauma Analysis*, Wiley, 156-166, 2015.
[3] Martens, M et al., *J Biomech*, 19:443-454, 1986.
[4] Reber, SL and Simmons, T, *J Forensic Sci*, 60:1401-1411, 2015.
[5] Isa, MI et al., *J Forensic Sci*, 63:38-46, 2018.
[6] Vaughan, PE et al., *J Clin Orthop Trauma* (2018), In Press.

SB^{3}C2019
Summer Biomechanics, Bioengineering and Biotransport Conference
June 25 -28, Seven Springs, PA, USA

THE IMPORTANCE OF SKULL MORPHOLOGY IN REMOTE BLUNT IMPACT INDUCED FRACTURE INITIATION

Paul J. Snyder (1,2,3), Steven A. Rundell (2), Todd W. Fenton (4) Roger C. Haut (1), Feng Wei (1,3)

(1) Orthopaedic Biomechanics Laboratories
Michigan State University
East Lansing, MI, USA

(2) Explico Engineering Company
Novi, MI, USA

(3) Department of Biomedical Engineering
Michigan State University
East Lansing, MI, USA

(4) Department of Anthropology
Michigan State University
East Lansing, MI, USA

INTRODUCTION

Forensic evaluations of blunt force trauma to the human head have traditionally relied on investigator experience and comparisons with case studies, rather than on controlled experimental data. Experimental and computational head impact research typically focuses on fracture tolerance, skull force-deflection response under quasi-static and dynamic loads, and the effects of blunt head trauma on the tissues of the brain, while the patterns of cranial fracture resulting from head trauma have yet to be investigated in depth [1-3].

Recent research from our group has investigated the influence of multiple extrinsic impact variables on initiation and propagation of cranial fracture, such as impactor geometry, energy of impact, number of impacts, and location of impact [4]. While the results generally indicate that extrinsic factors play a significant role in determining the final fracture pattern, they unfortunately do not fully explain the variability between skulls. These types of studies do not account for the potential significance of the skull's intrinsic properties, i.e. skull morphology, on the resulting fracture pattern.

The objective of the current study was to investigate the comparative contribution of intrinsic skull properties, such as skull morphology, and extrinsic impact properties, such as impactor geometry, to the prediction of remote fracture site initiation. It was hypothesized that areas of remote high tensile stress would correspond to locations of remote fracture initiation observed experimentally, and that the magnitude and pattern of tensile stress contours would be affected by skull morphology.

METHODS

Thirty-three unembalmed, adult male human crania were included in this study. Twenty-four impacts were administered laterally towards the anterior/posterior center of the parietal bone, superior to the temporoparietal suture, while nine impacts were administered superiorolaterally towards the geometric center of the parietal bone. Impacting implements included a flat 3-inch diameter implement, a flat 1-inch diameter implement, a cylindrical curved 2.5-inch diameter implement, a 2-inch diameter hemisphere implement, and a 1-inch edge length square implement. A high-speed 10,000 fps camera captured video of fracture initiation and propagation throughout each impact test.

Each specimen underwent a pre-impact high-resolution computed tomography (CT) scan (GE 750HD; 120 kVp; 125 mAs; 0.625-mm slice thickness; 0.49 mm pixels; 512x512 matrix), from which 3D finite element models of the specimens were created. Wrapping operations were performed to eliminate cancellous cavities between the interior and exterior cortical layers of the skull cranium. A thickness analysis was performed to evaluate the average thickness of each specimen in the region enclosed by the sphenoid to the coronal suture, sagittal suture, occipital suture, and the region superior to the mastoid, external auditory meatus, and zygomatic arch on the ipsilateral side of impact.

Three specimens, representing a wide range of average skull thicknesses (thin, average, and thick) were meshed using tetrahedral elements. Cortical bone material properties were assigned to the elements using a linear elastic material law. Laterally applied dynamic impacts were simulated for each specimen using the cylindrical 2.5-inch diameter, flat 3-inch diameter, and flat 1-inch diameter implements. The speed, mass, and orientation of the impacting implement with respect to the anatomical features of the skull were held constant in each simulation. The impacting mass was 6.349 kg and the impacting velocity was 6.455 m/s for all simulations. Signed von Mises stresses at maximum impactor engagement were generated and compared for each test setup to the experimental results.

Poster Presentation #P205

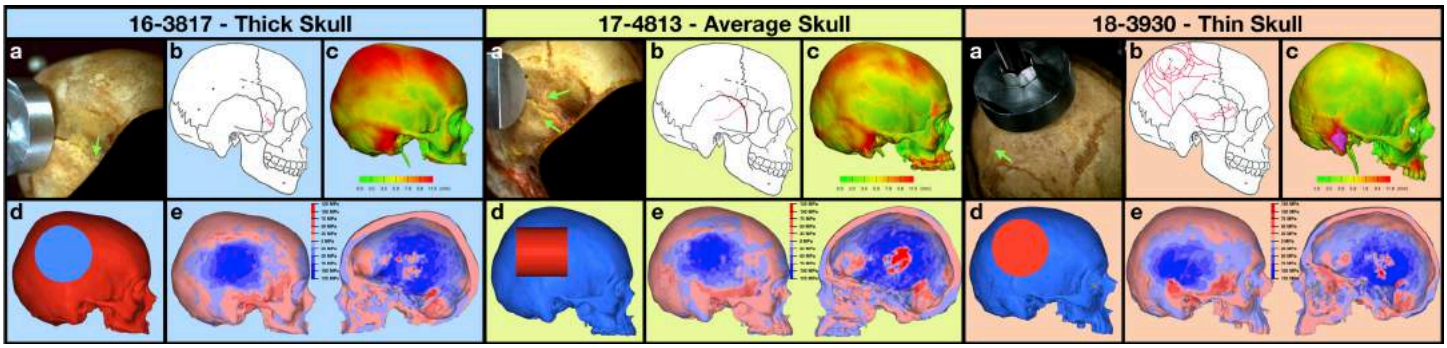

Figure 1: (a) Fracture initiation during experimental impact, (b) Resulting fracture pattern after experimental impact, (c) Thickness map of specimen, (d) Impactor orientation in computational simulation, (e) Peak signed von Mises stress distribution in computational simulation.

RESULTS

Thickness analyses on all thirty-three specimens yielded a maximum average thickness of 9.6 mm, a mean average thickness of 7.0 mm (SD ± 0.9 mm), and a minimum average thickness of 5.1 mm. The thickest specimen contained a significant defect on the contralateral side of the skull, and was excluded from being chosen for mesh model creation in favor of the second thickest specimen (8.6 mm). Specimens 16-3817, 17-4813, and 18-3930 represent the thickest, average, and thinnest computational models used in the simulation, respectively. Thickness maps of the computational models are shown in Figure 1c.

Impactor orientation and results of selected dynamic simulations are shown in Figure 1d and 1e. Red shaded areas represent regions under tensile stress, while blue shaded areas represent regions under compressive stress (Figure 1e). Peak tensile stress concentrations remote to the origin of impact on the exterior of the skull tended to occur in the area of the sphenoid near the zygoma in all specimens, independent of impacting implement. Extension of this peak tensile stress region occurred posteriorly superior to the zygomatic arch, external auditory meatus, and mastoid. The magnitude and span of stress in these regions tended to increase as the overall thickness of the skull decreased. Peak tensile stress concentrations remote to the origin of impact on the interior of the skull tended to occur in the area of the petrous ridge.

High-speed camera footage of the experimental fracture data confirmed the identified high tensile stress concentration regions on the exterior of the skull as common sites of remote fracture initiation, as shown in Figure 1a. The resulting fracture pattern for each specimen is shown in Figure 1b.

DISCUSSION

The hypothesis that localized geometric features of the skull contribute to the generation of remote peak tensile stress concentrations was confirmed. Independent of impacting implement, peak tensile stresses remote to the location of impact occurred in regions of geometric transition or discontinuity. Gross skull morphologies, such as the transition from the convex frontal, parietal, and squamous temporal bone to the concavity of the sphenozygomatic suture, the relative reduced thickness in the sphenozygomatic region, the presence of a hole in the external auditory meatus, and the transition from an area of increased thickness near the mastoid to an area of reduced thickness superior in the temporal squama, are thought to be responsible for these peak tensile stresses concentrations on the exterior of the skull. Similarly, the crease geometry of the petrous ridge is thought to be responsible for peak tensile stresses on the interior of the skull.

While the magnitude and span of the tensile stress concentrations on the exterior of the skull tended to increase as the thickness of the skull decreased, the magnitude and span of the tensile stresses on the interior of the skull did not follow this trend. The magnitude and span of the tensile stress on the petrous ridge of the thinnest specimen appeared to be smaller than those of the thickest specimen. One possible explanation for this is the geometric prominence of the petrous ridge, which appears less prominent in the thin specimen as compared to the thick specimen.

Results of these analyses indicate that, in the absence of additional fracture pattern information near the identified or suspected location of impact, impacting implement identification may be difficult to achieve given that intrinsic skull morphology tends to drive the initiation sites of remote fractures. This study identifies the likely locations of remote fracture initiation based on skull morphology, but does not guarantee fracture will occur in that location, especially if fracture initiation occurs local to the point of impact. Experimental results have demonstrated initiation and propagation of fracture from the location of impact in some cases.

Limitations of the current model include the absence of varying properties for the three-layer composition of the skull, and consideration of the subject-specific intrinsic density distribution in the CT scans. Further refinements of the computational model may be required to explain the differences in fracture patterns observed experimentally local to the point of impact due to extrinsic impactor shape properties. Failure criteria and transient response of the computational model to developing fractures are necessary to continue to model the development of fracture patterns after initiation.

ACKNOWLEDGEMENTS

The study was supported by an NIJ grant 2015-DN-BX-K013 and Explico Engineering Company. The authors thank Mr. Clifford Beckett for technical assistance in the experiments.

REFERENCES

[1] Yoganandan, N et al., *J Neurotrauma*, 12(4):659-68.
[2] Nahum, A et al., *SAE Technical Paper*, 770922.
[3] Mao, H et al., *J Biomech Eng.*, 135(11):111002.
[4] Isa, M et al., *Forensic Sci Int*, In Review.

SB^{3}C2019
Summer Biomechanics, Bioengineering and Biotransport Conference
June 25 -28, Seven Springs, PA, USA

SUBJECT-SPECIFIC MADYMO ANALYSIS OF A LOW SPEED REAR-END COLLISION

D. Sproule (1), S. Rossman (1), P. Snyder (1), K. Button (1), B. Weaver (1), S. Rundell (1)

(1) Explico Engineering Co.
Novi, Michigan, USA

INTRODUCTION

The available kinematic and kinetic data with respect to low speed rear-end collisions are limited to volunteer, cadaver, and anthropomorphic test device (ATD) tests. Biomechanical analyses involving these collisions can be made more robust through the consideration of the occupant's specific anthropometry, interior vehicle geometry, and occupant position. The MAthematical Dynamic Modeling (MADYMO) software suite can be utilized to conduct such subject-specific analyses. MADYMO is widely used in automotive safety, research, and forensic engineering for evaluating occupant dynamics utilizing multi-body, finite element, and computational fluid dynamic solvers.

To demonstrate the presented methods, a belted, female occupant involved in a rear-end collision while driving a 2004 Toyota Highlander was evaluated. Specifically, the collision was evaluated to determine the potential for biomechanically causing intervertebral disc herniations. Previous biomechanical studies have demonstrated that axial compression is imperative to the causation of, or significant contribution to, a traumatic disc herniation [1,2]. Therefore, the objective of the current study was to outline a methodology for conducting a subject-specific analysis of a low speed rear-end collision in the evaluation of spinal compression. It was predicted that the results from the current study would be consistent with previously published rear-end crash data.

METHODS

The Event Data Recorder (EDR) of the Toyota was imaged from the Airbag Control Module (ACM) directly through the Diagnostic Link Controller (DLC) utilizing Bosch's Crash Data Retrieval (CDR) software. One event was recovered during retrieval, and was determined to be consistent with the subject collision. The EDR reported a maximum longitudinal change in velocity (Delta-V) of 9.0 kph (5.6 mph) with a peak acceleration of 3.5 g's over a pulse duration of approximately 120 ms (Figure 1).

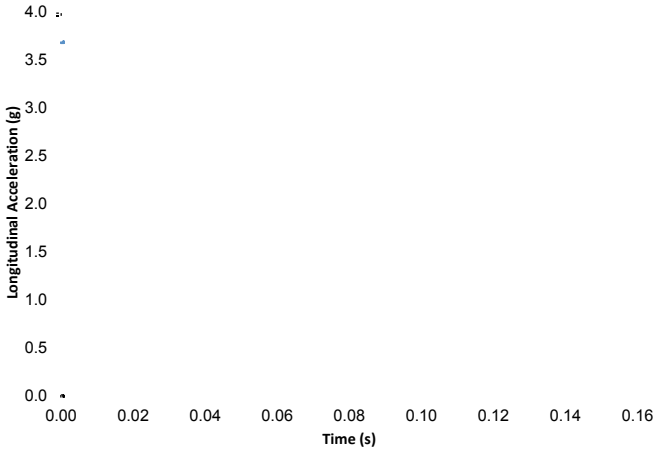

Figure 1: Collision pulse downloaded from the subject vehicle

The subject driver, demonstrating her body positioning in the driver seat of the subject vehicle, was imaged using a Faro Focus 3D laser scanner. The MADYMO seat model was created using a series of ellipsoids connected by joints to geometrically match the 3D laser scan data (Figure 2). The contact stiffness characteristics and seatback joint rotational characteristics were applied based on prior data from static tests on mechanical car seats [3]. MADYMO provides ellipsoid dummy models that have the ability to be scaled to specified

anthropometry. For the subject analysis, a Hybrid III 5th percentile dummy was scaled based on the height and weight of the subject female driver. The scaled dummy was aligned with the 3D laser scan data to match the position demonstrated by the subject, and belted using a three-point harness utilizing multi-body elements positioned to correspond with the 3D laser scan data (Figure 2).

The collision pulse retrieved from the EDR of the subject vehicle was applied to the vehicle system in MADYMO. For the subject analysis, linear head acceleration, upper cervical spine compression, and lower lumbar spine compression were recorded and filtered according to SAE J211 specifications.

For comparison, an analysis was conducted utilizing previously published volunteer and dummy low speed rear-end crash data evaluating the variables of interest. The Delta-V's in these tests ranged from 1 to 24.4 kph (0.6 – 15 mph). A linear interpolation of the datasets was performed to determine generalized results applicable to the subject collision [4-9]. Interpolated spinal loads were appropriately scaled to the occupants weight and added to static loads determined from anthropomorphic databases and simulation software (MICH3DSSP).

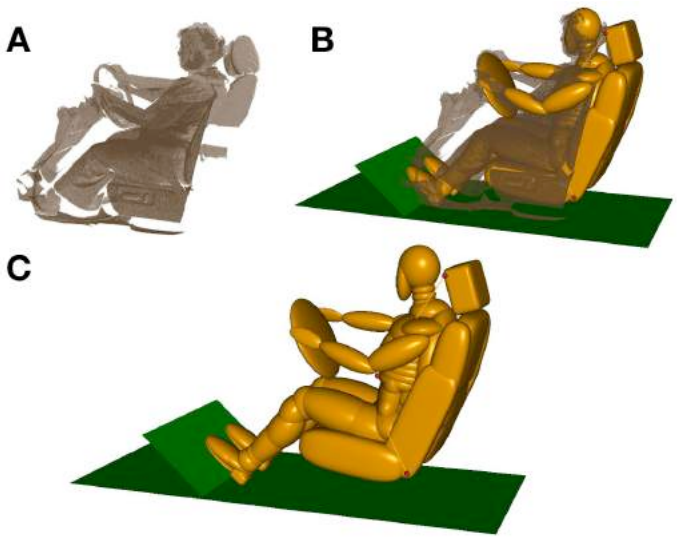

Figure 2: (A) 3D scan data of seat and subject, (B) model built to match 3D scan data, and (C) final model.

RESULTS

The occupant kinematics of the subject simulation were consistent with kinematics demonstrated in previously conducted volunteer, cadaver, and dummy tests (Figure 3). Specifically, the occupant remained stationary as the seat was accelerated forward. The occupant therefore moved rearward relative to the seat into the seatback and head restraint. The peak linear head acceleration was 8.4 g's, the peak cervical spine compression was 71.2 N, and the peak lumbar spine compression was 457.9 N.

A correlation analysis of 43 volunteer tests and 8 dummy tests indicated a strong linear relationship between Delta-V and linear head acceleration (R^2 = 0.87). Furthermore, select dummy tests exhibited correlation between Delta-V and both cervical spine compression (R^2 = 0.95) and lumbar spine compression (R^2 = 0.79). Based on the linear interpolations the subject Delta-V would produce a linear head acceleration of 8.4 g's, a cervical spine compression of 69.0 N, and a lumbar spine compression of 547.3 N.

Figure 3: Occupant position (A) pre-impact, (B) impact, and (C) rebound.

DISCUSSION

The results from the present study indicate that MADYMO can be utilized to evaluate collisions with a subject-specific analysis. The results from the simulation were consistent with previously conducted low speed rear-end crash test data. These data indicated that the use of a subject-specific model accurately predicted results of a generalized rear-end collision. Furthermore, the effects of occupant and vehicle specific geometries did not have a significant effect on the metrics evaluated, i.e. spinal compression and linear head acceleration. This indicates that MADYMO is a useful tool when predicting results of real-world collisions. These data also provide the methodological framework for evaluating real-world collisions that may be less characteristic of generalized testing performed for collinear rear-end collisions with a normally seated driver.

The present study evaluated a Hybrid III 5th percentile dummy scaled using anthropomorphic databases. Scaling can be improved through scaling factors specific to the occupant in place of the scaling algorithms determined through the anthropomorphic databases. Additionally, MADYMO offers scalable human models in conjunction with the scalable dummy models used in the present study. The MADYMO manual indicates that the human models have improved biofidelity in comparison to the dummy models and can be utilized in a wider range of loading conditions [10]. Future work will utilize the human body models and evaluate in comparison with the dummy models. Furthermore, these outlined methodologies will continue to be developed to analyze a wide range of occupant anthropometries, body positions, and interior vehicle geometry.

REFERENCES

[1] Adams, M., Hutton, W., *Spine,* 10:524-31, 1985.
[2] Adams, M., Hutton, W., *Int Orthopaedics,* 6:249-53, 1982.
[3] Erikkson, L. *Traf Inj Prev,* 3:75-87, 2002.
[4] Welch, T., et al, *SAE 2010-01-1031.*
[5] Erickson, M., *SAE 2012-01-0570.*
[6] West, D., et al, Acc Recon Journal, May/June:22-26, 1993.
[7] Goodwin, V., et al, *SAE 1999-01-0442.*
[8] Fugger, T., et al, *SAE 2003-01-0158.*
[9] Ruberte, L., et al, *Collision Magazine, 11(1):32-45, 2016.*
[10] *MADYMO Human Body Models Release 7.7*. TASS Int. 2017

SB³C2019
Summer Biomechanics, Bioengineering and Biotransport Conference
June 25 -28, Seven Springs, PA, USA

DEVELOPMENT OF A PORTABLE SUCTION DEVICE FOR COMBAT MEDICS

F. Akhter (1), A. Schoppe (2), O. Navarro (1), C. Carroll (1), P. Jain (2), R. Pescador (1), R. De Lorenzo (3), B. D. Adams (3), Y. Feng (1), R. L. Hood (1)

(1) Department of Mechanical Engineering
University of Texas at San Antonio
San Antonio, Texas, United States

(2) Department of Biomedical Engineering
University of Texas at San Antonio
San Antonio, Texas, United States

(3) Department of Emergency Medicine
University of Texas Health Science Center at San Antonio
San Antonio, Texas, United States

INTRODUCTION

Airway obstruction and compromise is the second leading cause of preventable battlefield death (77 out of 976 preventable battlefield deaths studied) [1], a fact attributed to unavailability of sufficiently powerful portable suction systems, insufficient training of combat medics, and improper use of airway securement devices, among others [2]. As such, airway securement is one of the foremost challenges for combat medics responding to traumatic injury [3]. This lifesaving intervention involves quickly assessing the severity of airway injury, which is immediately followed by insertion of a suction catheter in the oropharyngeal area to evacuate any accumulated obstacles, which may include saliva, vomit, and blood. Process improvements directed toward pre-hospital care can improve survival rate from combat injury. Emergency care facilities and field hospitals are equipped with powerful suction systems which are non-portable, bulky, and heavy to carry manually. As a combat medic's kit routinely weighs in excess of 45 kg, this is not a practical device for them to manage [4]. There are different types of portable suction devices available on the market, including both manually powered and automatic systems. The former is frequently unable to remove sufficient material in a timely manner, while the latter are more powerful, but too cumbersome for the combat medic to carry in their kits [4]. Also, these devices are orientation dependent i.e. these will stop working if they are put upside down or in sideways as the hydrophobic filter inside will get clogged by the back flow of liquid [5]. Market assessments and surveys conducted by this group have demonstrated that combat medics require a light weight, compact, efficient, and reliable portable suction alternative for the battlefield [6, 7]. Discussion with emergency physicians and combat medics revealed the design specifications i.e. size (30 x 10 x 10 cm), weight (<1 kg), vacuum pressure (450-550 mmHg), fluid flowrate (16 ml/s) etc. Also, the device should work independent of its position on the ground. This research describes the initial design, fabrication, and characterization of a suction platform focused on bridging this gap in combat casualty care. Characterization experiments include flowrate testing, solid particle lift tests, comparative analysis of the flowrate between commercially available suction tips, and evaluation of design criteria for maximum flowrate and minimum obstruction resistance at a given vacuum pressure.

METHODS

The prototype was designed and fabricated in line with the derived specifications. This orientation independent prototype includes three major sections: a compact, rectangular, and durable housing, a canister, and a suction pipe with catheter. The housing stores the diaphragm type Parker suction pump which is connected to the cylindrical canister (1L) by a hydrophobic filter (0.2 micron) to protect the pump from getting contaminated by the backflow of liquid. The canister is supported by 2 sets of ball bearing at two ends for rotating freely irrespective of the position of the device on the ground. The other end of the canister is connected to the suction pipe (10 mm inner diameter) and catheter (Yankauer suction tip, model#298, Busse Hospital

Disposables, Hauppauge, NY). The Arduino Uno circuit board was used to control the pump-motor. The user can regulate the motor speed as per requirement through a potentiometer attached to the main housing. An overdrive switch has also been integrated with the assembly to run the pump at full capacity whenever necessary. The rechargeable 12 V battery can provide power for approximately 3 h of continuous use. This device was utilized to evaluate the maximum vacuum pressure and flowrate while evacuating simulated vomitus liquid prepared by mixing 1L of distilled water with 10g Xanthan gum and 100 g of 1 mm diameter glass beads. Then five different commercially available suction catheters: Yankauer (4 mm inlet diameter), Wide Yank (11 mm), Flange (3.8 mm), Argyle (3.2 mm), and Poole (3 mm) were compared in terms of suction flowrate while evacuating water (baseline), blood phantom, and simulated vomit. The blood phantom solution was prepared by mixing 276 ml of glycerol into 1224 ml of distilled water [8]. The dynamic viscosity of water, blood phantom, and vomitus solution was measured as 0.89, 3.68, 22.71 mPa.s respectively at room temperature of 22°C (viscosity measured with DV1 digital viscometer, AMETEK Brookfield, Middleborough, MA). Finally, a solid particle lift test was carried out using the 10 mm diameter suction pipe only without the catheter. The device was used to lift three sets of stainless steel spheres (set 1: 6 mm diameter, 0.9 g; set 2: 8 mm diameter, 2.7g, set 3: 14 mm diameter, 11.3g) submerged in the water.

RESULTS

Figure 1.A depicts the orientation independent design which is 30 x 15 x 15 cm and weighs 1.2 kg with a 1L waste canister and 10 mm (inner diameter) suction tube. Performance tests revealed the device generated a maximum of 560 and 650 mmHg vacuum pressure with and without the hydrophobic filter, respectively. The suction flow rate of vomitous solution without the filter was 13.5 ml/sec, while inclusion of the filter reduced this to 11.7 ml/sec. In next test, the Wide Yank demonstrated higher flow rates than Yankauer, whereas the Poole demonstrated lower flow rates than Yankauer for each of the fluid solutions which revealed that bigger diameter suction catheter without sharp bends generate higher suction flowrate. Solid particles lift test demonstrated that the device could evacuate submerged metal spheres of set 1 and set 2. The third set of spheres (14 mm diameter, 11.3 g) were larger than the tubing's diameter (10 mm). However, the tubing could lift the largest spheres while they were submerged, but released once being lifted into the air.

DISCUSSION

Structurally, the present airway suction device achieves a smaller footprint than commercially available devices, such as Laerdal Compact Suction Unit® 4 (LCSU4, 800 ml) that measures 24 x 20 x 24 cm and weighs 1.95 kg [5]. The max vacuum pressure, and flowrate test of simulated vomit also support its achievement of clinical reliability and durability. The drop in maximum vacuum pressure and flowrate observed during the test can be reduced in the future through replacing the 0.2 µm filter, which is more restrictive than necessary, with a larger pore size alternative. Another solution would be utilization of a liquid compatible vacuum pump, eliminating the need for the filter altogether. Future work will focus on carrying out a drop test of the device to evaluate the durability and utilizing alternate design to minimize the footprint while enhancing the maximum vacuum pressure.

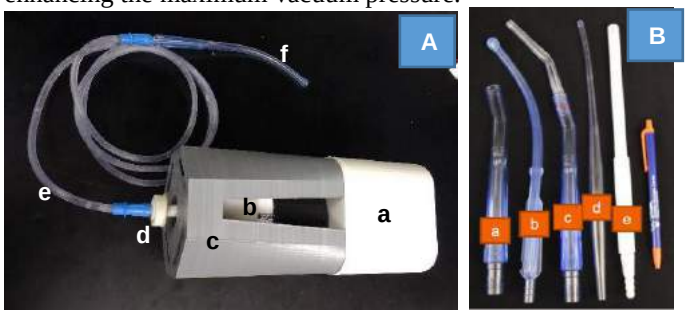

Figure 1: A. Combat airway suction device (a) housing for pump/motor, (b) cylindrical canister (c) outer cover of canister, (d) bearing support of canister, (e) suction tube, (f) Yankauer catheter; B. Five different types of suction tips used to compare fluid flow rate (a) Wide Yank, (b) Yankauer, (c) Flange Type, (d) Argyle, (e) Poole

ACKNOWLEDGEMENTS

The funding from NSF I-Corps Program, the Office of Commercialization at the University of Texas at San Antonio, San Antonio Life Science Institute, and the University of Texas Health Science Center are greatly appreciated.

REFERENCES

[1] Eastridge, B.J. et al, *"Death on the battlefield (2001-2011): Implications for the future of combat casualty care"* J Trauma & Acute Care Surg, 73(6), S431-S437, 2012.

[2] Peake, J. B., *"Beyond the Purple Heart--continuity of care for the wounded in Iraq"*, N Engl J Med, 352(3), pp. 219-222, 2005

[3] Prokakis, C., Koletsis, E. N., Dedeilias, P., Fligou, F., Filos, K., and Dougenis, D., *"Airway trauma: a review on epidemiology, mechanisms of injury, diagnosis and treatment"*, J Cardiothorac Surg, 9, p. 117, 2014

[4] Cloonan, C. C., *"Don't just do something, stand there!": to teach or not to teach, that is the question--intravenous fluid resuscitation training for Combat Lifesavers*, J Trauma., 54 (5 Suppl):S20-5, 2003

[5] http://www.laerdal.com/us/doc/2115/Laerdal-Compact-Suction-Unit-4-LCSU-4#/Specifications

[6] De Lorenzo, R. A. et al., *"Summary of Findings and Recommendations for Suction Devices for Management of Prehospital Combat Casualty Care Injuries"*, Defense Technical Information Center (DTIC), 2017

[7] Committee on Tactical Combat Casualty Care (TCCC), "*Tactical Combat Casualty Care Guidelines for Medical Personnel*," 2017

[8] Temptime, *"Simulated Blood Products: 10% Glycerol in water may not be 'One Size Fits All."*, 2012

SB^{3}C2019
Summer Biomechanics, Bioengineering and Biotransport Conference
June 25 -28, Seven Springs, PA, USA

FINITE ELEMENT MODEL OF NEONATAL BRACHIAL PLEXUS AND SPINAL CORD

Christian D'Andrea (1), Anita Singh (2), Sriram Balasubramanian (1),

(1) School of Biomedical Engineering, Sciences and Health Systems
Drexel University
Philadelphia, PA, USA

(2) Department of Biomedical Engineering
Widener University
Chester, PA, USA

INTRODUCTION

Limitations with studying birth-related brachial plexus (BP) injuries in humans warrant the use of highly biofidelic (human-like) physical surrogates or computational models. Such models can help develop preventative strategies in complicated birthing scenarios. Very few models exist with none having the ability to report spinal cord (SC) responses to BP stretch. In this aim, we propose to develop a 3D Finite Element Model (3D FEM) of the neonatal SC and BP complex.

METHODS

Geometry and Mesh Development: Using average dimensions for the individual structures of the SC-BP complex obtained from 110 fetuses (Wozniak 2012), a precise 3D unilateral geometric model of the SC-BP complex with dura was created (Figure 1). This model also includes spinal nerve roots of C5-T1. The extracted geometries were meshed to generate high-quality tetrahedral solid elements (total 420,799 elements) using Hypermesh v.11 (Altair Inc, MI) and ICEM CFD v.14.5 (ANSYS, Canonsburg, PA).

Biomechanical Properties: The elastic moduli (E) for the BP complex were based on in vitro tensile tests performed on neonatal BP structures (Singh et al., 2018). Additionally, we tested a total of six spinal cord (with dura) samples obtained from neonatal (3-5 days old) piglets (Figure 2). The maximum failure load for SC was found to be 6.5±2.2 N at a failure strain of 31.7±7.2% with an elastic modulus of 1.1 MPa. These biomechanical data were used in the neonate 3D FEM of the SC-BP complex.

Boundary / Loading Conditions and Simulations: The superior and inferior ends of the spinal cord were fixed, and a load of 1 N and 3.5 N were applied to the end of the C5 BP nerve segment at 10 mm/sec. Simulations were run on ANSYS v.18 (ANSYS, Canonsburg, PA), and the maximum principal stress and maximum principal strain values were recorded at the SC-BP junction (i.e. at rootlets) at all levels.

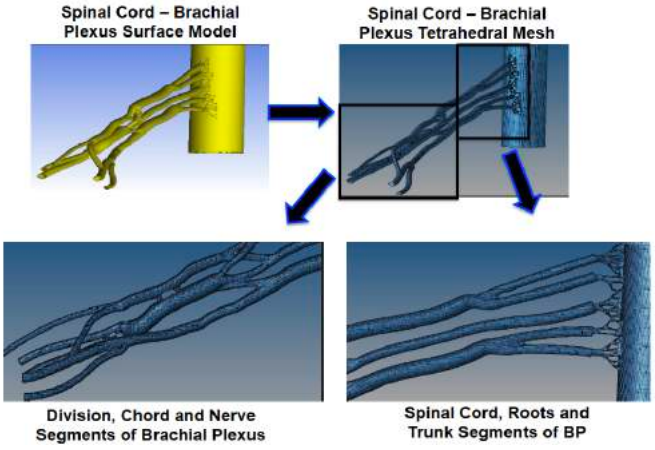

Figure 1: FE models of spinal cord and brachial plexus complex

Figure 2: In vitro mechanical testing of neonatal spinal cord

RESULTS & DISCUSSION

For a 1 N applied force, a maximum principal stress of 25.4 MPa and maximum principal strain of 19.3% was observed at the SC-rootlet junction at the C5 level (Figure 3). The 3.5 N traction force resulted in approximately 300 MPa max principal stress and 32% max principal strain at the rootlets at the C5 level. Based on preliminary in vitro testing performed on SC-BP complex with similar boundary and loading conditions, a failure at the rootlets at approximately 3.5 N was observed. However, it is unknown if the stresses from the simulation are similar to those experienced during failure during the in vitro experiment.

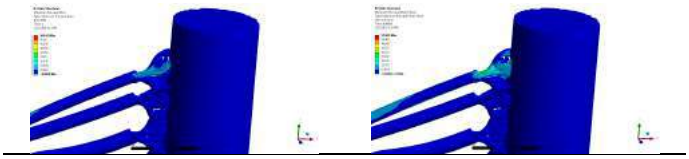

(a) (b)

Figure 3: Simulation results from 1 N traction force applied to the C5 nerve segment (a) Maximum principal stress distribution, and (b) Maximum principal strain distribution.

CONCLUSION

This is the first reported 3D FEM of the neonatal SC-BP complex with a simulation of in vivo loading. Such 3D FEMs may serve as useful tools that provide quantitative metrics for the assessment of BP and concomitant SC injury.

ACKNOWLEDGEMENTS

This study was supported by the Eunice Kennedy Shriver National Institute of Child Health and Human Development of the National Institutes of Health (R15HD093024).

REFERENCES

1) Woźniak J, Kedzia A, Dudek K.. Adv Clin Exp Med. 2012 Mar-Apr;21(2):151-67.
2) Singh A, Shaji S, Delivoria-Papadopoulos M, Balasubramanian S. J Brachial Plex Peripher Nerve Inj. 2018;13(1):e8-e14.

SB³C2019
Summer Biomechanics, Bioengineering and Biotransport Conference
June 25 -28, Seven Springs, PA, USA

DEVELOPMENT OF VISUAL ANALYSIS TRACKING METHOD FOR USE IN CONJUNCTION WITH NOVEL ANIMAL MODEL OF MTBI

Allison J. Gleason (1), Lisa A. Pruitt (1), Daniela Kaufer (2), Ellen Parker (3)

(1) Mechanical Engineering
University of California - Berkeley
Berkeley, CA, USA

(2) Hellen Wills Neuroscience Institute
University of California - Berkeley
Berkeley, CA, USA

(3) Medical Neuroscience
Dalhousie University
Halifax, Nova Scotia, Canada

INTRODUCTION

According to the CDC, head injury is one of the leading causes of death and disability among the population of the United States [1]. Mild TBI (mTBI) accounts for most of the head injuries sustained each year, and until recently the clinical impact of mTBI on function and quality of life has been thought to be low [2]. However, a multitude of recent studies have shown that mTBI is not only difficult to detect using current diagnostic imaging modalities [3,4,5] but is also linked to negative neurological outcomes [6,7,8]. The mechanics and biological sciences communities have approached the TBI problem from different perspectives for some time now without any significant bridge between the fields. The mechanics community focuses on the macro level mechanics of the head upon impact by using human headforms equipped with high sampling frequency accelerometers that yield accurate acceleration measurements [9,10]. However, these models do not allow for study of damage to tissue or microvasculature nor do they allow for following neurological outcomes post-injury. Biological science fields that utilize animal models enable such benefits, but these studies are focused predominately on the cellular level processes that occur downstream of the mechanical injury itself [11]. The separation between these fields leaves an open question regarding whether the mechanical parameters of an impact are linked to a patient's outcome post-injury. This project is novel in that it utilizes a customized visual tracking analysis method in conjunction with a new animal model of TBI. This combination of techniques allows for kinematic analysis of a living subject being exposed to an impact scenario and allows for the animals to be followed post-impact and tested for impairment.

METHODS

This study used a closed-head animal model that was optimized in parallel with the development of the tracking technique. Previously, TBI literature has been dominated by open-head injury models. In these models the animal's head is held still while damage is induced directly on the brain tissue [12]. This eradicates the affects of the kinematic interactions likely at play in acceleration/deceleration dominated TBI scenarios, which make up the majority of human TBIs treated in emergency departments every year [1]. This new model, adapted from the Shohami model [13], more accurately mimics injuries humans experience in the field.

In this study, rats and mice sustained controlled head impacts using a drop tower style test rig [9,10]. In this model the animals are initially suspended over a catch-box by support material. Upon impact, the animal is forced through the support material, falls and lands on a layer of foam lining the bottom of the catch-box. A single view of the impacts (side view) is filmed. The rat and mouse impacts for this study were filmed at 60 and 240 frames per second (fps) respectively. The impact videos are uploaded to an opensource motion analysis tool, Tracker. The videos are calibrated within Tracker and then an anatomical feature on the animal (usually the eye) is traced through each frame of the video (fig. 1). Tracker takes the position data of the tracers to calculate the linear and angular acceleration of the animal's head during impact using the finite difference method.

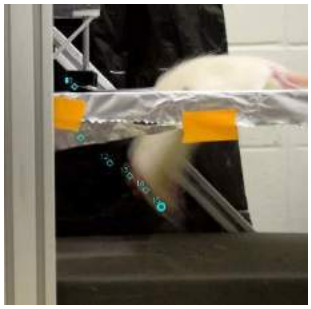

Figure 1 : Tracer placement through rat impact video

RESULTS

Repeatability of Tracking*:* Tracking features on the animals in the impact videos by-eye introduced some error to the method. The repeatability of the method was analyzed by tracking a cohort of rat impact videos (n=4) three times each. The peak linear and angular

accelerations were compared between the three tracks for each animal (table 1). The standard deviations of the peak accelerations were all found to be under ten percent of the mean values for the animals. The animal with the highest standard deviation also had the largest amount of out-of-plane (toward the viewer) motion during impact, which was not accounted for with the current method.

Table 1 : Linear ($^{m}/_{s^2}$) and Angular ($^{rad}/_{s^2}$) Acceleration Repeatability Data for Rat Cohort Filmed at 60fps

Animal ID	Linear [mean±SD(%)]	Angular [mean±SD(%)]
S1	70.51±2.49(3.53)	2366.17±174.95(7.39)
S3	49.86±2.51(5.04)	1354.92±71.46(5.27)
S4	41.12±4.03(9.79)	1276.02±99.49(7.80)
S5	48.89±1.89(3.86)	1331.88±34.26(2.57)

Sensitivity to Camera Capture Rate*:* The technique was developed as the animal model was being optimized on different species so several cameras were used to film impacts. During analysis the capture rate of the camera became a limiting factor. This was most obvious between the rat cohort discussed above and filmed at 60fps and a mouse cohort (n=4) filmed at 240fps (fig. 2).

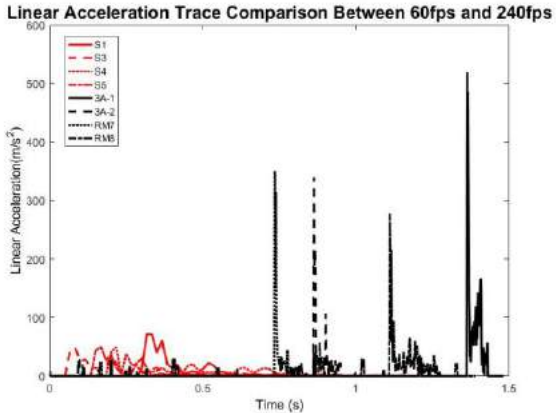

Figure 2 : Linear acceleration traces for rats (red) filmed at 60fps and mice (black) filmed at 240fps

The average peak linear acceleration of the mouse impacts was 6.8 times higher than that of the rats, even though the rats were struck at a higher impact velocity to compensate for their larger size. The average time over impact for the mouse impacts was also much lower, 33ms compared to 120ms, and approached what has been previously reported for times over impact [14]. There were also noticeable dips in the linear acceleration traces filmed at 60fps that were not characteristic of previously reported impact acceleration traces recorded using accelerometers [9,14].

Comparative Ability between Animals*:* Each of the animals in the rat cohort that has been described were exposed to the same impact parameters (drop height:85cm, impactor weight:120g). However, their trajectories and landings varied, and this was identifiable in the acceleration traces (fig.3) of the animals after the video analysis. Animal S1 experienced a typical impact and subsequent fall through the support material and landing in the catch-box. In comparison, animal S3 landed in a position that caused whipping of the head, which was reflected by multiple secondary acceleration peaks in the trace of linear acceleration where the animal's head contacted the foam lining the bottom of the catch-box multiple times. Animal S5 landed directly on its head and neck and came to an abrupt stop, which was reflected in the sharp secondary acceleration peak for that animal that then dropped to zero acceleration.

Normally animals land on their backs and bounce slightly before coming to rest. Also note that animal S4 experienced the most out-of-plane motion, which is reflected by the amount of noise in the animal's acceleration trace.

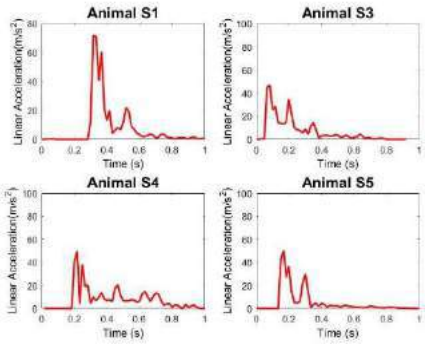

Figure 3 : Linear acceleration traces for rats filmed at 60fps

The animals in the mouse cohort were also exposed to the same impact parameters (60cm, 100g), however animal 3A-1 experienced an atypical flip. The animal turned 360 degrees after impact before contacting the foam lining the catch-box. This case was especially interesting because this animal's peak acceleration was noticeably higher than the other animals in the cohort (fig. 2) and upon sacrifice this animal had a skull fracture and brain bleed while the other animals did not display these findings.

DISCUSSION

The results from this early testing showed that the tracking method is sensitive to capture rate, and that by-eye tracking of the videos were repeatable and provided valuable comparisons between animals even at this low-fidelity stage. The current method was able to be developed and tuned quickly and cost-efficiently as the impact experiments were being optimized, however the accuracy of acceleration magnitudes suffered due to low capture speed of the camera equipment used. The effects described between capture rates were likely due to a type of aliasing: the camera was not capturing frames quickly enough to accurately capture the motion of the head during impact at lower frame rates. This would explain why the traces for the videos filmed at 240fps have a more characteristic shape and the peak acceleration values are approaching those previously reported in human headform testing using accelerometers at similar impact velocities [9]. Increasing the capture rate of the camera to mimic those used in some previous related studies should increase the accuracy of the acceleration results, however, will come at a cost, both monetarily and in labor. The current method could also be improved by adding another camera view to each impact video to account for out-of-plane movement of the animal after impact.

ACKNOWLEDGEMENTS

Funded through the NSF GRFP (AJG), and grants through BSF and CDMRP (DK).

REFERENCES

[1] Thurman, D. J. et al., *J of Head Trauma Rehab*, 14(6):602-615, 1999. [2] Bazarian, J. J. et al., *Brain Injury*, 19(2):85-91, 2005. [3] Johnston, K. M. et al., *Clinical Journal of Sport Med*, 11(3):166-175, 2001. [4] Talavage, T. M. et al., *J of Neurotrauma*, 31(4):327-338, 2014. [5] Gong, N. J. et al., *Neurobiology of Disease*, 119:79-87, 2018. [6] Weissberg, I. et al., *Neurobiology of Disease*, 78:115-125, 2015. [7] McKee, A. C. et al., *J of Neuropath & Experimental Neuro*, 68(7):709-735, 2009. [8] Gavett, B. E. et al., *Clinics in sports med*, 30(1):179-188, 2011. [9] King, A. I. et al., *IRCOBI conf*, pp. 1-12, 2003. [10] Camarillo, D. B. et al., *Annals of Biomed Engr*, 41(9):1939-1949, 2013. [11] Chodobski, A. et al., *Translational Stroke Research*, 2(4):492-516, 2011. [12] Xiong, Y. et al., *Nature Rev Neurosci*, 14(2):128, 2013. [13] Flierl, M. A. et al., *Nat Protoc 4*(9):1328, 2009. [14] Zhang, J. et al., *Biomed Sci Instrum*, 42:501-506, 2006.

SB³C2019
Summer Biomechanics, Bioengineering and Biotransport Conference
June 25 -28, Seven Springs, PA, USA

BIOMECHANICAL RESPONSE OF THE MANDIBLE TO BLUNT IMPACT AND CORRESPONDING BIOFIDELITY OF THE FOCUS HEADFORM

Charles A. Weisenbach (1,2), Jodie A. Gomez (1,3), Andrea S. Dargie (1,2), Ray W. Daniel (1,2), Valeta Carol Chancey (1), Frederick T. Brozoski (1)

(1) U.S. Army Aeromedical Research Laboratory,
Fort Rucker, AL, USA

(2) Katmai Government Services
Orlando, FL, USA

(3) Oak Ridge Institute for Science and Education,
Oak Ridge, TN, USA

INTRODUCTION

Within the U.S. Military, approximately 25% of injuries during recent conflicts were craniomaxillofacial (CMF) in nature [1]. To predict injury risk and evaluate potential countermeasures, the Facial and Ocular CountermeasUres Safety (FOCUS) headform was developed with segmented facial regions for measuring facial and ocular insults [2]. The biofidelity of a headform is essential for this purpose, and the FOCUS headform has been shown to respond similarly to cadaveric subjects for anterior-posterior (A-P) blunt impacts to the frontal bone, nasal bone, and maxilla [3]. For mandibular A-P impacts, however, large displacements of the unrestrained mandible prohibited the appropriate evaluation of the FOCUS headform mandible [4].

Recently, a method was developed to evaluate the mandible under a restrained jaw condition that more realistically mimics the response of a helmeted individual [5]. The current study used this method to determine the cadaveric response of the restrained jaw to A-P blunt impacts and assess the biofidelic response of the FOCUS headform.

METHODS

Impacts to the cadaveric mandible and mandible region of the FOCUS headform were performed using a gravity-driven guided cylindrical impactor with a 6.45 cm^2 surface area and 3.2 kg mass to remain consistent with previous investigations [3-5].

The impactor was instrumented with a load cell (Model 53; Honeywell) directly behind the impact surface and an accelerometer atop the impactor mass (Model 7264C; Endevco). Data were collected using a Synergy Data Acquisition System (Hi-Techniques Inc.) at 1 MHz and filtered in MATLAB (Mathworks) using a 4th order low-pass Butterworth filter with a 500 Hz cutoff frequency [4,6]. Tests were recorded using a high-speed camera (Vision Research Inc.) at 10,000 frames per second.

Cadaver Test Series. Twenty-five fresh-frozen male post-mortem human surrogate (PMHS) heads were used. All specimens were handled in accordance with institutional standard operating procedures and U.S. Army Policy for Use of Human Cadavers [7]. Specimens were secured in a potting fixture using polyurethane resin (Golden West Manufacturing) with the Frankfort plane vertical. Strain gauges were attached to the skull and acoustic emission sensors were secured at the angle of the mandible (bilaterally) to assist with fracture detection.

The impactor was centered on the symphysis of the mandible with the edge of the impactor below the alveolar process (Figure 1). A restraint fixture was used to prevent the jaw from opening during impact [5]. Impacts were repeated in 5 J increments until fracture was detected through review of sensor data and comparison to baseline assessment impacts (5 J).

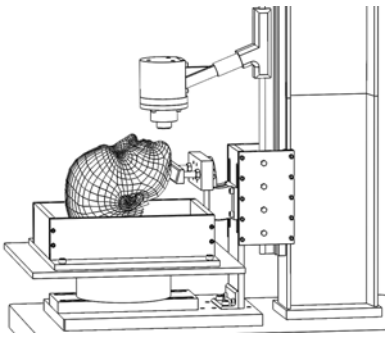

Figure 1. Schematic of the specimen mounted in the test fixture with the impactor positioned above the mandible.

Poster Presentation #P210

FOCUS Test Series. The FOCUS headform was attached to a Hybrid III neck and mounted to the test device. Five impacts were conducted at each of 5, 10, 15, and 20 J energy levels. The internal mandible load cell data were collected and filtered in the same manner as the impactor data [4,6].

Analysis. Mandible force-displacement response was computed from the time of initial impactor contact (defined as 10N of contact force) to 90% of the peak force. Impactor accelerometer data was double integrated to obtain position data. The cadaveric response was defined using the characteristic average and corridors calculated using methods described by Lessley et al. [8].

RESULTS

Cadaver Test Series. Sixty-five tests were performed on 25 mandibles and used to determine the PMHS biomechanical response. Impact velocity ranged from 1.7 to 4.4 m/s, corresponding to impact energies from 4.5 to 31.4 J. Maximum force and displacement increased with increasing impact energy (Table 1). Force-displacement data for all impact energies were used to obtain the PMHS characteristic average and corridors (Figure 2).

Table 1. Average peak force and displacement by impact energy.

Energy (J)	PMHS		FOCUS	
	Force (N)	Disp (mm)	Force (N)	Disp (mm)
5	1795 ± 315	6.5 ± 1.3	990 ± 3.5	7.7 ± 0.1
10	2320 ± 296	8.0 ± 2.0	1403 ± 6.3	10.1 ± 0.6
15	2779 ± 550	9.8 ± 2.7	1768 ± 8.1	11.4 ± 0.4
20	3465 ± 758	12.0 ± 3.5	2117 ± 10.9	12.7 ± 0.1
25	4167 ± 947	14.7 ± 2.1	–	–
Overall	2476 ± 837	8.6 ± 3.0	–	–

Data given as mean ± standard deviation. Disp: displacement.

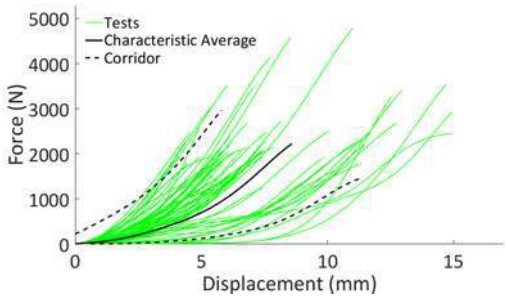

Figure 2. PMHS characteristic average and corridors for all tests.

FOCUS Test Series. Twenty A-P impacts on the FOCUS headform were performed at four energy levels. The headform produced repeatable loading responses. The peak force and displacement were dependent on the impact energy but the overall stiffness was independent of energy (Table 1; Figure 3).

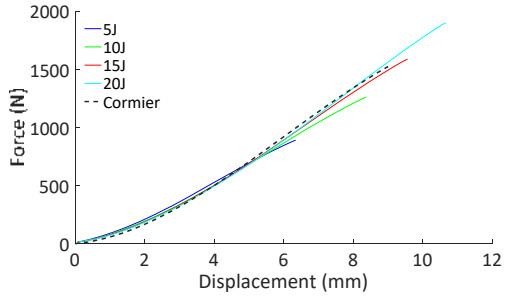

Figure 3. FOCUS headform average response by impact energy overlaid with the average response from Cormier [4].

The PMHS showed a bilinear response with initial (0-20% peak force) and secondary (20-80% peak force) stiffnesses of 152.3 and 324.6 N/mm, respectively. The FOCUS headform response was linear and fell within the PMHS response corridors (Figure 4).

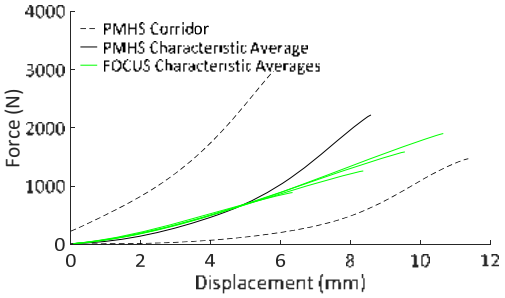

Figure 4. Average PMHS response and corridors overlaid with the average FOCUS headform responses at each energy.

DISCUSSION

When overlaid, the PMHS corridors from Cormier [4] fall within the PMHS corridors from the current study (Figure 5). Our tests exhibited much larger reaction forces than Cormier [4] due to the restrained chin condition. Cormier [4] observed more jaw motion, lower forces, and fewer mandible fractures. The differences in secondary stiffness could be attributed to their lower forces that did not cause fracture and perhaps indicate that their data reflect the initial PMHS response.

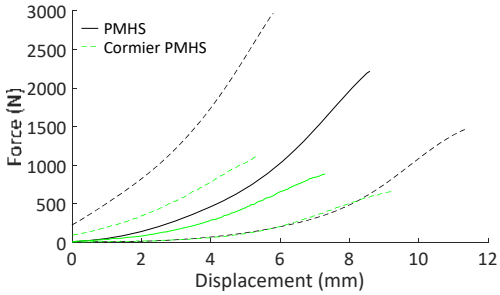

Figure 5. Average PMHS response and corridors overlaid with the corresponding response and corridors from Cormier [4].

The FOCUS headform response was consistent with the results of A-P impact testing performed by Cormier [4], whose impact energies ranged from 12.7 to 15.7 J (Figure 3). Thus, the FOCUS headform gives a consistent mechanical response that is biofidelic and useable in evaluating facial insults to the mandible.

ACKNOWLEDGEMENTS

This research was supported in part by an appointment to the Postgraduate Research Participation Program at the U.S. Army Aeromedical Research Laboratory administered by the Oak Ridge Institute for Science and Education through an interagency agreement between the U.S. Department of Energy and US Army Medical Research and Materiel Command.

REFERENCES

[1] Lew, T et al., *J Oral Maxillofac Surg*, 68:3-7, 2010.
[2] Crowley, J et al., *Aviat Space Environ Med*, 80(9):831, 2009.
[3] Cormier, J et al., SAE 2010-01-1317, 2010.
[4] Cormier, J, Ph.D. Dissertation, Dept. of Biomedical Engineering, Virginia Polytechnic Institute and State University, 2009.
[5] Weisenbach, C et al., Poster presentation at American Society of Biomechanics Annual Meeting, 2017.
[6] Cormier, J et al., *Biomed Sci Instrum*, 44:147-152, 2008. (AE)
[7] United States Army, *Army Policy for Use of Human Cadavers for Research, Development, Test and Evaluation, Education or Training*, 20APR2012.
[8] Lessley, D et al., *SAE International*, No. 2004-01-0288, 2004.

SB³C2019
Summer Biomechanics, Bioengineering and Biotransport Conference
June 25 -28, Seven Springs, PA, USA

CONVERTING THE WORCESTER HEAD INJURY MODEL FROM ABAQUS INTO LS-DYNA FORMAT

Kianoosh Ghazi (1), Wei Zhao (1), Songbai Ji (1,2)

(1) Department of Biomedical Engineering
Worcester Polytechnic Institute
Worcester, MA, USA

(2) Department of Mechanical Engineering
Worcester Polytechnic Institute
Worcester, MA, USA

INTRODUCTION

Traumatic brain injury (TBI), including sports-related concussion that occurs in 1.6 to 3.8 million athletes a year, is a major health problem in the United States (1). This necessitates accurate and reliable prediction of brain injury. In the past, head impact kinematics including peak magnitudes of linear or rotational accelerations have been extensively used as injury predictors. Lately, efforts to employ finite element (FE) models of the human head are increasing. These models translate impacts into tissue strains thought to cause injury and are generally believed to potentially improve the prediction performance.

Numerous efforts exist to improve FE models of the human head, including optimizing brain material properties, enhancing the quality of brain meshes, etc. Still, a significant disparity between the various human head injury models is the different simulation packages. This may preclude a meaningful comparison between simulation results and injury analyses using different head injury models.

Abaqus and LS-DYNA that are the most common choices in TBI impact simulations. In this study, we converted our latest anisotropic Worcester Head Injury Model (WHIM) developed in Abaqus into LS-DYNA format. This conversion process allowed us to understand the differences between the two most commonly used software packages in brain injury studies. This would facilitate the comparisons between models developed in these two packages in the future.

METHODS

The latest WHIM served as a baseline for model conversion. The model uses a re-meshed brain (202.8 k high-quality hexahedral elements of the brain (2)) and implements brain material property anisotropy in Abaqus using the HGO hyperelastic model coupled with viscoelasticity (3). It was successfully validated against both high-rate cadaveric head impacts and *in vivo* head rotation. Unfortunately, LS-DYNA currently does not have an equivalent anisotropic material. Therefore, a material optimization scheme was conducted to convert the Abaqus HGO anisotropic material model into an isotropic model in LS-DYNA while minimizing differences between model simulation responses. It was necessary to model the gray matter (GM) and white matter (WM) separately in order to preserve their response differences arising from brain material anisotropy.

The 50 deep white matter regions of interest (ROIs) were localized in the WHIM by registering the JHU-ICBM-DTI 81 WM atlas with the T1-weight MRI used to develop the baseline WHIM (3). Similarly, a GM neuroimaging atlas (4) was used to identify 54 cerebral GM regions within the WHIM space. A recorded loss of consciousness impact (5) was simulated to aid the model conversion.

Specifically, we started with the baseline WHIM based on a full integration element with incompatible modes (C3D8I) in Abaqus. This type of element often serves as a benchmark in simulation that is free from shear locking, immune to hourglass deformation, and with minimal volumetric locking (2, 6). However, this element is computationally rather expensive. Therefore, we first converted the model into reduced integrated elements (C3D8R) using relax stiffness hourglass control (HG) with a high scaling factor (SF) of 200 for GM and 100 for WM to maximize model simulation efficiency.

Next, an Ogden isotropic hyperealastic model was selected to approximate the previous anisotropic response. The initial shear modulus, G_0, was determined *via* iterative adjustment so that a linear regression slope between the peak maximum principal strains in the GM and WM regions obtained from the two models was within 1.00±0.05.

With the same G_0 value for the entire brain as a new starting point, the G_0 values for the GM and WM were further iteratively adjusted so that the linear regression slope between GM regions, as well as that for the WM regions, were both within 1.00±0.05.

Poster Presentation #P211

Next, the two isotropic GM and WM material models were directly converted into LS-DYNA format without alteration. As there were quite some different integration schemes available in LS-DYNA, we sought to identify the best option to maximize the match between simulation results with respect to that from Abaqus. Specifically, we examined the selectively reduced integration (S/R; element types 2, -1, and -2) and all of the reduced integration schemes in LS-DYNA, enumerating each HG type with three hourglass coefficients (QM) (0.01, 0.1 (default), and 1), with a maximum QM of 1 to avoid unstable simulations.

Table 1 summarizes the overall procedure of this study, including the type of material properties and element types used in each step.

Table 1: Summary of six simulation steps to convert the baseline WHIM using anisotropic brain material properties in Abaqus into LS-DYNA counterpart with isotropic properties.

Step	Software	Hourglass Control (HG)	Elm. Type	Material
1	Abaqus	Not needed	C3D8I	Anisotropic
2	Abaqus	Relaxed stiffness WM SF of 100 GM SF of 200	C3D8 R	ibid.
3	Abaqus	Relaxed stiffness WM SF of 100 GM SF of 200	C3D8 R	Isotropic (same for GM/WM)
4	Abaqus	Relaxed stiffness WM SF of 100 GM SF of 200	C3D8 R	Isotropic (with GM/WM heterogeneity)
5	LS-DYNA	Not needed for S/R	{2, -1, -2}	ibid.
6	LS-DYNA	Type 1 to 10, excluding 8/QM of 0.01, 0.1, 1	1	ibid.

RESULTS

After converting the baseline WHIM (step 1 in Table 1) into isotropic and heterogeneous GM/WM with C3D8R (step 4 in Table 1), element-wise comparisons led to the following linear regression slopes (k) and Pearson correlation coefficients (r): k_{WM} = 0.91 and r_{WM} = 0.71 for the 50 WM ROIs; k_{GM} = 0.96 and r_{GM} = 0.86 for the 54 GM ROIs. Step-wise comparisons are reported in Table 2. Converting anisotropy into isotropy mostly affected the WM (a low r_{WM} of 0.78), as expected. These results suggested that the reduced integration scheme was able to preserve the simulation accuracy while maximizing computational efficiency (2h 24 min versus 38 min on a computer cluster: 15 CPUs + 2 GPUs). **Fig.1** (a, b, c) compares their fringe plots of accumulated maximum principal strain.

Table 2: Summary of the results from the experiments.

Reference	Target	54 GM ROIs		50 WM ROIs	
		k_{GM}	r_{GM}	k_{WM}	r_{WM}
Anisotropic/ C3D8I	Anisotropic/ C3D8R	0.97	0.92	0.93	0.95
Anisotropic/ C3D8R	Isotropic /C3D8R	0.99	0.92	0.98	0.78
Isotropic /C3D8R	LS-DYNA HG = 1	0.93	0.88	0.98	0.85
Anisotropic/ C3D8I	LS-DYNA HG = 1	0.90	0.87	0.89	0.64

When further converting into LS-DYNA, results from the S/R integration (element types 2, -1, -2; step 4 in Table 1) did not match the Abaqus counterpart (e.g., k_{WM} = 1.32, r_{WM} = 0.72 and k_{GM} = 1.12, r_{GM} = 0.42 with element type 2). The closest response was obtained using reduced integration with HG types 1, 2, or 3 with the default QM of 0.1 (e.g., step 6 in Table 1; **Fig. 1d**). A QM of 1 led to unstable simulations in most cases. Results from HG type 6, 9 and 10 were always unstable regardless of the QM (type 8 for shell elements was not applicable here).

These findings were further re-confirmed by simulating a separate impact case (self-reported concussion case (5)). This suggested that the observations may be applicable more broadly in other impacts as well.

DISCUSSION AND CONCLUSION

In this study, we used the benchmark element type, C3D8I (full integration element with incompatible modes), as the baseline to convert the latest WHIM into LS-DYNA format step-by-step. Our results suggested that reduced integration with HG types 1, 2, and 3 coupled with the default QM of 0.01 produced the most similar results relative to the Abaqus baseline. S/R did not yield comparable results.

However, even with the most similar results (**Fig. 1d**), significant differences were apparent in both strain magnitude (underestimated by ~10% w.r.t. C3D8I baseline) and distribution. While the magnitude may be compensated for *via* scaling, the distribution disparity was likely a result of the two different material properties used in the two WHIM variants. Nevertheless, this study enhances our understanding of the differences between Abaqus and LS-DYNA in impact simulation.

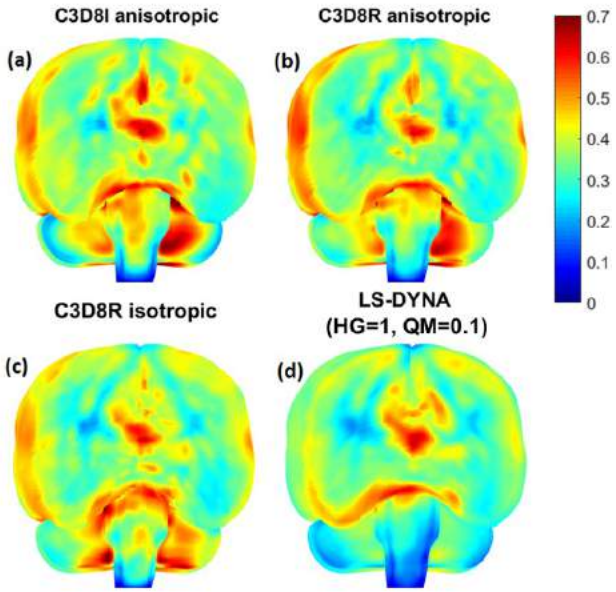

Fig. 1: Cumulative maximum principal strain from C3D8I with an anisotropic material model (a), same anisotropic material with C3D8R and high SFs (b), optimized isotropic material with GM/WM heterogeneity using C3D8R and high SFs (c), and same isotropic materials converted into LS-DYNA (d).

ACKNOWLEDGEMENT

Funding is provided by the NIH grant R01 NS092853.

REFERENCES

1. Thomas et al. 2015. *Centers Dis. Control Prev.*, pp. 1–72
2. Zhao et al. 2018. *Ann. Biomed. Eng.* in press
3. Zhao et al. 2018. *J. Neurotrauma*. 36(2) 250–263
4. Shattuck et al. 2008. *Neuroimage*. 39:1064–80.
5. Hernandez et al. 2015. *Ann. Biomed. Eng.* 43(8):1918–34
6. Abaqus. 2016. Abaqus Online Documentation, Abaqus 2016

SB³C2019
Summer Biomechanics, Bioengineering and Biotransport Conference
June 25 -28, Seven Springs, PA, USA

QUASI-LINEAR VISCOELASTIC FITTING OF THORACIC TISSUES AND BALLISTICS GEL FOR MODELING BEHIND ARMOR BLUNT TRAUMA

Madelyn A. K. Eaton (1), Robert S. Salzar (1)

(1) Center for Applied Biomechanics
University of Virginia
Charlottesville, VA, USA

INTRODUCTION

Injuries resulting from the non-penetrating energy dispersion of a projectile missile into body armor is a phenomenon known as behind armor blunt trauma (BABT). Characterized as an emerging problem in the military and law enforcement,[1] BABT occurs when the body armor stops the projectile without penetration but deforms into the body of the wearer. This back-face deformation (BFD) results in blunt-type injuries ranging in severity to include death. BABT has been shown to result in numerous thoracic injuries, the most lethal being rib fractures and injuries to the cardiac and pulmonary tissues.[2–4]

The pass/fail of body armor is almost solely dependent on its BFD. The official measuring of BFD comes from the National Institute of Justice (NIJ), and uses an oil-based clay (Roma Plastilina No.1) as a backing material and measuring standard. The passing limit of the armor is set at 44 mm: the BFD cannot exceed 44 mm in more than 20% of the hits with a confidence of 95%, and the armor fails if BFD reaches 50 mm or higher.[5] However, this method for testing armor, specifically using a single measure of BFD, has never been correlated with injury risk or severity. The clay used in NIJ standard testing was picked for its close material response to that of 20% ballistics gel. 20% ballistics gel was the first medium used to measure the effects of BABT, but was replaced with clay to lower cost, omit the need of high speed cameras, and to be able to utilize a reusable material. The 44 mm BFD limit was picked based on data from a .38 caliber round and for soft body armor, and has no proven relevance to higher velocity rounds.[6]

Since the clay standard was chosen for its closeness to 20% ballistics gel, many studies have turned to using gels as a backing material since its progress can be tracked with video.[7–9] The goal of this study is to find the material properties associated with the lungs and heart at certain strain rates and compare their responses to those of the 20% ballistic gel (comparable to the clay standard). In order to further the knowledge of the response of these organs under BABT the data will be processed for future use in a finite element model (FEM). The intermediate step between experimental findings and modeling will be through quasi-linear viscoelastic (QLV) fitting, which will allow the data to be implemented into the FEM. Furthermore, the elastic (Young's) modulus of lung tissue has not been thoroughly discussed in the literature, so this study attempts to bridge the gap by reporting the elastic moduli for the tested strain levels.

METHODS

The tissue samples tested were acquired from whole porcine organs ~1 hour after death and were never frozen. The porcine lungs were sectioned into 4 cylindrical samples (2 left, 2 right), and the heart into 6 cylindrical samples: 4 from the ventricles (2 left, 2 right) and 2 from the atriums (1 left, 1 right). The gel was from standard 20% clear ballistics gelatin, and was also sectioned into cylindrical samples. The samples' radii were such that when the 1/8 inch (3.175 mm) cylindrical indenter was used for compression, the infinite plane scenario was maintained. The samples were placed on an aluminum mounting plate and uniaxially compressed using a displacement/force driven bench-top test machine (ElectroForce® 3100, Bose Corporation – ElectroForce, Eden Prairie, MN). A 1000 g load cell was used and velocity was set to 1 m/s. On each compression sample, four strain levels where achieved in a step-hold fashion: 10% strain, 20% strain, 35% strain, and 45% strain. The strain level was held for 30 s, and between each strain level the sample was decompressed and allowed to relax until the load cell read zero. The strain levels went in ascending order: a sample was first tested at 10% strain, held for 30 s, allowed to relax, then tested at 20% strain, etc.

Poster Presentation #P212

The testing resulted in force/displacement time histories, and the force response to an arbitrary displacement input, $\delta = \delta(t)$, was modeled using a quasi-linear viscoelastic (QLV) mathematical framework:

$$F(\delta, t) = \int_0^t G_{red}(t - t') \frac{dF^e(\delta)}{d\delta} \frac{d\delta}{dt'} dt' \quad (1)$$

where $F^e(\delta)$ is the instantaneous elastic response modeled with:

$$F^e(\delta) = A[e^{B\delta} - 1] \quad (2)$$

and $G_{red}(t)$ is the reduced relaxation function:

$$G_{red}(t) = G_\infty + \sum_{n=1}^{5} G_n e^{-t/\tau_n} \quad (3)$$

The reduced relaxation function has been normalized so that $0 \leq G_{red}(t) \leq 1$. The elastic coefficients, A and B, and the viscoelastic coefficients, G_n, were determined by minimizing the sum squared error (SSE) between the experimental data set and the predicted model fitting (Excel Solver®, Microsoft®, Redmond, WA). The time constants, τ_n, were set as decades to simplify and improve stability: $\tau_1 = 0.001$, $\tau_2 = 0.01$, $\tau_3 = 0.1$, $\tau_4 = 1$, $\tau_5 = 10$.

RESULTS

All samples were tested successfully for all strain levels; engineering stress vs. strain curves were found and no sample had any obvious failure of material. Elastic (Young's) moduli were found based on the engineering stress-strain curves, and the strain rates were found to be consistent among samples for the same strain levels (Table 1). The force and displacement data for each set of samples (tissues/gel) was averaged within the separate strain levels, so that each material tested had one data set per level of strain.

Table 1: The right column details the tested strain levels, while the table depicts the elastic moduli of lung, heart ventricles, heart atriums, 20% ballistics gel in kPa, and the strain rates in %/ms

	E, Lung	E, Heart-V	E, Heart-A	E, BGel	Strain Rate
10%	0.28	2.11	0.97	2.95	0.9
20%	0.56	2.96	1.03	3.38	1.9
35%	0.70	6.06	1.16	5.11	3.2
45%	0.77	7.52	1.19	5.08	4.0

For the QLV fitting of the experimental force, all data for each material was modeled together; the average curves for each strain level were fit all as one. In this way, there is one set of coefficients for each material that predict a model that fits all strain levels (Figure 1).

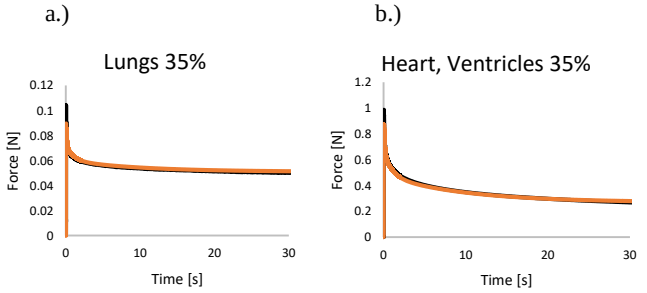

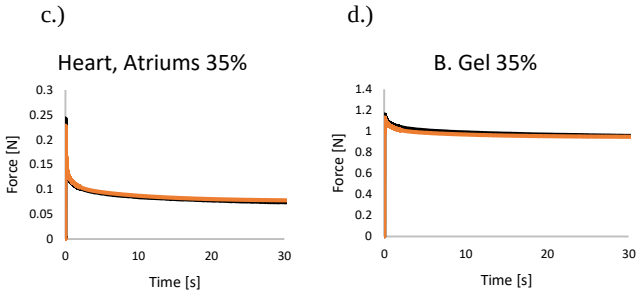

Figure 1: QLV results at strain level 35% for a.) lung, b.) heart ventricles, c.) heart atriums, and d.) 20% ballistics gel. Experimental data is shown in black, the model fit is shown in red.

DISCUSSION

As expected, the results of the 20% ballistics gel didn't match either the lungs or the heart completely, a large factor being that the three materials are very different in density and material structure. However, it could be said that the ballistics gel has too high of an elastic modulus to compare with inner organs, yet way too low to compare with bone; it is close to cardiac muscle in magnitude, but the relaxation curve is more similar to lung. This could account for the discrepancies found when the 20% ballistics gel or clay standard is compared with human surrogates (animal, FEM, etc.).[6,8,10]

As for the constitutive modeling of the materials, a QLV fit was found readily for all materials for all strain levels. The r^2 values, for the experimental force and the fitted model force, were: 0.997 for lung, 0.997 for heart ventricles, 0.996 for heart atriums, and 0.998 for 20% ballistics gel.

Future courses of action include using the QLV data obtained from these materials at these strain rates, and improving FE models of organs to improve current methods of determining risks and injuries associated with BABT.

ACKNOWLEDGEMENTS

This effort was funded by MTEC Project Award No. 2018-652-001, sponsored by the Office of Naval Research. The views and conclusions contained herein are those of the authors and should not be interpreted as necessarily representing the official policies or endorsements, either expressed or implied, of the U.S. Government.

REFERENCES

[1] Cannon, L. et al., *J. R. Army Med. Corps* **147**, 87–96 (2001).
[2] Bass, C. R. et al. *Int. J. Occup. Saf. Ergon.* **12**, 429–442 (2006).
[3] Cooper, G. J. et al., *J. Trauma* **22**, 994–1008 (1982).
[4] Carr, D. J. et al., *J. R. Army Med. Corps* **162**, 8–11 (2016).
[5] U.S. Department of Justice. Ballistic Resistance of Body Armor NIJ Standard-0101.06. (2008).
[6] Hanlon, E. et al., *Mil. Med.* **177**, 333–339 (2012).
[7] Bracq, A. et al., *Research Gate.* 12 (2018)
[8] Merkle, A. C. et al., *J. Trauma Inj. Infect. Crit. Care* **64**, 1555–1561 (2008).
[9] Mauzac, O. et al. Comparative assessment of Behind Armour Blunt Trauma (BABT) by means of a novel transparent synthetic gel (2012).
[10] Roberts, J. C. et al., *J. Trauma Inj. Infect. Crit. Care* **62**, 1127–1133 (2007).

SB^{3}C2019
Summer Biomechanics, Bioengineering and Biotransport Conference
June 25 -28, Seven Springs, PA, USA

INHIBITITNIG SPINAL PHOSPHOLIPASE A_2 PREVENTS PAIN AND MODIFIES SPINAL NEURON ACTIVITY & GLUTAMATE SIGNALING EARLY AFTER NERVE ROOT COMPRESSION

Julia C. Quindlen-Hotek (1), Sonia Kartha (1), Prabesh Ghimire (1), Beth A. Winkelstein (1,2)

(1) Department of Bioengineering
University of Pennsylvania
Philadelphia, PA, USA

(2) Department of Neurosurgery
University of Pennsylvania
Philadelphia, PA, 19146

INTRODUCTION

Chronic pain is a debilitating disorder affecting nearly 1/3 of American adults [1]. The cervical nerve root is a common source of pain from its compression during neck trauma and/or disc disease [2]. Nerve root compression (NRC) induces a host of inflammatory mediators, including pro-inflammatory cytokines, prostaglandins, in the spinal cord that initiate and maintain neuronal hyperexcitability and pain [3-5]. NRC induces persistent pain within 1 day [6]. Spinal glial activation and cytokine upregulation also occur early after a painful insult [3,7], which directly and indirectly induce and modulate spinal neuronal hyperexcitability [4,8]. Although hyperexcitability of spinal neurons is evident at later times after NRC when pain persists and is attenuated by neuromodulatory drugs that provide pain relief [8,9], it is unknown if spinal neuronal hyperexcitability is established as early as day 1.

Spinal phospholipase A_2 ($sPLA_2$) has been implicated in painful NRC [7]. $sPLA_2$ is an enzyme that releases arachidonic acid from cell membranes and is involved in production of inflammatory mediators like prostaglandins [10]. $sPLA_2$ has been implicated as an early pain mediator in inflammation and neural injury [10,11]; it modulates neuronal regulation of nociception, excitotoxicity, and excitatory signaling [12,13]. Yet, its involvement and/or its effects on spinal neuronal changes that lead to early central sensitization after painful root injury are not known. This study investigated whether inhibiting spinal $sPLA_2$ modulates pain, spinal neuron hyperexcitability, and/or spinal genes involved in glutamate signaling early after NRC injury. At day 1 after NRC, with or without $sPLA_2$ inhibitor, behavioral sensitivity and extracellular potentials in the spinal cord were measured to assess onset of pain and spinal neuronal activity. Because glutamate signaling has a role in synaptic plasticity and central sensitization [14], RT-PCR probed genes in glutamate regulation [15-17]: a metabotropic glutamate receptor (mGluR5), a subunit of the NMDA glutamate receptor (NR1), and a transporter involved in glutamate uptake (GLT-1).

METHODS

All procedures were IACUC-approved. Male Holtzman rats underwent a unilateral C7 dorsal nerve root compression (NRC) by a 10-gf clip [8]. Immediately after root compression, rats received the $sPLA_2$ inhibitor thioetheramide-PC (Cayman) dissolved in PBS (0.25mg/kg) intrathecally by lumbar puncture (40-60µL) (NRC+TXT; n=4) [12]. Additional groups of rats underwent root compression only (NRC; n=3) or a sham surgical procedure (SHAM; n=3) with the C7 nerve root exposed but not compressed. Behavioral sensitivity was measured as the ipsilateral paw withdrawal threshold (PWT) to a series of von Frey filaments with increasing weight before (baseline) and 1 day after surgery [8]. PWTs were normalized to baseline and compared between groups by a two-way ANOVA with Tukey's HSD test.

One day after behavioral testing, electrophysiology recordings measured spinal extracellular potentials [8]. Rats were anesthetized with sodium pentobarbital (45mg/kg; i.p.). A recording electrode was lowered in the C6/C7 dorsal horn on the same side as surgery [8]. After identifying mechanosensitive neurons, nonnoxious and noxious von Frey filaments (1.4g, 4g, 10g, 26g) were applied for 5 consecutive 1s-intervals [8]. Voltage potentials were measured during each stimulation, spike-sorted and counted using Spike2 software (CED). Evoked responses were compared between groups by an ANOVA with Tukey's HSD test. Each neuron was classified [8]: wide dynamic range (WDR) neurons respond in a graded manner, low-threshold mechano-receptive (LTM) neurons respond more to nonnoxious stimuli, and nociceptive specific (NS) neurons respond only to noxious stimuli. A Pearson's chi-squared test compared the proportion of neuron types across groups. After recording, rats were transcardially perfused with PBS. The

ipsilateral C6 spinal cord was collected and homogenized in Trizol for RT-PCR. Total RNA was extracted and reverse-transcribed into cDNA [3]. RT-PCR was carried out in duplicate with primers specific to mGluR5, GLT-1, NR1, and CyA (Table 1) [3,15-17]. Genes were normalized to CyA and calculated as fold-changes over normal levels. Quantification was performed by the comparative ΔΔCt method [3] and levels for each gene were compared between groups using ANOVAs.

Table 1: Primer Sequences for Genes Probed.

Gene	Sequence
mGluR5	F: 5´-GTAACCAAGACCAACCG-3´
	R: 5´-CGCATAGAACGTGCAA-3´
GLT-1	F: 5´-AACCGAGGGTGCCAACAA-3´
	R: 5´-AAGCAGCCCGCCACATAC-3´
NR1	F: 5´-AGATGGCCCTGTCAGTGTGT-3´
	R: 5´-GTGAAGTGGTCGTTGGGAGT-3´
CyA	F: 5´-TATCTGCACTGCCAAGACTGAGTG-3´
	R: 5´-CTTCTTGCTGGTCTTGCCATTCC-3´

RESULTS

Inhibiting spinal $sPLA_2$ at NRC prevents pain at day 1, with normalized PWT (0.78±0.30) significantly higher ($p<0.01$) than NRC (0.17±0.10). The PWT after treatment is not different from sham (0.85±0.29) at day 1. Although NRC significantly reduces ($p<0.01$) the PWT at day 1 from baseline, the withdrawal thresholds for NRC+TXT at day 1 (0.78±0.30) are not different from its baseline (1.0±0.33).

Neuronal activity in the dorsal horn is also reduced by inhibitor treatment (Fig. 1). Recordings were made at a depth of 533±238µm below the pial surface, with no difference in recording depth between groups. At day 1 after NRC (20 neurons), neuronal activity evoked by all stimuli increases over normal (16 neurons) levels ($p<0.04$), and sham (34 neurons) levels ($p<0.02$) for all filaments except the nonnoxious 1.4g filament (Fig. 1). However, NRC with $sPLA_2$ inhibitor treatment (37 neurons) decreases neuron firing for all stimuli, with significant reductions ($p<0.04$) for the 4g, 10g, and 26g filaments.

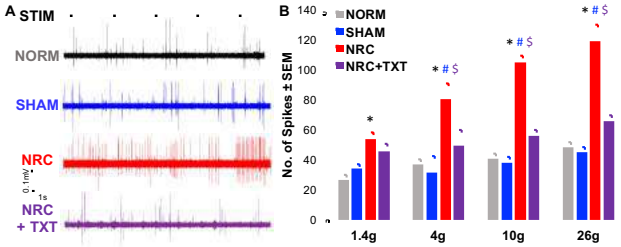

Fig. 1: (A) Representative recordings for the 26g filament stimulus (STIM). (B) Evoked firing increases (*p<0.04) after NRC over normal levels for all filaments and is higher than SHAM (#p<0.02) and NRC+TXT ($p<0.04) for the 4g, 10g, and 26g filaments.

Inhibiting spinal $sPLA_2$ with NRC also rescues the shift in neuronal phenotype distribution that occurs with NRC (Fig. 2). After NRC, the majority (78%) of neurons are classified as WDR, which is higher ($p<0.04$) than in normal (33%) and sham (38%) rats. In those control groups, the majority of neurons are LTM (53.3% NORM; 52.9% SHAM) (Fig. 2). However, with inhibitor treatment, the phenotypic distribution resembles that in SHAM, with 49% of neurons classified as LTM and 43% as WDR (Fig. 2). The distribution for NRC+TXT is significantly different ($p<0.05$) from that of NRC alone.

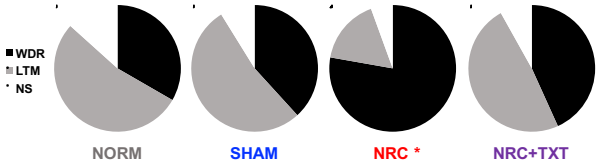

Fig. 2: The distribution of neurons after NRC is different (*p<0.05) from that of normal, sham, and NRC+TXT.

All genes (mGluR5, GLT-1, NR1) were detected in the ipsilateral spinal cord in all groups (Fig. 3). Although expression of mGluR5 mRNA at day 1 after NRC is higher than SHAM and NRC+TXT, the difference is only significant ($p<0.05$) for NRC+TXT which is not different from SHAM (Fig. 3). GLT-1 mRNA is significantly lower ($p<0.04$) than SHAM after both treated and untreated NRC, which are not different from each other (Fig 3). NR1 mRNA is not different between groups and more variable in the NRC groups (Fig. 3).

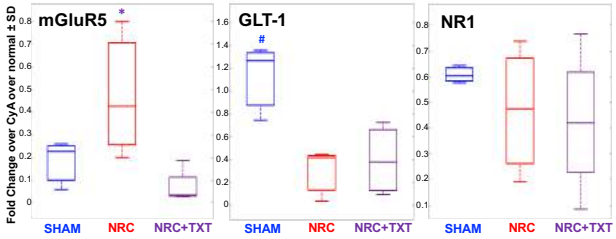

Fig. 3: Spinal mGluR5 mRNA is higher (*p<0.05) after NRC than NRC+TXT. GLT-1 mRNA is greater (#p<0.04) after SHAM than both NRC and NRC+TXT. NR1 mRNA is unchanged.

DISCUSSION

$sPLA_2$ inhibition at the time of nerve root compression prevents the early development of pain and spinal neuron hyperexcitability (Fig. 1) [7,8]. It also prevents upregulation of mRNA for mGluR5 at that time (Fig. 3). These data suggest spinal $sPLA_2$ may directly modulate neuron activity early after painful NRC. The apparent reversal of neuronal phenotypic changes (Fig. 2) is consistent with other reports of neuromodulatory drugs preventing the shift to WDR neurons [8,9]. However, the downregulation of GLT-1 mRNA that is observed after painful root injury is *not* reversed with $sPLA_2$ inhibition (Fig. 3). Since mGluR5 is expressed on both neurons and astrocytes and GLT-1 is expressed *only* on astrocytes [4,8], and spinal astrocytic activation occurs later after painful NRC [7], the differences observed here may be due to the early time point and direct relationship between neuronal hyperexcitability and the genes probed in this study. The variability between the RT-PCR and electrophysiology results (Figs. 1-3) also may be due to differences in the assays themselves. RT-PCR was performed on *whole* C6 spinal cord tissue but recordings were made only from the dorsal horn but at both C6 and C7 levels. Studies at later times, of protein, and of additional regulators are needed. Also, glutamate levels were not measured directly but genes for receptors and transporters *do* provide a proxy measure of signaling [16,17]. Nevertheless, the fact that its inhibition prevents pain and neuronal hyperexcitability after NRC suggests that $sPLA_2$ has a role in early nociceptive transmission and central sensitization for painful injury.

ACKNOWLEDGEMENTS

Funding provided by the Catherine D. Sharpe Foundation and the National Institutes of Health (R01NS199892; T32NS043126).

REFERENCES

[1] Johannes C et al, *Pain* 11:1230-9, 2010. [2] Abbed K et al, *Neurosurgery* 60:S28-S34, 2007. [3] Rothman S et al., *J Pain* 10:90-9, 2009. [4] Nicholson K et al, *Neurosci* 209:187-95, 2012. [5] Vasquez E et al, *J Neurosci* 21:9001-8, 2001. [6] Chang Y et al, *J Neurotrauma* 28:2429-38, 2011. [7] Kartha S et al, *Neurosci* 388:393-404, 2018. [8] Nicholson K et al, *J Neurosci Res* 92:116-29, 2014. [9] Nicholson K et al, *J Neurosurg:Spine* 20:751-62, 2014. [10] Svensson C et al, *Neurosci* 133:543-53, 2005. [11] Titsworth W et al, *Glia* 57:1251-37, 2009. [12] Morioka N et al, *J Neurochem* 80:989-97, 2002. [13] DeCoster M et al, *J Neurosci Res* 67:634-45, 2002. [14] Latremoliere A et al, *J Pain* 10:895-926, 2009. [15] Mantilla C et al, *Exp Neurol* 234:191-9, 2012. [16] Cui X et al, *Mol Neurobiol* 51:1322-33, 2015. [17] Labombarda F et al, *Neurosci Lett* 447:115-9, 2008.

SB³C2019
Summer Biomechanics, Bioengineering and Biotransport Conference
June 25 -28, Seven Springs, PA, USA

VISCOELASTIC RESPONSE OF SHOCK WAVE IMPACTED BRAIN TISSUE

Annastacia McCarty (1), Ling Zhang (1), Sarah Hansen (1), William J. Jackson (1), Sarah A. Bentil (1)

(1) Department of Mechanical Engineering
Iowa State University
Ames, Iowa, USA

INTRODUCTION

In recent years, there has been an escalation of blast-induced traumatic brain injuries (bTBI) caused by improvised explosive devices (IEDs) during global conflict. Blast injuries are attributed to the blast wave and has the capability to cause life-threatening injuries and fatalities. However, the mechanical behavior of brains subjected to shock wave impact is still unknown. Thus, hindering improved countermeasure development to mitigate bTBI. This study aims to understand the viscoelastic response of shock wave impacted brain tissue. *Postmortem* porcine brain tissue was subjected to shock wave impact, prior to unconfined compression experiments at a linear rate of 5 and 50 mm/min to a strain of 20%. The shock wave impacted tissue was allowed to relax for two minutes, after being compressed to 20% strain. Coefficients of the fractional Zener (FZ) constitutive model was optimized to obtain the viscoelastic material properties of the brain tissue.

METHODS

Porcine brains, chosen due to availability and anatomical similarity to human brains [1], were extracted from the skull immediately after the porcine was harvested. Afterwards, the freshly extracted brains were subjected to shock wave impact using a 0.177 cal Crosman Pumpmaster Classic air pistol. The pistol was pumped five (5) times before firing a single shock of air at the temporal region of the brain to achieve a reflected pressure of 138 kPa (20 psi). A pellet was not used with the air pistol. After the shock wave impact, each brain was prepared for unconfined compression tests by coring both the left and right cerebral hemisphere (Figure 1). Due to the brain's heterogeneous and anisotropic properties, care was taken to core a sample with a consistent composition [2].

Cored brains, with an average height of 12 mm, were subjected to stress relaxation using unconfined compression experiments (Figure 2). Unconfined compression occurred at a linear rate of either 5 or 50 mm/min to a strain of 20%, at which the strain was held constant for two minutes. Brain samples that were unimpacted by a shock wave were also subjected to unconfined compression experiments, for comparison. All porcine brains were tested less than 8 hours *postmortem*.

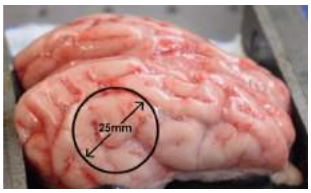

Figure 1. The black circle, overlaid on the right hemisphere of the porcine brain, illustrates the region and diameter cored.

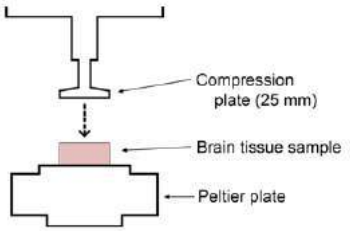

Figure 2. Schematic diagram of test setup.

The viscoelastic brain was described using the fractional Zener (FZ) constitutive model. The FZ coefficients were optimized by fitting the FZ model with the experimental data, using a nonlinear least squares

method in the software MATLAB [3]. Equation 1 describes the FZ viscoelastic model, where the coefficients are composed of E_∞, the long-term modulus of the tissue; E_0, the brain's instantaneous modulus; τ_0, the relaxation time; and α, representing the brain tissue's location on the viscoelastic spectrum. $\alpha = 0$ represents an elastic (Hookean) solid and $\alpha = 1$ describes a Newtonian fluid.

$$\sigma(t) + \tau_0^\alpha D^\alpha \sigma(t) = E_\infty \epsilon(t) + E_0 \tau_0^\alpha D^\alpha \epsilon(t), \quad (1)$$

where σ is stress and D is a differentiation/integration operator from fractional calculus [4].

The FZ model coefficients, describing the material properties of both shock wave impacted and unimpacted brain tissue, were quantitatively compared using a standard least squares regression that was fit to a linear fixed effect model. The statistical software JMP [5] was applied for the standard least squares regression analysis. The linear fixed effect model was used to understand the relationship between independent variables, such as shock wave impact and compressive loading rate, on the dependent variables (i.e. FZ coefficients). An analysis of variance (ANOVA) was then used to identify the FZ coefficients that were significantly dependent on the shock wave impact and/or the compressive rate. The significance level (p-value) was 0.05. As a result, p-values less than 0.05 were considered significant.

RESULTS

Fresh porcine brains, less than 8 hours *postmortem*, have a lower average instantaneous modulus (Figure 3) and lower average long-term modulus (Figure 4) after shock wave impact.

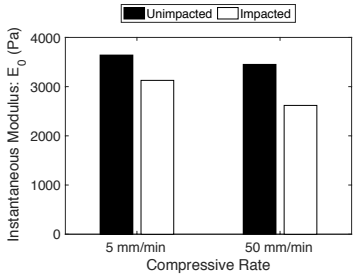

Figure 3. Average instantaneous modulus E_0 for brain unimpacted and impacted by a shock wave, at compressive rates of 5 mm/min and 50 mm/min.

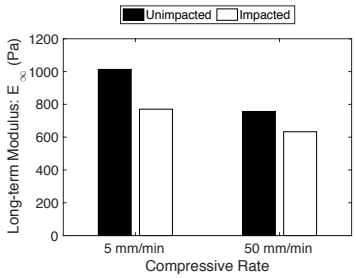

Figure 4. Average long-term modulus E_∞ for brain unimpacted and impacted by a shock wave, at compressive rates of 5 mm/min and 50 mm/min.

Coefficient values describing the relaxation time τ_0 and fractional order α were statistically influenced by the independent variables (i.e. whether or not the brains were subjected to a shock wave impact and also the applied compressive rate). The instantaneous modulus E_0 and long-term modulus E_∞ of the tissue was not statistically dependent on the compressive rate applied or whether or not the brain samples were impacted by a shock wave. Table 1 summarizes the results from the ANOVA.

Table 1: Influence of shock wave impact and compressive rate on the FZ coefficients. A p-value < 0.05 is statistically significant.

	Fractional Zener Coefficients			
Linear Fixed Effects Model Parameters	E_∞	E_0	τ_0	α
Shock wave Impact	0.3805	0.0978	0.0374	0.0114
Compressive Rate	0.5005	0.4024	<0.0001	<0.0001

DISCUSSION

In this paper, whole porcine brains were impacted by a shock wave, as would occur during a blast impact, to investigate the viscoelastic properties of the brain after a bTBI. The coefficients of a fractional Zener constitutive model were used to describe the viscoelastic response of shock wave impacted brain tissue. The brain tissue is softer after shock wave impact, as evidenced by lower average elastic modulus values (i.e. E_0 and E_∞). Additionally, the coefficients for the relaxation time and fractional order statistically depend on the compressive rate considered and whether or not the brain was impacted by a shock wave. Coefficients for the elastic modulus were not statistically influenced by shock wave impact status of the brain or compressive rate. This may due to variance in the distribution of gray and white matter of the cored inhomogeneous brain sample, even though the samples were extracted from the same region of the brain to achieve a consistent anatomical structure.

Previous study by Bentil et al. [4] and Davis et al. [6] also considered the fractional Zener model to characterize the brain's material response following unconfined compression experiments. However, this is the first study the authors are aware of that examined the mechanical response of brain tissue after a simulated blast-induced TBI. Thus, the results of this study will advance the knowledge of the brain's material properties due to bTBI.

ACKNOWLEDGEMENTS

This research was financially supported by the Roy J. Carver Charitable Trust under Grant #18-5021 and is acknowledged gratefully.

REFERENCES

[1] A. Säljö, F. Arrhén, H. Bolouri, M. Mayorga, and A. Hamberger, "Neuropathology and pressure in the pig brain resulting from low-impulse noise exposure," *J. Neurotrauma*, vol. 25, no. 12, pp. 1397–1406, Dec. 2008.

[2] F. Boudjema, B. Khelidj, and M. Lounis, "Dynamical properties of the brain tissue under oscillatory shear stresses at large strain range," *J. Phys.: Conf. Ser.*, vol. 790, no. 1, p. 012002, 2017.

[3] MATLAB, *MATLAB*. Natick, Massachusetts: The MathWorks Inc., 2016.

[4] S. A. Bentil and R. B. Dupaix, "Exploring the mechanical behavior of degrading swine neural tissue at low strain rates via the fractional Zener constitutive model," *Journal Of The Mechanical Behavior Of Biomedical Materials*, vol. 30, no. Journal Article, p. 83, 2014.

[5] JMP, *JMP*. Cary, North Carolina: SAS, 2015.

[6] G. B. Davis, M. Kohandel, S. Sivaloganathan, and G. Tenti, "The constitutive properties of the brain paraenchyma: Part 2. Fractional derivative approach," *Medical Engineering and Physics*, vol. 28, no. 5, pp. 455–459, Jun. 2006.

SB³C2019
Summer Biomechanics, Bioengineering and Biotransport Conference
June 25 -28, Seven Springs, PA, USA

EFFECTS OF EXCESSIVE IMPACT ON BONE CONDUCTION IN CONTACT SPORTS

Shinji Hamanishi (1), Namkeun Kim (2), Seongho Mo (2),

Takashi Watanabe (1), Yoshihiro Aoki (1)

(1) Department of Mechanical Engineering
Sendai National College of Technology
Natori, Miyagi, Japan

(2) Department of Mechanical Engineering
Incheon National University
Incheon, Korea

INTRODUCTION

Kendo, Japanese fencing, is a modern martial art, which descended from swordsmanship, and is widely practiced in Japan, Korea, U.S. and many other countries today. In order to get points and win matches, each player tries to hit one of the four target areas on opponent's body with a bamboo sword.

Many audiometric studies have shown that kendo training over many years often causes sensorineural hearing loss at 2000 Hz and/or 4000 Hz. Although the risk of kendo-associated hearing loss has long been known, its mechanism is still unclear.

Our hypothesis is that the cause of hearing loss by kendo may possibly be related to accumulation of small concussions in the human head by the excessive impact-induced bone conduction. We evaluated this hypothesis by a simplified impact experiments and Finite Element (FE) simulation using a skull bone and a kendo helmet models.

METHODS

1) Impact experiments

As shown in Figure 1(a), impact experiments were performed using a skull bone model (BONElike™, 3B Scientific), which has similar mechanical properties of the human skull bone. Strain gauges (KFG120Ω2, KYOWA) were then attached at 9 points of the skull model. Time history responses of strain at each points to impact by a bamboo sword were measured. Frequency responses were also analyzed based on time history data.

2) Bone conduction simulation

We introduced a computational approach to simulate bone conduction using a newly constructed FE model of a human head. The head model contains the skull, brain, soft tissue, cartilage and auditory peripheries, including the middle ear, cochlea and semicircular canals. In order to validate the newly constructed model, an impulse force, which were the same as the impact experiments, were applied only on FE skull model directly as shown in Fig. 1(b) and amplitude of bone conduction were calculated.

2) Kendo helmet model

A newly constructed FE model of kendo helmet is shown in Fig. 2. Kendo helmet consists of anterior and side parts and made by Titanium alloy and thick cotton fabric, respectively. Time history of impact distribution was simulated by applying impulse force on the impact area, which is surrounded by white dashed line in Fig. 2.

Simulation of bone conduction and impact simulation using FE models were performed by COMSOL Multiphysics.

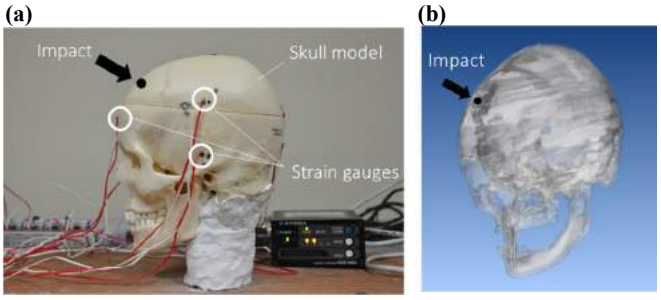

Figure 1: Experimental and computational approaches for evaluating bone conduction by kendo impact. (a) Experimental setup for bone conduction map using a skull bone model. Impact force was applied by a device with miniature shinai (bamboo sword) and strain at each points were measured. (b) Simulation of bone conduction using FE skull model. An impulse force was applied on the forehead area and velocity amplitude was calculated.

Poster Presentation #P215

RESULTS AND DISCUSSION

Figure 3(a) shows frequency characteristics of the strain amplitude at impact area, ear area and back of head area. At the impact area, impact by shinai causes bone conduction, which consists of frequency domains of 10, 100, and 200 Hz. Curves of ear area and back of the head are also showed that frequency components of bone conduction around 100 Hz are dominant.

Figure 3(b) is frequency response of velocity amplitude by FE skull model. Frequency component of bone conduction is approximately 100 Hz, which is correspond to that in experiments using the skull model. These results therefore indicate that an excessive bone conduction may possibly affect physical damages on brain and auditory peripheries.

Impact simulation using FE model of kendo helmet showed that excessive impact propagates to especially side part of kendo helmet, which may cause damage on brain and auditory system.

CONCLUSIONS

An excessive bone conduction may possibly affect physical damages on brain and auditory peripheries and frequency components around 100 Hz are dominant. Further simulation of bone conduction using a coupled model of human head and men are needed in order to evaluate relationship between bone conduction of 100 Hz and previously reported hearing loss at 2000 and/or 4000 Hz.

ACKNOWLEDGEMENTS

This work was supported by JSPS KAKENHI Grant Number 26350826 and 17K01775.

REFERENCES

[1] Takahashi M, Udaka J and Takeda N: Cases with Sensorineural Hearing Loss Associated with Japanese Fencing, Kendo. *Otology Japan*, 16(3), 178-182, 2006.

[2] Kato E, and Tono T: Audiometric Findings of Senior High School Students Belonging to a Kendo Club. Nippon Jibiinkooka Gakkai Kaiho, 115, 842-848, Oto-Rhino-Laryngological Society of Japan, Inc. 2012.

[3] Kato E, Tono T and Morimitsu T: Sensorineural Hearing Loss with a 2 kHz-dip in Kendo Athletes. Otologia Fukuoka, 42, 761-765, 1996.

[4] Kim N, You C and Stenfelt S: Quantification of the Contribution of Fluid Inertia and Bone Compression for the Hearing of Bone Conducted Sound, 7th Symposium on Middle Ear Mechanics in Research and Otology (MEMRO2015), 60, 2015.

[5] Kim N, Steele C and Puria S: The Importance of the Hook Region of the Cochlea for Bone-Conduction Hearing, Biophysical Journal, 107, 233-241, 2014.

[6] Kim N, You C and Stenfelt S: A Three-Dimensional Finite-Element Model of a Human Dry Skull for Bone-Conduction Hearing, BioMed Research International, Article ID 519429, 2014.

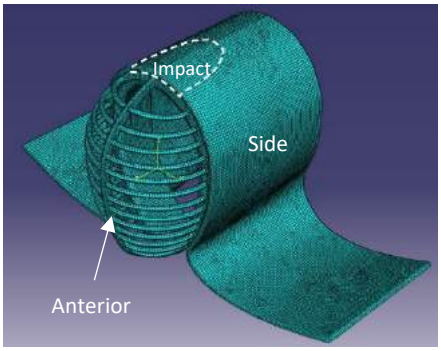

Figure 2: FE model of kendo helmet model. Impact area is shown by white dashed line.

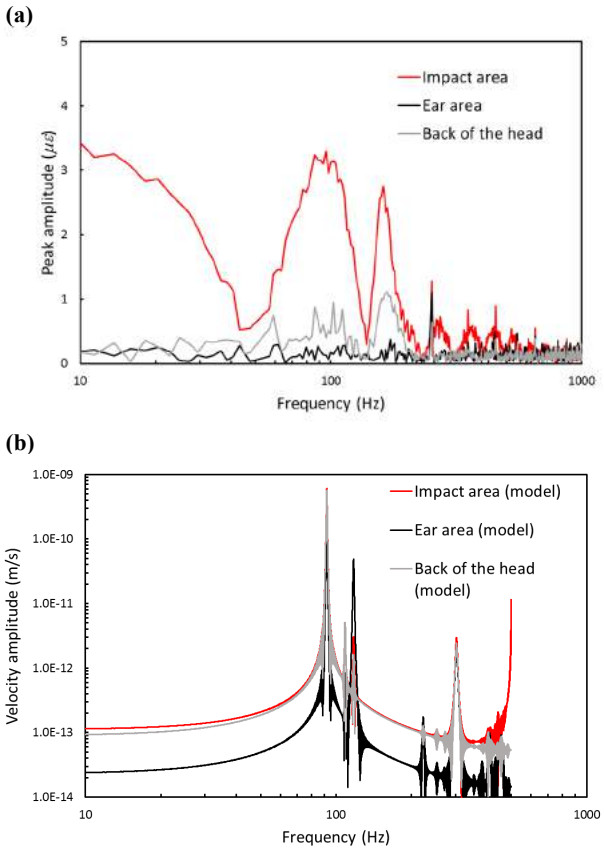

Figure 3: Comparison between experimental and computational results of bone conduction by impact. (a) Frequency response of the strain amplitude at impact, ear, and back of the head areas. (b) Simulation for frequency response of the velocity amplitude at impact, ear, and back of the head areas.

SB³C2019
Summer Biomechanics, Bioengineering and Biotransport Conference
June 25 -28, Seven Springs, PA, USA

PROPERTIES OF THE SIX LAYERS OF THE GRAY MATTER

Arpad Bakonyi[1], Alan Faitelewicz[2], Siavash Hashemi[2], Ali Sadegh[2]

(1) Department of Advanced Engineering Systems, University of Applied Sciences Technikum Vienna

(2) Department of Mechanical Engineering The City College of the City Univ. of New York New York, NY United States

INTRODUCTION

The grey matter neocortex contains most of the brain's neuronal cell bodies and plays an important role in the causation of traumatic brain injury (TBI). The function of grey matter (GM) includes muscle control, sensory perception, as well as information storage and cognitive abilities. The grey matter consists of six layers of neuronal tissue with different histological constitution. Brodmann [1] and Vogt [2] first described and mapped the cyto- and myeloarchitecture of neocortical grey matter (GM) in different regions, identifying at least six distinct histological layers of the GM neocortex. In their computational models, investigators have used a single layer representing the grey matter which would lead to inaccuracy in their TBI analyses [3]. As several studies have shown [4], [5], the resulting mechanical strains in the brain, induced by a head injury, are responsible for the injury of the brain tissue at the microscale. The detailed material properties of each layer of the grey matter as they relate to the outcomes of TBI have not been investigated yet.

The objectives of this study are to identify the six distinct layer of the gray matter and to determine the elastic and viscoelastic properties of each layer. It is further the goal of this study is to investigate the inaccuracy (error) in the computational TBI models when considering the grey matter as one uniform layer versus six distinct layers.

METHODS

Microscopy: A brain cadaver from a 67-year-old male was obtained from the anatomy lab of CUNY School of Medicine. A cubic cut-out segment was extracted with a scalpel from the cortex of the right hemisphere, containing GM neocortex and a significant amount of white matter, from the region of Brodmann's area 9 [1] of the superior frontal cortex, as shown in Fig. 1. After immersing into paraffin wax (Histoplast LP) using the tissue processor Leica ASP 300S, slices of 1.5 μm thickness were produced using the microtome Leica RM 2265 for microscopic analysis, and one 12 μm thick slice for indentation. The obtained slices were laid on a conventional glass plate and washed out from paraffin wax. The microscopic slices were stained with hematoxylin-eosin (H&E) and hermetically covered with a transparent thin covering plate, thus prepared for microscopic analysis. The thicker slice determined for indentation analysis was also washed out from paraffin and put into filtered water for storage, at 15 °C temperature.

The microscopic sample was examined under a ZEISS Axiocam HRc microscope using 10x and 20x zoom, and the tissue structure was visually analyzed, after post-processing (AxioVision), shown in Fig.2

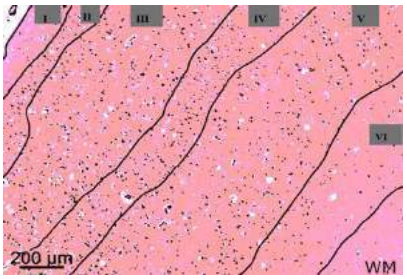

Fig.2: stained cross-section of the neocortical specimen showing the six layers of the grey matter from layer I adjacent to the pia matter

Fig.1: Location of the extraction of the sample

Indentation: The instrumented AFM nanoindenter MFP-3D™ (Asylum Research, Inc, USA) was utilized to conduct experiments on the 12 μm specimen slice. A silicon cantilever type SICONG-TL-SIO2-D5 (Applied NanoStructures, Inc, USA) with a spherical silica glass tip

was installed into the cantilever holder. The apparent radius was measured visually with the AFM instrument and was found to be R= 19 μm. After calibration of the instrument, the spring constant of the actual cantilever was measured k= 0.28 N/m. After finding the different layers based on the microscopic analysis, measurements were conducted across the entire GM cross-section, to obtain data from all layers of the neocortex. One series of measurements across the thickness of GM was declared as one sample. Six different sample regions were defined on the specimen containing several measurements in each layer. Elastic moduli from force-displacement curves were yielded by defining the contact stiffness [6] and using the Oliver-Pharr method [7].

The AFM nanoindenter was then utilized to create relaxation curves at all sample positions, by applying a pre-set displacement (1 μm) of the cantilever tip held for 10 s, followed by an unloading phase. The apparent force (Fig 3) was registered for all measurements and analyzed using the software Igor Pro 6.37 (WaveMetrics, Inc.). The force decays were fitted by a two-term exponential function and a Prony-series representation of viscoelasticity was established for each layer by conversion to shear values [8] and building layer averages.

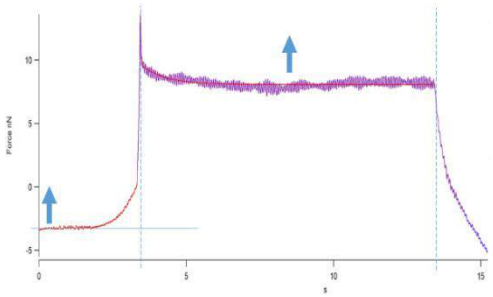

Fig. 3: Time dependent force plot (AFM), relaxation experiments

RESULTS

The microscopic image on Fig. 2 shows a cross-section of the obtained specimen from the superior frontal cortex. With the combination of Harris hematoxilyn and eosin, the neural cell nuclei, colored dark purple, could be distinguished from the network of axons and dendrites having light pink colors. Thus, different cell types and densities became apparent based on which the six different layers after Brodmann [1] were identified (Fig.2). The specimen was examined for its material properties with AFM nanoindentation, focusing on the differences in the outcomes of material properties between the layers. The elastic moduli and viscoelastic properties of the six layers of the gray matter were determined and are shown in Figs. 4 and 5, respectively.

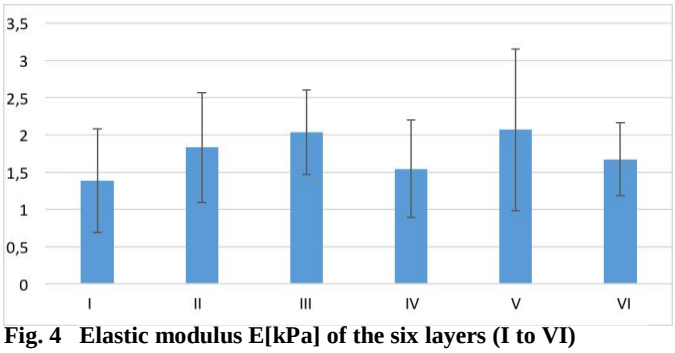

Fig. 4 Elastic modulus E[kPa] of the six layers (I to VI)

DISCUSSION

This study reveals difference (p=0.14) between the elastic modulus of layer III and layer I of the GM. The calculated average value E=1.78 lies close to the value 1.389 kPa±0.289 kPa found by Budday et al. [9], strengthening the feasibility of the measurements in this study.

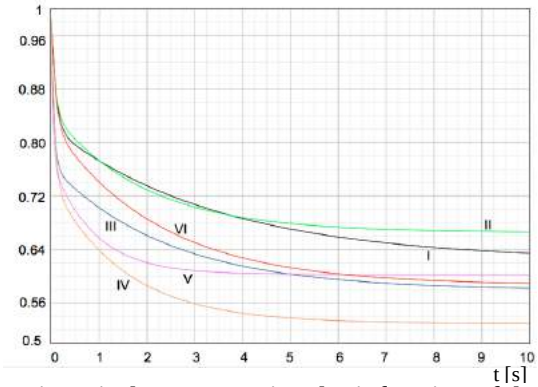

Fig. 5 Dimensionless average viscoelastic functions of the layers

The disparity of E among the layers can be connected to variations in the cytoarchitecture and the presence of pyramidal neurons in a dense fibrous network in layer III, while they are completely absent in layer I, as well as very scarcely populated in layers II and IV [1].

The analyses of the average viscoelastic properties of the GM reveal a sharp relaxation with a fast decay in layers III and V, indicating a more elastic, fibrous material, while layers I and II demonstrate a comparably slower decay implying more viscous characteristics than III and V. Regarding the comprising Prony-parameters, it was apparent that the overall average across all layers for parameters g_1 (0.2003) and g_2 (0.1983) yields almost the same values. The two relaxation times $\tau_1$and τ_2 were different in every layer with 2 orders of magnitude (avg. values 0.069 and 2.17) and could be associated with the viscous and the porous nature of brain tissue [10].

We have also used the results of this study in our FE head model and determined the inaccuracy (error) in the computational TBI models when considering the gray matter as one uniform layer verses six layers. The significant application of this study is to provide the ability to analyze the specification of TBI, i.e. the strain in each layer that is associated with specific dysfunction of the brain such as muscle control and sensory perceptions.

ACKNOWLEDGEMENTS

This research was supported by PSC-CUNY grant and the Marshall Plan Scholarship of the Austrian Marshall Plan Foundation.

REFERENCES

[1]K.Brodmann, et.al. Leipzig: J.A. Barth, 1909.
[2]. O. Vogt, J. Psychol. Neurol., vol. 15, no. 221–232, 1910.
[3]Hashemi, et.al. Int. J. Exp Comp Bio, V4, No1, 2018.
[4] T. W. McAllister et al., Ann. Biomed. Eng., v40, no1, pp. 127–140, 2012.
[5]. F. A. O. Fernandes et al. Proc. Inst. Mech. Eng. Part H J. Eng. Med., vol. 229, no. 8, pp. 592–608, 2015.
[6] J. C. Benech et al., "Am. J. Physiol. Physiol., vol. 307, no. 10, pp. C910–C919, 2014.
[7] W. C. Oliver etal. "Measurement of hardness and elastic modulus by instrumented indentation," 2004.
[8] Efremov et al Sci. Rep., vol. 7, no. 1, p. 1541, May 2017.
[9] Budday et al., Mech. Behav. Biomed. Mater., vol. 46, pp.318–330, 2016.
[10] . D. Finan, etal. Acta Biomater., vol. 55, pp. 333–339, 2017.

SB³C2019
Summer Biomechanics, Bioengineering and Biotransport Conference
June 25 -28, Seven Springs, PA, USA

HELMETED HEAD-NECK KINEMATICS WITH LOCALIZED IMPACTS AND IMPLICATIONS FOR BRAIN INJURY METRICS: A MILITARY APPLICATION

Narayan Yoganandan (1), John Humm (1), Mark Meyer (1), Frank Pintar (1), Tyler F. Rooks (2), Frederick T. Brozoski (2), B. Joseph McEntire (2), Valeta Carol Chancey (2)

(1) Department of Neurosurgery
Medical College of Wisconsin
Milwaukee, WI USA

(2) Injury Biomechanics and Protection Group
U.S. Army Aeromedical Research Laboratory
Fort Rucker, AL, USA

INTRODUCTION

It is known in biomechanical and clinical literatures that angular kinematics play a major role in traumatic brain injuries[1]. Contact loading to the head may be a necessary condition to achieve the levels of angular kinematics required to produce brain injuries[2]. Sporting events such as American football, at the professional or collegiate level, have shown that contact loading to helmeted athletes can result in mild traumatic injuries, termed as mTBI or concussion[3 4]. This is also true in the military[5]. To determine helmet injury mitigating capability, helmet test standards use drop techniques that do not include the neck structure, which would enable the angular motions of the head-helmet system. The overall objectives of the present study are to develop a test methodology using a hybrid helmeted-head-neck system, and to determine the linear and angular kinematics under impact loads delivered at four distinct sites, around the head circumference.

METHODS

Specimen preparation: The study was conducted using a hybrid helmeted-head-neck system. The anthropomorphic neck surrogate from the widely used Hybrid III test device in automotive environments was attached to the Facial and Ocular CountermeasUres for Safety (FOCUS) headform, with an army combat helmet. This headform is used for evaluating head and facial loads[6]. The helmet was donned to the head with straps per Army guidelines (TM 10-8470-211-10, active 08/01/2015). Care was taken to ensure that the helmet was placed horizontally when viewed from the sagittal plane and with bilateral symmetry from the coronal plane. The helmeted-head-neck system was attached to a load cell at the base of the neck and fixed to the custom platform of a mini-sled (Figure 1). The Frankfort plane of the head-helmet system was maintained horizontal in all tests. This was ensured with a laser beam. A velocity gate was used to measure the impact velocity, and a light sensor was used to trigger the high-speed camera and data acquisition system simultaneously.

Impact sites and loading: Four sites were chosen to apply the impact loading to the helmeted-head-neck system: front, rear, left side, and left nape. These sites corresponded to the current locations for evaluating helmets and obtaining head linear accelerations from drop tests. Repeat tests were done at each of the four sites. The target impact velocity was 3 m/s, also according to the current standards in the military[9]. Sufficient time was allowed between tests to permit full relaxation of the viscoelastic components in the system: the neck and helmet.

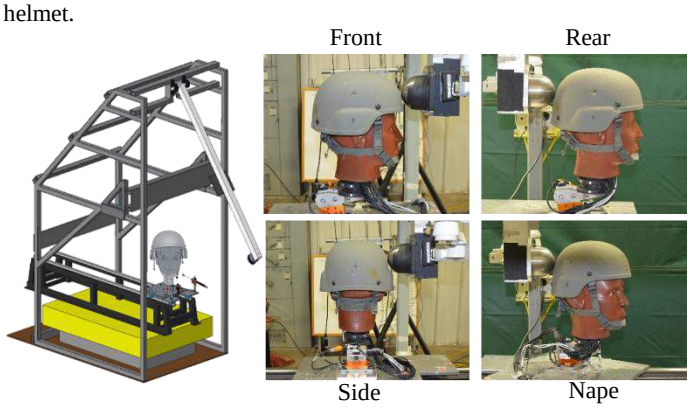

Figure 1: Left: mini-sled test device. Right: four impact sites with the helmeted-head-neck system, and the impactor is also shown.

Instrumentation: A triaxial accelerometer (Endevco 7264B-2000, San Juan Capistrano, CA) was attached to the center of gravity of the head, and a triaxal angular velocity sensor was also attached to the same

block. An accelerometer placed at the base of the neck was used to record the applied acceleration. All data was gathered according to the Society of Automotive Engineers J211 specifications: at a sampling rate of 20,000 Hz and filtering using SAE class 1000 filter[7].

RESULTS

Figure 2 shows a representative set of linear acceleration and angular velocity profiles from repeat tests for the side impact case. The maximum anteroposterior (X) and superior-to-inferior vertical accelerations (Z) for the rear impact tests were 33.0 ± 1.5 g and 11.7 ± 0.02 g. For the frontal impact tests, they were 27.3 ± 2.1g and 10.2 ± 0.7 g, respectively, and the lateral accelerations (Y) were the minimal off-axis components. In contrast, for the side impact tests the anteroposterior accelerations were off-axis and minimal, while the lateral and vertical accelerations were 28.5 ± 1.2 g and 8.2 ± 0.05 g, respectively. All 3 components were comparable for the nape impact tests. Table 1 shows the peak data from all tests. Figure 3 compares the peak angular velocities from all tests. Standard deviations are shown in in red bars for each impact site in the figure.

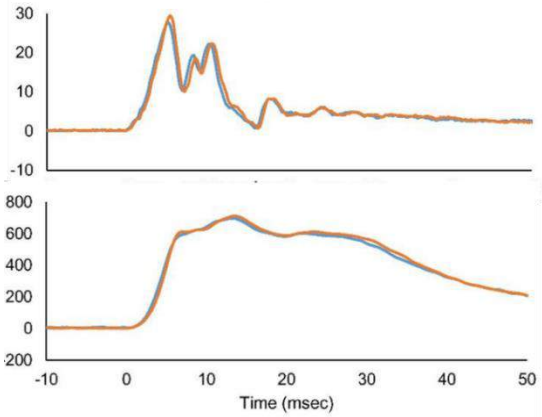

Figure 2: Linear acceleration (g, top) and angular velocity (deg/sec, bottom) for the side impact. Data are from repeated tests.

Table 1: Mean peak linear acceleration magnitudes from all tests. Off-axis values are not shown.

Impact Site	Values	Linear acceleration (g)		
		X	Y	Z
Rear	Mean	33.03	Off-axis	-11.67
	SD	1.50	Off-axis	0.02
Front	Mean	-27.34	Off-axis	10.18
	SD	2.15	Off-axis	0.75
Side	Mean	Off-axis	28.49	-8.22
	SD	Off-axis	1.22	0.05
Nape	Mean	29.36	16.72	-14.46
	SD	0.50	0.66	0.69

DISCUSSION

The linear and angular kinematics of the helmeted-head-neck system, as demonstrated by the morphologies of the time histories, were very repeatable for all impact sites. Further, both kinematic histories were confined to the principal plane in all cases except the nape site, which is to be expected as this location is off-principal planes. The coefficients of variations were low, less than 8% in all cases for both types of peak kinematics. This shows that the developed protocols for donning the helmet, maintaining the fit within the FOCUS headform, and the testing methodology using the mini-sled are appropriate for evaluating the combat helmet to assess its injury mitigating characteristics and traumatic brain injuries from impact loading. It should be noted this method is novel, and it is not in the current military standards. Further, greater magnitudes of the angular kinematics from the present hybrid system shows the importance of including the neck to induce angular motions, paralleling a recent analysis albeit using a different model[10].

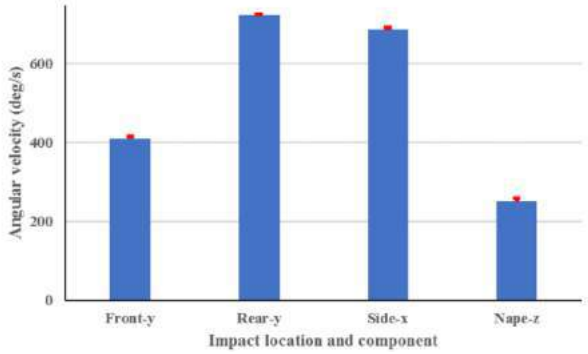

Figure 3: Angular velocities from all tests.

The presently used 3 m/s impact velocity was based on the isolated helmet drop tests that includes a headform used in the automotive standards, FMVSS 218, for motorcycle helmets. The FOCUS headform used in this study was designed to have realistic ears, chin, and nape for proper mounting of spectacles and helmets, and it attaches to a standard Hybrid III neck. Other details of the headform are given elsewhere[6]. The present helmeted-head-neck preparation is therefore, applicable to the military, and it also uses biofidelic head and neck surrogates. This hybrid system can be used for other conditions such as those simulating parachute drops and determine the linear and angular kinematics[8]. The present data and results can also be used to exercise finite element models to compute regional and local brain metrics such as cumulative strain damage measures and brain injury criteria, BrIC[11].

In summary, this study has provided a methodology for testing military helmets using military-developed headform to induce angular kinematics and reported a set of metrics that are traditionally correlated with brain injuries, hitherto not considered in helmet evaluations in this discipline. The military helmet-FOCUS headform together with the widely used biofidelic neck can be used to conduct additional tests for evaluating the helmet performance and mitigation of brain injuries, as applied to this important group of our populations.

ACKNOWLEDGEMENTS

This material is the result of work supported with resources and use of facilities at the Zablocki VA Medical Center in Milwaukee, Wisconsin, the U.S. Army Medical Research and Materiel Command in Fort Detrick, Maryland, under agreement number W81XWH-16-1-0010. Any views expressed in this article are those of the authors and not necessarily representative of the funding organizations.

REFERENCES

1. Yoganandan N, et al. Accidental Injury: Springer, NY, 2015.
2. Yoganandan N, et al. J Trauma 2009;66(2):309-15
3. Guskiewicz KM, et al. Neurosurgery 2007;61(6):1244-52
4. Rowson S, Duma SM. Ann Biomed Eng 2011;39(8):2130-40.
5. Brozoski F. USAARL Report 2010-10
6. Crowley J, et al. Aviation, Space, Envir. Med. 2009;80(9):831.
7. SAE. Warrendale, PA. 2014
8. McEntire BJ, Whitley P. USAARL Report, 2005
9. CO/PD-05-04. Dept Army Fort Belvoir, VA. 2007
10. Begonia, MB, et al., J Biomech, 2018 (In Press)
11. Takhounts EG, et al. Stapp Car Crash J 2013;57:243-66

SB^{3}C2019
Summer Biomechanics, Bioengineering and Biotransport Conference
June 25 -28, Seven Springs, PA, USA

INVESTIGATE THE VARIATIONS OF THE HEAD IMPACT RESPONSE IN A RODENT HEAD IMPACT ACCELERATION MODEL BY FINITE ELEMENT MODELING

Runzhou Zhou, Liying Zhang

Biomedical Engineering
Wayne State University
Detroit, MI, USA

INTRODUCTION

Diffuse axonal injury (DAI) is a severe form of traumatic brain injury (TBI) and often induced by direct external forces as in motor vehicle accidents. DAI is generally associated with mechanical disruption of innumerable axons throughout the brain i.e. in the cerebral hemispheres (subcortical white matter) as well as focal lesions in the corpus callosum and in the dorsolateral quadrants of the rostral brainstem [1]. There were many in vivo models proposed to study DAI. Marmarou head impact acceleration model [2] is the most widely used. This model can reliably produce axonal changes in a closed head injury in rodents. However, this model suffers large variations of the injury results [3]. Recently, the impact device/system was modified to improve the consistency and repeatability of the impact energy [4,5]. Furthermore an in-house made miniature sensor was added to the rat head to monitor the real-time rat head motion in response to each impact. In addition, the degradation characteristics and reusability of foam after repeated was quantified to assure the consistent support offered by the foam bed during impact. Even by precisely control the impact velocity, the material properties of the foam bed [4], the variations of the head impact kinematics and subsequent brain injuries were still observed. This study was aimed to utilize a Finite Element (FE) model of a rat head/body to investigate the potential factors, e.g. the initial inclination angle of the helmet on the rat skull, the variation of the skull properties which could influence the impact energy transferring to the head. Therefore, it could affect the resulting head kinematics and its resulting injury severity in this rodent head impact model.

METHODS

FE rat head model development and validation: A detailed FE rat head model was developed based on the MRI, micro CT and atlas data. The skull was meshed with three-layer solid elements with various thicknesses. The brain mesh included all essential anatomical structures i.e. cerebral white matter, gray matter, olfactory bulb, corpus callosum, hippocampus, cerebellum, brainstem with pyramidal tract (py), medial lemniscus (ml) and medial lemniscus fasciculus (mlf), ventricles, CSF, pial, arachnoid and dural mater (**Error! Reference source not found.**). The mass of the brain and head was 1.9g and 36g, respectively. The FE rat head model consists of over 722,000 elements of which 310,000 being the brain.

The white matters structures e.g. corpus callosum and brainstem consisting of highly aligned axonal fibers were assigned with transversely-isotropic material. The rest of the brain were assigned as linear viscoelastic. A simplified rat body were also modeled to provided realistic boundary to the head at the spine-medulla junction.

Three sets of experimental data including dynamic cortical deformation (DCD), brain scar length from head rotation, and impact acceleration kinematics [6-8] were simulated to validate rat model.

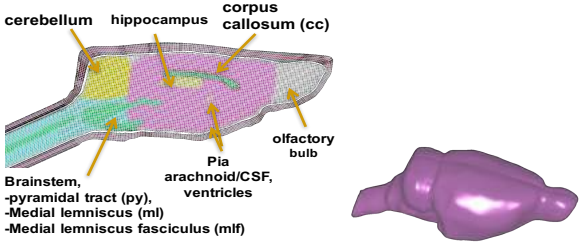

Figure 1 A FE rat head and brain model

Effect of the helmet angle, skull stiffness and impact: The validated rat head FE model along with a simplified rat body was applied to

simulate the rat head impact experiments using the modified Marmarou model reported previously [4,9]. Briefly, the rat was placed on the foam bed in prone position where the top surface of the helmet (stainless disc) glued to the skull was aligned with the horizontal plane. The flat end of the cylindrical impactor impacted to the helmet at 6.5m/s causing a downward head excursion first followed by the entire body pressing into the foam bed until the foam returned to its original height. The experimentally measured head kinematics showed large variations. A several factors might influence the test results. The helmet surface inclination angle might vary from test to test (Figure 2). The skull stiffness between the rats could vary and therefore the local deformation may vary. In order to understand the effect of the initial contact condition and the skull property on the resulting head motion, we conducted two studies. For helmet surface inclination effect: the helmet was inclined backward (Rb), forward (Rf) and sideward (Rs) by 2-5 degrees, respectively and compared to the helmet inclined at 0 degree (baseline) (Figure 2D,E). For the skull property effect, the skull elastic modulus was increased/decreased by 25% of the baseline value and also as rigid material (simulate no skull deformation). The resulting head kinematics and brain strain in the corpus callosum (cc) and pyramidal tract (py) of the brainstem, were compared.

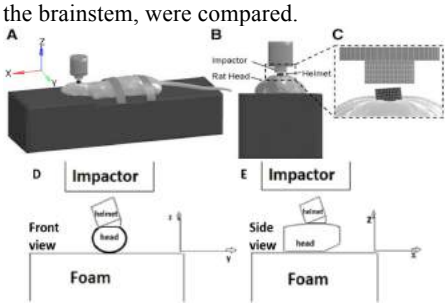

Figure 2: Simulation setup to investigate the effects of the helmet surface inclination angles and variations of the skull stiffness on the resulting head kinematics in a closed head injury model

RESULTS

Rat head model validation: The DCD validation results showed that both the pia-arachnoid material property and the contact interface defined between the brain and skull had effects on resulting brain displacement profile under DCD loadings. The viscoelastic pia-arachnoid material along with the auto-tiedbreak matched not only to the peak but also the temporal patterns of the displacements measured from experiments (Figure 3) achieving CORA rating score of 0.74.

The brain scar length validation was aimed to validate the deeper brain responses due to head rotation. Explicitly modeling the pin was found to be essential to match the brain movement as measured by the pin. At the 2 mm below the brain surface, the model predicted strain scar length of 0.64 mm which matched well to tests (0.6±0.06mm).

For the validation of rat head kinematics, the model predicted the peak and patterns of the head linear acceleration and rotational velocity-histories matched to the typical experimental curves characteristics. The excursion of rat head into the foam and its displacement was also matched quite well with the experimental data.

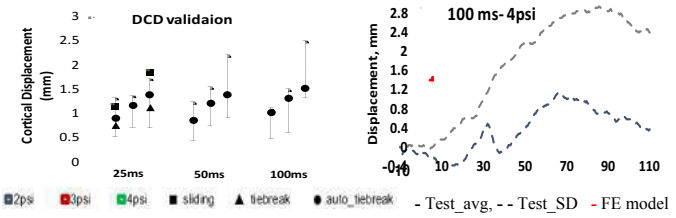

Figure 3 DCD brain displacement validation results

Effect of the helmet surface inclination angle: At a given impact energy, by changing inclination angle of the helmet surface from 0 to 2 degrees anteriorly, laterally or posteriorly, respectively, the head linear acceleration varied by 2-8% but increased to 8-31% at 5-degree inclination angle (Table 1). The change in rotational velocity was inversely related to the change in linear acceleration in all cases.

Table 1 Head kinematics affected by helmet inclination

Linear acceleration changes							
	Baseline(Flat)	Rb-2D	Rb-5D	Rf-2D	Rf-5D	Rs-2D	Rs-5D
Acceleration		4%	8%	-8%	-31%	-2%	-11%
Rotational velocity changes (*(p): positive value; (n): negative value)							
	Baseline(Flat)	Rb-2D	Rb-5D	Rf-2D	Rf-5D	Rs-2D	Rs-5D
R-y (p)		0%	1%	-1%	-4%	0%	0%
R-y (n)		-7%	-19%	7%	14%	0%	-2%
Ry (p+n)		-4%	-9%	3%	5%	0%	-1%

Effect of the skull stiffness: By changing the skull' Young's modulus either increase or decrease by 25%, it was observed only 3% changes in head linear acceleration and velocity was unaffected (<1%). The brain MPS responses in the cc were unaffected. But for brainstem, MPS in the py near caudal end was increased by 10% as a result of softer skull. As the skull was defined as rigid, linear acceleration and rotational velocity were both increased by 8% suggesting that the skull deformation could have absorb some impact energy. The MPS in the cc and py were increased by 16% and 29%, respectively.

DISCUSSION AND CONCLUSIONS

The FE models of impact head injury once validated can assist in exploring various biomechanical factors influencing the head impact response and subsequently the internal brain response such as occurred in this rodent closed head impact TBI model. Identification of these variables may help explain the variability of injury severities observed between the samples from an injury model and across different labs.

For Marmarou's rodent head impact TBI model, in addition to improve the repeatability and consistence of the impact device by engineering design, the changes in initial boundary conditions from the helmet surface angle have shown to have impact on the head kinematics following the impact. The current study has shown that the helmet inclination angles could affect the head kinematics up to 19% and with more effect on the brain strain in terms of spatial pattern and magnitude. This may explain the variations of the head kinematics reported and DAI severities in our previous studies [3,7].

For the biomechanical responses within the brain, the MPS in the brainstem was affected by the local skull deformation but cc was not. The MPS in the cc was affected by the head rotation. The MPS in the brainstem was affected by the combined head kinematics (linear and rotation), local skull deformation and head-neck position. The ongoing analysis focuses on the correlation of the biomechanical response map in the FE rat brain model to the DAI injury map and ultimately to establish the tissue level thresholds for predicting white matter injury.

ACKNOWLEDDGEMENTS

The work was supported by NIH R01 EB006508.

REFERENCES

[1] Wright, R. Biomech and Modeling in Mechanobiology, 2012. 11:245-260.
[2] Marmarou, A., et al.,Journal of neurosurgery, 1994. 80(2):291-300.
[3] Piper, I. et al. Journal of neuroscience methods, 1996. 69(2):171-174.
[4] Li, Y. et al., Stapp Car Crash Journal, 2011. 55:25.
[5] Zhang, L., et al. J Neuroscience Method, 2010,
[6] Shreiber, D. et al. 1997, SAE Technical Paper.
[7] Davidsson, J. and M. Risling, Frontiers in neurology, 2011. 2.
[8] Antona-Makoshi, J. et al., Int J Automot Eng, 2014. 5: p. 31-7.
[9] Li, Y. et al., Journal of Neurotrauma, 2011. 28(9): p. 1767-1782.

SB³C2019
Summer Biomechanics, Bioengineering and Biotransport Conference
June 25 -28, Seven Springs, PA, USA

INJURY RISK CURVES USING A NOVEL (BAYESIAN) TECHNIQUE TO DESCRIBE HUMAN TOLERANCE IN IMPACT BIOMECHANICS

Nicholas DeVogel (1), Anjishnu Banerjee (1), Narayan Yoganandan (2)

(1) Division of Biostatistics
Medical College of Wisconsin
Milwaukee, WI USA

(2) Department of Neurosurgery
Medical College of Wisconsin
Milwaukee, WI USA

INTRODUCTION

Injury risk curves (IRCs) are needed to quantify human tolerance and develop countermeasures to advance safety in environments such as automotive, military, and aviation [1]. Historical developments have focused on binary regression methods such as the Weibull, logistic, and probit models. These models cannot account for censored data that are typical in impact biomechanics. More recent developments in the field include non-parametric and parametric survival regression methods. The International Standards Organization has recommended procedures to perform survival analysis for developing IRCs [2]. This process has been adopted in a variety of loading scenarios and applied to automotive and military disciplines [3-4]. This study presents a semi-parametric Bayesian technique for survival analysis, novel in the context of IRCs and impact biomechanics. Its effectiveness is demonstrated using tests with Post Mortem Human Subject lower leg-foot-ankle complexes.

METHODS

A published dataset was used from the senior authors [5]. It consisted of delivering axial impacts applied to the plantar surface of the foot to the below knee-foot preparations. The experimental test design included repeated tests on the same specimen resulting in injury and non-injury data points for each specimen. In some cases, only one test was conducted yielding a single injury or non-injury data point. Thus, the dataset consisted of a combination of interval censored, right censored, and left censored observations. The axial force was treated as the response variable. The IRC was developed using a semi-parametric Bayesian survival model, termed B-IRC. The transformed Bernstein polynomial prior was used [6]. Mathematical representation of the chosen technique is as follows.

$$\begin{aligned} S_0(\cdot) \mid \alpha, \theta &\sim TBP_L\big(\alpha, S_\theta(\cdot)\big) \\ \alpha &\sim \Gamma(a_0, b_0) \\ \theta &\sim N_2(\theta_0, V_0), \end{aligned} \tag{1}$$

where $S_0(\cdot)$ is a non-parametric baseline survival function, α and θ are prior parameters, a_0, b_0, θ_0, and V_0 are prior hyperparameters, and $S_\theta(\cdot)$ is a parametric family of survival functions. The transformed Bernstein polynomial prior is given as

$$\begin{aligned} S_0(t) &= \textstyle\sum_{j=1}^{L} w_j I\left(S_{\theta_j}(t) \mid j, L-j+1\right) \\ w_L &\sim Dirichlet(\alpha, \dots, \alpha), \end{aligned} \tag{2}$$

where $I(\cdot \mid a, b)$ is the cumulative distribution function for a beta random variable with parameters a and b. The 95% credible intervals (CIs) were calculated with this method and were also used to calculate the Normalized Confidence/Credible Interval Size (NCIS) at a few levels of injury risk. This resultant B-IRC was compared to the IRCs developed using the standard parametric survival approach, denoted PS-IRCs, using Weibull (WB), lognormal (LN), and loglogistic (LL) distributions. Appropriate 95% confidence intervals (also noted CIs) were constructed and were used to calculate corresponding NCIS values.

RESULTS

The B-IRC and PS-IRCs are presented in Figure 1. Forces of 2.9 kN, 2.6 kN, 2.4 kN, and 2.3 kN were associated with 10% risk injury for the Bayesian, PS-LL, PS-LN, and PS-WB IRCs, respectively. Figure 2 shows difference between the PS-IRCs and the B-IRC for pre-chosen risk levels. The maximum change occurred at lower risk levels ($<LD_{50}$) with the PS-LL IRC and at higher risk levels with the PS-WB IRC. Figure 3 shows the NCIS values for the pre-chosen risk levels for each IRC. The NCIS values were the lowest for the B-IRC (0.55), and this was followed by PS-LL (0.91), PS-WB (0.93), and PS-LN (0.94),

at the same level of injury probability. The NCIS data are shown in Figure 3, for other risk levels.

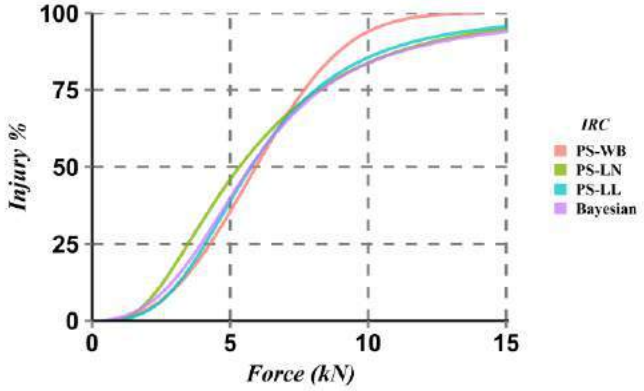

Figure 1: IRCs

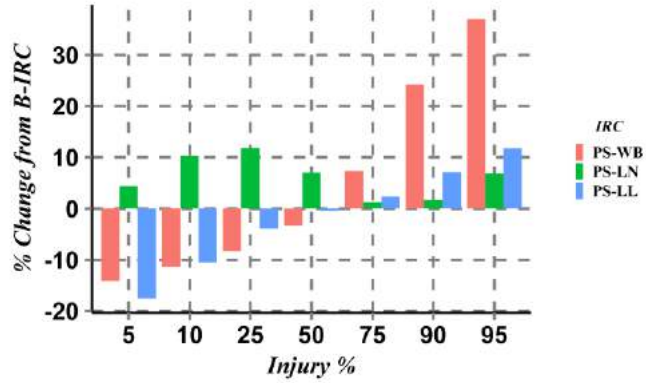

Figure 2: % Change from B-IRC

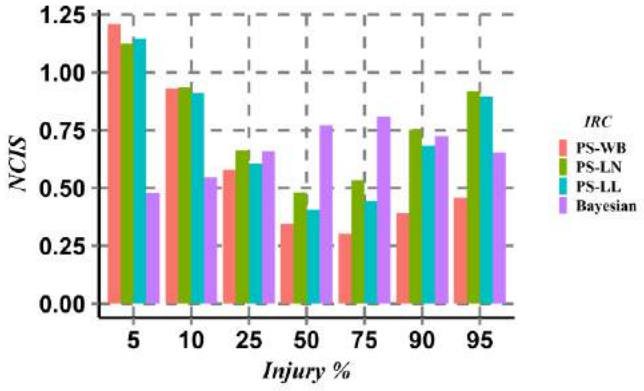

Figure 3: NCIS

DISCUSSION

Injury risk curves in recent years have been derived using parametric survival methods. In the absence of covariates, this involves estimating two scalar parameters of a chosen parametric distribution, typically labeled shape and scale, which would define the entire curve. This dependence on just two parameters puts strong constraints on the shape of the IRC. Even in the presence of three typical distributional choices for PS (Weibull, lognormal, loglogistic), the constraints may not allow enough flexibility to unbiasedly estimate the true underlying IRC. An entirely new paradigm for estimating IRCs is by using semi-parametric Bayesian survival methods, which are gaining increasing acceptance in the statistical literature, owing to their flexibility. The semi-parametric Bayesian model presented in the present study is equivalent to estimating an IRC with an infinite number of parameters, allowing much greater flexibility compared to PS models. The flexibility is achieved through the prior, specified in equations (1) and (2).

All the PS-IRCs were relatively similar to the B-IRC around the LD_{50} level risk of injury. The PS-IRC based on the Weibull distribution showed the greatest deviation from the B-IRC in general, especially at higher risk levels with a 37% increase compared to the B-IRC in force required for 95% risk of injury. The PS-IRC based on the lognormal distribution generally had a higher force required while that based on loglogistic was generally lower at lower risk values and higher at higher risk values. These are therefore dependent on the distribution, e.g., lognormal versus Weibull.

In constructing an IRC, it is intuitive that there should exist greater variability in the middle (LD_{50} level) and less at the extreme ends (low/high force), as a very low force magnitude should have a very low probability of injury. Thus, the NCIS should be generally smaller at the extreme ends and larger in the middle region. The B-IRC showed this pattern, while the PS-IRCs did not demonstrate this level of association (Figure 3). In fact, the PS-IRCs showed the opposite pattern, with greater variability at the extreme ends and less towards the middle. These results, while derived for one set of experimental data, shows that the Bayesian method may be the more appropriate technique to construct IRCs that are a more robust estimate of the true risk curve.

The novel approach presented here not only allows greater flexibility in estimating IRCs but uses a methodology, Bayesian, that is growing in popularity in the statistics community. As such it is a rich area for future development, resulting in even more benefits over typical PS-IRCs. The Bayesian technique presented in this study has the potential to replace or confirm the validity of the PS methods that have been used for IRCs in impact biomechanics and safety engineering applications.

ACKNOWLEDGEMENTS

The project described was supported by the National Center for Advancing Translational Sciences, National Institutes of Health, Award Number UL1TR001436. The content is solely the responsibility of the author(s) and does not necessarily represent the official views of the NIH. This study was also funded by the Research and Education Program Fund, a component of the Advancing a Healthier Wisconsin endowment at the Medical College of Wisconsin. This material is the result of work supported with resources and use of facilities at the Zablocki VA Medical Center in Milwaukee, Wisconsin, the U.S. Army Medical Research and Materiel Command in Fort Detrick, Maryland, W81XWH-16-1-0010. Any views expressed herein are those of the authors and not necessarily representative of the funding organizations.

REFERENCES

[1] Yoganandan, Narayan, Alan M. Nahum, and John W. Melvin, eds. Accidental injury: biomechanics and prevention. Springer, 2014.

[2] Petitjean, Audrey, et al. Injury risk curves for the WorldSID 50th male dummy. No. 2009-22-0016. SAE Technical Paper, 2009.

[3] Yoganandan, Narayan, and Anjishnu Banerjee. "Survival analysis-based human head injury risk curves: focus on skull fracture." Journal of neurotrauma 35.11 (2018): 1272-1279.

[4] Yoganandan N, et al. Traffic Inj Prev, 2014, 2015, 2018.

[5] Yoganandan N. Stapp car crash journal, 1996.

[6] Zhou, Haiming, and Timothy Hanson. "A Unified Framework for Fitting Bayesian Semiparametric Models to Arbitrarily Censored Survival Data, Including Spatially Referenced Data." Journal of the American Statistical Association 113.522 (2018): 571-581.

SB³C2019
Summer Biomechanics, Bioengineering and Biotransport Conference
June 25 -28, Seven Springs, PA, USA

DESIGNING AN IMPACT PENDULUM TO TEST DIFFERENT CONCUSSION PREVENTION HELMET ACCESSORIES

F. Groder (1), E. Ozkaya (1), L. Conetta (3), M. Kurt (1, 2)

(1) Department of Mechanical Engineering
Stevens Institute of Technology
Hoboken, NJ, USA

(2) Translational and Molecular Imaging Institute (TMII)
Mount Sinai Hospital
New York, NY, USA

(3) The Packer Collegiate Institute
Brooklyn, NY, USA

INTRODUCTION

Approximately 1.6 million to 3.8 million sport-related mild traumatic brain injuries (mTBI) occur in the United States each year [1]. Of particular concern is football, which not only has one of the highest rates of concussion but also the largest participation [2]. Between 2012-2014 NFL regular seasons, there were 292 reported concussions in 480 games giving an average concussion per game ratio of 0.61 [3]. There is also now evidence linking long-term neurodegenerative mechanisms such as Chronic Traumatic Encephalopathy (CTE) in former NFL players with repeated concussions [4].

These worrisome statistics in football led to many rule changes and emphasis on tackling form [5], as well as emphasis on novel helmet technologies [6]. There are three typical methods used for football helmet testing: a linear impactor [7], a drop tester [8] and an impact pendulum [9]. The NFL ranks helmets every year based on linear impactor tests and drop tests at speeds varying from 25.37 mph to 44.07 mph (11.34 m/s to 19.7 m/s). They look at peak rotational acceleration as well their own severity index values [10]. For the purpose of this study, we designed an impact pendulum that would mimic the mechanics of a football impact at speeds reaching up to 6.4 m/s. We constructed the impact pendulum and installed all of the supplemental pieces to match the previously stated NFL testing standards so we can research, design and test the different concussion prevention helmet accessories.

METHODS

This section will go into detail on the design and implementation of all of the supplemental components. The parameters of the impact pendulum were based on Virginia Tech's custom impact pendulum [9]. These components include: a scissor lift/slider assembly, an electromagnet lifting mechanism, four accelerometers and an inclinometer. The scissor lift assembly consists of two motorcycle hand-crank lifts with a 30" x 5" x 0.5" steel plate welded between. The scissor lifts are bolted to the floor and the slider is bolted to the metal plate (Figure 1). The slider includes an attachment for the Hybrid-III 50th Male head form that includes the capability to change the angular orientation of the head form. The scissor lift allows for a wide range of impact heights on the Hybrid-III 50th Male head form depending on the helmet that is being used during testing.

Figure 1: Scissor Lift/ Slider/ Hybrid-III 50th Male Head Form and Neck Assembly

For the lift/release mechanism, an electromagnet was implemented into the supplemental design of the pendulum. An electric hoist, which is connected to the top horizontal frame of the pendulum, draws power from a ceiling outlet through an extension cord and is controlled by the yellow toggle switch. Connected to the hoist is the electromagnet which draws power from the electrical cart through a retractable extension cord and an on/off switch. The electrical cart is the hub of the controls for the

pendulum as it draws power from a wall outlet and allows for easy access to the drop mechanism when conducting impact tests. When the electromagnet is on, it connects to a u-bracket that is bolted to the pendulum arm, this connection allows for a safe lifting mechanism (Figure 2). Furthermore, an inclinometer will be attached to the pendulum arm and its display will be attached to the pendulum frame directly under the hoist control and near the electrical cart so the user can see the drop angle as the arm is being lifted.

Figure 2: Electromagnet Connection to Hoist and Electrical Cart

Finally, the impact data would be obtained by DTS sensors placed in the center of mass of the Hybrid-III 50th Male head form. These sensors include one tri-axial accelerometer (ACC3 PRO) and three uniaxial accelerometers (ARS PRO-8K 2000 Hz) placed into a mounting block. Figure 3 below shows the wiring diagram for the sensors while Figure 4 shows a wiring diagram for all of the electrical components connected to the cart. Initial drop test data was done with the sensors through the provided user interface, SLICEWare (Seal beach, CA, USA).

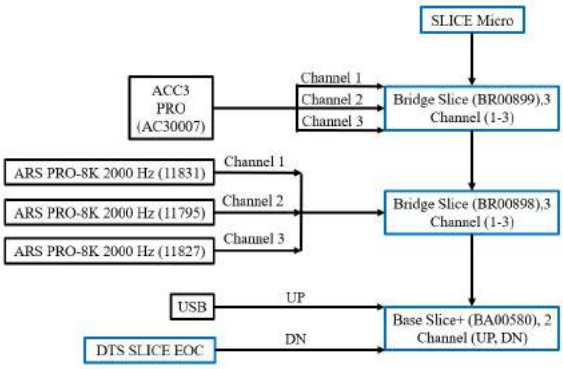

Figure 3: DTS Sensor Wiring Diagram

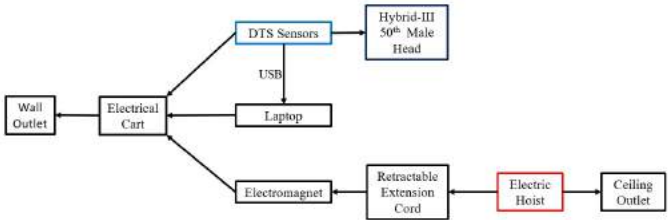

Figure 4: Electrical Cart Wiring Diagram

The pendulum frame is 11' 2" x 5' 4" x 8'and is made of hollow square steel tubing. The pendulum arm consists of three hollow square aluminum tubes, two being 2' 11" long, weighing 9.37 lbs. (4.25 kg) each and the third being 6' 3" long, weighing 20.11 lbs. (9.12 kg). The arm is connected to an aluminum cylinder at the top of the frame that is 3' 8" long and 4" in diameter. At the end of the arm is a steel hammer head form that is 5" in diameter and can fit six 4.5" diameter steel disks allowing for a maximum hammer weight of 40.79 lbs. (18.5 kg). These discs are removable allowing for weight variation during testing. In total the arm and hammer weigh 79.63 lbs. (36.12 kg) and carries an inertia of 3.51×10^5 lbs. in^2 (102.72 kg m^2).

The size and weight of the pendulum arm and hammer were designed to replicate the inertia of the average NFL player's torso [9]. The maximum pendulum starting angle is about 90 degrees from vertical and can reach a maximum impact speed of 14.32 mph (6.4 m/s).

RESULTS

We have conducted six impact tests at 90 degrees and measured the impact speed of the pendulum arm right at the contact point of the Hybrid-III 50^{th} Male head form through a photogate sensor (ENFTG137). The impact speeds resulted in 14.32 +/- 0.67 mph (6.4 +/- 0.3 m/s), confirming our initial estimates about the system.

DISCUSSION

The future direction of this project is to use the pendulum to test the capabilities of different helmets and helmet accessories that are still in the design phase. This includes but is not limited a neck webbing design to prevent whiplash type concussions [11] and an electrical system to prevent direct impact type concussions [12].

ACKNOWLEDGEMENTS

Thank you to Metal Supermarket for assistance in building the impact pendulum frame and the scissor lift assembly.

REFERNCES

[1] Langlois J.A, Rutland-Brown W, Wald M.M. *J Head Trauma Rehabil.*, 21(5):375-378, 2006

[2] Daneshvar D.H. et al. *Clin. Sports Med.* 30(1):1–17, 2011

[3] Nathanson, John T., et al. *Journal of Sports Medicine*, 4(1):1-6, 2016

[4] Mez J, Daneshvar DH, Kiernan PT, et al. JAMA. 318(4):360-370, 2017

[5] Heck, Jonathan F. et al. *Journal of Athletic Training*, 39(1):101-111, 2004

[6] Nakatsuka A.S., Yamamoto L.G. *Hawai'i Journal of Medicine & Public Health* ,72(9 Suppl. 4):66, 2013

[7] Viano, D.C. et al., *Annals of Biomed Engineering*, 40(1):160-174, 2012

[8] Meyer, J.J. et al., *Defense Technical Information Center*, 1-15, 2014

[9] Rowson, B., Rowson, S. & Duma, S.M. *Ann Biomed Eng*, 43(10):2429-2443, 2015

[10] Standard Performance Specification For Newly Manufactured Football Helmets, NOCSAE DOC (ND) 002-17m18

[1] Kurt, M., Laksari, K., Kuo, C. et al. *Ann Biomed Eng*, 45(4):1148-1160, 2017

[12] Hernandez F., Camarillo D.B. et al. *J Neurotrauma*, 1-37, 2018

SB³C2019
Summer Biomechanics, Bioengineering and Biotransport Conference
June 25 -28, Seven Springs, PA, USA

HEAD IMPACT CHARACTERIZATION IN MEN'S AND WOMEN'S COLLEGIATE RUGBY

Emily E. Kieffer, Grace Pierce, Chase Vaillancourt, Steven Rowson

Biomedical Engineering and Mechanics
Virginia Tech
Blacksburg, VA, US

INTRODUCTION

Concussion is a serious concern in sports, especially those that are full-contact sports, such as rugby [1]. Worldwide, rugby is the most popular team sport, and its physicality and competitiveness leads to a high concussion rate [1]. It has been reported that 13-17% of rugby players will sustain a concussion in a season, depending on style of play [2]. Players sometimes choose to wear mouthguards and soft-shelled headgear while playing [3]. Headgear use is limited, as the design is not optimized to the type of head impacts sustained during play [4]. Effective headgear would reduce accelerations during real-world events, but there is need to characterize the types of head impacts rugby players experience. The objective of this study was to quantify and characterize head impacts experienced by collegiate rugby players in attempts to understand mechanism of head injury.

METHODS

The study was approved by and conducted according to the ethical guidelines of the Virginia Tech Institutional Review Board (IRB). During the fall of 2018, athletes were recruited from the Virginia Tech club women's and men's rugby teams. There were 35 women and 38 men enrolled in the study. Written informed consent was obtained from each participant after explaining the purpose, associated benefits, and risks of the study. All participants were identified with a unique study ID to maintain confidentiality of study measures. The athletes were studied over the course of six weeks, in the middle of their fall season. Video was recorded for each game and practice for the purpose of visual identification of head impacts. A head impact was recorded if a player's head impacted another player, the ground, or another object on the field. Two research personnel identified each head impact in the videos, and their reports were compared and finalized to quantify head impact frequency. The categories differentiated the object the athlete's head was impacting: another head, a body, the ground, or equipment (the goal post or the ball). The two analyses were compared and disparities were reconciled by reviewing video clips to determine the presence and category of a head impact.

RESULTS

Over the six week span, there were 587 video-identified head impacts. The men's team sustained 403 of those impacts, while the women's team accounted for the other 184 (Table 1). More than 71% of the women and 92% of the men who were enrolled in the study sustained a head impact.

The women's team had three games in the six week period, with head impacts occurring at a rate of 3.04 ± 2.09 impacts/player/game. Their games were played in weeks four, eight, and nine. During practices, the impact rate was 1.0 ± 0.54

impacts/player/practice. The men's team played a game each week in the six weeks and sustained impacts at a rate of 2.95 ± 1.59 impacts/player/game. The impact rate for practices was 1.53 ± 0.78 impacts/player/practice. The number of head impacts per player varied by week and by team (Figure 1).

Table 1: Cumulative number of head impacts sustained each of the six weeks for each rugby team. Data collection started 4 weeks into the women's season and 3 weeks in to the men's season. The men's team experienced head impacts each week, while the women played two weeks without head impacts.

	Women	Men
Week 3	N/A	122
Week 4	66	85
Week 5	0	44
Week 6	5	37
Week 7	0	53
Week 8	39	62
Week 9	74	N/A
Total	184	403

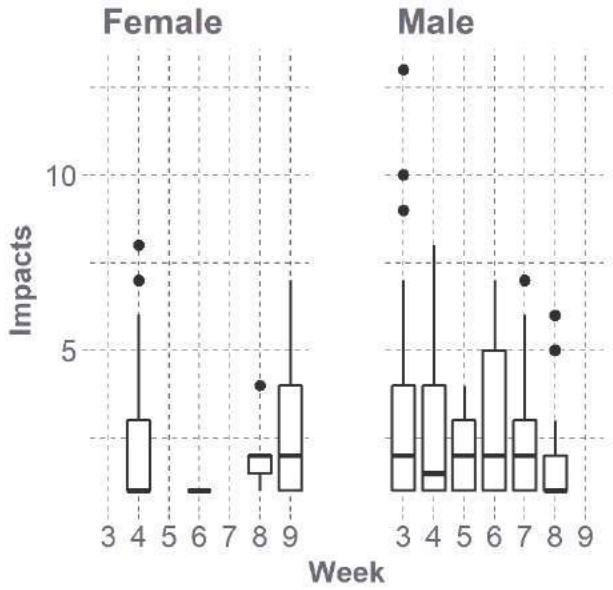

Figure 1: Box plots of head impacts sustained for the female and male athletes over course of six weeks in-season. Data collection started 4 weeks into the women's season and 3 weeks in to the men's season. On average, the athletes sustained less than five impacts per week, but some outliers experienced many more.

The majority of head impacts the women's team sustained were head to body (82.6%), with the remaining impacts to the ground (17.4%). Head to body was the most common impact scenario for the men's team (84.9%), followed by head to ground (13.2%), head to head (1.7%), and head to equipment (0.25%).

DISCUSSION

The objective of this study was to quantify and characterize head impacts in men's and women's collegiate rugby players. Number of head impacts sustained varied by team, player, and week. The men's team experienced more head impacts than the women's team, but this could be due to style of play and the semester schedule. The women only had three games in the six week study period, but the men had a game each week (six in total). There were no clinically diagnosed concussions in the study period.

For both teams, head to body was the most common mechanism of a head impact. Rugby players are taught to tackle by driving their shoulder into the ball carrier's leg, wrapping their arms around the opponent's thighs, and bringing them down with momentum. The head should not be involved, but the speed and physicality of the sport can result in tackles in which the tackler's head, instead of the shoulder, makes contact first. Head to ground was the second most common mechanism for both sexes. The most frequent scenario for this impact is the ball carrier being tackled and thrown back to the ground with enough force that he or she cannot stop the momentum, and their head impacts the ground. A vast majority of head impacts were sustained during games compared to those sustained at practice. This disparity is likely because neither team had many full-contact practices. When they did include contract drills, head impacts were still infrequent because the pace was slower and they focused on tackling form, making it less likely that a player tackled with their head first.

The main limitation of this study is the use of researchers to video identify head impacts. At some points of play, obstructions on the field, video angle, and camera resolution made it difficult to identify a head impact. We attempted to minimize this error by using the two independent video observers. This study does not take into consideration the attrition on either teams; players who were enrolled but quit mid-way through the season were still included in the analysis.

The purpose of this study was to quantify and characterize head impacts sustained by collegiate rugby players. The frequency and characterization are similar for both men and women. Understanding how rugby players sustain head impacts could provide insight into mechanisms of injury and strategies on methods of reducing injury risk and improving clinical management of concussions.

ACKNOWLEDGEMENTS

We would like to thank Virginia Tech Institute for Critical and Translational Science (ICTAS) for their support in the project.

REFERENCES

[1] Fuller, C. W et al., *Br J Sports Med.* 2014. [2] Lopez, V et al., *Am J Sport Med,* 2012. [3] Marshall S. W. et al., *J Athl Train*, 2001 [4] Marshall S. W. et al., *Int J Epidemiol*, 2005.

SB³C2019
Summer Biomechanics, Bioengineering and Biotransport Conference
June 25 -28, Seven Springs, PA, USA

HISTORY DEPENDENT DAMAGE MODELLING FOR AXONAL FIBER TRACTS OF THE BRAIN

Ritika R. Menghani (1,3), Ouniol T. Aklilu (2,3), Reuben H. Kraft (1,2,3)

(1) Department of Mechanical Engineering
The Pennsylvania State University
University Park, Pennsylvania, United States of America

(2) Department of Biomedical Engineering
The Pennsylvania State University
University Park, Pennsylvania, United States of America

(3) Institute of Cyberscience
The Pennsylvania State University
University Park, Pennsylvania, United States of America

INTRODUCTION

In an effort to design safer products and study the underlying mechanisms of brain injury, there has been a significant push to develop biofidelic finite element (FE) models of the human head. At this time, a number of FE brain studies have specifically focused on the prediction of DAI. Using a variety of methods, these models predict axonal strains, which are then compared with functional and mechanical tissue thresholds. While these studies are extremely useful, they have been restricted to simulating separate isolated events with elastic material properties. At this time, there is no accepted method to account for the accumulated damage that is caused by multiple head trauma events. In order to overcome this issue, this study is focused on the design, implementation and experimental validation of tract level damage models that provides a first step towards realizing history-dependent brain modeling. In this study, we present mechanisms of stress softening, fatigue damage, fiber rupture damage and a healing model that can be used together to understand the effect of successive loading on the axonal bundles. Here, we develop our damage models at the tract level so that we can compare predicted axonal fiber damage with experimentally observed diffusion tensor imaging disruption. Our ultimate vision is that these models will enable personized computational-enabled brain medicine in the future.

METHODS

Damage accumulation is subdivided into different mechanisms commonly observed in brain tissue. There are some mechanisms where more experimental data is available. For example, material parameters for stress rupture in brain tissue are reported, but parameters for modeling brain tissue fatigue are not found to be abundant. Our approach was to conduct a thorough literature search on material models for brain models, as well as other soft tissues, then employ the mechanisms that we identified.

In previous studies [1], brain tissue has been observed to experience significant **stress softening**, also called **the Mullins effect**, after the initial loading cycle. This stress softening behavior has been successfully modeled for brain tissue [2] using the pseudo-elasticity theory [3]. The material softens after the initial loading cycle and the degree of softening depends on the previous strain history. However, the degree of softening is unaffected by the number of loading cycles. To represent this mechanism, we employ a scalar damage variable η, which ranges from 0 to 1 to soften the Cauchy stress response of the fibers as follows:

$$\boldsymbol{\sigma_{fiber}} = \boldsymbol{\eta}\left[\frac{\boldsymbol{2\mu}}{\boldsymbol{\alpha}}\left(\boldsymbol{\lambda^{\alpha}} - \boldsymbol{\lambda^{-\frac{\alpha}{2}}}\right)\right] \quad (1)$$

Where μ and α are material constants and λ is the fiber stretch computed using the embedded finite element method as we have previously developed [4].

In order to introduce cycle-dependent degradation and finite life, we have also implemented a **fatigue-induced stress softening model**. At this time, the functional and mechanical fatigue properties of brain tissue have not yet been experimentally studied. However, based on the prevalence of fatigue damage in other soft biological tissues, we assume that brain tissue also experiences this mechanism. We calculate a damage parameter and update using the following linear damage accumulation model:

$$\boldsymbol{D_f} = \sum_{\boldsymbol{n=1}}^{\boldsymbol{N_{cycles}}} \frac{\boldsymbol{1}}{\boldsymbol{n_{tot}}} \quad (2)$$

where n_{tot} is the number of cycles to failure. This damage parameter is then applied to the fiber elements which gives us the following stress response:

$$\sigma_{fiber} = \left(1 - D_f\right)[\eta(\frac{2\mu}{\alpha}\left(\lambda^{\alpha} - \lambda^{-\alpha/2}\right))] \quad (3)$$

The next mechanism we implemented is for **tissue rupture**. In both the previous models, information from the initial loading cycle is used alter the response of the second loading cycle. These methods progressively degrade the tissue but cannot predict complete failure from a single cycle tissue tensile test to rupture. Interestingly, it seems that the most experimental data is available for this damage mechanism, even though it is the least relevant for mTBI (i.e., complete separation of tissue is severe). To remain brief, we do not present the damage equation for this mechanism since it is less relevant. We assume a linear evolution of fiber rupture damage, based on the fiber stretch history. The total fiber damage, D_{tot}, which ranges from 0 to 1, is then calculated for each fiber as the sum of the fatigue and fiber rupture damage parameters:

$$D_{tot} = D_f + D_r \tag{4}$$

and the stress becomes

$$\sigma_{fiber} = (1 - D_{tot})[\eta(\frac{2\mu}{\alpha}(\lambda^{\alpha} - \lambda^{-\alpha/2}))] \tag{5}$$

Finally, we have provided a mechanism to account for the **healing process between two successive events**. When the next simulation is initialized, a healing duration can be specified, which then partially or completely reverses the accumulated damage in each fiber element. Due to the lack of experimental data, a constant healing rate is typically assumed. In addition, we have assumed exponential recovery functions. It is important to recognize that healing is an extremely complex remodeling process that involves many interacting biochemical and biomechanical processes. It is also important to note that damage modeling is concerned with mechanical behavior and structural integrity, while most recovery studies are concerned with patient symptoms and functional restoration. Therefore, in order to accurately model damage recovery, future research is needed to understand how mechanical damage recovers over time.

RESULTS:

Our vision requires us to carry out simulations on head models with the entire fiber tractography included. Fig 1(a) shows one such test head model that highlights the fiber tractography. This tractography was obtained from an open source database at http://brain.labsolver.org; it has been constructed using diffusion MRI data of 842 subjects.

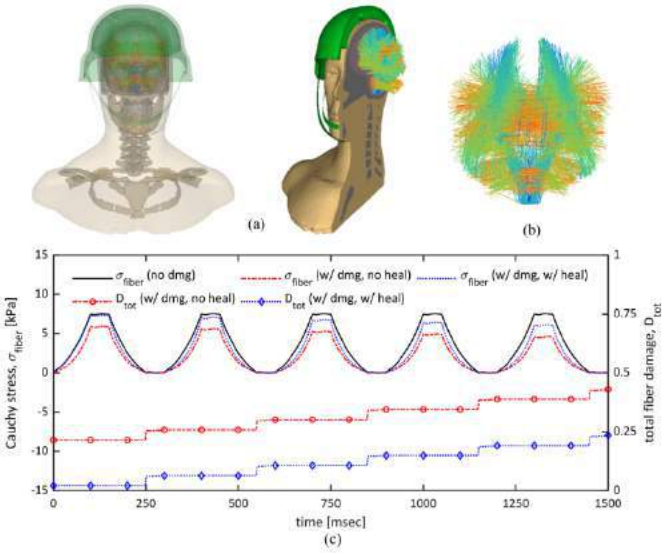

Figure 1: (a) Model showing the fiber tractography; the color of each fiber is a combination of red, green and blue where left-right is red, anterior-posterior is green and superior-inferior is blue (b) Entire fiber tractography (c) Damage evolution in a small fiber section.

Fig 1(c) shows preliminary results for a small section of brain tissue near the corpus collosum. It consists of multiple curves representing the Cauchy stress over time (or cycles) with and without including the healing function. Consider that the fiber tracts have been damaged in a previous event that was also simulated and the damage data has been stored. If further damage is experienced due to exposure from cyclic loads, the damage parameter continues from previous damage level (in this case, the red curve). However, if we consider some time has passed between both simulations and we enable healing, the effect of damage is reduced (the blue curve). It can be observed that as more cycles of load are applied, the damage increases and the stress carrying capacity of the fibers reduces. Therefore, by introducing damage, we are now able to view the consequence of successive impacts.

DISCUSSION:

In this study we designed, implemented and tested a modeling framework for computing the history-dependent mechanical damage of axonal fiber tracts in the brain. In its current form, the proposed framework should be regarded as a first step in a necessary direction of tracking neurotrauma over time. While we are able to validate some of the mechanisms to experimental data (e.g. tissue rupture), validation remains a challenge for other mechanisms (e.g. cyclic fatigue) due to the lack of experimental data. Continuing efforts from our research group seek to validate the predicted disruption in fiber tractography with diffusion tensor imaging. Preliminary results are expected for the meeting.

The implication of this work is that it further motivates the need for new measurements in experimental brain tissue mechanics that is critical for the modeling framework. A new metric (i.e., inelastic damage) that captures both the magnitude and frequency of successive fiber tract strains would be a significant advance in computational brain biomechanics.

ACKNOWLEDGEMENTS:

The authors gratefully acknowledge the support provided by the U.S. Army Research Laboratory (ARL) at Aberdeen Proving Grounds under contracts W15P7T-10-D-D416 and DOTC-17-01-INIT0086, and CFD Research Corporation under a subcontract funded by the Department of Defense, Department of Health Program through contract W81XWH-17-C-0216.

CONFLICT OF INTEREST:

Kraft has a financial interest in Digital Brain Technologies LLC, a company which could potentially benefit from the results of this research. This interest has been reviewed by Penn State University in accordance with its Individual Conflict of Interest policy for the purpose of maintaining the objectivity and integrity in research and is being managed.

REFERENCES:

[1] S. Budday *et al.*, "Mechanical characterization of human brain tissue," *Acta Biomater.*, vol. 48, pp. 319–340, Jan. 2017.

[2] G. Franceschini, D. Bigoni, P. Regitnig, and G. A. Holzapfel, "Brain tissue deforms similarly to filled elastomers and follows consolidation theory," *J. Mech. Phys. Solids*, vol. 54, no. 12, pp. 2592–2620, Dec. 2006.

[3] Ogden R. W. and Roxburgh D. G., "A pseudo–elastic model for the Mullins effect in filled rubber," *Proc. R. Soc. Lond. Ser. Math. Phys. Eng. Sci.*, vol. 455, no. 1988, pp. 2861–2877, Aug. 1999.

[4] H. T. Garimella, R. R. Menghani, J. I. Gerber, S. Sridhar, and R. H. Kraft, "Embedded Finite Elements for Modeling Axonal Injury," *Ann. Biomed. Eng.*, Dec. 2018.

SB³C2019
Summer Biomechanics, Bioengineering and Biotransport Conference
June 25 -28, Seven Springs, PA, USA

CHESTBAND-BASED INJURY METRICS IN FAR-SIDE IMPACTS

Yuvaraj Purushothaman (1,2), John Humm (1), Hans Hauschild (1), Klaus Driesslein (1), Frank Pintar (1), Narayan Yoganandan (1)

(1) Department of Neurosurgery
Medical College of Wisconsin
Milwaukee, WI USA

(2) School of Mechanical and Building Science
VIT University, Chennai Campus
Chennai, Tamil Nadu, India

INTRODUCTION

Previous experimental biomechanical studies using Post Mortem Human Subjects and animal models have shown that the chest deflection correlates well with thoracic and abdominal injuries[1-2]. The normalized peak chest deflection (C_{max}), velocity of compression (V_{max}), and viscous criterion (VC_{max}) are derived from deflections. They serve as injury criteria in frontal and side impacts[3-4]. Anthropomorphic test devices (also known as crash test dummies) are used as human surrogates to assess crashworthiness of vehicles, design restraint systems, and improve safety[1]. The Test Device for Human Occupant Restraint (THOR) is shown to be an appropriate dummy for far-side occupant protection[6]. This dummy can record rib deflections using internal Infrared Telescope Rods for Assessment of Chest Compression (IR-TRACC). The aims of this study are to determine whether the IR-TRACCs location accurately measure the injury metrics, C_{max}, V_{max}, and VC_{max} in pure lateral and oblique far-side impact using sled test results.

METHODS

The 3-point belt restrained mid-size male THOR dummy was seated upright in a sled buck consisting of a rigid flat seat, simulated center console, dash board, far-side side door structure, and an armrest, and they were covered with energy absorbing materials. A center-mounted airbag was mounted to the right side of the seat, and two chestbands were routed around the circumference at the level of the third rib and sixth ribs. Oblique and pure lateral tests with and without airbags were conducted at a velocity of 8.3 m/s. An accelerator sled was used to deliver the impact to the dummy in the right far-side mode. The temporal contours were processed using custom software to determine the maximum chest deflections from three methods. The first method paralleled the computations of deflections from Post Mortem Human Subject (PMHS) studies[7]. The second method used the actual anchor point location and actual alignment of the IR-TRACC to compute the deflections. The third method used the same anchor location at the rear of the internal sensor but, determined the location of the peak chest deflection on the contour and confining to the aspect (right or left) of the sensor to compute the deflections. These were termed as the SD, ID, and TD metrics, respectively (Figure 1).

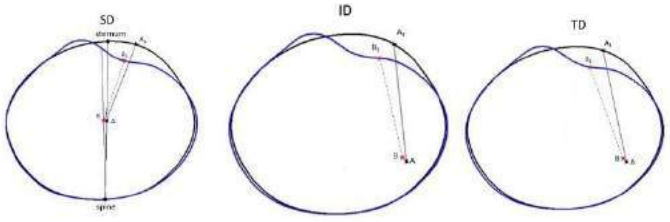

Figure 1: Chest deflection calculation methods, SD, ID, and TD. A and B refer to the origin in the undeformed and deformed contours. The peak deflection is the difference between vectors AA1 and BB1.

The C metric was obtained by normalizing the compression of the respective widths. The C corresponding to the SD metric used the one-half of spine-sternum distance. The C corresponding to the ID metric used the initial length between the points of attachment (origin to the tip), physically corresponding to the location of the sensors. The C corresponding to the TD metric used the distance between the origin (physical attachment of the sensors inside the dummy rear) and the transformed location of the peak deflection (identified in the deformed contour) on the undeformed contour. The V metric was obtained by differentiating the deflection signal, and VC_{max} was obtained as the peak of the product of the C and V signals in the time domain. The peak

magnitudes of the metrics were obtained for the three methods, and an evaluation of the accuracy was made based on the SD method.

RESULTS

Briefly, the average SD-based C_{max}, for the upper and lower chest levels were 0.124 and 0.173, the V_{max} were 5.31 m/s and 1.75 m/s, and VC_{max} were 0.24 m/s and 0.15 m/s, respectively. Other data are given (Figure 2-4) for all metrics at the two levels of the thorax. Consistently, the peak metrics were the lowest for the ID method, and this was true regardless of the aspect, right or left side. In contrast, the SD method produced the greatest magnitudes of the metrics. The VC_{max} had the greatest percentage difference between ID or TD and SD (normalized based on SD) among all the three metrics.

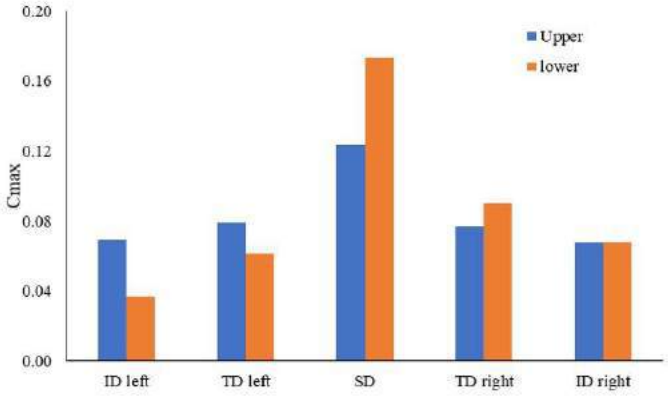

Figure 2: Averaged C_{max} metric for the different methods

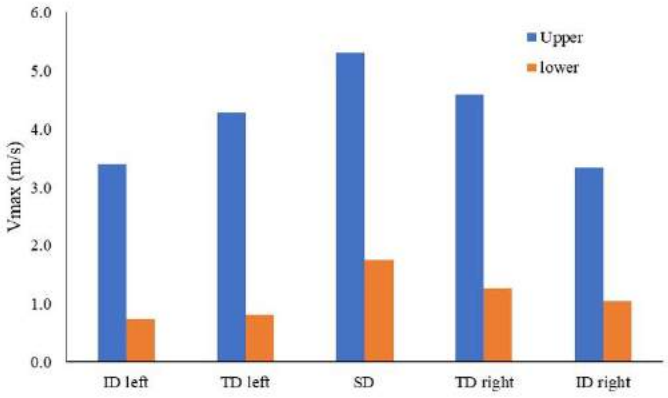

Figure 3: Averaged V_{max} for the different methods

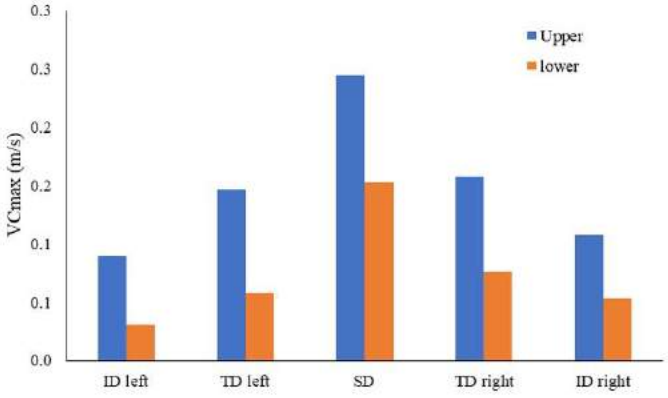

Figure 4: Averaged VC_{max} metric for the different methods

DISCUSSION

Using the processed chestband contours at two levels, this study determined different types of deflection measures from the THOR dummy. While the data from the actual IR-TRACC sensors were not obtained, they were calculated using the contours (ID method). The effectiveness or accuracy of the 'sensor-predicted' C_{max}, V_{max}, and VC_{max} injury metrics were evaluated. It was based on the chestband deflection contours that paralleled procedures used in the PMHS tests, i.e., SD method[7,8]. The underlying hypothesis is that the sensor-predicted deflection represents a lower bound estimate of the true deflections, and it is also true for the derived metrics, i.e., C_{max}, V_{max}, and VC_{max}. This is because the actual location of the peak deflections on the dummy ribs depends on factors such as the obliquity of the impact vector, interaction with the airbag, and belt restraint conditions. The *a priori* locations of the anchor point (origin) that is inside the ribcage (mounting) and the tip of the sensor that is attached to the inner surface of the ribs are fixed in the ID measures. Because of this, it also expected that all the three derived injury metrics would be lower than the SD method. This was proved in the present study as SD metrics were consistently greater than ID deflections in all cases, i.e., upper and lower thorax levels, lateral and oblique impacts, and presence and absence of airbags.

The TD method, instead, relaxed one assumption, i.e., the tip of the sensor was changed from the *a priori* location to the actual point where the deflection was found to be the maximum. This also produced lower deflections than the SD method in all cases. Thus, the hierarchical sequence was SD (actual true deflections and derived metrics), followed by the TD and ID methods, for all metrics. In addition, the $VC_{max.}$ was found to be more sensitive than the other two metrics, C_{max} and V_{max}.

Under the conditions tested in the present study, the computational chestband contour-based results indicate that the *a priori* placement of IR-TRACC sensors under predicts chest deflection-related parameters, and the viscous criterion is the least reliable metric (among the three metrics) in lateral and oblique far-side impacts. While additional studies are needed to reinforce these observations, these results lay a foundation to investigate other methods such as optical tracking for a better prediction of deflection metrics that describe human chest response to injury in far-side impact scenarios[9]. Such systems may prove to be more efficacious for improved assessments of crashworthiness and far-side occupant protection.

ACKNOWLEDGEMENTS

This material is the result of work supported with resources and use of facilities at the Zablocki VA Medical Center in Milwaukee, Wisconsin. It was supported by the US Department of Transportation, NHTSA, DTNH22-13-D-00290L, and U.S. Army Medical Research and Materiel Command in Fort Detrick, Maryland, W81XWH-16-1-0010. Any views expressed in this article are those of the authors and not necessarily representative of the funding organizations.

REFERENCES

1. Kuppa S, et al., Stapp Car Crash Journal, 2003, 47:189-210
2. Viano DC, and Lau IV: J. Biomechanics, 1988, 21:387-389
3. Directive 96/79/EC european parliament and of the council, 1996
4. Yoganandan N, et al., J Biomechanics, 2007, 40: 227-243
5. Hobbs C, ESV Conference, 1998, 2439-2453
6. Umale S, et al., IRCOBI Conference, 2018, 608-629
7. Yoganandan N, et al., Stapp Car Crash Journal, 2011, 55:351-378
8. Yoganandan N, et al., Med. Eng. Phy., 2013, 35:1181-1187
9. Belcher T, and Terrel M, ESV Conference, 2013, paper 11-133

SB³C2019
Summer Biomechanics, Bioengineering and Biotransport Conference
June 25 -28, Seven Springs, PA, USA

APPLICATION OF SIX-YEAR-OLD CHILD HUMAN BODY FINITE ELEMENT MODELS WITH ACCURATE ANATOMICAL CHARACTERISTICS FOR UNDERSTANDING THE INJURY MECHANISMS

HY Li (1) (2), YQ Huang (1), WL Lv (1) (2), SH Cui (1) (2), LJ He (1) (2), SJ Ruan (1), CX Wang (3)

(1) International Joint Research Centre of modern automobile safety technology, Tianjin University of Science and Technology, Tianjin, China

(2) College of Mechanical Engineering, Tianjin University of Science and Technology, Tianjin, China

(3) Tianjin Children Hospital, Tianjin, China

INTRODUCTION

In 2012, the pedestrian fatalities increased up to 14%, compared with 11% in 2003, in the United States [1]. At the same time, 22% of children aged 5-15 who died in traffic accidents were pedestrians. The traffic accidents were the second-leading cause of death for children aged 4-7 in U.S in 2015[2]. Therefore, the protection for child deserves further researches.

Nowadays, computational simulations such as finite element modeling (FE), multi-body modeling, are among the most important ways to investigate injury mechanism. In 2003, Okamoto[3] developed a six-year-old child pedestrian lower extremity model based on MRI scans, but the model was not a full-scale model. The 10-year-old occupant and pedestrian human body FE models (CHARM-10) with detailed anatomical structures were constructed and validated by Shen Ming [4]. Recently, a 6-year-old 6YO-PS FE model was developed by scaling and morphing the GHBMC adult pedestrian model[5]. However, child is not a scaled adult due to their anatomical differences, and some detailed anatomical structures such as abdominal organs, growth plates, should be constructed in the FE models.

The aim of this study was to investigate pediatric injury mechanisms by using of the 6-year-old occupant and pedestrian child human body finite element models with high-biofidelity and accurate anatomical characteristic.

METHODS

The human body 6YO-TUST FE models of pediatric pedestrian and occupant contained 858,190 nodes/801,926 elements and 767,475 nodes/732,595 elements respectively (Figure 1). The stature/weight of the pediatric pedestrian and occupant is 1135mm/26.8kg and 845.0mm/28kg, respectively.

Definition of 6-year-old pediatric occupant Impact Simulation

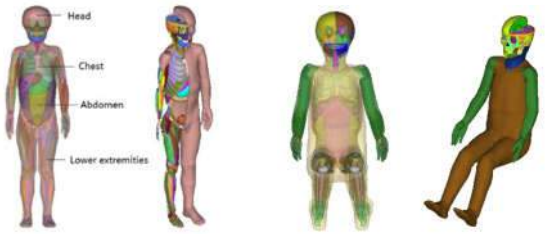

(a) **(b)**

Figure 1: The 6YO-TUST FE models of 6-year-old pedestrian and occupant. (a) Pediatric pedestrian (b) Pediatric occupant

In Figure 2, the 6-year-old occupant FE model was seated using the CRS with forward-facing car seat and the booster. The parameters of restriction system were referred from the Hybrid III dummy simulation by Tanya Kapoor[6]. The simulation was setup according to ECER44 regulation. The initial speed of all the models was set as 50km/h.

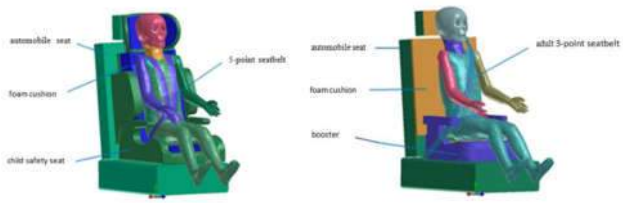

(a) **(b)**

Figure 2: Simulation setup of occupant 6YO-TUST FE models with different CRS（a）Forward-facing car seat（b）Booster seat.

Poster Presentation #P224

Definition of Car-to-Pedestrian Impact Simulation

A validated Ford Taurus sedan FE model from National Crash Analysis Center (NCAC) was applied in this simulation. The child FE model was positioned laterally 4mm offset from the vehicle's centerline in a midstance gait posture (Figure 3). The developed 6YO-TUST FE model was impacted laterally by the vehicle model moving at a 40 km/h initial velocity.

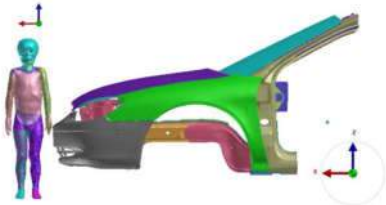

Figure 3: The initial position of the pedestrian 6YO-TUST model relative to the sedan vehicle.

RESULTS

Figure 4 showed the kinematics and dynamic response of the child occupant restricted by two different CRS system.

90ms **120ms**

Figure 4: Kinematics of pediatric 6YO-TUST occupant FE models restricted by forward-facing car seat and booster seat

Figure 5 showed the while-body kinematics of 6-year-old pedestrian during the impact.

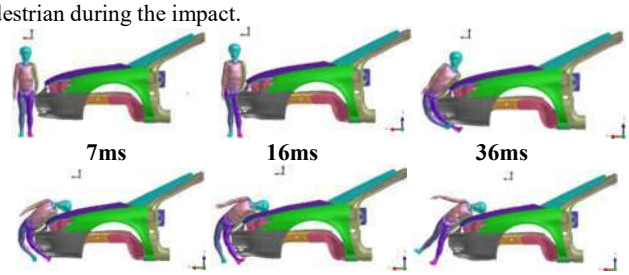

7ms **16ms** **36ms**

55ms **61ms** **77ms**

Figure 5: Pedestrian Kinematic during Car-to-Pedestrian Impact simulation

DISCUSSION

Figure 6 showed the maximum first principal strain of internal organs in two occupant restraint systems. It can also be seen that the maximum first principal strain of internal organs restricted with 5-point seatbelt is usually lower than that of 3-point seatbelt, which means that the forward facing child safety seat usually has a better protection to child than the booster.

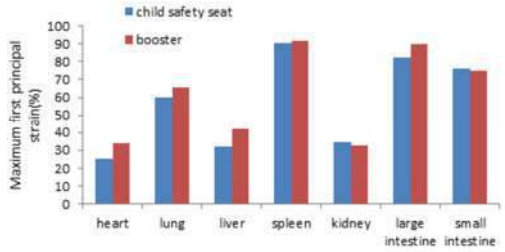

Figure 6: Maximum first principal strain of internal organs under two occupant restraint systems

The results suggested in the E-NCAP Technical Bulletin of Pedestrian Human Model Certification were output. As figure 7, the first peak of contact force occurs at 3ms and then decreases because of the free moving of upper limb. When the upper limb contacts the thigh muscle at 7ms, the contact force increases again along with the compression of thigh muscles. Then the contact force increases sharply to 3.47KN at 13ms when the thigh muscles are compressed to the limit. The maximum force is up to 4.23KN at 15ms, which leads to the fracture of femur (Figure 8).

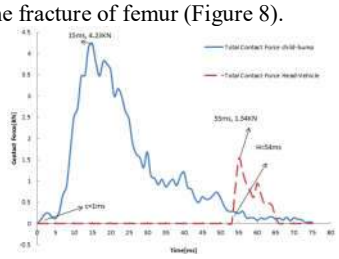

Figure 7: The contact force history during the car-pedestrian crash

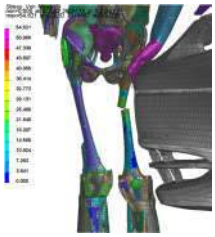

Figure 8: The fracture of femur at 15ms

The Z-direction acceleration rises sharply at 54ms, which means that the head hits the engine hood (Figure 9). The maximum contact force between head and engine is 1.54kN at 55ms. The maximum acceleration of head is 164g. The head hits the hood reinforcement panel at 61ms. There's a second peak acceleration at 61ms, leading to the HIC 1339, which means that the head has a high risk of injury. Figure 10 showed the trajectory of head COG, T1 and T12. It can be shown that the child pedestrian moves slightly upward during the impact. According to the definition of Head Impact Time (HIT), the HIT is 53ms. The WAD of head impact location is 1062mm, .

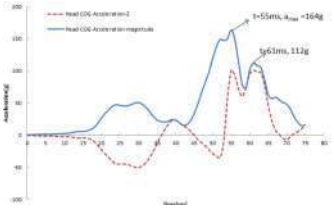

Figure 9: The resultant and Z-direction acceleration history of head COG during the Car-to-Pedestrian impact

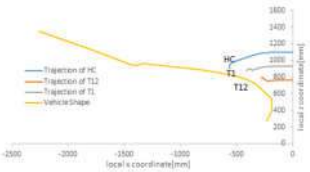

Figure10: The trajectory of head COG, T1 and T12 during the Car-to-Pedestrian impact

ACKNOWLEDGEMENTS

This work was supported by the National Natural Science Foundation of China (81471274 and 81371360).

REFERENCES

[1] NHTSA. Traffic Safety Fact, 2012.

[2] Traffic Safety Fact. Motor Vehicle Traffic Crashes as a Leading Cause of Death in the United States, 2015

[3] Okamoto M, et al. Development of finite element model for child pedestrian protection. The 18th ESV, 2003.

[4] Shen M, et al. Introduction of Two New Pediatric Finite Element Models for Pedestrian and Occupant Protections. SAE International,2016.

[5] Meng Y, et al. A finite element model of a six-year-old child for simulating pedestrian accidents. Accident Analysis & Prevention, 2017, 98:206-213.

[6]Kapoor T, et al. Injury potential of a three-year-old Hybrid III dummy in forward and rearward facing positions under CMVSS 208 testing conditions [J]. Accident; analysis and prevention, 2006, 38(4): 786-800.

EFFECT OF MICROSTRUCTURAL VARIATION IN THE BIOMECHANICS OF OLIGODENDROCYTE-NEURON CO-CULTURES

Zeynep M. Suar (1), Mateusz Urbanski (2), Gloria Fabris (1), Carmen V. Melendez-Vasquez (2), Mehmet Kurt (1,3)

(1) Dept. of Mechanical Engineering,
Stevens Institute of Technology,
Hoboken, NJ, USA.

(2) Biological Sciences,
Hunter College,
New York, NY, USA.

(3) Translational and Molecular Imaging Institute (TMII),
Mount Sinai Hospital,
New York, NY, USA.

INTRODUCTION

Even though computational models provide significant insights into the impact mechanics of the brain, correlating this mechanical response to biological outcomes is not straightforward. Here, we implemented an *in vitro* model mimicking the various myelination levels observed in the pediatric brain, and the different anisotropy levels observed in white and gray matter in order to examine their response to mechanical compression tests under different loading conditions. Despite the fact that true organ function cannot be recreated *in vitro*, we seeded oligodendrocyte progenitor cells in co-culture with DRG neurons as well as on one of the most biofidelic scaffolds known, namely a 3D-fiber matrix, in order to render the culturing environment as physiological as possible. Mechanically testing such samples will allow us to obtain the mechanical thresholds for inducing axonal damage and microtubule rupture for age and brain-region specific cellular model systems, as well as to study the variations occurring in cell physiology at sub damage-inducing rates.

METHODS

DRG neurons were isolated following a well-established protocol [1] and either dissociated or directly plated as explants on electrospun 3D-PCL scaffolds. Neurons were allowed to extend axons for 2-3 weeks in either anisotropic (highly aligned axons in DRG explants) or isotropic (non-aligned axons in dissociated DRG neurons) patterns prior to their use in myelinating co-culture experiments. Primary oligodendrocyte progenitor cells (OPC) were purified from mixed glial cultures of postnatal day 1 rat cerebral cortices using immunopanning [1, 2]. Freshly purified OPC (Ran2-, A2B5+) were seeded directly onto X-micron thick network of DRG neurons for co-cultures or onto 3D-PCL scaffolds (50-100,000 cells). OPC alone cultures were maintained in Sato media with 10 ng/ml PDGF and 10 ng/ml bFGF for proliferation, or induced to differentiate into mature oligodendrocytes (OL) in Sato containing T3 (30 ng/ml) for 1-3 days. All animal work was with IACUC regulations and under approved animal protocols.

The OPC proliferation, survival and differentiation were evaluated by staining in order with Ki-67, caspase 3, and MBP over the course of 1 week [1, 2]. We also used immunostaining for PDGFRα (immature OPC), Olig2 (immature and mature OL), CC1 (mature OL), NeuN (for mature neurons) β-III tubulin (Tuj1) or neurofilament (NF) to follow axon development.

Myelination was induced by changing DRG-OL co-cultures to MEM media containing 10% FBS, 2 mM L-glutamine, and 4 mg/mL glucose. Cultures were fixed at different time points (3, 7, 14 and 21 days) and confocal microscopy was used to check for the extent of myelination using antibodies to myelin basic protein (MBP), in combination with Olig2, NeuN and NF.

Electrospun fiber alignment and axonal directionality were assessed based on calculations of 3D directional variance from confocal Z-stacks as reported in [3]. This approach provided us with easy and powerful metrics to correlate variations in the stress-strain response curve of 3D cell culture samples with variations in the structural organization of tissue at the microscale.

We performed atomic force microscopy (AFM) indentations coupled with live cell imaging using SiR-Tubulin, Sir-Actin (Cytoskeleton) and/or Fluromyelin™ (Invitrogen) to enable visualization of the cellular structures and number of myelin segments. 4 experimental groups were established, 2 of which (Group III and IV) were used for AFM experiments as shown in Table 1. These include isotropic and anisotropic samples, which are prepared by using dissociated DRG neurons (isotropic) and DRG explants (anisotropic). Different myelination levels are obtained by imaging at

varying culturing times. We hypothesized that the microstructural variation within the tissue will manifest as mechanical differences in elasticity modulus and viscoelastic relaxation at microscales.

Table 1: Experimental groups for AFM indentations

Fiber alignment \ Myelination level	Low	High
Isotropic	Group I	Group II
Anisotropic	Group III	Group IV

RESULTS

DRG/Oligodendrocyte co-culture

A reproducible method for the controlled myelination of primary DRGs in oligodendrocyte co-cultures was established [1, 2]. Cultures analyzed at different time points reveal a clear pattern of myelination, as indicated by the increased immunofluorescent signal for myelin basic protein (MBP). Markers such as Olig2 and neurofilament (NF) recognize cells of the OL lineage (mature and immature) and axons respectively. An increase in the number of myelin segments with time in culture is clearly observed (Fig. 1).

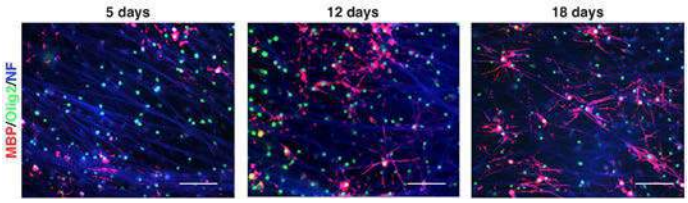

Figure 1: DRG-OL co-cultures displaying different myelination levels *in vitro*: Representative images showing the increase in CNS myelin formation over time in organotypic OL-DRG co-cultures grown in Matrigel. (Red: myelin basic protein. Blue: neurofilaments. Green: Olig2).

At the same time, a variation of the protocol (seeding whole DRG explants as well as dissociated DRG neurons) allowed to control the degree of axonal alignment: axon bundles in organotypic cultures displayed axons tightly packed in anisotropic bundles, while dissociated cultures showed thinner axon bundles arranged in a more isotropic pattern. Despite similar numbers of OLs, as shown by staining with Olig2+ (red) more myelin segments (green) were observed in organotypic compared to dissociated cultures (see Fig. 2).

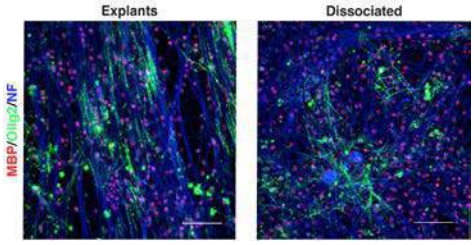

Figure 2: Aligned vs. random DRG/OL co-cultures. Representative images of 18 days-old myelinating OL-DRG cocultures showing the differences in the extent of myelination (red: MBP stain) and axonal alignment (blue: neurofilament stain) in organotypic vs. dissociated cultures despite similar number of OL (green).

AFM indentation of DRG-OL co-cultures for mechanical characterization

Samples from different myelination levels for co-cultures with DRG explants (Group III and Group IV) were imaged with an AFM to obtain stiffness measurements. Group IV (higher myelination) had significantly higher stiffness values (1.58 ± 1.1594 kPa, $p<0.05$) than Group III (lower myelination, 0.959 ± 0.51 kPa).

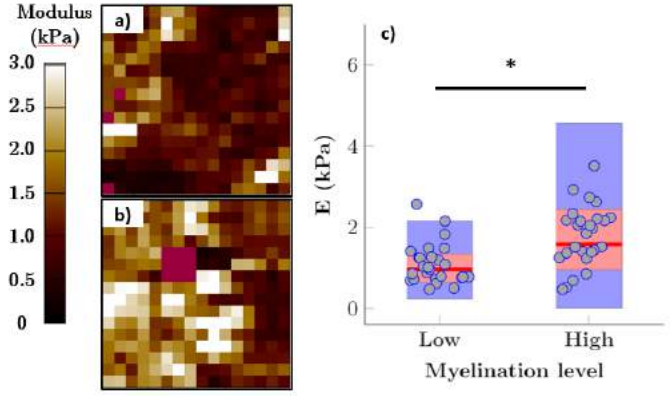

Figure 3: a) Stiffness map of anisotropic fiber alignment with low level myelination (Group III) sample obtained through AFM. b) Modulus map of anisotropic fiber alignment with high level myelination (Group IV) sample obtained through AFM. c) Comparison of stiffness values between Group III and Group IV.

Oligodendrocyte culture on electrospun scaffolds

Primary rat OL were seeded on a network of randomly aligned, electrospun polycaprolactone (PCL) fibers (*cf.* Fig. 4). The good adhesion and cell viability observed after 7 days in culture indicate the feasibility of the approach.

DISCUSSION

Our preliminary results confirm the strong link between myelin content and mechanical stiffness in neuronal tissues, as consistent with prior literature [4].

The measured samples were prepared using co-cultures prepared with DRG explants, yielding highly aligned hence anisotropic samples. Moving on, to obtain different degrees of anisotropy and isotropy, we will perform AFM analysis on co-cultures prepared with dissociated DRG neurons planted on PCL-scaffolds (Fig. 4). The purpose here is to mimic the differing levels of anisotropy in the human brain.

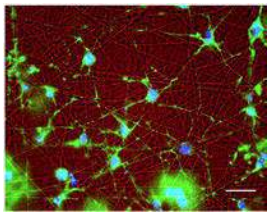

Figure 4: Primary rat oligodendrocytes growing on PCL electrospun scaffold. 7 DIV rat OL (green: phalloidin-actin) align and extend processes over a network on electrospun PCL fibers (red). Blue: DAPI.

REFERENCES

[1] H. Wang, A. Tewari, S. Einheber, J.L. Salzer, C.V. Melendez-Vasquez, J. Cell Biol. 182 (2008) 1171–1184.

[2] H. Wang, T. Rusielewicz, A. Tewari, E.M. Leitman, S. Einheber, C.V. Melendez-Vasquez, J. Neurosci. Res. 90 (2012) 1547–1556.

[3] Z. Liu, D. Pouli, D. Sood, A. Sundarakrishnan, C.K. Hui Mingalone, L.M. Arendt, C. Alonzo, K.P. Quinn, C. Kuperwasser, L. Zeng, T. Schnelldorfer, D.L. Kaplan, I. Georgakoudi, Biomaterials 116 (2017) 34–47.

[4] J. Weickenmeier, R. de Rooij, S. Budday, P. Steinmann, T.C. Ovaert, E. Kuhl, Acta Biomater. 42 (2016) 265–272.

SB³C2019
Summer Biomechanics, Bioengineering and Biotransport Conference
June 25 -28, Seven Springs, PA, USA

AN ATLAS-BASED FINITE ELEMENT MODEL OF MOUSE BRAIN FOR CONTROLLED CORTICAL IMPACT

Changxin Lai , Suhao Qiu, Yuan Feng

School of Biomedical Engineering
Shanghai Jiao Tong University
Shanghai, China

INTRODUCTION

Traumatic brain injury (TBI) is one of the leading causes of death and injuries affecting millions of people [1]. To understand process and mechanism of the injury, many experimental work has been carried out [1-3]. However, human experiment can only be conducted in the non-injury level. Therefore, animal model is indispensable for injury-level studies. Although animal experiments could provide important data and insights, computational models could help guide the experiment and are crucial for translational studies.

Typical finite element (FE) models for animal studies include mouse [4], rat [5], and pig [6]. Among them, mouse could provide various genotypes, is easy to handle and is ideal for translational study. However, most of the computational studies of the mouse brain had simplified geometries of the brain structure. An accurate model with anatomically accurate geometry could improve the computational results.

Although there are many different ways to induce injury, controlled cortical impact (CCI) is able to provide well-controlled injury and is widely used for mouse model. In this study, we constructed an atlas-based model of mouse brain for CCI. The anatomically accurate FE model will provide helpful insights into the injury process.

METHODS

FE Mesh: The FE mesh was constructed from a set of probability MR images of mouse brain (UCLA Brain Mapping Center, CA) [7]. Custom written MATLAB (Mathworks, Natick, MA) codes were used for segmentation of images and generation of FE meshes. Mask images labelling different tissues were first generated. Each voxel was labelled as either white matter (WM) or gray matter (GM) with greater probability. The volumetric mesh was generated based on the generated mask image. The mesh composed of a total of 577, 824 hexahedral solid elements, where GM had 484,647 elements and WM had 93,177 elements. The element size was 0.1 mm isotropic. The mesh was imported to ABAQUS 6.17 (SIMULIA, Providence, RI) for simulation.

Material Properties: A neo-Hookean material model was adopted for the brain tissue. Prony series were adapted to describe the viscoelastic behavior of the brain tissue.

$$G(t) = G_0\left(1 - \sum_{i=1}^{N} \bar{g}_i^p\left(1 - e^{-t/\tau_i}\right)\right) \quad (1)$$

where $G(t)$ is the time-dependent shear relaxation modulus, G_0 is the instantaneous shear modulus, τ_i is the characteristic relaxation time, and $\bar{g}_i^p$ is the Prony series coefficients. The relationship between long-term shear modulus G_∞ and the instantaneous shear modulus G_0 is

$$G_\infty = G_0\left(1 - \sum_{k=1}^{N} \bar{g}_k^p\right) \quad (2)$$

We adopted the viscoelastic properties of the brain tissues from MacManus et al. (2017) [2], where GM (G_∞=1533Pa, $\bar{g}_1^p$=0.568, τ_1=13ms, $\bar{g}_2^p$=0.264, τ_2=184ms) and WM (G_∞=1834Pa, $\bar{g}_1^p$=0.578, τ_1=11ms, $\bar{g}_2^p$=0.267, τ_2=176ms) were separated based on the cortex and pons regions.

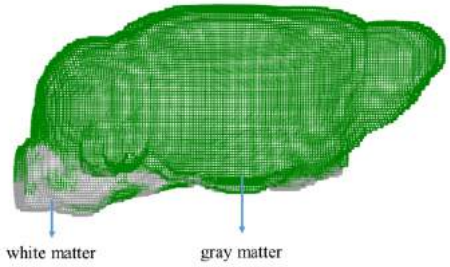

Figure 1. A sagittal view of the FE model.

Poster Presentation #P226

CCI Simulation: To simulate the CCI process, a cylindrical impactor with a diameter of 3 mm were used to induce injury to the brain. Three different velocities (0.6 m/s, 0.8 m/s, and 1.0 m/s) were applied. The impact process was simulated as follows. First, the impactor hit the brain with a constant velocity, and held still for 0.001s at a maximum depth of 2mm. Then, the impactor retracted with the same velocity. The impactor was treated as a rigid body. A frictionless general contact mode was adopted for the interaction between the impactor and brain. The impact process was simulated with ABAQUS/Explicit.

RESULTS

Simulation results from different impact depths and velocities are shown in Figure 2. In all cases, the maximum stresses and strains were observed at the region of brain tissue that in contact with the impactor. For the impact velocity of 1.0 m/s, the brain tissue had the highest average von Mises stress and logarithmic strain.

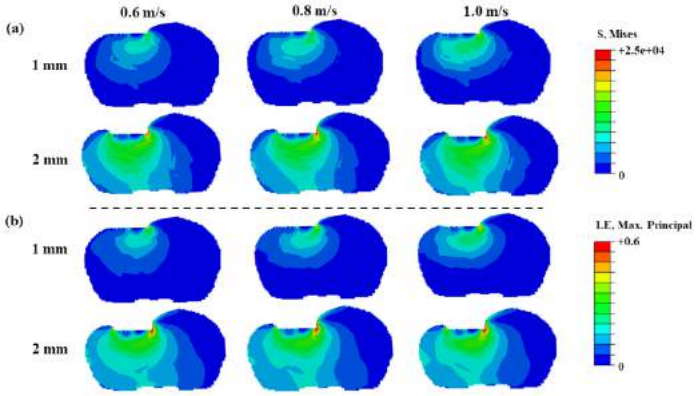

Figure 2. (a) Von Mises stress and (b) logarithmic strain of the brain from different impact depths and velocities.

A clear wave propagation of stress was observed (Figure 3). When the impactor reached its maximum depth, the stress kept propagating throughout time due to the viscoelastic properties of the tissue.

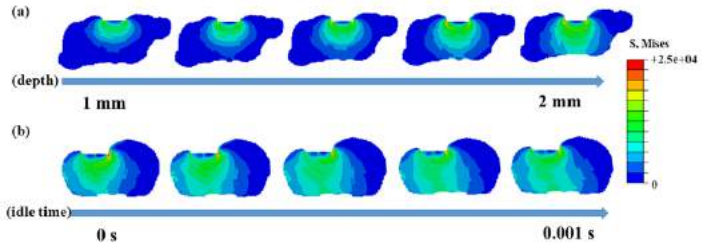

Figure 3. Propagation of von Mises stress (a) when the impactor moved from 1mm to 2mm, and (b) when the impactor reached its maximum depth of 2 mm.

A plot of maximum principal stress over depth showed a similar pattern from different impact velocities (Figure 4). However, the stress propagation after the impactor reached its maximum depth differs from each other.

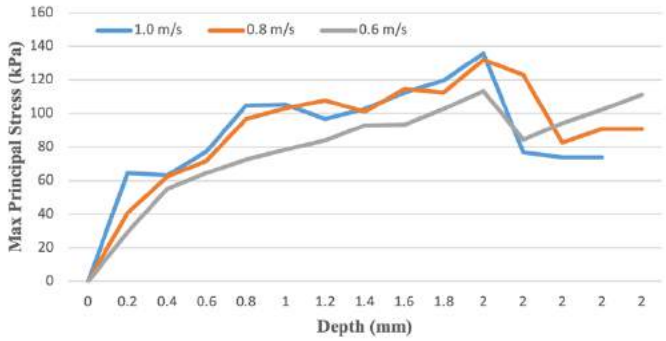

Figure 4. Maximum principal stress in brain tissue. The multiple "2"s of the depth axis refer to different time points when the impactor reached maximum depth of 2 mm.

DISCUSSION

In this study, an anatomically detailed FE mouse brain model was developed for CCI simulation. Using image-based modeling, the anatomical structure of the brain was preserved. We noticed that it was crucial to use viscoelastic material property for simulating dynamic responses of the brain. A clear time-dependent stress propagation pattern was observed. Sullivan et al. (2015) used an Ogden material model with 2nd order Prony series for the piglet brain [6]. In our case, a neo-Hookean material model with 2nd order Prony series was also used.

For CCI, the impact velocities could alter the biomechanical responses of the brain tissue. A larger velocity will introduce a larger distribution of stress and strain with the same impact depth. The simulation results are consistent with that from Sutton et al. (1993), where they found a greater velocity led to a greater contusion volume [8]. In addition, our observation of the biomechanical responses is also consistent with that by Mao et el. [5]. Future work includes animal experiments to validate this model. Also, influences of different impact configurations will be analyzed.

In summary, we developed a protocol to construct an image-based FE model of mouse brain. The simulation results are consistent with experimental observations and showed a clear time-dependent behavior of the brain tissue during CCI.

ACKNOWLEDGEMENTS

Grant 31870941 (YF) from National Natural Science Foundation of China (NSFC). The authors would like to thank Zheyu Ye for his help in Abaqus and Prof. Philip V. Bayly for helpful discussions.

REFERENCES

[1] P. V. Bayly *et al. Annu. Rev. Biomed. Eng.*, 14: 369–396, 2012.
[2] S. Budda *et al. J Mech Behav Biomed Mat*, 74:463–476, 2017.
[3] Y. Feng *et al. J Mech Behav Biomed Mat*, 71:407–415, 2017.
[4] H. Zhao *et al. IMECE*, 2018.
[5] H. Mao *et al. Stapp Car Crash Journal*, p. 18, 2006.
[6] S. Sullivan *et al.*, *Biomech Model Mechanobiol*, 14:877–896, 2015.
[7] C. E. Meyer *et al.*, *NeuroImage*, 163:197–205, 2017.
[8] R. L. Sutton *et al. J Neurotrauma*, 10:135–149, 1993.

SB³C2019
Summer Biomechanics, Bioengineering and Biotransport Conference
June 25 -28, Seven Springs, PA, USA

BIOMECHANICAL CHARACTERIZATION OF OVINE PIA ARACHNOID COMPLEX

Gabryel Conley Natividad [1], Sophia Theodossiou[1], Nathan R. Schiele[1], Gordon Murdoch[2], Goutham Burla[1], Gabriel Potirniche[3], Bryn A. Martin[1]

(1) Department of Biological Engineering
The University of Idaho, Moscow, ID, USA

(2) Department of Animal and Veterinary Science
The University of Idaho, Moscow, ID, USA

(3) Department of Mechanical Engineering
The University of Idaho, Moscow, ID, USA

INTRODUCTION

The pia arachnoid complex (PAC) is a cerebrospinal fluid-filled tissue that surrounds the brain and spinal cord. Within the PAC, arachnoid trabeculae (AT) fibers, AT sheets, and blood vessels span the space between the arachnoid and pial surfaces. These microstructures help hold the delicate central nervous system tissue in place [1]. Due to its structural role, alterations to the biomechanical properties of the PAC caused by sub-concussive hits could impact stresses acting on the brain during traumatic brain injury (TBI). Relatively few studies have investigated PAC biomechanics [2-4]. However, relatively little is known about PAC biomechanical properties causing a gap in knowledge making it difficult to accurately model TBI using finite element modeling (FEM) [5, 6]. The aim of this study was to quantify the mechanical and structural properties of ovine PAC.

METHODS

Ovine brain samples (n=10) were harvested from the University of Idaho Vandal Brand Meats. All samples were removed from the skull within 30 minutes post-mortem. To access the brain tissue, skulls were split medially. To expose the base of the skull, the lower jaw was removed. A shearing knife was used to make clean proximal cuts through the buccal tissue. Once all connective tissue was cut, the lower mandible was removed and discarded. Subsequently, the skull was positioned with the hard and soft pallet of the mouth exposed. The hard and soft pallets where completely separated medially. A similar procedure was employed to split the top of the skull from the occipital region down to the nose. The skull was flipped, and the lower skull cavity was split. Final separation was achieved by breaking the occipital portion of the skull with the halves being carefully separated so as not to damage the brain. Using flat head forceps and a scalpel the brain was removed from the skull. A ~25x40x3 mm template was placed on the frontal right (FR), frontal left (FL), occipital right (OR), and occipital left (OL) region of the brain surface (**Figure 1b**). Each section was cut and removed using a disposable surgical scalpel and bent flat head tweezers. During removal, the brain was kept moist with artificial cerebrospinal fluid (aCSF). Immediately following the removal, each specimen was submerged in aCSF inside a 50 mL conical centrifugal tube and kept on ice. At <2-hours post-mortem all samples were taken back to the laboratory. Upon arrival, each PAC sample was removed and tested separately. It was necessary to remove the PAC from the underlying brain tissue. To do this, the sample was submerged in aCSF (~25ml) with the soft brain matter facing up. Using a scalpel and flat-head tweezers the brain matter was removed until all that was left was the clear PAC. The PAC was then placed in a C-shaped template made of thick paper (10 mm opening) and glued shut (**Figure 2a**). Kimwipes™ were soaked with aCSF and placed in the bottom of 50ml tubes and the PAC samples where gently placed inside and set on ice until testing. The prepared sample was then placed in the bioreactor system developed by Raveling et. al [7] (**Figure 2b**). Once clamped inside the rig, the samples were pulled in uniaxial tension at 2 mm/s until failure. The force and displacement data were acquired at 100 Hz using LabVIEW. To evaluate the stress and strain values, the length and width of the specimens were measured from photographs using ImageJ. PAC thickness was measured using a micrometer (Model 293-340-30 Mitutoyo, Japan). Each sample was measured three times. An Olympus Fluoview 1000 confocal/multiphoton microscope, with second harmonic imaging (860 nm excitation wavelength) was used to visualize collagen microstructure including sheets, pillars, and blood vessel walls. 4,6-diamidino-2-phenylindole (DAPI) was used to visualize cell nuclei.

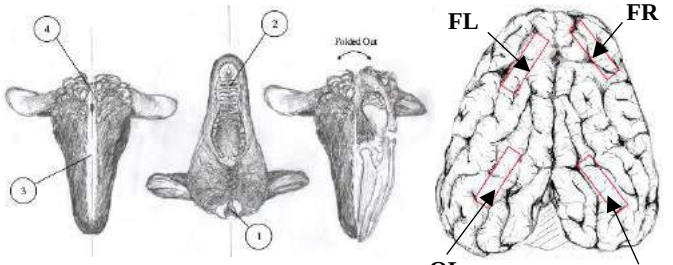

Figure 1: (a) Sheep head with lower mandible removed showing order of cranial cuts (1-4). (b) Location of PAC specimen removal sites.

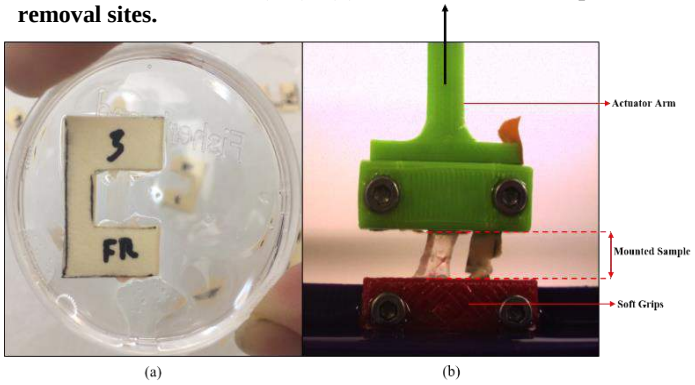

Figure 2: (a) C-shaped template used to mount into the bioreactor (10 mm opening). (b) Bioreactor apparatus with mounted sample prior to testing.

Poster Presentation #P227

RESULTS

All data collected from the bioreactor was read into and analyzed with MATLAB to generate stress-strain curves. **Figure 3** shows the stress-strain behavior of the PAC samples, when subjected to uniaxial tension at an average strain rate of 0.59 s^{-1}**.** A Mooney-Rivlin model (Eq.1) was fit to the average stress-strain curve (**Eq.1)** with stretch ratio $\lambda = \varepsilon + 1$.

$$\sigma_{Uniaxial}^{Eng} = 2C_{10}\left(\lambda - \frac{1}{\lambda^2}\right) + 2C_{01}\left(\lambda - \frac{1}{\lambda^3}\right) + 4C_{20}\left(\lambda - \frac{1}{\lambda^2}\right)\left(\lambda^2 + \frac{2}{\lambda} - 3\right) \quad \textbf{(Eq.1)}$$

The nonlinear least-squares fit for the Mooney-Rivlin constants were estimated to be 1, -1.004 and 0.629 MPa for C_{10}, C_{01}, C_{20} respectively (SSE = 0.6552, R^2 = 0.985). The linear region Young's modulus (E), of the stress-strain curves was found to be 7.68±3.0 MPa. The mean ultimate stress and strain were found to be 2.69±0.76 MPa and 0.60±0.13, respectively. The limited samples collected did not reveal significant differences across sample locations. Mean PAC thickness was found to be 69.7±29.7µm. Using SHG imaging, trabecular fibers and sheets were found to range from ~5 to 30 µm in thickness and showed both straight and crimp-like morphology (**Figure 4**). Cell nuclei appeared to be organized along blood vessel lumens traversing the PAC.

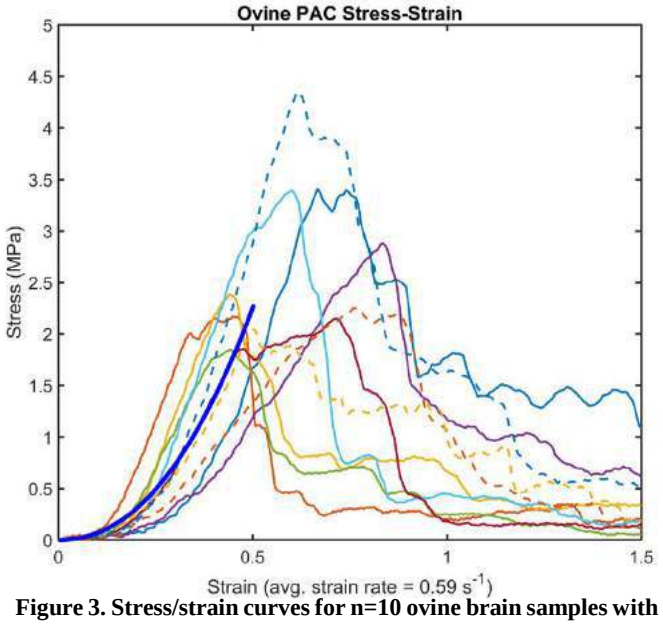

Figure 3. Stress/strain curves for n=10 ovine brain samples with a superimposed curve fit using the Mooney-Rivlin model.

DISCUSSION

To our knowledge, this preliminary study represents the first biomechanical characterization of ovine PAC tissue. Brain sample harvesting and uniaxial tension testing methods of fresh ovine PAC specimens (n=10 animals) were successfully developed. These methods required a detailed series of preparation steps to secure the samples in place for mechanical testing. Our results collected at a strain rate of 0.59 s^{-1} reasonably agree to those found by Jin et al., [3] with a Young's modulus of 11.33 MPa and ultimate stress of 1.44 MPa. We did not observe significant differences in Young's modulus with location on the brain surface. These properties can be used as input data in finite element models of the brain during TBI simulations. Albeit, the strain rate analyzed was relatively slow compared to those often seen in TBI-related circumstances. Future studies should clarify if the stress-strain behavior of PAC tissue depends on strain rate or cyclic loading, representing repeated TBI scenarios.

Collagen folding was visible on SHG imaging, albeit, to a lesser degree than in many other biologic tissues. We found the PAC tissue to be pre-stressed on the surface of the brain. To our knowledge, pre-stress of PAC on the brain surface has not been previously reported in the literature. Upon removal from the surface of the brain from the PAC, the tissue contracted in length and became flaccid making it difficult to determine the physiological zero-strain state. For our testing, a threshold of 0.05 N was defined to determine the zero stress/strain state. Specimen length was found to change by as much as 63% between its pre-stressed condition situated on the brain, to its unstressed condition situated in a C-shaped template. This resulted in significant variation when calculating Young's Modulus. However, the ultimate stress/strain (failure point) of each sample under uniaxial tension were similar between cases.

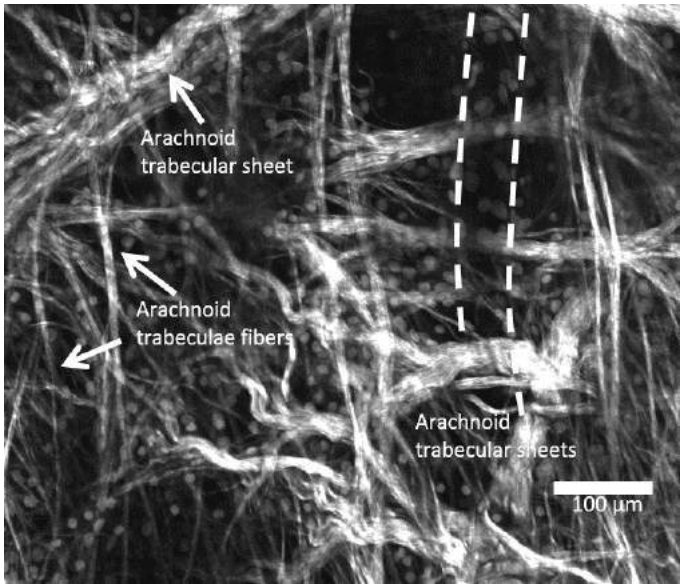

Figure 4. Second harmonic imaging of the pia-arachnoid complex showing collagen microstructures.

ACKNOWLEDGEMENTS

Institutional Development Award (IDeA) from the National Institute of General Medical Sciences (NIGMS) of the National Institutes of Health (NIH) under Grants #P20GM1033408, #4U54GM104944-04TBD, and #1R44MH112210-01A1, and University of Idaho Vandal Ideas Project.

REFERENCES

[1] J. J. Malloy and F. N. Low, *J Comp Neurol*, vol. 157, Sep 1 1974.
[2] X. Jin *et al.*, *Stapp Car Crash J*, vol. 51, Oct 2007.
[3] X. Jin, J. B. Lee, L. Y. Leung, L. Zhang, K. H. Yang, and A. I. King, *Stapp Car Crash J*, vol. 50, Nov 2006.
[4] X. Jin, K. H. Yang, and A. I. King, *J Biomech*, vol. 44, Feb 3 2011.
[5] X. Jin, H. Mao, K. H. Yang, and A. I. King, *Ann Biomed Eng*, vol. 42, Apr 2014.
[6] G. Scott and B. Coats, *IEEE Trans Med Imaging*, vol. 34, Jul 2015.
[7] A. R. Raveling, S. K. Theodossiou, and N. R. Schiele, *MethodsX*, vol. 5, 2018.

SB³C2019
Summer Biomechanics, Bioengineering and Biotransport Conference
June 25 -28, Seven Springs, PA, USA

TEMPLATE MODELS FOR SURFACE MANIPULATION OF MUSCULOSKELETAL EXTREMITY REGIONS

Sean B. Doherty, Ben Landis, Tammy Owings, Ahmet Erdemir

Computational Biomodeling (CoBi) Core, Department of Biomedical Engineering
Lerner Research Institute, Cleveland Clinic
Cleveland, Ohio, USA

INTRODUCTION

Virtual representations of the musculoskeletal extremities that faithfully replicate the behavior of tissue's surface mechanics would advance simulation-based surgical assessment, medical training, and prototyping of protective gear. The musculoskeletal extremities, consisting of the upper leg, lower leg, upper arm, and lower arm, are of particular interest because they account for more combat wounds than any other region of the body [1]. This study aims to develop template models for these regions that can accommodate simulations of indentation and other surface interactions, which are necessary for haptic feedback in virtual training.

METHODS

Finite element representations of cadaver arm and leg regions were generated for one male and one female donor (Table 1). The specimens were put through a series of experiments which tested the loads observed on an ultrasound probe during indentation trials [2]. Computed tomography (CT) images of these specimens were also collected at a resolution of 0.5 mm x 0.5 mm x 0.6 mm.

Table 1: Specifications of donors.

Sex	Age (years)	Weight (kg)	Height (m)	BMI (kg/m^2)
Male	65	77.1	1.778	24
Female	62	68.0	1.803	21

Anatomy of eight regional models was reconstructed from manual segmentation of the CT images using 3D Slicer [https://www.slicer.org]. Surface representations for both the lumped flesh and the bone were created by Poisson surface reconstruction on the 3D Slicer output using Meshlab [http://www.meshlab.net]. The surface meshes were then parameterized, remeshed, and smoothed to improve mesh quality.

A three-dimensional scan of a Siemens 9L4 transducer, the ultrasound probe used during tissue indentation experiments, was generated to replicate its geometry for simulations. The ultrasound probe and the bone were both assumed to be rigid bodies and were modeled as 3 node triangular shell elements. The flesh volume was meshed with 10-node quadratic tetrahedral elements using Gmsh [gmsh.info]. The flesh component was modeled using an uncoupled Neo-Hookean constitutive model, with C_1 set to 0.01 MPa, based on a literature based effective Young's modulus [3]. K was set to 10 MPa to enforce near incompressibility, i.e., K was 1000 times larger than C_1. The model was then assembled for simulation in FEBio [https://febio.org].

Contact between the ultrasound probe and the flesh was modeled with a frictionless, penalty-based, sliding-elastic contact formulation. The ultrasound probe was positioned based on the initial point of the experimental data and was given a prescribed displacement based on the displacement vector between the initial and end position during the indentation trials. Simulations were performed in FEBio v2.8.0 on the high performance computing cluster at the Cleveland Clinic. Figure 1 shows the basic setup of the upper leg models at the start of the simulation, as well as the flesh and bone components for the other six regions.

Prior to running simulations reproducing experimental conditions, a mesh sensitivity study was performed on the female donor's upper leg to determine the appropriate remeshing sampling rate. Convergence was considered reached after simulated reaction forces did not vary by more than 5% in consecutive densities. For these simulations the probe was displaced 15 mm and the material

parameters were set as C_1 at 0.0018 MPa and K at 1.795 MPa. These values were used as an approximation of material properties early in the model development process. Material properties are not expected to influence the mesh convergence results obtained (Table 2).

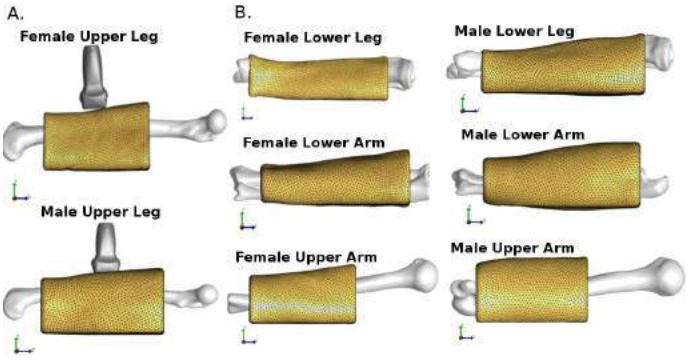

Figure 1: A. Layout of the probe, bone, and flesh components for the female and male upper leg models. B. Bone and flesh components for the remaining six models.

RESULTS

Table 2 shows the results of the mesh sensitivity study, highlighting the converged mesh, which had a remeshing sample rate of 5.

Table 2:Mesh sensitivity of female upper leg model. The bold row highlights the converged mesh density (remeshing sample rate 5).

Node Count	Predicted Reaction Force (N)	Percent Difference
44968	20.8	-
72904	19.9	-4.3
113836	**18.1**	**-9.1**
173068	17.5	-3.0
244551	17.6	0.3

Table 3 compares the experimental force data against predictions from simulations conducted with literature based material properties.

Table 3:Experimental vs. simulation predicted probe reaction forces.

Model Region	Experimental (N)	Predicted (N)
Male Upper Leg	13.1	25.7
Male Lower Leg	13.3	15.8
Male Upper Arm	9.6	24.9
Male Lower Arm	14.4	22.5
Female Upper Leg	9.9	13.4
Female Lower Leg	6.1	12.7
Female Upper Arm	7.9	20.1
Female Lower Arm	6.6	23.8

Figure 2 shows the effective stress distribution for the female upper leg model at the end of indentation. Other field metrics such as Lagrange strain and contact pressures are also available.

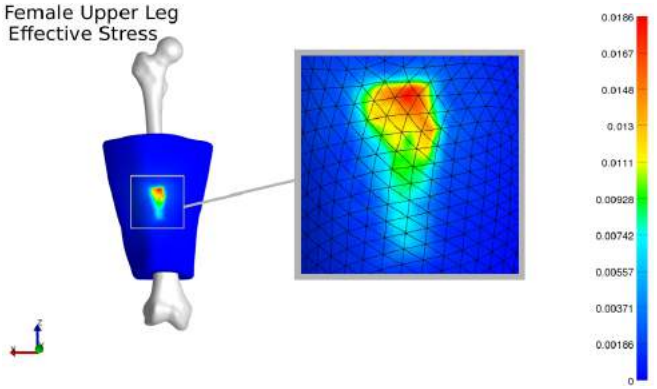

Figure 2: Effective stress (MPa) distributed across the surface of the flesh of the female upper leg model at full indentation.

DISCUSSION

Lumped tissue models for the musculoskeletal extremities were built and simulated with probe indentation for prediction of surface mechanics. While the reaction forces obtained from simulation do not match closely with experimental data, a close match was not expected at this point. Soft tissue material properties are known to differ based on a variety of factors, including gender and body region [4]. The literature based effective Young's modulus does not attempt to control for either of these variables and resulted in a simulated reaction force that is consistently an overestimation, by a factor ranging from 1.18 to 3.61. The variability in overestimation highlights the need to assign each flesh component its own material properties to obtain more representative surface mechanics.

Future work will include calibration of these models through inverse finite element analysis, where each model's material parameters will be determined based on the force-displacement data obtained from experimentation. This step will improve the accuracy of the representation of surface mechanics for each model. Once calibrated, these models may serve as the the basis for individualized surgical simulation tools.

Beyond calibration of the lumped tissue models, additional model development is planned as a part of this project. Models that explicitly represent the skin, fat, muscle, and the interactions between these layers are currently under development. Additional model features such as gravity compensation and model incorporation with haptic feedback devices are also planned.

All models, data, and scripts that were used in this study are available online, in the source code repository at https://simtk.org/projects/multis. A more detailed set of modeling specifications is also available on this website's wiki. The open availability of this data through public dissemination aims to reduce the barrier of entry for other researchers to adapt these models to their own work.

ACKNOWLEDGEMENTS

This study has been supported by USAMRMC, DoD (W81XWH-15-1-0232, PI: Erdemir). The views, opinions and/or findings contained in this document are those of the authors and do not necessarily reflect the views of the funding agency. The authors thank Tyler Schimmoeller and Erica Neumann for their work on experimentation.

REFERENCES

[1] Eskridge, Susan L., et al. Injury 43.10 (2012): 1678-1682.
[2] Schimmoeller, Tyler, et al. Journal of Biomechanics (2018).
[3] J. W. Steege et al. in Proc. Symp. Biomech ASME (1987): 39–43.
[4] Choi, A. et al. Medical and Biological Engineering and Computing 43.2 (2005): 258-264.

SB³C2019
Summer Biomechanics, Bioengineering and Biotransport Conference
June 25 -28, Seven Springs, PA, USA

A PARAMETRIC STUDY OF TRANSCONDYLAR SCREW EFFECTIVENESS TO ENHANCE HEALING OF SUBCHONDRAL BONE CYSTS OF VARIED SIZES

Lance L. Frazer (1), Elizabeth M. Santschi (2), Kenneth J. Fischer (1, 3)

(1) Bioengineering Program
University of Kansas
Lawrence, KS, USA

(2) Equine Surgery
Kansas State University,
Manhattan, KS, USA

(3) Mechanical Engineering
University of Kansas
Lawrence, KS, USA

INTRODUCTION

Subchondral bone cysts (SBCs) are frequently diagnosed in young horses bred for racing. They occur most often in the medial femoral condyle (MFC). SBCs can result in lameness and cause secondary injuries such as meniscal and cartilage damage. Traditional treatments of SBCs aim to reduce local inflammation and promote bone healing by use of anti-inflammatory agents, cyst debridement and/or regenerative substances [1]. Reported success rates vary greatly and reflect short-term lameness reduction only. Radiographic healing rates of SBC after treatment are rarely reported, and when they occur, are described as a reduction in SBC size rather than complete healing [2].

A recently developed treatment which places a transcondylar lag screw across the void has shown high success rates in both lameness resolution and radiographic healing [3], and recent work in our laboratory indicates the mechanism of healing is increased bone stress stimulus combined with reorientation of the compressive principal stresses. However, these results were obtained using a single 2 cm^3 void. As such, it is of clinical interest to study the effectiveness of the standard screw placement for several different cyst sizes.

In this study, finite element analysis was utilized to quantify the bone remodeling stimulus with a proximodistal oblique transcondylar lag screw through an equine MFC with SBC voids of varying proximal-distal height, medial-lateral width, and anterior-posterior depth. We hypothesized that the lag screw treatment strategy stimulates bone formation in cysts where the screw passes through the cysts, but not for small cysts that the screw does not penetrate.

METHODS

Previous work by our lab developed a finite element model of an equine stifle joint in extension with a 2 cm^3 void in the MFC under joint loading to simulate stall confinement, hand walking and light exercise [4]. The present study used this model with an added sclerotic region of bone of thickness 5 mm (as seen clinically) outside of the SBC. The sclerotic density was assumed to be 1.0 g/cm^3 and given a corresponding modulus of 3770 MPa using

$$E = 3770\,\rho^3 \quad (1)$$

for the density-modulus relationship [5]. The remaining bone tissue was assigned properties using the same relationship. Cartilage material properties were lowered from our previous study to better represent the tissue response at lower loads and strain rates experienced in a post-operative environment (E = 8 MPa, $\nu = 0.45$).

Criteria for Effectiveness: To evaluate the efficacy of various surgical treatment strategies, Beaupre, Orr, and Carter's theory of bone remodeling was adopted [6, 7]. The standard tissue stimulus (Ψ) was calculated to predict bone resorption, apposition, or no net change,

$$\Psi = \left(\sum_{day} n_i \sigma_{b_i}^m\right)^{\frac{1}{m}} \quad (2)$$

where n_i is the number of cycles per day (for a given load), σ_{b_i} is a bone tissue-level effective stress based on strain energy density, and m is an empirical constant assumed to be 6 for the horse [8]. We assumed the standard attractor state (ideal reference stimulus) of 50 MPa and a "dead zone" of ± 20% (i.e. 40-60 MPa). Thus, values of $\Psi > 60$ MPa predict bone apposition, and values of $\Psi < 40$ MPa predict bone resorption.

General Boundary Conditions and Analysis Procedures: A 900 N load was applied as uniform pressure on the proximal femur to simulate stall-confinement loading that occurs for the first few weeks post-surgery. The quadriceps tensile force on the superior aspect of the patella to prevent unrealistic femoral anterior translation was scaled down from our previous study to 100 N [5]. The proximal aspect of the

Poster Presentation #P229

femur was constrained in varus-valgus (0°) and flexion/extension rotations (155°). The tibia was fully constrained, and all femoral translations and internal rotation were allowed. Frictionless contact was defined between all articulating surfaces using general contact in ABAQUS. Stimulus, Ψ, was calculated on the interior surface elements of the SCL, and the percentage of the available cyst surface area exceeding 60 MPa, bone formation area (BFA), was calculated.

For all models, a simplified screw (40 mm length and 4.5 mm diameter cylinder, E = 200 GPa) was constructed with a 6 mm head and tapered at the axial end. The head was constrained by contact with the outside of the bone and the tip was tied to the bone. Screw compression of 300 N was applied axially to simulate tightening. The screw was placed from abaxial to axial in the MFC (i.e. from medial surface toward central femur), to simulate the clinical proximodistal oblique transcondylar screw placement, such that the screw passes through larger SBC voids. The number of steps, cycles per day (cpd) or n_i in Equation 2, was chosen as 3000 cpd for the applied joint load of 900 N.

Parametric Study Design: Each spatial dimension of the cyst was varied between 3 different levels that represent the minimum, median, and maximum lengths observed clinically [9]. The proximal-distal height of the SBC void was 2 mm, 14 mm, or 26 mm. The medial-lateral width of the SBC void was 2 mm, 8 mm, or 14 mm. The anterior-posterior depth of the SBC void was 2 mm, 10 mm, or 20 mm. The study design was a full 3^k (k=3) factorial evaluation of all 27 combinations. Previous work has shown that at 900 N load, a neutral screw with 0 N of compression does not differ from using no screw at all. Therefore, the models were run with 0 N of compression and then again with 300 N compression. The change in BFA was calculated to demonstrate the effectiveness of the compression on the lag screw.

RESULTS

The results clearly show that the size of the cyst is the primary predictor of the increase in bone formation area (BFA) caused by the screw (Table 1). For all cysts with a 2 mm height, the BFA increased a negligible 0-3 %. For cysts with a 14 mm height, the BFA increased by 6-31%. For cysts with a 26 mm height, the BFA increased 5-34%. In particular, the height of the cyst had the largest effect. Regression analysis showed that the cyst height alone accounts for 56% of the variation (increase) in the BFA, followed by cyst depth (12%) and cyst width (negligible). For small height cysts (Figure 1A), the screw does not penetrate the cyst, but simply goes over the top of it, producing little stress stimulus for bone formation. For cysts with a 14 mm height, the screw penetrates and crosses the top of the cyst. Depending on the cyst width and depth (Table 1), the screw increased the bone stimulus and BFA substantially.

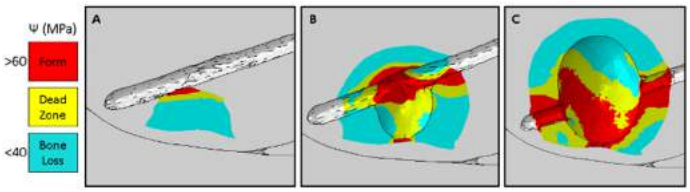

Figure 1. Bone tissue stress stimulus in the medial femoral condyle region of interest 900 N joint load, 300 N stainless lag screw compression, and 3000 cpd for three different sizes of cyst.
A) 2 mm height, 2 mm width, 2 mm depth
B) 14 mm height, 8 mm width, 10 mm depth
C) 26 mm height, 14 mm width, 20 mm depth

DISCUSSION

The BFA is affected by the screw position in the cyst, and the PDO screw position is constrained by the regional anatomy, as the screw head cannot contact the cartilage or meniscus. Given that limitation, the cyst height is the most important factor affecting the increase in BFA provided by the screw. While the 14 mm cyst height did see substantial increases in BFA with the screw (Figure 1 and Table 1), this cyst height may be near the minimum for the screw to be effective using the standard screw placement. When the screw goes above the cyst, it has little effect on the BFA (Figure 1A).

Table 1: Predicted bone formation area (BFA) increase as a percent of void surface area with a 900 N joint load, 300 N screw compression, and 3000 daily cycles (steps).

Height	Depth	Width	BFA % Increase
14	10	2	12
14	10	8	15
14	10	14	27
14	20	2	10
14	20	8	20
14	20	14	31
26	10	2	34
26	10	8	28
26	10	14	24
26	20	2	34
26	20	8	22
26	20	14	29

Cyst depth (anterio-posterior) had a moderate impact on BFA and the impact of cyst width was minor. Because the screw goes primarily medial-lateral and proximal-distal, a larger depth is important so that the screw will pass through the cyst. Thus, the secondary factor affecting the increase in BFA is cyst depth. But if the cyst is high enough and deep enough, it will pass through a cyst regardless of the medial-lateral width. In order to reach lower cysts, a lower and more horizontal screw would be required, but the screw head would interfere with the medial meniscus. It may be possible to reach and stimulate bone formation in such cysts with a dual pitch headless screw, if enough compression can be achieved across the cyst.

There are a number of limitations to this study. All configurations tested were variations of a single finite element model based on a single healthy stifle joint. The SBC shape and the sclerotic region were idealized to match what is commonly observed clinically. The joint loading was estimated, as there are no kinetic data for the equine stifle. Also, the bone remodeling theory framework is based on limited samples that do not include equine data. While absolute values may be questioned, the relative values of stress stimulus clearly indicate the relative effectiveness of the lag screw for various sized cysts.

ACKNOWLEDGEMENTS

Supported by the Madison and Lila Self Graduate Fellowship.

REFERENCES

[1] Howard RD, et al., *J Am Vet Med Assoc*. 1995;206:842-850.
[2] Ortved KF, et al., *Equine Vet J.* 2012;44:606-13.
[3] Santschi EM, et al., *Veterinary Surgery* 2015;44:281-8.
[4] Frazer LL, et al., *Vet Surg* 2018; DOI: 10.1111/vsu.13139
[5] Carter DR, Hayes WC. *J Bone Joint Surg* [Am] 1977;59:954-62.
[6] Beaupre GS, et al.. *J Orthopaedic Research* 1990;8:651-61.
[7] Beaupre GS, et al.. *J Orthopaedic Research* 1990;8:662-70.
[8] Whalen RT, et al., *Journal of Biomechanics* 1988;21:825-37.
[9] Walker WT, et al., *Am J Vet Res* 2016;77:265-274

SB³C2019
Summer Biomechanics, Bioengineering and Biotransport Conference
June 25 -28, Seven Springs, PA, USA

Reducing Kinematic Data Uncertainty During Mechanical Testing of Orthopaedic Implants: The Benefits and Pitfalls of Auxiliary Motion Capture Systems

Callan Gillespie (1), Quinn N Saluan (1), Tara F Nagle (1), Joe Little (2), Willy Theodore (2), Robb W Colbrunn (1)

(1) The Cleveland Clinic Foundation
Cleveland, OH, USA

(2) 360 Knee Systems
Sydney, Australia

INTRODUCTION

Understanding *in vivo* motion of orthopaedic implants is an important part of evaluating performance. Simulation of these situations is often done via multi-axis mechanical simulators. As with any mechanical testing, the compliance of the machine and associated fixtures are sources of uncertainty in acquiring kinematic data. Compliance is often compensated for in 1 degree of freedom (DOF) applications with an extensometer (e.g. Instron machine for tensile testing). The extensometer, measures movement without the influence of machine deformation and thus provides a more accurate displacement measurement compared to the output of the machine itself. In this study, motion capture was used as a 6-DOF extensometer to eliminate machine compliance in the kinematic data during testing of orthopaedic implants. The aim of this study was to understand the kinematic differences in implant motion when reported by the testing machine vs. the motion capture system.

METHODS

A single knee implant was tested using a robotic musculoskeletal simulator that consisted of a pedestal base, ATI Omega 85 load cell, total knee replacement, and a Kuka KR300 robot. An active motion tracking sensor was mounted to the femur and tibia implants so as to be seen by the NDI Optotrak Certus stereoscopic motion tracking camera (**Figure 1**). Femur and tibia component coordinate systems were created relative to the robot, load cell, and motion tracking sensor by digitizing the implants, load cell, and robot. The relative relationship of the femur and tibia coordinate systems was defined by the Grood and Suntay knee joint coordinate system (JCS) [1]. The implant was then biomechanically tested using simVITRO® software by applying various motions and loads specified by a standard gait profile (ISO 14243-1) and constraint test (ASTM F1223) [2, 3]. The two versions of JCS kinematic data (i.e. measured by the motion tracking sensors and the robot) were collected throughout the tests and analyzed.

Figure 1: simVITRO Robotic Test System

RESULTS

Differences between JCS kinematics from motion capture and robot data were identified. The measurement noise was more favorable using robot data (60-800µm, 5-40µm noise range for motion tracking and robot respectively). Robot data accuracy decreased with increasing forces, as the differences in measurement was a function of force, and therefore due to system compliance (**Figure 2**). Compliance was identified in several degrees of freedom, however the difference between the motion capture and robot data was greatest in the inferior-superior direction (877 N/mm), and likely due to large applied compression forces. At high loads, the robot data suggested ~3 mm of reported penetration of the femur into the tibia (**Figure 3**).

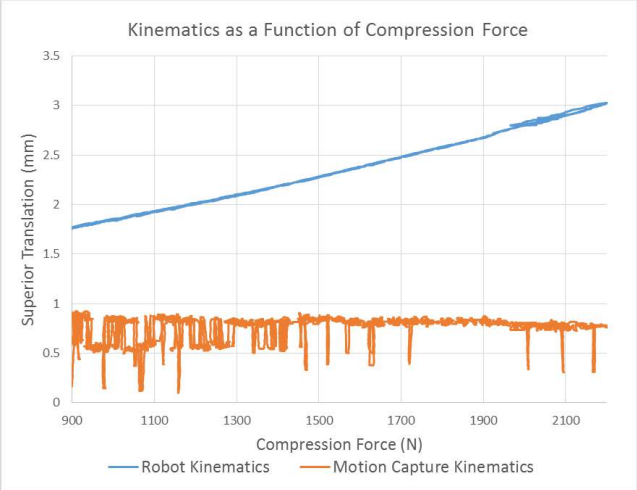

Figure 2: Compression Force vs Kinematic Error

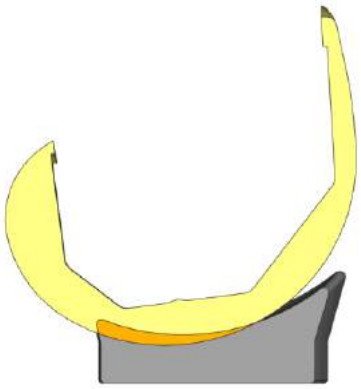

Figure 3: Incorrect (Orange) Penetration of Components

DISCUSSION

While the robot kinematic data was considerably more precise than motion capture, it was found to suffer from compliance induced accuracy problems. The linear relationship with force is likely due to machine and fixture compliance (**Figure 2**). When utilizing this data for kinematic control of biomechanical simulations, wear testing systems, or computational model validation, the machine compliance inaccuracies will degrade the kinematic integrity of the results. **Figure 3** shows the non-linear contact relationship between implant components and how model reconstructions of the kinematic data can produce inaccurate results if using machine kinematic data only. Wear testing, for example, is performed by applying the same kinetic/kinematic profile to implants millions of times to characterize how the component changes. Kinematic controlled testing assumes the desired and actual kinematics match. If they don't, then the forces applied to the component will change, and introduce uncertainty in the results. However, motion tracking based kinematic measurement and control is no panacea and possesses two major pitfalls to be aware of: visibility and noise.

Each rigid body motion tracking sensor is made up of 3 or more 3D markers which can be combined together through a least-squares fit algorithm to determine the position and orientation of the rigid body. Occlusion of one or more markers so that there is less than 3 visible will result in no knowledge of rigid body location. In addition, occlusion of any one of the markers can affect the least squares fit result. Also, each of the markers has some stochastic noise associated with the measurement. This measurement (i.e. sensor location) is then transformed to the femur and tibia to calculate the JCS. Depending on the spatial relationship of the sensor and bone, this process can amplify noise and visibility uncertainty in the resulting JCS kinematics. Lastly, kinematic control of a testing machine using an external measurement of position (e.g. motion capture) is difficult due to these measurement uncertainties as well as other issues regarding control communication rates and robustness to noise and data dropouts.

Neither the robot or motion capture based kinematics are ideal, but each have beneficial properties. In the future, a potential solution for remedying the shortcomings of robot kinematic data and lessening the pitfalls of motion capture systems lies in a hybrid algorithm that combines data from both sensors in real-time.

In conclusion, the compliance of mechanical testing machines can generate incorrect kinematic data which when coupled to wear testing, superposition testing, or mathematical modeling can lead to incorrect conclusions about implant performance. By utilizing motion capture and accounting for its limitations, improved accuracy in testing results can be achieved thus providing meaningful research that can be more directly translated to patient care in any mechanical testing system in which compliance exists.

ACKNOWLEDGEMENTS

The authors would like to thank 360 Knee Systems for funding the study.

REFERENCES

[1] Grood ES, Suntay WJ., *J Biomech Eng* 105:136-144, 1983
[2] ISO 14243-1, 2009
[3] ASTM F-1223-14, 2014

SB³C2019
Summer Biomechanics, Bioengineering and Biotransport Conference
June 25 -28, Seven Springs, PA, USA

EFFECT OF PELVIS AND LIMB POSITION ON RADIOGRAPHIC LEG LENGTH DISCREPENCY MEASUREMENT: A SAWBONES MODEL

Isaac Livshetz, MD (1), Awais K. Hussain, MD (1), Matthew Robinson, MD (1), Farid Amirouche, PhD (1),

Mark Gonzalez, MD, PhD (1)

(1) Orthopedic Surgery
University of Illinois College of Medicine
at Chicago
Chicago, IL, USA

INTRODUCTION

Leg length discrepancy (LLD) after total hip arthroplasty is a challenging problem which can result in nerve palsy, abnormal gait and hip instability among other complications.[1–3] Measuring LLD on pelvis radiographs can be challenging, especially because the obliquity of the pelvis and position of the corresponding limb can affect the measured leg length. A perfect pelvis x-ray with a level pelvis and neutral femur abduction is not always available or attainable. We sought to determine how varying pelvis and limb position would affect LLD measurement and devise a method to estimate true leg length discrepancy.

METHODS

A size large pelvis and bilateral femur sawbones model with equal leg lengths and a high resolution radiopaque cortical shell was utilized with fluoroscopy. Leg lengths were measured with a medical imaging software from the acetabular tear drop to the tip of the lesser trochanter, as is established in clinical practice.[2] Leg length discrepancy was measured with intentional malpositioning of pelvic obliquity 0°, 5°, 10° and 15° and femur malpositioning from 15° adduction to 15° abduction in 5° increments. We then calculated the LLD measurement error resulting from all combinations of pelvic obliquity and femur malpositioning.

RESULTS

Pelvic obliquity changes of 5° or less typically result in LLD measurement error <1 cm. As pelvic obliquity increases to 10°, resultant LLD measurements errors are <1cm if the femora remain neutral. At pelvic obliquity of 10° and 15°, even minor limb malposition results in clinically significant measurement errors >1cm. Greatest LLD measurement error occurs when femur on high side of obliquity is adducted and low side femur is abducted.

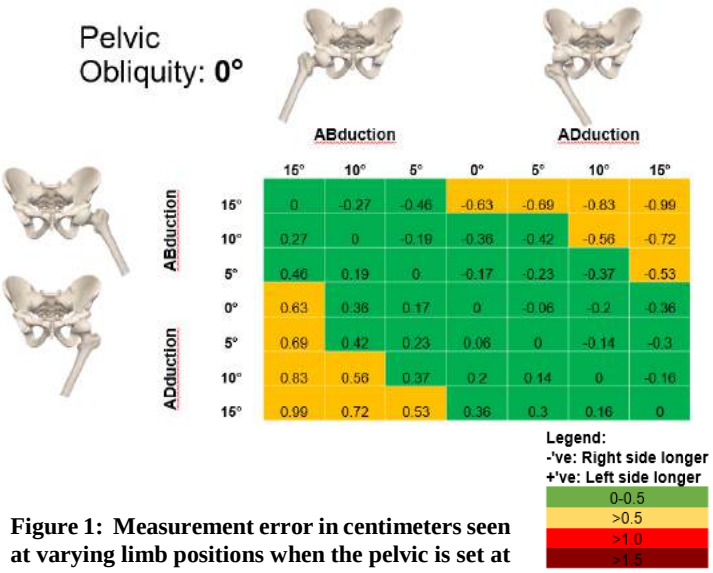

Figure 1: Measurement error in centimeters seen at varying limb positions when the pelvic is set at

0 degrees obliquity. The legend explains a negative ME implies a longer right side and positive ME implies longer left side

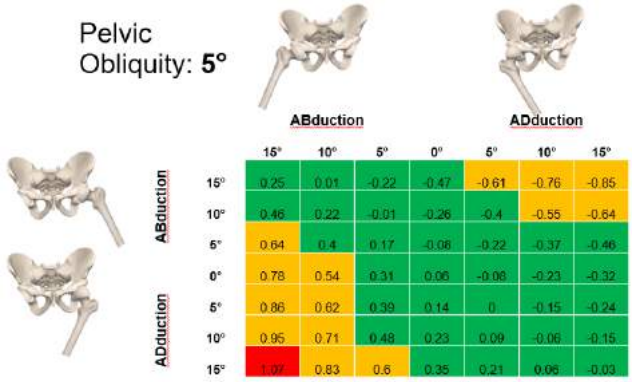

Figure 2: Measurement error in centimeters seen at varying limb positions when the pelvic is set at 5 degrees obliquity. The legend explains a negative ME implies a longer right side and positive ME implies longer left side.

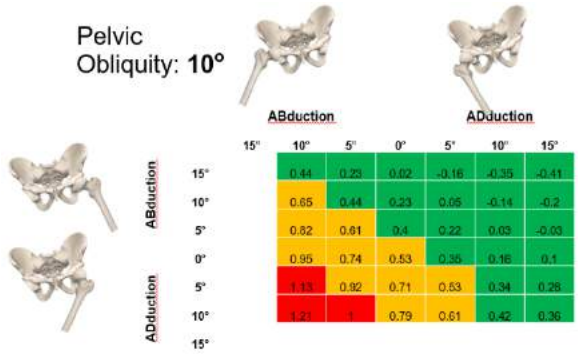

Figure 3: Measurement error in centimeters seen at varying limb positions when the pelvic is set at 10 degrees obliquity. The legend explains a negative ME implies a longer right side and positive ME implies longer left side.

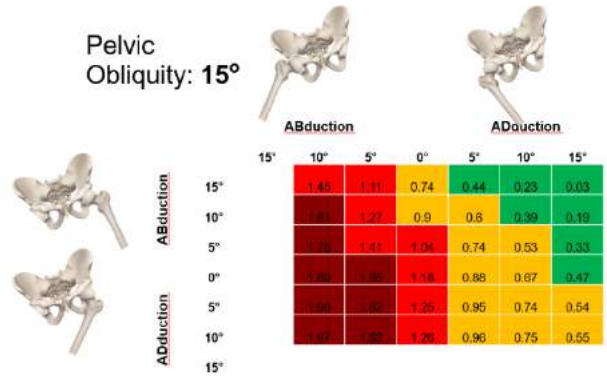

Figure 4: Measurement error in centimeters seen at varying limb positions when the pelvic is set at 15 degrees obliquity. The legend explains a negative ME implies a longer right side and positive ME implies longer left side.

DISCUSSION

LLD after total hip arthroplasty is a challenging problem for patient and surgeon alike and careful leg length measurement on pelvis radiographs is critical. Pelvic obliquity greater than 10° can lead to significant LLD measurement errors >1cm even with minor limb malposition.[4] Error is increased in lower limb positions typically seen in a standing radiograph with pelvic obliquity where one femur is adducted and the other abducted. Accurate LLD measurement is critical but perfect radiographs are not always attainable. We offer methods to estimate true LLD using simple geometric calculations or correction tables obtained from our results.

The findings of our study are clinically relevant, as up until now CT, MRI, and X-ray scanograms have been shown to have more validity and reliability than AP radiographs.[5,6] However, our method of measurement correction allows the use of quickly obtainable, cheap, AP radiographs to similar accuracy levels of the previously mentioned modalities.

ACKNOWLEDGEMENTS: There are no current acknowledgements

REFERENCES

1. Austin MS, Hozack WJ, Sharkey PF, Rothman RH. Stability and leg length equality in total hip arthroplasty. J Arthroplasty [Internet] 2003 [cited 2018 Sep 6];18(3):88–90. Available from: http://www.ncbi.nlm.nih.gov/pubmed/12730937
2. Woolson ST. Leg length equalization during total hip replacement. Orthopedics [Internet] 1990 [cited 2018 Sep 6];13(1):17–21. Available from: http://www.ncbi.nlm.nih.gov/pubmed/2300514
3. Amstutz HC, Ma SM, Jinnah RH, Mai L. Revision of aseptic loose total hip arthroplasties. Clin Orthop Relat Res [Internet] 1982 [cited 2018 Sep 6];(170):21–33. Available from: http://www.ncbi.nlm.nih.gov/pubmed/7127949
4. Parvizi J, Sharkey PF, Bissett GA, Rothman RH, Hozack WJ. Surgical treatment of limb-length discrepancy following total hip arthroplasty. J Bone Joint Surg Am [Internet] 2003 [cited 2018 Sep 6];85–A(12):2310–7. Available from: http://www.ncbi.nlm.nih.gov/pubmed/14668499
5. Woolson ST, Hartford JM, Sawyer A. Results of a method of leg-length equalization for patients undergoing primary total hip replacement. J Arthroplasty [Internet] 1999 [cited 2018 Sep 6];14(2):159–64. Available from: http://www.ncbi.nlm.nih.gov/pubmed/10065720
6. Kjellberg M, Al-Amiry B, Englund E, Sjödén GO, Sayed-Noor AS. Measurement of leg length discrepancy after total hip arthroplasty. The reliability of a plain radiographic method compared to CT-scanogram. Skeletal Radiol [Internet] 2012 [cited 2018 Jul 28];41(2):187–91. Available from: http://www.ncbi.nlm.nih.gov/pubmed/21491155

SB³C2019
Summer Biomechanics, Bioengineering and Biotransport Conference
June 25 -28, Seven Springs, PA, USA

CLINICAL REPRESENTATION OF JOINT COORDINATE SYSTEM FORCES

Callan Gillespie (1), Tara Nagle (1), Robb Colbrunn (1)

(1) BioRobotics Lab
Cleveland Clinic
Cleveland, Ohio, US

INTRODUCTION

There is currently no standard way of describing knee joint kinetics unlike kinematics, in the field of biomechanics. Practically, this means that two identical tests can produce different kinetic results because the results are displayed in different coordinate systems (CS). Three common ways to report knee loads are in the JCS reference frame, the tibia reference frame, and a third hybrid approach.

In the knee JCS a single translation and rotation is applied starting at the local femur CS followed by a second translation and rotation, and a third, as seen in the left of Figure 1. The JCS is a non-orthogonal CS, meaning that its axes, specifically the first and third do not have to be perpendicular [1, 2]. This knee JCS definition by Grood & Suntay was standardized by the International Society of Biomechanics and is now the accepted method to describe clinically meaningful representations of motion [2]. Alignment of the kinetic and kinematic CSs provides a direct mapping between kinetics and kinematics. However, JCS kinetics are non-orthogonal which creates the possibility of loads being overstated if components of the force aligns with multiple axes, or being understated if components are not aligned with any of the JCS axes. For normal knee motion these amounts may not be clinically significant, but they are real.

For this reason, kinetics are often described in an orthogonal tibia based CS where there is no possibility of under- or overstating loads. The downside is that anatomical loads and kinematic directions do not match. For example, if a patient is sitting on an exam table and the tibia is internally rotated 20 degrees, then when the clinician sitting across from the patient pulls the tibia towards them, it is clinically considered an anterior translation. However, the forces, as represented in the tibia reference frame, include components of anterior and lateral loads (figure 1, right).

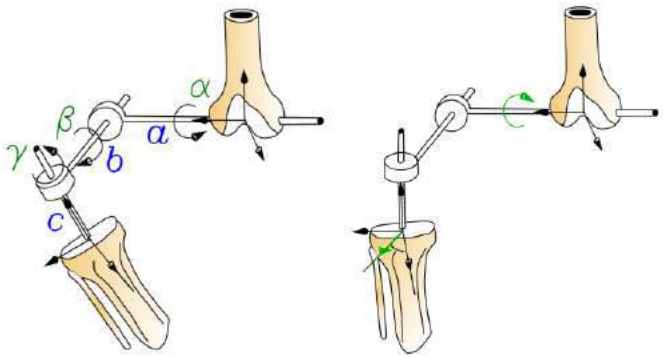

Figure 1: Knee Joint Coordinate System

Left: Knee JCS, Right: Knee JCS with Anterior Drawer Force

The third approach in literature is reporting orthogonal forces in the tibial reference frame, and projecting the torques onto the non-orthogonal JCS axes. This provides some benefits, retains some of the original limitations, and introduces a new limitation. Typically torques are projected onto the JCS without taking into account moment arms [3]. In the example described above, an anterior pull will create an extension torque about the flexion axis of the JCS (figure 1, right). However, if kinetics are initially computed in the orthogonal tibial plateau reference frame and then projected into the JCS, there will be a smaller torque because the calculations only include the moment arm

from the application of force to the tibial plateau, and not the femur flexion axis. To overcome the limitation of this approach, the moment arms from the orthogonal CS to each link of the JCS would need to be taken into account when calculating JCS moments.

The goals of this study were to understand the effect using different kinetic reference frames has on reported loads and to convey the importance of properly reporting kinetic reference frames.

METHODS

Freely available data from the Open Knees project was examined to determine the effect of different kinetic CSs [4]. Open Knees was a research project conducted at the Cleveland Clinic using a simVITRO® universal musculoskeletal simulator (Cleveland Clinic, Cleveland, OH) to apply forces and torques to cadaveric knee joints. The tests were performed by controlling kinetics in the tibial reference frame. Data collected from specimen oks008 was utilized. Combined loading states were applied to the knee joint yielding 27 different kinetic states at 90 degrees of flexion (**Table 1**).

Condition	Loads
Lateral Drawer Force	0 N
Anterior Drawer Force	100, 0, -100 N
Distraction Force	-20 N
Extension Torque	0 Nm
Varus Torque	10, 0, -10 Nm
External Rotation Torque	5,0,-5 Nm

Table 1: Open Knees Combined Loading Conditions

Kinetics were considered in the native tibia reference frame, the projected reference frame (by projecting moments to the JCS reference frame (Eqn. 1)), and the JCS reference frame (by transforming forces and moments to the JCS reference frame (Eqn. 2-3)).

$$\overline{M_i} = \bar{M} \cdot \overline{e_i} \quad (1)$$

$$\overline{F_i} = \bar{F} \cdot \overline{e_i} \quad (2)$$

$$\overline{M_i} = \bar{M} \cdot \overline{e_i} + (\overline{r_i} \otimes \bar{F}) \cdot \overline{e_i} \quad (3)$$

In the above equations, M is the moment vector and F is the force vector represented on the orthogonal tibia CS of the knee. M_i and F_i are the kinetics about or along the ith JCS axis. r is the moment arm vector between the origin of the tibia reference frame and the ith JCS axis of interest. Similarly, $\overline{e_i}$ is the unit vector of the ith JCS axis represented in the tibia CS.

RESULTS

Tables 2 and **3** present the average difference between kinetics represented by either the tibial reference frame, or projected reference frame, compared to the JCS reference frame.

	Mediolateral JCS Force	Ant/Post JCS Force	Distraction Force	Resultant JCS Force
Tibia	33%	12%	0%	2%

Table 2: Average Force Differences per DOF

	JCS Extension Torque	JCS Varus Torque	JCS I/E Torque	Resultant JCS Force
Tibia	31%	12%	0%	5%
Projection	6%	1%	0%	4%

Table 3: Average Torque Differences per DOF

Distraction forces and external rotation torques were identical between all kinetic references frames because the internal rotation axes were the same in all cases. For all other loads, differences were observed between the JCS reference frame and the tibia and projected reference frames. The alignment of JCS coordinate axes is demonstrated by the differences in resultant force and torque between JCS and tibial plateau kinetics.

DISCUSSION

Forces

The anterior and lateral forces were different in the JCS as opposed to the tibia and projected reference frames. These differences, can be attributed to internal/external rotation altering the anterior direction between the tibia and JCS reference frames. Large applied anterior forces between 100 and -100 N in the tibia reference frame are partly distributed as a medial/lateral force in the JCS reference frame when the tibia is rotated. Lateral force differences can be attributed to alignment between compression and mediolateral axes. Varus rotation causes the compression axis to be partially aligned with the mediolateral axis resulting in tibia compression creating mediolateral force.

Torques

Similar to the force, there was a trend of increasing kinetic differences when moving up the kinematic chain. Varus torques in the tibia were redistributed as varus and extension torques in the JCS, as a function of internal rotation. External rotation torques in the tibia were reported as extension torque of the JCS, due to alignment between the mediolateral and compression axes.

Table 3 demonstrates the relationship between tibial forces and moment arms applied to the different JCS axis. Including moment arms in torque calculations does produce noticeable differences as can be seen in the bottom of table 2. The Open Knees Protocol prescribes a tibia component ML force of 0. If this were higher differences would most likely be greater in both tables.

In conclusion, it can be convenient to describe kinetics in an orthogonal coordinate system especially when experimental methods obtain kinetics there directly [5]. However, this study shows there are significant differences between kinetics reported in these coordinate systems and the JCS reference frame. Kinetics possess more clinical meaning when described in the JCS and moment arms should be included in calculations so that the contribution of forces to JCS torques is captured. For studies where knee loads are controlled and kinematics are reported using the ISB Standards it is recommended to use the same JCS reference frame to control kinetics.

ACKNOWLEDGEMENTS

This material is based upon work supported by the NIH under Grant No. R01GM104139.

REFERENCES

[1] Grood ES, Suntay WJ., *J Biomech Eng* 105:136-144, 1983
[2] Wu, G et al., *J. Biomechanics* 35 (4), 543–548.
[3] Kristianslund et al., *J. Biomechanics*, 47(1) pp. 193-199. 2014.
[4] Erdemir, A. *J Med. Devices*, 7 (2013)
[5] Bergman G, et al., PLoS ONE 9(1): e86035, 2014

SB³C2019
Summer Biomechanics, Bioengineering and Biotransport Conference
June 25 -28, Seven Springs, PA, USA

BIOMECHANICS OF THREE-LEVEL CERVICAL FUSION COMPARING A STAND-ALONE CAGE CONSTRUCT TO ANTERIOR PLATE AND CAGES CONSTRUCT - A CADAVERIC STUDY

R. McGuire (1), A. Al-Barghouthi (2,4), L. Latta (2,4), F. Travascio (2,3,4)

(1) Department of Orthopaedic Surgery & Rehabilitation
University of Mississippi
Jackson, MS, USA

(2) Max Biedermann Institute for Biomechanics
Mount Sinai Medical Center
Miami Beach, FL, USA

(3) Department of Industrial Engineering
University of Miami
Coral Gables, FL, USA

(4) Department of Orthopaedic Surgery
University of Miami
Miami, FL, USA

INTRODUCTION

Anterior cervical discectomy and fusion (ACDF) is the current established surgical treatment for cervical disk disease, such as herniated discs or stenosis. ACDF removes the damaged intervertebral disc and employs an anterior plate for cervical spine fusion to reduce graft-related complications. A common problem with cervical plates is the fixed spaced of rigid plate design, which was thought to promote bone fixation and healing, but has been shown to have a tendency to detach from the bone [1-4]. Recent designs utilize dynamic plates, which allow screws to glide between bone anchor points during early graft settling. In this study, we compare the load transmission between vertebral bodies and cages of the self-correcting feature of stand-alone cages (SAC) to conventional anterior plate-cage configuration (APC). Specifically, we aim at evaluating the biomechanical safety and efficacy of a 3 level construct from C3 to C6 using a SAC compared to an APC.

METHODS

Cadaver cervical spines from T1 – C2 were DEXA scanned for general bone density evaluation. Five non-osteoporotic spines were chosen. All soft tissues were removed except for ligaments and joint capsules. All spines were stored frozen and thawed on the day of the surgical procedures for testing at room temperature. The C2 level was held in a fixture that allows translations in the sagittal plane and rotations in 3 planes at each level. The C7 and T1 levels were potted and fixed to the testing bench. Mechanical tests were performed via a servo-hydraulic testing system MTS 858 Mini Bionix II (MTS Systems Corp., Eden Prairie, MN, USA). The mount at C2 was preloaded posteriorly and the MTS applied a compression load anteriorly through a linear bearing system that followed the movement of C2 as the spine cycled from 1 Nm extension to 1 Nm flexion while range of motion (ROM) of each level was recorded by fluoroscopy (OEC 6600 Mini C-arm) in the sagittal plane, see Figure 1. Each spine had a discectomy performed at 3 levels. A SAC was applied at each level with a Tekscan 6900CR (Tekscan, In.c Boston, MA) pressure map placed between the inferior end plate and the cage, and a 1 cm wide strip of X-ray film (shim) was be placed between the superior end plate and the cage. This construct was repeated at all 3 levels of the spine. After the first mechanical loading regimens and recordings were complete, the shims, 0.18 mm thick, were removed to simulate minor bone resorption in early healing, and the loading regimen and all recordings were repeated. After that testing with the SAC was complete, an anterior plate and cages (APC) were applied with the same construct of pressure maps and shims. The whole battery of loading regimens and recordings were repeated before and after removal of the shims with the APC construct. Peak pressures, average pressures, center of pressure movements, contact areas and forces were calculated for each pressure map at critical points of the cycle loading and for each condition tested. Analysis from the fluoroscopic images provided

measures of the ROM in sagittal plane for each motion segment unit.

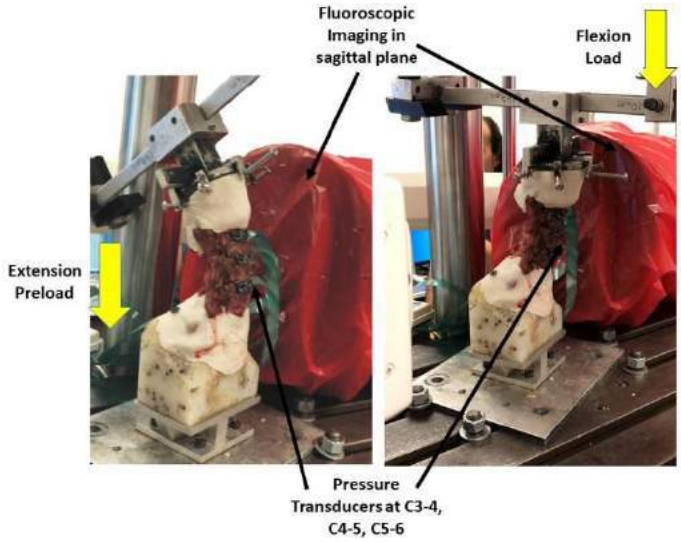

Figure 1 – Experimental setup: the location of the pressure transducer and the orientation of the fluoroscope, as well as the loading conditions are shown

RESULTS

The ROM of the SAC and APC constructs were not significantly different. Comparison with vs. without shims showed no change in ROM for SAC, but there was a significantly larger ROM in extension for APC after shim removal ($p < 0.05$). Since the plated construct tends to create more compression on the cage in extension (plate in tension band mode) than in flexion, and the stand-alone cage is the opposite, we focused on analysis of the constructs in both extreme positions. None of the investigated levels of the spine lost significant contact area or average pressure with removal of the shim in the SAC constructs in both flexion and extension. There was significant loss of contact area and average pressure at 2 of 3 levels in the APC constructs in flexion and at 1 of 3 levels in extension. The combined losses at all 3 levels for SAC were not significant ($p > 0.05$). In contrast, for the APC constructs, the combined losses were statistically significant ($p < 0.05$), see Figure 2.

DISCUSSION

The ROM measures suggested that the rigidity of SAC was at least as good as APC constructs in flexion-extension despite the simulated loss of bone. Resorption of bone in early healing has been blamed for lack of healing with APC constructs [5].

It was impossible to measure the whole foot print of the cage-endplate interface. The contact area was variable since the cage's flat surface contacted a non-flat end plate surface. So we made the assumption that the measured area on each construct was a reasonable representation of the whole contact surface. Moreover, the main goal of the study was to measure the change associated with the simulated loss of a thin layer of bone expected in early phases of healing, and those changes were consistent, reinforcing our assumption.

Overall, the results indicate that SAC provides an alternative construct that can "adjust" to the early loss of bone at the interfaces, without compromising the rigidity of a 3-level construct.

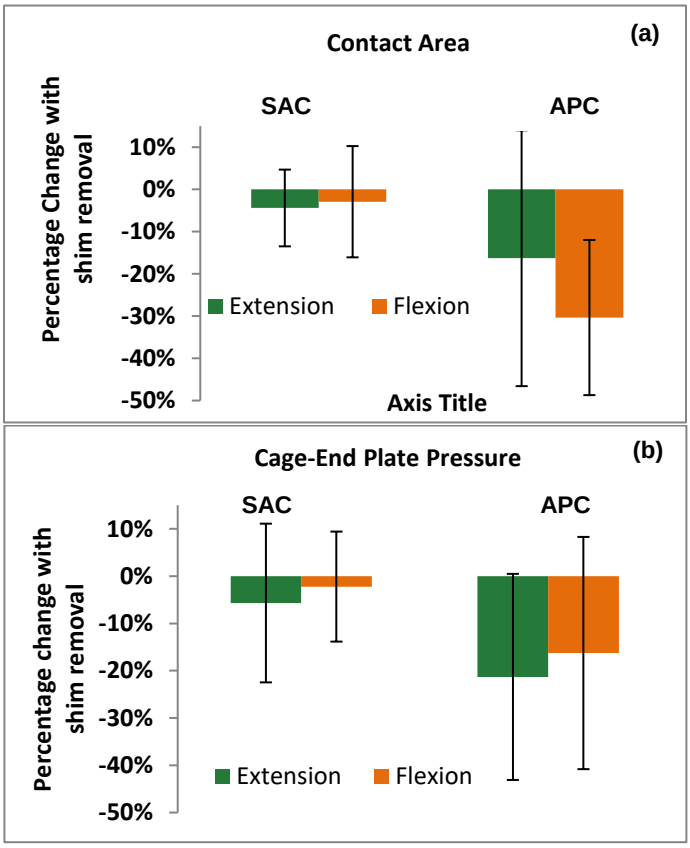

Figure 2 – Contact pressure measurements: (a) Loss of contact area; (b) average pressure. Data are reported at maximum extension and maximum flexion. Statistically significant changes only occurred for APC.

ACKNOWLEDGEMENTS

Zavation, Inc. provided research support to conduct this research.

REFERENCES

[1] Geisler FH, et al., *Spine*, 23:911–920, 1998.
[2] Gruss P and Tannenbaum H, *Arch Orthop Trauma Surg*, 101:283–286, 1983.
[3] Liao Z, et al, *Med Sci Monit*, 23;21:4006-14, 2015.
[4] Smith SA1, et al., *Eur Spine J*, 1(4):222-5, 1993.
[5] McClellan JW, et al., J Spinal Disord Tech. 19:483–486, 2006

SB³C2019
Summer Biomechanics, Bioengineering and Biotransport Conference
June 25 -28, Seven Springs, PA, USA

A POSTURE CONTROLLING TEST DEVICE TO DYNAMICALLY LOAD LUMBAR SPINAL COLUMNS

John R. Humm (1,2), Narayan Yoganandan (1)

(1) Department of Neurosurgery
Center for Neurotrauma Research
Medical College of Wisconsin
Milwaukee, WI

(2) Department of Biomedical Engineering
Marquette University
Milwaukee, WI

INTRODUCTION

Current US Federal Motor Vehicle Safety Standards in frontal impacts regulate occupant safety criteria for the head acceleration, neck loads, and thorax compression [1]. To date, human tolerances have not been similarly defined for the lumbar spine as the mechanisms of injury are not well understood. Several epidemiology studies have reported on lumbar spine injuries in motor vehicle accidents. One study examined crashes from 1993-2010 using National Automotive Sampling System-Crashworthiness Data System (NHTSA NASS-CDS) and Crash Injury Research Engineering Network (CIREN) databases and found an increasing trend in the number of occupants with lumbar spine fractures and vehicle model year [2]. Injuries were observed at all levels with the majority occurring at L1 and L5. A similar study was performed using the same databases and found 2.5 times increase in frontal crash occupants with major compression lumbar spine fractures in newer model vehicles compared to occupants of vehicles from the previous decade [3]. Likewise, burst fractures were mainly observed at L1 and L5. Both studies reported the occurrence of lumbar spine burst fractures in purely horizontal impacts indicating compression of the spine without a direct vertical input to the vehicle. Determining the tolerance of the lumbar spine to complex loading will help delineate the mechanisms of injury and establish new occupant safety thresholds. The aim of the current study is to simulate combined loading of the lumbar spine by conducting compression tests on isolated post mortem human surrogates in a flexed posture using a custom designed fixture.

METHODS

Nine specimens were procured and isolated from T12 to sacrum. The inferior end of the spine was potted in polymethyl-methacrylate (PMMA) such that the L5/S1 disc was free and the top surface of the PMMA was parallel to the S1 endplate in the sagittal plane. Superior end of the spine was fixed in PMMA such T12/L1 joint was unconstrained. Six-axis load cells were mounted proximal to the superior PMMA and distal to the inferior PMMA. Sets of three non-collinear retroreflective targets were placed into the anterior vertebral body at L1-L5. Additionally, three targets were mounted on the anterior surface of the inferior and superior PMMA. A set of CT scans were obtained following instrumentation.

The superior end of the upper load cell was attached to a single-axis electro-hydraulic piston which applied a rostral to caudal compressive load to spine. The inferior end of the lower load cell was fixed to a spinal position device (SPD) which consisted of 3-axis translation platform and a dual axis rotation mechanism (Figure 1).

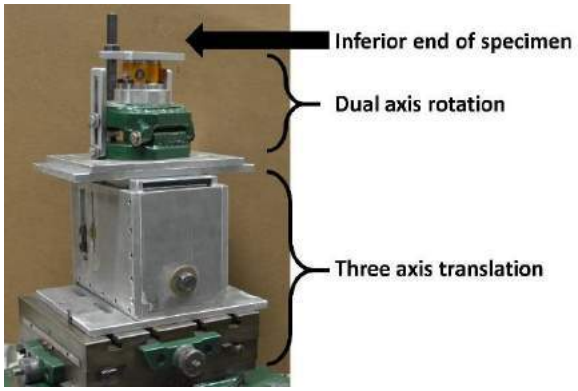

Figure 1: Spinal position device showing three axis translation (anterior/posterior, left/right, and superior/inferior) and dual axis rotation (flexion/extension, axial rotation) components.

Flexed posture of the spine was achieved by using the SPD to rotate the distal PMMA in the sagittal plane and translate it forward to minimize sacral slope. Height of the sacrum was adjusted so that vertical preload was approximately zero. Figure 2 shows radiographs of a specimen in its unstressed or natural position and pre-test position

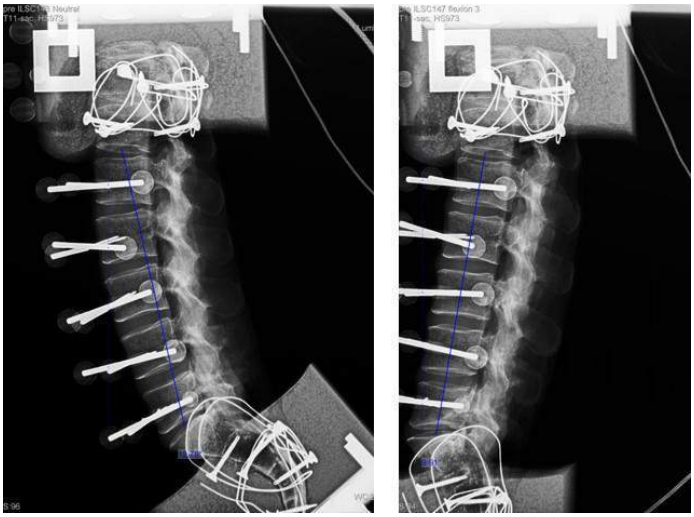

Figure 2: Unstressed alignment of lumbar spine (left) and pre-test position (right).

Superior end of the specimen was compressed at a rate of 1 m/s for 30 mm. Piston displacement and linear acceleration, and upper and lower loadcells were collected at 20 kHz. Specimen preloads were accurately recorded and incorporated into load-time history curves by measuring the sensor offsets in an unloaded condition. Three-dimensional motion of the vertebral markers was recorded at 1 kHz using a six-camera motion capture system. Marker data was combined with anatomic information collected from pre-test CT's to calculate three-dimensional kinematics of each vertebral level. Posttest CT's and radiographs were obtained, and specimens were dissected to determine injury.

RESULTS

Injuries from the nine specimens are summarized in Table 1. Posttest CT is shown in Figure 2.

Table 1: Injuries

PMHS	Injuries
1	Vertebral body fractures at T12 and L2
2	Disc disruption L2-3, L3-4, L4-5, and L5-S1
3	L5 and S1 spinous process fractures, S1 body fracture
4	L5-S1 fracture dislocation; L5 vertebral body fracture
5	L1 compression fracture; L2 superior endplate fracture
6	T12 inferior end plate fracture; L1 superior end plate fracture; T12-L1 disc disruption
7	Transverse fracture S1
8	L1-2-disc disruption with herniation; L1and L2 compression fracture
9	T12 inferior end plate fracture, T12-L1 disc disruption

Average peak failure was 5068 ± 2370 N and 347 ± 112 Nm for force and moment.

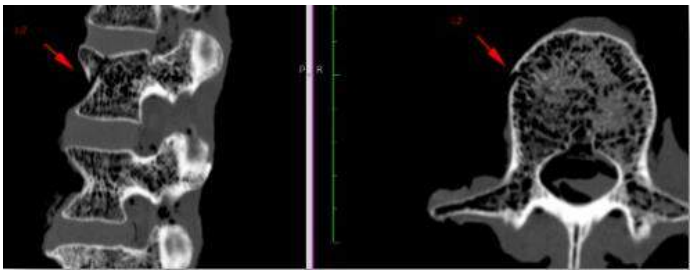

Figure 3: Posttest CT showing L2 vertebral body fracture

DISCUSSION

Design of the current study was to examine the effect of posture on the compression failure tolerance of the lumbar spine. Results from the CIREN studies revealed the occurrence of lumbar spine fractures in pure-horizontal frontal motor vehicle accidents. These studies hypothesized that compressive loading to the occupant was from the seat bottom or restraints and later in the event when the lumbar spine is in a flexed posture. Injuries from the current study were generally at the distal and proximal segments of the lumbar spinal column and agree with field observations.

One published study from two isolated lumbar spines reported higher peak compressive failure force, (5460 vs 5069 N) but lower peak flexion moment (201 vs 347 Nm) [4] compared to the current study. This may be due to differences in test setup and posture. In the previous study, specimens were isolated from T12-L5 and the distal end was potted at a 15-degree angle in the sagittal plane to represent the orientation of the spine in an upright seated position. The current study included the L5-S1 joint and placee the spine in a more flexed posture which may explain the differences in peak injury loads.

Data from this study has been used to derive preliminary injury risk curves (although not reported herein due to page constraints) using survival analysis for force, moment and interactive force-moment (N_{ij}-type). This methodology may assist in the development of human tolerance to advance vehicle crashworthiness and tolerance criteria hitherto not available to this region of the spine. With increasing advancement toward automated vehicles and autonomous driving, the present results may assist future safety standards.

ACKNOWLEDGEMENTS

This material is the result of work supported with resources and use of facilities at the Zablocki VA Medical Center in Milwaukee, Wisconsin. This study was supported by the US Department of Transportation, NHTSA, DTNH22-13-D-00290L, and the U.S. Army Medical Research and Materiel Command in Fort Detrick, Maryland, W81XWH-16-1-0010. Any views expressed in this article are those of the authors and not necessarily representative of the funding organizations.

REFERENCES

1. NHTSA, *FMVSS No. 208*. 2012. p. 29247-29249.
2. Pintar, F.A., et al., *Thoracolumbar spine fractures in frontal impact crashes.* Annals of advances in automotive medicine. Association for the Advancement of Automotive Medicine. Annual Scientific Conference, 2012. **56**: p. 277-283.
3. Kaufman, R.P., et al., *Burst fractures of the lumbar spine in frontal crashes.* Accid Anal Prev, 2013. **59**: p. 153-63.
4. Duma, S.M., et al., *Biomechanical response of the lumbar spine in dynamic compression.* Biomed Sci Instrum, 2006. **42**: p. 476-81.

SB³C2019
Summer Biomechanics, Bioengineering and Biotransport Conference
June 25 -28, Seven Springs, PA, USA

3D SURFACE KINEMATICS OF THE LUMBAR FACET CAPSULAR LIGAMENT DURING INFLATION TESTING

Elizabeth Gacek (1), Emily A. Bermel (1), Arin M. Ellingson, PhD (2), Victor H. Barocas, PhD (1)

(1) Biomedical Engineering Department
University of Minnesota – Twin Cities
Minneapolis, MN., USA

(2) Rehabilitation Medicine
University of Minnesota – Twin Cities
Minneapolis, MN., USA

INTRODUCTION

The facet joints articulate between the superior and inferior articular processes of adjacent vertebrae of the spine. The facet capsular ligament (FCL) encloses a facet joint with a capsule and encases the lubricating synovial fluid in the joint space between[1]. The FCL contains a region of highly aligned collagen fibers on the outer (posterior) portion and is innervated with nociceptors that can trigger pain signals under stress[1]. These structural and mechanosensory characteristics present the FCL as a likely culprit for low back pain (LBP)[1], a debilitating disease that affects 70 to 85% of Americans at some point in their lives[2]. Among these patients, 90% are diagnosed with non-specific LBP, and treatment is often unsatisfactory. To provide better patient care, we must first understand how the various components of the lumbar spine work together in a healthy state and then extend this model to the diseased state. Specifically, this work seeks to define the relationship between the FCL ligament and the joint pressure.

Very little is known about the mechanics of the synovial fluid and how the inner capsular pressure changes with spinal motion. Defining the underlying mechanics of the synovial fluid will further our understanding of ligament-fluid interaction. An inflation test, where the specimen is injected with a known volume of solution and the subsequent change in pressure is recorded, can help provide this insight. Coupling the inflation test with 3D strain tracking of the FCL surface allows us to determine differences in the mechanical behavior of the FCL under load[3].We can extend this experiment to record changes in pressures and strains to determine ligament-fluid interactions under prescribed spinal motions such as flexion or extension. We can also further expand this study to observe regional mechanical adaptations of the FCL in a diseased spinal state and increase our understanding of how FCL degeneration changes ligament loading.

In the current study, we conducted an inflation test while simultaneously recording 3D ligament surface kinematics on porcine lumbar spines. We hypothesized that we would observe higher stresses in the ligament that spans across the facet joint space as more solution is injected into the joint space.

METHODS

Sample Preparation

Three porcine lumbar spines were obtained from the Visible Heart Lab at the University of Minnesota. The samples were dissected to expose the posterior surface of the FCLs, and a total of 14 FCLs were viable for testing. These samples were then speckled by airbrushing for stereo imaging analysis.

Inflation Test

Pressure within the facet capsular space was measured using a pressure transducer (Harvard Apparatus) while saline was injected by a syringe pump. The pump injected 250 μL of 1% PBS at a rate of 1,000 μL/min into the joint space between facet joint pairs. The pressure transducer was zeroed by recording the voltage with the needle near the point of injection but not piercing the tissue. The needle was then pierced through the FCL such that the needle tip was within the facet joint space for interstitial pressure recording. All subsequent pressure recordings were determined by normalized the initial baseline pressure.

3D Strain Tracking

Concurrently with the inflation test, strain tracking was done on the speckled surface of the FCL using stereo imaging analysis. A two-camera system was utilized to obtain stereo images of the surface as it deformed during the inflation test. Surface displacements and strains were calculated using MultiDIC[4].

Data Analysis

Data for four of the 14 samples were discarded because damage during set-up led to significant joint leakage. The pressure data from the remaining 10 FCL samples were analyzed (Fig 1). Tissue compliance β was defined as the slope of the linear portion of the pressure-volume curve, as given by equation 1 where V is capsule volume (μL) and P is pressure (mmHg):

$$\beta = \frac{dV}{dP} \quad (1)$$

Compliance was determined using four samples that displayed similar pressure-volume behavior. Average pressure and standard deviation were calculated using all ten samples.

The curvature for a single sample was obtained from the results of MultiDIC (Fig 3A). Using the locations of the speckles in 3D space, we are able to obtain two principal radii of curvature (R_1 and R_2) and approximate the facet capsule as an ellipsoid. R_1 is the radial direction and R_2 is in the longitudinal direction. Positions of the speckles were obtained from MultiDIC and a surface map of the underformed and deformed FCL was analyzed using MATLAB R2018a (Fig 3B-C). Displacements of the speckles were obtained from MultiDIC(Fig. 3D-F).

RESULTS

Pressure-volume curves for each sample and the mean are shown in Figure 1. The compliance was 0.776 μL/mmHg, 95% CI [0.757, 0.794]. In some cases, the pressure begins to decrease due to ligament failure. This trend is observed after injecting 150 μL or more of saline.

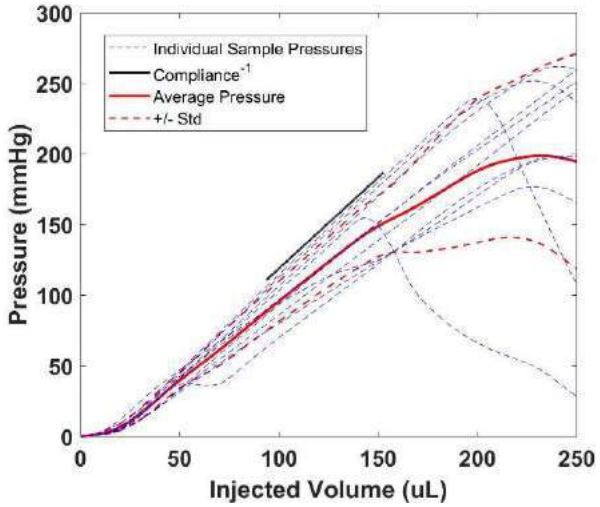

Figure 1: The solid red line is the average pressure of all individual sample pressure-volume relationships (dashed blue). The black line is FCL compliance.

A function of the radii of curvature with respect to injection volume is shown in Figure 2. R_1 is smaller than R_2 at all volumes of injected saline. This denotes a higher degree of curvature in the radial direction. An increase in R_1 near 200 μL may be due to ligament failure.

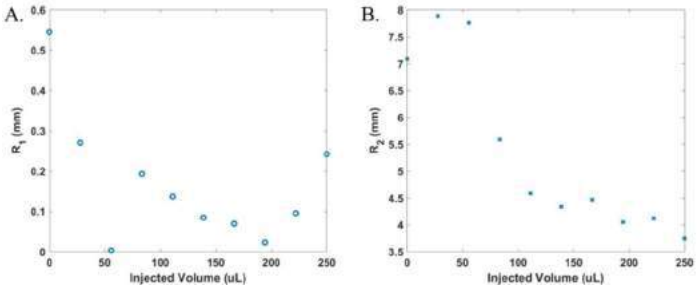

Figure 2: The principal radii of curvature (A.) R_1 and (B.) R_2.

Figure 3A outlines the region of interest on the FCL for analysis and we observe the highest speckle displacement after inflation in the y-direction (Fig 3B-F).

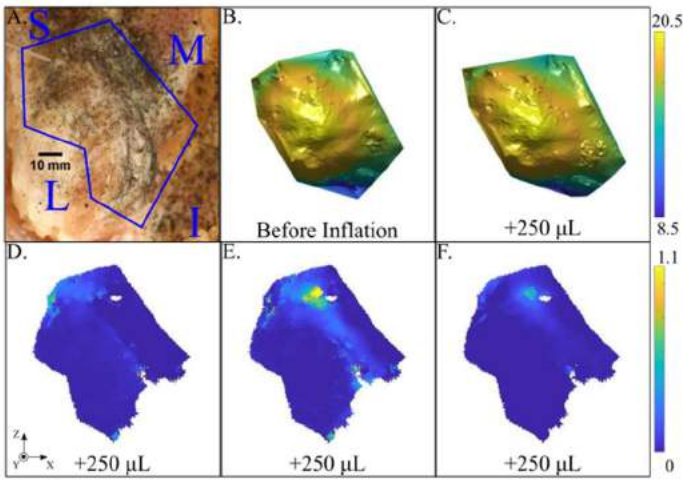

Figure 3: (A.) 3D surface outline on the sample where S=superior, I=inferior, M=medial and L=lateral. Surface map in XZ plane with color denoting Y of the (B.) reference and (C.) deformed sample. Speckle displacement (mm) in the (D.) x, (E.) y, and (F.) z direction.

DISCUSSION

We used inflation testing and 3D strain tracking to determine ligament-fluid interaction of a porcine FCL. Specifically, the pressure-volume response remained linear unless ligament failure occurs (Fig 1). We observed similar pressure-volume relationships for almost half of our samples despite differences in the vertebral levels of the FCLs. Concurrently with inflation, speckle displacements showed swelling of the facet capsule (Fig 3B-F). We conclude that the stress induced from facet capsule swelling will be similar across all lumbar levels.

Interestingly, we observe a lower radius of curvature in the radial, or bone-to-bone, direction (Fig 2). In this direction, the ligament is bounded on either end by facet joint. As the sample is inflated, the ligament displaces up and out (Fig 3E). The curvature along the radial direction increases at a higher rate than the curvature in the longitudinal direction. This trend is significance because it denotes a higher ligament strain in the bone-to-bone direction, which is believed to be the direction of primary fiber alignment in the collagen layer.

The results of this study further our understanding the relationship between interstitial fluid pressure and the FCL. We found that as the ligament swelled, the degree of curvature in the radial direction increased. This may lead to higher stresses along the primary fiber orientation and excess stretch of the nerves within the ligament, causing LBP.

ACKNOWLEDGEMENTS

Funding provided by the NIH grant U01EB016638 and the NIH/NICHD grant K12HD073945.

REFERENCES

1. Yamashita, T. et al. A Morphological Study of the Fibrous Capsule of the Human Lumbar Facet Joint. *Spine* **21** 538–543 (1996).
2. Andersson, G. B. J. Epidemiological features of chronic low-back pain. *Lancet* **354,** 581–85 (1999).
3. Kim, J. & Ã, S. B. Circumferential variations of mechanical behavior of the porcine thoracic aorta during the inflation test. *J. Biomech.* **44,** 1941–1947 (2011).
4. Solav, D. et al. M. MultiDIC : An Open-Source Toolbox for Multi-View 3D Digital Image Correlation. *IEEE Access* **6,** 30520–30535 (2018).

SB³C2019
Summer Biomechanics, Bioengineering and Biotransport Conference
June 25 -28, Seven Springs, PA, USA

DORSAL SUBLUXATION OF THE FIRST METACARPAL AT THE BASILAR THUMB JOINT DURING KEY PINCH: COMPARISON TO OSTEOARTHRITIS GRADING SYSTEMS

Nolan M. Norton (1), Brandon Barnds (2), Terence E. McIff (1, 2), E. Bruce Toby (2), Kenneth J. Fischer (1,2,3)

(1) Bioengineering Program
University of Kansas
Lawrence, KS, USA

(2) Orthopedic Surgery
University of Kansas Medical Center
Kansas City, KS, USA

(3) Mechanical Engineering
University of Kansas
Lawrence, KS, USA

INTRODUCTION

The basilar thumb joint, also known as the trapeziometacarpal (TMC) joint, is commonly affected by osteoarthritis (OA) The standard imaging views used for radiographic evaluation of the hand are posterior-anterior (PA) or anterior-posterior (AP), lateral, and oblique. Special positioning techniques are also used to image the TMC joint. The PA view of the hand approximates a lateral view of the TMC joint.

Instability of the joint has been believed to be a factor in the development and progression of OA [1, 2]. Eaton and Littler first proposed a stress radiograph in 1973 to characterize laxity (instability) of the stabilizing ligaments, measuring metacarpal lateral subluxation [1]. A recent study reported that the basilar thumb joint experienced greater instability during key pinch than other functional tasks [3]. Thus, key pinch stress radiographs may be clinically useful.

The role of subluxation in diagnosing OA or evaluating OA risk in the TMC joint has been debated. The TMC joint lacks substantial geometric constraint and relies on muscles, ligaments and other soft tissue for stability. The palmar anterior oblique ligament (AOL) and the dorsoradial ligament (DRL) are thought to be most important in preventing dorsoradial translation of the metacarpal with respect to the trapezium [2]. Increased metacarpal dorsoradial translation has been reported increased arthritic wear in the TMC joint [2]. But, studies have reported poor agreement between radiographic and arthroscopic/visual measures of TMC joint OA, such as the Outerbridge system and International Cartilage Repair Society (ICRS) system [4].

The first objective of this study was to determine the imaging angle that best measures lateral subluxation during key pinch. The second objective was to compare the lateral subluxation of the metacarpal during key pinch with the Eaton-Littler radiographic OA grade and the visual OA grades from the Outerbridge and ICRS systems. The third objective was to determine the effect that opening the joint capsule and cutting the AOL had on the lateral subluxation of the metacarpal during key pinch. We hypothesized that the percent of subluxation would significantly correlate with the radiographic and arthroscopic/visual classifications and that sectioning the capsule and/or the AOL would significantly increase the amount of lateral subluxation.

METHODS

Eleven frozen cadaveric forearms (10 males, 1 female, mean age at death 72 years, 54-88 years) were obtained with no known history of connective tissue disease. The mid-forearm was dissected to isolate tendons for the extensor pollicis longus (EPL), flexor pollicis longus (FPL), and abductor pollicis longus (APL). The hand was dissected to isolate and elevate the origins of the abductor pollicis brevis (APB) along with the radial portion of the flexor pollicis brevis (FPB) as one group. The adductor pollicis (ADP) along with the ulnar portion of the FPB were also isolated as a group [2]. The forearm was fixed in a neutral rotation. Kirschner wires were used to fix the wrist in 30° of extension, the thumb metacarpophalangeal (MP) joint in 20° of flexion, and the index finger MP joint at 90°. Krackow suture loops secured the end of each tendon/muscle group to for loading through a pulley system using weights. The loads applied followed Pellegrini et al. and were 0.8 N, 4.2 N, 5.0 N, 8.4 N, and 13.4 N for the EPL, ADP group, APB group, FPL, and APL, respectively, to simulate static key pinch [2].

During load application, a mobile C-Arm unit (OrthoScan HD model 1000-0004) was used to acquire three sets of radiographs. Images were recorded from 0° (the hand AP view) with the top of the C-arm rotated by 5° increments towards the ulnar aspect of the arm up to 60. The first set of images was recorded with an intact TMC joint capsule. The best angle to measure lateral subluxation for subsequent analyses

Poster Presentation #P236

was determined from the first set of images. The joint capsule was opened between the AOL and the APL, and another set of key pinch images was recorded. The AOL was sharply transected, and the final set of images was recorded. Specimen tissues were kept moist by saline mist. Grading of the specimens was performed by an orthopedic resident using the Eaton-Littler scale as a radiographic grading system, and the Outerbridge and ICRS systems for arthroscopic/visual grades.

Percent lateral subluxation of the metacarpal base was measured in Adobe Photoshop 6.0 (Figure 1-Left). Maximum subluxation was used to normalize subluxations from the other image views to reduce the effect of inter-specimen variability. A frequency analysis of the maximum normalized subluxation by image angle was performed. Further, we evaluated percent errors in the normalized maximum subluxation measurements for every angle and each specimen. The imaging angle that most frequently captured maximum subluxation and with smallest percent error was used for all further comparisons. Regression was used to evaluate the relationship between subluxation for each specimen and OA grades. Repeated measures ANOVA with Brown-Forsythe post-hoc analysis was used to evaluate differences between the subluxation measurements for the intact joint capsule, the open joint capsule, and the transected AOL. Statistical significance was set at $p < 0.05$.

RESULTS

Because lateral subluxation could not be consistently measured for image angles greater than 25^0, only data from 0^0 (AP view) to 25^0 were used for analysis of the imaging angle (Figure 1). The most common view that displayed the maximum subluxation was the AP (0^0) view (Figure 2-L). The mean percent difference from the measured maximum subluxation was also smallest for the AP view. Mean subluxation error increased as the imaging angled increased (Figure 2-R).

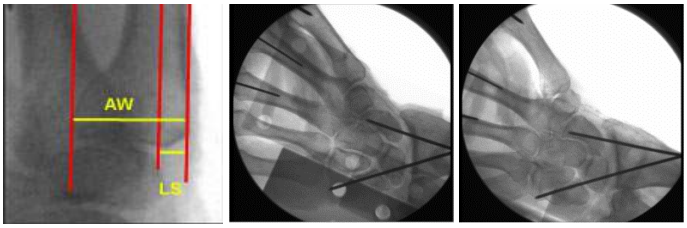

Figure 1: Left: Percent subluxation during key pinch calculated as lateral subluxation (LS) divided by the metacarpal articular width (AW). Red lines parallel to the metacarpal long axis. Mid: Typical AP (0°) X-ray. Right: Typical X-ray 25° supination.

Visual OA grades indicated the majority of the specimens had cartilage fragmentation or erosion to the bone. The remaining specimens had superficial fissures or lesions less than 50% of the cartilage depth. Only one specimen was found to be Grade 1 (cartilage swelling and softness). There was no correlation between lateral subluxation and the ICRS or Outerbridge classifications.

For the Eaton-Littler radiographic classification system three specimens were Stage I, three were Stage II, three were Stage III, and two were Stage IV. There was a significant correlation between lateral subluxation and the Eaton-Littler stage (p= 0.0003, R^2 = 0.779).

No significant difference was found between subluxation with an intact joint capsule, with the joint capsule opened, or with the AOL cut.

For the Eaton-Littler radiographic classification system three specimens were Stage I, three were Stage II, three were Stage III, and two were Stage IV. There was a significant correlation between lateral subluxation and the Eaton-Littler stage (p= 0.0003, R^2 = 0.779).

No significant difference was found between subluxation with an intact joint capsule, with the joint capsule opened, or with the AOL cut.

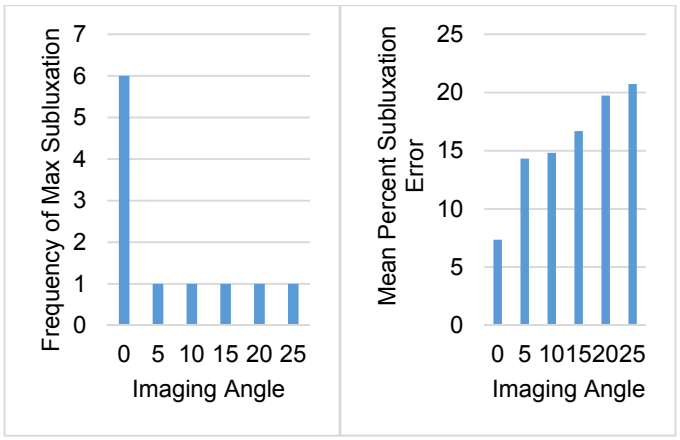

Figure 2: Left: For the majority of specimens, the maximum subluxation was measured in the AP view. Right: The AP view had the lowest mean error (7%) for specimens whose maximum subluxation was measured at a different angle.

DISCUSSION

Stress view radiographs provide insight that can help quantify the instability of the joint noted during physical examinations. Few studies have focused on subluxation of the first metacarpal during key pinch. Our study sought to verify the best view for subluxation analysis for future studies like these. The oblique orientation of the basilar thumb joint created some difficulties when attempting to analyze subluxation in the images due to its position and overlap between other osseous structures. Still, our findings suggest that the AP view provides the best assessment of lateral subluxation during key pinch.

While we did find a significant correlation between Eaton-Littler stage and lateral subluxation, this was expected, as the Eaton-Littler stage uses subluxation (during a different stress view) as one of the factors affecting the classification. Our results are consistent with other studies that have found poor agreement between subluxation and either pain or visual classification. While subluxation may not be as accurate for OA classification, we believe it is useful as a measure of the risk of developing OA.

That we found no significant difference in maximum subluxation with sectioning the capsule or AOL appears to support more recent studies indicating that the AOL may play a lesser role in the prevention of dorsal subluxation of the metacarpal [5]. However, the older age of our specimens and generally advanced arthritic states could have influenced the subluxation results [2]. Also, stability of the joint during simulated key pinch may be supported by (simulated) muscular activity.

This study has several limitations. Both visual and radiographic OA grades were assigned by only one investigator. An increased number of investigators grading the joints could produce more accurate averaged OA grades. Subluxation was also measured by only one of the investigators. Most cadaveric specimens were quite old and were kept frozen before the experiments and moist during the experiments. Only one specimen was female so no analysis of gender effects was possible.

ACKNOWLEDGEMENTS

Supported by the Department of Orthopedics and Sports Medicine at Kansas University.

REFERENCES

[1] Eaton, et al., *J Bone Joint Surg Am*, 1973. **55**(8):1655-66.
[2] Pellegrini, et al., *J Hand Surg Am*, 1993. **18**(2):238-44.
[3] Halilaj, et al., *J Orthop Res*, 2015. **33**(11):1639-45.
[4] North, et al., *J Hand Surg Am*, 1983. **8**(2):160-6.
[5] Colman, et al., *J Hand Surg Am*, 2007. **32**(3):310-7.

SB³C2019
Summer Biomechanics, Bioengineering and Biotransport Conference
June 25 -28, Seven Springs, PA, USA

WHEELCHAIR SEAT POSITION AND FOOTPRINT LENGTH EFFECTS ON SHOULDER AND ELBOW ANGLES ON GRADED SURFACES

Amogha Vijayvargiya (1,3), Sarah Bass (1,2), Hailee Kulich (1,2), Alicia Koontz, PhD (1,2)

(1) Human Engineering Research Laboratories
Department of Veteran's Affairs
Pittsburgh, PA, USA

(2) Department of Rehabilitation Science and Technology
University of Pittsburgh
Pittsburgh, PA, USA

(3) Department of Bioengineering
University of Pittsburgh
Pittsburgh, PA, USA

INTRODUCTION

Full time manual wheelchair users rely entirely on their upper extremities for essential activities of daily living, including propulsion and transfers. Upper extremity pain and injury are highly prevalent among manual wheelchair users due to the repetitive movements and stresses associated with these activities [1, 2]. Previous studies have shown that between 30-70% of manual wheelchair users experience shoulder pain [3, 4], including pain related to wheelchair propulsion [5]. Moreover, manual wheelchair users must be able to navigate different terrain conditions that require differences in propulsion effort, including smooth level surfaces, indoor/outdoor carpets and sloped surfaces such as ramps [3,6]. Ramp propulsion specifically increases the biomechanical risk factors associated with wrist and shoulder injuries and pain [7]. When ascending a ramp, recovery time decreases while cadence increases, increasing the risk for carpal tunnel syndrome [6, 8]. Forward trunk flexion increases as the ramp incline becomes steeper to move the center of mass forward to prevent the wheelchair from tipping [9]. Forward lean of the trunk increases shoulder flexion, which can lead to shoulder pain/injury [10]. The combination of these factors makes ramped propulsion an activity with increased risk for upper extremity injury and pain.

Although clinical practice guidelines with specific recommendations concerning wheelchair setup and propulsion techniques have been published related to preserving upper limb function, the guidelines were based on research collected during level ground propulsion. It is therefore unclear if they are applicable to other types of mobility tasks on non-level surfaces [11]. On level ground, studies have collectively shown that positioning the seat more posterior with respect to the rear wheels reduces the biomechanical risk factors for upper limb injuries by lowering forces, lessening cadence, increasing the push angle, and reducing muscular effort. However, this configuration is not ideal for ramps as the CoG shifts rearward due to the effects of gravity resulting in a compensatory forward lean to bring the CoG ahead of the rear wheels to prevent tipping. Additionally, posterior forces and internal rotation moments at the shoulder are higher with a more posterior seat during ramped propulsion [12]. A wheelchair configuration that helps to support better trunk and arm positioning on ramps may help mitigate the joint forces during ramp propulsion and preserve upper limb function.

A wheelchair that could enable the user to modify their configuration in real time depending on the terrain may reduce overall effort and promote biomechanically favorable propulsion patterns. Potential modifiable configuration parameters include the positioning of the footrest and seat relative to the rear wheel axle, respectively known as the footprint and seat position. The aim of this study was to compare joint range of motion (ROM) at the shoulder, elbow, wrist and trunk between four different wheelchair configurations over three different inclines. We hypothesized that a more stable configuration, with an elongated footprint and a more posterior rear axle would increase the ranges of motion at the shoulders, elbows and wrists and trunk during ramped propulsion.

METHODS

This study was approved by the VA Pittsburgh Healthcare System's Institutional Review Board. Six participants were recruited and signed informed consent forms prior to study procedures. In order to participate in the study, individuals had to have had a spinal cord injury, be at least one-year post injury or diagnosis, primarily use a manual wheelchair for mobility (over 40 hours/week), and had to be over 18 years in age. Participants were excluded from the study if they had upper limb pain or injury that interferes with the ability to propel,

Poster Presentation #P237

had cardiopulmonary disease, were unable to be fitted in the ICON test wheelchair, or were women who self-reported to be pregnant.

Data Collection

Measurements of participants' personal wheelchairs were taken by the investigators and used to make the customizable ICON A1® chair (ICON Wheelchairs) as close to their personal wheelchair as possible by adjusting features such as seat height, wheel camber, backrest height, and seat width. Kinematic data were collected using a ten-camera Vicon motion capture system (Version 1.8). Passive reflective markers were placed on bony landmarks of the chest, back and non-dominant side upper extremity including the third metacarpophalangeal joint, radial styloid, ulnar styloid, lateral epicondyle and acromion. Markers were also placed on the wheel hubs. Data was collected at 100 Hz.

The configurations evaluated in the order of most stable to least stable were: anterior long (AL), anterior short (AS), posterior long (PL), posterior short (PS). Each of these configurations was tested on 3 inclines at controlled speeds: level at 1 m/s, 3 degrees at 0.8 m/s, and 6 degrees at 0.6 m/s. Participants were fitted to a harness on the Computer Assisted Rehabilitation Environment (CAREn) platform, which was attached to a four-point tie down system. The CAREn is an integrated system consisting of a platform with 6 degrees of freedom, a custom dual belt treadmill (each of which are 2m long and 0.5m wide), and embedded force plate. They performed a 2-3-minute warm-up followed by 1 minute of data collection in each configuration and incline.

Data Analysis

Data was post processed in the Vicon software to fill gaps in markers. The post processed data was then analyzed using a custom Matlab 2018a code to calculate joint angle ranges. Nine consecutive strokes from steady state data from the middle of the trials were analyzed and the average range is reported. Missing data due to Vicon marker drop out (less than 10%) were handled by group mean imputation. A two-way repeated measures ANOVA with Bonferroni post-hoc correction using SPSS (Version 25, IBM) was performed on the data with a significance level of 0.05.

RESULTS

The level ground trials showed the smallest ROM in lateral trunk bending compared to both the three-degree incline ($p=0.035$) and the six-degree incline ($p=0.022$). In addition, level ground trials showed the least ROM in trunk flexion and axial rotation compared to the three-degree ($p=0.041$ and $p<0.001$ respectively) and six-degree ($p=0.049$ and $p=0.022$ respectively) inclines. No significant differences were seen in trunk angles between wheelchair configurations.

The AL configuration had more ROM at the shoulder in adduction and abduction compared to PS ($p=0.029$). The AL and AS configuration both had larger ROM than the PS configuration ($p=0.009$ and $p=0.017$ respectively) in internal/external rotation of the shoulder. Elbow flexion showed that there was an interaction between wheelchair configuration and incline, wherein the AL and PS configurations had a larger ROM with the 6-degree incline in contrast to the AS and PL configurations showing a decrease at 6 degrees ($p=0.02$).

DISCUSSION

A smaller ROM at the trunk, as seen with level trials, is associated with increased trunk stability. Individuals had more stability on level ground because they had to be less concerned with the chair tipping backwards during propulsion. For the shoulder angles, it is ideal to have a larger ROM because a larger ROM will make it more likely for individuals to use a biomechanically favorable stroke pattern due to the increased time in which they have contact with the pushrim. The increased ROM in the AL and AS configurations allows individuals to grip the pushrim at more locations, thus increasing the amount of time their hands stay on the pushrim. Elbow flexion ROM is dependent on both footprint and incline, as the forward lean of the trunk to compensate for the shift in CoG in the AL and PS configurations on inclines changes the nature of elbow flexion and results in increased ROM.

In contrast to studies showing posterior seat positioning as more beneficial for level ground propulsion [12], the anterior seat position seems to have greater biomechanical consequences on wheelchair propulsion on various inclines. Additional analyses may shed insight into the benefits of adjustable seating configuration during level and ramped wheelchair propulsion.

ACKNOWLEDGEMENTS

Funding was provided by VA VISN CPPF Pilot Funds. The contents of this paper do not represent the views of the Department of Veterans Affairs or the United States Government.

REFERENCES

[1] Morrow, M.M., et al., Shoulder demands in manual wheelchair users across a spectrum of activities. Journal of Electromyography and Kinesiology, 2010. 20(1): p. 61-67

[2] Brose, S.W., et al., Shoulder ultrasound abnormalities, physical examination findings, and pain in manual wheelchair users with spinal cord injury. Archives of physical medicine and rehabilitation, 2008. 89(11): p. 2086-2093.

[3] Hurd, W.J., et al., Wheelchair propulsion demands during outdoor community ambulation. Journal of Electromyography and Kinesiology, 2009. 19(5): p. 942-947.

[4] Curtis, K.A., et al., Shoulder pain in wheelchair users with tetraplegia and paraplegia. Archives of physical medicine and rehabilitation, 1999. 80(4): p. 453-457.

[5] Gironda, R.J., et al., Upper Limb Pain in Anational Sample of Veterans With Paraplegia. The journal of spinal cord medicine, 2004. 27(2): p. 120-127.

[6] Chow, J.W., et al., Kinematic and electromyographic analysis of wheelchair propulsion on ramps of different slopes for young men with paraplegia. Archives of physical medicine and rehabilitation, 2009. 90(2): p. 271-278.

[7] Boninger, M.L., et al., *Pushrim biomechanics and injury prevention in spinal cord injury: recommendations based on CULP-SCI investigations.* Journal of rehabilitation research and development, 2005. 42(3): p. 9

[8] Boninger ML, Waters R.L., Chase T., Dijkers M.P.J.M., Gellman H., Gironda R.J., Goldstein B., Johnson-Taylor S., Koontz A. and McDowell S. Preservation of upper limb function following spinal cord injury: a clinical practice guideline for healthcare professionals. *Consortium for Spinal Cord Medicine* 2005.

[9] Howarth SJ, Polgar JM, Dickerson CR, Callaghan JP. Arch Phys MedRehabil. 2010 Mar;91(3):436-42. doi: 10.1016/j.apmr.2009.10.016

[10] Gagnon, D., Babineau, A.-C., Champagne, A., Desroches, G., & Aissaoui, R. (2015). Trunk and Shoulder Kinematic and Kinetic and Electromyographic Adaptations to Slope Increase during Motorized Treadmill Propulsion among Manual Wheelchair Users with a Spinal Cord Injury. BioMed Research International, 2015, 636319.

[11] Medicine, P.V.o.A.C.f.S.C., *Preservation of upper limb function following spinal cord injury: a clinical practice guideline for health-care professionals.* The journal of spinal cord medicine, 2005. 28 p. 434.

[12] Mulroy SJ, Newsam CJ, Gutierrez DD, Requejo P, Gronley JK, Haubert LL and Perry J. Effect of fore-aft seat position on shoulder demands during wheelchair propulsion: part 1. A kinetic analysis. *J Spinal Cord Med* 28: 214-221, 2005.

SB³C2019
Summer Biomechanics, Bioengineering and Biotransport Conference
June 25 -28, Seven Springs, PA, USA

AN ALTERNATIVE METHOD TO CHARACTERIZE POROELASTIC MATERIAL PROPERTIES OF MURINE ARTICULAR CARTILAGE

Alexander Kotelsky (1), Joseph S. Carrier (1), Mark R. Buckley (1)

(1) Department of Biomedical Engineering
University of Rochester
Rochester, NY, USA

INTRODUCTION

Articular cartilage (AC) is a load-bearing tissue that covers bones in synovial joints. Due to its unique biphasic/poroelastic mechanical properties, AC serves as a shock absorber and attenuates contact forces that are transmitted across joints. Alterations in these mechanical properties can indicate functional loss and degradation of AC in the form of osteoarthritis (OA). For example, when proteoglycan loss occurs in the AC of degraded joints, the equilibrium Young's modulus (E) and hydraulic permeability (k) – measures of intrinsic stiffness and the ability of water to flow in and out of the tissue – are reduced and elevated, respectively [1]. Since OA can be easily induced through genetic or surgical means, murine models provide a valuable, low-cost research platform to study AC degradation. However, alterations in the mechanical properties of murine articular cartilage are challenging to measure due to its small size (thickness ~ 50 μm). Only a few research groups have quantified the mechanical properties of murine cartilage through nano- and micro-indentation techniques [1, 2]. Though effective, these indentation techniques provide characterization of local mechanical properties and may overlook the overall mechanical response of AC, especially when it is focally damaged. Building off our previously described method for measuring the static mechanical properties of articular cartilage [3], here we describe an alternative method to measure the *biphasic* mechanical properties (k, E) of large regions of intact murine AC under compression through inverse finite element modeling and confocal microscope-based 3D stretch mapping.

METHODS

All experiments were conducted using our previously established custom microscope-mounted mechanical testing device (Fig. 1a) [3, 4]. Briefly, carefully dissected, fully intact cartilage-on-bone specimens from 8-10 week-old BALB/c female mice were placed onto the cover glass slide of the testing device and loaded with a prescribed force F on top of the specimen such that the cartilage on the distal femoral condyles was compressed against the cover glass (Fig. 1a). Fluorescence micrographs of the articular surface and 3D z-stacks of AC were obtained using either an inverted epifluorescence microscope or an inverted confocal laser scanning microscope, respectively. Specimens were hydrated at room temperature in Hank's Balanced Salt Solution (HBSS) at 302 mOsm and a pH of 7.4 throughout the experiment.

Biphasic material properties (E, k) were characterized using a combination of experimental and computational methods (Fig. 1b). These methods and their sequence are as follows: 1) establishment of the correlation between cell death area across the articular surface and the peak cartilage compressive deformation; 2) characterization of transient cartilage deformation (boundary displacements) using the correlation established in step 1; 3) implementation of inverse finite element analysis (iFEA) based on the boundary displacement at equilibrium and the measured condylar boundary force to characterize E; 4) implementation of iFEA based on the transient boundary displacements and the contact boundary force to characterize k of AC with a pre-determined E.

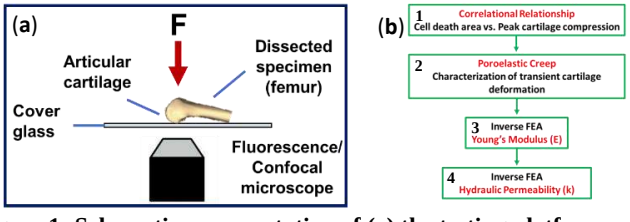

Figure 1: Schematic representation of (a) the testing platform and (b) the experimental methods.

1. Correlation between tissue compressive deformation and cell death. While slow acquisition of confocal z-stacks allows for

characterization of tissue deformation at equilibrium [3], it is virtually impossible to quantify transient boundary displacements during poroelastic creep of murine AC. Thus, transient tissue deformation was characterized by determining the extent of cell death at different loading times (quantified in step 2) and converting to deformation using the correlation between peak tissue compressive deformation and the extent of cell death. To first establish this correlation, in step 1, areas of chondrocyte death were induced on articular surfaces of proximal humeri and distal femurs through application of different load magnitudes (0.1N, 0.5N, or 1N, n= 5/group) on top of the specimens for 5 min. The specimens were vitally stained with calcein AM (an indicator of live cells) at baseline and with propidium iodide (PI) (an indicator of dead cells) after the load was removed and prior to imaging under fluorescent illumination. Cells that lost calcein fluorescence (green) and became PI-positive (red) were considered to be dead (Fig. 2a). Radii of cell death ($r_{cell\ death}$) were quantified assuming the areas were circles.

After assessment of cell vulnerability, the specimens were stored at -20ºC for 1-2 weeks and then used to quantify the peak tissue deformation induced by each prescribed load. Specimens were then thawed, and the AC was fluorescently stained with 5'-DTAF to enable visualization of the extracellular matrix (ECM). AC on the lateral femoral condyles and on the humeral heads was imaged with a 40X dry lens on a laser scanning confocal microscope. 3D image stacks were obtained before compression and 5 min after the application of the corresponding load (Fig. 2b-c). From the acquired z-stacks, spatially varying tissue stretch (λ_z) was quantified by normalizing 2D thickness maps of compressed specimens by the corresponding thickness maps obtained at the baseline using custom MATLAB algorithms (Fig. 2d). Note that lower stretch means more compression. Therefore, the peak tissue compression (i.e., minimal value of λ_z (λ_z^{min})) was correlated to the corresponding $r_{cell\ death}$ using a Pearson correlation (Fig. 2e).

2. Characterization of transient cartilage deformation during poroelastic creep. Distal femurs vitally stained with calcein AM were subjected to 1 N statically applied for 0, 5, 10, 30, 60, 300, and 900 s (n = 5-6/group), and $r_{cell\ death}$ on lateral femoral condyles was analyzed as a function of loading duration (Fig. 2f). The transient apical boundary displacement (i.e., λ_z^{min}) was obtained using the equation from step 1 relating $r_{cell\ death}$ to λ_z^{min} (Fig. 2e, g). Specimens that did not exhibit cell death on lateral femoral condyles were discarded since λ_z^{min} could not be quantified.

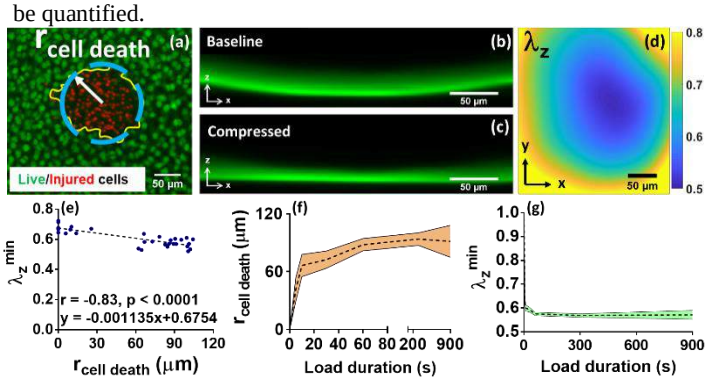

Figure 2: (a) Representative fluorescent micrographs of viable/non-viable cells after the compression of AC. (b, c) Representative (side-view) confocal micrographs of murine AC on the lateral femoral condyle (b) before and (c) after specimen compression. (d) the resultant compressive stretch (λ_z) map for the specimen shown in (b-c). (e) Correlation between λ_z^{min} and $r_{cell\ death}$. (f) $r_{cell\ death}$ as a function of load duration (mean ± SD). (g) A creep curve estimated based on $r_{cell\ death}$ (mean ± SD).

3. iFEA to determine E. A 3D finite element model (FEM) of murine cartilage on the lateral femoral condyle was constructed using the FEBio software suite [5] (Fig. 3a). To account for inter-specimen variability in geometry, a specimen-specific radius of curvature and thickness were measured from confocal z-stacks of specimens (n = 5) exposed to a 1 N load in step 1 (Fig. 2b). The cartilage was approximated as an ideal hemispherical shell with a measured outer radius (877.8 ± 48.4 μm) and a uniform thickness (30.13 ± 1.67 μm). The top surface (cartilage-bone interface) was constrained to be stationary, and a rigid platen on the bottom surface (cartilage-glass interface) compressed the cartilage in the z-direction with a prescribed λ_z^{min} determined from the equilibrium of the creep curve at 900 s generated in step 2 (Fig. 2g). The solid matrix was taken to be a neo-Hookean hyperelastic material with a previously determined Poisson ratio (ν) of 0.25 [3]. To estimate E, an iterative optimization algorithm implemented in FEBio was used to match the boundary force of 0.43 N exerted on the lateral femoral condyle corresponding to the 1 N load applied on top of the specimen [3].

4. iFEA to determine k. Poroelastic FEMs with specimen-specific geometry and corresponding E from step 3 were used to estimate k. Under a constant prescribed force of 0.43 N, an iterative optimization algorithm was used to match temporally varying mean λ_z^{min} (Fig. 3b), also determined in step 3.

RESULTS

With the pre-determined ν of 0.25 [3], the mean E and k of mouse AC were measured to be 17.54 MPa and 0.86×10^{-16} m^4/N-s, respectively (Fig. 3 c-d).

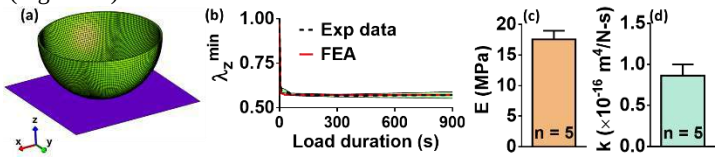

Figure 3: (a) Representative FEM of murine AC used to estimate k and E. (b) A creep curve response from step 2 with the corresponding curve fit from FEA (mean ± SD). (c, d) Measured poroelastic material properties of murine AC (mean ± SD).

DISCUSSION

In this study, we developed an alternative method to characterize poroelastic material properties (E and k) of murine AC. Assuming a previously determined ν, the method involves fitting one parameter at a time by first focusing on AC equilibrium behavior to determine E, and then fitting the entire creep curve to determine k using iFEA. The measured k in this study (0.86×10^{-16} m^4/N-s) is consistent with the value reported in literature (k = 1.1±0.4 $\times10^{-16}$ m^4/N-s) determined from micro-indentation [2]. However, E was not previously assessed for applied loads as high as the 0.43 N. As expected, due to the non-linear mechanical behavior of AC, E was found to be higher than the values reported in literature for lower applied loads [1-3].

We also established a strong relationship between AC deformation and cell vulnerability (Fig. 2e). This relationship may depend on mouse strain, age and/or gender. However, once this relationship is established, future studies using this method can bypass step 1 (the only step that requires the use of a confocal microscope), thereby reducing the cost and time associated with the characterization of E and k. Hence, $r_{cell\ death}$ quantification is the only requirement to determine E and k.

Future studies will expand the method to assess non-linearity of murine AC and will apply this method to assess how different stages of experimentally-induced OA alter k and E.

REFERENCES

[1] Nia, H. et al., *J Biomech*, 48(1):162-65, 2015; [2] Cao, L. et al., *J Biomech Eng*, 128:766-71, 2006; [3] Kotelsky, A. et al., *J Biomech Eng*, 140:1-9, 2018; [4] Kotelsky, A et al., *J. Vis. Exp*,143:1-7, 2018; [5] Maas, S et al., *J Biomech Eng*, 134:1-10, 2012.

SB³C2019
Summer Biomechanics, Bioengineering and Biotransport Conference
June 25 -28, Seven Springs, PA, USA

COMPARISON OF THE EFFECTS OF BOUNDARY LUBRICANTS ON THE TRIBOLOGICAL REHYDRATION OF ARTICULAR CARTILAGE

Margot S. Farnham (1), David L. Burris (2), Christopher Price (1,2)

(1) Biomedical Engineering
University of Delaware
Newark, DE, USA

(2) Mechanical Engineering
University of Delaware
Newark, DE, USA

INTRODUCTION

Articular cartilage is unique in that it retains exceptionally low frictional properties through the millions of articulation cycles we expose it to yearly. Healthy cartilage is composed of ~80% water, with the remaining ~20% consisting mostly of a deformable matrix of collagen and negatively charged proteoglycans[1], and it is thought that cartilage's unique tribomechanical properties stem from this biphasic composition. A major goal of the field has been to understand how this soft biological material can maintain phenomenally low friction values (μ<0.02) under usage conditions that can be considered extreme[2–8]. Recently, our team rediscovered an *ex vivo* cartilage testing configuration, the convergent stationary contact area (cSCA), that helps to shed light on these mechanisms due to its unique ability to promote and sustain physiologically-consistent levels of cartilage strain, deformation recovery, hydration, and lubricity over unprecedentedly-long time scales (hours). The cSCA configuration uses large (∅19mm) articular cartilage explants that retain the joint's natural radius of curvature thought necessary for promoting hydrodynamically-driven interfacial behaviors when explants are slid again a counterface. These hydrodynamic forces, through a mechanism termed 'tribological rehydration'[8–10], can 'pump' fluid exuded from cartilage during compression back into the tissue during sliding, enabling the recovery of interstitial fluid pressures and fluid-load support needed to maintain interstitial lubrication and physiologically low friction coefficients.

Previous cSCA studies have used 1X phosphate buffered saline (PBS) as the hydrating/lubricating solution, representing a 'worst-case' lubrication condition. Despite this, we have consistently observed remarkable tribological rehydration-driven strain recovery and frictional outcomes. However, the effect of other bathing solutions containing lubricants such as synovial fluid (SF), hyaluronic acid (HA), bovine serum albumin (BSA), or culture media, on tribological rehydration have not been fully explored. The *goal of this study was to investigate the effect of boundary lubricants on tribological rehydration and tribomechanical outcomes in the cSCA configuration.* Four 'lubricants' were chosen for their presence *in vivo* (SF), and as common additives to articular cartilage testing (HA) and explant culture solutions (BSA, media). We hypothesized that the more viscous lubricants, HA and SF, would increase both the effectiveness of tribological rehydration and lubrication in articular cartilage by enhancing fluid uptake (strain recovery) and reducing friction over sustained bouts of sliding. We also wished to ask the question of *whether low viscosity PBS and standard chondrogenic culture media are suitable bathing solutions for ex vivo tribology studies or if boundary lubricants should be added to produce physiological 'safe' frictional responses.*

METHODS

Tissue Specimens and Tribological Testing: ∅19mm osteochondral cores were removed from the femoral condyles of mature bovine stifle joints (procured from Bowman's Butcher Shop, Churchville, MD)[10]. Cores were trimmed to ~12mm in height and the *in vivo* sliding direction noted[11]. Following extraction, explants were stored in PBS + protease inhibitors (referred to herein as PBS) at 4°C[12]. Explants were tested in a custom-built reciprocating materials device (a.k.a. tribometer)[8] in which explants were compressed and slid against a reciprocating slide.

Boundary Lubricants: Four different boundary lubricants were tested in this study: SF, PBS+HA, PBS+BSA, and chondrogenic culture media. SF was extracted from healthy equine stifle joints within 2 hrs of euthanasia and stored at -20°C. PBS+HA was prepared by dissolving high-molecular weight (1350 kDa, 5mg/mL) hyaluronan in PBS. PBS+BSA was prepared at 3% wt/vol. Chondrogenic culture media was prepared using DMEM supplemented with 1% ITS+Premix (Corning), 20 μg/mL ascorbic acid, 1% pen-strep, and 1% amphotericin-B.

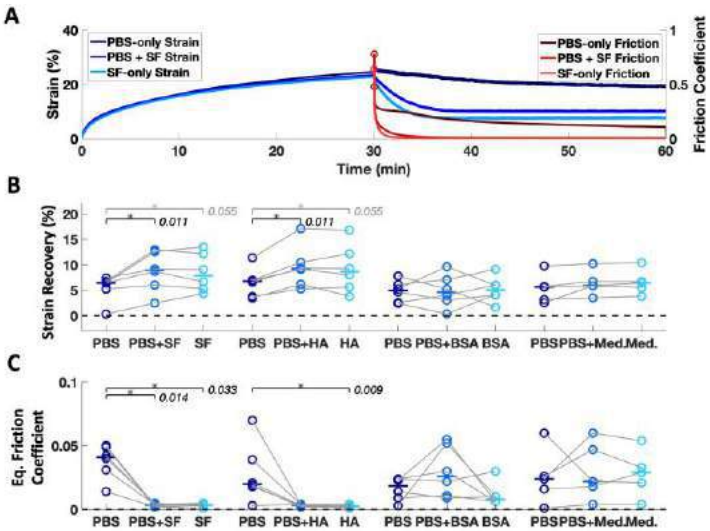

Figure 1. A) Overlaid traces from a random SF explant show increased strain recovery and lower friction after addition of lubricant. Collated data shows B) sliding-induced strain recovery (i.e. tribological rehydration) is greater, and C) sliding equilibrium friction coefficient is lower in in the samples treated with the more viscous lubrication solutions (SF, HA).

Testing Protocols: Prior to testing, each sample was inspected for surface damage using India Ink and a stereomicroscope; visible damage was an exclusionary criterion. Samples then underwent a diagnostic test consisting of 10min compression at 7N (~0.25MPa), followed by 2min of reciprocal sliding at 80mm/s (~walking speed) to identify if samples exhibited adequate tribological rehydration for inclusion in the study, i.e. friction coefficients $\mu<0.2$, and sliding-induced recovery/reversal of deformation (<10% of samples were excluded in this manner). Samples were then assigned to one of four lubricant study arms.

A tribological rehydration characterization scheme, with a repeated-measures design, was used for each lubricant testing group. This protocol started with 30min of static compression at 7N, followed by 30min of reciprocal sliding at 80mm/s under 7N compression[11]. Characterization was first performed in the presence of a *PBS-only* bath, followed by a 1-hr free-swell period in PBS. Next, characterization was repeated with the PBS bath replaced by one of the four lubricant baths immediately prior to sliding. After these *PBS+lubricant* tests, each explant was free-swelled in lubricant bath for 1-hr before a final characterization in the presence of *lubricant only*. Repeated-measures testing was utilized to improve statistical power and to determine if brief lubricant application or extensive lubricant soaking differentially influenced tribomechanical outcomes in the cSCA. After testing, explants were again assessed for damage using stereomicroscopy, and then bisected to measure cartilage thickness (h).

Data Analysis: Deformation (δ), normal force (F_N), and friction coefficients (μ) recorded and analyzed using MATLAB[11]. Tissue strain ($\varepsilon = \delta/h$) and friction magnitudes were analyzed at the beginning and end of active sliding, and strain recovery (i.e. tribological rehydration) during sliding was calculated. Friedman's Test, a nonparametric test with replication, was used to identify statistically significant changes between the repeated *PBS-only*, *PBS+lubricant*, and *lubricant-only* tests. Kruskal-Wallis' test was used to identify differences among the *PBS-only* test groups and the *lubricant-only* test groups.

RESULTS

The most pronounced changes occurred in samples where SF and HA were present (representative SF deformation and friction traces shown in **Fig. 1A)**; BSA and culture media did not meaningfully affect the tribomechanical behavior of explants. In the repeated tests, strain recovery increased when SF ($p=0.011$) and HA ($p=0.011$) were added as lubricants (**Fig. 1B)**. Friction coefficients at the end-of-sliding (i.e. sliding equilibrium) were, relatively speaking, quite low for all groups (on average <0.04), but high-viscosity lubricants (SF and HA) drove a significant reduction in sliding equilibrium friction (μ = 0.03 to 0.003, $p=0.033$ & 0.009, respectively; **Fig. 1C**). There were no significant changes in strain recovery or end-of-sliding friction for the samples lubricated with BSA or chondrogenic media.

When comparing across lubricant testing groups, no significant differences in strain recovery magnitude (i.e. tribological rehydration) or rate of strain recovery were observed either prior to the addition of lubricant (*PBS-only* tests) or following the addition of the lubricants (*PBS+lubricant* or *lubricant-only*). However, the presence of both SF and HA led to, on average, significantly reduced end-of-sliding and time averaged friction compared to PBS, BSA, and culture media (BSA and culture media outcomes were no different from PBS outcomes). Start-of-sliding strain, end-of-sliding strain, time-average strain, start-of-sliding friction, and deformational time-constants were also investigated (data not shown), and showed similar results to strain recovery and end-of-sliding friction, with the majority of changes occurring when SF and HA were present as lubricants.

DISCUSSION

These results illustrate that viscous lubricants, e.g. SF and HA, create an environment that enhances tribological rehydration and lubrication during high-speed sliding in the cSCA. This was reflected in increased overall strain recovery and reduced sliding equilibrium friction when compared to the BSA, chondrogenic media, and PBS-lubricated groups. These findings suggest that SF and HA may aid cartilage function through two distinct, but complementary mechanisms. First, as traditionally-understood boundary-mode lubricants[1], and second, as viscous bathing solutions that enhance fluid pressurization (and thus tribological rehydration) within the convergent contacts (e.g. the cSCA) by purely hydrodynamic means. Enhanced tribological rehydration supports both the recovery of tissue deformation (i.e. strain recovery) and the promotion of very-low friction coefficients via the maintenance and replenishment of interstitial lubrication. Lastly, we have seen that even PBS and chondrogenic media can mediate, under high-speed sliding in the cSCA, equilibrium friction outcomes ($\mu<0.03$) that are below those previously shown to induce chondrocyte 'dysfunction' ($\mu>0.1$)[13]. Together, these findings suggest that highly-viscous solutions like HA and SF *enhance* the lubrication of articular cartilage *ex vivo*, however these *lubricants are not necessary for maintaining physiologically-consistent and safe tribomechanical behavior in the cSCA.* When possible, we recommend adding lubricants to bathing solutions, however due to increased cost of these solutions, lubrication with PBS and media is sufficient.

ACKNOWLEDGEMENTS - This work was supported by the NSF BMMB [1635536] & GRFP [1247394]. All opinions, findings, and conclusions are those of the authors and do not reflect views of the NSF.

REFERENCES - [1] Mansour, J.M., *Kines*, 66-79, 2009. [2] Wright, V. et al., *J Anat*, 121:107-18, 1976. [3] Ateshian, G.A. et al., *J Tribol*, 120:241-8, 1976. [4] Ateshian, G.A., *J Biomech*, 42:1163-76, 2009. [5] Pawaskar, S.S. et al., *J Eng Tribol*, 221: 165-74, 2007. [6] Moore, A.C. et al., *OA&C*, 23:161-9, 2015. [7] Kienle, S. et al., *J Biomech*, 48:3052-8, 2015. [8] Moore, A.C. et al., *OA&C*, 25:99-107, 2016. [9] Burris, D.L. et al., *Biotribol*, 12:8-14, 2017. [10] Graham, B.T. et al., *OA&C*, 2017. [11] Farnham, M.S. et al., *JMBBM*, under review. [12] Stewart, R.C. et al., *Cart*, 2016. [13] Bonnevie, E.D. et al., *JOR*, 2018.

SB^{3}C2019
Summer Biomechanics, Bioengineering and Biotransport Conference
June 25 -28, Seven Springs, PA, USA

EFFECT OF COUNTERFACE SURFACE ROUGHNESS ON TRIBOLOGICAL REHYDRATION OF ARTICULAR CARTILAGE

Meghan E. Kupratis (1), Margot S. Farnham (1), David L. Burris (2), Christopher Price (1,2)

(1) Biomedical Engineering
University of Delaware
Newark, DE, USA

(2) Mechanical Engineering
University of Delaware
Newark, DE, USA

INTRODUCTION — Articular cartilage comprises the load-bearing region of synovial joints and, in the absence of injury or degradation, is able to support smooth articulation over decades of repetitive use. Cartilage's multiphasic structure, consisting of ~80% fluid and ~20% solid collagen and proteoglycan matrix, allows for its exceptionally low coefficient of friction (μ <0.02) and high wear resistance.[1-8] The fluid phase in particular is key to the tissue's phenomenal lubrication properties becaue sit can support large fractions of contact stress while also shielding the solid matrix from excessive shear. In previous studies, our team has characterized usage of an *ex vivo* testing configuration known as the convergent stationary wedge (cSCA) that allows assessment of cartilage biomechanics under sustained, physiologically-consistent values of cartilage strain, strain recovery, hydration, and lubricity over multiple hours of testing.[6] In the cSCA configuration, glass counterfaces are slid against large (∅19mm) articular cartilage explants, which retain the cartilage's natural radius of curvature and allow hydro-dynamically driven fluid flow from the bathing solution into the tisse during sliding. Through a mechanism we have termed 'tribological rehydration,' hydro-dynamically driven fluid flow during sliding competes with, and often exceeds, the rate of load-inuduced fluid exudation associated with stationary compression. As a result, high interstitial fluid pressure is retained in the tissue during sliding and provides sufficient load support for sustaining cartilage hydration and low coefficients of friction over the duration of active sliding.[8]

In our previous cSCA-based studies, only one type of glass counterface, standard lass microscope slides was used. In order to further characterize the biomechanical response of cartilage under the cSCA configuration, *the goal of this study was to investigate the effect of glass counterfaces of different surface roughnesses on tribological rehydration and resultant cartilage tribomechanical outcomes.* Specifically, counterfaces of three asperity heights were investigated, including super-polished quartz slides, plain microscope slides (those used in our previous investigations), and frosted microscope slides.

METHODS

Tissue Specimens and Tribological Testing: ∅19mm osteochondral cores were removed from the femoral condyle centerline of thawed, mature bovine stifle joints (procured frozen from Bowman's Butcher Shop, Churchville, MD)[10]. Cores were trimmed to ~12mm in height and the *in vivo* sliding direction noted[11]. Following extraction, explants were stored in PBS + protease inhibitors (referred to herein as PBS) at 4°C[12]. Explants were tested using a custom-built reciprocating materials device ('tribometer')[8] in which explants were compressed and slid against a reciprocating glass slide. Glass Surfaces: Glass surfaces of three different different asperity heights were tested in this study: super-polished quartz microscope slides of roughness ~2 nm (SPI Supplies, West Chester, PA), plain microscope slides of roughness ~200 nm (Fisher Scientific), and frosted microscope slides of roughness >200 nm (Fisher). Testing Protocols: Prior to testing, each sample was inspected for surface damage using India Ink and a stereomicroscope; visible damage was an exclusionary criterion. Samples then underwent a diagnostic test: 10 min compression at 7N, followed by 2 min of reciprocal sliding at 80 mm/s (~walking speed) to identify if samples exhibited adequate tribological rehydration for inclusion in the study, i.e. friction coefficients μ<0.2, and sliding-induced recovery/reversal of deformation (<10% of samples were excluded in this manner).

A tribological rehydration characterization scheme, with a repeated-measures design, was used for each lubricant testing group. This protocol started with 30 min of static compression at 7N (~0.25 MPa), followed by 30 min of reciprocal sliding at 80 mm/s (~walking speed)

under 7N compression[11]. Characterization was first performed sliding against a plain microscope slide, followed by two hours of free swelling in PBS. Characterization was then repeated with polished, plain, and frosted slides. Between each sliding test, each explant free-swelled in PBS for two hours. After testing, explants were again assessed for damage using stereomicroscopy, and then bisected to measure cartilage thickness (h). Data Analysis: Deformation (δ), normal force (F_N), and friction coefficients (μ) recorded by the tribometer were analyzed using MATLAB.[11] Measures of tissue strain ($\varepsilon = \delta/h$) were calculated, and strain and friction magnitudes were analyzed at the beginning and end of active sliding, and strain recovery (i.e. tribological rehydration) during sliding was calculated. Characteristic deformation rates were obtained from linear regression fits of the time-dependent deformation data. Negative deformation rates are respresentative of recovery of compressive deformation (i.e., tribological rehydration), while positive deformation rates are representative of pure compression-induced deformation (during static loading) or continued compressive deformation, and thus, compromised tribological rehydration (during sliding). Friedman's Test, a nonparametric test with replication, was used to identify statistically significant changes between the repeated surface roughness tests

RESULTS — The deformation and friction responses were similar with sliding against regular glass slides and polished slides and strain recovery (i.e., tribological rehydration) was observed under both of these conditions ($p=0.97$). The most pronounced changes occurred when explants were tested against the rough glass counterface, under which strain recovery (i.e., tribological rehydration) did not occur. Under sliding against the rough counterface, strain recovery was significantly impaired relative to regular and polished surfaces ($p<0.0001$), as was deformation recovery. For regular and polished glass surfaces, explants recovered an average of 14.5 and 17.6 µm, respectively, while explants had not recovered any deformation at the end of 30 minutes of sliding against the rough glass, and instead compressed an additional 64.5 µm on average. Friction coefficients at the end of sliding (i.e., sliding equilibrium, were similar for all three surfaces (μ = 0.04 - 0.07). However, there was a significant difference in start of sliding friction coefficient for sliding against rough glass (μ = 0.5288, $p<0.0001$) compared to regular and rough surfaces (μ= 0.288 and 0.289, respsectively; $p=0.9996$).

Surface roughess had no effect on the static deformation time constant ($p>0.1$); however, increased surface roughness had a significant effect on the sliding deformation time constant relative to regular and polished glass surfaces ($p<0.0001$), consistent with the lack of strain recovery observed under this condition.

DISCUSSION — The results of this study illustrate that decreasing surface roughness of the glass counterface has no appreciable effect on the tribomechanical response of articular cartilage under the cSCA testing configuration. This was reflected in similar values of strain recovery, deformation recovery, and start- and end-of-sliding friction coefficients for both regular glass and polished glass. These findings suggest that regular microscope slides are of sufficient frictional properties to assess the tribological behavior of articular cartilage under the cSCA and ultrapolished glass is not necessary for these experiments. Conversely, the use of frosted glass, which is of a greater asperity height, and thus, surface roughness, prevents cartilage from sustaining tribological rehydration under reciprocal sliding in the cSCA configuration. Under this condition of increased microscale porosity of the counterface surface, reciprocal sliding leads to wearing of the cartilage surface, and as the uppermost layer of cartilage matrix is being removed, lubrication is not actively occurring. This is reflected in an overall increase in deformation during sliding for the rough surface, whereas a recovery of deformation is seen for polished and regular glass, meaning that tribological rehydration is not occurring when cartilage is slid against rough glass. In addition, increased surface roughness (i.e., increased nanoscale porosity) leads to a greater number of fluid flow pathways, thereby increasing compression-induced excudation and preventing tribological rehydration during reciprocal sliding.

These findings suggest that ultrapolished glass is not necessary for creating physiologically analogous behavior under the cSCA configuration and that plain microscope slides provide a sufficient surface roughness to sustain tribologial rehydration in these experiments, while increasing counterface surface roughness defeats the tissue's ability to recover compressive deformation under sliding.

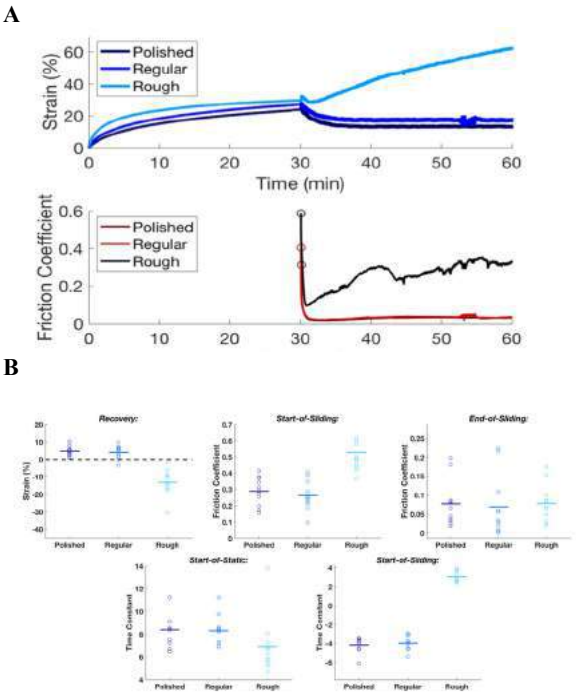

Figure 1. A) Overlaid traces from a representative explant show similar strain and friction behavior for regular and polished glass, and continued compressive deformation during sliding for rough glass. B) Sliding-induced strain recovery occurs with both polished and regular, but not rough glass (top row); the static compression time constants were similar for polished and regular glass while explants reached characteristic deformation faster when compressed against rough glass; end-of-sliding deformation time constants show that strain recovery occurred for polished and regular glass while sliding against rough glass resulted in continued deformation (bottom row).

REFERENCES — [1] Mansour, J.M., *Kines*, 66-79, 2009. [2] Wright, V. et al., *J Anat*, 121:107-18, 1976. [3] Ateshian, G.A. et al., *J Tribol*, 120:241-8, 1976. [4] Ateshian, G.A., *J Biomech*, 42:1163-76, 2009. [5] Pawaskar, S.S. et al., *J Eng Tribol*, 221: 165-74, 2007. [6] Moore, A.C. et al., *OA&C*, 23:161-9, 2015. [7] Kienle, S. et al., *J Biomech*, 48:3052- 8, 2015. [8] Moore, A.C. et al., *OA&C,* 25:99-107, 2016. [9] Burris, D.L. et al., *Biotribol*, 12:8-14, 2017. [10] Graham, B.T. et al., *OA&C*, 2017. [11] Farnham, M.S. et al., *JMBBM*, in review. [12] Stewart, R.C. et al., *Cart*, 2016.

SB^{3}C2019
Summer Biomechanics, Bioengineering and Biotransport Conference
June 25 -28, Seven Springs, PA, USA

MAINTAINING CARTILAGE HYDRATION DURING SLIDING PART I: THE EFFECT OF MIGRATION LENGTH

Jamie M. Benson(1), Caroline Kook(2), Axel C. Moore(1,3), Steven Voinier(2), Christopher Price(1,2), David L. Burris(1,2)

(1) Department of Biomedical Engineering
University of Delaware
Newark, DE, USA

(2) Department of Mechanical Engineering
University of Delaware
Newark, DE, USA

(3) Department of Bioengineering
Imperial College London
London, UK

INTRODUCTION

The remarkable fact that cartilage can withstand contact stresses (0.5-10 MPa) that exceed its modulus (0.1-1 MPa) with minimal strains (5-20 %) and friction coefficients (0.001-0.05) is attributed to load support through interstitial fluid pressurization. The maximum fluid load fraction (F'_{max}) varies for cartilage but is typically between 70 and 99%, depending largely on the tensile stiffness of the matrix. Sustaining high interstitial pressure is necessary to sufficiently maintain the mechanical and lubrication functions of the joint.

Because interstitial pressure drives exudation, fluid load support subsides temporally during static loading. Fortunately, as both theory and experiments have shown, cartilage achieves and maintains maximum fluid load support if the contact migrates across the cartilage surface faster than the interstitial fluid can escape. According to the literature, maximum fluid load support is achieved when Pe>>1, which corresponds to sliding speeds exceeding 100 nm/s in a typical human joint. Thus, there is a school of thought that even "fidgeting" (Pe>>1) during nominally static loading can be sufficient to sustain interstitial fluid pressure.

While the role of migration speed on fluid load support is well-studied, the theory, experiments and discussions have only considered migration paths that greatly exceed the characteristic size of the contact. Clearly, maximum fluid load support cannot be sustained when a portion of the contact area remains in a stationary contact—which occurs whenever the path length falls below the characteristic size of the contact. Furthermore, full range of motion for most joints in vivo is comparable to the size of the contact area. This transitional response in migration length has yet to be studied in a systematic way and the literature provides little insight into how load, contact area, contact stress and limited ranges of motion affect fluid load support and joint function. This experimental study was designed to quantify these migration length effects and elucidate their possible contributions to joint dysfunction and disease.

METHODS

Materials: Adult bovine stifles were obtained from a local abattoir. Full thickness ϕ19 mm osteochondral plugs (n=5) were extracted along the centerline of the medial and femoral condyles from 3 joints. Samples were rinsed in phosphate buffered saline (PBS) and stored in protease inhibitor solution at 4°C. The samples were CNC-milled, mounted into a custom tribometer, and lubricated in a 1X PBS bath. Borosilicate glass spheres (ϕ 2.4, 3.9, 6.4mm) were used as the counter-body. The material properties of each sample were quantified before and after tribological testing. All tests were completed within 24hr of extraction to minimize the risk of enzymatic digestion-induced changes in material properties.

In-situ characterization: Normal force and indentation depth were quantified during sliding in the migrating contact area (MCA) configuration. Our previous in-situ observations with cartilage [1] showed that the contact geometry is best described by Hertzian mechanics, which we used to relate the contact radius (a) to the known probe radius (R) and the measured indentation depth (δ_s) with Eq. (1).

$$a = \sqrt{\delta_s \cdot R} \quad (1)$$

The effective contact modulus (E_c), which depends on the material properties and sliding speed among other variables, is quantified experimentally with measured/known values of load (F), equilibrium tissue deformation (δ_s), and probe radius (R), as described in Eq. (2):

$$E_c = \frac{3}{4}\frac{F}{R^{0.5}\cdot{\delta_s}^{1.5}} \quad (2)$$

At equilibrium under static contact conditions, load is supported entirely by osmotic pressure. With Eq. (2), the equilibrium contact modulus (E_{c0}) can be quantified by the force or deformation response during ***static equilibrium*** contact. During sliding, interstitial pressurization increases E_c and reduces friction. At ***dynamic equilibrium***, interstitial pressure, the fluid load fraction, the effective contact modulus, and the friction coefficient depend on material properties and the sliding conditions. We quantify the magnitude of fluid load support using the fluid load fraction (F'), which varies between 0 and maximum fluid load fraction (F'_{max}). As we have shown in a previous paper [2], the fluid load support can be quantified experimentally based on E_c and E_{c0} using Eq. (3):

$$F' = \frac{E_c - E_{c0}}{E_c} \quad (3)$$

Tribological Testing: Each sample was first indented with a borosilicate glass sphere to a target load under static conditions until reaching equilibrium (<0.3 μm/min), as shown in Figure 1A.

Following equilibration, the next minute of data was used with Eq. (2) to determine the mean and standard deviation of the equilibrium modulus. Immediately following static equilibration, a lateral stage began reciprocating at 1.5 mm/s (Pe > 100) over a maximum track length (S = 7 mm) to establish the large Pe number and long track length baseline (F'_{max}). Following equilibrium (<0.3 μm/min), the next minute of data was used to determine the mean and standard deviation in the maximum effective contact modulus and then the maximum fluid load fraction using Eqs. (2) and (3), respectively.

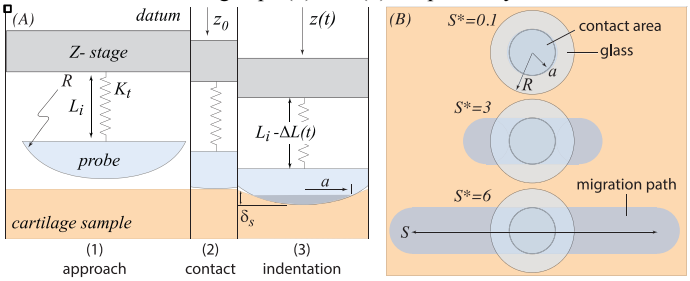

Figure 1: (A) Definition of measured variables and illustration of the indentation measurement. Force is quantified with deflection of a pre-calibrated spring and indentation depth is quantified with spring deflection and stage position. (B) Definition of path length (S) and migration length (S*=S/2a).

The track length was then reduced to 4 mm and the system re-equilibrated to determine the corresponding fluid load fraction. This procedure was repeated for 2, 1, 0.5, 0.2, 0.1, and 0.05 mm track lengths in that order. Following the final equilibration, sliding was terminated, the probe retracted, and the sample left to free-swell in the PBS bath for 10 min before being subjected to another indentation measurement to establish the variability in the equilibrium response. Each sample was subjected to each of the three target loads (5, 20, and 100 mN) and probe sizes (ϕ 2.4, 3.9, 6.4mm) in random order to test for load, area, and stress effects on the transition response.

Analysis: The fluid load fraction in an MCA of an infinite track depends on F'_{max}—which depends on sample-specific elastic properties, and the Pe number—which depends on speed [3], as follows in Eq. (4):

$$F'_{inf} = F'_{max} \cdot \left[\frac{Pe}{Pe+1}\right] \quad (4)$$

When Pe > 100 (1.5 mm/s), F'_{inf} is within 1% of F'_{max}. Therefore, the 7 mm baseline measurement, which is many times the contact diameter, provides a reliable measurement of F'_{max}. To isolate path effects from material effects, each variable path-length measurement of F' is normalized by its 7 mm (effectively infinite) path length counterpart (F'_{max}). Given the similarities in the physical effects of speed and migration length, we propose that the normalized fluid load fraction ($F^*=F'/F'_{max}$) varies between 0 and 1 as a sigmoidal function of the migration length (S^* = path length normalized by contact diameter, Figure 1B) and reaches 0.5 at a critical migration length (S^*_c), as described in Eq. (5):

$$F^* = \frac{F\prime}{F\prime_{max}} = \frac{S^*}{S^*+S_c^*} \quad (5)$$

The results were used to determine (1) if track length affects fluid load support, (2) the quantitative relationship between the two variables, (3) the necessary migration length for an effectively infinite track, (4) S^*_c, and (5) the directional effects of load, probe size, contact stress, and contact size on S^*_c.

RESULTS

The normalized fluid load fraction (F*) is plotted against the migration length (S*) for N=5 independent samples at all 7 track conditions, at all 9 combinations of load and probe radius in Figure 2A. We observed no significant reduction in fluid load support when the track length was an order of magnitude longer than the contact diameter (S*>10). The fluid load fraction decreased with decreased track length below this threshold. On average, the fluid load fraction only decreased by ~20% when the track length matched the contact diameter (S*=1). The fit to the entire dataset gave $S^*_c = 0.12$.

To determine if and how the critical migration length varied with probe diameter, load, contact area, and contact stress, we first binned the results into low, medium, and high groups within each category. Then, we determined the mean critical migration length and its statistical uncertainty by fitting each group within each category using Eq. (5). The dependence of the critical length on each variable is shown in Figure 2B. The critical migration length (the length needed to maintain 50% of F'_{max}), increased with decreased probe diameter (p>0.05), increased load (p<0.05), increased contact area (p<0.05), and increased stress (p<0.05).

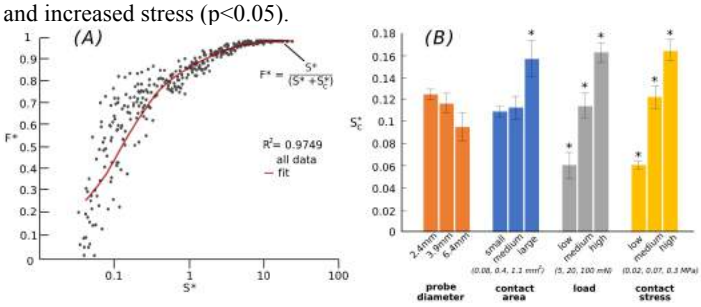

Figure 2: (A) Plot of N=5 for entire dataset—varied load, track length and probe size. (B) Transition migration length (S_c^*) for each variable— *denotes significance of p<0.05.

DISCUSSION

The results of this study demonstrate that restricted ranges of motion defeat interstitial hydration, pressure, and lubrication. Previous studies have hinted at this effect [4, 5]. Our results show that Eq. (5) yields a reasonable estimate of the fluid load fraction with $S^*_c = 0.12$ over a fairly broad range of tested conditions. For small-scale MCA conditions typical of cartilage friction studies, it seems safe to assume that a migration length of S* = 10 results in full fluid load support. However, the results also suggest that the transition response varies significantly with changes in contact conditions. Unfortunately, the variables are inter-dependent, which makes it difficult to tease out the dominant contributor. For example, a non-significant probe radius effect might be best explained by its effect on stress (at fixed load). Our results are consistent with stress as the dominant variable; this explanation is also intuitive since stress drives exudation.

The clinical implications of these results are fairly obvious but it's important to establish without ambiguity: full or near full range of motion appears necessary to fully disrupt exudation and its functional consequences. On the joint level, these results dismiss the possibility that small-scale fidgeting preserves interstitial hydration even if Pe>>1. While these data cannot be used to predict the transition behavior of joints with any certainty, extrapolating the stress trend suggests that $S^*_c \sim 0.20–1.2$ for contact stresses between 1 and 5 MPa. This analysis reinforces the suggestion that full range-of-motion movements are important for maximizing tissue hydration and function. These results also suggest that the heaviest and least active populations are more likely to experience tissue and joint dysfunction.

Finally, these results leave little doubt that joints lose interstitial fluid in the absence of intentional activity, which composes only about 5-10% of a typical day. Part 2 of this paper considers the mechanisms and competitive rates of fluid recovery following static exudation.

ACKNOWLEDGEMENTS

The authors acknowledge support from the NSF BMMB 1635536.

REFERENCES

[1] Moore, A. C. et. al., *J Biomech, 47*(1), 148-153, 2014
[2] Bonnevie, E. D. et. al., *J Biomech*, *45*(6), 1036-1041, 2012
[3] Moore, A. C., et. al., *Osteoarthr Cartilage*, *23*(1), 161-169, 2015
[4] Bell, C. J., et. al., *P I Mech Eng H, 220(1)*, 23-31, 2006
[5] Accardi, M. A., et. al., *Tribol Int, 44(5)*, 565-578, 2011

SB³C2019
Summer Biomechanics, Bioengineering and Biotransport Conference
June 25 -28, Seven Springs, PA, USA

IMPROVED METHODS FOR MECHANCIALLY TESTING FOOT AND ANKLE LIGAMENTS: PREPARATION, LENGTH ESTIMATION, ENVIRONMENTAL MAINTENANCE, AND SEMI-AUTOMATION

Alexander T. Berardo-Cates (1,2), Christopher T. Prasanna (1), Levi D. Davis (1), Matthew W. Kindig (1), William R. Ledoux (1,2,3), Joseph M. Iaquinto (1,2)

(1) VA RR&D
Center for Limb Loss and MoBility
Seattle, WA, USA

(2) Department of Mechanical Engineering
University of Washington
Seattle, WA, USA

(3) Department of Orthopedics & Sports Medicine
University of Washington
Seattle, WA, USA

INTRODUCTION

Ligaments are collagenous structures that connect the bones of the body and form the joints which are critical to overall foot function, including the ankle joint complex and the medial arch of the foot. Understanding the material properties of the ligaments supporting some of these key joints will help to predict how the structures of the foot respond to external loads and locomotion. Mechanical testing of soft tissues can provide these material properties; however, the small size and unique shape of the foot and ankle ligaments makes determining these properties technically challenging. One such challenge is that it is often difficult to load irregularly-shaped ligaments in their anatomic orientation, yielding material properties that are not representative of *in vivo* loading [1]. Additionally, the process of maintaining environmental conditions while running precise mechanical tests is exacting, demanding work that is subject to errors. The following is a presentation of methods developed to determine the viscoelastic properties of foot and ankle ligaments. These methods address a way to maintain anatomical alignment of a neutrally flexed foot, estimate the length of a small irregularly shaped ligaments, and maintain the specimen environmental conditions while partially automating the mechanical testing procedure.

METHODS

The calcaneofibular, anterior tibiofibular, calcaneonavicular, tibiocalcanear, and interosseous ligament between the talus and calcaneus will be tested from eight fresh-frozen cadaveric specimens. The ligament viscoelastic response will be characterized at a range of loading frequencies (0.5, 1, 2, 5, 10 Hz) at several non-destructive strain targets using a mechanical testing machine (ElectroPuls 3000, Instron, Norwood MA), followed by a stress relaxation test, and concluding with a load to failure test. A 10-minute rest interval is prescribed between each of these tests. Pilot ligaments were used to develop further experimental methods.

Specimen Length Estimate

In preparing the ligaments for mechanical testing, the soft tissues surrounding the ligaments are removed and the foot is placed in a custom radiotransparent acrylic loading jig where the foot is loaded through the tibia to approximately 50 lbs. of body weight. The foot and loading jig are then scanned using cone beam computed tomography (CT) (PedCAT, Curvebeam, Hatfield PA; 0.37 mm isotropic volume). The relevant bones and each ligament of the resulting DICOM images are segmented in Mimics (Materialise, Leuven Belgium) and imported as point clouds into a custom Matlab program.

In that program, two surfaces are created from the intersection of the ligament and bone point clouds at both insertion sites. The linear distance between the centers of each surface defines a rough ligament length. The line between these points is adjusted to intersect the cross-sectional center of the ligament at 10% intervals along the line's length. This process iterates bi-directionally until the length of the ligament changes by less than 5% (Figure 1).

Specimen Preparation

To maintain *in vivo* pose, a rigid wooden brace is fixed to each boney insertion with several 1mm wires while the ankle is flexed to ~90 degrees (Figure 2). Once secured with a polyurethane adhesive (Gorilla glue, Cincinnati OH.), the externally fixed bone-ligament-bone sample is excised using a surgical saw (Stryker, Kalamazoo MI.).

An alignment jig was used to visually align the ligament and external fixation in the potting and the rigid wooden brace are cut once the ligament has been positioned in the mechanical testing machine.

Poster Presentation #P242

To compare the strain applied by the actuator to the true ligament orientation, fiducial marker clusters are placed on the potted ends. The potted bone-ligament-bone specimen complete with external fixation and fiducial marker clusters are CT scanned a second time. The relative positions of the bone-ligament surface centroids in relation to fiducial marker clusters can be used to relate the origin and insertion to actuator position and therefore applied strain to anatomical strain.

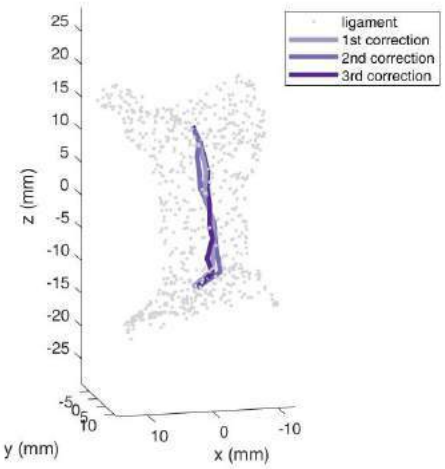

Figure 1: CT point cloud of a representative tibiocalcaneal ligament (grey) with last 3 length estimates.

Maintain Environmental Conditions

A custom-made insulated chamber is used to enclose potted ligaments during mechanical testing. The chamber is fitted with a ceramic heating element and a saline sprayer system. A data acquisition system (National Instruments BNC 2090, Austin TX) was used to control the environmental temperature, saline spray, record and trigger high-speed cameras (Phantom v641, Vision Research, Wayne NJ.), download high-speed video, and record analog signals from mechanical testing equipment. Temperature from 6 thermistors surrounding the ligament was recorded and compiled with mechanical testing data.

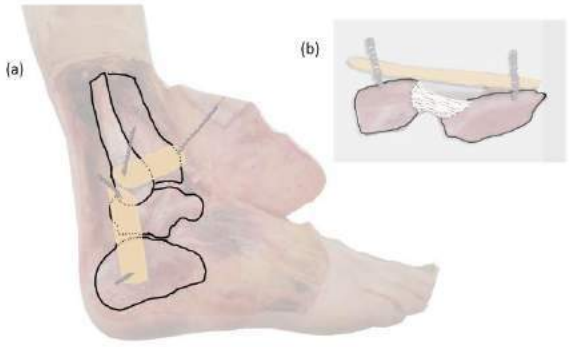

Figure 2: (a) Example of a calcaneofibular and tibiofibular external fixation before and (b) after removal with fixation maintaining *in vivo* ligament pose.

Semi-Automated Mechanical Testing

A mechanical testing sequence with randomized loading frequencies and increasing strain targets is programed in testing software (Wavematrix, Norwood MA). During testing, a custom LabView program integrates the materials testing machine, cameras, sprayers, heater and data acquisition system. As each test in the sequence begins, the program interrupts the sprayers and starts the cameras. At the conclusion of each test, the program saves the displacement, force, and video data maintaining consistent naming conventions. The program inputs the next test parameters into the materials testing system, and this process repeats until all tests have been completed. The calibrated video data collected by the high-speed cameras will be used to perform 2d digital image correlation and to track proximal and distal marker clusters

RESULTS

Visual comparison of the intact and potted ligaments show that pose was maintained after ligament was excised.

After a total of 3 1-hour long pilot tests, the semi-automated mechanical testing system successfully performed sets of 5 loading frequencies followed by ramp and hold tests. The resulting video data, loadcell data, displacement data, and temperature data were successfully saved, and each next test was input and ran without user interaction. During this 3-hour long session temperatures were maintained within (37 ± 2.21 ^{o}C) while the specimens were kept constantly moist.

DISCUSSION

Length estimation is dependent on high contrast CT scan data, reliable feature detection, point cloud density, and operator variability. Removing soft tissues surrounding the bone and ligament produces CT images with high contrast since contrast is dependent on changes in relative density. To improve point cloud density, a surface subdivision routine can be applied to interpolate between points. Poor point cloud density and subsequent mesh resolution can cause inaccuracies in cross-section definition resulting in poor length estimations or an inability to converge to a final length after multiple bidirectional iterations.

The ability to maintain pose with external fixation requires healthy bone. If the bone is osteoporotic, the wire base may not stay in place while the bone is cut. While the comparison between the pose and the potted ligaments showed good alignment, a method is needed to determine the optimal potting orientation that best represents the common directions of *in vivo* tensile loading. Finally, the irregular shapes of these ligaments can make visual alignment during potting a challenge which can cause inconsistencies in ligament loading directions between specimens.

Ligament mechanical properties are sensitive to changes in temperature and moisture during long testing sessions which can fluctuate within an environmental chamber. The presented semi-automated testing methodology successfully maintained constant hydration and temperature during a long testing series.

The methods outlined here are now being applied to establish material properties for a series of ligaments from eight cadaveric specimens, this work is ongoing.

ACKNOWLEDGEMENTS

This work is supported by NICHD grant #HD075997 and a VA Puget Sound pilot grant.

REFERENCES

[1] Woo, S et al., *Am J Sports Med*, 19:217-225, 1991.

SB^{3}C2019
Summer Biomechanics, Bioengineering and Biotransport Conference
June 25 -28, Seven Springs, PA, USA

TESTING MEDIAL ULNAR COLLATERAL LIGAMENT FATIGUE FAILURE

David B. Jordan (1); Alexander Kharlamov (2); Patrick J. Schimoler (1,2); Patrick J. DeMeo; Mark Carl Miller (1,2)

(1) Mechanical Engineering and Materials Science
University of Pittsburgh
Pittsburgh, PA, USA

(2) Allegheny General Hospital
Pittsburgh, PA, USA

INTRODUCTION

Fatigue failure occurs with repetitive loading and, in baseball pitchers, such cyclic loads are applied at the elbow as a result of repeated pitches thrown. During the cocking phase of pitching, a large valgus torque is generated that can potentially damage the medial ulnar collateral ligament (mUCL). In that the mUCL is the primary stabilizer to valgus loading [1], the threat of injury to the ligament as a result of the repeated application of these valgus loads is evidenced by the growing number of mUCL surgeries.

The effect of fatigue has been studied in regard to human and animal ligaments. Lipps et al. [2] experimentally simulated cyclic pivot landings on knee joints and showed that the anterior cruciate ligament is indeed susceptible to failure by fatigue. Thornton et al. [3] showed that the degree of modulus reduction resulting from fatigue is more severe, as compared to creep, when studying rabbit medial collateral ligaments.

The current study seeks to introduce and test a custom designed fatigue testing machine to study the fatigue properties of the mUCL. In previous work, the ligament was instrumented in three distinct bands, posterior, middle and anterior, and strain data obtained with application of load. To study fatigue failure, strain data from cyclic testing can be compared to the quasistatic testing results and to any known failure values. The purpose of the current work was to perform initial testing of a valgus loading cyclic test machine for the mUCL so that the subsequent analyses could be performed. The basic hypotheses were that the custom device could impose failure loads and that strains would quantitatively match the quasistatically obtained values before failure.

METHODS

Three cadaveric elbows were prepared for testing by stripping away all muscle, nerve and soft tissue except the mUCL and that part of the lateral ligament complex lateral to the radial head. The humerus and ulna with the radius were each set within a PVC container and polyester resin was poured into the PVC and allowed to harden, securing the two bones. Screws were placed through the PVC and bone to ensure that the specimen could not rotate within the PVC. Optical markers were placed along the length of the mUCL in three equally-spaced columns, posterior to anterior.

Each elbow was mounted in the testing device (Figure 1). The device accommodates a variable flexion angle but the first tests were performed at a single fixed angle. The PVC containers were then placed inside two custom designed metal sleeves and loaded into the fatigue tester at 90º of elbow flexion. Each sleeve was connected to a shaft. The shaft with the humerus was held stationary and the shaft with the ulnar was connected to a torsional load cell that was driven by a 10:1 gear reducer. The gear reducer included an encoder to quantify angular motion and was driven by a servomotor. The axis of the shaft connected to the driving motor was positioned to align with the center of the capitellum in order to rotate the ulna/radius construct around the natural axis of valgus motion. The housing holding the PVC sleeves could translate along the swing arm attached to the drive shaft in order to minimize binding. For the current tests, internal-external rotation was completely constrained, although complete rotational freedom could have been allowed. With the specimen in place, two high-resolution cameras were calibrated and testing begun.

Poster Presentation #P243

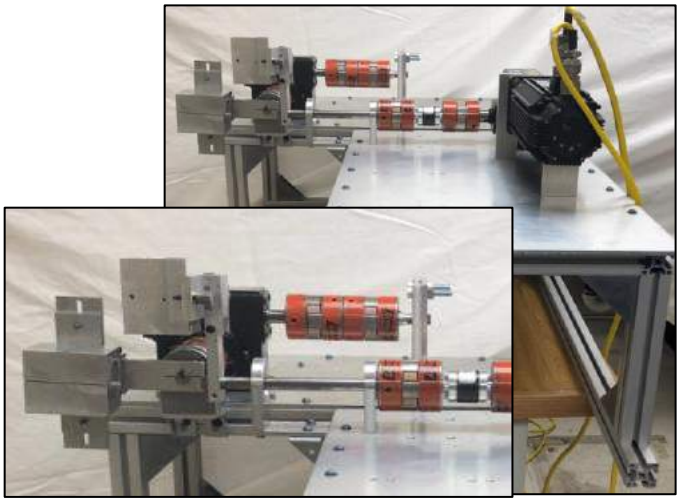

Figure 1: Fatigue Testing Apparatus; the lower expended view shows the elbow housings attached to shafts with a load cell in line with the v-v axis

Testing began with an initial load-controlled valgus rotation of 2 Nm of torque. Three slow cycles were followed by a fourth cycle during which toque, angular displacement and ligament displacements were recorded. The recorded cycle was followed by one-hundred fast cycles and a final recorded slow cycle. This procedure was repeated for increments of 2 Nm of valgus torque, until failure of the ligament. A test length of 100 cycles was chosen because that number is the current expectation for the number of pitches thrown in a game.

The recorded camera footage was used to quantify the longitudinal displacement of the length of the mUCL. The ligament lengths at the beginning of each load cycle were used as the reference lengths in the strain calculations of each band.

RESULTS

Each of the three tested specimens ruptured completely in valgus loading. The failure torques were 50 Nm, 20Nm and 30Nm for specimens 1, 2 and 3, respectively. Specimens 1 and 3 failed with posterior band avulsion at the ulnar joint line and subsequent tearing to the mid-substance; specimen 2 failed by complete ulnar sided avulsion. Figure (2) shows the maximum strain in each band, for each specimen, at the start of the cyclic load step just before the cyclic load step where failure occurred. The maximum valgus loads for these cycles were 48 Nm, 18 Nm and 28 Nm. Except for the posterior band of specimen 1, the strain in each band at the at the end of the load step was larger than the strain at the beginning of the load step.

DISCUSSION

The fatigue tester successfully carried valgus testing to failure after multiple steps of loading. The device integrated features that allowed for adjustability of the specimen position, which kept the radial head pivoting on the capitellum. The valgus loads were able to be applied repeatedly for a prescribed number of cycles, consistent with what a major league baseball pitcher may perform during a single game.

The different torques at which each specimen experienced failure was a testament to the variability in the geometric and mechanical properties between the specimens. The specimen which failed at 50 Nm had significantly greater thickness than the other two specimens. This showed that these geometric attributes do affect the fatigue life of the mUCL.

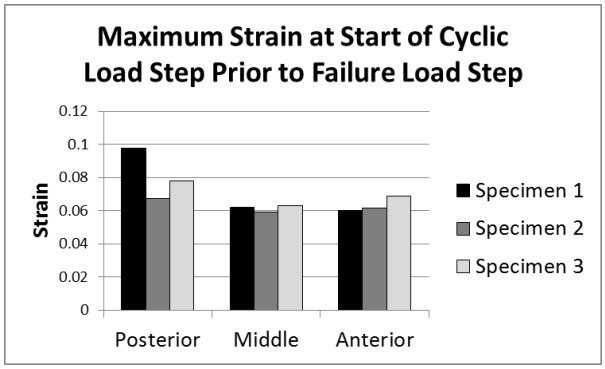

Figure 2: Maximum Strain for each Band during the Start of the Cycle before Failure

The three failure modes were similar in the origination of failure at the posterior insertion on the ulna. For specimens 1 and 3, the failure was observed to originate at the posterior band near the mid-substance of the ligament. This was evident from the complete rupture of the posterior band fibers, which proceeded across the mid-substance of the ligament toward the anterior band, which had a few fibers still intact. The failure of specimen 2 originated at the posterior band near the ulnar end of the ligament. The initiation of the failure at the posterior band seemed to agree with the strain results of Figures (2), which show the posterior band strain to be approximately equal to, if not greater than, the strain in the middle and anterior bands.

The difference in failure location with one specimen could be a result of the variation of the ligament properties between specimens, as well as the valgus rotation angle. Because the test was load-controlled, the angular valgus displacement could have been different for each specimen at any particular magnitude of valgus torque. More tests need to be performed to determine the consistency of the observed failure nature.

Figure (2), showing the maximum strain for the cyclic load step just before the failure load step showed an indicator of stiffness reduction in the bands of the mUCL. The maximum strain was greater at the end of the cycle than at the beginning of the cycle for eight of the nine bands. This meant that, for the same value of valgus load, a higher amount of deformation was achieved. This showed that, due to cyclic loading, the stiffness of the mUCL was gradually reduced over the course of the cyclic load step. This stiffness, or modulus, reduction is a criterion that has been used to show the presence of damage accumulation within a solid body [3]. Viscoelastic deformation could also be the source of this additional stretch.

Similar to the results presented in the previous studies [2-3] on ligament fatigue of the human ACL and rabbit MCL, fatigue seemed to play a definite role in the degradation of the mechanical properties of the bands of the human mUCL as well. This degradation effect continued up until the ultimate failure of the ligament. Further experimental and computational modeling will seek to implement these fatigue results in an effort to predict injury, relating to baseball pitchers who regularly experience these types of loadings.

REFERENCES

[1] Floris, S et al., *J Shoulder Elbow Surg.*, 7:345-51, 1998.
[2] Lipps, DB et al., *Am J Sports Med.*, 41:1058-1066, 2013.
[3] Thornton, GM et al., *J Annals of Biomech Eng.*, 35:1713-1721, 2007.

SB³C2019
Summer Biomechanics, Bioengineering and Biotransport Conference
June 25 -28, Seven Springs, PA, USA

EXPERIMENTAL MEASUREMENT OF EMBRYONIC TENDON MULTISCALE MECHANICS

Benjamin E. Peterson (1), Spencer E. Szczesny (1,2)

(1) Department of Biomedical Engineering
Pennsylvania State University
University Park, PA

(2) Department of Orthopaedics and Rehabilitation
Pennsylvania State University
Hershey, PA

INTRODUCTION

During embryonic and neonatal development, there is a rapid change in tendon structure and mechanics. Previous studies demonstrate that the tendon tensile modulus and ultimate strength dramatically increase as the collagen fibrils grow in diameter and length.[1,2,3] Additionally, there is a substantial decrease in the cellular volume fraction as more extracellular matrix is deposited.[2] These developmental changes are critical for the establishment of the load-bearing capacity of mature tendon. However, how tenocytes carefully orchestrate and regulate this process is unknown. Since tenocytes are sensitive to mechanical stimuli,[4,5] there is likely a feedback loop between tenocyte behavior and the changes in their mechanical microenvironment that drives tendon development.[5,6] Identifying the nature of this feedback loop and the role of cellular mechanotransduction in producing functional tendons will provide insight into the nature of tenogenesis and new opportunities for regenerative medicine.

A first step in identifying the interplay between tissue mechanics and cell behavior during tendon development is to determine the local tissue strains that cells experience in embryonic tissue. Previous studies only examined the macroscale mechanical properties of embryonic tendons.[2,3,6] However, the observed macroscale tendon behavior likely does not reflect the local microscale mechanics. Recent studies investigating the multiscale mechanics of rat tail tendon fascicles reported that the microscale tissue strains are significantly less that those applied at the tissue level, which can be explained by relative sliding between collagen fibrils.[7,8] However, it is unclear if the same phenomenon occurs within embryonic tissue and to what degree. Possible changes in fibril strains and sliding during development may have important implications for the mechanobiological pathways that are activated during tenogenesis.

The objective of this study is to measure the multiscale mechanics of embryonic tendons. We hypothesize that the fibril strains will be less than the applied tissue strains, suggesting that the fibrils are discontinuous and exhibit interfibrillar sliding under tensile load.

METHODS

Four digitorum longus tendons (n=4) were isolated from the tarsometarsal region of the hindlimbs from white Leghorn day 20 (E20) chicken embryos. Samples were stained with DTAF at 10 ug/ml and secured in the grips of a tensile testing device mounted on a confocal microscope with a 5 mm reference length **(Fig. 1)**.

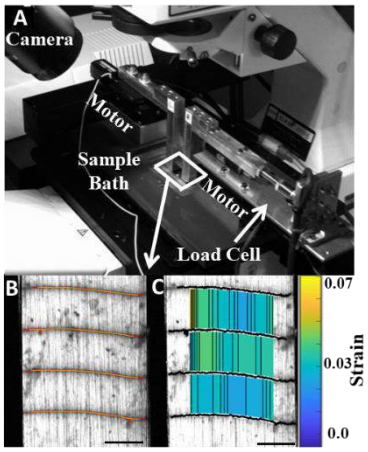

Figure 1: Experimental setup for multiscale tension testing. (A) Uniaxial tension device mounted atop a confocal microscope. (B,C) Representative image of the photobleached lines at 15% strain and their corresponding microscale strains. Scale bar = 100 μm.

Prior to testing, the samples were rotated in order to image the major and minor diameters, which were used to calculate the cross-sectional area. Samples were then untwisted and preconditioned to 1% strain for 5 cycles at 0.03 Hz. Three sets of photobleached lines (PBL) (4 lines, 125 μm apart) were bleached at the sample center and ± 2 mm from the center. Samples were then loaded

to 20% grip-to-grip strain in 5% increments at 10%/min followed by a 15 min stress relaxation. At the end of the relaxation, z-stack images were acquired at all three PBL locations and the stage positions were recorded.

All images were processed utilizing a series of custom MATLAB scripts to precisely track the photobleached lines and quantify the microscale fibril strains and interfibrillar sliding **(Fig. 1B-C)**.[5] Additionally, a MATLAB code was utilized to optically quantify the macroscale strain by tracking the spatial displacement of the peripheral PBL sets relative to one another (PBL-to-PBL strain). The coefficient of variance for the ratio between the fibril and PBL-to-PBL tissue strains was calculated across the three PBL locations for each sample.

The applied load was collected during the entire ramp and stress relaxation period. The load during the last 30 seconds of the relaxation was averaged to determine the quasi-static stress at each incremental strain. The macroscale tissue modulus was calculated using a linear regression fit to the quasi-static stress versus both the grip-to-grip and PBL-to-PBL strains.

The fibril:tissue strain ratio was averaged across all strain increments and a Student's t-test was used to determine if the value was different from one. A linear regression was used to determine if the values were dependent on the applied tissue strain. Similar statistical tests were used for the interfibrillar sliding, except t-tests were used to determine if the average value was different from zero. Significance for all tests was set at $p < 0.05$.

RESULTS

The fibril:tissue strain ratio had an average coefficient of variance of 0.139 across the tendon length. The fibril strains were significantly lower than the applied tissue strain ($p < 0.01$) but were not significantly different with increasing strain ($p = 0.43$) **(Fig. 2A)**. The interfibrillar sliding was significantly greater than zero ($p < 0.05$) and there was an increase in fibril sliding observed with increasing strain ($p < 0.01$) **(Fig. 2B)**.

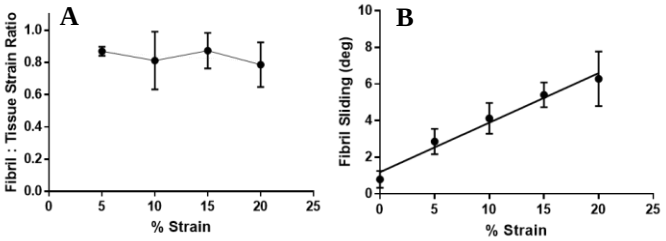

Figure 2: Multiscale behavior of embryonic day 20 chick tendon. (A) Fibril:tissue strain ratio and (B) interfibrillar sliding as a function of the applied grip-to-grip strain.

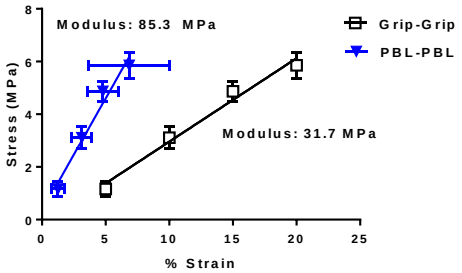

Figure 3: Plots and linear regressions of the quasi-static tendon behavior as a function of both the grip-to-grip and optical (PBL-to-PBL) strains.

Linear regressions of the quasi-static stress versus the PBL-to-PBL ($p < 0.01$) and grip-to-grip ($p < 0.02$) tissue strains indicated an average quasi-static modulus of 85.3 MPa and 31.7 MPa respectively **(Fig. 3)**.

DISCUSSION

This study provides the first measurement of the local microscale tissue strains that cells are exposed to during embryonic development. Consistent with our hypothesis, the microscale strains were less than the applied macroscale tissue strains **(Fig. 2A)**. Together with the observed non-zero interfibrillar sliding measurements **(Fig. 2B)**, this suggests that the fibrils are discontinuous in E20 tissue and that they slide relative to each other during tendon elongation. While previous studies reported that discontinuous fibrils could not be extracted in tendons from chicken embryos beyond E17,[1] our current data are consistent with previous testing of mature rat tail tendons.[5] However, in contrast to mature tendon, the fibril:tissue strain ratio was unaffected by increasing tissue strain and remained high with an average of 0.84 ± 0.04. This suggests that a different mechanism governing interfibrillar sliding may exist in embryonic versus mature tendon; however, additional work needs to be conducted to investigate this phenomenon further.

It is worth noting that there was a large discrepancy between the tendon behavior depending on whether the grip-to-grip or optical (PBL-to-PBL) strains were considered. In general, the optical strain measurements were less than 50% of the grip-to-grip strains, suggesting that the bulk of the strain occurred near the grips. This resulted in a nearly three-fold difference between our calculated modulus values. While our modulus values calculated from the grip-to-grip strains are comparable to previous tests of late embryonic chick tendons,[2] our optical strain data suggest that prior studies may underestimate the stiffness of embryonic tendon. It may be useful to develop alternative grip designs that transmit more of the applied tensile strains to the central portion of the sample. Nevertheless, our results suggest that cells are exposed to complex mechanical stimuli in developing tendons. Future work will be conducted across additional developmental time points to determine how changes in local tissue mechanics influence cell behavior and subsequent tendon development.

ACKNOWLEDGEMENTS

We thank Scott Kephart of the Penn State University Poultry Education and Research Center for supplying the chicken embryos.

REFERENCES

1. Birk, D. E., Nurminskaya, M. V. & Zycband, E. I. Collagen fibrillogenesis in situ: Fibril segments undergo post-depositional modifications resulting in linear and lateral growth during matrix development. *Dev. Dyn.* **202,** 229–243 (1995).
2. McBride, D. Structural and mechanical assessment of developing chick tendon. *Int. J. Biol. Macromol.* **10,** 194–200 (1988).
3. Heather L. Ansorge, Sheila Adamns, David Birk, L. S. Mechanical , Compositional , and Structural Properties of the Post-natal Mouse Achilles Tendon. *Annals of Biomedical Engineering*. **39,** 1904–1913 (2011).
4. Maeda, E. & Ohashi, T. Biochemical and Biophysical Research Communications Mechano-regulation of gap junction communications between tendon cells is dependent on the magnitude of tensile strain. *Biochem. Biophys. Res. Commun.* **465,** 281–286 (2015).
5. Richardson, S. H. *et al.* Tendon Development Requires Regulation of Cell Condensation and Cell Shape via Cadherin-11-Mediated Cell-Cell Junctions. *Mol. Cell. Biol.* **27,** 6218–6228 (2007).
6. Kalson, N. S. *et al.* An experimental model for studying the biomechanics of embryonic tendon: Evidence that the development of mechanical properties depends on the actinomyosin machinery. *Matrix Biol.* **29,** 678–689 (2010).
7. Szczesny, S. E. & Elliott, D. M. Interfibrillar shear stress in the loading mechanism of collaen fibrils in tendon. *Acta Biomater.* **10,** 2582–2590 (2014).
8. Screen, H. R. C., Lee, D. A., Bader, D. L. & Shelton, J. C. An investigation into the effects of the hierarchical structure of tendon fascicles on micromechanical properties. *Proc Inst Mech Eng H.* **218,** 109–119 (2014)

SB³C2019
Summer Biomechanics, Bioengineering and Biotransport Conference
June 25 -28, Seven Springs, PA, USA

FEMORAL TUNNEL LOCATION AFFECTS ACL EXCURSION DURING KNEE FLEXION

Patrick J. Schimoler (1,2), J. Jared Guth (1), Alexander Kharlamov (1), J. Daniel Thompson (1), Sam Akhavan (1), Mark Carl Miller (1,2)

(1) Department of Orthopaedic Surgery
Allegheny General Hospital
Pittsburgh, PA, USA

(2) Department of Mechanical Engineering
and Materials Science
University of Pittsburgh
Pittsburgh, PA, USA

INTRODUCTION

Anterior cruciate ligament (ACL) rupture is a common sports injury, and active patients often undergo surgical reconstruction using a tendon graft. Isometry in the graft placement would reduce the chances of graft damage, but the existence of isometric points for graft insertion is far from certain due to the complex motion patterns of the knee. Isometric placement is technically demanding when it is possible [1]. Anatomic placement of a graft would seem to have an intuitive advantage, but the tension in the native ACL is known to vary considerably. A small deviation from the native location may offer stability and isometry, potentially reducing risk of post-operative graft rupture. Existing studies have compared ACL excursion for proposed isometric tunnel locations [2] and have determined that transtibial reconstructions are more isometric than anatomic reconstructions [3]. While previous authors' works have examined tunnel placement, this work investigated ACL excursion for different pairings of femoral and tibial tunnels spaced evenly in and around the native ACL footprint in the same knee. Additionally, the knee flexion angle of minimum ACL excursion was determined.

METHODS

Nine cadaveric knee specimens, mid femur to mid shank, were dissected, removing skin, adipose tissue, and muscle tissue. The patella and patellar tendon were also removed. Care was taken to preserve all ligamentous structures of the knee. The ACL was transected and six tunnels were drilled centered around the ACL's femoral footprint and five tunnels were drilled around and in the middle of the ACL's tibial footprint (Figure 1). The center of the femoral footprint was identified as a point 50% of the distance from proximal to distal on the femoral footprint and 8mm anterior to the posterior articular margin of the lateral femoral condyle. Additional tunnels were drilled 5mm proximal and distal to this point, and 3 additional tunnels 5mm anterior to the first 3 tunnels. The center of the tibial footprint was identified as 9mm posterior to the posterior edge of the intermeniscal ligament and exactly midway between the tibial spines. Additional tunnels were placed 5mm anterior, lateral, posterior, and medial to the central tunnel.

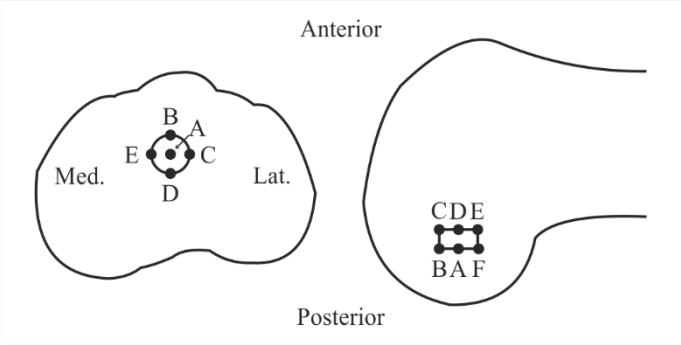

Figure 1: Tibial (left) and femoral (right) tunnel locations.

Each knee was mounted in a horizontal plane in a custom test fixture that maintained knee flexion with the knee's lateral side up. The fixture held the femur rigidly and allowed the shank to move freely. A swingarm connected to an incremental encoder rotated with the shank, measuring knee flexion. A string potentiometer was mounted to the fixture. Near the knee, the potentiometer's string was routed from the lateral side of the femur, into the intra-articular space, out through the medial side of the tibia, and clamped.

Poster Presentation #P245

The knee was moved through ten flexion cycles from full extension to at least 120°. The first five cycles were treated as preconditioning, the next three cycles were used for analysis, and the last two cycles were not used. The ACL excursion was calculated as the difference between minimum and maximum string potentiometer excursion seen during the three analysis cycles. Data was analyzed for flexion angles between 20° and 120° to ensure all knees were analyzed over the same range of motion. Additionally, the flexion angle between 20° and 120° of smallest ACL excursion for each knee was recorded.

Two separate two-way repeated measures ANOVAs were performed. The first ANOVA compared ACL excursions across 20° to 120° of knee flexion with factors of femoral tunnel location (6 levels, A-F) and tibial tunnel location (5 levels, A-E). The second ANOVA compared flexion angles of minimum ACL excursion with the same factors and across the same flexion angles as the first ANOVA. Significance was determined by a p-value below 0.05. In the case of significance, Tukey's Test was used for post hoc comparisons.

RESULTS

Femoral tunnel location significantly affected both ACL excursion between 20° and 120° of knee flexion ($p < 0.01$) and flexion angle of minimum ACL excursion ($p < 0.01$). Femoral tunnels D and B had the smallest average ACL excursions, 3.7±1.5mm and 4.0±1.7mm, respectively (Figure 2). ACL excursion for femoral tunnel D was significantly smaller than at all other locations except B and ACL excursion for femoral tunnel B was significantly smaller than at locations C, A, and F. The smallest ACL excursion, 3.4±1.9mm, resulted from femoral tunnel D and tibial tunnel C (Figure 3). Femoral tunnel locations D (79.4±38.9°) and B (83.4±26.7°) had knee flexion angles with the smallest ACL excursion significantly different than the other femoral tunnel locations as well (Figure 4).

Tibial tunnel location had no significant effect on either ACL excursion or flexion angle of minimum ACL excursion.

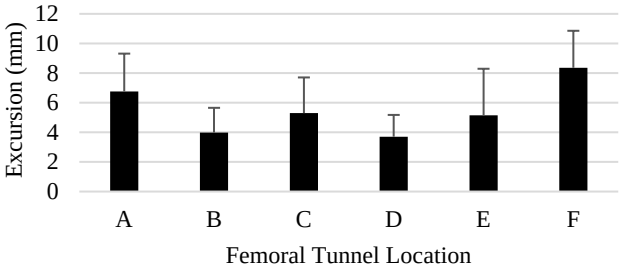

Figure 2: ACL excursion as a function of femoral tunnel location.

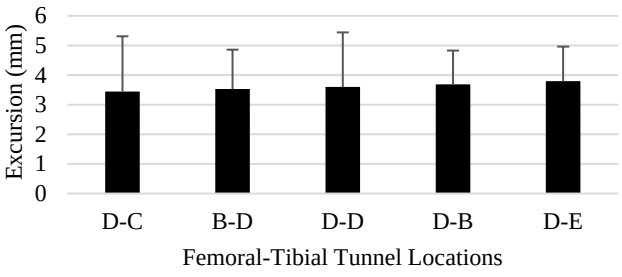

Figure 3: The five smallest ACL excursions.

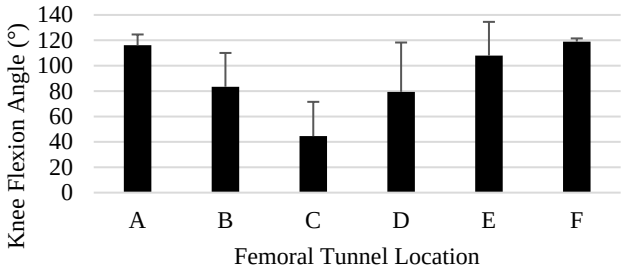

Figure 4: Knee flexion angle of smallest ACL excursion as a function of femoral tunnel location.

DISCUSSION

This work found femoral tunnel location significantly affected both ACL excursion over the knee flexion range of 20° and 120° and the flexion angle of minimum ACL excursion over the same knee flexion range.

Zavras et al. [2] compared tunnel locations that have been suggested throughout the literature for isometric graft behavior. They found ACL excursions as large as 6mm for geometrically placed tunnels and 3mm for anatomically placed tunnels. They found several tunnel locations that had less than 1mm total ACL excursion. The smallest ACL excursion found in our study was 3.4±1.9mm for femoral tunnel D and tibial tunnel C.

Lubowitz [3] compared anatomic and transtibial ACL reconstructions and found approximately 7.3mm and 5mm excursions, respectively, when the current method, ACL excursion as the difference between maximum and minimum change in ACL length across the knee's flexion range, was applied to his data. Both measurements are within the range of what was found in our study, although he included data to full knee extension.

Both Zavras et al. (full extension to 140°) and Lubowitz (full extension to 120°) used larger knee flexion ranges than our study which may have affected our flexion angle of minimum excursion because some minima were found to be at 120° of flexion.

Another consideration in a cadaveric study is the effect of muscular structures on knee stability. Only ligamentous structures were maintained during this study, and we cannot account for the complex patterns of musculotendinous units in the stabilization of the knee joint in vivo.

Finally, the motion measured in this study was limited to flexion and extension, and did not include imposed rotatory motion. Many prior works have demonstrated the importance of a reconstructed ACL to withstand a pivot shift type motion, and femoral tunnels drilled trans-tibially are more likely to result in grafts that fail to prevent this pathologic motion. Thus, less excursion of the graft during flexion and extension should not be inferred as clinically superior. Our results may explain the roughly 5% rate of post-operative rupture with anatomic reconstruction given the forces on the graft.

REFERENCES

[1] Kohn, D, *Knee Surg, Sports Traumatol, Arthrosc*, 6 [Suppl 1]: S13-S15, 1998.

[2] Zavras, TD, et al., *Knee Surg, Sports Traumatol, Arthrosc*, 9: 28-33, 2001.

[3] Lubowitz, JH, *Knee Surg Sports Traumatol Arthrosc*, 22: 1190-1195, 2014.

SB³C2019
Summer Biomechanics, Bioengineering and Biotransport Conference
June 25 -28, Seven Springs, PA, USA

Utilization of Multi-Foci ARFI Imaging to Generate Larger Tendon Displacement

**Gerald A. Ferrer (1), Waqas Khalid (1),
Volker Musahl (1,2), Kang Kim (1,3), Richard E. Debski (1,2)**

(1) Department of Bioengineering
University of Pittsburgh
Pittsburgh, PA, USA

(2) Department of Orthopaedic Surgery
University of Pittsburgh
Pittsburgh, PA, USA

(3) Department of Medicine
University of Pittsburgh
Pittsburgh, PA, USA

INTRODUCTION

Ultrasound is a non-invasive, reliable and cost-effective tool often used by clinicians to diagnose musculoskeletal injuries (ie. tendon and ligament injuries). Currently, evaluation of tissue quality based on ultrasound images is mostly qualitative and depends on the user. Acoustic Radiation Force Impulse (ARFI) imaging is an ultrasound technique that generates a localized force onto the tissue of interest at a precise location and the resulting tissue displacement is measured. Information about the resulting tissue displacement could lead to insights about tissue quality. ARFI imaging is primarily utilized for compliant, isotropic biological tissues such as the breast and liver, where tissue displacement measurements are <10μm. The utility of ARFI imaging is not well understood for stiff, anisotropic biological tissues such as a tendon (tendon modulus: ~100s of MPa in long axis and ~1MPa in transverse axis vs breast/liver ~kPa), where tissue displacements may be too small to differentiate between un-injured and injured tendons. Conventional ultrasound imaging (full-frame imaging) utilizes narrow beams for better image resolution. However, utilizing narrow beams limits the acoustic radiation force applied to the tissue. Multi-foci beamforming is an imaging technique that allows for a more powerful and focused beam of acoustic radiation force by dividing the ultrasound transducer into multiple sub-apertures and programming each sub-aperture to focus at a specific axial and lateral position [4]. Therefore, the objective of this study was to assess the ability of the multi-foci and full-frame approach to push onto the tendons. It was hypothesized that tendon displacement will increase compared to full-frame ARFI imaging.

METHODS

Four fresh-frozen porcine knees were dissected, and the extensor tendons were harvested and prepared for tensile testing and ARFI imaging of the tendon midsubstance. The cross-sectional area of the tendon midsubstance was determined using a laser scanner (Next Engine, Desktop 3D Scanner, Santa Monica, CA, USA).

Mechanical Testing: Each tendon underwent a uniaxial tensile testing protocol (Preload = 1N, Preconditioning = 1-10N for 10 cycles, Load to 100N) to determine its modulus in the linear region. The ends of the tendon were clamped with custom soft tissue clamps and aligned for tensile loading in the materials testing machine (Instron, Model 5965, Norwood, MA, USA). The midsubstance strain in the tendon was

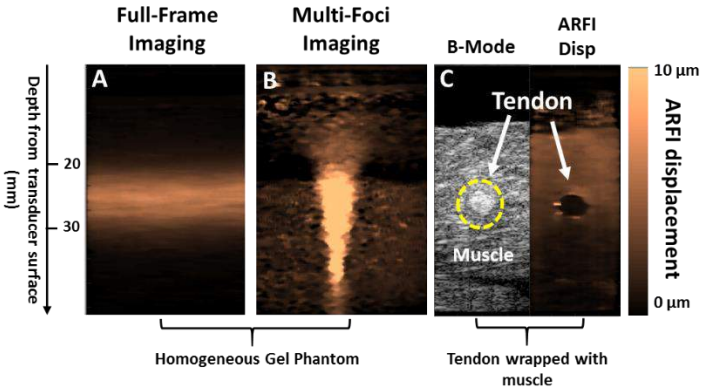

Figure 1: Control images of the regions of excitation (bright areas) for a (A) full-frame and (B) multi-foci ARFI push in a homogeneous gelatin phantom. Multi-foci imaging focuses the acoustic radiation force to a precise location. (C) ARFI displacement within the stiff tendon is less compared to the surrounding softer muscle after a full-frame ARFI push.

Poster Presentation #P246

measured with an optical tracking system (DMAS, Spica Technology, Kihei, HI, USA).

ARFI Imaging: Each tendon was wrapped with a layer of muscle and loaded into a custom tensioning jig immersed in distilled water to more closely mimic physiologic conditions. The tendon was loaded to five different stress levels (0.1, 0.25, 0.5, 0.75 and 1.0 MPa), where 3 full-frame and 3 multi-foci ARFI images were acquired at each stress level using a research ultrasound platform (Verasonics, VDAS V-1 Model, Redmond, WA, USA) and commercial linear array transducer (ATL L7-4). The average tendon displacement across the 3 images for both the full-frame and multi-foci approach was used for analysis.

For full-frame ARFI imaging, an ARFI push across the entire width of the transducer aperture was generated using a localized radiation force (spatial resolution = 148 μm) at the tendon midsubstance located at the elevation focus of the transducer (25 mm) for 1000 cycles at 5.2 MHz (duration = 192 μs). For multi-foci ARFI imaging, a multi-foci push is generated using the same parameters as full-frame ARFI imaging (spatial resolution = 298 μm). That is, the ultrasound transducer aperture is divided into 3 focused beams (foci), which all focus at the elevation focus and in the center of the transducer simultaneously (Figure 1B). ARFI tendon displacement was measured from post-ARFI push images and measured by manually selecting a region of interest at the center area of the tendon to minimize boundary effects (Figure 1C).

Mechanical Damaged Protocol: Cyclic compressive loading (40 cycles from 1-100N) was applied to the tendon midsubstance to damage the collagen fibers and injure the tendon. Loading conditions were determined based on preliminary tests that resulted in a decrease in the modulus of the linear region by ~40%. After injury, the same mechanical testing and ARFI imaging protocol performed for the un-injured tendon was repeated.

Statistics: A related samples Wilcoxon signed rank test was performed to assess the effect of ARFI technique (full-frame vs multi-foci) on ARFI tendon displacement. Significance was set at $p < 0.05$.

RESULTS

Multi-foci ARFI imaging resulted in significantly more tendon displacement compared to full-frame ARFI imaging (Figure 2). Across both tendon injury states and stress levels tested, multi-foci ARFI imaging was on average 2.7 times larger than the tendon displacement measured using full-frame ARFI imaging (multi-foci = 1.6 ± 0.4 μm and full-frame = 0.6 ± 0.3 μm, $p < 0.01$). The average linear region modulus for the 4 un-injured tendons was 347.0 ± 100.7 MPa. Following the mechanical testing damage protocol, the modulus of the linear region dropped by an average of 43% (injured tendons = 195.4 ± 47.8 MPa). The average difference of ARFI tendon displacement between un-injured and injured tendons was 0.2 μm when using the multi-foci approach (Figure 2). For the full-frame approach, the average difference in ARFI tendon displacement between un-injured and injured tendons across all stress levels was < 0.1 μm (Figure 2).

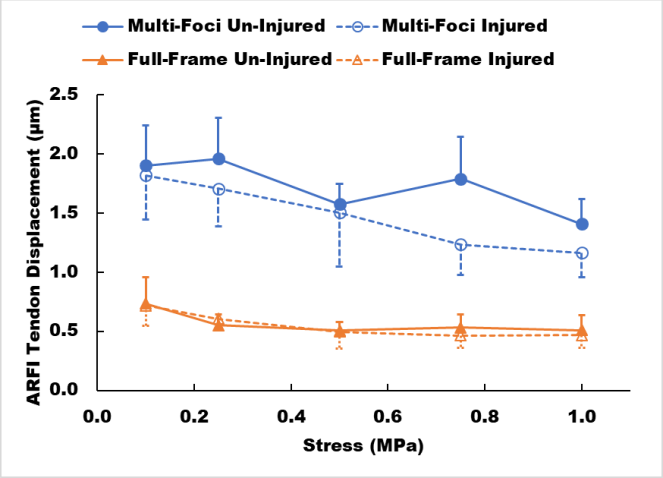

Figure 2: ARFI tendon displacement data (Avg ± SD). Blue circles indicate multi-foci approach. Orange triangles indicate full-frame approach. Dashed lines indicate injured tendons.

DISCUSSION

The results of this study demonstrate the utility of multi-foci ARFI imaging to generate larger tendon displacement compared to full-frame ARFI imaging. On average across all stress levels, multi-foci ARFI imaging generated nearly 3 times more tendon displacement (Table 1), which was expected since the multi-foci ARFI imaging approach divided the transducer into 3 focused beams to push onto the tendon at a precise location. Our study shows that both full-frame and multi-foci ARFI imaging can displace the tendon enough to be measured, though lower than the magnitude of displacement reported for breast and abdominal tissues (up to 10 μm) [1-3].

Different ultrasound techniques such as shear wave elastography have been used by researchers to better understand tendon health [5]. The advantage of ARFI imaging is that it provides local information while shear wave elastography provides averaged information over the region where shear wave speed was taken. Previous studies have used ARFI imaging to identify the presence of tumors, by detecting changes in ARFI displacement to indicate a change in the tissue stiffness [1,2]. Our study establishes a novel methodology for ARFI imaging by focusing the ultrasound beams to a precise location (Figure 1B) and at a higher force. Developing a method that generates more force is important since tendons are much stiffer than tissues traditionally used for ARFI imaging (tendon modulus: ~100s of MPa vs breast/liver ~kPa).

In addition, the larger magnitude displacement using the multi-foci may be beneficial to differentiating the degree of injury or degeneration in tendons. Our results also show that distinguishing differences in tendon mechanical properties might be possible. At certain stress levels, differences greater than the repeatability (0.2 μm) of ARFI displacements measurements were found when using the multi-foci approach (Figure 2). With further development, multi-foci ARFI imaging may be a viable approach to target specific locations where a musculoskeletal soft tissue may be damaged and evaluate mechanical properties non-invasively.

ACKNOWLEDGEMENTS

Support from the University of Pittsburgh Swanson School of Engineering, Department of Bioengineering, Orthopaedic Surgery, and NSF-GRFP No. 1247842 is gratefully acknowledged.

REFERENCES

[1] Nightingale, K et al., *Ultrasound Med Biol*, 28(2): 227-35. 2002.
[2] Nightingale, K et al. *Ultrason Imaging*, 24(2): 129-38. 2002.
[3] Fahey, BJ et al. *Ultrasound Med Biol*, 31(9): 1185-98. 2005.
[4] Nguyen, MM et al., *Ultrasound Med Biol*, 43(6): 1263-74, 2017.
[5] Baumer, TG et al., *J Orthop Res*, 36(1): 282-288. 2017.

SB³C2019
Summer Biomechanics, Bioengineering and Biotransport Conference
June 25 -28, Seven Springs, PA, USA

USING OPTICAL TRACKING TO CALCULATE NON-RECOVERABLE STRAIN IN THE GLENOHUMERAL CAPSULE

J. Hawk(1), C. Chan (1), R. Tisherman (2), R. Debski (1,2)

(1) Bioengineering
University of Pittsburgh
Pittsburgh, Pennsylvania, USA

(2) Department of Orthopaedic Surgery
University of Pittsburgh
Pittsburgh, Pennsylvania, USA

INTRODUCTION

The glenohumeral joint is the most commonly dislocated joint, usually by an anterior shoulder dislocation [1]. This type of injury can result in non-recoverable strain of the glenohumeral capsule, increasing the chances of recurrent shoulder instability [2]. In order to minimize the risk of recurrent shoulder instability, a common surgical procedure is to plicate the capsule, reducing its size [3]. Currently, how the capsule is plicated depends on the surgeon's personal experience rather than taking into account the magnitude or location of non-recoverable strain in the capsule. Previous work has looked at non-recoverable strain in the glenohumeral capsule following multiple shoulder subluxations, while this study will examine non-recoverable strain following multiple severe anterior shoulder dislocations, with a severe dislocation being defined as the humeral head crossing the entire width of the glenoid. Optical tracking was used to measure non-recoverable strain, which allows non-recoverable strain in all directions to be accounted for, unlike other methods, such as strain gauges, which only allow stain to be measured along one axis. The objective of this study is to determine if performing 10 severe anterior shoulder dislocations without tearing the joint capsule is possible, as well as develop a method that utilizes optical tracking to calculate the magnitude and location of non-recoverable strain in the glenohumeral capsule following multiple severe anterior shoulder dislocations.

METHODS

Experimental Setup: Healthy cadaveric shoulders were dissected of all soft tissue except for the glenohumeral capsule. A 7x11 grid of black strain markers were glued to the inferior side of the capsule spanning from the anterior band to the posterior band of the IGHL. The scapula and humerus were potted in epoxy putty and then mounted in the FRS2010 6 degree of freedom robotic testing system (Chino, Japan) (**Figure 1**).

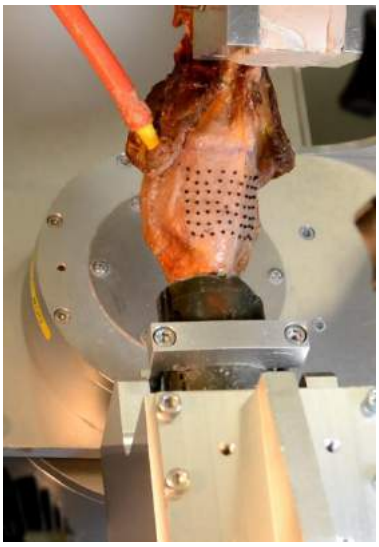

Figure 1: Specimen mounted in the FRS2010 robotic testing system

The capsule was inflated to 0.7 psi and 0.9 psi at five different joint positions to determine at which position the capsule had the fewest wrinkles and folds. The joint positions that were tested were 60 degrees of abduction and 0, 5, and 10 degrees of internal and external rotation. Four cameras were clamped to the robot and captured the movement of the markers, and the coordinates of the strain markers at each of these positions were recorded using a motion capture software, DMAS7 (Spicatek, HI). The joint position that had the least average marker movement between 0.7 and

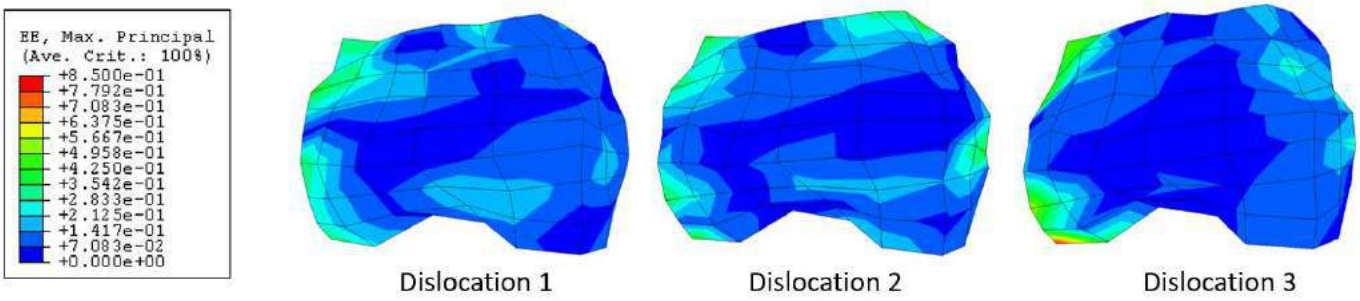

Figure 2: Strain distributions after 1, 2, and 3 severe anterior shoulder dislocations shown on a right shoulder. The posterior side of the capsule is on the right, and the anterior side of the capsule is on the left.

0.9 psi was the joint position used for all following dislocations. The marker position of the intact joint at 0.9 psi was used as the reference position for calculating non-recoverable strain.

Data Acquisition: The specimen underwent 1, 2, 3, 4, 5, and 10 dislocations performed by the FRS2010. After each of these dislocations, the capsule was given 30 minutes of recovery time to account for the viscoelasticity of the tissue and was then inflated to 0.9 psi. The marker position at 0.9 psi was recorded by the four cameras and served as the strained state after each dislocation. Non-recoverable strain was defined as the maximum principal strain calculated from the marker configurations of the reference state and of the strained state.

Data Analysis: The marker coordinates from each of these states were used in ABAQUS (ABAQUS/CAE Student Version 6.4; Simulia, Providence RI) to generate strain maps. The 7x11 grid of markers produces a 6x10 grid of 60 elements The capsule was split into six sub regions, for each of which the average magnitude of maximum principal strain were calculated. The six regions were the glenoid side of the anterior band, the humeral side of the anterior band, the glenoid side of the axillary pouch, the humeral side of the axillary pouch, the glenoid side of the posterior band, and the humeral side of the posterior band.

RESULTS

Preliminary testing was performed on 4 specimens. The joint capsules of two of the four specimens tore following the third dislocation, making collection of data for dislocations 4-10 not possible for those two trials. 10 dislocations were successfully performed on the other two specimens. Non-recoverable strain was calculated at the centroid of each element, and the average non-recoverable strain of each sub-region of the capsule was recorded. Strain maps were generated for each dislocation to show non-recoverable strain distribution (**Figure 2**). Repeatability between specimens was calculated using one-way ANOVA to be 45.8%. A large increase in non-recoverable strain was observed in one specimen from the second to third dislocation on the posterior side of the capsule. The non-recoverable strain increased from 4.3% and 4.1% to 22.5% and 21.9% on the glenoid and humeral side of the posterior band, respectively.

DISCUSSION

This study was motivated by a need to quantify non-recoverable strain in the glenohumeral capsule following multiple severe anterior shoulder dislocations. Preliminary testing has proven that performing ten severe anterior shoulder dislocations without tearing the joint capsule is possible. The large increase in non-recoverable strain in one specimen suggests a possible error made when collecting data, such as a camera being moved after calibration. Any slight movement of the cameras after calibration greatly affected recording of the marker coordinates and created inaccurate strain readings when the data was processed in ABAQUS. The repeatability was calculated to be 45.8% and indicates unreliability in the data collected. Preliminary testing will continue with a focus on camera stability to ensure accurate data collection. More specimens will be tested on to determine the magnitude and location of non-recoverable strain in the glenohumeral capsule following multiple severe anterior shoulder dislocations.

ACKNOWLEDGEMENTS

This project was supported by the Department of Bioengineering and the Department of Orthopaedic Surgery at the University of Pittsburgh.

REFERENCES

[1] Abrams et al. JBJS. 2014 [2] Malicky et al. JSES 2002 [3] Alberta et al. JBJS. 2006

SB³C2019
Summer Biomechanics, Bioengineering and Biotransport Conference
June 25 -28, Seven Springs, PA, USA

3D STRAIN COMPONENTS AND THEIR VISCOELASTIC BEHAVIOR FOR KNEE MENISCUS TISSUE IN CIRCUMFERENTIAL TENSION UNDER STRESS RELAXATION AND CREEP

John M. Peloquin (1), Michael H. Santare (2), Dawn M. Elliott (1)

(1) Dept. of Biomedical Engineering
University of Delaware
Newark, DE, USA

(2) Dept. of Mechanical Engineering
University of Delaware
Newark, DE, USA

INTRODUCTION

The knee meniscus supports 3D loads in vivo and exhibits time-dependent (viscoelastic) material properties. The circumferential (x) direction is loaded in tension. This tensile hoop stress serves to restrain tibial translation. The radial (y) direction is loaded in a mix of moderate tension and compression, and the axial (z) direction is loaded in compression. The meniscus is also fluid-saturated. Accordingly, in joint-scale FEA simulations, the meniscus is typically modeled as a transversely isotropic, poroelastic material [1]. Compression in the z-axis is well-studied. However, key aspects of the meniscus' tensile properties remain unknown. In tensile tests, meniscus strain has only been measured in the plane of the specimen, not in 3D. The z-strain and hence volume change are not known. Volume change is a fundamental aspect of a poroelastic material's behavior because it sets the amount of fluid flux. Furthermore, although tensile viscoelasticity has been investigated using stress relaxation tests and attributed to poroelasticity [2], tests of the other tensile viscoelastic limiting case—creep—have not been performed, and it is unknown if results obtained from tensile stress relaxation generalize to tensile creep. In addition, the recoverability of tensile viscoelastic changes is not known, and is needed to distinguish normal mechanical function from damage. This study was designed to provide this missing fundamental data by testing the meniscus in circumferential tension, with test segments of both stress relaxation and creep and with continuous measurement of 3D strain in x, y, and z. Specifically, we sought to answer the following questions: (a) Does the meniscus' volume change under tension? (b) Is the 3D strain consistent with transversely isotropic material symmetry? (c) Do stress relaxation and creep differ in their effects on y-strain, z-strain, and volume? (d) Are volume changes during a loaded hold faster than during unloaded recovery?

METHODS

Tensile test specimens (n = 3) were cut from fresh-frozen adult bovine meniscus in the circumferential–radial plane. Cross-sectional area was measured using a laser interferometer. Specimens were cut in the expanded tab shape [3]. Midsubstance width (y, radial) = 8 mm and thickness (z, axial) = 2 mm. Specimens were mounted on an Instron 5943 with a grip-to-grip length (x) of 16 mm for circumferential uniaxial tensile testing, matching the direction of physiologic tension.

The test protocol consisted of preload to 20 kPa, preconditioning, stress relaxation at $\lambda x = 1.08$ for 10 minutes, unloaded recovery for 30 minutes, creep for 10 minutes at the σ_{xx} value reached by a ramp to $\lambda x = 1.07$, unloaded recovery for 30 minutes, and a repeat stress relaxation. The repeat stress relaxation verified that the specimen's properties did not change during the test. Preconditioning consisted of 30 minutes unloaded swelling followed by an identical stress relaxation at $\lambda x = 1.08$. All ramps were done at 0.1 mm/s. Throughout the entire test, the x–y face of the specimen was videoed using a Basler a102f CCD camera (1392×1000 px, 1 fps) and the y–z side of the specimen was videoed using a Canon T7i (6016×4010 px, 1/30 fps). Tests were done in PBS.

λx was measured using grip-to-grip displacement. (There was no significant grip slip.) λy was measured using Vic-2D (Correlated Solutions, Inc.) to track the edge-to-edge width of the specimen in the CCD images at the midpoint between the two grips. λz was measured by manually tracing the specimen edges in each DSLR photo and calculating the median edge-to-edge thickness. Strain was referenced to the last value in the unloaded hold segment immediately prior to stress relaxation/creep. Volumetric strain was measured as $J = \lambda x \cdot \lambda y \cdot \lambda z$.

Statistical analysis was performed using the initial and final strain values of each strain ratio in each loaded hold (stress relaxation, creep) and each unloaded recovery (Figure 1). The rapidity of change for each strain component was quantified as $t_{\Delta 63\%}$, the time to change by 63% of

final − initial. (The time dependency was often not exponential, so exponential decay fits were not used.) Null hypothesis significance tests were done using repeated measures ANOVAs for objectives a, b, and d and paired t-tests for objective c. Significance was set as $p < 0.05$ and trends as $p < 0.10$. In figures, * ≠ 1, $p < 0.05$; · ≠ 1, $p < 0.1$; — $p < 0.05$ between groups; - - - $p < 0.1$ between groups.

RESULTS

In both stress relaxation and creep, volume increased during the ramp loading segment to $J = 1.02 \pm 0.01$ ($J \neq 1$, $p < 0.05$), then decreased significantly by a greater amount during the loaded hold segment, such that final $J = 0.98 \pm 0.02$ ($\Delta J \neq 0$, $p < 0.05$; final $J \neq 1$, $p = 0.06$) (Figs 1 and 2). Volume decrease during the hold was mediated by both λy and λz, which were ≤ 1 throughout, and exhibited further contraction during the loaded hold. This further contraction was sufficient to overcome the initial volumetric expansion caused by the applied x-extension and, by the end of the loaded hold, to produce overall volumetric contraction.

During unloaded recovery following stress relaxation and creep, volume increased significantly to a final $J = 1.007 \pm 0.006$ ($J \neq 1$, $p < 0.05$), indicating a final volume slightly greater than when the ramp to the loaded hold began (Fig 3). λy and λz also increased during recovery to final $\lambda y = 1.004 \pm 0.004$ ($\lambda y \neq 1$, $p < 0.05$) and final $\lambda z = 1.003 \pm 0.003$ ($\lambda z \neq 1$, $p < 0.10$).

Asymmetry was observed between the y and z axes. The final λz value in the loaded hold for both stress relaxation and creep was significantly less than the final λy value (Fig 2). During unloaded recovery after stress relaxation and creep, λz increased significantly more than λy ($p < 0.05$), such that both had a final value ≈ 1.0035 at the end of recovery. The kinetics of λy and λz also differed. As quantified by $t_{\Delta 63\%}$, λy tended to change faster than λz during the loaded hold ($p < 0.10$) and slower during the unloaded recovery ($p < 0.05$) (Fig 4).

Stress relaxation and creep overall produced similar changes in J, λy, and λz, with only two slight differences. In the loaded holds, J tended to be slightly smaller (more contracted) at the end of stress relaxation than at the end of creep ($p < 0.10$, paired t-test) (Fig 2). In unloaded recovery, $t_{\Delta 63\%}$ for λy was slightly shorter for stress relaxation than for creep ($p < 0.05$, paired t-test) (Fig 4).

Kinetics for J and λy differed greatly between loaded hold and unloaded recovery (Fig 4), with a much shorter $t_{\Delta 63\%}$ (faster change) during the loaded hold ($p < 0.05$). λz displayed a similar pattern, but the difference in $t_{\Delta 63\%}$ between loaded hold and unloaded recovery was small and not statistically significant.

DISCUSSION

Measured volume was found to significantly increase during the circumferential tensile ramps and decrease during the loaded holds, which is a new finding. This implies that the meniscus takes up fluid during rapid circumferential extension and loses fluid under static loading. Cycling of synovial fluid may benefit the meniscus by increasing exchange of metabolic or signaling factors. Fluid exudation from the meniscus during static loading may also serve, in the knee joint, to pressurize fluid in the cartilage–meniscus contact and force fluid into the cartilage.

Concerning symmetry, λy and λz were not equal, suggesting that the meniscus may not be transversely isotropic. Since the meniscus functions under 3D constraints in vivo, even slight asymmetry may meaningfully alter its internal stresses and limits of safe function.

Stress relaxation and creep produced similar changes in strain at similar rates, indicating that it is plausible to treat both as the consequence of the same viscoelastic mechanism. Strain and volume recovered much slower during unloaded recovery than they changed during stress relaxation/creep, taking almost 10 minutes to recover by 63%. This recovery is too slow to be useful in vivo for restoration of volume and fluid content; load-induced fluid pumping mechanisms are likely to be more relevant physiologically.

The observations made here of (a) a switch between volumetric dilation to contraction, (b) y/z asymmetry, (c) similarity between stress relaxation and creep, and (d) slow unloaded recovery compared to relaxation/creep are all new findings and fill a fundamental gap pertaining to meniscus tensile mechanics and poroelasticity. This data provides a foundation for future work to understand meniscus function in native 3D joint loading.

ACKNOWLEDGEMENTS

Funded by NIH NIAMS R21AR070966.

REFERENCES

[1] Spilker, R et al., *J Biomech*, 25:1027–45, 1992.
[2] LeRoux, M et al., *J Biomech*, 124:315–21, 2002.
[3] Peloquin, J et al., *J Biomech Eng*, 138:021002, 2016.

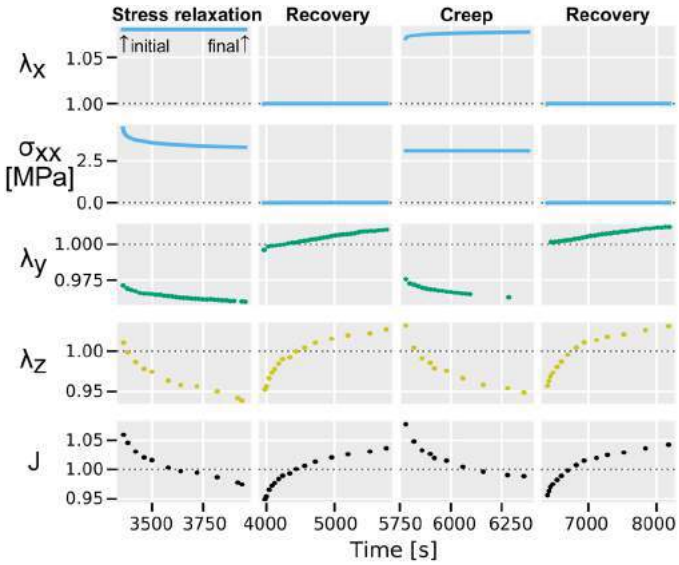

Figure 1: Test segments used for analysis (representative).

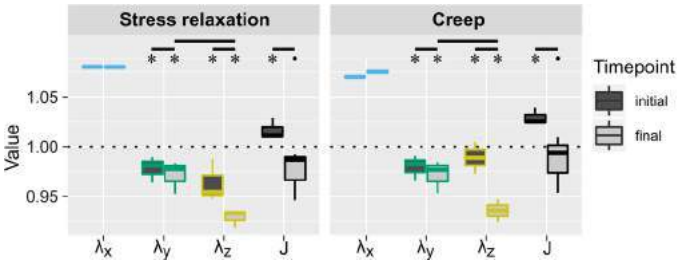

Figure 2: Stretch ratio changes during loaded hold.

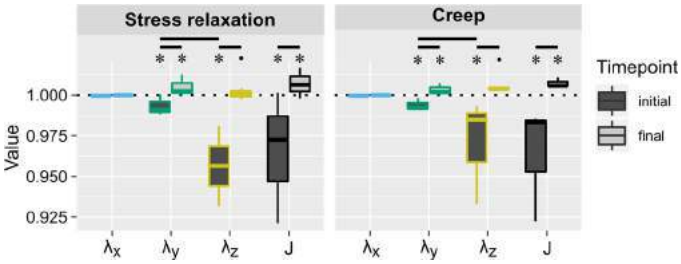

Figure 3: Stretch ratio changes during unloaded recovery.

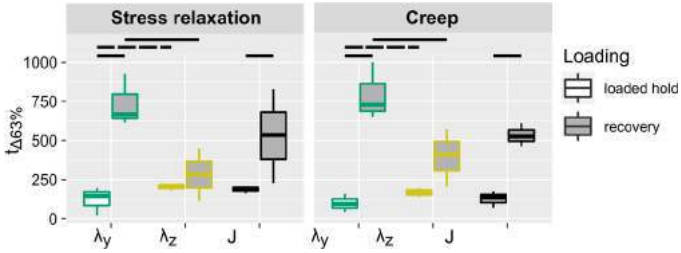

Figure 4: Time constants.

SB³C2019
Summer Biomechanics, Bioengineering and Biotransport Conference
June 25 -28, Seven Springs, PA, USA

INTRAMUSCULAR PRESSURE AND SHEAR MODULUS OF LOWER-LEG MUSCLES ARE CORRELATED

S. Sadeghi (1), D. Bader (2), D. Cortes (1,3)

(1) Mechanical Engineering Department
Penn State University
State College, PA, USA

(2) Department of Orthopaedics & Rehabilitation, Penn State College of Medicine
State College, PA, USA

(3) Biomedical Engineering Department
Penn State University
State College, PA, USA

INTRODUCTION

Intramuscular pressure (IMP) is the hydrostatic regional stress in a muscle [1]. IMP is linearly correlated to muscle force during isometric, concentric and eccentric muscle contractions, as well as dynamic exercises such as running and walking [2]. Therefore, IMP is a good estimator of individual muscle force. Shear wave elastography (SWE) is an ultrasound-based imaging technique developed to non-invasively provide information about the shear modulus of soft tissues [3]. The shear modulus of the muscles is linearly correlated to force during isometric contraction [4] over the full range of 0–100% of maximum voluntary contraction. This similarity between IMP and shear modulus strongly suggest that these parameters are related. The objective of this study was to quantify the dependency of shear modulus within the lower-leg muscles on IMP in healthy individuals. This dependency is important to improve interpretation of ultrasound elastograms and to potentially use it as a biomarker for more accurate diagnosis of pathologies related to increased IMP.

METHODS

Nineteen healthy participants (eight males and eleven females; Mean age ± SD, 23.84±6.64; Mean BMI ± SD, 23.00±2.89) were recruited in this study. An initial SWE measurement was performed within the lower leg muscles (Tibialis Anterior, TA; Peroneus Longus, PL). The IMP of TA and PL was then increased using a blood pressure cuff placed around the thigh and inflated to 40, 80 and 120 mmHg (Figure 1 (a)). Elastography measurements were taken at each cuff pressure level (40, 80 or 120 mmHg). Additionally, one of the legs was elevated using a leg holder and the knee and hip joints were flexed to 90° and SWE was performed (Figure 1(b)). To directly measure the IMP corresponding to each cuff pressure level, an intramuscular pressure system was used (Figure 1(c)). For the statistical analysis, a linear mixed effects model was used, with the cuff pressure condition, muscle type and gender as fixed variables, while the shear modulus was used as the dependent variable. The spearman's rank correlation coefficient was applied to analyze the correlation between the TA muscle shear modulus and IMP.

RESULTS

The change in shear modulus relative to the shear modulus at zero pressure (median and interquartile range) at elevated leg, 40 mmHg, 80 mmHg and 120 mmHg cuff pressure was -2.35 (4.08) kPa, 1.22 (2.09) kPa, 3.02 (4.94) kPa and 5.10 (5.02) kPa, respectively, for the TA muscle; and -1.06 (1.15) kPa, 1.12 (1.64) kPa, 3.02 (3.74) kPa and 3.22 (4.96) kPa for the PL muscle. From the linear mixed effects model, it was observed that muscle and cuff pressure had a significant effect on muscle shear modulus ($P < 0.01$ and $P < 0.01$, respectively), while gender did not. Figure 2 and 3 show representative shear modulus maps of the TA and PL muscles at each cuff pressure level. Additionally, the shear modulus for both the TA and PL muscles were found to increase as a function of IMP (Figure 4 and 5). Specifically, there were significant positive correlations found between the median shear modulus and IMP for the TA muscle ($rho = 0.99$, $p < 0.01$), and

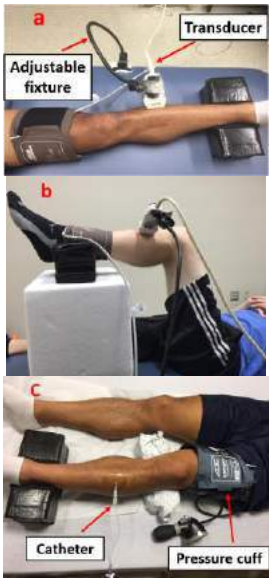

Figure 1: Setup for: (a) elastography while the TA muscle was pressurized, (b) elastography while leg was elevated and (c) IMP measurement.

the PL muscle (rho = 0.99, $p < 0.01$).

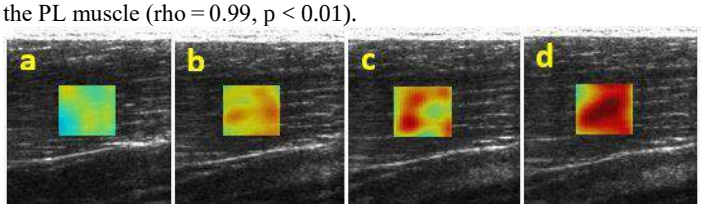

Figure 2: The shear modulus maps of the TA muscle at each cuff pressure level: (a) 0 (b) 40 mmHg (c) 80 mm Hg and (d) 120 mmHg).

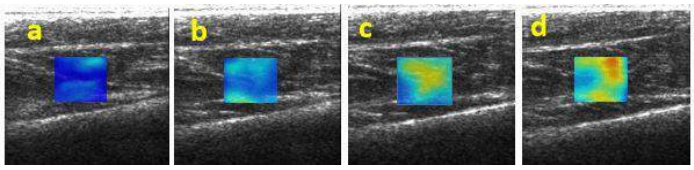

Figure 3: The shear modulus maps of the PL muscle at each cuff pressure level: (a) 0 (b) 40 mmHg (c) 80 mm Hg and (d) 120 mmHg).

DISCUSSION

The results from this study suggest that there is a linear correlation between shear modulus and IMP. This correlation is significant because IMP is an important parameter for evaluating function of muscle as well as some pathological conditions. IMP changes linearly during concentric and eccentric contraction. Therefore, IMP has been used to predict force during these type of muscle actions. The linear correlation shown here suggests that shear modulus can also be used to predict individual muscle force in the same way as IMP. So far, muscle shear modulus has been shown to correlate to force in isometric contraction only. However, the relationship to IMP suggests that shear modulus can potentially be used to measure individual muscle force during concentric and eccentric muscle contractions as well. Our results may also have several potential clinical applications. Shear modulus may also help clinicians diagnose or monitor the recovery process of compartment syndrome disease. Methods to measure IMP, such as needle manometry, suffer from significant variability depending on the depth of needle insertion, amount of fluid introduced, and soft tissue occlusion of the needle. The blood pressure cuff inflation around the thigh may also be used to simulate compartment syndrome with reversible neuromuscular dysfunction. Therefore, the results of this study may be beneficial for practitioners to consider the contribution of shear modulus changes on the diagnosis of compartment syndrome using ultrasound SWE.

The contact pressure between the transducer and the skin has been shown to affect the shear modulus of muscles. Kot et al. [5] evaluated the shear modulus of the rectus femoris muscle when different transducer pressures were applied to the muscle, reporting an increase in shear modulus from 13.33 kPa to 18.88 kPa when transducer's pressure increased from light to high. These results are in line with our observations. The pressure applied with the transducer may change the IMP and consequently the shear modulus measured.

Leg position is also an important factor affecting the shear modulus of lower leg muscles. Dubois et al. [6] quantified the shear modulus of the anterior and posterior lower limb muscles at rest and during passive stretching postures using a protocol that involved different body positions. They reported that shear modulus was significantly higher when muscle was stretched compared to rest posture. Results of our study showed that the elevated leg decreased shear modulus of the TA and PL muscles' due to the reduction in IMP. These observations can help giving a proper interpretation to changes in shear modulus in evaluation of protocols that use limb or body positions with changes in elevation.

Several studies evaluated effect of interstitial pressure on the shear modulus of soft tissues. Millonig et al. [7] studied the relationship between intravenous hydrostatic pressure and liver shear modulus in the isolated pig liver, reporting that the stepwise increase of intravenous pressure to 3.5 kPa linearly and reversibly increased liver shear modulus to the upper detection limit of 75 kPa. Nguyen et al. [8] evaluated the influence of the intraocular pressure on the elasticity of cornea in an ex vivo porcine model, reporting an increase in shear modulus of cornea with an increase in intraocular pressure. Gennisson et al. [9] measured elasticity of renal compartments at the baseline and urinary pressure levels from 5 to 40 mm Hg in in-vivo pig kidney, reporting that the increase in shear modulus of renal compartments is linearly correlated to the increased urinary pressure. In this study, we revealed a similar relationship between IMP and shear modulus of lower-leg muscles using SWE. The limitation of this study was that the majority of the subjects recruited were under age 30. Consequently, it is unknown if the observed relationship is affected by age. In conclusion, this preliminary study suggest that changes in shear modulus could serve as a surrogate non-invasive measurement of IMP levels.

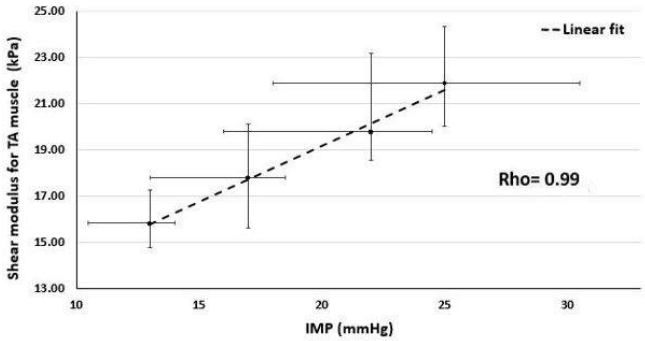

Figure 4: The shear modulus of TA increased as function of IMP (median, interquartile range) ($p < 0.01$).

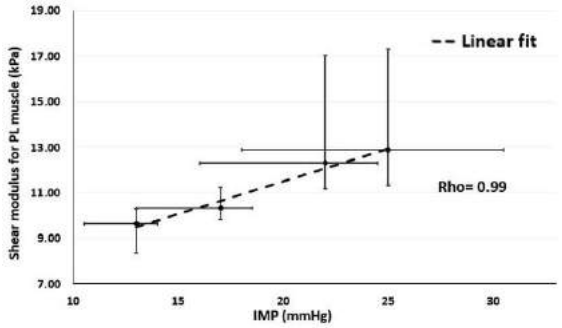

Figure 5: The shear modulus of PL increased as function of IMP (median, interquartile range) ($p < 0.01$).

ACKNOWLEDGEMENTS: NIH UL1 TR002014.

REFERENCES

[1] Baumann, J et al., *Clin Orthop Relat Res*, 145: 292-299, 1979.
[2] Parker, P et al., *Med Biol Eng Comput*, 22: 453-457, 1984.
[3] Cortes D et al., *Ultrasound Med Bio*, 41: 1518-1529, 2015.
[4] Shinohara M et al., *Muscle & nerve*, 42: 438-441, 2010.
[5] Kot B et al., *PloS one*, 7, e44348, 2012.
[6] Dubois G et al., *Ultrasound Med Bio*, 41: 2284-2291, 2015.
[7] Millonig G et al., *J Hepatol*, 52: 206-210, 2010.
[8] Nguyen T et al, *Invest Ophthalmol Vis Sci*, 55, 7545-7552, 2014.
[9] Gennisson J et al., *Ultrasound Med Bio*, 38: 1559-1567, 2012.

SB³C2019
Summer Biomechanics, Bioengineering and Biotransport Conference
June 25 -28, Seven Springs, PA, USA

DEVELOPMENT OF DISPLACEMENT-CONTROLLED MULTIAXIAL STRETCHING DEVICE FOR CHARACTERISING VISCOELASTIC PROPERTIES OF FEMALE PELVIC FLOOR TISSUE

Katie Harte (1), Gary Menary (1), Alex B. Lennon (1)

(1) School of Mechanical and Aerospace Engineering,
Queen's University Belfast,
United Kingdom

INTRODUCTION

Up to 20-30% of women over the age of 20 may suffer from pelvic floor disorders and up to 50% of women over the age of 50.[1] Furthermore, injuries as a result of childbirth can lead to varying types of incontinence, pelvic organ prolapse (POP), and avulsions[2 3]. A strong association has been found between parity (the number of times a woman has carried pregnancies to a viable gestational age) and developing pelvic organ prolapse (POP).[4] Given the strong evidence for injury during childbirth leading to later prolapse and recent developments in biomechanical understanding of the female pelvic floor, better understanding of the mechanical properties of the muscles are required to improve risk assessment for child birth induced injury. As pelvic floor muscle is an anisotropic material, mechanical characterisation requires multi-axial testing. Pelvic floor sample sizes are small (<20mm) and expected forces are low (<15N).

Many commercially available machines can be large and expensive, designed to apply relatively high loads to structural materials. The aim of this project is to develop a displacement-controlled multiaxial stretching device for characterising mechanical properties of female pelvic floor tissue.

METHODS

A low cost, desktop radial stretching device was developed, based on an open source design by Schausberger et al[5], with adaptations to make it suitable for soft tissue testing. Specific adaptations include modifying grips for smaller soft-tissue samples, digital image correlation (DIC), and an environmental chamber for biological tissue testing. Samples can be clamped onto 18 arms to create a radial stretch during testing (Figures 1 & 2).

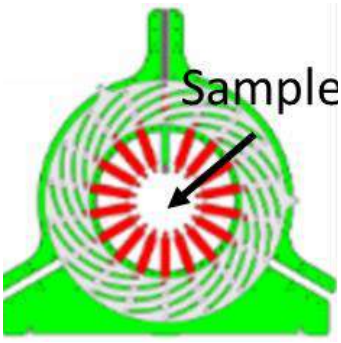

Figure 1 – Radial Stretch Tester

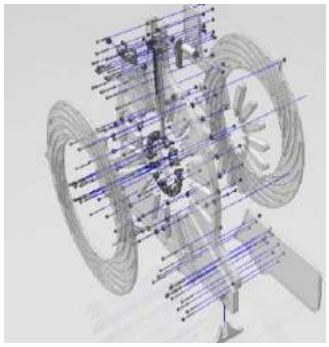

Figure 2 – Radial Stretch Tester Assembly

The radial stretch tester has been fitted with a 20N load cell (FSJ03829, Futek Inc., USA) to obtain load data and modified to incorporate smaller samples sizes and DIC to obtain strain data (Figure 3). Initial tests have been carried out using a sample of Versaflex ™ CL2000X (Polyone Corporation). A displacement rate of 12mm/min was used for all tests. Uniaxial tests were carried out on a Lloyds instruments (Company info?) uniaxial tester with a 50 N load cell and repeated in the radial stretch tester in both uniaxial and radial mode. Grip-to-grip displacement was used to calculate strain in the Lloyd test while DIC was carried out to record strain for the radial stretch tests and Labview (National Instruments Corp., UK) was used to analyse data from the load cell. Further tests have been carried out comparing clamping systerms using a sample of Chronoprene™ 40A (Dunn Industries, Manchester). Uniaxial tests repeated in the radial stretch tester using hooked clamps and Velcro clamps.

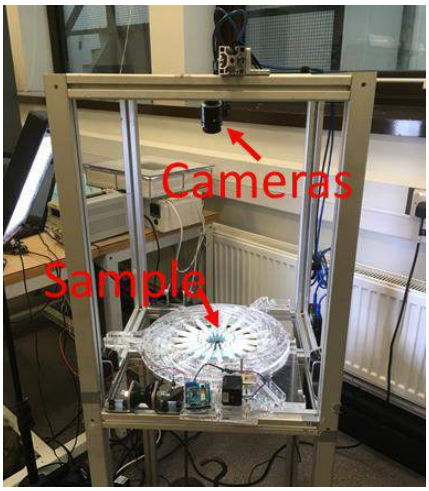

Figure 3 – Radial Stretch Tester with DIC

(Figure 4a,b). The radial stretch test with DIC was repeated in radial mode using the hook clamps (Figure 4c).

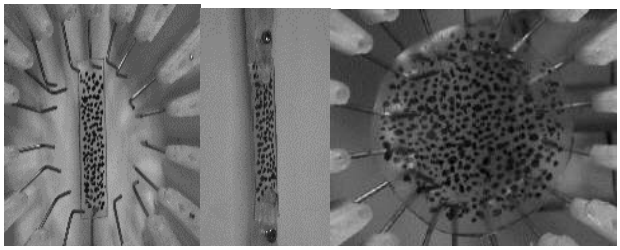

Figure 4 - uniaxial with hooks (a) uniaxial with velcro clamps(b),and (c) radial with hooks (all with speckle for DIC)

RESULTS

True stress results from the uniaxial tests in the rig were slightly higher than in the Lloyd test (Figure 5) due to friction in the rig which is being rectified. The true stress increased significantly for the radial sample compared with uniaxial testing as expected (Figure 5).

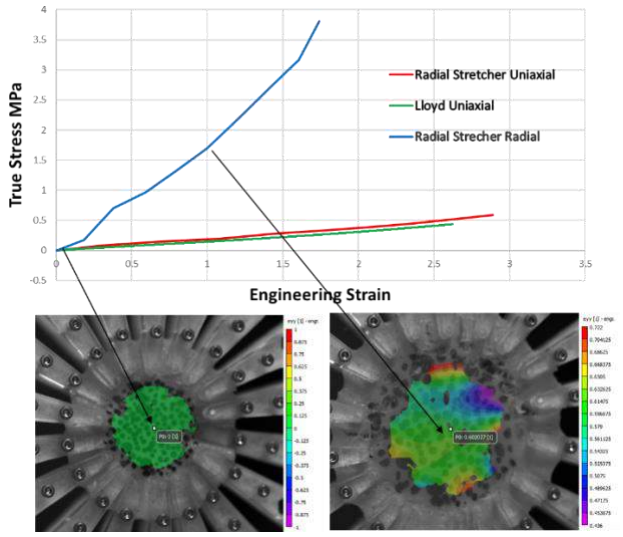

Figure 5 –True stress vs engineering strain data for three tests of Versaflex™ CL2000X

Similar results were found using the radial stretch tester in a uniaxial format for both the hooks and velcro clamps and the Lloyd test (Figure 6). However, the sample began to tear at the hooks before a strain of 0.4 in the uniaxial test and just after a strain of 0.3 in the radial test.

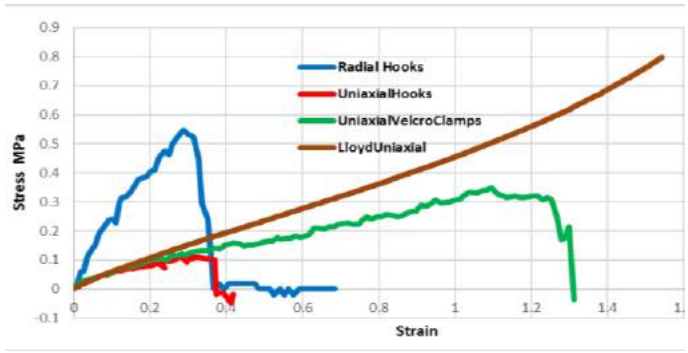

Figure 6 –True stress vs engineering strain data for three tests of Chronoprene™ 40A

DISCUSSION

Results verify basic functionality of the radial stretcher in both uniaxial and radial modes. Initial tests with soft tissue are now being carried out, incorporating adjustments in the form of a temperature controlled bath to incorporate an environmental chamber (Figure 7). Ovine pelvic floor tissue samples will be used as it is readily available and has many similar anatomical and ultrastructural anatomies to the human pelvic floor.[6]

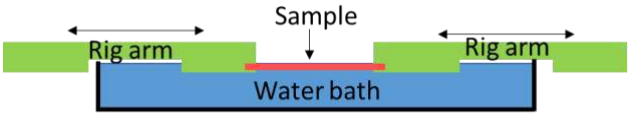

Figure 7 – Environmental chamber for sample

Due to tearing at the hooks, peak strains are below reported maximum strains of 70–100% from analogous multiaxial tests in the literature[7,8] and clamps are being redesigned to achieve higher stretch ratios before tearing. Additionally, alternatives to a load cell on each of the arms are being investigated to reduce costs of obtaining load data in multiple directions for anisotropic samples. Standard tension-to-failure and stress relaxation testing of pelvic floor tissue will be carried out following satisfactory performance in all verification tests.

ACKNOWLEDGEMENTS

This project is funded by the Department for the Economy Northern Ireland with additional financial support from the School of Mechanical Engineering, Queen's University Belfast.

REFERENCES

[1] Wilson, D. et al,. Obstet. Gynecol. 2001;98:398–406
[2] Boyles, S.H. et al, *AJOG*, *188*(1), 108–115.(2003)
[3] Subak, L.L. et al, Obstet. Gynecol, 98(4), 646–651.
[4] Mant, J et al., BJOG, 104(5), 579-585, (1997).
[5] Schausberger, S.E. et al, IEEE Access, 555-561 (2015).
[6] Urbankova, I et al., Gynecol Obstet Inves, 82(6), 582-591 (2017).
[7]. Lally, C et al, Ann Biomed Eng. 32(10), 1355-1364 (2004).
[8]. Jing, Dejun, PhD, Univeristy of Michigan (2010).

SB^{3}C2019
Summer Biomechanics, Bioengineering and Biotransport Conference
June 25 -28, Seven Springs, PA, USA

BODY POSITION EFFECTS ON THIGH SOFT TISSUE PROPERTIES

Justin Scott, Sheng Chen, Sara Roccabianca PhD, and Tamara Reid Bush PhD

Mechanical Engineering, Michigan State University, East Lansing, MI, USA

INTRODUCTION

Seating interface design has significant impacts on the everyday lives of people, particularly those in wheelchairs. This is due to the fact that well designed interfaces distribute pressures, reducing pressure concentrations. For populations who spend the majority of their time in a seated position, such as wheelchair users or the elderly, the ability of seating interface to distribute pressure well can reduce the likelihood of tissue damage due to prolonged sitting [1]. The ability of seating interfaces to distribute pressure is often evaluated by finite element models. These models rely on accurate tissue properties to obtain realistic outcomes. Yet there is limited data on human soft tissue available for use in these models.

Current finite element models of human buttocks and thigh regions use material properties determined from animal tests of soft tissue and limited data from human tissue [2,3]. Current data is limited in that the material properties obtained from human thigh have been determined from studies where the participants were in a supine or prone position, not the seated position that is being modeled [4]. Second, these data sets come from only two points of deflection. There is a dearth of information on the mechanical properties of the human thigh while in the seated position as well as a need for data at multiple points of deflection. Models that simulate people sitting need representative properties of the thigh soft tissue while seated, through the full range of deflection to accurately represent body responses. *Thus, the goal of this study was to determine if differences occurred in the thigh material properties with changes in body posture.* The seated, quadruped, and prone postures were evaluated.

METHODS

Ten males and ten females volunteered for our study with Institutional Review Board approvals. A custom indenting tool with an embedded load cell was used to obtain force and deflection measurements on three regions of the thigh. To obtain deflection measures, a linear potentiometer was attached to the indenter to track its location.

All participants wore snug fitting, stretchy athletic attire for all test positions. For the seated position, a section of the chair with a opening more than 3 times the size of the indenter head was removed to permit access of the indenter without inducing tissue tensions in the region (Figure 1). The indenting tool was held perpendicular to each test location. The thigh was indented using a constant load rate until a physiological barrier (ie. the femur) was felt, at which point the load was removed. This indentation process was followed for the proximal, middle, and distal thigh regions.

Figure 1. Indentation test set up in the seated (left), quadruped (middle), and prone (right) positions.

After a five minute period to permit tissue recovery, the participants moved to the quadruped position (Figure 1). In that position, the chest and legs were supported with the hips and knees flexed at 90º. The same three thigh regions were tested as in the seated position. After five minutes, the participants laid in the prone position with their hips and knees extended at 180º (Figure 1). The same

indentation process was followed in the prone position as for the other two.

Force and deflection data were converted into stress and stretch data which were then used to optimize the parameters of an Ogden based material model [5]. Stress data were obtained by dividing the indentation force by the cross sectional area of the indenting surface (25 cm^2). Deflection was converted into stretch using a relationship between the thigh circumference and tissue thickness between the femur and posterior surface of the thigh. The strain energy density of the Ogden model is described by equation 1.

$$W(\lambda) = \frac{\mu}{\alpha}(\lambda_1^\alpha + \lambda_2^\alpha + \lambda_3^\alpha - 3) \quad (1)$$

In this equation, λ_1, λ_2, and λ_3 are the stretches in the principal directions. μ is a stiffness parameter with units of Pascals, and α is a unit-less nonlinearity parameter. Two conditions placed on this model were that of transverse isotropy and incompressibility, meaning that stress in the loaded direction is described by equation 2.

$$\sigma = \mu(\lambda^\alpha - \lambda^{-\frac{\alpha}{2}}) \quad (2)$$

In this equation λ is the stretch in the loaded direction. Stress and stretch data from each of the three thigh regions was used to determine μ and α parameter values so that comparisons could be made.

RESULTS

Average μ and α parameter values for each region and body position were reported for each sex (Tables 1 and 2). In all regions, for both males and females, the μ parameter values for the prone position were significantly smaller than the values in the seated and quadruped positions. The α values in the prone position, for both males and females, were significantly higher than those in the seated and quadruped positions. Higher stresses were consistently needed in the prone position to produce the same amount of stretch as the seated and quadruped positions (Figure 2).

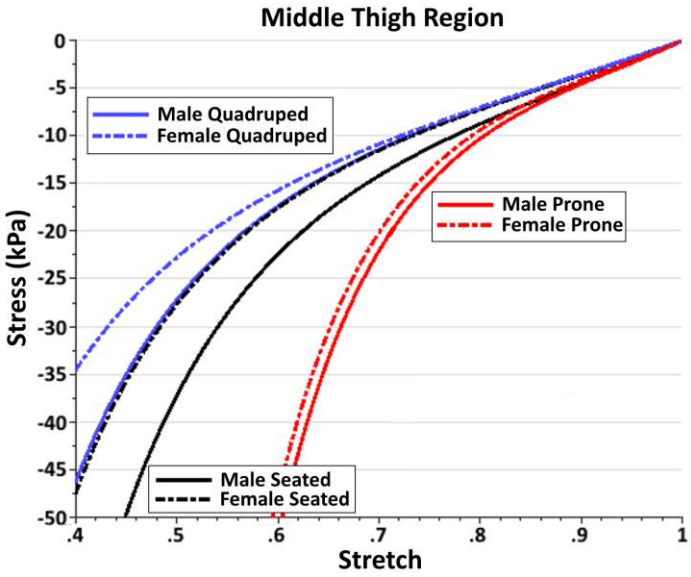

Figure 2. Predicted stress and stretch values for the average middle thigh region in males and females.

Table 1. Average μ values in Pascals for the proximal, middle, and distal thigh in each position for males (left) and females (right).

	Male			Female		
	Prox	Mid	Dist	Prox	Mid	Dist
Seated	4720	5676	5785	5469	5292	5383
Quadruped	4908	5345	4777	5239	6651	4388
Prone	3828	3054	2732	3138	2761	2385

Table 2. Average α values for the proximal, middle, and distal thigh regions in each position for males (left) and females (right).

	Male			Female		
	Prox	Mid	Dist	Prox	Mid	Dist
Seated	7.39	5.44	4.10	5.78	4.79	3.66
Quadruped	5.72	4.72	3.84	5.53	3.61	3.26
Prone	10.2	11.11	13.38	9.71	11.17	13.26

DISCUSSION

The motivation for this work was to determine if body posture had any effect of the material properties of thigh tissue. To this end, force and deflection data were collected from the proximal, middle, and distal regions of the thigh while in the seated, quadruped, and prone postures. Parameters of an Ogden material model were then optimized to fit the soft tissue in the each region of the thigh while participants were in these three postures. The results of the model fitting indicated that all three thigh regions were stiffer in the prone position as compared to the seated and quadruped positions. *Thus, the body position does affect the material stiffness, indicating that the soft tissue in the thighs of finite element models used to simulate sitting should be represented by material properties obtained from thighs in the seated position.* The thighs and buttocks experience large external pressures while seated, making them sites of tissue damage. Accurately representing the tissues will change the internal stresses predicted in models to better predict the likelihood of tissue damage.

Material properties were also obtained for the thigh while in the quadruped position because the lower body joint articulations in that position were similar to those of the seated position. As such, the quadruped position produced parameters that were similar to the seated position. The adaptation of a quadruped position for the determination of material properties of the thigh will allow the collection of data to expand to those who use wheelchairs. While our results indicating body position matters when determining soft tissue properties can inform cushion design for able bodied individuals, another concern is the health of wheelchair users. Tissue damage is a costly issue, and cushions designed to prevent damage are a common solution. Expanding this work to obtain material properties that represent wheelchair users can inform that design process as well.

ACKNOWLEDGEMENTS

This work was supported by NSF CBET, grant number 1603646.

REFERENCES

[1]Shoham, N et al. *Advances in Skin & Wound Care*, 28: 303-316, 2015.
[2] Makhsous, M et al. *IEEE*, 15: 517-525, 2007.
[3]Al-Dirini, R et al. *Annals of Biomedical Eng.*, 44: 2805-2816, 2016.
[4] Then, C et al. *Technology & Health Care*, 15: 385-398, 2007.
[5] Bosboom, E et al. *Journal of Biomechanics*, 34:1365-1368, 2001.

SB^{3}C2019
Summer Biomechanics, Bioengineering and Biotransport Conference
June 25 -28, Seven Springs, PA, USA

PYTHON-INSPIRED GRASPING TEETH FOR TENDON-TO-BONE REPAIR

Iden Kurtaliaj (1), Ethan Hoppe (2), Dong Hwan Yoon (2), Lester Smith (3), Victor Birman (4), Guy Genin (2), Stavros Thomopoulos (1)

(1) Columbia University
New York, NY, USA

(2) Washington University
St. Louis, MO, USA

(3) Indiana University
Indianapolis, IN, USA

(4) Missouri Science & Technology
St. Louis, MO, USA

INTRODUCTION

Rotator cuff tears are common, affecting more than 50% of patients over the age of 65 and resulting in pain and loss of shoulder function [1]. Rotator cuff surgical repair is one of the most common shoulder procedures performed clinically. Unfortunately, healing after rotator cuff repair is a well-known clinical challenge, with reported failure rates as high as 94% [2]. In the current standard double-row suture bridge repair, the suture punctures through bone and tendon at only two anchor points, thus leading to high concentrated forces being transferred from tendon to bone, in shear at these two points (Fig. 1B) [3]. In the current study, we propose a new approach for tendon-to-bone repair inspired by the remarkable grasping ability of python teeth on their prey. Unlike shark teeth, which are triangular and function to cut their prey, python teeth have a curvature that grasps prey, prevents escape, and enables ingestion of entire, intact animals. To test the hypothesis that tooth shape drives the balance between cutting and grasping, finite element models and experiments were performed to quantify the interaction between tendon and seven different tooth designs, ranging from shark-like to python-like (Fig. 1A).

METHODS

Finite Element Model (FEM): 2D and 3D models of a frictionless tooth in a homogeneous tendon were studied using Abaqus (Dassault Systems). Images and microCT scans were used to determine the radii of python moluris teeth. 7 different tooth geometries were examined in 2D, as defined by the dimensionless ratio w'/w, which ranged from 0.5 to 3.5 (Fig. 1A). A hard contact interaction was applied in the normal direction between the tooth and the tissue surfaces. Load was applied as a displacement of the tendon boundaries; periodic boundary conditions were applied to model an infinite row of teeth. The mesh was refined at the (rounded) tip of the tooth until convergence was reached. The maximum principal stress

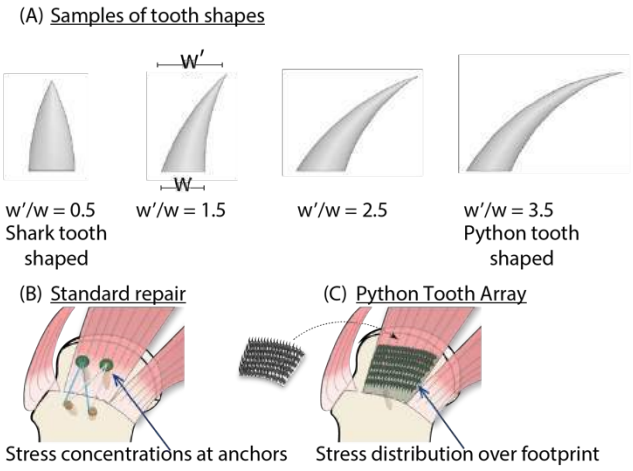

Figure 1. (A) Representative tooth geometries, defined by the ratio w'/w. (B) Schematics of standard rotator cuff repair. (C) Schematics of a python-inspired array of teeth to be used for tendon-to-bone repair.

concentration, the contact area beneath the tooth (Fig. 2A), and the average tissue/gum contact pressure were estimated.

Experimental Model: A modified single lap shear test was developed to test the grasping capacity of a tooth in bovine deep digital flexor tendon (3.9" x 2.4" x 0.125", N = 14). Each fixture contained one 3D printed tooth (EDEN 260VS, Stratasys LTD) made with VeroWhitePlusTM, a rigid and durable material with a modulus of elasticity of 2500 MPa. Each 3D printed tooth shape (N = 6) was inserted into the precut tendon block so that the entire tooth was fully within the tendon. A uniaxial tension test was then performed at 0.05 mm/sec for up to 10 mm of displacement (TA instruments, ElectroForce). From the force elongation curves, peak force for 5 mm elongation, stiffness, and energy to yield were determined. Tooth engagement with the tendon was determined by visual inspection and verified through video captured during testing. Groups were compared using ANOVA with a threshold for statistical significance defined at $p < 0.05$.

RESULTS

FEM results showed that the contact area between the tooth and the tendon increased with increasing w'/w, consistent with the hypothesis that python-shaped teeth are designed for grasping (Fig. 2B). The maximum principal stress concentration remained constant for tooth shapes of w'/w = 1, 1.5, 2, and 2.5 and decreased for w'/w = 3 and 3.5. There was a significant increase in maximum force with increasing w'/w (Fig. 3B, * $p < 0.05$, when compared to w'/w = 0.5). There was a dramatic decrease in the number of teeth that completely disengaged from the tendon with increasing w'/w (Fig. 3C). There was no significant difference between groups for stiffness and energy to yield.

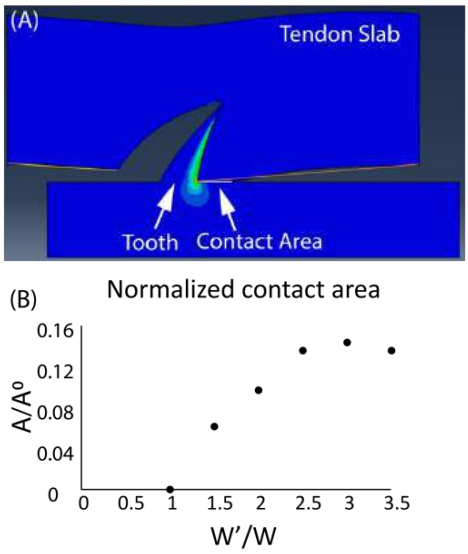

Figure 2. (A) Representative FEM result of the interaction between a python tooth and tendon showing stress (color map), contact area (white line) and average stress in the downward direction (orange lines). (B) Normalized contact area graph for tooth geometries of w'/w = 1-3.5.

DISCUSSION

FEM and experimental results revealed a strong non-linear relationship between tooth curvature and tendon grasping, implying an optimal tooth shape for the design of a tooth array device for tendon-to-bone repair. An optimal tooth shape maximizes contact area without increasing the maximum principal stress concentration. From the modelling results, a shape with w'/w = 2.5 was optimal, as contact area did not increase with further increases in curvature. This shape was supported by experimental results, where the maximum force through 5 mm of displacement increased through w'/w = 2.5. In addition, as evidenced by the force-displacement curves and the visual determination of tooth engagement, the tooth completely disengaged from the tendon at low values of w'/w. Ultimately, the device for enhanced tendon-to-bone repair will include an array of teeth, as shown in Fig. 1C. The particular arrangement of these teeth will require optimization as well to effectively solve the tissue-level shear lag problem inherent to tendon-to-bone repair. To successfully translate this theoretical and experimental work into a clinically relevant device for tendon to bone repair, future studies will test an array of teeth in a cadaver rotator cuff repair model.

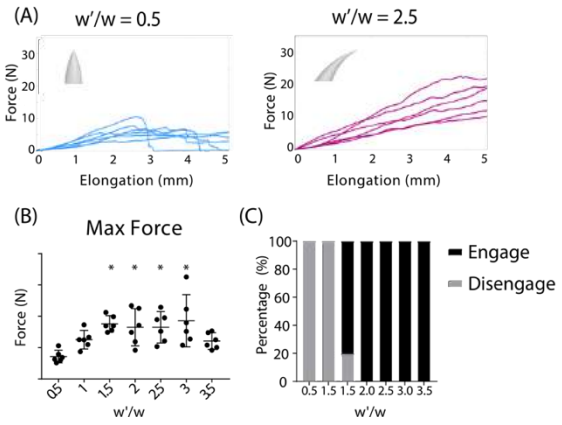

Figure 3. (A) Representative force -displacement curves for two tooth geometries (w'/w = 0.5 and 2.5). (B) Peak force for up to 5 mm of tendon elongation (* $p < 0.05$, when compared to w'/w = 0.5). (C) Percentage of teeth engaging vs. disengaging from tendon.

SIGNIFICANCE

The bioinspired tendon fixation system designed, analyzed, and tested here may have a significant effect on healing and functional recovery following rotator cuff repair, and holds potential the high post-surgery rupture rates.

ACKNOWLEDGMENTS

This work was supported by Nationals Institute of Health (EB016422).

REFERENCES

[1] Sher, et al., *J Bone Joint Surg Am* 77(1):10-5, 1995.
[2] Galatz, et al., *J Bone Joint Surg Am* 86-A:219-24, 2004.
[3] Linderman, et al., *Acta Biomater* 70:165-176, 2018.

SB³C2019
Summer Biomechanics, Bioengineering and Biotransport Conference
June 25 -28, Seven Springs, PA, USA

OPTIMIZING NON-LINEAR MECHANICAL BEHAVIOR OF SOFT TISSUES IN FINITE ELEMENT MODEL OF HUMAN THIGH

Eli Broemer (1), Sheng Chen (1), Justin Scott (1), Tamara R. Bush (1), Sara Roccabianca (1)

(1) Mechanical Engineering
Michigan State University
East Lansing, MI, USA

INTRODUCTION

Pressure ulcers (PUs) are a soft tissue injury caused by sustained pressure and/or shear near a bony prominence, more commonly in the thigh and buttocks area [1]. The injury most commonly develops in those with reduced mobility such as hospitalized patients and wheelchair users. Formation of PUs can lead to pain, infection, and even death. A recent 10-year study found that PUs are prevalent in 9% to 13% of patients in health care facilities in the United States [2].

The clinical setting is also lacking effective prediction methods for PUs [1]. Specifically, an interpretive scoring evaluation is the widely recommended tool for assessing PU risk. And there is not strong evidence showing that scoring tools are more effective at reducing the risk of PUs when compared to a medical practitioner's judgement alone.

Finite element methods estimating pressure distributions in soft tissues surrounding bony prominences may be used as a novel PU prevention tool for patients in the future. Such models have been previously developed in literature ranging from 2D linear models with 34 nodes [3] to detailed 3D non-linear models with over 250,000 nodes [4]. These commonly focus on the thigh and buttock region, so that the material properties of the bulk soft tissue in the area may be estimated.

A significant limitation to most of these thigh-buttock studies is lack of validation and error estimation, or the use of only two data points to validate highly non-linear material models (i.e. an unloaded and a body weight-bearing configuration) [4, 5].

This preliminary study aims to find the best fitting material parameters using a finite element model of a thigh whose geometry is generated from subject-specific MRI scans. The innovation is that the material parameters are estimated by comparing the model prediction with *in vivo* indentation tests at multiple load configurations. The goal of the model is to study the material behavior of soft tissues in seated individuals. Further research may investigate the material behavior as it relates to the prevention of PUs in wheelchair users.

METHODS

Experimental Setup. A single subject (Male, 185 lbs., 73 in.) participated for the purposes of this pilot study.

Force-deflection measurements were collected by indentation tests performed on the subject's thigh. Since it is difficult to collect indentation data from the posterior thigh of a seated individual, a quadruped posture was adopted for this procedure. The quadruped position has the same hip and knee flexion as the sitting position with the advantage of access to the thigh for indentation tests.

To setup the quadruped posture, the subject kneeled on both legs behind a small panel placed to constrain the forward movement of the thigh. The panel height was short of the subject's anterior superior iliac spine allowing them to lean forward, and a table in front of the panel supported their chest and head. The table was adjusted such that the subject's knee and hip angles were ~ 90° to mimic the seated position.

Indentation tests gave force-deflection measurements of the thigh via a six-axis load cell and a linear potentiometer respectively. The deformation was applied manually at a constant rate, and the system was calibrated to have zero force and deflection when the indenter was flush with the undeformed thigh [6]. Three locations on the posterior thigh were tested (i.e., proximal, middle, and distal), and between 60 N and 100 N of force was applied before the indenter was removed.

Geometry Generation. MRI scans of the subject in a supine position provided cross-sectional data for the thigh geometry. The images were segmented with Photoshop CS6 (Adobe – 2012) in order to obtain cross-sections of the bone, muscle, and fat. **Figure 1** shows 3D geometry for the three tissues, which was generated by interpolating the cross-sections in NX 12.0 (Siemens – 2017).

Poster Presentation #P253

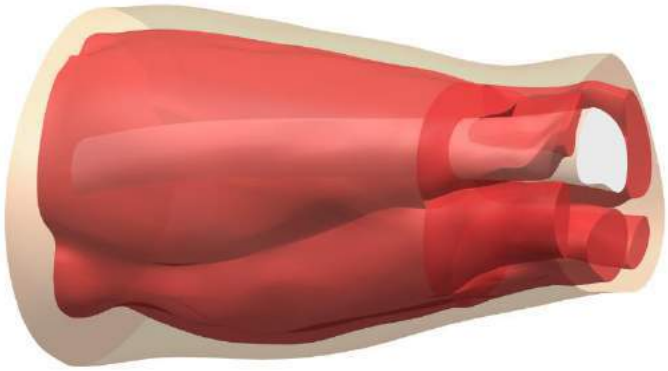

Figure 1: Geometry of subject's left thigh. Leftmost plane is just after buttocks and rightmost plane is just before the kneecap.

Finite Element Model. The model was meshed in HyperMesh (Altair – 2017) with second order tetrahedral elements. The mesh had 58,848 elements and 85,272 nodes. The model was setup and solved with the FEBio suite [7].

A previous study by our research group showed that the first order Ogden material model can accurately represent the non-linear mechanical behavior of these soft tissues *in vivo*. **Equation 1** shows the first order strain energy function for an Ogden material, where λi are the principle stretches, μ is a parameter with units of Pascals, and α is a unit-less parameter. Initial material parameters for the muscle and fat were taken from literature [4]. Soft tissues were assumed nearly incompressible (i.e., ν = 0.485) [5]. The femur was assumed to be a rigid body.

$$W(\lambda_1, \lambda_2, \lambda_3) = {}^{\mu}/_{\alpha}\,(\lambda_1^{\alpha} + \lambda_2^{\alpha} + \lambda_3^{\alpha} - 3) \quad (1)$$

Four boundary conditions constrained the model solution: 1) the femur was fixed in all directions and rotations; 2) a no-slip constraint on all material contact surfaces; 3) the left and right planes in **Figure 1** were fixed in their normal axis; 4) nodes with forces applied, at the three testing locations, had their movement constrained to the anterior - posterior axis (i.e. the direction of the force). Three load conditions were applied to model the mechanical test performed *in vivo*.

Optimization. The goal of the optimization protocol was to minimize the difference between the model force-deflection curves and the experimental data for each of the three test locations. A simplex search function (i.e., fminsearch) in MATLAB (MathWorks – 2018) minimized the objective function by adjusting material parameters μ and α and then re-solving the model in FEBio at each iteration.

Equation 2 shows the objective function where NRMSDprx, NRMSDmid, and NRMSDdis are the normalized root mean square deviations estimated for each of the three test locations.

$$e = NRMSD_{prx} + NRMSD_{mid} + NRMSD_{dis} \quad (2)$$

RESULTS

Optimized material parameters were estimated by fitting the model to the *in vivo* experimental data (**Table 1**). The values of the material parameters are in reasonable agreement with recent studies investigating the same tissue behavior [4]. The first order Ogden model fit the experimental data well. Error, measured as the normalized root mean square deviations between the model and *in vivo* data, was 5.47%, 1.48%, and 9.96% for proximal, middle, and distal locations respectively (**Figure 2**).

DISCUSSION

This pilot study investigates the mechanical properties of fat and muscle tissues in the human thigh. An anatomically detailed FE model was used to determine optimized material parameters. This model represents the first attempt to inform a finite element thigh model by precise tissue geometry and non-linear *in vivo* experimental data.

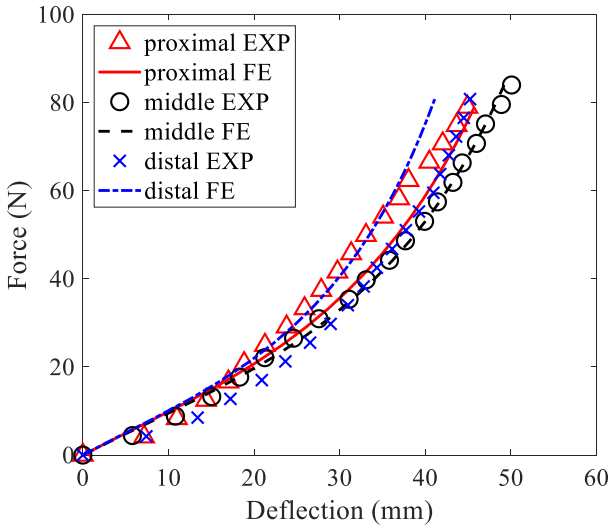

Figure 2: Simulated material behavior (continuous lines) fitted to non-linear *in vivo* indenter data (markers) for proximal, middle, and distal locations on the thigh.

Bulk material properties found in this study are limited to the thigh in a quadruped position. Model error was smallest in the middle thigh. Larger error at proximal and distal thigh locations may be due to the close proximity to fixed boundaries. Material contact surfaces assumed to have no slip could also affect the accuracy of this model, however there is sparse literature on this material interaction.

The optimization and model approach in this pilot study is useful to others interested in non-linear soft tissue mechanical behavior modeling.

Table 1: Initial and optimized material parameters for this model

Material Parameter		μ (kPa)	α
Muscle	Initial	1.91	4.6
	Optimized	1.43	6.16
Fat	Initial	1.17	16.2
	Optimized	1.01	14.54

ACKNOWLEDGEMENTS

NSF CBET 1603646.

REFERENCES

[1] Qaseem, A et al., *Ann Intern Med*, 162(5):359-69, 2015.
[2] VanGilder, C et al., *J Wound Ostonomy Continence Nurs*, 44(1):20-28, 2017.
[3] Chow, WW et al., *J Biomech Eng*, 100(2):79-87, 1978.
[4] Al-Dirini, RM et al., *Ann Biomed Eng*, 44(9):2805-16, 2016.
[5] Makhsous, M et al., *IEEE Trans Neural Syst Rehabil Eng*, 15(4):517-25, 2007.
[6] Sadler, Z et al., *Int J Non-Linear Mech*, 107:77-85.
[7] Maas, SA et al., *J of Biomech Eng*, 134(1):011005, 2012.

SB³C2019
Summer Biomechanics, Bioengineering and Biotransport Conference
June 25 -28, Seven Springs, PA, USA

DESIGN OF A NOVEL BIAXIAL MECHANICAL TESTING SYSTEM AND PROTOCOLS FOR ANALYSIS OF BIOLOGIC TISSUES AND TISSUE-ENGINEERED CONSTRUCTS

Mingliang Jiang (1), Michael R. Moreno (1,2)

(1) Mechanical Engineering
Texas A&M University
College Station, TX, USA

(2) Biomedical Engineering
Texas A&M University
College Station, TX, USA

INTRODUCTION

Recent advances in tissue engineering include the ability to "tune" the mechanical properties of engineered tissues. In the current paradigm, it is common to assess how well an engineered tissue mimics the mechanical behavior of its native counterpart by performing uniaxial mechanical tests designed to produce stiffness and/or strength measures. This type of material testing is founded in linear elasticity theory, however biologic tissues are generally non-linear viscoelastic inhomogeneous anisotropic materials that are subjected to large deformations and complex loading conditions, i.e. they violate every premise of linear elasticity theory. Nevertheless, there is some utility in using concepts from linear elasticity when attempting to engineer a tissue. The stiffness and strength parameters represent physically meaningful design targets. The challenge is to develop a theoretical framework that captures a more comprehensive set of the mechanical characteristics observed in biologic tissues and incorporates physically meaningful parameters in so doing. Conventional non-linear elasticity theories produce indeterminant equations that employ constants that are purely mathematical. Such models have utility for analysis applications (e.g. computational modeling), but offer little insight for synthesis applications, i.e. they lack physically meaningful parameters that might serve as design targets in tissue engineering applications. This work is focused on the development of experimental tools, methods, and protocols for the mechanical characterization of biologic tissues based on a novel theoretical framework that has been used to produce a 2D constitutive, or membrane model, that incorporates physically meaningful parameters [1].

The development of the new theoretical framework has required the development of a novel biaxial testing system and protocols. The membrane model describes deformation based on three stress-strain conjugate pairs. The results in three unique physically meaningful parameters: dilation, squeeze, and shear. Thus, a biaxial system must facilitate testing of biologic tissues in a manner that allows determination of these three parameters.

When conducting mechanical tests on biologic tissues other practical concerns arise. First, an appropriate method for fixing the material in the testing system must be developed. Clamping has been widely employed in mechanical testing of soft tissues from animal/human skin, connective tissues to ligaments and tendons [2,3]. It ensures a continuous and uniform lateral load distribution at the junction of the clamp and the sample by constraining all the clamped edges of the sample; however, soft tissues pose a concern. The central difficulty arises from the low friction between the surface of the clamping device and the soft biological tissue specimen, leading to slippage.

In addition to the challenges related to clamping or fixing a material in the mechanical testing system, strain measurement is also a practical challenge that must be addressed. A number of strain measurement techniques have been developed for soft tissues [4,5]. Most of the research has been focused on only one side of the tissue (usually the side with less connective tissues and cleaner). But what happened to the other side? Considering the complexity of biological tissues, it might be necessary to take into consideration deformation of both sides.

METHODS

Biaxial System Design: It consists of four motorized linear actuators, each driven by a servo motor. All linear actuators and the

bioreactor are rigidly affixed to a breadboard table to alleviate vibration. A camera is mounted above the specimen to record the markers' movement on the specimen. The system incorporates a custom four-axis controller that will employ a centroid control algorithm to enable load and displacement control on each axis. The versatile system can be configured to conduct conventional uniaxial, equi-biaxial, general biaxial, and shear tests.

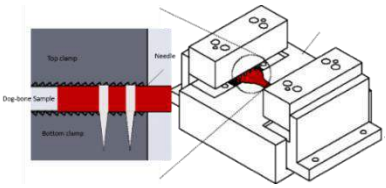

Figure 1: Novel clamping design.

Novel Clamping Design: After reviewing the successes and failures of alternatives, we present a novel clamp design. This design combines serrated clamps with needles. A schematic drawing of the clamps is shown in Figure 1. It was validated by 45 uniaxial tensile tests performed on rat abdominal wall muscles at 1% per second or 10% per second stretch rate. Dog-bone specimens were obtained from fresh and frozen samples. Load and displacement data were acquired at the grips. The clamping area was marked by India ink to check the slippage.

Strain Measurement from Both Sides: Rectangular specimens were cut out from rat abdominal skin specimens. A total of 20 uniaxial tests with 30% stretch were conducted. 14 tests showed no slippage. A custom-written program was used to calculate the strain. Strain at the inner side (the side connected to inner connective tissues) and outer side (the side open to the air) of the specimens were measured and compared.

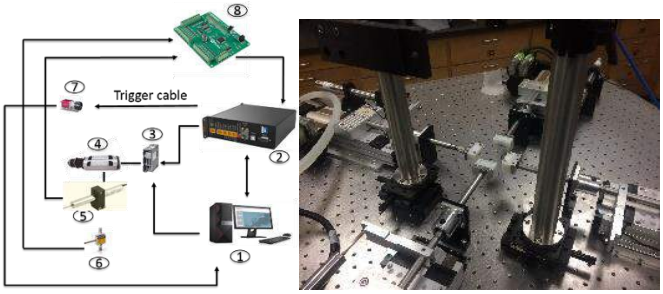

Figure 2: Biaxial system setup.

RESULTS

Biaxial System: An experimental apparatus was designed with the intention of performing both biaxial and simple shear tests. The testing platform is shown in Figure 2. A number of mechanical considerations were taken into account in the design of this setup. Proof-Of-Principle tests have been conducted to evaluate this system.

Novel Clamping Design: The 3D printed clamps with needles attached demonstrate their overall reliability in fixing rat abdominal wall tissues in this study. Additionally, it is quite easy to operate and could be used in a wide array of testing environments (for example, a 37ºdegree C saline bath), compared with freezing clamps. The effects of loading rate, anisotropy, and freezing on mechanical properties of rat abdominal wall muscles are also studied. The test result of specimens under 10% per second stretch rate is shown in Figure 3.

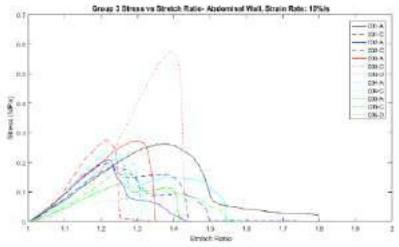

Figure 3: Clamping validation test (specimen tested under 10%/s strain rate)

Strain Measurement from Both Sides: This work shows that by measuring and comparing the strain of the inner surface and outer surface of rat skin specimens, we noticed that even when skin specimens are very thin, the strains are not always the same under the same loading condition. Thus it might be necessary to take into consideration the deformation of the inner side of soft tissues when trying to characterize their mechanical properties. One of the test result is shown in Figures 4~6.

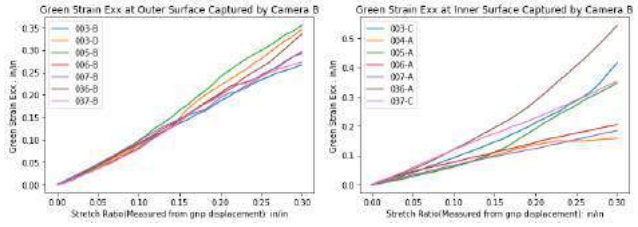

Figure 4: Green strain (Exx) measurement for outer surface(left) and inner surface(right)

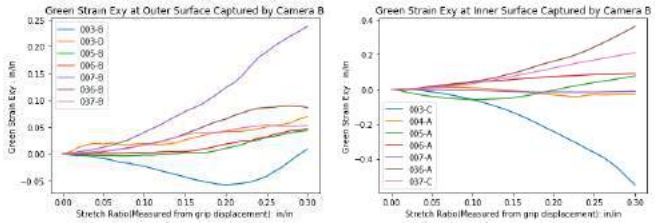

Figure 5: Green strain (Exy) measurement for outer surface (left) and inner surface (right)

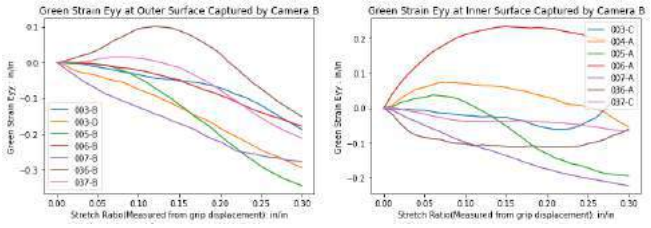

Figure 6: Green strain (Eyy) measurement for outer surface (left) and inner surface (right)

DISCUSSION

The results from future work with this system could lead to a better understanding of the mechanical properties of soft tissues under complex loading environments. It may also provide tissue engineers with additional practical design information in the form of physically meaningful parameters that could enable the engineering of a more comprehensive set of the mechanical properties of the native tissue counterpart. We suspect that the needles employed in the clamping system help fix the center core to prevent slippage. However, this potential effect was not quantified in the current study. The specimens were cut along the cranial-caudal direction directly. In the future study, the fiber orientation of the sample will be determined prior to testing. This might help understand potential shear behavior in tests.

REFERENCES

[1] Freed, AD et al., *J Mech Mater Struct*, 12(2): 219-247, 2016.
[2] Shi, D et al., *Med Eng Phys*, 34(4):516-520, 2012.
[3] Riemersa, DJ et al., *J Biomech*, 15(8):619-620, 1982.
[4] Yin, FCP et al., *J Biomech*, 19(1):27-37, 1986.
[5] Zhang, D et al., *J Biomed Opt*, 9(4):691-699. 2004.

DISSIMILAR LINEAR FRICTION WELDING (LFW) TECHNOLOGY FOR MANUFACTURING OF FUNCTIONAL MATERIALS: BI-METALLIC TI6AL4V-COCRMO JOINT IMPLANTS

David L. Irwin (1), Christina Seydlorsky (1), Agraha Gautam (1), Aspen Glaspell (2), Kyosung Choo (1, 2), Jae Joong Ryu (1)

(1) Mechanical, Industrial & Manufacturing Engineering
Youngstown State University
Youngstown, OH 44555 USA

(2) Materials Science and Engineering
Youngstown State University
Youngstown, OH 44555 USA

INTRODUCTION

Functional materials include metallic, intermetallic, ceramic or polymers in nature. Fabrication of an integrated material system from such a diverse subset of materials has created challenges to produce an engineered material that is able to act upon the exposed environments [1]. For example, in order to produce a prosthetic implant system, mechanical and electrochemical properties must be considered. The greater fatigue strength of the bearing element and higher corrosion resistance at the modular interfaces in total joint replacements (TJR) are the most important characteristics of the constituents. Therefore, it is necessary to design a functional implant material that possess a good resistivity against fatigue, wear, and corrosion [2].

Metallic implant materials have fascinated with a desirable combination of superior strength and ductility as summarized in Table 1. For example, the greater stiffness and strengths of CoCrMo would be suitable for the load bearing component of modular total joint replacements. The stable oxide layer of Ti6Al4V successfully protects implants from corrosion damage. However, the higher elastic modulus of metals compared to the bone tissue leads to bone loss and ultimately fails integrity at the implant-tissue interface, known as stress-shielding [3, 4]. Therefore, the ideal structural response of implants would be an optimum combination of superior mechanical strength and chemical inertness with lower stiffness. Consequently, the current study aims to utilize linear friction welding (LFW) technology to develop a bi-metallic Ti6Al4V-CoCrMo functional implant material to achieve the desirable properties.

Traditional fusion welding utilizes high energy input to produce weld pool mixing and solidify. Generally, the fusion welded metals result in defects including porosity, hot cracking and segregation. However, LFW is a solid-state joining process that utilizes friction heat to soften the workpieces and bonding by applied pressure [5]. It is a significant advantage of LFW in nature as the solid-state and forging plasticized materials remove surface oxides and other impurities.

Therefore, in this report, bi-metallic Ti6Al4V-CoCrMo joints were manufactured using linear friction welding process and analyzed the weldability and bonding strength.

Table 1. Mechanical Properties of Metallic Implant Materials

Materials	Yield Strength (MPa)	Ultimate Strength (MPa)	Elastic Modulus (GPa)
Ti6Al4V (F136)	924	1000	116
CoCrMo (F1537)	958	1338	210
TiMo-β (F2066)	483	690	78
Ti45Nb	480	546	62
Human cortical bone	-	-	25.8 [4]

METHODS

Ti6Al4V and CoCrMo cylinders were manufactured to a standard size of tensile specimens and cut into two identical pieces. The surfaces to be welded were polished and cleaned before performing welding.

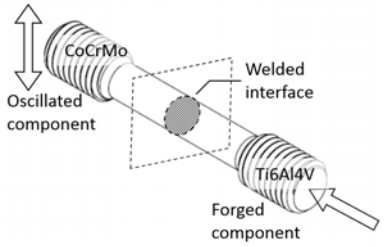

Figure 1. LFW of dissimilar components

CoCrMo cylinder was oscillated and Ti6Al4V cylinder was pushed to obtain axial shortening. A representative diagram of process parameters are summarized in Figure 2. Pressures were administered at 62 MPa to apply initial friction force and at 110 MPa to join the plasticized workpieces. An additional burn-off was applied to investigate the effect of the burn-off on bonding strength. A series of quasi-static tensile tests were performed on the dissimilar LFW CoCrMo-Ti6Al4V specimens to measure the bonding strength.

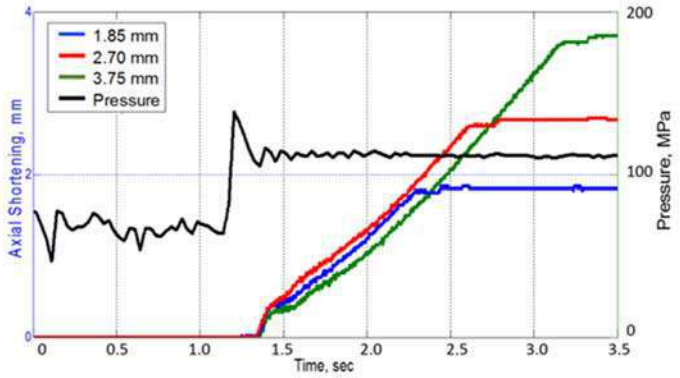

Figure 2. Measured burn-off (1.85 mm, 2.70 mm, and 3.75 mm) and forging pressure (110 MPa).

A mathematical transient heat transfer model was developed for the bi-metallic LFW process in order to obtain the temperature variation in the workpieces over time. Figure. 4 (a) shows a schematic of heat transfer paths including conduction, convection and radiation. Straight arrows indicate conduction heat transfer paths and curved arrows indicate convection and radiation heat transfer paths.

The energy balance method was used to determine the temperature variation of the bi-metallic joint over time, which was based on subdividing the medium into a sufficient number of volumetric elements and then applying energy balance for each [6]. Conduction, convection, and radiation heat transfer were considered for each metal. The transient heat transfer equation is given by:

$$\rho V c_p \frac{dT}{dt} = hA_s\left(T_s - T_\infty\right) + \varepsilon\sigma A_s\left(T_s^4 - T_{surr}^4\right) + kA_c\frac{\left(T_s - T_{contact}\right)}{L} \qquad (1)$$

where σ is Stefan-Boltzmann constant, c_p is the heat capacity of the each material, ρ is metal density, and V is metal volume, ε is the emissivity of the metal surface, k is thermal conductivity of the metal, T_∞ is the room temperature, and T_{surr} is the temperature of the surroundings to which the element radiates.

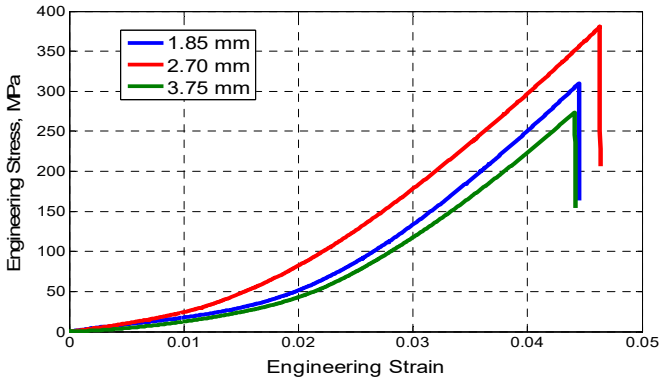

Figure 3. Tensile test result with variable burn-off

RESULTS

The visual inspection illustrated the produced flash was from plasticized Ti6Al4V. According to the phase transformation diagram Ti6Al4V, β-transus temperature is below 1000°C and therefore softened Ti6Al4V produced the flash [7]. However, CoCrMo phase diagram illustrated phase transformation barely takes place at the welding temperature. It implies that the majority of plasticization would occur on Ti6Al4V. The forged Ti6Al4V surrounds the joint area and then solidified. This prevents two materials from mixing to form strong bond. Tensile test results presented in Figure 3 describes a large scale plastic strain and catastrophic failure of the weldment.

The results of the thermal modeling for the joint are shown in Figure. 5, which illustrate that the model predicted the thermal profile of the friction process when compared to thermography with ± 10 % error.

DISCUSSION

Mechanical bonding of the two biomedical implant materials were not successfully formed. The high temperature properties are critical to obtain mixing of two alloys. It is suggested to use different process parameters to induce a slow temperature gradient and lower shortening pressure. Having an interlayer may improve alloying and mixture of the elements to create strong bonding.

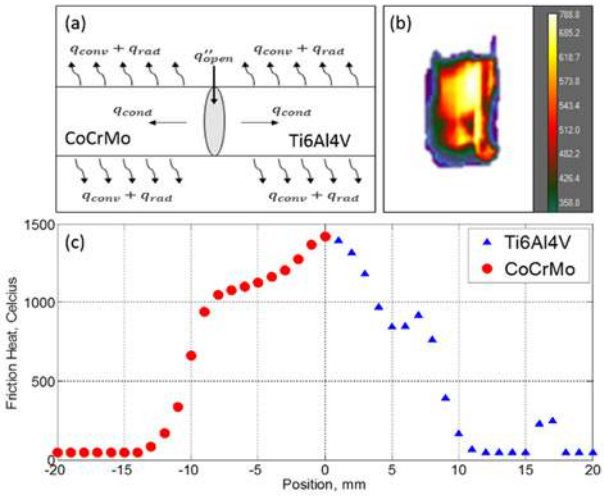

Figure 4. (a) Schematic of modeling strategy; (b) infrared imaging of the joint (in Celsius); and (c) thermal profile at maximum temperature.

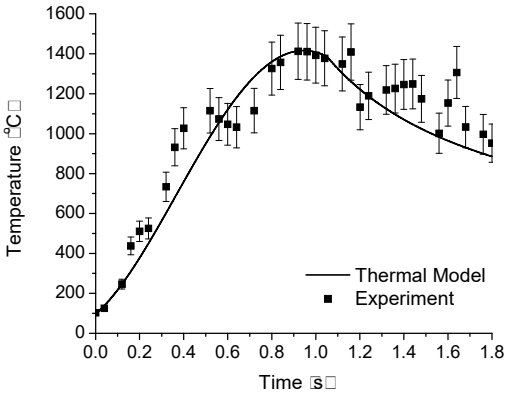

Figure 5. Comparison of the thermal model to the interface temperature of the two materials

ACKNOWLEDGEMENTS

Authors' thanks to Mr. Frank Deley and Michael Gaskill from Taylor-Winfield (Youngstown, OH) for their technical support and assistance in developing specimens. Authors gratefully acknowledge financial support of Center for Excellence program at Youngstown State University.

REFERENCES

[1] Momoda, L.A., *Bridge*, 34:18–21, 2004
[2] Oladokun, A. et al., *Trib-Mat, Surf & Inter,* 9:4, 165-173, 2015
[3] Avval, P.T. et al., *J Mech Behav Biomed Mater*, 41: 56-67, 2015
[4] Rho, J.-Y. et al., *Biomaterials*, 18:1325-1330, 1997
[5] McAndrew, A.R. et al., *Prog. Mater. Sci.* 9: 225-257, 2018
[6] Yunus, C. & Ghajar, A., *McGraw-Hill*. 3rd ED, 2014.
[7] Liu, X. et al., *Addit Manuf*, 21: 30-40, 2018

SB³C2019
Summer Biomechanics, Bioengineering and Biotransport Conference
June 25 -28, Seven Springs, PA, USA

AUTOMATED FIBER ORIENTATION QUANTIFICATION IN THREE DIMENSIONAL IMAGES

Jeremy D. Eekhoff (1), Spencer P. Lake (1,2,3)

(1) Department of Biomedical Engineering
Washington University in St. Louis
St. Louis, MO, USA

(2) Department of Mechanical Engineering and Materials Science
Washington University in St. Louis
St. Louis, MO, USA

(3) Department of Orthopaedic Surgery
Washington University in St. Louis
St. Louis, MO, USA

INTRODUCTION

Fibrous constituents of the extracellular matrix (ECM), such as collagen and elastic fibers, are essential for imparting tensile strength to biological tissues. Moreover, the mechanical properties of the tissue are dependent on the organization of such fibers. Tissues such as tendons and ligaments with strongly aligned collagen have high tensile strength along the direction of the fibers [1], whereas tissues with more randomly oriented fibers, such as skin, have reduced mechanical anisotropy in comparison [2]. In addition to dictating tissue mechanics, fiber topography has also been shown to affect the behavior of resident cells within the ECM [3-5]. Therefore, the ability to quantify fiber organization in biological tissues is a valuable tool with applications across a breadth of biomedical research.

Open-source programs to quantify fiber orientations in two-dimensional (2D) images are widespread throughout the literature, with options such as the FibrilTool and OrientationJ plugins in ImageJ [6,7], CT-FIRE [8], and CytoSpectre [9]. However, analyzing three-dimensional (3D) tissues in 2D has limitations: the results are dependent on the location and orientation of the imaging plane and low-density fiber networks are not readily visible in a single plane. While 3D orientation estimation is superior to analysis in 2D, options in 3D are limited and often constrained to particular imaging modalities [10-12]. To address this gap, we developed a novel 3D fiber orientation estimation technique for use on images with distinguishable fibers or fiber-like structures.

METHODS

A MATLAB script was written to calculate fiber orientations at each non-zero voxel in 3D image stacks. On a voxel-wise basis, a spherical window is generated around each voxel of interest by including all voxels at a distance less than a given radius from the voxel of interest. Within the window, all non-zero voxels which are not connected to the voxel of interest are set to zero. A line is fit to the remaining voxels in the spherical window such that the sum of the squared perpendicular distances from the line to each non-zero voxel, weighted by the intensity of the voxel, is minimized (Fig 1). This process is defined in Eq. (1), where $\mathbf{x}_\alpha$ is the vector defining the intersection of the fit line with the surface of the spherical window, $\mathbf{v}$ is the vector defining the orientation of the fit line, $\mathbf{x}_i$ is the vector defining the location of each non-zero voxel in 3D space relative to the voxel of interest, w_i is the weight of that point, and n is the number of non-zero voxels in the reduced spherical window.

$$\min_{\mathbf{x}_\alpha,\mathbf{v}} \sum_{i=1}^{n} w_i \left|(\mathbf{x}_\alpha - \mathbf{x}_i) \times (\mathbf{x}_\alpha + \mathbf{v} - \mathbf{x}_i)\right|^2 \quad \text{such that} \quad \begin{cases} |\mathbf{x}_\alpha| = \text{window radius} \\ |\mathbf{v}| = 1 \end{cases} \tag{1}$$

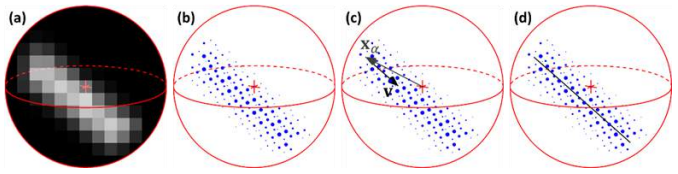

Figure 1: Pictorial demonstration of orientation finding algorithm. (a) A spherical window is generated around a voxel of interest. (b) Non-zero voxels are represented as points in 3D space weighted by the intensity of the voxel. (c) A line within the spherical window is defined by the vectors $\mathbf{x}_\alpha$ and $\mathbf{v}$. (d) The line is fit to the points through minimization of the sum of the squared and weighted perpendicular distances from each point to the line.

The technique was validated on a complex image phantom comprised of forty fibers following periodically rotating sine waves

with randomly assigned orientations, amplitudes (range: 0-30 voxels), periods (range: 50-200 voxels), diameters (range: 2-12 voxels), and maximum intensities (range: 0.4-1.0 a.u.). Where fibers intersected within the phantom, the actual orientation of the voxel was set to the mean orientation of the fibers passing through the voxel weighted by fiber diameter and intensity. The phantom stack was analyzed using different window radii (4-16 voxels) to evaluate the accuracy of the technique and determine the effect of window radius on performance.

Following validation of the technique, the orientation quantification technique was demonstrated on biological images. The superficial digital flexor tendon and a patch of skin were harvested from a bovine hind limb. The fresh tendon was flash frozen in optimal cutting temperature (OCT) compound and sectioned longitudinally to a thickness of 100 μm. The dermis of the skin was exposed and imaged without freezing or sectioning. Both samples were imaged using label-free two-photon microscopy: collagen was visualized using second-harmonic generation (excitation: 840nm, emission: 420-460nm) and elastin was visualized using two-photon excited autofluorescence (excitation: 840nm, emission: 495-540nm). The elastin channel images were background subtracted and thresholded to fully isolate the elastic fibers within the image for analysis. Orientation distributions were determined for the elastic fibers (not collagen) using the algorithm described above and visually represented with spherical histograms.

RESULTS

The algorithm performed well on the complex image stack with randomized fibers (Fig 2(a)). With the window radius set to eight, the median and mean error of the orientation estimation were 0.720° and 4.782°, respectively. The distribution of errors was highly skewed to the right, with more than 61% of voxels having orientation errors less than 1° (Fig 2(b)). Voxels with greater errors were located in regions near the edge of the phantom, near fiber intersections, or in regions of high fiber curvature. Using a small window radius increased error due to fewer available voxels within the window for line fitting. Increasing the window radius from eight voxels also increased the error of orientation estimates because more voxels became affected by fiber intersections and regions of high curvature. Therefore, the algorithm achieved the best performance when the window radius was approximately equal to the average fiber diameter of the image being analyzed. Still, even with a broad range of window sizes, the median error remained below 2.5°, demonstrating the robust nature of the algorithm.

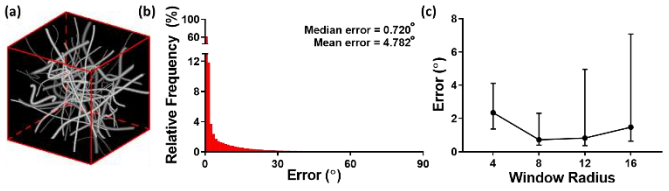

Figure 2: (a) Complex phantom image with forty randomized, curved fibers. (b) Histogram of errors from the orientation-finding algorithm with the window radius set to eight. The y-axis was broken to help visualize lower frequency bins and bin width = 1°. (c) Effect of window radius on algorithm performance on a complex phantom. Data are shown as median and interquartile range.

Application of the orientation algorithm was demonstrated on bovine tendon and dermis. The collagen fibers in the tendon displayed a strongly aligned and crimped structure, while the elastic fibers were sparsely distributed yet aligned with the collagen network: this alignment was represented in the sharply bipolar distribution determined by the algorithm (Fig 3(a-c)). In contrast to the tendon, both the collagen and elastic fibers in the dermis were found in a range of orientations within the plane of the skin (Fig 3(d-f)). The distinct topographies of these tissues are directly related to the mechanical loads they are typically subjected to *in vivo*.

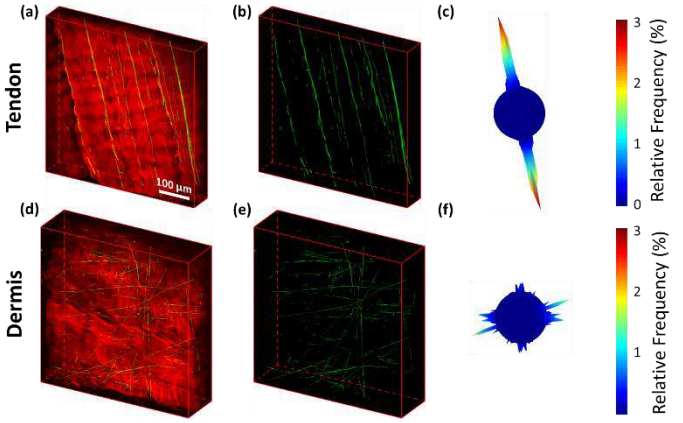

Figure 3: (a) Image stack of collagen (red) and elastin (green) in bovine superficial digital flexor tendon. (b) Isolated elastin channel from (a). (c) Spherical histogram representing the bipolar orientation distribution of elastic fibers in the tendon. (d) Image stack of collagen (red) and elastin (green) in bovine dermis. (e) Isolated elastin channel from (d). (f) Spherical histogram representing the orientation distribution of elastic fibers in the dermis. The peaks of the distribution are aligned within the plane parallel to the surface of the dermis.

DISCUSSION

We have presented and demonstrated a novel technique to find the voxel-wise orientation of fibers in three dimensions. While fiber intersections and regions with high curvature mildly impact the performance of the algorithm, a median error less than 1° was still achieved on a highly complex phantom image stack, exemplifying the high accuracy achievable with the algorithm. This technique is not dependent on imaging modality; however, it is limited to images with distinguishable fibers or fiber-like structures and may require minimal image post-processing prior to analysis. With these minor limitations, the algorithm still has potential applications across a large breadth of biomedical research including studying structure-function relationships in various tissues and in investigating fiber topography-dependent cell-ECM relationships. Further work extracting quantitative parameters describing the orientation distribution within single images or sets of images could augment the orientation algorithm by providing a simple measure to compare between study groups for statistical analysis.

ACKNOWLEDGEMENTS

We thank the National Science Foundation (1562107) and the National Institutes of Health (T32EB018266) for funding.

REFERENCES

[1] Quapp K et al, *J Biomech Eng*, 120:757-763, 1998.
[2] Ní A et al, *JMBBM*, 5:139-148, 2012.
[3] Wang S et al, *J Mater Chem*, 3:3358-3366, 2015.
[4] Newman P et al, *Sci Rep*, 6:1-12, 2016.
[5] Fraley SI et al, *Sci Rep*, 5:1-13, 2015.
[6] Püspöki Z et al, *Focus on Bio-Image Informatics*, 69-93, 2016.
[7] Boudaoud A et al, *Nat Prot*, 9:457-463, 2014.
[8] Bredfeldt JS et al, *J Biomed Opt*, 19:016007, 2014.
[9] Kartasalo K et al, *BMC Bioinformatics*, 16:1-23, 2015.
[10] Kuhnt D et al, *Neurosurgery*, 75:E913, 2013.
[11] Galvis L et al, *PLoS One*, 8:e63518, 2013.
[12] Axer M et al, *Front Neuroanat*, 10:1-12, 2016.

SB³C2019
Summer Biomechanics, Bioengineering and Biotransport Conference
June 25 -28, Seven Springs, PA, USA

THE EFFECT OF COMPOSITION AND HYDRATION ON THE ELASTIC PROPERTIES OF CARBONATED APATITE

Brian Wingender (1), Masashi Azuma (1), Christina Krywka (2), Paul Zaslansky (3), John Boyle (4), Alix Deymier (1)

(1) Biomedical Engineering
UConn Health
Farmington, CT, USA

(2) Helmholtz-□entrum Geesthacht
□entrum f□r Material- und
K□stenforschung GmbH
Geesthacht, Germany

(3) Dept. Operative and Preventive Dentistry
Charit□ - Universit□tsmedizin Berlin
Berlin, Germany

(4) Dept. of Orthopedic Surgery
Columbia University
New York, NY, USA

INTRODUCTION

Bone is composed of 65 wt% mineral surrounded by hydrated proteins and aqueous body fluid[1]. The mineral provides mechanical strength to the bone in addition to acting as an ionic reservoir. Despite composing a majority of bone mass, bone mineral continues to be misidentified as, and assigned the properties of geological hydroxyapatite. Instead, bone mineral is carbonate-substituted, hydroxyl and calcium depleted apatite that forms nano-crystals of yet unknown properties. Studies have shown that chemical changes in composition, specifically the addition of carbonate, significantly affect mineral crystal size, atomic structure, and solubility. Recent *in silico* studies have indicated that the moduli of bone apatite should decrease with increased carbonate content[2].

In addition to the changes in mineral composition, it has been suggested that the aqueous environment present in bone may also serve to give bone mineral unique properties. Bone apatite in the presence of water has been shown to form a hydrated surface layer that resembles amorphous calcium phosphate (ACP)[3]. This layer appears to disappear with dehydration in air. The presence of this amorphous surface layer would be expected to modify many of the crystals chemical and mechanical properties.

Despite theoretical and structural data indicating that the mechanical properties of bone apatite are different from those of geological hydroxyapatite, it has been difficult to experimentally probe the modulus of bone-like mineral due to its nanometer-scale size. Here, we have employed X-ray Diffraction (XRD) in conjunction with fluid-mediated hydrostatic loading to measure the effects of composition and hydration on the mechanical properties of apatite.

METHODS

Aqueous precipitation methods were used to create five carbonated apatite powders. Powders were precipitated from $NaHCO_3$, $Ca(NO_3)_2$, and NaH_2PO_4 in water at a pH of 9 and a temperature of 60°C. Carbonate content was confirmed via Carbon-Hydrogen-Nitrogen analysis to be 3.6, 9.2, 11.3, 13.6 and 17.8 wt% for the 5 samples. Powders were maintained and prepared in a dry glove box to minimize effect of environmental humidity. X-ray Diffraction and Raman Spectroscopy confirmed that the 5 samples were apatitic[2].

High Energy XRD and fluid-mediated hydrostatic loading were used to measure the deformation of these powders at P07 materials science beamline of Petra III synchrotron (DESY, Hamburg, DE) as previously described[4]. Powders were packed into a 7 mm^2 sample chamber with two flexible, xray-transparent kapton windows. The chamber was then filled with one of three liquids: phosphate buffered saline (PBS), ethanol (EtOH), or a 50/50 PBS/EtOH mixture (MIX) and sealed. The loaded sample holders were mounted into a custom made pressure chamber [4, 5] into which water was introduced and pressurized to hydrostatically compress the powders. Powders were gradually compressed in increments of ~100 GPa up to ~370 MPa.

The pressure chamber was aligned such that a collimated X-ray beam passed through pairs of diamond kapton windows, interacting with the pressurized powder thereafter exiting towards the detector. The x-ray beam had an energy of 60 or 71.8 keV with a 1x1 mm cross-section. XRD data was captured following each load increment on a 2048x2048 pixel Si detector with an acquisition time of 5x10sec. At each load both apatite (002) and (310) peaks were fully visible.

The full width at half maximum of the (002) and (310) diffraction rings were measured from the FWHM of the pseudo-Voigt fit peaks. The peak FWHM is inversely proportional to the atomic order of the crystals. The radial position of the (002) and (310) diffraction ring, R, was determined from the location of the center of the pseudo-Voigt fit for the peaks. The strains in the mineral, ε, were calculated from $\varepsilon=R-R_o/R_o$, where R_o is the radial position for the unstrained mineral. C-axis

strain was determined from the (002) peak while a-axis strain was determined from the (310) peak at each load.

The experimental results provide a direct measure of strain along the a and c-axes; however, due to the hydrostatic loading the compliance of the powders had to be found via optimization. From the strain measured and the load applied, we are able to calculate the bulk modulus, K, and the ratio η, which are related to the elastic constants C_{11}, C_{12}, C_{13}, and C_{33} according to the following equations:

$$K = \frac{\sigma}{(\frac{\Delta V}{V})} = \frac{\sigma}{2\varepsilon_1+\varepsilon_3} = \frac{[(C_{11}+C_{12})C_{33}]-2C_{13}^2}{C_{11}+C_{12}+2C_{33}-4C_{13}} \quad (1)$$

$$\eta = \frac{\varepsilon_1}{\varepsilon_3} = \frac{C_{33}-C13}{C_{11}+C_{12}-2C_{13}} \quad (2)$$

With these known values, the elastic constants were optimized such that (1) the calculated K and η matched the experimental values and (2) that the residual sum of squares differences between the optimized and guessed values of C_{xx} were minimized. Preliminary guesses (seed values) for the elastic constants as a function of carbonate content were obtained from molecular dynamics (MD) data previously reported for carbonated apatite[2]. To account for variability in the original guess, the MD results were interpolated across all CO_3 values. The experimental results were similarly interpolated and used to run the optimization 10,000 times to determine the spread in the calculated constants. The Young's moduli could then be calculated:

$$E_{11} = \frac{[C_{33}(C_{11}+C_{12})-2C_{13}^2](C_{11}-C_{12})}{C_1C_{33}-C_{13}^2} \quad (3)$$

$$E_{33} = \frac{C_{33}(C_{11}+C_{12})-2C_{13}^2}{C_{11}+C_{12}} \quad (4)$$

The true experimental values were averaged for the results reported here.

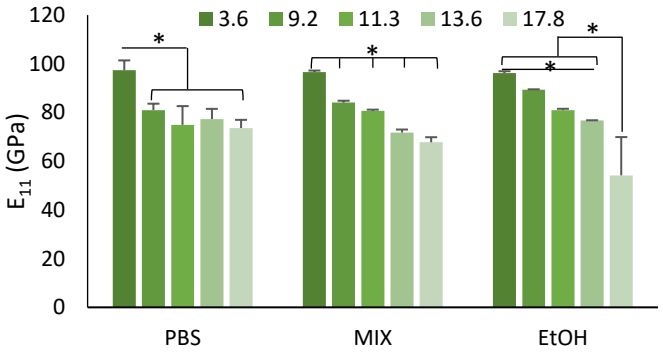

Figure 1: Effect of composition and hydration on E_{11}

RESULTS

The Young's moduli of the carbonated apatites were significantly decreased ($p<0.05$) with increasing carbonate content. Irrespective of the surrounding fluid, both the E_{11} and E_{33} exhibited a decrease with increasing carbonate concentration. The FWHM of both the (002) and (310) peaks increased significantly with increasing carbonate content. This indicates that there is greater atomic disorder in the more highly substituted samples. The bulk modulus, K, of the mineral powders exhibited no significant change as a function of carbonate content.

Overall, fluid composition in the loading chamber had no significant effects on the Young's moduli of the powers. The FWHM of the (002) peak does exhibit a trend towards a decrease in FWHM with increasing water content in the fluid. All compositions except that with the highest carbonate content (17.8 wt% CO_3) exhibited a significant decrease in (002) FWHM in PBS compared to EtOH. The bulk modulus showed no change with fluid composition.

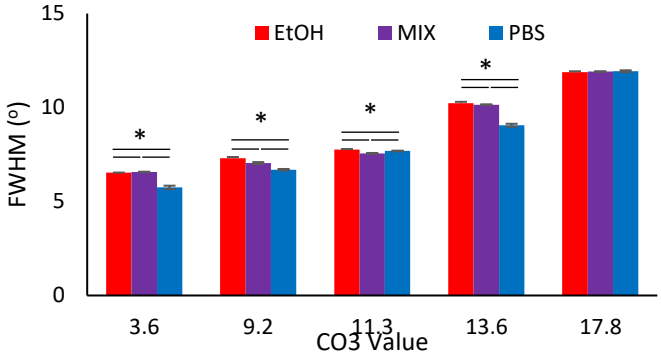

Figure 2: Effect of composition and hydration on FWHM

DISCUSSION

The Young's modulus of geological hydroxyapatite, 114 GPa [6], is often used in bone modelling. However, our XRD results present the first direct evidence that the composition of the bone mineral can reduce mineral particle stiffness by 20% or more. Thus, small % changes in carbonate composition must be accounted for in determining its elastic properties. The addition of carbonate to the atomic lattice of hydroxyapatite causes a significant decrease in the longitudinal and axial Young's modulus of the crystals. Considering that the carbonate content of bone apatite ranges from 2-8 wt% in mammals, this suggests that E_{11} could vary from ~88-105 GPa and ~100-140 GPa for E_{33}. These are very different results than the commonly used isotropic 114 GPa. This stiffness change is likely caused by a decrease in atomic order associated with the carbonate substitution. The FWHM results clearly show that higher carbonate content is associated with an increase in atomic disorder.

It has been previously suggested that bone mineral forms an amorphous surface layer in the presence of water[3]. If such a layer was present, we would expect that the FWHM of the crystals would increase with additional hydration. However, the FWHM data indicates that the atomic order of the crystals actually increases in PBS as compared to EtOH at most carbonate contents. It is unclear whether this indicates that PBS acts to increase the atomic order of the crystals or if EtOH has some unknown interaction with the apatite that would cause a decrease in crystallinity. It has been reported that ethanol can better stabilize ACP as compared to aqueous media[7]. This stabilizing effect may cause ACP to remain present in the crystals in the presence of EtOH while it may recrystallize in PBS. Regardless of this change in atomic order, it appears to negligibly affect the mechanical properties of the crystals. The main change in elastic moduli of the crystals was due to carbonate composition and not by changes in the surrounding fluid.

ACKNOWLEDGEMENTS

Funding was provided by Dr. Deymier's Startup at UConn Health. We acknowledge Helmholtz-Zentrum Geesthacht and DESY (Hamburg, Germany), both members of the Helmholtz Association HGF, for the provision of experimental facilities, beamtime and travel funding. We thank Norbert Schell for valuable support at the beamline.

REFERENCES

1. Currey, J.D., *Bones: structure and mechanics*. 2002, Princeton, NJ: Princeton University Press.
2. Deymier, A.C., et al. Biomaterials. **127**: p. 75-88
3. Wang, Y., et al. Nature Materials. **12**: p. 1144
4. Forien, J.B., et al. J Mech Behav Biomed Mater. **50**: p. 171-9
5. Krywka, C., et al. ChemPhysChem. **9**: p. 2809-2815
6. Gilmore, R.S., et al. J. Mater. Sci. **17**: p. 1131-1141
7. Tung, M.S., et al. Colloids and Surfaces A: Physicochemical and Engineering Aspects. **110**: p. 191-198

SB³C2019
Summer Biomechanics, Bioengineering and Biotransport Conference
June 25 -28, Seven Springs, PA, USA

APPLICATION OF MICRO-RAMAN SPECTROSCOPY TO MECHANICAL CHARACTERIZATION OF HYDROGELS

Hui Zhou (1), John M. Maloney (1), Alexander M. Knapp (1), Chelsey S. Simmons (1,2,3,4), Ghatu Subhash (1), Malisa Sarntinoranont (1,2,4)

(1) Mechanical and Aerospace Engineering, University of Florida
Gainesville, Florida, United States

(2) J. Crayton Pruitt Family Department of Biomedical Engineering, University of Florida
Gainesville, Florida, United States

(3) Division of Cardiovascular Medicine, Department of Medicine, University of Florida
Gainesville, Florida, United States

(4) Institute for Cell Engineering and Regenerative Medicine, University of Florida
Gainesville, Florida, United States

INTRODUCTION

Unlike conventional inanimate composites, biological tissue composites contain dynamic inclusions: biological cells that actively generate contractile forces that act on the surrounding matrix.[1] Non-destructive determination of these active internal stresses is necessary to build and validate accurate constitutive models. Micro-Raman spectroscopy (μRaman) has been applied to non-destructively determine residual stresses and strains in ceramics previously.[2-3] Here, we apply μRaman to characterize the effect of applied stress on polyacrylamide (PA) hydrogels as a first step toward characterization of engineered tissues. μRaman was performed on PA with increasing tension, and various features of the resulting spectra were compared to determine changes under strain.

METHODS

Fabrication of PA on Silicone Substrates. Silicone sheets (~250 μm thick, HT-6240, Stockwell Elastomerics) were cut into approximately 42 mm × 42 mm strips. PA gels were polymerized and attached to a silicone handle layer using benzophenone as previously reported.[4] Briefly, a 5 mL prepolymer solution of 10% w/v acrylamide (99% pure, Bio-Rad), 1% w/v bisacrylamide (molecular grade, Promega Corporation), ammonium persulfate (0.1 g/ml, Bio-Rad), tetramethylethylenediamine (1:2000 vol/vol, Bio-Rad) and deionized water were mixed, and 100 μl of this solution was pipetted onto benzophenone-functionalized silicone, covered with a 12 mm diameter coverslip, and exposed to UV (10.8 J/ cm^2, λ = 383 nm) for 263 seconds. Subsequently, the coverslip was removed and phosphate buffered saline (PBS, pH 7.4) was used to rehydrate the gel for more than 10 min at room temperature. This formulation resulted in a gel with an effective modulus of ~100 kPa as determined by millimeter-scale indentation on a custom cantilever-based system.[5]

μRaman Spectroscopy. Raman spectroscopy was performed with a 532nm argon-ion laser at 50 mW (Renishaw InVia). The spectra were recorded with a spatial resolution of approximately 1 μm (20× objective, 200× total magnification). Spectra were obtained from 300 cm^{-1} to 4000 cm^{-1} with a resolution less than 0.1 cm^{-1}. Measurements were performed at room temperature, and 30 scans were acquired at each location. Thermal effects such as heating were neglected under the assumption that the hydrogel dissipated heat rapidly, as water would. Using a custom LabVIEW program (National Instruments), the 30 scans at each location were averaged and fit with Lorentzian distribution curves to determine peak locations.

Applied Strain. The PA gel was mounted into a "micro-vice" holder (S.T. Japan) via the silicone handle. Stress was applied by turning the drive screws by hand and calculating the resulting strain between edges of vice clamps. Previous calibration of the

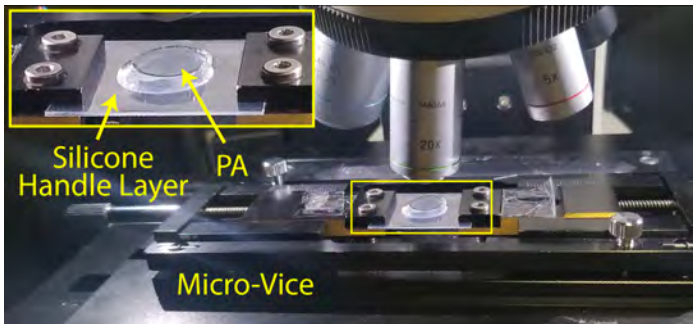

Figure 1: PA gel undergoes uniaxial tension while positioned in μRaman microscopy configuration.

Table 1: Select wavenumbers of interest assigned to bonds present in PA hydrogels

Assignments	*Peaks identified in this work [cm^{-1}]*	*Peaks identified by Gupta et al.[6,a] [cm^{-1}]*
Skeletal bending	486	478
C-O out-of-plane bending	636	639
Polymer vibration	708	766
CH_2 rocking	793	794
C-C side chain bending	841	841
C-H bending	1325	1327
C-N stretching (amide III)	1430	1428
CH_2 bending	1456	1456
NH_2 bending (amide II)	1617	1618

[a] *Gupta et al. used a 514.5 nm laser, while we used a 532 nm laser.*

PA-co-silicone system demonstrates full strain transfer from the silicone layer to the PA surface.[4] Spectra were acquired from the approximate center of the sample at 0 and 44 kPa estimated stress.

RESULTS AND DISCUSSION

The goal of this study was to determine the effect of controlled stresses on peak wavenumber shifts with the overarching goal to correlate shifts to stress states in this material. At baseline, the peak wavenumbers we identified matched reasonably with published data from Gupta et al., who validated their simulations with PA in solution and cross-linked with bis-acrylamide[6] (see Table 1). Under applied stress, the wave number and relative intensity of multiple peaks changed. For example, we observed that the 486 cm^{-1} peak associated with skeletal bending shifted to a higher wavenumber and higher Raman intensity, while the 1430 cm^{-1} peak associated with C-N stretching shifted to a lower wavenumber (Figure 2). While up-shifting of wavenumbers typically indicate bonds under tension and down-shifting of wavenumbers indicates bonds in compression, the physical interpretation of these data is still being clarified.

These findings suggest that uniaxial stress induces changes in molecular conformation that can be detected by μRaman spectroscopy, but additional characterization and analysis is warranted. Namely, experimental determination of stress-strain curves for PA will help us correlate applied strains to internal stresses in necessary detail. Additional analysis and comparison of Raman spectra across gel formulations will build a foundation for applying μRaman spectroscopy to cell-laden biomaterials for non-invasive or non-destructive evaluation of contractile stress, with the ultimate goal of improving computational models to support active inclusions.

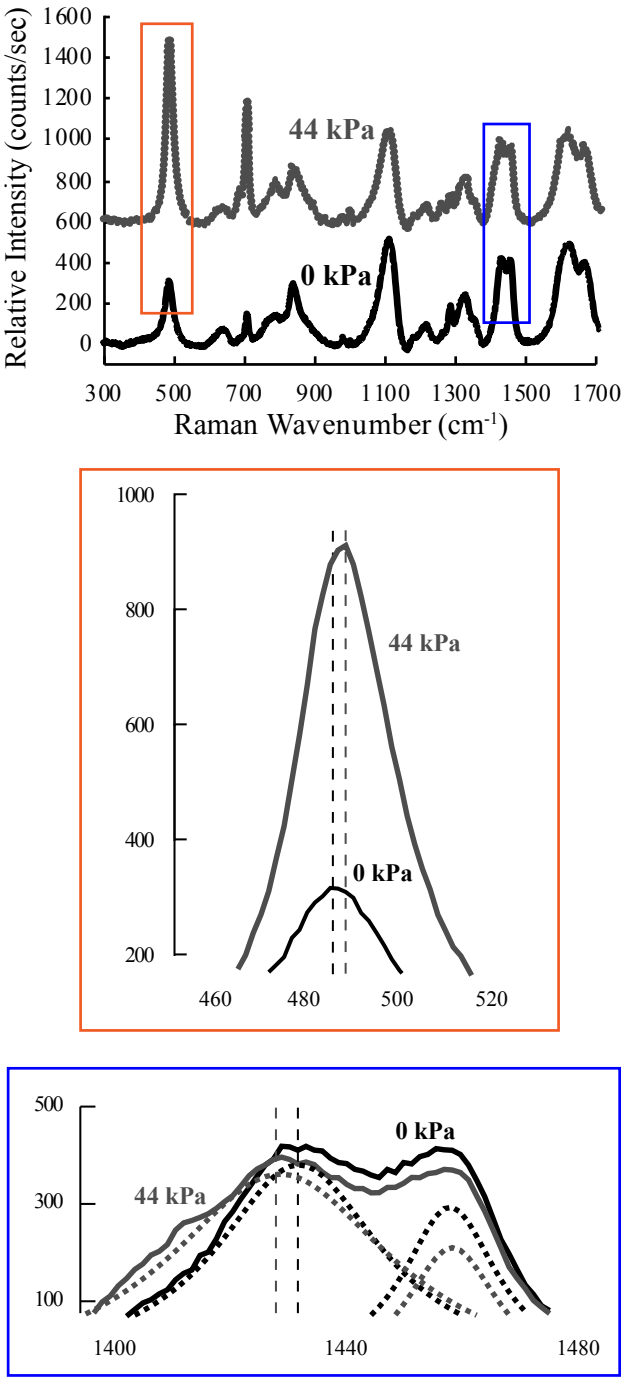

Figure 2: Raman spectra of polyacrylamide hydrogels at different levels of tension (averaged from n = 30 measurements each). Stress estimated from measured strain (44%) and nominal effective modulus of polyacrylamide gel (100 kPa). Details of shifts in skeletal bending (orange inset) and C-N stretching (blue inset) are shown magnified. Vertical dashed lines indicate wavenumber calculated from Lorentzian fit, and dashed curves in bottom panel reflect deconvolved peaks. Future work will include determination of experimental stress-strain curves for polyacrylamide to compare to Raman spectra.

ACKNOWLEDGMENTS

This work was supported by NSF CMMI 1762791.

REFERENCES

[1] Ciarletta, P et al., *Nat. Sci. Rep.* 6: 24390, 2016.
[2] Ghosh, D et al., *Acta Materialia*. 56:5345,2008.
[3] Washer, G et al., *AIP Conference Proceedings*. 975:964-969, 2008.
[4] Simmons, C et al., *Lab Chip*. 13(4): 646–649, 2013.
[5] Rubiano, A et al. *Acta Biomat.*67:331-340, 2017.
[6] Gupta, M et al., *J. Polym. Sci.(B): Polym. Phys.* 19:353-360, 1981.

SB^{3}C2019
Summer Biomechanics, Bioengineering and Biotransport Conference
June 25 -28, Seven Springs, PA, USA

HIGH FIDELITY MODELING OF 3D EULER BUCKLING AND STRESS TRANSMISSION THROUGH MOTHER-DAUGHTER CROSSLINK CAPTURES REVERSIBLE COLLAPSE IN COMPRESSING DENDRITIC ACTIN MESH

Jyothirmai Simhadhri, Preethi L. Chandran

Department of Chemical Engineering
Howard University
Washington, DC, USA

INTRODUCTION

Natural to man-made supporting structures, such as the cytoskeleton of cells to the transmission towers in the power grid, consist of intricate arrangements of slender filaments. The deformation physics of these structures are largely governed by the bending of the slender members, which being a low-resistance deformation mode, is quickly tipped into the nonlinear conformations and large deflections even as the overall strains and forces remain small. While the physics of shear-free nonlinear bending has been described since the 18 century, discretized simulations of arbitrary filamentous media have relied on the linear and jointed approximations to the Euler bending equations. These approximations decouple the proportionality between bending mechanics and conformation inherent in the theory. The systematic error due to the de-coupling has not been investigated. We present the String-of-Continuous-Beams approach to modeling slender elements in 3D, which prevents the decoupling by retaining the nonlinear contour/mechanics terms without approximations as primary variables. The approach reproduces Euler bending mechanics and geometry with high accuracy for less computational cost, and is easily extendable to buckling scenarios with mother and daughter strands such as that occurring in dendritic actin meshes.

METHODS

In classic Euler theory for shear-free beam bending (Eq. 1, 2), the mechanics variables (i.e., bending force F and moment M) are directly proportional to the geometric variables (i.e., curvature $d\theta(s)/ds$ and its differential $d\theta^2(s)/ds^2$). They are coupled in that solving one, directly gives the other. However in modeling filamentous networks, it is common to approximate the curvature as small-strain or 'jointed' (i.e., hinged straight rods) (Eq. 3) to make the geometric variables tenable for rectangular coordinates [1]. $\theta(s)$ is the in-plane bending angles along contour s.

$$M(s) = EI \, d\theta(s)/ds \quad (1)$$

$$F(s) = - EI \, d^2\theta(s)/d^2s \quad (2)$$

$$d\theta/ds = d^2y/dx^2 \approx \frac{1}{L}\Delta\left[dy/dx\right] = \frac{1}{L}\Delta[\theta] \quad (3)$$

To avoid the approximation, the String of Continuous Beams (SOCB) approach retains the contour angle and its differentials as primary variables (does not express in terms of displacements), and instead fits the angle contour to a fifth-order polymer in s. The displacements are then determined by numerically-integrating the angle polynomial as part of a mass or length conservation equation, which is solved simultaneously with the mechanics equations. The solution is generalized to arbitrary filament conformations by aligning the bending line with an in-plane x' axis, at where the filament shadow on each axis of the x'- y' - z' frame becomes the moment arm of the x', y', and z' components of the in-plane, out-plane, and axial forces [2]. An axial force at the end of a flexed filament can cause the filament to fold inwards or outwards, in both in- and out-plane directions. In-plane moment arms have to be compressed by the cos projection to compensate for an artificial increase brought about by the rotation.

RESULTS

Fidelity in capture Euler buckling mechanics: During axial buckling, the segment contour, forces, and moment arms undergo large changes and reverse direction, thereby serving as a good test case for stringently validating a generalized bending model (Fig. 1A). A filament can resist axial compressive force with stable axial bending

until a tipping configuration is reached. Beyond this configuration, filament buckles, passing through low-resistance states till tension in the opposite direction resists the compressive force (Fig. 1B). The SOCB model is able to capture the segment contours during the course of bucking (Figs. 1B and C) and the magnitude of the tipping force (scaled for filament length and EI) with <10% error using only 4 nodes, and with < 1% error by 8 nodes (Fig. 1C).[3] The jointed approach over-predicts the tipping force with >100% error with 4 nodes; the error stabilizes to 5% beyond 40 nodes.

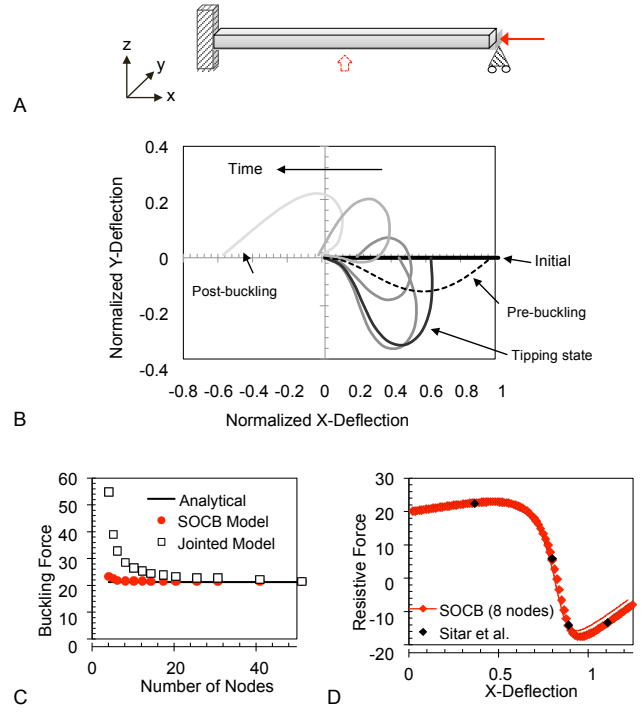

Figure 1: Axial application of force (A) produces a tipping force beyond which the filament buckles. The SOCB approach captures the geometry and forces of buckling (B and D) with high fidelity. Approximated Euler beam mechanics in jointed approaches over-predicts the buckling force (C).

Buckling in dendritic actin unit-mesh: In a buckling filament, the resistance-force increases linearly as long as stable bending occurs, but at the tipping force it takes a gradual downturn and decreases rapidly (Fig. 1D). However when a dendritic actin mesh that is outgrown from an AFM probe is compressed, the linear force region (constant elasticity) is followed by a nonlinear force increase and a sharp downturn that is reversible. The dendritic mesh consists of 'daughter' filaments off-shooting from pre-existing mother filaments at 70° angle. Can simulating Euler bending mechanics for the simplest unit of a dendritic actin mesh (mother filament with a cross branch added at 70° angle) reproduce the nonlinear reversible-collapse observed in experiments? Since the geometry variables in the Euler equation are retained, force transfers in crosslinks between mother and daughter strands can be easily imposed (i.e., internal shear and moment continuity for the two interconnecting mother filaments, overall force continuity between all interconnecting filaments in Fig. 2B). The compression of a single mother filament with a daughter appendage-filament produced an initial region of low-force development followed by a nonlinear increase and a sharp downturn (Fig. 2A). The force increase occurs because the bending of the mother filament is resisted by the daughter appendage. The force downturn occurs as the mother filament buckles when the daughter filament is no longer able to prop the mother filament. The force collapse is reversible.

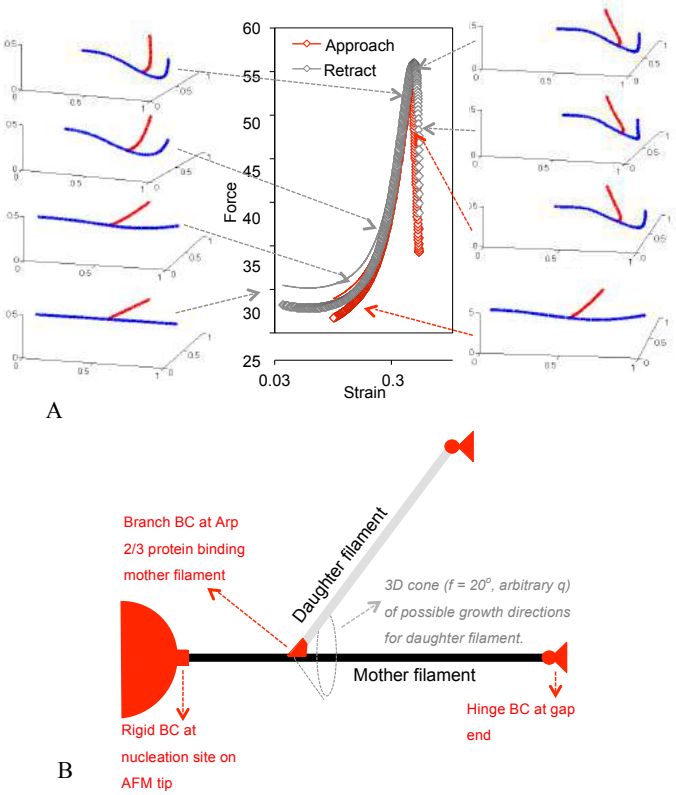

Figure 2: Force profile and configurations (A) of a buckling strand when cross-linked with an appendage strand (B).

DISCUSSION

We present a technique for capturing the non-linear 3D bending of filaments within arbitrary meshes. Single or two-jointed rods are typically used to simulate bending filaments in semiflexible and structural networks. Fig. 1C suggests that insufficient joints will over-predict the buckling force. Since buckling is a tipping event (i.e., crossing a force threshold produces disproportionally large deformations), modest errors in estimated the tipping force can produce large errors in the perceived compliance and rearrangements of the network. The SOCB approach can accommodate complex force transfer between filaments in a crosslinks, compared to the oft-used pin-joint idealization used in semiflexible networks modeling. By attaching adaughter strand as an appendage to a mother-filament, the force vs. deflection of buckling filaments changes from gradual increase and gentle turnover (Fig. 1D) to nonlinear increase and sharp turnover (Fig. 2A). The nonlinear force increase occurs without the filaments being in classic tension. Compared to Fig. 1D, the buckling force in Fig. 2B is increased by the presence of a branch support. However the compressive strain at which buckling occurs is considerably lowered, possibly because the filament contour is constrained at the branch point.

REFERENCES

[1] Berro et al., *Biophysical Journal*, **92**: 2546-2558, 2007
[2] Simhadhri, J et al., *in revision*
[3] Sitar, M et al., *Archive of Applied Mechanics*, 2: 263–275, 2014
[4] Chaudhuri, O et al., *Nature,* **445**: 295-298, 2007

SB³C2019
Summer Biomechanics, Bioengineering and Biotransport Conference
June 25 -28, Seven Springs, PA, USA

ULTRASHORT LASER FRAGMENTATION OF PLASMONIC GOLD NANOPARTICLES: COULOMB EXPOLSOION VERSUS PHOTOTHERMAL EVAPORATION

P. Kang (1), D. Sarkar (1), Z. Qin (1, 2, 3)

(1) Department of Mechanical Engineering
University of Texas at Dallas
Richardson, Texas, USA

(2) Department of Bioengineering
University of Texas at Dallas
Richardson, Texas, USA

(3) Department of Surgery
University of Texas at Southwestern Medical Center
Dallas, Texas, USA

INTRODUCTION

Plasmonic nanoparticles including gold nanoparticles (AuNPs) have created a tremendous impact on broad areas of research such as optics[1], catalysis[2] and biomedicine[3], due to their superior optical properties. The interaction between AuNP and light, due to the resonant oscillation of light and free electrons in gold, results in numerous interesting phenomenon. Particularly, short laser pulses (femtosecond (fs) to nanosecond (ns)) irradiation makes AuNPs undergo various morphology changes including reshaping, fragmentation and welding[4].

Two distinctive models have been proposed to explain the single AuNP fragmentation caused by short laser pulses[5]. The Coulomb explosion model, as a non-thermal effect, interprets that the fission is caused by the charge repulsion within the AuNP due to the ejection of electrons. On the other hand, the photothermal evaporation model suggests that laser plasmonic heating of gold brings the AuNP temperature to melting even boiling point to cause the fragmentation of AuNP thermally. Interestingly, dominance of these two mechanisms is highly dependent on laser duration, *i.e.* Coulomb explosion for fs laser irradiation, while photothermal evaporation usually prevails in ns laser case. Previous theoretical study suggests that both mechanisms are possible in ps laser excitation[5]. It remains unclear which mechanism dominates AuNP fragmentation under picosecond (ps) laser pulse.

Here, we experimentally studied the AuNP fragmentation induced by both ns and ps laser pulses. By systematically analyzing the extinction spectra change of AuNP before and after single laser pulse irradiation, we developed a method to determine the fragmentation threshold of AuNP which is highly size dependent for single ns laser pulse. This spectrum analysis further confirmed transmission electron microscope (TEM) imaging. Furthermore, we observed that the laser fragmentation behavior for ps laser irradiation is independent on size of AuNPs, suggesting a Coulomb explosion mechanism from ns laser scenario. Further experiments and modeling will be required to better understand the mechanism of ps laser induced AuNP morphology change. This study is an important step for understanding the plasmonic processing of AuNP by ultrashort laser pulses.

METHODS

AuNP with different sizes were synthesized following the modified Frens' method [6] and seed growth method. AuNP solutions (optical density @532 nm < 0.1) were loaded in 96 well plate with 115 µL/well. Single ns pulsed laser (full width half maximum FWHM = 6 ns) or ps pulsed laser (FWHM = 28 ps) was used to irradiate AuNP solution in each well. Wavelengths for both lasers were set at 532 nm. After single pulse irradiation, AuNP solution was transferred in to a 384 well plate to measure the extinction spectra (400 - 800 nm). The control group are AuNPs without laser irradiation. The data was processed with MATLAB 2018a. We firstly calculated the wavelength ratio matrix [R] by the following equation.

$$R_{ijk} = A_{ik}/A_{jk} \quad (1)$$

Where, A_{ik} and A_{jk} are absorbances of AuNP at i nm and j nm respectively, k represents laser fluence applied on the sample. We then normalized [R] for the same wavelength ratio with following equation.

$$R_{ijk}^{Norm.} = \frac{(R_{ijk} - R_{ij}^{Min.})}{(R_{ij}^{Max.} - R_{ij}^{Min.})} \quad (2)$$

Where, $R_{ij}^{Min.}$ and $R_{ij}^{Max.}$ are minimum and maximum ratio value for all laser fluences when wavelengths were fixed. We then compared the normalized R for the laser irradiation and control groups and selected the ratio that changes most with increasing of laser fluence.

TEM imaging was used to confirm the AuNP fragmentation after laser. 10 µL AuNP solution was added on a copper mesh, and air dried

overnight. Images were taken on TEM-JEOL 1400+ microscope (100 keV).

RESULTS AND DISCUSSION

Firstly, we observed that single ns laser pulse induces AuNP deformation and fragmentation. We checked the AuNP morphology by TEM imaging. As shown in Fig. 1A, AuNPs (15 nm diameter) remain spherical shape after laser irradiation at low fluence range (17, 65 mJ/cm^2). The normalized wavelength ratio of AuNP (450nm /500 nm) indicates that the ratio change is very small when the laser fluence is below 130 mJ/cm^2, while it increases dramatically above 130 mJ/cm^2 (Fig. 1B). This result agrees with what we observed in TEM images (Fig. 1A), in which fragmentations start appearing when laser fluence is higher than 128 mJ/cm^2. Interestingly, fragmented parts appear as twisted strings or horns on particle surface. This can be interpreted by the model of photothermal evaporation of AuNPs. Laser plasmonic heating of the AuNP causes the formation of gold vapor and boiling bubbles on the gold surface which were later cooled down by surrounding medium and formed the fragmentation around the AuNP. We then tested the fragmentation damage thresholds of AuNPs with different sizes. Larger particles can generate more heat during laser irradiation due to their larger absorption cross section area. Consequently, it is easier for large AuNPs to reach boiling point than small particles. This is evidenced by experimental results that larger particle has lower threshold for fragmentation induced by single ns laser pulse (Fig. 1C).

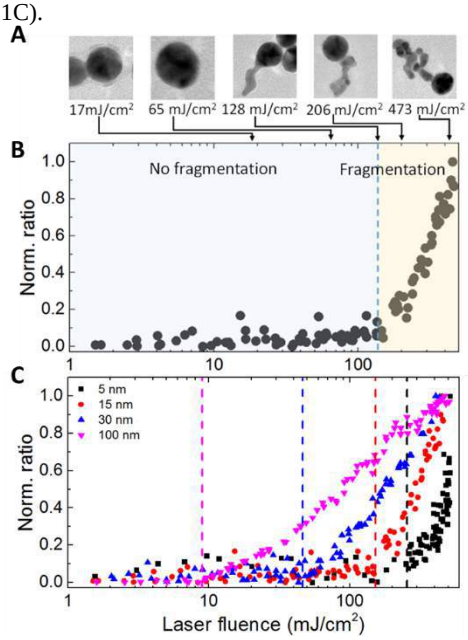

Figure 1. Nanosecond (ns) laser pulse induced AuNP fragmentation. A). TEM images for AuNP (diameter 15 nm) after single ns laser pulse irradiation. B) The normalized absorbance ratio ($R_{ijk}^{Norm.}, i = 450, j = 500$) indicates the fragmentation fluence threshold for AuNP (15 nm) C) The normalized absorbance ratio for different AuNP size. Larger particle has lower fragmentation threshold.

Next, we investigated the AuNP fragmentation induced by single ps laser pulse. Here we examined TEM imaging for two different sizes (5 and 100 nm). In both cases, irradiation at low (0.5 mJ/cm^2) and high (25 mJ/cm^2) laser pulse energies lead to particle fragmentation (Fig. 2A-L). Different from ns laser pulse irradiation, ps laser pulse leads to formation of small particles, for instance 2 nm population from 5 nm AuNP and 10 nm population from 100 nm AuNP. As laser pulse energy increases, the population of small particle also increases (Fig 2D-E, J-L). Further examination suggests that the absorbance ratio change is independent of AuNP sizes (Fig. 2M). This bimodal size distribution and AuNP size-independent fragmentation strongly indicate a different mechanism, possibly by Coulumb explosion for ps laser induced fragmentation, different from the photothermal evaporation in ns laser fragmentation.

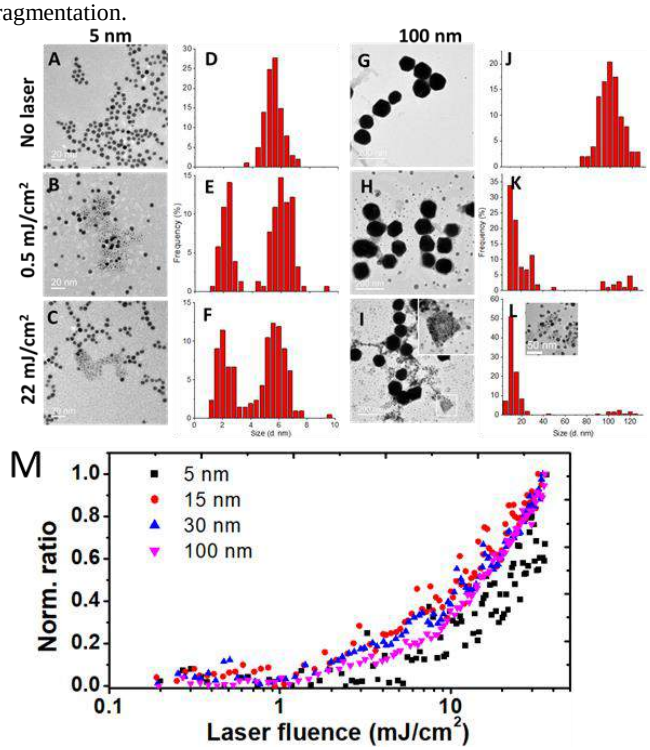

Figure 2. Picosecond (ps) laser pulse induced AuNP fragmentation. A-C) TEM images for AuNP (diameter 5 nm). D-F) Size distribution of AuNP in TEM images. G-I) TEM images for AuNP (d=100 nm) before and after laser. J-L) Size distribution in TEM images. The insert in L is TEM image for background of I which shows small particles. M) The normalized absorbance ratio ($R_{ijk}^{Norm.}$) for different size AuNP.

In conclusion, we demonstrated that the ns laser and ps laser single pulse can both lead to AuNP fragmentation. However, the fragmentation behaviors of AuNP for these two cases are different and can be attributed to distinctive mechanisms (photothermal evaporation vs. Coulomb explosion). Further computational modeling and experiments are required to validate this finding.

ACKNOWLEDGEMENTS

We acknowledge National Science Foundation (1631910), and startup fund from The University of Texas at Dallas.

REFERENCES

[1] L. Lin, et al., Acc Chem Res 2018, 51, 1465.
[2] E. L. Keller, R. R. Frontiera, ACS Nano 2018.
[3] M. R. K. Ali, et al., Proc Natl Acad Sci U S A 2017, 114, E5655.
[4] G. Gonzalez-Rubio, et al., Acc Chem Res 2016, 49, 678.
[5] D. Werner, S. Hashimoto, J. Phys. Chem. C 2011, 115, 5063.
[6] G. Frens, Nature Physical Science 1973, 241, 20; C. Ziegler, A. Eychmüller, J. Phys. Chem. C 2011, 115, 4502.

SB³C2019
Summer Biomechanics, Bioengineering and Biotransport Conference
June 25 -28, Seven Springs, PA, USA

IN VIVO ESTIMATION OF OPTIC NERVE SHEATH STIFFNESS USING NONINVASIVE MRI MEASUREMENTS AND FINITE ELEMENT MODELING

Chanyoung Lee (1), Jesse Rohr (2), Austin Sass (2), Stuart Sater (2), Bryn Martin (2), Arslan Zahid (1,3), John Oshinski (1,3), C. Ross Ethier (1)

(1) Wallace H. Coulter Department of Biomedical Engineering
Georgia Institute of Technology and Emory University
Atlanta, GA, USA

(2) Department of Biological Engineering
University of Idaho
Moscow, ID, USA

(3) Department of Radiology and Imaging Sciences
Emory University
Atlanta, GA, USA

INTRODUCTION

Approximately 40% of astronauts exposed to microgravity during long-duration space flight experience ocular changes, including change in visual acuity, in a condition known as space flight-associated neuro-ocular syndrome (SANS). The pathophysiology of SANS is poorly understood. However, the preponderance of evidence points to an important role of alterations in cerebrospinal fluid (CSF) pressure resulting from exposure to microgravity [1]. The optic nerve is surrounded by the subarachnoid space, which is filled with CSF, and the subarachnoid space is in turn encased in the optic nerve sheath (ONS), an anatomical extension of the dura mater. It has been reported that the elevated CSF pressure induces expansion of ONS [2], and that ONS tension can lead to significant mechanical insult to the optic nerve head (ONH) [3] where sight-influencing pathologies likely occur.

To explore the effects of microgravity and the possible effects of elevated CSF pressure on ocular function, it is useful to know the material properties of the ONS, e.g. to investigate ONS deformation and its effect on neighboring ocular tissues such as the ONH and optic nerve axons. Studies have measured the response of the ONS *ex vivo* [3-6]. However, to the best of our knowledge, there has been no effort to estimate the material properties of human ONS *in vivo*. In this study, we attempt to measure human ONS stiffness *in vivo* using MRI scans acquired during supine and head-down-tilt (HDT) postures, coupled with an inverse finite element approach.

METHODS

We acquired high-resolution MR scans of each eye in 4 healthy human subjects (7 eyes; 1 eye's scan had technical issues) in the supine position, followed by an identical scan during 15-degree HDT. The acute change in CSF pressure at the level of the eye associated with this postural change was estimated based on the hydrostatic indifference level and a typical subject height (Δp = 569.5 Pa). The MR scans in both supine and HDT positions were then segmented using semi-automated tools to extract cross-sectional profiles of the inner surface of the dura mater as 3D point clouds. Segmented ONS contours from the MR scan in the supine position were used to reconstruct the outer ONS surface in the intraorbital region using open-source software (MeshLab). A typical dural thickness of t = 0.4 mm was specified to create a 3D finite element model (Fig.1), which was meshed using hexahedral finite elements (ICEM CFD). The increased CSF pressure due to postural change from supine to HDT was then applied as a loading condition to the inner surface of the dura in the finite element model, allowing dura expansion due to elevated CSF pressure to be computationally simulated. We also applied boundary conditions at the

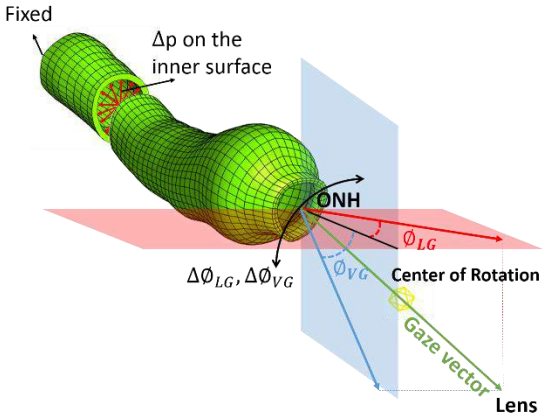

Figure 1: Finite element model of optic nerve sheath (ONS) attachment to the ONH with boundary conditions.

Poster Presentation #P261

anterior margin of the ONS (where it joins to the posterior globe) and at the optic foramen, as follows. At the anterior margin, a displacement (rotational) boundary condition was applied by computing the measured gaze angle change ($\Delta\phi_{LG}$, $\Delta\phi_{VG}$; Fig. 1) during position change from supine to HDT, as extracted from MR scans. At the foramen, the ONS was fixed, since its movement is tightly constrained at this location *in vivo*. In some cases, we were unable to segment the entire intraorbital length of the ONS due to artefacts in the MRI scans and scan resolution limitations; in such situations, we extended the length of ONS FE model by extruding the posterior margin of the segmented ONS to the location of the optic foramen and applied the fixed condition to the extended margin to reduce end effects. The dura mater was modelled as an incompressible, hyperelastic, neo-Hookean material assuming uniform material property along the entire ONS length. We computed the cross-sectional area of the ONS in HDT as a function of axial position. The FEM and MRI results were aligned using the most bulbous cross-section of the ONS as a reference location. Using an inverse FEM technique with the surrogate optimization algorithm (Matlab), we determined ONS stiffness (Young's modulus, *E*) that minimized the difference between computed and measured cross-sectional areas, evaluated using an objective function defined as the sum of root mean square differences calculated at uniformly sampled axial locations along the optic nerve axis.

RESULTS

Figure 2 shows a representative FEM result and comparison with HDT MRI data. Increased CSF pressure resulted in expansion of the ONS cross-sectional area during posture change from supine (black line) to HDT (red line), as measured by MRI. The FEM result (blue line) shows good agreement (RMS difference in cross-sectional area = 1.27 mm^2) with the result measured from MRI data (red line). The estimated ONS stiffness for all 7 eyes was 96.26 ± 49.10 kPa (mean ± SD; Fig. 3). Inter-individual differences in ONS stiffness (40-127 kPa) were larger than intra-individual differences (left vs. right eyes in a subject; 22-36 kPa; Fig. 3(b)).

DISCUSSION

We noninvasively estimated *in vivo* human ONS stiffness using an inverse FEM approach. Direct comparison of the estimated ONS stiffness to other published references is difficult because there is no information about *in vivo* measurement of human ONS stiffness, although there are *ex vivo* studies using animal eyes (porcine, bovine, ovine, and rat eye; [3-6]) and tensile testing. These studies report much larger stiffness (order 1 MPa) than our estimation; this difference may be due in part to the *ex vivo* conditions creating a reference stress state in the ONS differing markedly from that of the *in vivo* environment.

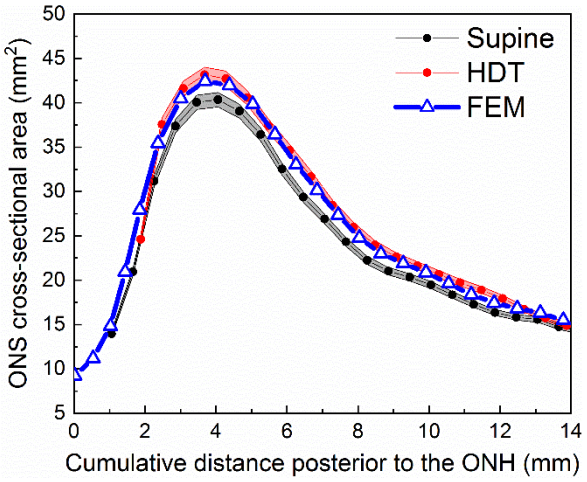

Figure 2: Experimentally measured ONS inner cross-sectional area as a function of axial position along the optic nerve in supine (black) and HDT (red) postures, and computed HDT values (blue).

This work is subject to certain limitations. First, our preliminary research revealed that a more complex material model (collagen fibers embedded in ground substance) did not give significantly better agreement between experimental and computed results (up to 3% difference between fiber model and neo-Hookean model), likely due to resolution limitations in the MR scans. Therefore, in this study we simply used a neo-Hookean model to characterize the behavior of the ONS. Second, we assumed an identical CSF pressure increase, Δp, for all subjects as a loading condition. The use of individual-specific conditions based on the height of each subject could improve the accuracy of estimates. Third, in this study, the sex and age of the subjects were not considered as factors, which may contribute to the large inter-individual differences we observed. Fourth, we note that since the ONS was modeled as a hollow cylinder-like structure with uniform thickness, the stiffness that we extracted is an effective value ("structural stiffness"), which: (i) lumps together the effects of the dura mater and the arachnoid trabeculae, and (ii) does not account for subject-specific variations in dura mater thickness. However, the tension exerted on the ONH tissues during microgravity will depend primarily on exactly this structural stiffness, and thus this may be a suitable outcome measure for use in the future study exploring the complete pathophysiology of SANS.

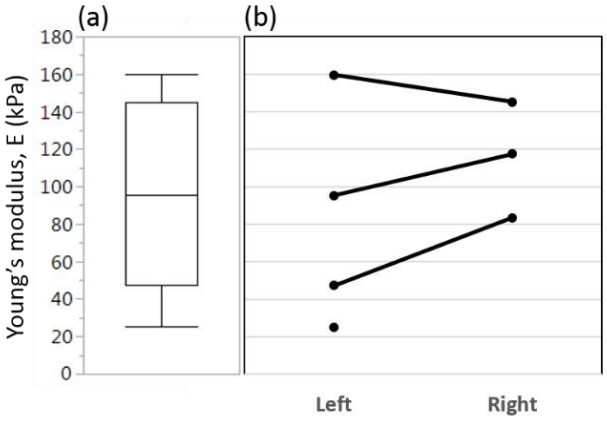

Figure 3: Estimated ONS stiffnesses. (a) Box plot for all eyes (N = 7). The bottom and top of the box represent the 1st and 3rd quartiles, respectively. The line inside the box represents the median. The bottom and top bars represent the minimum and maximum values, respectively. (b) Scatter plot showing stiffness values in left and right eyes. Connected points are from the same subject.

ACKNOWLEDGEMENTS

This work is supported by NASA grant NNX16AT06G, the Georgia Research Alliance, and the Idaho Space Grant Consortium.

REFERENCES

[1] Mader, TH et al., *J Neuroophthalmol*, 37: 133–139, 2017.
[2] Hansen, HC and Helmke, K, *J Neurosurg*, 87(1):34-40, 1997.
[3] Wang, X et al., *Invest Ophthalmol Vis Sci*, 57:2452-2462, 2016.
[4] Shin, A et al., *J Biomech Eng*, 139(10):101010-101010-10, 2017.
[5] Shetye, SS et al., *J Mech Behav Biomed Mater*, 34:146-153, 2014.
[6] Maikos, JT et al., *J Neurotrauma*, 25(1):38-51, 2008.

SB³C2019
Summer Biomechanics, Bioengineering and Biotransport Conference
June 25 -28, Seven Springs, PA, USA

PERIPAPILLARY DEFORMATION AND ITS RELATION TO MATERIAL PROPERTIES OF THE EYE GLOBE

Jafar A. Mehr (1), Heather E. Moss (2), Hamed Hatami-Marbini (1)

(1) Department of Mechanical and Industrial Engineering, University of Illinois at Chicago, Chicago, IL USA
Email: hatami@uic.edu

(2) Departments of Ophthalmology and Neurology & Neurosciences, Stanford University, Palo Alto, CA

INTRODUCTION

Idiopathic intracranial hypertension (IIH), which is related to pseudotumour cerebri (PTC), is a state of increased intracranial pressure (ICP) with unknown cause. Common symptoms of IIH are headache, pulsatile tinnitus, nausea, transitory visual obscurations, diplopia and blurred vision. Signs of intracranial hypertension (IH) on magnetic resonance (MR) images of the eye include flattening of the posterior globe and inward protrusion of the optic nerve head. Optic nerve head protrusion, i.e. peripapillary deformation (PD), is mostly due to papilledema, which reflects swelling of the retinal ganglion cells that form the optic nerve due to axoplasmic stasis. However, there may also be a mechanical component related to the inverted 'U' shape that peripapillary Bruch's membrane takes in states of high ICP [1]. In this work, we performed a finite element (FE) analysis to investigate the important parameters that affect the mechanical response of the posterior globe. Furthermore, we used the FE model in order to determine mechanical properties of ocular tissues as well as IOP and ICP pressures, which might facilitate the observed nerve protrusion in patients with idiopathic intracranial hypertension.

METHODS

The geometry of the posterior globe and intra-orbital optic nerve, Figure 1, was created from the available information in the literature -2-4]. The ANSYS APDL was used for conducting the finite element (FE) analysis. In the FE model, nodes on the axis of symmetry were constrained to deform such that they remain on the symmetry axis. In addition, because of anterior–posterior restraint of the extraocular muscles, nodes on the equator were constrained to radial deformation. Finally, since the degree to which the optic nerve is constrained is not fully known, a spring with normalized spring constant k was defined at the posterior ends of the dura mater and optic nerve, Figure 1.

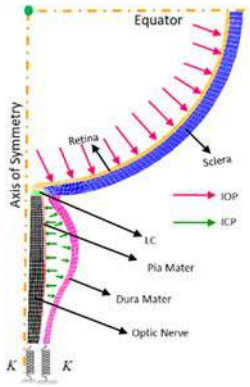

Figure 1: A schematic showing the computational model of the posterior globe. The model is radially symmetric and linear springs are used for end boundary conditions.

In order to assign the material parameters of the numerical model, a mid-axial MR image at the level of the optic nerve head was identified and measures of posterior eye NP (measured at the posterior scleral boundary) were obtained. The selection of a patient with high resolution MR imaging was done retrospectively based on the review of patients seen in the neuro-ophthalmology division at Byers Eye Institute at Stanford. This work followed the tenets of the Declaration of Helsinki and is approved by an institutional review board at Stanford University with a waiver of informed consent.

In order to relate the results of the MR image and the FE simulation, we used the angle-distance analysis technique [5] for characterizing the amount of PD. In this method, the actual boundary of the optic nerve head was considered in the MR image (shown by green color in Figure 2) and the displacement of peripheral nodes on the

inner retinal surface from the center of the eye globe was plotted versus the angle θ. The same analysis was done for the finite element model, in which the model parameters were changed until the results matched those obtained from the MR image.

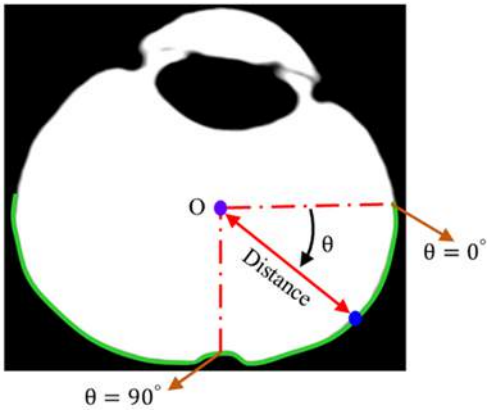

Figure 2: An MR image from a patient with high intracranial pressure. The outer boundary of the MR image is determined and was used for the angle-distance analysis.

RESULTS

Figure 3 shows the angle-distance graph obtained from the FE model matched very well with the curve obtained for a typical MR image shown in Figure 2. The numerical model showed that the amount of IOP and ICP and the material properties of lamina cribrosa, optic nerve, retina and pia mater were the most important parameters causing PD, i.e. the values of these parameters were significantly different than their default values. Furthermore, it was found that the end boundary conditions, modelled by linear springs, significantly influenced the amount of peripapillary deformation, Figure 4.

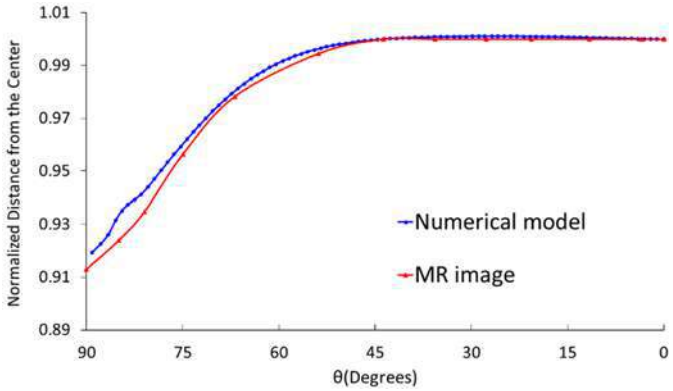

Figure 3: The Angle-Distance analysis of the finite element simulation of the MR image shown in Figure 2. The finite element results are obtained with IOP = 30 mm-Hg, and ICO = 70 mm-Hg. Furthermore, the modulus of pia mater, lamina cribrosa, optic nerve, and retina was 250, 25, 5, and 10 KPa, respectively.

DISCUSSION

Numerical models allow the isolation of mechanical from biological processes as well as enable researchers to manipulate parameters and measure outputs that cannot be accessed experimentally. Through manipulation of material properties, very good agreement was achieved between the numerical results and the MR image analysis of a patient with IH. These results supported the strength and suitability of developed characterization angle-distance technique for quantitative characterization of the contributing factors to the PD. Furthermore, it suggested that the proposed numerical model can be used in future studies to analyze MR images of patients with IH in order to estimate the average changes in the mechanical properties of tissues surrounding the ONH. Though it has been proposed that biological changes in the optic nerve head contributes significantly to nerve protrusion seen on MR images, the present numerical analysis suggests that there may exist a mechanical contribution as well. In other words, material properties as well as increased pressure loads could play a critical role in susceptibility to PD. This could occur due to either an individual's congenital variation in material properties of ocular tissues or acquired variation caused by tissue remodeling. The boundary conditions used at the bottom of the optic nerve and the dura mater were found important to the mechanical response of the globe.

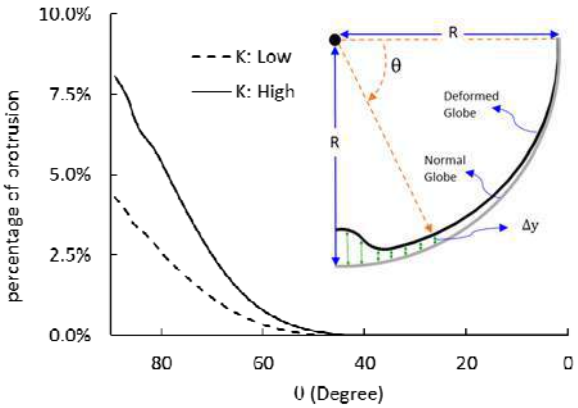

Figure 4: The effect of end boundary conditions on the amount of PD. The fixed boundary condition is obtained when the value of the spring constant is high. Except the spring constant, all other model parameters were the same as those used in Figure 3. Percentage of protrusion is $\frac{\Delta y}{R} \times 100$.

ACKNOWLEGMENTS

The support in part by NSF CMMI-1635290, NIH K23 EY 024345 and P30 EY 026877, and a Research to Prevent Blindness unrestricted grant to the Stanford Department of Ophthalmology is acknowledged.

REFERENCES

[1] Mader, T. H. et al. Optic disc edema, globe flattening, choroidal folds, and hyperopic shifts observed in astronauts after long-duration space flight. Ophthalmology 118, 2058-2069 (2011).

[2] Sigal, I. A. & Ethier, C. R. Biomechanics of the optic nerve head. Experimental eye research 88, 799-807 (2009).

[3] Hua, Y., Voorhees, A. P. & Sigal, I. A. Cerebrospinal Fluid Pressure: Revisiting Factors Influencing Optic Nerve Head Biomechanics. Investigative ophthalmology & visual science 59, 154-165 (2018).

[4] Sigal, I. A., Flanagan, J. G., Tertinegg, I. & Ethier, C. R. Finite element modeling of optic nerve head biomechanics. Investigative ophthalmology & visual science 45, 4378-4387 (2004).

[5] Mehr, J. A. A., Moss, H. E. & Hatami-Marbini, H. Mechanical Factors contributing to ocular globe flattening in states of elevated intracranial pressure: A Finite Element Analysis. Investigative Ophthalmology & Visual Science 59, 2192-2192 (2018).

SB^{3}C2019
Summer Biomechanics, Bioengineering and Biotransport Conference
June 25 -28, Seven Springs, PA, USA

THE EFFECTS OF SIZE AND LOCATION OF LASER PERIPHERAL IRIDOTOMY ON THE CHANGES IN PRESSURE DIFFERENCE ACROSS THE IRIS FOLLOWING DILATION

Anup D. Pant (1), Rodolfo Repetto (2), Syril K. Dorairaj (3), Rouzbeh Amini (1)

(1) Department of Biomedical Engineering
The University of Akron
Akron, OH, US

(2) Department of Civil, Chemical and Environmental Engineering
University of Genoa
Genoa, Italy

(3) Department of Ophthalmology
Mayo Clinic
Jacksonville, FL, US

INTRODUCTION

In angle-closure glaucoma, the anterior chamber angle (i.e., the angle between the iris and cornea) is closed or narrowed. Such a closure may lead to an increase in the intraocular pressure (IOP) due to the blockage of the aqueous humor outflow pathway. Laser peripheral iridotomy (LPI) is a common treatment method for angle closure [1]. In this procedure, a hole is made across the iris to redirect the aqueous humor flow and open the anterior chamber angle. However, LPI may not always be a successful treatment. IOP increases have been observed in patients undergone LPI, requiring additional interventions [2, 3]. In fact, the success rate of LPI may be as low as 24% [4, 5].

In our previous study, we showed that patients who continued to suffer from occludable angles post-LPI had stiffer irides [6]. While iris mechanical properties are important factors, the size and location of the LPI on the iris could also affect the surgical outcomes [7]. Although no gold standard exists, some clinicians have advocated for a hole size of at least 150-200 μm in diameter for the LPI candidates [8]. Such diameters, however, could change because of light-induced iris deformations. Using a computational approach we examined how the LPI hole size and location, as well as its deformation due to pupil dilation affect the pressure difference across the iris (i.e., between the anterior and posterior chambers of the eye).

METHODS

A three-dimensional finite element model of the iris similar to our previous two-dimensional axisymmetric model [6] was constructed using geometry obtained from an anterior segment optical coherence tomography image. Similar to our previous work [6], the iris was modeled as a neo-Hookean solid governed by the stress balance equations. A dilator region of 0.2 mm was manually identified in which the dilator stress was applied to simulate pupillary dilation. Holes with diameters of 200 μm and 400 μm were made in the iris to simulate LPI. Three different case studies were conducted:

i) To examine the effect of the hole location on the pressure difference, holes were placed in the iris at locations adjacent to the pupil, near the iris mid-periphery, and near the periphery of the iris (Figure 1).
ii) To examine the role of the hole size on the pressure difference, hole sizes with diameters of 200 μm and 400 μm were used.
iii) To examine the potential effect of iris compressibility on the pressure difference, Poisson's ratios of 0.35 and 0.49 were used for the iris model.

The geometry of the hole before and after dilation was imported into SolidWorks (Dassault Systèmes, Vèlizy-Villacoublay, France) and a flow simulation was performed using Flow Simulation add-in in SolidWorks. Pressure difference across the two ends of the hole before and after dilation was calculated. For boundary conditions, the inlet surface of the hole had a volumetric flow rate Q of 3.0 μL/min (5×10^{-11} m^3/s) [9] and the outlet surface had a known predefined pressure (P_o) (Figure 2).

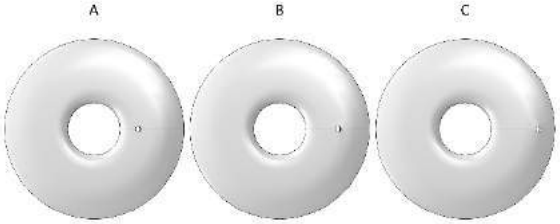

Figure 1: Holes with a diameter of 400 μm placed (A) near the pupil, (B) near the iris mid-periphery, and (C) near the periphery of the iris.

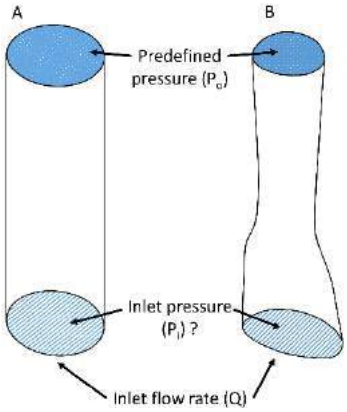

Figure 2: Geometry and corresponding boundary conditions of (A) an undeformed and (B) a deformed hole for CFD analysis.

Reynolds number was calculated to be 0.32; hence, the flow was considered laminar. Using the simulated values (e.g., see Figure 3), the pressure difference (ΔP) required to drive the flow through the hole was calculated for each of the abovementioned case studies.

RESULTS

In the presence of a 200 µm hole, the pressure difference between the posterior and anterior chambers were 0.85 Pa, 0.80 Pa, and 0.92 Pa when the hole was placed near the pupil, at the iris mid-periphery, and near the iris periphery, respectively. These predictions were consistent with published simulated data by Dvoriashyna and Repetto [7].

Following pupil dilation, the pressure difference increased in all cases (Table 1). For the compressible model, the pressure increased by 4.70%, 63.75%, and 52.17% near the pupil, at the iris mid-periphery, and near the iris periphery, respectively. For the nearly incompressible model, the pressure increased by 7.06%, 51.25%, and 55.43% near the pupil, at the iris mid-periphery, and near the iris periphery, respectively. The pressure differences for the 400 µm diameter hole were extremely smaller compared to the 200 µm diameter hole, both before and following dilation (Table 2).

Table 1: Pressure difference between the posterior and anterior chambers of the eye using a LPI hole size of 200 µm.

Hole location	ΔP (Pa) before dilation	ΔP (Pa) following dilation for a compressible iris	ΔP (Pa) following dilation for a nearly incompressible iris
Pupillary Region	0.85	0.89	0.91
Mid-periphery	0.80	1.31	1.21
Periphery	0.92	1.40	1.43

Table 2: Pressure difference between the posterior and anterior chambers of the eye using a LPI hole size of 400 µm

Hole location	ΔP (Pa) before dilation	ΔP (Pa) following dilation for a compressible iris	ΔP (Pa) following dilation for a nearly incompressible iris
Pupillary Region	0.05	0.05	0.05
Mid-periphery	0.05	0.07	0.08
Periphery	0.06	0.08	0.09

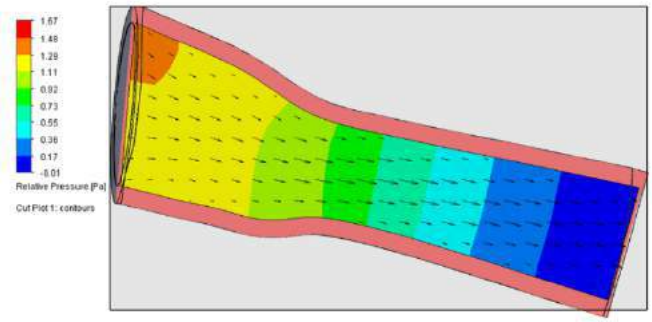

Figure 3: Relative pressure difference across the hole ends and the flow profile for a presentative simulated case following dilation-induced deformation.

DISCUSSION

The increased pressure difference between the anterior and posterior chambers as a result of changes in the LPI hole size following dilation could be a potential reason as why the angle does not always open following LPI. The main purpose of LPI is to release the excessive pressure in the posterior chamber and move the iris more towards the posterior. The higher pressure difference following dilation may inadvertently lead to more anterior apposition of the iris periphery and thus blocking the outflow pathway.

Our study showed that the LPI hole size/location has a pronounced effect in both compressible and nearly incompressible irides. To determine the reason behind variations in pressure difference among different locations, the thickness of the iris was also calculated. Not surprisingly, we found that the pressure difference was directly proportional to the thickness. Therefore, the iris thickness should also be taken into consideration when performing LPI. In other words, thicker irides may require larger hole sizes to achieve the same pressure difference.

We also observed that holes that are larger in diameter provide better results in terms of pressure differences following dilation-induced iris deformations. While a tempting idea, increasing the size of the hole could generate a *second* pupil and negatively affects the optics of the eye. Similar argument is valid for the holes closer to the pupil: while their dimeters do not change significantly with the pupil dilation, close proximity of the LPI hole to the pupillary margin could negatively affect the vision.

ACKNOWLEDGEMENTS

Computations were facilitated by a supercomputing resource grant from the Ohio Supercomputer Center (Columbus, OH). Funding for this study was provided in part by a grant from BrightFocus Foundation (G2018177).

REFERENCES

[1] Radhakrishna, S et al., *Ophthalmology*, 125:1110–1120, 2018.
[2] Aung, T et al., *JAMA*, 311:1901–1911, 2004.
[3] Alsagoff, Z et al., *Ophthalmology*, 107:2300–2304, 2000.
[4] Han, S et al., *Investigative Ophthalmology & Visual Science*, 55:6795–6801, 2014.
[5] Rao, A et al., *Seminars in Ophthalmology*, 28:4–8, 2013.
[6] Pant, AD et al., *Investigative Ophthalmology & Visual Science*, 59:4134–4142, 2018.
[7] Dvoriashyna, M., et al. *Mathematical Medicine and Biology*, 35: 447–467, 2017.
[8] Fleck BW, *British Journal of Ophthalmology*, 74:583–588, 1990.
[9] Goel, M et al., *The Open Ophthalmology Journal*, 4:52–59, 2010.

SB³C2019
Summer Biomechanics, Bioengineering and Biotransport Conference
June 25 -28, Seven Springs, PA, USA

IN VIVO MEASUREMENTS OF TRABECULAR MESHWORK STIFFNESS

C. Ross Ethier (1), Guorong Li (2), Chanyoung Lee (1), Ke Wang (1), Iris Navarro (2), Joseph M. Sherwood (3), Karen Crews (4), Sina Farsiu (2,5), Cheng-Wen Lin (4), W. Daniel Stamer (2,5)

(1) Biomedical Engineering
Georgia Tech/Emory University
Atlanta, GA, USA

(2) Department of Ophthalmology
Duke University
Durham, NC, USA

(3) Bioengineering
Imperial College London
London, United Kingdom

(4) Aerie Pharmaceuticals, Inc.
Durham, NC, USA

(5) Biomedical Engineering
Duke University
Durham, NC, USA

INTRODUCTION

Glaucoma is the leading cause of irreversible blindness worldwide. Loss of vision occurs due to progressive damage and eventual death of retinal ganglion cells, responsible for transmitting visual information from the eye to the brain. Although glaucoma can occur at any level of intraocular pressure (IOP), elevated IOP is a known risk factor [1]. Moreover, all current glaucoma treatments seek to reduce IOP, since sustained and significant IOP reduction is the only treatment that is known to slow or halt vision loss [1].

IOP is largely determined by the hydrodynamic resistance of the trabecular meshwork (TM), a porous, connective tissue through which aqueous humor fluid drains from the eye. The fluid conductance of this tissue (mathematical inverse of resistance) is referred to as the outflow facility, and is the most important measure of TM function. There is thus significant clinical and research benefit to knowing outflow facility, yet it is difficult to determine. Existing measurement techniques are either highly invasive, or are inaccurate, difficult to carry out, and time consuming; accordingly they are almost never used clinically.

We have recently shown that aqueous outflow facility and trabecular meshwork stiffness are closely correlated in both mouse and human eyes [2, 3], implying that TM stiffness may be a useful indirect measure of TM function and outflow facility. However, most previous work, including ours, has used invasive techniques on post mortem eyes to determine TM stiffness. Exceptions include the imaging-based studies of Pant et al. [4] and Johnson et al. [5]. To clinically exploit the link between TM stiffness and outflow facility, a non-invasive method of measuring TM stiffness is needed. Here our goals are to: (i) describe a minimally-invasive technique for optical coherence tomography (OCT)-based measurements of TM stiffness that overcomes many of the simplifying assumptions used in previous studies, and (ii) apply it to living mouse eyes.

METHODS

We used adult C57BL/6 mice for all studies due to well-documented structural and functional similarities between TMs in mice and humans. Studies were conducted with two cohorts of animals: one group received peri-ocular injections of dexamethasone (DEX)-containing nanoparticles, while the second group received vehicle-loaded nanoparticles (control). DEX is a glucocorticoid that causes a form of glaucoma similar to the most common form of human glaucoma, and thus DEX-treated mice are a good model of human disease. Methods are described in more detail in reference [6].

The TM and surrounding tissues were imaged using an Envisu R2200 high-resolution spectral domain (SD)-OCT system (Bioptigen). Images were acquired at a series of IOP steps (10, 12, 15, 17 and 20 mmHg), set by direct ocular cannulation with a glass micropipette attached to a reservoir.

A finite element model of a typical cross-section through the anterior eye was created and used to simulate the deformation of the TM as IOP was varied, quantified through the change in cross-sectional area of Schlemm's canal (SC), a fluid-containing vessel immediately adjacent to the TM (Figure 1A). We carried out an inverse FEM study, varying Young's modulus of the TM to match computed SC cross-sectional areas with values extracted from OCT images (Figure 1A). Due to the limited resolution of OCT images, we simply treated all tissues as linearly elastic, isotropic and incompressible, with TM modulus varied parametrically in the range 20-240 kPa and the moduli of other tissues taken from literature values [6]. Within the model, pressure loads were applied to surfaces exposed to aqueous humor, including an estimated pressure within the lumen of Schlemm's canal [6]. It was important to account for the biomechanical effects of the iris

Poster Presentation #P264

and cornea through specification of forces and moments at the virtual cut plane corresponding to the edge of the OCT image (Figure 1B).

RESULTS

Simulations predicted significant iris deformations, matching the OCT images reasonably well (Figure 1C). The inclusuion of iridial forces and moments at the virtual cut plane was critical to match computed predictions and experimental mesurements of SC collapse, emphasizing the importance of properly accounting for complex iris-TM mechanical interactions in the mouse eye. The TM in DEX-treated eyes was predicted by inverse FEM to be approximately twice as stiff as in control eyes (69 kPa vs. 29 kPa; Figure 1D), a ratio generally consistent with reported effects of DEX on TM stiffness in rabbit [7] and mouse [3], obtained via ex vivo measurements.

DISCUSSION

The determination of TM stiffness in mice is feasible using a combination of OCT imaging and inverse FEM. Technical issues include the small size of the outflow tissues in the mouse eye and the deformation delivered to the TM/SC by iris-TM interactions. Such effects are expected to be less influential in human eyes, and thus this non-destructive approach to monitoring TM stiffness in vivo shows potential for both mouse and human studies. These data strongly motivate further studies to compare TM stiffness measured as described above with direct measurements in mouse and human eyes.

ACKNOWLEDGEMENTS

Georgia Research Alliance, BrightFocus foundation, Research to Prevent Blindness Foundation, the National Eye Institute (EY005722 and EY019696)

REFERENCES

[1] M. C. Leske, A. Heijl, M. Hussein, B. Bengtsson, L. Hyman, and E. Komaroff, "Factors for glaucoma progression and the effect of treatment: the early manifest glaucoma trial," *Arch Ophthalmol*, 121(1):48-56, 2003.

[2] Wang K, Johnstone MA, Xin C, et al. Estimating Human Trabecular Meshwork Stiffness by Numerical Modeling and Advanced OCT Imaging. Invest Ophthalmol Vis Sci. 2017;58(11):4809-4817.

[3] Wang K, Li G, Read AT, et al. The relationship between outflow resistance and trabecular meshwork stiffness in mice. Sci Rep. 2018;8(1):5848.

[4] Pant AD, Kagemann L, Schuman JS, Sigal IA, Amini R. An imaged-based inverse finite element method to determine in-vivo mechanical properties of the human trabecular meshwork. J Model Ophthalmol. 2017;1(3):100-111.

[5] Johnson M, Schuman JS, Kagemann L. Trabecular Meshwork Stiffness in the Living Human Eye. Investigative Ophthalmology & Visual Science, ARVO Annual Meeting Abstract. 2015;Vol.56 3541.

[6] Li G, Lee C, Agrahari V, Wang K, Navarro I, Sherwood JM, Crews K, Farsiu S, Gonzalez P, Lin C-W, Mitra AK, Ethier CR and Stamer WD, "In vivo measurement of trabecular meshwork stiffness in a corticosteroid-induced ocular hypertensive mouse model", in press, Proceedings of the National Academy of Sciences USA, pp. 1-9, 2019.

[7] Raghunathan VK, Morgan JT, Park SA, Weber D, Phinney BS, Murphy CJ, Russell P. Dexamethasone Stiffens Trabecular Meshwork, Trabecular Meshwork Cells, and Matrix. Invest Ophthalmol Vis Sci. 2015;56(8):4447-59.

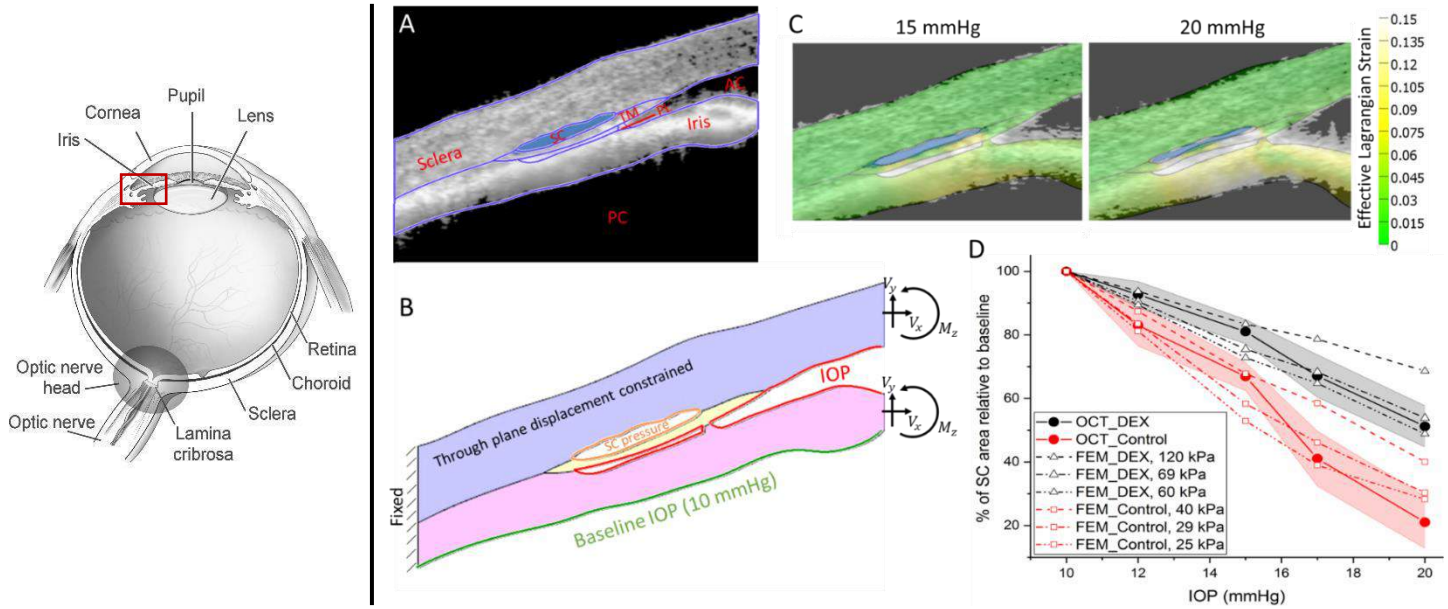

Figure 1: (Left): Overview of an eye, with red rectangle enclosing approximate extent of panel A at right. (Right) Summary of modeling approach and results. (A) Representative OCT image of TM and surrounding tissues in a mouse, overlain with tissue regions used to construct the finite element model. SC, Schlemm's canal; PL, pectinate ligament; AC, anterior chamber; PC, posterior chamber. (B) Resulting geometric model, indicating location where loads were specified in FEM, namely the lumen of SC, the anterior chamber, and the posterior iris, as well as the effective loads (Vx, Vy) and moment (Mz) acting on the virtual cut plane at the image boundary, arising from pressures acting on the iris and cornea. (C) Predicted tissue deformations and effective Lagrange strains (color) overlain on corresponding OCT images at IOPs of 15 and 20 mmHg. (D) Comparison between experimentally measured SC luminal area, and modeling results for different assumed TM stiffness values for DEX-treated and control mice. The shaded regions show 95% confidence intervals. Left: adapted from the National eye Institute. Right: adapted from [6].

SB³C2019
Summer Biomechanics, Bioengineering and Biotransport Conference
June 25 -28, Seven Springs, PA, USA

A COMPARISON OF TWO CONTINUUM MODELING APPROACHES FOR CORNEAL STROMA MECHANICAL RESPONSE

Shuolun Wang, Hamed Hatami-Marbini

Department of Mechanical and Industrial Engineering
University of Illinois at Chicago
Chicago, Illinois, USA
Email: hatami@uic.edu

INTRODUCTION

The cornea tissue covers the front of the eye and plays an important role in its proper function. For example, it is essential for protecting the inner contents of the eyeball. The precise shape and strength of the cornea are provided by mechanical properties of its extracellular matrix, which is composed of collagen fibers embedded in a proteoglycan matrix [1]. Experimental evidence shows that the collagen fibers in the corneal stromal are distributed with dispersion [2-3]. The mechanical contribution of these fibers into the mechanical behavior of the cornea tissue can be primarily captured via two different computational techniques, i.e. angular integration (AI) and generalized structure tensor methods. The angular integration method is based on the addition of the contribution of infinitesimal fractions of fibers oriented in different directions [4]. On the other hand, the GST method uses a generalized structure tensor for approximating the contribution of collagen fibers in order to avoid the required tedious angular integrations of AI approaches [5-6]. Although the GST approach is extremely friendly in terms of numerical implementation and computational cost, it is believed that its predictions include approximation and may produce unrealistic results. The primary objective of this study is to conduct a critical comparison between the GST and AI methods. Both methods are first implemented numerically in a commercial finite element software Abaqus/Standard by writing user-defined material subroutines (UMAT). They are then compared side by side by numerically simulating the experimental measurements conducted on the cornea [7].

METHODS

Both GST and AI approaches are implemented in Abaqus/Standard by writing user-defined material subroutines. The required energy functions are obtained from previous studies in the literature [4-5].

GST approach

The Total free energy could be decomposed into: 1) contributions from the soft matrix, and 2) contributions from *N* families of collagen fibers. In particular, the total free energy ψ_R is written as [5-6]

$$\psi_R = \psi_R^m(\bar{I}_1, J) + \sum_{\alpha=1}^{N} \psi_R^{f(\alpha)}\left(\bar{I}_1, \boldsymbol{A}_0^{(\alpha)}\right), \qquad (1)$$

where ψ_R^m and $\psi_R^{f(\alpha)}$ are free energies of the matrix and of the collagen fibers, respectively. The structure tensor $\boldsymbol{A}_0^{(\alpha)}$ for $\alpha's$ family of fibers is given by

$$\boldsymbol{A}_0 = \kappa\mathbf{1} + (1-3\kappa)\boldsymbol{a}_0 \otimes \boldsymbol{a}_0, \qquad (2)$$

with κ denotes the dispersion parameter, and $\boldsymbol{a_0}$ denotes the referential unit vector pointing in the preferred fibers' orientation. For the derivation of κ, refer to Gasser et al. [6]. The nearly-incompressible Neo-Hookean model is used to describe the free energy of the matrix material,

$$\psi_R^m = \frac{1}{2}G_0(\bar{I}_1 - 3) + K(\ln J)^2, \qquad (3)$$

where $\bar{I}_1$ denotes the distortional part of the first invariant, *J* is the determinant of the deformation gradient, G_0 denotes the shear modulus, and *K* denotes the bulk modulus.

As for the fibers' free energy form, collagen fibers found in the cornea fall into type I category and are unable to withstand significant amount of compression; thus, the free energy is written as

Poster Presentation #P265

$$\psi_R^f = \begin{cases} \frac{k_1}{k_2}\left(e^{k_2(\bar{I}_4^*)^2} - 1\right) & if\ \bar{I}_4 \geq 1 \\ 0 & otherwise \end{cases} \quad (4)$$

with $\bar{I}_4$ is the distortional part of the fourth invariant for α's family, and k_1 and k_2 denote the model parameters.

AI approach

Compared to the GST approach, AI methods take into account more detailed information about the cornea architecture. The free energy of stroma per its unit un-deformed volume is given by

$$\psi_R^{stroma} = \psi_R^m + \frac{1}{m}\iint_0^\pi \rho(\theta,\phi)\psi_R^f\, d\omega, \quad (5)$$

where $\rho(\theta,\phi)$ denotes the PDF of fibers' orientations, and $d\omega$ denotes the differential solid angle. Figure 1 shows the 3-D scatter plot of $\rho(\theta,\phi)$ at three different cornea depths, i.e. the AI approach is able to capture the variation in fiber orientation through the thickness of the cornea extracellular matrix.

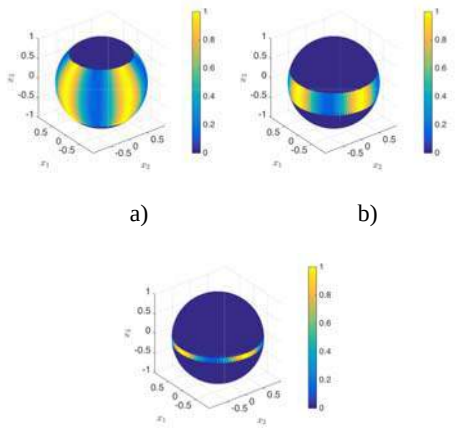

a) b)

c)

Figure 1: 3-D scatter plots of the PDFs for AI approach. PDFs are demonstrated at three different normalized depths of a) s = 0, b) s=0.5, and c) s = 0.9.

RESULTS

In simple tension tests, both approaches are capable of capturing the anisotropic behavior of the cornea. For both simple shear and torsional shear tests, which are designed to probe the in-depth properties of the cornea, AI approach is a clear winner. Both approaches are able to capture the apical rise-IOP curve (shown in Figure 2), but the difference in Von-Mises distribution between two approaches (shown in Figure 3) suggests that the internal architecture within the cornea plays an important role in terms of the mechanical response.

DISCUSSION

The simulated experimental results confirm that both approaches have their merits and disadvantages. For example, the AI approach is able to capture more realistic features of the cornea – variation of in-depth properties, but extremely expensive in terms of numerical simulation time. On the other hand, the GST approach requires no numerical integration of complex PDFs over the unit sphere at each material point, which makes it relatively cheap numerically, but due to fact that it is only an approximation of the true integral, the results it provides include some levels of inaccuracy.

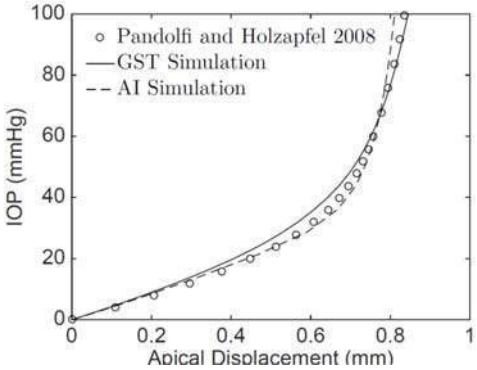

Figure 2: The apical displacement - IOP curves obtained from the GST and AI approaches are compared with that of a previous study [5].

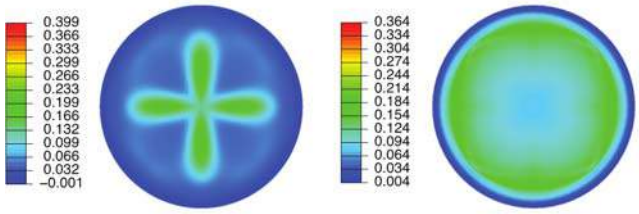

a) b)

Figure 3: The simulated contours of the maximum principal stress (MPa) for both approaches at an internal pressure of 100 mmHg. a) The GST approach, and b) The AI approach.

ACKNOWLEDGEMENTS

The support in part by NSF CMMI-1635290 is acknowledged

REFERENCES

[1] Hatami-Marbini, H., Etebu, E., Hydration dependent biomechanical properties of the corneal stroma, *Experimental Eye Research.* 116:47-54, 2013.

[2] Boote, C. et al. Lamellar orientation in human cornea in relation to mechanical properties, *Journal of structural biology*, 149(1):1–6, 2005.

[3] Aghamohammadzadeh, H., et al., X-ray scattering used to map the preferred collagen orientation in the human cornea and limbus. *Structure*, 12(2):249–256, 2004.

[4] Petsche, S. J., Pinsky P., The role of 3-d collagen organization in stromal elasticity: a model based on x-ray diffraction data and second harmonic-generated images *Biomechanics and modeling in mechanobiology*, 12(6):1101–1113, 2013.

[5] Pandolfi, A., Holzapfel, G.A., Three-dimensional modeling and computational analysis of the human cornea considering distributed collagen fibril orientations *Journal of biomechanical engineering*, 130(6):061006, 2008.

[6] Gasser, T. C., et al. Hyperelastic modelling of arterial layers with distributed collagen fibre orientations, *Journal of the royal society interface*, 3(6):15–35, 2006.

[7] Hatami-Marbini, H., Rahimi A., The relation between hydration and mechanical behavior of bovine cornea in tension, *Journal of the mechanical behavior of biomedical materials* 36, 90-97, 2014.

SB³C2019
Summer Biomechanics, Bioengineering and Biotransport Conference
June 25 -28, Seven Springs, PA, USA

MICROSTURCTURAL CHANGES AT THE VITREORETINAL INTERFACE WITH REGION AND AGE IN HUMAN EYES

Christopher J. Creveling (1), Yousef M Alsanea (1), Brittany Coats (1)

(1) Department of Mechanical Engineering
University of Utah
Salt Lake City, Utah, USA

INTRODUCTION

Vitreoretinal adhesion plays an integral role in trauma and disease. In trauma, adhesion between the vitreous and retina dictates the distribution of loading to the retina. In disease, vitreoretinal traction and adhesion can modulate clinical outcomes [1]. Despite its importance, very little is known about the mechanisms and mechanics of the vitreoretinal interface. Recently, we measured changes in vitreoretinal adhesion with age and in different regions of the eye [2]. We found disruption to the inner limiting membrane (ILM) due to vitreoretinal separation was not dictated by strong adhesive force, but rather by the mechanism of adhesion. We hypothesize that collagen interaction with the ILM, including orientation and density, dictate the mechanics and failure mechanism of vitreoretinal adhesion. The objective of this study was to test this hypothesis by quantifying the collagen density, orientation, and ILM thickness at the vitreoretinal interface and identify relationships with vitreoretinal adhesive strength and failure. If correlated, collagen structure may provide insight into those at greatest risk for lingering adhesion and inform strategies to modulate adhesion to affect disease outcomes.

METHODS

Previously, we measured the adhesive strength between the vitreous and retina in sheep (n=43) and human (n=17) eyes [2]. The sheep eyes were used to evaluate adhesion differences between immature (infant to young child) and mature (young adult) eyes. A sheep model was selected because they have well-defined retinal structure and holangiotic vasculature, and vitreous composition similar to human eyes [3].

Following the rotational peel test described in [2], 2x2 mm specimens were collected from an unpeeled retinal region immediately adjacent to the peeled retina. These specimens were placed in a 1% buffered formaldehyde and 1.25% glutaraldehyde solution, and processed as described in [2]. After embedding, 70 nm sections were cut and put on 150 copper mesh grids using a microtome (Leica UC6 Ultramicrotome, Leica Microsystems, Wetzlar, Germany). Sections were coated with uranyl acetate and lead citrate and were imaged on a 120kV FEI Tecnai T12 Spirit TEM. The magnification was set to 6500x with a beam size of 4 for optimal contrast and an exposure time of 0.5 seconds on the Gatan digital micrograph charge-coupled device. Approximately 25-35 TEM images were taken of each specimen. Specimens were obtained from the posterior pole and equator regions of each eye. A representative TEM image is shown in Figure 1.

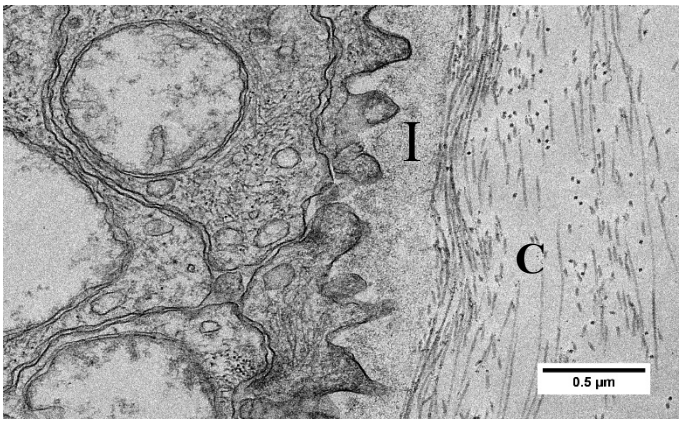

Figure 1: TEM image of a human vitreoretinal interface from the equator of a 69-year old donor. Collagen fibers (C) can be seen running parallel to the ILM (I).

Poster Presentation #P266

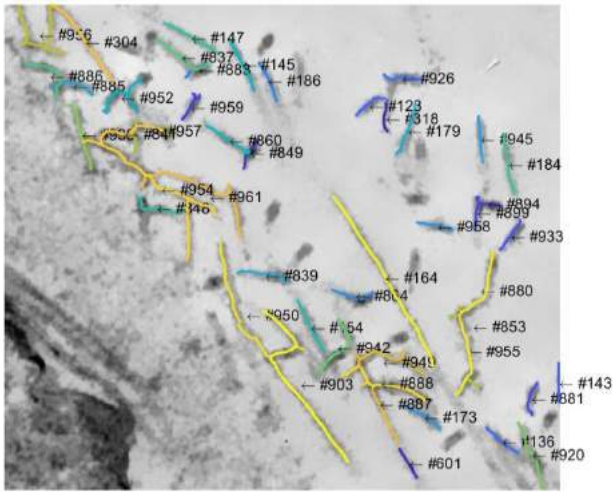

Figure 2: Collagen identification using ridge detection (Fiji) and a custom unionization MATLAB code. Collagen fibers are given unique ID numbers and color coded according to length. Specimen from the equator of a 69-year-old donor.

Ridge Detection [4], a Biomedgroup plugin from Fiji, was used to segment collagen fibers. Images were first smoothed using a non-local means denoising filter with a smoothing parameter $\sigma = 10$. Then, the width of the collagen fibers (w) and the fiber edge contrast, h, were identified in each image. Using these variables in equations (1) and (2) from [4], the smoothing parameter, σ, and upper threshold, U, were calculated and input to the Ridge Detection Fiji plugin. In these equations, x is the pixel location in the image and g'_σ is the derivative of the Gaussian kernel.

$$\sigma \geq \frac{w}{\sqrt{3}} \quad (1)$$

$$\mathrm{U} = h\left(g'_\sigma(x+w) - g'_\sigma(x-w)\right) \quad (2)$$

Output data from Ridge Detection were saved and input into a semi-automated MATLAB code to clean-up segmentation errors by the Fiji program. Segmented fibers from the Fiji algorithm often were segments of single long collagen fibers. The custom MATLAB code identified overlapping segments by iteratively comparing the coordinates of fiber segments. Fiber segments with a unique set of coordinates were counted as a unique fiber. For segments with non-unique coordinates, a least squares regression was fit to each fiber segment. If the slope and y-intercept were within a fiber distance, they were combined into a single fiber. Figure 2 presents an example output after images had been run through the custom MATLAB program.

Collagen density was defined as the number of segmented pixels divided by the length of the vitreoretinal interface. Collagen orientation was obtained using the Ridge Detection results. Any segmented fiber less than $0.04496\mu m$ in length was assumed to be primarily out-of-plane and eliminated from the analysis. ILM thickness was measured in 5 locations on an image, and averaged. For this preliminary assessment, three TEM images were selected from the image stack for each specimen, and all of the above metrics (collagen density, collagen orientation and ILM thickness) were averaged across the images.

For human data, a correlation analysis was performed for each variable (collagen density, collagen orientation, and ILM thickness) by donor age for each region (equator and posterior pole). Age was then categorized as $<$ or $\geq$ 60 years of age, and ANOVAs were used to evaluate the effects of age and region on each variable. For sheep data, ANOVAs were performed to evaluate the effects of age (immature and mature) and region (posterior pole and equator) on collagen density, orientation, and ILM thickness. A linear regression analysis was performed on both data sets to see if output variable were correlated to the maximum peel force measured previously by our group [2].

RESULTS and DISCUSSION

Collagen density was greatest in the equator ($p=0.0561$) and had a thinner ILM ($p=0.0675$). No difference in collagen orientation with region was noted. With age, ILM thickness decreased in both the equator and posterior pole ($p=0.0624$). Very little changes in collagen density and orientation occurred in the posterior pole, but the angle of the fibers relative to the retina in the equator increased with age ($p=0.0835$), perhaps due to syneresis effects. The density of collagen in the equator significantly decreased after 60 years of age ($p=0.029$) compared to the posterior pole.

When comparing the collagen and ILM measurements to measurements of adhesion, smaller collagen angles and higher collagen densities tended to have higher maximum adhesion forces. ILM thickness did not appear to have any correlation to peel adhesion force. This suggests that stronger adhesion is likely created by adhesion proteins along the vitreoretinal boundary rather than collagen fibers penetrating the retina. In sheep eyes, there were no differences in collagen orientation or ILM thickness between the immature and mature eyes. However, collagen density was greater in the posterior pole in mature eyes compared to immature eyes ($p=0.066$). The relationship between adhesive strength and collagen characteristics were similar to those seen in the human eyes. Specifically, maximum adhesion significantly increased with increasing collagen density ($p=0.0423$) and decreasing collagen angles ($p=0.0441$). Increasing ILM thickness resulted in significantly increased adhesion ($p=0.006$), but this finding was only in immature eyes. Due to limited specimens at this time, few statistics in the human specimens were significant. However, trends in the human eyes were statistically captured in sheep eyes and support continued analysis of human tissue. Once complete, this study will provide a unique insight into the mechanisms and mechanics of adhesion at the vitreoretinal interface.

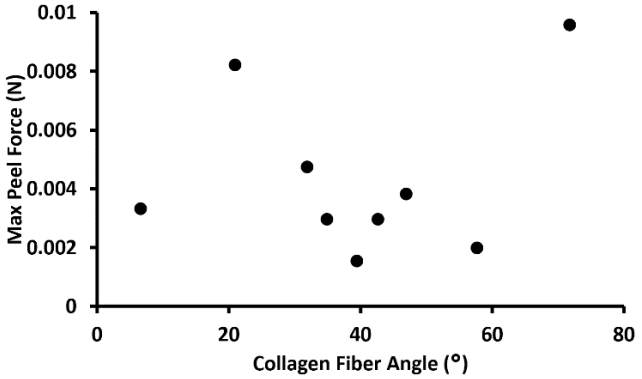

ACKNOWLEDGEMENTS

Support for this work was provided from the National Eye Institute with the National Institutes of Health award no. R21EY025813. The authors thank the Utah Lions Eye Bank, and donor families, for providing human donor eyes.

REFERENCES

[1] Sebag and Balazs, *Surv. Ophthalmol.*, 28:493–498, 1984.
[2] Creveling et al. *Front. Bioeng. Biotechnol.*, 6:1–11, 2018.
[3] Balazs and Denlinger.*Aging and human visual function*, NY, 1982,
[4] Steger, *IEEE Trans.Pattern Anal. Mach. Intell.*, 20:113–125, 1998.

SB³C2019
Summer Biomechanics, Bioengineering and Biotransport Conference
June 25 -28, Seven Springs, PA, USA

DEVELOPMENT OF A FINITE ELEMENT SIMULATION TO ESTIMATE CORNEAL ELASTICITY

U. Siddiqui (1), N. D. Gallant (2)

(1) Chemical and Biomedical Engineering
University of South Florida
Tampa, FL

(2) Mechanical Engineering
University of South Florida
Tampa, FL

INTRODUCTION

Cornea elasticity plays an central role in the proper function of the eye, yet it is not well understood. Therefore, the development of approaches to characterize ocular mechanical properties will impact numerous eye disorders. For example, Keratoconus (KC) is a progressive corneal ectatic disorder caused by degeneration of the collagen fibril network. Changes in the corneal stroma leads to topographic changes which results in a distinct bulging shape unique to patients with KC.[1] Due to the lack of proper stiffness measurements in vivo, KC can only be clinically diagnosed by detecting the bulging shape.

Keratoconus is halted using a procedure known as corneal crosslinking (CXL). The current FDA approved procedure (KXL) utilizes a potentially damaging ultraviolet light at 365 nm wavelength which can damage the endothelium layer leading to a corneal transplant.[2] Beginning with these observations, we initiated a long-term study which involves conducting mechanical testing on *ex vivo* corneas crosslinked at shorter UV wavelengths which are safer for the endothelium.

Unique to this study is the utilization of nanoindentation (NI) as a non-destructive, local mechanical measurement of corneal stiffness. This allows for repeated measurements on the same cornea, including before and after treatment and depth profiling. Building upon the ability to stiffen corneas with UV, we have created an in vitro experimental platform where corneal stiffness, thickness and intraocular pressure can be measured and manipulated on a single human cornea. There are, however, no established methods of extracting the mechanical properties of a pressurized membrane with the nanoindenter. Thus, the creation of a model, which takes into account both the bending and compression components, is required.

The purpose of the current work is to create a reliable model to estimate the mechanical properties of a pressurized thin wall shell. In order to complete this task, a finite element simulation of the experimental setup was constructed. To fine tune the model, complimentary experiments were conducted with silicone elastomer membrane with varied stiffness and thickness either laid on a rigid support or mounted on an artificial anterior chamber which enables the controlled simulation of intraocular pressure.

METHODS

A finite element simulation was constructed on COMSOL Multiphysics, utilizing the Structural Mechanics Module. The model consists of geometry and boundary conditions such as a flat punch indenter tip with a 500 μm diameter and loading stages to mimic the Hysitron Triboindenter (Bruker) setup. To gauge

the efficacy of the simulation and evaluate candidate models for estimating elastic modulus, the computational model is currently being evaluated with a tunable elastomer, polydimethylsiloxane (PDMS). PDMS is an ideal elastic tissue mimic because the material properties can be easily manipulated such as thickness and crosslink density.

PDMS was purchased from Dow Corning Corporation. The samples were prepared by first mixing the base and crosslink components at a 10:1 ratio. The two components were then manually mixed for 15 minutes and poured onto petri glass dishes. The samples were then placed in a vacuum pump to remove air bubbles and were then cured in the oven at 65 ℃ for 24 hours.

The Young's Modulus and Poisson's ratio from the samples PDMS were measured using the nanoindenter and subsequently entered into the COMSOL program. Before introducing pressure, a rigid compression experiment was conducted, and the displacement for specific applied forces in the computational model was compared to the experimental results.

RESULTS

To interpret data from the indenter, a force versus displacement graph is plotted, displaying a line following the loading, hold and unloading stages of the indentation, shown in Figure 1. The slope of the unloading stage (S), the contact area of the tip (A), and the Poisson's ratio, υ, are then used to compute the compressive elastic modulus (Eq. 1). 0.49 was used as Poisson's ratio for the incompressible tissue.[3]

$$E_{Comp} = (1-\upsilon)^2 \frac{S*\sqrt{\pi}}{2*\sqrt{A}} \quad (1)$$

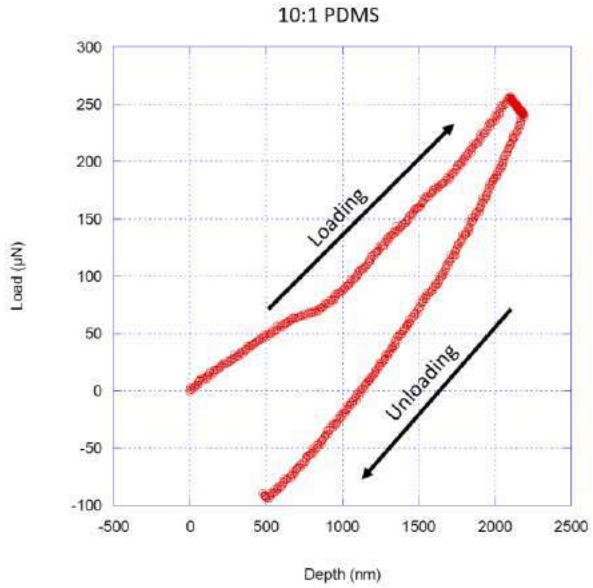

Figure 1: Raw data from nanoindenter

The force versus displacement data collected by the nanoindenter can be compared to the COMSOL model displacement field shown in Figure 2. From Equation 1, the data can then be converted to Young's Modulus. Experimental Young's modulus was calculated as 188 kPa while the COMSOL modulus is 130.5 kPa.

Force (μN)	Experimental (μm)	COMSOL (μm)	% Difference
120	1.88	1.37	29.3
100	1.753	1.14	34.9

Table 1: Linear elastic material model

Figure 2: COMSOL displacement field for rigid compression

DISCUSSION

The current finite element model deviates approximately 30% from the empirical result indicating that a linear elastic model does not completely replicate the experimental setup. In an effort to improve the model, we hypothesize that a hyperelastic material model will more accurately simulate the properties of PDMS as it is subjected to large deformations. By shifting to a hyperelastic material model, data from other modes of deformation such as uniaxial testing will provide a more accurate material behavior of PDMS for the finite element simulation. The aim of this study is to extract the material properties of a pressurized membrane through nanoindentation methods. After rigid compression has been accurately replicated, pressurized boundary conditions replicating fluidic intraocular pressure will be introduced and the combined bending and compression response will be analyzed. The proposed comprehensive model will greatly improve ophthalmic diagnosis of various ocular disorders by utilizing patient-specific cornea properties and may lead to new diagnostic instruments.

REFERENCES

[1] Piñero DP, et al. J Cataract Refract Surg. 2012;38(12):2167–83
[2] Badawi AE. Clinical ophthalmology (Auckland, NZ). 2016;10:1891.
[3] Timoshenko, S.; Goodier, J. N. Theory of Elasticity 1970

SB³C2019
Summer Biomechanics, Bioengineering and Biotransport Conference
June 25 -28, Seven Springs, PA, USA

CLOT CONTRACTION: INVESTIGATING THE IMPACT ON CLOT MECHANICAL BEHAVIOR AND MICROSTRUCTURE

S. Johnson (1), J.Y. Chueh (3), M.J. Gounis (3), M. Gilvarry (2), R. McCarthy (2), J.P. McGarry (1), P.E. McHugh (1)

(1) Biomedical Engineering, College of Engineering and Informatics, National University of Ireland Galway, Galway, Ireland

(2) Cerenovus, Johnson & Johnson, Galway, Ireland

(3) New England Centre for Stroke Research (NECStR), University of Massachusetts Medical School, MA, USA

INTRODUCTION

Thrombus material is a critically important tissue component that has the essential role of preventing blood loss in the human organism. Thrombus or blood clots can form through various pathways in vivo; due to insufficient blood flow (stasis), very high shear flow conditions or as a result of exposed tissue factor coming in contact with flowing blood due to a vascular injury [1]. Many life-threatening conditions are associated with abnormal clotting, such as acute ischemic stroke (AIS), which accounts for 85% of all strokes [2].

Mechanical thrombectomy has been firmly established as the new standard of care for the treatment of AIS [3]. In-vitro thrombus analogs are very useful in the pre-clinical testing of devices intended for use in thrombectomy, where amongst other things they can be used to evaluate the number of attempts required to remove the thrombus and the risk of embolization [3]–[5]. Some key determinants for success of the thrombectomy procedure are the mechanical properties of the clot.

The mechanical properties of clots are influenced by the composition of the clot, the arrangement of these components in the clot and internal contractile forces. Clot contraction/retraction is the tightening and shrinking of the clot network. It occurs as activated platelets rearrange within the clot structure, pulling on the fibrin threads, thus causing the fibrin network to contract and reduce in volume. This helps to create an impermeable seal at the site of vessel injury to prevent bleeding. It has also been found that the extent of clot contraction is hematocrit-dependent [6].

The aim of this study is to investigate the effect of clot contraction on the microstructure of clot analogs with varying hematocrit levels, and to determine how this impacts the mechanical behavior of the material.

METHODS

Sample Preparation

Venous blood was collected from sheep for the preparation of the clot analogs, and a 3.2% sodium citrate anticoagulant solution was added. All clots were prepared within 5 hours of blood collection.

Two types of clot analogs were produced – non-contracted and platelet contracted. Non-contracted clots were produced by mixing platelet poor plasma (PPP) with red blood cells in controlled ratios to represent clots with a low, medium and high red blood cell composition; the quantity of red blood cell used in the blood mixtures were: 0% hematocrit (plasma only), 5% hematocrit and 40% hematocrit. Similarly, platelet contracted clots formed from blood mixtures with the same hematocrit levels were formed by mixing red blood cells with platelet rich plasma (PRP).

Once the various blood mixtures were produced, coagulation was initiated by the addition of a 2.06% calcium chloride solution to the blood mixture in a 1:9 ratio. The clots were allowed to mature overnight at 37°C. The samples were formed in cylindrical shaped vessels and cut to an appropriate height for testing. The samples were placed in PBS for 30 minutes prior to mechanical testing.

Clot Weight

The weight of the clots was measured after contraction and expressed as a percentage of the mass of the original blood mixture/non-contracted clot.

Compression Testing

Unconfined compression was used to determine the material behavior of the clot samples. The testing was performed on a Zwick uniaxial tensile machine (Zwick Z2.5, Ulm, Germany), with the samples

tested in PBS. The samples were placed between two platens and the crosshead position of the machine was adjusted so that the top platen was slightly touching the top of the sample at the beginning of the test. The clot specimens were loaded to a compressive nominal strain of 30% at a strain rate of 10% per second and then unloaded to their initial configuration at the same rate (n=5 for each group).

DMA testing

DMA (Q800; TA Instruments, New Castle, Delaware), which was carried out at UMASS, was also used to investigate the mechanical properties of the clot analogs. The test was carried out using a submersion compression clamp in the controlled force mode, in saline at 37°C. The samples were cut to have an approximate height of 3mm and a calipers was used to measure the diameter. The samples (n=5 for each group) were first subjected to a preload force of 0.01N followed by a compression force ramp to 15N at a rate of 0.5N/min, according to [5].

Histology

Sections of both the contracted and non-contracted clot analogs were fixed in a 10% buffered formalin solution after removal from the incubator, and left for 48 hours. The samples were then embedded in a paraffin wax and cut into 5µm sections. The section were the dewaxed and hydrated with distilled water in preparation for staining. MSB staining was selected as an appropriate method to stain for fibrin and erythrocytes [3], [4].

SEM

The analog samples were fixed with 2.5% glutaraldehyde and dehydrated in a series of ethanol concentrations up to 100%. The samples were frozen in liquid nitrogen and fractured so that the interior surface of the clot analogs could be examined. The samples were then critical-point dried, mounted and sputter-coated with iridium.

RESULTS

The results for the DMA testing are shown in Figure 1. The contracted clots were found to be stiffer than the non-contracted clots across all 3 hematocrits. The contracted clots were found to fall within the range of behavior the human red emboli.

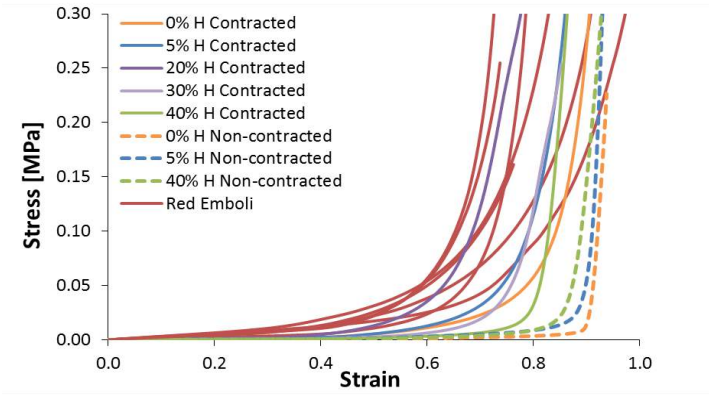

Figure 1: Stress-strain plot for the DMA testing comparing the contracted and non-contracted clot analogs, with varying hematocrit, with human red emboli tested by Chueh et al. [4] shown in red.

Figure 2 compares SEM images from both non-contracted and contracted clots with a 40% hematocrit. The microstructure of the two clot analogs were found to vary significantly.

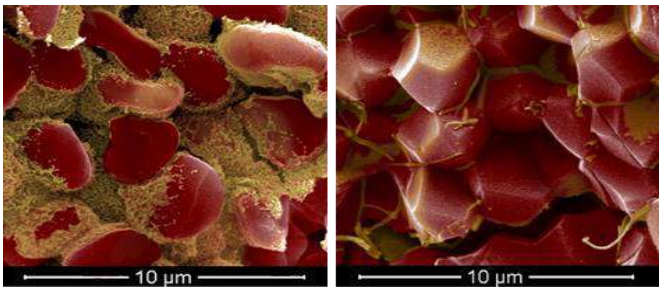

Figure 2: SEM images of non-contracted (left) and contracted clots (right) with a 40% hematocrit, with fibrin shown in yellow and RBCs in red.

DISCUSSION

Overall, the contracted clot analogs were found to be stiffer in compression than the non-contracted analogs across all hematocrits. The contracted clot analogs were also found to fall within the range of behavior of the human red emboli, previously tested by Chueh et al. [4] following the same protocol.

Importantly the histological study determined that there was little difference in the fibrin and RBC content when comparing the contracted and non-contracted groups at the same hematocrit levels. However, the SEM images show that the microstructure of both groups varied significantly. Taken together, the significant difference in mechanical properties and microstructure but without an appreciable difference in histology, implies that examination of the histology of explanted human clots alone may not prove to be predictive of the mechanical behavior of the clots in thrombectomy.

The extent of clot contraction was found to depend on the hematocrit, as clots with a greater hematocrit were found to exhibit less mass loss than clots with a lower hematocrit. The RBCs were found to be compacted into the core in all analogs, with the redistribution of platelets and fibrin to the outside of the clot [7]. The non-contracted clots were found to consist of a loose fibrin mesh with typical biconcave-shaped RBCs throughout, whereas the contracted clots consisted of compressed fibrin structures, compacted around polyhedrocyte-shaped RBCs [6]. The remarkable packing and reorganization of red blood cells into polyhedrocytes from there typical bi-concave discoid shape clearly demonstrates the internal contractility of clots brought about by platelets pulling on the fibrin matrix. Polyhedrocyte-shaped RBCs have previously been observed in cardiac-originating human thrombi [7] and it is hypothesized that this shape allows for more efficient packing of RBCs within the clots, thus creating an impermeable seal at the site of vessel injury to prevent bleeding.

In conclusion, it was found that platelet contraction significantly effects the clot microstructure, which in turn can cause an increase in clot stiffness. As this can also affect the clot permeability, it is hypothesized that this may impact the effectiveness of stroke treatments such as thrombolysis and mechanical thrombectomy respectively. We hope to investigate this further in future work.

ACKNOWLEDGEMENTS

The authors would like to acknowledge the support of Cerenovus, the Irish Research Council Enterprise Partnership Scheme (Grant No. EPSPG/2015/92), the NUI Travelling Studentship and the NUI Galway Hardiman Research Scholarship for this research.

REFERENCES

[1] Johnson et al., *Ann. Biomed. Eng*., 45(11):2494-2508, 2017. [2] Van Der Worp et al., *N. Eng. J. Med*, 357(6):572-9, 2007. [3] Duffy et al., *JNIS*., 0:1-7, 2016. [4] Chueh et al., *AJNR*, 32(7):1237–44, 2011. [5] Liebig et al., *Neuroradiology*, 50(1):43-52, 2007. [6] Tutwiler et al., *Sci. Rep.*, 8(1):17907, 2018. [7] Cines et al., Blood. 123(10): 1596-1603, 2014.

SB³C2019
Summer Biomechanics, Bioengineering and Biotransport Conference
June 25 -28, Seven Springs, PA, USA

ARTERIAL STIFFNESS COMPARED ACROSS SCALES: FROM CELLS TO EXTRACELLULAR MATRIX TO VESSELS

Bart Spronck (1), Jay D. Humphrey (1,2)

(1) Department of Biomedical Engineering, Yale University, New Haven, CT, USA

(2) Vascular Biology and Therapeutics Program, Yale School of Medicine, New Haven, CT, USA

INTRODUCTION

The importance of increased arterial stiffness in human disease, although anticipated at the turn of the 20th century, was confirmed in a seminal clinical study that revealed that an increased pulse wave velocity (PWV) is an initiator and indicator of all-cause mortality [1]. There is increasingly greater interest in measuring and understanding arterial stiffness both in basic science studies and clinical assessments. Therefore, in this study, we examine and contrast different methods that have been used to measure and interpret arterial stiffness.

METHODS

Atomic Force Microscopy. Atomic force microscopy (AFM) uses a laser to detect small deflections of a cantilever probe as it interacts with the surface of a specimen. Associated data consist primarily of the applied force (f) and the imposed motion of the probe, often the depth of penetration into the surface (δ). $f-\delta$ data are often interpreted using a Hertz solution for the localized indentation of a semi-infinite half-space that exhibits a linearly elastic and isotropic material behavior under small strains and rotations [2]. This yields a Young's modulus E, a measure of the intrinsic compressive material stiffness for this specialized class of material behaviors. The Hertz solution assumes that the half-space is unloaded prior to indentation, a condition that is neither met in vivo (arteries are axially stretched, and distended due to blood pressure) nor ex vivo (loading in cell or organ culture). In particular, the $f-\delta$ relationship, and thus the inferred stiffness, depends strongly on the pre-existing state of stress in the material [3, 4].

Biaxial Biomechanical Testing. In biaxial testing, arteries are subjected to axial as well as circumferential tensile loads, thus mimicking in vivo loading. Associated pressure-diameter and axial force-length data provide direct insight into the structural stiffness of these vessels. A global equilibrium solution reveals that the loads measured during standard biaxial tests on excised cylindrical samples can be related to principal components of the Cauchy stress [5]. Constitutive behavior is typically captured by fitting a strain energy function W to the measured data, from which a linearized spatial material stiffness obtained using the theory of small deformations superimposed on large deformations can be computed, namely:

$$\mathbb{C}_{ijkl} = 2\delta_{ik}F^{\mathrm{o}}_{lA}F^{\mathrm{o}}_{jB}\frac{\partial W}{\partial C_{AB}} + 2\delta_{jk}F^{\mathrm{o}}_{iA}F^{\mathrm{o}}_{lB}\frac{\partial W}{\partial C_{AB}} + 4F^{\mathrm{o}}_{iA}F^{\mathrm{o}}_{jB}F^{\mathrm{o}}_{kP}F^{\mathrm{o}}_{lQ}\frac{\partial^2 W}{\partial C_{AB}\,\partial C_{PQ}}\bigg|_{\mathrm{o}}, \quad (1)$$

where δ_{ij} is the Kronecker delta and a superscript or subscript o denotes a quantity that is associated with an original finite deformation about which the small superimposed deformation occurs.

Pulse Wave Velocity and Distensibility. Whereas AFM, biaxial testing, and similar methods are used in vitro on excised samples, which generally enables significant experimental control, clinical studies necessarily require less invasive in vivo methods and measurements. The current clinical gold standard measure of arterial stiffness is the carotid-to-femoral PWV [6]. This metric of stiffness is best measured by dividing the centerline distance between two recording sites by the time that it takes the pressure pulse wave to travel between these sites. Nevertheless, intuitive understanding of the PWV often comes from the Moens-Korteweg equation, $\mathrm{PWV} = \sqrt{Eh/2\rho a}$, where E is an intrinsic (linear) material stiffness, h is wall thickness, a is luminal radius, and ρ is the mass density of the fluid. Understood in this way, we see that PWV depends on both the intrinsic material stiffness and geometry of the wall, hence rendering it an integrated measure of structural, not material, stiffness. There are,

in addition, other local metrics of structural stiffness that are used clinically. One such metric is the so-called distensibility

$$D = (d_{\mathrm{sys}}^n - d_{\mathrm{dias}}^n)/d_{\mathrm{dias}}^n(P_{\mathrm{sys}} - P_{\mathrm{dias}}) \,, \quad (2)$$

where d is luminal diameter and P is pressure, with sys and dias denoting values at systole and diastole, respectively. The parameter n = 1 or 2, yielding D values that numerically differ by approximately a factor of 2. Note that the Bramwell-Hill form of PWV can be written

$$\mathrm{PWV} = \sqrt{1/\rho D} \quad (3)$$

for $n = 2$, hence localizing the value of the PWV.

Quantitative Comparison of Methods. To illustrate the effect of different loading regimens of AFM and biaxial testing, we proceeded as follows. First, we assessed the difference in compressive vs. tensile stress-strain behavior by simulating isochoric uniaxial compression in the radial direction (traction-free circumferentially and axially) as well as equibiaxial stretching in the circumferential and axial directions (traction-free radially) of rabbit thoracic aorta described by Fung strain energy functions specifically parameterized under compressive and tensile conditions [7, 8]. Second, we simulated inflation and axial extension of a cylindrical tube consisting of a Fung material [8] to illustrate effects of axial stretching on circumferential linearized stiffness (biaxial coupling; Eq. 1). Third, we simulated the effect of in-plane equibiaxial stretching of an isotropic Fung material (parameterized by minimizing the circumferential and axial Cauchy stress difference to simulated anisotropic data [8]) on out-of-plane compression tests [3]. Fourth, we quantitatively compared literature values for these metrics.

RESULTS

Compressive and Tensile behaviors Intrinsically Differ. 10% uniaxial compression ($\lambda_r = 0.90$) leads to a compressive Cauchy stress of 19.9 kPa, whereas 10% equibiaxial tension ($\lambda_\theta = \lambda_z = 1.10$) yields much lower stresses of 3.36 kPa (circumferentially) and 1.41 kPa (axially).

Circumferential Material Stiffness Depends on Axial Stretch. At a physiological luminal pressure of 120 mmHg, increasing axial stretch from 1.0 to 1.7 causes $\mathbb{C}_{\theta\theta\theta\theta}$ (Eq. 1) to increase from 1.13 MPa to 1.95 MPa.

In-plane Pre-stretch Has a Dramatic Effect on Out-of-plane Indentation Stiffness. With an increase in equibiaxial in-plane stretch from $\lambda_\theta = \lambda_z = 1.0$ to 1.7 (i.e., from an unloaded to a physiologically stretched state), indentation stiffness increases 152-fold, from 0.095 kN/m to 14.41 kN/m.

Stiffness Values Reported in Literature for the Same Species and Vessel Show Large Dispersion. Results are shown in Table 1. Note the vast difference in material stiffness values derived from AFM (~20 kPa) and biaxial testing (~2 MPa). As PWV is a structural stiffness metric, PWV values cannot be directly compared to material stiffness metrics.

DISCUSSION

The many different metrics of arterial stiffness reported in the literature have different theoretical underpinnings and thus different meanings. Values of stiffness reported in literature (some compressive, some shear, most tensile) differ by orders of magnitude. In this study, we show that these differences can indeed be expected for highly nonlinear material behaviors when assessed relative to different configurations, ranging from otherwise unloaded to in vivo relevant. Caution is thus warranted when comparing values of stiffness across studies and interpreting fundamental implications of a particular metric.

ACKNOWLEDGMENTS

This work was supported by grants from the US NIH (R01 HL105297, P01 HL134605) as well as by Rubicon grant 452172006 by the Netherlands Organisation for Scientific Research (NWO).

REFERENCES

[1] Laurent, S et al., *Hypertension*, 37:1236-1241, 2001.
[2] Vinckier, A, Semenza G, *FEBS Lett*, 430:12-16, 1998.
[3] Humphrey, J et al., *J Appl Mech*, 58:1108-1111, 1991.
[4] Costa, KD, Yin FC, *J Biomech Eng*, 121:462-471, 1999.
[5] Humphrey, JD. Cardiovascular Solid Mechanics: Cells, Tissues, and Organs: Springer, NY; 2002.
[6] Laurent, S et al., *Eur Heart J*, 27:2588-2605, 2006.
[7] Chuong, CJ, Fung YC, *J Biomech*, 17:35-40, 1984.
[8] Chuong, CJ, Fung YC, *J Biomech Eng*, 108:189-192, 1986.
[9] Liu, SL et al., *Sci Rep*, 5:17189, 2015.
[10] Hayenga, HN et al., *J Vasc Res*, 48:495-504, 2011.
[11] Weisbrod, RM et al., *Hypertension*, 62:1105-1110, 2013.
[12] Lee, JJ et al., *Ann Biomed Eng*, 44:2994-3006, 2016.
[13] Bellini, C et al., *J Biomech Eng*, 139, 2017.
[14] Haskett, D et al., *J Biomech*, 45:772-779, 2012.
[15] Leloup, AJ et al., *Hypertension*, 64:195-200, 2014.
[16] Fujikura, K et al., *Ultrason Imaging*, 29:137-154, 2007.
[17] Trachet, B et al., *PLoS One*, 10:e0129007, 2015.

Table 1: Murine wild-type aortic stiffness values depend strongly on used methodology.

Aortic region	Modality/Definition/State		Value/Units	Ref.
Thoracic	Atomic force microscopy, in vitro, compressive	Unloaded, cut open, radially indented luminally	E=16.9 kPa (age 12 months)	[9]
Suprarenal abdominal		Unloaded or pressurized (100 mmHg) + elongated to in vivo stretch, ring, axially indented	E=18.7 kPa (unloaded) E=12.3/76.4 kPa (loaded; bimodal distribution)	[10]
Not specified		Unloaded, cut open, radially indented luminally	E=24 kPa	[11]
Ascending thoracic		Unloaded, cut open, radially indented luminally	E=4.4/36.7 (age 3.5 months)*	[12]
Ascending thoracic	Biaxial testing, in vitro, tensile	Loaded, intact, pressure 128 mmHg, in vivo axial stretch	$C_{\theta\theta\theta\theta}$=2.76 MPa, C_{zzzz}=2.26 MPa	[13]
Suprarenal abdominal		Loaded, intact, pressure 100 mmHg, in vivo axial stretch	$\partial S_{\theta\theta}/\partial E_{\theta\theta}$=1.33 MPa, $\partial S_{zz}/\partial E_{zz}$=0.082 MPa	[14]
Carotid-to-femoral arterial bed	Applanation tonometry	In vivo, loaded, sevoflurane or Nembutal anesthesia, non-invasive	PWV=3.96 m/s (sevoflurane)† PWV=2.89 m/s (Nembutal) †	[15]
Abdominal	Ultrasound	In vivo, loaded, tribromoethanol anesthesia, non-invasive	PWV=2.70 m/s‡	[16]
Region depends on metric	Ultrasound/ catheter	In vivo, loaded, isoflurane anesthesia, non-invasive (ultrasound)/invasive (catheter)	PWV=5.2 m/s§, PWV=3.0 m/s# PWV=3.5 m/sΔ	[17]

E, Young's modulus. *computationally separated into intimal/medial moduli. PWV, pulse wave velocity; $C_{\theta\theta\theta\theta}$ and C_{zzzz}, linearized circumferential and axial spatial material stiffness (theory of small on large). $\partial S_{\theta\theta}/\partial E_{\theta\theta}$ and $\partial S_{zz}/\partial E_{zz}$, material stiffness defined as the derivative of second Piola-Kirchhoff stress with respect to Green strain; †carotid-to-femoral transit-time PWV; ‡PWV in window of ultrasound probe; §aortic arch-to-femoral bifurcation transit-time PWV (ultrasound); #abdominal transit-time PWV (blood pressure catheter); Δdistensibility-based abdominal PWV (Bramwell-Hill, Eq. 3).

SB^{3}C2019
Summer Biomechanics, Bioengineering and Biotransport Conference
June 25-28, Seven Springs, PA, USA

REVIEW OF HYPERELASTIC MODELING OF BRAIN TISSUE

Kristen M. Cirincione and Joshua H. Smith

Department of Mechanical Engineering
Lafayette College
Easton, PA, USA

INTRODUCTION

Efforts to determine the mechanical behavior of brain tissue have occurred over the past several decades. Brain tissue was initially modeled as a linearly elastic material, with efforts limited to measuring a Young's modulus and shear modulus. However, researchers quickly determined that the behavior was more complex, with nonlinear stress-strain and time-dependent responses being observed in experiments. In addition, brain tissue is porous, and flow through the tissue has been connected to the physiology of the tissue and to diseases and their treatments. This has motivated researchers to model brain tissue as either single phase or biphasic and to model the mechanical behavior as hyperelastic and/or viscoelastic. In addition, researchers have considered the effect of the species, age of the tissue (i.e., infant vs. adult), region of the brain, homogeneity and directionality of extracted samples, and other experimental parameters such as how the tissue is preserved.

Despite a long history of experimental studies, there continues to be new contributions each year, with limited consistency amongst the results. Therefore, in order to make further progress in the field of brain tissue modeling, it is necessary to investigate the differences in modeling choices that arise among research groups. We focus our efforts on the modeling of the nonlinear mechanical behavior through the use of hyperelastic strain energy functions.

METHODS

Due to our interest in modeling the medical procedure convection-enhanced delivery [1] and the disease of hydrocephalus [2], we were familiar with a multitude of studies that report on the mechanical behavior of brain tissue. However, for completeness, we conducted a literature review using the search engine Web of Science on the following keywords: brain hyperelastic, brain compression testing, brain tension testing, brain shear testing, and brain indentation testing. Additionally, we conducted a cited reference search on each of the previously identified articles to find any other articles that were not found through the keyword search.

RESULTS

Through our literature review, we found a total of 41 articles that reported on the hyperelastic material properties of brain tissue, with the earliest article dating from 1997. While there are many other articles on the mechanical behavior of brain tissue, they focus on viscoelasticity or report experimental stress-strain or stress-relaxation data without any mathematical characterization. In the articles that report hyperelastic parameter fittings, the strain energy functions include, but are not limited to, the Fung, Gent, hyperfoam, Maxwell, Mooney-Rivlin, Neo-Hookean, Ogden, and polynomial. Of these, the Ogden strain energy function was the most used (Table 1), so we focus the remainder of this abstract on that one function.

The most commonly used expression of the Ogden strain energy function for incompressible tissue is

$$W = \sum_{i=1}^{N} \frac{\mu_i}{\alpha_i^2} \left(\lambda_1^{\alpha_i} + \lambda_2^{\alpha_i} + \lambda_3^{\alpha_i} - 3 \right), \tag{1}$$

where λ_i are the principal stretch ratios, α_i govern the shape of the stretch-stress curve, and μ_i relate to the infinitesimal shear modulus.

Poster Presentation #P270

Table 1. **Number of articles that report hyperelastic material properties for brain tissue. Some articles considered more than one function.**

Strain Energy Function	Articles
Ogden	26
Mooney-Rivlin	8
Gent	5
Fung	4
Maxwell	2
Neo-Hookean	2
Hyperfoam	1
Polynomial	1

Table 2. **Parameter values for the one-term incompressible Ogden strain energy function for human brain tissue.**

	α_1		
Test	Min	Max	Reference
Compression	−1.8	−1.9	[7]
	−15.5	−22.8	[15]
	−25.71	−50.0	[16]
	−12.67	−19.54	[17]
Tension	−26.6	−43.6	[15]
	−0.01	−0.16	[16]
	+4.52	+15.54	[17]
Shear	−21.7	−25.6	[15]
	−19.13	−28.74	[16]
Multiple Modes	−18.7	−25.3	[15]
	−20.47	−30.64	[16]
	−21.27	−28.41	[19]

While some researchers fit this Ogden strain energy function to a single loading mode [3–17], others fit it simultaneously to multiple loading modes [15, 16, 18, 19]. Each of the studies that fit data from a single loading mode used a single term in the Ogden function (i.e., $N = 1$). While three studies fit multiple loadings using a single term [15, 16, 19], one used multiple terms [18].

Focusing on studies that modeled brain tissue with the one-term Ogden function, values for the parameter α_1 in Equation 1 varied quite extensively in terms of both value and sign (see Table 2 for representative values for human brain tissue). Some researchers found α_1 to be negative [4, 7, 11, 15, 16, 19], others found it to be positive [3, 5, 6, 8–10, 12–14], and some found it could be either [17]. Even among studies from the same research group, the sign of α_1 was not always found to be consistent [10, 11].

DISCUSSION

The parameter values associated with the Ogden strain energy function vary quite extensively, most likely due to differences in experimental testing protocols. At least for human brain tissue, fitting parameter values to multiple loading modes showed more consistency across different studies than did fitting a single mode (Table 2).

While Equation 1 is the most commonly used form of the Ogden strain energy function, other researchers (for example, [20–23]) have utilized a compressible form based on the deviatoric stretch ratios $\bar{\lambda}_i$,

$$W = \sum_{i=1}^{N} \frac{2\mu_i}{\alpha_i^2}\left(\bar{\lambda}_1^{\alpha_i} + \bar{\lambda}_2^{\alpha_i} + \bar{\lambda}_3^{\alpha_i} - 3\right) - \sum_{i=1}^{N} \frac{1}{D_i}(J-1)^{2i}, \qquad (2)$$

that is found in the finite-element solver ABAQUS. While Equation 2 reduces to Equation 1 under the assumption of incompressibility, modelers adopting parameter values from literature must be careful to use values that are consistent with the form of the Ogden function that they have selected.

ACKNOWLEDGMENT

J. H. Smith thanks the Clare Boothe Luce Scholars program at Lafayette College for funding support for K. M. Cirincione during Summer 2018.

REFERENCES

[1] Smith and García, *J Biomech*, 44:524–531, 2011.
[2] Lefever et al., *J Biomech*, 46:1447–1453, 2013.
[3] Prange et al., *Stapp Car Crash Jo*, 44:205–213, 2000.
[4] Miller and Chinzei, *J Biomech*, 35:483–490, 2002.
[5] Prange and Margulies, *J Biomech Eng*, 124:244–252, 2002.
[6] Coats and Margulies, *J Biomech*, 39:2521–2525, 2006.
[7] Kohandel et al., *Med Eng Phys*, 28:449–454, 2006.
[8] Elkin et al., *J Biomech Eng*, 132:011010, 2010.
[9] Rashid et al., *J Mech Behav Biomed*, 10:23–38, 2012.
[10] Rashid et al., *J Mech Behav Biomed*, 14:163–171, 2012.
[11] Rashid et al., *Comp Mater Sci*, 64:295–300, 2012.
[12] Rashid et al., *J Biomech*, 46:1276–1281, 2013.
[13] Rashid et al., *J Mech Behav Biomed*, 28:71–85, 2013.
[14] Rashid et al., *J Mech Behav Biomed*, 33:43–54, 2014.
[15] Budday et al., *Acta Biomater*, 48:319–340, 2017.
[16] Budday et al., *J Mech Behav Biomed*, 74:463–476, 2017.
[17] Voyiadjis and Samadi-Dooki, *J Mech Behav Biomed*, 83: 63–78, 2018.
[18] Franceschini et al., *J Mech Phys Solids*, 54:2592–2620, 2006.
[19] Budday et al., *Acta Biomater*, 60:315–329, 2017.
[20] Begonia et al., *Ann Biomed Eng*, 38:3043–3057, 2010.
[21] Moran et al., *J Biomech*, 47:3762–3766, 2014.
[22] MacManus et al., *Sci Rep*, 6:21569, 2016.
[23] Forte et al., *Biomech Model Mechanobiol*, 16:907–920, 2017.

SB^{3}C2019
Summer Biomechanics, Bioengineering and Biotransport Conference
June 25 -28, Seven Springs, PA, USA

ON THE VISCOELASTICITY OF EXTRA- AND INTRA-PARENCHYMAL BRONCHI

S. Sattari (1), M. Eskandari (1, 2)

(1) Department of Mechanical Engineering
University of California, Riverside
Riverside, CA, USA

(2) BREATHE Center, School of Medicine
University of California, Riverside
Riverside, CA, USA

INTRODUCTION

Lung disease is the third leading cause of death in the United States, following cancer and heart disease, and costs over $50 billion annually [1]. Lung mechanics is still in its nascency; the escalating number of fatalities accentuates the importance of understanding pulmonary structure and function, and how disease alters tissue properties. Characterization of bronchial material response is practically nonexistent while fundamental for the creation of future technological and bioengineering tools capable of improving diagnosis and personalizing therapies. To address this need, here we explore the mechanical viscoelasticity of the lung.

One unique feature of the lung is the regulation of each breath: inhalation can be short or fast and deep or shallow in response to stimulus or conscious control. Investigating the temporal loading of this organ can produce a potential biomarker and clinical metric to contrast healthy and diseased states. However, only one other viscoelastic airway study has been conducted to date; and it was limited to the trachea, whereas distal intra-parenchymal airways are the site of chronic lung disease. Viscoelastic aspects of the lung, experimentally measured from proximal and distal airways, are analyzed in this study. Notable hysteresis and preconditioning effects are observed. Multiple discrete rheological element models are proposed to evaluate airway stress relaxation. Anisotropic and heterogeneous trends are examined with respect to recent microstructural and tissue composition results.

METHODS

Samples were obtained from five fresh pig lungs and collected from three regions (trachea, large bronchi, and small bronchi) and two directions per region (axial and circumferential) with N>20 per category (circumferential trachea, large bronchi, small bronchi: CT, CLB, CSB; axial trachea, large bronchi, small bronchi: AT, ALB, ASB). Uniaxial tensile tests were conducted (Instron 5848 Microtester, 10N load cell), with samples preconditioned five times to 35% elongation at a strain rate of 1%/sec (Fig. 1A) [2]. Energy dissipation (kPa/kPa) was defined as the hysteresis area (region between loading and unloading stress-strain curves) normalized by the cycle stress range (Fig. 1B). The effect of preconditioning between the first and fifth cycles was compared. The sixth loading curve held for 300s informed stress relaxation response per tissue category.

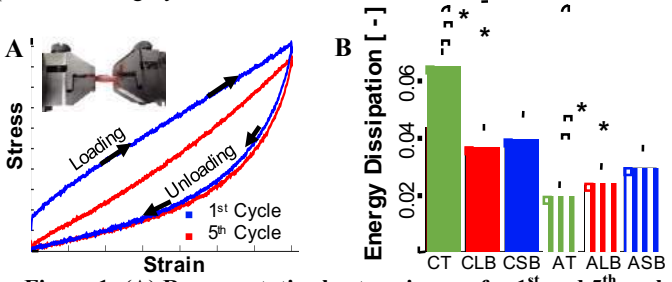

Figure 1: (A) Representative hysteresis area for 1st and 5th cycle of loading and unloading; (B) Energy dissipation per region and orientation.

Discrete rheological element models, including Maxwell, Kelvin-Voigt, Standard Linear Solid (SLS) and Standard Linear Fluid, were used to describe the tissue relaxation modulus E_{relax} (diminishing stress normalized by fixed strain). Amongst these models, SLS was most appropriate yet unable to capture the initial stress reduction (Figure 2A). Better representative of biological tissues with varying sequentially engaged molecular segments are the Maxwell-Weichart (MW) and the fractional order derivative SLS (FSLS) models (Table 1). The latter model defined a merged spring-dashpot with power α, which behaved between a pure elastic (α=0) and viscous material (α=1) [3]. Linear

viscoelastic models were only considered as tracheal soft connective tissue was previously documented as insignificantly nonlinear [4]. MATLAB's non-linear least squares algorithm, *lsqnonlin*, was used to minimize the difference between the model stress and experimentally measured stress. The averaged correlation coefficient R^2 and residuals determined the best fit model. All results were subject to a Box-Cox transformation, followed by one-way ANOVA and Bonferroni post-hoc analysis with significance set at $p<0.05$ (MATLAB Statistics Toolbox, Mathworks Inc.). Results presented as mean ± standard error, and *denotes $p<0.001$.

RESULTS

Preconditioning effects were notable between the first and fifth hysteresis samples (Fig. 1A). Circumferential samples were more subject to the effects of preconditioning than axial tissues: hysteresis area was seen to narrow and stress range decreased. Trachea samples required more preconditioning than large or small bronchi samples reproducibly behave. As preconditioning effects mirrored that of energy loss, results are not shown.

Energy dissipation was significantly higher in circumferential specimens compared to axial counterparts (Fig. 1B, $p<0.001$). Amongst regions (combined axial and circumferential response), the trachea displayed significantly greater energy dissipation compared to large and small bronchi ($p<0.001$).

Table 1 summarized model schematics, fit performances, and $E_{relax}(t)$. Of the three select models, all performed reasonably well with R^2 greater than 0.90. FSLS demonstrated superior fit to experimental stress relaxation data (R^2=0.994) and replicated the initial stress decay and asymptotic response the best, all with fewer parameters than MW.

The FSLS α parameter significantly differed for various regions and orientations (Fig. 2B). Anisotropy was only observed between circumferential and axial samples of the trachea and large bronchi ($p<0.001$), not amongst small bronchi specimens. Trachea samples exhibited heterogeneity with significantly greater α than either the large or small bronchi ($p<0.001$).

Table 1: Schematic, governing equations, and fit performance (R^2 and residual) for each viscoelastic model

	SLS	MW	FSLS
Schematic	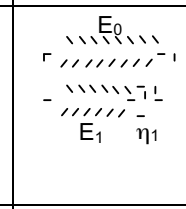	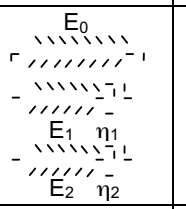	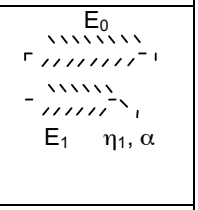
Relaxation Modulus	$E_{relax}(t) = E_0 + E_1 e^{-\frac{t}{\tau}}$ where $\tau_1 = \eta_1/E_1$	$E_{relax}(t) = E_0 + E_1 e^{-\frac{t}{\tau_1}} + E_2 e^{-\frac{t}{\tau_2}}$; where $\tau_1 = \eta_1/E_1$ $\tau_2 = \eta_2/E_2$	$E_{relax}(t) = E_0 + E_1 \sum_{k=0}^{\infty} \frac{\left(-\frac{t}{\tau}\right)^k}{\Gamma(\alpha k + 1)}$ where $\tau = (\eta_1/E_1)^{\frac{1}{\alpha}}$
{R^2} Residual	{ 0.935 } -2.5×10^{-10} [MPa]	{ 0.986 } -3.7×10^{-8} [MPa]	{ 0.994 } 4.6×10^{-9} [MPa]

DISCUSSION

Energy dissipation is found to be associated with glycosaminoglycan (GAG) content. Previous studies reveal GAG degradation results in reduced energy efficiency [5]; additionally, GAG bronchial heterogeneity uniformly increases from the trachea to the small bronchi [6]. These past studies speculate the energy inefficiency of the trachea; our viscoelastic study substantiates these inferences, finding energy dissipation and GAG are directly and inversely related.

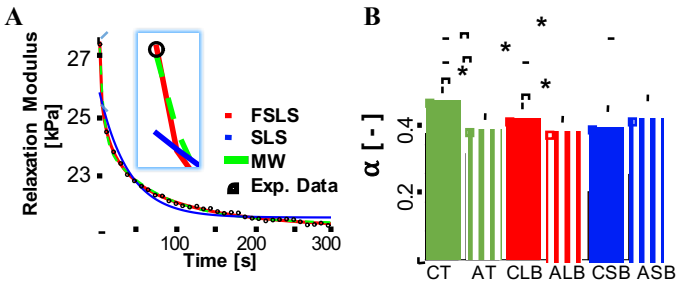

Figure 2: (A) SLS, MW, and FSLS fit to experimental data; (B) FSLS α parameter per region and orientation.

Measures of GAG content combine circumferential and axial behavior, however, the reduction of axial energy dissipation indicates the engagement of collagen and elastin fibers (Fig. 1B). The potential energy efficiency of these axially aligned elastic components drastically reduces the energy loss seen in axial tension [2].

Conversely, amongst the various regions of axial specimens, small bronchi are observed to have the greatest energy loss despite exhibiting greatest GAG content. Fiber architecture could potentially explain the counterintuitive results: small bronchi have taut and straightened fibers, whereas crimped fibers in the trachea need to be unwound before conducting stress [6]. Therefore, the reversed hysteresis trends axially can be due to taut fibers in small bronchi extending beyond their ideal physiological elastic regime and becoming inefficient.

Similar to parenchymal indentation tests with comparable α values, fits indicate pulmonary tissue relaxation is better represented by the FSLS power law than exponential decay [3]. α's are likewise more elastic (closer to 0) than viscous [3]. Regional α dependencies could possibly stem from thicker fibers in larger proximal airways, with increased viscous cross-links causing greater fluidic response; regional histology images substantiating this speculation are lacking in the literature but would elucidate the potential role of microstructure in mechanics. Energy efficiency heterogeneity is echoed in α, but overarching tissue anisotropy is insignificant; this suggests behavioral partitioning, where other discrete elements harbor the anisotropic response (indeed E_1 and η_1 present distinct direction-dependency).

This first assessment of proximal and distal bronchi viscoelasticity highlights significant anisotropy and heterogeneity, and establishes a novel relationship between tissue microstructure and energy dissipation. The intra-parenchymal results emphasize notable regional dependency, limiting extrapolation of tracheal mechanics to distal bronchi. Rheological models of bronchial viscoelasticity have the potential to yield novel diagnostic metrics of lung disease, as seen for breast tumors [3]; future studies, including dynamic viscoelasticity to represent the active breathing cycle, along with characterization and simulation of asthmatic and bronchitis human pulmonary tissue, can hold the same promise for advancements in pulmonary research.

REFERENCES

[1] Guarascio, A.J. et al. *J Clinicoecon Outcomes Res*, 5: 235-245, 2013. [2] Eskandari, M. et al. *J Appl Physiol*, 125: 878-888, 2018. [3] Dai, Z. et al. *J Med Eng Phys*, 37: 752-758, 2015. [4] Safshekan, F. et al. *J Biomech Eng*, 139: 1-8, 2017. [5] Al Jamal, R. et al. *Am J Physiol Lung Cell Mol Physiol*, 280: 306-315,2001. [6] Eskandari, M. et al., *submitted*, 2019.

SB³C2019
Summer Biomechanics, Bioengineering and Biotransport Conference
June 25 -28, Seven Springs, PA, USA

DOES THE RANDOM GENERATION ALGORITHM AFFECT THE RESULTS OF NUMERICAL MODELS FOR MECHANICAL RESPONSE OF FILAMENTOUS NETWORKS?

Hamed Hatami-Marbini

Department of Mechanical and Industrial Engineering
University of Illinois at Chicago
Chicago, Illinois, USA
Email: hatami@uic.edu

INTRODUCTION

Fibrous protein networks are the building blocks of many different biological systems such as the extracellular matrix of soft tissues. There have been different numerical and experimental studies in order to better understand the unique mechanical response of fiber networks [1-2]. It is found that the mechanical response of these networks is a function of mechanical properties of individual fibers and their arrangement with respect to each other. Furthermore, it is known that the mechanical behavior of fibrous structures is non-affine, which means that displacement gradients measured locally are different from the uniform applied far-field strains.

In numerical simulations, the microstructure of these networks is often represented by the Mikado algorithm [3-4]. This algorithm is based on depositing randomly oriented filaments of a given length into a simulation domain. However, the Mikado model may not properly represent the microstructure of all natural systems as there exist fibrous structures whose microstructure is clearly different from than the one obtained from the Mikado algorithm [5-7]. For example, extracellular matrix is created from the assembly and growth of collagen monomers from many nucleation sites. The microstructure of these networks cannot be represented by the Mikado algorithm.

Here, we create random fiber networks by growing filaments from randomly positioned nucleation sites as well by using the Mikado algorithm. We will then conduct numerical simulations and characterize the mechanical response of these fiber networks in order to determine the similarities and differences in the behavior of networks constructed by these two different generation algorithms.

METHODS

Two-dimensional (2D) random fiber networks are created by two different algorithms. In the first method, fibers of length L_0 are deposited in a square domain in random directions. Rigid crosslinks are defined at the intersection of two fibers. The coordination number of these networks is about four as two fibers cross each other at crosslinks. Note that the presence of dangling ends, which will be deleted later because they do not contribute to the elastic energy, will slightly reduce the actual coordination number.

We also generate another type of 2D fiber networks by first distributing a given number of seed points into a square domain. Fibers are grown at a constant rate from each of these seed points in random directions. We stop the growth of a filament when it reaches another fiber or the boundary of the simulation domain. The coordination number of these networks will be three, which is lower than that of the networks created by the Mikado algorithm.

We write the total free energy of the structures in terms of the bending and axial energy of their constituting filaments, i.e.

$$U = \frac{1}{2}\sum\int\left(\eta u'^2 + \kappa\phi'^2\right)ds$$

In the above equation, the filaments are represented as cylindrical rods with axial stiffness η and bending stiffness κ. Furthermore, ϕ' and u' are the curvature and axial strain of the filaments, respectively. The networks are subjected to displacement boundary conditions and their deformation field is obtained from an energy minimization procedure.

Poster Presentation #P272

The mechanical behavior of these networks will be a function of fiber density and the ratio of bending stiffness and axial stiffness of the filaments. The fiber density is a measure of how many fibers exist in the simulation box. The ratio of bending stiffness and axial stiffness represents the amount of flexibility of the filaments, i.e. the lower this ratio is, the more flexible the filaments are. Here, we use numerical simulations in order to characterize the effects of these parameters on the mechanical response of the Mikado fiber networks and the networks that are created by growing filaments from nucleation sites.

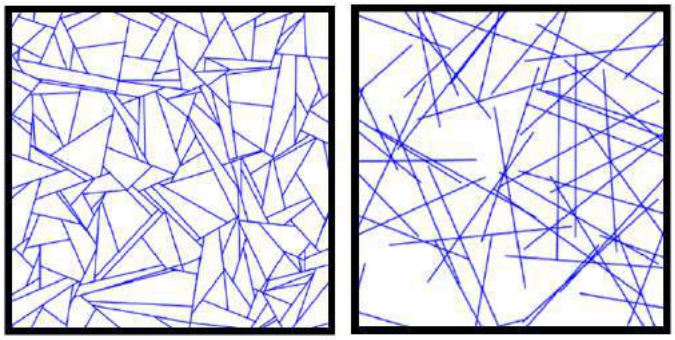

Figure 1: Typical random fiber networks created by different generation algorithm. The network shown on the right is created by the Mikado algorithm and the one on the left is created from the growth of random lines from nucleation sites.

RESULTS

The normalized Young's modulus of the fiber networks created by the Mikado algorithm and the growing one, as a function of the fiber density, is shown in Figure 2. The fiber density represents the amount of filaments per unit area in each structure. It is seen that the elasticity of both network types increases with increasing the fiber density and gets closer to its affine estimate. The affine effective Young's modulus of each network is obtained from assuming the deformation of each crosslink follows the applied macroscopic displacement. Thus, the amount of stretch in each filament is known and their energy can be found in order to determine the affine Young's modulus [7].

DISCUSSION

Figure 2 shows that there exists a significant difference in the effective elasticity of the networks generated by different algorithms. The effective Young's modulus of Mikado networks reaches the affine estimate with increasing the fiber density. Nevertheless, the effective Young's modulus of the other network type does not reach the affine estimate. This difference might be because the coordination number of these network is three and much lower than what required per by the Maxwell central-force isostatic threshold. Thus, the bending energy of filaments will be higher than their stretching energy.

Despite the above difference, Figure 2 shows that the effective Young's modulus of both networks shows a similar scaling behavior, i.e. their Young's modulus scales as a power law when the fiber density is smaller than a critical value. This observation is possibly because with decreasing the fiber density, the bending mode of deformation becomes prominent in both network types. Nevertheless, with increasing the fiber density, which accompanies a significant reduction of fiber segment length, the stretching mode of deformation starts to become more prominent and the power-law dependence of the effective Young's modulus on fiber density disappears.

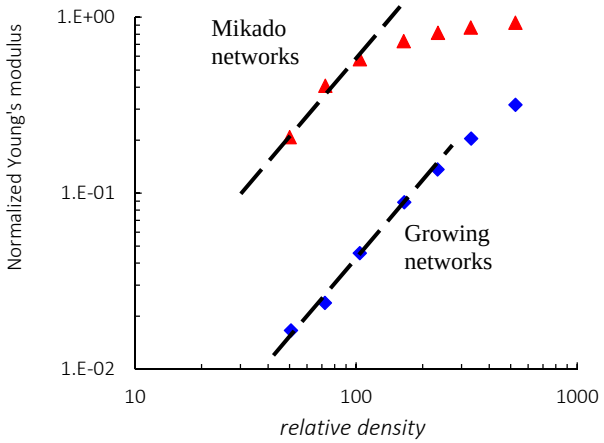

Figure 2: The normalized effective Young's moduli of different types of random fiber networks as a function of their fiber density. It is seen that increasing the line density causes the mechanical response of both fiber networks to become more affine. A similar power law dependence on the fiber density is also observed. The Mikado fiber networks shows a significantly higher effective Young's modulus compared to the other type of fiber networks when the fiber density is kept constant.

ACKNOWLEDGEMENTS

The authors would like to acknowledge the support in part by the National Science Foundation through the grant number CMMI-1351461.

REFERENCES

[1] C. P. Broedersz and F. C. MacKintosh, Modeling semiflexible polymer networks, *Rev. Mod. Phys.*, 2014, **86**, 995.

[2] H. Hatami-Marbini and C. Picu, Modeling the mechanics of semiflexible biopolymer networks: non-affine deformation and presence of long-range correlations, in *Advances in Soft Matter Mechanics*, eds. S. Li and B. Sun, Springer Heidelberg, 2012, ch. 4, pp. 119-145.

[3] J. Wilhelm and E. Frey, Elasticity of stiff polymer networks, *Phys. Rev. Lett.*, 2003, **91**, 108103.

[4] H. Hatami-Marbini and R. Picu, Scaling of nonaffine deformation in random semiflexible fiber networks, *Phys. Rev. E*, 2008, **77**, 062103.

[5] P. L. Chandran and V. H. Barocas, Affine versus non-affine fibril kinematics in collagen networks: theoretical studies of network behavior, *Journal of biomechanical engineering*, 2006, **128**, 259-270.

[6] H. Hatami-Marbini, V. Shriyan, Topology effects on nonaffine behavior of semiflexible fiber networks, *Phys. Rev. E, 2017,* **96**, 062502.

[7] H. Hatami-Marbini, Simulation of the mechanical behavior of random fiber networks with different microstructure, *Eur. Phys. J. E 2018, **41**, 65.*

SB³C2019
Summer Biomechanics, Bioengineering and Biotransport Conference
June 25−28, Seven Springs, PA, USA

VASCULAR REMODELING AND PROTEOGLYCAN ACCUMULATION IN THE AORTA OF PROGERIA MICE RESULT IN FATAL CARDIOVASCULAR EFFECTS

Sae-Il Murtada (1), Yuki Kawamura (1), Alexander W. Caulk (1), Nicole Guerrera (2), Hossein Ahmadzadeh (1), Nathan Maulding (3), Kristin Zimmerman (3), Dar Weiss (1), Marcos Latorre (1), Dillon Kavanagh (3), Zhenwu Zhuang (2), Demetrios T. Braddock (3), Jay D. Humphrey (1,4)

(1) Department of Biomedical Engineering
Yale University
New Haven, CT, USA

(2) Translational Research Imaging Center
Yale School of Medicine
New Haven, CT, USA

(3) Department of Pathology
Yale School of Medicine
New Haven, CT, USA

(4) Vascular Biology and Therapeutics Program
Yale School of Medicine
New Haven, CT, USA

INTRODUCTION

Increased central artery stiffness is an initiator and indicator of cardiovascular disease and a strong predictor of all-cause mortality, particularly deaths due to myocardial infarction, stroke, and heart failure [1]. Such stiffening is frequently associated with hypertension and aging. Hutchinson-Gilford progeria syndrome (HGPS) is an ultra-rare genetic disorder characterized by accelerated aging and premature death due to cardiovascular disease. Essential features of cardio-vascular conditions in HGPS include arterial stiffening and remodeling. Nevertheless, the development of microstructural changes in HGPS arteries involved in this process are not well characterized. Our objective was to evaluate cardiac function and biomechanically phenotype the aorta in a murine model of HGPS.

METHODS

We used the *Lmna*$^{G609G/G609G}$ knock-in mouse model which mimics the genetics and pathophysiology of HGPS [2]. Female and male wild-type control (*Lmna*$^{+/+}$) and HGPS (*Lmna*$^{G609G/G609G}$) mice were studied at 14 weeks (100 days) and 20 weeks (140 days) of age. Noninvasive echocardiographic and vascular ultrasonic data were collected from which systolic and diastolic function as well as wall thickness of the left ventricle were quantified. The pulse wave velocity was calculated from estimates of the aortic path length traveled by the pulse wave obtained from micro-CT scans, and pulse wave transit times were assessed from pulse wave Doppler measurements near the aortic root and iliac bifurcation [3].

We used a custom experimental testing system and theoretical framework to biomechanically phenotype central arteries from HGPS mice [4]. In particular, we assessed *in vivo* extensibility and distensibility, multiaxial wall stiffness, elastic stored energy capacity, and smooth muscle capacity among other metrics, and we correlated our findings with quantitative histology and *in vivo* measurements using ultrasound.

These findings were compared with similar data from mouse models of normal aging (up to 2 years) as well as from mice with severe elastopathy, noting that loss of elastic fiber integrity is a hallmark of normal aging in human central arteries.

RESULTS

HGPS (*Lmna*$^{G609G/G609G}$) mice survived to the intended 140 days of age but with significantly lower body mass than the age-matched wild-type controls (*Lmna*$^{+/+}$). Cardiac function was intact with trends of diastolic dysfunction and left ventricular wall thickening. Pulse wave velocity increased significantly due to marked shortening of pulse transit time, with no significant differences in aortic length.

In contrast to otherwise notable changes due to normal vascular aging or severe elastopathy, the biomechanical phenotype of the HGPS mice at 140 days was extreme and independent of sex: there was a dramatic loss of distensibility and extensibility, a striking reduction in wall stress and material stiffness, an unprecedented loss of elastic energy storage capacity, and a near total loss of vasoactive capacity in all central vessels from the *Lmna*$^{G609G/G609G}$ progeria mice when assessed at 140 days of age. Of particular note, there was also excessive thickening of the arterial wall due to significant increases in medial and adventitial proteoglycans/glycosaminoglycans as well as reduced undulation in fibrillar collagen.

Notwithstanding similar body mass between 100- and 140-day-old HGPS mice, the vascular biomechanical phenotype at 100 days of age was significantly milder when compared with 140-day-old HGPS mice. Importantly, little proteoglycan/glycosaminoglycan was observed in the aorta at 100 days of age, and only a slight loss in smooth muscle contractile function was observed in response to either high potassium

Poster Presentation #P273

chloride or phenylephrine. Given these observations, we then built a particle-based computational model of the arterial wall that enabled us to simulate changes in the overall biomechanical phenotype as a function of stochastically distributed local changes in cell contraction or matrix composition.

DISCUSSION

A primary function of central arteries is to store elastic energy during systole and to use this energy during diastole to augment blood flow, including both retrograde flow to perfuse the heart and antegrade flow to reduce the pulsatility to end organs. The loss of energy storage capacity we observed in HGPS mice is unprecedented even when compared to the marked losses seen in normal aging and severe elastopathy, which is expected to compromise its Windkessel effect.

Moreover, there was a significant accumulation of proteoglycans / glycosaminoglycans in the aortic wall, resulting in increased wall thickness and structural stiffness. Consistent with this, our results revealed marked increases in pulse wave velocity, a clinical indicator of central artery stiffness and all-cause morbidity and mortality. Our study suggests that accumulation of proteoglycans / glycosaminoglycans plays a critical role in vascular remodeling in the aorta and the cardiovascular disease in HGPS.

ACKNOWLEDGEMENTS

Funded in part by NIH grant HL105297

REFERENCES

[1] Mitchell, G.F. et al., *Circulation*, 121(4):505-11, 2010
[2] Osorio, F.G. et al., *Sci. Transl. Med.*, 3(106):106ra107, 2001
[3] Cuomo, F. et al., *Proc. R Soc Lond. A*, 475, 2019
[4] Gleason, R.L., Humphrey, J.D., *J. Biomech*, 38: 1255–1261, 2005.

SB³C2019
Summer Biomechanics, Bioengineering and Biotransport Conference
June 25 -28, Seven Springs, PA, USA

MECHANICAL EFFECTS OF FIBER INTERWEAVING

Bingrui Wang (1,3), Yi Hua (1,2), Fengting Ji (1,2), Ian A. Sigal (1,2)

(1) Department of Ophthalmology
University of Pittsburgh
Pittsburgh, PA, USA

(2) Department of Bioengineering
University of Pittsburgh
Pittsburgh, PA, USA

(3) School of Mechanical Engineering,
Southwest Jiaotong University,
Chengdu Sichuan, China

INTRODUCTION

Collagen fibers play a central role in the biomechanical behavior of connective tissues, and is therefore important in physiology and pathophysiology. [1, 2] Studies using scanning electron, polarized-light or multi-photon microscopy have shown that the collagen fibers of many connective tissues, such as sclera, skin and articular cartilage, are interwoven. [3, 4] However, the effects of this interweaving on the mechanical behavior of the tissues remain unknown. We hypothesized that tissue formed by interweaving fibers will have a stiffer behavior than if the fibers are not interwoven.

Our primary goal was to quantify the effects of the interweaving architecture of collagen fibers on the structural stiffness of connective tissues. A secondary goal was to determine how the effects of interweaving change with collagen volume fraction, fiber cross-section, and fiber bending stiffness.

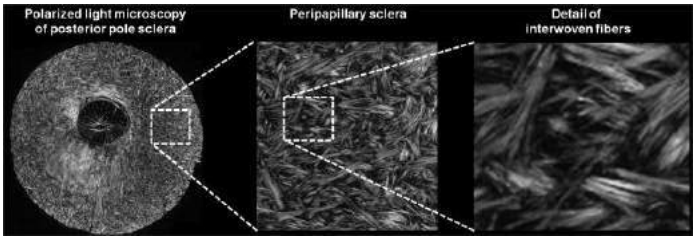

Figure 1. Example of interwoven collagen fibers in the human posterior sclera imaged with polarized light microscopy.

METHODS

To have full control of the model geometry and boundary conditions, we decided to do the study using finite element modeling.

Modeling. We reconstructed a model representing a region of interest 100 µm × 100 µm × 12 µm. All fibers in a given model were identical. The model has fibers in two directions: warp and weft. The number of fibers (N) was the same in both directions. As a first approximation the fibers were modeled as linear isotropic and homogeneous, with Young's modulus of 3 MPa, and incompressible (Poisson's ratio = 0.49).We assigned an equi-biaxial stretch of 20% as displacement boundary conditions to the ends of each fiber.

Virtual experiments: To test the effects of collagen volume fraction, we varied the number of fibers within the same region of interest: N = {2, 3, 4, 5, 6, 7}, resulting in models with collagen volume fractions of 9%, 14%, 19%, 24%, 28% and 33%.

To test the effects of fiber bending stiffness, we solved two families of models. First models without bending stiffness by using truss elements. Second, models with bending stiffness by using solid elements.

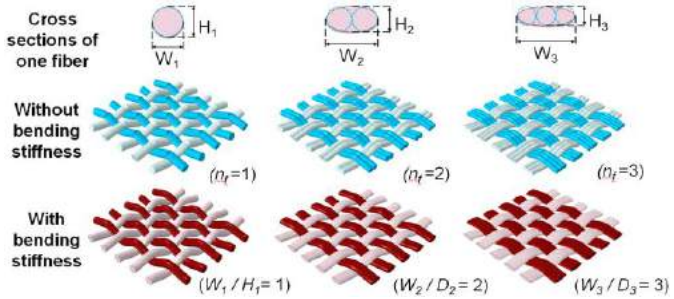

Figure 2. Example models of interweaving fibers (left column) and fibril bundles (middle and right columns) with collagen volume fraction of 24%. Top row: models with truss elements without bending stiffness. Bottom row: models with solid elements with bending stiffness.

Poster Presentation #P274

To test the effect of collagen fiber cross-section, we did the following: In models without bending stiffness (truss elements), fibers were split into two (nf = 2) or three (nf = 3) "fibril" bundles of smaller cross-section. In models with bending stiffness (solid elements), fiber cross section shape was varied from the original circular cross section, to elliptical cross sections with major axis W and minor axis H. The values of W and H were selected to be consistent with the width and height of the fibril groups in the models without bending stiffness. Total cross-sectional area was the same in all models, with single fibers or multiple fibrils, and independent of elliptical shape. Equivalent non-interweaving were also developed for comparison.

Outcome measures: Structural stiffness was computed as the sum of the response forces (the forces necessary to obtain the prescribed displacement). A stiffness increase ratio was computed by dividing the structural stiffness of a model with interweaving fibers by the stiffness of the corresponding model one without interweaving fibers (non-interweaving).

RESULTS

Example results obtained from the models without bending stiffness are shown in Figures 3 and 4. Results from models with bending stiffness are shown in Figures 5 and 6.

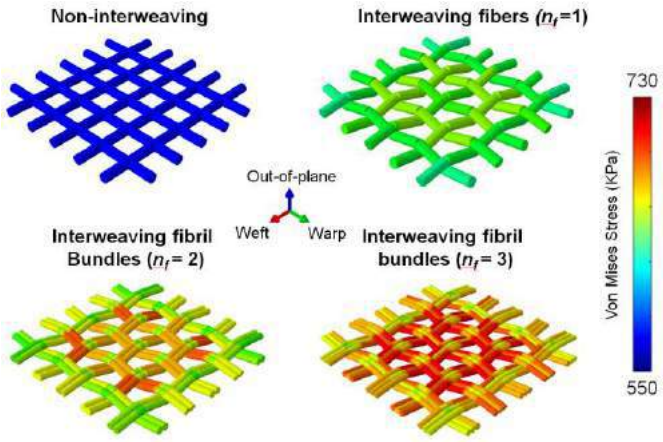

Figure 3. Contour plots of von Mises stress in models without bending stiffness. Interweaving fibers (top right) carried more load (stress) than non-interweaving ones (top left). The load-carrying capacity of the interweaving architecture was further enhanced by splitting fibers into fibrils (bottom row).

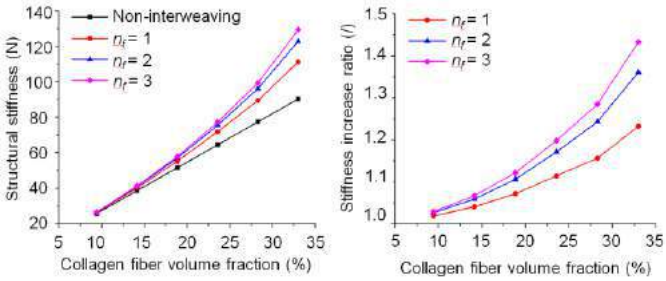

Figure 4. Structural stiffness (left) and stiffness increase ratio (right) as a function of collagen volume fraction in models without bending stiffness. Structural stiffness of interweaving fibers was higher than that of non-interweaving fibers. Stiffness increase ratio grew nonlinearly with collagen volume fraction and was higher in fibril bundles.

..

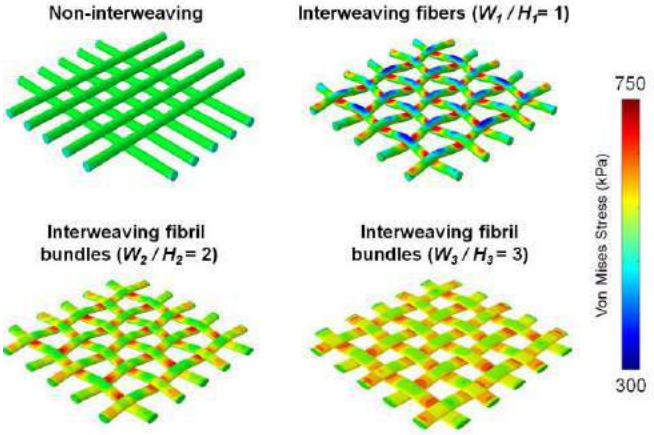

Figure 5. Contour plots of von Mises stress in models with bending stiffness. The interweaving effects were similar to those in models without bending stiffness (Figure 3). The major difference was that the high stress in models with bending stiffness was mainly located at the intersection of two fibers/fibril bundles, compared with between the intersections in models without bending stiffness

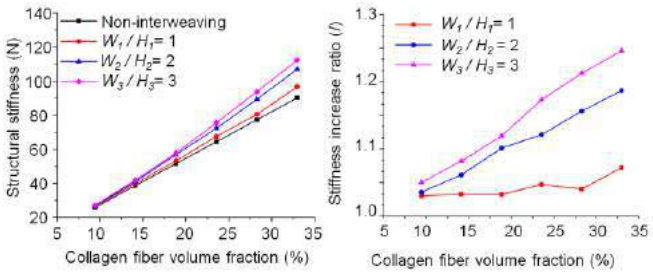

Figure 6. Structural stiffness (left) and stiffness increase ratio (right) as a function of collagen volume fraction in models with bending stiffness. In general, the magnitude and trend of structural stiffness is similar to that observed in models without bending stiffness (Figure 4). The stiffness increase ratios were lower, than in the models with no bending stiffness.

DISCUSSION

Four main findings arise from this work. First, the interweaving architecture of collagen fibers can enhance the structural stiffness of connective tissues. Second, the interweaving effects are small for low collagen volume fractions, but increase rapidly suggesting that for collagen-rich tissues the effects may be much larger. Third, collagen fiber bending stiffness can affect the stress distribution of the interweaving architecture, but its influence on the structural stiffness is limited. Fourth, the interweaving effects can be further enhanced if fibers are split into fibril bundles.

The results from our simulations should be confirmed experimentally. Also, models with geometries and mechanical properties more closely resembling biological tissues should be studied.

Our results suggest that characterizing fiber interweaving may be of important to understand how collagenous soft tissues bear loads.

ACKNOWLEDGEMENTS

Supported by National Institutes of Health Grants R01-EY023966, T32-EY017271, and P30-EY008098; Research to Prevent Blindness; and the Eye and Ear Foundation (Pittsburgh, PA, USA).

REFERENCES

[1] Voorhees, A. et al., Acta Biomater. 2017. 58: 278-290.
[2] Fratzl, P., Collagen. Springer, Boston, MA, 2008. 1-13.
[3] Jan, N.J. et al., IOVS, 2017. 58: 735-744.
[4] Gottardi, R. et al, PloS one, 11(10), e0163552.

SB³C2019
Summer Biomechanics, Bioengineering and Biotransport Conference
June 25 -28, Seven Springs, PA, USA

A CONNECTOME-BASED NETWORK MODEL TO SIMULATE PRION-LIKE PROTEIN PROPAGATION IN NEURODEGENERATIVE DISEASES

Xuesong Zhang (1), Johannes Weickenmeier (1)

(1) Department of Mechanical Engineering
Stevens Institute of Technology
Hoboken, NJ 07030

INTRODUCTION

The prion-like spreading of toxic proteins in the brain plays a crucial role in the pathogenesis of neurodegenerative diseases (ND) such as Alzheimer's disease (AD), Parkinson's disease (PD), amyotrophic lateral sclerosis or Lou Gehrig's disease (ALS), and chronic traumatic encephalopathy (CTE) [1]. Once this particular group of proteins, including amyloid-beta and tau in AD and CTE, and alpha-synuclein in PD, start misfolding, they aggregate in plaques and tangles, that cause structural and functional dysfunction of the brain [2]. Accelerated recruitment of healthy brain tissue produces common propagation patterns of principal biomarkers in ND.

Based on the development of animal models for Alzheimer's disease, it has been shown that there is a distinct chronology in the development of the disease and the spreading of toxic proteins. There is growing evidence, that these characteristic modes of progression are linked to the structural anatomy of the brain [3]. Amyloid-beta plaques in AD are sticky aggregations of misfolded amyloid beta protein that have been found to be highly neurotoxic. Neighboring neuron cells will ultimately die, leading to cerebral atrophy on the organ level [4]. As AD progresses, healthy brain tissue is progressively infested and leads to significant changes in behavior, the loss of memory and motor control, and ultimately death.

The second dominant prion associated with AD is tau [5]. Tau can turn toxic and form neurofibrillary tangles, that causes healthy axonal pathways to breakdown. The resulting disruption of regular nutrient transport along the axon network manifests in the accelerated spreading of the disease and the progressive recruitment of functional connected regions of the brain. Animal studies have shown that misfolded proteins emerge downstream of regular transport pathways associated with the axon network [6].

The spreading of toxic amyloid beta and tau are fundamental contributors to the progression of AD; yet, we know very little about their inter- and intracellular mechanisms behind the prion-like progression in ND and our understanding of progression patterns on the organ level is primarily based on studies of diseased patients [1].

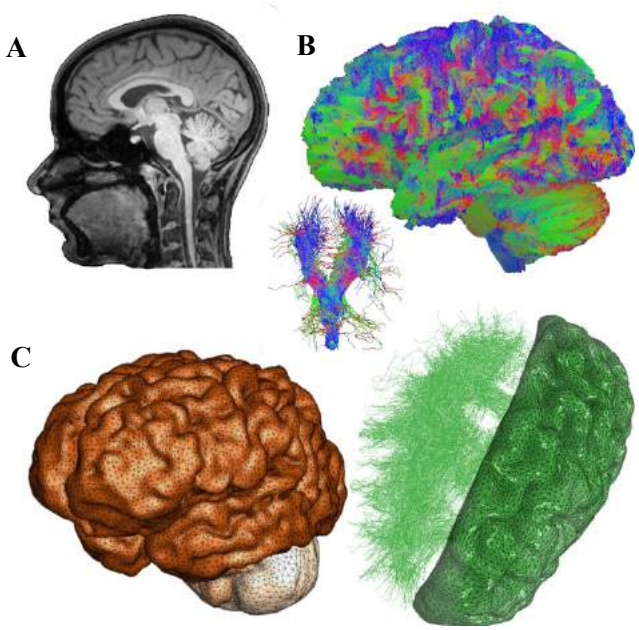

Figure 1: Segmentation and tractography of an anatomical scan (A) and of diffusion tensor imaging (B) provides a three-dimensional reconstruction of the brain (C) and allows so incorporate a physical representation of the axon network.

Poster Presentation #P275

The lack of experimental data and quantitative tools to model and predict the progression of NDs on the organ level, motivates the development of mathematical and computational models capable of representing known progression mechanisms. Thus far, most models use a graph-theory based representation of the structural and functional connectivity of the axon network [3]. While many of these models are able to capture hallmark features of cerebral atrophy, most remain limited in studying the relation between inter- and intracellular propagation mechanisms.

We created a high-fidelity finite element (FE) of the brain to study the propagation of misfolded tau along the axon network. Our ultimate goal is to predict the temporal and spatial distribution of toxic tau on the whole organ level. In a first step, we demonstrate that a reaction-diffusion equation-based propagation model is capable of reproducing characteristic progression patterns. Data-driven calibration and validation of the model will be part of future work.

METHODS

Our patient-specific high-fidelity model is based on medical images of a 32-year male volunteer. We obtained a T2-weighted magnetic resonance imaging scan with 160 transverse slices at a 1mm slice distance and an in-plane resolution of 256x256 voxels of edge size 0.938mm. We segmented gray matter, white matter, ventricles, and the cerebellum using Simpleware and generated a triangulated mesh of the patient's brain with a total of 395,409 elements [7]. The volunteer's connectome was reconstructed from accompanying diffusion tensor images (DTI) on a 7T Siemens scanner. We used the open source image processing library FSL to obtain the tractogram.

By co-registering the T2-weighted and DTI scan, we were able to merge the tractogram and the volumetric brain model, see Fig. 1. We convert each fiber track into a string of trusses and physically connect the brain and axon network models by merging nodes in both meshes that are closer together than a physically meaningful distance ϵ. In this way, we establish connectivity between the axon network and gray matter tissue, see Fig 1C.

We postulate that prions diffuse along the inter- and intra-cellular space of the brain. This mimics the aggregation and spreading of prions in the extracellular space of gray and white matter as well as the diffusion of toxic tau along the functionally and structurally connected axon network.

The toxic concentration c of both misfolded proteins is governed by the reaction diffusion equation [4]

$$\frac{\mathrm{dc}}{\mathrm{dt}} = \mathrm{Div}(\boldsymbol{D} \cdot \boldsymbol{\nabla} c) + \alpha\, c\,(1 - c), \qquad (1)$$

where D denotes the anisotropic spreading of misfolded protein. Our source term follows the classical Fisher–Kolmogorov equation and is a popular nonlinear reaction-diffusion equation that was initially proposed to model the spreading of a favored gene in population dynamics. Parameter α determines the growth rate, i.e. the speed at which healthy tissue is recruited by the propagating toxic proteins. The simulation is driven by initially seeding a minimal concentration of toxic protein in a disease specific region known from literature and will progress until the entire brain is affected, see Fig. 2A. We investigate the impact of seeding in regions associated with AD, PD, and ALS for which we have qualitative data from literature [1,2].

RESULTS AND DISCUSSION

We present our first results for the example of tau inclusions and their progression pattern in AD. Fig 2A shows the clinically observed spreading found in AD patients [1]. We note, that our three-dimensional brain model- in combination with the simple physics-based prion diffusion model- properly reproduces the clinically observed response [7]. Although we were not able to fully quantify the influence of the axon network model on the organ-level progression pattern, our initial analysis suggests that the integration of the high-fidelity brain mesh together with the axon network model, will allow us to predict tau progression on a local scale, see Fig. 2D. As a next step, we will calibrate our model parameters using toxic tau progression data obtained from animal models [5]. Our ultimate goal is to investigate the role of intercellular amyloid beta progression and intracellular tau propagation in order to understand the dominating disease mechanisms in AD.

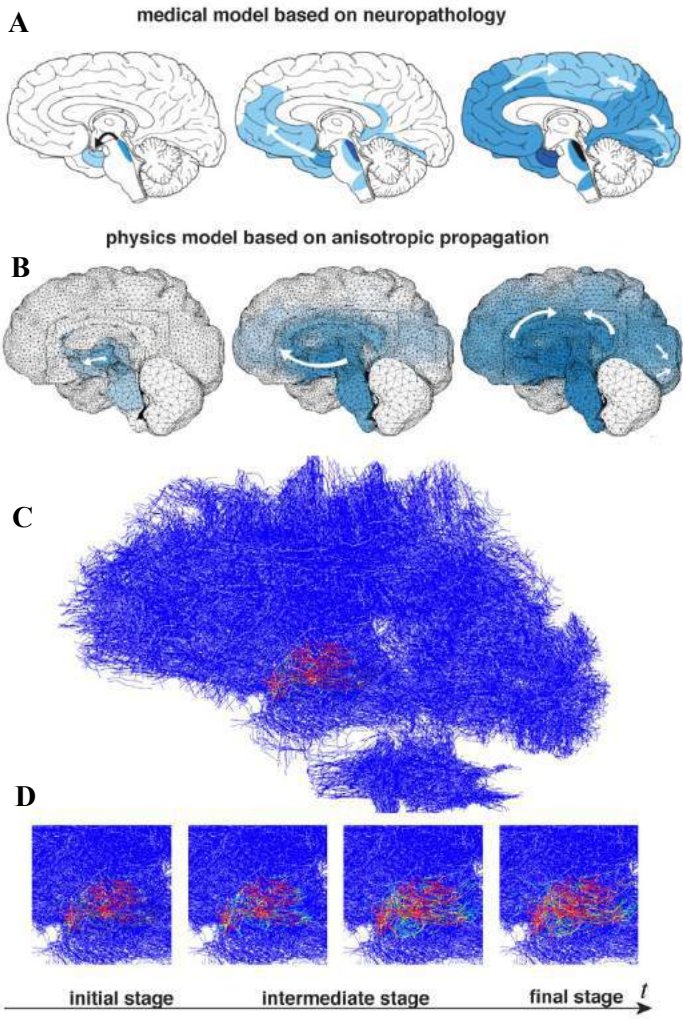

Figure 2: (A) Propagation pattern of tau inclusions observed in AD. The characteristic temporal progression of brain infestation was identified on the basis of AD patient brains []. (B) Prediction obtained using our three-dimensional ND model. Seeding of toxic tau in the entorhinal cortex (EC) accurately reproduces the clinically observed progression. (C) The progression of tau inclusion along the axon network based on initial seeding in the EC. (D) Progression along the axon network in the EC during the initial stages of AD.

REFERENCES

[1] Jucker, M and Walker L., *Nature*, 501:45, 2013.
[2] Jack, C. et al., *Lancet Neurol*, 12:207-216, 2013.
[3] Raj, A. et el., *Neuron*, 73:1204-1215, 2012.
[4] Weickenmeier, J. et al., *PRL*, 121:158101, 2018.
[5] Goedert, M, *Science*, 349:1255555, 2015.
[6] Braak, H. and Braak, E., *Acta Neuropathol*, 82:239-259, 1991.
[7] Weickenmeier, J. et al., *JMPS*, 124:264-281, 2019.

SB³C2019
Summer Biomechanics, Bioengineering and Biotransport Conference
June 25 -28, Seven Springs, PA, USA

DETERMINATION OF THE LINEAR VISCOELASTIC BEHAVIOR OF APONEUROSIS

Keith L. Grega (1), Benjamin B. Wheatley (2)

(1) Department of Biomedical Engineering
Bucknell University
Lewisburg, PA, United States

(2) Department of Mechanical Engineering
Bucknell University
Lewisburg, PA, United States

INTRODUCTION

Aponeuroses are strong elastic components that transmit force efficiently from muscle to bone to assist with locomotion. The aponeurosis acts as a transition site from muscle to tendon, which then attaches to bone [1]. The mechanical behavior of the aponeurosis is thus of great interest, as its role in the body is force transmission. There have been relatively few studies of aponeurosis material properties to date [2]. Ongoing debate exists regarding the similarities and differences of the aponeurosis and tendon, which are clouded by a lack of data on aponeurosis material properties. The specific contributions that each fibrous tissue has on muscle-tendon unit mechanics is not fully understood [3]. Determining the material properties of the aponeurosis will provide evidence of its structure and function to identify how it contributes to the movement of the musculoskeletal system.

To further complicate the role of the aponeurosis in the body, many soft tissues exhibit time dependent behavior. To the best of the authors' knowledge, there have been no previous studies investigating the stress relaxation of aponeurosis. The goal of this work is to determine how the rate of relaxation of a sample undergoing stress is affected at different strain levels. This experiment will show if the level of strain affects the relaxation behavior of the aponeurosis.

METHODS

Porcine shoulders were obtained from a local abattoir to extract the triceps brachii muscle for testing. The triceps brachii aponeurosis was dissected from the muscle and the tissue was cut into dog bone samples approximately 20 mm in height by 5 mm in width. All samples were cut parallel to the muscle fiber direction (n=10). Each sample's thickness was measured using a light microscope by taking images across the entire length of the aponeurosis and averaging all of the measurements.

Tensile stress relaxation was performed on each sample with a 5965 Instron uniaxial testing system. Images were taken throughout each trial to determine the precise strain of each sample using a digital image and correlation software. Each sample was coated with graphite powder to enhance strain tracking. The test procedure was as follows: 20 cycles of preconditioning (between 0.5 N and 1 N), then two consecutive stress relaxation steps of approximately 1-2% engineering strain at a rate of 1-2%/sec and 300 seconds of relaxation.

The data was analyzed by first determining stress (equation 1) and the strain values through a digital image and correlation software.

$\sigma = \text{stress}$
$F = \text{force}$
$A = \text{area}$

$$\sigma = \frac{F}{A} \qquad (1)$$

Then the data was examined through the power series equation of stress (equation 2):

$$\sigma = at^b + C \qquad (2)$$

The goal was to determine if the power coefficient (b) in equation 2 was strain dependent or independent at varying strain levels. Also, the power law coefficient (b) that resulted from the first and second strains of each test were compared through a paired two sample t-test for means ($p<0.05$) using equation 3.

$$t_{n-1} = \frac{\bar{y}-\mu_0}{SE(\bar{y})} \qquad (3)$$

The paired two sample t-test would determine whether the relaxation after the first and second strains of each sample were

comparable. Lastly, the strain and power law coefficient were examined to determine if there was a trend or relationship between the two values. This presents a repeated approach to evaluating if relaxation behavior is dependent on strain level.

RESULTS

The output data from the 5965 Instron uniaxial testing system shows consistent, smooth stress relaxation behavior (Figure 1). The average power law constant of the 10 samples during the first relaxation phase was -0.0952 ± 0.0246 (SD) with an average R^2 value of 0.957 and during the second relaxation phase the average power law constant was -0.0869 ± 0.0077 (SD) with an average R^2 value of 0.977 (Figure 2).

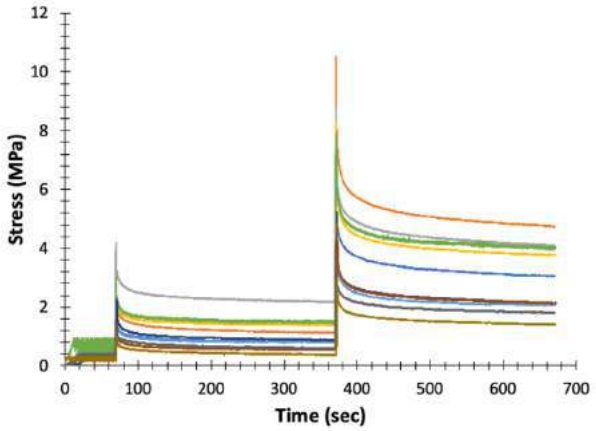

Figure 1: Instron's stress vs. time output data for each sample

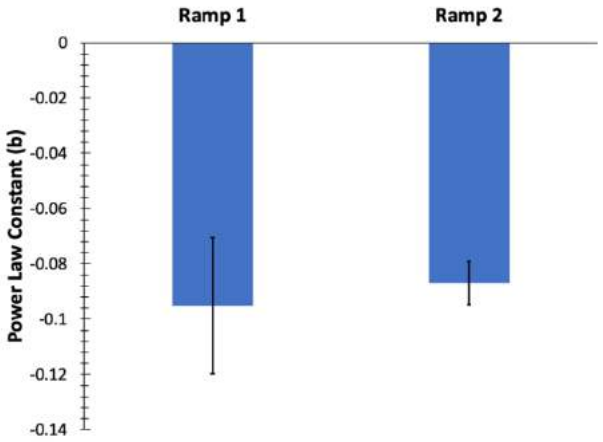

Figure 2: Comparison between Ramp 1 and Ramp 2 power law constants with standard deviation error bars

The paired t-test comparing the first and second relaxation phases were not significantly different (p=0.22). Comparison between strain and the power law coefficient of the samples yielded an R^2 value of 0.0016 with a linear slope of 0.0005 (Figure 3).

DISCUSSION

While previous studies have investigated the elastic material properties of the aponeurosis [2], we have investigated for the first time the viscoelastic relaxation behavior of the tissue. Our findings show that the rate of relaxation of the aponeurosis between strain levels of 1-4% engineering strain is independent of strain level and does not affect the relaxation behavior of the aponeurosis (Figures 2 and 3). This is supported through two statistical analyses, one comparing the two separate stress relaxation steps and one investigating the relationship between digital image correlation strain and relaxation rate.

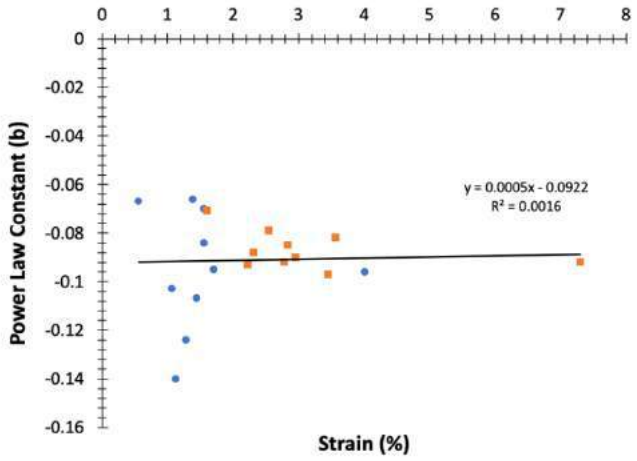

Figure 3: Strain vs. power law coefficient for each relaxation phase (blue circles – Ramp 1, orange squares – Ramp 2)

Future steps include investigation of directional viscoelasticity and fitting of hyperelastic and viscoelastic constitutive models. A more comprehensive material model for aponeurosis could then be applied to a more advanced computational model with attached aponeuroses to a full muscle-tendon unit. Implementations of these models, such as finite element analyses, could investigate how weak or diseased muscle versus healthy muscle interact with the aponeurosis, and potentially use these for post-surgery prediction of muscle function. For example, Rehorn and Blemker concluded that computational models of muscles tested with different dimensions of the aponeurosis impacted the overall location and magnitude of the peak stretches that were conducted within the muscle [4]. Thus, it is clear that the aponeurosis properties play a significant role in *in vivo* muscle function.

It is imperative to determine the material properties of the aponeurosis to ensure similar computational modeling of muscles with attached aponeurosis to *in vivo*. Once the material properties of the aponeurosis are known and studied more thoroughly, it will help improve the overall knowledge of how the aponeurosis contributes to the movement of the musculoskeletal system.

ACKNOWLEDGEMENTS

This work was supported in part by Bucknell University's Program for Undergraduate Research (PUR).

REFERENCES

[1] Eng, C. M., & Roberts, T. J. (2018). Aponeurosis influences the relationship between muscle gearing and force. *Journal of Applied Physiology*.

[2] Azizi, E., Halenda, G. M., & Roberts, T. J. (2009). Mechanical properties of the gastrocnemius aponeurosis in wild turkeys. *Integrative and comparative biology*, *49*(1), 51-58.

[3] Herzog, W. (2017). Skeletal muscle mechanics: questions, problems and possible solutions. *Journal of neuroengineering and rehabilitation*, *14*(1), 98.

[4] Rehorn, M. R., & Blemker, S. S. (2010). The effects of aponeurosis geometry on strain injury susceptibility explored with a 3D muscle model. *Journal of biomechanics*, *43*(13), 2574-2581.

SB^{3}C2019
Summer Biomechanics, Bioengineering and Biotransport Conference
June 25 -28, Seven Springs, PA, USA

MRI-BASED ANALYSIS OF 3D PRINTED PATIENT SPECIFIC PROSTATE SLICING MOLDS

David R. Rutkowski (1,2), Shane A. Wells (2), Brian Johnson (3), Wei Huang (4), David F Jarrard (5), Joshua M Lang (6), Steve Cho (2), Alejandro Roldán-Alzate (1,2,3),

(1) Mechanical Engineering
University of Wisconsin
Madison, WI, United States

(2) Radiology
University of Wisconsin
Madison, WI, United States

(3) Biomedical Engineering
University of Wisconsin
Madison, WI, United States

(4) Pathology
University of Wisconsin
Madison, WI, United States

(5) Urology
University of Wisconsin
Madison, WI, United States

(6) Medicine
University of Wisconsin
Madison, WI, United States

INTRODUCTION

Prostate cancer, one of the most common forms of cancer in America, affects nearly 165,000 men and leads to about 29,000 deaths annually.(1) Magnetic resonance imaging (MRI) has been successful at detecting prostate cancer and locating cancer lesions. However, the spatial accuracy of MR prostate images must still be validated, and appropriate correlation between MRI and histopathology should be made to display the clinical utility of MRI in prostate cancer diagnosis and treatment. Past studies have addressed this problem through the use of MRI-based prostate cutting devices that allow correlation between MRI data and histopathology data from excised prostates.(2-7) The purpose of this study was to address some limitations presented by previous studies and develop a method for 3D comparison between pre-prostatectomy MRI data and post-prostatectomy histological slices.

METHODS

Prostate Specific Membrane Antigen (PSMA) Positron Emission Tomography (PET)/MRI was performed on 10 patients with prostate cancer, both before and after chemohormonal treatment, with an imaging slice thickness of 2.5mm. The post-treatment images were imported into MIMICS (Materialise, Leuven, Belgium), where the boundary of the prostate was contoured under the guidance of an experienced radiologist (Figure 1). The prostate dimensions were measured on each MR image slice and saved for later pathological investigation. The prostate surface was then interpolated between MR image slices and a 3D volume was generated. A 3D model of the prostate was exported into 3-matic design software (Materialise, Leuven, Belgium).

To create a device that consistently cuts the prostate at 2.5mm increments, a mold template was designed in Solidworks (Dassault Systèmes, Waltham, MA). The patient specific prostate surface was subtracted from the mold template volume (Figure 2a). The mold was labeled with the patient study number and anterior/posterior, right/left, and base/apex notations. The model was exported to a steriolothography 3D printer (Form2, Formlabs, Somerville, MA). When the print was finished, it was cleaned, sterilized, and cured in isopropyl alcohol and UV light.

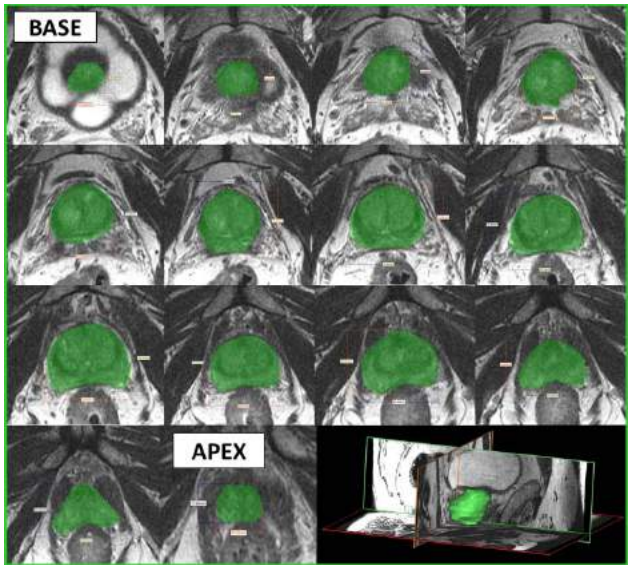

Figure 1: MR images obtained after chemohormonal therapy. Prior to prostatectomy, the prostate was contoured for definition of patient-specific prostate mold boundaries.

The mold was taken to surgical pathology, where it was used to section the prostate following prostatectomy. The slices of prostate were then oriented on the MRI-derived 2D contours, and a picture was taken for later analysis. The prostate slices were then taken for histological analysis.

To analyze the 3D accuracy of the MRI-based prostate mold, the post-resection prostate volume was reconstructed based on the prostate slices from surgical pathology. To do this, contours of the prostate slices were stacked on planes 2.5mm apart (Figure 2b), and lofted to create a 3D volume in Solidworks. A part comparison analysis was then performed in 3-matic to generate quantitative and qualitative regional difference maps comparing the MRI-derived prostate geometry with the representative post-prostatectomy geometry.

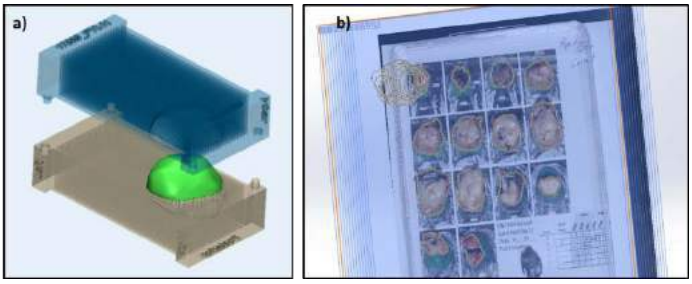

Figure 2: a) Mold template to guided parallel 2.5mm cuts in the prostate. After sectioning, outlines of the prostate slices lofted to create a representative post-prostatectomy 3D geometry for surface comparison

RESULTS

The patient-specific molds were used to effectively slice the unfixed prostate at 2.5mm increments. When compared to pre-prostatectomy MRI contours, the post-prostatectomy reconstructed volumes displayed patient-specific variation, as displayed in Table 1 and Figure 3. On average, the post-prostatecomy reconstructed volume dimensions were about 2mm smaller than the predicted MRI volume dimensions. This difference lies below the imaging slice resolution of 2.5mm.

Table 1: Statistics for surface point comparison between pre-prostatectomy MRI and post-prostatecomy slice reconstruction prostate geometries

Subject	Q1 (mm)	Median (mm)	Q3 (mm)	Mean (mm)	Standard Deviation (mm)
1	-0.72	0.85	2.39	1.16	2.37
2	-2.51	-0.99	0.94	-1.05	2.35
3	2.10	3.42	5.08	3.62	1.98
4	1.81	3.32	5.06	3.25	2.16
5	0.53	0.53	0.53	0.57	0.35
6	2.07	3.12	4.28	3.21	1.58
7	0	1.99	2.31	2	2.38
8	-0.21	1.43	3.67	2.17	3.34
9	1.20	3.09	5.30	4.2	9.91
10	-1.05	0.47	2.12	0.80	5.39
Average	**0.32**	**1.73**	**3.17**	**1.99**	**3.19**

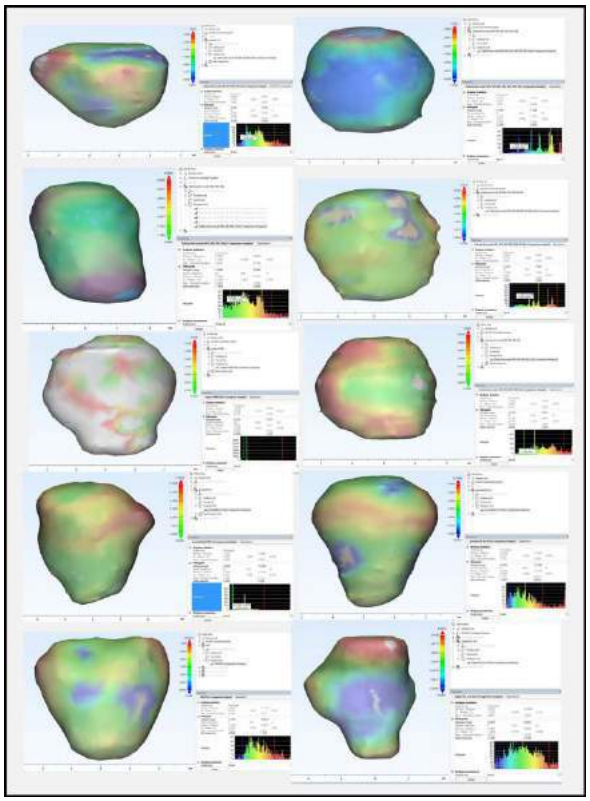

Figure 3: Comparison between pre-prostatectomy MRI and post-prostatecomy slice reconstruction prostate geometries.

DISCUSSION

Pre-prostatectomy MRI data can be compared post-prostatectomy histopathological prostate slices to determine the utility of MRI for prostate cancer detection and location. This study looked to build upon other studies focused on comparing prostate partitioning and MRI to histology. It has been noted that the fit of the mold to the resected prostate, the slicing technique, and the thickness of the image slices are major factors that affect image-based model performance.(3) Accordingly, this study employed patient-specific molds based upon individualized prostate contours, image slice thickness of 2.5mm (vs 3-6mm used in previous studies) that matched pathology slice thickness, and cutting of unfixed prostate on the day of surgery to evaluate masking of the MR image and geometric ex-vivo changes to the shape of the prostate. Through the remainder of this study, more subjects will be enrolled to analyze the effectiveness of these devices for histopathological prostate analysis with MRI and PET/MRI.

ACKNOWLEDGEMENTS

The research presented was supported by the NIH (UL1TR000427, TL1TR000429) and DOD IMPACT award PC15053. The authors also wish to acknowledge support from GE Healthcare who provides research support to the University of Wisconsin.

REFERENCES

[1] Prostate Cancer Facts. *Prostate Cancer Foundation*; 2018.
[2] Drew B, et al., *J Magn Reson Imaging* 2010;32(4):992-996.
[3] Shah V, et al. *Rev Sci Instrum* 2009;80(10):104301.
[4] Jackson AS, et al. *Br J Radiol* 2009;82(974):148-156.
[5] Kimm SY, et al. *J Magn Reson Imaging* 2012;36(1):206-212.
[6] Yamamoto H, et al. *Acad Radiol* 2014;21(8):1009-1019.
[7] Hughes C, et al. *IEEE Trans Biomed Eng* 2013;60(2):281-291

SB^{3}C2019
Summer Biomechanics, Bioengineering and Biotransport Conference
June 25 -28, Seven Springs, PA, USA

MURINE VAGINAL WALL BIAXIAL CONTRACTILE RESPONSE FOLLOWING ELASTASE DIGESTION

Gabrielle L. Clark (1), Laurephile Desrosiers (2), Leise R. Knoepp (2), Kristin S. Miller (1)

(1) Biomedical Engineering
Tulane University
New Orleans, LA, USA

(2) Female Pelvic Medicine and
Reconstructive Surgery
Ochsner Clinical School
New Orleans, LA, USA

INTRODUCTION

In the United States 1 in 10 women undergo surgical intervention for pelvic organ prolapse (POP) [1]. POP is characterized as the descent of the pelvic organs into the vaginal canal, which decreases quality of life. Although aging, child birth, and increased abdominal load are well established risk factors, the underlying mechanisms for POP are not fully understood. Elastin content and contractile function are decreased in vaginal tissues from patients with POP [2-3]. Disruption of elastin induced dilatation of the vaginal caliber and decreased tissue compliance [4]. Furthermore, the loss of elastin diminished the contractile response of the aortic wall under biaxial mechanical loading [5]. In the vaginal wall, however, the interaction between elastin and smooth muscle is not fully elucidated. Further, the effect of biaxial mechanical loading on the contractile response has not been investigated. Therefore, the objective of this study was to investigate the role of elastin and mechanical loading on the contractile response of the murine vaginal wall. It was hypothesized that decreased elastin content and increased mechanical loading will decrease the contractile response.

METHODS

Female C57BL6 mice at 4-6 months of age (at estrus) were euthanized by guillotine without anesthesia (IACUC approved). Vaginal tissue was freshly isolated and separated from the cervovaginal complex. **Biaxial Contractility.** Isobaric-axially isometric contraction of the vaginal tissue (n=5) under physiologically-relevant loads was performed with a pressure-myograph system (Danish MyoTechnologies, Aarhus, Denmark) [5]. The unloaded configuration was identified, followed by determination of the physiologic length where the transducer-measured force remained constant over an increasing range of pressure [4, 6, 7]. The tissue was preconditioned with cyclic pressurization and axial extension. The smooth muscle cells were preconditioned under low loads with 40 mM of KCl inducing maximum contraction. Isobaric-axially isometric contraction was assessed at the physiologic length (l_{pl}) under 3 constant pressures (0, 7, and 15 mmHg). Further, contraction was assessed under the *in vivo* measured pressure (7mmHg) at 2 additional fixed axial lengths (4% below and above the physiologic length). Maximum contraction was induced with 40 mM of KCl. Change in outer diameter and axial force was recorded. The tissue was incubated with 15U of porcine elastase for 45 minutes and the testing protocol was repeated [4]. **Ultrasound.** Short-axis B-mode ultrasound images were acquired during testing to measure vaginal wall thickness. Images were acquired with a 40MHz transducer at the physiologic length and pressure (7 mmHg) under basal tone and when maximally contracted. This was performed for the control and elastase treated samples. Vaginal wall thickness was measured in ImageJ. **Histology and Immunohistochemistry.** Histological and immunohistochemical analysis for the control (n=4) samples were performed on 4μm circumferential and axial cross-sections. Tissue sections were stained with Harts Elastin stain and for alpha-smooth muscle actin. Area fractions were quantified by ImageJ Color Deconvolution plugin and a custom GNU Image Manipulation Program protocol [4]. **Statistical Analysis.** A 2-way ANOVA evaluated the effects of treatment and load on the contractile response. When necessary, this was followed by a 1-way ANOVA with Tukey post-hoc to identify the significant effect of loading and paired t-test comparing the control and elastase treated response. Change in vaginal wall thickness with contraction between the control and elastase treatment was evaluated with paired t-test. Paired t-test were used to

Poster Presentation #P278

compare circumferential and axial area fraction. Statistical significance was set to $p<0.05$ and data reported as mean +/- standard error of mean.

RESULTS

The 2-way ANOVA identified significant differences in the change in axial force with respect to treatment ($p<0.003$) and pressure ($p<0.001$) (Figure 1A). Elastase treatment significantly decreased the changes in axial force with contraction at 0 ($p<0.007$), 7 ($p<0.03$), and 15 ($p<0.005$) mmHg. Further, the axial force was significantly reduced at 7 and 15 mmHg compared to 0 mmHg for the control ($p<0.003$) and treated ($p<0.02$) tissue. The 2-way ANOVA identified significant differences in the change in axial force with respect to treatment ($p<0.003$) and axial length ($p<0.001$) (Figure 1B). Elastase treatment significantly decreased the change in axial force with contraction at the physiologic length ($p<0.01$) and 4% below ($p<0.03$). For the control ($p<0.001$) and elastase ($p<0.03$) treated tissue, axial force was significantly reduced between 4% below and above the physiologic length (l_{pl}).

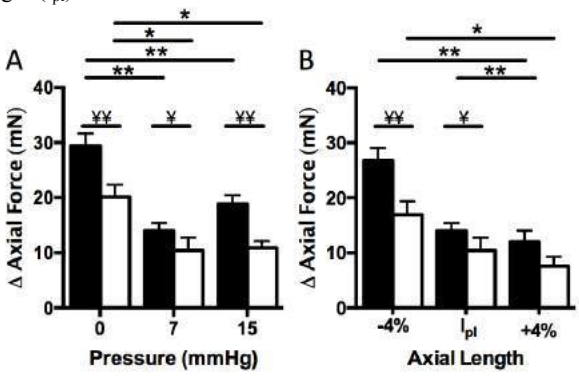

Figure 1: Change in axial force with contraction at 3 (A) constant pressures and (B) fixed lengths pre- (black) and post- (white) elastase digestion. Elastase treatment and mechanical loading significantly reduced the change in axial force. Statistical significance denoted by load (*p<0.05, **p<0.01) and treatment (¥p<0.05, ¥¥p<0.01).

The 2-way ANOVA identified significant differences in the change in outer diameter with respect to pressure ($p<0.001$) (Figure 2A). The change in outer diameter was significantly ($p<0.001$) reduced at 7 and 15 mmHg compared to 0 mmHg for the control and treated tissue.

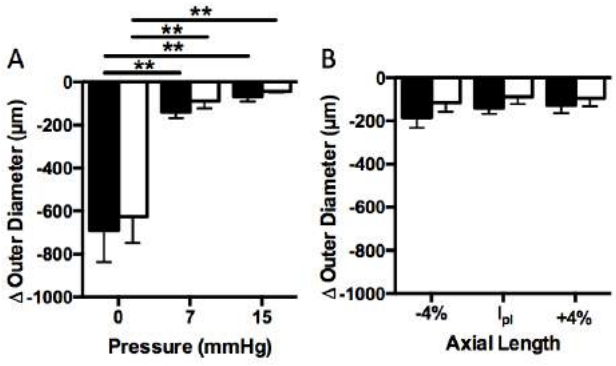

Figure 2: Change in outer diameter with contraction at 3 (A) constant pressures and (B) fixed lengths pre- (black) and post- (white) elastase digestion. Mechanical loading by pressure significantly reduced the change in outer diameter. Statistical significance denoted by load (p<0.01).**

Elastin area fraction was significantly greater for axial sections compared to circumferential sections (Figure 3). Statistical significance was not identified between the two orientations for alpha smooth-muscle actin. Significant change in vaginal wall thickness under contraction was not identified between the control and elastase treatment.

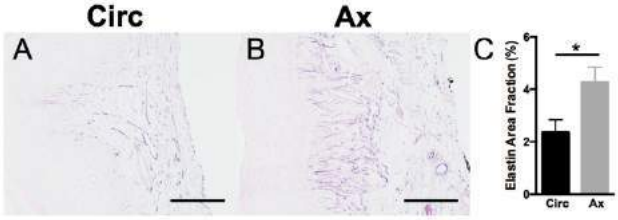

Figure 3: Histological analysis on (A) circumferential (circ) and (B) axial (ax) vaginal wall cross-sections with Hart's Elastin stain. (C) Elastin area fraction was significantly larger on axial sections compared to circumferential. Statistical significance denoted by *p<0.05. Scale=100μm.

DISCUSSION

This study investigated the effect of elastase digestion on vaginal wall contractile response as a function of mechanical loading. Elastase digestion significantly reduced the change in axial force observed with contraction (Figure 1). This finding is supported by prior work in the aorta from elastopathic mice, wherein a decrease in axial force with contraction compared to control was observed [4]. Note that in contrast to the findings from the murine aorta with elastin deficiency, the change in outer diameter was not significantly affected by elastase treatment in the murine vagina. This finding, however, is similar to the behavior of the murine mesentery artery following elastase digestion [8]. The significant decrease in axial force may be described by elastin composition with respect to orientation. Elastin area fraction was greater along the axial compared to the circumferential direction (Figure 3), suggesting that vaginal smooth muscle may interact with elastin. Further, increased pressure and axial length significantly decreased the change in axial force under contraction (Figure 1). Significant decreases in outer diameter, however, were only observed under increased pressures (Figure 2). These findings demonstrate that increased mechanical loading decreases the contractile response.

The findings of this study highlight the role of elastin and mechanical loading on vaginal wall contraction. This study investigated the immediate response to the loss of elastin and increased loading, however, further investigation is needed to quantify the long-term biochemical and biomechanical mediated effects. Characterizing the interaction between smooth muscle and elastin in response to mechanical loading may provide further insight into the etiology of POP and improve treatment strategies.

ACKNOWLEDGEMENTS

We acknowledge funding from the NSF CAREER Award Program (CMMI-1751050) (KSM) and Louisiana Board of Regents Fellowship (GLC). We acknowledge Sae-Il Murtada, PhD (Yale University) for training on the biaxial contractile protocol.

REFERENCES

[1] Olsen, A et al., *Obstet Gynecol*, 89:501–506, 1997. [2] Karam, J et al., *BJU Int*, 100: 346-50. 2007. [3] 27. Northington, G et al., *Reprod Sci*, 18:296-303. 2011.[4] Akintunde, A et al., *J Biomech Eng*, 2018. [5] Murtada, S et al., *J Biomech Eng*, 138: 0510081-7, 2016. [6] Robison, K et al., *J Biomech Eng*, 139: 1045041-8, 2017. [7] Ferruzzi, J et al., *Ann Biomed Eng*, 41: 1311-1330, 2013. [8] Tuna, B et al., *J Biomech*, 46: 1420-1426, 2013.

TOWARD FAST AND ACCURATE AUTOMATED FEMALE PELVIC FLOOR 3D GEOMETRIC MODEL RECONSTRUCTION BASED ON DEEP CONVOLUTIONAL NEURAL NETWORKS

Fei Feng (1), James A. Ashton-Miller (2), John O.L. DeLancey (3), Jiajia Luo (1)

(1) University of Michigan – Shanghai Jiao Tong University Joint Institute
Shanghai Jiao Tong University
Shanghai, 200240, China

(2) Department of Mechanical Engineering
University of Michigan
Ann Arbor, MI, USA

(3) Department of Obstetrics and Gynecology
University of Michigan
Ann Arbor, MI, USA

INTRODUCTION

3D geometric models reconstructed from medical imaging dataset of CT or MRI play an important role in surgery previsualization and intervention procedures[1, 2]. This technique has been widely applied in neurosurgery and oral and maxillofacial surgery[3, 4]. It has also been applied to the pelvic floor-related field for clinical use.

3D geometric pelvic floor model reconstructions are vital for the conduct of accurate 3D finite element analysis[5-7]. However, 3D model reconstruction based on manual segmentation is often time-consuming for personalized modeling, simulation and surgical planning.

Therefore, several authors have tried to apply automated segmentation and reconstruction method to pelvic floor organs[8-11]. Edge detection and pattern recognition methods were proposed to finish this task and have shown promising results. However, there still exist problems with generalization and efficiency. For example, reconstruction algorithms constructed from images from a few patients may not generalize well to other patients. In addition, non-parametric methods are time consuming at the inference stage.

Recently, deep convolutional neural networks (CNN) have shown great promise in computer vision[12], so many biomedical researchers have successfully applied these techniques to their domain[13]. Thus in this paper we developed a 3D geometric model reconstruction method for pelvic floor organs and muscle based on MR images, including bladder, rectum, and levator ani muscle, using an automated segmentation model based upon deep convolutional neural networks.

METHODS

MR images of 6 women with anterior and 6 with posterior vaginal prolapse were selected from University of Michigan institutional review board-approved (IRB #HUM00056743) study. 3D models of bladder,

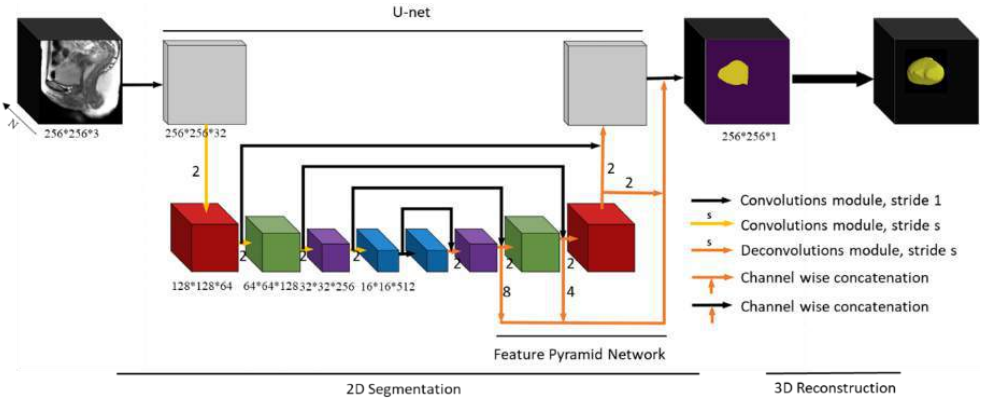

Figure 1: Automated MR images 3D modeling Pipeline. N means slices numbers for one series of MR images. 256*256*32 means height*width*channel. Feature map with same color has same size.

rectum, and levator ani muscle were reconstructed manually from the sagittal slices at both rest and Valsalva based on our previous work[14]. The MR images had the same resolution and image size (256*256 pixels).

We adopted the modeling method that segmented the structures into slices first, followed by the reconstruction. A pipeline is shown in Fig.1. The pipeline includes two parts: the 2D segmentation part and the post processing part for 3D reconstruction. The 2D segmentation model was constructed using deep convolutional neural networks. U-Net was used as the basic network architecture for segmentation feature extraction[15]. A transfer learning technique was then used to train the U-Net. At the end of the upsampling stage we adopted the feature pyramid network idea for the pixelwise prediction by concatenating the feature map at 4 different resolution configurations to make the final prediction[16]. After that the 3D models were reconstructed using the contours in all slices with interpolation and the surface smoothing.

A dice coefficient was used for segmentation performance evaluation[17]. However, if there are no regions of interest for segmentation some slices, the original dice coefficient would always be zero. To solve this problem, therefore, we proposed to use a loss function in Eq. (1).

$$Loss = \frac{GT \cap (1-PR) + (1-GT) \cap PR}{GT \cup PR} \qquad (1)$$

where GT represents the ground truth segmentation labeling, PR represents the prediction labeling. Another cross-entropy term was added to punish the situation that predicts a segmentation map with a blank interest region and vice versa.

RESULTS

The results for 2D segmentation model on testing dataset are summarized in Table 1.

Table 1: Evaluation result on testing dataset.

Class	Dice Coefficient	Presence accuracy
Bladder	**0.907**	**0.947**
Rectum	0.849	**0.917**
Levator ani muscle	0.619	**0.879**

Segmentation of the bladder had the best performance among the three classes. With our proposed loss function, average prediction presence accuracy for the three classes were all above 0.87.

The model prediction on testing sample images is shown in Fig. 2, and the 3D geometric model reconstructed on testing sample data is shown in Fig.3.

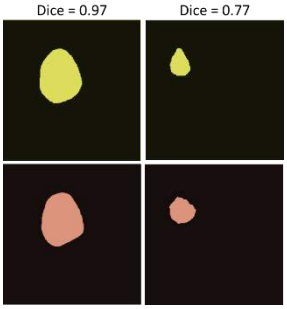

Figure 2: Visual results of segmentation map between ground truth and CNN model prediction on bladder. First row: Ground truth, Second row: Prediction map. Dice=0.97 shown good prediction. Dice=0.77 shown weak prediction on the contour.

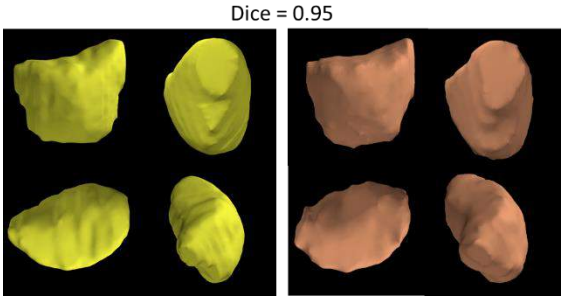

Figure 3: 3D geometric model reconstruction result by manual segmentation and model prediction. Left: Ground truth Right: Predicted model.

DISCUSSION

In this study we developed a technique which applied deep CNN for patient-specific pelvic floor organs 3D automated reconstruction based on MR images. Compared to the previous methods[8-11], it showed promising segmentation performance and faster processing speed, which could be useful for faster finite element modeling and virtual surgical planning.

The segmentation performance for the bladder was better than the rectum and levator ani muscle, this being best explained by the structure shape and volume. The bladder has the largest contour on each slice and with its large volume, we had more slices to use as the training samples.

In the future we need to add more segmentation classes, and more images into our study to improve the segmentation performance.

ACKNOWLEDGEMENTS

NSFC General Program grant 31870942, NIH R01 HD 038665 and P50 044406.

REFERENCES

[1] Y. L. Hu et al., *Injury* 42(10), 1121-1124, 2011.
[2] Š. Janda et al., *J Biomech* 36(6), 749-757, 2003.
[3] H. R. Malone et al., *Neurosurgery* 67(4), 1105-1116, 2010.
[4] J. Xia et al., *Int J Oral Max Surg* 29(1), 11-17, 2000.
[5] K. F. Noakes et al., *J Biomech* 41(14), 3060-3065, 2008.
[6] L. Chen et al., *J Biomech* 42(10), 1371-1377, 2009.
[7] J. Luo et al., *J Biomech* 48(9), 1580-1586, 2015.
[8] Z. Ma et al., *Comput Method Biomec* 13(2), 235-246, 2010.
[9] L. Hoyte et al., *J Magn Reson Imaging* 33(3), 684-691, 2011.
[10] Z. Ma et al., *Int J Numer Meth Bio* 28(6-7), 714-726, 2012.
[11] Z. Ma et al., *Comput Biol Med* 43(4), 248-258, 2013.
[12] A. Krizhevsky et al., *NIPS 2012*, 25(2), 2012.
[13] A. Esteva et al., *Nature* 542(7639), 115-118, 2017.
[14] J. Luo et al., *Am J Obstet Gynecol*, 391.e1-391.e2, 2011
[15] O. Ronneberger et al., *MICCAI 2015*, 234-241, 2015.
[16] T.-Y. Lin et al., *arXiv preprint arXiv:1612.03144*, 2016.
[17] Dice, Lee R. *Ecology* 26.3 : 297-302, 1945.

SB³C2019
Summer Biomechanics, Bioengineering and Biotransport Conference
June 25 -28, Seven Springs, PA, USA

VISCOELASTIC MECHANICAL BEHAVIOR OF DECORIN KNOCKOUT MOUSE CERVICAL TISSUE

Nicole Lee (1), Charles Jayyosi (1), Shanmugasundaram Nallasamy (2), Mala Mahendroo (2), Kristin M. Myers (1)

(1) Department of Mechanical Engineering
Columbia University
New York, NY, USA

(2) Department of Obstetrics and Gynecology and Green Center for Reproductive Biology Sciences
University of Texas Southwestern Medical Center
Dallas, TX, USA

INTRODUCTION

The dramatic remodeling of the soft tissues in the reproductive system are critical in a healthy pregnancy. One of these tissues is the cervix, which acts as a barrier between the fetus and environment. It must remodel sufficiently by term to allow for delivery [1]. One of the major medical challenges in obstetrics is preterm birth (PTB), which is defined as birth before 37 weeks. Much of current research focuses on the premature remodeling of the cervix, which is a final common pathway for many causes of PTB [2]. In the mouse, the cervix is shown to undergo a dramatic softening from day 6 to 12 of a 19-day pregnancy and a gradual softening later in pregnancy. These changes have been attributed to collagen reorganization in the tissue [3], but the contributions of other extracellular components to remodeling is not completely understood.

Cervical tissue is comprised of many components, including cells, collagen, elastin, proteoglycans, hyaluronan, and matricellular proteins [4]. Collagen fibers are shown to be the major load-bearing component of tissue, given its higher stiffness compared to other components [5]. Decorin is a major proteoglycan in the cervix and plays a role in collagen synthesis and formation [6]. A recent paper demonstrated a decorin knockout (DcnKO) mouse cervix had a significantly lower maximum stiffness and tissue strength compared to wild-type (WT) under a load-to-failure mechanical test. Moreover, this difference was only present at the early stages of pregnancy (non-pregnant (NP) and day 6) and disappeared in late pregnancy. The behavior was supported by TEM images, which showed NP mice exhibited disrupted collagen fibers, but were recovered at day 18 (d18) of pregnancy [7].

While differences are observed between WT and DcnKO models under load-to-failure mechanical tests, this test is a first step in understanding the mechanical behavior of the cervix. Hydrated soft tissue typically presents a hyperviscoelastic behavior, hence we designed a viscoelastic mechanical test. A viscoelastic response is more likely observed *in vivo* as the cervix experiences repeated loads from the fetus or other external forces. This research aims to implement a viscoelastic protocol and identify how decorin affects the behavior of NP and late pregnancy mouse cervical tissues.

METHODS

Mouse cervix samples were collected from two time points in pregnancy, NP and d18. At the NP time point, 3 WT and 3 DcnKO were collected. At the d18 time point, 3 WT and 2 DcnKO with biglycan heterozygous were collected. Samples were prepared for whole-specimen ring tensile loading as previously described [8].

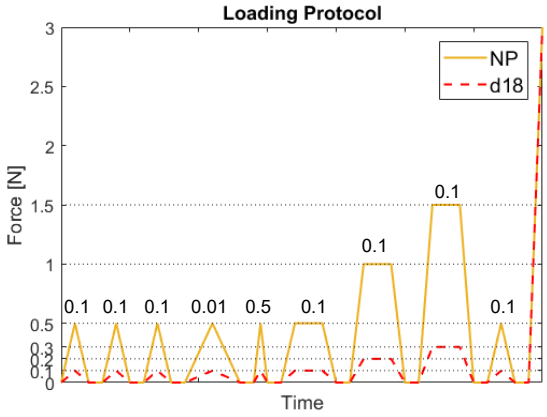

Figure 1: Loading Protocol for NP and d18 samples. Numbers above each load, denote its loading rate in mm/s. Time not to scale.

The sample was first allowed to swell for 2 hours in phosphate buffered saline with 2 mM ethylenediaminetetraacetic acid. A preload of 0.001 N was applied to ensure the sample was in contact with threaded sutures. The loading protocol consists of 2 main sections: 1) strain rate sensitivity cyclic load-unloads and 2) stress relaxation ramp-holds (Fig.1). Different load levels were applied for NP and d18 to ensure each sample could sustain a majority of the test without breaking. Between each loading, the sample was held at zero displacement for 20 minutes to recover and equilibrate. Images were taken 1/s while loading and 1/60s while holding to record deformation of the sample.

For this initial mechanical analysis, we compared raw force-extension curves of the load-unload section and raw force-time curves of the stress relaxation section. Comparison is contained to within each gestation point as the NP and D18 samples are taken to different load levels.

RESULTS

The average loading curve of the 3rd, 4th, and 5th load cycle (corresponding to loading rates of 0.1,0.01, and 0.5mm/s) are shown in Fig.2. A linear fit was applied to the data after the toe region to obtain a slope. At the NP time point, the WT and DcnKO exhibit similar slopes and no strain rate sensitivity. At the d18 time point, the WT samples have a larger toe region and lower slopes compared to DcnKO at all strain rates. The slopes increase with increasing strain rate. However, this increase in slope at d18 may be the result of damage – see Discussion.

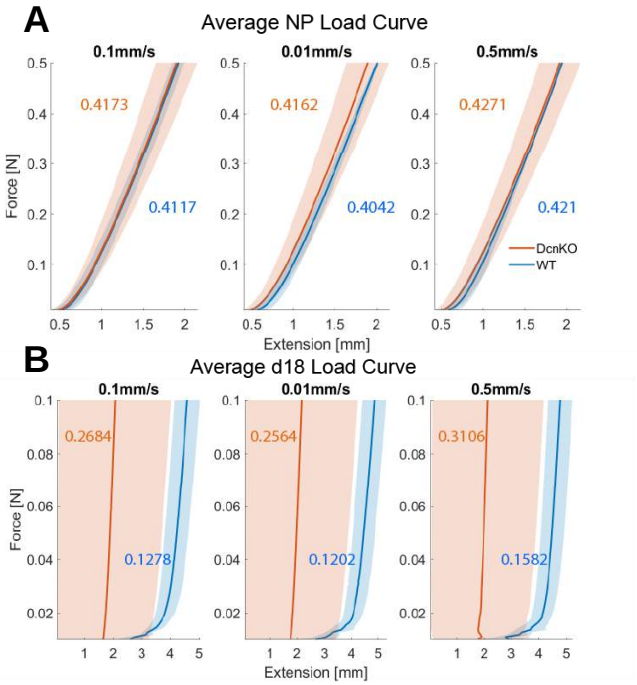

Figure 2: Average Load Response A) NP samples B) d18 samples. Shading represents standard deviation of average load curve. Numbers to the left of each line denote slope in N/mm of linear fit.

For the average stress relaxation curve, differences are more apparent between WT and DcnKO at the NP time point under the highest load level (Fig.3). Only 1 of 3 DcnKO samples made it to the highest 1.5N load level. At the 2 lower load levels, there are no differences, in part due to a large standard deviation. For d18 samples, there is no apparent difference between DcnKO and WT. All samples made it through the load cycles and the equilibrium forces are similar.

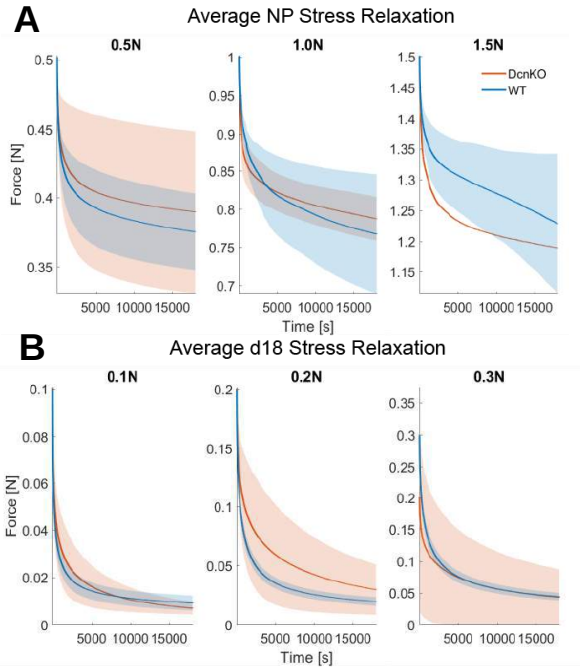

Figure 3: Average Stress Relaxation Response. A) NP samples B) d18 samples. Shading represents standard deviation.

DISCUSSION

These preliminary results are a portion of what is explored in this mechanical test. Decorin has a complex effect on viscoelastic behavior that can manifest differently at each gestation point. Overall, the NP DcnKO samples could not sustain the full loading regimen. The trend between NP samples observed in the stress relaxation section are similar to those observed in mouse patellar tendon. DcnKO tendon samples had higher percent relaxation than WT; a difference that was augmented with increasing prescribed strain [9]. In soft tissue, there are various mechanisms that can contribute to a tissue's viscoelasticity, such as unraveling and reforming of the collagen crimps. Decorin's effect on viscoelasticity and how it manifests structurally needs to be explored.

There are limitations on the experiment to be considered. For d18 samples, there is considerable softening and we are unable to separate this effect from the genotypic effects. The d18 DcnKO samples were also biglycan heterozygous. Future studies will include a d18 only DcnKO and increase sample size for all groups. This initial analysis reveals slight differences between WT and DcnKO samples. Further analysis will be conducted on the dataset, including damage parameters and model fit, to tease out differences between genotypes.

ACKNOWLEDGEMENTS

Research in this abstract was funded by the National Science Foundation CAREER award (CMMI 1454412) to K. Myers.

REFERENCES

[1] Timmons, B. et al., *Trends in Endocrinology & Metabolism*, 21(6): 353-361, 2010.
[2] Vink, J. et al., *Seminars in Perinatology*, 41:427-437, 2017.
[3] Yoshida K. et al. *PLOS One*, 9(11): e112391, 2014.
[4] House M. et al. *Seminars in Perinatology*, 33(5): 300-307, 2009.
[5] Kadler KE. et al. *Biomech J*, 316:1-11, 1997.
[6] Danielson K.G. et al. *J Cell Biol.* 136(3): 729-743. 1997.
[7] Nallasamy S. et al., *Endocrinology*, 158(4):950-962, 2017.
[8] Jayyosi C. et al., *Acta Biomaterialia*, 78:308-319, 2018.
[9] Dourte LM. Et al. *J Biomech Eng*, 134(3):03100, 2012.

SB³C2019
Summer Biomechanics, Bioengineering and Biotransport Conference
June 25 -28, Seven Springs, PA, USA

DETERMINATION OF THE ACTIVE AND PASSIVE MECHANICAL PROPERTIES OF THE NON-PREGNANT MURINE CERVIX

Cassandra K. Conway (1), Gabrielle L. Clark (1), Mala Mahendroo (2), Kristin S. Miller (1)

(1) Biomedical Engineering
Tulane University
New Orleans, LA, USA

(2) Obstetrics and Gynecology
University of Texas Southwestern Medical Center
Dallas, TX, USA

INTRODUCTION

Smooth muscle cells (SMC) work in coordination with the extracellular matrix (ECM) to carry out normal mechanical function of the reproductive system [1, 2]. The non-pregnant cervix undergoes regular phasic contractions through the estrous cycle to contribute to processes such as fertilization [1, 2]. Uniaxial strips or rings are traditionally used to independently investigate the maximum contractile response from the longitudinal and circumferential cervical SMCs [1,2,3]. While maximum contractile tone can provide insights into the function of the organ, the resting or basal tone of the organ may further inform our understanding of the mechanical properties of the cervix. Additionally, explant of strips and rings alter the native cell-matrix interactions and inhibits simultaneous assessment of axial and circumferential SMC. To overcome these limitations, an inflation-extension system can be used to assess multiaxial SMC contractility and basal tone while preserving native tissue geometry and cell-matrix interactions. Therefore, the objective of this study was to quantify differences in geometry and SMC contractile tone in the circumferential and axial orientations within the non-pregnant murine cervix.

METHODS

Reproductive systems from C57/BL/6 female mice at estrus (n=9, Tulane IACUC approved) were freshly isolated immediately post-euthanasia via guillotine in order to preserve SMC contractility closest to the physiological state. Post-explant tissue was bathed in 4°C Hanks Balanced Saline Solution (HBSS) and connective tissue was fine dissected from the organs. Cuts immediately posterior of the bifurcation of the uterine horns and superior to the vaginal introitus were made. The wall between the remainder of the uterine horns was cut to allow for cannulation. Cervical complexes were cannulated within an inflation-extension device and bathed in aerated Krebs Ringer Buffer at 37°C. **Dose Response (n=5)** To determine the normal contractile function of the cervix, an isobaric dose response protocol was performed at an estimated physiological (EP) length and pressure [4, 5]. At the constant length and pressure, tissues were subjected to increasing concentrations of potassium chloride (KCl) while circumferential and axial contractions were measured via diameter changes tracked at the mid-cervix through a digital camera and changes of force read by the force transducer, respectively. Contractile response was normalized with respect to cross sectional area (Fig. 1A). Ultrasound images (B-mode, 40MHz transducer) were made at the unloaded state to calculate thickness and student's t-tests were used to identify changes in geometry, force, circumferential stress (σ_θ), and axial stress (σ_z). **Basal-Passive (n=4)** Post-explant and cleaning, cervical complexes were cannulated in the extension-inflation device in aerated Krebs Ringer Buffer at 37°C. Unloaded geometry was recorded via a digital camera and digital micrometer. Samples were preconditioned circumferentially (P=0-7mmHg) for five cycles. An estimated physiological length was determined based on the assumption that soft tissues seek to maintain force over a range of pressures at an approximate *in vivo* length [4, 5]. Samples were subjected to secondary preconditioning at the EP length (P=0-15mmHg). Force-extension preconditioning was excluded as pilot studies showed a notable decrease in SMC contractility after the force-extension protocol. Following preconditioning, the unloaded length was re-determined as the length in which there was minimal changes in force with decreasing axial length. Three cycles of the pressure-inflation protocol was performed from (P=0-15mmHg) at -2% EP, EP, 1% EP, and 2% EP length. Samples were treated with 20mM KCl after the basal experiment

Poster Presentation #P281

to incite phasic contractions to confirm continued SMC activation. Samples were then treated with 2mM EGTA within the bath and intraluminally in a solution of calcium free Krebs Buffer for 30 minutes to de-activate SMC. Cervices were washed out with calcium free Krebs Buffer and the experimental protocol was repeated for the passive state. Ultrasound B-mode images of the tissue at the unloaded configuration were taken after the pressure-inflation cycles for both the basal and passive experiments. The inner canal and outer circumference excluding the vaginal fornix were traced in Image-J and lines drawn between the inner and outer perimeters were used to calculate thickness. Paired t-tests were used to compare geometry between location and active state (Fig. 1B). Bilinear curve fits were applied to the basal and passive experimental data. Two-way ANOVAs (axial extension, state) followed by student's t-tests were performed for basal and passive data [6].

RESULTS

Dose Response Maximum contraction was identified at 20mM KCl (Fig. 1A). At this concentration, phasic activity was maintained and there was a significant increase in axial stress (*p<0.001)* and an inverse effect on the circumferential stress *(p<0.05)*. **Basal Passive** Unloaded geometry and volume between the basal and passive state was not found to be significantly different (Fig. 1B). However, physiologic length was found to be significantly greater *(p<0.05)* in the passive state and passive outer diameter was larger compared to the basal state at matched pressures *(p<0.05,* Fig 1B). Bilinear curve fits did not reveal any significant differences in mechanical properties between the basal and passive state. Although no significance was found, the passive state trended to have a larger transition-stretch (*p<0.1*, Fig. 1C). Circumferential linear-modulus in the basal and passive state was significantly greater than the axial linear modulus (*p<0.05*, Fig. 1D). Spontaneous contractile response was observed and an adapted pressure-inflation protocol was designed to observe how the spontaneous contraction effected the tissue in comparison to contractile reaction incited by KCl in the dose response protocol (Fig. 2) [7].

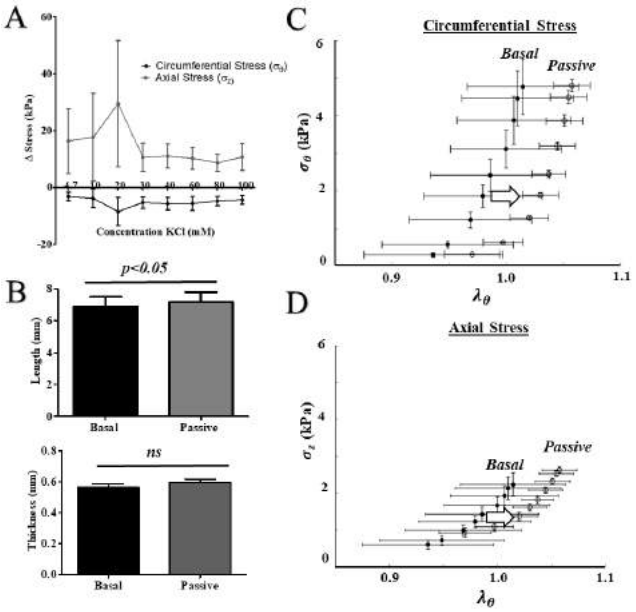

Figure 1: Dose Response (A) Maximum contraction was identified at 20mM KCl. At this concentration phasic activity was maintained resulting in a significant increase in axial stress (*p<0.001)* and decrease in circumferential stress (*p<0.05)*. **Basal-Passive Geometry (B)** A significant increase in the physiologic length for the passive state was measured (*p<0.05)*. However, no significant changes were identified in the thickness or volume between the basal and passive state. **Basal-Passive σ_θ (C)** Stress-stretch curves of the basal and passive response at the estimated physiological length. No significant differences between basal and passive properties were found. A trend towards a greater circumferential stretch in the passive state was identified. **Basal-Passive σ_z (D)** Circumferential linear modulus in the basal and passive state was larger than the axial linear modulus (*p<0.05*).

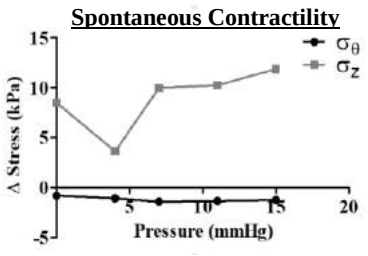

Figure 2: Spontaneous contractile response (n=2) was analyzed with an adapted pressure-inflation protocol [7]. Similar to the dose response, an increase in axial stress and decrease circumferential stress was observed in the representative sample shown.

DISCUSSION

Comparing basal and passive states within the cervix, there was a noted increase in the physiologic length (*p<0.05)* and an increase in diameter at matched pressures in the passive state (*p<0.05)*. However, no significant changes in the thickness, volume, and mechanical properties between the basal and passive state were identified. There was a trend for a larger transition-stretch (*p<0.1)* in the passive state that can be visualized as the rightward shift from the basal to passive state in Figure 1C suggesting an increase in distensibility with loss of basal tone. A minimal change in mechanical properties between the basal and passive state may be related to the phasic nature of the cervix. During dose response and spontaneous contractility protocols, the phasic nature of the cervix incited dramatic changes in force in a consistent pattern. The role of basal tone may be minimal in the non-pregnant cervix. Additionally, the non-pregnant cervix is a dense fibrous tissue that is composed of approximately 80-90% collagen and the basal tone of SMC within the tissue may contribute minimally to maintain rigidity [8, 9]. Interestingly, SMCs in the cervix are quiescent mid-pregnancy and a phenotypic change activates the SMCs during labor [1, 2]. An increase in the SMC content within the cervix during pregnancy may result in different behavior between the basal tone and passive state. Further work is needed to elucidate the role of basal and max contractile tone in comparison to the passive state to inform mathematical models of the non-pregnant cervix. Understanding the role of SMC in the non-pregnant cervix may contribute to our understanding of the role of SMC in the pregnant cervix.

ACKNOWLEDGEMENTS

Thank you to Dylan Lawrence and Carolyn Bayer for assistance in ultrasound imaging. This work was supported by NSF CMMI 1751050 (KSM).

REFERENCES

[1] Darios *et al*., 2012, J of Pharm and Exp Therapeutics, 341(3), p. 587. **[2]** Gravina *et al*, 2014, PLoS ONE, 9(10). **[3]** Ferland *et al*, 2015, Am J Obstet Gynecol, 212(2), pp. 244.e241-248. **[4]** Van Loon, P., 1976, Biorheology, 14(4), pp. 181-201. **[5]** Akintunde *et al*., Journal of biomech eng **[6]** Gosling, R. G., and Budge, M. M., 2003, Hypertension, 41(6), pp. 1180-1182. **[7]** Caulk *et al.*, 2015, Journal of The Royal Society Interface, 12(108), p. 20150280. **[8]** Myers *et al*, 2010, Journal of biomech eng, 132(2), p. 021003. **[9]** Vink *et al*, 2016, Am J Obstet Gynecol, 215(4), pp. 478.e471-478.e411.

SB³C2019
Summer Biomechanics, Bioengineering and Biotransport Conference
June 25 -28, Seven Springs, PA, USA

TRACTION FORCE MICROSCOPY ON HUMAN AORTIC SMOOTH MUSCLE CELLS

C. Petit (1), A. Guignandon (2), S. Avril (1)

(1) INSERM, U 1059 SAINBIOSE
Universit□ de Lyon, Mines Saint-Etienne
F - 42023 Saint-Etienne France

(2) INSERM, U 1059 SAINBIOSE
Universit□ de Lyon, Universit□ Jean Monnet
F - 42023 Saint-Etienne France

INTRODUCTION

It is now widely acknowledged that the biomechanical behavior of smooth muscle cells (SMC) in the aorta plays a key role in growth, remodeling, and homeostasis [1–4]. Through mechanosensitivity and mechanotransduction, aortic SMCs remain highly sensitive to biomechanical and mechanical stimuli from their extracellular matrix (ECM) [1, 5–12]. In fact, these cells can sense the state of their environment and react to the variation of its biophysical properties in some pathologies such as aortic aneurysms, but also in genetics, hemodynamics or biomechanics [6, 13–15]. SMCs undergo therefore alterations such as apoptosis, or even phenotypic switching from a mature quiescent and contractile phenotype towards a synthetic and proliferative one [1, 5, 10, 11]. A synthetic SMC is able to proliferate and migrate more than a contractile one, but it can also degrade the current "pathological" ECM and produce new ECM components in return in order to repair the tissue [2, 11]. In fact, in adulthood, only collagen of the ECM may be synthesized efficiently [12]. The collagen has a protective role for the other ECM components because it can withstand higher stress, but the increase of collagen leads to an increased stiffness and weakening of the aortic wall [1, 13]. These changes irreversibly affect the mechanical properties of the aortic tissue that becomes more vulnerable to rupture.

Since the SMC tend to maintain the preferred tension they exert on the ECM at homeostasis [2, 8, 13, 16], any biochemical or biomechanical imbalance results in a variation of this basal tone [17]. The cell tension, behavior and response, are therefore altered by pathological conditions, which leads to a vicious circle. In this way, the contractility of SMCs appears as a determinant parameter of the aortic wall state, but quantitative values of SMC basal tone have never been characterized precisely on individual cells.

METHODS

We developed an in vitro technique based on Traction Force Microscopy (TFM). Aortic SMCs from a human lineage (AoSMC, Lonza) at low passages (4-7) were cultured 2 days in conditions promoting preservation of their contractile apparatus. We performed fluorescent microscopy (FM) on these cells, notably by staining the α-Smooth Muscle Actin (α-SMA) that constitutes the contractile thin filaments of the cytoskeleton. The cells were seeded on hydrogels of varying elastic modulus (from 0.5 to 50kPa) with embedded fluorescent microbeads. During the experiment, SMCs were detached from the gels by a trypsin treatment. Since the unbinding cell no longer exerted a force on the gel, the microbeads movement was tracked using TFM. Then, using Digital Image Correlation (DIC) with the *NCorr* algorithm [18], we obtained the corresponding displacement fields. Then we used a mechanical model based on the Boussinesq solution [19], assuming linear elasticity, isotropy and plane strain, to extract the associated traction force applied by individual SMCs on the gel.

The first series of experiments consisted in one sample of each stiffness, in order to screen the range of stiffness values appropriate for SMC adhesion. Then, we performed experiments wthin this stiffness range using 24-well plates and achieved an advanced statistical analysis. We examined the distribution of the traction force values according to each stiffness by plotting histograms in Matlab®. Then, these histograms were fitted with an exponential law such as:

$$y_{model} = \frac{1}{\lambda} e^{-\lambda x} \qquad (1)$$

Where x is the center of the different classes of traction force values from the histograms and y its probability. The λ parameter was determined by a nonlinear least square method that minimizes the difference between the model and experimental data.

Poster Presentation #P282

RESULTS

SMCs showed a clear spindle shape on the gels (Fig. 1.a), with α-SMA fibers, oriented according to the direction of the cell (Fig. 1.b).

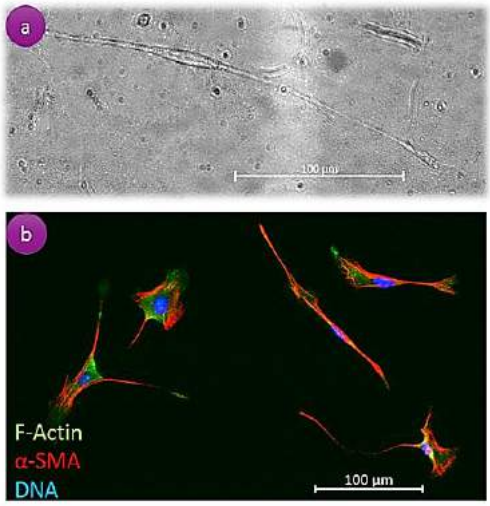

Figure 1: (a) Observation of cell morphology in bright light and (b) internal architecture using FM, for human aortic SMCs (AoSMC, Lonza). Microscope: Carl Zeiss Axio Observer.Z1/7, Objectives : Plan-Neofluar 10x/0.30.

Two major interesting and original observations about SMC traction forces were deduced from the obtained results (Fig. 2): a. they were stochastic and showed an exponential distribution, with 40% to 80% of traction forces in the range 0-10µN. b. They depend on the substrate stiffness: the fraction of adhesion forces below 10 µN tend to decrease when the substrate stiffness increases, whereas the fraction of larger adhesion forces increases.

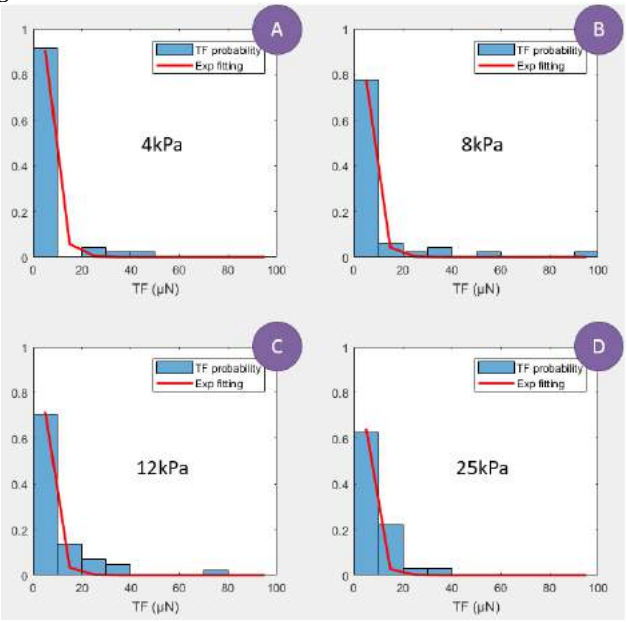

Figure 2: Histograms representing the distribution of the measured TF (Traction Force) values for each stiffness value: A) 4kpa, B) 8kPa, C) 12kPa, D) 25 kPa. Each of these histograms is represented in probability according to the classes of forces (width: $0.1*10^{-4}$N). The red curve represents the exponential model (Exp fitting) applied to experimental data.

DISCUSSION

Since human SMCs are particularly sensitive, specific culture conditions are required to preserve their contractility. In this way, we used cells at low passages, cultured in a differentiation medium, and they showed both the typical elongated morphology they have in the aorta and high α-SMA expression. Moreover, their contractile behavior was confirmed during TFM experiments. In fact, the adhering cells on the gels exert naturally a force on their substrate. Once removed, SMCs induced a displacement field on the fluorescent microbeads. We developed an algorithm that allowed extracting the corresponding local traction force at each cell anchorage point.

Measured adhesion forces are in good agreement with previous data on vascular SMCs [6, 20], although previous results were not obtained on single cells. We also showed that they could be predicted well by the motor-clutch model of Chan & Odde [21], that had never been extended to SMCs. Further studies will consider stimulated contractility and primary culture of cells extracted from aneurysmal human aortic tissue.

ACKNOWLEDGEMENTS

This research was supported by the European Research Council (ERC grant biolochanics, grant number 647067).

REFERENCES

[1] Humphrey JD. *Cardiovascular Solid Mechanics*. New York, NY: Springer New York. 2002.
[2] Hayashi K, Kamiya A, Ono K. *Biomechanics: Functional Adaption and Remodeling*. Springer Science & Business Media. 314 pp. 2012.
[3] Hong Z et al. *J Physiol*. 592[Pt 6]:1249. 2014.
[4] Lacolley P et al. *Cardiovasc. Res.* 95[2]:194. 2012.
[5] Thyberg J et al. *Arteriosclerosis*. 10[6]:966. 1990.
[6] Sazonova OV et al. *Matrix Biology*. 41:36. 2015.
[7] Murtada S-I, Ferruzzi J, Yanagisawa H, Humphrey JD. *Journal of Biomechanical Engineering*. 138[5]:051008. 2016.
[8] Bellini C et al. *Ann Biomed Eng*. 42[3]:488. 2014.
[9] Tsamis A, Krawiec JT, Vorp DA. *J R Soc Interface*. 10[83]:. 2013.
[10] Owens GK, Rabinovitch PS, Schwartz SM. *Proc Natl Acad Sci U S A*. 78[12]:7759. 1981.
[11] Mao N et al. *Interactive CardioVascular and Thoracic Surgery*. 21[1]:62. 2015.
[12] Arribas SM, Hinek A, González MC. *Pharmacology & Therapeutics*. 111[3]:771. 2006.
[13] Humphrey JD, Schwartz MA, Tellides G, Milewicz DM. *Circulation Research*. 116[8]:1448. 2015.
[14] Karšaj I, Sorić J, Humphrey JD. *Int J Eng Sci*. 48[11]:1357. 2010.
[15] Guo D-C et al. *Nat. Genet.* 39[12]:1488. 2007.
[16] Schildmeyer LA et al. *FASEB J.* 14[14]:2213. 2000.
[17] Murtada S-I, Lewin S, Arner A, Humphrey JD. *Biomech Model Mechanobiol*. 15[3]:579. 2016.
[18] Blaber J, Adair B, Antoniou A. *Exp Mech*. 55[6]:1105. 2015.
[19] L.D. Landau & E.M. Lifshitz. *Theory of Elasticity*
[20] Balasubramanian L, Lo C-M, Sham JSK, Yip K-P. *Am J Physiol Cell Physiol*. 304[4]:C382. 2013.
[21] Chan CE, Odde DJ. *Science*. 322[5908]:1687. 2008.

SB³C2019
Summer Biomechanics, Bioengineering and Biotransport Conference
June 25 -28, Seven Springs, PA, USA

EFFECTS OF SOLVENT AND GELATIN CONCENTRATION NEAR-FIELD, DIRECT-WRITE ELECTROSPINNING OF GELATIN

Zachary G. Davis (1), Paul B. Warren (1), Matthew B. Fisher (1,2)

(1) Department of Biomedical Engineering, University of North Carolina-Chapel Hill and North Carolina State University, Raleigh, NC, USA

(2) Department of Orthopaedics, University of North Carolina Chapel Hill, NC, USA

INTRODUCTION

Musculoskeletal (MSK) fibrous tissues, such as tendons and ligaments, are formed via a hierarchical collagen fiber structure which is responsible for these tissues' anisotropy and specialized mechanical properties [1]. Current treatment methods for injuries to these tissues use auto-or allografts to replace the injured tissue. Tissue engineering has been advanced as a means to overcome the limitations of auto-and allografts [1].

Two methods for attempting to replicate the structure and function of MSK fibrous tissue are 3D printing and electrospinning. There are a variety of different forms of 3D printing which use single fibers to create complex structures like MSK fibrous tissues including fused deposition modeling (FDM) and bioprinting [2]. Each method provides high resolution modelling capabilities using software and multi-axis control to deposit individual fibers. The fibers from these systems typically have a minimum range of 100µm-400µm in diameter, which is on the scale of a fascicle [1,2]. Though 3D printing has the potential to replicate the macroscale structure of MSK fibrous tissues it lacks the ability to replicate the smaller fibers and fibrils.

Electrospinning uses an electric potential to draw out a stream of fibers from a polymer solution creating a sheet of randomly oriented fibers with diameters that range from nanometers to microns, which approaches the range of fibrils and fibers [1,3]. Orientation can be manipulated by using a rotating mandrel to align fibers along a single axis [3]. One limitation of electrospinning is that the lack of control over fiber placement can prevent the creation of complex structures.

Direct-write, near-field electrospinning (DWNFE) combines the software and multi-axis control of 3D printing with the electrohydrodynamic fiber formation of near-field electrospinning to create complex, 3D scaffolds (Fig. 1) [4]. This combines the advantages of the two previous methods allowing for the fabrication of a structure with fibers similar in size to the fibers of collagen while also meeting the macroscopic requirements needed to replicate MSK fibrous tissue.

To date, however, DWNFE has been limited to synthetic polymers which provide a biocompatible environment but lack the bioactivity of natural polymers [1, 5]. Gelatin is an appropriate candidate for MSK tissue engineering, as it is collagen based, similar to MSK tissues, maintaining much of the enzymatic active sites while being more readily available [6]. Thus, the objective of this study was to determine the impact of acetic acid (solvent) and gelatin concentrations for the DWNFE of gelatin solutions.

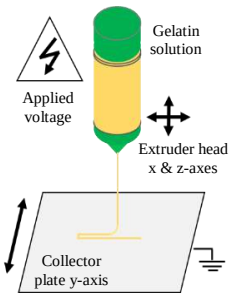

Figure 1: Schematic of direct-write, near-field electrospinning.

METHODS

Type A, 300 bloom, porcine gelatin (Sigma-Aldrich Saint Louis, MO, USA) was dissolved at a constant 45(w/v)% gelatin in five different acetic acid (Fisher Scientific, Fair Lawn, NJ, USA)-diH_2O concentration groups (% acetic acid groups): 60(v/v)%, 70(v/v)%, 80(v/v)%, 90(v/v)%, and 98(v/v)%. Three gelatin concentration groups (% gel groups) were also made, 30(w/v)% , 37.5(w/v)%, and 60(w/v)%, at a constant acetic acid concentration of 70(v/v)%. A custom modified Lulzbot mini (Lulzbot Inc., Loveland, CO, USA) FDM 3D printer with applied pneumatic pressure for extrusion was used to print 10mmX10mm 2-layer grid scaffolds with 1mm intended spacing. MATLAB was used to create the G-code for the grid structure. These scaffolds were imaged using a JEOL scanning electron microscope (SEM) and fibers diameters were measured using ImageJ. Three scaffolds were printed per day for three days for a total of nine scaffolds

Poster Presentation #P283

for each group. Six fibers from each scaffold were measured. All statistics were calculated using Prism (7.05, GraphPad, San Diego, CA, USA). Normality was determined via the D'Agostino-Pearson test. Nonparametric Kruskal-Wallis tests with Dunn's post hoc analysis (α=0.05) were run to determine statistically significant differences between the acetic acid and gelatin groups separately.

RESULTS

In terms of varying acetic acid concentration, the 60%AA group fibers, which resembled puddles, failed to form a coherent fiber structure (Fig. 2A). The 80%AA group fibers were not consistent with discontinuities in the fibers and an irregular form (Fig. 2A). The 90%AA and 70%AA groups both created continuous fibers with no discernible irregularities (Fig. 2A). A consistently printable solution could not be made for the 98%AA group. Statistical tests revealed significance between all %AA groups except between the 70%AA and 80%AA groups ($p<0.05$). The 45%gel, 70%AA group had the smallest diameter fibers with a median of 3.97 µm followed by the 80%AA group at 5.74 µm, then 90%AA with a median of 19.34 µm and finally the 60%AA with a median of 92.43 µm.

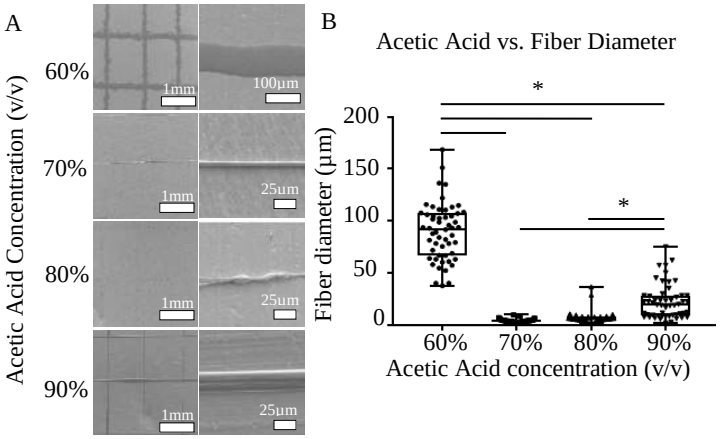

Figure 2: Effect of acetic acid concentration on fiber formation using DWNFE. A) SEM images at lower (left) and higher (right) magnification. B) Fiber diameter as a function of acetic acid concentration. '*' indicates statistically significant difference between groups connected by the black bar.

Once establishing that small fibers could be formed at 45% gelatin and 70%AA, the gelatin concentration was varied while holding the acetic acid concentration at 70%AA. The 30%gel group showed the presence of puddles instead of fibers (Fig. 3A). The 37.5%gel group also showed puddles that were smaller and inconsistent (Fig. 3A). The 60% gel group is not shown because it failed to print at the speeds used for the other groups. The median diameter for the 30%gel group was 154.50 µm which was significantly different from the 45%gel group (3.97 µm) ($p<0.05$, Fig. 3B). The 37.5%gel group is statistically significantly different from both the 30%gel and the 45%gel with a median of 72.00 µm ($p<0.05$).

DISCUSSION

From the data, we found that acetic acid and gelatin concentrations impact the ability to direct-write, near-field electrospin gelatin. The 70%AA and 90%AA groups were on par with synthetic polymers (polyvinylidene fluoride) in relation to fiber diameter [4]. The 70%AA was considered the best group as it created the most stable fibers while also remaining an appropriate size for replicating physiologic dimensions. The gelatin concentration groups showed a "goldilocks"

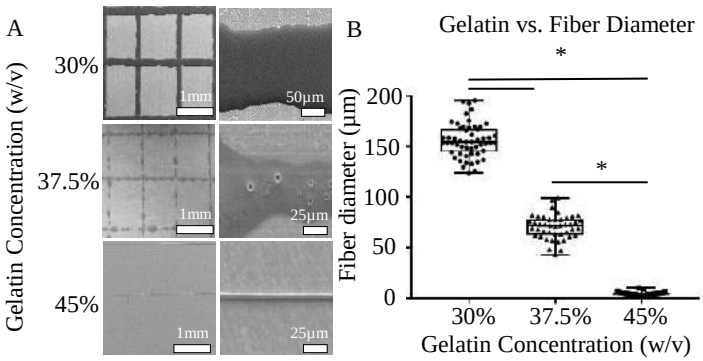

Figure 3: The effect of gelatin concentration, at constant 70% acetic acid, on fiber formation using DWNFE. A) SEM images at lower (left) and higher (right) magnification. B) Fiber diameter as a function of gelatin concentration.'*' indicates statistically significant difference between groups connected by the black bar.

zone at the 45%gel concentration as decreasing the concentration formed puddles instead of fibers, while increasing the concentration prevented fiber formation. These findings confirmed that the 45%gel group is the best concentration of those tested. From these results, we concluded that 45%gel/70%AA provides the best parameters of those tested. Further studies will be conducted with groups between 45%gel and 60%gel to see if this trend is continuous. Future work entails optimizing crosslinking of the gelatin and building larger 3D structures to allow for testing of the scaffolds' mechanical properties as well as their impact on cells.

ACKNOWLEDGEMENTS

We acknowledge the NC State, Game-Changing Research Incentive Program for their support and the NC State Analytical Instrumentation Facility and Food Rheology Laboratory for their expertise and equipment.

REFERENCES

[1] Yunoki S, et al, *J Biomed Mater Res B Part B*, 00B:1-13, 2018.; [2] Daly AC, et al. *Adv. Healthcare Mater.*,6:1-20, 2017.; [3] Li WJ, et al, *J. Biomech.*, 40:1686-1693, 2006.; [4] Luo G, et al, *Appl. Mater. Interfaces*, 7:27765-27770, 2015.; [5] Costa A, et al, *Principles of regenerative medicine*, "Biologic Scaffolds," 587-622, 2011.; [6] Erencia M, et al, *Journal of Applied Polymer Science*, 132:1-11, 2015.

SB³C2019
Summer Biomechanics, Bioengineering and Biotransport Conference
June 25 -28, Seven Springs, PA, USA

VOLUMETRIC INTENSITY HISTOGRAM ANALYSIS METHOD FOR QUANTIFICATION OF FATTY INFILTRATION FOLLOWING ROTATOR CUFF REPAIR

Victoria A. Webster-Wood (1,2), Phillip E. McClellan (3), Lekha Y. Kesavan (1,2), Greg D. Learn (4), Ozan Akkus (3,4,5)

(1) Dept. of Mechanical Engineering
Carnegie Mellon University
Pittsburgh, PA, USA

(2) Dept. of Biomedical Engineering
Carnegie Mellon University
Pittsburgh, PA, USA

(3) Dept. of Mechanical Engineering
Case Western Reserve University
Cleveland, OH, USA

(4) Dept. of Biomedical Engineering
Case Western Reserve University
Cleveland, OH, USA

(5) Dept. of Orthopaedic Surgery
University Hospitals of Cleveland
Cleveland, OH, USA

INTRODUCTION

Fatty infiltration is a progressive degeneration of muscle/connective tissue, which entails conversion to an adipose-like state, that occurs as a result of muscle disuse upon injury to the adjacent tendon. This process is commonly associated with tendon lesions and repairs in the rotator cuff [1]. With existing repair strategies, this fatty infiltration is associated with muscle atrophy, decreased functional outcomes, and may predict future injuries [2]–[4]. As such, accurate quantification of fatty infiltration pre- and post-operatively may be a useful biomarker for tendon repair success. However, fatty infiltration is currently assessed by a clinician or blinded observer through visual inspection and scoring the level of fatty infiltration on single slices in the coronal, sagittal, and axial [3], [5], despite the extension of fatty infiltration into the muscle belly. Here, we present a method for volumetric quantification of fatty infiltration based on anatomical landmarks and intensity histogram analysis.

METHODS

CT Dataset - Intensity histograms were assessed for micro-computed tomography (CT) scans of the operative and contralateral intact shoulder for rabbits having undergone infraspinatus repair as previously described [6]. Briefly, a gap defect was introduced in the infraspinatus of the operative shoulder and either left unrepaired (gap), repaired via reattachment of the remnant tendon to the bone (direct), or repaired using a woven collagen biotextile (scaffold). Scapulohumeral complexes were isolated post-euthanasia after 6 months and stored hydrated at 4°C for a maximum of 14 hours prior to scanning. CT scans of specimens were obtained (75-80kV, 470-500µa, 630-670ms exposure time, 42 µm voxel edge length, Inveon PET/CT, Siemens) and reconstructed (Inveon Acquisition Workplace, Siemens).

ROI Selection – Volumetric fatty infiltration metrics were investigated using an oblique cylindrical region of interest (ROI) within the muscle belly. To select a comparable ROI in each animal and minimize the effect of differences in overall animal size, ROIs were defined based on user identification of predefined anatomical features. The mid plane of the oblique cylinder is located by identification of the CT slice wherein the bifurcation in the scapula as seen from the sagittal plane first appears. Using this slice, the user identifies and selects two points, as shown in Figure 1, thereby defining the relative anatomical length (L_A) in pixels that will subsequently be used to scale and position the ROI. The radius of the oblique cylinder is calculated as:

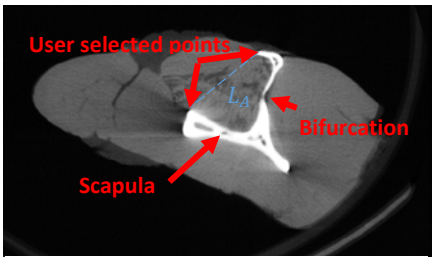

Figure 1. Characteristic operative shoulder central slice of the ROI. The anatomical length is defined by the user selection of the points shown. White = bone, light gray = muscle, dark gray = fat, black = air

$$r_c = 0.2L_A \quad (1)$$

Where the scaling factor of 0.2 was determined manually through a bisection search approach to identify an ROI diameter that did not result in the ROI projection intersecting with the bone on any slice in the volume. The height of the ROI is calculated as:

$$h_c = L_A \quad (2)$$

The CT slices corresponding to the bottom and top of the ROI are the used to position the ROI with their slice numbers being determined as:

$$n_{bot/top} = n_{mid-plane} \pm {}^{h_c}/_{2} \quad (3)$$

To position the ROI, a line is defined based on consistent anatomical features in the bottom and top slices as shown in Figure 2. The positions of the center of the ROI projection are located at the midpoint of the line defined by the selected features on each slice. The points are then used to define a unit vector along the axis of the oblique cylinder ROI, allowing calculation of the center of the ROI projection on each slice.

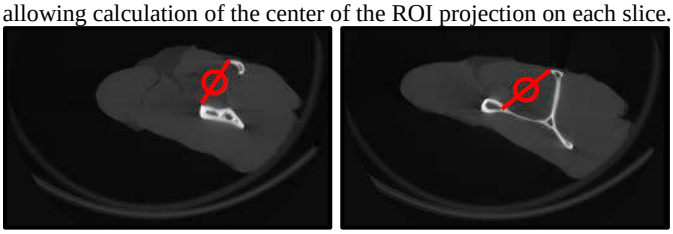

Figure 2. Anatomical feature selection and positioning of the ROI on the bottom (left) and top (right) slices of the volume.

Image Calibration **–** Images were calibrated prior to intensity histogram identification to ensure all images were within comparable intensity ranges. Calibration was performed by taking the average intensity of a user selected region of air, and the average intensity of a region of the carbon fiber tube housing as control intensities and scaling the image such that the mean air and mean tube values were rescaled to -1000 and 250, respectively.

Intensity Histogram Generation **–** Intensity histograms were generated for both the intact and operative shoulder of each rabbit three times to assess repeatability of the proposed method. For each test, the intensities contained within the ROI projection on each slice between the identified bottom and top slice were stored and the resulting histogram was produced via the built in MATLAB "histogram( )" function. For each intensity histogram the mean, skew, standard deviation, and kurtosis were calculated for assessment as potential markers of fatty infiltration.

Fatty Infiltration Quantification **–** The percentage of voxels within the ROI that contained fat were estimated by masking the ROI in each slice of the defined volume and thresholding for intensities between -200 and 150. These thresholds were determined experimentally based on user identification of fatty regions in Slicer3D.

Statistical Analysis **–**Kruskal–Wallis followed by Mann-Whitney testing was used to assess statistical differences (significance set at $p \leq 0.05$).

RESULTS

Characteristic intensity histograms of the operative should for each repair type and the intact control are shown in Figure 3. Comparison of all histogram assessment metrics (mean, skew, standard deviation, and kurtosis) between the intact and operative shoulders for each repair type was statistically significant. There was no significant difference in the kurtosis or standard deviation of the operative shoulders between repair types. However, the difference in skew between both direct vs. scaffold and gap vs. scaffold repairs

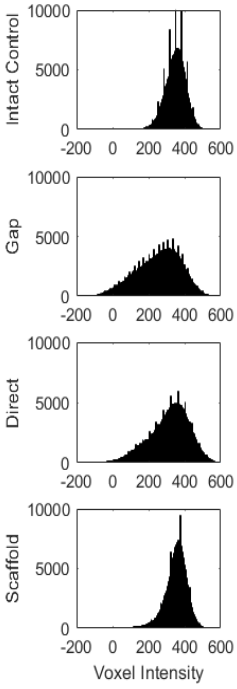

Figure 3. Characteristic intensity histograms

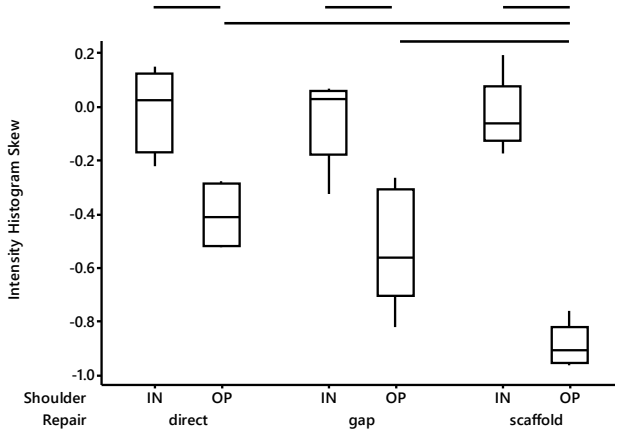

Figure 4. Intensity Histogram Skew. Overhead bars indicate significant differences based on Mann-Whitney analysis ($p < 0.05$)

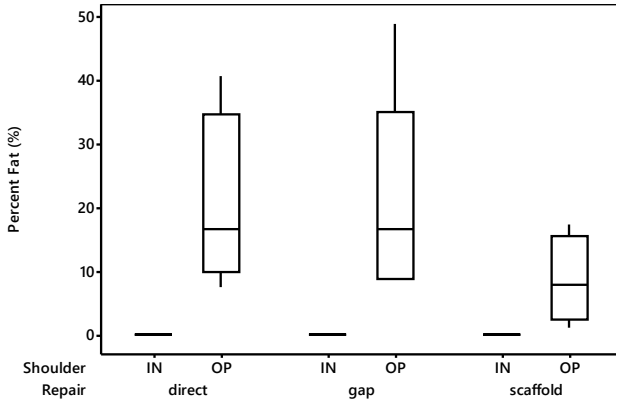

Figure 5. The volume percentage of the ROI identified as fat based on the specified threshold.

was significant for both comparisons (Fig. 4). Finally, the percentage of the ROI which was thresholded as fat was significantly different between intact and operative shoulders (Fig. 5), though substantial standard deviations in the direct and gap repair conditions prevent statistical assessment between repair conditions given the limited sample sizes in this pilot study.

DISCUSSION

The presented volumetric intensity histogram analysis demonstrates the ability to distinguish intact and operative shoulders based on the mean, skew, standard deviation, and kurtosis of the intensity histogram. Furthermore, the significant difference in skew observed between the repair conditions may be a useful fatty infiltration marker. Further work is needed to assess the correlation between intensity histogram metrics and functional outcomes following repair.

ACKNOWLEDGEMENTS

This study was supported by grants from National Institutes of Health (NIH): R01 AR063701 and T32 AR007505. LK and PM contributed equally to this work.

REFERENCES

[1] Osti, L. et al., *Muscles. Ligaments Tendons J.*, 3(4):351–354, 2013.
[2] Gerber, C. et al., *Shoulder Elb. Surg.*, 16(6):691–696, 2007.
[3] Melis, B. et al., *Orth. Traumatol. Surg. Res.*, 95(5):319–324, 2009.
[4] Barry, J. et al., *J. Shoulder Elb. Surg.*, 22(1):18–25, 2013.
[5] Somerson, J. et al., *Clin. Orthop. Relat. Res.*, 474(5):1328–32, 2016.
[6] Learn, G. et al., *J. Biomed. Mater. Res. Part B Appl. Biomater*, 2018.

SB³C2019
Summer Biomechanics, Bioengineering and Biotransport Conference
June 25 -28, Seven Springs, PA, USA

FIBER MORPHOLOGY AND TENSILE MODULUS OF MELT ELECTROWRITTEN SCAFFOLDS ARE DEPENDENT ON PROCESS PARAMETERS

Paul B. Warren (1), Zachary G. Davis (1), Matthew B. Fisher (1,2)

(1) Department of Biomedical Engineering
North Carolina State University and
University of North Carolina – Chapel Hill
Raleigh, NC, USA

(2) Department of Orthopaedics
University of North Carolina – Chapel Hill
Chapel Hill, NC, USA

INTRODUCTION

Musculoskeletal soft tissues within and around joints are critical for effective load transmission and movement. Their anisotropic tensile properties are determined by the organization of a fibrous matrix containing highly aligned networks of collagen fibers. For example, fibers in the meniscus run primarily in one of two orthogonal directions to withstand complex, multidirectional loads [1].

Because endogenous repair is limited when these tissues are injured, surgical removal and replacement with auto- or allografts is common, but function is not totally restored due to incomplete cellular integration and nonphysiological mechanical properties of the graft [2,3]. Thus, there is a need for alternative treatment strategies based on tissue engineering approaches that aim to better reproduce the biological and mechanical characteristics of native tissue.

Electrospinning and extrusion-based 3D printing are advantageous for musculoskeletal soft tissue scaffolds because they inherently produce fibrous structures [4,5]. Melt electrowriting (MEW, Fig. 1) in particular allows greater control over scaffold architecture than electrospinning and produces smaller fiber sizes compared to conventional 3D printing methods, which has led to interest in MEW for tissue engineering [6]. Numerous studies have evaluated MEW process parameters, though these studies tend to focus on optimizing fiber diameter [7,8]. The direct effect of varying processing conditions on the mechanical properties of MEW structures is not well understood. Furthermore, there are few investigations of MEW scaffolds with geometries relevant for musculoskeletal tissue engineering [9,10], which may require high aspect ratios on the macro-scale. Therefore, this study aimed to determine how scaffold geometry and processing conditions impact fiber morphology and whole scaffold mechanical properties.

METHODS

Scaffold fabrication: A desktop fused deposition modeling 3D printer (Aleph Objects, USA) was adapted to be capable of MEW. Three process variables – stage translation speed (1, 3, or 5 mm/s), melt extrusion temperature (70, 80, or 90°C), and working distance between the nozzle and stage (1.5, 5, or 10 mm) – were investigated by systematically varying one while holding the other two constant (Fig. 1) for a total of seven unique experimental groups. MATLAB-generated G-code was used to print 12x12 mm (square) or 35x5 mm (rectangular) scaffolds (Fig. 2) consisting of alternating layers of polycaprolactone (43 kDa, Polysciences, USA) fibers oriented in the longitudinal (0°) or transverse (90°) directions and spaced 0.2 mm apart (2 or 10 layers).

Imaging: ImageJ was used to quantify fiber diameter (10 fibers per image) and interfiber spacing (30 per image) from scanning electron microscopy (SEM, Hitachi, Japan) images of 10-layer square and rectangular scaffolds (n=3/group). 2-layer scaffolds were imaged but not quantified (n=1/group).

Mechanical testing: Uniaxial tension was applied to rectangular scaffolds (n=6/group) in a universal testing system (Instron, USA) with a clamp-to-clamp length of 20 mm and a strain rate of 0.1 mm/s until failure. To track local strains more accurately, videos of each tensile test were converted to image series and input into the MATLAB-based digital image correlation program Ncorr [11]. Using a custom script, strains were determined from the Ncorr-calculated displacements representing the middle 50% of the rectangular scaffold geometry to avoid any skewing of the data related to clamping effects. Apparent tensile modulus was calculated as the slope of the linear region of each stress-strain curve. Yield strain was estimated from each curve.

Statistical analysis: Statistical analyses were performed using Prism (GraphPad, USA). Normality of datasets was evaluated via the D'Agostino-Pearson test. For fiber diameter, interfiber spacing,

Poster Presentation #P285

apparent tensile modulus, and yield strain, nonparametric Kruskal-Wallis tests were performed using stage speed, melt temperature, or working distance as the independent variable ($\alpha = 0.05$). Dunn's post hoc tests were then performed.

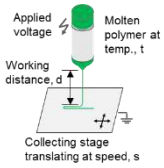

Experimental Groups	
Stage Speed Groups	**s = 1, 3, or 5 mm/s**; constant t (80°C) and d (1.5 mm)
Melt Temperature Groups	**t = 70, 80, or 90°C**; constant s (3 mm/s) and d (1.5 mm)
Working Distance Groups	**d = 1.5, 5.0, or 10 mm**; constant s (3 mm/s) and t (80°C)

Figure 1: Melt electrowriting diagram and experimental groups

RESULTS

Fiber organization was more consistent in 2-layer structures than 10-layer scaffolds. Nevertheless, fiber stacking, which suggests stable and repeatable deposition (Fig. 2), was observed in 10-layer scaffolds of all but the 5 and 10 mm working distance groups. On the other hand, many groups of rectangular scaffolds displayed angled and less consistent transverse fibers (Fig. 2), with exceptions being the 70 and 90°C groups. In terms of accuracy of fiber spacing, most groups had no more than 14% error relative to the target value of 0.2 mm, with the 3 and 5 mm/s groups being the most accurate.

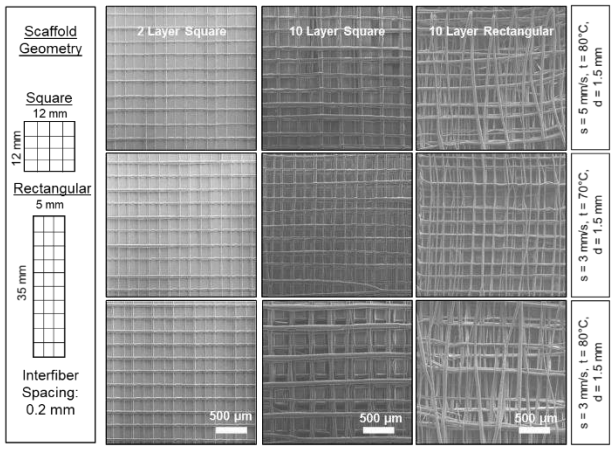

Figure 2: Representative SEM images show differences in fiber architecture between square and rectangular scaffolds, though some conditions resulted in more consistent fiber architecture between geometries (middle row).

In rectangular scaffolds, when melt temperature and working distance were held constant (Fig. 3, top row), median fiber diameter decreased 49% when stage speed increased from 1 to 3 mm/s ($p<0.05$) and decreased 56% from 1 to 5 mm/s ($p<0.05$). Median spacing decreased 43% between 1 and 3 mm/s ($p<0.05$) and 48% between 1 and 5 mm/s ($p<0.05$). Similarly, median apparent tensile modulus decreased 65% from 1 to 5 mm/s ($p<0.05$). When stage speed and working distance were held constant (Fig. 3 middle row), diameter increased 33% when melt temperature was increased from 70 to 80°C ($p<0.05$). Spacing increased 33% from 70 to 80°C ($p<0.05$) and 10% from 70 to 90°C ($p<0.05$). Altering melt temperature did not result in statistically significant differences in apparent modulus ($p>0.05$). When stage speed and melt temperature were held constant (Fig. 3 bottom row), working distance did not affect diameter or apparent modulus ($p>0.05$). Spacing could not be measured consistently for the 5 and 10 mm groups, preventing direct comparisons. For all groups, yield strain was independent of process parameters ($p>0.05$), with median values ranging from 3-4.5%.

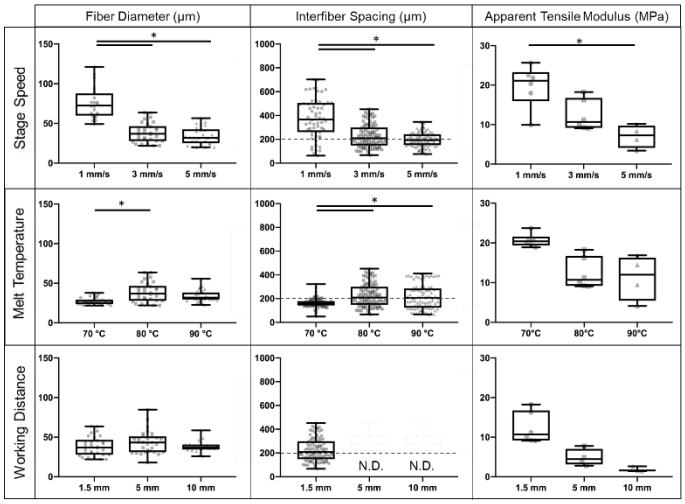

Figure 3: Fiber diameter, spacing, and apparent modulus in rectangular scaffolds are dependent on processing conditions. Data are presented as median with interquartile range (box) and outliers (whiskers). Irregular architecture in the 5 and 10 mm working distance groups prevented consistent measurement of spacing (no data, N.D.). The dashed line in the spacing plots indicates the intended spacing of 0.2 mm. '*' indicates a significant difference between groups linked by a black bar.

DISCUSSION

These data suggest that tensile modulus, along with fiber diameter and spacing, in scaffolds with geometries relevant for musculoskeletal tissue engineering is determined by multiple factors, including MEW process parameters. The largest effects were due to stage speed, though similar changes in modulus with respect to melt temperature and working distance are clear, if not statistically significant, due to limited sample size. Given the specific relevance of rectangular scaffolds to tissue engineering, tensile testing was performed only on those groups, many of which displayed angled transverse fibers, which likely arose from viscoelastic "lag" during printing that was compounded by rapid changes in nozzle direction due to scaffold geometry. It is possible that these fibers contribute to the overall tensile response. Furthermore, the apparent modulus calculations permit comparisons between groups, but assume tension is applied to a homogeneous cross-section. In reality, because the fibers are arranged in a three-dimensional "logpile" structure, cross-sections are heterogeneous and contain void space. Local fiber moduli are greater than those shown in these data. These findings highlight the potential of MEW to create anatomically relevant structures that reproduce architectural elements of native collagen networks and provide a foundation for further studies involving rectangular MEW scaffolds for musculoskeletal tissue engineering.

ACKNOWLEDGEMENTS

We gratefully acknowledge support from the NC State University Game-Changing Research Incentive Program (GRIP).

REFERENCES

[1] Makris EA+, *Biomater*, 32:7411-31, 2011. [2] Rodeo SA+, *J Bone Joint Surg*, 82:1071-82, 2000. [3] To JT+, *Arthroscopy*, 15:379-87, 1999. [4] Mauck RL+, *Tiss Eng B*, 15:171-93, 2009. [5] Gianitelli SM+, *Acta Biomater*, 24:1-11, 2015. [6] Dalton PD+, *Curr Opin Biomed Eng*, 2:49-57, 2017. [7] Hochleitner G+, *Biofabrication*, 7:(035002), 2015. [8] Hrynevich A+, *Small*, 14:(1800232), 2018. [9] Eichholz KF+, *Acta Biomater*, 75:140-51, 2018. [10] Castilho M+, *Adv Funct Mater*, 28:(1803151), 2018. [11] Blaber J+, *Exp Mech*, 55:1105-22, 2015.

SB³C2019
Summer Biomechanics, Bioengineering and Biotransport Conference
June 25 -28, Seven Springs, PA, USA

TRANSLATION OF AN ENGINEERED PORCINE ACCESSORY CARPAL OSTEOCHONDRAL UNIT AS A MODEL FOR TREATMENT OF THUMB OA

Brendan D. Stoeckl (1,2), Hannah M. Zlotnick (1,2,4), Megan J. Farrell (1), Liane M. Miller (1), Josh R. Baxter (1), Thomas P. Schaer (3), Michael W. Hast (1), David R. Steinberg (1,2), Robert L. Mauck (1,2,4)

(1) Department of Orthopaedic Surgery
University of Pennsylvania
Philadelphia, PA, USA

(2) Translational Musculoskeletal Research Center
Philadelphia VA Medical Center
Philadelphia, PA, USA

(3) Comparative Orthopaedic Research Lab
School of Veterinary Medicine
University of Pennsylvania,
Kennett Square, PA, USA

(4) Department of Bioengineering
University of Pennsylvania
Philadelphia, PA, USA

INTRODUCTION

Trapeziometacarpal (TMC) osteoarthritis (OA) is one of the most common conditions affecting middle and older aged adults.[1] Conservative treatments often fail in the long term, and many patients will eventually require destructive surgical intervention involving removal of all or part of the trapezium and replacement with tendon, fascia, or an artificial implant.[2] While effective at reducing pain, these procedures compromise grip strength and can result in subsidence and disfigurement of the hand.[2] Efforts to replace articular cartilage (and bone) with living, functional tissue have matured substantially over the last two decades[3], as has technology for generating constructs that can match the anatomical complexity and geometry of native articulating surfaces.[3,4] For these technologies to progress towards translation, appropriate large animal models are required. Here, we evaluate the porcine accessory carpal (AC) bone as a model for the human trapezium and develop and implement methods for its replacement with an engineered replica to advance treatment of human TMC OA.

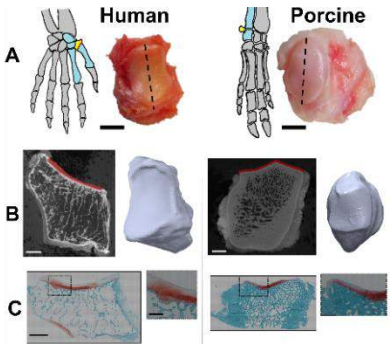

Figure 1: (A) Diagram and gross view of the human trapezium and porcine AC. Dotted line represents sectioning plane. Scale = 3mm. (B) µCT slices in ITK-SNAP showing cartilage segmentation in red and 3D renderings. Scale = 3mm. (C) Safranin-O/fast green staining. Scale = 3mm (1mm for insets).

METHODS

Assessment of the AC: Eight AC bones were isolated from the right forelimbs of adult Yucatan minipigs, and four human trapezia were isolated from cadaveric donors. A custom indentation testing setup was used to evaluate cartilage mechanics of the AC via stress relaxation tests. The saddle-shaped articular cartilage surface was indented with a 2 mm diameter spherical indenter in three locations (superior, middle, and inferior). Four compressive ramps (10% strain each) were applied, with a 600s relaxation between each step. The equilibrium modulus was calculated from the second step. Human and porcine samples were fixed and imaged via µCT (VivaCT 75, Scanco), before immersion in Lugol's solution (5% I_2 10% KI in water) to enhance cartilage contrast. DICOMs from the initial scan were imported into ITK-SNAP[5] and bone was segmented. A surface mesh was exported to Meshlab (ISTI) for simplification. Post-Lugol's scans were manually registered with the bone and processed similarly, with the cartilage layer segmented in a semi-automated manner. Samples were analyzed histologically with Safranin-O/fast green to visualize cartilage, bone, and fibrous tissue. AC Contact Mechanics: CT images of the forelimb of skeletally mature Yucatan minipigs were obtained and 3D models of the bones were generated. A musculoskeletal model was generated in OpenSim, and the relative motion of the AC and its contact forces was evaluated through a passive range of motion. In 3 additional minipig forelimbs, a TekScan iScan 6900 pressure sensor was inserted between the accessory carpal and the ulnar carpal. The carpus was moved through a range of angles from 90 degrees to full extension, while contact forces were measured. Development of AC Replacements: In Solidworks, an implant of the articulating cartilage surface and first third of the AC bone was designed using the µCT data. A 2mm thick by 5mm deep "keel" was added for fixation. Positive molds were 3D printed out of an ABS-like photopolymer (Figure 3B). To fabricate elastomeric negative molds,

Sylgard 184 (polydimethylsiloxane, PDMS) was poured over the 3D printed designs, degassed, and allowed to cure at 40°C overnight. To fabricate porous anatomical implants, poly(ε-caprolactone) (PCL) was dissolved in chloroform at 20% wt/vol and mixed with NaCl crystals sieved to ~106 µm. Zirconium nanoparticles were included for radioopacity. The slurry was poured into the mold and the solvent was evaporated. The units were demolded and the salt was leached. Implantation of Engineered AC: Next, a proof-of-concept implantation in an adult minipig was performed. The carpus was exposed and rotated so that the articulating surface of the AC was in view. A reciprocating saw and osteotome were used to remove the surface of the AC and a 2mm burr was used to create a slot in the remaining bone, matching the keel on the implant. The construct was fixed in place with two 1mm Ø by 8mm bicortical screws oriented normally to the plane of the keel. Fluoroscopy confirmed implant positioning. After 1 week, the animal was sacrificed and the implant was retrieved and evaluated by µCT.

RESULTS

The porcine AC bone shows marked anatomical similarity to the human trapezium in both its size and saddle shape of its major articulating surface (Fig 1A-B). Both showed strong staining for proteoglycans on their cartilage surfaces and fibrous tissue at their peripheries (Fig 1C). The average thickness of the AC articular cartilage ranged from 350-500 µm within the contour of the main articulating surface (Fig 2A). The equilibrium modulus in the superior, middle, and inferior regions was 0.93 +/- 0.54, 1.40 +/- 0.67, and 1.36 +/- 0.60 MPa, respectively.

In the OpenSim model, contact force remained ~0N as the carpus was extended, until ~20° flexion. After this point, force increased and reached a peak of 67N at full extension (Figure 2C). In the *ex vivo* experiment (Fig 2D), contact area across the joint remained close to 0 mm^2 until 15° of flexion, and then rose rapidly as the angle approached 0° (Fig 2E). Force (Fig 2F) followed the same pattern, reaching its maximum of 29.1±10.5N at 0°.

Using anatomic renderings generated from µCT, an implant was designed to replace the articular surface of the porcine AC (Fig 3A).

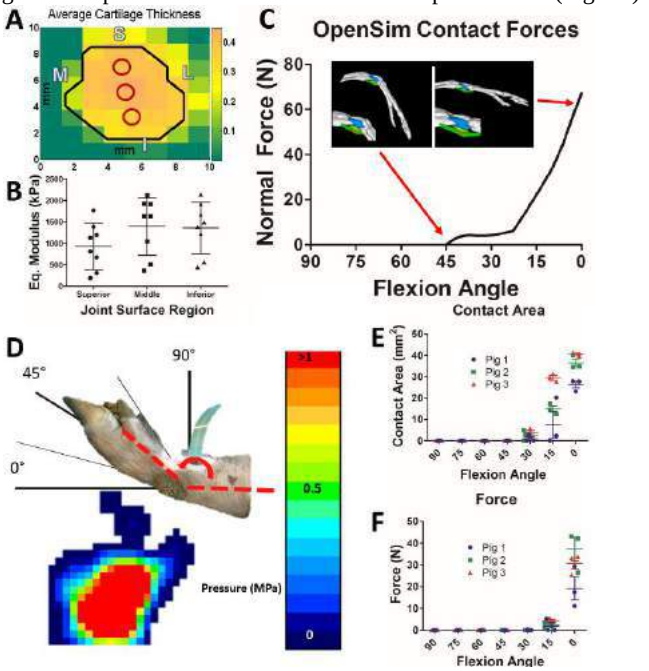

Figure 2: (A) Average thickness of the articulating surface of the AC on top of a profile indicating the average cartilage perimeter (black line). Indentation test location indicated by red circles. (B) Equilibrium modulus at three locations along the midline of the AC articular cartilage. N=8. (C) Plot of contact forces predicted by OpenSim model. (D) Example pressure map of the AC contact. (E-F) Plots of contact area and force with respect to flexion angle as measured using a TekScan sensor.

Using a 3D printed positive mold, a PDMS negative mold was produced (Fig 3B) which was used to create a porous PCL implant (Fig 3C). This was implanted into a living pig (Fig 4A-C), which began weight bearing soon after surgery (Fig 4D). The implant remained intact and in place after 1 week. (Fig 4E-G).

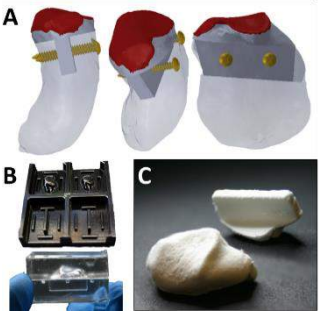

Figure 3: (A) Design of composite implant with keel, bicortical screws, parent bone, and engineered cartilage surface (in red). (B) ABS positive mold (top) and PDMS negative mold (bottom) used to create a PCL

DISCUSSION

In this study, we compared the porcine AC and the human trapezium. The two showed remarkable anatomic and compositional similarities. To better understand the loading of this joint, we analyzed the tissue-level mechanics of the cartilage as well as the load transfer across this joint. Loading patterns measured *ex vivo* matched that predicted via OpenSim. These models and data show that the AC is essentially unloaded, except when the carpus is fully extended. This means that when implanted into a living animal, the construct will only experience loads when the animal is standing, or in the stance phase of the gait cycle. Next, from µCT data, we designed an implant that recapitulates the articulating surface of the AC and a process to fabricate such an implant using a porous PCL foam. This we surgically implanted into a living animal, which recovered well from surgery and was weight bearing following recovery from general anesthesia. After one week, the implant remained in place and intact, demonstrating that this approach of implant fabrication and surgical fixation is feasible for the resurfacing of the AC. Future studies will evaluate the long-term function of a cell seeded osteochondral implant (with a stem cell-laden hydrogel cap to form a cartilage layer) in a living animal. Future studies will also use clinical CT to produce anatomic renderings of the AC, allowing us to fabricate the implant to patient-specific geometry. By using the porcine AC as a model for the human trapezium, evaluating its composition, mechanics, and function, designing and fabricating an anatomic construct, and implanting it in a living animal, this study advances our work towards total biologic resurfacing of this joint as an analog for the treatment of TMC OA in humans.

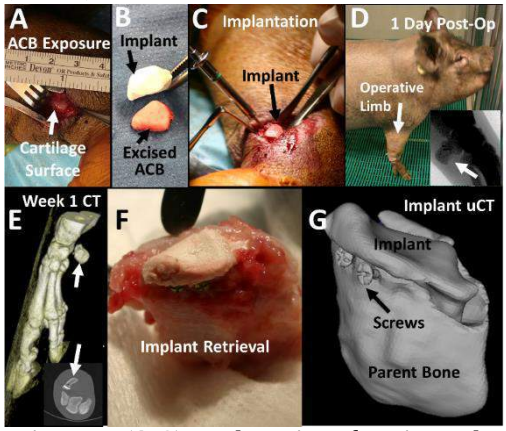

Figure 4: (A-C) Implantation of engineered ACB in a living animal. (D) Post-Op day 1 showing weight bearing and fluoroscopy showing implant. (E) Week 1 CT. (F) Implant retrieval and (G) implant µCT at week 1.

ACKNOWLEDGEMENTS

The National Institutes of Health and the Department of Veteran's Affairs supported this work.

REFERENCES

[1] Becker+, Clin Orthop Relat Res, 2013. [2] Wajon+, Cochrane Database Syst Rev, 2015. [3] O'Connell+ J Knee Surg, 2012. [4] Saxena+ Tissue Eng Part A, 2016. [5] Yushkevich+, Neuroimage, 2006.

SB³C2019
Summer Biomechanics, Bioengineering and Biotransport Conference
June 25 -28, Seven Springs, PA, USA

MUSCLE AND TENDON DERIVED EXTRACELLULAR MATRIX PROMOTES EXPRESSION OF MYOTENDINOUS JUNCTION SPECIFIC INTEGRINS IN MYOBLAST CELL CULTURE

Lewis Gaffney [1], Donald O. Freytes [1,] Matthew B. Fisher [1,2]

(1) Department of Biomedical Engineering
North Carolina State University and
University of North Carolina- Chapel Hill
Raleigh, NC, USA

(2) Department of Orthopedics
University of North Carolina-Chapel Hill
Chapel Hill, NC, USA

INTRODUCTION

Musculoskeletal disorders, such as muscular dystrophies and acute volumetric muscle loss, are prevalent and often debilitating. [1] The specific effects of muscular disorders are more understood in muscle tissue, however tendon tissue is also affected and contributes to the decreased function of the muscle tissue. [2] In parallel to muscular diseases, tendinopathies are more understood in tendon tissue, but there is little understanding how they affect muscle tissue. While importance of mechanical signaling has been established in skeletal tissue, the endocrine function and communication ("cross-talk") in tissues like muscle and bone are becoming increasingly recognized. [3] Specifically, at the myotendinous junction (MTJ), muscle cells express integrin proteins like paxillin and talin that integrate with tendon matrix.[4] In addition to cell-matrix interactions, cross-talk between cells may be an important aspect in the maintenance of the MTJ cell population and matrix structure. For instance, during development, tendon cells provide signals to muscle cells that help to anchor muscle to tendon, indicating this cross-talk is extremely important to the organization of muscle tissue. [5] A multi-phasic tissue may produce a gradient of growth factors sufficient to induce higher level organization and may be a key component for the synthesis of an *in vitro* MTJ model.

The development of multi-tissue platforms can enable researchers to understand how the cross-talk of muscle and tendon affects the regeneration in healthy or diseased muscle and tendon tissue. Currently *in vitro* models are often composed of one tissue and do not re-capitulate the complexity, especially at the interface of the muscle and tendon. The overlap of the two tissues may provide cross-talk crucial to the expression of MTJ specific proteins (e.g. paxillin). [6] As a first step toward developing an *in vitro* MTJ model, this research aims to determine the effects of muscle or tendon extracellular matrix on mouse myoblast cells grown in monolayer or cultured in a 3D hydrogel. Furthermore, to develop a multi-phasic tissue, special inserts were designed to create a tunable overlap region between extracellular matrix hydrogels seeded with tendon and muscle cells.

METHODS

Porcine muscle and tendon tissues were decellularized, lyophilized and digested according to previous methods to yield muscle derived extracellular matrix (mECM) or tendon derived extracellular matrix (tECM). [7] C2C12 mouse myoblasts were cultured on tissue culture plastic in either regular growth media (RGM) consisting of DMEM supplemented with 10% FBS and 1% Penicillin/Streptomyocin or muscle differentiation media (mdiff) consisting of DMEM, 1% Horse Serum, 1% FBS and 1% Penicillin/Streptomyocin.

To determine effects of ECM conditioned media, cells were cultured for 5 days in monolayer in both medias, alone and supplemented with 400ug/ml of either type I collagen, mECM or tECM (Figure 1A). To determine effects of culturing cells within tissue specific matrix, mouse myoblasts were suspended in type 1 collagen, mECM or tECM hydrogels before cross-linking, which resulted in a stable 3D engineered tissue with seeded cells following cross-linking (Fig. 2A). Tissue constructs were cultured in either RGM or mdiff media for 5 days. In both scenarios, RNA from cells were isolated and processed. Relative gene expression analysis for Paxillin was determined through q-PCR. Furthermore, samples were normalized to cells in RGM or Collagen tissues cultured in RGM.

To create an *in vitro* MTJ model that mimics the native interface, custom inserts with engineered tissues were utilized. Mouse myoblasts and mouse primary tendon fibroblasts were seeded in various hydrogel environments prior to cross-linking. Cell-laden hydrogels at concentrations of 4.5, 5.0, 5.5 and 6.0 mg/ml were seeded on either side of a removable barrier and allowed to partially cross-link. After 5, 10 or 15 minutes the barriers were removed allowing the gels to partially mix. This resulted in biphasic gels with an overlapping region containing

both myoblasts and tendon fibroblasts of varying widths depending on time and concentration.

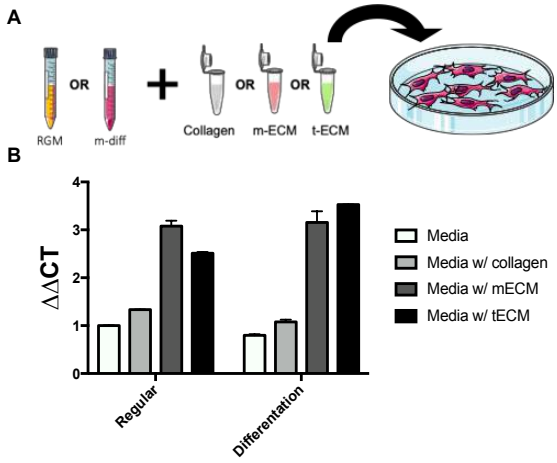

Figure 1: C2C12 cells cultured on tissue culture plastic cultured in RGM or Diff medias supplemented with digested type I Collagen, m-ECM or t-ECM had increased expression of Paxillin compared to cultures with non-supplemented medias or medias supplemented with collagen. ΔΔCT is relative to GAPDH and normalized to C2C12s cultured in regular growth media.

RESULTS

Myoblast Monolayers Cultured with Conditioned Media: Mouse myoblasts cultured in monolayer increased varying levels of paxillin expression when media was supplemented with mECM or tECM, relative to controls (Figure 1B). Fold increases of 1-2 were observed in ECM conditioned media and this shift also occurred in both media types (RGM and mDiff).

Engineered Tissues with Myoblasts: Myoblasts encapsulated in 3D hydrogel environments had increased levels of relative paxillin expression in ECM environments compared to the collagen environment (Figure 2). Fold changes of 2-4 occurred in cells within ECM hydrogels cultured in RGM. Lower fold changes occurred in tissues cultured in mDiff, but the rank order of groups was similar.

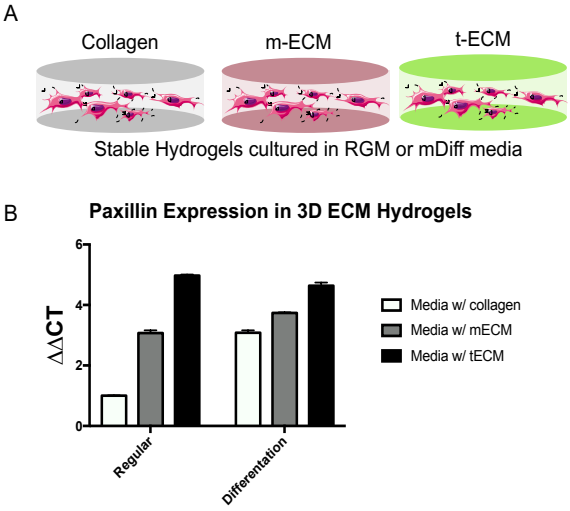

Figure 2: Myoblast cells cultured in type I collagen and ECM derived hydrogels for a period of 5 days have increased expression of MTJ protein Paxillin in ECM hydrogels compared to collagen. A) Briefly cells were encapsulated in self-assembling hydrogels and cultured in either RGM or Diff media. B) q-PCR results of Paxillin expression relative to housekeeping gene GAPDH and normalized to samples cultured in collagen gels with RGM.

Creating Biphasic Tissues with Tunable Interfaces: After determining the effect of tissue specific microenvironments on myoblasts, we designed a way to culture and examine cells in an interface zone with different microenvironments and different cell types. Gels were allowed to self-assemble separately before divider removal resulted in biphasic gels with varying regions of mixed hydrogels (Figure 3). In all 4 concentrations of hydrogels, time had a significant effect on the width of the overlap region, while the effect of gel concentration was not as pronounced. 15 minutes of isolated self-assembly in 5.5 and 6.0 mg/ml hydrogels yielded physiologically relevant overlaps of 200-600 μm.

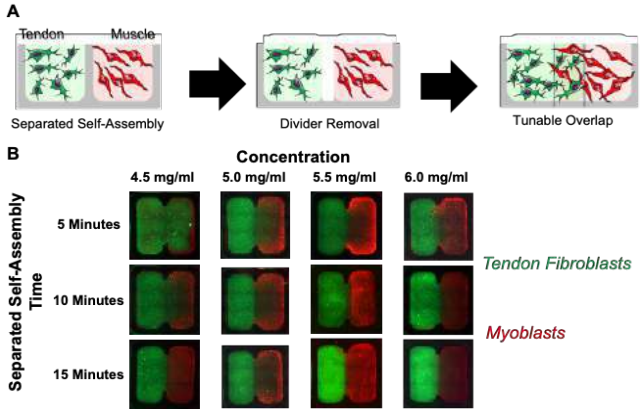

Figure 3: Overlapping interface regions of tendon and myoblast cells suspended in 3D hydrogels were achved with custom cell culture inserts. A) Cell culture inserts were modified to have a removable divider. Cells were seeded on either side of insert divider and incubated separately for specific times, after which the divider was removed allowing the gels to overlap. B) Images of gels of varying concentration and separated incubation times. Both time and concentration of gels had an effect on gel overlap.

DISCUSSION

Tissue specific derived matrix increased paxillin expression in myoblasts cultured in monolayer and 3D hydrogels, suggesting that mECM or tECM contained signals that helped promote MTJ expression in myoblast cells. Interestingly the highest levels of paxillin expression was seen in myoblast cells exposed to tECM, suggesting interaction with tendon matrix may be important in MTJ signaling *in vivo*. After establishing the effect of the microenvironment on myoblast cells the next step is to study the interface of myoblasts with tendon cells. Our tissue culture insert allows hydrogels to partially self-assemble, separately allowed for the creation of a tunable overlap region with a mix of both hydrogels. This will allow us to study interactions of cells in an overlap region, and possibly examine cross-talk effects between muscle and tendon cells.

ACKNOWLEDGEMENTS

The authors would like to acknowledge the Joint Department of Biomedical Engineering North Carolina State University and the University of North Carolina- Chapel Hill.

REFERENCES

[1] Romitti, P. A. *Pediatrics* **2015,** *135* (3), 513-21. [2] Merceron, T. K. *Biofabrication* **2015,** *7* (3), 035003. [3] Brotto, M.; *Bone* **2015,** *80*, 109-114. [4] Larkin, L. M. *Tissue Eng* **2006,** *12* (11), 3149-58. [5] Rodriguez-Guzman, M. *Dev Biol* **2007,** *302* (1), 267-80. [6] Jarvinen, T. A. *The American journal of sports medicine* **2005,** *33* (5), 745-64. [7] Freytes, D. O. *Methods Mol Biol* **2014,** *1181*, 69-81.

SB³C2019
Summer Biomechanics, Bioengineering and Biotransport Conference
June 25 -28, Seven Springs, PA, USA

SMOOTH MUSCLE DIFFERENTIATION ACTIVELY PATTERNS THE AIRWAY EPITHELIUM DURING BRANCHING MORPHOGENESIS

Katharine Goodwin (1), Andrej Kosmrlj (2), Celeste M. Nelson (3)

(1) Lewis-Sigler Institute for Integrative Genomics
Princeton University
Princeton, NJ, USA

(2) Department of Mechanical and Aerospace Engineering
Princeton University
Princeton, NJ, USA

(3) Department of Chemical and Biological Engineering and Department of Molecular Biology
Princeton University
Princeton, NJ, USA

INTRODUCTION

Branching morphogenesis begins with a simple tube or cluster of cells that grow and undergo rounds of budding and/or bifurcation, leading to the formation of a complex, arborized network. The final form and function of each branched organ varies, but the molecular programs responsible for their development are often similar. In most branched epithelial tissues, growth factors from the surrounding mesenchyme signal to the epithelium to elicit cellular behaviors required for growth and branching [1]. However, growth factor signaling alone cannot fully explain how the different architecture of each organ is achieved. To understand how branched networks are generated, we require a deeper understanding of the physical mechanisms of branching morphogenesis [2]. Equipped with such knowledge, we may be able to better diagnose and treat developmental disorders, and further, to recapitulate the mechanisms employed by the embryo to engineer branched tissues ex vivo.

In the mouse lung, branching is highly stereotyped and is achieved by repeated use of simple branching modes: the overall architecture is established by domain branching, in which new branches form laterally off the side of an existing branch, while bifurcations build a space-filling network [3]. The airway epithelium develops concomitantly with a layer of smooth muscle, which is derived from the embryonic mesenchyme and wraps circumferentially around the airways. We previously showed that stereotyped patterns of smooth muscle differentiation are required for terminal bifurcation [4]. Here, we examined the role of smooth muscle differentiation in shaping emerging domain branches during early murine lung development.

METHODS

Embryonic mouse lungs were isolated at embryonic day 11.5 (*E*11.5) and cultured ex vivo at an air-liquid interface for 24 hours. Pharmacological inhibitors or adenoviruses were added to the culture medium to manipulate smooth muscle differentiation. Genetic ablation of smooth muscle was achieved by selectively expressing the human diphtheria toxin receptor in smooth muscle cells and then treating lung explants ex vivo with diphtheria toxin. Immunostaining and EdU pulses were then used to assess the effects of these treatments on airway epithelial morphology, smooth muscle coverage, and epithelial proliferation. Time-lapse imaging was used to track epithelial morphology over the course of branching, and embryos expressing fluorescent reporters were used to visualize smooth muscle differentiation. Finally, a computational model of domain branching based on continuum mechanics of growing tissues was created to explore the role of smooth muscle-mediated constraint.

RESULTS

Our studies reveal a role for airway smooth muscle in sculpting emerging domain branches in the embryonic mouse lung. We have shown that domain branching is highly

Poster Presentation #P288

stereotyped and accompanied by evolving spatial patterns of smooth muscle. Perturbing these patterns of differentiation with pharmacological, adenoviral, or genetic approaches disrupts domain branching. Enhanced wrapping of smooth muscle around the epithelium suppresses branch initiation and extension, whereas decreased smooth muscle coverage leads to ectopic and dilated branches. Ablation of smooth muscle cells using transgenic mouse models at earlier stages of differentiation affects domain branching, but ablation of mature smooth muscle cells does not. Based on these findings, we propose that domain branching is primarily regulated by the pattern of newly forming smooth muscle and not by the existing smooth muscle sheath.

Our data suggest two possible mechanisms by which smooth muscle regulates branch formation. Firstly, we identified an evolving pattern of epithelial proliferation that is complementary to the pattern of smooth muscle differentiation and perturbed when the latter is disrupted. Secondly, we determined that the primary bronchus adjacent to an emerging branch is gradually constricted, and that this thinning depends on smooth muscle differentiation. These data suggest that smooth muscle affects local epithelial behaviors (i.e. proliferation rate) and overall epithelial morphology. We hypothesized that if smooth muscle was indeed required to physically shape the growing epithelium, then epithelial volume might be unchanged between treated lungs and controls. In line with this, we found that the volume of the epithelium is conserved even in lungs where smooth muscle differentiation is disrupted and that have wider epithelial branches and even ectopic branches.

Overall, our data suggest a model in which the airway epithelium expands uniformly into the mesenchyme and is guided into a branched morphology by spatially patterned smooth muscle differentiation (**Fig. 1**). These conclusions are supported by computational modeling: domain branches only form correctly when provided with the appropriate smooth muscle constraint. In the absence of a stiff smooth muscle layer, the simulated epithelium forms multiple ectopic branches and buckles, similar to the effects observed when smooth muscle differentiation is inhibited experimentally. These data support our assertion the local presence of smooth muscle exerts a physical force to direct the expansion of the growing epithelium.

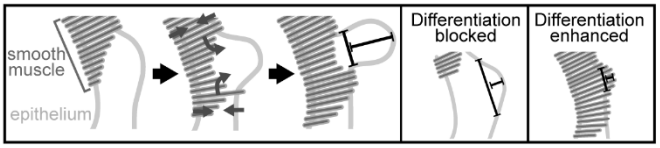

Figure 1: Differentiation of smooth muscle around the primary bronchus leads to thinning of elongating branches by physically constricting the epithelium. When differentiation is blocked, epithelial growth is unconstrained and the epithelium becomes dilated. When differentiation is enhanced, a sheath of smooth muscle envelops the epithelium, preventing branch initiation and extension.

DISCUSSION

Our work uncovers a role for smooth muscle differentiation in sculpting domain branches, and sheds additional light on the physical mechanisms of branching morphogenesis in the mouse lung. There is still much to be uncovered if we are to truly understand the complex relationships between epithelial branching and smooth muscle differentiation, and in particular, how signaling networks and mechanical forces may cooperate to achieve patterned differentiation. We show a clear spatiotemporal correlation between emerging domain branches and localized smooth muscle differentiation, and point to possible mechanisms by which this pattern of smooth muscle might guide the epithelium into its final morphology. We establish smooth muscle as a critical regulator of early lung branching morphogenesis, and anticipate that it may play similar roles in other smooth muscle-encircled epithelial tissues.

ACKNOWLEDGEMENTS

This work was supported by an NIH/NHLBI R01 grant, an NSF grant and an HHMI Faculty Scholar's award.

REFERENCES

[1] Wang, S et al., *J Cell Biol*, 216(3): 559-570, 2017.
[2] Varner, VD and Nelson, CM, *Development*, 141(14): 2750-2759, 2014.
[3] Metzger, RJ et al., *Nature*, 453(7196): 745-750, 2008.
[4] Kim, HY et al., *Dev Cell*, 34(6): 719-726, 2015.

SB³C2019
Summer Biomechanics, Bioengineering and Biotransport Conference
June 25 -28, Seven Springs, PA, USA

THE EFFECTS OF OXYGEN AND AIR-LIQUID-INTERFACE CULTURE ON HUMAN BRONCHIAL EPITHELIAL CELL DIFFERENTIATION

S. Kouthouridis (1), J. Goepp (2), C. Martini (3), E. Matthes (3), J. Hanrahan (2,3), C. Moraes (1,2,4,5)

(1) Department of Chemical Engineering
McGill University
Montreal, □c, Canada

(2) Cystic Fibrosis Translation Research Centre
McGill University
Montreal, □c, Canada

(3) Department of Physiology
McGill University
Montreal, □c, Canada

(4) Department of Biomedical Engineering
McGill University
Montreal, □c, Canada

(5) Rosalind and Morris Goodman Cancer Research Centre
McGill University
Montreal, □c, Canada

INTRODUCTION

Inhalable drug and respiratory toxicity assays are conventionally performed on human bronchial epithelial cells (HBECs) that have been differentiated for several weeks at an air-liquid interface (ALI). Porous filters have been used as ALI culture models for decades, since they were shown to promote differentiation into ciliated cells and mucus-producing goblet cells [1]. However, ALI filter culture is expensive, labor-intensive, and difficult to scale for high-throughput applications. It also remains unclear as to which biophysical cues prompt differentiation. Understanding these signals could lead to greatly simplified designs of culture platforms optimized for airway studies compatible with high-throughput methods.

The assumption that complete ALI is a uniquely necessary condition for HBEC differentiation was recently challenged by Gerovac et al. who demonstrated that a thin layer of culture media over lung cells at ALI can further improve differentiation [2]. This suggests that differentiation in submerged culture is not only possible, but that the increased availability of soluble nutrients may enhance differentiation efficiency under appropriate culture conditions. Eliminating the need for ALI could eliminate the need for filter culture platforms, and reduce the cost of drug discovery,

Limited diffusion of oxygen through culture media causes an oxygen-depleted zone to form at the cell surface during submerged culture. In contrast, ALI provides cells with increased oxygen access. Here, we hypothesize that exposure to increased oxygen levels present on the air-side of the ALI culture triggers differentiation, and that appropriately designed hyperoxic culture conditions would allow differentiation under submerged conditions. Here, we cultured HBECs on filters at standard/hyperoxic conditions, and at ALI/submerged conditions (Fig. 1) to determine the necessity of ALI cultures for differentiated studies.

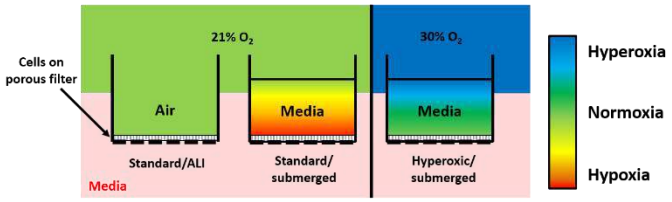

Figure 1: Comparison of the three culture conditions.

METHODS

Parametric finite element simulations were performed to determine the optimal incubator oxygen level to achieve ambient (21%) oxygen concentrations at the cell surface, when cultured with 3 mm of fluid in the apical chamber in submerged culture.

Primary bronchial cells from three otherwise-healthy trauma patients were isolated at the Cystic Fibrosis Translational Research core at McGill University, seeded onto polyester Transwell® filters at ALI, and cultured until confluent. Atmospheric oxygen levels and liquid levels were then controlled for standard O_2/ALI, standard O_2/submerged and hyperoxic O_2/submerged cultures for a subsequent 25 days.

To characterize cultures, transepithelial electrical resistance (TEER) was monitored to assure epithelial layer integrity. Epithelial morphology and function were assessed via immunofluorescent labels for nuclei, the microtubule element cilia β-tubulin III strongly expressed in cilia, the tight junction marker zonula occludens-1 (ZO-1), and nuclear levels of the oxygen-sensitive marker hypoxia-inducible factor 1-alpha (HIF-1a). Differentiation was determined by measuring epithelial layer thickness, ciliated surface area, and beat speed. Functional ciliation was verified using particle movement assays.

Poster Presentation #P289

RESULTS

Simulations demonstrated that that an incubator oxygen concentration of 30% would theoretically allow for the cells to experience normoxic conditions (21%) at the cell surface when submerged in 3 mm of media (Fig. 2A). Other combinations of media layer height, cell oxygen consumption rate and incubator oxygen concentrations to achieve normoxic cell conditions were plotted (Fig. 2B).

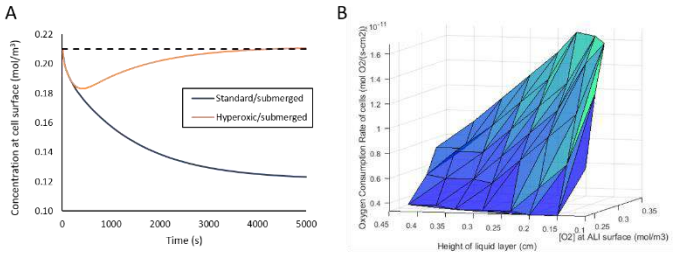

Figure 2: Finite element simulation (A) Time-dependent oxygen concentration at the cell surface for standard and hyperoxic atmospheric oxygen levels. (B) Parametric variation of cell oxygen consumption rate, media layer thickness, and atmospheric oxygen to achieve normoxic oxygen concentrations at the cell layer.

Validation. Average cell spread area was statistically similar in all three culture conditions, and cells closest to the porous filter surface adapted a flatter morphology, that is typical of basal epithelial cells. Nuclear HIF-1a was elevated in standard/submerged culture and reduced in standard/ALI and in hyperoxic/submerged (Fig. 3A), confirming that HBECs are sufficiently sensitive to oxygenation differences caused by submersion, and that oxygen levels at the cell surface that have been reduced by submerged culture can be rescued by hyperoxic exposure. In all three conditions, TEER measurements stabilized around day 7 (Fig. 3B), and tight junction ZO-1 expression was consistently observed (Fig. 3C), confirming that cultures do not suffer adverse effects at this level of oxygen exposure. In contrast, higher oxygen levels resulted in cell death and barrier permeabilization (data not shown).

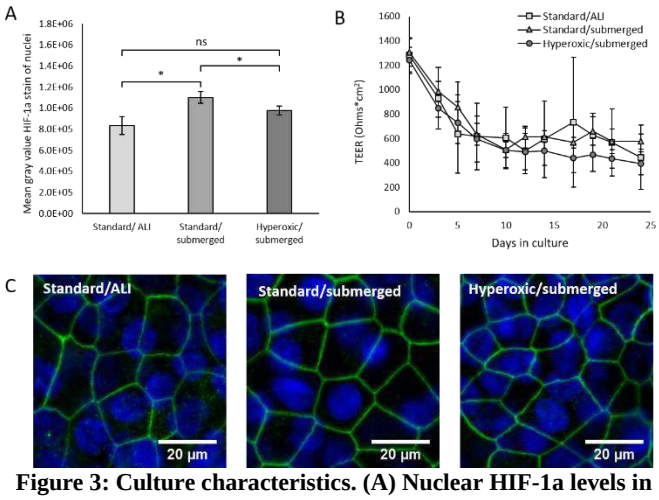

Figure 3: Culture characteristics. (A) Nuclear HIF-1a levels in HBECs after 25 days in culture (* p < 0.05). (B) TEER and (C) ZO-1 (green) / nuclei (blue) from standard/ALI, standard/submerged, and hyperoxic/submerged conditions.

Differentiation. For cells from all three patient donors, the hyperoxic/submerged condition exhibited the highest rates of ciliation; while cells under standard/ALI exhibited the lowest (Fig. 4A), which was surprising given that ALI culture is the standard for HBEC differentiation. Beat frequency of cilia was found to be lowest in standard/ALI conditions, likely a result of the presence of more concentrated levels of mucus on the epithelial surface. Moreover, both submerged conditions produced statistically thicker epithelial cell layers than the ambient-ALI cultures (Fig. 4BC). Taken together, these metrics indicate that hyperoxic/submerged culture promotes the highest rates of HBEC differentiation on filters.

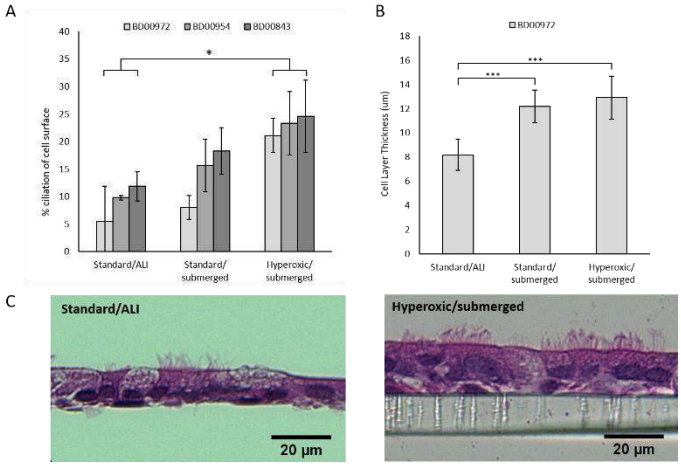

Figure 4: HBEC differentiation. (A) Ciliated area of cell surface after 18 days in culture (n=3, * p<0.05). (B) Cell layer thickness of histology slices (n=5, *** p<0.001). (C) H&E stain of cell layer histology cross-sections for standard/ALI and hyperoxic/submerged conditions.

DISCUSSION

The finite element simulation and nucleic HIF-1a levels confirm that controlled hyperoxic ambient conditions can compensate for the oxygen diffusion gradient present in submerged conditions. Our results show that submerged HBEC culture triggers higher rates of ciliation and allows for thicker epithelial layer formation in all three primary donors, which contradicts the widely accepted assumption that ALI is necessary for HBEC differentiation. Both increased ciliation and thicker epithelium can be a result of increased nutrient availability in submerged culture. The lower cilia beating speed observed in the standard/ALI condition is likely due to a thick mucosal layer on top of the cells, which offers resistance to cilia movement. Throughout submerged culture, these mucins excreted by goblet cells likely dissolve into the surrounding media and thus do not form the viscous dampening layer necessary for mucociliary clearance studies. Interestingly, the ability of these cell types to differentiate at all under hypoxic and hyperoxic submerged conditions suggests that improved media formulations may have already reduced the need for ALI cultures, and that hyperoxic conditions may be sufficient to eliminate ALI entirely. Intriguingly, these conditions might reflect the rapid increase in differentiated lung cells that occurs during the first trimester of fetal development, before ALI conditions exist in the lung [3].

ACKNOWLEDGEMENTS

Natural Sciences & Engineering Research Council of Canada; Canada Research Chair in Adv. Cellular Microenvironments to CM.

REFERENCES

[1] de Jong, P.M., Am J Respir Cell Mol Biol. 1994 Mar;10(3):271-7.
[2] Gerovac, B., Am J Respir Cell Mol Biol. 2014 Oct; 51(4): 516–525.
[3] Jeffery, P., Am J Respir Crit Care Med. 1998 May; 157(5 Pt 2):S174-80.

SB^{3}C2019
Summer Biomechanics, Bioengineering and Biotransport Conference
June 25 -28, Seven Springs, PA, USA

ECTOPIC SOURCES OF FIBROBLAST GROWTH FACTOR 10 DRIVE EPITHELIAL BUCKLING AND SUPERNUMERARY BUD FORMATION IN CULTURED EMBRYONIC LUNGS

Kara E. Peak (1), Victor D. Varner (1)

(1) Department of Bioengineering
The University of Texas at Dallas
Richardson, TX, USA

INTRODUCTION

Ramified networks form the basic architecture for many organs in the body including the lung, kidney, and salivary gland. In the developing lung, these structures are formed via a process known as branching morphogenesis. The embryonic lung bud arises as an out-pocketing of foregut endoderm, which undergoes a series of recursive branching events to build the bronchial tree [1]. A complex network of signaling pathways regulates this process, but fibroblast growth factor (FGF) signaling has emerged as a particularly important regulator of airway branching. Focal regions of FGF-10 expression in the pulmonary mesenchyme are thought to specify the locations of new epithelial branches and thereby control the overall branching pattern [2]. Recent experiments, however, have shown that mechanical forces can also regulate lung development [3-5], but it is unclear how growth factor signaling is integrated with these biophysical cues to direct the formation of the bronchial tree.

Here, we used growth factor-loaded beads to create ectopic sources of FGF-10 and implanted them in the mesenchyme of embryonic lung explants along regions of the airway epithelium that do not normally form branches. These focal sources of exogenous FGF-10 were sufficient to induce the formation of multiple supernumerary buds in explants cultured ex ovo. The supernumerary buds formed simultaneously, as revealed by time-lapse microscopy, and were found to depend crucially on cell proliferation. We did not observe changes in cellular contractility during the formation of ectopic buds, despite previous work suggesting that apical constriction, downstream of FGF-10 signaling, initiates the formation of new epithelial branches during normal lung development. Taken together, our results suggest that supernumerary buds arise via an FGF-10-induced buckling mechanism. These data will help elucidate how specific patterns of FGF-10 expression give rise to the macroscopic changes in tissue form that build the bronchial tree during embryonic development.

METHODS

Fertilized White Leghorn chicken eggs were incubated at 37 °C in a forced-draft incubator to Hamburger and Hamilton (HH) stage 26. Embryonic lungs were dissected in phosphate-buffered saline (PBS) supplemented with antibiotics using fine forceps and a dissecting stereomicroscope. Small agarose beads, soaked in either PBS or 100 μg/ml FGF-10 for 1.5 hr at room temperature, were then implanted into the pulmonary mesenchyme adjacent to unbranched regions of the airway epithelium. The explants were then cultured on porous membranes at the air-liquid interface in DMEM/F12 medium (without HEPES) supplemented with 5% fetal bovine serum (FBS) and antibiotics. In some experiments, the medium was also supplemented with either 1 μM aphidicolin or 5 μM blebbistatin, to inhibit cell proliferation or non-muscle myosin II contractility, respectively.

Bright field images of cultured explants were captured at 0 and 24 hr to quantify the number of ectopic buds, as well as changes in epithelial morphology. Relative changes in epithelial contour length, as well as an epithelial tortuosity index, defined as the ratio of the contour length relative to the length of a straight line connecting the end-points of the contour, were measured after 0 and 24 hr of culture. In other experiments, to determine the role of cell proliferation during supernumerary bud formation, we used the Click-iT EdU Imaging Kit to detect proliferating cells in explants cultured with either control or FGF-10-containing beads. These explants were fixed, stained for LCAM (E-cadherin) immunofluorescence and DAPI, dehydrated in a methanol series, optically cleared with Murray's clear, and imaged as whole-mounts using a laser scanning confocal microscope. Additional explants were stained with phalloidin to visualize F-actin.

Poster Presentation #P290

To quantify the dynamics of supernumerary bud formation, we also conducted time-lapse experiments using a stage-top incubator. Bright field images of cultured lung explants were captured every 30 minutes for 24 hr, and epithelial morphologies were quantified as described above.

RESULTS

Agarose beads containing 100 µg/ml FGF-10 were embedded in the pulmonary mesenchyme of embryonic chicken lungs adjacent to unbranched regions of the developing airway epithelium. These FGF-10-loaded beads induced the formation of several ectopic buds after 24 hr of culture, as compared to explants cultured with control beads (Figure 1). Quantitative morphological measurements revealed an increase in both the contour length and tortuosity index at 24 hr of the airway epithelium in explants cultured with FGF-10-loaded beads. To determine the role of cell proliferation in this process, we then cultured lung explants containing FGF-10 loaded beads in the presence and absence of the cell cycle inhibitor, aphidicolin. Explants treated with aphidicolin exhibited a decreased number of supernumerary buds and showed concomitant decreases in the counter length and tortuosity index at 24 hr of the airway epithelium, which suggested that cell proliferation is required for the formation of supernumerary buds. We also quantified rates of proliferation along the airway epithelium in explants treated with control beads, FGF-10-loaded beads, and FGF-10-loaded beads + aphidicolin. Confocal imaging of fixed explants stained for EdU incorporation and LCAM immunofluorescence revealed increased levels of epithelial proliferation in the FGF-10-induced supernumerary buds (Figure 2). Time-lapse culture of lung explants containing either control or FGF-10-loaded beads further showed that the supernumerary buds formed simultaneously, a result suggestive of an epithelial buckling event [5].

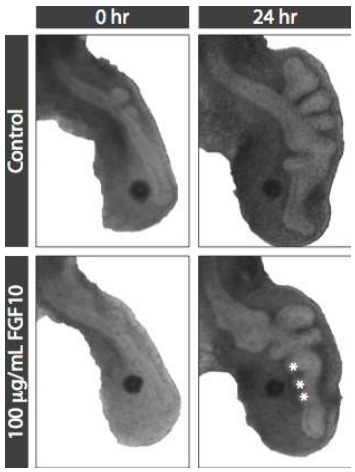

Figure 1: FGF-10-loaded beads induce the formation of supernumerary buds (white asterisks) in cultured embryonic chick lungs.

Other cultured explants were stained with phalloidin to visualize F-actin and to assess the role of apical constriction during the formation of ectopic buds, since earlier work had shown apical constriction to initiate budding events during normal lung development [6]. The FGF-10-induced supernumerary buds contained no discernible increases in F-actin staining, suggesting that apical constriction is not involved in their formation. However, explants containing FGF-10-loaded beads, which were treated with the non-muscle myosin-II inhibitor, blebbistatin, exhibited a reduction in the number of supernumerary buds. The treatment with blebbistatin did not modulate rates of cell proliferation, as determined by EdU incorporation, suggesting a role for cell contractility in suppressing the buckling morphogenesis of the airway epithelium.

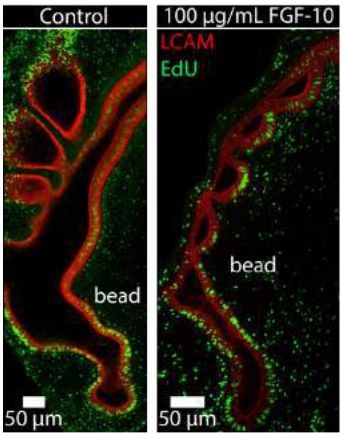

Figure 2: FGF-10-loaded beads induce elevated levels of EdU incorporation in supernumerary buds.

DISCUSSION

Previous studies have used grafts of distal pulmonary mesenchyme to stimulate the formation of supernumerary buds along the (unbranched) trachea of cultured embryonic mouse lungs [7]. The distal mesenchyme expresses a variety of growth factors that have been shown to regulate airway branching morphogenesis [8], but it is not clear how specific growth factors drive the changes in the epithelial cell behavior that result in the formation of a new branch. In these experiments, FGF-10-loaded beads were sufficient to induce the formation of numerous ectopic buds, which formed simultaneously, with branching dynamics redolent of the buckling instability previously shown to govern the branching morphogenesis of cultured mesenchyme-free explants [5]. Future work will investigate how epithelial buckling is integrated with growth factor signaling to direct the formation of these supernumerary buds. These data will help uncover the mechano-regulatory mechanisms that control airway branching morphogenesis.

ACKNOWLEDGMENTS

This work was supported, in part, by the NIH grant R01HL145147 to VDV.

REFERENCES

[1] Cardoso WV, Lü J, *Development*, 133:1611-1624, 2006.
[2] Bellusci S, et al., *Development*, 124:4867-4878, 1997.
[3] Varner VD, Nelson CM, *Development*, 141:2750-2759, 2014.
[4] Nelson CM, et al., *Development*, 144:4328-4335, 2017.
[5] Varner VD, et al., *Proc Natl Acad Sci U S A*, 112:9230-9235, 2015.
[6] Kim HY*, Varner VD*, et al., *Development*, 140:3146-3155, 2013.
[7] Goldin GV, Wessells NK, *J Exp Zool.*, 208:337-346, 1979.
[8] Morrisey EE, Hogan BLM, *Dev Cell*, 18(1):8-23, 2010.

SB³C2019
Summer Biomechanics, Bioengineering and Biotransport Conference
June 25 -28, Seven Springs, PA, USA

BIOELECTRIC GRADIENTS EMERGE DOWNSTREAM OF MECHANICAL FORCES IN EPITHELIAL TISSUES

Brian B. Silver (1), Celeste M. Nelson (1,2)

(1) Molecular Biology
Princeton University
Princeton, NJ, USA

(2) Chemical & Biological Engineering
Princeton University
Princeton, NJ, USA

INTRODUCTION

Communication between cells at the tissue scale is critical not only for development, but also for processes such as wound healing[1] and maintenance of the epithelial barrier. Disrupting the delicate balance between proliferation and cell death can lead to diseases such as cancer[2]. It is well known that not only biochemical but also mechanical cues contribute to the establishment of growth patterns across an epithelial sheet. For example, the geometry of an epithelial tissue dictates gradients of mechanical stresses that control the location of dividing cells via forces exerted on the tissue edge[3]. Specifically, higher geometric forces at the edges of convex epithelial tissues lead to increased proliferation in cells within these regions.

Not only can cells communicate via biochemical and mechanical means, but it is becoming increasingly clear that bioelectric gradients also play a role in coordinating growth at the tissue scale. Bioelectricity describes the membrane voltage (Vm) of cells across a tissue. Vm is defined simply as the electric potential difference across the plasma membrane[4]. This difference arises due to the different concentrations of ions such as K^+, Na^+, and Cl^- that exist in the cytoplasm and extracellular medium. Cells tune Vm by regulating the concentrations of such ions via channels and transporters within the plasma membrane, which open in response to various cues such as ion concentration or changes in Vm[5]. Some ion channels even respond to physical cues that exert forces across the plasma membrane[6]. These mechanosensitive ion channels establish a possible link between mechanical and bioelectric regulatory cues. However, it is unclear to what extent mechanical and bioelectric forces influence each other and coordinate cellular behavior across the tissue to control growth, healing, and prevention of cancer.

Bioelectricity has been documented to control striking phenotypes at the tissue scale, including organogenesis[7] and tumor formation[8], as well as properties of individual cells such as proliferation and apoptosis[4]. However, it is still unclear exactly what specific manipulations of Vm will lead to a desired outcome. This is not entirely surprising given the complexity of biochemical and mechanical cues surrounding the cell. We therefore wished to more thoroughly examine how mechanical factors influence the establishment of bioelectric gradients across a tissue. Since decreased Vm (depolarization) has been correlated with increased proliferation[4], we hypothesized that the convex edges of epithelial tissues constrained to specific geometries would be more depolarized at these highly proliferating regions[3]. We found that this bioelectric gradient is formed by forces exerted on the tissue, which activate the mechanosensitive ion channel Piezo1. Finally, our data suggest that decreased Vm is required for increased proliferation in these high-stress regions due to enhanced entry of Ca^{2+} ions, which affect signaling through the Yap/Taz[9] pathway.

METHODS

Mouse mammary epithelial cells were cultured to confluence on islands of fibronectin formed by microcontact printing[10]. Proliferation was visualized using EdU incorporation,

and immunofluorescence analysis was used to label E-cadherin, Yap/Taz, or Piezo1. The voltage reporter dyes DiBac4(3) or DiBac4(5) were used to visualize gradients of cellular Vm throughout the tissues. These molecular dyes more easily enter the plasma membrane of depolarized cells. The percent difference in mean fluorescence intensity was calculated for the outermost 2-3 cell border and innermost 5-10 cell regions of an average intensity stack comprised of at least 15 tissues. Ionic calcium was visualized using Calcium Green 1 (Thermo Fisher). Tissues were incubated for 24 hr in 10 μM dye concentration prior to imaging. Average intensity stacks were prepared as described above.

RESULTS

Square mammary epithelial tissues show increased proliferation at their edges as visualized with EdU incorporation (**Figure 1A, B**). This is in agreement with previously published work[3]. Tissues treated with $DiBac_4(3)$ to visualize Vm show increased fluorescence, indicating depolarization, along the edge and convex corners, where mechanical stress is highest (**Figure 1C, D**). These results are in agreement with our hypothesis that regions of increased mechanical stress correlate with depolarized regions of the tissue. Notably, we did not observe increases in either proliferation or depolarization in concave tissue regions of low mechanical stress. We next examined tissues comprised of cells in which we knocked out the cell adhesion protein E-cadherin (ΔE). These tissues are unable to establish the gradient of mechanical stress present in parental tissues. Knocking down E-cadherin abolished the geometric proliferation gradient (**Figure 1E**). As expected, ΔE tissues did not show a gradient of depolarization along the tissue edge and corners (**Figure 1F**). In addition to these data, we observe increased expression of the mechanosensitive ion channel Piezo1 in cells at the tissue periphery. Also, we observe increased intracellular calcium as visualized with Calcium Green 1. Nuclear localization of Yap/Taz are also increased along the tissue periphery. The patterns of both Piezo1 and Yap/Taz nuclear localization were disrupted in tissues comprised of ΔE cells.

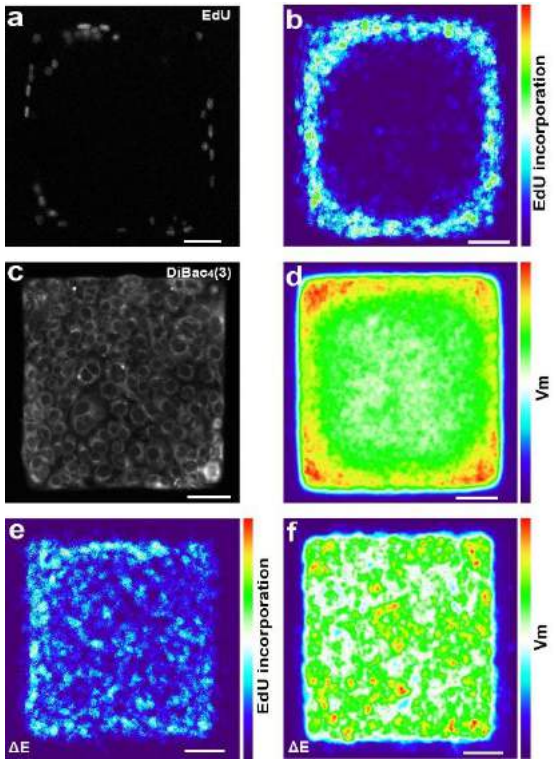

Figure 1: Epithelial tissue geometry dictates the location of proliferative cells as visualized by EdU analysis (a). This trend persists across multiple images (b). Further, depolarization occurs at convex tissue regions, where mechanical stresses are highest (c). Averaging multiple tissues reveals this pattern (d). Finally, E-cadherin is required for establishment of both the proliferation (e) and Vm (f) gradients.

DISCUSSION

We observe increased depolarization in convex regions of epithelial tissues constrained to specific geometries, consistent with our hypothesis that mechanical stresses are connected to Vm. Our data implicate the mechanosensitive ion channel Piezo1, increased intracellular Ca^{2+} concentration, and nuclear localization of Yap/Taz as key nodes in the link between mechanics and Vm. In the absence of mechanical stress gradients, we no longer see increased proliferation or depolarization. Further, we no longer observe the same patterns of Piezo1 expression or Yap/Taz activation. To our knowledge, this is the first study to directly establish a role for mechanical forces in Vm alteration.

ACKNOWLEDGEMENTS

The authors' work was supported in part by the NIH, the David & Lucile Packard Foundation and the Camille & Henry Dreyfus Foundation. BBS was supported in part by the NSF GRFP. CMN was supported in part by a Faculty Scholars Award from the HHMI.

REFERENCES

[1] Chifflet S et al., *Am. J. Physiol*, 288:C1420-C1430, 2005.
[2] Rosenblatt J et al., *Curr. Biol*, 11:1847-1857, 2001.
[3] Nelson CM et al., *Proc. Natl. Acad. Sci*, 102:11594-11599, 2005.
[4] Levin M et al., *Stem Cell Rev*, 5:231-246, 2009.
[5] Levin M. *Trends Cell Biol*, 17:261-270, 2007.
[6] Coste B et al., *Science*, 330:55-60, 2010.
[7] Adams DS et al., *Development*, 134:1323-1335, 2007.
[8] Chernet BT et al., *Oncotarget*, 7:19575-19588, 2016.
[9] Pathak MM et al., *PNAS*, 111:16148-16153, 2014.
[10] Tan J et al., *Tissue*, 10:865-872, 2004.

SB³C2019
Summer Biomechanics, Bioengineering and Biotransport Conference
June 25 -28, Seven Springs, PA, USA

CHARACTERIZATION OF COLLAGEN/KERATIN HYDROGELS AS AN EXTRACELLULAR MATRIX FOR 3D IN VITRO THERMAL STRESS STUDIES

K. Isaac (1), N. Ghousifam (2), S. Brocklehurst (1), M. Van Dyke (3), M.N. Rylander (1,2)

(1) Department of Biomedical Engineering
The University of Texas at Austin
Austin, TX, United States

(2) Department of Mechanical Engineering
The University of Texas at Austin
Austin, TX, United States

(3) School of Biomedical Engineering and Sciences
Virginia Tech
Blacksburg, VA, United States

INTRODUCTION

Biomimetic engineering has become critical for use in testing drugs and other treatments before moving forward with *in vivo* models and human clinical trials. Although *in vivo* models have normally been used, many drugs risk failure in clinical trials due to the significantly dissimilar microenvironments between humans and other animals and in addition are cost extensive. Biomimetic 3D *in vitro* models can serve as an early testing platform with carefully-designed parameters that can more closely model the human tissue microenvironment.

Collagen is commonly used to create 3D *in vitro* models to serve as the ECM. However it cannot be used to study cell behavior in response to thermal changes. Collagen has a denaturing temperature of approximately 40 °C and starts melting at even lower temperatures [1]. As a consequence, many in vitro hyperthermic models utilize a cell monolayer approach, which is not an accurate representation of heat transfer through an organ or tissue. Therefore, an ECM with greater thermal stability is needed.

Keratin is a more thermally stable natural biomaterial that can easily be extracted from animal wool and horn and human hair and can be used to as a biologically representative ECM component; therefore it can potentially be used for thermal stress studies without compromising the ECM with a denaturing temperature between 120 and 150 °C when wet [2]. Specific keratin extracts from the hair cortex have been shown to promote cellular attachment and proliferation in numerous studies, and have been shown to promote cell growth [3]. Kerateine (KTN), a form of reduced keratin, contains cysteine residues and is capable of disulfide crosslinking and self-assembly and has been shown to be more stable than its oxidative counterpart, keratose [3].

In the present study, we hypothesized that adding kerateine to collagen may increase the thermal stability of *in vitro* scaffolds and tissue platforms. This mixture will serve as a potentially-useful system to study the effect of thermal stress various doses and exposure time on cells behavior.

METHODS

Working collagen solutions of 3 and 7 mg/ml was prepared from the collagen stock solution of 6 and 14 mg/ml, respectively, by neutralizing with 10x DMEM, 1x DMEM, and 1 N NaOH. These concentrations of collagen were used because healthy tissue is less dense (3 mg/ml), whereas tumor tissue is denser in collagen and results in a stiffer ECM (7 mg/ml). 50/50, 30/70, and 20/80 w%/w% collagen/kerateine (C/KTN) hydrogels were prepared by combining both stock collagen (6 and 14 mg/ml) and KTN dissolved in neutralizing buffer of equal volume. After mixing thoroughly with a spatula, gels were added to cell culture-treated 96 well-plates and incubated at 37ºC for 40 minutes to allow polymerization. For cell culture experiments, gels were seeded with 0.5 million cells/ml and supplied with 100 µl of complete media. Media was changed every 2 days.

ECM structure was observed with dehydrated acellular gels through scanning electron microscopy (SEM). In addition, the thermal denaturation temperature of wet hydrogels were evaluated using differential scanning calorimetry (DSC) from 30 to 80°C at a rate of 5°C/min. For rheology, hydrogels underwent a frequency sweep at 1% strain from 1 to 15 Hz. Results were evaluated from 1 to 1.43 Hz.

Cellular studies were conducted to quantify cell viability and observe cell growth and morphology. Cell viability was quantified though CellTiter Blue viability assay at days 1, 3, 5, and 7 post-seeding. Cell viability was measured by reading fluorescence intensity with a spectrophotometer at $560_{ex}/590_{em}$. Sample readings were normalized to blank solutions (no sample). Additional samples were prepared for the same time points, fixed, and stained for actin to observe morphology.

Poster Presentation #P292

All experiments were repeated 3 times with n=3 and quantitative data was analyzed for significance with one-way ANOVA.

RESULTS

SEM images showed that the increase in keratin content corresponded with higher level of bundling of fibers as the gel becomes more porous and the fibers become thicker as shown in Figure 1. Fibers in C/KTN hydrogels are also aligned straighter than the 100% collagen gels, altering overall fiber organization.

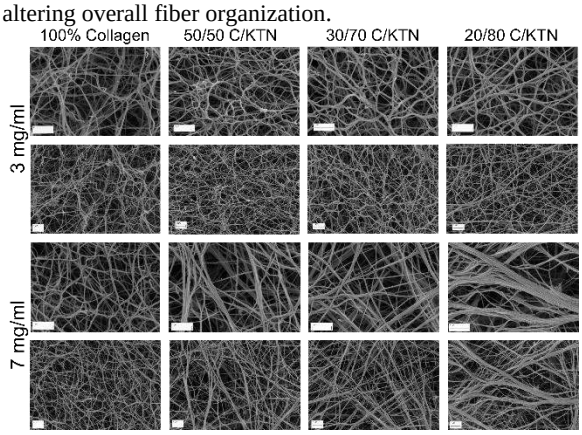

Figure 1. SEM images of 3 and 7 mg/ml collagen and C/KTN hydrogels from high to low magnifications (top to bottom).

Higher keratin content also increased the denaturing temperature of C/KTN hydrogels for both 3 and 7 mg/ml hydrogels demonstrated by DSC in Figure 2A. Significance was observed between 100% collagen and all C/KTN hydrogels. Although there were only slight increases, C/KTN hydrogels remained stable when incubated at 42°C for 1 hour whereas collagen melted completely.

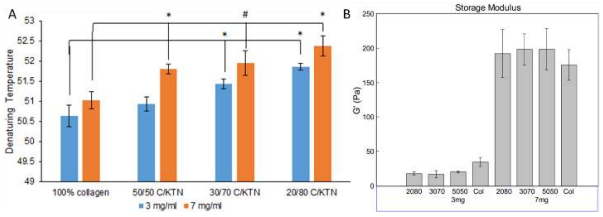

Figure 2. Thermal denaturing temperature measured by DSC (A) and storage modulus measured by rheology of various gels (B). # = p<0.05 and * = p<0.01.

Rheology measurements of the different hydrogels using a frequency sweep showed that there was no significant difference when adding keratin to the hydrogel (Figure 2B). However, for 7 mg/ml hydrogels, there appears to be a trend of increasing stiffness as keratin content increases. The 3 mg/ml hydrogels may not show any trend due to the fact that there is not enough keratin in the hydrogel blends.

Cell viability of C/KTN hydrogels were comparable with 100% collagen gels as shown in Figure 3A and B. Significance was only observed at days 3 and 7 between collagen and 20/80 C/KTN 50/50 C/KTN hydrogels, respectively for breast cancer cells (Figure 3B). Although 50/50 and 30/70 C/KTN hydrogels had higher viability than collagen at day 7 for both NHDF and breast cancer cells, 20/80 hydrogels had the lowest viability. However this was not significant, and at day 7, 20/80 C/KTN viability remained higher than day 5. Stained samples were also imaged and showed that the presence of kerateine caused both NHDF and breast cancer cells to appear more elongated than 100% collagen hydrogels, possibly promoting cell spreading (data not shown).

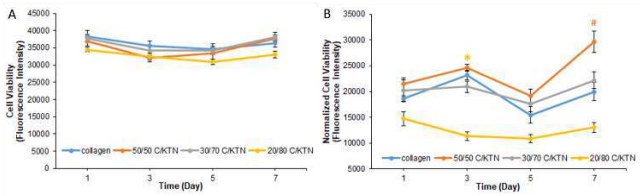

Figure 3. Cell viability measurements for 3 mg/ml NHDF (A) and 7 mg/ml breast cancer cell hydrogels (B). # = p<0.05 and * = p<0.01.

DISCUSSION

In this study, C/KTN hydrogels of various kerateine concentrations were fabricated to determine whether kerateine was able to increase the thermal stability of collagen hydrogels and whether it supported cell growth and proliferation so this blend can be used for hyperthermic or thermal stress studies without compromising the ECM. The different blends, with increasing kerateine content, was able to increase the thermal denaturing temperature of the ECM as shown by DSC when compared to pure collagen hydrogels. Although one previous study did create a C/KTN blend using animal horn, DSC analysis was performed on dry hydrogels and there were no comparisons with pure collagen hydrogels [4]. Because the samples were dried, one significant peak with similar shape as this study was observed at a temperature of approximately 80ºC. Keratin has been shown to have a thermal denaturing temperature of up to 150ºC. Therefore blending of collagen and keratin was able to increase the thermal denaturing temperature significantly as shown in this study.

In addition, presence of kerateine resulted in an ECM structure of aligned and bundled fibers whereas pure collagen hydrogels were more disorganized. This may have caused the cells to spread more throughout the C/KTN hydrogels along the aligned and thicker fibers. Previous studies have also demonstrated that cells seeded on top of KTN hydrogels displayed morphology characterized by spreading whereas cells grown on top of collagen was not as spread and linear [5]. In addition, keratin derived from human hair contain binding motifs such as leucine-aspartic acid-valine (LDV) which supports cell attachment and subsequently spreading [3]. Although cell viability of C/KTN hydrogels is similar to that of pure collagen hydrogels, slight increases in viability of 50/50 and 30/70 C/KTN may reflect the elongation and spreading of cells promoted by kerateine. Without SEM analysis with cellular gels however, this cannot be confirmed until further SEM studies are conducted.

In this study we were able to demonstrate the blended hydrogels' potential utility for hyperthermic in vitro testing increasing thermal stability and promoting cell growth with addition of kerateine. With a more thermally stable biomaterial, this hydrogel can potentially be used for developing 3D *in vitro* models for thermal stress studies or testing hyperthermic treatments without compromising the ECM.

ACKNOWLEDGEMENTS

This work was possible by generous funding from the Battelle Institute Grant US001-0000544452 (U.S. Army Natick Soldier Research, Development, and Engineering Research Center).

REFERENCES

[1] Drury, J et al., *Biomat,* 24:4337-4351, 2003.
[2] Wortmann, F et al., *J Appl Polym Sci,* 48:137-150, 1993.
[3] Rouse, J et al., *Materials,* 32:8205-8217, 2010.
[4] Balaji, S et al., *Polym Adv Tech,* 23:500-507, 2011.
[5] Tomblyn, S et al., *J Biomed Mater Res B Appl Biomater,* 104:864-879, 2016.

SB^{3}C2019
Summer Biomechanics, Bioengineering and Biotransport Conference
June 25 -28, Seven Springs, PA, USA

MICRORNA SEQUENCING OF ASCS UNDERGOING ENDOTHELIAL-GENESIS

S. Shaik (1), E. Martin (2), D. Hayes (3), J. Gimble (4) & R. Devireddy (5)

(1, 5) Bioengineering Laboratory, Department of Mechanical Engineering, Louisiana State University, Baton Rouge, LA.

(2) Biological & Agricultural Engineering, Louisiana State University, Baton Rouge, LA.

(3) Department of Biomedical Engineering, Pennsylvania State University, University Park, PA.

(4) La Cell LLC, New Orleans, LA.

INTRODUCTION

Adipose derived stem cells (ASCs) are multipotent that can be differentiated into adipogenic, chondrogenic, and osteogenic lineages with an appropriate stimulus [1]. miRNAs are short nucleotides which regulate various cell mechanisms such as differentiation [2]. For example, the upregulation of miRNA 148b in ASCs results in the induction of osteogenesis [3]. However, no miRNAs have been evidently shown to induce the endothelial differentiation in ASCs. In this article, we used next generation sequencing to sequence the miRNAs expressed in CD34+ ASCs treated with endothelial media during the period of endothelial differentiation. Using bioinformatics techniques, we identify several miRNAs (both upregulated and downregulated) that could potentially induce endothelial-genesis in ASCs.

METHODS

Magnetic bead sorting of CD34+ cells: ASCs from 3 different donors at P0 were counted and pooled together in equal amounts. The sorting of CD34+ cells from ASCs was done using CD34 MicroBead kit (Miltenyi Biotec) by following manufacturer's instructions. Briefly, the ASCs were treated with FcR blocking reagent and then with CD34 microbeads followed by incubation at 4°C for 30 minutes. After incubation the cells were washed and added to the magnetic separation column on the magnetic stand. The CD34 depleted ASCs and CD34+ ASCs were then collected and counted. The sorted cells were then plated in 6 well plates at a density of 8000 cells per cm^2 and cultured till 80-90% confluence was obtained in stromal media.

CD34 surface marker characterization: The CD34+ sorted cells and CD34 depleted ASCs were stained with CD34-PE antibody during the magnetic bead sorting process. Both the sorted cell populations were analyzed by flow cytometry for the expression CD34 antibody.

Induction of endothelial differentiation: Upon reaching confluence the CD34+ cells were treated with endothelial medium containing 50 ng/ml of VEGF, 2% FBS, and 1% antibiotic in DMEM/F12 media. For controls, CD34+ cells and CD34 depleted ASCs treated with stromal medium. The media was replaced for every 3 days till 14 days.

UEA I lectin Staining: The cells were fixed with 4% paraformaldehyde for 20 min at room temperature (RT) and later blocked with 1% BSA in PBST for 30 min at RT. UEA I lectin FITC was then added in the dilution of 1:200 and incubated for 1hr at 4°C in dark. After this step the cells were washed with PBS and imaged.

miRNA isolation and quantitation: miRNAs were isolated using Purelink miRNA isolation kit (Thermofisher) following manufacturer's instructions. The quality and purity of miRNAs was analyzed using fragment analyzer.

miRNA library preparation and sequencing: An ion proton sequencer was used to perform the miRNA sequencing. Library preparation and multiplexing with adapters was done using the kit compatible with the Ion proton sequencer.

miRNA sequencing data analysis: The obtained sequencing data was aligned to HG38 genome using STAR program [4] and interspersed with mature human miRNA sequences from miRbase.org using bedtools [5]. The miRNAs with P values < 0.05 were considered significant for further analysis. The miRNAs with fold change above 1.2 or below 0.8 are only considered as either upregulated or downregulated. Targetscan [6] and miRwalk [7] were used to identify miRNA target genes and the target genes were later used to determine pathways through Kegg analysis [8].

RESULTS

The endothelial differentiation of CD34 sorted ASCs was confirmed by UEA-I lectin staining and measuring the expression of endothelial genes (eNOS, VWF, and CD31) by qPCR

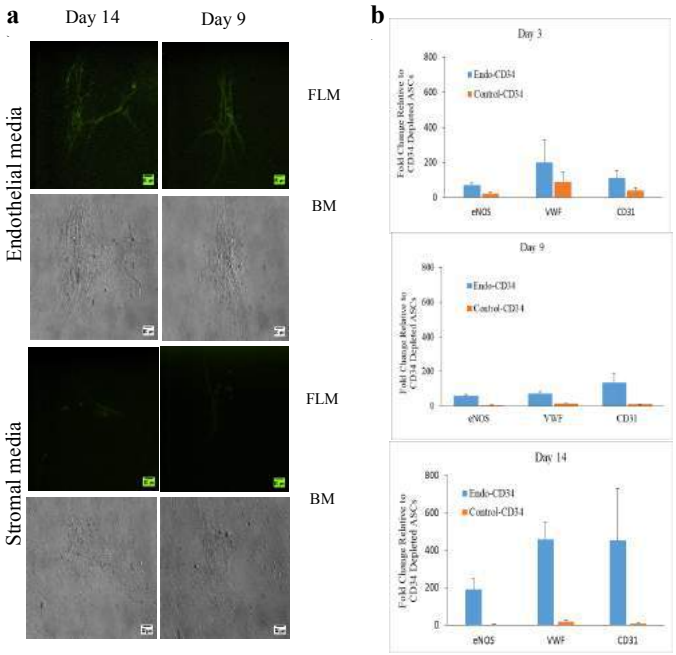

a) UEA I lectin-FITC staining: Left column: CD34 sorted ASCs treated with either endothelial or stromal media for 14 days; First row-fluorescent images (FLM), second row- bright field images (BM). Right column: CD34 sorted ASCs treated with either endothelial or stromal media for 9 days; third row-fluorescent images (FLM), last row- bright field images (BM). FLM and BM images are taken from the same cells. **b) qPCR:** The bar graphs shown indicate the expression of endothelial genes (eNOS, VWF, CD31) in CD34 sorted ASCs treated with endothelial media (Endo-CD34) in relation to control CD34 sorted ASCs (Control-CD34) on Day 3, Day 9, and Day14.

The heat maps below indicate the expression of miRNAs on day 3, day 9, and day 14 with P values < 0.05. To track the temporal expression of those significantly up/down regulated miRNAs on a particular time point we have also shown their expression on the other time points even though some of them have higher P-values.

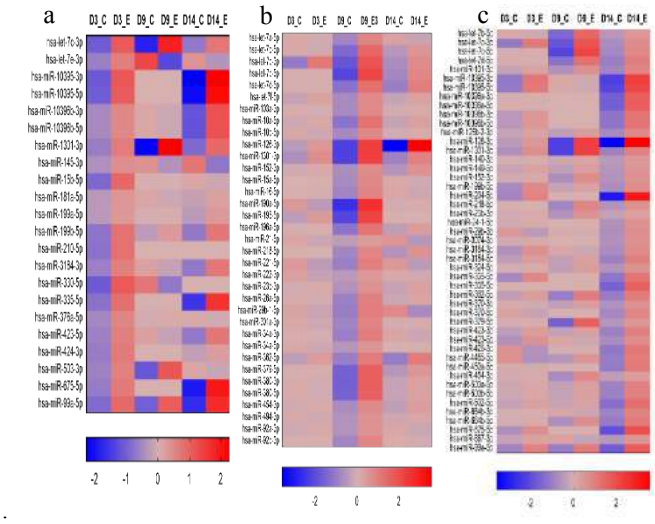

Upregulated miRNAs on **a)** day3, **b)** day9 and **c)** day14; the temporal expression of those miRNAs was also shown.

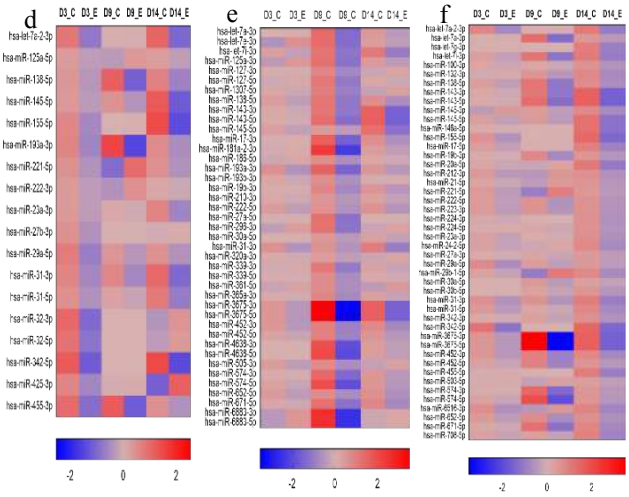

Downregulated miRNAs on **d)** day3, **e)** day9 and **f)** day14; the temporal expression of those miRNAs was also shown.

Kegg analysis of the up and down-regulated miRNAs on day 3 targeting most of the pathways involved with regulation of endothelial and angiogenic differentiation

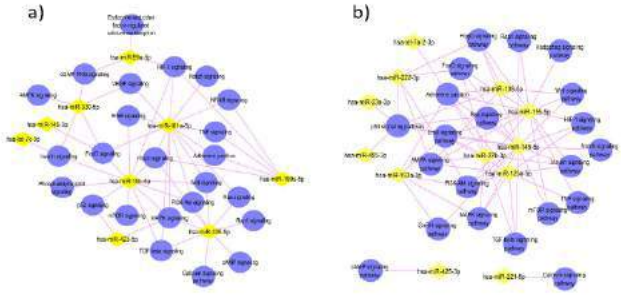

a) Upregulated miRNAs: hsa-miR-181a-5p, hsa-miR-335-5p, and hsa-miR-15b-5p
b) Downregulated miRNAs: hsa-miR-155-5p, hsa-miR-145-5p, hsa-miR-27b-3p, and hsa-miR-125a-5p

DISCUSSION

The Kegg analysis of the miRNA targeted genes enriched several signaling pathways such as ErbB, NF-KB, Notch, HIF-, PI3K-AKT, P53, VEGF, Hippo, Ras, Rap1, mTOR, TNF, TGF-B, Insulin, MAPK, cGMP-PKG, and cAMP signaling etc. which play regulatory role in the endothelial differentiation and angiogenic proliferation. Based on these results, we hypothesize that either upregulating hsa-miR-181a-5p, hsa-miR-335-5p, and hsa-miR-15b-5p or downregulating hsa-miR-155-5p, hsa-miR-145-5p, hsa-125a-5p and hsa-miR-27b-3p using antagomirs could result in the induction of ASCs into endothelial lineage.

ACKNOWLEDGEMENTS

Supported by NIDDK R21DK91852 & by NIDCR R01DE024790. The content is solely the responsibility of the authors and does not necessarily represent the official views of the NIH. The authors thank Dr. Chouljenko at the GeneLab of LSU-SVM for his technical assistance in preparing cDNA libraries.

REFERENCES

[1] Gimble, J et al., *Cytotherapy*, 5.5:362-369, 2003.
[2] Croce, C et al., *Cell,* 122(1): 6-7, 2005.
[3] Qureshi, A et al., *Biomaterials,* 34.31: 7799-7810, 2013.
[4] Dobin, A et al., *Bioinformatics* 29.1: 15-21, 2013.
[5] Quinlan, A et al., *Bioinformatics* 26.6: 841-842, 2010.
[6] Lewis, B et al., *Cell*, 120(1):15-20, 2005.
[7] Dweep, H et al., *Nature Methods*, 12(8): 697-697, 2015.
[8] Huang, D et al., *Nature Protocols*, 4(1):44-57, 2009

SB³C2019
Summer Biomechanics, Bioengineering and Biotransport Conference
June 25 -28, Seven Springs, PA, USA

IN VITRO DEGRADATION OF ELECTROSPUN POLYCAPROLOCATONE TISSUE ENGINEERING SCAFFOLDS UNDER CYCLICAL DYNAMIC LOADING

Johane Bracamonte, Sarah K. Saunders, Sam Cole, Gilbert Annohene, Gary Tepper, Joao S. Soares

Engineered Tissue Multiscale Mechanics & Modeling Laboratory
Department of Mechanical and Nuclear Engineering
Virginia Commonwealth University
Richmond, Virginia, USA

INTRODUCTION

The employment of biodegradable and implantable medical materials presents numerous potential advantages. In some applications, the need for additional interventions to remove the implant can be avoided.[1] In other situations, in which permanent implants represent the state-of-the-art, biodegradable designs offer the potential to eliminate problems associated with long-term tolerance of the implant. Biodegradable materials can be used to carry biologically active agents to be delivered locally such that healing/growing is promoted or enhanced. Biodegradable materials also offer great potential as scaffolding in tissue engineering (TE), as extracellular matrix (ECM) synthesized naturally by seeded cells can gradually replace them and take over supporting roles. Biodegradable scaffolds do not only perform acutely after cell seeding providing stress-shielding and mechanical support and function, but should also follow a designed load-transfer path from the degrading scaffold to the developing dense connective tissue over time.[2,3] This load-transfer can also provide mechanical cues that are transferred downscale to impart mechano-stimulation on the cells and to guide growth of de novo tissue with appropriate mechanical properties to remain in function once the scaffold is fully absorbed.

The employment of biodegradable materials is particularly challenging in TE because scaffolds are expected to bear and withstand mechanical loads, and in addition, are inherently evolving over time. Tissue engineers must optimize the appropriate scaffold characteristics or the material formulation (among many other design parameters) which result in scaffolds that satisfy the immediate need of stress-shielding on seeded cells, yet gradually continue to provide support for an appropriate period as de novo tissue is formed, and ultimately, fade away undergoing controllable absorption. This complex and challenging design process is largely based on empirical guesswork and trial-and-error approaches that often fail.[4]

Designing biodegradable scaffolds that provide acute support for a sufficient time, allow for a smooth load-transfer to the developing tissue, and finally degrade away in a controllable manner, requires extensive understanding and modeling tools that account for the change of properties as the material degrades. Our objective is to develop rigorous and quantitative understanding of the morphological and functional events occurring during mechanically-stimulated tissue engineering scaffold degradation during in vitro incubation, and ultimately, post-implantation in vivo function subjected to physiologic loading. Ultimately, these tools can be employed to optimize TE scaffold design, to tailor the stress-transfer between the degrading scaffold and the growing de novo ECM, and to guide the development of in vitro training protocols to better stimulate growing cells into favorable synthetic behaviors to result in successful in vivo integration.

METHODS

Scaffold Manufacture. Scaffolds were manufactured with (Mn) 80,000 g/mol Polycaprolactone (PCL) by electrospinning. Electrospinning parameters used are: electric potential of 12 kV; collector diameter of 3mm, rotational speed of 820 rpm, axial velocity of 1 cm/s and 30 cm displacement. The process was carried for 1 hour and 21 minutes. Samples were cut into 15 x 9.3 mm and 35 x 9.3 mm rectangular samples for static and dynamic experiments respectively.

Degradation protocol. Samples were dried in a vacuum oven at 40 °C and at a 2.06 bar vacuum for 24 hours and weighted afterwards. Static degradation consisted in submerging the sample in 10mL of solution, and rest at 37 C. The liquid media tested were distilled water and NaOH solutions with pHs of 9.15, 11.75, 12.45, 13.0 and 13.3 to accelerate the degradation rate into feasible time periods. Dynamic

degradation was carried at fixed 10% nominal strain with a sinusoidal function at 1 Hz frequency. Solutions were changed weekly. The samples were dried, weighted, and tested after degradation.

Table 1. Weight loss and thickness at different degradation conditions.

Time [days]	Degradation condition		Weight loss [%]	Thickness [μm]
	Exposure	pH		
0	--	--	0	165±11
7	Static	6.4	0.06±2.44	316±27
		11.75	1.16±1.40	263±16
		12.45	1.16±1.01	238±15
		13.0	22.0±1.6	195±16
		13.3	100±1.7	--
21	Static	6.4	-0.1±1.5	254±12
	Dynamic		1.10±1.02	164±56
	Static	11.75	1.5±1.0	209±17
		12.45	3.6±1.4	207±14
		13.0	61.5±1.4	--
42	Static	6.4	-2.58±0.08	188±9
		11.75	2.12±1.25	220±14
		12.45	17.5±1.2	230±16
		13.0	100±1.2	--

Mechanical properties. Elastic properties were measured with a custom-made uniaxial-extension mechanical tester. Mechanical testing was carried at 1mm/min under wet conditions after 10 preconditioning cycles, for all periods of degradation. The deformation gradient components were calculated from the relative distance between four markers located at the vertexes of a 2mm side square. The fixed and moving ends of the mechanical tester were attached to the samples through 3 hooks and a long single-loop suture to minimize force differentials and lateral components. Samples were stretched by imposing on the actuator a displacement equivalent to 30% of the original length. From the stress-strain graph, the linear region was identified and elastic modulus calculated as the slope of the linear region. Sample thickness was measured at multiple locations with a micrometer and employed to define stress.

Microstructure. Scanning Electron Microscopy (SEM) images were taken at 3000x magnification. Images were processed using ImageJ and DiameterJ plugging to determine fiber orientation, diameter, intersection density and superficial porosity.[5]

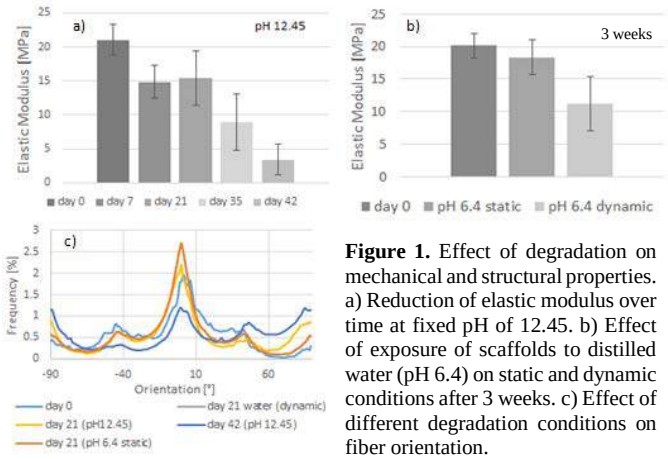

Figure 1. Effect of degradation on mechanical and structural properties. a) Reduction of elastic modulus over time at fixed pH of 12.45. b) Effect of exposure of scaffolds to distilled water (pH 6.4) on static and dynamic conditions after 3 weeks. c) Effect of different degradation conditions on fiber orientation.

RESULTS

Static degradation. The thickness of the scaffolds increased for all scaffolds tested. Swelling peaked at 1 week after exposition to liquid media and decreased afterwards. Swelling is reduced as the pH of the media is increased. For distilled water (pH 6.4), the increase in thickness reached 90%, whereas it was only of 18% for pH 13.0. Largely alkaline environments significantly affected scaffolds properties during early exposure. After 7 days of accelerated degradation, a pH of 13.0 was required to produce a significant weight loss (22%) and significant elastic modulus reductions, and a pH 13.3 achieved complete dissolution. No significant changes were found with pH below 13 (Table 1). At fixed pH 12.45, a reduction of 30% on elastic modulus was observed at 14 days of exposition, due to the increase of the cross section rather than degradation of mechanical properties. After 42 days, elastic modulus dropped to 16% of its original value (Figure 1a), along with a 18% weight loss, and homogenization of fiber orientation (Figure 1c). Weight losses larger than 20% produced structural collapse of the scaffold, SEM imaging revealed that scaffold fibers were mostly broken (Figure 2c) or fused in a single mass (Figure 2d). Macroscopically, scaffolds were prone to delaminate, and did not present sufficient elastic behavior to render mechanical testing significant. Static exposition to distilled water showed no significant effect on mass, fiber orientation or mechanical properties for all tested periods.

Dynamic vs static degradation. Scaffolds exposed to distilled water under dynamic conditions showed no significant mass loss or changes in the microstructure other than fiber swelling (Figure 2b). SEM images showed no evidence of damage on fibers and pH of solution did not change supporting no evidence for chemical reactions. Nevertheless, a decrease in elastic modulus of 45% was observed (Figure 1b).

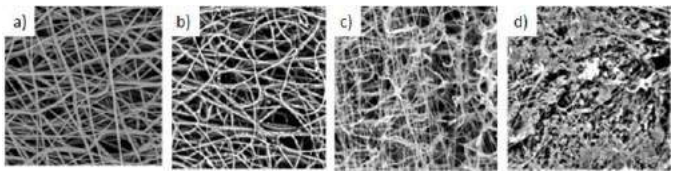

Figure 2. Representative SEM images at: a) original conditions. b) dynamically degraded in distilled water. c) statically degraded at pH 13.0 after one week. d) statically degraded at pH 13.0 after 3 weeks.

DISCUSSION

PCL electrospun scaffolds will not significantly degrade during a first week of exposition to liquid media, unless highly aggressive alkaline environments are used. This means that PCL scaffolds are not likely to change properties during cell seeding process for TE applications. Significant loss of properties were achieved within 3 weeks for pHs larger than 11.75 due to damage in the microstructure and changes in chemical composition. On the other hand, dynamic loading produced a reduction in mechanical properties not related to observable structural damage or chemical reactions.

The complex environment-dependent behavior, time-evolving properties, and multi-faceted performance requirements of biodegradable scaffolds for tissue engineering demand sophisticated theoretical, experimental and computational methods to their design. Yet, tissue engineers have been limited by sub-optimal analyses based on empiricism and costly trial- and-error, mainly due to the inexistence of proper frameworks to describe polymer degradation under physiological conditions.

ACKNOWLEDGEMENTS

We thank Robert Fricke and Federica Potere for assisting with the experimental program. This work was in part supported by the Virginia Commonwealth University Presidential Research Quest Fund.

REFERENCES

[1] Devan Ohst, J. J. Development of Novel, Bioresorbable, Small-Diameter Electrospun Vascular Grafts. *J. Tissue Sci. Eng.* **6,** (2015).; [2] Soares, J. S., Rajagopal, K. R. & Moore, J. E. Deformation-induced hydrolysis of a degradable polymeric cylindrical annulus. *Biomech. Model. Mechanobiol.* **9,** 177–186 (2010).; [3].Sailema-Palate, G. P., Vidaurre, A., Campillo, A. F. & Castilla-Cortázar, I. A comparative study on Poly(ϵ-caprolactone) film degradation at extreme pH values. *Polym. Degrad. Stab.* **130,** 118–125 (2016).; [4] Soares, J. S., Moore, J. E. & Rajagopal, K. R. Modeling of Deformation-Accelerated Breakdown of Polylactic Acid Biodegradable Stents. *J. Med. Device.* **4,** 41007 (2010).; [5] Hotaling, N. A., Bharti, K., Kriel, H. & Simon, C. G. DiameterJ: A validated open source nanofiber diameter measurement tool. *Biomaterials* **61,** 327–338 (2015).

SB³C2019
Summer Biomechanics, Bioengineering and Biotransport Conference
June 25 -28, Seven Springs, PA, USA

TRANSCORNEAL ELECTRICAL STIMULATION SHOWN TO REDUCE THE SIGNS OF GLAUCOMA

M. Cavanaugh (1*), A. H. Jassim (2*), L. Coughlin (2), J. Stukel (1), R. K. Willits (1), D. M. Inman (2)
* Both authors contributed equally to this work

(1) Department of Biomedical Engineering
University of Akron
Akron, Ohio, United States

(2) Department of Pharmaceutical Sciences
Northeast Ohio Medical University
Rootstown, Ohio, United States

INTRODUCTION

Glaucoma is among the group of neurodegenerative diseases that lead to irreversible blindness in approximately 39 million people worldwide [1]. Current therapies target the rejuvenation of the trabecular meshwork that is damaged due to increased intraocular eye pressure (IOP) [3]. Other therapies target the revival of ocular cells, such as retinal ganglion cells (RGC). However, none of the proposed therapies have proven to restore visual capacity to the pre-disease state. The irreversible nature of these cases is due to damage to critical tissues including the optic nerve (ON) and retina. During normal disease progression axonal death is followed by the retraction and death of RGCs [2], loss of oligodendrocytes [3], and activation of astrocytes [3]; all of which are accompanied by mitochondrial dysfunction, inflammation, and oxidative stress [6].

Recently, transcorneal electrical stimulation (TES) has been shown to have positive effects in an *in vivo* model as well as several clinical trials as a non-invasive therapy to revitalize cells in other neurogenerative diseases [1]. Therefore, we hypothesized that TES would slow glaucoma progression in the model. In this study, we used a DBA/2J (D2) mouse model to examine the effect of minimally invasive TES on the revitalization of diseased tissues by examining the health of the ON, retina, and changes in visual acuity (VA).

METHODS

The study is approved by the Animal Care and Use Committee at NEOMED. The model of study, the D2, is an inbred mouse that is genetically predisposed to develop glaucoma, which mirrors the disease progression that is seen in humans [7]. At approximately 8-11 months of age, animals were randomly divided into two groups: experimental and an age match control. A third group was added as a younger control at 5 months of age, as the disease likely has not had any affects by 5 months in most animals [7]. Visual acuities were established in all three groups of mice using a forced-choice swim behavioral task consisting of 2 sessions of 10 trials per day over a period of approximately 5 weeks. The visual discrimination task used was developed and characterized by Prusky [8]. Mouse VA thresholds were determined by systematically increasing the cycles/degree until animals chose lower than 7/10 trials correct. IOP was measured for both groups prior to stimulation. TES was applied to mice eyes for 10 minutes every three days for 8 weeks. Each eye was stimulated separately with a ground wire placed in the back of the neck. A symmetric biphasic square wave was applied at a current of 100 μA, 1 ms pulse duration, at a frequency of 20 Hz. After 8 weeks, VA tests and IOP measurements were repeated after stimulation. Post transcardially perfused superior colliculus (SC) was harvested for analysis Cholera toxin β-subunit (CTB) was used as an anterograde tracer to examine retinal uptake and transmission to the SC [9,10]. C-fos, which is an intermediate early gene upregulated in response to stimulation, is used to show activation in the SC due to the stimulation paradigm [11]. RGC soma and axon number were determined using unbiased stereological analysis. Whole mount retinas were labeled with RBPMS (RNA-binding protein with multiple splicing) to visualize RGCs [12]. ON were embedded in polybed resin and sectioned for quantification. Synapse revitalization in the retina was evaluated by co-localization of PSD95 and VGLUT1, which label pre- and post-synaptic markers in the inner plexiform layer of the retina [13]. Inflammation was measured in the ON and retina by labeling for NFκB p65, a master regulator of cytokine production [14]. ATP availability was quantified by the ratio of AMPK to pAMPK levels in the retina and ON [15]. Growth factor receptors, such as p75, were measured at the protein level to determine efficacy and cell death markers were evaluated via protein analysis. Data were analyzed using immunohistochemistry, stereological analysis, capillary

electrophoresis, and ImageJ quantification tools. Data is represented as mean ± stdev and evaluated for normalcy. One-way ANOVA and student's *t*-test were used to compare differences between groups, with $p<0.05$ considered significant.

RESULTS

After 8 weeks, the VA of TES-stimulated mice increased, decreased or maintained, while the control group mice only decreased or maintained (Figure 1A). RGC numbers were significantly higher in the young control, but no statistical differences in RGC number were found between the TES-stimulated and control age-matched groups (Figure 1B). However, CTB labeling in the SC of TES-stimulated mice was increased over age-matched controls (Figure 1C). Increased levels of ATP, noted by a reduction in the ratio of pAMPK/AMPK, were found in both the retina and ON via protein analysis (Figure 1 D and E) in the TES-stimulated mice. As we continue to gather more information, we will learn more about the axon count, synapse revitalization, inflammatory markers and growth factor receptors.

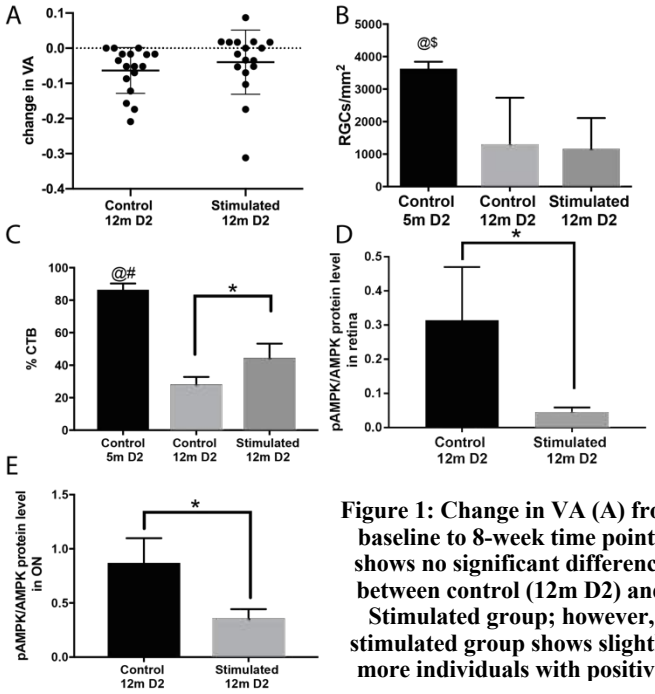

Figure 1: Change in VA (A) from baseline to 8-week time points shows no significant difference between control (12m D2) and Stimulated group; however, stimulated group shows slightly more individuals with positive change in VA (n=17 and n=17 respectively). RGC number(B) from whole mount retinas stained with RBPMS. 5m D2 had significantly (@, ****p < 0.0001, n=19) than 12 m D2 (n=22) and stimulated 12m D2 ($, ****p < 0.0001, n = 18). CTB transport to SC (C) Found to be significantly more for Stimulated group. 5m D2 (n=7) transported significantly more CTB compared to 12m D2 (@, ****p < 0.0001, n=27) and stimulated 12m D2 (#, **p < 0.01, n=16). Stimulated 12m D2 showed significant increase in CTB transport compared to control 12m D2 (* p < 0.05). Significantly more ATP available in the stimulated retina (D) and ON (E) compared to the age matched tissue. The ratio of pAMPK/APMK was significantly reduced with stimulation in the retina and ON (*p < 0.05, n=5 control retina and 6 control ON, and n=6 stimulated retina and 5 stimulated ON)

DISCUSSION

These findings exemplify a positive regenerative response in D2 mice to TES over an 8-week period that could reduce the signs of glaucoma progression. While the approach did not rescue RGCs, we nevertheless have shown mice that have demonstrated an increase in VA. The increase in VA, while not significant, demonstrated a limitation in determining VA through behavior tasks and can be improved upon in further trials. Furthermore, our previous studies indicated that metabolic vulnerability play a critical role in glaucoma progression [15]. TES was able to restore ATP level in both the retina and ON. Providing more ATP to the energy-demanding RGCs is expected to improve their function [15]. It was also shown to increase transmission of CTB to the SC, which indicated a revitalized ON giving it the ability to respond to signals from the retina and transmit them to the SC [6]. Collectively, these results reflect improvement in RGC function and therefore glaucoma pathology. Our current work is focused on gathering further results regarding synaptic revitalization, changes to inflammation, and examining cell death in the ON and retina in the D2 model. Our current results combined with future work aims to show the regenerative effects of minimally invasive TES in the D2 model, thus validating it as a possible treatment strategy for future investigation.

ACKNOWLEDGEMENTS

RKW acknowledges generous support through the Margaret F. Donovan Endowed Chair for Women in Engineering. DMI acknowledges the National Institute of Health (EY26662).

REFERENCES

[1] Sehic, A, et al., *The American J of Pathology*, 186: 2783-2797, 2016.
[2] Buckingham B et al. *J Neurosci*, 28 :2735-2744, 2008.
[3] Inman, D.M., *Glia*, 55 :942-953, 2007.
[4] Abu-Hassan, D.W., *J Ocul Biol*, 2: 2334-2838, 2014.
[5] Son, J. L, et al., *Glia,* 58: 780-9, 2010.
[6] Ng, T. K., *World J of Stem Cells*, 6:11-9, 2014.
[7] Libby, R.T., et al., *Visual Neuroscience*, *22*:637-648, 2005.
[8] Prusku, G.T., et al., *Vision Research*, 40: 2201-2209, 2000.
[9] Calkins, D.J., et al., *Invest. Ophthalmol. Vis. Sci,*50: 4317, 2009
[10] Jassim A. H., *Invest. Ophthalmol. Vis. Sci,* 60: 1-15, 2019.
[11] Sheng, M., et al., *Neuron*, *4*: 477-485, 1990.
[12] Kwong, J, et al., *Invest. Ophthalmol. Vis. Sci,*52: 9694-9702, 2011.
[13] Agostinone, J., et al., *Brain*, *141*: 1963-1980. 2018.
[14] Harun-Or-Rashid, M., et al., *J Neuroinflammation*, *15*:12974-018-1346-7, 2018.
[15] Harun-Or-Rashid, M., et al., *J Neurosci*, *38*: 5122-5139,2018.
[16] Baltan, S., et al., *J Neurosci*, 30: 5644-52, 2010.

SB³C2019
Summer Biomechanics, Bioengineering and Biotransport Conference
June 25-28, Seven Springs, PA, USA

OPTIMIZATION OF TOPOGRAPHICAL AND MECHANICAL PROPERTIES OF PEG-DA BASED HYDROGELS FOR PROMOTING NEUROREGENERATION

David Hall (1), Sourav S. Patnaik (2), Ender A. Finol (2), Gabriela R. Uribe (1)

(1) Department of Biomedical Engineering/Chemical Engineering Program
University of Texas at San Antonio
San Antonio, TX, USA

(2) Department of Mechanical Engineering
University of Texas at San Antonio
San Antonio, TX, USA

INTRODUCTION

When significant tissue damage to the spinal cord occurs and neuronal connectivity does not ever fully recover, this can lead to severe pain, partial, or full paralysis. To combat the effects of spinal cord injury, we propose promoting neuroregeneration using a seeded biomimetic polyethylene glycol diacrylate (PEGDA) hydrogel scaffold to deliver neural progenitor cells (NPC) to the injured spinal tissue. It has been shown that axonal outgrowth, neural cell growth, and NPC differentiation, which are components of broader neuroregeneration, occur on materials with an average pore area ranging from 0.07 to 7854 μm^2 [1, 2]. Instead of considering the broad range of ideal pore areas, we focused on developing scaffolds with a mean pore area between 100 and 200 μm^2, and an elastic modulus in the range of 40-60 kPa [3, 4]. We further enhanced the neuronal growth environment by incorporating iron oxide nanoparticles into the hydrogel matrix to provide physiological electromagnetic stimulation. To promote neuroregeneration in spinal tissue, we optimized the mechanical, chemical, and topographical characteristics of a biomimetic PEGDA scaffold. We hypothesize that by increasing cross-linking time, we can improve the PEGDA scaffold's biomechanical and cellular properties, and ultimately assist in improving neuronal growth in the spinal cord.

METHODS

The base components of the hydrogel consist of PEGDA, triethanolamine (TEA), vinylpyrrolidone (VP), eosin isothiocyanate, and iron oxide nanoparticles (IONPs). Hydrogels were photopolymerized using a 20 mW LED Lamp, with polymerization time itself tested as a variable. The ratio of PEGDA, TEA, and VP was optimized to generated gels with desired pore areas. Two molecular weights of PEGDA (575 and 700 kDa) were compared to study the effect of molecular weight on pore area and degradation. As control sample for comparison, a 575 kDa PEGDA hydrogel fabricated following commercially available protocols was used. The hydrogel degradation rate was measured in different environments over a period of 60 days at a temperature of 37°C, on a shaking platform. These environments include a culture media (pH 7.4), millipore water (pH 7.12), and culture media adjusted to a pH of 5 and 2.

Hydrogel topography and pore area were characterized via scanning electron microscopy and images were analyzed in ImageJ with a sample size of 8 for all groups tested. Thresholding was used to identify pore area in the hydrogel and the size of these pores was measured using the particle analysis tool.

The swelling ratio of the hydrogels was found using Eq. (1) [5],

$$Q_v = 1 + \frac{\rho_P}{\rho_s}\left(\frac{M_w}{M_d} - 1\right) \quad (1)$$

where M_w is the wet weight and M_d is the dry weight. The mass swelling ratio is equal to M_w/M_d. The volumetric swelling ratio (Q_v) is, therefore, calculated from the mass swelling ratio and the densities of the hydrogel polymer (ρ_p) and solvent (ρ_s).

Mechanical characterization of hydrogel specimens was performed via unconfined compression testing (Electro Force 3200, TA Instruments, New Castle, DE). The mechanical properties of the hydrogels were tested as function of polymerization time (crosslinking rate of either 8 or 10 minutes) and hydrogels loaded with different concentrations (0, 0.029, 0.058, and 0.116 mg/mL) of iron oxide nanoparticles (IONPs). Hydrogel samples were hydrated in milipore water to for 24 hours before testing to emulate swelling *in vitro*.

Data was reported as mean ± standard deviation for porosity, degradability, mechanics, and physical parameters. One-way ANOVA was performed to test the differences in data across the groups and Tukey's test was performed to evaluate pairwise differences in the data. Significance level was set to $\alpha = 0.05$.

Poster Presentation #P296

RESULTS

Topographical analysis of the hydrogel matrix shows that there is no difference between the 575 and 700 Mw PEGDA hydrogels ($p = 0.97$); however, there was a significant difference between the unoptimized control and the two optimized formulations ($p = 0.007$) (Fig. 1a). Of the two molecular weights of PEGDA tested (575 and 700 Mw) containing IONPs, the 575 PEGDA hydrogels displayed a mean pore area of 163 ± 42 μm^2, the 700 PEDGA had 164 ± 41 μm^2, and the control showed a pore area of 90 ± 58 μm^2. Degradation studies showed that PEGDA based hydrogels deteriorate faster in cell culture media with pH 5 than at pH 7.4 (Fig. 1b). The average degradation kinetics of PEGDA-based hydrogels are shown to have a negative trend in all test environments, excluding media. The average swelling ratio of the hydrogel scaffold in Millipore® water was found to be 4:1.

Compression testing of the cross-linked hydrogel specimens showed that the Young's' modulus of the 58 μL group was higher than the 29 μL and 10 minute groups (55.7 ± 37.5 kPa vs. 52 ± 13.7 kPa vs. 23.91 ± 8.45 kPa; $p = 0.0039$, as shown in Fig 2a). Conversely, maximum compressive stress was higher for the 29 μL hydrogel group followed by 116 μL and 8 minute groups, respectively (28.4 ± 15.8 kPa vs. 10.5 ± 6.37 kPa vs. 6.36 ± 0.95 kPa; $p = 0.0085$, as seen in Fig. 2b). The thickness of the 10 minute hydrogel specimens was found to be lower than specimens of 8 minutes, 116 μL, 58 μL, and 29 μL groups, respectively (6.38 ± 0.21 mm < 6.48 ± 0.58 mm < 7.08 ± 0.20 mm < 7.14 ± 0.23 mm < 7.23 ± 0.16 mm; $p = 0.0008$, as seen in Fig. 2c). Further, the diameter of the 29 μL hydrogel specimens was found to be the highest across the groups, whereas 10 minute specimens had the lowest diameter (4.89 ± 0.35 mm vs. 3.83 ± 0.18 mm; $p = 0.001$, as seen in Fig. 2d).

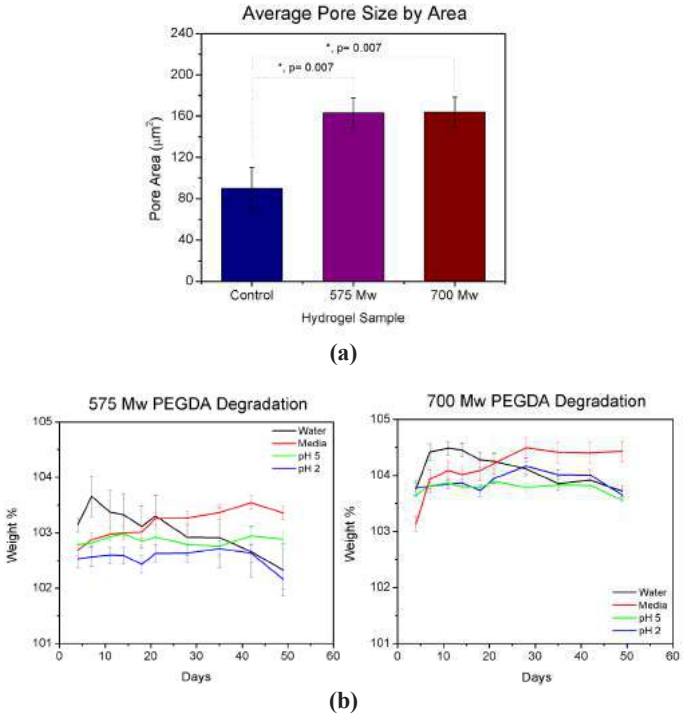

Figure 1: (a) Porosity - Average pore area of optimized 575 Mw and 700 Mw PEG-DA was found to be 81.7% and 82.5% higher than control specimens ($p = 0.007$). (b) Degradation - 575 and 700 Mw PEG-DA degradation study results; error bars indicate standard error and the sample size is ($n = 6$). * denotes significant level of $p < 0.05$.

DISCUSSION

While optimizing the hydrogels, it was found that the nanoparticles and the initial amount of water present in the gels did not play a large role in the overall structural properties of the gel. The ratio between PEGDA, TEA and VP, determined the rigidity and structure of the gels. These factors were further optimized to form hydrogels with proper structural properties and a mean pore area in the range of 100-200 μm^2. Environments with a pH of 2 mimic the biological environment of infected and inflamed tissues, and it is shown that the degradation of the 575 Mw hydrogel in this environment has a negative trend. After saturation, a downtrend was observed in all samples except the hydrogels kept in media during the degradation study. We will improve the degradation study in the future by incorporating enzymes into the different environments. Photopolymerization time and IONP concentration was optimized to synthesize 575 kDa PEGDA hydrogels with a Young's modulus like that of native spinal tissue. Mechanical testing of the hydrogel scaffolds has shown that polymerization time and IONP concentration play a significant role in determining the material's compressive behavior. Hydrogels allowed to polymerize for 7 minutes that contain a concentration of 0.029 or 0.058 mg/mL of IONPs fall within the desired range of 40-60 kPa. In conclusion, we have created a biomimetic hydrogel scaffold that displays similar mechanical characteristics to native spinal tissue and has optimal pore areas for neural growth. Future work includes gauging the biocompatibility of these hydrogels and evaluate the effects of electromechanical stimulation on neuroblast cells seeded in the scaffolds.

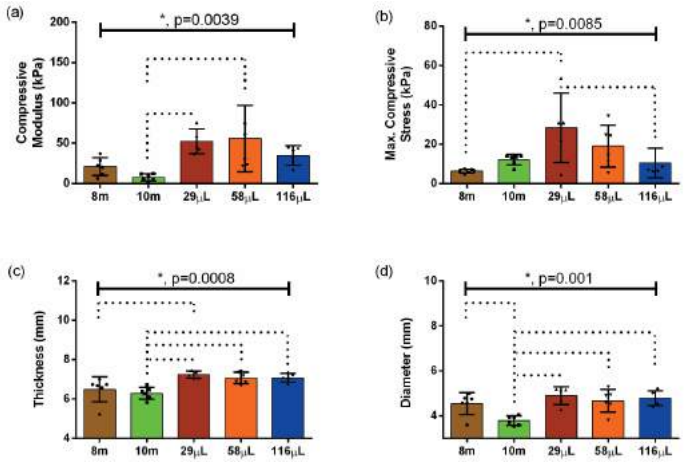

Figure 2: Compression testing of hydrogel specimens. (a) Compressive modulus was higher in hydrogel specimens from the 58 μL group compared to the 29 μL and 10 min groups. (b) Maximum compressive stress is highest in the 29 μL group in comparison to the 116 μL and 8 min groups. (c-d) Thickness and diameter were found to be lower for regular hydrogels vs. IONP hydrogels, respectively. * denotes significant level of $p < 0.05$.

REFERENCES

[1] Bružauskaitė, I et al., *Cytotechnology,* 68(3):355-369, 2016.
[2] De Bartolo, L et al., *J Memb Sci, 325(1): 139-149,* 2008
[3] Karimi, A et al., *J Chem Neuroanat,* 86:15-18, 2017.
[4] Koser, D et al., *Biophys J,* 108(9):2137-47, 2015.
[5] Caliari, S et al., *Nat Methods,* 13(5): 405-414, 2016.

SB³C2019
Summer Biomechanics, Bioengineering and Biotransport Conference
June 25 -28, Seven Springs, PA, USA

Maintaining Multipotency of Neural Stem Cells Using Synthetic FGF Peptide Microenvironments

Diana L. Philip (1†), Elena A. Silantyeva (2†), Matthew L. Becker (1,2), Rebecca K. Willits (1,3)
† Both authors contributed equally to this work

(1) Department of Biomedical Engineering
The University of Akron
Akron, Ohio, U.S.A.

(2) Department of Polymer Science
The University of Akron
Akron, Ohio, U.S.A.

(3) Department of Mechanical Engineering
The University of Akron
Akron, Ohio, U.S.A.

INTRODUCTION

Stem cell niches play a crucial role in regulating cellular response, including both maintenance and differentiation. By mimicking stem cell niches in a defined manner, better *in vitro* models can be developed to understand various diseased conditions. In addition, these *in vitro* niche models can be used to investigate drugs and can be utilized to investigate other therapies. Our group is interested in using synthetic materials to develop consistent culture environments to specifically control stem cell culture and differentiation. Using nanofibers and peptide mimics of whole proteins, these culture substrates have been shown to mimic laminin [1] and alter neural precursor protein presentation [2] during differentiation. To further develop these substrates for stem cell investigations, we are interested in investigating their ability to maintain potency.

Neural stem cells require a number of soluble proteins to maintain potency and proliferate in culture. A critical protein to maintain potency of neural stem cells is fibroblast growth factor 2 (FGF2) [3]. The FGF2 utilized for maintaining potency for human stem cells is typically a recombinant or purified human protein. These human proteins are expensive and difficult to isolate, increasing the cost and variability of stem cell culture components [4]. However, by utilizing synthetic peptides that mimic the functions of whole proteins, we can control the presentation of the signaling motif, fabricate consistent *in vitro* culture conditions, and reduce the cost of stem cell culture conditions.

The aim of this study is to utilize synthetic alternatives to current growth components in order to maintain multipotency of human induced pluripotent neural stem cells (hNSCs). Current hNSC growth conditions require the use of FGF2 for potency and Matrigel® for cellular adhesion. Matrigel® is derived from mouse tumors and consists of primarily laminin, in addition to variable amounts of other proteins and growth factors [5]. However, by utilizing synthetic alternatives such as YIGSR for laminin and FGF peptide (FGFp) for FGF2, we seek to fabricate a controlled and consistent stem cell culture condition that mimics whole protein conditions.

METHODS

Substrates were pretreated with UVO for 2 hr and placed in a solution of 4-chlorobutyldimethylchlorosilane (5% v/v) and 5-hexenyldimethylchlorosilane (5% v/v) in toluene for 5 hr. To immobilize alkyne functionality on the surface, glass slides were then placed in a methylene chloride solution with propargyl alcohol and pyridine for 2 hr. For GYIGSR immobilization *via* copper-mediated azide−alkyne cycloaddition (CuAAC), glass slides were placed into a solution of N_3-GYIGSR peptide, sodium ascorbate and $CuSO_4$ for 2 hr. For surface functionalization with FGFp, cysteine-FGFp and Irgacure 2959 were dissolved in H_2O/DMF (10:1 v/v) solution. The substrates were immersed in the peptide solution and exposed to UV (254 nm) for 1 hr at room temperature. The substrates were washed with methanol, toluene and then methanol and blown dry under N_2 after each reaction. XPS was utilized to determine the concentration of the peptides. All the reactions were carried out at room temperature.

Human induced pluripotent NSCs (GlobalStem) were maintained multipotent under growth conditions as previously published [6]. The manufacturer recommended growth conditions required the use of FGF2 at 1.16 nM. Doubling time was determined after replacement of FGF2 with synthetic FGFp at 1.16 nM, 2.32 nM, and 11.6 nM. hNSC multipotency was measured by $\%NES^+$ cells *via* flow cytometry. Cultures were maintained until ready for passage and proliferation rate was measured by doubling time (hr). One-way ANOVA, with Tukey's correction was utilized to determine significance between culture groups, with $p \leq 0.05$ considered significant. Our current work is focused on substituting Matrigel® with YIGSR-functionalized

substrates, and investigating the use of YIGSR and FGFp dual-functionalized substrates as a culture substitute.

RESULTS

GYIGSR and FGFp dual-functionalized glass slides were fabricated *via* sequential "click" CuAAC and thiol-ene reaction. The difference between C_{1s} peak areas before (Figure 1A) and after CuAAC reaction (Figure 1B) results from the covalent bonding of the GYIGSR peptide on the surface, and C_{1s} peak area after the thiol-ene reaction results from the covalent bonding of FGF peptide (Figure 1C). The concentration of GYIGSR on the glass surface was measured to be ~52.3 pmol/cm^2 for single-functionalized glasses and ~48.5 pmol/cm^2 for dual-functionalized glasses. The concentration of FGF peptide was measured to be ~62.6 pmol/cm^2. The nitrogen peak increased significantly on peptide-functionalized substrates.

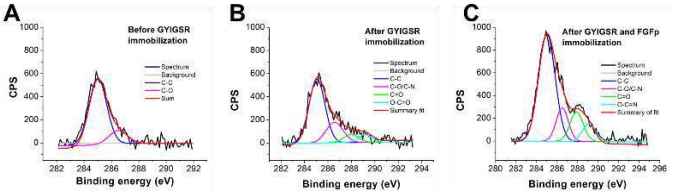

Figure 1: High resolution C_{1s} signals of (A) before any peptide immobilization, (B) after the GYIGSR covalent bonding and (C) after GYIGSR and FGF peptide surface modification. The area under the peak increased due to peptide attachment.

hNSCs were cultured under normal growth conditions that included Matrigel® and FGF2 as the control. Our findings suggested that FGFp at 2.32 nM best mimicked normal FGF2 culture conditions, where similar %NES positive cells, 90.8 ± 13.7% and 92.65 ± 8.4%, were found for FGF2 and FGFp at 2.32 nM, respectively (Figure 2A). In addition, a similar doubling time was also found between FGF2 and FGFp at 2.32 nM, 42.9 ± 10.9 hr and 58.69 ± 6.4 hr, respectively (Figure 2B). No significant differences were found between these proliferation rates.

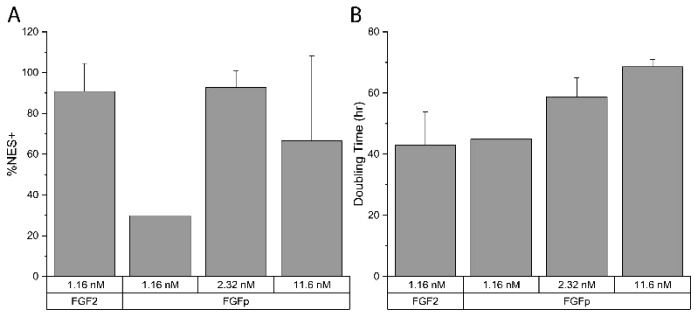

Figure 2: Multipotency (A) and proliferation rate (B) comparison between different concentrations of synthetic FGF peptide (1.16 nM, 2.32 nM, and 11.6 nM) and normal FGF2 concentration.

DISCUSSION

Current culture conditions for hNSCs require the use of Matrigel® for cell adhesion. However, approximately 60% of Matrigel® is composed of laminin [5], and laminin has been shown to be more favorable than Matrigel® for maintaining stemness of human induced pluripotent stem cells [7]. In addition, expansion conditions for hNSCs require whole protein FGF2, to keep hNSCs multipotent. Our findings suggest that soluble FGFp can be used as a culture substitute for FGF2, as similar hNSC potency and proliferation rates were found for the two culture conditions. Our next step is to culture hNSCs on FGFp-tethered substrates, to ensure cells are presented with the required signaling motif in bound form compared to soluble form. In addition, these substrates will be functionalized with GYISGR to mimic laminin [1] to assure the cells are adherent to the culture substrates. Future work will determine if utilizing this dual-functionalized substrate could eliminate the use of both bound, Matrigel®, and soluble, FGF2, factors in hNSC culture conditions.

ACKNOWLEDGEMENTS

This work was funded by the National Institutes of Health (R15-GM113155) and the National Science Foundation (CBET BME 1603832).

REFERENCES

[1] Silantyeva, E.A., et al., Acta Biomater., 75:129-39, 2018.
[2] Philip, D.L., et al., In submission, 2019
[3] Chen, G., et al., Nature Methods, 8:424, 2011.
[4] Lotz, S., et al., PLOS ONE, 8(2):e56289, 2013.
[5] Kleinman, H.K., et al., Biochemistry, 21(24): p. 6188-93, 1982.
[6] Stukel, J.M., et al., Biomed Mater, 13(2):024102, 2018.
[7] Lam, M.T., et al., J Tissue Eng and Regen M, 6(S3):80-6, 2012.

SB³C2019
Summer Biomechanics, Bioengineering and Biotransport Conference
June 25 -28, Seven Springs, PA, USA

HUVEC TUBULAR FORMATION ON BIO-INSPIRED VASCULARIZATION SUBSTRATE

Luis M. Garcia (1), Patrick N. Charron (2), Rachael A. Oldinski (1,2)

(1) Electrical and Biomedical Engineering
University of Vermont
Burlington, Vermont, USA

(2) Mechanical Engineering
University of Vermont
Burlington, Vermont, USA

INTRODUCTION

While possessing many desired properties for a biomaterial capable of cell encapsulation, alginate lacks the ability to interact with mammalian cells; however, alginate can be chemically modified with RGD- peptides, which promote cell adhesion, proliferation and ingrowth. Heparin, a glycosaminoglycan naturally found in the body, plays a role in preventing the formation of a thrombosis due to its anticoagulant activity and is a component of the extracellular matrix of blood vessels that has been shown to promote the growth of endothelial cells *in vitro*.[1]

The aim of this study was to determine the feasibility heparin and arginyl-glycyl-aspartic acid (RGD) conjugated alginate hydrogels encapsulated with vascular endothelial growth factor (VEGF) as a wound dressing to promote vascularization. VEGF is an important component in angiogenesis that binds to heparin, and RGD promotes cell adhesion. Alginate hydrogels consisted of methacrylic anhydride (MA), RGD, and heparin, and were crosslinked with visible light. The material properties and burst pressure mechanics were evaluated to determine the structural integrity and adhesiveness of the hydrogels.

METHODS

Methacrylated Alginate (Alg-MA) Synthesis: Methacrylated alginate (Alg-MA) was synthesized as previously described.[2,3] Briefly, sodium alginate was dissolved in PBS [1% (w/v)] solution at room temperature. A 10-fold molar excess of methacrylic anhydride was added to the alginate solution, pH 8.5, and the reaction was carried out for eight hours. The Alg-MA solution was purified via dialysis against deionized water for five days and lyophilized to yield a dry product.

Alg-MA-RGD Synthesis: Alg-MA was placed in DI water and conjugated with cysteine-L-arginyl–glycyl-L-aspartic acid (CRGD) using carbodiimide chemistry.

Methacrylated Heparin (Hep-GM) Synthesis: Sodium heparin was dissolved in deionized water [1.5g, (1% w/v)] at 60°C. Glycidyl methacrylate (GM) (1.5g) was added to the solution and stirred overnight. Hep-GM was purified via dialysis against deionized water for five days and lyophilized to obtain a dry polymer.

Hydrogel Preparation and VEGF Encapsulation: Polymer solutions were prepared in deionized water to form 3% (w/v) polymer precursor solutions. Human VEGFA was added to the copolymer solution at a ratio of 10^6:1 (polymer:VEGF). Hydrogels without VEGF were formed as controls. Control and modified solutions were blended with photo-activators to the following concentrations: 1 mM eosin Y, 125 mM triethanolamine, and 20 mM 1-vinyl-2-pyrrolidinone.[2-6] Crosslinking was achieved using LED arrays (525 nm).[2]

Mechanical Analysis: Rheometry was performed with a Peltier plate maintained at 37°C Hydrogel precursor solution was loaded onto the plate and crosslinked utilizing an LED ring for 5 minutes prior to collection of shear storage (G′) and loss (G″) moduli. Oscillatory time sweeps were performed at 10% radial strain and 1 Hz. Burst pressure values were collected using a custom burst pressure device and collagen-based materials; the hydrogels were tested as sealants on compromised collagen substrates.

Cell Culture: Human umbilical vein endothelial cells (HUVECs, Angio Proteomie) were suspended in complete medium (0.2% Bovine brain extract, 5 ng/mL recombinant human endothelial growth factor, 10 nM L-glutamine, 0.75 units/mL heparin sulfate, 1 μg/mL hydrocortisone, 50 μg/mL asorbic acid, 2% fetal bovine serum). HUVECs were seeded in complete media directly onto the green light polymerized hydrogels in a 96-well tissue culture polystyrene (TCPS) plate.

Cytotoxicity Assay: The cytotoxicity of VEGF-loaded RGD-modified alginate-heparin hydrogels were evaluated to observe the

Poster Presentation #P298

effects of VEGF, RGD and heparin on cell mitochondrial activity. After 24 hours, HUVECs were analyzed using a WST-8 Cell Proliferation Assay. The optical density was measured at 450 nm; absorbance values for the samples (alginate-heparin hydrogels with and without VEGF loading) were normalized to the non-modified controls.

Tubular Assay: The angiogenic properties of alginate-heparin hydrogels modified with RGD and loaded with VEGF were evaluated qualitatively by observing the effects on microtubule network formation. Analysis was conducted following a modified Angiogenesis Tube Formation Assay protocol. Hydrogel solutions were injected into and spread to evenly coat the bottom of each well of the 96-well TCPs (0.05 mL/well) and polymerized with visible green light for 5 minutes at room temperature (23°C). HUVECs were seeded directly onto hydrogels both modified and unmodified with heparin and loaded and unloaded with VEGF in 96-well TPCs and allowed to incubate to form microtubule networks. Tissue culture plates were prepared for each of the subsequent time points (6, 12, 24, and 72 hours). At each time point, the respective 96-well plate was removed from the incubator (37°C and 5% Co_2) and qualitatively analyzed with phase contrast microscopy to observe and capture the effects on HUVEC tube formation.

RESULTS

The shear moduli (Figure 1) and burst pressure values (Figure 2) indicate appropriate structural integrity and adhesion of the alginate-heparin hydrogels. Compared to the base Alg-MA, modifications with RGD, heparin, and RGD and heparin all showed increased mitochondrial activity. Those with the RGD modification demonstrated a greater degree of activity compared to non-modified alginate. In addition, there was no observable difference in activity between VEGF-loaded hydrogels and their corresponding controls. Despite some groups demonstrating increased amounts of mitochondrial activity over other groups, all hydrogels resulted in lower activity levels compared to the non-modified controls (Figure 3).

After 6 hours, unmodified Alg-MA showed little to no signs of tube formation or cell adhesion, demonstrated by the round morphology of the HUVECs. In comparison, Alg-MA modified with RGD and heparin and loaded with VEGF promoted cell adhesion and angiogenesis via the formation of a microtubule network between adjacent cells (Figure 4).

Table 1. List of material groups and their corresponding abbreviations for labeling.

Material Group	Abbreviation
Cell Control	Cells
Alg-MA	AM
Alg-MA-RGD	AMR
Alg-MA/Hep-GM	AMH
Alg-MA-RGD/Hep-GM	AMRH
Alg-MA/VEGF	AMV
Alg-MA-RGD/VEGF	AMRV
Alg-MA/Hep-GM/VEGF	AMHV
Alg-MA-RGD/Hep-GM/VEGF	AMRHV

DISCUSSION

The rheological properties and burst pressures for the modified alginate-heparin hydrogels indicate advantageous properties for use as wound dressing materials. HUVECs seeded gels were imaged at 6, 12, 24 and 72 hours, with 24 hours showing the greatest increase in tube formation. The effects of the released VEGF on angiogenesis remain qualitative as additional drug release studies and quantitative analysis of the phase contract images is necessary. The expected drug release profile of VEGF from the RGD modified methacrylated alginate-heparin hydrogel would be that of zero-order profile as previously reported; release studies are planned for the future. Also, tissue adhesion with excised skin and confocal imaging are ongoing studies to further analyze the effectiveness of the novel materials as wound dressings.

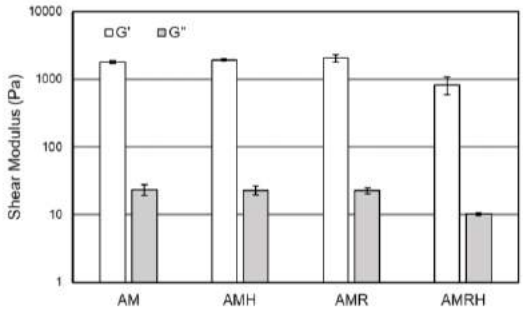

Figure 1. Storage and loss shear moduli of green light crosslinked alginate-heparin hydrogels, demonstrating viscoelastic properties.

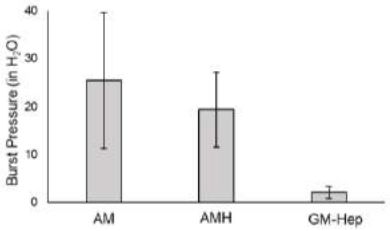

Figure 2. Burst properties of various hydrogels indicating adhesive strength to collagen-based substrates.

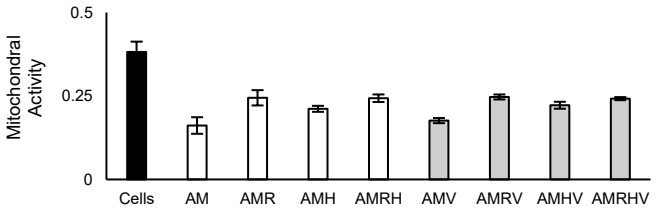

Figure 3. WST-8 assay demonstrating the HUVEC mitochondrial activity after culturing on alginate-heparin hydrogels for 24 hours.

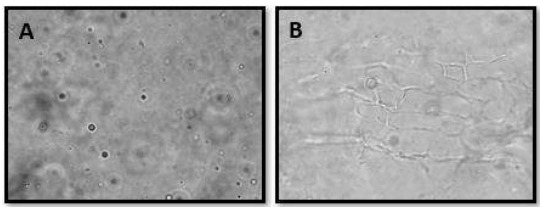

Figure 4. Phase contrast images of HUVECs cultured on (A) AM and (B) AMR hydrogels loaded with VEGF - demonstrating tubular formation.

ACKNOWLEDGEMENTS

Funding was provided by NIH Grant R01 EB020964 (Oldinski).

REFERENCES

[1] Na, K et al., *Biotechnology letters*, 25.5:381-385, 2003.
[2] Charron, P et al., *J. Mech. Behav. Biomed. Mater.*, 59:314-21, 2016.
[3] Fenn, S et al., *J. Biomed. Mater. Res.* 106.6:1229-1236, 2016.
[4] Smeds, K et al., *J. Biomed. Mater. Res.*, 54:115-121, 2001.
[5] Nettles, D et al., *Ann. Biomed. Eng.*, 32:391-397, 2004.
[6] Park, Y et al., *Biomaterials*, 24:893-900, 2003.

SB³C2019
Summer Biomechanics, Bioengineering and Biotransport Conference
June 25 -28, Seven Springs, PA, USA

COUPLED THERMAL AND ISCHEMIC STRESS INJURY TO SOFT TISSUE

Kenneth R. Diller, Gary L. McGregor

Biomedical Engineering Department
University of Texas
Austin, Texas, USA

INTRODUCTION

This paper is presented in support of the symposium/workshop at 2019 SB3C to celebrate the 70th birthday of Professor John Pearce who has been a prominent researcher in the field of thermal damage processes in tissues for many decades. He has been a faculty colleague of the senior author at the University of Texas Cockrell School of Engineering since 1982 and was an integral member of a large cohort of researchers who studied many aspects of thermal injury to living tissues. He has made many novel and ground breaking contributions to this field including developing a microscopic scale imaging technology to quantify the spatial distribution of protein denaturation (as a marker for injury) as a heat wave penetrates through tissue[1] and extensive theoretical and computational modeling analyses of thermal injury kinetics[2-4]. In particular, he has performed a series of in-depth evaluations of the relative efficacy and drawbacks of different mechanistic models for simulating the development of burns under defined conditions of thermal stress, including both accidental and surgical processes[2].

The Arrhenius formulation for modeling the kinetics of thermal injury in living tissues has been applied with success for well over a half century[5]. The rate of injury accrual, Ω, is modeled as a simple Arrhenius function of exposure time and temperature (eq. 1), and total injury is determined by integrating the rate function over the total insult time.

$$\Omega(\tau) = \int_0^{\tau} A e^{\left[\frac{-E_a}{RT}\right]} dt \qquad (1)$$

where A is a frequency factor (s^{-1}), τ the total heating time (s), E_a an activation energy barrier (J/ mole), R the universal gas constant (8.314 J/mole/K), and T the absolute temperature (K). Subsequently, many engineers have contributed to the measurement and modeling of the kinetics of thermal injury, including Stoll[6] and Bischof[7], and Pearce has demonstrated that more sophisticated models are often required[2].

Background

In addition to pure thermal injury that occurs via molecular denaturation processes that occur above a threshold of about 43°C, lower temperatures may also have an effect on tissue injury that derives from a different mechanism caused by applied mechanical stress. Physical deformation can result in strains that directly cause cellular injury, plus compressive stress can oppose the hydraulic pressure of blood perfusion, occluding vessels and resulting in ischemia[8]. Models for this injury process tend to involve complex constitutive equations[9]. Iaizzo and colleagues conducted very insightful experiments to identify and quantify injury that results when thermal and mechanical stresses are applied to soft tissues simultaneously[10]. As the temperature of tissue increases, the rate of metabolism increases proportionally, exacerbating the requirement for supply of nutrients and oxygen and for removal of toxic metabolic byproducts. Thus, Iaizzo showed that at elevated temperatures pressure sores develop more rapidly, and at depressed temperatures they are delayed. This type of injury, which may be termed a thermally enhanced pressure sore, is associated with only a mild increase in temperature and has a different mechanism than does a true thermal injury. The former is via ischemia; the latter via molecular denaturation. However, they may have a similar clinical presentation. Thus, thermal boundary conditions (even below the nominal 43°C threshold for thermal injury risk) for which it would be impossible to produce a full thickness burn, are fully consistent with causing a thermally enhanced pressure sore that may be misinterpreted as being a pure thermal injury. The relatively recent advent of heated vehicle seats has given rise to one such class of misclassified incidents[11], leading to confusion and misdirected interpretations[12], but there are many other scenarios in which the combination of applied pressure in combination with mild heating may produce similar results. This paper addresses developing a transient nonlinear fully coupled ischemic injury model of tissue under combined thermal and mechanical loading.

METHODS

The system consists of a person seated on a rigid heated surface that causes compression of superficial soft tissue against an internal skeletal structure. Heat transfer within the soft tissue is influenced by blood perfusion as described by the Pennes[13] equation. As a mechanical stress field develops in the soft tissue, a localized spatial distribution of ischemia is produced that effect convection between flow blood and tissue, giving rise to a nonlinear coupling between the thermal and

mechanical domains. Also, the total contact area between the tissue and the heated surface will expand as the interface flattens under load, altering the heat transfer boundary conditions.

This nonlinear, coupled process was modeled with finite elements using the ANSYS software platform. Fig. 1 shows a tissue grid deformed from an initial circular geometry.

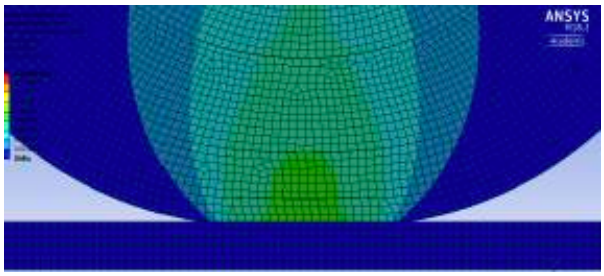

Figure 1: Finite element grid of soft tissue deformed under mechanical loading from a planar surface.

$$W = \frac{G}{2}\left[\lambda_1^2 + \lambda_2^2 + \lambda_3^2 - 3 - 2\ln\left(\lambda_1\lambda_2\lambda_3\right)\right] + \frac{K}{2}\ln\left(\lambda_1\lambda_2\lambda_3\right)^2 \quad (2)$$

$$\sigma_i = G\left(\lambda_1\lambda_2\lambda_3\right)^{-5/2}\left[\lambda_i^2 - \frac{\lambda_1^2 + \lambda_2^2 + \lambda_3^2}{3}\right] + K(\lambda_1\lambda_2\lambda_3 - 1); i = 1,2,3 \quad (3)$$

Eqs. (2) and (3) present a neoHookean model applied to describe the stress strain relationship in the deformed tissue[14]. W is internal strain energy, G is shear modulus, K is bulk modulus, λ is principle strain and σ is principle stress. Internal stress causes a pattern of ischemia that may persist over time to cause ischemic injury. The kinetics depend on the local tissue temperature that varies with distance from the heated external surface. Thus, there is a nonlinear coupling between the stress and temperature fields that directs the rate at which ischemic injury occurs. A constitutive function for the coupling of temperature and stress describes the progressive occurrence of ischemic injury over time.

RESULTS

Internal stress causes a pattern of ischemia that may persist over time to govern the kinetics of ischemic injury formation. The kinetics are a direct function of the local tissue temperature field that varies as a function of distance from the heated external surface. Thus, there is a nonlinear coupling between the stress and temperature fields that directs the rate at which ischemic injury occurs. We have developed an initial constitutive relationship for the coupling of temperature and stress leading to the progressive occurrence of ischemic injury over time.

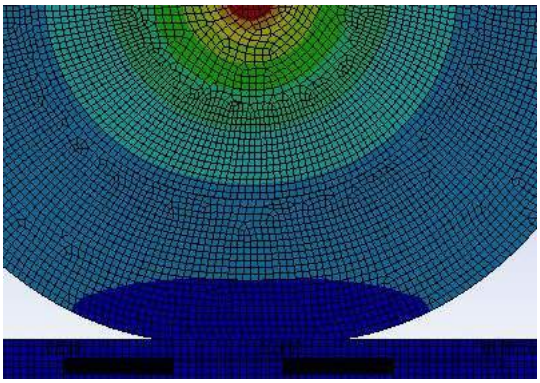

Figure 2: Mechanical deformation of elastic tissue effects the heat transfer boundary conditions and temperature field.

DISCUSSION

Pressure ulcers most commonly develop outward from the interface of soft tissue with a rigid skeletal structure where the stress/strain values are highest under an external load. When the load embodies a heating element, the temperature gradient will be inward from the surface in the opposite direction of the stress gradient. Under these conditions, the ischemic injury may be accelerated closer to the skin surface at higher temperature even though the stress loading is lower there. Depending on the relative characteristics of the mechanical and thermal loadings, a full thickness ischemic injury may occur from the outside to inward rather than the normal inside to outward direction. The clinical presentation of such an injury may be diagnosed as a burn even though it occurred by an ischemic rather denaturation process. Our model provides a predictive tool that may be applied to interpret injury causation as well as to design human interfaces for reduced injury risk.

ACKNOWLEDGEMENTS

This study was supported in part by the Robert M. and Prudie Leibrock Professorship in Engineering at the University of Texas.

REFERENCES

1. Thomsen S, Pearce JA, Cheong W-F. Changes in Birefringenece as Markers of Thermal Damage in Tissues. *IEEE Trans Biomedical Engineering.* 1989;36(12):1174-1179.
2. Pearce JA. Improving Accuracy in Arrhenius Models of Cell Death: Adding a Temperature-Dependent Time Delay. *J Biomech Eng.* 2015;137(12):121006.
3. Pearce JA. Comparative Analysis of Mathematical mModels of Cell Death and Thermal Damage Processes. *Int J Hyperthermia.* 2013;29(4):262-280.
4. Ryan TP, Pearce JA. Relationship Between Arrhenius Models of Thermal Damage and the CEM 43 Thermal Dose. SPIE Energy-based Treatment of Tissue and Assessment V; 2009.
5. Henriques FC. Studies of Thermal Injury. V. The Predictability and the Significance of Thermally Induced Rate Processes Leading to irreversible Epidermal Injury. *Archives of Pathology.* 1947;43:489-502.
6. Stoll AM, Greene LC. Relationship Between Pain and Tissue Damage Due to Thermal Radiation. *Journal of Applied Physiology.* 1959;14(3):373-382.
7. He X, Bischof J. Quantification of Temperature and Injury Response in Thermal Therapy and Cryosurgery. *Critical Reviews in Biomedical Engineering.* 2003;31(5&6):355-421.
8. Oomens CW, Bader DL, Loerakker S, Baaijens F. Pressure induced deep tissue injury explained. *Annals of Biomedical Engineering.* 2015;43(2):297-305.
9. Gefen A. Mathematical Functions and Their Properties as Relevant to the Biomechanical Modeling of Cell and Tissue Damage. *Journal of Applied Biomechanics.* 2010;26(1):93-103.
10. Kokate JY, Leland KJ, Held AM, et al. Temperature-modulated Pressure Ulcers: A Porcine Model. *Archives of Physical Medicine and Rehabilitation.* 1995;76:666-673.
11. Maguiña P, Palmieri TL, Greenhalgh DG. Car Seat Heaters: A Potential Hazard for Burns. *Journal of Burn Care & Rehabilitation.* 2003;24(5):315-316.
12. Diller KR. Car Seat Heaters As a Potential Burn Hazard: a Clarification. *J Burn Care Res.* 2011;32(2):e33-34; author reply e35-36.
13. Wissler EH. Pennes' 1948 Paper Revisited. *Journal of Applied Physiology.* 1998;85(1):35-41.
14. Linder-Ganz E, Shabshin N, Itzchak Y, Gefen A. Assessment of Mechanical Conditions in Sub-Dermal Tissues During Sitting: A Combined Experimental-MRI. *Journal of Biomechanics.* 2007;40:1443-1454.

SB³C2019
Summer Biomechanics, Bioengineering and Biotransport Conference
June 25 -28, Seven Springs, PA, USA

SUPRAPHYSIOLOGICAL AND SUBZERO TEMPERATURE DRIVEN KINETIC PROCESSES IN BIOHEAT TRANSFER

John C. Bischof (1,2)

(1) Department of Mechanical Engineering
University of Minnesota
Minneapolis, MN, USA

Department of Biomedical Engineering
University of Minnesota
Minneapolis, MN, USA

ABSTRACT: Classical work in bioheat transfer focused on heat transfer in blood perfused tissues at physiological temperatures [1 2-3] and the ability of blood perfusion to regulate temperature for comfort within humans and animals [4 5]. While thermal physiology remains important especially in understanding how species can adapt to climate change [6], there are now myriad applications of non-physiological temperatures that can be used to either destroy or protect biological systems at supra-physiological or subzero temperatures respectively [7 8 9].

This talk is inspired by the work of John Pearce who has pioneered different experimental and analytical techniques to understand supra-physiological kinetic processes that drive irreversible changes in molecules, cells and tissues [10 11]. To complement this work, we focus on kinetic processes at both high and low temperatures [12 13]. More specifically, I will review models and properties (thermal and kinetic) that determine whether the biological system will remain viable or be destroyed at both high and low non-physiological temperatures [13]. This information can prove critical to our ability to control numerous important biomedical applications ranging from burn injury and thermal therapy to cryo and biopreservation. A brief discussion of the importance of pressure on changing these kinetic processes will also be explored [14 15]. Finally, several new applications of bioheat transfer in both thermo-regulation and nanoparticle heating for diagnostics, therapy and cryopreservation will be reviewed [16].

1. Pennes, H. H., *J. Appl. Physiol.* **1948,** *1*, 3–122.
2. Chato, J., *Journal of biomechanical engineering* **1980,** *102* (2), 110-118.
3. Weinbaum, S.; Jiji, L.; Lemons, D., *J of biomechanical engineering* **1984,** *106* (4), 321-330.
4. Rupp, R. F.; Vásquez, N. G.; Lamberts, R., *Energy and Buildings* **2015,** *105*, 178-205.
5. Silanikove, N., *Livestock production science* **2000,** *67* (1-2), 1-18.
6. Buckley, L. B.; Ehrenberger, J. C.; Angilletta Jr, M. J., *Functional Ecology* **2015,** *29*, 1038-1047.
7. Chu, K. F.; Dupuy, D. E., *Nat Rev Cancer* **2014,** *14* (3), 199-208.
8. Giwa, S.; Lewis, J. K.; Alvarez, L.; Langer, R.; Roth, A. E.; Church, G. M.; Markmann, J. F.; Sachs, D. H.; Chandraker, A.; Wertheim, J. A.; Rothblatt, M.; Boyden, E. S.; Eidbo, E.; Lee, W. P. A.; Pomahac, B.; Brandacher, G.; Weinstock, D. M.; Elliott, G.; Nelson, D.; Acker, J. P.; Uygun, K.; Schmalz, B.; Weegman, B. P.; Tocchio, A.; Fahy, G. M.; Storey, K. B.; Rubinsky, B.; Bischof, J.; Elliott, J. A. W.; Woodruff, T. K.; Morris, G. J.; Demirci, U.; Brockbank, K. G. M.; Woods, E. J.; Ben, R. N.; Baust, J. G.; Gao, D.; Fuller, B.; Rabin, Y.; Kravitz, D. C.; Taylor, M. J.; Toner, M., *Nat Biotechnol* **2017,** *35* (6), 530-542.
9. Diederich, C. J., *International journal of hyperthermia* **2005,** *21* (8), 745-753.
10. Pearce, J. A., *International Journal of Hyperthermia* **2013,** *29* (4), 262-280.
11. Pearce, J., *Int J Hyperthermia* **2011,** *27* (8), 741-50.
12. He, X.; Bischof, J. C., *Crit Rev Biomed Eng* **2003,** *31* (5-6), 355-422.
13. Diller, K. R.; Valvano, J. W.; Pearce, J. A., Bioheat transfer. In *Thermal Engineering*, 2000; Vol. 4, pp 114-215.
14. Kokate, J. Y.; Leland, K. J.; Held, A. M.; Hansen, G. L.; Kveen, G. L.; Johnson, B. A.; Wilke, M. S.; Sparrow, E. M.; Iaizzo, P. A., *Arch Phys Med Rehabil* **1995,** *76* (7), 666-73.
15. Powell-Palm, M. J.; Zhang, Y.; Aruda, J.; Rubinsky, B., *Cryobiology* **2019**.
16. Bischof, J. C.; Diller, K. R., *Annu Rev Biomed Eng* **2018,** *20*, 301-327.